

Engineering Materials

Ahmed Esmail Shalan
Abdel Salam Hamdy Makhlouf
Senentxu Lanceros-Méndez *Editors*

Advances in
Nanocomposite
Materials
for Environmental and
Energy Harvesting
Applications

 Springer

Engineering Materials

This series provides topical information on innovative, structural and functional materials and composites with applications in optical, electrical, mechanical, civil, aeronautical, medical, bio- and nano-engineering. The individual volumes are complete, comprehensive monographs covering the structure, properties, manufacturing process and applications of these materials. This multidisciplinary series is devoted to professionals, students and all those interested in the latest developments in the Materials Science field, that look for a carefully selected collection of high quality review articles on their respective field of expertise.

Indexed at Compendex (2021)


More information about this series at <https://link.springer.com/bookseries/4288>


Ahmed Esmail Shalan ·
Abdel Salam Hamdy Makhlouf ·
Senentxu Lanceros-Méndez
Editors

Advances in Nanocomposite Materials for Environmental and Energy Harvesting Applications


 Springer

Editors

Ahmed Esmail Shalan 
Advanced Materials
BCMaterials—Basque Center for Materials,
Applications, and Nanostructures
Leioa, Spain

Abdel Salam Hamdy Makhlouf 
Vice President of Advanced Material
Research
Stanley Black & Decker, Inc.
New Britain, CT, USA

Central Metallurgical Research
and Development Institute
Cairo, Egypt

Senentxu Lanceros-Méndez 
Advanced Materials
BCMaterials—Basque Center for Materials,
Applications, and Nanostructures
Leioa, Spain

IKERBASQUE, Basque Foundation
for Science
Bilbao, Spain

ISSN 1612-1317

Engineering Materials

ISBN 978-3-030-94318-9

<https://doi.org/10.1007/978-3-030-94319-6>

ISSN 1868-1212 (electronic)

ISBN 978-3-030-94319-6 (eBook)

© The Editor(s) (if applicable) and The Author(s), under exclusive license
to Springer Nature Switzerland AG 2022

This work is subject to copyright. All rights are solely and exclusively licensed by the Publisher, whether the whole or part of the material is concerned, specifically the rights of translation, reprinting, reuse of illustrations, recitation, broadcasting, reproduction on microfilms or in any other physical way, and transmission or information storage and retrieval, electronic adaptation, computer software, or by similar or dissimilar methodology now known or hereafter developed.

The use of general descriptive names, registered names, trademarks, service marks, etc. in this publication does not imply, even in the absence of a specific statement, that such names are exempt from the relevant protective laws and regulations and therefore free for general use.

The publisher, the authors and the editors are safe to assume that the advice and information in this book are believed to be true and accurate at the date of publication. Neither the publisher nor the authors or the editors give a warranty, expressed or implied, with respect to the material contained herein or for any errors or omissions that may have been made. The publisher remains neutral with regard to jurisdictional claims in published maps and institutional affiliations.

This Springer imprint is published by the registered company Springer Nature Switzerland AG
The registered company address is: Gewerbestrasse 11, 6330 Cham, Switzerland

A special dedication is to my beloved father's soul (Esmail Shalan), who taught me the meaning of life. He passed away, during writing and collecting the current book.

Actually, no words can explain how he was a kind, helpful, and awesome person. He is the main reason for what I am currently now. I hope that he is now resting in peace in the upper level in Paradise.

Ahmed Esmail Shalan

Preface

Nanocomposite materials are one of the most exciting and fastest-growing areas of research with new materials and novel properties being continuously developed which are previously unknown in the constituent materials. Therefore, nanocomposite materials have enormous potential for new applications including aerospace, automotive, electronics, biomedical implants, nonlinear optics, mechanically re-enforced lightweight materials, sensors, nanowires, batteries, bioceramics, energy conversion, and many other systems with smart functionalities.

Nanocomposite materials are formed by mixing two or more dissimilar materials at the nanoscale in order to control and develop new and improved structures and properties. The properties of nanocomposites depend not only on the individual components used but also on the morphology and the interfacial characteristics.

This book is a comprehensive review to discuss the current state of the art on nanocomposite materials. In particular, the fundamentals, synthesis, characterization, and production of nanocomposites materials for two critical applications mainly environment and energy fields were explored. The book was divided into three main parts.

Part I: Fundamental of Nanocomposite Materials Synthesis and Production

Nanocomposite materials can be generated from different organic and inorganic materials as well as polymers and hence have altered properties and applications. Nanocomposite materials are the most auspicious nanomaterials that can be fashioned on a large scale. The improvement of nanocomposite materials-based systems has improved the possibility for applying these nanocomposites in a wide range of applications, from the fields of health, environment, and energy to automotive and aerospace.

Nanocomposite materials are progressively being industrialized for technological applications together with environmental directions, energy storage, production and conversion, sensing and actuation, water treatment, air purification, biomedical

applications, structural health reinforcement, drug delivery systems, health monitoring, and monitoring, among others. Consequently, the exhaustive current research in this area is motivated toward the fabrication, characterization, and application of nanocomposite materials systems for several environmental and energy dedications.

In this part, the current state of the art on nanocomposite materials is presented, as well as their assembly methods and applications in environmental and energy directions. This part highlights the recent advances in nanocomposite materials, also including their preparation and incorporation via innovative dispensation models such and preservative engineering.

This part covers the fundamentals of nanocomposite materials synthesis and production, features, and characterization of different nanocomposite materials-based systems. In particular, this part highlights in detail the following topics:

- The production of new multi-functional and composite nanomaterials by means of cold plasma–liquid interactions to allow practical applications
- Recent aspects of carbon nanostructure-based composites, from experimental setup to industrial applications in environmental and energy directions
- New physical and chemical techniques for graphene and its nanocomposites derivatives, synthesis, properties, and characterization
- Bio-nanocomposites and their applications in energy harvesting and deletion of environmental pollutions
- The properties and morphology of several kinds of nanocomposite materials, such as metal oxides, natural polymers, synthetic polymers, and hybrid inorganic polymers and carbon-based materials
- The challenges in nanocomposite materials-based systems and the interdisciplinary perspectives of science, biology, engineering, and technology, incorporating both fundamentals and applications.

Part II: Advances in Nanocomposite Materials for Environmental Applications

This part discusses the advances in nanocomposite materials for environmental applications. Nanocomposite materials are the most promising nanomaterials that can be produced on a large scale. A huge amount of ongoing research and development and technology implementation in academia and industry are aiming to utilize nanocomposite materials-based systems in a wide range of industrial applications, e.g., catalysis, photocatalysis, energy harvesting, energy storage, water/waste treatment, textiles, and many more. This part highlights in detail the following topics:

- Polymeric nanocomposite membranes for water remediation: from classic approaches to 3D printing

- Recent progress in the biodegradable polymeric nanocomposites and their potential applications for wastewater treatment
- Functionality–structure relationship into functional polymeric nanocomposite membranes for removal and monitoring of pollutants in fluid phases
- An in-depth look at the nature of green nanocomposite materials in terms of their applicability for environmental pollution problems
- Polymeric, carbon, metallic, and metal oxide, and ceramic nanocomposite materials that are prepared by direct and/or indirect synthetic routes
- In-depth insight and review on the most recent advances and industrial applications of the different types of nanocomposite materials-based systems with unique structures and compositions
- The challenges and interdisciplinary perspective of nanocomposite materials-based systems in science, environmental, engineering, and technology, incorporating both fundamentals and applications.

Part III: Advances in Nanocomposite Materials for Energy Harvesting Applications

This part discovers the advances in nanocomposite materials for energy harvesting applications. This part highlights in detail the following topics:

- The major applications of nanocomposite materials for energy storage applications
- Recent progress in the direct/indirect synthesis of nanocomposite materials and their potential applications in energy harvesting directions
- Advanced neutron and synchrotron characterization techniques for nanocomposite perovskite materials toward solar cells applications
- Incorporation of nanocomposite thin films as effective electrodes for photovoltaic devices applications
- Polymeric, carbon, metallic, and metal oxide, and ceramic nanocomposite materials and their applications in energy harvesting routes
- Supramolecular structures of organic molecules–single-walled carbon nanotube nanocomposites
- The challenges and interdisciplinary perspective of nanocomposite materials-based systems in science, energy, engineering, and technology, incorporating both fundamentals and applications.

Indeed, this book with all its parts launches how cutting-edge developments in nanocomposite materials interpret real-world innovations in a range of industry sectors. It is also a valuable reference for materials scientists; biologists; physicians; chemical, biomedical, manufacturing, and mechanical engineers working in R&D industry; and academia, who want to learn more about how nanocomposite materials-based systems are commercially applied in different environmental and energy aspects.

This book would not have been possible without the dedicated and insightful work to author different high-quality chapters a list of the world's leading scientists.

Finally yet importantly, being the first book in this area to be published in Springer publisher, the editors truly hope that this book will become a milestone to further foster increasing scientific and engineering efforts toward applying the nanocomposite materials for environmental and energy directions for supporting a more sustainable and interconnected better world.

Leioa, Spain/Cairo, Egypt
Edinburg, USA
Leioa, Spain
October 2021

Ahmed Esmail Shalan
Abdel Salam Hamdy Makhoulouf
Senentxu Lanceros-Méndez
Editors-in-Chief

Contents

Fundamental of Nanocomposite Materials Synthesis and Production	
Nanocomposites Materials and Their Applications: Current and Future Trends	3
Ahmed Esmail Shalan, Abdel Salam Hamdy Makhlouf, and Senentxu Lanceros-Méndez	
Versatile Production of New Multi-functional and Composite Nanomaterials by Means of Cold Plasma - Liquid Interactions	15
Anna Dzimitrowicz, Piotr Cyganowski, Piotr Jamroz, Dorota Jermakowicz-Bartkowiak, and Pawel Pohl	
Carbon Nanostructure Based Composites for Environmental and Energy Applications	35
Murthy Muniyappa, Prasanna Doddakunche Shivaramu, Siddabasave Gowda B. Gowda, Navya Rani Marilingaiah, and Dinesh Rangappa	
A Novel Synthesis of Gold Nanoparticles-Layered Double Hydroxides Nanocomposites Through <i>In-situ</i> Reductive Adsorption of Gold(III) Ion on Organic Acid-Functionalized Mg/Al Layered Double Hydroxides	75
Sri Juari Santosa, Philip Anggo Krisbiantoro, Rahma Hidaiyanti, Afini Muawanah, Ria Afifah Almas, Nur Raisah Maddeppungeng, Mike Rahayu, Sri Sudiono, Nuryono, and Sutarno	
Graphene and Its Nanocomposites Derivatives: Synthesis, Properties, and Their Applications in Water Treatment, Gas Sensor, and Solar Cell Fields	95
Sahar A. Mousa, Sohaila Z. Noby, and Ahmed Esmail Shalan	

Bionanocomposites and Their Applications in Energy Harvesting and Deletion of Environmental Pollutions	129
Parinaz Ghadam	
A Comparative Study of Cellulose Nanocomposite Derived from Algae and Bacteria and Its Applications	151
Ragaa A. Hamouda and Marwa Salah Abdel-Hamid	
Advances in Nanocomposite Materials for Environmental Applications	
Polymeric Nanocomposite Membranes for Water Remediation: From Classic Approaches to 3D Printing	191
Leire Ruiz Rubio, Rubén Tejjido, Antonio Veloso-Fernández, Sonia Pérez-Yáñez, and José Luis Vilas-Vilela	
Biodegradable Polymeric Nanocomposites for Wastewater Treatment	245
Mahmoud H. Abu Elella, Emad. S. Goda, Mohamed. A. Gab-Allah, Sang Eun Hong, Yared G. Lijalem, and Kuk Ro Yoon	
Functionality-Structure Relationship into Functional Polymeric Nanocomposite Membranes for Removal and Monitoring of Pollutants in Fluid Phases	299
Manuel Palencia, Jina M. Martínez-Lara, Nazly G. Chate-Galvis, and Jorge M. Durango-Petro	
Polymer-Based Nanocomposites for Removal of Pollutants from Different Environment Using Catalytic Degradation	331
Atul Kumar Maurya, Rupam Gogoi, and Gaurav Manik	
Role of Graphene Oxide Based Nanocomposites in Arsenic Purification from Ground Water	369
Debasree Ghosh, Sujata Kumari, and Sudip Majumder	
Green Nanocomposites: Magical Solution for Environmental Pollution Problems	389
Noor Hadi Aysa and Ahmed Esmail Shalan	
Recent Developments in Wastewater Treatment Using Polymer/Clay Nanocomposites	419
Atika Alhanish and Gomaa A. M. Ali	
Applications of Nanocomposites in Environmental Remediation	453
Riham R. Mohamed	
Removal of Radioactive Waste from Water Using Polymer Nanocomposites	473
Soliman M. A. Soliman and Mohsen E. Mohamed	

Advances in Nanocomposite Materials for Energy Harvesting Applications

Mixed Ionic-Electronic Conductors Based on Polymer Composites	493
Rafael Del Olmo, Maria Forsyth, and Nerea Casado	
Nanocomposites for Energy Storage Applications	533
J. Barbosa, R. Gonçalves, C. M. Costa, and S. Lanceros-Mendez	
Metal Sulfide Nanocomposites for Energy Harvesting Applications	567
Maqzia Bashir, Summan Aman, Aneesa Awan, Muhammad Faizan Nazar, Muhammad Zubair, Raziya Nadeem, and Muhammad Nadeem Zafar	
Advanced Neutron and Synchrotron Characterization Techniques for Nanocomposite Perovskite Materials Toward Solar Cells Applications	613
Jose M. Porro, Ahmed Esmail Shalan, and Manuel Salado	
Development of Hierarchical Nanostructures for Energy Storage	663
Jitha S. Jayan, Appukuttan Saritha, and Kuruvilla Joseph	
Polymer Nanocomposites for Energy Storage Applications	697
Arij Naser Abougreen, Ahmed Esmail Shalan, Esraa Samy Abu Serea, and Mustafa K. A. Mohammed	
Incorporation of Nanocomposite Thin Films as Effective Electrodes for Photovoltaic Devices Applications	725
Soraya Abdelhaleem and M. R. Balboul	
Recent Advances of TiO₂ Nanocomposites for Photocatalytic Degradation of Water Contaminants and Rechargeable Sodium Ion Batteries	757
Alaa El Din Mahmoud	
Major Trends and Mechanistic Insights for the Development of TiO₂-Based Nanocomposites for Visible-Light-Driven Photocatalytic Hydrogen Production	771
Ayat N. El-Shazly, Mahmoud A. Hamza, and Ahmed Esmail Shalan	
Polymer/Carbon Nanocomposites: Synthesis, Properties and Application in Solar Energy	795
Ali Boumeftah, Abdelkader Belmokhtar, and Abdelghani Benyoucef	
Graphene Based Nanocomposites: Synthesis, Characterization and Energy Harvesting Applications	817
Summan Aman, Maqzia Bashir, Muqaddas Baigum, Muhammad Faizan Nazar, Sajjad Hussain Sumrara, Syed Salman Shafqat, and Muhammad Nadeem Zafar	

Design of New High Energy Near Field Nanophotonic Materials for Far Field Applications	859
A. Guillermo Bracamonte	
Supramolecular Structures of Organic Molecules-Single Walled Carbon Nanotube Nanocomposites	921
Ahmed I. A. Abd El-Mageed and Takuji Ogawa	
Structure and Properties Manipulations of Graphene: Towards Developing High Sensitivity Optical and Electrical Sensors	941
Mai Desouky, Ahmed Medhat, Mona Samir, Dina Salah, and Amal Kasry	
Bulk and Nanocomposite Thermoelectrics: Synthesis, Properties, and Applications	959
Mustafa Shalaby, Salwa Hamdy, Ishtihadah Islam, Kulwinder Kaur, Aamer Nazir, and Shakeel Ahmad Khandy	
Nanodiamond/Conducting Polymer Nanocomposites for Supercapacitor Applications	1017
Abdelrahman Zkria, Ali M. Ali, Imtenan Mahmoud, Abdalla Abdelwahab, Waleed M. A. El Rouby, and Tsuyoshi Yoshitake	
Supercapacitors: Current Trends and Future Opportunities	1047
Amira M. Bakry, M. M. Moharam, and F. Abdel Mouez	

About the Editors



Dr. Ahmed Esmail Shalan, PhD

¹ BCMaterials—Basque Center for Materials, Applications, and Nanostructures, Martina Casiano, UPV/EHU Science Park, Barrio Sarriena s/n, 48940 Leioa, Spain

² Central Metallurgical Research and Development Institute, Cairo, Egypt

Dr. Ahmed Esmail Shalan is currently Research Associate at the Basque Center for Materials, Applications and Nanostructures (BCMaterials), UPV/EHU, Spain. He is graduated in Chemistry (2008) and later finished his Master's degree in "Renewable Materials Engineering" (2012) from Ain Shams University, Cairo, Egypt. His master thesis was focused on dye-sensitized solar cells. After finishing his master's degree, he obtained a fellowship from DAAD as Visiting Scholar for internship in (i-MEET-FAU), Erlangen, Germany, for 6 months and CIN2, UAB, Barcelona, Spain as internship student for 3 months. During this period, he gained hands of experience in laboratory skills as well as in scientific management. He pursued his research and joined Hokkaido University (2013), Japan, to pursue his PhD funded by Japanese government grant (MEXT) in Research Institute for Electronic Science. During his PhD, he also completed 6-month stay at National Chao Tung University, Taiwan, and obtained internship grant through collaboration project [NCTU, Taiwan Elite Internship Program (Taiwan, 2015 and 2016)]. He worked on the synthesis and functionalization

of different nanoparticles to assemble different types of perovskite solar cells. Subsequently, he returned to Egypt and worked as Assistant Professor at Central Metallurgical Research & Development Institute, CMRDI (2017), for tenured position (currently on leave). During this time, he was involved in different projects related to solar cells and succeeded to have several publications. After that, he work as Postdoctoral Research Associate at the Basque Center for Materials, Applications and Nanostructures (BCMaterials). The main goal of his research is to attain new materials with different structures and use them for different optoelectronic applications.

His research can be summarized in almost 100 peer-reviewed publications (>2000 times cited (Google Scholar)), one edited book, and >15 chapters. In addition, he has presented his work at many conferences and workshops (12 oral communications). He has received the Best Presentation Award at an International Scientific Conference, Egypt (2018). He has participated in 13 funded research projects and collaborated in the organization of several conferences. He also acts as Referee and Editorial Board Member for several peer-reviewed scientific journals. It is worth to mention that he got many awards, the best PhD thesis at Hokkaido University and Egyptian Academy Prize in Advanced Materials and Technology 2018 and 2020 as well as CMRDI prize for Distinguished Young Scientist 2017. In addition, he was selected to attend the 69th Lindau Nobel Laureate Meeting (June 30 – July 5, 2019, Lindau, Germany).

**Prof. Dr. Abdel Salam Hamdy Makhlof**

Vice President of Advanced Material Research Stanley Black & Decker, Inc. 1000 Stanley Dr, New Britain, CT 06053, USA

Professor Makhlof is an internationally recognized leader with more than 28 years of independent research project management, teaching, and consulting in industry and academia. He is the Vice President of Advanced Material Research, Stanley Black & Decker, Inc., USA. Before joining Stanley Black & Decker, he was the President of EMC3 - USA, VP of IM2C - USA, Full Professor of Materials Science at Central Metallurgical Research and Development Institute - Egypt, and Full Professor of Manufacturing and Industrial Engineering at the University of Texas - USA.

Prof. Makhlof has been included in Stanford University's List of World's Top 2% of Scientists, USA, 2020 & 2021. He is also the recipient of numerous national and international prizes and awards including the Humboldt Research Award for Experienced Scientists, at Max Planck Institute, Germany; Fulbright Scholar, NSF, and Dept. of Energy Fellowships, USA; Shoman Award in Engineering Science; and the State Prize of Egypt in Advanced Science and Technology, and more. He is a member of TMS-USA, EPSRC-UK, European Science Foundation - College of Expert Reviewers, Fulbright Alumni, Max Planck Institute Alumni, Alexander von Humboldt Alumni. He has served as both a Senior Editor and board member of many international journals, as well as a reviewer for several international funding agencies. He has excellent knowledge of USA, EU, and UK research landscape. He is a Consultant and Reviewer for several universities, and Advisory Editor for Elsevier USA.

**Prof. S. Lanceros-Mendez**

¹ BCMaterials—Basque Center for Materials, Applications, and Nanostructures, Martina Casiano, UPV/EHU Science Park, Barrio Sarriena s/n, 48940 Leioa, Spain

² IKERBASQUE, Basque Foundation for Science, 48009 Bilbao, Spain

Prof. S. Lanceros-Mendez graduated in physics at the University of the Basque Country, Leioa, Spain. He obtained his Ph.D. degree at the Institute of Physics of the Julius-Maximilians-Universität Würzburg, Germany. He is Associate Professor at the Physics Department of the University of Minho, Portugal (on leave) and Professor and Scientific Director of BCMaterials, Basque Center for Materials, Applications and Nanostructures.

His work is focused in the area of smart and multifunctional materials for sensors and actuators, environmental monitoring and remediation, energy and biomedical applications, with over 700 papers and 12 patents in the field. In all these research areas S. Lanceros-Méndez has achieved novel and relevant contributions published in high ranked journals, such as *Progress in Polymer Science*, *Progress in Energy and Combustion Science*, *Nature Protocols*, *Nature Communications*, *Advanced Functional Materials*, *Nanoscale*, *ChemSusChem*, *Applied Materials and Interfaces*, among others. Several of his papers have reach the marks of “highly cited papers” and/or “most downloaded papers” in their area/journal. He has published over 20 topical reviews and has given over 70 invited talks in major conferences, seminars and workshops. Overall he has over 600 conference presentations. He has written over 40 book chapter is his areas of expertise and, in particular, he has been co-editor of the first book on *Polymer Based Magnetoelectric Materials* (Wiley), the first book on *Printed Batteries* (Wiley) and the first book on *Advanced Lightweight Multifunctional Materials*. Over than 180 students have obtained expertise/ degree under his supervision, including post-doctoral fellows (over 20), PhD (over 30), master (over 120) and undergraduate degrees. Together with the scientific achievements, the technologies developed in his group resulted in 12

patents and four spin-off companies, Somática M&S, Acutus, NanoPaint and W4A, in the areas of sensors, materials and equipment's, active inks for active materials printing and electronics, respectively. Finally, he has participated in over 60 European, national and regional R&D projects, including private projects funded by national and international companies.

Fundamental of Nanocomposite Materials Synthesis and Production

Nanocomposites Materials and Their Applications: Current and Future Trends



Ahmed Esmail Shalan , Abdel Salam Hamdy Makhlouf,
and Senentxu Lanceros-Méndez 

Abstract Different nanostructures responsiveness and processability in exact shapes or dimensions are becoming increasingly important in a variety of applications, including environmental remediation (e.g., wastewater treatment), energy generation, and storage (e.g., biomedicine).

Nanotechnology and nanoscience have risen to the top of the list of the most intriguing fields of research being conducted today. By providing regulated functional building blocks into the nanomaterial society, graphene, an incomparable morphological 2-D carbon material, has sparked a gold rush in the nanomaterial society. Furthermore, the mechanical, electrical, and optical properties of graphene make it a promising candidate for use in solar energy conversion and electrochemical energy devices, among other uses.

1 Introduction

Nanocomposite materials are being progressively in request in different directions including environmental and wastewater treatment applications, energy generation, and storage or biomedicine, where different nanostructures response and processability in precise shapes or dimensions are indispensable to encounter detailed application difficulties.

A. E. Shalan (✉) · S. Lanceros-Méndez

BCMaterials, Basque Center for Materials, Applications and Nanostructures, Martina Casiano, UPV/EHU Science Park, Barrio Sarriena S/N, 48940 Leioa, Spain
e-mail: ahmed.shalan@bcmaterials.net

A. E. Shalan · A. S. H. Makhlouf

Central Metallurgical Research and Development Institute (CMRDI), P. O. Box 87, Helwan 11421, Cairo, Egypt

A. S. H. Makhlouf

Engineering, Metallurgy, Coatings and Corrosion Consultancy (EMC3), Austin, TX, USA

S. Lanceros-Méndez

IKERBASQUE, Basque Foundation for Science, 48009 Bilbao, Spain

© The Author(s), under exclusive license to Springer Nature Switzerland AG 2022

A. E. Shalan et al. (eds.), *Advances in Nanocomposite Materials for Environmental and*

Energy Harvesting Applications, Engineering Materials,

https://doi.org/10.1007/978-3-030-94319-6_1

The desire for usage of nanocomposites through combination with other materials is reinforced because of their high stability regarding environmental and mechanical aspects [1–5]. These aspects are supported by their ability of accountable availability as well as remaining pore-forming characteristics, possession of a large number of the functional groups, and low-cost contribution. There are many benefits of nanocomposites compared with bare nanoparticles including their easy recovery, inhibition of aggregation and loss during reaction procedure, and consequent environmental protection. For the application of nanomaterials on a heterogeneous system with constant flow, setup needs that it must be fixed on a support. Despite using bare nanoparticles, the use of composite contains the advantage of enhanced monitoring potential and treatment procedure [6]. For the preparation of composites, the nanoparticles are assembled with other materials like metals, nanoparticles, polymers, and organic or inorganic materials [7]. This assembly is formulated in such a way that there is maximum interactivity between the materials. It contains great importance because the final size and properties of composites depend on this interaction. Nanocomposites also contain pronounced properties including prevention from poisoning, enhanced permeability of the membrane, the potential for catalysis and sorption, and stability to mechanical and higher thermal application. These improved properties contribute to hybrid properties of final material and their versatility for monitoring performance in environmental and energy harvesting applications [8–11].

2 Definition of Nanocomposite Materials

A composite is a combination of two or more different materials that are mixed in an effort to blend the best properties of both. A nanocomposite is a composite material, in which one of the components has at least one dimension that is nanoscopic in size that is around 10^{-9} m. A scaling might be helpful: a coin is on the order of 1–2 mm thick, or 10^{-3} m; a carbon fiber, commonly used as a reinforcement in sporting goods, is approximately 7 μm in diameter, or 10^{-6} m; a carbon–carbon chemical bond, the basic unit of life, is about 1.5 Å, or 10^{-10} m.

The field of nanocomposites is burgeoning. A brief look at new, common commercial uses reveals automotive panels for sports utility vehicles, polypropylene nanocomposites for furniture, appliances, and bulletin board substrates. Advanced technologies implemented include magnetic media, bone cement, filter membranes, aerogels, and solar cells. Nanocomposites represent one area of nanoscale research that has led to marketable products.

Nanocomposites science and engineering have touched all fields of materials, metals, plastics, ceramics, biomaterials, electronic materials, and more.

Since nanomaterials possess exceptional properties, they are widely used to mix with the bulk polymeric material to improve their properties. By definition, nanocomposites are materials that are reinforced with nanoparticles. Based on the matrix material, nanocomposites are classified into polymer matrix composites, metal matrix composites, and ceramic matrix composites. In polymer matrix composites, the

most important topic to be considered is the dispersion of the nanofillers in bulk polymer matrix. Homogeneous distribution of nanomaterials results in improved properties. But the tendency of particle agglomeration due to the weak van der Waals forces between the nanomaterials results in deterioration in properties. For example, homogeneous dispersion of CNTs, graphene, CNFs, and clay in the polymer matrix improved mechanical, thermal, electrical, optical, gas barrier, and flame retardancy properties of nanocomposites [12–20]. It is now well established that for better dispersion of the nanomaterials in a polymer matrix, the nanomaterials can be surface modified or functionalized [21–26]. Recently, it has been shown that addition of compatibilizer also improved dispersion of the nanomaterials in the polymer matrix [27–30]. Surface modification and functionalization of nanomaterials improve the interfacial interaction or compatibility between the filler and matrix, which results in better dispersion which in turn facilitates effective stress transfer of the matrix and filler to develop high performance lightweight composites for advanced applications. A number of techniques such as TEM, SEM, AFM, STM, XRD, and FTIR can be used to find the size and distribution of filler in polymer matrix.

Over the last three decades, both industry and academics have developed a strong interest in nanomaterials. The impetus was the requirement for solutions in real-world situations, when conventional methodologies encountered limits (e.g., in electronics, catalysis, medicine, etc.). The advancement of characterisation and processing techniques aided scientists in their efforts to evaluate theoretical research on nanomaterials. This advancement resulted in the development of increasingly sophisticated instruments for investigating and manipulating the nanoscale world.

In general, nanomaterials are categorized into numerous kinds based on their composition and morphology. Their classification is practical in terms of the structural characteristics of their primary units and the number of dimensions beyond the nanoscale. Thus, they can be zero-dimensional (0-D) in nature, similar to nanoparticles, one-dimensional (1-D) in nature, similar to nanorods, or two-dimensional (2-D) in nature, similar to nanolayers. Numerous combinations of nanomaterials can be used to create a diverse range of nanostructures with identifiable form and dimension. Thus, for example, a linear or planar bonding of nanoparticles with a given composition results in the formation of a one- or two-dimensional nanostructured material. Additionally, the latter classification requires the presence of size effects. Additionally, the development of ordered arrays of nanostructures can provide methodologies for nanodevice fabrication.

Additionally, the combination of two or more components or phases with dissimilar physical or chemical properties, at least one of which is on the nanoscale scale, and which results in properties that are differentiated from the constituents individually, introduces the class of nanocomposites. These exhibit superior qualities to their respective microcomposites, owing primarily to the size effects of the nanomaterials used. Polymeric nanocomposites are a distinct class of nanocomposites in which at least one discontinuous nanosized phase is spread in a continuous polymeric media (i.e., matrix). This chapter will discuss polymeric nanocomposites in detail. Due to the close proximity of the nanofillers and the large surface area per mass, considerable property enhancement occurs.

3 Applications of Nanocomposite Materials

Nanocomposite materials and coatings have extensively been used in many industrial and medical applications [12–33]. In 2015, one of our editorial team members prepared a Handbook of nanoceramic and nanocomposite coatings and materials, published by Butterworth-Heinemann, Elsevier [33]. The handbook highlighted and discussed the applications of nanocomposites in many industrial applications including aerospace, automotive, medical, oil & gas, chemical, petrochemical, marine, etc.

Among the several applications of nanocomposite materials, this paper focuses on two main applications related to energy and environment.

4 Applications of Nanocomposite Materials in Energy Harvesting

The exhaustion of many resources of fossil fuel and the occurrence of consequential pollution problems in the environment is due to the rational development of human society [34]. The discerning solution to this credible support which covers all the world's energy demand for today and future generation is the direct transformation of light energy into electrical energy [35]. The exploration of solar cells, hybrid of nanoparticles (NPs) or polymers, is extensively reported due to capable perceptions of many uniting advantages of the nanocomposites which contain convenient solution-based practices and large absorption coefficient including semiconductors made of inorganic nanoparticles including modifiable shapes (nanorods, tetrapod, and nanodots), large conductivity and adjustable absorption properties [36]. For the recovery of waste heat and solid-state cooling, the advancements for evolving diverse thermoelectric materials have been documented in the past few decades [37]. The distinctive outcome of quantum confinement of small 3D-structures and exposure to nanotechnology has stimulated the use of the metal chalcogenides for many applications like light absorption and luminescence and the development of photodetectors and solar cells [38]. The realization of the probable global crisis arose due to energy deficiency and serious environmental pollution due to the rapid development of industrialization [39]. Human society demands clean and reliable energy sources due to the depletion of conventional sources of fossil fuels along with the downturn of the global climate. Recently, pronounced efforts are made by researchers worldwide for the development of technologies for energy harvesting by solar irradiation and wind turbines [40]. The biggest problem of the twenty-first century is the shortage of energy resources and thoughtful environmental pollution due to rapid industrialization and unspectacular advancement of the living standards of human beings [41]. There is a need of the hour for the development of innovative technologies that contain low cost and environment-friendly features that can harness the expanding depletion of fossil fuels along with exceedingly huge demand of energy resources

by the society for profound benefits [42]. The harvesting of solar H_2 is a low-cost, viable and clean approach for high potential demonstration of water splitting via photocatalysis by employing photocatalytic semiconductors [43].

There is increasing research interest for the exertion of renewable energy due to the consumption of untenable fossil fuel accompanied by issues related to the environment and growing energy needs around the globe [44]. To equip with energy depletion issues, the storage and transformation of irregular sustainable energy like wind energy and solar energy, etc. to chemical energy are regarded as a captivating approach [45]. For the conversion of renewable energy into the chemical fuel, the water-splitting strategy providing an evolution of H_2 and O_2 is conventionally reported as an absolute strategy [46, 47]. Furthermore, many industrial procedures on a global scale like ammonia synthesis and petroleum refining contain usage of H_2 . Another attractive procedure is the storage of renewable energy in supercapacitors in the form of electrical charge. The areas of interest nowadays are the development of proficient materials used for application in supercapacitors and water splitting because of their number of advantages for storage and conversion of renewable energy such as high power intensity, large lifetime, and friendliness to environment, and great efficiency [48–50].

We are living in a world that requires clean and environment-friendly energy resources. For this energy harvesting and environmental treatment, many technologies that are based upon nanomaterials are used. The knowledge regarding the behaviour of nanomaterials when they enter the environment is poor. As far as environmental protection is concerned, the occurrence of nanoparticles into the environment is unwelcome even when we are looking for environmental toxicology, energy depletion, or water treatment. Therefore, safe and operative procedures for the consumption of these particles are of great interest which leads to the development of nanocomposites [51]. Researchers sometimes have to face great challenges arising due to the utilization of the bare nanoparticles including; nanoparticle loss while performing treatment procedures, trouble in the recovery of these nanoparticles, reduction of the active surface area of nanoparticles due to their aggregation tendency, and their probable health concerns due to their release in the environment [52, 53].

5 Applications of Nanocomposite Materials in Environmental Pollution Control

The urge for use of nanocomposites by incorporation with other materials is supported due to their high stability regarding environmental, mechanical, and thermal aspects. These aspects are supported by their ability of liable accessibility and outstanding pore-forming characteristics, possession of a large number of the functional groups, and low-cost contribution. There are many benefits of nanocomposites compared with bare nanoparticles including their easy recovery, inhibition of aggregation and

loss during reaction procedure, and consequent environmental protection. For the application of nanomaterials on a heterogeneous system with constant flow setup needs that it must be fixed on a support. Despite using bare nanoparticles, the use of composite contains the advantage of enhanced monitoring potential and treatment procedure [6]. For the preparation of composites, the nanoparticles are assembled with other materials like metals, nanoparticles, polymers, and organic or inorganic materials [7]. This assembly is formulated in such a way that there is maximum interactivity between the materials. It contains great importance because the final size and properties of composites depend on this interaction. Nanocomposites also contain pronounced properties including prevention from poisoning, enhanced permeability of the membrane, the potential for catalysis and sorption, and stability to mechanical and higher thermal application. These improved properties contribute to hybrid properties of final material and their versatility for monitoring performance in energy harvesting applications.

6 Outlook and Future Trends

With prompt growth of living standards, there are increasing risks for the depletion of sources and energy crises along with environmental pollution [54]. Incessant improvement of society is cumulative the risk for environmental pollution and fossil fuel depletion. There is a need for green synthesis and developing effective technologies to check pollution accompanying the development of renewable and clean energy sources. As solar energy is a natural green energy resource that can be utilized through a number of devices including semiconductors, photoanodes, photo and electrochemical energy harvesting devices. Nanocomposite materials can degrade toxic chemicals existing in the environment to environment-responsive constituents along with the generation of fuel through a number of processes like production of hydrocarbon fuel from reduction of carbon dioxide and photocatalytic water splitting, and the conversion of sunlight into electrical energy [34]. The photothermal materials are getting attention due to their promising applications in photothermal therapy [55], harvesting solar energy, and photo-thermal imaging [56].

For applications of solar cells in energy harvesting and also its transformation, metal sulfides have proven to contribute the most in both cases i.e. photoelectrochemically and photovoltaically, because of possession of low bandgap, high abundance, and low cost [57]. With the development of nanotechnology metal chalcogenides show improved applications for light absorption including photodetectors, solar cells, luminescence, and even more accelerated because of the quantum confinement effect present in 3D structures. For production of solar cells aimed at energy harvesting applications include investigation of both un-doped and doped, nanoparticles and nanocomposites from which doped materials and nanocomposites show pronounced applications for energy harvesting purpose [38].

The feasibility and development of any energy-harvesting device must face serious economic, environmental, and operational challenges, as they must play a dynamic

role. Therefore, for the wide range of applications, fabrication of the nanocomposites is mandatory including large potential for their reusability. To overcome the energy depletion by excessive use of energy sources, careful investigations are being done to fabricate solar devices with nanomaterials and design new synthetic methods that contain reusability and minimal decrease in their working capabilities with time. It must be proven that they contain their regeneration capabilities and properties like cheap, simple, and fast, and accommodate with economy scale. Additionally, there is the need for the development of comprehensive and entirely safe technologies for the treatment and regeneration of spent materials and their safe disposal. The functional properties of nanoparticles can be advanced by the fabrication or formation of composites. Future advances will include the aspects of nanocomposites for removal of environmental contaminants, acting as catalysts and adsorbents for the study of combined functionalities of these composites.

There is increasing environmental and energy demands due to the increasing population of the world because of increased power consumption which is predicted to become double in coming few decades. Hence, there is a need for researchers and scientists to advance clean, sustainable and renewable environmental and energy technology, they can meet the growing challenges and demands of energy economically and should be environment friendly. [44]. The extensive use of the carbon fuels and their unfortunate environmental effects pushed this world in a paragon where there is need for the application of green methods and systems. Many of the environmental issues including acid rain and global warming are due to the unmediated response of excessive use of fossil fuels. The nanocomposites are based on graphene containing appreciable growth in the technology due to its applications based on its properties like lightweight, chemical stability, large surface area and the pronounced on board reversibility [58].

For the production of the photocatalytic hydrogen, the photocatalysts based on graphene are demonstrated as favourable photocatalytic materials. In this regard, many researches are made to prove the use of photocatalytic graphene-based materials for designing the procedure to produce photocatalytic H_2 . Presence of graphene proven to be important in these materials for hydrogen production [59]. The effectiveness of the multicomponent photocatalysts based on graphene in the photocatalytic reactions is proven to be effective by recent results [60]. The effective charge distribution in different energy levels in multicomponent nanocomposites can be facilitated by adjusting band gap in energy levels of constituent materials. Significant improvement in photocatalysis can be achieved by optimal selection of shape, size and the composition of the multicomponent nanocomposites based on graphene. For designing and developing the photocatalytic material containing high performance, the best solution is the effective transfer of electron between the interfaces. Efforts are being made for the development of controlled and cost-effective methods to fabricate the 3D framework and its transformation along with development of the graphene doped with heteroatoms for the practical applications [61].

However, there are few challenges to be managed in order to manifest the capability of nanocomposites based on graphene regarding its applications, cost and synthetic methods. One of the main challenges is production of graphene and its

composites on a large scale, which comprises enormous effects. Some of the challenges present are: (i) how we can prevent the formation of graphene clusters in matrix, (ii) how we can control most defects on the surface; and (iii) how we can tune application-based characteristics. Anyhow, there are many techniques to produce graphene, few methods have been reported for commercialization of the energy storage appliances of graphene. To address these challenges, new methods and setups are needed for improvement of performance and properties of the graphene [62].

Certainly, the utilization of nanocomposite materials in above mentioned applications is a new attempt presenting that research efforts in future will be profound. One challenge is the maintenance of the outstanding physical properties of the graphene for the synthesis of the nanocomposites. One prediction is the development of elementary route via direct oxidation method of graphene by soft templating method for production of little bit functionalities as to furnish active sites of graphene with the nanoparticles. One important characteristic is that it has no need for composite reduction due to its lower oxidation condition, producing graphene framework with lesser defects [63].

The development in the field of hybrids and nanocomposites of graphene is notable. However, significant work is to be done in the field where they show applications as electrochemical devices and catalysts [64]. However, new probabilities are opened for utilization and better understanding of the graphene to overcome the knowledge gap [65]. Still, for the understanding of the fundamental application of the composites, significant attention is still needed.

Acknowledgements The authors 1 & 3 gratefully acknowledge the support from BCMaterials to pursue that work. Furthermore, Author 1 thanks the National Research grants from MINECO, Spain, “Juan de la Cierva” [FJCI-2018-037717] and he is currently on leave from CMRDI. The authors 1&3 acknowledge funding by the Spanish State Research Agency (AEI) and the European Regional Development Fund (ERFD) through the project PID2019-106099RB-C43/AEI/<https://doi.org/10.13039/501100011033> and from the Basque Government Industry and Education Department under the ELKARTEK and PIBA (PIBA-2018-06) programs, respectively.

References

1. Abdel Maksoud, M.I.A., Fahim, R.A., Shalan, A.E., et al.: Advanced materials and technologies for supercapacitors used in energy conversion and storage: a review. *Environ. Chem. Lett.* **19**, 375–439 (2021)
2. Abdel Messih, M.F., Shalan, A.E., Sanad, M.F., Ahmed, M.A.: Facile approach to prepare ZnO@SiO₂ nanomaterials for photocatalytic degradation of some organic pollutant models. *J. Mater. Sci: Mater. Electron.* **30**, 14291–14299 (2019)
3. Abdelbasir, S.M., Shalan, A.E.: An overview of nanomaterials for industrial wastewater treatment. *Korean J. Chem. Eng.* **36**, 1209–1225 (2019)
4. Batool, M., Nazar, M.F., Awan, A., et al.: Bismuth-based heterojunction nanocomposites for photocatalysis and heavy metal detection applications. *Nano-struct. Nano-obj.* **27**, 10072 (2021)
5. El-Shazly, A.N., Shalan, A.E., Rashad, M.M., et al.: Solid-state dye-sensitized solar cells based on Zn1–xSnxO nanocomposite photoanodes. *RSC Adv.* **8**, 24059–24067 (2018)

6. Tang, L., et al.: Synergistic effect of iron doped ordered mesoporous carbon on adsorption-coupled reduction of hexavalent chromium and the relative mechanism study. *Chem. Eng. J.* **239**, 114–122 (2014)
7. Khezri, K., Mahdavi, H.: Polystyrene-silica aerogel nanocomposites by in situ simultaneous reverse and normal initiation technique for ATRP. *Microporous Mesoporous Mater.* **228**, 132–140 (2016)
8. Sanad, M.F., Shalan, A.E., Bazid, S.M., Abdelbasir, S.M.: Pollutant degradation of different organic dyes using the photocatalytic activity of ZnO@ZnS nanocomposite materials. *J. Environ. Chem. Eng.* **6**, 3981–3990 (2018)
9. Sanad, M.F., Shalan, A.E., Abdellatif, S.O., et al.: Thermoelectric energy harvesters: a review of recent developments in materials and devices for different potential applications. *Top Curr. Chem.* **378**, 48 (2020)
10. Reddy, B., Dadigala, R., Bandi, R., et al.: Microwave-assisted preparation of a silver nanoparticles/N-doped carbon dots nanocomposite and its application for catalytic reduction of rhodamine B, methyl red and 4-nitrophenol dyes. *RSC Adv.* **11**, 5139–5148 (2021)
11. Sanad, M.M.S., Shalan, A.E., Rashad, M.M., Mahmoud, M.H.H.: Plasmonic enhancement of low cost mesoporous Fe₂O₃-TiO₂ loaded with palladium, platinum or silver for dye sensitized solar cells (DSSCs). *Appl. Surf. Sci.* **359**, 315–322 (2015)
12. Hamdy, A.S., Shoeib, M., Butt, D.: A novel approach in designing environmentally compliant sol-gel based ceramic coatings and nanocomposite coatings for industrial applications. In: Malik, A., Rawat, R.J. (eds.) *New Nanotechniques*, chap. 20, pp. 649–659. Nova Science Publishers, USA (2009). ISBN: 978-1-60692-516-4.
13. Hamdy, A.S., Soliman, H.: Effect of nano-additives (Al₂O₃ and NaF) on the performance of ceramic coatings formed by microarc oxidation on magnesium alloys. In: Makhlof, A.S.H., Scharnweber, D. (eds.) *Handbook of Nanoceramic and Nanocomposite coatings and materials*, chap. 18, pp. 383–395. Elsevier, USA (2015). <https://doi.org/10.1016/B978-0-12-799947-0.00018-3>
14. Abu-Thabit, N.Y., Hamdy, A.S.: Recent advances in nanocomposite coatings for corrosion protection applications. In: Makhlof, A.S.H., Scharnweber, D. (eds.) *Handbook of Nanoceramic and Nanocomposite Coatings and Materials*, chap. 24, pp. 509–543. Elsevier, USA (2015). <https://doi.org/10.1016/B978-0-12-799947-0.00024-9>
15. Hamdy, A.S.: Novel approaches in designing high performance nano and nano-composite coatings for industrial applications. *Int. J. Nanomanuf.* **4**(1/2/3/4), 235–241 (2009). <https://doi.org/10.1504/IJNM.2009.028130>
16. Hamdy, A.S., Shoeib, M.A., Hady, H.: The effect of grain refining and phosphides formation on the performance of advanced nanocomposite and ternary alloy coatings on steel. *Mater. Lett.* **80**, 191–194 (2012). <https://doi.org/10.1016/j.matlet.2012.04.085>
17. Abdal-hay, A., Hamdy, A.S., Khalil, K.A.: Novel, facile, single-step technique of polymer/TiO₂ nanofiber composites membrane for photodegradation of methylene blue. *ACS Appl. Mater. Interf.* **7**(24), 13329–13341 (2015). <https://doi.org/10.1021/acsami.5b01418>
18. Abdal-hay, A., Hamdy, A.S., Abdel-Jaber, G.T., Barakat, N., Ebnalwaled, A.A., Khalil, K.A.: A facile manufacturing of Ag/SiO₂ nanofibers and nanoparticles composites via a simple hydrothermal plasma method. *Ceram. Int.* **41**, 12447–12452 (2015). <https://doi.org/10.1016/j.ceramint.2015.06.082>
19. Abdal-hay, A., Hasan, A., Yu-Kyoung, M.-H.L., Hamdy, A.S., Khalil, K.A.: Biocorrosion behavior of biodegradable nanocomposite fibers coated layer-by-layer on AM50 magnesium implant. *Mater. Sci. Eng. C* **58**, 1232–1241 (2016). <https://doi.org/10.1016/j.msec.2015.09.065>
20. Abdal-hay, A., Khalil, K.A., Hamdy, A.S., Al-Jassir, F.F.: Fabrication of highly porous biodegradable biomimetic nanocomposite as advanced bone tissue scaffold. *Arab. J. Chem.* **10**(2), 240–252 (2017). <https://doi.org/10.1016/j.arabjc.2016.09.021>
21. Gupta, V.K., Agarwal, S., Sadegh, H., Ali, G.A.M., Bharti, A.K., Hamdy, A.S.: Facile route synthesis of novel graphene oxide-β-cyclodextrin nanocomposite and its application as adsorbent for removal of toxic bisphenol A from the aqueous phase. *J. Mol. Liq.* **237**, 466–472 (2017). <https://doi.org/10.1016/j.molliq.2017.04.113>

22. Sadegh, H., Ali, G.A.M., Makhlof, A.S.H., Chong, K.F., Alharbi, N.S., Agarwal, S., Gupta, V.K.: MWCNTs-Fe₃O₄ nanocomposite for Hg(II) high adsorption efficiency. *J. Mol. Liq.* **258**, 345–353 (2018). <https://doi.org/10.1016/j.molliq.2018.03.012>
23. Soliman, H., et al.: Hydroxyquinoline/nano-graphene oxide composite coating of self-healing functionality on treated Mg alloys AZ31. *Surf. Coat. Tech.* **1**, 125395 (2020). <https://doi.org/10.1016/j.surfcoat.2020.125395>
24. Farag, M.M., Liu, H.H., Makhlof, A.H.: New nano-bioactive glass/magnesium phosphate composites by sol-gel route for bone defect treatment. *Silicon* **13**(3), 857–865 (2020). <https://doi.org/10.1007/s12633-020-00485-3>
25. Hamdy, A.S., Hady, H., Shoeib, M., Abdel Salam, O.: Electrochemical impedance studies on Ni-P-W and Ni-P-Al₂O₃ nano-composite alloy coatings in 3.5% NaCl. In: Proceedings of European Corrosion Congress, Germany (2007)
26. Hamdy, A.S., Shoeib, M., Hady, H., Abdel Salam, O.F.: Effect of the experimental parameters on the coating performance of Ni-P nano-composite alloy coatings. In: Processing and Product Manufacturing: Innovative Processing and Synthesis of Ceramics, Glasses and Composites Symposium, Proceedings of MS&T '07, Michigan, 16–20 September 2007 (2007)
27. Hamdy, A.S., Hady, H., Shoeib, M.A., Abdel Salam, O.F.: Newly developed corrosion resistant nano-composite alloy coatings for steels. In: Symposium “Corrosion and Coatings Challenges in Industry”, AAAS Pacific Division 88th Annual Meeting, Boise, ID (2007)
28. Hamdy, A.S., Shoeib, M.A., Hady, H.: Nano-composite and ternary-alloy protective coatings for steel. In: Proceedings of 14th NACE Middle East Corrosion Conference & Exhibition, Bahrain, 12–15 February 2012, Paper: 75-CR-12 (2012)
29. Hamdy, A.S.: Smart self-healing eco-friendly nano and nano-composite protective coatings. In: Invited Speaker at the Plenary Session of the International Conference on Nanotechnologies and Biomedical Engineering (ICNBE), Chisinau, Moldova, 6–9 July 2011 (2011)
30. Hamdy, A.S.: Nano-composites and nano-ceramic protective coatings for steel and aluminum alloys. In: Invited talk at UNESCO Workshop on “Awareness of Nanotechnology”, Cairo, Egypt, 27–29 November 2011 (2011)
31. Hamdy, A.S.: A novel composite nanofibres-based biomaterials for biomedical applications. In: Invited speaker, the Latin America IDEIA Partnership “La Idea” Incubator Program, 2–13 February 2015, Advanced Manufacturing Session at the Coastal Bend Business Innovation Center hosted by Texas A&M University in Corpus Cristi, Texas, USA, Sponsored by the U.S. Department of State (2015)
32. Hamdy, A.S., Shoeib, M., Butt, D.: Challenges in designing high performance anti-corrosion nano-sized thin films and nano-composite coatings for industrial applications. In: International Conference of Nanoscience, King Abdul Aziz University, Saudi Arabia, 17–19 June 2008 (2008)
33. Makhlof, A.S.H., Scharnweber, D. (eds.): Handbook of nanoceramic and nanocomposite coatings and materials, p. 688. Butterworth-Heinemann, Elsevier (2015). <https://doi.org/10.1016/C2013-0-13073-5>
34. Zheng, L., Teng, F., Ye, X., Zheng, H., Fang, X.: Photo/electrochemical applications of metal sulfide/TiO₂ heterostructures. *Adv. Energy Mater.* **10**(1), 1902355 (2020)
35. Dunst, S., Rath, T., Reichmann, A., Chien, H.-T., Friedel, B., Trimmel, G.: A comparison of copper indium sulfide-polymer nanocomposite solar cells in inverted and regular device architecture. *Synth. Met.* **222**, 115–123 (2016)
36. Fradler, C., et al.: Flexible polymer/copper indium sulfide hybrid solar cells and modules based on the metal xanthate route and low temperature annealing. *Sol. Energy Mater. Sol. Cells* **124**, 117–125 (2014)
37. Yang, H., Jauregui, L.A., Zhang, G., Chen, Y.P., Wu, Y.: Nontoxic and abundant copper zinc tin sulfide nanocrystals for potential high-temperature thermoelectric energy harvesting. *Nano Lett.* **12**(2), 540–545 (2012)
38. Krylova, V., Baltrusaitis, J.: Synthesis and properties of polyamide–Ag₂S composite based solar energy absorber surfaces. *Appl. Surf. Sci.* **282**, 552–560 (2013)

39. Ke, F., Wang, L., Zhu, J.: Facile fabrication of CdS-metal-organic framework nanocomposites with enhanced visible-light photocatalytic activity for organic transformation. *Nano Res.* **8**(6), 1834–1846 (2015)
40. Luo, Y., Que, W., Yang, C., Tian, Y., Yin, X.: Hydrothermal synthesis of transition metal sulfides/MWCNT nanocomposites for high-performance asymmetric electrochemical capacitors. *Electrochimica Acta* **322**, 134738 (2019)
41. Ren, Y., Zeng, D., Ong, W.-J.: Interfacial engineering of graphitic carbon nitride (g-C₃N₄)-based metal sulfide heterojunction photocatalysts for energy conversion: a review. *Chin. J. Catal.* **40**(3), 289–319 (2019)
42. Wang, J., Guan, Z., Huang, J., Li, Q., Yang, J.: Enhanced photocatalytic mechanism for the hybrid gC₃N₄/MoS₂ nanocomposite. *J. Mater. Chem. A* **2**(21), 7960–7966 (2014)
43. Ran, J., Gao, G., Li, F., Ma, T., Du, A., Qiao, S.: Ti₃C₂ MXene co-catalyst on metal sulfide photo-absorbers for enhanced visible-light photocatalytic hydrogen production (2017)
44. Chu, S., Majumdar, A.: Opportunities and challenges for a sustainable energy future. *Nature* **488**(7411), 294–303 (2012)
45. McCrory, C.C., Jung, S., Ferrer, I.M., Chatman, S.M., Peters, J.C., Jaramillo, T.F.: Benchmarking hydrogen evolving reaction and oxygen evolving reaction electrocatalysts for solar water splitting devices. *J. Am. Chem. Soc.* **137**(13), 4347–4357 (2015)
46. Yang, Y., Fei, H., Ruan, G., Tour, J.M.: Porous cobalt-based thin film as a bifunctional catalyst for hydrogen generation and oxygen generation. *Adv. Mater.* **27**(20), 3175–3180 (2015)
47. Wang, X., Kolen, K., Bao, Y.V., Kovnir, X.-Q., Liu, L.K.: One-step synthesis of self-supported nickel phosphide nanosheet array cathodes for efficient electrocatalytic hydrogen generation. *Angew Chem. Int. Ed.* **54**(28), 8188–8192 (2015)
48. Fahmy, H.M., Mosleh, A.M., Elghany, A.A., et al.: Coated silver nanoparticles: synthesis, cytotoxicity, and optical properties. *RSC Adv.* **9**, 20118–20136 (2019)
49. Abu Elella, M.H., Goda, E.S., Abdallah, H.M., et al.: Innovative bactericidal adsorbents containing modified xanthan gum/montmorillonite nanocomposites for wastewater treatment. *Int. J. Biol. Macromol.* **167**, 1113–1125 (2021)
50. Akman, E., Shalan, A.E., Sadegh, F., Akin, S.: Moisture-resistant FAPbI₃ perovskite solar cell with 22.25 % power conversion efficiency through pentafluorobenzyl phosphonic acid passivation. *Chemsuschem* **14**, 1176–1183 (2021)
51. Abdellatif Soliman, S.M., Sanad, M.F., Shalan, A.E.: Synthesis, characterization and antimicrobial activity applications of grafted copolymer alginate-g-poly(N-vinyl imidazole). *RSC Adv.* **11**, 11541–11548 (2021)
52. Elseman, A.M., Zaki, A.H., Shalan, A.E., et al.: TiO₂ nanotubes: An advanced electron transport material for enhancing the efficiency and stability of perovskite solar cells. *Ind. Eng. Chem. Res.* **59**, 18459–18557 (2020). <https://doi.org/10.1021/acs.iecr.0c03415>
53. Eivazzadeh-Keihan, R., Taheri-Ledari, R., Mehrabad, M.S., et al.: Effective combination of rGO and CuO nanomaterials through poly(p-phenylenediamine) texture: utilizing it as an excellent supercapacitor. *Energy Fuels* **34**, 8316–8324 (2021). <https://doi.org/10.1021/acs.energyfuels.1c01132>
54. Gong, H., Li, Z., Chen, Z., Liu, Q., Song, M., Huang, C.: NiSe/Cd_{0.5}Zn_{0.5}S composite nanoparticles for use in p–n heterojunction-based photocatalysts for solar energy harvesting. *ACS Appl. Nano Mater.* **3**(4), 3665–3674 (2020)
55. Jaque, D., et al.: Nanoparticles for photothermal therapies. *Nanoscale* **6**(16), 9494–9530 (2014)
56. Zhang, J., Yu, J., Jaroniec, M., Gong, J.R.: Noble metal-free reduced graphene oxide-Znx Cd_{1-x}S nanocomposite with enhanced solar photocatalytic H₂-production performance. *Nano Lett.* **12**(9), 4584–4589 (2012)
57. Guo, Q., et al.: Fabrication of 72% efficient CZTSSe solar cells using CZTS nanocrystals. *J. Am. Chem. Soc.* **132**(49), 17384–17386 (2010)
58. Chen, M.-L., Park, C.-Y., Choi, J.-G., Oh, W.-C.: Synthesis and characterization of metal (Pt, Pd and Fe)-graphene composites. *J. Korean Ceram. Soc.* **48**(2), 147 (2011)
59. Li, Q., Guo, B., Yu, J., Ran, J., Zhang, B., Yan, H., Gong, J.R.: Highly efficient visible-light-driven photocatalytic hydrogen production of CdS-cluster-decorated graphene nanosheets. *J. Am. Chem. Soc.* **133**(28), 10878–10884 (2011)

60. Xiang, Q., Yu, J., Jaroniec, M.: Enhanced photocatalytic H₂-production activity of graphene-modified titania nanosheets. *Nanoscale* **3**(9), 3670–3678 (2011)
61. Kumar, N.A., Baek, J.-B.: Doped graphene supercapacitors. *Nanotechnology* **26**(49), 492001 (2015)
62. Lightcap, I.V., Kamat, P.V.: Graphitic design: prospects of graphene-based nanocomposites for solar energy conversion, storage, and sensing. *Acc. Chem. Res.* **46**(10), 2235–2243 (2013)
63. Terrones, M., et al.: Interphases in graphene polymer-based nanocomposites: achievements and challenges. *Adv. Mater.* **23**(44), 5302–5310 (2011)
64. Chen, S., Zhu, J., Wang, X.: One-step synthesis of graphene–cobalt hydroxide nanocomposites and their electrochemical properties. *J. Phys. Chem. C* **114**(27), 11829–11834 (2010)
65. Zhou, M., et al.: Highly conductive porous graphene/ceramic composites for heat transfer and thermal energy storage. *Adv. Func. Mater.* **23**(18), 2263–2269 (2013)

Versatile Production of New Multi-functional and Composite Nanomaterials by Means of Cold Plasma - Liquid Interactions



Anna Dzimitrowicz, Piotr Cyganowski, Piotr Jamroz,
Dorota Jermakowicz-Bartkowiak, and Pawel Pohl

Abstract Nowadays, a rapid economic growth is observed, which is associated with series of technological and economic challenges, including development of new (nano)materials dedicated to diverse applications in environmental protection, energy storage, food sanitization, and medicine. The use of cold atmospheric pressure plasma (CAPP) systems, particularly those operated in contact with liquids, opens a quite new route for synthesis and modification of such specialized materials. CAPP-based production of new multi-functional and composite nanomaterials is usually eco-friendly and involves single-step processes, considerably lowering the labor investment and costs. It can also be carried out on a much larger scale, as compared to other methods and procedures that are based on complex chemical treatments and processes. The size and morphology as well as structural and optical properties of such new composite nanomaterials are tunable and tailorable. In addition, having reproducible physical dimensions, crystallinity, functionality, and spectral properties, they are ready for their specific applications without any initial pre-treatments.

In this review, a series of new synthetic routes for fabrication of modern multi-functional and composite nanomaterials for applications in environmental protection and biomedicine by means of CAPP systems is described. It includes production of (i) efficient nanocatalysts for catalytic decomposition of organic pollutants, (ii) new nanocomposites increasing the heat transfer rate, (iii) and unique nanomaterials revealing antimicrobial and cytotoxic properties.

A. Dzimitrowicz and P. Cyganowski—These authors contributed equally to this work.

A. Dzimitrowicz · P. Jamroz · P. Pohl (✉)
Faculty of Chemistry, Department of Analytical Chemistry and Chemical Metallurgy, Wrocław University of Science and Technology, Wybrzeże St. Wyspińskiego 27, 50-370 Wrocław, Poland
e-mail: pawel.pohl@pwr.edu.pl

P. Cyganowski · D. Jermakowicz-Bartkowiak
Faculty of Chemistry, Department of Process Engineering and Technology of Polymer and Carbonaceous Materials, Wrocław University of Science and Technology, Wybrzeże St. Wyspińskiego 27, 50-370 Wrocław, Poland

Keywords Non-thermal plasma · Nanocomposites · Catalysis · Heat transfer · Antimicrobial · Cytotoxicity

Abbreviations List (Alphabetical Order)

4-AP	4-aminophenol
4-NP	4-nitrophenol
AOETAC	[(2-acryloyloxy)ethyl]trimethylammonium chloride
CAPP	cold atmospheric pressure plasma
EDX	energy dispersive X-ray spectroscopy
km	mass-normalized first order kinetics constant
MBA	N,N-methylenebisacrylamide
NCats	nanocatalysts
NCs	polymeric nanocomposites
NMs	nanomaterials
NPs	nanoparticles
O/W	oil-in-water
PVA	poly(vinyl alcohol)
PVP	poly(vinyl pyrrolidone)
RNS	reactive nitrogen species
ROS	reactive oxygen species
SAED	selected area energy diffraction
SAM	self-assembled monolayer
SDS	sodium dodecyl sulphate
TEM	transmission electron microscopy
TMA	11-(mercaptoundecyl)-N,N,N-trimethylammonium chloride
UV/Vis	Ultraviolet/Visible
VBAC	vinylbenzyl trimethylammonium chloride

1 Introduction

Currently, a special attention is paid to fabrication of nanomaterials (NMs) having outstanding physical, chemical, mechanical, and optical properties [1], as compared to the macroscopic form of these materials. Due to listed properties of such NMs, they have found applications in a wide range of fields. This comprises their usage as: *i*) new nanocatalysts (NCats) for catalytic decomposition of organic pollutants [2, 3] and heat conductive processes [4] in addition to *ii*) antimicrobial and anticancer agents, fulfilling various roles in biomedicine [5–7].

Affordable and efficient methods for synthesis of NMs with the desirable morphology and functionality, as well as spectral, antibacterial and cytotoxic properties are the most important challenges of contemporary nanotechnology. Among different methods used for synthesis of the above-mentioned NMs, the most common are solvothermal, precipitation, and chemical reduction methods [8]. A promising alternative to these methods of NMs production is utilization of cold atmospheric pressure plasma (CAPP)-based approaches.

In the case of CAPPs-based protocols of NMs synthesis, appropriate metal ions (acting as NMs precursors) are reduced in their solutions by specific reducing agents that are generated during CAPP-liquid interactions. These specific reducing agents are reactive oxygen species (ROS) and reactive nitrogen species (RNS), in addition to solvated electrons (e^-_{aq}) and hydrogen radicals (H^\bullet) [9]. Moreover, CAPP-based production of NMs is controlled not only by the composition of NMs precursors solutions (e.g. a precursor form, its concentration), but also by appropriate CAPP operating parameters (e.g. a discharge current, a solution flow rate, a noble gas flow rate) [10]. As a result, it is possible to obtain NMs of desirable physical, chemical, mechanical, and optical properties [10].

So far, only few research groups have developed CAPP-based reaction-discharge systems and used them in the last few years for synthesis of metallic nanoparticles (NPs) [11–23]. In this case, CAPPs are either operated between two solid metallic electrodes [11–15] or in contact with liquids, *i.e.* in gaps between the surface of precursors solutions and stainless steel capillaries delivering appropriate discharge gases [16–23]. As a result, noble metals NPs are obtained, including AuNPs, AgNPs, and Au@Ag core-shell nanostructures [11–23]. Despite the above uses of CAPPs, a little attention has been paid to CAPP-based synthesis of PtNPs. To the best of our knowledge, only three scientific groups have reported efficient production of PtNPs, including Koo et al. [24], Hu et al. [25], and Ichin et al. [26].

In all the above-cited works [11–26], synthesis of NMs is exclusively carried out in stationary, non-flow-through mode systems. For that reason, the mentioned noble metals NPs have been produced in these systems in limited amounts, hindering their broaden application. To improve the CAPP-based synthesis process of NPs reported by others scientists, a highly-through-put, continuous-flow CAPP-based reaction-discharge system has been lately developed in our scientific group [2, 4–7, 10–34]. It is suspected that the CAPP-liquid interface would be a rich source of reactive species, which can react with precursors of noble metals to reduce them to their NPs. Figure 1 shows such CAPP-based reaction-discharge system, in which CAPP is operated between a sharpened pin-type metallic electrode [2, 4–7, 10, 30–34] and the surface of flowing solutions containing NPs precursors. In a similar system, the pin-type solid metallic electrode is replaced by a gaseous needle jet [27–29], however, the use of CAPP sustained under a noble gas atmosphere is associated with increased operating costs. In the CAPP-based reaction-discharge system given in Fig. 1, CAPP operating parameters can be easily controlled and appropriately adjusted. As a result, it is possible to control the course of CAPP-liquid interactions and produce NPs of defined properties [10, 28, 33]. However, in the case of uncoated AuNPs and AgNPs, unexpected problems associated with their uncontrolled agglomeration, aggregation,

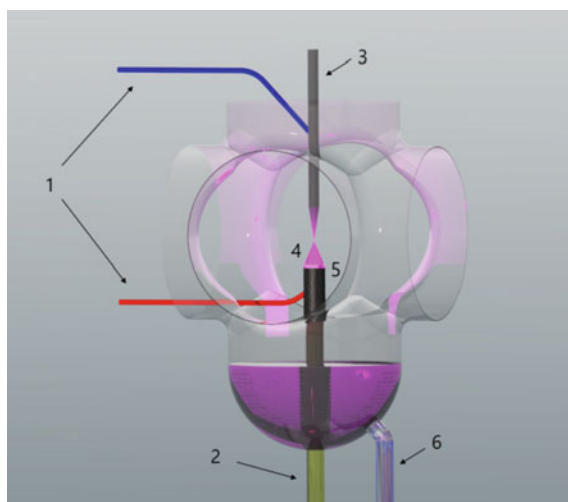


Fig. 1 A representative diagram of the CAPP-based reaction-discharge system used for continuous-flow production of metallic nanostructures. In this system, CAPP is operated between the surface of a flowing solution (containing precursors of metallic nanostructures) and a pin-type tungsten electrode. **1** high voltage inputs (\pm); **2** a flowing solution; **3** a metallic electrode or a gaseous needle; **4** CAPP; **5** a graphite tube inserted onto a quartz tube; **6** a sample reservoir. The figure reproduced from ref. [35] with permission of the MDPI under the CC BY license

and sedimentation are noted [2, 7, 30, 31, 33]. As such, raw-AuNPs and raw-AgNPs exhibit rather a limited applicability in real life uses. To combat this problems, two experimental approaches have also been developed in our group, successfully lifting the limitations of uncoated NPs in real life applications.

In the first approach, a proper stabilizer, *i.e.* gelatine [10, 27–30], fructose [6], pectin [5, 34], sodium dodecyl sulphate (SDS) [5], 11-(mercaptoundecyl)-N,N,N-trimethylammonium chloride (TMA) [7], polyvinylpyrrolidone (PVP) [4, 29] or poly(vinyl alcohol) (PVA) [29], is added to solutions of NPs precursors in order to protect synthesized nanostructures *versus* such uncontrolled processes like formation, aggregation, agglomeration, and sedimentation. In the second approach, polymeric nanocomposites (NCs) are fabricated using new *in-situ* or *ex-situ* synthetic routes [2, 3, 31, 36, 37]. These NCs include uncoated NPs that are dispersed within polymeric matrices. The latter type of NMs resolves undesirable problems related to instability of uncoated NPs, such NMs can also be easily separated from media they are used in. These two experimental approaches certainly enable to develop quite new and innovating synthetic strategies that address modern challenges of process engineering and biomedicine, and significantly broaden practical applications of metallic NPs.

The main objective of the present chapter is to present versatile CAPP applications for production of new multi-functional and composite NMs characterized by extended applicability in processes related to the heat transfer, catalysis and biomedicine.

2 Synthetic Routes for Obtaining New Multi-functional and Composite Nanomaterials

2.1 Stabilization of Uncoated Nanostructures

The most important goal in synthesis of stable-in-time NMs is to select a proper stabilizer that may prevent an uncontrolled growth of NPs [38]. To reach this aim, various stabilizers have been used in the NPs formation process supported by CAPP-liquid interactions (see above for more details). The appropriate choice of the stabilizer allows to obtain NPs that are stable in time and do not change their structural integrity and characteristics.

Due to an inherent nature of CAPP operation under defined conditions (ambient temperature, atmospheric pressure), suitable capping agents can be introduced into CAPP-based reaction-discharge systems directly in solutions of NPs precursors. Based on reported research, stabilizing agents should preferably contain chelating O-, N- and S-based functionalities that, after passing through CAPP-based reaction-discharge systems, tend to spontaneously orient themselves towards the surface of resultant NPs. As such, different proteins, carbohydrates, amino- and thiol-based reagents can be utilized. This approach allows to obtain hybrid materials, *i.e.* AuNPs, AgNPs, or PtNPs, that are stabilized by gelatine [10, 27–30], fructose [6], pectin [5, 34], SDS [5], TMA [7], PVP [4, 29] or PVA [29]. Figure 2 displays exemplary transmission electron microscopy (TEM) photomicrographs of AgNPs stabilized by fructose. As can be seen, almost all (95%) of analyzed NPs are spherical in size, with an average dimension about 14.9 ± 7.9 nm [6]. However, although fructose is added to a NPs precursor solution as a capping agent, efficiency of nanostructures stabilization by fructose has not been effective, likely due to sample preparation before TEM measurements.

Chelating functionalities of these compounds cause self-orientation of stabilizers particles towards the surface of NPs, enhancing their further stability and characteristics. For instance, (11-mercaptoundecyl)-N,N,N-trimethylammonium chloride (TMA) can be used as a stabilizer that enables to synthesize stable-in-time and ultra-small AgNPs. The corresponding TEM photomicrographs and selected area energy diffraction (SAED) of nanostructures are displayed in Fig. 3. As can be seen, the application of TMA as a capping agent leads to formation of self-assembled monolayers (SAMs) onto the AgNPs surface. The occurrence of such SAMs onto the Ag nanostructures surface determines their unique structural properties – in this case, ultra-small AgNPs of an average dimension of 1.21 ± 0.80 nm can be

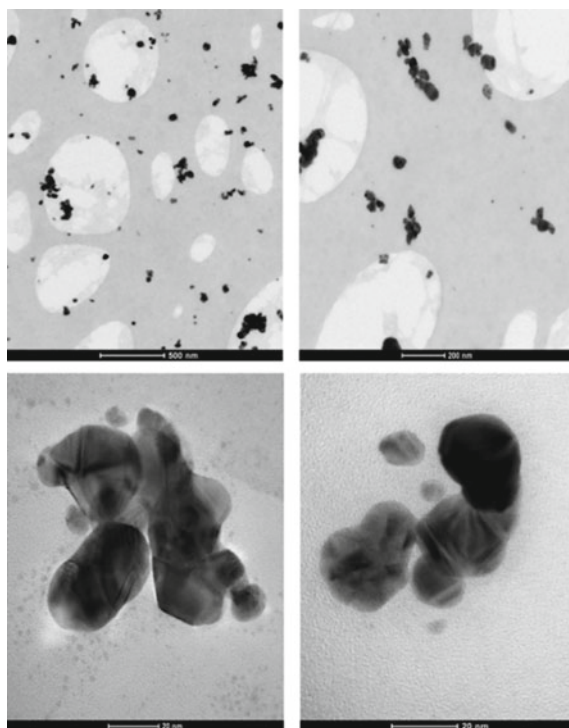


Fig. 2 Exemplary TEM photomicrographs of Ag nanostructures obtained with the aid of CAPP and stabilized by fructose. The figure reproduced from ref. [6] with permission of the MDPI under the CC BY license

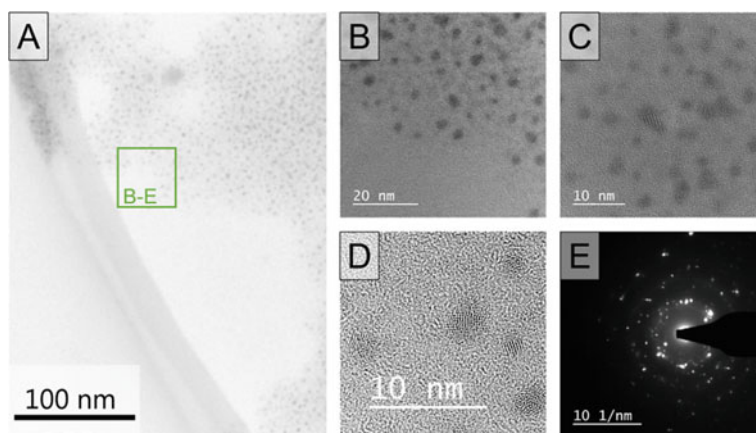


Fig. 3 a–d High resolution TEM photomicrographs, and e the SAED pattern of TMA-stabilized AgNPs. The figure reproduced from ref. [7] with permission of the John Wiley and Sons

obtained [7]. Additionally, excellent antimicrobial properties of such Ag nanostructures towards such microorganisms as *Staphylococcus aureus*, *Escherichia coli*, and *Candida albicans* are observed [7].

Considering the application of CAPP for synthesis of stable-in-time Ag nanostructures, not only AgNPs capped by TMA [7], but also Ag nanostructures stabilized by pectin [5], SDS [5] or fructose [6] have then useful biological properties and can be successfully applied as antimicrobials agents, inactivating microorganisms from different genera.

2.2 Polymeric Nanocomposites

Polymeric NCs combine both required structural, optical and physicochemical properties of typical NPs with an ease of uses of polymeric matrices. Nanostructures are stabilized in the polymeric matrix and this prevents their aggregation, while some properties (*e.g.* catalytic, antimicrobial) are not affected at all [3, 39]. For that reason, incorporation of raw-NPs within polymeric matrices appears to be an interesting approach to increase their stability and stability of resultant NCs. Synthesis of NCs can be carried out *via* two synthetic routes, *i.e.* applying *in-situ* or *ex-situ* approaches. When NPs are produced on polymer functionalities, such synthesis of NCs is called *in-situ* [36, 40]. Contrary, if production of NCs involves immobilization of pre-formed NPs into a polymeric matrix, this kind of synthesis is called *ex-situ*. Although these two approaches can be simply used for fabrication of NCs, they have some limitations. The *in-situ* approach results in a good yield of immobilization of NPs, but it is difficult to control it because the average size distribution of NPs depends on a variety of factors [41]. On the other hand, the *ex-situ* approach enables to controllably synthesize NPs, but the yield of their immobilization is often non-effective [41].

Because of this, a new method, combining both *in-situ* and *ex-situ* approaches, has been developed in our group for efficient synthesis of NCs. This method consists of two steps. In the first one, raw metallic NPs are produced with the aid of CAPP that is operated in a continuous-flow reaction-discharge system (see Fig. 1). In the next step, resultant uncoated metallic NPs are immobilized into a water phase of quaternary-ammonium monomers. Then, the resultant mixture is subjected to free radical polymerization, which leads to production of NCs hydrogels that contain stable-in-time and well dispersed metallic NPs [31]. The suggested method allows to avoid any diffusion limitations of NPs within a polymeric network and enables to efficiently use them as new catalysts for the heat conductive process [31] as well as for heterogeneous catalysis purposes [2].

3 Nanomaterials Dedicated to Increase Heat Transfer

CAPP-based technology does not need to use any reducing agents, hence, uncoated nanostructures can be efficiently produced [2, 10, 18, 30, 42]. Because CAPP is generated under defined operating conditions, there is a possibility to tune optical and granulometric properties of fabricated NMs [10, 28, 33]. This results in obtaining nanostructures of strictly defined properties [2, 42]. As an example, CAPP-based synthesis of raw-AuNPs of controlled granulometric properties can be provided, which are then immobilized into a quaternary ammonium hydrogel based on vinylbenzyl trimethyl ammonium chloride (VBTA) using the modified *ex-situ* approach [31]. In more details, raw-AuNPs, obtained using a continuous-flow CAPP reaction-discharge system, are added to a water phase that contains hydrophilic monomers. This resultant mixture can be further subjected to free radical polymerization as it is given in Fig. 4.

So-designed polymerization-driven immobilization of raw-AuNPs results in synthesis of NCs based on a VBTA and N,N-methylenebis(acryl amide) (MBA) copolymer (VBTA-co-MBA) [31]. The described method enables to efficiently stabilize raw-AuNPs but unfortunately it leads either to an undesired anion-exchange reaction between VBTA functional groups and AuCl_4^- ions. As a result, excessive HCl is formed, which gradually digests NPs [31]. Thus, the method has been modified to force the anion-exchange process by using NaOH, as is schematically given in Fig. 5.

Successful elimination of the anion-exchange reaction enables to neutralize excessive Cl^- anions located on VBTA and prevented formation of HCl and subsequent digestion of AuNPs. As displayed in Fig. 6D, the sample obtained in the presence of NaOH is the only one that can be described by ruby-red color, characteristic for colloidal suspensions of Au nanostructures, being a sign of the successfully synthesized NC [31].

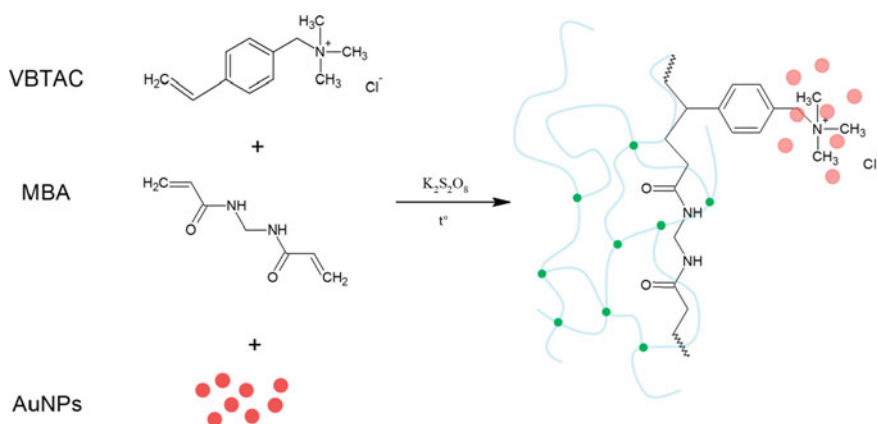


Fig. 4 A simplified synthetic route for production of the hydrogel NC containing raw-AuNPs. The figure reproduced from ref. [31] with permission of the MDPI under the CC BY license

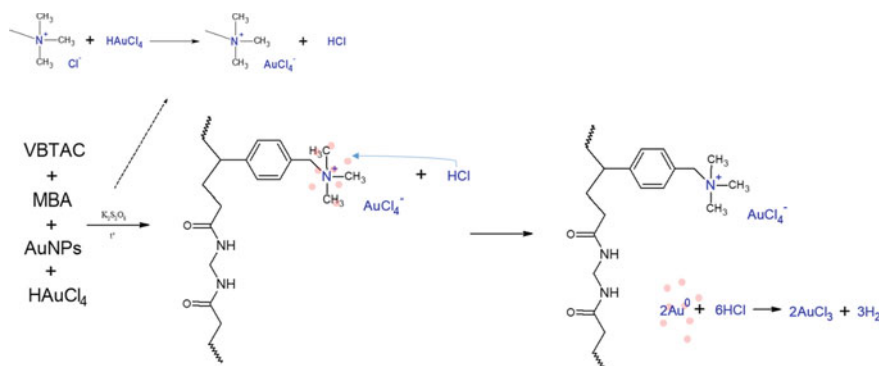
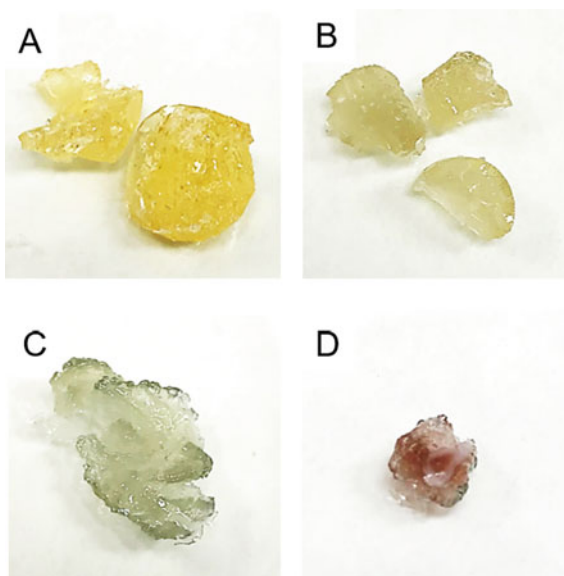


Fig. 5 Reactions occurring during synthesis of the hydrogel-based NC in the presence of NaOH. The figure reproduced from ref. [31] with permission of the MDPI under the CC BY license

Fig. 6 a VBTAAC-co-MBA copolymer, **b, c** samples of resultant NCs with AuNPs obtained without application of NaOH, **d** final NCs with AuNPs after applying NaOH into the VBTAAC monomer. The figure reproduced from ref. [31] with permission of the MDPI under the CC BY license



Successful and efficient stabilization of AuNPs in the VBTAAC-co-MBA hydrogel leads to synthesis of the NC characterized by increased hydrophilicity and enriched functionality attributed to the presence of metallic NPs within its structure. The NC, shown in Fig. 6D, can be used in a system simulating a cooling unit of a modern electronic device. As a result, an increase of the cooling rate by 300% is noted, which well complies with other reports [39, 43, 44]. Research on NCs for heat management systems have also been expanded by producing a NC with PtNPs. In this case, stable-in-time PtNPs are synthesized by using CAPP-based technology [4]. The reaction mixture, consisting of a PtNPs precursor (PtCl₆²⁻) and PVP as a stabilizer, is treated

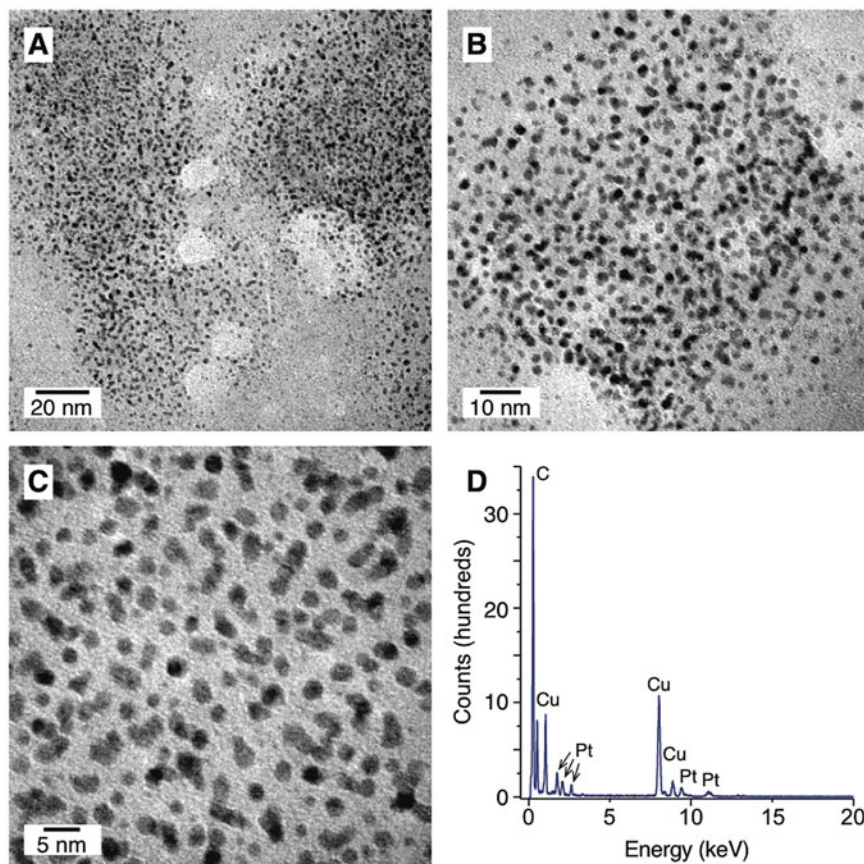


Fig. 7 a TEM photomicrographs, and **d** the EDX spectrum of PVP-PtNPs synthesized with the aid of CAPP. The figure reproduced from ref. [4] with permission of the MDPI under the CC BY license.

by CAPP operated in a continuous-flow reaction-discharge system. Because N and O donor atoms are present in the structure of PVP, stable PVP-PtNPs are produced. It is possible due to self-orientation of PVP towards the surface of PtNPs, providing successful surface stabilization of thereof and Fig. 7 displays these NPs. In this case, capsules of an average size of 111.4 ± 22.6 nm are formed and encapsulate PtNPs having 2.9 ± 0.6 nm [4].

A fluid containing these NCs can be used then as a cooling medium in a unit simulating an internal combustion chamber. Achieved heat exchange rates are greater by 800% as compared to those obtained with water that is used for cooling the system. These heat exchange rate are also comparable to those established for commercial NPs-based cooling liquids even though PtNPs are present in the fluid at a very low concentration, *i.e.* 0.0001% [4].

Both described NCs, containing AuNPs or PtNPs, reveal a very satisfactory activity in systems simulating cooling units. They are more efficient as compared to others reported in relevant literature, *i.e.* CuONPs immobilized into polyaniline (heat exchange rate increased by 12–38%) [43], graphene oxide stabilized in poly(N-isopropylacrylamide) (heat exchange rate increased by 200%) [44], carbon nanotubes immobilized into stearic acid (heat exchange rate increased by 91%) [39], and a Cu/Al₂O₃ nanofluid (heat exchange rate increased by 80%) [43, 45]. Although the price of Pt and Au exceeds this of Cu and Al, established exchange rates, particularly this one for very small amounts of PtNPs, make the proposed method of synthesis of NCs a very tempting alternative towards currently applied strategies [4, 31].

4 Nanocatalysts

There is a growing concern nowadays about environmental hazards derived from aromatic nitro compounds. These chemicals are accounted as major organic pollutants due to a vast number of waste sources and an increased discharge into water. Environmental contamination with these compounds becomes a serious problem because of their long-term toxic character [46–48]. For that reason, catalytic decomposition of nitroarenes in water under mild conditions is of a greatest concern. As such, catalytic reduction of 4-nitrophenol (4-NP) to 4-aminophenol (4-AP) is treated as a relevant model of this process. This is because 4-NP reveals toxic, inhibitory and potentially carcinogenic character [46–48] while the product of its reduction (4-AP) is an important by-product in production of *e.g.* paracetamol [49]. Due to unfavorable thermodynamics, decomposition of 4-NP cannot be carried out under mild conditions without any catalyst.

To address this issue, modified *ex-situ* protocols for synthesis of NCs have been used in our research group to immobilize raw-AuNPs, obtained with the aid of CAPP, into a polymeric matrix consisting of [(2-acryloyloxy)ethyl]trimethylammonium chloride (AOETAC) and MBA [2] via the synthetic route displayed in Fig. 8.

So-obtained NCs can be used then as heterogenous NCats for catalytic reduction of 4-NP to 4-AP under mild conditions in water environment. The developed NCs also reveal an increased pseudo-first order reaction rate constant being facilitated by an increased water uptake that is characteristic for the hydrogel-based NC [2]. Table 1 compares mass-normalized rate constants (k_m) found for different NMs and reported in literature with those established for developed NCs.

Developed NCs [2, 37] reveal a facilitated catalytic activity. Although there are more active catalysts [56], it must be noted that the form of developed NCs (hydrogel particles) makes their application and re-use very easy. An alternative approach to synthesis of new NMs is also proposed in work [32]. In this case, a CAPP-based reaction-discharge system is used to activate plant extracts prepared from *Ginkgo biloba* or *Panax ginseng*. Such CAAP-activated plant extracts can be used next to fabricate stable-in-time AuNPs. In this case, the CAPP treatment alters organic compounds present in both plant extracts, enhancing then reduction of

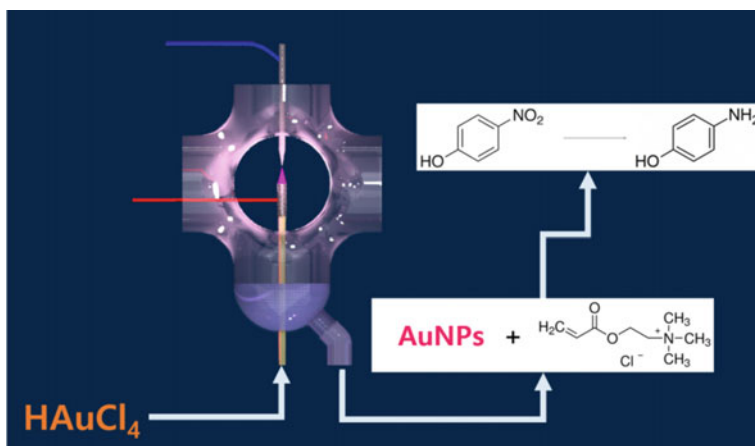


Fig. 8 The synthetic route for production of a AOETAC-co-MBA hydrogel nanocomposite with AuNPs revealing a catalytic activity. The figure reproduced from ref. [2] with permission of Elsevier

Table 1 Nanocomposite AuNPs-based catalysts for catalytic decomposition of 4-NP [37]. The table reproduced from ref. [35] with permission of the MDPI under the CC BY license

Support	Average size of AuNPs [nm]	k_m [$\text{mg}^{-1} \text{min}^{-1}$]	Ref.
Aryl diazonium-modified olive waste	n.a	0.02	[50]
PMMA	7.0	0.37	[51]
Magnetite microspheres	5.0–7.0	1.22	[52]
Reductive carbon dots	15.0	0.10	[53]
ZrO_2	17.0 ± 5.1	0.06	[54]
Egg-shell	6.2 ± 4.0	1.07	[55]
Fe_3O_4	15.0	13.8	[56]
Sulphur doped graphitic carbon nitride	12.0	1.50	[57]
VBC/DVB with 1-amino-4-methylpiperazine ligands	4.5 ± 2.1	1.46	[37]*
Quaternary ammonium hydrogel	6.2 ± 1.2	0.10	[2]*

* Authors' works

AuCl_4^- ions to AuNPs. Moreover, it has been found that amide species present in these CAPP-activated plant extracts indeed participate in formation and stabilization of AuNPs. Therefore, AuNPs are efficiently fabricated and stabilized in these conditions. Morphologies of so-obtained Au nanostructures are shown in Figs. 9 and 10.

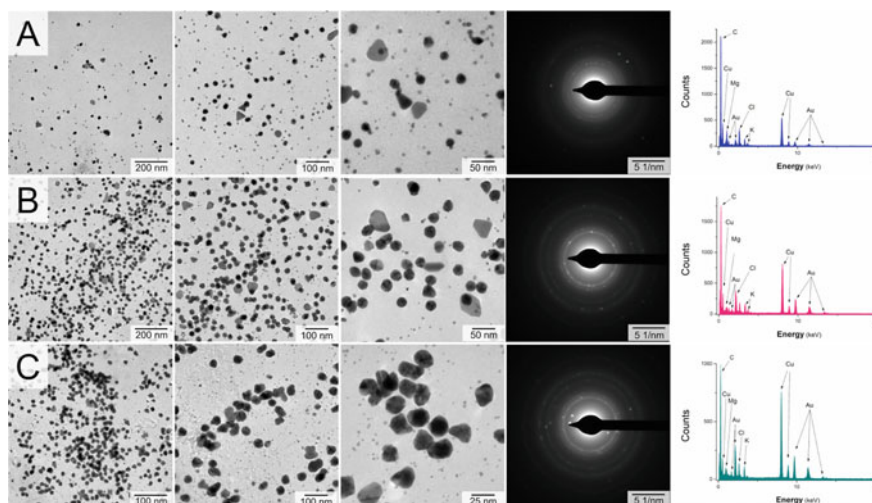


Fig. 9 TEM photomicrographs, electron diffraction (SAED) patterns, and energy dispersive X-ray (EDX) spectra of AuNPs obtained using **A** untreated, and CAPP-activated plant extracts by its operation between the surface of a flowing *G. biloba* extract, acting as the anode **B** or the cathode **C**. The figure reproduced from ref. [32] with permission of the MDPI under the CC BY license

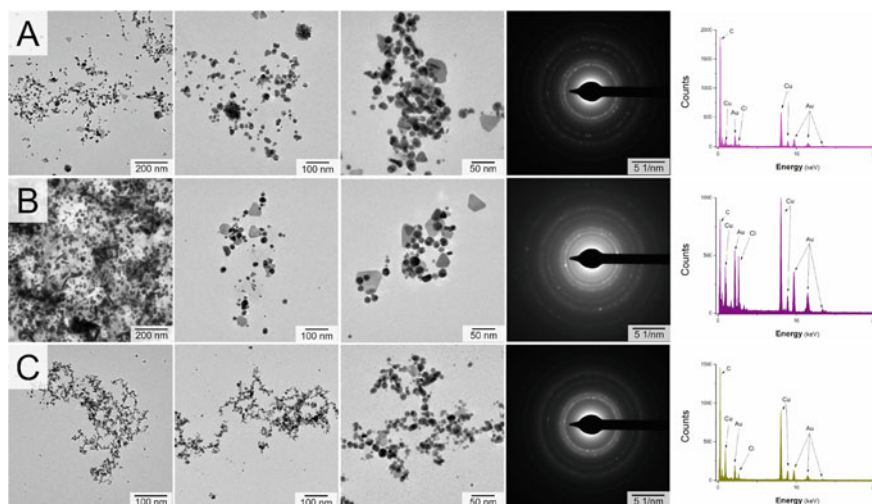


Fig. 10 TEM photomicrographs, electron diffraction (SAED) patterns, and energy dispersive X-ray (EDX) spectra of AuNPs obtained using **a** untreated, and CAPP-activated plant extracts by its operation between the surface of a flowing *P. ginseng* extract, acting as the anode **b** or the cathode **c**. The figure reproduced from ref. [32] with permission of the MDPI under CC BY license

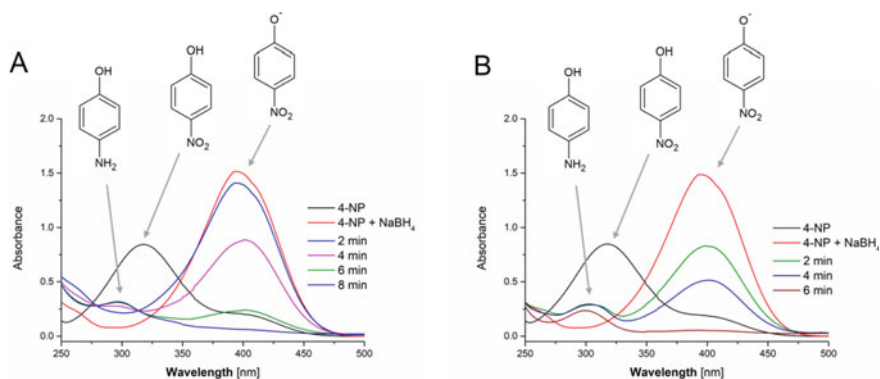


Fig. 11 UV/Vis absorption spectra of 4-NP to 4-AP reduction using homogenous catalysts containing AuNPs fabricated by the aqueous **a** *G. biloba* leaves extract and **b** *P. ginseng* root extract, activated by CAPP. The figure reproduced from ref. [32] with permission of the MDPI under the CC BY license

AuNPs obtained using CAPP-activated *G. biloba* and *P. ginseng* extracts can be used as homogenous NCats for decomposition of 4-NP to 4-AP. The catalytic activity of these homogenous catalysts are evidenced by Ultraviolet/Visible (UV/Vis) spectra displayed in Fig. 11. Based on them, it can be found that AuNPs obtained using the activated *P. ginseng* extract reveal the rate constant of 0.52 s^{-1} for reduction of 4-NP. These outcomes make the mentioned catalytic system a very tempting alternative to other systems because its mass-normalized rate constant is 10-times greater as compared to those reported in relevant literature [32, 58–61].

Based on other examples found in literature, including the application of dielectric barrier discharge (DBD) for production of a AgNPs-based NC [42] that reveals a catalytic activity towards photocatalytic degradation of methylene blue, applicability of NCs developed by our research group [32] is not limited only to degradation of 4-NP. Similar NMs can be used for eradication of *Escherichia coli* and *Staphylococcus aureus* microorganisms [42], suggesting that applied CAPP-based protocols may be easily pushed further, not only towards heat management and catalysis.

5 Nanomaterials Suitable for Biomedical Applications

Approaches associated with production of hybrid NMs allow to preserve or even enhance properties of NPs, involving them in processes related to heat transfer [4, 31] and catalysis [2, 3, 32, 37]. However, it is also possible to extend their possible applications in biomedicine by immersing them into non-toxic matrices, including biopolymers [33], saccharides [5, 6, 34], alkenothiol [7] or surfactants [5].

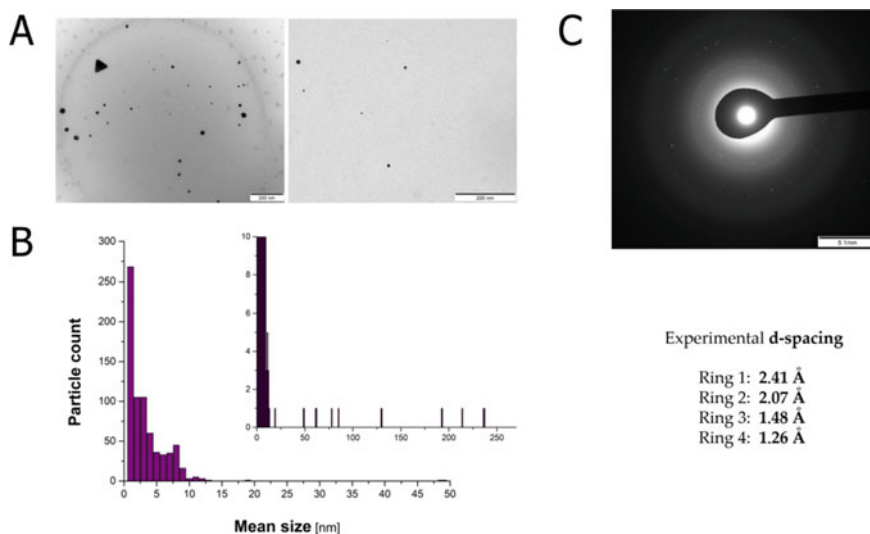


Fig. 12 **a** TEM photomicrographs and **b** the average mean size of AuNPs, and **c** SAED pattern recorded for the AuNPs-loaded nanoemulsion. The figure reproduced from ref. [33] with permission of Springer under Creative Commons CC BY license

The above-mentioned approach enables to enhance bioavailability and biocompatibility of AuNPs. To exploit this significant issue, a synthetic protocol has been developed in our research group for obtaining an oil-in-water (O/W) nanoemulsion that consists of gelatin, turmeric oil, and uncoated AuNPs [33]. The characteristics of the latter ones can be fully tailored by CAPP operating parameters, and hence, AuNPs of controlled optical and granulometric properties are only produced, as displayed in Fig. 12.

The synthesis procedure leads to functionalization of the AuNPs surface inducing their activity towards breast cell lines. Based on obtained results, the resultant O/W nanoemulsion with AuNPs induces apoptosis of breast cancer cells, confirming in this way its unique anti-cancer activity [33].

Referring to NMs exhibiting antimicrobial properties, the use of such innovative NMs is a remedy to problems associated with conventional antibiotics-based therapies used for inactivation of skin pathogens such as *e.g.* *Staphylococcus aureus*, *S. epidermidis*, *Streptococcus pyogenes*, *Pseudomonas aeruginosa*, *Pasteurella multocida*, *Capnocytophaga canimorsus*, *Klebsiella rhinoscleromatis*, and *Vibrio vulnificus* [62]. In order to limit a multidrug resistance among virulent pathogens, CAPP can be used, as reported by our research group, to produce AgNPs stabilized by TMA [7]. By performing multivariate optimization of the applied CAPP-based reaction-discharge system, optimal operating conditions found facilitate production of the smallest TMA-AgNPs. AgNPs obtained under these conditions are approximately spherical in shape and have the size of 1.2 ± 0.8 nm. So-resulted Ag nanostructures can be then applied towards *E. coli*, *S. aureus*, and *C. albicans*

and exhibit minimal bactericidal/fungicidal concentrations of 3.9 ± 0.2 , 7.8 ± 0.3 , and $3.9 \pm 0.2 \text{ mg L}^{-1}$, respectively [7]. It can be expected that this type of Ag nanostructures may be used in the future for inactivation of different human pathogens, limiting a widespread and dangerous with time application of antibiotics.

Additionally, AgNPs can also be applied for inactivation of plant pathogenic bacteria. When the CAPP-based approach is used for flow-through synthesis of AgNPs, stabilized either by fructose [6], pectins [5] or SDS [5], resultant NMs can be successfully used latter on to inactivate different types of plant pathogenic bacteria, including *Erwinia amylovora* [6], *Clavibacter michiganensis* [6], *Ralstonia solanacearum* [6], *Dickeya solani* [5, 6], *Pectobacterium atrosepticum* [5], *Pectobacterium carotovorum* subsp. *brasiliense* [5], *Pectobacterium carotovorum* subsp. *carotovorum* [5], and *Pectobacterium parmentieri* [5]. In this way, CAPP produced and stabilized AgNPs may find their applications in plant disease prevention. AgNPs can be also applied in biomedicine as anticancer agents. Pectin-stabilized AgNPs, produced with the aid of CAPP, are an example of NMs that can be applied for necrosis of human melanoma cancer cell lines [34]. In this case, so-obtained Ag nanostructures are of $10.4 \pm 4.5 \text{ nm}$ in size and monodispersed, and exhibit necrosis of 70–90% of cancerous cells of human melanoma [34].

Examples presented in this section seem to only open a much longer list of potential applications of AgNPs, mostly in drug delivery systems, but also in chemical formulas involved in production of cosmetics and toiletries.

6 Conclusions

CAPP-based technology offers unique approaches towards synthesis of modern and multifunctional NMs. This includes a sufficient and reproducible control over structural, optical and physicochemical properties of so-obtained NPs, as well as a vital possibility to synthesis of hybrid and composite NMs containing metallic NPs.

All presented approaches led to fabrication of stable-in-time composite and hybrid materials that preserve or enhance properties of uncoated AuNPs, AgNPs, and PtNPs. Furthermore, addition of proper capping agent to the analyzed reaction mixture, lead to conjugate onto the surface of nanostructures, produced with the aid of CAPP, other large molecules such as natural or synthetic polymers or surfactants. The adsorption of the capping agents on the surface of the nanostructures provides a protective layer, which allows NPs to be well-dispersed in the colloidal suspension. However, the selection of proper capping agents, containing amino functionalities and/or donor atoms, such as O, N and S, which effectively stabilize and functionalize metallic NPs, is required. Resultant polymeric NCs as well as organic/inorganic hybrids facilitate and extend their uses in processes related to heat transfer, catalysis and biomedicine, outperforming other solutions proposed in literature.

7 Perspectives

The presented here CAPP-based approaches for synthesis of multi-functional and composite nanomaterials are highly desired and very promising in reference to their potential use. Produced polymer-based nanomaterials are developed for controlled applications in heat transfer, catalysis, and biomedicine. In the case of multi-functional nanomaterials that exhibit antimicrobial properties, we believe that their utilization can reduce the amount of applied antibiotics overwhelmingly used for inactivation of pathogenic microorganisms from different genera. For that reason, utilization of CAPP-based technologies described in the present paper in industry, agriculture and medicine is very developmental and forward-looking, and it can be expected that more and more often applied.

Acknowledgement This work is co-financed by a subsidy from the Polish Ministry of Science and Higher Education for the Faculty of Chemistry of Wrocław University of Science and Technology. The research activity of Dr. A. Dzimitrowicz is supported by the Polish Ministry of Science and Higher Education, program Outstanding Young Scientists (532/STYP/13/2018). Prof. P. Pohl acknowledges the National Science Centre (Poland) for the financial support (UMO-2019/33/B/ST4/00356). A. Dzimitrowicz and P. Cyganowski also acknowledge the National Science Centre (Poland) for the financial support (the projects nos. UMO-2019/35/D/ST8/04107 and UMO-2019/33/B/NZ9/00940).

References

1. Khan, I., Saeed, K., Khan, I.: Nanoparticles: properties, applications and toxicities. *Arab. J. Chem.* **12**(7), 908–931 (2019)
2. Cyganowski, P., Jermakowicz-Bartkowiak, D., Jamroz, P., Pohl, P., Dzimitrowicz, A.: Hydrogel-based nanocomposite catalyst containing uncoated gold nanoparticles synthesized using cold atmospheric pressure plasma for the catalytic decomposition of 4-nitrophenol. *Colloid Surf. A* **582**, 123886 (2019)
3. Cyganowski, P., Lesniewicz, A., Dzimitrowicz, A., Wolska, J., Pohl, P., Jermakowicz-Bartkowiak, D.: Molecular reactors for synthesis of polymeric nanocomposites with noble metal nanoparticles for catalytic decomposition of 4-nitrophenol. *J. Colloid Interface Sci.* **541**, 226–233 (2019)
4. Dzimitrowicz, A., Cyganowski, P., Pohl, P., Jermakowicz-Bartkowiak, D., Terefinko, D., Jamroz, P.: Atmospheric pressure plasma-mediated synthesis of platinum nanoparticles stabilized by poly(vinylpyrrolidone) with application in heat management systems for internal combustion chambers. *Nanomaterials* **8**(8), 619 (2018)
5. Dzimitrowicz, A., Motyka, A., Jamroz, P., Lojkowska, E., Babinska, W., Terefinko, D., Pohl, P., Sledz, W.: Application of silver nanostructures synthesized by cold atmospheric pressure plasma for inactivation of bacterial phytopathogens from the genera *Dickeya* and *Pectobacterium*. *Materials* **11**(3), 331 (2018)
6. Dzimitrowicz, A., et al.: Antibacterial activity of fructose-stabilized silver nanoparticles produced by direct current atmospheric pressure glow discharge towards quarantine pests. *Nanomaterials* **8**(10), 751 (2018)
7. Dzimitrowicz, A., et al.: Production of antimicrobial silver nanoparticles modified by alkanethiol self-assembled monolayers by direct current atmospheric pressure glow discharge generated in contact with a flowing liquid anode. *Plasma Process. Polym.* **16**(10), 1900033 (2019)

8. Ealias, A.M., Saravanakumar, M.P.: A review on the classification, characterisation, synthesis of nanoparticles and their application. *IOP Conf. Ser. Mater. Sci. Eng* **263**, 032019 (2017)
9. Chen, Q., Li, J., Li, Y.: A review of plasma-liquid interactions for nanomaterial synthesis. *J. Phys. D Appl. Phys.* **48**, 424005 (2015)
10. Dzimitrowicz, A., Greda, K., Lesniewicz, T., Jamroz, P., Nyk, M., Pohl, P.: Size-controlled synthesis of gold nanoparticles by a novel atmospheric pressure glow discharge system with a metallic pin electrode and a flowing liquid electrode. *RSC Adv.* **6**(84), 80773–80783 (2016)
11. Heo, Y.K., Lee, S.Y.: Effects of the DC pulse duty ratio on the characteristics of nanoparticles in gold nanofluids. *Metals Mater. Int.* **17**(6), 943–947 (2011)
12. Saito, N., Hieda, J., Takai, O.: Synthesis process of gold nanoparticles in solution plasma. *Thin Solid Films* **518**(3), 912–917 (2009)
13. Bratescu, M.A., Cho, S.-P., Takai, O., Saito, N.: Size-controlled gold nanoparticles synthesized in solution plasma. *J. Phys. Chem. C* **115**(50), 24569–24576 (2011)
14. Hu, X.L., Takai, O., Saito, N.: Synthesis of gold nanoparticles by solution plasma sputtering in various solvents. *J. Phys. Conf. Ser.* **417**, 01230 (2013)
15. Valadi, K., Gharibi, S., Taheri-Ledari, R., et al.: Metal oxide electron transport materials for perovskite solar cells: a review. *Environ. Chem. Lett* **19**, 2185–2207 (2021)
16. Vijai Anand, K., Reshma, M., Kannan, M., et al.: Preparation and characterization of calcium oxide nanoparticles from marine molluscan shell waste as nutrient source for plant growth. *J Nanostruct. Chem.* (2021). <https://doi.org/10.1007/s40097-020-00376-4>
17. Taheri-Ledari, R., Esmaili, M.S., Varzi, Z., et al.: Facile route to synthesize Fe₃O₄@acacia-SO₃H nanocomposite as a heterogeneous magnetic system for catalytic applications. *RSC Adv.* **10**, 40055–40067 (2020)
18. Taheri-Ledari, R., Rahimi, J., Maleki, A., Shalan, A.E.: Ultrasound-assisted diversion of nitrobenzene derivatives to their aniline equivalents through a heterogeneous magnetic Ag/Fe₃O₄-IT nanocomposite catalyst. *New J. Chem.* **44**, 19827–19835 (2020)
19. Richmonds, C., Sankaran, R.M.: Plasma-liquid electrochemistry: Rapid synthesis of colloidal metal nanoparticles by microplasma reduction of aqueous cations. *Appl. Phys. Lett.* **93**(13), 131501 (2008)
20. Shalan, A.E., Afifi, M., El-Desoky, M.M., Ahmed, M.K.: Electrospun nanofibrous membranes of cellulose acetate containing hydroxyapatite co-doped with Ag/Fe: morphological features, antibacterial activity and degradation of methylene blue in aqueous solution. *New J. Chem.* **45**, 9212–9220 (2021)
21. Ruixue, W., Shasha, Z., Dong, W., Jue, Z., Weidong, Z., H. BK, Jing F.: Microplasma-assisted synthesis of colloidal gold nanoparticles and their use in the detection of cardiac troponin I (cTn-I). *Plasma Process. Polym.* **12**(4), 380–391 (2015)
22. Sanad, M.F., Shalan, A.E., Bazid, S.M., Abdelbasir, S.M.: Pollutant degradation of different organic dyes using the photocatalytic activity of ZnO@ZnS nanocomposite materials. *J. Environ. Chem. Eng.* **6**, 3981–3990 (2018)
23. Thong, Y.L., Chin, O.H., Ong, B.H., Huang, N.M.: Synthesis of silver nanoparticles prepared in aqueous solutions using helium dc microplasma jet. *Jpn. J. Appl. Phys.* **55**(1S), 01AE19 (2015)
24. Reddy, B., Dadigala, R., Bandi, R., et al.: Microwave-assisted preparation of a silver nanoparticles/N-doped carbon dots nanocomposite and its application for catalytic reduction of rhodamine B, methyl red and 4-nitrophenol dyes. *RSC Adv.* **11**, 5139–5148 (2021)
25. Hu, X., Takai, O., Saito, N.: Simple synthesis of platinum nanoparticles by plasma sputtering in water. *Jpn. J. Appl. Phys.* **52**, 01AN05 (2013)
26. El-Shazly, A.N., Rashad, M.M., Abdel-Aal, E.A., et al.: Nanostructured ZnO photocatalysts prepared via surfactant assisted Co-Precipitation method achieving enhanced photocatalytic activity for the degradation of methylene blue dyes. *J. Environ. Chem. Eng.* **4**, 3177–3184 (2016)
27. Dzimitrowicz, A., Jamroz, P., Nyk, M., Pohl, P.: Application of direct current atmospheric pressure glow microdischarge generated in contact with a flowing liquid solution for synthesis of Au-Ag core-shell nanoparticles. *Materials* **9**(4), 268 (2016)

28. Dzimitrowicz, A., Lesniewicz, T., Greda, K., Jamroz, P., Nyk, M., Pohl, P.: Production of gold nanoparticles using atmospheric pressure glow microdischarge generated in contact with a flowing liquid cathode - a design of experiments study. *RSC Adv.* **5**(110), 90534–90541 (2015)
29. Dzimitrowicz, A., Jamroz, P., Greda, K., Nowak, P., Nyk, M., Pohl, P.: The influence of stabilizers on the production of gold nanoparticles by direct current atmospheric pressure glow microdischarge generated in contact with liquid flowing cathode. *J. Nanopart Res.* **17**(4), 185 (2015)
30. Dzimitrowicz, A., Jamroz, P., Pogoda, D., Nyk, M., Pohl, P.: Direct current atmospheric pressure glow discharge generated between a pin-type solid cathode and a flowing liquid anode as a new tool for silver nanoparticles production. *Plasma Process Polym.* **14**(10), 1600251 (2017)
31. Cyganowski, P., Dzimitrowicz, A., Jamroz, P., Jermakowicz-Bartkowiak, D., Pohl, P.: Polymerization-driven immobilization of dc-APGD synthesized gold nanoparticles into a quaternary ammonium-based hydrogel resulting in a polymeric nanocomposite with heat-transfer applications. *Polymer* **10**(4), 377 (2018)
32. Dzimitrowicz, A., Cyganowski, P., Pohl, P., Milkowska, W., Jermakowicz-Bartkowiak, D., Jamroz, P.: Plant extracts activated by cold atmospheric pressure plasmas as suitable tools for synthesis of gold nanostructures with catalytic uses. *Nanomaterials* **10**(6), 1088 (2020)
33. Dzimitrowicz, A., et al.: Application of oil-in-water nanoemulsion carrying size-defined gold nanoparticles synthesized by non-thermal plasma for the human breast cancer cell lines migration and apoptosis. *Plasma Chem. Plasma Process.* **40**, 1037–1062 (2020)
34. Dzimitrowicz, A., Bielawska-Pohl, A., diCenzo, G., Jamroz, P., Macioszczyk, J., Klimczak, A., Pohl, P.: Pulse-modulated radio-frequency alternating-current-driven atmospheric-pressure glow discharge for continuous-flow synthesis of silver nanoparticles and evaluation of their cytotoxicity toward human melanoma cells. *Nanomater* **8**(6), 398 (2018)
35. Cyganowski, P., Dzimitrowicz, A.: A mini-review on anion exchange and chelating polymers for applications in hydrometallurgy, environmental protection, and biomedicine. *Polymer* **12**(4), 784 (2020)
36. Cyganowski, P., Leśniewicz, A., Polowczyk, I., Chęcmanowski, J., Koźlecki, T., Pohl, P., Jermakowicz-Bartkowiak, D.: Surface-activated anion exchange resins for synthesis and immobilization of gold and palladium nano- and microstructures. *React. Funct. Polym.* **124**, 90–103 (2018)
37. Cyganowski, P., Jermakowicz-Bartkowiak, D., Leśniewicz, A., Pohl, P., Dzimitrowicz, A.: Highly efficient and convenient nanocomposite catalysts produced using in-situ approach for decomposition of 4-nitrophenol. *Colloid Surf. A* **590**, 124452 (2020)
38. Stevenson, A.P., Bea, D.B., Civit, S., Contera, S.A., Cerveto, A.I., Trigueros, S.: Three strategies to stabilise nearly monodispersed silver nanoparticles in aqueous solution. *Nanoscale Res Lett.* **7**(1), 1–8 (2012)
39. Li, T., Lee, J.-H., Wang, R., Kang, Y.T.: Enhancement of heat transfer for thermal energy storage application using stearic acid nanocomposite with multi-walled carbon nanotubes. *Energy* **55**, 752–761 (2013)
40. Paul, D.R., Robeson, L.M.: Polymer nanotechnology: nanocomposites. *Polymer* **49**(15), 3187–3204 (2008)
41. Jeon, I.-Y., Baek, J.-B.: Nanocomposites derived from polymers and inorganic nanoparticles. *Materials* **3**(6), 3654 (2010)
42. Dong, P., et al.: Plasmon enhanced photocatalytic and antimicrobial activities of Ag-TiO₂ nanocomposites under visible light irradiation prepared by DBD cold plasma treatment. *Mater. Sci. Eng. C* **96**, 197–204 (2019)
43. Bhanvase, B.A., Kamath, S.D., Patil, U.P., Patil, H.A., Pandit, A.B., Sonawane, S.H.: Intensification of heat transfer using PANI nanoparticles and PANI-CuO nanocomposite based nanofluids. *Chem. Eng. Process. Process. Intens.* **104**, 172–180 (2016)
44. Lo, C.-W., Zhu, D., Jiang, H.: An infrared-light responsive graphene-oxide incorporated poly(N-isopropylacrylamide) hydrogel nanocomposite. *Soft Mater.* **7**(12), 5604–5609 (2011)

45. Moghaieb, H.S., Abdel-Hamid, H.M., Shedid, M.H., Helali, A.B.: Engine cooling using Al₂O₃/water nanofluids. *Appl. Therm. Eng.* **115**, 152–159 (2017)
46. Electronic document. <https://www.epa.gov/sites/production/files/2016-09/documents/4-nitrophenol.pdf>, Access 21 Jan 2019
47. Urben, P.G.: B. Bretherick's Handbook of Reactive Chemical Hazards, 7th edn., pp. 65–133. Academic Press, Oxford (2007)
48. Urben, P.G.: C. Bretherick's Handbook of Reactive Chemical Hazards, 7th edn., pp. 133–1565. Academic Press, Oxford (2007)
49. Zhao, P., Feng, X., Huang, D., Yang, G., Astruc, D.: Basic concepts and recent advances in nitrophenol reduction by gold-and other transition metal nanoparticles. *Coord. Chem. Rev.* **287**, 114–136 (2015)
50. Belbekhouche, S., et al.: Aryl diazonium-modified olive waste: a low cost support for the immobilization of nanocatalysts. *Colloid Surf. A* **529**, 541–549 (2017)
51. Kuroda, K., Ishida, T., Haruta, M.: Reduction of 4-nitrophenol to 4-aminophenol over Au nanoparticles deposited on PMMA. *J. Mol. Catal. A Chem.* **298**(1–2), 7–11 (2009)
52. Ma, M., et al.: Gold nanoparticles supported by amino groups on the surface of magnetite microspheres for the catalytic reduction of 4-nitrophenol. *J. Mater. Sci.* **54**(1), 323–334 (2019)
53. Zheng, B., et al.: Surfactant-free gold nanoparticles: rapid and green synthesis and their greatly improved catalytic activities for 4-nitrophenol reduction. *Inorg. Chem. Front.* **4**(8), 1268–1272 (2017)
54. Acosta, B., Evangelista, V., Miridonov, S., Fuentes, S., Simakov, A.: The decoration of gold core in Au@ZrO₂ nanoreactors with trace amounts of Pd for the effective reduction of 4-nitrophenol to 4-aminophenol. *Catal. Lett.* **149**(6), 1621–1632 (2019)
55. Ding, Q., Kang, Z., Cao, L., Lin, M., Lin, H., Yang, D.-P.: Conversion of waste eggshell into difunctional Au/CaCO₃ nanocomposite for 4-nitrophenol electrochemical detection and catalytic reduction. *Appl. Surf. Sci.* **510**, 145526 (2020)
56. Yang, Y., et al.: Facile fabrication of Au/Fe₃O₄ nanocomposites as excellent nanocatalyst for ultrafast recyclable reduction of 4-nitrophenol. *Chem. Eng. J.* **381**, 122596 (2020)
57. Balakumar, V., Kim, H., Ryu, J.W., Manivannan, R., Son, Y.-A.: Uniform assembly of gold nanoparticles on S-doped g-C₃N₄ nanocomposite for effective conversion of 4-nitrophenol by catalytic reduction. *J. Mater. Sci. Technol.* **40**, 176–184 (2020)
58. Massaro, M., et al.: Gold nanoparticles stabilized by modified halloysite nanotubes for catalytic applications. *Appl. Organomet Chem.* **33**(3), e4665 (2019)
59. Nadaf, N.Y., Kanase, S.S.: Biosynthesis of gold nanoparticles by *Bacillus marisflavi* and its potential in catalytic dye degradation. *Arab. J. Chem.* **12**(8), 4806–4814 (2019)
60. Ahmad, A.A., et al.: Synthesis of water-soluble gold–aryl nanoparticles with distinct catalytic performance in the reduction of the environmental pollutant 4-nitrophenol. *Catal. Sci. Technol.* **9**(21), 6059–6071 (2019)
61. Larm, N.E., Thon, J.A., Vazmitsel, Y., Atwood, J.L., Baker, G.A.: Borohydride stabilized gold–silver bimetallic nanocatalysts for highly efficient 4-nitrophenol reduction. *Nanoscale Adv.* **1**(12), 4665–4668 (2019)
62. Chiller, K., Selkin, B.A., Murakawa, G.J.: Skin microflora and bacterial infections of the skin. *J. Invest. Dermatol. Symp. Proceed.* **6**(3), 170–174 (2001)

Carbon Nanostructure Based Composites for Environmental and Energy Applications



Murthy Muniyappa, Prasanna Doddakunche Shivaramu, Siddabasave Gowda B. Gowda, Navya Rani Marilingaiah, and Dinesh Rangappa

Abstract In the twenty-first century, rapid industrialization, urbanization, and fossil fuel consumption have made a big impact on environmental pollution. At the same time due to increased population, energy consumption per capita has also increased globally. Therefore, energy generation from renewable sources is most promising to overcome energy demand across the world. Carbon nanostructure based composite materials have been applied in various technologies, because of their unique optical, electrical, mechanical properties. They are also potential in mitigating environmental remediation and energy harvesting applications. These include Fullerenes, carbon nanotubes, graphene or reduced graphene oxide (RGO), and its composites with metal oxides or sulfides.

In this chapter, we present an overview of recent progress in the various synthesis and characterization techniques of carbon nanostructure-based composites, including metal oxide–carbon based material composite, and metal sulfides–carbon based composite material. Further, discussed the applications of these carbon nanostructure-based composites in environmental remediation as adsorbents for organic and inorganic pollutants and catalysis. However, the energy harvesting applications of carbon-based nanostructures for battery and hydrogen generation are discussed.

Keywords Fullerene · CNT · Graphene · Adsorbents · Li-ion Battery H₂ generation

M. Muniyappa · P. Doddakunche Shivaramu (✉) · D. Rangappa (✉)
Department of Applied Sciences (Nanotechnology), Visvesvaraya Technological University,
Center for Postgraduate Studies, Bengaluru Region, Muddenahalli, Chikkaballapur 562 101, India

S. G. B. Gowda
Faculty of Health Sciences, Hokkaido University, Kita-12 Nishi-5, Kita-Ku, Sapporo 060-0812,
Japan

N. R. Marilingaiah
School of Basic and Applied Sciences, Dayanand Sagar University, Bengaluru 560111, India

Abbreviations

0 D	Zero dimensional
1 D	One Dimensional
2 D	Two Dimensional
3 D	Three Dimensional
GO	Graphene Oxide
RGO	Reduced Graphene Oxide
C ₆₀	Fullerene
CNT	Carbon Nanotubes
MWCNT	Multiwalled Carbon nanotubes
TPa	Tera Pascal
g-C ₃ N ₄	Graphitic carbon nitride
CVD	Chemical vapour deposition
FTO	Fluorine doped tin oxide
ZIF	Zeolite imidazole framework-8
SDS	Sodium dodecyl sulfide
VSS	(Vapour- Solid -Solid)
LDH	Layered double hydroxide

1 Introduction

A Global increase in rapid industrialization, urbanization, and fossil fuel consumption has made a huge impact on environmental pollution. At the same time due to increased population, energy consumption per capita also has increased globally. Further, by 2035 the energy demand will be increased by 40% of the current demand, therefore the energy generation from renewable sources is attracting very much interest to overcome the energy demand across the world. In mitigating environmental remediation and energy harvesting applications, suitable materials play a predominant role. Among various materials, carbon-based composite has attracted the entire scientific community, because of their unique optical, electrical, and mechanical properties. Carbon is an essential building block of all living organisms, but as an elemental carbon exists in two natural forms as graphite and diamond. Both are different in their chemical and physical properties. For example, graphite is a soft material, whereas, diamond is the hardest element. Despite these, in the late twentieth century, emerging nanotechnology has opened up many allotropes of carbon as shown in Fig. 1.

Based on the size, carbon allotropes can be classified into zero-dimensional (0 D,) one dimensional (1 D), two dimensional (2 D), and three-dimensional materials (3 D). Some of the most familiar allotropes of carbon are fullerene (0 D), carbon nanotubes (1 D), and graphene (2 D). These materials show unique optical, electrical, mechanical, and chemical properties. However, these properties do not meet the required

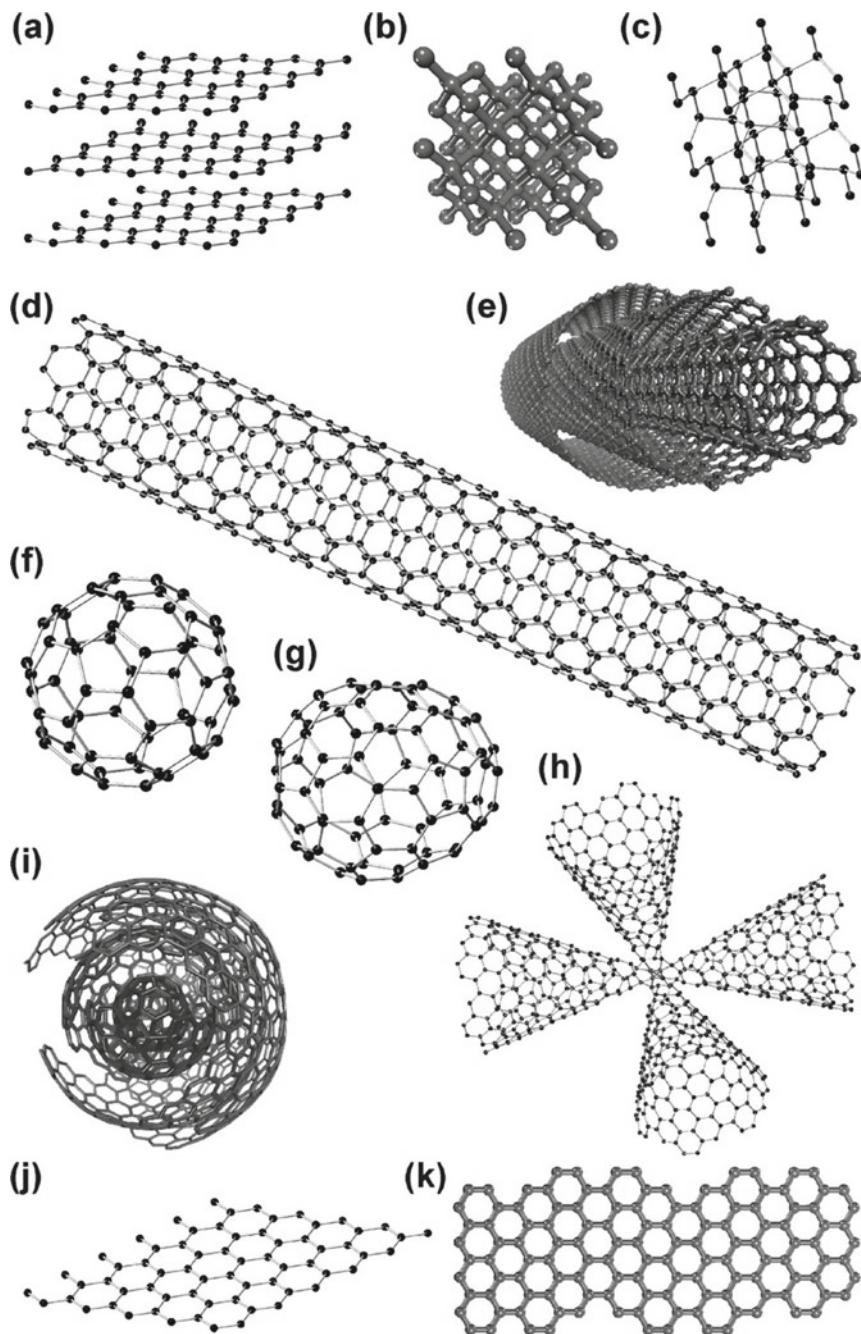


Fig. 1 Allotropes of Carbon **a** Graphite, **b** Diamond, **c** Ionsdaleite, **d** Single-walled carbon nanotube, **e** Multiwalled carbon nanotube, **f** Fullerene (C_{60}), **g** Fullerene C_{76} , **h** Carbon nanohorns, **i** Onion like carbon, **j** Graphene, **k** Carbon nanoribbons. Reprinted with permission from Ref [1]. Copyright © 2014 American Chemical Society

set of properties for particular applications. Carbon materials are loaded or modified with various functional materials which are known as carbon-based composites. When the carbon materials are added with other materials to form composites, these composite materials display some unique properties, which is better than the base material. For example, graphene alone is not suitable for photocatalytic applications because of its non-semiconducting nature. But, when it is made composite with any other semiconductors like TiO_2 or ZnO , due to the synergistic effect of both, the photocatalytic efficiency will increase enormously. Therefore, it is very much essential to study, carbon nanostructure-based composites, which, are potential materials for environmental remediation and energy harvesting applications.

Carbon nanostructures such as fullerenes, carbon nanotubes, graphene, or reduced graphene oxide (rGO) can be modified with various metal oxides, metal sulfides, and carbonitrides, phosphates, and polymers to form carbon-based nanocomposites.

1.1 Fullerenes

In 1985, a new carbon allotrope known as fullerene was introduced by Kroto et al. When he was studying the properties of carbon in interstellar space. It is named after pioneering architect Richard Buckminster Fuller, famous for its geodesic dome design, whose structural characteristics resemble spherical fullerenes. In fullerenes, the structure of a closed-cell is established by the presence of a five-membered ring. Among the known forms of fullerene, C_{60} is considered the most symmetrical and stable form. It consists of 20 hexagons and 12 non-intersecting pentagonal faces, with carbon atoms at each corner of an individual polygon. Further, polygons consist of a very symmetric truncated icosahedron. The van der Waals diameter of C is ~ 1.1 nm and the core-to-core diameter is ~ 0.71 nm.

Molecule C is often referred to as non-“super aromatic” because it tends to avoid double bond formation in the pentagonal ring. As a result, weak delocalization of electrons is observed, so that C molecule behaves like electrophiles themselves, with high electron acceptor capacity (i.e., can reversibly accept up to 6 electrons), readily react with electron-rich particles. Besides C_{60} , other fullerenes have been identified, such as C_{70} , C_{76} , C_{82} , and C_{84} .

Fullerenes and their derivatives are attracted to researchers due to their unique properties such as optical features, superconductivity, resistance to heat, and ferromagnetic applications. The C_{60} molecules can be termed as soft organic ferromagnets due to their lower curie temperature and high magnetic ordering. To enhance their potential applications in the field of biomedical, sensors, catalysis, and electronics, fullerenes have been functionalized with various substances. The development of fullerenes subsequently leads to discover the other carbon allotropes such as carbon nanotubes and graphene.

1.2 Carbon Nanotubes

In 1991, for the first time Ijima invented the multiwalled carbon nanotubes (MWCNT) by arc discharge method. After two years, the single-walled carbon (SWCNTs) nanotubes were discovered. In single-walled carbon nanotubes, the one-atom thickness sheet (graphene) rolled into a single-cylinder with a diameter ranging from 0.4 to 2 nm with sp^2 hybridized carbon atoms. But in the case of MWCNT, multiple single-walled carbon nanotubes are cylindrically rolled one above the other with weak Van der Waals forces as shown in Fig. 1(e). The diameter of MWCNT's is ranging from 0.34 to 2.5 nm with a high aspect ratio of up to 10,000. Hence, it is known as one of the best anisotropic materials. Based on the chirality for the nanotube axis, CNT's are classified as zig-zag, armchair, and chiral that influence the electronic properties of CNT (metal or semiconductor). The CNT's are considered as one of the strongest and stiffest materials because of their highest young's modulus (1.2 TPa) and tensile strength (100 GPa). The carbon nanotubes exhibit unique optical properties such as absorption, Raman scattering, and photoluminescence. The superior stability in thermal and chemical properties are noticeable in CNT's. However, CNT's have a large surface-to-volume ratio, which enables functionalization with various nanocomposites to improve the properties.

The CNT's have applications in energy storage (Batteries and supercapacitors), energy generation (H_2 generation and fuel cells), electronic applications (transistors, logic gates, sensors, and memory devices), medical applications (gene therapy, drug delivery vehicles), and other filler materials in construction technology to increase strength. The CNT's are also used in quantum modelings such as ballistic transport, single-electron charging, and quantum interference studies.

1.3 Graphene

A atomic thick 2D carbon layer consisting of sp^2 hybridized carbon atoms arranged in the hexagonal crystal structure. First discovered in 2004 by A. K. Geim et. al by the scotch tape method. Graphene is considered as one of the building blocks of different carbon allotropes such as Fullerenes (0D), CNTs (1D), and Graphite (3D). Graphite is the parent material for graphene because the graphite is made up of graphene sheets bonded together by weak Van der Waals force as shown in Fig. 1(j). The graphene sheets possess a unique property that includes Young's Modulus (1 TPa), large theoretical surface area ($2630 \text{ m}^2 \text{ g}^{-1}$) and intrinsic mobility ($200\,000 \text{ cm}^2 \text{ V}^{-1} \text{ S}^{-2}$), optical transmittance (97.7%), and thermal conductivity ($5000 \text{ Wm}^{-1} \text{ K}^{-1}$) [1].

Graphene is widely used in the field of electronics such as display screens, field-effect transistors, conductive electrodes in liquid crystal displays, organic light-emitting diodes, and ultracapacitors. In the biomedical field, graphene has many applications that include bioimaging, biosensors, cancer treatment, gene therapy,

and targeted drug delivery, etc., Therefore, graphene and its composites have been a hot research topic in this decade.

2 Synthetic Methods for Carbon Nanostructure-Based Composites

The semiconductor materials such as metal oxides, metal chalcogenides, Bi-based semiconductors, graphitic carbon nitride ($g\text{-C}_3\text{N}_4$), and Ag-based semiconductors, and different polymers have been used for energy and environmental applications. These materials have limitations such as low conductivity, less surface area, wider bandgap, photo corrosion, and mechanical instability. To overcome these limitations the carbon nanostructure-based compounds such as fullerene, graphene, and CNT's have been incorporated. The synergistic effect of the composites and the carbon nanostructures improves the mechanical, electrical, optical, thermal, properties. Therefore, it is paramount to know the synthesis of carbon nanostructure-based composites for various environmental and energy-related applications.

Depending on the materials, size, morphology, diverse techniques have been adopted for synthesizing fullerene, CNT's, and graphene associated carbon-based nanocomposites. Some of the synthesis techniques such as hydro or solvothermal, mechanochemical, precipitation, and ball milling methods are discussed in the following sections.

2.1 Synthesis of Fullerene Based Nanocomposites

A hydrothermal method is a well-studied technique for preparing fullerene-based nanocomposite because of its versatility in getting well-defined shape, size, and morphology. Fullerenes are hydrophobic, therefore, it should be functionalized or modified by acid treatment before adding into the hydrothermal autoclave for the synthesis of the fullerene-based nanocomposite. In the hydrothermal method, after complete dissolution of the precursors in water, the dissolved solution is kept in a sealed vessel above the boiling point of water ($>100\text{ }^\circ\text{C}$). Due to the fixed volume of the precursor-containing vessel and the constant temperature above $100\text{ }^\circ\text{C}$ maintains constant pressure. At this particular point, the precursor solution attains a subcritical state, where, the dissolved precursors reach supersaturation and initiate nucleation of cations and ions, further growth into nanosized particles. For example, CdS/ C_{60} nanocomposite synthesis, Cd $(\text{CH}_3\text{COO})_2$, L-cysteine used as Cd and S source respectively. the raw fullerenes are functionalized by treating with hydrochloric acid at $140\text{ }^\circ\text{C}$ for 4 h. Then, neutralized by washing with water until neutral pH to achieve better dispersibility [2]. After complete dissolution of the precursors transferred into

the hydrothermal autoclave at 200 °C for 10 h. At subcritical temperature supersaturation of precursors occurs then, start to nucleate cations (Cd^+) and anions (S^-) and growth on the surface of fullerenes. Similarly, different fullerene-based metal oxides and polymers can be synthesized by using the hydrothermal method.

The sol–gel method is one type of bottom-up approach for synthesizing nanocomposites. The complete dissolution of the precursors is called a sol. The sols are converted into a gel by the addition of gelating agents hence the name Sol-Gel. For the prepared sols, the addition of a gelating agent causes the formation three-dimensional network. Where the sols are nucleated and grow into nanoparticles in an uncontrolled manner. For instance, $\text{CdS-C}_{60}/\text{TiO}_2$ nanocomposite is synthesized by the Sol-Gel method. As usual, the fullerene molecules are surface modified with m-chloroperbenzoic acid. The functionalized fullerenes are mixed with Cd and S precursors and stirred for 7 h followed by filtration and washing in water, to get CdS-C_{60} composite, then mixed with titanium butoxide and reflux at 343 K along with stirring to get the gel. As the obtained gel is heat-treated at 873 K to synthesize $\text{CdS-C}_{60}/\text{TiO}_2$ nanocomposite.

Thermal decomposition is one of the chemical approaches for the synthesis of fullerene-based nanocomposites. Where a chemical reaction takes place with the aid of heat treatment. In this method, the precursors are evaporated in a high vacuum chamber and deposited as thin films on the substrate. Usually, by this method, thin films can be coated. The Cu-fullerene thin films can be synthesized by evaporation of Cu and fullerene powder kept in a separate boat in a high vacuum (5×10^{-6} Torr) in a reaction chamber [3]. The fullerenes-magnetic Iron nanocomposites can be synthesized by thermal decomposition technique by decomposing waste plastic bottles. Here, ferrocene acts as both precursors for Iron as well as a catalyst for fullerene formation [4]. The thermal decomposition requires high vacuum as well as high temperature which, are the limitations of this technique.

Ball milling is one type of top-down approach, it has been considered as an eco-friendly technique for synthesizing solid-state composites. In the ball-milling technique, bulk particles are grinded into nanosized particles. The synthesis of C_3N_4 -fullerene nanocomposite by ball milling method is shown in Fig. 2. In this technique, the pristine $\text{g-C}_3\text{N}_4$ and fullerene (with different weight ratio) are ball-milled under LiOH catalyst with 500 rpm rotation speed for 24 h. The LiOH catalyst helps to break

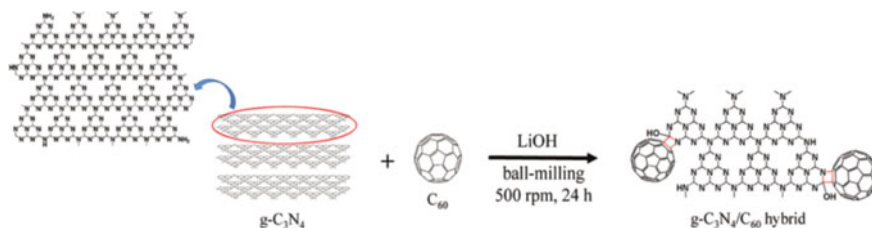


Fig. 2 Schematic representation of $\text{g-C}_3\text{N}_4$ -fullerene nanocomposite by ball milling method. Reprinted with permission from Ref [5]. Copyright © 2017 Royal Society of Chemistry

the π bonding of carbon atoms in fullerene and form bonds with $g\text{-C}_3\text{N}_4$. Therefore solid-solid reaction occurs and forms the $g\text{-C}_3\text{N}_4$ -fullerene nanocomposite [5]. In the same strategy, MoS_2 -fullerene nanocomposite can be synthesized in a planetary high-speed ball milling jar, at a rotation speed of 500 rpm for 48 h [6]. Ball milling does not require any surface modification as in the chemical reaction because of solid-state reaction.

The synthesis of fullerene-based nanocomposite hydro or solvothermal approach is preferred because of a simple, less time consuming, and energy expendable method compared to sol-gel, ball milling, and thermal deposition methods.

2.2 Synthesis of CNT Based Nanocomposites

Based on the composite materials and applications, different methods were reported for the synthesis of CNT based nanocomposites. The commonly used methods are hydro or solvothermal, coprecipitation, chemical bath deposition, and direct blending method. Generally, the synthesis of CNT with other composites (metal oxide, sulfides, nitrides) consists of the two-step method. In the first step, CNT synthesis in the CVD process, in the second step the addition of CNT into other metal oxides, sulfides, and nitrides by different techniques. In the next section, some of the CNT-based nanocomposite synthesis methods are discussed.

A hydrothermal method is one of the handiest approaches for synthesizing metal oxides or sulfide nanostructures. In most cases, the hydrothermal method has been preferred in synthesizing CNT based nanocomposite either as thin films or powder. To synthesize ZnO nanowires grown on CNT coated photoanode hydrothermal method can be preferred [7]. In this method, the CNT's are grown on 1 cm^{-2} silicon wafers by a CVD method and further transferred to the FTO glass substrate by a contact printing technique. After CNT coating on FTO glass, it is dipped into the aqueous solution of zinc nitrate and ammonia. After complete dissolution of the zinc nitrate and ammonia transferred to hydrothermal autoclave at $175\text{ }^\circ\text{C}$ for 12 h. During the reaction, the dissolved precursors are saturated in the subcritical temperature of the water and start to nucleate and grow nanowires on CNT coated FTO glass. Further, to remove dissolved impurities the coated CNT-ZnO nanowires on FTO glass are subjected to heat treatment at $300\text{ }^\circ\text{C}$ for 30 min. For the preparation of zeolite imidazole framework-8 (ZIF-8) coated CNT nanocomposite, the multiwalled carbon nanotubes are acid treated at $120\text{ }^\circ\text{C}$ for 6 h to functionalize. Further, zinc nitrate and functionalized MWCNT's are ultrasonicated in methanol solution until complete dispersion and transferred to hydrothermal autoclave at $90\text{ }^\circ\text{C}$ for 6 h then, calcinated in an inert atmosphere to get ZnO-CNT nanocomposite[8]. The schematic of the ZnO-CNT nanocomposite synthesis process is shown in Fig. 5.

Similarly, ZnO-CNT/GO nanocomposite are synthesized by the hydrothermal method [9]. In this process, ZnO, GO and CNT are prepared separately then, 1:1 weight ratio of ZnO: CNT, 1:1 wight ratio of GO: C transfer into hydrothermal

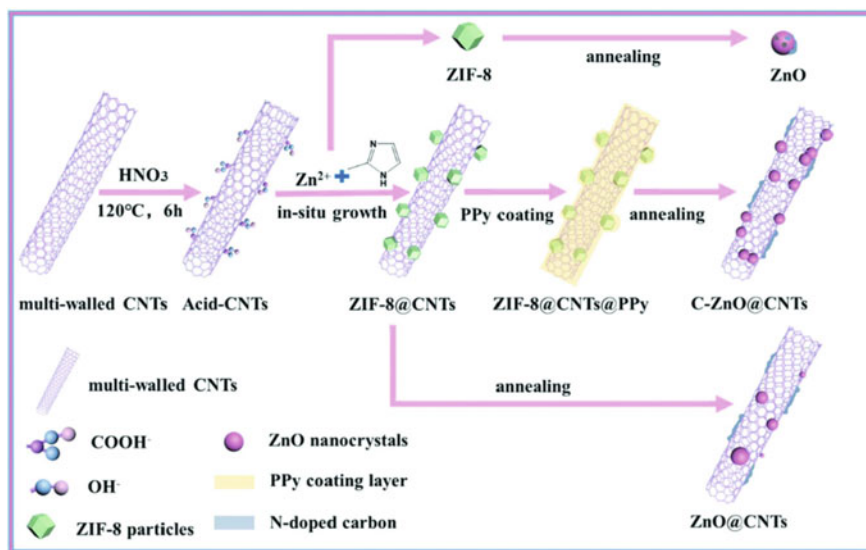


Fig. 3 A schematic representation of the ZnO-CNT nanocomposite synthesis process. Reproduced from Ref [8]. copyright © 2019, Royal Society of Chemistry

autoclave kept at 150 °C for 18 h for growing ZnO nanorods followed by reduction of GO into RGO by eliminating various functional groups present on the GO.

The precipitation method is a simple synthesis method to obtain metal oxide–carbon based nanocomposites. The precipitation of metal salts starts in the presence of a precipitating agent in basic conditions. To prepare CNT/CuO nanocomposite, functionalized CNT, copper chloride, SDS is dissolved in an aqueous medium. After complete dissolution, aqueous ammonia is added as a precipitating agent. Then, the obtained precipitate is washed in water and calcinated in a muffle furnace at 400 °C for 2 h to get CNT/CuO nanocomposite [10] (Fig. 3).

In the above methods, two steps are involved in synthesizing CNT-metal oxide nanocomposite which is a very tedious and time-consuming process. Therefore, a one-pot synthesis process for the development of CNT based nanocomposites is advantageous. X. Jin et. al reported a novel one-step synthesis of CNT-MnO nanocomposite at a lower temperature at 500 °C with a time duration of 20 h and also depicted the effect of catalyst (MnO) morphology on the growth of the CNT [11]. The exfoliated MnO₂ nanosheets (2D) acts as a catalyst which, provides enough adsorption sites due to large surface area compared to 0 D nanocrystals, 1 D nanostructures. The adsorbed carbon atoms started to diffuse into the particular MnO planes and start to nucleate in the form of hexagonally arranged tubular-shaped carbon atoms by the VSS (Vapour-solid_solid) mechanism. They noticed that due to high reductive condition MnO₂ becomes MnO and at the same time the morphology was not changed. This approach could be a better technique for CNT-metal oxide nanocomposite synthesis, but this method is limited to a few metal oxides only.

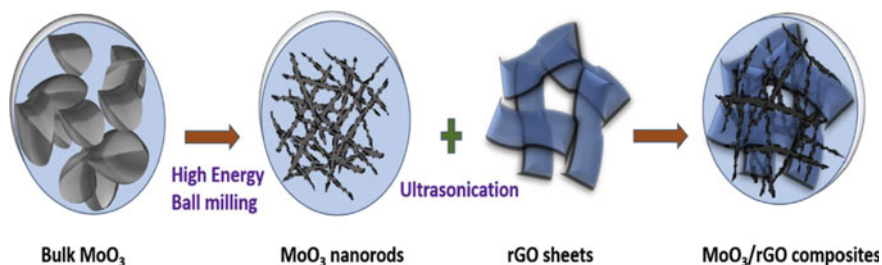


Fig. 4 Schematic representation of MoO₃-RGO nanocomposite synthesis by ball milling assisted ultrasonication. Reprinted from Ref [12]. Copyright © (2019), with permission from Elsevier

2.3 Synthesis of RGO Based Nanocomposites

To obtain controlled morphology, size, and shape various methods have been adopted for the synthesis of RGO based nanocomposite. The currently emerging methods are Ball milling assisted ultrasonication, Hydro or solvothermal method, chemical vapor deposition method, photochemical reaction, chemical electrolysis, etc. some of the most studied and easy methods are discussed as follows.

2.3.1 Ball Milling Assisted Ultrasonication Method

Ball milling assisted ultrasonication method is one type of top-down approach, where micro size particles grinded into nano-size by application of high energy ball milling process. For the synthesis of MoO₃-RGO nanocomposite bulk MoO₃ powder is grinded in high energy zirconia balls in ethanol at 300 rpm for 12 h with clockwise and anti-clockwise rotation (60 s each). The obtained nano MoO₃ powder was dispersed by ultrasonication in ethanol, for 1 h. Further, the graphene oxide (GO) is transferred to the dispersed MoO₃ and ultrasonicated for 1 h followed by 30 min stirring [12]. Then drying at 80 °C in the oven for 24 h results in MoO₃(10 wt% & 15 wt%)-RGO nanocomposite as shown in Fig. 4. Compared to wet-chemical and other physical methods ball milling method was found to be quite an easy method and the yield of the final product also relatively high.

2.3.2 Chemical Vapor Deposition

Chemical vapor deposition is one of the most studied and efficient methods for the synthesis of graphene-based nanocomposites. Normally, in this method, Ni or Cu metallic foam was used as both catalyst and substrate for growing graphene. By decomposing gaseous carbon sources such as CH₄, C₂H₂, etc., in a controlled atmosphere at high temperature in the presence of catalyst graphene sheets are grown. Then, metallic foams are removed by chemical etching. By varying the reaction

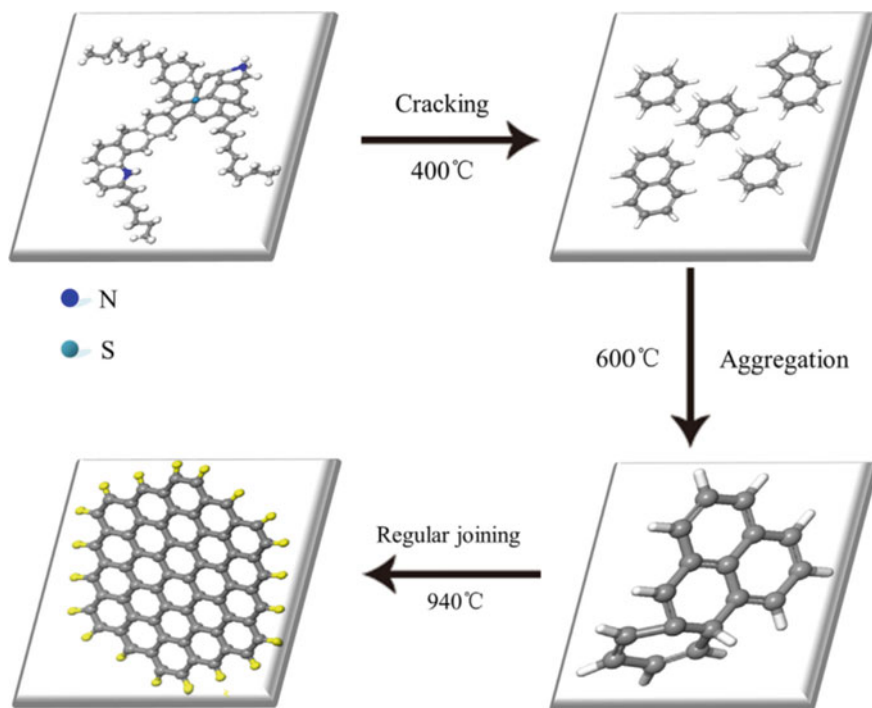


Fig. 5 Mechanism of graphene growth by CVD process by asphalt as a carbon source. Reprinted from Ref [14], Copyright © (2014), with permission from Elsevier

parameters, the shape and size of the graphene sheets can be controlled through this method.

For the first time, Z. Chen et. al reported template-assisted CVD growth of graphene by pyrolyzing methane (CH_4) gas at 1000 °C at a controlled atmosphere [13]. The use of pure carbon sources is expensive and hazardous. Therefore, the Z. Liu group developed a new strategy by taking asphalt, which is a petroleum by-product with higher carbon content [14]. The carbon content (aromatic ring structure) in the asphalt consists of various functional groups such as alkyl, nitrogen, and sulfur compounds. These functional groups are removed at 400 °C by the influence of H_2 gas in the presence of Ni catalyst. The outer surface branches converted into aromatic rings as shown in Fig. 5. At 600 °C the aromatic rings are fragmented, which were bonded through C-C bonding, finally at 940 °C, regularly joined and stacked into graphene sheets.

2.3.3 Hydro/Solvothermal Method

The hydrothermal process is on a type of bottom-up approach synthesis, where, water or organic solvents were used as a reaction medium. Usually, this method is carried out at a low temperature just above the boiling point of the solvents. If it is water above the water boiling point temperature i.e. $>100\text{ }^{\circ}\text{C}$. By this method, 1D and 2D nanostructures can be easily obtained by varying the reaction parameters such as solvents, surfactants, temperature, pressure, and reaction time. The hydrothermal method is one of the versatile and emerging synthesis processes especially, for RGO-based nanocomposite. The graphene with metal-oxides, sulfides, carbonitrides, and metallic nanoparticles were also synthesized by the Hydro or Solvothermal method.

For the first time, C. Yuxi et. al reported the one-step hydrothermal reduction of GO into graphene hydrogel [15]. Later, J. Shen et. al studied a one-pot synthesis of Ag nanoparticles deposited RGO nanocomposite under hydrothermal conditions [16]. The silver nitrate and GO were taken as a starting material and ascorbic acid as a reducing agent. The dissolved precursors in the water solution were added into the hydrothermal autoclave at $160\text{ }^{\circ}\text{C}$ for 4 h. The steps involved in synthesizing Ag-RGO nanocomposite are shown in Fig. 6. The silver ions are reduced into metallic silver particles and at the same time GO is reduced to RGO sheets by eliminating the functional groups present on them.

The 3D graphene aerogel decorated Iron oxide nanoparticles can be synthesized using the extended hydrothermal method [17]. The ready Iron oxide and GO were placed in the hydrothermal autoclave at $125\text{ }^{\circ}\text{C}$ for 2 h followed by freeze-drying to get 3D graphene- Fe_3O_4 aerogel. Not only metal oxides, metal dichalcogenides were also prepared by the hydrothermal method. Y. Zhang et al. synthesized MoS_2 -RGO nanocomposite by the one-step hydrothermal method [18]. In this process,

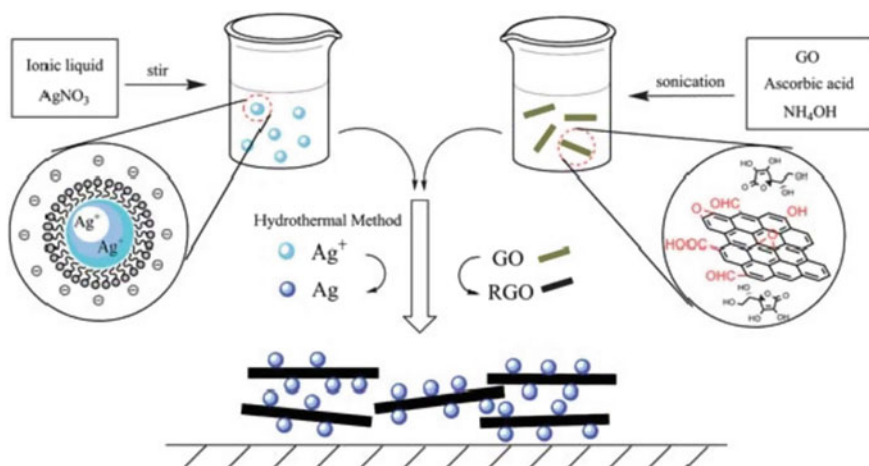


Fig. 6 Schematic representation of Ag-RGO nanocomposite synthesis by hydrothermal method. Reproduced from, Ref [16]. Copyright © (2011), Royal Society of Chemistry

sodium molybdate, thiourea used as Mo and S source. The pre-synthesized GO by modified Hummer's method is mixed in water with the precursors, transferred into hydrothermal autoclave and placed at 180 to 240 °C for 12, 18, and 24 h.

Even the complex structures like LiFePO₄ decorated graphene/C synthesized by the one-step hydrothermal method without sintering at high temperatures. The preparation of exact stoichiometric ratios of precursors is very important for synthesizing LiFePO₄ [19].

From the last decade, many reports are reported on graphene-based nanocomposites by hydro/solvothermal method because of its simple process, low temperature, efficient control in size, and morphology for energy and environmental applications.

2.3.4 Electrochemical Deposition Method

In an electrochemical deposition, the metal salts are deposited as a thin film on the substrate by a simple electrolysis process. Where, the cations in the precursor's solution are coated on the surface of the electrode as a thin film by the influence of an electric current. For example, in preparation of RGO-ZrO nanocomposite, GO and ZrOCl₂ solution added with chitosan solution. The cleaned glassy carbon electrode dipped into cyclic voltammetry setup as working electrode and application of current between -1.1 to +0.7 V at 20 mV S⁻¹ scan rate continuously. On the glassy carbon electrode, RGO-ZrO₂ is deposited as a thin film [20]. This is further confirmed by TEM, XRD, and Raman spectroscopy. In another study, reduced GO by the application of electric field and deposited on the gold wire that was suspended in a lithium perchlorate solution and formed 3D interpenetrating graphene network [21].

3 Environmental Applications

3.1 Environmental Applications of Fullerene Based Nanocomposites

In the twenty-first century, rapid industrialization, urbanization, and fossil fuel consumption have been a big impact on environmental pollution. The major source of environmental pollution is due to water contamination. The untreated water from industries such as plastic, leather, paper, textiles, electronic chip, electroplating, etc., contains various toxic chemicals which, contaminates the water sources [117]. Nowadays, particularly, carbon-based nanocomposites have been used for environmental remediation applications. Among the different forms of carbon, one of the unique and very fascinating types are fullerene-based nanocomposites. It is attracting researchers to treat wastewater through various techniques such as photocatalysis,

adsorption, electrocatalysis, electrochemical oxidation, etc. Some of the wastewater treatment applications are discussed below.

3.1.1 Wastewater Treatment by Photocatalysis

The photocatalytic degradation of water contaminants includes organic chemicals, coloring agents, and other heavy metals from different industries. Conventional techniques such as coagulation, filtration, flocculation, and sedimentation are practically not viable processes. Photocatalysis is one of the most widely studied approaches for treating wastewater. Usually for photocatalytic applications semiconducting metal oxides, sulfides, carbides are preferred, but these are having limitations such as UV light active, electron–hole recombination, low conductivity, less photosensitivity, etc. To overcome these problems fullerene-based composites have been reported for various photocatalytic applications as shown in Fig. 7. The fullerenes can reversibly accept up to six electrons due to the delocalization of electrons in it. In fullerenes the bandgap is narrow, and it is ranging from 1.5–1.9 eV. Which, acts as visible light active, higher photosensitizer as well as quantum efficient material [22]. Due to its electron trapping affinity, the excited electrons are trapped before recombining with holes. the excited electrons participate in the photocatalytic reaction. The increased photosensitization in the visible region automatically increases the charge carriers. Another advantage is the enhancement in the conductivity which, merely increases the rate of the charge transfer process thereby fast redox reaction takes place. These are some of the advantages of fullerene-based semiconductors in the photocatalytic degradation of wastewater. In the next section, discuss the fullerene-based nanocomposites for photocatalytic applications.

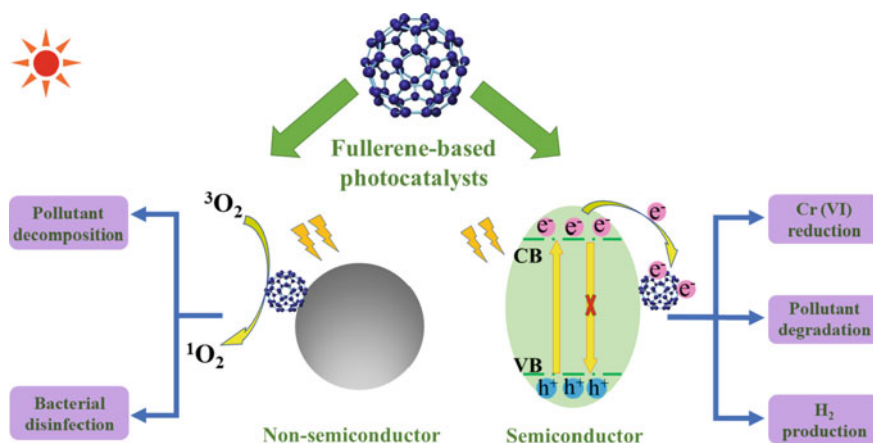


Fig. 7 Environmental applications of the fullerene-based nanocomposite. Adapted from ref [23]

Metal oxides such as TiO_2 and ZnO are wide-bandgap semiconductors that are active under a limited wavelength of light. To enhance the absorption range fullerenes are an alternative class of material.

The TiO_2 -fullerene nanocomposite is used for visible light active photocatalytic degradation of methylene blue dye. When compared to pure TiO_2 due to the synergistic effect of both TiO_2 and fullerene. The adsorbed fullerenes on the surface of TiO_2 causes a rapid charge transfer from the conduction band of TiO_2 to the surface of the catalyst to generate OH^- radicals without wasting as recombination with a hole. Which causes a 24% enhancement in photocatalytic degradation [24]. Similarly, ZnO -fullerene (1.5 wt%) nanocomposite is used for the degradation of methylene blue dye [25]. The results show that the ZnO -fullerene (1.5 wt%) nanocomposite shows 1.5 times higher photocatalytic activity than pure ZnO . The addition of fullerene reduces the photo corrosion of ZnO .

Not only do oxides take part in dye degradation, but even sulfides can also contribute to photocatalytic activity. The CdS -fullerene (0.4–8 wt%) nanocomposite shows enhanced photocatalytic degradation of Rhodamine B solution [2]. The 0.4 wt% loaded fullerene sample exhibit 1.5 times higher photocatalytic activity than pure CdS . The main reason attributed to effective suppression of charge carriers along with the fast charge transfer process.

3.1.2 Wastewater Treatment by Adsorption Process

The main causes of water pollution are due to untreated wastewater coming from various industries that contain a large number of dye molecules, heavy metal ions, pharmaceutical wastes, etc. For treating dye molecules, the adsorption process was found to be a promising method because of its simplicity, efficiency, affordability, and easy recoverability compared to other conventional techniques like flocculation, coagulation, filtration, and anodic oxidation. Even though, fullerene-based nanocomposites have limitations such as hydrophobicity, dissolution in nonpolar solvents, and less surface area. Very minimum efforts have been made on the fullerene-based nanocomposites for the adsorption process. The Iron nanoparticles incorporated fullerene nanocomposites have been used for adsorption of anionic (methylene blue) and cationic (Acid blue 25) dye adsorption process [4]. The dye adsorption parameters like contact time, pH, the concentration of dye, and catalyst loading amount certainly influence the adsorption ability of the nanoparticles. Usually, laboratory-scale batch adsorption experiments are preferred for adsorption studies, where, 500 ppm stock solutions of both anionic and cationic dye molecules are used for adsorption studies. kinetic studies determine the type of adsorption happening between dye molecules and fullerene-based nanocomposites. The cyclability of the magnetic-fullerene nanocomposite shows more than 90% adsorption capacity retention up to 10 cycles. Which is an economical and efficient adsorbent material.

3.2 Environmental Applications of CNT Based Nanocomposites

Environmental pollution is a major concern all over the world due to the rapid growth of industries. Among various constituents of environmental pollution, water pollution is becoming a major issue in the current situation. The main contaminants of water are pharmaceuticals, fertilizers, pesticides, textile dyes, etc. There are various conventional techniques for treating wastewater such as reverse osmosis, adsorption, ion-exchange, flocculation, advanced oxidation process, and membrane filtration. CNT based nanocomposites have been applied in dye degradation, filtration, adsorption, sensors, and monitoring systems because of their unique physical and chemical properties. The various applications of CNT's as scaffolds are shown in Fig. 8.

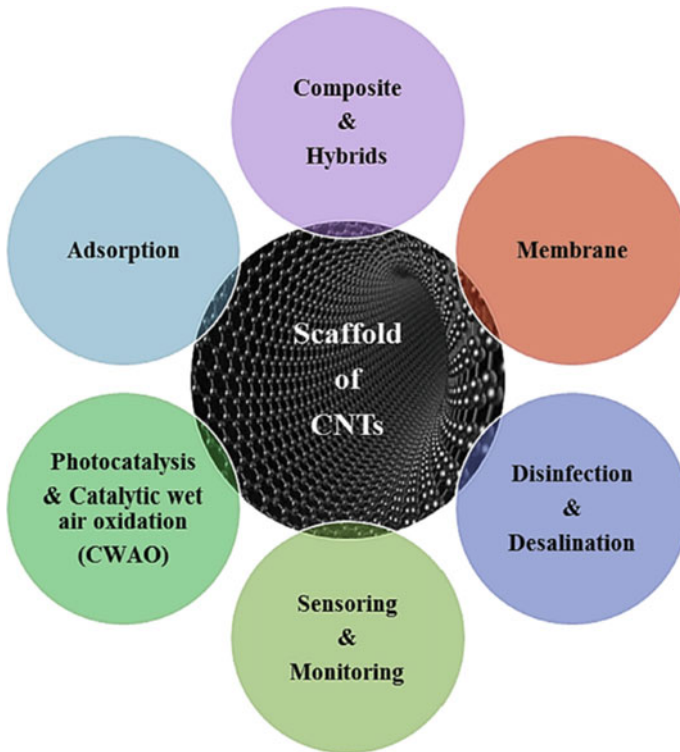


Fig. 8 Applications of CNT's in wastewater treatment. Reprinted from Ref [26]. Copyright © (2020), with permission from Elsevier

3.2.1 Photocatalytic Degradation of Pollutants

CNT based nanocomposites have been considered as superior photocatalysts for the degradation of organic dyes, pharmaceutical wastes, heavy metal reduction, etc. The photocatalytic advanced oxidation process has been considered an effective technique for wastewater treatment. In conventional treatment methods, secondary pollutants come out as by-products. Which are sometimes more dangerous than primary pollutants. The semiconducting metal oxides and sulfides have been studied for photocatalytic applications, but due to electron–hole recombination, UV activity, short absorption range, low surface area, an alternative class of materials attracted a lot of researchers. The carbonaceous material-based composites emerged as good photocatalysts [120]. Compared to other carbon materials, CNT's act as an efficient adsorbent for pollutants as well as an electron reservoir, which causes reduced charge carrier recombination thereby, enhanced photocatalytic activity was observed.

The mechanism of CNT based nanocomposite encompasses, the free electrons jump from conduction band to valance band by absorbing appropriate light energy. The excited electrons are captured by CNT without allowing them to recombine with valance band holes. The captured electrons will generate reactive oxygen species which, decompose the pollutants into CO_2 and water as shown in Fig. 9.

Some of the reported CNT based nanocomposites for the degradation of pollutants are discussed in the next section. K. Hemalatha et. al synthesised CNT-TiO₂ (up to 10%) nanocomposite by sol–gel process for the degradation of Indigo carmine dye under visible light [27]. Within 1 h Indigo carmine dye was degraded because of the synergistic effect of CNT and TiO₂. The addition of CNT enhances the photo-sensitivity, photoexcitation, and trapping of electrons increased the degradation rate. In 2019 A. Abega et. al synthesised the CNT-TiO₂ nanocomposite by improved

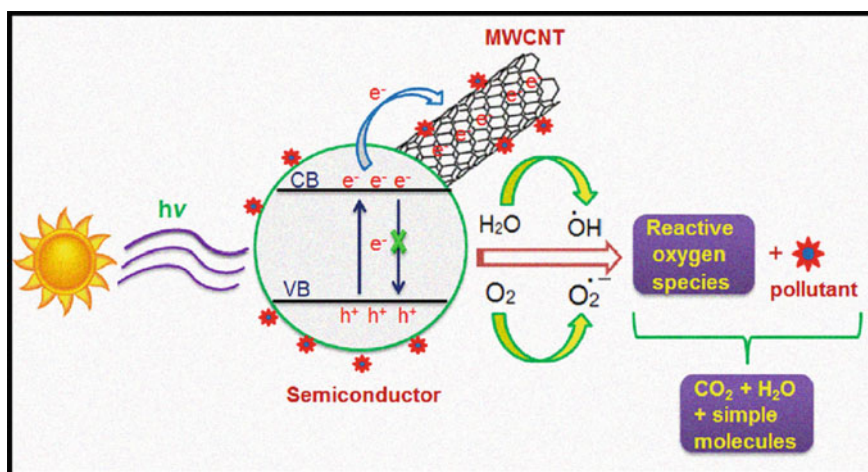


Fig. 9 CNT-Semiconductor based photocatalytic mechanism of pollutants degradation. Reprinted from Ref [30]. Copyright © (2018) with permission from Elsevier

sol–gel process for degradation of methyl orange dye [28]. The direct oxidation of Ti^{3+} ions in titanium tetrachloride rendered increased surface area, pore size, optical properties, and dispersion of TiO_2 in CNT which enables, enhanced degradation of methyl orange dye under visible light. W. Lee et. al reported CNT- TiO_2 core–shell nanowires by efficient and environmental friendly, approach for the degradation of methylene blue and p-nitrophenol [29]. The process was same as the natural biomineralization. The nitrogen-doped sites attract titanium precursors where nucleation and condensation of Ti–O taken place into a uniform shell-like structure on the surface of the CNT. In the resulted nanostructures the CNT act as a backbone for TiO_2 . It shifts the bandgap of TiO_2 towards the visible light region and the enhanced charge separation process. It resulted in increased photocatalytic activity. There are many reports on CNT- semiconductor-based nanocomposite for photocatalytic degradation of pollutants as shown in Table 1.

3.2.2 Adsorption of Pollutants

Adsorption is another type of water purification method for the removal of organic dyes, heavy metals such as arsenic, zinc, lead, fluorine, etc. The wastewater treatments like precipitation, coagulation, reverse osmosis, ion exchange, nanofiltration were used for wastewater remediation application but these methods are low efficient, high cost, and practically not a viable process. Adsorption by carbonaceous materials has attracted researchers because of its high surface-to-volume ratio, which enhances the sorption properties. The hydrophobicity of CNT's limits their application in the adsorption process. The functionalization of CNT is essential for better wettability. The loading of other low-cost metal oxides further enhances the adsorption capacity by chemical interaction with pollutants. Therefore, many efforts have been made on the CNT based nanocomposites for the removal of pollutants in water.

MWCNT- MnO_2 nanocomposite has been applied for the removal of arsenite (As [III]) toxic heavy metal by simultaneous adsorption and oxidation process. The oxidation properties of MnO_2 and sorption property of MWCNT combined to oxidize arsenite successfully [56]. Further, the amount of loading metal oxide into CNT or the attachment of carbon atoms significantly improves the adsorption capability. For example, Iron oxide coated CNT's nanocomposite shows significant adsorption capacity for the removal of arsenic due to a greater number of carbon atoms (11%) attached to the Iron oxide [57]. In a similar context, the CNT- ZrO_2 nanocomposite used to remove fluoride content in water, the abundant carboxylic group grafted on CNT enables high zirconium loading which, leads to enhanced adsorption capacity. Both physisorption and chemisorption are responsible for high sorption capacity [58].

Biocompatibility of CNT based nanocomposite attracting considerable attention as adsorbents. L. Yan et. al synthesized biocompatible magnetic guar gum attached MWCNT for adsorption of neutral red and methylene blue dye molecules [59]. The guar gum was extracted by the endosperm of the guar plant. It acts as a natural polysaccharide which, is biocompatible and nontoxic. The extracted guar gum was

Table 1 Some of the recent studies on CNT- semiconductor-based nanocomposite for photocatalytic degradation of pollutants

Sl. no	CNT-semiconductor composite	Pollutant (g/ml)	% of Photocatalytic activity (Time)	Reference
1	MWCNT-TiO ₂	Methyl orange (50 mM)	100% (100 min) UV light	[31]
2	N-CNT/TiO ₂	Methyl orange (10 ppm)	100% (240 min) UV light	[29]
3	CNT-TiO ₂	Indigo carmine dye (50 ppm)	100% (60 min) UV light	[27]
4	CNT-TiO ₂ nanotubes	Methyl orange (20 mg/L)	100% (300 min) UV light	[32]
5	MWCNT/MOF-In ₂ S ₃	Tetracycline (30 mg/L)	100% (120 min) visible	[33]
6	MWCNT/BiVO ₄	Oxytetracycline (10 mg/L)	88.8% (60 min) visible	[34]
7	Cd-ZnO/CNT	Methyl orange (20 mg/L)	93% (50 min) UV light	[35]
8	C ₆₀ /CNT-BiVO ₄	Rh B (0.01 mmol L ⁻¹)	96.1% (30 min) visible light	[36]
9	MWCNT-CdS-DETA	Methylene blue (20 mg/L)	0.034 min ⁻¹ (60 min) visible	[37]
10	Ag-ZnO/MWCNT	Acid orange (20 mg/L)	98% (60 min) visible	[38]
11	Zn ₂ SnO ₄ /MWCNT	Basic red-46 (14 mg/L)	94% (120 min) UV light	[39]
12	Boron doped TiO ₂ /CNT	Methylene blue (5 ppm)	97% (4 h) UV light	[40]
13	CuFe ₁₂ O ₁₉ -CNT	Erythrosine, Methylene blue and white (20 ppm)	88% (50 min) UV light 77.4% (50 min) UV light 72.2% (50 min) UV light	[41]
14	TiO ₂ (nanotube)/SWCNT	4-chlorophenol (50 mg/L)	100% (240 min) UV light	[42]
15	g-C ₃ N ₄ /GO-N-CNT	Tetracycline hydrochloride (10 mg/L)	94.30% (360 min) visible light	[43]
16	CaFe ₂ O ₄ /g-C ₃ N ₄ /CNT	Cr (VI) (10 ppm)	98% (60 min) visible light	[44]
17	g-C ₃ N ₄ /CNT/BiVO ₄	Phenol (10 mg/L)	80.6% (120 min) solar light	[45]
18	Cu-TiO ₂ -CNT	Methylene blue (5 ppm)	81.5% (60 min) visible light	[46]

(continued)

Table 1 (continued)

Sl. no	CNT-semiconductor composite	Pollutant (g/ml)	% of Photocatalytic activity (Time)	Reference
19	NiFe ₂ O ₄ /MWCNT/ZnO	Methylene blue (20 mg/L)	73.02% (300 min) solar light	[47]
20	WO ₃ /CNT	Tetracycline (60 mg/L)	90.6% COD (60 min) Visible light with ultrasound	[48]
21	Ho ₂ O ₃ /CNT	Tetracycline (20 mg/L)	98% (60 min) UV light	[49]
22	CNT-BiOBr /RGO	Rhodamine B (10 mg/L)	97.9% (100 min) visible light	[50]
23	ZnO-CNT	Malachite green (30 ppm)	79% (60 min) visible light	[51]
24	CNT/Zno-Ag	Methylene blue (4 mg/L)	81% (30 min) visible light	[52]
25	CNT/LaVO ₄	Sulfamethazine (30 mg/L)	88% (180 min) visible light	[53]
26	CNT-Ag-TiO ₂	Methylene blue (10 mg/L)	99.2% (40 min) UV light	[54]
27	SnSe-SnO ₂ /CNT	Methylene blue (10 mg/L)	100% (60 min) visible light	[55]

grafted onto functionalized MWCNT by just stirring in thionyl chloride and dimethyl-formamide solvents at 110 °C for 24 h. Then iron precursors were precipitated to get magnetic guar gum MWCNT nanocomposite. The prepared sample shows a significant adsorption capacity. The presence of magnetite helps to remove the sample easily from an aqueous solution by applying an external magnetic field.

3.3 Environmental Applications of RGO Based Nanocomposites

The RGO-based nanocomposites have been a hot topic for environmental applications because of their excellent physical and chemical properties. RGO-based nanocomposites have been applied in dye degradation, adsorption, filters, etc. in mitigating environmental-related problems.

3.3.1 Adsorption of Pollutants

Most of the water pollution is due to contamination of untreated organic dyes from various industries. There have been numerous efforts are made to decontaminate the

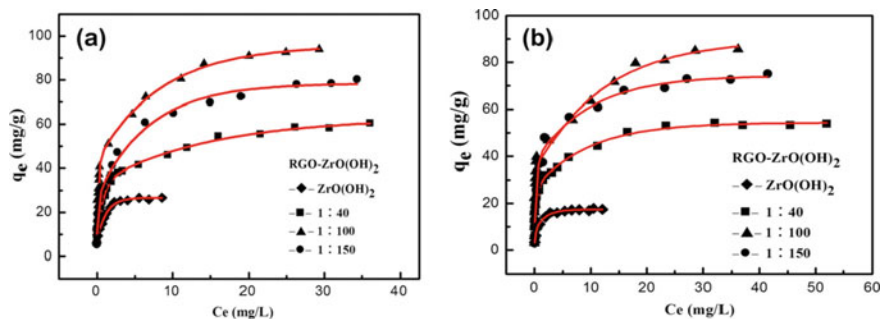


Fig. 10 Adsorption isotherms of **a** As (III), **b** As (V), RGO-Zr (OH)₂ (1:100 mass ratio) nanocomposite. Reprinted from Ref [60]. Copyright © (2013), with permission from Elsevier

water from organic dye molecules, azo dyes, hazardous solvents, pharmaceutical wastes, and heavy metals by the adsorption process. The adsorption process is one of the simple, low cost, and convenient technology compared to other conventional techniques such as biological treatment, chemical reduction, electrochemical oxidation, and membrane filtration. The high surface area, mechanical stability due to π conjugated structure, and high porosity of RGO-based nanocomposites are considered emerging materials in the adsorption of liquid and gas-phase contaminants. Some of the RGO-based nanocomposites are discussed below.

The pristine metal oxides have a low surface area and stability which, are the major concerns in the adsorption process. Therefore, many metal oxides-RGO composites have been studied. For the removal of As (III) and As (V) ions in aqueous solution hydrated RGO-Zr(OH)₂ nanocomposite have been studied with 95.15 and 84.89 mg/g of As (III), As (V) adsorption efficiency respectively as shown in Fig. 10.

Four times increase in surface area of the RGO-Zr (OH)₂ (1:100 mass ratio) nanocomposite compared to bare Zr (OH)₂ attributed to the addition of RGO and enhanced adsorption capacity of Arsenate ions were due to well dispersion of Zr (OH)₂ over RGO surface [60]. Further, to improve the separation of the nanocatalyst magnetic based materials have been incorporated with RGO. the M-RGO nanocomposite showed excellent adsorption capacity of 12.5 mg/g with 99.9% removal ability in neutral pH over the time duration of 2 h due to increased adsorption sites. By the external magnetic field, the adsorbent was easily separated from arsenite solution within 10 s and the synthesized M-RGO nanocomposite can be a practically viable process for arsenic removal [61].

A significant amount of adsorption studies was reported for the removal of organic dyes through the adsorption process. H. Xie. et. al reported MoS₂-RGO nanocomposites synthesized by one-step hydrothermal method for the adsorption of congo red dye [62]. The maximum adsorption reported was 440.9 mg/g at pH 3. The maximum adsorption was attributed to the increased surface area, high porosity, and π - π conjugation of MoS₂ and RGO.

3.3.2 Photocatalytic Degradation of Pollutants

Organic pollutants such as azo dyes, organic solvents, heavy metals, pesticides, and pharmaceutical wastes, are considered the most hazardous chemicals. These hazardous chemicals cause stern damage to the living organisms in the world. The photocatalytic advanced oxidation process is one of the efficient, low cost and most studied techniques for the efficient degradation of such hazardous chemicals [118]. The short absorption range, electron-hole recombination, low conductivity was the main limitations in conventional semiconductors such as metal oxide and sulfides [115]. To overcome these limitations graphene or RGO has been incorporated into the semiconductors.

The metal oxides are having the limitations such as low conductivity, wider bandgap, lower adsorption, higher recombination of charge carriers, etc. to overcome these issues RGO has been loaded to the metal oxides for the photocatalytic oxidation of organic pollutants. The graphene -TiO₂ nanocomposite is used to degrade malachite green dye under visible light irradiation [63]. The 10 wt% of RGO-TiO₂ nanocomposite shows 100% photocatalytic degradation of malachite green for 80 min. The enhanced photocatalytic activity is attributed to reduced recombination of charge carriers and the addition of RGO rendered increased surface area. Which leads to increased adsorption of dye molecules on the surface of the RGO-TiO₂ catalyst. The photocatalytic degradation mechanism of RGO-TiO₂ is shown in Fig. 11.

The 7 wt% loaded RGO-TiO₂ shows 98.6% degradation, attributed to the highest Ti/C ratio because of the better dispersion of RGO sheets on TiO₂. The increased amount of RGO resulted in the aggregation of RGO sheets and TiO₂ particles, which causes less absorption of light and Ethylparaben [64]. Therefore, an optimum amount of RGO loading is beneficial for effective dye degradation. To increase the range of absorption, charge separation, and conductivity a series of metal oxide heterostructured composites with RGO show promising results in photocatalytic dye

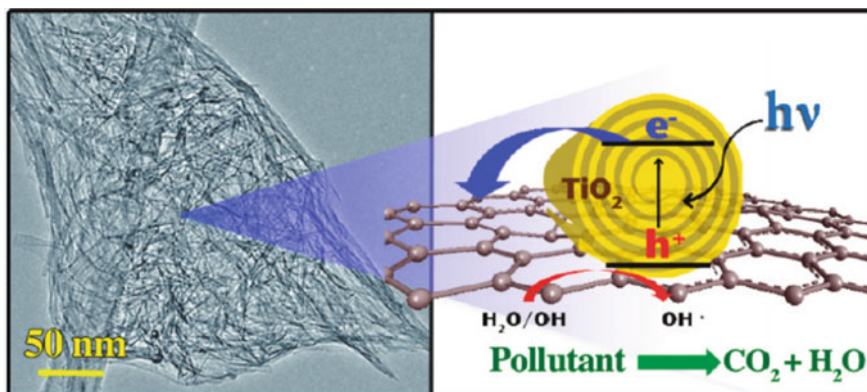


Fig. 11 Photocatalytic degradation of the graphene-TiO₂ nanocomposite. Reprinted with permission from Ref [63]. Copyright © (2012) American Chemical Society

degradation. For example, in the case of $\text{TiO}_2/\text{Nb}_2\text{O}_5/\text{SnO}_2$ -RGO heterostructured nanocomposite, the SnO_2 and Nb_2O_5 reduced the bandgap of TiO_2 for enhanced visible light absorption and charge separation. However, RGO supports the charge carrier's kinetics as well as surface area [65].

To enhance light absorption properties, charge separation, and electron transfer rate, even conductive polymers such as poly-pyrrole (PPy), polythiophene (PTH), polyaniline (PANI), is also introduced into the semiconductor-RGO based nanocomposite. Recently, In 2020, J. Ma et. al fabricated PANI- RGO- TiO_2 nanocomposite for photocatalytic degradation of RhB and photocatalytic hydrogen generation [66]. The addition of PANI into the matrix of RGO extends the light absorption range, kinetics of charge carriers, and effectively reduces the charge separation. By these advantages, 90.5% of dye was degraded within 90 min which, was 1.8 times higher than RGO- TiO_2 nanocomposite. However, M. Nawaz et. al 2020, instead of synthetic polymers, biopolymer such as sodium alginate was conjugated into RGO- TiO_2 nanocomposite for the efficient degradation of pharmaceutical pollutants under UV light [67]. The 99% of degradation of ibuprofen and sulfamethoxazole was achieved in the period of 45 to 90 min (Table 2) [115].

4 Energy Applications

4.1 Energy Applications of Fullerene Based Nanocomposites

4.1.1 Hydrogen Generation

Hydrogen is considered as one of the alternative renewable energy sources because of its zero-emission and most abundant in nature. Hydrogen generation by photocatalysis attracted researchers all over the world. Among many carbon-based nanocomposites, fullerene-based nanocomposites were used as semiconducting photocatalysis for hydrogen generation because of the strong electron affinity, which was beneficial for transferring photon-induced charge carriers for improving redox reactions. The fullerene-based metal oxide, sulfides, carbon nitrides have been studied for photocatalytic hydrogen generation [116].

Various metal oxides such as WO_3 -fullerene [96], $\text{Fe}_2\text{O}_3/\text{C}_{60}$ [97], TiO_2 - C_{60} -CNT's [98] were employed as photocatalyst for enhanced hydrogen generation. Usually, metal oxides are active in the only UV region, for shifting absorption range from UV region to visible region less band gap CdS (2.44 eV) materials are preferred for visible light photocatalytic hydrogen generation. For photocatalytic hydrogen generation, few reports on metal sulfides-fullerene nanocomposites are reported. The metal sulfides-fullerene nanocomposites were used as photocatalysts or co-catalysts due to their interesting electrical and optical properties compared to metal oxides-fullerene nanocomposite. The C_{60} coated CdS/ TiO_2 heterojunction nanocomposite have been studied for photocatalytic hydrogen generation, the bandgap shift into a

Table 2 Recent studies on RGO based nanocomposite for photocatalytic degradation of pollutants

Sl. No	RGO-based nanocomposite	Pollutant	Photocatalytic activity	References
1	Cu/Bi ₂ Ti ₂ O ₇ /RGO	Tetracycline and ibuprofen (5 mg/L)	92%, 84% (90 min) Visible light	[68]
2	RGO/Ag ₂ CO ₃	Tetracycline (10 ppm)	90% (60 min) visible light	[69]
3	WO ₃ -Fe ₂ O ₃ -RGO	Rhodamine B (RhB) Methylene blue (MB) (30 mg/L)	RhB-94%, MB-98% (30 min) Solar light	[70]
4	S-RGO/ZnS	2-chlorophenol (50 mg/L)	99.3% (4 h) sunlight	[71]
5	RGO/ZnO-Cu	Methylene blue (1*10 ⁻⁵ M)	95.14% (60 min) UV light	[72]
6	ZnFe ₂ O ₄ -RGO	Ciprofloxacin (20 ppm)	73.4% (60 min) solar light	[73]
7	ZrO ₂ /Fe ₂ O ₃ /RGO	Cango Red ()	98.43% (60 min) visible light	[74]
8	TiO ₂ -RGO-g-C ₃ N ₄	Remazol Turquoise Blue (10 ppm)	51.43% (90 min) sunlight	[75]
9	SnS ₂ -RGO	Remazol brilliant red (RBR) and Remazol brilliant blue (RBB) (10 ppm each 140 min)	RBR 97% () RBB 99.7% (140 min) Visible light	[76]
10	RGO-ZnO @Bi ₂ MoO ₆	RhB dye (10 mg/L)	79% (150 min) solar light	[77]
11	Tetra-4-carboxyphenyl porphyrin (TCPP)RGO-Bi ₂ WO ₆	Tetracycline (15 mg/L)	100% (60 min) visible light	[78]
12	NiFe-layered double hydroxide/RGO	Moxifloxacin (20 mg/L)	90.4% (60 min, sonophotocatalytic) visible light [79]	[79]
13	AgI/RGO-BiVO ₄	Tetracycline TC (20 ppm) RhB (20 ppm)	TC 84% (25 min) sunlight RhB 99% (25 min) sunlight	[80]
14	Cu ₂ O/ZnO-RGO	p-Nitrophenol (PNP, 10 mg/L) polyacrylamide (PAM, 10 mg/L)	PNP 98% (90 min) solar light PAM 99.6% (30 min) solar light	[81]
15	Tetraphenylporphyrin (TPP)/WO ₃ /RGO	Acid blue 25 (20 ppm)	85% (4 h) visible light	[82]

(continued)

Table 2 (continued)

Sl. No	RGO-based nanocomposite	Pollutant	Photocatalytic activity	References
16	ZnO dumbbell-RGO	methyl orange (MO, 10 mg/L) methylene blue (MB, 10 mg/L)	MO 89.78% (180 min) UV-Visible MB 97% (180 min) UV-Visible	[83]
17	Fe ₃ O ₄ @RGO@AgI	Phenol (50 ppm)	99% (9 h) UV-C light	[84]
18	NiFe-LDH/N-RGO/g-C ₃ N ₄	RhB (20 ppm)	RhB 95% (120 min) sunlight	[85]
19	N, F-TiO ₂ /SiO ₂ /RGO	Methyl red (10 mg/L)	95% (60 min) visible light	[86]
20	Au-B-TiO ₂ /RGO	Tetracycline (15 ppm)	100% (60 min) visible light	[87]
21	ZnFe-RGO	Phenol (10 mg/L)	100% (120 min) visible light	[88]
22	CQD-TiO _{2-x} /RGO	Bisphenol A (BA, 10 mg/L) Phenol (10 mg/L)	BA 82% (5 min) visible light Phenol 76% (20 min) visible light	[89]
23	RGO/In ₂ TiO ₅	RhB (10 mg/L)	97.5% (120 min) sunlight	[90]
24	BiOCl/RGO aerogel	Oxytetracycline (20 mg/L)	93.3% (120 min) UV light	[91]
25	Fe ₃ O ₄ @RGO	2-nitrophenol (20 ppm)	95.85% (30 min) visible light	[92]
26	ZnSnO ₃ /RGO	Methylene blue (10 mg/L)	84% (35 min) visible light	[93]
27	RGO/Bi ₂ WO ₆	Levofloxacin (0.00045 m mol)	74.3% (120 min) visible light	[94]
28	SnO ₂ /Fe ₂ O ₃ /RGO	Methylene blue (10 mg/L)	98.3% (3 h) visible light	[95]

visible light region and the coating of fullerene resulted fast transfer of charges to the surface of the photocatalyst thereby, an efficient photocatalytic hydrogen evolution was resulted with $120 \mu\text{mol h}^{-1} \text{g}^{-1}$. Which is 8.5 times higher than CdS/TiO₂ nanocomposite.. J. Guan et. al reported MoS₂-C₆₀ nanocomposite by mechanochemical ball milling method with optimised amount of fullerene-MoS₂ ratio (1:1) [6]. The resulted nanocomposite exhibited $6.89 \text{ mmol h}^{-1} \text{g}^{-1}$, 9.3 times higher than pure MoS₂, due to the formation of heterostructure with fullerene the conduction band edge was further shifted to the more negative region as shown in Fig. 12. When the light was irradiated, Eosin Y dye absorbs light energy and generates the electrons and holes at the conduction band and valance band, respectively. The conduction band electrons were easily captured by fullerenes for reducing the water molecules into H₂

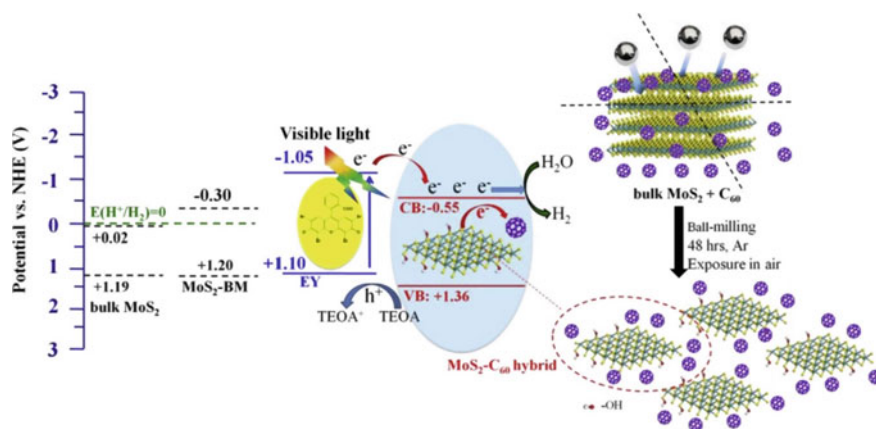


Fig. 12 Mechanism of photocatalytic hydrogen generation by MoS₂-C₆₀ nanocomposite reprinted with permission from ref [6], Copyright © 2011 with permission from Elsevier

and holes in the valance band will be scavenged by TEOAs hole scavengers. Which resulted in the suppression of charge recombination thereby enhanced production of H₂ was reported.

The g-C₃N₄ is another fascinating material because of its unique optical properties. The photocatalytic activity of g-C₃N₄ is quite low due to its relatively large bandgap and charge transfer resistance between the layers. Therefore, fullerene has been incorporated for overcoming these limitations. For the first time, X. Chen et. reported g-C₃N₄ -fullerene hybrid nanocomposite for photocatalytic hydrogen generation by mechanochemical ball milling process [5]. Which resulted in 266 μmol h⁻¹ g⁻¹ of photocatalytic hydrogen generation with an improved factor of four, compared to pure g-C₃N₄. The enhanced photocatalytic activity was due to the covalent bonding between the g-C₃N₄ and fullerene influenced enhanced conductivity and formation of heterojunction resulted in suppression of the electron–hole recombination process.

4.2 Energy Applications of CNT Based Nanocomposites

4.2.1 H₂ Generation

Due to the rapid increase in energy demand people searching for clean and renewable energy sources to avoid fossil fuels. Hydrogen generation has been considered as one of the cleanest form energies because of zero-emission. Hydrogen generation is an efficient (220 kJ/g) fuel for electric vehicles and devices. Nowadays, a lot of interest has been given to hydrogen generation by catalytic reactions that include photocatalysis, electrocatalysis, and photoelectrochemical catalysis, etc. Usually, semiconductors, noble metals are preferred for catalytic activity, but due to low

conductivity, high cost, and less surface area, the catalytic activity was negligible. To overcome these issues CNT's have been anchored on various semiconductors or noble metals for catalytic HER.

The addition of CNT extends the absorption range and shift the bandgap of the TiO_2 or other wide bandgap materials into a visible region with enhanced conductivity hence, results in enhanced photocatalytic hydrogen generation [99]. But metal oxide-based composites show limitations such as low conductivity, charge recombination, less active sites. To overcome these, transition dichalcogenides have been loaded to CNT for enhanced electrocatalytic hydrogen evolution reaction without using noble metals as cocatalyst [100]. The addition of N doped CNT significantly enhances the conductivity, surface area, and active sites of the catalyst therefore, the synthesized $\text{MoS}_2/\text{N-CNT}$ nanocomposite shows 110 mV onset potential and 40 mV/dec Tafel slope. This signifies an efficient electrocatalyst for hydrogen evolution without expensive Pt noble metal. However, $\text{Co}_3\text{Se}_4/\text{N-CNT}$ hybrid nanocomposite used for electrocatalytic hydrogen evolution reaction. The prepared catalyst shows 174, 240 mV over potential both in alkaline and acidic medium, respectively with 73.2, 43.8 mV/dec Tafel slope [101]. The doping of Co significantly reduces the barrier potential for hydrogen adsorption on the catalyst surface. However, the addition of CNT influences the higher conductivity and increased active sites to achieve 120 mV overpotential with 46 mV/dec Tafel slope in the case of FeS_2/CNT nanocomposite [102]. The chemical and electrical coupled core-shell cobalt phosphate-phosphosulphide, nitrogen-doped CNT ($\text{CoP} @ \text{PS} / \text{NCNT}$) hybrid nanostructures attracted considerable attention for electrocatalytic hydrogen evolution reaction [101]. Nitrogen-doped CNT ($\text{CoP} @ \text{PS} / \text{NCNT}$) hybrid nanostructures are one of the efficient non-noble metal-based electrocatalysts for hydrogen generation.

4.2.2 Battery Applications

To mitigate energy demand for electronic gadgets and other movable instruments, Li-ion/sulfur batteries have been considered as a fabulous energy storage application. Due to high theoretical capacities many metal oxides, sulfides are being used as an alternative to graphite, as an anode. However, poor kinetics, low electric conductivity, the formation of solid electrolyte interphase during conversion reactions, low-rate capability offered capacity fading [119]. To overcome these limitations, many carbonaceous materials have been incorporated among such materials CNT-based nanocomposites show excellent specific capacity because of impressive physio-chemical properties.

The enhanced electrochemical and physical interface between M13 phage bio nanonetworks of CNT (32:1 molar ratio of SWCNT and M13), Co_3O_4 nanoflowers resulted in a high specific capacity of 1283.5 mAh g^{-1} rate at 2 A g^{-1} after 500 cycles as shown in Fig. 13. The specific capacity is one of the highest values ever reported for Co_3O based nanocomposites as anodes for Li-ion battery applications [103].

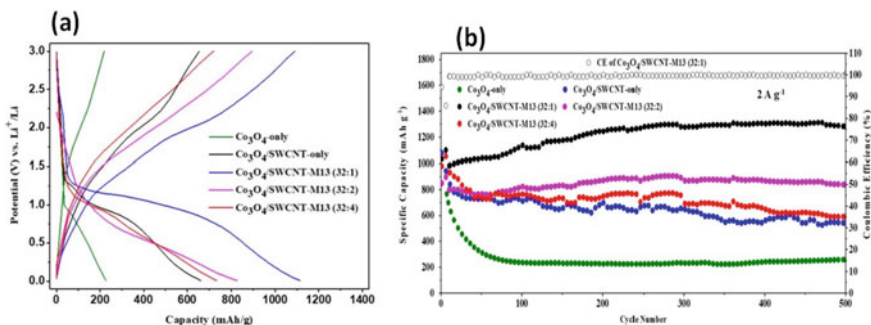


Fig. 13 Electrochemical performance of bio-templated (M13 phage) Co_3O_4 -CNT nanocomposite, **a** Charge–discharge curves, **b** rate capability at 2 A g^{-1} up to 500 cycles of Co_3O_4 -CNT. Reprinted with permission from Ref [103]. Copyright © (2020) American Chemical Society

Due to high theoretical energy (1675 mAh g^{-1} capacity) and power (2600 Wh kg^{-1}) density, Li-sulfur batteries are emerged as a potential battery technology for mitigating energy crisis. When considering the cost sulfur batteries found to be less compared to Li-ion batteries because of the abundant availability of sulfur. The stability of the Li-sulfur batteries at higher sulfur loading is quite concerned because of capacity fading due to the shuttling effect. In the shuttle effect, throughout charge–discharge cycles, the formation of polysulfides results in low conductivity with material instability. So to overcome these limitations CNT based nanocomposites are reported. Among such materials, the 3D hierarchical Co intercalated nitrogen-doped CNT grown on cobalt alumina layered double hydroxide (CoAl-LDH) @ sulfur (80 wt%) nanocomposite has shown, 860 mAh g^{-1} rate capability at 2 C current rate with 0.04% capacity decay in Li-sulfur battery anodes [104]. Usually at higher sulfur content due to the shuttling effect, the capacity of Li–S batteries decreases unevenly. In this case, high rate capability was achieved due to the strong affinity of cobalt particles and LDH nanosheets with elemental sulfur. Which, improves the polysulfide adsorption without leaching or shuttling effect and improved reaction kinetics.

4.3 Energy Applications of RGO Based Nanocomposites

4.3.1 Battery Applications

Recently, more attention has been given to Li-ion or sulfur batteries to mitigate energy storage problems in electronic gadgets and other movable instruments. The major issues in conventional battery materials are poor kinetics, low electric conductivity, the formation of solid electrolyte interphase during conversion reactions, low-rate capability, and capacity fading. To overcome these limitations, many carbonaceous

materials have been incorporated, among such materials, RGO-based nanocomposites show excellent properties in Li-ion batteries, Because of their high surface area, chemical, and mechanical stability, high electronic conductivity [121]. Some of the recent studies on RGO-based nanocomposites for Li-ion, Zn-ion batteries are discussed below.

Some of the metal oxides and sulfides have been studied for Li-ion batteries. The mesoporous nanocube TiO_2 -RGO nanocomposite exhibit improved anode capacity of 180 mAh g^{-1} at a 1.2 C rate after 300 cycles, because the addition of RGO enhanced both ionic and electronic conductivity. The volume expansion, charge transfer resistance, and structural stability of MnO_2 are enhanced by the incorporation of RGO [105]. The MnO_2 -GO nanotube hybrid structure exhibited a specific capacity of 1290 mAh g^{-1} at 0.1 A g^{-1} with higher columbic efficiency (68%) compared to pure MnO_2 (46%) because of increased material stability and conductivity due to the addition of RGO [106]. The transition metal chalcogenides are attracted as an excellent anode for Li-ion batteries due to their higher electrochemical properties and theoretical capacity. The in-situ grown Co_{1-x}S on RGO sheets enhance the conductivity and volume expansion compared to ex-situ grown Co_{1-x}S on RGO sheets because of better anchoring of Co_{1-x}S on RGO sheets [107].

The RGO-based nanocomposites have been used as cathode material as well for Li-ion battery applications. The redox kinetics of the $\text{LiFePO}_4/\text{C}/\text{Graphene}$ nanocomposite shows better performance compared to pure LiFePO_4/C . Which, shows the specific capacity of 165 mAh g^{-1} at a 0.1 C rate [19]. Further, the $\text{LiMn}_{0.8}\text{Fe}_{0.2}\text{PO}_4$ embedded nitrogen-doped RGO formed an interconnected three-dimensional conductive network which, enables the faster diffusion of electrons and Li ions and yielded the specific capacity of 160 mAh g^{-1} at 0.2 C rate further, decreased to 70 mAh g^{-1} at 10 C rate [108], as shown in Fig. 14. The formation of the 3D conductive network by RGO retained specific capacity even at a higher current rate [109]. This material offered a high rate of cathode material for high power density Li-ion batteries. Therefore, the addition of RGO improved the electrical and mechanical properties of both anode and cathode of Li-ion batteries.

Recently, aqueous Zn-ion batteries are attracting researchers because of environmental friendliness, low cost, and more safety compared to other battery technologies. The main issue in the zinc-ion battery is the sluggish mechanism of Zinc ion diffusion and dissolution of the cathode. To address these issues some of the RGO-based nanocomposites are studied. The MnO/C -RGO nanocomposite is used as cathode material for an aqueous zinc-ion battery. The addition of RGO enhanced the ionic conductivity, results in the discharge capacity of 170.6 mAh g^{-1} at 500 Ma g^{-1} , even after 300 cycles [109].

The VO_2/RGO nanocomposite results in a superior capacity of 456 mAh g^{-1} at 100 mA g^{-1} and an excellent rate capability of 292 mAh g^{-1} at 5 A g^{-1} . The uniform deposition of VO_2 belts on RGO leads to improve ionic kinetics as well as structural stability [110]. However, graphene wrapped hollow microspheres of ZnMn_2O_4 suppressed the charge transfer resistance and thereby increases the conductivity of the cathode results in a specific capacity of 146.9 mAh g^{-1} at 0.3 A g^{-1} [111]. From

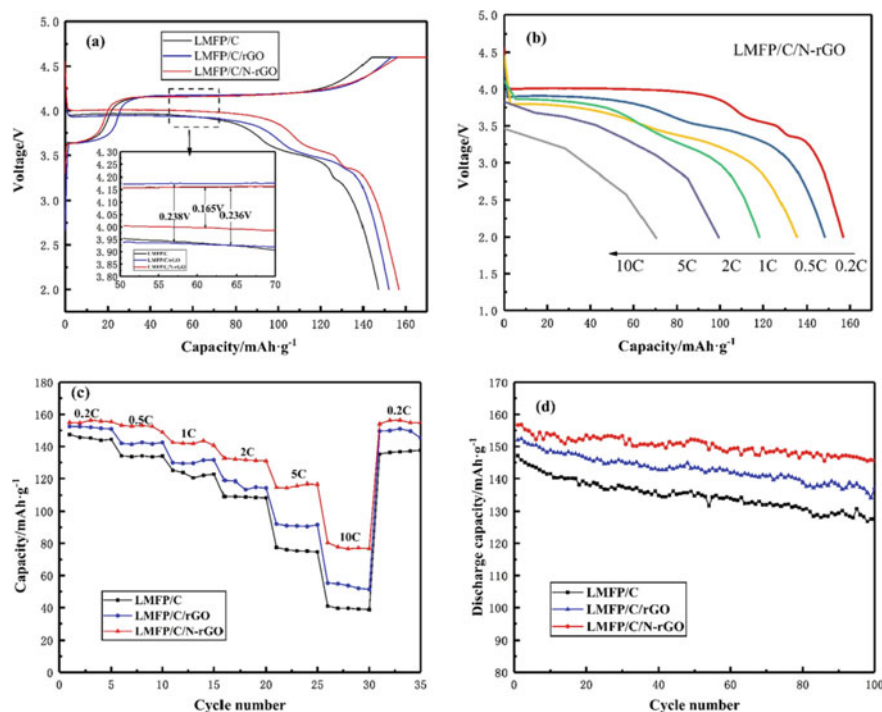


Fig. 14 a The charge–discharge profiles, b The discharge capacity at different C rates, c Rate performance at different C rates d Cycling rates of $\text{LiMn}_{0.8}\text{Fe}_{0.2}\text{PO}_4/\text{C}/\text{N}/\text{RGO}$ nanocomposite. Reprinted from Ref [108]. Copyright © (2019) with permission from Elsevier

the above facts, it is confirmed that the addition of RGO significantly influences the performance of the Zn-ion battery.

4.3.2 Hydrogen Generation

The ever increase in consumption of fossil fuel resulted in climate change which, leads to global warming. To mitigate these issues, renewable, and clean energy sources have to be explored, among such energy sources H_2 was considered as an excellent one. Presently, most of the H_2 is getting from steam reforming of natural gas at higher temperature and pressure and the remaining is from electrocatalysis and biofuel reformation. Photocatalytic H_2 generation is one of the alternative techniques. In this regard, RGO-based nanocomposites played a vital role as electrocatalyst as well as photocatalysts.

In the photoelectrochemical water splitting process, upon irradiation of light onto the anode (working electrode) the electrons will be generated and transferred to the cathode (counter electrode) via an external circuit. At the cathode surface, the

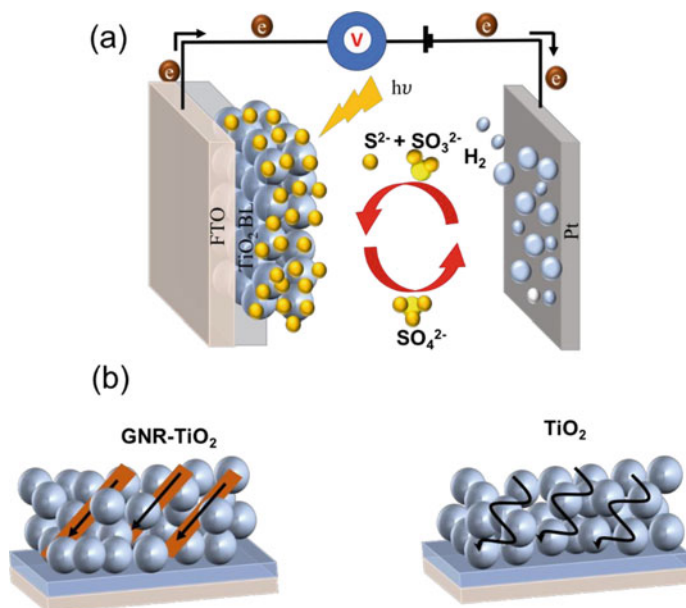


Fig. 15 **a** Mechanism of photoelectrochemical water splitting process, **b** electrons transport process in GNR-TiO₂ and without GNR. Reprinted from Ref [112], Copyright © (2020) with permission from Elsevier

adsorbed water molecules split into H₂ and oxygen. The amount of photocurrent generated, directly proportional to the H₂ generation rate. The charge neutrality is achieved by the electrolyte by scavenging the generated holes [112]. The schematic of the photo-electrochemical water splitting process is shown in Fig. 15. The 0.02 wt% GNR's loaded TiO₂ sample shows 5.51 mA/cm² current density. Which is 30% higher activity than without RGO loaded sample. This improved activity is attributed to a decrease in the charge transfer resistance by the addition of RGO. Usually, the electrons flow randomly in TiO₂ but in GNR-TiO₂ the unidirectional flow of electrons resulted in improved conductivity as shown in Fig. 15(b), thus enhances the H₂ generation activity.

The RGO based nanocomposites also have applications in photocatalytic hydrogen generation. The nitrogen-doped RGO increases the conductivity and active sites of the electrode. The addition of nitrogen into the crystal structure of TiO₂ suppresses the electron-hole recombination. The nitrogen-doped RGO shows 21.347 mmol h⁻¹ g⁻¹ of H₂ generation. The addition of conductive polymer and RGO benefitted in reduced charge recombination as well as increased surface area. Which, causes enhanced hydrogen generation of 0.806 mmol h⁻¹ g⁻¹ upon irradiation of visible light for 8 h duration and about 1.8 times higher activity than TiO₂-RGO [113]. For practically viable process membrane-type electrodes are preferred for photocatalytic H₂ generation. The RGO-TiO₂ nanocomposite immobilized on Nafion membrane by three different approaches such as solvent-casting (SC), dip

coating (DC), and spraying (SP). Among these methods, the spraying method results in better efficiency because of non leaching of the sample on the membrane which, resulted higher photocatalytic hydrogen generation ($0.012_{\text{mmol}} \text{H}_2 \text{ gcat}^{-1}$) [114]. Therefore, RGO based nanocomposites have been considered promising materials for hydrogen generation.

5 Summary and Future Perspective

In this chapter, the basic properties of carbon allotropes such as fullerene, CNT, and graphene were discussed to understand the importance of carbon-based materials. Mainly, focused on the synthesis and characterization techniques of carbon-based nanostructures composites explicitly on fullerene, CNT, and graphene-based nanocomposites. The synthesis methods such as ball milling, sol-gel, electrodeposition, hydro, or solvothermal methods were explored. Hydro or solvothermal method was found to be the most versatile, simple technique for getting controlled shape, morphology, and size of the carbon-based nanocomposites. The formation of the three-dimensional network between metal oxides, transition metal dichalcogenides based semiconducting materials with fullerene, CNT, and Graphene. These influence the mechanical, optical, and electrical properties, which are essential for applications in the energy and environmental sectors. Nowadays, fullerenes and CNT's are treated with concentrated acid for functionalization and make it hydrophilic which is not a green approach. Therefore more attention should be given towards the development of a suitable environmentally friendly approach for surface modification of these carbon-based nanostructures and their composites. In most of the studies, the hydro/solvothermal method was used for synthesizing carbon-based nanocomposites. But the long reaction time and less yield are the disadvantages of the Solvo/Hydrothermal method. There are no reports on the simple, low cost, and scale-up of the synthesis process for synthesizing carbon-based nanocomposites. Therefore, alternative simple, low cost and scale-up synthesis methods should be developed for the synthesis of carbon-based nanocomposites.

Recent studies on the environmental and energy applications of fullerene, CNT, and graphene-based nanocomposites are illustrated in the chapter. The environmental remediation applications such as adsorption of organic and inorganic pollutants, pharmaceutical wastes, heavy metals were discussed along with recent progress made in these applications. For repeatable use of catalyst recovering the catalyst is a more important aspect. So, efforts should be made on the magnetic materials loaded carbon composites for the easy recovery of catalyst, and importance should be given to a higher amount of carbon loading in the composites to increase the number of adsorption sites. The Photocatalytic degradation of organic chemicals, coloring agents, and other heavy metals were discussed. Deliberated few important and recent studies on photocatalytic degradation of Azo dyes, organic solvents, heavy metals, pesticides, and pharmaceutical wastes by carbon-based nanocomposites. Still, these photocatalytic applications of carbon-based nanocomposites are limited to lab scale.

For commercialization, major issues such as the impact on the ecosystem, stability, viability, repeatability, etc. are yet to be addressed.

The last part of the chapter discussed the latest energy generation and harvesting applications such as photocatalytic and electrocatalytic H₂ generation, Li-ion, Zn-ion batteries, fullerene, CNT, and graphene-based nanocomposites. In most of the battery materials, even the addition of carbon allotropes like fullerenes, CNT, and Graphene conductivity, dissolution of the electrodes, the formation of solid electrolyte interface (SEI) layer leads to capacity fading, low cycle rate as well as low coulombic efficiency which should be addressed. There is a lot of scope for Li-S, Zn-ion, Mg-ion, Na-ion and K-ion batteries due to their low cost when compared to Li-ion batteries. Carbon based nanocomposite are explored more on low cost battery technologies for the commercialization of battery technologies to mitigate energy needs in the world.

References

1. Tuçek, J., Kemp, K.C., Kim, K.S., Zbořil, R.: Iron-oxide-supported nanocarbon in lithium-ion batteries, medical, catalytic, and environmental applications. *ACS Nano* **8**, 7571–7612 (2014). <https://doi.org/10.1021/nn501836x>
2. Cai, Q., Hu, Z., Zhang, Q., Li, B., Shen, Z.: Fullerene (C₆₀)/CdS nanocomposite with enhanced photocatalytic activity and stability. *Appl. Surf. Sci.* **403**, 151–158 (2017). <https://doi.org/10.1016/j.apsusc.2017.01.135>
3. Vishnoi, R., Gupta, S., Kumar, U., Singhal, R.: Optical and structural modifications of copper-fullerene nanocomposite thin films by 120 MeV Au ion irradiation. *Radiat. Phys. Chem.* **166**, 108442 (2020). <https://doi.org/10.1016/j.radphyschem.2019.108442>
4. Ellessawy, N.A., El-Sayed, E.M., Ali, S., Elkady, M.F., Elnouby, M., Hamad, H.A.: One-pot green synthesis of magnetic fullerene nanocomposite for adsorption characteristics. *J. Water Process. Eng.* **34**, 101047 (2020). <https://doi.org/10.1016/j.jwpe.2019.101047>
5. Chen, X., Chen, H., Guan, J., Zhen, J., Sun, Z., Du, P., et al.: A facile mechanochemical route to a covalently bonded graphitic carbon nitride (g-C₃N₄) and fullerene hybrid toward enhanced visible light photocatalytic hydrogen production. *Nanoscale* **9**, 5615–5623 (2017). <https://doi.org/10.1039/c7nr01237c>
6. Guan, J., Wu, J., Jiang, D., Zhu, X., Guan, R., Lei, X., et al.: Hybridizing MoS₂ and C₆₀ via a van der Waals heterostructure toward synergistically enhanced visible light photocatalytic hydrogen production activity. *Int. J. Hydrogen Energy* **43**, 1–9 (2018). <https://doi.org/10.1016/j.ijhydene.2018.03.148>
7. Kilic, B.: Produce of carbon nanotube/ZnO nanowires hybrid photoelectrode for efficient dye-sensitized solar cells. *J. Mater. Sci. Mater. Electron.* **30**, 3482–3487 (2019). <https://doi.org/10.1007/s10854-018-00624-y>
8. Li, X., Wang, L., You, W., Li, X., Yang, L., Zhang, J., et al.: Enhanced microwave absorption performance from abundant polarization sites of ZnO nanocrystals embedded in CNTs: Via confined space synthesis. *Nanoscale* **11**, 22539–22549 (2019). <https://doi.org/10.1039/c9nr07895a>
9. Mohamed, M.M., Ghanem, M.A., Reda, S.M., Khairy, M., Naguib, E.M., Alotaibi, N.H.: Photovoltaic and capacitance performance of low-resistance ZnO nanorods incorporated into carbon nanotube-graphene oxide nanocomposites. *Electrochim. Acta* **307**, 430–441 (2019). <https://doi.org/10.1016/j.electacta.2019.03.226>
10. Cui, P., Wang, A.J.: Synthesis of CNTs/CuO and its catalytic performance on the thermal decomposition of ammonium perchlorate. *J. Saudi Chem. Soc.* **20**, 343–348 (2016). <https://doi.org/10.1016/j.jscs.2014.09.010>

11. Jin, X., Lim, J., Ha, Y., Kwon, N.H., Shin, H., Kim, I.Y., et al.: A critical role of catalyst morphology in low-temperature synthesis of carbon nanotube-transition metal oxide nanocomposite. *Nanoscale* **9**, 12416–12424 (2017). <https://doi.org/10.1039/c7nr03598e>
12. Naresh, N., Jena, P., Satyanarayana, N.: Facile synthesis of MoO₃/rGO nanocomposite as anode materials for high performance lithium-ion battery applications. *J. Alloys Compd.* **810**, 151920 (2019). <https://doi.org/10.1016/j.jallcom.2019.151920>
13. Chen, Z., Ren, W., Gao, L., Liu, B., Pei, S., Cheng, H.M.: Three-dimensional flexible and conductive interconnected graphene networks grown by chemical vapour deposition. *Nat. Mater.* **10**, 424–428 (2011). <https://doi.org/10.1038/nmat3001>
14. Liu, Z., Tu, Z., Li, Y., Yang, F., Han, S., Yang, W., et al.: Synthesis of three-dimensional graphene from petroleum asphalt by chemical vapor deposition. *Mater. Lett.* **122**, 285–288 (2014). <https://doi.org/10.1016/j.matlet.2014.02.077>
15. Xu, Y., Sheng, K., Li, C.: Self-assembled graphene hydrogel. *ACS Nano* **4**, 4324–4330 (2010)
16. Shen, J., Shi, M., Yan, B., Ma, H., Li, N., Ye, M.: One-pot hydrothermal synthesis of Ag-reduced graphene oxide composite with ionic liquid. *J. Mater. Chem.* **21**, 7795–7801 (2011). <https://doi.org/10.1039/c1jm10671f>
17. Xu, X., Li, H., Zhang, Q., Hu, H., Zhao, Z., Li, J., et al.: Self-sensing, ultralight, and conductive 3D graphene/iron oxide aerogel elastomer Deformable in a Magnetic Field. *ACS Nano* **9**, 3969–3977 (2015). <https://doi.org/10.1021/nn507426u>
18. Zhang, Y., Ju, P., Zhao, C., Qian, X.: In-situ grown of MoS₂/RGO/MoS₂@Mo nanocomposite and its supercapacitor performance. *Electrochim. Acta* **219**, 693–700 (2016). <https://doi.org/10.1016/j.electacta.2016.10.072>
19. Shi, Y., Chou, S.L., Wang, J.Z., Wexler, D., Li, H.J., Liu, H.K., et al.: Graphene wrapped LiFePO₄/C composites as cathode materials for Li-ion batteries with enhanced rate capability. *J. Mater. Chem.* **22**, 16465–16470 (2012). <https://doi.org/10.1039/c2jm32649c>
20. Du, D., Liu, J., Zhang, X., Cui, X., Lin, Y.: One-step electrochemical deposition of a graphene-ZrO₂ nanocomposite: preparation, characterization and application for detection of organophosphorus agents. *J. Mater. Chem.* **21**, 8032–8037 (2011). <https://doi.org/10.1039/c1jm10696a>
21. Li, Y., Sheng, K., Yuan, W., Shi, G.: A high-performance flexible fibre-shaped electrochemical capacitor based on electrochemically reduced graphene oxide. *Chem. Commun.* **49**, 291–293 (2013). <https://doi.org/10.1039/c2cc37396c>
22. Kumar, I., Sharma, R., Kumar, R., Kumar, R., Sharma, U.: C70 fullerene-catalyzed metal-free photocatalytic ipso-hydroxylation of aryl boronic acids: synthesis of phenols. *Adv. Synth. Catal.* **360**, 2013–2019 (2018). <https://doi.org/10.1002/adsc.201701573>
23. Barhoum, A., Shalan, A.E., El-Hout, S.I., et al.: A broad family of carbon nanomaterials: Classification, properties, synthesis, and emerging applications. In: *Handbook of Nanofibers*, pp. 1–40. Springer International Publishing, Cham (2019)
24. Oh, W.-C., Jung, A.-R., Ko, W.-B.: Preparation of fullerene/TiO₂ composite and its photocatalytic effect. *J. Ind. Eng. Chem.* **13**, 1208–1214 (2007)
25. Messih, M.F.A., Shalan, A.E., Sanad, M.F., Ahmed, M.A.: Facile approach to prepare ZnO@SiO₂ nanomaterials for photocatalytic degradation of some organic pollutant models. *J. Mater. Sci. Mater. Electron.* **30**, 14291–14299 (2019)
26. Nasrollahzadeh, M., Sajjadi, M., Irvani, S., Varma, R.S.: Carbon-based sustainable nanomaterials for water treatment: state-of-art and future perspectives. *Chemosphere* **263**, 128005 (2021). <https://doi.org/10.1016/j.chemosphere.2020.128005>
27. Hemalatha, K., Ette, P.M., Madras, G., Ramesha, K.: Visible light assisted photocatalytic degradation of organic dyes on TiO₂-CNT nanocomposites. *J. Sol-Gel Sci. Technol.* **73**, 72–82 (2014). <https://doi.org/10.1007/s10971-014-3496-0>
28. Abega, A.V., Ngomo, H.M., Nongwe, I., Mukaya, H.E., Kouoh Sone, P.M.A., Yangkou, M.X.: Easy and convenient synthesis of CNT/TiO₂ nanohybrid by in-surface oxidation of Ti³⁺ ions and application in the photocatalytic degradation of organic contaminants in water. *Synth. Met.* **251**, 1–14 (2019). <https://doi.org/10.1016/j.synthmet.2019.03.012>

29. Lee, W.J., Lee, J.M., Kochuveedu, S.T., Han, T.H., Jeong, H.Y., Park, M., et al.: Biomaterialized N-doped CNT/TiO₂ core/shell nanowires for visible light photocatalysis. *ACS Nano* **6**, 935–943 (2012). <https://doi.org/10.1021/nn204504h>
30. Gangu, K.K., Maddila, S., Jonnalagadda, S.B.: A review on novel composites of MWCNTs mediated semiconducting materials as photocatalysts in water treatment. *Sci. Total Environ.* **646**, 1398–1412 (2019). <https://doi.org/10.1016/j.scitotenv.2018.07.375>
31. Saleh, T.A., Gupta, V.K.: Photo-catalyzed degradation of hazardous dye methyl orange by use of a composite catalyst consisting of multi-walled carbon nanotubes and titanium dioxide. *J. Colloid Interface Sci.* **371**, 101–106 (2012). <https://doi.org/10.1016/j.jcis.2011.12.038>
32. Paquin, F., Rivnay, J., Salleo, A., Stingelin, N., Silva, C.: Multi-phase semicrystalline microstructures drive exciton dissociation in neat plastic semiconductors. *J. Mater. Chem. C* **3**, 10715–10722 (2015). <https://doi.org/10.1039/b000000x>
33. Pi, Y., Jin, S., Li, X., Tu, S., Li, Z., Xiao, J.: Encapsulated MWCNT@MOF-derived In₂S₃ tubular heterostructures for boosted visible-light-driven degradation of tetracycline. *Appl. Catal. B Environ.* **256**, 117882 (2019). <https://doi.org/10.1016/j.apcatb.2019.117882>
34. Ye, S., Zhou, X., Xu, Y., Lai, W., Yan, K., Huang, L., et al.: Photocatalytic performance of multi-walled carbon nanotube/BiVO₄ synthesized by electro-spinning process and its degradation mechanisms on oxytetracycline. *Chem. Eng. J.* **373**, 880–890 (2019). <https://doi.org/10.1016/j.cej.2019.05.109>
35. Azghandi, M.H.A., Vashghani, F.B., Rajabi, F.H., Keramati, M.: Synthesis of Cd doped ZnO/CNT nanocomposite by using microwave method: photocatalytic behavior, adsorption and kinetic study. *Results Phys.* **7**, 1–9 (2017). <https://doi.org/10.1016/j.rinp.2017.02.033>
36. Lin, X., Xi, Y., Zhao, R., Shi, J., Yan, N.: Construction of C₆₀-decorated SWCNTs (C₆₀-CNTs)/bismuth-based oxide ternary heterostructures with enhanced photocatalytic activity. *RSC Adv.* **7**, 53847–53854 (2017). <https://doi.org/10.1039/c7ra11056a>
37. Lv, J., Li, D., Dai, K., Liang, C., Jiang, D., Lu, L., et al.: Multi-walled carbon nanotube supported CdS-DETA nanocomposite for efficient visible light photocatalysis. *Mater. Chem. Phys.* **186**, 372–381 (2017). <https://doi.org/10.1016/j.matchemphys.2016.11.008>
38. Moradi, M., Haghghi, M., Allahyari, S.: Precipitation dispersion of Ag–ZnO nanocatalyst over functionalized multiwall carbon nanotube used in degradation of Acid Orange from wastewater. *Process Saf. Environ. Prot.* **107**, 414–427 (2017). <https://doi.org/10.1016/j.psep.2017.03.010>
39. Seyed Dorraji, M.S., Amani-Ghadim, A.R., Rasoulifard, M.H., Taherkhani, S., Daneshvar, H.: The role of carbon nanotube in zinc stannate photocatalytic performance improvement: experimental and kinetic evidences. *Appl. Catalysis B Environ.* **205**, 559–568 (2017). <https://doi.org/10.1016/j.apcatb.2017.01.002>
40. Koli, V.B., Mavengere, S., Kim, J.S.: Boron-doped TiO₂-CNTs nanocomposites for photocatalytic application. *J. Mater. Sci. Mater. Electron.* **29**, 16660–16672 (2018). <https://doi.org/10.1007/s10854-018-9759-8>
41. Mahdiani, M., Soofivand, F., Ansari, F., Salavati-Niasari, M.: Grafting of CuFe₂O₄ nanoparticles on CNT and graphene: eco-friendly synthesis, characterization and photocatalytic activity. *J. Clean Prod.* **176**, 1185–1197 (2018). <https://doi.org/10.1016/j.jclepro.2017.11.177>
42. Payan, A., Fattahi, M., Jorfi, S., Roozbehani, B., Payan, S.: Synthesis and characterization of titanate nanotube/single-walled carbon nanotube (TNT/SWCNT) porous nanocomposite and its photocatalytic activity on 4-chlorophenol degradation under UV and solar irradiation. *Appl. Surf. Sci.* **434**, 336–350 (2018). <https://doi.org/10.1016/j.apsusc.2017.10.149>
43. Qu, L., Zhu, G., Ji, J., Yadav, T.P., Chen, Y., Yang, G., et al.: Recyclable visible light-driven O-g-C₃N₄/graphene oxide/N-carbon nanotube membrane for efficient removal of organic pollutants. *ACS Appl. Mater. Interfaces* **10**, 42427–42435 (2018). <https://doi.org/10.1021/acsami.8b15905>
44. Liu, F., Dong, S., Zhang, Z., Li, X., Dai, X., Xin, Y., et al.: Synthesis of a well-dispersed CaFe₂O₄/g-C₃N₄/CNT composite towards the degradation of toxic water pollutants under visible light. *RSC Adv.* **9**, 25750–25761 (2019). <https://doi.org/10.1039/c9ra05005a>

45. Samsudin, M.F.R., Bacho, N., Sufian, S., Ng, Y.H.: Photocatalytic degradation of phenol wastewater over Z-scheme g-C₃N₄/CNT/BiVO₄ heterostructure photocatalyst under solar light irradiation. *J. Mol. Liq.* **277**, 977–988 (2019). <https://doi.org/10.1016/j.molliq.2018.10.160>
46. Shafei, A., Sheibani, S.: Visible light photocatalytic activity of Cu doped TiO₂-CNT nanocomposite powder prepared by sol-gel method. *Mater. Res. Bull.* **110**, 198–206 (2019). <https://doi.org/10.1016/j.materresbull.2018.10.035>
47. Hezam, F.A., Nur, O., Mustafa, M.A.: Synthesis, structural, optical and magnetic properties of NiFe₂O₄/MWCNTs/ZnO hybrid nanocomposite for solar radiation driven photocatalytic degradation and magnetic separation. *Colloids Surf. A Physicochem. Eng. Asp.* **592**, 124586 (2020). <https://doi.org/10.1016/j.colsurfa.2020.124586>
48. Isari, A.A., Mehregan, M., Mehregan, S., Hayati, F., Rezaei Kalantary, R., Kakavandi, B.: Sono-photocatalytic degradation of tetracycline and pharmaceutical wastewater using WO₃/CNT heterojunction nanocomposite under US and visible light irradiations: a novel hybrid system. *J. Hazard Mater.* **390**, 122050 (2020). <https://doi.org/10.1016/j.jhazmat.2020.122050>
49. Jiang, Z., Feng, L., Zhu, J., Li, X., Chen, Y., Khan, S.: MOF assisted synthesis of a Ho₂O₃/CNT nanocomposite photocatalyst for organic pollutants degradation. *Ceram. Int.* **46**, 19084–19091 (2020). <https://doi.org/10.1016/j.ceramint.2020.04.242>
50. Tie, W., Du, Z., Yue, H., Sarathi Bhattacharyya, S., Zheng, Z., He, W., et al.: Self-assembly of carbon nanotube/graphitic-like flake/BiOBr nanocomposite with 1D/2D/3D heterojunctions for enhanced photocatalytic activity. *J. Colloid Interface Sci.* **579**, 862–871 (2020). <https://doi.org/10.1016/j.jcis.2020.06.088>
51. Arsalani, N., Bazazi, S., Abuali, M., Jodeyri, S.: A new method for preparing ZnO/CNT nanocomposites with enhanced photocatalytic degradation of malachite green under visible light. *J. Photochem. Photobiol. A Chem.* **389**, 112207 (2020). <https://doi.org/10.1016/j.jphotochem.2019.112207>
52. Mohammed, M.K.A.: Carbon nanotubes loaded ZnO/Ag ternary nanohybrid with improved visible light photocatalytic activity and stability. *Optik (Stuttg)* **217**, 164867 (2020). <https://doi.org/10.1016/j.ijleo.2020.164867>
53. Samy, M., Ibrahim, M.G., Alalm, M.G., Fujii, M.: Effective photocatalytic degradation of sulfamethazine by CNTs/LaVO₄ in suspension and dip coating modes. *Sep. Purif. Technol.* **235**, 116138 (2020). <https://doi.org/10.1016/j.seppur.2019.116138>
54. Zhao, C., Guo, J., Yu, C., Zhang, Z., Sun, Z., Piao, X.: Fabrication of CNTs-Ag-TiO₂ ternary structure for enhancing visible light photocatalytic degradation of organic dye pollutant. *Mater. Chem. Phys.* **248**, 122873 (2020). <https://doi.org/10.1016/j.matchemphys.2020.122873>
55. Karpuraranjith, M., Chen, Y., Wang, X., Bo, Yu., Rajaboopathi, S., Yang, D.: Hexagonal SnSe nanoplate supported SnO₂-CNTs nanoarchitecture for enhanced photocatalytic degradation under visible light driven. *Appl. Surf. Sci.* **507**, 145026 (2020). <https://doi.org/10.1016/j.apsusc.2019.145026>
56. Saleh, T.A., Agarwal, S., Gupta, V.K.: Synthesis of MWCNT/MnO₂ and their application for simultaneous oxidation of arsenite and sorption of arsenate. *Appl. Catal. B Environ.* **106**, 46–53 (2011). <https://doi.org/10.1016/j.apcatb.2011.05.003>
57. Addo Ntim, S., Mitra, S.: Removal of trace arsenic to meet drinking water standards using iron oxide coated multiwall carbon nanotubes. *J. Chem. Eng. Data* **56**, 2077–2083 (2011). <https://doi.org/10.1021/je1010664>
58. Ramamurthy, S.S., Chen, Y., Kalyan, M.K., Rao, G.N., Chelli, J., Mitra, S.: Carbon nanotube-zirconium dioxide hybrid for defluorination of water. *J. Nanosci. Nanotechnol.* **11**, 3552–3559 (2011). <https://doi.org/10.1166/jnn.2011.3806>
59. Yan, L., Chang, P.R., Zheng, P., Ma, X.: Characterization of magnetic guar gum-grafted carbon nanotubes and the adsorption of the dyes. *Carbohydr. Polym.* **87**, 1919–1924 (2012). <https://doi.org/10.1016/j.carbpol.2011.09.086>

60. Luo, X., Wang, C., Wang, L., Deng, F., Luo, S., Tu, X., et al.: Nanocomposites of graphene oxide-hydrated zirconium oxide for simultaneous removal of As(III) and As(V) from water. *Chem. Eng. J.* **220**, 98–106 (2013). <https://doi.org/10.1016/j.cej.2013.01.017>
61. Chandra, V., Park, A., Lee, Y.W., Hwang, I.C., Kim, K.S.: Water-dispersible magnetite-reduced graphene oxide composites for arsenic removal. *ACS Nano* **4**, 3979–3986 (2010). <https://doi.org/10.1016/j.scitotenv.2019.02.376>
62. Batool, M., Nazar, M.F., Awan, A., et al.: ismuth-based heterojunction nanocomposites for photocatalysis and heavy metal detection applications. *Nano-Struct. Nano-Objects* **27**, 100762 (2021)
63. Perera, S.D., Mariano, R.G., Khiem, Vu., Nour, N., Seitz, O., Chabal, Y., Balkus, K.J.: Hydrothermal synthesis of graphene-TiO₂ nanotube composites with enhanced photocatalytic activity. *ACS Catal.* **2**(6), 949–956 (2012). <https://doi.org/10.1021/cs200621c>
64. Ruidíaz-Martínez, M., Álvarez, M.A., López-Ramón, M.V., Cruz-Quesada, G., Rivera-Utrilla, J., Sánchez-Polo, M.: Hydrothermal synthesis of rGO-TiO₂ composites as high-performance UV photocatalysts for ethylparaben degradation. *Catalysts* **10**(5), 520 (2020). <https://doi.org/10.3390/catal10050520>
65. Raja, A., Rajasekaran, P., Selvakumar, K., Arivanandhan, M., Asath Bahadur, S., Swaminathan, M.: Rational fabrication of needle with spherical shape ternary reduced Graphene Oxide-HoVO₄-TiO₂ photocatalyst for degradation of ibuprofen under visible light. *Appl. Surf. Sci.* **513**, 145803 (2020). <https://doi.org/10.1016/j.apsusc.2020.145803>
66. Zarrin, S., Heshmatpour, F.: Facile preparation of new nanohybrids for enhancing photocatalytic activity toward removal of organic dyes under visible light irradiation. *J. Phys. Chem. Solids* **140**, 109271 (2020). <https://doi.org/10.1016/j.jpcs.2019.109271>
67. Nawaz, M., Khan, A.A., Hussain, A., Jang, J., Jung, H.Y., Lee, D.S.: Reduced graphene oxide–TiO₂/sodium alginate 3-dimensional structure aerogel for enhanced photocatalytic degradation of ibuprofen and sulfamethoxazole. *Chemosphere* **261**, 127702 (2020). <https://doi.org/10.1016/j.chemosphere.2020.127702>
68. Shanavas, S., Priyadharsan, A., Gkanas, E.I., Acevedo, R., Anbarasan, P.M.: High efficient catalytic degradation of tetracycline and ibuprofen using visible light driven novel Cu/Bi₂Ti₂O₇/rGO nanocomposite: kinetics, intermediates and mechanism. *J. Ind. Eng. Chem.* **72**, 512–528 (2019). <https://doi.org/10.1016/j.jiec.2019.01.008>
69. Reheman, A., Kadeer, K., Okitsu, K., Halidan, M., Tursun, Y., Dilinuer, T., et al.: Facile photo-ultrasonic assisted reduction for preparation of rGO/Ag₂CO₃ nanocomposites with enhanced photocatalytic oxidation activity for tetracycline. *Ultrason. Sonochem.* **51**, 166–177 (2019). <https://doi.org/10.1016/j.ultsonch.2018.10.030>
70. Priyadharsan, A., Vasanthakumar, V., Shanavas, S., Karthikeyan, S., Anbarasan, P.M.: Crumpled sheet like graphene based WO₃-Fe₂O₃ nanocomposites for enhanced charge transfer and solar photocatalysts for environmental remediation. *Appl. Surf. Sci.* **470**, 114–128 (2019). <https://doi.org/10.1016/j.apsusc.2018.11.130>
71. Alafif, Z.O., Anjum, M., Ansari, M.O., Kumar, R., Rashid, J., Madkour, M., et al.: Synthesis and characterization of S-doped-rGO/ZnS nanocomposite for the photocatalytic degradation of 2-chlorophenol and disinfection of real dairy wastewater. *J. Photochem. Photobiol. A Chem.* **377**, 190–197 (2019). <https://doi.org/10.1016/j.jphotochem.2019.04.004>
72. Asgharian, M., Mehdipourghazi, M., Khoshandam, B., Keramati, N.: Photocatalytic degradation of methylene blue with synthesized rGO/ZnO/Cu. *Chem. Phys. Lett.* **719**, 1–7 (2019). <https://doi.org/10.1016/j.cplett.2019.01.037>
73. Behera, A., Kandi, D., Mansingh, S., Martha, S., Parida, K.: Facile synthesis of ZnFe₂O₄@RGO nanocomposites towards photocatalytic ciprofloxacin degradation and H₂ energy production. *J. Colloid Interface Sci.* **556**, 667–679 (2019). <https://doi.org/10.1016/j.jcis.2019.08.109>
74. Anjaneyulu, R.B., Mohan, B.S., Naidu, G.P., Muralikrishna, R.: ZrO₂/Fe₂O₃/RGO nanocomposite: good photocatalyst for dyes degradation. *Phys. E Low-Dimension. Syst. Nanostruct.* **108**, 105–111 (2019). <https://doi.org/10.1016/j.physe.2018.12.007>

75. Das, S., Mahalingam, H.: Dye degradation studies using immobilized pristine and waste polystyrene-TiO₂/rGO/g-C₃N₄ nanocomposite photocatalytic film in a novel airlift reactor under solar light. *J. Environ. Chem. Eng.* **7**, 103289 (2019). <https://doi.org/10.1016/j.jece.2019.103289>
76. Dashairya, L., Sharma, M., Basu, S., Saha, P.: SnS₂/RGO based nanocomposite for efficient photocatalytic degradation of toxic industrial dyes under visible-light irradiation. *J. Alloys Compd.* **774**, 625–636 (2019). <https://doi.org/10.1016/j.jallcom.2018.10.008>
77. Hejazi, R., Mahjoub, A.R., Cheshme Khavar, A.H., Zeynab, K.: Novel visible-light-responsive rGO-ZnO@Bi₂MoO₆ nanocomposite with enhanced light harvesting and Z-scheme charge transfer for photodegradation and detoxification of RhB. *Solid State Sci.* **95**, 105934 (2019). <https://doi.org/10.1016/j.solidstatesciences.2019.105934>
78. Hu, K., Chen, C., Zhu, Y., Zeng, G., Huang, B., Chen, W., et al.: Ternary Z-scheme hetero-junction of Bi₂WO₆ with reduced graphene oxide (rGO) and meso-tetra (4-carboxyphenyl) porphyrin (TCPP) for enhanced visible-light photocatalysis. *J. Colloid Interface Sci.* **540**, 115–125 (2019). <https://doi.org/10.1016/j.jcis.2019.01.013>
79. Khataee, A., Sadeghi Rad, T., Nikzat, S., Hassani, A., Aslan, M.H., Kobya, M., et al.: Fabrication of NiFe layered double hydroxide/reduced graphene oxide (NiFe-LDH/rGO) nanocomposite with enhanced sonophotocatalytic activity for the degradation of moxifloxacin. *Chem Eng J* **375**, 122102 (2019). <https://doi.org/10.1016/j.cej.2019.122102>
80. Lakhera, S.K., Hafeez, H.Y., Venkataramana, R., Veluswamy, P., Choi, H., Neppolian, B.: Design of a highly efficient ternary AgI/rGO/BiVO₄ nanocomposite and its direct solar light induced photocatalytic activity. *Appl. Surf. Sci.* **487**, 1289–1300 (2019). <https://doi.org/10.1016/j.apsusc.2019.05.201>
81. Liu, F., Che, Y., Chai, Q., Zhao, M., Lv, Y., Sun, H., et al.: Construction of rGO wrapping Cu₂O/ZnO heterostructure photocatalyst for PNP and PAM degradation. *Environ. Sci. Pollut. Res.* **26**, 25286–25300 (2019). <https://doi.org/10.1007/s11356-019-05814-7>
82. Malefane, M.E., Ntsendwana, B., Mafa, P.J., Mabuba, N., Feleni, U., Kuvarega, A.T.: In-situ synthesis of tetraphenylporphyrin/tungsten (VI) oxide/reduced graphene oxide (TPP/WO₃/RGO) nanocomposite for visible light photocatalytic degradation of acid blue 25. *ChemistrySelect* **4**, 8379–8389 (2019). <https://doi.org/10.1002/slct.201901589>
83. Prabhu, S., Megala, S., Harish, S., Navaneethan, M., Maadeswaran, P., Sohila, S., et al.: Enhanced photocatalytic activities of ZnO dumbbell/reduced graphene oxide nanocomposites for degradation of organic pollutants via efficient charge separation pathway. *Appl. Surf. Sci.* **487**, 1279–1288 (2019). <https://doi.org/10.1016/j.apsusc.2019.05.086>
84. Rehman, G.U., Tahir, M., Goh, P.S., Ismail, A.F., Khan, I.U.: Controlled synthesis of reduced graphene oxide supported magnetically separable Fe₃O₄@rGO@AgI ternary nanocomposite for enhanced photocatalytic degradation of phenol. *Powder Technol.* **356**, 547–558 (2019). <https://doi.org/10.1016/j.powtec.2019.08.026>
85. Nayak, S., Parida, K.M.: Deciphering Z-scheme charge transfer dynamics in heterostructure NiFe-LDH/N-rGO/g-C₃N₄ nanocomposite for photocatalytic pollutant removal and water splitting reactions. *Sci. Rep.* **9**, 1–23 (2019). <https://doi.org/10.1038/s41598-019-39009-4>
86. Samadi, S., Khalili, E., Allahgholi Ghasri, M.R.: Degradation of methyl red under visible light using N, F-TiO₂/SiO₂/rGO nanocomposite. *J. Electron. Mater.* **48**, 7836–7845 (2019). <https://doi.org/10.1007/s11664-019-07585-w>
87. Vinesh, V., Shaheer, A.R.M., Neppolian, B.: Reduced graphene oxide (rGO) supported electron deficient B-doped TiO₂ (Au/B-TiO₂/rGO) nanocomposite: an efficient visible light sonophotocatalyst for the degradation of Tetracycline (TC). *Ultrason. Sonochem.* **50**, 302–310 (2019). <https://doi.org/10.1016/j.ultsonch.2018.09.030>
88. Wei, Y., Liang, J., Yao, Y., Xu, X., Zheng, X., He, G., et al.: Synthesis of visible light-driven graphene based ZnFe mixed metal oxide for efficient degradation of tetracycline. *J. Mater. Sci. Mater. Electron.* **30**, 8931–8943 (2019). <https://doi.org/10.1007/s10854-019-01221-3>
89. Xu, L., Yang, L., Bai, X., Du, X., Wang, Y., Jin, P.: Persulfate activation towards organic decomposition and Cr(VI)reduction achieved by a novel QDs-TiO₂-x/rGO nanocomposite. *Chem. Eng. J.* **373**, 238–250 (2019). <https://doi.org/10.1016/j.cej.2019.05.028>

90. Zhang, Q., Han, F., Yan, Y., Dai, Q., Proctor, G., Cheah, P., et al.: Preparation and properties of visible light responsive RGO/In₂TiO₅ nanobelts for photocatalytic degradation of organic pollutants. *Appl. Surf. Sci.* **485**, 547–553 (2019). <https://doi.org/10.1016/j.apsusc.2019.04.185>
91. Zhang, J., Wang, Z., Fan, M., Tong, P., Sun, J., Dong, S., et al.: Ultra-light and compressible 3D BiOCl/RGO aerogel with enriched synergistic effect of adsorption and photocatalytic degradation of oxytetracycline. *J. Mater. Res. Technol.* **8**, 4577–4587 (2019). <https://doi.org/10.1016/j.jmrt.2019.08.002>
92. Mansingh, S., Padhi, D.K., Parida, K.: Bio-surfactant assisted solvothermal synthesis of Magnetic retrievable Fe₃O₄@rGO nanocomposite for photocatalytic reduction of 2-nitrophenol and degradation of TCH under visible light illumination. *Appl. Surf. Sci.* **466**, 679–690 (2019). <https://doi.org/10.1016/j.apsusc.2018.10.056>
93. Gnanamoorthy, G., Yadav, V.K., Latha, D., Karthikeyan, V., Narayanan, V.: Enhanced photocatalytic performance of ZnSnO₃/rGO nanocomposite. *Chem. Phys. Lett.* **739**, 137050 (2020). <https://doi.org/10.1016/j.cplett.2019.137050>
94. Arya, M., Kaur, M., Kaur, A., Singh, S., Devi, P., Kansal, S.K.: Hydrothermal synthesis of rGO-Bi₂WO₆ heterostructure for the photocatalytic degradation of levofloxacin. *Opt. Mater. (Amst)* **107**, 110126 (2020). <https://doi.org/10.1016/j.optmat.2020.110126>
95. Botsa, S.M., Naidu, G.P., Ravichandra, M., Rani, S.J., Anjaneyulu, R.B., Ramana, C.V.: Flower like SnO₂-Fe₂O₃-rGO ternary composite as highly efficient visible light induced photocatalyst for the degradation of organic pollutants from contaminated water. *J. Mater. Res. Technol.* **9**, 12461–12472 (2020). <https://doi.org/10.1016/j.jmrt.2020.08.087>
96. Tahir, M.B., Ghulam Nabi, M., Rafique, N.R.K.: Role of fullerene to improve the WO₃ performance for photocatalytic applications and hydrogen evolution. *Int. J. Energy Res.* **42**(15), 4783–4789 (2018). <https://doi.org/10.1002/er.4231>
97. Song, T., Zhang, P., Zeng, J., Wang, T., Ali, A., Zeng, H.: Boosting the photocatalytic H₂ evolution activity of Fe₂O₃ polymorphs (α-, γ- And β-Fe₂O₃) by fullerene [C₆₀]-modification and dye-sensitization under visible light irradiation. *RSC Adv* **7**, 29184–29192 (2017). <https://doi.org/10.1039/c7ra03451b>
98. Lian, Z., Xu, P., Wang, W., Zhang, D., Xiao, S., Li, X., et al.: C₆₀-decorated CdS/TiO₂ mesoporous architectures with enhanced photostability and photocatalytic activity for H₂ evolution. *ACS Appl. Mater. Interfaces* **7**, 4533–4540 (2015). <https://doi.org/10.1021/am5088665>
99. Dai, Ke., Zhang, X., Fan, Ke., Zeng, P., Peng, T.: Multiwalled carbon nanotube-TiO₂ nanocomposite for visible-light-induced photocatalytic hydrogen evolution. *J. Nanomater.* **2014**, 1–8 (2014). <https://doi.org/10.1155/2014/694073>
100. Li, D.J., Maiti, U.N., Lim, J., Choi, D.S., Lee, W.J., Oh, Y., et al.: Molybdenum sulfide/N-doped CNT forest hybrid catalysts for high-performance hydrogen evolution reaction. *Nano Lett.* **14**, 1228–1233 (2014). <https://doi.org/10.1021/nl404108a>
101. Bose, R., Patil, B., Rajendiran Jothi, V., Kim, T.H., Arunkumar, P., Ahn, H., et al.: Co₃Se₄ nanosheets embedded on N-CNT as an efficient electroactive material for hydrogen evolution and supercapacitor applications. *J. Ind. Eng. Chem.* **65**, 62–71 (2018). <https://doi.org/10.1016/j.jiec.2018.04.013>
102. Wang, D.Y., Gong, M., Chou, H.L., Pan, C.J., Chen, H.A., Wu, Y., et al.: Highly active and stable hybrid catalyst of cobalt-doped FeS₂ nanosheets-carbon nanotubes for hydrogen evolution reaction. *J Am Chem Soc* **137**, 1587–1592 (2015). <https://doi.org/10.1021/ja511572q>
103. Kim, S., Lim, Y., Kang, T.H., Moon, J., Choi, I.S., Lee, Y.J., et al.: Biotemplated nanocomposites of transition-metal oxides/carbon nanotubes with highly stable and efficient electrochemical interfaces for high-power lithium-ion batteries. *ACS Appl. Energy Mater.* **3**, 7804–7812 (2020). <https://doi.org/10.1021/acsaem.0c01208>
104. Qiu, Y., Wu, X., Wang, M., Fan, L., Tian, D., Guan, B., et al.: 3D Hierarchical CNT-based host with high sulfur loading for lithium-sulfur batteries. *ChemElectroChem* **6**, 5698–5704 (2019). <https://doi.org/10.1002/celec.201901609>

105. Yue, Z., Zhen, X., Ai, J., Shi, Q., Mao, T., Zhen, M., et al.: Three-dimensional mesoporous nanocube TiO₂/reduced graphene oxide composites with enhanced lithium storage properties. *J. Renew. Sustain. Energy* **12**, 044101 (2020). <https://doi.org/10.1063/5.0013254>
106. Muhammad, N., et al.: Volumetric buffering of manganese dioxide nanotubes by employing 'as is' graphene oxide: An approach towards stable metal oxide anode material in lithium-ion batteries. *J. Alloys Compd.* **842**, 155803 (2020). <https://doi.org/10.1016/j.jallcom.2020.155803>
107. Lu, S.J., Wang, Z.T., Zhang, X.H., He, Z.J., Tong, H., Li, Y.J., et al.: In situ-formed hollow cobalt sulfide wrapped by reduced graphene oxide as an anode for high-performance lithium-ion batteries. *ACS Appl. Mater. Interfaces* **12**, 2671–2678 (2020). <https://doi.org/10.1021/acsami.9b18931>
108. Guo, L., Ren, L., Wan, L., Li, J.: Heterogeneous carbon/N-doped reduced graphene oxide wrapping LiMn_{0.8}Fe_{0.2}PO₄ composite for higher performance of lithium ion batteries. *Appl. Surf. Sci.* **476**, 513–520 (2019). <https://doi.org/10.1016/j.apsusc.2018.12.227>
109. Guan, Y., Shen, J., Wei, X., Zhu, Q., Zheng, X., Zhou, S., et al.: High-rate performance of a three-dimensional LiFePO₄/graphene composite as cathode material for Li-ion batteries. *Appl. Surf. Sci.* **481**, 1459–1465 (2019). <https://doi.org/10.1016/j.apsusc.2019.03.213>
110. Cui, F., Zhao, J., Zhang, D., Fang, Y., Hu, F., Zhu, K.: VO₂(B) nanobelts and reduced graphene oxides composites as cathode materials for low-cost rechargeable aqueous zinc ion batteries. *Chem. Eng. J.* **390**, 124118 (2020). <https://doi.org/10.1016/j.cej.2020.124118>
111. Chen, L., Yang, Z., Qin, H., Zeng, X., Meng, J., Chen, H.: Graphene-wrapped hollow ZnMn₂O₄ microspheres for high-performance cathode materials of aqueous zinc ion batteries. *Electrochim. Acta* **317**, 155–163 (2019). <https://doi.org/10.1016/j.electacta.2019.05.147>
112. Akilimali, R., Selopal, G.S., Benetti, D., Mohammadnezhad, M., Zhao, H., Wang, Z.M., et al.: Graphene nanoribbon-TiO₂-quantum dots hybrid photoanode to boost the performance of photoelectrochemical for hydrogen generation. *Catal. Today* **340**, 161–169 (2020). <https://doi.org/10.1016/j.cattod.2018.10.052>
113. Ma, J., Dai, J., Duan, Y., Zhang, J., Qiang, L., Xue, J.: Fabrication of PANI-TiO₂/rGO hybrid composites for enhanced photocatalysis of pollutant removal and hydrogen production. *Renew. Energy* **156**, 1008–1018 (2020). <https://doi.org/10.1016/j.renene.2020.04.104>
114. Corredor, J., Perez-Peña, E., Rivero, M.J., Ortiz, I.: Performance of rGO/TiO₂ photocatalytic membranes for hydrogen production. *Membranes (Basel)* **10**, 1–13 (2020). <https://doi.org/10.3390/membranes10090218>
115. Babu, J., et al.: Carbon-based TiO₂-x heterostructure nanocomposites for enhanced photocatalytic degradation of dye molecules. *Ceram. Int.* **47**(7), 10314–10321 (2021). <https://doi.org/10.1016/j.ceramint.2020.12.014>
116. Murthy, M.S., et al.: Cocatalyst free nickel sulphide nanostructure for enhanced photocatalytic hydrogen evolution. *Int. J. Hydrog. Energy* **47**(8), 5307–5318 (2022). <https://doi.org/10.1016/j.ijhydene.2021.11.171>
117. Chitranu, C., et al.: Silver nanoparticles anchored TiO₂ nanotubes prepared using saponin extract as heterogeneous and recyclable catalysts for reduction of dyes. *Ceram. Int.* **47**(10), 14750–14759 (2021). <https://doi.org/10.1016/j.ceramint.2020.11.173>
118. Prasanna, D., et al.: Magnetic substrate supported ZnO-CuO nanocomposite as reusable photo catalyst for the degradation of organic dye. *Mater. Today: Proc.* **4**(11), 12314–12320 (2017). <https://doi.org/10.1016/j.matpr.2017.09.165>
119. Mahesh, S.M., et al.: Reduced graphene oxide wrapped sulfur nanocomposite as cathode material for lithium sulfur battery. *Ceram. Int.* **47**(10), 14790–14797 (2021). <https://doi.org/10.1016/j.ceramint.2020.10.215>
120. Ravi, M.C., et al.: Copper zinc tin sulfide and multi-walled carbon nanotubes nanocomposite for visible-light-driven photocatalytic applications. *Mater. Res. Bull.* **146**, 111606 (2022). <https://doi.org/10.1016/j.materresbull.2021.111606>
121. Manjunath, S.C., et al.: One-pot supercritical water synthesis of Bi₂MoO₆-RGO 2D heterostructure as anodes for Li-ion batteries. *Ceram. Int.* **47**(7), 10274–10283 (2021). <https://doi.org/10.1016/j.ceramint.2020.12.061>

A Novel Synthesis of Gold Nanoparticles-Layered Double Hydroxides Nanocomposites Through *In-situ* Reductive Adsorption of Gold(III) Ion on Organic Acid-Functionalized Mg/Al Layered Double Hydroxides



Sri Juari Santosa, Philip Anggo Krisbiantoro, Rahma Hidaiyanti, Afini Muawanah, Ria Afifah Almas, Nur Raisah Maddeppungeng, Mike Rahayu, Sri Sudiono, Nuryono, and Sutarno

Abstract Owing to their favorable physical, chemical and optical properties, gold nanoparticles (AuNPs) are one of the most intensively studied and applied nanoparticles (NPs) in the modern era. However, the application of bare AuNPs is subject to aggregation and agglomeration, which reduce their function and performance. Solid support, which may be used as a host to facilitate a uniform growth and well-dispersion of AuNPs without covering their surface should be beneficial to prevent this drawback. Here, we compiled research activities dealing with reductive adsorption of Au(III) ion on organic acid-functionalized Mg/Al layered double hydroxides (Mg/Al LDHs) as a novel synthesis method for AuNPs-LDHs nanocomposites. Organic acids employed to functionalize Mg/Al LDHs are organic acids capable of reducing Au(III) ion to metallic Au. Due to the still very few studies on this novel method, the organic acids employed to functionalize Mg/Al LDHs were limited to ascorbic (AA), gallic (GA) and salicylic (SA) acids. In this chapter, a detailed overview of the synthesis methods, characterizations and properties of the composites was given. Furthermore, the mechanism of the functionalization of

S. J. Santosa (✉) · R. Hidaiyanti · A. Muawanah · R. A. Almas · N. R. Maddeppungeng · S. Sudiono · Nuryono · Sutarno

Department of Chemistry, Faculty of Mathematics and Natural Sciences, Universitas Gadjah Mada, Bulaksumur, Yogyakarta 55281, Indonesia
e-mail: sjuari@ugm.ac.id

P. A. Krisbiantoro

International Graduate Program of Molecular Science and Technology (NTU-MST), National Taiwan University, Taipei 10617, Taiwan

Molecular Science and Technology, Taiwan International Graduate Program, Academia Sinica, Taipei 11529, Taiwan

M. Rahayu

Department of Chemistry Education, Faculty of Education and Teacher Training, IAIN Tulungagung, Tulungagung, East Java 66221, Indonesia

© The Author(s), under exclusive license to Springer Nature Switzerland AG 2022

A. E. Shalan et al. (eds.), *Advances in Nanocomposite Materials for Environmental and Energy Harvesting Applications*, Engineering Materials,
https://doi.org/10.1007/978-3-030-94319-6_4

Mg/Al LDHs and that of reductive adsorption of Au(III) ion on the functionalized Mg/Al LDHs was critically elucidated. While the usage possibility of waste electric and electronic equipment (WEEE) as sources of Au(III) ion in the preparation of AuNPs-Mg/Al LDHs nanocomposites was considered, the potency of the method to produce stable AuNPs-Mg/Al LDHs nanocomposites for a variety of applications was also discussed.

Keywords Reductive adsorption · Mg/Al layered double hydroxides · Gold nanoparticles · Ascorbic acid · Gallic acid · Salicylic acid

Abbreviations

AA	Ascorbic acid
AuNPs	Gold nanoparticles
AuNPs-Mg/Al LDHs	Gold nanoparticles Mg/Al layered double hydroxides
<i>b</i>	Adsorption capacity (mol g^{-1})
FTIR	Fourier transform infra-red
GA	Gallic acid
GluA	Glutamic acid
k_{2p}	Pseudo-second order adsorption rate constant ($\text{g mol}^{-1} \text{min}^{-1}$)
LDH	Layered double hydroxide
Mg/Al LDH	Mg/Al layered double hydroxides
Mg/Al LDH-AA	Ascorbic acid-functionalized Mg/Al layered double hydroxides
Mg/Al LDH-GA	Gallic acid-functionalized Mg/Al layered double hydroxides
Mg/Al LDH-SA	Salicylic acid-functionalized Mg/Al layered double hydroxides
MO _x s	Metal oxides
NPs	Nanoparticles
PANI	Polyaniline
PCB	Print circuit board
pK_{a1}	The first acid dissociation constant
SA	Salicylic acid
TA	Tartaric acid
TEM	Transmission electron microscopy
VOC	Volatile organic compound
WEEE	Waste electrical and electronic equipment
XPS	X-ray photoelectron microscopy
XRD	X-ray diffraction
ΔH°	Standard enthalpy of adsorption

1 Introduction

It is apparent that engineered NPs are the major reason for the recent advances in nanotechnology. By definition, NPs are a class of materials, including particulate substances, with particle sizes less than 100 nm, while nanotechnology is any design, method or technology that produces the NPs [1, 2]. In terms of application, NPs have reached the core of many fields; from drug delivery to cancer imaging and therapy, from the development of pollution sensors to the engineering of ultra-active catalysts or photocatalysts and adsorbents, and from battery to energy-harvesting solar-cell. Among NPs, AuNPs are one of the most widely studied and utilized due to their intrinsic physical, chemical and optical features that can be changed by altering their shape, size, aspect ratio and environment [3]. In terms of stability, AuNPs are stable against oxidation and degradation *in vivo*, enabling them to be used as potential theranostic tools.

Procedures for the synthesis of AuNPs are generally divided into chemical, physical and biological methods. Among them, the chemical method, which is a technique in which AuNPs are prepared through a chemical reaction with a reducing agent in an aqueous solution, is favorable due to the ease of synthesis, controllable size and high colloidal stability of AuNPs [3, 4]. So far, the pioneer Turkevich method is the intensively utilized one [5, 6]. This method employs citrate anion to reduce Au(III) ion into colloidal AuNPs. Later, this method was refined by Frens [7, 8]. Afterward, many organic acids were studied as reducing agents for AuNPs, including AA [9], GA [10], glutamic acid (GluA) [11], SA [12] and tartaric acid (TA) [13]. However, colloidal AuNPs from chemical synthesis with organic acids are still subject to aggregation and agglomeration which indeed reduce their function and performance. To prevent this drawback, a solid support that can be used as a host to facilitate uniform growth and well-dispersion of AuNPs is indispensable.

Support materials that can be used for AuNPs are including metal oxides (MOx) [14, 15], carbonaceous [16] and siliceous materials [17] and organic compounds such as cellulose [18] and polyaniline (PANI) [19]. Among them, MOx are the most popular ones owing to their easy preparation, stability and ability to alter the properties of AuNPs. LDHs as a class of layered materials with a general formula of $[M_{1-x}^{II}M_x^{III}(\text{OH})_2]^{x+}(\text{A}_{x/n}^{n-}) \cdot m\text{H}_2\text{O}$, where M^{II} and M^{III} are divalent and trivalent metal ions, respectively, while x is the ratio of M^{II} to $(M^{II} + M^{III})$ [20, 21], has been used intensively to support AuNPs. Unlike other MOx, LDHs possessed a shape memory effect, large surface area, excellent ion exchange capacities, low toxicity, ability to intercalate various anions and easily synthesized with various metal cation types and compositions [22, 23]. Therefore, the use of LDHs as supports for AuNPs is highly advantageous from the standpoint of green chemistry.

In this chapter, we describe the recent activities on the synthesis of AuNPs by using organic acid-functionalized Mg/Al LDHs as a novel synthesis method for AuNPs-LDHs nanocomposites. Because the study on this matter is still very few, the organic acids used to functionalize Mg/Al LDH are limited to AA, GA and SA, summarized from our published works with the addition of unpublished works of the students in

our research group [24, 25]. While a detailed summary on the synthesis methods, characterizations and properties of the composites was given, the mechanism of the functionalization of Mg/Al LDH and that of reductive adsorption of Au(III) ion on the organic acid-functionalized Mg/Al LDHs was also critically elucidated. The usage possibility of WEEE as a source of Au(III) ion in the preparation of AuNPs-Mg/Al LDHs nanocomposites was also considered. Moreover, the potency of the method to make stable AuNPs-Mg/Al LDHs nanocomposites for a variety of applications was also discussed.

2 Synthesis of AA-, GA- and SA-Functionalized Mg/Al LDHs

So far, the functionalization of organic acids on Mg/Al LDH in our studies has been done by a simple adsorption technique under pre-determined optimum conditions, while pure Mg/Al LDH was prepared through the conventional co-precipitation method. For the preparation of Mg/Al LDH, the molar ratio of Mg:Al = 2:1 is indispensable to obtain layered structure material with chemical formula close to that general formula of LDH [26]. In general, the preparation of Mg/Al LDH was done according to the following procedure. Firstly, the salts of Mg^{2+} (0.1 mol) and Al^{3+} (0.05 mol) were dissolved into a certain volume of CO_2 -free pure water and the mixture was vigorously stirred under N_2 atmosphere. Into the mixture, a precipitating agent (NaOH or $NH_3 \cdot H_2O$) was added dropwise until the pH of the reaction solution reached pH 10-11 to initiate the co-precipitation process. During this process, N_2 gas was constantly flowed to prevent the formation of interlayer CO_3^{2-} ion from free CO_2 which later may affect the adsorption process of organic acids [27]. Afterward, the formed solid was washed CO_2 -free pure water to neutral pH, heated hydrothermally at 120 °C for 5 h and followed by separation and mild temperature drying to obtain Mg/Al LDH. We reported that from the above method, Mg/Al LDH with the chemical formula of $Mg_{0.75}Al_{0.25}(OH)_2(NO_3)_{0.25} \cdot 0.32H_2O$ was obtained [26].

After Mg/Al LDH was obtained, AA, GA and SA were immobilized on Mg/Al LDH through an adsorption process at room temperature. In the process, the medium acidity of the reaction solution plays a key role in maximizing the amount of adsorbed AA, GA and SA since the surface charges of Mg/Al LDH and the chemical form of these organic acids are pH-dependent. Figure 1 demonstrates the effect of the reaction solution pH on the amount of immobilized AA, GA and SA on Mg/Al LDH [24, 26]. The immobilization processes of these organic acids were apparently optimum under weakly acidic condition, i.e., pH 5. It is understandable that, at such condition, the edge Mg-OH and Al-OH on the surface of Mg/Al LDH are protonated (Eqs. 1–2), and thus they can interact with the deprotonated vinyllic -OH of AA and the carboxyl group of GA or SA through hydrogen bonding (Fig. 2). It must be noted that AA, GA and SA possessed low values of pK_{a1} , e.g., 4.1 [28], 4.4 [29] and 3.0 [30], respectively, making them readily deprotonated even under

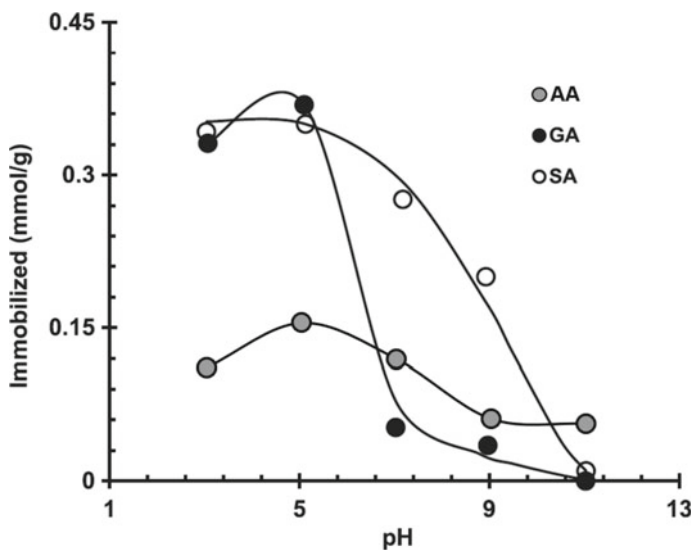
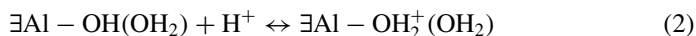
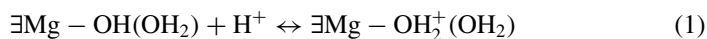


Fig. 1 Effect of pH on the immobilization of AA, GA and SA on Mg/Al LDH (the picture was edited with permission from [26], while AA was obtained from [24])

weakly acidic condition to form mono deprotonated species. Under strongly acidic condition, AA, GA, SA and Mg/Al LDH are highly protonated. Consequently, the repulsive interaction between AA, GA or SA and Mg/Al LDH is occurred and leads to a decrease in the immobilization amount of the organic acid. Meanwhile, under basic condition, the competition between OH^- in the reaction solution and mono deprotonated adsorbate is severe. So far, this is the most plausible reason for such a very low amount of immobilized AA, GA and SA on Mg/Al LDH at $\text{pH} > 5$ (Fig. 1). Moreover, since the vinylic $-\text{OH}$ of AA and carboxyl group of GA or SA are the responsible functional groups for the binding with Mg/Al LDH, the only active functional group available for the adsorption of Au(III) ion is the aliphatic $-\text{OH}$ on Mg/Al LDH-AA and phenolic $-\text{OH}$ on Mg/Al LDH-GA and Mg/Al LDH-SA.



3 Characterization of the Composites

To confirm that Mg/Al LDH and organic acid-functionalized Mg/Al LDH composites were successfully synthesized, two basic characterizations, e.g., Fourier transform

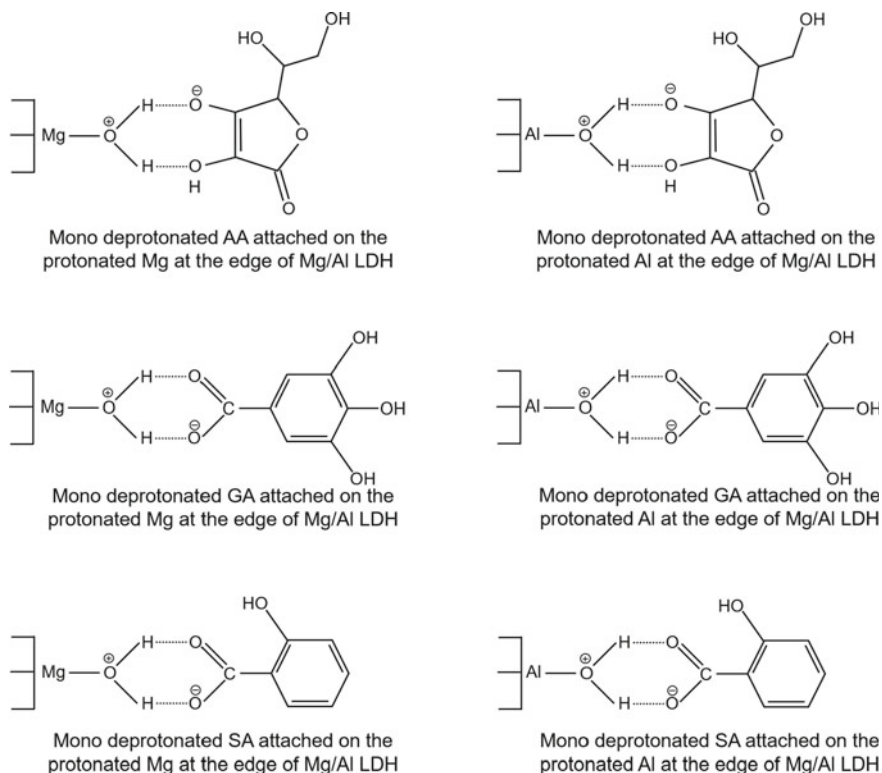


Fig. 2 Schematic illustration of the functionalization of AA, GA and SA on the Mg and Al metal ions at the edge of Mg/Al LDH under weakly acidic condition (for GA and SA, the illustration was adapted with permission from [26])

infra-red (FTIR) and X-ray diffraction (XRD) spectrometer, were performed. Here, we summarized the characterization results of Mg/Al LDH-AA, Mg/Al LDH-GA and Mg/Al LDH-SA from our recently published works as well as the unpublished works of the students in our research group [24, 25].

From FTIR spectra, a common indication that Mg/Al LDH has been successfully synthesized is the appearance of an absorption band due to interlayer anionic species, i.e., NO_3^- or CO_3^{2-} ion. For NO_3^- -intercalated Mg/Al LDH, the presence of interlayer NO_3^- ion is indicated by the appearance of a sharp peak at 1380 cm^{-1} , which is the absorption band of the antisymmetric stretching N–O vibration of free NO_3^- ion. It is also supported by the appearance of N = O stretching vibration at 670 cm^{-1} [26, 31–33]. Meanwhile, for CO_3^{2-} -intercalated Mg/Al LDH, C–O can be found at wavenumber 1334 cm^{-1} [34]. After the functionalization process with organic acids, generally, only a small modification is observed. For instance, on Mg/Al LDH-AA, only two absorption bands at 2931 and 1049 cm^{-1} ascribed to the stretching vibration of C–H (sp^3) and bending C–O, respectively, were observed in addition to the main absorption bands of Mg/Al LDH [32]. On the other hand, for Mg/Al LDH-GA and

Table 1 Basal spacing of Mg/Al LDH before and after functionalization with AA, GA and SA

Plane	d/Å		
	Mg/Al LDH/Mg/Al LDH-AA [32]	Mg/Al LDH/Mg/Al LDH-GA [33]	Mg/Al LDH/Mg/Al LDH-SA [25]
003	8.14/8.23	8.67/8.48	8.08/7.96
006	4.01/3.98	4.44/3.97	3.97/3.88
009	2.58/2.61	2.60/2.61	2.59

Mg/Al LDH-SA, three absorption bands at 2930, 1470 and 1265 cm^{-1} corresponded to stretching vibration of C–H, aromatic C = C and C–O, respectively, were appeared [26, 33]. Since Mg/Al LDH is a layered structure material with no moieties other than surface hydroxyl, those peaks observed after the functionalization process were true should be contributed by functionalized AA, GA or SA.

From XRD spectra, the layered structure of Mg/Al LDH can be verified by the appearances of typical (003), (006) and (009) diffraction lines [24–26, 31–33]. After functionalization with organic acids, those diffraction lines are generally broadened and the intensities are significantly decreased. This indicates that the functionalization with organic acids may decrease the crystallinity of the layered structure. Moreover, no increase or no significant increase in the interlayer spacing of Mg/Al LDH after the functionalization process with AA [24, 31, 32], GA [26, 33] and SA [25, 26] (Table 1) imply that these organic acids are interacted dominantly on the outer layer of the layered structure of Mg/Al LDH through hydrogen bonding on their mono deprotonated forms as illustrated in Fig. 2.

4 Reductive Adsorption of Au(III) Ion by AA-, GA- and SA-Functionalized Mg/Al LDHs

Reductive adsorption is an adsorption process of an adsorbate followed by the reduction of adsorbed species on the surface of an adsorbent. In terms of reductive adsorption of Au(III) ion by using Mg/Al LDH-AA, Mg/Al LDH-GA and Mg/Al LDH-SA, we have published several papers [26, 31–33]. In this section, the effect of initial pH, adsorption kinetics and adsorption isotherms as well as thermodynamic study are briefly discussed.

4.1 Effect of Initial pH

In the present study, medium acidity is an important parameter since it affects the form of the functional group of AA, GA and SA on the surface of Mg/Al LDH as well as the speciation of Au(III) ion in the reaction solution. It was revealed that

the adsorption of Au(III) ion on those adsorbents was increased with the increase of the medium acidity, in which pH 3 was found to be the optimum condition for all reactions at room temperature. The experiment at pH lower than that value should be avoided since Mg/Al LDH is a basic material that is readily dissolved into the reaction solution under strongly acidic conditions [35]. By considering the previously mentioned assumption in Sect. 2 that the aliphatic $-OH$ of AA and phenolic $-OH$ of GA and SA on Mg/Al LDH are the functional groups left available for adsorption, the effect of pH on the adsorption of Au(III) ion can be described as follows. Under acidic condition, the aliphatic $-OH$ of AA and phenolic $-OH$ of GA and SA on the surface of Mg/Al LDH remain un-deprotonated. At such condition, the gold ion in the reaction solution predominantly exists as Au(III) ion. The interaction between Au(III) ion and the un-deprotonated $-OH$ group is further established through a hydrogen bonding between acidic H on $-OH$ group and electronegative Cl on Au(III) ion. The adsorption of Au(III) ion on humin [36] and humic acid [37], which were governed by the hydrogen bonding, has been shown to be similar. When the pH of reaction solution increases from strong to weakly acidic condition, the deprotonation of adsorbents also increases. As a result, the total amount of adsorbed Au(III) ion decreases due to the repulsive interaction between $AuCl_4^-$ and the deprotonated functional groups of organic acids on Mg/Al LDH. In addition, the increase of reaction pH also leads to the substitution of Cl^- from $AuCl_4^-$ to form $AuCl_{4-x}(OH)_x^-$ complex. This substitution reaction with hydroxyl anion increases the inclination of the complex to remain in the reaction solution due to the strong hydrogen bond with water molecules [38]. Under weakly acidic condition, for instance at pH 5, this substitution effect may not be severe since, according to Usher et al. [39], gold ion at such pH exist predominantly as $AuCl_4^-$ and $AuCl_3(OH)^-$. However, under basic condition ($pH > 7$), $Au(OH)_4^-$ is predominant, and thus it should strongly contribute to the decrease of the adsorbed amount of gold ion in addition to the strong repulsive interaction between the complex and negatively charged adsorbent. These two factors are the most plausible reason to explain such low adsorption on Mg/Al LDH-AA, Mg/Al LDH-GA and Mg/Al LDH-SA under basic condition.

4.2 Adsorption Kinetics

The effect of the contact time on the adsorption of Au(III) ion on Mg/Al LDH-AA, Mg/Al LDH-GA and Mg/Al LDH-SA was examined in order to determine the kinetic parameters of the process. Interestingly, the adsorption process on Mg/Al LDH-GA and Mg/Al LDH-SA reached equilibrium at 120 min [26], despite GA showing a higher amount of adsorbed Au(III) ion under all given times than SA. The equilibrium time by using Mg/Al LDH-AA, on the other hand, was reached at 300 min ([24]). We tested three different kinetic models for the process, e.g., pseudo-first-order, pseudo-second-order and second-order by Lagergren [40], Ho and McKay [41] and Santosa [42]. It was observed that the adsorption process on those adsorbents were all followed pseudo-second order with pseudo-second order adsorption rate constant

Table 2 Kinetic and isotherm parameters for the adsorption of Au(III) ion on AA-, GA and SA-functionalized Mg/Al LDH at room temperature

Adsorbent	$k_{2p} \times 10^4$	$b \times 10^{-4}$	Ref.
Mg/Al LDH	23.13	0.38	[26]
Mg/Al LDH-AA	7.79	1.06	[24]
Mg/Al LDH-GA	0.06	3.10	[26]
Mg/Al LDH-SA	4.74	2.08	[26]

(k_{2p}) was in the range 0.06 to $23.13 \times 10^4 \text{ mg mol}^{-1} \text{ min}^{-1}$ (Table 2). This may imply that the adsorption of Au(III) on Mg/Al LDH-AA, Mg/Al LDH-GA and Mg/Al LDH-SA is prone to chemisorption and that the number of active adsorbent sites, as well as the concentration of Au(III) ion, might be the two parameters govern the adsorption process.

The unit of k_{2p} written in Table 2 is $\text{g mol}^{-1} \text{ min}^{-1}$ or can be converted to $\text{min}^{-1} (\text{mol/g})^{-1}$. It means the higher k_{2p} value the slower Au(III) ion adsorbed to the adsorbent every minute. Accordingly, the adsorption of Au(III) ion on Mg/Al LDH-GA was the fastest and then followed by that on Mg/Al LDH-SA, Mg/Al LDH-AA and Mg/Al LDH, respectively. The ability of Mg/Al LDH-GA and Mg/Al LDH-SA to adsorb Au(III) ion faster than Mg/Al LDH-AA has been indicated above, in which the adsorption of Au(III) ion on Mg/Al LDH-GA and Mg/Al LDH-SA reached equilibrium at 120 min, while that on Mg/Al LDH-AA at 300 min.

4.3 Adsorption Isotherms

Two classic adsorption isotherms models, e.g., Langmuir and Freundlich, were used to evaluate the surface behavior of each adsorbent as well as their capacity in adsorbing Au(III) ion. Again, all adsorbents showed similar behavior at room temperature, in which they followed the Langmuir isotherm model with parameters obtained from the model are shown in Table 2. The suitability of the effect of concentration data to the Langmuir isotherm model means that the coverage of Au(III) ion on Mg/Al LDH-AA, Mg/Al LDH-GA and Mg/Al LDH-SA is monolayer owing to the homogeneously distributed active sites of the adsorbents, i.e., aliphatic $-\text{OH}$ on Mg/Al LDH-AA and phenolic $-\text{OH}$ on Mg/Al LDH-GA and Mg/Al LDH-SA. These results support the previous assumption illustrated in Fig. 2 that those functional groups are the only available active site for the adsorption of Au(III) ion. In terms of adsorption capacity, as summarized in Table 2, Mg/Al LDH-GA showed the highest capacity ($3.10 \times 10^{-4} \text{ mol g}^{-1}$) or 2.9 and 1.5 times higher than that of Mg/Al LDH-AA and Mg/Al LDH-SA, respectively. This suggests that for the adsorption of Au(III) ion, GA is the best organic acid to be immobilized on Mg/Al LDH. This is presumably because GA possessed more free $-\text{OH}$ group than that of AA and SA (Fig. 2).

4.4 Thermodynamic Study

In this section, the discussion will be focused on Mg/Al LDH, Mg/Al LDH-GA and Mg/Al LDH-SA since the thermodynamic study on Mg/Al LDH-AA has not yet been performed. As described in our recently published paper [26], it has been observed that the adsorption of Au(III) ion to Mg/Al LDH-GA and Mg/Al LDH-SA was decreased with the increasing temperature. This strongly indicates that the adsorption process of Au(III) ion on both adsorbents is an exothermic process. In fact, the estimated enthalpy standard (ΔH°) of Mg/Al LDH-GA and Mg/Al LDH-SA was -25.23 and -15.74 kJ mol⁻¹, respectively. Also, the fact that ΔH° value of Mg/Al LDH before functionalization was positive (4.36 kJ mol⁻¹) means that GA and SA on Mg/Al LDH play a pivotal role in the thermodynamic behavior of the adsorbents. On the other hand, the values of Gibbs free energy of these adsorbents at all temperatures were negative, suggesting that the adsorption of Au(III) ion on these adsorbents is a spontaneous process [26].

5 Characterization of Adsorbents After Adsorption

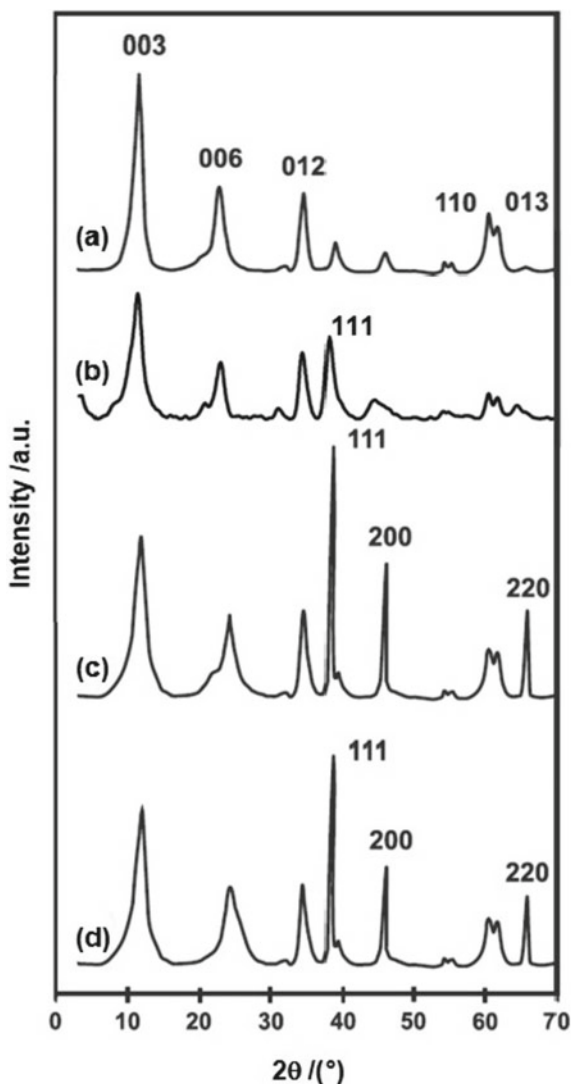
5.1 XRD

To confirm that Au(III) ion was successfully reduced into Au, characterization using XRD spectrometry was performed in all studies. As shown in Fig. 3, after adsorption of Au(III) ion, three diffraction lines corresponded to cubic Au, e.g., 38 (111), 44 (200) and 64° (220), were observed on Mg/Al LDH-GA and Mg/Al LDH-SA, but only one diffraction line on Mg/Al LDH-AA and none on bare Mg/Al LDH. This implies that the functionalization of Mg/Al LDH with AA, GA and SA gives a new ability of Mg/Al LDH to reduce Au(III) ion into Au. Furthermore, GA and SA are stronger than AA in reducing Au(III) ion. This may be correlated to the fact that the oxidation potential of GA (+1.16 to +1.84 V) [43] and SA (+1.0 to +1.1 V) [44] is higher than AA (+0.40 to +0.50 V) [45]. We also confirmed that the adsorption of Au(III) ion on bare Mg/Al LDH gave only peak broadening at $2\theta = 11.02$ and 22.90° [26], indicating that the removal of Au(III) ion from the reaction solution was governed solely by the adsorption process.

5.2 FTIR

Murugadoss et al. [46] reported that two vinylic -OH groups positioned at 3 and 4 of furan ring are responsible for the reduction of Au(III) ion with AA. It was pointed out that 3 mol of AA is required to reduce 2 mol of Au(III) ion. As the result, 3 mol of dehydroascorbic acid is produced in addition to 2 mol of Au [46].

Fig. 3 XRD spectra of **a** Mg/Al LDH, **b** Mg/Al LDH-AA, **c** Mg/Al LDH-GA and **d** Mg/Al LDH-SA after being used for the adsorption of Au(III) ion. Note: the picture was edited with permission from [26], while AA was obtained from [24]



Therefore, the reduction of Au(III) ion can be confirmed through the appearance of C = O ketone and the decreasing intensity of the absorption band of stretching and bending -OH. However, as shown in Fig. 4, there is no indication of the formation of C = O ketone on spent Mg/Al LDH-AA. The only change that might support the consumption of -OH group on the furan ring of AA is the decreasing intensity of the absorption band of stretching and bending -OH at 3471 and 1635 cm^{-1} , respectively. Therefore, although it had been confirmed through XRD in Fig. 3 that Au was formed on the spent Mg/Al LDH-AA, the reduction of Au(III) ion may be insignificant. This lack of indication from FTIR spectra could also be related to the

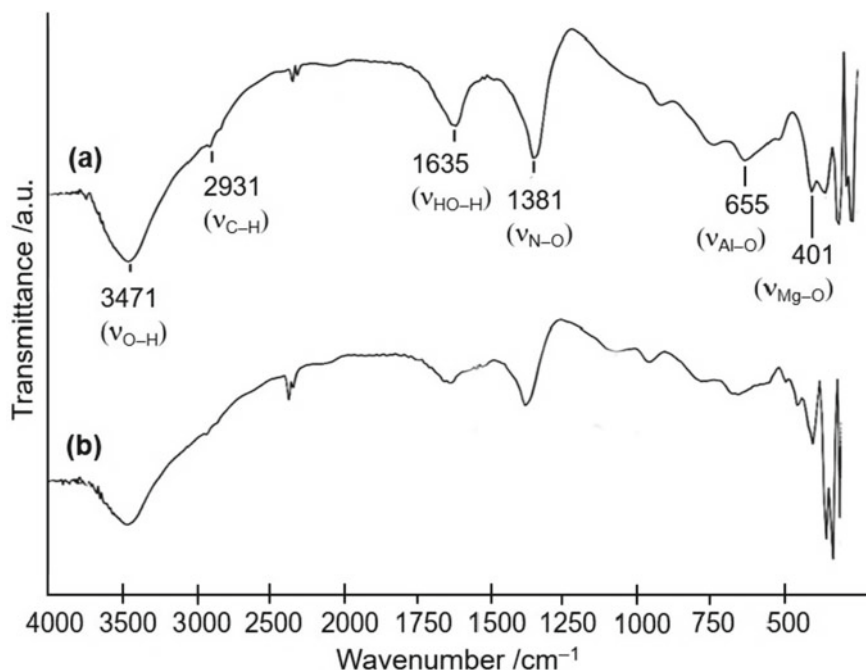


Fig. 4 FTIR spectra of Mg/Al LDH-AA **a** before and **b** after adsorption of Au(III) ion [24]

fact that unlike the spent Mg/Al LDH-GA and Mg/Al LDH-SA that produced three diffraction lines due to cubic Au after (Fig. 3), only (111) plane of Au was observed from the XRD spectra of the spent Mg/Al LDH-AA. In contrast, the oxidation of phenolic $-\text{OH}$ on Mg/Al LDH-GA and Mg/Al LDH-SA was well confirmed by the disappearance of the absorption band of $\text{C}-\text{O}$ at $1265\text{--}1273\text{ cm}^{-1}$ [26, 33] and the decreasing intensity of absorption bands due to stretching and bending $-\text{OH}$ at 3470 and 1635 cm^{-1} , respectively [26].

Meanwhile, the intensity of a sharp absorption band at wavenumber 1380 cm^{-1} on all adsorbents was always decreased and broadened after being used for the adsorption of Au(III) ion [24, 26, 33]. On Mg/Al LDH-AA, this absorption band is solely due to the asymmetric stretching vibration of $\text{N}-\text{O}$ from free NO_3^- , while on Mg/Al LDH-GA and Mg/Al LDH-SA, this may also be due to the binding between $-\text{COOH}$ group that may still remain on that GA or SA with Au(III) ion in addition to that stretching vibration of $\text{N}-\text{O}$ [26]. So far, the most plausible reason for the decreasing intensity and broadening absorption band at 1380 cm^{-1} on all adsorbents is that the interlayer NO_3^- may be exchanged with Au(III) ion during the adsorption process. While, notably for Mg/Al LDH-GA and Mg/Al LDH-SA, the interaction between their free $-\text{COOH}$ and Au(III) ion from reaction solution may also contribute to the phenomena in addition to that anion exchange reaction.

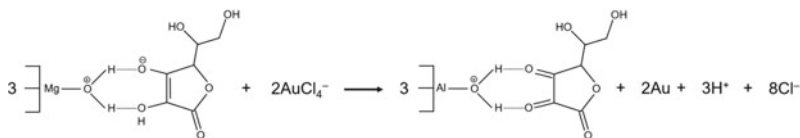
6 Reductive Adsorption Mechanism of Au(III) Ion

In this section, while the mechanism for the reductive adsorption of Au(III) ion on Mg/Al LDH-AA is predicted from the aforementioned data, which based on the unpublished work of the student in our research group [24], the mechanisms on Mg/Al LDH-GA and Mg/Al LDH-SA are the summaries of our recently published papers [26, 33].

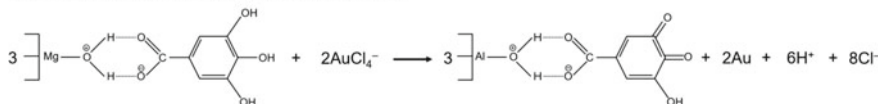
To elucidate the reductive adsorption of Au(III) ion on Mg/Al LDH-AA, it should first be noted that two vinylic –OH groups of AA are the only functional groups able to reduce Au(III) ion into Au [46]. This is understandable since they are the only moieties bonded with electron-rich C (sp^2), making them readily undergo oxidation reaction in the presence of a species with high reduction potential. Such redox reaction should not be possible on the electron-poor aliphatic –OH from the ethyl group of AA. Therefore, aliphatic –OH of AA on Mg/Al LDH must only contribute at most as an adsorption site for Au(III) ion. However, since the pK_{a1} of AA is contributed by the vinylic –OH, which is positioned at 3 of the furan ring of AA, it should interact with Mg and Al ions at the surface of Mg/Al LDH under preparation condition (Fig. 2) [24]. Therefore, although the reduction of Au(III) ion might occur, the hydrogen bond between vinylic –OH and Mg/Al LDH may hinder the reduction process of the adsorbed Au(III) ion. This could be why after being used for the adsorption of Au(III) ion, the spent Mg/Al LDH-AA lacks diffraction lines due to Au and that no clear evidence for the oxidation of AA on the surface of Mg/Al LDH. By considering the fact above, it is plausible to predict that the reductive adsorption of Au(III) ion on Mg/Al LDH-AA under acidic condition is initiated by the adsorption of Au(III) ion on aliphatic –OH of AA which is subsequently followed by reduction process of that adsorbed Au(III) ion by vinylic –OH groups of AA (Fig. 5).

As previously explained, phenolic –OH is the only possible active site on both Mg/Al LDH-GA and Mg/Al LDH-SA available for the adsorption of Au(III) ion since their –COOH group should be used for binding with Mg/Al LDH during synthesis. This is supported by the fact that the adsorption isotherm for both Mg/Al LDH-GA and Mg/Al LDH-SA, as shown in Table 2, followed the Langmuir isotherm model, which means that only one type of active site is active for the adsorption of Au(III) ion. By taking the fact that phenolic –OH is able to reduce Au(III) ion into Au [47], the reductive adsorption of Au(III) ion on Mg/Al LDH-GA and Mg/Al LDH-SA can be explained as follows. Firstly, under acidic condition, Au(III) ion interacts with phenolic –OH of GA or SA on Mg/Al LDH through hydrogen bonding. Afterward, the adsorbed Au(III) ion is spontaneously reduced into Au by that phenolic –OH, leading to the oxidation of that phenolic –OH into quinone (Fig. 5) [26, 33].

Reduction of AuCl_4^- with AA-functionalized Mg/Al LDH:



Reduction of AuCl_4^- with GA-functionalized Mg/Al LDH:



Reduction of AuCl_4^- with SA-functionalized Mg/Al LDH:

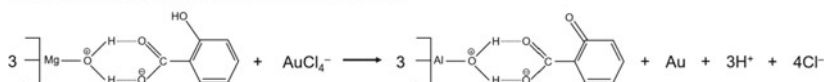


Fig. 5 Reduction of AuCl_4^- with Mg/Al LDH-AA, Mg/Al LDH-GA or Mg/Al LDH-SA based on the experimental results in [24, 46] for Mg/Al LDH-AA, [26, 33] for Mg/Al LDH-GA and [25, 26] for Mg/Al LDH-SA

7 Synthesis of Mg/Al LDH-Supported AuNPs from Au(III) Ion Obtained from Electronic Waste Solution

As it is apparent that the number of electronic wastes, namely e-waste, has rapidly increased in recent years [48], the recycling of Au from e-waste in the form of AuNPs is becoming more interesting and potentially reduces environmental pollution with gold ion. Previously, we have used Mg/Al LDH-AA for synthesizing of AuNPs from Au(III) ion obtained from the dissolution of printed circuit board (PCB) waste using aqua regia [31, 32]. The results showed that AuNPs were indeed formed on Mg/Al LDH-AA. Apparently, when the spent Mg/Al LDH-AA that has been used to adsorb Au(III) ion obtained from PCB was then exposed into the solution of sodium citrate, AuNPs with particle sizes ranging from 26.8 to 34.5 nm were released from the adsorbent (Fig. 6) [31]. The same behavior was also observed on the spent Mg/Al LDH-GA [49] and Mg/Al LDH-SA [25] when they are exposed to sodium citrate solution. This means that organic acid-functionalized Mg/Al LDHs are not only potential for the synthesis of AuNPs-Mg/Al LDHs nanocomposites but also potentially used for gold recovery. Notably for gold recovery, Mg/Al LDH can always be refunctionalized with a new organic acid and then subsequently reused for another recovery, as we demonstrated in our previous paper on the reductive adsorption of Au(III) ion by Mg/Al LDH-GA and calcined Mg/Al LDH GA [33]. However, it should be noted that since aqua regia is generally used for the dissolution process of metals in PCB, the solution is strongly acid ($\text{pH} < 1$). Therefore, pH adjustment of the reaction solution to less acidic, such as pH 3, is necessary to avoid the dissolution

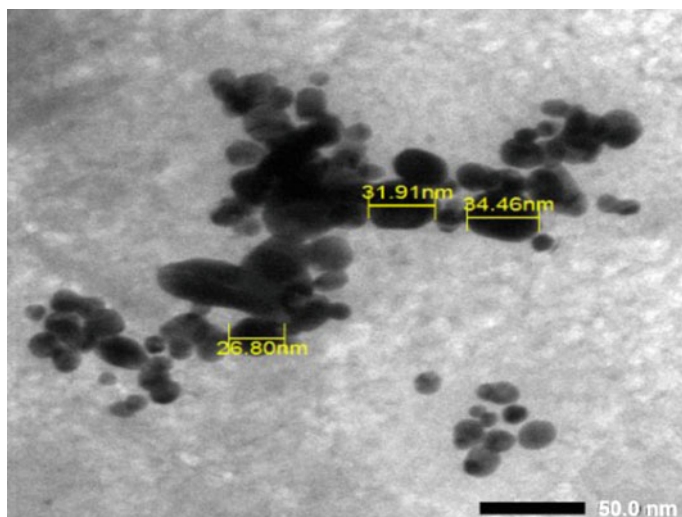


Fig. 6 Transmission electron microscopy (TEM) image of AuNPs recovered from Mg/Al LDH-AA by using sodium citrate solution (adapted with permission from [31])

of Mg/Al LDH. Meanwhile, the effect of other metal ions in PCB's solution for the adsorption of Au(III) ion is still under investigation.

8 Future Potentials and Challenges

So far, we have demonstrated that Au(III) ion is readily adsorbed and reduced by AA-, GA- and SA-functionalized Mg/Al LDHs, thus this reductive adsorption method is highly potential for the *in-situ* synthesis of AuNPs supported on Mg/Al LDH. Just like any other MO_x-supported AuNPs, Mg/Al LDH-supported AuNPs synthesized through this method are potential for a wide range of applications, particularly in catalysis and environment. In catalysis science, Mg/Al LDH-supported AuNPs is highly active for the oxidation of primary alcohols into methyl esters and imines [50], dehydrogenative synthesis of amide from alcohol [51], olefin epoxidation [52] and furfural liquid-phase oxidation [53]. All these reactions, most importantly, were effective even under mild temperatures. Meanwhile, for environmental applications, AuNPs-Mg/Al LDH may also be used as a catalyst for low-temperature cataluminescence sensing of volatile organic compounds (VOCs) [54].

Although we have found the best conditions for the preparation of AuNPs-Mg/Al LDH, some drawbacks need to be addressed in the future. Unlike the direct deposition technique, the amount of AuNPs on Mg/Al LDH cannot be precisely controlled. Although the amount of AuNPs can be controlled by altering the amount of the organic acid on the surface of Mg/Al LDH, it is time-consuming. The other way

is by investigating more organic acids and determining their adsorption capacities, which we are currently doing in our lab. In terms of applications, since Mg/Al LDH is used as a support for AuNPs, the material cannot be used for liquid reaction under strongly acidic and basic conditions since Mg/Al LDH is subject to dissolution under those conditions [35]. Moreover, more characterizations, such as TEM and X-ray photoelectron microscopy (XPS), should be performed to confirm the formation, more precise particle sizes and oxidation state of gold other than AuNPs on the surface of organic acid-functionalized LDHs.

9 Summary

It is obvious that organic acid-functionalized Mg/Al LDH is highly potential for the *in-situ* synthesis of Mg/Al LDH-supported AuNPs. The use of organic acids for the reductive adsorption process provides cheap, easy handling and environmentally friendly way for the synthesis of Mg/Al LDH-supported AuNPs. Among three organic acids, e.g., AA, GA and SA, used for the functionalization of Mg/Al LDH, GA exhibited the highest adsorption capacity and strongest ability in reducing Au(III) ion. While the high adsorption capacity on Mg/Al LDH-GA was presumably due to the possession of more –OH group than AA and SA, the strong ability to reduce Au(III) ion may be caused by the high oxidation potential. Further, the fact that the study in this matter is rarely reported means that the window in the *in-situ* synthesis of Mg/Al LDH-supported AuNPs is widely open.

Acknowledgements We thank Exceed-Swindon, Germany, for the seed money to conduct research which had been initially done by students in our research group for their undergraduate and master theses and to the Directorate General of Higher Education, Republic of Indonesia for the financial support for the completion of this research through a research scheme of World Class Research with contract number 892/UN1/DITLIT/DIT-LIT/PT/2020.

References

1. Laurent, S., Forge, D., Port, M., Roch, A., Robic, C., Elst, L.V., Muller, R.N.: Magnetic iron oxide nanoparticles: synthesis, stabilization, vectorization, physicochemical characterizations, and biological applications. *Chem. Rev.* **108**(6), 2574–2574 (2010)
2. Khan, I., Saeed, K., Khan, I.: Nanoparticles: properties, applications and toxicities. *Arab J. Chem.* **12**(7), 908–931 (2019)
3. Elahi, N., Kamali, M., Baghersad, M.H.: Recent biomedical applications of gold nanoparticles: a review. *Talanta* **184**, 537–556 (2018)
4. Wang, J., Zhu, G., You, M., Song, E., Shukoor, M.I., Zhang, K., Altman, M.B., Chen, Y., Zhu, Z., Huang, C.Z., Tan, W.: Assembly of aptamer switch probes and photosensitizer on gold nanorods for targeted photothermal and photodynamic cancer therapy. *ACS Nano* **6**(6), 5070–5077 (2012)

5. Turkevich, J., Stevenson, P.C., Hillier, J.: A study of the nucleation and growth processes in the synthesis of colloidal gold. *Discuss Faraday Soc.* **11**, 55–75 (1951)
6. Kimling, J., Maier, M., Okenve, B., Kotaidis, V., Ballot, H., Plech, A.: Turkevich method for gold nanoparticle synthesis revisited. *J. Phys. Chem. B* **110**(32), 15700–15707 (2006)
7. Frens, G.: Particle size and sol stability in metal colloids. *Kolloid-Zeitschrift Und Zeitschrift Für Polymere*. **250**, 736–741 (1972)
8. Frens, G.: Controlled nucleation for the regulation of the particle size in monodisperse gold suspensions. *Nat. Phys. Sci.* **241**, 20–22 (1973)
9. Malassis, L., Dreyfus, R., Murphy, R.J., Hough, L.A., Donnio, B., Murray, C.B.: One-step green synthesis of gold and silver nanoparticles with ascorbic acid and their versatile surface post-functionalization. *RSC Adv.* **6**, 33092–33100 (2016)
10. Kim, D.-Y., Kim, M., Shinde, S., Sung, J.-S., Ghodake, G.: Cytotoxicity and antibacterial assessment of gallic acid capped gold nanoparticles. *Colloids Surf. B Biointerfaces* **149**, 162–167 (2017)
11. Inbaraj, B.S., Chen, B.-Y., Liao, C.-W., Chen, B.-H.: Green synthesis, characterization and evaluation of catalytic and antibacterial activities of chitosan, glycol chitosan and poly(γ -glutamic acid) capped gold nanoparticles. *Int. J. Biol. Macromol.* **161**, 1484–1495 (2020)
12. Memon, S.S., Nafady, A., Solangi, A.R., Al-Enizi, A.M., Sirajuddin, S.M.R., Sherazi, S.T.H., Memon, S., Arain, M., Abro, M.I., Khattak, M.I.: Sensitive and selective aggregation based colorimetric sensing of Fe^{3+} via interaction with acetyl salicylic acid derived gold nanoparticles. *Sens. Actu. B Chem.* **259**, 1006–1012 (2018)
13. Liu, N., Wang, K., Gao, Y., Li, D., Lin, W., Li, C.: Tartrate as a substitute of citrate to prepare gold colloids from chloroauric acid. *Colloids Surf. A Physicochem. Eng. Asp.* **535**, 251–256 (2017)
14. Zheng, N., Stucky, G.D.: A general synthetic strategy for oxide-supported metal nanoparticle catalysts. *J. Am. Chem. Soc.* **128**(44), 14278–14280 (2006)
15. Tang, H., et al.: Classical strong metal–support interactions between gold nanoparticles and titanium dioxide. *Sci. Adv.* **3**(10), e1700231 (2017)
16. Zhang, X., Zheng, J.: Amperometric hydrazine sensor based on the use of a gold nanoparticle-modified nanocomposite consisting of porous polydopamine, multiwalled carbon nanotubes and reduced graphene oxide. *Microchim. Acta.* **187**, 89 (2020)
17. Fazzini, S., Nanni, D., Ballarin, B., Cassani, M.C., Giorgetti, M., Maccato, C., Trapananti, A., Aquilanti, G., Ahmed, S.I.: Straightforward synthesis of gold nanoparticles supported on commercial silica-polyethyleneimine beads. *J. Phys. Chem. C* **116**(48), 25434–25443 (2012)
18. Chen, M., Kang, H., Gong, Y., Guo, J., Zhang, H., Liu, R.: Bacterial cellulose supported gold nanoparticles with excellent catalytic properties. *ACS Appl. Mater. Interfaces* **7**(39), 21717–21726 (2015)
19. Han, J., Li, L., Guo, R.: Novel approach to controllable synthesis of gold nanoparticles supported on polyaniline nanofibers. *Macromolecules* **43**(24), 10636–10644 (2010)
20. Cavani, F., Trifirò, F., Vaccari, A.: Hydrotalcite-type anionic clays: preparation, properties and applications. *Catal. Today* **11**(2), 173–301 (1991)
21. Extremera, R., Pavlovic, I., Pérez, M.R., Barriga, C.: Removal of acid orange 10 by calcined Mg/Al layered double hydroxides from water and recovery of the adsorbed dye. *Chem. Eng. J.* **213**, 392–400 (2012)
22. Mishra, G., Dash, B., Pandey, S.: Layered double hydroxides: a brief review from fundamentals to application as evolving biomaterials. *Appl. Clay Sci.* **153**, 172–186 (2018)
23. Daud, M., et al.: A review on the recent advances, challenges and future aspect of layered double hydroxides (LDH) – Containing hybrids as promising adsorbents for dyes removal. *J. Mol. Liq.* **288**, 110989 (2019)
24. Hidayanti, R.: Immobilization of ascorbic acid on Mg/Al hydrotalcite and its application for the reductive adsorption of AuCl_4^- . Master Thesis, Universitas Gadjah Mada, Yogyakarta, Indonesia (2013)
25. Mu'awanah, A.: Sodium citrate assisted recovery of gold from gold obtained from reductive adsorption of AuCl_4^- on salicylic acid immobilized Mg/Al hydrotalcite. Undergraduate Thesis, Universitas Gadjah Mada, Yogyakarta, Indonesia (2016)

26. Santosa, S.J., Fitriani, D., Aprilita, N.H., Rusdiarso, B.: Gallic and salicylic acid-functionalized Mg/Al hydrotalcite as highly effective materials for reductive adsorption of AuCl_4^- . *Appl. Surf. Sci.* **507**, 145115 (2020)
27. Bouhent, M.M., Derriche, Z., Denoyel, R., Prevot, V., Forano, C.: Thermodynamical and structural insights of orange II adsorption by Mg_RAlNO_3 layered double hydroxides. *J. Solid State Chem.* **184**(5), 1016–1024 (2011)
28. Gray, D., Brameld, J., Tucker, G.: Vitamins C and E. *Phytonutr. Chap.* **5**, 146–172 (2012)
29. Sławińska, D., Polewski, K., Rolewski, P., Sławiński, J.: Synthesis and properties of model humic substances derived from gallic acid. *Int. Agrophys.* **21**(2), 199–208 (2007)
30. Friedrich, D.M., Wang, Z., Joly, A.G., Peterson, K.A., Callis, P.R.: Ground-state proton-transfer tautomer of the salicylate anion. *J. Phys. Chem. A* **103**(48), 9644–9653 (1999)
31. Andreani, A.S., Suyanta, S., Kunarti, E.S., Santosa, S.J.: Synthesis of gold nanoparticle from adsorbed Au on hydrotalcite using SDS and sodium citrate as capping agent and its recovery into pure gold. *Mater. Sci. Forum* **901**, 32–36 (2017)
32. Andreani, A.S., Suyanta, S., Kunarti, E.S., Santosa, S.J.: Synthesis of citrate-capped gold nanoparticles from reduced $[\text{AuCl}_4]^-$ on ascorbic acid-immobilized Mg/Al hydrotalcite. *Indones. J. Chem.* **18**(3), 434–440 (2018)
33. Santosa, S.J., Krisbiantoro, P.A., Elianasari, S.: Functionalization of Mg/Al hydrotalcite and calcined Mg/Al hydrotalcite with gallic acid for reductive adsorption of tetrachloroaurate(III) ion in aqueous solution. *Int. J. Environ. Anal. Chem.*, 1–17 (2020)
34. Bhojaraj, H.P., Rajamathi, M.: Cannizzaro reactions over calcined hydrotalcite. *Appl. Clay Sci.* **174**(2019), 86–89 (2019)
35. Santosa, S.J., Kunarti, E.S., Karmanto: Synthesis and utilization of Mg/Al hydrotalcite for removing dissolved humic acid. *Appl. Surf. Sci.* **254**(23), 7612–7617 (2008)
36. Santosa, S.J., Sudiono, S., Siswanta, D., Kunarti, E.S., Dewi, S.R.: Mechanism of the removal of AuCl_4^- ions from aqueous solution by means of peat soil humin. *Adsorpt. Sci. Technol.* **29**(8), 733–746 (2011)
37. Sudiono, S., Yuniarti, M., Siswanta, D., Kunarti, E.S., Triyono, T., Santosa, S.J.: The role of carboxyl and hydroxyl groups of humic acid in removing AuCl_4^- from aqueous solution. *Indones. J. Chem.* **17**(2017), 95–104 (2017)
38. Nuryono, N., et al.: Chitosan-functionalized natural magnetic particle@silica modified with (3-chloropropyl) trimethoxysilane as a highly stable magnetic adsorbent for gold(III) ion. *Mater. Chem. Phys.* **255**, 123507 (2020)
39. Usher, A., McPhail, D.C., Brugger, J.: A spectrophotometric study of aqueous Au(III) halide-hydroxide complexes at 25–80°C. *Geochim. Cosmochim. Acta* **73**(11), 3359–3380 (2009)
40. Lagergren, S.: Zur Theorie der sogenannten Adsorption gelöster Stoffe. *Zeitschrift Für Chemie Und Industrie Der Kolloide.* **2**, 15 (1907)
41. Ho, Y.S., McKay, G.: Pseudo-second order model for sorption processes. *Process Biochem.* **34**(5), 451–465 (1999)
42. Batool, M., Nazar, M.F., Awan, A., et al.: Bismuth-based heterojunction nanocomposites for photocatalysis and heavy metal detection applications. *Nano-Struct. Nano-Objects* **27**, 100762 (2021)
43. Carter, M.K.: Correlation of electronic transitions and redox potentials measured for pyrocatechol, resorcinol, hydroquinone, pyrogallol, and gallic acid with results of semi-empirical molecular orbital computations – a useful interpretation tool. *J. Mol. Struct.* **831**(1–2), 26–36 (2007)
44. Colucci, J., Montalvo, V., Hernandez, R., Poulet, C.: Electrochemical oxidation potential of photocatalyst reducing agents. *Electrochim. Acta* **44**(15), 2507–2514 (1999)
45. Matsui, T., Kitagawa, Y., Okumura, M., Shigeta, Y.: Accurate standard hydrogen electrode potential and applications to the redox potentials of vitamin C and NAD/NADH. *J. Phys. Chem. A* **119**(2), 369–376 (2015)
46. Murugadoss, A., Pasricha, R., Chattopadhyay, A.: Ascorbic acid as a mediator and template for assembling metallic nanoparticles. *J. Colloid Interface Sci* **311**(1), 303–310 (2007)

47. Hamamoto, K., Kawakita, H., Ohto, K., Inoue, K.: Polymerization of phenol derivatives by the reduction of gold ions to gold metal. *React. Func. Polym.* **69**(9), 694–697 (2009)
48. Kiddee, P., Naidu, R., Wong, M.H.: Electronic waste management approaches: an overview. *Waste Manag.* **33**(5), 1237–1250 (2013)
49. Almas, R.A.: Recovery of gold from gold nanoparticles produced by reductive adsorption of AuCl_4^- on gallic acid immobilized Mg/Al hydrotalcite and desorption using sodium citrate. Undergraduate Thesis, Universitas Gadjah Mada, Yogyakarta, Indonesia (2016)
50. Liu, P., Li, C., Hensen, E.J.M.: Efficient tandem synthesis of methyl esters and imines by using versatile hydrotalcite-supported gold nanoparticles. *Chem. Eur. J.* **18**(38), 12122–12129 (2012)
51. Zhu, J., Zhang, Y., Shi, F., Deng, Y.: Dehydrogenative amide synthesis from alcohol and amine catalyzed by hydrotalcite-supported gold nanoparticles. *Tetrahedron Lett.* **53**(25), 3178–3180 (2012)
52. Leandro, S.R., Mourato, A.C., Łapińska, U., Monteiro, O.C., Fernandes, C.I., Vaz, P.D., Nunes, C.D.: Exploring bulk and colloidal Mg/Al hydrotalcite–Au nanoparticles hybrid materials in aerobic olefin epoxidation. *J. Catal.* **358**, 187–198 (2018)
53. Thuriot-Roukos, J., Khadraoui, R., Paul, S., Wojcieszak, R.: Raman spectroscopy applied to monitor furfural liquid-phase oxidation catalyzed by supported gold nanoparticles. *ACS Omega* **5**(24), 14283–14290 (2020)
54. Li, Z., Xi, W., Lu, C.: Hydrotalcite-supported gold nanoparticle catalysts as a low temperature cataluminescence sensing platform. *Sens. Actu. B Chem.* **219**, 354–360 (2015)

Graphene and Its Nanocomposites Derivatives: Synthesis, Properties, and Their Applications in Water Treatment, Gas Sensor, and Solar Cell Fields



Sahar A. Mousa, Sohaila Z. Noby, and Ahmed Esmail Shalan 

Abstract Graphene and its derivatives have remarkable properties such as high electrical conductivity, mechanical strength, large surface area, excellent hydrophilicity, and significant thermal and barrier properties. Graphene oxides and its composites can be synthesized using simple top-down procedures. Graphene is a 2D material that consists of SP^2 carbon atoms arranged in a honeycomb structure. Graphene oxides can be prepared from graphene, which allows functionalizing the material to achieve more significant advantages via controlling the role of the oxygen groups. Moreover, it reveals a desirable ability to form nanocomposites with various materials categories such as metals, semiconductors, metal oxides, and polymers. Graphene and its derivatives nanocomposites have been applied in extensive technological applications in electronic, biological, engineering, energy production, and energy storage. Herein, we will briefly introduce Graphene and its derivatives nanocomposites synthesis techniques, and impressive properties. We will specifically show their promising performance in separated applications such as water treatment gas sensors, and solar cell applications.

Keywords Graphene · Graphene oxides · Reduced graphene oxides · Nanocomposite · Synthesis · Water treatment · Gas sensor · Solar cell device

S. A. Mousa

Faculty of Science, Department of Physics, Cairo University, Giza 12613, Egypt

S. Z. Noby

Department of Physics, University of Konstanz, 78457 Konstanz, Germany

Department of Solid State of Physics, National Research Center NRC, Cairo 12622, Egypt

A. E. Shalan (✉)

BCMaterials—Basque Center for Materials, Applications and Nanostructures, Martina Casiano, UPV/EHU Science Park, Barrio Sarriena s/n, 48940 Leioa, Bizkaia, Spain

Central Metallurgical Research and Development Institute CMRDI, Cairo 11421, Egypt

© The Author(s), under exclusive license to Springer Nature Switzerland AG 2022

95

A. E. Shalan et al. (eds.), *Advances in Nanocomposite Materials for Environmental and Energy Harvesting Applications*, Engineering Materials,

https://doi.org/10.1007/978-3-030-94319-6_5

Abbreviations

Symbol	Meaning
MOS	Metal oxide semiconductors
GO	Graphene oxide
RGO	Reduced Graphene oxide
N ₂ H ₄ borohydride	Hydrazine NaBH ₄
UV	Ultraviolet
E _g	Energy bandgap
e ⁻ /h ⁺	Electron hole pairs
CB	Conduction band
VB	Valence band
XRD	X ray diffraction
NPs	Nanoparticles
MB	Methylene blue
FESEM	Field emission scanning electron microscope
CNTS	Carbon nanotubes
COD	Chemical oxygen demand
TOC	Total oxygen
MO	Methyl orange
PVDF	Polyvinylidene fluoride
NRGT	Nitrogen-doped graphene/TiO ₂ nanocomposites with
PSF	Poly sulfone
CS	Chitosan
TMC	Trimesoylchloride
PES	Polyethersulfone
SGO	Single-layer Graphene oxide
MGO	Multilayered Graphene oxide
CTA	Cellulose triacetate
N-PGO	N-doped porous graphene oxide
<i>D</i>	The grain diameter
λ_D	Is Debye length
<i>n_b</i>	Free carrier concentration of the bulk material
<i>R_a</i>	The initial resistance in air
<i>R_g</i>	The resistance under gas exposure
PMMA	Polymethyl methacrylate
PDMS	Polydimethylsiloxane
PI	Polyimide
PEN	Polyethylenenaphthalate
PET	Polyethylene terephthalate
RGO/LN	Reduced nanographene oxide directly on linen
DOPA	Dopamine
DGY	DOPA- graphene flakes- Yarn hybrid

CEs	Counter electrodes
HTL	Hole transport layers
ETL	Electron transport layers
PV	Photovoltaic
DSSCs	Dye-sensitized solar cells
PSCs	Perovskite solar cells
OSCs	Organic solar cells
MEHPPV	2-Methoxy, 5-(2'-ethylhexyloxy)-p-phenylenevinyl
P3HT	Poly(3-hexylthiophene)
MWCNTs	Multi-walled carbon nanotubes
L-AA	Ascorbic Acid
EPD	Electrophoretic deposition
Psi	Porous silicon
PAni	Polyaniline
EG	Ethylene glycol
SC	Sodium citrate
SrGO	Sulfonic acid functionalized graphene oxide
PEDOT: PSS/SrGO	Poly(3,4-ethylenedioxythiophene): poly(styrenesulfonate) sulfonic acid functionalized graphene oxide

1 Introduction

Different researchers have discovered a lot of energy for metal oxide semiconductors (MOS) materials because of their smart benefits in designing applications [1–3]. Graphene is a substantial carbon structure got from graphite and lately, it is considered a viable semiconductor material with zero energy gap [4, 5]. It is prepared in a monolayer or a little of layers of a 2D planar sheet of sp^2 mongrelized carbon atoms with hexagonal construction [6, 7]. Graphene oxide (GO) and its products have a great surface area, excessive electrical conductivity, reliable mechanical properties, extraordinary thermal stability, and respectable optical properties [8]. Subsequently, they associated with different applications, including high-energy storing, electronic sensors nanomachines, [9], medication [10], water decontamination [11], and superior photovoltaics [12]. These applications resulting from its exceptionally low sheet film resistance, thermal conductivity, high optical transmittance, and great mechanical stability [13]. GO is a form of graphene functionalization. GO has unique compensations such as easy functionalization, solution processability, large-scale manufacturing, and minimal effort; as a result, it is an attractive nanomaterial [14]. GO material has oxygen interceded carbon network, enormous work function, and insulating properties, which is valuable for conductive electrode submissions, for example, solar cells [15], touch screens [16], organic optoelectronic strategies [17], and hole transport in organic electronic devices [18]. The oxidation level of GO is thusly constrained by different reductants like hydroiodic acid, L-ascorbic acid,

sodium borohydride, and hydrazine [19]. In particular, GO is effectively dispersed in the solvent and utilized in solution-processed organic photonic devices due to oxygen-containing functional group [20]. Therefore, reducing some of the functional groups of GO sheets is an effective way to enhance their electrical properties. The reduced graphene oxide (RGO) has applications than GO or even pure graphene, such as an electrode for Li-ion batteries [21], photoconductive switching [22], catalyst [4], water desalination [23], supercapacitors, and fuel cells [24, 25], gas separation [26], transparent conductive films [27], sensors [28], biological imaging [5], etc. Annealing of GO at high temperatures has been used as a thermal reduction technique [29]. Likewise, the chemical reduction can be obtained using strong reducing chemicals, such as hydrazine (N_2H_4) [30] and borohydride ($NaBH_4$) [31]. Moreover, radio frequency plasma is one of the new directions for reducing the numeral of functional groups in GO materials to form RGO [32, 33]. It's difficult to disperse The RGO due to its tendency to make aggregates. Graphite oxide and GO are very much like chemically; however, they are different structurally. The most elevated difference between themes is the interplanar space between the individual layers of the compounds, as a result of water intercalation. As a result of the increased spacing, an oxidization process, also disorders the sp^2 bonding system so, the number of layers is different also.

2 Synthesis of GO and RGO

Numerous advanced processes for the GO preparation are based on the process reported at first by Hummers wherein a solution of potassium permanganate in sulfuric acid was used to oxidized graphite [34]. GO is produced as a byproduct of this oxidation, so there is an increase in the interplanar spacing between the layers of graphite after the reaction between the oxidizing agents with graphite. The completely oxidized compound would then be able to be dispersed in a base solution for example water, and GO is then manufactured.

A few potential strategies are utilized to transform graphite oxide into GO. The most common methods by utilizing stirring, sonication, and a blend of the two. Sonication can be a quick and very time-efficient methodology of exfoliating graphite oxide, and it is immensely effective at exfoliating graphene; nonetheless, it can likewise significantly damage the graphene flakes, decreasing them in surface size from microns to nanometers, and it delivers a wide changeability of graphene platelet sizes [35].

3 Application of Graphene and Its Derivatives

3.1 Usage of Graphene Nanocomposites and Their Derivatives in Waste Water Treatment

Between all sources accessible on earth water, is the unique source. this substance accepts a key part to keep up earth nature and individual fulfillment and no presence of any kind can exist without water. Nowadays the world is facing many of serious environmental problems such as energy, pollution, and water problem. The water problem is due to two reasons;

i) The fast and relatively uncontrolled population growth and also industrial, agricultural and technological developments which affect the environment and human health. Especially wastewater effluents of industrial manufacturing companies contain toxic organic compounds and heavy metals. Additionally, the combustion of fossil fuels has caused global warming due to the increase of CO₂ concentration in the atmosphere.

ii) The natural resources of freshwater became very limited about 97% of the world's water is saltwater in the seas, and oceans and only 3% is freshwater just 0.25% of the freshwater on earth is enclosed in-stream frameworks, lakes, and supplies, which are the water we are generally acquainted with and the most reachable water source to fulfill human requirements in our everyday lives. Subsequently, saving water to protect the planet and to make the fate of humanity safe establishes a central point of contention for current cultures.

So clean water remains one of the major societal concerns and as the requirement for clean water expands the interest for new purification advancements with a low eco-friendly effect develops. Perceiving these necessities, advancement of proficient, manageable, and harmless to the ecosystem water treatment advances is serious for our future [36].

Organic dyes are One of the dangerous pollutants on water which represent a central source of environmental contamination as they are toxic and cause serious damage to human beings even at very low concentrations and mostly non-biodegradable because it is very stable to oxidation and light which makes it very challenging to biodegrade.

So, the elimination of dangerous organic dyes from industrial waste is considered effectively a great environmental challenge. Recently Different advanced oxidation processes, AOPs, have been technologically advanced to enhancement the oxidation of uncontrollable contaminants, through the generation of extremely reactive oxygen (O₂) and hydroxyl (OH) free radicals. Recently heterogeneous semiconductor photocatalysis presented as a promising technology to eliminate different types of organic compounds in the existence of either artificial or natural light [37].

MOS exhibit amazing properties such as high energy bandgap (E_g), and hydrophobic nature, therefore it can be suitable for different applications for example solar cell, photocatalysis, antibacterial products, microelectronics, charge spreading devices, chemical sensors, and textiles especially, in the Nano level because of their

extraordinary surface to volume ratio [38]. Recently different metal oxides such as GO, ZnO, TiO₂, and SnO₂, etc. were widely used in the photocatalytic degradation of organic pollutants. Although the benefits of using metal oxide as a photocatalyst but there is some limitation can effect on its photocatalytic effect such as i) fast recombination between photogenerated e/h⁺ pairs followed by radiative or nonradiative decay and energy release. ii) most stable semiconductors have high bandgap so it needs high energy to excite so only ultraviolet (UV) light and limited number of MOS excited by visible light. The solar spectrum reaching earth contains only about 50% of visible light and 4% of UV light so, many researchers focus on finding solutions to the incapacity to absorb light from the visible.

i) To reduce the bandgap.

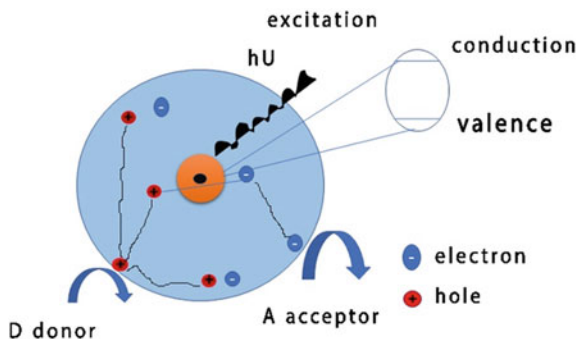
Doping is mostly considered to improve the photocatalytic activity of high-bandgap semiconductors. doping especially with transition metals can tunes the electronic structure of semiconductors and shifts the light absorption from the UV region to the visible light region. However, doping of TiO₂ often increases in concentration of trap sites, responsible for the recombination of electrons and holes. Even without doping, recombination is already a significant problem. A reduction in the recombination rate can be achieved by a reduction of the number of trap sites within the photocatalyst. Annealing of the catalysts in general will increase the crystallinity, and in this way reduce the number of defects or traps Fig. 1 a new electron state is generated inside the electronic structure of the high-band gap when the transition metal used [39].

ii) To increase the separation of holes and electrons, two different methods are used:

a) The use of Nobel metal co-catalysts, like Pt, Pd, Ag, and Au. By adding these metals in the form of nanoparticles to the photocatalyst, electrons will be transferred to the Nobel metal whereas the holes remain in the photocatalyst. Also, electron transfer to the reactant will occur catalytically over the metal surface Fig. 2.

b) Semiconductor coupling has a beneficial role in the improvement of the charge separation because the combination of dissimilar semiconductor nanoparticles can enable the separation and the transference of the photogenerated carrier's Fig. 3.

Fig. 1 Doping with transition metals



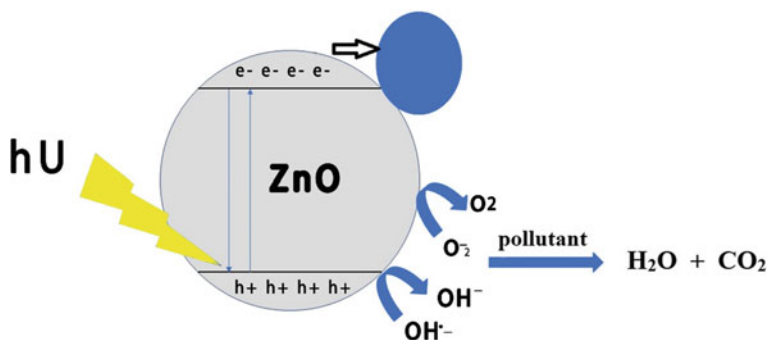


Fig. 2 Using Nobel metal co-catalysts

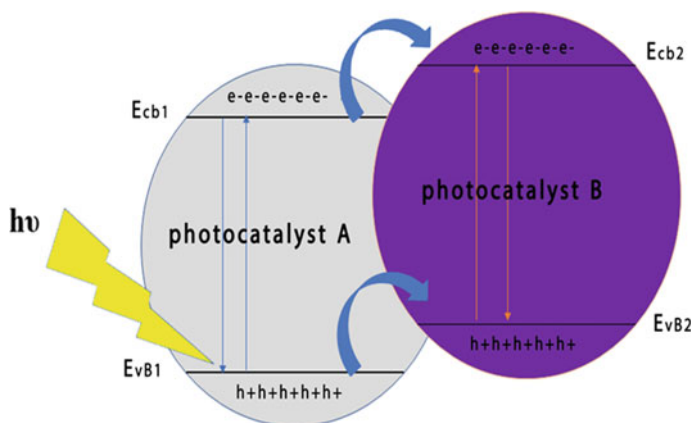


Fig. 3 Coupling of semiconductor

Lately, photocatalysis of graphene under UV- visible light has developed as an effective, ecofriendly, and economical technique for water decontamination and different visible-light photocatalysts have been synthesized and used for wastewater treatment. Nevertheless, the efficiency of the single semiconductor photocatalyst is still limited [40].

3.1.1 GO Nanocomposites as a Photocatalyst

Graphene- metal nanoparticles composites or Graphene-semiconductor have produced the new promises of technology in the water purification process. Lately, the studies showed that heterogeneous photocatalysis plays an effective and important role to improve the efficiency of the photocatalytic process. However, as mentioned

a lot of photocatalysts have a different limitation which confines their useful application combining graphene with MOS and other nanoparticles produce an effective strategy to improve the photocatalytic activity and stabilities. But the applied applications are limited because of the e^-/h^+ recombination process which reducing their photocatalytic efficiency. However, these difficulties have been solved by coupling different semiconductors which exceed the charge separation besides increases the photocatalytic efficiency [41].

Semiconductor coupling has a beneficial role in the improvement of the charge separation because the combination of different semiconductor NPs could enable the separation of the photogenerated carriers. Moreover, Heterojunction development in double and triple nanostructure MOS nanocomposites shows a vital role to make the separation of e^-/h^+ pairs for improved photocatalytic activity. When illuminated under light, the photogenerated electrons from the first photocatalyst with the CB at the highest negative potential side are transferred to the second photocatalyst with CB at the highest positive potential side. Likewise, the photogenerated holes are moved from the VB with the highest positive potential side to the VB with the highest negative potential side to decrease e^-/h^+ pair recombination and improve photocatalytic activity Fig. 4.

Also, there are a lot of advantages of graphene-based nanocomposites, graphene rises the surface area, enhances the mechanical strength, decreases the aggregation, hinders corrosion, leakage, and electron scavengers, becomes more photosensitive, etc. which improve the everyday application of photocatalysts [42].

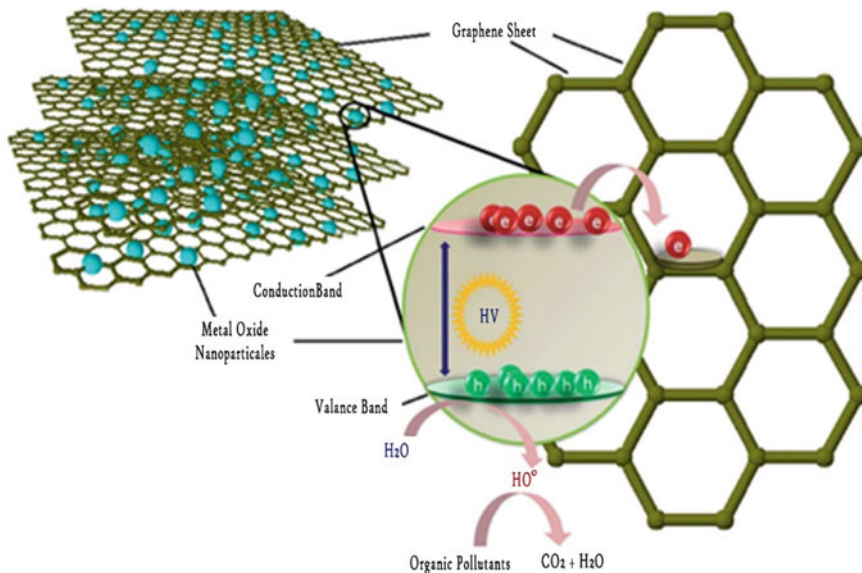


Fig. 4 Graphene-based nanocomposites photocatalyst [42]

Consequently, presenting a new band between the two levels will modify the semiconductor from a wide bandgap semiconductor into a slight bandgap semiconductor besides, expand the absorption from UV to visible region. The supplement of semiconductors with graphene additionally has arisen as a conspicuous option for enhancing the photoactivity of the nanocomposites. The movement of photogenerated e^-/h^+ pair from semiconductor to graphene relies on the interfacial connection or linking between the coupled semiconductor [43].

So, developing multi-junction nanocomposites of graphene have likewise been given a lot of consideration. Because of its interesting and unique properties, recently, more researches have been done on the synthesis of numerous multi-junction nanocomposites of graphene for different application. Different quaternary, and ternary, multi-junction nanocomposites have been synthesized.

In the synthesis of graphene-based nanocomposites as photocatalysts, different approaches have been engaged for enhancing the photocatalytic efficiency include doping, surface sensitization, coupling graphene with the semiconductor, improving the electrical conductivity of graphene, increasing active sites on graphene, constructing nanostructure of graphene, fabricating multi-junction nanocomposites, and enhancing photo-stability of graphene-based nanocomposites.

Ting-Ting Chen et al. 2013 Prepared ZnO/RGO nanocomposite have many oxygens, and zinc vacancies, via a simple Solvothermal method. The prepared nanocomposites exhibit an excellent photocatalytic activity as a result of generation vacancies from zinc and oxygen on the surface of ZnO NPs, which were essential to the photocatalytic performance as they induced effective charge separation which enhance ZnO/RGO photocatalytic activity. electron paramagnetic resonance and Photoluminescence were used to confirm zinc, and oxygen vacancies [44].

Eric S. Agorku et al. 2015 Used the coprecipitation method to prepare a sequence of Pd-decorated ZnS/RGO nanocomposites. XRD and Raman analysis confirmed a pure crystalline ZnS with fcc phase. The DRS and UV–vis spectral analysis showed a red shift in the absorption that caused a reduction in band gaps for both RGO and Pd. The Pd–ZnS/RGO nanocomposite have a highly photocatalytic effect in the degradation of indigo carmine under visible light. the 1.0% Pd–ZnS/RGO sample showed the highest photocatalytic activity. The enhancement in the photocatalytic activity was mostly recognized by the strong absorption in the visible spectrum, the small crystallite size, and slight bandgap energy [45].

Jinfen Niua et al. (2017) synthesized a novel and excellent visible-light photocatalyst BiOI/RGO nanocomposite using a different, simple, and fast microwave hydrothermal method. There is an enhancement in the photodegradation of levofloxacin and methylene blue under visible light was observed for BiOI/RGO nanocomposite than that of BiOI, and RGO. It enhanced by 1.6, and 7.3 times than that of BiOI, RGO respectively. The enhancement is due to the higher specific surface area and the morphology of the nanocomposites [46].

R. Suresh et al. (2018) synthesized an RGO/Fe₂O₃ hybrids in low concentrations of RGO (1, 3, and 5 wt%) by functionalization of Fe₂O₃ nanoparticles with RGO using thermal decomposition method, and applying it as a photocatalyst and adsorbent to remove acid blue 113 (AB113) from water. by adding RGO to Fe₂O₃

nanoparticles the RGO hindered the growth of Fe_2O_3 rods so hematite ($\alpha\text{-Fe}_2\text{O}_3$) phase was changed to maghemite ($\gamma\text{-Fe}_2\text{O}_3$) phase and distortion of nanocuboid Fe_2O_3 rods into spherical nanoparticles was also detected. The functionalization of Fe_2O_3 by 5% RGO enhanced the adsorption of AB113 from water as a result of the increasing in its surface area. The functionalized nanocomposite shows high photocatalytic activity than pure Fe_2O_3 under visible light. So, this material with low RGO concentrations has a great application in environmental remediation using solar light [47].

G. Jeevitha et al. 2018 used a simple ultrasonication method to synthesize a WO_3 -GO nanocomposite. The prepared WO_3 and WO_3 -GO nanocomposite were demonstrated as a photocatalyst in degradation of both cationic and anionic dye and as antibacterial towards both *E. coli* and *B. subtilis* and also as anticancer for human lung cancer cells (A-549). the prepared WO_3 -GO nanocomposites showed a good photodegradation efficiency, excellent anticancer against A-549 good antibacterial agent towards *E. coli* and *B. subtilis*. The antibacterial and photocatalytic activities of the prepared WO_3 -GO nanocomposite were higher than that of WO_3 because of the existence of GO that improves electron-hole pair separation rate and inhibits the electron-hole pair recombination [48].

T.P. Shende et al. 2018 used the ultrasound method to prepare Graphene- Fe-TiO_2 and Graphene- Ce-TiO_2 nanocomposites. The XRD analysis showed the existence of anatase TiO_2 on graphene nanosheets and the presence of Fe in the Graphene- Fe-TiO_2 and Ce in Graphene- Ce-TiO_2 nanocomposite. the prepared Graphene- Fe-TiO_2 , graphene- TiO_2 , and Graphene- Ce-TiO_2 nanocomposites have been used in the photodegradation of crystal violet dye. The result showed that doping the graphene- TiO_2 with Ce or Fe enhanced the degradation efficiency. The Graphene- Fe-TiO_2 showed the best photocatalytic activity than Graphene- TiO_2 , or Graphene- Ce-TiO_2 as it has the highest surface area. also doping of iron and cerium with graphene- TiO_2 caused a redshift in the bandgap of the Ce and Fe-doped graphene- TiO_2 nanocomposite which improves the intensity of absorption in the UV-visible light region. a decrease in the energy band gap was also observed as a result to doping of the graphene- TiO_2 with Fe and Ce in which reduce the recombination rate of the photo-generated hole-electron pair. The enhancement in the degradation of crystal violet dyes results from the high percentage of anatase phase in TiO_2 that limits TiO_2 crystallite size growth and increases its specific surface area. The study also showed that the photocatalytic degradation of the prepared NPs follows the first-order kinetics [49].

Afshin Ziarati Saravani et al. 2019 used the hydrolysis method to synthesize a new ternary magnetic nanocomposite from ($\text{TiO}_2/\text{NiFe}_2\text{O}_4/\text{RGO}$) with diverse quantities of graphene. the photocatalytic activities of the prepared nanocomposite in degradation of methylene blue (MB) in presence of U-V and visible light were studied. The FESEM and XRD investigation showed that TiO_2 and NiFe_2O_4 NPs cover the RGO surface. Experimental results showed that the photocatalytic degradation was increased with increasing graphene amount inside nanocomposites. Also, $\text{TiO}_2/\text{NiFe}_2\text{O}_4/\text{RGO}$ NPs with (0.120 g) of graphene quantity exhibited the highest

photocatalytic performance than binary ($\text{TiO}_2/\text{NiFe}_2\text{O}_4$ and TiO_2/RGO) nanocomposites or single TiO_2 NPs and it could be reused by put it on an external magnetic field because of the presence of NiFe_2O_4 NPs [50].

Shakeel Ahmad Khan et al. 2019 synthesized Titanium dioxide/Graphene oxide (TiO_2/GO) nanocomposites via deposition liquid phase of Titania on GO nanosheets with different ratios (2, 4, 6, and 8%). the Photocatalytic activities of the prepared nanocomposites against MB and ciprofloxacin under the sunlight were studied also. the synthesized TiO_2/GO (8%) photocatalyst exhibited a faster and higher rate in the degradation of the MB than other composites and pure TiO_2 because it has the largest surface area and the narrowest energy bandgap. the photocatalyst demonstrated good stability and recyclability with a small reduction in photocatalytic efficiency with increasing the number of cycles. it was stable even at the sixth cycle above 91% [51].

Parisa Ghasemipour et al. 2020 used a usual hydrothermal method to prepare $\text{RGO}/\text{ZnO}/\text{MoS}_2$ and $\text{CNTs}/\text{ZnO}/\text{MoS}_2$ nanocomposites with diverse quantities from RGO and CNTs. And study their photodegradation of aniline under various operational parameters. The $\text{RGO}/\text{ZnO}/\text{MoS}_2$ exhibited higher efficiency than MoS_2 , ZnO/MoS_2 , and $\text{CNTs}/\text{ZnO}/\text{MoS}_2$. From their study, they recommended that RGO has a substantial effect on the catalytic activity of ZnO/MoS_2 . The $\text{RGO}/\text{ZnO}/\text{MoS}_2$ show an extended visible absorption according to UV-vis and PL analysis, that caused by the photo-induced charges separation. The surface area was increased greatly in the presence of RGO. Good reusability and stability for the prepared nanocomposites were observed after five repeated cycles. The degradation of aniline was reached completely after 120 min of radiation-exposed, 4 pH value, 0.7 g/L of catalyst dosage, and aniline concentration of 80 ppm. under the same operational conditions, the COD and TOC ratios were decreased to zero and 7%, respectively after 440 min using $\text{RGO}/\text{ZnO}/\text{MoS}_2$ in the photodegradation of the real wastewater sample [52].

Xin Jin et al. 2020 developed a green and simple method (in-situ ionothermal precipitation) to prepare highly efficient ZnO/NG nanohybrids with high and stable photocatalytic activity for wastewater treatment. The obtained ZnO/NG nanohybrids showed a highly photocatalytic efficiency in photodegradation of MB as there is a significant enhancement in the light absorption in the visible range which as a result of the decrease in the bandgap of ZnO nanoparticles after the combination of graphene [53].

R. Shyamala, and L. Gomathi Devi, 2020 prepared RGO/SnO_2 nanocomposites by attaching the reduced graphene oxide on the surface of SnO_2 to increase the absorption in the visible region. for SnO_2 and $\text{RGO}-\text{SnO}_2$, Rutile structure is confirmed. $\text{RGO}-\text{SnO}_2$ reduced the recombination of charge carriers by 30%. The photocatalytic activity of $\text{RGO}-\text{SnO}_2$ was improved as a result of the electron transfer inside the RGO network with a great surface area. the $\text{RGO}-\text{SnO}_2$ has an excellent photoresponse under both visible light and UV irradiation. As a result, to the extent of light absorption in the range of visible light region, excellent charge transport efficiency, and charge separation. The prepared $\text{RGO}-\text{SnO}_2$ photocatalyst indicates good stability [54].

Muhammad Aqeel Ashraf et al. 2020 prepared an innovative nickel sulfide/molybdenum trioxide nanocomposite (NiS–MoO₃/GO) by a simple hydrothermal route. The Structural analysis indicated that the synthesized NiS–MoO₃/GO NPs were a mixture of two different crystalline phases hexagonal, and orthorhombic. the photocatalytic activity of the prepared nanocomposite was studied for The MO under UV and visible light. Next, the antioxidant test and antibacterial were studied also against *S. pyogenes*, *E. coli*, and DPPH analysis. The experimental result indicated that the photocatalysis efficiency, and the photodegradation activity, under UV light, were greater than that under visible light as a result, to its the prepared photocatalyst has the highest absorption intensity of the UV light region. The NiS–MoO₃/GO nanocomposites showed the highest photocatalytic activity on the MO degradation in comparison with MoO₃ and NiS–MoO₃ nanocomposites as GO narrowed the energy bandgap of the prepared composites which inhibits the recombination of electron/hole pair and improves photodegradation efficiency [55].

3.1.2 Usage of GO Nanocomposites as Water Filter

To address challenges in photocatalyst recovery, the epitome of photocatalysts in some support materials (like ceramic, activated carbon, magnetic materials, glass, and membranes) has been investigated. Photocatalytic membranes are viewed as a decent support selection. immobilization the Photocatalyst on the membrane avoids wasting and enhance its use. improving the Membranes by photocatalysts may influence different membrane properties, for example, hydrophilicity, the rejection rate of contamination, water permeability, and fouling resistance. Incorporation of photocatalysis with the membrane is a hopeful and perfect technique to decrease the membrane fouling and progress membrane properties.

GO has pulled in much consideration on membrane separation because of their innovative properties. Numerous membrane improvement strategies incorporating blending GO with membrane and layered GO layer have been accounted for to create GO-containing layers with particular constructions. At the point when GO or altered GO is mixed in the membrane, the efficiency of the membrane will enhance. Addition GO to the photocatalytic membrane is vital; the carbonyl, hydroxyl, and carboxylic functional groups of the GO lead to make the membrane more hydrophilic and enhance its mechanical properties. Also, deposition MOS NPs with GO stopping the membrane fouling.

Wentai Wang et al. 2013 made up of TiO₂ and Cu₂O nanowires between reduced graphene oxide (RGO) sheets from colloidal suspension via a simple method to prepare a heterojunction photocatalytic membrane. The fabrication method concluded as 1) mixing the well-dispersed GO, TiO₂, and Cu₂O nanowire suspensions after that, vacuum filtration on a Mixture from Cellulose Ester membrane ($\phi = 47$ mm, 0.22 μ m), finally it dried on-air and peeled from the Mixed Cellulose Ester membrane. The fabricated membrane displays considerable enhancement in activity under the UV–Vis region, exceeding nanowires dispersions, due to heterojunction construction and separate electron and hole transference on RGO sheets.

permeability and photocorrosion resistance of the membrane were increased also. the RGO layers appear to enable simultaneous electrons and holes transfer, so the electron-hole separation was enhanced in addition to there is an increase in its surface area. Because of the presence of RGO sheets a hole transfer to RGO revealed an influence on overpowering photocorrosion of Cu_2O in heterojunction structure. The RGO/ Cu_2O / TiO_2 , and RGO membranes and show good conductivity and display the highest degradation rate. The result showed that: in comparison with the binary RGO/ Cu_2O (2.5 mg), the ternary scheme only shows a small enhancement in photocatalytic activity and in the rate of degradation under visible light. Excellent stability on photocatalytic activity was noticed on MO photodegradation efficiency after four cycling trials [56].

Yong Gao et al. 2014 used TiO_2 -GO to modify the surface of membranes and improve their photocatalytic activities towards methylene blue under both U.V light and sunlight. GO nanosheets and TiO_2 NPs also were deposited on a polysulfone membrane using the layer-by-layer method. the TiO_2 -GO membrane revealed good enhancement in MB photodegradation (3-4 times faster) under sunlight and (60-80% faster) under UV light Contrasted with polysulfone membranes surface-adjusted with TiO_2 and GO only. the membrane flux was improved also because of the photo-improved hydrophilicity [57].

Zhiwei Xua et al. 2016 supplied GO/ TiO_2 nanocomposites into the PVDF matrix to construct an innovative multifunctional GO/ TiO_2 -PVDF hybrid membrane using the phase inversion technique. The GO/ TiO_2 -PVDF membrane revealed a perfect morphology, i.e. higher surface pore size, porosity, lower surface roughness, and extra porous structure constructed with TiO_2 -PVDF, pristine PVDF, and GO-PVDF membranes. GO/ TiO_2 -PVDF membrane showed an enhancement in antifouling properties and separation performance because it has an ideal morphology, higher surface pore size, lower surface roughness, and porous structure than TiO_2 -PVDF, pristine PVDF, and GO-PVDF membranes. GO/ TiO_2 -PVDF. The GO/ TiO_2 -PVDF membrane showed noteworthy enhancement in water permeability and hydrophilicity as a result of the decrease in contact angle. the photodegradation efficiency of GO/ TiO_2 -PVDF membrane was increased also toward BSA, in comparison with TiO_2 -PVDF, and GO-PVDF membranes. the GO/ TiO_2 -PVDF membrane allowed to reach a high recovery of membrane performance after fouling, as a result of the UV static irradiation subsequent water washing, confirming their self-cleaning ability [58].

Hang Xua et al. 2017 Fabricated an innovative photocatalytic membrane by combining nitrogen-doped graphene/ TiO_2 nanocomposites (NRGT) with polysulfone (PSF) using a non-solvent-induced phase-separation technique. The study showed that the NRGT nanocomposites enhanced the photocatalytic properties and it has anti-fouling resistance under UV and sunlight. NRGT-PSF membrane exposed higher efficiency in MB photodecomposition under UV light and sunlight by (20-50%), and (30-80%) respectively than that result by the (PSF) membranes, (GO, or TiO_2 membrane), and graphene/ TiO_2 (RGT). the NRGT-PSF membrane exhibited an enhancement in hydrophilicity, increasing in photodegradation of pollutants, smoothing in the surface, and higher flux and antifouling resistance. Along these

lines, the NRGT-PSF layer could recuperate higher water transition after fouling and accordingly present upgraded fouling obstruction [59].

Wei Chen et al. 2017 fabricated a photocatalytic membrane using a polysulfone membrane and N-TiO₂/graphene oxide nanoparticles by grafting it on the membrane surface. The prepared membrane displayed an enhancement in photocatalytic activity, specifically under sunlight than UV light, as a result of it has a rougher surface leads to enhances the photodegradation activity and a lesser water-contact angle, which improve the hydrophilicity. The photocatalysis and filtration of the prepared membrane were tested toward methylene-blue. a better methylene-blue removal ability was observed using the photocatalytic membrane than the pure membrane for a lower concentration of the methylene blue. the photocatalytic membrane exhibits a great improvement in recyclability than powder photocatalyst [60].

Xiaoju Yan et al. 2019 used a layer-by-layer technique to blend GO on polyacrylonitrile support and connecting GO nanosheets through polyethyleneimine to fabricated GO/TiO₂ membrane. The prepared GO-TiO₂ membrane exhibited good photocatalytic activity to remove methylene blue under UV with a 58.8% removal rate for 250 min. The results indicated that an enhancement in the J/J₀ percentage from 41 to 54% of the fouled GO-TiO₂ membrane after the membrane was irradiated with UV light for 30 min. The flux of the GO-TiO₂ membrane was improved from 1.67 to 1.88 L/m²-h when it irradiated with UV light for 40. This improvement may be caused because of the photoinduced superhydrophilicity of TiO₂ NPs. the flux of the treated GO-TiO₂, and GO membranes with and without UV treatment before filtration was studied also. the water flux of the treated GO membrane by the UV before filtration did not influence. However, the water flux of the treated GO-TiO₂ membrane with UV was increased. UV treatment enhanced the hydrophilicity of the GO-TiO₂ membrane which quick the spread of water everywhere on the membrane surface and among layers, which degrade the methylene blue that fouled on the surface [61].

A. M. Croitoruo et al. 2020 fabricated CS/EDTA/GO composite membranes using graphene oxide (GO) and chitosan (CS) by functionalization of CS with GO, and EDTA and used it as an excellent adsorbent material to adsorb and remove inorganic contaminants for example heavy metal ions, especially Pb⁺² from aqueous. Mixing EDTA with CS solution can support and raise the adsorption procedure for Pb⁺² ions [62].

Madhubonti Pal et al. 2020 synthesized graphene oxide-based nanocomposites membrane by using graphene oxide (GO) nanomaterials to modify polyethersulfone (PES) membrane using a layer-by-layer method. Trimesoylchloride (TMC) was used as a cross-linking reagent in the manufacturing process to help the adhesion of the GO layer strongly onto the surface of the membrane over strong ester bonds. This Tanique is a combination between advanced oxidation and downstream membrane separation by a new GO-based nanocomposite membrane. Experimental results expose hydrophilic nature, high mechanical strength, high flux, High rejection efficiency, and high selectivity in the elimination of ionic impurities [63].

Meng You et al. 2020 used the solution casting technique to fabricate graphene-based nanocomposite membranes using a different reduction degree of RGO prepared by the hydrothermal reduction process and cellulose triacetate (CTA). The water/salt conveyance properties of the membranes that blended with different reduction degrees and diverse morphologies of GO, including single-layer GO (SGO), multi-layered (MGO) and RGO were investigated. Moreover, the microstructure variation, free volume, thermal properties, and crystallinity of the prepared nanocomposite membranes were also investigated to picture the effect of RGO and GO on properties. An enhancement in the prepared membrane density and glass transition temperature was observed as a result of the interface of the polar group in GO/RGO through CTA chains. The water permeability was increased also as a result to the increase in its diffusivity because of the decrease in crystallinity and supplementary channel from RGO through the addition of RGO. The decrease in the salt permeability according to reducing its diffusivity is a result of the interactions of ions through GO/RGO and the membrane densification also. Both the water/salt selectivity, and the water permeability were increased with the decrease degree because of the declined water transference resistance [64].

Vahid Vatanpour et al. 2021 Fabricate N-doped porous graphene oxide (N-PGO) and used it by way of hydrophilic nanosheets to improve the efficiency of the polyethersulfone membranes. The prepared membrane was used for the separation of bovine serum albumin and protein Sensitive Red 195 dye. As the amount of porous graphene oxide exceeds the membrane hydrophilicity was improved because of the presence of nitrogen and hydrophilic hydroxyl groups on the porous graphene oxide surface which caused a high efficiency in the separation layer of membranes caused by the simultaneously promoted hydrogen bond between the N-PGO nanosheets and polymers. The pure water flux increased as the antifouling appearances of PES membranes improved [65].

Hifza Nawaz et al., 2021 Incorporated PANI-GO as a nanofiller to polyvinylidene fluoride (PVDF) To fabricate and improve the permeation properties of a novel hybrid PVDF/PANI/GO composite membranes via the phase inversion process. The experimental result indicated that PVDF/PANI/GO composite membranes have a slighter shrinkage ratio besides pore size with modest roughness of membrane surface than the blend PVDF membrane. The contact angle decreased, which ensure the presence of GO functional groups on the PVDF/PANI/GO composite membrane surface. The Pure water flux, the hydrophilicity of membranes, mechanical stability (The Young's Modulus and tensile strength), and the BSA rejection, of PVDF, were enhanced with the addition of GO and PANI. Degradation temperature was increased. the flux recovery ratio and dye rejection were improved also [66].

Layered GO membranes are assumed as a promising membranes filtration strategy to get high efficiency, selectivity, permeability, and anti-fouling capacity. The specific properties of GO don't get more attention. membrane fouling is a significant issue in membrane applications, while some GO membranes are now utilized in wastewater treatment applications. The membrane fouling result from the use of GO was not studied sufficiently.

3.2 Usage of Graphene Nanocomposites and Their Derivatives in Sensor

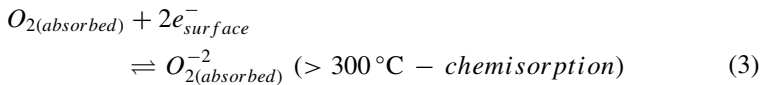
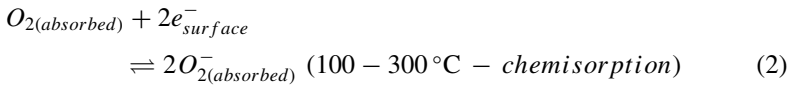
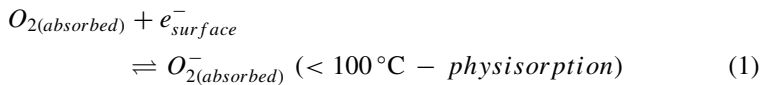
Within the growing, the emphasis on environment, a potential interest in the detection of hazard toxic gases is facing a high challenge to monitor industrial chemical processing such as in medicine, food, and agriculture industries. The detection of harmful gases can be achieved via a gas sensor device, which converts traces of such gases to a detectable electrical signal. A chemical sensor is a chemiresistive device configuration, which provides a signal in a form of change in the resistivity or in the conductivity [67, 68]. Changes in the conductivity occur due to exposure to different gases with a different concentrations in humid and non-humid atmospheres [69]. The sensor device can be classified by various parameters such as; the sensor working temperature, stability besides the lifetime, selectivity to a certain kind of gas, sensitivity with a detectable signal, and production cost of the sensitive layer [70, 71]. MOS are widely dominated by the commercial gas sensor market due to their high sensitivity and fast response [67]. The sensing mechanism of MOS has been explained and understood through the reduction or the oxidation reactions that occur on their surfaces [69]. However, a short lifetime, poor selectivity, and the high working temperature consider the main hindering disadvantages of their usage. One approach has been performed to overcome these problems, which is a fabrication of nanostructure materials to obtain a higher surface area and results in a higher sensitivity. Even though, still, the working temperature of the MOS is the main obstacle for their usage and makes them unsuitable for battery-operated applications due to their high power consumption [70]. Recent alternatives to overcome the drawbacks of MOS are GO, RGO and their nano-derivative have been given [70]. Since, GO is a monolayer material that offers a huge surface area, which allows higher possibilities for gas-surface interaction [72, 73]. In addition to, its high electron mobility at room temperature and lower resistivity in order of $20,000 \text{ cm}^2/\text{Vs}$ and $10^{-6} \Omega\text{cm}^{-1}$, respectively [74]. Various approaches are widely applied to functionalize the graphene, RGO with MOS to obtain highly sensitive hybrid graphene nanosheets such as Fe_2O_3 , NiO , WO_3 and SnO_2 decorated graphene nanosheets [75]. Additionally, hybrid graphene-based nanocomposites and noble metals have been employed [76].

The sensing mechanism is based on two types of gas-surface interaction, physisorption and chemisorption, as a weak van der Waals force and strong chemical bond, respectively. Those types of interactions reflect the bond nature, which is formed between the gas molecules and the surface of the sensing material. The bonding varies from van der Waals to a strong covalent bond, which can change the electrical conductivity drastically. To monitor those reactions a sensor device needs to fabricate. Generally speaking, the sensing device consists of a receptor and transducer [68]. The receptor is the material in use, which is in our case is the graphene, RGO, and its nano-derivatives. Whereas, the transducer is the component that transfer the gas-graphene material to an electrical signal (through an electrical metal electrode).

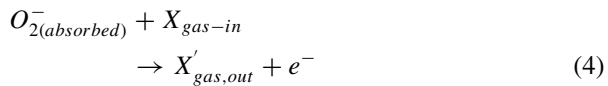
3.2.1 Gas-Sensor Working Mechanism

The decisive mechanism of gas- MOS sensors is very controversial [77]. However, the conventional depletion layer model is widely used [67]. In the standard depletion layer model, it is assumed that all kinds of receptors consist of large grains for bulk films and small grains for nanomaterials. The interaction between the reduced gas and the adsorbed oxygen ions on the surface of the n-type materials (e^- is the majority carriers) results in returning free carriers to the conduction band of the active sensing material and form a narrow depletion region on its surface [78]. On the contrary, for oxidizing gases, the depletion region on the surface of the n-type material is found to be wide due to electron attraction by the adsorbed gas species. This interaction leads to a decrease in the free carrier concentration in the conduction band (Fig. 5).

These influences of the gases can be seen as a form of tuning the electrical conductivity from lower to higher values corresponding to oxidizing and reducing gases, respectively. Hence, the oxygen molecules in the atmosphere are adsorbed on the surface and form oxygen ion molecules by attracting electrons from its conduction band. This effect depends strongly on the working temperature of the sensor device. The reaction is known as a ‘chemisorption reaction’ and can be given in form of the following relations [67, 79]:



where the target gas X (‘gas-in’ period) reacts with adsorbed ions on the surface according to the following relation [79]:



At the terminals (M-electrodes), a fixed independent barrier height forms as a result of metal/semiconductor junction. It is given as (eV_{m-s}) Fig. 5. Whereas, another barrier height of (eV_{s-g}) can be formed between the grains as a result of an interaction between the grain surface and the surrounding target gas. It is known as barrier height at the grain boundaries [80].

A well-defined semiquantitative model, given by Xu et al. 1991 for nanomaterials, states the relationship between the grain size, width (W) of the depletion region, and the sensitivity (S) through the following relations [67, 71, 81]:

$$\lambda_D = \left(\frac{\epsilon k_B T}{e^2 n_b} \right)^{\frac{1}{2}} \tag{5}$$

$$W = 2\lambda_D \left(\frac{e V_{s-g}}{k_B T} \right)^{\frac{1}{2}} \tag{6}$$

$$e V_{s-g} = \frac{e n_s^2}{2\epsilon n_b} \tag{7}$$

$$S = \frac{R_a}{R_g} = \left\{ (1-x)^2 + \frac{n_s}{n_b} [1 - (1-x)^2] \right\}^{-1} \tag{8}$$

where λ_D is Debye length as a material character, n_b is the free carrier concentration of the bulk material Fig. 5, n_s is the carrier concentration of the charges attached to the surface of the sensing material's grains (bound to the depletion region as surface states), R_a is the initial resistance in air, and R_g is the resistance under gas exposure. Whereas, x is a factor related to the grain size through the relation $x = 2\lambda_D/rD$ where D is the grain diameter or size and r is a constant.

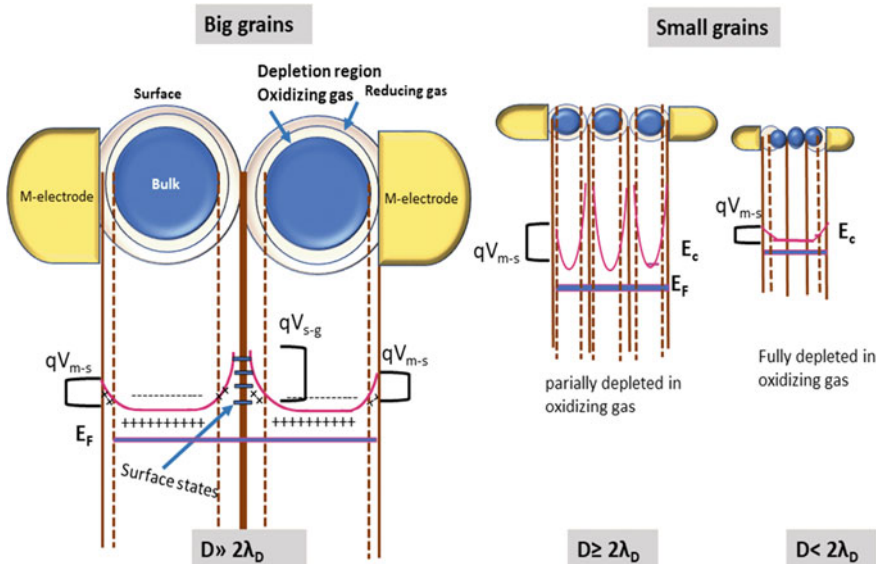


Fig. 5 Schematic illustration of depletion layer model and nick model for large and small grains, respectively

- We can deduce from these equations that the widest space charge region, which dominates the whole grains, can be formed when $D < 2\lambda_D$. In this case, no significant barrier height can be obtained between the small grains at a certain temperature, which is known as fully depleted grains. Therefore, the highest sensitive performance can be obtained [81]. Hence, the reaction between oxidizing and reducing atmospheres and the sensing material causes noticeable changes in the resistance even for a short exposure time to these atmospheres.
- In the case of $D \gg 2\lambda_D$, the total resistance of the device is controlled by the inner or bulk carrier concentration. Therefore, it is less sensitive to the interacted carriers at the surface.
- For $D \geq 2\lambda_D$, the space charge region shows nick-like conduction channels around each grain. Therefore, the resistance shows dependence not only on the grain boundaries but also on the cross-section area of every conduction channel around the grains. This leads to better sensitivity [82].

The metal–semiconductor junction barrier height (eV_{m-s}) for all cases is independent of the sensitive performance. However, the electrode material must be highly stable, do not diffuse into the semiconductor at high temperature, do not form an oxide layer in the interface, and do not corrode due to exposure to the target gases, because this could reduce the conductivity of our sensor device. For more information, see [83]. The graphene-based materials is favorable to be applied as ultrasensitive material due to their nanograins [74]. Whereas, the atoms in the graphene are a surface atom, which offers a large area for gas adsorption and interaction. As well as, their low operating temperature which mostly operates at room temperature. However, the weak chemical interaction between the carbon material and the gas molecules hinders the widespread usage of gas sensors based on graphene [84]. Therefore, a lot of strategies are applied to functionalize hybrid nanocomposites based on graphene, their derivatives, MOS, and polymers, not only to optimize a lower working temperature but also to improve the selectivity and sensitivity of the sensor device. In the next section, different nanocomposites based on hybrid graphene materials have been introduced.

3.2.2 Wearable Gas Sensor Based on Graphene Nanocomposites and Derivatives

Wearable device with functional groups are emerging widely in tremendous applications such as health monitoring [85, 86], in military purposes, and external stimuli as gas sensor [87]. The wearable sensing device usually deposited or fabricated on different flexible substrates such as poly(methyl methacrylate) (PMMA) [85, 88], poly(dimethylsiloxane) (PDMS), polyimide (PI) poly(ethylenephthalate) (PEN), poly(ethylene terephthalate) (PET) [89], Lenin [90], and cotton fabrics [87, 91]. great attention has been paid to sensor applications based on graphene-based material in wearable electronic textiles (e-textiles) due to their high reactivity with the oxygen groups in the textile fibers [89, 91]. E-textiles are gaining a considered attraction in

this field of gas sensors because of their low-cost fabrication and convenience to use with clothes and portable smart electronics.

The promising finding by Listya Utari et al. 2020 revealed on a wearable gas sensor device based on hybrid p-type graphene nanostructure/n-type ZnO nanowires grown on cotton fabric. The deposition of the graphene layer was utilized by using the dry-dipping method. Following the seed layer deposition of Zn.

O by a solution-based method on the graphene-coated cotton fabric, the ZnO nanowires are grown via chemical bath deposition technique Fig. 6. The device electrodes were designed to be a silver top-coplanar electrodes configuration [92].

The flexible wearable gas sensor based on graphene/vertically aligned ZnO nanowires coated cotton fabric performs well and providing a good sensitivity to CO gas in low concentrations (10–90 PPM) at room temperature as can be seen in Fig. 7a. It is worth to mention, that the sensor device based only on graphene

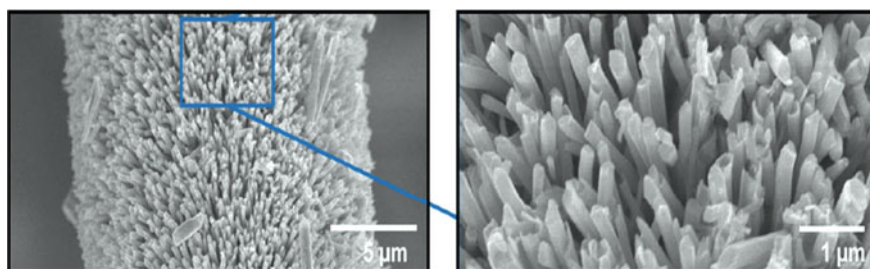


Fig. 6 SEM micrographs of cotton coated graphene flakes covered with vertically aligned ZnO nanowires. Reused by the license under a Creative Commons Attribution 4.0 License, L. Utari *et al.* “Wearable Carbon Monoxide Sensors Based on Hybrid Graphene/ZnO Nanocomposites,” in IEEE Access, vol. 8, pp. 49169–49179, 2020

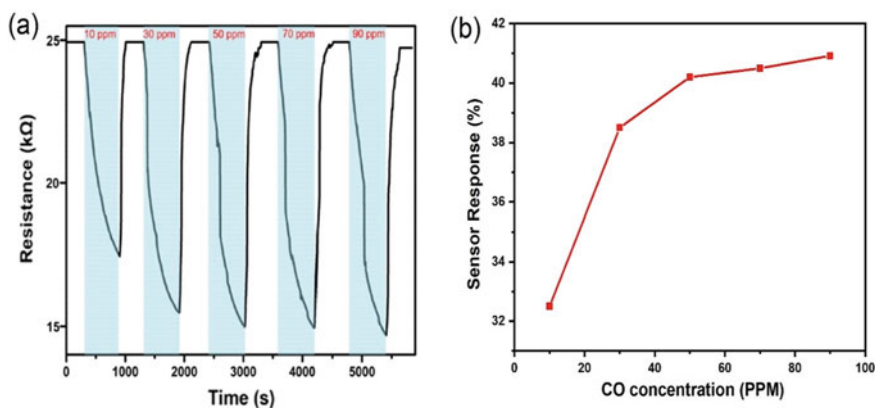
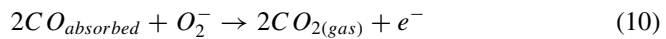


Fig. 7 **a** The resistance versus the time of the different concentrations of CO exposure of graphene/ZnO nanowires coated cotton fabric. **b** The corresponding sensor response to different CO concentrations

material shows the lowest sensitivity compared to graphene/vertically aligned ZnO nanowires. Moreover, the graphene/vertically aligned ZnO nanowires sensor device demonstrates a good selectivity toward Co gas at a value of $\approx 40\%$ (using Eq. at room temperature significantly more than common hazard gases detected by MOS materials (e.g., NO, ethanol, acetone, and methanol), whereas the sensor device based on MOS material show a poor selectivity behavior.

This result suggests the advantages to apply such hybrid graphene/MOS nanostructures coated fabric devices. The graphene material causes an enhancement in the conductivity of the MOS material, which it provides the MOS with additional electrons. In this case of the composite of p-type graphene/p-type ZnO nanowires, a potential barrier forms and band bending because of carrier's diffusion until an equilibrium state is reached [93]. Based on the working mechanism of the gas sensor, the adsorption of oxygen species happens to the surface of the MOS (ZnO) and attract free electrons from its conduction band. Under the exposure to CO gas (reducing gas), the gas molecules interact with these adsorbed oxygen species (Eq. 1) and consequently release back free electrons to the composite's conduction band (increase the conductivity) as can be seen in the following relations [78]:



Deepak Punetha et al. 2020 reported on a novel hybrid ternary nanocomposite based on a combination of graphene-based material (RGO), metal oxide (SnO_2), and additional polymer (polyvinylidene fluoride PVDF). The device was prepared by using different weight percentages of RGO, SnO_2 , and PVDF nanocomposites via the hot press method. The interactions between these tertiary compounds are formed when the π -electrons of RGO are attached to CH_2 dipoles of PVDF followed by F/H atoms of PVDF attached to the OH, carbonyl, and carboxyl groups in RGO [94] (Fig. 8a).

The sensor device has been deposited on Cr-electrodes, which shows a flexible nature (Fig. 8b). The wearable sensor device has been exposed to different H_2 gas concentrations (10–1000 PPM), which showed the highest response in comparison to exposure of N_2O , NH_3 , H_2S , CO, and CO_2 (Fig. 8c). Hence, the H_2 gas considers as a reduced gas, which interacts with the adsorbed oxygen species as mentioned in Eq. (1) and release back free electron to the nanocomposite and increase the conductivity. Interestingly, the wearable hybrid tertiary device based on RGO, SnO_2 , and PVDF introduces a well stable sensing performance under different concentration of H_2 gas continuously for a period of several days (Fig. 8d).

However, Xia HE et al. 2019 reported a multifunctional reduced nanographene oxide directly on linen (RGO/LN). The sensor device showed significant sensitivity, fast response, fast recovery, and feasibility. Various CH_4 gas concentrations (100–200 PPM) have been used as a target gas at room temperature, whereas the resistance ascends with the increase in the gas concentration (Oxidizing target gas). The high

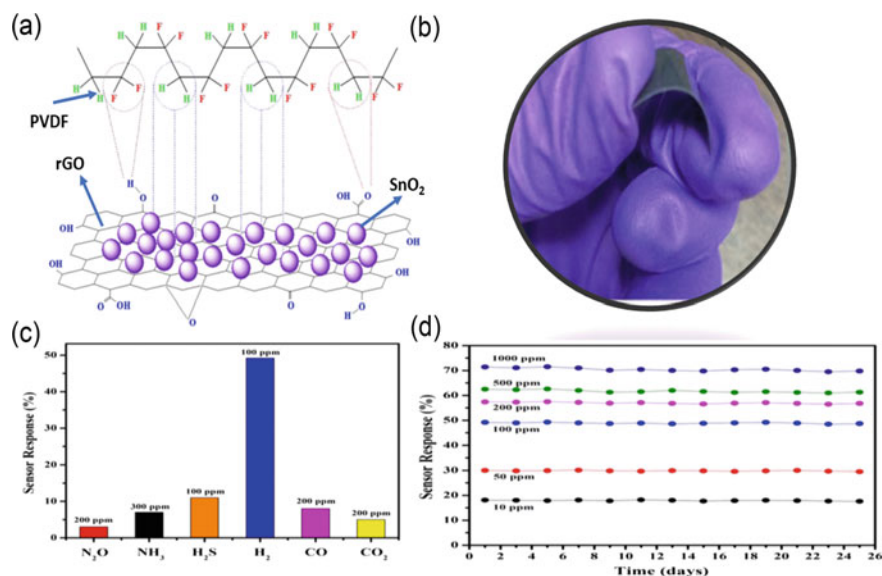


Fig. 8 **a-** The formation mechanism of the hybrid tertiary nanocomposites (RGO/SnO₂/PVDF) gas sensor. **b-** A wearable gas sensor device of (RGO/SnO₂/PVDF) nanocomposite. **c-** The sensitivity response to different hazard gases. **d-** The stability performance of the hybrid tertiary device versus the exposure time to different H₂ gas concentrations, Copyright © 2020, Springer [94]

sensitivity of (RGO/LN) is found to be attributed to the ionized oxygen attached to the surface of LN. When the RGO/LN exposes to the CH₄ gas, the latter decomposes into CH₃ and radical H ions, which interact with the ionized oxygen ions on the surface to form water molecules and release oxygen gas. This reaction shows a good moisture permeability as well as gas permeability [90].

After introducing some strategies to obtain a remarkable sensor, still another limitation of these implementations, which is the electrical conductivity of the e-textile as a transducer. Prior studies have emphasized that attaching graphene and its nanocomposites on the textile via an adhesive layer can improve the electrical conductivity. An apparent limitation of this method is the unfeasible fabrication method of the adhesion layer such as low acidic media necessary to obtain protein (e.g. bovine serum albumin) attached graphene [95]. Moreover, using organic adhesive can utilize the fabrication method, but was found to reduce the sensor performance (e.g. low sensitivity and selectivity) [91, 96]. Sang Won Lee et al. 2020 successfully introduced a new adhesive material, which can lead to highly conduction graphene-based e-textiles [96]. Dopamine (DOPA) has been used as a bio-inspired adhesive biomolecule. Hence, DOPA has been known as a reducing agent for graphene to form a RGO. Sang Won Lee et al. 2020 showed an improved DOPA- graphene flakes- Yarn (DGY) hybrid e-textiles gas sensor device for NO₂ gas detection. Figure 8 shows the schematic of the preparation of DGY via dip-coating at room temperature followed by a reduction process of the graphene at 40 °C.

The gas sensor device based on RGO-DOPA yarn shows higher sensitivity and selectivity to different concentrations of NO₂ gas (0–100 PPM) in comparison to RGO directly coated yarn. Moreover, the response time is found to be ≈2 min for RGO-DOPA yarn, contrary to RGO yarn which needs double the response time. These results demonstrate the better adhesion and reactivity of RGO flakes to DGY more than directly to yarn.

3.3 Usage of Graphene Nanocomposites and Their Derivatives in Solar Cell Devices

Nowadays, the different types of solar cells based on nanomaterials composited from pure graphene or its derivatives (GO, RGO) and other active metal oxides show high potential. These Carbon composites are used as counter electrodes (CEs), photoanodes, photoactive layers, hole transport layers (HTL), or electron transport layers (ETL) in various solar cells. Solar cell performance is improved by optimizing the carrier's generation and increasing their transportation between electrodes due to the presence of Carbon materials.

In all generations of photovoltaic (PV) technology, graphene, and its derivative materials were thoroughly examined for characteristics such as high optical transparency, high carrier mobility, and a zero-band gap. Besides it has been applied in various forms in the cells: graphene flakes, monolayer graphene, multilayer GO, and RGO have all been introduced. Herein, the developments of graphene-based materials in PV devices for example dye-sensitized solar cells (DSSCs), perovskite solar cells (PSCs), and organic solar cells (OSCs) are analytically reviewed [97–99]. The important roles of graphene-based materials in PV devices are studied by reviewing the most convincing results.

3.3.1 Photo-Anode or Counter Electrodes (CEs)-Based GO or RGO Materials

Graphene derivatives represent a promising substitute for traditional metallic electrodes e.g., in the bifacial different types of solar cell where both top and bottom electrodes can be substituted with a graphene sheet.

To dope RGO thin film surface effectively, Low et al. (2019) have investigated the effects of titanium (Ti) atoms sputtered from various sources on substrate area. To increase the performance of dye-sensitized solar cells (DSSCs), RGO-TiO₂ nanocomposites have been successfully manufactured as photo-anodes. Using RF magnetron sputtering procedure, RGO-TiO₂ nanocomposites were gotten using various sputtering distances between the Ti⁺³ target and RGO nanosheets. The Ti target allocated with 10 cm-apart FTO glass-coated RGO nanosheet and 0.67 cm² active area showed an ideal PCE of 6.60% after optimization, which is substantially

higher than the normal sputtering distance of 5 cm obtained by the sample (1.90%). These results were due to poor catalytic light absorption at the interface between photo-anode/FTO [100].

Javed et al. (2019) have used a solvothermal method for efficient plasmonic dye-sensitized solar cells (PDSSCs) to build advanced Ag/RGO/TiO₂ ternary nanocomposite-based photo-anode. In PDSSCs, the nanocomposite showed improved productivity of power variation of 6.87%, which was 15% greater than that of the pure photoanode based on TiO₂ NPs. Also, relative to pure TiO₂, an improved IPCE of 68% was also observed. The plasmonic effect of Ag NPs and the remarkable conductivity of RGO could be due to improved performance [101].

The molybdenum sulfide (MoS₂)/RGO composite was synthesized by Pang et al. (2019) via a hydrothermal technique to attend as a cheap and non-platinum counter electrode (CE) to enhance DSSC photovoltaic efficiency. A higher power conversion efficiency (PCE) of 6.72% is achieved by the fabricated cells than with Pt CE (5.74%) under normal sunlight radiation. The result shows that the hydrothermal MoS₂/RGO composite CE processed in one step has excellent electrocatalytic properties to accelerate the reduction of I⁻³ and showed an improvement in recombination rate with MoS₂/RGO CE than with Pt CE [102].

Using the electrodeposition process, Bahrami et al. (2019) have investigated the electrocatalytic behavior of Pt-Ni/RGO CEs. The thin films of the Pt-Ni alloy with different concentrations of Ni on FTO were prepared by electrodeposition. Then, using spin coating on Pt-Ni alloy thin films, GO film was deposited, and then thermal reduction was performed. The highest electrocatalytic activity corresponding to higher J_{Red1} ($-26.79 \text{ mA cm}^{-2}$), lower V_{Red1} (-1.28 V), and lower E_{pp} (0.26 V) compared to pure Pt and Pt/RGO CEs is obtained at Pt_{0.29}Ni_{0.71}/RGO CE [103].

A TiO₂-RGO composite has been produced by K. A Kumar et al. (2019) using the hydrothermal technique to reduce GO to RGO directly. In the photo-anodes of liquid junction DSSCs, those composite structures were then used. Because of the presence of electron acceptors in metal-based compounds, the measured PCE from the J-V curve is improved from 5.02 to 5.69%. Devices based on metal-free and metal-based complex co-sensitization display a PCE in the range of 2.29–2.65% [104]. Along these lines, Yalcin and Yakuphanoglu (2020) have used the same material in the QDSSCs. Finding the optimal doping ratio is the most significant influence in the manufacture of RGO-doped composites. For the doped pattern with 0.12 g of GO, the highest efficiency was obtained, as a result to the electrons lifetimes in this pattern were four times longer on average than those of the TiO₂ pattern. This increase suggests that thanks to RGO, new electron transport pathways have developed within the composite, that a major reduction in electron back-transfer has been achieved and that recombination has been repressed [105].

The Co_xSn_{1-x}/RGO nanohybrids CEs in DSSCs have been reported as inexpensive, stable, and earth-abundant by Omelianovych et al. (2020). NPs were prepared by reducing the functional oxygen groups of GO in the plasma-assisted type and by immobilization of the bimetallic NPs. The optimization of the PCE structure for DSSCs based on Co_{0.9}Sn_{0.1}/RGO contributed to a 5.36% improvement in PCE. The increased catalytic activity of the CEs indicated that efficiency was achieved [106].

The modification of both functional electrodes of a PDSSC to create an effective solar system structured with Cu/TiO₂ and RGO/Fe₃O₄ nanocomposites has been demonstrated by Qureshi et al. (2020). PCE was shown in PDSSCs by the Cu/TiO₂ nanocomposite-based photo-anode of 3.89% with platinum (Pt) and 2.20% with hybrid RGO/Fe₃O₄ CEs, respectively. The PDSSC based hybrid RGO/Fe₃O₄ CE achieved 57% of the efficiency of the conventional Cu/TiO₂ platinum electrode and 70% of that of pristine photoanodes based on TiO₂. The rational efficiency increase could be attributed to the uniform dispersion on the surface of RGO nanosheets of catalytic Fe₃O₄ nanoparticles (NPs) and due to the plasmonic effect of Cu NPs [107].

In the configuration of a perovskite solar cell with RGO contact Zandi et al. (2020) have provided 3D similar photogeneration, thermal/heat distribution, and electrical characteristics. The RGO contact does not greatly affect cell optical efficiency and electrical output but speeds up heat dissipation. The thermal pattern of the cell was improved due to heat conductivity and the thin thickness of the RGO layer [108].

3.3.2 Photoactive Layers-Based Composites of Carbon Materials

To achieve an effective active layer in organic PV material, (OPV) polymer device manufacturing was carried out by S. Kumar et al. (2019), and comparative analysis of RGO incorporated with polymers [2-methoxy, 5-(2'-ethylhexyloxy)-p-phenylenevinyl] (MEHPPV) and poly(3-hexylthiophene) (P3HT). After reduction from GO successfully, the RGO nanocomposites were developed using a simple ultrasound technique. To confirm the reduction of GO, the synthesized RGO was defined using different techniques. The I-V results suggested a 0.045% performance of the RGO composites mixed with P3HT polymer [109].

By introducing 1-dimensional (1D) multi-walled carbon nanotubes (MWCNTs) and 2-dimensional (2D) RGO in P3HT:PC60BM blends, bulk heterojunction (BHJ) photovoltaic cells (PVCs) have been manufactured by Mahakul et al. (2019). A maximum Jsc of ~11.01 mA/cm², Voc of ~0.63 V, and FF of ~0.5 were found in the manufactured solar cells, providing efficiency of ~4.13%. In addition to PC₆₀BM with P3HT, the increased performance was due to the effective exciton dissociation of CNTs and RGO junctions. The faster transportation of PC60BM electron and the hole through the CNT/RGO network in combination, which impedes the recombination of the carrier, significantly contribute to improved PVCs efficiency [110].

The photoactivated layer of an organic nanocomposite-based system in which the conductive polymer MEHPPV acts as an electron donor and the green route RGO as an acceptor material through L-Ascorbic Acid (L-AA) was materialized by S. Kumar et al. (2020). The highest efficiencies are found in the devices developed with 0.1 wt% RGO-AA, while those with 0.8 wt% display the greatest current characteristics, and those manufactured with 0.5% wt gives the least current and voltage. Therefore, it is obvious that the RGO-AA is a nanocomposite acceptor in the form of the MEHPPV and that charging is transferred at the donor: accepting interfaces which show that the RGO-AA can be used for the OPV applications [111].

Organic solar cells with a photoactive layer structured by P3HT and PCBM blend, reduced graphene oxide-germanium dioxide nanocomposite (RGO-GeO₂) were designed by Amollo et al. (2020). An increase in PCE from 1.5 to 2.2% was observed by BHJ SCs with RGO-GeO₂ composite in the active layer. By integrating RGO-GeO₂ into the active layer, improvement in the measured photocurrent is achieved. The high J_{sc} (up to 17 mA/cm²) indicates that the RGO-GeO₂ inlay in the active layer promotes the separation of excitons and generates percolation pathways for electrode charge transport. A built-in potential difference between the donor and acceptor phases of the active layer is energetically preferred by Charge separation. Therefore, the incorporation of composite RGO-GeO₂ into the active layer enhances the photogeneration, separation, and transport of its charge to yield high J_{sc} and improved PCE. In photovoltaic applications, the findings presented here extend the functionality of graphene derivatives [112].

Two sets of devices were manufactured by Fallahazad et al. (2020), photovoltaic characteristics of graphene/Si heterojunction solar cells based on flat and pyramid structure of Si. For the development of the pyramidal skeleton, selective chemical dissolution of Si wafers was carried out. Via electrophoretic deposition (EPD) techniques, RGO was then transferred to pyramidal Si. Compared to a solar cell based on a flat Si substrate, the conversion efficiency and current density of this system have been increased. It is due to the increased interface area between active layers of Si and graphene and improved surface roughness that improved light absorption on the surface [113].

Porous silicon (pSi) surface enhances light trapping in which improves the silicon solar cell performance. Rai et al. (2020) have determined the photoresponsivity of the devices designed of pSi heterojunction with GO, RGO, GO-polyaniline (PAni), and RGO-PAni are 0.053, 0.124, 0.348, and 1.25 mA/w, respectively. The photosensitivity as well as the photo responsivity, is found to be highest for pSi/RGO-PAni. This may be due to the enhanced π - π stacking forces between the π orbitals of sp² carbons of the aromatic ring of RGO and the quinoid ring of PAni. However, in the case of pSi/GO-PAni because the GO possesses a lesser number of sp² C atoms compared to RGO there are fewer π - π stacking forces [114].

3.4 Hole Transport Layer (HTL) or Electron Transport Layer (ETL)-Based Carbon Materials

As an ETL on perovskite solar cell efficiency, Patil et al. (2019) have investigated the effects of RGO-TiO₂ composite nanofibers. An efficiency = 17.66% of the PCE of Voc 1.070 V, J_{sc} of 22.16 mAcm⁻² and FF of 2.754, the optimum system with the configuration FTO/Bi-TiO₂/RGO-TiO₂/(FAPbI₃)_{0.85}(MAPbBr₃)_{0.15}/spiro-MeOTAD/Au, which might help to eliminate electrons and bring them from perovskite sheet. The effectiveness of mesoporousTiO₂ (14.39%), pristine-TiO₂ nanofibers (15.82%), and other nanofibers-based composite RGO-TiO₂ materials

was much higher. The results shown by RGO encourage better charge collection and quick electron transport leading to a considerably increased PCE. These results can be attributed to the charging transport results [115].

The performance of OSCs using the GO derivative as HTL has been reported by Nicasio-Collazo et al. (2019). OSCs are based on the PTB7:PC71BM blend as active layer and the alternative top electrode Field's metal (Bi/In/Sn: 32.5, 51, 16.5%). GO was chemically functionalized and reduced to form fluorinated (F5)-RGO with pentafluorophenyl hydrazine. Because of the strong electrostatics of the fluorine atoms embedded in the GO sheets, the working function of F5-RGO is 5.1 eV. The most active PCE of OSCs manufactured for one F5-RGO layer was 5.82%. An enhanced PCE of 7.67% was achieved when the F5-GO was used as an interlayer between ITO and PEDOT: PSS was reached 7.29%. These results have shown that this F5-RGO is an acceptable candidate for HTL use in the manufacture of OSCs or other electronic devices [116].

Hosseini et al. (2020) have synthesized P-type nanocomposites of RGO/Pt NPs through an in-situ crystallization method and used it as HTL in OSCs. By applying ethylene glycol (EG), sodium citrate (SC), and ascorbic acid (AA) as reducing agents through the in-situ crystallization process, three types of RGO/Pt nanocomposites were produced. Results have shown that the reduction of the form of agent has a significant effect on the removal levels from GO nanosheets of the oxygen-containing functional groups and structural disorders of the resulting RGO. Due to the lowest energy barrier between the P3HT and RGO/Pt NPs-EG, the PSCs were improved by 210%, making the extraction of a hole from the active layer easier and the resulting PCE improvement. The increased energy difference at the interface of the photoanode/HTL also improves the hole extraction and thus their photovoltaic efficiency [117].

To enhance the conductivity of the designed perovskites solar cells, Ding et al. (2020) have synthesized the RGO/NiO composites with different doping ratios of RGO using a simple hydrothermal process. The carrier transport in the cell was significantly improved by carbon PSCs, resulting in a 32% increase in J_{sc} , further reducing series resistance (R_s). Doping of the HTL improved the efficiency of carbon-based perovskite solar cells and increased the cell's PCE from 5.48 to 8.5%. These findings suggest carbon solar cells that will help improve the efficiency of these cells in the future [118].

Mann et al. (2020) have produced an effective planar perovskite solar cell with two layers of poly(3,4-ethylenedioxythiophene): poly(styrenesulfonate) (PEDOT: PSS) and sulfonic acid functionalized graphene oxide (SrGO) as HTL. The PEDOT: PSS/SrGO interlayer treated at low temperature and solution provided a better PCE of 16.01% than other single layers. Comprehensive analysis indicates that the increased PCE is mainly due to the reduction in recombination and the enhanced built-in potential for better transport and extraction of charges. The device also demonstrated excellent long-term stability in ambient air conditions with PEDOT: PSS/SrGO. Those findings, therefore, help the promising approach for high performance and cost-effective solar devices by incorporating graphene materials into interlayers [119].

4 The Present Challenges and Future Research in Graphene and Its Derivatives

As a summary, we have realized the importance of fabrication of GO and its derivative as it has a varied application such as wastewater treatment, sensor, and solar cell...etc. so, develop of an ecofriendly, fast, simple and cost-effective methods to prepare GO, RGO with excellent and suitable properties is highly demanded and it is still an interesting and challenging field. It has been confirmed that the addition of GO nanocomposites to membrane leads to improve the efficiency of the photocatalysis, and separation process. Nevertheless, there also exist problems in the practical application of GO nanocomposites in the removal of heavy metal ions and industrial waste, which must be solved. NPs tend to aggregate into large-size particles which decreases their activity so used a highly efficient method to solve this problem and getting better dispersion NPs is highly demanded. GO membranes can suffer from potential fouling caused by the matching between the carboxyl groups on the surface of the membrane, as well as cationic foulants. The fouling problem exists in subsequent filtration steps, which effect on membrane efficiency must be solved to get long-term stability of membranes. we have realized also the importance of fabrication of a high conductive, wearable e-textiles gas sensor based on hybrid graphene and its derivatives. Hence, they revealed a high sensitivity, selectivity, and scalability. These studies bring a new perspective to investigate more in a useful sophisticated modified hybrid nanocomposite based on graphene material and its derivatives in some multifunction applications.

References

1. Shen, S., Meng, Y.: A novel running-in method for improving life-time of bulk-fabricated silicon MEMS devices. *Tribol. Lett.* **47**(2), 273–284 (2012)
2. Tambe, N.S., Bhushan, B.: Scale dependence of micro/nano-friction and adhesion of MEMS/NEMS materials, coatings and lubricants. *Nanotechnology* **15**(11), 1561 (2004)
3. Alfeeli, B., Cho, D., Ashraf-Khorassani, M., Taylor, L.T., Agah, M.: MEMS-based multi-inlet/outlet preconcentrator coated by inkjet printing of polymer adsorbents. *Sens. Actuators B Chem.* **133**(1), 24–32 (2008)
4. Huang, H., Zhang, J., Jiang, L., Zang, Z.: Preparation of cubic Cu₂O nanoparticles wrapped by reduced graphene oxide for the efficient removal of rhodamine B. *J. Alloy. Compd.* **718**, 112–115 (2017)
5. Zang, Z., Zeng, X., Wang, M., Hu, W., Liu, C., Tang, X.: Tunable photoluminescence of water-soluble AgInZnS–graphene oxide (GO) nanocomposites and their application in-vivo bioimaging. *Sens. Actuators B Chem.* **252**, 1179–1186 (2017)
6. Subramani, K., Sathish, M.: Facile synthesis of ZnO nanoflowers/reduced graphene oxide nanocomposite using zinc hexacyanoferrate for supercapacitor applications. *Mater. Lett.* **236**, 424–427 (2019)
7. Rafiee, M.A., Rafiee, J., Wang, Z., Song, H., Yu, Z.Z., Koratkar, N.: Enhanced mechanical properties of nanocomposites at low graphene content. *ACS Nano* **3**(12), 3884–3890 (2009)

8. Park, J.W., Lee, C., Jang, J.: High-performance field-effect transistor-type glucose biosensor based on nanohybrids of carboxylated polypyrrole nanotube wrapped graphene sheet transducer. *Sens. Actuators B Chem.* **208**, 532–537 (2015)
9. Asadi, K., et al.: Up-scaling graphene electronics by reproducible metal–graphene contacts. *ACS Appl. Mater. Interfaces* **7**(18), 9429–9435 (2015)
10. Shen, H., Zhang, L., Liu, M., Zhang, Z.: Biomedical applications of graphene. *Theranostics* **2**, 283–294 (2012)
11. Zhang, P., et al.: Enhanced permeability of rGO/S-GO layered membranes with tunable inter-structure for effective rejection of salts and dyes. *Sep. Purif. Technol.* **220**, 309–319 (2019)
12. Park, S., Ruoff, R.S.: Chemical methods for the production of graphenes. *Nat. Nanotechnol.* **4**(4), 217–224 (2009)
13. Chen, S., et al.: Synthesis and characterization of large-area graphene and graphite films on commercial Cu–Ni alloy foils. *Nano Lett.* **11**(9), 3519–3525 (2011)
14. Liu, X., Kim, H., Guo, L.J.: Optimization of thermally reduced graphene oxide for an efficient hole transport layer in polymer solar cells. *Org. Electron.* **14**(2), 591–598 (2013)
15. Feng, T., et al.: Graphene based Schottky junction solar cells on patterned silicon-pillar-array substrate. *Appl. Phys. Lett.* **99**(23), 233505 (2011)
16. Bae, S., et al.: Roll-to-roll production of 30-inch graphene films for transparent electrodes. *Nat. Nanotechnol.* **5**(8), 574 (2010)
17. Jo, G., et al.: Large-scale patterned multi-layer graphene films as transparent conducting electrodes for GaN light-emitting diodes. *Nanotechnology* **21**(17), 175201 (2010)
18. Liu, L., et al.: Enhanced performance of ultraviolet organic light-emitting diode by using graphene oxide and MoO₃ dual hole injection layer. *Physica Status Solidi C* **14**(12), 1600131 (2017)
19. Pei, S., Zhao, J., Du, J., Ren, W., Cheng, H.M.: Direct reduction of graphene oxide films into highly conductive and flexible graphene films by hydrohalic acids. *Carbon* **48**(15), 4466–4474 (2010)
20. Barhoum, A., Shalan, A.E., El-Hout, S.I., et al.: A broad family of carbon nanomaterials: classification, properties, synthesis, and emerging applications. In: *Handbook of Nanofibers*, pp. 1–40. Springer International Publishing, Cham (2019)
21. Abdellatif Soliman, S.M., Sanad, M.F., Shalan, A.E.: Synthesis, characterization and antimicrobial activity applications of grafted copolymer alginate-g-poly(N-vinyl imidazole). *RSC Adv* **11**, 11541–11548 (2021)
22. Eivazzadeh-Keihan, R., Taheri-Ledari, R., Mehrabad, M.S., et al.: Effective combination of rGO and CuO nanomaterials through poly(p-phenylenediamine) texture: utilizing it as an excellent supercapacitor. *Energy Fuels* **35**, 10869–10877 (2021). <https://doi.org/10.1021/acs.energyfuels.1c01132>
23. Mohammed, M.K.A., Dehghanipour, M., Younis, U., et al.: Improvement of the interfacial contact between zinc oxide and a mixed cation perovskite using carbon nanotubes for ambient-air-processed perovskite solar cells. *New J. Chem.* **44**, 19802–19811 (2020)
24. Sanad, M.F., Shalan, A.E., Abdellatif, S.O., et al.: Thermoelectric energy harvesters: A review of recent developments in materials and devices for different potential applications. *Top Curr. Chem. (J)* **378**, 48 (2020)
25. Aytug, T., et al.: Vacuum-assisted low-temperature synthesis of reduced graphene oxide thin-film electrodes for high-performance transparent and flexible all-solid-state supercapacitors. *ACS Appl. Mater. Interfaces* **10**(13), 11008–11017 (2018)
26. Yoo, B.M., Shin, J.E., Lee, H.D., Park, H.B.: Graphene and graphene oxide membranes for gas separation applications. *Curr. Opin. Chem. Eng.* **16**, 39–47 (2017)
27. Moharam, M.M., El Shazly, A.N., Anand, K.V., et al.: Semiconductors as effective electrodes for dye sensitized solar cell applications. *Top Curr. Chem. (J)* **379**, 20 (2021)
28. Sanad, M.F., Shalan, A.E., Bazid, S.M., Abdelbasir, S.M.: Pollutant degradation of different organic dyes using the photocatalytic activity of ZnO@ZnS nanocomposite materials. *J. Environ. Chem. Eng.* **6**, 3981–3990 (2018)

29. Shalan, A.E., Afifi, M., El-Desoky, M.M., Ahmed, M.K.: Electrospun nanofibrous membranes of cellulose acetate containing hydroxyapatite co-doped with Ag/Fe: morphological features, antibacterial activity and degradation of methylene blue in aqueous solution. *New J. Chem.* **45**, 9212–9220 (2021)
30. Jung, I., et al.: Characterization of thermally reduced graphene oxide by imaging ellipsometry. *J. Phys. Chem. C* **112**(23), 8499–8506 (2008)
31. Shin, H.J., et al.: Efficient reduction of graphite oxide by sodium borohydride and its effect on electrical conductance. *Adv. Func. Mater.* **19**(12), 1987–1992 (2009)
32. Hui, L.S., Whiteway, E., Hilke, M., Turak, A.: Synergistic oxidation of CVD graphene on Cu by oxygen plasma etching. *Carbon* **125**, 500–508 (2017)
33. Zhao, Y., Yu, B., Yu, G., Li, W.: Study on the water-heat coupled phenomena in thawing frozen soil around a buried oil pipeline. *Appl. Therm. Eng.* **73**(2), 1477–1488 (2014)
34. Kim, K.K., et al.: Enhancing the conductivity of transparent graphene films via doping. *Nanotechnology* **21**(28), 285205 (2010)
35. Yang, K., Wang, J., Chen, X., Zhao, Q., Ghaffar, A., Chen, B.: Application of graphene-based materials in water purification: from the nanoscale to specific devices. *Environ. Sci. Nano* **5**(6), 1264–1297 (2018)
36. Uddin, M.T.: Metal oxide heterostructures for efficient photocatalysts (Doctoral dissertation, Université Sciences et Technologies-Bordeaux I; Technische Universität (Darmstadt, Allemagne)) (2013)
37. Hadjitaief, H.B., Zina, M.B., Galvez, M.E., Da Costa, P.: Photocatalytic degradation of methyl green dye in aqueous solution over natural clay-supported ZnO–TiO₂ catalysts. *J. Photochem. Photobiol. A* **315**, 25–33 (2016)
38. Kokila, P., Rameshababu, M., Senthilkumar, V.: Antibacterial and photocatalytic activation of pomegranate rind extract doped TiO₂ nanoparticles by sol-gel method. *Int. J. Dev. Res.* **1**(7) (2016)
39. Ni, M., Leung, M.K., Leung, D.Y., Sumathy, K.: A review and recent developments in photocatalytic water-splitting using TiO₂ for hydrogen production. *Renew. Sustain. Energy Rev.* **11**(3), 401–425 (2007)
40. Lamba, R., Umar, A., Mehta, S.K., Kansal, S.K.: ZnO doped SnO₂ nanoparticles heterojunction photo-catalyst for environmental remediation. *J. Alloy. Compd.* **653**, 327–333 (2015)
41. Derikvandi, H., Nezamzadeh-Ejehieh, A.: A comprehensive study on electrochemical and photocatalytic activity of SnO₂-ZnO/clinoptilolite nanoparticles. *J. Mol. Catal. A Chem.* **426**, 158–169 (2017)
42. Singh, P., Shandilya, P., Raizada, P., Sudhaik, A., Rahmani-Sani, A., Hosseini-Bandegharai, A.: Review on various strategies for enhancing photocatalytic activity of graphene-based nanocomposites for water purification. *Arab. J. Chem.* **13**(1), 3498–3520 (2020)
43. Sakhivel, S., Kisch, H.: Daylight photocatalysis by carbon-modified titanium dioxide. *Angew. Chem. Int. Ed.* **42**(40), 4908–4911 (2003)
44. Chen, T.T., Chang, I.C., Yang, M.H., Chiu, H.T., Lee, C.Y.: The exceptional photo-catalytic activity of ZnO/RGO composite via metal and oxygen vacancies. *Appl. Catal. B* **142**, 442–449 (2013)
45. Agorku, E.S., Mamo, M.A., Mamba, B.B., Pandey, A.C., Mishra, A.K.: Palladium-decorated zinc sulfide/reduced graphene oxide nanocomposites for enhanced visible light-driven photodegradation of indigo carmine. *Mater. Sci. Semicond. Process.* **33**, 119–126 (2015)
46. Niu, J., Dai, P., Zhang, Q., Yao, B., Yu, X.: Microwave-assisted solvothermal synthesis of novel hierarchical BiOI/rGO composites for efficient photocatalytic degradation of organic pollutants. *Appl. Surf. Sci.* **430**, 165–175 (2018)
47. Suresh, R., et al.: Effect of reduced graphene oxide on the structural, optical, adsorption and photocatalytic properties of iron oxide nanoparticles. *New J. Chem.* **42**(11), 8485–8493 (2018)
48. Jeevitha, G., Abhinayaa, R., Mangalaraj, D., Ponpandian, N.: Tungsten oxide-graphene oxide (WO₃-GO) nanocomposite as an efficient photocatalyst, antibacterial and anticancer agent. *J. Phys. Chem. Solids* **116**, 137–147 (2018)

49. Shende, T.P., Bhanvase, B.A., Rathod, A.P., Pinjari, D.V., Sonawane, S.H.: Sonochemical synthesis of Graphene-Ce-TiO₂ and Graphene-Fe-TiO₂ ternary hybrid photocatalyst nanocomposite and its application in degradation of crystal violet dye. *Ultrason. Sonochem.* **41**, 582–589 (2018)
50. Saravani, A.Z., Nadimi, M., Aroon, M.A., Pirbazari, A.E.: Magnetic TiO₂/NiFe₂O₄/reduced graphene oxide nanocomposite as a recyclable photocatalyst for photocatalytic removal of methylene blue under visible light. *J. Alloy. Compd.* **803**, 291–306 (2019)
51. Khan, S.A., et al.: Synthesis of TiO₂/Graphene oxide nanocomposites for their enhanced photocatalytic activity against methylene blue dye and ciprofloxacin. *Compos Part B Eng.* **175**, 107120 (2019)
52. Ghasemipour, P., Fattahi, M., Rasekh, B., Yazdian, F.: Developing the ternary ZnO doped MoS₂ nanostructures grafted on CNT and reduced graphene oxide (RGO) for photocatalytic degradation of aniline. *Sci. Rep.* **10**(1), 1–16 (2020)
53. Jin, X., Ma, Z., Liu, G., Hu, D., Song, C., Huang, Q.: In-situ ionothermal precipitation of well-dispersed ZnO nanoparticles onto 2-dimension neat graphene sheets with excellent photocatalytic activity. *J. Environ. Chem. Eng.* **8**(4), 104030 (2020)
54. Shyamala, R., Devi, L.G.: Reduced graphene oxide/SnO₂ nanocomposites for the photocatalytic degradation of rhodamine B: preparation, characterization, photosensitization, vectorial charge transfer mechanism and identification of reaction intermediates. *Chem. Phys. Lett.* **748**, 137385 (2020)
55. Ashraf, M.A., Yang, Y., Fakhri, A.: Synthesis of NiS–MoO₃ nanocomposites and decorated on graphene oxides for heterogeneous photocatalysis, antibacterial and antioxidant activities. *Ceram. Int.* **46**(6), 8379–8384 (2020)
56. Wang, W., et al.: High performance heterojunction photocatalytic membranes formed by embedding Cu₂O and TiO₂ nanowires in reduced graphene oxide. *Catal. Sci. Technol.* **8**(6), 1704–1711 (2018)
57. Gao, Y., Hu, M., Mi, B.: Membrane surface modification with TiO₂–graphene oxide for enhanced photocatalytic performance. *J. Membr. Sci.* **455**, 349–356 (2014)
58. Xu, Z., et al.: Photocatalytic antifouling PVDF ultrafiltration membranes based on synergy of graphene oxide and TiO₂ for water treatment. *J. Membr. Sci.* **520**, 281–293 (2016)
59. Xu, H., Ding, M., Liu, S., Li, Y., Shen, Z., Wang, K.: Preparation and characterization of novel polysulphone hybrid ultrafiltration membranes blended with N-doped GO/TiO₂ nanocomposites. *Polymer* **117**, 198–207 (2017)
60. Chen, W., Ye, T., Xu, H., Chen, T., Geng, N., Gao, X.: An ultrafiltration membrane with enhanced photocatalytic performance from grafted N-TiO₂/graphene oxide. *RSC Adv.* **7**(16), 9880–9887 (2017)
61. Yan, X., Huo, L., Ma, C., Lu, J.: Layer-by-layer assembly of graphene oxide-TiO₂ membranes for enhanced photocatalytic and self-cleaning performance. *Process Saf. Environ. Prot.* **130**, 257–264 (2019)
62. Croitoru, A.M., et al.: Chitosan/graphene oxide nanocomposite membranes as adsorbents with applications in water purification. *Materials* **13**(7), 1687 (2020)
63. Pal, M., Malhotra, M., Mandal, M.K., Paine, T.K., Pal, P.: Recycling of wastewater from tannery industry through membrane-integrated hybrid treatment using a novel graphene oxide nanocomposite. *J. Water Process Eng.* **36**, 101324 (2020)
64. You, M., Wang, B., Singh, P., Meng, J.: Water and salt transport properties of the cellulose triacetate/reduced graphene oxide nanocomposite membranes. *Polymer* **210**, 122976 (2020)
65. Vatanpour, V., et al.: Efficient removal of dyes and proteins by nitrogen-doped porous graphene blended polyethersulfone nanocomposite membranes. *Chemosphere* **263**, 127892 (2021)
66. Nawaz, H., Umar, M., Ullah, A., Razzaq, H., Zia, K.M., Liu, X.: Polyvinylidene fluoride nanocomposite super hydrophilic membrane integrated with Polyaniline-Graphene oxide nano fillers for treatment of textile effluents. *J. Hazardous Mater.* **403**, 123587 (2021)
67. Ahmad, R., Majhi, S.M., Zhang, X., Swager, T.M., Salama, K.N.: Recent progress and perspectives of gas sensors based on vertically oriented ZnO nanomaterials. *Adv. Coll. Interface. Sci.* **270**, 1–27 (2019)

68. Izawa, K., Ulmer, H., Staerz, A., Weimar, U., Barsan, N.: Application of SMOX-based sensors. In: *Gas Sensors Based on Conducting Metal Oxides*, pp. 217–257. Elsevier (2019)
69. Shankar, P., Rayappan, J.B.B.: Gas sensing mechanism of metal oxides: the role of ambient atmosphere, type of semiconductor and gases—a review. *Sci. Lett. J* **4**(4), 126 (2015)
70. Tian, W., Liu, X., Yu, W.: Research progress of gas sensor based on graphene and its derivatives: a review. *Appl. Sci.* **8**(7), 1118 (2018)
71. Ponzoni, A., et al.: Metal oxide gas sensors, a survey of selectivity issues addressed at the SENSOR Lab, Brescia (Italy). *Sensors* **17**(4), 714 (2017)
72. Thomas, N.J.S., Tomer, V.K.: *Functional Nanomaterials. Materials Horizons: From Nature to Nanomaterials*. Springer, Singapore (2020)
73. Smith, A.T., LaChance, A.M., Zeng, S., Liu, B., Sun, L.: Synthesis, properties, and applications of graphene oxide/reduced graphene oxide and their nanocomposites. *Nano Mater. Sci.* **1**(1), 31–47 (2019)
74. Latif, U., Dickert, F.L.: Graphene hybrid materials in gas sensing applications. *Sensors* **15**(12), 30504–30524 (2015)
75. Gu, F., Nie, R., Han, D., Wang, Z.: In₂O₃–graphene nanocomposite based gas sensor for selective detection of NO₂ at room temperature. *Sens. Actuators B Chem.* **219**, 94–99 (2015)
76. Yun, Y.J., Ah, C.S., Hong, W.G., Kim, H.J., Shin, J.H., Jun, Y.: Highly conductive and environmentally stable gold/graphene yarns for flexible and wearable electronics. *Nanoscale* **9**(32), 11439–11445 (2017)
77. Kwak, D., Wang, M., Koski, K.J., Zhang, L., Sokol, H., Maric, R., Lei, Y.: Molybdenum trioxide (α -MoO₃) nanoribbons for ultrasensitive ammonia (NH₃) gas detection: integrated experimental and density functional theory simulation studies. *ACS Appl. Mater. Interfaces.* **11**(11), 10697–10706 (2019)
78. Ayesh, A.I.: Metal/metal-oxide nanoclusters for gas sensor applications. *J. Nanomater.* **2016**, 1–17 (2016). <https://doi.org/10.1155/2016/2359019>
79. Choopun, S., Hongsith, N., Wongrat, E.: Metal-oxide nanowires for gas sensors. In: *Nanowires-Recent Advances*, pp. 3–24 (2012)
80. Barsan, N., Weimar, U.: Conduction model of metal oxide gas sensors. *J. Electroceram.* **7**(3), 143–167 (2001)
81. Xu, C., Tamaki, J., Miura, N., Yamazoe, N.: Grain size effects on gas sensitivity of porous SnO₂-based elements. *Sens. Actuators B Chem.* **3**(2), 147–155 (1991)
82. Sun, Y.F., Liu, S.B., Meng, F.L., Liu, J.Y., Jin, Z., Kong, L.T., Liu, J.H.: Metal oxide nanostructures and their gas sensing properties: a review. *Sensors* **12**(3), 2610–2631 (2012)
83. Lee, S.P.: Electrodes for semiconductor gas sensors. *Sensors* **17**(4), 683 (2017)
84. Li, W., et al.: Reduced graphene oxide/mesoporous ZnO NSs hybrid fibers for flexible, stretchable, twisted, and wearable NO₂ E-textile gas sensor. *ACS sensors* **4**(10), 2809–2818 (2019)
85. Karfa, P., Majhi, K.C., Madhuri, R.: Flexible substrate-based sensors in health care and biosensing applications. In: *Nanosensor Technologies for Environmental Monitoring*, pp. 431–454 (2020)
86. Liu, Y., Wang, H., Zhao, W., Zhang, M., Qin, H., Xie, Y.: Flexible, stretchable sensors for wearable health monitoring: sensing mechanisms, materials, fabrication strategies and features. *Sensors* **18**(2), 645 (2018)
87. Singh, E., Meyyappan, M., Nalwa, H.S.: Flexible graphene-based wearable gas and chemical sensors. *ACS Appl. Mater. Interfaces* **9**(40), 34544–34586 (2017)
88. Jia, X.S., et al.: Flexible polyaniline/poly (methyl methacrylate) composite fibers via electrospinning and in situ polymerization for ammonia gas sensing and strain sensing. *J. Nanomater.* **2016**, 1–8 (2016)
89. Baeg, K.J., Lee, J.: Flexible electronic systems on plastic substrates and textiles for smart wearable technologies. *Adv. Mater. Technol.* **5**(7), 2000071 (2020)
90. He, X., Liu, Q., Wang, J., Chen, H.: Wearable gas/strain sensors based on reduced graphene oxide/linen fabrics. *Front. Mater. Sci.* **13**(3), 305–313 (2019)

91. Kang, M.A., et al.: Highly sensitive and wearable gas sensors consisting of chemically functionalized graphene oxide assembled on cotton yarn. *RSC Adv.* **8**(22), 11991–11996 (2018)
92. Utari, L., Septiani, N.L.W., Nur, L.O., Wasisto, H.S., Yulianto, B.: Wearable carbon monoxide sensors based on hybrid graphene/ZnO nanocomposites. *IEEE Access* **8**, 49169–49179 (2020)
93. Liu, R., et al.: Gate modulation of graphene-ZnO nanowire Schottky diode. *Sci. Rep.* **5**(1), 1–6 (2015)
94. Punetha, D., Kar, M., Pandey, S.K.: A new type low-cost, flexible and wearable tertiary nanocomposite sensor for room temperature hydrogen gas sensing. *Sci. Rep.* **10**(1), 1–11 (2020)
95. Yun, Y.J., Hong, W.G., Choi, N.J., Kim, B.H., Jun, Y., Lee, H.K.: Ultrasensitive and highly selective graphene-based single yarn for use in wearable gas sensor. *Sci. Rep.* **5**(1), 1–7 (2015)
96. Lee, S.W., et al.: Highly conductive and flexible dopamine-graphene hybrid electronic textile yarn for sensitive and selective NO₂ detection. *ACS Appl. Mater. Interfaces* **12**(41), 46629–46638 (2020)
97. Huang, X., Zeng, Z., Fan, Z., Liu, J., Zhang, H.: Graphene-based electrodes. *Adv. Mater.* **24**(45), 5979–6004 (2012)
98. Huang, X., et al.: Graphene-based materials: synthesis, characterization, properties, and applications. *Small* **7**(14), 1876–1902 (2011)
99. Mahmoudi, T., Wang, Y., Hahn, Y.B.: Graphene and its derivatives for solar cells application. *Nano Energy* **47**, 51–65 (2018)
100. Low, F.W., et al.: An investigation on titanium doping in reduced graphene oxide by RF magnetron sputtering for dye-sensitized solar cells. *Sol. Energy* **188**, 10–18 (2019). <https://doi.org/10.1016/j.solener.2019.05.069>
101. Javed, H.M.A., et al.: Advanced Ag/rGO/TiO₂ ternary nanocomposite based photoanode approaches to highly-efficient plasmonic dye-sensitized solar cells. *Opt. Commun.* **453**, 124408 (2019). <https://doi.org/10.1016/j.optcom.2019.124408>
102. Pang, B., et al.: Triiodide reduction activity of hydrangea molybdenum sulfide/reduced graphene oxide composite for dye-sensitized solar cells. *Mater. Res. Bull.* **117**, 78–83 (2019). <https://doi.org/10.1016/j.materresbull.2019.04.034>
103. Bahrami, A., Kazeminezhad, I., Abdi, Y.: Pt-Ni/rGO counter electrode: electrocatalytic activity for dye-sensitized solar cell. *Superlattices Microstruct.* **125**, 125–137 (2019). <https://doi.org/10.1016/j.spmi.2018.10.026>
104. Kumar, K.A., Subalakshmi, K., Senthilselvan, J.: Effect of co-sensitization in solar exfoliated TiO₂ functionalized rGO photoanode for dye-sensitized solar cell applications. *Mater. Sci. Semicond. Process.* **96**, 104–115 (2019). <https://doi.org/10.1016/j.mssp.2019.02.027>
105. Yalcin, M., Yakuphanoglu, F.: An investigation of recombination processes in liquid junction solar cells by transient photocurrent measurements. *Optik (Stuttg.)* **210**, 164609 (2020). <https://doi.org/10.1016/j.ijleo.2020.164609>
106. Omelianovych, O., Larina, L.L., Oh, H.J., Park, E., Dao, V.D., Choi, H.S.: Plasma-processed CoSn/RGO nanocomposite: a low-cost and sustainable counter electrode for dye-sensitized solar cells. *Sol. Energy* **201**, 819–826 (2020). <https://doi.org/10.1016/j.solener.2020.03.057>
107. Qureshi, Akbar Ali, Javed, Sofia, Javed, Hafiz Muhammad Asif., Aftab Akram, M., Jamshaid, Asma Shaheen: Strategic design of Cu/TiO₂-based photoanode and rGO-Fe₃O₄-based counter electrode for optimized plasmonic dye-sensitized solar cells. *Opt. Mater.* **109**, 110267 (2020). <https://doi.org/10.1016/j.optmat.2020.110267>
108. Zandi, Soma, Saxena, Prateek, Gorji, Nima E.: Numerical simulation of heat distribution in RGO-contacted perovskite solar cells using COMSOL. *Solar Energy* **197**, 105–110 (2020). <https://doi.org/10.1016/j.solener.2019.12.050>
109. Kumar, Sumit, Kumar, Jitendra, Sharma, Shailesh Narayan, Srivastava, Shubhda: rGO integrated MEHPPV and P3HT polymer blends for bulk hetero junction solar cells: a comparative insight. *Optik* **178**, 411–421 (2019). <https://doi.org/10.1016/j.ijleo.2018.09.148>
110. Mahakul, P.C., Sa, K., Subramanyam, B.V.R.S., Mahanandia, P.: Mesoscopic investigation of the effect of MWCNT/rGO network on the performance of P3HT:PC60BM solar cells. *Mater. Chem. Phys.* **226**, 113–117 (2019). <https://doi.org/10.1016/j.matchemphys.2019.01.012>

111. Kumar, S., Kumar, J., Sharma, S.N.: Investigation of charge transfer properties in MEHPVV and rGO-AA nanocomposites for Green organic photovoltaic application. *Optik (Stuttg.)* **208**, 164540 (2020). <https://doi.org/10.1016/j.ijleo.2020.164540>
112. Amollo, T.A., Mola, G.T., Nyamori, V.O.: Improved short-circuit current density in bulk heterojunction solar cells with reduced graphene oxide-germanium dioxide nanocomposite in the photoactive layer. *Mater. Chem. Phys.* **254**, 123448 (2020). <https://doi.org/10.1016/j.matchemphys.2020.123448>
113. Fallahzad, P., Naderi, N., Eshraghi, M.J.: Improved photovoltaic performance of graphene-based solar cells on textured silicon substrate. *J. Alloys Compd.* **834**, 155123 (2020). <https://doi.org/10.1016/j.jallcom.2020.155123>
114. Rai, S., Bhujel, R., Biswas, J., Deka, U., Swain, B.P.: Dark and photocurrent response of porous Si/GO-PANI and Si/rGO-PANI heterojunctions for photovoltaics applications. *Mater. Today Proc.* **39**, 1848–1851 (2020). <https://doi.org/10.1016/j.matpr.2020.07.373>
115. Patil, J.V., Mali, S.S., Patil, A.P., Patil, P.S., Hong, C.K.: Highly efficient mixed-halide mixed-cation perovskite solar cells based on rGO-TiO₂ composite nanofibers. *Energy* **189**, 116396 (2019). <https://doi.org/10.1016/j.energy.2019.116396>
116. Nicasio-Collazo, J., et al.: Functionalized and reduced graphene oxide as hole transport layer and for use in ternary organic solar cell. *Opt Mater (Amst.)* **98**, 109434 (2019). <https://doi.org/10.1016/j.optmat.2019.109434>
117. Hosseini, M., Naji, L., Fakharan, Z.: Influences of synthesis parameters on the physicochemical and electrochemical characteristics of reduced graphene oxide/Pt nanoparticles as hole transporting layer in polymer solar cells. *Synth. Met.* **263**, 116366 (2020). <https://doi.org/10.1016/j.synthmet.2020.116366>
118. Ding, L., et al.: P-type doping of rGO/NiO composite for carbon based perovskite solar cells. *Mater. Sci. Semicond. Process.* **107**, 104798 (2020). <https://doi.org/10.1016/j.mssp.2019.104798>
119. Mann, D.S., Seo, Y.H., Kwon, S.N., Na, S.I.: Efficient and stable planar perovskite solar cells with a PEDOT:PSS/SrGO hole interfacial layer. *J. Alloys Compd.* **812**, 152091 (2020). <https://doi.org/10.1016/j.jallcom.2019.152091>

Bionanocomposites and Their Applications in Energy Harvesting and Deletion of Environmental Pollutions



Parinaz Ghadam

Abstract Force creation and accordingly the subsequent natural obliteration are among the premier significant issues of the twenty-first century. Around the world, over 6.5 billion individuals need around 13 Terawatts of energy for their ordinary requirements. Hence there's a need for qualified arrangements which bionanocomposites are crucial among them. Bionanocomposites are composite materials comprising of biodegradable polymers, regular or engineered, and nano-scale materials. A composite material's properties rely upon its segment materials like characteristic biopolymers or manufactured biodegradable polymers and inorganic or natural nanomaterials or minerals of a nano-scale type. The properties of a bionanocomposite frequently rely upon the attributes of the biopolymers, the stoichiometric proportion of the constituent materials, and along these lines the cross-connecting between the constituent materials, similarly as on the macromolecular lattice of the biopolymer. This audit communicates a few normal polymers, similar to cellulose, chitosan, lignin, pullulan, PHA, and protein, zeroed in on their wellspring of source, synthetic arrangement, practical gathering, conceivable surface alterations, and nanoscaled materials and their applications related with ecological and energy pathways.

Keywords Bionanocomposites · Energy harvesting · Nanoremediation

Abbreviations

(NCs)	Nanocomposites
(BNCs)	Bionanocomposites
(CAP)	Cellulose acetic acid derivation propionate
(CA)	Cellulose acetic acid derivation
(CAB)	Cellulose acetic acid derivation butyrate

P. Ghadam (✉)

Department of Biotechnology, Faculty of Biological Sciences, Alzahra University, Tehran, Iran
e-mail: pghadam@alzahra.ac.ir

(PLA)	Poly lactic Acid
(PEO)	Poly(ethylene oxide)
(OLA)	Oligomer lactic acid
(PEG)	Polyethylene glycol
(PHAs)	Polyhydroxyalkanoates
(HV)	Hydrovalerate
(PCL)	Polycaprolactone
(PHEE)	Polyhydroxy ester ethers
(PEA)	Polyesteramide
(PA)	Polyamide
(PVA)	Poly(vinyl alcohol)
(NFC)	Nanofibrillated cellulose
(CNT)	Carbon nanotube
(HNT)	Halloysite nanotubes
(MEL)	Mixtures containing melamine
(MCA)	melamine cyanurate
(DPG)	diphenylguanidine
(PV)	Photovoltaics
(PLLA/MWCNT)	Poly (L-lactide)/multi-walled CNTs
(EMI)	electromagnetic impedance
(PGS)	poly (glycerol-co-sebacate)
(MOF)	Metal–oxygen framework

1 Introduction

“Bionanocomposite” was frequently alluded to as “nanobiocomposites,” “characteristic composites,” or “biohybrids” is utilized from 2004 [1]. Nanocomposites (NCs) containing normally happening polymers (biopolymers) in combination with an inorganic nanomoiety make another class of materials called Bionanocomposites (BNCs) [2]. Bionanocomposites are composite substances made out of natural or regular, biodegradable polymer, and nano materials (nanofillers) (Fig. 1). The properties of it frequently rely upon the biopolymer characters, the stoichiometric proportion of its substances and thus the limiting between the materials and the grid of the biopolymer [3].

Bionanocomposites are another class of present day, biohybrid materials. They are additionally being taken a gander at by industrialists and analysts to fix natural concerns and discover expected elective hotspots for petrol related synthetic substances. Through utilizing amazing green innovations, they have created bionanocomposite materials with extraordinary biocompatibility and biodegradability. In any case, biopolymers additionally have relatively low mechanical and boundary properties that limit their modern utilization as of now. These days an

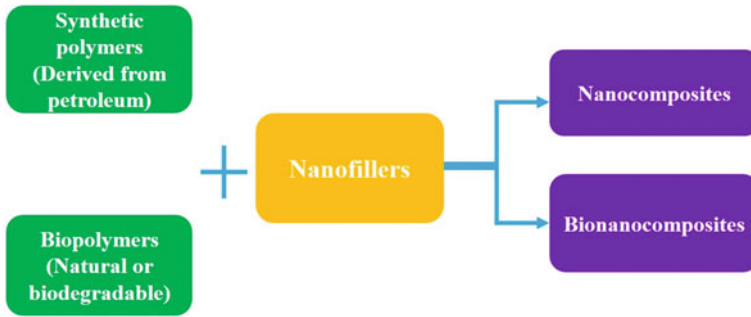


Fig. 1 Components of nanocomposite and bionanocomposite

expanding challenge is the creation of bio-based polymers and inventive cycle innovations that can diminish dependence on petroleum product and progress to a green crude material base. Bionanocomposites offer a capacity to supplant traditional oil based non-biodegradable plastic bundling materials with present day, superior, lightweight, maintainable nanocomposites [4].

Gold and silver nanoparticles have diverse physical and compound properties opening the focus on bionanocomposites to fabricate new items. Polymers with these nanoparticles are known as one of the fundamental courses for growing new materials with a wide scope of qualities, like high antimicrobial action, synergist action, and conductiveness. So these sort of nanocomposites have a wide scope of uses [5].

This section talks about the highlights of nanocomposite biopolymer/nanoparticles and surveys their use in energy recuperation, water the executives, and ecological discharge cancellation applications.

2 Biopolymers in Bionanocomposites

Biopolymers might be sorted as (a) agropolymers (cellulose and starch), (b) microbial polymers (polyhydroxyalkanoates) and (C) synthetically orchestrated polymers utilizing biomass monomers (poly[lactic acid]) [6, 7].

Fundamentally improved biopolymer properties by the expansion of nanofillers make resulting bionanocomposites a successful up-and-comer substrate for various applications [8]

Regardless of biopolymers' possibly good properties like the wide wealth of crude materials and their improved biodegradability, some key properties are normally lower than those of customary polymers, including their mechanical, and warm properties. Biodegradable and biosynthesized polymers have a huge impact in the creation of bionanocomposite. A few common polymers are utilized for bionanocomposite amalgamation and every one of these substances has characteristically different

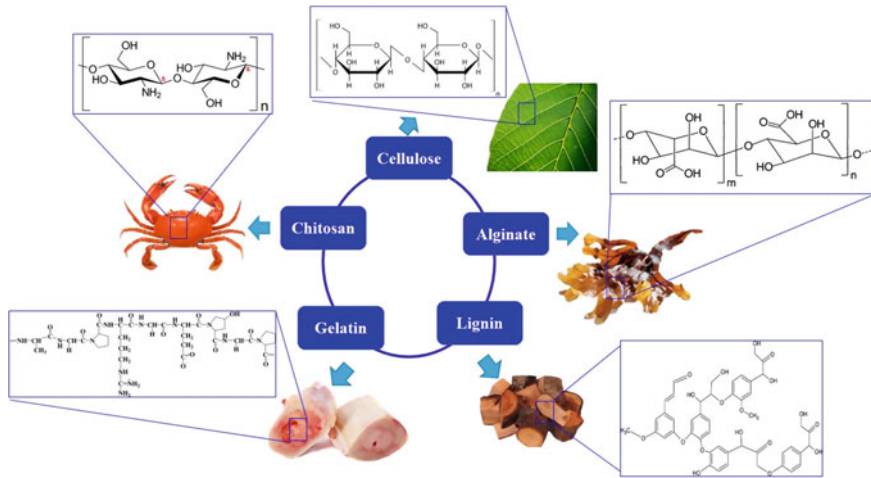


Fig. 2 Some of biosynthesized and biodegradable polymers as constituent of bionanocomposite

attributes, as atomic construction, useful gatherings, warm movement, holding plan and solubility [9]. Any of such polymers are found in Fig. 2.

2.1 Cellulose

Cellulose shows up as a cell biocomposite mixed in a few materials, including lignin, hemicelluloses, waxes, oils, and minor components, especially in wood and plant materials. The properties of it rely upon the climate, but at the same time are influenced during fiber handling [3]. Cellulose is a composite medium with long stringy cells and very tough normal polymer. Additionally, they are ecofriendly and basic of reusing by burning. Cellulose nanofibers are moderately minimal effort and promptly open material. Cellulose can ordinarily create two structures, stubbles and microfibrils [10, 11]

Acetobacter xylinum likewise produce bacterial cellulose with a high pliable force and biodegradability [7].

Various assets, like cellulose of wood and cotton, might be utilized as crude materials for the cellulose ester polymers union by utilizing reasonable added substances and plasticizers.

In explicit, cellulose acetic acid derivation propionate (CAP) as a thermoplastic celluloses, cellulose acetic acid derivation (CA), and cellulose acetic acid derivation butyrate (CAB) within the sight of reasonable acids and anhydride are orchestrated by cellulose esterification [6, 8].

2.2 Starch

The chief starch source is potato, corn, wheat. Normally starch is helpful for energy preservation in plants and microorganisms. Starch has two amylose-and amylopectin parts [12]. Amylose is a straight polysaccharide comprising of D-Glucose with α -(1 \rightarrow 4) glycosidic bond. Amylopectin like glycogen is a fanned polysaccharide comprising of D-Glucose with α -(1 \rightarrow 4) glycosidic bond in spine and α -(1 \rightarrow 6) bond in intersection. The dissolving purpose of unadulterated dry starch is the scope of 220–240 °C and is near the decay temperature of starch. In this way materials like water, glycerol and polyols are normally expected to decrease the liquefying purpose of starch.

The least difficult kind of starch in the sort of protected granules is helpful for energy stockpiling in miniature life forms and plants [13].

2.3 Alginate

Alginate is a polysaccharide viewed as a (1 \rightarrow 4) connected polyuronic, containing three kinds of square construction: M square (β -D-mannuronic acid), G block (poly α -L-guluronic acid), and MG block (containing both polyuronic acids) [14]. The most powerful restorative and clinical employments of alginates (algal polysaccharide) were accounted for in huge quantities of writing. It is intriguing that nanoalginate filaments or particles are not hypothetically usable for various applications with no other polymer or double segments (solvents, surfactants, polymers). Green polymer materials like creatures, plants, microorganisms, green growth and organisms have been broadly utilized, as they are usable, modest, harmless to the ecosystem and biocompatible [15].

2.4 Curcumin

Curcumin is a significant lipophilic phenolic and normally happening segment acquired from *Curcuma longa* (turmeric rhizomes) plant. Researchers have exhibited a wide cluster of helpful exercises (restorative properties) against different problems, disorder, and infections throughout the long term. Little fluid curcumin solvency brings about diminished bioavailability of this high pharmacological possible substance. On account of their obstruction and powerless mechanical properties, normal materials, (for example, curcumin, and so forth) have little applications. Subsequently it is essential to add various nanosized fillers and mixtures to fortify and improve their properties and execution. Bionanocomposite innovation was

applied to address the restrictions of curcumin, and curcumin-based bionanocomposites were made. Due to improved biodegradability, biocompatibility and wellbeing contemplations, curcumin is utilized in numerous bionanocomposite items [15].

2.5 Glycogen

Glycogen is a spread polysaccharide comprising of D-Glucose with α -(1 \rightarrow 4) glycosidic bond in spine and α -(1 \rightarrow 6) glycosidic bond in intersection. Bionanocomposites dependent on glycogen show famous therapeutic uses and are earth practical inexhaustible biopolymers on a nanoscale. In spite of the fact that phytyglycogen is gotten from plant sources, glycogen can be extricated from different creature sources. Heretofore few bionanocomposites dependent on glycogen have been recognized. Diverse nanofillers were additionally used to help the properties of these composites and to upgrade the biocompatibility. The sluggish biodegradable existence of bionanocomposites reliant on glycogen can be abused to make manures with moderate supplement delivery and furthermore to control herbicide and pesticide releases [15].

2.6 Chitin

Chitin is a straight polysaccharide which framed by N-acetylglucosamine units with β -(1 \rightarrow 4)- glycosidic linkage. It is principally utilized as a significant fastener in colorants and textures [12]. Chitin has a piece near cellulose [13]. Normally, chitin is found in exoskeletons and spineless creatures' inner construction, and its action is near that of glasslike nanofibrils and nanowiskers [6, 7, 13].

2.7 Chitosan

Chitosan is a straight polysaccharide comprising of D-glucosamine with β -(1 \rightarrow 4)-linkage and N-acetyl-D-glucosamine appropriated haphazardly. It is made utilizing an antacid material, like sodium hydroxide, to treat the chitin shells of shrimps and different scavengers. The dynamic hydroxyl and essential amine chitosan bunches grant their primary change with sufficient cross-linkers. Notwithstanding, a few procedures are acclimated improve the properties of chitosan, such as utilizing salt and plasticizers, hydroxyl bunches synthetic change, polysaccharides crosslinking, reasonable solvents work, pH improvement, the occasion of fluctuating polysaccharides and subsequently the mixing of other polymers [3]. Chitosan has various helpful uses, for instance wound dressings and absorbable stitches [12]. It is regularly delegated a semicrystalline polymer and its level of crystallinity relies upon the quantity

of deacetylation. Its mass relies upon the wellspring of the fixings, typically inside the scope of 100–1100 kg/mol [7].

2.8 Lignin

Lignins are regularly a classification of complex natural polymers that structure principle underlying materials in tissues and some green growth supporting plants. In the shaping of cell dividers, lignins are especially significant, particularly in bark and wood, as they give inflexibility and don't decay without any problem. Also, lignin normally has UV-engrossing abilities and presentations solid mechanical opposition, hydrophobic properties, and stubbornness to biodegradation. Thusly, lignin is considered a ground-breaking added substance for the gathering of biodegradable composite items, further as a pottery settling specialist and as a truly significant alumina suspension for cutting edge material processing [3].

2.9 Pullulan

Pullulan is frequently a polysaccharide polymer comprising of α -(1 \rightarrow 4)-; α -(1 \rightarrow 6)- glucan segments. Three glucose units of maltotriose are associated by a glycosidic obligation of α -(1 \rightarrow 4) and a glycosidic bond in α -(1 \rightarrow 6). Pullulan is amazingly water-dissolvable, non-hydroscopic in natural solvents and incorporates a consistency that is genuinely unique in relation to different polysaccharides, which is relatively little contrasted with different gums, especially Arabic gum [3].

2.10 Poly Lactic Acid (PLA)

PLA is one among the bioplastics which is most commonly created. It has various applications including clinical gadgets, materials, and food bundling. It's a direct thermoplasty polymer got fundamentally from sustainable assets like sugar beets or maize [12]. Blending in with different polymers, for example, poly(ethylene oxide) (PEO) utilizing a plasticizer, for example, oligomer lactic acid (OLA), low atomic weight polyethylene glycol (PEG) citrate ester can improve the deficiency of some PLAs regarding warm steadiness, sway opposition and flexibility [6, 16].

2.11 *Polyhydroxyalkanoates (PHAs)*

PHAs are polyesters shaped by numerous normally happening microorganisms, including the bacterial maturation of sugars or lipids [3]. PHA is grouped into 3 significant classes as indicated by their chain length, in different terms short length (C3-C5), medium length (C6-C14) and long length (carbon number more noteworthy than C14) [17].

Then again, expanding the measure of hydrovalerate (HV) brings about an expansion in effect strength, with coming about decreases in liquefying temperature, crystallinity, change temperature [18, 19], penetrability of water [20], and tractable force [21].

2.12 *Proteins*

They have more grounded oxygen hindrance properties and lower water-fume porousness comparative with other nonionic materials, due to their more polar presence and more roundabout (non-ring) shape, and lower free space. Keratin, casein, whey protein, white egg, collagen, and gelatin are extricated from creatures, while soy protein, zein (corn protein) are plant protein [3].

2.13 *Synthetic Biodegradable Polymers*

Aliphatic polyester-based polymers, among biodegradable polymers, have a fast hydrolytic debasement because of the practical ester bunch in its fundamental chain. Poly buildup and ring opening polymerization are the ways for the creation of biodegradable polyesters [3].

Polycaprolactone (PCL) is a biodegradable polyester with a low dissolving purpose of roughly 60 °C and a glass change temperature of around – 60° C. This polymer is utilized as a sap added substance to support dealing with properties of the pitches. PCL can be joined with starch to decrease its expense and improve biodegradability, or it tends to be added to polyvinyl chloride (PVC) as a polymeric plasticizer. PCL is a direct polyester orchestrated within the sight of metal alcoxides by ring-opening polymerisation of ϵ -caprolactone [13]. The critical drawback of this polymer is its helpless liquefying point that can be relieved by consolidating polymers (Averous et al. 2000; Bastioli et al. 1995) or by upgrades, for example, the cross-connecting [23].

Aliphatic polyester A with countless aliphatic copolyesters might be accomplished by joining diols like 1, 2-ethanediol, 1, 3-propanediol or 1, 4-butadenediol with dicarboxylic acids, for example, adipate and succinate [7, 13].

As another type of fragrant copolyester, polyhydroxy ester ethers (PHEE) can be gotten from the combination of adipate and diglycidal bisphenol [22, 24].

Polyesteramide (PEA) might be blended by the monomer and adipic acid measurable polyamide copolycondensation (PA6 or PA6-6) [22, 25].

Poly(vinyl alcohol) (PVA) with alluring properties like natural dissolvable opposition, water solvency (remembering for cold water), minimal effort, great mechanical strength and remarkable boundary properties [26] make it an attractive contender for bionanocomposite creation [27, 28].

2.14 Regular Polyester Filaments

The biodegradability, biocompatibility, cost-viability and non-poisonousness of reused regular polymers, for example, biopolyester filaments, polynucleotides, and polyisoprene strands make them appealing for bionanocomposite combination. Additionally, regular polymers have gigantic underlying capacities with regards to creating extraordinary properties for synthetic modifications [15].

3 Nano-Scale Fillers

Nano fillers, for example, nanorods, nanotubes, nanoparticles, nanowires, etc. are progressively utilizing in nanotechnology and contribute as significant materials in the bionanocomposite improvement which are depicted in this segment.

3.1 Layered Silicates

Layered silicates are otherwise called dirt minerals and are important for the silicate minerals and phyllosilicate class [2]. Natural or manufactured mineral-layered silicates are mainstream as a significant support for frameworks of nanocomposite [12]. These layers might be associated along with counter particles. Such kinds of fillers contain sheet stacks isolated by van der Waals holes. The layer comprises of a tetrahedral sheet including a silicon particle encompassed by four oxygen molecules and an octahedral sheet covered by eight oxygen atoms in metals like Al or Mg hydroxide [29].

3.2 *Nanocellulose*

By utilizing customary cellulose, the common adaptability, sturdiness and consistency required for most mechanical applications can't be accomplished [30, 31]. The option in contrast to this issue is to utilize nanocellulose and wipe out a significant part of the various leveled primary imperfections. Nanocellulose has some fantastic properties, like its low thickness, high viewpoint proportion, low coefficient of warm development and high ductile force [31]. This has added to different utilizations comprise of antimicrobial movies, drug appropriation, textures and materials, batteries and supercapacitors [31]. All in all, nanofibrillated cellulose (NFC) comprises of ultrafine cellulose fibrils created by different mechanical methods like the homogenisation of high pressing factor, granulating, cryocrushing and microfluidisation [32].

3.3 *Carbon Nanotubes (CNT)*

CNTs are among the most fascinating carbon allotropes organized by moving graphite sheets looking like chambers [33]. CNTs have been especially concerned due to their different capacity for supercapacitors [34], control actuators in mechanical turn of events [35], and capacity energy (e.g., hydrogen storage) [36]. CNTs can possibly balance out all thermosets and thermoplastics [37, 38] produce fantastic mechanical properties and a decent substance fondness [39], yet its poisonousness will influence their applications [12, 40].

3.4 *Halloysite Nanotubes (HNT)*

HNT ($\text{Al}_2\text{Si}_2\text{O}_5(\text{OH})_4 \cdot n\text{H}_2\text{O}$) hydrated or dried out halloysite might be available in different shapes, like rounded, spheroidal and plateous halloysite, contingent upon the land and crystallization conditions [41]. HNTs are a sort of rounded dirt normally happening due to aqueous movements in aluminum–silicate minerals [12, 42].

The critical advantages of HNTs are its wide accessibility [42], minimal effort, biological system agreeableness [43], their fantastic mechanical properties, and high warmth opposition.

In any case, the functionalization of the outside of HNTs is needed to expand their similarity with polymers to guarantee ideal pressure move from polymer frameworks to HNTs in nanocomposites [42, 44]. Hydrogen holding association is a non-covalent procedure of modification by which natural mixtures containing melamine (MEL), melamine cyanurate (MCA) or diphenylguanidine (DPG) are associated with structure filler networks inside polymer lattices [45].

Phosphonic acid joining is another covalent change strategy that outcomes in significant expansions in interlayer separating for HNTs (from 7 to 15.1 Å) bringing about expanded HNT scattering and improved execution for last nanocomposites [46].

3.5 Nanoparticles

The three elements of the particles in nanoparticles are of nanometer scale. The attributes of nanoparticles, for example electrical, optical, warm, machanical, and synthetic reactivity properties, differ with mass kinds on the grounds that their proportion of surface territory to volume increments. It very well may be circular, cubic, and amorphou. They are manufactured, and inorganic.

An extraordinary instance of nanoparticles as nanofiller is the hydroxyapatite ($\text{Ca}_{10}(\text{PO}_4)_6(\text{OH})_2$). It is a huge part of bones in minerals. On account of its magnificent biocompatibility, nano-scale hydroxyapatite as the dynamic part of platforms and inserts is generally utilized in muscular medical procedure and dentistry to recuperate the mineralized hard tissues of the living organism [47].

3.6 Nanofibers

Nanofibers, nanorods, nanotubes, and bristles are two dimensional nanoparticulates inside the nanometer scale range. While cellulose has been broadly utilized in the material business for quite a few years, its utilization as nanofibrillar just as starch and chitin has as of late pulled in impressive consideration for reinforcing composite materials. Such plants as cotton, soy, corn, banana and kenaf go about as wellsprings of nanofibers for cellulose and starch [47]. Perhaps the most popular model is carbon nanotubes comprising of a solitary sheet of graphene or more sheets [48, 49].

3.7 Nanoplatelets

Layered or plate like mud minerals are the most widely recognized nanoplatelets utilized in bionanocomposite plans [50, 51]. The thickness of nanoplatelets is just in the nanometer scale range. This classification incorporates phyllosilicates, silicic acid (magadiite), layered twofold hydroxides [$\text{M}_6\text{Al}_2(\text{OH})_{16}\text{CO}_{3n}\text{H}_2\text{O}$; M = Mg, Zn], zirconium phosphates [$\text{Zr}(\text{HPO}_4)_2\text{H}_2\text{O}$], and di-chalcogenides [$(\text{PbS})_{1.18}(\text{TiS}_2)_2, \text{MoS}_2$] [52].

3.8 Nanotubes

Various types of nanotubes are conceivable however frequently carbon nanotubes are utilized. It is carbon allotropes, which has a place with the progressive class of fullerenes. The distance across of the nanotubes is in a nanosize. Carbon nanotubes-supported composites may deliver light-weight material [2].

4 Ex Situ Versus In Situ Synthesis of Bionanocomposites

Bionanocomposite amalgamation utilizing explicit methodologies that are as per the following:

A) Ex situ: in this strategy, the biopolymer or biopolymer, like starch and protein, is applied to a dissolvable that is completely solvent in dissolvable. As swollen nanoparticles are joined with the biopolymer and water, the polymer chains are intercalated and the dissolvable eliminated (Fig. 3).

B) In situ: in this interaction nanomaterial union and polymerization happen in one stage so the incorporated nanoparticles scatter in a fluid monomer or monomer arrangement so the shaping of polymers between the intercalated sheets can happen [2]. The ex situ union methodology is more appropriate for business applications on wide scale than the in situ strategy [53].

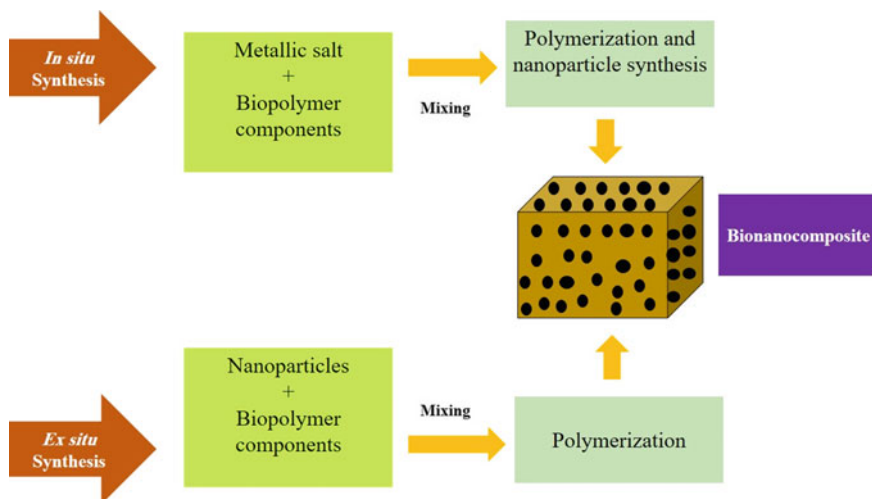


Fig. 3 In situ vs Ex situ synthesis of bionanocomposite

5 Applications

There are so many applications for bionanocomposite, from food packaging to energy storage, as shown in Fig. 4. Any of them are explained in the following below.

5.1 Electronic and Sensor Applications

The utilization of nanofiller in biopolymers improves bionanocomposites' mechanical and warm properties, yet additionally their optical, attractive and electrical properties [54].

Besides, clear nanocellulose containing bionanocomposites is utilized in various applications, from diodes delivering natural light to sun powered cells.

Bionanocomposites are utilized as electromagnetic protecting specialist, which fills in as an obstruction to proficient conductivity and attractive properties by catching electromagnetic fields in vacuum [55].

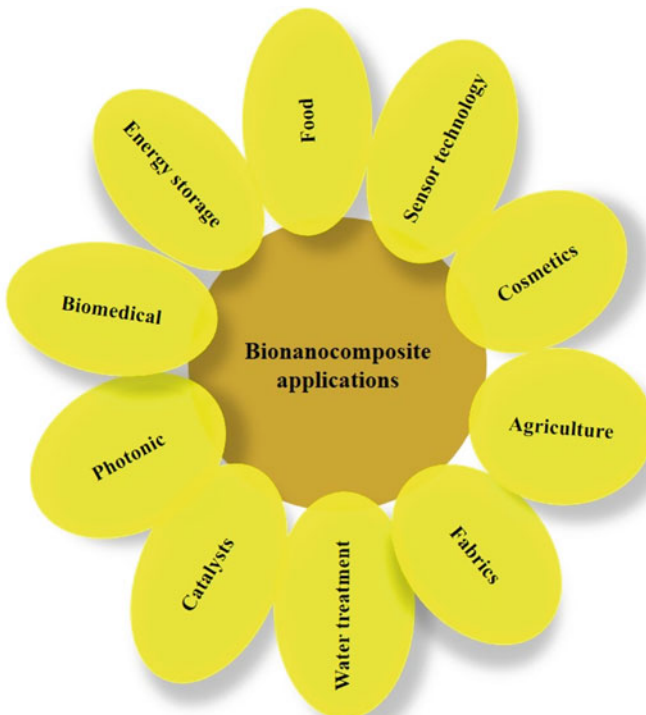


Fig. 4 Bionanocomposite applications

The solid electrical exhibition, light weight, minimal effort and ecological kind disposition of bionanocomposites would profit straightforwardly from adaptable sensor innovation. Bionic composites supported by cellulose nanowhiskers are thermally steady up to 220 °C and are ideal for assembling of electronic devices [56].

5.2 *Photovoltaics (PV)*

Photovoltaics are most popular as a methods for delivering power by utilizing sun based boards to change energy from the light by the photovoltaic impact into a rush of electrons. The mass blending of a polymer giver with semiconductor nanoparticles brings about a solid benefactor/acceptor interface number, increments exciton separation and in this way upgrades the progress from photon to control [57]. These nanomaterials incorporate zinc oxide nanorods, Cadmium selenide nanorods, Cadmium selenide tetrapods, Gallium arsenide nanorods, titanium oxide nanorods, and carbon nanotubes (Zhang et al., 2018). The joining of these electron-acceptant nanomaterials into electron-giving polymers and the design of the nanomaterials opposite to the sun powered cell anode are relied upon to improve energizing separation and the conductivity of the charge carrier [59]. Consequently, natural inorganic mixture PV materials like mass heterojunction have gotten extensive consideration as the reason for quick preparing and genuinely minimal effort sun based cells [60].

5.3 *Piezo-Electric Energy Preparing*

A convincing one is the possibility of gathering energy from encompassing mechanical vibrations as compact piezoelectric nano-generators. The utilization of anisotropic piezoelectric nanomaterials empowers the change of little pressing factors created by surrounding vibrations or human movement into flow stream. In this regard, single translucent, high-viewpoint nanorods or nanowires of materials, for example, zinc oxide, barium titanate, gallium nitride and cadmium sulfide are of concern [61]. The nanorods should be joined into adaptable plainly visible gadgets to change the individual, acoustic and other minor movement into survivable extending and twisting of piezoelectric materials [62]. Actually, it is again the work of guaranteeing that substrate-appended inorganic nanorods or nanowires are vertically adjusted over huge zones and blending these developments in with suitable polymer matrices (Zhang et al. 2018).

5.4 *Electronic*

In electronic gadgets, the dynamic materials are regularly semiconducting to get a level of controllable conductivity, which is the principal idea of most hardware. The new biodegradable and biocompatible polymers utilized as separators or (semi)conductors and the biodegradable and biocompatible nanocomposites utilized as substrates in gadgets [63].

The readied biodegradable poly (L-lactide)/multi-walled CNTs (PLLA/MWCNT) nanocomposites froths are reasonable for electromagnetic impedance (EMI) protecting in hardware bundling. Nanocomposites additionally have critical advantages in antistatic measurements of bundling rather than plain polymers. Nanocomposites have critical focal points in the electromagnetic protecting field of electronic bundling comparative with unadulterated polymers, attributable to the incorporation of conductive nanofillers [64–67].

Other than the above polymers, there are numerous biodegradable or biocompatible disconnected polymers which can be utilized in hardware like starch [68, 69], chitosan [70, 71], egg whites [72], and poly (glycerol-co-sebacate) (PGS) [73].

5.5 *Nanoremediation*

Lacking admittance to drinking water and disinfection is quite possibly the most widely recognized issues that worry individuals around the world. Water poisonousness from various cytotoxic contaminations, for example hefty metal particles, synthetic compounds, poisons, paints, deposits a genuine general medical condition for people; subsequently, this subject has acquired a ton of center for various strategies and procedures to kill hazardous substances from water and wastewater. Treatment of wastewater is critical for likely requests to get it back to a feasible sort. Techniques for water purging have been the subject and interest of various researchers and government divisions lately. Explicit methodologies for treating wastewater have been utilized, and a blend of current nanotechnology-arranged arrangement with conventional procedures has yielded significant advantages. Bionanocomposite items are the most reasonable assets for water remediation inferable from their sustainable and biodegradable presence, in other words, eliminate microorganisms, compound pollutants, and hefty metals, and so on from dirtied water. Significant bionanocomposites incorporate mud hydrogel nanocomposites, bionanocomposites dependent on gum polysaccharides, chitosan based polymer bionanocomposites, cellulosic nanocomposites, and they are utilized in wastewater treatment. The silver nanoparticles found in slender chitosan films are utilized for different purposes including photograph oxidation of natural pollutants, decrease of weighty metals (Cd, Cr, Pb, and Fe) and antibacterial activity [74]. The multidirectional work is expected to quicken the enormous scope use of bionanocomposites to successfully eliminate various sorts of foreign substances from wastewater [15, 75, 76].

Among the accessible methods, the adsorptive evacuation by nanomaterials, for example, metallic nanoparticles, zeolite and carbon-based materials has pulled in significant interest because of the enormous dynamic surface region, countless practical gatherings, solid synthetic and warm dependability bringing about phenomenal adsorption proficiency [77]. Metal–oxygen framework (MOF) are crossover inorganic/natural permeable materials containing a heap of metal – oxygen and natural atoms and, as a result of their fascinating properties, are turning into an option in contrast to ordinary inorganic permeable materials, like zeolite and silica. Specifically, a promising system is additionally centered on the synergistic impact of adsorption-concentrated photocatalytic oxidation of vaporous toxins with this recently created MOF, as it has extensive potential in the treatment of great vaporous poisons, minimal effort and optional contamination free [78].

Various types of normal adsorbents have been broadly read for the adsorption of arsenic, for example dirt, squander materials and carbon based items. Treatment of handled water can be accomplished utilizing various techniques including actual strategies (film filtration, adsorption, and so forth), compound strategies (precipitation, oxidation), and organic techniques (initiated muck, circulated air through natural channels and others). These days, carbon nanomaterials, for example, graphene and subordinates, carbon nanofibers, carbon nanotubes, nanoporous carbon, fullerene, nanodiamonds, and graphite carbon nitride are broadly utilized as adsorbents due to their remarkable surface properties, speedy change, gigantic explicit surface region, controlled primary varieties, porosity, high substance strength, low thickness, simplicity of recovery, and reusability [77].

Contrasted with customary adsorbents like initiated charcoal, chitosan can be created in a more affordable style, bringing about high adsorption effectiveness because of an enormous number of practical amino and hydroxyl bunches that empower the expulsion of a scope of toxins from water [79–81].

Considering the high capability of joining photocatalytic nanoparticles with polymeric nanofibers to give porosity and an expansive receptive surface region for the adsorption and photodecomposition of natural color particles, the likely photodegradation of the polymeric base ought to likewise be noted [80].

Other than graphene oxide, nanosheets with decreased graphene oxide are additionally material to water adsorption of colors. The adsorption effectiveness of the nanosheets has been accounted for to be related with their electronic properties and this capacity can be improved by nano hybridization with profoundly conductive metal nanoparticles like silver [82].

In these cycles, initiated carbon fills in as a cradle for nanoparticles and furthermore gives extra responsive restricting locales, like hydroxyl, carboxyl, carbonyl and amide gatherings, which alongside the nanoparticles improve the capacity to adsorb [83].

6 Perspective and Future Trends

A wide assortment of inorganic nanoparticles and biopolymers accessible are utilized to create different types of bionanocomposites with assorted shapes, properties, and applications [47].

Biodegradable polymers are viewed as a satisfactory substitution medium to customary engineered polymers to decrease both energy utilization and carbon contamination. Essentially improved warm solidness of bionanocomposites happens with the presentation of nanofillers that go about as warmth obstructions in its plan. The properties and arrangement of the particular bionanocomposites improved with carbon nanotubes, and halloysite nanotubes [12]. Controlling the direction and area of bionic composites in an assortment of uses is significant for the total use of their trademark properties in perceptible congregations [58].

Inferable from natural conditions and their biodegradability, bionanocomposite covering films have been utilized with different angles in numerous new applications. Notwithstanding the constituent materials and the bionanocomposite stoichiometric proportion, the accomplishment of these covering films depends on the territory where such movies are utilized. These procedures expanded the working territory and the physico-synthetic properties and mechanical properties of bionanocomposite covering films. Also, the chance of creating novel quality covering films is energizing.

Albeit the general presentation of biodegradable polymers has been fundamentally improved by useful nanomaterials, certain essential properties should be additionally evolved including electrical conductivity and life span, just as biodegradability and biocompatibility. The electrical conductivity is exceptionally liked by the scattering condition of the polymer framework nanofillers just as the interfacial morphology that has been concentrated by numerous analysts will in any case be a significant field of study. Normal based conductive polymers can be advantageously biodegradable, however they do experience the ill effects of unsatisfied conductivity and powerless mechanical properties that truly limit their applications. The improvement of new polymers got from regular materials with better mechanical properties, or the union of plant-based polymers and engineered polymers, might be promising methodologies for future headway [63].

References

1. Khan, A.K., et al.: Carrageenan based bionanocomposites as drug delivery tool with special emphasis on the influence of ferromagnetic nanoparticles. *Oxid. Med. Cell. Long.* **2017**, 1–13 (2017). <https://doi.org/10.1155/2017/8158315>
2. Pande, V.V., Sanklecha, V.M.: Bionanocomposite: a review. *Austin J. Nanomed. Nanotechnol.* **5**(1), 1045 (2017)
3. Mhd Haniffa, M.A.C., Ching, Y.C., Abdullah, L.C., Poh, S.C., Chuah, C.H.: Review of bionanocomposite coating films and their applications. *Polymers (Basel)*. **8**(7), 246 (2016)
4. Akbar, M.U., Huma, Z., Salman, M., Hussain, R., Zahoor, A.F., Mansha, A., et al.: Synthetic materials to bionanocomposites: an overview. In: *Bionanocomposites*, pp. 1–20. Elsevier (2020)

5. Tamayo, L., Palza, H., Bejarano, J., Zapata, P.A.: Polymer composites with metal nanoparticles: synthesis, properties, and applications. In: *Polymer Composites with Functionalized Nanoparticles*, pp. 249–286. Elsevier (2019)
6. Averous, L.: Biodegradable multiphase systems based on plasticized starch: a review. *J. Macromol. Sci. Part C Polym. Rev.* **44**(3), 231–274 (2004)
7. Ray, S.S., Bousmina, M.: Biodegradable polymers and their layered silicate nanocomposites: in greening the 21st century materials world. *Prog. Mater. Sci.* **50**(8), 962–1079 (2005)
8. Averous, L., Boquillon, N.: Biocomposites based on plasticized starch: thermal and mechanical behaviours. *Carbohydr. Polym.* **56**(2), 111–122 (2004)
9. Darder, M., Aranda, P., Ruiz-Hitzky, E.: Bionanocomposites: a new concept of ecological, bioinspired, and functional hybrid materials. *Adv. Mater.* **19**(10), 1309–1319 (2007)
10. De Azeredo, H.M.C.: Nanocomposites for food packaging applications. *Food Res. Int.* **42**(9), 1240–1253 (2009)
11. Oksman, K., Aitomäki, Y., Mathew, A.P., Siqueira, G., Zhou, Q., Butylina, S., et al.: Review of the recent developments in cellulose nanocomposite processing. *Compos. Part A Appl. Sci. Manuf.* **83**, 2–18 (2016)
12. Mousa, M.H., Dong, Y., Davies, I.J.: Recent advances in bionanocomposites: preparation, properties, and applications. *Int. J. Polym. Mater. Polym. Biomater.* **65**(5), 225–254 (2016)
13. Reddy, M.M., Misra, M., Mohanty, A.K.: Bio-based materials in the new bio-economy. *Chem. Eng. Prog.* **108**(5), 37–42 (2012)
14. Schacht, E., Vandichel, J.V., Lemahieu, A., De Rooze, N., Vansteenkiste, S.: The use of gelatin and alginate for the immobilisation of bioactive agents. *Spec. Publ. Soc. Chem.* **138**, 18 (1993)
15. Zia, K.M., Jabeen, F., Anjum, M.N., Ikram, S.: *Bionanocomposites: Green Synthesis and Applications*. Elsevier, Amsterdam (2020)
16. Martin, O., Avérous, L.: Poly (lactic acid): plasticization and properties of biodegradable multiphase systems. *Polymer (Guildf)* **42**(14), 6209–6219 (2001)
17. Lenz, R.W., Marchessault, R.H.: Bacterial polyesters: biosynthesis, biodegradable plastics and biotechnology. *Biomacromolecules* **6**(1), 1–8 (2005)
18. Amass, W., Amass, A., Tighe, B.: You have full text access to this contentA review of biodegradable polymers: uses, current developments in the synthesis and characterization of biodegradable polyesters, blends of biodegradable polymers and recent advances in biodegradation studies. *Polym. Int.* **47**, 89–144 (1998)
19. Williams, S.F., Martin, D.P., Horowitz, D.M., Peoples, O.P.: PHA applications: addressing the price performance issue: I. *Tissue Eng. Int. J. Biol. Macromol.* **25**(1–3), 111–121 (1999)
20. Shogren, R.: Water vapor permeability of biodegradable polymers. *J. Environ. Polym. Degrad.* **5**(2), 91–95 (1997)
21. Kotnis, M.A., O'Brien, G.S., Willett, J.L.: Processing and mechanical properties of biodegradable poly (hydroxybutyrate-co-valerate)-starch compositions. *J. Environ. Polym. Degrad.* **3**(2), 97–105 (1995)
22. Bastioli, C., Cerutti, A., Guanella, I., Romano, G.C., Tosin, M.: Physical state and biodegradation behavior of starch-polycaprolactone systems. *J. Environ. Polym. Degrad.* **3**(2), 81–95 (1995)
23. Sasikala, C.H., Ramana, C.V.: Biodegradable polyesters. In: *Advances in Applied Microbiology*, pp. 97–218. Elsevier (1996)
24. Fujimaki, T.: Processability and properties of aliphatic polyesters, 'BIONOLLE', synthesized by polycondensation reaction. *Polym. Degrad. Stab.* **59**(1–3), 209–214 (1998)
25. Grigat, E., Koch, R., Timmermann, R.: BAR 1095 and BAK 2195: completely biodegradable synthetic thermoplastics. *Polym. Degrad. Stab.* **59**(1–3), 223–226 (1998)
26. Gross, R.A., Kalra, B.: Biodegradable polymers for the environment. *Science* **297**(5582), 803–807 (2002)
27. Baker, M.I., Walsh, S.P., Schwartz, Z., Boyan, B.D.: A review of polyvinyl alcohol and its uses in cartilage and orthopedic applications. *J. Biomed. Mater. Res. Part B Appl. Biomater.* **100**(5), 1451–1457 (2012)

28. Jose, T., George, S.C., Maria, H.J., Wilson, R., Thomas, S.: Effect of bentonite clay on the mechanical, thermal, and pervaporation performance of the poly (vinyl alcohol) nanocomposite membranes. *Ind. Eng. Chem. Res.* **53**(43), 16820–16831 (2014)
29. Miranda-Trevino, J.C., Coles, C.A.: Kaolinite properties, structure and influence of metal retention on pH. *Appl. Clay Sci.* **23**(1–4), 133–139 (2003)
30. Moon, R.J., Martini, A., Nairn, J., Simonsen, J., Youngblood, J.: Cellulose nanomaterials review: structure, properties and nanocomposites. *Chem. Soc. Rev.* **40**(7), 3941–3994 (2011)
31. Postek, M.T., Vladár, A., Dagata, J., Farkas, N., Ming, B., Wagner, R., et al.: Development of the metrology and imaging of cellulose nanocrystals. *Meas. Sci. Technol.* **22**(2), 24005 (2010)
32. Saito, T., Hirota, M., Tamura, N., Kimura, S., Fukuzumi, H., Heux, L., et al.: Individualization of nano-sized plant cellulose fibrils by direct surface carboxylation using TEMPO catalyst under neutral conditions. *Biomacromolecules* **10**(7), 1992–1996 (2009)
33. Baughman, R.H., Zakhidov, A.A., de Heer, W.A.: Carbon nanotubes--the route toward applications. *Science* **297**(5582), 787–792 (2002). <https://doi.org/10.1126/science.1060928>
34. An, K.H., Kim, W.S., Park, Y.S., Moon, J., Bae, D.J., Lim, S.C., et al.: Electrochemical properties of high-power supercapacitors using single-walled carbon nanotube electrodes. *Adv. Funct. Mater.* **11**(5), 387–392 (2001)
35. Niu, C., Sichel, E.K., Hoch, R., Moy, D., Tennent, H.: High power electrochemical capacitors based on carbon nanotube electrodes. *Appl. Phys. Lett.* **70**(11), 1480–1482 (1997)
36. Zandonella, C.: Is it all just a pipe dream? *Nature* **410**(6830), 734–735 (2001). <https://doi.org/10.1038/35071183>
37. Ma, P.-C., Siddiqui, N.A., Marom, G., Kim, J.-K.: Dispersion and functionalization of carbon nanotubes for polymer-based nanocomposites: a review. *Compos. Part. A Appl. Sci. Manuf.* **41**(10), 1345–1367 (2010)
38. McEuen, P.L., Bockrath, M., Cobden, D.H., Yoon, Y.-G., Louie, S.G.: Disorder, pseudospins, and backscattering in carbon nanotubes. *Phys. Rev. Lett.* **83**(24), 5098 (1999)
39. Baur, J., Silverman, E.: Challenges and opportunities in multifunctional nanocomposite structures for aerospace applications. *MRS Bull.* **32**(4), 328–334 (2007)
40. Mingo, N., Stewart, D.A., Broido, D.A., Srivastava, D.: Phonon transmission through defects in carbon nanotubes from first principles. *Phys. Rev. B.* **77**(3), 33418 (2008)
41. Zhang, J., Zhang, Y., Chen, Y., Du, L., Zhang, B., Zhang, H., et al.: Preparation and characterization of novel polyethersulfone hybrid ultrafiltration membranes bending with modified halloysite nanotubes loaded with silver nanoparticles. *Ind. Eng. Chem. Res.* **51**(7), 3081–3090 (2012)
42. Liu, M., Jia, Z., Jia, D., Zhou, C.: Recent advances in halloysite research. *Prog. Polym. Sci.* **39**, 1498–1514 (2014)
43. Hassan-Nejad, M., Ganster, J., Bohn, A., Pinnow, M., Volkert, B.: Bio-based nanocomposites of cellulose acetate and nano-clay with superior mechanical properties. *Macromol. Symp.* **280**(1), 123–129 (2009)
44. Du, M., Guo, B., Jia, D.: Newly emerging applications of halloysite nanotubes: a review. *Polym. Int.* **59**(5), 574–582 (2010)
45. Du, M., Guo, B., Liu, M., Jia, D.: Formation of reinforcing inorganic network in polymer via hydrogen bonding self-assembly process. *Polym. J.* **39**(3), 208–212 (2007)
46. Yah, W.O., Takahara, A., Lvov, Y.M.: Selective modification of halloysite lumen with octadecylphosphonic acid: new inorganic tubular micelle. *J. Am. Chem. Soc.* **134**(3), 1853–1859 (2012)
47. Kushwaha, R.K., Srivastava, A.: Recent developments in bio-nanocomposites: a review. *Res. J. Nanosci. Eng.* **2**(2), 1–4 (2018)
48. Srivastava, A., Maiti, P., Kumar, D., Parkash, O.: Mechanical and dielectric properties of CaCu₃Ti₄O₁₂ and La doped CaCu₃Ti₄O₁₂ poly (vinylidene fluoride) composites. *Compos. Sci. Technol.* **93**, 83–89 (2014)
49. Srivastava, A., Jana, K.K., Maiti, P., Kumar, D., Parkash, O.: Poly (vinylidene fluoride)/CaCu₃Ti₄O₁₂ and La doped CaCu₃Ti₄O₁₂ composites with improved dielectric and mechanical properties. *Mater. Res. Bull.* **70**, 735–742 (2015)

50. Alemdar, A., Sain, M.: Isolation and characterization of nanofibers from agricultural residues—wheat straw and soy hulls. *Bioresour. Technol.* **99**(6), 1664–1671 (2008)
51. Zimmermann, T., Bordeanu, N., Strub, E.: Properties of nanofibrillated cellulose from different raw materials and its reinforcement potential. *Carbohydr. Polym.* **79**(4), 1086–1093 (2010)
52. Kumar, A., Srivastava, A.: Preparation and mechanical properties of jute fiber reinforced epoxy composites. *Ind. Eng. Manag.* **6**, 1–4 (2017)
53. Guo, Q., Ghadiri, R., Weigel, T., Aumann, A., Gurevich, E.L., Esen, C., et al.: Comparison of in situ and ex situ methods for synthesis of two-photon polymerization polymer nanocomposites. *Polymers (Basel)* **6**(7), 2037–2050 (2014)
54. Nogi, M., Yano, H.: Transparent nanocomposites based on cellulose produced by bacteria offer potential innovation in the electronics device industry. *Adv. Mater.* **20**(10), 1849–1852 (2008)
55. Gahlawat, G., Shikha, S., Chaddha, B.S., Chaudhuri, S.R., Mayilraj, S., Choudhury, A.R.: Microbial glycolipoprotein-capped silver nanoparticles as emerging antibacterial agents against cholera. *Microb. Cell Fact.* **15**(1), 25 (2016)
56. Forrest, S.R.: The path to ubiquitous and low-cost organic electronic appliances on plastic. *Nature* **428**(6986), 911–918 (2004)
57. Günes, S., Neugebauer, H., Sariciftci, N.S.: Conjugated polymer-based organic solar cells. *Chem. Rev.* **107**(4), 1324–1338 (2007)
58. Zhang, S., Pelligra, C.I., Feng, X., Osuji, C.O.: Directed assembly of hybrid nanomaterials and nanocomposites. *Adv. Mater.* **30**(18), 1705794 (2018)
59. Borchert, H., Witt, F., Chanaewa, A., Werner, F., Dorn, J., Dufaux, T., et al.: Vertically oriented carbon nanostructures and their application potential for polymer-based solar cells. *J. Phys. Chem. C* **116**(1), 412–419 (2012)
60. Moulé, A.J., Chang, L., Thambidurai, C., Vidu, R., Stroeve, P.: Hybrid solar cells: basic principles and the role of ligands. *J. Mater. Chem.* **22**(6), 2351–2368 (2012)
61. Dagdeviren, C., Li, Z., Wang, Z.L.: Energy harvesting from the animal/human body for self-powered electronics. *Ann. Rev. Biomed. Eng.* **19**, 85–108 (2017)
62. Qi, Y., McAlpine, M.C.: Nanotechnology-enabled flexible and biocompatible energy harvesting. *Energy Environ. Sci.* **3**(9), 1275–1285 (2010)
63. Liu, H., Jian, R., Chen, H., Tian, X., Sun, C., Zhu, J., et al.: Application of biodegradable and biocompatible nanocomposites in electronics: current status and future directions. *Nanomaterials* **9**(7), 950 (2019)
64. Gupta, T.K., Singh, B.P., Mathur, R.B., Dhakate, S.R.: Multi-walled carbon nanotube–graphene–polyaniline multiphase nanocomposite with superior electromagnetic shielding effectiveness. *Nanoscale* **6**(2), 842–851 (2014)
65. Kuang, T., Chang, L., Chen, F., Sheng, Y., Fu, D., Peng, X.: Facile preparation of lightweight high-strength biodegradable polymer/multi-walled carbon nanotubes nanocomposite foams for electromagnetic interference shielding. *Carbon* **105**, 305–313 (2016)
66. Pawar, R., Lee, C.S.: Heterogeneous Nanocomposite-Photocatalysis for Water Purification. William Andrew (2015)
67. Wang, G., Zhao, G., Wang, S., Zhang, L., Park, C.B.: Injection-molded microcellular PLA/graphite nanocomposites with dramatically enhanced mechanical and electrical properties for ultra-efficient EMI shielding applications. *J. Mater. Chem. C* **6**(25), 6847–6859 (2018)
68. Jeong, H., Baek, S., Han, S., Jang, H., Kim, S.H., Lee, H.S.: Novel eco-friendly starch paper for use in flexible, transparent, and disposable organic electronics. *Adv. Funct. Mater.* **28**(3), 1704433 (2018)
69. Misman, M.A., Azura, A.R., Sidek, O.: Validation of an electronic sensor network (ESN) control chamber for monitoring the soil decomposition process of sago starch-filled natural rubber latex films. *J. Test. Eval.* **43**(5), 1037–1046 (2015)
70. Chao, J.Y., Zhu, L.Q., Xiao, H., Yuan, Z.G.: Protonic/electronic hybrid oxide transistor gated by chitosan and its full-swing low voltage inverter applications. *J. Appl. Phys.* **118**(23), 235301 (2015)

71. Lin, Y.-H., Kang, P.-L., Xin, W., Yen, C.-S., Hwang, L.-C., Chen, C.-J., et al.: Preparation and evaluation of chitosan biocompatible electronic skin. *Comput. Ind.* **100**, 1–6 (2018)
72. Chang, J., Wang, C., Huang, C., Tsai, T., Guo, T., Wen, T.: Chicken albumen dielectrics in organic field-effect transistors. *Adv. Mater.* **23**(35), 4077–4081 (2011)
73. Najafabadi, A.H., Tamayol, A., Annabi, N., Ochoa, M., Mostafalu, P., Akbari, M., et al.: Biodegradable nanofibrous polymeric substrates for generating elastic and flexible electronics. *Adv. Mater.* **26**(33), 5823–5830 (2014)
74. Al-Sherbini, A.S.A., Ghannam, H.E.A., El-Ghanam, G.M.A., Amr, A., Youssef, A.M.: Utilization of chitosan/Ag bionanocomposites as eco-friendly photocatalytic reactor for Bactericidal effect and heavy metals removal. *Heliyon* **5**(6), e01980 (2019). <https://doi.org/10.1016/j.heliyon.2019.e01980>
75. Alves, N.M., Mano, J.F.: Chitosan derivatives obtained by chemical modifications for biomedical and environmental applications. *Int. J. Biol. Macromol.* **43**(5), 401–414 (2008)
76. Repo, E., Warchoń, J.K., Bhatnagar, A., Mudhoo, A., Sillanpää, M.: Aminopolycarboxylic acid functionalized adsorbents for heavy metals removal from water. *Water Res.* **47**(14), 4812–4832 (2013). <https://doi.org/10.1016/j.watres.2013.06.020>
77. Srivastava, V., Zare, E.N., Makvandi, P., Zheng, X., Iftekhar, S., Wu, A., et al.: Cytotoxic aquatic pollutants and their removal by nanocomposite-based sorbents. *Chemosphere.* **2020**, 127324 (2020)
78. Wen, M., Li, G., Liu, H., Chen, J., An, T., Yamashita, H.: Metal–organic framework-based nanomaterials for adsorption and photocatalytic degradation of gaseous pollutants: recent progress and challenges. *Environ. Sci. Nano.* **6**(4), 1006–1025 (2019)
79. Bhatnagar, A., Sillanpää, M.: Applications of chitin-and chitosan-derivatives for the detoxification of water and wastewater—a short review. *Adv. Colloid Interface Sci.* **152**(1–2), 26–38 (2009)
80. Homaeigohar, S.: The nanosized dye adsorbents for water treatment. *Nanomaterials* **10**(2), 295 (2020)
81. Miretzky, P., Cirelli, A.F.: Fluoride removal from water by chitosan derivatives and composites: a review. *J. Fluor. Chem.* **132**(4), 231–240 (2011)
82. Pang, J., Chao, Y., Chang, H., Li, H., Xiong, J., Zhang, Q., et al.: Silver nanoparticle-decorated boron nitride with tunable electronic properties for enhancement of adsorption performance. *ACS Sustain. Chem. Eng.* **6**(4), 4948–4957 (2018)
83. Asfaram, A., Ghaedi, M., Hajati, S., Goudarzi, A., Bazrafshan, A.A.: Simultaneous ultrasound-assisted ternary adsorption of dyes onto copper-doped zinc sulfide nanoparticles loaded on activated carbon: optimization by response surface methodology. *Spectrochim. Acta Part A Mol. Biomol. Spectrosc.* **145**, 203–212 (2015)

A Comparative Study of Cellulose Nanocomposite Derived from Algae and Bacteria and Its Applications



Ragaa A. Hamouda  and Marwa Salah Abdel-Hamid 

Abstract Cellulose nanofibers have a highest promise of nanocomposites in many different fields. Nanocomposites are systems in, which at least one component in the nanorange needs to be present. In different types of composites, including the most recent nanocomposites, cellulose is used. Cellulose is a renewable, higher plant-based, algae-based, and bacterial polysaccharide. Cellulose is composed of repeating units of β -D-glucopyranose. According to cellulose sources and extraction methods, and the properties of cellulose vary. Properties and scale can be influenced by cellulose sources. The cellulose molecular structure of different sources is identical, but its physical and chemical properties differ. The algae's cell wall is made up of polysaccharides, which are organized into amorphous and plenty of matrixes as microfibrils. Acid hydrolysis and mechanical refinement can be consumed to extract cellulose from cell wall of the various types of algae. The structure of bacterial cellulose is a glucose monomer that displays good characteristics such as a unique nanostructure. Acetic acid bacteria in synthetic and non-synthetic media that assimilate various sugars produce bacterial cellulose and produce nanocellulose in liquid media. The nanofibrillary, highly crystalline, high surface area, high fiber and tense strength appearance ratio, higher capacity for water maintenance, and high purity because of a lack of lignin and hemicellulose is the bacterial cellulose. Because of their motivating properties and potential applications, nanocellulose fibers composit received increasing attention.

Keywords Algae · Bacteria · Cellulose nanocomposite · Cellulose

R. A. Hamouda (✉)

University of Jeddah, College of Sciences and Arts Khulais, Department of Biology, Jeddah, Saudi Arabia

R. A. Hamouda · M. S. Abdel-Hamid

Microbial Biotechnology Department, Genetic Engineering and Biotechnology, Research Institute, University of Sadat City, El Sadat City, Egypt

e-mail: marwa.salah@gebri.usc.edu.eg

© The Author(s), under exclusive license to Springer Nature Switzerland AG 2022

151

A. E. Shalan et al. (eds.), *Advances in Nanocomposite Materials for Environmental and*

Energy Harvesting Applications, Engineering Materials,

https://doi.org/10.1007/978-3-030-94319-6_7

Abbreviations

<i>A. baumannii</i>	<i>Acetobacter baumannii</i>
a-CC	Anionic <i>Cladophora</i> nanocellulose
AC	Algal cellulose
AFM	Atomic force microscopy
Ag	Silver
Alg	Alginate
ANC	Amorphous Nanocellulose
Au	Gold
BC	Bacterial Cellulose
BHA	Boron-Doped Hydroxyapatite
BNC	Bacterial Nanocellulose
BNC	Bacterial Nano Cellulose
CC	<i>Cladophora</i> Nanocellulose
c-CC	Cationic <i>Cladophora</i> nanocellulose
Cds	Cadmium
<i>C. albicans</i>	<i>Candida albicans</i>
CMCase	Carboxymethyl cellulase
CMF	Cellulose Microfibril
CNC	Cellulose Nanocrystalline
CNF	Cellulose Nanofibril
CNP	Cellulose Nanocomposites
CNY	Cellulose Nanoyarn
Co	Cobalt
CrI	Crystallinity
Cu	Copper
Dcr	Type of Crystalline Allomorph, Degree Size of Nanocrystallites
DP	Degree of polymerization
DSC	Differential scanning calorimetry
DTA	Differential thermal analysis
<i>E. coli</i>	<i>Escherichia coli</i>
FT-IR	Fourier Transform Infrared
GEL	Gelatin
GPa	The unit of tensile strength
H ₂ O ₂	Hydrogen Peroxide
H ₂ SO ₄	Sulfuric acid
H ₃ O ⁺	Hydronium ions
H ₃ PO ₄	Phosphoric acid
H ₃ PO ₄	Phosphoric acid
HA	Hydroxyapatite
HAp-BC	Hydroxyapatite bacterial cellulose composite
HCHO	HCHO reducing agents

HCl	Hydrochloric acid
HNO ₃	Nitric acid
LLS	Laser light scattering
LPS	Lipopolysaccharide
MCC	Microcrystalline Cellulose
MNPs	Metals nanoparticles
NABH ₄	NABH ₄ reducing agents
NaClO ₂	Sodium Chlorite
NC	Nanocellulose
NFC	Nanofibrillated Cellulose
NMR	Nuclear Magnetic Resonance
NPs	Nanoparticles
PANI	Polyaniline
PEO	Polyethylene Oxide
PEO _x -PPO _y -PEO _x	Tri Block Structure
PPO	Polypropylene Oxide
PPy	Polymer polypyrrole or polyaniline
Pt	Platinum
PVA-CNC	Polyvinyl alcohol based nanocomposite derived from red alga
PVP	Polyvinylpyrrolidone
RS	Raman spectroscopy
RSM	Response Surface Methodology
SaOs-2	Human osteoblast-like cells
SEM	Scanning Electron Microscopy
<i>Staphy. aureus</i>	<i>Staphylococcus aureus</i>
TEA	Triethanol amine
TEM	Transmission Electron Microscopy
TEMPO	2,2,6,6-Tetramethylpiperidine-1-oxyl radical
TiO ₂	Titanium oxide
TGA	Thermogravimetric analysis
UV	Ultra Violete
WAXS	Wide-angle X-ray scattering
XRD	X-ray powder diffraction
ZnO	Zinc oxide
ZnO/CNC	Cellulose/Zinc oxide nanocomposite

1 Introduction

Cellulose is one of the richest biopolymers on the world, are extant in the plants, specific types of bacteria, fungi, and algae [1]. Cellulose is a most vital skeletal constituent in plants; the polysaccharide containing cellulose is a nearly unlimited

polymeric raw substance with interesting characteristics and structure [2]. The cellulose fibrils consist of crystalline in addition to amorphous regions, the amorphous cellulose despoiled to liberate nano-scaled constituents from the cellulose resource by chemical, mechanical, or blend and may also be by enzymes [3]. Algae are promising sources of cellulose and hence nanocellulose, cellulose has been effectively isolated from various groups of algae such as green, red, and brown macroalgae [4, 5]. The inner layer of brown algae cell wall is composed of cellulose that represents 2 to 20% of dry biomass [6]. He et al. [7] isolated highly crystalline cellulose from *Saccharina japonica* brown alga. Cellulose was extracted from macrogreen alga *Ulva lactuca* with a crystallinity index of 48% [8]. NC was efficaciously extracted from red alga *Gelidium elegans* dry biomass, with higher crystallinity (73%). Cellulose nanofibers obtained from marine algae have many applications as food industry [9]. Many bacteria also produce cellulose; the bacterial genera such as *Gluconacetobacter*, *Sarcina*, and *Agrobacterium* are produced cellulose [10, 11]. Bacteria produce cellulose by using synthetic and non-synthetic media through fermentation processes [12]. Bacterial cellulose microfibrils are nearly 100-times smaller than the fibrils of cellulose extracted from plants [13, 14]. BC has many applications; such as membranes for audio machines that are used in the production of electronic paper and coating paper, as well as many other applications [15, 16]. Nanocomposites are substances that composed of more one distinct material to devolve the properties of nanoparticles; such as the stiffness, strength and toughness [17]. Many applications of cellulose nanocomposites derived from macrogreen alga *Cladophora* such as ion-exchange membranes, the isolation and purification of biomolecules, gas-sensor machines, energy-storage machines and diagnostics [5]. Bacterial cellulose is an exceptional biopolymer for the synthesis of nanocomposites. BC has been applied in medicine field such as wound dressing and regeneration of damaged tissue, ease of wound observation, drug application, and accelerate the epithelialization process [18, 19]. The current review describes the structure, types and characterization of cellulose and nanocellulose and cellulosic nanocomposite and their applications. This chapter focuses on the advantages, structure and characterizations of nanocellulose extracted from algae and secreted from bacteria. Futhermore, the characterisations and applications of nanocomposite derived from algae and bacteria and potential uses in the future.

2 Cellulose

Cellulose is global and rich, represenating 1.5×10^{12} tons of overall yearly biomass yielding; so, cellulose from new sources is reflected an unlimited resource of raw substances for the growing mandate for replacing indesterial substances with ones that are more eco-friendly and bio-compatible [20]. Cellulose has interesting material properties such as worthy bio-compatibility, economy, low density, high force, and better mechanical estate [21]. Wood is a natural cellulose material used in industries for ancient era in the worldwide such as paper, textiles and cellulose derivatives

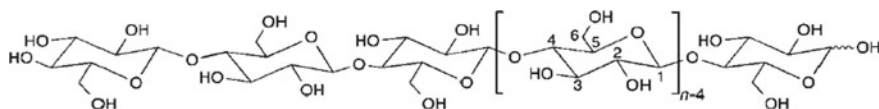


Fig. 1 Molecular structure of cellulose $nd =$ degree of polymerization [2]

are recycled for coverings, protects, optical films as well as additive on it making, composites and nanocomposites, that are used in pharmaceuticals, foodstuffs and cosmetics [22]. Cellulose is composed of a carbohydrate polymer produced from duplicating B-D-glucopyranose that is connected by covalent bonds, as shown in Fig. 1 [2]. Cellulose chain length can be indicated by the (degree of polymerization, DP), which can differ according to origin and the methods of extraction, the DP of cellulose ranged from many hundreds to many thousands of glucose units related to nature and treatments [23, 24].

3 Cellulose Structure and Composition

The most important nanostructured component occurring in plant-based material is cellulose [25]. The whole of tree is up to hundreds of meter and the cross-section in the centimeter scale containing of growth rings in millimeter, the cellular is tens of micrometers, cell wall consists of lignin besides hemicelluloses embedded in the cellulose microfibrils that length tens of nanometers, so the cellular construction measure by nanometric [26] Cellulose is stabilized by hydrogen bonds in addition to van der Waal forces [27]. The cellulose fibrils consist of crystalline as well as amorphous regions [20].

4 Nanocellulose

Cellulose nanomaterial classified into various subdivisions depending on shape, dimension, function, extraction methods, nature sources and conditions for processing [28]. NC is characterized into six groups by using the next expressions: 1) microcrystalline cellulose (MCC), 2) Cellulose microfibril (CMF), 3) Cellulose nanofibril (CNF), 4) cellulose nanocrystal (CNC), 5) amorphous nanocellulose (ANC), and 6) cellulose nanoyarn (CNY) [29]. According to their morphology, nanocellulose is divided into three forms; “i) cellulose nanocrystals (CNCs), ii) nanofibrillated cellulose (NFC) and iii) bacterial nanocellulose (BNC)” [30]. The preparation of NC is impacted by cellulosic nature, their type of strong acid hydrolysis, temperature, time, agitation and ratio of acid to cellulose fibers, the producing suspension washed by double distilled water (DD water) numerous times with successive centrifugation, dialysis with made against D. D water to eliminate any free acid

molecules [31]. Cherian et al. [32, 33] investigated that nanocellulose prepared by dilute acid linked with steam. The production of nanocellulose depends on the type of acid was used, if used hydrochloric acid, the dispersion of NC yield is inadequate and the aqueous suspensions leads to flocculate [34], charged surface sulfate esters are produce, when the hydroxyl group of cellulose reacts with sulfuric acid that stimulate spreading of the nanocellulose in water [35], and there is a change in the rheological parameters, when used sulfuric acid (H_2SO_4) and hydrochloric acid (HCL) [32]. Blending of both (H_2SO_4) and (HCL) during hydrolysis during Fig. 2 demonstrated different methods using for synthesis of cellulose nanofibers.

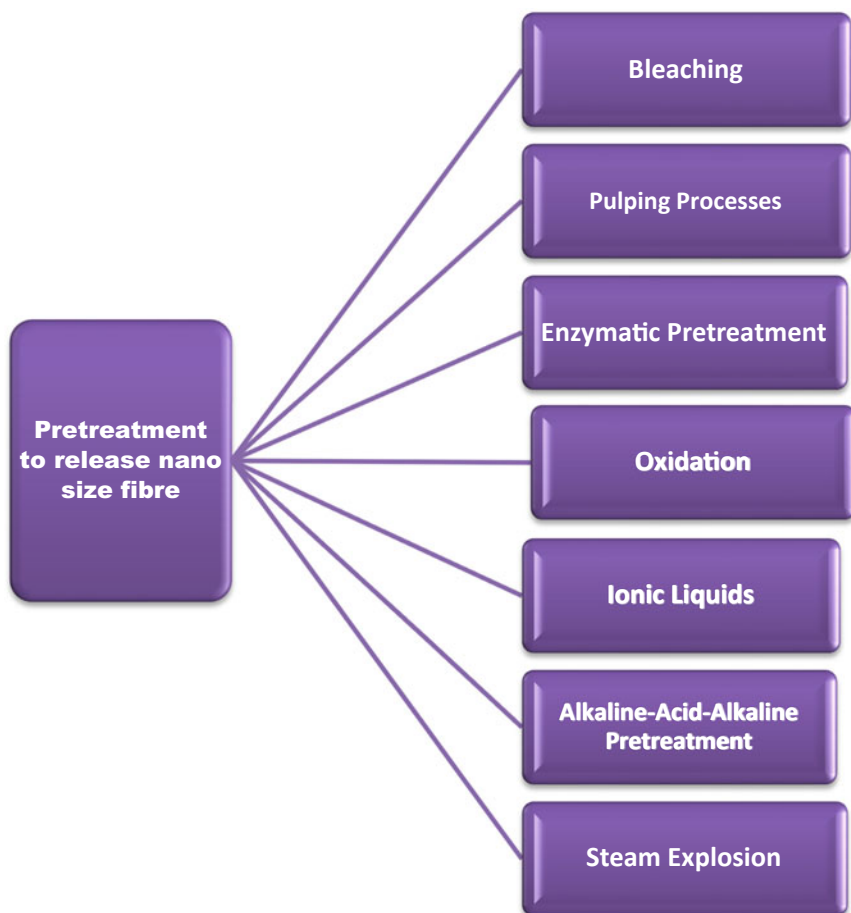


Fig. 2 Schematic diagrams of different pretreatments to release cellulose nanofibers

5 Cellulose Nanocrystals

Cellulose nanocrystals (CNCs) acquired from organically arising cellulose fibers, they are bio-degradable, renewable in quality, environmentally friendly and hydrophilic in nature [36]. The nature of CNCs are rigid bar-like particles composed of chain slices of cellulose in a closely accurate crystalline components, which described as nanoparticles whiskers, nanofibers, microcrystallites, along with some others, but the maximum broadly acknowledged nomenclature is CNCs [37, 38]. CNCs have superior amorphous fractions, high special strength, superior surface area, and exclusive liquid crystalline belongings [36]. CNCs can be yielded in various shapes such as sphere, ribbon, rod and needle shape that having dense cellulose chains and can be steadied by hydrogen bonding, which build identical remarkable solid crystalline nanoparticles and possess exceptional characteristics [3, 37–40]. CNCs shows great fascinating advantages such as low cost, and density, good homogeneity, stability, bio-degradability, elevated strength, toughness, nontoxicity, excellent mechanical properties and the minor dimensions of nanocrystalline cellulose inform valuable possessions to composite substances strengthened with these fibers, which successively be expended in broad area of applications [41]. The length and width of CNCs, differ according to the natural of cellulose microfibrils, the methods and circumstances of extractions [36]. The range of diameter and length of cellulose nanocrystals (CNCs) attained from wood 3–5 nm and 100–300 nm, cotton 5–10 nm and 100–150 nm, Ramie 70–200 nm and 5–15 nm, sisal 3–5 nm and 100–300 nm [37–44]. The relation between lengths and diameter (L/D) of CNCs is referred to geometrical aspect ratio that is very useful to determine the reinforcing ability of CNCs and is useful in the configuration of infiltrated networks that enhance the mechanical routines of nanocomposites [45]. The vital CNC properties can be distinguished by three main sorts, like mechanical, rheological and nature of liquid crystalline. The important devices were used to determine and calculate the tensile modulus and strength of CNC are “Atomic force microscopy (AFM), X-ray diffraction analysis, Inelastic X-ray scattering and Raman scattering microscopy” [22], and they also reported that the tensile strength of CNCs is much more than that of the steel wire. The unit of tensile strength is GPa. Iwamoto et al. [46] found that the elastic moduli of CNCs were 150 GPa, and the calculated modulus of tunicate cellulose whiskers CNC is 143 GPa [47]. All asymmetric nanocrystal bar-like or plate-like particles impulsively form regular configures, under suitable conditions and also, at critical concentrations that refer to liquid crystalline nature of CNCs, that guiding to the creation of a nematic phase [36]. Liquid crystalline can be affected by many aspects such as shape, disparity, size, charge, electrolyte, external conditions and the acids used in hydrolysis, the liquid crystallinity of nanocrystals beside the birefringent nature producing vital optical phenomena [36, 48, 49]. CNC rheological parameters are impacted by many factors such as liquid crystallinity, gelation possessions, aspect ratio of CNCs, and acid type that consumed for hydrolysis [36, 50]. CNC yielded by acid hydrolysis due to hydronium ions diffuse into the cellulose strings in the amorphous regions stimulating individual crystallites after mechanical

pretreatment like sonication, homogenizer [51]. Several numbers of acids were used in hydrolysis processes such as (H_2SO_4), (HCL), nitric acid (HNO_3) and phosphoric acid (H_3PO_4), while (H_2SO_4) and (HCL) acids are widely consumed [52, 53]. Meanwhile H_2SO_4 was the most widely used, especially in the U.S., which was nearly 10-folds in comparison to compare to (HCL), so (H_2SO_4) economic due to the larger amount [54]. CNC differ in structure and aspect ratio owing to the nature sources of cellulose [21]. Cellulose nanocrystalline is highly used in biomedical industry, for instance, drug release systems, skin replacements for wound and wounds, scaffolds for tissue engineering, gum, wrappers and bone reconstruction nerves, and blood vessel repair [55]. CNC can transfer medicine or antibiotics into the healing because it's porous network structure and acts as barrier against any external pathogenic microorganisms [56].

6 Cellulose Nanofibrillar (CNFs)

Cellulose nanofibrillar can be shaped “spaghetti-like” and include mechanically and chemically isolated microfibrils and bacterial cellulose, which differ from CNCs form liquid crystal suspensions, needle shaped, and maximum crystalline, strong ($E = 150$ GPa) [57]. CNFs involves stretched packets of elementary nanofibrils (aggregation), that are assembled from alternating amorphous to crystalline fields, the length of CNFs is 500–2000 nm and the width 20–50 nm [29]. CNFs is characterized by high surface area in contrast to native cellulose, forms aqueous gel with low concentration [29]. Cellulose nanofibrillar has several properties such as biocompatibility that make them appropriate for different biomedical and environmental applications [58], does not degrade or liberate toxic material so it has used in water purification and high purity that enhance thermal stability so it used in the sensor fabrications and decompositions of several pollutants [59]. The CNFs have used in many applications due to flexibility, high strength, aspect ratio (length to width ratio), and rheology [60–63]. CNFs has high quantities of $-OH$ groups that present on their surface that helps cationic groups attached to CNF surface that improves anions from wastewater [64]. Physical, chemical, biological and oxidation methods can be used to extract cellulose nanofibrillar (CNF) [65]. The extraction of CNFs required high energy that causes the problem in commercialization [1, 66]. CNF yielding required high energy, which increased up to 30,000 kWh/ton with a extreme-pressure homogenizer [61]. Important development has been created in diminishing the energy to yield CNF, such as enzymatic pretreatment or carboxymethylation of wood cellulose, a diminution of energy demand for the nanofibrillation method operating following mechanical management [67–70]. CNF has limit applications due to low dewatering, and poor compatibility of hydrophilic reinforcers with hydrophobic polymers [70]. Several studies had been conducted to overcome the problem of energy, such as the researcher in the University of Tokyo, Japan, that announced a new treatment to develop CNF by treated cellulose fibers by 2, 2, 6, 6-tetramethylpiperidine-1-oxyl radical (TEMPO)- intermediated oxidation [71–74]. The pervious methods is not

only convert cellulose into nanofibrils with thickness 3–4 nm and little microns in length, and reformed the CNF surface into the anionic charge, the carboxylate group were replaced by the hydroxyl group of cellulose, with supplying functional groups for further functionalization [75]. CNFs hydrogels use as a 3D scaffold on, which to culture hepatic cells stem cells [76, 77] Cellulose nanofibrillar/nanocrystalline have been used in a wide range in drug delivery [78–85]. NC preventing bacterial infections due to permit to transfer of antibiotics and it can act as a physical barrier [86]. NC is developing as an appealing solution for improving unique and operative bone grafting techniques [87]. NC has been used as a filler in many dental materials and composites [87]. Different types of nanocellulose possessed a vital role in drug delivery and advanced pelleting systems, due to low cost, renewable and sustainable resources [88, 89]. Nanocellulose has been used as scaffold cornea tissue engineering [90]. Nanocellulosic blanket had been used for nasal reconstruction, displayed good bio-compatibility and steady over time, thus a better material to improve the nose bone [91].

7 Cellulose Nanocomposites

Nanocomposites concept are more than one materials in, which at least one material in the nanometer range [92]. The merging of inorganic NPs (Ag, Cu, Au, Cd, etc.) only or with polymers by supporting their homogeneous combination to form nanocomposites substances has been broadly utilized [93]. The polymer chains perform a vital role leading to a restrict size dissemination besides carefully distinct shape for the metal nanoparticles (MNPs) [94]. CNF has been combined with several metals and nonmetals such as carbon, nanoparticles, polymers etc. to produce composites used for numerous applications [68]. NC have concerned an abundant material in the nanocomposite substances in regard to their important properties for instance nanoscale, high aspect ratio, high surface area, unique morphology and low density (1.61 g/cm^3) [95]. Cellulosic fibers can be recycled to composites that enhances the strength and dimensional stability characteristics [96]. Various applications of cellulose nanocomposites such as water purification, food packaging, tissue engineering etc., [59]. Carbon nanotubes associated with CNF and blended with polyaniline (PANI) to form cellulose nanocomposites and combination with Titanium oxide (TiO_2), produced fibers with diameters of 10–30 nm that used in various applications [97]. The CNF has been associated with different nanoparticles such as silver, gold, hydroxyapatite (HAp), (Cadmium) Cds nanoparticles that have been used in various applications [68]. Cellulose with silver nanoparticles (cellulose/silver nanocomposite) has been applied in biosensors to detect catechol, antibacterial fibers and catalytic materials [98]. Several studies have been advanced to blend metal nanoparticles (NPs) with cellulose fibers to synthesis cellulose/metal nanocomposites, such as blending of components, the reduction of metal salts, addition of reducing agents, the reduction of metal salts by cellulose-reducing groups, photo-induced metal growth using irradiation, and electrostatic assembly [99]. Methods for

blending inorganic NPs into polymers to form a homogeneous mixture of nanocomposites have been widely applied; the advantage of this method is simplicity, but does not cause a homogeneous allocation of MNPs onto cellulose [100]. The reduction of metal salts involved utilization of a soluble metal as forerunner, a reducing agent and a co-stabilizer, reduction of metal salts can be retained lacking adjunct of an external mediator due to adsorption of metals on the cellulose surfaces that reduce metal by aldehyde, carboxylic and hydroxyl groups in cellulose fibres [101, 102], the advantage of this process, benefits to enhance their dissemination interior the cellulose matrix and avoids the formation of accumulates [94]. Reducing agent performance as co-stabilizer with cellulose fibers, such as Sodium borohydride, trisodium citrate, hydrazine, hydroxylamine, triethanol amine (TEA) and ascorbic acid with gelatine or polyvinylpyrrolidone (PVP) as colloidal stabilizers has been examined to yield small spherical particles with 8.5 nm average sizes [103, 104]. The reduction applying UV irradiation is easy treatment to yield M-NPs on the surface of cellulose fibres to produce nanocomposites, the mechanism is investigated by the UV photons are activated reducing sites at the surface of cellulose, the time of irradiation and light intensity are the vital parameters that vital parameters to control the numbers of metals incorporated into cellulose fibres [105, 106]. The electrostatic methods depend on the adsorption of oppositely charged species on the solid material, the advantages of this method that improved control of inorganic content, control of NPs size, morphology, and prevent agglomeration nanoparticles [107].

8 Cellulose Nanocrystalline or Nanofiber Characterization

Cellulose, cellulose nanocrystalline, nanofiber can be characterized by different devices such as X-ray scattering, which determine the allomorph type by investigated locations of the chief diffraction peaks, investigated the crystalline unit cell, investigated lateral sizes of nanocrystallites, length and width of crystalline cellulose, Another device such as cross-polarization magic angle spinning ^{13}C NMR spectroscopy (CP/MAS ^{13}C NMR), which can be measure index of crystallinity (CrI), their accumulates, the kind of crystalline allomorph, a measure of substitution and lateral size of nanocrystallites (Dcr). Electron microscopy "transmission electron microscopy (TEM) and scanning electron microscopy (SEM)" that produce images of an object offer data concerning to the size, features of surface and content of the sample [108–110]. Atomic force microscopy contains a sharp tip used to scan the object surface [111]. Laser light scattering (LLS) clears predominantly a longitudinal size. Fourier Transform Infrared (FT-IR) investigated the functional groups of samples, IR-spectroscopy can be worked for determinations the crystallinity of cellulose [111, 112]. Raman spectroscopy (RS) evaluate the crystallinity, also there are many methods can give some informations about the chemicals and physical properties of cellulose, Differential thermal analysis (DTA), Thermogravimetric analysis (TGA) beside Differential scanning calorimetry (DSC) [113–115]. Mechanical characterization of nanocellulose can be obtained using different treatments [116, 117].

Experimental approaches for investigation of the moduli of NC include WAXS, Raman spectroscopy and AFM [118].

9 Cellulosic Nanocomposite and Their Applications

A various number of cellulose metal nanocomposites have taken much attention owing to their unique properties, such as optical electronic, minor size and large specific surface that vary from the bulk material [25]. The merged of MNPs and cellulose is an unlimited significance to obtain molecular recognition and biosensing stages [119]. Ag nanoparticles have strong cytotoxicity against a broad number of bacteria, fungi and algae [120]. Many research proved that cellulose/Ag nanocomposite materials have antibacterial agents against both Gram-positive besides to Gram-negative bacteria [121, 122]. Rac-Rumijowska et al. [123] proved that cellulose/Ag nanocomposite has good antimicrobial activities against the following microorganisms *Staphy.aureus*, *E. coli*, *A. baumannii*, and *C. albicans* and the flammability reduction was obtained. Cellulose/Ag nanocomposite used as antiseptic solution and more concentrated, in wound healing gels [124]. Cellulose/Ag nanocomposite various in colour from yellow to orange to brown, due to Ag concentrations and their size because optical properties of Ag-NPs in, which restricted surface plasmon resonance [125]. Nanocellulose has no antimicrobial activity but it become antimicrobial agent when incorporated with silver nanoparticles (Ag-NPs) and CNC nanohybrid materials containing dendritic nanostructured silver [126]. Cellulose/Zinc oxide (ZnO) nanocomposite (ZnO/CNC) were antimicrobial properties and is more effective than ZnO nanoparticles [127]. Au NPs-cellulose nanocomposite has been fabricated by electronic conduction [52, 128]. Cellulose /Ag nanocomposites showed significant biocidal activity against Gram-negative *E. coli*, which was 95.5%, *A. baumannii* and Gram-positive bacteria *Staph. aureus* the reduction was 99% [124]. Smiechowicz et al. [129] fabricated cellulose fibers coated with silver or silver nanoparticles (Ag-NPs) and both coated with nanosilica, the cellulose fibers were obtained have high effective as antibacterial agent versus *E. coli* and *S. aureus*, and tested the cellulose composite against survival of L929 and HeLa cells, they noticed that cellulose fibers blend with silver nanoparticles and nanosilica were safe for humans and environment that leads to appliance in medical applications. Cellulose/Au nanocomposites have been consumed as catalysts in glucose oxidation [130], and better catalysts for reducing 4-nitrophenol [131]. Cu NPs with cellulose have been formed via electrostatic association via chemical pretreatments was applied to perform surface charge on the cellulose that attend to band with copper ions, followed by chemical reduction to produce Cu/nanocomposite [132]. Cu/nanocomposite has antibacterial activity against multi-drug resistant pathogen *A. baumannii* [99]. A variety of methods are using to synthesis Pt NPs that has been used in various application processes [133].The fabrication of Pt/cellulose nanocomposites required the additive of reducing agent with cellulose, which may be act as structural-directing agent [134].The Pt-nanoparticles were good spread and steadied

in the cellulose network, and thus prevent particle accumulation. Cationic cellulose assuming ammonium ions at the surface has been spent to yield of nanocomposites, so, the connection of negatively charged Pt-NPs with cationic cellulose material was stimulated via electrostatic interactions, which yield to strong surface exposure of the fibres [135]. The production of hydrogen from cyclohexene may be caused by Cellulose/Pt nanocomposites catalysis [136, 137]. Potential using Co NPs was embedded in cellulose matrices as magnetic nanocomposites [138]. CNC/Ag developed the tensile and antimicrobial properties of chitosan [139]. The cellulose nanocomposite has been used for ligament or tendon substitutes [140, 141]. NFC was merged with poloxamers, polyethylene oxide (PEO)/polypropylene oxide (PPO) and form tri block structure as PEO_x-PPO_y-PEO_x, these compounds using as control bacterial disease for the time demands to the wound heal [142]. The mechanical strength of NFC filaments had been improved by addition glutaraldehyde, which originated bridges with various filaments, the originated filaments caused mechanically strong enough to pass through various tissues such as muscle, fat and skin [143]. The extracted cellulose from cotton has been associated with nano- (HAp) to organize scaffolds for bone tissue engineering [144]. Cellulose has been associated with pullulan (polymer of glucose) to form a 3D bone grafting scaffold and has the capability to enhance osteogenic discrimination in vitro [145, 146]. Figure 3 represents the applications of cellulose nanofibers, Fig. 4) represents the various applications of cellulose nanocomposites.

10 Algal Cellulose

Most potential sources of nanocellulose are algal biomass. The improvements of consuming marine biomasses over lignocellulosic plant for biopolymer yields are (i) low or zero substance of natural physicochemical hurdles in algae biomass, thus no strict chemical for treatment is demands to eliminate their natural disobedient construction so as to rise the cellulose convenience [147]; (ii) seaweeds consist of higher incomes of preserve carbohydrates, and able to develop under natural necessities by using carbon dioxide (CO₂), light and inorganic nutrients professionally, which no charge are demands for offering [148]; (iii) seaweeds have a fast growth rate and can be collected within a low period of time, and thus accomplished to rise the demand of yielding nanocellulose [149]. Many algal cell walls consist of a vital content such as cellulose, which are well crystalline. The cellulose extracted from macroalgae are pure due to lack of lignin so is used in many biomedical applications [87]. Microalgae have content a very high quantities of cellulose, that is possible substitution of plant sources and can present numerous advantages such as microalgae growth is fast and harvesting in any time and can grow in saline aqueous areas wastewater and in harsh condition [150] *Nannochloropsis gaditana* is a microgreen algae inner cell wall composed of 75% cellulose covered by an outer hydrophobic algaenan layer [151]. Dry weight of the microalgae *N. gaditana* consists of 25% cellulose [152]. Red, green, and yellow algae are recognized for cellulose yields;

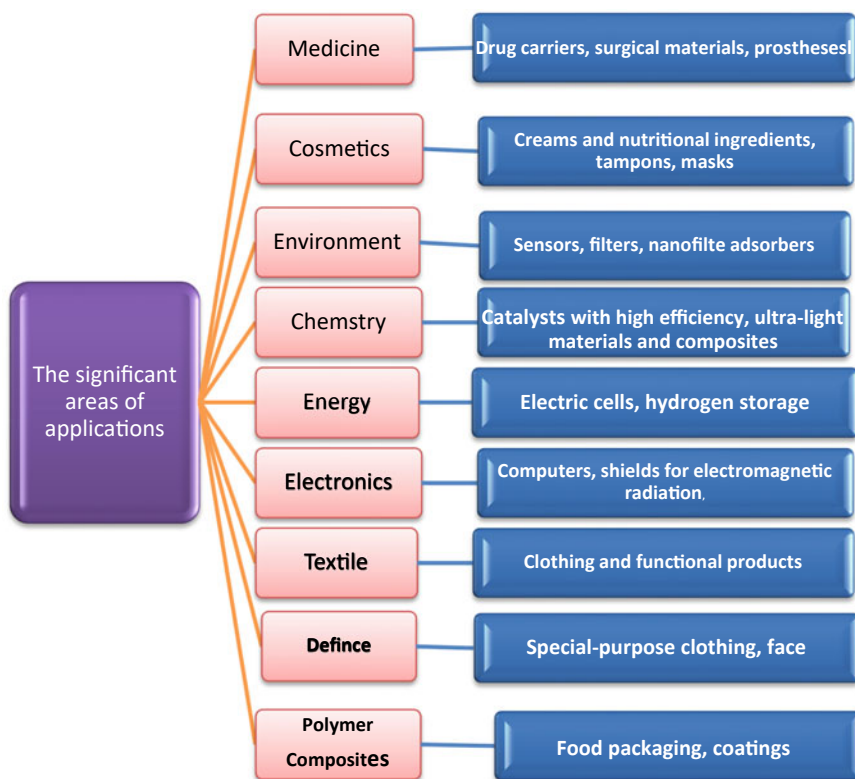


Fig. 3 A significant area of applications cellulose nanofibers

meanwhile, green algae are the best favoured ones for cellulose production. The cellulose content of some species of green algae are reached 70% of dry weight, the cell wall of algae in general content of xylan, mannan or cellulose and are described as microfibrillar (crystalline) phase that unassociated of lignin so it economic in extraction processes [153–158]. Common cellulose-yielding algae related to green algae *Cladophora*, *Chaetomorpha*, *Rhizoclonium*, *Microdyction*, *Valonia*, *Dictyosphaeria*, *Siphonocladus*, and *Boergesenia*. A precious and distinct properties of nanocellulose is algal cellulose (AC) that is extracted from green algae such as *Cladophora*, *Micrasterias denticulata*, *Siphonocladales*, *Valonia* and *Boergesenia* [5, 22]. Cellulose and nanocellulose have originated from numerous species of algae (red, green, brown...), such as *Valonia*, *Micrasterias denticulate*, *Micrasterias rotata*, *Boerogesenia*, *Coldophora* [159–161]. According to the cell wall, the algae can be classified into three groups [161]. The first group is green algae that the cell wall consist of high major contents of cellulose that is usually crystalline, the second groups are also green algae that cell walls contain large amounts of cellulose, that has little grade of crystallinity, the third groups are heterogeneous algae in, which cellulose is a minor

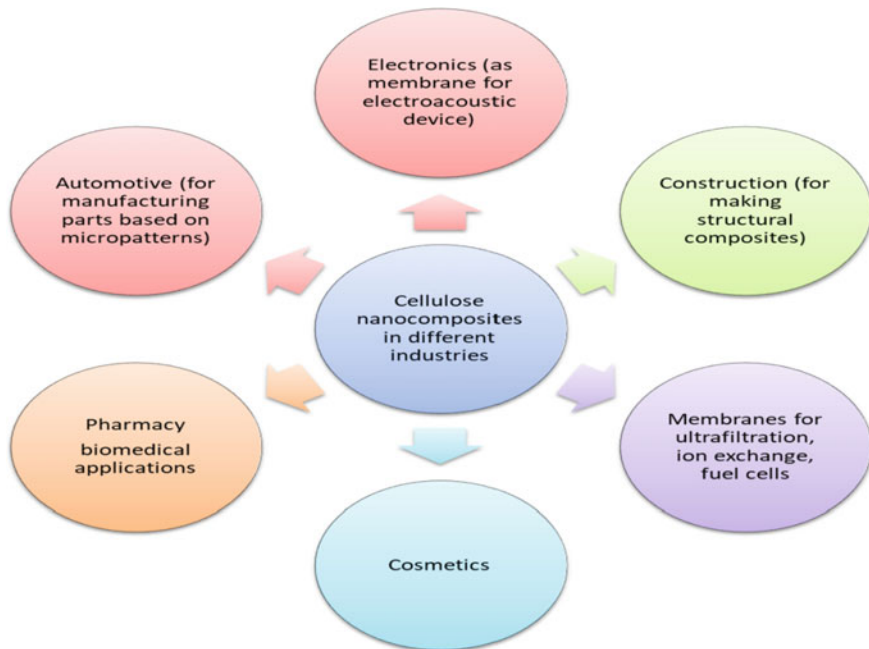


Fig. 4 The applications of cellulose nanocomposites in different fields

constituent of the cell walls and low crystallinity [22]. The crystallinity degrees are differing according to algal species [162]. The cell wall of filamentous green algae contains about 20 to 30% cellulose [163, 164]. Some studies revealed that cell wall of *Cladophora glomerata* contains about 45 wt % cellulose [165]. *Cladophora* cellulose was highly crystalline, high porous, nonhygroscopic and showed frequency-independent conductivity [166]. Marine green algae, *Valonia* and *Cladophora*, have a high degree of cellulose crystallinity was reached 95% and determined by XRD [167, 168]. *Valonia ventricosa* yields cellulose nanocrystallins with sizes in the range of 20 nm diameter and length 1,000–2,000 nm [49]. The cellulose fibrils extracted from *Cladophora* sp reach 100% crystallinity, high specific surface area, mechanical and rheological properties [5, 22, 169]. The cellulose content of *Cladophora* manages to absorb a little amount of moisture from the air at ambient relative humidity due to its, high degree of crystallinity [169]. Little amount of moisture of cellulose is due to only disordered constituencies of the cellulose fibers is absorbance of the humidity from an ambient area, so that is proved cellulose are obtained from *Cladophora* are crystalline [169]. *Gelidium* is a red marine alga has greatly capability of biomass for different purposes owing to its high carbohydrate content, which is chiefly contents cellulose and agar [148, 170, 171]. *Gelidium* play a novel favorable applicant for NC yield due to their profusion and accessibility than global biomass. Seo et al. [172] reported two species of red algae, (*G. amansii* and *G. corneum*) consumed as bleached pulp in paper making manufacturing. The outcomes exposed that the paper

created by the extraction of red algae pulp held off remarkably well softness and obscurity than standard wood pulp. Meanwhile, physicochemical characterizations such as “surface morphological studies, crystallinity structure and thermal properties” of extracted cellulose pulp did not assess. In recent decades, new nanomaterials such as nanocellulose fiber effectively extracted from marine sources such as *Posidonia oceanica* [173]. The crystallinity index of cellulose extracted from *Ulva lactuca* is 48% and it is free from inorganic ash and has thermal stability up to 260 °C [8]. The high-level of cellulose crystallinity degree derived from algae is supposed to be associated with the presence of thick microfibrils [174–176]. The cellulose derived from algae is microfibrils, and the width is 10–30 nm [174–177]. Solid crystalline nanoparticles “NC” and water-soluble sugar monomers can be acquired under manageable hydrolysis circumstances and energy compact substrates such as cellulose material [171]. *Chaetomorpha crassa* gives a higher amount of nanofibrillated cellulose and can be easily extracted, the cellulose was obtained highly crystalline and average diameter was 25 nm [178].

11 Cellulose/nanocellulose Extractions from Algae

Cellulosic substances can be attended as a possible feedstock for bio-transformation to nanocellulose. Similar to other cellulosic biomass derived from terrestrial plants, the long chains cellulose polymer isolated from algae can also be hydrolyzed into minor solid particles with nanodimension NC by consuming strong mineral acid “i.e. H₂SO₄ and HCl acid”. To extract high quality and more efficiently cellulose from algae, it should be eliminated noncellulosic constituents from the algae through the treatment procedure [179]. For the removal of components other than cellulose, the dry algae treated by alkalization processes, 7% NaOH had a noteworthy and helpful impact in solubilize the agar from the marine alga “*Gracilaria vermiculophylla*” at 85 °C for 2 h. The nanocellulose color plays a vital factor due to it can influence in the purchaser approval in several appliances [180]. The rhizoidal filaments content in the fiber of red algae dented reddish color of it [181]. Therefore for yield highly purified, whiteness-isolated cellulose pulp, it is necessary to eliminate the natural pigment and chlorophyll from the red algae by treatments with successive bleaching. Fundamentally, the algae biomass fiber was bleached by two chief oxidizing bleaching agents such as sodium chlorite (NaClO₂) and hydrogen peroxide (H₂O₂) to yield bleached red algae pulp [172, 180]. Green algae such as *Ulva lactuca* biomass had been treated by methanol and hypochlorite to remove pigments [181]. The most common methods for extraction NC are acid hydrolysis [182, 183], TEMPO-mediated oxidation [184], mechanical fragmentation [185] and enzyme-supported hydrolysis [186]. Until now acid hydrolysis like (H₂SO₄), (HCl), and (H₃PO₄) is reflected the most operative and extremely effective in the function of cellulose depolymerization route for alteration of cellulose into its NC materials, acids disrupted cellulose polymeric chain into minor lengths and widths, under the regulated hydrolysis circumstances such as “time, temperature, acid concentration and agitation”, the amorphous dominions of

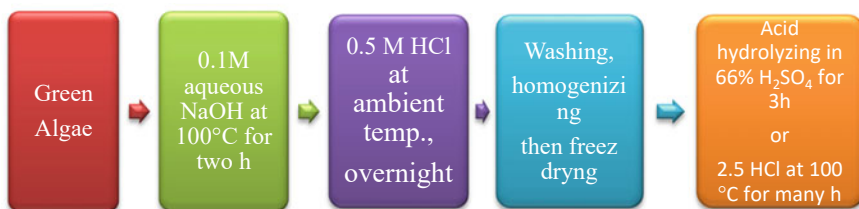


Fig. 5 Nanocellulose derived from green algae

cellulose matrix are better hydrolyzed by the Hydronium ions (H_3O^+) and consent the exceedingly crystalline segments unaltered [187]. Compared with other hydrolysis techniques, highly crystalline nanocellulose was made by acid hydrolysis. H_2SO_4 hydrolysis method has been commonly used for extracting exceedingly crystalline NC [188].

NC can be obtained, from green algae as show in Fig. 5. High crystalline cellulose nanocrystals (CNC) have been effectively extracted from red algae by alkalization, bleaching and acid hydrolysis treatments [189, 190].

12 Cellulose Composites from Algae

When cellulose material derived from alga *Cladophora* is coated with conductive polymer polypyrrole or polyaniline (PPy) form cellulose composite, the fractions of *Cladophora* cellulose in this composite are 1/3 [191]. This cellulose composite become conductive properties, black paper sheets thickness merely 50 nm thick, bent, large surface area and high ion-exchange capacity [5]. *Cladophora* cellulose (PPy) composite had conductivity about 1 S/cm and specific surface area of 70–80 m^2/g [192]. The PVA-CNC nano-composites synthesized by adding 8 wt % CNC derived from red alga into PVA matrix had good tensile strength and toughness were amplified and clear a high level of optical transparency [190].

13 The Application of Cellulose Composites/Nanocomposites Derived from Algae

The applications of cellulose PPy/composite derived from *Cladophora* had many applications due to their conductive properties, elevated ion-exchange capacity and small inorganic and moderately large organic ions [193], these applications includes diagnostics extraction and purification of biomolecules gas-sensor instrument, ion-exchange membranes and energy-storage devices [5]. A bioink based on NFC and alginate (alg) (unbranched polysaccharides isolated from brown algae) has been

used to operate the bioprinting technology [149, 194]. The NCF/A (80/20) (w/w) bionk was entrenched with human bone marrow–resulting stem cells, human nasal chondrocytes and consumed in cartilage generation [195, 196]. CC was used in wide applications due to unique properties, such as reinforcement fibres in formation materials, drug carriers, rheology enhancers and energy storage composite [197–199]. NC extracted from *Cladophora* had been used in wastewater treatments in Japan [5]. Metreveli et al. [200] reported the filters made from nanocellulose extracted from *Cladophora* have efficiency for confining swine influenza virus particles and match industrial filters. And the beads fabricated from *Cladophora* nanocellulose proven efficiency due to the absorption of Palladium (II) ions of reach to 80% supreme capacity in 2 h [201]. The PVA-CNC nan-composite that cellulose derived from red alga waste had with excellent belongings are therefore superior candidates for use in food packaging purposes [190]. Nanosilver-coated cellulose sheets extracted from filamentous seaweed *Chaetomorpha crassa* has a good antibacterial activity versus *Staph. aureus* and *E. coli*, the antimicrobial activities of Ag/cellulose sheet can effectively use in different purposes such as food packing, water treatment, biomedical and in pharmaceutical [167]. CC films repressed the inflammatory response stimulated by lipopolysaccharide (LPS), and the anionic-CC (a-CC) substances with its accumulated, associated fibre structure initiated a more distinct reduction levels compared to the cationic-CC (c-CC) film that displayed non-aggregated, randomly positioned fibres, so its possible usage of CC materials in the biomedical field such as dressing for treated chronic wounds [160] Cellulose nanocrystal/silver/alginate (CNC/Ag/Alg) bionanocomposite films can be consumed as a UV barrier in food packaging substances [202].

14 Bacterial Cellulose

Bacterial cellulose (BC) was first recognized by Brown [203] as an extracellular gram-negative secretion. Biologists have speculated on why microorganisms manufacture cellulose. It is considered that aerobic bacteria yield pellicles to survive and succeed near the surface of the culture medium. A small set of bacterial species such as *Agrobacterium*, *Achromobacter*, *Pseudomonas*, *Salmonella*, *Acetobacter*, *Azotobacter*, *Sarcina*, and *Rhodococcus* yield cellulose. Unlike the top-down methods for NFC and CNC, BC is synthesized from different bacteria from glucose or other carbon sources (e.g. xylinus of gluconacetobacter) [204]. Acetic acid bacteria can convert glucose, sugar, glycerol, or other substances to pure cellulose. Each cell is a spinner, and produces a bundle of sub-microscopic fibrils, which collects polymer in a series of pores [204]. Figure 6 denoted the methods used for production of bacterial cellulose.

Illa et al. [205] reported that BC have highly conductive carbon films electric conductivity elevated to 6×10^3 S/cm with high surface area, volume 670 m²/g and 0.83 cc/g, respectively and displayed a typical graphitic structure with graphene layers organized along the fibrillary axis. BC displayed interesting results and has a



Fig. 6 The methods of producing cellulose by some types of bacteria

broad range of applications, such as “oil clean up absorbents, fire-resistant materials, stretchable conductors as well as electrode material in LIBs and supercapacitors besides lithium-ion batteries”.

15 Characterizations of Bacterial Cellulose

BC fibril is usually 20–100 nm in diameter and length several microns, with various morphologies, depending on the form of bacteria and the conditions of cultivation [5, 206]. Features such as its highly hydrophilic field, elevated voltage strength besides biological affinity create BC attractive in bio-medical material like wound dressing, antimicrobial material, for example, or scaffold for fabric engineering [206–209]. BC also has a greater capacity to retain water, a superior degree of polymerization “up to 8,000”, and a better network than plant cellulose [104, 210]. Bacterial cellulose is economical, can be yielded in meniscus and supports cell migration, making it desirable to be considered a meniscus implant [211].

Brown and Laborie, [212] reported that there are significant properties differences between BC and plant cellulose, the BC is secreted in the ribbon format, lower than “100 nm” long, consisting of nanofibrils much finer 2–4 nm. Information about biopolymerisation processes and simultaneous crystallization is well understood in the elongated, parallel rows of stretched chains. The intrinsic properties of bacterial cellulose bundles are excellently crystallinized (up to 84–89%) [213]. Both elastic modulus and glass fibers have the same order (70 GPa) [214, 215]. The most bacterial species produced cellulose is *Gluconacetobacter xylinus*. BC crystallites are principally of the C1 α crystalline type, and the degree of polymerization (DP) of BC is in range 2000 to 6000. Another significant characteristic of BC is its elevated chemical purity, which separates it from the forms of cellulose extracted from plants generally accompanying with hemicellulose and lignin. Both bacterial synthesized cellulose and cellulose derived from different plants have identical molecular structures [5, 51, 216].

Dar et al. [217] clarified that the cellulolytic bacterial strain *Bacillus tequilensis* G9 was appraised for CMCCase yielding on agricultural waste illustrated its involved enzyme activities generating pores and deconstruction, thereby valorizing GS as significant carbon source for biorefinery.

Another presupposes that bacteria manufacture cellulose to shield themselves from ultraviolet or heavy-metal ions [206]. Contrary to the yielding of NC from CNF and CNC, in the absence of some other components such as hemicelluloses and lignin, BC is an upward method that generates NC from glucose monomers. Furthermore, BC has much stronger mechanical characterize, involving tensile resistance and modulus, and great bio-compatibility with nano-cellulose with high crystallinity, which is very thermally stable. BC has high cost, approximately 100 times more than plant cellulose, thus reducing its possible applications for advanced materials and relatively low production power [218]. BC was endangered to incubation cycles in chemical substances that enclose calcium besides phosphate minerals [219].

16 The Application of Cellulose Composites/Nanocomposites Derived from Bacteria

Bioconjugated plasmonic NPs are excellent biocompatibility and their physiochemical characteristics are highly desirable choices for nanomaterials for enhanced Skin Penetration designed for biomedical applications [220]. Bacterial cellulose (BC) is used as a model for yielding biohybrid inorganic/organic nanocomposites that assemble the good belongings of biocellulose that exhibited by inorganic nanoparticles, such as optical, glowing, magnetic, photorefractive beside photochromic [221].

BC, HA, Boron-doped hydroxyapatite (BHA), beside to gelatin (GEL) including scaffolds were deliberated as well applicant to improve tissue assistance and reinforcement in a practical method for the engineering of bone tissue [222]. Nogi and Yano, [223] achieved in putting an electroluminescent layer on these transparent BC nanocomposites, low coefficient of thermal expansion, required 60–70 wt% cellulose nanofibers of high Young's modulus, 138 GPa. Bayir et al. [224] revealed BC extracted from *Gluconacetobacter xylinus* was improved to 275 μm by a new shredded agar technique, and SaOs-2 cells were displayed to transfer between the fibers of the reformed BC. It was observed that mineralization of SaOs-2 cells was enriched on in situ yielded HAp-BC nanocomposites comparison to BC scaffolds. Xu et al. [225] investigated carbon nanofibers derived from bacterial cellulose were used as the anode besides the cathode in hybrid dual carbon sodium ion capacitor. Fillat et al. [226] clarified the BC was made by *Komagataeibacter xylinus* had lengthier size fibers and significant impact in reducing the wettability of composites than the BC was extracted from *Gluconacetobacter sucrofermentans* that had short fibers, in general BC-paper fibers are strongly attached in a composite, offering higher barrier belongings to air and water than in a bilayer biomaterial.

Electrospun nanofibers had synthesis by BC made by *Staph.aureus* and *E.coli*, which are used in removal-radiating metal ions, Uranium (VI), these nanofibres replaced the commercial filtration membranes because it cost effectiveness and high performance [227–230]. Soares da Silva et al. [231] used combined of non-recyclable

fibres, as a carbon source for bacterial (BNC) production by using *K. xylinus* by application response surface methodology (RSM), where BNC composites can be simply designed by varying the polymer percentage contents.

In industrial applications, including water purification and in electronic, magnetic and optical composite materials, BC has also been used [232–235]. BC membranes with antimicrobial characteristics were obtained from the nanofibrillar network using chemical greasing of aminoalkyl groups [236]. BC has shown encouraging results in vitro as a material for replacing of damaged blood vessels and in vivo [236, 237]. In the soft tissue substitution, BC also considered potential applications. In the instance, because of its comparable elongation and tensile fracture potential to the ligaments, a BC/polyacrylamide gel was identifiable as an attractive candidate for ligament replacement [238], whereas BC gel was suggested for meniscus implants as a material [239]. NC application, in particular BC, is a common research field for the treating of injuries. BC membranes are characterized by important characterizations for ideal wound care (e.g., high water holding power, elasticity, flexibility besides high strength) [240]. Several commercial wound-dressing products based on BC, such as XCell®, Bioprocess® and Biofill®, have been launched Jorfi and Foster [241]. BC wound-dressing products have been formulated with Ag for increased antimicrobial activity [102, 241–243].

Cu/NPs are prepared with inorganic fillers in bacterial cellulose, stable Cu/cellulose composites. Researchers have reported that these nanocomposites are attractive in emerging electronic paper technologies [99]. In situ confession of Pt NPs with BC membranes through liquid phase chemical deoxidization in the existence of NABH₄ or HCHO as reducing agents and thermally stable proton-conducting membranes have been established [244]. The low cytotoxicity, high porosity and 3D network of BC have been explored for tissue engineering use [245], hydrogels [246] and composites with bioactive compounds [247], or conductive polymers [248] (Table 1).

Table 1 A comparative between major cellulose/nanocellulose derived from algal and bacteria, insight cellulose nanocomposite applications

Comparison	Source of cellulose			
	Algae	Ref.	Bacteria	Ref.
Sources	<i>Gelidium amansii</i> <i>G. corneum</i> <i>Posidonia oceanica</i> <i>Ulva lactuca</i> <i>Cladophora</i> , <i>Chaetomorpha</i> , <i>Rhizoclonium</i> , <i>Microdyction</i> , <i>Valonia</i> , <i>Dictyosphaeria</i> , <i>Siphonocladus</i> , <i>Boergesenia</i> , <i>Valonia</i> , <i>Micrasterias</i> <i>denticulate</i> , <i>Micrasterias</i> <i>rotate</i> , <i>Boergesenia</i> , <i>Coldophora</i>	[170] [161] [25] [5, 22, 148]	<i>Agrobacterium</i> , <i>Achromobacter</i> , <i>Pseudomonas</i> , <i>Salmonella</i> , <i>Acetobacter</i> , <i>Azotobacter</i> , <i>Sarcina</i> , <i>Rhodococcus S. aureus</i> <i>Bacillus</i> and <i>E. coli</i>	[203, 258, 259]

(continued)

Table 1 (continued)

Comparison	Source of cellulose			
	Algae	Ref.	Bacteria	Ref.
Methods of extractions	Mechanical or chemo-mechanical methods	[61]	Chemo-mechanical methods	[61]
Advantages	1. low or zero content of natural physicochemical barriers in algae biomass	[147]	1. High thermal conductivity, inherent fibrous nature and mechanical flexibility	[205]
	2. Seaweeds consist of higher yields of stored carbohydrates	[148]	2. Bacterial cellulose is high purity (with no associated substances like hemicelluloses, lignin, or pectin)	[2]
	3. seaweeds have efficient to increase the demand of yielding nanocellulose	[149]		
The degrees of crystallinity	filamentous green algae contain about 20 to 30% cellulose	[164]	BC is in range to 2000 and 6000 has a greater capacity to retain water, a higher degree of polymerization (up to 8,000)	[41, 215]
	<i>Cladophora glomerata</i> 45 wt % cellulose	[165]	A better network than plant cellulose 60–70 wt% cellulose	[104, 210]
	High porous, nonhygroscopic and showed frequency-independent conductivity	[166]	The low cytotoxicity, high porosity and 3D network of BC have been explored for tissue engineering use	[243]
	<i>Valonia ventricosa</i> yields cellulose nanocrystallins with dimensions in the range of 20 nm width and length 1,000–2,000 nm	[49]		
Types of Nanocomposite and applications	Algal cellulose with polypyrrole and graphene applied in electrode for supercapacitor relevance	[257]	Bacterial cellulose-hydroxyapatite (BC-HA) nanocomposite used in bone regeneration	[249]
	PVA nanocomposite films with CNC extracted from red algae for possible applications	[190]	Bacterial cellulose nanofibrils (BCNs) and protein zein nanoparticles (ZNs) display BCN-ZN nanocomposites has antibacterial properties and postulated used in food packaging	[174]
	<i>Cladophora</i> cellulose–PPy nanocomposite uses in paper battery cell	[5]	Polyvinyl acetate and bacterial cellulose BC/PVA nanocomposites can supplant cardiovascular tissues	[209]

(continued)

Table 1 (continued)

Comparison	Source of cellulose			
	Algae	Ref.	Bacteria	Ref.
	A bioink based on NFC derived from algae and alginate from red algae formed nanocomposite used to operate the bioprinting technology	[146, 194]	BC/polyethylene glycol (PEG) nanocomposites are used in wound dressing and tissue-building	[250]
	The NCF/A (80/20) (w/w) nanocomposite used in cartilage generation	[195, 196]	BC nanofibers and chitin nanocrystals (ChNCs), (BC/D-ChNC nanocomposites) have Bactericidal activities	[251, 252]
	The PVA-CNC nanocomposite that cellulose derived from red alga waste uses in food-packaging applications	[190]	BC-silica nanocomposites can benefit material applications	[253]
	Cellulose nanocrystal/silver/alginate (CNC/Ag/Alg) bionanocomposite films can be used as a UV barrier in food packaging materials	[202]	BC/methylglyoxal (BC/MGO nanocomposite) as antimicrobial dressing in chronic wound care	[254]
			Bacterial-cellulose/silver nanocomposites have antibacterial activities as a candidate for future wound-healing applications	[255]
			Bacterial cellulose/gelatin the persistent growth of brain cell and human mesenchymal stem cells (hMSCs)	[256]
			Bacterial cellulose/alginate and nanocomposite has antibacterial activities and potential application in medicine as a wound-dressing	[257]

17 Conclusions

Cellulose is the most widespread natural polymer on the earth; cellulose has the most important biosources in the earth. Algae and bacteria are the most common organisms in the world and abundant of cellulose. The extractions of algal cellulose need

mechanical and chemical methods, which need high economical cost for extractions and conversion to nanocellulose, meanwhile bacterial secretions nanocellulose in media needs different source of fermented sugar. CNFs are produced from algae and bacteria used in synthesis nanocomposite material and there are numerous applications are obtained by using CNFs and CNCs derived from algae and bacteria. Recent studies were conducted on nanocomposite cellulose derived from bacteria meanwhile minor studies conducted on nanocomposite cellulose derived from algae. Both Algal and bacterial cellulose nanocomposite have many applications. More research into microbial cellulose nanocomposite and its applications as a safe and cost-effective source is still needed.

18 Future Prospective

Nanocomposite research should be search of the economy media for growing bacteria that secreted nanocellulose and economic methods for extracting nanocellulose from algae. Nanocellulose market reached 60 billion dollars in 2020 in the world, and another technological development is urgent in NC research. The NC market will soar in the future as a result of this form of technological revolution. Furthermore, commercialization, management and standardization of NC for safety and properties will be needed.

References

1. Siro, I., Plackett, D.: Microfibrillated cellulose and new nanocomposite materials: a review. *Cellulose* **17**(3), 459–494 (2010). <https://doi.org/10.1007/s10570-010-9405-y>
2. Taheri-Ledari, R., Esmaeili, M.S., Varzi, Z., et al.: Facile route to synthesize Fe₃O₄@acacia-SO₃H nanocomposite as a heterogeneous magnetic system for catalytic applications. *RSC Adv.* **10**, 40055–40067 (2020)
3. Taheri-Ledari, R., Rahimi, J., Maleki, A., Shalan, A.E.: Ultrasound-assisted diversion of nitrobenzene derivatives to their aniline equivalents through a heterogeneous magnetic Ag/Fe₃O₄-IT nanocomposite catalyst. *New J. Chem.* **44**, 19827–19835 (2020)
4. Chen, Y.W., Lee, H.V., Juan, J.C., Phang, S.M.: Production of new cellulose nanomaterial from red algae marine biomass *Gelidium elegans*. *Carbohydr. Polym.* **151**, 1210–1219 (2016). <https://doi.org/10.1016/j.carbpol.2016.06.083>
5. Vijai Anand, K., Reshma, M., Kannan, M., et al.: Preparation and characterization of calcium oxide nanoparticles from marine molluscan shell waste as nutrient source for plant growth. *J. Nanostruct. Chem.* **11**, 409–422 (2021). <https://doi.org/10.1007/s40097-020-00376-4>
6. Davis, T.A., Volesky, B., Mucci, A.: A review of the biochemistry of heavy metal biosorption by brown Algae. *Water Res.* **37**(18), 4311–4330 (2003). [https://doi.org/10.1016/S0043-1354\(03\)00293-8](https://doi.org/10.1016/S0043-1354(03)00293-8)
7. He, Q., Wang, Q., Zhou, H., Ren, D., He, Y., Cong, H., Wu, L.: Highly crystalline cellulose from brown seaweed *Saccharina japonica*: isolation, characterization and micro-crystallization. *Cellulose* **25**(10), 5523–5533 (2018). <https://doi.org/10.1007/s10570-018-1966-1>

8. Abdellatif Soliman, S.M., Sanad, M.F., Shalan, A.E.: Synthesis, characterization and antimicrobial activity applications of grafted copolymer alginate-g-poly(N-vinyl imidazole). *RSC Adv.* **11**, 11541–11548 (2021)
9. Gao, H., Duan, B., Lu, A., Deng, H., Du, Y., Shi, X., Zhang, L.: Fabrication of cellulose nanofibers from waste brown algae and their potential application as milk thickeners. *Food Hydrocolloids* **79**, 473–481 (2018). <https://doi.org/10.1016/j.foodhyd.2018.01.023>
10. Donini, Í.A.N., Salvi, D.T.B., Fukumoto, F.K., Lustrì, W.R., Barud, H.S., Marchetto, R., et al.: Biosynthesis and recent advances in production of bacterial cellulose. *Eclética Quím* **35**, 165–178 (2010). <https://doi.org/10.1590/S0100-46702010000400021>
11. Huang, Y., Zhu, C.L., Yang, J.Z., Nie, Y., Chen, C.T., Sun, D.P.: Recent advances in bacterial cellulose. *Cellulose* **21**, 1–30 (2014). <https://doi.org/10.1007/s10570-013-0088-z>
12. Abu Elella, M.H., Goda, E.S., Abdallah, H.M., et al.: Innovative bactericidal adsorbents containing modified xanthan gum/montmorillonite nanocomposites for wastewater treatment. *Int. J. Biol. Macromol.* **167**, 1113–1125 (2021)
13. Chawla, P.R., Bajaj, I.B., Survase, S.A., Singhal, R.S.: Microbial cellulose: fermentative production and applications. *Food Technol. Biotechnol.* **47**, 107–124 (2009). <https://hrcak.srce.hr/38098>
14. Gayathry, G., Gopalswamy, G.: Production and characterization of microbial cellulosic fibre from *Acetobacter xylinum*. *Indian J. Fibre Text Res.* **39**, 93–96 (2014)
15. Pascoal Neto, C., Freire, C.S.R., Fernandes, S.C.M., Silvestre, A.J.D., Gandini, A.: Aqueous Coating Compositions for Use in Surface Treatment of Cellulosic Substrates. Patent WO/2011/012934 (2011)
16. Gomes, F.P., Silva, N.H.C.S., Trovatti, E., Serafim, L.S., Duarte, M.F., Silvestre, A.J.D., et al.: Production of bacterial cellulose by *Gluconacetobacter sacchari* using dry olive mill residue. *J. Biomass Bioenergy* **55**, 205–211 (2013). <https://doi.org/10.1016/j.biombioe.2013.02.004>
17. Huber, T., Müssig, J., Curnow, O., Pang, S., Bickerton, S., Staiger, M.P.: A critical review of all-cellulose composites. *J. Mater. Sci.* **47**(3), 1171–1186 (2012). <https://doi.org/10.1007/s10853-011-5774-3>
18. Czaja, W., Krystynowicz, A., Bielecki, S., Brown, R.J.: Microbial cellulose—the natural power to heal wounds. *Biomaterials* **27**, 145–151 (2006)
19. Czaja, W.K., Young, D.J., Kawecki, M., Brown, R.M.: The future prospects of microbial cellulose in biomedical applications. *Biomacromolecules* **8**, 1–12 (2007). <https://doi.org/10.1021/Bm060620d>
20. Klemm, D., Kramer, F., Moritz, S., Lindström, T., Ankerfors, M., Gray, D., Dorris, A.: Nanocelluloses: a new family of nature-based materials. *Angew. Chem. Int. Ed.* **50**, 5438–5466 (2011). <https://doi.org/10.1002/anie.201001273>
21. Börjesson, M., Westman, G.: Crystalline nanocellulose preparation, modification, and properties. *Cellulose-Fund. Aspects Curr. Trends*, 159–191 (2015). <https://doi.org/10.5772/61899>
22. Moon, R.J., Martini, A., Nairn, J., Simonsen, J., Youngblood, J.: Cellulose nanomaterials review: structure, properties and nanocomposites. *Chem. Soc. Rev.* **40**, 3941–3994 (2011). <https://doi.org/10.1039/C0CS00108B>
23. Brett, C.T.: In *International Review of Cytology*. Academic Press, San Diego (2000)
24. Somerville, C.: Cellulose synthesis in higher plants. *Ann. Rev. Cell Dev. Biol.* **22**, 53–78 (2006). <https://doi.org/10.1146/annurev.cellbio.22.022206.160206>
25. Thomas, V., Namdeo, M., Mohan, Y.M., Bajpai, S.K., Bajpai, M.: Review on polymer, hydrogel and microgel metal nanocomposites: a facile nanotechnological approach. *J. Macromol. Sci. Part A-Pure Appl. Chem.* **45**(1), 107–119 (2008). <https://doi.org/10.1080/10601320701683470>
26. Moon, R.J.: *McGraw-Hill Yearbook in Science & Technology*, pp. 225–228. McGraw-Hill, New York (2008)
27. Boy, R., Narayanan, G., Kotek, R.: Formation of cellulose and protein blend biofibers. In: *Polysaccharide-based Fibers and Composites*, pp. 77–117. Springer, Cham (2018). https://doi.org/10.1007/978-3-319-56596-5_5

28. Mariano, M., El Kissi, N., Dufresne, A.: Cellulose nanocrystals and related nanocomposites: review of some properties and challenges. *J. Polym. Sci. Part B Polym. Phys.* **52**, 791–806 (2014). <https://doi.org/10.1002/polb.23490>
29. Kargarzadeh, H., Ioelovich, M., Ahmad, I., Thomas, S., Dufresne, A.: Methods for extraction of nanocellulose from various sources. *Handb. Nanocellulose Cellulose Nanocompos.* **1**, 1–51 (2017). <https://doi.org/10.1002/9783527689972.ch1>
30. Nechyporchuk, O., Belgacem, M.N., Bras, J.: Production of cellulose nanofibrils: a review of recent advances. *Ind. Crops Prod.* **93**, 2–25 (2016). <https://doi.org/10.1016/j.indcrop.2016.02.016>
31. Elazzouzi-Hafraoui, S., Nishiyama, Y., Putaux, J.L., et al.: The shape and size distribution of crystalline nanoparticles prepared by acid hydrolysis of native cellulose. *Biomacromolecules* **9**, 57–65 (2008). <https://doi.org/10.1021/bm700769p>
32. Cherian, B.M., Pothan, L.A., Nguyen-Chung, T., et al.: A novel method for the synthesis of cellulose nanofibril whiskers from banana fibres and characterization. *J. Agric. Food Chem.* **56**, 5617–5627 (2008). <https://doi.org/10.1021/jf8003674>
33. Cherian, Bibin Mathew, Leão, Alcides Lopes, Ferreira, Sivoney, de Souza, Sabu, Thomas, Laly A., Pothan, M. Kottaisamy.: Isolation of nanocellulose from pineapple leaf fibres by steam explosion. *Carbohydr. Polym.* **81**(3), 720–725 (2010). <https://doi.org/10.1016/j.carbpol.2010.03.046>
34. Araki, J., Wada, M., Kuga, S., et al.: Flow properties of microcrystalline cellulose suspension prepared by acid treatment of native cellulose. *Colloids Surf. A* **142**, 75–82 (1998). [https://doi.org/10.1016/S0927-7757\(98\)00404-X](https://doi.org/10.1016/S0927-7757(98)00404-X)
35. Revol, J.F., Bradford, H., Giasson, J., et al.: Helicoidal self-ordering of cellulose microfibrils in aqueous suspension. *Int. J. Biol. Macromol.* **14**, 170–172 (1992). [https://doi.org/10.1016/s0141-8130\(05\)80008-x](https://doi.org/10.1016/s0141-8130(05)80008-x)
36. George, J., Sabapathi, S.N.: Cellulose nanocrystals: synthesis, functional properties, and applications. *Nanotechnol. Sci. Appl.* **8**, 45–54 (2015). <https://doi.org/10.2147/NSA.S64386>
37. Habibi, Y., Lucia, L.A., Rojas, O.J.: Cellulose nanocrystals: chemistry, self-assembly, and applications. *Chem. Rev.* **110**, 3479–3500 (2010). <https://doi.org/10.1021/cr900339w>
38. Tonoli, G.H.D., et al.: Cellulose micro/nanofibres from Eucalyptuskraft pulp: preparation and properties. *Carbohydr. Polym.* **89**, 80–88 (2012). <https://doi.org/10.3390/polym11111785>
39. Grishkewich, N., Mohammed, N., Tang, J., Tam, K.C.: Recent advances in the application of cellulose nanocrystals. *Curr. Opin. Colloid Interface Sci.* **29**, 32–45 (2017). <https://doi.org/10.1016/j.cocis.2017.01.005>
40. Tang, J., Sisler, J., Grishkewich, N., Tam, K.C.: Functionalization of cellulose nanocrystals for advanced applications. *J. Colloid Interface Sci.* **494**, 397–409 (2017). <https://doi.org/10.1016/j.jcis.2017.01.077>
41. Bhat, A.H., Dasan, Y.K., Khan, I., Soleimani, H., Usmani, A.: Application of nanocrystalline cellulose: processing and biomedical applications. In: *Cellulose-Reinforced Nanofibre Composites*, pp. 215–240 (2017). <https://doi.org/10.1016/B978-0-08-100957-4.00009-7>
42. Beck-Candanedo, S., Roman, M., Gray, D.G.: Effect of reaction conditions on the properties and behaviour of wood cellulose nanocrystal suspensions. *Biomacromolecules* **6**, 1048–1054 (2005). <https://doi.org/10.1021/bm049300p>
43. Araki, Jun, Wada, Masahisa, Kuga, Shigenori: Steric stabilization of a cellulose microcrystal suspension by poly(ethylene glycol) grafting. *Langmuir* **17**(1), 21–27 (2001). <https://doi.org/10.1021/la001070m>
44. De Menezes, A.J., Siqueira, G., Curvelo, A.A., Dufresne, A.: Extrusion and characterization of functionalized cellulose whiskers reinforced poly-ethylene nanocomposites. *Polymer* **50**, 4552–4563 (2009). <https://doi.org/10.1016/j.polymer.2009.07.038>
45. Peng, B.L., Dhar, N., Liu, H.L., Tam, K.C.: Chemistry and applications of nanocrystalline cellulose and its derivatives: a nanotechnology perspective. *Can. J. Chem. Eng.* **9999**, 1–16 (2011). <https://doi.org/10.1002/cjce.20554>
46. Iwamoto, S., Kai, W., Isogai, A., Iwata, T.: Elastic modulus of single cellulose microfibrils from tunicate measured by atomic force microscopy. *Biomacromolecules* **10**, 2571–2576 (2009). <https://doi.org/10.1021/bm900520n>

47. Sturcova, A., Davies, G.R., Eichhorn, S.J.: Elastic modulus and stress-transfer properties of tunicate cellulose whiskers. *Biomacromolecules* **6**, 1055–1061 (2005). <https://doi.org/10.1021/bm049291k>
48. Orts, W.J., Godbout, L., Marchessault, R.H., Revol, J.F.: Enhanced ordering of liquid crystalline suspensions of cellulose microfibrils: a small angle neutron scattering study. *Macromolecules* **31**, 5717–5725 (1998). <https://doi.org/10.1021/ma9711452>
49. Revol, J., Ventricosa, V., Carboh, F.: On the cross-sectional shape of cellulose crystallites in *Valonia ventricosa*. *Carbohydr. Polym.* **2**(2), 123–134 (1982). [https://doi.org/10.1016/0144-8617\(82\)90058-3](https://doi.org/10.1016/0144-8617(82)90058-3)
50. Azizi, S., Alloin, M.A.S., Sanchez, F., El Kissi, J.Y.N., Dufresne, A.: Preparation of cellulose whiskers reinforced nanocomposites from an organic medium suspension. *Macromolecules* **37**, 1386–1393 (2004). <https://doi.org/10.1021/ma030532a>
51. Dufresne, A.: Nano-cellulose: from nature to high performance tailored materials. Walter de Gruyter GmbH (2013). <https://doi.org/10.1016/j.mattod.2013.06.004>
52. Zhang, P.P., et al.: Effects of acid treatments on bamboo cellulose nanocrystals. *Asia Pac. J. Chem. Eng.* **9**(5), 686–695 (2014). <https://doi.org/10.1002/apj.1812>
53. Liu, Z., et al.: Self-assembly of electrically conducting biopolymer thin films by cellulose regeneration in gold nanoparticle aqueous dispersions. *Chem. Mater.* **22**(8), 2675–2680 (2010). <https://doi.org/10.1021/cm1001863>
54. Wittcoff, H.A., Reuben, B.G., Plotkin, J.S.: *Industrial Organic Chemicals*, 3rd edn., pp. 44–45. John Wiley & Sons Inc., Hoboken (2013)
55. Kalia, S., Dufresne, A., Cherian, B.M., Kaith, B., Averous, L., Njuguna, J., et al.: Cellulose-based bio-and nanocomposites: a review. *Int. J. Polym. Sci.* **2011**, 1–35 (2011). <https://doi.org/10.1155/2011/837875>
56. Andresen, M., Stenstad, P., Moretro, T., Langsrud, S., Syverud, K., Johansson, L.S., et al.: Nonleaching antimicrobial films prepared from surface-modified microfibrillated cellulose. *Biomacromolecules* **8**(7), 2149–2155 (2007). <https://doi.org/10.1007/s10570-013-9914-6>
57. Das, M., Bhattacharyya, R.: Cellulose nanofibers: synthesis, properties and applications. In: *Polymer Nanocomposites Based on Inorganic and Organic Nanomaterials*, pp. 1–37 (2015). <https://doi.org/10.1002/9781119179108.ch1>
58. Salama, A.: Cellulose/calcium phosphate HYBRIDS: NEW MATERIALS FOR biomedical and environmental applications. *Int. J. Biol. Macromol.* **127**, 606–617 (2019). <https://doi.org/10.1016/j.ijbiomac.2019.01.130>
59. Menon, M.P., Selvakumar, R., Ramakrishna, S.: Extraction and modification of cellulose nanofibers derived from biomass for environmental application. *RSC Adv.* **7**(68), 42750–42773 (2017). <https://doi.org/10.1039/C7RA06713E>
60. Jonoobi, M., Oladi, R., Davoudpour, Y., Oksman, K., Dufresne, A., Hamzeh, Y., Davoodi, R.: Different preparation methods and properties of nanostructured cellulose from various natural resources and residues: a review. *Cellulose* **22**(2), 935–969 (2015). <https://doi.org/10.1007/s10570-015-0551-0>
61. Nakagaito, A.N., Yano, H.: The effect of morphological changes from pulp fiber towards nano-scale fibrillated cellulose on the mechanical properties of high-strength plant fiber-based composites. *Appl. Phys. A* **78**, 547–552 (2004). <https://doi.org/10.1007/s00339-003-2453-5>
62. Oksman, K., Sain, M.: Cellulose nanocomposites: processing, characterization and properties. In: *Acs Symposium Series (Book 938)*. American Chemical Society, Washington (2006). <https://doi.org/10.1021/bk-2006-0938>
63. Hubbe, M.A., Rojas, O.J., Lucia, L.A., Sain, M.: Cellulosic nanocomposites: a review. *Bioresources* **3**, 929–980 (2008)
64. Najib, N., Christodoulatos, C.: In: *Proceedings of the 13th International Conference of Environmental Science and Technology*, Athens, Greece (2013)
65. Luo, Y., Zhang, J., Li, X., Liao, C., Li, X.: The cellulose nanofibers for optoelectronic conversion and energy storage. *Nanomater. J.* **2014**, 11 (2014). <https://doi.org/10.1155/2014/654512>
66. Ioelovich, M.: Peculiarities of cellulose nanoparticles. *Tappi J.* **13**(5), 45–52 (2014)

67. Paakko, M., et al.: Enzymatic hydrolysis combined with mechanical shearing and high-pressure homogenization for nanoscale cellulose fibrils and strong gels. *Biomacromolecules* **8**(6), 1934–1941 (2007). <https://doi.org/10.1021/bm061215p>
68. Filson, P.B., Dawson-Andoh, B.E., Schwegler-Berry, D.: Enzymatic-mediated production of cellulose nanocrystals from recycled pulp. *Green Chem.* **11**, 1808–1814 (2009). <https://doi.org/10.1039/B915746H>
69. Wagberg, L., Winter, L., Odberg, L., Lindstrom, T.: On the charge stoichiometry upon adsorption of a cationic polyelectrolyte on cellulosic materials. *Colloids Surf.* **27**, 163–173 (1987). [https://doi.org/10.1016/0166-6622\(87\)80335-9](https://doi.org/10.1016/0166-6622(87)80335-9)
70. Missoum, K., Belgacem, M.N., Bras, J.: Nanofibrillated cellulose surface modification: a review. *Materials* **6**, 1745–1766 (2013). <https://doi.org/10.3390/ma6051745>
71. Saito, T., Isogai, A.: TEMPO-mediated oxidation of native cellulose. The effect of oxidation conditions on chemical and crystal structures of the water-insoluble fractions. *Biomacromolecules* **5**, 1983–1989 (2004). <https://doi.org/10.1021/bm0497769>
72. Saito, T., Nishiyama, Y., Putaux, J.L., Vignon, M., Isogai, A.: Homogeneous suspensions of individualized microfibrils from TEMPO-catalyzed oxidation of native cellulose. *Biomacromolecules* **7**, 1687–1691 (2006). <https://doi.org/10.1021/bm060154s>
73. Saito, T., Kimura, S., Nishiyama, Y., Isogai, A.: Cellulose nanofibers prepared by TEMPO-mediated oxidation of native cellulose. *Biomacromolecules* **8**, 2485–2491 (2007). <https://doi.org/10.1021/bm0703970>
74. Isogai, A., Saito, T., Fukuzumi, H.: TEMPO-oxidized cellulose nanofibers. *Nanoscale* **3**, 71–85 (2011). <https://doi.org/10.1039/C0NR00583E>
75. Leung, A.C.W., Hrapovic, S., Lam, E., Liu, Y., Male, K.B., Mahmoud, K.A., Luong, H.T.: Characteristics and properties of carboxylated cellulose nanocrystals prepared from a novel one-step procedure. *Small* **7**(3), 302–305 (2011). <https://doi.org/10.1002/sml.201001715>
76. Lou, Yan-Ru., Kanninen, Liisa, Kuisma, Tytti, Niklander, Johanna, Noon, Luke A., Burks, Deborah, Urtti, Arto, Yliperttula, Marjo: The use of nanofibrillar cellulose hydrogel as a flexible three-dimensional model to culture human pluripotent stem cells. *Stem Cells Dev.* **23**(4), 380–392 (2014). <https://doi.org/10.1089/scd.2013.0314>
77. Bhattacharya, M., Malinen, M.M., Lauren, P., Lou, Y.R., Kuisma, S.W., Kanninen, L., et al.: Nanofibrillar cellulose hydrogel promotes three-dimensional liver cell culture. *J. Control Release* **164**, 291–298 (2012). <https://doi.org/10.1016/j.jconrel.2012.06.039>
78. Cozzolino, C.A., Nilsson, F., Iotti, M., Sacchi, B., Piga, A., Farris, S.: Exploiting the nano-sized features of microfibrillated cellulose (MFC) for the development of controlled-release packaging. *Colloid Surf. B* **110**, 208–216 (2013). <https://doi.org/10.1016/j.colsurfb.2013.04.046>
79. Huang, L., Chen, X., Nguyen, T.X., Tang, H., Zhang, L., Yang, G.: Nano-cellulose 3D-networks as controlled-release drug carriers. *J. Mater. Chem. B* **1**, 2976–2984 (2013). <https://doi.org/10.1039/C3TB20149J>
80. Jackson, J.K., Letchford, K., Wasserman, B.Z., Ye, L., Hamad, W.Y., Burt, H.M.: The use of nanocrystalline cellulose for the binding and controlled release of drugs. *Int. J. Nanomed.* **6**, 321–330 (2011). <https://doi.org/10.2147/IJN.S16749>
81. Kolakovic, R., Peltonen, L., Laukkanen, A., Hirvonen, J., Laaksonen, T.: Nanofibrillar cellulose films for controlled drug delivery. *Eur. J. Pharm. Biopharm.* **82**, 308–315 (2012). <https://doi.org/10.1016/j.ejpb.2012.06.011>
82. Müller, A., Ni, Z., Hessler, N., Wesarg, F., Müller, F.A., Kralisch, D., et al.: The biopolymer bacterial nanocellulose as drug delivery system: Investigation of drug loading and release using the model protein albumin. *J. Pharm. Sci. US* **102**, 579–592 (2013). <https://doi.org/10.1002/jps.23385>
83. Valo, H., Arola, S., Laaksonen, P., Torkkeli, M., Peltonen, L., Linder, M.B., et al.: Drug release from nanoparticles embedded in four different nanofibrillar cellulose aerogels. *Eur. J. Pharm. Sci.* **50**, 69–77 (2013). <https://doi.org/10.1016/j.ejps.2013.02.023>

84. Villanova, J., Ayres, E., Carvalho, S., Patrício, P., Pereira, F., Oréface, R.: Pharmaceutical acrylic beads obtained by suspension polymerization containing cellulose nanowhiskers as excipient for drug delivery. *Eur. J. Pharm. Sci.* **42**, 406–415 (2011). <https://doi.org/10.1016/j.ejps.2011.01.005>
85. Xiang, C., Taylor, A.G., Hinestroza, J.P., Frey, M.W.: Controlled release of non-ionic compounds from poly (lactic acid)/cellulose nanocrystal nanocomposite fibers. *J. Appl. Polym. Sci.* **127**, 79–86 (2013). <https://doi.org/10.1002/app.36943>
86. Lin, Yung-Kai., Chen, Ko-Hua., Keng-Liang, Ou., Liu, Min: Effects of different extracellular matrices and growth factor immobilization on biodegradability and biocompatibility of macroporous bacterial cellulose. *J. Bioact. Comp. Polym.* **26**(5), 508–518 (2011). <https://doi.org/10.1177/0883911511415390>
87. Halib, N., Perrone, F., Cemazar, M., Dapas, B., Farra, R., Abrami, M., Murena, L.: Potential applications of nanocellulose containing materials in the biomedical field. *Materials* **10**(8), 977 (2017). <https://doi.org/10.3390/ma10080977>
88. Baumann, M.D., Kang, C.E., Stanwick, J.C., et al.: An injectable drug delivery platform for sustained combination therapy. *J. Control. Release* **138**, 205–213 (2009). <https://doi.org/10.1016/j.jconrel.2009.05.009>
89. Watanabe, Y., Mukai, B., Kawamura, K.I., et al.: Preparation and evaluation of press-coated aminophylline tablet using crystalline cellulose and polyethylene glycol in the outer shell for timed-release dosage forms. *Yakugaku Zasshi* **122**, 157–162 (2002). <https://doi.org/10.1248/yakushi.122.157>
90. Huia, J., Yuanyuan, J., Jiao, W., Yuan, H., Yuan, Z., Shiru, J.: Potentiality of bacterial cellulose as the scaffold of tissue engineering of cornea. In: Proceedings of the 2nd International Conference on Biomedical Engineering and Informatics, (BME'09), China (2009). <https://doi.org/10.1109/BMEI.2009.5305657>
91. Amorim, W.L., Costa, H.O., Souza, F.C., Castro, M.G., Silva, L.: Experimental study of the tissue reaction caused by the presence of cellulose produced. *Braz. J. Otorhinol.* **75**, 200–207 (2009). <https://doi.org/10.1016/j.jvoice.2010.07.005>
92. Khalil, H.A., Bhat, A.H., Yusra, A.I.: Green composites from sustainable cellulose nanofibrils: a review. *Carbohydr. Polym.* **87**(2), 963–979 (2012). <https://doi.org/10.1016/j.carbpol.2011.08.078>
93. Balazs, A.C., Emrick, T., Russell, T.P.: Nanoparticle polymer composites: where two small worlds meet. *Science* **314**(5802), 1107–1110 (2006). <https://doi.org/10.1126/science.1130557>
94. Dallas, P., Sharma, V.K., Zboril, R.: Silver polymeric nanocomposites as advanced antimicrobial agents: classification, synthetic paths, applications, and perspectives. *Adv. Colloid Interface Sci.* **166**(1–2), 119–135 (2011). <https://doi.org/10.1016/j.cis.2011.05.008>
95. Nishiyama, Y., Langan, P., Chanzy, H.: Crystal structure and hydrogen-bonding system in cellulose Ib from synchrotron X-ray and neutron fibre diffraction. *J. Am. Chem. Soc.* **124**, 9074–9082 (2002). <https://doi.org/10.1021/ja0257319>
96. Dominkovics, Z., Danyadi, L., Pukanszky, B.: Surface modification of wood flour and its effect on the properties of PP/wood composites. *Compos. A Appl. Sci. Manuf.* **38**(8), 1893–1901 (2007). <https://doi.org/10.1016/j.compositesa.2007.04.001>
97. Wang, Y., Liao Chia-Hung, Y., Jiashing, L., Jung-Chih, Y., ChenKevin, C., Wu, W.: Fabrication of inorganic hydroxyapatite nanoparticles and organic biomolecules-dual encapsulated alginate microspheres. *Biointer. Phases* **10**(2), 1–8 (2015). <https://doi.org/10.1116/1.4919561>
98. Fu, J., Li, D., Li, G., Huang, F., Wei, Q.: Carboxymethyl cellulose assisted immobilization of silver nanoparticles onto cellulose nanofibers for the detection of catechol. *J. Electroanal. Chem.* **738**, 92–99 (2015). <https://doi.org/10.1016/j.jelechem.2014.11.025>
99. Pinto, R.J., Neves, M.C., Neto, C.P., Trindade, T.: Composites of cellulose and metal nanoparticles. In: *Nanocomposites—New Trends and Developments*, chap. 4, pp. 1–25 (2012). IntechOpen Limited, London. <https://doi.org/10.5772/50553>
100. Ngo, Y.H., Li, D., Simon, G.P., Gamier, G.: Paper surfaces functionalized by nanoparticles. *Adv. Colloid Interface Sci.* **163**(1), 23–38 (2011). <https://doi.org/10.1016/j.cis.2011.01.004>

101. He, J.H., Kunitake, T., Nakao, A.: Facile in situ synthesis of noble metal nanoparticles in porous cellulose fibers. *Chem. Mater.* **15**(23), 4401–4406 (2003). <https://doi.org/10.1021/cm034720r>
102. Maneerung, T., Tokura, S., Rujiravanit, R.: Impregnation of silver nanoparticles into bacterial cellulose for antimicrobial wound dressing. *Carbohydr. Polym.* **72**(1), 43–51 (2008). <https://doi.org/10.1016/j.carbpol.2007.07.025>
103. De Santa, M.L.C., Santos, A.L.C., Oliveira, P.C., Barud, H.S., Messaddeq, Y., Ribeiro, S.J.L.: Synthesis and characterization of silver nanoparticles impregnated into bacterial cellulose. *Mater. Lett.* **63**(9–10), 797–799 (2009). <https://doi.org/10.1016/j.matlet.2009.01.007>
104. Barud, H.S., Barrios, C., Regiani, T., et al.: Self supported silver nanoparticles containing bacterial cellulose membranes. *Mater. Sci. Eng. C-Biomim. Supramol. Syst.* **28**, 515–518 (2008). <https://doi.org/10.1016/j.msec.2007.05.001>
105. Omrani, A.A., Taghavinia, N.: Photo-induced growth of silver nanoparticles using UV sensitivity of cellulose fibers. *Appl. Surf. Sci.* **258**(7), 2373–2377 (2012). <https://doi.org/10.1016/j.apsusc.2011.10.038>
106. Son, W.K., Youk, J.H., Park, W.H.: Antimicrobial cellulose acetate nanofibers containing silver nanoparticles. *Carbohydr. Polym.* **65**(4), 430–434 (2006). <https://doi.org/10.1016/j.carbpol.2006.01.037>
107. Hubsch, E., Ball, V., Senger, B., Decher, G., Voegel, J.C., Schaaf, P.: Controlling the growth regime of polyelectrolyte multilayer films: changing from exponential to linear growth by adjusting the composition of polyelectrolyte mixtures. *Langmuir* **20**(5), 1980–1985 (2004). <https://doi.org/10.1021/la0361870>
108. Egerton, R.: *Physical Principles of Electron Microscopy*. Springer, Heidelberg (2005). <https://doi.org/10.1007/b136495>
109. Hall, J.L., Hawes, C.R.: *Electron Microscopy of Plant Cells*. Academic Press, London (1991)
110. Fultz B, Howe J (2007) *Transmission Electron Microscopy and Diffractometry of Material*, Springer-Verlag, Heidelberg <https://doi.org/10.1007/978-3-642-29761-8>
111. Binnig, G., Quate, C.F., Gerber, C.: Atomic force microscope. *Phys Rev Letters* **56**(9), 930–933 (1986). <https://doi.org/10.1103/PhysRevLett.56.930>
112. Levдик, I.Y., Nikitin, V.N.: Determination of cellulose mercerization using IR-spectroscopy. *Cell. Chem. Technol.* **11**(3), 259–268 (1968)
113. Mochalov, A., Chlustova, T., Ioelovich, M., Kaimin, I.: Effect of the crystallinity degree on the heat capacity of cellulose. *Wood Chem.* **4**, 66–68 (1982)
114. Kaimin, I., Ioelovich, M.: *Methods of Cellulose Investigation*, Science Riga (1981)
115. Ioelovich, M., Luksa, R.: Changes of cellulose crystalline structure during thermal treatment. *Wood. Chem.* **3**, 18–20 (1990). <https://doi.org/10.1007/BF00765800>
116. Eichhorn, S.J., Davies, G.R.: Modeling the crystalline deformation of native and regenerated cellulose. *Cellulose* **13**(3), 291–307 (2006). <https://doi.org/10.1007/s10570-006-9046-3>
117. Tanaka, F., Iwata, T.: Estimation of the elastic modulus of cellulose crystal by molecular mechanics simulation. *Cellulose* **13**(5), 509–517 (2006). <https://doi.org/10.1007/s10570-006-9068-x>
118. Nishino, T., Takano, K., Nakamae, K.: Elastic modulus of the crystalline regions of cellulose polymorphs. *J. Polym. Sci. Part B* **33**, 1647–1651 (1995). <https://doi.org/10.1002/polb.1995.090331110>
119. Marques, P.A.A.P., Nogueira, H.I.S., Pinto, R.J.B., Neto, C.P., Trindade, T.: Silver-bacterial cellulosic sponges as active SERS substrates. *J. Raman Spectrosc.* **39**(4), 439–443 (2008). <https://doi.org/10.1002/jrs.1853>
120. Carlson, C., Hussain, S.M., Schrand, A.M., Braydich-Stolle, L.K., Hess, K.L., Jones, R.L., Schlager, J.J.: Unique cellular interaction of silver nanoparticles: size-dependent generation of reactive oxygen species. *J. Phys. Chem. B* **112**(43), 13608–13619 (2008). <https://doi.org/10.1021/jp712087m>
121. Barud, H.S., Regiani, T., Marques, R.F., Lustrì, W.R., Messaddeq, Y., Ribeiro, S.J.: Antimicrobial bacterial cellulose-silver nanoparticles composite membranes. *J. Nanomater.* **2011**, 1–10 (2011). <https://doi.org/10.1155/2011/721631>

122. Bober, P., Liu, J., Mikkonen, K.S., Ihalainen, P., Pesonen, M., Plumed-Ferrer, C., et al.: Biocomposites of nanofibrillated cellulose, polypyrrole, and silver nanoparticles with electroconductive and antimicrobial properties. *Biomacromolecules* **15**(10), 3655–3663 (2014). <https://doi.org/10.1021/bm500939x>
123. Shi, Z., Tang, J., Chen, L., Yan, C., Tanvir, S., Anderson, W.A., et al.: Enhanced colloidal stability and antibacterial performance of silver nanoparticles/cellulose nanocrystal hybrids. *J. Mater. Chem. B* **3**(4), 603–611 (2015). <https://doi.org/10.1039/C4TB01647E>
124. Rac-Rumijowska, O., Maliszewska, I., Fiedot-Toboła, M., Karbownik, I., Teterycz, H.: Multi-functional nanocomposite cellulose fibers doped in situ with silver nanoparticles. *Polymers* **11**(3), 562 (2019). <https://doi.org/10.3390/polym11030562>
125. Drogat, N., Granet, R., Sol, V., Memmi, A., Saad, N., Koerkamp, C.K., et al.: Antimicrobial silver nanoparticles generated on cellulose nanocrystals. *J. Nanopart. Res.* **13**(4), 1557–1562 (2011). <https://doi.org/10.1007/s11051-010-9995-1>
126. Xiong, R., Lu, C.H., Zhang, W., Zhou, Z.H., Zhang, X.X.: Facile synthesis of tunable silver nanostructures for antibacterial application using cellulose nanocrystals. *Carbohydr. Polym.* **95**, 214–219 (2013). <https://doi.org/10.1016/j.carbpol.2013.02.077>
127. Azizi, S., Ahmad, M., Mahdavi, M., Abdolmohammadi, S.: Preparation, characterization, and antimicrobial activities of ZnO nanoparticles/cellulose nanocrystal nanocomposites. *Bio Resour.* **8**(2), 1841–1851 (2013). <https://doi.org/10.2147/IJN.S60274>
128. Turyanska, L., Makarovskiy, O., Patanè, A., Kozlova, N.V., Liu, Z., Li, M., Mann, S.: High magnetic field quantum transport in Au nanoparticle–cellulose films. *Nanotechnology* **23**(4), 045702 (2012). <https://doi.org/10.1088/0957-4484/23/4/045702>
129. Smiechowicz, E., Niekraszewicz, B., Kulpinski, P., Dzitko, K.: Antibacterial composite cellulose fibers modified with silver nanoparticles and nanosilica. *Cellulose* **25**(6), 3499–3517 (2018). <https://doi.org/10.1007/s10570-018-1796-1>
130. Ishida, T., Watanabe, H., Bebeko, T., Akita, T., Haruta, M.: Aerobic oxidation of glucose over gold nanoparticles deposited on cellulose. *Appl. Catal. A-Gen.* **377**(1–2), 42–46 (2010). <https://doi.org/10.1016/j.apcata.2010.01.017>
131. Koga, H., Tokunaga, E., Hidaka, M., Umemura, Y., Saito, T., Isogai, A., Kitaoka, T.: Topochemical synthesis and catalysis of metal nanoparticles exposed on crystalline cellulose nanofibers. *Chem. Commun.* **46**(45), 8567–8569 (2010). <https://doi.org/10.1039/C0C02754E>
132. Cady, Nathaniel C., Behnke, Jason L., Strickland, Aaron D.: Copper-based nanostructured coatings on natural cellulose: nanocomposites exhibiting rapid and efficient inhibition of a multi-drug resistant wound pathogen, *A. baumannii*, and mammalian cell biocompatibility *In Vitro*. *Adv. Funct. Mater.* **21**(13), 2506–2514 (2011). <https://doi.org/10.1002/adfm.201100123>
133. Benaissi, K., Johnson, L., Walsh, D.A., Thielemans, W.: Synthesis of platinum nanoparticles using cellulosic reducing agents. *Green Chem.* **12**(2), 220–222 (2010). <https://doi.org/10.1039/B913218J>
134. Cai, J., Kimura, S., Wada, M., Kuga, S.: Nanoporous cellulose as metal nanoparticles support. *Biomacromolecules* **10**(1), 87–94 (2009). <https://doi.org/10.1021/bm800919e>
135. Dong, H., Hinestroza, J.P.: Metal nanoparticles on natural cellulose fibers: electrostatic assembly and in situ synthesis. *ACS Appl. Mater. Interfaces* **1**(4), 797–803 (2009). <https://doi.org/10.1021/am800225j>
136. Gelesky, M.A., Scheeren, C.W., Foppa, L., Pavan, F.A., Dias, S.L.P., Dupont, J.: Metal nanoparticle/ionic liquid/cellulose: new catalytically active membrane materials for hydrogenation reactions. *Biomacromolecules* **10**(7), 1888–1893 (2009). <https://doi.org/10.1021/bm9003089>
137. Himeshima, N., Amao, Y.: Photoinduced hydrogen production from cellulose derivative with chlorophyll-a and platinum nanoparticles system. *Energy Fuels* **17**(6), 1641–1644 (2003). <https://doi.org/10.1021/ef034006w>
138. Pirkkalainen, K., et al.: Nanocomposites of magnetic cobalt nanoparticles and cellulose. *Eur. Phys. J. D* **49**(3), 333–342 (2008). <https://doi.org/10.1140/epjd/e2008-00180-5>

139. Dong, F., Li, S.: Wound dressings based on chitosan-dialdehyde cellulose nanocrystals-silver nanoparticles. *Mech. Strength Polym.* **10**(6), 673 (2018). <https://doi.org/10.3390/polym10060673>
140. Mathew, A.P., Oksman, K., Pierron, D., Harmad, M.F.: Cross linked fibrous composites based on cellulose nanofibers and collagen with in situ pH induced fibrillation. *Cellulose* **19**, 139–150 (2012). <https://doi.org/10.1007/s10570-011-9624-x>
141. Mathew, A.P., Oksman, K., Pierron, D., Harmand, M.F.: Fibrous cellulose nanocomposite scaffolds prepared by partial dissolution for potential use as ligament or tendon substitutes. *Carbohydr. Polym.* **87**, 2291–2298 (2012). <https://doi.org/10.1016/j.carbpol.2011.10.063>
142. Dumortier, G., Grossiord, J.L., Agnely, F., Chaumeil, J.C.: A review of poloxamer 407 pharmaceutical and pharmacological characteristics. *Pharm. Res.* **23**, 2709–2728 (2006). <https://doi.org/10.1007/s11095-006-9104-4>
143. Mertaniemi, H., et al.: Human stem cell decorated nanocellulose threads for biomedical applications. *Biomaterials* **82**, 208–220 (2016). <https://doi.org/10.1016/j.biomaterials.2015.12.020>
144. Ao, C., Niu, Y., Zhang, X., He, X., Zhang, W., Lu, C.: Fabrication and characterization of electrospun cellulose/nano-hydroxyapatite nanofibers for bone tissue engineering. *Int. J. Biol. Macromol.* **97**, 568–573 (2017). <https://doi.org/10.1016/j.ijbiomac.2019.11.029>
145. Atila, D., Keskin, D., Tezcaner, A.: Crosslinked pullulan/cellulose acetate fibrous scaffolds for bone tissue engineering. *Mater. Sci. Eng. C* **69**, 1103–1115 (2016). <https://doi.org/10.1016/j.msec.2016.08.015>
146. Fricain, J.C., et al.: A nano-hydroxyapatite: Pullulan/dextran polysaccharide composite macroporous material for bone tissue engineering. *Biomaterials* **34**, 2947–2959 (2015). <https://doi.org/10.1016/j.biomaterials.2013.01.049>
147. Korzen, L., Pulidindi, I.N., Israel, A., Abelson, A., Gedanken, A.: Single step production of bioethanol from the seaweed *Ulva rigida* using sonication. *RSC Adv.* **5**(21), 16223–16229 (2015). <https://doi.org/10.1039/C4RA14880K>
148. Jeong, T.S., Choi, C.H., Lee, J.Y., Oh, K.K.: Behaviors of glucose decomposition during acid-catalyzed hydrothermal hydrolysis of pretreated *Gelidium amansii*. *Bioresour. Technol.* **116**, 435–440 (2012). <https://doi.org/10.1016/j.biortech.2012.03.104>
149. Kim, H.M., Wi, S.G., Jung, S., Song, Y., Bae, H.J.: Efficient approach for bioethanol production from red seaweed *Gelidium amansii*. *Bioresour. Technol.* **175**, 128–134 (2015). <https://doi.org/10.1016/j.biortech.2014.10.050>
150. Gouveia, L.: *Microalgae as a Feedstock for Biofuels*, pp. 1–69. Springer, London (2011). https://doi.org/10.1007/978-3-642-17997-6_1
151. Scholz, M.J., et al.: Ultrastructure and composition of the Nannochloropsis gaditana cell wall. *Eukaryot. Cell* **13**(11), 1450–1464 (2014). <https://doi.org/10.1128/EC.00183-14>
152. Hamed, S.B., Hamed, M.B.B., Kassouar, S., Abi Ayad, S.M.E.A.: Physicochemical analysis of cellulose from microalgae *Nannochloropsis gaditana*. *Afr. J. Biotechnol.* **15**(24), 1201–1206 (2016). <https://doi.org/10.5897/AJB2016.15321>
153. Kloareg, B., Quatrano, R.: Structure of the cell walls of marine algae and ecophysiological functions of the matrix polysaccharides. *Oceanogr. Mar. Biol. Ann. Rev.* **26**, 259–315 (1988). http://scholar.google.com/scholar_lookup?&title=Structure%20of%20the%20cell%20walls%20of%20marine%20algae%20and%20ecophysiological%20functions%20of%20the%20matrix%20polysaccharides&journal=Oceanogr%20Mar%20Biol%20Annu%20Rev%20vol%20ume=26&pages=259-315&publication_year=1988&author=Kloareg%2CB&author=Quatrano%2CRS
154. Tsekos, I., Okuda, K., Brown, R.: The formation and development of cellulosesynthesizing linear terminal complexes (TCs) in the plasma membrane of the marine red alga *Erythrocladia subintegra*. *Rosenv. Protoplasma.* **193**(1–4), 33–45 (1996). <https://doi.org/10.1007/BF01276632>
155. Tsekos, I.: The sites of cellulose synthesis in algae: diversity and evolution of cellulose synthesizing enzyme complexes. *J. Phycol.* **35**(4), 635–655 (1999). <https://doi.org/10.1046/j.1529-8817.1999.3540635.x>

156. Goswami, G., BangV, A.S.: Diverse applications of Algae. *Int. J. Adv. Res. Sci. Eng.* **4**(1), 1102–1109 (2015)
157. Imai, T., Sugiyama, J.: Nanodomains of α and β cellulose in algal microfibrils. *Macromolecules* **31**(18), 6275–6279 (1998). <https://doi.org/10.1021/ma980664h>
158. Kim, N.H., Herth, W., Vuong, R., Chanzy, H.: The cellulose system in the cell wall of *Micrasterias*. *J. Struct. Biol.* **117**(3), 195–203 (1996). <https://doi.org/10.1006/jsbi.1996.0083>
159. Sugiyama, J., Harada, H., Fujiyoshi, Y., Uyeda, N.: Lattice images from ultrathin sections of cellulose microfibrils in the cell wall of *Valonia macrophysa* Kütz. *Planta* **166**(2), 161–168 (1985). <https://doi.org/10.1007/bf00397343>
160. Hua, K., Stromme, M., Mhryanyam, A., Ferraz, N.: Nanocellulose from green algae modulates the *in vitro* inflammatory response of monocytes/macrophages. *Cellulose* **22**, 3673–3688 (2015). <https://doi.org/10.1007/s10570-015-0772-2>
161. Nicolai, E., Preston, R.D.: Cell-wall studies in the Chlorophyceae. I. A general survey of submicroscopic structure in filamentous species. *Proc. Roy. Soc. Lond. Ser. B Biol. Sci.* **140**(899), 244–274 (1952)
162. Koyama, M., Sugiyama, J., Itoh, T.: Systematic survey on crystalline features of algal celluloses. *Cellulose* **4**, 147–160 (1997). <https://doi.org/10.1023/A:1018427604670>
163. Kreger, D.R.: *Cell Walls, Physiology and Biochemistry of Algae*. Academic, New York (1962)
164. Sjöstrom, E.: *Wood Chemistry-Fundamentals and Applications*. Academic, San Diego (1993)
165. Bold, H., Wynne, M.: *Introduction to the Algae*, 2nd edn. Prentice Hall Int, Englewood Cliffs (1985)
166. Le Bras, D., Strømme, M., Mhryanyan, A.: Characterization of dielectric properties of nanocellulose from wood and algae for electrical insulator applications. *J. Phys. Chem. B* **119**(18), 5911–5917 (2015). <https://doi.org/10.1021/acs.jpcc.5b00715>
167. Ek, R., Gustafsson, C., Nutt, A., Iversen, T., Nystrom, C.: Cellulose powder from *Cladophora* sp. algae. *J. Mol. Recogn.* **11**, 263–265 (1998). [https://doi.org/10.1002/\(SICI\)1099-1352\(199812\)11:1/6%3C263::AID-JMR437%3E3.0.CO;2-G](https://doi.org/10.1002/(SICI)1099-1352(199812)11:1/6%3C263::AID-JMR437%3E3.0.CO;2-G)
168. Wada, M., Okano, T., Sugiyama, J.: Synchrotron-radiated X-ray and neutron diffraction study of native cellulose. *Cellulose* **4**(3), 221–232 (1997). <https://doi.org/10.1023/A:1018435806488>
169. Mhryanyan, A., Andersson, S.B., Ek, R.: Sorption of nicotine to cellulose powders. *Eur. J. Pharm. Sci.* **22**, 279–286 (2004). <https://doi.org/10.1016/j.ejps.2004.03.012>
170. Cunha, A.G., Zhou, Q., Larsson, P.T., Berglund, L.A.: Topochemical acetylation of cellulose nanopaper structures for biocomposites: mechanisms for reduced water vapour sorption. *Cellulose* **21**(4), 2773–2787 (2014)
171. Yoon, J.J., Kim, Y.J., Kim, S.H., Ryu, H.J., Choi, J.Y., Kim, G.S., Shin, M.K.: Production of polysaccharides and corresponding sugars from red seaweed. *Adv. Mater. Res.* **93**, 463–466 (2010). <https://doi.org/10.4028/www.scientific.net/AMR.93-94.463>
172. Seo, Y.B., Lee, Y.W., Lee, C.H., You, H.C.: Red algae and their use in papermaking. *Bioresour. Technol.* **101**(7), 2549–2553 (2010). <https://doi.org/10.1016/j.biortech.2009.11.088>
173. Bettaieb, F., Khiari, R., Dufresne, A., Mhenni, M.F., Belgacem, M.N.: Mechanical and thermal properties of *Posidonia oceanica* cellulose nanocrystal reinforced polymer. *Carbohydr. Polym.* **123**, 99–104 (2015). <https://doi.org/10.1016/j.carbpol.2015.01.026>
174. Bayer, E.A., Chanzy, H., Lamed, R., Shoham, Y.: Cellulose, cellulases and cellulosomes. *Curr. Opin. Struct. Biol.* **8**, 548–557 (1998). [https://doi.org/10.1016/S0959-440X\(98\)80143-7](https://doi.org/10.1016/S0959-440X(98)80143-7)
175. Brett, C.T.: Cellulose microfibrils in plants: biosynthesis, deposition, and integration into the cell wall. *Int. Rev. Cytol.* **199**, 161–199 (2000). [https://doi.org/10.1016/s0074-7696\(00\)99004-1](https://doi.org/10.1016/s0074-7696(00)99004-1)
176. Larsson, P.T., Wickholm, K., Iversen, T.: A CP/MAS13C NMR investigation of molecular ordering in celluloses. *Carbohydr. Res.* **302**, 19–25 (1997). [https://doi.org/10.1016/S0008-6215\(97\)00130-4](https://doi.org/10.1016/S0008-6215(97)00130-4)
177. O'sullivan, A.C.: Cellulose: the structure slowly unravels. *Cellulose* **4**(3), 173–207 (1997). <https://doi.org/10.1023/A:1018431705579>

178. Bhutiya, P.L., Misra, N., Rasheed, M.A., Hasan, S.Z.: Silver nanoparticles deposited algal nanofibrous cellulose sheet for antibacterial activity. *BioNanoScience* **10**, 23–33 (2020). <https://doi.org/10.1007/s12668-019-00690-4>
179. Arvizu-Higuera, D.L., Rodríguez-Montesinos, Y.E., Murillo-Álvarez, J.I., Muñoz-Ochoa, M., Hernández-Carmona, G.: Effect of alkali treatment time and extraction time on agar from *Gracilaria vermiculophylla*. *J. Appl. Phycol.* **20**(5), 515–519 (2008). <https://doi.org/10.1007/s10811-007-9258-4>
180. Saelee, K., Yingkamaeng, N., Nimchua, T., Sukyai, P.: An environmentally friendly xylanase-assisted pretreatment for cellulose nanofibrils isolation from sugarcane bagasse by high-pressure homogenization. *Ind. Crops Prod.* **82**, 149–160 (2016). <https://doi.org/10.1016/j.indcrop.2015.11.064>
181. Siddhanta, A.K., Chhatbar, M.U., Mehta, G.K., Sanandiya, N.D., Kumar, S., Oza, M.D., Meena, R.: The cellulose contents of Indian seaweeds. *J. Appl. Phycol.* **23**(5), 919–923 (2011). <https://doi.org/10.1007/s10811-010-9599-2>
182. Ching, Y.C., Rahman, A., Ching, K.Y., Sukiman, N.L., Cheng, H.C.: Preparation and characterization of polyvinyl alcohol-based composite reinforced with nanocellulose and nanosilica. *BioResources* **10**(2), 3364–3377 (2015)
183. Liew, S.Y., Thielemans, W., Hewakandamby, B.: Separation of sulphuric acid from an acid suspension of cellulose nanocrystals by manual shaking. *J. Nano Res.* **38**, 58–72 (2016). <https://doi.org/10.4028/www.scientific.net/JNanoR.38.58>
184. Tanaka, Reina, Saito, Tsuguyuki, Isogai, Akira: Cellulose nanofibrils prepared from softwood cellulose by TEMPO/NaClO/NaClO₂ systems in water at pH 4.8 or 6.8. *Int. J. Biol. Macromol.* **51**(3), 228–234 (2012). <https://doi.org/10.1016/j.ijbiomac.2012.05.016>
185. Li, J., Wei, X., Wang, Q., Chen, J., Chang, G., Kong, L., Su, J., Liu, Y.: Homogeneous isolation of nanocellulose from sugarcane bagasse by high pressure homogenization. *Carbohydr. Polym.* **90**(4), 1609–1613 (2012). <https://doi.org/10.1016/j.carbpol.2012.07.038>
186. Janardhan, S., Sain, M.M.: Isolation of cellulose microfibrils—an enzymatic approach. *BioResources* **1**(2), 176–188 (2006)
187. Yahya, M.B., Lee, H.V., Hamid, S.B.A.: Preparation of nanocellulose via transition metal salt-catalyzed hydrolysis pathway. *BioResources* **10**(4), 7627–7639 (2015)
188. De Rodriguez, N.L.G., Thielemans, W., Dufresne, A.: Sisal cellulose whiskers reinforced polyvinyl acetate nanocomposites. *Cellulose* **13**, 261–270 (2006). <https://doi.org/10.1007/s10570-005-9039-7>
189. Hayashi, N., Kondo, T., Ishihara, M.: Enzymatically produced nano-ordered short elements containing cellulose I- crystalline domains. *Carbohydr. Polym.* **61**, 191–197 (2005). <https://doi.org/10.1016/j.carbpol.2005.04.018>
190. El Achaby, M., Kassab, Z., Aboulkas, A., Gaillard, C., Barakat, A.: Reuse of red algae waste for the production of cellulose nanocrystals and its application in polymer nanocomposites. *Int. J. Biol. Macromol.* **106**, 681–691 (2018). <https://doi.org/10.1016/j.ijbiomac.2017.08.067>
191. Nystrom, G., Razaq, A., Strømme, M., Nyholm, L., Mihranyan, A.: Ultrafast all-polymer paper-based batteries. *Nano Lett.* **9**(10), 3635–3639 (2009). <https://doi.org/10.1021/nl901852h>
192. Mihranyan, A., Nyholm, L., Bennett, A.E.G., Strømme, M.: Novel high specific surface area conducting paper material composed of polypyrrole and *Cladophora* cellulose. *J. Phys. Chem. B* **112**, 12249–12255 (2008). <https://doi.org/10.1021/jp805123w>
193. Gelin, K., Mihranyan, A., Razaq, A., Nyholm, L., Strømme, M.: Potential controlled anion absorption in a novel high surface area composite of *Cladophora* cellulose and polypyrrole. *Electrochim. Acta* **54**(12), 3394–3401 (2009). <https://doi.org/10.1016/j.electacta.2009.01.010>
194. Turco, G., Donati, I., Grassi, M., Marchioli, G., Lapasin, R., Paoletti, S.: Mechanical spectroscopy and relaxometry on alginate hydrogels: a comparative analysis for structural characterization and network mesh size determination. *Biomacromolecules* **12**, 1272–1282 (2011). <https://doi.org/10.1021/bm101556m>
195. Möller, T., et al.: *In vivo* chondrogenesis in 3D bioprinted human cell-laden hydrogel constructs. *Plast. Reconstr. Surg. Glob. Open* **5**, 1–7 (2017). <https://doi.org/10.1097/gox.0000000000001227>

196. Martinez, A.H., et al.: Novel bilayer bacterial nanocellulose scaffold supports neocartilage formation *in vitro* and *in vivo*. *Biomaterials* **44**, 122–133 (2015). <https://doi.org/10.1016/j.biomaterials.2014.12.025>
197. Johnson, M., Shivkumar, S.: Filamentous green algae additions to isocyanate based foams. *J. Appl. Polym. Sci.* **93**, 2469–2477 (2004). <https://doi.org/10.1002/app.20794>
198. Strømme, M., Mihranyan, A., Ek, R.: What to do with all these algae? *Mater. Lett.* **57**, 569–572 (2002). [https://doi.org/10.1016/S0167-577X\(02\)00831-5](https://doi.org/10.1016/S0167-577X(02)00831-5)
199. Mihranyan, A., Edsman, K., Strømme, M.: Rheological properties of cellulose hydrogels prepared from *Cladophora* cellulose powder. *Food Hydrocolloid.* **21**, 267–272 (2007). <https://doi.org/10.1016/j.foodhyd.2006.04.003>
200. Metreveli, G., Wågberg, L., Emmoth, E., Belák, S., Strømme, M., Mihranyan, A.: Virus removal: a size-exclusion nanocellulose filter paper for virus removal. *Adv. Healthcare Mater.* **3**, 1546–1550 (2014). <https://doi.org/10.1002/adhm.201300641>
201. Ruan, C., Strømme, M., Jonas, L.: A green and simple method for preparation of an efficient palladium adsorbent based on cysteine functionalized 2, 3-dialdehyde cellulose. *Cellulose* **23**(4), 2627–2638 (2016). <https://doi.org/10.1007/s10570-016-0976-0>
202. Yadav, M., Liu, Y.K., Chiu, F.C.: Fabrication of cellulose nanocrystal/silver/alginate bionanocomposite films with enhanced mechanical and barrier properties for food packaging application. *Nanomaterials* **9**(11), 1523–1532 (2019). <https://doi.org/10.3390/nano9111523>
203. Brown, A.J.: On an acetic ferment, which forms cellulose. *J. Chem. Soc. Trans.* **49**, 432–439 (1986). <https://doi.org/10.1039/CT8864900432>
204. Iguchi, M., Yamanaka, S., Budhiono, A.: Bacterial cellulose - a masterpiece of nature's arts. *J. Mater. Sci.* **35**, 261–270 (2000). <https://doi.org/10.1023/A:1004775229149>
205. Illa, M.P., Khandelwal, M., Sharma, C.S.: Bacterial cellulose-derived carbon nanofibers as anode for lithium-ion batteries. *Emerg. Mater.* **1**, 105–120 (2018). <https://doi.org/10.1007/s42247-018-0012-2>
206. Lin, N., Dufresne, A.: Nanocellulose in biomedicine: Current status and future prospect. *Eur. Polym. J.* **59**, 302–325 (2014). <https://doi.org/10.1016/j.eurpolymj.2014.07.025>
207. Kucinska-Lipka, J., Gubanska, I., Janik, H.: Bacterial cellulose in the field of wound healing and regenerative medicine of skin: recent trends and future prospectives. *Polym. Bull.* **72**, 2399–2419 (2015). <https://doi.org/10.1007/s00289-015-1407-3>
208. Feng, J., et al.: Antimicrobial activity of silver nanoparticles in situ growth on TEMPO-mediated oxidized bacterial cellulose. *Cellulose* **21**(6), 4557–4567 (2014). <https://doi.org/10.1007/s10570-014-0449-2>
209. Dugan, J.M., Gough, J.E., Eichhorn, S.J.: Bacterial cellulose scaffolds and cellulose nanowhiskers for tissue engineering. *Nanomedicine* **8**, 287–298 (2013). <https://doi.org/10.2217/nmm.12.211>
210. Wan, W.K., Hutter, J.L., Millon, L.E., et al.: Bacterial cellulose and its nanocomposites for biomedical applications. In: Oksman, K., Sain, M. (eds.) *Cellulose Nanocomposites. Processing Characterization and Properties*. American Chemical Society, Washington, DC (2006)
211. Cherian, B.M., Leao, A.L., De Souza, S.F., Thomas, S., Pothan, L.A., Kottaisamy, M.: Cellulose nanocomposites for high-performance applications. In: *Cellulose Fibers: Bio Nano Polymer Composites*, pp. 539–587 (2011). https://doi.org/10.1007/978-3-642-17370-7_21
212. Brown, E.E., Laborie, M.P.G.: Bioengineering bacterial cellulose/poly(ethylene oxide) nanocomposites. *Bio Macromol.* **8**, 3074–3081 (2007). <https://doi.org/10.1021/bm700448x>
213. Czaja, W., Romanovicz, D., Brown, R.M.: Structural investigations of microbial cellulose produced in stationary and agitated culture. *Cellulose* **11**, 403–411 (2004). <https://doi.org/10.1023/B:CELL.0000046412.11983.61>
214. Guhados, G., Wan, W.K., Hutter, J.L.: Measurement of the elastic modulus of single bacterial cellulose fibres using atomic force microscopy. *Langmuir* **21**, 6642–6646 (2005). <https://doi.org/10.1007/s10570-008-9206-8>
215. Juntaro, J., Pommert, M., Mantalaris, A., et al.: Nanocellulose enhanced interfaces in truly green unidirectional fibre reinforced composites. *Compos. Interface* **14**, 753–762 (2007). <https://doi.org/10.1163/156855407782106573>

216. Ashjarian, Ali, Yazdanshenas, Mohammad Esmail, Rashidi, Abosaeed, Khajavi, Ramin, Rezaee, Abbas: Overview of bio nanofabric from bacterial cellulose. *J. Text. Inst.* **104**(2), 121–131 (2013). <https://doi.org/10.1080/00405000.2012.703796>
217. Dar, M.A., Pawar, K.D., Chintalchere, J.M., Pandit, R.S.: Statistical optimization of ligno-cellulosic waste containing culture medium for enhanced production of cellulase by *Bacillus tequilensis* G9. *Waste Disp. Sustain. Energy* **1**, 213–226 (2019). <https://doi.org/10.1007/s42768-019-00016-w>
218. Singh, I., Sharma, A., Park, B.D.: Drug-delivery applications of cellulose nanofibrils. In: *Nanoarchitectonics for Smart Delivery and Drug Targeting*, pp. 95–117. Elsevier, Amsterdam (2016). <https://doi.org/10.1016/B978-0-323-47347-7.00004-5>
219. Favi, P.M., Ospina, S.P., Kachole, M., Gao, M., Atehortua, L., Webster, T.J.: Preparation and characterization of biodegradable nano hydroxyapatite–bacterial cellulose composites with well-defined honeycomb pore arrays for bone tissue engineering applications. *Cellulose* **23**, 1263–1282 (2016). <https://doi.org/10.1007/s10570-016-0867-4>
220. Alba-Molina, D., Giner-Casares, J.J., Cano, M.: Bioconjugated plasmonic nanoparticles for enhanced skin penetration. *Top. Curr. Chem.* **8**, 378 (2020). <https://doi.org/10.1007/s41061-019-0273-0>
221. Xiaobing, L., Hamid, S., Yudong, Z., Yajie, X., Wei-Hong, Z., Cai, W.: Soy protein isolate bacterial cellulose composite membranes for high efficiency particulate air filtration. *Compos. Sci. Technol.* **138**, 124–133 (2017). <https://doi.org/10.1016/j.compscitech.2016.11.022>
222. Atila, D., Karatas, A., Evcin, A., Keskin, D., Tezcaner, A.: Bacterial cellulose-reinforced boron-doped hydroxyapatite/gelatin scaffolds for bone tissue engineering. *Cellulose* **26**, 9765–9785 (2019). [https://doi.org/10.1007/s10570-019-02741-1\(012345678](https://doi.org/10.1007/s10570-019-02741-1(012345678)
223. Nogi, M., Yano, H.: Transparent nanocomposites based on cellulose produced by bacteria offer potential innovation in the electronics device industry. *Adv. Mater.* **20**, 1849–1852 (2008). <https://doi.org/10.1002/adma.200702559>
224. Bayir, E., Bilgi, E.E., Hames, E., Sendemir, A.: Production of hydroxyapatite–bacterial cellulose composite scaffolds with enhanced pore diameters for bone tissue engineering applications. *Cellulose* **26**, 9803–9817 (2019). <https://doi.org/10.1007/s10570-019-02763-9>
225. Xu, J., Liu, Z., Zhang, F., Tao, J., Shen, L., Zhang, X.: Bacterial cellulose-derived carbon nanofibers as both anode and cathode for hybrid sodium ion capacitor. *RSC Adv.* **10**, 7780–7790 (2020). <https://doi.org/10.1039/C9RA10225F>
226. Fillat, A., et al.: Bacterial cellulose for increasing barrier properties of paper products. *Cellulose* **25**, 6093–6105 (2018). [https://doi.org/10.1007/s10570-018-1967-0\(0123456789\(,-volV\(0123456789\(,-volV](https://doi.org/10.1007/s10570-018-1967-0(0123456789(,-volV(0123456789(,-volV)
227. Jiji, S., Thenmozhi, S., Kadirvelu, K.: Comparison on properties and efficiency of bacterial and electrospun cellulose nanofibers. *Fibers Polym.* **19**(12), 2498–2506 (2018). <https://doi.org/10.1007/s12221-018-8527-y>
228. Thavasi, V., Singh, G., Ramakrishna, S.: Electrospun nanofibers in energy and environmental applications. *Energy Environ. Sci.* **1**, 205–221 (2008). <https://doi.org/10.1039/B809074M>
229. Aliabadi, Majid, Irani, Mohammad, Ismaeili, Jabir, Piri, Hossein, Parnian, Mohammad Javad: Electrospun nanofiber membrane of PEO/Chitosan for the adsorption of nickel, cadmium, lead and copper ions from aqueous solution. *Chem. Eng. J.* **220**, 237–243 (2013). <https://doi.org/10.1016/j.cej.2013.01.021>
230. Keshtkar, Ali Reza, Irani, Mohammad, Moosavian, Mohammad Ali: Removal of uranium (VI) from aqueous solutions by adsorption using a novel electrospun PVA/TEOS/APTES hybrid nanofiber membrane: comparison with casting PVA/TEOS/APTES hybrid membrane. *J. Radioanal. Nucl. Chem.* **295**(1), 563–571 (2012). <https://doi.org/10.1007/s10967-012-2110-6>
231. Soares da Silva, F.A.G., Fernandes, M., Pedro Souto, A., Ferreira, E.C., Gama, D.F.M.: Optimization of bacterial nanocellulose fermentation using recycled paper sludge and development of novel composites. *Appl. Microbiol. Biotechnol.* **103**, 9143–9154 (2019). <https://doi.org/10.1007/s00253-019-10124-6>
232. Sun, D.P., Yang, J.Z., Li, J., Yu, J.W., Xu, X.F., Yang, X.J.: Novel Pd-Cu/bacterial cellulose nanofibers: preparation and excellent performance in catalytic denitrification. *Appl. Surf. Sci.* **256**, 2241–2244 (2010). https://doi.org/10.1007/978-3-319-58538-3_71-1

233. Muller, D., Rambo, C.R., Recouvreux, D.O.S., Porto, L.M., Barra, G.M.O.: Chemical in situ polymerization of polypyrrole on bacterial cellulose nanofibers. *Synth. Met.* **161**, 106–111 (2011). <https://doi.org/10.1016/j.synthmet.2010.11.005>
234. Cai, Z.J., Yang, G.: Optical nanocomposites prepared by incorporating bacterial cellulose nanofibrils into poly (3-hydroxybutyrate). *Mater. Lett.* **65**, 182–184 (2011). <https://doi.org/10.1016/j.matlet.2010.09.055>
235. Zhang, W., Chen, S.Y., Hu, W.L., Zhou, B.H., Yang, Z.H., Yin, N.: Facile fabrication of flexible magnetic nanohybrid membrane with amphiphobic surface based on bacterial cellulose. *Carbohydr. Polym.* **86**, 1760–1767 (2011). <https://doi.org/10.1016/j.carbpol.2011.07.015>
236. Fernandes, S.C.M., Sadocco, P., Aonso-Varona, A., Palomares, T., Eceiza, A., Silvestre, A.J.D., et al.: Bioinspired antimicrobial and biocompatible bacterial cellulose membranes obtained by surface functionalization with aminoalkyl groups. *Acs Appl. Mater. Inter.* **5**, 3290–3297 (2013). <https://doi.org/10.1021/am400338n>
237. Schumann, D.A., Wippermann, J., Klemm, D.O., Kramer, F., Koth, D., Kosmehl, H., et al.: Artificial vascular implants from bacterial cellulose: preliminary results of small arterial substitutes. *Cellulose* **16**, 877–885 (2009). <https://doi.org/10.1007/s10570-008-9264-y>
238. Wippermann, J., Schumann, D., Klemm, D., Kosmehl, H., Salehi-Gelani, S., Wahlers, T.: Preliminary results of small arterial substitute performed with a new cylindrical biomaterial composed of bacterial cellulose. *Eur. J. Vasc. Endovasc.* **37**, 592–596 (2009). <https://doi.org/10.1016/j.ejvs.2009.01.007>
239. Hagiwara, Y., Putra, A., Kakugo, A., Furukawa, H., Gong, J.P.: Ligament-like tough double-network hydrogel based on bacterial cellulose. *Cellulose* **17**, 93–101 (2010). <https://doi.org/10.1007/s10570-009-9357-2>
240. Bodin, A., Concaro, S., Britberg, M., Gatenholm, P.: Bacterial cellulose as a potential meniscus implant. *J. Tissue Eng. Regen. M* **1**, 406–408 (2007). <https://doi.org/10.1002/term.51>
241. Jorfi, M., Foster, E.J.: Recent advances in nanocellulose for biomedical applications. *J. Appl. Polym. Sci.* **132**, 41719 (2015). <https://doi.org/10.1002/app.41719>
242. Jung, R., Kim, Y., Kim, H.S., Jin, H.J.: Antimicrobial properties of hydrated cellulose membranes with silver nanoparticles. *J. Biomater. Sci. Polym.* **20**(3), 311–324 (2009). <https://doi.org/10.1163/156856209X412182>
243. Abdel-Hamid, M.S., Saad, M.W., Badawy, G.A., Haroun, H.H.A.: Synthesis and examination of hydroxyapatite nanocomposites based on alginate extracted from *Azotobacter chroococcum* new strain MWGH-ShKB *in vitro*. *Biosci. Res.* **15**(4), 3293–3306 (2018)
244. Yang, J., et al.: In situ deposition of platinum nanoparticles on bacterial cellulose membranes and evaluation of PEM fuel cell performance. *Electrochim. Acta* **54**(26), 6300–6305 (2009). <https://doi.org/10.1016/j.electacta.2009.05.073>
245. Watanabe, K., Eto, Y., Takano, S., Nakamori, S., Shibai, H., Yamanaka, S.: A new bacterial cellulose substrate for mammalian-cell culture - a new bacterial cellulose substrate. *Cytotechnol* **13**, 107–114 (1993). <https://doi.org/10.1007/bf00749937>
246. Favi, P.M., Benson, R.S., Neilsen, N.R., Hammonds, R.L., Bates, C.C., Stephens, C.P., et al.: Cell proliferation, viability, and *in vitro* differentiation of equine mesenchymal stem cells seeded on bacterial cellulose hydrogel scaffolds. *Mat. Sci. Eng. C Mater.* **33**, 1935–1944 (2013). <https://doi.org/10.1016/j.msec.2012.12.100>
247. Kim, J., Cai, Z., Lee, H.S., Choi, G.S., Lee, D.H., Jo, C.: Preparation and characterization of a bacterial cellulose/chitosan composite for potential biomedical application. *J. Polym. Res.* **18**, 739–744 (2011). <https://doi.org/10.1007/s10965-010-9470-9>
248. Muller, D., Silva, J.P., Rambo, C., Barra, G., Dourado, F., Gama, F.: Neuronal cells' behavior on polypyrrole coated bacterial nanocellulose three-dimensional (3D) scaffolds. *J. Biomater. Sci. Polym. E* **24**, 1368–1377 (2013). <https://doi.org/10.1080/09205063.2012.761058>
249. Saska, S., Barud, H.S., Gaspar, A.M.M., Marchetto, R., Ribeiro, S.J.L., Messaddeq, Y.: Bacterial cellulose-hydroxyapatite nanocomposites for bone regeneration. *Int. J. Biomater.* **2011**, 175362 (2011). <https://doi.org/10.1155/2011/175362>

250. Cai, Z., Kim, J.: Bacterial cellulose/poly (ethylene glycol) composite: characterization and first evaluation of biocompatibility. *Cellulose* **17**, 83–91 (2010). <https://doi.org/10.1007/s10570-009-9362-5>
251. Butchosa, N., Brown, C., Larsson, P.T., Berglund, L.A., Bulone, V., Zhou, Q.: Nanocomposites of bacterial cellulose nanofibers and chitin nanocrystals: fabrication, characterization and bactericidal activity. *Green Chem.* **15**(12), 3404–3413 (2013)
252. Soemphol, W., Charee, P., Audtatar, S., Sompech, S., Hongsachart, P., Dasri, T.: Characterization of a bacterial cellulose-silica nanocomposite prepared from agricultural waste products. *Mater. Res. Exp.* **7**(1), 015085 (2020)
253. Yang, M., Ward, J., Choy, K.L.: Nature-Inspired Bacterial Cellulose/Methylglyoxal (BC/MGO) nanocomposite for broad-spectrum antimicrobial wound dressing. *Macromol. Biosci.* **20**(8), 2000070 (2020). <https://doi.org/10.3390/polym11111785>
254. Fadakar Sarkandi, A., Montazer, M., Harifi, T., Mahmoudi Rad, M.: Innovative preparation of bacterial cellulose/silver nanocomposite hydrogels: in situ green synthesis, characterization, and antibacterial properties. *J. Appl. Polym. Sci.* **138**, 49824 (2020). <https://doi.org/10.1002/app.49824>
255. Xing, Q., Zhao, F., Chen, S., McNamara, J., DeCoster, M.A., Lvov, Y.M.: Porous biocompatible three-dimensional scaffolds of cellulose microfiber/gelatin composites for cell culture. *Acta Biomater.* **6**(6), 2132–2139 (2010)
256. Liyaskina, E.V., Revin, V.V., Paramonova, E.N., Revina, N.V., Kolesnikova, S.G.: Bacterial cellulose/alginate nanocomposite for antimicrobial wound dressing. *KnE Energy* **3**(2), 202 (2018). <https://doi.org/10.18502/ken.v3i2.1814>
257. Daels, N., et al.: Potential of a functionalised nanofibre microfiltration membrane as an antibacterial water filter. *Desalination* **275**, 285–290 (2011). <https://doi.org/10.1016/j.desal.2011.03.012>
258. Islam, M.T., Alam, M.M., Patrucco, A., Montarsolo, A., Zoccola, M.: Preparation of nanocellulose: a review. *AATCC. J Res* **1**(5), 17–23 (2014). <https://doi.org/10.1007/s10570-019-02312-4>
259. Aphale, A., Chattopadhyay, A., Mahakalakar, K., Patra, P.: Synthesis and electrochemical analysis of algae cellulose-polypyrrole-graphene nanocomposite for supercapacitor electrode. *J Nanosci. Nanotechnol.* **15**(8), 6225–6229 (2015). <https://doi.org/10.1166/jnn.2015.10280>

Advances in Nanocomposite Materials for Environmental Applications

Polymeric Nanocomposite Membranes for Water Remediation: From Classic Approaches to 3D Printing



Leire Ruiz Rubio, Rubén Tejjido, Antonio Veloso-Fernández, Sonia Pérez-Yáñez, and José Luis Vilas-Vilela

Abstract Limited water resources are one of the most important global issues. Among the possible techniques devoted to water purification, polymeric membranes are of particular interest to the industry due to their versatility and cost-effectiveness. Among them, nanocomposite-based membranes have been successfully developed for many applications, such as seawater desalination, water softening or pollutant removal. There are several methodologies described for the membrane fabrication from more classical approaches such as solvent evaporation or precipitation to more advanced techniques such as electrospinning or 3D printing. In addition, hybrid nanocomposites that include inorganic nanocompounds such as titanium or aluminium oxides or more recently metal-organic frameworks (MOFs) present great applicability due to their capacity for pollutant capture and degradation. This chapter reviews the most recent advances in nanocomposite based membranes, the new materials developed, the fabrication methods and their application for the improvement of water resources and water remediation.

Abbreviations

3DP Liquid binding jetting
6FDA-DAM 4,4'-(Hexafluoroisopropylidene)diphthalic anhydride

L. R. Rubio (✉) · R. Tejjido · A. Veloso-Fernández · J. L. Vilas-Vilela
Macromolecular Chemistry Group (LQM), Department of Physical Chemistry, Faculty of Science and Technology, University of the Basque Country (UPV/EHU), Barrio Sarriena s/n, 48940 Leioa, Spain
e-mail: leire.ruiz@ehu.eus

L. R. Rubio · R. Tejjido · S. Pérez-Yáñez · J. L. Vilas-Vilela
BCMaterials, Basque Center for Materials, Applications and Nanostructures, UPV/EHU Science Park, 48940 Leioa, Spain

S. Pérez-Yáñez
Departamento de Química Inorgánica, Facultad de Farmacia, Universidad del País Vasco UPV/EHU, 01006 Vitoria-Gasteiz, Spain

ABS	Acrylonitrile butadiene styrene
AIBN	2,2-Azobisisobutyronitrile
AM	Advanced manufacturing
BSA	Bovine serum albumin
CLIP	Continuous liquid interface production
CMC	Carboxymethylcellulose
CNC	Cellulose nanocrystals
CNT	Carbon nanotube
DC	Direct current
DMF	N,N-dimethylformamide
DWA	Direct writing assembly
EC	Emerging contaminant
ENM	Electrospun nanofibrous membrane
FDM	Fused deposition modelling
FTIR	Fourier transform infrared
G	α -L-guluronic acid
GO	Graphene oxide
HFP	Hexafluoropropylene
HKUST-1	Hong Kong University of Science and Technology
LOM	Laminated object manufacturing
M	β -D- mannuronic acid
MIL-100	Materials Institute Lavoisier
MMM	Mixed matrix membranes
MMT	Montmorillonite
MOF	Metal-organic framework
MWCNT	Multi-walled carbon nanotube
NIPS	Non-solvent induced phase inversion
NP	Nanoparticles
PA	Polyamide
PA6	Polyamide-6
PAA	Polyacrylic acid
PAN	Polyacrylonitrile
PANI	Polyaniline
PC	Polycarbonate
PCL	Polycaprolactone
PDA	Polydiacetylene
PDMS	Poly(dimethylsiloxane)
PEG	Poly(ethylene glycol)
PEI	Poly(ether imide)
PES	Polyethersulfone
PHB	Poly(hydroxybutyrate)
PLA	Poly(lactic acid)
PLGA	Poly(lactic-co-glycolic acid)
PNC	Polymer nanocomposites
POPs	Persistent organic pollutants

PP	Polypropylene
PPG	Poly(propylene glycol)
PS	Polystyrene
PSF	Polysulfone
PSS	Polystyrene sulfonate
PTFE	Polytetrafluorethylene
PTMSP	Poly(1-trimethylsilyl-1-propyne)
PU	Polyurethane
PVA	Polyvinylalcohol
PVDF	Polyvinylidene fluoride
PVP	Polyvinylpyrrolidone
rGO	Reduced graphene oxide
SLM	Selective laser melting
SLS	Selective laser sintering
SPS	Sulfonated polystyrene
St	Starch
SWNT	Single walled nanotubes
TEOS	Tetraethoxysilane
TFC	Thin film nanocomposite
T_g	Glass transition temperature
TIPS	Thermally induced phase inversion
TTP	Two-photon polymerization
UiO-66	Universitetet i <i>Oslo</i>
UV	Ultraviolet
XPS	X-ray photoelectron spectroscopy
ZIF	Zeolitic imidazole framework

1 Introduction

The ever-increasing human population and the limited clean water resources have arisen the problem for more than two billion people to access to a clean water [1–3]. In addition, the industrialization, agriculture and the modern urbanization have increase the water use and water waste generation until unsustainable levels. Water scarcity and pollution has become a global problem. Indeed, the water quality deterioration and water resource scarcity have induced the incorporation of “clean water and sanitation” as one of the 17 Sustainable Development Goals (SDGs) described in the Agenda 2030 launched in 2015 by the United Nations [4]. In this context, there is an imperious necessity to find out efficient forms to conserve water resources and to remediate water in case it is contaminated.

Table 1 Summary of the main causes of water pollution

Surface water	Ground water
Untreated animal waste	Untreated water waste
Spreading pathogens (bacteria, viruses,...)	Industrial waste stored close to aquifers
Oxygen-depleting waste	Compounds derived from the agriculture (fertilizers and pesticides)
Inorganic plant nutrients	Leaks from storage tanks
Organic chemicals (water soluble and non-soluble)	Leachate form landfills
Water soluble radioactive isotopes	Mining
Hot water release	Leaks from septic tanks
Acid release	

The water pollution could induce several harmful effects not only in an aquatic environment but also for the biodiversity and humans. In this sense, Sadhu et al. [5] reviewed the main causes for water pollution both at surface and ground level, being the main points summarized in Table 1.

Until recently, persistent organic pollutants (POPs) and heavy metals were the main target contaminants when soil or water remediation was carried out [6]. However, these compounds have become less important in aquatic media since many industrialized countries have taken strict measures to reduce their presence. This fact has significantly reduced its presence in wastewater, providing a more pronounced amount of these pollutants mainly on the soils of former industrial areas [7].

The variation in industrial and agricultural activity, as well as the occurrence of new products and drugs, has increased the emergence of a new class of pollutants. These pollutants that were not relevant before or simply did not exist are becoming both an environmental and human health problem. These compounds are known as emerging contaminants (ECs) [8, 9]. There are many compound that could be considered as ECs, for example: artificial sweeteners and food additives, perfluorinated compounds, drinking water and swimming pool disinfection by-products, pesticides, veterinary products, industrial compounds/by-products, sunscreens and UV filters, pharmaceuticals and personal care products, among others [10, 11].

In order to reduce this problem and recover water to be reused again, many water purification methods have been developed. However, not all the classical water purification processes could remove ECs from the wastewater [12]. Regarding this issue, membranes stand out among the possible wastewater purification technologies due to their versatility and low cost. Polymeric membranes are market leaders membranes because of their excellent properties and reasonable price compared with other materials. Nonetheless, this type of membranes has some limitations, such as thermal, mechanical and chemical resistance, which could limit their application. In this context, hybrid nanocomposites represent an excellent alternative to overcome these drawbacks. The combination of the polymer matrix with inorganic nanofillers could improve many of the properties of the material, such as chemical

resistance, thermal and mechanical properties and the purification capability [13]. It is worthy to mention, the advantageous properties of the inorganic nanomaterials used in nanocomposite membranes, which include large surface area, high reactivity, strong sorption, specific interaction with contaminants, etc.

This chapter reviews the most common polymer matrices and nanofillers (inorganic nanoparticles, graphene derivatives, and metal-organic frameworks) used for the development of nanocomposite membranes for water remediation. The main methods used for the fabrication of hybrid inorganic polymer nanocomposite membranes are summarized, from the classic fabrication methods to more innovative methods, such as electrospinning and 3D printing. Finally, the main applications of these hybrid nanocomposite membranes for water remediation are revised.

2 Polymers as a Matrix for Hybrid Nanocomposite Membranes

Many of the properties of a nanocomposite depend on the ones of the polymer matrix. Furthermore, adequate mechanical and chemical properties, such as hydrophobicity or hydrophilicity of the membrane or chemical resistance, biocompatibility or even the capability to absorb some of the contaminants are crucial to design a successful membrane. Considering this, it is mandatory to select the most adequate polymer matrix for each application, such as water remediation, filtration, disinfection, etc. This selection could amplify the properties of the employed nanofillers and vice versa [14, 15].

Both synthetic and biopolymers have been used in nanocomposite-based membranes (Table 2), being among the synthetic polymers the most used polymers: polysulfone (PSF), polyethersulfone (PES), polyacrylonitrile (PAN), polyethylene (PE) polypropylene (PP), polytetrafluoroethylene (PTFE), and polyvinylidene fluoride (PVDF). On the other hand, many examples of membranes based biopolymers have been reported until date, using alginate, chitosan, cellulose derivatives and poly(hydroxybutyrate) (PHB).

Thus, among the biopolymer used for membrane applications, several of them are polysaccharides. Alginate is an anionic polysaccharide obtained from some algae or microorganisms. It presents an unbranched binary structure formed by a copolymer of 1–4 linked β -D-mannuronic acid (M) and α -L-guluronic acid (G) [16]. Carboxymethylcellulose (CMC) is a water soluble derivative of the cellulose often used as a superabsorbent [17]. Chitosan is a cationic biopolymer derived from the deacetylation of chitin. It presents antibacterial properties, which added to other chemical properties made it highly suitable for membrane applications [18]. Other polysaccharides, such as pectin and starch, have also been used in membrane preparation but in a more restricted fashion. On the other hand, poly(hydroxybutyrate) is biocompatible and biodegradable polyester [19]

Table 2 Summary of some of the main polymer matrices and inorganic nanofillers used to fabricate nanocomposite membranes for water remediation

Polymer matrix	Nanofillers	Reference
<i>Synthetic polymers</i>		
PES	TiO ₂	[23–27]
	SiO ₂	[28–32]
	ZnO	[33–35]
	Fe ₃ O ₄	[36–38]
	Ag	[39, 40]
	MOF	[41]
	Multi-walled carbon nanotubes (MWCNTs)	[42–44]
	Graphene oxide (GO)	[45, 46]
PVDF	TiO ₂	[47–50]
	SiO ₂	[51–53]
	ZnO	[54–56]
	Fe ₃ O ₄	[57–59]
	Ag	[60]
	Multi-walled carbon nanotubes (MWCNTs)	[61]
	Graphene oxide (GO)	[48, 59]
	MOF	[62]
<i>Biopolymers</i>		
CMC	Polyvinyl alcohol/ZSM-5 zeolite	[63]
	Fe ₃ O ₄	[64]
Cellulose acetate	TiO ₂	[65, 66]
	SiO ₂	[67–69]
	ZnO	[70]
	Ag with poly(N-vinylpyrrolidone)	[71]
	Multi-walled carbon nanotubes (MWCNTs)	[72–74]
	Graphene oxide (GO)	[75, 76]
	MOF	[77, 78]
Chitosan	TiO ₂	[79, 80]
	ZnO	[80]
	Ag	[80]
	Fe ₃ O ₄	[81]
	Multi-walled carbon nanotubes (MWCNTs)	[82]
	Graphene oxide (GO)	[83]
	MOF	[84]

There have been many synthetic polymers used in the development of membranes. Among all of them, the polyvinylidene fluoride (PVDF) stands out as one of the most used polymers for membrane development both at research and development level and at industrial level. It presents high favourable properties such as thermal stability, hydrophobicity that could be tailored by modifying the polymer, chemical resistance and adequate mechanical strength, being all these properties not present in many of the synthetic polymers [20].

Other synthetic polymers are also used in membranes, for example, polyethylene that is a neutral polymer with good chemical stability and mechanical strength, and polyether sulfone presents high hydrolytic, oxidative and thermal stability and good mechanical strength, being both of them commercially available [21, 22].

3 Hybrid Inorganic-Polymeric Based Membranes for Water Remediation

Most of the methods employed up to date for environmental remediation show disadvantages mainly related to a lack of the properties, which are closely linked to the use of conventional materials, such as polymers. Therefore, during the last years there has emerged an alternative to these materials, which relies on the use of hybrid materials, in order to overcome these drawbacks. In this quest for the ideal material, the development of membranes built up from the incorporation of inorganic nanoparticles into polymeric materials is catching the eye of the researchers. In the following lines, there is a brief description of some of the usually employed inorganic nanoparticles and the latest advances in these nanocomposite membranes with their performance in water remediation technologies. Worthy to mention the burgeoning area of metal-organic frameworks (MOFs) which provides an excellent opportunity because of their potential application and the processing of MOF-polymer composites by means of 3D printing technologies.

3.1 Polymeric Membranes with Titanium Dioxide Nanoparticles

Titanium dioxide (TiO_2) is a special semiconductor that has been widely used for different applications because of its hydrophilicity and photocatalytic properties, as well as its stability, low price and availability. Thus, the use of titania in the design of hybrid inorganic-polymeric membranes has been widely explored, in such a way that the resulting membranes show an improved performance in terms of increased hydrophilicity and reduced fouling [85, 86].

The most explored advantage of using polymeric/TiO₂ composite membranes deals with antifouling properties. Regarding this issue, Vatanpour et al. [87] explored the influence of different types of nanoparticles and sizes on the morphology, performance and fouling control of hybrid membranes.

On the other hand, the treatment of humic acid has been widely studied because of its amount in natural waters which leads to environmental problems. Related to this matter, Teow et al. studied the mechanism of polyvinylidene fluoride-TiO₂ mixed matrix membranes in order to identify the fouling mechanism applied to humic acid treatment. They concluded that the fine and well TiO₂ dispersion on membrane polymeric matrix have a significant effect on the membrane antifouling property [88].

Concerning the photocatalytic activity, Damodar et al. explored the bactericidal ability of composite PVDF-TiO₂ membranes in order to provide new materials for detoxifying water [89]. More recently, Al-Ghafri et al. provided a new hybrid membrane able to simultaneously separate and degrade organic pollutants. More concisely, they incorporated TiO₂ into a highly porous nanofiber made of UV-resistant polyetherimide. The best performing membrane resulted in significant removal rate of *Escherichia coli* (99%) and humic acid (ca. 80%) along with 85% methylene blue degradation during photocatalytic process [90].

As previously mentioned, during the last years, the amount of drugs in water has significantly increased. In this sense, Zhou et al. developed a modified ultrafiltration membrane for the treatment of antibiotics containing sulfanilamide groups in water. They fabricated a PVDF-PVP-TiO₂-dopamine membrane which, compared to the original PVDF membrane, increased the porosity and average pore size of membranes, resulting in improved hydrophilicity. The degradation experiments showed that membrane filtration-photocatalysis system had significant potential for controlling sulfadiazine as water pollutant [91].

3.2 Polymeric Membranes with Aluminium Oxide Nanoparticles

Aluminium oxide (Al₂O₃) nanoparticles are another alternative for developing nanocomposite membranes based on their properties such as availability, stability, hydrophilicity and mechanical strength. The inclusion of this inorganic material provides, compared to the pristine membrane, superior thermal and chemical resistance, better separation performance, and high adaptability to wastewater conditions [92].

Some years ago, Yan et al. studied the antifouling performance in some PVDF-alumina nanocomposite membranes. For this study, they prepared different membranes changing the concentration of Al₂O₃. They observed that the inorganic particles increased the permeability due to the increasing surface hydrophilicity of

the membrane [93]. In another work, Maximous et al. [94] studied PES ultrafiltration membranes modified by the dispersion of alumina nanoparticles. In this case, the membranes with the alumina captured within them revealed lower flux decrease compared to bare polymeric membranes.

In a recent study, Rajeswary et al. studied ultrafiltration mixed matrix membranes based on aluminium oxide nanoparticles and cellulose acetate-polysulfone. They studied the material, prepared by phase inversion, for the removal of dyes and metal ions from wastewater. This membrane showed high water permeability due to porosity and hydrophilicity. Moreover, the addition of Al_2O_3 promoted an increase in rejection percentage for methylene blue and Cu(II) compared to the bare membrane [95].

3.3 Polymeric Membranes with Clay Nanoparticles

Clay nanoparticles are another inorganic fillers widely employed in the preparation of polymer nanocomposites. Among the different types of nanoclays the most common one is montmorillonite, but others such as kaolinite, illite, chlorite, and halloysite are also usual. Nanoclays are built up from stacked metal-silicate layers in which substances of low molecular weight, such as water, can permeate, which in turn promotes its swelling [96]. Based on the degree of penetration into the interlayer, a classification into intercalated or exfoliated nanoclays can be performed. Intercalated nanoclays are those in which the expansion of the layers is less than 20–30 Å, while in the case of exfoliated nanoclays the expansion reaches 80–100 Å or more [97].

The layered structure of silicate is responsible for the hydrophilic properties and good thermal stability at high temperatures. Therefore, the effects of the inclusion of these nanoclays into polymeric membranes have been widely investigated. In general, the common methods used for obtaining composites based on polymeric membranes with nanoclays are in situ polymerization, melt intercalation, and solution dispersion. All these methodologies provide polymer-clay nanocomposite materials, which can be used in applications such as sensing, adsorption of pollutant gases or catalysis [98].

3.4 Polymeric Membranes with Silver Nanoparticles

The interest on the employment of silver nanoparticles into membrane matrix relies on its bactericidal nature. The use of silver nanoparticles is increasing since some researchers have highlighted that silver is non allergic, nontoxic and environmentally friendly [99]. Despite providing a bactericidal membrane, the inclusion of silver nanoparticles into polymeric membranes also affords an improvement in virus removal [100]. Some years ago, the antibacterial mechanism provided by silver

nanoparticles was described in detail as: (i) firstly, reactive oxygen species are indirectly generated, (ii) then, Ag interacts directly with proteins and lipids in the cell wall and, also, proteins in the cytoplasmic membrane, and (iii) finally, there is an interaction with deoxyribonucleic acid [101]. Other researchers suggested that the mechanism implied that silver nanoparticles pass through cell barriers releasing Ag^+ cations, which interact with the thiol groups of enzymes and cell proteins, and in turn, damage bacterial respiration and transport systems across the cell membrane [102].

Thus, the polymeric membranes with silver nanoparticles are gaining attention due to their bactericidal nature and low toxicity towards humans. Their inclusion into membranes provides as well an improvement in the hydrophilicity and selectivity, together with antifouling performance under proper conditions [103].

3.5 Polymeric Membranes with Iron Oxide Nanoparticles

During the last years, Fe_3O_4 has gained great attention in a wide variety of fields. This iron oxide has properties such as good magnetic performance, excellent thermal and chemical stability, and good biocompatibility and biodegradation ability [104]. Based on its magnetic properties, these nanoparticles have been widely studied in drug and gene targeting, cell separation and hyperthermia [105].

Some works have pointed out that the insertion of these Fe_3O_4 nanoparticles into polymeric membranes has provided materials with increased porosity and thermal stability but decreased hydrophilicity. Their inclusion made the nanocomposite membranes able to separate some substances by modifying the magnetic intensity. The magnetic nature of these nanocomposites has been employed in water remediation for arsenic removal [106] and adsorption of heavy metals [107].

Recently, some authors have synthesized $\text{Fe}_3\text{O}_4@ \text{TiO}_2$ particles that have been included into polymeric membranes [108]. Therefore, the magnetic properties of the Fe_3O_4 particles together with the photocatalytic activity of TiO_2 particles can provide a good way towards water remediation technologies.

3.6 Polymeric Membranes with Zinc Oxide Nanoparticles

Another type of inorganic nanoparticles that it is gaining attention in the field of composite membranes are ZnO nanoparticles, since they confer the polymeric membranes antifouling efficiency as well as they supply a photocatalytic self-cleaning capacity [33]. These nanoparticles show, in combination with their physical and chemical properties, antibacterial properties and high catalytic activity [35]. Besides their elevated surface-to-volume ratio, which make them appealing in different fields, their lower cost compared to TiO_2 and Al_2O_3 make these nanoparticles an alternative to more conventionally used ones [109]. Considering their

reactivity, zinc oxide nanoparticles show strong hydrophilicity towards hydrophilic functional groups such as $-\text{OH}$, $-\text{COOH}$, and $-\text{SO}_3\text{H}$ [34].

Therefore, these low-cost ZnO nanoparticles can confer polymeric membranes antimicrobial properties, considerable hydrophilic nature, and photocatalytic activity. All these properties makes them suitable for wastewater treatments.

3.7 Polymeric Membranes with Carbon Nanotubes

Carbon nanotubes (CNTs) are also in the spotlight of the nanocomposite membranes. Their properties such as high surface area, good chemical stability, electrical and mechanical properties, and high hydrophilicity provide the nanocomposite membranes with increased porosity and high antibacterial properties [110]. Although CNTs are efficient sorbents, they have some limitations such as the sorption activation energy and low surface active sites. These restraints can be overcome by modifying the surface functional groups of the CNTs. In the event that the adsorption of polar compounds has to be enabled, CNTs should be functionalized with higher surface acidity (e.g. carboxylic, lactonic or phenolic groups) [111]; while when a higher adsorption of non-polar compounds is desired the unfunctionalized CNTs will be used [112].

Considering the area of water purification technologies CNTs have been employed to remove or decrease pollutant species. Notwithstanding the hydrophobic nature of CNTs, they are good water transporters. Apart from the applications of CNTs as nanofilters and sorbents, they have shown high antimicrobial properties in water purification [113].

3.8 Polymeric Membranes with Metal-organic Frameworks

Metal-organic frameworks (MOFs) are ordered crystalline porous materials, which fulfil several applications mainly due to their elevated surface areas, tuneable pores, as well as intriguing functionalities [114]. Although these innovative materials have lot of applications [115] their processability is, unfortunately, low due mainly to their general insolubility and lack of thermoplasticity [116]. Therefore, integrating MOFs with polymer composites [117] seems to provide an opportunity for significantly enhance processability of the resulting materials, thus, increasing their range of applications. Despite these advanced materials have proven beneficial for different applications, their use in water remediation is in a nascent stage. In the next lines, we provide some of the recent advances in this area.

An emerging type of MOF composite material is that of polysaccharide based MOFs, which are featured as a self-assembled highly ordered functional nanostructure [118]. The presence of polysaccharides provides biocompatibility and flexible nature to the hybrid material, as well as biosafety and bioavailability. In this regard,

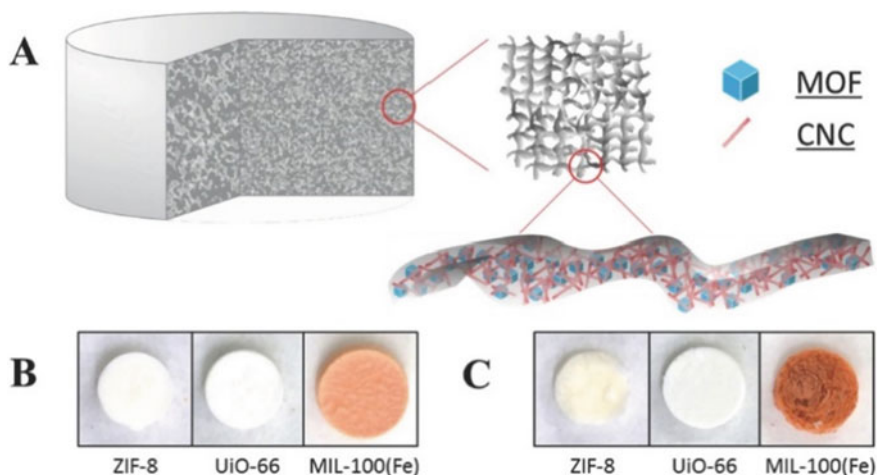


Fig. 1 a Scheme of the hybrid membranes based on cellulose/MOF. b Images CNC-CMC aerogels with different MOFs. c Images of CNC aerogels with different MOFs. Reproduced with permission from Zhu et al. [119]. Copyright (2016) Wiley

Zhu et al. combined different MOFs (ZIF-8, UiO-66 and MIL-100, Fig. 1) with cellulose nanocrystals (CNC) and carboxymethylcellulose (CMC) aerogels obtaining a flexible and porous materials with hierarchical structure [119]. The integration of these MOFs into the cellulose provided a platform able to separate Cr(VI) from water. The resulting MOF-cellulose composites were also tested for eliminating other hazardous materials including benzotriazole and rhodamine B.

Another lightweight cellulose-based foam with ZIF-8 was employed for the removal of pollutants from water [120]. In this sense, composite foam showed high adsorption capacity for fluorescent dyes (24.6 mg g^{-1} for rhodamine B), heavy metal ions (35.6 mg g^{-1} for Cr(VI)) and organic solvents (45.2 g g^{-1} for DMF). On another stage, a biomimetic composite material built up of cellulose acetate integrated with the well-known HKUST-1 was introduced by Rickhoff et al. [121]. In this case, the incorporation of this copper-based metal-organic framework into cellulose acetate enhanced the stability of the MOF in water, thus giving rise to a flexible and tuneable polymeric material. The authors studied the adsorption of the textile dye methylene blue to the cellulose-HKUST-1 composite and they obtained lower overall adsorption compared to cellulose. However, the integration of this MOF into cellulose acetate inhibited the growth of *Escherichia Coli*.

4 Membrane Preparation Methods

Hybrid inorganic polymer membranes or polymer nanocomposites membranes (PNC) are economical and high-performance membranes where it is relatively easy to prepare and disperse many kind of inorganic nanomaterials in the organic matrix.

In this section, the main processing methods to prepare hybrid inorganic/polymer membranes are summarized. First, classical routes are presented, followed by new preparation methods such as electrospinning and 3D printing.

4.1 Classic Preparation Methods of Nanocomposite Membranes

Currently, the traditional methods to fabricate hybrid nanocomposite membranes can be classified into three types: 1) in situ polymerization, 2) sol-gel and 3) physical blending methods. These three processes could be used individually or combined in order to obtain desired membrane structures [122–124].

4.1.1 In Situ Polymerization

In-situ polymerization or infiltration method is a widespread method for the preparing of PNC membranes. The nanofillers are mixed with the monomer in bulk or in solution, and then, is polymerized (Fig. 2). Some functional groups on the surface of nanofillers, such as hydroxyl and carboxyl groups, can create activated species (radicals, cations or anions) by heating, high-energy radiation or plasma, among others. These activated species could initiate the polymerization of the monomer on the surface. After the initiation process, the polymer chain grows and the inorganic fillers could be physically or chemically bonded to polymer matrix or be embedded into it. This method is very useful when the nanocomposite membranes have inorganic exfoliated structures because the monomer penetrates inside the inorganic galleries of the exfoliated structure and, after polymerization, a better dispersion of fillers inside the polymer matrix is obtained. In addition to the classical polymerization methods, some

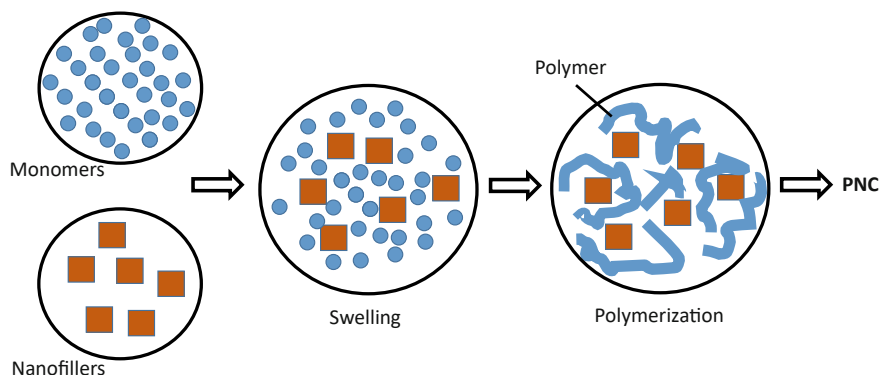


Fig. 2 Steps for fabricating PNC via in situ polymerization method

possible polymerizations used in this technique include ring-opening, atom transfer radical, living anionic/cationic and nitroxide-mediated polymerizations [125–128]. However, this method presents one significant disadvantage since it is still difficult to avoid or reduce the aggregation of inorganic nanofillers in the formed membranes [124, 129–132].

As it has been mentioned, different polymerization methods can be used during this preparation method, for instance polystyrene (PS), usually, polymerizes by forming radicals. This type of polymerization can be performed in bulk, solution or suspension. For this reason, many factors should be taken into account in the selection of the appropriate surfactant. The first one is due to the fact that the surfactant modifies the inorganic filler reactivity so that it can react with the monomer. The second one relies on the fact that surfactant need to have in its structure long alkyl chains or tetrahedral structures in order to make possible to increase the interlayer space [133]. A group from Toyota research institute first utilized the in situ polymerization method in the fabrication of Nylon-6/clay hybrid nanocomposite membranes. Polymerization occurs between the layers and long macromolecular chains are formed. As these chains grow, they detach the disoriented layers of clay and an exfoliated structure is achieved [134].

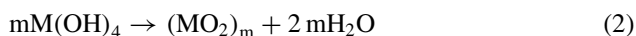
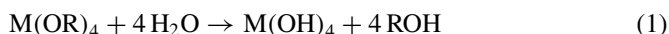
Doucouré et al. [135] prepared some gas permeation membranes by in situ plasma polymerization using mesoporous silica with different fluorinated monomers in each of them. The used monomers were octafluorocyclobutane (C_4F_8), trifluoromethane (CHF_3) and 1,1,1,2-tetrafluoroethane (CF_3-CH_2F) and argon was used as carrier gas. The Fourier transform infrared (FTIR) spectra and X-ray photoelectron spectroscopy (XPS) results showed that the most crosslinked polymers are obtained using CF_3-CH_2F and the least crosslinked using C_4F_8 , that is, the most flexible polymer. Using permeability and selectivity techniques, it was able to see that N_2 molecules permeated in this least crosslinked polymer. On the contrary, using CF_3-CH_2F , it was difficult to permeate small atoms such as He.

In another example, Patel et al. [136, 137] synthesized different hybrid membranes using dispersed silica nanofillers and diacrylate-terminated poly(ethylene glycol) (PEG) or poly(propylene glycol) (PPG) and performing radical polymerization adding 2,2-azobisisobutyronitrile (AIBN) as initiator. After incorporating silica, the elastic modulus of the polymer was improved and the gas permeability was reduced, but the CO_2/H_2 selectivity was almost not affected. In addition, Nunes et al. [138] fabricated PNC for gas separation using also dispersed silica, but in poly(ether imide) (PEI). The polymer nanocomposite membranes were obtained by in situ hydrolysis and condensation of tetraethoxysilane (TEOS). In order to disperse silica, aminosilanes, which have a strong interaction with imide groups of PEI, were incorporated in this inorganic polymer network. By measuring glass transition temperature (T_g) it was observed that aminosilanes increased the T_g , which is directly related with the increase in the rigidity and this rigidity explains the better stability of PNC under pressure. Moreover, with the addition of silica the morphology of the membrane changed from finger-like to a sponge-like structure.

4.1.2 Sol-gel

The sol-gel method is a low temperature synthesis method and has been widely used to prepare PNC since the 1980s. The dissolved inorganic nanofillers and dissolved monomers, oligomers or polymers are mixed in this method. Then, the inorganic precursors hydrolyse and condense into well-dispersed nanofillers in the polymer matrix (Fig. 3). In this method, the mild reaction conditions such as room temperature and pressure, is an advantage. Moreover, in the solution the concentration of the different species is easy to control. Finally, the obtained membranes are homogeneous due to the dispersion of the reagents at molecular or nanometer level [139–143].

Pomogailo [144] reported the main reactions for this process, (1) and (2), which consist in acid hydrolysis followed by condensation for alkoxides $M(OR)_n$, where M could be Si, Ti, Zr, V, Zn, Al, Sn, Ce, Mo or W:



Obviously, the real process is more complex and intermediate products can be formed, such as metal oxoalkoxides. For example, to form the monodisperse TiO_2 powder first, hydrolysis is performed, followed by condensation, to continue with nucleation, and finish with particle growth. Oxo-oligomers, polymers and crosslinked macromolecules are also formed and coexist with the sol [145]. Usually, monomers and oligomers in gels condense and reprecipitate and a subsequent phase transition occurs. Some inorganic fillers are not very sensitive to hydrolysis and if water is added in some days the gelation can happen. Therefore, hydrolysis and condensation

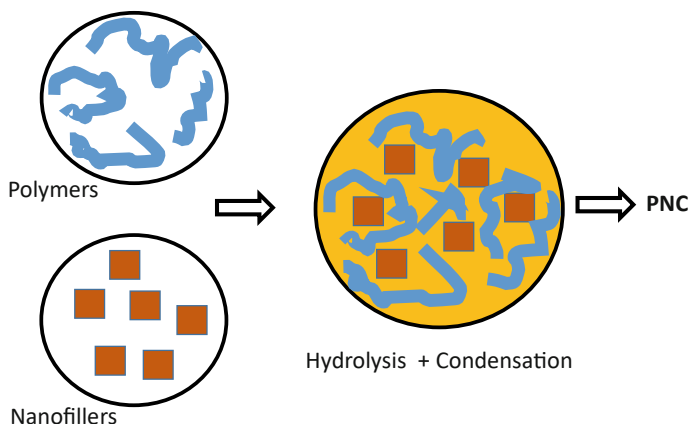


Fig. 3 Steps for fabricating PNC via sol-gel method

proceed without catalysts for non-silicate metal alkoxides, whereas acid or base catalysts are required for silicon alkoxides [146].

Using this method, Iwata et al. [147] synthesized gas permeable PNC to separate N_2 and O_2 made by tetraethoxysilane (TEOS) with 1.3 to 20 wt % fumed silica in polyacrylonitrile (PAN) membranes. Using TEOS, Si–O–Si network is formed. The authors demonstrated a really good separation of the O_2/N_2 mixture by this PNC increasing silica content, that is, obtaining dense Si–O–Si network. In another case, Gomes et al. [148] used sol-gel copolymerization of TEOS with different organoalkoxysilanes to obtain poly(1-trimethylsilyl-1-propyne) (PTMSP)/silica PNC. The type and concentration of organoalkoxysilanes, temperature and time of the synthesis reaction and the gas permeation of the PNC were evaluated. Using 20–40 nm particle size and increasing the silica content in the PNC, butane permeability and butane/methane selectivity increased.

Moreover, using this technique prevents the use of high temperatures in the growth of the MOF, as it can be the following example of a uniform growth of ZIF-8 is achieved at room temperature. For example, Guo et al. [149] used this method to obtain PNC of MOFs at room temperature to remove Rhodamine B dye molecule from wastewater. Using this technique, the macroporous surface of the hollow PVDF fibre was covered with a layer of ZIF-8. First, for 12 h and at room temperature, all the components were immersed in a methanol/water solution. Then, the preparation was immersed in $Zn(NO_3)_2 \cdot 6H_2O$ using an ethanol/water solution at 30 °C for 6 h. In this way, the preparation of ZIF-8 membranes on the inner or outer surface of the hollow PVDF fibres can be controlled as long as the pre-coating of one or the other surface with the Zn precursor or the ZIF-8 seeds is controlled.

4.1.3 Physical Blending

Physical blending or casting method is considered the simplest method for the fabrication of hybrid polymer membranes. In this method, the nanofillers and polymer matrix are directly mixed (Fig. 4). The mixture could be obtained by two main methods: solution blending and melt blending. These two blending methods are going to be studied separately.

Solution Blending

Solution blending or solution casting method is a simple way to fabricate PNC membranes and effective for any inorganic material. Moreover, reagents concentrations in the mixture can be controlled easily [150]. However, the inorganic components can aggregate in membranes [151]. In this method, the inorganic material is dissolved in a solvent and the polymer must be soluble in this solvent. The two compounds can be mixed and dispersed by stirring in different steps: a) dissolving the polymer and adding the nanofillers, b) dissolving the nanofillers and adding the polymer, and c) dissolving both species to finally mix them. The polymer chains interchange with solvent molecule to intercalate into the inorganic structures. Afterwards, the solvent is evaporated by precipitation or under vacuum to form the membrane.

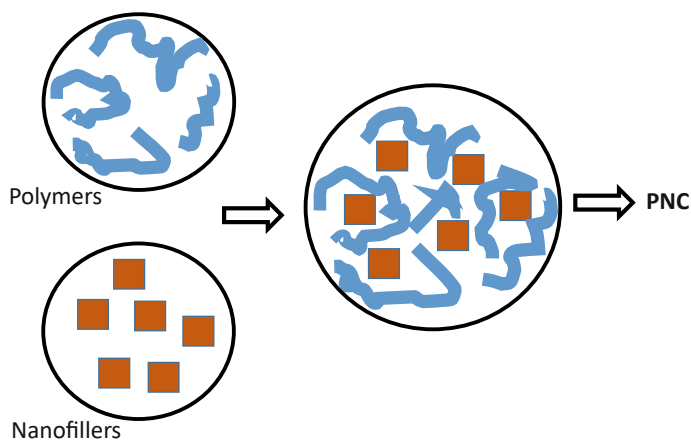


Fig. 4 Steps for fabricating PNC via physical blending method

[152]. However, this technique uses a large amount of solvent, reducing its industrial viability due to health, cost and environmental concerns. Nevertheless, water soluble polymers are available for use with this technique in water solution, this is the case of poly(ethylene glycol) and polyvinyl alcohol. Moreover, by this method, low or non-polar polymers can be used for producing intercalated nanocomposites [130, 132].

Panwar et al. [133] explained that by this method immersing the clay in the appropriate solvent, the solvent molecules penetrate the clay channels and expand. On the other hand, they also mentioned that one of the greatest benefits of this method compared to melt mixing is the decrease in viscosity. This fact allows the polymer molecules to move easily to the surface of the platelets. However, the solvent is also adsorbed on the surface of the clay so the polymer must better adsorb on the surface of the clay and thus displace the solvent. This last reason is the one that shows that this method is more suitable to prepare hybrid membranes from weak polar polymers.

Ragab et al. [153] used polytetrafluoroethylene (PTFE) double layer membrane with ZIF-8 for the removal of micropollutants from water. For the hybrid membrane synthesis, different concentrations of ZIF-8 (20 wt%) were used and PTFE membrane was dipped. In a comparison between the modified and unmodified membranes, it was observed that the modified membranes increase 40% the adsorption capacity of micropollutants, doubling its permeability to water. This permeability is also very interesting since it would reduce energy consumption during the process. Moreover, after three regeneration cycles and using poly(ethylene glycol)-400, it was observed that the membrane maintained 95% of its efficiency.

Low et al. [154] synthesized a new two-dimensional ZIF with leaf-shaped morphology (ZIF-L). This ZIF-L was incorporated into polyethersulfone (PES) membranes to investigate the impact on its ultrafiltration properties. The best results were obtained from the membrane modified with 0.5% ZIF-L, as it increased the water flux to 75% and showed an increase of almost twice the resistance to fouling with bovine serum albumin (BSA). These results obtained in the modified membrane

can be explained as a consequence of obtaining a lower value of zeta potential, an increase in hydrophilicity and a lower surface roughness, which made it difficult for the BSA to bind to the membrane surface.

Melt Blending

Melt blending method also called melt compounding, melt casting or melt intercalation method among other techniques, this is the most widely used, versatile and preferred method for the synthesis of PNCs and also industrially accepted because no solvent is used in the entire process so it is environmentally friendly. Further, it is also one of the best methods due to its compatibility with today's industrial processing equipment, such as injection moulding and extrusion, making this method the most interesting procedure to PNC synthesis with industrial applications [124]. Moreover, it is simpler than in situ polymerization, sol-gel or solution blending methods because it does not require any solvent selection [124, 130, 131, 155] and it is accessible for commercial polymers that are not suitable for these methods. This method involves blending by forces thermoplastic polymers with nanofillers. Different processing techniques can be used: single- or double screw extrusion, internal mixers, and manual mixing. The applied external forces during the processing make easier and more homogeneous the dispersion of the nanofillers into the polymer matrix. Paul et al. [127] studied the dispersion and intercalation of nanofillers in polymers, and they concluded that shear forces due to the extrusion melt processing and mixing conditions due to screw speed, mixing time and temperature are both important parameters. Moreover, the polymer nature, molecular weight and polarity affect to the inter-action between phases, which is really important to obtain a homogeneous filler dispersion [157]. The blended hybrid material anneals at a temperature higher than T_g of the polymer allowing proper mixing of compounds to fabricate membranes. However, this high temperature could be a limitation, because sometimes the high temperatures could decompose the polymers. Van der Hart et al. [131] investigated several exfoliated nylon-6/clay membranes mixtures and compared with pure nylon-6 using solid-state NMR. The membranes were generated by two methods: blending and in situ polymerization. The clays were first treated with a cationic modifier, which ionically adheres to the surface of the clay layers to expand them. The results obtained showed similar results for the modified hybrid membranes using both preparation methods in terms of the spacing, crystallinity and mobility of the non-crystalline nylon 6 segments. By this method, Bhiwankar and Weiss [155] used tetra-octyl and tetra-decyl ammonium salts of sulfonated polystyrene (SPS) as ionic compatibilizers of polymer PS and pristine Na-montmorillonite clay. After mixing all the components, compatibilizers showed good exfoliation and dispersion of the clay, probably due to the separation caused by the quaternary ammonium ion which exchanges with the Na in the channels. Furthermore, it was observed that exfoliation increased with increasing the length of the alkyl chain of the counterion of the compatibilizer. In addition, a greater storage modulus of the membranes with compatibilizer was also observed. In another research, Motamedi and Bagheri [156] based on this preparation method studied the structure and properties of polymer composite membranes using the following components: polypropylene (PP), nanoclay and polyamide-6

(PA6), in order to prepare this PNC: PP/organoclay, PA6/organoclay, mixtures of PP/PA6 and PP/PA6/layered silicate. Among this PNC, the PA6/organoclay PNC presented an exfoliated structure because the clay was concentrated within the PA6 particles, so the viscosity was also increased. On the other hand, in the PP/PA6 PNC the silicate layers were aligned close to the PP/PA6 interface. In this sample, it was also observed that PA6 particles changed in shape and size when the organic clay was introduced. Finally, the obtained samples with two components showed better mechanical properties. In another study, Yoon et al. [157] investigated the effect of the polar comonomers in the PS chains on the intercalation in the organosilicate galleries by melt. The comonomer content of styren/organosilicates membranes and two preparation methods were studied. The polymers used were PS and three different styrenic copolymers with methylvinyl oxazoline and acrylonitrile units. The two synthesis methods were used at the same temperature with and without shearing. In all cases and very quickly, the polymers perfectly intercalate in the organosilicate structure. It seems that the structural stability of polymer/organosilicate hybrids depends on the interactions between both components. The weak interactions between components resulted in an unstable hybrid because polymer chains do not diffuse well into organosilicate layers. Nevertheless, using polar comonomers, the obtained PNC were stable due to the strong interaction between components.

4.2 *Electrospinning*

The electrospinning technique is considered one of the most relevant methods to obtain polymeric (or composite) nanofibers, with diameter between the nanometric and micrometric scale [158]. One of the most important advantages is its versatility, which allows an easy, cheap and tuneable membrane fabrication, with a variable pore size and distribution, aspect ratio, flexibility and stiffness, among others. This technique has been extensively used for membrane fabrication, including thin-film nanocomposites, mixed matrix hybrids, two- or three-layered composites, and metal-organic membranes using different component materials [159]. Membranes obtained by electrospinning have been used in many environmental applications, such as microfiltration [160], ultrafiltration [161], nanofiltration [162], reverse osmosis [163], oil/water separation [164], membrane distillation [165], and bio-separation [166].

The use of electrospun nanofibrous membranes (ENMs) for many different applications makes crucial the control of their structural integrity, stability and functionality under a wide range of operating conditions, including temperature, fluid pressure or pH [159]. These characteristics are intrinsically related both to the different polymeric or composite systems and to the morphology/topology of the electrospun fibers. There are over 200 polymers that have been successfully used for the development of fibres by electrospinning [167], offering a wide range of compositions for membrane fabrication. Furthermore, electrospinning is compatible with different inorganic fillers, such as nanoparticles (NPs) of different nature (SiO_2 , TiO_2 ,

ZnO, carbon nanotubes...) [168, 169]. The wide range of combinations within reach allows the improvement and/or adjustment of membrane mechanical properties to fulfil different operational conditions and, in some cases, provide secondary functionalities as a photocatalytic activity [169]. In comparison with other traditional fabrication methods as non-solvent induced phase inversion (NIPS) and thermally induced phase inversion (TIPS), electrospun membranes present an interconnected open pore structure and an easy tailorable thickness, granting them better porosity and permeability [170].

4.2.1 Instrumentation and Theoretical Background

A great advantage of electrospinning methodology is simplicity of the required equipment (Fig. 5), making it accessible for almost any research laboratory. The main components are: i) a static DC high voltage power supply source between 1–30 kV, ii) a syringe pump that allows the control of the fluid flux between 0.01–2 mL/h, iii) syringes and needles, in general, hypodermic blunt tip type needles are used, with different lengths and inner diameters between 0.3–1 mm, and iv) a metallic collector, usually, an aluminium foil [171]. The grounded collector can be fixed perpendicular to the needle, for obtaining materials with random orientated nanofibers, or in a rotatory system to generate materials with oriented fibers upon a preferred deposition direction.

Electrospinning is based in an electrohydrodynamic process in which a drop of a polymer solution or melt, coming out the needle at a controlled flux rate, is subjected to the electric potential difference generated by the electrical field in which it is

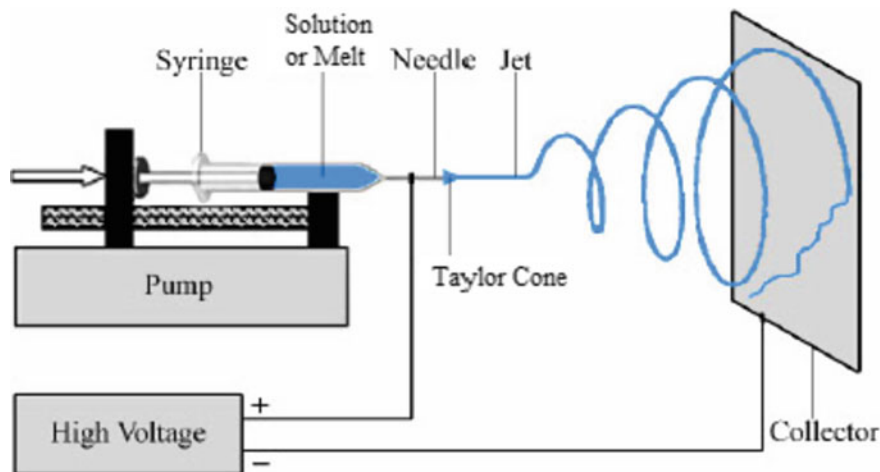


Fig. 5 Basic setup of an electrospinning equipment Reprinted with permission from Ziabari et al. [172]. Creative Commons CC-BY

immersed. The drop adopts a conical or “jet” shape, similar to the tip of a fountain pen, known as the Taylor’s cone. This cone undergoes elongation and flapping processes due to electrostatic tensile forces that exceed the surface tension of the fluid. These forces cause the polymer to be pushed into a connected metal manifold, where the polymeric fibres are deposited to shape the final membrane upon their superposition.

4.2.2 Control Parameters in an Electrospinning Process

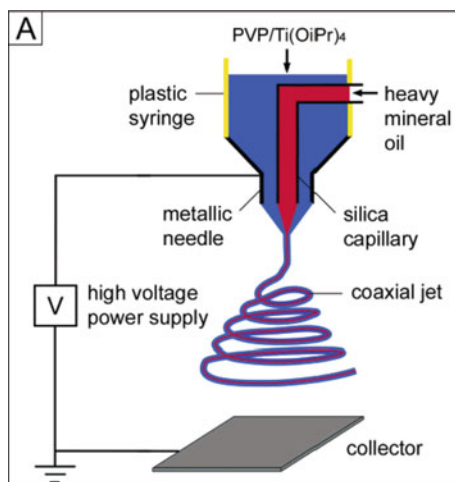
Each electrospinning process is governed by a series of parameters of three different natures: i) electrospinning parameters, namely, voltage applied, distance needle tip-collector, needle inner diameter and fluid flux speed. ii) fluid parameters, including viscosity, conductivity and, in solution electrospinning, type of solvent and polymer concentration. iii) environmental parameters, temperature and humidity [159]. The optimization of these parameters to obtain fibres of a determined diameter and morphology is the real challenge of this methodology. Each of these parameters possesses a discrete critical value for each different electrospun system. Setting up a parameter far from this value will always be translated into fibres of undesired morphologies, pearl beaded structures, discontinuous fibres or the deficient solidification of the fluid prior to its deposition over the collector. The simplicity of typical electrospinning equipment allows the introduction of multiple variants to the process. Examples of these are multi-needle electrospinning and coaxial electrospinning [159]. Multi-needle electrospinning offers a great increase in productivity, as high as 18 m²/h [173], but introduces new control parameters to be considered as the number of needles, the spacing among them or their layout [174]. Formed by two concentric needles, a coaxial spinneret allows the extrusion of two different systems that, when meeting with each other at the tip of the needle, form a core-sheath structure, (Fig. 6) [175]. Coaxial electrospinning introduces the parameter of miscibility between the two extruded fluids to be considered and makes desirable that both fluids have similar dielectric properties to ensure similar electrical pullings [176].

4.2.3 Electrospinning of Composite Membranes

Focusing on composite nanofiber membranes, the two are the more common methods for obtaining membranes by electrospinning. On one hand, the addition of sol-gel precursors, mostly used when obtaining ceramic based composite fibres [177] is commonly used. And on the other hand, the incorporation of nanoscale components to polymeric solutions [178], which is the most used for composite fibres with polymeric matrices. With these two methods, successful composite nanofibers materials have been extensively reported over the past years for water treatment applications.

In Table 3, some examples of nanocomposite membranes and their applications are summarized. It is important to acknowledge that the introduction of the presented or other nanocomponents will always have a final effect of modifying the aspect ratio, the mechanical properties, the water flux [173] and/or the hydrophobicity [179] of

Fig. 6 a Scheme of the setup for coaxial electrospinning. Reproduced with permission from Li et al. [175]. Copyright (2004) American Chemical Society



the material, making the optimization of the proportion to use essential to adjust these properties to their optimal values for each application. Some of the most important parameters to select the correct composite system for each application will be its chemical compatibility, contact angle, pore size, porosity and surface roughness [180].

4.3 3D Printing Technology

Additive manufacturing or 3D printing technology has arisen as highly versatile and promising techniques for many applications. The diversity of areas in which this technology could be applied has impressively arisen, from aerospace [198–200], automotive [201, 202] or construction [203] to biomedicine [204, 205] or food industry [206]. Even if, comparatively, it is still less studied, the amount of membranes fabricated by 3D printing technologies for desalination and water remediation increases year by year.

The need to eliminate new pollutants such as emergent contaminants, in addition to the reduction of membrane fouling and the chemical stability of the membrane are one of the key factors that impulse the investigation on more efficient and profitable membranes. With the improvement and expansion of 3D printing technologies, a manufacturing system capable of regulating the structure of the membrane has been implemented as relatively low cost and solvent free technique for the development of new membranes. Thus, 3D printing capable of producing complex structures of reduced size is presented as one of the techniques with the greatest potential in the coming years in the manufacture of membranes. However, this technique still presents some crucial drawbacks that prevent its massive use. Table 4 summarizes

Table 3 Examples of the application of composite nanofibrous membranes based on polymeric matrixes in water treatment

Nanocomponent	Composite System	Application	Ref.
TiO ₂ NPs	poly(vinylpyrrolidone) (PVP)-co-poly(vinylidene fluoride) (PVDF)/P25-TiO ₂ NPs	Photocatalytic degradation of organic contaminants	[181]
	poly(ethersulfones) (PES)/TiO ₂ NPs/water soluble porphyrins	Fast detect and removal of heavy metals	[182]
Carbon Nanotubes (CNT)	poly(acrylonitrile) (PAN)/CNT/TiO ₂ -NH ₂ NPs	Photocatalytic reduction of metal ions	[183]
	PES/single walled CNT (SWNTs)	Antimicrobial activity membranes	[184]
	poly(vinyl alcohol) (PVA)/bovine seroalbumin (BSA)/SWNTs	Increased enzyme adsorption and ester hydrolysis activity	[185]
SiO ₂ NPs	PVDF/SiO ₂ NPs	Increase of water flux (24L·m ⁻² ·h ⁻¹) in water-oil separations	[186]
	PVDF/Amorphous SiO ₂ NPs	Increased water flux (83L·m ⁻² ·h ⁻¹) in forward osmosis desalination	[187]
	PVDF/SiO ₂ NPs	Membrane distillation processes	[188]
Ag NPs	Cellulose acetate/Ag NPs	Antimicrobial activity	[189]
	poly(lactide-co-glycolide) PLGA/Chitosan (10%)/Graphene-oxide-Ag decorated NPs (GO-Ag NPs)	Antimicrobial activity	[190]
	Policaprolactone (PCL)/TiO ₂ -Ag NPs	Photocatalytic and antibacterial membranes	[191]
ZnO	Nylon 6,6/ZnO core-shell nanofibers	Highly stable and flexible photocatalytic membranes	[192]
	polyurethane (PU)/polydopamine/ZnO nanorods	Anti-fouling membranes with photocatalytic activity	[193]
	PAN/ZnO-Ag heterostructured NPs	Antibacterial activity	[194]
Fe NPs	Poly(acrylic acid) (PAA)/polyvinylalcohol (PVA)/FeCl ₃ (aq)	Complexation of Fe ³⁺ ions and synthesis of new Fe NPs. Dye degradation	[195]
Fe ₂ O ₃ NPs	poly(lactic acid)/γ-Fe ₂ O ₃ NPs	Highly efficient oil adsorption/separation	[196]
Yeast Cells	Core: PVP/Yeast Cells Sheath: PVDF-co-hexafluoropropylene (HFP)/poly(ethylen glycol) (PEG)	Phenol degradation	[197]

Table 4 Comparison of the most significant advantages and disadvantages of the main membrane fabrication techniques

Fabrication technique	Advantage	Disadvantage
Interfacial polymerization	Low cost High simplicity and reproducibility Uniform pore size Good antifouling properties	Low flux High retention
Phase inversion	Stability Film-forming is fast High simplicity and reproducibility High flux	Non uniform pore size Limited materials
Track-etching	Controlled structure Uniform pore size High reproducibility Precise structure	High cost Low simplicity Low flux
Electrospinning	High flux Mass production	Non uniform pore size Medium cost Solvent required Low mechanical stability
3D printing	Cost-effective Complex and controlled structures Flexibility Chemical and mechanical stability	Limited materials Size limitations Post-processing time

the advantages and disadvantages of the most widely used membrane fabrication techniques to date [207, 208].

Commonly, the 3D printing technologies are classified in four groups (Fig. 7), considering the material feed or deposition technique: 1) powder, 2) material extrusion, 3) lamination and 4) photopolymerization. The most common 3D printing method is fused deposition modelling (FDM), a filament extrusion technique which usually prints thermoplastics (PC, ABS, PLA,...) and presents a resolution around 50–200 μm . Among the powder processing based methods, selective laser sintering (SLS), selective laser melting (SLM) or liquid binding jetting in three-dimensional printing (3DP) are used. In these technologies the powder is spread on the building platform and selectively joint forming material layers. The resolution for SLS is close to 80 μm , whereas 3DP presents a resolution of 100–250 μm . In lamination-based 3D printing, laminated object manufacturing (LOM) and selective deposition lamination (SDL) uses polymer sheets as feedstock that are cut and laminated together. Finally, photopolymerization based 3D printing, that is, stereolithography (SLA) uses UV light to initiate the polymerization process, a polymer/resin layer is solidified and holds

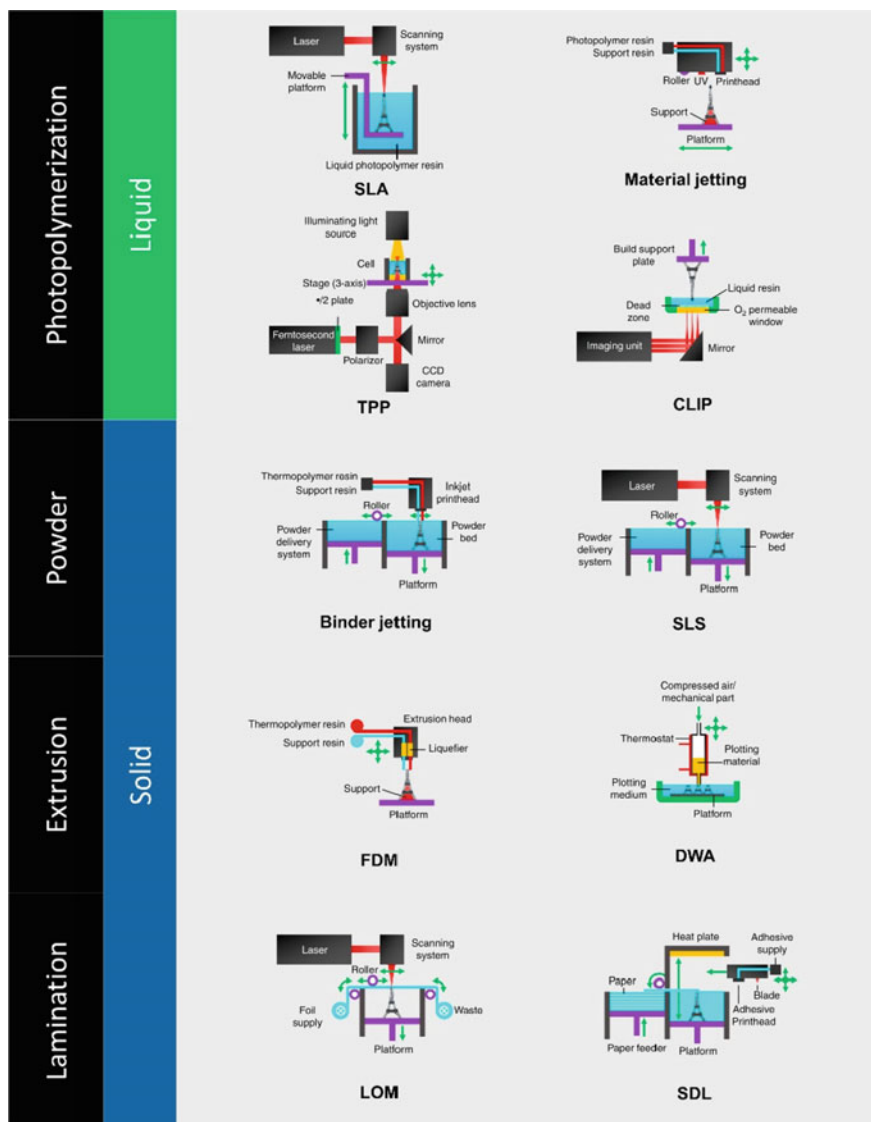


Fig. 7 Summary of the main 3D printing groups and the printing methods. Stereolithography (SLA), two-photon polymerization (TPP), continuous liquid interface production (CLIP), fused deposition modeling (FDM), direct writing assembly (DWA) (DWA could be used both in liquid and in solid), laminated object manufacturing (LOM) and selective deposition. Reproduced from [210], Creative Commons CC-BY license

the subsequent layers. In this case, the resolution is close to 10 μm . In addition to the common 3D printing technologies, in the last years new printing technologies have been improved. Among the novel methods it could be highlight two-photon polymerization (TPP) and continuous liquid interface production (CLIP) due to their high resolution and increased mechanical properties compared to the classical approaches [209]. Besides, all the techniques are widely used in many applications when it comes to the membrane fabrication the photopolymerization has arisen as the more used technique until date [210].

Until now, considering the materials based on 3D printing for water remediation, the present technological limitations, resolution above 10 μm , have been reduced their use to the fabrication of module spacers more than into the fabrication of membranes [211]. However, recently, the great progress of advanced manufacturing (AM) technologies has expanded the potential of 3D printing for the manufacture of membranes and several examples of membranes based in this technology have been reported [212]. For example, Koh and co-workers fabricated an antifouling oil/water cellulose membrane by direct printing. Created cellulose mesh present a pore average smaller than 240 μm and its separation efficiency was around 95% [213].

This evolution also has improved the development of hybrid materials capable to be printed by the different available methodologies. Sangiorgi et al. [214] developed hybrid membranes of polylactic acid (PLA) and TiO_2 by FDM technology.

5 Applications

As it has been described above hybrid polymer nanocomposite membranes offer better mechanical, thermal, electrical and barrier properties than conventional composites. In this section, the most relevant applications of these hybrid materials for water remediation are summarized.

Few years ago, Singh et al. [215] have reviewed different methods used for water purification mainly categorized on the separation techniques like physical adsorption, chemical degradation, and biological treatment. All the methods have some advantages and disadvantages but no single process is able to purify the water adequately. For this reason, combination of processes is recommended to ensure adequate quality of water. In the following lines, different examples of hybrid membranes used for water purifications are described.

5.1 Desalination

Due to the demand for drinking water and the increasing scarcity of it in the world, it has been necessary to promote the development of technologies to use alternative water resources, such as seawater. Desalination is the most effective process to overcome the increasing global water demand situation, consisting on removing salt ions

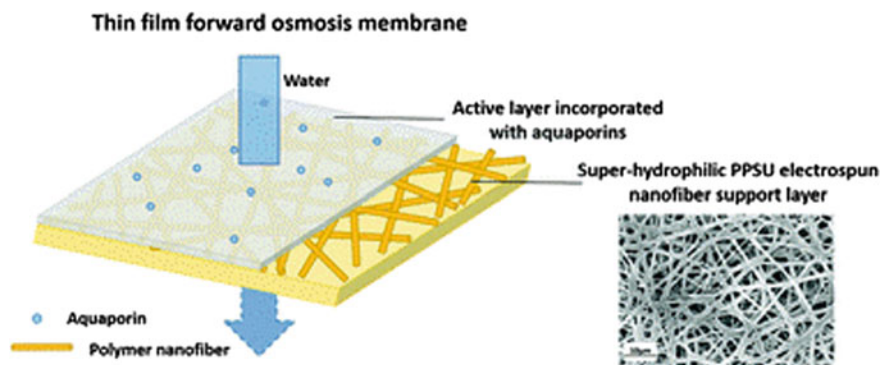


Fig. 8 Scheme of the osmosis membrane developed by electrospinning of polyphenylsulfone. Reproduced from Wang et al. [220]. Published by The Royal Society of Chemistry (2019). Creative Commons 3.0

from sodium chloride and others through energy-efficient processes [216]. Although desalination methods already exist, the scientific community has increased interest in membrane desalination techniques because it has multiple advantages compared to other processes such as low energy consumption, low pressure requirement and high salt rejection [217, 218]. Salt water from ocean and brackish water represents the majority of the world's water resources and can be used as a source of drinking water using desalination processes. Recent studies show that PNC allows to obtain higher performance than commercial osmosis membranes, and also allows greater water flow and have high rejection of salts with antifouling activity [35].

During the past two decades, electrospun membranes have been successfully used in desalination tasks as the supportive layer on the three layered structured of thin film composite (TFC) membranes, attracting worldwide attention [219]. As reported by Wang et al. [220], a superhydrophilic membrane can be prepared of polyphenylsulfone and chitosan by means of a low pressure plasma treatment modifying its contact angle from 137 to 0° (Fig. 8). They suggest that these membranes may be used as support in forward osmosis processes at higher water fluxes ($14 \text{ L} \cdot \text{m}^{-2} \cdot \text{h}^{-1}$) than commercially available aquaporin membranes ($>10 \text{ L} \cdot \text{m}^{-2} \cdot \text{h}^{-1}$).

Emadzadeh et al. [221] prepared hybrid membranes of polysulfone (PSF)/TiO₂ incorporating different amounts of nanoparticles (from zero to 1 wt%). After characterizing the membranes, it was observed that both the hydrophilicity and the porosity of the substrate increased when the nanoparticles were added. Furthermore, finger-shaped structures were obtained by increasing the percentage of TiO₂, resulting in a higher water permeability. Since the final desalination application required the fabrication of membrane films, a thin layer of polyamide was formed on the surface of PSF/TiO₂ by interfacial polymerization between phenylene-1,3-diamine and benzene-1,3,5-tricarbonyl trichloride. The film membrane prepared with 0.5 wt% TiO₂ showed the best results: high water permeability and low reverse solute flux. Compared to the control membrane, the water flux of this hybrid membrane was

improved to 86.93%. This variation depends on the orientation of the membrane and the concentration of draw solution. On the other hand, by increasing the concentration of TiO_2 from 0.75 to 1 wt%, the salt rejection of the film membrane decreased from 95.4 to 72.8% due to a lower degree of crosslinking of polyamide layer. The authors concluded that the performance of the film membrane could be improved during desalination as long as an adequate amount of TiO_2 nanoparticles were added in PSF.

In another work, Zirehpour et al. [222] used hydrophilic MOF in a cellulosic membrane in order to improve the performance in desalination. The incorporated MOF allowed the control of the porosity, interconnectivity of pores and hydrophilicity of the obtained membrane. The modification improved the antifouling properties of the membrane compared to unmodified membranes and the nanoparticles produced better water transport across the membrane and better selectivity due to their hydrophilic character.

Another PNC film for water desalination was synthesized by Kebria et al. [218] with ultrathin zeolitic imidazolate (ZIF-8)/chitosan layer coated on the surface of the polyvinylidene fluoride (PVDF). The ZIF-8/chitosan layer did not improve the hydrophobicity of the film membrane. However, the liquid inlet pressure of the water increased, being this increase attributed to the porosity increase and decrease of average pore size of the surface, which allowed water vapour to penetrate through the membrane. The permeate water flux also increased up to 350% using NaCl 3.5 wt% solution compared to the unmodified PVDF membrane. The ZIF-8/chitosan modified membrane showed NaCl rejection higher than 99.5%. The antifouling properties of the membranes were also investigated using a seawater feed solution. The chitosan layered membrane gave better antifouling properties reducing the flux to 16% and a flux recovery of 90% compared to the obtained values for unmodified PVDF membrane (41 and 67%).

5.2 Membrane Distillation

Membrane distillation is a thermally induced process with the objective to effectively separate salty from pure water that permeates. For membrane distillation processes is important that the membranes are hydrophobic in nature. Although electrospinning methodology focuses the attention of many research groups for the obtaining of such commercial devices, no commercial membranes are currently available for this purpose. Amongst these many researching efforts it is worth to mention the advances for the achievement of superhydrophobic membranes by introducing different NPs, as in the work reported by Khraisheh et al. [223] where styrene-butadiene-styrene electrospun membranes with functionalized and activated Al_2O_3 nanoparticles were obtained. The wettability of these systems was investigated with respect to the liquid entrance pressure (16.87 psi) and the contact angle ($141^\circ \pm 2^\circ$) and their efficiency tested against salt (NaCl) containing waters as well as heavy metals (Cr(VI), Cd, Pb) in various concentrations and in single and multicomponent systems.

Another good example of membranes adequate for this technology has been reported by Tijging et al. [224]. In their research nanofiber membranes based on polyvinylidene fluoride and hexafluoropropylene copolymer (PcH) were fabricated with different concentrations (1–5 wt%) of carbon nanotubes incorporated as nanofillers. The pore size of the as prepared membranes was comparable with a commercial flat-sheet PVDF membrane but with an increased porosity (>85%). The superhydrophobicity was assessed through higher contact angle values of 158.5°, with increased water fluxes (24–29.5 L m⁻² h⁻¹) higher than those of commercial PVDF membranes (18–18.5 L m⁻² h⁻¹) and a salt rejection >99.99%.

5.3 Ultrafiltration/Nanofiltration

Ultrafiltration and nanofiltration process are membrane separation processes, similar to microfiltration with the only difference of their pore size. While microfiltration membranes are able to separate bacteria and suspended solids, ultrafiltration membranes, with pore sizes around 0.01 micron, can separate viruses, often requiring an increased pressure. Nanofiltration membranes with pore size on the nanometer scale (≈ 0.001 micron) are also able to separate individual ions as chloride or sodium. The limiting pore size of typically electrospun membranes render them useless in filtration processes under the microfiltration scale [2]. Nonetheless, they have been successfully employed as supportive layer for membrane separation composite films as reported by K. Yoon et al. [225] in their three layer composite membrane with a hydrophilic water permeable chitosan layer, an electrospun nanofibrous support of polyacrylonitrile and a microfibrillar substrate of polyethylene terephthalate. For the electrospun component, the polyacrylonitrile solution (4–12 wt% in DMF) was directly deposited over the polyethylene terephthalate non-woven substrate set on a rotating metal drum with 9 cm diameter and a speed of 300 rpm. The rest of electrospinning parameters were set as follows: i) applied voltage 14–20 kV, ii) needle inner diameter 0.7 mm, iii) distance tip-collector 10–18 cm (depending on the polymer concentration), and the process was kept going until ≈ 1.2 mg·cm⁻² of polyacrylonitrile were deposited. Tang et al. [227] also reported in 2009 a similar multilayered system consisting on UV-cured polyvinyl alcohol hydrogel barrier layer, an electrospun nanofibrous PVA mid-layer scaffold and polyethylene terephthalate (PET) as non-woven substrate.

5.4 Oil/Water Separation

Oil/Water separation consists on the separation by different physicochemical processes (coagulation-flocculation, air flotation, ultrasonic separation...) of the oily contaminants present in wastewater currents. Nanofiber sorbent/filter materials, with high specific surface areas and high sorption capacity for oily substances have lately

focused an increasing interest for this endeavour. Due to the dependence of oil/water separation processes in interfacial phenomena, electrospun nanofibrous composite materials must also have a high wettability to be good candidates. As reported by Tang et al. [227] superhydrophobic/superoleophilic membranes for oil-removing operations have been prepared by introducing a multiscale roughness, to a high-strength poly(m-phenylene iso-phthalamide) nanofibers membrane reinforced with multi-walled carbon nanotubes. Electrospinning control parameters for obtaining these reinforced fibres were a feed rate of $0.15 \text{ mL}\cdot\text{h}^{-1}$, 30 kV of applied voltage and with fibres deposition over a rotating aluminium foil at 200 rpm at a 15 cm distance from the needle tip. Superficial roughness was achieved by the introduction of an in situ polymerized polybenzoxazine layer containing SiO_2 NPs. Their high efficiency oil separation membranes achieved a superhydrophobic water contact angle of 161° and a superoleophilic oil contact angle of 3° . Another recent example of a hybrid electrospun membrane for gravity assisted oil/water separation process is the system reported by Arslan et al. [228]. In their work, cellulose acetate nanofibers were modified with perfluoroalkoxysilanes (Fig. 9). The modification of the outer surface of the fibres with these groups granted them a superhydrophobic characteristic ($\approx 155^\circ$ contact angle). The fibres were obtained from an alkoxy silane modified cellulose acetate solution, at 1:2 mixture of dimethylacetamide:acetone. The mixture was electrospun with a 15 kV applied voltage, 15 cm distance between tip and grounded collector and $0.5 \text{ mL}\cdot\text{h}^{-1}$ flow rate. The followed method allowed them to reduce the diameter of the fibres from $850 \pm 230 \text{ nm}$ for pristine cellulose acetate nanofibers to $290 \pm 110 \text{ nm}$ for the alkoxy silane cellulose fibres, thus greatly increasing the specific active surface of the membranes.

3D printing technology has been also employed for the development of oil/water separation membranes. Lv et al. [229] reported the fabrication of poly(dimethylsiloxane) (PDMS) nanosilica nanocomposites for oil/water separation. In their study, Sylgard184 (vinyl-ended PDMS) with a methylhydrosiloxane with Pt catalyst (as curing agent) were mixed with different amounts of silica NPs. It is important to notice that but-3-yn-1-ol were added to the mixture in order to delay the polymerization, allowing the printability of the mixture. The ink was plotted by a syringe extrusion printing a mesh structure of 0.8 mm thick. Once printed the structure was cured at 120°C for 1 h. Membranes, with a pore size of 0.37 μm , present excellent separation efficiency at all pH range and around 90% for water and kerosene, bean oil, corn oil and silicone oil mixtures (1:1 v/v).

5.5 Ion Exchange

Ion exchange membranes are nanofibrous materials containing functional groups able to generate electrically charged active sites where target species contained on the feed water may remain attached by an ionic exchange process [230]. The employing of these materials in wastewater decontamination processes is still in its infancy with only a few groups investigating their potential. Nevertheless, in the past few years

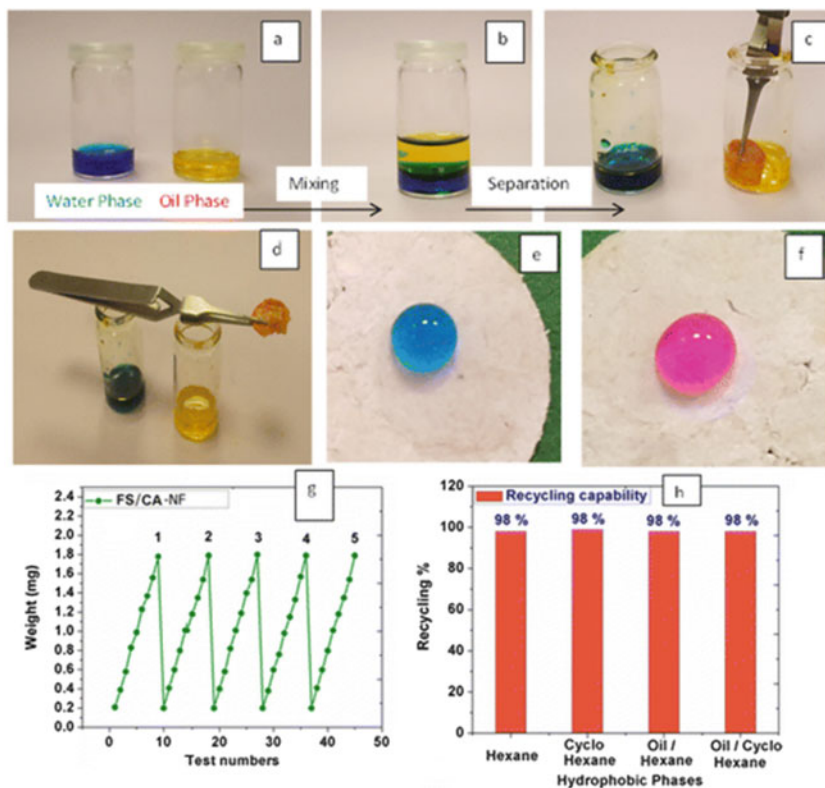


Fig. 9 Summary of the separation process carried out in this study: **a** separated oil and water phases, **b** mixture of oil/water, **c** phase separation. **d** Demonstration that perfluorinated fibre do not absorb methylene blue. **e** and **f** Wettability of the fabricated fibres. **g** Study of the effectiveness of the separation for different cycles and **h** separation effectiveness for different mixtures. Reproduced from Arslan et al. [220]. Published by American Chemical Society (2016)

some interesting works have been reported. Tran et al. [231] investigated the ion-exchange capability of a composite system of zeolite NPs embedded in a cellulose acetate matrix. Their electrospinning process involved the mixing of the precursor solutions, Linde type A zeolites (10 wt%) and cellulose acetate (5 wt%), using a 1:1 mixture of acetone/chloroform as solvent, to be electrospun as an unique solution with 15 kV of applied voltage and 10 cm between the spinneret and the collector. This process allowed them to produce nanofibrous membranes with fibre diameter ranging from 50 to 200 nm (139 ± 54 nm). These membranes presented a good ion exchange activity between Na^+ and $\text{Cu}^{2+}/\text{Pb}^{2+}$ cations. Thus, these cheap fibre materials could be used in heavy metals removal operations.

5.6 Adsorption of Pollutants

Another useful approach for water treatment is based on the absorption of pollutant that cannot be filtrated from the wastewater. The adsorption effectiveness of these materials is greatly increased with high surface area and porosity, which can be easily provided by electrospinning, not only via optimization of the process parameters for the desired morphologies but also modifying surface properties and textures [160]. Among the examples of electrospun composite membranes for adsorption of pollutants those reported by Zhao et al. [232] can be found. Their work was based on coating with activated carbon, electrospun polyacrylonitrile (PAN) nanofibers for adsorption of herbicide-like substances from water streams, reaching a removal efficiency of 83% after five cycles. Similarly, Habiba et al. [234] prepared chitosan/polyvinyl alcohol/zeolite nanofibrous composite membranes. The blended electrospun solution during this work was composed on a 7 wt.% chitosan solution in concentrated acetic acid with an aqueous PVA solution in various weight ratios. The electrospun parameters, 10 kV of voltage applied and 0.2 mL h⁻¹ flow rate, allowed them a nanofibrous membrane with a high capability for adsorption of ionic metallic species as Cr⁶⁺, Fe³⁺ and Ni²⁺. This material could be reusable during heavy metals recovering and recycling operations.

5.6.1 Removal of Heavy Metal Ions

The contamination of water with heavy and radioactive metals is due to anthropogenic sources or geological reasons. These contaminants are very dangerous because they can be responsible of some human diseases if they enter by food chain in the human body [234]. A hybrid membrane is a good option to remove these contaminants from water. It is well known that the removal efficiency of inorganic contaminants is affected by membrane pore size [235], surface electrical charge [236], and surface area [237]. The interaction between adsorbent and adsorbed molecules is usually physical and chemical. In nature, the physical adsorption is reversible, but not chemical adsorption. Lim and Aris [238] have summarized low cost adsorbents for heavy metals from wastewater reporting different techniques such as adsorption, coagulation, flocculation, ion exchange, and membrane filtration. They also reported that there some factors which affect adsorption capacity such as pH, contact times, temperature and initial concentration of adsorbate [238].

Ghaemi et al. [36] modified Fe₃O₄ nanoparticles surface and using different concentration, they mixed with polyethersulfone (PES) to form hybrid membranes. A significantly better Cu²⁺ removal was observed for hybrid membranes with Fe₃O₄ compared to the bare PES. The best result was obtained with 0.1 wt% nanoparticle concentration removing 92% Cu²⁺, while using unmodified PES membrane only 25% of Cu²⁺ was removed. The inclusion of the nanoparticles increased the flow of water. This is due to changes in the mean pore radius, porosity, and hydrophilicity

of membranes. Furthermore, the Cu^{2+} rejection capacity was improved due to the nanoparticles due to its hydrophilicity.

One year later, Ghaemi [239] employed the same polymer and alumina (Al_2O_3) nanoparticles for adsorption of Cu^{2+} but in order to improve its removal efficiency. Polymer and nanoparticles were mixed by phase inversion method, and the same characterization methods and also reusability test were used. In this case, the best results were obtained using less than 1 wt% of alumina to adsorb 59% Cu^{2+} . Increasing nanoparticles concentration no effect on Cu^{2+} adsorption was observed. It was concluded that the addition of these nanoparticles increases the membrane porosity and hydrophilicity. Moreover, the removal efficiency was the same after four cycles of filtration.

In another work, Kim et al. [240] through a sol-gel system fabricated multifunctional composite polyurethane (PU) membranes using titanium dioxide (TiO_2) nanoparticles and fly ash. For this, varying the composition of nanoparticles in blend solution, different PU nanofiber mats were prepared. The good incorporation of both nanoparticles into PU mat was confirmed by different techniques, and adsorption of Hg, Pb, and methylene blue dye, antibacterial activity, and water flux of the modified PU was evaluated and the results showed a good improvement in all the parameters. The authors conclude that fly ash gives good adsorptive property and TiO_2 nanoparticles good photocatalytic/hydrophilic property to the modified PUs.

Radioactive waste generates also important metallic pollutants. These compounds are discharged during operations and reprocess of nuclear fuel from nuclear plants [241]. Some authors have reported a good adsorption of radioactive metal ions by magnetic PNCs [242, 243]. Wen et al. [244] synthesized a membrane for the adsorption in different conditions of Sr(II) from radiation contaminated water by using multifunctional flexible sodium titanate nanobelt. The results showed that a good absorption coefficient was obtained (107 mL g^{-1}) and the cation permanently trapped inside PNC. Other PNC examples used for removal of radioactive metals are potassium zinc hexacyanoferrate loaded PNC for Cs^+ [245], ammonium molybdophosphate-polyacrylonitrile for removal of Co^{2+} , Sr^{2+} , and Cs^+ [246]. In all of them, the adsorption is due to physical interactions and ion exchange.

5.6.2 Removal of Dyes

The ability to modify the surface and catalytic properties of PNC make them of great interest in removing one of the most serious contaminants from water, dyes. Given the large number of dyes used by various sectors and taking into account that most of them are released into water, these molecules are becoming a serious problem [247–249]. Therefore, techniques such as adsorption, coagulation, filtration, photo-, catalytic degradation and biochemistry for the removal of these molecules from water are really important. To apply these techniques, hybrid membranes are gaining scientific interest due to the good results that are obtained. The hybrid structures of the PNC have as advantages for the elimination of dyes: high adsorption capacity, catalytic and magnetic properties. This is because the addition of nanoparticles to the

membranes increases their functionality. In addition, the hybrid membranes show a porous structure of adequate size for adsorbents such as dyes, a large contact surface, high mechanical resistance, easy regeneration, biocompatibility, profitability, optimal energy consumption and high selectivity, making them very suitable for dye removal [211, 250–252]. Usually, the main mechanism of the PNC to eliminate the colorants is based on the electrostatic interaction between both components [253].

Among the different nanoparticles used in hybrid membrane, metal-organic framework (MOF) structures have created great expectations given the properties of these porous solids and the possibility of incorporating them into membranes. However, the preparation of these hybrid membranes is not trivial and it is difficult to obtain their homogeneous dispersion in the membranes. Zhang et al. [254] synthesized a hybrid membrane to remove the methylene blue dye from water by nanofiltration process. To do this, the authors proposed the dispersion of MOF in polystyrene sulfonate (PSS) polymer and its growth in situ on a polyacrylonitrile (PAN) surface. In this way, a very good dispersion of the MOFs was obtained due to the new coordination bonds between the metals, the organic ligand and the polymer. Due to this reason, the hybrid membrane has also better compatibility, stability, selectivity, hydrophilicity and adsorption. The particle size of the MOF structure depends on the initial concentrations of precursor used. In the specific case of zeolitic imidazolate framework (ZIF-8), if the concentration of the precursor $\text{Zn}(\text{NO}_3)_2$ increased from 0.05 to 0.5 mol L⁻¹, the particle size decreased from 150 to 50 nm, so membrane surface roughness and density increase, and few cracks were observed. The ZIF-8/PSS membranes showed high flux and high rejection values for methylene blue and methyl orange (with a smaller molecular size) dyes.

Maroofi and Mahmoodi [255] prepared ZIF-8/polyvinylpyrrolidone (PVP)/PES PNC for malachite green dye removal. For this, ZIF-8 was mixed in different proportions (1, 2 and 3%) with PVP/PES and the mixture was processed as films. Using scanning electron microscopy, it was observed that ZIF-8 particles inside the membrane pores and on the surface were homogeneously dispersed, thus increasing the roughness of the surface and improving the hydrophobicity of the membrane. In addition, good efficiency and stability were obtained in the dye removal process using different test pressures.

In another work, Wan et al. [256] manufactured membranes using graphene oxide (GO) nanoparticles dispersed in water in combination with polydiacetylene (PDA)/modified PSS (PSPSH) membrane. The obtained membranes were used for the adsorption and removal of organic dyes in water. Good adsorption times of the dyes were obtained for maximum adsorption efficiency at pH 7, specifically for the methylene blue dye it was obtained at 58 min. It was also observed that the adsorption process is endothermic since raising temperature, the efficiency of hybrid membranes increased. In addition, a higher adsorption capacity was obtained than most GO-based nanocomposites.

In another study, Safarpour et al. [257] developed a modified PES nanofiltration membrane with partially reduced graphene oxide (rGO)/TiO₂. The rGO/TiO₂ content was studied on the morphology and performance of the membranes, obtaining in all

of them, in comparison with the unmodified PES membranes, better water permeability and resistance to incrustations. Furthermore, with an rGO/TiO₂ content of 0.15 wt%, the water flow was doubled with respect to the unmodified membrane. On the other hand, the 0.1 wt% rGO/TiO₂ membrane had the best antifouling property as it showed the highest resistance to fouling using bovine serum albumin (BSA). The rGO/TiO₂/PES membranes showed better removal performance of three organic dyes (Reactive Green 19, Direct Yellow 12, and Reactive Blue 21) compared to unmodified ones. rGO/TiO₂/PES membranes presented the best water permeation rate, antifouling ability, and dye rejection compared to TiO₂/PES and GO/PES membranes.

Nevertheless, in order to be able to apply the PNC membranes correctly in the removal of dyes, it is important to take into account their biocompatibility. To do so, biopolymer-based PNC systems are being studied. For this reason, compounds based on chitosan, alginate and starch have been used as polymeric compounds. Among these three compounds, chitosan, which is a multifunctional polysaccharide-based biopolymer with primary and secondary hydroxyl and reactive amino groups, appears to be an optimal candidate as a support material that involves adsorption processes. However, to be able to use them the most important thing is to stabilize them chemically [258]. For this, modifications of the polysaccharide are carried out that also lead to an improvement in the adsorption, mechanical and physical properties of chitosan. Vakili et al. [258] investigated chitosan and its derivatives for their application in dyes removal from water. In this field, modifying chitosan allows to increase the adsorption of dyes. Among the derivatives of chitosan through chemical and physical modifications, crosslinking, grafting and impregnation of its structure are used. Knowing the affinity between these modified compounds and dyes, much more interesting studies can be carried out in this field.

In another study, Olad and Azhar [259] synthesized a hybrid membrane based on starch (St)/montmorillonite (MMT)/polyaniline (PANI) by oxidative polymerization of aniline in St/MMT dispersion. The PNC characterization results showed that there was intercalation of MMT in the St matrix and PANI grew on the surface of the St/MMT. The St/MMT/PANI hybrid was used for the adsorption of a reactive navy blue dye and in a very short time, total removal of the dye was observed. This effect is because the removal was due to two physical processes between PNC and dye: adsorption and electrostatic attraction. All the results obtained showed that the St/MMT/PANI membrane was highly effective in removing reactive dyes in water.

3D printing is a breakthrough technology, which has received huge attention as a powerful tool to develop complex geometries for a variety of materials. Regarding this area, 3D printed MOF-polymer composites provide an excellent opportunity towards their implementation in manufacturing technologies. In this sense, Figuerola et al. incorporated the ZIF-67 on intricate 3D printed devices, which were obtained by stereolithography using PVDF as binder. The effect of this cobalt based MOF/polymer mixed-matrix coating for the peroxymonosulfate activation to enhance the degradation of organic dyes in water was evaluated. The authors showed that 3D printed hybrid material showed excellent reusability and reproducibility after using rhodamine B (5 mg L⁻¹) after 30 min of degradation time and observing 97–98%

degradation of the dye after 10 cycles [260]. Worthy to mention that dye degradation was analysed both in stirred-tank and flow-through column formats. The effect of the shape was studied in 3D printed adsorbents in the work of Pei et al. [261]. More concisely, square, hexagon and circles of 3D printed HKUST-1 were analysed in the adsorption of methylene blue, methyl violet, malachite green, rhodamine B and auramine O. The hexagonally shaped material showed the best adsorptive performance towards the analysed organic dyes. Moreover, these printed hybrids could be regenerated, up to 7 times, by immersing them in HCl solution for one hour.

Other 3D printed hybrid MOF-polymer composites has been also used for methylene blue (MB) removal. Wang and co-workers printed acrylonitrile butadiene styrene (ABS) structures by FDM printer, and them, Cu-BTC (also known as HKUST-1) was formed in the structures by in situ growth method (Fig. 10) [262]. The membranes were tested with two MB solutions, 5 and 10 mg/mL. This system presents a good absorption of methylene blue, being amount of MB (mg) absorbed per gram of MOF of 33.9 mg/g (for 5 mg/mL solution) and 64.3 mg/g (for 10 mg/mL). On the other hand, the removal efficiencies, after only 10 min, were 93.3 and 98.3% for 5 and 10 mg/L solutions, respectively. It is important to notice the regeneration capacity of this membrane. The membrane was evaluated in 5 consecutive cycles, removing the

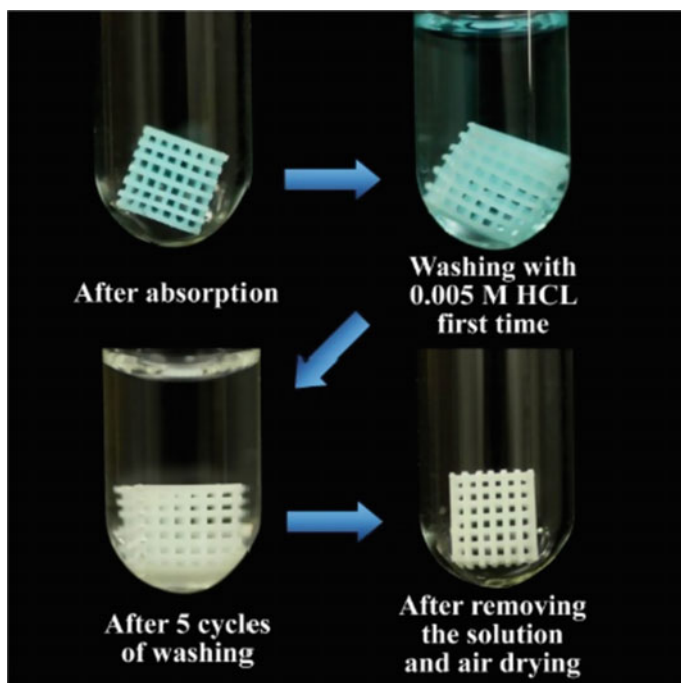


Fig. 10 Images of the absorption and recovery process of the ABS/HKUST-1 hybrid membrane. Reprinted with permission from Wang et al. [262]. Creative Commons CC-BY

MB after each cycle with methanol, and the efficiency only decreased to 58% (for 10 mg/L) and 68% (for 5 mg/L).

5.6.3 Removal of Drugs

Basu and Balakrishnan [143] prepared hybrid polymeric membranes of ZIF-8 for the removal of paracetamol analgesic using this method. A hydrophobic, microporous nanomaterial (ZIF-8) was investigated as filler in thin film nanocomposite (TFC) membrane. Nano sized (0.4–0.5 μm) ZIF-8 was synthesized and two different types of TFC membranes with ZIF-8 were prepared, (i) ZIF-8 in polyamide (PA) with polysulfone (PSF) support, and (ii) in-situ growth of ZIF-8 on PSF support with PA top layer. The addition of ZIF-8 created defects on TFC membranes and also improves the separation of paracetamol and MgSO_4 solutions.

5.7 Other Applications and Secondary Functionalities

The wide range of combinations between matrices and fillers that can be employed in the preparation of electrospun nanofibrous materials allow the introduction of secondary functionalities in membranes aimed at one of the already mentioned applications. Such functionalities could include specific substances detection, antimicrobial activity or photocatalytic degradation activity [263]. As an example, in the work reported by Blanco et al. [264] a nanofibrous material, based on polyamide 6 modified with titanium dioxide nanoparticles, was prepared. During this work, a multijet electrospinning setup was used making the process easily scalable to higher dimensions. The electrospun blend was a 12 wt.% polyamide 6 solution with a 25 wt.% of TiO_2 NPs, stabilized with SDS as surfactant in a 1:1 ratio with the NPs, altogether in a 2:1 acetic acid:formic acid mixture as solvent. The applied voltage was 75 kV consequently higher as it is required by multijet processes and with a separation distance of 17 cm between the needles and the rotating (6.7 rpm) grounded collector. This setup and conditions allowed the obtaining a membrane composed of 110–260 nm diameter nanofibers and an aerial weight of 4.3 $\text{g}\cdot\text{m}^{-2}$ which presented a photocatalytic activity being able to degrade 80% of the Remazol Black B dye employed as model pollutant after 240 min and irradiation with UV-light (365 nm).

6 Conclusions and Future Work

As it has been described in this chapter, very important advances have been done in the water remediation field due to the development of the hybrid polymer/inorganic nanofillers membranes. These membranes join the best properties of the inorganic nanofillers, such as the photocatalytic degradation capacity, bactericide properties or

absorption capacity, to the improved mechanical, absorption and chemical properties of the polymer matrices, being these combination a key factor to the wide range of application described for these hybrid membranes. However, their evaluation for large-scale applications is still quite limited, being most of the studied restricted to laboratory scale, and only some of them to pilot scale. This lack on full-scale test have limited their commercial applications. In this context, the increasing interest of the European Union for reducing and remediating water pollution, arisen from the 2030 Agenda for Sustainable Development in which “Clean Water and Salination” is one of the 17 Sustainable Development Goals, could boost the progress on the research of a wide number of hybrid membranes and their industrial transfer.

Acknowledgements Authors acknowledge UPV/EHU and Fundación Vital funding within the project “PROYECTOS DE INVESTIGACIÓN UPV/EHU-FUNDACIÓN VITAL FUNDAZIOA 2020” (VITAL20/26).

References

1. United Nations Development Programme: Human development report 2019: beyond income, beyond averages, beyond today. United Nations Development Programme (2019)
2. World Health Organization: Drinking-water (2018). <https://www.who.int/news-room/fact-sheets/detail/drinking-water>. Accessed 18 Jul 2020
3. Rijsberman, F.R.: Water scarcity: fact or fiction? *Agric. Water Manag.* **80**(1–3), 5–22 (2006). <https://doi.org/10.1016/j.agwat.2005.07.001>
4. United Nations: The sustainable development goals report 2016. United Nations (2016)
5. Sadhu, S.D., Garg, M., Kumar, A.: Major environmental issues and new materials. In: *New Polymer Nanocomposites for Environmental Remediation*, pp 77–97. Elsevier Inc. (2018)
6. Jones, K.C., de Voogt, P.: Persistent organic pollutants (POPs): state of the science. *Environ. Pollut.* **100**(1–3), 209–221 (1999). [https://doi.org/10.1016/S0269-7491\(99\)00098-6](https://doi.org/10.1016/S0269-7491(99)00098-6)
7. Varjani, S.J., Chaithanya, S.M.: *Treatment Technologies for Emerging Organic Contaminants Removal from Wastewater*, pp. 91–115 (2018)
8. Deblonde, T., Cossu-Leguille, C., Hartemann, P.: Emerging pollutants in wastewater: a review of the literature. *Int. J. Hygiene Environ. Health* **214**(6), 442–448 (2011). <https://doi.org/10.1016/j.ijheh.2011.08.002>
9. Rivera-Utrilla, J., Sánchez-Polo, M., Ferro-García, M.Á., Prados-Joya, G., Ocampo-Pérez, R.: Pharmaceuticals as emerging contaminants and their removal from water. a review. *Chemosphere* **93**(7), 1268–1287 (2013). <https://doi.org/10.1016/j.chemosphere.2013.07.059>
10. Abdelbasir, S.M., Shalan, A.E.: An overview of nanomaterials for industrial wastewater treatment. *Korean J. Chem. Eng.* **36**(8), 1209–1225 (2019). <https://doi.org/10.1007/s11814-019-0306-y>
11. Abu Elella, M.H., Goda, E.S., Abdallah, H.M., et al.: Innovative bactericidal adsorbents containing modified xanthan gum/montmorillonite nanocomposites for wastewater treatment. *Int. J. Biol. Macromol.* **167**, 1113–1125 (2021)
12. Batool, M., Nazar, M.F., Awan, A., et al.: Bismuth-based heterojunction nanocomposites for photocatalysis and heavy metal detection applications. *Nano-struct. Nano-objects* **27**, 100762 (2021)
13. Bassyouni, M., Abdel-Aziz, M.H., Zoromba, M.S., Abdel-Hamid, S.M.S., Drioli, E.: A review of polymeric nanocomposite membranes for water purification. *J. Ind. Eng. Chem.* **73**, 19–46 (2019). <https://doi.org/10.1016/j.jiec.2019.01.045>

14. Ucanus, G., Ercan, M., Uzunoglu, D., Culha, M.: Methods for Preparation of Nanocomposites in Environmental Remediation. Elsevier Inc. (2018)
15. Jhaveri, J.H., Murthy, Z.V.P.: Nanocomposite membranes. *Desalin. Water Treat.* **57**(55), 26803–26819 (2016). <https://doi.org/10.1080/19443994.2015.1120687>
16. Aburabie, J.H., Puspasari, T., Peinemann, K.-V.: Alginate-based membranes: paving the way for green organic solvent nanofiltration. *J. Membr. Sci.* **596**, 117615 (2020). <https://doi.org/10.1016/j.memsci.2019.117615>
17. Chang, C., Duan, B., Cai, J., Zhang, L.: Superabsorbent hydrogels based on cellulose for smart swelling and controllable delivery. *Eur. Polym. J.* **46**(1), 92–100 (2010). <https://doi.org/10.1016/j.eurpolymj.2009.04.033>
18. Cui, L., et al.: Preparation and characterization of chitosan membranes. *RSC Adv.* **8**(50), 28433–28439 (2018). <https://doi.org/10.1039/C8RA05526B>
19. Villegas, M., Castro Vidaurre, E.F., Gottifredi, J.C.: Sorption and pervaporation of methanol/water mixtures with poly(3-hydroxybutyrate) membranes. *Chem. Eng. Res. Des.* **94**, 254–265 (2015). <https://doi.org/10.1016/j.cherd.2014.07.030>
20. Kang, G.-D., Cao, Y.-M.: Application and modification of poly(vinylidene fluoride) (PVDF) membranes – a review. *J. Membr. Sci.* **463**, 145–165 (2014). <https://doi.org/10.1016/j.memsci.2014.03.055>
21. Tan, R.: A review on porous polymeric membrane preparation. Part II: production techniques with polyethylene, polydimethylsiloxane, polypropylene, polyimide, and polytetrafluoroethylene. *Polymers* **11**(8), 1310 (2019). <https://doi.org/10.3390/polym11081310>
22. Zhao, C., Xue, J., Ran, F., Sun, S.: Modification of polyethersulfone membranes - a review of methods. *Prog. Mater. Sci.* **58**(1), 76–150 (2013). <https://doi.org/10.1016/j.pmatsci.2012.07.002>
23. Razmjou, A., Mansouri, J., Chen, V.: The effects of mechanical and chemical modification of TiO₂ nanoparticles on the surface chemistry, structure and fouling performance of PES ultrafiltration membranes. *J. Membr. Sci.* **378**(1–2), 73–84 (2011). <https://doi.org/10.1016/j.memsci.2010.10.019>
24. Rahimpour, A., Madaeni, S.S., Taheri, A.H., Mansourpanah, Y.: Coupling TiO₂ nanoparticles with UV irradiation for modification of polyethersulfone ultrafiltration membranes. *J. Membr. Sci.* **313**(1–2), 158–169 (2008). <https://doi.org/10.1016/j.memsci.2007.12.075>
25. Wu, G., Gan, S., Cui, L., Xu, Y.: Preparation and characterization of PES/TiO₂ composite membranes. *Appl. Surf. Sci.* **254**(21), 7080–7086 (2008). <https://doi.org/10.1016/j.apsusc.2008.05.221>
26. Ehsani, M., Aroujalian, A.: Fabrication of electrospun polyethersulfone/titanium dioxide (PES/TiO₂) composite nanofibers membrane and its application for photocatalytic degradation of phenol in aqueous solution. *Polym. Adv. Technol.* **31**(4), 772–785 (2020). <https://doi.org/10.1002/pat.4813>
27. Parvizian, F., Ansari, F., Bandehali, S.: Oleic acid-functionalized TiO₂ nanoparticles for fabrication of PES-based nanofiltration membranes. *Chem. Eng. Res. Des.* **156**, 433–441 (2020). <https://doi.org/10.1016/j.cherd.2020.02.019>
28. Shen, J., Ruan, H., Wu, L., Gao, C.: Preparation and characterization of PES–SiO₂ organic–inorganic composite ultrafiltration membrane for raw water pretreatment. *Chem. Eng. J.* **168**(3), 1272–1278 (2011). <https://doi.org/10.1016/j.cej.2011.02.039>
29. Yu, H., Zhang, X., Zhang, Y., Liu, J., Zhang, H.: Development of a hydrophilic PES ultrafiltration membrane containing SiO₂@N-Halamine nanoparticles with both organic antifouling and antibacterial properties. *Desalination* **326**, 69–76 (2013). <https://doi.org/10.1016/j.desal.2013.07.018>
30. Kusworo, T.D., Qudratun, U.D.P.: Performance evaluation of double stage process using nano hybrid PES/SiO₂-PES membrane and PES/ZnO-PES membranes for oily waste water treatment to clean water. *J. Environ. Chem. Eng.* **5**(6), 6077–6086 (2017). <https://doi.org/10.1016/j.jece.2017.11.044>

31. Lin, J., Ye, W., Zhong, K., Shen, J., Jullok, N., Sotto, A., Van der Bruggen, B.: Enhancement of polyethersulfone (PES) membrane doped by monodisperse Stöber silica for water treatment. *Chem. Eng. Process. Process Intensif.* **107**, 194–205 (2016). <https://doi.org/10.1016/j.cep.2015.03.011>
32. Ghandashtani, M.B., Zokaei Ashtiani, F., Karimi, M., Fouladitajar, A.: A novel approach to fabricate high performance nano-SiO₂ embedded PES membranes for microfiltration of oil-in-water emulsion. *Appl. Surf. Sci.* **349**, 393–402 (2015). <https://doi.org/10.1016/j.apsusc.2015.05.037>
33. Shen, L., et al.: Polymeric membranes incorporated with ZnO nanoparticles for membrane fouling mitigation: a brief review. *Front. Chem.* **8**, 224 (2020). <https://doi.org/10.3389/fchem.2020.00224>
34. Shen, L., et al.: Preparation and characterization of ZnO/polyethersulfone (PES) hybrid membranes. *Desalination* **293**, 21–29 (2012). <https://doi.org/10.1016/j.desal.2012.02.019>
35. Balta, S., Sotto, A., Luis, P., Benea, L., Van der Bruggen, B., Kim, J.: A new outlook on membrane enhancement with nanoparticles: the alternative of ZnO. *J. Membr. Sci.* **389**, 155–161 (2012). <https://doi.org/10.1016/j.memsci.2011.10.025>
36. Ghaemi, N., et al.: Polyethersulfone membrane enhanced with iron oxide nanoparticles for copper removal from water: application of new functionalized Fe₃O₄ nanoparticles. *Chem. Eng. J.* **263**, 101–112 (2015). <https://doi.org/10.1016/j.cej.2014.10.103>
37. Bavasso, I., et al.: Effect of pretreatment of nanocomposite PES-Fe₃O₄ separator on microbial fuel cells performance. *Polym. Eng. Sci.* **60**(2), 371–379 (2020). <https://doi.org/10.1002/pen.25292>
38. Ouda, M., Ibrahim, Y., Banat, F., Hasan, S.W.: Oily wastewater treatment via phase-inverted polyethersulfone-maghemite (PES/γ-Fe₂O₃) composite membranes. *J. Water Process. Eng.* **37**, 101545 (2020). <https://doi.org/10.1016/j.jwpe.2020.101545>
39. Mukherjee, M., Bandyopadhyaya, R.: Silver nanoparticle impregnated polyethersulfone ultra-filtration membrane: optimization of degree of grafting of acrylic acid for biofouling prevention and improved water permeability. *J. Environ. Chem. Eng.* **8**(2), 103711 (2020). <https://doi.org/10.1016/j.jece.2020.103711>
40. Lee, S.Y., Kim, H.J., Patel, R., Im, S.J., Kim, J.H., Min, B.R.: Silver nanoparticles immobilized on thin film composite polyamide membrane: characterization, nanofiltration, antifouling properties. *Polym. Adv. Technol.* **18**(7), 562–568 (2007). <https://doi.org/10.1002/pat.918>
41. Mohammadnezhad, F., Feyzi, M., Zinadini, S.: A novel Ce-MOF/PES mixed matrix membrane; synthesis, characterization and antifouling evaluation. *J. Ind. Eng. Chem.* **71**, 99–111 (2019). <https://doi.org/10.1016/j.jiec.2018.09.032>
42. Vatanpour, V., Madaeni, S.S., Moradian, R., Zinadini, S., Astinchap, B.: Fabrication and characterization of novel antifouling nanofiltration membrane prepared from oxidized multiwalled carbon nanotube/polyethersulfone nanocomposite. *J. Membr. Sci.* **375**(1–2), 284–294 (2011). <https://doi.org/10.1016/j.memsci.2011.03.055>
43. Son, M., Choi, H., Liu, L., Celik, E., Park, H., Choi, H.: Efficacy of carbon nanotube positioning in the polyethersulfone support layer on the performance of thin-film composite membrane for desalination. *Chem. Eng. J.* **266**, 376–384 (2015). <https://doi.org/10.1016/j.cej.2014.12.108>
44. Nikita, K., Karkare, P., Ray, D., Aswal, V.K., Singh, P.S., Murthy, C.N.: Understanding the morphology of MWCNT/PES mixed-matrix membranes using SANS: interpretation and rejection performance. *Appl. Water Sci.* **9**(7), 154 (2019). <https://doi.org/10.1007/s13201-019-1035-4>
45. Marjani, A., Nakhjiri, A.T., Adimi, M., Jirandehi, H.F., Shirazian, S.: Effect of graphene oxide on modifying polyethersulfone membrane performance and its application in wastewater treatment. *Sci. Rep.* **10**(1), 2049 (2020). <https://doi.org/10.1038/s41598-020-58472-y>
46. Zinadini, S., Zinatizadeh, A.A., Rahimi, M., Vatanpour, V., Zangeneh, H.: Preparation of a novel antifouling mixed matrix PES membrane by embedding graphene oxide nanoplates. *J. Memb. Sci.* **453**, 292–301 (2014). <https://doi.org/10.1016/j.memsci.2013.10.070>

47. Razmjou, A., Arifin, E., Dong, G., Mansouri, J., Chen, V.: Superhydrophobic modification of TiO₂ nanocomposite PVDF membranes for applications in membrane distillation. *J. Membr. Sci.* **415–416**, 850–863 (2012). <https://doi.org/10.1016/j.memsci.2012.06.004>
48. Safarpour, M., Khataee, A., Vatanpour, V.: Preparation of a novel poly(vinylidene fluoride) (PVDF) ultrafiltration membrane modified with reduced graphene oxide/titanium dioxide (TiO₂) nanocomposite with enhanced hydrophilicity and antifouling properties. *Ind. Eng. Chem. Res.* **53**(34), 13370–13382 (2014). <https://doi.org/10.1021/ie502407g>
49. Zhang, F., Zhang, W., Yu, Y., Deng, B., Li, J., Jin, J.: Sol-gel preparation of PAA-g-PVDF/TiO₂ nanocomposite hollow fiber membranes with extremely high water flux and improved antifouling property. *J. Membr. Sci.* **432**, 25–32 (2013). <https://doi.org/10.1016/j.memsci.2012.12.041>
50. Bae, T.-H., Tak, T.-M.: Effect of TiO₂ nanoparticles on fouling mitigation of ultrafiltration membranes for activated sludge filtration. *J. Membr. Sci.* **249**(1–2), 1–8 (2005). <https://doi.org/10.1016/j.memsci.2004.09.008>
51. Yu, S., Zuo, X., Bao, R., Xu, X., Wang, J., Xu, J.: Effect of SiO₂ nanoparticle addition on the characteristics of a new organic–inorganic hybrid membrane. *Polymer (Guildf)* **50**(2), 553–559 (2009). <https://doi.org/10.1016/j.polymer.2008.11.012>
52. Liao, C., Zhao, J., Yu, P., Tong, H., Luo, Y.: Synthesis and characterization of low content of different SiO₂ materials composite poly (vinylidene fluoride) ultrafiltration membranes. *Desalination* **285**, 117–122 (2012). <https://doi.org/10.1016/j.desal.2011.09.042>
53. Li, Li., et al.: Preparation and electrochemical characterization of organic–inorganic hybrid poly(vinylidene fluoride)-SiO₂ cation-exchange membranes by the sol-gel method using 3-mercaptopropyl-triethoxysilane. *Materials* **12**(19), 3265 (2019). <https://doi.org/10.3390/ma12193265>
54. Roshani, R., Ardeshtiri, F., Peyravi, M., Jahanshahi, M.: Highly permeable PVDF membrane with PS/ZnO nanocomposite incorporated for distillation process. *RSC Adv.* **8**(42), 23499–23515 (2018). <https://doi.org/10.1039/C8RA02908C>
55. Radwan, A.B., Mohamed, A.M.A., Abdullah, A.M., Al-Maadeed, M.A.: Corrosion protection of electrospon PVDF–ZnO superhydrophobic coating. *Surf. Coat. Technol.* **289**, 136–143 (2016). <https://doi.org/10.1016/j.surfcoat.2015.12.087>
56. Ayyaru, S., Dinh, T.T.L., Ahn, Y.-H.: Enhanced antifouling performance of PVDF ultrafiltration membrane by blending zinc oxide with support of graphene oxide nanoparticle. *Chemosphere* **241**, 125068 (2020). <https://doi.org/10.1016/j.chemosphere.2019.125068>
57. Rahimi, Z., Zinatizadeh, A.A., Zinadini, S.: Milk processing wastewater treatment in a bioreactor followed by an antifouling O-carboxymethyl chitosan modified Fe₃O₄/PVDF ultrafiltration membrane. *J. Ind. Eng. Chem.* **38**, 103–112 (2016). <https://doi.org/10.1016/j.jiec.2016.04.011>
58. Huang, Z.-Q., Zheng, F., Zhang, Z., Xu, H.-T., Zhou, K.-M.: The performance of the PVDF-Fe₃O₄ ultrafiltration membrane and the effect of a parallel magnetic field used during the membrane formation. *Desalination* **292**(15), 64–72 (2012). <https://doi.org/10.1016/j.desal.2012.02.010>
59. Huang, Y., Xiao, C., Huang, Q., Liu, H., Hao, J., Song, L.: Magnetic field induced orderly arrangement of Fe₃O₄/GO composite particles for preparation of Fe₃O₄/GO/PVDF membrane. *J. Membr. Sci.* **548**, 184–193 (2018). <https://doi.org/10.1016/j.memsci.2017.11.027>
60. Park, S.Y., Chung, J.W., Chae, Y.K., Kwak, S.-Y.: Amphiphilic thiol functional linker mediated sustainable anti-biofouling ultrafiltration nanocomposite comprising a silver nanoparticles and poly(vinylidene fluoride) membrane. *ACS Appl. Mater. Interfaces* **5**(21), 10705–10714 (2013). <https://doi.org/10.1021/am402855v>
61. Ma, J., et al.: Role of oxygen-containing groups on MWCNTs in enhanced separation and permeability performance for PVDF hybrid ultrafiltration membranes. *Desalination* **320**, 1–9 (2013). <https://doi.org/10.1016/j.desal.2013.04.012>
62. Sun, H., et al.: PEG@ZIF-8/PVDF nanocomposite membrane for efficient pervaporation desulfurization via a layer-by-layer technology. *ACS Appl. Mater. Interfaces* **12**(18), 20664–20671 (2020). <https://doi.org/10.1021/acsami.0c02513>

63. Sabarish, R., Unnikrishnan, G.: Polyvinyl alcohol/carboxymethyl cellulose/ZSM-5 zeolite biocomposite membranes for dye adsorption applications. *Carbohydr. Polym.* **199**, 129–140 (2018). <https://doi.org/10.1016/j.carbpol.2018.06.123>
64. Gong, G., Zhang, F., Cheng, Z., Zhou, L.: Facile fabrication of magnetic carboxymethyl starch/poly(vinyl alcohol) composite gel for methylene blue removal. *Int. J. Biol. Macromol.* **81**, 205–211 (2015). <https://doi.org/10.1016/j.ijbiomac.2015.07.061>
65. Abedini, R., Mousavi, S.M., Aminzadeh, R.: A novel cellulose acetate (CA) membrane using TiO₂ nanoparticles: preparation, characterization and permeation study. *Desalination* **277**(1–3), 40–45 (2011). <https://doi.org/10.1016/j.desal.2011.03.089>
66. Gebru, K.A., Das, C.: Removal of chromium (VI) ions from aqueous solutions using amine-impregnated TiO₂ nanoparticles modified cellulose acetate membranes. *Chemosphere* **191**, 673–684 (2018). <https://doi.org/10.1016/j.chemosphere.2017.10.107>
67. Liu, T., An, Q.-F., Wang, X.-S., Zhao, Q., Zhu, B.-K., Gao, C.-J.: Preparation and properties of PEC nanocomposite membranes with carboxymethyl cellulose and modified silica. *Carbohydr. Polym.* **106**, 403–409 (2014). <https://doi.org/10.1016/j.carbpol.2014.01.040>
68. Rakhshan, N., Pakizeh, M.: The effect of functionalized SiO₂ nanoparticles on the morphology and triazines separation properties of cellulose acetate membranes. *J. Ind. Eng. Chem.* **34**, 51–60 (2016). <https://doi.org/10.1016/j.jiec.2015.10.031>
69. Cai, Y., Hou, X., Wang, W., Liu, M., Zhang, J., Qiao, H., Huang, F., Wei, Q.: Effects of SiO₂ nanoparticles on structure and property of form-stable phase change materials made of cellulose acetate phase inversion membrane absorbed with capric-myristic-stearic acid ternary eutectic mixture. *Thermochim. Acta* **653**, 49–58 (2017). <https://doi.org/10.1016/j.tca.2017.03.027>
70. Anitha, S., Brabu, B., Thiruvadigal, D.J., Gopalakrishnan, C., Natarajan, T.S.: Optical, bactericidal and water repellent properties of electrospun nano-composite membranes of cellulose acetate and ZnO. *Carbohydr. Polym.* **87**(2), 1065–1072 (2012). <https://doi.org/10.1016/j.carbpol.2011.08.030>
71. Kendouli, S., et al.: Modification of cellulose acetate nanofibers with PVP/Ag addition. *Mater. Sci. Semicond. Process.* **28**, 13–19 (2014). <https://doi.org/10.1016/j.mssp.2014.03.010>
72. El Badawi, N., Ramadan, A.R., Esawi, A.M.K., El-Morsi, M.: Novel carbon nanotube–cellulose acetate nanocomposite membranes for water filtration applications. *Desalination* **344**, 79–85 (2014). <https://doi.org/10.1016/j.desal.2014.03.005>
73. Moghadassi, A.R., Rajabi, Z., Hosseini, S.M., Mohammadi, M.: Fabrication and modification of cellulose acetate based mixed matrix membrane: gas separation and physical properties. *J. Ind. Eng. Chem.* **20**(3), 1050–1060 (2014). <https://doi.org/10.1016/j.jiec.2013.06.042>
74. Ahmad, A.L., Jawad, Z.A., Low, S.C., Zein, S.H.S.: A cellulose acetate/multi-walled carbon nanotube mixed matrix membrane for CO₂/N₂ separation. *J. Membr. Sci.* **451**, 55–66 (2014). <https://doi.org/10.1016/j.memsci.2013.09.043>
75. Ghaseminezhad, S.M., Barikani, M., Salehirad, M.: Development of graphene oxide–cellulose acetate nanocomposite reverse osmosis membrane for seawater desalination. *Compos. Part B Eng.* **161**, 320–327 (2019). <https://doi.org/10.1016/j.compositesb.2018.10.079>
76. Shi, Y., Li, C., He, D., Shen, L., Bao, N.: Preparation of graphene oxide–cellulose acetate nanocomposite membrane for high-flux desalination. *J. Mater. Sci.* **52**(22), 13296–13306 (2017). <https://doi.org/10.1007/s10853-017-1403-0>
77. Su, Z., Zhang, M., Lu, Z., Song, S., Zhao, Y., Hao, Y.: Functionalization of cellulose fiber by in situ growth of zeolitic imidazolate framework-8 (ZIF-8) nanocrystals for preparing a cellulose-based air filter with gas adsorption ability. *Cellulose* **25**(3), 1997–2008 (2018). <https://doi.org/10.1007/s10570-018-1696-4>
78. Zhao, X., et al.: Porous cellulose nanofiber stringed HKUST-1 polyhedron membrane for air purification. *Appl. Mater. Today* **14**, 96–101 (2019). <https://doi.org/10.1016/j.apmt.2018.11.012>
79. Yang, D., Li, J., Jiang, Z., Lu, L., Chen, X.: Chitosan/TiO₂ nanocomposite pervaporation membranes for ethanol dehydration. *Chem. Eng. Sci.* **64**(13), 3130–3137 (2009). <https://doi.org/10.1016/j.ces.2009.03.042>

80. Bui, Vu., Park, D., Lee, Y.-C.: Chitosan combined with ZnO, TiO₂ and Ag nanoparticles for antimicrobial wound healing applications: a mini review of the research trends. *Polymers* **9**(12), 21 (2017). <https://doi.org/10.3390/polym9010021>
81. Dorraji, M.S.S., et al.: Fenton-like catalytic activity of wet-spun chitosan hollow fibers loaded with Fe₃O₄ nanoparticles: batch and continuous flow investigations. *J. Mol. Catal. A Chem.* **398**, 353–357 (2015). <https://doi.org/10.1016/j.molcata.2015.01.003>
82. Xu, R., Tang, R., Zhou, Q., Li, F., Zhang, B.: Enhancement of catalytic activity of immobilized laccase for diclofenac biodegradation by carbon nanotubes. *Chem. Eng. J.* **262**, 88–95 (2015). <https://doi.org/10.1016/j.cej.2014.09.072>
83. Bagheripour, E., Moghadassi, A.R., Hosseini, S.M., Van der Bruggen, B., Parvizian, F.: Novel composite graphene oxide/chitosan nanoplates incorporated into PES based nanofiltration membrane: chromium removal and antifouling enhancement. *J. Ind. Eng. Chem.* **62**, 311–320 (2018). <https://doi.org/10.1016/j.jiec.2018.01.009>
84. Casado-Coterillo, C., Fernández-Barquín, A., Zornoza, B., Téllez, C., Coronas, J., Irabien, Á.: Synthesis and characterisation of MOF/ionic liquid/chitosan mixed matrix membranes for CO₂/N₂ separation. *RSC Adv.* **5**(124), 102350–102361 (2015). <https://doi.org/10.1039/C5RA19331A>
85. Li, D., Yan, Y., Wang, H.: Recent advances in polymer and polymer composite membranes for reverse and forward osmosis processes. *Prog. Polym. Sci.* **61**, 104–155 (2016). <https://doi.org/10.1016/j.progpolymsci.2016.03.003>
86. Madaeni, S.S., Ghaemi, N.: Characterization of self-cleaning RO membranes coated with TiO₂ particles under UV irradiation. *J. Membr. Sci.* **303**(1–2), 221–233 (2007). <https://doi.org/10.1016/j.memsci.2007.07.017>
87. Vatanpour, V., Madaeni, S.S., Khataee, A.R., Salehi, E., Zinadini, S., Monfared, H.A.: TiO₂ embedded mixed matrix PES nanocomposite membranes: influence of different sizes and types of nanoparticles on antifouling and performance. *Desalination* **292**, 19–29 (2012). <https://doi.org/10.1016/j.desal.2012.02.006>
88. Teow, Y.H., Ooi, B.S., Ahmad, A.L.: Fouling behaviours of PVDF-TiO₂ mixed-matrix membrane applied to humic acid treatment. *J. Water Process. Eng.* **15**, 89–98 (2017). <https://doi.org/10.1016/j.jwpe.2016.03.005>
89. Damodar, R.A., You, S.-J., Chou, H.-H.: Study the self cleaning, antibacterial and photocatalytic properties of TiO₂ entrapped PVDF membranes. *J. Hazard Mater.* **172**(2–3), 1321–1328 (2009). <https://doi.org/10.1016/j.jhazmat.2009.07.139>
90. Al-Ghafri, B., Lau, W.-J., Al-Abri, M., Goh, P.-S., Ismail, A.F.: Titanium dioxide-modified polyetherimide nanofiber membrane for water treatment. *J. Water Process. Eng.* **32**, 100970 (2019). <https://doi.org/10.1016/j.jwpe.2019.100970>
91. Zhou, A., et al.: Abatement of sulfadiazine in water under a modified ultrafiltration membrane (PVDF-PVP-TiO₂-dopamine) filtration-photocatalysis system. *Sep. Purif. Technol.* **234**, 116099 (2020). <https://doi.org/10.1016/j.seppur.2019.116099>
92. Madaeni, S.S.S., Ghaemi, N., Rajabi, H.: Advances in polymeric membranes for water treatment. In: *Advances in Membrane Technologies for Water Treatment*, pp. 3–41. Elsevier (2015)
93. Yan, L., Li, Y.S., Xiang, C.B.: Preparation of poly(vinylidene fluoride)(pvdf) ultrafiltration membrane modified by nano-sized alumina (Al₂O₃) and its antifouling research. *Polymer (Guildf)* **46**(18), 7701–7706 (2005). <https://doi.org/10.1016/j.polymer.2005.05.155>
94. Maximous, N., Nakhla, G., Wong, K., Wan, W.: Optimization of Al₂O₃/PES membranes for wastewater filtration. *Sep. Purif. Technol.* **73**(2), 294–301 (2010). <https://doi.org/10.1016/j.seppur.2010.04.016>
95. Rajeswari, A., Christy, E.J.S., Mary, G.I.C., Jayaraj, K., Pius, A.: Cellulose acetate based biopolymeric mixed matrix membranes with various nanoparticles for environmental remediation-a comparative study. *J. Environ. Chem. Eng.* **7**(4), 103278 (2019). <https://doi.org/10.1016/j.jece.2019.103278>
96. Rother, R. (ed.): *Fillers for Polymer Applications. Polymers and Polymeric Composites: A Reference Series*, Springer, Cham (2017). <https://doi.org/10.1007/978-3-319-28117-9>

97. Rallini, M., Kenny, J.M.: Nanofillers in polymers. In: *Modification of Polymer Properties*, pp. 47–86. Elsevier (2017)
98. *Advances in Membrane Technologies for Water Treatment*. Elsevier (2015)
99. Danilczuk, M., Lund, A., Sadlo, J., Yamada, H., Michalik, J.: Conduction electron spin resonance of small silver particles. *Spectrochim. Acta Part A Mol. Biomol. Spectrosc.* **63**(1), 189–191 (2006). <https://doi.org/10.1016/j.saa.2005.05.002>
100. Zodrow, K., Brunet, L., Mahendra, S., Li, D., Zhang, A., Li, Q., Alvarez, P.J.J.: Polysulfone ultrafiltration membranes impregnated with silver nanoparticles show improved biofouling resistance and virus removal. *Water Res.* **43**(3), 715–723 (2009). <https://doi.org/10.1016/j.watres.2008.11.014>
101. Chamakura, K., Perez-Ballesteros, R., Luo, Z., Bashir, S., Liu, J.: Comparison of bactericidal activities of silver nanoparticles with common chemical disinfectants. *Colloids Surf. B Biointerfaces* **84**(1), 88–96 (2011). <https://doi.org/10.1016/j.colsurfb.2010.12.020>
102. Koseoglu-Imer, D.Y., Kose, B., Altinbas, M., Koyuncu, I.: The production of polysulfone (PS) membrane with silver nanoparticles (AgNP): physical properties, filtration performances, and biofouling resistances of membranes. *J. Memb. Sci.* **428**, 620–628 (2013). <https://doi.org/10.1016/j.memsci.2012.10.046>
103. Li, J.-H., Shao, X.-S., Zhou, Q., Li, M.-Z., Zhang, Q.-Q.: The double effects of silver nanoparticles on the PVDF membrane: surface hydrophilicity and antifouling performance. *Appl. Surf. Sci.* **265**, 663–670 (2013). <https://doi.org/10.1016/j.apsusc.2012.11.072>
104. Dudek, G., Turczyn, R., Strzelewicz, A., Rybak, A., Krasowska, M., Grzywna, Z.J.: Preparation and characterization of iron oxides – polymer composite membranes. *Sep. Sci. Technol.* **47**(9), 1390–1394 (2012). <https://doi.org/10.1080/01496395.2012.672519>
105. Wei, Y., Han, B., Hu, X., Lin, Y., Wang, X., Deng, X.: Synthesis of Fe₃O₄ nanoparticles and their magnetic properties. *Procedia Eng.* **27**, 632–637 (2012). <https://doi.org/10.1016/j.proeng.2011.12.498>
106. Dutta, S., Manna, K., Srivastava, S.K., Gupta, A.K., Yadav, M.K.: Hollow polyaniline microsphere/Fe₃O₄ nanocomposite as an effective adsorbent for removal of arsenic from water. *Sci. Rep.* **10**(1), 4982 (2020). <https://doi.org/10.1038/s41598-020-61763-z>
107. Badruddoza, A.Z.M., Shawon, Z.B.Z., Tay, W.J.D., Hidajat, K., Uddin, M.S.: Fe₃O₄/cyclodextrin polymer nanocomposites for selective heavy metals removal from industrial wastewater. *Carbohydr. Polym.* **91**(1), 322–332 (2013). <https://doi.org/10.1016/j.carbpol.2012.08.030>
108. Sun, J., Li, S., Ran, Z., Xiang, Y.: Preparation of Fe₃O₄@TiO₂ blended PVDF membrane by magnetic coagulation bath and its permeability and pollution resistance. *J. Mater. Res. Technol.* **9**(3), 4951–4967 (2020). <https://doi.org/10.1016/j.jmrt.2020.03.014>
109. Hong, J., He, Y.: Polyvinylidene fluoride ultrafiltration membrane blended with nano-ZnO particle for photo-catalysis self-cleaning. *Desalination* **332**(1), 67–75 (2014). <https://doi.org/10.1016/j.desal.2013.10.026>
110. Davood Abadi Farahani, M.H., Vatanpour, V.: Polymer/carbon nanotubes mixed matrix membranes for water purification, pp 87–110. In: *Nanoscale Materials in Water Purification*. Elsevier (2019)
111. Rao, G., Lu, C., Su, F.: Sorption of divalent metal ions from aqueous solution by carbon nanotubes: a review. *Sep. Purif. Technol.* **58**(1), 224–231 (2007). <https://doi.org/10.1016/j.seppur.2006.12.006>
112. Yang, K., Zhu, L., Xing, B.: Adsorption of polycyclic aromatic hydrocarbons by carbon nanomaterials. *Environ. Sci. Technol.* **40**(6), 1855–1861 (2006). <https://doi.org/10.1021/es052208w>
113. Savage, N., Diallo, M.S.: Nanomaterials and water purification: opportunities and challenges. *J. Nanopart. Res.* **7**(4–5), 331–342 (2005). <https://doi.org/10.1007/s11051-005-7523-5>
114. Rowsell, J.L.C., Yaghi, O.M.: Metal–organic frameworks: a new class of porous materials. *Microporous Mesoporous Mater.* **73**(1–2), 3–14 (2004). <https://doi.org/10.1016/j.micromeso.2004.03.034>

115. Jiao, L., Seow, J.Y.R., Skinner, W.S., Wang, Z.U., Jiang, H.-L.: Metal–organic frameworks: structures and functional applications. *Mater. Today* **27**, 43–68 (2019). <https://doi.org/10.1016/j.mattod.2018.10.038>
116. Chen, Y., et al.: Shaping of metal–organic frameworks: from fluid to shaped bodies and robust foams. *J. Am. Chem. Soc.* **138**(34), 10810–10813 (2016). <https://doi.org/10.1021/jacs.6b06959>
117. Li, S., Huo, F.: Metal–organic framework composites: from fundamentals to applications. *Nanoscale* **7**(17), 7482–7501 (2015). <https://doi.org/10.1039/C5NR00518C>
118. Nadar, S.S., Vaidya, L., Maurya, S., Rathod, V.K.: Polysaccharide based metal organic frameworks (polysaccharide–MOF): a review. *Coord. Chem. Rev.* **396**, 1–21 (2019). <https://doi.org/10.1016/j.ccr.2019.05.011>
119. Zhu, H., Yang, X., Cranston, E.D., Zhu, S.: Flexible and porous nanocellulose aerogels with high loadings of metal–organic–framework particles for separations applications. *Adv. Mater.* **28**(35), 7652–7657 (2016). <https://doi.org/10.1002/adma.201601351>
120. Ma, S., Zhang, M., Nie, J., Tan, J., Song, S., Luo, Y.: Lightweight and porous cellulose-based foams with high loadings of zeolitic imidazolate frameworks-8 for adsorption applications. *Carbohydr. Polym.* **208**, 328–335 (2019). <https://doi.org/10.1016/j.carbpol.2018.12.081>
121. Rickhoff, T.A., Sullivan, E., Werth, L.K., Kissel, D.S., Keleher, J.J.: A biomimetic cellulose-based composite material that incorporates the antimicrobial metal–organic framework HKUST-1. *J. Appl. Polym. Sci.* **136**(3), 46978 (2019). <https://doi.org/10.1002/app.46978>
122. Cong, H., Radosz, M., Towler, B., Shen, Y.: Polymer–inorganic nanocomposite membranes for gas separation. *Sep. Purif. Technol.* **55**(3), 281–291 (2007). <https://doi.org/10.1016/j.seppur.2006.12.017>
123. Pourzare, K., Mansourpanah, Y., Farhadi, S.: Advanced nanocomposite membranes for fuel cell applications: a comprehensive review. *Biofuel Res. J.* **3**(4), 496–513 (2016). <https://doi.org/10.18331/BRJ2016.3.4.4>
124. Bee, S.-L., Abdullah, M.A.A., Bee, S.-T., Sin, L.T., Rahmat, A.R.: Polymer nanocomposites based on silylated-montmorillonite: a review. *Prog. Polym. Sci.* **85**, 57–82 (2018). <https://doi.org/10.1016/j.progpolymsci.2018.07.003>
125. Anado, P.: Clay-containing polysulfone nanocomposites. In: *Advances in Nanocomposite Technology*. InTech (2011)
126. Alateyah, A.I., Dhakal, H.N., Zhang, Z.Y.: Processing, properties, and applications of polymer nanocomposites based on layer silicates: a review. *Adv. Polym. Technol.* **32**(4), 21368 (2013). <https://doi.org/10.1002/adv.21368>
127. Paul, D.R., Robeson, L.M.: Polymer nanotechnology: nanocomposites. *Polymer (Guildf)* **49**(15), 3187–3204 (2008). <https://doi.org/10.1016/j.polymer.2008.04.017>
128. Sheikholeslami, S.N., Rafizadeh, M., Taromi, F.A., Bouhendi, H.: Synthesis and characterization of poly(trimethylene terephthalate)/organoclay nanocomposite via in situ polymerization. *J. Thermoplast. Compos. Mater.* **27**(11), 1530–1552 (2014). <https://doi.org/10.1177/0892705712475000>
129. Alexandre, M., Dubois, P.: Polymer-layered silicate nanocomposites: preparation, properties and uses of a new class of materials. *Mater. Sci. Eng. R Rep.* **28**(1–2), 1–63 (2000). [https://doi.org/10.1016/S0927-796X\(00\)00012-7](https://doi.org/10.1016/S0927-796X(00)00012-7)
130. Pavlidou, S., Papispyrides, C.D.: A review on polymer–layered silicate nanocomposites. *Prog. Polym. Sci.* **33**(12), 1119–1198 (2008). <https://doi.org/10.1016/j.progpolymsci.2008.07.008>
131. VanderHart, D.L., Asano, A., Gilman, J.W.: Solid-state NMR investigation of paramagnetic nylon-6 clay nanocomposites. 2. Measurement of clay dispersion, crystal stratification, and stability of organic modifiers. *Chem. Mater.* **13**(10), 3796–3809 (2001). <https://doi.org/10.1021/cm011078x>
132. Gao, F.: Clay/polymer composites: the story. *Mater. Today* **7**(11), 50–55 (2004). [https://doi.org/10.1016/S1369-7021\(04\)00509-7](https://doi.org/10.1016/S1369-7021(04)00509-7)
133. Panwar, A., Choudhary, V., Sharma, D.K.: Review: a review: polystyrene/clay nanocomposites. *J. Reinf. Plast. Compos.* **30**(5), 446–459 (2011). <https://doi.org/10.1177/0731684411399132>

134. Usuki, A., et al.: Synthesis of nylon 6-clay hybrid. *J. Mater. Res.* **8**(5), 1179–1184 (1993). <https://doi.org/10.1557/JMR.1993.1179>
135. Doucouré, A., Guizard, C., Durand, J., Berjoan, R., Cot, L.: Plasma polymerization of fluorinated monomers on mesoporous silica membranes and application to gas permeation. *J. Membr. Sci.* **117**(1–2), 143–150 (1996). [https://doi.org/10.1016/0376-7388\(96\)00052-X](https://doi.org/10.1016/0376-7388(96)00052-X)
136. Patel, N.P., Miller, A.C., Spontak, R.J.: Highly CO₂-permeable and selective polymer nanocomposite membranes. *Adv. Mater.* **15**(9), 729–733 (2003). <https://doi.org/10.1002/adma.200304712>
137. Patel, N.P., Aberg, C.M., Sanchez, A.M., Capracotta, M.D., Martin, J.D., Spontak, R.J.: Morphological, mechanical and gas-transport characteristics of crosslinked poly(propylene glycol): homopolymers, nanocomposites and blends. *Polymer (Guildf)* **45**(17), 5941–5950 (2004). <https://doi.org/10.1016/j.polymer.2004.06.024>
138. Nunes, S., Peinemann, K., Ohlrogge, K., Alpers, A., Keller, M., Pires, A.T.: Membranes of poly(ether imide) and nanodispersed silica. *J. Membr. Sci.* **157**(2), 219–226 (1999). [https://doi.org/10.1016/S0376-7388\(98\)00379-2](https://doi.org/10.1016/S0376-7388(98)00379-2)
139. Bounor-Legaré, V., Cassagnau, P.: In situ synthesis of organic-inorganic hybrids or nanocomposites from sol-gel chemistry in molten polymers. *Prog. Polym. Sci.* **39**(8), 1473–1497 (2014). <https://doi.org/10.1016/j.progpolymsci.2014.04.003>
140. Brzesowsky, R., de With, G., van den Cruissem, S., Snijkers-Hendrickx, I.J., Wolter, W.A., van Lierop, J.: Glass strengthening by silica particle reinforced organic-inorganic coatings. *J. Non Cryst. Solids* **241**(1), 27–37 (1998). [https://doi.org/10.1016/S0022-3093\(98\)00750-9](https://doi.org/10.1016/S0022-3093(98)00750-9)
141. Livage, J., Sanchez, C.: Sol-gel chemistry. *J. Non Cryst. Solids* **145**, 11–19 (1992). [https://doi.org/10.1016/S0022-3093\(05\)80422-3](https://doi.org/10.1016/S0022-3093(05)80422-3)
142. Kioul, A., Mascia, L.: Compatibility of polyimide-silicate ceramers induced by alkoxy silane silane coupling agents. *J. Non Cryst. Solids* **175**(2–3), 169–186 (1994). [https://doi.org/10.1016/0022-3093\(94\)90009-4](https://doi.org/10.1016/0022-3093(94)90009-4)
143. Smaïhi, M.: Organic-inorganic gas separation membranes: preparation and characterization. *J. Membr. Sci.* **116**(2), 211–220 (1996). [https://doi.org/10.1016/0376-7388\(96\)00042-7](https://doi.org/10.1016/0376-7388(96)00042-7)
144. Pomogailo, A.D.: Polymer sol-gel synthesis of hybrid nanocomposites. *Colloid J.* **67**(6), 658–677 (2005). <https://doi.org/10.1007/s10595-005-0148-7>
145. Day, V.W., Eberspacher, T.A., Chen, Y., Hao, J., Klemperer, W.G.: Low-nuclearity titanium oxoalkoxides: the trititanates [Ti₃O](OPrⁱ)₁₀ and [Ti₃O](OPrⁱ)₆(OMe). *Inorg. Chim. Acta* **229**(1–2), 391–405 (1995). [https://doi.org/10.1016/0020-1693\(94\)04270-6](https://doi.org/10.1016/0020-1693(94)04270-6)
146. Livage, J.: Basic principles of sol-gel chemistry. In: Aegerter, M.A., Mennig, M. (eds.) *Sol-Gel Technologies for Glass Producers and Users*, pp. 3–14. Springer, Boston (2004). https://doi.org/10.1007/978-0-387-88953-5_1
147. Iwata, M., Adachi, T., Tomidokoro, M., Ohta, M., Kobayashi, T.: Hybrid sol-gel membranes of polyacrylonitrile-tetraethoxysilane composites for gas permselectivity. *J. Appl. Polym. Sci.* **88**(7), 1752–1759 (2003). <https://doi.org/10.1002/app.11895>
148. Gomes, D., Nunes, S.P., Peinemann, K.-V.: Membranes for gas separation based on poly(1-trimethylsilyl-1-propyne)-silica nanocomposites. *J. Membr. Sci.* **246**(1), 13–25 (2005). <https://doi.org/10.1016/j.memsci.2004.05.015>
149. Guo, Y., Wang, X., Hu, P., Peng, X.: ZIF-8 coated polyvinylidene fluoride (PVDF) hollow fiber for highly efficient separation of small dye molecules. *Appl. Mater. Today* **5**, 103–110 (2016). <https://doi.org/10.1016/j.apmt.2016.07.007>
150. Stephen, R., Ranganathaiah, C., Varghese, S., Joseph, K., Thomas, S.: Gas transport through nano and micro composites of natural rubber (NR) and their blends with carboxylated styrene butadiene rubber (XSBR) latex membranes. *Polymer (Guildf)* **47**(3), 858–870 (2006). <https://doi.org/10.1016/j.polymer.2005.12.020>
151. Mascia, L., Zhang, Z., Shaw, S.J.: Carbon fibre composites based on polyimide/silica ceramers: aspects of structure-properties relationship. *Compos. Part A Appl. Sci. Manuf.* **27**(12), 1211–1221 (1996). [https://doi.org/10.1016/1359-835X\(96\)00082-6](https://doi.org/10.1016/1359-835X(96)00082-6)
152. Gacitua, W., Ballerini, A., Zhang, J.: Polymer nanocomposites: synthetic and natural fillers a review. *Maderas Cienc. y Tecnol.* **7**(3), 159–178 (2005). <https://doi.org/10.4067/S0718-221X2005000300002>

153. Ragab, D., Gomaa, H.G., Sabouni, R., Salem, M., Ren, M., Zhu, J.: Micropollutants removal from water using microfiltration membrane modified with ZIF-8 metal organic frameworks (MOFs). *Chem. Eng. J.* **300**, 273–279 (2016). <https://doi.org/10.1016/j.cej.2016.04.033>
154. Low, Z.-X., Razmjou, A., Wang, K., Gray, S., Duke, M., Wang, H.: Effect of addition of two-dimensional ZIF-L nanoflakes on the properties of polyethersulfone ultrafiltration membrane. *J. Membr. Sci.* **460**, 9–17 (2014). <https://doi.org/10.1016/j.memsci.2014.02.026>
155. Bhiwankar, N.N., Weiss, R.A.: Melt intercalation/exfoliation of polystyrene–sodium-montmorillonite nanocomposites using sulfonated polystyrene ionomer compatibilizers. *Polymer (Guildf)* **47**(19), 6684–6691 (2006). <https://doi.org/10.1016/j.polymer.2006.07.017>
156. Motamedi, P., Bagheri, R.: Investigation of the nanostructure and mechanical properties of polypropylene/polyamide 6/layered silicate ternary nanocomposites. *Mater. Des.* **31**(4), 1776–1784 (2010). <https://doi.org/10.1016/j.matdes.2009.11.013>
157. Yoon, J., Jo, W., Lee, M., Ko, M.: Effects of comonomers and shear on the melt intercalation of styrenics/clay nanocomposites. *Polymer (Guildf)* **42**(1), 329–336 (2001). [https://doi.org/10.1016/S0032-3861\(00\)00333-5](https://doi.org/10.1016/S0032-3861(00)00333-5)
158. Huang, Z.-M., Zhang, Y.-Z., Kotaki, M., Ramakrishna, S.: A review on polymer nanofibers by electrospinning and their applications in nanocomposites. *Compos. Sci. Technol.* **63**, 2223–2253 (2003). [https://doi.org/10.1016/S0266-3538\(03\)00178-7](https://doi.org/10.1016/S0266-3538(03)00178-7)
159. Xue, J., Wu, T., Dai, Y., Xia, Y.: Electrospinning and electrospun nanofibers: methods, materials, and applications. *Chem. Rev.* **119**(8), 5298–5415 (2019). <https://doi.org/10.1021/acs.chemrev.8b00593>
160. Wang, Z., Crandall, C., Sahadevan, R., Menkhaus, T.J., Fong, H.: Microfiltration performance of electrospun nanofiber membranes with varied fiber diameters and different membrane porosities and thicknesses. *Polymer (Guildf)* **114**, 64–72 (2017). <https://doi.org/10.1016/j.polymer.2017.02.084>
161. Dolina, J., Jifčák, T., Lederer, T.: Biocide modification of ultrafiltration membranes using nanofiber structures. *Desalin. Water Treat.* **56**(12), 3252–3258 (2015). <https://doi.org/10.1080/19443994.2014.981923>
162. Wang, X., Fang, D., Hsiao, B.S., Chu, B.: Nanofiltration membranes based on thin-film nanofibrous composites. *J. Membr. Sci.* **469**, 188–197 (2014). <https://doi.org/10.1016/j.memsci.2014.06.049>
163. Wang, X., Ma, H., Chu, B., Hsiao, B.S.: Thin-film nanofibrous composite reverse osmosis membranes for desalination. *Desalination* **420**, 91–98 (2017). <https://doi.org/10.1016/j.desal.2017.06.029>
164. Li, J.J., Zhu, L.T., Luo, Z.H.: Electrospun fibrous membrane with enhanced switchable oil/water wettability for oily water separation. *Chem. Eng. J.* **287**, 474–481 (2016). <https://doi.org/10.1016/j.cej.2015.11.057>
165. Tijing, L.D., Choi, J.S., Lee, S., Kim, S.H., Shon, H.K.: Recent progress of membrane distillation using electrospun nanofibrous membrane. *J. Membr. Sci.* **453**, 435–462 (2014). <https://doi.org/10.1016/j.memsci.2013.11.022>
166. Najafi, M., Frey, M.W.: Electrospun nanofibers for chemical separation. *Nanomaterials* **10**(5), 982 (2020). <https://doi.org/10.3390/nano10050982>
167. Bhardwaj, N., Kundu, S.C.: Electrospinning: a fascinating fiber fabrication technique. *Biotechnol. Adv.* **28**(3), 325–347 (2010). <https://doi.org/10.1016/j.biotechadv.2010.01.004>
168. Hou, D., Lin, D., Ding, C., Wang, D., Wang, J.: Fabrication and characterization of electrospun superhydrophobic PVDF-HFP/SiNPs hybrid membrane for membrane distillation. *Sep. Purif. Technol.* **189**, 82–89 (2017). <https://doi.org/10.1016/j.seppur.2017.07.082>
169. Yar, A., et al.: Electrospun TiO₂/ZnO/PAN hybrid nanofiber membranes with efficient photocatalytic activity. *RSC Adv.* **7**(47), 29806–29814 (2017). <https://doi.org/10.1039/c7ra03699j>
170. Essalhi, M., Khayet, M.: Self-sustained webs of polyvinylidene fluoride electrospun nanofibers: effects of polymer concentration and desalination by direct contact membrane distillation. *J. Membr. Sci.* **454**, 133–143 (2014). <https://doi.org/10.1016/j.memsci.2013.11.056>

171. Soares, R.M.D., Siqueira, N.M., Prabhakaram, M.P., Ramakrishna, S.: Electrospinning and electrospray of bio-based and natural polymers for biomaterials development. *Mater. Sci. Eng. C* **92**, 969–982 (2018). <https://doi.org/10.1016/j.msec.2018.08.004>
172. Ziabari, M., Mottaghitalab, V., Haghi, A.K.: Application of direct tracking method for measuring electrospun nanofiber diameter. *Braz. J. Chem. Eng.* **26**(1), 53–62 (2009). <https://doi.org/10.1590/S0104-66322009000100006>
173. Biswas, P., Bandyopadhyaya, R.: Biofouling prevention using silver nanoparticle impregnated polyethersulfone (PES) membrane: E. coli cell-killing in a continuous cross-flow membrane module. *J. Colloid Interface Sci.* **491**, 13–26 (2017). <https://doi.org/10.1016/j.jcis.2016.11.060>
174. Zheng, Y., Gong, R.H., Zeng, Y.: Multijet motion and deviation in electrospinning. *RSC Adv.* **5**(60), 48533–48540 (2015). <https://doi.org/10.1039/c5ra06049d>
175. Li, D., Xia, Y.: Direct fabrication of composite and ceramic hollow nanofibers by electrospinning. *Nano Lett.* **4**(5), 933–938 (2004). <https://doi.org/10.1021/nl049590f>
176. Lee, G.H., Song, J.C., Yoon, K.B.: Controlled wall thickness and porosity of polymeric hollow nanofibers by coaxial electrospinning. *Macromol. Res.* **18**(6), 571–576 (2010). <https://doi.org/10.1007/s13233-010-0607-9>
177. Li, D., Xia, Y.: Fabrication of titania nanofibers by electrospinning. *Nano Lett.* **3**(4), 555–560 (2003). <https://doi.org/10.1021/nl034039o>
178. Malwal, D., Gopinath, P.: Fabrication and characterization of poly(ethylene oxide) templated nickel oxide nanofibers for dye degradation. *Environ. Sci. Nano J.* **2**(1), 78–85 (2015). <https://doi.org/10.1039/c4en00107a>
179. Rezaei, M., Samhaber, W.: Wetting behaviour of superhydrophobic membranes coated with nanoparticles in membrane distillation. *Chem. Eng. Trans.* **47**, 373–378 (2016). <https://doi.org/10.3303/CET1647063>
180. Ray, S.S., Chen, S.S., Li, C.W., Nguyen, N.C., Nguyen, H.T.: A comprehensive review: electrospinning technique for fabrication and surface modification of membranes for water treatment application. *RSC Adv.* **6**(88), 85495–85514 (2016). <https://doi.org/10.1039/c6ra14952a>
181. Lee, C.G., et al.: Porous electrospun fibers embedding TiO₂ for adsorption and photocatalytic degradation of water pollutants. *Environ. Sci. Technol.* **52**(7), 4285–4293 (2018). <https://doi.org/10.1021/acs.est.7b06508>
182. Ognibene, G., Gangemi, C.M.A., D’Urso, A., Purrello, R., Cicala, G., Fragalà, M.E.: Combined approach to remove and fast detect heavy metals in water based on PES-TiO₂ electrospun mats and porphyrin chemosensors. *ACS Omega* **3**(7), 7182–7190 (2018). <https://doi.org/10.1021/acsomega.8b00284>
183. Mohamed, A., et al.: Visible light photocatalytic reduction of Cr(VI) by surface modified CNT/titanium dioxide composites nanofibers. *J. Mol. Catal. A Chem.* **424**(Vi), 45–53 (2016). <https://doi.org/10.1016/j.molcata.2016.08.010>
184. Schiffman, J.D., Elimelech, M.: Antibacterial activity of electrospun polymer mats with incorporated narrow diameter single-walled carbon nanotubes. *ACS Appl. Mater. Interfaces* **3**(2), 462–468 (2011). <https://doi.org/10.1021/am101043y>
185. Ford, E.N.J., Suthiwangcharoen, N., D’Angelo, P.A., Nagarajan, R.: Role of single-walled carbon nanotubes on ester hydrolysis and topography of electrospun bovine serum albumin/poly(vinyl alcohol) membranes. *ACS Appl. Mater. Interfaces* **6**(14), 11741–11748 (2014). <https://doi.org/10.1021/am502495e>
186. Liao, Y., Loh, C.H., Wang, R., Fane, A.G.: Electrospun superhydrophobic membranes with unique structures for membrane distillation. *ACS Appl. Mater. Interfaces* **6**(18), 16035–16048 (2014). <https://doi.org/10.1021/am503968n>
187. Obaid, M., Ghouri, Z.K., Fadali, O.A., Khalil, K.A., Almajid, A.A., Barakat, N.A.M.: Amorphous SiO₂ NP-incorporated poly(vinylidene fluoride) electrospun nanofiber membrane for high flux forward osmosis desalination. *ACS Appl. Mater. Interfaces* **8**(7), 4561–4574 (2016). <https://doi.org/10.1021/acsaami.5b09945>
188. Li, X., Yu, X., Cheng, C., Deng, L., Wang, M., Wang, X.: Electrospun superhydrophobic organic/inorganic composite nanofibrous membranes for membrane distillation. *ACS Appl. Mater. Interfaces* **7**(39), 21919–21930 (2015). <https://doi.org/10.1021/acsaami.5b06509>

189. Son, W.K., Youk, J.H., Park, W.H.: Antimicrobial cellulose acetate nanofibers containing silver nanoparticles. *Carbohydr. Polym.* **65**(4), 430–434 (2006). <https://doi.org/10.1016/j.carbpol.2006.01.037>
190. De Faria, A.F., Perreault, F., Shaulsky, E., Chavez, L.H.A., Elimelech, M.: Antimicrobial electrospun biopolymer nanofiber mats functionalized with graphene oxide-silver nanocomposites. *ACS Appl. Mater. Interfaces* **7**(23), 12751–12759 (2015). <https://doi.org/10.1021/acsami.5b01639>
191. Karagoz, N.S., et al.: Synthesis of Ag and TiO₂ modified polycaprolactone electrospun nanofibers (PCL/TiO₂-Ag NFs) as a multifunctional material for SERS, photocatalysis and antibacterial applications. *Ecotoxicol. Environ. Saf.* **188**, 109856 (2020). <https://doi.org/10.1016/j.ecoenv.2019.109856>
192. Kayaci, F., Ozgit-Akgun, C., Donmez, I., Biyikli, N., Uyar, T.: Polymer-inorganic core-shell nanofibers by electrospinning and atomic layer deposition: flexible nylon-ZnO core-shell nanofiber mats and their photocatalytic activity. *ACS Appl. Mater. Interfaces* **4**(11), 6185–6194 (2012). <https://doi.org/10.1021/am3017976>
193. Kim, J.H., Joshi, M.K., Lee, J., Park, C.H., Kim, C.S.: Polydopamine-assisted immobilization of hierarchical zinc oxide nanostructures on electrospun nanofibrous membrane for photocatalysis and antimicrobial activity. *J. Colloid Interface Sci.* **513**, 566–574 (2018). <https://doi.org/10.1016/j.jcis.2017.11.061>
194. Barhoum, A., Bechelany, M., Makhlof, A.S.H. (eds.): *Handbook of Nanofibers*. Springer, Cham (2019). <https://doi.org/10.1007/978-3-319-53655-2>
195. Xiao, S., Shen, M., Guo, R., Wang, S., Shi, X.: Immobilization of zerovalent iron nanoparticles into electrospun polymer nanofibers: synthesis, characterization, and potential environmental applications. *J. Phys. Chem. C* **113**(42), 18062–18068 (2009). <https://doi.org/10.1021/jp905542g>
196. Zhang, D., et al.: Electrospun fibrous membranes with dual-scaled porous structure: super hydrophobicity, super lipophilicity, excellent water adhesion, and anti-icing for highly efficient oil adsorption/separation. *ACS Appl. Mater. Interfaces* **11**(5), 5073–5083 (2019). <https://doi.org/10.1021/acsami.8b19523>
197. Letnik, I., Avrahami, R., Rokem, J.S., Greiner, A., Zussman, E., Greenblatt, C.: Living composites of electrospun yeast cells for bioremediation and ethanol production. *Biomacromol* **16**(10), 3322–3328 (2015). <https://doi.org/10.1021/acs.biomac.5b00970>
198. Yap, C.Y., et al.: Review of selective laser melting: materials and applications. *Appl. Phys. Rev.* **2**(4), 041101 (2015). <https://doi.org/10.1063/1.4935926>
199. Fasel, U., Keidel, D., Baumann, L., Cavolina, G., Eichenhofer, M., Ermanni, P.: Composite additive manufacturing of morphing aerospace structures. *Manuf. Lett.* **23**, 85–88 (2020). <https://doi.org/10.1016/j.mfglet.2019.12.004>
200. Lewandowski, J.J., Seifi, M.: Metal additive manufacturing: a review of mechanical properties. *Ann. Rev. Mater. Res.* **46**, 151–186 (2016). <https://doi.org/10.1146/annurev-matsci-070115-032024>
201. Schmitt, M., Mehta, R.M., Kim, I.Y.: Additive manufacturing infill optimization for automotive 3D-printed ABS components. *Rapid Prototyp. J.* **26**(1), 89–99 (2020). <https://doi.org/10.1108/RPJ-01-2019-0007>
202. Lim, C.W.J., Le, K.Q., Lu, Q., Wong, C.H.: An overview of 3-D printing in manufacturing, aerospace, and automotive industries. *IEEE Potentials* **35**(4), 18–22 (2016). <https://doi.org/10.1109/MPOT.2016.2540098>
203. Tay, Y.W.D., Panda, B., Paul, S.C., Noor Mohamed, N.A., Tan, M.J., Leong, K.F.: 3D printing trends in building and construction industry: a review. *Virtual Phys. Prototyp.* **12**(3), 261–276 (2017). <https://doi.org/10.1080/17452759.2017.1326724>
204. Lin, K., Zhang, D., Macedo, M.H., Cui, W., Sarmiento, B., Shen, G.: Advanced collagen-based biomaterials for regenerative biomedicine. *Adv. Funct. Mater.* **29**(3), 1–16 (2019). <https://doi.org/10.1002/adfm.201804943>
205. Derakhshanfar, S., Mbeleck, R., Xu, K., Zhang, X., Zhong, W., Xing, M.: 3D bioprinting for biomedical devices and tissue engineering: a review of recent trends and advances. *Bioact. Mater.* **3**(2), 144–156 (2018). <https://doi.org/10.1016/j.bioactmat.2017.11.008>

206. Sun, J., Zhou, W., Huang, D., Fuh, J.Y.H., Hong, G.S.: An overview of 3D printing technologies for food fabrication. *Food Bioprocess Technol.* **8**(8), 1605–1615 (2015). <https://doi.org/10.1007/s11947-015-1528-6>
207. Lalia, B.S., Kochkodan, V., Hashaikh, R., Hilal, N.: A review on membrane fabrication: structure, properties and performance relationship. *Desalination* **326**, 77–95 (2013). <https://doi.org/10.1016/j.desal.2013.06.016>
208. Issac, M.N., Kandasubramanian, B.: Review of manufacturing three-dimensional-printed membranes for water treatment. *Environ. Sci. Pollut. Res.* **27**(29), 36091–36108 (2020). <https://doi.org/10.1007/s11356-020-09452-2>
209. Ngo, T.D., Kashani, A., Imbalzano, G., Nguyen, K.T.Q., Hui, D.: Additive manufacturing (3D printing): a review of materials, methods, applications and challenges. *Compos. Part B Eng.* **143**, 172–196 (2018). <https://doi.org/10.1016/j.compositesb.2018.02.012>
210. Low, Z.X., Chua, Y.T., Ray, B.M., Mattia, D., Metcalfe, I.S., Patterson, D.A.: Perspective on 3D printing of separation membranes and comparison to related unconventional fabrication techniques. *J. Membr. Sci.* **523**, 596–613 (2017). <https://doi.org/10.1016/j.memsci.2016.10.006>
211. Yusuf, A., et al.: A review of emerging trends in membrane science and technology for sustainable water treatment. *J. Clean. Prod.* **266**, 121867 (2020). <https://doi.org/10.1016/j.jclepro.2020.121867>
212. Tijing, L.D., Dizon, J.R.C., Ibrahim, I., Nisay, A.R.N., Shon, H.K., Advincula, R.C.: 3D printing for membrane separation, desalination and water treatment. *Appl. Mater. Today* **18**, 100486 (2020). <https://doi.org/10.1016/j.apmt.2019.100486>
213. Koh, J.J., Lim, G.J.H., Zhou, X., Zhang, X., Ding, J., He, C.: 3D-printed anti-fouling cellulose mesh for highly efficient oil/water separation applications. *ACS Appl. Mater. Interfaces* **11**(14), 13787–13795 (2019). <https://doi.org/10.1021/acsami.9b01753>
214. Giorgi, A., et al.: 3D printing of photocatalytic filters using a biopolymer to immobilize TiO₂ nanoparticles. *J. Electrochem. Soc.* **166**(5), H3239–H3248 (2019). <https://doi.org/10.1149/2.0341905jes>
215. Singh, N.B., Agarwal, S.: Nanocomposites: an overview. *Emerg. Mater. Res.* **5**(1), 5–43 (2016). <https://doi.org/10.1680/jemmr.15.00025>
216. Ma, H., Hsiao, B.S.: *Electrospun Nanofibrous Membranes for Desalination*. Elsevier Inc. (2018)
217. Elimelech, M., Phillip, W.A.: The future of seawater desalination: energy, technology, and the environment. *Science* **333**(6043), 712–717 (2011). <https://doi.org/10.1126/science.1200488>
218. Kebria, M.R.S., Rahimpour, A., Bakeri, G., Abedini, R.: Experimental and theoretical investigation of thin ZIF-8/chitosan coated layer on air gap membrane distillation performance of PVDF membrane. *Desalination* **450**, 21–32 (2019). <https://doi.org/10.1016/j.desal.2018.10.023>
219. Subramanian, S., Seeram, R.: New directions in nanofiltration applications - are nanofibers the right materials as membranes in desalination? *Desalination* **308**, 198–208 (2013). <https://doi.org/10.1016/j.desal.2012.08.014>
220. Wang, Y., et al.: Preparation of super-hydrophilic polyphenylsulfone nanofiber membranes for water treatment. *RSC Adv.* **9**(1), 278–286 (2019). <https://doi.org/10.1039/C8RA06493H>
221. Emadzadeh, D., Lau, W.J., Matsuura, T., Rahbari-Sisakht, M., Ismail, A.F.: A novel thin film composite forward osmosis membrane prepared from PSf–TiO₂ nanocomposite substrate for water desalination. *Chem. Eng. J.* **237**, 70–80 (2014). <https://doi.org/10.1016/j.cej.2013.09.081>
222. Zirehpour, A., Rahimpour, A., Khoshhal, S., Firouzjaei, M.D., Ghoreyshi, A.A.: The impact of MOF feasibility to improve the desalination performance and antifouling properties of FO membranes. *RSC Adv.* **6**(74), 70174–70185 (2016). <https://doi.org/10.1039/C6RA14591D>
223. Khraisheh, M., AlMomani, F., Al-Ghouti, M.: Electrospun Al₂O₃ hydrophobic functionalized membranes for heavy metal recovery using direct contact membrane distillation. *Int. J. Energy Res.* **45**(6), 8151–8167 (2020). <https://doi.org/10.1002/er.5710>

224. Tijing, L.D., et al.: Superhydrophobic nanofiber membrane containing carbon nanotubes for high-performance direct contact membrane distillation. *J. Membr. Sci.* **502**, 158–170 (2016). <https://doi.org/10.1016/j.memsci.2015.12.014>
225. Yoon, K., Kim, K., Wang, X., Fang, D., Hsiao, B.S., Chu, B.: High flux ultrafiltration membranes based on electrospun nanofibrous PAN scaffolds and chitosan coating. *Polymer (Guildf)* **47**(7), 2434–2441 (2006). <https://doi.org/10.1016/j.polymer.2006.01.042>
226. Tang, Z., et al.: UV-cured poly(vinyl alcohol) ultrafiltration nanofibrous membrane based on electrospun nanofiber scaffolds. *J. Memb. Sci.* **328**(1–2), 1–5 (2009). <https://doi.org/10.1016/j.memsci.2008.11.054>
227. Tang, X., et al.: In situ polymerized superhydrophobic and superoleophilic nanofibrous membranes for gravity driven oil-water separation. *Nanoscale* **5**, 11657–11664 (2013). <https://doi.org/10.1039/c3nr03937d>
228. Arslan, O., Aytac, Z., Uyar, T.: Superhydrophobic, hybrid, electrospun cellulose acetate nanofibrous mats for oil/water separation by tailored surface modification. *ACS Appl. Mater. Interfaces* **8**(30), 19747–19754 (2016). <https://doi.org/10.1021/acsami.6b05429>
229. Lv, J., et al.: 3D printing of a mechanically durable superhydrophobic porous membrane for oil-water separation. *J. Mater. Chem. A* **5**(23), 12435–12444 (2017). <https://doi.org/10.1039/c7ta02202f>
230. Tijing, L.D., Woo, Y.C., Yao, M., Ren, J., Shon, H.K.: 1.16 Electrospinning for Membrane Fabrication: Strategies and Applications. Elsevier Ltd. (2017)
231. Tran, D.N., Marti, A.M., Balkus, K.J.: Electrospun zeolite/cellulose acetate fibers for ion exchange of Pb²⁺. *Fibers* **2**(4), 308–317 (2014). <https://doi.org/10.3390/fib2040308>
232. Zhao, R., et al.: Surface activated hydrothermal carbon-coated electrospun PAN fiber membrane with enhanced adsorption properties for herbicide. *ACS Sustain. Chem. Eng.* **4**(5), 2584–2592 (2016). <https://doi.org/10.1021/acssuschemeng.6b00026>
233. Habiba, U., Afifi, A.M., Salleh, A., Ang, B.C.: Chitosan/(polyvinyl alcohol)/zeolite electrospun composite nanofibrous membrane for adsorption of Cr⁶⁺, Fe³⁺ and Ni²⁺. *J. Hazard. Mater.* **322**, 182–194 (2017). <https://doi.org/10.1016/j.jhazmat.2016.06.028>
234. Pandey, N., Shukla, S.K., Singh, N.B.: Water purification by polymer nanocomposites: an overview. *Nanocomposites* **3**(2), 47–66 (2017). <https://doi.org/10.1080/20550324.2017.1329983>
235. Fu, F., Wang, Q.: Removal of heavy metal ions from wastewaters: a review. *J. Environ. Manage.* **92**(3), 407–418 (2011). <https://doi.org/10.1016/j.jenvman.2010.11.011>
236. Hua, M., Zhang, S., Pan, B., Zhang, W., Lv, L., Zhang, Q.: Heavy metal removal from water/wastewater by nanosized metal oxides: a review. *J. Hazard. Mater.* **211–212**, 317–331 (2012). <https://doi.org/10.1016/j.jhazmat.2011.10.016>
237. Al-Rashdi, B.A.M., Johnson, D.J., Hilal, N.: Removal of heavy metal ions by nanofiltration. *Desalination* **315**, 2–17 (2013). <https://doi.org/10.1016/j.desal.2012.05.022>
238. Lim, A.P., Aris, A.Z.: A review on economically adsorbents on heavy metals removal in water and wastewater. *Rev. Environ. Sci. Bio/Technol.* **13**(2), 163–181 (2014). <https://doi.org/10.1007/s11157-013-9330-2>
239. Ghaemi, N.: A new approach to copper ion removal from water by polymeric nanocomposite membrane embedded with γ -alumina nanoparticles. *Appl. Surf. Sci.* **364**, 221–228 (2016). <https://doi.org/10.1016/j.apsusc.2015.12.109>
240. Kim, H.J., Pant, H.R., Kim, J.H., Choi, N.J., Kim, C.S.: Fabrication of multifunctional TiO₂–fly ash/polyurethane nanocomposite membrane via electrospinning. *Ceram. Int.* **40**(2), 3023–3029 (2014). <https://doi.org/10.1016/j.ceramint.2013.10.005>
241. Valsala, T.P., Roy, S.C., Shah, J.G., Gabriel, J., Raj, K., Venugopal, V.: Removal of radioactive caesium from low level radioactive waste (LLW) streams using cobalt ferrocyanide impregnated organic anion exchanger. *J. Hazard. Mater.* **166**(2–3), 1148–1153 (2009). <https://doi.org/10.1016/j.jhazmat.2008.12.019>
242. El-Magied, M.O.A., Tolba, A.A., El-Gendy, H.S., Zaki, S.A., Atia, A.A.: Studies on the recovery of Th(IV) ions from nitric acid solutions using amino-magnetic glycidyl methacrylate resins and application to granite leach liquors. *Hydrometallurgy* **169**, 89–98 (2017). <https://doi.org/10.1016/j.hydromet.2016.12.011>

243. Zach-Maor, A., Semiat, R., Shemer, H.: Synthesis, performance, and modeling of immobilized nano-sized magnetite layer for phosphate removal. *J. Colloid Interface Sci.* **357**(2), 440–446 (2011). <https://doi.org/10.1016/j.jcis.2011.01.021>
244. Wen, T., et al.: Multifunctional flexible free-standing titanate nanobelt membranes as efficient sorbents for the removal of radioactive $^{90}\text{Sr}^{2+}$ and $^{137}\text{Cs}^+$ ions and oils. *Sci. Rep.* **6**(1), 20920 (2016). <https://doi.org/10.1038/srep20920>
245. Sheha, R.R.: Synthesis and characterization of magnetic hexacyanoferrate (II) polymeric nanocomposite for separation of cesium from radioactive waste solutions. *J. Colloid Interface Sci.* **388**(1), 21–30 (2012). <https://doi.org/10.1016/j.jcis.2012.08.042>
246. Park, Y., Lee, Y.-C., Shin, W.S., Choi, S.-J.: Removal of cobalt, strontium and cesium from radioactive laundry wastewater by ammonium molybdophosphate–polyacrylonitrile (AMP–PAN). *Chem. Eng. J.* **162**(2), 685–695 (2010). <https://doi.org/10.1016/j.cej.2010.06.026>
247. Ahmad, A., et al.: Recent advances in new generation dye removal technologies: novel search for approaches to reprocess wastewater. *RSC Adv.* **5**(39), 30801–30818 (2015). <https://doi.org/10.1039/C4RA16959J>
248. Moussavi, G., Mahmoudi, M.: Removal of azo and anthraquinone reactive dyes from industrial wastewaters using MgO nanoparticles. *J. Hazard. Mater.* **168**(2–3), 806–812 (2009). <https://doi.org/10.1016/j.jhazmat.2009.02.097>
249. Yagub, M.T., Sen, T.K., Afroze, S., Ang, H.M.: Dye and its removal from aqueous solution by adsorption: a review. *Adv. Colloid Interface Sci.* **209**, 172–184 (2014). <https://doi.org/10.1016/j.cis.2014.04.002>
250. Elrasheedy, A., Nady, N., Bassyouni, M., El-Shazly, A.: Metal organic framework based polymer mixed matrix membranes: review on applications in water purification. *Membranes (Basel)* **9**(7), 88 (2019). <https://doi.org/10.3390/membranes9070088>
251. Dulman, V., Cucu-Man, S.-M., Bunia, I., Dumitras, M.: Batch and fixed bed column studies on removal of Orange G acid dye by a weak base functionalized polymer. *Desalin. Water Treat.* **57**(31), 14708–14727 (2016). <https://doi.org/10.1080/19443994.2015.1065767>
252. Chong, M.N., Jin, B., Chow, C.W.K., Saint, C.: Recent developments in photocatalytic water treatment technology: a review. *Water Res.* **44**(10), 2997–3027 (2010). <https://doi.org/10.1016/j.watres.2010.02.039>
253. Striemer, C.C., Gaboroski, T.R., McGrath, J.L., Fauchet, P.M.: Charge- and size-based separation of macromolecules using ultrathin silicon membranes. *Nature* **445**(7129), 749–753 (2007). <https://doi.org/10.1038/nature05532>
254. Zhang, R., Ji, S., Wang, N., Wang, L., Zhang, G., Li, J.-R.: Coordination-driven in situ self-assembly strategy for the preparation of metal-organic framework hybrid membranes. *Angew. Chemie. Int. Ed. Engl.* **53**(37), 9775–9779 (2014). <https://doi.org/10.1002/anie.201403978>
255. Maroofi, S.M., Mahmoodi, N.M.: Zeolitic imidazolate framework-polyvinylpyrrolidone-polyethersulfone composites membranes: from synthesis to the detailed pollutant removal from wastewater using cross flow system. *Colloids Surf. A Physicochem. Eng. Asp.* **572**, 211–220 (2019). <https://doi.org/10.1016/j.colsurfa.2019.03.093>
256. Wan, Q., et al.: Facile and highly efficient fabrication of graphene oxide-based polymer nanocomposites through mussel-inspired chemistry and their environmental pollutant removal application. *J. Mater. Sci.* **52**(1), 504–518 (2017). <https://doi.org/10.1007/s10853-016-0349-y>
257. Safarpour, M., Vatanpour, V., Khataee, A.: Preparation and characterization of graphene oxide/TiO₂ blended PES nanofiltration membrane with improved antifouling and separation performance. *Desalination* **393**, 65–78 (2016). <https://doi.org/10.1016/j.desal.2015.07.003>
258. Vakili, M., et al.: Application of chitosan and its derivatives as adsorbents for dye removal from water and wastewater: a review. *Carbohydr. Polym.* **113**, 115–130 (2014). <https://doi.org/10.1016/j.carbpol.2014.07.007>
259. Olad, A., Azhar, F.F.: Eco-friendly biopolymer/clay/conducting polymer nanocomposite: Characterization and its application in reactive dye removal. *Fibers Polym.* **15**(6), 1321–1329 (2014). <https://doi.org/10.1007/s12221-014-1321-6>
260. Figuerola, A., et al.: Metal–organic framework mixed-matrix coatings on 3D printed devices. *Appl. Mater. Today* **16**, 21–27 (2019). <https://doi.org/10.1016/j.apmt.2019.04.011>

261. Pei, R., et al.: 3D-Printed metal-organic frameworks within biocompatible polymers as excellent adsorbents for organic dyes removal. *J. Hazard. Mater.* **384**, 121418 (2020). <https://doi.org/10.1016/j.jhazmat.2019.121418>
262. Wang, Z., Wang, J., Li, M., Sun, K., Liu, C.J.: Three-dimensional printed acrylonitrile butadiene styrene framework coated with Cu-BTC metal-organic frameworks for the removal of methylene blue. *Sci. Rep.* **4**, 4–10 (2014). <https://doi.org/10.1038/srep05939>
263. Chen, H., Huang, M., Liu, Y., Meng, L., Ma, M.: Functionalized electrospun nanofiber membranes for water treatment: a review. *Sci. Total. Environ.* **739**, 139944 (2020). <https://doi.org/10.1016/j.scitotenv.2020.139944>
264. Blanco, M., et al.: TiO₂-doped electrospun nanofibrous membrane for photocatalytic water treatment. *Polymers (Basel)* **11**(5), 1–11 (2019). <https://doi.org/10.3390/polym11050747>

Biodegradable Polymeric Nanocomposites for Wastewater Treatment



Mahmoud H. Abu Elella, Emad. S. Goda, Mohamed. A. Gab-Allah, Sang Eun Hong, Yared G. Lijalem, and Kuk Ro Yoon

Abstract Safe drinking water is one of the fundamental necessities for all living being on the earth. Ever-growing population, industrialization, water sources disorganization, and global warming are among the multiple factors which have contributed to the shortage of clean water resources worldwide. Commonly, water has been contaminated with different water-soluble and non-biodegradable substances such as toxic organic dyes, metal ions, persistent organic pollutants, bacteria, etc. Thus, ensuring sufficient resources of fresh water is of a great environmental challenge. Various attempts have been undertaken to purify wastewater by advanced strategies utilizing smart and multifunctional materials. Among these materials, biodegradable polymers-based nanocomposites (PNCs) have received a great deal of attention in wastewater treatment owing to their outstanding properties such as high specific surface area, stability, bio-compatibility, cost-effectiveness, and easy interaction with micro-pollutants. PNCs generally demonstrate a rapid decontamination potential paired with a high specificity for a wide array of contaminants. This chapter was mainly organized to provide overview insights on the importance and application of PNCs for treating and removal of several toxic substances such as organic dyes, metal

E. S. Goda—Co-author.

M. A. Gab-Allah, S. E. Hong, Y. G. Lijalem and K. R. Yoon—Contributing authors.

M. H. A. Elella (✉)

Chemistry Department, Faculty of Science, Cairo University, Giza 12613, Egypt

Emad. S. Goda · S. E. Hong · K. R. Yoon

Organic Nanomaterials Lab, Department of Chemistry, Hannam University, Daejeon 34054, Republic of Korea

e-mail: kryoon@hnu.kr

Emad. S. Goda

Fire Protection Laboratory, National Institute of Standards, 136, Giza 12211, Egypt

Mohamed. A. Gab-Allah

Reference Materials Lab, National Institute of Standards, 136, Giza 12211, Egypt

Y. G. Lijalem

Industrial Metrology Department, National Metrology Institute of Ethiopia, 5722 Addis Abeba, Ethiopia

© The Author(s), under exclusive license to Springer Nature Switzerland AG 2022

245

A. E. Shalan et al. (eds.), *Advances in Nanocomposite Materials for Environmental and Energy Harvesting Applications*, Engineering Materials,

https://doi.org/10.1007/978-3-030-94319-6_9

ions, persistent organic pollutants, bacteria, and spilled oils from polluted water. The procedure involved in the elimination of aforementioned contaminants is based on the adsorption process, which turns out to be more efficient and economically inexpensive. The polymer nanocomposites reviewed in this chapter have successfully eliminated methyl violet, methylene blue, Pb, Cd, Cr(VI), phenolic compounds, pesticides, oil matrices, etc. with removal percentages reaching almost 100% in some instances. Furthermore, the data presented herein exhibits the effectiveness of PNCs in wastewater purification over the existing conventional singular materials, and can be considered as a good base for the researchers and ecologists in exploring new avenues in wastewater treatment.

Keywords Drinking water · Synthetic dyes · Metal ions · Microbial contamination · Nanocomposites

List of Abbreviations

2,4-DNP	2,4-Dinitrophenol
AB	Acid blue 74
AF	Acid fuchsin
AL ₂ O ₃	Alumina
Alg	Alginate
AY	Acid yellow 36
BB	Bismarck brown Y
BC	Black cumin
BET	Brunauer–Emmett–Teller
ChNWs	Chitin nanowisker
CMC	Carboxymethyl cellulose
CNCs	Cellulose nanoparticles
CNCs	Cellulose nanocrystals
CNTs	Carbon nanotubes
COF	Covalent organic frameworks
Co-MCM	Chitosan/cobalt-silica
CR	Congo red
Cs	Chitosan
CTX	Cefotaxime
CV	Crystal violet
DB71	Direct Blue 71
DR	Direct red 80
DY12	Direct yellow 12
EDX	Energy-dispersive X-ray spectroscopy
FESEM	Field emission scanning electron microscopy
FTIR	Fourier-transform infrared spectroscopy
GA	Glutaraldehyde

Gel	Gelatin
GG	Guar gum
GO	Graphene oxide
HA	Humic acid
Hap	Hydroxyapatite
KPS	Potassium persulphate
MB	Methylene blue
MC	Mica
MG	Malachite green
MNPs	Magnetic nanoparticles
MO	Methyl orange
MOFs	Metal–organic frameworks
MV	Methyl violet
MWCNs	Multi-wall carbon nanotubes
NaAlg	Sodium alginate
NAC	Nacetyl cysteine
Nc	Nanocomposite
NPRI	National Pollutant material Release Inventory
PAA	Polyacrylic acid
PAA	Polyacrylic acid
PAAm	Polyacrylamide
PAM	Polyacrylamide
PANI	Polyaniline
PEI	Polyethyleneimine
PMMA	Poly(methylmethacrylate)
PNCs	Polymers-based nanocomposites
POPs	Persistent organic pollutants
Ppy	Polypyrrole
PVA	Poly(vinyl alcohol)
PVI	Poly(vinyl imidazole)
PVK	Polyvinyl-N-carbazole
Q_{\max}	Maximum adsorption capacity
RB	Rhodamine B
RB19	Reactive Blue 19
ROS	Reactive oxygen species
SCNTs	Single-walled carbon nanotubes
SGR	Simultaneous gelation and reduction
SMCS	Superhydrophobic magnetic cellulose sponge
TC	Tetracycline
TEOS	Tetraethyl orthosilicate
TFC	Thin film composite
TFN	Thin-film nanocomposite nanofiltration
TGA	Thermogravimetric analysis
TMC	Trimesoyl chloride
TPA	Terephthalaldehyde

TS	Total solids
USEPA	United States Environmental Protection Agency
VSM	Value-stream mapping
XG	Xanthan gum
XRD	X-ray diffraction

1 Introduction

Water is a very essential source for all living organisms and it represents around 70% of the total earth area). It is indispensable in multiple fields of human life include food, energy, economy, and health fields [1, 2]. In this regard, the contamination of freshwater is considered as a crucial environmental problem that causes a distressing situation for both ecosystems and human individuals. Indeed, the intensive growth of industrialization activities, increasing population, urbanization, global warming, and globalization have all contributed to the shortage of safe drinking water sources. The world health organization reported that 62% of the total global population will suffer from water lack by 2030, besides most of the wastewater reaches around 95% especially in the developing countries [3–10].

It is well known that there are more than 700 pollutants which can induce water contamination. Among these contaminants, toxic heavy metals, organic pollutants, oil pollutants, and microbial infection. These pollutants are highly toxic, carcinogenic, water-soluble, and non-biodegradable inside the body of living organisms [11–13]. Thus, the purification of wastewater is anticipated as a critical dilemma worldwide, and the researchers unit their efforts to find new strategies for the purification of contaminated water to preserve fresh-water resources. There were several established techniques such as adsorption, ion-exchange, reverse osmosis, chemical precipitation, electrolysis, conventional coagulation, membrane filtration, photocatalytic oxidation, and phytoremediation which have been used for obtaining well-cleaned water [14–16]. Nowadays, nanotechnology is considered as one of the important research areas that is covering a broad range of various applications such as wastewater treatment. It can enable the design of innovative adsorbents to remediate the problems associated with water pollution. Especially, the cost-effective and eco-friendly adsorbents consisting of nanomaterials have gained attention from scientific researchers around the world to treat and eliminate various hazardous materials from polluted water [5, 17–25]. Recently, biodegradable polymers-based nanocomposites containing various nanomaterials are receiving great interest in the water research due to their outstanding properties such as low cost, abundance, and easy to interact for pollutants.

2 Classification of Biodegradable Polymeric Nanocomposites

Biodegradable polymers can be classified into three categories; natural polymers, synthetic polymers, and polymer nanocomposites (see Fig. 1). The natural biodegradable polymers are divided into natural polysaccharides and proteins. Polysaccharides are long chains of carbohydrate polymeric oligosaccharides which are linked together through glycosidic bonds between monosaccharide repeating units. The extraction of polysaccharides depends on their origin sources; plant, animal, microbial and algal origin. Also, they can be categorized based on the composition of monosaccharide repeating units into homopolymers such as starch and heteropolymers such as chitosan [26–28].

Additionally, proteins are defined as natural polymers with polyamide structure. They are mainly formed of sequenced amino acids through peptide bonds and are considered as one of the main components in the human body due to its essential roles of controlling cell fates, catalyzing reactions, and building cellular structures. In these days, different proteins such as collagen, gelatin, silk fibroin, and bovine serum albumin have been widely employed in wastewater treatment due to their excellent properties such as non-toxic, low cost, biocompatibility, and biodegradability [19, 29].

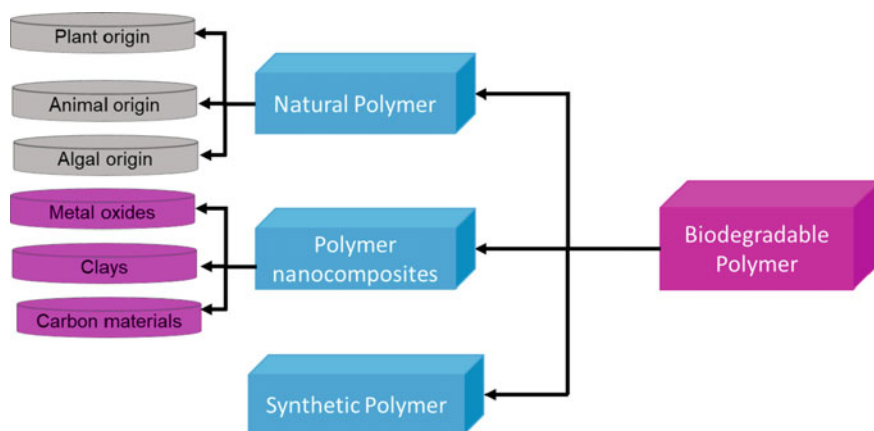


Fig. 1 Schematic representation showing the classification of biodegradable polymers

3 Removal of Dyes

Over the past few years, the use of dyes in a wide array of industrial fields such as inks, textiles, leather, paper mills, food, medical products, and cosmetics have been dramatically increased owing to their ease accessibility and affordable price [30, 31]. Worryingly, industrial effluents discharged from such industries are comprising massive amounts of dye contents [30, 32]. Most of existing dyes are organic compounds with complex composition; this can explain their chemical stability against degradation, and thus they persist in the environment for protracted periods. Additionally, they are soluble in water, highly toxic, mutagenic, and carcinogenic, thereby eliciting harmful effects on human health even at low concentrations [33]. For instance, dyes can provoke dermatitis, skin irritation, serious damage to human reproductive and central nervous systems, as well as kidney and liver malfunctions [34, 35]. On the other hand, when released into the environment, dyes have a detrimental ecological effect on the marine life since they can block sunlight from penetrating water, thus hampering the photosynthesis process [35, 36].

Methyl violet (MV), methylene blue (MB), methyl orange (MO), crystal violet (CV), congo red (CR), malachite green (MG), bismarck brown Y (BB), azo dye, acid fuchsin (AF), Direct Blue 71 (DB71) and Reactive Blue 19 (RB19), and rhodamine B (RB) are among the most prominent industrially relevant toxic dyes with known adverse effects on human beings. From both toxicological and ecological standpoints, adequate and efficient treatment of dye-containing industrial effluents before their discharge is therefore of a paramount environmental issue [37].

Different conventional strategies are currently available, as recently reviewed by Singh et al. [38] such as ozonation, reverse osmosis, coagulation, flocculation, biological treatment, chemical oxidation, electrochemical precipitation, ion-exchange, membrane filtration, etc. for remediation of industrial effluents and dyes removal from aqueous solutions. Nevertheless, such techniques are either costly and/or ineffective for entire dye removal [33, 39]. Adsorption has been the most promising and widely used technique because it is cost-effective, simple, yet efficient, and the applied adsorbent can be selected from a wide array of natural and rather bio-degradable materials [32, 40].

Recently, nanotechnology has provided an innovative and critical means of tremendous potential for industrial wastewater treatment with improved efficiency compared with conventional techniques. In this regards, polymer nanocomposites (PNCs) have attracted intense attention of the researchers and ecologists as another class of adsorbents for the purification of contaminated water (Table 1). In PNCs, nanoparticles (inorganic/organic fillers at the nanometer scale) spread into a polymer matrix via surface functionalization leading to the formation of novel materials which can have innovative chemical and physical properties such as high specific surface area, tunable porosity, binding property, thermal stability, good mechanical strength, bio-compatibility, cost-effectiveness, and potential to eliminate micro-pollutants [40–42]. Thus, they are considered as advanced tools in wastewater purification technology and suitable for efficient remediation of industrial effluents. A variety of

Table 1 An overview of the utilization of nanocomposite bio-adsorbents in the removal of dyes and heavy metals from contaminated water (adsorption kinetics, pseudo-second order)

Bio-adsorbents	Contaminant	Q _{max} (mg/g)	Ref.
XG-cl-P(AA-co-AAm)/Fe ₃ O ₄ hydrogel nanocomposite	Malachite green	497.15	[30]
SA-g-PAA/TiO ₂ hydrogel nanocomposite	Methyl violet	1156.61	[31]
XG-g-poly(AA-co-AAm) superporous hydrogel nanocomposite	Methyl violet	302.15	[35]
XG-cl-PAA/Fe ₃ O ₄ hydrogel nanocomposite	Methyl violet	642.00	[33]
h-XG/SiO ₂ nanocomposite	Methylene blue Methyl violet	497.50 378.80	[37]
GK-cl-PAA/silicon carbide hydrogel nanocomposite	Malachite green Rhodamine B	757.57 497.51	[39]
CMS-g-PVI/PVA/Fe ₃ O ₄ hydrogel beads	Congo red Crystal violet	83.66 91.58	[47]
CS/silica/ZnO nanocomposite	Methylene blue	293.30	[53]
CS/n-ZnO nanocomposite	Direct Blue 78 Acid Black 26	– –	[54]
Chitosan-epichlorohydrin/TiO ₂ nanocomposite	Reactive red 120	220.00	[56]
Chitosan/SiO ₂ /CNTs nanocomposite	Direct Blue 71 Reactive Blue 19	61.35 97.08	[57]
Magnetic chitosan/Al ₂ O ₃ /Fe ₃ O ₄ nanocomposite	Acid fuchsin	1666.67	[61]
Magnetic β-cyclodextrin–chitosan/graphene oxide nanocomposite	Methylene blue	84.32	[64]
XG-cl-pAA/rGO hydrogel nanocomposite	Methyl violet Methylene blue	1052.63 793.65	[66]
GO–Chitosan nanocomposite	Acid yellow Acid blue	68.86 85.70	[69]
Zeolite/nickel ferrite/sodium alginate bio-nanocomposite	Methylene blue	54.05	[71]
XG/SiO ₂ hybrid nanocomposite	Congo red	209.21	[72]
Magnetic polypyrrole decorated chitosan-based nanocomposite	Crystal violet Methylene blue	62.89 89.29	[76]
PAM-g-CS@γ-Fe ₂ O ₃ nanocomposite	Malachite green	86.28	[79]
XG-cl-pAA/o-MWCNTs hydrogel nanocomposite	Methylene blue	521.00	[80]
CS–PANI–CuO nanocomposite	Methyl orange	–	[81]
Fe ₃ O ₄ –gelatin nanocomposite	Direct yellow 12	1250	[83]
Gel-CNT-MNPs nanocomposite	Direct red 80 Methylene blue	465.50 380.70	[84]

(continued)

Table 1 (continued)

Bio-adsorbents	Contaminant	Q _{max} (mg/g)	Ref.
GO-cellulose nanocomposite	Azo dye	751.88	[102]
CMC-cl-pAA/Fe ₃ O ₄ -Cloisite 30B magnetic hydrogel nanocomposite	Methylene blue	1081.60	[103]
Starch/polyaniline nanocomposite	Reactive Black 5 Reactive Violet 4	811.30 578.39	[104]
CMS-g-PVI/PVA/Fe ₃ O ₄ hydrogel beads	Pb(II) Cu(II) Cd(II)	65.00 83.60 53.20	[47]
CS-Fe ₂ O ₃ nanocomposite	Pb(II) Cd(II) Pb(II) in Pb(II)+Cd(II)	214.923 204.318 173.218	[60]
XG-g-PAM/SiO ₂ nanocomposite	Pb(II)	537.634	[86]
XG/n-acetyl cysteine modified mica bio-nanocomposite	Pb(II) Cu(II) Ni(II)	530.54 177.20 51.48	[87]
CS-GO nanocomposite	Cr(VI)	104.16	[91]
CMC-Fe ₃ O ₄	Pb(II)	152.00	[92]
NaAlg-hydroxyapatite-CNT nanocomposite	Co(II)	347.8	[93]
CS-Alg nanocomposite	Cr(VI)	147.15	[105]
Magnetic chitosan/graphene oxide nanocomposites	Cu(II)	217.4	[106]
(h-GG/SiO ₂)	Pb(II) Cd(II)	645.16 709.21	[107]
HAp/Alg/gelatin nanocomposites	Pb(II) Cd(II)	616 388	[108]

polymeric resins are currently available as adsorbents via ion exchange mechanism such as polystyrene amidoxime, sulfonated polystyrene, polystyrene phosphonate, phenolic resin, sulfonated phenolic resin, aminopolystyrene, and epoxy-polyamine. Such polymeric resins can provide efficient removal capacity of dyes [34]. Nonetheless, lack of bio-degradability is a persisting issue throughout their long-term uses [43, 44].

Indeed, both environmental regulation and sustainability have triggered the need of PNCs hybrid to be prepared from renewable sources with bio-degradable nature and practical life cycle. Accordingly, a broad range of natural and synthetic bio-degradable polymer-based matrices have been utilized in the synthesis of nanoscale materials. Chitin/chitosan, xanthan gum (XG), guar gum (GG), gelatin (Gel), carboxymethyl cellulose (CMC), alginate (Alg), starch, polyvinylalcohol, polyaniline, polyacrylamides, polyvinyl imidazole, etc. have been widely explored for the

fabrication of PNCs for further removal of different dyes [34, 45–51]. Especially chitosan is the second-most prevalent natural polysaccharide with multifunctional character [52]. It comprises reactive primary and secondary hydroxyl groups, as well as amino groups which facilitate its uses as a convenient supporting material for adsorption purpose. However, this biopolymer suffers from chemical instability [45, 53]. Nano-porous particles such as ZnO [53, 54], TiO₂ [55, 56], SiO₂ [57], CuO [58], CdS [59], and Fe₂O₃ [60] have been extensively utilized for chemical modification in order to improve physical and chemical stability, as well as specific surface area and catalytic efficiency. Most recently, Hassan et al. [53] fabricated an efficient and cost-effective adsorbent for MB dye based on chitosan/silica/zinc oxide nanocomposite. Chitosan (Cs)/silica hybrid was prepared via the hydrolysis of tetraethyl orthosilicate (TEOS), and the sol-gel process was utilized for the formation of silica gel networking structure. Thereafter, the incorporation and immobilization of ZnO nanoparticles into the developed network structure were performed with the aid of the reactive hydroxyl and amino groups of chitosan as well as the residual hydroxyl groups in silica network as shown in Fig. 2. The adsorption data agreed with Langmuir isotherm, and the maximum adsorption capacity (Q_{\max}) of MB dye was 293.3 mg/g at pH 7, contact time 120 min, MB concentration of 550 ppm.

Moreover, the incorporation of Fe₃O₄ magnetic nanoparticles (MNPs) into polymer composites have been extensively applied as a nanostructured material, and generally provide beneficial characteristics for efficient purification of water due to their special magnetic characteristics, high surface area, strong adsorption, and easy separation under external magnetic field [34, 61]. However, Fe₃O₄ NPs have poor chemical stability and can be easily oxidized in the air which hinders their applications [62]. Hence, Alumina (Al₂O₃) is commonly used to improve their stability due to good chemical and physical characteristics and low cost [63]. Akbarnejad et al. [61] performed a brilliant work for the preparation of magnetic bio-degradable Chitosan/Al₂O₃/Fe₃O₄ nanocomposite (CSAF) for efficient adsorption of acid fuchsin (AF) dye from aqueous solutions. A co-precipitation method was utilized for the synthesizing of magnetic NPs. A graphical representation for the preparation procedure of CSAF nanocomposite, and the proposed mechanism for AF onto CSAF adsorbent are depicted in Fig. 3(a, b). Characterization of the polymer-based nanocomposite was performed by fourier-transform infrared spectroscopy (FTIR), energy-dispersive X-ray spectroscopy (EDX), field emission scanning electron microscopy (FESEM), Brunauer–Emmett–Teller (BET) analysis, X-ray diffraction (XRD) analysis, value-stream mapping (VSM) analysis, and thermogravimetric analysis (TGA) techniques. Spherical shapes of the magnetic Fe₃O₄ and Al₂O₃/Fe₃O₄ nanoparticles were confirmed by FESEM characterization with 51 and 69 nm size diameters, respectively (see Fig. 3c). The adsorption behavior was spontaneous, and well-fitted to the pseudo-second order and Langmuir isotherm models. Q_{\max} of 1666.67 mg/kg was obtained at pH 3, AF dye concentration 200 mg/L, and contact time 15 h. Figure 3d shows the AF dye removal by the developed adsorbent and its magnetic separation property. The authors suggested that this adsorption process could be controlled by intra-particle diffusion and film diffusion [61].

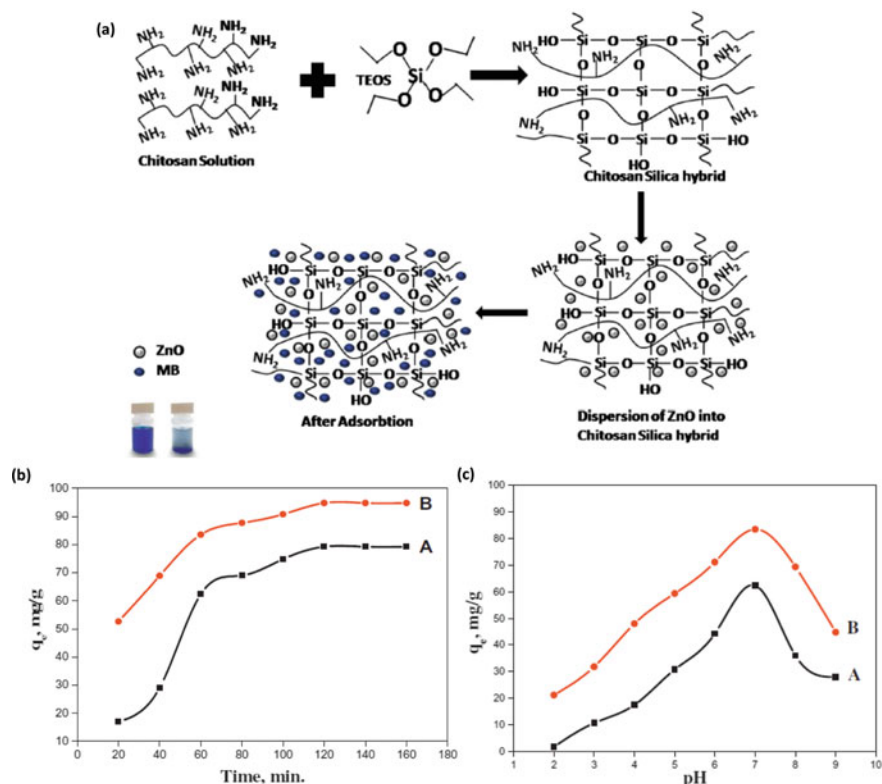


Fig. 2 a Graphical illustration of the synthesis of chitosan/silica/ZnO polymer nanocomposite as a bio-degradable adsorbent, **b** and **c** effects of contact time and pH, respectively on the adsorption capacity of CS/silica (A) and CS/silica/ZnO nanocomposite (B). Reprinted with permission [53]. Copyright 2019, Elsevier

On the other hand, carbon nanotubes (CNTs) possess outstanding properties such as unique tubular structures, high electrical and thermal conductivity as well as improved mechanical properties. In view of this, a novel magnetic nanocomposite based on chitosan/SiO₂/CNTs has been developed via the gelation method, which can be applied as an efficient bio-degradable adsorbent for the removal of toxic anionic dyes (direct blue 71 (DB71) and reactive blue 19) from contaminated aqueous solutions [57]. The developed magnetic chitosan nanocomposite proved to have important features since they demonstrated high stability over different pH conditions, high thermal stability, low toxicity, and ease separation from aqueous solution. Graphene oxide (GO)-based polymer nanocomposites have also been considered as effective adsorbents for organic dyes capturing from the contaminated wastewater due to its high surface area, hydrophilic nature, and functional properties which allow a broad spectrum of chemical modifications [64–67]. The technological applications of graphene-based polymer nanocomposite adsorbents were thoroughly presented

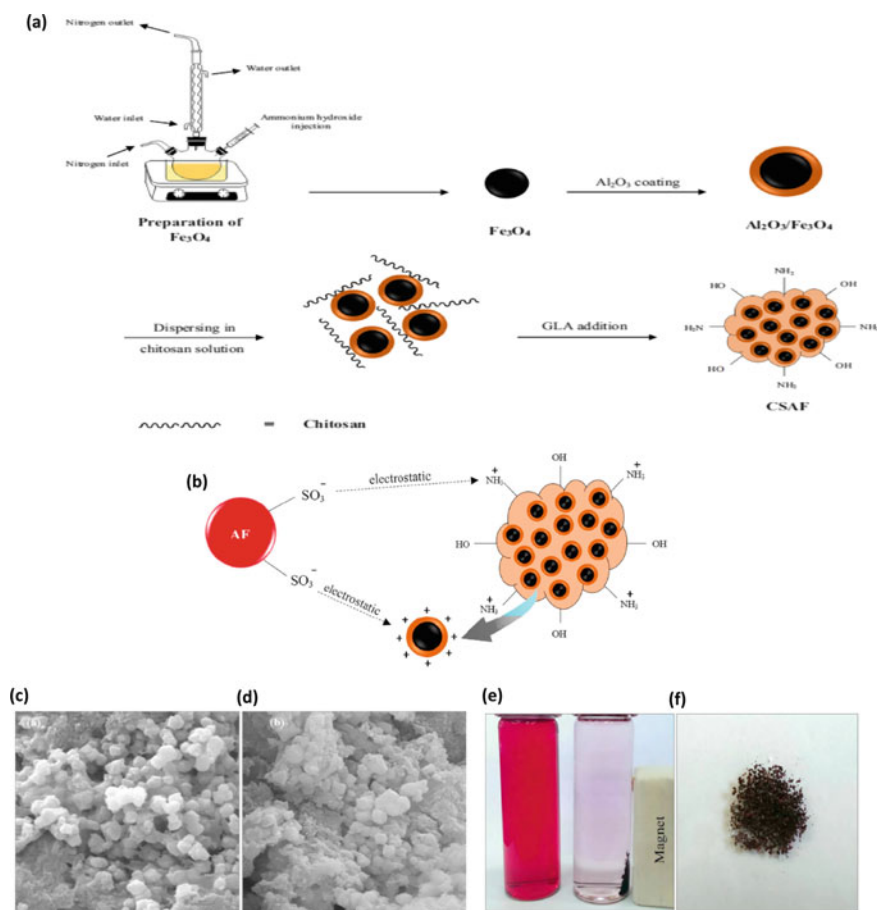


Fig. 3 **a** Graphical representation of the preparation procedure of CSAF adsorbent, **b** proposed mechanism for the AF dye adsorption onto CSAF adsorbent, **c** FESEM micrographs of the nanocomposite before and after the adsorption process, and **(d)** AF dye removal by the developed adsorbent and its magnetic separation property. Reprinted with permission [61]. Copyright 2019, Elsevier

in detail by Ali and co-workers, emphasizing the potential outlook of this fascinating adsorbent in the efficient removal of contaminants from wastewater [68]. In this respect, an inspiring work was conducted by Banerjee and co-workers for the preparation of excellent bio-degradable adsorbent based on GO chitosan nanocomposite prepared by incorporation of GO nanoparticles into chitosan matrix (GO-Cs-Nc) with the assistance of ultrasound irradiation [69]. GO was prepared from exfoliated graphite powder via Hummers method. The obtained GO was allowed to form a homogeneous suspension through ultrasound exposure for 20 min. Thereafter chitosan flakes were added, stirred for two hours, and subjected to further ultrasound exposure for 1 h. The final polymer nanocomposite was then vigorously washed, and

then allowed to dryness in a vacuum at 40 °C. The developed bio-degradable and rather a cost-effective polymer nanocomposite allowed the removal of acid yellow 36 (AY) and acid blue 74 (AB) from industrial effluent with adsorption efficiency reached 98.18 and 98.80%, respectively, with initial concentrations of 21.47 (AY) and 22.15 mg/L (AB). The authors concluded that ultrasound exposure of GO for 6.48 min caused improvement in its adsorption efficiency and considerably shorten the time needed for maximum adsorption of the target dyes from industrial effluents [69].

It has been proven that biocompatibility, biodegradability, renewable nature, nontoxicity, the abundance of alginate-based composites have promoted its applications in the removal of water pollutants such as dyes, heavy metals, and antibiotics from industrial effluents [70]. Physical and chemical features of the alginate nanocomposite have controlled its adsorption efficiency. Zeolite/nickel ferrite in conjunction with sodium alginate (NaAlg) was synthesized and elucidated as bio-nanocomposite adsorbent utilizing a co-precipitation technique for efficient removal of water-soluble MB dye. The adsorption systems of MB dye were in line with Langmuir isotherms with Q_{\max} of 54.05 mg/g, and thermodynamic investigations indicated the spontaneity of the process. Moreover, the developed bio-nanocomposite adsorbent revealed to be efficient and environmentally friendly [71].

On the other hand, hydrogels have gained immense popularity in recent researches. Combining the inorganic materials and organic polymers to synthesize nanocomposite hydrogels generally results in innovative physical, and chemical properties (i.e., high strength, enhanced swelling properties, high heat resistance, high chemical stability, and good modulus. An alginate nanocomposite hydrogel (NaAlg-g-polyacrylic acid (PAA)/TiO₂) was prepared by free radical graft copolymerization of sodium alginate (NaAlg) with AA and TiO₂. The introduction of TiO₂ NPs allowed the formation of the hydrogel nanocomposite with high pore volume, tunable surface and unique structure. This bio-adsorbent was suitable for the efficient removal of MV dye with high Q_{\max} (1156.61 mg/g), and adsorption efficiency of 99.6% at pH 7, temperature of 25 °C [31].

Xanthan gum (XG), a natural exopolysaccharide which is produced by Gram-negative bacterium namely *Xanthomonas campestris*, has gained a paramount importance in recent years in many technological applications due to biodegradable nature, non-toxicity, abundance, swelling, hydration, high viscosity and gelation ability. To extend its potential uses, XG has been chemically modified to form xanthan-based nanocomposites and hydrogels which have been extensively employed as a biopolymer adsorbent in the purification of contaminated water [30, 33, 37, 41, 72–74]. Incorporation of Fe₃O₄ MNPs into XG-g-PAA to form nanocomposite hydrogel was found effective in capturing of MV dye from contaminated water with efficiency of 99%, and Q_{\max} of 642 mg/g at a contact time of 60 min, optimum pH of 6.5 at 25 °C [33]. In another interesting study, Ghorai et al. [37] utilized biodegradable hydrolyzed polyacrylamide grafted xanthan gum/silica nanocomposite (h-XG/SiO₂) as an excellent adsorbent for wastewater purification. The nanofiller was prepared via sol-gel process and the prepared adsorbent was applied for the

effective removal of toxic cationic dyes including methyl violet (MV) and methylene blue (MB) from aqueous solution. The adsorption mechanism of MB and MV using the developed polymer nanocomposite (h-XG/SiO₂) is presented in Fig. 4. The efficiencies of removal for both MB and MV were 99.4 and 99.1%, respectively. The maximum specific removal (Q_{\max}) for MB was 497.5 mg/g at pH 8 at contact time

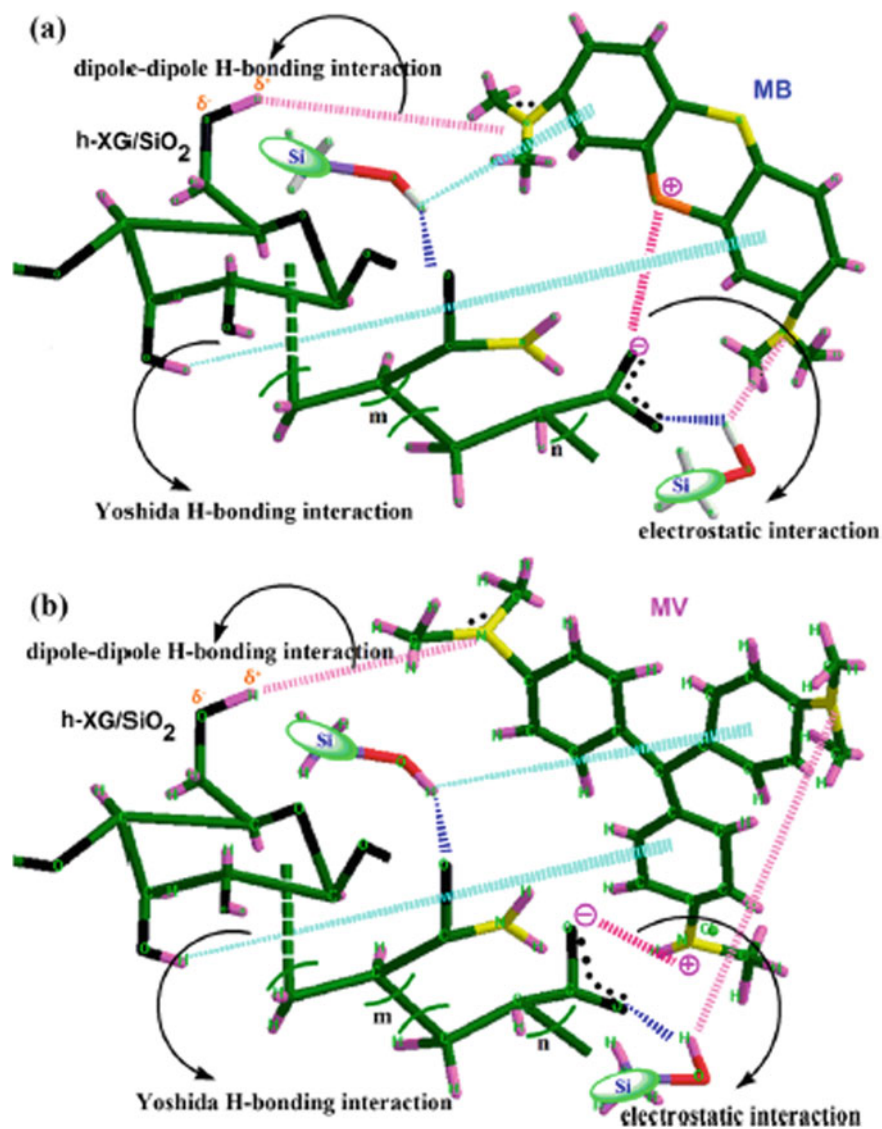


Fig. 4 Schematic layout of the adsorption mechanism for MB **a** and MV **b** using the developed polymer nanocomposite (h-XG/SiO₂). Reprinted with permission [37]. Copyright 2014, Elsevier

of 20 min, and temperature of 323 K, meanwhile, Q_{\max} for MV was 378.8 mg/g at pH 9 at contact time of 15 min, and temperature of 313 K.

In addition to the above, biopolymers such as chitosan, alginate, xanthan gum, guar gum or starch have been combined with various synthetic polymers such as polyacrylamide (PAAm) polyacrylic acid (PAA), polypyrrole (Ppy), and polyaniline (PANI) to optimize the limitation of these synthetic polymers and expand their features in terms of biodegradability and eco-friendly nature [75–82]. The blending or grafting of the synthetic polymer onto the backbone of the biopolymer and incorporation of nanoparticles have enhanced both the adsorption efficiency of contaminants and the water absorption rate of the systems. As reported by Mashkoo and Nasar [76], polypyrrole decorated chitosan-based adsorbent facilitated the highly efficient removal of the cationic CV and anionic MO dyes from contaminated wastewater with removal efficiency reached up to 88.11 and 92.89%, respectively, at the optimum conditions. Furthermore, the maximum monolayer sorption capacities of CV and MO dyes were recorded as 62.893 and 89.286 mg/g, respectively at 303 K. On the same track, poly(vinyl alcohol) (PVA) and poly(vinyl imidazole) (PVI) are water-soluble, non-toxic, and biodegradable synthetic polymers which have been commonly employed in different blend formations for water treatment and biomedical applications. Pour and Ghaemy [47] synthesized a new bio-adsorbent hydrogel (m-CVP) beads via a gelation method of CMS-g-PVI, PVA, and Fe_3O_4 blend in boric acid solution with further crosslinking using glutaraldehyde (GA). Based on characterization data, Fe_3O_4 nanoparticles were successfully incorporated into the crosslinked hydrogel beads. The developed magnetic nanocomposite hydrogel has been efficient in capturing of CR and CV dyes with Q_{\max} of 83.66 and 91.58 mg/g, respectively, at optimum pH of 7.4, and the adsorption rate fitted well with the pseudo-second order kinetics. This study was proved to be beneficial in the fabrication of high capacity magnetic biodegradable nanocomposite adsorbents with appropriate recovery [47].

Furthermore, the development of protein-based materials for potent water decontamination has been gaining pace. Gelatin is a protein produced from controlled hydrolysis of native collagen. In recent times, this protein has been exploited in the fabrication of nanocomposites-based polymers for the elimination of dyes from wastewater [50, 83, 84]. A uniform and high efficient nanoadsorbent based on iron oxide and gelatin was prepared from gelatin powder, iron salts, and ammonium hydroxide solution by means of controlled co-precipitation technique [83]. The characterization analysis revealed that the Fe_3O_4 -gelatin was efficiently prepared with crystallite size 82 nm, and particle diameter of 81 nm. Fe_3O_4 -gelatin has shown to be efficient for direct yellow 12 (DY12) dye removal with an excellent adsorption capacity of 1250 mg/g, at pH 2, and contact time 600 min. This nano adsorbent proved to have better adsorption efficiency compared with activated carbon in similar conditions due to the activity of its functional groups. The authors concluded that this efficient and affordable material had the potential to be applied for the removal of other colored contaminants, with ease separation by external magnetic field after the adsorption process could be reused in further treatments [83]. On the same track, another magnetic nanocomposite adsorbent synthesized from gelatin,

CNT, and Fe_3O_4 nanoparticles (Gel-CNT-MNPs) was applied for the elimination of anionic direct red 80 (DR) dye and cationic MB dye from aqueous solutions [84]. The proposed mechanism for DR and MB adsorption by using the synthesized nanocomposite bead is depicted in Fig. 5a. The nanocomposite bead removed 96 and 76% of DR and MB dyes, respectively (Fig. 5b, c). Additionally, the maximum adsorption capacities for DR and MB dyes were noted as 465.5 and 380.7 mg/g, respectively, which revealed that this novel nanocomposite adsorbent could have substantial capacity in the applications of wastewater treatment.

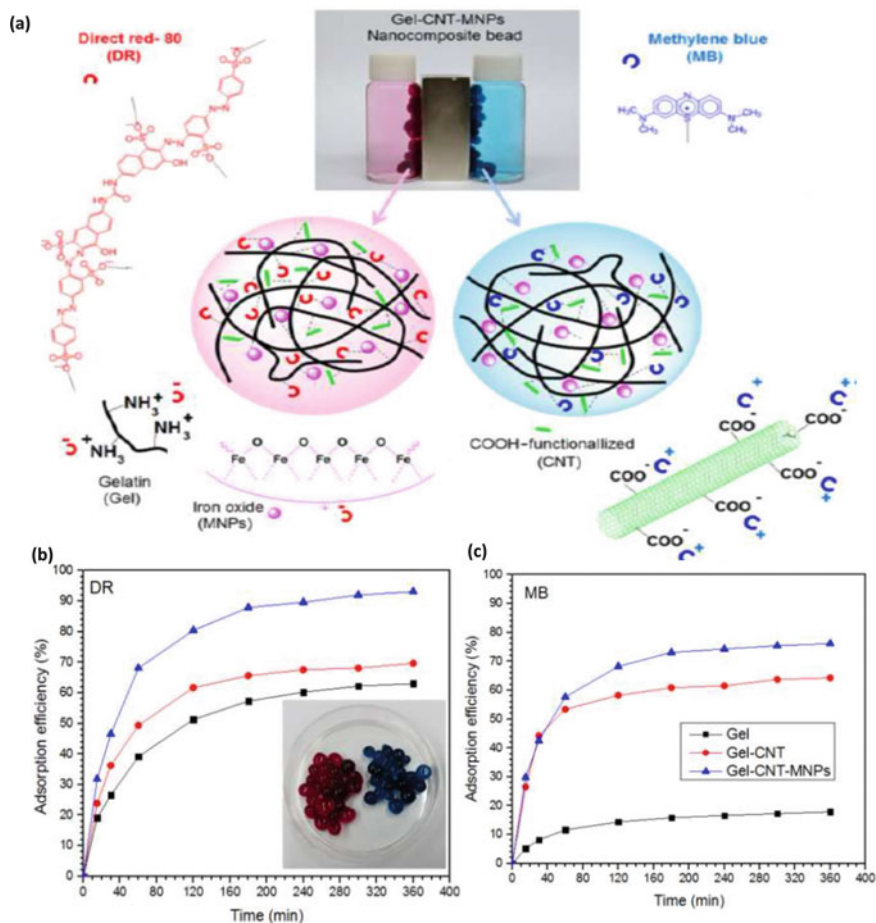


Fig. 5 a Graphical illustration for the proposed mechanism for DR and MB adsorption by using the synthesized nanocomposite bead (Gel-CNT-MNPs), and b–e effects of time and initial dyes concentration on adsorption performance of DR and MB by the gelatin, synthesized bead, and the nanocomposite beads. Reprinted with permission [84]. Copyright 2017, Elsevier

4 Removal of Metals

Heavy metals such as mercury, lead, arsenic, gold, chromium, zinc, copper, cadmium, nickel, palladium, platinum, and silver, etc. are naturally occurring elements possessing relatively high density. They can be released into the environment through water streams and soils as a result of human activities including mining, agricultural, industrial processes, as well as improper waste disposal [85, 86]. Unlike dyes and other organic contaminants, heavy metals have gained a significant deal of attention due to non-degradability, toxicity even at trace amounts, carcinogenic nature, and their accumulation tendency in the food chain and living beings. This causes a long term risk to human health [87]. For instance, the intake of such heavy metals can elicit nerve damage as well as a malfunction in the liver, brain, kidney, and endocrine system, and in a serious situation, they can induce death [87]. Considering non-degradability, accumulation tendency, and further severe adverse effects of these heavy metals, establishing suitable methods for efficient removal of these toxic contaminants from industrial effluents using eco-friendly and cost effective materials has become of significant importance in the current frontier research. Lim and Aris [88] have explained the development of affordable and suitable adsorbents for the removal of heavy metals from contaminated water using a variety of techniques. For these techniques, there is a requirement for proper adsorbent with design versatility and functional capability for generating high-quality treated effluent. In this sense, the catalytic properties, bio-degradability, biocompatibility and tunable surface of bio-degradable polymer nanocomposites also find enormous potential as bio-adsorbents in the elimination of metals from contaminated water (see Table 1).

As noted earlier, the nanocomposite-based adsorbents have been synthesized via infusing or incorporation of the inorganic nanoparticles onto the polymers such as xanthan gum, alginate, chitosan, cellulose, ion-exchangers, and porous resins to develop hybrid adsorbents which can facilitate the rapid removal of metals from contaminated water [34, 86, 88]. In this view, XG-g-polyacrylamide (PAM)/SiO₂ was fabricated as a novel hybrid bio-adsorbent for efficient elimination of Pb²⁺ from contaminated water [86]. XG-g-PAM was prepared through a radical polymerization method using potassium persulphate (KPS) as initiator. In situ dehydration and sol-gel processes were utilized for the synthesis of the hybrid nanocomposite. The nanocomposite adsorbent exhibited excellent adsorption capacity ($Q_{\max} = 537.634$ mg/g) of Pb²⁺ (400 ppm) at pH 5.5 in comparison to XG-g-PAM and XG. This was attributed to the enhanced hydrodynamic radius and high intrinsic viscosity of the nanocomposite as a result of the uniform distribution of SiO₂ in XG-g-PAM polymer. Figures 6(a, b) show the adsorption mechanism of Pb²⁺ by grafted polymer and the nanocomposite, and the influence of contact time on the adsorption efficiency using nanocomposite, different graft copolymers, and XG adsorbents.

Another recent and ecofriendly bio-nanocomposite adsorbent based on xanthan gum/nacetyl cysteine-Mica (XG/NAC-MC) was developed by Ahmad et al. [87]. The fabricated adsorbent was found efficient in the capturing of toxic heavy metals including Cu(II), Pb(II), and Ni(II) from aqueous solutions. The adsorption of the

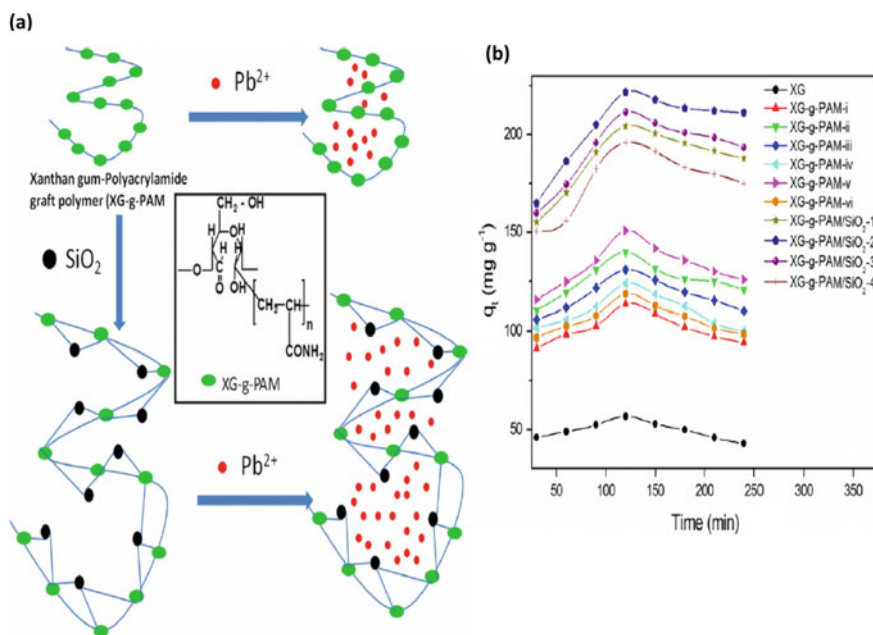


Fig. 6 **a** Schematic illustration of the adsorption mechanism of Pb²⁺ by grafted polymer and the nanocomposite, **b** influence of contact time on the efficiency of Pb²⁺ adsorption using nanocomposite, different graft copolymers, and XG adsorbents. Reprinted with permission [86]. Copyright 2012, Elsevier

target metal ions was considerably improved due to the new functionality illustrated by the interaction of various functional groups on NAC-MC with XG functional groups. The % removal of Cu(II), Pb(II), and Ni(II) were 97, 99, and 93%, respectively and the Q_{\max} were 177.2, 530.54, and 51.48 mg/g, respectively at 323 K. The optimal conditions for adsorption of Cu(II), Pb(II), and Ni(II) (Conc. 50 mg/L) were acquired at pH of 5, 4 and 4; and contact time of 60 min, 60 min and 120 min, respectively [87].

In another study, modified guar gum/SiO₂ was synthesized by grafting synthetic PAM chains on guar gum (GG) backbone via the sol-gel process. The nanocomposite flocculant was found suitable for the elimination of diverse metal ions (Mn²⁺, Fe³⁺, Ca²⁺ and Mg²⁺) along with turbidity, total solids (TS), total suspended solids, and total dissolved solids from industrial wastewater [89].

Reportedly, chitosan can be used as an excellent bio-adsorbent, after implementing physical and chemical treatments, for the removal of targeted metal ions from contaminated water with coveted bio-sorption selectivity and capacity [34, 45]. An extensive review on this regard was conducted by Shukla et al. reviewing most of its technological and scientific facets [90]. Most recently, Ahmad et al. [60] investigated the eco-friendly synthesis of a novel CS-Fe₂O₃ nanocomposite via a facile green approach. This nanoadsorbent was employed for the uptake of Pb (II), Cd (II) in a single

system, and Pb (II) in binary system from aqueous solution. The Q_{\max} for Pb(II), Cd(II) and Pb(II) in Pb(II)+Cd(II) was reached 214.923, 204.318 and 173.218 mg/g, respectively. These results were obtained at pH 5 and 6 for single and binary systems, respectively. Contact time, initial metal concentration, and temperature were 180 min, 100 mg/L and 323 K, respectively, for both systems. The adsorption kinetics of metals were in accordance with Pseudo-second order and Langmuir isotherm kinetic model. Thermodynamic data exhibited that the process was spontaneous and endothermic, being chemical sorption as the rate determining step. Furthermore, the nanocomposite adsorbent revealed superior regenerability and can be successfully reused up to five cycles as an ecofriendly adsorbent for toxic elements elimination from contaminated water.

Chromium (VI) removal from aqueous solutions was facilitated by chitosan grafted GO (CS-GO) nanocomposite [91]. The fabrication of this adsorbent was carried out by modified Hummer's method with ultrasonic irradiation technique. SEM micrographs of CS-GO nanocomposite confirmed the mounting of chitosan polymer onto GO layers by exhibiting surface roughness, and heterogeneous morphology as can be seen from Fig. 7a. Meanwhile, after adsorption, the CS-GO nanocomposite showed a dense porous morphology owing to the accumulation of Cr(VI) between the GO layers (Fig. 7b). The fabricated CS-GO adsorbent showed a good monolayer adsorption capacity of 104.16 mg/g at 50 mg/L of the target metal ion. The optimum results were acquired at pH 2 and contact time of 420 min (Fig. 7c and d). The desorption study indicated that CS-GO material can be recycled up to 10 cycles with a slight loss in the adsorption efficiency, confirming good regeneration ability.

Magnetic nanoparticles have also gained considerable scientific attention and been commonly employed in the removal of heavy metals from wastewater. Fan and co-worker facile fabricated magnetic CMC/Fe₃O₄ nanocomposite from 1 g of CMC, FeCl₃·6H₂O (0.321 M, 500 ml) and FeCl₂·4H₂O (0.179 M, 500 ml) via one-step high-gravity technology using an IS-RPB reactor (Fig. 8) [92]. The adsorption capacity of the nanocomposite for Pb (II) (200 mg/L) was investigated using the Langmuir isotherm model for adsorption, and the maximum sorption capacity obtained was 152.0 mg/g. The fabricated CMC-Fe₃O₄ adsorbent revealed both enhanced adsorption capacity and faster rate for Pb(II) than the pure Fe₃O₄ NPs.

On the other hand, hydroxyapatite (HAp) has been broadly researched as a sorbent due to its properties such as high adsorption capacity and low water solubility. HAp can also be uniformly distributed in polymer matrices, such as Alg to improve their mechanical properties. However, lack of sufficient porosity and low surface area limits its application. To overcome this limitation, Karkeh-abadi et al. [93] introduced a new nanocomposite bead by the utilization of NaAlg, hydroxyapatite (HAp), and CNTs for the synthesis of NaAlg/HAp/CNTs as nanocomposite adsorbent for the elimination of Co(II) ion pollutants from contaminated water. The obtained results reflected about 347.8 mg/g maximum adsorption capacity of Co(II) ion with a concentration of 400 mg/L and pH 6.8; indicating high metal ion affinity. The results demonstrated that the adsorption capacity of NaAlg/HAp/CNTs nanocomposite beads was enhanced owing to the inclusion of CNT with the large surface area into the network

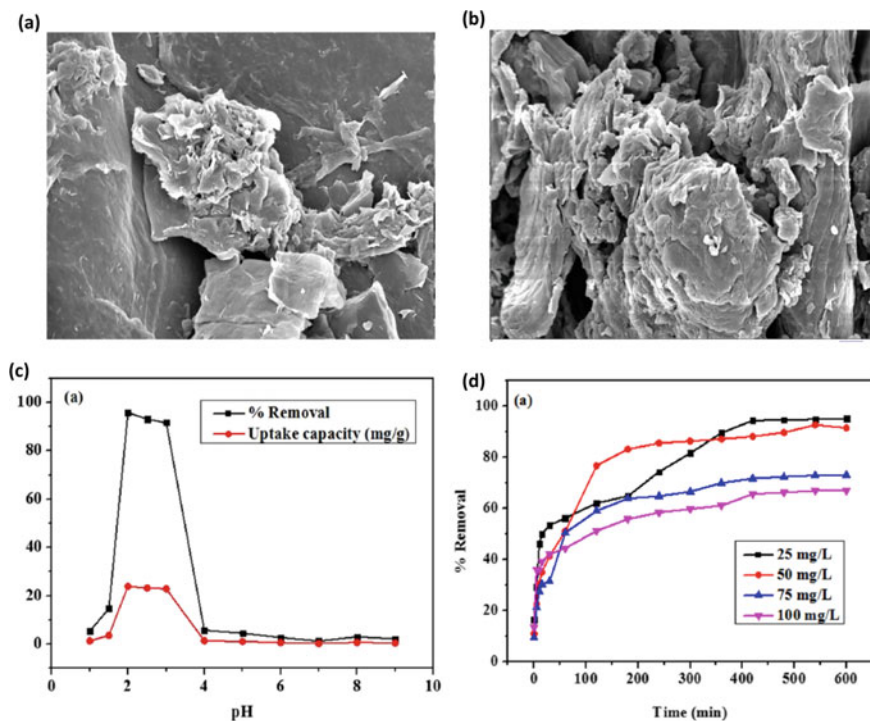


Fig. 7 a Synthesis of CS-GO nanocomposite adsorbent and the proposed mechanism of Cr(VI) removal, b, c SEM micrographs of CS-GO before and after adsorption of Cr(VI), d pH effect on the adsorption process, and e contact time effect on % removal of Cr(VI) on CS-GO. Reprinted with permission [91]. Copyright 2019, Elsevier

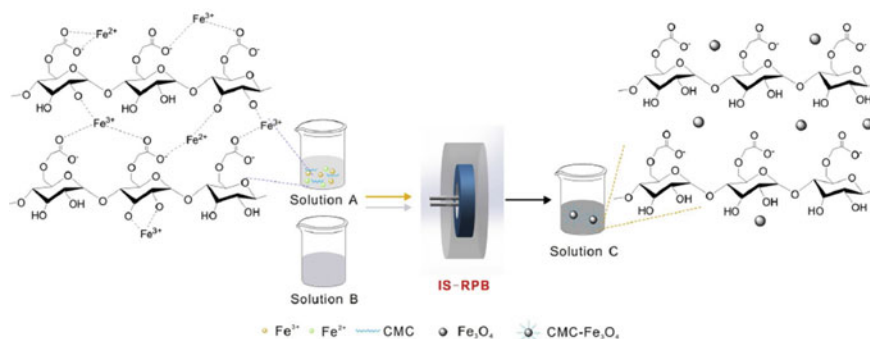


Fig. 8 Schematic diagram for the fabrication of CMC- Fe_3O_4 through IS-RPB reactor. Reprinted with permission [92]. Copyright 2019, Elsevier

of NaAlg-HAp, and the adsorption kinetics of Co(II) ions was consistent with a pseudo-second-order model [93].

Another study devoted to the contribution of polymer nanocomposite adsorbents for water purification was presented based on the combination of CMS-g-PVI, PVA, and Fe₃O₄ via a gelation method with further crosslinking using glutaraldehyde (GA) to synthesize new bio-adsorbent hydrogel beads [47]. Fe₃O₄ nanoparticles were efficiently introduced into the crosslinked hydrogel beads. The developed magnetic nanocomposite hydrogel has been used as efficient adsorbent for Pb(II), Cu(II), and Cd(II) with Q_{max} of 65.00, 83.60, and 53.20 mg/g, respectively, at optimum pH of 7.4, and the adsorption rate fitted well with the pseudo second order kinetics. This study was proved to be beneficial in the fabrication of high capacity magnetic biodegradable nanocomposite adsorbents with appropriate recovery [47].

Furthermore, membrane separation systems have received a great deal of attention in recent times for the elimination of toxic contaminants from water. The integration of a variety of nanomaterials as particular chemical functionalities onto the activated carbon surface has promoted the fabrication of extremely selective nano-adsorbent materials for hybrid membranes applications. Such nanomaterials include zeolite nanoparticles [94], cellulose nanoparticles [95], TiO₂ [96], silica [97], silver [98], graphene oxide [99], carbon nanotubes [100], and metal-organic frameworks (MOFs) [101]. Cellulose nanocrystals (CNCs) are regarded as excellent candidates for the modification of thin film composite (TFC) owing to their hydrophilic, renewable, bio-degradable nature as well as non-toxic characteristics. Most recently, Hoang and co-worker have done a brilliant work by preparation of a novel positively charged thin-film nanocomposite nanofiltration (TFN) membrane from trimesoyl chloride (TMC) and polyethyleneimine (PEI) via interfacial polymerization and inclusion of cellulose nanoparticles (CNCs). The findings revealed acceptable and competitive removal efficiency for toxic heavy metal ions of CuSO₄, CuCl₂, and PbCl₂ (200 mg/L) with rejection (%) of 98.0, 96.5, and 90.8%, respectively. The author concluded that the inclusion of green and affordable CNCs as nanofillers for membrane technology resulted in an enhancement in membrane permeability, hydrophilicity, surface roughness as well as surface area, thereby improving the general performance of TFN membranes.

5 Removal of Persistent Organic Pollutants

Among the common pollutants, persistent organic pollutants (POPs) such as poly(chlorinated biphenyls), antibiotic residues, pesticides, and humic acid are toxic aromatic contaminated compounds that can cause serious environmental problems for human individuals and living organisms worldwide [109–111]. Concerningly, POPs could be discharged into the environment via industrial effluents and contaminate drinking and ground water. Therefore, they can be ingested by human beings through food chains exerting harmful effects due to their bioaccumulation and non-biodegradability [112, 113].

5.1 Removal of Phenols

In recent years, water surfaces have been contaminated with highly poisonous organic pollutants such as phenolic compounds including 2,4-dinitrophenol, bisphenol A, gallic acid, catechol, picric acid, polyphenols, and poly(chlorinated biphenyls) causing a grave risk on the body health and a severe diseases such as cancer, malformation, and poisoning [114–117]. United States Environmental Protection Agency (USEPA) and the National Pollutant material Release Inventory (NPRI) in Canada have reported the phenolic compounds as priority pollutants [118]. Moreover, phenols are a weak acid and can spread into water surfaces from the outlets of various industrial activities such as oil refining, capacitors, paper, transformers, paint, pharmaceutical, plastics, pesticides, petroleum, polymeric resins, coal conversion, pulp, wood products, and petrochemical industries [119–121]. Consequently, their discharge into drinking water and groundwater without purification process causes serious risks to the eco-system.

There are many available techniques for the purification of phenols from water such as ozonolysis, photocatalytic decomposition, electrochemical and chemical oxidation, ion-exchange, distillation, redox reactions, precipitation, membrane separation, and solvent extraction techniques but the research results showed their low purification efficiency with a low rate of purification. Nevertheless, the prominent adsorption technique has been widely applied for the removal of phenols from wastewater due to its excellent properties such as low cost, high flexibility, easy operation, and design simplicity. Additionally, adsorption technique can be carried out through different three adsorption mechanisms including chemical, physical, and ion-exchange adsorptions [114, 122, 123]. Usually, the adsorption technique involves adsorption of the contaminated molecules onto adsorbent surface to separate them from the water surface. A different class of adsorbent materials has been utilized for purifying water including multi-walled carbon nanotubes [124], modified diatomite [125], and mesoporous silica [126]. However, they are suffering from the high cost, difficult regeneration, high disposal cost, and poor adsorption ability. As a result, biodegradable polymers-based adsorbents have recently drawn a great attention of global scientific researchers for wastewater purification to reduce the disposal cost and enhance the regeneration ability. The presence of more functional groups on their surfaces have led to ease derivatization to many useful forms. For example, natural polysaccharides such as xanthan gum, chitosan, and modified cellulose, in addition to β -cyclodextrin and synthetic biodegradable polymers such as poly(methylmethacrylate) and Poly(N-vinyl-2-pyrrolidone-co-N-isopropyl acrylamide), but they still have distress in their chemical instability, and mechanical properties. To improve their properties, various nanomaterials can be widely used as incorporated fillers such as ZnO [127, 128], activated carbon [129], silica [122], Fe₃O₄ [130–132], alumina [133], and multi-wall carbon nanotubes [134].

For instance, ZnO/XG-grafted-Poly(aniline) nanocomposite has been recently synthesized with oxidative free radical grafting copolymerization method according

to Ahmed and Hasan [127] to be used as an efficient adsorbent for the capture of 2,4-dinitrophenol (2,4-DNP). The adsorption data illustrated the endothermic and spontaneous adsorption process. Q_{\max} was mentioned as 123.15 mg/g for 2,4-dinitrophenol at pH 4 according to Langmuir isotherm model. Also, the pseudo-second order kinetic was found to be the best model for describing the chemical adsorption data according to its high R^2 and low χ^2 values.

Moreover, Campagnolo et al. [128] mentioned the synthesis of photocatalyst poly(methylmethacrylate)/zinc oxide/gold (PMMA/ZnO/Au) hybrid porous nanocomposite via the thermal and dipping treatment for removing bisphenol-A. The authors reported that maximum adsorption efficiency was to be 63.5% using PMMA/ZnO/Au nanocomposite compared to that of the PMMA/ZnO nanocomposite (34%) due to the higher adsorption on the surface of gold nanoparticles. Wang et al. [135] reported the synthesis of a core-shell magnetic β -cyclodextrin layer ($\text{Fe}_3\text{O}_4 @ \beta\text{-CD}$) nanocomposite for removing 2,4,4'-trichlorobiphenyl (PCB-28) and 2,2', 5,5'-tetrachlorobiphenyl (PCB52). The adsorption of PCB-28 was a little higher than that of PCB-52. Langmuir adsorption isotherm data demonstrated that Q_{\max} was 40.01 mg/g for PCB-28 and 30.32 mg/g for PCB-52.

In this respect, more recently, Khammar et al. [136] prepared carboxymethyl- β -cyclodextrin nanocomposite modified by novel magnetic nanoparticles through the grafting onto the as-prepared core-shell structure of magnetic silica nanoparticles for removing a high concentration of PCBs as decachloro biphenyl (PCBs 209) as depicted in Fig. 9b. As shown in Fig. 9a, the average size of nanoparticles was found to be 51.2 nm. While EDX data supported the preparation of nanocomposites by seeing both Si and Fe peaks. The as-mentioned findings demonstrated that the optimum conditions for the removal of maximum PCBs value of 82% were 10 mg/mL and 30 min at 50 °C (Fig. 9c). From the thermodynamic parameters ($\Delta H^0 > 0$, $\Delta G^0 > 0$, and $\Delta S^0 > 0$), the adsorption process was confirmed to be nonspontaneous and endothermic.

5.2 Removal of Antibiotics

Antibiotics are considered as humans and veterinary drugs for curing the fetal bacterial infections and can be used for growing animal promotion purposes. Nowadays, the antibiotic consumption has increased sharply around the world (10,000 tons in Europe, 13,000 tons in USA, and 162,000 tons in China). Environmental sources (surface water, groundwater, and soil) are mainly contaminated with a trace of active antibiotic residues within agricultural, domestic, and industrial effluents that can cause toxic impact through the possible cause of different infectious diseases on human bodies and surrounding flora [137–143].

Conventional wastewater treatment techniques such as membrane filtration, coagulation, sedimentation, biological treatment, and flocculation are were found to be ineffective methods for capturing the water contaminants from antibiotics [144–147].

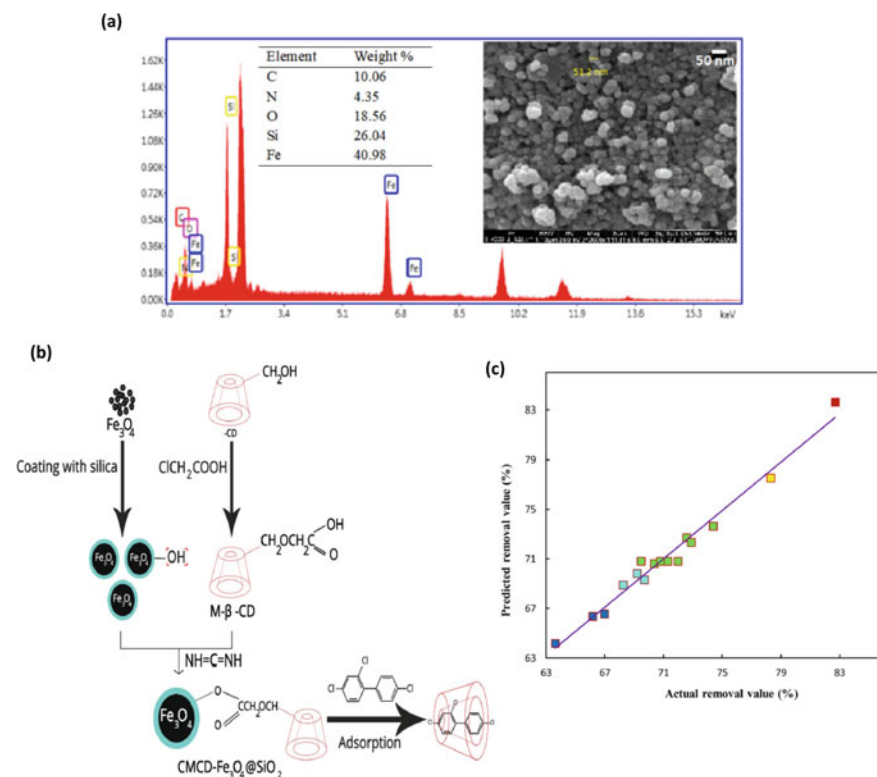


Fig. 9 **a** SEM and EDX images for the elucidation of the nanocomposite, **b** Graphical illustration for using biodegradable core-shell magnetic silica/carboxymethyl- β -cyclodextrin nanocomposite as an adsorbent for PCBs, and **c** maximum adsorption of PCBs (82%). Reprinted with permission [136]. Copyright 2020, Elsevier

Additionally, advanced oxidation technique has great attention for separating antibiotic by using oxidizing agents such as UV photolysis, Fenton' reagent, ozone, H_2O_2 , and ionizing radiation to produce hydroxyl radicals that can be utilized for actively and non-selectively decomposing pollutants. However, the this technique has the main disadvantages of such as high cost, residual toxicity in treated water effluents, and resulting byproducts [147–149].

Whereas, the adsorption technique is the best choice for fully eliminating residual antibiotics from wastewater surfaces due to its low cost, simple design, easy operation and high removal efficiency [150, 151]. For example, Danalıoğlu et al. [152] reported the potential capture of three antibiotic drugs: erythromycin, ciprofloxacin, and amoxicillin using magnetic biodegradable polymeric nanocomposite (chitosan/activated carbon/ Fe_3O_4) which was prepared via co-precipitation method. The adsorption data was well fitted with the Langmuir isotherm model that presented the maximum adsorption capacity value of 178.57, 90.10, and 526.31 mg/g for erythromycin, ciprofloxacin, and amoxicillin, respectively, and the adsorption

kinetic mechanism fitting with a pseudo-second kinetic model. Not so far, the removal of tetracycline (TC) and cefotaxime (CTX) have been reported by Li et al. [153] using NiFe_2O_4 - covalent organic frameworks (COF)-chitosan nanocomposites film (NCCT) prepared using terephthalaldehyde (TPA) as a crosslinking agent and can reveal blocking for the possible acid degradation of the structure (Fig. 10a). SEM images showed severely agglomerated of NiFe_2O_4 particles with a diameter ranged from 30 to 250 nm (Fig. 10 bi) that converted to 100–240 nm when it is incorporated within COF nanocomposite (Fig. 10bii). While, TEM image in Fig. 10biii exhibited NiFe_2O_4 nanoparticles with a diameter size of 8 nm. Also, the NCCT thickness measured from the SEM image was recorded as $7.5 \pm 0.5 \mu\text{m}$ (Fig. 10biv) producing accessible active groups onto the chitosan surface for the as developed NCCT nanocomposite along with the high surface area and highly obtained roughness; leading to enhancing the adsorption efficiency of antibiotics (Fig. 10bv). As a result, the adsorption data showed that the maximum adsorption of TC and CTX was 388.52 (pH 8) and 309.26 mg/g (pH 4), respectively using pseudo-second order kinetic model through different interactions as complexation cationic exchange, electrostatic, π - π , and H-bonding interactions (Fig. 10c).

Furthermore, various adsorbent systems for antibiotics using different biodegradable polymeric nanocomposites are tabulated in Table 2. For instance, tetracycline antibiotics can be removed from contaminated water surfaces using nanocomposites-based on biodegradable polymers such as chitosan in the presence of effective inorganic fillers like magnetic carbon nanotube [154], a mixture of $\text{Fe}_3\text{O}_4/\text{SiO}_2/\text{graphene}$ oxide [155], and Fe_3O_4 [156]. Also, they could be captured by using modified alginate (natural anionic polysaccharide) incorporated with $\text{Fe}_3\text{O}_4/\text{TiO}_2$ [157] and blended mixture between starch and polyurethane [158]. Moreover, clindamycin, tylosin, and amoxicillin antibiotics have been previously removed by chitosan/ Ag_2S [159], chitosan/cellulose/ activated carbon [160], and Mg-Al layered double hydroxide/cellulose [161], respectively. On the other hand, magnetic chitosan can be applied as an effective adsorbent for removing ciprofloxacin [162] from an aqueous solution, while magnetic cellulose has been used for the capture of metronidazole [163] using graphene oxide/ β -cyclodextrin/Ag nanocomposite [164]. Additionally, diclofenac and dorzolamide antibiotics have been isolated using modified chitosans such as chitosan-glyoxal/polyvinylpyrrolidone/ MoS_2 [165] and graphite oxide/poly (acrylic acid) grafted chitosan [166], respectively.

5.3 Removal of Pesticides

Pesticides have gained a great interest in the last decades because they are widely exploiting in agricultural production to protect the plant against fungi, pests, and weeds. So, pesticide residues are dispersed extensively in soils, drinking water, and groundwater which cause serious environmental hazard problems [167–169]. The quality of fresh water for human consumption, according to the drinking water

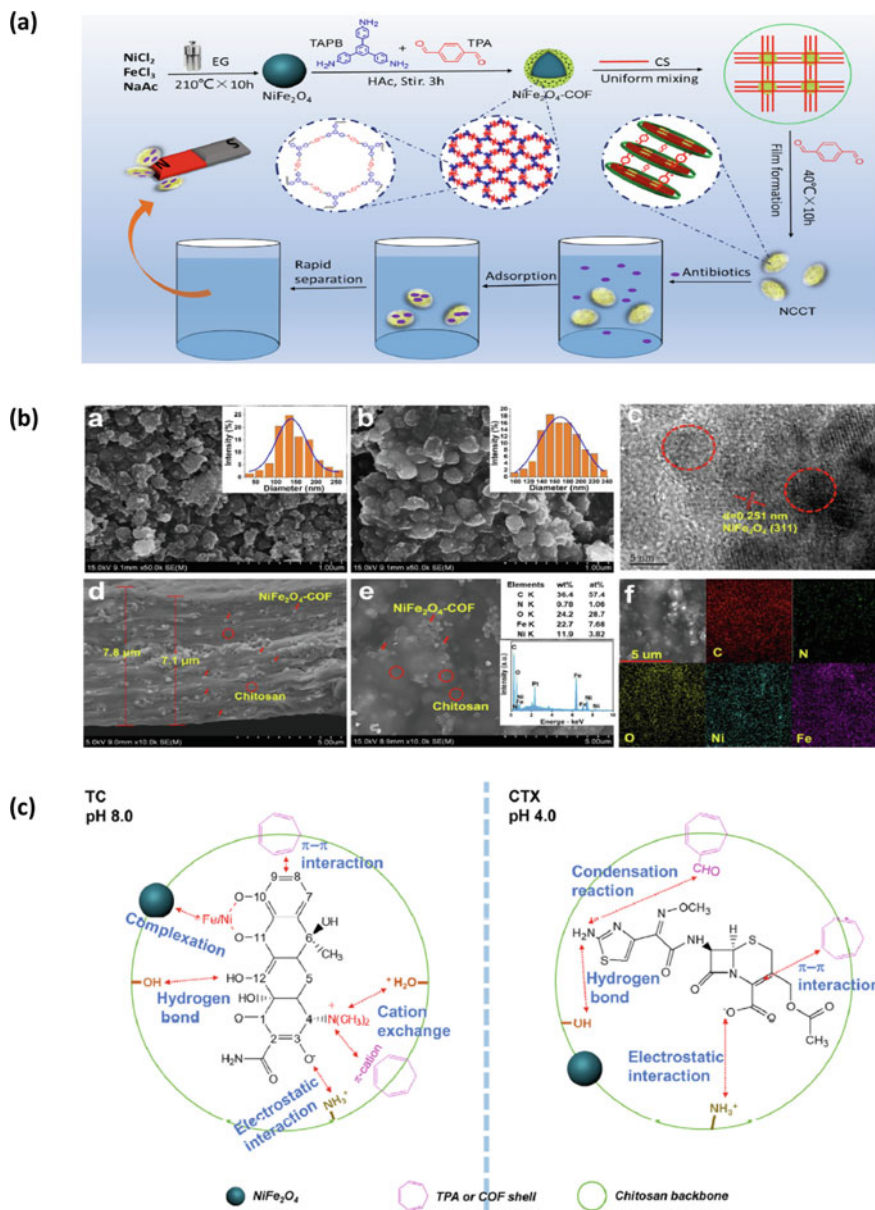


Fig. 10 **a** Graphical illustration of the preparation of $NiFe_2O_4$ - covalent organic frameworks (COF)-chitosan nanocomposites film (NCCT), **b** SEM, TEM and EDX images for $NiFe_2O_4$ and NCCT nanocomposites, **c** maximum adsorption of TC and CTX in different pHs, and **d** the adsorption mechanism for removal of TC and CTX antibiotics. Reprinted with permission [153]. Copyright 2020, Elsevier

Table 2 Removal of persistent organic pollutants by different biodegradable polymer-based nanocomposite

Adsorbate	Adsorbent	Maximum adsorption (mg/g or %)	Ref.	
Phenols	Chitosan/Activated carbon	409.0 mg/g	[129]	
	Chitosan/Silica	149.3 mg/g	[122]	
	Magnetic porous β -cyclodextrin	21.0 mg/g	[132]	
	Magnetic chitosan/hydroxyapatite	48.1 mg/g	[130]	
	Catechol	Cellulose acetate phthalate/alumina	91%	[133]
	Picric acid	Chitosan/multi-wall carbon nanotubes	90%	[134]
	Polyphenols	Poly(N-vinyl-2-pyrrolidone-co-N-isopropylacrylamide)/tannic acid/Fe ₃ O ₄	92.1%	[131]
	Antibiotic	Tetracycline	Chitosan/magnetic carbon nanotube	125 mg/g
			Magnetic starch polyurethane	13.12 mg/g
			Fe ₃ O ₄ /SiO ₂ /Chitosan/graphene oxide	183.47 mg/g
		Alginate/Fe ₃ O ₄ /TiO ₂	98%	
		Fe ₃ O ₄ /Chitosan	91.23%	
		Chitosan/Ag ₂ S	153.21 mg/g	
		Chitosan/cellulose/activated carbon	59.26 mg/g	
		Mg-Al layered double hydroxide/cellulose	138.3 mg/g	
		Chitosan-glyoxal/Polyvinylpyrrolidone/MoS ₂	94.5%	
		Fe ₃ O ₄ /Chitosan	142 mg/g	
Pesticides	Metomidazole	Fe ₃ O ₄ /Cellulose	332 mg/g	
		Graphene oxide/ β -cyclodextrin/Ag	72%	
	Dorzolamide	Graphite oxide/poly (acrylic acid) grafted chitosan	447 mg/g	
	Permethrin	Chitosan/ZnO nanoparticles	99%	

(continued)

Table 2 (continued)

Adsorbate	Adsorbent	Maximum adsorption (mg/g or %)	Ref.
	Chitosan/AgO	99%	[178]
Methomyl	Alginate-g-poly(acrylic acid)/xonotlite	64%	[180]
Pendimethalin	Poly N-isopropylacrylamide/MWCNTs /TiO ₂	57.4 mg/g	[182]
Neonicotinoid	Fe ₃ O ₄ /graphene oxide/ β -cyclodextrin	2.88 mg/g	[181]
Rotenone	Graphene oxide/Chitosan	92.59 mg/g	[179]
Humic acid	Cellulose acetate/MMT	91.85%	[197]
	Fe ₃ O ₄ /Chitosan	32.6 mg/g	[198]
	Polyethyleneimine/Fe ₃ O ₄ /graphene oxide	49.87 mg/g	[199]
	Cellulose acetate /Polyvinylpyrrolidone and activated carbon	23.32 mg/g	[200]

Directive (98/83/EC) stated that the concentration of pesticide should be individually limited to 0.1 $\mu\text{g/L}$ and for the sum of all used pesticides 0.5 $\mu\text{g/L}$ [170]. Also, USEPA announced that around 90% of pesticides found in the market are toxic organic contaminations [171, 172]. Hence, the research interest of pesticides pollutants such as permethrin, methomyl, pendimethalin, neonicotinoid, rotenone, organophosphorus, diazinon, chlorpyrifos, and pirimiphos-methyl in water sources is one of the major challenges for global scientists these days because they cause many of human health infections due to their high mobility, toxicity and persistence in eco-system [173, 174].

Recently, polymeric nanocomposites have gained attention to remove pesticide pollutants from wastewater surfaces due to their high surface area, mechanical properties, and thermal stability. For example, graphene oxide/polyamide nanocomposite was prepared according to Ayazi and Jaafarzadeh [175] by the solvent blending method and then coated on stir bar substrate via solvent changed method to remove three organophosphorus pesticides as ethion, chlorpyrifos, and phosalone. The target pesticides were monitored using gas chromatography/flame ionization detector. The findings showed that the as-developed method could capture three pesticides successfully with relative recovery range of 82.0–95.6%. Youssef et al. [176] had reported the preparation of efficient antimicrobial hydrophobic nanocomposite films based on poly(vinyl alcohol)/multi-wall carbon nanotubes (f-MWCNTs) using citric acid as crosslinker via casting method. The nanocomposite was then used for removing four organophosphorus harmful pesticides (OPPs) residues including diazinon, chlorpyrifos, pirimiphosmethyl, and malathion. The high loading of f-MWCNTs with 4 wt.% could remove the highest amount of pesticides reached up to 99% and enhanced the inhibition of bacteria and fungi growth species. Besides, the regeneration and reusability studies of loaded f-MWCNTs/pesticides were investigated via consequence adsorption-desorption cycles as shown in Fig. 11, and the data showed that nanocomposites exhibited both good regeneration performance and stability.

Table 2 includes other different polymeric nanocomposites which have also been applied for the removal of various toxic pesticides such as chitosan nanocomposites (chitosan/ZnO [177] and chitosan/AgO [178] for removal of permethrin and chitosan/graphene oxide for the capture of rotenone [179]), alginate-g-poly(acrylic acid)/xonotlite nanocomposite for adsorping methomyl pesticide from an aqueous solution [180], neonicotinoid using Fe_4O_3 /graphene oxide/ β -cyclodextrin nanocomposite [181], and poly N-isopropylacrylamide/MWCNTs/ TiO_2 nanocomposite for separating pendimethalin from wastewater [182].

5.4 Removal of Humic Acid

Humic acid (HA) is a known natural organic pollutant extracted from the decomposition of both animal and plant materials that are found in water surfaces and can affect both the taste and color of the water. HA has a complex structure that includes many functional groups such as carboxylic, hydroxyl, phenolic, and carbonyl groups. As a

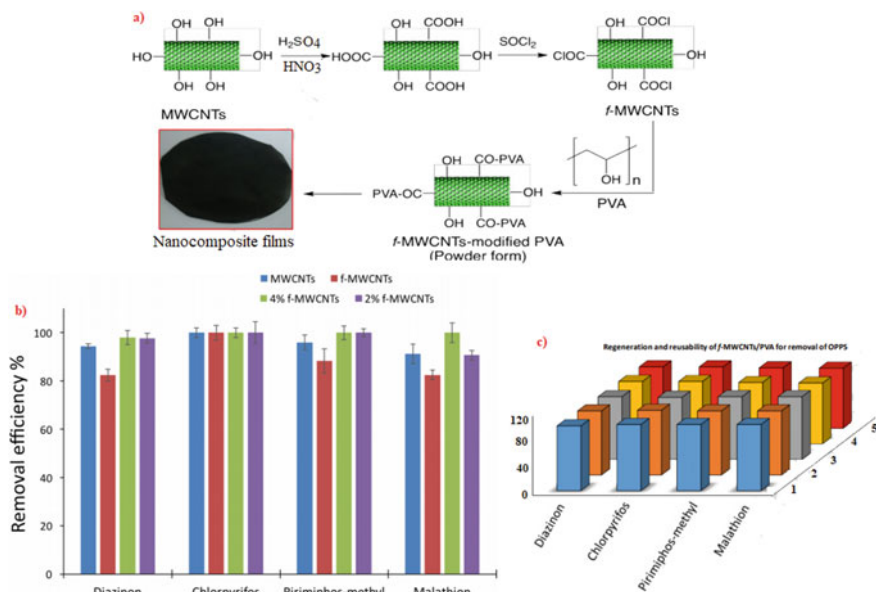


Fig. 11 **a** Schematic preparation of f-MWCNTs/PVA nanocomposite films, **b** removal efficiency %, and **c** regeneration study of four pesticide residues; diazinon, chlorpyrifos, pirimiphosmethyl, malathion, respectively. Reprinted with permission [176]. Copyright 2020, Elsevier

consequence, the research on HA removal from water is of a great challenge [183–187]. Various traditional processes have been used for purifying wastewater such as advanced oxidation, chemical coagulation, biodegradation, and membrane separation [188–191], but these processes cause interaction of HA with both toxic heavy metals and synthetic organic compounds leading to damaging the distribution of the as-used systems [192]. In addition, HA can react in drinking water with chlorine molecules producing very toxic byproducts such as trihalomethanes and haloacetic acids [193, 194]. Recently, the adsorption technique has revealed an efficient method for the adsorption of HA due to the possibility of using the polymer nanocomposite as adsorbents [195]. For instance, Etemadi et al. [196] reported an efficient adsorbent nanocomposite for HA-based on cellulose acetate/polyethylene glycol-grafted nano-diamond. Authors found that the as-prepared nanocomposite showed good mechanical properties, rejection, hydrophilicity, permeability, abrasion resistance, and anti-fouling performance. Also, the adsorption study exhibited maximum HA adsorption of 2.15 mg/g. Moreover, different types of polymeric nanocomposites applied to the removal of HA from aqueous solutions are listed in Table 2.

5.5 Removal of Oil Pollutions

Oil pollutions coming from the petroleum industry are considered one of the main sources for polluting water. The amount of transported oils over an international sea accounts for around five million tonnes annually. Worryingly, spilled-oil tankers participate 33 thousand tonnes of oils in the marine environment. These oils can block sunlight from penetrating water, thus hampering the photosynthesis process and causing harmful effects on human life through adversely impacting on coastal beaches, fishing, and resorts [201–205]. There are different types of spilled oils such as motor oil, gasoline oil, crude oil, corn oil, diesel oil, soybean oil, pump oil, silicon oil. Additionally, petroleum hydrocarbons such as ethylene glycol and xylene (BTEX) which includes benzene, toluene, ethylbenzene, and isomers of xylene are also related subjects [204, 206–212]. Consequently, the purification of oily contaminated water is an essential challenge today to stop these environmental disasters [213].

Recently, most of the researchers have a great concern with the fabrication of nanocomposites as adsorbents to treat and purify the contaminated water due to their high surface area and stability [214]. In this respect, Zheng et al. [215] reported the green synthesis of silane/poly (vinyl alcohol)/ cellulose nanofibril nanocomposite aerogels using the freeze-drying method in the presence of methyl trichlorosilane as superabsorbent for different organic solvents and oils as diesel oil, gasoline, crude oil, corn oil, pump oil, hexane, chloroform, and toluene. Also, Peng et al. [216] developed the preparation of superhydrophobic magnetic cellulose sponge (SMCS) nanocomposite by both sol-gel and freeze-drying methods using in-situ incorporated magnetic Fe_3O_4 nanoparticles for removing toluene from oily contaminated water. The adsorption measurements showed that SMCS had a maximum separation of toluene capacity of ~98%. In this track, superhydrophobic silylated cellulose/ SiO_2 NPs aerogels nanocomposites were prepared according to Zhou et al. [217] via the freeze-drying method. The as-prepared nanocomposite possessed high roughness, flux ($1910 \text{ Lm}^{-2} \text{ h}^{-1}$), and porous structure ($\geq 99.60\%$), along with low surface energy of contact angle 168.4° . The separation oil capacity was investigated against various oil types such as petroleum ether, gasoline oil, silicone oil, isooctane, hexane, trichloromethane, dichloromethane, soybean oil, toluene, and motor oil, and the separation results indicated that the efficiency was 99.5% for different mixture with a controlled stable efficiency even after 20 removal cycles.

Another eco-friendly reusable and recycled superhydrophilic nanocomposite membrane was modulated by Wu et al. [218] via in-situ co-crosslinked hydrophilic poly(*N*-isopropylacrylamide-co-*N*-methylolacrylamide)(PNIPAm-co-NMA)/chitin nanowisker (ChNWs) (Fig. 12a–c). The as-prepared nanocomposite membrane had a high flux varied between 1100 and $1300 \text{ Lm}^{-2} \text{ h}^{-1}$ and was exploited for oil separation mixture containing petroleum ether, gasoline oil, hexadecane, edible oil, and isooctane with a separation efficiency of 99.90, 99.53, 99.85, 99.14, and 99.93%, respectively at two different pH (1 and 13) as shown in Fig. 12d&e. Also,

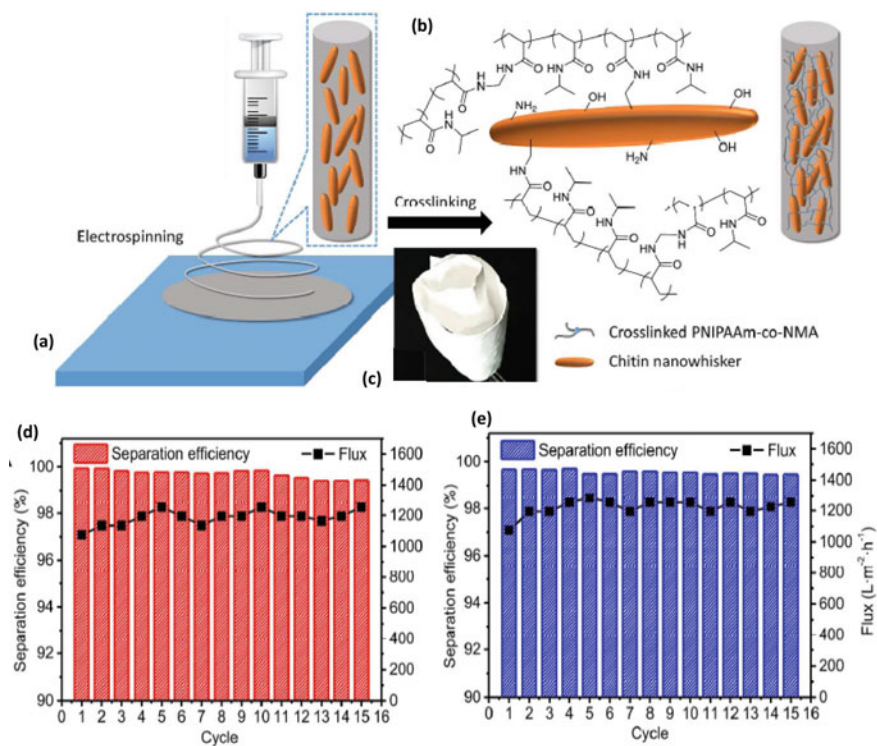


Fig. 12 **a** graphical illustration of the preparation of poly(*N*-isopropylacrylamide-co-*N*-methylolacrylamide)/chitin nanowisker, **b** illustration of the cross-linked nanofibrous membranes, **c** photograph of the robust flexibility of ChNWs-10% membranes, **d** flux and separation efficiency of ChNWs-10% NF membrane at different separation cycles with an emulsion pHs: **d** pH 1 and **e** pH 13. Reproduced with permission [218]. Copyright (2020), American Chemical Society

the regeneration ability of as-prepared nanocomposite was evaluated and the findings exhibited effectively separated-emulsions after regenerating at least 5 removing cycles.

Moreover, a biodegradable anionic polysaccharide such as xanthan gum-based nanocomposite has been mentioned by Saha et al. [219] in the presence of SiO₂ nanoparticles to enhance the heavy crude oil recovery. They overcame the main limitation of crude oil as it has a high interfacial tension against an aqueous phase. They synthesized the nanocomposite based on xanthan gum (XG) and extracted natural Reetha surfactant in the presence of different concentrations (0.1–0.5 wt%) of SiO₂ nanoparticles (15 nm). The adsorption studies investigated that the oil recovery increased from 18.5% using Reetha/XG matrix to 27.3% of XG/Reetha/SiO₂ (0.3 wt%) nanocomposite.

More recently, crude oil has been removed from water by Dong et al. [220] using the biodegradable glucose-grafted poly(ethylene glycol)-*b*-dopamine-functionalized poly(ethyl propargyl glucose carbonate)-*b*-poly(ethyl glucose carbonate)/magnetic

Fe₃O₄ nanoparticles nanocomposites through the sequential ring-opening polymerization (Fig. 13a&b). The maximum adsorption value of oil was found to be 5 mg/mg and the regeneration study showed that 60–80% of the total weight nanocomposite was able to be recovered each cycle. Additionally, more various biodegradable polymeric nanocomposites have been applied for the removal of different oily contaminated water as summarized in Table 3.

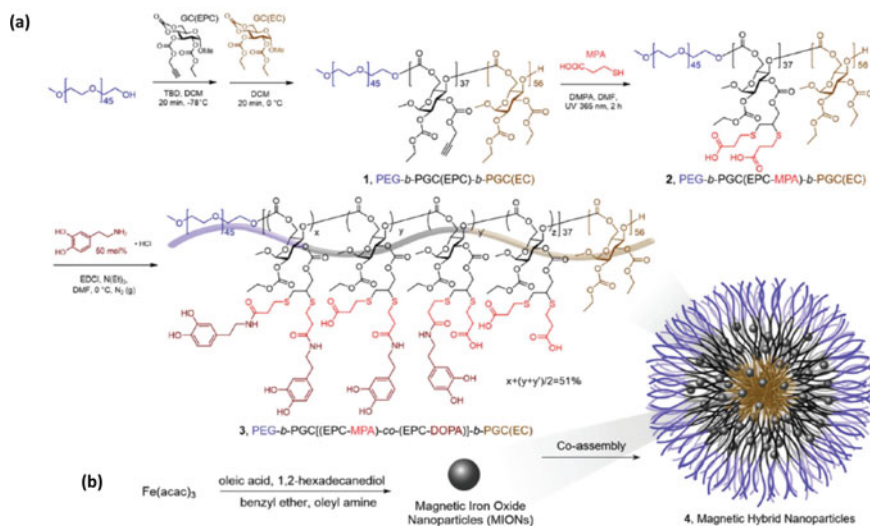


Fig. 13 (a) Graphical representation for the preparation of a glucose-grafted poly(ethylene glycol)-b-dopamine-functionalized poly(ethyl propargyl glucose carbonate)-b-poly(ethyl glucose carbonate) by sequential ROPs and (b) magnetic hybrid nanocomposite. Reprinted with permission [220]. Copyright 2020, Royal Society of Chemistry

Table 3 Removal of different oils that contaminated the freshwater using biodegradable polymeric nanocomposites

Adsorbate (Oil)	Nanocomposite (adsorbent)	Oil recovery	Ref.
Crude oil	Polyvinylpyrrolidone/Fe ₃ O ₄	100%	[221]
	Poly(methyl methacrylate)/Fe ₃ O ₄	21.2 g/g (98%)	[222]
	Polyurethane/Cloisite 20A nanoclay	19.569 g/g (56%)	[223]
Petroleum ether	Cellulose/SiO ₂ NP/polyethylene	99.9%	[224]
Benzene	Cellulose/SiO ₂ /polyethylene	99.0%	[224]
Motor oil	Collagen/Fe ₃ O ₄	2 g/g	[225]
Diesel oil	Chitosan/Fe ₃ O ₄	157.739 mg/g	[226]
Chloroform	Chitosan/rectorite	81 mg /g	[227]

6 Bacteria Removal

Water quality could be spoiled with the existence of hazardous microorganisms partially, bacteria. Generally, pathogens such as *S. aureus* (gram-positive) and *E. coli* (gram-negative) were known as very infectious and drug-resistant organisms that can contaminate the drinking water. As a result, they can be a cause for many infectious diseases besides the gastrointestinal illness [228, 229]. The outer membrane in the bacterium structure plays a vital role in resisting the entry of compounds such as antibiotics, dyes, and detergents to their body via the penetration of the inner wall of the cell [230]. Therefore, it is very crucial to treat the water against the microorganisms using disinfectants to retard their growth. There are various effective techniques for the disinfection of water bacteria such as chlorination, UV radiation, and ozonation. Even though these methods were found to be exorbitant, time-consuming, and accompanied by harmful disinfection byproducts as in the case of the chlorination method, whereby chlorine could interact with the organic compounds in water to get trihalomethanes that are mutagenic and carcinogenic species [231, 232]. Hence, an urgent necessity for cost-effective, and safe disinfectant alternatives with fewer byproducts is required to obtain immaculate drinking water. As a solution for that problem, various efforts have been united for the development of antibacterial sorbent nanocomposites obtaining attractive properties such as biodegradability, renewability, and environmental non-toxic. Recently, the prosperous progress in altering nanomaterials in the matrix of natural or synthetic polymers is of a great interest and can be effectively utilized for overcoming the challenges that are facing the field of water purification. In general, the main target for making polymer nanocomposites is to enhance the properties of the virgin polymer by the addition of small amounts from nanomaterials. Nanomaterials such as graphene, carbon nanotubes, layered silicate, and metal oxides can be incorporated into the polymer as nanofillers because of their high surface area, thermal stability, physicochemical properties that could improve the polymer properties [19, 233, 234].

Nevertheless, the usage of nanomaterials alone for the purification of water could be of probable toxicity and safety hazards. The nanoparticles need to be specifically wrapped with polymer molecules in which the particles will be incorporated ensuring no further addition of pollutants and good dispersion during the water remediation.

In general, nanoparticles can be synthesized using two different approaches; bottom-up, and top-down techniques. The bottom-up method involves the building of complex nanoclusters from the usage of molecular precursors as the starting reactants accompanied by the nucleation and growth procedures. Whereas, the top-bottom one relates to the disintegration of bulk materials into nanoparticles using methods like milling, quenching, and photolithography. Importantly, both natural, and synthetic polymers can be utilized for the functionalization of nanomaterials for water treatment. For instance, the natural polymer, chitosan, was mixed with the hybrid cobalt-silica to give different nanocomposites for the good adsorption toward dyes of methyl orange, congo red, and indigo carmine. However, these composites showed no significant efficiency against the dye of the acridine orange dye

[235]. Furthermore, chitosan/cobalt-silica (Co-MCM-15) nanocomposite revealed the strongest antimicrobial performance against various gram-positive and gram-negative bacteria as well as multidrug-resistant bacteria suggesting the best dispersion of Co-MCM in chitosan polymer that is in charge of the superior adsorption and biological performance. It was motivating to know that methyl orange dye shows a better selectivity and strong adsorption on chitosan/Co-MCM-15, unlike the other dyes. Additionally, the dye removal was found to be approximately constant at pH 3–5 due to the chitosan and nanomaterial solvation in the acidic medium [22]. However, the maximum dye adsorption was detected at pH 6–8, and the further increase of the pH value above 8 resulting in the decline behavior of dye adsorption because there is a competition between hydroxyl ions and the dyes for occupying the active sites of the composite layer.

Additionally, titanium dioxide (TiO_2) can be chelated with chitosan to obtain photocatalyst nanocomposites which can be used for removing congo red, and rhodamine B dyes. The as-developed nanocomposites could be utilized as an efficient antibacterial agent for Gram-positive and Gram-negative bacteria along with their activity against fungus. They can achieve inhibition diameter values ranged from 10.333 ± 0.5773 to 25.667 ± 1.5275 (mm) [236].

It was mentioned that chitosan action against bacteria could be related to the amino groups presented in the structure that can interact electrostatically with the bacteria cell wall resulting in destroying the outer membrane. Individually, TiO_2 could also decay the bacteria's outer membrane through the reactive oxygen species (ROS) giving a rise for the permanent damage of bacteria. With a synergism phenomenon, the good dispersion of chitosan/ TiO_2 nanocomposite paired with the high surface area can result in more adsorption of nanoparticles on the wall of bacteria leading to the disturbance of function of cellular nucleus and the cell death.

In another study, zinc oxide nanoparticles were supported by using the natural bentonite and then were encapsulated using sodium alginate in novel adsorbent nanocomposites that can reveal an outstanding antibacterial behavior against staphylococcus aureus for both the synthetic and surface water. It was found that in case of using only 0.5 g of the as-prepared nanocomposites, the bacteria concentration of 200 cfu/ml was changed to null bacteria after 70 min and within a min when the bacteria was in contact with the synthetic and surface water, respectively as shown in Fig. 14 illustrating different bacteria concentration and composite amounts [231].

Additionally, silver is commonly known as the most toxic nanoparticles to bacteria of various kinds, and hence can be found in various fields such as wound dressing, air filtration, water disinfection, and antimicrobial filter.

Previously, alginate was used to prepare silver-alginate nanocomposites with three different techniques for being used for the water disinfection as alginate was utilized previously for the immobilization of silver and gold nanoparticles for the catalysis application [237].

The first method involved the reduction of silver ions on the preformed beads of alginate, the second one was made by the incorporation of previously prepared silver nanoparticles, while the formation of beads using gelation, and the last one reveals the occurrence of reduced silver nanoparticles along with the simultaneous gelation

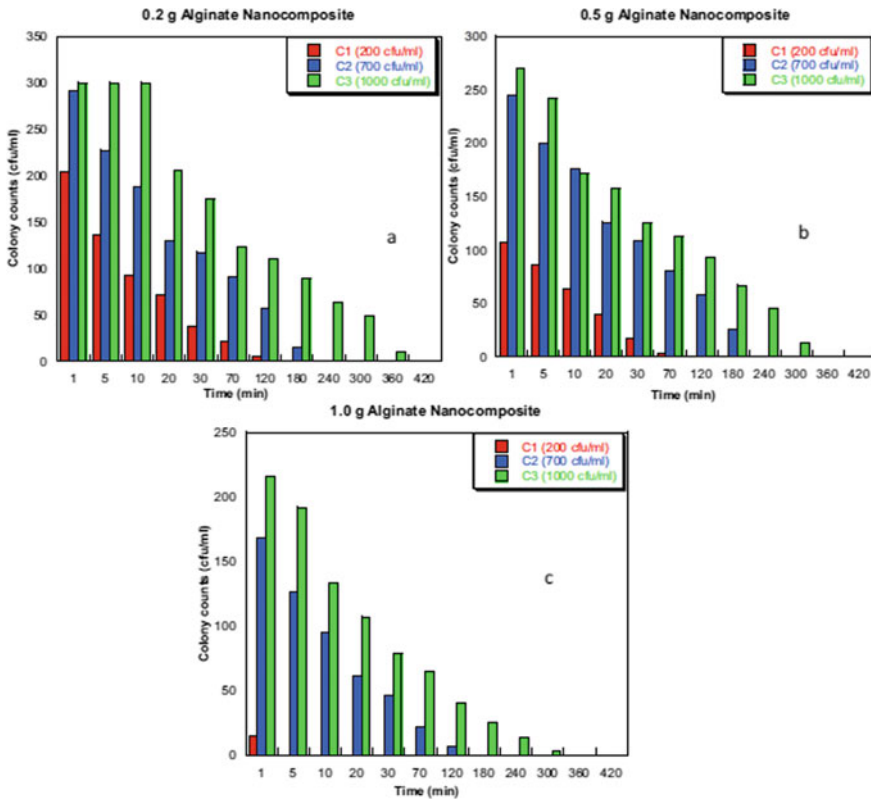


Fig. 14 Antimicrobial performance of alginate nanocomposites against a set of nanocomposite amount, bacterial concentration. Reprinted with permission [231]. Copyright 2020, Elsevier

of alginate. The former composites were then used to fill columns in which the water contaminated with bacteria was passed through.

From measuring the Ag concentrations found in the three composites, the AR beads showed relatively higher concentration ranging from 4 to 22 ppm compared to the other beads, based on the hydraulic retention time. However, SGR depicted the excellent behavior in bacterial removal in a relation to other beads due to containing the lower size of silver nanoparticles. On the other hand, the nanocomposite fabricated from synthetic polymers with nanomaterials is of a great efficiency to improve their dispersion for high-performance adsorbent and antibacterial agents.

In another developed study by sharf et al. [238] that showed the premier preparation of antimicrobial nanocomposites using manganese dioxide (MnO₂), black cumin (BC) and was found to purify the water from bacteria and methylene blue dye along with their photocatalytic degradation as depicted by Fig. 15.

For instance, poly(methyl methacrylate) (PMMA) nanocomposite was prepared by embedding titanium dioxide nanoparticles (TiO₂) with single-walled carbon nanotubes (SCNTs), as an acceptor of electrons for having high photocatalytic

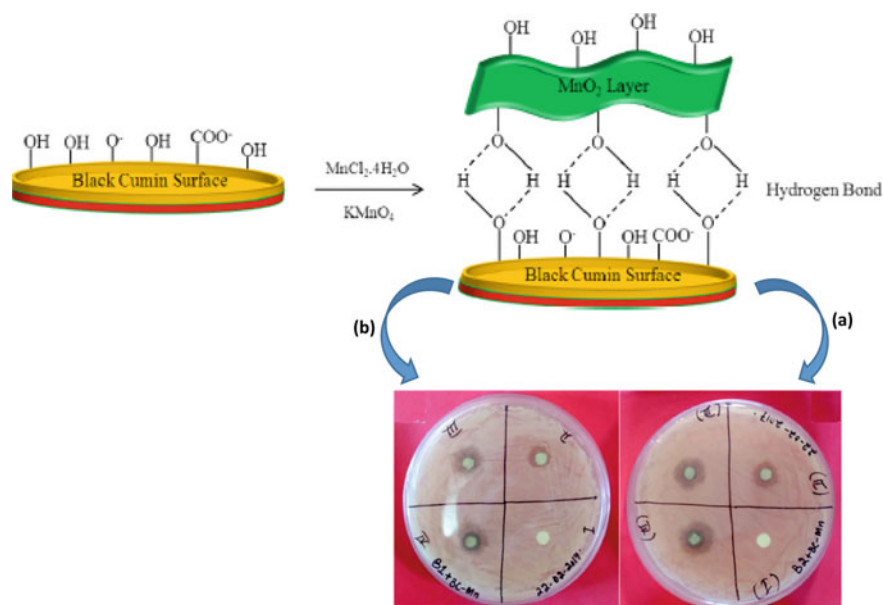


Fig. 15 Scheme showing the formation of MnO₂/BC composite for the water purification and **a** antibacterial activity against Gram –ve and **b** antibacterial activity against Gram +ve. Reprinted with permission [238]. Copyright 2020, Elsevier

and antibacterial behavior. The Antibacterial properties of the as-prepared films containing 15 wt.% TiO₂ were investigated through the measurement of *E. coli* survival rate after the exposure to UV radiation for 1 h. The survival rate of bacteria for PMMA-TiO₂ was lowered by 30%. While, exposure of bacteria to both PMMA and UV achieved the highest rate of 98%. On the other hand, the rate of 90% was obtained by exposure of *E. coli* to UV irradiation only. Further, for better estimating the influence of UV radiation on the antibacterial behavior, the PMMA-TiO₂ composite was measured without the exposure to the radiation condition, and it was found to achieve only 60% reduction in the survival rate indicating that the exposure to UV catalyzed the antimicrobial effect of nanoparticles [239].

In another interesting study, the nitrocellulose was firstly coated with antibacterial nanocomposite containing 97 wt.% of polyvinyl-N-carbazole (PVK) and only 3 wt.% of SCNTs against *B. subtilis*, and *E. coli* bacteria. It was previously reported that SCNTs could inhibit the growth of bacterium and virus most remarkably in water [240]. PVK-SWNT membranes revealed a bacteria inhibition by 70% for *E. coli* and ~65% for *B. subtilis* as shown in Fig. 16; suggesting that bacteria lost their ability to grow on the membrane filters [241]. Hussein et al. succeeded to prepare new series of antimicrobial hybrid nanocomposites from the conducting polyaniline, graphene, and CNTs for the disinfection of water via the in situ polymerization method in acid medium. The data of bacterium removal before and after adsorption stated that *S. aureus* and *E. coli* were removed by 99.5 and 99.2%, respectively confirming the

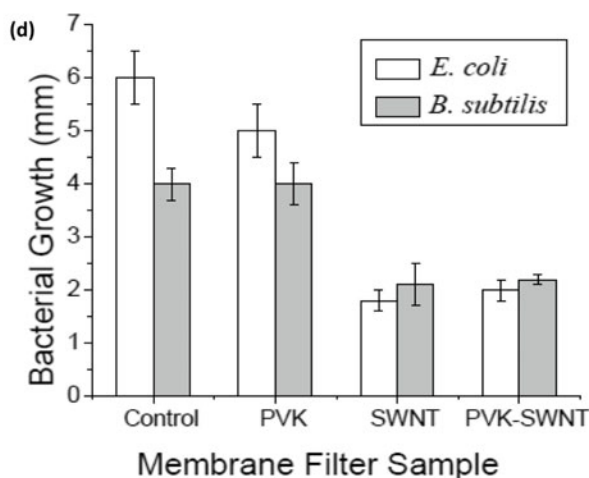
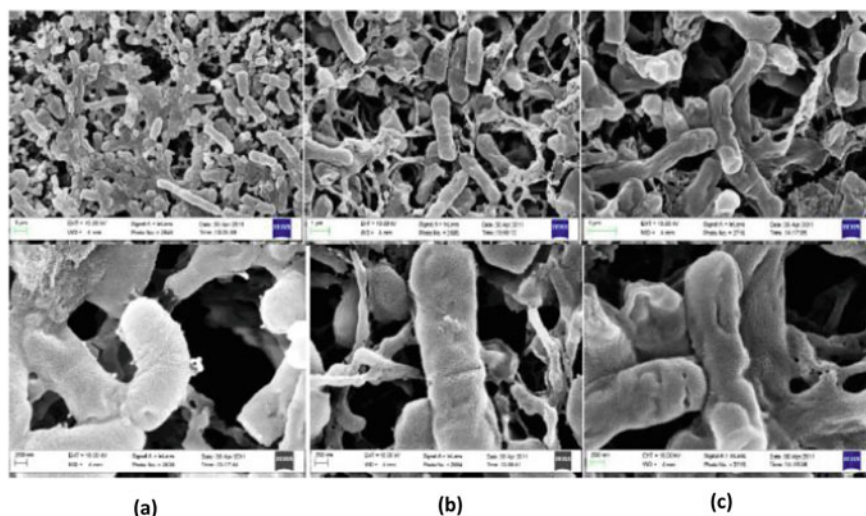


Fig. 16 SEM images of the bacterial behavior (*E. coli*) on **a** unmodified membrane (control), **b** membrane coated with SCNTs, **c** membrane coated with PVK-SCNTs at the scale: top is 1 μm , and bottom is 200 μm , and **d** the bacterial growth curve of the pure membrane, the membrane coated with PVK, SCNTs, and PVK-SCNTs. Reprinted with permission [241]. Copyright 2020, Elsevier

occurred synergism between the three individual materials. More importantly, the reuse measurement after doing 4 cycles was still providing the same percentage of bacteria removal [242].

Using another conducting polymer (polypyrrole) doped with thioglycolic acid to prepare magnetic nanocomposite containing Fe_3O_4 for the adsorption of silver ions has been also investigated. Interestingly, the silver adsorbent could be used for

Table 4 Reports describing the usage of various polymer nanocomposites in the water disinfection

Polymer	Nanomaterials	Antimicrobial activity against	Observation	Ref.
Chitosan	Cobalt-silica	<i>E. coli</i> , <i>P. stutzeri</i> , <i>E. faecium</i> , <i>B. subtilis</i> , <i>S. epidermidis</i>	Inhibition zone diameter (3 mm)	[235]
Chitosan	TiO ₂	<i>S. Pneumoniae</i> <i>P. vulgaris</i>	Zone of inhibition ranged between 10.333 ± 0.5773 and 25.667 ± 1.5275 (mm)	[236]
Sodium alginate	Zinc oxide-bentonite	<i>S. aureus</i>	At 0.2 g, the reduction of bacteria was observed after 120 min of contact time	[231]
Chitosan/biochar-	Silver nanoparticles	<i>E. coli</i>	The antibacterial rate reached over 90%	[244]
Black cumin seed	MnO ₂	<i>E. coli</i> , <i>S. aureus</i>	Diameters of the zones of inhibition were 25, and 19 mm	[238]
Basil granular mucilage	Co _{0.3} Zn _{0.7} Fe ₂ O ₄ @Ag NPs	<i>S. aureus</i> , <i>B. cereus</i> , <i>E. coli</i> , <i>S. typhimurium</i>	The inhibition diameters were 10.5, 10.7, 11.7, 11.9 respectively	[245]
PMMA	TiO ₂	<i>E. coli</i>	Survival rate has been reduced up to ~30% w	[239]
PVK	SCNTs	<i>E. coli</i> and <i>B. subtilis</i>	~90% inactivation for both bacteria	[241]
Polyaniline	Graphene, and CNTs	<i>S. aureus</i> and <i>E. coli</i>	The removal percentages of <i>S. aureus</i> and <i>E. coli</i> were 99.5 and 99.2%	[242]

(continued)

Table 4 (continued)

Polymer	Nanomaterials	Antimicrobial activity against	Observation	Ref.
Polypyrrole	Fe ₃ O ₄	E. coli	The concentration of bacteria was reduced from 10 ⁷ to 1.4 × 10 ³ CFU/ml	[243]
Polyacrylonitrile	Carbon nitride	A. baumannii, E. coli, S. aureus	The bacteria can be inactivated within 120 min	[246]
N-halamine	Silica	E. coli, S. aureus	No survival bacteria was observed within 3 min of contact	[247]
Polyacrylonitrile/polyurethane/polyaniline	SWNTs	E. coli, S. aureus	Electrolysis led to inactivate the bacteria within 20 min	[248]

the removal of *E.coli* bacterium according to a former report [243]. The maximum adsorption function toward Ag^+ was found to be 806.4 mg/g and the kinetics data showed the fast adsorption process on the nanocomposite. Some researchers also reported the utilization of other various polymer nanocomposites for killing bacteria found in water as given in Table 4.

7 Conclusions

One of the major challenges the environment is facing is the scarcity of drinking water of adequate quality due to growing population and global climate change. Contamination of water with various pollutants including organics, metal ions, microorganism, etc. has been regarded as a serious environmental issue. Over recent years, utilizing nanomaterials in water remediation has been increased. However, due to instability, agglomeration and non-compatibility, biodegradable polymer-based nanocomposites are now being favored as high-performance biodegradable materials. This chapter provides up to date overview on the recent advances of various polymer nanocomposites which have been developed for uses wastewater treatment industry. These multifunctional adsorbent materials have found various applications such as the elimination of toxic dyes, metal ions, spilled oils, bacteria, and other organic pollutants from water. Additionally, they have been revealed to possess antimicrobial and antibacterial properties.

New fabrication strategies, characterization and properties of PNCS have been also explained. Studies affirmed that proper incorporation of nanoparticles at optimal dose into several polymer and biopolymer composites in the nanometer range for the fabrication of PNCs improved their efficiency for contaminants removal in aqueous systems. Nearly, all the adsorption mechanisms discussed herein have shown to be endothermic with a rise in spontaneity. Critical data evaluation have evidenced that polymeric nanocomposites based on magnetic nanoparticles and activated carbon have been extensively investigated and considered as promising materials for removal of various pollutants from wastewater due to high surface area, strong adsorption, cost effectiveness and easy separation under external magnetic field in the case for magnetic nanoparticles. Other polymeric nanocomposites including graphene oxide, single-walled carbon nanotubes, multi-walled carbon nanotubes, etc. are also advantageous due to their greater durability, selective elimination features and regeneration capacity. Ultimately, the chapter clearly points out that, over the last decade, there has been a significant leap in the exfoliation of PNCs in water remediation compared to other conventional singular materials.

8 Future Perspective

As noted earlier, the high decontamination efficiency of a wide array of pollutants, cost effectiveness and their regeneration potential have made the PNCs as one of the most important and innovative materials. This makes it apparent that these fast burgeoning improved materials seem to have a very bright future and their emergence in purification of wastewater would witness a revolution in the forthcoming years; this would fortunately contribute in overcoming the global water issues. Undoubtedly, the unique characteristics derived from the controlled nanostructure of these materials provide a basis for a much broader range of applications.

Although a remarkable work have already been carried out on various facets of PNCs, several research studies still remain to be conducted to better address structure–property relationship in various PNCs. Remarkably, the applicability of these material have commonly investigated at the laboratory scale, but their utilization must be extended to industrial purposes and large-scale production. Therefore, further research studies which reflect cost-effectiveness of the provided nanomaterials and strategies for integrating nanomaterials into polymeric matrices are also required. It would be preferable that these research studies can be directed at the fabrication of a single biodegradable polymer-based nanocomposite material capable of removing all the potential contaminants from a given source. Despite, these innovations can pave the way for a sustainable future, in practise a comprehensive technological analysis is still needed to cross the gap between laboratory-scale and industrial implementations.

As far as legislations and human health are firmly concerned, several regulation and comprehensive evaluation of the toxicity of nanomaterials have to be carefully established, especially in the large scale uses to verify their real applications, since these nanoparticles might be released to the environment inducing harmful consequences on human health.

References

1. Mhlanga, S.D., Mamba, B.B., Krause, R.W., Malefetse, T.J.: Removal of organic contaminants from water using nanosponge cyclodextrin polyurethanes. *J. Chem. Technol. Biotechnol.* **82**(4), 382–388 (2007)
2. Elella, M.H.A., Goda, E.S., Gamal, H., El-Bahy, S.M., Nour, M.A., Yoon, K.R.: Green antimicrobial adsorbent containing grafted xanthan gum/SiO₂ nanocomposites for malachite green dye. *Int. J. Biol. Macromol.* **191**, 385–395 (2021)
3. Abdel Messih, M.F., Shalan, A.E., Sanad, M.F., Ahmed, M.A.: Facile approach to prepare ZnO@SiO₂ nanomaterials for photocatalytic degradation of some organic pollutant models. *J. Mater. Sci. Mater. Electron.* **30**, 14291–14299 (2019)
4. Abu-Thabit, N.Y., Uwaezuoke, O.J., Elella, M.H.A.: Superhydrophobic nanohybrid sponges for separation of oil/water mixtures. *Chemosphere* **294**, 133644 (2022)
5. Abu Elella, M.H., et al.: Xanthan gum-derived materials for applications in environment and eco-friendly materials: a review. *J. Environ. Chem. Eng.* **9**(1), 104702 (2021)
6. Shehata, A.B., Mohamed, G.G., Gab-Allah, M.A.: Simple spectrophotometric method for determination of iron in crude oil. *Pet. Chem.* **57**(12), 1007–1011 (2017)

7. Goda, E.S., Gab-Allah, M.A., Singu, B.S., Yoon, K.R.: Halloysite nanotubes based electrochemical sensors: a review. *Microchem. J.* **147**, 1083–1096 (2019)
8. Gab-Allah, M.A., Choi, K., Kim, B.: Development of isotope dilution-liquid chromatography/tandem mass spectrometry for the accurate determination of type-A trichothecenes in grains. *Food Chem.* **344**, 128698 (2021)
9. Gab-Allah, M.A., Goda, E.S., Shehata, A.B., Gamal, H.: Critical review on the analytical methods for the determination of sulfur and trace elements in crude oil. *Crit. Rev. Anal. Chem.* **50**(2), 161–178 (2020)
10. Gab-Allah, M.A., Choi, K., Kim, B.: Accurate determination of type B trichothecenes and conjugated deoxynivalenol in grains by isotope dilution-liquid chromatography tandem mass spectrometry. *Food Control* **121**, 107557 (2021)
11. Abdellatif Soliman, S.M., Sanad, M.F., Shalan, A.E.: Synthesis, characterization and antimicrobial activity applications of grafted copolymer alginate-g-poly(N-vinyl imidazole). *RSC Adv.* **11**, 11541–11548 (2021)
12. Beyene, H.D., Ambaye, T.G.: Application of sustainable nanocomposites for water purification process. In: Inamuddin, T.S., Kumar Mishra, R., Asiri, A. (eds.) *Sustainable Polymer Composites and Nanocomposites*, pp. 387–412. Springer, Cham (2019). https://doi.org/10.1007/978-3-030-05399-4_14
13. Zhu, H., Qiu, S., Jiang, W., Wu, D., Zhang, C.: Evaluation of electrospun polyvinyl chloride/polystyrene fibers as sorbent materials for oil spill cleanup. *Environ. Sci. Technol.* **45**(10), 4527–4531 (2011)
14. Pandey, S.A.: comprehensive review on recent developments in bentonite-based materials used as adsorbents for wastewater treatment. *J. Mol. Liq.* **241**, 1091–1113 (2017)
15. Zhou, Y., Zhang, L., Cheng, Z.: Removal of organic pollutants from aqueous solution using agricultural wastes: a review. *J. Mol. Liq.* **212**, 739–762 (2015)
16. Gutiérrez, A., Atilhan, M., Aparicio, S.A.: nanoscopic approach on benzene-toluene-xylenes extraction by sulfolane. *J. Mol. Liq.* **249**, 1039–1046 (2018)
17. Bi, X., Reed, R., Westerhoff, P.: Control of nanomaterials used in chemical mechanical polishing/planarization slurries during on-site industrial and municipal biological wastewater treatment. *Front. Nanosci.* **8**, 247–265 (2015)
18. Lee, J., Goda, E.S., Choi, J., Park, J., Lee, S.: Synthesis and characterization of elution behavior of nonspherical gold nanoparticles in asymmetrical flow field-flow fractionation (AsFFFF). *J. Nanoparticle Res.* **22**(9), 256 (2020)
19. Abu Elella, M.H., ElHafeez, E.A., Goda, E.S., Lee, S., Yoon, K.R.: Smart bactericidal filter containing biodegradable polymers for crystal violet dye adsorption. *Cellulose* **26**(17), 9179–9206 (2019)
20. Goda, E.S., Lee, S., Sohail, M., Yoon, K.R.: Prussian blue and its analogues as advanced supercapacitor electrodes. *J. Energy Chem.* **50**, 206–229 (2020)
21. Attia, N.F., Goda, E.S., Hassan, M.A., Sabaa, M.W., Nour, M.A.: Preparation and certification of novel reference material for smoke density measurements. *Mapan* **33**(3), 297–306 (2018)
22. Elella, M.H.A., et al.: Novel vapor polymerization for integrating flame retardant textile with multifunctional properties. *Compos. Commun.* **24**, 100614 (2021)
23. Goda, E.S., Hong, S.E., Yoon, K.R.: Facile synthesis of Cu-PBA nanocubes/graphene oxide composite as binder-free electrodes for supercapacitor. *J. Alloys Compd.* **859**, 157868 (2020)
24. Elella, M.H.A., Goda, E.S., Abdallah, H.M., Shalan, A.E., Gamal, H., Yoon, K.R.: Innovative bactericidal adsorbents containing modified xanthan gum/montmorillonite nanocomposites for wastewater treatment. *Int. J. Biol. Macromol.* **167**, 1113–1125 (2021)
25. Singu, B.S., Goda, E.S., Yoon, K.R.: Carbon Nanotube–Manganese oxide nanorods hybrid composites for high-performance supercapacitor materials. *J. Ind. Eng. Chem.* **97**, 239–249 (2021)
26. Ngwuluka, N.C., et al.: Natural polymers in micro-and nanoencapsulation for therapeutic and diagnostic applications: part i: lipids and fabrication techniques. In: *Nano-and Micro-Encapsulation-Techniques and Applications*, pp. 3–54. Intech Open (2020)

27. Mittal, H., Alili, A.A., Morajkar, P.P., Alhassan, S.M.: Graphene oxide crosslinked hydrogel nanocomposites of xanthan gum for the adsorption of crystal violet dye. *J. Mol. Liq.* **323**, 115034 (2021)
28. Elella, M.H.A., Shalan, A.E., Sabaa, M.W., Mohamed, R.R.: One-pot green synthesis of antimicrobial chitosan derivative nanocomposites to control foodborne pathogens. *RSC Adv.* **12**(2), 1095–1104 (2022)
29. Sabaa, M.W., Hanna, D.H., Abu Elella, M.H., Mohamed, R.R.: Encapsulation of bovine serum albumin within novel xanthan gum based hydrogel for protein delivery. *Mater. Sci. Eng. C* **94**, 1044–1055 (2019)
30. Mittal, H., Parashar, V., Mishra, S., Mishra, A.: Fe₃O₄ MNPs and gum xanthan based hydrogels nanocomposites for the efficient capture of malachite green from aqueous solution. *Chem. Eng. J.* **255**, 471–482 (2014)
31. Thakur, S., Arotiba, O.: Synthesis, characterization and adsorption studies of an acrylic acid-grafted sodium alginate-based TiO₂ hydrogel nanocomposite. *Adsorpt. Sci. Technol.* **36**(1–2), 458–477 (2018)
32. Goda, E.S., Abu Elella, M.H., Gamal, H., Hong, S.E., Yoon, K.R.: Two-dimensional nanomaterials as smart flame retardants for polyurethane. In: *Materials and Chemistry of Flame-Retardant Polyurethanes Volume 1: A Fundamental Approach*, pp. 189–219. ACS Publications (2021)
33. Mittal, H., Kumar, V., Ray, S.S.: Adsorption of methyl violet from aqueous solution using gum xanthan/Fe₃O₄ based nanocomposite hydrogel. *Int. J. Biol. Macromol.* **89**, 1–11 (2016)
34. Pandey, N., Shukla, S., Singh, N.: Water purification by polymer nanocomposites: an overview. *Nanocomposites* **3**(2), 47–66 (2017)
35. Mittal, H., Babu, R., Alhassan, S.M.: Utilization of gum xanthan based superporous hydrogels for the effective removal of methyl violet from aqueous solution. *Int. J. Biol. Macromol.* **143**, 413–423 (2020)
36. Elella, M.H.A., Aamer, N., Mohamed, Y., El Nazer, H.A., Mohamed, R.R.: Innovation of high-performance adsorbent based on modified gelatin for wastewater treatment. *Polym. Bull.*, 1–17 (2022)
37. Ghorai, S., Sarkar, A., Raoufi, M., Panda, A.B., Schönherr, H., Pal, S.: Enhanced removal of methylene blue and methyl violet dyes from aqueous solution using a nanocomposite of hydrolyzed polyacrylamide grafted xanthan gum and incorporated nanosilica. *ACS Appl. Mater. Interfaces* **6**(7), 4766–4777 (2014)
38. Singh, N.B., Agarwal, S.: Nanocomposites: an overview. *Emerg. Mater. Res.* **5**(1), 5–43 (2016)
39. Mittal, H., Maity, A., Ray, S.S.: Gum karaya based hydrogel nanocomposites for the effective removal of cationic dyes from aqueous solutions. *Appl. Surf.* **364**, 917–930 (2016)
40. Fosso-Kankeu, E., Mittal, H., Mishra, S.B., Mishra, A.K.: Gum ghatti and acrylic acid based biodegradable hydrogels for the effective adsorption of cationic dyes. *J. Ind. Eng. Chem.* **22**, 171–178 (2015)
41. Thakur, S., Pandey, S., Arotiba, O.A.: Sol-gel derived xanthan gum/silica nanocomposite—a highly efficient cationic dyes adsorbent in aqueous system. *Int. J. Bio. Macromol.* **103**, 596–604 (2017)
42. Jaspal, D., Malviya, A.: Composites for wastewater purification: a review. *Chemosphere* **246**, 125788 (2020)
43. Zhang, X., Li, A., Jiang, Z., Zhang, Q.: Adsorption of dyes and phenol from water on resin adsorbents: effect of adsorbate size and pore size distribution. *J. Hazard. Mater.* **137**(2), 1115–1122 (2006)
44. Yu, Y., Zhuang, Y.Y., Wang, Z.H.: Adsorption of water-soluble dye onto functionalized resin. *J. Colloid Interface Sci.* **242**(2), 288–293 (2001)
45. Dongre, R.S., et al.: Natural polymer based composite membranes for water purification: a review. *Polym. Plast. Technol. Mater.* **58**(12), 1295–1310 (2019)
46. Inamuddin: Xanthan gum/titanium dioxide nanocomposite for photocatalytic degradation of methyl orange dye. *Int. J. Biol. Macromol.* **121**, 1046–1053 (2019)
47. Pour, Z.S., Ghaemy, M.: Removal of dyes and heavy metal ions from water by magnetic hydrogel beads based on poly (vinyl alcohol)/carboxymethyl starch-g-poly (vinyl imidazole). *RSC Adv.* **5**(79), 64106–64118 (2015)

48. Zhijiang, C., Cong, Z., Ping, X., Jie, G., Kongyin, Z.: Calcium alginate-coated electrospun polyhydroxybutyrate/carbon nanotubes composite nanofibers as nanofiltration membrane for dye removal. *J. Mater. Sci.* **53**(20), 14801–14820 (2018)
49. Jaseela, P., Garvasis, J., Joseph, A.: Selective adsorption of methylene blue (MB) dye from aqueous mixture of MB and methyl orange (MO) using mesoporous titania (TiO₂)-poly vinyl alcohol (PVA) nanocomposite. *J. Mole. Liq.* **286**, 110908 (2019)
50. Thakur, S., Govender, P.P., Mamo, M.A., Tamulevicius, S., Thakur, V.K.: Recent progress in gelatin hydrogel nanocomposites for water purification and beyond. *Vacuum* **146**, 396–408 (2017)
51. Sabet, S., et al.: The interactions between the two negatively charged polysaccharides: Gum Arabic and alginate. *Food Hydrocoll.* **112**, 106343 (2021)
52. Aizat, M.A., Aziz, F.: Chitosan nanocomposite application in wastewater treatments. In: *Nanotechnology in Water and Wastewater Treatment*, pp. 243–265. Elsevier (2019)
53. Hassan, H., Salama, A., El-ziaty, A.K., El-Sakhawy, M.: New chitosan/silica/zinc oxide nanocomposite as adsorbent for dye removal. *Int. J. Biol. Macromol.* **131**, 520–526 (2019)
54. Salehi, R., Arami, M., Mahmoodi, N.M., Bahrami, H., Khorramfar, S.: Novel biocompatible composite (chitosan-zinc oxide nanoparticle): preparation, characterization and dye adsorption properties. *Colloids Surf. B* **80**(1), 86–93 (2010)
55. Masilompane, T.M., Chaukura, N., Mishra, S.B., Mishra, A.K.: Chitosan-lignin-titania nanocomposites for the removal of brilliant black dye from aqueous solution. *Int. J. Biol. Macromol.* **120**, 1659–1666 (2018)
56. Jawad, A.H., Mubarak, N.S., Abdulhameed, A.S.: Hybrid crosslinked chitosan-epichlorohydrin/TiO₂ nanocomposite for reactive red 120 dye adsorption: kinetic, isotherm, thermodynamic, and mechanism study. *J. Polym. Environ.* **28**(2), 624–637 (2020)
57. Abbasi, M.: Synthesis and characterization of magnetic nanocomposite of chitosan/SiO₂/carbon nanotubes and its application for dyes removal. *J. Clean Prod.* **145**, 105–113 (2017)
58. Haldorai, Y., Shim, J.J.: Multifunctional chitosan-copper oxide hybrid material: photocatalytic and antibacterial activities. *Int. J. Photoenergy* **2013**, 245646 (2013)
59. Zhu, H., et al.: Photocatalytic decolorization and degradation of Congo Red on innovative crosslinked chitosan/nano-CdS composite catalyst under visible light irradiation. *J. Hazard. Mater.* **169**(1–3), 933–940 (2009)
60. Ahmad, R., Mirza, A.: Facile one pot green synthesis of Chitosan-Iron oxide (CS-Fe₂O₃) nanocomposite: removal of Pb (II) and Cd (II) from synthetic and industrial wastewater. *J. Clean Prod.* **186**, 342–352 (2018)
61. Akbarnejad, S., Amooey, A.A., Ghasemi, S.: High effective adsorption of acid fuchsin dye using magnetic biodegradable polymer-based nanocomposite from aqueous solutions. *Microchem. J.* **149**, 103966 (2019)
62. Ramalingam, B., Khan, M.M., Mondal, B., Mandal, A.B., Das, S.K.: Facile synthesis of silver nanoparticles decorated magnetic-chitosan microsphere for efficient removal of dyes and microbial contaminants. *ACS Sustain. Chem. Eng.* **3**(9), 2291–2302 (2015)
63. Huang, C.P., Stumm, W.: Specific adsorption of cations on hydrous γ -Al₂O₃. *J. Colloid Interface Sci.* **43**(2), 409–420 (1973)
64. Fan, L., Luo, C., Sun, M., Qiu, H., Li, X.: Synthesis of magnetic β -cyclodextrin-chitosan/graphene oxide as nanoadsorbent and its application in dye adsorption and removal. *Colloids Surf. B* **103**, 601–607 (2013)
65. Jiang, Y., et al.: Magnetic chitosan-graphene oxide composite for anti-microbial and dye removal applications. *Int. J. Biol. Macromol.* **82**, 702–710 (2016)
66. Makhado, E., Pandey, S., Ramontja, J.: Microwave assisted synthesis of xanthan gum-cl-poly (acrylic acid) based-reduced graphene oxide hydrogel composite for adsorption of methylene blue and methyl violet from aqueous solution. *Int. J. Biol. Macromol.* **119**, 255–269 (2018)
67. Ma, Y., Yu, F., Ma, J.: Design of graphene/organic composite adsorbent and its application in water treatment. *Prog. Chem.* **29**(6), 582–592 (2017)

68. Ali, I., et al.: Graphene based adsorbents for remediation of noxious pollutants from wastewater. *Environ. Int.* **127**, 160–180 (2019)
69. Banerjee, P., Barman, S.R., Mukhopadhyay, A., Das, P.: Ultrasound assisted mixed azo dye adsorption by chitosan–graphene oxide nanocomposite. *Chem. Eng. Res. Des.* **117**, 43–56 (2017)
70. Wang, B., et al.: Alginate-based composites for environmental applications: a critical review. *Crit. Rev. Environ. Sci. Technol.* **49**(4), 318–356 (2019)
71. Bayat, M., Javanbakht, V., Esmaili, J.: Synthesis of zeolite/nickel ferrite/sodium alginate bionanocomposite via a co-precipitation technique for efficient removal of water-soluble methylene blue dye. *Int. J. Biol. Macromol.* **116**, 607–619 (2018)
72. Ghorai, S., Sarkar, A.K., Panda, A.B., Pal, S.: Effective removal of Congo red dye from aqueous solution using modified xanthan gum/silica hybrid nanocomposite as adsorbent. *Bioresour. Technol.* **144**, 485–491 (2013)
73. Makhado, E., Pandey, S., Nomngongo, P., Ramontja, J.: Xanthan gum-cl-poly (acrylic acid)/reduced graphene oxide hydrogel nanocomposite as adsorbent for dye removal. In: *ASETWM-17*, pp. 159–164 (2017)
74. Tanzifi, M., Esmizadeh, E., Bazgir, H., Nazari, A., Vahidifar, A.: Adsorption of methylene blue dye from aqueous solution using polyaniline/xanthan gum nanocomposite: kinetic and isotherm studies. *J. Polym. Compos.* **7**, 17–26 (2019)
75. Bhatti, H.N., Mahmood, Z., Kausar, A., Yakout, S.M., Shair, O.H., Iqbal, M.: Biocomposites of polypyrrole, polyaniline and sodium alginate with cellulosic biomass: Adsorption-desorption, kinetics and thermodynamic studies for the removal of 2, 4-dichlorophenol. *Int. J. Biol. Macromol.* **153**, 146–153 (2020)
76. Mashkoor, F., Nasar, A.: Facile synthesis of polypyrrole decorated chitosan-based magsorbent: characterizations, performance, and applications in removing cationic and anionic dyes from aqueous medium. *Int. J. Biol. Macromol.* **161**, 88–100 (2020)
77. Midya, L., Chettri, A., Pal, S.: Development of a novel nanocomposite using polypyrrole grafted chitosan-decorated CDs with improved photocatalytic activity under solar light illumination. *ACS Sustain. Chem. Eng.* **7**(10), 9416–9421 (2019)
78. Nasar, A., Mashkoor, F.: Application of polyaniline-based adsorbents for dye removal from water and wastewater—a review. *Environ. Sci. Pollut. Res.* **26**(6), 5333–5356 (2019)
79. Hasan, I., Bhatia, D., Wallia, S., Singh, P.: Removal of malachite green by polyacrylamide-g-chitosan γ -Fe₂O₃ nanocomposite—an application of central composite design. *Groundw. Sustain. Dev.* **11**, 100378 (2020)
80. Makhado, E., Pandey, S., Nomngongo, P.N., Ramontja, J.: Preparation and characterization of xanthan gum-cl-poly (acrylic acid)/o-MWCNTs hydrogel nanocomposite as highly effective re-usable adsorbent for removal of methylene blue from aqueous solutions. *J. Colloid Interface Sci.* **513**, 700–714 (2018)
81. Rathore, B.S., Chauhan, N.P., Rawal, M.K., Ameta, S.C., Ameta, R.: Chitosan–polyaniline–copper (II) oxide hybrid composite for the removal of methyl orange dye. *Polym. Bull.* **77**, 4833–4850 (2019)
82. Karthikeyan, P., Elanchezhian, S.S., Meenakshi, S., Park, C.M.: Magnesium ferrite-reinforced polypyrrole hybrids as an effective adsorbent for the removal of toxic ions from aqueous solutions: preparation, characterization, and adsorption experiments. *J. Hazard. Mater.* **408**, 124892 (2021)
83. Alinejad-Mir, A., Amooey, A.A., Ghasemi, S.: Adsorption of direct yellow 12 from aqueous solutions by an iron oxide-gelatin nanoadsorbent; kinetic, isotherm and mechanism analysis. *J. Clean Prod.* **170**, 570–580 (2018)
84. Saber-Samandari, S., Saber-Samandari, S., Joneidi-Yekta, H., Mohseni, M.: Adsorption of anionic and cationic dyes from aqueous solution using gelatin-based magnetic nanocomposite beads comprising carboxylic acid functionalized carbon nanotube. *Chem. Eng. J.* **308**, 1133–1144 (2017)
85. Yadav, M., Gupta, R., Sharma, R.K.: Green and sustainable pathways for wastewater purification. In: *Advances in Water Purification Techniques*, pp. 355–383. Elsevier (2019)

86. Ghorai, S., Sinhamahapatra, A., Sarkar, A., Panda, A.B., Pal, S.: Novel biodegradable nanocomposite based on XG-g-PAM/SiO₂: application of an efficient adsorbent for Pb²⁺ ions from aqueous solution. *Bioresour. Technol.* **119**, 181–190 (2012)
87. Ahmad, R., Mirza, A.: Application of Xanthan gum/n-acetyl cysteine modified mica bionanocomposite as an adsorbent for the removal of toxic heavy metals. *Groundw. Sustain. Dev.* **7**, 101–108 (2018)
88. Lim, A.P., Aris, A.Z.: A review on economically adsorbents on heavy metals removal in water and wastewater. *Rev. Environ. Sci. Biotechnol.* **13**(2), 163–181 (2014)
89. Pal, S., Patra, A.S., Ghorai, S., Sarkar, A.K., Das, R., Sarkar, S.: Modified guar gum/SiO₂: development and application of a novel hybrid nanocomposite as a flocculant for the treatment of wastewater. *Environ. Sci. Water Res. Technol.* **1**(1), 84–95 (2015)
90. Shukla, S.K., Mishra, A.K., Arotiba, O.A., Mamba, B.B.: Chitosan-based nanomaterials: a state-of-the-art review. *Int. J. Biol. Macromol.* **59**, 46–58 (2013)
91. Samuel, M.S., Bhattacharya, J., Raj, S., Santhanam, N., Singh, H., Singh, N.P.: Efficient removal of Chromium (VI) from aqueous solution using chitosan grafted graphene oxide (CS-GO) nanocomposite. *Int. J. Biol. Macromol.* **121**, 285–292 (2019)
92. Fan, H., Ma, X., Zhou, S., Huang, J., Liu, Y., Liu, Y.: Highly efficient removal of heavy metal ions by carboxymethyl cellulose-immobilized Fe₃O₄ nanoparticles prepared via high-gravity technology. *Carbohydr. Polym.* **213**, 39–49 (2019)
93. Karkeh-abadi, F., Saber-Samandari, S., Saber-Samandari, S.: The impact of functionalized CNT in the network of sodium alginate-based nanocomposite beads on the removal of Co (II) ions from aqueous solutions. *J. Hazard. Mater.* **312**, 224–233 (2016)
94. Lind, M.L., et al.: Influence of zeolite crystal size on zeolite-polyamide thin film nanocomposite membranes. *Langmuir* **25**(17), 10139–10145 (2009)
95. Hoang, M.T., et al.: Fabrication of thin film nanocomposite nanofiltration membrane incorporated with cellulose nanocrystals for removal of Cu (II) and Pb (II). *Chem. Eng. Sci.* **228**, 115998 (2020)
96. Rajaeian, B., Rahimpour, A., Tade, M.O., Liu, S.: Fabrication and characterization of polyamide thin film nanocomposite (TFN) nanofiltration membrane impregnated with TiO₂ nanoparticles. *Desalination* **313**, 176–188 (2013)
97. Zargar, M., Hartanto, Y., Jin, B., Dai, S.: Polyethylenimine modified silica nanoparticles enhance interfacial interactions and desalination performance of thin film nanocomposite membranes. *J. Membr. Sci.* **541**, 19–28 (2017)
98. Liu, X., Qi, S., Li, Y., Yang, L., Cao, B., Tang, C.Y.: Synthesis and characterization of novel antibacterial silver nanocomposite nanofiltration and forward osmosis membranes based on layer-by-layer assembly. *Water Res.* **47**(9), 3081–3092 (2013)
99. Xia, S., Yao, L., Zhao, Y., Li, N., Zheng, Y.: Preparation of graphene oxide modified polyamide thin film composite membranes with improved hydrophilicity for natural organic matter removal. *Chem. Eng. J.* **280**, 720–727 (2015)
100. Zarrabi, H., Yekavalangi, M.E., Vatanpour, V., Shockravi, A., Safarpour, M.: Improvement in desalination performance of thin film nanocomposite nanofiltration membrane using amine-functionalized multiwalled carbon nanotube. *Desalination* **394**, 83–90 (2016)
101. Zhao, D.L., Yeung, W.S., Zhao, Q., Chung, T.S.: Thin-film nanocomposite membranes incorporated with UiO-66-NH₂ nanoparticles for brackish water and seawater desalination. *J. Membr. Sci.* **604**, 118039 (2020)
102. Zaman, A., et al.: Facile one-pot in-situ synthesis of novel graphene oxide-cellulose nanocomposite for enhanced azo dye adsorption at optimized conditions. *Carbohydr. Polym.* **246**, 116661 (2020)
103. Malatji, N., et al.: Synthesis and characterization of magnetic clay-based carboxymethyl cellulose-acrylic acid hydrogel nanocomposite for methylene blue dye removal from aqueous solution. *Environ. Sci. Pollut. Res.* **27**, 1–17 (2020)
104. Janaki, V., et al.: Starch/polyaniline nanocomposite for enhanced removal of reactive dyes from synthetic effluent. *Carbohydr. Polym.* **90**(4), 1437–1444 (2012)

105. Gokila, S., Gomathi, T., Sudha, P., Anil, S.: Removal of the heavy metal ion chromium (VI) using Chitosan and Alginate nanocomposites. *Int. J. Biol. Macromol.* **104**, 1459–1468 (2017)
106. Hosseinzadeh, H., Ramin, S.: Effective removal of copper from aqueous solutions by modified magnetic chitosan/graphene oxide nanocomposites. *Int. J. Biol. Macromol.* **113**, 859–868 (2018)
107. Patra, A.S., Ghorai, S., Sarkar, D., Das, R., Sarkar, S., Pal, S.: Anionically functionalized guar gum embedded with silica nanoparticles: an efficient nanocomposite adsorbent for rapid adsorptive removal of toxic cationic dyes and metal ions. *Bioresour. Technol.* **225**, 367–376 (2017)
108. Sangeetha, K., Vidhya, G., Vasugi, G., Girija, E.: Lead and cadmium removal from single and binary metal ion solution by novel hydroxyapatite/alginate/gelatin nanocomposites. *J. Environ. Chem. Eng.* **6**(1), 1118–1126 (2018)
109. Richardson, S.D., Ternes, T.A.: Water analysis: emerging contaminants and current issues. *Anal. Chem.* **86**(6), 2813–2848 (2014)
110. Jones, K.C., De Voogt, P.: Persistent organic pollutants (POPs): state of the science. *Environ. Pollut.* **100**(1–3), 209–221 (1999)
111. Zhang, Z., Feng, S.S.: The drug encapsulation efficiency, in vitro drug release, cellular uptake and cytotoxicity of paclitaxel-loaded poly (lactide)–tocopheryl polyethylene glycol succinate nanoparticles. *Biomaterials* **27**(21), 4025–4033 (2006)
112. Dang, V.D., Walters, D.M., Lee, C.M.: Historical changes in polychlorinated biphenyls contaminated sediments. *Am. J. Environ. Sci.* **8**(1), 11–15 (2012)
113. Hopf, N.B., Ruder, A.M., Succop, P.: Background levels of polychlorinated biphenyls in the US population. *Sci. Total Environ.* **407**(24), 6109–6119 (2009)
114. Sun, X., Wang, C., Li, Y., Wang, W., Wei, J.: Treatment of phenolic wastewater by combined UF and NF/RO processes. *Desalination* **355**, 68–74 (2015)
115. Calace, N., Nardi, E., Petronio, B., Pietroletti, M.: Adsorption of phenols by papermill sludges. *Environ. Pollut.* **118**(3), 315–319 (2002)
116. Akbal, F., Onar, A.N.: Photocatalytic degradation of phenol. *Environ. Monit. Assess.* **83**(3), 295–302 (2003)
117. Liao, Q.G., Wang, D.G., Luo, L.G.: Chitosan-poly (m-phenylenediamine)@ Fe₃O₄ nanocomposite for magnetic solid-phase extraction of polychlorinated biphenyls from water samples. *Anal. Bioanal. Chem.* **406**(29), 7571–7579 (2014)
118. Villegas, L.G., Mashhadi, N., Chen, M., Mukherjee, D., Taylor, K.E., Biswas, N.: A short review of techniques for phenol removal from wastewater. *Curr. Pollut. Rep.* **2**(3), 157–167 (2016)
119. Kazemi, P., Peydayesh, M., Bandegi, A., Mohammadi, T., Bakhtiari, O.: Stability and extraction study of phenolic wastewater treatment by supported liquid membrane using tributyl phosphate and sesame oil as liquid membrane. *Chem. Eng. Res. Des.* **92**(2), 375–383 (2014)
120. Mohammadi, S., Kargari, A., Sanaeepur, H., Abbassian, K., Najafi, A., Mofarrah, E.: Phenol removal from industrial wastewaters: a short review. *Desalin. Water Treat.* **53**(8), 2215–2234 (2015)
121. Busca, G., Berardinelli, S., Resini, C., Arrighi, L.: Technologies for the removal of phenol from fluid streams: a short review of recent developments. *J. Hazard. Mater.* **160**(2–3), 265–288 (2008)
122. Fathy, M., Selim, H., Shahawy, A.E.: Chitosan/MCM-48 nanocomposite as a potential adsorbent for removing phenol from aqueous solution. *RSC Adv.* **10**(39), 23417–23430 (2020)
123. Ofomaja, A.E.: Kinetic study and sorption mechanism of methylene blue and methyl violet onto mansonia (*Mansonia altissima*) wood sawdust. *Chem. Eng. J.* **143**(1–3), 85–95 (2008)
124. Deb, A.S., Dwivedi, V., Dasgupta, K., Ali, S.M., Shenoy, K.: Novel amidoamine functionalized multi-walled carbon nanotubes for removal of mercury (II) ions from wastewater: combined experimental and density functional theoretical approach. *Chem. Eng. J.* **313**, 899–911 (2017)
125. Li, S., Li, D., Su, F., Ren, Y., Qin, G.: Uniform surface modification of diatomaceous earth with amorphous manganese oxide and its adsorption characteristics for lead ions. *Appl. Surf. Sci.* **317**, 724–729 (2014)

126. Fellenz, N., Martin, P., Marchetti, S., Bengoa, F.: Aminopropyl-modified mesoporous silica nanospheres for the adsorption of Cr (VI) from water. *J. Porous Mater.* **22**(3), 729–738 (2015)
127. Ahmad, R., Hasan, I.: Efficient remediation of an aquatic environment contaminated by Cr (VI) and 2, 4-dinitrophenol by XG-g-polyaniline@ ZnO nanocomposite. *J. Chem. Eng. Data* **62**(5), 1594–1607 (2017)
128. Campagnolo, L., Lauciello, S., Athanassiou, A., Fragouli, D.: Au/ZnO hybrid nanostructures on electrospun polymeric mats for improved photocatalytic degradation of organic pollutants. *Water* **11**(9), 1787 (2019)
129. Soni, U., Bajpai, J., Singh, S.K., Bajpai, A.: Evaluation of chitosan-carbon based biocomposite for efficient removal of phenols from aqueous solutions. *J. Water Process Eng.* **16**, 56–63 (2017)
130. Fan, S., et al.: Magnetic chitosan-hydroxyapatite composite microspheres: preparation, characterization, and application for the adsorption of phenolic substances. *Bioresour. Technol.* **274**, 48–55 (2019)
131. Cai, H., Feng, J., Wang, S., Shu, T., Luo, Z., Liu, S.: Tannic acid directed synthesis of Fe₃O₄@ TA@ P (NVP-co-NIPAM) magnetic microspheres for polyphenol extraction. *Food Chem.* **283**, 530–538 (2019)
132. Hu, X., et al.: Green synthesis of a magnetic β -cyclodextrin polymer for rapid removal of organic micro-pollutants and heavy metals from dyeing wastewater. *Environ. Res.* **180**, 108796 (2020)
133. Mukherjee, R., De, S.: Adsorptive removal of phenolic compounds using cellulose acetate phthalate–alumina nanoparticle mixed matrix membrane. *J. Hazard. Mater.* **265**, 8–19 (2014)
134. Khakpour, R., Tahermansouri, H.: Synthesis, characterization and study of sorption parameters of multi-walled carbon nanotubes/chitosan nanocomposite for the removal of picric acid from aqueous solutions. *Int. J. Biol. Macromol.* **109**, 598–610 (2018)
135. Wang, M., et al.: Core–shell superparamagnetic Fe₃O₄@ β -CD composites for host–guest adsorption of polychlorinated biphenyls (PCBs). *J. Colloid Interface Sci.* **447**, 1–7 (2015)
136. Khammar, S., Bahramifar, N., Younesi, H.: Optimization using the response surface methodology for adsorption of polychlorinated biphenyls (PCBs) from transformer oil by magnetic CMCD-Fe₃O₄@ SiO₂ nanoparticles. *Mater. Chem. Phys.* **252**, 123195 (2020)
137. Alnajrani, M.N., Alsager, O.A.: Removal of antibiotics from water by polymer of intrinsic microporosity: isotherms, Kinetics, thermodynamics, and adsorption mechanism. *Sci. Rep.* **10**(1), 1–14 (2020)
138. Castanon, J.: History of the use of antibiotic as growth promoters in European poultry feeds. *Poult. Sci. J.* **86**(11), 2466–2471 (2007)
139. Mathers, J.J., Flick, S.C., Cox, L.A.: Longer-duration uses of tetracyclines and penicillins in US food-producing animals: indications and microbiologic effects. *Environ. Int.* **37**(5), 991–1004 (2011)
140. Heberer, T.: Occurrence, fate, and removal of pharmaceutical residues in the aquatic environment: a review of recent research data. *Toxicol. Lett.* **131**(1–2), 5–17 (2002)
141. Prestinaci, F., Pezzotti, P., Pantosti, A.: Antimicrobial resistance: a global multifaceted phenomenon. *Pathog. Glob. Health* **109**(7), 309–318 (2015)
142. Aarestrup, F.M., Wegener, H.C.: The effects of antibiotic usage in food animals on the development of antimicrobial resistance of importance for humans in *Campylobacter* and *Escherichia coli*. *Microb. Infect.* **1**(8), 639–644 (1999)
143. Schwarz, S., Kehrenberg, C., Walsh, T.: Use of antimicrobial agents in veterinary medicine and food animal production. *Int. J. Antimicrob. Agents* **17**(6), 431–437 (2001)
144. Batt, A.L., Bruce, I.B., Aga, D.S.: Evaluating the vulnerability of surface waters to antibiotic contamination from varying wastewater treatment plant discharges. *Environ. Pollut.* **142**(2), 295–302 (2006)
145. Gulkowska, A., et al.: Removal of antibiotics from wastewater by sewage treatment facilities in Hong Kong and Shenzhen, China. *Water Res.* **42**(1–2), 395–403 (2008)
146. Watkinson, A., Murby, E., Costanzo, S.: Removal of antibiotics in conventional and advanced wastewater treatment: implications for environmental discharge and wastewater recycling. *Water Res.* **41**(18), 4164–4176 (2007)

147. Alsager, O.A., Alnajrani, M.N., Alhazzaa, O.: Decomposition of antibiotics by gamma irradiation: kinetics, antimicrobial activity, and real application in food matrices. *Chem. Eng. J.* **338**, 548–556 (2018)
148. Alsager, O.A., Alnajrani, M.N., Abuelizz, H.A., Aldaghmani, I.A.: Removal of antibiotics from water and waste milk by ozonation: kinetics, byproducts, and antimicrobial activity. *Ecotoxicol. Environ. Saf.* **158**, 114–122 (2018)
149. Klavarioti, M., Mantzavinos, D., Kassinos, D.: Removal of residual pharmaceuticals from aqueous systems by advanced oxidation processes. *Environ. Int.* **35**(2), 402–417 (2009)
150. Ahmed, M., Hameed, B.: Removal of emerging pharmaceutical contaminants by adsorption in a fixed-bed column: a review. *Ecotoxicol. Environ. Saf.* **149**, 257–266 (2018)
151. Akhtar, J., Amin, N.A., Shahzad, K.: A review on removal of pharmaceuticals from water by adsorption. *Desalin. Water Treat.* **57**(27), 12842–12860 (2016)
152. Danalioğlu, S.T., Bayazit, Ş.S., Kuyumcu, Ö.K., Salam, M.A.: Efficient removal of antibiotics by a novel magnetic adsorbent: Magnetic activated carbon/chitosan (MACC) nanocomposite. *J. Mol. Liq.* **240**, 589–596 (2017)
153. Li, Z., et al.: Removal and adsorption mechanism of tetracycline and cefotaxime contaminants in water by NiFe₂O₄-COF-chitosan-terephthalaldehyde nanocomposites film. *Chem. Eng. J.* **382**, 123008 (2020)
154. Ma, J., Zhuang, Y., Yu, F.: Equilibrium, kinetic and thermodynamic adsorption studies of organic pollutants from aqueous solution onto CNT/C@ Fe/chitosan composites. *New J. Chem.* **39**(12), 9299–9305 (2015)
155. Huang, B., et al.: Effect of Cu (II) ions on the enhancement of tetracycline adsorption by Fe₃O₄@ SiO₂-Chitosan/graphene oxide nanocomposite. *Carbohydr. Polym.* **157**, 576–585 (2017)
156. Mohammadi, A.M., Nourisepehr, M., Dehghanifard, E.: Evaluation the efficiency of magnetic-metallic chitosan nanocomposite adsorbent in the removal of tetracycline antibiotic from aqueous solutions. *J. Environ. Health Eng.* **6**(4), 356–374 (2019)
157. Gopal, G., Roy, N., Chandrasekaran, N., Mukherjee, A.: Photo-assisted removal of tetracycline using bio-nanocomposite-immobilized alginate beads. *ACS Omega* **4**(17), 17504–17510 (2019)
158. Okoli, C.P., Ofomaja, A.E.: Development of sustainable magnetic polyurethane polymer nanocomposite for abatement of tetracycline antibiotics aqueous pollution: response surface methodology and adsorption dynamics. *J. Clean. Prod.* **217**, 42–55 (2019)
159. Gupta, V.K., Fakhri, A., Agarwal, S., Azad, M.: Synthesis and characterization of Ag₂S decorated chitosan nanocomposites and chitosan nanofibers for removal of lincosamides antibiotic. *Int. J. Biol. Macromol.* **103**, 1–7 (2017)
160. Luo, X., Liu, L., Wang, L., Liu, X., Cai, Y.: Facile synthesis and low concentration tylosin adsorption performance of chitosan/cellulose nanocomposite microspheres. *Carbohydr. Polym.* **206**, 633–640 (2019)
161. Yang, C., et al.: Highly efficient removal of amoxicillin from water by Mg-Al layered double hydroxide/cellulose nanocomposite beads synthesized through in-situ coprecipitation method. *Int. J. Biol. Macromol.* **149**, 93–100 (2020)
162. Rasoulzadeh, H., Mohseni-Bandpei, A., Hosseini, M., Safari, M.: Mechanistic investigation of ciprofloxacin recovery by magnetite-imprinted chitosan nanocomposite: isotherm, kinetic, thermodynamic and reusability studies. *Int. J. Biol. Macromol.* **133**, 712–721 (2019)
163. Azizi, A.: Green synthesized Fe₃O₄/cellulose nanocomposite suitable adsorbent for metronidazole removal. *Polym. Sci. Ser. B* **62**, 572–582 (2020)
164. Jafarzadeh, N., et al.: Taguchi optimization approach for metronidazole removal from aqueous solutions by using graphene oxide functionalized β-cyclodextrin/Ag nanocomposite. *Water Sci. Technol.* **2017**, 36–47 (2017)
165. Li, X., Zhang, Z., Fakhri, A., Gupta, V.K., Agarwal, S.: Adsorption and photocatalysis assisted optimization for drug removal by chitosan-glyoxal/Polyvinylpyrrolidone/MoS₂ nanocomposites. *Int. J. Biol. Macromol.* **136**, 469–475 (2019)

166. Kyzas, G.Z., Bikiaris, D.N., Seredych, M., Bandosz, T.J., Deliyanni, E.A.: Removal of dorzolanamide from biomedical wastewaters with adsorption onto graphite oxide/poly (acrylic acid) grafted chitosan nanocomposite. *Bioresour. Technol.* **152**, 399–406 (2014)
167. Taghizade, F.T., Mehrdadi, N., Baghdadi, M., Nabi, B.G.: Application of nanotechnology in pesticides removal from aqueous solutions—a review. *Int. J. Nanosci. Nanotechnol.* **14**(1), 43–56 (2018)
168. Nasrabadi, T., Bidhendi, G.N., Karbassi, A., Grathwohl, P., Mehrdadi, N.: Impact of major organophosphate pesticides used in agriculture to surface water and sediment quality (Southern Caspian Sea basin, Haraz River). *Environ. Earth Sci.* **63**(4), 873–883 (2011)
169. Maddah, B., Hasanzadeh, M.: Fe₃O₄/CNT magnetic nanocomposites as adsorbents to remove organophosphorus pesticides from environmental water. *Int. J. Nanosci. Nanotechnol.* **13**(2), 139–149 (2017)
170. Plakas, K.V., Karabelas, A.J.: Removal of pesticides from water by NF and RO membranes—a review. *Desalination* **287**, 255–265 (2012)
171. Schäfer, R., Ohe, P., Kühne, R., Schüürmann, G., Liess, M.: Occurrence of 331 organic pollutants in four rivers of North Germany between 1994 and 2004 and risk assessment for algae, invertebrates and fish. *Environ. Sci. Technol.* **45**(14), 6167–6174 (2011)
172. Shen, X., Zhu, L., Wang, N., Ye, L., Tang, H.: Molecular imprinting for removing highly toxic organic pollutants. *Chem. Comm.* **48**(6), 788–798 (2012)
173. Arias-Estévez, M., López-Periago, E., Martínez-Carballo, E., Simal-Gándara, J., Mejuto, J.C., García-Río, L.: The mobility and degradation of pesticides in soils and the pollution of groundwater resources. *Agric. Ecosyst. Environ.* **123**(4), 247–260 (2008)
174. Kim, K.H., Kabir, E., Jahan, S.A.: Exposure to pesticides and the associated human health effects. *Sci. Total Environ.* **575**, 525–535 (2017)
175. Ayazi, Z., Jaafarzadeh, R.: Graphene oxide/polyamide nanocomposite as a novel stir bar coating for sorptive extraction of organophosphorous pesticides in fruit juice and vegetable samples. *Chromatographia* **80**(9), 1411–1422 (2017)
176. Youssef, A.M., El-Naggar, M.E., Malhat, F.M., El Sharkawi, H.M.: Efficient removal of pesticides and heavy metals from wastewater and the antimicrobial activity of f-MWCNTs/PVA nanocomposite film. *J. Clean Prod.* **206**, 315–325 (2019)
177. Dehaghi, S.M., Rahmanifar, B., Moradi, A.M., Azar, P.A.: Removal of permethrin pesticide from water by chitosan–zinc oxide nanoparticles composite as an adsorbent. *J. Saudi Chem. Soc.* **18**(4), 348–355 (2014)
178. Rahmanifar, B., Dehaghi, S.M.: Removal of organochlorine pesticides by chitosan loaded with silver oxide nanoparticles from water. *Clean Technol. Environ. Policy* **16**(8), 1781–1786 (2014)
179. Muda, M.S., et al.: Chitosan-graphene oxide nanocomposites as water-solubilising agents for rotenone pesticide. *J. Mol. Liq.* **318**, 114066 (2020)
180. Mahmoud, G.A., El-kelesh, N.A., Badway, N.A., Kamal, F.H., Abdel Aziz, A.M.: Characterisation of alginate-based nanocomposites prepared by radiation for removal of pesticides. *IJNP* **7**(3–4), 213–230 (2014)
181. Liu, G., et al.: Metal–organic framework preparation using magnetic graphene oxide– β -cyclodextrin for neonicotinoid pesticide adsorption and removal. *Carbohydr. Polym.* **175**, 584–591 (2017)
182. Shahnazi, A., Nabid, M.R., Sedghi, R., Heidari, B.: A thermosensitive molecularly imprinted poly-NIPAM coated MWCNTs/TiO₂ photocatalyst for the preferential removal of pendimethalin pesticide from wastewater. *J. Photochem. Photobiol. A* **402**, 112802 (2020)
183. Wei, Y., Chu, H., Dong, B., Li, X.: Evaluation of humic acid removal by a flat submerged membrane photoreactor. *Sci. Bull.* **56**(32), 3437–3444 (2011)
184. Szymański, K., Morawski, A.W., Mozia, S.: Humic acids removal in a photocatalytic membrane reactor with a ceramic UF membrane. *Chem. Eng. J.* **305**, 19–27 (2016)
185. Hebbar, R.S., Isloor, A.M., Ismail, A., Shilton, S.J., Obaid, A., Fun, H.K.: Probing the morphology and anti-organic fouling behaviour of a polyetherimide membrane modified with hydrophilic organic acids as additives. *New J. Chem.* **39**(8), 6141–6150 (2015)

186. Wen, T., et al.: A core-shell structure of polyaniline coated protonic titanate nanobelt composites for both Cr (VI) and humic acid removal. *Polym. Chem.* **7**(4), 785–794 (2016)
187. Wang, L., Han, C., Nadagouda, M.N., Dionysiou, D.D.: An innovative zinc oxide-coated zeolite adsorbent for removal of humic acid. *J. Hazard. Mater.* **313**, 283–290 (2016)
188. Collado, S., Oulego, P., Suárez-Iglesias, O., Díaz, M.: Biodegradation of dissolved humic substances by fungi. *Appl. Microbiol. Biotechnol.* **102**(8), 3497–3511 (2018)
189. Yuan, S., et al.: Hydrophilic nanofiltration membranes with reduced humic acid fouling fabricated from copolymers designed by introducing carboxyl groups in the pendant benzene ring. *J. Membr. Sci.* **563**, 655–663 (2018)
190. Cheng, M., et al.: Hydroxyl radicals based advanced oxidation processes (AOPs) for remediation of soils contaminated with organic compounds: a review. *Chem. Eng. J.* **284**, 582–598 (2016)
191. Jin, P., Song, J., Yang, L., Jin, X., Wang, X.C.: Selective binding behavior of humic acid removal by aluminum coagulation. *Environ. Pollut.* **233**, 290–298 (2018)
192. Li, C., Dong, Y., Wu, D., Peng, L., Kong, H.: Surfactant modified zeolite as adsorbent for removal of humic acid from water. *Appl. Clay Sci.* **52**(4), 353–357 (2011)
193. Wang, S., Gong, W., Liu, X., Gao, B., Yue, Q.: Removal of fulvic acids using the surfactant modified zeolite in a fixed-bed reactor. *Sep. Purif. Technol.* **51**(3), 367–373 (2006)
194. Santosa, S.J., Kunarti, E.S.: Synthesis and utilization of Mg/Al hydrotalcite for removing dissolved humic acid. *Appl. Surf. Sci.* **254**(23), 7612–7617 (2008)
195. Liang, X.X., et al.: Efficient adsorption of diclofenac sodium from aqueous solutions using magnetic amine-functionalized chitosan. *Chemosphere* **217**, 270–278 (2019)
196. Etemadi, H., Yegani, R., Seyfollahi, M., Rabiee, M.: Synthesis, characterization, and anti-fouling properties of cellulose acetate/polyethylene glycol-grafted nanodiamond nanocomposite membranes for humic acid removal from contaminated water. *Iran Polym. J.* **27**(6), 381–393 (2018)
197. Rodríguez, F.J., Galotto, M.J., Guarda, A., Bruna, J.E.: Modification of cellulose acetate films using nanofillers based on organoclays. *J. Food Eng.* **110**(2), 262–268 (2012)
198. Dong, C., Chen, W., Liu, C.: Preparation of novel magnetic chitosan nanoparticle and its application for removal of humic acid from aqueous solution. *Appl. Surf. Sci.* **292**, 1067–1076 (2014)
199. Zhang, J., Kang, M., Zhou, Y., Ma, C., Ning, F., Qiu, Z.: Facile synthesis of polyethyleneimine modified magnetic graphite: an effective adsorbent for the removal of humic acid from aqueous solution. *Mater. Chem. Phys.* **255**, 123549 (2020)
200. Sid-Sahtout, N., Hank, D., Hellal, A.: Characterization and performance of polymer composite membranes for the removal of humic substances from water. *Environ. Eng. Manage. J.* **19**(5), 733–746 (2020)
201. Sarbatly, R., Krishnaiah, D., Kamin, Z.: A review of polymer nanofibres by electrospinning and their application in oil-water separation for cleaning up marine oil spills. *Mar. Pollut. Bull.* **106**(1–2), 8–16 (2016)
202. Anisuddin, S., Al Hashar, N., Tahseen, S.: Prevention of oil spill pollution in seawater using locally available materials. *Arab J. Sci. Eng.* **30**(2B), 143–152 (2005)
203. Gao, J., Song, X., Huang, X., Wang, L., Li, B., Xue, H.: Facile preparation of polymer microspheres and fibers with a hollow core and porous shell for oil adsorption and oil/water separation. *Appl. Surf. Sci.* **439**, 394–404 (2018)
204. Kizil, S., Sonmez, H.B.: Oil loving hydrophobic gels made from glycerol propoxylate: efficient and reusable sorbents for oil spill clean-up. *J. Environ. Manag.* **196**, 330–339 (2017)
205. Costa Cunha, G., et al.: Removal of heavy crude oil from water surfaces using a magnetic inorganic-organic hybrid powder and membrane system. *J. Environ. Manag.* **247**, 9–18 (2019)
206. Wu, J., Wang, N., Wang, L., Dong, H., Zhao, Y., Jiang, L.: Electrospun porous structure fibrous film with high oil adsorption capacity. *ACS Appl. Mater. Interfaces* **4**(6), 3207–3212 (2012)
207. Lin, J., et al.: Co-axial electrospun polystyrene/polyurethane fibres for oil collection from water surface. *Nanoscale* **5**(7), 2745–2755 (2013)

208. Lee, M.W., An, S., Lathe, S.S., Lee, C., Hong, S., Yoon, S.S.: Electrospun polystyrene nanofiber membrane with superhydrophobicity and superoleophilicity for selective separation of water and low viscous oil. *ACS Appl. Mater. Interfaces* **5**(21), 10597–10604 (2013)
209. Shang, Y., et al.: An in situ polymerization approach for the synthesis of superhydrophobic and superoleophilic nanofibrous membranes for oil–water separation. *Nanoscale* **4**(24), 7847–7854 (2012)
210. Singh, H., Bhardwaj, N., Arya, S.K., Khatri, M.: Environmental impacts of oil spills and their remediation by magnetic nanomaterials. *Environ. Nanotechnol.* **14**, 100305 (2020)
211. Bolden, A.L., Kwiatkowski, C.F., Colborn, T.: New look at BTEX: are ambient levels a problem? *Environ. Sci. Technol.* **49**(9), 5261–5276 (2015)
212. Sheikholeslami, Z., Kebria, D.Y., Qaderi, F.: Nanoparticle for degradation of BTEX in produced water; an experimental procedure. *J. Mol. Liq.* **264**, 476–482 (2018)
213. Lee, K.P., Arnot, T.C., Mattia, D.: A review of reverse osmosis membrane materials for desalination—development to date and future potential. *J. Membr. Sci.* **370**(1–2), 1–22 (2011)
214. Wang, J., Wang, H., Geng, G.: Highly efficient oil-in-water emulsion and oil layer/water mixture separation based on durably superhydrophobic sponge prepared via a facile route. *Mar. Pollut. Bull.* **127**, 108–116 (2018)
215. Zheng, Q., Cai, Z., Gong, S.: Green synthesis of polyvinyl alcohol (PVA)–cellulose nanofibril (CNF) hybrid aerogels and their use as superabsorbents. *J. Mater. Chem. A* **2**(9), 3110–3118 (2014)
216. Peng, H., et al.: Preparation of superhydrophobic magnetic cellulose sponge for removing oil from water. *Ind. Eng. Chem. Res.* **55**(3), 832–838 (2016)
217. Zhou, S., You, T., Zhang, X., Xu, F.: Superhydrophobic cellulose nanofiber-assembled aerogels for highly efficient water-in-oil emulsions separation. *ACS Appl. Nano Mater.* **1**(5), 2095–2103 (2018)
218. Wu, J.X., Zhang, J., Kang, Y.L., Wu, G., Chen, S.C., Wang, Y.Z.: Reusable and recyclable superhydrophilic electrospun nanofibrous membranes with in situ co-cross-linked polymer–chitin nanowhisker network for robust oil-in-water emulsion separation. *ACS Sustain. Chem. Eng.* **6**(2), 1753–1762 (2018)
219. Saha, R., Uppaluri, R.V., Tiwari, P.: Impact of natural surfactant (Reetha), polymer (xanthan gum), and silica nanoparticles to enhance heavy crude oil recovery. *Energy Fuels* **33**(5), 4225–4236 (2019)
220. Dong, M., et al.: Degradable sugar-based magnetic hybrid nanoparticles for recovery of crude oil from aqueous environments. *Polym. Chem.* **11**(30), 4895–4903 (2020)
221. Mirshahghassemi, S., Cai, B., Lead, J.R.: A comparison between the oil removal capacity of polymer-coated magnetic nanoparticles in natural and synthetic environmental samples. *Environ. Sci. Technol.* **53**(8), 4426–4432 (2019)
222. Barroso-Solares, S., Zahedi, M., Pinto, J., Nanni, G., Fragouli, D., Athanassiou, A.: Oil removal from water–oil emulsions using magnetic nanocomposite fibrous mats. *RSC Adv.* **6**(75), 71100–71107 (2016)
223. Nikkhah, A.A., Zilouei, H., Asadinezhad, A., Keshavarz, A.: Removal of oil from water using polyurethane foam modified with nanoclay. *Chem. Eng. J.* **262**, 278–285 (2015)
224. Satapathy, M., Varshney, P., Nanda, D., Panda, A., Mohapatra, S.S., Kumar, A.: Fabrication of superhydrophobic and superoleophilic polymer composite coatings on cellulosic filter paper for oil–water separation. *Cellulose* **24**(10), 4405–4418 (2017)
225. Thanikaivelan, P., Narayanan, N.T., Pradhan, B.K., Ajayan, P.M.: Collagen based magnetic nanocomposites for oil removal applications. *Sci. Rep.* **230**(2), 1–7 (2012)
226. Singh, H., Jain, A., Kaur, J., Arya, S.K., Khatri, M.: Adsorptive removal of oil from water using SPIONs–chitosan nanocomposite: kinetics and process optimization. *Appl. Nanosci.* **10**, 1281–1295 (2019)
227. Shiqian, L., Peijiang, Z., Ling, D.: Adsorption application for removal of hazardous chloroform from aqueous solution by nanocomposites rectorite/chitosan adsorbent. *J. Water Resour. Prot.* **3**, 448–455 (2011)

228. Chang, F.T., Bently, W.: Toxicogenomic response of staphylococcus aureus to peracetic acid. *Environ. Sci. Technol.* **40**, 5124–5131 (2006)
229. Tsai, Y.T., Cheng, P.C., Pan, T.M.: Immunomodulating activity of *Lactobacillus paracasei* subsp. *paracasei* NTU 101 in enterohemorrhagic *Escherichia coli* O157H7-infected mice. *J. Agric. Food. Chem.* **58**(21), 11265–11272 (2010)
230. Wang, Y., Jett, S.D., Crum, J., Schanze, K.S., Chi, E.Y., Whitten, D.G.: Understanding the dark and light-enhanced bactericidal action of cationic conjugated polyelectrolytes and oligomers. *Langmuir* **29**(2), 781–792 (2013)
231. Motshekga, S.C., Ray, S.S., Maity, A.: Synthesis and characterization of alginate beads encapsulated zinc oxide nanoparticles for bacteria disinfection in water. *J. Colloid Interface Sci.* **512**, 686–692 (2018)
232. Krasner, S.W., et al.: Occurrence of a new generation of disinfection byproducts. *Environ. Sci. Technol.* **40**(23), 7175–7185 (2006)
233. Goda, E.S., Yoon, K.R., El-sayed, S.H., Hong, S.E.: Halloysite nanotubes as smart flame retardant and economic reinforcing materials: a review. *Thermochim. Acta* **669**, 173–184 (2018)
234. Goda, E.S., Singu, B.S., Hong, S.E., Yoon, K.R.: Good dispersion of poly(δ -gluconolactone)-grafted graphene in poly(vinyl alcohol) for significantly enhanced mechanical strength. *Mater. Chem. Phys.* **254**, 123465 (2020)
235. Khan, S.A., Khan, S.B., Kamal, T., Yasir, M., Asiri, A.M.: Antibacterial nanocomposites based on chitosan/Co-MCM as a selective and efficient adsorbent for organic dyes. *Int. J. Biol. Macromol.* **91**, 744–751 (2016)
236. Karthikeyan, K.T., Nithya, A., Jothivenkatachalam, K.: Photocatalytic and antimicrobial activities of chitosan-TiO₂ nanocomposite. *Int. J. Biol. Macromol.* **104**, 1762–1773 (2017)
237. Saha, S., Pal, A., Kundu, S., Basu, S., Pal, T.: Photochemical green synthesis of calcium-alginate-stabilized Ag and Au nanoparticles and their catalytic application to 4-nitrophenol reduction. *Langmuir* **26**(4), 2885–2893 (2010)
238. Siddiqui, S.I., Manzoor, O., Mohsin, M., Chaudhry, S.A.: *Nigella sativa* seed based nanocomposite-MnO₂/BC: an antibacterial material for photocatalytic degradation, and adsorptive removal of Methylene blue from water. *Environ. Res.* **171**, 328–340 (2019)
239. Cantarella, M., et al.: Immobilization of nanomaterials in PMMA composites for photocatalytic removal of dyes, phenols and bacteria from water. *J. Photochem. Photobiol. A* **321**, 1–11 (2016)
240. Kang, S., Pinault, M., Pfefferle, L.D., Elimelech, M.: Single-walled carbon nanotubes exhibit strong antimicrobial activity. *Langmuir* **23**(17), 8670–8673 (2007)
241. Ahmed, F., Santos, C.M., Mangadlao, J., Advincula, R., Rodrigues, D.F.: Antimicrobial PVK:SWNT nanocomposite coated membrane for water purification: performance and toxicity testing. *Water Res.* **47**(12), 3966–3975 (2013)
242. Hussein, M.A., El-Shishtawy, R.M., Alamry, K.A., Asiri, A.M., Mohamed, S.A.: Efficient water disinfection using hybrid polyaniline/graphene/carbon nanotube nanocomposites. *Environ. Technol.* **40**(21), 2813–2824 (2019)
243. Mahlangu, T., Das, R., Abia, L.K., Onyango, M., Ray, S.S., Maity, A.: Thiol-modified magnetic polypyrrole nanocomposite: an effective adsorbent for the adsorption of silver ions from aqueous solution and subsequent water disinfection by silver-laden nanocomposite. *Chem. Eng. J.* **360**, 423–434 (2019)
244. Hu, Z., Zhang, L., Zhong, L., Zhou, Y., Xue, J., Li, Y.: Preparation of an antibacterial chitosan-coated biochar-nanosilver composite for drinking water purification. *Carbohydr. Polym.* **219**, 290–297 (2019)
245. Allafchian, A., Jalali, S.A., Hosseini, F., Massoud, M.: *Ocimum basilicum* mucilage as a new green polymer support for silver in magnetic nanocomposites: production and characterization. *J. Environ. Chem. Eng.* **5**(6), 5912–5920 (2017)
246. Yuan, M., et al.: Polymeric carbon nitride modified polyacrylonitrile fabrics with efficient self-cleaning and water disinfection under visible light. *Chem. Eng. J.* **391**, 123506 (2020)

247. Liu, C., et al.: Novel Inorganic-based n-halamine nanofibrous membranes as highly effective antibacterial agent for water disinfection. *ACS Appl. Mater. Interfaces* **10**(51), 44209–44215 (2018)
248. Xie, L., Shu, Y., Hu, Y., Cheng, J., Chen, Y.: SWNTs-PAN/TPU/PANI composite electrospun nanofiber membrane for point-of-use efficient electrochemical disinfection: New strategy of CNT disinfection. *Chemosphere* **251**, 126286 (2020)

Functionality-Structure Relationship into Functional Polymeric Nanocomposite Membranes for Removal and Monitoring of Pollutants in Fluid Phases



Manuel Palencia, Jina M. Martínez-Lara, Nazly G. Chate-Galvis, and Jorge M. Durango-Petro

Abstract Pressure-driven membrane methods are a well-established technology based on the use of porous membranes and pressure, to produce the separation of substances from water or gaseous effluents. In these methods, membrane is a passive component acting as separation barrier of substances contained in a transporting medium; thus, a membrane separation process is characterized by the transport of matter through the membrane phase which can be porous or dense. The use of membranes as an active component of the separation process leads to the generation of a wide range of new and innovative systems based on porous polymeric nanocomposite materials with multiple applications, such as: surface sensing for monitoring of pollutant and low-pressure systems (air, water, blood, etc.), removal of heavy metals, pharmaceutical products and sub-products (emerging pollutants), among other. Though, for “passive” porous membranes, the separation mechanistic description is based on the transport through the membrane, by size-exclusion or dissolution-diffusion mechanisms, for “active” membranes, the bulk properties, superficial phenomena, and nanoconfinement of the matter are influenced by the nanometric component constituting the membrane material, which not only affects the macroscopic properties of them, but also the response of this material to superficial changes inherent in the separation process. Here, a comprehensive description

M. Palencia (✉)

Research Group in Science With Technological Applications (GI-CAT),
Department of Chemistry, Universidad del Valle, Cali, Colombia
e-mail: manuel.palencia@correounivalle.edu.co

J. M. Martínez-Lara

Mindtech Research Group (Mindtech-RG), Mindtech S.A.S., Cali, Colombia
e-mail: jina.martinez@correounivalle.edu.co

J. M. Martínez-Lara · N. G. Chate-Galvis

Research Group in Science With Technological Applications (GI-CAT),
Department of Chemistry, Universidad del Valle, Cali, Colombia
e-mail: nazly.chate@correounivalle.edu.co

J. M. Durango-Petro

Department of Material Engineering, Universidad de Concepción, Concepción, Chile

of compositional and structural factors associated with the properties of functional-polymer nanocomposite membranes are described and analyzed from a wide vision of their applications and potentialities.

Keywords Nanocomposite membrane · Active polymeric membrane · Emerging pollutant · Sensing surface

Acronyms

AgNPs	Silver nanoparticles
DNA	Deoxyribonucleic acid
MF	Microfiltration
NF	Nanofiltration
PNC	Polymer nanocomposite
PNCM	Polymeric nanocomposite membrane
RO	Reverse osmosis
UF	Ultrafiltration
ZnONPs	Zinc oxide nanoparticles

1 Introduction

The three more important concepts for the proper understanding of what is a polymeric nanocomposite membrane (PNCM) are: (i) nanomaterial, (ii) polymer nanocomposite (PNC) and (iii) membrane. Thus, a *nanomaterial* is defined to be a matter fraction characterized because at least one of its dimensions can be described in the nanoscale, i.e., with a size lower than 100 nm, whereas a *polymer nanocomposite* is a composite material containing at least two components where one of them is a nanomaterial which is physically or chemically included in a polymer phase (i.e., second component).

In particular, the third concept, *membrane*, has an important difference with respect to the other two. Although a nanomaterial and a nanocomposite are fully understood in terms of their properties or composition, the concept of the membrane is distanced from this principle, since neither the properties nor the composition alone, or in combination, are sufficient criteria for the proper understanding of what a membrane is. While a nanomaterial can be unequivocally defined in terms of the nanoscale and the resulting properties of it, and a PNC can be defined through the combined use of its properties (for example, solid mixture) and its components (at least one of its components must be a nanomaterial), the concept ‘membrane’ requires the explicit specification of its use. Thus, a ‘membrane’ is a functional concept due to that ‘something’ is conceived to be a membrane when it is used as membrane, in

consequence, the concept 'membrane' is intimately linked to the function it fulfills [1–3]. By instance, a nano-porous film of polypropylene can be used for several applications including, the adsorption of hydrophobic molecules on its surface, or the separation of substances when a fluid containing suspended solids passes through it. In the first case, nano-porous film of polypropylene is an adsorbent, however, in the second one, the nano-porous polypropylene film is used as a separating element by mass transport through it, and in consequence, it can be stated that it is a membrane. Therefore, from previous example, it is identified that a membrane it is understood to be a material separating two flows or 'streams' (feeding flow, or inflow, and permeate flow, or outflow), but also, a membrane permits the passing of substances from feeding to the permeate and, at the same time, avoids or restricts the pass of some substances contained in the feeding, consequently, a third stream called retentate is produced. These is also called retentate flow, concentrate or retained. Depending on the configuration and design of the system, the retentate can be separated from the feeding, but specifically, the main difference between feeding and retentate is the change in its composition by effect of separation process [1]. Some authors add morphological features to the membrane definition, and in this way, a membrane is a material region characterized by showing a large lateral dimension in comparison with its thickness, that is an important aspect because it helps to visualize a membrane from morphologic characteristics [4, 5]. From a functional overview, the transfer and restriction of the passage of matter through membrane is the most important, and it has been the main characteristic from which numerous applications have been proposed and developed [6–9]. However, recently, this idea of membrane as a passive element in the separation process has been abandoned, and the functionality of membrane is being strongly rethought with the advance of science and technology of materials both at the structural and compositional levels, being, for the technology of active or multifunctional membranes very important the advances performed from the field of nanomaterials, in particular, in relation with those advances related with PNCs [10–14].

Based on the above, a PNCM can be defined as a membrane made of PNCs, which it is a solid colloidal system, i.e., a multiphase solid material where one of the phases is in nanometric scale in at least one dimension, and whose properties are determined by properties of their components, composition, structure and interfacial interactions [15]. However, despite the wide range of possibilities offered by the use of nanocomposite materials for the development of active membranes, the main use of the nanocomponent or nanofiller in the development of this type of membrane has been focused towards the enhancement of thermal, mechanical and antifouling properties of the material, being, therefore, a conventional approach under which, although undoubtedly improved membranes are obtained, these remain as passive elements within the separation process [1, 15]. Some examples of active nanocomposite membranes are those membranes made of polyesters, poly(vinyl acetate), polyamides, poly(vinylidene difluoride), polysulfones, poly(ether ether ketone), poly(ether sulfone), and poly(acrylonitrile) having as nanofiller SiO₂ zeolite, TiO₂, SiO₂, graphene oxide, zeolite, CaCO₃, carbon nanotubes, among others [15]. However, it is important to recognize that the use of nanocomposite materials is

not the single way for the obtaining of active membranes, since several strategies for the making of multifunctional membranes have been described, for example, the building of porous interpenetrating polymer networks [16, 17], modification of membrane surface by polymer-chains grafting [18, 19], or by the assembly of an active layer from polymers with special properties [20–22].

Some authors refer to PNCMs as all kinds of membranes containing nanoparticles; however, that approach contains inaccuracies that must be carefully analyzed because a PNCM is, in principle, expected to be made of some PNC. If the above condition is not met, the use of other more generic terms such as nanostructured membrane is suggested. Note that a PNCM is a nanostructured membrane but not every nanostructured membrane is a PNCM. By instance, the membrane surface can be modified by the adsorption of metallic nanoparticles in order to produce new membranes with novel surface properties, therefore, materials resulting can be considered surface-modified membranes; however, the nanoparticles were included on the surface and they are not part of the polymer phase, but rather they are located at the interface in contact with the feeding, and in this sense, the membrane can best be described as a nanostructured multilayer system instead of a PNCM. It can be concluded, the PNCM concept is the directly linked to PNC definition.

Finally, this chapter aims to give a comprehensive description of compositional and structural factors associated with the properties of functional PNCMs, as well as, offer a wide vision of their applications and potentialities.

2 Polymeric Nanocomposite Membranes (PNCMS)

It is possible to classify the PNCMs in three types depending on membrane functionality: (i) Type I: Conventional PNCMs, which are PNCMs made from polymeric nanocomposites, in order to improve their properties, but without giving to the membrane an additional function, in this case, membrane is improved but it follows being a passive element in the separation systems whose main and unique function is the separation of components of the feed phase by two possible mechanisms: dissolution-diffusion or size exclusion [23–28]; (ii) Type II: Active-bulk phase PNCMs, which are PNCMs made from polymeric nanocomposites giving to the membrane the possibility to take double functionality, one main function related with the mass transfer between two phases separated, and a second function related to specific properties of material from which is manufactured, an example is the PNCMs made from inorganic nanoparticles dispersed in a polymeric phase based on some conductive polymer like to poly(aniline) or poly(pyrrrole) [29–33]; and (iii) Type III: Active-surface PNCMs which are characterized to show a second functionality, which can be observed on the surface in contact with the feed phase, or in the inner of the pores, but on the surface of them and not in the bulk of the material [34–39]. Examples of types of PNCMs are shown in the Table 1. The classification previously proposed is implicitly based on the nature of the active layer, and therefore, a same

Table 1 Examples of types of polymeric nanocomposite membranes

Type	Polymeric phase	Nanophase	Functionality	Ref.
Type I: Conventional PNCMs	Poly(vinyl alcohol) and chitosan	Cellulose nanocrystals/ZnO	Improving of mechanical properties	[23]
	Poly(vinyl alcohol)	Nanofibrillated cellulose	Improving of mechanical, thermal, and chemical properties	[24]
	Poly(vinyl alcohol)	Phosphorylated nanocellulose fibrils	Improving of mechanical, thermal, and chemical properties	[25]
	Poly(vinyl alcohol)	Cellulose nanocrystals	Improving of mechanical, thermal and swelling properties	[26]
	Nafion®	Zirconium phosphates+carbon nanotubes	Improving of mechanical, properties	[27]
	Nafion®	Zirconium phosphates	Mechanical properties	[28]
Type II: Active-bulk phase PNCMs	Poly(vinyl alcohol) crosslinked with glutaraldehyde	Nanostructured Fe ₃ O ₄ /polystyrene core shell	Regulating of permeability in response to external temperature	[29]
	Poly(acrylamide)	Graphene oxide and reduced graphene oxide	Increase of thermal conductivity	[30]
	Poly(aniline)	Graphene oxide	NH ₃ gas sensitive	[31]
	Conductive poly(vinylidene fluoride)	Carbon nanofiber+ionic liquid	Strain sensitive	[32]
	Cellulose	Copper Oxide	Detection of gaseous substances at low temperatures (e.g., H ₂ S)	[33]
Type III: Active-surface PNCMs	Aromatic polyamide	Carbon nanotubes	Antifouling, increase of permeability and resistant to chlorine	[34]
	Polyethersulfone	Fe ₂ O ₃ nanoparticles	Ionic strength sensitive	[35]
	Polyamide	Natural zeolite nanoparticles	Increase of permeability and nitrate rejection	[36]

(continued)

Table 1 (continued)

Type	Polymeric phase	Nanophase	Functionality	Ref.
	Polyphenylsulfone	Carboxylated graphene	Anti-biofouling and protein antifouling	[37]
	Polyamide	Highly hydrophilic clay mineral+Ag	Anti-biofouling, increase of and NaCl rejection	[38]
	Polyamide	Silica nanoparticles functionalized with quaternary ammonium groups	Superhydrophilic, antifouling, high water permeable	[39]

membrane could be classified in two types since polymeric surface properties can be influenced by polymer bulk properties.

From membrane structure and position of nanomaterials, some authors have proposed another classification in order to group the different types of PNCMs: (i) Mix-matrix PNCMs, which are membranes made from some nanocomposite material, (ii) Nanomaterial thin-film PNCMs, which are membranes surface coated by some type of nanomaterial, (iii) Thin-film PNCMs with nanocomposite substrate, which are defined to be membranes formed by a thin-film on some support made from nanocomposite material, (iv) Nanocomposite thin-film PNCMs, which are membranes coated by some type polymer nanocomposite and (v) Surface coated PNCMs which are described to be a porous support coated by a thin film which is coated by a some type of nanomaterial [40].

However, though this classification is very useful because it helps to visualize the configuration of membrane layers, it is seen not to be completely suitable for the description of structure-functionality relationship of PNCMs since all separation properties of porous membrane depend on ‘active layer’, which is characterized to be the layer with the smallest pore size distribution forming the membrane structure, and consequently, porous substrate must be understood to be only a support layer. By instance, an asymmetric polymeric membrane is defined to be a porous polymeric support coated on its surface by a thin-film with a pore-size distribution smaller than pore-size distribution of support, therefore, all retention properties in this kind of membrane are determined by the thin-film constituting the active layer since the function of porous polymeric support is the improving of mechanical properties of multilayer system [1]. By the above, it is noted that previous classification is really describing multilayer membranes instead of PNCMs for the following cases: ‘nanomaterial thin-film PNCMs’ (symmetric membrane | nanomaterial), ‘thin-film PNCMs with nanocomposite substrate’ (nanocomposite support | active layer) and ‘surface coated PNCMs’ (support | active layer | nanomaterial). Note that the vertical bar was used to indicate the interface between the different layers that make up the membrane. But also, note that ‘mix-matrix PNCMs’ corresponds to symmetric PNCMs whereas ‘thin-film PNCMs’ corresponds to asymmetric PNCMs.

3 Separation Mechanism of PNCMs

Separation mechanism of conventional membranes and PNCMs is, in general terms, the same; however, small changes in their description can take place by the presence of the nanocomponent both on the surface and in the internal structure of the pores, or in the case of dense membranes, by the occlusion of nanophase inside the membrane. The nanocomponent effect on separation based on the use of PNCMs can be analyzed from the separation mechanisms or from the membrane operative performance. In general, a wide numerous of publications have focused their attention in the antifouling properties and operative performance (i.e., improving of mechanical and thermal properties for their use in operations at high temperatures and high pressures) [15, 40–43]. Thus, for example, a porous polymeric membrane, which is used for the separation of analyte dissolved in water, is characterized by the rejection coefficient and its permeability. Therefore, for a given initial temperature, the description of process has associated the corresponding initial values of rejection coefficient and permeability. Since permeability is increased with the increase on temperature, changes on process temperature helps to the increase of permeability, however, as temperature is increased, the polymer phase expands and as a result the effective pore size is increased. If the separation mechanism is size exclusion, then the increasing of effective pore size will be related with a strong decreasing in rejection coefficient. On the other hand, if porous polymeric membrane is nanostructured, then thermal properties can be significantly improved and, in consequence, for PNCMs could be possible the increase of permeability by the increase on temperature without impacts negatively the values of rejection coefficient. The global result of this generic example is that the membrane performance is improved into PNCMs compared with non-nanostructured membranes. However, the improving of properties depend on the nature and content of nanomaterial, properties of polymeric phase, and interaction between nanostructured and polymeric phases.

An important aspect for the correct understood of PNCMs is the analysis of separation mechanisms. In general, for separation processes by membranes two mechanisms can be defined: (i) separation by size-based exclusion and (ii) separation by dissolution-diffusion [1]. In the first case, particles larger than the membrane pore are retained whereas particles smaller than membrane pore pass through them. This mechanism occurs in porous membranes used in nano-, ultra-, and microfiltration (NF, UF and MF, respectively), being the main fluid phase the liquid phase, specifically water. The liquid phase forming the feed stream can be homogeneous (e.g., aqueous dissolution for removal of macromolecules) or heterogeneous (e.g., aqueous dispersion for the removal of suspended solids). In some conditions, it can be visualized to be a gaseous fluid containing suspended solids (e.g., air filtration) [1, 4]. In the second mechanism, separation by dissolution-diffusion, the permeating substance is dissolved in the inside of the membrane (i.e., dissolution stage), and subsequently, it is diffused through it (i.e., diffusion stage). This mechanism is used to describe the separation process in dense membranes (e.g., bulk, emulsion, and supported liquid membranes), however, it can be used for the description of separation by

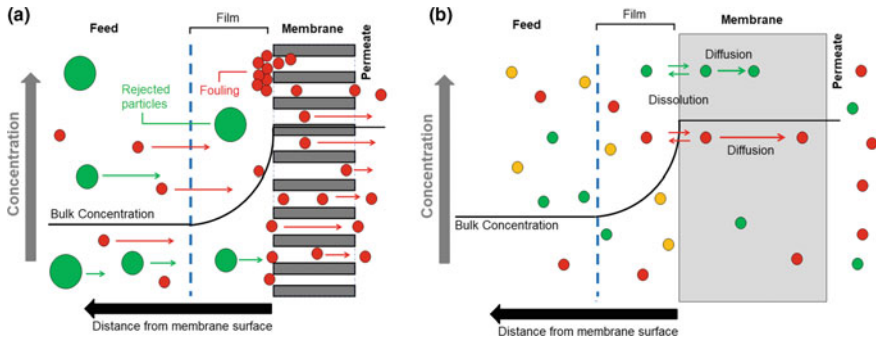


Fig. 1 **a** separation by size-based exclusion, and **b** separation by dissolution-diffusion © Image made by the authors

porous membranes of reverse osmosis (RO) because the matter nanoconfinement in the inner of very small pores produces the increasing of the interaction between permeant substance and membrane phase [1, 4]. An illustration of main mechanisms of membrane separation methods is shown in the Fig. 1.

3.1 Effect on Size Exclusion Mechanism

The effect of nanometric component on separation by porous PNCMs must be understood by the visualizing of the process and not only the membrane. In this way, if it is imagined a system in which the fluid and the species contained in it do not interact with the membrane, which can be NF, MF, or UF membranes, the nature of the membrane lacks importance in the separation process. That is, regardless of whether it is a ceramic, polymeric or nanocomposite membrane, the separation will be determined by the cut-off of the membrane, which is defined by the pore size, and the relative size distribution of particle in the fluid. Note that this hypothetical ‘zero interaction membrane’ or ‘non-interacting membrane’, it should not be confused with the concept ‘zero retention membrane’ that is used for the modeling of hybrid methods of membrane separation such as polymer enhanced ultrafiltration, micellar ultrafiltration, and liquid membranes enhanced with liquid-phase polymer-based retention [44, 45]; because the separation mechanism that is being analyzed is size exclusion, as the process proceed, the composition of the retentate and the permeate will change over time which does not happen in a zero retention system.

On contrary, when membrane interacts with one or more components of the fluid, if the interaction is significant then the nature of the membrane becomes into a main component since it will be associated with the interaction type among the membrane and solutes, and among membrane and solvent, but also, with the phenomena that are triggered as a result of these interactions. These can be positive and negative

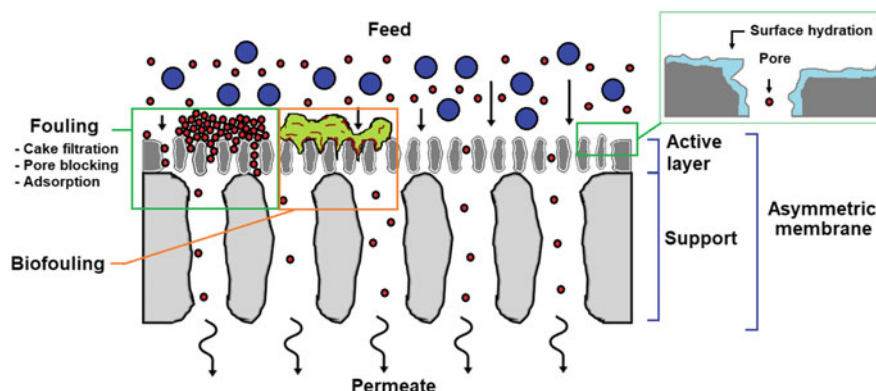


Fig. 2 a Illustration of several processes occurring into membrane separation by size exclusion mechanism, b Surface hydration (solvent = water), c fouling and (D) biofouling. © Image made by the authors

phenomena, being the main negative effect the increase of the fouling and, consequently, the decrease in the operating capacity by the decreasing of permeability and selectivity. Positive effects could be the decrease of fouling, increase of permeability and disinfection, increase in operating times, decrease of secondary cleaning stages, increase of half-life time, or improving of microbiological quality of retentate and permeate [34–39] (see Fig. 2).

On the other hand, when a non-interacting PNCM is analyzed, several situations can be identified: (i) If the nanomaterial constituting the PNCM improves only mechanical and thermal properties, then, it is expected that the operativity of membrane is increased, but no effect on separation mechanism is obtained and, therefore, the PNCM is not active element during the separation (see Fig. 3A). (ii) If nanomaterial constituting the PNCM improves the operativity of the membrane and the separation, then, some type of favorable interaction is produced with one or more solutes; by instance, PNCMs based on silver nanoparticles (AgNPs) are an active element during the separation due to the decreasing of biofouling. In these systems, surface of nanocomposite constituting the active layer of the membrane has AgNPs partially exposed and in contact with the feed stream, therefore, one or more additional interactions at level surface could be occurring in comparison with the respective non-nanostructured membrane. For the specific case of AgNPs, nanoparticle surface chemically links molecules with thiol groups on their structure, and therefore, though a small molecules like to cysteine, with 0.64 nm (length) and 0.37 nm (width) [46], cannot be removed by size exclusion mechanism using NF, UF or MF membranes, it is observed that, the formation of bonds $RSH-Ag^0$ can produce the retention of cysteine molecules without produce changes in the effective pore diameter of membrane using NF, UF or MF PNCMs based on AgNPs. In addition, the recovery of cysteine linked to the membrane can be easily carry out by the washing under specific conditions of pH [17, 47] (see Fig. 3B). In addition,

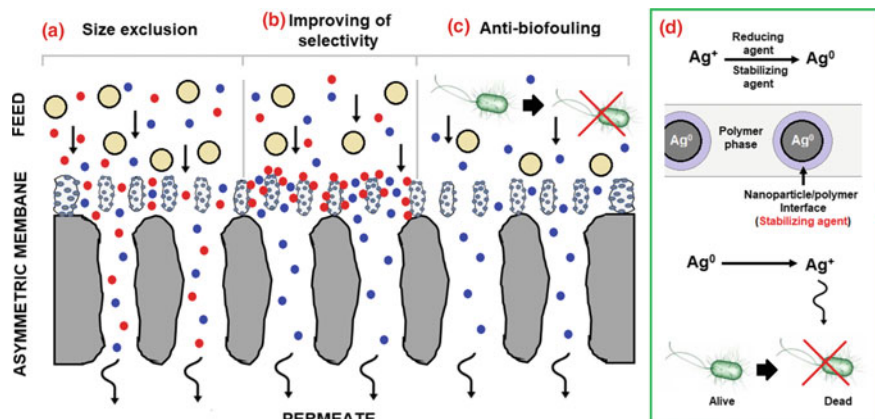


Fig. 3 **a** Schematic representation of nanocomposite asymmetric membrane without effect on separation mechanisms, **b** Improving of selectivity as a result of interaction of surface nanomaterial with some specific solute, **c** Improving of functionality as a result of antibiofouling properties resulting of the presence of surface nanomaterial and **d** schematic representation of stages required for the making of nanocomposite asymmetric membrane with antibiofouling properties. © Image made by the authors

anti-biofouling properties of PNCMs based on AgNPs have been widely described in several publications. In general, AgNPs can act as reservoir of Ag^+ ions and diffuse from the membrane surface and achieve the bacterium where it interacts with several biomolecules producing the death of microorganism [45] (see Fig. Fig. 3C and Fig. 3D).

In these membranes, AgNPs are reduced and stabilized using some adequate stabilizing agent (e.g., citrate, glucamine, poly(vinyl alcohol), etc.), later, nanoparticles are introduced to polymer phase in order to produce the nanocomposite, which is later used for the making of the membrane. In addition, selective retention of thiolated compounds and antibiofouling properties, it is evident that other properties of material were changed by the addition of AgNPs, among them, the dielectric properties. However, studies focused on the description of the dielectric response of PNCMs in term of chemical composition of polymer phase and nanomaterial are scarce, despite the potential of this type of membrane as sensing surfaces both for monitoring a specific effluent and for process self-control operations [48, 49]. Note that, AgNPs can be added only at surface level in which case in order to produce antibiofouling membranes or anchoring surface of thiolated compounds, however, this type of membranes could be denominated 'nanostructured' and 'active' but not PNCM since active polymer phase is not a nanocomposite.

3.2 *Effect on Dissolution-Diffusion Mechanism*

The analysis shown below is restricted to polymeric membranes and therefore liquid membrane are not included. In the dissolution-diffusion mechanism two main stages are defined: one dissolution stage and one diffusion stage. Note that dissolution stage is a stage depending of phases in contact, and therefore, it is intimately related with the nature of solute and membrane. If the feed phase has a high affinity to the membrane phase then interfacial contact is favorable and transfer of analytes to the membrane phase is promoted. In fact, this stage can be considered analogous to the size exclusion when the size is defined as an affinity criterion. In this way, particles with size larger than the membrane cut-off have to low affinity with membrane phase, since they cannot penetrate it, while particles with sizes smaller than the membrane cut-off have a high affinity to the membrane phase since they can penetrate it. Note that, likewise, analyte dissolution in the membrane phase generates an exclusion criterion, thus, solutes with low affinity to the membrane phase are excluded while analytes with high affinity to the membrane phase can penetrate it. This affinity is associated to the structural similarity between the membrane-forming polymer and the solute, or in molecular terms, it is associated with the set of intermolecular interactions existing between the membrane material, analyte and transporting phase [1, 4, 5, 15]. Therefore, it is not easy to visualize the influence of the nanomaterial on this first stage. However, a careful analysis reveals some interesting aspects helping to the mechanistic understanding of the process.

To further develop the above idea, it is necessary to imagine the simplest possible system, which corresponds to a feed without solute, in this case for the dissolution stage, a single interaction should be analyzed for both non-nanostructured membranes and PNCMs: solvent-membrane interaction, understanding as ‘solvent’ the fluid phase in the feed. In the case of gases, the analysis is limited to considering a single gas penetrating the membrane. In the case of porous membranes, i.e., OR membranes, the gas molecules would have a high affinity under the premise that the molecular diameter of the molecules is smaller than the membrane cut-off. For very particular situations where the gas molecules are large compared with the membrane cut-off, the affinity can be considered significantly decreased. However, in dense membranes (that is, a crosslinked polymer embedded with a liquid), the affinity will depend on the solubility of the gas in the liquid, so the polymeric structure would be equivalent to a hydrogel when the solvent is water. However, the solubility of the gas will be defined by operating parameters such as pressure and concentration (chemical potential) which are the key parameters that influence the Henry constant of the gas [1, 4, 5, 15].

On the other hand, if the feeding stream is a liquid, in the case of dense membranes, three situations are possible: (i) liquid contained in the membrane has a high to the feeding phase, (ii) Feeding phase and the liquid in the inner of membrane are the same and (iii) feeding phase has not affinity with the liquid in the membrane phase. In the first case, the solvent will be able to penetrate the membrane, and the membrane stability will be determined by on the mechanical strength of polymer network. In this

point the nano-structuring of membrane becomes very important. In the second case, no change occurs. In consequence, in order to deepen the analysis, it is necessary to introduce at least one solute in the simplification carried out. Therefore, if the solute is structurally similar to the medium, and the medium is structurally similar to the membrane, it is evident that the solute will have a high affinity by membrane phase. However, the membrane surface properties can be used to provide greater selectivity to this first stage in the specific case in which the solute has a net charge. In this way, if the membrane has charges, even though two solutes have a high affinity with the medium, and although the medium contained in the inner of the membrane has a high affinity with the membrane, it is possible, by means of the adequate selection of polymer structure, to increase the rejection of one of the solutes with respect to the other. It is the case of the use of an anionic membrane to restrict the passage of negatively charged particles. In the third case, in which the liquids contained are not structurally related, the affinity of the solute is defined by the partition, or distribution, coefficient between the phases [1, 4, 5, 15].

In the case of porous membranes, specifically RO membranes, the solvent will penetrate the membrane structure, from which two situations are identified, the polymer phase have a high affinity with the membrane, and therefore, it is possible that strong solvation interactions occur and promotes the decrease of the permeability producing a decreasing of the effective pore radius, but also, it is very probable that under these conditions the membrane shows poor mechanical properties analogously to the hydrogels. In this case, for PNCMs, the nanocomponent contributes to mitigate this effect [23–28]. The next situation is that the affinity between the solvent and the membrane is non-existent, and therefore solvation does not occur, the mechanical properties of the membrane material will be stable, and the solute dissolution in the membrane phase can be easily understood by means of the solute-membrane affinity in terms of the relative size with respect to the membrane cut-off.

4 Effect of Nanocomponent on the Membrane Functionality

The main limitation of membrane technology is the fouling, in consequence, many studies have been focused in the decrease of fouling and its impact on membrane integrity or continuity of the process [34, 37–39]. Fouling can occur in the inside of the pores (e.g., standard blocking and intermediate blocking) or on the membrane surface (e.g., cake filtration and complete fouling), but, whereas fouling by cake filtration or complete fouling are promoted, the interaction between components of feeding stream and membrane surface, fouling by pore blocking, besides of surface interactions, can be resulting of mechanical obstruction of particles inside the pores [50]. A typical case exemplifying the above is the ultrafiltration of polymer dissolutions. In addition, a special type of fouling is very common in natural systems

is the biofouling, which is the fouling produced by microorganisms. In consequence, the nature of membrane material plays an important role on the susceptibility to the fouling, but also, on antifouling properties of them. In relation with the above, it has been described that PNCMs based on nanomaterials such as carbon nanotubes, graphene oxide and metal inorganic nanoparticles improve the resistance to biofouling, chlorine resistance, permeability and selectivity [34, 37–39].

4.1 Effect on Mechanical and Thermal Properties

Several publications have evidenced that polymer-based nanocomposites have improved mechanical and physical properties in comparison to non-nanostructured polymers [23–28, 40]. Though the effect of nanomaterial is directly related with the nature of polymeric phase and nanocomponent, and therefore, those results obtained for a specific polymer are not the same when different nanofillers are used, it is clear that the incorporation of nanoparticles introduces new interactions impacting the properties of all system. These interactions can be physical or chemical in its nature, and they are the key point for the understanding of the effect of nano-structuration of polymer. In both cases, the positive effect of physical or chemical interactions between nanofiller and polymer phase is the formation of crosslinking points in the inner of the phase. These crosslinking points acts as an internal molecular network distributed in all the polymer phase. However, if interactions are not attractive, the interactions go directed toward the separation of phases, which is a phenomenon observed when a mixture is formed by two immiscible solids or liquids, e.g., polyethylene and poly(vinyl alcohol) or water and heptane. The crosslinking points can be chemical or physical depending on whether interactions of polymer with nanofiller are covalent or non-covalent, respectively [3, 51]. This internal molecular network model describes the change of mechanical and thermal properties analogously to it evidenced for linear and crosslinked polymers (resins), where the presence of crosslinking point in the resin structure impacts the thermal and mechanical properties of material [52, 53].

On the other hand, it is not only the promotion of attractive interactions the single aspects determining the final properties of PNC. PNC is basically, in the case of physical interactions, a disperse system or a solid dissolution, or in the case of chemical interactions, a multiphasic network. In consequence, in order to obtain uniform properties is needed that total system can be defined as an isotropic material. Given that the successful results are those that tend to be published, the impact of the incorrect dispersion of the nanofiller in the polymer phase and the consequent anisotropy of the material on the properties of the PNCMs is not widely documented [54, 55]. However, it is possible to make inferences from analog systems and from system models (e.g., clay-polymer systems). A widely nanomaterial-polymer system which has been studied are the PNC produced by the use of layered silicate as nanofiller. In these systems have been evidenced that for a same type of clay, the result on mechanical properties depend on whether clay particles are intercalated, exfoliated

or aggregated being an important evidence of the importance of surface area on final properties of material [54]. In addition, studies on clay-based PNC for the formation of multifunctional materials have evidenced that the amount of clay incorporated in to PNC strongly impacts the cohesion of polymer phase [56–58], evidencing that, the simple addition of high amounts of nanofiller in order to increase the number of crosslinking points and produce the improving of mechanical properties is not adequate for the synthesis of PNCs. For the making of PNCMs, the nanocomposite is required to be a continuous phase instead of being a particulate material or a disaggregated system. In consequence, the adequate dispersion of nanofiller, their amount and size, and the extend of interaction surface area are main aspects which must be analyzed.

4.2 *Effect on Permeability*

Permeability of membrane depends on intrinsic properties of membrane materials (i.e., hydrophobic or hydrophilic nature), operation conditions (e.g., pressure, temperature, concentration), fluid characteristics (e.g., concentration and viscosity) and morphological characteristics such as thickness, surface porosity, pore diameter, surface roughness, and fluid trajectory inside of the membrane (tortuosity); therefore, any characteristic of the nanocomponent present in a PNCM affects one of the characteristics previously described and will influence the permeability. For example, a hydrophilic nanofiller will give the membrane surface a greater hydrophilicity and contribute to the flow of water. But also, the nanofiller could also affect the internal morphology of the pore, increasing the tortuosity or its effective pore diameter, in both cases, decreasing the permeability. Some nanofillers introduced to polyacrylamide membranes which have shown an increase on permeability are zeolites, functionalized silica, carbon nanotubes, silver nanoparticles, graphene oxide, and alumina nanoparticles among other [15]. For example, membranes PNCMs based on poly(vinyl alcohol)/polysulfone showed an increased on permeability when carbon nanotubes functionalized with aluminosilicate were incorporated to polymer phase. Researcher explained the permeability changes by an increase on membrane surface hydrophilicity and a decrease on membrane roughness; they supported their conclusions by changes of contact angles (which decreased from ~ 64 to ~ 59 , and $\sim 50^\circ$), atomic force microscopy analysis, and permeability test [59]. Similar results have been described when sulfonated multiwall carbon nanotubes were added as nanofiller to poly(ether sulfone) membranes [60].

Despite strong and recurring experimental evidence of the nanocomponent's effect on permeability, the mechanism through which this improvement in transport properties occurs is often oversimplified; thus, hidden contributions of parameters not considered may be influencing the results and they go unnoticed. Unfortunately, much of the current scientific information does not take into account the multiparameter contributions in explaining the causes of observations made. In the case of permeability, for example, the incorporation of a hydrophilic nanofiller can impact

hydrophilicity, superficial roughness, tortuosity and pore diameter, however, due to the spatial variability of the pore diameters, their shape polydispersity, and the internal heterogeneous of them, the difficulty of having a direct pore measurement characterizing the total of the membrane, which is not based on the microscopic analysis of small fractions that involve the breaking off thereof, are not available. In consequence, small changes in the effective pore diameter can be overlooked, which have an enormous impact on permeability. The above is easily understood through the Hagen-Poiseuille model. Note that, by this model, a membrane with a specific permeability can be transformed into a Hagen-Poiseuille membrane, as a result of this, it is observed that the product porosity-pore size depends on the fourth power of the pore radius, therefore, a small change in this leads to a highly significant effect in terms of permeability [1, 7, 44]. Indirectly, it is evident that, by improving of the membrane's thermal properties, the separation operation is carried out at higher temperatures whereby the viscosity of the fluid is decreased and the permeability is increased.

4.3 Effect on Anti-fouling and Biofouling Properties

Fouling and biofouling are concepts differentiated only for the origin of fouling. Thus, a fouling resulting of physical or chemical processes is usually named 'fouling' whereas fouling originated by any biological entity is named 'biofouling' [61]. Though the differentiation is apparently simple, the implications and impacts about the membrane integrity and separation process are very important. In general terms, three types of fouling can be defined: (i) Reversible fouling or concentration polarization, (ii) irreversible fouling which is usually denominated simply fouling and (iii) biofouling [1].

The concentration polarization is a result of flux, and it can be defined to be a gradient of concentration experimenting the substances in the fluid as these are transported toward the membrane surface. It is denominated 'reversible' because if process is stopped then the gradient of concentration disappears. Its main effect is the promoting of irreversible fouling since, as substances contained in the fluid get closer to the membrane, their concentration at the surroundings of the surface, and the possible solute-membrane interactions, are significantly increased in comparison with the process in absence of concentration polarization. Thus, in the proximity of the surface at least three types of interactions can be identified: solute-solvent, solute-solute, solute-membrane, where the solute-membrane interaction includes solute-polymer and solute-nanocomponent due to the two possible phases which can be on the surface of PNCMs [1, 61–63]. A short description of main macroscopic interactions and their effects on fouling formation is summarized in the Table 2.

Table 2 Description of interactions in membrane separation processes and their effects on fouling formation [62, 64–66]

Interaction	Effects	Important parameters
Solute-solvent	Strong interaction is associated with a low fouling Weak interaction is associated with: Precipitation or adsorption on the surface Promotion of cake formation and complete fouling	It is influenced by the temperature, pH, concentration, concentration polarization, ionic strength, molecular structure, solvent polarity, among other
Solute-solute	Strong interaction is associated with the formation of aggregates in the inner of fluid phase. The size of aggregates promotes a decrease of selectivity and an increase of retention If aggregates are mechanically anchored on the surface then filtration cake is produced	It is influenced by the temperature, pH, concentration, concentration polarization, ionic strength, molecular structure, solvent polarity, among other
Solute-membrane	<i>Solute-polymer</i> Strong attractive interactions between solutes and polymer phase promote the adsorption on the surface and consequently surface fouling. The same could be occur in the inner of the pores. On contrary, repulsive interactions are associated with antifouling properties	It is influenced by the molecular structure, solute-solvent and solute-solute interactions
	<i>Solute-nanocomponent</i> Strong attractive interactions between solutes and nanostructured phase promote the adsorption or anchoring on the surface or inside the pores promoting the surface fouling. On contrary, repulsive or 'non-favorable' interactions are associated with antifouling properties	It is influenced by the molecular structure, solute-solvent and solute-solute interactions Its magnitude will largely depend on the superficially exposed nanocomponent fraction

The irreversible fouling is resulting of mechanical, chemical and physical interactions, it is associated mainly with solute-membrane interaction and, as result of its progressive accumulation, the affection of membrane and the stopping of the separation process are produced. Since nanofiller used in the making of PNCMs is relatively low, lower than 20%, a low fraction of nanomaterial is exposed on the surface, suggesting that the impact of nanocomponent on the surface properties is expected to be low, and therefore, the impact on irreversible fouling should not be significant. However, the results show that this is not the case. PNCMs are obtained

Table 3 Examples of PNCMs with antifouling and antibiofouling properties

Type of fouling	Polymer phase	Nanofiller	Ref.
Fouling	Aromatic polyamide	Carbon nanotubes	[34]
	Polysulfone	Al ₂ O ₃ nanoparticles	[72]
	Polyamide	Titanate nanotubes	[73]
	Polyamide	Silica nanoparticles functionalized with quaternary ammonium groups	[39]
Biofouling	Poly(ethylenimine)/poly(acrylic acid)/polyamide	Copper nanoparticles	[74]
	Polyethersulfone	Silver nanoparticles	[75]
	Poly(vinylidene fluoride) (PVDF)	Carbon functionalized with ammonium quaternary groups	[76]
	Polyamide	Graphene oxide-silver nanocomposites	[77]
	Polyphenylsulfone	Carboxylated graphene	[37]
	Polyamide	Highly hydrophilic clay mineral+Ag	[38]

from a large number of different systems that have shown the best antifouling properties compared to their non-nanostructured counterparts (see Table 3). Although the results in principle show the advantages of nano-structuring, the results must be carefully analyzed because the mechanism for this improvement of antibiofouling properties is not usually discussed in terms of interactions, but in addition, each separation system has its own particularities, and therefore, the decrease in fouling with respect to a specific component may affect the increase in fouling of another component in the feeding stream. In contrast, mechanical, thermal and chemical resistance of polymer membrane are enhanced by the addition of adequate nanocomponent. Therefore, the improving in these properties positively impact the cleaning operations, the durability of the membrane by allowing a greater number of cleaning cycles, as well as, the use of more severe conditions [67].

As previously indicated, biofouling is an important operational problem in membrane separation processes, being particularly important during separations in the food, biomedical and pharmaceutical industries, in the treatment of environmental effluent, outdoor use membrane-based devices, and process based on membrane bioreactors. Biofouling is defined as the formation of undesirable microbial biofilms resulting of anchoring, growth, and modification of surfaces by action of bacterial metabolism. Biofilms is formed by sequential stages including: (i) attachment of one or more planktonic cells onto membrane or any adequate surface, (ii) formation of small colonies which are bioadhered, (iii) modification of surface by extracellular secretions, and (iv) growth of mature biofilms [68, 69]. Biofouling may be uniformly or partially covering the surface, and usually, it is formed by extracellular polysaccharides, polypeptides, microbial living and dead layers, and other extracellular substances such as lipids and deoxyribonucleic acid (DNA). In general, two

processes have been described for the bacterial accumulation on membrane: attachment of microbial cells (i.e., processes combined of adhesion and adsorption) and biofilm growth (i.e., modification of surface and cellular multiplication) [62, 70, 71].

The bioadhesion stage depends on the factors like the type of microorganism, environment factors, and the type of surface, being very common the secretion of polysaccharides and other extracellular biomolecules by the bacteria, e.g., adhesins, which form a coating on the membrane surface, transforming it into a new surface with a high bioaffinity to the microorganism and, therefore, it is the first step for growth and colonization. Through the mechanism previously described, any surface effect of some intrinsic component of the membrane can be blocked by the microorganism, and therefore, biofilms from a biological point of view are usually described to be an efficient survival mechanism based on the transformation of the environment [68, 69]. However, PNCMs have shown enhanced antibiofouling capabilities in comparison with non-nanostructured membranes, and despite the importance of these observations, in many publications the description of these properties is only descriptive, with little detailed information on the mechanism by which the nanocomponent can achieve this effect (see Table 3 and Fig. 4).

The best documented cases are those related with the effect of AgNPs on the susceptibility of membrane to biofouling, not only at the level of membranes but also at the level of the material that constitutes it. In the case of surface made of Ag⁰-based PNCs, it has been shown that the antimicrobial effect of the nanomaterial is rather passive, that is, the silver nanoparticles act only as a reservoir of silver ions that generate a biocidal and disinfecting effect on the material and the closer environment. Because in Ag⁰-based PNCMs, nanoparticles are occluded in the material, no disruptive effect at the membrane level, or penetration at the cellular level occurs; however, partial oxidation of silver nanoparticle produces the release of Ag⁺ which is a potent no-selective antimicrobial agent [13, 38, 75, 78], in consequence,

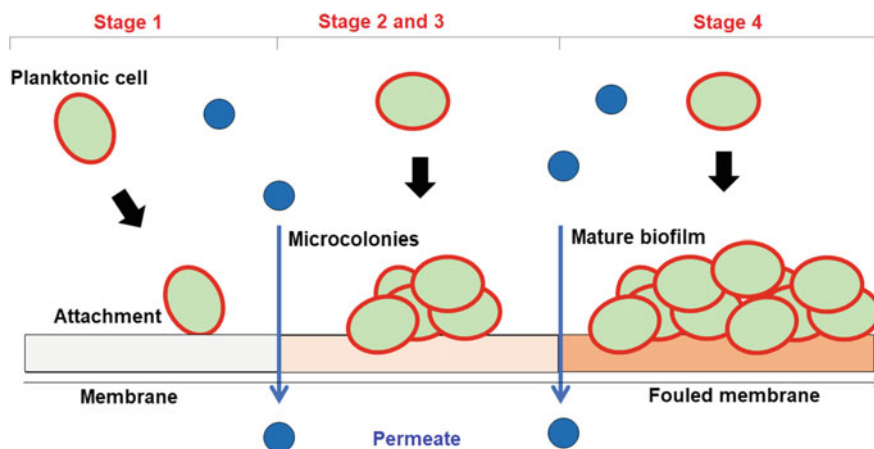


Fig. 4 Schematic illustration of biofilm formation. © Image made by the authors

microorganisms are killed before bioadhesion, in addition, due to its small size, the Ag^+ ions can diffuse through extracellular secretions and reach the cell, making it a very efficient mechanism for biofouling control and microbiological control of biomedical surfaces [51, 79, 80].

4.4 Effect on Other Functional Properties

A polymer membrane is a complex structure combining several technologic aspects which are required to carry out the desired function. However, these systems can be used for other functions simultaneously with their main function: Separation. Thus, additional properties incorporated to the membrane structure have a higher technological value, and these novel properties in the case of PNCMs are directly related with the PNC. Thus, by instance, PNC based on inorganic nanoparticles (e.g., ZnO, TiO_2 , $\text{Fe}_3\text{O}_4/\text{Fe}/\text{SiO}_2$, Fe_2O_3 and Si powders) have shown interesting optical, electric, and magnetic properties [81, 82], but also, electric properties, by the use of MoS, SnS_2 and SiO_2 [83]. Therefore, in principle, if PNCMs are made using these novel material then multifunctional membranes can be obtained in order to take advantage of properties like absorption of visible and ultraviolet light, photoluminescence by application of some stimulus, and significant changes of refractive index, among others [81, 82].

To exemplify the potential applications of PNCMs, a particular example will be explored since this can serve to show the benefits of directing researches toward the concept of active membranes. Recently, several researchers have been working with ZnO nanoparticles (ZnONPs), which can be synthesized and obtained to have various morphologies, therefore, it is important to know that nanoparticle properties not only are determined by the size and the distribution of them but also by the shape and shape variability. An important aspect for us example the ZnO is that it is a multifunctional semiconductor characterized by a wide bandwidth (3.4 eV) and a great exciton binding energy (60 meV), in addition, ZnO absorbs efficiently ultraviolet light, is no-toxic, and shows an excellent chemical stability under outdoor conditions including the exposition to sunlight, air, and water. But also, ZnO have been described in several applications associated with the manufacture of semiconductors, solar cells, polymer coating, UV laser emitters, cosmetics, among others [84].

In general, with a good dispersion, a small size, and low size and shape polydispersity, the addition of ZnONPs improve the tensile strength, the elongation capacity, and the Young' modulus of PNCs. Therefore, it is logic to think that ZnONPs-based PNCM could be obtained and used for new and novel applications related with the improving of mechanical properties. The above have been evidenced with polypropylene, poly(sulfone), poly(vinyl alcohol), poly(thiourethane), poly(acrylonitrile), poly(vinylidene fluoride) and chitosan [84]. Therefore, there is experimental evidence that suggests that lamellar porous structure can be made from ZnONPs-based PNC and, through the functional concept of membrane, these structures can

be used as separating elements during some filtration process by the use of a proper driver force, such as pressure, concentration gradient or an electric field. From the set of properties of ZnONPs, the dielectric properties will be selected for this example, the reason for the above is that they can be used for applications in the electronics and electrical industry, and therefore, this property could be used for applications as sensing surface or as a devices for the generation of charges. Note that, from an overview, the dielectric behavior of PNCs depends on the nature of polymer and nanomaterial, the making technique, the morphological features, and the interfacial interaction. By instance, when poly(vinyl alcohol) was used as polymer phase for the making of PNCs, the value of dielectric constant was lower than 400 (0.5% of nanofiller, ZnONPs with average particle size of 10–100 nm which were classified as nanopowders) [85] whereas, for poly(vinylidene fluoride) as polymeric phase, the value was 13 (25% of nanofiller, ZnONPs with $\sim 1 \mu\text{m}$ in length and $\sim 20\text{--}30 \text{ nm}$ in diameter are usually classified to be nanowires) [86].

5 Applications of PNCMs

PNCMs are complex systems having multiples configurations depending of making method they can be dense or porous. In addition, these can be modified in order to add some special characteristic. In general, the making of conventional membranes can be carried out by phase-inversion method, by dissolution-evaporation method, or other techniques directed to the formation of porous structure, e.g., electrospinning. Comprehensive review about methods of fabrication have been published [3, 6, 10, 15, 40, 42]. An illustration of several methods of membrane fabrication is shown in the Fig. 5. Usually, membranes are made and after their properties are evaluated in order to stablish their functionality; however, it is clear that depending of application the better preparation method must be selected. Thus, if it PNCMs with excellent thermal properties are required, then surface modification is not the better method since all membrane will be submitted to the working temperature. Similar analysis should be performed in all cases previous to the beginning of research. Below a brief review of the PNCMs applications is shown in order to illustrate their technological potential.

5.1 PNCMs for Treatment of Aqueous Effluents

Technologies based on PNCMs have been of special interest in wastewater treatment and purification since the incorporation of nano-scale substances such as nanoparticles, nanofibers, nanotubes or nanoplates in the polymeric phase improve some properties that result useful in this type of treatment such as its flexibility, thermal, mechanical and chemical properties, permeability, selectivity among other [87]. It has been published that the inclusion of aluminosilicates, such as zeolites, which

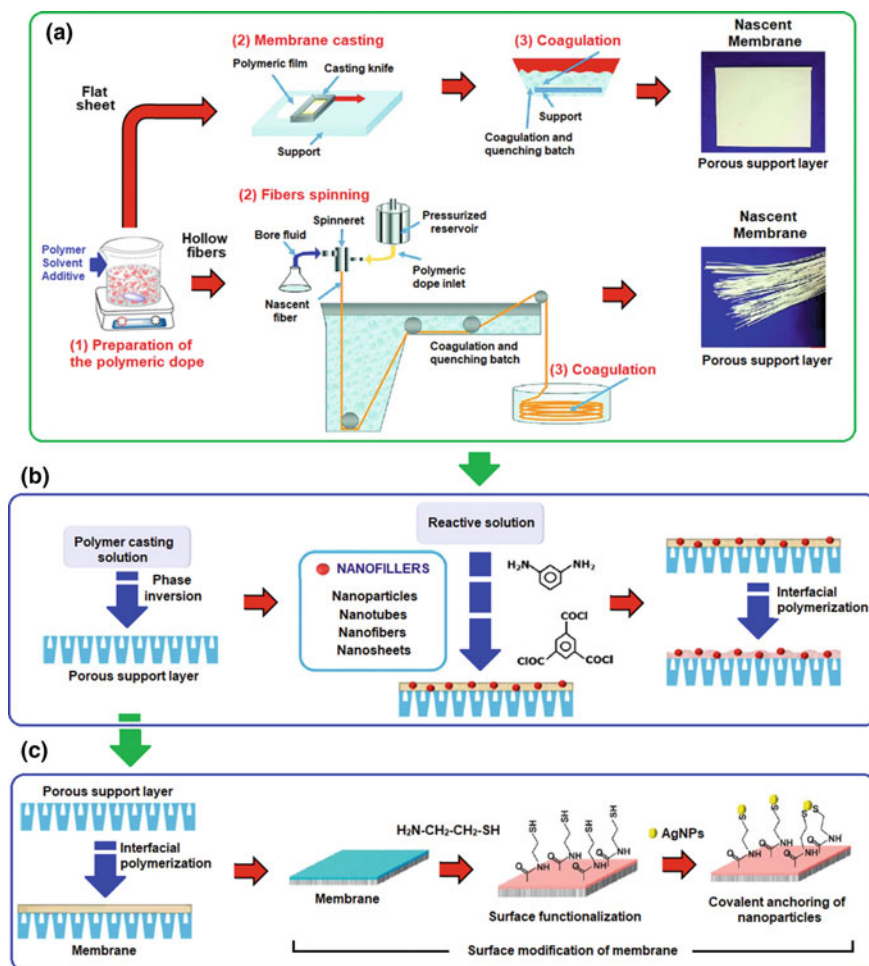


Fig. 5 Illustration of different method for PNCM fabrication: **a** Conventional membrane making, **b** in situ formation of nanocomposite layer by interfacial polymerization and **c** surface modification of membranes. © Adapted from Amin and Kargari 2018 [15]

have a negative surface charge and uniform nanopores can be used to increase the separation efficiencies during the filtration of contaminants, but also, the addition of metallic oxide nanoparticles (e.g., TiO_2 , ZnO , CuO , ZrO_2) can generate high fluxes and improve antimicrobial properties and antifouling of the membranes, in addition, the use of PNCs as active layer of membrane can ease the cleaning operation and increase the reuse. In desalination operations, the use of OR-PNCMs has shown to be a promising way to improve process performance. By instance, the use of thin-film PNCMs based on a thin layer of polyamide supported on a polysulfone- TiO_2 layer showed that the flow of water was increased. However, also it was observed that the

rejection of salt is decreased as the concentration of TiO_2 is increased, evidencing the importance to establish the optimum content of nanofiller in the inner of polymeric phase. In the same way, for desalination of sea water, reduced graphene oxide and TiO_2 have been used as nanofiller of PNCMs. For these materials, rejections upper to 99% of NaCl and water flow 51.3 LMH were achieved using only weight ratio of 0.02% of nanomaterials [88, 89]. An important characteristic of example previous is the use of TiO_2 ; therefore, it should be noted that one of the advantages of TiO_2 over other nanoparticles is that antiviral and antibacterial properties can be induced by the activation of them with UV radiation. By this photocatalytic process, the reactive oxygen species generated oxidize organic compounds and eliminate microbial pathogens [88].

On the other hand, the incorporation of carbon nanotubes has also been addressed within researches focused in the treatment of aqueous effluents since these have interesting electrical properties which can be used for the making of active membranes, in addition, selective nanopores and a certain degree of antimicrobial activity has been reported for these nanomaterials. Besides, the hydrophilicity of carbon nanotubes contributes with the obtaining of greater pure water flows with lower fouling rates. An example of the above is the addition of carbon nanotubes in poly(ether sulfone) or cellulose acetate membranes [90].

On the other hand, the removal and recovery of metal ions is a technological problem that is still in force due to the growing needed of having environmentally friendly processes, both from the energy point of view, and the waste generated from these. Thus, for a certain sector it may be of interest to remove a certain ion from an effluent, but also, for another sector, the interest may be directed towards the recovery of a certain ion, often for economic or analytical interests. In this context, one of the main challenges is the elimination of heavy metals since they show a high toxicity, bioaccumulation in the food chain, and the serious impact on human health. Active PNCMs emerge as an alternative as it seeks to take advantage of physical or chemical adsorption phenomena to increase process retention and selectivity. In this way, the control of surface phenomena that take place in the membrane are highly relevant, and play a central role in the separation process. An example that allows visualizing how to carry out the previous strategy is presented below. Abdalia et al. [19] prepared PNCMs for the recovery and elimination of metal ions such as Cd^{2+} , Zn^{2+} , Pb^{2+} and Cu^{2+} . For that, they prepared an asymmetric PNCM from PNC based on poly(vinyl alcohol)/ Fe_3O_4 and using as porous support poly(vinylidene fluoride)/poly(ether sulfone) containing 8-hydroxyquinoline which was used as a complexing agent. The researchers were able to determine that the Cu^{2+} and Pb^{2+} ions had better membrane adsorption affinity compared with Cd^{2+} and Zn^{2+} ions, in addition, they established that the membrane's maximum performance was achieved using 3% in weight of the nanomaterial in the poly(vinylidene fluoride)/poly(ether sulfone) support [91].

5.2 PNCMs for Removal of Organic Compounds

The removal of organic compounds from aqueous and non-aqueous effluents is of importance in sectors such as the textile, pharmaceutical and agricultural industries. In membrane separation systems, systems range from simple configuration methods (two phases separated by a membrane) to more complex configuration methods, where typical examples are hybrid membrane separation methods where the global separation mechanism is consisting of sub-stages. In simple setup methods, one of the strategies is to use the membrane as the adsorbent surface, which is a frequently used approach to dye removal. An example is the removal of Direct Red 16 using PNCMs based on poly(ether sulfone) nanostructured with Fe_3O_4 /carboxymethyl chitosan. By using the PNCM an increase in retention was observed with respect to the membrane without nano-structuring (10%), in addition, a greater permeability and flow of pure water were achieved. The authors of the research concluded that the main cause associated to the increase of retention was due to the increasing of negative surface charge of the membrane [92]. Note that a quick analysis allows to conclude that the use of PNCM based on Fe_3O_4 /carboxymethyl chitosan represents an unnecessary effort due to that the use of cellulose membranes could produce a similar result because, chemically, the dyes are designed to achieve a strong adsorption on surfaces. However, it is important to indicate that due to the above, a strong adsorption on surfaces, membranes should be cleaned using aggressive methods that are not compatible with membranes with poor chemical, thermal and mechanical properties. Similar experiments have been performed with clay-chitosan PNCMs for the removal of Bezatic Orange [93] and cellulose membranes modified with chitosan crystals for the removal of dyes such as Victoria Blue, Methyl Violet, and Rhodamine 6G [94], among others.

On the other hand, other type of organic compounds with increasing interest in the scientific community are the so-called emerging contaminants, which is a term that is used to describe to group the products and by-products of pharmaceutical compounds for use in humans and veterinary medicine, and also, personal care products. Some PNCMs used for this application are: epichlorohydrin-poly(ether sulfone) nanostructured with silver nanoparticles for removal of atenolol, carbamazepine and ibuprofen, polysulfone membrane with graphite nanoplates decorated with gold nanoparticles for removal of dextran which is widely used in drugs [90, 95, 96], and montmorillonite-poly(vinyl alcohol) film supported on a polysulfone membrane for the removal of cephalixin, amoxicillin and ibuprofen [97].

5.3 PNCMs as Adsorption Surface

A membrane can be used to be adsorption surface simultaneously with the separating process. The above is a strategy involving the incorporation of functional groups on the polymer phase constituting the membrane. Some polymers alike sodium alginate,

cellulose, poly(acrylic acid), poly(styrene sulfonate), poly(vinyl benzyl-N-methyl-D-glucamine), chitosan, among other, improve the adsorption in terms of selectivity for metal-ion, anions, and non-charged species due to the presence of some functional groups which can interact by electrostatic-type interactions and by the forming of coordinating links [17, 66, 97]. Therefore, an 'active' surface may be obtained by the insertion of surface functional groups on the membrane or into intrinsic structure of material, however, as a result of interaction of functional groups with the fluid, component of fluid or environmental conditions, different no-desired processes impacting negatively the permeability and mechanical properties can be produced, by instance, surface hydration or internal hydration with the subsequent polymer-phase swelling and pore constriction. In this context, the addition of nanofiller to the polymer phase is an interesting alternative to decrease the collateral negative effects resulting of insertion of functional groups during the improving of membrane absorption properties, thus, by the use of nanomaterials, despite the presence of functional groups, its resistance to the environmental conditions associated with its use, and reducing the impact of hydration on the mechanical properties in highly hydrophilic systems can be easily achieved.

Passive sampling technology will be taken as an example in order to expand previous ideas since it permits define a specific application but also it shows the importance of material properties as the great potential of PNCMs [98–101].

Passive sampling consists in a monitoring operation applied on natural or artificial systems where samplers are placed during a time interval at one or several sampling points, by this procedure is carried out the in-situ extraction of sub-samples or analytes, including in some cases direct analytical information on target one or several chemical species or physicochemical properties of system under study. Thus, per sampling point, temporal-average information is obtained, which is influenced by the specific conditions associated with place and the specific changes that have taken place during the time interval that the sampler was in operation [98, 101]. Two types of membrane-based passive sampling are referred semi-permeable membrane devices and diffusion membrane being their properties defined in function of target analyte and operating conditions; in addition, these can contain a receiving phase or act simultaneously as separating component and receiving phase. Thus, for the making of membrane-type absorbing passive sampler for, by instance, the removal of polar pharmaceutical products dissolved in natural water, polar functional groups interacting with analyte should be added in the polymer phase, but also, adequate mechanical and anti-biofouling properties are required to avoid the rupture of the membrane by action of the flow and increase the sampling time minimizing its deterioration as a result of microbial colonization, respectively. As can be concluded from previous sections of this chapter, the PCNMs offer the capacity to satisfy all the minimum requirements previously exposed.

5.4 PNCMs for Separation and Sensing

An interesting and promissory field of work in the membrane technology is the making of smart membranes and sensing surface. For the adequate achievement of this type of applications, membrane systems offer the advantage that they can, simultaneously with the separation, react to stimuli in the process that generate a response associated with some type of action or desired information. Implicitly, these applications require materials with special properties such as shape memory, sensitivity to pH, temperature or ionic strength, electrical conductivity, and magnetic, optical or dielectric properties, among others. Some example of smart PNCMs are shown below.

The use of dielectric electro-active polymers is an alternative to obtain electro-active surfaces which can be used as electro-active membranes. Basically, electroactive polymers are those able to change their shape and size by action of an electric field. A wide number of dielectric electro-active polymers can be used as actuators, sensors or energy harvesters, among other interesting applications. In particular, these membranes can be used as sensor through two mechanisms: capacitive sensing mechanism and resistive sensing mechanism. In this context, an interesting example of PNCMs was developed by Lee et al. [102]. They made membrane nanocomposite based on the combination of one sulfonated styrene pentablock copolymer, montmorillonite as nanofiller and an ionic liquid for charge transporting [102]. In addition, gel-based composite membranes able to regulate their permeability by a change on the external temperature have been developed. These membranes are based on ordered nanochannels acting like “on - off” switches or “permeability valves”. They are based on polystyrene latex particles that can change with magnetic properties and core-shell morphology [29, 103]. Zwitterionic membranes based on a copolymer from poly(acrylonitrile) and poly(N,N-dimethyl-N-methacryloxyethyl-N-(3-sulfopropyl)) have been described as electrolyte-sensitive smart membranes [104]. In order to produce PNCMs with electroactive properties not only metal nanoparticles are used. For example, electroactive dense membranes have been made by the dispersion of polyaniline nanoparticles in a matrix of poly(vinyl alcohol)-g-poly(2-acrylamido-2-methyl-1-propanesulfonic acid); for these membranes an increase on conductivity was observed as polyaniline nanoparticle content was increased [105]. PNCMs based on poly(vinyl alcohol) and poly(diaminonaphtalene) nanoparticles; these PNCMs were denominated to be chemical-response electroactive PNCMs since they showed different responses when different metal ions were used, (e.g., Ag⁺, Hg²⁺ and Cu²⁺ in HClO₄) [106].

On the other hand, thermosensitive smart PNCMs have been developed from polyurethane and SiO₂ nanoparticles and poly(vinylidene fluoride) and TiO₂ nanoparticles [107], whereas membranes sensitive to variations of external magnetic field were made by coating via grafting, and coating by direct blending of magnetic materials; usually these membranes are based on Fe₃O₄ nanoparticles due to their magnetic properties. Thus, by instead, PNCMs based on poly(2-hydroxyethyl methacrylate) supported on polyamide, and using Fe₃O₄ nanoparticles as nanofiller,

showed an increased permeation and salt rejection in the presence of a magnetic field [108]. Also, environmentally-sensitive magnetic nanocomposite membranes like capsules were prepared for controlled-release of nitrate. These were made of poly(ether sulfone) and Fe_2O_3 as nanofiller [35, 109].

Other interesting examples are found in the field of piezoelectric materials which are those able to show an accumulation of electric charges within certain materials when some type of mechanical stress is applied. Thus, piezoelectric electroresponsive PNCMs have been made from piezoelectric polymers, however, usually, the piezoelectric effect is produced by the use of an intense electric field at high temperature, therefore, these systems require high thermal properties which can be obtained by NCPs [110–113]. Some polymers with piezoelectric properties are poly(vinylidene fluoride), poly(lactic acid), and poly(vinylidene fluoridene-trifluoroethylene) which show modulus of the maximum piezoelectric coefficient of 24–34, 10, and 38 pC/N, respectively, whereas clays, hydrated salts, barium titanate, and titanium dioxide have been used as nanofiller for several applications [114].

6 Conclusions and Perspectives

PNCMs are versatile systems with a great number of applications in many fields of science and technology. Its development goes hand in hand with the advances in the field of materials both at the level of polymer science as at the level of nanomaterials. However, two trends are clearly identified: (i) the use of biopolymers and bio-based polymers for the making of functional materials, including, membranes, and (ii) the making of PNCMs with two or more functional applications. In consequence, multifunctional biobased PNCMs can be defined to be the new frontier in the membrane science, with the advantage that they combine the concepts of sustainability and multifunctionality. At the present, membrane technology based on these concept is limited and practically null.

On the other hand, from a conceptual and mechanistic viewpoint, there are still many challenges due to the intrinsic complexity of these systems in which, by example, the categorization of biphasic, that is, a polymeric phase and a nanostructured phase, would be an oversimplification that can overlook many key aspects, which are associated with the fact that PNCMs can be, by instance, porous or dense systems, with modulable properties, sensitive to a wide variety of stimuli, systems transcending their use as separation elements, having an internal polymer-nanomaterial interface, and properties associated both with polymeric phase and nanoparticulate, as well as, synergic properties resulting of combination of materials; in addition these systems are able to contain active components such as ionic liquids, biomolecules, catalysts, among others.

In relation with their properties, these systems are often described by unifactorial analysis and from descriptive characterization strategies that do not allow the stablishing of synergistic effects. In general, much of the research on this topic focuses on the manufacture, characterization and identification of properties and

their application in specific fields, therefore, mechanistic information is limited to the extrapolation of fundamental concepts from the field of membranes and from the field of materials used to manufacture them. To improve the understanding of these systems and expand their rational design as well as the control of their properties and expand their applications, it is necessary to advance with the study at a fundamental level, being important, the subdivision of these systems both at the compositional level and at the level of properties due to the extensive, in terms of knowledge, that a single of these systems is.

References

1. Palencia, M., Córdoba, A., Vera, M.: Membrane technology and chemistry. In: Visakh, P.M., Nazarenko, O. (eds.) *Nanostructured Polymer Membranes*, vol. 1, PP 27–54. Scrivener Publishing LLC (2016)
2. Sharma, V.P., Sharma, U., Chattopadhyay, M., Shukla, V.N.: Advance applications of nanomaterials: a review. *Mat. Today Proc.* **5**(1), 6376–6380 (2018)
3. Fu, S., Sun, Z., Huang, P., Li, Y., Hu, N.: Some basic aspects of polymer nanocomposites: a critical review. *Nano Mat. Sci.* **1**, 2–30 (2019)
4. Kaushik, N.: *Membrane Separation Processes*, p. 336. Prentice-Hall of India, New Delhi (2008)
5. Drioli, E., Giorno, L., Fontananova, E. (eds.): *Comprehensive Membrane Science and Engineering*, vol. 1, p. 1720. Elsevier, Oxford (2017)
6. Maksoud, M.I.A.A., Fahim, R.A., Shalan, A.E., et al.: Advanced materials and technologies for supercapacitors used in energy conversion and storage: a review. *Environ. Chem. Lett.* **19**, 375–439 (2021)
7. Rivas, B.L., Pereira, E.D., Palencia, M., Sánchez, J.: Water-soluble functional polymers in conjunction with membranes to remove pollutant ions from aqueous solutions. *Prog. Polym. Sci.* **36**, 294–322 (2011)
8. Messih, M.F.A., Shalan, A.E., Sanad, M.F., Ahmed, M.A.: Facile approach to prepare ZnO@SiO₂ nanomaterials for photocatalytic degradation of some organic pollutant models. *J. Mater. Sci. Mater. Electron.* **30**, 14291–14299 (2019)
9. Abdelbasir, S.M., Shalan, A.E.: An overview of nanomaterials for industrial wastewater treatment. *Korean J. Chem. Eng.* **36**, 1209–1225 (2019)
10. Abdellatif Soliman, S.M., Sanad, M.F., Shalan, A.E.: Synthesis, characterization and antimicrobial activity applications of grafted copolymer alginate-g-poly(N-vinyl imidazole). *RSC Adv.* **11**, 11541–11548 (2021)
11. Elella, M.H.A., Goda, E.S., Abdallah, H.M., et al.: Innovative bactericidal adsorbents containing modified xanthan gum/montmorillonite nanocomposites for wastewater treatment. *Int. J. Biol. Macromol.* **167**, 1113–1125 (2021)
12. Barhoum, A., et al.: A broad family of carbon nanomaterials: classification, properties, synthesis, and emerging applications. In: Barhoum, A., Bechelany, M., Makhlof, A. (eds.) *Handbook of Nanofibers*, pp. 1–40. Springer, Cham (2019). https://doi.org/10.1007/978-3-319-42789-8_59-1
13. Palencia, M., Berrio, M.E., Melendez, M.: Nanostructured polymer composites with potential applications into the storage of blood and hemoderivates. *J. Sci. Technol. Appl.* **1**, 4–14 (2016)
14. Batool, M., Nazar, M.F., Awan, A., et al.: Bismuth-based heterojunction nanocomposites for photocatalysis and heavy metal detection applications. *Nano-struct. Nano-objects* **27**, 100762 (2021)
15. Amin, M., Kargari, A.: Nanocomposite membranes. In: *Emerging Technologies for Sustainable Desalination Handbook*, pp. 285–330. Oxford, Elsevier (2018)

16. Lerma, T.A., Collazos, S., Córdoba, A.: Effect of side chain length of carbamates on the surface properties of porous interpenetrating networks. *J. Sci. Technol. Appl.* **1**, 30–38 (2016)
17. Lerma, T.A., Martínez, G., Palencia, M.: Generation of thiolated porous surfaces by interpenetrating polymeric networks: study of their surface properties. *J. Sci. Technol. Appl.* **3**, 56–65 (2017)
18. Arbelaez, N., Lerma, T.A., Córdoba, A.: Modification of membranes by insertion of short-chain alcohols on reactive porous substrates: effect of chain length on the surface free energy. *J. Sci. Technol. Appl.* **2**, 75–83 (2017)
19. Benitez, E.F., Lerma, T.A., Córdoba, A.: Making of porous ionic surfaces by sequential polymerization: polyurethanes + grafting of polyelectrolytes. *J. Sci. Technol. Appl.* **2**, 44–53 (2017)
20. Bessbousse, H., Rhlalou, T., Verchere, J.F., Lebrun, L.: Novel metal-complexing membrane containing poly(4-vinylpyridine) for removal of Hg(II) from aqueous solution. *J. Phys. Chem. B* **113**, 8588–8598 (2009)
21. Palencia, M., Lerma, T.A., Berrio, M.E.: Thin-film composite by in situ polymerization of 4-chloromethyl styrene functionalized with N-methyl-D-glucamine in pore-type microreactors. *J. Sci. Technol. Appl.* **3**, 66–76 (2017)
22. Rastgar, M., Shakeri, A., Salehi, H.: Study of polyamide thin film characteristics impact on permeability/selectivity performance and fouling behavior of forward osmosis membrane. *Environ. Sci. Pollut. Res. Int.* **26**, 1181–1191 (2019)
23. Azizi, S., Ahmad, M.B., Ibrahim, N.A., Hussein, M.Z., Namvar, F.: Cellulose nanocrystals/ZnO as a bifunctional reinforcing nanocomposite for poly(vinyl alcohol)/chitosan blend films: fabrication, characterization and properties. *Int. J. Mol. Sci.* **15**, 11040–11053 (2014)
24. Poyraz, B., Tozluoğlu, A., Candan, Z., Demir, A., Yavuz, M.: Influence of PVA and silica on chemical, thermo-mechanical and electrical properties of Celluclast-treated nanofibrillated cellulose composites. *Int. J. Biol. Macromol.* **104**, 384–392 (2017)
25. Niazi, M.B.K., Jahan, Z., Berg, S.S., Gregersen, Ø.W.: Mechanical, thermal and swelling properties of phosphorylated nanocellulose fibrils/PVA nanocomposite membranes. *Carbohydr. Polym.* **177**, 258–268 (2017)
26. Jahan, Z., Khan, M., Gregersen, O.W.: Mechanical, thermal and swelling properties of cellulose nanocrystals/PVA nanocomposites membranes. *J. Ind. Eng. Chem.* **57**, 113–124 (2018)
27. Sigwadi, R., Dhlamini, M.S., Mokrani, T., Nemavhola, F.: Enhancing the mechanical properties of zirconia/Nafion® nanocomposite membrane through carbon nanotubes for fuel cell application. *Heliyon* **5**, e02112 (2019)
28. Sigwadi, R., Dhlamini, M.S., Mokrani, T., Nemavhola, F., Nonjola, P.F., Msomi, P.F.: The proton conductivity and mechanical properties of Nafion®/ZrP nanocomposite membrane. *Heliyon* **5**, e02240 (2019)
29. Csetneki, I., Filipcsei, G., Zrinyi, M.: Smart nanocomposite polymer membranes with on/off switching control. *Macromol* **39**, 1939–1942 (2006)
30. Shemehadi, R., Ghafarian, R., Gorji, M., Avazverdi, E.: A smart thermoregulatory nanocomposite membrane with improved thermal properties: simultaneous use of graphene family and micro-encapsulated phase change material. *Textile Res. J.*, 1–9 (2018)
31. Lee, C.T., Wang, Y.S.: High-performance room temperature NH₃ gas sensors based on polyaniline-reduced graphene oxide nanocomposite sensitive membrane. *J. Alloys Comp.* **789**, 693–696 (2019)
32. Prasad, B., Singh, F., Panwar, V., Anoop, G.: Development of strain sensor using conductive poly(vinylidene fluoride) (PVDF) nanocomposite membrane reinforced with ionic liquid (IL) & carbon nanofiber (CNF). *Compos. B Eng.* **173**, 106990 (2019)
33. Hittini, W., Abu-Hani, A.F., Reddy, N., Mahmoud, S.T.: Cellulose-Copper Oxide hybrid nanocomposites membranes for H₂S gas detection at low temperatures. *Sci. Rep.* **10**, 2940 (2020)
34. Inukai, S., et al.: High-performance multi-functional reverse osmosis membranes obtained by carbon nanotube-polyamide nanocomposite. *Sci. Rep.* **5**, 13562 (2015)

35. Emami, N., Razmjou, A., Noorisafa, F., Habibnejad, A., Zarrabi, A., Ji, C.: Fabrication of smart magnetic nanocomposite asymmetric membrane capsules for the controlled release of nitrate. *Environ. Nanotechnol. Monit. Manag.* **8**, 233–243 (2017)
36. Ghaee, A., Zerafat, M.M., Askari, P., Sabbaghi, S., Sadatnia, B.: Fabrication of polyamide thin-film nanocomposite membranes with enhanced surface charge for nitrate ion removal from water resources. *Environ. Technol.* **38**, 772–781 (2017)
37. Shukla, A.K., Alam, J., Ansari, M.A., Alhoshan, M., Ali, F.A.A.: Antimicrobial and antifouling properties of versatile PPSU/carboxylated GO nanocomposite membrane against Gram-positive and Gram-negative bacteria and protein. *Environ. Sci. Pollut. Res. Int.* **25**, 34103–34113 (2018)
38. Wang, W., Li, Y., Wang, W., Gao, B., Wang, Z.: Palygorskite/silver nanoparticles incorporated polyamide thin film nanocomposite membranes with enhanced water permeating, antifouling and antimicrobial performance. *Chemosphere* **236**, 124396 (2019)
39. Shakeri, A., Salehi, H., Ghorbani, F., Amini, M., Naslhajian, H.: Polyoxometalate based thin film nanocomposite forward osmosis membrane: superhydrophilic, anti-fouling, and high water permeable. *J. Colloid Interface Sci.* **15**, 328–338 (2019)
40. Wen, Y., Yuan, J., Ma, X., Wang, S., Liu, Y.: Polymeric nanocomposite membranes for water treatment: a review. *Environ. Chem. Lett.* **17**, 1539–1551 (2019)
41. Kononova, S.V., et al.: Polymer nanocomposite membranes. *Appl. Sci.* **8**, 1181 (2018)
42. Liang, C.Z., Chung, T.S., Lai, J.Y.: A review of polymeric composite membranes for gas separation and energy production. *Prog. Polym. Sci.* **97**, 101141 (2019)
43. Bassyouni, M., Abdel-Aziz, M.H., Zoromba, M., Abdel-Hamid, S.M.S., Drioli, E.: A review of polymeric nanocomposite membranes for water purification. *J. Ind. Eng. Chem.* **73**, 19–46 (2019)
44. Palencia, M.: Fundamental and methodological aspects of porous membrane characterization by hydrodynamic permeability test - a review. *J. Sci. Technol. Appl.* **7**, 17–25 (2019)
45. Palencia, M.: Liquid-phase polymer-based retention: theory, modeling and applications for the removal of pollutant inorganic ions. *J. Chem.* **965624**, 1–9 (2015)
46. Ching, C.B., Hidajat, K., Uddin, M.S.: Evaluation of equilibrium and kinetic parameters of smaller molecular size amino acids on KX zeolite crystals via liquid chromatographic techniques. *Sep. Sci. Technol.* **24**, 581–597 (1989)
47. Palencia, M.S., Berrio, M.E., Palencia, S.L.: Effect of capping agent and diffusivity of different silver nanoparticles on their antibacterial properties. *J. Nanosci. Nanotechnol.* **17**, 1–8 (2017)
48. Ambrosio, R., et al.: Polymeric nanocomposites membranes with high permittivity based on PVA-ZnO nanoparticles for potential applications in flexible electronics. *Polymers* **10**, 1370 (2018)
49. Nizamuddin, S., et al.: Electrical properties of sustainable nano-composites containing nanofillers: dielectric properties and electrical conductivity. In: Inamuddin, S.T., Mishra, R.K., Asiri, A.M. (eds.) *Sustainable Polymer Composites and Nanocomposites*, pp. 899–914. Springer, Cham (2019). https://doi.org/10.1007/978-3-030-05399-4_30
50. Palencia, M., Rivas, B.L., Valle, H.: Size separation of silver nanoparticles by dead-end ultrafiltration: description of fouling mechanism by pore blocking model. *J. Membr. Sci.* **455**, 7–14 (2014)
51. Palencia, M., Cordoba, A., Combatt, E.M.: Synthesis and characterization of biofouling-resistant nanocomposites based on glucamine polymers and silver/acrylic acid nanoparticles. *Polym. Bull.* **75**, 4555–4569 (2018)
52. Bandyopadhyay, A., Valavala, P.K., Clancy, T.C., Wise, K.E., Odegard, G.M.: Molecular modeling of crosslinked epoxy polymers: the effect of crosslink density on thermomechanical properties. *Polymer* **52**, 2445–2452 (2011)
53. Balani, K., Verma, V., Agarwal, A., Narayan, R.: *Biosurfaces: A Materials Science and Engineering Perspective*, pp. 329–344. The American Ceramic Society, Wiley (2015)
54. Hussain, S.A., Chakraborty, S.: Organoclay hybrid films with improved functionality. In: Jassi, K., Chehimi, M.M., Thomas, S. (eds.) *Clay-Polymer Manocomposites*, pp. 273–305. Elsevier (2011)

55. Wypych, F., Bergaya, F., Schoonheydt, R.A.: From polymers to clay polymer nanocomposites. *Dev. Clay Sci.* **9**, 331–359 (2018)
56. Lerma, T.A., Palencia, M., Combatt, E.M.: Soil polymer conditioner based on montmorillonite-poly(acrylic acid) composites. *J. Appl. Polym. Sci.* **135**, 46211 (2017)
57. Lerma, T.A., Combatt, E., Palencia, M.: Soil-mimicking hybrid composites based on clay, polymers and nitrogen-fixing bacteria for the development of remediation systems of degraded soil. *J. Sci. Technol. Appl.* **4**, 17–27 (2018)
58. Lerma, T.A., Garces, V., Palencia, M.: Novel multi- and bio-functional hybrid polymer hydrogels based on bentonite-poly(acrylic acid) composites and sorbitol polyesters: structural and functional characterization. *Eur. Polym. J.* **128**, 109627 (2020)
59. Baroña, G.N.B., Choi, M., Jung, B.: High permeate flux of PVA/PSf thin film composite nanofiltration membrane with aluminosilicate single-walled nanotubes. *J. Colloid. Interf. Sci.* **386**, 189–197 (2012)
60. Zheng, J., Li, M., Yu, K., Hu, J., Zhang, X., Wang, L.: Sulfonated multiwall carbon nanotubes assisted thin-film nanocomposite membrane with enhanced water flux and anti-fouling property. *J. Membr. Sci.* **524**, 344–353 (2017)
61. Guo, W., Ngo, H.H., Li, J.: A mini-review on membrane fouling. *Biores. Technol.* **122**, 27–34 (2012)
62. Al-Juboori, R.A., Yusaf, T.: Biofouling in RO system: mechanisms, monitoring and controlling. *Desalination* **302**, 1–23 (2012)
63. Jian, S., Li, Y., Ladewing, B.P.: A review of reverse osmosis membrane fouling and control strategies. *Sci. Total Environ.* **595**, 567–583 (2017)
64. Palencia, M., Rivas, B.L., Pereira, E.: Metal ion recovery by polymer-enhanced ultrafiltration using poly(vinyl sulfonic acid): fouling description and membrane–metal ion interaction. *J. Membr. Sci.* **345**, 191–200 (2009)
65. Palencia, M., Rivas, B.L., Pereira, E., Hernandez, A., Prádanos, P.: Study of polymer–metal ion–membrane interactions in liquid-phase polymer-based retention (LPR) by continuous diafiltration. *J. Membr. Sci.* **336**, 128–139 (2009)
66. Palencia, M., Rivas, B.L.: Adsorption of linear polymers on polyethersulfone membranes: Contribution of divalent counterions on modifying of hydrophilic–lipophilic balance of polyelectrolyte chain. *J. Membr. Sci.* **372**, 355–365 (2011)
67. El-Dessouky, H.T., Ettouney, H.M.: Reverse osmosis feed treatment, biofouling, and membrane cleaning. In: *Fundamentals of Salt Water Desalination*, pp. 439–452 (2002)
68. O’Toole, G., Kaplan, H.B., Kolter, R.: Biofilm formation as microbial development. *Ann. Rev. Microbiol.* **54**, 49–79 (2000)
69. Donlan, R.M.: Biofilms: microbial life on surfaces. *Emerg. Infect. Dis.* **8**, 881–890 (2002)
70. Lopez, D., Vlamakis, H., Kolter, R.: Biofilms. *Cold Spring Harb. Perspect. Biol.* **2**(7), a000398–a000398 (2010). <https://doi.org/10.1101/cshperspect.a000398>
71. Du, X., Shi, Y., Jegatheesan, V., Haq, I.: A review on the mechanism, impacts and control methods of membrane fouling in MBR system. *Membr. (Basel)* **10**, 24 (2020)
72. Homayoonfal, M., Mehrnia, M.R., Rahmani, S., Mohades, Y.: Fabrication of alumina/polysulfone nanocomposite membranes with biofouling mitigation approach in membrane bioreactors. *J. Ind. Eng. Chem.* **22**, 357–367 (2015)
73. Emadzadeh, D., et al.: A novel thin film nanocomposite reverse osmosis membrane with superior anti-organic fouling affinity for water desalination. *Desalination* **368**, 106–113 (2015)
74. Ma, A., Van Anh, L.T., Brennan, G., Rahaman, M.S., Asadishad, B., Tufenkji, N.: Spray and spin-assisted layer-by-layer assembly of copper nanoparticles on thin-film composite reverse osmosis membrane for biofouling mitigation. *Water Res.* **99**, 188–199 (2016)
75. Zirehpour, A., Rahimpour, A., Shamsabadi, A.A., Sharifian, M.G., Soroush, M.: Mitigation of thin-film composite membrane biofouling via immobilizing nano-sized biocidal reservoirs in the membrane active layer. *Environ. Sci. Technol.* **51**, 5511–5522 (2017)
76. Zhang, X., Wang, Z., Chen, M., Ma, J., Chen, S., Wu, Z.: Membrane biofouling control using polyvinylidene fluoride membrane blended with quaternary ammonium compound assembled on carbon material. *J. Membr. Sci.* **539**, 229–237 (2017)

77. Faria, A.F., et al.: Thin-film composite forward osmosis membranes functionalized with graphene oxide–silver nanocomposites for biofouling control. *J. Membr. Sci.* **525**, 146–156 (2017)
78. Palencia, S.L., Buelvas, A.M., Palencia, M.S.: Interaction mechanisms of inorganic nanoparticles and biomolecular systems of microorganisms. *Curr. Chem. Biol.* **9**, 11–23 (2015)
79. Palencia, M., Cordoba, A., Melendez, M.F.: Nanocomposites based on cationic polyelectrolytes and silver nanoparticles: synthesis, characterization, molybdate retention and antimicrobial activity. *Arab. J. Chem.* **12**, 825–834 (2019)
80. Palencia, M., Lerma, T.A., Afanasjeva, N.: Antibacterial cationic poly(vinyl chloride) as an approach for in situ pathogen-inactivation by surface contact with biomedical materials. *Eur. Polym. J.* **115**, 212–220 (2019)
81. Althues, H., Henle, J., Kaskel, S.: Functional inorganic nanofillers for transparent polymers. *Chem. Soc. Rev.* **36**, 1454–1465 (2007)
82. Li, S., Lin, M.M., Toprak, M.S., Kim, D.K., Muhammed, M.: Nanocomposites of polymer and inorganic nanoparticles for optical and magnetic applications. *Nano Rev.* **1**(1), 5214 (2010). <https://doi.org/10.3402/nano.v1i0.5214>
83. Kirmayer, S., Aharon, E., Dovgolevsky, E., Kalina, M., Frey, G.L.: Self-assembled lamellar MoS₂, SnS₂ and SiO₂ semiconducting polymer nanocomposites. *Philos. Trans. A Math. Phys. Eng. Sci.* **365**, 1489–1508 (2007)
84. Ponnamma, D., et al.: Synthesis, optimization and applications of ZnO/polymer nanocomposites. *Mater. Sci. Eng. C Mater. Biol. Appl.* **98**, 1210–1240 (2019)
85. Roy, A.S., Gupta, S., Sindhu, S., Parveen, A., Ramamurthy, P.C.: Dielectric properties of novel PVA/ZnO hybrid nanocomposite films. *Compos. B: Eng.* **47**, 314–319 (2013)
86. Wang, G., Deng, Y., Guo, L.: Single-crystalline ZnO nanowire bundles: synthesis, mechanism and their application in dielectric composites. *Chem. Eur. J.* **16**, 10220–10225 (2010)
87. Nasir, A., Masood, F., Yasin, T., Hameed, A.: Progress in polymeric nanocomposite membranes for wastewater treatment: preparation, properties and applications. *J. Ind. Eng. Chem.* **79**, 29–40 (2019)
88. Safarpour, M., Khataee, A., Vatanpour, V.: Thin film nanocomposite reverse osmosis membrane modified by reduced graphene oxide/TiO₂ with improved desalination performance. *J. Membr. Sci.* **489**, 43–54 (2015)
89. Rabbani, M., et al.: Nanocomposite membranes for water separation and purification: fabrication, modification and applications. *Sep. Purif. Technol.* **213**, 465–499 (2019)
90. Ursino, C., Castro-Muñoz, R., Drioli, E., Gzara, L., Albeirutty, M.H., Figoli, A.: Progress of nanocomposite membranes for water treatment. *Membr. (Basel)* **8**(2), 18 (2018)
91. Abdalia, N., Marjani, A., Heidary, F., Adimi, M.: Fabrication of PVA coated PES/PVDF nanocomposite membrane embedded with in-situ formed magnetite nanoparticles for removal of metal ions from aqueous solutions. *New J. Chem.* **41**, 6405–6414 (2017)
92. Zinadini, S., Zinatizadeh, A.A., Rahimi, M., Vatanpour, V., Zangeneh, H., Beygzadeh, M.: Novel high flux antifouling nanofiltration membranes for dye removal containing carboxymethyl chitosan coated Fe₃O₄ nanoparticles. *Desalination* **349**, 145–154 (2014)
93. Nestic, A.R., Velickovic, S.J., Antonovic, D.G.: Characterization of chitosan/montmorillonite membranes as adsorbents for Bezactiv Orange V-3R dye. *J. Hazard. Mater.* **209–210**, 256–263 (2012)
94. Karim, Z., Mathew, A.P., Grahn, M., Mouzon, J., Oksman, K.: Nanoporous membranes with cellulose nanocrystals as functional entity in chitosan: removal of dyes from water. *Carbohydr. Polym.* **112**, 668–676 (2014)
95. Crock, C.A., Rogensues, A.R., Shan, W., Tarabara, V.V.: Polymer nanocomposites with graphene-based hierarchical fillers as materials for multifunctional water treatment membranes. *Water Res.* **47**, 3984–3996 (2013)
96. Bojnourd, F.M., Pakizeh, M.: Preparation and characterization of a nanoclay/PVA/PSf nanocomposite membrane for removal of pharmaceuticals from water. *Appl. Clay Sci.* **162**, 326–338 (2018)
97. Ulbricht, M.: Advanced functional polymer membranes. *Polymer* **47**, 2217–2262 (2006)

98. Gorecki, T., Namiesnik, J.: Passive sampling. *TrAC Trends Anal. Chem.* **21**, 276–291 (2002)
99. Martinez, J.M., Troches, E., Paez, M.I.: Evaluation of poly(ethylene-co-vinylacetate) as polymeric adsorbent of polychlorinated biphenyls in water. *J. Sci. Technol. Appl.* **2**, 94–107 (2017)
100. Martínez, J., Paez, M., Palencia, M., Peña, M.: Sampling devices of pesticides in surface waters based on glass fiber poly(ethylene-co-vinyl acetate) adsorbents. *Rev. LatinAm. Metal. Mat.* **38**, 9–20 (2018)
101. Taylor, A.C., Fones, G.R., Vrana, B., Mills, G.A.: Applications for passive sampling of hydrophobic organic contaminants in water—a review. *J. Critical. Rev. Anal. Chem.* **51**, 1–36 (2019)
102. Lee, J.W., Hong, S.M., Koo, C.M.: Electroactive nanostructured polymer actuators fabricated using sulfonated styrenic pentablock copolymer/montmorillonite/ionic liquid nanocomposite membranes. *Jpn. J. Appl. Phys.* **53**, 1–6 (2014)
103. Gu, S., Shiratori, T., Konno, M.: Synthesis of monodisperse, magnetic latex particles with polystyrene core. *Colloid Polym. Sci.* **281**, 1076–1081 (2003)
104. Su, Y., Zheng, L., Li, C., Jiang, Z.: Smart zwitterionic membranes with on/off behavior for protein transport. *J. Phys. Chem. B* **112**, 11923–11928 (2008)
105. Soni, S.N., Bajpai, J., Bajpai, A.K.: Investigation of electroactive behaviour of polyaniline containing polyelectrolyte nanocomposite membranes. *J. Nanosci. Meth.* **1**, 164–182 (2012)
106. Li, X.G., Zhang, J.L., Huang, M.R.: Chemical response of nanocomposite membranes of electroactive polydiaminonaphthalene nanoparticles to heavy metal ions. *J. Phys. Chem.* **118**, 11990–11999 (2014)
107. Kumar, M., Kumar, M., Mondal, P., Singh, R.: Temperature-responsive membranes. In: *Stimuli Responsive Polymeric Membranes: Smart Polymeric Membranes*, pp. 25:67–113. Elsevier (2018)
108. Kumar, M., Kumar, M., Mondal, P., Singh, R.: Magnetic-responsive membranes. In: *Stimuli Responsive Polymeric Membranes: Smart Polymeric Membranes*, pp. 25:193–219. Elsevier (2018)
109. Vatanpour, V., et al.: Nanostructured polyethersulfone nanocomposite membranes for dual protein and dye separation: lower antifouling with lanthanum (III) vanadate nanosheets as a novel nanofiller. *Polym. Testing* **94**, 107040 (2021)
110. Coster, H.G.L., Farahani, T.D., Chilcott, T.C.: Production and characterization of piezoelectric membranes. *Desalination* **283**, 52–57 (2011)
111. Darestani, M.T., Coster, H.G.L., Chilcott, T.C., Fleming, S., Nagarajan, V., An, H.: Piezoelectric membranes for separation processes: fabrication and piezoelectric properties. *J. Membr. Sci.* **434**, 184–192 (2013)
112. Darestani, M.T., Coster, H.G.L., Chilcott, T.C.: Piezoelectric membranes for separation processes: operating conditions and filtration performance. *J. Membr. Sci.* **435**, 226–232 (2013)
113. Kumar, M., Kumar, M., Mondal, P., Singh, R.: Electric field-responsive. In: *Stimuli Responsive Polymeric Membranes: Smart Polymeric Membranes*, pp. 173–191. Elsevier (2018)
114. Castro, N., Pereira, N., Cardos, V., Ribeiro, C., Lanceros-Mendez, S.: Micro- and nanostructured piezoelectric polymers: fundamentals and application. *Front. Nanosci.* **14**, 35–65 (2019)

Polymer-Based Nanocomposites for Removal of Pollutants from Different Environment Using Catalytic Degradation



Atul Kumar Maurya, Rupam Gogoi, and Gaurav Manik

Abstract Thermal power plants, polymer and paper industries have been growing at an accelerated pace to fulfil the basic human needs and energy requirements. However, these industries release harmful and carcinogenic pollutants like fly-ash, heavy metals, biphenyls, dyes, water-soluble impurities, and greenhouse gases, which are increasingly deteriorating our environment. Hence, the use of a relatively economic catalytic degradation process that targets and degrades both organic and inorganic pollutants is the need of the hour. This chapter covers the use of advanced nanomaterials and speciality polymer nanocomposites for catalytic degradation due to availability of high surface area and potential high efficiency. Nanomaterials such as nano-particles, nano-fibers, nano-tubes, and polymeric nanocomposites are widely used for the removal of contaminants from different environments. Organic contaminants such as halogenated alkanes, brominated methane, other polychlorinated hydrocarbons, pesticides, and dyes can be degraded by nanomaterials such as zero valence metals Fe, Cu, Zn and bimetals like Fe/Pd, Fe/Ni and Pd/Zn, etc. Likewise, nano-semiconductors such as ZnO, CdS, and WO₃, also serve as catalysts for the selective degradation of targeted pollutants. However, an aqueous solution of fine nano-particles cannot be used directly for catalytic degradation because there is a possibility of their agglomeration. To solve this problem, immobilization of such nanocatalysts can be achieved on the surface of porous resin, ion exchange, and polymeric membranes, which minimizes particle loss and their agglomeration. Applications involving such polymer nanocomposites, require the matrix to exhibit high antioxidant behaviour during illumination by the ultraviolet (UV) light for the production of highly reducing and oxidation agents to eliminate environmental pollutants. In line with this, recent fabrication procedures, advances in research and prospects of polymer based-nano composites for environmental remediation and protection are discussed, in details.

A. K. Maurya · R. Gogoi · G. Manik (✉)
Department of Polymer and Process Engineering, Indian Institute of Technology Roorkee,
Saharanpur Campus, Paper Mill Road, Saharanpur, UP 247001, India
e-mail: gaurav.manik@pe.iitr.ac.in

A. K. Maurya
e-mail: amaurya@pe.iitr.ac.in

Keywords Catalytic degradation · Polymer nano composite · Environmental remediation

List of Abbreviations

UV	Ultraviolet
CMC	Carboxymethyl Cellulose
PVA	Polyvinyl alcohol
PANI	Polyaniline
PEDOT	Poly (3,4-ethylenedioxythiophene)
PMMA	Poly (methylmetha-acrylate)
PVP	Poly (vinyl pyrrolidone)
PHB	Poly(hydroxybutyrate)
PDMS	Poly (dimethyl siloxane)
PVDF	Poly (vinylidene fluoride)
nZV	Nano zero-valent
CdS	Cadmium sulphide
PE	Polyethene
PP	Polypropylene
CIP	Ciprofloxacin (CIP)
RhB	Rhodamine B
PNA	1-Naphthylamine
MB	Methyl Blue
TCE	Trichloroethene

1 Introduction

With the modernization of civilization, the material need of human is also increasing day by day. To simplify services and to make them available for a large number of masses new technologies are being developed at an accelerated pace. With the growing population and urbanization, demand and use of different products, and thereby, generation of waste by-products have been increasing exponentially. To meet the high demand of products and services numerous industries and plants have been set up by both the government and private entities in almost all the countries worldwide. These manufacturing units use many chemical-based products such as dyes, fertilizers, pesticides, conventional energy reserves, agrochemicals, polymers, and composites. Subsequently, such industries generate fly-ash, heavy metals, biphenyls, dyes, water-soluble impurities which are very harmful to water and our environment [1]. Conventional techniques like adsorption, biological oxidation, incineration, supercritical water oxidation and catalytic degradation have been used to treat

and reduce the aforementioned organic and toxic wastes [2–4]. In parallel to the mentioned remediation techniques for pollutant degradation, nano-technology also gained popularity due to nanomaterials' immense capability for adsorption, catalytic degradation, and sensing material to detect waste [5]. Large specific surface area and high interfacial reactivity of nanomaterials make them ideal candidates for pollutant degradation and waste treatment. The surface area of nanomaterials increases exponentially with the reduction of their size. The small size of the nanomaterials provides them good mobility when added to a solution. Hence, they can scan and detect waste in a huge volume of solution in a brief period of time and with the use of a tiny quantity [6]. Similarly, the presence of high coordination atoms at the surface, edges, and vortices of nanomaterial makes it highly reactive [6]. These properties of the nanomaterial can be used to degrade and scavenge pollutants from both water and air [7]. Synthesised engineered nanomaterials for example- zero-valent metals [8–11], bimetals [12–14], metal oxides [15–17], bio-polymers [18–20], single enzyme nanoparticles [21–23], all possess highly reactive and disordered surfaces, catalytic effect, and have proved to possess strong antimicrobial properties and ability to degrade pollutants. Metals from the iron group, Co, Cu, Fe, and Ni possess excellent magnetic and chemical catalytic properties and attract researchers to work and tailor their properties further for remediation of various pollutants. Hence, composites between these nanoparticles and host matrix-like polymer, carbon, silica, and novel metals are suitable for contaminant degradation. Polymers such as cellulose [24, 25], carboxymethyl cellulose (CMC) [4], chitosan [26, 27], alginate [28, 29], polyvinyl alcohol (PVA) [26, 30], polyaniline (PANI) [30–32], poly(3,4-ethylenedioxythiophene (PEDOT) [30], polythiophene [30] and polypyrrole [30, 33, 34] could be reinforced by these nanoparticles depending upon the mechanical and thermal behaviour of the host organic resin. This chapter focuses on review and an analysis of the application of polymer nanocomposites for the distillation or purification of the water and air contaminants like dyes, heavy metals, greenhouse gases, coal fly ash etc. using the process of catalytic degradation.

2 Nanomaterials and Polymers Used for Removal of Pollutants from Different Environment Using Catalytic Degradation

2.1 Available Nano Materials

Some of the nanomaterials which have already been used for the catalytic degradation have been explained briefly in the next section.

2.1.1 Zero Valent Metals

Zero valent metals [8–11] are reduced down to nano level and then used for the catalytic degradation, which increases the efficiency of the pollutant removal. Zero valent metals such as Fe^0 and Cu^0 has been successfully studied previously for environmental remediation. Fe and Cu are acknowledged for their change in volume due to change of several factors such as rust, bio-opportunity, ecotoxicity, bioaccumulation, translocation potential and distant future activity properties [35]. Also, as things go to the nanosized metals' excessive specific surface area, it provides rapid degradation of the contaminant with higher ability.

Iron (Fe^0)

Fe^0 can coordinate with small atoms like oxygen, nitrogen, and sulfur and bind as a small molecule. The outstanding electron donor property ($\text{Fe}^{+2} \rightarrow \text{Fe}^{+3}$) of the Fe^0 supports the degradation, sorption, or adsorption of contaminants. One of the finest adsorbents is iron oxyhydroxide due to its high surface area. Polymeric nanocomposites of Fe^0 with CMC, Poly (methylmetha-acrylate) (PMMA), and poly (vinyl pyrrolidone) (PVP) were previously prepared for effective contaminant degradation [35].

Copper (Cu^0)

Another excellent example of zero-valent metals for environmental remediation is copper, although, an excessive use of some may contaminant and pollute groundwater. To reduce toxicity levels various forms of copper has been improved for their biosuitability and activity properties. Like iron, zero-valent copper is also a perfect electron donor, and hence, used for the catalytic degradation or dechlorination of the pollutant like CCl_4 . It is sometimes used as a reducing agent due to its stable in situ measurement for resin/Cu grain along with a temperature-programmed reduction (TPR). Nano zero-valent (nZV) copper is more stable in water. And hence, the occurrence of unavoidable reactions is very rare. The high adsorption capacity of chitosan towards Cu (II) makes Cu/chitosan composite satisfactory for environmental remediation. Another advantage of using nZV copper is its lower price than noble metals like Pt, Au, and Ag [36–38].

2.1.2 Metal Oxide

Metal oxides can also be categorized as semiconductors. Semiconductors have suitable band energy gaps (example, 3.2 eV for TiO_2) [35] and possess excellent physicochemical properties [39], which are collectively helpful in deteriorating contaminants. For example, a nanocomposite of TiO_2 with PANI has been fabricated, with the help of electrospinning, for water treatment. Interfacial interaction between polymer and metal oxides is gaining interest and opening a new window for the researchers. Wide applications of metal oxides with conductive polymers are yet to be explored.

However, electrospinning polymeric fiber requires the adoption of insoluble polymers for water treatment.

2.1.3 Cadmium Sulphide (CdS)

Despite being very toxic in nature, CdS is used for biological, optical, and electronic applications [40]. CdS can be synthesized by template-free solution-phase synthesis, which is very efficient for contaminant degradation [41]. Water treatment through photocatalysis hosted by CdS has been preferred. Also, its photocatalytic degradation ability for the methyl tertiary butyl ether was excellent when the CdS microsphere was used with the aqueous solution under visible light [42]. Hence, CdS microspheres play an important role in the detoxification of the environment via photocatalysis.

2.1.4 Bimetals

Bimetals such as Cu/Fe [13], Ni/Fe [12], and Pd/Fe [14] are very interesting due to their ability to rapidly degrade contaminants. Due to their excellent catalytic properties, these bimetallics are attracting researchers consistently. However, aggregation of the nanoparticles of the bimetallics can reduce their reactivity, surface area, catalytic degradation and may also generate waste products. Making nanocomposites of these bimetallics can mitigate many of these issues, for example, loading Pd/Fe nanoparticles with PMMA controlled these drawbacks and increased their physicochemical applications [43].

2.2 *Hosting Polymers*

Several choices have been used previously and are available to host the nanoparticles described earlier.

2.2.1 Polyaniline (PANI)

PANI is a conductive polymer used for various applications, including organic electrodes, sensors, and actuators [44]. Based upon the choice of preparation methods, PANI may have either of synthesized three structures, which are shown in Table 1, named as Leucoemeraldine (LEB), Emeraldine (EB), and Pernigraniline (PB) [45]. PANI has been used for removing chromium (VI) very effectively. Its easy availability, large surface area, and low cost make it one of the finest materials for removing Cr (VI). It was a challenging task for the researcher to degrade Cr (VI). However,

the invention of polymeric nanocomposites improved its ability to destroy contaminants [46–48]. Various research articles have already been published with PANI-nanocomposite for removing pollutants from water and air. Nanocomposites of PANI as a matrix with TiO_2 , Fe_3O_4 , graphene, urease immobilized over PANI/PVA-AgNP, SrTiO_3 and thulium titanate as selective nanoparticles have been used to remove phenol, Cr (VI), rose bengal dye, urea, methyl blue (MB) and Rhodamine B (RhB) respectively (Table 2).

2.2.2 Poly(Hydroxybutyrate) (PHB)

PHB is a naturally existing polyester with a linear backbone, also identified as *p*-hydroxyacid [49]. Eco-friendly PHB is attracting researchers due to its 100% biodegradability and its use in agriculture, industrial and marine applications. Degradation study of the PHB has been reported in various environments wherein it has been observed to degrade in a few weeks. However, its high production cost makes it difficult to be used as a general-purpose plastic like PP. Researchers are continually trying to synthesize low-cost PHB with methods like bacterial strain improvement, fermentation/recovery process, and other renewable sources. Mechanical and other catalytic properties of composites have been improved by fabricating them with PHB, which also degrades specific pollutants. Methylene blue and acetaldehyde have been degraded by the TiO_2 /PHB composites [50]. Also, Niobium oxyhydroxide and HH/TiO_2 have been used to reinforce PHB to remove methylene blue and inhibit bacterial growth from different media (Table 2).

2.2.3 Poly (Dimethyl Siloxane) (PDMS)

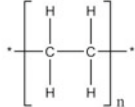
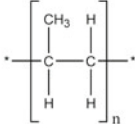
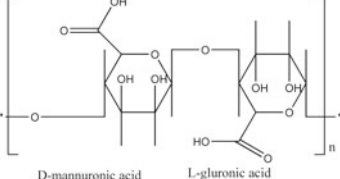
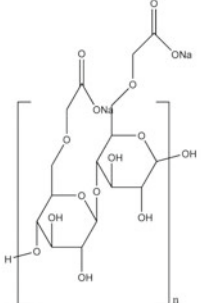
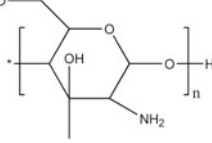
PDMS is a polymer with Si-O as the backbone shown in Table 1. Property wise PDMS is an inert, non-toxic, and highly flexible material that has been used in various product applications. Lab synthesis of PDMS sponges do not need any complex process, and it can be synthesized by the sugar template method. The molecular structure (Table 1) of the PDMS makes it highly oleophilic in nature, making it suitable for oil adsorption. Sponges of PDMS can be deformed in any shape in the liquid and air media without damaging its properties. The PDMS sponge's unique property makes it different and preferred for repeatedly removing oils and organic solvents. The spongy PDMS's pollutant removal property can be fine-tuned by controlling sugar particle quantity into its structure, thereby making it the most convenient technique to remove harmful (lethal) chemicals from grease discharge and organic pollutants from water [51]. However, people also reported the removal of methylene blue and acetaldehyde, Rhodium B, thalianosole, and the odor, by fabricating composites of PDMS with the inclusion of nanoparticles like TiO_2 , carbon nitride and nanosheet, gold (Au), and zinc oxide (ZnO) (Table 2).

Table 1 Structures of different polymeric hosts for polymer-based nanocomposite

S.No.	Name	Structure
1.	PANI	<p> Pyraziniline (blue/violet) Reduction / Oxidation Emeraldine (blue) Reduction / Oxidation Leucoemeraldine (White or colorless) </p>
2.	PHB	<p>hydroxybutyrate</p>
3.	PDMS	<p>dimethylsiloxane</p>
4.	PVP	<p>vinyl pyrrolidone</p>
5.	PMMA	
6.	PVDF	

(continued)

Table 1 (continued)

7.	PE	
8.	PP	
9.	Alginate	 <p style="text-align: center;">D-mannuronic acid L-guluronic acid</p>
10.	CMC	
11.	Chitosan	

2.2.4 Poly (Vinyl Pyrrolidone) (PVP)

PVP is one of the most preferred polymers for contaminant degradation, which is water-soluble and possesses good physiochemical properties such as chemical inertness, mechanical stability, and optical transparency (Table 1). The colloidal suspension of the PVP reflects good binding and adhesive characteristics [52, 53]. Another industrial application of the PVP is as suspension stabilizer, pigment dispersant and binding agent [54, 55]. Presence of a saturated carbon in its structure makes PVP's composites chemically resistant and mechanically stable. The presence of polar and ionic groups in its structure offers a polar nature to PVP, removing polar contaminants like bromates from the water with ease [56]. The nanocomposite of PVP with nanoparticles of natural rubber-b-PVP/Ag, ZnO, Ag/ZnO, and FeO has been already

Table 2 Details of important examples of use of polymers and nanoparticles for environmental remediation via catalytic degradation

Polymer matrix	Nano particle	Target pollutant	Preparation method	Effectiveness	Ref.
PANI	TiO ₂	Phenol	Solvent-cast	Solar illumination for 5 h leads to degradation of an aqueous solution of phenol	[93]
	Fe ₃ O ₄	Cr(VI)	Surface initiated polymerization (SIP)	100% degradation in 5 min	[103]
	Graphene	Rose Bengal Dye (RB)	In-situ preparation	56% degradation within 3 h	[104]
	Urease immobilized over PANI/PVA-AgNP	Urea	Chemical deposition followed by drop coating	Occurrence of degradation	[105]
	SrTiO ₃	MB	In-situ oxidative polymerization	97% degradation in 90 min	[106]
	Thulium titanate	Dyes (RhB)	Sol-gel assisted sonochemical method	99% degradation for 100 min	[107]
	TiO ₂	MB	Solvent casting	96% degradation of methylene blue subsequently 1 h in solar light	[50]
PHB	Niobium oxyhydroxide -HH/TiO ₂	MB	Solvent casting	Almost 100% degradation in a flow bath	[108]
		Inhibits bacterial growth	Solvent casting	100% degradation in 5 h under black light	[109]
	TiO ₂	Methylene Blue and acetaldehyde	Sol-gel	Lower than 60% degradation under UV radiation for both the pollutants	[110]
	Carbon Nitride Nano Sheet	RhB (Self-cleaning and high reusability after 5 use)	Sugar templating method	100% degradation after 1 h illumination the visible light	[111]
	Au (Gold)	Thioanisole and odour	Solution casting	Occurrence of degradation	[111]
PVP	ZnO	Methyl Blue	Sugar template method	93% degradation with UV-visible and 85% with visible light illumination	[111]
	Natural rubber-b-PVP/Ag	Methyl orange	Solution casting	70% degradation after 15 min at pH 7	[111]
	ZnO, Ag/ZnO	Methyl Orange and terephthalic acid	Hydrothermal	85% degradation of Methyl Orange in 80 min and less than 50% terephthalic acid in 1 h	[112]
	Fe ⁰	Bromate	Electrospinning	PVP/Fe ⁰ composites gives closer activity value to 90% of the activity of raw bare Fe ⁰ and kept 78% of the activity after 28 days of storage under the dry state	[56]

(continued)

Table 2 (continued)

Polymer matrix	Nano particle	Target pollutant	Preparation method	Effectiveness	Ref.
PMMA	Au/ZnO	Methylene Blue and BPA	In-situ	MB: 60% degradation BPA: 63.5% degradation	[58]
	Graphene-SnO ₂	MB	One-pot synthesis	99% degradation methylene blue under sunlight	[59]
	Fe ⁰	TCE	In situ synthesis with MMA monomer and FeSO ₄ ·7H ₂ O as precursors	62.3% degradation	[60]
PVDF	Fe ₂ O ₃ and MWCNT	Cyclohexanoic acid	In-situ	48% after 24 h when exposed to H ₂ O ₂	[62]
	TiO ₂ with PVDF: PVP(2:1)	BPA	Electrospinning	96% within 2 h	[63]
	Fe/Pd	Trichloroacetic acid	Reduction-deposition	100% dechlorination within 180 min	[64]
PE	TiO ₂	MB	Hot pressing	A solution of 200 ppm of PE/TiO ₂ degrades 0.3 mg of methylene blue per cm ⁻² within 1 h at room temperature under visible light	[66]
PE and PP	TiO ₂	Paraquat	Hot-press	Polyethylene/TiO ₂ : Photocatalytic degradation was maximum with a TiO ₂ loading of 8.8 × 10 ⁻⁵ g/cm ² provided ultraviolet lamps and sunlight. Polypropylene/TiO ₂ : Photocatalytic degradation was maximum with a TiO ₂ loading of 3.1 × 10 ⁻⁵ g/cm ² provided ultraviolet lamps and sunlight	[68]
Alginate	TiO ₂	Methyl orange	Sol-gel	More than 87% in 6 h even after 6 cycles	[113]
	CMC/TiO ₂	Congo red dye	Dissipative convective	91.5% in 240 min	[114]
	Magnetic alginate/Cds/Fe ₂ O ₃	Congo red dye	Solution casting	91.6% in 300 min under xenon lamp	[114]
	Fe ⁰	Trichloroethylene	Fe ⁰ has been synthesized from Fe ³⁺ precursor in alginate bead via in-situ synthesis	The degradation efficiency of TCE was >99.8% within 4 h with a reported rate constant (k _{obs}) of 6.1 l per hour	[115]

(continued)

Table 2 (continued)

Polymer matrix	Nano particle	Target pollutant	Preparation method	Effectiveness	Ref.
CMC	Fe ⁰	Cr(VI)	In situ synthesis with FeSO ₄ ·7H ₂ O as a precursor	After 60 min, reported Cr(VI) degradation efficiency of Fe ⁰ nanoparticle and CMC-Fe ⁰ composite was 22 and 94%, respectively. This reduction process happened within a broad pH range	[116]
	Fe ⁰	TCE	Solvent-cast	Most effective degradation of TCE was observed when 80 mg/l TCE aqueous solution was used, increased iron zero valent nanoparticle increases dechlorination. The interdependent effect of pre-concentration of TCE by the CA was indicated	[117]
	Sodium-CMC/Fe/Pd	Para nitro chlorobenzene	FeSO ₄ ·7H ₂ O and K ₂ PdCl ₆ was used as precursors for in-situ synthesis	At a dose of 0.2 g/L, the composites removed 100% of p-NCB (C0 = 50 mg/L) within 40 min, with a pseudo-first-order the rate constant 4 times greater than that for the non-stabilized iron	[25]
Chitosan	CdS	Congo Red	Simulating bio-mineralization	85.9% of degradation rate was achieved within 180 min of irradiation for 20 mg/L CR the solution at natural pH of 6.0 in the presence of 1.5 g/L composite catalyst under simulated visible light	[117]
	Cu ⁰	Cr(VI)	Cu(SO ₄) ₂ ·5H ₂ O was used as a precursor for in-situ synthesis	Pollutant degradation was more than 99% when Cr(VI) concentration was 5 mg/l after 1 day. However, it decreases when Cr(VI) concentration increased to 50 mg/l. Cr(VI) reported value in solution degrades to 2.21 from 50 mg/l after 1 day at initial pH of 2.85	[38]

(continued)

Table 2 (continued)

Polymer matrix	Nano particle	Target pollutant	Preparation method	Effectiveness	Ref.
	Fe ⁰	Cr(VI)	Mixing in solution	In a time span of 30 min Cr(VI) has been degraded up to 82%. An increase in temperature and pH increases the degradation but decreased when increase in Cr(VI) concentration	[118]
Nafion	TiO ₂	Victoria blue R	Solution mixing	93.85 degradation after 24 h in UV radiation	[119]
Cellulose acetate	Ni/Fe	Trichloroethylene	Solvent-cast	Degradation rate constant calculated at metal mass normalization shows proportional to the Ni content between 0–14.3%. The maximum value reached was between 14.3 and 21.4% and decreased rate constant on further adding Ni content	[120]
PEG/nylon membrane	Fe ⁰	Nitrobenzene	FeSO ₄ ·7H ₂ O was used as a precursor for in-situ synthesis	68.9% of the nitrobenzene has been degraded within the first 20 min in the groundwater, and in the next 20 to 80 min, it decreases only 15% NB in groundwater	[121]

used to remove methyl orange, terephthalic acid, and potassium bromate (KBrO_3), respectively (Table 2).

2.2.5 Poly (Methyl Metha Acrylate) (PMMA)

PMMA is a brittle polymer that contains methyl metha acrylate linkage with good dimensional stability. It has various applications in the optical industry due to its good transparency and compatibility with ceramics. Table 1 demonstrates the chemical structure of PMMA. Non-toxic, easy synthesis and cheap manufacturing cost make it a suitable material for industrial application. Various nanocomposites using nanomagnetic particles have been developed by researchers with PMMA for environmental remediation [57]. PMMA coated nZV metals have been also used for environmental remediation. Nanoparticles like Au/ZnO, graphene/SnO₂, and Fe⁰ have been used with PMMA to remove contaminants like methylene blue, BPA [58], methylene blue [59], and trichloroethylene [60]. Different methods like in-situ and one-pot synthesis have been used for composite fabrication.

2.2.6 Poly (Vinylidene Fluoride) (PVDF)

Unlike other polymers, PVDF is the most favorable polymer for membrane synthesis. It can be used for micro and ultra-filtration processes for different purposes. Property wise PVDF possesses good thermal stability, chemical resistance, mechanical strength, and hydrophobicity. Membrane contactor and membrane distillation is the current use of the PVDF membranes. Significant advancements in the field of PVDF membrane synthesis for wastewater remediation have happened. However, the PVDF's hydrophobicity is still less than that of polyolefins (PP) and their derivatives (PTFE). The polymer's high mechanical strength and thermal stability can be attributed to the crystallinity and morphology of the polymer. PVDF may also show higher thermal stability than other hydrocarbon polymers due to higher electronegative lead to durable C-F bond, thereby making a further balanced structure. However, PVDF stability may show a decrease at higher reaction temperatures [61]. Previously nanoparticles of Fe₂O₃ and MWCNT have been reinforced with PVDF by the in-situ process to remove cyclohexanol acid [62]. TiO₂ with PVDF: PVP(2:1) has also been synthesized via the electrospinning process to use the composite to remove 96% of BPA within 2 h [63]. Bimetals like Fe/Pd with PVDF have been used for removing trichloroacetic acid up to 100% within 180 min [64].

2.2.7 Polyethylene (PE)

PE is one of the most common type of polymer, which comes in the category of commodity plastics, and is synthesized by the polymerization of ethylene gas. PE structure has been shown in Table 1. PE contributes to the environmental remediation

as a stabilizer encapsulation for nanoparticles. UV radiation may break its chain, and as a result, PE loses its plasticity [65]. Being easily available and economic researchers have shown interest in PE as an effective host for nanoparticles. PE/TiO₂ nanocomposite has been synthesized earlier by immobilizing TiO₂ powder on a PE sheet via hot pressing. This nanocomposite can degrade several organic dyes including methylene blue, and show suitability for treating wastewater [66].

2.2.8 Polypropylene (PP)

PP comes under the category of polyolefins like PE but exhibits higher stiffness. PP may exist in three forms based on their chirality of the methyl group such as isotactic, atactic and syndiotactic [67]. Based on the substituents' orientation -CH₃, isotactic PP have all the -CH₃ groups on the same side, random arrangement of -CH₃ in atactic PP, and alternate pattern of -CH₃ in syndiotactic PP. Like PE it suffers from the same problem as of chain scission under UV and sunlight and loses its plastic property. Compared to PE, PP exhibits higher temperature stability and has been used with TiO₂ to fabricate PP/TiO₂ nanocomposite to remove paraquat under the UV lamp [68].

2.2.9 Alginate

Many of the polymers described yet are synthetic polymers (except few degradable ones) and have been regarded as a concern to the environment. Natural polymers like alginate have attracted massive attention of the researchers. Microbial activity over some algae or microorganisms may lead to the formation of polysaccharides like alginate. Most alginates used these days for different research purposes have been produced from brown algae (Phaeophyceae) [69]. The alginate linear polymer's backbone contains mannuronic and guluronic acid linkage termed as M and G groups. Its open lattice structure provides high porosity to the polymer, ultimately suitable for encapsulation [70]. The basic application of alginate is in biomedicine, such as drug delivery, tissue engineering, wound and cut healing, and biosensor [71].

Along with molecular weight, this M and G group of the alginate plays a crucial role in deciding the physical properties of polymer. Properties like hydrophilicity, nontoxicity, biocompatibility and chelating ability make it the most suitable polymer for environmental remediation [72]. Alginate nanocomposites prepared with different nanoparticles have been listed in Table 2. The nanoparticles of zero-valent metals such as Fe⁰ solutes diffuse in the alginate matrix due to the porous nature of calcium alginate and serve to remove trichloroethylene. Also, alginate nanocomposites reinforced with nanoparticles such as TiO₂, CMC/TiO₂, and magnetic alginate/CdS/Fe₂O₃ have been used for degrading contaminants like methyl orange, congo red, and congo red again, respectively (Table 2).

2.2.10 Carboxymethyl Cellulose (CMC)

CMC is a derivative of cellulose shown in Table 1 where available primary alcohol may convert into carboxylic acid under a strong oxidizing agent. Industrially available CMC is generally applicable in the form of sodium salts known as (cellulose gum). Easily available water-soluble CMC salts are sodium (Na), potassium (K), and ammonium (NH_4). However, among all the above-mentioned salts for thickening purposes, Na salt has been widely used for many industrial applications [73]. Steric repulsive force, induced by CMC, which is larger than electrostatic repulsion, helps in the stabilization of Fe^0 nanoparticle via the carboxylic group. CMC/ Fe^0 nanocomposite [74, 75]. CMC/ Fe^0 nanocomposite has been used to successfully remove Cr (VI) and trichloroethylene from different media. In contrast, its Na salt with bimetal (Fe/Pd) has been used to degrade *p*-nitro chlorobenzene.

2.2.11 Chitosan

Another interesting biopolymer that is used for the formulation of polymeric nanocomposite used in environmental remediation is chitosan. Complete or partial deacetylation of chitin produces chitosan. Capability to share electrons via coordination bond with metals, biodegradability, and activity against microbial action and non-toxicity makes it the most superior polymeric material for contaminant degradation. Other application areas where chitosan has been used successfully are agriculture, pharmacy, and nanocomposite for environmental remediation [76]. It has also been used in fabrication and controlled releasing formulations (CRF) of the chemicals attributed to the polycationic and chelating properties of the chitosan towards various organic and inorganic compounds. The chitosan's good physico-chemical and biological properties promote the use of chitosan for environmental remediations [77]. Using bulk chitosan in water results in an insoluble system that shows relatively low biostimulant activity and further limits its application as environment remediation [36]. Table 1 mentions the details of the nanocomposites of chitosan with Fe^0 , Cu^0 , and CdS for removal of metals and various organic dyes such as Cr(VI) and congo red, respectively.

2.2.12 Other Lesser-Known Polymers

Apart from the polymers mentioned earlier, some of the other less known polymers used in the preparation of nanocomposites for environmental remediation are cellulose acetate, nafion, nylon, etc. Nanocomposites such as Nafion/ TiO_2 to remove victoria blue R, cellulose acetate/Ni/Fe for degrading trichloroethylene, and PEG/nylon membrane to remove nitrobenzene are some of the exciting examples for the removal of various contaminants (Table 2).

3 Fabrication of Polymer Nanocomposites

The formation process, polymer nanocomposite, can be categorized into two major sections; direct compounding and in situ synthesis, as shown in Fig. 1.

3.1 Direct Compounding/Blending/Mixing

On an industrial scale, the direct mixing of the nanoparticles with polymer resin has been used extensively. Due to ease and convenience, this fabrication process is economical and sustainable for production. Reinforcing nanomaterials are prepared separately and then incorporated in the resin with the help of solution evaporation [30], fusion [79], co-precipitation [30], hydrothermal [30], and injection moulding [80]. However, these processes have several disadvantages, including poor dispersion of the nanoparticles within the polymer. Nanoparticles tend to make larger aggregates limiting their advantage of larger surface area when mixing or blending with any polymers or resins. Another disadvantage of using nanocomposite for environmental remediation is the degradation of the base polymer itself. Also, there is a possibility of phase separation of nanoparticles from the polymer phase due to

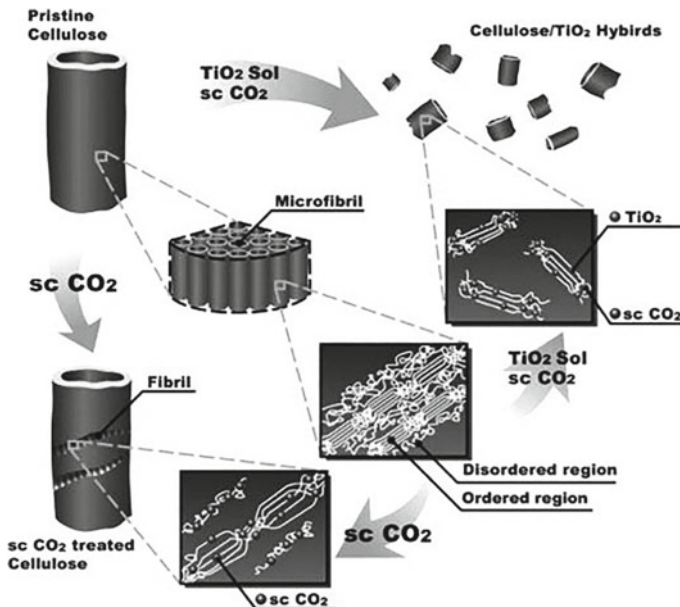


Fig. 1 Simplified exemplary for penetration of supercritical CO₂ and TiO₂ nanoparticles into cellulose matrix. Used with permission from the Elsevier reference [78]

poor compatibility. To avoid the problem mentioned earlier and make good dispersion of the nanoparticles into the polymer, a coupling agent and surface treatment of the nanoparticles has been endorsed [81, 82]. Temperature, melt rheology, time, and shear forces of the reactor also decide the nanoparticles' good dispersion into the polymer matrices [83, 84]. Figure 1 is the illustration of the impregnation of nanoparticles into the cellulose matrix.

3.2 *In-situ* Synthesis

For preparing polymer nanocomposite, required nanoparticles, for example, metal sulphide or halide, could be readily preloaded into the polymeric state using the *in-situ* process. These are categorized into three types depending upon precursor and monomer of both the polymer nanocomposite constituents. An illustration of the *in-situ* process has been given in Fig. 2, and the same is explained below.

- (1) In this method (Fig. 2(a)), the synthesis of nanoparticle from the precursor takes place within the host polymer matrix. Polymer matrix already loaded with the uniformly distributed metal ion in the form of a precursor is exposed to the corresponding liquid or gas (S^{2-} , OH^- , or Se^-) for the *in-situ* synthesis of desired nanomaterials [85–87].
- (2) This method, as depicted in Fig. 2(b), follows almost the same approach as the previous. Instead of taking the nanoparticle precursor, monomers of the

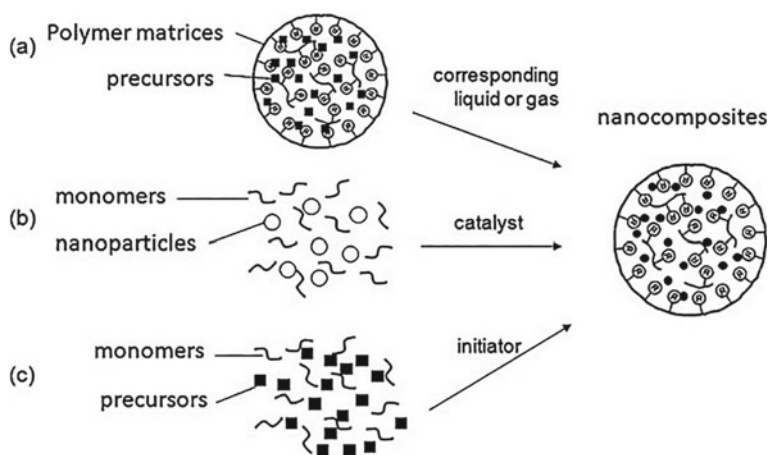


Fig. 2 Simplified model image of *in-situ* procedure of preparing polymer nanocomposites. **a** Precursor of nano-particle are precharged into the host polymer initially; **b** monomers of polymer matrix and the desired nanomaterial as the initial components; **c** both nanoparticles and polymer matrix are processed together by mixing the desired precursors of nanomaterials and the monomers of polymer adding an initiator in a suitable solvent. Used with permission from the Elsevier ref. [78]

polymer are taken along with nanoparticles. The nanoparticles are initially distributed within the host polymer monomers, and then polymerization of the composite takes place with the desired catalytic condition [88–90]. The physical and mechanical properties can be altered and accurately controlled with the help of this method.

- (3) In the method depicted in Fig. 2(c), both the polymer and targeted nanoparticles are synthesized simultaneously using the precursor of the nanoparticle and monomers of the polymer together with desired conditions [91–94]. Hence, the preparation of nanoparticles, as well as polymerization of host resin, co-occurs.

3.3 Other Methods

Other than the direct compounding and in-situ synthesis process, the scientist also tried template synthesis, self-assembly [95, 96], phase separation, and electrospinning [97, 98] upon their needs. A nanomaterial filler can be used as a filler in the tubules or shapes of the desired materials' porous template [99, 100]. Phase separation consists of dissolution, gelation, and extraction using different solvents and freezing or drying results in nano-scale porous foam [101, 102]. A schematic representation of the electrospinning process has been given in Fig. 3.

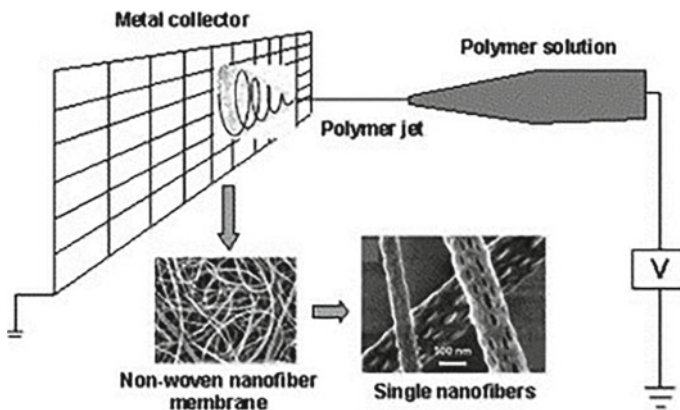


Fig. 3 Schematic diagram to show polymer nanofibers by electrospinning, Used with the permission from Elsevier ref. [98]

4 Catalytic Degradation Techniques for Environmental Remediation

Polymer nanocomposites play an essential role in reducing pollutant from different media like water and industrial effluents. Nanoparticles present in polymer nanocomposite destroy the target pollutant through catalytic degradation and adsorption. Our environment can be protected from different contaminants with the help of polymer nanocomposite since it can sense and detect the pollutant even at trace level. Based on their chemical activity and functionality, environmental remediation can be divided into 4 basic types (i) Catalytic and redox degradation (ii) Adsorption of the pollutant (iii) Pollutant sensing and detection (iv) Green chemistry. However, this chapter is concisely limited to focus on remediation via catalytic degradation.

Catalytic degradation is a process where a pollutant is decomposed into harmless components via chemical degradation with the action of a catalyst. Based on their catalytic and chemical activity, such modes of degradation have been divided into ten types that are discussed under Sect. 4.1 to 4.10. Some of the relevant examples of using specific polymers and nanoparticles for environmental remediation via catalytic degradation are detailed in Table 2.

4.1 *Ozone/UV Radiation/H₂O₂ Oxidation*

This method uses oxidation and photolysis routes collectively to remove the foreign contaminants present in the wastewater. This method helps in the degradation of individual pollutants and enhances the biodegradability of industrial wastewater. In this process, along with UV radiation, ozone and hydrogen peroxide were used, which directly degrades the pollutant from the water by oxidation mechanism, and hydroxyl free radicals are generated through in situ process. The most extensive standard redox potential of the hydroxyl radicals can rapidly react with common water contaminants like phenols and pesticides and destruct the pollutant by reacting with contaminants present in water and air [122, 123] (Fig. 4).

4.2 *Photocatalytic Degradation*

As the term implies, this process uses photocatalytic degradation using semiconductor photocatalysts and involves a photon and a catalyst. In any material, either conductor, semiconductors, or insulator presence of different energy levels has been found. These energy levels result due to the electronic movement of electrons and their presence in the atom. Similarly, in crystals, these bands split into many bands that are very close to each other and are divided into valence and conduction bands

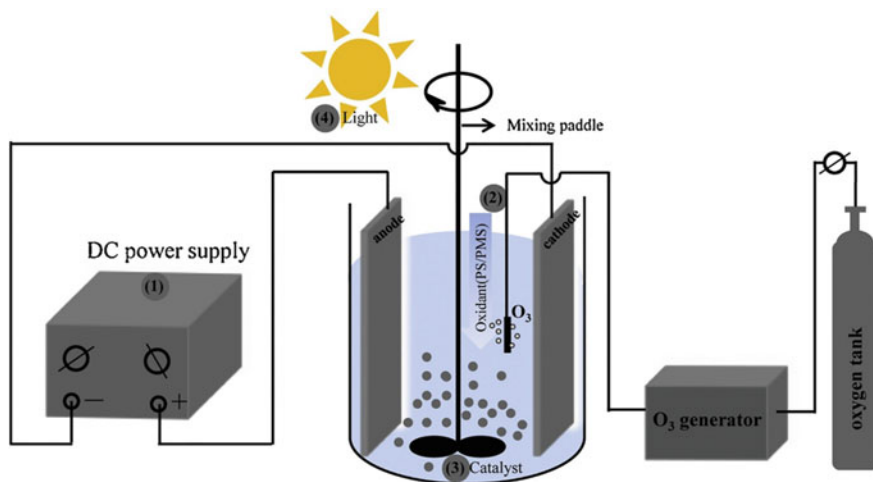
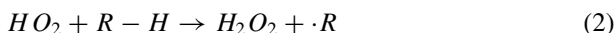
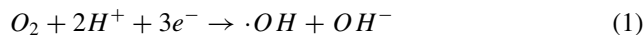


Fig. 4 Scheme of the (photo)electro-oxidants system used for organic compounds degradation [149]. Used with permission from Elsevier

depending upon their energy levels. A material where the conduction band is half-filled or requires very little energy to jump an electron from the valence band to the conduction band is known as a conductor. Whereas, for semiconductors and insulators, an electron needs high energy to jump from valence band to conduction band at least at 0 K. Chemistry of different reactions occurring at the photo-excited surface semiconductor is based on the radicals generated from the O₂, H₂O, and electron-rich organic compounds. Similarly, cations in the solution can also be directly reduced by the conduction band electron if the redox potential is less than the conduction band energy [123]. Generation of ·OH by the reduction of O₂ can be illustrated through 1 and 2.



Where, R-H stands for an organic species with a liable H atom; however, the reaction could have also been complete with H atom abstraction from R-H by the OH radical.

Based on their chemical activity, the photocatalytic activity occurring in the adsorbed phase and happens in five steps-

- (i) Transfer of the reactant on the catalyst surface from the fluid phase.
- (ii) Adsorption of the reactants
- (iii) A reaction in the adsorbed phase.
- (iv) The desorption of the products
- (v) Removal of the products from the interfacial region (Fig. 5).

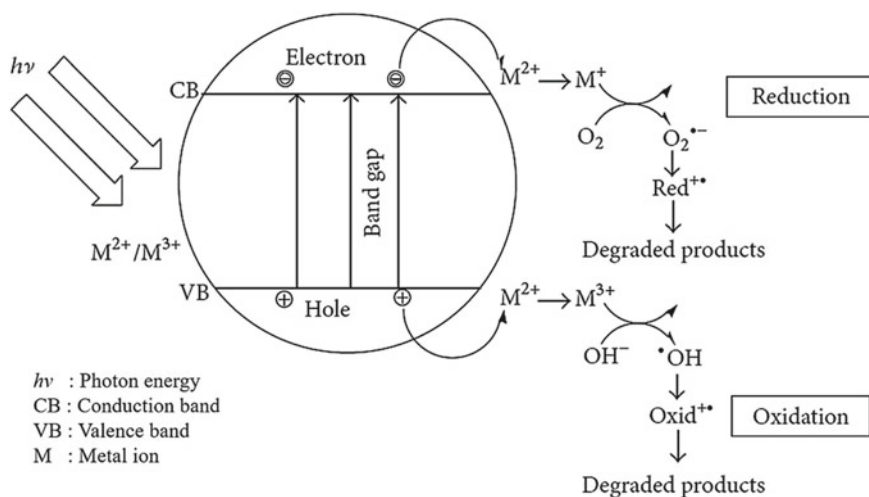


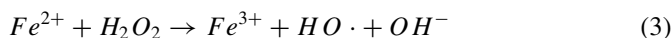
Fig. 5 Activation and degradation process of pollutant via semiconductors under sunlight [124]. Used with permission from Elsevier

4.3 Supercritical Water Oxidation

In this method, wastewater and oxygen are heated and pressurized in a reactor above the critical point (374 °C, 218 atm) of the water. Above mentioned condition is suitable for the increment of the organic solubility and reduction in the inorganic solubility of the water. Thus, at this high-pressure media, rheology changes and gives gas-like properties, thereby ultimately increasing the mass transfer properties. This high pressure and generation of a single-phase for both oxygen and organics pulls them in contact, and thus, organics (pollutant) get oxidized rapidly. More than 99.99% of the organic pollutants have been degraded by supercritical water oxidation at 400–650 °C and 255 atm (Fig. 6).

4.4 The Fenton Method

The Fenton method uses the Fenton reagent, the mixture of Fe (II) and hydrogen peroxide. Generation of hydroxyl free radicals takes place by the following reaction (Eq. 3), precisely termed as Fenton reaction (Fig. 7)-



Many reactions take place through the Fenton method for removing pollutants. However, the primary reaction involves the generation of HO· free radicals, capable of oxidizing a wide array of contaminants [123, 125].

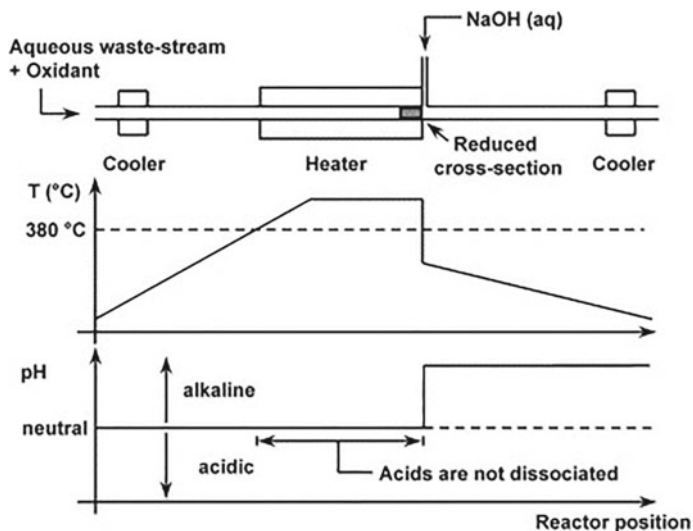


Fig. 6 Modified SCWO process with quenching the supercritical reaction mixture [150]. Used with the permission from Elsevier

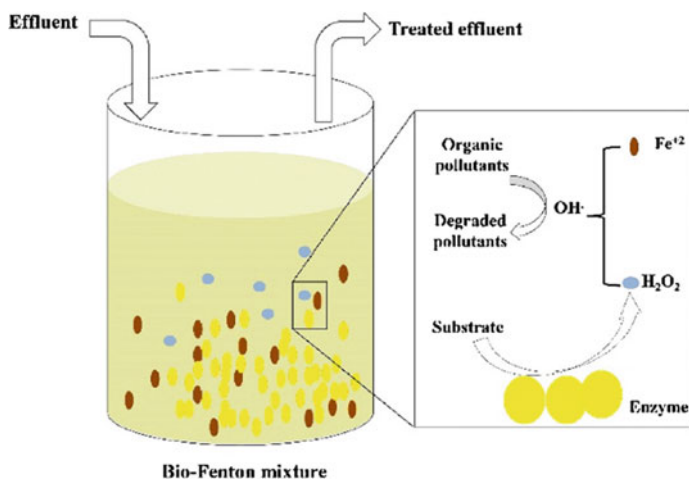


Fig. 7 Schematic of a Bio-Fenton process [151]. Used with the permission from Elsevier

4.5 Sonochemical Degradation

Insertion of mechanical effect due to the sonication which enhances the heterogeneous reaction in the fluid system. This effect provides more surface area among reactants, a rapid restoration of catalysts, and dissolution and mixing. Being different from other degradation methods, it helps in accelerated and environmentally secured

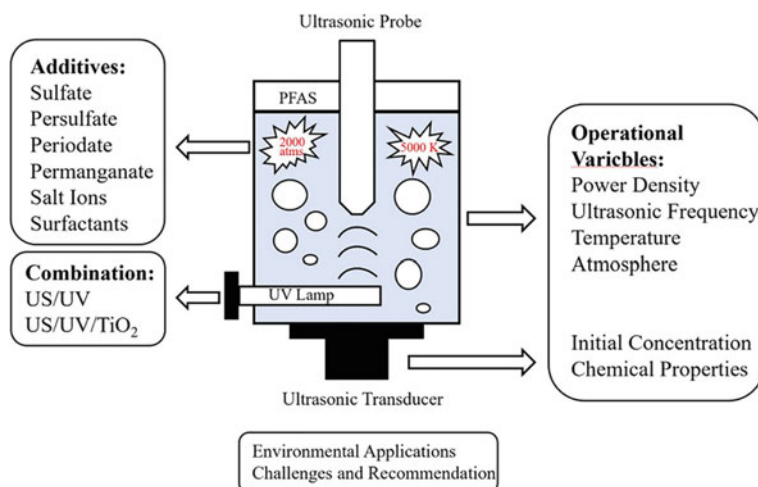


Fig. 8 A schematic of ultrasonic degradation of pollutants [152]. Used with the permission from Elsevier

deterioration of the pollutants. Chemistry of sonochemical degradation of CCl_4 yields $\cdot\text{Cl}$ and $\cdot\text{CCl}$ initial transitional radicals where its thermolysis of CCl_4 occurs into unique, high-temperature gaseous cavitation bubbles. These radicals further react with $\text{HO}\cdot$ or O_2 radicals to give further relatively more environment-friendly final products such as HOCl , HCl , CO_2 , and Cl_2 [123, 126, 127] (Fig. 8).

4.6 The Electrochemical Method

Electrochemical treatments involve two types of processes depending upon pollutant reaction media (i) Direct and (ii) Indirect. Direct electrochemical treatment involves cathodic reduction and anodic oxidation (Fig. 9(a)), where the reaction of the pollutant at the electrode surface occurs due to the presence of $\text{HO}\cdot$ produced from water oxidation at a high O^{2-} overpotential anode. The indirect method uses a solution where a cationic species (B^+) reacts with the pollutant, as shown in Fig. 9(b). The irreversible B^+ has been produced from the oxidation of B at the anode. These B compounds could be Cl , ClO_2 , O_3 , etc. [123, 128].

4.7 The Electron Beam Process

It is already explained about the oxidative nature of $\text{HO}\cdot$ free radicals towards pollutants. Hence, for water treatment, an effective method is to ionize the water with

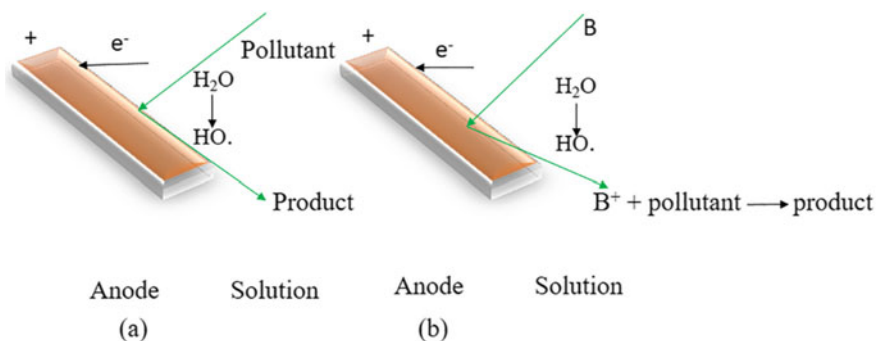
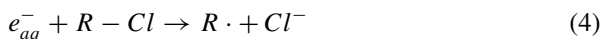


Fig. 9 Electrochemical chemical treatments of contaminants via **a** Direct electrolysis **b** Indirect electrolysis

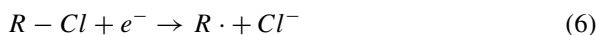
radiation (electronic beams) [123, 130]. In the presence of such radiations, reducing and oxidizing agents present in ionized water can degrade or destroy any pollutants present in the water. For reliable and safe e-beams, machine-generated e-beams has been used on a process size scale. The number of electrons, beam size, and energy of the beams each can be controlled by the machine. A generalized equation can be given as for treating halogenated organic pollutants is mentioned below-



This e_{aq}^- species have been used for to de-halogenation of the organic compounds having halogen groups (Fig. 10).

4.8 Solvated Electron Reduction

In this method, a deep blue solution is formed by dissolving alkali and alkaline earth metals (group I-Na, K and group II-Ca, Li, etc.) in the ammonia. Such solutions have been used for reducing many pollutants, including chloro organic compounds [123, 131, 132]. For example, electropositive potassium gives one electron to chloro organic compound, which converted to hydrocarbon and released a less toxic chlorine ion, as shown in Eqs. 5 and 6 (Fig. 11).



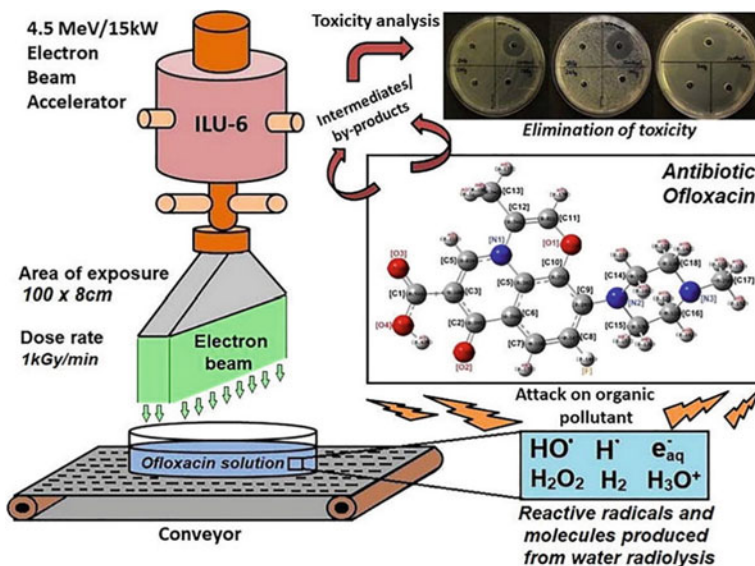


Fig. 10 Illustration of electron beam induced catalytic degradation process of pollutant [153]. Used with the permission from Elsevier

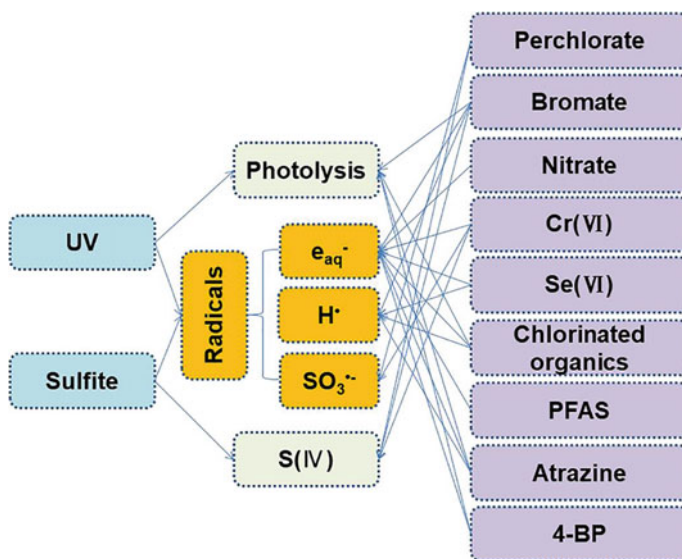


Fig. 11 The crucial roles of various radicals and mechanisms during the degradation of selected contaminants using UV/SO₃²⁻ advanced solvated electron reduction processes [154]. Used with the permission from Elsevier

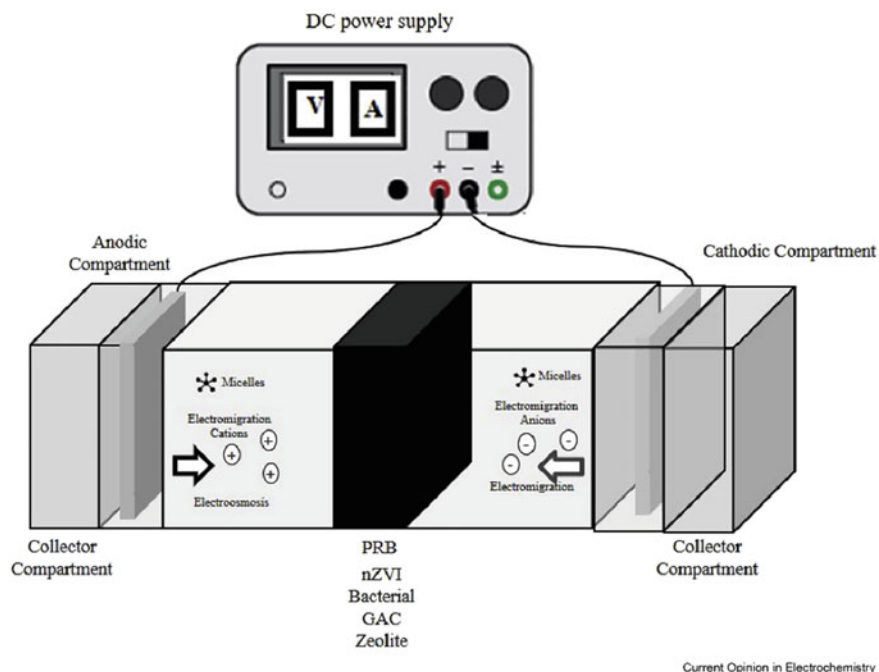


Fig. 12 Schematic diagram of coupled EK–PRB for soil remediation. **PRB**: permeable reactive barrier; **EK**: electrokinetic [155]. Used with the permission from Elsevier

4.9 Permeable Reactive Barriers (PRB) of Iron and Other Zero-Valent Metals

This technique of decontamination involves physical contact between contaminants and reactive barriers. Likewise, zero-valent metals, PRBs also need physical removal of contaminants from the solutions using adsorption, reduction, co-precipitation, pore diffusion, and polymerization [123]. Figure 12 shows an illustration of coupled EK–PRB for soil remediation.

4.10 Enzymatic Treatment Methods

Enzymatic degradation of the contaminants involves catalysis of a pollutant that resist or create problems in degradation. Such catalytic degradations can be performed over the toxic pollutants that are toxic to microbes. Some enzymes can also perform a wide range of temperatures, pH values, and salinity ranges compared to cultured microorganisms and are not be affected by the concentration of the pollutant, which can inactivate the microbial cells [123, 133] (Fig. 13).

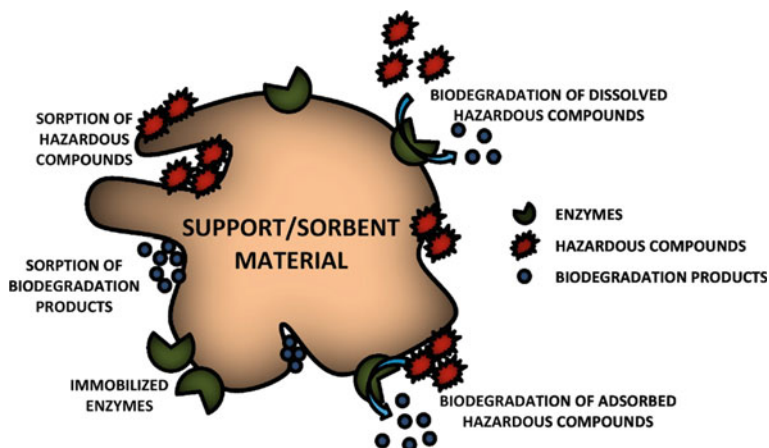


Fig. 13 Schematic diagram of simultaneous enzyme immobilization and sorption/biodegradation processes of environmental pollutants [156]. Used with the permission from Elsevier

5 Need for Polymer Nanocomposite for Environmental Remediation

The use of nano-particles for any application may pose some risk to human health and eco-system due to the release of nano-particles into the environment. There has also been a limit to reuse and difficulty in the separation of nanoparticles. Hence, using only an aqueous solution of the nanoparticle limits separation and recyclability and so their wide applications. Immobilization of different nanoparticles on the polymer surface has helped resolve this issue. Porous resins, ion-exchange, and polymeric membrane have been effectively used for this purpose [134, 135]. Polymer host helps in preventing particle loss, agglomeration, and application in convective flow occurring by free-standing particles. Researchers have reported many host materials for reinforcing purposes, such as- cellulose, silica, sand, and polymers. Host materials must have good mechanical strength for long time use. Choice of host polymer depends on their mechanical and thermal behavior, hydrophobic or hydrophilic, bio-compatibility, optical or electronic, chemical functionalities, and the pollutant requirement to be degraded [136]. Table 2 summarizes some of the polymer nanocomposites used for environmental remediation. For redox degradation of pollutants common nanosize semiconductors (TiO_2 , ZnO , CdS), zero valence metals (Fe^0 , Cu^0 , Zn^0) and bimetallic particles (Fe/Pd , Fe/Ni , Fe/Al and Zn/Pd) are used. Pollutants like biphenyls, dyes, aliphatics pesticides, herbicides, and nitroaromatics can be destroyed by the above-mentioned nano-particles [136–140].

Also, TiO_2 has been used extensively in removing a wide range of pollutants [30]. Illumination with the visible light promotes one electron to move from valence band to conduction band and leaving a hole in the valence band, and insertion of highly reducing and the oxidizing agent takes during the reaction. Hence, the need

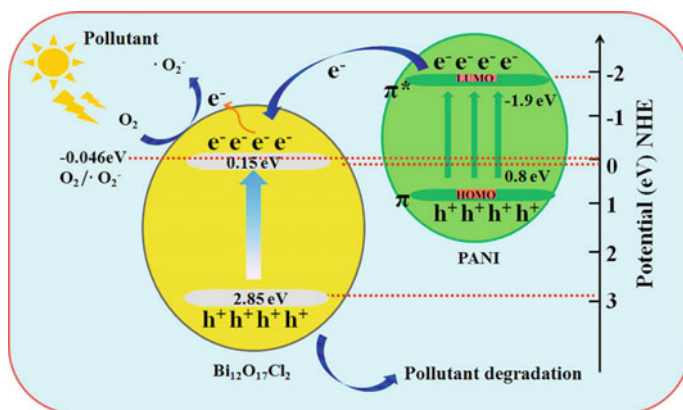


Fig. 14 Schematic diagram for photocatalysis of contaminants by PANI/ $\text{Bi}_{12}\text{O}_{17}\text{Cl}_{12}$ composites. Used with permission from Elsevier ref. [142]

for an antioxidative substrate or polymer must resolve illumination with the visible light. Some of the common examples of the substrates are PDMS, PVP, PE, PP, poly (3-hexylthiophene) (P3HT), PANI, poly (tetrafluoroethene), and neffion.

PANI-supported-bismuth oxyhalide composite has been used for removing ciprofloxacin (CIP) and RhB. However, it has been observed when a composite based on $\text{Bi}_{12}\text{O}_{17}\text{Cl}_{12}$ and PANI was used, CIP and RhB removal increased 3 and 1.5 times, respectively, compared to pristine $\text{Bi}_{12}\text{O}_{17}\text{Cl}_{12}$ [30]. The reason behind increased degradation is the extension in light response range and visible light degradation performance of the pollutants. Also, 1-naphthylamine (PNA)/ TiO_2 shows improved methyl blue degradation under visible light illumination [141]. This high rate of photo-degradation is attributed to the efficient charge separation of the electron (e^-) and hole (h^+) pair at the interface of PNA and TiO_2 . This is because the PNA extends the visible light response range, and hence, light-driven photo-degradation of the MB occurs. The proposed mechanism of PANI/ $\text{Bi}_{12}\text{O}_{17}\text{Cl}_{12}$ has been given in Fig. 14.

Literature indicates other pollutants such as chlorinated methanes, brominated methanes, trihalomethanes, chlorinated ethenes, chlorinated benzenes, polychlorinated hydrocarbons, pesticides, and dyes can be degraded using zero valence metals and bimetals. Zero valence metals Fe, Cu, Zn, and bimetals Pd/Fe, Ni/Fe, Zn/Pd have already been used for degrading these pollutants. However, to protect their chemical essence and inhibit oxidation as far as they interact with contaminants, a host polymer must be added.

Cation exchange resin has been used as a matrix to reinforce zero-valent copper [141]. This composite has been used to remove carbon tetrachloride (CCl_4) from the water. Host polymer helped maintain the increased surface area of the Cu^0 by inhibiting the nanoparticles' agglomeration. Host polymer helped in the recycling of the Cu^0 nanoparticle by neutralizing copper ion originated from the interaction among CCl_4 and Cu^0 and decreased the CCl_4 by sorption. In this reaction pseudo

first order was normalized by the surface area, and mass concentration was almost 20 times more than powdered zero valence copper.

A composite with CMC and bimetals Fe/Pd nanoparticles has been reported. It has been observed that the chemical reactivity, aggregation, and soil transportability has been decreased in the composite compared to pristine Fe/Pd nanoparticles. Initial pseudo-first-order reaction constant confirms that pollutant trichloroethene degraded 17times faster by CMC stabilized Fe/Pd composite than pristine Fe/Pd [25].

Biocatalytic Nanocomposite

Enzymes and catalytic antibodies are natural nanoreactors to the specific and targeted pollutants. Due to their environmental benign, they could have been a more attractive choice than the synthetic catalyst. However, their short life and sensitivity towards pH, temperature, and other chemical and mechanical factors, prevent their wide application in the industries. To reuse, increase lifetime, and reduce the amount of enzymes used the stability of the enzymes must be increased. Researches have reported immobilization, modification, and genetic modification of the enzymes to increase their stability and widen the application. Enzyme immobilization by loading or entrapping into a natural or synthetic polymer (polysaccharides, polyacrylamides, alginates, resins, chitosan, etc.) is the most successful approach [18–20, 143–146]. Tripathi et al. [144] used amber lite MB 150 and chitosan beads to immobilize α -amylase from mung beans. It was observed that the activity loss for free amylase was ~70% after 100 days at 4 °C. Amylases immobilized with amberlite and chitosan show an activity loss of 45 and 55%, respectively, under the same laboratory conditions. Also, polymer-based amylases performed residual activity of 43 and 27% even after ten uses.

Protecting enzymes from the environment helped minimize the effect of gas bubbles, mechanical shear, and hydrophobic solvents with enzyme entrapment. However, low enzyme loading and mass transfer limitation was the biggest drawback for this method. However, the invention of enzyme stabilization methods like single

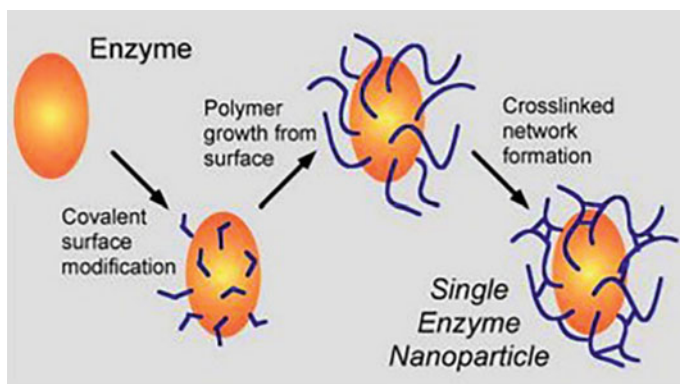


Fig. 15 Schematic of single enzyme nanoparticle polymer composites. Used with permission from Elsevier ref. [78]

enzyme nanoparticles [147, 148] resolved the issue. The Schematic for the process, as mentioned earlier, has been given in Fig. 15.

6 Conclusion and Perspective

For a safe and hazard-free environment, industrial pollutants need to be controlled and disposed of in the least possible toxic form. Many methods have been invented to resolve the issue and destroy the pollutant while forming the least toxic products. The use of nanomaterials in environmental remediation can drastically and positively alter the results. The presence of larger surface areas and more reactive nanomaterials sites makes them the most suitable remedial pollutants. Nanomaterials such as nano-particles, nano-fibres, nano-tubes, and polymeric nanocomposites are widely used for the removal of contaminants from different environments. Organic pollutants such as halogenated alkanes, brominated methane, other polychlorinated hydrocarbons, pesticides, and dyes can be degraded by nanomaterials such as zero valence metals Fe, Cu, Zn and bimetals like Fe/Pd, Fe/Ni and Pd/Zn, etc. Likewise, nano-semiconductors such as ZnO, CdS, and WO₃, also serve as catalysts for the selective degradation of targeted pollutants. Photo- and chemical degradation process that targets and degrades both organic and inorganic pollutants is the need of the hour. The biggest disadvantage of nanomaterials is agglomeration, mobilization, instability, and high reactivity to environmental gases. Also, applications involving polymer nanocomposites require the matrix to be highly antioxidant during illumination by the UV light for the production of highly reducing and oxidizing agents to eliminate environmental pollutants. Hence, the use of a host matrix has been introduced, and from there, an active role of polymer nanocomposite came into the focus. Numerous polymer nanocomposites are already available in the market, but the cost is still an issue. Researchers are looking for more efficient and cost-effective polymer nanocomposites for environmental remediation purposes. The use of thermoplastic polymer as a matrix also has a disposable problem since they are non-biodegradable. Hence, researchers are looking for an environment-friendly option for both of them. Similarly, no studies have been found on the recyclability of the polymer nanocomposite, which is still a hot topic for research. It is also important to study the interfacial adhesion between encapsulated nanoparticles and host matrix and its effect on polymer nanocomposite's application performance. Furthermore, the role of the host polymer in the dispersion and distribution of the nanoparticles in the composite must be studied more precisely to control the effectiveness and cost of the polymer nanocomposite. Most of the polymer nanocomposites reported are still on a laboratory scale of evaluation, and to scale them up for industrial use, and their aforementioned inherent drawbacks must be eliminated.

References

1. Náráy-Szabó, G., Mika, L.T.: Conservative evolution and industrial metabolism in Green Chemistry. *Green. Chem.* **20**(10), 2171–2191 (2018)
2. Fu, F., Wang, Q.: Removal of heavy metal ions from wastewaters: a review. *J. Environ. Manage.* **92**(3), 407–418 (2011)
3. Wang, Y.H., Lin, S.H., Juang, R.S.: Removal of heavy metal ions from aqueous solutions using various low-cost adsorbents. *J. Hazard. Mater.* **102**(2–3), 291–302 (2003)
4. O’Connell, D.W., Birkinshaw, C., O’Dwyer, T.F.: Heavy metal adsorbents prepared from the modification of cellulose: a review. *Bioresour. Technol.* **99**(15), 6709–6724 (2008)
5. Khare, P., Kumar Patel, R., Shankar, R.: Recent Developments in Nanocarbon-Polymer Composites for Environmental and Energy Applications. *IntechOpen* (2019). <https://doi.org/10.5772/INTECHOPEN.85626>
6. Abdelbasir, S.M., Shalan, A.E.: An overview of nanomaterials for industrial wastewater treatment. *Korean J. Chem. Eng.* **36**, 1209–1225 (2019)
7. Batool, M., Nazar, M.F., Awan, A., et al.: Bismuth-based heterojunction nanocomposites for photocatalysis and heavy metal detection applications. *Nano-struct. Nano-objects* **27**, 100762 (2021)
8. Abdel Messih, M.F., Shalan, A.E., Sanad, M.F., Ahmed, M.A.: Facile approach to prepare ZnO@SiO₂ nanomaterials for photocatalytic degradation of some organic pollutant models. *J. Mater. Sci. Mater. Electron.* **30**, 14291–14299 (2019)
9. Morshed, M.N., Bouazizi, N., Behary, N., Guan, J., Nierstrasz, V.: Stabilization of zero valent iron (Fe₀) on plasma/dendrimer functionalized polyester fabrics for Fenton-like removal of hazardous water pollutants. *Chem. Eng. J.* **374**, 658–673 (2019)
10. Lumbaqué, E.C., Tiburtius, E.R.L., Barreto-Rodrigues, M., Sirtori, C.: Current trends in the use of zero-valent iron (Fe₀) for degradation of pharmaceuticals present in different water matrices. *Trends Environ. Anal. Chem.* **24**, e00069 (2019)
11. Xiong, Z., Zhao, D., Pan, G.: Rapid and complete destruction of perchlorate in water and ion-exchange brine using stabilized zero-valent iron nanoparticles. *Water Res.* **41**(15), 3497–3505 (2007)
12. Han, Y., Li, W., Zhang, M., Tao, K.: Catalytic dechlorination of monochlorobenzene with a new type of nanoscale Ni(B)/Fe(B) bimetallic catalytic reductant. *Chemosphere* **72**(1), 53–58 (2008)
13. Zhu, N., Luan, H., Yuan, S., Chen, J., Wu, X., Wang, L.: Effective dechlorination of HCB by nanoscale Cu/Fe particles. *J. Hazard. Mater.* **176**(1–3), 1101–1105 (2010)
14. Barhoum, A., et al.: A broad family of carbon nanomaterials: classification, properties, synthesis, and emerging applications. In: Barhoum, A., Bechelany, M., Makhlof, A. (eds.) *Handbook of Nanofibers*, pp 1–40. Springer, Cham (2019). https://doi.org/10.1007/978-3-319-42789-8_59-1
15. Cumbal, L., Sengupta, A.K.: Arsenic removal using polymer-supported hydrated iron(III) oxide nanoparticles: role of Donnan membrane effect. *Environ. Sci. Technol.* **39**(17), 6508–6515 (2005)
16. Zouboulis, A.I., Katsoyiannis, I.A.: Arsenic removal using iron oxide loaded alginate beads. *Ind. Eng. Chem. Res.* **41**(24), 6149–6155 (2002)
17. Sylvester, P., Westerhoff, P., Möller, T., Badruzzaman, M., Boyd, O.: A hybrid sorbent utilizing nanoparticles of hydrous iron oxide for arsenic removal from drinking water. *Environ. Eng. Sci.* **24**(1), 104–112 (2007)
18. Jordan, B.J., Hong, R., Gider, B., Hill, J., Emrick, T., Rotello, V.M.: Stabilization of α -chymotrypsin at air-water interface through surface binding to gold nanoparticle scaffolds. *Soft Matter* **2**(7), 558–560 (2006)
19. Chico, B., et al.: Polyelectrostatic immobilization of gold nanoparticles-modified peroxidase on alginate-coated gold electrode for mediatorless biosensor construction. *J. Electroanal. Chem.* **629**(1–2), 126–132 (2009)

20. Tang, Z.X., Qian, J.Q., Shi, L.E.: Characterizations of immobilized neutral proteinase on chitosan nano-particles. *Process Biochem.* **41**(5), 1193–1197 (2006)
21. Fahmy, H.M., Mosleh, A.M., Elghany, A.A., et al.: Coated silver nanoparticles: synthesis, cytotoxicity, and optical properties. *RSC Adv.* **9**, 20118–20136 (2019)
22. Taheri-Ledari, R., Rahimi, J., Maleki, A., Shalan, A.E.: Ultrasound-assisted diversion of nitrobenzene derivatives to their aniline equivalents through a heterogeneous magnetic Ag/Fe₃O₄-IT nanocomposite catalyst. *New J. Chem.* **44**, 19827–19835 (2020)
23. Shalan, A.E., Afifi, M., El-Desoky, M.M., Ahmed, M.K.: Electrospun nanofibrous membranes of cellulose acetate containing hydroxyapatite co-doped with Ag/Fe: morphological features, antibacterial activity and degradation of methylene blue in aqueous solution. *New J. Chem.* **45**, 9212–9220 (2021)
24. Wang, J., Liu, M., Duan, C., Sun, J., Xu, Y.: Preparation and characterization of cellulose-based adsorbent and its application in heavy metal ions removal. *Carbohydr. Polym.* **206**, 837–843 (2019)
25. Dong, T., Luo, H., Wang, Y., Hu, B., Chen, H.: Stabilization of Fe-Pd bimetallic nanoparticles with sodium carboxymethyl cellulose for catalytic reduction of para-nitrochlorobenzene in water. *Desalination* **271**(1–3), 11–19 (2011)
26. Alshabanat, M.N., Al-Anazy, M.M.: An experimental study of photocatalytic degradation of Congo red using polymer nanocomposite films. *J. Chem.* **11**, 1–8 (2018). <https://doi.org/10.1155/2018/9651850>
27. Alizadeh, B., Delnavaz, M., Shakeri, A.: Removal of Cd(II) and phenol using novel cross-linked magnetic EDTA/chitosan/TiO₂ nanocomposite. *Carbohydr. Polym.* **181**, 675–683 (2018)
28. Nguyen, T.D., Dang, C.H., Mai, D.T.: Biosynthesized AgNP capped on novel nanocomposite 2-hydroxypropyl-β-cyclodextrin/alginate as a catalyst for degradation of pollutants. *Carbohydr. Polym.* **197**, 29–37 (2018)
29. Mohamed, S.K., Hegazy, S.H., Abdelwahab, N.A., Ramadan, A.M.: Coupled adsorption-photocatalytic degradation of crystal violet under sunlight using chemically synthesized grafted sodium alginate/ZnO/graphene oxide composite. *Int. J. Biol. Macromol.* **108**, 1185–1198 (2018)
30. Lee, S., Chang, C.-J.: Recent developments about conductive polymer based composite photocatalysts. *Polymers (Basel)* **11**(2), 206 (2019)
31. Carević, M.V., et al.: Properties of Zirconia/Polyaniline hybrid nanocomposites and their application as photocatalysts for degradation of model pollutants. *Mater. Chem. Phys.* **205**, 130–137 (2018)
32. Selvin, S.S.P., et al.: Photocatalytic degradation of Rhodamine B using zinc oxide activated charcoal polyaniline nanocomposite and its survival assessment using aquatic animal model. *ACS Sustain. Chem. Eng.* **6**(1), 258–267 (2018)
33. Krehula, L.K., et al.: Conducting polymer polypyrrole and titanium dioxide nanocomposites for photocatalysis of RR45 dye under visible light. *Polym. Bull.* **76**(4), 1697–1715 (2019)
34. Liu, X., Cai, L.: Novel indirect Z-scheme photocatalyst of Ag nanoparticles and polymer polypyrrole co-modified BiOBr for photocatalytic decomposition of organic pollutants. *Appl. Surf. Sci.* **445**, 242–254 (2018)
35. Ucanus, G., Ercan, M., Uzunoglu, D., Culha, M.: Methods for preparation of nanocomposites in environmental remediation. In: *New Polymer Nanocomposites for Environmental Remediation*, pp. 1–28. Elsevier (2018)
36. Saharan, V., Pal, A.: *Chitosan Based Nanomaterials in Plant Growth and Protection*. Springer, New Delhi (2016). <https://doi.org/10.1007/978-81-322-3601-6>
37. Lin, C.J., Lo, S.L., Liou, Y.H.: Degradation of aqueous carbon tetrachloride by nanoscale zerovalent copper on a cation resin. *Chemosphere* **59**(9), 1299–1307 (2005)
38. Wu, S.J., Liou, T.H., Mi, F.L.: Synthesis of zero-valent copper-chitosan nanocomposites and their application for treatment of hexavalent chromium. *Bioresour. Technol.* **100**(19), 4348–4353 (2009)

39. Wang, X., Han, M., Bao, J., Tu, W., Dai, Z.: A superoxide anion biosensor based on direct electron transfer of superoxide dismutase on sodium alginate sol-gel film and its application to monitoring of living cells. *Anal. Chim. Acta.* **717**, 61–66 (2012)
40. Bowers, M.J., McBride, J.R., Rosenthal, S.J.: White-light emission from magic-sized cadmium selenide nanocrystals. *J. Am. Chem. Soc.* **127**(44), 15378–15379 (2005)
41. Rengaraj, S., et al.: CdS microspheres composed of nanocrystals and their photocatalytic activity. *J. Nanosci. Nanotechnol.* **11**(10), 2090–2099 (2011)
42. Selvaraj, R., Al-Kindy, S.M.Z., Silanpaa, M., Kim, Y.: Nanotechnology in environmental remediation: degradation of volatile organic compounds (VOCs) over visible-light-active nanostructured materials. *Rev. Environ. Health* **29**(1–2), 109–112 (2014)
43. Zhu, M., Wang, X., Yang, J., Liu, H., Ma, J.: Study on the physicochemical properties of poly(methylmethacrylate) (PMMA) modified Pd/Fe nanocomposites: roles of PMMA and PMMA/ethanol. *Appl. Surf. Sci.* **282**, 851–861 (2013)
44. Sotomayor, P.T., Raimundo, I.M., Zarbin, A.J.G., Rohwedder, J.J.R., Neto, G.O., Alves, O.L.: Construction and evaluation of an optical pH sensor based on polyaniline-porous Vycor glass nanocomposite. *Sens. Actuators B Chem.* **74**(1–3), 157–162 (2001)
45. Ogoshi, T., Hasegawa, Y., Aoki, T., Ishimori, Y., Inagi, S., Yamagishi, T.A.: Reduction of emeraldine base form of polyaniline by pillar[5]arene based on formation of poly(pseudorotaxane) structure. *Macromolecules* **44**(19), 7639–7644 (2011)
46. Guo, X., Tao Fei, G., Su, H., De Zhang, L.: High-performance and reproducible polyaniline nanowire/tubes for removal of Cr(VI) in aqueous solution. *J. Phys. Chem. C* **115**(5), 1608–1613 (2011)
47. Samani, M., Borghei, S., Olad, A., Chaichi, M.: Removal of chromium from aqueous solution using polyaniline–poly ethylene glycol composite. *J. Hazard. Mater.* **184**(1–3), 248–254 (2010)
48. Kumar, P., Chakraborty, S., Ray, M.: Removal and recovery of chromium from wastewater using short chain polyaniline synthesized on jute fiber. *Chem. Eng. J.* **141**(1–3), 130–140 (2008)
49. Doyle, C., Tanner, E., Bonfield, W.: In vitro and in vivo evaluation of polyhydroxybutyrate and of polyhydroxybutyrate reinforced with hydroxyapatite. *Biomaterials* **12**(9), 841–847 (1991)
50. Yew, S.P., Tang, H.Y., Sudesh, K.: Photocatalytic activity and biodegradation of polyhydroxybutyrate films containing titanium dioxide. *Polym. Degrad. Stab.* **91**(8), 1800–1807 (2006)
51. Choi, S.-J., et al.: A polydimethylsiloxane (PDMS) sponge for the selective absorption of oil from water. *ACS Appl. Mater. Interfaces* **3**(12), 4552–4556 (2011)
52. Gniewek, A., Trzeciak, A., Ziółkowski, J.J., Kępiński, L., Wrzyszczyk, J., Tylus, W.: Pd-PVP colloid as catalyst for Heck and carbonylation reactions: TEM and XPS studies. *J. Catal.* **229**(2), 332–343 (2005)
53. Huang, L., Peng, F., Yu, H., Wang, H.: Synthesis of Cu₂O nanoboxes, nanocubes and nanospheres by polyol process and their adsorption characteristic. *Mater. Res. Bull.* **43**(11), 3047–3053 (2008)
54. Li, D., Wang, Y., Xia, Y.: Electrospinning of polymeric and ceramic nanofibers as uniaxially aligned arrays. *Nano Lett.* **3**(8), 1167–1171 (2003)
55. Basha, M.A.F.: Spectroscopic, magnetic, and optical characterization of nanocomposite films of polyvinylpyrrolidone doped with cerium disulphate. *J. Appl. Polym. Sci.* **122**(3), 2121–2129 (2011)
56. Xu, X., Wang, Q., Choi, H.C., Kim, Y.H.: Encapsulation of iron nanoparticles with PVP nanofibrous membranes to maintain their catalytic activity. *J. Membr. Sci.* **348**(1–2), 231–237 (2010)
57. Li, S., Qin, J., Fornara, A., Toprak, M., Muhammed, M., Kim, D.K.: Synthesis and magnetic properties of bulk transparent PMMA/Fe-oxide nanocomposites. *Nanotechnology* **20**, 185607 (2009). <https://doi.org/10.1088/0957-4484/20/18/185607>
58. Campagnolo, L., Lauciello, S., Athanassiou, A., Fragouli, D.: Au/ZnO hybrid nanostructures on electrospun polymeric mats for improved photocatalytic degradation of organic pollutants. *Water* **11**(9), 1787 (2019)

59. Shanmugam, M., Alsalmeh, A., Alghamdi, A., Jayavel, R.: Photocatalytic properties of graphene-SnO₂-PMMA nanocomposite in the degradation of methylene blue dye under direct sunlight irradiation. *Mater. Exp.* **5**(4), 319–326 (2015)
60. Wang, W., Zhou, M., Jin, Z., Li, T.: Reactivity characteristics of poly(methyl methacrylate) coated nanoscale iron particles for trichloroethylene remediation. *J. Hazard. Mater.* **173**(1–3), 724–730 (2010)
61. Liu, F., Hashim, N.A., Liu, Y., Abed, M.R.M., Li, K.: Progress in the production and modification of PVDF membranes. *J. Membr. Sci.* **375**(1–2), 1–27 (2011)
62. Alpatova, A., Meshref, M., McPhedran, K.N., Gamal El-Din, M.: Composite polyvinylidene fluoride (PVDF) membrane impregnated with Fe₂O₃ nanoparticles and multiwalled carbon nanotubes for catalytic degradation of organic contaminants. *J. Membr. Sci.* **490**, 227–235 (2015)
63. Lee, C.G., et al.: Porous electrospun fibers embedding TiO₂ for adsorption and photocatalytic degradation of water pollutants. *Environ. Sci. Technol.* **52**(7), 4285–4293 (2018)
64. Wang, X., Chen, C., Liu, H., Ma, J.: Preparation and characterization of PAA/PVDF membrane-immobilized Pd/Fe nanoparticles for dechlorination of trichloroacetic acid. *Water Res.* **42**(18), 4656–4664 (2008)
65. Lehr, J.H.: *Wiley's Remediation Technologies Handbook: Major Contaminant Chemicals and Chemical Groups*. Wiley (2004). <https://doi.org/10.1002/0471655473>
66. Naskar, S., Pillay, S.A., Chanda, M.: Photocatalytic degradation of organic dyes in aqueous solution with TiO₂ nanoparticles immobilized on foamed polyethylene sheet. *J. Photochem. Photobiol. A Chem.* **113**(3), 257–264 (1998)
67. Ute, K., Miyatake, N., Hatada, K.: Glass transition temperature and melting temperature of uniform isotactic and syndiotactic poly(methyl methacrylate)s from 13 mer to 50 mer. *Polymer (Guildf)* **36**(7), 1415–1419 (1995)
68. Tennakone, K., Kottegoda, I.R.M.: Photocatalytic mineralization of paraquat dissolved in water by TiO₂ supported on polythene and polypropylene films. *J. Photochem. Photobiol. A Chem.* **93**(1), 79–81 (1996)
69. Smidsrod, O., Skjåkbrk, G.: Alginate as immobilization matrix for cells. *Trends Biotechnol.* **8**, 71–78 (1990)
70. Lee, K.Y., Mooney, D.J.: Alginate: properties and biomedical applications. *Prog. Polym. Sci.* **37**(1), 106–126 (2012)
71. Polyak, B., Geresh, S., Marks, R.S.: Synthesis and characterization of a biotin-alginate conjugate and its application in a biosensor construction. *ACS Publ.* **5**(2), 389–396 (2004)
72. Ding, S.N., Shan, D., Xue, H.G., Zhu, D.B., Cosnier, S.: Glucose oxidase immobilized in alginate/layered double hydroxides hybrid membrane and its biosensing application. *Anal. Sci.* **25**(12), 1421–1425 (2009). <https://doi.org/10.2116/analsci.25.1421>
73. Hollabaugh, C.B., Burt, L.H., Walsh, A.P.: Carboxymethylcellulose. Uses and applications. *Ind. Eng. Chem.* **37**(10), 943–947 (1945)
74. Geng, B., Jin, Z., Li, T., Qi, X.: Preparation of chitosan-stabilized Fe(0) nanoparticles for removal of hexavalent chromium in water. *Sci. The Total Environ.* **407**(18), 4994–5000 (2009)
75. Kanel, S.R., Goswami, R.R., Clement, T.P., Barnett, M.O., Zhao, D.: Two dimensional transport characteristics of surface stabilized zero-valent iron nanoparticles in porous media. *Environ. Sci. Technol.* **42**(3), 896–900 (2008)
76. Galván Márquez, I., Akuaku, J., Cruz, I., Cheetham, J., Golshani, A., Smith, M.L.: Disruption of protein synthesis as antifungal mode of action by chitosan. *Int. J. Food Microbiol.* **164**(1), 108–112 (2013)
77. Kong, M., Chen, X.G., Xing, K., Park, H.J.: Antimicrobial properties of chitosan and mode of action: a state of the art review. *Int. J. Food Microbiol.* **144**(1), 51–63 (2010)
78. Zhao, X., Lv, L., Pan, B., Zhang, W., Zhang, S., Zhang, Q.: Polymer-supported nanocomposites for environmental application: a review. *Chem. Eng. J.* **170**(2–3), 381–394 (2011)
79. Lee, D.K., Kang, Y.S., Lee, C.S., Stroeve, P.: Structure and characterization of nanocomposite Langmuir-Blodgett films of poly(maleic monoester)/Fe₃O₄ nanoparticle complexes. *J. Phys. Chem. B* **106**(29), 7267–7271 (2002)

80. Chan, C.M., Wu, J., Li, J.X., Cheung, Y.K.: Polypropylene/calcium carbonate nanocomposites. *Polymer (Guildf)* **43**(10), 2981–2992 (2002)
81. Yu, Q., Wu, P., Xu, P., Li, L., Liu, T., Zhao, L.: Synthesis of cellulose/titanium dioxide hybrids in supercritical carbon dioxide. *Green Chem.* **10**(10), 1061–1067 (2008)
82. Su, X., et al.: The relationship between microstructure and properties in PP/rubber powder/nano-CaCO₃ ternary blends. *Macromol. Mater. Eng.* **289**(3), 275–280 (2004)
83. Zha, L., Fang, Z.: Polystyrene/CaCO₃ composites with different CaCO₃ radius and different nano-CaCO₃ content-structure and properties. *Polym. Compos.* **31**(7), 1258–1264 (2010)
84. Wang, G., Chen, X.Y., Huang, R., Zhang, L.: Nano-CaCO₃/polypropylene composites made with ultra-high-speed mixer. *J. Mater. Sci. Lett.* **21**(13), 985–986 (2002)
85. Luo, Y.B., Da, L.W., Wang, X.L., Xu, D.Y., Wang, Y.Z.: Preparation and properties of nanocomposites based on poly(lactic acid) and functionalized TiO₂. *Acta Mater.* **57**(11), 3182–3191 (2009)
86. Tong, Y., Li, Y., Xie, F., Ding, M.: Preparation and characteristics of polyimide-TiO₂ nanocomposite film. *Polym. Int.* **49**(11), 1543–1547 (2000)
87. Wei, W., He, T., Chen, J.-F., Zhang, X., Chen, Y.: Study on in situ preparation of nano calcium carbonate/PMMA composite particles. *Mater. Lett.* **60**(19), 2410–2415 (2006)
88. Guan, C., Lü, C.-L., Liu, Y.-F., Yang, B.: Preparation and characterization of high refractive index thin films of TiO₂/epoxy resin nanocomposites. *J. Appl. Polym. Sci.* **102**(2), 1631–1636 (2006)
89. Tang, E., Cheng, G., Ma, X.: Preparation of nano-ZnO/PMMA composite particles via grafting of the copolymer onto the surface of zinc oxide nanoparticles. *Powder Technol.* **161**(3), 209–214 (2006)
90. Tang, E., Cheng, G., Pang, X., Ma, X., Xing, F.: Synthesis of nano-ZnO/poly(methyl methacrylate) composite microsphere through emulsion polymerization and its UV-shielding property. *Colloid Polym. Sci.* **284**(4), 422–428 (2006)
91. Utracki, L.A., Sepehr, M., Boccaleri, E.: Synthetic, layered nanoparticles for polymeric nanocomposites (PNCs). *Polym. Adv. Technol.* **18**(1), 1–37 (2007)
92. Cai, L.F., Huang, X.B., Rong, M.Z., Ruan, W.H., Zhang, M.Q.: Fabrication of nanoparticle/polymer composites by in situ bubble-stretching and reactive compatibilization. *Macromol. Chem. Phys.* **207**(22), 2093–2102 (2006)
93. Li, X., Wang, D., Cheng, G., Luo, Q., An, J., Wang, Y.: Preparation of polyaniline-modified TiO₂ nanoparticles and their photocatalytic activity under visible light illumination. *Appl. Catal. B Environ.* **81**(3–4), 267–273 (2008)
94. Liaw, W.C., Chen, K.P.: Preparation and characterization of poly(imide siloxane) (PIS)/titania(TiO₂) hybrid nanocomposites by sol-gel processes. *Eur. Polym. J.* **43**(6), 2265–2278 (2007)
95. Hua, F., Cui, T., Lvov, Y.: Lithographic approach to pattern self-assembled nanoparticle multilayers. *Langmuir* **18**(17), 6712–6715 (2002)
96. Wang, D., Kou, R., Choi, D., et al.: Ternary self-assembly of ordered metal oxide-graphene nanocomposites for electrochemical energy storage. *ACS Nano J.* **4**(3), 1587–1595 (2010)
97. Deitzel, J.M., Kleinmeyer, J.D., Hirvonen, J.K., Beck Tan, N.C.: Controlled deposition of electrospun poly(ethylene oxide) fibers. *Polymer (Guildf)* **42**(19), 8163–8170 (2001)
98. Huang, Z.M., Zhang, Y.Z., Kotaki, M., Ramakrishna, S.: A review on polymer nanofibers by electrospinning and their applications in nanocomposites. *Compos. Sci. Technol.* **63**(15), 2223–2253 (2003)
99. Feng, L., Li, S., Li, H., Zhai, J., Song, Y., Jiang, L., Zhu, D.: Super-hydrophobic surface of aligned polyacrylonitrile nanofibers. *Angew. Chemie Int. Ed.* **41**(7), 1221–1223 (2002)
100. Martin, C.R.: Membrane-based synthesis of nanomaterials. *Chem. Mater.* **8**(8), 1739–1746 (1996)
101. Ma, P.X., Zhang, R.: Synthetic nano-scale fibrous extracellular matrix. *J. Biomed. Mater. Res.* **46**(1), 60–72 (1999)
102. Zhou, S., Wu, L.: Phase separation and properties of UV-curable polyurethane/zirconia nanocomposite coatings. *Macromol. Chem. Phys.* **209**(11), 1170–1181 (2008)

103. Gu, H., Rapole, S.B., Sharma, J., et al.: Magnetic polyaniline nanocomposites toward toxic hexavalent chromium removal. *RSC Adv.* **2**(29), 11007–11018 (2012)
104. Ameen, S., Seo, H.K., Shaheer Akhtar, M., Shin, H.S.: Novel graphene/polyaniline nanocomposites and its photocatalytic activity toward the degradation of rose Bengal dye. *Chem. Eng. J.* **210**, 220–228 (2012)
105. Crespilho, F.N., Iost, R.M., Travain, S.A., Oliveira, O.N., Zucolotto, V.: Enzyme immobilization on Ag nanoparticles/polyaniline nanocomposites. *Biosens. Bioelectron.* **24**(10), 3073–3077 (2009)
106. Shahabuddin, S., Muhamad Sarih, N., Mohamad, S., Joon Ching, J.: SrTiO₃ nanocube-doped polyaniline nanocomposites with enhanced photocatalytic degradation of methylene blue under visible light. *Polymers (Basel)* **8**(2), 27 (2016)
107. Sobhani-Nasab, A., Behpour, M., Rahimi-Nasrabadi, M., Ahmadi, F., Pourmasoud, S., Sedighi, F.: Preparation, characterization and investigation of sonophotocatalytic activity of thulium titanate/polyaniline nanocomposites in degradation of dyes. *Ultrason. Sonochem.* **50**, 46–58 (2019)
108. Heitmann, A.P., et al.: Nanostructured niobium oxyhydroxide dispersed Poly (3-hydroxybutyrate) (PHB) films: highly efficient photocatalysts for degradation methylene blue dye. *Appl. Catal. B Environ.* **189**, 141–150 (2016)
109. Oliver Fundador, E.V., Lagmay, G.B., de Cadiz, A.E., Grace Fundador, N.V., Iwata, T.: Photocatalytic and antibacterial studies on poly(hydroxybutyrate-co-hydroxyhexanoate)/titanium dioxide composites. *BANWA Seri. B* **12**, res006 (2017)
110. Iketani, K., De, S.R., Toki, M., Hirota, K., Yamaguchi, O.: Sol-gel-derived TiO₂/poly(dimethylsiloxane) hybrid films and their photocatalytic activities. *J. Phys. Chem. Solids* **64**(3), 507–513 (2003)
111. Abdelhafeez, I.A., Zhou, X., Yao, Q., Yu, Z., Gong, Y., Chen, J.: Multifunctional edge-activated carbon nitride nanosheet-wrapped polydimethylsiloxane sponge skeleton for selective oil absorption and photocatalysis. *ACS Omega* **5**(8), 4181–4190 (2020)
112. Mavrič, T., Emin, S., Valant, M., Peng, W., Štangar, U.L.: The role of polyvinylpyrrolidone in hydrothermally synthesized Ag/ZnO Nanocomposites and their photocatalytic activities. *J. Nanosci. Nanotechnol.* **15**(9), 6541–6549 (2015)
113. Dai, J., et al.: TiO₂-alginate composite aerogels as novel oil/water separation and wastewater remediation filters. *Compos. Part B Eng.* **160**, 480–487 (2019)
114. Thomas, M., Naikoo, G.A., Sheikh, M.U.D., Bano, M., Khan, F.: Effective photocatalytic degradation of Congo red dye using alginate/carboxymethyl cellulose/TiO₂ nanocomposite hydrogel under direct sunlight irradiation. *J. Photochem. Photobiol. A Chem.* **327**, 33–43 (2016)
115. Kim, H., Hong, H.J., Jung, J., Kim, S.H., Yang, J.W.: Degradation of trichloroethylene (TCE) by nanoscale zero-valent iron (nZVI) immobilized in alginate bead. *J. Hazard. Mater.* **176**(1–3), 1038–1043 (2010)
116. Wang, Q., Qian, H., Yang, Y., Zhang, Z., Naman, C., Xu, X.: Reduction of hexavalent chromium by carboxymethyl cellulose-stabilized zero-valent iron nanoparticles. *J. Contam. Hydrol.* **114**(1–4), 35–42 (2010)
117. Wu, L., Shamsuzzoha, M., Ritchie, S.M.C.: Preparation of cellulose acetate supported zero-valent iron nanoparticles for the dechlorination of trichloroethylene in water. *J. Nanopart. Res.* **7**(4–5), 469–476 (2005)
118. Liu, T., Zhao, L., Sun, D., Tan, X.: Entrapment of nanoscale zero-valent iron in chitosan beads for hexavalent chromium removal from wastewater. *J. Hazard. Mater.* **184**(1–3), 724–730 (2010)
119. Chen, K.T., et al.: Comparison of photodegradative efficiencies and mechanisms of Victoria Blue R assisted by Nafion-coated and fluorinated TiO₂ photocatalysts. *J. Hazard. Mater.* **174**(1–3), 598–609 (2010)
120. Wu, L., Ritchie, S.M.C.: Removal of trichloroethylene from water by cellulose acetate supported bimetallic Ni/Fe nanoparticles. *Chemosphere* **63**(2), 285–292 (2006)

121. Tong, M., Yuan, S., Long, H., Zheng, M., Wang, L., Chen, J.: Reduction of nitrobenzene in groundwater by iron nanoparticles immobilized in PEG/nylon membrane. *J. Contam. Hydrol.* **122**(1–4), 16–25 (2011)
122. Andreozzi, R., Caprio, V., Ermellino, I., Insola, A., Tufano, V.: Ozone solubility in phosphate-buffered aqueous solutions: effect of temperature, tert-butyl alcohol, and pH. *Ind. Eng. Chem. Res.* **35**(4), 1467–1471 (1996)
123. Tarr, M.A. (eds.): *Chemical Degradation Methods for Wastes and Pollutants* (2003). <https://doi.org/10.1201/9780203912553>
124. Lum, P.T., Foo, K.Y., Zakaria, N.A., Palaniandy, P.: Ash based nanocomposites for photocatalytic degradation of textile dye pollutants: a review. *Mater. Chem. Phys.* **241**, 122405 (2020)
125. Kim, C.G., Il, Y.T., Seo, H.J., Yu, Y.H.: Hybrid treatment of tetramethyl ammonium hydroxide occurring from electronic materials industry. *Korean J. Chem. Eng.* **19**(3), 445–450 (2002)
126. Anandan, S., Ashokkumar, M.: Sonochemical synthesis of Au-TiO₂ nanoparticles for the sonophotocatalytic degradation of organic pollutants in aqueous environment. *Ultrason. Sonochem.* **16**(3), 316–320 (2009)
127. Ondruschka, B., Lifka, J., Hofmann, J.: Aquasonolysis of ether – effect of frequency and acoustic power of ultrasound. *Chem. Eng. Technol.* **23**(7), 588–592 (2000)
128. Comminellis, C., Pulgarin, C.: Electrochemical oxidation of phenol for wastewater treatment using SnO₂ anodes. *J. Appl. Electrochem.* **23**, 108–112 (1993)
129. Khin, M.M., Nair, A.S., Babu, V.J., Murugan, R., Ramakrishna, S.: A review on nanomaterials for environmental remediation. *Energy Environ. Sci.* **5**(8), 8075–8109 (2012)
130. Chitose, N., Ueta, S., Seino, S., Yamamoto, T.A.: Radiolysis of aqueous phenol solutions with nanoparticles. 1. Phenol degradation and TOC removal in solutions containing TiO₂ induced by UV, γ -ray and electron beams. *Chemosphere* **50**(8), 1007–1013 (2003)
131. Holm, T.: Kinetic isotope effects in the reduction of methyl iodide. *J. Am. Chem. Soc.* **121**(3), 515–518 (1999)
132. Pittman, C.U., He, J., Sun, G.R.: Solvated electron (Na/NH₃) dechlorination of model compounds and remediation of PCB-and CAH-contaminated wet soils. *ACS Symp. Ser.* **806**, 419–433 (2002)
133. Klibanov, A.M., Tu, T.M., Scott, K.P.: Peroxidase-catalyzed removal of phenols from coal-conversion waste waters. *Science* **221**(4607), 259–261 (1983)
134. Kim, H., Hong, H.J., Lee, Y.J., Shin, H.J., Yang, J.W.: Degradation of trichloroethylene by zero-valent iron immobilized in cationic exchange membrane. *Desalination* **223**(1–3), 212–220 (2008)
135. Yuan, J., Liu, X., Akbulut, O., Hu, J., Suib, S.L., Kong, J., Stellacci, F.: Superwetting nanowire membranes for selective absorption. *Nat. Nanotechnol.* **3**(6), 332–336 (2008)
136. Blaney, L.M., Cinar, S., SenGupta, A.K.: Hybrid anion exchanger for trace phosphate removal from water and wastewater. *Water Res.* **41**(7), 1603–1613 (2007)
137. Ngomsik, A.F., Bee, A., Siaugue, J.M., Talbot, D., Cabuil, V., Cote, G.: Co(II) removal by magnetic alginate beads containing Cyanex 272®. *J. Hazard. Mater.* **166**(2–3), 1043–1049 (2009)
138. Zhang, Y.X., et al.: Self-assembled, monodispersed, flower-like γ -AlOOH hierarchical superstructures for efficient and fast removal of heavy metal ions from water. *CrystEngComm* **14**(9), 3005–3007 (2012)
139. Barnes, R.J., Riba, O., Gardner, M.N., Scott, T.B., Jackman, S.A., Thompson, I.P.: Optimization of nano-scale nickel/iron particles for the reduction of high concentration chlorinated aliphatic hydrocarbon solutions. *Chemosphere* **79**(4), 448–454 (2010)
140. Sinsawat, A., Anderson, K.L., Vaia, R.A., Farmer, B.L.: Influence of polymer matrix composition and architecture on polymer nanocomposite formation: coarse-grained molecular dynamics simulation. *J. Polym. Sci. Part B Polym. Phys.* **41**(24), 3272–3284 (2003)
141. Ameen, S., Akhtar, M.S., Kim, Y.S., Shin, H.S.: Nanocomposites of poly(1-naphthylamine)/SiO₂ and poly(1-naphthylamine)/TiO₂: comparative photocatalytic activity evaluation towards methylene blue dye. *Appl. Catal. B Environ.* **103**(1–2), 136–142 (2011)

142. Xu, Y., et al.: Conjugated conducting polymers PANI decorated Bi₁₂O₁₇C₁₂ photocatalyst with extended light response range and enhanced photoactivity. *Appl. Surf. Sci.* **464**, 552–561 (2019)
143. Da Silva, V.C.F., Contesini, F.J., De Oliveira, C.P.: Enantioselective behavior of lipases from *Aspergillus niger* immobilized in different supports. *J. Ind. Microbiol. Biotechnol.* **36**(7), 949–954 (2009)
144. Tripathi, P., Kumari, A., Rath, P., Kayastha, A.M.: Immobilization of α -amylase from mung beans (*Vigna radiata*) on Amberlite MB 150 and chitosan beads: a comparative study. *J. Mol. Catal. B Enzym.* **49**(1–4), 69–74 (2007)
145. Bin, S.G., Xing, J.M., Zhang, H.Y., Liu, H.Z.: Biotransformation of dibenzothiophene by microbial cells coated with magnetite nanoparticles. *Appl. Environ. Microbiol.* **71**(8), 4497–4502 (2005)
146. Da Silva, L.R.D., Gushikem, Y., Kubota, L.T.: Horseradish peroxidase enzyme immobilized on titanium(IV) oxide coated cellulose microfibers: study of the enzymatic activity by flow injection system. *Colloids Surf. B Biointerfaces* **6**(4–5), 309–315 (1996)
147. Yan, M., Ge, J., Liu, Z., Ouyang, P.: Encapsulation of single enzyme in nanogel with enhanced biocatalytic activity and stability. *J. Am. Chem. Soc.* **128**(34), 11008–11009 (2006)
148. Kim, J., Grate, J.W.: Single-enzyme nanoparticles armored by a nanometer-scale organic/inorganic network. *Nano Lett.* **3**(9), 1219–1222 (2003)
149. Li, J., Li, Y., Xiong, Z., Yao, G., Lai, B.: The electrochemical advanced oxidation processes coupling of oxidants for organic pollutants degradation: a mini-review. *Chin. Chem. Lett.* **30**(12), 2139–2146 (2019)
150. Kritzer, P., Dinjus, E.: An assessment of supercritical water oxidation (SCWO): existing problems, possible solutions and new reactor concepts. *Chem. Eng. J.* **83**(3), 207–214 (2001)
151. Kahoush, M., Behary, N., Cayla, A., Nierstrasz, V.: Bio-Fenton and Bio-electro-Fenton as sustainable methods for degrading organic pollutants in wastewater. *Process Biochem.* **64**, 237–247 (2018)
152. Cao, H., Zhang, W., Wang, C., Liang, Y.: Sonochemical degradation of poly- and perfluoroalkyl substances – a review. *Ultrason. Sonochem.* **69**, 105245 (2020)
153. Changotra, R., Guin, J.P., Khader, S.A., Varshney, L., Dhir, A.: Electron beam induced degradation of ofloxacin in aqueous solution: kinetics, removal mechanism and cytotoxicity assessment. *Chem. Eng. J.* **356**, 973–984 (2019)
154. Yang, L., He, L., Xue, J., Ma, Y., Shi, Y., Wu, L., Zhang, Z.: UV/SO₃²⁻ based advanced reduction processes of aqueous contaminants: current status and prospects. *Chem. Eng. J.* **397**, 125412 (2020)
155. Andrade, D.C., dos Santos, E.V.: Combination of electrokinetic remediation with permeable reactive barriers to remove organic compounds from soils. *Curr. Opin. Electrochem.* **22**, 136–144 (2020)
156. Zdarta, J., Meyer, A.S., Jesionowski, T., Pinelo, M.: Multi-faceted strategy based on enzyme immobilization with reactant adsorption and membrane technology for biocatalytic removal of pollutants: a critical review. *Biotechnol. Adv.* **37**(7), 107401 (2019)

Role of Graphene Oxide Based Nanocomposites in Arsenic Purification from Ground Water



Debasree Ghosh, Sujata Kumari, and Sudip Majumder

Abstract In twenty-first century the major and most concerned environmental challenge faced by the developing countries is providing pure and cost-effective water through shields and decontaminating it from pollutants. The major contaminant in water is arsenic which is seriously a threat to human health and long exposure to arsenic is responsible for causing skin lesions and hyperkeratosis. Graphene oxide and graphene are new carbonaceous nanomaterials. Graphene oxide (GO) nanomaterials have accomplished extensive advancement in effective pollution treatment due to the inherent advantages of large specific surface area, abundant functional groups and their distinctive physicochemical characteristics. Coupling of GO-based nanomaterials with other nanomaterials have been done for removal of pollutants from water. This chapter shows developments in the synthesis of graphene oxides and their composites, and focuses on its applications in the removal of arsenic from arsenic contaminated ground water. Additionally, parameters affecting the efficiency of adsorption have been discussed. Furthermore, the trials for the commercial uses are also discussed.

Keywords Graphene oxide · Heavy metals · Adsorption · Pollutants · Pollution treatment

Abbreviations

GO	Graphene oxide
RGO	Reduced Graphene oxide
As	Arsenic
M-GO	Fe ₃ O ₄ -graphene oxide composite
M-rGo	Fe ₃ O ₄ -reduced graphene oxide composite
M-nOG	Magnetite/non-oxidative graphene

D. Ghosh · S. Kumari · S. Majumder (✉)
Department of Chemistry, Amity School of Applied Science, Amity University, Gurgaon,
Haryana, India

© The Author(s), under exclusive license to Springer Nature Switzerland AG 2022
A. E. Shalan et al. (eds.), *Advances in Nanocomposite Materials for Environmental and Energy Harvesting Applications*, Engineering Materials,
https://doi.org/10.1007/978-3-030-94319-6_12

GO-COOH	Arboxylic graphene oxide nano-composite
CDs	β -Cyclodextrins
β -CDs@GO	β -Cyclodextrins (CDs) functionalized GO
pDADMAC	Poly (diallyl dimethylammonium chloride)
GN-MNP-TNT	Graphene-doped titanium nano tube
PDOS	Partial density of states
TDOS	Total density of states
ZPC	Zero-point charge

1 Introduction

Nowadays, the most common global environmental concern is water pollution [1–5]. The major pollutants in the aqueous environment are heavy metals and metalloids like Arsenic (As), Selenium (Se) etc. Constant exposure to them leads to critical and life-threatening health disorders to individuals. Heavy metals and metalloids are widely distributed throughout the crust of Mother Earth [6]. Activities indispensable to human civilization including mining operation, archaeological and geographical research, use of metal and metalloid based compounds in agriculture act as key contributing factors to the ground water pollution [7]. Henceforth, water does act one significant channel through which these toxic elements get into human system [8]. Currently available methods for purifying water are usually capable of removing these toxic elements to a trace level [8]. Among the available techniques in market adsorption technology is extremely popular due to its cost effectiveness [9–12]. Especially, use of activated charcoal provides higher efficiency and better-quality assurance but unfortunately its present on field application range is relatively limited because of complex operation mechanism and severely high maintenance cost [13]. Therefore, these shortcomings are strong motivators for extensive research to develop new generation materials for water purification, which will simultaneously be effective and reusable. The 2D materials especially GO-based nanocomposites have shown significant promises in this field as reported by various researchers [14].

1.1 Arsenic Contamination and Toxicity

One of major source of ground water pollution is arsenic (As) and this problem is really prevalent in South-Asian countries including Indian subcontinent and China. A significant percentage of population in these countries are revealed to the risk of arsenic poisoning [15–18]. In India, the eastern states like West Bengal and Orissa are among the worst affect zones by arsenic poisoning.

Arsenic poisoning slowly leads to symptoms like skin lesions and hyperkeratosis [19]. Sustainable contact to arsenic contamination causes severe health disorders including neurological, cardiovascular diseases and cancer of multiple organs [20–26]. Furthermore, arsenic has an influence on calcium signalling, induces redox imbalance, have a negative impact on the normal functioning of the mitochondria leading the cell towards apoptosis and also inders the progression of the cell-cycle. [20, 27, 28]. Arsenic is commonly found as rock mineral, which gets mobilized into groundwater by natural processes and anthropogenic activities like mineralization, mining and smelting [24, 25, 29, 30]. Hence, production of arsenic free drinking water is absolutely essential to reduce the health hazard for a huge percentage of world population. Numerous treatment methods like oxidation-coagulation, electro-coagulation and co-precipitation, oxidation-precipitation, reverse osmosis, electro-dialysis, and ion exchange has been operated. Though, most of them remains practically unemployable due to huge maintenance cost and difficulties in execution [31–33].

Instead of these techniques, adsorption being low-cost; does not involve refined instrumentation and do not require long procedure [34–36]. The scheme is simple, safe to handle, and efficiently work at low and high arsenic concentrations in water [37–40]. Thus, adsorption of arsenic from water is a superior method of making water arsenic-free (Fig. 2).

1.2 Graphene Oxide

Graphene oxide (GO) is a monolayer sheet of graphite that assists as a precursor for the synthesis of reduced graphene oxide (rGO) [41]. GO is graphite that has been oxidized to intersperse the carbon layers with oxygen molecules, and then reduced, to discrete the carbon layers completely into individual or few-layer graphene. In GO, the interplanar spacing between the graphitic layers has been increased by surface functionalization of GO [42–45] which makes it a water-soluble nanomaterial [46]. Similarly, in graphene, a large number of oxygen-containing functional groups have been presented onto both sides of a single graphite sheet. Like graphite oxide, GO is normally termed as an electrical insulator, because of interrupted sp² bonding network. However the electrical conductivity of GO primarily depends on the state of oxidation, highly oxidised GO molecules are worst conductors of electricity. Although highly reduced GO might be able to conduct electricity, it will be still be a much poorer conductor compared to purified GO monolayer.

The graphite sheets in such an expanded structure are then easily pulled open using a peripheral force such as sonication. Usually, the oxidized graphene sheets, namely, GO acquires multiple defect related to addition of oxidant and oxidation duration [47]. GO is produced by the oxidative treatment of graphite by one of the principal methods established by Brodie, Hummers, or Staudenmaier (Fig. 3).

1.3 Adsorption Technology

Adsorption is an eminent mechanism used in the purification of water. It works on the physiochemical interaction between pollutants and a solid surface. The solid surface is the adsorbent which must possess low particle size, high surface area, and high active sites for efficient removal of pollutants [33, 48–51]. A huge number of adsorbents removes arsenic (arsenite, As^{3+} , and arsenate, As^{5+}), however for removing As^{3+} , pre-oxidation of As^{3+} to As^{5+} using oxidizing agents is required, which leads to the formation of toxic by-products and is not cost effective [22, 52]. The surface area of graphene oxide is large, porous with many active sites for capturing arsenic from water [53–56]. Graphene oxide contains bulky acidic groups while graphene comprises a hydrophobic surface that results in greater attraction for cations [57]. Graphene oxide have the capability of trapping pollutants by coordination, electrostatic, and covalent interactions ascribed to the epoxy, hydroxyl, and carboxyl groups present on it [53, 58, 59]. Thus, the best choice for arsenic removal is GO-based adsorbents. In this chapter the recent developments of GO and its various forms in arsenic removal from water has been discussed. Additionally, the role of various GO-based adsorbents with their arsenic adsorption capacity have been discussed.

2 Preparation of GO

Discovery of graphene took place in 2004 [60] and its exclusive properties have caused huge importance in diverse exploration fields. GO has attracted prodigious consideration in environmental pollution treatment as it is the derivate of graphene. Generally, GO was synthesized by different methods such as Brodie method [61], Staudenmaier method [62], and Hummers' method [63] or some variations of these methods.

Brodie synthesized GO for the first time in 1859. For synthesizing GO, he used a mixture of definite quantity of graphite and potassium chlorate in the ratio 1:3 (w/w) and kept in a distiller. To which fuming nitric acid was added and kept at 60 °C in water bath till no yellow vapours were evolved. Later, the mixture was diluted by an adequate amount of deionized water, and washed several times to remove excess salt and acid. Finally, drying of the GO was done at 100 °C.

Staudenmaier in 1898 synthesized GO where concentrated sulfuric acid was added in addition to fuming nitric acid along with potassium chlorate. The approach triggered improved synthetic yield. The Staudenmaier method was risky and required more time than the earlier one.

In 1958, Hummers and Offeman used concentrated sulphuric acid and potassium permanganate for the synthesis of GO. According to this method, graphite, sodium nitrate and concentrated sulphuric acid were mixed in a pre-chilled flask at 0 °C. After that, potassium permanganate was added slowly to the mixture. Then the ice-bath was removed, and the mixture was maintained at a temperature of 35 °C that

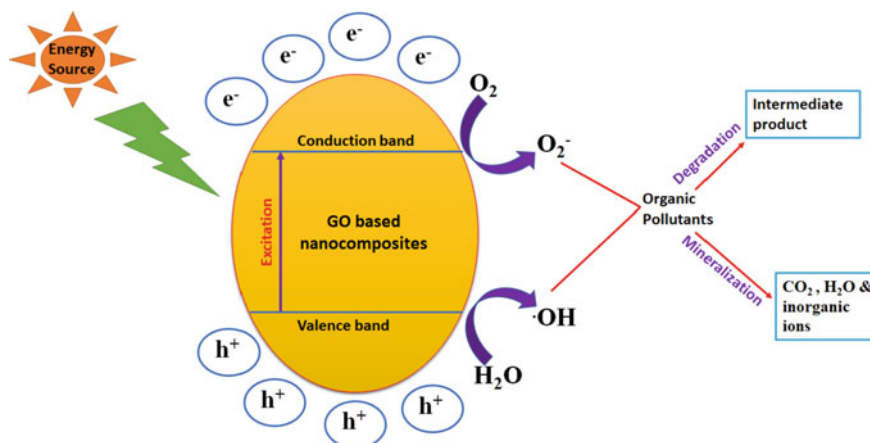


Fig. 1 General mechanism of toxic organic pollutants degradation via GO-based nanocomposites

Table 1 Characteristic absorption peaks for GO

Stretching frequency (cm^{-1})	Information (65–68, 72)
3420–3200	ν_{O-H} stretching
2850–2950	Hydrogen bonding with oxygenous groups
1710–1730	$\nu_{C=O}$ stretching
1620–1640	$\nu_{C=C}$ in-plane stretching
1415–1550	ν_{O-H} deformation
1230–1400	ν_{C-O} Alkoxy stretching
1020–1070	ν_{C-O} Epoxy stretching

was retained for 30 min. Later, it was kept at a temperature of 98 °C for 15 min. 3% hydrogen peroxide was added to convert the left over manganese dioxide and permanganate to colourless soluble manganese sulphate. The product obtained was washed with distilled water and resuspended in it and the pH was checked to be 7. The above mentioned methods of synthesis include the foremost pathways for developing GO (Fig. 4).

3 Characterization of GO

FT-IR, Raman, and XRD techniques were certified for the preparation of GO and its composites. Table 1 represents the FTIR spectrum of GO.

Kumari et al. [64] described the FTIR peaks of GO at 1729, 1620, 1415, 1046, and 1236 cm^{-1} respectively (Fig. 1(c)). The C=O group is verified through the presence of peak at 1729 cm^{-1} in IR spectrum and C=C stretching was allotted by the appearance of peak at 1620 cm^{-1} . The band at 1415 cm^{-1} confirms C-H bond deformation. Bands at 1046 and 1236 cm^{-1} appeared because of C-O stretching vibration for epoxy and alkoxy groups, respectively.

Analogous outcome was observed by Khatamian et al. [65], Kumar and Jiang [66], Peng et al. [54]. Su et al. [52] established the distribution of iron oxide species onto GO matrix by assigning the absorption peaks for Fe-O, between the 750–400 cm^{-1} . The two bands appeared at 552 and 442 cm^{-1} due to Fe-O and one band at 1578 cm^{-1} for C=C stretch in GO; it was confirmed the formation of FeO_x -GO nano-composite. FTIR spectrum of GO- MnFe_2O_4 (Fig. 1(c)) displayed absorption peaks at 490 and 577 cm^{-1} due to Metal-Oxygen stretching vibrations of manganese ferrite [64]. Comparable consequence was observed from the studies of Huang et al. [67], Kumar et al. [64], and Marcano et al. [68].

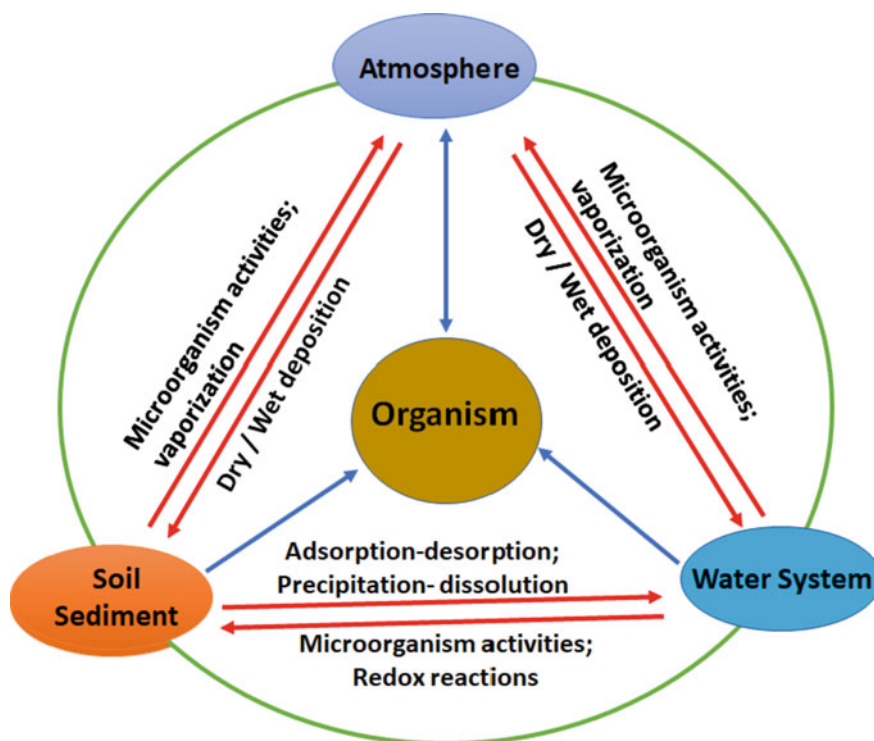


Fig. 2 Geochemical cycle of arsenic in Nature

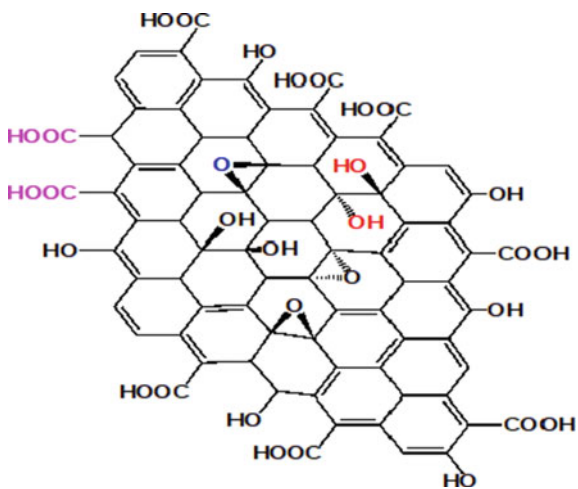


Fig. 3 Structure of GO (Adapted from Kumari et al. ACS OMEGA, 2020)

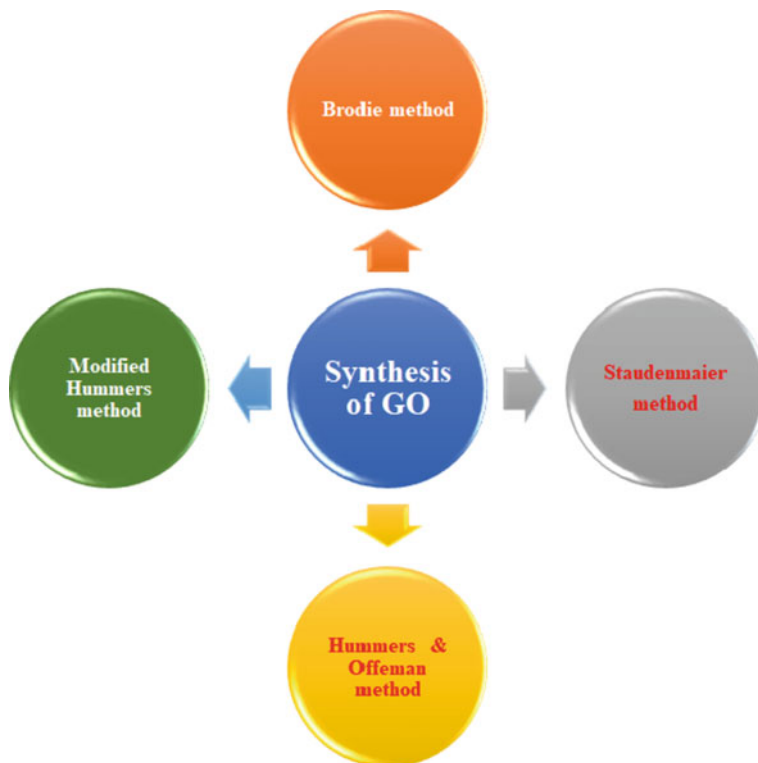


Fig. 4 Different synthesis routes of GO

XRD data of GO provides the characteristic peak at $2\theta = 9.4\text{--}10.50^\circ$ conforming the (001) plane of GO. However, usually for the composites of GO with metal the intensity of these peaks significantly decreases due to reduction in crystalline structure. This effect probably originates from the bonding interaction between GO with metal. Comparable result was observed by Huang et al. [67], Kumar et al. [64], Kumar and Jiang [66], Marcano et al. [68] and Kumari et al. [69]. XRD data of GO and its composite is shown in Fig. 1(a).

Raman spectra is an excellent technique for characterization of GO based material. Raman spectrum of GO exhibited two prominent peaks at $1580\text{--}1620$ and $1340\text{--}1365\text{ cm}^{-1}$ correlated to the first order E_{2g} mode from sp^2 carbon domains (G-band) and disorder mode (D-band), respectively. Kumar and Jiang [66] reported strong peaks at 1610 and 2445 cm^{-1} for GO associated to G band and D' band, and one broad peak at 1360 cm^{-1} corresponding to D band. The functionalization of GO with chitosan display additional peaks arising at 718 and 1047 cm^{-1} due to the interaction of COOH of the GO and OH group of chitosan Fig. 1(b). Analogous outcomes were described by Chen et al. [70], Kumar et al. [64], and Yang et al. [71]. SEM and TEM of GO and GO based nanomaterials were done by different groups of researchers [52, 64, 71, 72] (Fig. 5, 6, 7, 8 and 9).

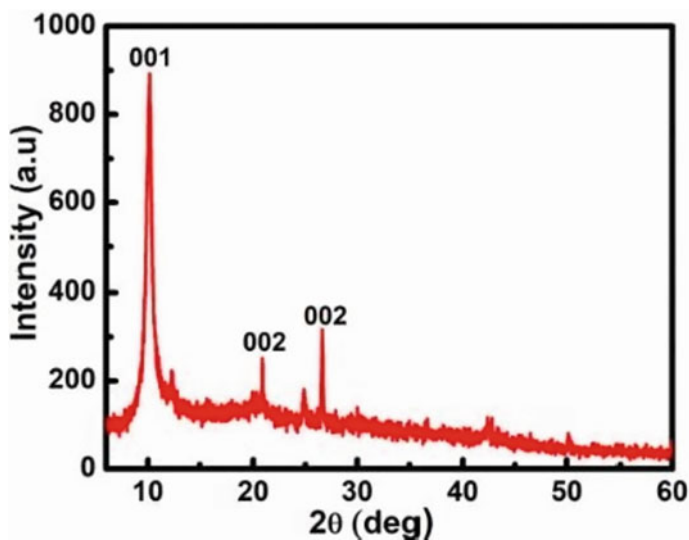


Fig. 5 PXRD micrographs of GO (Adapted from Kumari et al. ACS OMEGA, 2020)

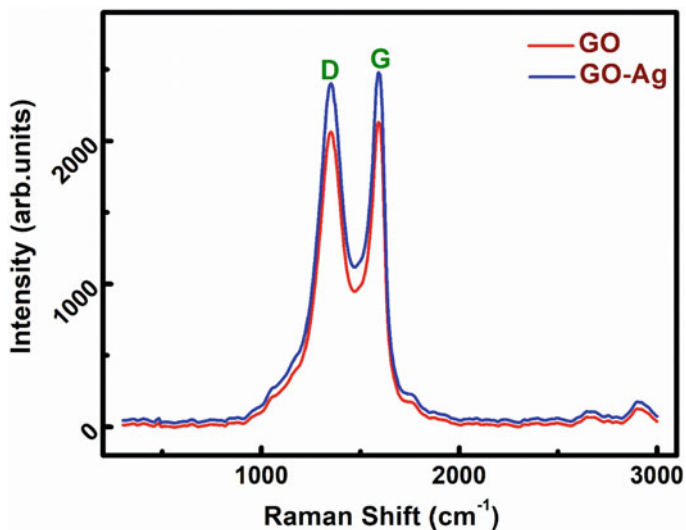


Fig. 6 RAMAN micrographs of GO (Adapted from Kumari et al. ACS OMEGA, 2020)

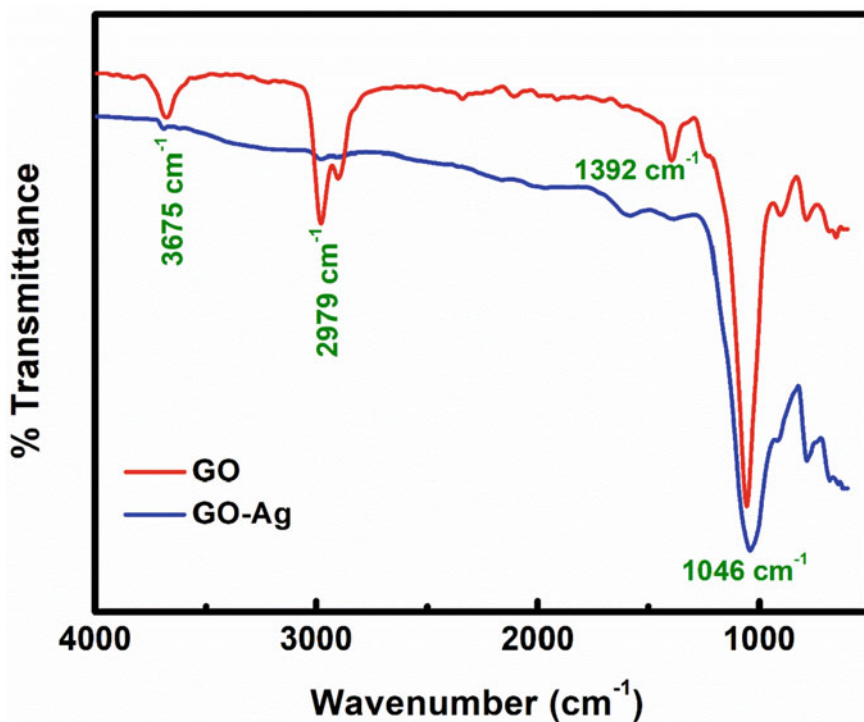


Fig. 7 FTIR micrographs of GO (Adapted from Kumari et al. ACS OMEGA, 2020)

Fig. 8 SEM micrographs of GO (Adapted from Kumari et al. ACS OMEGA, 2020)

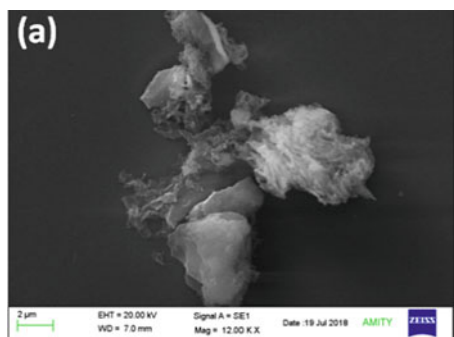
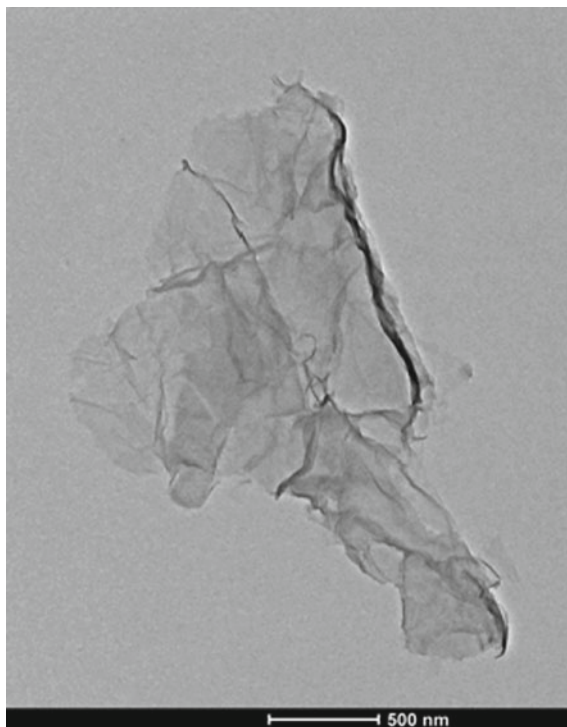


Fig. 9 TEM micrographs of GO (Adapted from Kumari et al. ACS OMEGA, 2020)



4 GO as Adsorbent for Arsenic

With the fast advancement of industrialization, heavy metal toxicity has increased a lot which has been a major ecological concern. The exclusive physicochemical properties along with high surface area and abundant oxygen-containing functional groups of GO and GO-based nanomaterials is important in waste water management.

Binary and ternary composites of transition metal oxides (especially magnetite and MnO_2) with GO and rGO are widely used for arsenic treatment [64, 72]. These composites exhibit large sorption capacity towards arsenic and become magnetic in nature. These composites are found to be highly ion selective and effective at low concentration and over wide pH range. As compared to MnFe_2O_4 nanoparticles, Graphene oxide MnFe_2O_4 nano-composite exhibited higher efficacy in removing arsenic from water. Adsorption capacity of graphene oxide- MnFe_2O_4 for As (III) and As (V) was 146 and 207 mg/g, respectively [64]. Because of electrostatic interaction and preoxidation step, Fe_3O_4 -RGO- MnO_2 nano-composite was found to be more efficient than the graphene- FeMnO_x [73, 74]. Yoon et al. [75] mentioned the synthesis of Fe_3O_4 -graphene oxide composite (M-GO) and Fe_3O_4 -reduced graphene oxide composite (M-rGO) where the non-reduced form exhibited better arsenic removal efficiency. Chen et al. [76] described the efficient adsorption capability of β - FeOOH @GO-COOH composite.

Thus, Su et al. [52] described the use of FeO_x -GO nanocomposites having different amounts of iron oxide as efficient adsorbents. In this method, he prepared GO sheets on which iron oxide was coupled by Coprecipitation method. Increase in iron oxide content have a direct correlation with increasing the adsorption efficiency due to an increase in the surface area. FeO_x -GO-80 was found to exhibit the highest adsorption capacity.

Similarly, for arsenic removal Yoon et al. [77] reported the large scale production of non-oxidative graphene and magnetite/non-oxidative graphene (M-nOG) composite among which the one having magnetite had better adsorption capability. The characteristic features of the adsorbent surface influenced the adsorption of As (III) whereas As (V) displayed intraparticle diffusion mechanism. Additionally, efficient arsenic removal has been exhibited by three dimension (3D)-magnetite (Fe_3O_4)-graphene macroscopic composites [78]. Polydopamine has been used in synthesizing these composites as they increase the adsorbent efficiency.

Dubey et al. [79] reported, engineered graphene based metallic composites for removing.

As (V). Correspondingly, Arriagada and Labbe [80] described the use of Al and Fe-doped graphene in removing methylated As (III) and As (V). The synthesis of chitosan functionalized GO has been reported by Kumar and Jiang [66]. For incoming arsenic oxy-anion the chitosan functionalized GO functioned as good host. Several interaction mechanisms like charge transfer and electrostatic interactions have been proposed to explain the interaction among arsenic and GO moieties. Mishra and Ramaprabhu [81] described the synthesis of GO sheets which have been used in removing high concentrations of As (III) and As (V) from aqueous solution.

Super capacitor based on graphene have been proved to have efficient water filtration capacity. Kumar and Jiang [82] magnetic nanoparticles coupled with β -cyclodextrin functionalized for arsenic removal.

Lin et al. prepared Graphene-doped titanium nano tube coated to super paramagnetic nanoparticles (GN-MNP-TNT) for removal of As (III) [83] (Fig. 10).

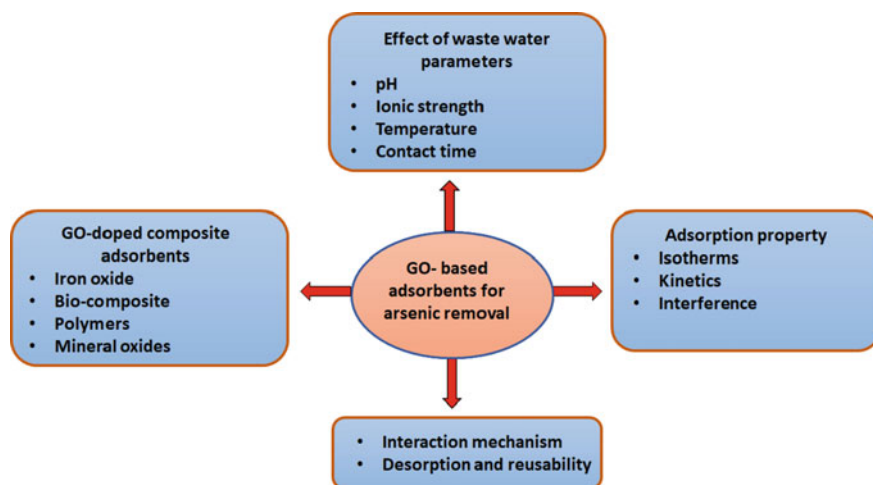


Fig. 10 Flow chart of GO-based adsorbents for arsenic removal

5 Effects of Wastewater Parameters

Generally, the parameters like pH, temperature, contact time, pollutant concentration, type of pollutants and parameters associated with the adsorbant surface are responsible for the interaction of the pollutants with the GO based adsorbents [84].

5.1 Effect of pH

The pH value of the solution very important in controlling the adsorption of metal ion on solid particles. Mainly protonation-deprotonation reactions at altered pH values is important [85]. Madadrang et al. [86] described that at the solution pH > 2.0, a negative charge develops on GO. Research report illustrates that adsorption of Cr (VI) increases at pH value from 1.0 to 2.0 and decreases between pH 2.0 to 6.0. According to Gercel et al. [87], decrease in the adsorption potential at low pH is due to the presence of H^+ and H_3O^+ in solution in greater amounts which competes with the heavy metal ions for binding to GO and GO-based nanomaterials. At high pH, the functional groups on GO containing oxygen are easily protonated facilitating the adsorption process [88]. On the other hand, Gu et al. [89] reported that electrostatic interaction among the negatively charged surfaces of GO nanosheets and the positively charged metal ions was improved, on increasing the solution pH, an alternative inspiration in increasing adsorption capacity. Moreover, at altered pH values, the ions of the heavy metals could exist as $M(OH)^{2-n+2}$, $M(OH)^{-n+1}$, $M(OH)^{+n-1}$, $M(OH)_n$, and M^{n+} etc., [90]. Adsorption reduces on increasing the pH due to electrostatic repulsion amongst the $M(OH)^{-n+1}$, $M(OH)^{2-n+2}$ species, and

functional groups containing oxygen [88]. The adsorption efficiency depends on the type of metal ions, the functional groups and the surface properties of GO-based nanomaterials in addition to pH [90–93]. Hence, solution pH values is fundamental in determining the pollutant removal efficiency from water.

5.2 *Effect of Ionic Strength*

External ions have an important role in the adsorption process. Ionic strength influences adsorption of pollutants on GO or GO-based nanomaterials in the following ways:

- (1) The external ions competes with the pollutants for getting adhered on the surface of the adsorbents.
- (2) Particle aggregation was influence by the electrostatic interactions which could unusually disturb by the concentration of external ions.
- (3) The activity coefficient of the pollutants is affected by the presence of the external ions which reduces the efficiency of adsorption [93].

The influence of the external ions on the adsorption efficiency has been studied in great details [94, 95]. Normally, the strength of the ions directly influences the adsorption of pollutants having low valency which is not the case with the pollutants with high valency. Inner-sphere surface interaction is an important parameter in determining the adsorption efficiency of the adsorbents when pH or ionic strength do not play any role. Outer-sphere surface complexation is the main determinant in the adsorption process if ionic strength is mainly influences the process and the pH having only a minor role.

5.3 *Effect of Temperature*

Temperature also is an important parameter in determining adsorption efficiency. Earlier, Chen et al. mentioned different isothermal models like Dubinin-Radushkevich (D-R), Freundlich, Langmuir and Sips sorption models [96]. The kinetics of adsorption is dependent on the solubility of the pollutants and their molecular interactions with the adsorbent which is influenced by temperature [97]. The rise in temperature increases the accessibility of the pollutants on the solid nanomaterials leading to an increase in the adsorption efficiency. Managing the temperature of wastewater is very tough and thus treating waste water by temperature variation.

5.4 Effect of Contact Time

Throughout the adsorption process, time is a significant factor that influences the mass transfer rate of pollutants. The exclusion efficacy of the metal ions at first rises intensely followed by a gradual rise till the contact time is prolonged to attain equilibrium. On increasing the contact duration the adsorption performance decreases finally leading to saturation. [98] lesser time to attain the sorption equilibrium recommends the greater efficacy.

6 Interaction Mechanism

Study of this mechanism between the adsorbent and the pollutants is important in the purification of water. For monitoring the removal of the metal ions at the solid-liquid interfaces, a variety of interaction mechanisms play major role, like ion exchange, surface complexation, and precipitation. Macroscopic group investigations cannot ultimately and adequately provide a microscopic insight into the mechanism, hence, spectroscopic techniques comprising Fourier-transform infrared spectroscopy (FT-IR), X-ray photoelectron spectroscopy (XPS), and X-ray absorption fine structure (XAFS) and computational methods have been suggested [99–101]. The broadly utilized surface chemical analysis technique is FT-IR and XPS spectroscopy, which can suggest molecular information of materials with a high spatial resolution. These techniques to detect the state of GO before and after import of distinct metal ions. The results specified the binding of the positively charged ions with GO [102]. The XPS spectra of the GO-CS at different pH are reported by Huang et al. [103], described adsorption is due to inner-sphere surface coordination among U (VI) and -NH_2 ,

-COO- , and -OH groups of the GO-CS. Hu et al. [104] established that the outer-sphere complexes of Cu (II) on LDH were converted to inner-sphere complexes on LDH_GO through the EXAFS analysis. Hence, it is extremely suggested to use collective multiple methods comprising experimental, spectroscopic and theoretical examinations to get a better view of the interaction mechanism.

7 Desorption and Reusability

High exclusion rate is an important parameter in managing waste water. The Desorption/regeneration feature of the adsorbent ominously decreases charge of the overall process and rises the adsorbent efficacy. Hence, for the implementation of an adsorbent redevelopment of adsorbent is very essential.

Adsorption is dependent on surface charge which is determined by solution pH. At zero-point charge (ZPC), the net charge on the surface of the adsorbent is 0. At $\text{pH} > \text{ZPC}$, and $\text{pH} < \text{ZPC}$, the adsorbent charge becomes negative and positive

respectively [22, 23, 25]. Additionally, as previously discussed, arsenic species have been found to possess oxy-anions. Mostly, in basic environment, adsorption of the oxygen containing anions decreases due to the detachment of these anions from the adsorbent surface. [22, 105]. Kumar et al. reported that after 3 adsorption-desorption cycles, Chitosan GO was renewed with 10 ml of 1.0 M NaOH whereby a 15% reduction in the efficiency was observed [66]. Magnetic receptive GO have been found to be superior to be used as adsorbents in managing water pollution [64, 106]

8 Conclusions and Future Perspectives

In this review, synthesis along with improvement of GO-based nanocomposites and their applications have for purifying polluted water have been discussed. Furthermore, GO-based composite materials have high efficiency and strong affinity for the metal ions due to which they are now being used as novel adsorbent materials. GO based materials have been proved to be extremely efficacious in the removal of arsenic from water. The surface binding ability of GO based material are responsible for their increased efficiency as adsorbents in water purification. The thickness and the porous nature of GO are also responsible in influencing the adsorption process. Modifying the surface of GO helps in improving the adsorption efficiency, selectivity and stability. This also aids in improved performance of the magneto-responsive adsorbent materials. GO based materials are inexpensive and can be reused which makes them promising material.

8.1 Limitations

GO and GO based nanomaterials promises to be efficient adsorbants a few limitations like high cost and large scale production has to be dealt with before it can be used widely for commercial purposes.

Acknowledgements DG, SK, and SM would like to thanks Amity University, Haryana for supporting this work. SM and DG would like to acknowledge the support provided under the DST-FIST Grant No.SR/FST/PS-I/2019/68 of Govt. of India.

References

1. Rezakazemi, M., Dashti, A., Harami, H.R., Hajilari, N., Inamuddin: Fouling-resistant membranes for water reuse. *Environ. Chem. Lett.* **16**(3), 715–763 (2018)
2. Rezakazemi, M., Ghafarinazari, A., Shirazian, S., Khoshshima, A.: Numerical modeling and optimization of wastewater treatment using porous polymeric membranes. *PolymEng. Sci.* **53**, 1272–1278 (2013)

3. Rezakazemi, M., Khajeh, A., Mesbah, M.: Membrane filtration of wastewater from gas and oil production. *Environ. Chem. Lett.* **16**, 367–388 (2018)
4. Rezakazemi, M., Shirazian, S., Ashrafizadeh, S.N.: Simulation of ammonia removal from industrial wastewater streams by means of a hollow-fiber membrane contactor. *Desalination* **285**, 383–392 (2012)
5. Shirazian, S., Rezakazemi, M., Marjani, A., Moradi, S.: Hydrodynamics and mass transfer simulation of wastewater treatment in membrane reactors. *Desalination* **286**, 290–295 (2012)
6. Azimi, A., Azari, A., Rezakazemi, M., Ansarpour, M.: Removal of heavy metals from industrial wastewaters: a review. *ChemBioEng. Rev.* **4**, 37–59 (2017)
7. Tangahu, B.V., Abdullah, S.R.S., Basri, H., Idris, M., Anuar, N., Mukhlisin, M.: A review on heavy metals (As, Pb, and Hg) uptake by plants through phytoremediation. *Int. J. Chem. Eng.* **20**(11), 1–31 (2011)
8. Abbas, A., et al.: Heavy metal removal from aqueous solution by advanced carbon nanotubes: critical review of adsorption applications. *Sep. PurifTechnol.* **157**, 141–161 (2016)
9. Vijai Anand, K., Reshma, M., Kannan, M., et al.: Preparation and characterization of calcium oxide nanoparticles from marine molluscan shell waste as nutrient source for plant growth. *J. Nanostruct. Chem.* **11**, 409–422 (2021). <https://doi.org/10.1007/s40097-020-00376-4>
10. Taheri-Ledari, R., Rahimi, J., Maleki, A., Shalan, A.E.: Ultrasound-assisted diversion of nitrobenzene derivatives to their aniline equivalents through a heterogeneous magnetic Ag/Fe₃O₄-IT nanocomposite catalyst. *New J. Chem.* **44**, 19827–19835 (2020)
11. Shalan, A.E., Afifi, M., El-Desoky, M.M., Ahmed, M.K.: Electrospun nanofibrous membranes of cellulose acetate containing hydroxyapatite co-doped with Ag/Fe: morphological features, antibacterial activity and degradation of methylene blue in aqueous solution. *New J. Chem.* **45**, 9212–9220 (2021)
12. Shalan, A.E., Mohammed, M.K.A., Govindan, N.: Graphene assisted crystallization and charge extraction for efficient and stable perovskite solar cells free of a hole-transport layer. *RSC Adv.* **11**, 4417–4424 (2021)
13. Reddy, B., Dadigala, R., Bandi, R., et al.: Microwave-assisted preparation of a silver nanoparticles/N-doped carbon dots nanocomposite and its application for catalytic reduction of rhodamine B, methyl red and 4-nitrophenol dyes. *RSC Adv.* **11**, 5139–5148 (2021)
14. El-Shazly, A.N., Rashad, M.M., Abdel-Aal, E.A., et al.: Nanostructured ZnO photocatalysts prepared via surfactant assisted Co-Precipitation method achieving enhanced photocatalytic activity for the degradation of methylene blue dyes. *J. Environ. Chem. Eng.* **4**, 3177–3184 (2016)
15. Batool, M., Nazar, M.F., Awan, A., et al.: Bismuth-based heterojunction nanocomposites for photocatalysis and heavy metal detection applications. *Nano-struct. Nano-objects* **27**, 100762 (2021)
16. Kao, A.C., Chu, Y.J., Hsu, F.L., Liao, V.H.C.: Removal of arsenic from groundwater by using a native isolated arsenite-oxidizing bacterium. *J. ContamHydro.* **155**, 1–8 (2013)
17. Chaudhry, S.A., Zaidi, Z., Siddiqui, S.I.: Isotherm, kinetic and thermodynamics of arsenic adsorption onto Iron-Zirconium Binary Oxide-Coated Sand (IZBOCS): modelling and process optimization. *J. Mol. Liq.* **229**, 230–240 (2017)
18. Ng, J.C., Wang, J., Shraim, A.: Global health problems caused by arsenic from natural sources. *Chemosphere* **52**, 1353–1359 (2003)
19. Matschullat, J.: Arsenic in the geosphere—a review. *Sci. Total Environ.* **249**, 297–312 (2000)
20. Abdul, K.S., Jayasinghe, S.S., Chandana, E.P., Jayasumana, C., De-Silva, P.M.: Arsenic and human health effects: a review. *Environ. ToxicolPharmacol.* **40**, 828–846 (2015)
21. Biswas, B.K.: Adsorptive removal of As(V) and As(III) from water by a Zr(IV)-loaded orange waste gel. *J. Hazard. Mater.* **154**, 1066–1074 (2008)
22. Siddiqui, S.I., Chaudhry, S.A.: Arsenic removal from water using nano-composites: a review. *Cur. Environ. Eng.* **4**, 81–102 (2017)
23. Siddiqui, S.I., Chaudhry, S.A.: Arsenic: toxic effects and remediation. In: Islam, S.U. (ed.) *Advanced Materials for Wastewater Treatment*, pp. 1–27. Wiley (2017)

24. Siddiqui, S.I., Chaudhry, S.A.: Iron oxide and its modified forms as an adsorbent for arsenic removal: a comprehensive recent advancement. *Process Saf. Environ. Protect.* **111**, 592–626 (2017)
25. Siddiqui, S.I., Chaudhry, S.A.: Removal of arsenic from water through adsorption onto metal oxide-coated material. *Mater. Res. Found.* **15**, 227–276 (2017)
26. Watanabe, C.H., et al.: Toxicity assessment of arsenic and cobalt in the presence of aquatic humic substances of different molecular sizes. *Ecotoxicol. Environ. Saf.* **139**, 1–8 (2017)
27. Flora, S.J.S.: Arsenic-induced oxidative stress and its reversibility. *Free Rad. Biol. Med.* **51**, 257–281 (2011)
28. Kulshrestha, A., Jarouliya, U., Prasad, G.B.K.S., Flora, S.J.S., Bisen, P.S.: Arsenic-induced abnormalities in glucose metabolism: biochemical basis and potential therapeutic and nutritional interventions. *World J. Trans. Med.* **3**, 96–111 (2014)
29. Chaudhry, S.A., Ahmed, M., Siddiqui, S.I., Ahmed, S.: Fe(III)-Sn(IV) mixed binary oxide-coated sand preparation and its use for the removal of As(III) and As(V) from water: application of isotherm, kinetic and thermodynamics. *J. Mol. Liq.* **224**, 431–441 (2016)
30. Anastopoulos, I., Karamesouti, M., Mitropoulos, A.C., Kyzas, G.Z.: A review for coffee adsorbents. *J. Mol. Liq.* **229**, 555–565 (2017)
31. Chaudhry, S.A., Khan, T.A., Ali, I.: Adsorptive removal of Pb(II) and Zn(II) from water onto manganese oxide-coated sand: Isotherm, thermodynamic and kinetic studies. *Egypt J. Basic Appl. Sci.* **3**, 287–300 (2016)
32. Devi, P., Saroha, A.K.: Utilization of sludge-based adsorbents for the removal of various pollutants: a review. *Sci. Total Environ.* **578**, 16–33 (2017)
33. Mohan, D., Pittman, C.U., Jr.: Arsenic removal from water/wastewater using adsorbents: a critical review. *J. Hazard. Mater.* **142**, 1–53 (2007)
34. Alqadami, A.A., Naushad, M., Abdalla, M.A.: Synthesis and characterization of Fe₃O₄ @TSC nanocomposite: highly efficient removal of toxic metal ions from aqueous medium. *RSC Adv.* **6**, 22679–22689 (2016)
35. Khan, T.A., Chaudhry, S.A., Ali, I.: Equilibrium uptake, isotherm and kinetic studies of Cd (II) adsorption onto iron oxide activated red mud from aqueous solution. *J. Mol. Liq.* **202**, 165–175 (2015)
36. Sharma, G., et al.: Fabrication and characterization of chitosan-crosslinked-poly(alginic acid) nanohydro-gel for adsorptive removal of Cr(VI) metal ion from aqueous medium. *Int. J. BiolMacromol.* **95**, 484–493 (2017)
37. Gupta, A., Chauhan, V.S., Sankaramakrishnan, N.: Preparation and evaluation of iron-chitosan composites for removal of As (III) and As (V) from arsenic contaminated real life groundwater. *Water Res.* **43**, 3862–3870 (2009)
38. Han, C., et al.: Synthesis and characterization of mesoporous alumina and their performances for removing arsenic (V). *Chem. Eng. J.* **217**, 1–9 (2013)
39. Mondal, P., Balomajumder, C., Mohanty, B.: A laboratory study for the treatment of arsenic, iron, and manganese bearing ground water using Fe³⁺ impregnated activated carbon: effects of shaking time, pH and temperature. *J. Hazard. Mater.* **144**, 420–426 (2007)
40. Maliyekkal, S.M., Philip, L., Pradeep, T.: As(III) removal from drinking water using manganese oxide-coated-alumina: performance evaluation and mechanistic details of surface binding. *Chem. Eng. J.* **153**, 101–107 (2009)
41. Ranjan, P., Agrawal, S., Sinha, A., Rao, T.R., Balakrishnan, J., Thakur, A.D.: A low-cost non-explosive synthesis of graphene oxide for scalable applications. *Sci. Rep.* **8**, 12007 (2018)
42. Balaprasad, F.: Water soluble graphene synthesis. *Chem. Sci. Trans.* **10**, 500–507 (2012)
43. Ban, F.Y., Majid, S.R., Huang, N.M., Lim, H.N.: Graphene oxide and its electrochemical performance. *Int. J. Electrochem. Sci.* **7**, 4345–4351 (2012)
44. Geim, A.K., Novoselov, K.S.: The rise of graphene. *Nat. Mater.* **6**, 183–191 (2007)
45. Grzegorz, S., Jaroslaw, S., Joanna, J., Rafal, K., Mariusz, Z.: Graphene oxide vs reduced graphene oxide as saturable absorbers for Er-doped passively mode-locked fiber laser. *Opt. Exp.* **20**, 19463–19473 (2012)

46. Ramakrishnan, M.C., Thangavelu, R.R.: Synthesis and characterization of reduced graphene oxide. *Adv. Mater. Res.* **678**, 56–60 (2013)
47. Ling, S., Bunshi, F.: Massive production of graphene oxide from expanded graphite. *Mater. Lett.* **109**, 207–210 (2000)
48. Bai, L., Ma, X.J., Liu, J.F., Sun, X.M., Zhao, D.Y., Evans, D.G.: Rapid separation and purification of nanoparticles in organic density gradients. *J. Am. Chem. Soc.* **132**, 2333–2337 (2010)
49. Sansone, V., Pagani, D., Melato, M.: Chronic arsenicals dermatoses from tube-well water in West Bengal during 1983–87. *Clin. Cases Miner. Bone Metab.* **10**, 34–40 (2013)
50. Sherman, D.M., Randall, S.R.: Surface complexation of arsenic (V) to iron (III) hydroxides: structural mechanism from ab initio molecular geometries and EXAFS spectroscopy. *GeochimCosmochim. Acta* **67**, 575–580 (2003)
51. Su, H., Ye, Z., Hmidi, N.: High-performance iron oxide–graphene oxide nanocomposite adsorbents for arsenic removal efficient removal of arsenic using graphene-zeolite based composites. *Colloids Surf. A PhysicochemEng. Asp* **522**, 161–172 (2017)
52. Zhang, G., Qu, J., Liu, H., Liu, R., Wu, R.: Preparation and evaluation of a novel Fe-Mn binary oxide adsorbent for effective arsenite removal. *Water Res.* **41**, 1921–1928 (2007)
53. Peng, W., Li, H., Liu, Y., Song, S.: A review on heavy metal ions adsorption from water by graphene oxide and its composites. *J. Mol. Liq.* **230**, 496–504 (2017)
54. Platero, E., Fernandez, M.E., Bonelli, P.R., Cukierman, A.L.: Graphene oxide/alginate beads as adsorbents: influence of the load and the drying method on their physicochemical-mechanical properties and adsorptive performance. *J. Colloid Interface Sci.* **491**, 1–12 (2017)
55. Kumar, S., Nair, R.R., Pillai, P.B., Gupta, S.N., Iyengar, M.A.R., Sood, A.K.: Graphene oxide–MnFe₂O₄ magnetic nano-hybrids for efficient removal of lead and arsenic from water. *ACS Appl. Mater. Interfaces* **6**, 17426–17436 (2014)
56. Sheshmani, S., Nematzadeh, M.A., Shokrollahzadeh, S., Ashori, A.: Preparation of grapheme oxide/chitosan/FeOOH nanocomposite for the removal of Pb (II) from aqueous solution. *Int. J. BiolMacromol.* **80**, 475–480 (2015)
57. Zhou, Q., Zhong, Y.H., Chen, X., Liu, J.H., Huang, X.J., Wu, Y.C.: Adsorption and photocatalysis removal of fulvic acid by TiO₂-graphene composites. *J. Mater. Sci.* **49**, 1066–1075 (2014)
58. Ray, S.K., Majumdera, C., Saha, P.: Functionalized reduced graphene oxide (RGO) for removal of fulvic acid contaminant. *RSC Adv.* **7**, 21768–21779 (2017)
59. Machida, M., Mochimaru, T., Tatsumoto, H.: Lead(II) adsorption onto the graphene layer of carbonaceous materials in aqueous solution. *Carbon* **44**, 2681–2688 (2006)
60. Novoselov, K., et al.: Electric field effect in atomically thin carbon films. *Science* **306**, 666–669 (2004)
61. Brodie, B.C.: On the atomic weight of graphite. *Philos. Trans. Roy. Soc. Lond* **149**, 249–259 (1859)
62. Staudenmaier, L.: Verfahrenzurdarstellung der graphits. *Ber. Dtsch. Chem. Ges.* **31**, 1481–1487 (1898)
63. Hummers, W.S., Offeman, R.E.: Preparation of graphitic oxide. *J. Am. Chem. Soc.* **80**, 1339 (1958)
64. Fu, F., Wang, Q.: Removal of heavy metal ions from wastewaters: a review. *J. Environ. Manage.* **92**, 407–418 (2011)
65. Khatamian, M., Khodakarampoor, N., Oskoui, M.S.: Efficient removal of arsenic using graphene-zeolite based composites. *J. Colloid Interface Sci.* **498**, 433–441 (2017)
66. Kumar, S.K., Jiang, S.J.: Chitosan-functionalized graphene oxide: a novel adsorbent an efficient adsorption of arsenic from aqueous solution. *J. Environ. Chem. Eng.* **4**, 1698–1713 (2016)
67. Huang, N.M., Lim, H.N., Chia, C.H., Yarmo, M.A., Muhamad, M.R.: Simple room temperature preparation of high-yield large-area graphene oxide. *Int. J. Nanomed.* **6**, 3443–3448 (2011)

68. Marcano, D.C., et al.: Improved synthesis of graphene oxide. *ACS Nano* **4**, 4806–4814 (2010)
69. Chen, J., Yao, B., Li, C., Shi, G.: An improved Hummers method for eco-friendly synthesis of graphene oxide. *Carbon* **64**, 225–229 (2013)
70. Kumari, S., et al.: A Novel Synthesis of the Graphene Oxide-Silver (GO-Ag) Nanocomposite for Unique Physiochemical Applications. *ACS Omega* **5**, 5041–5047 (2020)
71. Yang, G., Cao, J., Li, L., Rana, R.K., Zhu, J.J.: Carboxymethyl chitosan-functionalized graphene for label free electrochemical cytosensing. *Carbon* **51**, 124–133 (2013)
72. Yu, L., Ma, Y., Ong, C.N., Xie, J., Liu, Y.: Rapid adsorption removal of arsenate by hydrous cerium oxide–graphene composite. *RSC Adv.* **5**, 64983–64990 (2015)
73. Xubiao, L., Cheng, W., Shenglian, L., Ruizhi, D., Xinman, T., Guisheng, Z.: Adsorption of As(III) and As(V) from water using magnetite Fe₃O₄-reduced graphite oxide-MnO₂ nano composites. *Chem. Eng. J.* **187**, 45–52 (2012)
74. Jin, Z., Zimo, L., Yu, L., Ruiqi, F., Shams, A.B., Xinhua, X.: Adsorption behavior and removal mechanism of arsenic on graphene modified by iron-manganese binary oxide (FeMnOx/RGO) from aqueous solutions. *RSC Adv.* **5**, 67951–67961 (2015)
75. Yoon, Y., et al.: Comparative evaluation of magnetite–graphene oxide and magnetite-reduced graphene oxide composite for As(III) and As (V) removal. *J. Hazard. Mater.* **304**, 196–204 (2016)
76. Chen, M.L., Sun, Y., Huo, C.B., Liu, C., Wang, J.H.: Akaganeite decorated graphene oxide composite for arsenic adsorption/removal and its pre-concentration at ultra-trace level. *Chemosphere* **130**, 52–58 (2015)
77. Yoon, Y., Zheng, M., Ahn, Y.T., Park, W.K., Yang, W.S., Kang, J.W.: Synthesis of magnetite/non-oxidative graphene composites and their application for arsenic removal. *Sep. Pure Technol.* **178**, 40–48 (2017)
78. Guo, L., Ye, P., Wang, J., Fu, F., Wu, Z.: Three-dimensional Fe₃O₄-graphene macroscopic composites for arsenic and arsenate removal. *J. Hazard. Mater.* **298**, 28–35 (2015)
79. Dubey, S.P., Nguyen, T.T.M., Kwon, Y.N., Lee, C.: Synthesis and characterization of metal-doped reduced graphene oxide composites, and their application in removal of *Escherichia coli*, arsenic and 4-nitrophenol. *J. Ind. Eng. Chem.* **29**, 282–288 (2015)
80. Arriagada, D.C., Labbe, A.T.: Aluminum and iron doped graphene for adsorption of methylated arsenic pollutants. *Appl. Surf. Sci.* **386**, 84–95 (2016)
81. Mishra, A.K., Ramaprabhu, S.: Functionalized graphene sheets for arsenic removal and desalination of sea water. *Desalination* **282**, 39–45 (2011)
82. Kumar, S.K., Jiang, S.J.: Synthesis of magnetically separable and recyclable magnetic nanoparticles decorated with β -cyclodextrin functionalized graphene oxide an excellent adsorption of As(V)/(III). *J. Mol. Liq.* **237**, 387–401 (2017)
83. Lin, Y.J., Cao, W.Z., Ouyang, T., Chen, B.Y., Chang, C.T.: Developing sustainable graphene-doped titanium nano tube coated to super paramagnetic nanoparticles for arsenic recovery. *J. Taiwan Inst. Chem. Eng.* **70**, 311–318 (2017)
84. Yu, S., Wang, X., Tan, X., Wang, X.: Sorption of radionuclides from aqueous systems onto graphene oxide-based materials: a review. *Inorg. Chem. Front.* **2**, 593–612 (2015)
85. Yu, S., et al.: Efficient removal of uranium (VI) by layered double hydroxides supported nanoscale zerovalent iron: a combined experimental and spectroscopic studies. *Chem. Eng. J.* **365**, 51–59 (2019)
86. Madarang, C., et al.: Adsorption behavior of EDTA-graphene oxide for Pb(II) removal. *ACS. Appl. Mater. Inter.* **4**, 1186–1193 (2012)
87. Gercel, O., Gercel, H.: Adsorption of lead (II) ions from aqueous solutions by activated carbon prepared from biomass plant material of *Euphorbia rigida*. *Chem. Eng. J.* **132**, 289297 (2007)
88. Wang, X., Chen, Z., Yang, S.: Application of graphene oxides for the removal of Pb(II) ions from aqueous solutions: experimental and DFT calculation. *J. Mol. Liq.* **211**, 957–964 (2015)
89. Dungang, Gu., Fein, J.B.: Adsorption of metals onto graphene oxide: surface complexation modeling and linear free energy relationships. *Colloids Surf. A Physicochem. Eng. Asp.* **481**, 319–327 (2015)

90. Xu, D., Tan, X., Chen, C., Wang, X.: Adsorption of Pb(II) from aqueous solution to MX80 bentonite: effect of pH, ionic strength, foreign ions and temperature. *Appl. Clay Sci.* **41**, 37–46 (2008)
91. Lim, J., Mubarak, N., Abdullah, E., Nizamuddin, S., Khalid, M.: Recent trends in the synthesis of graphene and graphene oxide based nanomaterials for removal of heavy metals—a review. *J. Ind. Eng. Chem.* **66**, 29–44 (2018)
92. Lim, J., Mubarak, N., Khalid, M., Abdullah, E., Arshid, N.: Novel fabrication of functionalized graphene oxide via magnetite and 1-butyl-3-methylimidazolium tetrafluoroborate. *Nano-Struct. Nano-Objects* **16**, 403–411 (2018)
93. Zhao, G., et al.: Removal of Pb(II) ions from aqueous solutions on few-layered graphene oxide nanosheets. *Dalton Trans. J.* **40**, 10945–10952 (2011)
94. Wu, Y., et al.: Environmental remediation of heavy metal ions by novel-nanomaterials: a review. *Environ. Pollut.* **246**, 608–620 (2019)
95. Gu, P., et al.: Recent advances in layered double hydroxide-based nanomaterials for the removal of radionuclides from aqueous solution. *Environ. Pollut.* **240**, 493–505 (2018)
96. Chen, L., Feng, S., Zhao, D., Chen, S., Li, F., Chen, C.: Efficient sorption and reduction of U(VI) on zero-valent iron-polyaniline-graphene aerogel ternary composite. *J. Colloid Interf. Sci.* **490**, 197–206 (2017)
97. Ahmaruzzaman, M., Sharma, D.: Adsorption of phenols from wastewater. *J. Colloid. Interf. Sci.* **287**, 14–24 (2005)
98. Chen, J., et al.: Highly effective removal of Cu(II) by triethylenetetramine-magnetic reduced graphene oxide composite. *Appl. Surf. Sci.* **356**, 355–363 (2015)
99. Gao, Y., Chen, K., Ren, X., Alsaedi, A., Hayat, T., Chen, C.: Exploring the aggregation mechanism of graphene oxide in the presence of radioactive elements: experimental and theoretical studies. *Environ. Sci. Technol.* **52**(21), 12208–12215 (2018)
100. Zhao, D., et al.: Amino siloxane oligomer modified graphene oxide composite for the efficient capture of U (VI) and Eu (III) from aqueous solution. *ACS Sustain. Chem. Eng.* **5**, 10290–10297 (2017)
101. Zhao, G., Huang, X., Tang, Z., Huang, Q., Niu, F., Wang, X.: Polymer-based nanocomposites for heavy metal ions removal from aqueous solution: a review. *Polym. Chem.* **9**, 3562–3582 (2018)
102. Gao, Y., et al.: Graphene oxide interactions with co-existing heavy metal cations: adsorption, colloidal properties and joint toxicity. *Environ. Sci. Nano.* **5**, 362–371 (2018)
103. Huang, Z., et al.: Interaction mechanism of uranium (VI) with three-dimensional graphene oxide-chitosan composite: insights from batch experiments, IR, XPS, and EXAFS spectroscopy. *Chem. Eng. J.* **328**, 1066–1074 (2017)
104. Hu, B., et al.: Macroscopic and spectroscopic insights into the mutual interaction of graphene oxide, Cu (II), and Mg/Al layered double hydroxides. *Chem. Eng. J.* **313**, 527–534 (2017)
105. Siddiqui, S.I., Chaudhry, S.A., Islam, S.U.: Green adsorbents from plant sources for the removal of arsenic: an emerging wastewater treatment technology. In: Islam, S.U. (ed.) *Plant-Based Natural Products: Derivatives and Applications*, pp. 193–215. Wiley (2017)
106. Kumar, A.S.K., Jiang, S.J.: Synthesis of magnetically separable and recyclable magnetic nanoparticles decorated with β -cyclodextrin functionalized graphene oxide an excellent adsorption of As (V)/(III). *J. Mol. Liq.* **237**, 387–401 (2017)

Green Nanocomposites: Magical Solution for Environmental Pollution Problems



Noor Hadi Aysa and Ahmed Esmail Shalan 

Abstract The utilization of several sequence of green nanocomposites, by different researchers via different preparation techniques, consider as an effective hygienic source of materials toward clean environment and to reduce different environmental pollution issues. The green nanocomposites are highlighted as a result of their elevated effectiveness due to their large surface area or the towering ratio of area to volume, which made them attractive materials for wide applications, especially in environmental issues. The current chapter will give attention to different pathways to attain clean environment via starting to distance the world from dependence on harmful polymeric materials as well as getting rid of heavy metals from water through introducing of green nanocomposite materials. The accumulation problem of the non-dissolving harmful polymeric material wastes responsible for the emission of dioxin, which is a substance that has a major role in the abundance of cancerous diseases because of its ability to settle in the fatty tissues of humans and animals, can be recycled through burning it via using environmentally friendly nanocomposite materials. In addition, we will summarize the recent developments in the use of different nanocomposites to purify the environment and to remove the heavy metals from water.

Keywords Green · Nanocomposites · Environmental · Heavy metals · Pollution

N. H. Aysa

College of Pharmacy, University of Babylon, Babylon, Iraq

e-mail: phar.noor.hadi@uobabylon.edu.iq

A. E. Shalan (✉)

Central Metallurgical Research and Development Institute (CMRDI), P.O. Box 87, Helwan 11421, Cairo, Egypt

e-mail: ahmed.shalan@bcmaterials.net

BCMaterials-Basque Center for Materials, Applications and Nanostructures, Martina Casiano, UPV/EHU Science Park, Barrio Sarriena s/n, 48940 Leioa, Spain

© The Author(s), under exclusive license to Springer Nature Switzerland AG 2022

A. E. Shalan et al. (eds.), *Advances in Nanocomposite Materials for Environmental and*

Energy Harvesting Applications, Engineering Materials,

https://doi.org/10.1007/978-3-030-94319-6_13

Abbreviations

GNC	Green Nano Composites
PVC	Polyvinyl Chloride
VCM	Monomer vinyl chloride
HCl	Hydrochloric acid
CD	Compact disc
UV	Ultra-violet
COVID-19	Coronavirus Disease 2019
PDE	Personal defensive equipment
DNA	Deoxyribonucleic acid
IR	Infra-red
APU	Amphiphilic polyurethane
CNTs	Carbon Nano Tubes
SWNTs	Single-walled nanotubes
MWNTs	Multi-walled nanotubes
NO ₂	Nitrogen Dioxide
NH ₃	Ammonia
ppt	Parts-per-trillion
ppm	Parts per million
TCDD	Tetraklorodibenzo-p-dioxin
NO _x	Blend of NO and NO ₂
NO	Nitrogen Oxide
SO ₂	Sulfur dioxide
LCD	Liquid-crystal display
PC	Personal computer
TiO ₂	Titanium dioxide
CO ₂	Carbon dioxide
CO	Carbon monoxide

1 Introduction

Plastic is one of the harmful materials create better and easier life for us. At the same time, the present international production of plastics (200 million tons/year) has generated a vast environmental consideration, primarily associated with the waste generation by plastic packaging, that are accountable for 35–40% share of annuli plastics consumption [1].

The issue of ecological contamination has become a hot calamity in this day and age. Natural contamination, basically brought about by poisonous synthetic substances, incorporates air, water, and soil contamination [2].

Wherever researchers looked, they were horrified from the harmful effects of the plastics on the environment which are multifaceted. It triggers many dramatic problems such as environmental change, biodiversity, species wellbeing and biological system administrations and normal assets [3].

Meanwhile the decomposition of the most widely recognized plastics utilized on the planet are delivering ozone harming substances, methane and ethylene, into the air when presented to encompassing sunlight based radiation. That badly deteriorates the purity and quality of water, air, and food which threatening man health [4].

This remembers plastics for the land and in the ocean, not, at this point being used, however adding to gas outflows and subsequently to environmental change more seriously exaggerated in summer due to temperature elevation above 40 °C [5].

Nanotechnology offers a few endowments to upgrade existing natural advancements, and assemble new innovation that is superior to current innovation [6].

Nanocomposites, afford a golden mine of materials with marked unusual property combinations and unique design possibilities. Economic and ecological viewpoints are adding to the developing enthusiasm for green nanocomposites (GNC), because of their biodegradability, low harmfulness, low production costs, low removal expenses and inexhaustibility [7, 8].

GNC proposed perfections over conventional composites in mechanical, electrical, thermal, healthier indoor climates, antimicrobial and Self-cleaning materials [9–11] (Fig. 1).

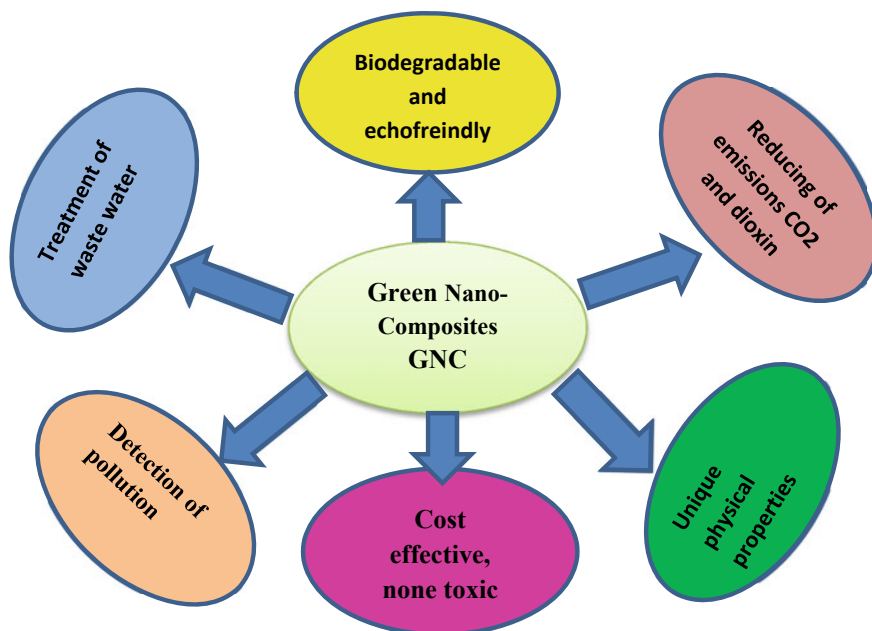


Fig. 1 A scheme showing the properties of GNC

2 Harmful Material

A considerable lot of us don't mull over the cosmetics we wear every day or the plastic compartment we use to put together our lunch. We realize natural food should be better for us, yet some of the time we simply would prefer not to pay the additional cash. Lamentably, the entirety of the above might be changing the manner in which our body normally works since they all contain endocrine disruptors called, xenoestrogens. Xenoestrogens like the phthalates do anyway not just mischief the male body. It has for since quite a while ago been seen that young ladies arrive at sexual development prior and prior [12–14]. Bosom malignant growth and augmentation of uterus (endometrium) is on the rising, not to ignore the higher movement of distortions. Climate maturing breaks greater plastic parts to littler pieces until just little conceded particles are left finished. The significant impact of plastics is the fermentation of our wellspring of water by the extensive increment of CO₂ air substance will be risky for marine life forms dependent on bones and limestone skeletons like corals [15].

Polyvinyl chloride (PVC) is a manufactured polymer material (or gum), which is developed by the rehashed expansion of the monomer vinyl chloride (VCM) with the formula (CH₂=CHCl) [16].

PVC has in this way a similar structure as polyethylene aside from the presence of chlorine. The chlorine in PVC speaks to 57% of the heaviness of the unadulterated polymer [13, 17]. Unadulterated PVC is an unbending material, which is precisely extreme, genuinely great climate safe, water and synthetic concoctions safe, electrically protecting, yet generally temperamental to heat and light [16–18].

The mechanical properties of PVC can be adjusted through the expansion of low sub-atomic weight aggravates that blend in with the polymer grid. Expansion of these purported plasticisers in different sums creates materials with a significant flexibility of characteristics that has prompted the utilization of (PVC) in a huge scope of uses [19].

So as to give the scope of properties required in the completed items, PVC polymer is blended in with various added substances. Contingent upon the expected application, the piece of the PVC compound (for example pitch+added substances) can fluctuate generally because of the various amounts of added substances which are fused within the polymer as fillers, stabilizers, ointments, plasticisers, shades or fire resistant [17, 20, 21]. So as to give the scope of properties required in the completed items, PVC polymer is blended in with various added substances. Contingent upon the planned application, the creation of the PVC compound (for example gum+added substances) can shift to a great extent because of the various amounts of added substances that are joined into the polymer as fillers, stabilizers, greases, plasticisers, shades or fire resistant [20, 22, 23].

The most significant classes of added substances, which should be evaluated logically as far as perilous qualities and dangers to people health and the environment, are stabilizers, specifically those which containing weighty metals, for example, lead and cadmium, and plasticisers, chiefly the phthalates [24].

Some of these plasticisers, specifically adipates, and organophosphates can likewise be utilized as conditioners in PVC. These plasticisers speak to just a little division of the utilization of plasticisers. Data on the impact of these plasticisers on the earth and on human prosperity from their utilization in PVC is restricted and further information would should be procured for an appropriate evaluation [20]. This part will hence focus on the most significant plasticisers in term of amount and the principle plasticisers right now evaluated in term This part will hence focus on the most significant plasticisers in term of amount and the principle plasticisers right now evaluated in term of ecological and wellbeing hazards [14, 22, 25–28].

Phthalates are high creation volume synthetic concoctions, five of which have been put, because of their possible dangers to human wellbeing and nature, on the initial three need records for hazard appraisal as per Regulation 793/93 on existing substances [12–14].

Long-chain length phthalates have a low biodegradability under typical states of sewage treatment and are just somewhat corrupted in common leachate and sewage treatment plants, where they gather on suspended solids [29–32]. Certain phthalates just as their (metabolites and debasement items) can cause unfavorable consequences for human wellbeing (specifically on liver and kidney). That way phthalates can be found in various items like floor coatings, pipes, rugs, counterfeit calfskin, nail clean, hues, cements, beautifiers and even food packings [12, 14, 33].

Adipates plasticizer used for things more relevant to human as toys, vinyl ground surface, wire and link, writing material, wood facade, covered textures, gloves, tubing, counterfeit cowhide, shoes, sealants, cover support and floor wax [34–36].

The term (dioxins) is utilized for individuals from the poly-halogenated fragrant hydrocarbons that are basically related, are diligent and bio-accumulative, and have a typical range of biologic reactions interceded by means of official to a particular high-partiality cell protein [37–39].

The most abnormal part of the poisonous activity of dioxin is that it influences numerous organs. Its belongings fluctuate extraordinarily, contingent upon the kind of cell, tissue, age and sex, species, and the circumstance and span of introduction [40–45].

Indeed, even inside a similar cell line, its harmfulness can differ enormously, contingent upon the way of life conditions and phase of development. Presentation to dioxin brings about various pathophysiological irregularities which seem, by all accounts, to be species just as organ or cell type explicit. These anomalies incorporate chloracne, thymic decay and safe brokenness, hepatic harm and steatosis, gastric epithelial [43, 44, 46–50] (Fig. 2).

In instances of over-warming during transformation of PVC through warming, framing and cooling, there is a danger of discharge of various debasement mixes, where HCl is the most significant one. In any case, the sums produced are little and have a low capability of unfavorable impacts on the earth [22]. PVC represents an issue at garbage removal since it can't be reused. When being singed dioxin rises in view of the high substance of chlorine. Salts staying in the channel should be arranged as uncommon perilous waste [22, 51]. PCBs (Polychlorinated Biphenyls) which have been used in concealing, fixing and plastic (in like manner in electrical

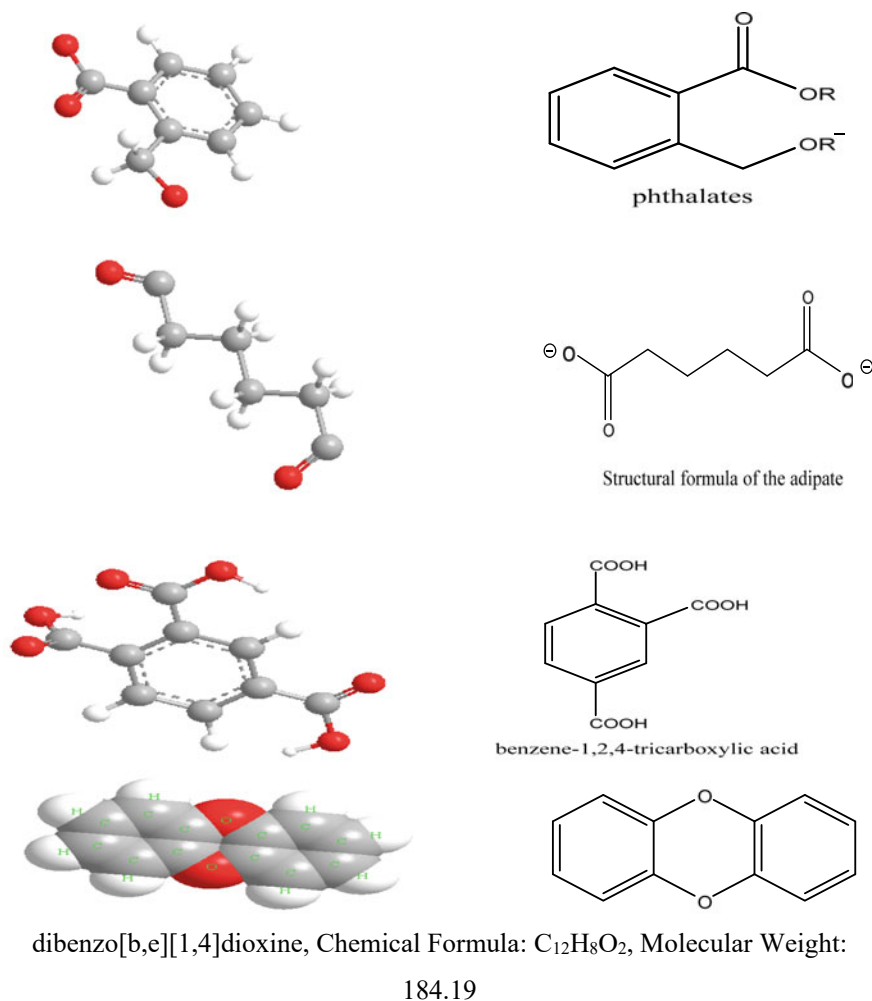


Fig. 2 A scheme illustrating some representative plasticizers identified in plastic or PVC

parts) as conditioners until the 80ies. The two substances are malignancy causing and endocrine disruptors upsetting the human hormone structure [39, 52].

Bisphenol A settles the plastic bundle and is besides the base material for a unique class of plastics, the polycarbonates. Polycarbonates are firm, semi rugged and highlight a high temperature resistance of up to 145 °C and obstruction against acids and oils (use in one manner and microwave plates, hard plastics, food bundles, clear family items like keys, infant jars, CD fronts, vehicle armatures) [22, 30, 53].

Both substance classes, (phthalates and bisphenol A) can be viewed as cancer-causing, can advance diabetes and corpulence and can go about as xenoestrogens; this implies they similarly affect the body as the hormone estrogen [14, 15] (Fig. 3).

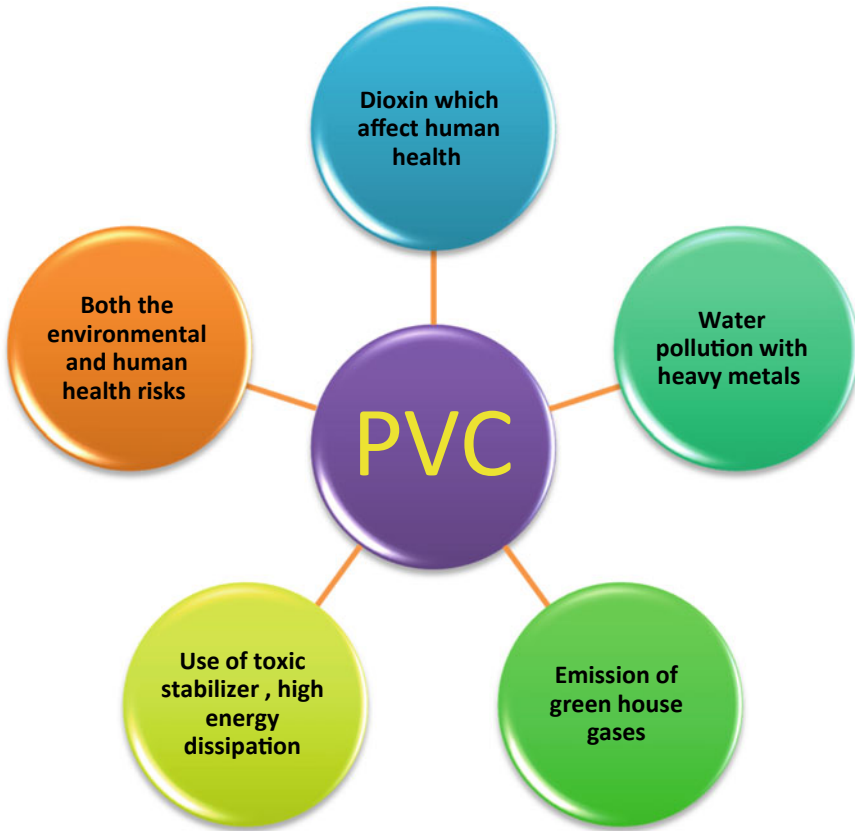


Fig. 3 A scheme illustrating some representative disadvantage identified in plastic or PVC

3 Physical Aging Degradation Factors (Weather- Uv- Ir- Water-Chemical)

Because of extraordinary climate related occasions (floods, heat waves, dry seasons, timberland fires, changes in vegetation, changes in the ocean and sea levels) are turning out to be increasingly visit. The difference in the worldwide atmosphere, its effects, and the requirement for arrangements speak to one of the most significant and broadly examined natural issues in mankind’s history. These variables impact upon the quality and dependability of polymer [54, 55].

Corruption is a convoluted non-straight time-subordinate procedure which influences straightforwardly or in a roundabout way a few properties of the material identified with its utilitarian attributes. In its last phase of debasement, a material doesn’t meet its practical prerequisites and is effectively inclined to mechanical disappointment. As a down to earth rule, the helpful existence of a material is viewed as arrived

at when its underlying mechanical quality is decreased by half. There are a few elements to screen and standards to characterize the level of debasement. Corruption of polymers is prompted by various outside components and instruments [56, 57].

Quickly, the different debasement types for polymers are the accompanying: Thermal corruption happens because of utilization or preparing of polymers at high temperatures, Photo-actuated corruption happens when, on introduction to the lively piece of the daylight, for example the bright (UV) radiation [30, 58, 59], or other high-vitality radiation, the polymer or polluting influences inside the polymer ingest the radiation and instigate compound responses [60, 61] (Fig. 4).

Additionally Mechanical corruption happens because of the impact of mechanical pressure strain. While hydrolytic debasement happens in polymers containing useful gatherings which are touchy with the impacts of water. Synthetic debasement happens when destructive synthetics, for example, ozone or the sulfur in agrochemicals, assault the polymer chain causing bond breaking or oxidation [56, 63–65]. Natural corruption is explicit to polymer with utilitarian gatherings that can be assaulted by microorganisms. Natural breakdown following landfill removal of biodegradable waste, including bioplastics, causes the arrival of ozone harming substances [2, 22, 45, 66] (Fig. 5).

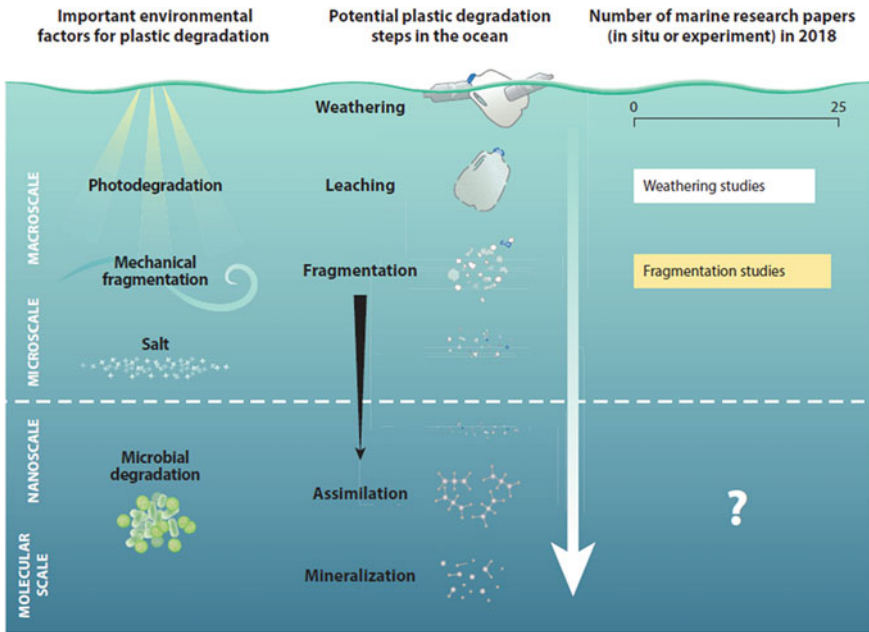


Fig. 4 Important natural factors that may conceivably catalyze diverse plastic debasement steps in the sea. The regions underneath the level ran line show steps that can be extrapolated from improved lab tests (left of the bolt) yet at the same time require affirmation for the sea (right of the bolt) [62]



Fig. 5 The harmful plastic material polluted water

4 The COVID-19 Pandemic and the New Challenges in Waste Management

The coming of the COVID-19 pandemic has improved the complexities of plastic waste administration. Our improved, hyper-clean lifestyle in the dread of transmission has helpfully moved our personal conduct standards like the utilization of PDE (Personal defensive equipment), expanded interest for plastic-bundled food and staple good, furthermore, the utilization of dispensable utensils. The insufficiencies and shortcomings of our present waste administration framework to manage the expanded reliance on plastic could irritate its fumble and spillage into nature, subsequently setting off another ecological emergency [67–70]. Ordering logical cleansing and the utilization of fixed sacks for safe removal of tainted plastic squanders ought to be a quick need to diminish the danger of transmission to sterilization laborers. Interests in round innovations like feedstock reusing, improving the foundation and ecological suitability of existing procedures could be the way to managing the plastic waste motions during such an emergency as shown in Fig. 6. Change towards ecologically inviting materials like bioplastics and holding new maintainable innovations would be significant to battling future pandemics.

Decrease in plastic contamination and simultaneously advancing reasonable plastic waste administration innovations can be accomplished by organizing our arrangements to impart individual conduct just as social, institutional changes [71–74] (Fig. 7).



Fig. 6 The ways in which covid-19 increasing plastic waste

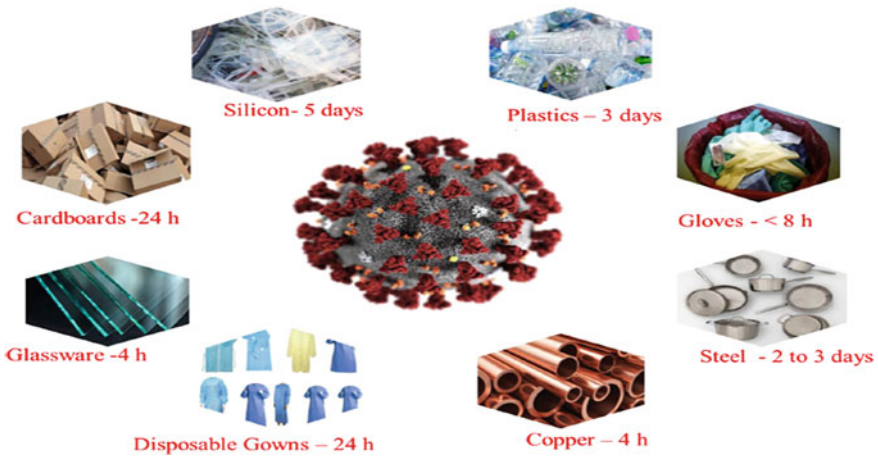


Fig. 7 Various sorts of waste and steadiness of Covid on its surface [Data were taken from (Kampf et al., 2020; van Doremalen et al., 2020) and delineation of the SARS-CoV-2 taken from (CDC, 2020) [72]

The COVID-19 emergency is featuring the basic function of plastic in day by day life. The board of the infection requires single-utilize plastic [71], regardless of whether superfluity is generally observed as a natural obligation in most different applications. A powerful evaluation apparatus can sum up the key environmental impressions of plastic items. Figure 8 shows an approach to reduce plastic pollution and to bring more inclusive and sustainable plastic waste management. Interest for clinical items and bundling is expanding pointedly during the COVID-19 pandemic. Different relief or concealment measures being executed in various nations are changing both the amount and nature of plastic waste. Single-use plastics are seen by purchasers as a sheltered option for some applications. In spite of the fact that plastics were demonstrated to be no superior to different materials as far as infection maintenance, superfluity is viewed as a significant preferred position by buyers organizing cleanliness. This has prompted an expansion in the utilization and removal of plastic items, in any event, for non-clinical applications [67, 68, 72, 73, 75, 76].

Waste covers, gloves, tissues and other defiled materials Furthermore, squander container food holders. It is normally delegated recyclable waste. At the present time It ought to be treated as a risky waste if there is a danger of pollution with microbes. As instances of COVID-19 develop catalyze the utilization of plastics and the age of blended waste. Than make strategic difficulties for waste the executives frameworks, among others monetary and ecological issues take a rearward sitting arrangement in the Coronavirus emergency [67, 68].

Burning and steam sanitization (an hour and a half, 120 °C) are normal ways for heat therapy of perilous clinical waste. Be that as it may, the remainders of these cycles can dispose of the infection, however aim natural contamination of another sort, as indicated by the outflows from the consuming (Fig. 9).

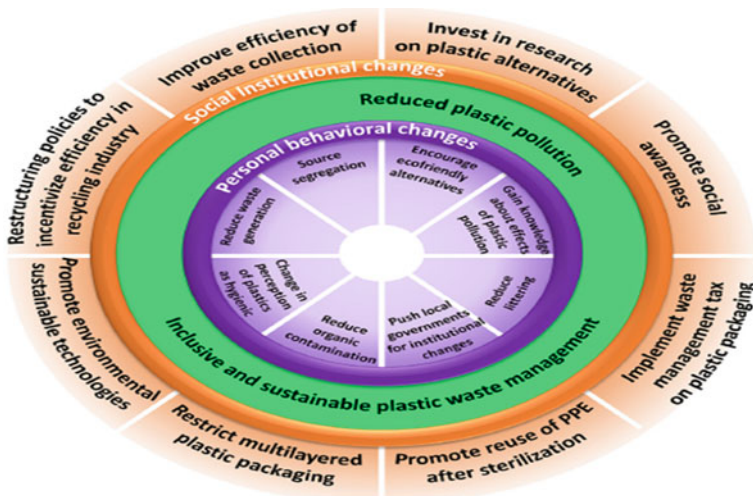


Fig. 8 Shows an approach to reduce plastic pollution and to bring more inclusive and sustainable plastic waste management [72]

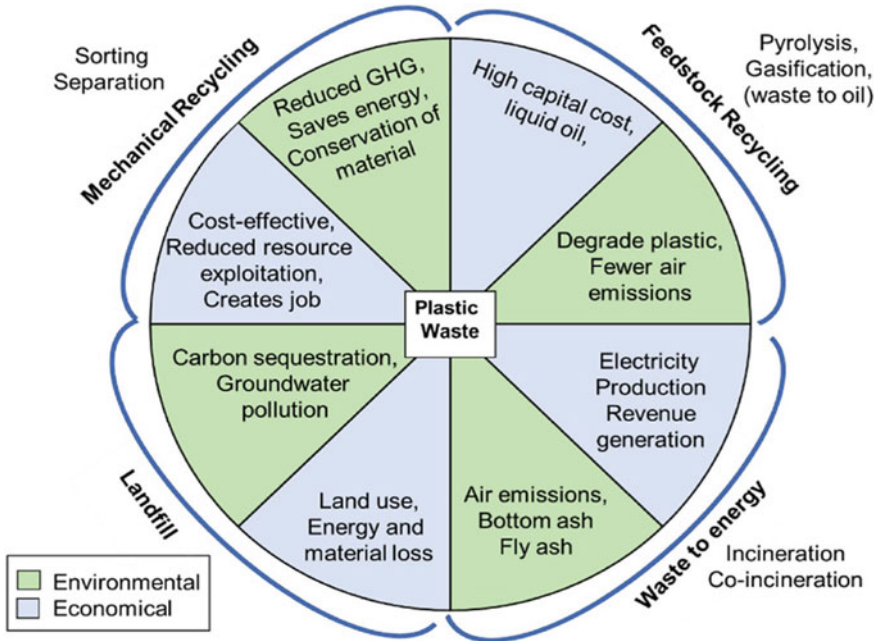


Fig. 9 Shows the ecological and monetary exhibition for different ways to deal with plastic waste administration [71]

5 Golden Solution After Detection of Pollution

Toward the start of the 21st Century, we are encountering a renaissance of inexhaustible polymers and a significant push towards the advancement of bio-based macromolecular materials [29, 30]. Is the fate of plastics going to be green? There are a few purposes behind this change in perspective and for the imagined progress from petro-science to bio-economy. From the financial perspective, in the wake of intersection the oil creation top, the lessening oil flexibly is probably going to additionally support the oil cost, particularly taking into account the normal flood in overall vitality request. This could radically affect the cost-adequacy and competitiveness of plastics.

Moving concoction crude material creation to sustainable assets or coal could defend plastics creation against this normal new future oil emergency [9, 17, 71, 77]. Thus, another significantly increasingly significant explanation is the developing worries of shoppers in regards to a dangerous atmospheric deviation, bringing about a flooding interest for feasible and “green” items [4, 9, 78]. Likewise, a wave of natural enactment and guidelines is impelling the improvement of earth well-disposed items with a low carbon impression. So as to diminish the impact of synthetics on the condition the utilization of biodegradable plastics would be important.



Fig. 10 The sample of degradable GNC

Human needs and employments of plastics in past decades have raised troublesome issues related to the earth and its assurance. Air defilement, helpless organization of waste, water pollution, and land/soil corruption, worldwide ecological change [57]. As for condition issues including tainting of air and water, pollution related to substantial metals, dioxin and ozone depleting substances that expansion worldwide warming [79]. Cause serious wellbeing perils, for example, malignant growth, harassed neural transmission, smothered safe frameworks, damaged reproductive systems, and affected mitochondrial functions [49].

GNC might be utilized as a promising and compelling apparatus to conquer significant difficulties in the improvement of remediation strategies that help in the assurance of the earth [80]. Right now, basic parts of natural issues will be audited and afterward the utilization of new nanomaterials, which can fill in as ecological cleaners, will be focused. Polymer-GNC have been utilized for the removal of many organic and inorganic contaminants such as heavy metals from wastewater [24]. GNC is easy to remove from the environment because it is degradable, none toxic as shown in figure below the degradable GNC prepared by us (Fig. 10).

6 Nanotechnology for Pollution Prevention

Counteraction of contamination alludes to a decrease in contamination sources and different practices that use crude materials, vitality, utilities and different assets successfully so as to lessen or wipe out waste age. Nanotechnology [5, 81] offers numerous imaginative techniques to lessen squander creation in different procedures, for example, improving assembling forms, decreasing unsafe synthetic substances, diminishing ozone depleting substance emanations and decreasing the utilization of biodegradable plastics [53, 54, 82]. The conversation underneath is only a couple of

numerous methodologies that should be possible to diminish natural contamination. Nanotechnology is effectively associated with this area, both for creating propelled materials that have low contamination levels and improving creation productivity in mechanical procedures (for example nanocatalysts) [3, 60].

7 Detection of Heavy Metals by Means of GNC Sensors

Heavy metal contamination is one of the most genuine natural issues, which subverts worldwide supportability. Numerous endeavors have been made to create convenient sensors for observing weighty metals in nature. Joining of nanomaterials and nanostructures into sensors prompts noteworthy improvement in the exhibition of gadgets regarding affectability, selectivity, multiplexed location capacity and versatility [83–86]. Likewise, little atoms, DNA (Deoxyribonucleic acid), proteins and microbes have been incorporated with inorganic materials to specifically tie substantial metals as the sub-atomic acknowledgment tests. This survey presents an ongoing development in optical, electrochemical and field-impact semiconductor sensors for substantial metal discovery [87].

The optical sensors are centered around colorimetric, fluorescent, surface-improved Raman dissipating and surface plasmon reverberation gadgets. What's more, optofluidic gadgets which incorporate optical parts with microfluidic chips are talked about. Moreover, nanoparticle-adjusted terminals, microelectrode (or nano-electrode) exhibits and microfluidic electrochemical sensors are summed up [84, 86] (Fig. 11).

GNC can discover application in different parts of industry, including food innovation. It have just been accounted for as promising nanosensors for the discovery of substantial metal particles in soil, water and food [88]. Novel GNC such as starch-based were set up in type of gels and thwarts of potato starch with inserted round quantum specks estimated 10–20 nm. They were portrayed utilizing photoluminescence, IR (Infra-red) and UV spectra. Pb^{2+} and Cu^{2+} particles diminished discharge power of the photoluminescent ghostly groups [53, 89]. The portrayed quantum dots have been gotten utilizing a straightforward, sheltered and minimal effort technique. Their properties make them elective sensors for Pb^{2+} and Cu^{2+} particles that could be applied in biotechnology and food innovation [84].

8 Water Remediation Using Green Polymer Nanocomposites

A great many creatures are murdered by plastics consistently, from winged animals to fish to other marine life forms. Almost 700 species, including jeopardized ones, are known to have been influenced by plastics [90]. Practically every types of seabird eats

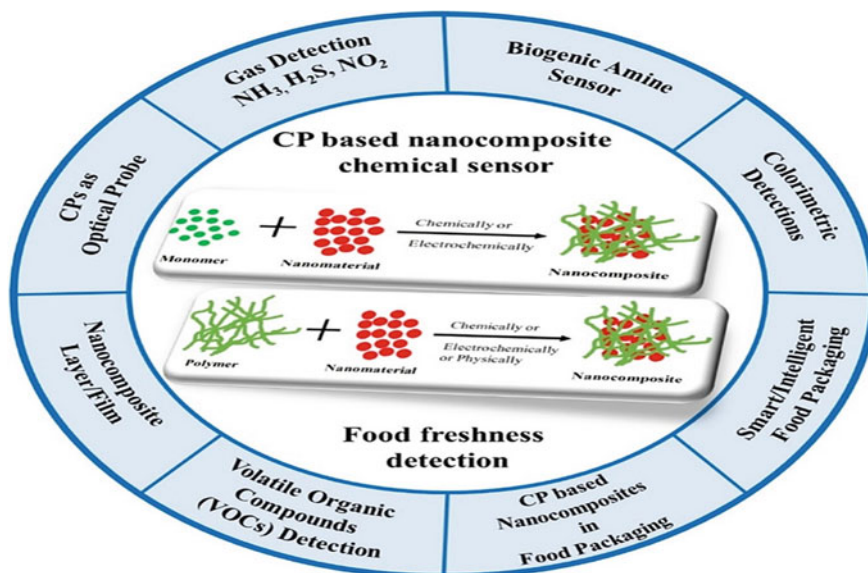


Fig. 11 The applications of highly sensitive and selective degradable GNC nanocomposite based chemosensors with Active/Intelligent technologies [85]

plastics Polymer nanoparticles have various usages, including water treatment and sunscreen. Using a practically identical principle as surfactant micelles, polymeric nanoparticles have amphiphilic properties, where each molecule has hydrophobic and hydrophilic parts [91]. At the point when water is accessible, the polymer will shape a polymer cell with a width of a couple of nanometers inside the hydrophobic part, while the hydrophilic part is outside. On polymer nanoparticles, crosslink happens going before the assortment of particles with the objective that their adequacy is kept up. Amphiphilic polyurethane (APU) nanoparticles [92] have good prospects as a remediation agent [91]. Countless animals are executed by plastics reliably, from winged creatures to fish to other marine living creatures. Very nearly 700 species, including risked ones, are known to have been impacted by plastics [35, 92].

In the application, GNC offer a reaction for regularly utilized ordinary surfactants to improve remediation of hydrophobic normal contaminants utilizing a siphon and treat framework. These contaminants are normally arranged into nonaqueous-stage fluid which sticks immovably to the ground with the target that it is hard to perfect, driving the remediation technique to be less and less appropriate. In this way, a surfactant is needed to tidy up these contaminants. Until this point, the utilization of polymeric nanoparticles is still in the examination stage [2, 93].

9 Application of GNC for Water Purenness

Various sorts of GNCs are at present being examined for use in cleaning of water. The major reason behind the usage of GNCs in any implementation lies in their individual features, which isn't exactly equivalent to their accomplices. The GNCs with upgraded porosity have capacity of mass trade, liquid support, and lighter weight. The penetrable materials have implementation in water cleaning yet restriction of permeable materials are low mechanical quality and strength. Physical adsorption is reversible in nature [94]. While, if the interest powers is a result of substance holding, it is complicated to desorb the chemisorbed species from the adsorbent surface. The GNC - based adsorbents were set up by infusing the inorganic nanoparticles onto the polymers, for instance, alginate, cellulose, porous tars, and molecule exchangers [8–10, 95] (Fig. 12).

Further, the expansion of attractive particles in nanocomposite make an invaluable element for effective cleaning of water [96–98]. Chitosan based attractive nanocomposites show enhanced adsorption rate and better adsorption proficiency for evacuation of different toxins. Their recuperation procedure is additionally exceptionally basic and simple [99–101].

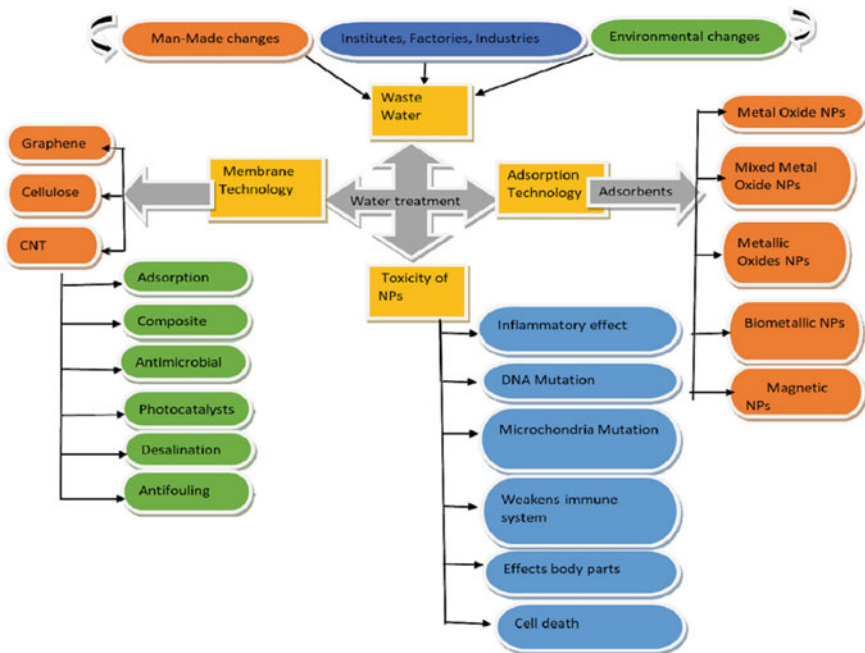


Fig. 12 The applications of nanomaterials in wastewater treatment. Such nanomaterial's which reasonable, eco-accommodating are, and effectively work everywhere scale is the need of the hour [81]

The other critical water harms are microscopic organism, especially a bacterium, virus, or fungus, pesticides, and other characteristic materials. The risks related with them fuse the plan of disinfection results and multidrug safe bacterial species and have incited the examination of forefront cleansing strategies [102–104].

The results revealed that GNC based Ag covering has basically redesigned antimicrobial activity, similarly as antifouling features of the layers. The microorganism departure limit in wastewater channel structures depends upon various components. These parts are (biotic and abiotic) in nature like clamminess, pH, temperature, kinds of microorganism. With respect to improving the methodology for water treatment containing regular and inorganic solutes, dendrite polymers are used as water-dissolvable ligands for filtration purposes [15, 79, 105].

Among all materials, GNC has been proposed to be the best natural impacts. Poisons released from consuming plastic waste in a consume the air either short or huge separations and are then kept onto land or into streams. Two or three these toxins, for instance, mercury, dioxins and furans proceed for critical intervals in the earth and tend to bio gather, which suggests they create in predators at the superior of the food web. Bioaccumulation of toxins typically occurs by suggestion through degraded water and food instead of breathing the dirtied air direct [22, 45, 107, 107].

In untamed life, the scope of impacts related with these poisons incorporates malignant growth, distorted posterity, conceptive disappointment, safe infections and inconspicuous neurobehavioral impacts [28]. Individuals can be revealed by suggestion essentially like untamed life, especially through usage of contaminated fish, meat and dairy things. Characteristic defilement can moreover be harmful to the fundamental uprightness of the polyethylene in light of manufactured attack of the polymer securities. Barometrical pollutions, for instance, nitrogen oxides, sulfur oxides, hydrocarbons [3, 108].

10 Nanotechnology(GNC) for the Adsorption of Venomous Gases

Water handling isn't the primary implementation for nanotechnology: noxious gases in the enveloping air can similarly be treated by GNC. A model nanotechnology application in noxious gas cleaning is the methodology of (Carbon Nano Tubes) CNTs with gold particles adsorption. The CNTs involve a hexagonal strategy of carbon particles in graphene sheets which incorporate the chamber rotate. There is a powerful cooperation between the two benzene rings of dioxin and the outside of CNTs [42, 57, 109–113].

These GNC materials have seemed to have extraordinary potential as predominant adsorbents to remove different kinds of characteristic and inorganic toxins, both in airstreams and in an aqueous situation. The adsorption breaking point of toxins by CNTs is essentially achieved by the pore structure and the presence of a wide extent of surface helpful get-togethers of CNTs that can be polished by changing the substance or warm treatment to tune the CNTs to have ideal execution for a specific clarification [114, 115].

11 GNC for Sensors and Detectors of Pollution

It has been perceived that long-life introduction to dirtied matter and substantial metal contamination is a critical driving element in messing wellbeing up as heart sicknesses, lung harm and different issues. Weighty metals could be found in different scopes of fixation. Also, heavy metals can't be separated by microorganisms (for example they are not being decomposed by bacteria or other living organisms). A serious extent of trouble in the recuperation of heavy-metal-contaminated land raises the pressure in developing on-site GNC sensors that can detect heavy metal ions before their concentration arrives at hazardous levels [103, 116].

Fast and exact nanosensors ready to recognize contaminations at the atomic level may upgrade the human capacity to ensure the supportability of human wellbeing and the earth. Huge increments in measure control, biological system checking and ecological based dynamic can happen if the accessible contaminant discovery innovation is most touchy and less costly [84, 86, 117].

A nano-contact sensor has been created and this sensor can possibly distinguish some metal particles without pre-concentration required. Specifically, this sensor is reasonable for the on location discovery of substantial metal particles, including radioactive components. Nano-contact sensors can be made in smaller than expected size and programmed mode with the goal which they are anything but difficult to utilize nearby or taken to the land. Likewise, the utilization of these sensors is additionally economical (savvy) since they are made with ordinary micro-electronics fabricating hardware utilizing straightforward electrochemical strategies [24, 84, 118].

12 GNC as Ultrasensitive Resistive Gas Sensor for Compound Responses Contemplates

A perfect sensor ought to have the accompanying noteworthy highlights: (i) activity at 70 °F; (ii) working in surrounding condition and no prerequisite of oxygen /air gracefully; (iii) no outer improvement, for example, Joule warming or UV enlightenment for reaction/recuperation; (iv) low discovery limit; (v) high affectability and re-productibility; (vi) quick reaction and recuperation; (vii) minimal effort and eco-accommodating, and so forth [97, 119, 120].

The sensor in all viewpoints meets all requirements to be considered as an incredible sensor. It must have affectability, solidness, reproducibility and strength. It considers uncovering fantastic gadget features that can be investigated as an alkali sensor for hazardous and clinical applications. The most significant preferences of the sensor are the 70 °F temperature activity in encompassing and wide scope of identification going from barely any parts-per-trillion (ppt) to hardly any hundred ppm [84, 87].

13 GNC and CNTs as (Gases) Dioxin and Green House Capture

One of contaminated gases is dioxin and related mixes (for example polychlorinated dibenzofuran and polychlorinated biphenyls) are steady and exceptionally poisonous contaminations [121–123]. Dioxins additionally influence the insusceptible and endocrine frameworks and fetal turn of events. Dioxin mixes are principally created from the burning of natural mixes in squander cremation. Dioxin mixes framed from burning have focuses in the scope of 10–500 ng/m³ [43]. Guidelines on dioxin discharges are mind boggling and differ across nations. By the by, it is commonly important to decrease dioxin fixations to under 1 ng/m³. Two basic audits have been distributed that talk about the counteraction and decrease of dioxin [3, 43, 44].

As of late, adsorption utilizing initiated carbon has been generally embraced to kill dioxins from squander burner in Europe and Japan. Evacuation of dioxin proficiency utilizing an enacted carbon-adsorbent is a more higher than different adsorbents in light of the fact that the bond vitality among dioxin and actuated carbon is greater than with different adsorbents [111].

Inferable from the extraordinary harmfulness of dioxin, a more effective adsorbent than initiated carbon is required with the goal that the dioxin outflows can be diminished to a lower level. Qazi et al. [110] have discovered that the cooperation of CNTs with dioxin is almost multiple times more grounded than the association of dioxin with initiated carbon. This improvement is presumably because of the nanotube bended surface contrasted and those for level sheets that gives more grounded connection powers among dioxin and CNTs [114, 115].

Poisonous emanations created during the extraction of materials for the creation of plastic staple packs, their assembling and their transportation add to corrosive down-pour, exhaust cloud and various other destructive impacts related with the utilization of oil, coal and flammable gas, for example, wellbeing states of coal excavators and ecological effects related with flammable gas and oil recovery [16, 22, 120]. Heavy metals might be delivered into nature from metal purifying and refining businesses, salvaged material, plastic and elastic enterprises, different shopper items and from consuming of waste containing these components. On delivery to the air, the components travel for huge separations and are saved onto the dirt, vegetation and water contingent upon their thickness. Once stored, these metals are not corrupted and continue in the earth for a long time harming people through inward breath, ingestion and skin retention. Intense presentation prompts queasiness, anorexia, spewing, gastrointestinal irregularities and dermatitis [14, 41, 44, 124].

14 NO_x Adsorption

There has been a significant exertion in the improvement of advances to dispose of the discharges of NO_x (blend of NO and NO₂) from non-renewable energy source ignition. Normal adsorbent used to expel NO_x at low temperatures incorporate particle trade zeolites, initiated carbon and FeOOH scattered on dynamic carbon nanofiber [63, 125]. (NO) can be feasibly adsorbed to started carbon in view of the surface reactivity helpful social affairs, regardless of the way that the proportion of adsorbed species is up 'til now not basic [63].

NO_x adsorption maybe associated to the individual structures, electronic properties and surface commonsense social occasions of CNTs. When NO and O₂ experience CNTs, NO is oxidized to NO₂ and a while later adsorbed outwardly of nitrate species. This idea was confirmed by [63, 125] who uncovered the oxidation of NO to NO₂ at 70 °F on incited carbon fiber. Differentiated and NO or NO₂, SO₂ can similarly be adsorbed on CNTs, regardless of the way that the adsorption rate isn't hopeful while CO₂ is extensively less adsorbed on CNTs [110].

15 Earth Benevolent Materials (Ecologically Agreeable Materials)

The utilization of nanotechnology can make a naturally genial substance, overriding commonly used destructive materials. An example, fluid translucent showcase (LCD) PC screens that are greater imperativeness profitable and less destructive have by and large displaced the screen cathode pillar tubes which include various noxious materials [126–128]. LCDs moreover don't contain lead and eat up less imperative-ness differentiated and PC screens. The use of CNTs in PC screens may furthermore decrease the impact on nature by murdering unsafe significant metals, lessening material and essentialness needs drastically, similarly as improving execution agreeing to client needs.

Also, the utilization of nanotechnology in composite materials can convey a substance with best mechanical and various features. This is because nanotechnology can convey structures that are humbler and lighter without defiling the idea of existing features. The utility of this advancement is the extended quality, diminutive system costs and a whole alteration, similarly as diminished ecological impact. Occurrences of earth all around arranged substances that can be conveyed using nano-technology are: the biodegradable plastics created utilizing polymers with a sub-nuclear structure that is simple to crumble; nanocomposite materials that are not unsafe to supersede the (lithium–graphite) anodes in battery-controlled batteries; and glass with self-purifying limit. An instance of a glass thing with self-purifying limit that has been made commonly open in the market has a layer (covering) made of uncommon TiO₂ nanocrystal [95, 129–132].

Exactly when introduced to sunlight, the glass is respond in two unique manners. At first, it crumbles each characteristic iota which are saved money on the surface of glass. Second, when introduced to rain, the movement of water will chop down the solid toxic substances through the surface of glass with no issue. In this thing, TiO_2 is as a humble film in the extent of 2–20 nm applied by high-temperature gas-stage declaration. The film thickness is basic to ensure the most extraordinary photograph reactant activity and straightforwardness .[131]

The surface covering has a tendency to mix with, dissolve in, or be wetted by water (contact point with water is 20° , more diminutive while differentiated and customary soda glass with 40° of water contact edge). Exactly when hard toxic substances are kept on the surface of glass, the contact edge surface grows then decays again because of light. Photochemical responses [127, 130, 133], that need oxygen, are erratic and incorporate different things between the revolutionaries. TiO_2 is simply going about as a driving force and isn't eaten up throughout the reaction. The reaction will achieve the crumbling of characteristic issue into CO_2 . At the same time, the contact point surface is diminished further in view of light (between 20° – 15°). After light, solid pollutions will be even more viably cleaned from the glass surface by storm. Water can be propagated effectively by confining a covering outwardly of the glass [129, 130].

16 Conclusions

Green -Nanotechnology has been made to fulfill the explanation of keeping up characteristic reasonability. For this situation, natural reasonability isn't obliged to human natural issues, yet also human clinical issues. Advances that have been made fuse progresses that can redesign and enhance the conventional inventive limits and new developments that supersede the common advancements.

Regardless of being used in purifying and water refinement, green nanotechnology can in like manner be utilized to purify the air from unsafe gases, for instance, CO and dioxins by using CNTs, gold nanoparticles and various adsorbents. Nanomaterials such as nanoparticles and nanotubes can similarly be used as a sensor for unsafe substances, particularly materials that are problematic to perceive with traditional advancement since they have an amazingly little in size and obsession. The use of nanotechnology concept in the natural field isn't obliged to the situations where ecological debasement has achieved. Nanotechnology can in like manner be used to thwart the arrangement of defilement. Its utilization join the association of green nanomaterials, coatings and biocides to hinder the appearance of dangerous materials into the condition.

17 Summary and Future View

Recently, after the emergence of the Corona pandemic, the increasing demand for single-use plastic materials to avoid transmitting the virus has led to a steady accumulation of plastic waste. Today for humans, a group called “dioxin” that inhabits fat cells in our bodies, disguises and acts as a hormone and disrupts the work of our natural hormones.

The burning of plastic is accompanied by the emission of dozens of dangerous substances, including: benzene, toxic heavy metals such as tin, chromium and other small particles that enter the body through the respiratory system and cause damage to the immune system, the nervous system, fertility, the liver and kidneys, and it has become scientifically stable that dioxin spreads in the body. Humans and animals occur, and chemical transformations occur that directly affect the body’s organs, the nervous system and the rest of the body’s systems.

From here comes the call through this article to act with the highest levels of self-responsibility and to refrain from the following: Refrain from burning any kind of waste, especially household waste because it contains a lot of nylon and plastic, as well as solid waste resulting from building or old electrical tools. Refrain from dumping waste on roadsides, fields, valleys, waterways and open places.

The blatant lack of knowledge of the dangers of plastics on the part of those concerned is very flawed. It is also of concern that plastic waste is treated in the worst possible way, which is open burning. Burning them will lead to the production of extremely dangerous gases, dioxin, and their attachment to crops, animals and the rest of our food chain.

Regardless of the authorities’ role in providing basic services owed to citizens, the primary responsibility remains with us, to protect ourselves and our children from the health damages caused by various environmental pests.

Therefore, the current study suggests several means to reduce the risks that the study referred to, including: Encouraging the adoption of sound alternatives such as bioplastic manufacturing processes derived from polylactic acid (polylactic), which is an environmentally friendly compound and a practical alternative to traditional plastics produced from petrochemicals.

Using materials extracted from nature to prepare plastics that are naturally degraded by nature factors and using nanotechnology in order for the prepared green materials to acquire the element of durability and strength to the extent that makes them biodegradable, makes them cheaper, environmentally friendly, reduces pollution and can help the global economy. A futuristic view of solving waste disposal issues has led to the challenge of manufacturing green nanocomposites using biodegradable polymers.

A series of interesting polymers has been achieved through several research activities ranging from thermoplastic starch and its blends, cellulose, gelatin, chitosan, etc.

In nanotechnology, to achieve maximum properties, these particles must be very thin (one nanometer) and very wide (500 nm). Achieving this task requires sophisticated machinery such as high pressure homogenizers and embedded dispersants. Although modern technology has made this possible, it has been observed that efforts to achieve nanoparticles that produce compounds of most biodegradable polymers possess poor mechanical properties and low thermal deformation temperatures, which limits their use in wide applications. Therefore, carbon nanotubes can be used as nanocomposites of degradable polymers to provide a range of composites with improved mechanical properties, extended durability and better thermal stability.

Another advantage that green nanocomposites provide is the ability to recycle the embedded carbon nanotubes due to the decomposition of the degradable polymer. Degradation of the biodegradable polymer can be achieved either through microbial degradation or enzymatic hydrolysis under specific conditions of pH and temperature. After decomposition, the recovered carbon nanotubes may act as stiffeners to produce new compounds. The reuse and recycling of carbon nanotubes can reduce waste disposal, while at the same time cost-effective for material processing.

References

1. Chatterjee, A.M., Salanitro, J.P.: Environmentally degradable polymer composition. Google Patents (1992)
2. Bhakta, J.N., et al.: Impact of nanomaterial in environmental remediation and toxicity. *Int. J. Environ. Technol. Sci.* **2**, 38–52 (2016)
3. Tue, N.M., et al.: Environmental contamination and human exposure to dioxin-related compounds in e-waste recycling sites of developing countries. *Environ. Sci. Process Impacts* **15**(7), 1326–1331 (2013)
4. Koshy, R.R., et al.: Environment friendly green composites based on soy protein isolate—a review. *Food Hydrocolloids* **50**, 174–192 (2015)
5. Rastogi, S., Sharma, G., Kandasubramanian, B.: Nanomaterials and the environment. In: *The ELSI Handbook of Nanotechnology*, pp. 1–23 (2020)
6. Diallo, C.M., Brinker, J.: Nanotechnology for sustainability: environment, water, food, minerals, and climate. In: Roco, M.C., Hersam, M.C., Mirkin, C.A. (eds.) *Nanotechnology Research Directions for Societal Needs in 2020*, pp. 221–259. Springer, Dordrecht (2011). https://doi.org/10.1007/978-94-007-1168-6_6
7. Batool, M., Nazar, M.F., Awan, A., et al.: Bismuth-based heterojunction nanocomposites for photocatalysis and heavy metal detection applications. *Nano-struct. Nano-objects* **27**, 100762 (2021)
8. Abu Elella, M.H., Goda, E.S., Abdallah, H.M., et al.: Innovative bactericidal adsorbents containing modified xanthan gum/montmorillonite nanocomposites for wastewater treatment. *Int. J. Biol. Macromol.* **167**, 1113–1125 (2021)
9. Barhoum, A., et al.: A broad family of carbon nanomaterials: classification, properties, synthesis, and emerging applications. In: Barhoum, A., Bechelany, M., Makhlof, A. (eds.) *Handbook of Nanofibers*, pp. 1–40. Springer, Cham (2019). https://doi.org/10.1007/978-3-319-42789-8_59-2
10. Abdellatif Soliman, S.M., Sanad, M.F., Shalan, A.E.: Synthesis, characterization and antimicrobial activity applications of grafted copolymer alginate-g-poly(N-vinyl imidazole). *RSC Adv.* **11**, 11541–11548 (2021)

11. Abdelbasir, S.M., Shalan, A.E.: An overview of nanomaterials for industrial wastewater treatment. *Korean J. Chem. Eng.* **36**, 1209–1225 (2019)
12. Abdel Messih, M.F., Shalan, A.E., Sanad, M.F., Ahmed, M.A.: Facile approach to prepare ZnO@SiO₂ nanomaterials for photocatalytic degradation of some organic pollutant models. *J. Mater. Sci. Mater. Electron.* **30**, 14291–14299 (2019)
13. Carlstedt, F., Jönsson, B., Bornehag, C.G.: PVC flooring is related to human uptake of phthalates in infants. *Indoor Air* **23**(1), 32–39 (2013)
14. Heudorf, U., Mersch-Sundermann, V., Angerer, J.: Phthalates: toxicology and exposure. *Int. J. Hyg. Environ. Health* **210**(5), 623–634 (2007)
15. Weidemann, E., et al.: 14th congress of combustion by-products and their health effects—origin, fate, and health effects of combustion-related air pollutants in the coming era of bio-based energy sources. *Environ. Sci. Pollut. Res.* **23**(8), 8141–8159 (2016)
16. Johnsen, T.: How Regulation and Industry Innovation Have Eliminated Dioxin Emissions from PVC Production and Waste Incineration (2011)
17. Yang, P., et al.: Novel environmentally sustainable cardanol-based plasticizer covalently bound to PVC via click chemistry: synthesis and properties. *RSC Adv.* **5**(22), 16980–16985 (2015)
18. Taverdet, J., Vergnaud, J.: Study of transfer process of liquid into and plasticizer out of plasticized PVC by using short tests. *J. Appl. Polym. Sci.* **29**(11), 3391–3400 (1984)
19. Van Oosterhout, J., Gilbert, M.: Interactions between PVC and binary or ternary blends of plasticizers. Part I. PVC/plasticizer compatibility. *Polymer* **44**(26), 8081–8094 (2003)
20. Da Silva, M.A., et al.: Polyvinylchloride (PVC) and natural rubber films plasticized with a natural polymeric plasticizer obtained through polyesterification of rice fatty acid. *Polym. Testing* **30**(5), 478–484 (2011)
21. Greco, A., et al.: Plasticizer for poly (vinyl chloride) from cardanol as a renewable resource material. *Polym. Degrad. Stab.* **95**(11), 2169–2174 (2010)
22. Alabi, O., et al.: Public and environmental health effects of plastic wastes disposal: a review. *J. Toxicol. Risk Assess.* **5**, 021 (2019)
23. Austin, H.P., et al.: Characterization and engineering of a plastic-degrading aromatic polyesterase. *Proc. Natl. Acad. Sci.* **115**(19), E4350–E4357 (2018)
24. Mahmoud, M.E., Fekry, N.A., El-Latif, M.M.: Nanocomposites of nanosilica-immobilized-nanopolyaniline and crosslinked nanopolyaniline for removal of heavy metals. *Chem. Eng. J.* **304**, 679–691 (2016)
25. Lithner, D., Larsson, Å., Dave, G.: Environmental and health hazard ranking and assessment of plastic polymers based on chemical composition. *Sci. Total Environ.* **409**(18), 3309–3324 (2011)
26. Milkov, L., et al.: Health status of workers exposed to phthalate plasticizers in the manufacture of artificial leather and films based on PVC resins. *Environ. Health Perspect.* **3**, 175–178 (1973)
27. Momani, B.L.: Assessment of the Impacts of Bioplastics: Energy Usage, Fossil Fuel Usage, Pollution, Health Effects, Effects on the Food Supply, and Economic Effects Compared to Petroleum Based Plastics (2009)
28. Pesatori, A.C., et al.: Dioxin exposure and non-malignant health effects: a mortality study. *Occup. Environ. Med.* **55**(2), 126–131 (1998)
29. Ahmad, N., et al.: Novel bio-nanocomposite materials for enhanced biodegradability and photocatalytic activity. *New J. Chem.* **41**(18), 10198–10207 (2017)
30. Ilyas, R., et al.: Thermal, biodegradability and water barrier properties of bio-nanocomposites based on plasticised sugar palm starch and nanofibrillated celluloses from sugar palm fibres. *J. Biobased Mater. Bioenergy* **14**(2), 234–248 (2020)
31. Tokiwa, Y., et al.: Biodegradability of plastics. *Int. J. Mol. Sci.* **10**(9), 3722–3742 (2009)
32. Vaezi, K., Asadpour, G., Sharifi, S.H.: Bio nanocomposites based on cationic starch reinforced with montmorillonite and cellulose nanocrystals: Fundamental properties and biodegradability study. *Int. J. Biol. Macromol.* **146**, 374–386 (2020)
33. Schulsinger, C., Møllgaard, K.: Polyvinyl chloride dermatitis not caused by phthalates. *Contact Dermatitis* **6**(7), 477–480 (1980)

34. Cano, J., et al.: Determination of adipate plasticizers in poly (vinyl chloride) by microwave-assisted extraction. *J. Chromatogr. A* **963**(1–2), 401–409 (2002)
35. Felder, J., Adams, W., Saeger, V.: Assessment of the safety of dioctyl adipate in freshwater environments. *Environ. Toxicol. Chem. Int. J.* **5**(8), 777–784 (1986)
36. Oriol-Hemmerlin, C., Pham, Q.: Poly 1, 3-butylene adipate Reoplex® as high molecular weight plasticizer for PVC-based cling films—microstructure and number-average molecular weight studied by ¹H and ¹³C NMR. *Polymer* **41**(12), 4401–4407 (2000)
37. Alcock, R.E., Jones, K.C.: Dioxins in the environment: a review of trend data. *Environ. Sci. Technol.* **30**(11), 3133–3143 (1996)
38. Behnisch, P.A., Hosoe, K., Sakai, S.-I.: Bioanalytical screening methods for dioxins and dioxin-like compounds—a review of bioassay/biomarker technology. *Environ. Int.* **27**(5), 413–439 (2001)
39. Bertazzi, P.A., et al.: Dioxin exposure and cancer risk: a 15-year mortality study after the “seveso accident.” *Epidemiology* **8**(6), 646–652 (1997)
40. Behnisch, P.A., Hosoe, K., Sakai, S.-I.: Brominated dioxin-like compounds: in vitro assessment in comparison to classical dioxin-like compounds and other polyaromatic compounds. *Environ. Int.* **29**(6), 861–877 (2003)
41. Bertazzi, P.A., et al.: Health effects of dioxin exposure: a 20-year mortality study. *Am. J. Epidemiol.* **153**(11), 1031–1044 (2001)
42. Kang, H.S.: Theoretical study of binding of metal-doped graphene sheet and carbon nanotubes with dioxin. *J. Am. Chem. Soc.* **127**(27), 9839–9843 (2005)
43. Mandal, P.K.: Dioxin: a review of its environmental effects and its aryl hydrocarbon receptor biology. *J. Comp. Physiol. B.* **175**(4), 221–230 (2005)
44. Mocarelli, P., et al.: Dioxin exposure, from infancy through puberty, produces endocrine disruption and affects human semen quality. *Environ. Health Perspect.* **116**(1), 70–77 (2008)
45. Van den Berg, M., et al.: The 2005 World Health Organization reevaluation of human and mammalian toxic equivalency factors for dioxins and dioxin-like compounds. *Toxicol. Sci.* **93**(2), 223–241 (2006)
46. Fiedler, H., Hutzinger, O., Timms, C.: Dioxins: sources of environmental load and human exposure. *Toxicol. Environ. Chem.* **29**(3), 157–234 (1990)
47. Huang, H., Buekens, A.: On the mechanisms of dioxin formation in combustion processes. *Chemosphere* **31**(9), 4099–4117 (1995)
48. Manz, A., et al.: Cancer mortality among workers in chemical plant contaminated with dioxin. *Lancet* **338**(8773), 959–964 (1991)
49. Mayani, A., et al.: Dioxin concentrations in women with endometriosis. *Human Reprod. (Oxf. Engl.)* **12**(2), 373–375 (1997)
50. Olsman, H., et al.: Formation of dioxin-like compounds as photoproducts of decabrominated diphenyl ether (DEBDE) during UV-irradiation. *Organohalogen Compd.* **58**, 41–44 (2002)
51. Al-Salem, S., Al-Samhan, M.: Plastic solid waste assessment in the state of Kuwait and proposed methods of recycling. *Am. J. Appl. Sci.* **4**(6), 354–356 (2007)
52. Heidari, A.: Biomedical resource oncology and data mining to enable resource discovery in medical, medicinal, clinical, pharmaceutical, chemical and translational research and their applications in cancer research. *Int. J. Biomed. Data Min.* **06**(02), e103 (2017)
53. Amalia, D., Saleh, D., Djonaedi, E.: Synthesis of biodegradable plastics using corn starch and corn husk as the fillers as well as chitosan and sorbitol. *J. Phys. Conf. Ser.* **1442**(1), 012007 (2020). <https://doi.org/10.1088/1742-6596/1442/1/012007>
54. Albertsson, A.-C., Karlsson, S.: Biodegradation and test methods for environmental and biomedical applications of polymers. In: Barenberg, S.A., Barenberg, S.A., Brash, J.L., Narayan, R., Redpath, A.E. (eds.) *Degradable Materials: Perspectives, Issues, and Opportunities*, pp. 263–294. CRC Press (2018). <https://doi.org/10.1201/9781351071321-11>
55. Nemphos, S.P., Kharas, G.B.: Higher heat degradable polymer alloys. Google Patents (1994)
56. Achrai, B., Wagner, H.D.: Micro-structure and mechanical properties of the turtle carapace as a biological composite shield. *Acta Biomater.* **9**(4), 5890–5902 (2013)

57. Ayatollahi, M.R., Shadlou, S., Shokrieh, M.M.: Mixed mode brittle fracture in epoxy/multi-walled carbon nanotube nanocomposites. *Eng. Fract. Mech.* **78**(14), 2620–2632 (2011)
58. Ray, S., Cooney, R.P.: Thermal degradation of polymer and polymer composites. In: *Handbook of Environmental Degradation of Materials*, pp. 185–206. Elsevier (2018)
59. Sen, S., Patil, S., Argyropoulos, D.S.: Thermal properties of lignin in copolymers, blends, and composites: a review. *Green Chem.* **17**(11), 4862–4887 (2015)
60. Bazgan, S., et al.: Propagation of UV radiation through meta-materials and its application in bio decontamination. *Romanian Rep. Phys.* **67**(4), 1602–1607 (2015)
61. Khan, M.A., et al.: Preparation and characterization of ultra violet (UV) radiation cured bio-degradable films of sago starch/PVA blend. *Carbohydr. Polym.* **63**(4), 500–506 (2006)
62. Oberbeckmann, S., Labrenz, M.: Marine microbial assemblages on microplastics: diversity, adaptation, and role in degradation. *Ann. Rev. Mar. Sci.* **12**(1), 209–232 (2020)
63. Carvalho, R.A., et al.: WPI and cellulose nanofibres bio-nanocomposites: effect of thyme essential oil on the morphological, mechanical, barrier and optical properties. *J. Polym. Environ.* **28**(1), 231–241 (2020)
64. Farah, S., Anderson, D.G., Langer, R.: Physical and mechanical properties of PLA, and their functions in widespread applications—a comprehensive review. *Adv. Drug Deliv. Rev.* **107**, 367–392 (2016)
65. Tavakoli, M., Karbasi, S., Bakhtiari, S.S.E.: Evaluation of physical, mechanical, and biodegradation of chitosan/graphene oxide composite as bone substitutes. *Polym. Plast. Technol. Mater.* **59**(4), 430–440 (2020)
66. Ragnarsdottir, K.V.: Environmental fate and toxicology of organophosphate pesticides. *J. Geol. Soc.* **157**(4), 859–876 (2000)
67. Fadare, O.O., Okoffo, E.D.: Covid-19 face masks: a potential source of microplastic fibers in the environment. *Sci. Total Environ.* **737**, 140279 (2020)
68. Hale, R.C., Song, B.: *Single-Use Plastics and COVID-19: Scientific Evidence and Environmental Regulations*. ACS Publications (2020)
69. Jessop, Z.M., et al.: Personal protective equipment for surgeons during COVID-19 pandemic: systematic review of availability, usage and rationing. *Brit. J. Surg.* **107**(10), 1262–1280 (2020). <https://doi.org/10.1002/bjs.11750>
70. Matava, C.T., Yu, J., Denning, S.: Clear plastic drapes may be effective at limiting aerosolization and droplet spray during extubation: implications for COVID-19. *Can. J. Anesth./Journal canadien d'anesthésie* **67**(7), 902–904 (2020)
71. Vanapalli, K.R., et al.: Emissions and environmental burdens associated with plastic solid waste management. *Plast. Energy* (2019)
72. Sharma, H.B., et al.: Challenges, opportunities, and innovations for effective solid waste management during and post COVID-19 pandemic. *Res. Conserv. Recycl.* **162**, 105052 (2020)
73. Silva, A.L.P., et al.: Rethinking and optimising plastic waste management under COVID-19 pandemic: policy solutions based on redesign and reduction of single-use plastics and personal protective equipment. *Sci. Total Environ.* **742**, 140565 (2020)
74. Patrício, A.L., et al.: Increased plastic pollution due to Covid-19 pandemic: challenges and recommendations. *Chem. Eng. J.* **405**, 126683 (2021)
75. Eroğlu, H.: Effects of Covid-19 outbreak on environment and renewable energy sector. *Environ. Dev. Sustain.* **23**(4), 4782–4790 (2020)
76. Saadat, S., Rawtani, D., Hussain, C.M.: Environmental perspective of COVID-19. *Sci. Total Environ.* **728**, 138870 (2020)
77. Khalil, H.A., et al.: Seaweed based sustainable films and composites for food and pharmaceutical applications: a review. *Renew. Sustain. Energy Rev.* **77**, 353–362 (2017)
78. Ebrahimezhad, A., et al.: Green synthesis of silver nanoparticles capped with natural carbohydrates using ephedra intermedia. *Nanosci. Nanotechnol. Asia* **7**(1), 104–112 (2017)
79. Bates, A.: *Transforming Plastic: From Pollution to Evolution*. GroundSwell Books (2019)
80. Kausar, A.: Progress in green nanocomposites for high-performance applications. *Mater. Res. Innov.* **25**(1), 53–65 (2020)

81. Deshpande, B., et al.: Prospective of nanotechnology in degradation of waste water: a new challenges. *Nano-Struct. Nano-Objects* **22**, 100442 (2020)
82. Song, J., et al.: Biodegradable and compostable alternatives to conventional plastics. *Philos. Trans. R. Soc. B Biol. Sci.* **364**(1526), 2127–2139 (2009)
83. Mascini, M., et al.: Piezoelectric sensors for dioxins: a biomimetic approach. *Biosens. Bioelectron.* **20**(6), 1203–1210 (2004)
84. Mousavi, S., et al.: Nanosensors for Chemical and Biological and Medical Applications. *Med. Chem. (Los Angeles)* **8**(8), 205–217 (2018)
85. Pavase, T.R., et al.: Recent advances of conjugated polymer (CP) nanocomposite-based chemical sensors and their applications in food spoilage detection: a comprehensive review. *Sens. Actuators B Chem.* **273**, 1113–1138 (2018)
86. Rani, V., Verma, M.L.: Biosensor applications in the detection of heavy metals, polychlorinated biphenyls, biological oxygen demand, endocrine disruptors, hormones, dioxin, and phenolic and organophosphorus compounds. In: Tuteja, S.K., Arora, D., Dilbaghi, N., Lichtfouse, E. (eds.) *Nanosensors for Environmental Applications*, pp. 1–28. Springer, Cham (2020). https://doi.org/10.1007/978-3-030-38101-1_1
87. Entezami, A.A., Massoumi, B.: Artificial muscles, biosensors and drug delivery systems based on conducting polymers: a review. *Iran. Polym. J.* **15**, 13–30 (2006)
88. Husen, A.: Gold nanoparticles from plant system: synthesis, characterization and their application. In: Ghorbanpour, M., Manika, K., Varma, A. (eds.) *Nanoscience and Plant–Soil Systems*, pp. 455–479. Springer, Cham (2017). https://doi.org/10.1007/978-3-319-46835-8_17
89. Swanson, C., et al.: Starch-plastic materials—preparation, physical properties, and biodegradability (a review of recent USDA research). *J. Environ. Polym. Degrad.* **1**(2), 155–166 (1993)
90. Watlington, K.: *Emerging nanotechnologies for site remediation and wastewater treatment*. Environmental Protection Agency, Washington DC (2005)
91. Nagappan, S., et al.: Bio-inspired, multi-purpose and instant superhydrophobic–superoleophilic lotus leaf powder hybrid micro–nanocomposites for selective oil spill capture. *J. Mater. Chem. A* **1**(23), 6761–6769 (2013)
92. Santamaria-Echart, A., et al.: Cellulose nanocrystals reinforced environmentally-friendly waterborne polyurethane nanocomposites. *Carbohydr. Polym.* **151**, 1203–1209 (2016)
93. Gaur, N., Narasimhulu, K., PydiSetty, Y.: Recent advances in the bio-remediation of persistent organic pollutants and its effect on environment. *J. Clean. Prod.* **198**, 1602–1631 (2018)
94. Bhattacharya, P., et al.: Physical adsorption of charged plastic nanoparticles affects algal photosynthesis. *J. Phys. Chem. C* **114**(39), 16556–16561 (2010)
95. Asempour, F., et al.: Synthesis and characterization of novel Cellulose Nanocrystals-based Thin Film Nanocomposite membranes for reverse osmosis applications. *Desalination* **439**, 179–187 (2018)
96. Bhawana, P., Fulekar, M.: Nanotechnology: remediation technologies to clean up the environmental pollutants. *Res. J. Chem. Sci.* **2**, 90–96 (2012)
97. Ghazemzadeh, K., Tilebon, S.S., Basile, A.: Membrane technologies for exhaust gas cleaning and carbon capture and sequestration. In: *Current Trends and Future Developments on (Bio-) Membranes*, pp. 97–123. Elsevier (2020)
98. Moharir, R.V., Kumar, S.: Challenges associated with plastic waste disposal and allied microbial routes for its effective degradation: a comprehensive review. *J. Clean. Prod.* **208**, 65–76 (2019)
99. Abdelkrim, S., et al.: Chitosan/Ag-bentonite nanocomposites: preparation, characterization, swelling and biological properties. *J. Inorg. Organomet. Polym. Mater.* **30**(3), 831–840 (2020)
100. Mallakpour, S., Rashidimoghadam, S.: Preparation, characterization, and in vitro bioactivity study of glutaraldehyde crosslinked chitosan/poly (vinyl alcohol)/ascorbic acid-MWCNTs bionanocomposites. *Int. J. Biol. Macromol.* **144**, 389–402 (2020)
101. Postnova, I., et al.: Chitosan bionanocomposites prepared in the self-organized regime. *Pure Appl. Chem.* **87**(8), 793–803 (2015)

102. Rahman, M.M., Netravali, A.N.: Aligned bacterial cellulose arrays as “Green” nanofibers for composite materials. *ACS Macro Lett.* **5**(9), 1070–1074 (2016)
103. Zawisza, K., et al.: Preparation and preliminary evaluation of bio-nanocomposites based on hydroxyapatites with antibacterial properties against anaerobic bacteria. *Mater. Sci. Eng. C* **106**, 110295 (2020)
104. Zhijiang, C., Guang, Y., Kim, J.: Biocompatible nanocomposites prepared by impregnating bacterial cellulose nanofibrils into poly (3-hydroxybutyrate). *Curr. Appl. Phys.* **11**(2), 247–249 (2011)
105. Sun, Y., Yuan, J., Zhou, T., Zhao, Y., Fei, Yu., Ma, J.: Laboratory simulation of microplastics weathering and its adsorption behaviors in an aqueous environment: a systematic review. *Environ. Pollut.* **265**, 114864 (2020). <https://doi.org/10.1016/j.envpol.2020.114864>
106. Dasari, A., Zhong-Zhen, Yu., Mai, Y.-W.: Ecological issues. In: Dasari, A., Zhong-Zhen, Yu., Mai, Y.-W. (eds.) *Polymer Nanocomposites*, pp. 263–277. Springer, London (2016). https://doi.org/10.1007/978-1-4471-6809-6_11
107. Rochman, C.M.: The complex mixture, fate and toxicity of chemicals associated with plastic debris in the marine environment. In: Bergmann, M., Gutow, L., Klages, M. (eds.) *Marine Anthropogenic Litter*, pp. 117–140. Springer, Cham (2015). https://doi.org/10.1007/978-3-319-16510-3_5
108. Truong, V., Blakey, I., Whittaker, A.K.: Hydrophilic and amphiphilic polyethylene glycol-based hydrogels with tunable degradability prepared by “click” chemistry. *Biomacromol* **13**(12), 4012–4021 (2012)
109. Moniruzzaman, M., Winey, K.I.: Polymer nanocomposites containing carbon nanotubes. *Macromolecules* **39**(16), 5194–5205 (2006)
110. Qazi, R.A., Khan, M.S., Shah, L.A., Ullah, R., Kausar, A., Khattak, R.: Eco-friendly electronics, based on nanocomposites of biopolyester reinforced with carbon nanotubes: a review. *Polym. Plast. Technol. Mater.* **59**(9), 928–951 (2020)
111. Mallakpour, S., Rashidimoghadam, S.: Carbon nanotubes for dyes removal. In: *Composite Nanoadsorbents*, pp. 211–243. Elsevier (2019)
112. Saththasivam, J., et al.: A novel architecture for carbon nanotube membranes towards fast and efficient oil/water separation. *Sci. Rep.* **8**(1), 7418 (2018)
113. Wang, Y., Hu, S.: Applications of carbon nanotubes and graphene for electrochemical sensing of environmental pollutants. *J. Nanosci. Nanotechnol.* **16**(8), 7852–7872 (2016)
114. Ilbasnis-Tamer, S., Degim, I.T.: A feasible way to use carbon nanotubes to deliver drug molecules: transdermal application. *Exp. Opin. Drug Deliv.* **9**(8), 991–999 (2012)
115. Tan, C.W., et al.: Energy and environmental applications of carbon nanotubes. *Environ. Chem. Lett.* **10**(3), 265–273 (2012)
116. Zhang, W., et al.: Strong, ductile and lightweight bionanocomposites constructed by bioinspired hierarchical assembly. *Compos. Commun.* **17**, 97–103 (2020)
117. Zhou, X.C., Cao, L.: High sensitivity microgravimetric biosensor for qualitative and quantitative diagnostic detection of polychlorinated dibenzo-p-dioxins. *Analyst* **126**(1), 71–78 (2001)
118. Cimboláková, I., et al.: Heavy metals and the environment. In *Environmental Factors Affecting Human Health*. IntechOpen (2019)
119. Mandal, S., et al.: Designing advanced biochar products for maximizing greenhouse gas mitigation potential. *Crit. Rev. Environ. Sci. Technol.* **46**(17), 1367–1401 (2016)
120. Zhang, C., et al.: Biochar for environmental management: mitigating greenhouse gas emissions, contaminant treatment, and potential negative impacts. *Chem. Eng. J.* **373**, 902–922 (2019)
121. Ema, M., et al.: Dioxin binding activities of polymorphic forms of mouse and human arylhydrocarbon receptors. *J. Biol. Chem.* **269**(44), 27337–27343 (1994)
122. Rappe, C.: Dioxin, patterns and source identification. *Fresenius’ J. Anal. Chem.* **348**(1–2), 63–75 (1994)
123. Roberts, L.: Dioxin risks revisited. *Science* **251**(4994), 624–627 (1991)

124. LeBoeuf, S.F., Tucker, J.B., Aumer, M.E.: Apparatus, systems, and methods for measuring environmental exposure and physiological response thereto. Google Patents (2019)
125. Gradinaru, I., Ignat, L., Dascalu, C.G., Soroaga, L.V., Antohe, M.E.: Studies regarding the architectural design of various composites and nanofibres used in dental medicine. *Rev. Chim.* **69**(2), 328–331 (2018)
126. Chen, H.W., et al.: Liquid crystal display and organic light-emitting diode display: present status and future perspectives. *Light Sci. Appl.* **7**(3), 17168–17168 (2018)
127. Chigrinov, V.G., Kozenkov, V.M., Kwok, H.-S.: Photoalignment of Liquid Crystalline Materials: Physics and Applications, vol. 17. Wiley (2008)
128. Ko, Y.-H., et al.: Super ultra-high resolution liquid-crystal-display using perovskite quantum-dot functional color-filters. *Sci. Rep.* **8**(1), 1–7 (2018)
129. Arora, R., Srivastav, A., Mandal, U.K.: Polyaniline based polymeric nanocomposite containing TiO₂ and SnO₂ for environmental and energy applications. *Int. J. Mod. Eng. Res. (IJMER)* **2**(4), 2384–2395 (2012)
130. Chen, L., et al.: Photoreduction of CO₂ by TiO₂ nanocomposites synthesized through reactive direct current magnetron sputter deposition. *Thin Solid Films* **517**(19), 5641–5645 (2009)
131. Li, G., Gray, K.A.: The solid–solid interface: explaining the high and unique photocatalytic reactivity of TiO₂-based nanocomposite materials. *Chem. Phys.* **339**(1–3), 173–187 (2007)
132. Yang, C., et al.: High photocatalytic degradation activity of the polyvinyl chloride (PVC)–vitamin C (VC)–TiO₂ nano-composite film. *J. Hazard. Mater.* **178**(1–3), 152–156 (2010)
133. Ökte, A.N., Karamanis, D.: A novel photoresponsive ZnO-flyash nanocomposite for environmental and energy applications. *Appl. Catal. B* **142**, 538–552 (2013)

Recent Developments in Wastewater Treatment Using Polymer/Clay Nanocomposites



Atika Alhanish and Gomaa A. M. Ali

Abstract Numerous reports on wastewater treatment techniques using polymer/clay nanocomposites (PCNs) are available in the literature. However, many of these endeavors are confined in enumerates the various efforts in the field. Thus, this work offers informative, direct, and straightforward insight into the topic by highlighting the research advances made in wastewater treatment using PCNs, the fundamental knowledge, and delivering some of the critical issues in this regard. A brief introduction is also provided, as well as an overview of those materials is presented. The different technologies using PCNs in water treatment, such as membranes, the main factors affecting them, and the future perspectives are discussed. A particular focus is placed on using PCNs as membranes and adsorbents. Scaling up the processes and regenerating PCNs are also covered.

Keywords Polymer/clay nanocomposites · Wastewater treatment · Nanomaterials · Environment

Abbreviations

DMAC16	[2-(Methacryloyloxy)ethyl]dimethylhexadecylammonium bromide
AG25	Acid Green 25 textile dye
AO	Acid orange 07
AR1	Acid red 1
BPA	Bisphenol A
BG	Brilliant green

A. Alhanish (✉)

Chemical Engineering Department, Faculty of Petroleum and Natural Gas Engineering,
University of Zawia, Zawia, Libya
e-mail: atika.alhanish@zu.edu.ly

G. A. M. Ali

Chemistry Department, Faculty of Science, Al-Azhar University, Assiut 71524, Egypt

© The Author(s), under exclusive license to Springer Nature Switzerland AG 2022
A. E. Shalan et al. (eds.), *Advances in Nanocomposite Materials for Environmental and Energy Harvesting Applications*, Engineering Materials,
https://doi.org/10.1007/978-3-030-94319-6_14

BET	Brunauer–Emmett–Teller
CV	Crystal violet
EOM	Effluent organic matter
GFZ	Gemfibrozil
HNTs	Halloysite nanotubes clay
MgFe-LDH	Layer double hydroxide
LDPE	Light density polyethylene
mMMT	Methyl dihydroxy ethyl hydrogenated tallow ammonium
MR	Methyl red
MB	Methylene blue
MF	Microfiltration
MMT	Montmorillonite
OMMT	Organically modified MMT
PMR	Photocatalytic membrane reactor
PVP	Poly(4-vinylpyridine)
PNIPAM	Poly(N-isopropylacrylamide)
OHPVP	Poly-4-vinyl(1-(2-hydroxyethyl)-pyridinium bromide
PVPcoS	Poly-4-vinylpyridine-co-styrene
PA	Polyamide
PANI	Polyaniline
pCD+-MMT and pCD0-MMT	Polycyclodextrin and MMT
PDADMAC	Polydiallyl dimethylammonium chloride
PES	Polyethersulfone
PEG	Polyethylene glycol
PEO	Polyethylene oxide
PNCs	Polymer nanocomposites
PCNs	Polymer/clay nanocomposites
PPSU	Polyphenylsulfone
PP	Polypropylene
PS	Polysulfone
PVA	Polyvinyl alcohol
PVC	Polyvinyl chloride
PVDF	Polyvinylidene fluoride
RB5	Reactive Black5
RR	Reactive red 02
Na-MMT	Sodium MMT
2D	Two-dimensional
UF	Ultrafiltration
WHO	World Health Organization

1 Introduction

Water is one of the essential natural resources. Despite the numerous water sources that exist on the earth, the scarcity of potable water is remaining one of the major challenges for humanity over time. The sustained developments in industrial as well as all modern activities cause a consistent release of different types of harmful contaminations in water bodies as they make the water unsuitable for consumption. Numerous pollutants have been reported in water bodies (Fig. 1). These pollutants are generally categorized into organic, inorganic, and biological contaminants, and most of these contaminants are non-degradable, carcinogenic, and highly toxic.

In this era, sustained civilization development is a prime source of creating new emerging pollutants that are not monitored regularly in the environment. A few years ago, more than 700 toxic, emerged pollutants in the aquatic environment had been listed by the World Health Organization (WHO) [1]. In 2014, another report by WHO estimated that about 748 million people still lack potable water, and every day about 3,900 children died due to consuming water with low quality and diseases [2].

Removal of these pollutants can provide humankind with potable water and generate clean water that can be used for various sectors such as industry and agriculture. Therefore, searching for effective treatment techniques to mitigate the water crisis had been continuously a critical and urgent issue.

Over the years, different techniques for wastewater treatment had been investigated, including adsorption, ion exchange, precipitation, advanced oxidation

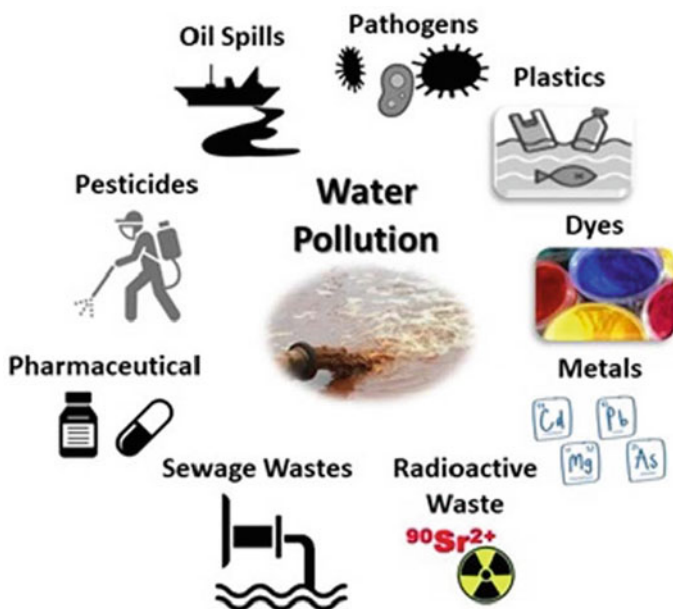


Fig. 1 Most common pollutants found in water sources

processes, membranes filtration, electro and photocatalysis, electro dialysis, biological approaches, reverse osmosis, coagulation, and hybrid processes that are combining two or more of the techniques above, among others [1, 3–7]. Several of these approaches showed demerits, such as the threat of forming secondary pollution, generation of sludge, high cost, and unproven performance in the large-scale application [3]. Researchers attempt to mitigate these challenges by exploring different materials to be implemented in various technologies to find the appropriate candidate for a specific treatment application.

Nowadays, scholars' attention has been paid to using nanostructured materials. Nanocomposites showed better performance than any other nanoparticles in wastewater treatment applications, particularly those based on polymers; this attributed to many features such as their high chemical stability, high surface area, and excellent selectivity cost-effectiveness, and good mechanical strength [8].

Different polymer nanocomposites (PNCs) were employed in wastewater treatment and desalination using various inclusions, including graphene, carbon, and clay [9]. According to the available literature, PCNs could be considered a promising material in wastewater treatment. Based on a very recent meta-analysis study, PCNs demonstrate a high adsorption performance for several organic and inorganic pollutants such as dyes, heavy metals, and oxyanions [10]. It was also reported that various biopolymer/clay nanocomposites showed comparable or even a higher adsorption performance to commercial adsorbents [11]. Different studies employed PCNs as decontamination agents in different ways to remove various contaminations, and most of these studies showed encouraging results. This chapter offers informative and straightforward insight into PCNs and their applications in wastewater treatment technologies.

2 Overview in Polymer/Clay Nanocomposites

PNCs are functional materials with tunable properties compared to their constituents. They are a combination of the polymer host (matrix) and dispersed nanofiller as reinforcement. The privilege of these materials is by using a filler, PNCs will mitigate the pristine polymer matrix's limitations without scarifying the original properties.

Among nanofillers used in synthesizing PNCs, clay can offer numerous improvements in polymer properties at very low loading (<5 wt. %), and in comparison, to traditional composites, these composites are lighter in weight.

These materials are considered a promising alternative to the traditional micro composites due to their unique characteristic, including nano-clay layers' ability to disperse in a polymer matrix with enhanced chemical, physical, thermal, electrical, optical, barrier, and mechanical properties [12].

Clay minerals originate from the earth's crust, having various geometry and morphology [13]. They are two-dimensional (2D) nanoparticles that possess a disk-like structure and unique characteristics, including abundance in nature, chemical stability, accessibility, high cation exchange, excellent sorption properties, low cost,

ion exchange properties, and large aspect ratio [14]. They have a crystalline flat platelet structure composed of stacked sheets (consisting of tetrahedral silicate and octahedral aluminate groups) from a few to as many as one thousand (Fig. 2). Furthermore, clay possesses a negative or positive layer along with interlayered cations or anions [9].

However, some clay particles possess fibrous geometry, including sepiolite or hollow nanotube such as halloysite.

Generally, clays are classified according to the ratio of existing layers to 1:1, and 2:1 (Table 1), where each group has different characteristics of swelling properties, ion exchange capacity, and the order of the crystal structure.

It worth mentioning that not all clays shown in Table 1 had been used as fillers for polymeric composites [16]. Besides being used as filler, clay could also be used as a host matrix to hold polymers [9]. To synthesize PCNs, there are three basic methods: melt blending, solution blending, and in-situ polymerization, and various routes based on these basic approaches are available in the literature [15].

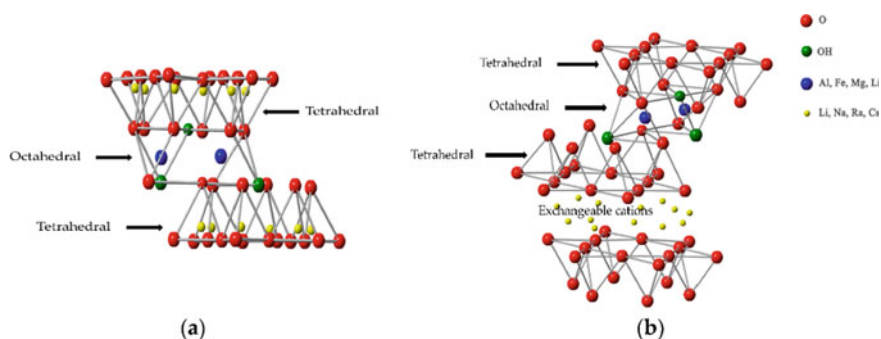


Fig. 2 Crystal Structure of clays: **a** 1:1, and **b** 2:1 (Reproduced from Ref. [15])

Table 1 Classification of natural clays [15]

The ratio of octahedral to tetrahedral layers	Clay group	Clay species
1:1	Rectorite, Kaolinite, Halloysite, Chrysotile	Lizardite, Berthierine, Cronstedtite, Kellyite, Fraipontite, Brindleyite, Dickite, Nacrite
2:1	Smectite, Vermiculite, Pyrophyllite, Talc, Mica, Brittle Mica	Montmorillonite (MMT), Laponite, Sepiolite, Hectorite, Bentonite, Vermiculite, Pyrophyllite, Talc, Muscovite, Paragonite, Clintonite, Bityite
2:1:1	Chlorite	Amesite, Cookeite, Donbassite, Sudoite, Chamosite
Amorphous – low crystalline		

Clay is known for the hydrophilic nature that responsible for the stacked layers structure. Owing to the existence of less or more layer charges, the hydrophilicity of pristine clay increases further following their saturation with cations such as Li^+ and Na^+ , and adsorbed water molecules [17]. Thus, direct physical mixing with most non-polar polymers is not possible. To synthesize PCNs, a modification step (pretreatment) of clay surface to have modified clay (commonly organoclay) is essential for both delaminate the layers and enhancing the compatibility between the chosen host and the clay. This step can be done in different ways such as grafting organic compounds, ion exchange with organic and inorganic cations, binding organic and inorganic anions at the edges, interparticle polymerization, calcination, and dihydroxylation, plasma and ultrasound treatment, among others [18]. However, the available literature describes the modification of clays in the laboratory using various experimental conditions, several treatment approaches and using clays from different regions. Thus, investigating the preparation of specifically modified clay, considering the origin (structure), is essential.

Depending on the polymer, the clay used, and the synthesis method, PCNs are classified into three categories based on the obtained morphology (Fig. 3). In phase separated, the clay layers separated from the polymer in an immiscible manner, producing composite materials with poor properties. In the second type, polymer chain intercalated into the galleries between the clay layers, increasing the inter-layer space and minimize the electrostatic force between the layers, which causes an improvement in the properties. Clay layers could be fully delaminated in exfoliated structures, which leads to superior enhancement of properties.

It is well known that PCNs possess better thermal, mechanical, physiochemical, and biodegradable properties compared to traditional composites [20]. These composites' structure and properties are governed by two main factors; interfacial interaction between the polymer host and clay particles and the dispersion quality. Hence, to reach the highest potential for a specific PCNs for a particular application is possible by controlling these factors.

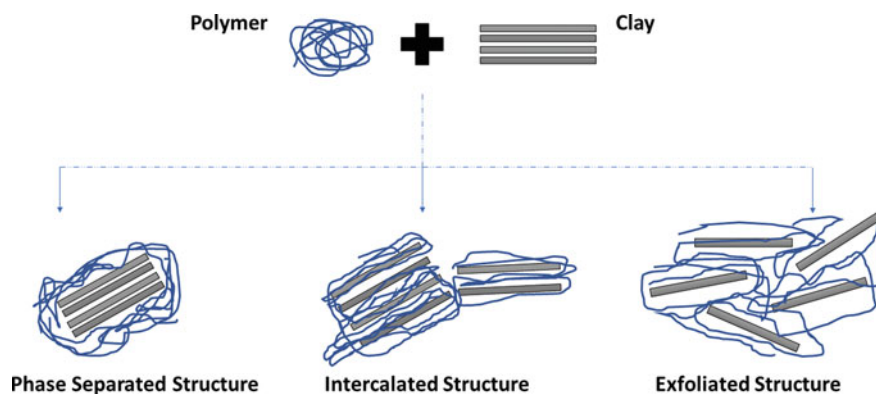


Fig. 3 Structures of polymer/clay nanocomposites. (Reproduced with permission from [19])

3 Polymer/Clay Nanocomposites Technologies for Wastewater Treatment

The continuous growth in publications can recognize the significance of PNCs in wastewater treatment. They gain this interest in wastewater treatment application due to their wide range of advantages such as good surface areas, pore structure, and ultralightweight congregated with high stiffness, film-forming ability, improved stability and processability, less installation space requirement, cost-effectiveness, good selectivity toward different contaminations, along with an easy process for recovering from treated water and almost no loss on regeneration for reuse [9, 21]. It was demonstrated by several reports that PCNs performance was superior to their counterparts. As well, PCNs are far more easily recovered from aqueous media compared to pristine clay. Also, exhibit better treatment cycles compared to both clay and polymer adsorbents [22]. The development of PCNs combines the advantages of clays and polymers that offer lightweight, pore structure, higher surface area, among others, paved the way for more economical and high-performance material.

PCNs offers many opportunities in the field of wastewater treatment. They could be used in different technologies by showing satisfactory results. It was reported using PCNs for wastewater treatment as adsorbents, membrane, coagulation/flocculation agents in barriers and columns to remove various types of harmful pollutants. They were also used in different physical states, e.g., solid and hydrogels, and different types of clays and polymers were explored, and some of these studies showed an excellent performance. Also, they were investigated in chemical decontaminations, including degradation. A study employed the combination of Ferroferric oxide (Fe_3O_4) and polypyrrole, which emerged recently as a p-n type semiconductor in the field of photocatalysis and used it as a semiconductor in the presence of halloysite nanotubes clay (HNTs) for loading dopants (Silver and Cobalt), to fabricate magnetic nanocomposite in order to be used for methylene blue (MB) degradation under the visible light [23]. This novel photocatalyst increased MB degradation under irradiation of simulated visible light. At 40 mg nanocatlyst and within 120 min., the maximum degradation percent of 91% was obtained.

The versatility offered by PCNs paved the way to explore many options for various decontaminations with promising results. However, the proper choice of a treatment technique depends on the chemical species in the water source, nature, the concentration of the ions, treatment costs, handling of residuals, ability to reuse, and the technique's versatility. In the following sections, we briefly provide the recent advances and the basic knowledge in using PCNs in wastewater treatment in the standard techniques: membrane, adsorption, coagulation, and flocculation technologies.

3.1 Membrane

The membrane is essentially working as a filter that permits the passage of only selective species (permeate) in solution while retaining other species (retentate). This process works by a combination of diffusion and sorption mechanisms (Fig. 4).

The membrane separates components with different sizes (molecular weights) selectively from monovalent ions such as sodium and potassium to macromolecules, including protein and starch. The transport of permeate through the membrane occurs due to driving force such as pressure difference, temperature difference, electrical potential difference, and concentration (chemical potential) difference [1]. Based on pore size and filtration process, membranes generally are divided into categories: Ultrafiltration (UF), Microfiltration (MF), and Reverse Osmosis [24]. UF and MF became popular for wastewater treatment applications due to low operating pressure, low energy consumption, compact design, effectiveness toward organic matters, pathogens, and turbidity [25].

Membranes employed in wastewater treatment, typically polymeric, endure several limitations such as low resistance to fouling and a trade-off relationship between selectivity and permeability. By introducing unique functionalities such as photocatalytic, adsorptive capabilities, and antibacterial, it could be possible to alter their structure and physicochemical properties, including charge density, porosity, hydrophilicity, thermal and mechanical stability, in order to be designed to meet various treatment application requirements [26].

Combining polymer with nanomaterials to create membrane emerged as a promising solution to mitigate these challenges, including biofouling and extending

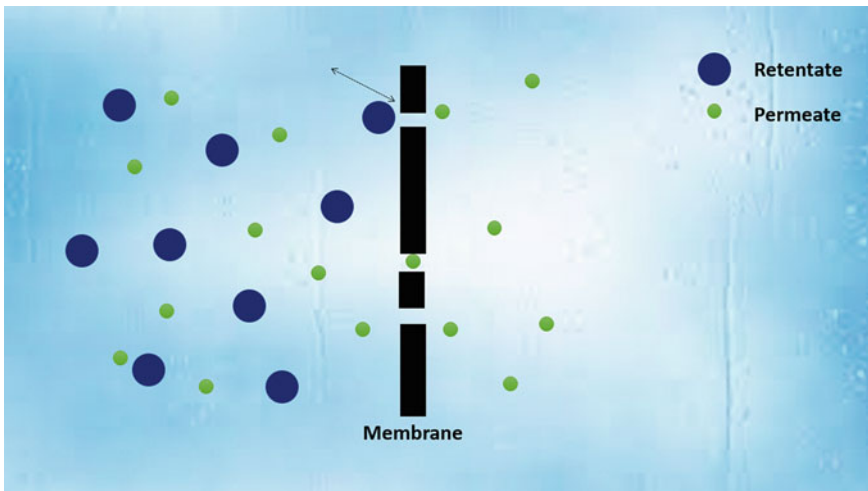


Fig. 4 General mechanism of membrane separation

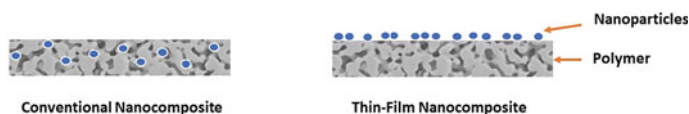


Fig. 5 Basic structures of polymer nanocomposite membranes

the lifetime of the membrane by improving their mechanical properties and resistance to cleaning [8]. Nanoparticles could be introduced into the structure of the most common polymers used for membranes such as polyvinylidene fluoride (PVDF), polyvinyl alcohol (PVA), polysulfone (PS), polyvinyl chloride (PVC), polyamide (PA), polypropylene (PP), and polyethersulfone (PES), during phase inversion to prepare the membrane with enhanced performance as a result of surface and internal pore modification [24, 25]. PNCs membranes are divided into two types; conventional (blended nanocomposite membrane) and thin-film nanocomposite membrane, and their structure are illustrated in Fig. 5.

Recently, PCNs membranes emerged as a promising class of PNCs membranes with enhanced performance and properties. They used clay particles during the fabrication of polymer composite membrane as reinforcement has been reported for different applications such as fuel cell, wastewater treatment, and gas separation [27]. Along with being economically beneficial, easy to synthesize, and effective in filtering contaminations from water, they showed better performance in wastewater treatment application than their counterpart due to the privilege of combined effects of organic-inorganic materials, which offer enhanced selectivity, permeability for mixed pollutants, strength, mechanical, chemical resistance, and thermal stability [1].

Usually, to obtain the best performance (adsorption capacity and selectivity), the current membranes sacrifice the mechanical properties [9]. However, nanocomposites membranes, in general, must possess enough mechanical strength to define stability and processability to endure the pressure during the treatment process [21]. In this regard, the functionalization of the PCNs membrane is proposed as a solution to enhance the performance as well as the chemical, mechanical, and thermal stability of the membrane. To fabricate a functional PCNs membrane, functionalization (modification) of clay is a practical approach to optimizing different related parameters [1]. There are many ways to achieve this task, like through chemical modifications, including grafting of organic compounds, calcination, reaction with acids, coupling agents, surfactants, and surface modification with polymers or by physical treatment such as plasma and ultrasound. However, it examines the use of modified and unmodified clays, particularly in PSF and PES composite ultrafiltration membrane were performed. The results of Ghaemi et al. [28] indicate that using modified clay, namely organically modified MMT (OMMT) in PES composite membrane, showed significant changes in the skin layer and sub-layer of the membrane as a result of increasing clay content, subsequently increases in membrane permeability was achieved. On the other hand, Mierzwa et al. [27] used unmodified MMT in PES composite membrane. The results revealed that introducing clay had reduced

the negative surface charge density with little effect on hydrophilicity, while an increase in contact angle was detected, and no effect on thickness and porosity of the membrane had been observed.

In general, various types of polymers and clays have been employed to synthesize PCNs membranes and investigated their potential ability to decontaminate over the past years. In a remarkable study, Ghaemi et al. [28] fabricated a nanocomposite membrane comprised of PES and OMMT via a hybrid method of phase inversion and solution dispersion techniques for the removal of pesticides (nitrophenols) in natural and acidic pHs mediums. The addition of clay showed an enhancement in hydrophilicity, and the performance was significantly improved. Also, improvement in thermal stability and mechanical properties were reported.

The effect of introducing clay on the structure and performance of different polymeric membranes had been investigated. Rodriquoés et al. [29] studied the role of introducing a commercial clay (MMT Nanomer®) as a nanofiller with common polymers used for membranes: PVDF, PS, and PES at similar conditions. Different clay loading (1–10 wt.%) was also explored. The presence of clay particles had changed the pore morphology of the membranes; as a result, a significant change in water permeability and fouling potential occurred. The optimum loading of clay varied for each polymer, 6, 1.5, and 2% for PVDF, PS, and PES, respectively. The authors explained that these differences appeared as a result of the difference in polymer's hydrophobicity (PVDF is more hydrophobic than PS and PES). Furthermore, the presence of clay affected the internal pore structure for all membranes. Finally, they concluded that the introducing clay showed a promising potential for enhancing the polymeric membrane regardless of the polymer matrix involved. Ma et al. [30] demonstrated that OMMT clay had little impact on the hydrophilicity of membranes.

In order to enhance the hydrophilicity of most hydrophobic polymers used in membranes, different additives are used, such as hydrophilic polymers as blend or pore-forming and inorganic molecules [31]. Morihama and Mierzwa [31] studied the effect of introducing MMT clay on the performance of PVDF-UF membranes, and then the performance was compared to clay/PVDF composite and clay/PVDF-poly(4-vinylpyridine) (PVP) composites membranes. The results showed that the presence of clay and pore maker (PVP) enhanced the water permeate flux compared to the pristine PVDF membrane. Furthermore, using clay alone showed the best result compared to all PVDF membranes compared. Also, the authors claimed that introducing PVP affected the kinetic and thermodynamic of the casting process, altering the morphology and pore size of the membrane.

Membrane fouling is a major challenge for the implantation of membranes in wastewater treatment. The fouling may be due to the deposition of organic or inorganic molecules, adsorption, biological growth, etc. The fouling causes an increase in feed pressure as well as reducing the lifespan of the membrane [32]. In order to reduce the fouling rate, a common pretreatment of the feed, optimization of operational conditions, and membrane modification are used to enhance anti-fouling properties. In a modification, there are different approaches that are involved, such as grafting or coating of a hydrophilic surface layer onto the membrane. The common method is to dope the membrane casting solution with hydrophilic molecules, which

are embedded into and onto the membrane. Adding organic and inorganic components as pore-forming agents, including polyethylene oxide (PEO), polyethylene glycol (PEG), glycerol, alcohols, and PVP to the casting solution affects membrane properties such as permeability, rejection capability, surface and internal pore structure, hydrophilicity, and mechanical/thermal/chemical resistance. This approach has the privilege of being performed in a single step during the synthesis process of membrane and hence can be easily introduced in the current industrial production of membranes [25].

However, different reports of influencing this method in the performance of PCNs membrane using modified and unmodified clay had been reported. Mierzwa et al. [27] reported the permeability of 2% of unmodified MMT clay (PGV®-10) content in composite membrane based on PES had increased by 121% compared to the undoped membrane, while the membrane fouling found to be reversible. On the contrary, Lai et al. [33] reported a reduction in water permeability of MMT clay (Cloisite® 15A) doped PVDF membranes, while improvement in mechanical strength and abrasion resistance was observed at 1 wt.% clay content. On the other hand, Rajabi et al. [34] prepared UF membrane by using clay doped membrane with PVDF and observed that the presence of clay (OMMT) had increased fouling resistance, hydrophilicity, and macrovoid size.

Using mixed matrix membranes also were explored to overcome the current limitations. Rodrigues et al. [25] examined the effect of using clay with and without the combination of PEO as the pore maker on the structure and performance of the mixed matrix PS-UF membrane. It was found that introducing clay improved the mechanical/thermal resistance and permeability with minimal loss in rejection. Furthermore, clay particles had significantly enhanced all the evaluated characteristics of the mixed membrane. On the contrary, Ma et al. [30] demonstrated the addition of clay with a combination of PEG to PS membrane reduces the mechanical resistance of the membrane while increasing the number of large pores was observed.

Jacob et al. [32] also worked in a mixed matrix UF membrane. They used PSF, clay, and PVP as pore makers to synthesis the membrane via phase inversion technique for Cr(VI) removal from wastewater and investigated the anti-fouling performance. Unlike other nanocomposites membranes prepared by using clay, this work deals with the introduction of pristine MMT and MMT modified with methyl dihydroxy ethyl hydrogenated tallow ammonium (mMMT) to the PSF matrix. Compared to the pristine PSF membrane, total fouling was reduced to 39% and, the flux recovery ratio of mMMT/PSF membrane with 3% mMMT has increased to 83%. Also, the presence of both MMT and mMMT improved the performance of the membrane by 89 and 95% rejection, along with the flux of 102 and 271 l/m²hr, respectively. The results demonstrated that 3% mMMT improved the thermal stability and enhanced the anti-fouling property in higher performance compared to pristine PSF and PSF/MMT membranes.

In notable work [35], Hosseini and his team prepared novel electrospun nanofibrous membranes based on MMT clay and chitosan/PVA for dye removal. The addition of MMT improved membrane resistance to compaction and Young's modulus by using clay content of 1 wt.% (0.89 MPa for chitosan/PVA to 2.09 MPa for MMT with

chitosan/PVA). At clay loading of 2 wt.%, both dye removal and water flux increased. The optimized removal performance was 95%, with a high flux of 1765 L/m² h under 0.4 bar operating pressure that overcoming the trade-off between selectivity and permeability. Furthermore, this anti-fouling membrane was also regeneratable for several cycles.

Clay embedded polymeric membranes were also prepared by using bentonite with different polymers: polyphenylsulfone (PPSU), PVDF, PSF, and PES for humic acid removal [36]. This study investigated the performance of this membrane in a circular crossflow filtration system and compared the results to commercial membranes. Introducing bentonite into the polymer matrix had affected the morphological structure, pore size, surface roughness of the membrane. High flux rate, low fouling, and low retention for humic acid in all the membranes tested were observed. The authors claimed that introduced charged bentonite for polymeric membranes with various surface roughness are the main targets to reduce undesirable fouling. In conclusion, based on all tests, the performance of these synthesized membranes was comparable to the commercial ones.

According to the aforementioned literature introducing modified clay into polymeric membranes showed remarkable enhancement in their performance. However, employing modified clays raises the cost of fabricating the membrane. A few efforts investigated the use of natural clay as a cost-effective approach. Recently, Barbosa et al. [37] introduced natural MMT into PES membrane in order to investigate their effect on membrane performance for the removal of effluents from the textile industry. Membrane with 1 wt.% clay loading showed the highest rejection performance of 94% of indigo blue (200% compared to pristine PES membrane).

A hybrid thin-film nanocomposite membrane based on HNTs and titanium dioxide (TiO₂) with PVDF was successfully prepared [38]. This membrane was used as a photocatalytic separator in the photocatalytic membrane reactor (PMR) to treat bilge water (composed of a corrosive mixture of different hydrocarbons from engine oil and fuel tank of ships that discharged in the sea). The performance of this photocatalytic membrane reactor has shown more than 99.9% of hydrocarbon removal from the bilge water. Immobilizing the TiO₂ nanoparticles on the HNTs surface provides a uniform dispersion of the photocatalysts when embedded in PVDF matrix, besides high photocatalyst activity, anti-fouling properties, and reasonable permeation.

Another hybrid UF membrane was fabricated by using layer double hydroxide (MgFe-LDH) generated on MMT layers with PSF-PVP blend for the separation of oil and water mixture [39]. This membrane showed remarkable results compared to modified MMT with PS-PVP blend and pristine PS-PVP blend membranes. The LDH-MMT/PSF-PVP membrane possesses good anti-fouling with a good flux recovery ratio. A rejection performance of 87.2 and 95.9% were found for transformer oil and motor oil, respectively. The authors claimed that by using this membrane, up to 96%, oil separation could be obtained.

As interest in sustainability is growing in almost every sector in modern industries. Using low cost and renewable resources in synthesizing PCNs is reported. In recent work [40], a hybrid porous ceramic membrane based on kaolinite and polystyrene foam waste have been prepared in various ratios for MB dye removal. The polymer

works as the pore maker in the membrane, which will affect the physical properties of the clay. The membrane that contains 20 wt% polystyrene showed the best adsorption performance and regeneration for 2 cycles. The authors claimed that the adsorption capacity of this membrane in the second cycle had decreased as a result of filling the free sites of the surface. Also, the presence of 20 wt.% of polystyrene waste decreased the bulk density and increased the porosity of the membrane.

As with any emerged technologies, understanding some criteria that affect the performance of PCNs is essential in order to expand their applications. More work is needed to develop a fundamental understanding of the impact of clay (type and content) on membrane structure. Also, the reported improvements in using these membranes in performance require further investigations based on pore size, charge density, and porosity [1]. It was also reported that clay casting solution dopants strongly influence membrane structure and performance [31]. Thus, exploring the effect of other techniques for comparison might be a good addition.

In general, the basic factors for evaluating membrane performance are fouling resistance, permeability, and separation capacity. However, evaluating the rate of treatment process using membrane is not reported because using clay that possesses a large aspect ratio in the membrane will alter the diffusion path of permeate that may affect the time of treatment and especially with well-dispersed filler.

One of the basic challenges is to fabricate PCNs with a uniform dispersion of clay particles for membrane, as the non-uniform dispersion causes agglomerates within the polymer matrix that might lead subsequently to cracking and failure in the membrane during operation. Among the techniques used in preparing PCNs, melt blend via screw and extruder configuration is might be a good choice to nominate in order to obtain PCNs with enhanced dispersion quality.

On the other hand, investigating the optimal clay loading is important to avoid basically losing essential mechanical properties. At high clay loading, the tensile strength of the membrane will decrease [37], while at low clay loading will increase [33]. It is well known also that agglomeration of clay particles in the membrane will weaken the mechanical strength [30]. It was reported increasing clay loading causes a decrease of surface charge and increases contact angle [27].

Membrane design is essential, as investigating the use of PCNs for different types of membranes may show different potentials. Thus, studying a certain polymer and clay for different types of membranes would contribute to the existing knowledge.

3.2 Adsorbents

The adsorption process is a surface phenomenon where contaminants are deposited over the surface of the adsorbent [41–46], and it is classified as chemisorption or physisorption depending on the interaction between contaminants (adsorbate) and the adsorbent surface (Fig. 6). This interaction might be through forces including hydrogen bonding, electrostatic, or van der Waals interactions [21, 44, 45, 47, 48].

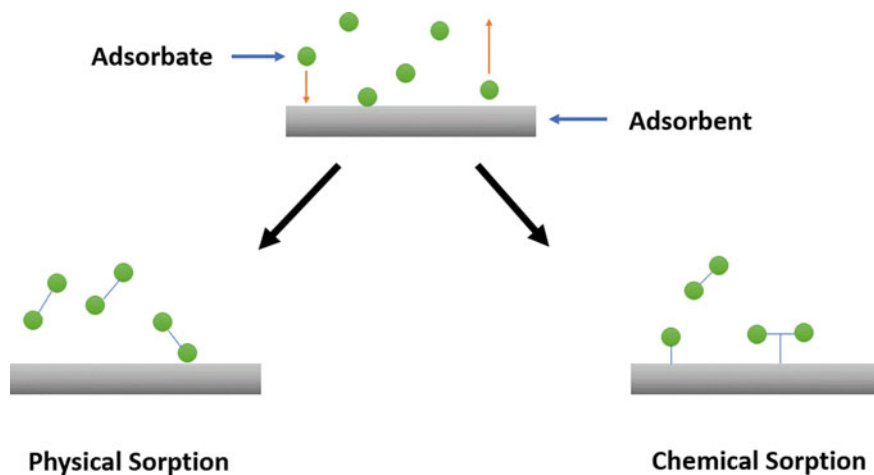


Fig. 6 General mechanism of adsorption phenomena

In wastewater treatment applications, adsorption is considered the most versatile technique [41, 42, 44, 49, 50]. It is simple, cost-effective, efficient, and producing water of high quality [51, 52]. In addition, it does not require the addition of any chemicals. There are different parameters controlling the adsorption process, such as pH of the solution, temperature, adsorbent dosage, contact time and ion concentration, etc. Despite this, the effectiveness of the decontamination process depends on the choice of the appropriate adsorbent [53].

Numerous materials (organic and inorganic) have been investigated as adsorbents such as activated carbon, agriculture wastes, biochar, polymeric resin, industrial waste, natural clay, and modified clay minerals [3, 49, 54–56]. However, most of them show slow kinetic, poor capacity, not regenerable, and in some cases, expensive [57]. On the other hand, most of the high adsorbents are the modification of classical adsorbents.

According to the literature, clays had been extensively explored as an adsorbent for various pollutants due to their characteristics, including surface area and porosity. Nevertheless, limited ability for removal of micro-pollutants, poor wettability, pH-dependence, and lack of standard protocol for recovery and regeneration in aqueous systems had limited their utility [3, 9]. On the other hand, organoclays (modified clays) possess enhanced adsorption capacity and increased surface positive charges [58]. However, several drawbacks hindered their use for some pollutants. For instance, the management of organic dyes after adsorption is not over wholly in the end, and how to deal with clay after treatment (adsorbed the dyes) is still a problem [59]. Also, when they are generated, these clays lose a substantial amount of their performance (adsorption capacity) [22].

To overcome most of these obstacles, clay composites and particularly PCNs had been offered as a promising alternative. These materials exhibit superior quality compared to traditional adsorbents in organic and inorganic pollutants elimination

[9, 57]. It was demonstrated that using PCNs showed improved performance in the removal selectivity of organic and inorganic pollutants from aqueous media [9]. Compared to activated carbon, which demonstrates the highest adsorption capacity among the commercial sorbents, PCNs had the advantage in real water circumstances; unlike activated carbon, their performance is less compromised in the presence of background organic matter [10].

The presence of functional groups in PCNs extends a better ability to adsorption as well as decontamination [21]. For instance, PCNs based on PVA and kaolinite were used for Pb(II) and Cd(II) removal. FTIR analysis revealed the presence of -OH functional group at the surface. This adsorbent showed good performance (56.18 mg/g for Pb(II) and 41.67 mg/g for Cd(II)) and excellent regeneration (99% within 5 min.). Table 2 demonstrated different studies with remarkable results for decontamination using various combinations of PCNs.

The removal of metal ions such as Pb(II), Hg(II), As(III), Cd(II), Cr(VI), etc., from wastewater could be done either by filtration using PCNs or by adsorption. However, adsorption is considered the most efficient and economical route [8].

There are different factors affecting the rate of adsorption, such as type of clay and polymer. For instance, phenol derivatives removal using PCNs adsorbents based on polydiallyl dimethylammonium chloride (PDADMAC) and poly-4-vinylpyridine-co-styrene (PVPcoS) with MMT clay was dramatically faster (2–4 h) compared to PCNs based on (PDADMAC) and (PVPcoS) polymers with sepiolite (3–4 days), as result of the porous structure according to authors [66].

Clay loading is also a determining factor. Erdem et al. [67] employed bentonite to synthesize PCNs via in-situ polymerization using a methacrylate-based quaternary

Table 2 Maximum efficiency of various PCNs adsorbents for different contaminations

Polymer	Clay	Contaminate	Efficiency (%)	Ref
Moringa oleifera	Bentonite	Cd(II) Cr(VI) Pb(II)	99.97–100 99.98–100 99.99–100	[58]
Polyaniline	MMT	Acid Green 25 dye	100	[14]
Chitosan	Halloysite	Cr(VI)	90	[20]
Chitosan	Silver–zinc oxide bentonite	Gram-negative Escherichia coli and Gram-positive Enterococcus faecalis bacteria	78	[60]
Polyacrylamide	Natural zeolite	Cr(VI)	76.3–100	[61]
Chitosan-g-polyacrylamide	MMT	MB dye	>88	[62]
Starch	Smectite	Pharmaceuticals	70	[63]
Bean starch	Sodium MMT (Na-MMT)	Ni(II) Co(II)	97.1 78.07	[64]
Polyacrylamide	Na-MMT	Ni(II) Co(II)	99.3% 98.7%	[65]

ammonium monomer ([2(methacryloyloxy)ethyl] dimethyl hexadecyl ammonium bromide) = "DMAC16" for Reactive Black5 (RB5) removal. At all pH tested values, the highest capacity 833.3 mg/g was obtained at 10% bentonite loading, which is high compared to poly(DMAC16), and with 15% loading, adsorption capacity decreased.

Seeking for more sustainable options is rising globally, and in this manner, bio-polymers had been employed in PCNs adsorbents to made them more eco-friendly, and the reported efforts showed a remarkable performance by utilizing it. For instance, a 684.8 mg/g capacity of MB dye was adsorbed within 30 min. by using sepiolite/gelatin nanocomposites [68].

Biopolymers offer a diversity of functional groups as well as being eco-friendly. Among biopolymers used, chitosan is one of the most bio-polymers used in synthesizing PCNs adsorbents, as the use of this polymer demonstrated a high potential. This polymer can be transformed into different shapes, such as films, membranes, beads, etc. This diversity in transformation helps in the ease of continuous operations [20].

It is a natural, abundant, hydrophilic, biodegradable, and biocompatible polymer. It contains many -OH and -NH₂ functional groups; as a result, chitosan is extremely reactive. These functional groups can adsorb anionic and cationic molecules; consequently, it has got a high adsorptive capacity for transition, heavy metals, and dyes. However, using chitosan as adsorbent faces challenges, it possesses low mechanical property, low specific gravity, and it swells and floats when dissolved in water, besides having low stability in acidic media [69]. To overcome these limitations, using fillers such as clay offered enhancement in their performance. For instance, it was reported that chitosan/MMT composite showed higher efficiency in the removal of selenium from water compared to the commercial ferric oxide and aluminum oxide adsorbents [58].

The authors suggest a recent review that discussed comprehensively the use of PCNs based on biopolymers for further information at this point [11]. Here, we provide the most recent works.

A remarkable performance was reported for chitosan/HNTs bionanocomposites film for decontamination of toxic hexavalent chromium Cr(VI) from wastewater [20]. At an initial concentration of 25 ppm and a pH of 3.0, removal of Cr(VI) increased with an increase in adsorbent dose. The maximum removal obtained was 92% at an adsorbent weight of 1.7 g/L. The results also showed that HNTs were dispersed well in chitosan and the adsorption capacity for this composite was higher compared to pristine chitosan under the same conditions.

PCNs based on chitosan and bentonite was also synthesized in order to remove Cr(VI) from aqueous media [70]. The study showed that the composite had better performance compared to its counterpart. Also, the removal increased with increasing adsorbent dosage at an optimum pH of 3.

Kumar et al. [71] also investigated the decontamination of Cr(VI) using bionanocomposite based on cellulose and Na-MMT. A maximum capacity of 22.2 mg/g with the ability to reuse for 10 cycles was reported. On the other hand, it was tested in a real aqueous environment (leather tannery unit) by using the adsorbent in a packed column. Effective adsorption of Cr(IV) about (97.5 ± 0.25%) was

achieved with negligible influence from the common anions and cations existing in the tannery, with the ability to regeneration by using sodium hydroxide (NaOH) as the eluent (desorbing agent).

In essence, Cr(VI) exists in five different forms in aqueous media which depend on the pH of the solution: H_2CrO_4 , HCr_2O_7^- , HCrO_4^- , $\text{Cr}_2\text{O}_7^{2-}$, CrO_4^{2-} , $\text{Cr}_2\text{O}_7^{2-}$; and an acidic medium; Cr(IV) is mostly present in the anionic form [53]. Hence, pH is a vital parameter to be considered in adsorption analysis. For PCNs adsorbents, the choice of a specific PCNs with certain zeta potential is depending on the pH of the solution.

For instance, the amine group in clay presented in PCNs is easily protonated at low pH to form cation (H_3N^+), and PCNs adsorbents with negative surface charge (negative zeta potential) are not suitable adsorbents for anionic molecules [53].

Amphoteric functionalization is a novel route that was developed to employ PCNs for both cationic and anionic pollutants. Azha et al. [72] synthesized PCNs coating with amphoteric functionality based on smectite powder, acrylic polymer emulsion, and poly-epichlorohydrin-di-methyleamine (cationic polyelectrolyte) supported on cotton cloth. The study evaluated the feasibility of this adsorbent for the removal of cationic (brilliant green, BG) and anionic (acid red 1, AR1) dyes. The ability to decontamination of both BG and AR1 for this adsorbent, despite the experimental data, was confirmed. However, the variation of temperature and concentration showed a different effect on both pollutants due to the nature of interaction that occurred during adsorption, which was discussed in the literature. It was reported that linking polymer to clay surface by grafting improves the adsorption capacity to remove negatively charged ions as well as preventing coagulation in aqueous media [61].

Zeolite and other aluminosilicate minerals are well-known adsorbents for the cationic metal ions removal from wastewater due to the permeant negative charge. For further application to remove other negatively charged ions, modification using polymers is achieved. Sallam et al. [61] prepared high efficient PCNs adsorbent for Cr(VI) removal. PCNs were prepared by using natural zeolite (clinoptilolite)/local clay deposits grafted using polyacrylamide. The highest removal of Cr(VI) achieved was 76.3–100%, with an initial concentration of 10–50 mg/L at pH of 2. The results revealed that polymerized samples showed a higher adsorption capacity of Cr(VI) than their counterpart. The authors also claimed that the level of salinity and other soluble ions (Na^+ , Cr^{2+} , Cl^- , and SO_4^{2-}) were reduced in tannery wastewater.

Using chitosan with modified bentonite clay nanocomposites adsorbents for removal of dyes, fertilizers, metals, pesticides, and other organic pollutants have also been extensively studied. It reveals high adsorption capacity for the removal of anionic and cationic dyes in wide temperature and pH ranges [69].

Yu et al. [73] investigated three different approaches for modifying bentonite clay: sulfuric acid, microwave, and calcination treatments in order to be used in synthesizing PCNs adsorbent with a combination of chitosan for heavy metal removal from wastewater. The study also explored the effect of different parameters on the loading amount of chitosan. The optimal chitosan loading on raw bentonite was 126.30 mg/L at an initial chitosan concentration of 1000 mg/L, pH of 4.9, 30 °C, and 60 min. The loading increased to 208.83, 233.70, 256.30 mg/g, when using modified

bentonite through a calculation at 600 °C, 10% sulfuric acid treatment, and 6 min of microwave irradiation (800 W), respectively. Also, it was observed that as the loading increased from 34.76 to 233.7 mg/g, the removal of pb(II), Cu(II), and Cr(VI) were improved, respectively, from 60.09 to 86.18%, from 78.90 to 95.5%, and from 82.22 to 98.74%. Thus, high chitosan loading improves the adsorption capacity of modified bentonite for heavy metal removal.

In the work of Eladlani et al. [74], chitosan was used as the host polymer with various ratios of MMT to prepare PCNs adsorbent for Cr(III) removals from tannery wastewater. The sample containing 2 wt.% of MMT showed acceptable performance in chromium solution and tannery water. It can adsorb 45% of Cr(III) in one day in tannery water, while in 70 min adsorbs, about 120 wt.% of Cr(III) in chromium solution. According to the authors, the reduction in capacity attributes to the presence of other metallic ions (Cd, Cu, Ni, etc.) in tannery water.

Another PCNs adsorbent based on chitosan and Na-MMT was fabricated in order to investigate their potential for selenium (Se) adsorption [75]. The results showed that 18.4 mg/g of Se was adsorbed from well water, which is higher compared to the metal oxide adsorbent, and the removal was effective as it removes Se below the standard levels. Also, the study showed that pH has no effect on Se uptake.

As shown in the literature, PCNs are able to reduce different contaminations significantly, often to safe levels. Despite this, this treated water would not be safe for consumption until biological contaminations such as microbes were removed. For this purpose, there are several attempts to develop PCNs with good antimicrobial activity to overcome the existence of filtration systems, including activated carbon [22]. One of these endeavors is introducing biocidal metals into clay structure in order to be used as an antibacterial agent. In recent work [76], MMT was modified with Cu(II) and used as a nanofiller to prepare light density polyethylene (LDPE) based nanocomposite via melt mixing approach. This nanofiller provides the composite with high thermal stability along with enhanced antibacterial activity, and optimum activity of 94% was obtained at low clay loading (4%). The authors reported that this enhancement comes as a result of the presence of Cu(II). It is well known that Cu in the oxidation state is highly effective against microbial. Thus, the idea of introducing molecules with antimicrobial properties into clay structures such as silver is a promising strategy to enhance the overall ability of the based nanocomposite for the targeted contamination. However, degradation assessments could give a valuable knowledge to determine if this treated water is safe for human consuming or not.

There are other approaches to develop PCNs with antimicrobial activity via modifying the clay, such as using biocides as it demonstrated the ability to remove microorganisms including *Pseudomonas aeruginosa*, *Escherichia coli*, *Candida albicans*, and *Staphylococcus aureus* from water [12] or using polymers that possess antimicrobial activity [60] or even both approaches at once.

Chitosan possesses several merits, such as higher antibacterial activity, higher killing rate, with lower toxicity toward mammalian cells over other disinfectants [22]. Motshekga et al. [60] developed a crosslinked chitosan (with glutaraldehyde) based nanocomposite with the presence of bentonite supported with zinc oxide and silver nanoparticles as nanofiller. The study investigated the inactivation of bacteria

(Gram-positive *Enterococcus* and Gram-negative *Escherichia coli faecalis*) in water. The study reveals that the inactivation of bacteria influenced by factors such as particle size, pH, and surface area when crosslinked chitosan is employed. For example, the antibacterial activity of crosslinked chitosan increased as the contact time increased. Also, introducing zinc oxide and silver into bentonite structure improves the inactivation of bacteria. Furthermore, the study concluded that the best removal efficiency was about 78%, and leaching tests demonstrated that the composite is stable, and the antibacterial activity was affected by the contact time, as the number of colonies decreases with time, the amount of composite, and concentration of bacteria.

In an earlier study [77], the antibacterial activity of hydrogel composite (superabsorbent composites) based on chitosan-g-poly(acrylamide) and Na-MMT in various contents against *Escherichia coli* (*E. coli*) and *Staphylococcus aureus* (*S. aureus*) was investigated. They were also hydrolyzed in order to enhance the swelling properties by obtaining functionalized pH-sensitive nanocomposites. The results confirmed the exfoliated structure with good dispersion and favorable compatibility for the samples, and the presence of low content of Na-MMT had enhanced the thermal stability and generate a more porous structure. Regardless of clay content, the swelling of these composites was affected by pH changes and salinity. All composites reveal moderate antibacterial activity in an acidic medium, and the sensitivity of *S. aureus* was higher compared to *E. coli*. The authors attributed this result to two reasons: (1) the antimicrobial activity of chitosan is related to the number of the free amino groups in the polymer backbone, and a less amino group in the network existed as a result of hydrogen attraction between some amino groups and the carbonyl group of poly(acrylamide), consequently less antimicrobial activity of the composite, and (2) the presence of less positive charges. For the removal of biological pathogens (viruses and bacteria) with positively charged membranes, it was reported that using negative PCNs based on anionic polymer and pristine clay might be useful [78].

In general, hydrogels have gained attention in wastewater treatment applications due to their high performance, and especially reuse and regeneration ability in a continuous process, along with low interfacial tension [18]. In general, the hydrogel is a polymer with 3D crosslinked network structure that holds a large quantity of water within its structure, containing hydrophobic and hydrophilic parts in a defined amount. However, hydrogel suffers from undesirable low mechanical properties and gel strength. Hence, the introduction of clay into the hydrogel was found to elaborate the properties of the corresponding hydrogels, such as adsorption and swelling capacities, as the presence of clay particles allows the amending of adsorbing ability since clay particles are fixed in the matrix [77]. Also, clay had offered enhancement of permeability and elasticity of hydrogels with improvement in adsorption capacity as a result of clays' ability to adsorb various substances [18].

A study showed that by introducing OMMT into hydrogel matrix-induced sorption capability for acid dye (Acid Orange 3). In this study [18], poly(*N*-isopropylacrylamide) (PNIPAM)/OMMT hydrogels were prepared using a photopolymerization technique. The results indicate that dye removal increased (30–59.9%) with the increase of OMMT content (0.25–1.00%), as the increase in OMMT particles provides a great number of active sites. The privilege here is the presence

of positively charged nitrogen offered by the modification that attracts the negatively charged ions of dyes via electrostatic forces. Despite this, no change in adsorption capacity is reported with increasing clay loading beyond 1% (maximum adsorption was about 60.3% at 5 wt.% clay). The authors claimed that agglomeration is formed; thus no more active sites are formed. Also, the study reveals that increasing the pH of the solution (4–7) will decrease the adsorption capacity (maximum capacity reported at pH 3), attributed to a decrease in active sites (positive charges) on the surface of clay while negatively charged increases, consequently, electrostatic repulsion occurred. Interestingly, the authors noticed a slight increase of adsorption at alkaline pH (8–9), which is still lower than the maximum adsorption at pH of 3. Interpretations of this phenomena were earlier introduced by [79, 80], they explained that at alkaline media, competition between dye anions and -OH ions on the external surface of the clay is expected, and another explanation is the formation of covalent bonds between -OH and negatively charged molecule.

Recently, hydrogel based on chitosan-g-poly(acrylamide) matrix and various contents of MMT nanofiller were prepared via free-radical grafting copolymerization for cationic MB dye removal from aqueous media [62]. These adsorbents showed remarkable performance at a fast rate, more than 88% of MB adsorbed after 50 min in 200 mg/L of dye media. On the other hand, at 2 wt.% of MMT a superior adsorption capacity of 1749 mg/g is obtained. Also, the process is highly pH-dependent. The kinetic data were described by the pseudo-second-order model, while equilibrium data represented perfectly via the Langmuir model.

Utilizing plastic wastes for fabricating PCNs adsorbent had also been explored. LLDPE waste was chemically modified with starch and acrylic acid through emulsion polymerization in the presence of OMMT to prepare hydrogel nanocomposite for Pb(II) removal from aqueous media [81]. A maximum adsorption capacity of 430 mg/g was obtained, and according to the authors, that value is comparable to other reported adsorbents. The adsorption was considered fast (at 312 mg/g within 20 min.). Also, adsorption/desorption studies were carried out. The results indicate that the adsorption process is reversible, and 93% in the first cycle, 88% in the second, and 82% at the third cycle were obtained, respectively. Furthermore, the adsorption was 97.5% in the first cycle, 93% in the second, and 88% in the third cycle, respectively. The desorption was carried out in 0.1 mol/L HNO₃ solution, and the authors explained the desorption mechanism as the protons competed with Pb(II) for carboxylic acid groups; as a result, a decrease in the ionic attraction between Pb(II) ions and carboxylate group, consequently desorption occurred. Despite the performance, the preparation process for the composite involved four steps that could affect the production cost.

Hydrogel nanocomposites based on 2-acrylamido-2-methylpropane sulfonic acid and acrylamide with Na-MMT and bis[2-methacryloyloxy] ethyl phosphate as a crosslinker poly(AAm-co-AMPS)/Na-MMT were synthesized in simple free radical polymerization for dyes removals such as methyl red (MR), crystal violet (CV), and MB from aqueous media [82]. Maximum adsorption capacities were 113, 155, and 176 mg/g for MR, CV, and MB, respectively. At pH 7, the uptakes of 51% for MR, 80% for CV, and 89% for MB in 50 mg/L of dye solution were observed, while

at pH 12, 23% MR, 86% for CV, and 93% MB were reported. The reusability studies showed that this nanocomposite hydrogel could be efficiently used as a reusable dye adsorbent agent as the dye molecules were easily desorbed from the hydrogel via ethanol for four cycles.

Modification of clay with an acid, surfactant, and magnetic for the preparation of PCNs adsorbents also showed a significant enhancement in the decontamination of different types of pollutants with good ability for regeneration, and this subject had been discussed elsewhere [83].

It worth mentioning that hydrolysis elaborates hydrogels swelling properties as well as functionalizes it by forming polyelectrolytic chains. In a study performed by [77], a comparison between hydrolyzed hydrogel composite based on chitosan-g-poly(acrylamide) and Na-MMT, and unhydrolyzed one. Water uptake on hydrolyzed hydrogel composites was higher than the unhydrolyzed one due to the existence of polyelectrolytic character (anionically charged chains) that cause electrostatic repulsive between anionic carboxylate led to the expansion of the network and consequently increases water absorbency. It was also reported that partial hydrolysis in alkaline media is more convenient than acidic hydrolysis.

Another route that was widely used in wastewater treatment is incorporating metals with bio-polymers and clay. Sirajudheen et al. [84] fabricated a Zr(IV) encapsulated carboxymethyl cellulose with MMT for reactive red 02 (RR) and acid orange 07 (AO) dyes. At 100 mg adsorbent and within 50 min, the dyes were removed successfully. The adsorption capacity of AO (96%) and RR (97.5%) were achieved.

PCNs based on using polyaniline (PANI) for wastewater treatment had been widely explored. Recently, Kalotra and Mehta investigated the synthesis of PANI and PANI/MMT nanocomposite via in-situ polymerization at 0 °C and using ammonium persulfate as an oxidizing agent for Acid Green 25 textile dye (AG25) removal [14]. About 100% of AG25 dye was removed in 30 min at an initial dosage of 50 mg/L, pH of 6, and at 20 °C. At higher temperatures (45–50 °C), 100% of AG25 dye removed in 10 min. Compared to pristine PANI, PANI/MMT composite showed higher adsorption capacity in less time. Despite the efficiency of this adsorbent, no regeneration studies were conducted. In another study, PANI was used with modified clay (Biotite 2 M1 represents nearly 55% of the clay composition) to synthesis via in-situ polymerization for Pb ions removal [85]. A maximum capacity of 70.4% was achieved at pH 5.0. The study investigated the removal efficiency by using real water samples: drinking water, seawater, and river. The study found that the presence of interfering ions had no effect on the removal efficiency, unlike the common adsorbent where it does.

Another study aimed to design a dual-site (neutral and cationic) PCNs based on polycyclodextrin and MMT (pCD⁺-MMT and pCD⁰-MMT) for simultaneous removal of non-ionic micropollutants [Bisphenol A (BPA)] in the presence of effluent organic matter (EOM) from wastewater in column filtration system [86]. Both sorbents showed different behavior, i.e., the adsorption capacity of pCD⁰-MMT was higher than that of pCD⁺-MMT, whereas the rate of adsorption for pCD⁺-MMT was more rapid. These differences attribute to the difference in the structure, as the

authors commented. The study also showed the ability of these sorbents for simultaneous removal of 38 micropollutants, including different types of pesticides and pharmaceuticals. Furthermore, effective regeneration for 2 cycles was achieved.

Fixed bed operations are known to produce treated water with high quality, and dense media are mandatory in fixed beds to avoid having large (in volume) beds [57]. Polymers alone are unsuitable for this as they possess very low densities; thus, PCNs are a good candidate. Onyango et al. [57] investigated the feasibility of using natural clay as a matrix to hold polymers (polypyrrole/OMMT nanocomposite) in order to remove Cr(VI) from wastewater. This study evaluated the removal efficiency in both batch and column mode. The results found that this process was endothermic (adsorption increases with temperature increases) and the maximum capacities of the Langmuir isotherm increased from 112.35 to 209.6 mg/g as the temperature increased from about 19 to 45 °C in batch mode. For the design of a fixed bed, initial concentration, flow rate, and bed mass are the most important parameters. It was found that the increases in the initial concentration of Cr(VI) showed a decrease in breakthrough time as a result of the rapid consumption of active sites at higher concentrations. The authors claimed that these results showed the suitability to use this composite in low Cr(VI) media. On the other hand, bed mass depending on the number of active sites available for decontamination. It was also observed that increasing the flow rate reduces performance. In conclusion, the authors concluded that a good bed performance could be achieved at a low flow rate, low initial concentration, and high bed mass.

A novel adsorbent made from bentonite clay embedded in polyacrylamide gel was used for the removal of Cu(II) from an aqueous medium. The results showed that the adsorption was dependent on pH, temperature, and ionic strength. The adsorption increased from 9 to 97% at pH range of (2.4–7.0). Also, the rate of adsorption increased as temperature increases and with decreasing ionic strength. In addition, an adsorption/desorption study was performed and indicates that the desorption of Cu(II) is difficult [87].

A new kind of PCNs adsorbent based on loess clay supported by in-situ polymerization of acrylic acid and 2-hydroxyethyl methacrylate was produced for the removal of Pb (II) from an aqueous medium [88]. A removal rate of 99% at room temperature was observed, and the adsorption capacity of 356.9 mg/g was achieved. Despite the excellent performance for this composite, the economic feasibility requires exploring the ability for regeneration.

On the other hand, Anirudhan & Suchithra explored the feasibility of utilizing the spent adsorbent for heavy metal removal [89]. Humic acid-immobilized-amine modified polyacrylamide/bentonite composite was used as an adsorbent for Zn(II), Cu(II), and Co(II) in wastewaters. At 30 °C, significant adsorption capacities were observed as follows: 106.2, 96.1, and 52.9 mg/g for Cu(II), Zn(II), and Co(II) ions, respectively. Also, reusability was investigated. Adsorption/desorption for three cycles without any loss in removal and recovery was conducted. However, it was noticed that the adsorbent's synthesis process is not simple and included several steps that may affect the cost for practical application.

Reusing treated wastewater is currently considered for the sustainable management of water resources. However, nano-concentrations of many pharmaceuticals were reported in this water. Efforts for resolving this issue were conducted with some drawbacks. In recent work, a novel PCNs was designed in order to remove gemfibrozil (GFZ: a lipid regulating drug) from treated wastewater [90]. This PCNs is based on poly-4-vinyl(1-(2-hydroxyethyl)-pyridinium bromide (OHPVP) at high or medium charge densities, adsorbed to MMT clay. The authors demonstrated that the configuration of polyelectrolyte is strongly affected by the charge density at adsorbed state; as the charge decreases, the polyelectrolyte adopts an extended configuration (tails and loops). Thus, this study investigated the effect of polymer charge density, loading (50 and 100% pyridine groups with bromo-ethanol), and configuration on PCNs structure and, consequently, the effect on removal of GFZ. The study showed that at high polymer loading, 100% PCNs adsorbed in flat configuration (trains), whereas 50% PCNs adsorbed in a more extended configuration (tails and loops). The adsorption capacity of GFZ was significantly higher by using 50% PCNs than the 100% PCNs. This affinity was explained in terms of more adsorption sites that existed due to the extended configuration.

Finally, it worth mentioning that there are important studies to be investigated regarding the adsorption phenomena. One of these is adsorption isotherm models that curves describe the phenomenon governing the release or mobility of species from aquatic environments or aqueous porous media to a solid at constant pH and temperature [8]. They provide valuable insight into the surface properties, adsorption mechanism, and the degree of attraction of adsorbents. A wide variety of equilibrium models such as Freundlich, Langmuir, Flory-Huggins, Temkin, Khan, and Brunauer–Emmett–Teller (BET) have been employed [91]. On the other hand, kinetic studies are vital in order to find the optimized conditions to perform efficient decontamination, such as solute uptake, mass transport, chemical interactions, and ionization. Adsorption kinetic can be both simple and sophisticated [8]. There are also a number of models that have been widely used in the literature. The thermodynamic analysis is another important assessment that shows the possible nature of the process. However, this chapter provides the basic knowledge and the recent contributions without discussing these studies. In the end, an ideal adsorbent for any pollutants should have typical criteria, including high capacity with minimum dosage, decontamination rapidly, and be able for regeneration.

3.3 Coagulation and Flocculation

Most agro-industries effluents are unsuitable for direct discharge into sewage treatment plants as they contain a significant quantity of suspended particles such as silts, bacteria, clay, and organic matter from the contaminated water [92]. The suspended particles remain in dispersed condition (colloidal), and using conventional adsorbents that are used commonly for the removal of organic and inorganic micropollutants is difficult. Hence, pretreatment is necessary to avoid clogging of filters by

suspended matter. The pretreatment involves three stages: coagulation (neutralization of colloidal charges), flocculation (several small particles linked together to form a larger flock aggregate that sinks and separated from the effluents), and separation by filtration processes [3, 92].

The current efforts in the coagulation/flocculation field are focused on designing new composite coagulants. According to the literature, the performance of composite coagulant is superior to their counterpart coagulants in wastewater treatment. The recent efforts focused on using natural resources as well as biodegradable materials. In particular, it was reported that chitosan/clay coagulants show better results compared to conventional synthetic coagulants [58].

Yadi et al. [93] produced PCNs coagulants based on chitosan/bentonite and chitin (deacetylated chitosan)/bentonite for the removal of ammonia. The chitosan/bentonite coagulant achieved maximum removal of 11.6 mg/g at an optimal pH of 6, which is higher compared to chitin/bentonite (1.04 mg/g) and the natural bentonite (0.75 mg/g). The uptake equilibrium was within 30 min. for chitosan/bentonite with a removal rate of 60%. The results showed that chitosan/bentonite coagulant is a better adsorbent compared to chitin/bentonite bead and pristine bentonite. This is attributed to the high surface area and high porosity, as well as the lower cost.

A novel composite coagulant based on natural polymer moringa oleifera seed as coagulant and bentonite as adsorbent was prepared for heavy metal ions from aqueous media [58]. This composite coagulant showed a considerable performance for Cr(VI), Cd(II), and Pb(II) removal. Coagulo-adsorption studies showed that maximum removal (100%) occurred at 5 g/L dosage of composite coagulant for all tested heavy metals. For a higher dosage, a decreased removal efficiency was observed. The authors attributed this behavior to the change in zeta potential of the solution. On the other hand, the desorption study showed an overall efficiency for Cr, Pb, and Cd, which was in the range of 97.9–98.87% for three adsorption/desorption cycles. The study also showed that this process was affected by pH variation, where the surface charge of this composite coagulant could be modified via changing the pH of the solution. The results showed that at a very low pH, the uptake of Cd(II) and Pb(II) was very low, whereas Cr removal was very high.

In another study performed by Amin et al. [94], they investigated the use of smectite clay and cationic starch flocculants for atrazine removal from demineralized water. Efficient flocculation was achieved (about 80% of atrazine removed) by using a combination of 40 mg/L smectite with 20 mg/L cationic starch with a dosage of 100 mg/L while increasing the dosage did not improve the atrazine removal. Generally, removal ranging from 10–99% based on clay concentration of 10–50 g/L was reported. The addition of cationic starch increased the settling of smectite, consequently increased the atrazine removal from demineralized water. Later, another study performed by the same team [63] was carried out to determine the ability of this composite flocculant for atrazine and other pharmaceuticals removal from wastewater treatment plant effluent. The study showed a significant drop in performance (30–40%) in wastewater treatment plant effluent media compared to the highest performance achieved in demineralized water. On the other hand, about

70% of the measured pharmaceuticals were removable by smectite/cationic starch composite. Also, the dosage of (20 mg/L cationic starch and 40 mg/L smectite) was sufficient for the removal of pharmaceuticals.

A rapid and efficient treatment could be achieved in one single step by using PNCs as “coago-flocculants” in order to reduce the suspended particles and turbidity in wastewater. These materials combine the merits of both coagulant and flocculent via neutralizing the charge of the colloids by polymer’s charged sites while accumulating them to denser particle (agglomerate), improving their precipitation [8]. In a single step, Rytwo [92] showed that using PCNs based on sepiolite clay and PDADMAC dramatically reduces total suspended particles and the chemical oxygen demand in effluents. The study reveals that at 0.1 wt.% of sepiolite, the suspended particles from a winery effluent (1610 mg/L) was removed completely at a rapid time (less than 2 min) while using the polymer individually revealed poor performance, while 24 h for pristane clay was reported. A subsequent study [95] uses different PCNs: chitosan/sepiolite, PDADMAC/sepiolite, and PDADMAC/Volclay® nanocomposites were to treat winery effluent that showed an efficient and rapid treatment (15–60 min.).

According to the literature, a polymer candidate for this kind of treatment should be a water-soluble polymer such as cationic polyacrylamide or PDADMAC, aromatic polymers such as styrene-based cationic copolymers, cationic biopolymers such as chitosan. Also, the study by [92] suggested the use of suitable anchoring particles for efficient coagoflocculation that possess the following properties: large surface area, using particle with a size of less than 0.5 μm in one dimension, density of the particle should be bigger than the effluents, and ability to adsorb the polymers with a strong bond. Generally, PCNs based on clay with relatively high density bonded to ionic polymers holding opposite charge to the effluent’s colloids had the ability to coagoflocculation in wastewater from different sources such as desalination of seawater and stream water [78]. These findings are promising for continuous flow in wastewater plant as the authors claimed, this technique will eliminate the large sedimentation tanks that used in traditional flocculation processes, which require a long time for sedimentation to occur [95]. Hence, rapid and efficient purification on a large scale with economical materials such as this is possible.

4 Regenerating of Polymer/Clay Nanocomposites

In order to commercialize PCNs adsorbents, the ability to regenerate is an essential factor. This factor affects the economics of the process, as well as the environmental aspect. Thus, adsorption/desorption studies are important in evaluating a prospective adsorbent for certain decontamination. In general, there are different approaches reported for the regeneration of PNCs include treatment of PNCs with various concentrations of alkaline solution, acidic solution, a combination of alkaline and acidic solutions, methanol, ethanol, hydrogen peroxide solution, buffer

Table 3 Regeneration efficiency of PCNs

Polymer	Clay	Pollutant	Eluent	Recovery (%)	Ref.
Moringa oleifera	Bentonite	Cd(II) Cr(IV) Pb(II)	–	97.9–98.8	[58]
Poly(AAm-co-AMPS)	Na-MMT	CV MB MR	Ethanol	80.54 89.74 51.94	[82]
Chitosan	Bentonite	Cr(IV)	NaOH	60.1	[70]
PVA	Kaolinite	Pb(II) Cd(II)	HCl	99	[97]
Chitosan-g-poly(acrylamide)	MMT	MB	NaCl solution 0.5 M of water/ethanol	87	[62]
PANI	Modified clay	Pb(II) Cd(II)	HCl and HNO ₃	80	[85]
Cellulose	Na-MMT	Cr(VI)	Ascorbic acid Na ₂ CrO ₄	85 (99 ± 0.3)	[71]
Polycyclodextrin	MMT	EOM BPA	brine (NaCl ₂ N) NaOH	60 95–75	[86]

solution, mannose solution, and petroleum ether [96]. Although chemical regeneration of PCNs is the most common method explored were almost in many cases, complete recovery was achieved [10]. However, combined regeneration approaches may represent a better alternative [83].

Compared to pristine clay, PCNs could be easily recovered from aqueous media and exhibit better life cycles [12]. Table 3 above demonstrates promising potentials for the regeneration of some PCNs.

Regardless of their abilities to regenerate, using effective and eco-friendly eluents is also important. On the other hand, a single cycle for adsorption/desorption study is not sufficient for accurate assessment of the recovery efficiency for a given adsorbent [97].

Despite the good results of some of the aforementioned studies in Table 3, the recovery rate was reduced in subsequent cycles. On the other hand, adsorbent with the ability to decontaminate does not grant the ability of good recovery. For instance, PCNs based on raw kaolinite and PVA showed a potential for the removal of Pb(II) from aqueous media, but this adsorbent showed reduction during the regeneration test [98]. In general, the regeneration procedure must be simple, cheap, and fast in order to be used on an industrial scale [96].

Recently, a novel approach to design PCNs with the ability to regenerate by responding to external stimuli was reported. Using covalently grafting stimuli-responsive polymer is a new way for this purpose, as polymers may respond to external stimuli such as temperature, pH, infrared light, and ionic strength for

adsorbing and desorb. A pH-responsive adsorbent based on PVP brushes grafted to MMT was fabricated and evaluated for adsorption and desorption of MB, selenate, sulfentrazone, arsenate, atrazine, and eosin-Y [99]. Successful in-column regeneration of the adsorbent was induced by pH as well, as excellent removal performance of organic and inorganic anionic micropollutants were achieved. The grafted polymer protonated at low/moderate pH and consequently promote pollutant adsorption, while at high pH, the polymer undergoes deprotonation and then promotes pollutant desorption.

Still, most of the regenerative procedures for PCNs re-introduce the pollutants into the solution [96]. Thus, separation of adsorbent from pollutants after adsorption is a major challenge, and for that magnetize the PCNs in order to separate the pollutant with the help of a magnet, it might be one of the promising solutions.

5 Scaling up the Processes

The practical application for any new technology relies on its cost over the potential benefits [96]. Thus, studying the ability to decontaminate from wastewater to a safe level without considering the cost and how fast is the process is not enough for scaling up [92]. Yet, the current research endeavors are limited to the laboratory and performed in synthetic polluted water (prepared in the laboratory) under controlled conditions, while the real contaminated water is sophisticated. However, as a step toward scaling up, several efforts have been made to study the performance of PCNs in real or simulated contaminated wastewater as previously noted in the aforementioned literature. These attempts are valuable as they provide fundamental knowledge to understand the mechanisms, chemistry, kinetics and limitations of the materials used in area in order to make final assessment possible.

However, understanding the PCNs stability and their toxicity and environmental impact must be evaluated to demonstrate their practical utility [3]. Hence, detailed studies are also essential to bridge the gap between laboratory findings and practical applications [100].

6 Conclusions

The performance of PCNs differs not only through the technique used but also on the type of the pollutants and the aqueous conditions, including pH of the solution. The composition of the basic materials (polymer and clay) and the method of synthesis can influence the morphological, structural, functional, physicochemical properties and adsorption efficiency of the produced PCN. Also, monitoring the long-term stability of these materials under practical conditions is crucial.

In practical application, the volume of wastewater to be treated is generally huge. Thus, adsorbents, membranes, or coagulants must have high selectivity or

targeted pollutant. Furthermore, it must be easily recovered. The continuous research in this area by exploring new polymers, clays, novel modifications, and even new technologies may induce new functions and characteristics of those materials. For instance, the photodegradation of pollutants was also explored by employing PCNs as photocatalyst.

Based on the available literature, these materials have excellent potentials. However, more attention should be paid to explore PCNs with novel architecture as it is constantly developed.

7 Future Prospectives

The contamination of water resources with various pollutants is a sustained issue. This global concern leads to extensive endeavors in order to find the best solution. Investigation of a wide range of techniques using various materials to overcome this global challenge in the most effective way is still a burning issue. Among the emerged materials used in this area, PCNs were employed in many techniques for wastewater treatment applications. This composite combines the features of their counterparts. It has been revealed by several studies that PCNs are suitable for the removal of organic, inorganic, and biological pollutants in wastewater. Furthermore, several efforts reveal that the performance of PCNs as adsorbents exceeds the commercially available adsorbents. The significant importance of these composites is the ability to tailored according to diverse requirements and also could be combined with other processes. However, various types of building units of PCNs have not yet been investigated. Therefore, a lot of work could be done to extend knowledge.

References

1. Buruga, K., Song, H., Shang, J., Bolan, N., Thimmarajampet, J., Kim, K.: A review on functional polymer-clay based nanocomposite membranes for treatment of water. *J. Hazard. Mater.* **379**, 120584 (2019)
2. Beyene, H.D., Ambaye, T.G.: Application of sustainable nanocomposites for water purification process. In: *Sustainable Polymer Composites and Nanocomposites*, pp. 387–412 (2019)
3. Batool, M., Nazar, M.F., Awan, A., et al.: Bismuth-based heterojunction nanocomposites for photocatalysis and heavy metal detection applications. *Nano-struct. Nano-objects* **27**, 100762 (2021)
4. Sadegh, H., Ali, G.A.M., Abbasi, Z., Nadagoud, M.N.: Adsorption of ammonium ions onto multi-walled carbon nanotubes. *Stud. Univ. Babeş Bolyai Chem.* **62**(2), 233–245 (2017)
5. Agarwal, S., et al.: Efficient removal of toxic bromothymol blue and methylene blue from wastewater by polyvinyl alcohol. *J. Mol. Liq.* **218**, 191–197 (2016)
6. Gupta, V.K., Agarwal, S., Sadegh, H., Ali, G.A.M., Bharti, A.K., Hamdy, A.S.: Facile route synthesis of novel graphene oxide- β -cyclodextrin nanocomposite and its application as adsorbent for removal of toxic bisphenol A from the aqueous phase. *J. Mol. Liq.* **237**, 466–472 (2017)

7. Sadegh, H., et al.: MWCNTs-Fe₃O₄ nanocomposite for Hg(II) high adsorption efficiency. *J. Mol. Liq.* **258**, 345–353 (2018)
8. Singh, N.B., Susan, A.B.H.: Polymer nanocomposites for water treatments. In: *Polymer-Based Nanocomposites for Energy and Environmental Applications*, pp. 569–595. Elsevier Ltd. (2018)
9. Berber, M.R.: Current advances of polymer composites for water treatment and desalination. *J. Chem.* **2020**, 7608423 (2020)
10. Shabtai, I.A., Lynch, L.M., Mishael, Y.G.: Designing clay-polymer nanocomposite sorbents for water treatment: a review and meta-analysis of the past decade. *Water Res.* **188**, 116571–116571 (2021)
11. Orta, M.D.M., Martín, J., Santos, J.L., Aparicio, I., Medina-Carrasco, S., Alonso, E.: Biopolymer-clay nanocomposites as novel and ecofriendly adsorbents for environmental remediation. *Appl. Clay Sci.* **198**, 105838–105838 (2020)
12. Abouchenari, A., Hardani, K., Abazari, S., Keleshteri, M.A., Chahardehi, A.M.: Clay-reinforced nanocomposites for the slow release of chemical fertilizers and water retention. *J. Compos. Compd.* **2**, 85–91 (2020)
13. Awasthi, A., Jadhao, P., Kumari, K.: Clay nano-adsorbent: structures, applications and mechanism for water treatment. *SN Appl. Sci.* **1**(9), 1076 (2019). <https://doi.org/10.1007/s42452-019-0858-9>
14. Kalotra, S., Mehta, R.: Synthesis of polyaniline/clay nanocomposites by in situ polymerization and its application for the removal of Acid Green 25 dye from wastewater. *Polym. Bull.* **78**(5), 2439–2463 (2020)
15. Guo, F., Aryana, S., Han, Y., Jiao, Y.: A review of the synthesis and applications of polymer-nanoclay composites. *Appl. Sci.* **8**, 1696 (2018)
16. Kotal, M., Bhowmick, A.K.: Polymer nanocomposites from modified clays: recent advances and challenges. *Prog. Polym. Sci.* **51**, 127–187 (2015)
17. Ali, F., Ullah, H., Ali, Z., Rahim, F., Khan, F., Ur Rehman, Z.: Polymer-clay nanocomposites, preparations and current applications: a review. *Curr. Nanomater.* **1**(2), 83–95 (2016)
18. Kurecic, M., Smole, M.S.: Polymer nanocomposite hydrogels for water purification. In: Farzad, E. (ed.) *Nanocomposites-New Trends and Developments*, pp. 161–185. IntechOpen (2012)
19. Babu Valapa, R., Loganathan, S., Pugazhenthii, G., Thomas, S., Varghese, T.O.: An overview of polymer-clay nanocomposites. In: Jlassi, K., Chehimi, M.M., Thomas, S. (eds.) *Clay-Polymer Nanocomposites*, pp. 29–81. Elsevier (2017)
20. Padmavathy, K.S., Murali, A., Madhu, G., Sahoo, D.K.: Adsorption of hexavalent chromium (Cr(VI)) from wastewater using novel chitosan/halloysite clay nanocomposite films. *Indian J. Chem. Technol.* **24**(6), 593–600 (2017)
21. Nasir, A., Masood, F., Yasin, T., Hameed, A.: Progress in polymeric nanocomposite membranes for wastewater treatment: preparation, properties and applications. *J. Ind. Eng. Chem.* **79**, 29–40 (2019)
22. Unuabonah, E.I., Taubert, A.: Clay-polymer nanocomposites (CPNs): adsorbents of the future for water treatment. *Appl. Clay Sci.* **99**, 83–92 (2014)
23. Rouhi, M., Babamoradi, M., Hajizadeh, Z., Maleki, A., Maleki, S.T.: Design and performance of polypyrrole/halloysite nanotubes/Fe₃O₄/Ag/Co nanocomposite for photocatalytic degradation of methylene blue under visible light irradiation. *Optik* **212**, 164721–164721 (2020)
24. Zahid, M., Rashid, A., Akram, S., Rehan, Z.A., Razaq, W.: A comprehensive review on polymeric nano-composite membranes for water treatment. *J. Membr. Sci. Technol.* **08**(01), 1–20 (2018)
25. Rodrigues, R., Mierzwa, J.C., Vecitis, C.D.: Mixed matrix polysulfone/clay nanoparticles ultrafiltration membranes for water treatment. *J. Water Process Eng.* **31**(2), 100788–100788 (2019)
26. Yin, J., Deng, B.: Polymer-matrix nanocomposite membranes for water treatment. *J. Membr. Sci.* **479**, 256–275 (2015)

27. Mierzwa, J.C., Arieta, V., Verlage, M., Carvalho, J., Vecitis, C.D.: Effect of clay nanoparticles on the structure and performance of polyethersulfone ultrafiltration membranes. *Desalination* **314**, 147–158 (2013)
28. Ghaemi, N., Madaeni, S.S., Alizadeh, A., Rajabi, H., Daraei, P.: Preparation, characterization and performance of polyethersulfone/organically modified montmorillonite nanocomposite membranes in removal of pesticides. *J. Membr. Sci.* **382**(1–2), 135–147 (2011)
29. Rodrigues, R., Morihama, A.C.D., Barbosa, I.M., Leocádio, G.N., Mierzwa, J.C.: Clay nanoparticles composite membranes prepared with three different polymers: performance evaluation. *J. Membr. Sep. Technol.* **7**(2), 1–11 (2018)
30. Ma, Y., Shi, F., Wang, Z., Wu, M., Ma, J., Gao, C.: Preparation and characterization of PSf/clay nanocomposite membranes with PEG 400 as a pore forming additive. *Desalination* **286**, 131–137 (2012)
31. Morihama, A.C.D., Mierzwa, J.C.: Clay nanoparticles effects on performance and morphology of poly(vinylidene fluoride) membranes. *Braz. J. Chem. Eng.* **31**(1), 79–93 (2014)
32. Jacob, L., Joseph, S., Varghese, L.A.: Polysulfone/MMT mixed matrix membranes for hexavalent chromium removal from wastewater. *Arab. J. Sci. Eng.* **45**(9), 7611–7620 (2020)
33. Lai, C.Y., Groth, A., Gray, S., Duke, M.: Preparation and characterization of poly(vinylidene fluoride)/nanoclay nanocomposite flat sheet membranes for abrasion resistance. *Water Res.* **57**, 56–66 (2014)
34. Rajabi, H., Ghaemi, N., Madaeni, S.S., Daraei, P., Khadivi, M.A., Falsafi, M.: Nanoclay embedded mixed matrix PVDF nanocomposite membrane: preparation, characterization and biofouling resistance. *Appl. Surf. Sci.* **313**, 207–214 (2014)
35. Hosseini, S.A., Vossoughi, M., Mahmoodi, N.M., Sadrzadeh, M.: Clay-based electrospun nanofibrous membranes for colored wastewater treatment. *Appl. Clay Sci.* **168**, 77–86 (2019)
36. Seshasayee, M.S., Yu, Z., Arthanareeswaran, G., Das, D.B.: Preparation of nanoclay embedded polymeric membranes for the filtration of natural organic matter (NOM) in a circular crossflow filtration system. *J. Water Process Eng.* **37**, 101408 (2020)
37. da Silva, R., et al.: Treatment of effluents from the textile industry through polyethersulfone membranes. *Water (Switz.)* **11**(12), 2540 (2019)
38. Moslehyani, A., Ismail, A.F., Othman, M.H.D., Matsuura, T.: Hydrocarbon degradation and separation of bilge water via a novel TiO₂-HNTs/PVDF-based photocatalytic membrane reactor (PMR). *RSC Adv.* **5**(19), 14147–14155 (2015)
39. Makwana, D., Poliseti, V., Castaño, J., Ray, P., Bajaj, H.C.: Mg-Fe layered double hydroxide modified montmorillonite as hydrophilic nanofiller in polysulfone- polyvinylpyrrolidone blend ultrafiltration membranes: separation of oil-water mixture. *Appl. Clay Sci.* **192**, 105636 (2020)
40. Khalil, A.M., Kenawy, S.H.: Hybrid membranes based on clay-polymer for removing methylene blue from water. *Acta Chim. Slov.* **67**(1), 96–104 (2020)
41. Sadegh, H., Ali G.A.M., Nia, H.J., Mahmoodi, Z.: Nanomaterial surface modifications for enhancement of the pollutant adsorption from wastewater. In: *Nanotechnology Applications in Environmental Engineering*, p. 143 (2019)
42. Hamidreza, S., Goma, A.M.A.: Potential applications of nanomaterials in wastewater treatment: nanoadsorbents performance. In: Athar, H., Sirajuddin, A. (eds.) *Advanced Treatment Techniques for Industrial Wastewater*, pp. 51–61. IGI Global, Hershey (2019)
43. Seyed Arabi, S.M., Lalehloo, R.S., Olyai, M.R.T.B., Ali, G.A.M., Sadegh, H.: Removal of congo red azo dye from aqueous solution by ZnO nanoparticles loaded on multiwall carbon nanotubes. *Phys. E* **106**, 150–155 (2019)
44. Sadegh, H., et al.: The role of nanomaterials as effective adsorbents and their applications in wastewater treatment. *J. Nanostruct. Chem.* **7**(1), 1–14 (2017)
45. Sadegh, H., Ali, G.A.M., Agarwal, S., Gupta, V.K.: Surface Modification of MWCNTs with carboxylic-to-amine and their superb adsorption performance. *Int. J. Environ. Res.* **13**(3), 523–531 (2019)
46. Abdel Ghafar, H.H., Ali, G.A., Fouad, O.A., Makhlof, S.A.: Enhancement of adsorption efficiency of methylene blue on Co₃O₄/SiO₂ nanocomposite. *Desalin. Water Treat.* **53**(11), 2980–2989 (2015)

47. Ali, G.A.M., et al.: High surface area mesoporous silica for hydrogen sulfide effective removal. *Curr. Nanosci.* **16**(2), 226–234 (2020)
48. Maazinejad, B., et al.: Taguchi L9 (34) orthogonal array study based on methylene blue removal by single-walled carbon nanotubes-amine: Adsorption optimization using the experimental design method, kinetics, equilibrium and thermodynamics. *J. Mol. Liq.* **298**, 112001 (2020)
49. Habeeb, O.A., Ramesh, K., Ali, G.A.M., Yunus, R.M.: Experimental design technique on removal of hydrogen sulfide using CaO-eggshells dispersed onto palm kernel shell activated carbon: experiment, optimization, equilibrium and kinetic studies. *J. Wuhan Univ. Technol. Mater. Sci. Ed.* **32**(2), 305–320 (2017)
50. Habeeb, O.A., Ramesh, K., Ali, G.A.M., Yunus, R.M.: Low-cost and eco-friendly activated carbon from modified palm kernel shell for hydrogen sulfide removal from wastewater: adsorption and kinetic studies. *Desalin. Water Treat.* **84**, 205–214 (2017)
51. Shayegan, H., Ali, G.A.M., Safarifard, V.: Amide-functionalized metal–organic framework for high efficiency and fast removal of Pb(II) from aqueous solution. *J. Inorg. Organomet. Polym. Mater.* **30**(8), 3170–3178 (2020)
52. Shayegan, H., Ali, G.A.M., Safarifard, V.: Recent progress in the removal of heavy metal ions from water using metal-organic frameworks. *ChemistrySelect* **5**(1), 124–146 (2020)
53. Soetaredjo, F.E., Ismadji, S., Foe, K., Woworuntu, G.L.: Removal of hazardous contaminants from water or wastewater using polymer nanocomposites materials. In: *Nanotechnology for Sustainable Water Resources*, pp. 103–139 (2018)
54. Abed, H.O., Kanthasamy, R., Ali, G.A.M., Sethupathi, S., Yunus, R.B.M.: Hydrogen sulfide emission sources, regulations, and removal techniques: a review. *Rev. Chem. Eng.* **34**(6), 837–854 (2017)
55. Habeeb, O.A., Ramesh, K., Ali, G.A.M., Yunus, R.M.: Isothermal modelling based experimental study of dissolved hydrogen sulfide adsorption from waste water using eggshell based activated carbon. *Malays. J. Anal. Sci.* **21**(2), 334–345 (2017)
56. Habeeb, O.A., Ramesh, K., Ali, G.A.M., Yunus, R.M., Olalere, O.A.: Kinetic, isotherm and equilibrium study of adsorption of hydrogen sulfide from wastewater using modified eggshells. *IJUM Eng. J.* **18**(1), 13–25 (2017)
57. Onyango, M.S., Mbakop, S., Leswif, T.Y., Mthombeni, N.H., Setshedi, K.: Application of polymer-natural clay composite in water treatment. In: *Proceedings of Sustainable Research and Innovation Conference* (2016)
58. Ravikumar, K., Udayakumar, J.: Preparation and characterisation of green clay-polymer nanocomposite for heavy metals removal. *Chem. Ecol.* **36**(3), 270–291 (2020)
59. Zhou, K., et al.: The integrated utilization of typical clays in removal of organic dyes and polymer nanocomposites. *J. Clean. Prod.* **81**, 281–289 (2014)
60. Motshega, S.C., Ray, S.S., Onyango, M.S., Momba, M.N.B.: Preparation and antibacterial activity of chitosan-based nanocomposites containing bentonite-supported silver and zinc oxide nanoparticles for water disinfection. *Appl. Clay Sci.* **114**, 330–339 (2015)
61. Sallam, A., Al-Zahrani, M., Al-Wabel, M., Al-Farraj, A., Usman, A.: Removal of Cr(VI) and toxic ions from aqueous solutions and tannery wastewater using polymer-clay composites. *Sustainability* **9**(11), 1993 (2017)
62. Ferfera-Harrar, H., Benhalima, T., Lerari, D.: Sustainable hydrogel nanocomposites based on grafted chitosan and clay for effective adsorption of cationic dye. *Int. J. Mater. Metall. Eng.* **14**, 5–15 (2020)
63. Amin, M.F.M., Heijman, S.G.J., Rietveld, L.C.: Clay-starch combination for micropollutants removal from wastewater treatment plant effluent. *Water Sci. Technol.* **73**(7), 1719–1727 (2016)
64. García-Padilla, Á., Moreno-Sader, K.A., Realpe, Á., Acevedo-Morantes, M., Soares, J.B.P.: Evaluation of adsorption capacities of nanocomposites prepared from bean starch and montmorillonite. *Sustain. Chem. Pharm.* **17**, 100292 (2020)
65. Moreno-Sader, K., García-Padilla, A., Realpe, A., Acevedo-Morantes, M., Soares, J.B.P.: Removal of heavy metal water pollutants (Co²⁺ and Ni²⁺) using polyacrylamide/sodium montmorillonite (PAM/Na-MMT) nanocomposites. *ACS Omega* **4**(6), 10834–10844 (2019)

66. Ganigar, R., Rytwo, G., Gonen, Y., Radian, A., Mishael, Y.G.: Polymer-clay nanocomposites for the removal of trichlorophenol and trinitrophenol from water. *Appl. Clay Sci.* **49**(3), 311–316 (2010)
67. Erdem, B., Erdem, M., Özcan, A.S.: Adsorption of reactive black 5 onto quaternized 2-dimethylaminoethyl methacrylate based polymer/clay nanocomposites. *Adsorption* **22**(4–6), 767–776 (2016)
68. Sabzi, M., Shafagh, N., Mohammadi, M.: Assembly of gelatin biopolymer to fibrous sepiolite clay for efficient dye removal from wastewater. *J. Appl. Polym. Sci.* **136**(48), 1–10 (2019)
69. Giannakas, A., Pissanou, M.: Chitosan/bentonite nanocomposites for wastewater treatment: a review. *SF J. Nanochem. Nanotechnol.* **1**, 1–17 (2018)
70. Yang, J., Huang, B., Lin, M.: Adsorption of hexavalent chromium from aqueous solution by a chitosan/bentonite composite: isotherm, kinetics, and thermodynamics studies. *J. Chem. Eng. Data* **65**, 2751–2763 (2020)
71. Kumar, A., Kalidhasan, S., Vidya, R., Rajesh, N.: Application of cellulose-clay composite biosorbent toward the effective adsorption and removal of chromium from industrial wastewater. *Ind. Eng. Chem. Res.* **51**, 58–69 (2012)
72. Azha, S.F., et al.: Synthesis and characterization of a novel amphoteric adsorbent coating for anionic and cationic dyes adsorption: experimental investigation and statistical physics modelling. *Chem. Eng. J.* **351**, 221–229 (2018)
73. Yu, T., Qu, C., Fan, D., Xu, R.: Effects of bentonite activation methods on chitosan loading capacity. *Bull. Chem. React. Eng. Catal.* **13**(1), 14–23 (2018)
74. Eladlani, N., et al.: “Chitosan/montmorillonite” nanocomposites: adsorption of Cr(III). *J. Water Chem. Technol.* **41**(3), 175–181 (2019)
75. Bleiman, N., Mishael, Y.G.: Selenium removal from drinking water by adsorption to chitosan-clay composites and oxides: batch and columns tests. *J. Hazard. Mater.* **183**(1–3), 590–595 (2010)
76. Bruna, J.E., Peñaloza, A., Guarda, A., Rodríguez, F., Galotto, M.J.: Development of MtCu²⁺/LDPE nanocomposites with antimicrobial activity for potential use in food packaging. *Appl. Clay Sci.* **58**, 79–87 (2012)
77. Ferfera-Harrar, H., Aiouaz, N., Dairi, N., Hadj-Hamou, A.S.: Preparation of chitosan-g-poly(acrylamide)/montmorillonite superabsorbent polymer composites: studies on swelling, thermal, and antibacterial properties. *J. Appl. Polym. Sci.* **131**(1), 1–14 (2014)
78. Rytwo, G.: Securing the future: clay-based solutions for a comprehensive and sustainable potable-water supply system. *Clays Clay Miner.* **66**(4), 315–328 (2018)
79. Baskaralingam, P., Pulikesi, M., Ramamurthi, V., Sivanesan, S.: Equilibrium studies for the adsorption of acid dye onto modified hectorite. *J. Hazard. Mater.* **136**(3), 989–992 (2006)
80. Baskaralingam, P., Pulikesi, M., Elango, D., Ramamurthi, V., Sivanesan, S.: Adsorption of acid dye onto organobentonite. *J. Hazard. Mater.* **128**(2), 138–144 (2006)
81. Irani, M., Ismail, H., Ahmad, Z., Fan, M.: Synthesis of linear low-density polyethylene-g-poly (acrylic acid)-co-starch/organo-montmorillonite hydrogel composite as an adsorbent for removal of Pb(II) from aqueous solutions. *J. Environ. Sci.* **27**, 9–20 (2015)
82. Nakhjiri, M.T., Marandi, G.B., Kurdtabar, M.: Effect of bis[2-(methacryloyloxy)ethyl] phosphate as a crosslinker on poly(AAm-co-AMPS)/Na-MMT hydrogel nanocomposite as potential adsorbent for dyes: kinetic, isotherm and thermodynamic study. *J. Polym. Res.* **25**(11), 1–19 (2018). <https://doi.org/10.1007/s10965-018-1625-0>
83. Han, H., Rafiq, M.K., Zhou, T., Xu, R., Mašek, O., Li, X.: A critical review of clay-based composites with enhanced adsorption performance for metal and organic pollutants. *J. Hazard. Mater.* **369**, 780–796 (2019)
84. Sirajudheen, P., Karthikeyan, P., Basheer, M.C., Meenakshi, S.: Adsorptive removal of anionic azo dyes from effluent water using Zr(IV) encapsulated carboxymethyl cellulose-montmorillonite composite. *Environ. Chem. Ecotoxicol.* **2**, 73–82 (2020). <https://doi.org/10.1016/j.enceco.2020.04.002>

85. Piri, S., Zanjani, Z.A., Piri, F., Zamani, A., Yaftian, M., Davari, M.: Potential of polyaniline modified clay nanocomposite as a selective decontamination adsorbent for Pb(II) ions from contaminated waters; kinetics and thermodynamic study. *J. Environ. Health Sci. Eng.* **14**(1), 1–10 (2016)
86. Shabtai, I.A., Mishael, Y.G.: Polycyclodextrin-clay composites: regenerable dual-site sorbents for bisphenol a removal from treated wastewater. *ACS Appl. Mater. Interfaces* **10**(32), 27088–27097 (2018)
87. Zhao, G., et al.: Sorption of copper(II) onto super-adsorbent of bentonite–polyacrylamide composites. *J. Hazard. Mater.* **173**(1), 661–668 (2010)
88. He, Y.F., Zhang, L., Wang, R.M., Li, H.R., Wang, Y.: Loess clay based copolymer for removing Pb(II) ions. *J. Hazard. Mater.* **227–228**, 334–340 (2012)
89. Anirudhan, T.S., Suchithra, P.S.: Heavy metals uptake from aqueous solutions and industrial wastewaters by humic acid-immobilized polymer/bentonite composite: kinetics and equilibrium modeling. *Chem. Eng. J.* **156**(1), 146–156 (2010)
90. Levy, L., Izbitski, A., Mishael, Y.G.: Enhanced gemfibrozil removal from treated wastewater by designed “loopy” clay-polycation sorbents: effect of diclofenac and effluent organic matter. *Appl. Clay Sci.* **182**, 105278 (2019)
91. Foo, K.Y., Hameed, B.H.: Insights into the modeling of adsorption isotherm systems. *Chem. Eng. J.* **156**(1), 2–10 (2010)
92. Rytwo, G.: The use of clay-polymer nanocomposites in wastewater pretreatment. *Sci. World J.* **2012**, 7–7 (2012)
93. Yadi, M.G., Benguella, B., Gaouar-Benyelles, N., Tizaoui, K.: Adsorption of ammonia from wastewater using low-cost bentonite/chitosan beads. *Desalin. Water Treat.* **57**(45), 21444–21454 (2016)
94. Amin, M.F.M., Heijman, S.G.J., Rietveld, L.C.: Clay-biodegradable polymer combination for pollutant removal from water. *Drink. Water Eng. Sci. Discuss.* **8**, 177–196 (2015)
95. Rytwo, G., Lavi, R., Rytwo, Y., Monchase, H., Dultz, S., König, T.N.: Clarification of olive mill and winery wastewater by means of clay–polymer nanocomposites. *Sci. Total Environ.* **442**, 134–142 (2013)
96. Akhrame, M.O., Fatoki, O.S., Opeolu, B.O.: Regeneration and reuse of polymeric nanocomposites in wastewater remediation: the future of economic water management. *Polym. Bull.* **76**, 647–681 (2019)
97. Unuabonah, E.I., Olu-Owolabi, B.I., Adebowale, K.O., Yang, L.Z.: Removal of lead and cadmium ions from aqueous solution by polyvinyl alcohol-modified kaolinite clay: a novel nano-clay adsorbent. *Adsorpt. Sci. Technol.* **26**(6), 383–405 (2008)
98. Unuabonah, E.I., El-Khaiary, M.I., Olu-Owolabi, B.I., Adebowale, K.O.: Predicting the dynamics and performance of a polymer-clay based composite in a fixed bed system for the removal of lead (II) ion. *Chem. Eng. Res. Des.* **90**(8), 1105–1115 (2012)
99. Gardi, I., Mishael, Y.G.: Designing a regenerable stimuli-responsive grafted polymer-clay sorbent for filtration of water pollutants. *Sci. Technol. Adv. Mater.* **19**(1), 588–598 (2018)
100. Pandey, N., Shukla, S.K., Singh, N.B.: Water purification by polymer nanocomposites: an overview. *Nanocomposites* **3**(2), 47–66 (2017)

Applications of Nanocomposites in Environmental Remediation



Riham R. Mohamed

Abstract Organic and inorganic contaminants polluting global water resources are concerning the world. Generally, being non-biodegradable synthetic and/or highly soluble in water, pollutants get easily mobilized in the environment. Their interaction with and accumulation in environment has adverse effects on ecosystems and human health.

Deterioration of environment thanks to human activities is increasing daily which results in the discharge of toxic effluents, like pesticides, heavy metals and toxic dyes into environment, causing serious health problems to humans and pollution to environment. *Nanocomposites* have wide applications in different fields like air purification, wastewater treatment via heavy metal removal, soil improvement, fertilizers delivery systems, food packaging and flame retardancy. Nanocomposite composition gives a large surface area with special properties. Lately nanocomposite structures are employed to purify water, develop fertilizer retention in soil, and enhances plant growth resulting in agricultural development, food packaging and flame retardancy. Properties of these nanocomposites rely upon both the properties of their constituents and also the combination between polymer/nano-filler.

This chapter covers the advances on nanocomposites aimed at water decontamination through remediation of metal ions and synthetic organic chemicals, especially dyes, from wastewater.

Keywords Nanocomposites · Metal uptake · Antimicrobial activity · Delivery system

Abbreviations

SAPs	SuperAbsorbent Polymers
PNC	Polymeric Nanocomposites
NC	Nanocomposites

R. R. Mohamed (✉)
Faculty of Science, Cairo University, Giza, Egypt

ACF	Activated Carbon Fibers
CNT	Carbon Nanotubes
CNF	Carbon NanoFibers
HEPA	High Efficiency Particulate Air
PISG	Plasma Induced Surface Grafting
PVDF	PolyVinylene DiFluoride
DMFC	Direct Methanol Fuel Cells
MWCNT	Multiwalled Carbon Nanotubes
PAA	PolyAcrylic Acid
PDADMAC	Poly(DiAllyl DiMethyl ammoniumchloride)
ZVI	Zero-Valent Iron
PCN	Polymer–Clay Nanocomposites
ROS	Reactive oxygen species
HRR	Heat release rate
PHRR	Peak of Heat Release Rate
POSS	Polyhedral oligomeric silsesquioxane

1 Introduction

Nanomaterials are materials having structural components sized 1–100 nm. Nanomaterials have special properties comparing with other normal materials due to small size and large surface area. Lately, They have been employed to various areas as catalysis, medicine [1, 2], sensors, and biology [3, 4]. They also are employed in many fields to solve different environmental problems like treatment of wastewater. Nanomaterials capable of removing several toxins like, organic pollutants, toxic metals, pathogens and inorganic ions. Nanocomposites (NCs) are synthesized through a reaction between many materials with different properties and special interface [5, 6]. Nanocomposites own many benefits than other conventional materials due to their special properties such as; rigidity, durability, gas-barrier properties, corrosion resistance, high strength, thermal stability and low density. Composite materials are defined as a combination between a continuous matrix phase and dispersed reinforced materials. Composite materials are materials which have multiple phase materials, each phase shows sizes in range of 10–100 nm [7, 8]. Nanocomposites have large surface area that recommend them for wide applications in different fields like; wastewater treatment, drug carrier systems, biological sciences, and soil development. Nanocomposite SAPs have been employed in water treatment, fertilizer retention improvement in soil, to enhance plant growth and agricultural development. This chapter deals with nanocomposites different environmental applications.

2 Polymer Nanocomposites for Water Treatments

Water is a valuable natural resource important for the life of all living organisms. Although, fast civilization is destroying water purity and threatening the entire biosphere due to contamination of water by high amounts of pollutants [9, 10].

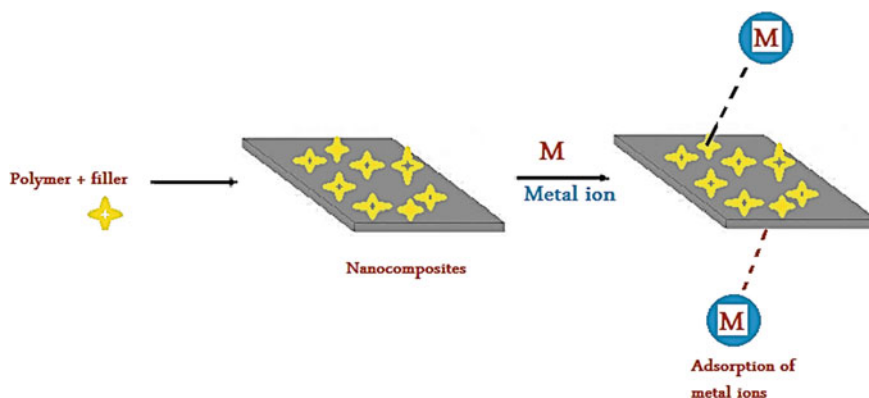
For water purification to be suitable, used materials with good purification capability, high porosity, low price and ability to be recovered should be used. Various kinds of nanocomposites were employed for water treatment. Water resources are polluted with radioactive or heavy metal ions, which are accumulated in the biosphere then in the human body causing severe health problems.

i) *Heavy metal ions removal*

Precipitation, adsorption, flocculation, coagulation, membrane filtration and ion exchange are various techniques for metal removal. Also, polymer-based nanocomposite is used for metal removal since they have unique properties in different forms such as; mat, beads, membrane ...etc.

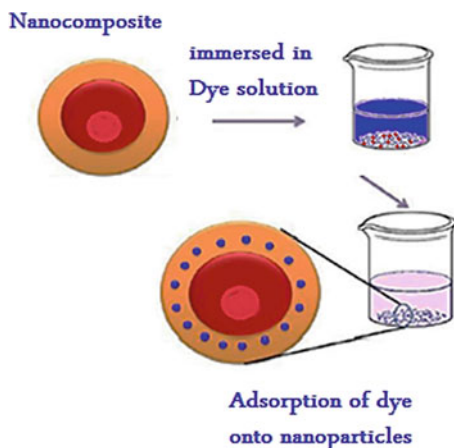
PNCs adsorbents were synthesized by combination of the inorganic nanoparticles with polymeric matrix such as; porous resins, cellulose, alginate and ion-exchangers. They were proved to be perfect adsorbents, for their good surface chemistry and excellent mechanical properties [11, 12].

Acrylic acid copolymerization in presence of bentonite gave a good superabsorbent suitable for various heavy metal ions removal with q_{\max} values 1666.67 for Pb^{2+} , 270.27 for Ni^{2+} and 416.67 mg/g for Cd^{2+} [13, 14]. Chitosan derivatives maybe considered as good physical remedy for water treatment of pollutants, as shown in Scheme 1. Besides, magnetic particles were added to the composites for efficient water purification. Magnetic chitosan composites increased both the removal efficiency and rate for different contaminants. Also, the recovery step is easy and simple [15, 16].



Scheme 1 Schematic diagram of adsorption of heavy metal ions using nanocomposites

Scheme 2 Schematic diagram of adsorption of dye using nanocomposites



ii) Dyes removal

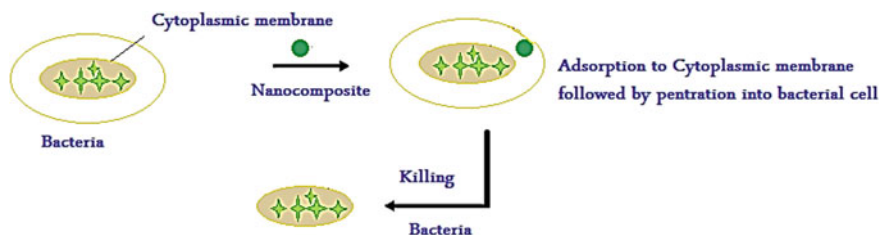
The adjustable catalytic and surface characters of nanocomposites find large application for dyes removal. Dyes discharge in water is one of the most severe toxins creating health problems. There are different techniques raised for getting rid of dyes like; catalytic and filtration. Recently, PNC are used for dyes removal.

PNC have different features as high adsorptivity for dyes. Metal insertion has also created more active centers for efficient dyes removal. Polypyrrole nanocomposite anode doped with metal had been tested to adsorb red dye up to 83–100% by oxidation [17, 18]. This method was efficient for getting rid of all dyes types. Fe_3O_4 nanoparticles dispersed in polymeric matrix has been employed due to Fe_3O_4 good efficiency and the ability of polymer -as being anionic- to remove cationic dyes from water [19, 20] - as shown in Scheme 2.

iii) Removal of pollutants

Pathogens, pesticides, microorganisms, and other organic materials are one of the most important water pollutants. Nanocomposites kill pathogens via liberation both toxic chemicals and reactive oxygen species. Also, metals antibacterial activity acts as a viable disinfectant. Most metals as; silver, gold, aluminum, lead and iron are considered as efficient disinfectants. However, some of these metals are toxic, so the safe metals are used, as shown in Scheme 3. Recently, nanocomposites became water decontaminators that replaced current chemical disinfectants [21, 22]. Metal/copolymer is used efficiently for killing wide spectrum pathogens up to 99.9%.

Cellulose acetate/Ag nanofibers were tested to kill bacteria. Filters for water, made of polyurethane/Ag nanofibers, have a high antibacterial activity towards (*E. coli*). Different composites with carbon nano fillers like; (ACFs) and (CNTs), are also efficient in getting rid of different pathogenic microorganisms [23, 24].



Scheme 3 Schematic diagram of adsorption of nanocomposites to bacterial cell

3 Polymer Nanocomposites for Fertilizers Delivery in Soil

Polymeric nanocomposites have special properties to be used in agriculture field like; biocompatibility and biodegradability, nutrients and fertilizers carriers in soil. Moreover, polymers encapsulation with various nanoparticles as; metal/metal-oxide and carbon increased the delivery rate and biocompatibility.

Metal nanomaterials are used for crops protection and plant growth, as shown in Scheme 4. Used nanomaterials are Fe, Zn, Cu, zinc oxide (ZnO), titanium dioxide (TiO₂), silicon dioxide (SiO₂), aluminum nitride (AlN) and boron nitride (BN),..... etc.

Prepared nanomaterials are aimed for: nutrients-controlled delivery, enhance solubility and protect nutrients against degradation, by increasing the agrochemicals efficiency.

Metal nanocomposites deposit onto the root and move less into the shoot and leaves. Moreover, the problem remains into accumulation, instability, and impossibility to use directly in land.

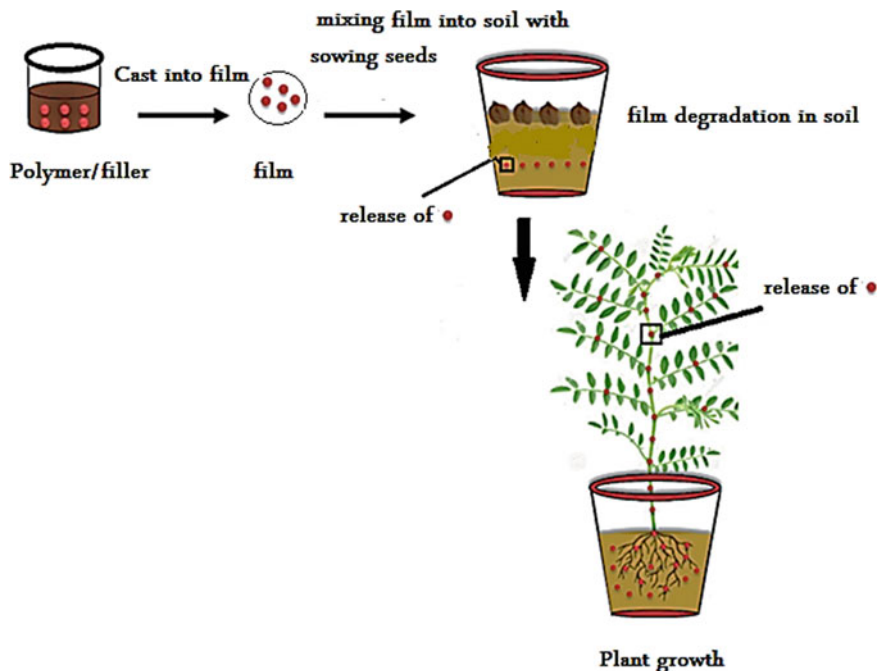
Nanocomposites containing different nanomaterials like fillers with polymer that have excellent features as nontoxicity, stability, controlled delivery and biocompatibility.

Synthesis of nanocomposites is done via polymers encapsulate metal/metal oxide. Composites developed characteristics came from interactions between filler–polymer on the interface and also the homogeneous distribution of nanofillers into the polymer.

Different methods to fulfill those requirements: (1) Fillers/polymer characters change, (2) Polymer properties change by functionalization or copolymerization and (3) required characters developing with mixed nanocomposite.

According to agricultural applications, a larger dose of nanomaterials may cause harms to the crops [25–28].

Nanocomposites interaction with plants depends on different parameters like; size stability, charge, shape, functional groups, chemistry and plants type. Plant cell wall is the major interaction site with nanomaterials/fertilizer. Cell wall never allow any odd substances like; nanocomposites or other nutrients as it represents a shield. Plant wall contains many groups like; hydroxyl, carboxylate, phosphate and imidazole moieties that yield large biomolecules, leading to absorption inside the plant.



Scheme 4 Schematic diagram for micronutrient delivery of polymer nanocomposites

Two important characters affecting nanomaterials/other micronutrients uptake and translocation: (i) charge on surface (ii) size. Negative charges on plant cell-wall will repel with the negative charges on nanomaterials or any other micronutrients, so nanomaterials will favor easily uptake within the plants. On the other hand, negative charges on plant cell wall will attract positive charges onto nanomaterials or any other micronutrients, thus will have large accumulation and lower motion so they will be accumulating on the root.

Due to accumulation, there is some phytotoxicity effect for those metal nanoparticles at higher doses [29]. Nanocomposites or any other nutrients size is the most essential parameter needed for translocation and uptake.

Translocation and uptake in plants favors small size (20–200 nm). Besides, nanomaterials like (CNFs) and (CNTs) ~500 nm or less move in plants easily because of easy motion through epidermis going to vascular bundle. Nanocomposites are transported to root, to shoot and finally to leaves. The osmotic pressure and capillary action are driving forces for nanomaterials translocation into plants. Nanomaterials chemical compositions and types affect the translocation and uptake into the plants. Nanomaterials functionalization can change the accumulation capability and adsorption of plants. Some nanomaterials might deposit in Casparian strip, whereas other nanomaterials can translocate towards root and shoot [30].

4 Recent Advances in Nanofibrous Composite Air Filters

Biological and chemical contaminants present in air have a serious consequence on man health. Elimination of these pollutants is very important from their sources. Conventional methods like adsorption with activated carbon were used to eliminate contaminants. However, some of these methods were good but still have some drawbacks. Several new trials have achieved new materials for such purpose.

The combination of some nanoparticles like; MgO, Al₂O₃, TiO₂ and other oxides into polymeric matrices was recently employed for air filtration purpose because of the special capability of those nanoparticles to eliminate toxic gases as chemical pollutants, bacteria or viruses as biological pollutants and pesticides [31]. These polymeric matrices doped with nanofillers will not just develop separation accuracy, but also nonselective decontamination efficiency, protection maintenance and weight decrease. Ahn et al. have examined separation accuracy of the films of nanofibrous nylon-6, to find they are more efficient the commercial HEPA filter.

From their defects is that they showed a large pressure drop through polymeric film [32]. However, it was suggested their usage as air filter with good efficiency in hygienic air zones like; hospitals where the polluted air can be filtered, as shown in Scheme 5.

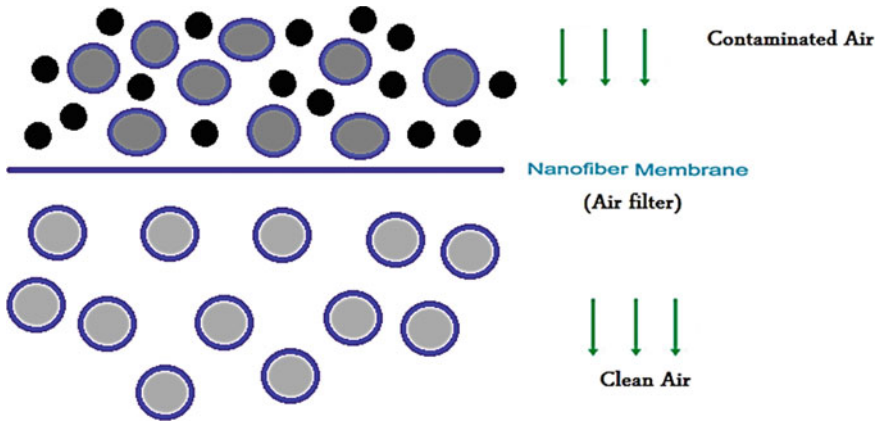
Today, a nanofiber electrospun into different novel matters in everyday life demands as; air, water and pharmaceuticals. Nonwoven electrospun fibers have large surface areas, very tiny pore sizes, much porosity with good elasticity. Ramakrishna et al. worked on nanofibrous membranes development for environmental applications [33]. Hydrophobic membranes can be transformed into hydrophilic ones via different methods. This method is known as *hydrophilization* and is divided into four kinds [34–37]:

- (a) PISG
- (b) Oxidation
- (c) Chemical functionalization
- (d) Radiation induced grafting method

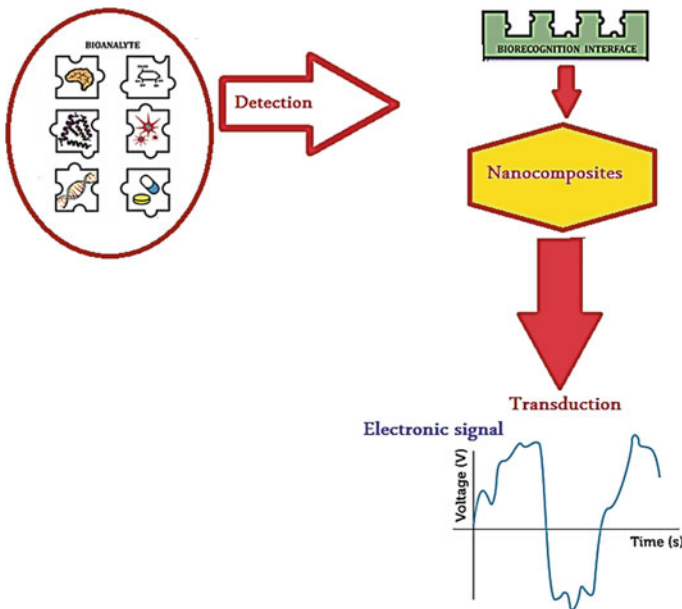
Methacrylic acid was PISG onto electro spun polyvinylidene difluoride PVDF, compared to commercially PVDF hydrophobic membranes. That performance is utilized to minimize PVDF membranes pores size [38].

5 Nanocomposites for Environmental Remediation

Biosensor mode of action is converting a biological induction into an electrical pulse - Scheme 6. They have been used in many fields of environmental pollution management by determining poisonous gases in air and poisonous substances in water. The biosensors depend on fixation fixing the enzyme on conducting polymer, as polypyrrole [39] and polyaniline [40, 41]. Cholesterol biosensor was finished



Scheme 5 Nanocomposites applications in air filtration for removal of particulates



Scheme 6 Biosensors mechanism by using nanocomposites

by cholesterol esterase, cholesterol oxidase and peroxidase fixation onto polyaniline films electrochemically prepared [41]. Response time of this biosensor is about 240 s and can regulate cholesterol concentration up to 500 mg/dl. These biosensors have a detection limit of 25 mg/dl with sensitivity of 0.042 $\mu\text{A mg/dl}$. They were found to be thermally stable up to 48 °C and they have a shelf-life of about 6 weeks when stored at 4 °C.

Nano-catalysts based on polymers allows chemical manufacturing easier and safer by giving higher selection for required products, removing side reactions and decrease energy intake [42, 43]. Polymer-coated bimetallic alloy was used as a catalyst to manage certain reactions, to reduce chemical reagents intake and hazardous substances yield [44].

NCs can be employed in energy manufacture and storage fields and in DMFC [45–47]. NCs have special properties like; high energy-conversion efficiency, low working temperature and low pollutants emission, DMFCs may contribute to solve future energy problem. However, a clear defect in DMFC is the slow reaction rate that decreases the power yield.

The main advantage of nanoparticles in polymer nanofibers is that it is easily separated from the impure water, which is a perfect character enabling their use as reusable and recyclable filtration or sorption substances, and simultaneously to avoid side contamination. The prepared Zirconia- and silica-supported ZVI nanoparticles onto (PAA/PDADMAC)₆ - covered cellulose acetate CAc have been used to decolorize dye-contaminated water [48]. In another study, MWCNT-reinforced PAA/PVA nanofibers having ZVI NPs were also used to adsorb dyes such as acridine orange, methyl blue and acid fuchsin AF [49].

Recently, a great interest in TiO₂/Carbon Nanotube NC catalyst synthesis was developed as a substitute for environmental pollution management. By the aid of that NC catalyst, some benefits in photocatalysis were obtained (i) a large surface area for pollutants removal, (ii) excitation wavelength outspreading over photosensitization and (iii) delaying the reaction of photo-generated hole pairs with electrons. This catalyst has good advantage in removing pollutants in aqueous and gaseous media [50].

Simple mixing and sonication sol–gel method were used to prepare TiO₂-graphene oxide (GO) nanocomposites with changing the hydrolysis rate of the TiO₂. The average particle sizes of NCs were 436 Å ± 59 nm for samples TL with large particle size TiO₂ and 251 Å ± 32 nm for samples TS with small particle size TiO₂.

Deterioration of methylene blue (MB) dye was examined via UV light irradiation ($\lambda = 365$ nm) via photocatalytic activity of the synthesized TiO₂-GO nanocomposites. TiO₂-GO NCs have more photocatalytic activity than blank TiO₂. This work gives new ideas about wastewater treatment via high-performance photocatalysts [51].

CuO-ZnO nanocomposite had been synthesized using different techniques like; thermal degradation, wet impregnation and sol–gel. Different kinds of CuO-ZnO nanocomposites with different structures had been obtained depending on the synthesis method used [52].

CuO-ZnO nanocomposite is considered an excellent gas sensor. Researchers [53] utilized the prepared CuO-ZnO as a sensor to decrease gases like; xylene, ethanol and acetone. CuO-ZnO sensor response for acetone was maximum ~2.8.

In literature it was reported [54] that the response for gas-sensing ability for nanocomposite for CO gas was found to be 7.6 at 300 °C for 300 ppm CO. Kim et al. [55] showed an enhancement in sensing ability of nanocomposites towards H₂S gas at a temperature ≤500 °C than pure ZnO, which was 890 for 50 ppm H₂S. It was also

indicated that CuO-ZnO nanocomposite was used as H₂S gas (10 ppm) sensor [56]. Furthermore, it was shown that nanocomposite can be applied for cataluminescence sensing (CL intensity counting ~400) of acetic acid [57].

NCs were shown to be applied as propane gas sensor, for 500 ppm at 300 °C working temperature [58]. NCs showed good gas-sensing ability than that of pure ZnO for a volatile organic compound like; ethanol, formaldehyde, and hydrogen sulfide [59].

Generally, nanocomposites gas-sensing response is much accurate than that of pure ZnO due to the 3D morphology of CuO-ZnO, which gives larger active sites with high porosity, which increases mass transportation, gas diffusion and catalytic reaction.

Kidowaki *et al.* [60] showed that CuO-ZnO NCs can be employed as solar cell with $1.1 \times 10^{-4}\%$ conversion efficiency.

Liu *et al.* [61] showed nanocomposites in methanol and water mixture can be applied in photocatalytic hydrogen generation. CuO-ZnO catalyst can yield hydrogen generation rate 1700 $\mu\text{mol/h}$ per g of, which is higher than other oxide catalysts [62–65]. Simon *et al.* showed CuO-ZnO catalyst application for photocatalytic hydrogen [66].

Kargar *et al.* [67] examined nanocomposites application for clean solar hydrogen generation. The higher hydrogen generation rate was because of the large surface area, providing more active centers, increases mass transmission, promoting electron relocation from ZnO to CuO, decreasing the reaction of electrons and holes, avoiding ZnO photo-corrosion.

Baek and Tuller [68] synthesized a CuO-ZnO NC for humidity sensor. Zain el abdin *et al.* [69] showed that CuO-ZnO NC sensitivity is larger than its separate components [70–74].

Gajendiran and Rajendran [75] indicated that CuO-ZnO NCs had great optical properties, to be used for optoelectronic devices. Better optical properties showed its better crystallinity and less intrinsic defect properties for optoelectronic devices. Transmittance of CuO-ZnO NC (~86%) is higher than its separate components (~76%), due to the greater crystallinity and structure compatibility of NCs.

6 Nanocomposites for Food Packaging Applications

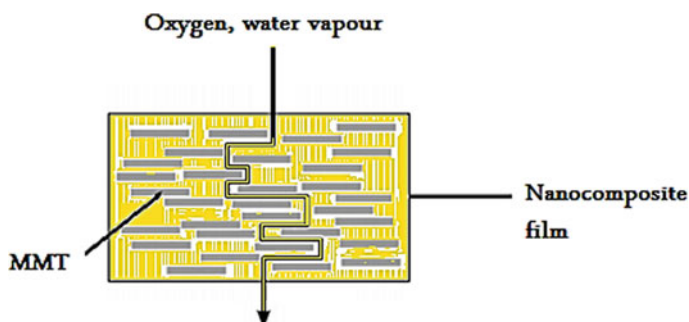
Food packaging current used materials are non-degradable which give rise to severe environmental problems. Several attempts had been made for biopolymers to be used as environmental food packaging. However, biopolymers use has been limited due to their low mechanical properties, which could be enhanced by reinforcing materials (fillers) addition forming NCs [76].

Antimicrobial compounds inclusion into food packaging substances has established great attention. Antimicrobial films could inhibit the expansion of infection and microorganisms. An antimicrobial NC film is preferable thanks to its suitable structure and barrier properties given by the nanocomposite matrix, and also the antimicrobial characters given by the antimicrobial agents infused in [77]. Nanoscale materials have the next surface-to-volume ratio compared with microscale materials. This allows nanomaterials to assign more biological molecules having greater efficiency [78]. Commonly used antimicrobial agents are metals and metal oxides nanomaterials as silver (Ag), gold (Au), titanium dioxide (TiO_2), zinc oxide (ZnO), alumina (Al_2O_3), silica (SiO_2) and iron oxides (Fe_3O_4 , Fe_2O_3). Nano- magnesium and zinc oxide have good antimicrobial properties that had recently been discovered.

Many researchers reported silver nanocomposites for their antimicrobial efficiency. It was reported that polyamide 6/silver nanocomposites with a lower silver content showed a higher activity against *Escherichia coli* than polyamide 6/silver microcomposites with a much higher silver content [79]. It was reported that polyamide 6/2 wt.% Ag nanocomposites was more effective against *E. coli* even after immersion in water for 100 days [80]. Ag nanocomposites absorb and decompose ethylene [81] which contribute to outspread shelf life of fruits and vegetables. Nanocomposites PE film/Ag was reported to retard the degradation of jujube, a Chinese fruit [82]. A Ag-nanoparticles containing coating was reported to be effective in reducing microbial growth and enhancing shelf life of asparagus [83].

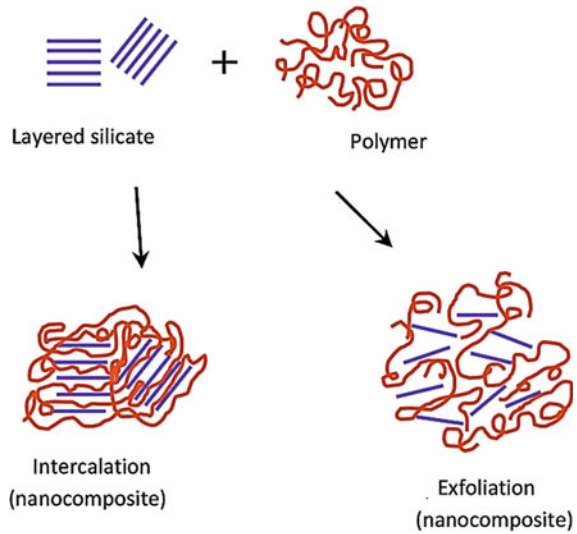
PCN were synthesized by 1980s. Researches were issued on the progress of PCN for food packaging [84]. The layered silicates were utilized in NCs of two-dimensional layers. Its presence in polymer matrices induces the tortuosity of the diffusion of any penetrant molecule - (Scheme 7) - giving excellent barrier properties.

Two kinds of composites are formed when clays layers are introduced within polymeric chains: a) intercalated nanocomposite and b) exfoliated nanocomposite. Intercalated nanocomposites are produced when the polymeric chains are implanted between clay layers as the interlayer space is expanded as shown in Scheme 8. Exfoliated nanocomposites are molded when the clay layers have been completely



Scheme 7 Tortuous path of any permeant in nanocomposite

Scheme 8 Types of composites formed by incorporation of layered clay with polymer



parted and the distinct layers are dispersed throughout the binder matrix as shown in Scheme 8.

Titanium dioxide (TiO_2) is extensively used as a photocatalytic sterilizing agent for external coatings [85]. TiO_2 photocatalysis, which advances peroxidation of the polyunsaturated phospholipids of microbial cell membranes [86], it has been utilized to kill several food-associated infective bacteria [87–89]. TiO_2 powder-covered wrapping film was created and affirmed its capacity to stop *E. coli* infection on food tops, proposing that the film may be utilized for fresh cut crop [90].

The disinfectant activity of nanoparticles may be linked to different mechanisms. The nanoparticles can either directly assign to the microbial cells, e.g. disturbing transmembrane electron transfer, disrupting/piercing the cell shell, or oxidizing cell components, or yield secondary products (e.g. ROS or dissolved heavy metal ions) that make harm [91].

7 Fire Retardancy of Polymer Nanocomposites

However, most of the polymers were basically flammable, which triggered the fire hazard. The enhancement in flame retardancy of polymeric supplies was crucial, so researchers started to combine flame retardants into polymeric skeleton to produce flame retardant composites. Commercially used flame retardants are endothermic additives like; halogenated compounds, phosphorus, graphite and melamine derivatives. Metal hydroxides have revealed good effectiveness, but they want a large amount of load. Besides, morphology and purity can easily affect productivity. However, Metal hydroxides have been restricted by high charge of manufacture.

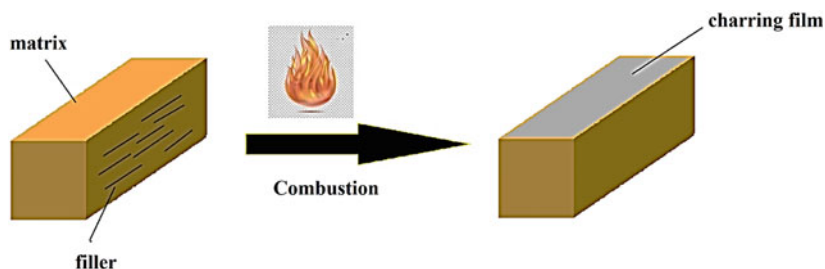
Nanoparticles decrease the polymers flammability owing to the reduction in HRR, increase in flame-out and their ability to auto-extinguish. The mode of action is related to both physical barrier and catalytic effects, which can improve the polymers degradation and form charred coating layers reinforced by the nanoparticles – Scheme 9. The characteristics of nanoparticles depend on both dispersion and compatibility with polymers to improve matrix characters. The decrease in the released heat during combustion is due to the effect of both nanoparticles and flame retardants.

The combination of nanoparticles has an excessive result on flame retardancy, by slowing down emission of combustible volatiles and by stabilizing the charred structures. The formation of charring coating film is generally noticed for polymers having aromatic groups or that undergo elimination reactions during thermal degradation [92, 93]. The formation of charring films is often necessary for developing the fire retardancy of polymers. Char formation is acting as a barrier for oxygen and heat transfer. Nanoparticles can enhance the carbonaceous residue and improve the polymers degradation.

POSS are constant till over 400 °C, which is more advanced than the thermal deterioration temperatures of most organic compounds [94]. Amine-functionalized POSS developed an ionic exchange reaction and the surfactant can be attached to clay spacing [95, 96]. The produced NCs had high thermal stability up to 300 °C due to existence of silicate clay. The intercalation of amine-POSS into clay spacing was shown by the rise in the interlayer space from 1.26 to 1.61 nm. The polystyrene/clay NCs, which were caused by combination of the amine-POSS/clay hybrid, gave an exfoliation of the clay platelets and enlarged thermal stability compared with original polystyrene [97].

Zanetti and Costa [98] examined the silicate nanoparticles outcome when using an EVA-based nanocomposite that shown high flammability, HRR was reduced 70–80% with silicate loading 2–5%. That was owing to the development of porous clay-burn. During the burning process, clay-char layer is molded by the silicate clay.

During combustion of polymeric binder, graphene improved the formation of condensed char layers. Furthermore, the char layer effectively stops thermal decomposition products into the flame region and that of the O₂ into the original polymeric matrix. Compared to pure PVA, PHRR of PVA-G3 (3 wt% graphene) is reduced by 49% and is lower than those of PVA-MMT and PVA-MWNTs [99].



Scheme 9 Combustion and flame-retardant mechanism

Graphene also has been attached in various organic–inorganic systems, and the resulted polymer composite has high thermal stability and flammability [100].

8 Conclusion

However, the worldwide existing stock of pure water is high to cover all existing and expectable water demands. There are several areas where the drinking water resources are insufficient to satisfy the basic, economic and domestic needs.

The inclination of nanomaterial for water treatment is growing owing to the very urgent request for fresh water worldwide. There is an important need for progressive water treatment methods, for drinking purpose, remove micro/macro pollutants and increase industrial production developments via advanced water treatment approaches.

Nanotechnology has shown great accomplishment for monitoring water purification contests and making some future advancements. Nanomaterial approaches like nanosorbents, nano- catalytic membranes,etc. are very efficient, less time required, less energy and eco-friendly methods but all these methods are expensive, and they are not used for wastewater purification at a larger scale yet.

References

1. Abdellatif Soliman, S.M., Sanad, M.F., Shalan, A.E.: Synthesis, characterization and antimicrobial activity applications of grafted copolymer alginate-g-poly(N-vinyl imidazole). *RSC Adv.* **11**,11541–11548 (2021)
2. Abdel Maksoud, M.I.A., Fahim, R.A., Shalan, A.E., et al.: Advanced materials and technologies for supercapacitors used in energy conversion and storage: a review. *Environ. Chem. Lett.* **19**, 375–439 (2021)
3. Abdel Messih, M.F., Shalan, A.E., Sanad, M.F., Ahmed, M.A.: Facile approach to prepare ZnO@SiO₂ nanomaterials for photocatalytic degradation of some organic pollutant models. *J. Mater. Sci. Mater. Electron.* **30**, 14291 (2019)
4. Eivazzadeh-Keihan, R., Taheri-Ledari, R., Mehrabad, M.S., et al.: Effective combination of rGO and CuO nanomaterials through poly(p-phenylenediamine) texture: Utilizing it as an excellent supercapacitor. *Energy Fuels* (2021). Doi: <https://doi.org/10.1021/acs.energyfuels.1c01132>
5. Batool, M., Nazar, M.F., Awan, A., et al.: Bismuth-based heterojunction nanocomposites for photocatalysis and heavy metal detection applications. *Nano-struct Nano-objects* **27**, 100762 (2021)
6. Barhoum, A., Shalan, A.E., El-Hout, S.I., et al.: A broad family of carbon nanomaterials: classification, properties, synthesis, and emerging applications. In: *Handbook of Nanofibers*, pp 1–40. Springer, Cham (2019)
7. Sharma, G., Amit, K., Shweta, Mu.N., Ram, P.D., Zeid, A.A., Genene, T.M.: Novel development of nanoparticles to bimetallic nanoparticles and their composites: a review. *J. King Saud Univ. Sci.* **31**(2), 257–269 (2019)

8. Sanad, M.F., Shalan, A.E., Abdellatif, S.O., et al.: Thermoelectric energy harvesters: a review of recent developments in materials and devices for different potential applications. *Top Curr. Chem.* (J.) **378**, 48 (2020)
9. Mark, A.S., Paul, W.B., Menachem, E., John, G.G., Benito, J.M., Anne, M.M.: Science and technology for water purification in the coming decades. *Nature* **452**, 337–346 (2009)
10. Masud, H., Ravi, N., Jianhua, D., Yanju, L., Fangjie, Q.: A Review, Critical review of magnetic biosorbents: their preparation, application, and regeneration for wastewater treatment. *Sci. Total Environ.* **702**, 134893 (2020)
11. Pan, B.C., Zhang, Q.R., Zhang, W.M., Pan, B.J., Du, W., Lv, L.Q., Zhang, J., Xu, Z.W., Zhang, Q.X.: Highly effective removal of heavy metals by polymer-based zirconium phosphate: a case study of lead ion. *J. Colloid Interface Sci.* **310**, 99–105 (2007)
12. Guixia, Z., Xiubing, H., Zhenwu, T., Qifei, H., Fenglei, N., Xiangke, W.: A review, Polymer-based nanocomposites for heavy metal ions removal from aqueous solution: *Polym. Chem.* **9**, 3562–3582 (2018)
13. Samiey, B., Cheng, C.H., Wu, J.: A review, Organic-inorganic hybrid polymers as adsorbents for removal of heavy metal ions from solutions. *Materials* **7**, 673–726 (2014)
14. Jinyue, Y., Baohong, H., Jinggang, W., Beiqian, T., Jingtao, B., Na, W., Xin, L., Xin, H.: A review, nanomaterials for the removal of heavy metals from wastewater. *Nanomaterials* **9**, 424(1–39) (2019)
15. Shi, J., Li, H., Lu, H., Zhao, X.: Use of carboxyl functional magnetite nanoparticles as potential sorbents for the removal of heavy metal ions from aqueous solution. *J. Chem. Eng. Data* **60**(7), 2035–2041 (2015)
16. Gholamhossein, M., Arnavaz, K.B.: A review, polymer matrix nanocomposites for heavy metal adsorption. *J. Iran. Chem. Soc.* **17**, 1259–1281 (2020)
17. Lopes, A., Martins, S.: Degradation of a textile dye C. I. Direct red 80 by electrochemical processes. *Portugaliae Electrochim. Acta* **22**, 279–294 (2004)
18. Laura, M.S., Romina, P.O., Jimena, S.G., Vera, A.A.: Chapter 51: nanocomposite materials for dyes removal. *Handbook of Nanomaterials for Industrial Applications Micro and Nano Technologies*, pp. 922–951 (2018)
19. Santos, S.C.R., Vilar, V.J.P., Boaventura, R.A.R.: Waste metal hydroxide sludge as adsorbent for a reactive dye. *J. Hazard. Mater.* **153**, 999–1008 (2008)
20. Simona, G.M., Maria, A.N., Eliza, M., Anamaria, T., Robert, I., Cornelia, P.: Removal of colored organic pollutants from wastewaters by magnetite/carbon nanocomposites: single and binary systems. *Hindawi Journal of Chemistry* 2018 16 pages (2018)
21. Jain, P., Pradeep, T.: Potential of silver nanoparticle-coated polyurethane foam as an antibacterial water filter *Biotechnol. Bioeng.* **90**, 59–63 (2005)
22. Theresa, A.D., Derek, G.G.: Bactericidal paper impregnated with silver nanoparticles for point-of-use water treatment *environ. Sci. Technol.* **45**(5), 1992–1998 (2011)
23. Rieger, K.A., Cho, H.J., Yeung, H.F., Fan, W., Schiffman, J.D.: Antimicrobial activity of silver ions released from zeolites immobilized on cellulose nanofiber mats *ACS Appl. Mater. Interf.* **8**(5), 3032–3040 (2016)
24. Lizzy, M.M., Nomcebo, H.M., Maurice, S.O., Maggy, N.B.M.: Cost-effective filter materials coated with silver nanoparticles for the removal of pathogenic bacteria in groundwater. *Int. J. Environ. Res. Public Health* **9**, 244–271 (2012)
25. Ponnamma, D., et al.: Synthesis, optimization and applications of ZnO/polymer nanocomposites. *Mater. Sci. Eng., C* **98**, 1210–1240 (2019)
26. Emad, M.M., Laijun, L., Biaolin, P.: Synthesis, characterization, and applications of polymer nanocomposites. *Hindawi J. Nanomater.*, 2 p. (2020)
27. Kumar, S., et al.: Nano-based smart pesticide formulations: Emerging opportunities for agriculture. *J. Control. Release* **294**, 131–153 (2019)
28. Sarlak, N., Taherifar, A., Salehi, F.: Synthesis of nanopesticides by encapsulating pesticide nanoparticles using functionalized carbon nanotubes and application of new nanocomposite for plant disease treatment. *J. Agric. Food Chem.* **62**(21), 4833–4838 (2014)

29. Pérez-de-Luque, A.: Interaction of nanomaterials with plants: What do we need for real applications in agriculture? *Front. Environ. Sci.* **5**(12), 1–7 (2017)
30. Tan, W., Peralta-Videa, J.R., Gardea-Torresdey, J.L.: Interaction of titanium dioxide nanoparticles with soil components and plants: Current knowledge and future research needs—a critical review. *Environ. Sci. Nano* **5**(2), 257–278 (2018)
31. Sundarrajan, S., Ramakrishna, S.: Fabrication of nanocomposite membranes from nanofibers and nanoparticles for protection against chemical warfare stimulants. *J. Mater. Sci.* **42**, 8400–8407 (2007)
32. Ahn, Y.C., Park, S.K., Kim, G.T., Hwang, Y.J., Lee, C.G., Shin, H.S.: Development of high efficiency nanofilters made of nanofibers. *Curr. Appl. Phys.* **6**, 1030–1035 (2006)
33. Ramakrishna, S., Jose, R., Archana, P.S., Nair, A.S., Balamurugan, R., Venugopal, J., Teo, W.E.: Science and engineering of electrospun nanofibers for advances in clean energy, water filtration, and regenerative medicine. *J. Mater. Sci.* **45**, 6283–6312 (2010)
34. Buldum, A., Busuladzic, I., Clemons, C.B., Dill, L.H., Kreider, K.L., Young, G.W., Evans, E.A., Zhang, G., Hariharan, S.I., Kiefer, W.: Multiscale modeling, simulations, and experiments of coating growth on nanofibers. Part I. Sputtering. *J. Appl. Phys.* **98**, 044303 (2005)
35. Ramakrishna, S., Fujihara, K., Teo, W.E., Lim, T.C., Ma, Z.: *An Introduction to Electrospinning and Nanofibers*. World Scientific Publishing Co., Singapore (2005)
36. Kim, B.C., Nair, S., Kim, J., Kwak, J.H., Grate, J.W., Kim, S.H., Gu, M.B.: Preparation of biocatalytic nanofibers with high activity and stability via enzyme aggregate coating on polymer nanofibers. *Nanotechnology* **16**, S382–S388 (2005)
37. Ma, Z., Kotaki, M., Ramakrishna, S.: Surface modified nonwoven polysulphone (PSU) fiber mesh by electrospinning: A novel affinity membrane. *J. Membr. Sci.* **272**, 179–187 (2006)
38. Kaur, S., Ma, Z., Gopal, R., Singh, G., Ramakrishna, S., Matsuura, T.: Plasma-induced graft copolymerization of poly (methacrylic acid) on electro spun poly (vinylidene fluoride) nanofiber membrane. *Langmuir* **23**, 13085–13092 (2007)
39. Kajiya, Y., Sugai, H., Iwakura, C., Yoneyama, H.: Glucose sensitivity of polypyrrole films containing immobilized glucose oxidase and hydroquinone sulfonate ions. *Anal. Chem.* **63**, 49–54 (1991)
40. Mu, S., Xue, H., Qian, B.: Bioelectrochemical responses of the polyaniline glucose oxidase electrode. *J. Electroanal. Chem. Interfac. Electrochem.* **304**, 7–16 (1991)
41. Singh, S., Solanki, P.R., Pandey, M.K., Malhotra, B.D.: Cholesterol biosensor based on cholesterol esterase, cholesterol oxidase and peroxidase immobilized onto conducting polyaniline films. *Sens. Actuator B Chem.* **115**(1), 534–541 (2006)
42. Sarkar, A., Mukherjee, T., Kapoor, S.: PVP-stabilized copper nanoparticles: a reusable catalyst for “click” reaction between terminal alkynes and azides in nonaqueous solvents. *J. Phys. Chem. C* **112**(9), 3334–3340 (2008)
43. Praharaj, S., Nath, S., Ghosh, S.K., Kundu, S., Pal, T.: Immobilization and recovery of Au nanoparticles from anion exchange resin: resin-bound nanoparticle matrix as a catalyst for the reduction of 4-nitrophenol. *Langmuir* **20**(23), 9889–9892 (2004)
44. Lu, P., Teranishi, T., Asakura, K., Miyake, M., Toshima, N.: Polymer-protected Ni/Pd bimetallic nano-clusters: Preparation, characterization and catalysis for hydrogenation of nitrobenzene. *J. Phys. Chem. B* **103**(44), 9673–9682 (1999)
45. Kalappa, P., Lee, J.H.: Proton conducting membranes based on sulfonated poly (ether ether ketone)/TiO₂ nanocomposites for a direct methanol fuel cell. *Polym. Int.* **56**, 371–375 (2007)
46. Wang, J., Zhao, Y., Hou, W., Geng, J., Xiao, L., Wu, H., Jiang, Z.: Simultaneously enhanced methanol barrier and proton conductive properties of phosphorylated titanate nanotubes embedded nanocomposite membranes. *J. Power Source* **195**(4), 1015–1023 (2010)
47. Rhee, C.H., Kim, Y., Lee, J.S., Kim, H.K., Chang, H.: Nanocomposite membranes of surface-sulfonated titanate and Nafion® for direct methanol fuel cells. *J. Power Source* **159**(2), 1015–1024 (2006)
48. Xiao, S., Wu, S., Shen, M., Guo, R., Huang, Q., Wang, S., Shi, X.: Polyelectrolyte multilayer-assisted immobilization of zero-valent iron nanoparticles onto polymer nanofibers for potential environmental applications. *ACS Appl. Mater. Interf.* **1**, 2848 (2009)

49. Xiao, S., Shen, M., Guo, R., Huang, Q., Wang, S., Shi, X.: Fabrication of multiwalled carbon nanotube-reinforced electro spun polymer nanofibers containing zero-valent iron nanoparticles for environmental applications. *J Mater Chem* **20**, 5700 (2010)
50. Sze-Mun, L., Jin-Chung, S., Ahmad, Z.A., Abdul, R.M.: Photocatalytic TiO₂/Carbon nanotube nanocomposites for environmental applications: an overview and recent developments fullerenes. *Nanotubes Carbon Nanostructures* **22**, 471–509 (2014)
51. Amr, M.T., Adham, R.R., Omar, A., El, S.: The American University in Cairo, Egypt. The University of São Paulo, Brazil. TiO₂-Graphene Oxide (GO) Nanocomposites: Synthesis, Environmental Applications and Surface Characterization using Perichromism. 7th World Nano Conference June 20–21, 2016 Cape Town, South Africa (2016)
52. Susmita, D., Vimal, C.S.: An overview of the synthesis of CuO-ZnO nanocomposite for environmental and other applications. *Nanotechnol. Rev.* **7**(3), 267–282 (2018)
53. Yang, C., Cao, X., Wang, S., Zhang, L., Xiao, F., Su, X., Wang, J.: Complex directed hybridization of CuO/ZnO nanostructures and their gas sensing and photocatalytic properties. *Ceram. Int.* **41**, 1749–1756 (2015)
54. Wang, J.X., Sun, X.W., Yang, Y., AKyaw, K.K., Huang, X.Y., Yin, J.Z., Wei, J., Demir, H.V.: Free-standing ZnO-CuO composite nanowire array films and their gas sensing properties. *Nanotechnology* **22**, 325704 (2011)
55. Kim, J., Kim, W., Yong, K.: CuO/ZnO heterostructured nanorods: photochemical synthesis and the mechanism of H₂S gas sensing. *J. Phys. Chem. C* **116**, 15682–15691 (2012)
56. Xu, Z., Duan, G., Li, Y., Liu, G., Zhang, H., Dai, Z., Cai, W.: CuO-ZnO micro/nanoporous array-film-based chemosensors: new sensing properties to H₂S. *Chem. Eur. J.* **20**, 6040–6046 (2014)
57. Xia, H., Zhou, R., Zheng, C., Wu, P., Tian, Y., Hou, X.: Solution-free, in situ preparation of nano/micro CuO/ZnO in dielectric barrier discharge for sensitive cataluminescence sensing of acetic acid. *Analyst* **138**, 3687–3691 (2013)
58. Gomez-Pozos, H., Arredondo, E.L., Álvarez, A.M., Biswal, R., Kudriavtsev, Y., Vega Pérez, J., Casallas-Moreno, Y.L., Amador, M.L.O.: Cu-doped ZnO thin films deposited by a sol-gel process using two copper precursors: gas-sensing performance in a propane atmosphere. *Materials* **87**, 1–16 (2016)
59. Huang, J., Dai, Y., Gu, C., Sun, Y., Liu, J.: Preparation of porous flowerlike CuO/ZnO nanostructures and analysis of their gas-sensing property. *J. Alloys Compd.* **575**, 115–122 (2013)
60. Kidowaki, H., Oku, T., Akiyama, T.: Fabrication and characterization of CuO/ZnO solar cells. *J. Phys: Conf. Ser.* **352**, 012022 (2012)
61. Liu, Z., Bai, H., Xu, S., Sun, D.D.: Hierarchical CuO/ZnO “corn-like” architecture for photocatalytic hydrogen generation. *Int. J. Hydrog. Energy* **36**, 13473–13480 (2011)
62. Kudo, A., Miseki, Y.: Heterogeneous photocatalyst materials for water splitting. *Chem. Soc. Rev.* **38**, 253–278 (2009)
63. Kudo, A.: Development of photocatalyst materials for water splitting. *Int. J. Hydrog. Energy* **31**, 197–202 (2006)
64. Zhou, H., Li, X., Fan, T., Osterloh, F.E., Ding, J., Sabio, E.M.: Artificial inorganic leafs for efficient photochemical hydrogen production inspired by natural photosynthesis. *Adv. Mater.* **22**, 951–956 (2010)
65. Wu, N.L., Lee, M.S.: Enhanced TiO₂ photocatalysis by Cu in hydrogen production from aqueous methanol solution. *Int. J. Hydrog. Energy* **29**, 1601–1605 (2004)
66. Simon, Q., Barreca, D., Gasparotto, A., Maccato, C., Montini, T., Gombac, V., Fornasiero, P., Lebedev, O., Turnere, S., Tendeloo, G.V.: Vertically oriented CuO/ZnO nanorod arrays: from plasma assisted synthesis to photocatalytic H₂ production. *J. Mater. Chem.* **22**, 11739–11747 (2012)
67. Kargar, A., Jing, Y., Joo Kim, S., Riley, C.T., Pan, X., Wang, D.: ZnO/CuO heterojunction branched nanowires for photoelectrochemical hydrogen generation. *ACS Nano* **7**, 11112–11120 (2013)

68. Baek, K.K., Tuller, H.L.: Atmosphere sensitive CuO/ZnO junctions. *Solid State Ionics* **75**, 179–186 (1995)
69. Zainelabdin, A., Amin, G., Zaman, S., Nur, O., Lu, J., Hultman, L., Willande, M.: CuO/ZnO nanocorals synthesis via hydrothermal technique: growth mechanism and their application as humidity sensor. *J. Mater. Chem* **22**, 11583–11590 (2012)
70. Zhang, Y., Yu, K., Jiang, D., Geng, H., Luo, L.: Zinc oxide nanorod and nanowire for humidity sensor. *Appl. Surf. Sci* **24**, 212–217 (2005)
71. Xu, J., Yu, K., Wu, J., Shang, D., Li, L., Xu, Y., Zhu, Z.: Synthesis, field emission and humidity sensing characteristics of honeycomblike CuO. *J. Phys. D Appl. Phys.* **42**, 075417 (2009)
72. Yoo, D.J., Park, S.J.: Electrolysis of water in CuO/ZnO heterocontact humidity sensor. *J. Electrochem. Soc.* **143**, L89–L91 (1996)
73. Qi, Q., Zhang, T., Zeng, Y., Yang, H.: Humidity sensing properties of KCl-doped Cu–Zn/CuO–ZnO nanoparticles. *Sens. Actuators B* **137**, 21–26 (2009)
74. Chakrabarti, D., Narayan, J.: Room temperature ferromagnetism in thin films. *Appl. Phys. Lett.* **90**, 062504 (2007)
75. Gajendiran, J., Rajendran, V.: Synthesis and characterization of coupled semiconductor metal oxide (ZnO/CuO) nanocomposite. *Mater. Lett.* **116**, 311–313 (2014)
76. Henriette, M.C.D.: A review; nanocomposites for food packaging applications. *Food Res. Int.* **42**, 1240–1253 (2009)
77. Rhim, J.W., Ng, P.K.W.: Natural biopolymer-based nanocomposite films for packaging applications. *Crit. Rev. Food Sci. Nutr.* **47**(4), 411–433 (2007)
78. Luo, P.G., Stutzenberger, F.J.: Nanotechnology in the detection and control of microorganisms. In: Laskin, A.I., Sariaslani, S., Gadd, G.M. (eds.) *Advances in Applied Microbiology*, vol. 63, pp. 145–181. Elsevier, London (2008)
79. Damm, C., Münsted, H., Rösch, A.: The antimicrobial efficacy of polyamide 6/silver-nano- and microcomposites. *Mater. Chem. Phys.* **108**, 61–66 (2008)
80. Damm, C., Münstedt, H., Rösch, A.: Long-term antimicrobial polyamide 6/ silver-nanocomposites. *J. Mater. Sci.* **42**(15), 6067–6073 (2007)
81. Hu, A.W., Fu, Z.H.: Nanotechnology and its application in packaging and packaging machinery. *Packaging Eng.* **24**, 22–24 (2003)
82. Li, H., Li, F., Wang, L., Sheng, J., Xin, Z., Zhao, L., et al.: Effect of nano-packing on preservation quality of Chinese jujube (*Ziziphus jujuba* Mill. var. *inermis* (Bunge) Rehd). *Food Chem.* **114**(2), 547–552 (2009)
83. An, J., Zhang, M., Wang, S., Tang, J.: Physical, chemical and microbiological changes in stored green asparagus spears as affected by coating of silver nanoparticles-PVP. *LWT – Food Sci. Technol.* **41**(6), 1100–1107 (2008)
84. Ray, S., Easteal, A., Quek, S.Y., Chen, X.D.: The potential use of polymer– clay nanocomposites in food packaging. *Int. J. Food Eng.* **2**(4), art. 5 (2006)
85. Fujishima, A., Rao, T.N., Tryk, D.A.: Titanium dioxide photocatalysis. *J. Photochem. Photobiol., C* **1**(1), 1–21 (2000)
86. Maness, P.C., Smolinski, S., Blake, D.M., Huang, Z., Wolfrum, E.J., Jacoby, W.A.: Bactericidal activity of photocatalytic TiO₂ reaction: toward an understanding of its killing mechanism. *Appl. Environ. Microbiol.* **65**(9), 4094–4098 (1999)
87. Kim, B., Kim, D., Cho, D., Cho, S.: Bactericidal effect of TiO₂ photocatalyst on selected food-borne pathogenic bacteria. *Chemosphere* **52**(1), 277–281 (2003)
88. Lee, S.K., Sheridan, M., Mills, A.: Novel UV-activated colorimetric oxygen indicator. *Chem. Mater.* **17**(10), 2744–2751 (2005)
89. Robertson, J.M.C., Robertson, P.K.J., Lawton, L.A.: A comparison of the effectiveness of TiO₂ photocatalysis and UVA photolysis for the destruction of three pathogenic micro-organisms. *J. Photochem. Photobiol., A* **175**(1), 51–56 (2005)
90. Chawengkijwanich, C., Hayata, Y.: Development of TiO₂ powder-coated food packaging film and its ability to inactivate *Escherichia coli* in vitro and in actual tests. *Int. J. Food Microbiol.* **123**(3), 288–292 (2008)

91. Li, Q., Mahendra, S., Lyon, Y.D., Michael, L.B., Li, P.L.V.D., Alvarez, J.J.: Antimicrobial nanomaterials for water disinfection and microbial control: potential applications and implications. *Water Res.* **42**(18) 4591–4602 (2008)
92. Lyon, R.E., Walters, R.N.: Pyrolysis combustion flow calorimetry. *J. Anal. Appl. Pyrolysis* **71**, 27–46 (2004)
93. Jiang, B.N., Costache, M., Wilkie, C.: The relationship between thermal degradation behavior of polymer and the fire retardancy of polymer/clay nanocomposites. *Polymer* **46**, 10678–10687 (2005)
94. Phillips, S.H., Haddad, T.S., Tomczak, S.J.: Developments in nanoscience: polyhedral oligomeric silsesquioxane (POSS)-polymers”. *Curr. Opin. Solid State Mater. Sci.* **8**, 21–29 (2004)
95. Yei, D.R., Kuo, S.W., Su, Y.C., Chang, F.C.: Enhanced thermal properties of PS nanocomposites formed from inorganic POSS-treated montmorillonite. *Polymer* **45**, 2633–2640 (2004)
96. Kuo, S.W., Chang, F.C.: POSS related polymer nanocomposites. *Prog. Polym. Sci.* **36**, 1649–1696 (2001)
97. Chiu, C.W., Huang, T.K., Wang, Y.C., Alamani, B.G., Lin, J.J.: Intercalation strategies in clay/polymer hybrids. *Prog. Polym. Sci.* **39**, 443–485 (2014)
98. Kashiwagi, T., Grulke, E., Hilding, J., Groth, K., Harris, R., Butler, K., Shields, J., Kharchenko, S., Douglas, J.: Thermal and flammability properties of polypropylene/carbon nanotube nanocomposites. *Polymer* **45**, 4227–4239 (2004)
99. Huang, G., Gao, J., Wang, X., Liang, H., Ge, C.: How can graphene reduce the flammability of polymer nanocomposites. *Mater. Lett.* **66**, 187–189 (2012)
100. Wang, Z., Wei, P., Qian, Y., Liu, J.: The synthesis of a novel graphene-based inorganic – organic hybrid flame retardant and its application in epoxy resin. *Composites: Part B* **60**, 341–349 (2014)

Removal of Radioactive Waste from Water Using Polymer Nanocomposites



Soliman M. A. Soliman  and Mohsen E. Mohamed

Abstract The continuous development and modernization of various projects have a significant human and environmental impact. The important environmental impact appears in contaminating of clean water because of the industrial wastes such as the organic one (e.g. chemicals, dyes, and pesticide), inorganic (e.g. heavy metal ions) and radioactive waste (e.g. Uranium ($U_{(VI)}$), $^{65}Zn(II)$ and $^{60}Co(II)$). This chapter will focus on radioactive and nuclear waste removal because it has a great effect on the environment. Radioactive waste is coming from the generation of nuclear power and producing of different radioactive materials in various commercial sectors. Nanocomposites based polymers have many advantages that enable exhibit the suggested solutions in environmental applications. Polymer nanocomposites have a high ability and selectivity to uptake different pollutants. Conducting polymers enhanced the efficiency of radioactive waste removal. Moreover, the incorporation of magnetic nanoparticles inside polymer nanocomposites shows an improvement in radioactive removal efficiency.

Keywords Nanocomposites · Removal · Waste · Radioactive · Magnetic · Conducting polymer

List of Abbreviations

NCs	Nanocomposites
PNCs	Nanoparticles
DHBF	Dihydroxybenzaldehyde-formaldehyde resin
AMP-PAN	Ammonium molybdophosphate-polyacrylonitrile
TEMPO	(2,2,6,6-Tetramethylpiperidin-1-yl) oxyl
LMT	Lignocellulose/montmorillonite
CP	Conducting polymer

S. M. A. Soliman (✉) · M. E. Mohamed
Chemistry Department, Faculty of Science, Cairo University, Giza 12613, Egypt
e-mail: sabdellatif@sci.cu.edu.eg

© The Author(s), under exclusive license to Springer Nature Switzerland AG 2022
A. E. Shalan et al. (eds.), *Advances in Nanocomposite Materials for Environmental and Energy Harvesting Applications*, Engineering Materials,
https://doi.org/10.1007/978-3-030-94319-6_16

PANI	Polyaniline
PEDOT	Poly(3,4-ethylenedioxythiophene)
PA	Polyacetylene
PPy	Polypyrrole
PT	Polythiophene
CoHCNF	Cobalt Hexacyanoferrate
P(AAm-SSS)	Poly(acrylamide-styrene sodium sulfonate)
SANCHs	Na-CMC-g-P(AMPS-co-AA-co-AM)/NanoFe ₃ O ₄
Na-CMC	Sodium Carboxymethyl cellulose
AMPS	2-Acrylamido-2-methyl-1-propane sulfonic acid
AM	Acrylamide
AA	Acrylic acid

1 Introduction

Water is a valuable natural resource that is important for the existence of every living creature. Unfortunately, the quality of water is reducing every day due to the rapid growth of the industry which leaks a lot of the pollution into water [1]. The removal of water pollutants has become very essential nowadays due to the various threats that face the entire biosphere [2]. One of the most essential human goals is credible access of clean water so, the substantial requirements during water purification is using conventional materials with high porosity, reusability and for sure with the recommended safety precautions [3]. Nanotechnology supply promising and effective modification for advanced materials for better water treatment purposes through improving their mechanical strength, hydrophilicity, porosity and hydrophobicity [4]. Nanomaterials have been shown effective progress in a lot of applications besides to water treatment like in medicine, catalysis and sensing application [5]. Nanomaterials have a size range from 1 to 100 nm according to their different structural nano-components [6]. Comparing to the normal materials, nanomaterials have the perfect properties which is convenient for the most of applications due to their challengeable electrical, mechanical and magnetic properties [7]. Although nanoparticles having large surface area which is actually very good for water treatment but may face some delimitations due to its agglomeration. This agglomeration could be reduced by modifying nanoparticles into nanocomposites which is showing magnificent results in water treatment in the last few years [8]. Nanocomposites are synthesized by the reaction of more than two materials which possess unique chemical and physical properties [9]. Adsorption is mightily used for the removal for different soluble pollutants from water so; different promising nanocomposites have been modified with polymer for the synthesis of next generation polymer nanocomposites for effective treatment of wastewater from radioactive wastes. Radioactive waste is by-product which generates from radioactive nuclear power materials. This radioactive waste is adjusted as extremely hazardous waste to the environment in general not only water. A

lot of recommendations have been announced about the importance of isolating these radioactive materials but the suggested steps accepted with slow progress towards isolating these dangerous materials. Due to the large scale use of nuclear power and the applications which depend on nuclear power technology, it was found that those technologies form radioactive isotopes which present in the form of radionuclide that has the ability to sustain in an aquatic ecosystem because of its long term half-life which is with no doubt can extremely contaminate the environment even in a small traces. The radionuclides can produce reactive species which could be reacting with biomolecules leading to the damaging of the whole biological life organization. To overcome this problem, Scientists nowadays play serious role in synthesizing nano-sized materials which have high reactivity, large surface area and also high selectivity and all of this special characters present in nanocomposites based polymers [10]. In this chapter, we will focus on radioactive waste removal by Polymer nanocomposites, Conducting polymer nanocomposites and magnetic polymer nanocomposites.

1.1 Nanocomposites

Nanocomposites (NCs) are multiple phasic nanomaterials in which one of the phases present in the nano range from 10 to 100 nm. Classification of nanocomposites depends on their dispersed phase and dispersed matrix. Nanocomposites have very unique characteristics so they have more advantages than any other materials such as their high durability, corrosion resistance, heat resistance, high strength materials and their low density [11]. Nanocomposites have large variety in many fields such as drug delivery, water treatment and other life science applications. Nanoparticles were integrated inside nanocomposites with different functionalized media like graphene oxide (GO), activated carbon and may other polymers to form polymer nanocomposites (PNCs) [12]. NCs are multiple materials in the solid state which include gels, colloids and copolymers. The process of selecting the host inside nanocomposites is very important as it widely effect on the performance of the final form of the resultant nanocomposite [13].

NCs with very large surface area show strong ability towards different interfacial reactions that is very essential for the adsorption of radionuclides from wastewater.

1.2 Polymer Nanocomposites (PNCs)

Polymer nanocomposites have attracted scientist's attention in the last few years especially in water treatment field due to their stability, process-ability, cost effectiveness and surface area [14]. Polymer nanocomposites showed high selectivity for removing different pollutants with promising water decontamination ability. In recent years, it was found that PNCs record magnificent decontamination ability against serious

wastewater like radioactive waste, metal ions, dyes and microorganisms. The traditional treatment technologies and the usual materials are not effective enough to overcome water pollution caused by the rapid industrialization. In the field of production of drinking water, Polymer nanocomposites (PNCS) have been the first choice a cost effective and efficient materials for removal of various wastewater pollutants [15]. Traditional method of preparation polymer nanocomposites has many drawbacks than bio-inspired method like not good dispersion, random structure, low content and weak interface [16].

Polymer nanocomposites (PNCs) are outstanding materials in which nanoparticles (NPs) diffuse in polymer matrix leading to unique materials with novel chemical and physical properties [17]. PNCs have outstanding mechanical and physical properties, porous structure and also chemically bonded functional groups so; they consider one of the recommended nanomaterials that support nanotechnology [18]. Due to the great dimensional variability and film forming ability, Polymer nanocomposites have become leading area of research and development [19]. The adsorption behavior of polymer nanocomposites granted them the tendency for various applications like drug delivery, chemical sensor, fuel cell technology and for water treatment [20]. PNCs which is previously synthesized from inorganic metal oxide nanoparticles that used in situ polymerization showed promising sorbent properties and also convenient as reducing agents, sensors and catalysts. PNCs possess effective magnetic properties which play an essential role in the removal of wastes from water. The addition of metal to polymer nanocomposites has created functional sites leading to hybrid structures which have the ability for the removal of pollutants from the water. As an example, Polypyrrole metal nanocomposites have been tested to decay Red 80 upto 835 through electrochemical oxidation [21]. Characterization of polymer nanocomposites (PNCs) has been done usually through wide angle (WAXS) either or small angle X-ray scattering (SAXS) which is generally recommended tools for the characterization of the structure of the nanocomposites [22]. PNCs characterization also has been focused onto the methods of the surface analysis and the determination of the topography of composition, shape surfaces, morphology and crystallinity of the prepared polymer nanocomposites [23]. Polymer nanocomposites can be synthesized through dispersion of nanoparticles into polymer matrix or by direct compounding which is used for the synthesis of different PNCs [24]. Polymer nanocomposites (PNCs) can be synthesized as shown in the modification of polyaniline with TiO_2 nanocomposite which showed promising adsorption performance and remarkable regeneration with maximum adsorption capacity 455 mg/g [25]. PNCs have been synthesized through various effective methods such as 1) Template synthesis, 2) Polymer Intercalation, 3) In-situ polymerization, 4) In-situ intercalative polymerization and 5) sol-gel polymerization [26]. The preparation of polymer-based nanocomposites through intercalative polymerization process that possess layered silicates has been occurred with production of nanocomposites with various structures from intercalated to exfoliated which generally depends on the penetration degree of the polymer chains within silicate layers. In-Siu polymerization, melt mixing and solution mixing techniques can be also used for the synthesis of CNT-Reinforced polymer-based nanocomposites [27]. Chemical and electrochemical methods for the preparation of polymer

nanocomposites have been announced to be the most recommended methods for best resultant PNCs. Polymer-based nanocomposites having layered reinforcements depends on the components nature such as (organic cation, Layered silicate and polymer matrix) and also on the interfacial interactions strength between the layered silicate and the polymer matrix. The injection of a polymer matrix within the layered silicate happens in a crystallo-graphically regular form and in general only fewer polymer layers have the ability to intercalate in this material [28].

When polymer-based nanocomposites present in the three dimensions within nano-metre scale, they are known as isodimensional polymer nanocomposites. While in the form of two dimensions within the nanometer scale it forms elongated structured polymer nanocomposites [29].

One of the most recommended polymer nanocomposites is polymer layered silicate-based nanocomposites which has showed great interest in the recent years for wastewater treatment due to its developed properties compared to the pure polymer such as increasing biodegradability and high strength and heat resistance [30].

2 Radioactive Waste Removal

Different methods have been used lately for water treatment which mainly depending on the basics of separation methods such as Physical–chemical methods (including Adsorption/Ion exchange, Advanced oxidation process and chemical precipitation), Evaporation, Electrochemical methods (including Electrodialysis, Electro-adsorption and Electrodeionization), Biological method, Membrane (including Seeded ultra- and micro filtration, Reverse Osmosis, Nanofiltration, Membrane distillation and Forward osmosis), and Integrated process (as chemical precipitation, flotation and adsorption) [7] (Fig. 1). All of the previously mentioned methods are very promising and effective but cannot totally purify the water so, a combination of the recommended methods can be applied for better results such as adsorption-biological treatments which exhibit the biodegradation of pollutant in the water [31]. Other forms of pollutants are radioactive wastes which are released in enormous amount throughout nuclear plants operations and the reprocessing of nuclear fuel [32].

The main components of radioactive wastes are neptunium, uranium, cesium and curium. The most serious fission products are cesium radioisotopes due to their long half-life and high fission yield which is seriously release hazard impacts to environments [33]. Cesium is a very active source for gamma radiation with has high solubility and migration ability from water to the biosphere so, the contamination occurred by cesium should be handled to reduce its dangerous effect on the environment [34]. In this concern, Scientists have great interest onto solid state extraction depending on polymer-based nanocomposites because of their rapid separation, high selectivity and their high heat and radiation resistance [35].

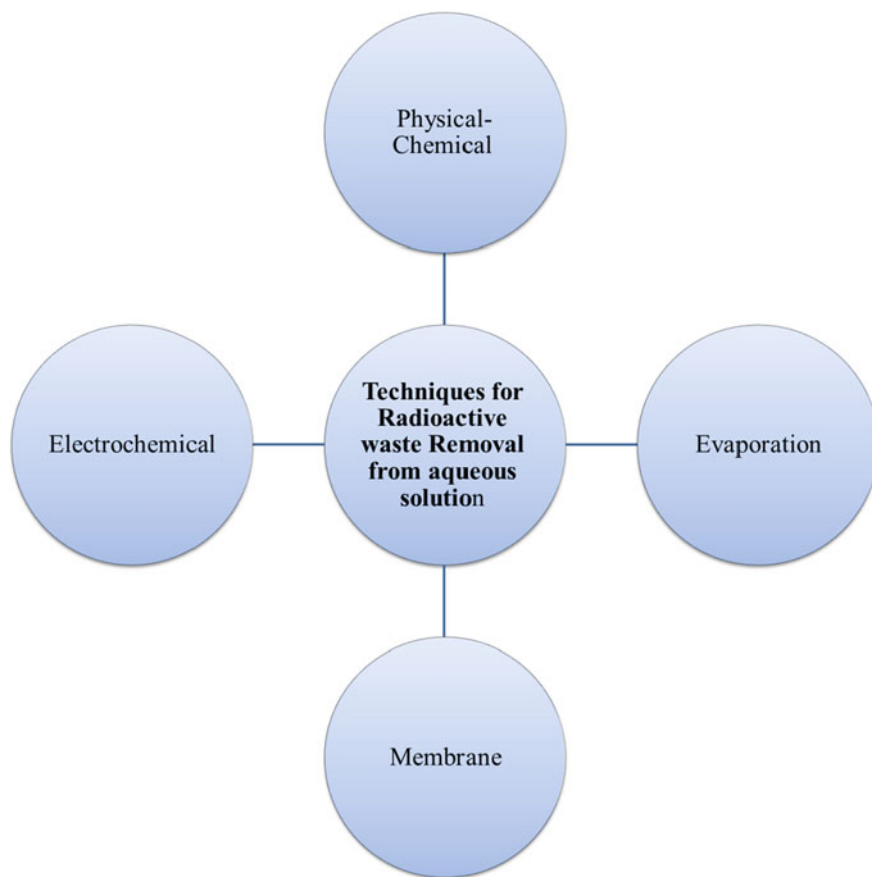


Fig. 1 Some examples of wastewater treatment methods

2.1 Polymer-Based Nanocomposites (PNCs)

The porous polymeric nanocomposite based on dihydroxybenzaldehyde-formaldehyde resin (DHBF) (Fig. 2) and CoFe_2O_4 nanoparticles (CoFe_2O_4 @DHBF) was synthesized by Ahamad et. al. [36]. The authors proved the fabricated nanocomposites have high surface area $370.24 \text{ m}^2/\text{g}$. CoFe_2O_4 @DHBF nanocomposite showed efficient U(VI) and Eu(III) removal with adsorption kinetics follow second order adsorption kinetics. Moreover, The adsorption isotherm was found to be fitting well with the adsorption isotherm of Langmuir (with the correlation coefficient $R^2 = 0.9913$ and 0.9920 for of Eu(III) and U(VI) adsorption, respectively). Authors observed highly regeneration ability of adsorbed U(VI) and Eu(III). The optimum conditions were reported of the E(III) and U(VI) removal as initial concentration of nanocomposite 100 mg/L at $\text{pH} = 7$ for 60 min in room temperature.

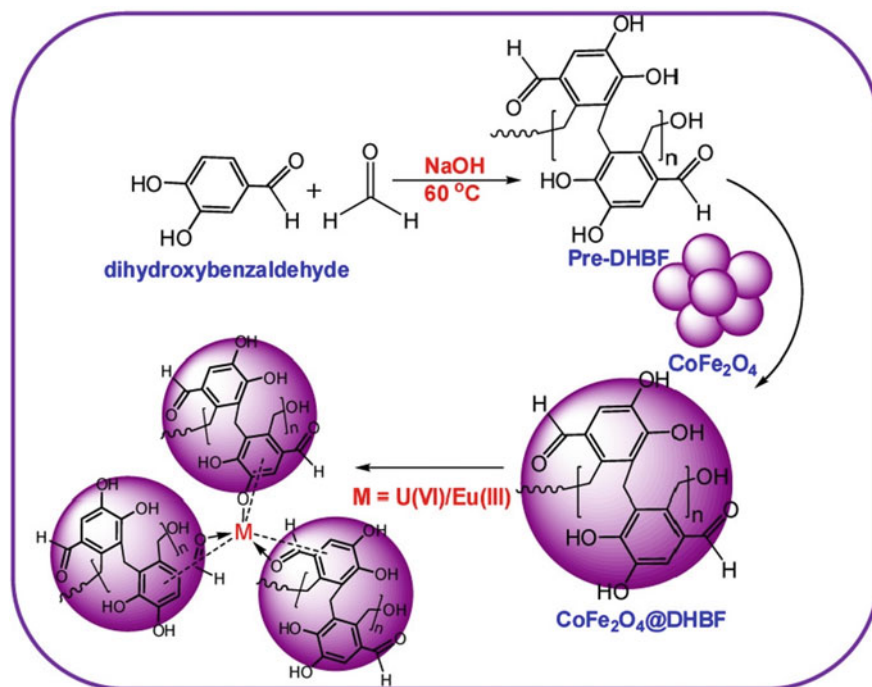


Fig. 2 The Fabrication method of CoFe₂O₄@DHBF [36]

Other polymer-based nanocomposites for different radioactive metals removal as following: potassium zinc hexacyanoferrate loaded polymer nanocomposite for Cs [37, 38] Ammonium molybdophosphate–polyacrylonitrile (AMP–PAN) uptake Co(II), Sr(II), and Cs(I) [39]. Ma et al. 115 fabricated cellulose nano fiber through two steps; first step is oxidation of (2,2,6,6-tetramethylpiperidin-1-yl)oxyl (TEMPO)/NaBr/NaClO process and second step through mechanical treatment [40]. The better adsorption capacity of UO₂²⁺ due to cellulose nanofibers compared to another adsorbent have not carbonyl groups.

A lignocellulose/montmorillonite (LMT) nanocomposite was fabricated and tested for removal of radioactive ⁶⁰Co(II) [41]. ⁶⁰Co(II) is affecting on the environment because it has long half-life, which is equal 5.27 years. There are various problems caused by high level of ⁶⁰Co(II) to human such as low blood pressure, diarrhea, paralysis, bone defects, and irritation of lung in humans [42]. Accordingly, ⁶⁰Co(II) removal is a critical process in industrial sector. There are various techniques for removal ⁶⁰Co(II) namely ion-exchange, coagulation, chemical precipitation, flocculation, reverse osmosis and adsorption [43–45]. The adsorption technique has many advantages than other technique. The advantages of adsorption are environmentally friendly, low cost and great efficiency [46, 47]. The authors observed that lignocellulose/montmorillonite (LMT) nanocomposites are efficient and reusable adsorbent for ⁶⁰cobalt(II) ions via chemical adsorption process. The adsorption kinetic result

well fit with the kinetic model of pseudo-second-order and also was found to be well fitting with the Langmuir isotherm equation. The authors reported that lignocellulose/montmorillonite (LMT) nanocomposites can be reusable with efficient removal capacity up to four times.

Polyacrylonitrile/nanozeolite based composite was fabricated and used as fixed-bed column operation for Cs^+ and Sr^{2+} removal [48]. Authors observed that bed capacity and total adsorbed Cs^+ and Sr^{2+} were affected by initial Cs^+ and Sr^{2+} ions concentration, bed height and flow rate. Authors reported maximum bed capacity of Cs^+ and Sr^{2+} are 0.085 and 0.128 meq/g for Cs^+ and Sr^{2+} , respectively and critical bed height (Z0) are 4.35 and 2.89 cm for Cs^+ and Sr^{2+} , respectively. Authors concluded based on the obtained results column based on Polyacrylonitrile/nanozeolite based composite show high column performance and adsorption capacity for Cs^+ and Sr^{2+} ions. The results showed that high bed height and initial Cs^+ and Sr^{2+} ions concentration lead to highest column performance and sorption capacity. The column based on Polyacrylonitrile/nanozeolite based composite showed higher column efficiency and adsorption capacity for Sr^{2+} than Cs^+ .

2.2 Conducting Polymer-Based Nanocomposites

Conducting polymer (CP) is polymer possessing π -conjugated polymeric chains. Conducting polymers have great academic and industrial interest due to their curious properties. CPs own properties like magnificent mechanical properties, high stable in the environment, low temperature of processing and cheap. CPs has characteristics of semiconductor without doping process. The electrical properties could be regulated by doping process through increasing charge carriers number in conducting polymers chains. There are a high number of CPs were used owing to their good conductivity such as polyaniline (PANI), poly(3,4-ethylenedioxythiophene) (PEDOT), polyacetylene (PA), polypyrrole (PPy), and polythiophene (PT) (Fig. 3).

Yousefi et al. synthesis Cobalt Hexacyanoferrate(CoHCNF)@polyaniline composite (HCNFe@polymer) using A chemical co-precipitation method [49]. Authors observed semi-spherical particles in range between 50–500 nm using Scanning electron microscope and transmission electron microscope. The prepared adsorbent HCNFe@polymer shows efficiently removal of Cs (I) ions from water. The uptake of Cesium by fabricated composite through two pathways a) coordination with amino groups and b) cation exchange of K^+ in cobalt hexacyanoferrate as shown in Fig. 4. The highest adsorption of cesium ions was found to be fitting with Langmuir model at ambient temperature and 60 °C. The kinetic adsorption of Cs(I) was followed to the pseudo-second-order kinetic models. Cs (I) ions adsorption onto the nanocomposite is endothermic and spontaneous that was proved by Thermodynamic parameters.

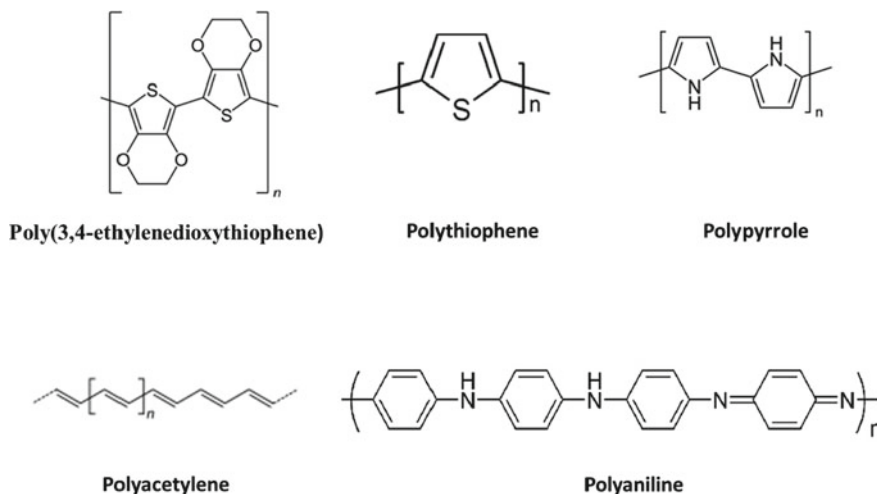


Fig. 3 Structures of some conducting polymers

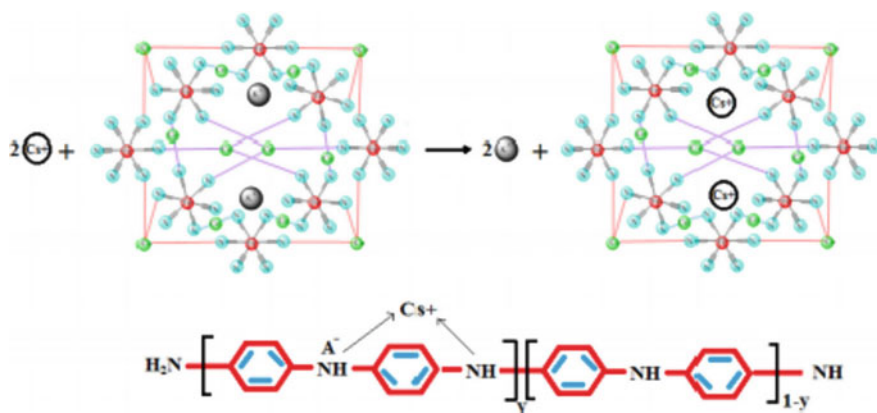


Fig. 4 Illustration of removal of Cesium ion by Hexacyanoferrate(CoHCNF)@poly aniline composite [49]

Anirudhan et al. synthesized composites based on rafted copolymer poly(methacrylic acid) onto chitosan incorporated with bentonite (PMAA-g-CTS/B) in presence of cross-linker N,N –methylenebisacrylamide (Fig. 5) [50]. Authors reported the efficient removal of thorium over range of pH from 5 to 6 and the kinetic adsorption was fitting with pseudo-second-order. The maximum adsorption capacity of Th(IV) was noted 110.5 mg.g⁻¹ at 30 °C. The proposed mechanism of removal Th(IV) was illustrated in same studied as shown in Figure. Authors studied the

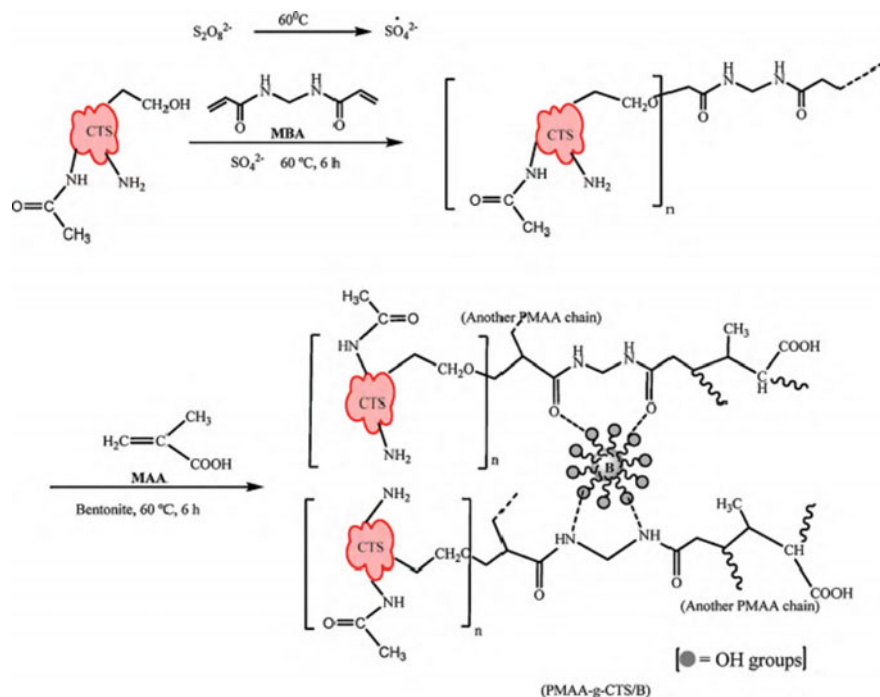


Fig. 5 Synthesis of poly(methacrylic acid)-grafted chitosan/bentonite composite and Proposed mechanism of removal Th(IV) [50]

reusability (Adsorption–desorption) up to 4 cycles of poly(methacrylic acid)-grafted chitosan/bentonite composite for the removal of thorium ion from water.

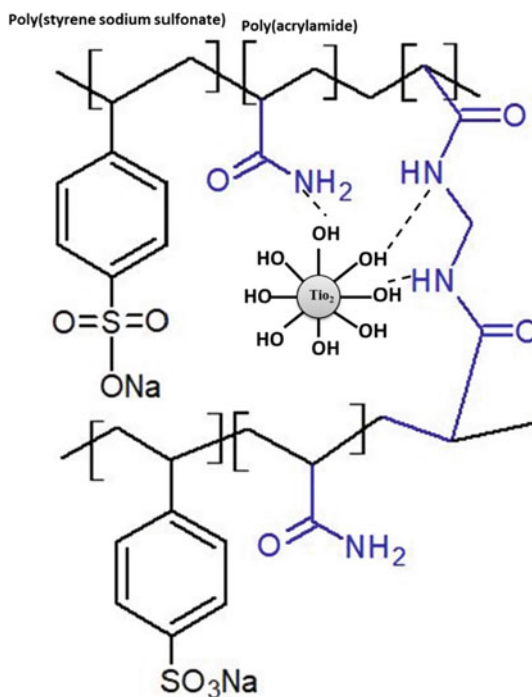
Different synthetic adsorbents have also been established for the getting rid of radionuclides, such as strontium (Sr^{2+}) [51], selenium (Se^{4+}) [52], iodide (I^-) [52, 53], Uranium (U) [53], Thallium (Tl) [54], Radium (Ra^{2+}) [54], and Actinium (Amc^{3+}) [54]. Thorium ion (Th(IV)) is one of the most radioactive metal ions which have long-lived and its removal of water is very interesting for radiation and nuclear field. There are many studies reported the removal of Th(IV) from aqueous solutions using different campsites as mentioned in the following Table [50, 55, 56].

There are different materials based on polymer nanocomposites as shown in table [1]

Radionuclide	Adsorbent
Sr^{2+}	Resorcinol formaldehyde polycondensate resin
$^{75}\text{Se}^{4+}$ and $^{125}\text{I}^{-}$	Microporous inorganic zirconium silicate (MZrSi) ion exchanger
Thorium (IV)	Poly (methacrylic acid)grafted chitosan/bentonite composite
Thorium (IV)	Polyvinyl alcohol/titanium oxide
Uranium	PVA/TEOS/APTES hybrid nanofiber
UO_2^{2+} , Tl^+ , Pb^{2+} , Ra^{2+} , and Ac^{3+}	Polyacrylamide–bentonite
Thorium (IV)	polyacrylamide–aluminosilicate composites

Different composites were fabricated as TiO_2/Poly (acrylamide-styrene sodium sulfonate) [$\text{TiO}_2/(\text{P}(\text{AAm-SSS}))$] composite was fabricated via in-situ intercalative polymerization technique using γ -radiation as initiator [57]. Another composite poly styrene- TiO_2 (PS- TiO_2) was synthesized using ionic polymerization technique. Prepared composites were tested for removal of (Cs(I)), cobalt (Co(III)) and europium (Eu(III)) ions from water (Fig. 6). Authors observed the equilibrium was

Fig. 6 Structure of TiO_2/Poly (acrylamide-styrene sodium sulfonate) [$\text{TiO}_2/(\text{P}(\text{AAm-SSS}))$] composite



achieved by composites for all metal ions up to 3 h. There is no considerable effect in metal ion removal between TiO_2 -PS and TiO_2 nanoparticles. But, TiO_2 /P (AAm-SSS) composite shows better metal Cs(I), Co(II) and Eu(III) ions removal. Authors concluded that by TiO_2 /P (AAm-SSS) composite has higher surface and various functional groups which improve the removal of metal Co(II), Cs(I) and Eu(III) ions.

Olatunji et. al. fabricated adsorbent based on conducting polymer polypyrrole and sawdust which is a biomass waste through simple chemical oxidative polymerization technique for radioactive ^{57}Co removal [58]. Authors observed removal of radioactive ^{57}Co was rapid and full saturation was achieved after 3 h in contact of polypyrrole-based Nanocomposite and ^{57}Co in aqueous solution at room temperature. Effect of Na^+ and K^+ coexisting ions on ^{57}Co adsorption was noted leads to decreasing the rate of removal from 54.9 to ~20% using 0.1 M for each Na^+ and K^+ ions. Authors concluded based on the results polypyrrole/sawdust composite could be used for removal of ^{57}Co instead of high cost materials from aqueous solution.

2.3 *Magnetic Polymer Nanocomposites*

Other form of polymer-based nanocomposite (PNCs) is a magnetic polymer nanocomposite which is very effective and promising adsorbents for various radioactive metal ions contaminants [59]. Magnetic Polymer nanocomposites-based potassium zinc hexacyanoferrate are effectively used for the removal of radioactive cesium (Cs) which is showed great water purification [60]. Other forms of polymer-based nanocomposites that used for the removal of radioactive Co(II), Sr(II) and Cs(I) wastes from water is ammonium molybdophosphate-poly(acrylonitrile) in which results showed great adsorption capacity of the prepared polymer nanocomposites which led to high water purification [61]. The effective adsorption back to ion-exchange ability and physical adsorption and the presence of alkali metals with all lead to magnificent adsorption ratio [62]. Titanium dioxide and zinc oxide are among the best catalysts that act as photo-catalysts to speed up the adsorption reaction of many polymer nanocomposites such as ZnO-based PMMA nanocomposites and this importance as result of their high stability and photo-catalytic activity [63].

One of the most effective polymer-based magnetic nanocomposites is magnetic Prussian blue NCs which can be synthesized through the fabrication of Prussian blue to the core of magnetite Fe_3O_4 NPs. The prepared magnetic polymer nanocomposites showed outstanding rapid separation of Cesium from water. Also PB nanocomposites achieved the maximum sorption capacity that is much more than any previous reports of PB nanomaterials. The advantages of the prepared magnetic PB-based polymer nanocomposites is their higher stability even in the highest ionic competition in the water and also PB-PNCs can be easily eliminated from the water after treatment by exposure the water to a magnet [64].

Increasing the concerns about the hazard effects caused by radioactive iodine waste, the scientists worked hard for the development of polymer nanocomposites to

be used for highly effective desalination process for the purification of the contaminated water with radioactive iodine. Due to the high affinity showed by silver towards iodine, silver nanoparticles was immobilized on the membrane of cellulose acetate for the synthesis of Polymer-based silver nanocomposites. The results showed that once the polymer-based silver nanocomposites exposed to the contaminated water, the radioactive iodine was rapidly attached to the prepared Ag-PNCs [65].

Na-CMC-g-P(AMPS-co-AA-co-AM)/NanoFe₃O₄ (SANCHs) superabsorbent composite was fabricated by El-saied et. al [66]. SANCHs composite was prepared by rafting process through free radical polymerization in the medium containing Fe₃O₄. Fabricated composite can be used for removal of radioactive ¹³⁴Cs, ⁸⁵Sr and ⁶⁰Co metal ions from aqueous solution. Authors observed that kinetic of the radioactive metal ions was fitting with pseudo-second-order. The maximum adsorption capacities of ⁸⁵Sr, ¹³⁴Cs, and ⁶⁰Co were equal 43, 23.9, and 47.2 mg.g⁻¹ respectively. Authors concluded SANCHs composite is an excellent adsorbent for the radioactive metal ions.

Han et al. synthesized composite porous microsphere based on polystyrene (PS) and trioctylamine (TOA) incorporated with Fe₃O₄ (Fe₃O₄/PS/TOA) by penetration-deposition and swelling-deswelling [67]. Microspheres magnetization was achieved and reached to 21.72 emu/g. Authors estimated the removal of Ce³⁺ using the prepared composite Fe₃O₄/PS/TOA as shown in Fig. 7. The maximum adsorption

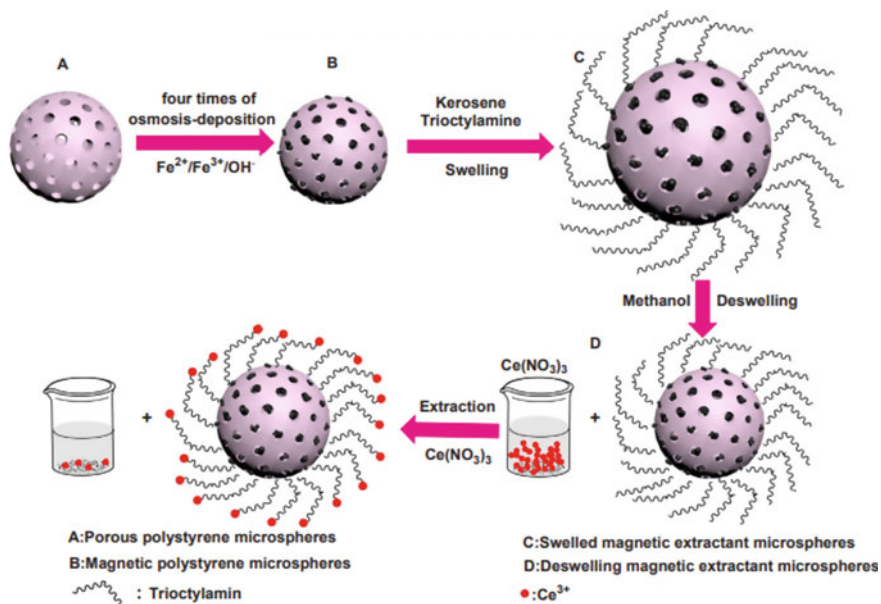


Fig. 7 Synthesis of composite porous microsphere Fe₃O₄/PS/TOA and proposed uptake of Ce³⁺ [67]

capacity was fitting with pseudo second-order found to be 74 mg.g^{-1} at 298 K. The kinetic isotherm adsorption of Ce^{3+} was followed to Langmuir model.

3 Conclusion

In this chapter discussed using of polymer nanocomposites in the field of wastewater treatment. Different types of composites used in wastewater treatment were reviewed polymer based nanocomposite, conducting polymer based nanocomposites and Magnetic polymer nanocomposites. Most of radioactive metal ions (such as Cesium Cs(I), Cobalt ($^{60}\text{Co(II)}$) and Europium (Eu(III)), U(VI), Thorium ion (Th(IV)), strontium (Sr^{2+}), selenium (Se^{4+}), Thallium (Tl), Radium (Ra^{2+}) and Actinium (Ac^{3+}) removal was considered. Efficiency of removal of radioactive metal ions from aqueous solution by composites was noted.

4 Future Perspective

The continuing progress of the international water situation is closely associated with the climate change and development of global population. The request of pure water is significantly increasing. Recently, nanomaterials are playing important role in water purification. Nanomaterials have special properties based on their size which enables to reach for materials with high efficient for wastewater treatment. Nanomaterial incorporated with polymer to improve the ability of polymer in water treatment and it is called nanocomposite. The dormant of nanocomposites in different district of research and implementation is encouraging and attention expanding investment from trade and Governments over worldwide. Definitely nanocomposites are based on polymer incorporated with magnetic materials enhance unique properties. Moreover, organoclay is a new material based on nature material. Despite many polymer nanocomposites advantages in water treatment, but there are various drawbacks that should be take in consideration. Finally, to produce nanocomposites with an efficient and low effective in water treatment should be study the interaction between polymer nanocomposites and the targeted contaminant or the matrix, nanomaterials and polymers used, adjusting conditions for water treatment and the effect on environment and human health.

References

1. Batool, M., Nazar, M.F., Awan, A., et al.: Bismuth-based heterojunction nanocomposites for photocatalysis and heavy metal detection applications. *Nano-Struct Nano-Objects* **27**, 100762 (2021)

2. Abu Elella, M.H., Goda, E.S., Abdallah, H.M., et al.: Innovative bactericidal adsorbents containing modified xanthan gum/montmorillonite nanocomposites for wastewater treatment. *Int. J. Biol. Macromol.* **167**, 1113–1125 (2021)
3. Bhatnagar, A., Sillanpaa, M.: Applications of chitin and chitosan derivatives for the detoxifications of water and wastewater- a short review. *Ad Colloid Interface Sci.* **152**, 26–38 (2009)
4. Abdellatif Soliman, S.M., Sanad, M.F., Shalan, A.E.: Synthesis, characterization and antimicrobial activity applications of grafted copolymer alginate-g-poly(N-vinyl imidazole). *RSC Adv.* **11**, 11541–11548 (2021)
5. Teow, Y.H., Mohammed, A.W.: New generation nanomaterials for water desalination; a review. *Desalination* **451**, 2–17 (2019)
6. Dargo, H., Ayaliew, A., Kassa, H.: Synthesis paradigm and applications of silver nanoparticles (AgNPs); a review. *Sustain. Mater. Technol.* **13**, 18–23 (2017)
7. Reddy, B., Dadigala, R., Bandi, R., et al.: Microwave-assisted preparation of a silver nanoparticles/N-doped carbon dots nanocomposite and its application for catalytic reduction of rhodamine B, methyl red and 4-nitrophenol dyes. *RSC Adv.* **11**, 5139–5148 (2021)
8. Ray, P.Z., Shipley, H.J.: Inorganic nano-adsorbents for the removal of heavy metals and arsenic: a review. *RSC Adv.* **5**, 29885–29907 (2015)
9. Ishida, H., Campbell, S., Blackwell, J.: General approach to nanocomposite preparation. *Chem. Mater.* **12**(5), 1260–1267 (2000)
10. Zhang, X., Liu, Y.: Nanomaterials for radioactive wastewater decontamination. *Environ. Sci. Nano.* **7**, 1008–1040 (2020)
11. Sharma, G., Kumar, A., Sharma, S., Naushad, M., Dwivedi, R.P., Allothman, Z.A., Mola, G.T.: Novel development of nanoparticles to bimetallic nanoparticles and their composites: a review. *King Saud Univ. J.* **31**(2), 257–269 (2019)
12. Othman, S.H.: Bio-nanocomposites materials for food packaging applications; types of biopolymer and nanosized filler. *AgricAgricSciProcedia* **2**, 296–303 (2014)
13. Zhang, Y., Wum, B., Liu, H., Wang, M., He, Y., Pan, B.: Nanomaterials-enabled water and wastewater treatment. *NanolImpact* **3**(4), 22–39 (2016)
14. Pandey, N., Shukla, S.K., Singh, N.B.: Water purification by polymer nanocomposites: an overview. *Nanocomposite* **3**(2), 47–66 (2017)
15. Singh, N.B., Susan, A.B.H.: Polymer-based nanocomposites for energy and environmental applications. *Wood head Publish Ser In composites Sci Eng*, pp. 569–595 (2018)
16. Huang, C., Cheng, Q.: Learning from nacre: constructing polymer nanocomposites. *Composites Sci. Technol.* **150**, 141–166 (2017)
17. Tian, T., Shi, X., Cheng, L., Luo, Y., Dong, Z., Gong, H., Xu, L., Zhong, Z., Peng, R., Liu, Z.: Graphene-based nanocomposites as an effective, multifunctional and recyclable antibacterial agent. *ACS. Appl. Mater. Interfaces* **6**(11), 8542–8548 (2014)
18. Zhao, S., Wang, Z., Wei, X., Zhao, B., Wang, J., Yang, S., Wang, S.: Performance improvement of polysulfoneultrafiltration membrane using well-dispersed polyaniline-poly(vinylpyrrolidone) nanocomposite as the additive. *Ind. Eng. Chem. Res.* **51**(12), 4661–4672 (2012)
19. Jordan, J., Jacob, K.I., Tannenbaum, R., Sharaf, M.A., Jasiuk, I.: Experimental trends in polymer nanocomposites: a review. *Mater. Sci. Eng. A* **1**(2), 1–11 (2005)
20. Shukla, S.K., Singh, N.B., Rastogi, R.P.: Efficient ammonia sensing over zinc oxide/polyaniline nanocomposite. *Ind. J. Eng. Mater. Sci.* **20**, 319–324 (2013)
21. Lopes, A., Martins, S.: Degradation of a textile dye C. I. Direct red 80 by electrochemical processes. *Portugaliae Electo. Chim. Acta* **22**, 279–294 (2004)
22. Alexandre, M., Dubois, P.: Polymer-layered silicate nanocomposites: preparation, properties and uses of a new class of materials. *Mater. Sci. Eng.* **28**(1–2), 1–63 (2000)
23. Laurent, S., Forge, D., Port, M., Roch, A., Robic, C., Vander, E., Muller, R.N.: Magnetic iron oxide nanoparticles: synthesis, stabilization, vectorization, physicochemical characterizations and biological applications. *Chem. Rev.* **108**, 2064–2110 (2008)

24. Zhang, Y., Wu, B., Xu, H., Liu, H., Wang, M., He, Y., Pan, B.: nanomaterials-enabled water and wastewater treatment. *NanoImpact* **3**(4), 22–39 (2016)
25. Wang, N., Li, J., Lv, W., Feng, J., Yan, W.: Synthesis of polyaniline/TiO₂ composite with excellent adsorption performance on acid red G. *RSC Adv.* **5**, 21132–21141 (2015)
26. Gangopadhyay, R., Amitabha, D.: Conducting polymer nanocomposites: a brief overview. *Chem. Mater* **12**(7), 608–622 (2000)
27. Sandler, J., Shaffer, M.S.P., Prasse, T., Bauhofer, W., Schulte, K., Windle, A.H.: Development of a dispersion process for carbon nanotubes in an epoxy matrix and the resulting electrical properties. *Polymer* **40**(21), 5967–5971 (1999)
28. Fernando, W., Satyanarayana, K.G.: Functionalization of single layers and nanofibers: a new strategy to produce polymer nanocomposites with optimized properties. *Colloid Int. Sci. J* **285**(1), 532–543 (2005)
29. Favier, V., Canova, C.R., Shrivastava, S.C., Cavaille, J.V.: Mechanical percolation in cellulose whisker nanocomposites. *Polymer Eng. Sci.* **37**(10), 1732–1739 (1997)
30. Ginnelis, E.P., Krishnamoorti, R., Manias, E.: Polymer-silica nanocomposites: model systems for confined polymers and polymer blends. *Polymers in confined environments. Adv. Polym. Sci.* **138**, 107–147 (1999)
31. Singh, N.B., Agarwa, I.S.: Nanocomposites: an overview. *Emerg. Mater Res.* **5**(1), 5–43 (2016)
32. Valsala, T.P., Roy, S.C., Shah, J.G., Gabriel, J., Raj, K., Venugopal, V.: Removal of radioactive caesium from low level radioactive waste (LLW) streams using cobalt ferrocyanide impregnated organic anion exchange. *Hazard Mater. J.* **166**, 1148–1153 (2009)
33. Nilchi, A., Atashi, H., Javid, A.H., Sberi, R.: Preparations of PAN-based adsorbents for separation of cesium and cobalt from radioactive wastes. *Appl. RadiatIsot.* **65**, 482–487 (2007)
34. Chang, C.Y., Chau, L.K., Hu, W.P., Wang, C.Y., Liao, J.H.: Nickel hexacyanoferrate multilayers on functionalized mesoporous silica supports for selective sorption and sensing of cesium. *Micro Meso Mater* **109**, 505–512 (2008)
35. Sheha, R.R., El-Shazly, E.A.: Kinetics and equilibrium modeling of Se(IV) removal from aqueous solutions using metal oxides. *Chem. Eng. J.* **160**, 63–71 (2010)
36. Ahamad, T., Naushad, M., Ubaidullah, M., Alshehri, S.: Fabrication of highly porous polymeric nanocomposite for the removal of radioactive U(VI) and Eu(III) ions from aqueous solution. *Polymers.* **12**(12), 2940 (2020)
37. Pandey, N., Shukla, S.K., Singh, N.B.: Water purification by polymer nanocomposites: an overview. *Nanocomposites* **3**(2), 47–66 (2017)
38. Sheha, R.R.: Synthesis and characterization of magnetic hexacyanoferrate (II) polymeric nanocomposite for separation of cesium from radioactive waste solutions. *J. Colloid Interface Sci.* **388**, 21–30 (2012)
39. Park, Y., Lee, Y.C., Shin, W.S., Choi, S.J.: Removal of cobalt, strontium and cesium from radioactive laundry wastewater by ammonium molybdophosphate–polyacrylonitrile (AMP–PAN). *Chem. Eng. J.* **162**, 685–695 (2010)
40. Ma, H., Hsiao, B.S., Chu, B.: Ultrafine cellulose nanofibers as efficient adsorbents for removal of UO₂²⁺ in water. *ACS Macro Lett.* **1**(1), 213–216 (2012)
41. Zhang, X., Wang, X., Chen, Z.: Radioactive Cobalt(II) removal from aqueous solutions using a reusable nanocomposite: kinetic, isotherms, and mechanistic study. *Int. J. Environ. Res. Public Health* **14**, 1453 (2017)
42. Ahluwalia, S.S., Goyal, D.: Removal of heavy metals by waste tea leaves from aqueous solution. *Eng. Life Sci.* **2**, 158–162 (2005)
43. LeeAYW, L.S.F., Chua, S.N.D., Bains, K.S.R., Abdullah, M.O.: Adsorption equilibrium for heavy metal divalent ions (Cu²⁺, Zn²⁺, and Cd²⁺) into zirconium-based ferromagnetic sorbent. *Adv. Mater. Sci. Eng.* **2017**, 1–13 (2017)
44. Louzao, M.C., Abal, P., Fernández, D.A., Vieytes, M.R., Legido, J.L., Gómez, C.P., Pais, J., Botana, L.M.: Study of adsorption and flocculation properties of natural clays to remove Prorocentrum lima. *Toxins* **7**, 3977–3988 (2015)
45. Mil, T.D., Devreese, M., Baere, S.D., Ranst, E.V., Eeckhout, M., Backer, D.P., Croubels, S.: Characterization of 27 mycotoxin binders and the relation with in vitro zearalenone adsorption at a single concentration. *Toxins* **7**, 21–33 (2015)

46. Shahat, A., Awual, M.R., Naushad, M.: Functional ligand anchored nanomaterial based facial adsorbent for cobalt(II) detection and removal from water samples. *Chem. Eng. J.* **271**, 155–163 (2015)
47. Yang, S.T., Zhao, D.L., Zhang, H., Lu, S.S., Chen, L., Yu, X.J.: Impact of environmental conditions on the sorption behavior of Pb(II) in Na- bentonite suspensions. *J. Hazard Mater.* **183**, 632–640 (2010)
48. Faghihian, H., Irvani, M., Moayed, M., Ghannadi-Maragheh, M.: A novel polyacrylonitrile–zeolite nanocomposite to clean Cs and Sr from radioactive waste. *Environ. Chem. Lett.* **11**, 277–282 (2013)
49. Yousefi, T., Torab-Mostaedi, M., Moosavian, M.A., Mobtaker, H.G.: Potential application of a nanocomposite: HCNFe@polymer for effective removal of Cs (I) from nuclear waste. *Prog. Nuclear. Energy* **85**, 631–639 (2015)
50. Sreenivasan, T., Sreenivasan, R., Tharunl, A.R.: Adsorptive removal of thorium(IV) from aqueous solutions using poly(methacrylic acid) grafted chitosan/bentonite composite matrix: process design and equilibrium studies. *Colloids Surf. A* **368**, 13–22 (2010)
51. Nur, T., Loganathan, P., Kandasamy, J., Vigneswaran, S.: Removal of strontium from aqueous solutions and synthetic seawater using resorcinol formaldehyde polycondensate resin. *Desalination* **420**, 283–291 (2017)
52. Hamed, M.M., Holiel, M., El-Aryan, Y.F.: Removal of selenium and iodine 699 radionuclides from waste solutions using synthetic inorganic ion exchanger. *J. Mol. Liq.* **242**, 722–731 (2017)
53. Keshtkar, A.R., Irani, M., Moosavian, M.A.: Removal of uranium (VI) from aqueous solutions by adsorption using a novel electrospun PVA/TEOS/APTES hybrid nanofiber membrane: comparison with casting PVA/TEOS/APTES hybrid membrane. *J. Radioanal. Nucl. Chem.* **295**, 563–571 (2013)
54. Simex, S., Ulusoy, U., Ceyhan, Ö.: Adsorption of UO_2^{2+} , Tl^+ , Pb^{2+} , Ra^{2+} and Ac^{3+} onto polyacrylamide-bentonite composite. *J. Radio Anal. Nucl. Chem.* **256**(2), 315–321 (2003)
55. Abbasizadeh, S., Keshtkar, A.R., Mousavian, M.A.: Preparation of a novel electrospun polyvinyl alcohol/titanium oxide nanofiber adsorbent modified with mercapto groups for uranium (VI) and thorium(IV) removal from aqueous solution. *Chem. Eng. J.* **220**, 161–171 (2013)
56. Baybaş, D., Ulusoy, U.: The use of polyacrylamide-aluminosilicate composites for thorium adsorption. *Appl. Clay Sci.* **51**, 138–146 (2011)
57. BoraiEH, B.M.M.E., Sayed, M.S., Abo-Aly, M.M.: Synthesis, characterization and application of titanium oxide nanocomposites for removal of radioactive cesium, cobalt and europium ions. *J. ColloidInter. Sci.* **450**, 17–25 (2015)
58. Olatunji, M.A., Khandaker, M.U., Amin, Y.M., Ekramul Mahmud, H.N.M.: Development and characterization of polypyrrole-based nanocomposite adsorbent and its applications in removal of radioactive materials. In: Ibrahim, F., Usman, J., Mohktar, M., Ahmad, M. (eds.) *International Conference for Innovation in Biomedical Engineering and Life Sciences. ICIBEL 2015. IFMBE Proceedings*, vol. 56. Springer, Singapore (2016)
59. Zach-Maor, A.Z., Semiat, R., Shemer, H.: Synthesis, performance and modeling of immobilized nano-sized magnetite layer for phosphate removal. *Colloid Inter. Sci. J.* **357**, 440–446 (2011)
60. Sheha, R.R.: Synthesis and characterization of magnetic hexacyanoferrate (II) polymeric nanocomposite for separation of cesium from radioactive waste solutions. *Colloid Inter. Sci. J.* **388**, 21–30 (2012)
61. Park, Y., Lee, Y.C., Shin, W.S., Choi, S.J.: Removal of cobalt, strontium and cesium from radioactive laundry wastewater by ammonium molybdophosphate-poly(acrylonitrile) (AMP-PAN). *Chem. Eng. J.* **162**, 685–695 (2010)
62. MaH, H.B.S., Chu, B.: Ultrafine cellulose nanofibers as efficient adsorbents for removal of UO_2^{2+} in water. *ACS Macro. Lett.* **1**(1), 213–216 (2012)
63. Di Mauro, A., Cantarella, M., Nicotra, G., Pellegrino, G., Gulino, A., Brundo, M.V., Privitera, V., Impellizzeri, G.: Novel synthesis of ZnO/PMMA nanocomposites for photocatalytic applications. *Sci. Rep.* **7**, 40895 (2017)

64. Jang, J., Lee, D.S.: Magnetic Prussian Blue nanocomposites for effective cesium removal from aqueous solution. *Ind. Eng. Chem. Res.* **55**(13), 3852–3860 (2016)
65. Shim, H.E., Yang, J.E., Jeong, S.W., Lee, C.H., Song, L., Mushtaq, S., Choi, D.S., Choi, Y.J., Jeon, J.: Silver nanomaterial-immobilized desalination systems for efficient removal of radioactive iodine species in water. *Nanomaterials* **8**(9), 660 (2018)
66. El-saied, H.A., Shahr El-Din, A.M., Masry, B.A., Ibrahim, A.M.: A promising superabsorbent nanocomposite based on grafting biopolymer/nanomagnetite for capture of ^{134}Cs , ^{85}Sr and ^{60}Co radionuclides. *J Polym Environ.* **28**, 1749–1765 (2020)
67. Han, Q., Du, M., Guan, Y., Luo, G., Zhang, Z., Li, T., Yanqin, J.: Removal of simulated radioactive cerium (III) based on innovative magnetic trioctylamine-polystyrene composite microspheres. *Chem. Phys. Lett.* **741**, 137092 (2020)

Advances in Nanocomposite Materials for Energy Harvesting Applications

Mixed Ionic-Electronic Conductors Based on Polymer Composites



Rafael Del Olmo, Maria Forsyth, and Nerea Casado

Abstract This chapter outlines the current state of mixed ionic-electronic conducting composite materials, and discusses the latest advances from a didactic point of view. Beginning with the fundamentals, the electronic conducting agent and its nature is described. This section progresses from previously studied inorganic composites to the latest updates in flexible and highly conducting organic systems, where radical and π -conjugated polymers are used. Then, the concept of dopants, which boosts the conductivity of these materials, will be expounded, in addition to the material characteristics depending on their nature (organic based and hybrid architectures). Finally, the electronic and ionic transport are explained. The main characterization techniques are discussed in the following section, highlighting electrochemical impedance spectroscopy. In the last section, the role and scope of these materials in different applications (thermocells, batteries, sensors/transistors and other devices) are explained.

R. Del Olmo · M. Forsyth (✉) · N. Casado (✉)

POLYMAT University of the Basque Country UPV/EHU, Joxe Mari Korta Center,
Avda. Tolosa 72, 20018 Donostia-San Sebastian, Spain
e-mail: maria.forsyth@deakin.edu.au

N. Casado

e-mail: nerea.casado@ehu.eus

R. Del Olmo

e-mail: rafael.delolmo@polymat.eu

M. Forsyth

Basque Foundation for Science, IKERBASQUE, 48011 Bilbao, Spain

Institute for Frontier Materials (IFM), Deakin University, Geelong, VIC 3217, Australia

ARC Centre of Excellence for Electromaterials Science (ACES), Deakin University, Burwood,
VIC 3125, Australia

© The Author(s), under exclusive license to Springer Nature Switzerland AG 2022

A. E. Shalan et al. (eds.), *Advances in Nanocomposite Materials for Environmental and*

Energy Harvesting Applications, Engineering Materials,

https://doi.org/10.1007/978-3-030-94319-6_17

List of Acronyms

4PP	Four-point probe
AC	Alternating current
AFM	Atomic force microscopy
BSCF	$\text{Ba}_{0.5}\text{Sr}_{0.5}\text{Co}_{0.8}\text{Fe}_{0.2}\text{O}_{3-\delta}$
CCTS	Carboxymethyl chitosan
CMC	Carboxymethyl cellulose
CNT	Carbon nanotubes
CP	Conducting polymer
DBSA	Dodecyl benzene sulfonic acid
DC	Direct current
DCA	Dicyanamide
DFT	Density functional theory
DSC	Differential scanning calorimetry
EIS	Electrochemical impedance spectroscopy
EMIM	1-Ethyl-3-methylimidazolium
FET	Field effect transistor
FSI	Bis(fluorosulfonyl)imide
FTIR	Fourier transform
GOPS	3-Glycidoxypropyltrimethoxysilane
IL	Ionic liquid
LFP	Lithium iron phosphate
LSCF	$\text{La}_{0.2}\text{Sr}_{0.8}\text{Co}_{0.8}\text{Fe}_{0.2}\text{O}_{3-\delta}$
LTM	Long-term memory
NCA	Lithium nickel cobalt aluminium oxide
NFC	Nanofibrillated cellulose
NMC	Lithium nickel manganese cobalt oxide
NMP	N-Methyl-2-pyrrolidone
NMR	Nuclear magnetic resonance
OECT	Organic electrochemical transistor
OFET	Organic field effect transistor
OIPC	Organic ionic plastic crystal
P3HT	Poly(3-hexylthiophene-2,5-diyl)
PA	Polyacetylene
PANI	Polyaniline
PEDOT	Poly(3,4-ethylenedioxythiophene)
PGSt	Poly(4-(2,6-di-tert-butyl- α -(3,5-di-tert-butyl-4-oxo-2,5-cyclohexadien-1-ylidene)-p-tolyloxy)styrene)
PolyDADMA	Poly(diallyldimethylammonium)
PProDOT	Poly(3,4-propylenedioxythiophene)
PPy	Polypyrrole
PROXYL	1-Pyrrolidnyloxy,2,2,5,5-tetramethyl
PSS	Polystyrenesulfonate

PTEO	Poly(4-glycidyoxy-2,2,6,6-tetramethylpiperidine-1-oxyl)
Pth	Polythiophene
PTHS	Poly(6-(thiophene-3-yl)hexane-1-sulfonate)
PTMA	Poly(2,2,6,6-tetramethyl-1-piperidinyloxy-4-yl methacrylate)
PTSA	P-toluene sulphonic acid
PVDF	Polyvinylidene fluoride
RH	Relative humidity
SA	Sodium alginate
SAXS	Small angle X-ray scattering
SPP	Symmetric polarization procedure
STM	Short-term memory
TCB	Tetracyanoborate
TE	Thermoelectronics
TEMPO	(2,2,6,6-Tetramethylpiperidin-1-yl)oxidanyl
TFSI	Bis(trifluoromethanesulfonyl)imide
WAXS	Wide angle X-ray scattering
XPS	X-ray photoelectron spectroscopy
XRD	X-ray diffraction

1 Introduction

Nowadays, ionic and electronic transport and their coupling are key to the performance of a large variety of electronic devices such as batteries, thermoelectric devices, actuators and sensors. The vast array of intricate physical mechanisms and their interrelations are still not completely deciphered, nonetheless, their successful implementation in multiple applications makes them a current hot topic.

The fundamentals of mixed ionic-electronic conductors (MIECs) will be explained in this chapter. Depending on their nature, MIECs are divided in two types: inorganic and organic (OMIECs). Up to now, this field has been dominated by ceramics; however, studies on inorganic mixed ionic and electronic conductors based on silver were already underway in 1966 [1] when the electronic transport in polymers were being described during the 1960s. [2] In 1977 Shirakawa, H. et al. [3] discovered the possibility of modifying the conductivity of polyacetylene to match that of metallic values, and was eventually awarded the Nobel Prize in Chemistry in 2000 for “the discovery and development of conductive polymers”. Ceramic mixed conductors have been thoroughly studied while research on organic materials has mostly focused on the electronic conductivity, optoelectronic properties, and enhancement of material flexibility and thermal stability but not on the mixed conduction. Ceramic compounds, despite being far from reaching the electronic conductivities of conducting polymers at room temperature, have shown high ionic conductivities. In fact, currently applicable fields like fuel cells, membranes for CO₂ reduction and thermoelectrics are mainly governed by inorganic compounds

because of their long thermal stability. On the other hand, conducting polymers which have recently been exploited with their coupled ionic transport, have been successfully employed in many specific fields because of their wide range of design, ease of processability and semi-metallic conductivity. Some of their applications include in energy storage devices, transistors and a large list of integrated circuits involving this kind of devices.

In this same section, examples and mechanisms of doping for OMIECs are introduced (again sorted into organic based and hybrid architectures), as well as their ionic transport, electronic transport and ionic-electronic coupling. The transport properties are described by the latest models, as reported by the authors and some of the more commonly used techniques to explain the different conductivity values are discussed, including: UV spectroscopy, X-ray spectroscopy, atomic force microscopy (AFM), solid state nuclear magnetic resonance (NMR) spectroscopy and differential scanning calorimetry (DSC). The highest and typical values of conductivities, as well as the key parameters used to compare different systems are highlighted in this part.

In a separate part, the most common techniques to measure conductivities are expounded. On one hand, electrochemical impedance spectroscopy (EIS) and on the other, four-point probe (4PP), Van der Pauw method and DC polarization. These techniques allow measurement of the ionic and electronic conductivities either along or across the sample. Besides, other important information can be obtained such as the transference number or in relation to the conduction mechanism by EIS.

Finally, the role and importance of the MIECs in the applications where they are more widely employed are discussed in the last section. The remarkably easy manufacturing and good electronic conductivities of conducting polymers are desirable properties for thermoelectrics, batteries and transistors, and additionally, their ionic conductivity has been shown to have a positive role in thermoelectrics, and a crucial role in all-solid-state batteries and organic electrochemical transistors (OECTs) with lower response times. Multiple examples can be found in this section as well as their common figures of merit.

2 Fundamentals of MIECs

2.1 Electronic Conducting Agent

Although the highest electronic conductivities reached belong to metals (apart from graphene), materials with a certain ionic character and solvation ability are required for yielding both ionic and electronic conducting pathways. Depending on the nature of the electronic conducting agent, MIECs can be sorted as either inorganic or organic based.

2.1.1 Inorganic Based MIECs

Ceramic mixed conducting materials developed for the separation of hydrogen and solid oxide fuel cells have shown high ionic and electronic conductivity values at high temperatures (>200 °C). For example, some research groups have dispersed insoluble metallic or another ceramic phase with high electron transfer properties into an ionic conducting phase, forming a dual-phase mixed ionic material [4, 5]. Many others work on the development of other compounds such as pyrochlore ($A_2B_2O_7$), brownmillerite ($A_2B_2O_5$), and strontium ferrite ($Sr_4Fe_{6-x}Co_xO_{13}$) [6, 7], but the most famous are fluorite ($AO_{2-\delta}$), perovskite ($ABO_{3-\delta}$) and their dual mixed-phase, where A and B are distinct metal cations. The ideal crystalline structures of fluorites and perovskites have long been known [8, 9], as represented in Fig. 1a–b, respectively.

The presence of defects in inorganic compounds enables the conduction of species and electrons along the material. There can be structural defects that involve atom and ion displacements or electronic defects consisting of the intrinsic ionization, excitation from the valence to the conduction bands or their formation to maintain electric neutrality. The structural defects can be sorted in point, line or plane defects. Thanks to point defects (that implies just a single lattice and its vicinity), lattice diffusion occurs by Schotky disorder (an atom/ion moves from its regular site to an interstitial hole as represented in Fig. 2a), Frenkel disorder, where a certain number of cation and anion vacancies exist to always maintain electroneutrality, (Fig. 2b) and also via vacancies pushing neighbour atoms or via interstitial sites (Fig. 2c). Line defects can result in dislocation because of the displacement in repeated patterns of the crystalline structure, while plane defects might lead to grain boundaries and surface diffusion. All these defects can occur internally but also by the addition of moieties that promote these motions and hence, the conduction pathways. For

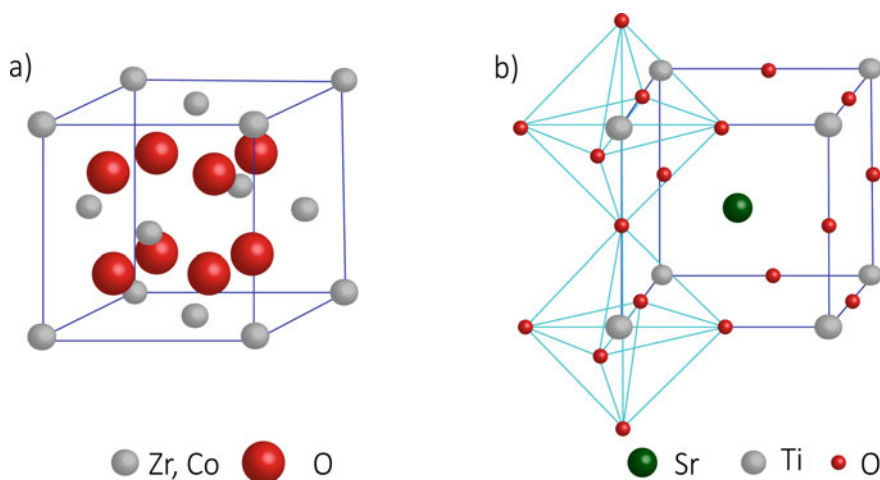


Fig. 1 Crystalline structures of **a** fluorite and **b** perovskite

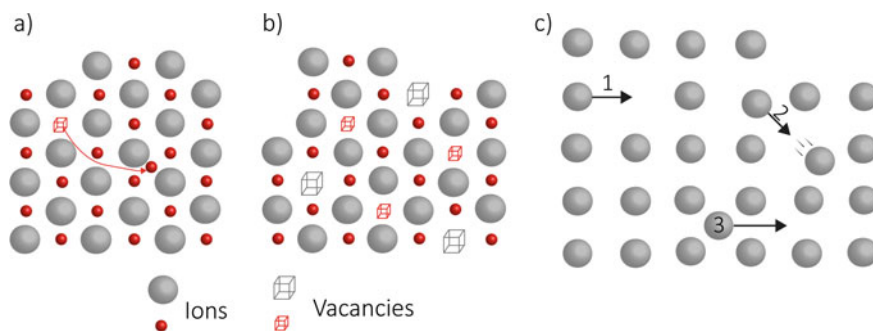


Fig. 2 Illustrations representing point defects formed by **a** Frenkel disorder, **b** Schottky disorder, and **c** 1- via vacancy, 2- via pushing of neighboring atoms and 3 - via an interstitial site. The big grey circles refer to anions, small black circles to cations, and the empty squares to vacancies

instance, the addition of La_2O_3 to CeO_2 or CaO to ZrO_2 increases the number of anion vacancies because La^{3+} and Ca^{2+} replace Ce^{4+} and Zr^{4+} , respectively, generating a negatively charged material that needs to be counterbalanced by removing oxygen anions (vacancy formation) or forming interstitial cations. In this regard, there can be stoichiometric oxides, whose number of negatively and positively charged defects occur equally, or non-stoichiometric, where the number of each defect depends on the pressure and the temperature of their components. Besides, non-stoichiometry might be caused by oxygen vacancies (or excess of cations), which result in n-type conductors (electrons), or an excess of oxygen (or deficiency of cations) leading to p-type conductors (holes). The non-stoichiometric oxygen can be measured, for example, by thermogravimetric analysis. The addition of multivalent cations in mixed oxides can also promote a polaron mechanism based on electron hopping [6]. The ion and electron conduction depends on different factors, where the ionic conductivity is usually related to the crystalline structure while the electronic conduction is more affected by the electronic bandgap.

Regarding the kind of MIECs, fluorite type oxides (e.g. HfO_2 , ZrO_2 , CeO_2 [10]) are good ionic carriers used widely in fuel cells and oxygen sensors, but poor electronic conductors, so they are typically blended with other conductors to obtain mixed-phase materials [11]. The addition of different dopants as well as changes in pressure and temperature, enable modification of their electronic conductivity, stability and crystalline structure.

For perovskites, combinations such as $\text{A}^{3+}\text{B}^{3+}\text{O}$, $\text{A}^{2+}\text{B}^{4+}\text{O}$ and $\text{A}^{1+}\text{B}^{5+}\text{O}$, with the total charge of +6 in the cations are usually used, but in most of the cases A is a 2+ large alkali earth metal like Sr, Ba or La, while B is a 4+ smaller cation of the first-row transition elements like Ce, Fe or Co. These last kind commonly exhibit a high electronic conductivity in contrast to their ionic conductivity [12]. The Ruddlesden–Popper (R-P) series ($\text{A}_{n+1}\text{B}_n\text{O}_{3n+1}$) are still sorted into perovskite-related intergrowth structures. They represent the most general formula for this family where the structural formula of the K_2NiF_4 and perovskite-type oxides can be obtained by $n = 1$ and $n = \infty$, respectively [13]. Perovskites do not show ionic conduction unless it

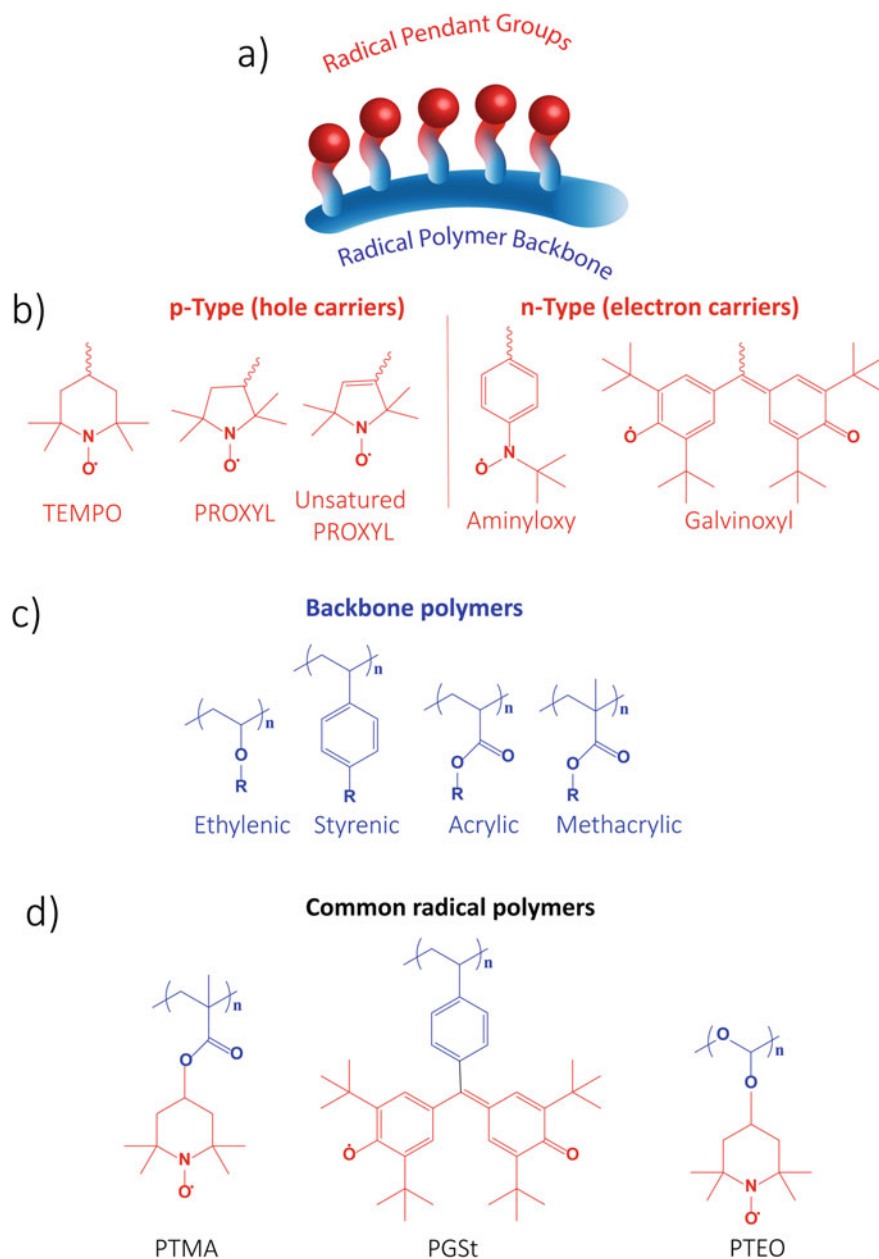


Fig. 3 **a** Typical structure of radical polymers and common examples, **b** radicals commonly used, **c** backbone polymers normally used and **d** examples of radical polymers. TEMPO: (2,2,6,6-tetramethylpiperidin-1-yl)oxidanyl, PROXYL: 1-pyrrolidnyloxy,2,2,5,5-tetramethyl, PTMA: poly (2,2,6,6-tetramethyl-1-piperidinyloxy-4-yl methacrylate, PGSt: poly(4-(2,6-di-tert-butyl- α -(3,5-di-tert-butyl-4-oxo-2,5-cyclohexadien-1-ylidene)-p-tolyloxy)styrene) and PTEO: poly(4-glycidyoxy-2,2,6,6-tetramethylpiperidine-1-oxyl)

presents intrinsically or extrinsically from added defects in their structure. Those defects can take the form of either vacancies, ion displacements along the lattice, impurities or ions in a valence state so that A and B do not sum up to +6. Then, each defect must be counterbalanced or accommodated, in order for the lattice to remain neutral. Doping with heterovalent cations is feasible at both A and B sites and yields to complex perovskite families derivated from the simple ABO_3 formula, for instance $A_xA'_{1-x}B_yB'_{1-y}O_{3-\delta}$, with the A-site generally doped by lanthanides and the B-site by first row transition elements. Among the wide range of doped perovskites that can be design, $La_{1-x}Sr_xCo_{1-y}Fe_yO_{3-\delta}$ (LSCF), $Ba_{1-x}Sr_xCo_{1-y}Fe_yO_{3-\delta}$ (BSCF) and its La-doped BLSCF as well as their composites have attracted interest for their use as cathodes for fuel cells [14].

Finally, mixed-phase materials involve more than one phase with a similar thermal expansion coefficient and compatibility between them, but exhibiting a dominant conductivity in each phase that can be optimized separately. For instance, the different material preparation methods cause exclusive microstructures, which influence the charge transport. The relationship between microstructures and species mobility has been reported in oxides with a predominant electronic conductivity, indicating that a larger grain size typically promotes better ionic conductivities [15].

Electronic transport in the order of 10^2 S cm^{-1} have been reported for LSCF systems in between 600–800 °C, showing higher values for Co-rich than for Fe-rich compositions [16]. In contrast, in terms of ionic transport, bismuth-based materials are an object of constant research, exhibiting values of 1 S cm^{-1} in its pure form (fluorite) at 800 °C. In order to make these bismuth- and also zirconia based mixed ionic–electronic conductors, some rare-earth and metal oxides such as CeO_2 , TiO_2 and CuO_2 , with multivalent-states cations, have typically been added [6].

Overall, in addition to the requirements of high electronic and ionic conductivity, a similar thermal expansion coefficient to the whole system is desirable for MIECs due to the high temperatures reached in their application where the thermal stability excludes the organic compounds.

2.1.2 Organic Based MIECs

Organic mixed ionic-electronic conductors (OMIECs) are entirely dominated by radical polymers and mainly π -conjugated polymers.

Radical polymers are macromolecules containing a stable radical group that is usually pending from the polymeric backbone, as shown in Fig. 3a–d. Conjugation doesn't necessarily exist in this kind of polymers, where the electron charge transfer occurs through hops facilitated by the dynamics of the redox-active pendant groups. Basically, the electron charges are transported by redox self-exchange reactions being able to transport charge across interfaces (e.g. at current-collecting electrodes) and also through heterogeneous redox reactions [17]. Depending on the choice of the pendant group chemistry, radicals can act as n-type (electron carriers) or p-type (hole carriers) (Fig. 3b), which enables the design and customization for a large variety of applications [18–20]. For instance, a nitronyl nitroxide based system has

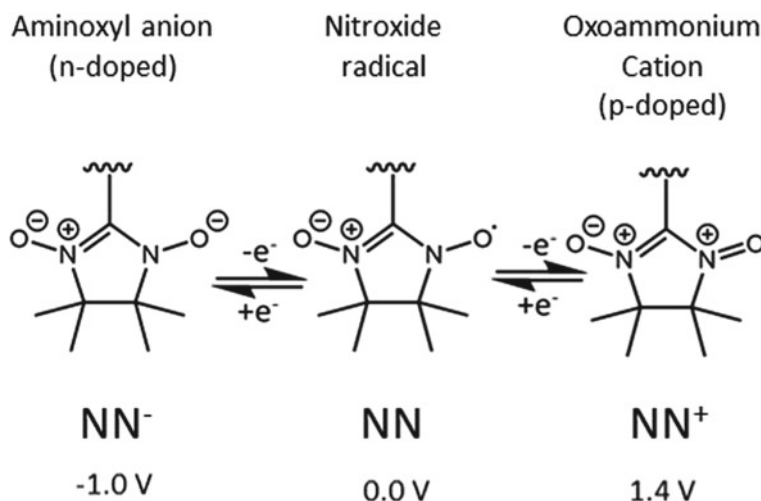


Fig. 4 Doping states of nitronyl nitroxide [21]

been demonstrated to have three redox states: p-doped state, neutral and an n-doped state, as depicted in Fig. 4, which is of special interest for rechargeable devices [21]. The electronic conductivity of radical polymers is around $10^{-3} - 10^{-5}\text{ S cm}^{-1}$ [17, 22], but values of 0.3 S cm^{-1} has been also obtained for poly(4-glycidyloxy-2,2,6,6-tetramethylpiperidine-1-oxyl) (PTEO) samples [23].

Since 2002, when Nakahara et al. [24] reported the first radical polymer based battery, radical polymers have been of great interest in the field of superfast charging-discharging batteries [25–28] and solar cells coupled with perovskites [29, 30].

Differently, conducting polymers necessarily must have a π -conjugated polymer backbone, which enables the electronic conductivity. Conducting polymers have been widely studied and their structure, electronic transport mechanisms and applications have been reported in several books and reviews [31, 32]. The most common conducting polymers are listed in Fig. 5. All the carbon atoms in a fully π -conjugated molecule are sp^2 hybridized, forming localized σ bonds that determine the geometrical structure of the molecule. The remaining $2p_z$ orbitals, which are perpendicular to the chain plane, overlap forming π orbitals through which the electrons are delocalized. The number of π and π^* formed orbitals is proportional to the number of carbon atoms, exhibiting a splitting of the energy levels as the number of carbons is doubled. Figure 6 represents an example of the simplest conjugated molecule based on trans-acetylene. For long conjugated chains (trans-polyacetylene), the difference of energy between levels becomes negligible and can be considered as continuous bands along the electrons that can flow better. The filled π band is named *valence band* and the empty π^* band, *conduction band*. Nonetheless, the conduction of the most famous polymers is facilitated by the induction of charge defects in the polymer, which reduces the energy gap between π band (HOMO) and π^* band (LUMO) levels, forming so-called polarons and bipolarons (two polarons close to each other) to create

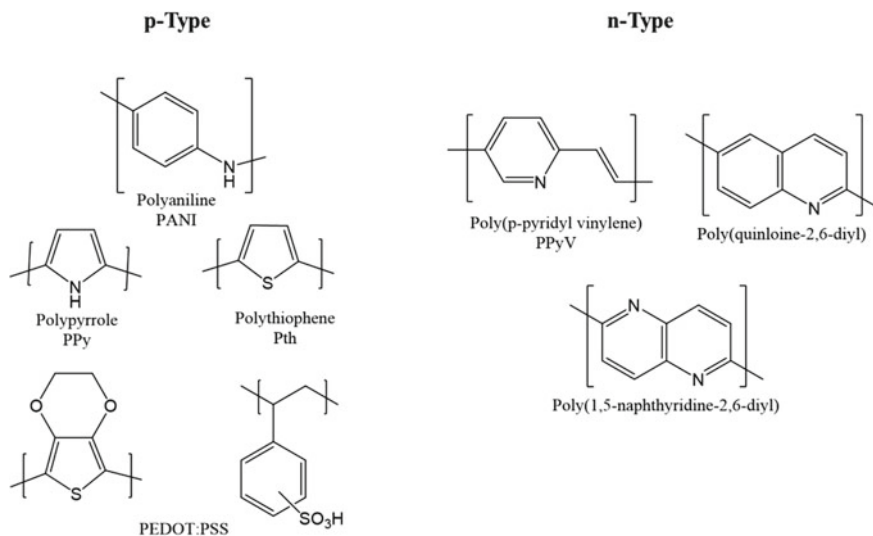


Fig. 5 Common p-type and n-type conducting polymers

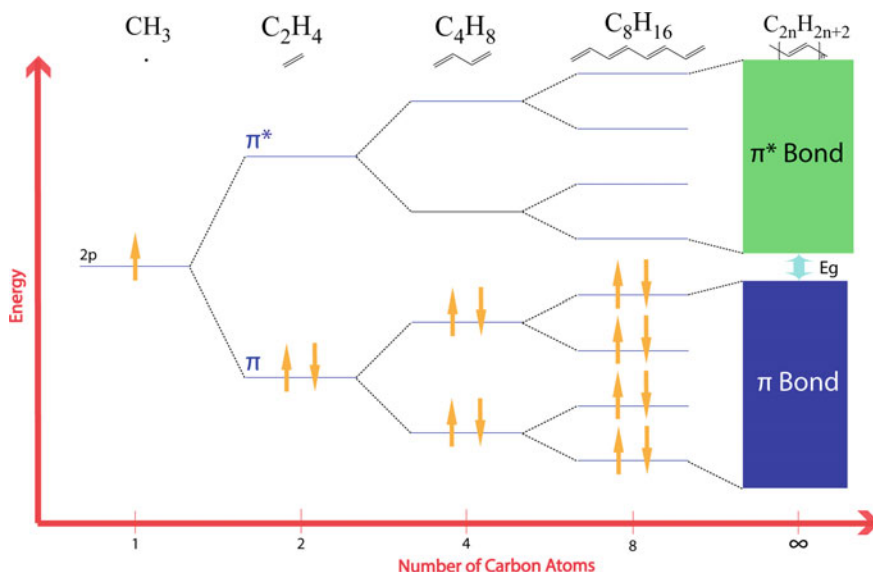


Fig. 6 Energy levels of π and π^* as a function of the number of carbon atoms

conjugated pathways (Fig. 7). A polaron can be described as a charged quasi-particle localized along the polymer chains, stabilized by other ions acting as dopants in a mechanism that receives the name of primary doping. Basically, the more doped the polymer is, the better the electronic conductivity, showing higher charge defects and hence also creating more electronic and ionic pathways. In Sect. 2.2, the various dopants that have been studied to date are introduced. Those who are interested in the understanding and prediction of polaronic density state by DFT (density functional theory) and pre-DFT approaches would do well by reading the article published by Zozoulenko et al., [33]. Until now, the progress and conductivity of p-type conducting polymers (hole transporting) is limited compared to n-type (electron transport).

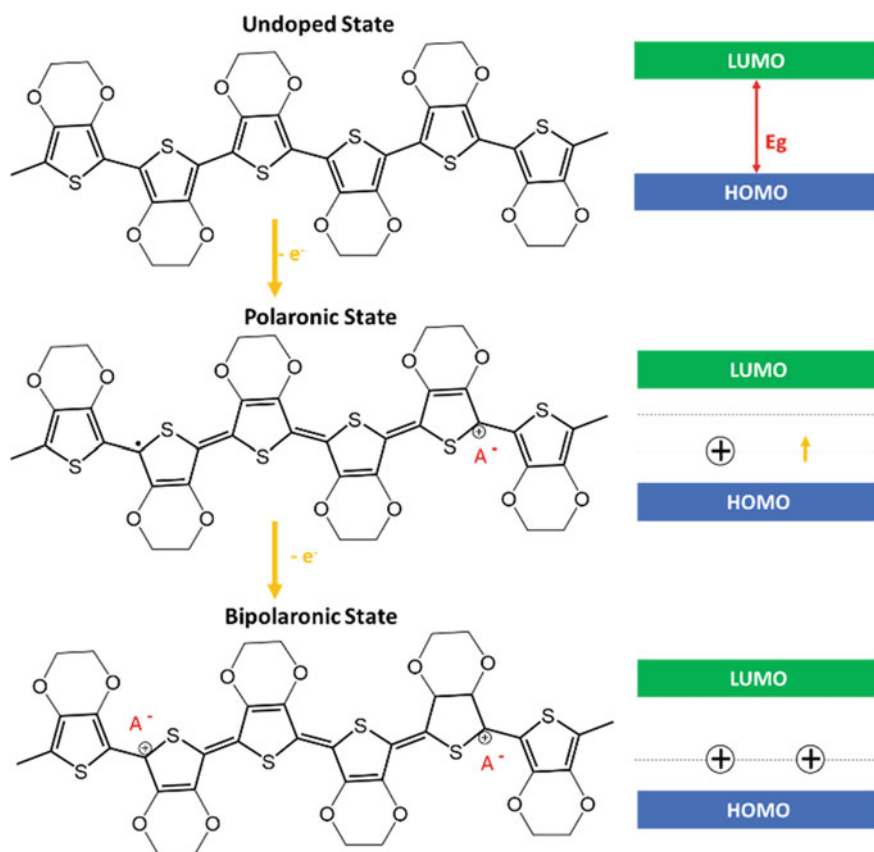


Fig. 7 Undoped, polaronic and bipolaronic states of PEDOT (poly(3,4-ethylenedioxythiophene)) with a representation of their HOMO and LUMO levels. A^- refers to a dopant which stabilizes the charge

Since the research conducted in the 1960s on the synthesis and electronic properties of π -conjugated trans-polyacetylene [2, 34, 35], considerable efforts have been paid to the characterization, improvement of electronic transport, design and application of this kind of polymers. Conducting polymers have attracted much attention in terms of mass production, due to their ease of manufacturing and low temperature processability relative to ceramic materials, as well as their semi-metallic electronic conductivity at room temperature, flexibility and binding effect. These features enable the design of wearable, light and versatile devices such as transistors [36], ion pumps [37], sensors [38], electrochromic displays [39] and energy storage systems [40].

Conducting polymers are typically brittle, so one effective way to produce them is to create a layer on a surface by vapour phase polymerization. This method results in materials with high electronic conductivities due to the good distribution of the material in a really thin film, which is less affected by internal mechanical stress and other kinds of physical defects. Many studies have focused on creating really thin layers revealing a huge impact on the final electronic conductivity, obtaining values above 6000 S cm^{-1} [41]. Another way to synthesize them is by oxidative chemical polymerization, which is more attractive in terms of scale up, and have resulted in high and air-stable electronic conductivities in bulky films. Among these conducting polymers, poly(3,4-ethylenedioxythiophene):poly(styrene sulfonate) (PEDOT:PSS) is one of the most ubiquitous ones. As shown in Fig. 5, the conducting agent, PEDOT, is accompanied by the polyelectrolyte polystyrene sulfonate (PSS), which acts not only as a dopant with its SO_3^- groups but also influences the water solubility of the final compound, the ability to create self-standing films and certain extra ion conduction.

There has been a fundamental development in the design of new functionalized OMIEC systems that can be sorted in different categories, as reported by (OMIECs). The stabilizer that accompanies the conducting polymer can be split into those that intrinsically have an ionic charge (polyelectrolyte) such as PSS and those whose ionic conduction mechanism is based on the solvation of external ions (polymer electrolyte) such as polyethylene oxide (PEO), where the ionic species need to be incorporated. This stabilizer can be attached to the conducting polymer forming block copolymers or just mixed to obtain blends, showing in both cases regions that are predominantly ion conductors and other areas that are predominantly electron conductors. This leads to different types of MIECs according to Paulsen et al. [42]: blends with either polyelectrolytes (Type I) [43], or polymer electrolytes (Type II) [44, 45], and block copolymers with polyelectrolytes (Type III) [46] or polymer electrolytes [47] (Type IV) [48]. Finally, the conducting polymer can exhibit the ionic and electronic conduction simultaneously throughout a single material, without segregation of the charge transfers, by functionalization of the conducting polymer. Two further types appear regarding this variable: the ones that form ionic charge-bearing compounds that contain a stable ionic moiety (Type V) [49] that is counterbalanced by either ions, or the electronic charge on a conjugated section, or forming a self-balanced zwitter ion; and the ones that contain polar moieties enabling the solvation of ions (Type VI) [50]. This classification isn't only taking into account the kind of

ion conduction of the electrolyte but also the addition of redox active moieties, more biocompatible stabilizers or even radical polymers could be considered [28].

The extensive range of OMIECs that can be designed reflects the large array of target applications and optimization variables that will be discussed in Sect. 4. The use of one OMIEC over another for a specific application is usually due to the compatibility with other parts of the device, physico-chemical or electrochemical stability, processability or conductivity values. For this reason, a more thorough characterization is required for the improvement of a wide variety of gadgets that whose performances are completely affected by the features of OMIECs and specifically where the ionic transfer is crucial. Even though there are some reports of the ionic and electronic characterization of OMIECs, there is still a gap in the full understanding of ionic transport and specially the ionic-electronic coupling due to their ion carrier properties being overlooked and unnoticed until quite recently.

2.2 Dopants and Additives

Conducting polymers in their oxidized state form positive charges that need to be counterbalanced by anions to stabilize this doped state, as represented in Fig. 7. These counter ions are called dopants. Acidic compounds have been commonly used to dope PEDOT, PANI (polyaniline) and Ppy (polypyrrole), such as hydrochloric acid (HCl), sulfuric acid (H_2SO_4), triflic acid ($\text{CF}_3\text{SO}_3\text{H}$), p-toluene sulphonic acid (PTSA) and dodecyl benzene sulfonic acid (DBSA) [51–55]. Besides, DFT calculations have shown that protons also dope PEDOT predominantly by the most favourable interaction with the α -position of thiophene in a doping/de-doping fully reversible mechanism [56]. Other ways to boost the electronic conductivity of these polymers is through electrochemical doping [57] or by the addition of polar solvents (methanol, dimethylsulfoxide, ethylene glycol) [58] to PEDOT:PSS to promote a phase segregation between PEDOT and PSS, namely secondary doping, as depicted in Fig. 8. Rich cores of PEDOT are normally surrounded by isolating PSS, which after a secondary doping, detach from PEDOT creating more continuous and conducting particles of PEDOT. In addition to all of these techniques to improve the electrical transport, organic based additives can be incorporated or hybrid systems can be designed as supplementary approaches.

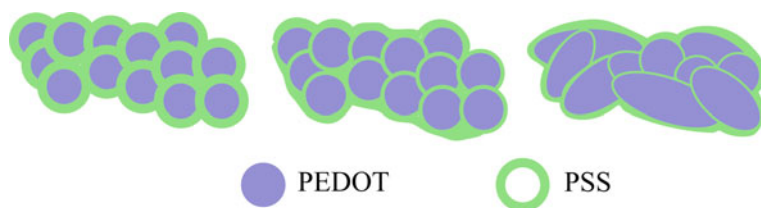


Fig. 8 Phase segregation between PEDOT and PSS

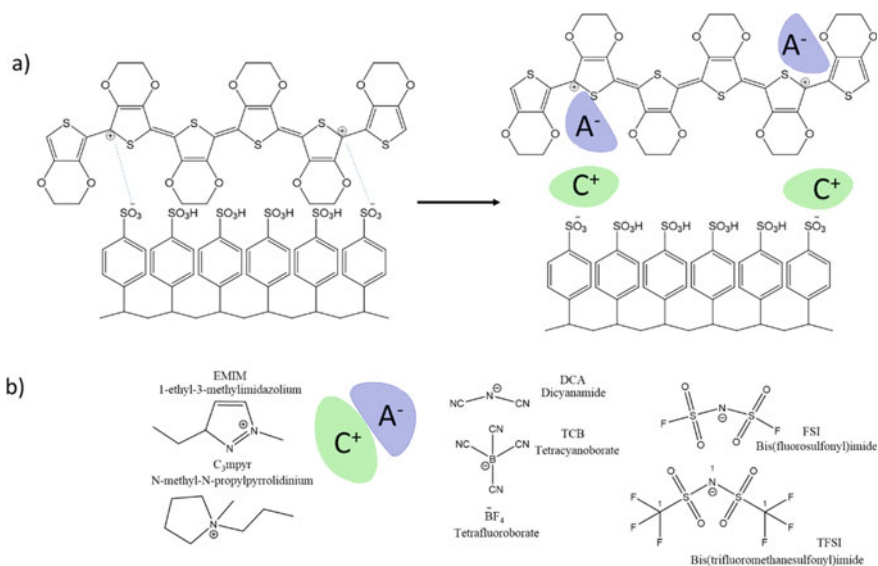


Fig. 9. **a** Ion exchange of PEDOT:PSS with ionic liquids and **b** commonly used ionic liquids.

2.2.1 Organic Based Additives

Ionic liquids (ILs) and their solid-state cousins, organic ionic plastic crystals (OIPCs), have emerged highlighting by their electrochemical stability, high ionic conductivity and safer properties versus the flammable and volatile conventional electrolytes [59, 60]. The addition of ILs to conducting polymers has improved ionic-electronic conductivities and Seebeck coefficient without losing mechanical properties [61, 62]. Although the mechanism is not fully clear, a secondary doping is believed to be coming from an ion exchange as depicted in Fig. 9, followed by the below described phase segregation, where PEDOT incorporates IL anions and PSS the cations. Through free energy calculations using DFT, Izarra et al. [63] showed that among various ILs the most efficient pairs were the ones with the lowest binding energies, meaning the least tightly bound, which lead to more favourable and spontaneous ion exchange, and also with p-doping power. The extra Seebeck coefficient has been explained by several authors by an ionic Seebeck effect [64].

Untreated, commercially available PEDOT:PSS (Clevios PH1000) typically presents an electronic conductivity lower than 1 S cm^{-1} at room temperature and a Seebeck coefficient of $12\text{--}16 \mu\text{V K}^{-1}$ [65], while the incorporation of an IL can successfully achieve values of $1000\text{--}2000 \text{ S cm}^{-1}$ [43, 66, 67] and $35 \mu\text{V K}^{-1}$ [62] respectively. The enhancement in the electronic conductivity typically comes accompanied by a higher electrochemical response as well.

Even though the use of OIPCs has not yet been applied in conducting polymers, the intrinsically solid-state nature of the compounds has a promising point for those applications where the presence of liquids must be avoided. Besides, the plastic

behavior of this kind of salts should help to improve the mechanical properties of particularly brittle conducting materials. There is only one report to date that has shown a doping behavior in a PEDOT based system that also influences the electrochemical response [68]. Nonetheless, OIPCs have been successfully combined with other polymers for solid electrolytes [69, 70], opening a promising approach for all-solid-state devices.

2.2.2 Hybrid Architectures

The use of carbon-nanostructures or inorganic additives leads to hybrid structures, which are widely used in the field of thermoelectronics (TE) due to their increase in electronic conductivity, Seebeck coefficient and mechanical stability.

Carbon-nanostructures, such as cellulose structures, have been successfully employed to obtain flexible and quite resistant films [71, 72], carbon nanotubes (CNTs) and graphene to improve the electrical response [73–75], and fullerenes because of their large Seebeck value of 2 mV K^{-1} [75].

The incorporation of inorganic compounds to organic electrolytes has been probed for a long time and has shown to boost ionic conductivity [76]. Mimicking this strategy, π -conjugated [45, 47] and radical [17] MIEC polymers have even exhibited a rise in the electron conduction. Those systems are based on the solvation of lithium or sodium salts (using for instance hexafluorophosphate (PF_6^-), triflate (CF_3SO_3^-), bis(fluorosulfonyl)imide (FSI^-), bis(trifluorosulfonyl)imide (TFSI^-) as anions) by ethers and carbonates. This effect leads to an ionic-electronic coupling that will be explained in Sect. 2.3. It is important to consider that there is a maximum quantity of salt that the organic part can solvate to obtain the best scenario. Once the perfect percolation threshold is reached, an excess of inorganic salt leads to a precipitation and huge ionic resistances. Another desirable goal is to improve the thermoelectric properties, where the low thermal conductivity and high electronic conductivity of conducting polymers fits well with the high Seebeck coefficient of inorganic compounds. The addition of different bismuth, tellurium or molybdenum-selenium morphologies varies between particles, nanowires or nanosheets, and is quite common in the field TE [77] as will be commented in Sect. 4.1.

With these kind of additives, Seebeck coefficient around $\sim 60 \mu\text{V K}^{-1}$ has been reported with germanium particles [78], with electronic conductivities in the range of $1000\text{--}3000 \text{ S cm}^{-1}$ being reported for multiple systems [77].

2.3 Ionic-Electronic Transport

The electronic conduction has been investigated for many years in π -conjugated polymers as well as the ionic transport in polymer electrolytes and polyelectrolytes. In the following sections their mechanisms of transport and coupling in MIECs will be expounded with the latest models and techniques of characterization.

2.3.1 Electronic Transport

In non-conjugated radical polymers, the electronic conduction occurs via electron hopping (Fig. 10a), which is thermally activated between pendant radical sites by self-exchange reactions. They can also transfer charge through heterogeneous redox reactions and across interfaces (e.g. at current-collecting electrodes) [17]. The distance between radical sites has been demonstrated to play a key role for efficient charge transfer to occur [20]. An electron transport assisted via segmental motion of the pendant groups has been proposed by Yu et al., [17] (Fig. 10f), which implies a disorder dependence. The addition of lithium salt to a TEMPO based polymer poly(4-glycidyloxy-2,2,6,6-tetramethylpiperidine-1-oxyl) (PTEO), increases the chain dynamics, promoting an improvement of the electronic conductivity across long channel lengths in a synergistic step where the ionic conductivity is enhanced as well.

In conducting polymers, in addition to the degree of doping, the ordering of the chains, which is directly influenced by the surrounding environment, also plays a key role in the efficiency of the charge transport. The movement of the electrons can take part along the backbone of the conducting polymer or across π -stacked backbones (Fig. 10b). A high degree of π -conjugation allows the electrons to move along less-interrupted pathways through delocalized π -orbitals and between molecules where there is sufficient π - π overlapping. DFT calculations on neat and crystallites of doped PEDOT have demonstrated that the intra-chain ordering is considerably more efficient than the inter-chain transfer [79]. The disorder of the conducting polymer normally limits the delocalization of charge carriers and overlap, what leads

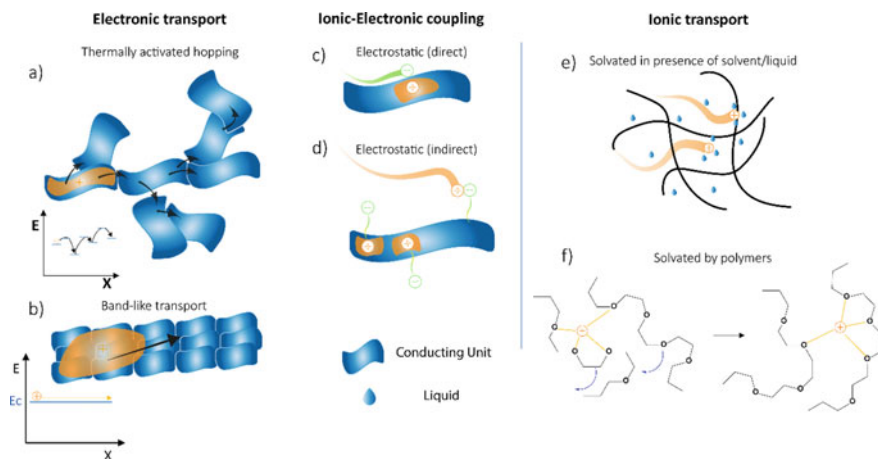


Fig. 10 Mechanisms of electronic and ionic transports and ionic-electronic coupling. Electronic conduction given by **a** thermally activated hopping and **b** band-like transport. Ionic-electronic coupling given by **c** directly electrostatic and **d** indirectly electrostatic. Ionic conduction **e** through liquid and **f** facilitated by the segmental motion of the polymer

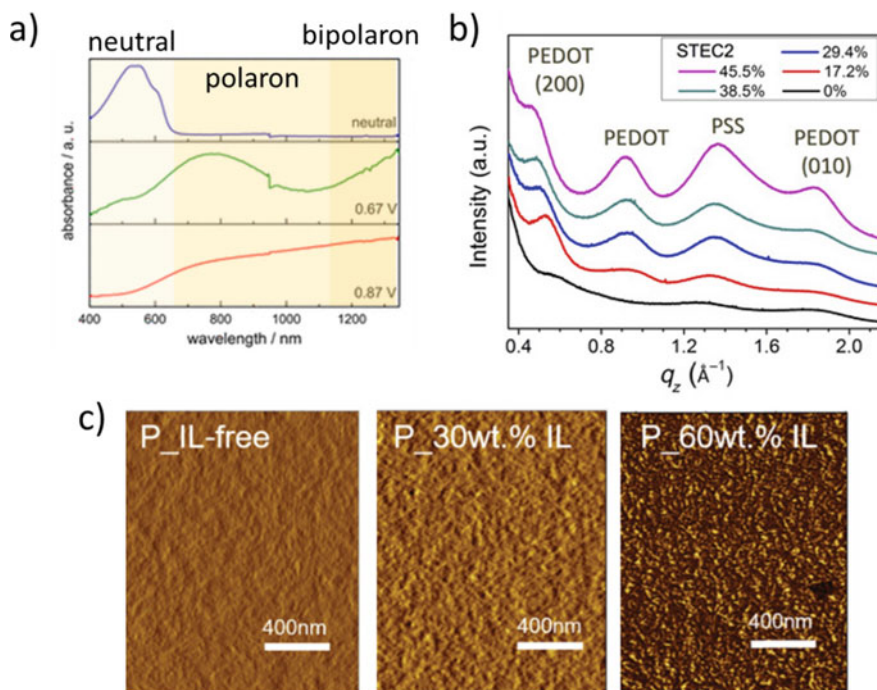


Fig. 11 **a** UV spectra of electrochemically doped P3HT. Reprinted with permission from [57]. Copyright 2020 American Chemical Society, **b** GIWAX measurements of PEDOT:PSS with different loadings of 4-(3-Butyl-1-imidazolium)-1-butananesulfonic acid triflate ionic liquid. Reprinted with permission from [73]. Copyright 2017, and **c** AFM images of the phase segregation created by doping PEDOT-PSS with LiTFSI. Reprinted with permission from [66]. Copyright 2017

to charge transport occurring as a series of thermally activated jumps between states with a favourable distance and energy that can be described by different models [80]. In contrast, when the ordering is good enough, the conducting polymer can display diffuse band-like electron transport. Electronic conductivity values of 8800 S cm^{-1} have been obtained for single-crystal PEDOT nanowires where highly ordered diffraction spots were observed [81]. Several works have reported the electronic conduction behavior versus temperature resulting in a typical semi-metallic behavior with a thermally activated mechanism [82, 83].

Several characterization techniques have been employed to explain the electronic transport. UV measurements are typically used to qualitatively quantify the amount of neutral, polaronic and bipolaronic states of a conducting polymer, which is directly related to the degree doping. Figure 11a shows an example of electrochemically doped poly(3-hexylthiophene-2,5-diyl) (P3HT), where the more oxidized compound shows no neutral states (below 600 nm), just polaronic (600–1200 nm) and bipolaronic states (>1200 nm) [57]. X-ray based systems, such as X-ray diffraction (XRD), wide-angle X-ray scattering (WAXS) and small-angle X-ray scattering

(SAXS) have been extensively employed to measure the degree of ordering of lamella interchain stacking and interchain π - π stacking, which is given by the intensity of the peaks related to the [1 0 0], [2 0 0] and [0 1 0], [0 2 0] signals respectively. In Fig. 11b, grazing incidence WAX spectra are shown which demonstrate ordering of PEDOT:PSS blends with different loads of 4-(3-Butyl-1-imidazolio)-1-butanefulfonic acid triflate, exhibiting a much better stacking of PEDOT chains with 45.5% loading [73]. Finally, in addition to FTIR (Fourier transform infrared) and X-ray photoelectron spectroscopy (XPS), which are commonly used to analyze structural changes and the interaction with different additives by the appearance of peaks or the shifting or intensity changes in the peaks, AFM is a useful technique to observe the PEDOT-PSS phase segregation, where an example is presented in Fig. 11c for a PEDOT:PSS LiTFSI system [66].

2.3.2 Ionic Transport

The ionic conduction can introduce new and diverse variables to a system that can sometimes result in a system too complex to analyse. Ions can be multivalent, exist in multiple species and induce ion exchange, form pairs and larger clusters, be solvated and interact with traces of solvent. The ionic transference in a certain material is quantified as ionic conductivity (σ_{ionic}), which represents the sum of the different ionic conductivity values of each mobile ionic specie, i . The contribution of each ion to the total conductivity is given by the transfer number (t_i). These parameters are mathematically related by Eq. 1.

$$\sigma_{ionic} = \sum_i t_i \sigma_{ionic,i} \quad (1)$$

The ionic conductivity of an ion, i , is a function of the ion charge (z_i), number density (n_i), elementary charge (e) and mobility (μ_i) as follows the next equation:

$$\sigma_{ionic,i} = |z_i| n_i e \mu_i \quad (2)$$

And finally, the ion mobility and diffusivity (D) are related by the Einstein equation (Eq. 3):

$$D_i = \frac{\mu_i k_B T}{e} \quad (3)$$

where k_B is the Boltzman's constant and T is temperature.

When one of the ions is a polymer, the mobility of such ion can be considered as negligible versus small molecules. This effect has a particular interest for some applications when only the movement of a specific ion is required or desirable for a good performance. For instance, lithium-ion batteries where a high transfer number of lithium is required for the electrolytes, to prevent polarization of the system which

typically ends up with the growth of lithium dendrites, causing a short circuit, or in ion pumps which delivery specific analytes.

The measurement of this parameter is quite sensitive to moisture and all the characterization related to it needs to be performed in a glovebox, under inert atmosphere. The presence of liquid electrolyte or solvent wets and swells OMIECs, causing ion transfer to occur more rapidly through solvated ion vehicle transport (Fig. 10e), making other contributions negligible. In dried films, the ion motion proceeds through ion hopping coupled with the segmental motion of the polymer side chains or backbone (Fig. 10f). Ions can be solvated by either carbonates or ethers, radicals, polyelectrolytes or any moiety that could interact with them adding more degrees of freedom to flow through.

The ionic conductivity is typically obtained by measuring the ionic resistance and taking into account the geometry of the sample as described in Eq. 4.

$$\sigma_{ionic} = \frac{t}{R_{ionic} A} \quad (4)$$

where t is the thickness and A is the area of the sample. Electrochemical impedance spectroscopy (EIS) has been widely used, not only to measure the ionic conductivity but also the number of transferances in the field of electrolytes, showing a totally different behavior than mixed conductors, and this will be explained in Sect. 3. Plots of $\log(\sigma_{ionic})$ versus $1000/T$ following the Arrhenius equation (Eq. 5) are typically presented in studies of ionic conductivity to evaluate the conductivity dependence with temperature.

$$\sigma_{ionic} = \sigma_0 \exp\left(\frac{-E_a}{RT}\right) \quad (5)$$

where σ_{ionic} is the ionic conductivity, σ_0 is the pre-exponential factor, E_a is the activation energy, R the universal gas constant and T the absolute temperature. In general, for a specific ion surrounded by different environments, lower activation energy corresponds to higher ionic conductivities. However, when there are different ions it is more complicated due to the intrinsic mobility of each ion and their ability to be solvated or packaged that might result in materials not necessarily with a lower activation energy being the best conductors.

Ionic conductivities of 0.02 S cm^{-1} have been reached for high relative humidity systems (PEDOT:PSS – nanofibrillated cellulose (NFC) at 80% relative humidity (RH)) [71]. Nonetheless, the bottleneck for dried systems is around the values of solid polyelectrolytes/polymer electrolytes, $10^{-3} - 10^{-4} \text{ S cm}^{-1}$.

In order to explain different ionic conductivities in different systems, several measurements can be done. For instance, with differential scanning calorimetry (DSC), the thermal behavior of a specific material can be determined, which is intimately related to the movement of the compounds. The ionic conductivity will always be higher close to the melting point (T_m) where some liquid particles may be present and the material is quite activated. At the same time, the further above

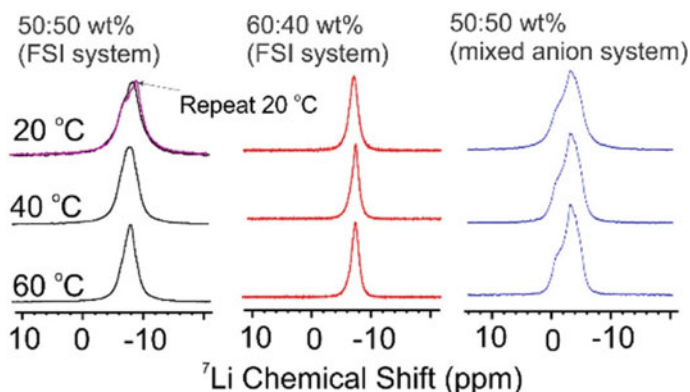


Fig. 12 Static ^7Li NMR measured at 20, 40, and 60 °C for 50:50 and 60:40 IL/Li salt: polyDADMA FSI system compared with the 50:50 polyDADMA TFSI mixed anion system. Reprinted from [84] with permission from Elsevier, Copyright 2018

the glass transition temperature (T_g) of the material, the greater the motions of the polymer are and hence, the conductivity is higher. That means that low T_g is desirable.

Solid-state NMR (static and magic angle spinning) enables the determination of the most favorable environment for a specific ion to flow through. In general, the sharper the NMR peak, the better the dynamics of the studied ion. In Fig. 12 [84], for a poly(diallyldimethylammonium) bis(fluorosulfonylimide) (PolyDADMA FSI) based system with ionic liquid and LiFSI salt, at higher temperatures and higher ionic liquid content (60:40 wt.%), the peak is much more abrupt.

2.3.3 Ionic-Electronic Coupling

Overall, while a high crystallization of the conducting polymer results in high σ_e in the electronic transfer, it limits the ionic dynamics. In fact, many works have used the suppression of crystallinity for the improvement of the σ_{ionic} [76, 85]. The addition of lithium salts to polymers that can solvate it, such as PEO; a common electrolyte, used from the 1980s thanks to Professor M. Armand [86], diminishes the crystallinity of the polymer (PEO) and gives ion conduction. However, there are studies reported that have included lithium salts to polymer electrolyte (e.g. polyvinylpyridine or polyethylene oxide) based OMIECs resulting in an enhancement of both conductivities [17, 44, 45, 47, 87]. The mechanism of this controversial behavior is not fully understood. In any case, the coupling between electronic and ionic species is fundamental for batteries, solid-state electronics and energy devices, though its study is in a steady state.

The addition of ionic dopants allows for strategic ionic – electronic coupling that could lead to electronic structural modifications and consequently modulate the electronic conduction in these materials. Due to the intrinsic demand of charge

balance in all systems, for there to be a presence of electronic charge, a stabilizing excess ionic charge with the net opposite sign is required. Conducting polymers combined with just polymer electrolytes need the inclusion of mobile ions to stabilize the doping state, while OMIECs stabilized by polyelectrolytes do not need extra ions. The ionic-electronic coupling can proceed directly (Fig. 10c), via electrostatically charge transference (for instance the protonation of PANI) [42] or is facilitated by a self-exchange reaction (radical polymers) [17], and the subsequent dragging of ions. But also can proceed indirectly as it is represented in Fig. 10d [42].

EIS has been used to deconvolute the electronic and ionic conductivities, which is explained in Sect. 3, and also the ionic-electronic coupling by measuring the volumetric capacitance or the electrochemical density of states [88–90].

The geometry, size, as well as the intended application govern the direction, speed and dimension along which the ions and electrons flow. The reason why conducting polymers are often employed as thin films (from nm to mm) is because the ionic/electron transport is always more favorable along the surface than across the defects and layers of thickness. For instance, in applications such as batteries, where the ionic and electronic transport take place across the film (see Fig. 13a), the best performances are reached for really thin films that show highly active cyclic voltammograms, while in thick films that activity drops. In organic electrochemical transistors (OECT), the electronic transport occurs along the film from the source to the drain, which is explained in Sect. 4.3. The ionic species flow through the film resulting in the limiting process (Fig. 13b). Not only the theoretical transport mechanisms matter, but also the dimension and geometry of the designed devices play key roles in the electronic transport, which should also be considered in their scalability and understanding.

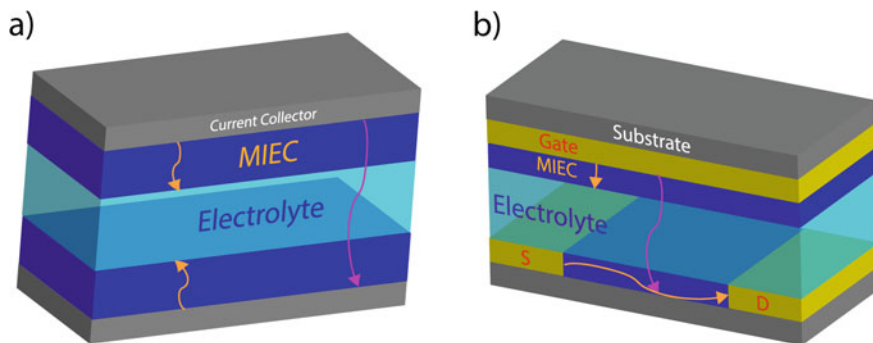


Fig. 13 Electronic and ionic transport in **a** batteries and **b** OECT. Yellow arrows refer to electronic transport and pink arrows to ionic transport

3 Characterization

3.1 Electrochemical Impedance Spectroscopy (EIS)

EIS is a powerful characterization technique which applies a small AC voltage to an electrochemical cell and then measures the frequency-dependent complex impedance through the cell. This kind of measurement results in real and imaginary components that are typically represented in Nyquist plots, providing information about the ionic resistance and store charge respectively, in different processes occurring in the sample. EIS has been largely used to extract the mobility and conductivities of ionic [71] and electronic transport [91]. Even though some systems are satisfactorily modelled with simple circuits, mixed conductors generally have some more complex impedance spectra.

These Nyquist plots must be interpreted by fitting an equivalent circuit that is a representation of what is happening electronically in a sample. That equivalent circuit must have a physical meaning, considering the involved processes in a certain material, and taking into account that complex equivalent circuits can fit to any Nyquist plot, but might not have a comprehensive sense. Different elements can be used such as resistances (R), capacitors (C), constant phase elements (Q), Warburg impedances (W) or inductors (L), that can be combined in serial or in parallel depending on the material and can have completely different meanings. Whereas serial connections are related to layer-by-layer materials or sequential elements, parallel ones refer to different pathways along which species can flow simultaneously. Although many systems are suitably modelled with simple circuits, OMIECs sometimes present some complications in finding the perfect equivalent circuit.

In ionic conductors, the common shape of graphs is a single semicircle followed by a tail at low frequencies, as represented in Fig. 14a with a common equivalent circuit for electrolytes. Contrarily, in OMIECs, when the order of the ionic and electronic conductivity values are similar to each other, two semicircles appear (see Fig. 14b). Nonetheless, ionic conductivity is usually much lower in conductive polymers than

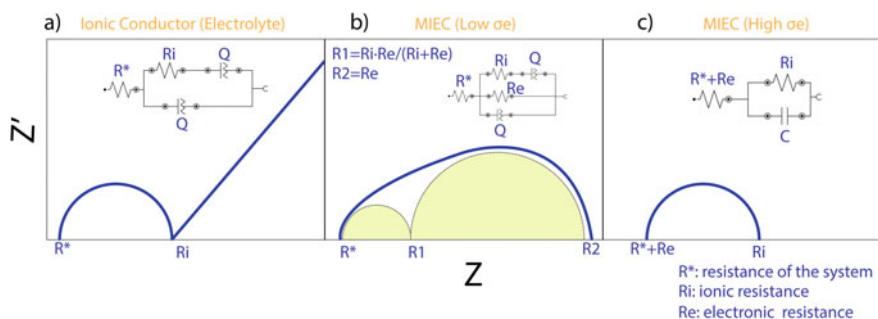


Fig. 14 Typical Nyquist plots obtained by EIS for **a** electrolytes, **b** MIECs with low σ_e and **c** MIECs with high σ_e , as well as their respective common equivalent circuits used

the electronic conduction and for this reason only one semicircle attributed to the ionic conduction appears because the electronic resistance is negligible and not possible to measure with this technique, as demonstrated in Fig. 14c. Another difference between ionic conducting polymers and mixed conductors worth mentioning is the absence of tails in MIECs, due to the fact that the interfacial capacitance is shunted by the electronic current at low frequencies. In Fig. 14, Nyquist plots of an ionic conductor and two different MIECs with their equivalent circuits, have demonstrated that the electronic conductivity can be measured for one MIEC but not for the other.

It is also possible to quantify the transference number of each ion by the Bruce-Vincent or Watanabe methods in a symmetric polarization procedure (SPP) that consist of applying a potentiostatic polarization to the cell until the current is stabilized between two EIS measurements and comparing the resistances, taking into account the initial and steady state currents [92]. Equation 6 is employed to calculate the transference number by using the Bruce-Vincent method.

$$t_i = \frac{I_{SS}(V - I_0 R_0)}{I_0(V - I_{SS} R_{SS})} \quad (6)$$

where I_0 is the initial current, I_{SS} is the steady state current, V the applied potential, R_0 the initial resistance of the passivation layer and R_{SS} the resistance of the passivation layer (steady state).

3.2 *Electronic Conductivity Measurements*

To quantify the electronic transport, several systems have been developed. The 4-point probe (4PP) and van der Pauw methods (see Fig. 15a and b, respectively) enable the measurement of the electronic conduction along different directions of a film by applying a potential between two points of the sample and recovering a current in another two different points. The electronic conductivity is then calculated according to Eq. 7, by taking into account the electronic resistance (R_e) and film thickness (t).

$$\sigma_e = \frac{1}{R_e \cdot t} \quad (7)$$

In these techniques, an electron diffusion across the thickness occurs making the electronic resistance higher in thick films than in thin ones. Several works have developed physical models as well as corrections factors to account for this [93, 94] which are included in current 4PP devices and their software, which should not be forgotten. Despite those corrections, it should be acknowledged that the resulting values are estimations and even nowadays thin films always show higher electronic conductivity.

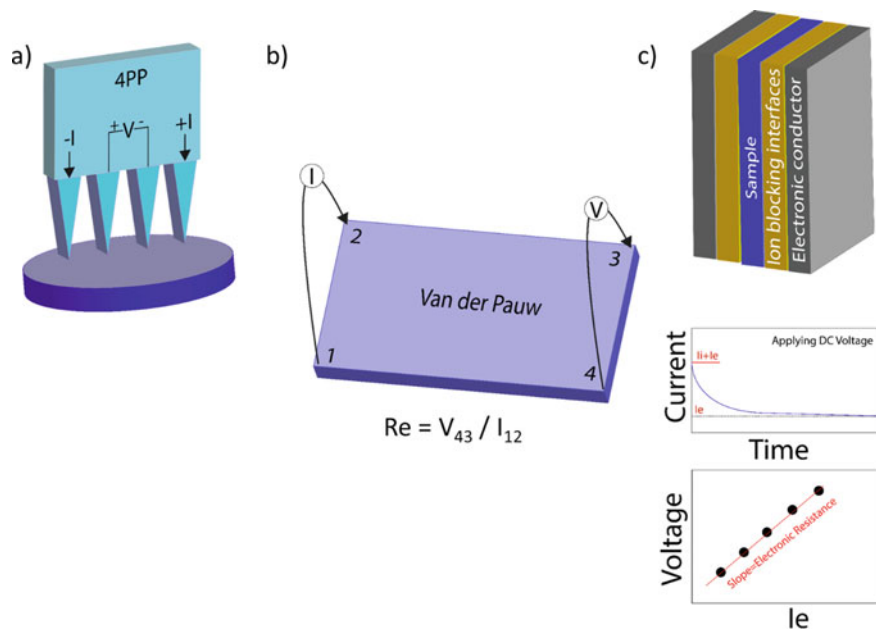


Fig. 15 Common approaches for the quantification of electronic transport include **a** the 4PP, **b** the Van der Pauw method and **c** via DC polarization

In contrast, DC polarization has been utilized to measure the electronic conductivity across a sample covered by ion-blocking Ag electrodes on both sides [95]. After applying a DC polarization, the steady state current is recorded and plotted versus the applied potential, obtaining linear graphs as shown in Fig. 15c.

4 Applications

The outstanding properties exhibited by mixed ionic-electronic conductors have led to a growing interest in them. The most important fields where MIECs highlight are thermoelectrics, energy storage systems and transistors. Moreover, the wide potential functionalization and versatility offered by these compounds have yielded to a large variety of devices based on transistors such as sensors of pressure, specific analytes and actuators. In the following sections, it will be expounded the most relevant advances in the application of MIECs in these fields with multiple examples.

4.1 Thermoelectric

The plenty of solar thermal energy and the demand for waste heat reuse make thermoelectric materials very attractive for both scientific and industrial societies as they can employ that thermal energy otherwise dissipated. The conversion of a difference of temperature into electricity occurs via the Seebeck effect. Thermoelectric generators (TEG) are a device that can function to produce energy (Fig. 16a). Additionally, there are heat pumps that are driven by the Peltier effect (Fig. 16b), which is basically the inverse process of the Seebeck effect. These thermoelectric devices generally consist of n- and p-type thermoelectric materials connected through conducting plates as depicted in Fig. 16.

However, the current commercialized TE modules suffer from surface rigidity which limits the contact area on both ends. Organic TE systems out-perform their conventional inorganic analogues in terms of light weight and flexibility. Additionally, their scalability, abundance of precursor options and fabrication advances (being printable by different techniques [96–98]) make them promising candidate materials. Among all the organic systems studied so far, PEDOT:PSS is undoubtedly the most developed p-type material that offers semi-metallic conductivity and quite low thermal conductivity, typical for polymers. These features are collected in the TE figure of merit according to the next equation (Eq. 8), which quantifies the goodness of a TE material:

$$ZT = S^2\sigma_e T/\kappa \quad (8)$$

where S (V K^{-1}) is the Seebeck coefficient, σ_e (S m^{-1}) is the electrical conductivity, T is the absolute temperature (K) and κ ($\text{W m}^{-1}\text{K}^{-1}$) is the total thermal conductivity.

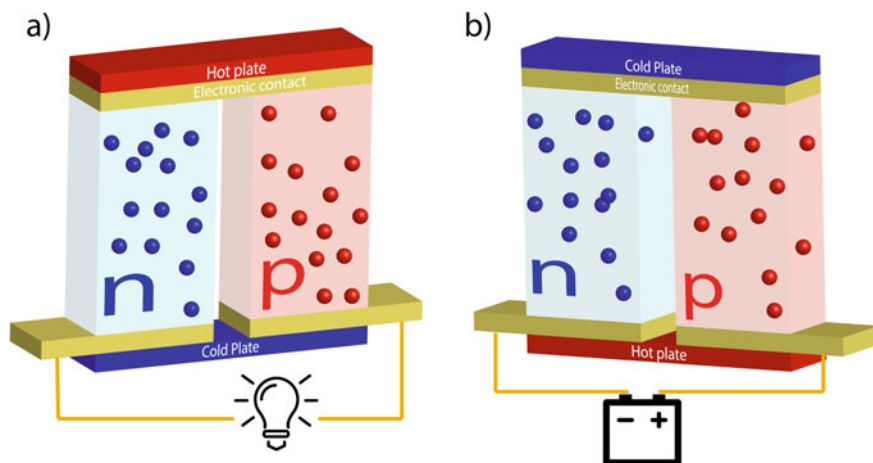


Fig. 16 Thermoelectric generators using p- and n-type thermoelectric materials based on **a** the thermoelectric effect and **b** a heat pump driven by the Peltier effect

Seebeck coefficient is quantified by the slope of several measurements of the open circuit voltage (ΔV) between two extremes of the film with distinct temperature differences (ΔT) along the sample. For instance, the intrinsic Seebeck coefficient of pure PEDOT:PSS is around $10\text{--}17\text{ mV K}^{-1}$, which is the main point for the improvement of the power factor ($S^2 \sigma_e$). The thermal conductivity is considered lower than $1\text{ W m}^{-1}\text{ K}^{-1}$, while the in-plane value remains challenging to quantify [99]. In Fig. 17, several examples of p-type and n-type compounds are expounded with their power factors listed by Luo et al. [100].

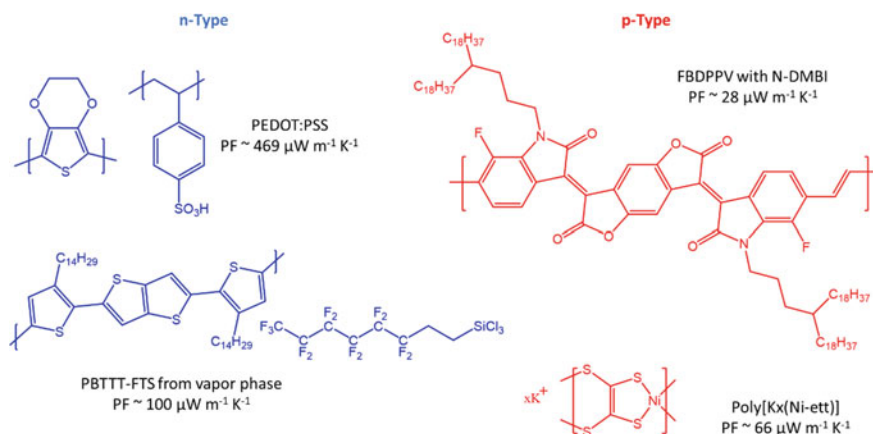


Fig. 17 Examples of n-type and p-type compounds and their power factors (PF)

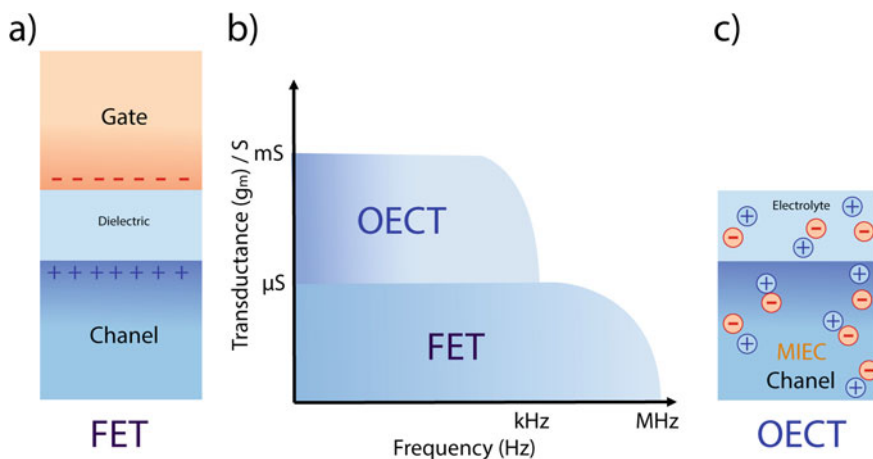


Fig. 18. **a** A typical field effect transistor (FET), **b** a comparison of the transductance and frequencies of OECT and FET, and **c** organic electrochemical transistor (OECT).

Although conducting polymers exhibit high electronic conductivity and low thermal conductivity, factors that lead to a promising figure of merit, a relatively low Seebeck coefficient is common for the neat material compared to inorganic compounds or faradaic systems.

Among the tremendous efforts to promote the thermoelectric properties of conducting polymers, the post-treatments, the addition of salts commented in Sect. 2.2 have significantly enhanced the electrical conductivity and in some cases, despite not being totally clear, the Seebeck coefficient [55, 61, 62]. The morphological rearrangement mechanisms do not necessarily influence the Seebeck coefficient. Those works which have used additives to successfully increase the Seebeck coefficient explain this effect by a favourable ion-exchange reaction such that: $M^+X^- + \text{PEDOT:PSS} \rightarrow M^-\text{PSS}^+ + \text{PEDOT}^+X^-$, driving to more diffuse compounds [61, 101], though it remains uncertain which features of the cation and anion in additives regulate this property. As previously mentioned, an ionic Seebeck effect has also been reported by the study of its dependence with relative humidity, showing a hump from $9.56 \mu\text{V K}^{-1}$ at 20% RH to $161 \mu\text{V K}^{-1}$ at 80% RH [64].

Owing to the characteristic low Seebeck coefficient of organic systems, different hybrids with nanostructured inorganic components have been designed, exhibiting outstanding performances compared to the traditional inorganic counterparts [77]. As previously commented (Sect. 2.2.2), morphologies of the incorporated additives of PEDOT:PSS vary from nanoparticles to nanosheets, forming advanced interfaces with looking for introducing percolation effects [102], band alignments [103] or energy filtering effects [104] that boost the Seebeck coefficient. With these hybrid compounds, Seebeck coefficients up to $160 \mu\text{V K}^{-1}$ (10 times higher than neat PEDOT:PSS), still with a high electronic conductivity have been reached in a PEDOT:PSS – Tellurium nanowire system [105]. Readers who are interested in the current state of the art of polymers and their composites for thermoelectric devices can gain further insight in the following reviews, where a discussion of the development of n-type polymers, essential to match with p-type compounds, is included [99, 106]. There have also been efforts to combine the good features of conducting polymers with redox active electrolytes to fabricate thermocells with a higher Seebeck coefficient, thanks to their faradaic processes. For instance, a PEDOT:PSS combined with CNTs and an aqueous potassium ferri/ferrocyanide electrolyte system has reached a Seebeck coefficient value of 1.5 mV/K , hundred times higher than neat PEDOT:PSS [107].

4.2 Batteries

The use of conductive polymers in batteries dates back to the 1980s when Yoshino et al. assembled a LiCoO_2 cathode with a polyacetylene (PA) anode to form LiCoO_2/PA full cell Li-ion batteries [108]. However, it had some deficiencies such as chemical instability and low density. In an attempt to overcome these performance issues, the same author replaced PA with carbonaceous materials, producing a new

family of batteries with a huge impact, due to their high-power density, low weight and versatile design. Even though conducting polymers show capacitive activity, the capacitance results are low compared to faradaic systems.

Immense efforts have been dedicated to devise more efficient active materials. At the anode, graphite competitors have grown, with materials such as silicon, tin and titanium-based nanostructures that possess higher theoretical capacity [109–112]. Nonetheless, the enhanced capacity means more lithium can be stored, which comes accompanied by larger volume changes during cycling that induce cracking of the anode. This phenomenon results in side reactions, contact loss and finally capacity fading [109, 113]. On the other hand, others cathode active materials have been developed such as LiFePO_4 (LFP) [114], $\text{Li}[\text{Ni},\text{Co},\text{Mn}]\text{O}_2$ (NMC) [115] and $\text{Li}[\text{Ni},\text{Co},\text{Al}]\text{O}_2$ (NCA) [116], satisfying the demands of cost and capacity.

To sustain those active materials, binders are required; polyvinylidene fluoride (PVDF) is the typically used binder material in conventional batteries. However, PVDF is isolating and presents drawbacks including the requirement of carbon additives to electronically connect all the active material, while the use of N-Methyl-2-pyrrolidone (NMP) solvent in the electrode fabrication is toxic. [117]. An ideal binder should create strong interactions with the active material but also stick to the current collector to prevent electrode delamination. Additionally, the binder should form a continuous electronically connected electrode, accommodate volume changes during cycling, and remain chemically and electrochemically stable, or show reversible processes in the application's conditions. Finally the binder material should be easily processed both in its synthesis and in the electrode fabrication. A number of studies have suggested that the cyclability problems of some of the most promising active materials could be overcome by selecting a more adequate binder [118–120].

Many materials have been investigated for their binder potential, such as sodium carboxymethyl cellulose (CMC) [119], sodium alginate (SA) [121], carboxymethyl chitosan (CCTS) [122] and nanofibrillated cellulose (NFC) [123]. Generally, these showed strong polar interactions and polar-solvent dispersability, making them processable from an aqueous system, but all of them still remain electronically isolating. The conventional quantities of each material in an electrode are at least 10 wt.% of carbon, 5–10 wt.% of binder and the rest is active material. Conducting polymers can play a dual role as both the binder and conductive additive, opening the possibility of using carbon free electrodes and hence, increasing the amount of active material used. In this regard, PEDOT:PSS has been successfully applied as the binder in carbon-free systems, including Li-ion [124] and Li-S [125], and it has also shown good electrochemical stability and performance as an additive in high voltage systems, including Lithium-ion batteries with NMC-111 [126].

Recent works have reported a new class of binders that combines conducting polymers such as PANI (polyaniline), Ppy (polypyrrole) or Pth (polythiophene) with the previously listed carboxylate-containing polymers (CMC, SA, CCTS, NFC), which form different morphologies including nanospheres [127, 128] and nanofibers [129]. This strategy offers continuous ionic and electronic transport doped by the carboxylate polymers with stronger binder properties. For instance, the interactions between

Si and CMC carboxyl-silanol; covalent and hydrogen bonding might mitigate the volume changes of Si-based advanced anodes [130].

Each kind of battery has intrinsic drawbacks that need to be solved. Although lithium-sulfur batteries offer superior energy storage capacity thanks to the high theoretical specific capacity of the sulfur cathode, they are still at a low technology readiness level. The growth of polysulfides and consequent cathode deformation makes it impossibly difficult to reach a reasonable life-span. Several studies point out the use of alternative binders like CP, whose interactions with sulfur and polysulfide species (Li_2S and Li_2S_2) can suppress shuttle effects, maintaining the electronic pathways at the same time [125, 131, 132].

Modified multifunctional conductive binders have also been synthesized and successfully applied in carbon-free electrodes, where processability and enhanced binding affinity are required. For instance, sodium alginate poly(3,4-propylenedioxythiophene) (SA-PProDOT), exhibited stronger adhesion versus CMC, SA or PVDF binders even though the mechanism for the improved mechanical properties is not yet elucidated [133]. It is also worth mentioning that redox activity has also been incorporated into conducting polymers either using redox polymers (PEDOT-TEMPO) [28] or biopolymers (PEDOT-lignin) [40], which can be used as direct electrodes or adding an extra capacity.

The porosity of electrodes is also known to impact performance. However, the recent progress on the synthesis of CPs, as mentioned above, enables a powerful control over microstructure, providing three-dimensional frameworks that may result in ideal electrodes for intercalation materials [117]. CPs have been in situ polymerized in the presence of active materials [134], and formed hydrogels with active materials by the use of crosslinkers and dopants [135, 136].

All the previously listed batteries are in liquid state, where the ionic conductivity is given by the liquid electrolyte and it is not intrinsically necessary in the electrode as it is going to be wet. In all-solid-state batteries the mechanism is totally different. Solid-state batteries were designed to be safer devices than liquid state batteries, which traditionally use volatile, flammable and leakable electrolytes. Solid electrolytes prevent the growth of metal dendrites that can result in fires and explosions. Good cycling performance has only been presented in thin film all-solid state cells where the active material is available on the surface but not in the electrode [117]. The development of thick and scalable devices passes directly through the development of mixed conductors, which are considered to play a key role by enabling ion transfer to occur throughout the entire electrode. For instance, PEDOT:PSS has been combined with the polymer electrolyte PEO and polyethylenimine (PEI), showing increased electronic and ionic conductivities and better mechanical strength than their neat forms, but these have not been tested in a full-cell solid Li-ion battery [137, 138].

The energy stored in MIEC-based batteries is dependant on the ionic-electronic coupling, but the adequate charging rates and the available power are limited by the ionic conductivity [42] being much more important in all-solid-state batteries where there is no liquid wetting the system, providing an all over ionic connection. The progress in all-solid-state batteries passes directly through that of MIECs.

4.3 Transistors, Sensors and Other Devices

The invention of the transistor in 1947 established the birth of microelectronics era, replacing the vacuum tubes. Nowadays, all the integrated circuits of each electronic device contain hundreds of those, which are based on field-effect doping (field effect transistors, FET). These FETs consist of a metal electrode (gate) separated from either an n-type or a p-type semiconductor by an insulating dielectric layer. The application of a potential between the semiconductor and the gate (V_G) generates an interfacial charge at the semiconductor surface, compensated by a counter charge at the electrode gate, like the capacitor mechanism in an electrical double layer. This changes the doping state of the semiconductor, creating a certain amount of charge stored in this way. Organic based (OFETs) transistors are highlighted by their facile manufacturing on different substrates and tuneable properties, making it possible to design for a wide range of applications [139].

In the 1980s, Wrighton et al. [140] developed the concept of organic electrochemical transistors (OECTs). The scheme of a typical OECT is depicted in Fig. 18 in comparison with FET and their different range of values of transductance and frequency. The gate is soaked in an electrolyte, which is in contact with the organic semiconductor, also called the channel, and finally two metal electrodes, namely the source (S) and drain (D), which are attached to the channel. The operating mechanism relies on the injection of ions from the electrolyte into the film, modulating the degree of doping of the whole film, resulting in a volumetric capacitance. The application of an input voltage between the gate and source (V_G) rules the entrance of ions into the semiconductor, thereby the redox state of the semiconductor and hence, the electronic conductivity. This change of conductivity has a response read into the current output (I_D) from the gate-drain circuit, proportional to the quantity of mobile holes or electrons in the channel. OECTs transduce a small input voltage applied into huge changes in the output current, described by a typical transfer curve (Fig. 19). The sharper the change, the better the efficiency of transduction, usually calculated by the first derivative of the transfer curve ($g_m = \partial I_D / \partial V_G$), which is the figure of merit next to the response time. OECTs achieve much higher transductance values than FET, attributed to the volumetric capacitance, but at the same time it limits their response time as depicted in Fig. 19b. These features result in OECTs to be powerful amplifiers and efficient switches [141].

In the simplest device, it works like a switch, where there can be two possible modes depending on the kind of semiconductor: depletion or accumulation. PEDOT:PSS has been by far the most studied organic semiconductor in these type of applications over two last decades. They show a depletion-mode [142] which consist on being switched ON at $V_G = 0$ and switched OFF when $V_G > 0$. The reason is because the entrance of cations to the channel, that react with the dopants of PEDOT, lead to a dedoping of the conducting chain and hence a drop in the output current. However, it has been recently employed as accumulation mode OECT as well by an over-oxidation process [36]. The accumulation-mode based systems are normally switched OFF in the absence of V_G . After applying a negative gate voltage, an

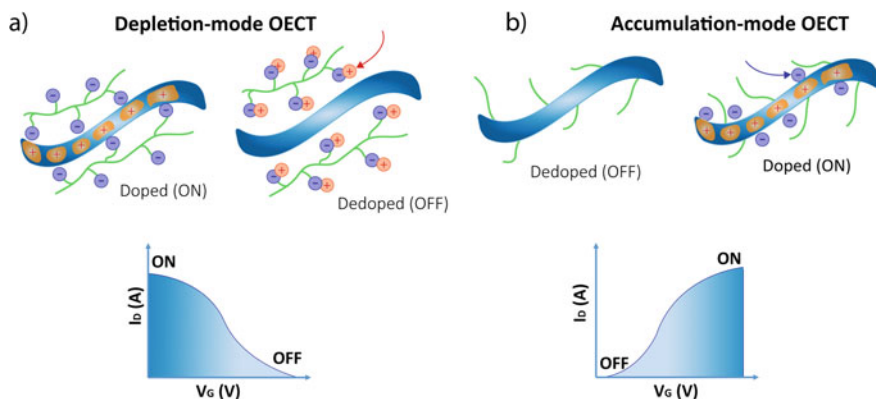


Fig. 19 Different mechanisms of working of OECTs. **a** Depletion-mode and **b** accumulation mode with their typical transfer curve and states of the conducting polymer in ON and OFF states

entrance of anions into the channel occurs, leading to an accumulation of holes and the ON state (e.g. poly(6-(thiophene-3-yl)hexane-1-sulfonate) (PTHS) [49], Fig. 2c).

Once again, the improvement of this kind of device is intimately related to the optimization of organic mixed conductors, which controls the response time, which is usually limited by the ionic conductivity. The design, synthesis, functionalization and optimization motivates researchers to continue the development of more sophisticated gadgets.

Nonetheless, the features of organic semiconductors make it technically quite simple to fabricate OECTs of high quality. The flexibility that these materials offer enables the design of devices on rigid substrates, flexible and stretchable gadgets, microfluidic systems [143], structured in fibres [144] or scaffolds [145] for a large range of applications (see Fig. 20a–c). Besides, many modifications can be done to tune the device for very specific applications as the group of Professor Malliaras at the University of Cambridge has shown over the past two decades. For instance, although the mechanical properties of PEDOT:PSS are good, it can be modulated by the addition of 3-glycidoxypropyltrimethoxysilane (GOPS) to reach a Young's modulus similar to that of biological tissue, for *in vivo* applications [146]. In fact, many applications have been designed and applied in the field of bioelectronics with electrically active tissues and organs, due to the local amplification of OECT. For example, *in vivo* measurements or stimulation of cell activity from the local signal amplification [147, 148], biosensors of analyte levels such as ions [38, 149] (see Fig. 20e) or even more complex molecules such as dopamine in the presence of interfering compounds [38], and ion pumps for *in vivo* drug delivery [37].

The relatively low switching speed versus FETs limits OECT application in computation [139] but there have been reports that focused in their implementation as pixel drivers in active matrix displays of PEDOT:PSS printed on paper [150], woven circuits [144], light-emitting electrochemical cells [45], pressure sensors [151] (see Fig. 20d), solar cells [152] and different techniques for easier manufacturing (printing

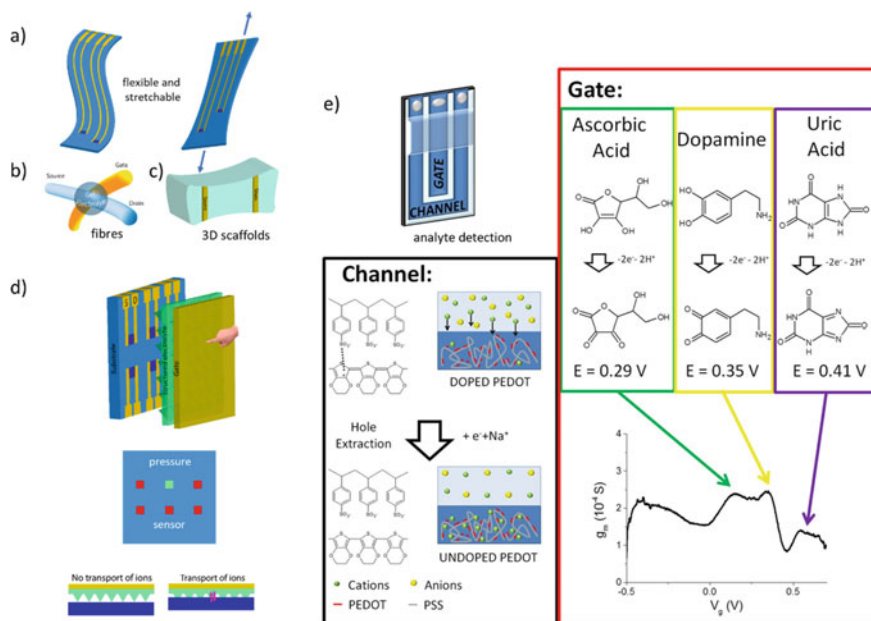


Fig. 20 Different OECT forms and designs to satisfy specific requirements or objectives. **a** Flexible and stretchable devices, **b** made of fibres, **c** 3D scaffolds for channels, **d** pressure sensors and **e** analyte detection. Reprinted with permission from [38]. Copyright 2016, Springer Nature

[96], screen printing [97] or even using a standard label printing press [98]). There are updated reviews available for those who are interested in specific applications and the current state of fabrication methods [139, 153].

The neuromorphic field mimics the nervous system by displaying either temporal or permanent alterations in electrical properties. For instance, Professor Malliaras research group has developed neuromorphic functions such as short-term depression, adaptation and dynamic filtering with PEDOT:PSS [154], which was improved by increasing the retention time from a few seconds to several hours with a modified polymer (poly(tetrahydrofuran) based PEDOT) that undergoes conformational changes when a high reduction voltage is applied [155]. Therefore, the drain current can be programmed to multiple discrete memory states with a device that can operate in short- (STM) and long-term memory (LTM).

5 Conclusions and Perspectives

Materials that efficiently transport and couple ionic and electronic charge are key to achieve a host of technological developments for next-generation energy storage and health technologies. In the last decades, organic materials that enable ionic

and electronic conduction have emerged as ideal candidates for several applications including thermoelectrics, batteries, sensors and organic electrochemical transistors due to their processability, enhanced charge storage and coupled transport properties. In this chapter, the state of art of mixed ionic and electronic conducting materials has been introduced, as well as the fundamentals of the field, such as the nature of materials, kinds of dopants and the transport mechanisms.

From a materials perspective, the area of organic mixed ionic-electronic conductors is mainly dominated by π -conjugated polymers, where the π -conjugated polymer backbone enables the electronic transport, while their ionic conductivity has been unnoticed for many years. However, due to the significant ionic-electronic coupling, ionic and electronic conductivities in OMIECs are not independent and should be studied together. The most employed characterization techniques for analysing the electronic and ionic conductivities have been described in this chapter. Among them, Electrochemical Impedance Spectroscopy is one of the most powerful techniques as both the ionic and electronic transports can be examined at the same time. This implies generally complex impedance spectra that has to be analysed with correct equivalent circuit models. Moreover, the conditions of the experiments are not established in the field, and thus, depending on the application, for example the ionic conductivity can be measured in dried or wet samples. This makes difficult to compare the properties of different MIEC materials of various applications. Thus, it is important to study the structure–property relationships of MIECs in order to understand the relations between ionic and electronic conductivities, and the influence of microstructure, morphology and processing on them.

MIECs have gained a great interest for a wide range of applications, starting from energy storage to healthcare technologies. In this chapter, we have outlined the most important applications of MIECs in the fields of thermoelectrics, batteries and transistors, as these have been the fields where they have been used the most. Nevertheless, MIECs are expected to find out many opportunities in other areas like sensors, actuators or artificial muscles.

References

1. Reuterand, B., Hardel, K., Bunsenges, B.: Silver sulfide bromide Ag_3SBr and silver sulfide iodide Ag_3SI III: semiconductor properties of Ag_3SBr and α - and β - Ag_3SI . *J. Phys. Chem.* **70**, 82 (1966)
2. Macpherson, A.S., Siudak, R., Weiss, D.E., Willis, D.: Electronic conduction in polymers. *Aust. J. Chem.* **18**, 493–505 (1965)
3. Shirakawa, H., Louis, E.J., MacDiarmid, A.G., et al.: Synthesis of electrically conducting organic polymers: halogen derivatives of polyacetylene, $(\text{CH})_x$. *JCS Chem. Commun.* **16**, 578–580 (1977)
4. Chena, C.S., Kruidhof, H., Verweij, H., Burggraaf, A.J.: Oxygen permeation through oxygen ion oxide-noble metal dual phase composites. *Solid State Electron.* **88**, 569–572 (1996)
5. Mazanec, T.J., Cable, T.L., Frye, J.G.: Electrocatalytic cells for chemical reaction. *Solid State Ionics* **56**, 111–118 (1992)

6. Sunarso, J., Baumann, S., Serra, J.M., et al.: Mixed ionic-electronic conducting (MIEC) ceramic-based membranes for oxygen separation. *J. Memb. Sci.* **320**, 13–41 (2008)
7. Zhang, C., Sunarso, J., Liu, S.: Designing CO₂-resistant oxygen-selective mixed ionic-electronic conducting membranes: guidelines, recent advances, and forward directions. *Chem. Soc. Rev.* **46**, 2941–3005 (2017)
8. Kingery, W.D., Pappis, J., Doty, M.E., Hill, D.C.: Oxygen ion mobility in cubic Zr_{0.85}Ca_{0.15}O_{1.85}. *J. Am. Chem. Soc.* **42**(8), 393–398 (1959)
9. Bhalla, A.S., Guo, R., Roy, R.: The perovskite structure – a review of its role in ceramic science and technology. *Matter. Res. Innov.* **4**, 3–26 (2000)
10. Kim, D.: Lattice parameters, ionic conductivities and solubility limits in fluorite-structure MO₂ Oxide (M = Hf⁴⁺, Zr⁴⁺, Ce⁴⁺, Th⁴⁺, U⁴⁺) solid solutions. *J. Am. Ceram Soc.* **72**(8), 1415–1421 (1989)
11. Garcia-fayos, J., Balaguer, M., Baumann, S., Serra, J.M.: Dual-phase membrane based on LaCo_{0.2}Ni_{0.4}Fe_{0.4}O_{3-X}-Ce_{0.8}Gd_{0.2}O_{2-X} composition for oxygen permeation under CO₂/SO₂-rich gas environments. *J. Memb. Sci.* **548**, 117–124 (2017)
12. Liu, Y., Tan, X., Li, K., et al.: Membrane processing mixed conducting ceramics for catalytic membrane processing. *Catal. Rev.* **48**, 145–198 (2006)
13. Yang, W., Wang, H., Zhu, X., Lin, L.: Development and application of oxygen permeable membrane in selective oxidation of light alkanes. *Top Catal.* **35**, 155–167 (2005)
14. Burnwal, S.K.: Review on MIEC cathode materials for solid oxide fuel cells. *J. Mol. Eng. Mater.* **4**(2), 1630001 (2016)
15. Kharton, V.V., Marques, F.M.B.: Mixed ionic – electronic conductors: effects of ceramic microstructure on transport properties. *Curr. Opin. Solid State Mater. Sci.* **6**, 261–269 (2002)
16. Maguire, E., Gharbage, B., Marques, F.M.B., Labrincha, J.A.: Cathode materials for intermediate temperature SOFCs. *Solid State Ionics* **127**, 329–335 (2000)
17. Yu, I., Jeon, D., Boudouris, B., Joo, Y.: Mixed Ionic and electronic conduction in radical polymers. *Macromolecules* **53**(11), 4435–4441 (2020)
18. Suga, T., Pu, Y.J., Kasatori, S., Nishide, H.: Cathode- and anode-active poly(nitroxylstyrene)s for rechargeable batteries: p- and n-type redox switching via substituent effects. *Macromolecules* **40**, 3167 (2007)
19. Nishide, H., Suga, T.: Organic radical battery. *Electrochem. Soc. Interface* **14**, 32–38 (2005)
20. Tomlinson, E.P., Hay, M.E., Boudouris, B.W.: Radical polymers and their application to organic electronic devices. *Macromolecules* **47**(2), 6145–6158 (2014)
21. Suga, T., Sugita, S., Ohshiro, H., et al.: p- and n-type bipolar redox-active radical polymer: toward totally organic polymer-based rechargeable devices with variable configuration. *Adv Mater* **23**, 751–754 (2011)
22. Rostro, L., Wong, S.H., Boudouris, B.W.: Solid state electrical conductivity of radical polymers as a function of pendant group oxidation state. *Macromolecules* **47**, 3713 (2014)
23. Joo, Y., Agarkar, V., Sung, S.H.: A nonconjugated radical polymer glass with high electrical conductivity. *Science* (80-) **359**, 1391–1395 (2018)
24. Nakahara, K., Iwasa, S., Satoh, M., et al.: Rechargeable batteries with organic radical cathodes. *Chem. Phys. Lett.* **359**, 351 (2002)
25. Song, Z., Zhou, H.: Towards sustainable and versatile energy storage devices: an overview of organic electrode materials. *Energy Environ. Sci.* **6**, 2280 (2013)
26. Wang, S., Li, F., Easley, A.D., Lutkenhaus, J.L.: Real-time insight into the doping mechanism of redox-active organic radical polymers. *Nat. Mater.* **18**, 69–76 (2019)
27. Tokue, H., Murata, T., Agatsuma, H., et al.: Charge – discharge with rocking-chair-type Li⁺ migration characteristics in a zwitterionic radical copolymer composed of TEMPO and tri fl uoromethanesulfonylimide with carbonate electrolytes for a high-rate Li-ion battery. *Macromolecules* **50**, 1950–1958 (2017)
28. Casado, N., Hernandez, G., Veloso, A., et al.: PEDOT radical polymer with synergetic redox and electrical properties. *ACS Macro Lett.* **5**, 59–64 (2016)
29. Suwa, K., Oyaizu, K., Segawa, H., Nishide, H.: Anti-oxidizing radical polymer-incorporated perovskite layers and their photovoltaic characteristics in solar cells. *Chemsuschem* **12**, 5207–5212 (2019)

30. Zheng, L., Mukherjee, S., Wang, K., et al.: Radical polymers as interfacial layers in inverted hybrid perovskite solar cells †. *J. Mater. Chem. Mater. Energy Sustain.* **5**, 23831–23839 (2017)
31. Dey, A., Singh, A., Das, D., Iyer, P.K.: Organic semiconductors: a new future of nanodevices and applications. In: Film, T. (ed.) *Babu Krishna Moorthy S*, pp. 97–128. *Structures in Energy Applications*. Springer International Publishing, Cham (2015)
32. Moon, J., Thapliyal, N., Khadim, K., Goyal, R.N.: Conducting polymer-based electrochemical biosensors for neurotransmitters: a review. *Biosens. Bioelectron.* **102**, 540–552 (2018)
33. Zozoulenko, I., Singh, A., Singh, S.K., et al.: Polarons, bipolarons, and absorption spectroscopy of PEDOT. *ACS Appl. Polym. Mater.* **1**, 83–94 (2018)
34. Tsuchida, E., Shih, C., Shinohara, I.: Synthesis of a polymer chain having conjugated unsaturated bonds by dehydrohalogenation of polyhalogen-containing polymers. *J. Polym. Sci.* **2**, 3347–3354 (1964)
35. Berets, D.J., Smith, D.S.: Electrical properties of linear polyacetylene. *Trans. Faraday Soc.* **64**, 823–828 (1967)
36. Valadi, K., Gharibi, S., Taheri-Ledari, R., et al.: Metal oxide electron transport materials for perovskite solar cells: a review. *Environ. Chem. Lett.* **19**, 2185–2207 (2021)
37. Taheri-Ledari, R., Rahimi, J., Maleki, A., Shalan, A.E.: Ultrasound-assisted diversion of nitrobenzene derivatives to their aniline equivalents through a heterogeneous magnetic Ag/Fe₃O₄-IT nanocomposite catalyst. *New J. Chem.* **44**, 19827–19835 (2020)
38. Taheri-Ledari, R., Esmaeili, M.S., Varzi, Z., et al.: Facile route to synthesize Fe₃O₄@acacia-SO₃H nanocomposite as a heterogeneous magnetic system for catalytic applications. *RSC Adv* **10**, 40055–40067 (2020)
39. Shalan, A.E., Sharmoukh, W., Elshazly, A.N., et al.: Dopant-free hole-transporting polymers for efficient, stable, and hysteresis-less perovskite solar cells. *Sustain. Mater. Technol.* **26**, e00226 (2020)
40. Shalan, A.E., Mohammed, M.K.A., Govindan, N.: Graphene assisted crystallization and charge extraction for efficient and stable perovskite solar cells free of a hole-transport layer. *RSC Adv.* **11**, 4417–4424 (2021)
41. Shalan, A.E., El-Shazly, A.N., Rashad, M.M., Allam, N.K.: Tin–zinc-oxide nanocomposites (SZO) as promising electron transport layers for efficient and stable perovskite solar cells. *Nanoscale Adv.* **1**, 2654–2662 (2019)
42. Shalan, A.E., Akman, E., Sadegh, F., Akin, S.: Efficient and stable perovskite solar cells enabled by dicarboxylic acid-supported perovskite crystallization. *J. Phys. Chem. Lett.* **12**, 997–1004 (2021)
43. Sanad, M.M.S., Shalan, A.E., Rashad, M.M., Mahmoud, M.H.H.: Plasmonic enhancement of low cost mesoporous Fe₂O₃-TiO₂ loaded with palladium, platinum or silver for dye sensitized solar cells (DSSCs). *Appl. Surf. Sci.* **359**, 315–322 (2015)
44. Sanad, M.F., Shalan, A.E., Abdellatif, S.O., et al.: Thermoelectric energy harvesters: a review of recent developments in materials and devices for different potential applications. *Top. Curr. Chem. J.* **378**, 48 (2020)
45. Van, R.S., Akatsuka, T., Tordera, D., et al.: Universal transients in polymer and ionic transition metal complex light-emitting electrochemical cells. *J. Am. Chem. Soc.* **135**, 886–891 (2013)
46. Erothu, H., Kolomanska, J., Johnston, P., et al.: Synthesis, thermal processing, and thin film morphology of poly(3-hexylthiophene) – poly(styrenesulfonate) block copolymers. *Macromolecules* **48**, 2107–2117 (2015)
47. Reddy, B., Dadigala, R., Bandi, R., et al.: Microwave-assisted preparation of a silver nanoparticles/N-doped carbon dots nanocomposite and its application for catalytic reduction of rhodamine B, methyl red and 4-nitrophenol dyes. *RSC Adv.* **11**, 5139–5148 (2021)
48. Patel, S.N., Javier, A.E., Beers, K.M., et al.: Morphology and thermodynamic properties of a copolymer with an electronically conducting block: poly(3-ethylhexylthiophene)-block-poly(ethylene oxide). *Nano Lett.* **12**, 4901–4906 (2012)
49. Inal, S., Rivnay, J., Leleux, P., et al.: A high transconductance accumulation mode electrochemical transistor. *Adv. Mater.* **26**, 7450–7455 (2014)

50. Giovannitti, A., Sbircea, D., Inal, S., et al.: Controlling the mode of operation of organic transistors through side-chain engineering. *Proc. Natl. Acad. Sci. USA* **113**(43), 12017–12022 (2016)
51. Jang, K.S., Lee, H., Moon, B.: Synthesis and characterization of water soluble polypyrrole doped with functional dopants. *Synth. Met.* **143**, 289–294 (2004)
52. Sinha, S., Bhadra, S., Khastgir, D.: Effect of dopant type on the properties of polyaniline. *J. Appl. Polym. Sci.* **112**(5), 3135–3140 (2009)
53. Polk, B.J., Potje-kamloth, K., Josowicz, M.: Role of protonic and charge transfer doping in solid-state polyaniline. *J. Phys. Chem. B* **106**, 11457–11462 (2002)
54. Yano, H., Kudo, K., Marumo, K., Okuzaki, H.: Fully soluble self-doped an electrical conductivity greater than 1000 S cm⁻¹. *Sci. Adv.* **5**, 1–10 (2019)
55. Wang, X., Ko, K., Yin, C., et al.: Enhancement of thermoelectric performance of PEDOT:PSS films by post-treatment with a superacid. *RSC Adv.* **8**, 18334–18340 (2018)
56. Shuzhong, H., Masakazu, M., Kazuhiro, K., et al.: Reversible protonic doping in poly(3,4-Ethylenedioxythiophene). *Polymers (Basel)* **10**, 1065 (2018)
57. Neusser, D., Malacrida, C., Kern, M., et al.: High conductivities of disordered p3ht films by an electrochemical doping strategy. *Chem. Mater.* **32**, 6003–6013 (2020)
58. Ikei, M.J., Amaya, T.Y., Ramoto, S.U., Atsumoto, K.M.: Conductivity enhancement of PEDOT/PSS films by solvent vapor treatment. *Int. J. Soc. Mater. Eng. Resour.* **20**(2), 158–162 (2014)
59. Pringle, J.M., Howlett, P.C., Macfarlane, D.R., Forsyth, M.: Organic ionic plastic crystals: recent advances. *J. Mater. Chem.* **20**, 2056–2062 (2010)
60. Basile, A., Hilder, M., Makhlooghiyazad, F., et al.: Ionic liquids and organic ionic plastic crystals: advanced electrolytes for safer high performance sodium energy storage technologies. *Adv. Energy Mater.* **8**, 1703491 (2018)
61. Mazaheripour, A., Majumdar, S., Hanemann-rawlings, D., et al.: Tailoring the seebeck coefficient of PEDOT: PSS by controlling ion stoichiometry in ionic liquid additives. *Chem. Mater.* **30**, 4816–4822 (2018)
62. Kee, S., Kim, H., Harish, S., et al.: Highly stretchable and air-stable PEDOT:PSS/Ionic liquid composites for efficient organic thermoelectrics. *Chem. Mater.* **31**, 3519–3526 (2019)
63. De, I.A., Park, S., Lee, J., et al.: Ionic liquid designed for PEDOT:PSS conductivity enhancement. *J. Am. Chem. Soc.* **140**, 5375–5384 (2018)
64. Wang, H., Ail, U., Gabrielsson, R., et al.: Ionic seebeck effect in conducting polymers. *Adv. Energy Mater.* **5**, 1500044 (2015)
65. Xiong, J., Liu, C., Xu, J.: Highly electrical and thermoelectric properties of a PEDOT:PSS thin-film via direct dilution – filtration †. *RSC Adv.* **5**, 60708–60712 (2015)
66. Li, Q., Deng, M., Zhang, S., et al.: Synergistic enhancement of thermoelectric and modulated PEDOT flexible films †. *J. Mater. Chem. C* **7**, 4374 (2019)
67. Kee, S., Kim, N., Kim, B.S., et al.: Controlling molecular ordering in aqueous conducting polymers using ionic liquids. *Adv. Mater.* **28**, 8625–8631 (2016)
68. Del Olmo, R., Casado, N., Olmedo-Martinez, J.L., et al.: Mixed ionic-electronic conductors based on PEDOT : PolyDADMA and organic ionic plastic crystals. *Polymers (Basel)* **12**, 1981 (2020)
69. Nti, F., Porcarelli, L., Greene, G.W., et al.: The influence of interfacial interactions on the conductivity and phase behaviour of organic ionic plastic crystal/polymer nanoparticle composite electrolytes. *J. Mater. Chem. A* **8**, 5350–5362 (2020)
70. Wang, X., Zhu, H., Greene, G.W., et al.: Organic ionic plastic crystal-based composite electrolyte with surface enhanced ion transport and its use in all- solid-state lithium batteries. *Adv. Mater. Technol.* **2**, 1700046 (2017)
71. Malti, A., Edberg, J., Granberg, H., et al.: An organic mixed ion – electron conductor for power electronics. *Adv. Sci.* **3**, 1500305 (2016)
72. Belaine, D., Andreasen, J.W., Palisaitis, J., et al.: Controlling the organization of PEDOT:PSS on cellulose structures. *ACS Appl. Polym. Mater.* **1**, 2342–2351 (2019)

73. Wang, Y., Zhu, C., Pfattner, R., et al.: A highly stretchable, transparent and conductive polymer. *Sci. Adv.* **3**, e1602076 (2017)
74. Chen, L., Liu, W., Su, X., et al.: Chemical synthesis and enhanced electrical properties of bulk poly (3,4- ethylenedioxythiophene)/reduced graphene oxide nanocomposites. *Synth. Met.* **229**(March), 65–71 (2017)
75. Zhang, K., Zhang, Y., Wang, S.: Enhancing thermoelectric properties of organic composites through hierarchical nanostructures. *Sci. Rep.* **3**, 3448 (2013)
76. Olmedo-Martinez, J.L., Meabe, L., Basterretxea, A., et al.: Effect of chemical structure and salt concentration on the crystallization and ionic conductivity of aliphatic polyethers. *Polymers (Basel)* **11**, 452 (2019)
77. Zheng, Y., Zeng, H., Zhu, Q., Xu, J.: Recent advances in conducting poly (3,4-ethylenedioxythiophene): polystyrene sulfonate hybrids for thermoelectric applications. *J. Mater. Chem. C* **6**, 8858–8873 (2018)
78. Ock, G., Wook, J., Kim, J., et al.: Enhanced thermoelectric properties of germanium powder/poly(3,4-ethylenedioxythiophene):poly(4-styrenesulfonate) composites. *Thin Solid Films* **566**, 14–18 (2014)
79. Franco-Gonzalez, J.F., Zozoulenko, I.V.: Molecular dynamics study of morphology of doped PEDOT: from solution to dry phase. *J. Phys. Chem. B* **121**, 4299–4307 (2017)
80. Tessler, N., Preezant, Y., Rappaport, N., Roichman, Y.: Charge transport in disordered organic materials and its relevance to thin-film devices: a tutorial review. *Adv. Mater.* **21**, 2741–2761 (2009)
81. Cho, B., Park, K.S., Baek, J., et al.: Single-crystal Poly(3,4-ethylenedioxythiophene) nanowires with ultrahigh conductivity. *Nano Lett.* **14**, 3321–3327 (2014)
82. Kim, J.Y., Jung, J.H., Lee, D.E., Joo, J.: Enhancement of electrical conductivity of poly(3,4-ethylenedioxythiophene)/poly(4-styrenesulfonate) by a change of solvents. *Synth. Met.* **126**, 311–316 (2002)
83. Kaisera, A.B., Subramaniam, C.K.: Electronic transport properties of conducting polymers and polymer blends *. *Synth. Met.* **69**, 197–200 (1995)
84. Yunis, R., Girard, G.M.A., Wang, X., et al.: The anion effect in ternary electrolyte systems using poly (diallyldimethylammonium) and phosphonium-based ionic liquid with high lithium salt concentration. *Solid State Ionics* **327**, 83–92 (2018)
85. Olmedo-Martinez, J.L., Porcarelli, L., Alegr, A., et al.: High Lithium Conductivity of Miscible Poly (ethylene oxide)/Methacrylic Sulfonamide Anionic Polyelectrolyte Polymer Blends. *Macromolecules* **53**, 4442–4453 (2020)
86. Armand, M.: Polymer solid electrolytes - an overview. *Solid State Ionics* **9**, 745–754 (1983)
87. Van, R.S., Kemerink, M.: Correcting for contact geometry in Seebeck coefficient. *Org. Electron.* **15**(10), 2250–2255 (2014)
88. Wiemhöfer, H.-D.: Coupling Between Electron and Ion Transport in Mixed Conductors. *Solid State Ionics* **41**, 530–534 (1990)
89. Barea, E.M., Palomares, E.: A review of recent results on electrochemical determination of the density of electronic states of nanostructured metal-oxide semiconductors and organic hole conductors. *Inorganica Chim. Acta* **361**, 684–698 (2008)
90. Savva, A., Wustoni, S., Inal, S.: Ionic-to-electronic coupling efficiency in PEDOT:PSS films operated in aqueous electrolytes. *J. Mater Chem. C* **6**, 12023–12030 (2018)
91. Garcia-Belmonte, G., Bisquet, J., Popkirov, G.S.: Determination of the electronic conductivity of polybithiophene films at different doping levels using in situ electrochemical impedance measurements. *Appl. Phys. Lett.* **83**(11), 2178–2180 (2003)
92. Pozyczka, K., Marzantowicz, M., Dygas, J.R., Krok, F.: IONIC CONDUCTIVITY AND LITHIUM TRANSFERENCE NUMBER OF POLY (ETHYLENE OXIDE): LiTFSI SYSTEM. *Electrochim. Acta* **227**, 127–135 (2017)
93. Waremra, R.S., Betaubun, P.: Analysis of electrical properties using the four point probe method. *E3S Web Conf.* **73**, 13019 (2018)
94. Catalano, S.B.: Correction factor curves for square-array and rectangular-array four-point probes near conducting or nonconducting boundaries *. *IEEE Trans. Electron. Devices* **10**(3), 185–188 (1963)

95. Wang, S., Yan, M., Li, Y., et al.: Separating electronic and ionic conductivity in mix-conducting layered lithium transition-metal oxides. *J. Power Sources* **393**(March), 75–82 (2018)
96. Brooke, R., Evans, D., Diemel, M., et al.: Inkjet printing and vapor phase polymerization: patterned conductive PEDOT for electronic applications †. *J. Mater. Chem. C* **1**, 3353–3358 (2013)
97. Hütter, P.C., Rothländer, T., Scheipl, G., Stadlober, B.: All screen-printed logic gates based on organic electrochemical transistors. *IEE Trans. Electron. Devices* **62**(12), 4231–4236 (2015)
98. Andersson, B.P., Forchheimer, R., Tehrani, P., Berggren, M.: Printable all-organic electrochromic active-matrix displays **. *Adv. Funct. Mater.* **17**, 3074–3082 (2007)
99. Bharti, M., Singh, A., Samanta, S., Aswal, D.K.: Progress in Materials Science Conductive polymers for thermoelectric power generation. *Prog. Mater. Sci.* **93**, 270–310 (2018)
100. Luo, X., Schroeder, B.C., Di, C., Mei, J.: Flexible and printed organic thermoelectrics: opportunities and challenges. *Mater Matters* **12**(3) (2017)
101. Fan, Z., Du, D., Yu, Z., et al.: Significant enhancement in the thermoelectric properties of PEDOT: PSS films through a treatment with organic solutions of inorganic salts. *ACS Appl. Mater. Interfaces* **8**, 23204–23211 (2016)
102. Hsu, J., Choi, W., Yang, G., Yu, C.: Origin of unusual thermoelectric transport behaviors in carbon nanotube filled polymer composites after solvent/acid treatments. *Org. Electron.* **45**, 182–189 (2017)
103. Zhang, T., Li, K., Li, C., et al.: Mechanically durable and flexible thermoelectric Films from PEDOT: PSS/PVA/Bi_{0.5}Sb_{1.5}Te₃ nanocomposites. *Adv. Electron. Mater.* **3**, 1600554 (2017)
104. Liang, Z., Boland, M.J., Butrouna, K., et al.: Increased power factors of organic-inorganic nanocomposite thermoelectric materials and the role of energy filtering. *J. Mater. Chem. A* **5**, 15891–15900 (2017)
105. See, K.C., Feser, J.P., Chen, C.E., et al.: Water-processable polymer-nanocrystal hybrids for thermoelectrics. *Nano Lett.* **10**, 4664–4667 (2010)
106. Yao, H., Fan, Z., Cheng, H., et al.: Recent development of thermoelectric polymers and composites. *Macromol. Rapid Commun.* **39**, 1700727 (2018)
107. Kazim, A.H., Cola, B.A., Soc, J.E., et al.: Electrochemical characterization of carbon nanotube and poly(3,4-ethylenedioxythiophene)—poly(styrenesulfonate) composite aqueous electrolyte for thermo-electrochemical cells. *J. Electrochem. Soc.* **163**(8), F867–F871 (2016)
108. Yoshino, A.: The birth of the lithium-ion battery. *Angew Chem. Int. Ed.* **51**, 5798 (2012)
109. Su, X., Wu, Q., Li, J., et al.: Silicon-based nanomaterials for lithium-ion batteries: a review. *Adv. Energy Mater.* **4**, 1300882 (2014)
110. Besenhard, E.O., Winter, M., Wachtler, M.: Tin and tin-based intermetallics as new anode materials for lithium-ion cells. *J. Power Sources* **94**, 189–193 (2001)
111. Zhao, Y., Yang, L., Liu, D., et al.: A conductive binder for high-performance sn electrodes in lithium-ion batteries. *ACS Appl. Mater Interfaces* **10**, 1672–1677 (2018)
112. Chen, Z., Belharouak, I., Sun, Y., Amine, K.: Titanium-based anode materials for safe lithium-ion batteries. *Adv. Funct. Mater.* **23**, 959–969 (2013)
113. Wu, M., Xiao, X., Vukmirovic, N., et al.: Toward an ideal polymer binder design for high-capacity battery anodes. *J. Am. Chem. Soc.* **135**, 12048–12056 (2013)
114. Liu, C., Neale, Z.G., Cao, G.: Understanding electrochemical potentials of cathode materials in rechargeable batteries. *Mater Today* **19**(2), 109–123 (2016)
115. Nayak, P.K., Grinblat, J., Levi, M., et al.: Multiphase LiNi_{0.33}Mn_{0.54}Co_{0.13}O₂ cathode material with high capacity retention for li-ion batteries. *Chem. Electron. Chem.* **2**(12), 1957–1965 (2015)
116. Purwanto, A., Yudha, C.S., Ubaidillah, U., et al.: NCA cathode material: Synthesis methods and performance enhancement efforts. *Mater. Res. Express* **5**, 122001 (2018)
117. Nguyen, V.A., Kuss, C.: Review — conducting polymer-based binders for lithium-ion batteries and beyond. *J. Electrochem. Soc.* **167**, 065501 (2020)
118. Bresser, D., Buchholz, D., Moretti, A., et al.: Alternative binders for sustainable electrochemical energy storage—the transition to aqueous electrode processing and bio-derived polymers. *Energy Environ. Sci.* **11**(11), 3096–3127 (2018)

119. Zhao, J., Yang, X., Yao, Y., et al.: Moving to aqueous binder: a valid approach to achieving high-rate capability and long-term durability for sodium-ion battery. *Adv. Sci.* **5**, 1700768 (2018)
120. Chen, H., Ling, M., Hencz, L., et al.: Exploring chemical, mechanical, and electrical functionalities of binders for advanced energy-storage devices. *Chem. Rev.* **118**(18), 8936–8982 (2018)
121. Ling, L., Bai, Y., Wang, Z., et al.: Remarkable effect of sodium alginate aqueous binder on anatase TiO₂ as high-performance anode in sodium ion batteries. *ACS Appl. Mater. Interfaces* **10**, 5560–5568 (2018)
122. Yue, L., Zhang, L., Zhong, H.: Carboxymethyl chitosan: a new water soluble binder for Si anode of Li-ion batteries. *J. Power Sources* **247**, 327–331 (2014)
123. Wang, A., Zhou, W., Huang, A., et al.: Modifying the Zn anode with carbon black coating and nanofibrillated cellulose binder: a strategy to realize dendrite-free Zn-MnO₂ batteries. *J. Colloid Interface Sci.* **577**, 256–264 (2020)
124. Das, P.R., Soc, J.E.: PEDOT:PSS as a functional binder for cathodes in lithium ion batteries. *J. Electrochem. Soc.* **162**(4), A674–A678 (2015)
125. Pan, J., Xu, G., Chang, Z., et al.: PAA/PEDOT:PSS as a multifunctional, water-soluble binder to improve the capacity and stability of lithium-sulfur batteries. *RSC Adv.* **6**, 40650–40655 (2016)
126. Kim, T., Ono, L.K., Qi, Y.: Elucidating the mechanism involved in the performance improvement of lithium-ion transition metal oxide battery by conducting polymer. *Adv. Mater. Interfaces* **6**, 1801785 (2019)
127. Sasso, C., Zeno, E., Petit-conil, M., et al.: Highly conducting polypyrrole/cellulose nanocomposite films with enhanced mechanical properties. *Macromol. J.* **295**, 934–941 (2010)
128. Xu, Y., Zhang, Y.: Synthesis of polypyrrole/sodium carboxymethyl cellulose nanospheres with enhanced supercapacitor performance. *Mater. Lett.* **139**, 145–148 (2015)
129. Su, N.: Improving electrical conductivity, thermal stability, and solubility of polyaniline-polypyrrole nanocomposite by doping with anionic spherical polyelectrolyte brushes. *Nanoscale Res. Lett.* **10**, 301 (2015)
130. Vogl, U.S., Das, P.K., Weber, A.Z., et al.: Mechanism of Interactions between CMC binder and si single crystal facets. *Langmuir* **30**, 10299–10307 (2014)
131. Luo, Y., Guo, R., Li, T., et al.: Application of polyaniline for li-ion batteries, lithium-sulfur batteries, and supercapacitors. *Chemsuschem* **12**, 1591–1611 (2019)
132. Kang, W., Deng, N., Ju, J., et al.: A review of recent developments in rechargeable lithium-sulfur batteries. *Nanoscale* **8**, 16541–16588 (2016)
133. Ling, M., Qiu, J., Li, S., et al.: Multifunctional SA-PProDOT binder for lithium ion batteries. *Nano Lett.* **15**, 4440–4447 (2015)
134. Shi, Y., Zhou, X., Zhang, J., et al.: Nanostructured conductive polymer gels as a general framework material to improve electrochemical performance of cathode materials in li-ion batteries. *Nano Lett.* **17**(3), 1906–1914 (2017)
135. Wu, H., Yu, G., Pan, L., et al.: Stable Li-ion battery anodes by in-situ polymerization of conducting hydrogel to conformally coat silicon nanoparticles. *Nat. Commun.* **4**, 1943 (2013)
136. Minudri, D., Mantione, D., Dominguez-alfaro, A., et al.: Water Soluble Cationic Poly (3,4-Ethylenedioxythiophene) PEDOT-N as a Versatile Conducting Polymer for Bioelectronics. *Adv Electron Mater.* **6**, 2000510 (2020)
137. Mcdonald, M.B., Hammond, P.T.: Efficient transport networks in a dual electron/lithium-conducting polymeric composite for electrochemical applications. *ACS Appl. Mater. Interfaces* **10**, 15681–15690 (2018)
138. Zeng, W., Wang, L., Peng, X., et al.: Enhanced Ion conductivity in conducting polymer binder for high-performance silicon anodes in advanced lithium-ion batteries. *Adv. Energy Mater.* **8**, 1702314 (2018)
139. Rivnay, J., Inal, S., Salleo, A., et al.: Organic electrochemical transistors. *Nat. Rev. Mater.* **3**, 17086 (2018)

140. Kittleesen, G.P., White, H.S., Wrighton, M.S.: Chemical derivatization of microelectrode arrays by oxidation of pyrrole and n-methylpyrrole: fabrication of molecule-based electronic devices. *J Am. Chem. Soc.* **106**, 7389–7396 (1984)
141. Braendlein, M., Lonjaret, T., Leleux, P., et al.: Voltage amplifier based on organic electrochemical transistor. *Adv. Sci.* **4**, 1600247 (2017)
142. Majak, D., Fan, J., Gupta, M.: Fully 3D printed OECT based logic gate for detection of cation type and concentration. *Sensors Actuators B Chem.* **286**, 111–118 (2019)
143. Bernardis, D.A., Malliaras, G.G., Toombes, G.E.S., Gruner, S.M.: Gating of an organic transistor through a bilayer lipid membrane with ion channels. *Appl. Phys. Lett.* **89**, 053505 (2006)
144. Hamedi, M., Forchheimer, R., As, O.I.: Towards woven logic from organic electronic fibres. *Nat. Mater.* **6**, 357–362 (2007)
145. Wan, A.M., Inal, S., Williams, T., et al.: 3D conducting polymer platforms for electrical control of protein conformation and cellular functions. *J. Mater. Chem. B* **3**, 5040–5048 (2015)
146. Elmahmoudy, M., Inal, S., Charrier, A., et al.: Tailoring the electrochemical and mechanical properties of PEDOT:PSS films for bioelectronics. *Macromol. Mater. Eng.* **302**, 1600497 (2017)
147. Bernard, C., Ghestem, A., Ismailova, E., et al.: In vivo recordings of brain activity using organic transistors. *Nat. Commun.* **4**, 1575 (2013)
148. Williamson, A., Ferro, M., Leleux, P., et al.: Localized neuron stimulation with organic electrochemical transistors on delaminating depth probes. *Adv. Mater.* **27**, 4405–4410 (2015)
149. Sessolo, M., Rivnay, J., Bandiello, E., et al.: Ion-selective organic electrochemical transistors. *Adv. Mater.* **26**, 4803–4807 (2014)
150. Andersson, B.P., Nilsson, D., Svensson, P., et al.: Active matrix displays based on all-organic electrochemical smart pixels printed on paper. *Adv. Mater.* **14**(20), 1460–1464 (2002)
151. Chen, S., Surendran, A., Wu, X., Leong, W.L.: Contact modulated ionic transfer doping in all-solid-state organic electrochemical transistor for ultra-high sensitive tactile perception at low operating voltage. *Adv. Funct. Mater.* **30**, 2006186 (2020)
152. Hu, X., Meng, X., Zhang, L., et al.: A mechanically robust conducting polymer network electrode for efficient flexible perovskite solar cells a mechanically robust conducting polymer network electrode for efficient flexible perovskite solar cells. *Joule*, pp. 1–14 (2019)
153. Chen, S., Surendran, A., Wu, X., et al.: Recent technological advances in fabrication and application of organic electrochemical transistors. *Adv. Mater. Technol.* **5**, 2000523 (2020)
154. Gkoupidenis, P., Schaefer, N., Garlan, B., Malliaras, G.G.: Neuromorphic functions in PEDOT:PSS organic electrochemical transistors. *Adv. Mater.* **27**, 7176–7180 (2015)
155. Gkoupidenis, P., Schaefer, N., Strakosas, X., et al.: Synaptic plasticity functions in an organic electrochemical transistor. *Appl. Phys. Lett.* **107**, 263302 (2015)

Nanocomposites for Energy Storage Applications



J. Barbosa, R. Gonçalves, C. M. Costa, and S. Lanceros-Mendez

Abstract Energy storage devices are essential to meet the energy demands of humanity without relying on fossil fuels, the advances provided by nanotechnology supporting the development of advanced materials to ensure energy and environmental sustainability for the future. The electrochemical energy storage devices that currently stand out the most are lithium-ion batteries and supercapacitors. Furthermore, the demand on higher performance devices and more efficient technologies has led to growing attention in advanced functional nanosized materials. In this chapter, the most relevant nanocomposite materials for lithium-ion batteries and supercapacitors are presented, together with the recent advances in this area.

Keywords Nanocomposites · Battery systems · Supercapacitors

Abbreviations

[DEME][TFSA]	(N,N-Diethyl-N-methyl-N-(2-methoxy-ethyl) ammonium bis (trifluoromethyl -sulfonyl)amide
2D	2-Dimensional
3D	3-Dimensional
AC	Activated carbon
CNF	Carbon nanofibers

J. Barbosa · C. M. Costa (✉)
Centro de Física, Universidade do Minho, 4710-057 Braga, Portugal
e-mail: cmscosta@fisica.uminho.pt

R. Gonçalves
Centro de Química, Universidade do Minho, 4710-057 Braga, Portugal

S. Lanceros-Mendez
BCMaterials, Basque Center for Materials, Applications and Nanostructures, Martina Casiano,
UPV/EHU Science Park, Barrio Sarriena s/n, 48940 Leioa, Spain

IKERBASQUE, Basque Foundation for Science, 48009 Bilbao, Spain

CNS	Carbon nanospheres
CNT	Carbon nanotubes
COF	Covalent organic frameworks
EDLC	Electric double layer capacitor
EIS	Electrochemical impedance spectroscopy
EMIMBF ₄	1-ethyl-3-methylimidazolium tetrafluoroborate
ESS	Energy storage systems
FAU	Faujasite
FG/ANA	Zeolitic analcime/functionalized spongy graphene
GA	Glutaraldehyde
Gly	Glycerol
GN	Graphite nanosheet
GPE	Gel polymer electrolyte
HPE	Hydrogel polymer electrolyte
IL	Ionic liquids
LCO	Lithium cobalt oxide (LiCoO ₂)
LFP	Lithium iron phosphate (LiFePO ₄)
LIB	Lithium-ion battery
LiTFSI	Lithium bis(trifluoromethylsulphonyl)imide
LLZO	Lithium lanthanum zirconium oxide
LLZTO	Tantalum doped lithium lanthanum zirconate
LMB	Lithium-metal battery
LMO	Lithium manganese oxide (LiMnO ₂)
LOB	Lithium-oxygen battery
MOF	Metal-organic framework
NCM	Lithium nickel cobalt manganese oxide (LiNiCoMnO ₂)
NIB	Sodium ion battery
NMR	Nuclear magnetic resonance
OMC	Organometallic complex
P(VDF-co-CTFE)-g-POEM)	Poly(vinylidene fluoride-co-chlorotri fluoroethylene)-g-poly (oxyethylene methacrylate)
PAA	Polyacrylic acid
PAN	Polyacrylonitrile
PANI	Polyaniline
PANI-NTs	Polyaniline nanotubes
PEDOT:PSS	Poly(3,4-ethylenedioxythiophene) polystyrene sulfonate
PEG	Polyethylene glycol
PEO	Polyethylene oxide
PP	Polypropylene
PPENK	Phthalazone ether nitril ketone
PVA	Polyvinyl alcohol
PVDF	Polyvinylidene fluoride
PVDF-HFP	Polyvinylidene fluoride-co-hexafluoropropylene

PVP	Polyvinyl pyrrolidone
R_{ct}	Charge-transfer resistance
rGO	Reduced graphene oxide
R_s	Surface resistance
SCE	Solid composite electrolyte
SEI	Solid electrolyte interface
SEM	Scanning electron microscopy
SPE	Solid polymer electrolyte
SWCNTs	Single-walled carbon nanotubes
TEM	Transmission electron microscopy
TMDC	Transition metal dichalcogenides
TNT	Titania nanotube
WIS	Water-in-salt
XPS	X-ray photoelectron spectroscopy
ZIF	Zeolite imidazolate framework
ZTC	Zeolite-templated carbon

1 Introduction

Energy storage is a field of growing interest. Since the First Industrial Revolution in the XVIII century, it has been aimed the development of technologies allowing the mechanization of the activities, leading to mass production of materials and products at reduced costs. However, the operation of these technologies needs vast amounts of energy to work properly. Over the years, different kinds of energy sources have been used, from coal to petroleum, and more recently, natural gas or nuclear power, leading nowadays, in the 4th Industrial Revolution, to a growing number of devices and applications connected altogether. These advances are categorized in four distinct industrial revolutions (Fig. 1) [1].

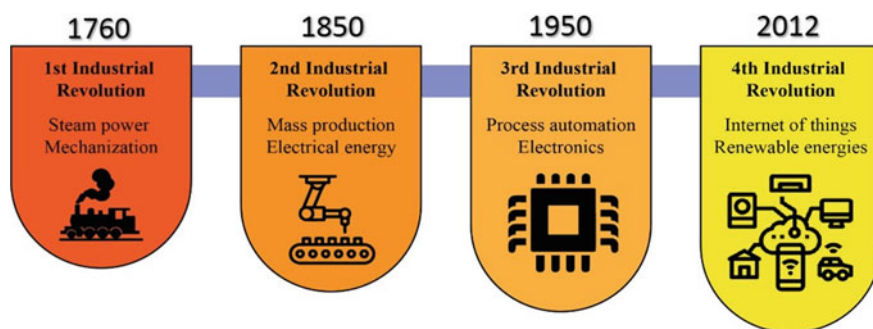


Fig. 1 The four industrial revolutions

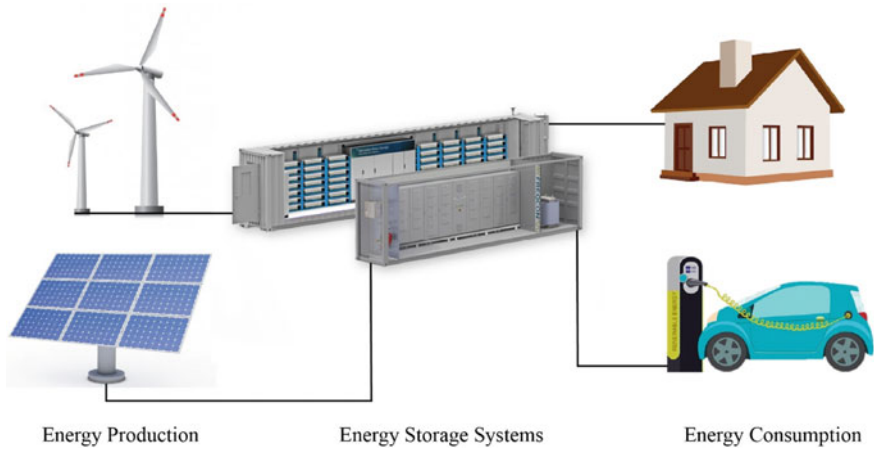


Fig. 2 Schematic representation of renewable energy production, storage, and consumption

In parallel to the industrial development, the growth of the environmental concerns due to pollution and climate change issues, brought a crescent interest in changing the way in which energy is produced and consumed. The current conventional way to produce energy, based on the burning of fossil fuels is highly damaging the environment due to the large amount of greenhouse gases that are emitted during the combustion [2]. So, the concept of renewable energies arose as an effective candidate to replace fossil fuels as the base of modern economy.

Renewable energies rely on inexhaustible sources in the human timescale, such as sun, wind, or water [3]. The harnessing of that energy warrants large amounts of energy with reduced environmental impacts, when compared to the fossil fuels. However, there is a major issue regarding the mass use of renewable energies, which is their irregularity. Because there is no sun or wind continuously in a given place, it is not possible to maintain a constant and regular output of the needed energy [4]. For this reason, the idea of storing energy become a central issue. Energy storage systems (ESS) allow the excess energy produced in a specific moment to be stored, and to be used later, whenever needed (Fig. 2). This is a perfect complement for renewable energy sources, as it allows a significant increase in their efficient use. For example, solar energy that can be stored during the daytime, and used at the end of the day.

2 Energy Storage Devices

As stated before, ESS allow the storage of energy to be used later. This is possible by converting the produced energy in different types of energy, such as potential or chemical energy, that are more easily stored. There are different kinds of energy

storage devices. Although their goal is similar, the way in which the energy is stored can vary substantially. For example, a pumping system can be used to pump water upwards a dam reservoir, converting electric energy, that would be lost if not used, in potential energy that can be converted again in electric energy when the dam is activated [5]. Another example of a common and effective ESS is the solar radiation energy, which is used to heat water, being stored as thermal energy. This energy can be used directly as thermal energy, for house heating, or can be converted in electric energy by boiling the water in solar power plants [6]. Fuel cells are also an effective ESS based on electrochemical reactions, and rely on a supply of fuel (usually hydrogen) and oxygen to produce electricity, with the production of water as byproduct [7]. However, the most common ESS are batteries and the supercapacitors. These devices convert electrical energy into chemical energy (also chemical energy into electrical energy) and are the most appropriate option for their use in smaller devices, such as laptops, smartphones, or even electric vehicles.

2.1 Battery Energy Storage Systems

Battery energy storage systems are the most used storage device worldwide, due to their versatility, high capacity, and relatively low costs, when compared with other ESS. However, their low durability is a drawback that needs to be addressed in years to come [6]. The history of the battery systems covers more than 200 years, since the first voltaic pile of Alessandro Volta, in 1800, until the latest developments in the field of solid-state batteries nowadays (Fig. 3). The first batteries were based on zinc and copper electrodes separated by a brine soaked cloth [8]. The problems associated with the electrolyte leakage and low durability of the batteries were improved by the works of Daniell [9] and Leclanché [10]. The first functional and commercial rechargeable batteries were the lead-acid batteries, developed in 1859 [11]. These batteries are still in use nowadays, based on the same working principle. It took about 50 years for the first nickel–cadmium batteries to be developed, and almost 100 years, until the development of the nickel-metal hydride technology. The lithium ion technology was developed in the XX century, with the first device fabricated by Stanley Whittingham in 1977 [12]. In the decade of the 80, John Goodenough solved a couple of issues related with the security of the Whittingham battery by developing new cathode active materials [13–15]. The first commercial battery entered the market in 1991, based on the work of Akira Yoshino [16]. The work of these three researchers granted them the Nobel prize in Chemistry in 2019, due to the importance of the energy storage systems in the modern society and, in particular, of lithium-ion batteries (LIBs). The research work in the battery field has been traditionally accompanied by the development of solid-state technologies, in order to eliminate the liquid components of the battery structure, leading to safer devices.

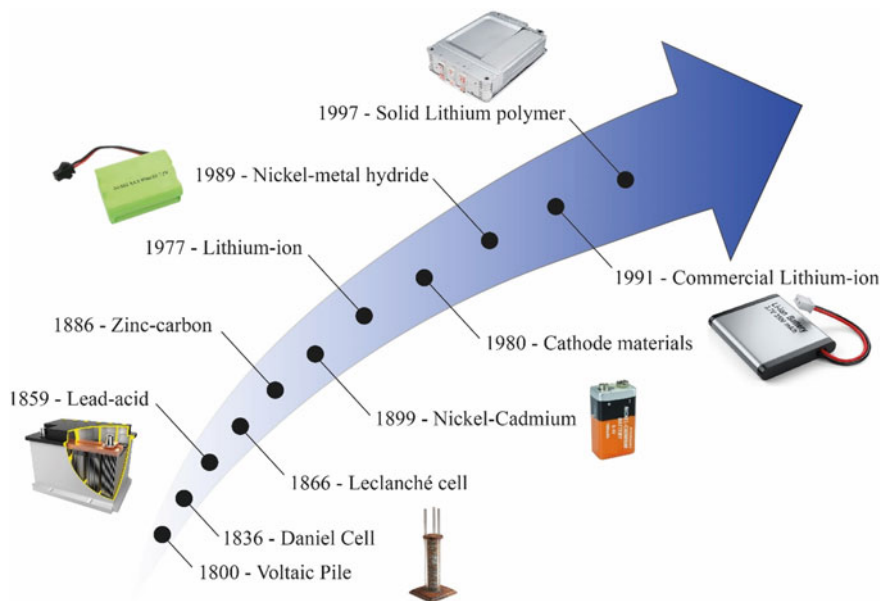
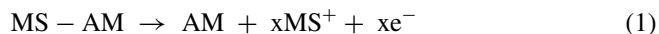


Fig. 3 Advances in battery development along time

A battery is an electrochemical device that allow the conversion between electrical energy into chemical energy, and the opposite [17]. The working principle of a battery is ruled by the redox reactions. A battery is typically composed by two electrodes, cathode and anode, physically separated by a separator membrane soaked in an electrolyte solution [18]. The electrodes are constituted by three basic components: active material, conductive material, and binder. The conductive material and the binder are similar for both electrodes and have the function of increasing the electrical conductivity and warranting the electrode's structural integrity, respectively. The active materials are responsible for the battery capacity, as they must have the capacity to donate the mobile species in the case of the cathode and to store them in the case of the anode [19]. The electrodes are deposited in metallic substrates, or current collectors, with high electric conductivity and different redox potentials [20]. This difference allows the occurrence of the redox reactions responsible for the charge and discharge process of the battery. The separator membrane avoids the physical contact between the electrodes, preventing the occurrence of short circuits, and simultaneously allows the passage of the mobile ion species during the charge and discharge process. It is usually a porous polymeric membrane embedded in the electrolyte, which is responsible for the ionic conductivity in the separator, facilitating the flow of the mobile species [21].

When a battery is charged, energy is provided to the system, which leads to the migration of the mobile species from the cathode to the anode. During the discharge process, the cell returns to its lower energy state, and the mobile species return to

the cathode, with the release of energy. This flow of the mobile ion species occurs to balance the charge difference generated in the electrodes by the flow of electrons in the charge and discharge processes, as stated in Eq. (1),



where MS is the mobile specie and AM is the active material.

As stated before, there are different types of batteries. LIBs are the most used nowadays, due to their high specific capacity, which makes them suitable for light and small devices without compromising their performance. They also possess long cycle life, and no memory effect [22]. These properties led to the progressive replacing of the older and less reliable nickel-metal hydride and nickel-cadmium batteries in the small devices, which allowed the development of improved portable devices, such as smartphones and laptops, as well as the first electric vehicles. LIBs use metal oxides such as LiFePO_4 (LFP), LiCoO_2 (LCO) or LiMnO_2 (LMO) as active materials, and usually graphite as anode active material. Though, LIBs have some limitations which include high prices, the necessity of protection circuits to maintain the voltage and current within safe limits, and their degradation through time [23].

However, there are several other types of batteries based on lithium technology, such as lithium-air or lithium-sulfur, with different properties and limitations. Lithium-air is a promising technology for applications that need significant amounts of energy, such as electric vehicles, due to its theoretical discharge capacity of about 1000 Wh/kg, against the current 200 Wh/kg of LIBs. However, some of the limitations of this technology include the difficulty of effectively establish reversible reactions, control over the volume changes in the cell, stabilization of the electrodes and warranting a supply of pure oxygen into the system [24]. Lithium-sulfur batteries have an even higher theoretic capacity (2572 Wh/kg), with their sulfur cathodes and metallic lithium anodes, but the low conductivity of sulfur is a major drawback that needs to be overcome, as well as the large expansion of sulfur during the charge and discharge process, and the lithium dendrites formation [25].

Beyond lithium, there are several promising technologies that can be suitable for the future of ESS but that still need significant improvements to be commercially viable (Table 1). Sodium ion batteries (NIBs) are one of the most promising systems for this purpose, due to the large amount of sodium available on Earth (it is the

Table 1 Comparative analysis of different battery technologies [28, 29] [25, 30] [31]

Technology	Specific Energy (Wh/kg)	Number of cycles	Efficiency (%)	Voltage (V)
Lithium ion	100–265	1000–2000	99.9	3.6
Lithium air	3860	700	65	2.91
Lithium sulfur	500	~ 500	85	3
Sodium ion	85–125	~ 500	> 90	2.7–3.2
Potassium ion	120–170	~ 4000	> 90	2.0–4.3
Magnesium ion	77	~ 2000	~ 95	1.1

4th most abundant element), allowing the possibility for much cheaper devices than lithium batteries. NIBs also rely in much less dangerous materials, making them a more environmentally friendly option. The major drawbacks of this technology are the high temperatures needed for operation, and the high reactivity of sodium, which leads to security issues. [26]. Magnesium ion batteries present similar advantages and disadvantages as the previous ones, as Magnesium is also an abundant element on Earth, but it possesses a high reactivity. Potassium ion batteries can offer a high operation voltage and realize high power densities due to the fast K^+ ion diffusion. Similarly, to Sodium and Magnesium, Potassium is highly reactive, which can cause safety problems in the batteries. The low melting point of Potassium metal can also be an issue in the case of operation at higher temperatures [27]. Despite the fact that there are some interesting alternatives to lithium ion technologies, these alternatives need further improvement in order to overcome the issues mentioned before and to become a viable and effective option for a diversification of the battery market.

2.2 Supercapacitor Energy Storage Systems

Super capacitors are ESS with some similarities with batteries. They are electro-chemical devices with a very high value of capacitance. The working principle of the two electrodes and a separator is similar to the battery, however, supercapacitors have higher power densities, can be charged and deliver much more energy in a smaller amount of time with high efficiency, and have a prolonged lifecycle (up to 500.000 cycles) with low maintenance, when compared to battery systems [32]. On the other hand, despite their high specific capacity, supercapacitors are not able to store large amounts of energy, which can vary between 3 to 30 times less than a conventional battery [33]. Table 2 summarizes the main differences between a typical battery and a supercapacitor. This makes supercapacitors an interesting option for applications that need frequent high-power bursts in a small timeframe, such as electric vehicle breaking and acceleration systems, stabilization of power grids, energy harvesting systems, or even in parallel with battery systems to increase their efficiency.

There are three main categories of super capacitors. The electric double layer capacitor (EDLC), the pseudocapacitor, and the hybrid supercapacitor, that combines the EDLC and the pseudocapacitor.

Table 2 Comparison of the main characteristics of battery and super capacitor systems. Adapted from [33]

Properties	Battery	Supercapacitor
Specific Energy (Wh/kg)	10–100	1–10
Specific Power (W/kg)	<1000	500–10,000
Charge/discharge time	20 min – 5 h	1 s–1 min
Coulombic efficiency (%)	85–98	70–85
Number of cycles	~1000	>500.000



Fig. 4 Main differences between a double layer capacitor (EDLC), a pseudocapacitor, and a lithium ion battery [41]

As stated before, a super capacitor has two electrodes and a separator soaked in an electrolyte solution. The role of each component is similar to those of batteries. The operation of the supercapacitor is based on the polarization of the electrodes when a voltage is applied. The main difference in the operation of EDLC and pseudocapacitors is that in the case of the EDLC, this polarization does not occur with transfer of charges between the electrodes and the electrolyte, while in the pseudocapacitor charge transfer occurs between the electrode and the electrolyte by electrosorption reactions (Fig. 4). This means that in EDLCs the energy is stored electrostatically, without reactions in electrodes, contrarily to the pseudocapacitor, where electrochemical reactions occur [34].

Energy storage, in EDLC, is based on intrinsic shell area and atomic charge partition length, which leads to low energy densities [35]. Pseudocapacitors rely on the occurrence of reactions in the electroactive unit present on the electrode's active material, with the help of an electrolyte solution, which allows for higher energy densities [36].

The first capacitor was developed in 1746 by Pieter van Musschenbroek. This device, known as Leiden jar, was made with a glass jar (dielectric) and metal foils (electrodes) where the charges were accumulated [37]. It took almost 200 years until the first EDLC electrolytic capacitor appeared, and only in 1957 the first super capacitor was patented by General Electric [38]. In the decade of the 70, studies on pseudocapacitors were carried out by Brian Evans Conway [39]. Hybrid lithium ion capacitors were obtained more recently, in 2007, in which carbon and lithium ion electrodes were combined, providing increased capacitance and energy density [40].

3 Nanocomposites for Battery Systems

Battery systems are one of the most used energy storage systems in the last decade. Their physical–chemical characteristic control, manipulation and knowledge, obtained over the years, allowed the development of advanced battery systems with increasing energy and power densities, higher storage capacity, long cycle life, lightweight and safety. Increasing interest in the development of new battery system concepts is also observed [42, 43]. Their applicability in medical devices, portable devices or vehicles, among others, demand specific and tailorable physical–chemical characteristics [44, 45].

Different battery systems, as already mentioned in the Sect. 2.1, and their intensive study to achieve improved properties and higher electrochemical performance can be found in the literature [46, 47]. One of the main problems of batteries systems is the degradation that occur over the time. The degradation mechanisms can be driven by high temperature, mechanical stress, current load, and other effects and promote some effect that usually are associated with high capacity and power fade (Fig. 5) [48]. The kinetic degradation behavior mainly involves an increase in the internal resistance or cell impedance measured by the voltage drop during a load [48].

Different approaches have been carried out to prevent these degradation mechanisms and also, to stabilize and improve the characteristics of these batteries. To prevent these issues, and enhance their properties, battery components have been modified and submitted to different methodologies including coating and encapsulation, control of their morphology, reduction of their dimensions, doping and functionalization, electrolyte modification and composite formation (Fig. 6) [49].

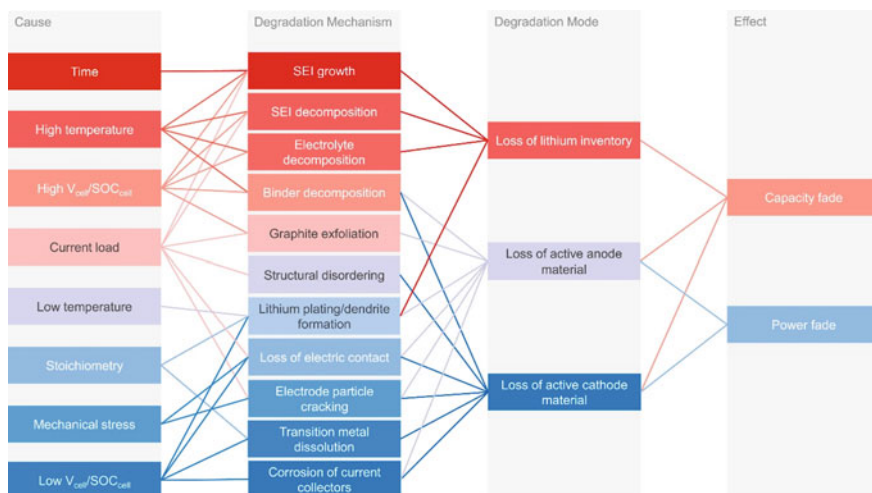


Fig. 5 Degradation mechanisms and degradation modes for the different causes [48]

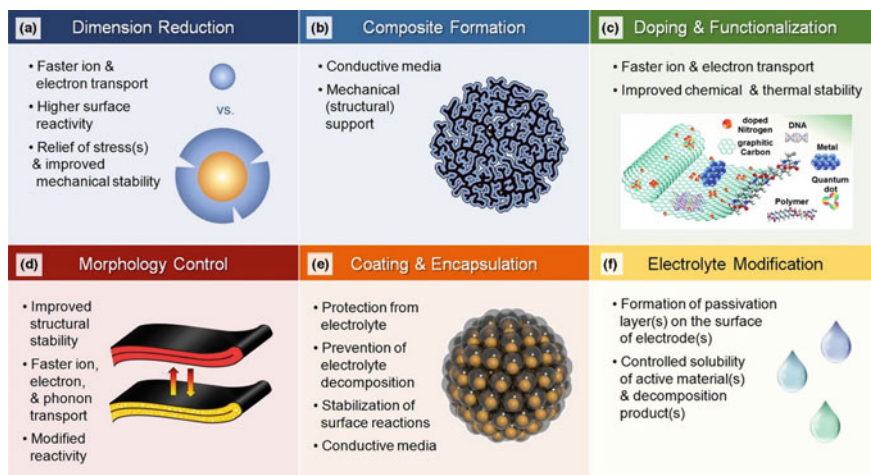


Fig. 6 Methodologies used to prevent battery degradation mechanisms and also to enhance their electrochemical properties [49]

Among the mentioned methodologies, composite formation has been intensively studied by the addition of new materials that not only provide stability but also new properties to the battery components. The use of this methodology can result in an improved synergy between energy, chemistry, physics and environmental areas resulting in a multidisciplinary materials approach [50].

Two approaches can be mentioned in order to achieve composite battery systems: multifunctional structures [51, 52] and multifunctional materials [53]. In multifunctional structures, new properties are implemented in each battery component and then assembled as a structure; with respect to multifunctional materials, the new property is added into the specific components, each constituent possessing multiple functions [51, 53]. Both approaches are intensively studied and different morphologies [54] and fillers such as organometallic complexes (OMCs) [55], zeolites [56, 57], carbon materials [58], ionic liquids (ILs) [59–61], polymers [62, 63] and others [64] have been used. In the following, different composite approaches for electrodes and separator components are presented.

3.1 Micro and Nanocomposites for Electrodes

The active material is the component of the electrode, which is responsible for the battery capacity. In this section, it will be discussed the studies performed into the other two elements, conductive and binder materials, to enhance the electrochemical performance of the electrodes in battery systems.

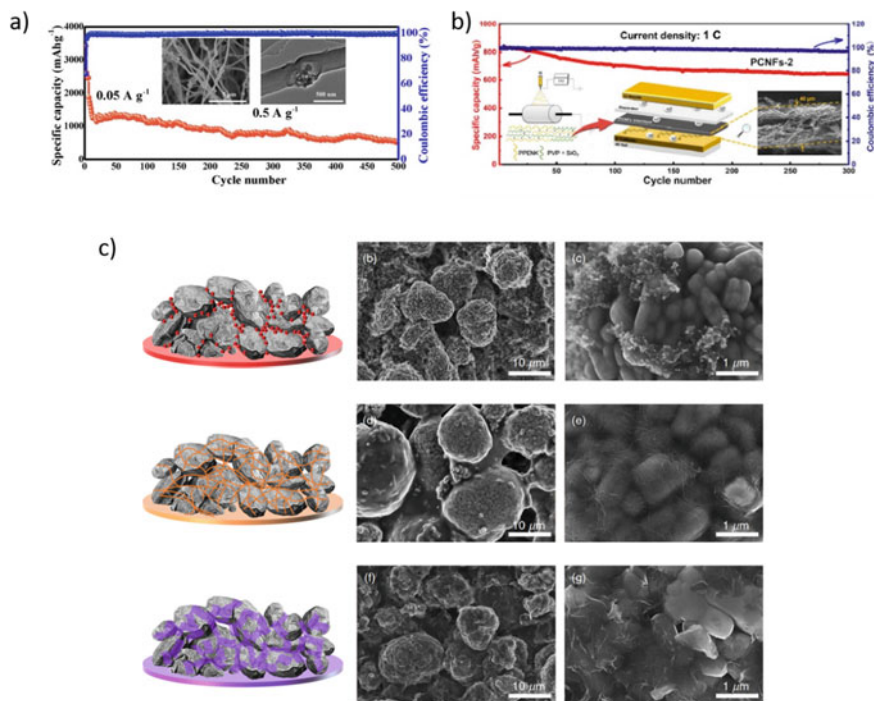


Fig. 7 **a** Self-standing pumpkin-like Si/C-ZIF-8/CNFs anode and its cycling performance [72]; **b** multifunctional structures N/O dual-doping porous CNFs [70] and **c** electrode architecture of (LiNi_{1/3}Co_{1/3}Mn_{1/3}O₂) NCM electrodes with Super P, SWCNTs, and GNs as conductive fillers and their respectively SEM images [83].

Carbonaceous particles including carbon nanosheets, core-shell sphere carbon and carbon nanofibers are intensively used to improve battery systems properties [65]. Once carbon particles are less capable of providing the necessary conductive networks, carbon materials with other geometries emerge to solve and provide high performance batteries [66, 67]. Thus, carbon nanofibers (CNFs) have been developed by different production methods including hydrogel-based template [68], electrospinning [69, 70], chemical vapor deposition [71] and hydrothermal synthesis [67]. CNFs are applied in different type of battery systems and composites. Yanfei Zeng et al. [72] studied free-standing N-doped porous CNFs sheathed pumpkin-like Si/C composites (Si/C-ZIF-8/CNFs) in lithium-ion battery anodes. Their results show that the studied structure reduce the volume variation, improve the electrical conductivity and stabilize the solid electrolyte interface (SEI) film. The obtained reversible capacity of 945.5 mAh·g⁻¹ at 0.2 A·g⁻¹ and a capacity retention of 64% (150 cycles) shows the suitability of the new process to fabricate Si-anode for LIBs (Fig. 7a). According with Fangyuan Hu et al. [70], multifunctional structures N/O dual-doping porous CNFs were applied into lithium-sulfur (Li-S) batteries, using phthalazone ether nitril ketone (PPENK) and polyvinyl pyrrolidone (PVP) as precursors, to reduce the

polarization reactions of the battery. This effect is observed through the chemical and physical adsorption of the polysulfide. The combination of the N/O dual-doping CNF interlayer with the S particles cathode lead to an improved electrochemical performance of $862.5 \text{ mAh}\cdot\text{g}^{-1}$ after 200 cycles (0.2 C) (Fig. 7b). The combination of CNFs with the transition metal dichalcogenides (TMDC) molybdenum disulfide (MoS_2) was studied due to their capacity of overcome the MoS_2 volume expansion and increase the conductivity [73]. Core-shell CNF comprising MoS_2 and iron oxide-based nanoparticles were used in anode material for both Li-ion and K-ion batteries presenting a high cycling performance of $1218 \text{ mAh}\cdot\text{g}^{-1}$ at $100 \text{ mA}\cdot\text{g}^{-1}$ for LIB and $320 \text{ mAh}\cdot\text{g}^{-1}$ at $50 \text{ mA}\cdot\text{g}^{-1}$ for KIB [74]. Furthermore, it was proven by cyclic voltammetry and X-ray photoelectron spectroscopy (XPS) that MoS_2 can accelerate the conversion of polysulfides in Li-S batteries [75]. Beyond battery systems, CNFs were studied for different energy applications [76]. Other carbonaceous materials such as graphene have been also combined with MoS_2 particles due to the large specific area, additional active sites, high stability and inhibition of volume expansion [77]. Si-based anodes for LIB present some issues related to volume variations during battery charge/discharge processes, unstable SEI and pulverization of Si particles. Different carbon-based materials including CNTs [78, 79], graphene [80] and graphite [81, 82] have been used to address those issues.

Graphite efficiently works as anode in LIB systems although in NIB systems this material does not show good performance due to the higher radius of the sodium ion, compared with lithium, that obstruct the intercalation of the Na^+ ion into the graphite structure. Once that, soft carbons, hard carbons and graphene have been studied to overcome and improve electrochemical performance of NIBs by their good Na^+ retention (larger intercalation distances) and better stability (less susceptible to formation the SEI) [84].

The conductive fillers of anode and cathode components are essential elements once provide the necessary conductivity for percolation. Comparing the main three conductive materials used in electrodes, single-walled carbon nanotubes (SWCNT's), Super P and graphene nanosheets (GN's) (Fig. 7c), Zhengy Ju et al. [83] studied the dimensionality effect of the fillers in commercial $\text{LiNi}_{1/3}\text{Co}_{1/3}\text{Mn}_{1/3}\text{O}_2$ (NCM). Their morphology, electrical percolation and electrochemical properties were compared, and the results show that the electrodes with SWCNTs present higher rate performance. Although the NCM/SWCNTs electrodes presented the lowest electrical percolation threshold and highest electrical conductivity, its rate capability is high with capacity of $142 \text{ mAh}\cdot\text{g}^{-1}$ at 0.2 C. The low surface resistance (R_s) and charge-transfer resistance (R_{ct}) from electrochemical impedance spectroscopy (EIS), high porosity and high percolation support the results, showing that in NCM/SWCNTs, not just the electrical properties but also the structural properties are key factors to ensure a suitable electrochemical performance.

Carbonaceous materials are the most studied fillers applied in electrode materials, but some other fillers are being also used. Metal-organic frameworks (MOFs) are porous materials with a periodic network structure, large surface area, high porosity, versatile chemistry and topological diversity [85]. Furthermore, their active metal

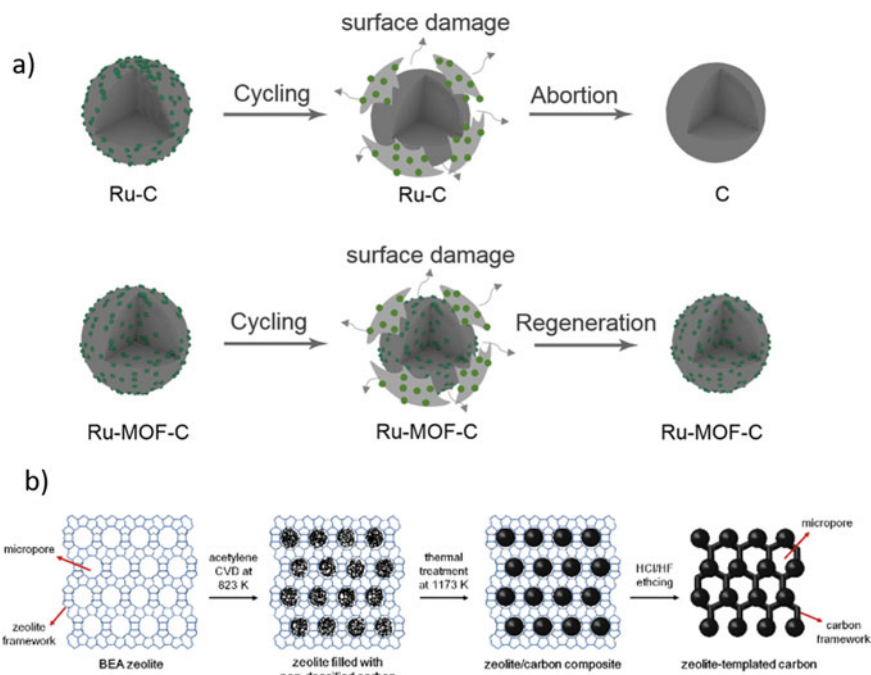


Fig. 8 a Graphic representation of (a) conventional Ru – C catalyst and (b) Ru-MOF – C catalyst, both after long-term cycling in LOBs [87]. **b** Schematic representation of the synthesis of zeolite template carbon (ZTCs) using beta (BEA) zeolite as a solid template [94].

sites, tunable particles/pore size, functional ligands and multidimensional properties allow these materials to be suitable for energy systems [86]. MOF structures are mostly studied in metal ion batteries, lithium-sulfur batteries, lithium oxygen batteries (LOBs) and sodium batteries. Ruthenium-carbon (Ru-C) is used as alternative oxygen catalyst in LOBs due to their high catalytic activity. Xiangkun Meng et al. [87] studied the addition of $\text{Ru}_3(\text{BTC})_2$ to improve the electrochemical performance of LOBs. The results show that with increasing MOF content, the particles were uniformly dispersed not only on the carbon surface but also inside, avoiding the decrease of the catalytic activity and further allow long-term cycling stability (Fig. 8a). Due to MOFs capability to host ions in their structure, these materials are particularly suitable as electrode material [88–91]. Also, electrolyte can be introduced in the porous structure characteristic of MOFs, that combined with the MOFs synthesis capabilities with multiple function containing organic active ligands and metal active centers, allow to improve the stability and capacity of battery systems [92].

Faujasite zeolite (FAU, $(\text{Na}_2, \text{Ca}, \text{Mg})_{3.5}[\text{Al}_7\text{Si}_{17}\text{O}_{48}] \cdot 32(\text{H}_2\text{O})$) was studied as a zeolite template carbon (ZTC) cathode in aluminum batteries in order to mitigate SEI formation [93]. The concept was based in the use of the NaY zeolite framework as

a template where carbon was deposited through chemical vapor deposition and then chemically/thermally treated. A dense and ultrahigh surface area was obtained with conductive network of homogeneous channels of 12 Å in width and 6 Å in diameter, that guarantee the storage of AlCl_4^- ions. Beta (BEA) zeolite crystallites were also studied as a ZTC (Fig. 8b), with different particles sizes ranging from 20 to 400 nm, in Li-S batteries [94]. It was verified that small particles promote high capacity retention (94.6%) at 200 cycles due to the easier penetration of lithium ions inside the pores, promoting a uniform Li_2S deposition on the surface of the micropores. Zeolites are also intensively used in different areas besides energy, including catalytic and environmental applications [95].

Metal iron was used as conductive network in iron-red phosphorus electrodes by mechanical ball milling process. EIS results show the increase of the electronic conductivity where the charge transfer resistance was lowered from 400 to 187 Ω in sodium storage systems, also enhancing their reversible capacity [96]. Other kind of composites (binder free) have been used to increase the electrochemical stability, including antimony (Sb) in NIB [97, 98] and both LIB / NIB [99].

Studies related to the electrode–electrolyte interface, such as SEI formation, have been carried out by different catechization techniques as situ ^7Li nuclear magnetic resonance (NMR) [100, 101], in-situ transmission electron microscopy (TEM) [102, 103] and optical microscopy [104, 105] for different batteries systems [65, 106]. These techniques allow to study the SEI formation by varying parameters that include the electrolytes and the electrode surface, allowing to further understand these processes. Today it is known that capacity losses in lithium metal batteries (LMBs) are mostly due to dead lithium formation (lithium that has not electronic contact with the current collector) [107].

It is thus essential to isolate and understand the effects of chemical and mechanical properties of materials within the battery during their operation at short and long time scales. This will provide insights on how mechanical mechanisms at nanoscale such as cracks and their propagation and interface effects. Mathematical modeling experiments and artificial intelligent predictions with extensive analytical data sets are an essential tool to successfully achieve this goal [108, 109].

3.2 *Micro and Nanocomposites in Battery Separators*

Commercial polyolefin porous separators are the main used ones in battery applications due to their mechanical strength, high porous structure, and cost-efficiency [110]. Nevertheless, this separator has some issues related to nonpolarity, low surface energy and high thermal shrinkage above 90 °C, the latter increasing the possibility of internal short circuit inside the battery at high temperatures [111]. Thus, different approaches have been devoted to enhance separator performance in battery systems [112–115]. Further, different materials such as ceramic [116] and polymer fibers [117, 118], have been widely studied.

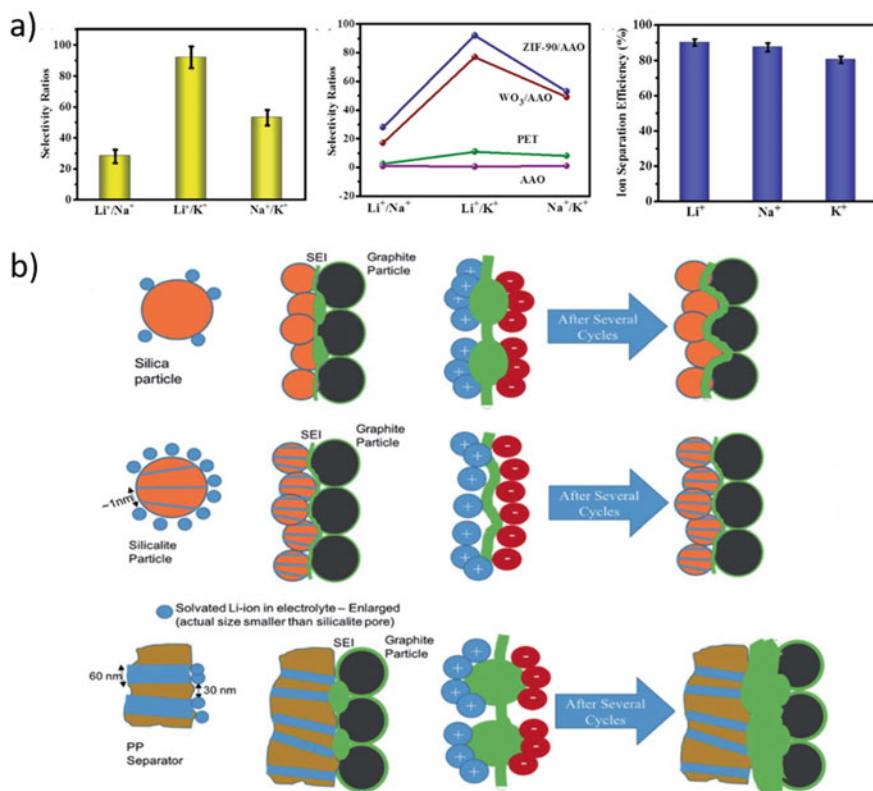


Fig. 9 **a** Ion selectivity ratios with angstrom-sized pores; ion separation efficiency and comparison of ion selectivity in asymmetrical membranes [122]. **b** Graphic representation of the SEI formation at the interface of the silicalite, silica and PP separators [57]

Ion separation and mass transport are the processes used in the separators composites, once selectively allows the passage of smaller ions, blocking the larger ones, and polarity selectivity allows ion movement. The main challenge still remains a high selectivity for specific ions due to the existence of ions with similar size, valence and polarity [50, 119]. Different composite structures have been studied for separators [120]. MOF particles such as UiO-66-(COOH)₂ revealed three orders of magnitude higher conduction to K⁺, Na⁺ and Li⁺ ions compared to Ca²⁺ and Mg²⁺ ions, in the subnanometer-to-nanometer channel direction. The process has been theoretically explained by the ion-carboxyl interactions that substantially reduce the energy barrier for monovalent cations [121]. The ZIF-90 structure also reveals permeability to K⁺, Na⁺ and Li⁺ ions showing different energy barrier for each one $E_{Li^+} < E_{Na^+} < E_{K^+}$, attributed to the strong electrostatic force interaction between the ions and the particle pores (Fig. 9a) [122]. Overall, ceramic particles used as fillers within the separator membranes improve the development of interconnected porous structures that increase lithium pathways, the high surface area of the fillers also increasing

the wettability. MOF-808 fillers have been studied as fillers for polyvinylidene fluoride (PVDF) polymer separator membranes for LIBs in order to enhance electrolyte affinity with the separator by increasing porosity and guaranteeing their interconnectivity [55]. All these properties facilitate lithium migration and resulted in a high discharge capacity of $68 \text{ mAh}\cdot\text{g}^{-1}$ at 2C for PVDF-MOF-808 10wt.%, together with long-term stability.

Zeolite structures have been used in separator membranes due to their tunable surface properties, high surface area, high mechanical strength and thermal stability [123]. Polymer composites with zeolites have been thus intensively studied. Kishen Rafiz et al. [57] presented pure zeolites as an electrode-coated separator (Fig. 9b). The SEI reduction allows to increase the electrochemical performance of the NMC/silicalite batteries, leading to an enhancement of the charge retention in more than 15% in long-term cycling compared with polypropylene separators. Polyethylene terephthalate composite separators with Al_2O_3 and with different structures (nonwoven and tri-layered separators) have been presented [98], demonstrating high thermal resistance and dimensional stability in the nonwoven separators. Nonetheless, the non-uniform ceramic particles distribution in the nonwoven separators lead to unbalanced current density distribution and cell failure.

Composites with Al_2O_3 [124, 125], SiO_2 [126, 127], TiO_2 [128, 129] and other particles are used to improve the thermotolerance of the separators, avoiding their degradation with the increasing temperature related to the charge/discharge processes. More information on thermotolerance in separators can be found in reference [130].

Separator composites have the advantage of enhanced hydrophilicity, allowing the incorporation ILs in its structure. The use of IL in battery systems present advantages compared with carbonated electrolytes, the most important being the lower volatility and flammability [59]. Furthermore, various ILs of imidazolium salts have demonstrated high lithium ion conductivity [131]. Solid composite electrolytes (SCEs) are also a class of solid-state electrolyte (SPEs). SCEs are typically composed by a polymer hosts with inorganic fillers and dissolved lithium salts. Polymers such as polyethylene oxide (PEO) [132] and polyvinylidene fluoride (PVDF) [133] and fillers from lithium lanthanum zirconium oxide (LLZO) [134] to MOFs [135] have been used. One of the main drawbacks of SCEs are the interface with the electrode and many efforts have been developed to address this problem [136, 137]. To a deeper and better understanding of these materials, some reviews can be found in literature [138–141].

Other polymers, including PVDF and co-polymers, polyacrylonitrile (PAN), cellulose [142, 143], or polyvinylalcohol (PVA), have been studied as separators due to their different mechanical, thermal, chemical and electric properties that allow enhancing electrochemical battery behavior. The necessity of developing advanced materials to overcome some drawbacks as the weak bonding forces in composite structures is relevant [144]. Dendrite inhibition through the separator component is also a relevant issue to be addressed [145–147]. Fillers, including magnesium nanoparticles, tantalum doped lithium lanthanum zirconate (LLZTO), hydroxyapatite nanorods, or silicon particles have been used as functionalization of separators

for lithium metal batteries. Although different efforts have been carried out to prevent dendrite formation, some drawbacks still need to be solved: preservation of flexibility after filler addition, avoiding the powdering of lithium and electrolyte consumption using mechanical barriers, or avoiding lithium dendrite formation in uneven surfaces [145]. To overcome these drawbacks new advanced characterization techniques have to be implemented to gain further understanding on the mechanism of dendrite formation, providing the directions for their effectively suppression [146]. Also, new materials with different morphological designs as the nano-shield can allow decreasing dendrites formation [148] and can represent a new way to prevent this issue. Until a full understanding of dendrite mechanism is achieved, studies such as the one in [149] allow to address the issue in a different way: the developed of smart batteries with improved safety with a bifunctional separator designed to in situ early detection of lithium dendrites.

4 Nanocomposites for Supercapacitors

Supercapacitors show a rapid growth in the electronic market due to their high power density, improved rate capability, fast charge/discharge rate, long cycle life (higher than 100 000 cycles), simple principles, rapid dynamics of charge propagation and lower maintenance cost [150, 151]. The components of the supercapacitors are current collectors, electrodes and electrolyte/separator [152].

As previously mentioned there are two main types of charge storage mechanism for supercapacitors: EDLC, based on electrostatic charge accumulation at the interface of electrode/electrolyte, and pseudocapacitor, based on charge transfer, via reversible (Faradaic) redox reaction(s), to redox materials on the surface of the electrode [151].

The performance of the supercapacitors is based on power density, energy density, cyclability, and charge/discharge rates, among others [153].

The electrode materials in EDLC supercapacitors are typically based on different forms of porous carbon materials in such as activated carbons (ACs), carbon nanotubes (CNTs) and nanofibres, mesoporous carbons, or graphene [154]. The specific surface structure of the electrodes, i.e., reduced pore tortuosity, interconnected pore structure, short pore length, and controlled surface chemistry, are critical parameters affecting the performance of supercapacitors. The association of graphene and metal oxides, mainly manganese oxides, has been extensively studied in order to improve the energy density of the supercapacitors [155].

For the pseudocapacitors, the electrodes materials most used are metal oxides (RuO_2 , MnO_2 , NiO , Co_3O_4 , Fe_3O_4 , V_2O_5 , etc.), metal hydroxides ($\text{Ni}(\text{OH})_2$, $\text{Co}(\text{OH})_2$, etc.) and conductive polymers (polyaniline (PANI), polypyrrole, etc.) [156].

Typically, the electrolytes used in supercapacitors are based on aqueous electrolytes (KOH, H₂SO₄, and Na₂SO₄ for alkaline, acidic and neutral solutions, respectively), organic electrolytes (Et₄NBF₄, (C₂H₅)₄PBF₄ and TEABF₄ in organic solvents) and ionic liquids.

4.1 *Micro and Nanocomposites for the Electrodes*

The materials most used as electrodes in supercapacitors are carbon-based materials due to their low cost, higher stability and high specific capacitance, i.e. 100–200 F·g⁻¹ [153]. Recently, 3-dimensional (3D)-heterostructured NiO nanofibers/ultrathin g-C₃N₄ holey nanosheets [157] and graphitic carbon nitride/iron oxide nanoparticles nanocomposites [158] have been presented for improving structural and electronic properties and, consequently, the specific capacitance of the supercapacitor. Also, carbon nanotubes doped with mesoporous Fe₃O₄ [159] nanospheres, ferrous tungstate (FeO₄W) [160], polyaniline nanotubes (PANI-NTs) [161] and aligned iron oxide [162], Co₃O₄/C composite [163], N-doped carbon spheres (NCSs)@Ni(OH)₂ [164] composites, NiSe₂@C nanocomposites [165], flower shaped NiS₂@regenerative graphene oxide [166], silicon nanowire-graphene nanowall-PANI composites [167], porous graphene-NiO nanocomposites [168] and nickel oxide/graphene/polypyrrole hybrid ternary nanocomposites [169] were developed for electrodes in supercapacitor devices. In order to improve the performance of graphene nanosheets, hybrid material were developed by the interaction of covalent organic frameworks (COFs) with reduced graphene oxide (rGO) films or fibers in which the optimal COF/rGO hybrid provides a high gravimetric specific capacitance of 321 F·g⁻¹ as shown in Fig. 10a) [170]. Also, nanocomposites based on reduced graphene oxide (rGO) and MnO₂/PEDOT:PSS on a carbon fiber substrate [171], NiCoAl-layered double hydroxide [172], graphene paper [173], graphene quantum dots/Ni(OH)₂ [174] and graphene nanosheets with MnO₂ [175] were developed. In addition, nanocomposites based on zeolitic analcime/functionalized spongy graphene (FG/ANA) were prepared by hydrothermal-aided process leading to a capacitance of 652 F·g⁻¹ at 5 mV·s⁻¹ and 1061.95 F·g⁻¹ at 0.5 A·g⁻¹ showing 92% cycling stability over 2000 cycles (1.5 A·g⁻¹) (Fig. 10b) [176]. Nanocomposites based on reduced graphene oxide and CuS/ZnS/sodium alginate were produced by physical crosslinking followed by one-step reduction, reaching a specific capacitance of 252.1 F·g⁻¹ at 5 mV·s⁻¹ [177].

Another materials for electrodes that are gaining special attention for supercapacitor devices are MXene nanosheets [179]. The two-dimensional (2D) hierarchical NiCoS/d-Ti₃C₂ (MXene) composites have been prepared by a co-precipitation synthesis and in situ sulfuration process. In these process, the synergistic interaction between the two components improves the specific capacity to 758.9 C·g⁻¹ at a current density of 1 A·g⁻¹ [180]. Also, this Ti₃C₂ (MXene) material was doped by polypyrrole nanospheres in order to increase the electrical conductivity [181]. Moreover, polymer conductors such as polyaniline (PANI) and

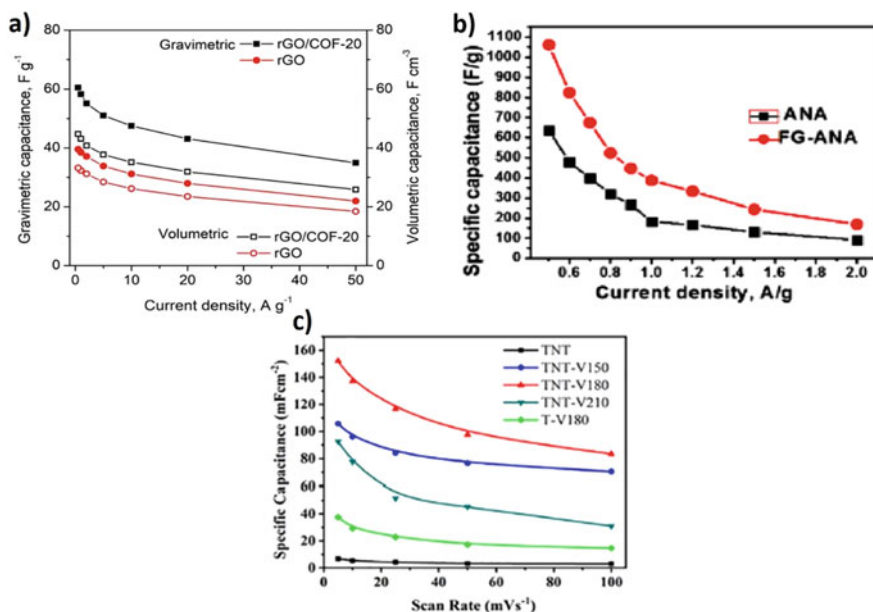


Fig. 10. **a** Comparison of the rate capability of rGO/COF-20 and rGO supercapacitors [170], **b** average specific capacitance (C_s) of Analcime (ANA) and functionalized spongy graphene (FG)/ANA in 0.5 M H₂SO₄ at several current densities [176] and **c** rate capabilities of various (titania nanotube (TNT)) -VO₂(M) nanocomposites at different scan rates [178].

polypyrrole [182] were used for supercapacitors devices, in which nanocomposites based on PANI wrapped boroncarbonitride [183], MnO₂/polyaniline/hollow mesoporous silica [184], polyaniline–titanium dioxide nanoparticles composite [185] and CuCo₂S₄/Polyaniline composites [186] allowed to increase capacitance.

Electrodes based on transitional metals are widely used in supercapacitors to enhance their electrochemical performance. Thus, Co(OH)₂@NiSe₂ was electroplated on metal co-coated textiles as conductive substrates, with a capacity retention of 86.7% after 20,000 cycles in all solid-state cells (PVA-KOH) [187]. Bi (nanoparticles)/CN_x(nanosheets) nanocomposites were synthesized for supercapacitor electrodes, leading to a specific capacity of 1251 F.g⁻¹, that is more than 90% of its theoretical value, at a current density of 500 mA.g⁻¹, with 6 M KOH as electrolyte [188]. Composites based on Cu₂Se nano-cauliflower with 2D CuS nanosheets on Ni foam were prepared by co-electrodeposition technique for supercapacitor application, the Cu₂Se@CuS composite delivering an ultra-high specific capacitance of 2727 F.g⁻¹, when compared to single compound materials as Cu₂Se (1925 F.g⁻¹) and CuS (1156 F.g⁻¹), respectively, on three-electrode configuration with current density of 2.5 mA.cm⁻² [189]. Also, CoNiSe₂/CoNiSe₂/Ti electrodes [190] and MoS₂-RuO₂ nanocomposites [191] were synthesized for supercapacitor devices.

Titania nanotube (TNT)-VO₂ (M) nanocomposites were developed through a combined potentiostatic anodisation-hydrothermal procedure, showing also a suitable specific capacity Fig. 10c) [178].

4.2 Micro and Nanocomposites for Separator/Electrolytes

The capacitance of supercapacitors is also affected by the electrolyte/separator due to its ionic conductivity and potential window. Thus, new electrolytes based on polyvinyl alcohol (PVA) and polyethylene glycol (PEG) with glutaraldehyde (GA) have been developed with high ionic conductivity ($67.1 \text{ mS}\cdot\text{cm}^{-1}$) as shown in Fig. 11 [192].

Further, gel polymer electrolyte (GPE) films based on poly(vinylidene fluoride-co-hexafluoropropylene) (PVDF-HFP), capable to immobilize a solution of lithium bis(trifluoromethane sulfonyl)imide in suberonitrile, was produced for quasi-solid-state carbon supercapacitors, with a specific capacitance of $220\text{--}230 \text{ F}\cdot\text{g}^{-1}$, corresponding

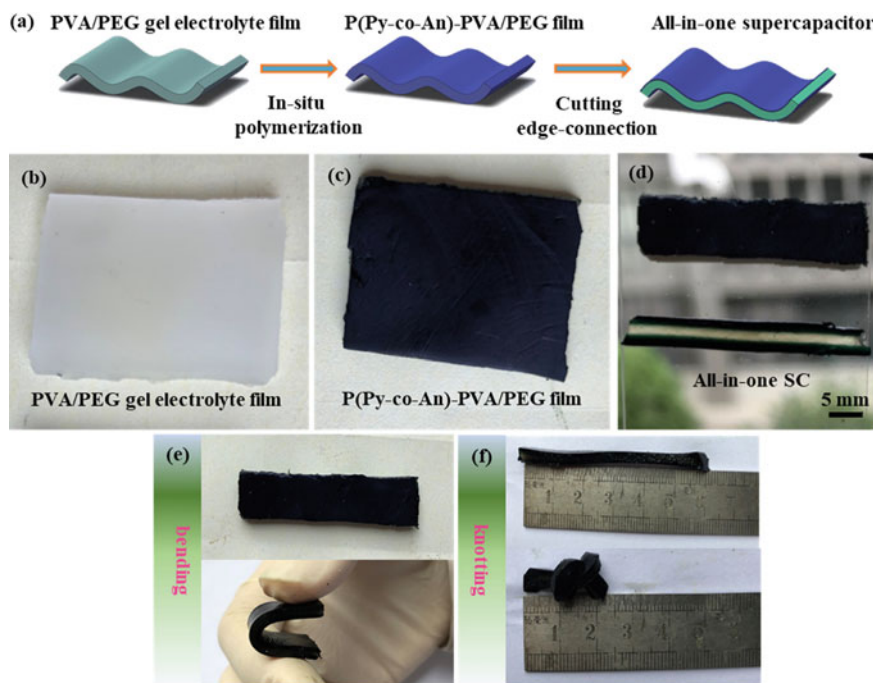


Fig. 11 a Schematic image of the fabrication of an all-in-one supercapacitor based on P(Py-co-An)-PVA/PEG film. Image of: **b** PVA/PEG gel electrolyte film, **c** P(Py1-co-An6)-PVA/PEG film and **d** electrode–electrolyte–electrode configuration of all-in-one supercapacitor based on P(Py1-co-An6)-PVA/PEG film. **e–f** Bending and knotting image of the all-in-one supercapacitor, with the respective scale [192]

to high specific energy and power of 27–32 Wh.kg⁻¹ and 12.5–13.5 kW.kg⁻¹, respectively [193]. PVDF-HFP composites with IL (N,N-Diethyl-N-methyl-N-(2-methoxy-ethyl)ammonium bis (trifluoromethyl-sulfonyl)amide [DEME][TFSA]) was used for GPE where the supercapacitor device presents a specific capacitance of 165F.g⁻¹ at 0.25 A.g⁻¹ [194]. Also, an 1- ethyl-3-methylimidazolium tetrafluoroborate (EMIMBF₄) ionic liquid was used for electrolytes [195].

In order to repair physical damages and preserve good electric contact at the electrode/electrolyte interface, self-healing hydrogel electrolytes were developed based on a 3D network structural gel electrolyte (PAA-g-EG50%) through the use of acrylic acid as monomer and glycol as cross-linked agent, respectively (Fig. 12a) [196]. In addition, glycerol (Gly) gel electrolyte with several fractions of potassium hydroxide (KOH) and ammonium molybdate, (NH₄)₂MoO₄ in the anhydrous state, was produced in which the doped glycerol matrix is used as a framework providing a stable gel electrolyte, creating hierarchical pathways for ion diffusion. This gel electrolyte reaches a specific capacitance of 328 F.g⁻¹ and an energy density of 45.6 Wh.kg⁻¹ as shown in Fig. 12b) [197].

Another hydrogel polymer electrolyte (HPE) was synthesized by the step-wise dissolution of polyvinyl alcohol (PVA) and redox additive KBr in a 5 m (mol kgwater⁻¹) lithium bis(trifluoromethylsulphonyl)imide (LiTFSI) “water-in-salt” WIS solution, being characterized by a wide operating voltage and exhibiting pseudocapacitance [199]. Other interesting solid-gel electrolytes were produced based on ZnO doped PVA-Borax, their cycle life behavior being shown in Fig. 12c) [198].

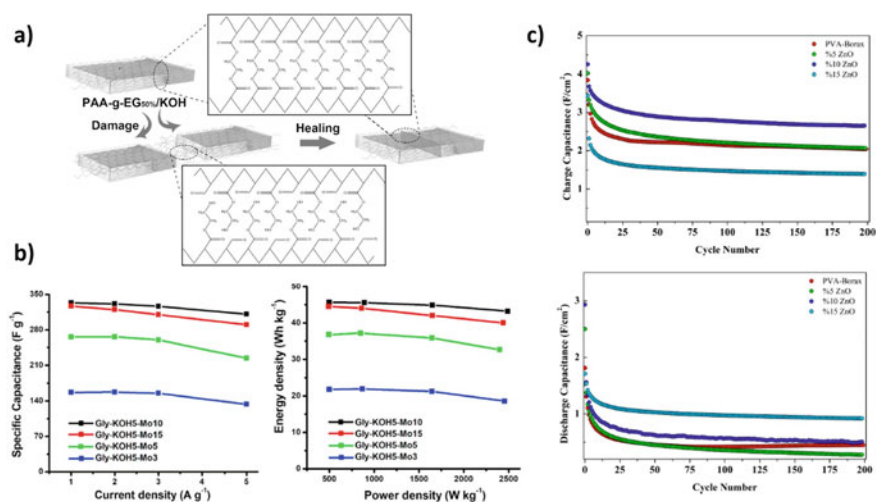


Fig. 12. a) Graphic illustration of the self-healing process of the PAA-g-EG50% [196], b) specific capacitance and Ragone plots of the Mo₃-, Mo₅-, Mo₁₀-, and Mo₁₅- containing Gly-KOH₅ gel electrolyte [197] and c) cycle life results of PVA-ZnO-Borax samples [198].

Finally, solid electrolytes for supercapacitor applications have been prepared from materials as amphiphilic CP, poly(vinylidene fluoride-co-chlorotrifluoroethylene)-g-poly (oxyethylene methacrylate) (P(VDF-co-CTFE)-g-POEM) comprising hydrophobic P(VDF-co-CTFE) main chains and hydrophilic POEM side chains, showing a high specific capacitance of $239.3 \text{ F}\cdot\text{g}^{-1}$ [200].

5 Final Remarks

In this chapter, recent developments on nanocomposites for lithium-ion batteries and supercapacitor devices have been presented for the different components. The focus of those nanocomposites is to improve performance, conversion efficiency, energy and power density, and extended lifetime, among other relevant properties of the corresponding energy storage systems. A wide variety of nanocomposite materials are shown for lithium-ion batteries and supercapacitor devices with a wide range of manufacturing methods and properties. Nanocomposites show as main advantages, the significant surface area to volume ratio, flexibility in tailoring surface functionalities and improved mechanical performance (stiffness and strength) when compared with the bulk material.

Future trends in nanocomposite development rely on introducing new functionalities to the materials (e.g. ion exchange and storage, sensing or healing capabilities) and further tailoring mechanical, electrical and electrochemical response.

This improvement can be only achieved through the understanding of their fundamental physical properties through a correlation of processing conditions with the nanostructure and macroscopic response of the materials. Finally, in the scope of improved sustainability, environmental material and processes will be a focus of the next developments in this field.

Acknowledgements Work supported by the Portuguese Foundation for Science and Technology (FCT): projects UID/FIS/04650/2020, UID/QUI/0686/2020, UID/CTM/50025/2020, UID/QUI/50006/2020, PTDC/FIS-MAC/28157/2017, and Grants SFRH/BD/140842/2018 (J.C.B.), CEECIND/00833/2017 (R.G.) and SFRH/BPD/112547/2015 (C.M.C.). Financial support from the Basque Government Industry and Education Departments under the ELKARTEK, HAZITEK and PIBA (PIBA-2018-06) programs, respectively, is also acknowledged.

References

1. Xu, M., David, J.M., Kim, S.H.: The fourth industrial revolution: Opportunities and challenges. *Int. J. Financ. Res.* **9**(2), 90–95 (2018)
2. Abdelkareem, M.A., Elsaid, K., Wilberforce, T., Kamil, M., Sayed, E.T., Olabi, A.: Environmental aspects of fuel cells: a review. *Sci. Total Environ.* **752**, 141803 (2021)
3. Kaltschmitt, M., Streicher, W., Wiese, A.: *Renewable Energy: Technology, Economics and Environment*. Springer Science & Business Media (2007)

4. Scrosati, B., Hassoun, J., Sun, Y.-K.: Lithium-ion batteries. A look into the future. *Energy Environ. Sci.* **4**, 3287–3295
5. Hunt, J.D., Byers, E., Riahi, K., Langan, S.: Comparison between seasonal pumped-storage and conventional reservoir dams from the water, energy and land nexus perspective. *Energy Convers. Manage.* **166**, 385–401 (2018)
6. Laing, D., Bahl, C., Bauer, T., Fiss, M., Breidenbach, N., Hempel, M.: High-temperature solid-media thermal energy storage for solar thermal power plants. *Proc. IEEE* **100**(2), 516–524 (2012)
7. Kirubakaran, A., Jain, S., Nema, R.K.: A review on fuel cell technologies and power electronic interface. *Renew. Sustain. Energy Rev.* **13**(9), 2430–2440 (2019)
8. Volta, A.X.V.I.I.: On the electricity excited by the mere contact of conducting substances of different kinds. In a letter from Mr. Alexander Volta, F. R. S. Professor of Natural Philosophy in the University of Pavia, to the Rt. Hon. Sir Joseph Banks, Bart. K.B. P. R. S. *Philos. Trans. R. Soc. Lond.* **90**, 403–431 (1800)
9. Spencer, J.N., Bodner, G.M., Rickard, L.H.: *Chemistry: Structure and Dynamics*. Wiley (2010)
10. Mertens P (1999) The theoretical batteries of Georges Leclanché.
11. Pavlov, D.: *Lead-Acid Batteries: Science and Technology*. Elsevier, Amsterdam (2011)
12. Whittingham, M.S.: Electrical energy storage and intercalation chemistry. *Science* **192**(4244), 1126 (1976)
13. Mizushima, K., Jones, P.C., Wiseman, P.J., Goodenough, J.B.: LiCoO_2 ($0 < x < 1$): a new cathode material for batteries of high energy density. *Mater. Res. Bull.* **15**(6), 783–789 (1980)
14. Thackeray, M.M., David, W.I.F., Bruce, P.G., Goodenough, J.B.: Lithium insertion into manganese spinels. *Mater. Res. Bull.* **18**(4), 461–472 (1983)
15. Padhi, A., Nanjundaswamy, K.S., Goodenough, J.: Phospho-Olivines as positive-electrode materials for rechargeable lithium batteries. *J. Electrochem. Soc.* **144**, 1188–1194 (1997)
16. Nishi, Y.: The development of lithium ion secondary batteries. *Chem. Rec.* **1**(5), 406–413 (2001)
17. Väyrynen, A., Salminen, J.: Lithium ion battery production. *J. Chem. Thermodyn.* **46**, 80–85 (2012)
18. Liu, C., Neale, Z.G., Cao, G.: Understanding electrochemical potentials of cathode materials in rechargeable batteries. *Mater. Today* **19**(2), 109–123 (2016)
19. Winter, M., Besenhard, J.O., Spahr, M.E., Novák, P.: Insertion electrode materials for rechargeable lithium batteries. *Adv. Mater.* **10**(10), 725–763 (1998)
20. Deng, W., Zhu, W., Zhou, X., Liu, Z.: Graphene nested porous carbon current collector for lithium metal anode with ultrahigh areal capacity. *Energy Storage Mater.* **15**, 266–273 (2018)
21. Miranda, D., Gören, A., Costa, C.M., Silva, M.M., Almeida, A.M., Lanceros-Méndez, S.: Theoretical simulation of the optimal relation between active material, binder and conductive additive for lithium-ion battery cathodes. *Energy* **172**, 68–78 (2019)
22. Abraham, K.M.: Prospects and limits of energy storage in batteries. *J. Phys. Chem. Lett.* **6**(5), 830–844 (2015)
23. Jiang, F., Peng, P.: Elucidating the performance limitations of lithium-ion batteries due to species and charge transport through five characteristic parameters. *Sci. Rep.* **6**(1), 32639 (2016)
24. Christensen, J., Albertus, P., Sanchez-Carrera, R.S., Lohmann, T., Kozinsky, B., Liedtke, R., et al.: A critical review of li/air batteries. *J. Electrochem. Soc.* **159**(2), R1–R30 (2011)
25. Li, T., Bai, X., Gulzar, U., Bai, Y.-J., Capiglia, C., Deng, W., et al.: A Comprehensive understanding of lithium-sulfur battery technology. *Adv. Func. Mater.* **29**(32), 1901730 (2019)
26. Slater, M.D., Kim, D., Lee, E., Johnson, C.S.: Sodium-Ion batteries. *Adv. Func. Mater.* **23**(8), 947–958 (2013)
27. Hosaka, T., Kubota, K., Hameed, A.S., Komaba, S.: Research development on K-Ion batteries. *Chem. Rev.* **120**(14), 6358–6466 (2020)
28. Nunes-Pereira, J., Costa, C.M., Lanceros-Méndez, S.: Polymer composites and blends for battery separators: state of the art, challenges and future trends. *J. Power Sources* **281**, 378–398 (2015)

29. Imanishi, N., Yamamoto, O.: Rechargeable lithium–air batteries: characteristics and prospects. *Mater. Today* **17**(1), 24–30 (2014)
30. Zhang, W., Liu, Y., Guo, Z.: Approaching high-performance potassium-ion batteries via advanced design strategies and engineering. *Sci. Adv.* **5**(5), eaav7412 (2019)
31. Canepa, P., Sai Gautam, G., Hannah, D.C., Malik, R., Liu, M., Gallagher, K.G., et al.: Odyssey of multivalent cathode materials: open questions and future challenges. *Chem. Rev.* **117**(5), 4287–4341 (2017)
32. Pandolfo, A.G., Hollenkamp, A.F.: Carbon properties and their role in supercapacitors. *J. Power Sources* **157**(1), 11–27 (2006)
33. González, A., Goikolea, E., Barrena, J.A., Mysyk, R.: Review on supercapacitors: technologies and materials. *Renew. Sustain. Energy Rev.* **58**, 1189–1206 (2016)
34. Conway, B.E., Pell, W.G.: Double-layer and pseudocapacitance types of electrochemical capacitors and their applications to the development of hybrid devices. *J. Solid State Electrochem.* **7**(9), 637–644 (2003)
35. Lu, Z., Chang, Z., Zhu, W., Sun, X.: Beta-phased Ni(OH)₂ nanowall film with reversible capacitance higher than theoretical Faradic capacitance. *Chem. Commun.* **47**(34), 9651–9653 (2011)
36. Xie, J., Sun, X., Zhang, N., Xu, K., Zhou, M., Xie, Y.: Layer-by-layer β-Ni(OH)₂/graphene nanohybrids for ultraflexible all-solid-state thin-film supercapacitors with high electrochemical performance. *Nano Energy* **2**(1), 65–74 (2013)
37. Heilbron, J.L.: *Electricity in the 17th and 18th Centuries: A Study of Early Modern Physics*. Univ of California Press, Berkeley (1979)
38. Becker, H.I.: Low voltage electrolytic capacitor. Google Patents (1957)
39. Conway, B.E.: Transition from “supercapacitor” to “battery” behavior in electrochemical energy storage. *J. Electrochem. Soc.* **138**(6), 1539–1548 (1991)
40. Muzaffar, A., Ahamed, M.B., Deshmukh, K., Thirumalai, J.: A review on recent advances in hybrid supercapacitors: design, fabrication and applications. *Renew. Sustain. Energy Rev.* **101**, 123–145 (2019)
41. Gulzar, U., Goriparti, S., Miele, E., Li, T., Maidecchi, G., Toma, A., et al.: Next-generation textiles: from embedded supercapacitors to lithium ion batteries. *J. Mater. Chem. A* **4**(43), 16771–16800 (2016)
42. Mezzomo, L., Ferrara, C., Brugnetti, G., Callegari, D., Quartarone, E., Mustarelli, P., et al.: Exploiting Self-Healing in Lithium Batteries: Strategies for Next-Generation Energy Storage Devices **10**(46), 2002815 (2020)
43. Chombo, P.V., Laoonual, Y.: A review of safety strategies of a Li-ion battery. *J. Power Sources* **478**, 228649 (2020)
44. Lopez, J., Gonzalez, M., Viera, J.C., Blanco, C.: Fast-charge in lithium-ion batteries for portable applications. In: INTELEC 2004 26th Annual International Telecommunications Energy Conference 2004, pp. 19–24 (2004)
45. Duan, J., Tang, X., Dai, H., Yang, Y., Wu, W., Wei, X., et al.: Building safe lithium-ion batteries for electric vehicles: a review. *Electrochem. Energy Rev.* **3**(1), 1–42 (2020)
46. He, J., Manthiram, A.: A review on the status and challenges of electrocatalysts in lithium-sulfur batteries. *Energy Storage Mater.* **20**, 55–70 (2019)
47. Bhatt, M.D., Lee, J.Y.: High capacity conversion anodes in Li-ion batteries: a review. *Int. J. Hydrogen Energy* **44**(21), 10852–10905 (2019)
48. Birkl, C.R., Roberts, M.R., McTurk, E., Bruce, P.G., Howey, D.A.: Degradation diagnostics for lithium ion cells. *J. Power Sources* **341**, 373–386 (2017)
49. Nitta, N., Wu, F., Lee, J.T., Yushin, G.: Li-ion battery materials: present and future. *Mater. Today* **18**(5), 252–264 (2015)
50. Wang, R., Chen, C., Zheng, Y., Wang, H., Liu, J.-W., Yu, S.-H.: Structure–property relationship of assembled nanowire materials. *Mater. Chem. Front.* **4**(10), 2881–2903 (2020)
51. Ladpli, P., Nardari, R., Kopsaftopoulos, F., Chang, F.-K.: Multifunctional energy storage composite structures with embedded lithium-ion batteries. *J. Power Sources* **414**, 517–529 (2019)

52. Gu, M., Kim, B.-S.: Electrochemistry of multilayer electrodes: from the basics to energy applications. *Acc. Chem. Res.* **54**(1), 57–69 (2021)
53. Asp, L.E., Greenhalgh, E.S.: Structural power composites. *Compos. Sci. Technol.* **101**, 41–61 (2014)
54. Kalimuldina, G., Nurpeissova, A., Adylkhanova, A., Adair, D., Taniguchi, I., Bakenov Z. Morphology and dimension variations of copper sulfide for high-performance electrode in rechargeable batteries: a review. *ACS Appl. Energy Mater.* **3**(12), 11480–11499 (2020)
55. Valverde, A., Gonçalves, R., Silva, M.M., Wuttke, S., Fidalgo-Marijuan, A., Costa, C.M., et al.: Metal-organic framework based PVDF separators for high rate cycling lithium-ion batteries. *ACS Appl. Energy Mater.* **3**(12), 11907–11919 (2020)
56. Xu, J., Xiao, X., Zeng, S., Cai, M., Verbrugge, M.W.: Multifunctional lithium-ion-exchanged zeolite-coated separator for lithium-ion batteries. *ACS Appl. Energy Mater.* **1**(12), 7237–7243 (2018)
57. Rafiz, K., Lin, J.Y.S.: Safe Li-ion batteries enabled by completely inorganic electrode-coated silicalite separators. *Sustainable Energy Fuels* **4**(11), 5783–5794 (2020)
58. Liu, X., Chen, Q., Li, Y., Chen, C., Xing, X., Huang, B., et al.: LiMn₂O₄ Cathode materials with excellent performances by synergistic enhancement of double-cation (Na⁺, Mg²⁺) doping and 3DG coating for power lithium-ion batteries. *J. Phys. Chem. C* **124**(48), 26106–26116 (2020)
59. Brutti, S., Simonetti, E., De Francesco, M., Sarra, A., Paolone, A., Palumbo, O., et al.: Ionic liquid electrolytes for high-voltage, lithium-ion batteries. *J. Power Sources* **479**, 228791 (2020)
60. Jónsson, E.: Ionic liquids as electrolytes for energy storage applications – a modelling perspective. *Energy Storage Mater.* **25**, 827–835 (2020)
61. Karuppasamy, K., Theerthagiri, J., Vikraman, D., Yim, C.-J., Hussain, S., Sharma, R., et al.: Ionic liquid-based electrolytes for energy storage devices: a brief review on their limits and applications. *Polymers* **12**(4), 918 (2020)
62. Sebastian, J., Samuel, J.M.: Recent advances in the applications of substituted polyanilines and their blends and composites. *Polym. Bull.* **77**(12), 6641–6669 (2020)
63. Gonçalves, R., Dias, P., Hilliou, L., Costa, P., Silva, M.M., Costa, C.M., et al.: Optimized printed cathode electrodes for high performance batteries. *Energy Technol.* **9**(1), 2000805 (2021)
64. Wang, Y., Niu, P., Li, J., Wang, S., Li, L.: Recent progress of phosphorus composite anodes for sodium/potassium ion batteries. *Energy Storage Mater.* **34**, 436–460 (2021)
65. Shi, Q., Zhou, J., Ullah, S., Yang, X., Tokarska, K., Trzebicka, B., et al.: A review of recent developments in Si/C composite materials for Li-ion batteries. *Energy Storage Mater.* **34**, 735–754 (2021)
66. Hong, Y.J., Lee, J.-K., Chan Kang, Y.: Yolk-shell carbon microspheres with controlled yolk and void volumes and shell thickness and their application as a cathode material for Li-S batteries. *J. Mater. Chem. A* **5**(3), 988–995 (2017)
67. Feng, S., Song, J., Fu, S., Zhu, C., Shi, Q., Song, M.-K., et al.: One-step synthesis of carbon nanosheet-decorated carbon nanofibers as a 3D interconnected porous carbon scaffold for lithium-sulfur batteries. *J. Mater. Chem. A* **5**(45), 23737–23743 (2017)
68. Zhang, K., Xiong, F., Zhou, J., Mai, L., Zhang, L.: Universal construction of ultrafine metal oxides coupled in N-enriched 3D carbon nanofibers for high-performance lithium/sodium storage. *Nano Energy* **67**, 104222 (2020)
69. Tiwari, A.P., Chae, S.-H., Ojha, G.P., Dahal, B., Mukhiya, T., Lee, M., et al.: Three-dimensional porous carbonaceous network with in-situ entrapped metallic cobalt for supercapacitor application. *J. Colloid Interface Sci.* **553**, 622–630 (2019)
70. Hu, F., Peng, H., Zhang, T., Shao, W., Liu, S., Wang, J., et al.: A lightweight nitrogen/oxygen dual-doping carbon nanofiber interlayer with meso-/micropores for high-performance lithium-sulfur batteries. *J. Energy Chem.* **58**, 115–128 (2021)
71. Cui, R., Xu, D., Xie, X., Yi, Y., Quan, Y., Zhou, M., et al.: Phosphorus-doped helical carbon nanofibers as enhanced sensing platform for electrochemical detection of carbendazim. *Food Chem.* **221**, 457–463 (2017)

72. Zeng, Y., Huang, Y., Liu, N., Wang, X., Zhang, Y., Guo, Y., et al.: N-doped porous carbon nanofibers sheathed pumpkin-like Si/C composites as free-standing anodes for lithium-ion batteries. *J. Energy Chem.* **54**, 727–735 (2021)
73. Tang, T., Zhang, T., Zhao, L., Zhang, B., Li, W., Xu, J., et al.: Multifunctional ultrasmall-MoS₂/graphene composites for high sulfur loading Li–S batteries. *Mater. Chem. Front.* **4**(5), 1483–1491 (2020)
74. Zaidi, S.D.A., Wang, C., Jin, Y., Zhu, S., Yuan, H., Yang, Y., et al.: Single-nozzle electrospun core-shell MoS₂@FexOy@CNF anodes for lithium and potassium-ion batteries. *J. Alloys Comp.* **848**, 156531 (2020)
75. Wang, H., Wei, D., Zheng, J., Zhang, B., Ling, M., Hou, Y., et al.: Electrospinning MoS₂-decorated porous carbon nanofibers for high-performance lithium-sulfur batteries. *ACS Appl. Energy Mater.* **3**(12), 11893–11899 (2020)
76. Zhou, X., Liu, B., Chen, Y., Guo, L., Wei, G.: Carbon nanofiber-based three-dimensional nanomaterials for energy and environmental applications. *Mater. Adv.* **1**(7), 2163–2181 (2020)
77. Liu, C., Bai, Y., Zhao, Y., Yao, H., Pang, H.: MoS₂/graphene composites: fabrication and electrochemical energy storage. *Energy Storage Mater.* **33**, 470–502 (2020)
78. Kong, X., Zheng, Y., Wang, Y., Liang, S., Cao, G., Pan, A.: Necklace-like Si@C nanofibers as robust anode materials for high performance lithium ion batteries. *Sci. Bull.* **64**(4), 261–269 (2019)
79. Wang, W., Kumta, P.N.: Nanostructured hybrid silicon/carbon nanotube heterostructures: reversible high-capacity lithium-ion anodes. *ACS Nano* **4**(4), 2233–2241 (2010)
80. Shi, L., Pang, C., Chen, S., Wang, M., Wang, K., Tan, Z., et al.: Vertical graphene growth on sio microparticles for stable lithium ion battery anodes. *Nano Lett.* **17**(6), 3681–3687 (2017)
81. Li, J.-Y., Li, G., Zhang, J., Yin, Y.-X., Yue, F.-S., Xu, Q., et al.: Rational design of robust Si/C microspheres for high-tap-density anode materials. *ACS Appl. Mater. Interfaces* **11**(4), 4057–4064 (2019)
82. Feng, Y., Wu, K., Deng, X., Ke, J., Yang, B., Dong, H., et al.: Exfoliated graphite nanosheets coating on nano-grained SnO₂/Li₄Ti₅O₁₂ as a high-performance anode material for lithium-ion batteries. *Langmuir* **36**(48), 14666–14675 (2020)
83. Ju, Z., Zhang, X., King, S.T., Quilty, C.D., Zhu, Y., Takeuchi, K.J., et al.: Unveiling the dimensionality effect of conductive fillers in thick battery electrodes for high-energy storage systems **7**(4), 041405 (2020)
84. Mishra, K., Yadav, N., Hashmi, S.A.: Recent progress in electrode and electrolyte materials for flexible sodium-ion batteries. *J. Mater. Chem. A* **8**(43), 22507–22543 (2020)
85. Yaghi, O.M., Li, G., Li, H.: Selective binding and removal of guests in a microporous metal–organic framework. *Nature* **378**(6558), 703–706 (1995)
86. Wang, H., Zhu, Q.-L., Zou, R., Xu, Q.: Metal-organic frameworks for energy applications. *Chem* **2**(1), 52–80 (2017)
87. Meng, X., Liao, K., Dai, J., Zou, X., She, S., Zhou, W., et al.: Ultralong cycle life Li–O₂ battery enabled by a MOF-derived ruthenium-carbon composite catalyst with a durable regenerative surface. *ACS Appl. Mater. Interfaces* **11**(22), 20091–20097 (2019)
88. Huang, Q., Wei, T., Zhang, M., Dong, L.-Z., Zhang, A.M., Li, S.-L., et al.: A highly stable polyoxometalate-based metal–organic framework with π – π stacking for enhancing lithium ion battery performance. *J. Mater. Chem. A* **5**(18), 8477–8483 (2017)
89. Peng, Z., Yi, X., Liu, Z., Shang, J., Wang, D.: Triphenylamine-based metal-organic frameworks as cathode materials in lithium-ion batteries with coexistence of redox active sites, high working voltage, and high rate stability. *ACS Appl. Mater. Interfaces* **8**(23), 14578–14585 (2016)
90. Jin, Y., Zhao, C., Sun, Z., Lin, Y., Chen, L., Wang, D., et al.: Facile synthesis of Fe-MOF/RGO and its application as a high performance anode in lithium-ion batteries. *RSC Advances* **6**(36), 30763–30768 (2016)
91. Wang, D.-Y., Liu, R., Guo, W., Li, G., Fu, Y.: Recent advances of organometallic complexes for rechargeable batteries. *Coordination Chemistry Rev.* **429**, 213650 (2020)

92. Baumann, A.E., Burns, D.A., Liu, B., Thoi, V.S.: Metal-organic framework functionalization and design strategies for advanced electrochemical energy storage devices. *Commun. Chem.* **2**(1), 86 (2019)
93. Stadie, N.P., Wang, S., Kravchuk, K.V., Kovalenko, M.V.: Zeolite-templated carbon as an ordered microporous electrode for aluminum batteries. *ACS Nano* **11**(2), 1911–1919 (2017)
94. Noh, H., Choi, S., Kim, H.G., Choi, M., Kim, H.-T.: Size Tunable Zeolite-Templated Carbon as Microporous Sulfur Host for Lithium-Sulfur Batteries **6**(2), 558–565 (2019)
95. Chen, L.-H., Sun, M.-H., Wang, Z., Yang, W., Xie, Z., Su, B.-L.: Hierarchically structured zeolites: from design to application. *Chem. Rev.* **120**(20), 11194–11294 (2020)
96. Chin, L.-C., Yi, Y.-H., Chang, W.-C., Tuan, H.-Y.: Significantly improved performance of red phosphorus sodium-ion anodes with the addition of iron. *Electrochim. Acta* **266**, 178–184 (2018)
97. Wan, F., Guo, J.-Z., Zhang, X.-H., Zhang, J.-P., Sun, H.-Z., Yan, Q., et al.: In situ binding Sb nanospheres on graphene via oxygen bonds as superior anode for ultrafast sodium-ion batteries. *ACS Appl. Mater. Interfaces.* **8**(12), 7790–7799 (2016)
98. Zheng, X.-M., You, J.-H., Fan, J.-J., Tu, G.-P., Rong, W.-Q., Li, W.-J., et al.: Electrodeposited binder-free Sb/NiSb anode of sodium-ion batteries with excellent cycle stability and rate capability and new insights into its reaction mechanism by operando XRD analysis. *Nano Energy* **77**, 105123 (2020)
99. Dashairya, L., Das, D., Saha, P.: Binder-free electrophoretic deposition of Sb/rGO on Cu foil for superior electrochemical performance in Li-ion and Na-ion batteries. *Electrochimica Acta* **358**, 136948 (2020)
100. Boukhvalov, D.W., Paolucci, V., D'Olimpio, G., Cantalini, C., Politano, A.: Chemical reactions on surfaces for applications in catalysis, gas sensing, adsorption-assisted desalination and Li-ion batteries: opportunities and challenges for surface science. *Physical Chemistry Chemical Physics* (2021)
101. Gunnarsdóttir, A.B., Amanchukwu, C.V., Menkin, S., Grey, C.P.: Noninvasive in situ NMR study of “dead lithium” formation and lithium corrosion in full-cell lithium metal batteries. *J. Am. Chem. Soc.* **142**(49), 20814–20827 (2020)
102. Woods, J., Bhattarai, N., Chapagain, P., Yang, Y., Neupane, S.: In situ transmission electron microscopy observations of rechargeable lithium ion batteries. *Nano Energy* **56**, 619–640 (2019)
103. Wu, X., Li, S., Yang, B., Wang, C.: In situ transmission electron microscopy studies of electrochemical reaction mechanisms in rechargeable batteries. *Electrochem. Energy Rev.* **2**(3), 467–491 (2019)
104. Sanchez, A.J., Kazyak, E., Chen, Y., Chen, K.-H., Pattison, E.R., Dasgupta, N.P.: Plan-view operando video microscopy of Li metal anodes: identifying the coupled relationships among nucleation, morphology, and reversibility. *ACS Energy Lett.* **5**(3), 994–1004 (2020)
105. Pang, Q., Liang, X., Shyamsunder, A., Nazar, L.F.: An in vivo formed solid electrolyte surface layer enables stable plating of Li metal. *Joule* **1**(4), 871–886 (2017)
106. Liu, W., Liu, P., Mitlin, D.: Review of emerging concepts in SEI analysis and artificial SEI membranes for lithium, sodium, and potassium metal battery anodes. *Adv. Energy Mater.* **10**(43), 2002297 (2020)
107. Fang, C., Li, J., Zhang, M., Zhang, Y., Yang, F., Lee, J.Z., et al.: Quantifying inactive lithium in lithium metal batteries. *Nature* **572**(7770), 511–515 (2019)
108. Zhang, S., Liu, Y., Liu, H.: Understanding lithium transport in SEI films: a nonequilibrium molecular dynamics simulation. *Mol. Simul.* **46**(7), 573–580 (2020)
109. Franco, A.A., Rucci, A., Brandell, D., Frayret, C., Gaberscek, M., Jankowski, P., et al.: Boosting rechargeable batteries R&D by multiscale modeling: myth or reality? *Chem. Rev.* **119**(7), 4569–4627 (2019)
110. Lagadec, M.F., Zahn, R., Wood, V.: Characterization and performance evaluation of lithium-ion battery separators. *Nature Energy* **4**(1), 16–25 (2019)
111. Croce, F., Focarete, M.L., Hassoun, J., Meschini, I., Scrosati, B.: A safe, high-rate and high-energy polymer lithium-ion battery based on gelled membranes prepared by electrospinning. *Energy Environ. Sci.* **4**(3), 921–927 (2011)

112. Man, C., Jiang, P., Wong, K.-w., Zhao, Y., Tang, C., Fan, M., et al.: Enhanced wetting properties of a polypropylene separator for a lithium-ion battery by hyperthermal hydrogen induced cross-linking of poly(ethylene oxide). *J. Mater. Chem. A* **2**(30), 11980–11986 (2014)
113. Dai, J., Shi, C., Li, C., Shen, X., Peng, L., Wu, D., et al.: A rational design of separator with substantially enhanced thermal features for lithium-ion batteries by the polydopamine–ceramic composite modification of polyolefin membranes. *Energy Environ. Sci.* **9**(10), 3252–3261 (2016)
114. Costa, C.M., Lizundia, E., Lanceros-Méndez, S.: Polymers for advanced lithium-ion batteries: State of the art and future needs on polymers for the different battery components. *Progress Energy Combustion Sci.* **79**, 100846 (2020)
115. Heidari, A.A., Mahdavi, H.: Recent development of polyolefin-based microporous separators for li-ion batteries: a review. *Chem. Rec.* **20**(6), 570–595 (2020)
116. Nestler, T., Schmid, R., Münchgesang, W., Bazhenov, V., Schilm, J., Leisegang, T., et al.: Separators - Technology review: Ceramic based separators for secondary batteries. *AIP Conf. Proc.* **1597**(1), 155–184 (2014)
117. Huang, X.: Separator technologies for lithium-ion batteries. *J. Solid State Electrochem.* **15**(4), 649–662 (2011)
118. Zhang, H., Zhou, M.-Y., Lin, C.-E., Zhu, B.-K.: Progress in polymeric separators for lithium ion batteries. *RSC Adv.* **5**(109), 89848–89860 (2015)
119. Dou, H., Xu, M., Wang, B., Zhang, Z., Wen, G., Zheng, Y., et al.: Microporous framework membranes for precise molecule/ion separations. *Chem. Soc. Rev.* **50**, 986–1029 (2021)
120. Barbosa, J.C., Dias, J.P., Lanceros-Méndez, S., Costa, C.M.: Recent advances in poly(vinylidene fluoride) and its copolymers for lithium-ion battery separators. *Membranes* **8**(3), 45 (2018)
121. Lu, J., Zhang, H., Hou, J., Li, X., Hu, X., Hu, Y., et al.: Efficient metal ion sieving in rectifying subnanochannels enabled by metal–organic frameworks. *Nat. Mater.* **19**(7), 767–774 (2020)
122. Li, R., Lu, B., Xie, Z., Zhai, J.: The Confinement Effect of Angstrom-Sized Pores in Asymmetrical Membrane Constructed by Zeolitic Imidazolate Frameworks: Partially Dehydrated Ion Transport Performance. **15**(52), 1904866 (2019)
123. Shekarian, E., Jafari Nasr, M.R., Mohammadi, T., Bakhtiari, O., Javanbakht, M.: Preparation of 4A zeolite coated polypropylene membrane for lithium-ion batteries separator **136**(32), 47841 (2019)
124. Li, W., Li, X., Yuan, A., Xie, X., Xia, B.: Al₂O₃/poly(ethylene terephthalate) composite separator for high-safety lithium-ion batteries. *Ionics* **22**(11), 2143–2149 (2016)
125. Xu, Q., Wei, C., Fan, L., Peng, S., Xu, W., Xu, J.: A bacterial cellulose/Al₂O₃ nanofibrous composite membrane for a lithium-ion battery separator. *Cellulose* **24**(4), 1889–1899 (2017)
126. Liu, H., Xu, J., Guo, B., He, X.: Effect of Al₂O₃/SiO₂ composite ceramic layers on performance of polypropylene separator for lithium-ion batteries. *Ceramics Int.* **40**(9, Part A), 14105–14110 (2014)
127. Liu, H., Xu, J., Guo, B., He, X.: Effect of SiO₂ content on performance of polypropylene separator for lithium-ion batteries **131**(23) (2014)
128. Khassi, K., Youssefi, M., Semnani, D.: PVDF/TiO₂/graphene oxide composite nanofiber membranes serving as separators in lithium-ion batteries. *J. Appl. Polym. Sci.* **137**(23), 48775 (2020)
129. Cao, J., Shang, Y., Wang, L., He, X., Deng, L., Chen, H.: Composite electrospun membranes containing a monodispersed nano-sized TiO₂@Li⁺ single ionic conductor for Li-ion batteries. *RSC Advances* **5**(11), 8258–8262 (2015)
130. Li, Y., Yu, L., Hu, W., Hu, X.: Thermotolerant separators for safe lithium-ion batteries under extreme conditions. *J. Mater. Chem. A* **8**(39), 20294–20317 (2020)
131. Salikolimi, K., Sudhakar, A.A., Ishida, Y.: Functional Ionic Liquid Crystals. *Langmuir* **36**(40), 11702–11731 (2020)
132. Huang, J., Huang, Y., Zhang, Z., Gao, H., Li, C.: Li_{6.7}La₃Zr_{1.7}Ta_{0.3}O₁₂ Reinforced PEO/PVDF-HFP based composite solid electrolyte for all solid-state lithium metal battery. *Energy Fuels* **34**(11), 15011–15018 (2020)

133. Wei, T., Zhang, Z.-H., Wang, Z.-M., Zhang, Q., Ye, Y.-S., Lu, J.-H., et al.: Ultrathin solid composite electrolyte based on $\text{Li}_6.4\text{La}_3\text{Zr}_{1.4}\text{Ta}_{0.6}\text{O}_{12}/\text{PVDF-HFP}/\text{LiTFSI}/\text{succinonitrile}$ for high-performance solid-state lithium metal batteries. *ACS Appl. Energy Mater.* **3**(9), 9428–9435 (2020)
134. Yang, T., Zheng, J., Cheng, Q., Hu, Y.-Y., Chan, C.K.: Composite polymer electrolytes with $\text{Li}_7\text{La}_3\text{Zr}_2\text{O}_{12}$ garnet-type nanowires as ceramic fillers: mechanism of conductivity enhancement and role of doping and morphology. *ACS Appl. Mater. Interfaces* **9**(26), 21773–21780 (2017)
135. Angulakshmi, N., Zhou, Y., Suriyakumar, S., Dhanalakshmi, R.B., Satishrajan, M., Alwarappan, S., et al.: Microporous Metal-Organic Framework (MOF)-Based Composite Polymer Electrolyte (CPE) mitigating lithium dendrite formation in all-solid-state-lithium batteries. *ACS Omega* **5**(14), 7885–7894 (2020)
136. Tong, Z., Wang, S.-B., Liao, Y.-K., Hu, S.-F., Liu, R.-S.: Interface between solid-state electrolytes and li-metal anodes: issues, materials, and processing routes. *ACS Appl. Mater. Interfaces* **12**(42), 47181–47196 (2020)
137. Pervez, S.A., Cambaz, M.A., Thangadurai, V., Fichtner, M.: Interface in solid-state lithium battery: challenges, progress, and outlook. *ACS Appl. Mater. Interfaces* **11**(25), 22029–22050 (2019)
138. Li, S., Zhang, S.-Q., Shen, L., Liu, Q., Ma, J.-B., Lv, W., et al.: Progress and perspective of ceramic/polymer composite solid electrolytes for lithium batteries. *Adv. Sci.* **7**(5), 1903088 (2020)
139. Li, L., Deng, Y., Chen, G.: Status and prospect of garnet/polymer solid composite electrolytes for all-solid-state lithium batteries. *J. Energy Chem.* **50**, 154–177 (2020)
140. Chen, X., Vereecken, P.M.: Solid and solid-like composite electrolyte for lithium ion batteries: engineering the ion conductivity at. *Interfaces* **6**(1), 1800899 (2019)
141. Yu, X., Manthiram, A.: A review of composite polymer-ceramic electrolytes for lithium batteries. *Energy Storage Mater.* **34**, 282–300 (2021)
142. Chun, S.-J., Choi, E.-S., Lee, E.-H., Kim, J.H., Lee, S.-Y., Lee, S.-Y.: Eco-friendly cellulose nanofiber paper-derived separator membranes featuring tunable nanoporous network channels for lithium-ion batteries. *J. Mater. Chem.* **22**(32), 16618–16626 (2012)
143. Lv, D., Chai, J., Wang, P., Zhu, L., Liu, C., Nie, S., et al.: Pure cellulose lithium-ion battery separator with tunable pore size and improved working stability by cellulose nanofibrils. *Carbohydrate Polymers* **251**, 116975 (2021)
144. Liu, J., Qin, J., Mo, Y., Wang, S., Han, D., Xiao, M., et al.: Polyphenylene sulfide separator for high safety lithium-ion batteries. *J. Electrochem. Soc.* **166**(8), A1644–A1652 (2019)
145. Ren, W., Zheng, Y., Cui, Z., Tao, Y., Li, B., Wang, W.: Recent progress of functional separators in dendrite inhibition for lithium metal batteries. *Energy Storage Mater.* **35**, 157–168 (2021)
146. Hao, Z., Zhao, Q., Tang, J., Zhang, Q., Liu, J., Jin, Y., et al.: Functional separators towards the suppression of lithium dendrites for rechargeable high-energy batteries. *Mater. Horizons* **8**, 12–32 (2021)
147. Zhang, T., Yang, J., Xu, Z., Li, H., Guo, Y., Liang, C., et al.: Suppressing dendrite growth of a lithium metal anode by modifying conventional polypropylene separators with a composite layer. *ACS Appl. Energy Mater.* **3**(1), 506–513 (2020)
148. Liang, J., Chen, Q., Liao, X., Yao, P., Zhu, B., Lv, G., et al.: A nano-shield design for separators to resist dendrite formation in lithium-metal batteries. *Angew. Chem. Int. Ed. Engl.* **59**(16), 6561–6566 (2020)
149. Wu, H., Zhuo, D., Kong, D., Cui, Y.: Improving battery safety by early detection of internal shorting with a bifunctional separator. *Nature Commun.* **5**(1), 5193 (2014)
150. Yan, J., Wang, Q., Wei, T., Fan, Z.: Recent advances in design and fabrication of electrochemical supercapacitors with high energy densities. *Adv. Energy Mater.* **4**(4), 1300816 (2014)
151. Chen, T., Dai, L.: Carbon nanomaterials for high-performance supercapacitors. *Mater. Today* **16**(7–8), 272–280 (2013)


152. Conway, B.E.: *Electrochemical Supercapacitors: Scientific Fundamentals and Technological Applications*. Springer, US (1999)
153. Zhang, L.L., Zhao, X.S.: Carbon-based materials as supercapacitor electrodes. *Chem. Soc. Rev.* **38**(9), 2520–2531 (2009)
154. Bose, S., Kuila, T., Mishra, A.K., Rajasekar, R., Kim, N.H., Lee, J.H.: Carbon-based nanostructured materials and their composites as supercapacitor electrodes. *J. Mater. Chem.* **22**(3), 767–784 (2012)
155. Yan, J., Wang, Q., Lin, C., Wei, T., Fan, Z.: Interconnected frameworks with a sandwiched porous carbon layer/graphene hybrids for supercapacitors with high gravimetric and volumetric performances. *Adv. Energy Mater.* **4**(13):n/a (2014)
156. Lu, P., Xue, D., Yang, H., Liu, Y.: Supercapacitor and nanoscale research towards electrochemical energy storage. *Int. J. Smart Nano Mater.* **4**(1), 2–26 (2012)
157. Paliwal, M.K., Meher, S.K.: 3D-heterostructured NiO nanofibers/ultrathin g-C₃N₄ holey nanosheets: An advanced electrode material for all-solid-state asymmetric supercapacitors with multi-fold enhanced energy density. *Electrochimica Acta.* **358**, 136871 (2020)
158. Yang, Z., Liu, Q., Zhang, L., Dai, J., Shen, Z.: Green one-pot synthesis of binder-free porous edge-functionalized graphitic carbon nitride/iron oxide nanoparticles nanocomposite as an outstanding electrode for supercapacitors. *J. Energy Storage* **32**, 101909 (2020)
159. Zhang, X., Yang, W., Liu, A., Guo, Z., Mu, J., Hou, J., et al.: Anchoring mesoporous Fe₃O₄ nanospheres onto N-doped carbon nanotubes toward high-performance composite electrodes for supercapacitors. *Ceram. Int.* **46**(14), 22373–22382 (2020)
160. Sathish Kumar, P., Prakash, P., Srinivasan, A., Karupiah, C.: A new highly powered supercapacitor electrode of advantageously united ferrous tungstate and functionalized multiwalled carbon nanotubes. *J. Power Sources* **482**, 228892 (2021)
161. Wu, X., Zheng, S., Huang, Y., Xu, Z., Liu, Z., Yang, W., et al.: Electrolyte permeation and ion diffusion enhanced architectures for high performance all-solid-state flexible supercapacitors. *J. Power Sources* **482**, 228996 (2021)
162. Avasthi, P., Arya, N., Singh, M., Balakrishnan, V.: Fabrication of iron oxide-CNT based flexible asymmetric solid state supercapacitor device with high cyclic stability. *Nanotechnology* **31**(43), 435402 (2020)
163. Iqbal, M.Z., Haider, S.S., Zakar, S., Alzaid, M., Afzal, A.M., Aftab, S.: Cobalt-oxide/carbon composites for asymmetric solid-state supercapacitors. *Mater. Res. Bull.* **131**, 110974 (2020)
164. Zhang, L., Li, G., Jing, L., Li, Z., Li, Z., Yao, H., et al.: Controllable and fast growth of ultrathin α -Ni(OH)₂ nanosheets on polydopamine based N-doped carbon spheres for supercapacitors application. *Synthetic Metals* **270**, 116580 (2020)
165. Mei, H., Zhang, L., Zhang, K., Gao, J., Zhang, H., Huang, Z., et al.: Conversion of MOF into carbon-coated NiSe₂ yolk-shell microspheres as advanced battery-type electrodes. *Electrochimica Acta* **357**, 136866 (2020)
166. Zhang, L., Guo, H., Xue, R., Yue, L., Li, Q., Liu, H., et al.: In-situ facile synthesis of flower shaped NiS₂@regenerative graphene oxide derived from waste dry battery nano-composites for high-performance supercapacitors. *J. Energy Storage* **31**, 101630 (2020)
167. Van Toan, N., Kim Tuoi, T.T., Li, J., Inomata, N., Ono, T.: Liquid and solid states on-chip micro-supercapacitors using silicon nanowire-graphene nanowall-pani electrode based on microfabrication technology. *Mater. Res. Bull.* **131**, 110977 (2020)
168. Sethi, M., Shenoy, U.S., Bhat, D.K.: Simple solvothermal synthesis of porous graphene-NiO nanocomposites with high cyclic stability for supercapacitor application. *J. Alloys Comp.* **854**, 157190 (2021)
169. Golkhatmi, S.Z., Sedghi, A., Miankushki, H.N., Khalaj, M.: Structural properties and supercapacitive performance evaluation of the nickel oxide/graphene/polypyrrole hybrid ternary nanocomposite in aqueous and organic electrolytes. *Energy* **214**, 118950 (2021)
170. Wang, C., Liu, F., Chen, J., Yuan, Z., Liu, C., Zhang, X., et al.: A graphene-covalent organic framework hybrid for high-performance supercapacitors. *Energy Storage Mater.* **32**, 448–457 (2020)

171. Naderi, L., Shahrokhian, S., Soavi, F.: Fabrication of a 2.8 V high-performance aqueous flexible fiber-shaped asymmetric micro-supercapacitor based on MnO₂/PEDOT:PSS-reduced graphene oxide nanocomposite grown on carbon fiber electrode. *J. Mater. Chem. A* **8**(37), 19588–602 (2020)
172. Wang, X., Li, X., Huang, C., Hao, C., Ge, C., Guo, Y.: Fabrication of NiCoAl-layered double hydroxide/N-GO for high energy all-solid-state asymmetric supercapacitors. *Appl. Surf. Sci.* **527**, 146891 (2020)
173. Khanam, Z., Liu, J., Song, S.: Flexible graphene paper electrode prepared via polyvinyl alcohol-assisted shear-exfoliation for all-solid-state polymer supercapacitor application. *Electrochimica Acta* **363**, 137208 (2020)
174. Hong, Y., Xu, J., Chung, J.S., Choi, W.M.: Graphene quantum dots/Ni(OH)₂ nanocomposites on carbon cloth as a binder-free electrode for supercapacitors. *J. Mater. Sci. Technol.* **58**, 73–79 (2020)
175. Zhou, Y., Cheng, X., Huang, F., Sha, Z., Han, Z., Chen, J., et al.: Hierarchically structured electrodes for moldable supercapacitors by synergistically hybridizing vertical graphene nanosheets and MnO₂. *Carbon* **172**, 272–282 (2021)
176. El-Gendy, D.M., Wahab, R.M.A.E., Selim, M.M., Allam, N.K.: A facile synthesis of zeolitic analcime/spongy graphene nanocomposites as novel hybrid electrodes for symmetric supercapacitors. *J. Energy Storage* **32**, 101953 (2020)
177. You, Y., Qu, K., Shi, C., Sun, Z., Huang, Z., Li, J., et al.: Binder-free CuS/ZnS/sodium alginate/rGO nanocomposite hydrogel electrodes for enhanced performance supercapacitors. *Int. J. Biol. Macromol.* **162**, 310–319 (2020)
178. Thulasi, K.M., Manikoth, S.T., Paravannoor, A., Palantavida, S., Bhagiyalakshmi, M., Vijayan, B.K.: Facile synthesis of TNT-VO₂(M) nanocomposites for high performance supercapacitors. *J. Electroanal. Chem.* **878**, 114644 (2020)
179. Garg, R., Agarwal, A., Agarwal, M.: A review on MXene for energy storage application: effect of interlayer distance. *Mater. Res. Express* **7**(2), 022001 (2020)
180. Luo, Y., Tian, Y., Tang, Y., Yin, X., Que, W.: 2D hierarchical nickel cobalt sulfides coupled with ultrathin titanium carbide (MXene) nanosheets for hybrid supercapacitors. *J. Power Sources* **482**, 228961 (2021)
181. Wei D, Wu W, Zhu J, Wang C, Zhao C, Wang L (2020) A facile strategy of polypyrrole nanospheres grown on Ti3C2-MXene nanosheets as advanced supercapacitor electrodes. *J. Electroanal. Chem.* **877**, 114538 (2020)
182. Xue, J., Yang, Q., Guan, R., Shen, Q., Liu, X., Jia, H., et al.: High-performance ordered porous Polypyrrole/ZnO films with improved specific capacitance for supercapacitors. *Mater. Chem. Phys.* **256**, 123591 (2020)
183. Krishnaiah, P., et al.: Fabrication of anode material for asymmetric supercapacitor device using polyaniline wrapped boroncarbonitride nanocomposite with enhanced capacitance. *J. Alloys Comp.* **848**, 156602 (2020)
184. Huang, Y., Bao, S., Lu, J.: Flower-like MnO₂/polyaniline/hollow mesoporous silica as electrode for high-performance all-solid-state supercapacitors. *J. Alloys Comp.* **845**, 156192 (2020)
185. Singh, G., Kumar, Y., Husain, S.: High charge retention and optimization of polyaniline–titanium dioxide nanoparticles composite nanostructures for dominantly stable pseudocapacitive nature. *J. Energy Storage* **31**, 101660 (2020)
186. Abuali, M., Arsalani, N., Ahadzadeh, I.: Investigation of electrochemical performance of a new nanocomposite: CuCo₂S₄/Polyaniline on carbon cloth. *J. Energy Storage* **32**, 101694 (2020)
187. Wang, L., Wang, X., Kannan, P., Ji, S., Wang, Z.: A highly-stable flexible electrode based on Co(OH)₂@NiSe₂ electroplated on metals co-coated textiles. *Mater. Lett.* **279**, 128492 (2020)
188. Butenko, D.S., Zhang, X., Zatonovsky, I.V., Fesych, I.V., Li, S., Chen, R., et al.: Bi(nanoparticles)/CN_x(nanosheets) nanocomposites as high capacity and stable electrode materials for supercapacitors: the role of urea. *Dalton Trans.* **49**(35), 12197–12209 (2020)

189. Raju, T.D., Gopalakrishnan, A., Badhulika, S.: Facile synthesis of 3D/2D Cu₂Se cauliflower/CuS nanosheets composite as a binder-free electrode for high-performance asymmetric solid-state supercapacitors. *J. Alloys Comp.* **845**, 156241 (2020)
190. Wang, Q., Tian, X., Zhang, D.: Flexible asymmetric supercapacitors and electrocatalytic water splitting based on CoNiSe₂/CoNiSe₂ nanoflowers. *Mater. Lett.* **276**, 128245 (2020)
191. Manuraj, M., Chacko, J., Narayanan Unni, K.N., Rakhi, R.B.: Heterostructured MoS₂-RuO₂ nanocomposite: a promising electrode material for supercapacitors. *J. Alloys Comp.* **836**, 155420 (2020)
192. Guo, L., Ma, W.-B., Wang, Y., Song, X.-Z., Ma, J., Han, X.-D., et al.: A chemically crosslinked hydrogel electrolyte based all-in-one flexible supercapacitor with superior performance. *J. Alloys Comp.* **843**, 155895 (2020)
193. Bhat, M.Y., Yadav, N., Hashmi, S.A.: A high performance flexible gel polymer electrolyte incorporated with suberonitrile as additive for quasi-solid carbon supercapacitor. *Mater. Sci. Eng. B* **262**, 114721 (2020)
194. Pochai, C., Sriprachuabwong, C., Sotdipinta, J., Lohitkarn, J., Pasakon, P., Primpray, V., et al.: Alpha-MnO₂ nanofibers/nitrogen and sulfur-co-doped reduced graphene oxide for 4.5 V quasi-solid state supercapacitors using ionic liquid-based polymer electrolyte. *J. Colloid Interface Sci.* **583**, 734–745 (2021)
195. Song, Z., Duan, H., Miao, L., Ruhlmann, L., Lv, Y., Xiong, W., et al.: Carbon hydrangeas with typical ionic liquid matched pores for advanced supercapacitors. *Carbon* **168**, 499–507 (2020)
196. Zhao, J., Gong, J., Wang, G., Zhu, K., Ye, K., Yan, J., et al.: A self-healing hydrogel electrolyte for flexible solid-state supercapacitors. *Chem. Eng. J.* **401**, 125456 (2020)
197. Cevik, E., Gunday, S.T., Bozkurt, A., Amine, R., Amine, K.: Bio-inspired redox mediated electrolyte for high performance flexible supercapacitor applications over broad temperature domain. *J. Power Sources* **474**, 228544 (2020)
198. Demirel, S., Akgun, M.R., Topkaya, R., Kocyigit, A., Cicek, K.: Fabrication and electrochemical properties of flexible ZnO doped PVA-Borax based solid-gel electrolytes. *Inorganic Chem. Commun.* **122**, 108268 (2020)
199. Fan, L.-Q., Geng, C.-L., Wang, Y.-L., Sun, S.-J., Huang, Y.-F., Wu, J.-H.: Design of a redox-active “water-in-salt” hydrogel polymer electrolyte for superior-performance quasi-solid-state supercapacitors. *New J. Chem.* **44**(39), 17070–17078 (2020)
200. Lee, C.S., Ahn, S.H., Kim, D.J., Lee, J.H., Manthiram, A., Kim, J.H.: Flexible, all-solid-state 1.4 V symmetric supercapacitors with high energy density based on comb polymer electrolyte and 1D hierarchical carbon nanotube electrode. *J. Power Sources* **474**, 228477 (2020)

Metal Sulfide Nanocomposites for Energy Harvesting Applications



Maqzia Bashir, Summan Aman, Aneesha Awan, Muhammad Faizan Nazar, Muhammad Zubair, Raziya Nadeem, and Muhammad Nadeem Zafar 

Abstract The global challenges relating to energy harvesting could be solved using nanotechnology, which provides progressively elaborated and ingenious geometric structures, which can incorporate an accrescent material surface. For this purpose of energy harvesting, metal sulfides are serving as an emerging generation. For the conversion of electrochemical energy, metal sulfides have gained considerable attention as favorable electrode material due to their remarkable electrochemical performance including broad potential windows and elevated theoretical capacities. The production of electricity from the waste heat by thermoelectric material is of great interest because of its reliability and simplicity, which enhances energy efficiency. There are some scientific and civil problems regarding the achievement of power densities and high energy for electrochemical conversion. The possible solution to increasing energy demand around the world, for today and to the next generation, is the production of electrical energy directly from light.

In this chapter, we have discussed the process by which metal sulfide nanocomposites can be used for energy harvesting, their utilization for eco-friendly and renewable energy demands, and its efficient storage from alternate sources. This chapter also includes different types of nanocomposites of metal sulfides, their synthetic route including one-step electrode coating method, atomic layer deposition method, one-step high-temperature solvothermal synthesis, hydrothermal method, metal sulfide deposition method, wet chemical method, low-temperature water bath technique and modified hummers method followed by hydrothermal method, hard templating method, soft templating method, and sacrificial templating method, and one step hydrothermal and sol-gel synthesis method. For the elucidation of their structural and morphological characteristics and functional properties, different techniques

M. Bashir · S. Aman · A. Awan · M. Zubair · M. N. Zafar (✉)
Department of Chemistry, University of Gujrat, Gujrat 50700, Pakistan
e-mail: nadeem.zafar@uog.edu.pk

M. F. Nazar
Department of Chemistry, University of Education Lahore, Multan Campus, Lahore, Pakistan

R. Nadeem
Department of Chemistry, University of Agriculture Faisalabad, Faisalabad 38000, Pakistan

including SEM, TEM, X-ray photoelectron spectroscopy (XPS), UV/Vis absorption spectroscopy, XRD, cyclic voltammetry (CV), FTIR, BET (surface and pore size studies) and TGA have been discussed. Analysis for application potential of metal sulfides is elaborated based on several modes of their applications including photo/electrochemical energy storage and conversion, semiconductor solar cells, photocatalytic hydrogen production, electrochemical capacitors, hybrid solar cells with enhanced photocurrent, and solar energy harvesting. Some of the future concerns are also discussed related to their feasibility, production of composites containing multifunctional hybrids, stability and life span of composite, solution or medium for their regeneration, and their safe dumping.

Keywords Metal sulfide nanocomposites · Energy · Hydrogen production · Solar cells

Abbreviations

SEM	Scanning Electron Microscopy
TEM	Transmission Electron Microscopy
XPS	X-Ray Photon Spectroscopy
XRD	X-Ray Diffraction
CV	Cyclic Voltammetry
FTIR	Fourier Transmission Infrared- Spectroscopy
BET	Brunauer-Emmett-Teller
TGA	Thermal Gravimetric Analysis
NMR	Nuclear Magnetic Resonance- Spectroscopy
EDX	Energy Dispersive X-Ray
ESCA	Electron Spectroscopy for Chemical- Analysis
AFM	Atomic Force Microscopy
STM	Scanning Tunneling Microscopy
XAS	X-Ray Absorption Spectroscopy
XRF	X-Ray Fluorescence
MFM	Magnetic Force Microscopy
DSC	Differential Scanning Calorimetry
GC	Gas Chromatography
DFT	Discrete Fourier Transform
APXPS	Ambient-Pressure X-Ray Photoelectron Spectroscopy
SILAR	Successive Ionic-Layer Adsorption and Reaction
DSC	Differential Scanning Calorimetry
LSPR	Local Surface Plasma Resonance
MSHNs	Metal Sulfide Hollow Nanostructures
MOFs	Metal–Organic Frameworks
NG	N-Dopped Graphene
TAA	Thioacetamide

ITO	Indium Tin Oxide
PVDF	Poly(Vinylidene Fluoride)
MMS	Double Metal Sulfide
MIP	Macrophage Inflammatory Protein
DLS	Dynamic Light Scattering
VSM	Vibrating Sample Magnetometer
SQUID	Superconducting Quantum Interference Device
DMTA	Dynamic Mechanical Thermal Analysis
TMA	Thermal Mechanical Analysis
TCD	Thermal Conductivity Detection
NPs	Nanoparticles
3D	3-Dimensional
MS	Metal Sulfides
TTP	Z-(9)-Tricosene, Tricosane, Pentacosane
RCF	Relative Centrifugal Force
DI	Deionized
SMC	Sheet Molding Compounds
GPa	Gigapascal
NP10	Nonylphenol
CTAB	Cetyltrimethylammonium Bromide
HER	Hydrogen Evolution Reaction
QDSC	Quantum Dot Sensitized Solar Cells
GO	Graphene Oxide
DMF	Dimethyl Formamide
IR	Infrared
r-GO	Reduced Graphene Oxide
FTO	F-Doped SnO ₂
QD	Quantum Dots
NCs	Nanocomposites
TBT	Tetra-Butyl Titanate
SDS	Sodium Dodecyl Sulfate
HSCs	Hybrid Supercapacitors
MWCNT's	Multiwalled Carbon Nanotubes

1 Introduction

The exhaustion of many resources of fossil fuel and the occurrence of consequential pollution problems in the environment is due to the rational development of human society [1]. The discerning solution to this credible support which covers all the world's energy demand for today and future generation is the direct transformation of light energy into electrical energy [2]. The exploration of solar cells, hybrid

of nanoparticles (NPs) or polymers, is extensively reported due to capable perceptions of many uniting advantages of the nanocomposites which contain convenient solution-based practices and large absorption coefficient including semiconductors made of inorganic nanoparticles including modifiable shapes (nanorods, tetrapod, and nanodots), large conductivity and adjustable absorption properties [3]. For the recovery of waste heat and solid-state cooling, the advancements for evolving diverse thermoelectric materials have been documented in the past few decades [4]. The distinctive outcome of quantum confinement of small 3D-structures and exposure to nanotechnology has stimulated the use of the metal chalcogenides for many applications like light absorption and luminescence and the development of photodetectors and solar cells [5]. The realization of the probable global crisis arose due to energy deficiency and serious environmental pollution due to the rapid development of industrialization [6]. Human society demands clean and reliable energy sources due to the depletion of conventional sources of fossil fuels along with the downturn of the global climate. Recently, pronounced efforts are made by researchers worldwide for the development of technologies for energy harvesting by solar irradiation and wind turbines [7]. The biggest problem of the twenty-first century is the shortage of energy resources and thoughtful environmental pollution due to rapid industrialization and unspectacular advancement of the living standards of human beings [8]. There is a need of the hour for the development of innovative technologies that contain low cost and environment-friendly features that can harness the expanding depletion of fossil fuels along with exceedingly huge demand of energy resources by the society for profound benefits [9]. The harvesting of solar H_2 is a low-cost, viable and clean approach for high potential demonstration of water splitting via photocatalysis by employing photocatalytic semiconductors [10].

There is increasing research interest for the exertion of renewable energy due to the consumption of untenable fossil fuel accompanied by issues related to the environment and growing energy needs around the globe [11]. To equip with energy depletion issues, the storage and transformation of irregular sustainable energy like wind energy and solar energy, etc. to chemical energy are regarded as a captivating approach [12]. For the conversion of renewable energy into the chemical fuel, the water-splitting strategy providing an evolution of H_2 and O_2 is conventionally reported as an absolute strategy [13, 14]. Furthermore, many industrial procedures on a global scale like ammonia synthesis and petroleum refining contain usage of H_2 . Another attractive procedure is the storage of renewable energy in supercapacitors in the form of electrical charge. The areas of interest nowadays are the development of proficient materials used for application in supercapacitors and water splitting because of their number of advantages for storage and conversion of renewable energy such as high power intensity, large lifetime, friendliness to environment, and great efficiency [15–17].

We are living in a world that requires clean and environment-friendly energy resources. For this energy harvesting and environmental treatment, many technologies that are based upon nanomaterials are used. The knowledge regarding the behavior of nanomaterials when they enter the environment is poor. As far as environmental protection is concerned, the occurrence of nanoparticles into the environment

is unwelcome even when we are looking for environmental toxicology, energy depletion, or water treatment. Therefore, safe and operative procedures for the consumption of these particles are of great interest which leads to the development of nanocomposites [18]. Researchers sometimes have to face great challenges arising due to the utilization of the bare nanoparticles including; nanoparticle loss while performing treatment procedures, trouble in the recovery of these nanoparticles, reduction of the active surface area of nanoparticles due to their aggregation tendency, and their probable health concerns due to their release in the environment [19, 20].

The urge for use of nanocomposites by incorporation with other materials is supported due to their high stability regarding environmental, mechanical, and thermal aspects. These aspects are supported by their ability of liable accessibility and outstanding pore-forming characteristics, possession of a large number of the functional groups, and low-cost contribution. There are many benefits of nanocomposites compared with bare nanoparticles including their easy recovery, inhibition of aggregation and loss during reaction procedure, and consequent environmental protection. For the application of nanomaterials on a heterogeneous system with constant flow setup needs that it must be fixed on a support. Despite using bare nanoparticles, the use of composite contains the advantage of enhanced monitoring potential and treatment procedure [21]. For the preparation of composites, the nanoparticles are assembled with other materials like metals, nanoparticles, polymers, and organic or inorganic materials [22]. This assembly is formulated in such a way that there is maximum interactivity between the materials. It contains great importance because the final size and properties of composites depend on this interaction. Nanocomposites also contain pronounced properties including prevention from poisoning, enhanced permeability of the membrane, the potential for catalysis and sorption, and stability to mechanical and higher thermal application. These improved properties contribute to hybrid properties of final material and their versatility for monitoring performance in energy harvesting applications.

2 Composition of Nanostructured Composites

There are several nanoparticles that are used for energy harvesting applications which include either bare nanoparticles or composites. Metal sulfide-based (MS) nanoparticles have gained special attention in this regard. Inorganic-transition metals are of special interest and other metal sulfides either contain transition metals incorporated to form composite or use transition metal catalysts. A detailed study of these nanocomposites has shown the contribution of a number of metals for energy harvesting applications as given in the Table 1 along with their reported applications.

Table 1 Contribution of nanoparticles for energy harvesting and other applications

Incorporated nanomaterials	Reported applications	References
CdS/CdSe-TiO ₂ , PbS/PbSe-TiO ₂ , MoS ₂ , CdS, CuS, PbS, Sn ₂ S, ZnS, Ag ₂ S, Bi ₂ S ₃ , In ₂ S ₃ , CdS/TiO ₂ , PbS/TiO ₂	Visible light photo degradation, Photo degradation of organic pollutants, Photocatalytic hydrogen production	[1]
MoS ₂ , ZnS, CdS, graphene/CdS	Solar light harvesting, Deactivation of water borne pathogens	[23]
NiSe/Cd _{0.5} Zn _{0.5} S, Cd _{0.5} Zn _{0.5} S, Pt/Cd _{0.5} Zn _{0.5} S, Ni ₂ P/Cd _{0.5} Zn _{0.5} S, NiS/Zn _{0.5} Cd _{0.5} SCu _{1.94} S Zn _{0.23} Cd _{0.77} S	Photo catalyst for solar energy harvesting	[24]
CdSe: PCPDTBT, CdS: P ₃ HT, Sb ₂ S ₃ , Sb ₂ S ₃ : P ₃ HT, (Sb (S ₂ COEt) ₃)	Solution processed polymer-inorganic semiconductor solar cells formation, Properties of light harvesting and electron transport	[25]
PbS/CdS QDSCs, PbS/CdS/ZnS	Polychromatic sensitized solar cells formation	[26]
Li ₂ S ₂ or Li ₂ S, TiS ₂ and MoS ₂	Formation of high energy lithium-sulfur cells	[27]
Bismuth-sulfide/spiro-OMeTAD, Bismuth sulfide/silver sulfide	Develop environment friendly panchromatic solar cells	[28]
CuS, CoS, NiS, and PbS, TiO ₂ /CdS/CdSe	Photo electrochemical performance or photocatalytic activity	[29]
ZnO, Fe ₂ O ₃ , WO ₃ , MoS ₂ , TiO ₂ , CdS MoS ₂ /CdS	Used in dye solar cell, Show photocatalytic activity	[30]
TiO ₂ /CdS, TiO ₂ /Cu ₂ S, TiO ₂ /FeS, TiO ₂ /Co ₉ S ₈ , and, TiO ₂ /ZnS	Visible light driven photocatalytic performance	[32]
CdS-TND-Ni NCs, TEA ⁺ -CdS-TND, CdS-TND	Photocatalytic hydrogen production	[33]
CdS/P ₃ HT, Cd (S ₂ COEt) ₂ .2C ₅ H ₅ N	Formation of inorganic-organic solar cells	[34]
CdS, CdSe, CdTe, Sb ₂ S ₃ , ZnO, CuInS ₂ (CIS)	Formation of hybrid solar cells in inverted and regular device architecture	[2]
CdSe, CdS, CdTe, CuInS ₂ (CIS), PbS, ZnO, polymer/CdS, polymer/CIS, polymer/Sb ₂ S ₃	Formation of hybrid solar cells, Low temperature annealing	[3]
copper zinc tin sulfide (CZTS)	Potential High Temperature, Thermoelectric Energy Harvesting	[4]
Sodium sulfide nonahydrate, CuS	Energy harvesting in thin film solar cells	[35]

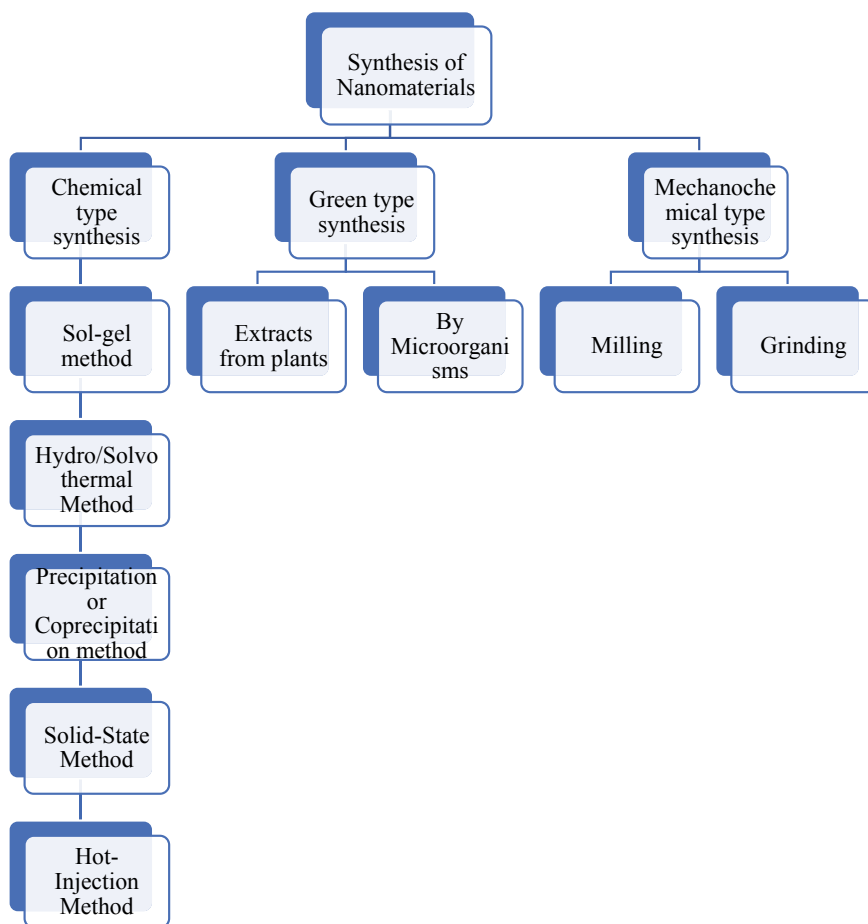
(continued)

Table 1 (continued)

Incorporated nanomaterials	Reported applications	References
1 T-MoS ₂ @HCS, 2H-MoS ₂ @HCS	Solar energy harvesting and storage	[36]
CdS NPs, CdSe/ZnS-MOF CdS-UiO-66(NH ₂)	Photocatalytic activity for organic transformation	[6]
Ag ₂ S, Sb ₂ S ₃ , SnS	Solar light absorption and conversion	[5]
nickel sulfides, cobalt sulfides, copper sulfides, iron sulfides, Na ₃ C ₃ N ₃ S ₃	High performance electrochemical capacitors	[7]
CoS ₂ /RGO-CNT, MoS ₂	Formation of flexible electrodes for hydrogen evolution	[37]
ZnS or Zn _x Cd _{1-x} S	Photocatalytic hydrogen production	[10]
CdS, ZnS, CuInS ₂	Formation of hybrid solar cells	[38]
N-doped graphene/Nickel sulfide	Electrochemical energy harvesting by supercapacitors	[39]
CuInS ₂ , Cu ₂ SnS ₃ , Cu ₁₂ Sb ₄ S ₁₃ , Cu ₂ ZnSnS ₄	Energy harvesting and sensing applications	[40]
SnS ₂ /g-C ₃ N ₄ , MoS ₂ /g-C ₃ N ₄	Photocatalytic energy conversion	[8]
Cu _x S, Cu _x Se, Cu _{2-x} Se _y S _{1-y} , Cu _{2-x} Te _y S _{1-y}	Ligand exchange approach, Energy harvesting applications	[41]
CdSe, PbS, PbSe, PbS (PbSe)/P ₃ HT	Formation of photovoltaic cell	[42]
Polyaniline-cadmium sulfide, CdS	Light harvesting applications	[43]
MoS ₂ , MoSe ₂ , WS ₂ , WSe ₂ , TiS ₂ , TaS ₂ , NbSe ₂	Energy harvesting in solar cells	[44]
Graphene CdS, Graphene ZnS	Photovoltaic applications	[45]
MoS ₂ /rGO	Photocatalytic applications	[9]
1 T and 2H MoS ₂	Electrochemical energy storage	[46]
CoS ₂ , NiS, CuS, CoS, Ag ₂ Se, CdSe, ZnS, CdS - Ag ₂ S	Electrochemical energy storage applications	[47]
Ni (OH) ₂ -CdS/rGO, CdS/rGO	Photocatalytic hydrogen production	[48]
NiCo ₂ S ₄ , MoS ₂	Electrochemical energy storage	[49]
(NH ₄) ₂ Mo(W)S ₄	Electrochemical energy storage and conversion	[50]
AgI-Ag ₂ S	Photothermal conversion and solar energy harvesting	[51]
(RGO)-Zn _x Cd _{1-x} S, Pt-Zn _{0.8} Cd _{0.2} S Zn _x Cd _{1-x} S, RGO-Zn _{0.8} Cd _{0.2} S, Zn _{0.8} Cd _{0.2} S	Photocatalytic hydrogen production	[52]
TiO ₂ /CdS	Photocatalytic hydrogen production and quantum-dot-sensitized solar cell applications	[53]

3 Synthesis Procedures of NPs

Depending on the synthetic strategy different techniques are used presently for the synthesis of nanoparticles as shown in Scheme 1. These are divided mainly into two types based on synthetic procedure, the ex-situ, and the in-situ type of synthesis. These are shown in Scheme 3.



Scheme 1 Routes for synthesis of nanomaterials

3.1 Ex Situ Synthesis

The ex-situ technique for the synthesis of nanoparticles is comparably cost-effective as well as operationally suitable technique employed where mass production is chosen and denoted as blending or direct compounding technique [54].

3.1.1 Blending Technique

In the blending method, firstly; we must prepare the solutions of TTP and Chitosan/Pectin. Now the TTP solution is mixed with pectin solution with continuous stirring (magnetic stirring) while both solutions have, unlike volume ratio. When stirring is continued, the nanoparticles immediately form with dropwise mixing of the cationic solution in anionic solution. These nanoparticles are centrifuged for separation from the solution. Centrifugation is done for 2 h at about 3270 RCF. Now discard the supernatant and wash the particles with DI-water, characterize them and mostly freeze-dried [55].

3.1.2 Direct Compounding Method

The direct compounding method was developed by Dieffenbacher which is used for the generation of the SMC compounds along with the successive production of MS particles using the flow molding method. In this technique, nanoparticles of Ag, Al, and Cu are prepared, filled in a mold which has high strength, at Vacuum gloves-chest of ZKSTX-1 type which is made inert by purging Ar gas. Now, this mold is transferred to the hydraulic press chamber of the type TDY 15–50 T. Later, nanoparticles are made compacted into the sample having disc shape and having 0.5–1.5 mm of thickness and 10 mm diameter by applying 1.0–1.75 GPa of uniaxial load for about 2–60 min [56]. As both of these are single-stage methods, they have the benefit of having no need for maturing of nanoparticles for several days. They have reduced the processing time to a few seconds from the introduction of raw material to the formation of the product by neglecting the intermediate step which contains the semi-finished products.

3.1.3 Reverse Emulsion Method

The synthesis of metal-sulfide catalysts containing ultrafine dispersions and nano-sized particles is done by reverse emulsion method in the presence of vacuum residue medium containing two components, one is metal and other the sulfiding agent, utilizing specific time and temperature for synthesis. In the reverse emulsion method, all the chemicals used are of the analytical grade except for chemical grade NP10. For the typical synthesis of FeS by this method, 14 mL of the 0.2 mol/L aqueous

solution of $\text{Fe}(\text{NO}_3)_3$, 7 mL of the 0.2 mol/L aqueous solution of $\text{Ni}(\text{NO}_3)_3$, 4 mL of the NP10, and hexane of 35 mL solution are mixed with continuous stirring and dropwise addition of 2.80 g of CTAB in the above emulsion was done. By the continuous stirring and addition of 2.10 g of thiourea in above emulsion, it changes to reverse emulsion. Now this solution is transferred into a stainless-steel autoclave with internal Teflon lining and having 16 mL of capacity and placed in the oven at 120 °C for about 2–30 h. After the removal of autoclave, the product was washed several times with distilled water and then dried in air at 90 °C [57].

The metal sulfide-containing catalysts which are synthesized by several ex-situ synthetic methods can be used for conducting hydro-conversion for the West Siberian vacuum residue. To explore the composition, size, structure and the dispersion phase of diffused particles and dependence of nanoparticles on the synthesis conditions is determined by the physicochemical methods. They are highly active in restricting reaction for poly-condensation resulting in coke formation [58]. Jung Wu et al. have synthesized the nanoparticle heterostructures of $\text{Ag}_2\text{S}/\text{ZnS}$ and the $\text{Ag}_2\text{S}/\text{CdS}$ by ex-situ synthesis using seed-mediated growth protocol [59]. Kadiev et al. also used the same medium with two components one is Mo-containing and the other is a sulfiding agent for synthesis of ultrafine nanosized composites via ex-situ condensation [58]. Casalongue et al. applied reaction conditions for ex-situ observation including HER (hydrogen evolution reaction) exposure and detected a change in the composition of nanoparticles from MoS_3 to the imperfect MoS_2 [60]. Chang et al. fabricated QDSC (quantum dot sensitized solar cells) by Cd-free CuInS_2 by the edge of ex-situ technique for assembly of chiefly crystalline quantum dots [61].

3.2 *In Situ Synthesis*

There are following perspectives for in-situ synthesis of nanoparticles based upon different starting materials and the fabrication processes:

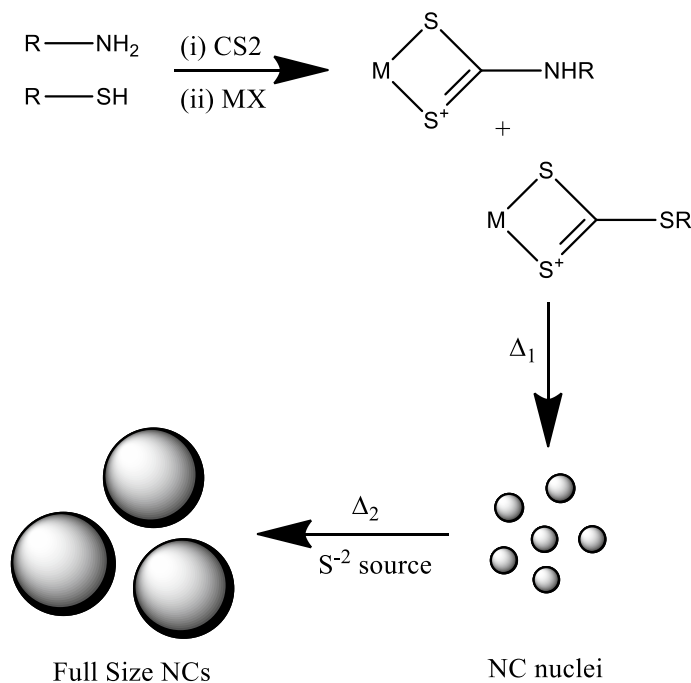
1. The in-situ synthesis comprises the loading of the metal sulfide within the substrate molecules mainly the graphene. For this purpose, oxidation of graphite is done in the formation of graphite oxide by applying the improved Hummers method. Then this graphite oxide of 6 mg weight was dissolved in water and then exfoliated to sheets of graphene oxide having a single layer using 30 min of ultrasonication. In this homogenized GO solution of 4 mL volume, added 15 mg sodium phosphor-tungstate hydrate which was purchased from Sigma-Aldrich and contains purity up to 99.9%. Then added absolute ethanol (5 mL) and anhydrous DMF (36 mL) in the above solution which then became light brown. Then Ar gas was purged from the system for about 30 min to make it inert before irradiation. Then continuous stirring was done along with 3 h irradiation by 300 W Xe arc lamp. Then cutoff and IR water filters were used to filter light, which was then focused on a 50 mL Pyrex reactor through the quartz window. Afterward, 5 mM of silver nitrate and 1 mM of gold chloride trihydrate were added along

- with 5 mM of Na_2S in an inert reactor with 30 min of Ar purging prior to their reaction with graphene oxide. Just after closing the lamp, about 1 mL solution of metal precursor was added in the solution where reduction of complete GO is done. A membrane filter was used to filter the suspension of $\text{Ag}_2\text{S}/\text{r-GO}$ and r-GO and washed several times by 2-propanol to remove unreacted ions of silver. r-GO sheet was obtained after its drying and conscientious peeling off the r-GO film from the membrane filter by using 2-propanol [62]. The electrical conductivity of sandwiched MS/rGO was improved by preventing self-aggregation thus establishing a connection between MS and graphene for achieving fast transport of electrons, the constancy of active material throughout the process of M^+ intercalation and de-intercalation and strengthen MS/rGO as substantial buffering substrate. The adequate electrochemical performance of MS/rGO was observed by in-situ preparation along with exceptional rate capability, cycling stability, and improved reversible capacity. Lu et al. described cobalt sulfide hollow spheres prepared through the in-situ loading technique with improved specific capacity and elevated Coulombic efficiency. Thus results clarify that in-situ synthesis is superior to ex-situ in improving conductivity and restrict volume expansion for CoS_x [63].
2. The other synthesis approach is by alteration of surface sites e.g. MS_x to MS_{x-1} in presence of HER conditions. The hydrothermal reaction is used for MS nanoparticle synthesis. It is shown by ex-situ synthesis that there occurs composition change in nanoparticles by the transformation of MoS_3 to MoS_2 and surface layer rich in MoS_2 utilized for HER. However, the real procedure of transformation is not clear that as it occurs entirely in operation conditions or there occurs any relation connecting catalytic currents and magnitude of the transformation. Moreover, there is also ambiguity in the type of catalytic site used i.e. which composition of S and Mo atoms expeditiously take part in HER, which is critical information in considering reaction steps and high catalytic activity source. Casalongue et al. revealed that by the combination of DFT with APXPS we can observe the change of chemical composition of the active site of Molybdenum Sulfide from MoS_3 to MoS_2 by applying HER conditions [60].
 3. The other approach of in-situ synthesis for establishing inflated surface coverage contains SILAR (successive ionic-layer adsorption and reaction). Firstly, the nanoparticles of TiO_2 of the size of $\sim 20_{\text{nm}}$ were deposited on FTO (F-doped SnO_2) glass substrate. Afterward, a transparent film was coated with scattered TiO_2 and annealed for 30_{min} at about 500 °C for the formation of TiO_2 film which is mesoporous and contains double layer of TiO_2 . The pretreatment of as prepared TiO_2 film is done by dipping it for 24 h in 45 mL of acetonitrile which contains 2 M MPA along with H_2SO_4 . For the sake of sensitization, this TiO_2 -electrode, again for 24_h was dipped in sensitized CuInS_2 solution. These prepared electrodes were then sequentially exposed to three nonidentical solutions as; (i) 1.25×10^{-1} M copper nitrate in CH_3OH for 30 s (ii) 1.35×10^{-1} M sodium sulfide in $\text{CH}_3\text{OH}/\text{H}_2\text{O}$ (iii) 10^{-1} M indium nitrate in CH_3OH for 1 min. Repetition of the SILAR process was done 2–6 times to get the desired

- photoanode. Chang et al. noticed the in-situ fabrication of Cd-free CuInS₂-QDSC by SILAR for the achievement of appreciable QD's surface coverage [61].
4. Another analogous approach for in-situ synthesis is the one-pot synthesis of a large amount of constitutionally tunable NC's by decomposition of MS precursors. When we use Cu and Pb precursors of the type Pb(II)[S₂CNC₄H₁₀]₂ and Cu(II)[S₂CNC₄H₁₀]₂, we can synthesize CuS₂ and PbS₂ nanoparticles by simple one-step thermal decomposition. Shortly, these precursors are prepared by a simple method by mixing solution of metal chloride i.e. Pb(II)Cl₂ and Cu(II)Cl₂ in the solution of Na(I)[S₂CNC₄H₁₀] in 2:1 molar ratio. The product form immediately. In the other method, a mixture of copper bis(diethyldithiocarbamate) was deposited on Si-substrate (6 mm × 6 mm) which was cleaned by isopropanol by sonication. Then the substrate was placed on a hot plate with a glass slide at ~240–250 °C in an inert environment until the evaporation of all the solvent. The as-prepared MS nanoparticles are collected, washed and dried [64]. This approach is suitable for the synthesis of numerous metal sulfides using precursors that are stable in air. The construction of particles, ligands, and precursors is also studied. Chesman et al. sketched the in-situ synthesis of CS₂ by precursors. Mainly the precursors are aliphatic amines, and the other component is thiol which is also the part of the reaction mixture employed for ligand synthesis. The ligand formation is explained by using FTIR, optical absorption spectroscopy, and ¹H and ¹³C NMR. The reaction progress is monitored by using XRD hence validating the kesterite (Cu₂ZnSnS₄) nanocomposite formation [65]. The steps for one-pot in situ synthesis are shown in Scheme 2.
 5. The advanced approach for the in-situ method contains starting material as nanofillers and the use of monomers of polymer hosts. The synthesis is done by the formation of dispersion from precursors and host monomers followed by exposure of mixture to suitable conditions by the introduction of appropriate metal ions [54]. Firstly, precursors are synthesized by the preloading of metal ions into the polymer matrix, where metal ions are assumed to be uniformly distributed. Thus the loading of resultant is done in nanofillers and their exposure to S⁻² is done for synthesizing desired nanoparticles [20]. Yang et al. described that by assimilation of the heterostructures of nanocomposites of dielectric material, semiconductor, and organic/inorganic metals, the lifetime of solar cells can be increased. Regarding this purpose CdS and Sb₂S₃ were synthesized in the presence of precursors [66].

3.3 Emerging Synthesis Methods

The chemicals used for preparation/synthesis purposes were all purchased from authentic resources (Acros or Aldrich, Alfa Aesar corporation, Aladdin Ltd. Shanghai, China) and were of AR grade and used as it is without further need of

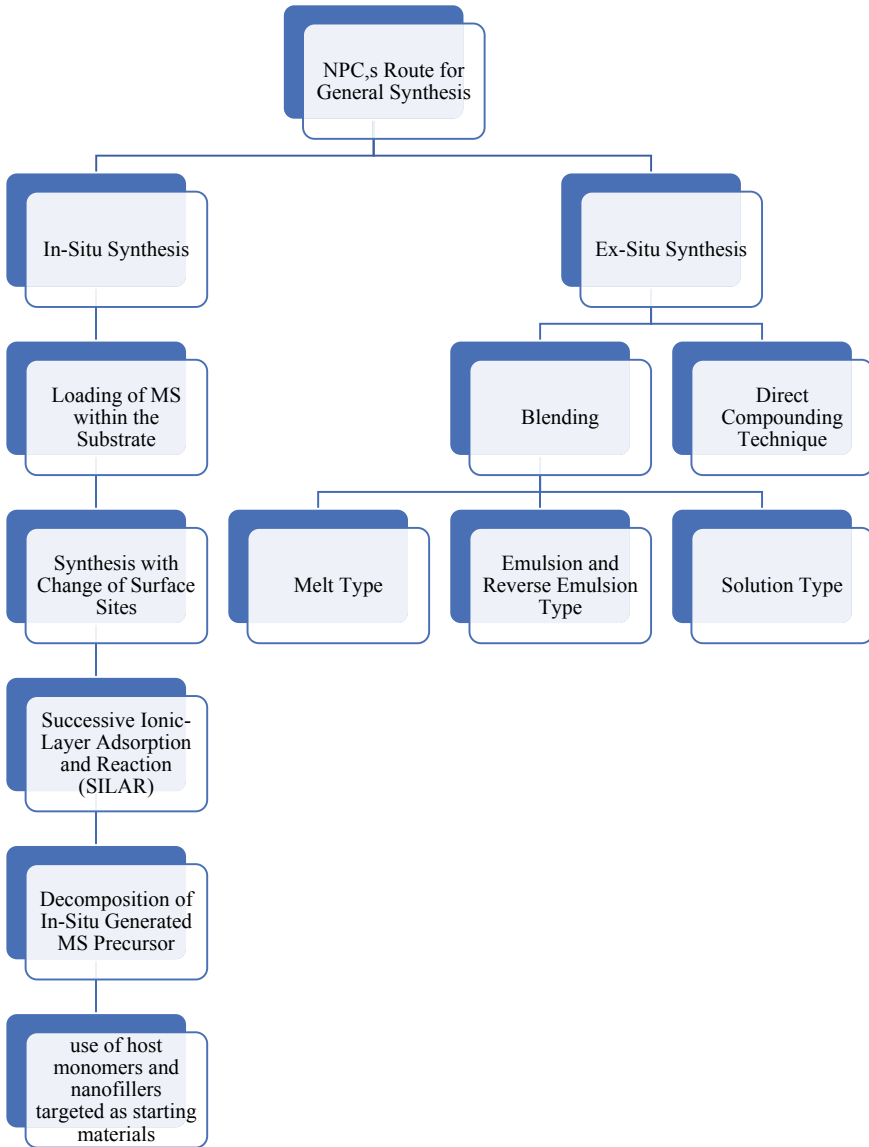


Scheme 2 A precise Three Stage, One-Pot in-situ synthesis of CZTS NC's (Reproduced with permission from [64])

purification. All the reagents used were of analytical grade. Aluminum foils have 99.99% purity with 0.3 mm thickness. For the purification of water, the Millipore system was used. Following methods were used so far:

3.3.1 One-Step Electrode Coating Method

Due to great operational performance of mesoporous photoanode of standard TiO_2 , formed by double-layer deposition of TiO_2 NPC's and two films of nanoparticles containing size differences, as one is transparent with 20 nm size and other opaque with the size 300–400 nm, is used as working anode in traditional DSC configuration with magnified light scattering phenomenon. The paste of TiO_2 NPC's was deposited onto the transparent photoanode with conducting material of F_1 -doped SnO_x . Before the sensitization of anode, it is calcined in muffle as well as TiCl_4 at 450 °C. Electrode thickness is measured with dispersion even lower than 10% by SEM using JSM-700F JEOL FEG-SEM system and found to be 14 μm , divided as a scattering layer of 5 μm and transparent layer of 9 μm . Now the single SILAR cycle is performed by dipping of working electrode in a solution of metal precursor for 1 min and then into the solution of sulfide. Minimum of 3–4 baths are required and photoanode is washed thoroughly

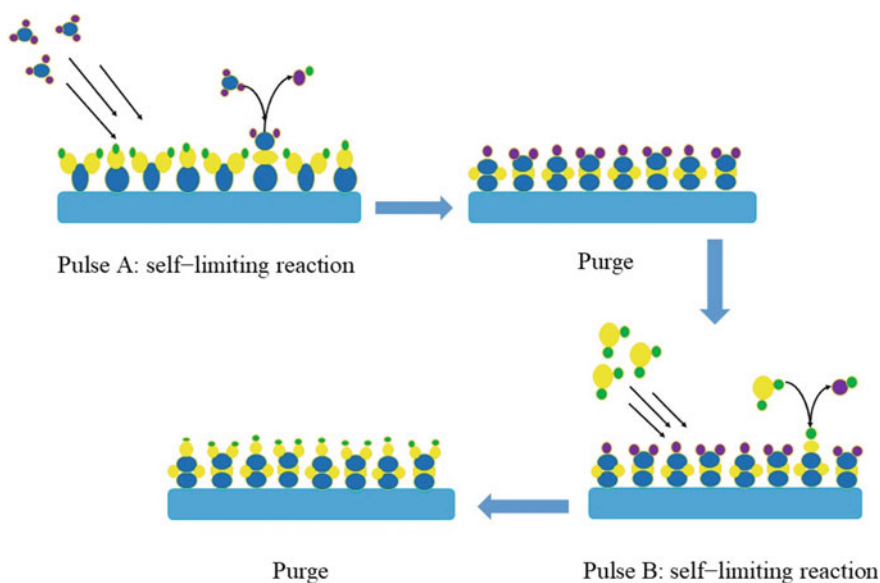


Scheme 3 Synthesis of polymeric nanocomposites

with the corresponding solvent (depending upon the nature of nanoparticles) for the subtraction of chemical residues from electrode surface afterward every bath and air-dried. In this way deposition of MS-nanoparticles is done on the electrode. For example; for samples of hybrid PbS/CdS, the deposition of CdS is done directly by PbS deposition [26].

3.3.2 Atomic Layer Deposition (ALD)

ALD is a robust technique with an accuracy of up to sub nanometers for depositing several materials. The ALD is a revised version of the chemical vapor deposition, which contains the consecutive exposure of a precursor (present in the gas phase) to the substrate in an inert environment maintained by inert-gas purging. ALD has the advantage that every precursor selectively reacts at the surface with a substrate having a specified functional group and prevents thermal decomposition. These precursors are self-limiting and after one species is saturated on the surface, the extra molecules are expelled out by introducing another precursor with the same self-limiting characteristic as evident from Scheme 4. By the repetition of these cycles develop continual material growth. In this method, a consistent coating of the ultrahigh-aspect-ratio structures to the surface without the establishment of a gradient in its composition of thickness is done. In the earliest times, elemental sulfur was used as a sulfur source (anion source) but nowadays, the majority of the ALD techniques make use of H_2S as a sulfur source because of its advantages like high volatility and ability to react with precursors containing metal-organic framework. Elemental Zn and S were used in the synthesis of ZnS by ALD in the earliest experiments using $\sim 500^\circ\text{C}$ temperature and synthesis of 1st monolayer make use of binding energy slightly higher than the succeeding layers during self-limiting growth. Afterward, the use of atomic precursors was replaced by molecular precursors like ZnCl_2 with H_2S , where more favorable self-limitations are obtained by the ligand-exchange reaction. Although, there are some limitations for halide precursors like the use of $300\text{--}400^\circ\text{C}$ source



Scheme 4 Design of ALD process (Reproduced with permission from [32])

temperature for vaporization which is very high and a temperature equal or higher than it for the deposition step. These limitations produce defiance for several applications. Moreover, the halide impurities contain some detrimental effects in several applications [31].

3.3.3 One-Step High-Temperature Solvothermal Synthesis

For the preparation of metal oxide/sulfide nanocomposites/hybrids, this methodology is employed. The metal sulfide used must be hydrated which was mixed with absolute ethanol with 4 h of constant stirring till the formation of a white-colored suspension and then TBT (tetra-butyl titanate) was added in this solution. It results in the formation of slurry which is further stirred for 1 h. This above solution was now added in an autoclave with an internal lining of quartz and placed in the oven for about 20 h at a temperature of 350 °C. After the removal from the oven, the product precipitates were intensively washed with ethanol as well as with deionized water several times after which it was set to dry for 12 h at 80 °C [32].

3.3.4 Hydrothermal Method

The aqueous solutions of all required components were prepared and set for ultrasonication for about 20 min. For example, for the synthesis of MoS₂ aqueous solution of about 16 mL is prepared which contain 0.466 mmol of sodium molybdate, 0.16 mmol of SDS, 0.528 mmol of glucose, and 2.15 mmol of cysteine, and then ultrasonicated. The resultant homogenized solutions were then shifted to autoclave, made of stainless steel with internal Teflon lining, and set for 24 h at 180 °C in an electrical oven for the hydrothermal reaction. After the removal of the autoclave, it was cooled at room temperature and the resultant material was washed several times with ethanol and deionized water and rested for air-dry [36].

The double metal sulfide (MMS) nanocomposites were assembled by a two-step hydrothermal reaction. Briefly describing, the required materials for the preparation of single metal sulfide were dissociated in an aqueous solution of acid-treated MWCNT's and set for 1 h stirring. After that, the homogeneous solution was shifted to a stainless-steel autoclave and set for 12 h at 120 °C. When the reaction was completed the resultant precipitates were washed several times with ultrapure water and dried overnight at 60 °C. Subsequently, the acquired precursor was mixed with an aqueous solution of the salt of 2nd metal with vigorous shaking and again set for 8 h at 120 °C in a Teflon-lined autoclave. Now the product formed is washed several times with ultrapure water and dried in a vacuum oven at 60 °C which contains the desired dual metal nanoparticles.

For the preparation of Ni-Fe-S/MWCNT composites, a 2-step hydrothermal procedure was adopted. The solutions of Ni(NO₃)₂·6H₂O (291 mg), Fe(NO₃)₂·9H₂O (404 mg), urea (300 mg), and NH₄F (74 mg) were prepared and mixed in about 50 mL aqueous solution of the acid-treated MWCNT with continuous stirring for 1 h. After

that, the mixture was poured into a stainless-steel autoclave of 100 mL capacity and retained in the oven for 12 h at 120 °C. After the removal of autoclave, precipitates formed were washed several times with the ultrapure water and set for drying in the vacuum oven at 60 °C overnight. These are the precursors obtained for MMS synthesis. These precursors were then mixed with $\text{Na}_2\text{S}\cdot 9\text{H}_2\text{O}$ (0.1 M) and again transferred to stainless-steel autoclave and again rested for 8 h at 120°C. After the autoclave was removed, the product formed was washed several times with the ultrapure water and dried in a vacuum oven at 60 °C. For the confirmation of the formation of Ni–Fe–S nanoparticles, these were synthesized again by the same procedure but this time without the use of MWCNT's [7].

3.3.5 Metal Sulfide Deposition Method

The preparation of sulfur cathodes is done by one side coating of the electrode with Al-foil material by use of mini-laboratory coater and by application of slurries made of 55 wt.% S, 40 wt.% C-black, 5 wt.% PVDF binder along with N-methyl-2-pyrrolidinone. In the case of metal sulfides, the cathode composition is 65% S, 15% MS, 15% C-black, and 5% binder. The preparation of cathode is done by using a doctor blade for the addition of a 100 μm thick layer of a mixture of C-ink and bare alumina and thus dried at 80 °C under vacuum. A mixture of about 5 g is prepared by adding PVDF, metal sulfides, S, and C-black in proper ratio with vigorous mixing for 15 min in Flacktek Speed Mixer. The resultant slurry was pasted onto the dried substrate utilizing the doctor blade to about 350–450 μm and set for drying overnight at 80–100 °C. The application of vacuum is avoided. After drying its weight is determined and desired pieces are cut off. Before coating to the electrode, the solution was thoroughly mixed for 18 h with the help of a magnetic stirrer. The surface coating is done with the help of a Pasteur pipette accompanied by the spin coating for roughly 15 s. The repetition of the process was done for 5 times by drying the sample every time in the oven and then weighed for calculation of loading which is generally 2 mg/cm^2 . In the case of a pristine cathode, S-loading is around 5 mg/cm^2 while approximately 12 mg/cm^2 in simple cathode blended with MS. The loading level of these electrodes is greater than what is reported in the literature with greater areal capacity for these S-cathodes. [27].

In the case of the SILAR method, the dipping method for electrode deposition is applied. Firstly, the ITO porous films were used to dip in metal nitrate aqueous solution of desired metal and then in 0.1 M NaS_2 each for 1 min . The washing is done with help of deionized water and repetition of the process is done 12 times. The name of ITO porous film is given after the number of times the cycle was performed as for x-cycles we give $\text{CuS}_{(x)}\text{CE}$. For comparison, Pt-CE makes use of Pt-wire [29].

3.3.6 Wet Chemical Synthesis Method

This wet-chemical synthesis method includes both the hydrothermal as well as solvothermal synthesis method with the use of precursor, like $(\text{NH}_4)_6\text{Mo}_7\text{O}_{24}\cdot 4\text{H}_2\text{O}$ and thiourea and substrate displaying benefit of easy coalescing capacity with s substrate including amorphous carbon coating, formation of graphene films, conductive coatings of polymer components, carbon nanofibers and nanotubes formation, CMK-3 formation, the formation of hollow carbon spheres and plentiful active sites but a disadvantage of comparatively reduced crystal quality [46]. In this method, firstly the metal precursors are mixed with a substrate molecule with continuous stirring and then transferred in stainless-steel autoclave which is tightly sealed and placed in an electrical oven for 24 h at 120°C. After the completion of time, the autoclave was removed, and the product formed was washed several times with DI-water and ethanol and dried in a vacuum oven at low temperature overnight.

3.3.7 Low Temperature Water Bath Technique

Aqueous solutions of required components for the synthesis of metal sulfide rGO are prepared as per requirement of reaction and mixed to form a clear solution by the continuous stirring of the solution in a water bath at about 40 °C for about 12 h. After the reaction was completed, the resultant mixture was centrifuged and washed several times with ethanol and distilled water and then set for drying at 353 °C in an electrical oven to obtain resultant MS/rGO nanocomposite. In many controlled experiments, the same procedure was followed for the preparation of metal sulfide nanoparticles [48].

For the preparation of Ag_2S nanoparticles, an ambient temperature water bath technique is required. Solutions are prepared as per requirement of reaction specifically in deionized water with continuous magnetic stirring. Stirring is done for about 30 min after that it is shifted to a water bath to maintain temperature as per requirement of experiment and dropwise added the TAA solution with continuous stirring of the solution. After 30 min of stirring the reaction is stopped and the resultant is centrifuged to get precipitates which are then washed with ethanol and deionized water for 3-times. If MS-suspension is required then resultant ppts are dissolved in deionized water [51].

3.3.8 Modified Hummers Method Followed by Hydrothermal Method

N-doped graphene/MS nanocomposites are prepared using this method. Modified Hummer's method was used to prepare graphite oxide by stirring the H_2SO_4 with graphite flakes for 10 min at room temperature. Then set this beaker in an ice bath with a temperature below 5 °C with constant stirring for 30 min and slowly added KMnO_4 with a 3:1 ratio. After the removal of the mixture from the ice bath, it was again stirred for 30 min at 35 °C with dropwise addition of deionized water in

it with which mixture changes its color to reddish-brown showing an exothermic reaction. Now the temperature of the solution was increased to 95 °C with 15 min stirring and continuous addition of a specific amount of DI-water after which 2 or 3 drops of H₂O₂ are introduced which changes its color to yellowish-orange. The resultant product obtained was removed and washed several times by using 10% HCl and deionized water and set for drying overnight. Now, this is ready for use in the synthesis of N-doped graphene/MS nanocomposites. For this purpose, as prepared NG is assimilated with MS with the use of hydrothermal technique. In short, prepare solution A by using a specific amount of NG as per requirement of reaction in ethanol with 30 min of continuous stirring and homogenize by using ultrasonication. Now the solution B was prepared by required components for the synthesis of MS and both solutions A and B are mixed with appropriate stirring to form solution C by maintaining 9.5 pH. Now this solution was transferred in a Teflon-lined autoclave and set for 12 h at 180 °C. After the removal of autoclave, the product was washed with ethanol and DI water and dried. The resultant product was categorized as NG/MS [39].

3.3.9 Hard Templating Method

It is one of the advanced methods including a coating on the outer surface of the hard template with precursor or shells of metal sulfide with successive careful elimination of template. There are insufficient hard templates available that are appropriate for MSHNs synthesis due to the vulnerability of MS to environmental temperature and acids. However, due to conflict between material available for templates and MS, the formation of invariable precursors or MS-shells on diversified templates is challenging in most cases.

3.3.10 Soft Templating Method

In this method, there is the introduction of gas bubbles or the surfactants in the solvothermal/hydrothermal system for the synthesis of MSHNs. In 2004, pioneer work was done by Alivisatos and his co-workers who preferred the sacrificial templating method superior to the soft templating method which depends upon nanoscale-Kirkendall effect along with ion-exchange which have proven to be much effective and adaptable for MSHNs synthesis via sulfidation in the gaseous or liquid phase.

3.3.11 Sacrificial Templating Method

The shape and size of the MSHNs can be directly identified by using self-involved sacrificial templates, e.g. to transmute solid structure to polyhedral as well as

nanotubes or hollow spheres. It is also possible to acquire MSHNs containing multiplex interior by applying controlled conditions for sulfidation reaction as well as precursor structure. Applying precursor templates containing several metal cations, it is possible to synthesize diversified MS-hollow structures. Another advanced technique for MSHNs synthesis is the template-free approach depending upon the inside-out Ostwald ripening method but have a difficulty in obtaining monodispersed, invariable and composite MSHNs [49].

3.3.12 One-Step Hydrothermal (Solvothermal) and Sol–Gel Synthesis

This method includes the preparation of metal sulfide nanocomposites with appropriate doping of another metal along with Si–OH as a substrate. Firstly, the solution A of the required salts for synthesis of desired metal sulfide was prepared in aqueous media as for the synthesis of Mn-doped ZnS, solutions of Zn(OAc)₂ and Mn(OAc)₂ are prepared in aqueous media. The substrates are rinsed with H₂O in an inert environment and dried with a stream of Ar. Now the substrate is immersed in an aqueous solution of Na₂S and thoroughly rinsed with H₂O and then dried in the Ar stream. The mixture is then homogenized by using ultrasonication and placed in a stainless-steel autoclave with internal Teflon lining and set in an electric oven for 24 h at about 180 °C. The resultant product was rinsed several times with ethanol and DI water and then dried with Ar-stream. These nanoparticles were then adsorbed on the Si–OH substrate film. For the synthesis of Si–OH film, mainly two methods are used. In 1st method, Si-surfaces terminating at OH are prepared by the sonification of the solution mixture of 4:1 of the conc. H₂SO₄ and 30% H₂O₂ and then rinsed with plentiful water. Ellipsometric data showed that there is the formation of about 2 nm thick film of Si–OH. In the 2nd method, for the synthesis of SiO₂ films loaded with Mn-doped ZnS, we place the Si–OH substrate in a beaker containing the aqueous solution of either 91 mM of Zn(OAc)₂ or the mixture containing 91 mM of Zn(OAc)₂ and the 98 mM of Mn(OAc)₂ respectively. Then rinsing of the substrate with water is done along with drying of the substrate with Ar-stream. Then these substrates were submerged in Na₂S-aqueous solution for about 2 min and again rinsed with a stream of water and then dried in Ar-stream. In the case of all these film preparations, rinsing is carefully done by using a parallel stream of water to the substrate. It was observed that the films containing longer rinsing time have no effect on their Ellipsometric thickness. By repetition of adsorption cycles, we can synthesize multilayer films. Every adsorption cycle is accompanied by ellipsometry measurements [36, 67].

4 Characterization Techniques for NPCs

The nanocomposites are a combination of multilayers of nanomaterial with matrix support of another compound [68]. Thus, their characterization contains several aspects [18]. Firstly, nanoscale dimensions of NPCs must be proven [69]; then the

presence of hybrid properties in between components of nanocomposites must be verified. Mittal et al. [70] described the explained properties of NPCs consist of: (i) The scattering and distribution level of NPCs within support material, (ii) the interactivity between NPCs and support material (iii) various structural changes within NPCs arise due to different synthetic routes, (iv) extensive performance of NPCs for their possible utilization. The characterization of NPCs based upon analysis of morphological, optical, elemental, structural, and functional properties is done by a number of techniques such as NMR, MS, FTIR, XRD, UV–vis spectroscopy, etc. as evident from Table 3. The optical properties of NPCs are recognized by two spectroscopic techniques, namely FTIR and UV–vis spectroscopy [54, 71].

4.1 UV–Vis Spectroscopy

The spectroscopic technique that makes use of UV and Visible range of electromagnetic spectra for absorption measurements in a molecule constitutes the UV–Vis spectroscopy. The concentration and absorption of NPCs are described by UV–Vis spectra. Only a small region of the wavelength and frequency of the electromagnetic spectrum is covered by UV and Visible light which is of interest to most chemists. However, the narrow range is of supreme importance because it causes the change in the electronic states of the atoms as well as molecules, thus also called electronic spectroscopy. Moreover, when interaction occurs in the visible region, color can be seen for that molecule. This concept assisted the early exploration of the method for measurement and its basic principle is still in use in today's experiments [71]. The wavelength range for electronic spectra is given in Fig. 1. UV–vis for Ni(OH)₂-CdS/rGO nanocomposites is shown in Fig. 2 [52].

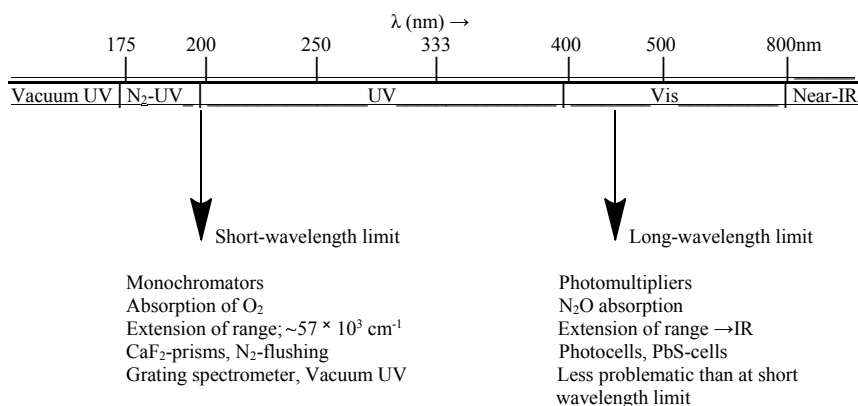
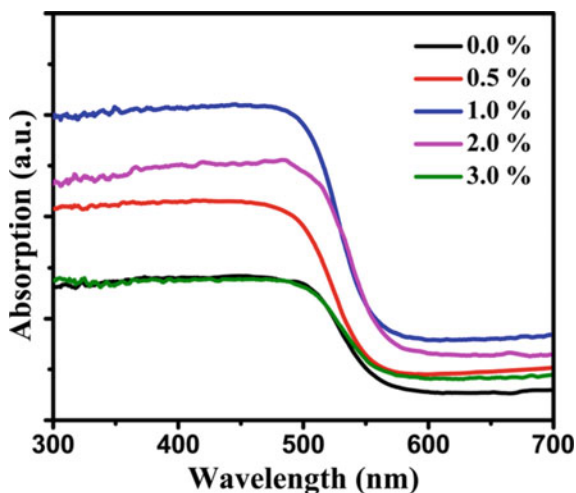


Fig. 1 The ranges and limits of electronic spectra (Reproduced with permission from [71])

Fig. 2 UV-vis for Ni(OH)₂-CdS/rGO nanocomposites (Reproduced with permission from [52])



4.2 FTIR Spectroscopy

FTIR spectra show the absorption measurements revealing interchange of different groups on the surface of substrate showing different vibrations specified for each functional group [31]. FTIR spectroscopy also regarded as vibrational spectroscopy is the technique used for the molecules to optically probe them for the sake of study. This is an accurate method to characterize a molecule, conservatively and effectively having a specified functional group, molecular confirmation, and bonding type. The spectral bands obtained in FTIR are molecule specific and give information about direct compounding as the spectra are called fingerprints of the molecule. FTIR contains narrow vibrational peaks. This technique has advantages as a simple, nondestructive, and reproducible technique requiring minimum sample preparation. The information obtained is about molecular levels, functional group, molecular confirmations, and bonding type. Bands obtained in FTIR are somewhat narrow, easily resolvable, and also sensitive towards molecular environment, conformation, and molecular structure [72]. Figure 3 shows FTIR spectra for in-situ measurement of Ga₂S₃ including different peaks at different wavelength ranges giving information about constituent molecules.

The XRD and XPS are used for the determination of the crystalline phase and composition of the proposed sample for analysis [7, 36]. The system used for XRD analysis was PANalytical X'Pert PRO MPD Alpha system [28]. For the investigation of morphologies of as-prepared samples, SEM, TEM, and EDX analysis are done [36].

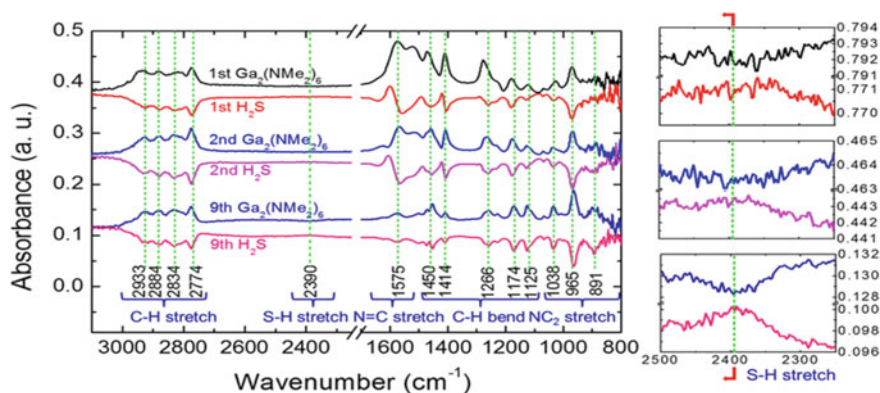


Fig. 3 FTIR spectra for in-situ measurement of Ga_2S_3 (Reproduced with permission from [31])

4.3 X-ray Diffraction Spectroscopy

The atomic structure as well as the molecular structure of a crystal can be determined by using XRD which contains the principle of diffraction of light from the crystalline structure in specific directions. The electronic density of the crystal can be determined by measuring the intensities and angles of diffracted beams by which a 3D picture can be produced. The information like atomic position within the crystal along with chemical bonds and crystallographic disorder can be obtained by studying electron density [73].

4.4 X-ray Photoelectron Spectroscopy

The X-ray photoelectron spectroscopy is generally used for the study of surface characteristics and for analyzing biomedical polymers. This is also regarded as ESCA technique i.e. Electron Spectroscopy of Chemical Analysis and used for the study of elements with mass ranging from 10–200, which are stable in vacuum conditions or made stable by simply cooling the molecule. It is not suitable for H_2 and He. This is the most informative surface technique providing other applications like most quantitative, informative about chemical information, and readily interpretable technique as compared to other techniques. Due to these reasons, this technique can be recommended for the study of medical polymers [74]. Figure 5 shows XPS spectra for $\text{Ni}(\text{OH})_2\text{-CdS/rGO}$ nanocomposites with different energy levels of C.

4.5 SEM Analysis

The other technique, the SEM is a versatile instrument used for the analysis of microstructures and their examination for determining morphologies and characterization of their chemical composition. It uses a high energy electron beam for the measurement. Compared to the optical microscope, it has high resolution due to diffracted electron beams [75]. As Fig. 4 shows results for SEM, TEM, and XRD analysis of MS nanocomposites.

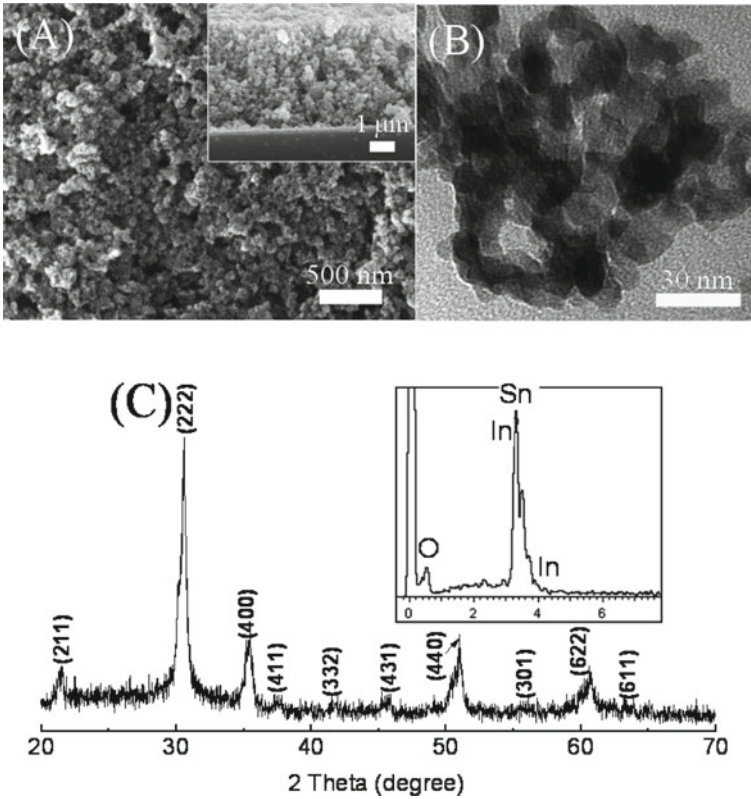


Fig. 4 (A) SEM (B) TEM (C) XRD pattern for ITO porous film of MS nanocomposites (Reproduced with permission from [29])

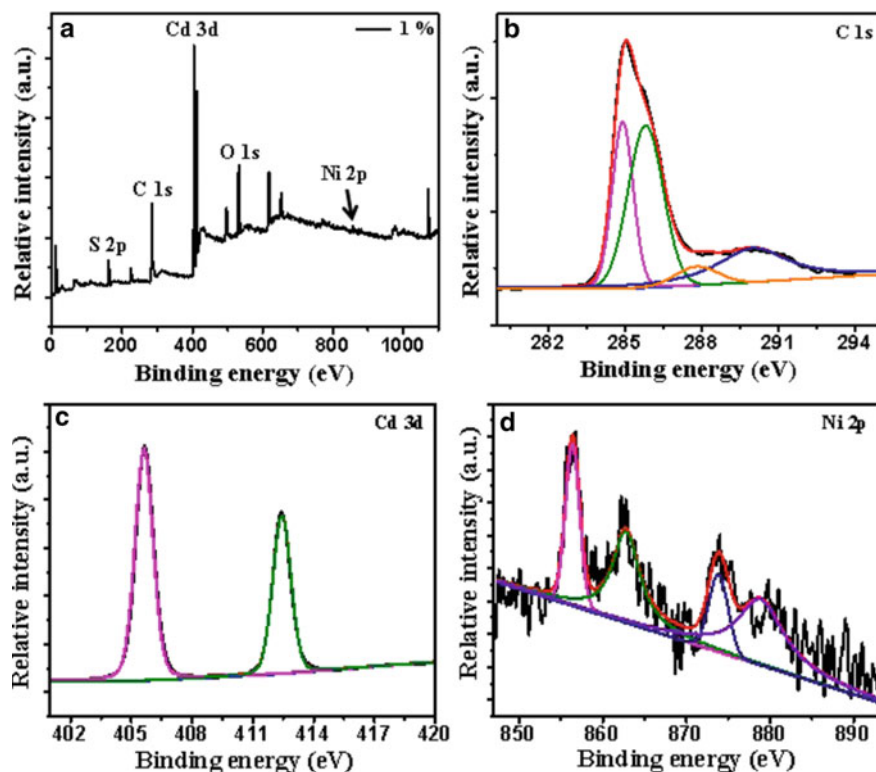


Fig. 5 XPS spectra for Ni(OH)₂-CdS/rGO nanocomposites with different energy levels of C (Reproduced with permission from [52])

4.6 TEM Analysis

The major reason for TEM development was the need to study anything below the atomic level which is possible only by using an electron beam which when diffract produces light that falls on the viewing screen and reveals even minor details of the object recorded photographically. Many of the details of the molecules are below the atomic level which can't be obtained by light microscope thus the need for TEM arrived. The x-ray spectrum obtained by TEM containing a very small portion gives characteristic peaks identifying specific molecules. This spectral information can be converted into quantitative data for which we can interpret the presence of elemental changes. By using fine e⁻-beam, signals can be localized. SEM and TEM can be combined to form STEM which contains combined properties and is a unique scanning imaging microscope [76].

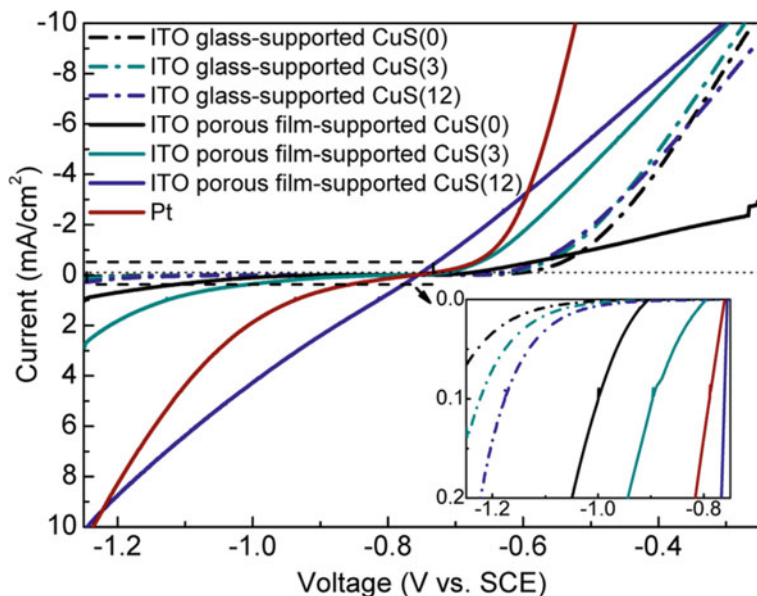


Fig. 6 CV-curve for ITO porous film supported CuS(X) and Pt CEs (Reproduced with permission from [29])

4.7 Cyclic Voltammetry

Cyclic voltammetry is regarded as a powerful technique, used for the study of oxidation and reduction processes occurring within the molecular species and the study of catalysis which includes chemical reactions initiated by electron transfer. The plot of CV is called voltammogram. X-axis represents the applied potential while y-axis represents the resulting current. CV data is mainly reported by two conversions i.e. oxidation and reduction [77]. The pseudo capacitive nature of MS Nano flakes is illustrated by the cyclic behavior of cyclic voltammetry. The scanning rate is observed by the as produced response current from MS. Figure 6 demonstrates the powerful peaks for oxidation as well as the reduction of NG/NiS nanocomposite [39]. For the first time, the CV-curves were studied for electroanalytical activities presented by ITO porous film supported MS nanocomposites.

4.8 Thermogravimetric Analysis

Thermogravimetry (TG) is the technique that measures the mass of a molecule/polymer as the function of time and temperature when we subject the sample to controlled and programmed conditions of temperature and atmosphere. The range of temperature for a commercial TGA ranges up to 1000 °C or above

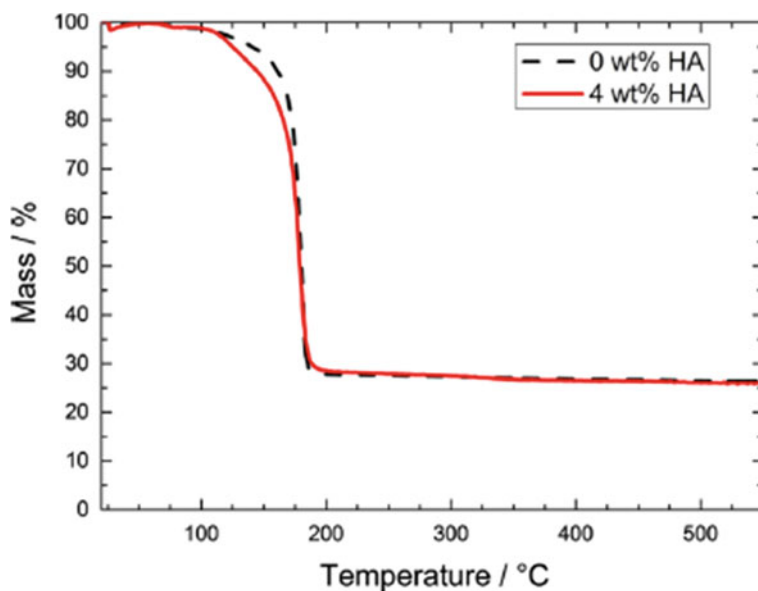


Fig. 7 TGA curve for analysis of PCDTBT/CIS precursor with and without n-hexylamine (Reproduced with permission from [3])

which indicates an adequate upper limit in case of its application for polymers. Its internal atmosphere is made inert by purging an inert gas like N_2 , Ar, or He; or oxidizing gases like O_2 or air; or reducing gases like forming gas which is 8.10% H_2 in N_2 . When we are dealing with polymers, we rarely need a reducing environment. If we consider the moisture content of purged gas, then they can fluctuate from dry conditions to saturated one. [78]. The impact of a specific temperature-dependent component on the formation of MS is determined by TG analysis. Figure 7 demonstrates the loss of mass for the precursor molecules in the presence and absence of n-hexylamine [3].

4.9 BET Analysis

For the demonstration of specific surface area, only two appropriate methods are used, first is MIP, and the other is BET analysis for inert gas adsorption. Adsorption of an inert gas like Ar, N, or Kr is the basic concept for BET analysis for the determination of surface area. In pioneer studies, the surface area of soil particles was determined and then a comparison for internal diameter difference for different clay particles was done as a consequence of adsorbate gas [79]. BET analysis for MS nanocomposites containing specific surface area, total pore volume and average pore diameter is given in Table 2.

Table 2 BET analysis for MS nanocomposites containing specific surface area, total pore volume and average pore diameter (Reproduced with permission from [7])

Sample	Specific surface area (m^2g^{-1})	Total pore volume (m^3g^{-1})	Average pore diameter (nm)
Ni-S	25.2	0.11	17.39
Ni-S/MWCNT	38.3	0.22	22.55
Ni-Fe-S	11.9	0.06	21.65
Ni-Fe-S/MWCNT	10.4	0.12	46.92

Table 3 The characterization techniques for NPCs reorganized by Mourdikoudis et al. [80] and Nasrollahzadeh et al. [18, 69]

NPCs properties	NPCs analysis types	Characterization technique
Optical	Concentration, size, agglomeration state, hints on NPCs shape	UV–Visible spectroscopy
	Surface composition, ligand binding, functional groups	Fourier transmission infrared spectroscopy (FT-IR)
Structural	Crystal composition and structure	X-ray diffraction (XRD)
	Crystallography, elemental analysis, energy binding	X-ray photon spectroscopy (XPS)
Morphological	Morphology, size, dispersion, topology, crystallography	Scanning electron microscopy (SEM)
	Shape, size, quantification, Topology, crystallographic structure	Transmission electron microscopy (TEM, HRTEM)
	Elemental composition, dispersion, morphology, surface roughness, size, shape, texture	Atomic force microscopy (AFM)
	Texture, topology, elemental Analysis	Scanning tunneling microscopy (STM)
	Size, agglomeration, dispersion	Dynamic light scattering (DLS)
Elemental	Elemental composition, purity	Energy dispersive X-ray (EDX)
	Chemical elements, materials and geometry	X-ray absorption spectroscopy (XAS)
	Elemental composition, Thickness, Concentration	X-ray fluorescence (XRF)
Surface	Surface charge, colloidal stability	Zeta potential
	Surface area active	Brunauer–Emmett–Teller (BET)

(continued)

Table 3 (continued)

NPCs properties	NPCs analysis types	Characterization technique
Magnetic	Magnetic behavior	Vibrating sample magnetometer (VSM)
	NPCs magnetization	Superconducting quantum interference device (SQUID)
	NPCs surface magnetic properties	Magnetic force microscopy (MFM)
Thermal	Amorphous status	Differential scanning calorimetry (DSC)
	Mass and composition of stabilizers	Thermal gravimetric analysis (TGA)
	Viscoelastic behavior	Dynamic mechanical thermal analysis (DMTA)
	Kinetic, physical and chemical properties	Thermal mechanical analysis (TMA)

5 Applications of Nanoparticles

With rapid industrialization, the living standard of peoples is increasing day by day. The shortage of energy with increasing energy demand and also the environmental pollution prevailing due to the rapid consumption of fossil fuels are the chief problems today in the twenty-first century. According to a report, the energy consumption in 2013 was about ca. 17TW and it was forecast that it will become two times its current demand in 2050 [81]. Nowadays, from the total energy demand of the globe, 90% is provided by C-based fuels which contain oil, coal, and natural gas [82]. Therefore, researches are held to utilize solar energy as a sustainable and chief energy source [8]. For the determination of the application potential of MS, several experiments are done which includes the following applications;

5.1 Photo/Electrochemical Energy Storage and Conversion

There are mainly three systems at present for solar energy harvesting namely, photocatalysis, photovoltaic-assisted electrolysis, and photoelectrochemical cells [83, 84]. Among these three technologies, the endless energy source for solar energy harvesting is photocatalysis [85, 86]. Graphene-based MS nanocomposites show enhanced photocatalytic activity than bare ones. Basically, the interaction between metal sulfide and graphene is the main strategy for energy harvesting by utilizing as produced e^- -hole pairs [8].

The study of electrochemical behavior of MS was done on CoS nanowires by using a galvanostatic charge–discharge test and CV in about 2 M KOH. As demonstrated by

these studies, this MS nanoarray contains large surface area as well as a high surface-to-volume ratio that favors the complete electron exchange reaction by S^{-2} -ions. It is demonstrated by CV analysis that CoS contains a reversible electrochemical reaction i.e. CoS nanowires can reversibly store electrochemical energy along with enhanced electrochemical activity and weaker polarizability. Conclusively, CoS nano-array possesses the improved high-rate capability and better specific capacity. From the electrochemical study, it is clear that free-standing CoS nano-array has enhanced electrochemical activity over its powder counterpart. This concept of formation of nanoarray or thin films has the advantage of a superior photoelectrochemical and photocatalytic application by the fabrication of additional MS nanostructures [47].

As with advancing research in the field of electrochemical energy harvesting, the performance of rechargeable systems is improving day by day by giving noteworthy hints for additional improvement of performance for energy storing devices. As many rechargeable devices for energy storage are developed including several electrolytes, electrodes, etc. nanocomposite materials have their own place due to the reasons; (i) newly designed nanostructures have high flexibility, enhanced traits like free-binder and free-standing capacity for endless performance, [87, 88] (ii) possess heightened catalytic activity by the possession of exceptionally reactive sites [89, 90] (iii) electrochemical resistance of core is reduced by adopting conductive material coating technique which enhances its conductivity [46, 91, 92]. The recent advantage of this electrochemical energy harvesting is the utilization of Li-ion batteries which have a capable system for energy storage in millions of electric vehicles and portable devices [93, 94]. Additionally, they can also store energy from clean energy sources like hydro-energy, solar energy, and wind energy in the form of chemical energy as well as capable of its release when needed [46, 95].

The storage and release of electrochemical energy in HSCs and LIBs is through the charge and discharge process at electrodes [96, 97]. Its working principle contains ionic movement between the electrodes from the electrolyte by stabilization of charge through the movement of electrons from an external circuit. Their performance is determined by the composition of their electrodes [49, 98–100]. The process of electrochemical energy storage as well as the conversion is recognized to be enhanced by the type of nanomaterial used and is promising in the case of MMSs. In contrast with bulk material, MMSs nanostructure has enhanced electrochemical energy storage capability due to great active sites with large surface area, small pathway for electronic and ionic transfer, decreased electrolytic diffusion resistance along with effective accommodation of strain due to structural changes during the course of electrochemical reaction.

Ternary $NiCo_2S_4$ has proven to possess a wide range of electrochemical energy storage and conversion due to diversified nanostructure and crystalline nature. Especially due to their huge conductivity they show quick charge and discharge phenomenon and enhanced activity due to possession of more active sites because of vast surface area because of nanobelt subunits. Its 3D structure has advantages of prevention of aggregation by shortening of diffusion length for electrolytes with good accessibility and cycling stability [50].

5.2 Semiconductor Solar Cells

In the presence of sunlight, photocatalysis is a basic reaction performed by the semiconductors for catalysis of oxidation–reduction reaction [101, 102]. The semiconductors contain a photocatalytic reaction which is divided into 3-steps. The first step is absorption of light: when solar energy is irradiated, electron generation in conductive band occurs if these absorbed photons have energy equal to or greater than optical bandgap, creating holes in valence band which are generally represented as e^- -holes or charge carriers. The second step is separation and transport of charge: it includes movement of charge carriers towards the surface. The third step contains surface reaction: the substances which are adsorbed on the photocatalytic surface take part in a redox reaction with as-produced holes and electrons [8, 103]. CuS contains great stability and an appropriate bandgap for photocatalysis as it is a p-type semiconductor [104]. When hybridization of CuS with graphene is done it enhances its charge transfer efficiency due to the formation of p–n junction which restricts the combination of holes and electrons generated and enhances light absorption range by making it a powerful photosensitizer to expand composite's response range [8].

The semiconductor NPs containing elevated photocatalytic activity and suitable storage size act as favorable photocatalytic materials [105–110]. Due to this reason, most of the semiconductor materials are transition metal nitrides, sulfides, or oxides which contain appropriate band position and bandgap [111]. The crystalline CdS is chosen from transition metals due to its small bandgap of about 2.4 eV which correlate well with a range of visible spectra for solar radiations along with high electronic and optical properties which depend upon particle size [112, 113], and diversified solar cell applications [114], decontamination of the environment [115], evolution of H_2 [116], and sensors especially chemical sensors [117].

Besides these captivating applications, metal organic framework (MOFs) contain highly active light-absorbing structures with energy harvesting applications associated with excited states [118]. MOFs are used as semiconductors for light-sensitive applications with metal oxide core interconnected with photon antenna [119]. Freshly, MOFs with the capability of converting solar radiations into chemical and electrical energy are reported [120]. When organic linkers are provided, MOF-5 show absorption spectra at 450 nm and encounter photochemical excitation [121]. Both MOFs and semiconductor nanoparticles possess several disadvantages along with their electrochemical applications; if they are combined to form a composite, their properties are enhanced along with overwhelming disadvantages. Their light-harvesting applications are also enhanced in the form of nanocomposites. But the use of MOFs as semiconductors is hardly investigated [6].

The use of solar cells which are solution-processed is assisted with inorganic semiconductors which enhances its efficiency for power conversion and greatly reduces its fabrication cost. The nanowires of inorganic semiconductors are indicated as high charge collecting devices and are promising in enhancing solar cell efficiency [122]. There is the requirement of the photovoltaic cells for their production at a large

scale because inorganic semiconductors have several advantages including facile fabrication, earth abundance, and low toxicity [28].

5.3 Photocatalytic Hydrogen Production

After the revelation of photo-induced H_2O splitting on electrodes made of TiO_2 , it has attracted interest towards the usage of semiconductors for water splitting phenomenon for the production of photocatalytic H_2 as it produces clean and sustainable energy from the solar radiations [123]. From all the sources used for the production of catalytic hydrogen from water splitting, metal sulfides are verified to be the best source utilizing visible light [124–126]. Among all, CdS have gained an advantage because of its high conduction band and efficiency to absorb visible light and reduce H^+ to H_2 [127–129]. The production of NCs is done by a combination of CdS, TNDs, and Ni-clusters. The water-soluble TNDs containing negative charge on their surface are crucial in the construction of active CdS-TND-Ni NCs. When visible light is irradiated, as produced electrons move from all the 3-components of the composite providing a better place for photocatalytic activity. It is found that when sunlight is irradiated, these nanocomposites can produce hydrogen even from the ethanol–water system with a high rate of 3.182 mmolh^{-1} making them the most efficient photocatalytic system even in the absence of the noble-metal catalysts [123]. The recycling experiments were done to prove the stability of NCs of CdS-TND-Ni and CdS-Ni. The production of photocatalytic hydrogen was reduced to 52% of the original production after the performance of the 5th cycle for CdS/Ni. On the other hand, there was not any activity loss observed in the case of CdS-TND-Ni NCs showing its great stability and ability to produce photocatalytic H_2 [33].

The doping of metal, non-metal and noble metal can enhance photocatalytic performance of TiO_2 to some extent as they are important in the production of catalytic hydrogen from the splitting of water. However, TiO_2/CdS nanocomposite is considered to be more effective for water splitting for the production of catalytic hydrogen and removal of pollutants from the environment. The efficiency and properties of TiO_2/CdS are much superior to the individual nanoparticles for water splitting which is related to its synthetic method and microstructure. The addition of Pt as a co-catalyst can enhance the photocatalytic activity of NC. The need for the formation of NiO_2/CdS NC's arises from the fact that CdS undergo photo-corrosion and is preserved from this corrosion due to NC formation with TiO_2 which also enhances its photocatalytic activity and stability [130]. The enhanced applications of these NC's for the solar cell was confirmed by determination of its cell efficiency and photocurrent generation after composite formation and the method adopted for photocatalysis was ideal for the production of H_2 -fuel. [131, 132].

Photocatalytic splitting of H_2O was investigated by Fujishima and Honda in 1972 [133], by then, this strategy has gained great attention due to the effective production of catalytic H_2 which can be utilized to solve environmental and energy problems in near future [134]. From all of these, metal sulfides have gained specific attention due

to pronounced catalytic properties and suitable bandgap. ZnS has gained pace overall due to the rapid production of its holes for photoexcitation purposes and has an advantage to show a photocatalytic reaction in UV light for the production of hydrogen without the need of any catalyst. Several attempts have been made to produce MS combined with graphene to enhance photocatalytic activity and succeeded to produce MS-graphene composites with enhanced photocatalytic water splitting activity [129, 135]. When $Zn_xCd_{1-x}S/rGO$ was irradiated with sunlight, noble metal-free photocatalytic activity was done for hydrogen production with 45% of upgraded production [113].

Recently, the most considered MS-material is CdS [129, 136, 137], which shows high production of hydrogen by photocatalytic activity due to the presence of low bandgap energy of about 2.4 eV. The reaction was studied in a Pyrex glass photoreactor with Xe-lamp for UV-irradiation. Solutions for Ni(OH)₂-CdS/rGO were prepared and stirred in dark for about 10_{min} by purging N₂ for 15 min just for the removal of air by then 5 ml methane was introduced to the above mixture as an internal standard. The production of catalytic hydrogen was then confirmed by determining its amount using GC assisted with a TCD detector [48, 138].

Due to pollution-free nature and recyclability of hydrogen, it is regarded as the best substitute for fossil fuel in near future [139]. The best source of hydrogen is splitting of water for its huge quantity and high purity [140]. The key step for water splitting is HER [37]. The energy crisis of the world can be resolved by the production and utilization of catalytic hydrogen from water by the use of solar irradiations [141, 142]. The use of semiconductors for photocatalytic activity is considered as a promising source with a sustainable, clean, and low-cost approach [10].

5.4 Electrochemical Capacitors

The electrochemical capacitors have advantages of high power density, cell potential, energy density, and cyclic stability when fabricated with Ni-S/MWCNT//Ni-Fe-S//MWCNT [7, 143].

It became the need of hour to develop energy storage devices which could be both electrochemical capacitors as well as rechargeable batteries [143–145]. The determination of energy density of ECs can be done by both voltage and capacitance window by using the equation $E^{1/4} 0.5CV_2$ [146, 147]. For the improvement of energy density without the sacrifice of cycling stability and power density, both voltage and capacitance can be increased. By the addition of isolated potential windows, there observed improvement in AEC of electrodes [148–151], and proved to be the most favorable approach for improvement of their energy density. The transition metal sulfides containing NiS [152], Co_xS_y [153], CuS [154], FeS [155], and mixed metal sulfides [50] are promising pseudo-capacitors with enhanced electrical capacity along with lower electronegativity and exceptional redox reversibility. Chiefly, NiS and FeS

gain significant attraction because of their wider potential windows and large theoretical capacities [50, 146, 156]. Due to extraordinary electrochemical and mechanical stability, high conductivity, and a large number of active sites available due to possession of elevated surface area, these are ideal for the preparation of nanocomposites. Fabrication of electrochemical capacitors containing Ni-S/MWCNT//Ni-Fe-S/MWCNT shows higher value up to 1.7 V for its potential window, 42.2 Whkg^{-1} of energy density, and 3.7 kWkg^{-1} of power density with possession of excellent cyclic stability. Specifically, the electrochemical capacitors of Ni-S/MWCNT show excellent properties and perform noteworthy action for energy harvesting with improved capacity, potential, and redox kinetics. By the comparison of doped and undoped Ni-S/MWCNT//Ni-Fe-S/MWCNT AEC, high capacitance and excellent performance can be achieved [7].

5.5 Hybrid Solar Cells with Enhanced Photocurrent

For the maximum generation of photocurrent, the expansion of solar spectra from UV to IR region with maximum light absorption range is needed in the formation of sensitive solar cells. The high potential and photocurrent generation is observed by the use of PbSe_9 and PbS_8 incorporated solar cells [157]. The conduction of these hybrid solar cells is also notably increased by the incorporation of TiO_2 [158]. The energy harvesting problems can dramatically be solved by the production of hybrid solar cells with PbS and PbS-QD which enhances their efficacy with the production of improved photocurrent in addition to their stability in presence of polysulfide electrolytes [26].

The hybrid solar cells with nanoparticles or polymers contain advantages of easy processability, large absorption coefficient, and production of photocurrent [159] including properties of semiconductors like easily adjustable shape including tetrapod, nanorods, and nanodots [160], many adjustable absorption properties [161], and also the high conductivity [162]. Recently, for many hybrid solar cells, the combining polymer or nanoparticles are recognized as absorber layers [159, 162, 163]. The examples of combining materials include poly para-phenylene-vinylene, polythiophenes, or polymers with low bandgap including CdS [164], CuInS_2 [165], PbS [42]. The power efficacy of hybrid solar cells is from 4–5.5% to a maximum [164, 166–168]. The processability of hybrid solar cells has many challenges that can be exploited by advancing the technology which benefited from cheap production, new modules with lightweight solar cell production, and high flexibility by advancing the field [3].

5.6 Solar Energy Harvesting

For the purpose of solar light harvesting, CdS are proven to be more effective compared to graphene including adequate negative potential for providing a sufficient quantity of electron–hole pairs for conduction and photocatalytic activity [169]. Thus CdS is used as an efficient photocatalyst for the production of photocatalytic H₂, degradation of both organic and inorganic pollutants from the water, and reduction of CO₂ [23].

The need for production of photocatalyst responsive for visible light is necessary for efficient harvesting of solar energy [170]. As metal sulfide nanocomposites contain sufficient bandgap thus used for energy harvesting applications utilizing visible light [171]. Among all the metal sulfides used, CdS is the most efficient photocatalyst for the production of catalytic hydrogen due to a reasonable band gap of about 2.4 eV and has suitable positions for band edges. They show pronounced photocatalytic activity when present in composite form than the CdS nanoparticles [172].

In the case of thin-film solar cells, the capability for energy harvesting depends upon the nature of the material used. Thus, polymers with band gaps in UV or near IR regions show better performance when irradiating sunlight. The need of the hour is the production of solar cells incorporating nanoparticles for energy harvesting applications using LSPR (local surface plasma resonance) absorption property [173]. Recently, di and trimetallic nanocomposites with Au, Ag for bimetallic and Ag, Zn, and Ni for trimetallic are effectively utilized for the production of thin-film solar cells for the improvement in their performance [174]. Generally, the nanohybrids contain more pronounced performance for energy harvesting applications [175–177]. Lei et al. used CuS film for the fabrication of solar cells due to the fact that it contains a small path-length for the mobility of electrons and holes along with pronounced stability, transparency, and power conversion efficiency [175].

Some of the hetero-structures have exactly the same range for absorption spectra needed for energy harvesting in UV and near-IR region when exposed to solar radiations, thus reported as the photothermal materials used for energy harvesting purposes [178]. Another report on separated AgI and Ag₂S and in the form of composite as AgI-Ag₂S showed that there is enhanced efficiency of solar cells using nanocomposites as compared to plasmonic nanoparticles, utilizing UV and near-IR region show possible utilization in photothermal therapy [51].

6 Summary and Future Outlook

With expeditious development of living standards, there are increasing risks for the depletion of sources and energy crises along with environmental pollution [24]. Continuous development of society is increasing the risk for environmental pollution

and fossil fuel depletion. There is a need for green synthesis and developing effective technologies to check pollution accompanying the development of renewable and clean energy sources. As solar energy is a natural green energy resource that can be utilized through a number of devices including semiconductors, photoanodes, photo and electrochemical energy harvesting devices. Semiconductors can degrade toxic chemicals existing in the environment to environment-responsive constituents along with the generation of fuel through a number of processes like production of hydrocarbon fuel from reduction of carbon dioxide and photocatalytic water splitting, and the conversion of sunlight into electrical energy as done in semiconductor solar cells [1]. The photothermal materials are getting attention due to their promising applications in photothermal therapy [179], harvesting solar energy, and photo-thermal imaging [52, 180].

For applications of solar cells in energy harvesting and also its transformation, metal sulfides have proven to contribute the most in both cases i.e. photoelectrochemically and photovoltaically, because of possession of low bandgap, high abundance, and low cost [181, 182]. With the development of nanotechnology metal chalcogenides show improved applications for light absorption including photodetectors, solar cells, luminescence, and even more accelerated because of the quantum confinement effect present in 3D structures. Presently, MSs are gaining pace due to the presence of active surfaces in them for the evolution of H_2 photochemically [183–185] with the addition of thermoelectric and photoelectric applications possessed by these MSs especially the Ag_2S , CuS , etc. Particularly, Ag-diffused In_2S_3 possesses various structural modifications in composite form showing low resistivity, decreased bandgap, and a dramatic increase in conductivity of composite-based solar cells [186]. Hence for production of solar cells for energy harvesting applications include investigation of both un-doped and doped, nanoparticles and nanocomposites from which doped materials and nanocomposites show pronounced applications for energy harvesting purpose [5].

The feasibility and development of any energy harvesting device must face serious economic, environmental, and operational challenges as they must play a dynamic role. Therefore, for the wide range of applications, fabrication of the nanocomposites is mandatory including large potential for their reusability. To overcome the energy depletion by excessive use of energy sources, careful investigations are being done to fabricate solar devices with nanomaterials and design new synthetic methods that contain reusability and minimal decrease in their working capabilities with time. It must be proven that they contain their regeneration capabilities and properties like cheap, simple, and fast, and accommodate with economy scale. Additionally, there is the need for the development of comprehensive and entirely safe technologies for the treatment and regeneration of spent materials and their safe disposal. From the literature review, it is evident that most of the information in this regard is either absent or very little work is reported. The functional properties of nanoparticles can be advanced by the fabrication or formation of composites. Future advances will include the aspects of nanocomposites for removal of environmental contaminants, acting as catalysts and adsorbents for the study of combined functionalities of these composites. Thus, for above-mentioned functionalities little knowledge is reported

in literature. Enhanced studies will prove the use of MS-nanocomposites for the production of multifunctional hybrids and their safe disposal [18, 54].

References

1. Zheng, L., Teng, F., Ye, X., Zheng, H., Fang, X.: Photo/electrochemical applications of metal sulfide/TiO₂ heterostructures. *Adv. Energy Mater.* **10**(1), 1902355 (2020)
2. Dunst, S., Rath, T., Reichmann, A., Chien, H.-T., Friedel, B., Trimmel, G.: A comparison of copper indium sulfide-polymer nanocomposite solar cells in inverted and regular device architecture. *Synth. Met.* **222**, 115–123 (2016)
3. Fradler, C., Rath, T., Dunst, S., Letofsky-Papst, I., Saf, R., Kunert, B., Hofer, F., Resel, R., Trimmel, G.: Flexible polymer/copper indium sulfide hybrid solar cells and modules based on the metal xanthate route and low temperature annealing. *Sol. Energy Mater. Sol. Cells* **124**, 117–125 (2014)
4. Yang, H., Jauregui, L.A., Zhang, G., Chen, Y.P., Wu, Y.: Nontoxic and abundant copper zinc tin sulfide nanocrystals for potential high-temperature thermoelectric energy harvesting. *Nano Lett.* **12**(2), 540–545 (2012)
5. Krylova, V., Baltrusaitis, J.: Synthesis and properties of polyamide-Ag₂S composite based solar energy absorber surfaces. *Appl. Surf. Sci.* **282**, 552–560 (2013)
6. Ke, F., Wang, L., Zhu, J.: Facile fabrication of CdS-metal-organic framework nanocomposites with enhanced visible-light photocatalytic activity for organic transformation. *Nano Res.* **8**(6), 1834–1846 (2015)
7. Luo, Y., Que, W., Yang, C., Tian, Y., Yin, X.: Hydrothermal synthesis of transition metal sulfides/MWCNT nanocomposites for high-performance asymmetric electrochemical capacitors. *Electrochimica Acta* **322**, 134738 (2019)
8. Ren, Y., Zeng, D., Ong, W.-J.: Interfacial engineering of graphitic carbon nitride (g-C₃N₄)-based metal sulfide heterojunction photocatalysts for energy conversion: a review. *Chin. J. Catal.* **40**(3), 289–319 (2019)
9. Wang, J., Guan, Z., Huang, J., Li, Q., Yang, J.: Enhanced photocatalytic mechanism for the hybrid gC₃N₄/MoS₂ nanocomposite. *J. Mater. Chem. A* **2**(21), 7960–7966 (2014)
10. Ran, J., Gao, G., Li, F., Ma, T., Du, A., Qiao, S.: Ti₃C₂ MXene co-catalyst on metal sulfide photo-absorbers for enhanced visible-light photocatalytic hydrogen production (2017)
11. Chu, S., Majumdar, A.: Opportunities and challenges for a sustainable energy future. *Nature* **488**(7411), 294–303 (2012)
12. McCrory, C.C., Jung, S., Ferrer, I.M., Chatman, S.M., Peters, J.C., Jaramillo, T.F.: Benchmarking hydrogen evolving reaction and oxygen evolving reaction electrocatalysts for solar water splitting devices. *J. Am. Chem. Soc.* **137**(13), 4347–4357 (2015)
13. Yang, Y., Fei, H., Ruan, G., Tour, J.M.: Porous cobalt-based thin film as a bifunctional catalyst for hydrogen generation and oxygen generation. *Adv. Mater.* **27**(20), 3175–3180 (2015)
14. Wang, X., Kolenko, Y.V., Bao, X.-Q., Kovnir, K., Liu, L.: One-step synthesis of self-supported nickel phosphide nanosheet array cathodes for efficient electrocatalytic hydrogen generation. *Angew. Chem. Int. Ed.* **54**(28), 8188–8192 (2015)
15. Abdel Maksoud, M.I.A., Fahim, R.A., Shalan, A.E., et al.: Advanced materials and technologies for supercapacitors used in energy conversion and storage: a review. *Environ. Chem. Lett.* **19**, 375–439 (2021)
16. Abdel Messih, M.F., Shalan, A.E., Sanad, M.F., Ahmed, M.A.: Facile approach to prepare ZnO@SiO₂ nanomaterials for photocatalytic degradation of some organic pollutant models. *J. Mater. Sci. Mater. Electron.* **30**, 14291–14299 (2019)
17. Abdelbasir, S.M., Shalan, A.E.: An overview of nanomaterials for industrial wastewater treatment. *Korean J. Chem. Eng.* **36**, 1209–1225 (2019)

18. Abdellatif Soliman, S.M., Sanad, M.F., Shalan, A.E.: Synthesis, characterization and antimicrobial activity applications of grafted copolymer alginate-g-poly(N-vinyl imidazole). *RSC Adv.* **11**, 11541–11548 (2021)
19. Elseman, A.M., Zaki, A.H., Shalan, A.E., et al.: TiO₂ nanotubes: an advanced electron transport material for enhancing the efficiency and stability of perovskite solar cells. *Ind. Eng. Chem. Res.* (2020). <https://doi.org/10.1021/acs.iecr.0c03415>
20. Batool, M., Nazar, M.F., Awan, A., et al.: Bismuth-based heterojunction nanocomposites for photocatalysis and heavy metal detection applications. *Nano-Struct Nano-Objects* **27**, 100762 (2021)
21. Tang, L., Yang, G.-D., Zeng, G.-M., Cai, Y., Li, S.-S., Zhou, Y.-Y., Pang, Y., Liu, Y.-Y., Zhang, Y., Luna, B.: Synergistic effect of iron doped ordered mesoporous carbon on adsorption-coupled reduction of hexavalent chromium and the relative mechanism study. *Chem. Eng. J.* **239**, 114–122 (2014)
22. Khezri, K., Mahdavi, H.: Polystyrene-silica aerogel nanocomposites by in situ simultaneous reverse and normal initiation technique for ATRP. *Microporous Mesoporous Mater.* **228**, 132–140 (2016)
23. Baig, U., Hawsawi, A., Ansari, M., Gondal, M., Dastageer, M., Falath, W.: Synthesis, characterization and evaluation of visible light active cadmium sulfide-graphitic carbon nitride nanocomposite: a prospective solar light harvesting photo-catalyst for the deactivation of waterborne pathogen. *J. Photochemistry Photobiol. B: Biol.* **204**, 111783 (2020)
24. Gong, H., Li, Z., Chen, Z., Liu, Q., Song, M., Huang, C.: NiSe/Cd_{0.5}Zn_{0.5}S composite nanoparticles for use in p–n heterojunction-based photocatalysts for solar energy harvesting. *ACS Appl. Nano Mater.* **3**(4), 3665–3674 (2020)
25. Bansal, N., O’Mahony, F.T., Lutz, T., Haque, S.A.: Solution processed polymer–inorganic semiconductor solar cells employing Sb₂S₃ as a light harvesting and electron transporting material. *Adv. Energy Mater.* **3**(8), 986–990 (2013)
26. Braga, A., Giménez, S., Concina, I., Vomiero, A., Mora-Seró, I.: Panchromatic sensitized solar cells based on metal sulfide quantum dots grown directly on nanostructured TiO₂ electrodes. *J. Phys. Chem. Lett.* **2**(5), 454–460 (2011)
27. Bugga, R.V., Jones, S.C., Pasalic, J., Seu, C.S., Jones, J.-P., Torres, L.: Metal sulfide-blended sulfur cathodes in high energy lithium-sulfur cells. *J. Electrochem. Soc.* **164**(2), A265 (2016)
28. Cao, Y., Bernechea, M., MacLachlan, A., Zardetto, V., Creatore, M., Haque, S.A., Konstantatos, G.: Solution processed bismuth sulfide nanowire array core/silver sulfide shell solar cells. *Chem. Mater.* **27**(10), 3700–3706 (2015)
29. Chen, H., Zhu, L., Liu, H., Li, W.: ITO porous film-supported metal sulfide counter electrodes for high-performance quantum-dot-sensitized solar cells. *J. Phys. Chem. C* **117**(8), 3739–3746 (2013)
30. Darsara, S.A., Seifi, M., Askari, M.B.: One-step hydrothermal synthesis of MoS₂/CdS nanocomposite and study of structural, photocatalytic, and optical properties of this nanocomposite. *Optik* **169**, 249–256 (2018)
31. Dasgupta, N.P., Meng, X., Elam, J.W., Martinson, A.B.: Atomic layer deposition of metal sulfide materials. *Acc. Chem. Res.* **48**(2), 341–348 (2015)
32. Ding, S., Yin, X., Lü, X., Wang, Y., Huang, F., Wan, D.: One-step high-temperature solvothermal synthesis of TiO₂/sulfide nanocomposite spheres and their solar visible-light applications. *ACS Appl. Mater. Interfaces* **4**(1), 306–311 (2012)
33. Dinh, C.-T., Pham, M.-H., Kleitz, F., Do, T.-O.: Design of water-soluble CdS–titanate–nickel nanocomposites for photocatalytic hydrogen production under sunlight. *J. Mater. Chem. A* **1**(42), 13308–13313 (2013)
34. Dowland, S., Lutz, T., Ward, A., King, S.P., Sudlow, A., Hill, M.S., Molloy, K.C., Haque, S.A.: Direct growth of metal sulfide nanoparticle networks in solid-state polymer films for hybrid inorganic-organic solar cells. *Adv. Mater.* **23**(24), 2739–2744 (2011)
35. Hamed, M.S., Mola, G.T.: Copper sulphide as a mechanism to improve energy harvesting in thin film solar cells. *J. Alloy. Compd.* **802**, 252–258 (2019)

36. Hsiao, M.-C., Chang, C.-Y., Niu, L.-J., Bai, F., Li, L.-J., Shen, H.-H., Lin, J.-Y., Lin, T.-W.: Ultrathin 1T-phase MoS₂ nanosheets decorated hollow carbon microspheres as highly efficient catalysts for solar energy harvesting and storage. *J. Power Sources* **345**, 156–164 (2017)
37. Peng, S., Li, L., Han, X., Sun, W., Srinivasan, M., Mhaisalkar, S.G., Cheng, F., Yan, Q., Chen, J., Ramakrishna, S.: Cobalt sulfide nanosheet/graphene/carbon nanotube nanocomposites as flexible electrodes for hydrogen evolution. *Angew. Chem.* **126**(46), 12802–12807 (2014)
38. Rath, T., Edler, M., Haas, W., Fischereder, A., Moscher, S., Schenk, A., Trattinig, R., Sezen, M., Mauthner, G., Pein, A.: A direct route towards polymer/copper indium sulfide nanocomposite solar cells. *Adv. Energy Mater.* **1**(6), 1046–1050 (2011)
39. Reddy, B.J., Vickraman, P., Justin, A.S.: Electrochemical performance of nitrogen-doped graphene anchored nickel sulfide nanoflakes for supercapacitors. *Appl. Surf. Sci.* **483**, 1142–1148 (2019)
40. Regulacio, M.D., Wang, Y., Seh, Z.W., Han, M.-Y.: Tailoring porosity in copper-based multi-nary sulfide nanostructures for energy, biomedical, catalytic, and sensing applications. *ACS Appl. Nano Mater.* **1**(7), 3042–3062 (2018)
41. Saldanha, P.L., Brescia, R., Prato, M., Li, H., Povia, M., Manna, L., Lesnyak, V.: Generalized one-pot synthesis of copper sulfide, selenide-sulfide, and telluride-sulfide nanoparticles. *Chem. Mater.* **26**(3), 1442–1449 (2014)
42. Seo, J., Cho, M.J., Lee, D., Cartwright, A., Prasad, P.N.: Efficient heterojunction photovoltaic cell utilizing nanocomposites of lead sulfide nanocrystals and a low-bandgap polymer. *Adv. Mater.* **23**(34), 3984–3988 (2011)
43. Singh, S., Deol, R.S., Singla, M., Jain, D.: Light harvesting efficiency of hybrid nanocomposite for photovoltaic application. *Sol. Energy Mater. Sol. Cells* **128**, 231–239 (2014)
44. Singh, E., Kim, K.S., Yeom, G.Y., Nalwa, H.S.: Atomically thin-layered molybdenum disulfide (MoS₂) for bulk-heterojunction solar cells. *ACS Appl. Mater. Interfaces* **9**(4), 3223–3245 (2017)
45. Wang, P., Jiang, T., Zhu, C., Zhai, Y., Wang, D., Dong, S.: One-step, solvothermal synthesis of graphene-CdS and graphene-ZnS quantum dot nanocomposites and their interesting photovoltaic properties. *Nano Res.* **3**(11), 794–799 (2010)
46. Wang, T., Chen, S., Pang, H., Xue, H., Yu, Y.: MoS₂-based nanocomposites for electrochemical energy storage. *Adv. Sci.* **4**(2), 1600289 (2017)
47. Xia, X., Zhu, C., Luo, J., Zeng, Z., Guan, C., Ng, C.F., Zhang, H., Fan, H.J.: Synthesis of free-standing metal sulfide nanoarrays via anion exchange reaction and their electrochemical energy storage application. *Small* **10**(4), 766–773 (2014)
48. Yan, Z., Yu, X., Han, A., Xu, P., Du, P.: Noble-metal-free Ni (OH)₂-modified CdS/reduced graphene oxide nanocomposite with enhanced photocatalytic activity for hydrogen production under visible light irradiation. *J. Phys. Chem. C* **118**(40), 22896–22903 (2014)
49. Yu, X.Y., Yu, L., Lou, X.W.: Metal sulfide hollow nanostructures for electrochemical energy storage. *Adv. Energy Mater.* **6**(3), 1501333 (2016)
50. Yu, X.Y., Lou, X.W.: Mixed metal sulfides for electrochemical energy storage and conversion. *Adv. Energy Mater.* **8**(3), 1701592 (2018)
51. Zeng, W., Suo, L., Zhang, C., Wu, D., Zhu, H.: AgI–Ag₂S heterostructures for photothermal conversion and solar energy harvesting. *J. Taiwan Inst. Chem. Eng.* **95**, 273–280 (2019)
52. Zhang, J., Yu, J., Jaroniec, M., Gong, J.R.: Noble metal-free reduced graphene oxide-Zn_xCd_{1-x}S nanocomposite with enhanced solar photocatalytic H₂-production performance. *Nano Lett.* **12**(9), 4584–4589 (2012)
53. Zhao, D., Yang, C.-F.: Recent advances in the TiO₂/CdS nanocomposite used for photocatalytic hydrogen production and quantum-dot-sensitized solar cells. *Renew. Sustain. Energy Rev.* **54**, 1048–1059 (2016)
54. Akhrame, M.O., Oputu, O.U., Pereao, O., Fagbayigbo, B.O., Razanamahandry, L.C., Opeolu, B.O., Fatoki, O.S.: Nanostructured Polymer Composites for Water Remediation, pp. 275–306. Springer, *Nanostructured Materials for Treating Aquatic Pollution* (2019)

55. Rampino, A., Borgogna, M., Bellich, B., Blasi, P., Virgilio, F., Cesàro, A.: Chitosan-pectin hybrid nanoparticles prepared by coating and blending techniques. *Eur. J. Pharm. Sci.* **84**, 37–45 (2016)
56. Wei, L., Yang, T.-Z., Guang, C., Luo, J.-S., Tang, Y.-j.: Synthesis and properties of nanocrystalline nonferrous metals prepared by flow-levitation-molding method. *Trans. Nonferrous Metals Soc. China* **17**(6), 1347–1351 (2007)
57. Zhang, J., Shi, J., Gong, M.: Synthesis of magnetic nickel spinel ferrite nanospheres by a reverse emulsion-assisted hydrothermal process. *J. Solid State Chem.* **182**(8), 2135–2140 (2009)
58. Kadiev, K.M., Khadzhiev, S., Kadieva, M.K., Dogova, E.: Ex situ synthesis of sulfided molybdenum-containing ultrafine hydroconversion catalysts. *Pet. Chem.* **57**(7), 608–617 (2017)
59. Wu, P.-J., Yu, J.-W., Chao, H.-J., Chang, J.-Y.: Silver-based metal sulfide heterostructures: synthetic approaches, characterization, and application prospects. *Chem. Mater.* **26**(11), 3485–3494 (2014)
60. Casalongue, H.G.S., Benck, J.D., Tsai, C., Karlsson, R.K., Kaya, S., Ng, M.L., Petterson, L.G., Abild-Pedersen, F., Nørskov, J., Ogasawara, H.: Operando characterization of an amorphous molybdenum sulfide nanoparticle catalyst during the hydrogen evolution reaction. *J. Phys. Chem. C* **118**(50), 29252–29259 (2014)
61. Chang, C.-C., Chen, J.-K., Chen, C.-P., Yang, C.-H., Chang, J.-Y.: Synthesis of eco-friendly CuInS₂ quantum dot-sensitized solar cells by a combined ex situ/in situ growth approach. *ACS Appl. Mater. Interfaces* **5**(21), 11296–11306 (2013)
62. Moon, G.-h, Park, Y., Kim, W., Choi, W.: Photochemical loading of metal nanoparticles on reduced graphene oxide sheets using phosphotungstate. *Carbon* **49**(11), 3454–3462 (2011)
63. Lu, S.-j, Wang, Z.-t, Zhang, X.-h, He, Z.-j, Tong, H., Li, Y.-j, Zheng, J.-c: In situ-formed hollow cobalt sulfide wrapped by reduced graphene oxide as an anode for high-performance lithium-ion batteries. *ACS Appl. Mater. Interfaces* **12**(2), 2671–2678 (2020)
64. Jen-La Plante, I., Zeid, T.W., Yang, P., Mokari, T.: Synthesis of metal sulfide nanomaterials via thermal decomposition of single-source precursors. *J. Mater. Chem.* **20**(32), 6612–6617 (2010)
65. Chesman, A.S., van Embden, J., Duffy, N.W., Webster, N.A., Jasieniak, J.J.: In situ formation of reactive sulfide precursors in the one-pot, multigram synthesis of Cu₂ZnSnS₄ nanocrystals. *Cryst. Growth Des.* **13**(4), 1712–1720 (2013)
66. Yang, C., Sun, Y., Li, X., Li, C., Tong, J., Li, J., Zhang, P., Xia, Y.: In situ growth of metal sulfide nanocrystals in poly (3-hexylthiophene):[6, 6]-Phenyl C₆₁-butyric acid methyl ester films for inverted hybrid solar cells with enhanced photocurrent. *Nanoscale Res. Lett.* **13**(1), 184 (2018)
67. Kovtyukhova, N.I., Buzaneva, E.V., Waraksa, C.C., Martin, B.R., Mallouk, T.E.: Surface sol-gel synthesis of ultrathin semiconductor films. *Chem. Mater.* **12**(2), 383–389 (2000)
68. Anandhan, S., Bandyopadhyay, S.: Polymer nanocomposites: from synthesis to applications. *Nanocomposites Polymers Analytical Methods* **1**, 1–28 (2011)
69. Nasrollahzadeh, M., Sajjadi, M., Dadashi, J., Ghafuri, H.: Pd-based nanoparticles: plant-assisted biosynthesis, characterization, mechanism, stability, catalytic and antimicrobial activities. *Adv. Colloid Interface Sci.* **276**, 102103 (2020)
70. Mittal, V.: *Characterization techniques for polymer nanocomposites*. Wiley (2012)
71. Caro, C.: *UV/VIS Spectrophotometry—Fundamentals and Application*. Mettler-Toledo Publication (2015)
72. Movasaghi, Z., Rehman, S., ur Rehman DI.: Fourier transform infrared (FTIR) spectroscopy of biological tissues. *Appl. Spectrosc. Rev.* **43**(2), 134–179 (2008)
73. Singh, R.: Sc Raman, Cv Raman and diffuse spots in laue photographs. *Science and culture*.
74. Andrade, J.D.: *X-ray photoelectron spectroscopy (XPS)*, pp. 105–195. Springer, Surface and interfacial aspects of biomedical polymers (1985)
75. Zhou, W., Apkarian, R., Wang, Z.L., Joy, D.: *Fundamentals of scanning electron microscopy (SEM)*, pp. 1–40. Springer, Scanning microscopy for nanotechnology (2006)

76. Williams, D.B., Carter, C.B.: The transmission electron microscope, pp. 3–17. Springer, Transmission Electron Microscopy (1996)
77. Elgrishi, N., Rountree, K.J., McCarthy, B.D., Rountree, E.S., Eisenhart, T.T., Dempsey, J.L.: A practical beginner's guide to cyclic voltammetry. *J. Chem. Educ.* **95**(2), 197–206 (2018)
78. Prime, R.B., Bair, H.E., Vyazovkin, S., Gallagher, P.K., Riga, A.: Thermogravimetric analysis (TGA). *Thermal analysis of polymers: Fundamentals and applications*, 241–317 (2009)
79. Odler, I.: The BET-specific surface area of hydrated Portland cement and related materials. *Cem. Concr. Res.* **33**(12), 2049–2056 (2003)
80. Mourdikoudis, S., Pallares, R.M., Thanh, N.T.: Characterization techniques for nanoparticles: comparison and complementarity upon studying nanoparticle properties. *Nanoscale* **10**(27), 12871–12934 (2018)
81. Ong, W.-J., Tan, L.-L., Ng, Y.H., Yong, S.-T., Chai, S.-P.: Graphitic carbon nitride (g-C₃N₄)-based photocatalysts for artificial photosynthesis and environmental remediation: are we a step closer to achieving sustainability? *Chem. Rev.* **116**(12), 7159–7329 (2016)
82. Li, P., Chen, W.: Recent advances in one-dimensional nanostructures for energy electrocatalysis. *Chin. J. Catal.* **40**(1), 4–22 (2019)
83. Lim, J., Kim, H., Park, J., Moon, G.-H., Vequizo, J.J.M., Yamakata, A., Lee, J., Choi, W.: How g-C₃N₄ works and is different from TiO₂ as an environmental photocatalyst: mechanistic view. *Environ. Sci. Technol.* **54**(1), 497–506 (2019)
84. Zhang, N., Han, C., Fu, X., Xu, Y.-J.: Function-oriented engineering of metal-based nanohybrids for photoredox catalysis: exerting plasmonic effect and beyond. *Chem* **4**(8), 1832–1861 (2018)
85. Li, Z., Meng, X., Zhang, Z.: Recent development on MoS₂-based photocatalysis: a review. *J. Photochem. Photobiol., C* **35**, 39–55 (2018)
86. Chen, Y., Xin, X., Zhang, N., Xu, Y.J.: Aluminum-based plasmonic photocatalysis. Part. Part. Syst. Charact. **34**(8), 1600357 (2017)
87. Zhang, Y., Ji, Q., Han, G.-F., Ju, J., Shi, J., Ma, D., Sun, J., Zhang, Y., Li, M., Lang, X.-Y.: Dendritic, transferable, strictly monolayer MoS₂ flakes synthesized on SrTiO₃ single crystals for efficient electrocatalytic applications. *ACS Nano* **8**(8), 8617–8624 (2014)
88. Xiong, X., Luo, W., Hu, X., Chen, C., Qie, L., Hou, D., Huang, Y.: Flexible membranes of MoS₂/C nanofibers by electrospinning as binder-free anodes for high-performance sodium-ion batteries. *Sci. Rep.* **5**(1), 1–6 (2015)
89. Alvarez, L.X., Sorokin, A.B.: Mild oxidation of ethane to acetic acid by H₂O₂ catalyzed by supported μ -nitrido diiron phthalocyanines. *J. Organomet. Chem.* **793**, 139–144 (2015)
90. Cong, Z., Shoji, O., Kasai, C., Kawakami, N., Sugimoto, H., Shiro, Y., Watanabe, Y.: Activation of wild-type cytochrome P₄₅₀BM₃ by the next generation of decoy molecules: enhanced hydroxylation of gaseous alkanes and crystallographic evidence. *Acs Catalysis* **5**(1), 150–156 (2015)
91. Wang, Z., Ma, L., Chen, W., Huang, G., Chen, D., Wang, L., Lee, J.Y.: Facile synthesis of MoS₂/graphene composites: effects of different cationic surfactants on microstructures and electrochemical properties of reversible lithium storage. *Rsc Adv.* **3**(44), 21675–21684 (2013)
92. Guo, Z., Zhou, D., Dong, X., Qiu, Z., Wang, Y., Xia, Y.: Ordered hierarchical mesoporous/macroporous carbon: a high-performance catalyst for rechargeable Li–O₂ batteries. *Adv. Mater.* **25**(39), 5668–5672 (2013)
93. Li, S.-R., Sun, Y., Ge, S.-Y., Qiao, Y., Chen, Y.-M., Lieberwirth, I., Yu, Y., Chen, C.-H.: A facile route to synthesize nano-MnO/C composites and their application in lithium ion batteries. *Chem. Eng. J.* **192**, 226–231 (2012)
94. Li, W., Yang, Z., Jiang, Y., Yu, Z., Gu, L., Yu, Y.: Crystalline red phosphorus incorporated with porous carbon nanofibers as flexible electrode for high performance lithium-ion batteries. *Carbon* **78**, 455–462 (2014)
95. Yu, Y., Chen, C., Shi, Y.: With a porous, spherical, multideck-cage morphology as a highly reversible anode material for lithium-ion batteries. *Adv. Mater.* **21**, 3541–3541 (2009)
96. Wang, G., Zhang, L., Zhang, J.: A review of electrode materials for electrochemical supercapacitors. *Chem. Soc. Rev.* **41**(2), 797–828 (2012)

97. Jiang, J., Li, Y., Liu, J., Huang, X., Yuan, C., Lou, X.W.: Recent advances in metal oxide-based electrode architecture design for electrochemical energy storage. *Adv. Mater.* **24**(38), 5166–5180 (2012)
98. Reddy, A.L.M., Gowda, S.R., Shaijumon, M.M., Ajayan, P.M.: Hybrid nanostructures for energy storage applications. *Adv. Mater.* **24**(37), 5045–5064 (2012)
99. Chen, W., Gong, Y.-F., Liu, J.-H.: Recent advances in electrocatalysts for non-aqueous Li–O₂ batteries. *Chin. Chem. Lett.* **28**(4), 709–718 (2017)
100. Yu, Z., Tetard, L., Zhai, L., Thomas, J.: Supercapacitor electrode materials: nanostructures from 0 to 3 dimensions. *Energy Environ. Sci.* **8**(3), 702–730 (2015)
101. Di, J., Xia, J., Li, H., Liu, Z.: Freestanding atomically-thin two-dimensional materials beyond graphene meeting photocatalysis: opportunities and challenges. *Nano Energy* **35**, 79–91 (2017)
102. Xu, Q., Li, W., Ding, L., Yang, W., Xiao, H., Ong, W.-J.: Function-driven engineering of 1D carbon nanotubes and 0D carbon dots: mechanism, properties and applications. *Nanoscale* **11**(4), 1475–1504 (2019)
103. Kong, D., Zheng, Y., Kobielski, M., Wang, Y., Bai, Z., Macyk, W., Wang, X., Tang, J.: Recent advances in visible light-driven water oxidation and reduction in suspension systems. *Mater. Today* **21**(8), 897–924 (2018)
104. Wang, M.-H., Guo, S.-P.: Highly uniform hollow CuCo₂S₄@ C dodecahedra derived from ZIF-67 for high performance lithium-ion batteries. *J. Alloys Comp.*, 154978 (2020)
105. Zhou, W., Li, T., Wang, J., Qu, Y., Pan, K., Xie, Y., Tian, G., Wang, L., Ren, Z., Jiang, B.: Composites of small Ag clusters confined in the channels of well-ordered mesoporous anatase TiO₂ and their excellent solar-light-driven photocatalytic performance. *Nano Res.* **7**(5), 731–742 (2014)
106. Park, S., Kim, D., Lee, C.W., Seo, S.-D., Kim, H.J., Han, H.S., Hong, K.S., Kim, D.-W.: Surface-area-tuned, quantum-dot-sensitized heterostructured nanoarchitectures for highly efficient photoelectrodes. *Nano Res.* **7**(1), 144–153 (2014)
107. Ong, W.-J., Tan, L.-L., Chai, S.-P., Yong, S.-T., Mohamed, A.R.: Self-assembly of nitrogen-doped TiO₂ with exposed 001 facets on a graphene scaffold as photo-active hybrid nanostructures for reduction of carbon dioxide to methane. *Nano Res.* **7**(10), 1528–1547 (2014)
108. Zhang, N., Yang, M.-Q., Tang, Z.-R., Xu, Y.-J.: Toward improving the graphene–semiconductor composite photoactivity via the addition of metal ions as generic interfacial mediator. *ACS Nano* **8**(1), 623–633 (2014)
109. Zhang, N., Zhang, Y., Xu, Y.-J.: Recent progress on graphene-based photocatalysts: current status and future perspectives. *Nanoscale* **4**(19), 5792–5813 (2012)
110. Kisch, H.: Semiconductor photocatalysis—mechanistic and synthetic aspects. *Angew. Chem. Int. Ed.* **52**(3), 812–847 (2013)
111. Liu, J., Wen, S., Hou, Y., Zuo, F., Beran, G.J., Feng, P.: Boron carbides as efficient, metal-free, visible-light-responsive photocatalysts. *Angew. Chem.* **125**(11), 3323–3327 (2013)
112. Li, H., Wang, X., Xu, J., Zhang, Q., Bando, Y., Golberg, D., Ma, Y., Zhai, T.: One-dimensional CdS nanostructures: a promising candidate for optoelectronics. *Adv. Mater.* **25**(22), 3017–3037 (2013)
113. Zhang, Y., Zhang, N., Tang, Z.-R., Xu, Y.-J.: Transforming CdS into an efficient visible light photocatalyst for selective oxidation of saturated primary C-H bonds under ambient conditions. *Chem. Sci.* **3**(9), 2812–2822 (2012)
114. Pan, Z., Zhang, H., Cheng, K., Hou, Y., Hua, J., Zhong, X.: Highly efficient inverted type-I CdS/CdSe core/shell structure QD-sensitized solar cells. *ACS Nano* **6**(5), 3982–3991 (2012)
115. Zhao, W., Bai, Z., Ren, A., Guo, B., Wu, C.: Sunlight photocatalytic activity of CdS modified TiO₂ loaded on activated carbon fibers. *Appl. Surf. Sci.* **256**(11), 3493–3498 (2010)
116. Chu, J., Han, X., Yu, Z., Du, Y., Song, B., Xu, P.: Highly efficient visible-light-driven photocatalytic hydrogen production on CdS/Cu₇S₄/g-C₃N₄ ternary heterostructures. *ACS Appl. Mater. Interfaces* **10**(24), 20404–20411 (2018)

117. Wang, H., Sun, Z., Lu, Q., Zeng, F., Su, D.: One-Pot Synthesis of (Au Nanorod)–(Metal Sulfide) core–shell nanostructures with enhanced gas-sensing property. *Small* **8**(8), 1167–1172 (2012)
118. Wang, C., Xie, Z., deKrafft, K.E., Lin, W.: Doping metal–organic frameworks for water oxidation, carbon dioxide reduction, and organic photocatalysis. *J. Am. Chem. Soc.* **133**(34), 13445–13454 (2011)
119. Lin, C.-K., Zhao, D., Gao, W.-Y., Yang, Z., Ye, J., Xu, T., Ge, Q., Ma, S., Liu, D.-J.: Tunability of band gaps in metal–organic frameworks. *Inorg. Chem.* **51**(16), 9039–9044 (2012)
120. Khajavi, H., Gascon, J., Schins, J.M., Siebbeles, L.D., Kapteijn, F.: Unraveling the optoelectronic and photochemical behavior of Zn₄O-based metal organic frameworks. *J. Phys. Chem. C* **115**(25), 12487–12493 (2011)
121. Alvaro, M., Carbonell, E., Ferrer, B., i Xamena, F.X.L., Garcia, H.: Semiconductor behavior of a metal-organic framework (MOF). *Chem.–Eur. J.* **13**(18), 5106–5112 (2007)
122. Law, M., Greene, L.E., Johnson, J.C., Saykally, R., Yang, P.: Nanowire dye-sensitized solar cells. *Nat. Mater.* **4**(6), 455–459 (2005)
123. Chen, X., Shen, S., Guo, L., Mao, S.S.: Semiconductor-based photocatalytic hydrogen generation. *Chem. Rev.* **110**(11), 6503–6570 (2010)
124. Tsuji, I., Kato, H., Kobayashi, H., Kudo, A.: Photocatalytic H₂ evolution reaction from aqueous solutions over band structure-controlled (AgIn)_xZn_{2(1-x)}S₂ solid solution photocatalysts with visible-light response and their surface nanostructures. *J. Am. Chem. Soc.* **126**(41), 13406–13413 (2004)
125. Zhang, J., Yu, J., Zhang, Y., Li, Q., Gong, J.R.: Visible light photocatalytic H₂-production activity of CuS/ZnS porous nanosheets based on photoinduced interfacial charge transfer. *Nano Lett.* **11**(11), 4774–4779 (2011)
126. Bao, N., Shen, L., Takata, T., Domen, K.: Self-templated synthesis of nanoporous CdS nanostructures for highly efficient photocatalytic hydrogen production under visible light. *Chem. Mater.* **20**(1), 110–117 (2008)
127. Ma, G., Yan, H., Shi, J., Zong, X., Lei, Z., Li, C.: Direct splitting of H₂S into H₂ and S on CdS-based photocatalyst under visible light irradiation. *J. Catal.* **260**(1), 134–140 (2008)
128. Hayden, S.C., Allam, N.K., El-Sayed, M.A.: TiO₂ nanotube/CdS hybrid electrodes: extraordinary enhancement in the inactivation of *Escherichia coli*. *J. Am. Chem. Soc.* **132**(41), 14406–14408 (2010)
129. Li, Q., Guo, B., Yu, J., Ran, J., Zhang, B., Yan, H., Gong, J.R.: Highly efficient visible-light-driven photocatalytic hydrogen production of CdS-cluster-decorated graphene nanosheets. *J. Am. Chem. Soc.* **133**(28), 10878–10884 (2011)
130. Sun, W.-T., Yu, Y., Pan, H.-Y., Gao, X.-F., Chen, Q., Peng, L.-M.: CdS quantum dots sensitized TiO₂ nanotube-array photoelectrodes. *J. Am. Chem. Soc.* **130**(4), 1124–1125 (2008)
131. Zhang, Q., Zhou, S., Li, Q., Li, H.: Toward highly efficient CdS/CdSe quantum dot-sensitized solar cells incorporating a fullerene hybrid-nanostructure counter electrode on transparent conductive substrates. *Rsc Adv.* **5**(39), 30617–30623 (2015)
132. Lin, K.-H., Chuang, C.-Y., Lee, Y.-Y., Li, F.-C., Chang, Y.-M., Liu, I.-P., Chou, S.-C., Lee, Y.-L.: Charge transfer in the heterointerfaces of CdS/CdSe cosensitized TiO₂ photoelectrode. *J. Phys. Chem. C* **116**(1), 1550–1555 (2012)
133. Fujishima, A., Honda, K.: Electrochemical photolysis of water at a semiconductor electrode. *Nature* **238**(5358), 37–38 (1972)
134. Xiang, Q., Yu, J., Wang, W., Jaroniec, M.: Nitrogen self-doped nanosized TiO₂ sheets with exposed 001 facets for enhanced visible-light photocatalytic activity. *Chem. Commun.* **47**(24), 6906–6908 (2011)
135. Jia, L., Wang, D.-H., Huang, Y.-X., Xu, A.-W., Yu, H.-Q.: Highly durable N-doped graphene/CdS nanocomposites with enhanced photocatalytic hydrogen evolution from water under visible light irradiation. *J. Phys. Chem. C* **115**(23), 11466–11473 (2011)
136. Li, J., Yang, J., Wen, F., Li, C.: A visible-light-driven transfer hydrogenation on CdS nanoparticles combined with iridium complexes. *Chem. Commun.* **47**(25), 7080–7082 (2011)

137. Zhong, M., Shi, J., Xiong, F., Zhang, W., Li, C.: Enhancement of photoelectrochemical activity of nanocrystalline CdS photoanode by surface modification with TiO₂ for hydrogen production and electricity generation. *Sol. Energy* **86**(2), 756–763 (2012)
138. Rufus, I.B., Ramakrishnan, V., Viswanathan, B., Kuriacose, J.: Rhodium and rhodium sulfide coated cadmium sulfide as a photocatalyst for photochemical decomposition of aqueous sulfide. *Langmuir* **6**(3), 565–567 (1990)
139. Walter, M.G., Warren, E.L., McKone, J.R., Boettcher, S.W., Mi, Q., Santori, E.A., Lewis, N.S.: Solar water splitting cells. *Chem. Rev.* **110**(11), 6446–6473 (2010)
140. Yang, S., Gong, Y., Zhang, J., Zhan, L., Ma, L., Fang, Z.: R. Vajtai, XC Wang and PM Ajayan. *Adv Mater* **25**, 2452–2456 (2013)
141. Ma, G., Hisatomi, T., Domen, K.: *Semiconductors for photocatalytic and photoelectrochemical solar water splitting*, pp. 1–56. Springer, From molecules to materials (2015)
142. Ran, J., Ma, T.Y., Gao, G., Du, X.-W., Qiao, S.Z.: Porous P-doped graphitic carbon nitride nanosheets for synergistically enhanced visible-light photocatalytic H₂ production. *Energy Environ. Sci.* **8**(12), 3708–3717 (2015)
143. Lin, D., Liu, Y., Cui, Y.: Reviving the lithium metal anode for high-energy batteries. *Nat. Nanotechnol.* **12**(3), 194 (2017)
144. Lukatskaya, M.R., Dunn, B., Gogotsi, Y.: Multidimensional materials and device architectures for future hybrid energy storage. *Nature Commun.* **7**(1), 1–13 (2016)
145. Wang, Y., Song, Y., Xia, Y.: Electrochemical capacitors: mechanism, materials, systems, characterization and applications. *Chem. Soc. Rev.* **45**(21), 5925–5950 (2016)
146. Zhao, H., Liu, L., Vellacheri, R., Lei, Y.: Recent advances in designing and fabricating self-supported nanoelectrodes for supercapacitors. *Adv. Sci.* **4**(10), 1700188 (2017)
147. Wang, X., Shi, B., Huang, F., Fang, Y., Rong, F., Que, R.: Fabrication of hierarchical NiCo₂O₄@ NiCo₂S₄ core/shell nanowire arrays by an ion-exchange route and application to asymmetric supercapacitors. *J. Alloy. Compd.* **767**, 232–240 (2018)
148. Shao, Y., El-Kady, M.F., Sun, J., Li, Y., Zhang, Q., Zhu, M., Wang, H., Dunn, B., Kaner, R.B.: Design and mechanisms of asymmetric supercapacitors. *Chem. Rev.* **118**(18), 9233–9280 (2018)
149. Wang, X., Wan, F., Zhang, L., Zhao, Z., Niu, Z., Chen, J.: Large-area reduced Graphene oxide composite films for flexible asymmetric Sandwich and microsized Supercapacitors. *Adv. Func. Mater.* **28**(18), 1707247 (2018)
150. Zhang, Q., Wang, X., Pan, Z., Sun, J., Zhao, J., Zhang, J., Zhang, C., Tang, L., Luo, J., Song, B.: Wrapping aligned carbon nanotube composite sheets around vanadium nitride nanowire arrays for asymmetric coaxial fiber-shaped supercapacitors with ultrahigh energy density. *Nano Lett.* **17**(4), 2719–2726 (2017)
151. Liu, Y., Zhou, Z., Zhang, S., Luo, W., Zhang, G.: Controllable synthesis of CuS hollow microflowers hierarchical structures for asymmetric supercapacitors. *Appl. Surf. Sci.* **442**, 711–719 (2018)
152. Dai, Z., Zang, X., Yang, J., Sun, C., Si, W., Huang, W., Dong, X.: Template synthesis of shape-tailorable NiS₂ hollow prisms as high-performance supercapacitor materials. *ACS Appl. Mater. Interfaces* **7**(45), 25396–25401 (2015)
153. Hu, H., Guan, B.Y., Lou, X.W.D.: Construction of complex CoS hollow structures with enhanced electrochemical properties for hybrid supercapacitors. *Chem* **1**(1), 102–113 (2016)
154. Guo, J., Zhang, X., Sun, Y., Zhang, X., Tang, L., Zhang, X.: Double-shell CuS nanocages as advanced supercapacitor electrode materials. *J. Power Sources* **355**, 31–35 (2017)
155. Karade, S.S., Dwivedi, P., Majumder, S., Pandit, B., Sankapal, B.R.: First report on a FeS-based 2 V operating flexible solid-state symmetric supercapacitor device. *Sustainable Energy Fuels* **1**(6), 1366–1375 (2017)
156. Wu, J., Shi, X., Song, W., Ren, H., Tan, C., Tang, S., Meng, X.: Hierarchically porous hexagonal microsheets constructed by well-interwoven MCo₂S₄ (M= Ni, Fe, Zn) nanotube networks via two-step anion-exchange for high-performance asymmetric supercapacitors. *Nano Energy* **45**, 439–447 (2018)

157. Luther, J.M., Law, M., Beard, M.C., Song, Q., Reese, M.O., Ellingson, R.J., Nozik, A.J.: Schottky solar cells based on colloidal nanocrystal films. *Nano Lett.* **8**(10), 3488–3492 (2008)
158. Pattantyus-Abraham, A.G., Kramer, I.J., Barkhouse, A.R., Wang, X., Konstantatos, G., Debnath, R., Levina, L., Raabe, I., Nazeeruddin, M.K., Gratzel, M.: Depleted-heterojunction colloidal quantum dot solar cells. *ACS Nano* **4**(6), 3374–3380 (2010)
159. Helgesen, M., Søndergaard, R., Krebs, F.C.: Advanced materials and processes for polymer solar cell devices. *J. Mater. Chem.* **20**(1), 36–60 (2010)
160. Gur, I., Fromer, N.A., Chen, C.-P., Kanaras, A.G., Alivisatos, A.P.: Hybrid solar cells with prescribed nanoscale morphologies based on hyperbranched semiconductor nanocrystals. *Nano Lett.* **7**(2), 409–414 (2007)
161. de Mello, D.C.: Synthesis and properties of colloidal heteronanocrystals. *Chem. Soc. Rev.* **40**(3), 1512–1546 (2011)
162. Gao, F., Ren, S., Wang, J.: The renaissance of hybrid solar cells: progresses, challenges, and perspectives. *Energy Environ. Sci.* **6**(7), 2020–2040 (2013)
163. Moulé, A.J., Chang, H., Thambidurai, C., Vidu, R., Stroeve, P.: Hybrid solar cells: basic principles and the role of ligands. *J. Mater. Chem.* **22**(6), 2351–2368 (2012)
164. Ren, S., Chang, L.-Y., Lim, S.-K., Zhao, J., Smith, M., Zhao, N., Bulovic, V., Bawendi, M., Gradedecak, S.: Inorganic–organic hybrid solar cell: bridging quantum dots to conjugated polymer nanowires. *Nano Lett.* **11**(9), 3998–4002 (2011)
165. Rath, T., et al.: Polymer/copper indium sulphide hybrid solar cells (2012)
166. Chen, Z., Zhang, H., Du, X., Cheng, X., Chen, X., Jiang, Y., Yang, B.: From planar-heterojunction to n–i structure: an efficient strategy to improve short-circuit current and power conversion efficiency of aqueous-solution-processed hybrid solar cells. *Energy Environ. Sci.* **6**(5), 1597–1603 (2013)
167. Zhou, R., Stalder, R., Xie, D., Cao, W., Zheng, Y., Yang, Y., Plaisant, M., Holloway, P.H., Schanze, K.S., Reynolds, J.R.: Enhancing the efficiency of solution-processed polymer: colloidal nanocrystal hybrid photovoltaic cells using ethanedithiol treatment. *ACS Nano* **7**(6), 4846–4854 (2013)
168. Liu, Z., Sun, Y., Yuan, J., Wei, H., Huang, X., Han, L., Wang, W., Wang, H., Ma, W.: High-efficiency hybrid solar cells based on polymer/PbS_xSe_{1-x} nanocrystals benefiting from vertical phase segregation. *Adv. Mater.* **25**(40), 5772–5778 (2013)
169. Ilyas, A.M., Gondal, M.A., Yamani, Z.H., Baig, U.: Facile synthesis of titanium dioxide-cadmium sulfide nanocomposite using pulsed laser ablation in liquid and its performance in photovoltaic and photocatalytic applications. *Int. J. Energy Res.* **41**(10), 1422–1435 (2017)
170. Xing, F., Liu, Q., Song, M., Huang, C.: Fluorine modified boron carbon nitride semiconductors for improved photocatalytic CO₂ reduction under visible light. *ChemCatChem* **10**(22), 5270–5279 (2018)
171. Jiang, X., Gong, H., Liu, Q., Song, M., Huang, C.: In situ construction of NiSe/Mn_{0.5}Cd_{0.5}S composites for enhanced photocatalytic hydrogen production under visible light. *Appl. Catalysis B Environ.* **268**, 118439 (2020)
172. Li, Q., Meng, H., Zhou, P., Zheng, Y., Wang, J., Yu, J., Gong, J.: Zn_{1-x}Cd_xS solid solutions with controlled bandgap and enhanced visible-light photocatalytic H₂-production activity. *ACS Catalysis* **3**(5), 882–889 (2013)
173. Atwater, H.A., Polman, A.: Plasmonics for improved photovoltaic devices. *Materials for Sustainable Energy: A Collection of Peer-Reviewed Research and Review Articles from Nature Publishing Group: World Scientific*, pp. 1–11 (2011)
174. Nishi, H., Asami, K., Tatsuma, T.: CuS nanoplates for LSPR sensing in the second biological optical window. *Optical Mater. Express* **6**(4), 1043–1048 (2016)
175. Lei, H., Fang, G., Cheng, F., Ke, W., Qin, P., Song, Z., Zheng, Q., Fan, X., Huang, H., Zhao, X.: Enhanced efficiency in organic solar cells via in situ fabricated p-type copper sulfide as the hole transporting layer. *Sol. Energy Mater. Sol. Cells* **128**, 77–84 (2014)
176. Oseni, S.O., Mola, G.T.: Effects of metal-decorated nanocomposite on inverted thin film organic solar cell. *J. Phys. Chem. Solids* **130**, 120–126 (2019)

177. Dlamini, M.W., Mola, G.T.: Near-field enhanced performance of organic photovoltaic cells. *Phys. B* **552**, 78–83 (2019)
178. Xuan, Y., Duan, H., Li, Q.: Enhancement of solar energy absorption using a plasmonic nanofluid based on TiO₂/Ag composite nanoparticles. *Rsc Adv.* **4**(31), 16206–16213 (2014)
179. Jaque, D., Maestro, L.M., Del Rosal, B., Haro-Gonzalez, P., Benayas, A., Plaza, J., Rodriguez, E.M., Sole, J.G.: Nanoparticles for photothermal therapies. *Nanoscale* **6**(16), 9494–9530 (2014)
180. Zoubos, H., Koutsokeras, L.E., Anagnostopoulos, D.F., Lidorikis, E., Kalogirou, S.A., Wildes, A.R., Kelires, P.C., Patsalas, P.: Broadband optical absorption of amorphous carbon/Ag nanocomposite films and its potential for solar harvesting applications. *Sol. Energy Mater. Sol. Cells* **117**, 350–356 (2013)
181. Guo, Q., et al.: Fabrication of 7.2% efficient CZTSSe solar cells using CZTS nanocrystals. *J. Am. Chem. Soc.* **132**(49), 17384–17386 (2010)
182. Guo, Q., Hillhouse, H.W., Agrawal, R.: Synthesis of Cu₂ZnSnS₄ nanocrystal ink and its use for solar cells. *J. Am. Chem. Soc.* **131**(33), 11672–11673 (2009)
183. Li, Y., Wang, H., Xie, L., Liang, Y., Hong, G., Dai, H.: MoS₂ nanoparticles grown on graphene: an advanced catalyst for the hydrogen evolution reaction. *J. Am. Chem. Soc.* **133**(19), 7296–7299 (2011)
184. Wu, M., Wang, Y., Lin, X., Yu, N., Wang, L., Wang, L., Hagfeldt, A., Ma, T.: Economical and effective sulfide catalysts for dye-sensitized solar cells as counter electrodes. *Phys. Chem. Chem. Phys.* **13**(43), 19298–19301 (2011)
185. Shen, S., Guo, L., Chen, X., Ren, F., Mao, S.S.: Effect of Ag₂S on solar-driven photocatalytic hydrogen evolution of nanostructured CdS. *Int. J. Hydrogen Energy* **35**(13), 7110–7115 (2010)
186. Capistrán, M.J., Nair, M., Nair, P.: Antimony sulfide and Silver antimony sulfide absorbers for thin film solar cells. *MRS Online Proceedings Library Archive* 1447 (2012)

Advanced Neutron and Synchrotron Characterization Techniques for Nanocomposite Perovskite Materials Toward Solar Cells Applications



Jose M. Porro, Ahmed Esmail Shalan , and Manuel Salado

Abstract Solar energy conversion represents one of the better options to replace carbon-based technology. Among a wide variety of available technologies, well established silicon solar cells entails almost 90% of the up-scale installed technology. Nevertheless, from a decade ago perovskite solar cells interrupted abruptly in the research community as an impressive material that triggers the power energy conversion from 3.9 to 20% in just five years, being currently above 25.5% and very close to silicon efficiencies. Its easy and cost-effective fabrication process as well as its tuneable opto-electronic properties make perovskite material very suitable to solar energy conversion. Although it presents an amphiphilic character and long carrier transport, usually two selective layers (hole and electron) are deposited to assist charge extraction. Therefore, the proper selection of those selective contacts contributes not only to the improvement of the final performance of the solar cells, but also to the intrinsic stability of the device. In addition, the layered structure nature of the perovskite devices requires a good connection and a perfect energy level alignment between layers. However, the lack of a deep understanding of the charge recombination process and some instability issues limit its implementation to industrial scale. This chapter gives a critical discussion about the materials and device design to improve opto-electronic properties and interfaces in different perovskites composition based solar cells. A discussion about the synthesis of perovskite solar cell devices is followed by a comprehensive dissertation on advanced neutron and synchrotron-based characterization techniques, which offer the possibility to disentangle the charge transport and degradation mechanism in perovskite solar cells.

J. M. Porro · A. E. Shalan · M. Salado (✉)

BCMaterials-Basque Center for Materials Applications and Nanostructures, Martina Casiano
UPV/EHU Science Park, Barrio Sarriena S/N, 48940 Leioa, Spain

e-mail: manuel.salado@bcmaterials.net

A. E. Shalan

Central Metallurgical Research and Development Institute (CMRDI), P.O. Box 87,
Helwan 11421, Cairo, Egypt

J. M. Porro

IKERBASQUE, Basque Foundation for Science Basque Foundation for Science, Plaza Euskadi 5,
48009 Bilbao, Spain

© The Author(s), under exclusive license to Springer Nature Switzerland AG 2022

A. E. Shalan et al. (eds.), *Advances in Nanocomposite Materials for Environmental and*

Energy Harvesting Applications, Engineering Materials,

https://doi.org/10.1007/978-3-030-94319-6_20

Keywords Perovskite solar cells · Interfaces · Neutron scattering · Synchrotron radiation · Charge extraction · Stability

Abbreviations

(Spiro-OMeTAD)	2,2',7,7'-tetrakis-(N,N-di-4-methoxyphenylamino)-9,9'spirobifluorene
(t-BP)	4-Tert-butylpyridine
(AFM)	Atomic force microscopy
(ALD)	Atomic layer deposition
(LiTFSI)	Bis-(trifluoromethanesulfonyl)imide lithium salt
(CMRR)	China Miyang Research Reactor
(DOS)	Density of states simulations
(DMF)	Dimethyl formamide
(DMSO)	Dimethyl sulfoxide
(DSSC)	Dye Sensitized Solar Cell
(ETM)	Electron Transport Material
(ETA)	Ethylammonium
(ESRF)	European Synchrotron Radiation Facility
(EXAFS)	Extended X-Ray absorption fine structure spectroscopy
FTO	Fluoro tin oxide
(FA ⁺)	Formamidinium
(GISANS)	Grazing-incidence SANS
(GISAXS)	Grazing-incidence small angle X-Ray scattering
(GIWAXS)	Grazing-incidence wide-angle X-Ray scattering
(GIXRD)	Grazing-incidence X-Ray diffraction
(GUA)	Guanidinium
(HNEXAFS)	Hard near-edge X-Ray absorption fine structure spectroscopy
(HXMCD)	Hard X-Ray magnetic circular dichroism
(HAXPES)	Hard X-Ray photoelectron spectroscopy
(HOMO)	Highest occupied molecular orbital
(HFBS)	High-flux backscattering spectrometer
(HTM)	Hole Transport Material Impedance spectroscopy
(IPCE)	Incident Photon-to-electron Conversion Efficiency
ITO	Indium tin oxide
(INS)	Inelastic neutron scattering
(ICP)	Intrinsic Conducting polymers
(LUMO)	Lowest unoccupied molecular orbital
(MBCP)	Mesoporous block-copolymer
(MA ⁺)	Methylammonium
(NSRRC)	National Synchrotron Radiation Research Center
(NEXAFS)	Near-edge X-Ray absorption fine structure spectroscopy
(NR)	Neutron reflectometry

(NMR)	Nuclear magnetic resonance
(NQR)	Nuclear quadrupole resonance
(OPV)	Organic photovoltaic
(OLEDs)	Organic solar cells
(PSC)	Perovskite Solar cell
(PEA ⁺)	Phenylethylammonium
(PL)	Photoluminescence
(PEDOT)	Poly(3,4 ethylene dioxythiophene)
(P3HT)	Poly(3-hexylthiophene-2,5-diyl)
PET	Poly(ethylene terephthalate)
(PTAA)	Poly(triarylamine)
(PCEs)	Power Conversion Efficiencies
(PCE)	Power conversion efficiency
(QENS)	Quasi-elastic neutron scattering Raman spectroscopy
RH	Relative humidity
(RIXS)	Resonant inelastic X-Ray scattering
(R2R)	Roll-to-roll
(SEM)	Scanning electron microscopy
(STEM)	Scanning transmission electron microscope
(SSRF)	Shanghai Synchrotron Radiation Facility
(SANS)	Small angle neutron scattering
(SAXS)	Small angle X-Ray scattering
(SXES)	Soft X-Ray emission spectroscopy
(TPNR)	Time-of-flight polarized neutron reflectometer
(TRS)	Time-resolved spectroscopy
(FK209)	Tris[2-(1H-pyrazol-1-yl)-4-tert-butylpyridine]cobalt(III)tris [bis(trifluoromethylsulfonyl) imide]
(TEM)	Tunneling electron microscopy
(WAXS)	Wide-angle X-Ray scattering
(XANES)	X-Ray absorption near-edge structure spectroscopy
(XRD)	X-Ray diffraction
(XMCD)	X-Ray magnetic circular dichroism
(XPS)	X-Ray photoemission spectroscopy
(GBL)	γ -Butyrolactone

1 Introduction

In the last ten years, the whole research community in the field of photovoltaics has been focused in the study and optimization of perovskite material for optoelectronic application. Even though this material was known in the past and its use in catalysis (especially oxides perovskites), their counterparts hybrid organic–inorganic have stirred up the field due to their outstanding properties and its easy fabrication

process. According to literature [1, 2], there have been an extraordinary effort in perovskite composition, device fabrication, characterization techniques and environmental cycling. All experts agree in the unprecedented development to achieve equal power conversion efficiency (PCE) that silicon solar cells in this short period [3]. However, due to the intrinsic and extrinsic instability, its jump to industrial scale has been limited until a consistent encapsulation method will be developed [4].

A multitude of measurement techniques were employed in order to probe the fundamental properties of single crystal, powder, and polycrystalline thin-films of perovskite material. Scanning microscopy techniques such as atomic force microscopy (AFM), [5] scanning electron microscopy (SEM) [6], and tunneling electron microscopy (TEM) [7] were extensively used in order to reveal the microstructure of perovskite thinfilm samples with subgrain resolution. Some of these studies revealed ordered domains within crystal grains, but no consensus has been reached about the interpretation of their crystallographic origins. In addition, techniques that probe full devices such as J–V characterization added some uncertainty due to the lack of reproducibility in batch-to-batch fabrication [8].

One important aspect to avoid intrinsic instability is to understand the charge recombination processes. Although lab techniques such as Incident Photon-to-electron Conversion Efficiency (IPCE), Impedance (IS) and Raman spectroscopy, Photoluminescence (PL) and time-resolved spectroscopy (TRS) can give a first insight in terms of charge mechanisms, need to be complemented with other techniques [9]. Large-scale facilities including neutron radiation and synchrotron X-Ray radiation have been used to study rotational states inside of the organic cations inside the perovskite crystal structure depending on the temperature [10].

Within this chapter, a profound insight into the different neutron and synchrotron X-Ray scattering techniques widely used to study perovskite solar cells will be offered. More concretely, experiments performed using neutron diffraction, neutron reflectometry, small angle neutron scattering, inelastic and quasielastic neutron scattering techniques will be discussed, alongside with brief introductions to each of these techniques. Similarly, science cases including synchrotron X-Ray diffraction, grazing-incidence small and wide angle synchrotron X-Ray scattering, and synchrotron X-Ray absorption spectroscopy experiments will be presented, also accompanied by explanations of each particular technique. This will be complemented by a couple of examples of muon spectroscopy measurements on perovskite solar cell devices, as well as by science cases where a combination of these aforementioned techniques provided with crucial information about the structure and dynamics of the studied perovskite solar cells.

2 Hybrid Perovskite Material

After ten years of research in organic–inorganic perovskite material, great advance has been done in terms of improve efficiency and new compositions has been synthesized allowing a better stability under real working conditions. However, degradation mechanisms are not well understood and the combination of a large variety of compositions and device configurations, make it difficult to compare and propose a consistent model, which explain this issues [11–13].

2.1 Structure

If we focus on the crystal structure, perovskite material possesses a 3D network composed by a divalent metal ion, which is octahedrally coordinated with halides anion. The centre of every eight octahedra is usually occupied by an organic cation that balances. Depending on the size of the organic cation, the symmetry of the octahedral network can be modified, being able to synthesized 2D or 3D perovskite structures [14]. In order to evaluate the distortion of the three-dimensional network, Goldschmidt proposed a tolerance factor depending on the ionic radii of the components that composes the perovskite. It follows the equation, $t = R_A * R_X / \sqrt{2(R_B + R_X)}$ where, subscripts indicate the position of the atom in the ABX_3 structure. Depending on the value of the tolerance factor, different crystal structures can be found giving rise to hexagonal structures ($t > 1$), cubic structure ($0.9 > t > 1$), octahedral rotations ($0.71 > t > 0.9$) and finally trigonal crystals ($t > 0.71$) [15]. Besides the Goldschmidt tolerance factor, the octahedral factor μ , defined by $\mu = r_B/r_X$ is usually used to evaluate the stability of the three-dimensional network [16].

The stability of the crystal structure with temperature has been deeply investigated as it affects the charge transfer and opto-electronic properties. One of the former hybrid perovskite used in solar devices was $CH_3NH_3PbI_3$. The organic cation in this perovskite composition with a ionic radii of 2.17 Å has a tolerance factor of $t = 0.89$. Nevertheless, after neutron diffraction experiments, it was demonstrated as depending on the temperature, the organic cation leads to an oriental disorder in the crystal [17].

According to the study, three different crystal phases were identified. At low-temperature ($T < -108$ °C), an orthorhombic phase with a space group Pnma is formed. The organic cation is fully ordered and it can be considered that it has barely no movement in just one axis. Closely to room temperature (-108 – 54 °C), the structure is altered to achieve a tetragonal phase with space group I4/mcm. In this situation, the organic cation possesses a two-dimensional disorder. Finally, when the temperature reaches values above 55 °C, the organic cation has a three-dimensional disorder entailing a cubic phase transition with a space group Pm3m.

A more stable three-dimensional network is achieved when a bigger organic cation is used. Although the size of the formamidinium cation is 2.53 Å and owns a tolerance factor near to 1, its based perovskite exhibits two phases depending on the temperature in which samples are annealed. It can be obtained a cornersharing α -perovskite structure (dark) or a δ -phase perovskite (yellow) not optically active, when the film is annealed above or under 160 °C, respectively [18]. The same issue has been also found in fully inorganic cesium based perovskites, where high temperature (330 °C) is needed to achieve a stable and optically active phase [19].

2.2 Composition

With the intention of stabilize the optical active phases in formamidinium and cesium based perovskite, different approaches were conducted [20]. In 2014, Pellet et al. [21] opened the door to a series of research works focused on the study the mixture of methylammonium (MA^+) and formamidinium (FA^+). The work concluded that only the addition of a small percentage of methylammonium cation avoided the unwanted formation of the non-active phase. Nevertheless, their best results were achieved with a percentage of 40. Nevertheless, the main aim of the work was obtained as they can anneal the perovskite to 100°C while maintaining the red-shifted band gap of α -FAPbI₃. Since that work, many research groups have been focused in composition engineering of perovskite material. In 2018, an impressive efficiency above 20% were obtained with the incorporation of only a 10% of methylammonium cation [22]. Expanding the research to a more complex perovskite composition, inorganic cations were also mixed with MA^+ and FA^+ such as cesium, potassium or rubidium [23–25]. Among them, the mixture of (MA)/(FA)/(Cs) perovskites have been studied by different research groups, showing that the addition of a low percentage of cesium (5–10%), benefits the stabilization of the structure and increases thermal stability [26–28]. The composition modification not only entail the combination of organic/inorganic cations but also in a rational mixture of halide components. In addition, the crystal growth has an important role in order to avoid charge accumulation. In this context, the combination of a mixture of the solvents (dimethyl formamide (DMF)/dimethyl sulfoxide (DMSO)) will lead to an intramolecular exchange, achieving high-efficiency perovskite devices [29]. It is well demonstrated as complex perovskite leads high-efficiency devices as well as induce better stability, however a nanoscale segregation of multiple perovskite compositions is expected to occurred [30–33]. In this regards, neutron experiments will contribute to extract the exact structure of mixed perovskite as we will explain in the following sections.

Another interesting approach focused on the improvement of long-term stability is the great flexibility that presents the perovskite structure, allowing the incorporation of large organic cation such as ethylammonium (ETA), or guanidinium (GUA). Generally, these bigger cations typically produce 2D structure, which is more stable than 3D, due to their superior stability and water resistance [34]. However, efficiency drops because of the uniaxial channel to charge extraction. Lately, mixture of

MA/GUA brought special attention due to its good performance [35, 36]. Although, large organic cations do not adjust the Goldschmidt tolerance factor, authors suggest that the low load of GU expand the crystal lattice and increase hydrogen bonding with the crystal network improving therefore the stability of the perovskite. Bearing this in mind, some authors suggested a multidimensional model so as to improve stability in perovskite solar cells. Basically it consists in the deposition of a 2D perovskite (general formula $R_2(A)_{n-1}B_nX_{3n+1}$) on top of a 3D perovskite, using isopropanol or chlorobenzene solvent to avoid 3D perovskite dissolution [37–39]. Very recently, Shikoh et al. [40] fabricated and characterized a 2D/3D perovskite solar cell with the deposition of 2D (PEA_2PbI_4) on top of (MA/FA/Cs) mixed perovskite, obtaining almost 20% PCE and structures more robust than the 3D ones.

Another method to improve stability and performance is the use of a passivating layer of a hydrophobic ionic liquid, on the perovskite/Hole Transport Material (HTM) interface, which has two main purpose; first, it reduces interface recombination improving charge transfer and second, it reduces perovskite degradation limiting the infiltration of water molecules [41–43]. Recently, Salado et al. [44] proposed the used of modified thiazolium compound in order to improve temperature stability. Results demonstrated the good performance of $MAPbI_3$ even above 140 °C, when it supposed to occur MAI segregation.

3 Fabrication Techniques

Due to the easy fabrication process of perovskite solar cells, several methods and its derivate have been utilized. Figure 2 summarized the common and successfully implemented methods that can be used so far, depending on the device architecture, substrate size, etc. selected. A controlled crystal growth is paramount in order to obtain relative low numbers of grain boundaries and therefore an efficient charge transfer. Considering lab scale samples, one-step with solvent-engineering is the easiest method and most commonly used, albeit dexter skills need to be developed to fabricate devices with high reproducibility. On the other hand, the vapour methods allow a better control of large perovskite film with respect to the crystallinity, morphology, and homogeneity.

3.1 Solution-Based Methods

3.1.1 One-Step Deposition with Solvent Engineering

The basics of this method lie in the dissolution of powdered reactants in aprotic polar solvents such as (γ -butyrolactone (GBL), dimethyl formamide (DMF), dimethyl sulfoxide (DMSO), to get a clear solution. Generally, MAI and PbI_2 are mixed in a ratio 1:1, however, some studies indicate that an excess of PbI_2 (around 8%) is

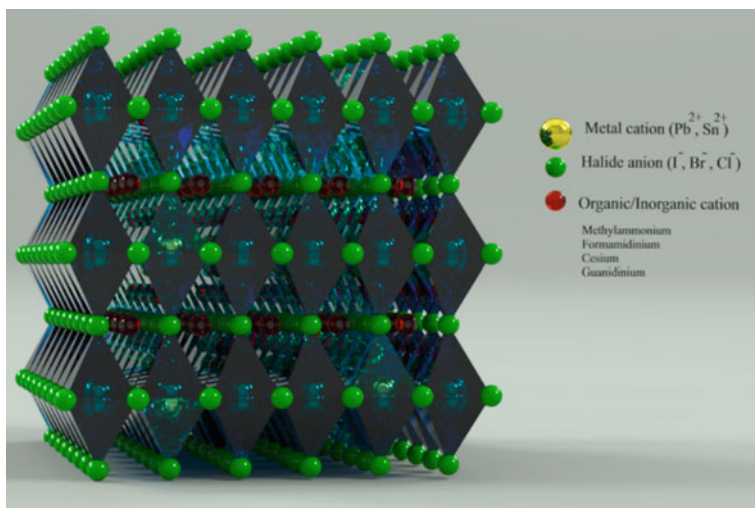


Fig. 1 Generic scheme of a 3D hybrid organic–inorganic perovskite crystal structure

beneficial to create a capping layer on top of the perovskite [45]. After spin-coating the solution, the film is annealed at approximately 100–150 °C to transform the precursor to crystalline perovskite. The use of an anti-solvent during the spinning step not only improve the crystal structure (optical properties) with the formation of an intermediate compound but also affects the electronic properties of the perovskite [46].

3.1.2 Sequential Deposition

Burschka et al. [47] used this method in 2013, as it improves the perovskite infiltration of the perovskite solution in the TiO₂ mesoporous layer. It was used before one-step deposition with efficiencies closed to 16%, however mixed perovskite does not present good performances with this method due to the complex of the composition and the environmental condition (generally out from the glove-box). The experimental details of this method entail, first the deposition of the inorganic PbI₂ dissolved in DMF and subsequently transformed into the perovskite by dipping into a solution of the organic halide in isopropanol. Usually, the ratio is 1:3 allowing a close contact with the organic excess during the dipping step. It also permits much better control over the perovskite morphology than achieved with the common one-step method, and consequently a much more reproducibility.

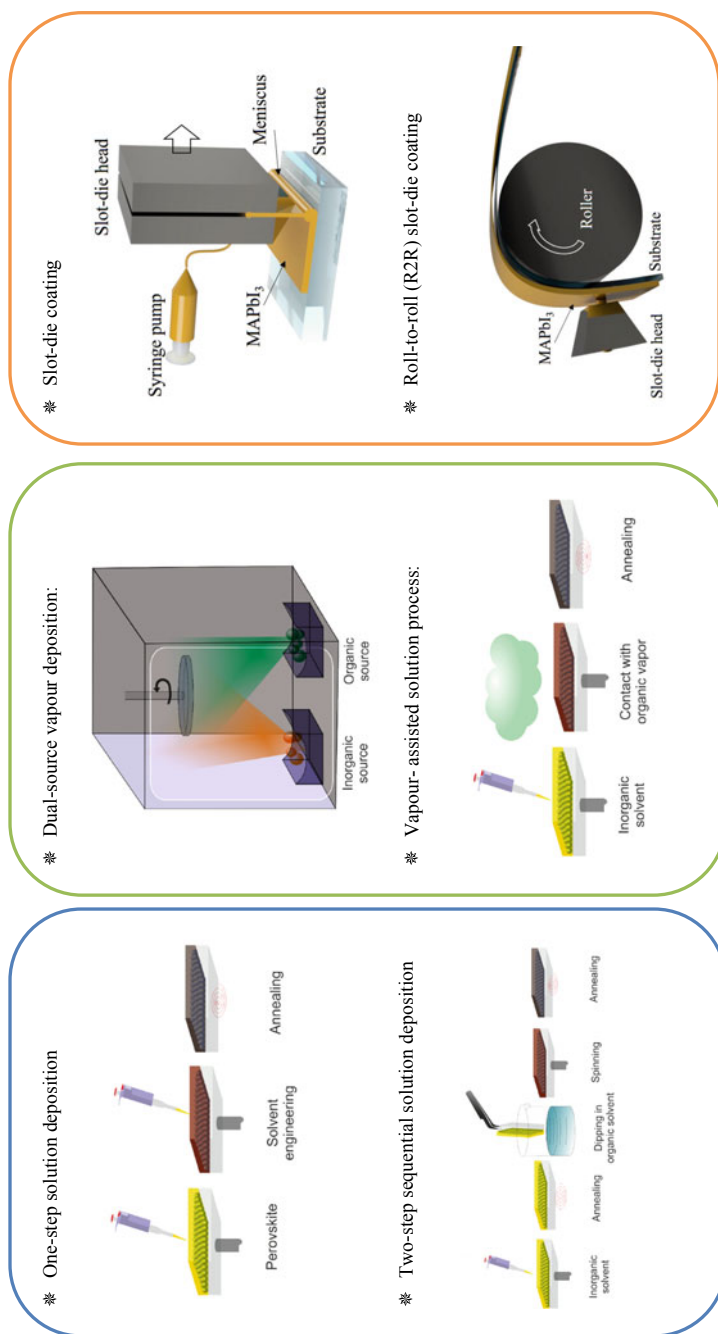


Fig. 2 Visual scheme of different perovskite deposition methods

3.2 *Evaporation Methods*

3.2.1 **Dual-Source Vapour Deposition**

With the perspective to fabricate large perovskite solar cells, evaporation techniques are one of the best options. This method evaporate simultaneously from separate sources the different reactants under high-vacuum conditions onto a rotating substrate. The main advantage is the possibility to deposited extremely uniform and nanocrystalline perovskite films without any voids between the perovskite crystals in big substrated, which is rarely observed in solution-processed films. However, the optimization on the fabrication of a full device entails great expertise to avoid the presence of voids in the different layers interfaces. As result of this optimization, Li et al. [48] achieved Power Conversion Efficiencies (PCEs) of 20.28% for 0.16 cm² and 19% for 1 cm² with MAPbI₃ perovskite. Besides, a novel method as vacuum-flash solution process [49] has obtained a maximum efficiency of above 20%. Recently, this method also has caught the attention for the possibility to evaporate novel lead-free perovskite compositions, which are difficult to obtain by wet chemistry. In particular, methylammonium bismuth iodide layers were deposited successfully by co-evaporation [50]. However, the final PCE of devices demonstrate that there is still much room for improvement.

3.2.2 **Vapour-Assisted Solution Process**

Following the same basics and the experimental steps, the vapour-assisted process can be seen as a variation of the sequential deposition. Though the simplest change in the reaction environment induces a full surface coverage, high surface smoothness, bigger grain sizes, and completely precursor transformation thanks to the incorporation of the organic through vapour phase. However, the first step with the deposition of the inorganic compound by spin-coating limits its use in large scale devices [51–53].

3.3 *Large Scale Methods*

Once the efficiency of perovskite solar cells is as competitive as silicon technology, the need to up-scale this technology to the industry has focused many attention in the recent years. However, the key parameter aforementioned, restrict its large-scale fabrication. Besides evaporation methods, numerous potentially scalable techniques have been explored for depositing the perovskite layer such as screen printing, spray coating, blade coating, slot-die coating and inkjet printing. Among these, slot-die coating is considered a flagship due to combine low material waste as well as high degree of film thickness control.

3.3.1 Slot-Die Coating

The main components of a slot-die coating system are illustrated in Fig. 2. It consists in the slot-die head, a dispensing unit for the perovskite solution, and a motor to control the movement of the slot-die head or substrate. The control of the movement entails the possibility to design such that various patterned coatings can be produced [54]. The thickness of the film can be controlled by three different ways; by adjusting the solution feed rate, the relative speed of the slot-die head and the substrate, the width of the meniscus, and the concentration of the coating solution. Regarding the feed rate, usually it involves of a syringe pump and a syringe, nevertheless, a precision pump is used to meter the coating solution from a reservoir. Nevertheless, the perovskite films that dry rapidly and the evaporation of toxic solvents are the main issues to be addressed. The blow of N_2 into the perovskite film to assist a fast crystallization process has resulted an interesting approach to improve the film quality [55]. As happens with the two-step method in solution-based methods, it is quite complicate to obtain good performance with mixed perovskite due to its complexity.

3.3.2 Roll-To-Roll (R2R) Slot-Die Coating

One-step forward to a fully automatized system to up-scale perovskite solar cells is the use of roll-to-roll deposition technique. Although this process have been employed widely for the fabrication of organic solar cells (OLEDs), the production of perovskite is now drawing increasing attention [56]. The main difference with slot-die coating is the use of a flexible substrate, which limits the use of TiO_2 mesoporous layer. Similar to solution-based two-step deposition, a PbI_2 solution was deposited onto the 10 cm^2 flexible PET/ITO substrate, blow-dried under N_2 , followed by coating with a MAI solution [57]. Nevertheless, the PCE of this module was low ($\sim 1\%$), indicating difficulty in maintaining film quality over this area. Further research has been focused on the chemistry to improve the film quality and avoid pinholes and voids. Recently, Dou et al. [58] fabricated efficient mixed perovskite by this method obtaining 14.1% PCE with an active area of 0.51 cm^2 and an impressive 17.3% with slot-die method.

The performance of PSCs strongly depends on the perovskite film quality. This comprises different properties such as grain size, crystallinity, homogeneous morphology as well as a full surface coverage. According to deposition methods aforementioned, perovskite deposition are carried out from very controlled to ambient environment.

- Perovskite layer deposition at controlled environment.

With the aim to achieve efficient perovskite films, many studies have preferred well-regulated inert conditions or a low-humidity atmosphere (relative humidity <30%) for fabricating highly efficient PSCs to avoid the adverse impact of humidity on a perovskite film. Nevertheless, there exist some discrepancies whether humidity during the perovskite deposition affects positive or negatively in the final device performance. Some studies [59] reported the independence of the annealing time with the perovskite layer is deposited at around 20%RH. However, the opto-electronic properties are highly affected within the annealing time when they are deposited at higher (30–40% RH) or lower (0–15% RH) humidity. On the other hand, Tai and co-workers [59] have obtained high-quality ($\text{CH}_3\text{NH}_3\text{PbBr}_{3-x}\text{SCN}_x$) perovskite films even at high 70%RH. Aranda et al. [60] focused on the recombination processes when the perovskite is deposited at different values of humidity. Specifically, the precursor's stoichiometry under non-ideal conditions affects the presence of hydrates that induces recombination processes and therefore a dropping in the open circuit voltage. Very recently, Watson et al. [61] reported good device performance by using ethyl acetate as an anti-solvent during deposition. The role of ethyl acetate as a moisture absorber during spin-coating, protect the perovskite from water inclusion. In addition, perovskite solar cells with power conversion efficiencies (PCEs) up to 15% were achieved in a high relative humidity (RH) environment (75%). It can be said that there is not a fully consensus on the optimal conditions to perovskite fabrication.

Herein we summarize the general procedure of mesoporous perovskite solar cell preparation, at lab scale, to obtain highly efficient devices [62].

After a proper substrate cleaning, a TiO_2 blocking layer is sprayed at 500 °C, using a titanium diisopropoxidebis(acetylacetonate) solution diluted in ethanol (v/v) with oxygen as carrier gas. After the samples are cooled down at room temperature, and after 15 min in UV-Ozone in order to improve hydrophilicity of the substrates, a mesoporous TiO_2 layer (in case of mesoscopic structure) is deposited by spin coating. TiO_2 nanoparticles are transformed from rutile phase to anatase phase by heating at 500 °C for 30 min using a progressive heating program. Perovskite films can be deposited by different methods, Fig. 3 shows one-step with solvent engineering. After deposition, the substrate is annealed at 100 °C (depending on the perovskite) for 40 min. Then, the hole-transporting material (HTM) is deposited by spin coating. Finally, a very thin layer (80 nm) of gold metal is thermally evaporated on top of the device to form the electrode contacts.

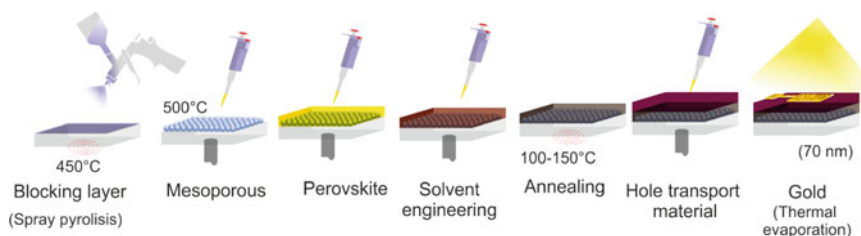


Fig. 3 General scheme of perovskite solar cell fabrication steps

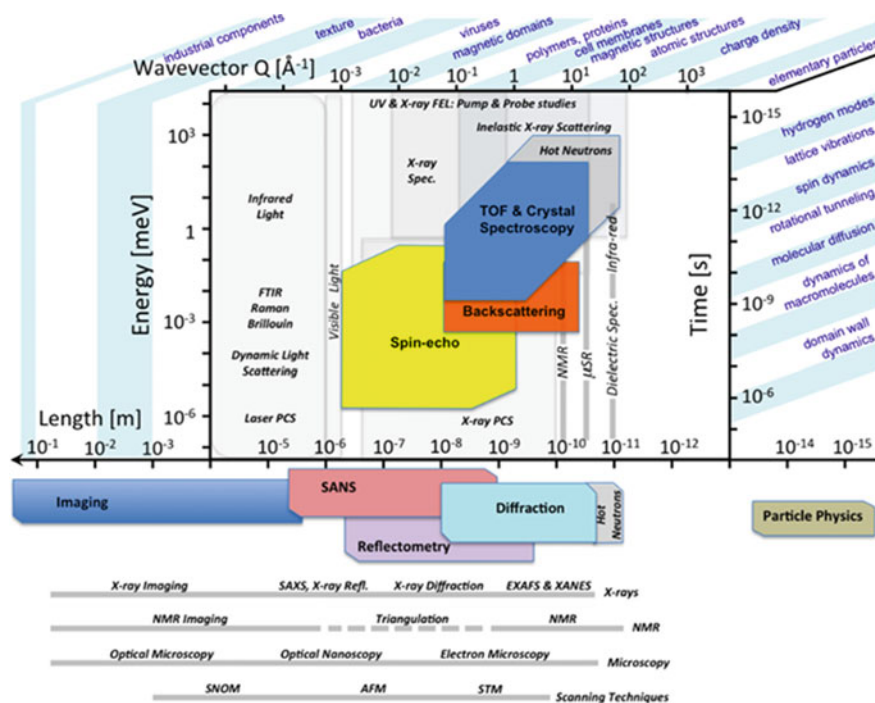
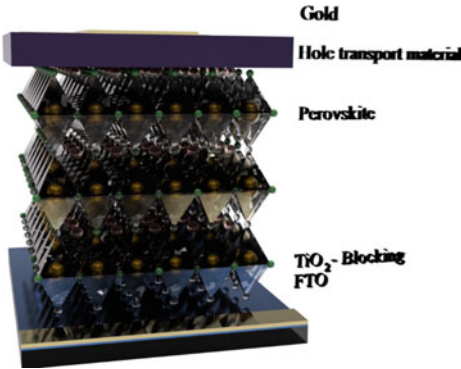


Fig. 4 Scheme of different characterization techniques, including neutron and synchrotron X-Ray scattering, as a function of the energy, wavevector/lengthscale and time ranges in which each technique is relevant, together with examples of phenomena that can be studied within the specific time and length scales. Reuse with permission from <https://europenspallationsource.se/science-using-neutrons>; ESS Technical Design Report 2013

4 Device Configuration

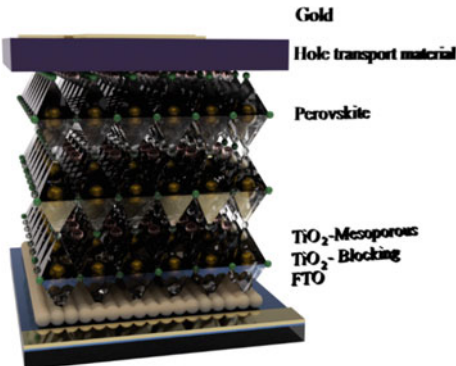
4.1 Planar



Best PCE: 21.6%[63]

- ✓ Simplified devices
- ✓ Low-temperature processing
- ✓ Large grains -> fast charge mobility
- ✓ Future applications: flexible devices
- ✗ Need of a fully coverage surface and large grain size
- ✗ High recombination

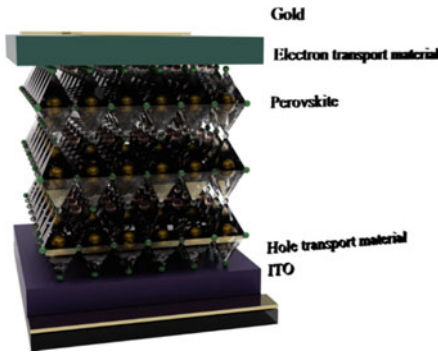
4.2 Mesoporous



Best PCE: 25.5%[3]

- ✓ Large contact area within perovskite
- ✓ Long-term stability
- ✓ Reduce the carrier transport length
- ✓ Prolong the light-absorption length
- ✗ Require high temperature

4.3 Inverted



Best PCE: 22.3%[64]

- ✓ Well define energy levels
- ✓ Low-temperature processing
- ✓ Negligible hysteresis behavior
- ✓ Future applications: flexible devices
- ✗ Difficult to obtain full surface coverage

5 Interfaces in Perovskite Solar Cell Devices

As it can be seen in the previous section, perovskite solar cells consist in a layered structure and therefore, interfaces between them are highly important in order to reduce charge accumulation. For that, a homogeneous contact and a good energy alignment are crucial to obtain high efficient perovskite solar cells. Depending on the device configuration, different materials extract electron and holes, nevertheless, the two main interfaces that need to be optimized and has focused more attention are the one closer to the perovskite layer.

5.1 ETM/Perovskite

Electron transport materials (ETM), particularly the inorganic semiconductor ones, can encourage the development of electron to the cathode after the charge partition when the light consumed by the sensitizer material. Various sorts of inorganic semiconductors ETMs advanced as delay of the Dye Sensitized Solar Cell (DSSC) and Perovskite Solar cell (PSC) solar cell headings. We checked the models just as the diverse creation pathways dependent on arrangement handled for metal oxides as transport materials for PSCs. The inorganic metal oxide materials are considered as the favorable substitutional materials for charge transport measure in PSCs. Incidentally, the obtained productivity and the dependability of the examined cells developed on exposed and doped inorganic semiconductors are featured. Thus, the great coordinating of these metal oxide materials energy levels with the valence band of perovskites can be required to build up the net productivity of the gathered cells.

In the end at this point critically, the financial practicality of PSCs utilizing these distinctive metal oxide materials is likewise obviously examined.

ETM diminishes the potential energy obstruction for electron move to the cathode and square the opening vehicle to manage the cost of a superior energy arrangement between the perovskite layer and the terminal material. ETMs utilized in perovskite sun oriented cells are isolated in two classes, inorganic and natural ones. Titanium dioxide, TiO_2 , has been the most well-known ETM changed as an augmentation of the solar cell innovation as a mesoporous layer. This mesoporous layer is essential for effective electrons assortment from the thick safeguard layer in light of the short transporter dissemination length. In any case, perovskite glasslike film includes a long dispersion length of more than $1 \mu\text{m}$, which shows that proficient electron extraction can be accomplished without utilizing mesoporous layer and that minimal TiO_2 layer.

5.2 HTM/Perovskite

Besides perovskite composition, the synthesis of an efficient hole transport material has been widely investigated to achieve high open circuit voltage (V_{OC}) [65]. Generally, HTLs can be categorized into inorganic and organic, which can be divided additional into polymers and small molecules. 2,2',7,7'-tetrakis-(N,N-di-4-methoxyphenylamino)-9,9'spirobifluorene (Spiro-OMeTAD) was the first HTL used in its solid-state form, its origins becomes from DSSC technology. Although its performance in perovskite solar cell is quite relevant, it needs to be doped with tris[2-(1H-pyrazol-1-yl)-4-tert-butylpyridine]cobalt(III)tris[bis(trifluoromethylsulfonyl) imide] (FK209), in order to improve the open circuit voltage and with 4-tert-butylpyridine (t-BP) and bis-(trifluoromethanesulfonyl)imide lithium salt (LiTFSI) due to its lack of good conductivity [66, 67]. This issue together with its hydrophobicity character limits its application in a commercial scale.

As a result, there is a consensus that spiro-OMeTAD by itself is not stable enough for long-term stable devices, and its market price makes its use in large-scale production costly. Due to large variety of possibilities of synthesis in conductive polymers and small molecules, the number of research works published on the development of Spiro-OMeTAD substitute since 2010 increased quantitative. The pioneering work was focused on well-understood organic semiconductor moieties such as quinolino acridine, carbazole, thiophenes or triazatruxenes [65, 68–70]. Those chemical structures were used in organic light-emitting (OLEDs) devices and need to be optimize to its use in perovskite solar cell. Although most research groups have reported the hole mobility values, only a few of them had used advanced spectroscopic techniques to determine these reference energy values directly. Moreover, after the interaction with the perovskite layer, those molecules often have different highest occupied molecular orbital (HOMO) and lowest unoccupied molecular orbital (LUMO) energies than the values estimated indirectly using solution-based electrochemical methods.

This mismatch give us an idea the need of accurate techniques that allow the characterization of materials in the same nature they will be used on the devices. Even though the usage of small molecules was demonstrated to be very fruitful with efficiencies over 23% PCE, their instability under high temperature conditions and under light stress need to be addressed.

Intrinsic Conducting polymers (ICP) have been already applied in organic photovoltaic (OPV) technology. According to their energetic levels, poly(3,4 ethylene dioxythiophene) (PEDOT), poly (3-hexylthiophene-2,5-diy1) (P3HT) [71] and poly(triarylamine) (PTAA) have been widely used as electron or hole transport layer [72]. Focusing on the HTL, with poly(triarylamine) (PTAA), yields over 21% has been achieved when used as charge separator in a PSC device. Besides, recent studies [73] have demonstrated that a passivation layer of MABr in ethanol reduce non-radiative recombination due to an enlargement of perovskite grains, improvement of the quality of the interface with the perovskite (see Sect. 4). Nowadays, carbon-based materials (e.g. graphene related materials, carbon nanotube, carbon paste) have been used in PSC for a wide range of roles, such as electron or hole transporting materials, electrodes or as additives within the perovskite light harvesting layer. Moreover, these materials were also proven favourable aspirants to replace organic molecules for overcoming instability issues as well as hysteresis behaviour in perovskite solar cells. For example, the addition of a small percentage of fullerene on the top of the perovskite can achieve efficiencies over 20% with negligible hysteresis behaviour due to a passivation of the recombination processes [74–76]. In addition, taking advantage of the impressive electric properties of graphene and carbon nanotubes, it is possible to improve the charge transport and therefore replace the costly gold metal electrode [77]. Nazeerudin et al. published a seminal work in 2018 where reported a perovskite based device with high stability over 10,000 h under 1 sun, using conductive carbon as electrode [78]. These outstanding results proved the attractive perspective of carbon materials as hole transport material. Recently, Kim et al. [79] first presented that an effective and rapid method used F plasma treatment for the production of a highly efficient carbon electrode-based perovskite solar cell with durable moisture resistance. Samples after F treatment retain 95% of efficiency after 1000 h of constant illumination at 80%RH.

Once inorganic HTMs have showed large improvement in power conversion efficiency (PCE) and stability [80]. However, the surface homogeneity is the bottleneck of this hole extraction layers. With the intention of avoid this, an ultrathin layer of NiO was deposited by atomic layer deposition (ALD) technique, achieving an impressive efficiency of 16.4% mainly due to the high open circuit voltage (1.04 V) [81, 82]. Copper oxide materials have reached a PCE of 19.0% with better stability, [83] suggesting that inorganic HTMs are better alternatives to the organic HTMs for next generation PSCs. On the other hand, cupper halides, specifically CuI, where successfully deposited, obtaining higher fill facto that the reference device with the organic molecule based Spiro-OMeTAD. Unfortunately, the improvement in stability, counteracted with his lack of high V_{OC} due to a high recombination rate [84]. Currently, one of the best candidates of inorganic HTM belongs to CuSCN. It has the main

advantage to operates in high temperature ranges mainly to stable crystalline structure. In order to demonstrate this, efficient perovskite devices (18%) were exposed to high temperature and high humidity conditions [85]. The results indicate as the samples that used organic molecule (Spiro-OMeTAD) as dropped considerably its initial efficiency, meanwhile the samples with CuSCN maintain the 60% of its initial efficiency after been exposed to 2 h at 125 °C and 40% RH.

6 Advanced Characterization Techniques at Large Scale Facilities

The amount of techniques accessible to characterize perovskite solar cell devices range from standard lab-based ones to advanced large scale facilities, where a wide variety of neutron and synchrotron radiation techniques are available to complement the basic characterization performed with lab-based techniques. Among the aforementioned standard techniques usually available at many laboratories studying photovoltaic and perovskite-based materials, one can find techniques for structural characterization such as X-ray diffraction and reflectometry, atomic force microscopy or differential scanning calorimetry, among others. A usual second-step characterization process of the perovskite solar cell devices comprises the study of their efficiency and performance, where techniques like, for instance, quantum efficiency equipment to measure external (incident photon-to-current efficiency)/internal quantum efficiencies, potentiostats, solar simulators or four-point probe measurement systems, provide a sufficient knowledge on the basic behaviour of the perovskite solar cells.

Nonetheless, beyond this basic knowledge on the composition, structure and behaviour of the perovskite solar cells, there are still a few aspects of these devices that need to be studied in depth in order to go beyond the state-of-the-art performance of the perovskite solar cell devices. Among them, the degradation processes and the charge transfer in perovskite solar cell devices are being intensively studied, as their advanced knowledge paves the way towards the implementation of more stable and more efficient devices. However, the study of these two interesting phenomena requires the usage of characterization techniques only available at large scale facilities across the globe, making the employment of neutron and synchrotron radiation based techniques a crucial aspect to further advance in the field of perovskite solar cells (PSCs). In this section of the present chapter, current developments on perovskite solar cell devices discovered by means of neutron and/or synchrotron related techniques will be discussed, alongside with brief introductions to each of the techniques employed within the aforementioned framework. Finally, an introduction to muon spectroscopy, a technique not so widely known, will also be provided, together with examples where this technique has been successfully employed to characterize perovskite solar cell devices.

6.1 Neutron Scattering Techniques

Due to the intrinsic properties of the neutron (they have no charge, their electric dipole moment is either zero or so small that is undetectable, and they possess non-zero magnetic spin) their penetration depth in matter is much higher than that of any other charged particle. This makes them a very unique tool to probe matter far from the surface, although there is a counterpart to this particular characteristic: they scatter weakly, meaning that a lot of scattering events are needed in order to detect these events with a strong enough signal. Furthermore, the neutron flux (number of neutrons per unit area and unit time) of the currently available neutron sources around the world is very limited compared to that of the photons coming out from synchrotron light sources (10^4 neutrons/mm.s compared to 10^{18} photons/mm²), forcing the count time for neutron scattering events to be long compared to synchrotron radiation sources. Even if these particular characteristics of neutron scattering and neutron sources would make one think that such signal-limited techniques should be discarded, the information provided with neutron scattering events is so unique that cannot be obtained by any other means.

The aforementioned properties of neutrons and of the neutron scattering phenomena lead to the impossibility to design a generic instrument in which all the different neutron scattering techniques can be applied. In fact, all the neutron scattering techniques are gathered into four different main groups: neutron imaging, neutron diffraction, large-scale structures (neutron reflectometry and small angle neutron scattering) and inelastic/quasielastic neutron scattering. While neutron imaging is widely applied in materials science to reveal the interior of materials and components thanks to its non-destructive nature, as there is no current need to image any component of the devices within the current state of development of PSCs technology, this technique has not been used so far in these devices. In the following sections, examples of neutron diffraction, reflectometry, small angle neutron scattering and inelastic/quasielastic neutron scattering experiments that have been performed in perovskite solar cells will be discussed, followed by a couple of examples where a combination of these techniques led to interesting phenomena in these devices.

6.1.1 Neutron Diffraction

Neutron diffraction is a very powerful technique to characterize the structure of samples both polycrystalline and in single-crystal form. While the usage of X-ray diffraction, both at laboratory-based equipment and in synchrotron radiation sources, is well established among the materials science community for structure determination in crystalline materials, the usage of neutrons to determine the crystal structure of materials presents a number of advantages with respect to X-rays. The fact that neutrons are scattered by the nuclei and not by the electrons of the atom, as it is the case for photons, makes the neutron scattering cross sections dependent on the properties

of the nuclei. This leads to the possibility of differentiating not only elements that are very close in the periodic table, but also isotopes within the same element, which is impossible to do with X-ray diffraction. Further to this, while X-ray diffraction struggles at determining materials composed by light elements, neutron diffraction excels in doing so.

In this section, representative examples of studies conducted on perovskite solar cells in powder and single crystal form within the last years will be introduced and discussed. To start with, a representative study of perovskite solar cell systems with powder neutron diffraction is the one performed by Mark T. Weller and colleagues, who studied the structure and cation orientation in $\text{CH}_3\text{NH}_3\text{PbI}_3$ perovskite solar cells between 100 and 352 K at the D20 high-intensity two-axis powder diffractometer of the Instituto Laue-Langevin (ILL) (Grenoble, France) [17]. They acquired diffractograms at 100 K, where the PSC shows an orthorhombic structure; 180 K, where the PSC is in a tetragonal structure; and at 352 K, where it shows a cubic structure, together with thermodiffractograms between 100 and 352 K, where the phase changes and lattice parameters expansions are evidenced, as observed in Fig. 5. As the $[\text{PbI}_3]^-$ framework becomes less distorted as the temperature is increased, the MA^+ cations migrate slowly towards the centre of the perovskite structure. In addition to this, they also showed how the MA^+ cations possess a high level of orientational motion at room temperature, hence attributing the excellent photovoltaic performance of this particular PSC to this behaviour of the cations.

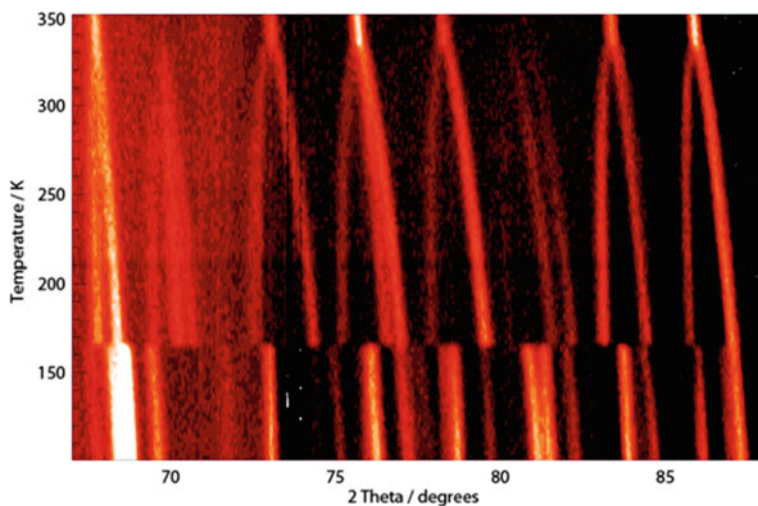


Fig. 5 Thermodiffractogram of a MAPbI_3 PSC collected with powder neutron diffraction experiments, where the phase changes at 165 K and 327 K are clearly evidenced. Republished with permission of the Royal Society of Chemistry, from [17]; permission conveyed through Copyright Clearance Center, Inc.

Oliver J. Weber and colleagues studied the phase behaviour and polymorphism of FAPbI_3 , combining data from two different powder diffractometers: the aforementioned D20 powder diffractometer at ILL, which is a constant-wavelength diffractometer, and the powder neutron diffractometer GEM located at ISIS, the neutron and muon source of the Rutherford Appleton Laboratory (Oxfordshire, UK), which is a time-of-flight diffractometer [86]. Their experiments consisted in studying the high and low temperature phases of formamidinium lead iodide combining powder neutron diffraction experiments with ab-initio molecular dynamics simulations, which led to determining not only the crystalline phases of the PSCs but also the dynamics of the cations in the studied temperature range: 430 K to 10 K. Both deuterated and fully-hydrogenated FAPbI_3 PSCs showed equivalent crystalline phase behaviours. Two low temperature phases related to the room temperature cubic α - FAPbI_3 were formed: a primitive tetragonal β -(FAPbI_3) cell around 285 K, and a second phase transition to γ -(FAPbI_3) evidenced by weak Bragg scattering peaks. They also reported on phase transitions across the δ to α polymorphs, attributing the observed phases of the PSCs to delicate synthesis conditions, sample environments and cycling temperatures. Finally, combining the powder neutron diffraction data with ab-initio calculations, the authors found greater stability for the non-cubic phases in the FAPbI_3 , due to significant FA^+ cation tumbling motion and on-axis rotations in the cubic phases, whereas in the tetragonal β -(FAPbI_3) there is restricted motion of the aforementioned cation with preferred orientations within the A-site cage. Further cooling the PSCs below 140 K demonstrate a high level of disorder of the FA^+ cations, forming a glassy-like state.

Sometimes the usage of neutron diffraction is not intended to study phase transitions and cation motion in PSCs, but to provide key insights into mechanisms that lead to exceptional photovoltaic performances. This is the case of the work performed by Jonathon R. Harwell and colleagues [87]. They combined powder neutron diffraction measurements with resonant ultrasound spectroscopy, differential scanning calorimetry and photoluminescence measurements to study the elastic and anelastic properties, together with structural instabilities, of MAPbX_3 , being X Cl, Br or I, and the corresponding fully deuterated compound $[\text{MA-d}]\text{PbI}_3$ ($\text{CD}_3\text{ND}_3\text{PbI}_3$) in the 5–380 K temperature range. They found that, upon deuteration of the MAPbI_3 , the role of hydrogen bonding plays a crucial role in the performance of the PSCs. While the temperature-dependent photoluminescence properties remain unaffected in the tetragonal to orthorhombic phase transition that the PSCs undergo upon cooling, a blueshift in the emission of the PSCs is observed, alongside with a moderate increase in the photoluminescence quantum yield below 150 K. The chlorinated PSC shows interesting changes in its photoluminescence, alongside with the observation of freezing processes in the temperature window from 150 to 170 K. These are attributed to freezing of the motion of the MA cations, a mechanism that could also be responsible of the photoluminescence changes observed in MAPbI_3 .

A recent study performed by Carlos A. López and colleagues [88] used powder neutron diffraction, together with STEM imaging and other standard widely used characterization techniques for PSCs, to demonstrate the influence of growing the PSCs by solvent-free ball milling on its properties, finding that the stability of the ball-milled PSCs is greater than that showed by wet chemistry. This enhanced stability

is attributed to the full iodine content found in the ball milled PSCs after imaging them with atomic-resolution scanning transmission electron microscope (STEM). The powder neutron diffraction measurements revealed the configuration of the MA⁺ cation in the temperature range 100 K to 298 K, where a phase transition from a tetragonal structure to an orthorhombic one upon cooling, being the organic cations fully localized in the latter. According to the powder neutron diffraction data, the changes on the MA⁺ behaviour are gradual and start before the aforementioned phase transition makes place. The ball milled PSCs also showed a more compact inorganic framework with a reduced unit cell volume, which is related to the bigger stability of these PSCs, and a photocurrent peak that is redshifted by 30 nm with respect to similar wet chemistry synthesized PSCs.

Although powder neutron diffraction measurements are widely used to determine structure phases, phase transitions and motions/positions of the organic cations within the PSCs, these PSCs are also fabricated in single crystal form in order to enhance and unify their excellent photovoltaic performance. One of the first single crystal neutron diffraction experiments in PSCs was performed by Hiroyuki Mashiyama and colleagues, who used this technique to study the disorder of the organic MA⁺ cations in MAPbBr₃ single crystal PSCs [89]. Mashiyama and co-workers measured the PSCs in the four-circle single crystal diffractometer FONDER of the JRR-3 research reactor of JAERI (Tohoku, Japan), where they identified the inorganic structure frame formed by eight PbBr₆ octahedrons with disordered MA⁺ ions centred in each cage. They also studied the low temperature phase transition leading to a partial ordering of the MA⁺ that reduces the site symmetry, together with the condensation of the rotational motion of the PbBr₆ octahedron around the axis formed by the Pb and Br atoms.

A more recent example of single crystal neutron diffraction measurements in PSCs is the one performed by Yixin Ren and colleagues, who used this technique to study the orientation of organic cations in MAPbI₃ with subatomic resolution at the TOPAZ beamline of the Spallation Neutron Source at the Oak Ridge National Laboratory (Oak Ridge, USA) [90]. Their studies provided with a detailed description of the crystal structure of the single crystal MAPbI₃ PSCs at 295 K, where the sample is in a tetragonal phase, and at 350 K, where it is in a cubic phase. In the tetragonal phase, the MA⁺ cations are disordered in a way it presents four possible orientations of the amine cation substituent on one extremity nearest the iodine neighbouring atom, whereas the methyl cation substituent presents eight possible positions, hence showing higher mobility. Finally, the authors also report on a key feature of the MA⁺ cation orientation: it resides mainly along the [011] direction, being this in good agreement with performed density functional theory calculations.

Another representative study of PSCs with neutron diffraction is the one performed by Bin Yang and colleagues, who performed real-time observations of the order-disorder transformation of the MA cations in MAPbBr₃ single crystal PSCs, which they measured also at the single crystal neutron diffractometer TOPAZ [91]. With real-time temperature-dependent neutron diffraction experiments, combined with photoluminescence measurements, Yang et al. found that the organic MA⁺ cation suffers from an order to disorder transition with increasing temperature, leading to

an anomalous increase in the photoluminescence intensity measured from the PSCs, together with observing fingerprints of a multidomain to a single-domain structural transition in the PSCs.

6.1.2 Neutron Reflectometry and Small Angle Neutron Scattering

The reflectometry and small angle neutron scattering beamlines are usually gathered together in the same group within the corresponding neutron source facility instrumental divisions, under a general name commonly similar to “large scale structures” instruments. Both in reflectometry and small angle neutron scattering the scattering processes take place not from nuclei of individual atoms, as it is the case of diffraction, but from aggregates of atoms, thus looking for characteristic length scales ranging from nanometres to microns. Small angle neutron scattering (SANS) is primarily focused on bulk materials, with a SANS measurement usually yielding information about sizes, shapes, ordering and other characteristic length scales of the materials under study. SANS has been successfully implemented to probe a wide variety of samples, including morphology and formation of polymers, biological structures such as the formation of micelles, the study of magnetic materials and the corresponding nature of their interactions, and voids and aggregates in metal alloys, among others. Neutron reflectometry (NR) is employed to investigate properties of interfaces and multilayers, with special attention to the quality and roughness of interfaces otherwise invisible to any other technique. The shape of the reflectivity curves collected in a NR experiment gives information about the thickness of layers, concentration of a certain material at an interface, the roughness of surfaces and interfaces, and the nature of the magnetic interactions in a magnetic material.

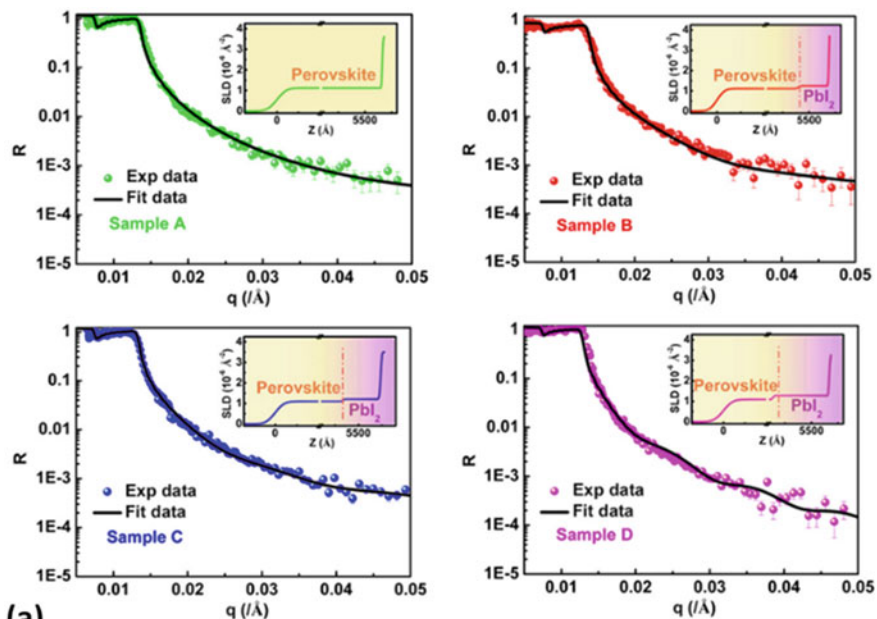
Although SANS and NR are not among the most used neutron scattering techniques to study perovskite solar cells, a few of these kind of experiments performed on PSCs will be presented hereafter. Johannes Schlipf and co-workers [92] performed in-situ grazing-incidence SANS (GISANS) experiments to study the degradation process of MAPbI₃ perovskite thin films at the D22 high dynamic range small-angle neutron scattering instrument of the ILL (Grenoble, France). Schlipf and colleagues exposed MAPbI₃ PSC thin films to different levels of humidity, and studied the water content, degradation products and morphological changes in the thin films during prolonged exposure to moisture. Depending on the humidity level, either monohydrate (MAPbI₃·H₂O; $\geq 73\%$ of room humidity) or dehydrate (MA₄PbI₆·2H₂O $\geq 93\%$) MAPbI₃ compounds are formed, happening in all the cases the water uptake in the form of water molecules adsorbed either on the amorphous parts of the PSCs or on the outside part of the crystalline domains. This water intake takes place together with a slight grain expansion, and is a reversible process even if the grain shapes suffer from a transformation from faceted to pebble-like particles. Besides this, they also found that relatively low humidity values of around 41% lead to an incorporation of around 10 times volume percentage of water into the PSC thin film by adsorption on the crystals, concluding that no hydrates are formed.

Again, Schlipf and colleagues [93] employed grazing-incidence SANS to depict the moisture stability of 3D and 2D PSC heterojunction thin films at the D22 beamline of the ILL. In this work, they study the degradation of a mixed-dimensional PSC/PSC heterojunction formed by a 2D perovskite on top of a 3D one, which enhances moisture resistance and solar cell performance, under different humidity conditions. Representative SANS plots are presented in Fig. 6(b). One of the 2D PSCs was made of $(\text{PEA})_2(\text{MA})_4\text{Pb}_5\text{I}_{16}$, $m = 5$, dubbed PEAMAPI, where PEA^+ is phenylethylammonium, whereas another 2D PSC was made of a more complex quadruplication system incorporating formamidinium, rubidium and caesium cations, dubbed FAMARC. In both cases, the 3D PSC was the standard MAPbI_3 . Their study found that there is a strong water uptake into the heterojunction PSC, even if PEA^+ is reportedly found to be hydrophobic. A first consequence of the exposure to humidity is the disproportionation of the initially formed $m = 5$ PEAMAPI into more stable 2D PSC with lower m values, being the FAMARC 2D PSC not altered. They also found that the reduced migration of MA^+ and I^- ions to the crystal surface is possibly responsible for the segregation of PbI_2 in the heterojunction PSCs. The reversibility of the degradation process induced by humidity is further increased by the 2D perovskites in the heterojunction containing MAPbI_3 , while this is not the case for the other heterojunction PSC studied, as the water-mediated segregation of the FAMARC compound involves an irreversible Rb-rich side phase that cannot be prevented on the long-term.

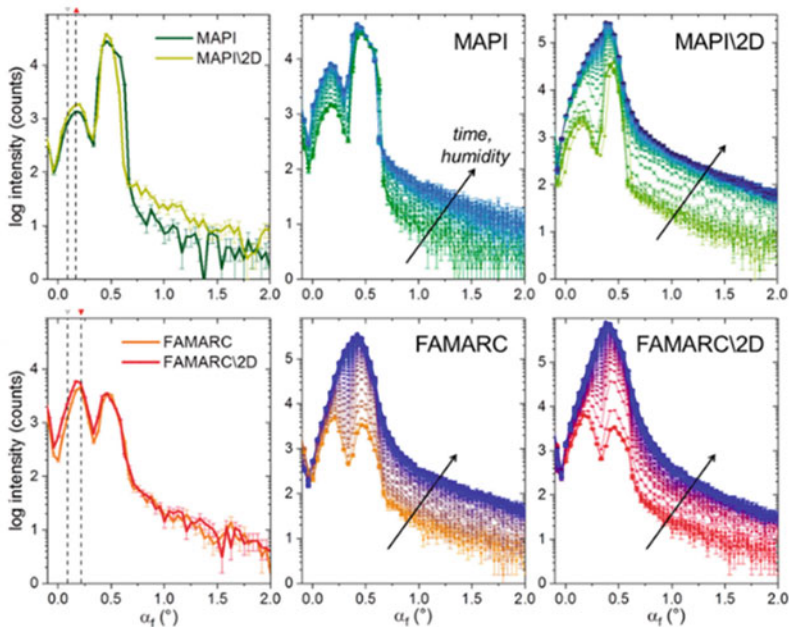
The usage of neutron reflectometry to study PSCs is, so far, very limited. One example where neutron reflectometry is employed in PSCs is found in the work shown by Yang Li and colleagues [94], who investigated the effect of residual PbI_2 layers formed during the solution process-based perovskite growth process at the time-of-flight polarized neutron reflectometer, TPNR, of the China Miyang Research Reactor (CMRR), part of the Key Laboratory of Neutron Physics (Miyang, China). Li and co-workers studied a series of $(\text{FAPbI}_3)_{1-x}(\text{MAPbI}_3)_x$ perovskite thin films with different buffer PbI_2 layers by neutron reflectometry, some of these reflectometry curves being represented in Fig. 6(a). They demonstrated that a layer of around 40 nm thick PbI_2 between the perovskite thin film and the SiO_2 substrate induce a better carrier behaviour at the interface, an effect that could lead to suppress the recombination processes that take place at the perovskite/ SiO_2 substrate interface. The authors combine these experimental results with theoretical predictions on different carriers in PSCs, concluding that higher efficient devices can be fabricated by interface engineering via the aforementioned inclusion of an intermediate PbI_2 layer of the appropriate thickness.

6.1.3 Inelastic and Quasi-Elastic Neutron Scattering

The neutron scattering techniques discussed so far in this chapter belong to the so-called group of *elastic neutron scattering* techniques, in which there is no momentum and/or energy transfer between the neutron beam and the sample being investigated. These techniques provide information about the structure of the materials



(a)



(b)

Fig. 6 **a** Neutron reflectometry curves of four different PSCs with their corresponding fittings, which lead to the composition distribution and thicknesses of the PSCs shown in the insets for each particular case. Reprinted with permission from [94]. Copyright 2020 American Chemical Society. **b** Vertical line cuts of GISANS experiments performed on different PSCs. Reprinted with permission from [93]. Copyright 2019 American Chemical Society

issue of study, but there is a way of obtaining information about the dynamics taking place in materials with neutron scattering: through inelastic (INS) and quasi-elastic (QENS) neutron scattering techniques. INS and QENS experiments deal with the analysis of the change in kinetic energy of neutrons after the neutron beam passes through a material. A number of processes that control many of the physical properties in condensed matter, such as chemical functionalization, transport phenomena, magnetism, catalytic processes or biological self-assembly processes, among others, depend on microscopic dynamical events that can be accessed through INS and QENS experiments. With these neutron scattering techniques, scientists can reveal displacements of atoms and/or molecules ranging from a few angstroms to dozens of nanometres, and accessing time scales that range from picoseconds to microseconds. Typical instrument types that serve to perform INS and QENS experiment include time-of-flight and backscattering spectrometers, and neutron spin-echo instruments.

In particular, INS and QENS experiments are very popular among the PSC community, as they provide information about lattice and cation dynamics in the devices. One example of an INS experiment performed with PSCs is the one described by Chen Wang and colleagues [95], who studied the tuning of giant phonons induced by pressure-mediated polar rotation in PSCs, combining INS experiments at the AMATERAS neutron spectrometer of J-PARC (Tokai, Japan) with molecular dynamics simulations. The authors found that the phonon scattering in MAPbI₃ PSCs is affected by the jumping rotational mode of the organic MA⁺ cations, which dramatically affect the properties of the phonons. They also found that the phase transition of the PSCs from orthorhombic to tetragonal, induced upon heating of the samples, considerably broadens the transition-fingerprint phonon line width, a broadening that is found to be mode-selective, as the four-fold rotation around the C-N axis of the organic cations is very sensitive to compression.

Another interesting study of PSCs with INS experiments is the one performed by Alfonso da Cunha Ferreira and his colleagues [96], who investigated the different low frequency acoustic phonons in four different perovskite single crystals at the Laboratoire Léon Brillouin (Paris, France). Their investigations comprised studying single crystal PSCs of MAPbI₃, FAPbBr₃, MAPbBr₃ and α -FAPbI₃ in their cubic phases, which they found to show, all of them, a very soft shear modulus C₄₄. The investigation of the low frequency structural excitations in the cubic phases of the aforementioned PSCs, where some of the recorded phonon spectra are shown in Fig. 7(a), provides a complete set of elastic constants for these materials, and the significant variation of their elastic bulk modulus. The softness differences shown between FA- and MA-based PSCs is linked to their structural stability and low thermal conductivities. The authors demonstrate with these experiments the hot phonon bottleneck phenomena that explains the relaxation of hot carriers.

Inelastic neutron scattering experiments performed by Aryeh Gold-Parker et al. [97] at the BT4 spectrometer of NIST Center for Neutron Research (NCNR, Maryland, USA) shows that acoustic phonons in MAPbI₃ possess very short lifetimes that have direct implications on the transport and on the cooling of charge carriers in these PSCs. The authors performed the INS experiments using fully deuterated MAPbI₃ single crystals with the objective of reducing the incoherent scattering from

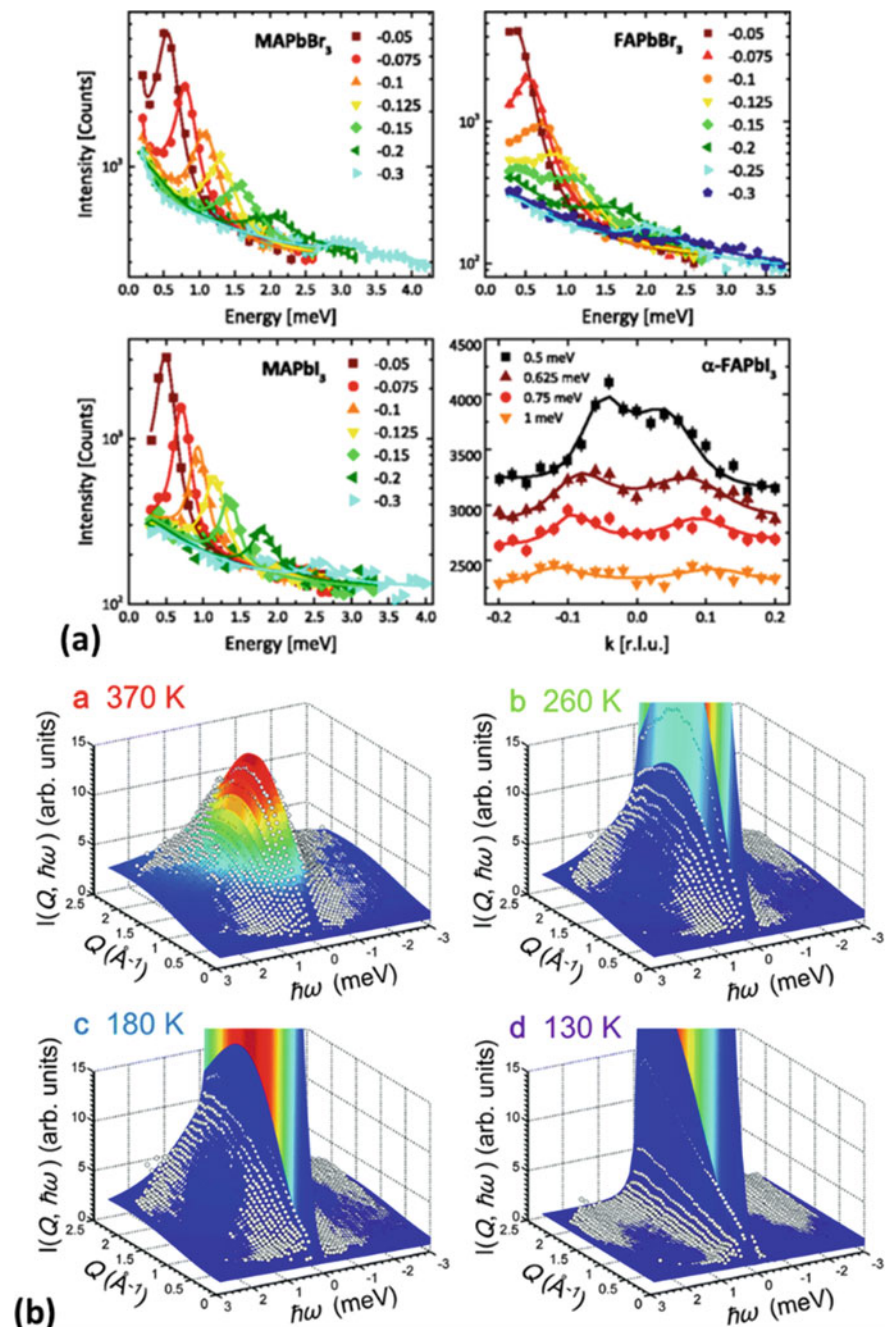


Fig. 7 **a** Phonon spectra in different PSCs in their cubic phases measured by inelastic neutron scattering. Reprinted (abstract/excerpt/figure) with permission from [96]. Copyright 2018 by the American Physical Society. **b** Quasi-elastic neutron scattering plots from MAPbI_3 samples measured at different temperatures. Republished with permission of the Royal Society of Chemistry, from [98]; permission conveyed through Copyright Clearance Center, Inc.

hydrogen. The INS measurements revealed extremely short acoustic phonon lifetimes of a few picoseconds, which are 50 to 500 times shorter than those found in conventional semiconductors. These lifetimes correspond to mean free paths of carriers on the nanometre lengths, demonstrating non-efficient heat dissipation processes. A combination of the INS results with lattice dynamics calculations show that the degrees of freedom of the MA^+ cation are responsible for a high density of low-energy optical phonon modes, together with a strong three-phonon interaction that is a fingerprint of the cation motion. Further to this, these investigations also infer that the short lifetimes of the acoustic phonons affect the cooling of the hot carriers.

QENS experiments are usually employed in PSCs to study slow processes such as cation reorientations or rotations. One example of such a study is the one presented by Aurelien M. A. Leguy and colleagues [99], who studied the dynamics of MA^+ cations in PSCs by QENS experiments performed at the OSIRIS spectrometer of the ISIS neutron and muon source. The authors studied the motion of the organic cations in $MAPbI_3$ PSCs, finding that both the methyl and amino groups rotate around the C-N axis within the structure formed by the PbI_3 octahedra that surround each cation. The characteristic timescale of these rotation movements is of around 14 picoseconds at room temperature, compatible with jumps between faces, corners or edges of the cations, whereas no evidence is found for translational motions of the cations. Non-expected rotations of the cations were found within the aforementioned time window irrespective of the temperature; these are attributed to C-N reorientations taking place in the vicinity of boundaries between antiferroelectric or ferroelectric domains, as elucidated from Monte Carlo simulations of dipole–dipole interactions between the organic cations. As antiferroelectric domains are believed not to affect charge carriers significantly, a crude estimate for a timescale of ferroelectric domain relaxation processes, deduced from the observations of the QENS experiments, corresponds to around 0.1 to 1 ms. This might have implications on the performance of PSC devices if ferroelectric effects influence the behaviour of such devices, a case in which the materials used as contacts in the PSCs should be carefully selected.

Alongside with QENS, sister spectroscopy techniques are generally employed in order to complement the neutron scattering experiments. This is the case of the experiments performed on $FAPbBr_3$ by Eve M. Mozur and colleagues [100], who combined nuclear magnetic resonance (NMR), nuclear quadrupole resonance (NQR) and QENS to study the cation dynamics of the aforementioned PSCs upon caesium substitution as cation. The QENS experiments were performed at the high-flux backscattering spectrometer (HFBS) of the NCNR. The authors attribute the changes to the dynamic degrees of freedom of the MA^+ cations to the five phase transitions of the $FAPbBr_3$. The addition of Cs^+ cations suppresses the four low-temperature phase transitions of the $FAPbBr_3$ due to the local compressive strain caused by the inorganic cation, which overrides the orientation driven by the MA^+ - MA^+ interactions. The mechanism proposed by the authors is that the caesium substitution causes the relief of geometric frustration derived from the possible orientations of the organic cations, which actually maintain their local dynamical degrees of freedom.

6.1.4 Complementarity of Neutron Scattering Techniques

In many cases the systems under study require not only one specific neutron scattering technique. Typical examples of this complementarity between different neutron scattering techniques are found in systems where a combination of inelastic and quasielastic neutron scattering techniques provide the scientists with a full knowledge about the dynamic processes that occur in that particular system. Other common complementarities are found when studying particular systems whose structure and dynamics are analysed together: in this case, a combination of neutron diffraction or large scale structures techniques with INS/QENS are employed, as it could be the case of magnetic materials whose crystal structure is studied with neutron diffraction and the magnon dispersions with inelastic neutron scattering.

This complementarity has also been employed by scientists studying perovskite solar cells. For instance, Bing Li and colleagues [101] employed complementary INS and QENS techniques, joined by density functional theory calculations and molecular dynamics simulations in order to present a complete atomic dynamic picture of MAPbI₃, joining together the study of the jumping rotational dynamics of molecules and phonons in the PSCs. They performed the neutron scattering experiments at the inverse-geometry time-of-flight chopper spectrometer DNA (BL02) and at the direct-geometry time-of-flight chopper spectrometer AMATERAS (BL14), both at J-PARC in Japan. The authors present high resolution INS and QENS experiments with which they obtained the characteristic timescales of all the dynamic processes that are involved in the studied PSCs, finding that around 165 K the ultrafast orientational disorder of molecular dynamics are activated, acting as an extra scattering source for optical phonons and charge carriers. They also found that it is the acoustic phonons who dominate the thermal transport happening in the PSCs rather than the optical phonons, as demonstrated by characteristic lifetimes in the sub-picosecond regime. All these findings are consistent with finite-temperature molecular dynamics simulations of the aforementioned processes.

Another good example of complementarity between INS and QENS in PSCs is found in the work performed by Jingrui Li et al. [102]. They employed these techniques jointly to study the effect of partial deuteration in MAPbI₃ on the activation energies of the organic cation rotation processes, which they studied at the D2AM and the D2A spectrometers of the ILL, also complemented with first-principles calculations. Li and colleagues studied the low temperature activation energies of the studied PSC, measuring an activation energy of the MA cation of around 48 meV, which is associated with the rotation of the methyl group without involving the amino group. In addition to this, they also found that in partially deuterated MA cations where the methyl group is deuterated and the amino group is hydrogenated, the activation energy for the rotation of the CD₃ is higher than that of the CH₃. The rotation of the NH₃ is unlikely to occur in any case due to its high energy barrier of around 120 meV, due to the strong hydrogen bondings of this group to the inorganic cage. All the experimentally obtained activation energies are in good agreement with those obtained from simulations performed taking into account nuclear quantum effects through path integral molecular dynamics simulations.

There is a further combination of neutron scattering techniques that is very popular among scientists studying perovskite solar cells: neutron diffraction, to study the structure of the PSCs, and INS/QENS, to study its dynamics. The account manuscript presented by Jarvist M. Frost and Aron Walsh [103] introduces a few examples where neutron diffraction and inelastic neutron scattering are combined, together with multiscale simulations of different nature (electronic structure, ab initio molecular dynamics and Monte Carlo simulations) and complementary ultrafast vibrational spectroscopy measurements. As previously mentioned in this chapter, neutron diffraction experiments provide scientists with extensive information about the different crystalline phases that occur in each particular PSC, together with the position of the organic cations within the crystal lattice in each phase. Through QENS measurements on the same PSCs, one can get information about the motion of hydrogen atoms, following the previously discussed examples of this kind of measurements in PSCs, due to the incoherent neutron scattering cross-section of the hydrogen nuclei. The authors of the manuscript discuss the multiscale simulations performed in hybrid halide PSCs, matching them with the aforementioned neutron scattering experiments and drawing conclusions about the atomistic origin of the dynamic processes in these PSCs, together with their associated chemical disorder that is a fingerprint of these systems.

A clear example of measurements performed with elastic and inelastic neutron scattering techniques to fully characterize PSCs is the one presented by Tianran Chen and colleagues [98], who studied MAPbI₃ with neutron diffraction experiments at the BT1 powder neutron diffractometer and QENS experiments at the DCS and HFBS spectrometers, the three instruments belonging to the NIST Center for Neutron Research, NCNR. After using neutron diffraction to fully characterize the crystallographic phases of the MAPbI₃, the authors managed to separate the dynamics of the rotation of the C-N axis, which presents a fourfold symmetry, from the dynamics of the rotation of the hydrogen atoms around the C-N atoms, with a threefold symmetry, in the cubic and tetragonal phases. Nonetheless, when the temperature of the PSC is decreased and it reaches the orthorhombic phase at around 165 K, the fourfold symmetry rotation is suppressed. The characteristic relaxation times for the fourfold and threefold rotation motions are determined to be five picoseconds and one picosecond, respectively. An interesting conclusion from this work is that the activation energy of the fourfold rotation motion, which is around 68 meV, is very close to the activation energy of 75 meV of the experimental charge recombination process, suggesting that the MA⁺ cations may be the rate-limiting step for the charge recombination processes in these PSCs.

One last experiment that involves high-resolution powder neutron diffraction and QENS measurements is the one presented by Eve M. Mozur and colleagues [104], who studied the dynamical phase transitions and photoconductivity dependent on the cation orientation in FAPbBr₃ PSCs at the NCNR of NIST. In this work, the authors report on three additional phase transitions that are not resolved crystallographically, which are deduced from calorimetry and neutron diffraction experiments, in addition to the two previously reported ones for FAPbBr₃. These three phase transitions are linked to the different changes that occur in the PSCs through

molecular reorientations of the FA^+ cations, and have an impact on the photoconductivity spectrum recorded and its intensity. The orientation of the organic FA^+ cation may be coupled to the inorganic PbBr_3^- framework through quadrupolar interactions, hydrogen bonding or pure geometric strain, which could lead to local lattice distortions that influence the electronic behaviour of the PSCs.

Besides the use of neutron scattering techniques to get information about the structure and dynamics of PSCs, there are other curious usages of neutron radiation to study PSCs. This is the case of Guiseppe M. Paternò and colleagues, who realized a first-time in-situ operando neutron irradiation experiment on PSCs at the VESUVIO spectrometer of the ISIS neutron and muon source [105]. Their experiment, a first of a kind in PSCs, wanted to shed light on the effects of outer space radiation on PSC devices. Although the experiment was performed in a spectrometer, this is not an INS experiment as the objective of the experiment is to mimic years of neutron exposure in space, and for that, the VESUVIO instrument is capable of mimicking around 80 years of radiation exposure at the International Space Station just within 8 h of beamtime. The results of the experiment demonstrates that fast neutron irradiation induces permanent defects in the PSCs, probably due to atomic displacements in the PSC layer, which are non-reversible. The decrease of leakage current can be a consequence of the formation of Frenkel-type defects that act as dopants within the PSCs. These results demonstrate that the PSC technology is strong against cosmic radiation, holding promises for their effective implementation in the aeronautic industry.

6.2 *Synchrotron X-Ray Scattering Techniques*

Synchrotron radiation is composed by electromagnetic radiation; i.e. photons, which is generated from electrons that are accelerated very close to the speed of light in a ring of electromagnets and that, upon curving their trajectories with dipolar electromagnets, they emit radiation in the form of photons in the direction tangential to their curved trajectories. Depending on the equipment installed right after the ejection of the synchrotron radiation from the ring, one can control the properties (intensity, polarization, etc.) of the synchrotron radiation before it hits the sample that will be studied. There are certain properties of the synchrotron radiation that make it a unique tool for scientific research: it is an extremely brilliant source of radiation, many orders of magnitude more brilliant than any laboratory-based X-Ray source, and the white nature of the synchrotron makes it a versatile source of possible monochromatic beams ranging from infrared to gamma rays. This radiation is very suitable to study the structure of solids, proteins, polymers or biological systems, among others, offering at the same time the possibility to investigate specific electronic transitions in the materials issue of study. Besides this, the fact that the electrons in the ring travel grouped in bunches opens the possibility to perform high-frequency dynamic pump-probe type experiments.

Similar to neutron radiation, the synchrotron radiation instruments are grouped into three different big instrument groups: X-Ray diffraction and scattering, which comprises both diffraction and small angle scattering, X-Ray spectroscopy, and X-Ray imaging and microscopy. Again, likewise with neutrons, imaging experiments with synchrotron radiation have not yet been reported, as these are not needed at this stage of development of current PSC technology. Nonetheless, both X-Ray diffraction/scattering and spectroscopy techniques have been widely implemented in the study of different PSC materials, and a few representative examples of these will be discussed in the next sections of this chapter hereafter.

6.2.1 Synchrotron X-Ray Diffraction

Synchrotron X-Ray diffraction (XRD) is a well-established synchrotron technique that sheds light into the structure of the materials that are being investigated, similar to the already discussed neutron diffraction techniques. As previously mentioned in Sect. 6.1.1, diffraction can be used to look at a wide variety of materials, such as metal alloys, chemical compounds, biological samples and magnetic materials, among others. Nonetheless, as the penetration of X-Rays is limited compared to that of neutrons, XRD are suited for surface analysis and for shallow depths or thin films, rather than giving information about bulk samples as it is the case of neutron diffraction. On the other hand, the scattering cross sections of the elements depend on their atomic number and are, generally and for non-light elements, much higher than these of neutrons for the same elements. This fact, coupled to the much higher flux of synchrotron radiation compared that of neutrons in neutron radiation sources, makes XRD more suitable for samples with reduced sizes and with non-light elements.

In this section, a few examples of synchrotron XRD experiments on PSCs will be presented. One representative example of such studies is the one given by the experiments performed by Jiangtao Zhao and colleagues [108], who employed synchrotron XRD to investigate the degradation processes in humidity conditions of powder MAPbI_3 at the BL14B end-station of the Shanghai Synchrotron Radiation Facility (SSRF, Shanghai, China). A combination of in-situ XRD, microscopy and gravimetric analysis provided the scientists with a complete study of the degradation process of MAPbI_3 under moisture. Their results reveal that the humidity conditions lead not only to the decomposition of MAPbI_3 into PbI_2 and $\text{CH}_3\text{NH}_3\text{I}$, but that moisture also affects the their relative distributions, resulting into an incompletely reversible reaction of the hydrolysis process in MAPbI_3 . Their analysis infer that a further decomposition of $\text{CH}_3\text{NH}_3\text{I}$ into volatile CH_3NH_2 , HI or I_2 is not likely to occur. The findings of their work sheds light into the role of the hydrolysis processes on the photoelectric properties of degraded PSCs.

A second comprehensive example of the use of synchrotron powder XRD on PSCs is found in the work developed by Frederike Lehmann et al. [106], who employed the diffraction technique to obtain a phase diagram of a mixed halide PSC at the KMC-2 beamline of the BESSY-II synchrotron (Berlin, Germany). The authors of this work fabricated and studied a series of $\text{MAPb}(\text{I}_{1-x}\text{Br}_x)_3$ PSCs and, by means of

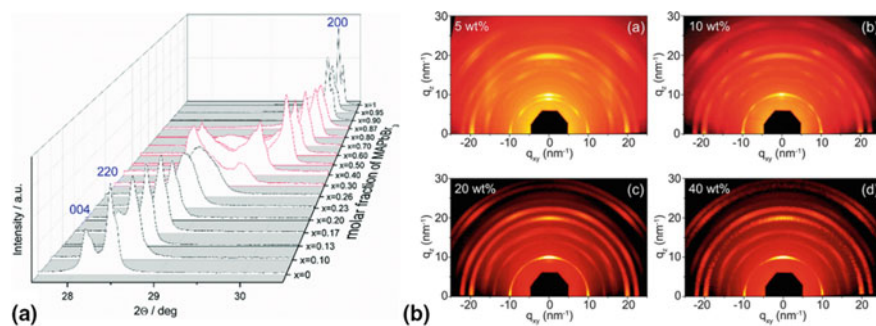


Fig. 8 **a** Powder X-Ray diffraction pattern evolutions for different $\text{MAPb}(\text{I}_{1-x}\text{Br}_x)_3$ PSCs, evidencing a phase change for increasing x values. Republished with permission of the Royal Society of Chemistry, from [106]; permission conveyed through Copyright Clearance Center, Inc. **b** 2D GIWAXS images of $\text{H}_3\text{NH}_3\text{PbI}_{3-x}\text{Cl}_x$ PSCs prepared from different wt% precursor solutions (a: 5%, b: 10%, c: 20% and d: 40%) annealed for 45 min at 100 °C. Reprinted with permission from [107]. Copyright 2014 American Chemical Society

synchrotron XRD, they studied their solubility and structural phase transitions over a temperature range between 30 and 350 K. For values of x between 0.29 and 0.92, the PSCs present an immiscible two-phase region, as observed in Fig. 8(a). Their lattice parameters were studied at different temperatures, showing a linear dependence of the chemical composition on the iodine rich PSCs, in good agreement with Vegard's law. Nonetheless, for the bromine rich PSCs this law is not followed probably due to the difference between the Br and I sizes. For the iodine rich PSCs, the phase transition temperatures follow a decreasing trend with the I content, attributed to the increasing Br-I substitution, leading to an increasing disorder in the crystal structure and to the stabilization of the cubic phase at higher temperatures. This is not the case for the bromine rich PSCs, which remain unaffected by the Br-I substitution. Regarding the photoluminescence properties of the PSCs, for compositions with $x < 0.29$ a tuneable bandgap between 1.56 eV to 1.66 eV appears, depending on the exact composition, while for compositions within the $0.29 < x < 0.92$ range the bandgap value does not significantly change.

Further to the study of powder PSCs with synchrotron XRD, information about the structure of PSC thin films can also be obtained when the X-Rays are hitting the sample under grazing incidence conditions (GIXRD). This is the case of the study performed by Liang Kuai and colleagues [109], a recent study about the crystallization dynamics and compositional control mechanism in 2D PSCs performed at the Shanghai Synchrotron Radiation Facility. The authors report on the incorporation of potassium cations to stabilize a vertically oriented quasi-2D $\text{BA}_2\text{MA}_3\text{Pb}_4\text{I}_{13}$, where BA stands for butylammonium, increasing the efficiency and the stability of these PSCs. They found that the doping cations fosters the crystallinity along the vertical orientation through in-situ GIXRD experiments. For PSC devices with 10%

K_+ incorporation to the initial $\text{BA}_2\text{MA}_3\text{Pb}_4\text{I}_{13}$ perovskite, the power conversion efficiency is around 11.3% while, at the same time, this PSC retains 90% of the initial performance after 1000 h in $40 \pm 10\%$ relative humidity conditions.

6.2.2 Grazing-Incidence Small and Wide Angle Synchrotron X-Ray Scattering

Similar to its sister technique with neutrons, the small angle X-Ray scattering technique (SAXS) is widely used in the characterization of materials at the nanoscale, and gives information about particle sizes, aggregates and size distributions present in the materials being investigated. In the case of perovskite solar cells, as many of these are usually produced in the form of thin films, the X-Rays need to be provided in grazing-incidence geometry (GISAXS) so that they can probe thin films. Sometimes SAXS experiments are well complemented with their counterpart wide-angle X-Ray scattering (WAXS) and the corresponding grazing-incidence WAXS (GIWAXS), which consists in measuring the scattering processes at higher incident angles than these used in SAXS, giving complementary information about the presence and size of nanocrystallites and the quantification of crystalline phases. A very nice review on grazing-incidence X-Ray scattering experiments performed in PSCs can be found in [110].

Due to the higher flux of the synchrotron light sources, the amount of small and wide angle X-Ray scattering experiments performed in PSCs is higher than these performed so far with neutrons. In this section, examples of GISAXS, GIWAXS and a combination of GIWAXS and GISAXS experiments performed in perovskite solar cell devices will be discussed. One example of GISAXS experiments in PSCs is the one performed by Johannes Schlipf and colleagues [111], who studied the growth of PSC thin films with a crystalline precursor PbI_2 at the Austrian SAXS beamline of the Elettra Synchrotron (Trieste, Italy). The researchers analysed both the precursor PbI_2 thin film before immersion in a mixed solution of methylammonium iodide and methylammonium chloride, and the final perovskite $\text{MAPbI}_{3-x}\text{Cl}_x$ after immersion, by GISAXS, finding a close correlation of the lateral crystal sizes present in both thin films. In addition to this, the careful analysis of the individual scattering signals recorded in each case revealed an increasing ratio of crystal sizes, from smaller to larger, from the top of the surface towards the bulk side of the PSC.

One of the first experiments reporting the use of GIWAXS to study PSCs is the one presented by Kwan W. Tan and colleagues [107]. They performed in-situ 2D GIWAXS to follow the structural evolution of $\text{CH}_3\text{NH}_3\text{PbI}_{3-x}\text{Cl}_x$ PSCs on mesoporous block copolymer Al_2O_3 thin films under thermal annealing, on the D1 beamline of the Cornell High Energy Synchrotron Source (CHESS, Ithaca, USA). With these experiments, the researchers found that the PSCs undergo transitions upon annealing, between three different crystalline phases: crystalline precursor, perovskite and PbI_2 resulting from the degradation process. Examples of GIWAXS images they obtained are shown in Fig. 8(b). Further to the study of the proper perovskite material, they also investigated the process of annealing the mesoporous

block-copolymer (MBCP)- Al_2O_3 by in-situ GIWAXS experiments, finding optimal conditions with which the full PSC device.

The origin of crystal orientations in hybrid halide perovskite thin films has also been investigated by means of GIWAXS by Lukas Oesinghaus and colleagues [112]. Although they performed the GIWAXS experiment with an 8 keV Cu-K X-Ray source without the needs of synchrotron radiation, their findings on the role of film morphology on the properties of the PSCs studied after one-step and two-step PSC fabrication processes, is of such a crucial interest to the PSC community using GIWAXS techniques that it deserves mentioning in this section.

The crystallization kinetics in PSCs was studied through GIWAXS experiments by David T. Moore et al. [113] at the D1 beamline at CHESS synchrotron, where they developed a method to obtain the time evolution of the transformed portion of MAPbI_3 during growth. With these measurements, the researchers developed a crystallization kinetics model that is applied successfully to extract the crystallization activation energy in each particular growth process. This model shows that the activation energies are strongly dependent on the precursor lead salt that, together with the methylammonium salt, contributes to the crystallization process. This work suggests that one should be very careful when choosing the right lead salt for the fabrication of PSCs by spin-coating techniques.

Another study dealing with in-situ GIWAXS experiments to analyse the PSC growth is the one carried out by Wei Zhang and colleagues [114], also at the D1 beamline at CHESS synchrotron. In this study, the authors found that the perovskite thin film morphology and device performance are affected by the kinetics of the crystal growth, on which the anions play a crucial role. Instead of using a halide lead source as it is usually employed, the use of a non-halide one, as it is lead acetate, results into a faster crystal growth that results into almost pinhole-free and ultra-smooth perovskite thin films. This effect is due to the easy removal of the excess $\text{CH}_3\text{NH}_3\text{AC}$, where AC is the acetate group.

The complementarity between GIWAXS and GISAXS is perfectly evidenced in the work developed by Alexander T. Barrows and co-workers [115], who studied PSCs with GIWAXS at the XMaS beamline of the European Synchrotron Radiation Facility, ESRF (Grenoble France), and GISAXS at the I22 beamline of the Diamond Light Source synchrotron (Oxfordshire, UK). They studied the formation of $\text{CH}_3\text{NH}_3\text{PbI}_{3-x}\text{Cl}_x$ from a precursor film, similar to other works presented before in this section, but making use of these grazing-incidence synchrotron X-Ray scattering techniques to gain information about the crystallization kinetics of the PSCs during thermal annealing. With GIWAXS the transition from the precursor to the perovskite structure was characterized and quantified, obtaining activation energies of this transformation around 85 kJ/mol, and observing an out-of-plane preferential growth orientation of the perovskite crystallites. With GISAXS, information about the evolution of crystallite sizes during annealing was obtained, presenting these crystallites sizes between 30 and 400 nm, increasing their sizes through the annealing process. The observed evolution in these crystallite sizes is positively correlated with an effective increase in thin film surface coverage, leading to an increase of the efficiency of the PSC devices.

6.2.3 Synchrotron X-Ray Absorption Spectroscopy

The synchrotron X-Ray absorption spectroscopy is the synchrotron sister technique to inelastic neutron scattering, as it consists in inelastic scattering events where the synchrotron photons interact with the electrons present in the material being investigated. With the aforementioned very wide range of photon energies provided by the synchrotron radiation source, absorption or fluorescence events may occur in the atoms constituting the materials issue of study. Every single atom absorbs X-Rays at certain specific wavelengths, corresponding to the energy needed by the electrons orbiting around it to change orbit or to be expelled from the atom: these are called the absorption edges, characteristic of each element. Hence, when a bunch of photons with different energies are shined onto a material, element-specific information for the atoms forming that material is obtained. In this way, characteristic vibrational modes of soft and hard condensed matter can also be investigated with synchrotron X-Ray spectroscopy techniques.

The synchrotron X-Ray absorption spectroscopy techniques can be divided into two main groups: soft X-Ray spectroscopy and hard X-Ray spectroscopy. Among the techniques within the first group, near-edge X-Ray absorption fine structure spectroscopy (NEXAFS), soft X-Ray emission spectroscopy (SXES), resonant inelastic X-Ray scattering (RIXS), X-Ray magnetic circular dichroism (XMCD) or X-Ray photoemission spectroscopy (XPS) can be found. The hard X-Ray spectroscopy group comprises techniques such as extended X-Ray absorption fine structure spectroscopy (EXAFS), hard X-Ray photoelectron spectroscopy (HAXPES), hard NEXAFS, X-Ray absorption near-edge structure spectroscopy (XANES) and hard XMCD, among others.

Examples of hard X-Ray absorption spectroscopy measurements on PSCs can be found in the work carried out by Rebecka Lindblad and colleagues, who performed HAXPES experiments in MAPbI₃ PSCs [116], and in both MAPbBr₃ and MAPbI₃ PSCs [117] performed at the KMC-1 beamline of BESSY-II synchrotron. In the first study, the authors disclose the electronic structure of MAPbI₃ at titanium dioxide interfaces. Through HAXPES measurements, information about different characteristics of the PSCs were obtained: the binding energy and the characteristics of the valence band of the PSCs, and the chemical composition of the PSC. A direct comparison of the spectroscopy measurements performed between PSCs grown by one-step and two-step processes is presented in Fig. 9, demonstrating that their stoichiometry and electronic structures are very similar in the two cases. Further to this, their work also shows that the bandgap states of the TiO₂ after the perovskite layer deposition are still present. Through a direct comparison of the measured valence bands and these obtained with density of states simulations (DOS), a good agreement between them is demonstrated, together with a correspondence of the outermost valence levels as lead and iodine orbitals. In their second study, the researchers use a combination of HAXPES with density functional theory and density of states calculations in order to investigate the differences between the electronic structures of MAPbBr₃ and MAPbI₃. The results of the spectroscopy measurements, which are supported by the aforementioned calculations, show a shift of the valence band edges

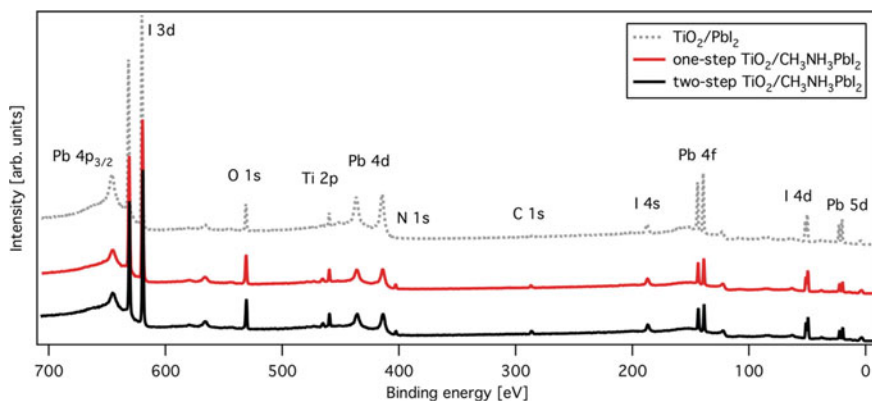


Fig. 9 Overview of the HAXPES spectra measured with a photon energy of 4 keV in MAPbI₃ PSCs prepared following one-step and two-step processes, together with the spectra of the PbI₂. Reprinted with permission from [116]. Copyright 2014 American Chemical Society

for both PSCs with a higher binding energy of the bromine-based perovskite. This energy shift towards higher binding energies is attributed to the nature of the Br ion.

The electronic structure of MAPbI₃ perovskite thin films fabricated using either one-step or two-step deposition protocols has also been studied by John A. McLeod and colleagues [118], who performed angle-resolved K-edge soft X-Ray absorption spectroscopy measurements at the BL24A beamline of the National Synchrotron Radiation Research Center, NSRRC (Hsinchu, Taiwan). The main results of their work show that the PSCs fabricated following a one-step fabrication process present angle-dependent characteristics, while the perovskites fabricated following a two-step process lack this angle-dependent feature. This leads to the presence of long-range alignment of the methylammonium molecules, being this angle-dependency decreased with increasing thin film thicknesses.

6.2.4 Complementarity of Synchrotron X-Ray Scattering Techniques

As it is the case with the different neutron scattering techniques and their complementarity, the different synchrotron radiation techniques also present a high degree of complementarity when it comes to study different advanced properties of a certain material. Typical combinations of characterization techniques involving synchrotron radiation include structural ones, like diffraction or wide/small angle neutron scattering, and spectroscopy, so that both static (structure) and dynamics are probed within the same material.

Nonetheless, in some cases two different synchrotron radiation techniques aiming at studying the structure of a certain material can be employed to obtain complementary information: this is the case of certain studies that combine synchrotron X-Ray diffraction and wide angle X-Ray scattering, where information about crystal

structures and textures (diffraction) and crystallite sizes and aggregates (wide angle scattering) are obtained. This is the case of the work performed by Hsinhan Tsai and colleagues [119], who employed grazing-incidence XRD and GIWAXS at the Advanced Photon Source of the Argonne National Laboratory (Illinois, USA), to study highly-efficient 2D Ruddlesden-Popper PSCs. More concretely, the authors showed that this type of 2D PSCs present promising stability properties, although their efficiencies were still far from those developed in their counterpart 3D PSCs. Through GIXRD, the authors demonstrate the most adequate fabrication processes for these 2D PSCs: the hot-cast thin films presented superior crystallinity degrees, whose finding motivated the need to perform GIWAXS with complementary imaging techniques. The main results derived from the joint analysis of the GIXRD and GIWAXS experiments are that the devices exhibit 60% efficiency after being continuously exposed to light during 2250 h without encapsulation. This behaviour is further improved if the PSCs are encapsulated: the PSCs showed no degradation under constant illumination or humidity exposure conditions.

As previously mentioned, examples of research activities combining structural and spectroscopy measurements are common when using synchrotron radiation techniques. This is the case of the work performed by Wenchao Huang et al. [120], where they employ a combination of GIWAXS and NEXAFS at the Australian Synchrotron (Melbourne, Australia) to probe molecular and crystalline orientations in solution-processed PSCs. In this case, the morphology of the crystallites of MAPbI₃ PSCs, which appears to be linked to the shape characteristics, thickness and kinetics of the underlying TiO₂ layer, was studied with GIWAXS experiments. For perovskite film thicknesses between 200 and 250 nm, the crystallites present a lack of preferential orientation, whereas for thinner films of around 60 nm, the crystallites are oriented. This indicates that the orientation of these crystallites is very sensitive to the kinetics of the process of solvent evaporation. NEXAFS experiments indicate that these methylammonium cations present a random molecular orientation with respect both to the substrate and to the perovskite unit cell. Nonetheless, measurements of the efficiencies in all the PSCs studied demonstrate that there is a limited sensitivity of the PSC performance with respect to the crystallite orientation.

Lastly, a comprehensive study of thermally induced degradation processes in MAPbI₃ PSCs using three different synchrotron techniques is presented hereafter. Nam-Koo Kim and colleagues [121] performed a combination of various in-situ synchrotron radiation surface analysis techniques in MAPbI₃: GIWAXD, at the PLS-II 9A U-SAXS beamline of the Pohang Accelerator Laboratory (PAL, Pohang, South Korea), high-resolution XPS and NEXAFS, both at the 4D PES beamline of PAL. Their study on the degradation process of MAPbI₃ PSCs confirmed the structural change of the PSCs upon 20 min exposure to 100° C, or upon exposure longer than 1 h to 80 °C, which led to a decomposition process to CH₃I, NH₃ and PBI₂. Further to this, the spectroscopy measurements demonstrate that the orientation of the MA⁺ cations with respect to the substrate changes in intermediate phases before degradation. These results indicate that the incorporation of the organic cation by the PSC structure is very sensitive to heat, being a possible solution to this problem the

substitution of the MA⁺ cations with other cations that should improve the thermal stability of the PSCs.

6.3 Examples of Combinations of Neutron and Synchrotron Radiation Characterization Techniques

The advantages and disadvantages that neutron and synchrotron X-Ray scattering possess with respect to each other put them often in situations in which a combination of techniques using both types of radiations is a perfect match. As previously mentioned in this chapter, neutrons interact with the nuclei of the atoms, whereas X-Rays interact with their electron clouds. Therefore, although both scattering processes have the same physical theory behind them, the different way both particles scatter often lead to complementary information after the analysis of the scattering events. Also, as neutrons can probe light elements with more contrast than X-Rays, these are usually employed to analyse in-depth the properties of soft matter and materials where light elements play a crucial role. Nonetheless, the usage of synchrotron radiation to probe these materials also gives complementary information to the scientists about the materials being studied.

In this section, a few examples of the complementarity between neutron and synchrotron radiation techniques to study perovskite solar cell devices will be introduced. To start with, Pamela S. Whitfield and colleagues [122] studied the structure, phase transitions and tricritical behaviour of MAPbI₃ by neutron powder diffraction, at the Nanoscale Ordered Materials diffractometer of the Spallation Neutron Source, ORNL (USA), and by synchrotron X-Ray powder diffraction, at the DND-CAT sector 5 of the Advanced Photon Source (USA). The researchers utilized fully deuterated MAPbI₃ to avoid the strong incoherent neutron scattering from hydrogen, with the objective of studying the structural complexity given by the MA⁺ cation. In this way, they managed to collect neutron diffraction data with superior signal-to-noise ratios, accessing better resolved higher Q diffractometers than previous studies performed with non-deuterated PSCs. The usage of synchrotron X-Ray powder diffraction complements the neutron powder diffraction due to the fact that the structural phase transitions of the PSC can be studied in more detail because of the higher resolution of the synchrotron-based diffraction technique. In their analysis of the recorded data, they found that the high temperature cubic phase of the PSC is transformed into a body-centered tetragonal phase around 330 K, scaling the order parameter Q with the temperature following $Q \sim (T_C - T)^\beta$, where T_C is the critical temperature and $\beta \sim 1/4$ is the value of the exponent predicted for a tricritical phase transition. They also reported on a phase coexistence of the cubic and tetragonal phases before the full transformation to the tetragonal one, a fingerprint of a first-order phase transition. Upon cooling towards 100 K, the PSC transformed into an orthorhombic phase around 160 K through another first-order phase transition.

Tianran Chen and colleagues [123] also combined neutron and synchrotron X-Ray diffraction measurements in MAPbI₃ and FAPbI₃ PSCs, at the NCNR neutron source and the CHESS synchrotron, respectively, to study the role of the organic cations on the extension of the lifetime of photoexcited charge carriers. Together with the diffraction experiments, they also performed photoluminescence measurements and discrete Fourier transform calculations in order to determine the emission spectra and the electronic band structures of the PSCs, respectively. The results from their research demonstrate that a major contribution to the extended charge carrier lifetimes is attributed to the screening of band-edge charge carriers, due to the rotation motions of the organic cations. This extended carrier lifetime is increased when the PSCs undergo a phase transition from a lower rotational entropy phase to a higher rotational entropy one. In this scenario, the screening of the charge carriers suppresses the recombination processes of the photoexcited electrons and the holes, resulting into the formation of polarons that extend the lifetime of the carriers.

Carlos A. López and co-workers [124] studied the conformation of the methylammonium cation on MAPbBr₃ PSCs through a combination of synchrotron X-Ray powder diffraction and neutron powder diffraction experiments, performed at the MSPD diffractometer of the ALBA synchrotron (Barcelona, Spain), and at the D2B powder diffractometer of the ILL, respectively. The synchrotron X-Ray powder diffraction experiments, which they performed in transmission geometry, provided with a better powder averaging that minimizes the preferred orientation that is observed with laboratory-based X-Ray diffraction equipment. The information on the positions of the carbon and nitrogen atoms within the MA⁺ cation were obtained through the powder neutron diffraction, which helped determining the organic cation conformation within the lattice. The structural phase transitions of the PSC were studied, finding a partial delocalization of the C and N atoms in the cubic phase at room temperature, which evolves upon cooling to localized positions within the orthorhombic phase at 120 K.

6.4 Muon Spectroscopy

Besides the well-established and widely known neutron scattering and synchrotron X-Ray scattering techniques that are implemented in large scale facilities, there is a third kind of measurements that are found in these facilities: muon spin spectroscopy. This experimental technique is based on the implantation of polarized muons in the material that is investigated. The muons, which are charged particles similar to electrons but with higher mass and a half-life time of around 2 μ s, start precessing around the local fields of the material where they are implanted and, when they decay, the positrons emitted from the decay process are detected and their properties analysed.

While muon spectroscopy, or muon spin relaxation (μ SR), was originally widely used to study magnetism and magnetic materials, in recent times this technique has been successfully employed to investigate processes like ion diffusion or superconducting properties. One of the key properties of μ SR is that the implantation depth of the muons can be tuned by changing the incident energy of the muon beam, therefore allowing to probe thin film depths in a range between 2 and 300 nm. Other advantages of this technique are that there is no need to employ photons, current or voltages to stimulate the material and measure its intrinsic diffusion process, and that there is no need to fabricate a full PSC device to measure diffusion. This allows measuring directly the diffusion processes in the perovskite material, not being impacted by interface properties or contact materials.

So far, there is one group that has implemented this technique to study the ion transport properties in PSCs, and is the one of Petra J. Cameron, from the University of Bath (UK), who performed the experiments at the ISIS neutron and muon source. In a first set of experiments, Dominic W. Ferdani and co-workers [125] employed μ SR to study the effect on the iodide ion transport of the incorporation of seven different sized cations (rubidium, caesium, azetidinium, formamidinium, dimethylammonium, acetamidinium and guanidinium, as ordered from smaller to bigger sizes) into MAPbI_3 . They combined the results of these experiments with impedance spectroscopy measurements and ab-initio simulations, finding that all of the studied cation substitutions increase the activation energy for the iodide ion transport with respect to pure MAPbI_3 . The results of this work involving muon spectroscopy measurements, which are shown in Fig. 10, included a first-time observation that partial (5%) guanidinium substitution into MAPbI_3 causes a strong suppression of the iodide ion transport.

The second μ SR set of experiments performed on PSCs by that group is the one led by Rodrigo García-Rodríguez [126], who studied the incorporation of bromide content on iodide migration in $\text{MAPb}(\text{I}_{1-x}\text{Br}_x)$ perovskite solar cells. In this work, the authors demonstrate that the increasing incorporation of Br in the PSCs affects strongly the low frequency impedance response of the devices, showing that for

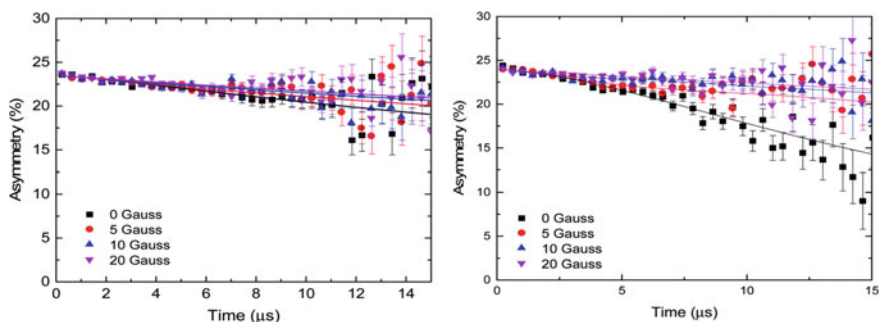


Fig. 10 Muon spectroscopy measurements performed at 400 K on PSCs with different compositions, obtained at different applied longitudinal fields. Republished with permission of the Royal Society of Chemistry, from [125]; permission conveyed through Copyright Clearance Center, Inc.

a critical Br content of 7.5% the slow impedance response is fully suppressed. The muon spin relaxation measurements in these PSCs demonstrated that a concentration of Br of 17%, typically used to increase the performance of these mixed PSCs, there is no fingerprint of the onset of iodide motion in the PSC.

7 New Challenges and Perspectives

The commercialization of PSCs requires scalability, device stability, low material cost and simple and low temperature manufacturing procedures. Therefore, in the hunt for stable and efficient PSCs, different architecture were explored which provides a large number of combinations in order to reduce resistances and increase open circuit voltage. Different possibilities are offered for both ETL and HTL. Nevertheless, it is important to optimize not only the different layer which compose the devices but also the ideal architecture for future commercial applications.

Perovskite solar cell technology has demonstrated to become one of the milestones in the latest years. Nevertheless, it is vital to continue its research in order to untangle the recombination processes of the different perovskite compositions and device configuration with the development of new characterization approaches. The development of combining different characterization techniques is an important direction, which will provide multidimensional, multimodal information about the materials and components of perovskite devices. Clearly, in situ/operando techniques developed for other technologies, such as batteries, can be expected to be easily adopted for studies of perovskite solar cell systems, making these developments of general importance for the field of photovoltaics.

References

1. Snaith, H.J.: Present status and future prospects of perovskite photovoltaics. *Nat. Mater.* **17**, 372–376 (2018)
2. Jena, A.K., Kulkarni, A., Miyasaka, T.: Halide perovskite photovoltaics: background, status, and future prospects. *Chem. Rev.* **119**, 3036–3103 (2019). <https://doi.org/10.1021/acs.chemrev.8b00539>
3. NREL efficiency chart - <https://www.nrel.gov/pv/cell-efficiency.html>
4. (2020) Perovskites take steps to industrialization. *Nat. Energy* **5**
5. Valadi, K., Gharibi, S., Taheri-Ledari, R., et al.: Metal oxide electron transport materials for perovskite solar cells: a review. *Environ. Chem. Lett.* **19**, 2185–2207 (2021)
6. Shalan, A.E., Sharmoukh, W., Elshazly, A.N., et al.: Dopant-free hole-transporting polymers for efficient, stable, and hysteresis-less perovskite solar cells. *Sustain. Mater. Technol.* **26**, e00226 (2020)
7. Shalan, A.E., Mohammed, M.K.A., Govindan, N.: Graphene assisted crystallization and charge extraction for efficient and stable perovskite solar cells free of a hole-transport layer. *RSC Adv.* **11**, 4417–4424 (2021)
8. Petrus, M.L., Schlipf, J., Li, C., et al.: Capturing the sun: a review of the challenges and perspectives of perovskite solar cells. *Adv. Energy Mater.* **7** (2017)

9. Shalan, A.E., El-Shazly, A.N., Rashad, M.M., Allam, N.K.: Tin–zinc-oxide nanocomposites (SZO) as promising electron transport layers for efficient and stable perovskite solar cells. *Nanoscale Adv.* **1**, 2654–2662 (2019)
10. Cheol, K.M., Ham, S.Y., Cheng, D., et al.: Advanced characterization techniques for overcoming challenges of perovskite solar cell materials. *Adv. Energy Mater.* **2001753**, 1–26. Doi: <https://doi.org/10.1002/aenm.202001753>
11. Wang, R., Mujahid, M., Duan, Y., et al.: A Review of Perovskites Solar Cell Stability. *Adv. Funct. Mater.* **29** (2019)
12. Shalan, A.E., Akman, E., Sadegh, F., Akin, S.: Efficient and stable perovskite solar cells enabled by dicarboxylic acid-supported perovskite crystallization. *J. Phys. Chem. Lett.* **12**, 997–1004 (2021)
13. Djurišić, A.B., Liu, F.Z., Tam, H.W., et al.: Perovskite solar cells - an overview of critical issues. *Prog. Quantum Electron.* **53**, 1–37 (2017)
14. Johnsson, M., Lemmens, P.: Crystallography and Chemistry of Perovskites. In: *Handbook of Magnetism and Advanced Magnetic Materials* (2007)
15. Goldschmidt, S.A.: Cover Page. *J. Am. Chem. Soc.* **1**, 311–312 (1879). <https://doi.org/10.1021/ja02148a600>
16. Li, C., Lu, X., Ding, W., et al.: Formability of ABX₃ (X = F, Cl, Br, I) halide perovskites. *Acta Crystallogr. Sect. B Struct. Sci.* **64**, 702–707 (2008). <https://doi.org/10.1107/S0108768108032734>
17. Weller, M.T., Weber, O.J., Henry, P.F., et al.: Complete structure and cation orientation in the perovskite photovoltaic methylammonium lead iodide between 100 and 352 K. *Chem. Commun.* **51**, 4180–4183 (2015). <https://doi.org/10.1039/c4cc09944c>
18. Petrov, A.A., Fateev, S.A., Khurstalev, V.N., et al.: Formamidinium haloplumbate intermediates: the missing link in a chain of hybrid perovskites crystallization. *Chem. Mater.* **32**, 7739–7745 (2020). <https://doi.org/10.1021/acs.chemmater.0c02156>
19. Fu, Y., Rea, M.T., Chen, J., et al.: Selective stabilization and photophysical properties of metastable perovskite polymorphs of CsPbI₃ in Thin Films. *Chem. Mater.* **29**, 8385–8394 (2017). <https://doi.org/10.1021/acs.chemmater.7b02948>
20. Fu, Y., Wu, T., Wang, J., et al.: Stabilization of the metastable lead iodide perovskite phase via surface functionalization. *Nano Lett.* **17**, 4405–4414 (2017). <https://doi.org/10.1021/acs.nanolett.7b01500>
21. Pellet, N., Gao, P., Gregori, G., et al.: Mixed-organic-cation perovskite photovoltaics for enhanced solar-light harvesting. *Angew. Chemie – Int. Ed.* **53**, 3151–3157 (2014). <https://doi.org/10.1002/anie.201309361>
22. Zhang, Y., Grancini, G., Feng, Y., et al.: Optimization of stable quasi-cubic FA_xMA_{1-x}PbI₃ perovskite structure for solar cells with efficiency beyond 20%. *ACS Energy Lett.* **2**, 802–806 (2017). <https://doi.org/10.1021/acsenerylett.7b00112>
23. Saliba, M., Matsui, T., Domanski, K., et al.: Incorporation of rubidium cations into perovskite solar cells improves photovoltaic performance. *Science (80-)* **354**, 206–209 (2016). <https://doi.org/10.1126/science.aah5557>
24. Abdi-Jalebi, M., Andaji-Garmaroudi, Z., Pearson, A.J., et al.: Potassium-and rubidium-passivated alloyed perovskite films: Optoelectronic properties and moisture stability. *ACS Energy Lett.* **3**, 2671–2678 (2018). <https://doi.org/10.1021/acsenerylett.8b01504>
25. Duong, T., Wu, Y.L., Shen, H., et al.: Rubidium multication perovskite with optimized bandgap for perovskite-silicon tandem with over 26% efficiency. *Adv. Energy Mater.* **7** (2017). Doi: <https://doi.org/10.1002/aenm.201700228>
26. Saliba, M., Matsui, T., Seo, J.Y., et al.: Cesium-containing triple cation perovskite solar cells: Improved stability, reproducibility and high efficiency. *Energy Environ. Sci.* **9**, 1989–1997 (2016). <https://doi.org/10.1039/c5ee03874j>
27. Zhang, T., Wu, J., Zhang, P., et al.: High speed and stable solution-processed triple cation perovskite photodetectors. *Adv. Opt. Mater.* **6** (2018). Doi: <https://doi.org/10.1002/adom.201701341>

28. Wang, C., Zhang, C., Wang, S., et al.: Low-temperature processed, efficient, and highly reproducible cesium-doped triple cation perovskite planar heterojunction solar cells. *Sol. RRL* **2** (2018). Doi:<https://doi.org/10.1002/solr.201700209>
29. Yang, W.S., Noh, J.H., Jeon, N.J., et al.: High-performance photovoltaic perovskite layers fabricated through intramolecular exchange. *Science* **80**(348), 1234–1237 (2015). <https://doi.org/10.1126/science.aaa9272>
30. Gratià, P., Grancini, G., Audinot, J.N., et al.: Intrinsic halide segregation at nanometer scale determines the high efficiency of mixed cation/mixed halide perovskite solar cells. *J. Am. Chem. Soc.* **138**, 15821–15824 (2016). <https://doi.org/10.1021/jacs.6b10049>
31. Kubicki, D.J., Prochowicz, D., Hofstetter, A., et al.: Phase segregation in Cs-, Rb- and K-Doped Mixed-Cation (MA)_x(FA)_{1-x}PbI₃ hybrid perovskites from solid-state NMR. *J. Am. Chem. Soc.* **139**, 14173–14180 (2017). <https://doi.org/10.1021/jacs.7b07223>
32. Hentz, O., Zhao, Z., Gradečák, S.: Impacts of ion segregation on local optical properties in mixed halide perovskite films. *Nano Lett.* **16**, 1485–1490 (2016). <https://doi.org/10.1021/acs.nanolett.5b05181>
33. Knight, A.J., Wright, A.D., Patel, J.B., et al.: Electronic traps and phase segregation in lead mixed-halide perovskite. *ACS Energy Lett* **4**, 75–84 (2019). <https://doi.org/10.1021/acsenergylett.8b02002>
34. Yan, J., Qiu, W., Wu, G., et al.: Recent progress in 2D/quasi-2D layered metal halide perovskites for solar cells. *J. Mater. Chem. A* **6**, 11063–11077 (2018)
35. De, M.N., Zhou, H., Chen, Q., et al.: Guanidinium: a route to enhanced carrier lifetime and open-circuit voltage in hybrid perovskite solar cells. *Nano Lett.* **16**, 1009–1016 (2016). <https://doi.org/10.1021/acs.nanolett.5b04060>
36. Jodłowski, A.D., Roldán-Carmona, C., Grancini, G., et al.: Large guanidinium cation mixed with methylammonium in lead iodide perovskites for 19% efficient solar cells. *Nat. Energy* **2**, 972–979 (2017). <https://doi.org/10.1038/s41560-017-0054-3>
37. Chen, P., Bai, Y., Wang, S., et al.: In situ growth of 2D perovskite capping layer for stable and efficient perovskite solar cells. *Adv. Funct. Mater.* **28** (2018). Doi:<https://doi.org/10.1002/adfm.201706923>
38. Wang, Z., Lin, Q., Chmiel, F.P., et al.: Efficient ambient-air-stable solar cells with 2D-3D heterostructured butylammonium-caesium-formamidinium lead halide perovskites. *Nat. Energy* **2** (2017). Doi:<https://doi.org/10.1038/nenergy.2017.135>
39. Grancini, G., Nazeeruddin, M.K.: Dimensional tailoring of hybrid perovskites for photovoltaics. *Nat. Rev. Mater.* **4**, 4–22 (2019)
40. Shikoh, A.S., Paek, S., Polyakov, A.Y., et al.: Assessing mobile ions contributions to admittance spectra and current-voltage characteristics of 3D and 2D/3D perovskite solar cells. *Sol. Energy Mater. Sol. Cells* **215** (2020). Doi: <https://doi.org/10.1016/j.solmat.2020.110670>
41. Salado, M., Fernández, M.A., Holgado, J.P., et al.: Towards extending solar cell lifetimes: addition of a fluorine cation to triple cation-based perovskite films. *Chemsuschem* **10**, 3846–3853 (2017). <https://doi.org/10.1002/cssc.201700797>
42. Salado, M., Jodłowski, A.D., Roldan-Carmona, C., et al.: Surface passivation of perovskite layers using heterocyclic halides: Improved photovoltaic properties and intrinsic stability. *Nano Energy* **50**, 220–228 (2018). <https://doi.org/10.1016/j.nanoen.2018.05.035>
43. Zhao, P., Kim, B.J., Jung, H.S.: Passivation in perovskite solar cells: a review. *Mater. Today Energy* **7**, 267–286 (2018). <https://doi.org/10.1016/j.mtener.2018.01.004>
44. Salado, M., Andresini, M., Huang, P., et al.: Interface engineering by thiazolium iodide passivation towards reduced thermal diffusion and performance improvement in perovskite solar cells. *Adv. Funct. Mater.* **30**, 1–11 (2020). <https://doi.org/10.1002/adfm.201910561>
45. Park B wook, Kedem N, Kulbak M, et al (2018) Understanding how excess lead iodide precursor improves halide perovskite solar cell performance. *Nat. Commun.* **9**. Doi: <https://doi.org/10.1038/s41467-018-05583-w>
46. Jeon, N.J., Noh, J.H., Kim, Y.C., et al.: Solvent engineering for high-performance inorganic-organic hybrid perovskite solar cells. *Nat. Mater.* **13**, 897–903 (2014). <https://doi.org/10.1038/nmat4014>

47. Burschka, J., Pellet, N., Moon, S.J., et al.: Sequential deposition as a route to high-performance perovskite-sensitized solar cells. *Nature* **499**, 316–319 (2013). <https://doi.org/10.1038/nature12340>
48. Li, J., Wang, H., Chin, X.Y., et al.: Highly efficient thermally co-evaporated perovskite solar cells and mini-modules. *Joule* **4**, 1035–1053 (2020). <https://doi.org/10.1016/j.joule.2020.03.005>
49. Zhu, X., Yang, D., Yang, R., et al.: Superior stability for perovskite solar cells with 20% efficiency using vacuum co-evaporation. *Nanoscale* **9**, 12316–12323 (2017). <https://doi.org/10.1039/c7nr04501h>
50. Momblona, C., Kanda, H., Sutanto, A.A., et al.: Co-evaporation as an optimal technique towards compact methylammonium bismuth iodide layers. *Sci. Rep.* **10** (2020). Doi: <https://doi.org/10.1038/s41598-020-67606-1>
51. Liu, M., Johnston, M.B., Snaith, H.J.: Efficient planar heterojunction perovskite solar cells by vapour deposition. *Nature* **501**, 395–398 (2013). <https://doi.org/10.1038/nature12509>
52. Lewis, D.J., O'Brien, P.: Ambient pressure aerosol-assisted chemical vapour deposition of (CH₃NH₃)PbBr₃, an inorganic-organic perovskite important in photovoltaics. *Chem. Commun.* **50**, 6319–6321 (2014). <https://doi.org/10.1039/c4cc02592j>
53. Bhachu, D.S., Scanlon, D.O., Saban, E.J., et al.: Scalable route to CH₃NH₃PbI₃ perovskite thin films by aerosol assisted chemical vapour deposition. *J. Mater. Chem. A* **3**, 9071–9073 (2015). <https://doi.org/10.1039/c4ta05522e>
54. Whitaker, J.B., Kim, D.H., Larson, B.W., et al.: Scalable slot-die coating of high performance perovskite solar cells. *Sustain. Energy Fuels* **2**, 2442–2449 (2018). <https://doi.org/10.1039/c8se00368h>
55. Kim, J.E., Jung, Y.S., Heo, Y.J., et al.: Slot die coated planar perovskite solar cells via blowing and heating assisted one step deposition. *Sol. Energy Mater. Sol. Cells* **179**, 80–86 (2018). <https://doi.org/10.1016/j.solmat.2018.02.003>
56. Krebs, F.C., Tromholt, T., Jørgensen, M.: Upscaling of polymer solar cell fabrication using full roll-to-roll processing. *Nanoscale* **2**, 873–886 (2010). <https://doi.org/10.1039/b9nr00430k>
57. Di Giacomo, F., Shanmugam, S., Fledderus, H., et al.: Up-scalable sheet-to-sheet production of high efficiency perovskite module and solar cells on 6-in. substrate using slot die coating. *Sol Energy Mater. Sol. Cells* **181**, 53–59 (2018). <https://doi.org/10.1016/j.solmat.2017.11.010>
58. Dou, B., Whitaker, J.B., Bruening, K., et al.: Roll-to-roll printing of perovskite solar cells. *ACS Energy Lett.* **3**, 2558–2565 (2018). <https://doi.org/10.1021/acseenergylett.8b01556>
59. Stanne, T.M., Sjögren, L.L.E., Koussevitzky, S., Clarke, A.K.: Identification of new protein substrates for the chloroplast ATP-dependent Clp protease supports its constitutive role in Arabidopsis. *Biochem. J.* **417**, 257–268 (2009). <https://doi.org/10.1042/BJ20081146>
60. Aranda, C., Cristobal, C., Shooshtari, L., et al.: Formation criteria of high efficiency perovskite solar cells under ambient conditions. *Sustain. Energy Fuels* **1**, 540–547 (2017). <https://doi.org/10.1039/c6se00077k>
61. Troughton, J., Hooper, K., Watson, T.M.: Humidity resistant fabrication of CH₃NH₃PbI₃ perovskite solar cells and modules. *Nano Energy* **39**, 60–68 (2017). <https://doi.org/10.1016/j.nanoen.2017.06.039>
62. Ma, C., Park, N.G.: A realistic methodology for 30% efficient perovskite solar cells. *Chem* **6**, 1254–1264 (2020)
63. Yang, D., Yang, R., Wang, K., et al.: High efficiency planar-type perovskite solar cells with negligible hysteresis using EDTA-complexed SnO₂. *Nat. Commun.* **9** (2018). doi:<https://doi.org/10.1038/s41467-018-05760-x>
64. Zheng, X., Hou, Y., Bao, C., et al.: Managing grains and interfaces via ligand anchoring enables 22.3%-efficiency inverted perovskite solar cells. *Nat. Energy* **5**, 131–140 (2020). <https://doi.org/10.1038/s41560-019-0538-4>
65. Calió, L., Kazim, S., Grätzel, M., Ahmad, S.: Hole-Transport Materials for Perovskite Solar Cells. *Angew. Chemie - Int. Ed.* **55**, 14522–14545 (2016)
66. Fabregat-Santiago, F., Bisquert, J., Cevey, L., et al.: Electron transport and recombination in solid-state dye solar cell with spiro-OMeTAD as hole conductor. *J. Am. Chem. Soc.* **131**, 558–562 (2009). <https://doi.org/10.1021/ja805850q>

67. Nguyen, W.H., Bailie, C.D., Unger, E.L., McGehee, M.D.: Enhancing the hole-conductivity of spiro-OMeTAD without oxygen or lithium salts by using spiro(TFSI)₂ in perovskite and dye-sensitized solar cells. *J. Am. Chem. Soc.* **136**, 10996–11001 (2014). <https://doi.org/10.1021/ja504539w>
68. Bi, D., Yang, L., Boschloo, G., et al.: Effect of different hole transport materials on recombination in CH₃NH₃PbI₃ perovskite-sensitized mesoscopic solar cells. *J. Phys. Chem. Lett.* **4**, 1532–1536 (2013). <https://doi.org/10.1021/jz400638x>
69. Bakr, Z.H., Wali, Q., Fakharuddin, A., et al.: Advances in hole transport materials engineering for stable and efficient perovskite solar cells. *Nano Energy* **34**, 271–305 (2017)
70. Xu, B., Sheibani, E., Liu, P., et al.: Carbazole-based hole-transport materials for efficient solid-state dye-sensitized solar cells and perovskite solar cells. *Adv. Mater.* **26**, 6629–6634 (2014). <https://doi.org/10.1002/adma.201402415>
71. Jung, E.H., Jeon, N.J., Park, E.Y., et al.: Efficient, stable and scalable perovskite solar cells using poly(3-hexylthiophene). *Nature* **567**, 511–515 (2019). <https://doi.org/10.1038/s41586-019-1036-3>
72. Ko, Y., Kim, Y., Lee, C., et al.: Investigation of hole-transporting poly(triarylamine) on aggregation and charge transport for hysteresisless scalable planar perovskite solar cells. *ACS Appl. Mater. Interfaces* **10**, 11633–11641 (2018). <https://doi.org/10.1021/acsami.7b18745>
73. Xu, W., Gao, Y., Ming, W., et al.: Suppressing defects-induced nonradiative recombination for efficient perovskite solar cells through green antisolvent engineering. *Adv. Mater.* **32** (2020). Doi: <https://doi.org/10.1002/adma.202003965>
74. Jeng, J.Y., Chiang, Y.F., Lee, M.H., et al.: CH₃NH₃PbI₃ perovskite/fullerene planar-heterojunction hybrid solar cells. *Adv. Mater.* **25**, 3727–3732 (2013). <https://doi.org/10.1002/adma.201301327>
75. Abrusci, A., Stranks, S.D., Docampo, P., et al.: High-performance perovskite-polymer hybrid solar cells via electronic coupling with fullerene monolayers. *Nano Lett.* **13**, 3124–3128 (2013). <https://doi.org/10.1021/nl401044q>
76. Liu, D., Wang, Q., Traverse, C.J., et al.: Impact of ultrathin C60 on perovskite photovoltaic devices. *ACS Nano* **12**, 876–883 (2018). <https://doi.org/10.1021/acsnano.7b08561>
77. Mahmoudi, T., Wang, Y., Hahn, Y.B.: Graphene and its derivatives for solar cells application. *Nano Energy* **47**, 51–65 (2018)
78. Grancini, G., Roldán-Carmona, C., Zimmermann, I., et al.: One-Year stable perovskite solar cells by 2D/3D interface engineering. *Nat. Commun.* **8**, 1–8 (2017). <https://doi.org/10.1038/ncomms15684>
79. Kim, J., Lee, G., Lee, K., et al.: Fluorine plasma treatment on carbon-based perovskite solar cells for rapid moisture protection layer formation and performance enhancement. *Chem. Commun.* **56**, 535–538 (2020). <https://doi.org/10.1039/c9cc07785e>
80. Qin, P., He, Q., Ouyang, D., et al.: Transition metal oxides as hole-transporting materials in organic semiconductor and hybrid perovskite based solar cells. *Sci. China Chem.* **60**, 472–489 (2017)
81. Abzieher, T., Moghadamzadeh, S., Schackmar, F., et al.: Electron-beam-evaporated nickel oxide hole transport layers for perovskite-based photovoltaics. *Adv. Energy Mater.* **9** (2019). Doi: <https://doi.org/10.1002/aenm.201802995>
82. Seo, S., Park, I.J., Kim, M., et al.: An ultra-thin, un-doped NiO hole transporting layer of highly efficient (16.4%) organic-inorganic hybrid perovskite solar cells. *Nanoscale* **8**, 11403–11412 (2016). <https://doi.org/10.1039/c6nr01601d>
83. Sun, W., Li, Y., Ye, S., et al.: High-performance inverted planar heterojunction perovskite solar cells based on a solution-processed CuOx hole transport layer. *Nanoscale* **8**, 10806–10813 (2016). <https://doi.org/10.1039/c6nr01927g>
84. Christians, J.A., Fung, R.C.M., Kamat, P.V.: An inorganic hole conductor for Organo-lead halide perovskite solar cells. improved hole conductivity with copper iodide. *J. Am. Chem. Soc.* **136**, 758–764 (2014). <https://doi.org/10.1021/ja411014k>
85. Jung, M., Kim, Y.C., Jeon, N.J., et al.: Thermal stability of CuSCN hole conductor-based perovskite solar cells. *Chemoschem* **9**, 2592–2596 (2016). <https://doi.org/10.1002/cssc.201600957>

86. Weber, O.J., Ghosh, D., Gaines, S., et al.: Phase behavior and polymorphism of formamidinium lead iodide. *Chem. Mater.* **30**, 3768–3778 (2018). <https://doi.org/10.1021/acs.chemmater.8b00862>
87. Harwell, J.R., Payne, J.L., Sajjad, M.T., et al.: Role of lattice distortion and a site cation in the phase transitions of methylammonium lead halide perovskites. *Phys. Rev. Mater.* **2**, 1–13 (2018). <https://doi.org/10.1103/PhysRevMaterials.2.065404>
88. López, C.A., Abia, C., Rodrigues, J.E., et al.: Enhanced stability in CH₃NH₃PbI₃ hybrid perovskite from mechano-chemical synthesis: structural, microstructural and optoelectronic characterization. *Sci. Rep.* **10**, 1–11 (2020). <https://doi.org/10.1038/s41598-020-68085-0>
89. Mashiyama, H., Kawamura, Y., Kasano, H., et al.: Disordered configuration of methylammonium of CH₃NH₃PbBr₃ determined by single crystal neutron diffractometry. *Ferroelectrics* **348**, 182–186 (2007). <https://doi.org/10.1080/00150190701196435>
90. Ren, Y., Oswald, I.W.H., Wang, X., et al.: Orientation of organic cations in hybrid inorganic-organic perovskite CH₃NH₃PbI₃ from subatomic resolution single crystal neutron diffraction structural studies. *Cryst. Growth Des.* **16**, 2945–2951 (2016). <https://doi.org/10.1021/acs.cgd.6b00297>
91. Yang, B., Ming, W., Du, M.H., et al.: Real-time observation of order-disorder transformation of organic cations induced phase transition and anomalous photoluminescence in hybrid perovskites. *Adv. Mater.* **30**, 1–7 (2018). <https://doi.org/10.1002/adma.201705801>
92. Schlipf, J., Bießmann, L., Oesinghaus, L., et al.: In situ monitoring the uptake of moisture into hybrid perovskite thin films. *J. Phys. Chem. Lett.* **9**, 2015–2021 (2018). <https://doi.org/10.1021/acs.jpcclett.8b00687>
93. Schlipf, J., Hu, Y., Pratap, S., et al.: Shedding light on the moisture stability of 3D/2D hybrid perovskite heterojunction thin films. *ACS Appl. Energy Mater.* **2**, 1011–1018 (2019). <https://doi.org/10.1021/acsaem.9b00005>
94. Li, Y., Cui, K., Xu, X., et al.: Understanding the essential role of PbI₂ films in a high-performance lead halide perovskite photodetector. *J. Phys. Chem. C* **124**, 15107–15114 (2020). <https://doi.org/10.1021/acs.jpcc.0c04488>
95. Wang, C., Liu, Y., Liu, S.F., et al.: Giant phonon tuning effect via pressure-manipulated polar rotation in perovskite MAPbI₃. *J. Phys. Chem. Lett.* **9**, 3029–3034 (2018). <https://doi.org/10.1021/acs.jpcclett.8b01101>
96. Ferreira, A.C., Létoublon, A., Paofai, S., et al.: Elastic softness of hybrid lead halide perovskites. *Phys. Rev. Lett.* **121**, 1–6 (2018). <https://doi.org/10.1103/PhysRevLett.121.085502>
97. Gold-Parker, A., Gehring, P.M., Skelton, J.M., et al.: Acoustic phonon lifetimes limit thermal transport in methylammonium lead iodide. *Proc. Natl. Acad. Sci. U S A* **115**, 11905–11910 (2018). <https://doi.org/10.1073/pnas.1812227115>
98. Chen, T., Foley, B.J., Ipek, B., et al.: Rotational dynamics of organic cations in the CH₃NH₃PbI₃ perovskite. *Phys. Chem. Chem. Phys.* **17**, 31278–31286 (2015). <https://doi.org/10.1039/c5cp05348j>
99. Leguy, A.M.A., Frost, J.M., McMahon, A.P., et al.: The dynamics of methylammonium ions in hybrid organic-inorganic perovskite solar cells. *Nat. Commun.* **6** (2015). Doi:<https://doi.org/10.1038/ncomms8124>
100. Mozur, E.M., Hope, M.A., Trowbridge, J.C., et al.: Cesium substitution disrupts concerted cation dynamics in formamidinium hybrid perovskites. *Chem. Mater.* **32**, 6266–6277 (2020). <https://doi.org/10.1021/acs.chemmater.0c01862>
101. Li, B., Kawakita, Y., Liu, Y., et al.: Polar rotor scattering as atomic-level origin of low mobility and thermal conductivity of perovskite CH₃NH₃PbI₃. *Nat. Commun.* **8**, 1–9 (2017). <https://doi.org/10.1038/ncomms16086>
102. Li, J., Bouchard, M., Reiss, P., et al.: Activation energy of organic cation rotation in CH₃NH₃PbI₃ and CD₃NH₃PbI₃: quasi-elastic neutron scattering measurements and first-principles analysis including nuclear quantum effects. *J. Phys. Chem. Lett.* **9**, 3969–3977 (2018). <https://doi.org/10.1021/acs.jpcclett.8b01321>

103. Frost, J.M., Walsh, A.: What is moving in hybrid halide perovskite solar cells? *Acc. Chem. Res.* **49**, 528–535 (2016). <https://doi.org/10.1021/acs.accounts.5b00431>
104. Mozur, E.M., Trowbridge, J.C., Maughan, A.E., et al.: Dynamical phase transitions and cation orientation-dependent photoconductivity in $\text{CH}(\text{NH}_2)_2\text{PbBr}_3$. *ACS Mater. Lett.* **1**, 260–264 (2019). <https://doi.org/10.1021/acsmaterialslett.9b00209>
105. Paternò, G.M., Robbiano, V., Santarelli, L., et al.: Perovskite solar cell resilience to fast neutrons. *Sustain. Energy Fuels* **3**, 2561–2566 (2019). <https://doi.org/10.1039/c9se00102f>
106. Lehmann, F., Franz, A., Töbrens, D.M., et al.: The phase diagram of a mixed halide (Br, I) hybrid perovskite obtained by synchrotron X-ray diffraction. *RSC Adv.* **9**, 11151–11159 (2019). <https://doi.org/10.1039/c8ra09398a>
107. Tan, K.W., Moore, D.T., Saliba, M., et al.: Thermally induced structural evolution and performance of mesoporous block copolymer-directed alumina perovskite solar cells. *ACS Nano* **8**, 4730–4739 (2014). <https://doi.org/10.1021/nn500526t>
108. Zhao, J., Cai, B., Luo, Z., et al.: Investigation of the hydrolysis of perovskite organometallic halide $\text{CH}_3\text{NH}_3\text{PbI}_3$ in humidity environment. *Sci. Rep.* **6**, 1–6 (2016). <https://doi.org/10.1038/srep21976>
109. Kuai, L., Li, J., Li, Y., et al.: Revealing crystallization dynamics and the compositional control mechanism of 2D perovskite film growth by in situ synchrotron-based GIXRD. *ACS Energy Lett.* **5**, 8–16 (2020). <https://doi.org/10.1021/acsenerylett.9b02366>
110. Schlipf, J., Müller-Buschbaum, P.: Structure of organometal halide perovskite films as determined with grazing-incidence X-Ray scattering methods. *Adv. Energy Mater.* **7**, 1–10 (2017). <https://doi.org/10.1002/aenm.201700131>
111. Schlipf, J., Docampo, P., Schaffer, C.J., et al.: A closer look into two-step perovskite conversion with X-ray scattering. *J. Phys. Chem. Lett.* **6**, 1265–1269 (2015). <https://doi.org/10.1021/acs.jpcclett.5b00329>
112. Oesinghaus, L., Schlipf, J., Giesbrecht, N., et al.: Toward tailored film morphologies: the origin of crystal orientation in hybrid perovskite thin films. *Adv. Mater. Interfaces* **3**, 1–11 (2016). <https://doi.org/10.1002/admi.201600403>
113. Moore, D.T., Sai, H., Tan, K.W., et al.: Crystallization kinetics of organic-inorganic trihalide perovskites and the role of the lead anion in crystal growth. *J. Am. Chem. Soc.* **137**, 2350–2358 (2015). <https://doi.org/10.1021/ja512117e>
114. Zhang, W., Saliba, M., Moore, D.T., et al.: Ultrasoft organic-inorganic perovskite thin-film formation and crystallization for efficient planar heterojunction solar cells. *Nat. Commun.* **6** (2015). Doi: <https://doi.org/10.1038/ncomms7142>
115. Barrows, A.T., Lilliu, S., Pearson, A.J., et al.: Monitoring the formation of a $\text{CH}_3\text{NH}_3\text{PbI}_3$ - xCl_x perovskite during thermal annealing using x-ray scattering. *Adv. Funct. Mater.* **26**, 4934–4942 (2016). <https://doi.org/10.1002/adfm.201601309>
116. Lindblad, R., Bi, D., Park, B.W., et al.: Electronic structure of $\text{TiO}_2/\text{CH}_3\text{NH}_3\text{PbI}_3$ perovskite solar cell interfaces. *J. Phys. Chem. Lett.* **5**, 648–653 (2014). <https://doi.org/10.1021/jz402749f>
117. Lindblad, R., Jena, N.K., Philippe, B., et al.: Electronic structure of $\text{CH}_3\text{NH}_3\text{PbX}_3$ perovskites: dependence on the halide moiety. *J. Phys. Chem. C* **119**, 1818–1825 (2015). <https://doi.org/10.1021/jp509460h>
118. McLeod, J.A., Wu, Z., Shen, P., et al.: Self-alignment of the methylammonium cations in thin-film organometal perovskites. *J. Phys. Chem. Lett.* **5**, 2863–2867 (2014). <https://doi.org/10.1021/jz501472d>
119. Tsai, H., Nie, W., Blancon, J.C., et al.: High-efficiency two-dimensional ruddlesden-popper perovskite solar cells. *Nature* **536**, 312–317 (2016). <https://doi.org/10.1038/nature18306>
120. Huang, W., Huang, F., Gann, E., et al.: Probing molecular and crystalline orientation in solution-processed perovskite solar cells. *Adv. Funct. Mater.* **25**, 5529–5536 (2015). <https://doi.org/10.1002/adfm.201502553>
121. Kim, N.K., Min, Y.H., Noh, S., et al.: Investigation of thermally induced degradation in $\text{CH}_3\text{NH}_3\text{PbI}_3$ perovskite solar cells using in-situ synchrotron radiation analysis. *Sci. Rep.* **7**, 1–9 (2017). <https://doi.org/10.1038/s41598-017-04690-w>

122. Whitfield, P.S., Herron, N., Guise, W.E., et al.: Structures, phase transitions and tricritical behavior of the hybrid perovskite methyl ammonium lead iodide. *Sci. Rep.* **6**, 1–16 (2016). <https://doi.org/10.1038/srep35685>
123. Chen, T., Chen, W.L., Foley, B.J., et al.: Origin of long lifetime of band-edge charge carriers in organic–inorganic lead iodide perovskites. *Proc Natl Acad Sci U S A* **114**, 7519–7524 (2017). <https://doi.org/10.1073/pnas.1704421114>
124. López, C.A., Martínez-Huerta, M.V., Alvarez-Galván, M.C., et al.: Elucidating the Methylammonium (MA) conformation in MAPbBr₃ perovskite with application in solar cells. *Inorg. Chem.* **56**, 14214–14219 (2017). <https://doi.org/10.1021/acs.inorgchem.7b02344>
125. Ferdani, D.W., Pering, S.R., Ghosh, D., et al.: Partial cation substitution reduces iodide ion transport in lead iodide perovskite solar cells. *Energy Environ. Sci.* **12**, 2264–2272 (2019). <https://doi.org/10.1039/c9ee00476a>
126. García-Rodríguez, R., Ferdani, D., Pering, S., et al.: Influence of bromide content on iodide migration in inverted MAPb(I1-: XBrx)₃ perovskite solar cells. *J. Mater Chem. A* **7**, 22604–22614 (2019). <https://doi.org/10.1039/c9ta08848b>

Development of Hierarchical Nanostructures for Energy Storage



Jitha S. Jayan, Appukuttan Saritha, and Kuruvilla Joseph

Abstract Energy storage and its usage is a major problem of the twenty-first century and hence this topic is increasingly gaining attention in academic and industrial fields. The development of advanced functional materials is highly mandatory for energy generation, storage and consumption. The growth of nanotechnology and the fabrication of nano devices have totally revolutionized the energy storage arena. Hierarchical nanostructures are capable of showing advanced properties over regular nanomaterials and hence are considered as distinguished candidates. Multicomponent hierarchical nanostructures exhibit enhanced cyclic performance, high energy density, high flexibility, fast charge–discharge capability, specific capacitance and sustained cycle life, which make them suitable for high end storage applications in fuel cells, solar cells, super capacitors etc. These unique properties can be augmented by logically altering the smart design and structure. More complex and fractal forming structures like branched nanoforests with nanopores could be judiciously applied even in renewable energy storage devices. This chapter primarily focuses on the fabrication and characterization of 2D and 3D hierarchical nanostructures and their application in different energy storage devices. This chapter also tries to throw light into the immense possibilities offered by hierarchical surfaces in fine tuning the properties of nanomaterials that will positively influence the applications in nanomechanics, nanoelectronics, and nanophotonics. This chapter is highly helpful in understanding the development, advancement and problems associated with the fabrication of nanostructured energy storage devices. It also helps to rule out the associated problems and brings light into the future perspectives of hierarchical nanostructures in energy storage.

Keywords Hierarchical nanostructures · Energy storage · Super capacitor

J. S. Jayan · A. Saritha (✉)

Department of Chemistry, Amrita VishwaVidyaapeetham, Amritapuri, Kollam, Kerala, India

K. Joseph

Department of Chemistry, Indian Institute of Space Science and Technology, Valiyamala PO, Thiruvananthapuram, Kerala, India

© The Author(s), under exclusive license to Springer Nature Switzerland AG 2022

A. E. Shalan et al. (eds.), *Advances in Nanocomposite Materials for Environmental and*

Energy Harvesting Applications, Engineering Materials,

https://doi.org/10.1007/978-3-030-94319-6_21

Abbreviations

SA	Surface Area
SEM	Scanning Electron Microscope
LIBs	Lithium-Ion Batteries
ATRP	Atom transfer radical polymerization
MOF	Metal Organic frame works
rMBs	Rechargeable Magnesium Batteries
EDLC	Electrical double layer capacitors
CV	Cyclic Voltametry
PEC	Photo-Electrochemical
DSSC	Dye-Sensitized Solar Cells
PSCs	Perovskite Solar Cells
ETL	Electron Transport Layer
J_{sc}	Current Density
V_{OC}	Open-Circuit Voltage
η	Photoelectrical Conversion Efficiency
I_{sc}	Photocurrent
INP	Inverted Nanopyramids
CV	Cyclic voltagrams
ECSA	Electrochemically Active Surface Area
PEMFCs	Polymer Electrolyte Membrane Fuel Cells
PEMFCs	Polymer Electrolyte Membrane Fuel Cells
GNPtNWs	Graphene Supported Pt Nanowires
GNPtNPs	Graphene Supported Pt Nanoparticles
ORR	Oxygen Reduction Reaction
LDH	Layered Double Hydroxides
OCV	Open-Circuit Voltage

1 Introduction

Energy generation, storage and consumption are the essential parts of an energy device. Each of the devices has its own importance in determining the efficiency and energy usage to a large extent. The development of extremely efficient energy device is of greater concern and the whole process in an energy device can be considered as an energy cycle as shown in Fig. 1. All the steps in the energy cycle are very relevant in determining the efficiency [1]. The structure and arrangement of each device plays an inevitable role in the energy cycle. The surface of the device is also playing an important role as almost all the energy devices are of interface or

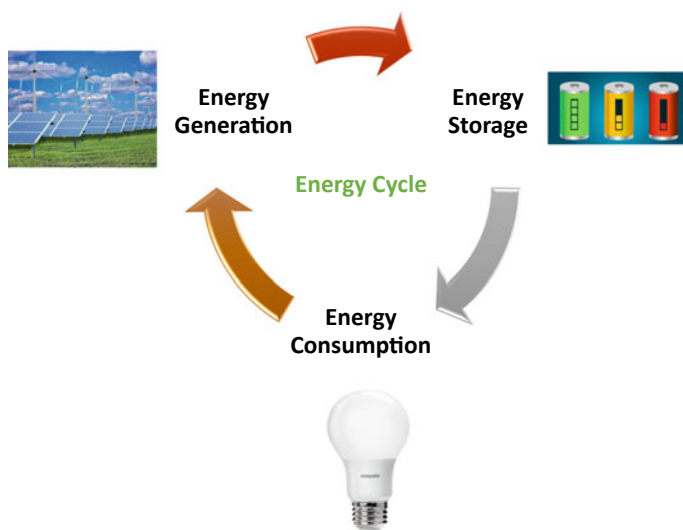


Fig. 1 Schematic representation of energy cycle

surface based. Hence the surface properties like surface area (SA) and porosity and the tuning of these properties are requires apt attention. Surface modification can bring about better transport of carriers, enhance surface area, porosity etc. and thus it can lift the efficiency of the device. The fabrication 3D building blocks with multi-functional characteristics are in its utmost demand and the incorporation of voids and disorder has also become a well experimented research topic. The importance of nanostructures in enhancing the efficiency of energy devices is now evident as it is capable of enhancing the surface area [2, 3]. Hierarchical and porous structured materials exhibit multiple levels of pores like micro, meso, macro and nano [4, 5]. Highly porous structure, high surface area, flexible chemical composition, higher amount of accessible space, low density and highly interconnected crossed hierarchical structures make the materials highly efficient in light harvesting, ensures electron and ion transport, diffusion and mass loading [6, 7]. These properties convert them into useful functional materials for different application like catalysis, energy storage, energy conversion, photocatalysis, gas sensing and biomedicine [8, 9]. The hierarchical nanostructures are having potential applications in energy conversion process like solar and chemical [10, 11]. In this chapter we are mainly focusing on the application of hierarchical nanostructures in various energy storage devices.

1.1 Fabrication of Hierarchical Nanostructures

There are different methods which are successfully being used for the fabrication of hierarchical nanostructures of which the most common methods are solvo-thermal, wet-Chemical, template, template free and controllable self-assembly.

Solvo-Thermal Method

Solvo-thermal synthesis can be considered as a chemical reaction taking place in a solvent at a pressure higher than 1 bar and temperature greater than the boiling point of the selected solvent. The medium can be either organic or inorganic solvents; hence it can be varied from water to alcohol. Generally, the solvo-thermal synthesis taking place in the water medium is called hydrothermal synthesis [12, 13]. Metal oxide and metal chalcogenides nanostructures are synthesized by following the solvo-thermal route. The use of eco-friendly solvents is considered as the major advantage of solvo-thermal method [14]. This method of synthesis generally proceeds through nucleation followed by particle growth. By varying the parameters like temperature, pressure, pH, time, concentration, and reaction medium, it is possible to tune the morphology, size, structure and properties [15]. Solvothermal methods are successful in synthesizing hierarchical nanostructured materials having sponge-like [16], tremella-like [17], spherical-like [18] and flower-like morphologies [19]. It is possible to make different nanostructures of same material by changing the solvent used and by altering the reaction time. As the reaction time is prolonged, it was observed that the morphology of the nanoparticle changes from spherical to hierarchical three dimensional sponge-like, flower-like and tramella like structures due to the self-assembly tendency. Figure 2 shows the Scanning Electron Microscope (SEM) images of different morphologies of spherical-like nanostructures obtained by the solvo-thermal treatment. The same method can also be utilized for obtaining metal doped hierarchical nanostructures having self-assembled layers, as the doping content increases the size of the microspheres decreases by inhibiting the crystal growth [20]. Temperature is also responsible for tuning the morphology of the synthesized nanostructures, it was observed that it is possible to change the morphology from rose like to chrysanthemum-like and sea-urchin-like titania nanoparticles by increasing the temperature [21]. The combination of solvo-thermal and other techniques like electrospinning could offer more advanced nanostructures, wherein nanoflowers and nanosphere can be attached to the nanofibers produced by the technique of electrospinning [22]. It is possible to make 3D hierarchical nanostructures by interconnecting 2D nanoplatlets via solvo-thermal process [23]. Two-step solvo-thermal methods are highly effective in making nanotree-like structures, initial solvo-thermal treatment lead to the formation of nanowires and the second step creates nanotree out of it [24]. Template free solvo-thermal treatment and subsequent thermal treatment were highly effective in making dandelion-like 3D hierarchical composite structure [25]. Highly porous waxberry-shaped nanostructures were also synthesized by interconnecting crystalline nanomaterials using ethylene glycol as solvent and hexamethylenetetramine as precipitant [26].

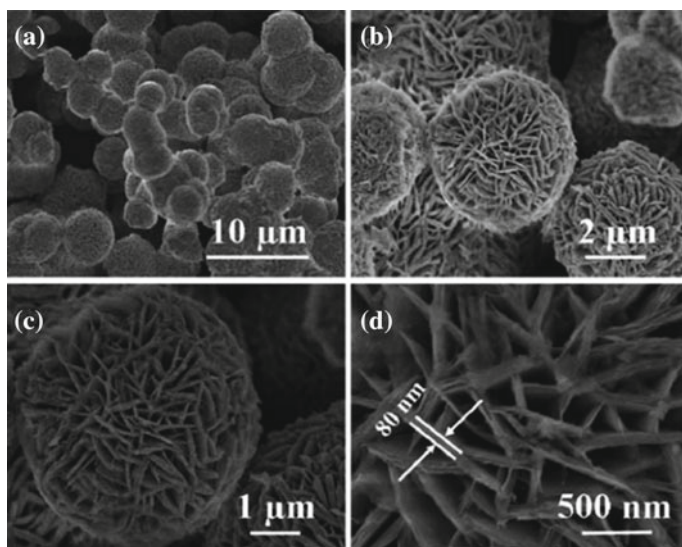


Fig. 2 SEM images **b–e** of the as-synthesized BiOCOOH product prepared by the solvothermal method at 150 C in mannitol solution[18]. Reproduced with permission from Royal society of Chemistry

Solvo-thermal method followed calcination process leads to the formation of carbon based hierarchical structures for functional application in energy storage. Self-template solvo-thermal synthesis of fern leaf like structured carbon-coated α -Fe₂O₃ particles binded to reduced graphene oxide ensures high surface area which is suitable for making anode of Lithium-Ion Batteries (LIBs) [27]. Nano-petal like structures of layered Double hydroxides prepared by solvo-thermal methods are highly efficient in the application of high-performance super capacitors [28]. The reaction scheme is represented in Fig. 3. Surface assisted solvo-thermal treatments comprise the advanced fabrication methodology for the synthesis of highly hierarchical porous 3D nanostructures. Surfactant plays an important role in determining the grain size, pore size and surface area of the synthesized porous structure [29]. Hence the solvo-thermal synthesis can be considered as an efficient method in making highly porous and hierarchical 3D nanostructures and by adjusting the reaction conditions it is possible to alter the morphology and pore size of the nanostructures. Solvo-thermal method is a still growing method for the advanced synthesis of hierarchical nanostructures.

Support/Template Method

Template synthesis is a simple and easy procedure for the synthesis of highly sophisticated hierarchical 3D nanostructures. It is an effective method for controlled synthesis and this method ensures unique characteristics like structure, property and morphology [30]. Large production and well controlled morphology can be attained by following the template method, especially hollow structured morphology using

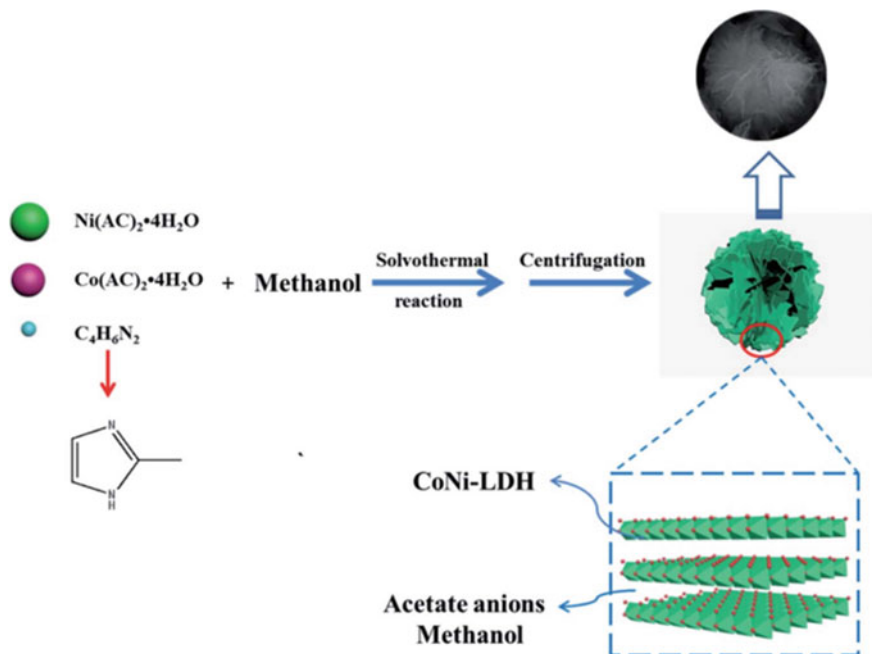


Fig. 3 Schematic diagram of the synthesis of CoNi LDH nano-petals [28]. Reproduced with permission from Royal Society of Chemistry

hard or soft templates. Polymers, carbon and silica are considered as hard templates whereas, bubbles and emulsion micelle are soft templates. Hard micelle can be removed either by chemical etching or thermal degradation methods [31]. Hierarchically porous nanostructures of MnO_2 can be successfully synthesized by mesoporous silica template; these materials are capable of showing enhanced capacitance due to the high surface area and porosity. The hierarchical nanostructures contain interlocked nanorods of MnO_2 and are the exact replica of the used mesoporous template [32]. Atom transfer radical polymerization (ATRP) based methods are used for fabricating templates for the successful preparation of nitrogen enriched highly porous carbon nanostructures. Graft polymer made by ATRP acted as a self-template and the second pyrolysis step lead to the formation of nitrogen rich carbon nanostructure [33]. Natural materials of biological origin have hierarchical nanostructures that can also be utilized as template, thus egg shell membranes are utilized for the preparation of highly porous Au nanoparticles [34]. Utilization of electrospinning can also be considered as an effective method of fabrication of template for the hierarchical nanostructures. Recently, multi-dimensional blocks were made by electrospinning as well as solution phase reaction for the fabrication of NiO based highly hierarchical nanostructures [35]. This method of synthesis is schematically represented in Fig. 4.

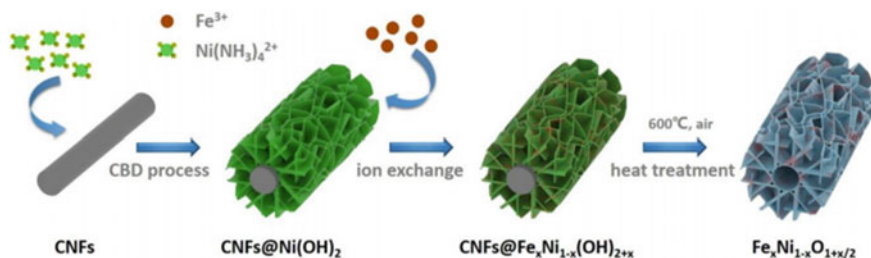


Fig. 4 Schematic representation for the fabrication of the hierarchical NiO based nanostructures [35]. Reproduced with permission from Royal Society of Chemistry

Metal Organic frame works (MOF) are now used as templates for the fabrication of highly sophisticated nanostructures due to the capability of the resultant materials to mimic the porous structure and the easy removal of templates. The nanostructures thus obtained generally possess small nanosized subunits with more active sites. By following a two way synthesis, Ren et al. [36] made Co_3O_4 hierarchical nanosheets. In the first step, MOFs are utilized as a template and later it is subjected to a thermal treatment as shown in Fig. 5. Zhang et al. [37] employed the template based method and hydrothermal synthesis for making hierarchical micro boxes of MoO_3 . Hollow structure of the MoO_3 micro boxes were further substantiated with the help of Transmission Electron Microscopy studies. Surface area, porosity and mesoporous structure was elucidated by the BET analysis. Freeze casting or ice-templated synthesis are getting much attention in the fabrication of hierarchical nanostructures, this technique is unique due to its controllability, flexibility and simplicity. Nanostructures having tunable properties and unidirectional and bidirectional ribbon like structures can be synthesized by this method [38–40]. This offers the generation of highly networked hierarchical nanostructures containing 2D and 3D micro networks. Energy storage materials made from these highly networked nanostructures and its composites are capable of showing high performance and reliability [41].

Template-Free method

Template based methods are being widely used for the fabrication of hierarchical nanostructures as we have discussed in the earlier section. But prolonged reaction process, template cost, morphology loss during template removal and the presence of impurities are considered as major disadvantages of the template synthesis [42, 43]. In order to avoid these drawbacks template-free method of fabrication of hierarchical nanostructures is highly recommended [44]. Template free fabrication method is highly efficient in making TiO_2 based micro-flowers like hierarchical nanostructures consisting of numerous nano belts. This multilayered structure confirms the possibility of making hierarchical structures without any surfactant or templates for light harvesting [45]. Core-shell like hollow structures of alumina were fabricated by Cai et al. [46] by following a facile hydrothermal treatment via a template-free method. The obtained pore size and surface area were higher and were suitable for the adsorption of CO_2 and phenol. This synthesis generally follows a three stage process like the

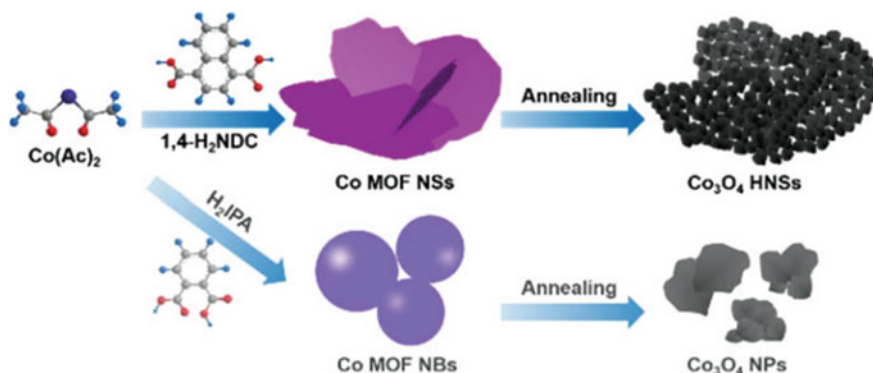


Fig. 5 Schematic illustration of the synthesis process of Co_3O_4 hierarchical nanosheets and Co_3O_4 nanoparticles [36]. Reproduced with permission from Royal Society of Chemistry

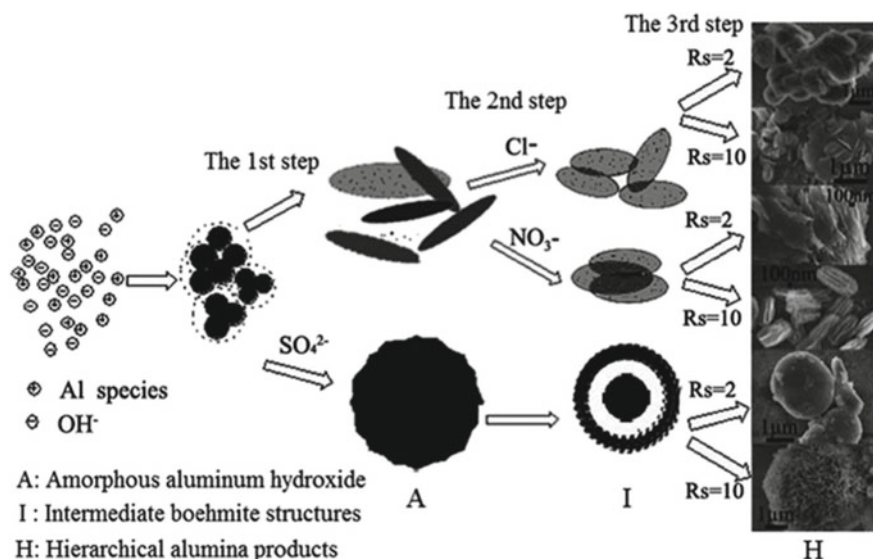


Fig. 6 Schematic illustration of the morphology evolution of the hierarchical alumina nanostructures [46]. Reproduced with permission from Royal society of Chemistry

formation and aggregation of particles, nucleation through ring opening and induced self-transformation and growth via self-assembly. The mechanism is schematically shown in Fig. 6. They have followed the same method for the fabrication of spindle like hierarchical alumina by the self-transformation and co-operative self-assembly. High surface area, large pore volume and porosity are the characteristics of the synthesized nanostructures [47]. Solvo-thermal treatments can also be carried out in

a template free method for the fabrication of microspheres via the process of hierarchical assembly where nanoparticles first assemble into plate-like structures and later into microspheres [48]. Supercritical treatment is yet another method of fabrication of highly hierarchical porous structure without any templates and surfactants. This microsphere structure together with the conductive coating enhance the discharge capacity of super capacitors [49]. Hydrothermal treatments without template help in attaining highly sophisticated hierarchical structures by adjusting the time and temperature. Moreover, the morphology with narrow band gap can be attained by the ring opening and self-assembly [50]. It was observed that non-templated urea assisted hydrothermal treatments are useful in making fibrous and urchin-like morphology in metal cobaltites. High surface area, pore size and flower-like structures of assembled nanosheets can be obtained by the template-free method using water and the source for nanoparticles. This method is considered as a simple, green and highly effective technique for sensing applications [51]. Nanoparticles having high surface area and suitable pore size for the adsorption of heavy metals can be prepared by the template-free method. Volume fraction in the selected solvent is the major factor in determining the pore structure of the nanostructure and thus the adsorption capacity. As the volume fraction increases, the possibility of formation of highly porous hierarchical structure improves. Ethanol-assisted solvo-thermal method can be considered as an effective method of fabrication of nanostructures with high surface area and pore size. As the volume fraction increases, the pore size also increases as the solvent plays an important role in growth process [52]. Multi-shell structures formed by the combination of hollow and core-shell structures with more layers of shell can be synthesized by the template-free fabrication method. Such structures are capable of showing high energy density and great volume change throughout the cycling process. Thus they can be employed as electrode materials for LIB [53, 54].

By Controllable Assembly

Self-assembly plays an important role in fabricating tailored nanostructures, this method is generally adopted for generating supramolecular architecture [55]. It can be considered as a spontaneous arrangement of molecules into different nano structures by non-covalent interactions at thermodynamic equilibrium [56]. The fundamental non-covalent interactions behind the self-assembly process include hydrogen bonding, van der Waals interaction, dipole-dipole interactions and other weak interactions between the functionalities. Hierarchical nanostructures formed by controllable self-assembly are capable of showing enhanced properties than the individual components [57–59]. The self-assembly ensures high complexity, tunable periodicity potential application in nanopatterning, molecular electronics and energy storage [60]. Different template-free methods like solvo-thermal method, electro deposition, sol-gel, micro-wave assisted and chemical precipitation are used for the fabrication of highly sophisticated hierarchical nanostructures of NiO [61–68]. But these techniques lead to the formation of crowded macro-balls with a solid core and disordered 2D nanosheets [69, 70]. The development of structures with high degree of orientation, controlled size and shape can be attained by the simplest controllable assembly [71]. The electrostatic assembly can be ensured by the use of surfactants for spherical

structures, whereas the use of non-ionic surfactants lead to the formation of lamellar shaped nanostructures [72, 73]. By adjusting the critical micellar concentration, it is possible to make different nanostructures [74]. Schematic representation showing the synthesis of hierarchical nanostructures by controllable self-assembly is shown in Fig. 7. Multi-level mesoporous structures fabricated by controllable assembly ensure high specific capacitance [75]. In one of our recent studies, it was observed that the block copolymer grafted nanoparticles are capable of self-assembling in the form of fractal like structure [76]. The self-assembly of the molecules ensure the formation of highly ordered micelle having different nanostructures like spherical, worm-like, vesicle and highly hierarchical octopus structures [77]. Urchin-like nanostructured spheres made by the method of controllable assembly (without any surfactants) having macropores with higher surface area are good enough in providing active sites for catalytic activity [78]. Surfactant functionalized graphene sheets are capable of forming highly hierarchical structures in water thereby showing enhanced biocompatibility and act as a platform for biomolecule assembly [79]. Self-assembled nanostructures thus integrate the advantages of nanostructures and make it appealing for advanced functional applications. The regulation of non-covalent bonds ensures the formation of nanostructures with different morphology. The formation and regulation of hierarchal nanostructures by the controlled self-assembly without any templates attained little success due to the difficulty in controlling the non-covalent interactions [80–82]. So the development of highly hierarchical nanostructures is a challenging area. Recently, by adjusting the formation ratio of hydrogen bonds, Li et al. [83] made louver-like hierarchical nanostructures having high charge separation capability and surface area in a controlled way.

1.2 Properties of Hierarchical Nanostructures

Hierarchical nanostructures are integrated architectures made of different nanoscale structures and these structures are seen in nature in the form of tree trunk, flowers and sea urchin. By mimicking these structures, it is possible to make highly hierarchical configurations and the properties of the materials can be modulated so as to make it fit for highly specific applications [84]. The low dimensional highly hierarchical nanostructures are getting attention due to large surface area, low density and surface permeability. These basic properties offer high end application to these nanostructures [85]. Hierarchical nanostructures improve the surface area and improve the electro chemical properties. High surface to volume ratio ensured by the hierarchical nanostructures are highly inevitable in tuning the electrochemical properties especially in controlling the kinetics of electrode reactions [86]. High uniformity and controlled density are the major advantages of these nanostructures [87]. Improved specific capacitance retention, coulombic efficiency and current density can be obtained by a judicious tuning of hierarchical nanostructures [88]. The perfect

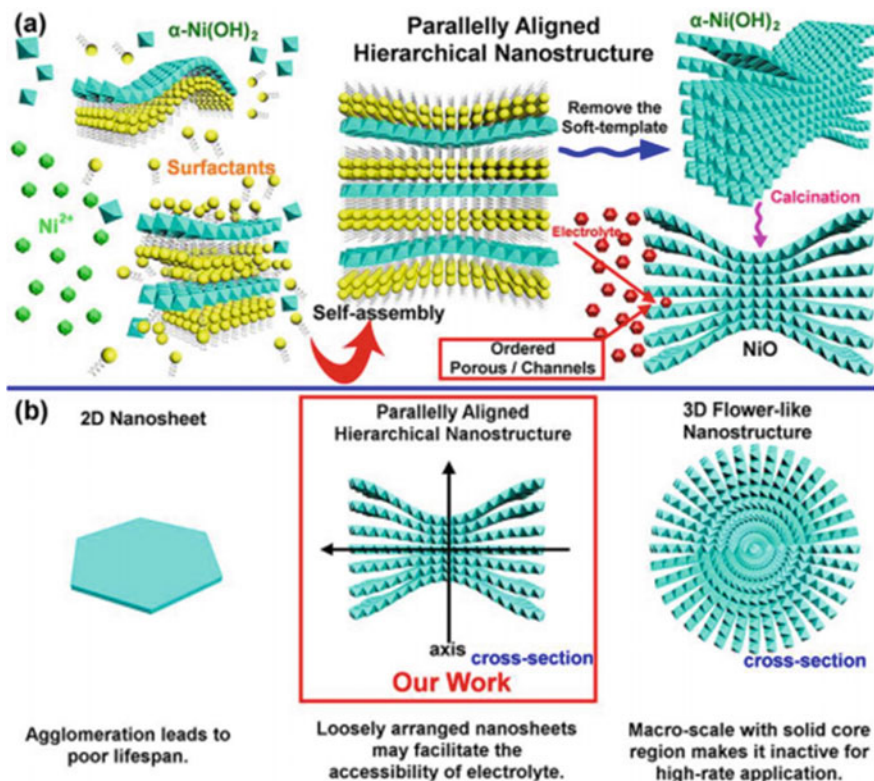
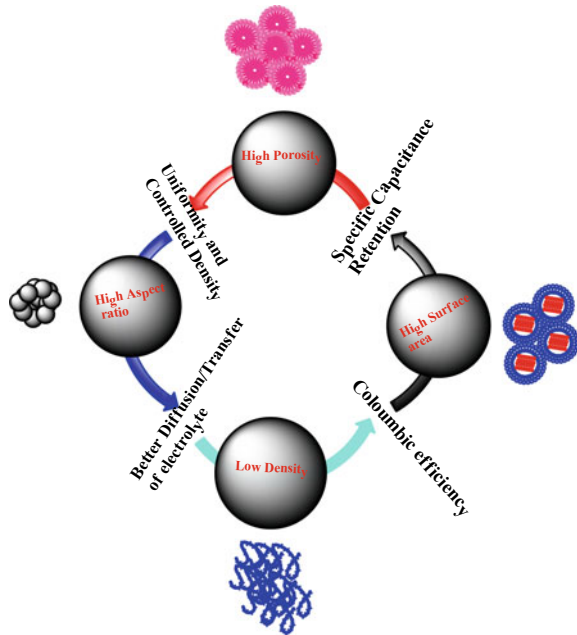


Fig. 7 Schematic representation of formation of hierarchical nanostructures by controllable assembly [75]. Reproduced with permission from American Chemical Society

hierarchical architecture ensures and maintains a synergistic effect among the components, and it improves the reactive sites. The highly porous nature promotes the diffusion and transfer of electrolyte [89]. Hierarchical nanostructures having high surface area, electrical conductivity, mechanical robustness and free standing configuration increases the utility for higher performance in electrodes [90]. Higher capacitive performance can be attained by the hierarchical structures due to faster transfer of electrons through the structure, higher reactivity and structural stability. The network structure improves the electrical conductivity and the nano dimensionality offers large surface area for improved activity [91]. Properties of hierarchical nanostructures' which make its application suitable in energy storage are schematically represented in Fig. 8. High energy storage, power density, storage capacity, high power density and cyclic performance are the general characteristics that should be possessed by an efficient energy storage device [92]. As these properties can be attained easily by the hierarchical nanostructures, it is widely used in energy storage applications and is discussed in detail in the coming section.

Fig. 8 Energy storage related properties of Hierarchical nanostructures



2 Applications of Hierarchical Nanostructures

2.1 Battery

Device performance directly depends on the size and morphology of the nanostructures used; hence the hierarchical structures are very relevant in determining the efficiency of battery. Renewable energy conversion and energy storage are of prime importance due to the increasing world inhabitants and industrialization [93]. Lithium ion batteries are considered as major energy storage devices due to its potential application in hybrid electric vehicle and portable devices. Generally, these batteries consist of three parts, electrodes (anode and cathode), electrolyte, and separator. Materials used in the electrodes determine the performance of the battery to a large extent. The working of LIBs is by the reversible intercalation and deintercalation of Li ions between the electrode materials which creates a Li ion difference in between and get charged and discharged by electron gain and loss process. Hence the cycling stability determines the performance of LIBs. The conventional LIBs are incapable to meet high power density and energy density, hence the need of highly efficient LIBs are needed for modern Electrical Energy Storages. Hence manipulation of LIBs and design shifting are taking place in order to attain high reversible capacity with long cycle life in an inexpensive way. The development of high performance electrode is considered as a vibrant research area in the energy community. Unique nanostructures are having promising role in the application of LIBs. Large surface area offered

by the hierarchical structures and the large contact interfaces of nanostructures makes the diffusion of Li more effective [94, 95]. Moreover, the contact between the electrolyte and the active material, diffusion length and area are the other important parameters which determine the performance of LIBs [96]. Galvanostatic charge–discharge studies are more importantly used for the determination of efficiency of an electrode material. The cyclic performance determines the reversible capacity of an electrode material in LIBs [97]. In order to prove the effect of morphology of the self-assembled hierarchical nanostructures in the LIBs, Xiang et al. [98] made different nanostructures of CuO like leaf, shuttle, flower, dandelion and caddice by adjusting the pH. The study revealed that dandelion and caddice like nanostructures displayed enhanced reversible discharge capacities and cycling performance due to enhanced surface area and porosity. It was observed that at lower pH, the initial discharge capacity was very less compared to other structures but as the pH increases the initial discharge ability got improved due to the advanced hierarchical structures. As shown in Fig. 9, the dandelion-like and caddice clew-like structures obtained at pH 11 and 11.5 are having higher reversible capacity and better retention. LIB electrodes made of star like hierarchical structures showed high reversibility and specific charge capacity due to the highly porous electrode structure. Reversible discharge–charge capability progressively improved to 1300 mA h g^{-1} and 1278 mA h g^{-1} due to interfacial storage and electrolyte decomposition. Compared to other nano structures like needles, wires, cages and tubes, the star like Co_3O_4 was capable of exhibiting high coulombic efficiency, initial capacity and was capable of maintaining the stabilities even after cycling due to the increased interfacial area [99]. Recently, hierarchically structured MOFs are found to be capable of showing enhanced storage application due to the easy electrolyte transfer through the interface [100]. Self-assembled hierarchical structures of hybrid nanomaterials are used as potential anode material in LIBs due to robust stability and active surface/interface [101–105].

These nanostructures are capable of showing enhanced performance by taking advantage of fascinating properties like nanometer size and secondary assembly [106, 107]. The combination of hierarchical nanostructures together with conducting materials can bring about tremendous changes like good rate capability, extreme reversible capacity and outstanding cyclic performance in LIBs [108]. It is observed that silicon based hierarchical porous structures are capable of avoiding the pulverization of silicon anodes used in LIBs. Mesoporous materials show enhanced performance by reducing swelling and alleviating pulverization with good cycling stability [109]. Ni-Zn batteries are having limited applications due to poor recyclability and low capacity, but Ni based hierarchical nanostructure configured cellulose fibers are capable of showing cycling stability which is attained by the presence of exposed active sites [110]. The hierarchical nanostructures are capable of displaying a lower storage plateau [111, 112]. The hierarchical nanostructures of cellulose materials offer an improvement in Li storage and recycle stability [113]. Hollow nanospheres containing nanosheets are capable of improving the performance of LIBs by the inherent characteristics like electrical conductivity of the core, active sites in shell materials and the reciprocal hybridization capable of reducing the agglomeration [114]. High theoretical capacity of cobalt chalcogenides/phosphides and the less

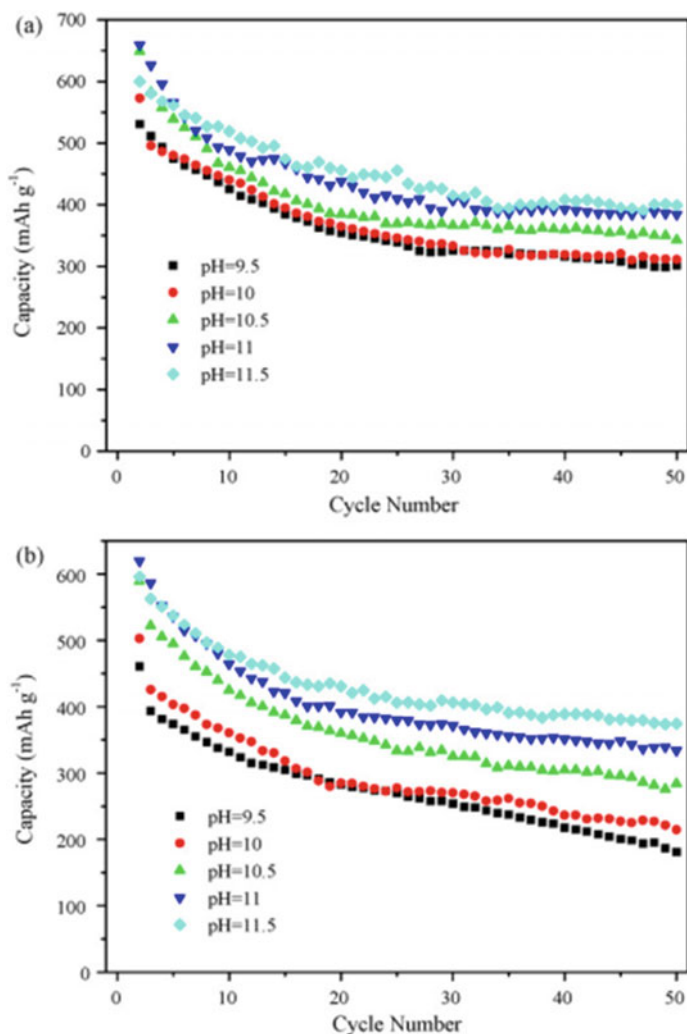


Fig. 9 Cycling performances of CuO electrodes at rates of: (a) 0.1 C and (b) 0.5 C (from the 2nd cycle to the 50th cycle) [98]. Reproduced with permission from Elsevier

cost of cobaltates makes it appropriate for LIBs but it is unsuitable for Li because of the lack of active sites for the insertion and storage of Li. It is also noteworthy that the hierarchical structures can accommodate the volume expansion during the lithiation process, shorten the pathway of diffusion and are capable of producing enormous active sites thereby improving the lithiation environment [115]. Rechargeable Magnesium Batteries (rMBs) are considered as next generation energy storage devices, the absence of cathodes with recyclability and high capacity are the major issues associated. But it was observed that the hierarchical characteristics can bring

about tremendous changes in the discharge capacity with a value of 300 mA h g^{-1} at 20 mA g^{-1} , and excellent cycling stability of about 200 cycles. Thus it was possible to make highly efficient rMBs by altering the conventional structure into hierarchical nano form. The structures offer increased contact area between electrolyte and electrodes, provides more active sites and avoids ion/electron migration barriers and accommodate volume expansion repetitive cycling [116]. Thus the hierarchical nanostructures are potential materials for the fabrication of batteries like LIBs, rMBs or Ni-Zn, Na ion, and Li-S [89, 117–119]

2.2 Super Capacitor

Super capacitors are electrochemical capacitors used for energy storage application that have greater energy density than the conventional capacitors [120–122]. These devices are having higher power density and greater life cycle than batteries [123, 124]. Depending on the charge transfer mechanism, the super capacitors can be categorized into two electrical double layer super capacitors and pseudocapacitors. Electrical double layer capacitors (EDLC) work based on the non-faradic and pseudocapacitors works according to the faradic redox reaction between the electro active materials [125–127]. Hierarchical nanostructures with highly porous structure are considered as the future of super capacitors [128, 129]. High surface area, mesoporous structure, large pore volume, and ultrathin structures of these materials are effective to facilitate the electron transport and insertion/extraction in the electrode and this leads to a greater enhancement in the specific capacitance (SC) [130–136]. The process of current accumulation will be slow and reduce the current density which leads to the utilization of all active spots whereby the capacitance get improved [88]. The mesoporous structured NiO materials were capable of showing a SC of 405 Fg^{-1} at the current density of 0.5 Ag^{-1} and offered good capacitance retention of ca. 91% after 1500 continuous charge–discharge cycles. Generally, mesoporous structures are considered as ‘ion-buffering reservoirs’, offer faradic reactions and store energy [137]. Hierarchical structures having multilevel mesopores and high surface area are capable of facilitating the accessibility of electrolyte and provide higher number of redox activation sites [75]. The hybrid nanomaterials having hierarchical architecture maximize the synergistic effect of the components and thus introduce more active sites and facilitate electrolyte transfer. These hierarchical structures with activated carbons enhance the energy density and function as an electrode material for the super capacitor applications [89]. Nest like structured hierarchical nanostructured Ni_3S_2 shows activity as a binder free electrode for the super capacitive applications. Cyclic Voltametry (CV) studies of the electrode material suggest the pseudo super capacitive behavior from the presence of redox peaks in the CV plots [138] as shown in Fig. 10.

Hierarchical nanostructures of chalcogenides directly on the Ni surface can bring about improved super capacitive behavior [139]. Core–shell hierarchical nanostructures containing mesopores nanowires as core and nano sheets as shells are capable

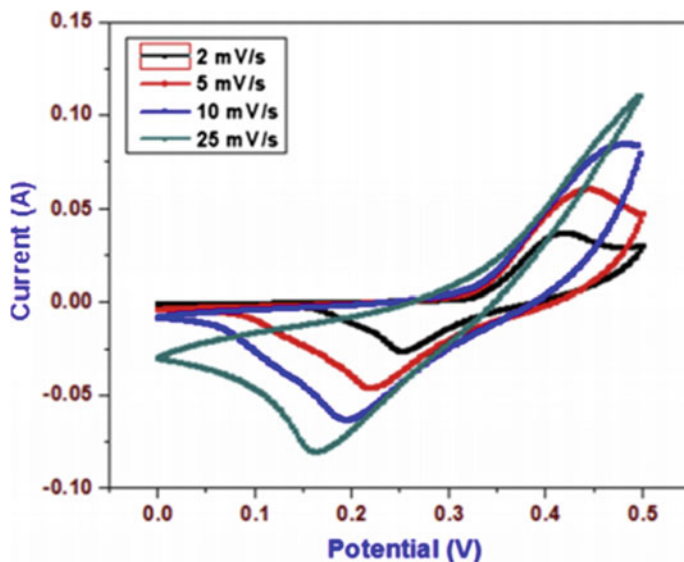


Fig. 10 Cyclic voltammetry curves of Ni₃S₂/Ni electrode with different scan rates measured in 1 M NaOH electrolyte [138]. Reproduced with permission from Elsevier

of providing highly effective contact and volume change during the electrochemical reactions [97, 140, 141]. 3D hierarchical nitrogen doped nanostructures derived from houttuynia is having flower-like unique structure with high SA and homogeneous micro/nano porous distribution. These materials were capable of showing 15.99 Wh/kg energy density at 500 W/kg and 95.74% capacitance retention even after a 10,000 repeated charge–discharge cycles in 6 M KOH electrolyte at 10 A/g. Thus the porous hierarchical nanostructures derived from biomass opens a way towards sustainable and green energy storage and conversion [142]. Excellent capacitive behavior and coulombic efficiency can be attained by the NiCo₂S₄@NiS/CF hierarchical nanostructures compared to the solitary ones. The rectangular CV curves and triangular shape of galvanostatic charge–discharge curves confirm the EDLC behavior [143]. Hierarchical core–shell hetero structure can be utilized for making asymmetric super capacitors using it as positive electrode and activated carbon as negative electrode due to the enhanced charge transfer offered by its surface area and its mechanical stability [144]. Nowadays ternary systems are used to generate highly hierarchical structures with conductivity, electro active surface area, and stability. The hybrid device made by using the hierarchical nanostructures as negative and positive electrodes are capable of showing enhanced electrochemical performance with an energy density of 62.13 Wh Kg⁻¹ at a power density of 789.66 W kg⁻¹. Thus the advantages of the hierarchical nanostructures are still explored by researchers for enhanced electrochemical performance [145]. The new insight in the super capacitive application is the insertion of novel hierarchical nanostructured atoms into the active material for high specific capacitance and long term cycling stability. The uniqueness

in the nanostructure provides high conductivity, efficient charge transport, rich redox reactions and short ion diffusion due to the homogeneous arrangement of co-axial hierarchical structures [146]. The tunable properties of the hierarchical nanostructures [89, 147] are playing an outstanding role in the development of more advanced super capacitive devices [146, 148–150] and thus the assortment of hierarchical nanostructures are indeed unavoidable for a highly sustainable future.

2.3 *Photo-Electro Chemical Cells*

Photo-electrochemical (PEC) solar energy conservation systems like water splitting and solar cells are under the rigorous progress of harvesting and utilizing solar energy. Photo-electrochemical performance can be improved by the incorporation of highly hierarchical structures by improving the charge separation and transport [151]. The photovoltaic cells which convert solar energy into electricity and PECs convert the solar energy into chemical fuels are now utilized in transportation [152, 153]. Indirect band gap, shorter carrier diffusion length and the inefficiency in absorbing the sun light are considered as the major issues associated with the conventional PEC [154]. The scope of PEC is still in the rear of the practical applications because of the low effectiveness of the physic-chemical processes which are generally multi-step/complex [155, 156]. PEC generally follows the mechanism of absorption of sunlight followed by separation of electron and hole pairs. The generated electron–hole(e–h) pairs then move to the surface and redox reactions will take place on the surface(reduction of carbon dioxide and water to form hydrogen and carbon fuels) [157]. The hierarchical core–shell nanostructures are capable of shortening the diffusion path, accelerating separation of the e–h pairs and its transfer to the surface; and thus it makes the surface redox reaction possible [158, 159]. Multi-light reflection and scattering of light in the interior cavity makes the absorption possible [160–162]. Hierarchical structures are capable of making active centers suitable for redox reaction [163, 164]. Moreover, these structures are highly effective in improving the photostability and the interfaces accelerate the charge separation process to a greater extent [165–167]. Nanostructures improve the current density and help to decrease the band gap and thus enable the recombination of electron–hole pair [168]. Moreover, these structures enhance the separation between the generated charge carriers, improve the photo activity and the nano branches present in the hierarchical structure will act as charge mediators to the electrolyte. Incorporation of Fe_2O_3 nanostructures into titania enhances the special separation which effect the recombination probability and enhance the performance [169]. The incorporation of hierarchical architecture enhances the internal surface area of Dye-sensitized solar cells (DSSC) and thus an enhancement in short-circuit current density can be observed which in turn improve the power conversion efficiency [170]. Core–shell nanostructures facilitate the charge separation and carrier transport by depressing the e–h recombination [171]. Perovskite solar cells (PSCs), whose electron transport layer (ETL) is made of hierarchical Zn_2SnO_4 based nanostructures improves the infiltration ability

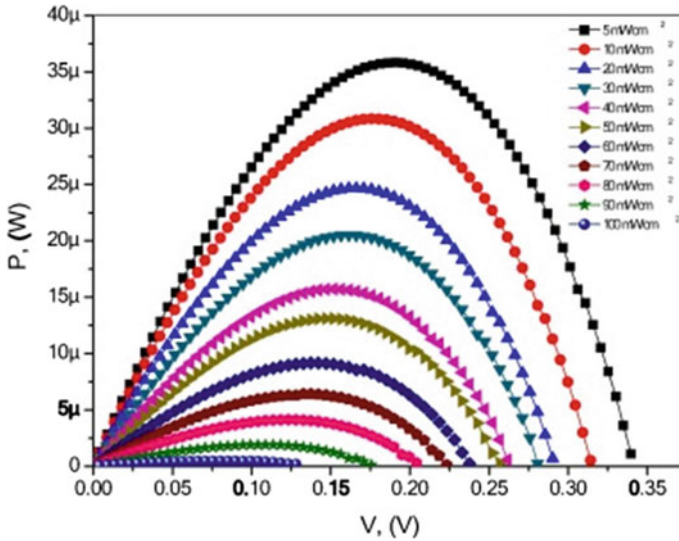


Fig. 11 P–V curve of the QDSS Cell at various intensities of light [173]. Reproduced with permission from Elsevier

and absorption due to the enhanced porosity and surface area of the material. The infiltration and charge separation ability of the ETL is capable of enhancing the electron transfer and thus the charge transport [172]. Flower like TiO_2 absorbs more light due to its enhanced surface area and produce charge carriers in the system. Power-voltage images shown in Fig. 11 indicates that with the illumination intensity maximum power point moves to a higher voltage [173]. Rational combination of multidimensional and multifunctional hierarchical structures is capable of solving the contradiction between the light absorption and charge collection [174].

Compactly arranged TiO_2 structures are capable of enhancing the charge transfer than the loosely bonded conventional structures [175]. Photo anodes prepared by the deposition of hierarchical structures improve the DSSC performance with a high power efficiency of about 1.81%. Short current density (J_{sc}) and open-circuit voltage (V_{oc}) can be improved with deposition duration because of the higher amount of dye absorbed by the enhanced surface area [176]. P^{H} assisted synthesis of nano structures show that the addition of HCl reduces the band gap energy and thus for a flower like hierarchical structure, the electron transport is comparatively easier [177]. Uniform morphology of the highly hierarchical nanoflowers attribute enhanced photoelectrical conversion efficiency (η) and highest photocurrent (I_{sc}) with 1.03% of conversion efficiency due to the high crystallinity and surface area [178]. The catalyst having high surface area and active sites can facilitate the transport velocity of reactants more importantly for the regeneration of dye in the DSSC. The controlled fabrication of hierarchical nanostructures with high surface area and pore size helps to tune the photovoltaic performance. The pore size of cobalt nickel selenides can be adjusted by the ratio of Co and Ni. Thus it is possible to accelerate the photoinduced electron

transfer to the photo anode from the dye molecules [179–181]. If the morphology of the hierarchical structures is almost similar, the pore size distribution determines the efficiency as it can offer different diffusion channels for the redox couple. Thus the photovoltaic performance can be tuned by the pore size distribution owing to the electrocatalytic activity [182]. Solar absorbing broad band surfaces are beneficial for fabricating devices like photo detectors, solar thermoelectric generators, thermo photovoltaic and for harvesting of solar energy [183, 184]. Randomly distributed hierarchical nanostructures of metal deposited self-aggregated Al_2O_3 were utilized as solar absorbers in the ultra-broad band range. The nanoporous aerogels with more than 80% of porosity lowered the thermal conductivity and showed an improved solar absorbance [185]. Yolk-shell structured nanoparticles can offer high catalytic activity to energy conversion due to the shorter charge transfer path attributed by the presence of efficient active sites offered by the enhanced SA. These nanostructures are capable of showing enhanced power conversion efficiency than the Pt based solar cells due to high SA and uniform size and thus it opens a way towards the advancement of Pt free solar cells [186]. Balance of light trapping is an important parameter in determining the application and superiority of solar cells. Increasing the light trapping efficiency without much enhancement in SA is a choice of great research interest for the commercial application of solar cells. Inverted nanopyramids (INP) are having high light trapping and conversion efficiency compared to other structures [187]. Hierarchical structured INPs are capable of showing a high efficiency of 19.8% than the conventional inverted and micro pyramids due to its high trapping efficiency, lower reflectance and lower sheet resistance [188]. The scope of hierarchical nanostructures in PEC is still in its infancy and active research using hierarchical nanostructures is still going on with the aim of attaining improved efficiency and photoelectrical performance of PEC [189–191]. The thirst for the development of highly efficient PEC from hierarchical nanostructures, inverted structures, aerogels and the manipulation of these structures for highly efficient energy conversion system is the need of the hour.

2.4 Fuel Cells

Fuel cells are considered as electrochemical devices that convert chemical energy produced by a chemical reaction to electrical energy and heat. It works similar to a battery but charging is not needed like battery [192]. The methanol and ethanol fuel cells have attracted wide interest due to high energy density, lower working temperature and environmental friendliness [193, 194]. Platinum based catalysts are mainly used in fuel cells due to the high efficiency in bringing out methanol and ethanol based oxidative reactions [195, 196]. But the less stability, high cost and the limited resources are the major concerns associated with Pt based catalysts [197, 198]. Morphology of the catalyst plays an important role in determining the catalytic activity, the improved SA, and porosity control the active sites and thus the catalytic activity [199, 200]. Hierarchical structures are capable of showing enhanced catalytic

performance in fuel cells by facilitating the mass-electron transfer through the active sites due to its enhanced stability and SA [201, 202]. The Cyclic Voltagram (CV) curves of thorn-like multi-metallic hierarchical structures exhibit a higher reduction peak area. Based on the area of the peak and the weight ratio it was found that the electrochemically active surface area (ECSA) was higher for such species. This enhancement in ESCA is due to the increased active sites and the intrinsic activity of the unique nanostructure with small particle size [203]. To enhance the mass transfer of polymer electrolyte membrane fuel cells (PEMFCs), Deng et al. [204] made hierarchical nanostructures with ultrathin Pt nano arrays. These structures were capable of showing enhanced mass transport, electrochemical activity compared to conventional Pt. Nanosized Pt and its alloy supported graphitic carbons are also employed in methanol and glucose fuel cells [205] due to electrical conductivity and stability [206]. Qazzazie et al. [207] made graphene supported Pt nanowires (GNPtNWs) and nanoparticles (GNPtNPs), and the study reveals that graphene supported hierarchical structures help in achieving enhanced cell performance due to the improved glucose transfer to the active sites. Improved roughness of surface helps in shifting the polarization limiting effect to higher current density and improves the cell performance. Thus the mass transport and the electrocatalytic activity is influenced by the surface roughness and leads to improved anodic activity. Compared to GNPtNPs and PtC electrodes, a45 fold improvement in current density was obtained for the hierarchical structure in the CV curves (Fig. 12) due to the improved roughness. Highly hierarchical CNT/Ni-SiC catalyst was capable of showing enhanced electrochemical performance depending on the pyrolysis temperature and it was noted that the temperature also affects the morphology. The enhanced catalytic activity is attributed to the uniformity of the particle size, enhanced SA of diffusion, better dispersion of Ni and enhanced mass-electron transportation [208]. Highly hierarchical and porous nanostructures based on MOF and nanoparticles composites are considered exceptional as oxygen reduction reaction (ORR) catalysts for cathodes. The wrapping of MOFs by the N-doped graphene create the active segments, these segments provide ORR active sites and the active sites increased by the porous structure enhances the transportation of H^+ , e^- , O_2 , OH^- [209]. Hollow hierarchical structures are capable of showing stable and enhanced catalytic performance following a fast electrochemical kinetics because the hollow structures facilitates the exposure of active sites [210].

Hollow structures generally expose the inner concave surfaces to the reaction medium and reduce the material density and charge carrier length and thus improve the catalytic activity [211, 212]. Ni based hollow structures made by self-assembly method are also capable of enhancing the oxygen evolution reaction and improved performance [213]. Hierarchical structured layered double hydroxides (LDH) based composites materials are effective in hindering the methanol permeability from the anode to cathode, and thus shows an enhanced open-circuit voltage(OCV) value [214]. Hierarchical TiN nanostructured electrode with Pt deposition, tunable porosity, high SA, chemical stability and conductivity can be employed as an active electrode material in fuel cell application. Enhanced ESCA and active sites improve the activity by enhancing the diffusion because of the presence of larger pores and smaller SA

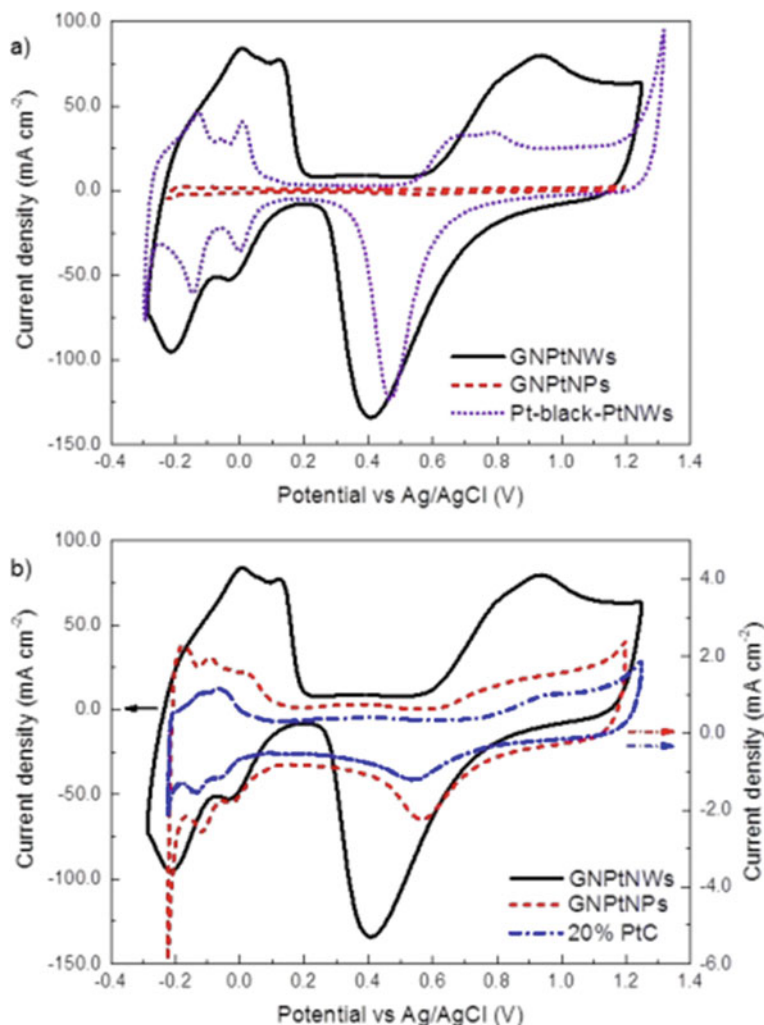


Fig. 12 Cyclic voltammograms in 0.5 M H_2SO_4 at 20 mV s^{-1} before (dashed curve) and after the electroless deposition of Pt nanowires on graphene and Pt-blackPtNWs (dotted curve) **a**; Comparison of CVs shape and current densities of GNPtNWs, GNPtNPs (dashed curve) and commercial 20% PtC (dashed-dotted curve) **b**. Please note the arrows marking the y-axis for the respective cyclic voltammogram [207]. Reproduced with permission from Royal Society of Chemistry

[215]. Biomass derived hierarchical nanostructures are also being used widely for fuel cell applications due to the presence of various hetero atoms, high SA, porosity, electrical conductivity, active sites and ESCA [216]. ORR catalytic activity of materials can be improved by the introduction of hierarchical materials capable of showing enhanced electrochemical activity and durability [217]. Scaling-up of hierarchical nanostructures for widening the path for highly stable and efficient fuel cells are

in its budding period. Hence for the commercialization of fuel cells, highly porous hierarchical nanostructures and hierarchical biomass derived nanostructures and its management should be studied in future.

3 Conclusion

Hierarchical nanostructures are potential materials for the fabrication of highly efficient energy storage devices from batteries to fuel cells. The inherent porosity and surface area of the hierarchical nanostructures are highly efficient in enhancing the active sites for charge transfer and diffusion. Self-assembled nanostructures can integrate the advantages of different nanostructured materials and thus can be made appealing for advanced functional applications. The electrochemical properties can be tuned by controlling the kinetics of electrode reactions and by adjusting the surface to volume ratio of hierarchical nanostructures. Moreover, high uniformity and controlled density are considered as the major advantages of nanostructures in ensuring the potential application. Improved specific capacitance retention, coulombic efficiency and current density can be tuned by adjusting the porosity, SA of hierarchical nanostructures and by the judicious selection of the appropriate hierarchical nanostructure. The perfect hierarchical architecture ensures and maintains a synergistic effect among the components, and it improves the reactive sites. Thus hierarchical nanostructures could bring tremendous changes in the energy storage applications.

4 Future Perspectives

The manipulation of hierarchical nanostructures for the improvement of catalytic, capacitive and conversion efficiency is still in its infancy. Hence the development of highly hierarchical hybrid nanostructures, aerogels and their further modifications can offer enhanced energy storage application with electrochemical stability. The development of highly inverted hierarchical structures and its manipulation can fulfill the future energy requirement to a greater extent. Scaling up of the nanostructures and fabrication of highly effective energy devices are the possibility for commercializing the energy storage devices. Novel 2D and 3D hierarchical structures from chalcogenides of transition metals which could revolutionize the energy storage arena is gradually replacing the first generation nanostructures. The development of advanced methods for the fabrication of defect free highly hierarchical nanostructures is the immediate need of the hour. Moreover, the fabrication and development of re-usable energy storage hierarchical nanostructures are highly essential and is still in its initial stage. Hence this area demands apt attention and upcoming research in the allied areas can bring tremendous changes in the field of energy storage.

References

1. Ko, S.H.: Introduction: Hierarchical Nanostructures for Energy Devices (2014)
2. Abdel Maksoud, M.I.A., Fahim, R.A., Shalan, A.E., et al.: Advanced materials and technologies for supercapacitors used in energy conversion and storage: a review. *Environ. Chem. Lett.* **19**, 375–439 (2021)
3. Akman, E., Shalan, A.E., Sadegh, F., Akin, S.: Moisture-resistant FAPbI₃ perovskite solar cell with 22.25 % power conversion efficiency through pentafluorobenzyl phosphonic acid passivation. *Chemosuschem* **14**, 1176–1183 (2021)
4. Bae, W., Kim, H.N., Kim, D., et al.: 25th anniversary article: scalable multiscale patterned structures inspired by nature: the role of hierarchy. *Adv. Mater.* **26**, 675–700 (2014)
5. Abdellatif Soliman, S.M., Sanad, M.F., Shalan, A.E.: Synthesis, characterization and antimicrobial activity applications of grafted copolymer alginate-g-poly(N-vinyl imidazole). *RSC Adv.* **11**, 11541–11548 (2021)
6. Jayan, J.S., Saritha, A., Deeraj, B.D.S., Joseph, K.: Synthesis of self-assembled and porous nano titania-graphene oxide hybrids for toughening the epoxy. *Polym Compos n/a*: <https://doi.org/10.1002/pc.25696>
7. Abdelbasir, S.M., Shalan, A.E.: An overview of nanomaterials for industrial wastewater treatment. *Korean J. Chem. Eng.* **36**, 1209–1225 (2019)
8. Fang, B., Kim, J.H., Kim, M.-S., Yu, J.-S.: Hierarchical nanostructured carbons with meso-macroporosity: design, characterization, and applications. *Acc. Chem. Res.* **46**, 1397–1406 (2013)
9. Abu Elella, M.H., Goda, E.S., Abdallah, H.M., et al.: Innovative bactericidal adsorbents containing modified xanthan gum/montmorillonite nanocomposites for wastewater treatment. *Int. J. Biol. Macromol.* **167**, 1113–1125 (2021)
10. Barhoum, A., Shalan, A.E., El-Hout, S.I., et al.: A broad family of carbon nanomaterials: classification, properties, synthesis, and emerging applications. In: *Handbook of Nanofibers*, pp. 1–40. Springer, Cham (2019)
11. Bataool, M., Nazar, M.F., Awan, A., et al.: Bismuth-based heterojunction nanocomposites for photocatalysis and heavy metal detection applications. *Nano-struct Nano-Objects* **27**, 100762 (2021)
12. Nunes, D., Pimentel, A., Santos, L., et al.: 2—Synthesis, design, and morphology of metal oxide nanostructures. In: Nunes, D., Pimentel, A., Santos, L., Barquinha, P., Pereira, L., Fortunato, E., Martins, R., eds. *Met Oxide Nanostructures*, pp. 21–57 (2019)
13. Saxena, V., Shukla, I., Pandey, L.M.: Hydroxyapatite: an inorganic ceramic for biomedical applications. In: *Materials for Biomedical Engineering*. Elsevier, pp. 205–249 (2019)
14. Ashik, U.P.M., Kudo, S., Hayashi, J.: An overview of metal oxide nanostructures. In: *Synthesis of Inorganic Nanomaterials*. Elsevier, pp 19–57 (2018)
15. Eivazzadeh-Keihan, R., Taheri-Ledari, R., Mehrabad, M.S., et al.: Effective combination of rGO and CuO nanomaterials through poly(p-phenylenediamine) texture: Utilizing it as an excellent supercapacitor. *Energy Fuels* (2021). <https://doi.org/10.1021/acs.energyfuels.1c01132>
16. Cheng, G., Xiong, J., Yang, H., et al.: Facile solvothermal synthesis of uniform sponge-like Bi₂SiO₅ hierarchical nanostructure and its application in Cr (VI) removal. *Mater. Lett.* **77**, 25–28 (2012)
17. Kang, W., Tang, Y., Li, W., et al.: High interfacial storage capability of porous NiMn 2 O 4/C hierarchical tremella-like nanostructures as the lithium ion battery anode. *Nanoscale* **7**, 225–231 (2015)
18. Xiong, J., Cheng, G., Lu, Z., et al.: BiOCOOH hierarchical nanostructures: shape-controlled solvothermal synthesis and photocatalytic degradation performances. *Cryst. Eng. Comm.* **13**, 2381–2390 (2011)
19. Mu, J., Shao, C., Guo, Z., et al.: Solvothermal synthesis and electrochemical properties of 3D flower-like iron phthalocyanine hierarchical nanostructure. *Nanoscale* **3**, 5126–5131 (2011)

20. Song, X.C., Zheng, Y.F., Yin, H.Y., et al.: The solvothermal synthesis and enhanced photocatalytic activity of Zn²⁺ doped BiOBr hierarchical nanostructures. *New. J. Chem.* **40**, 130–135 (2016)
21. Fan, Z., Meng, F., Zhang, M., et al.: Solvothermal synthesis of hierarchical TiO₂ nanostructures with tunable morphology and enhanced photocatalytic activity. *Appl. Surf. Sci.* **360**, 298–305 (2016)
22. Zhang, M., Shao, C., Guo, Z., et al.: Hierarchical nanostructures of copper (II) phthalocyanine on electrospun TiO₂ nanofibers: controllable solvothermal-fabrication and enhanced visible photocatalytic properties. *ACS Appl. Mater. Interfaces* **3**, 369–377 (2011)
23. Tian, F., Xiong, J., Zhao, H., et al.: Mannitol-assisted solvothermal synthesis of BiOCl hierarchical nanostructures and their mixed organic dye adsorption capacities. *Cryst. Eng. Comm.* **16**, 4298–4305 (2014)
24. Li, Y., McMaster, W.A., Wei, H., et al.: Enhanced electrochromic properties of WO₃ nanotree-like structures synthesized via a two-step solvothermal process showing promise for electrochromic window application. *ACS Appl. Nano Mater.* **1**, 2552–2558 (2018)
25. Xun, L., Gao, S., Xu, Y., et al.: Synthesis of dandelion-like V₂O₃/C composite with bicontinuous 3D hierarchical structures as an anode for high performance lithium ion batteries. *Ceram Int.* **44**, 14128–14135 (2018)
26. Sun, W., Li, Y., Liu, Y., et al.: Hierarchical waxberry-like LiNi_{0.5}Mn_{1.5}O₄ as an advanced cathode material for lithium-ion batteries with a superior rate capability and long-term cyclability. *J. Mater. Chem. A* **6**, 14155–14161 (2018)
27. Wu, X., Chen, W., Key, J., Wu, W.: One-pot solvothermal synthesis of fern leaf-like α -Fe₂O₃@C/graphene from ferrocene with enhanced lithium and sodium storage properties. *Powder Technol.* **323**, 424–432 (2018)
28. Chu, H., Zhu, Y., Fang, T., et al.: Solvothermal synthesis of cobalt nickel layered double hydroxides with a three-dimensional nano-petal structure for high-performance supercapacitors. *Sustain. Energy Fuels* **4**, 337–346 (2020)
29. Liu, W., Qu, Y., Li, H., et al.: Nanostructure Bi₂WO₆: Surfactant-assisted hydrothermal synthesis for high sensitive and selective sensing of H₂S. *Sensors Actuators B Chem.* **294**, 224–230 (2019)
30. Liu, Y., Goebel, J., Yin, Y.: Templated synthesis of nanostructured materials. *Chem. Soc. Rev.* **42**, 2610–2653 (2013)
31. Xia, Y., Wang, J., Chen, R., et al.: A review on the fabrication of hierarchical ZnO nanostructures for photocatalysis application. *Crystals* **6**, 148 (2016)
32. Chen, H., Dong, X., Shi, J., et al.: Templated synthesis of hierarchically porous manganese oxide with a crystalline nanorod framework and its high electrochemical performance. *J. Mater. Chem.* **17**, 855–860 (2007)
33. Wu, D., Li, Z., Zhong, M., et al.: Templated Synthesis of Nitrogen-Enriched Nanoporous Carbon Materials from Porogenic Organic Precursors Prepared by ATRP. *Angew Chemie Int. Ed.* **53**, 3957–3960 (2014)
34. Zhong, S.-L., Zhuang, J., Yang, D.-P., Tang, D.: Eggshell membrane-templated synthesis of 3D hierarchical porous Au networks for electrochemical nonenzymatic glucose sensor. *Biosens. Bioelectron.* **96**, 26–32 (2017)
35. Dong, S., Wu, D., Gao, W., et al.: Multi-dimensional templated synthesis of hierarchical Fe₂O₃/NiO composites and their superior ethanol sensing properties promoted by nanoscale p–n heterojunctions. *Dalt Trans.* **49**, 1300–1310 (2020)
36. Ren, J.-T., Zheng, Y.-L., Yuan, K., et al.: Self-templated synthesis of Co₃O₄ hierarchical nanosheets from a metal–organic framework for efficient visible-light photocatalytic CO₂ reduction. *Nanoscale* **12**, 755–762 (2020)
37. Zhang, J., Song, P., Li, J., et al.: Template-assisted synthesis of hierarchical MoO₃ microboxes and their high gas-sensing performance. *Sensors Actuators B Chem.* **249**, 458–466 (2017)
38. Sahoo, P.K., Aepuru, R., Panda, H.S., Bahadur, D.: Ice-templated synthesis of multifunctional three dimensional graphene/noble metal nanocomposites and their mechanical, electrical, catalytic, and electromagnetic shielding properties. *Sci. Rep.* **5**, 17726 (2015)

39. Romeo, H.E., Hoppe, C.E., Lopez-Quintela, M.A., et al.: Directional freezing of liquid crystalline systems: from silver nanowire/PVA aqueous dispersions to highly ordered and electrically conductive macroporous scaffolds. *J. Mater. Chem.* **22**, 9195–9201 (2012)
40. Scotti, K.L., Dunand, D.C.: Freeze casting—A review of processing, microstructure and properties via the open data repository. *FreezeCasting. net. Prog. Mater. Sci.* **94**, 243–305 (2018)
41. Zhang, L., Liu, X., Deb, A., Feng, G.: Ice-Templating synthesis of hierarchical and anisotropic silver-nanowire-fabric aerogel and its application for enhancing thermal energy storage composites. *ACS Sustain. Chem. Eng.* **7**, 19910–19917 (2019)
42. Kudo, A., Miseki, Y.: Heterogeneous photocatalyst materials for water splitting. *Chem. Soc. Rev.* **38**, 253–278 (2009)
43. Yan, S.C., Ouyang, S.X., Gao, J., et al.: A room-temperature reactive-template route to mesoporous ZnGa₂O₄ with improved photocatalytic activity in reduction of CO₂. *Angew Chemie* **122**, 6544–6548 (2010)
44. Zhang, Q., Wang, W., Goebel, J., Yin, Y.: Self-templated synthesis of hollow nanostructures. *Nano Today* **4**, 494–507 (2009)
45. Shao, F., Sun, J., Gao, L., et al.: Template-free synthesis of hierarchical TiO₂ structures and their application in dye-sensitized solar cells. *ACS Appl. Mater. Interfaces* **3**, 2148–2153 (2011)
46. Cai, W., Hu, Y., Yu, J., et al.: Template-free synthesis of hierarchical γ -Al₂O₃ nanostructures and their adsorption affinity toward phenol and CO₂. *RSC Adv.* **5**, 7066–7073 (2015)
47. Cai, W., Yu, J., Jaroniec, M.: Template-free synthesis of hierarchical spindle-like γ -Al₂O₃ materials and their adsorption affinity towards organic and inorganic pollutants in water. *J. Mater. Chem.* **20**, 4587–4594 (2010)
48. Zhang, J., Yao, B., Ping, H., et al.: Template-free synthesis of hierarchical porous calcium carbonate microspheres for efficient water treatment. *RSC Adv.* **6**, 472–480 (2016)
49. Permana, A.D.C., Nugroho, A., Chung, K.Y., et al.: Template-free synthesis of hierarchical porous anatase TiO₂ microspheres with carbon coating and their electrochemical properties. *Chem. Eng. J.* **241**, 216–227 (2014)
50. Wang, Z., Hou, J., Yang, C., et al.: Template-free synthesis of 3D Nb₃O₇F hierarchical nanostructures and enhanced photocatalytic activities. *Phys. Chem. Chem. Phys.* **15**, 3249–3255 (2013)
51. Wei, F., Zhang, H., Nguyen, M., et al.: Template-free synthesis of flower-like SnO₂ hierarchical nanostructures with improved gas sensing performance. *Sensors Actuators B Chem.* **215**, 15–23 (2015)
52. Huang, R., Wu, M., Zhang, T., et al.: Template-free synthesis of large-pore-size porous magnesium silicate hierarchical nanostructures for high-efficiency removal of heavy metal ions. *ACS Sustain. Chem. Eng.* **5**, 2774–2780 (2017)
53. Tang, S., Shen, C., Ji, W., et al.: Template-free synthesis of hierarchical MoO₂ multi-shell architectures with improved lithium storage capability. *Mater. Res. Bull.* **91**, 85–90 (2017)
54. Zhou, L., Han, Z., Li, G.-D., Zhao, Z.: Template-free synthesis and photocatalytic activity of hierarchical hollow ZnO microspheres composed of radially aligned nanorods. *J. Phys. Chem. Solids*, 109719 (2020)
55. Gong, C., Sun, S., Zhang, Y., et al.: Hierarchical nanomaterials via biomolecular self-assembly and bioinspiration for energy and environmental applications. *Nanoscale* **11**, 4147–4182 (2019)
56. Dahman, Y.: *Nanotechnology and functional materials for engineers*. Elsevier (2017)
57. Elsev, V.: Nuclear antiferromagnetism in a registered He₃ solid. *Phys. Rev. Lett.* **62**, 2405 (1989)
58. Pennec, Y., Auwärter, W., Schiffrin, A., et al.: Supramolecular gratings for tuneable confinement of electrons on metal surfaces. *Nat. Nanotechnol.* **2**, 99–103 (2007)
59. Lobo-Checa, J., Matena, M., Müller, K., et al.: Band formation from coupled quantum dots formed by a nanoporous network on a copper surface. *Science (80-)* **325**, 300–303 (2009)

60. Liu, J., Chen, T., Deng, X., et al.: Chiral hierarchical molecular nanostructures on two-dimensional surface by controllable ternary self-assembly. *J. Am. Chem. Soc.* **133**, 21010–21015 (2011)
61. Liu, X., Zhao, J., Cao, Y., et al.: Facile synthesis of 3D flower-like porous NiO architectures with an excellent capacitance performance. *Rsc Adv.* **5**, 47506–47510 (2015)
62. Kim, S.-I., Lee, J.-S., Ahn, H.-J., et al.: Facile route to an efficient NiO supercapacitor with a three-dimensional nanonetwork morphology. *ACS Appl. Mater. Interfaces* **5**, 1596–1603 (2013)
63. Yuan, C., Zhang, X., Su, L., et al.: Facile synthesis and self-assembly of hierarchical porous NiO nano/micro spherical superstructures for high performance supercapacitors. *J. Mater. Chem.* **19**, 5772–5777 (2009)
64. Zhang, X., Shi, W., Zhu, J., et al.: Synthesis of porous NiO nanocrystals with controllable surface area and their application as supercapacitor electrodes. *Nano Res.* **3**, 643–652 (2010)
65. Ren, Y., Gao, L.: From three-dimensional flower-like α -Ni(OH)₂ nanostructures to hierarchical porous NiO nanoflowers: microwave-assisted fabrication and supercapacitor properties. *J. Am. Ceram. Soc.* **93**, 3560–3564 (2010)
66. Meher, S.K., Justin, P., Ranga Rao, G.: Microwave-mediated synthesis for improved morphology and pseudocapacitance performance of nickel oxide. *ACS Appl. Mater. Interfaces* **3**, 2063–2073 (2011)
67. Cao, C.-Y., Guo, W., Cui, Z.-M., et al.: Microwave-assisted gas/liquid interfacial synthesis of flowerlike NiO hollow nanosphere precursors and their application as supercapacitor electrodes. *J. Mater. Chem.* **21**, 3204–3209 (2011)
68. Yang, W., Gao, Z., Ma, J., et al.: Two-step electrodeposition construction of flower-on-sheet hierarchical cobalt hydroxide nano-forest for high-capacitance supercapacitors. *Dalt Trans.* **42**, 15706–15715 (2013)
69. Wang, Y., Zhu, Q., Zhang, H.: Fabrication of β -Ni(OH)₂ and NiO hollow spheres by a facile template-free process. *Chem. Commun.*, 5231–5233 (2005)
70. Fu, M., Zhou, J., Xiao, Q., et al.: ZnO nanosheets with ordered pore periodicity via colloidal crystal template assisted electrochemical deposition. *Adv. Mater.* **18**, 1001–1004 (2006)
71. Zhong, L., Hu, J., Liang, H., et al.: Self-Assembled 3D flowerlike iron oxide nanostructures and their application in water treatment. *Adv. Mater.* **18**, 2426–2431 (2006)
72. Niu, C., Meng, J., Han, C., et al.: VO₂ nanowires assembled into hollow microspheres for high-rate and long-life lithium batteries. *Nano Lett.* **14**, 2873–2878 (2014)
73. Vijayakumar, S., Nagamuthu, S., Muralidharan, G.: Supercapacitor studies on NiO nanoflakes synthesized through a microwave route. *ACS Appl. Mater. Interfaces* **5**, 2188–2196 (2013)
74. Sun, Z., Liao, T., Dou, Y., et al.: Generalized self-assembly of scalable two-dimensional transition metal oxide nanosheets. *Nat. Commun.* **5**, 1–9 (2014)
75. Min, J., Liu, J., Lei, M., et al.: Self-assembly of parallelly aligned NiO hierarchical nanostructures with ultrathin nanosheet subunits for electrochemical supercapacitor applications. *ACS Appl. Mater. Interfaces* **8**, 780–791 (2016)
76. Jayan, J.S., Saritha, A., Deeraj, B.D.S., Joseph, K.: Triblock copolymer grafted Graphene oxide as nanofiller for toughening of epoxy resin. *Mater. Chem. Phys.* 122930 (2020)
77. Jayan, J.S., Saritha, A., Joseph, K.: Innovative materials of this era for toughening the epoxy matrix: a review. *Polym. Compos.* **39**, E1959–E1986 (2018)
78. Li, G.-R., Zheng, F.-L., Tong, Y.-X.: Controllable synthesis of Bi₂Te₃ intermetallic compounds with hierarchical nanostructures via electrochemical deposition route. *Cryst. Growth Des.* **8**, 1226–1232 (2008)
79. Zeng, Q., Cheng, J., Tang, L., et al.: Self-assembled graphene–enzyme hierarchical nanostructures for electrochemical biosensing. *Adv. Funct. Mater.* **20**, 3366–3372 (2010)
80. Zhuo, M.-P., Wu, J.-J., Wang, X.-D., et al.: Hierarchical self-assembly of organic heterostructure nanowires. *Nat. Commun.* **10**, 1–9 (2019)
81. Sun, H., Chen, Y., Zhao, J., Liu, Y.: Photocontrolled reversible conversion of nanotube and nanoparticle mediated by β -cyclodextrin dimers. *Angew. Chemie Int. Ed.* **54**, 9376–9380 (2015)

82. Wang, S.-P., Lin, W., Wang, X., et al.: Controllable hierarchical self-assembly of porphyrin-derived supra-amphiphiles. *Nat. Commun.* **10**, 1–12 (2019)
83. Li, B., Si, Y., Fang, Q., et al.: Hierarchical self-assembly of well-defined louver-like P-doped carbon nitride nanowire arrays with highly efficient hydrogen evolution. *Nano-Micro Lett.* **12**, 1–16 (2020)
84. Fang, M., Dong, G., Wei, R., Ho, J.C.: Hierarchical nanostructures: design for sustainable water splitting. *Adv. Energy Mater.* **7**, 1700559 (2017)
85. Sun, P., Mei, X., Cai, Y., et al.: Synthesis and gas sensing properties of hierarchical SnO₂ nanostructures. *Sensors Actuators B Chem.* **187**, 301–307 (2013)
86. Dubal, D.P., Gund, G.S., Holze, R., et al.: Surfactant-assisted morphological tuning of hierarchical CuO thin films for electrochemical supercapacitors. *Dalt Trans.* **42**, 6459–6467 (2013)
87. Krishnamoorthy, K., Kim, S.-J.: Growth, characterization and electrochemical properties of hierarchical CuO nanostructures for supercapacitor applications. *Mater. Res. Bull.* **48**, 3136–3139 (2013)
88. Zhang, X., Yu, P., Zhang, H., et al.: Rapid hydrothermal synthesis of hierarchical nanostructures assembled from ultrathin birnessite-type MnO₂ nanosheets for supercapacitor applications. *Electrochim. Acta* **89**, 523–529 (2013)
89. Feng, X., Huang, Y., Li, C., et al.: Construction of carnations-like Mn₃O₄@NiCo₂O₄@NiO hierarchical nanostructures for high-performance supercapacitors. *Electrochim. Acta* **308**, 142–149 (2019)
90. Zhang, Q., Wang, Y., Zhang, B., et al.: 3D superelastic graphene aerogel-nanosheet hybrid hierarchical nanostructures as high-performance supercapacitor electrodes. *Carbon N Y* **127**, 449–458 (2018)
91. Zhou, W., Kong, D., Jia, X., et al.: NiCo₂O₄ nanosheet supported hierarchical core–shell arrays for high-performance supercapacitors. *J. Mater. Chem. A* **2**, 6310–6315 (2014)
92. Yang, J., Gao, H., Kang, X.: Nanomaterials application in Li–Se and Na–Se batteries. In: *Advanced Nanomaterials for Electrochemical-Based Energy Conversion and Storage*. Elsevier, pp. 69–114 (2020)
93. Wang, X., Ahmad, M., Sun, H.: Three-dimensional ZnO hierarchical nanostructures: Solution phase synthesis and applications. *Materials (Basel)* **10**, 1304 (2017)
94. Zhang, Y., Sun, C., Lu, P., et al.: Crystallization design of MnO₂ towards better supercapacitance. *Cryst. Eng. Comm.* **14**, 5892–5897 (2012)
95. Chen, W., Xia, C., Alshareef, H.N.: One-step electrodeposited nickel cobalt sulfide nanosheet arrays for high-performance asymmetric supercapacitors. *ACS Nano* **8**, 9531–9541 (2014)
96. Park, J.C., Kim, J., Kwon, H., Song, H.: Gram-scale synthesis of Cu₂O nanocubes and subsequent oxidation to CuO hollow nanostructures for lithium-ion battery anode materials. *Adv. Mater.* **21**, 803–807 (2009)
97. Sun, D., Chen, J., Yang, J., Yan, X.: Morphology and crystallinity-controlled synthesis of MnO₂ hierarchical nanostructures and their application in lithium ion batteries. *Cryst. Eng. Comm.* **16**, 10476–10484 (2014)
98. Xiang, J.Y., Tu, J.P., Zhang, L., et al.: Self-assembled synthesis of hierarchical nanostructured CuO with various morphologies and their application as anodes for lithium ion batteries. *J. Power Sources* **195**, 313–319 (2010)
99. Li, L., Seng, K.H., Chen, Z., et al.: Self-assembly of hierarchical star-like Co₃O₄ micro/nanostructures and their application in lithium ion batteries. *Nanoscale* **5**, 1922–1928 (2013)
100. Xiao, X., Zou, L., Pang, H., Xu, Q.: Synthesis of micro/nanoscaled metal–organic frameworks and their direct electrochemical applications. *Chem. Soc. Rev.* **49**, 301–331 (2020)
101. Magasinski, A., Dixon, P., Hertzberg, B., et al.: High-performance lithium-ion anodes using a hierarchical bottom-up approach. *Nat. Mater.* **9**, 353–358 (2010)
102. Mai, L., Xu, L., Han, C., et al.: Electrospun ultralong hierarchical vanadium oxide nanowires with high performance for lithium ion batteries. *Nano Lett.* **10**, 4750–4755 (2010)

103. Sun, F., Yu, J.C., Wang, X.: Construction of size-controllable hierarchical nanoporous TiO₂ ring arrays and their modifications. *Chem. Mater.* **18**, 3774–3779 (2006)
104. Ariga, K., Hill, J.P., Lee, M.V., et al.: Challenges and breakthroughs in recent research on self-assembly. *Sci. Technol. Adv. Mater.* (2008)
105. Zhang, D.-F., Sun, L.-D., Jia, C.-J., et al.: Hierarchical assembly of SnO₂ nanorod arrays on α -Fe₂O₃ nanotubes: a case of interfacial lattice compatibility. *J. Am. Chem. Soc.* **127**, 13492–13493 (2005)
106. Chen, J.S., Tan, Y.L., Li, C.M., et al.: Constructing hierarchical spheres from large ultrathin anatase TiO₂ nanosheets with nearly 100% exposed (001) facets for fast reversible lithium storage. *J. Am. Chem. Soc.* **132**, 6124–6130 (2010)
107. Hu, Y., Adelhelm, P., Smarsly, B.M., et al.: Synthesis of hierarchically porous carbon monoliths with highly ordered microstructure and their application in rechargeable lithium batteries with high-rate capability. *Adv. Funct. Mater.* **17**, 1873–1878 (2007)
108. Sun, Y., Hu, X., Luo, W., Huang, Y.: Self-assembled hierarchical MoO₂/graphene nanoarchitectures and their application as a high-performance anode material for lithium-ion batteries. *ACS Nano* **5**, 7100–7107 (2011)
109. Jia, H., Li, X., Song, J., et al.: Hierarchical porous silicon structures with extraordinary mechanical strength as high-performance lithium-ion battery anodes. *Nat. Commun.* **11**, 1–9 (2020)
110. Jiang, L., Li, L., Luo, S., et al.: Configuring hierarchical Ni/NiO 3D-network assisted with bamboo cellulose nanofibers for high-performance Ni–Zn aqueous batteries. *Nanoscale* **12**, 14651–14660 (2020)
111. Yang, X., Wu, H., Feng, C.: Synthesis and electrochemical performance of Sb₂ WO₆@ PPy as novel anode material for lithium ion battery application. *J. Mater. Sci. Mater Electron.* **31**, 4761–4768 (2020)
112. Bao, L., Xu, G., Wang, M.: Controllable synthesis and morphology evolution of hierarchical LiFePO₄ cathode materials for Li-ion batteries. *Mater Charact* **157**, 109927 (2019)
113. Lin, Z., Huang, J.: Hierarchical nanostructures derived from cellulose for lithium-ion batteries. *Dalt Trans.* **48**, 14221–14232 (2019)
114. Xie, J., Zhu, K., Min, J., et al.: In-situ grown ultrathin MoS₂ nanosheets on MoO₂ hollow nanospheres to synthesize hierarchical nanostructures and its application in lithium-ion batteries. *Ionics (Kiel)* **25**, 1487–1494 (2019)
115. Liang, L., Li, J., Zhu, M., et al.: Cobalt chalcogenides/cobalt phosphides/cobaltates with hierarchical nanostructures for anode materials of lithium-ion batteries: improving the lithiation environment. *Small*, 1903418 (2019)
116. Wang, Z., Rafai, S., Qiao, C., et al.: Microwave-assisted synthesis of CuS hierarchical nanosheets as the cathode material for high-capacity rechargeable magnesium batteries. *ACS Appl. Mater. Interfaces* **11**, 7046–7054 (2019)
117. Chen, J., Pan, A., Wang, Y., et al.: Hierarchical mesoporous MoSe₂@ CoSe/N-doped carbon nanocomposite for sodium ion batteries and hydrogen evolution reaction applications. *Energy Storage Mater.* **21**, 97–106 (2019)
118. Bian, H., Li, Z., Xiao, X., et al.: Anodic synthesis of hierarchical SnS/SnO_x hollow nanospheres and their application for high-performance na-ion batteries. *Adv. Funct. Mater.* **29**, 1901000 (2019)
119. Zhang, H., Zou, M., Zhao, W., et al.: Highly Dispersed catalytic Co₃S₄ among a hierarchical carbon nanostructure for high-rate and long-life lithium-sulfur batteries. *ACS Nano* **13**, 3982–3991 (2019)
120. Wang, P., Wang, S., Zhang, X., et al.: Rational construction of CoO/CoF₂ coating on burnt-pot inspired 2D CNs as the battery-like electrode for supercapacitors. *J. Alloys Compd.* **819**, 153374 (2020)
121. Li, S., Yang, K., Ye, P., et al.: Three-dimensional porous carbon/Co₃O₄ composites derived from graphene/Co-MOF for high performance supercapacitor electrodes. *Appl. Surf. Sci.* **503**, 144090 (2020)

122. Kumar, Y.A., Kumar, K.D., Kim, H.-J.: Reagents assisted ZnCo₂O₄ nanomaterial for supercapacitor application. *Electrochim. Acta* **330**, 135261 (2020)
123. Pericola, D., Kötzt, R.: Hybridization of rechargeable batteries and electrochemical capacitors: principles and limits. *Electrochim Acta* **72**, 1–17 (2012)
124. Liu, C., Li, F., Ma, L., Cheng, H.: Advanced materials for energy storage. *Adv. Mater.* **22**, E28–E62 (2010)
125. Kotz, R.: Carlen M Principles and applications of electrochemical capacitors' *Electrochim. Acta* **45**, 2483 (2000)
126. Simon, P., Gogotsi, Y.: Materials for electrochemical capacitors. In: *Nanoscience and technology: a collection of reviews from Nature journals*. World Scientific, pp 320–329 (2010)
127. Zhang, L.L., Zhao, X.S.: Carbon-based materials as supercapacitor electrodes. *Chem. Soc. Rev.* **38**, 2520–2531 (2009)
128. Jiang, H., Zhao, T., Ma, J., et al.: Ultrafine manganese dioxide nanowire network for high-performance supercapacitors. *Chem. Commun.* **47**, 1264–1266 (2011)
129. Jiang, H., Sun, T., Li, C., Ma, J.: Hierarchical porous nanostructures assembled from ultrathin MnO₂ nanoflakes with enhanced supercapacitive performances. *J. Mater. Chem.* **22**, 2751–2756 (2012)
130. Zhang, Y., Wang, D., Lü, S., et al.: CoO@ CoS/Ni₃S₂ hierarchical nanostructure arrays for high performance asymmetric supercapacitor. *Appl. Surf. Sci.*, 147438 (2020)
131. Youssry, S.M., El-Hallag, I.S., Kumar, R., et al.: Synthesis of mesoporous Co(OH)₂ nanostructure film via electrochemical deposition using lyotropic liquid crystal template as improved electrode materials for supercapacitors application. *J. Electroanal Chem.* **857**, 113728 (2020)
132. An, G., Hong, J., Pak, S., et al.: 2D metal zn nanostructure electrodes for high-performance zn ion supercapacitors. *Adv. Energy Mater.* **10**, 1902981 (2020)
133. Raghavendra, K.V.G., Vinodh, R., Gopi, C.V.V.M., et al.: Facile synthesis of hierarchical agglomerated cauliflower-like ZnWO₄@ NiO nanostructures as an efficient electrode material for high-performance supercapacitor applications. *Mater. Lett.* 127594 (2020)
134. Gopi, C.V.V.M., Vinodh, R., Sambasivam, S., et al.: Recent progress of advanced energy storage materials for flexible and wearable supercapacitor: from design and development to applications. *J. Energy Storage* **27**, 101035 (2020)
135. Chen, X., Li, H., Xu, J., et al.: Synthesis and characterization of a NiCo₂O₄@ NiCo₂O₄ hierarchical mesoporous nanoflake electrode for supercapacitor applications. *Nanomaterials* **10**, 1292 (2020)
136. Prasad, K., Rajasekhara Reddy, G., Rajesh, M., et al.: Electrochemical performance of 2D-hierarchical sheet-like ZnCo₂O₄ microstructures for supercapacitor applications. *Crystals* **10**, 566 (2020)
137. Xiong, S., Yuan, C., Zhang, X., Qian, Y.: Mesoporous NiO with various hierarchical nanostructures by quasi-nanotubes/nanowires/nanorods self-assembly: controllable preparation and application in supercapacitors. *Cryst. Eng. Comm.* **13**, 626–632 (2011)
138. Krishnamoorthy, K., Veerasubramani, G.K., Radhakrishnan, S., Kim, S.J.: One pot hydrothermal growth of hierarchical nanostructured Ni₃S₂ on Ni foam for supercapacitor application. *Chem. Eng. J.* **251**, 116–122 (2014)
139. Kim, T.K., Chen, W., Wang, C.: Heat treatment effect of the Ni foam current collector in lithium ion batteries. *J. Power Sources* **196**, 8742–8746 (2011)
140. Huang, M., Zhang, Y., Li, F., et al.: Merging of Kirkendall growth and Ostwald ripening: CuO@ MnO₂ core-shell architectures for asymmetric supercapacitors. *Sci. Rep.* **4**, 4518 (2014)
141. Li, F., Li, G., Chen, H., et al.: Morphology and crystallinity-controlled synthesis of manganese cobalt oxide/manganese dioxides hierarchical nanostructures for high-performance supercapacitors. *J. Power Sources* **296**, 86–91 (2015)
142. Shang, Z., An, X., Zhang, H., et al.: Houttuynia-derived nitrogen-doped hierarchically porous carbon for high-performance supercapacitor. *Carbon N Y* **161**, 62–70 (2020)
143. Qu, G., Li, C., Hou, P., et al.: Hierarchically hollow structured NiCo₂S₄@ NiS for high-performance flexible hybrid supercapacitors. *Nanoscale* **12**, 4686–4694 (2020)

144. Zhang, A., Zheng, W., Yuan, Z., et al.: Hierarchical NiMn-layered double hydroxides@ CuO core-shell heterostructure in-situ generated on Cu(OH)₂ nanorod arrays for high performance supercapacitors. *Chem. Eng. J.* **380**, 122486 (2020)
145. Kshetri, T., Tran, D.T., Nguyen, D.C., et al.: Ternary graphene-carbon nanofibers-carbon nanotubes structure for hybrid supercapacitor. *Chem. Eng. J.* **380**, 122543 (2020)
146. Bhushan, M., Jha, R.: Surface activity correlations of mesoporous 3-D hierarchical ZnS nanostructures for enhanced photo and electro catalytic performance. *Appl Surf Sci.* **528**, 146988 (2020)
147. Reddy, G.R., Dillip, G.R., Sreekanth, T.V.M., et al.: Mechanistic investigation of defect-engineered, non-stoichiometric, and Morphology-regulated hierarchical rhombus-/spindle-/peanut-like ZnCo₂O₄ microstructures and their applications toward high-performance supercapacitors. *Appl. Surf. Sci.* **529**, 147123 (2020)
148. Yan, J., Li, S., Lan, B., et al.: Rational design of nanostructured electrode materials toward multifunctional supercapacitors. *Adv. Funct. Mater.* **30**, 1902564 (2020)
149. Shrestha, R.G., Maji, S., Shrestha, L.K., Ariga, K.: Nanoarchitectonics of nanoporous carbon materials in supercapacitors applications. *Nanomaterials* **10**, 639 (2020)
150. Lonkar, S.P., Pillai, V.V., Patole, S.P., Alhassan, S.M.: Scalable in situ synthesis of 2D–2D-type graphene-wrapped SnS₂ nano hybrids for enhanced supercapacitor and electrocatalytic applications. *ACS Appl. Energy Mater.* **3**(5), 4995–5005 (2020)
151. Chen, H., Yang, S.: Hierarchical nanostructures of metal oxides for enhancing charge separation and transport in photoelectrochemical solar energy conversion systems. *Nanoscale Horizons* **1**, 96–108 (2016)
152. Shah, A., Torres, P., Tscharnner, R., et al.: Photovoltaic technology: the case for thin-film solar cells. *Science* (80-) **285**, 692–698 (1999)
153. Surek, T.: Crystal growth and materials research in photovoltaics: progress and challenges. *J. Cryst. Growth* **275**, 292–304 (2005)
154. Bierman, M.J., Jin, S.: Potential applications of hierarchical branching nanowires in solar energy conversion. *Energy Environ. Sci.* **2**, 1050–1059 (2009)
155. Wang, Q., Hisatomi, T., Jia, Q., et al.: Scalable water splitting on particulate photocatalyst sheets with a solar-to-hydrogen energy conversion efficiency exceeding 1%. *Nat. Mater.* **15**, 611–615 (2016)
156. Chen, S., Takata, T., Domen, K.: Particulate photocatalysts for overall water splitting. *Nat. Rev. Mater.* **2**, 1–17 (2017)
157. Wang, S., Wang, Y., Zang, S., Lou, X.W.: Hierarchical hollow heterostructures for photocatalytic CO₂ reduction and water splitting. *Small Methods* **4**, 1900586 (2020)
158. In, S., Vaughn, D.D., Schaak, R.E.: Hybrid CuO-TiO₂– xN_x Hollow Nanocubes for Photocatalytic Conversion of CO₂ into Methane under Solar Irradiation. *Angew. Chemie Int. Ed.* **51**, 3915–3918 (2012)
159. Sun, J., Zhang, J., Zhang, M., et al.: Bioinspired hollow semiconductor nanospheres as photosynthetic nanoparticles. *Nat. Commun.* **3**, 1–7 (2012)
160. Zheng, D., Cao, X., Wang, X.: Precise formation of a hollow carbon nitride structure with a janus surface to promote water splitting by photoredox catalysis. *Angew. Chemie* **128**, 11684–11688 (2016)
161. Wang, D., Hisatomi, T., Takata, T., et al.: Core/Shell photocatalyst with spatially separated co-catalysts for efficient reduction and oxidation of water. *Angew. Chemie Int. Ed.* **52**, 11252–11256 (2013)
162. Qi, J., Zhao, K., Li, G., et al.: Multi-shelled CeO₂ hollow microspheres as superior photocatalysts for water oxidation. *Nanoscale* **6**, 4072–4077 (2014)
163. Liu, Y., Yu, L., Hu, Y., et al.: A magnetically separable photocatalyst based on nest-like γ -Fe₂O₃/ZnO double-shelled hollow structures with enhanced photocatalytic activity. *Nanoscale* **4**, 183–187 (2012)
164. Zhou, Y., Zhang, Y., Lin, M., et al.: Monolayered Bi₂ WO₆ nanosheets mimicking heterojunction interface with open surfaces for photocatalysis. *Nat. Commun.* **6**, 1–8 (2015)


165. Xing, M., Qiu, B., Du, M., et al.: Spatially separated CdS shells exposed with reduction surfaces for enhancing photocatalytic hydrogen evolution. *Adv. Funct. Mater.* **27**, 1702624 (2017)
166. Low, J., Yu, J., Jaroniec, M., et al.: Heterojunction photocatalysts. *Adv. Mater.* **29**, 1601694 (2017)
167. Cao, S., Shen, B., Tong, T., et al.: 2D/2D heterojunction of ultrathin MXene/Bi₂WO₆ nanosheets for improved photocatalytic CO₂ reduction. *Adv. Funct. Mater.* **28**, 1800136 (2018)
168. Khan, I., Abdalla, A., Qurashi, A.: Synthesis of hierarchical WO₃ and Bi₂O₃/WO₃ nanocomposite for solar-driven water splitting applications. *Int. J. Hydrogen Energy* **42**, 3431–3439 (2017)
169. Han, H., Riboni, F., Karlicky, F., et al.: α -Fe₂O₃/TiO₂ 3D hierarchical nanostructures for enhanced photoelectrochemical water splitting. *Nanoscale* **9**, 134–142 (2017)
170. Qiu, J., Guo, M., Wang, X.: Electrodeposition of hierarchical ZnO nanorod-nanosheet structures and their applications in dye-sensitized solar cells. *ACS Appl. Mater. Interfaces* **3**, 2358–2367 (2011)
171. Chen, X.-Y., Ling, T., Du, X.-W.: Low-temperature synthesis of ZnO/CdS hierarchical nanostructure for photovoltaic application. *Nanoscale* **4**, 5602–5607 (2012)
172. Zhang, M., Cui, X., Wang, Y., et al.: Simple route to interconnected, hierarchically structured, porous Zn₂SnO₄ nanospheres as electron transport layer for efficient perovskite solar cells. *Nano Energy* **71**, 104620 (2020)
173. Farooq, W.A., Atif, M., Fatehmulla, A., et al.: Photovoltaic and capacitance measurements of solar cells comprise of Al-doped CdS (QD) and hierarchical flower-like TiO₂ nanostructured electrode. *Results Phys.* **16**, 102827 (2020)
174. Tang, S., Qiu, W., Xiao, S., et al.: Harnessing hierarchical architectures to trap light for efficient photoelectrochemical cells. *Energy Environ. Sci.* **13**, 660–684 (2020)
175. Burungale, V.V., Bae, H., Kamble, A.S., et al.: Surfactant-free pH-assisted facile engineering of hierarchical rutile TiO₂ nanostructures by a single step hydrothermal method for water splitting application. *Cryst. Eng. Commun.* **22**, 2462–2471 (2020)
176. Yang S, Sha S, Lu H, et al (2020) Electrodeposition of hierarchical zinc oxide nanostructures on metal meshes as photoanodes for flexible dye-sensitized solar cells. *Colloids Surfaces A Physicochem Eng Asp* 124665
177. Quy, V.H.V., Kang, S.-H., Kim, H., Ahn, K.-S.: Cu₃Se₂ nanomeshes constructed by enoki-mushroom-like Cu₃Se₂ and their application to quantum dot-sensitized solar cells. *Appl. Surf. Sci.* **499**, 143935 (2020)
178. Mir, N., Salavati-Niasari, M., Davar, F.: Preparation of ZnO nanoflowers and Zn glycerolate nanoplates using inorganic precursors via a convenient route and application in dye sensitized solar cells. *Chem. Eng. J.* **181**, 779–789 (2012)
179. Qian, X., Li, H., Shao, L., et al.: Morphology-tuned synthesis of nickel cobalt selenides as highly efficient Pt-free counter electrode catalysts for dye-sensitized solar cells. *ACS Appl. Mater. Interfaces* **8**, 29486–29495 (2016)
180. Yun, S., Hagfeldt, A., Ma, T.: Pt-free counter electrode for dye-sensitized solar cells with high efficiency. *Adv. Mater.* **26**, 6210–6237 (2014)
181. Jiang, X., Li, H., Li, S., et al.: Metal-organic framework-derived Ni–Co alloy@ carbon microspheres as high-performance counter electrode catalysts for dye-sensitized solar cells. *Chem. Eng. J.* **334**, 419–431 (2018)
182. Huang, S., He, Q., Liu, M., et al.: Controlled synthesis of porous nanosheets-assembled peony-like cobalt nickel selenides for triiodide reduction in dye-sensitized solar cells. *J. Alloys Compd.* **818**, 152817 (2020)
183. Hussain, A.A., Sharma, B., Barman, T., Pal, A.R.: Self-powered broadband photodetector using plasmonic titanium nitride. *ACS Appl. Mater. Interfaces* **8**, 4258–4265 (2016)
184. Zhou, Z., Sakr, E., Sun, Y., Bermel, P.: Solar thermophotovoltaics: reshaping the solar spectrum. *Nanophotonics* **5**, 1–21 (2016)
185. Kim, C., Ryu, Y., Shin, D., et al.: Efficient solar steam generation by using metal-versatile hierarchical nanostructures for nickel and gold with aerogel insulator. *Appl. Surf. Sci.* **517**, 146177 (2020)

186. Huang, J., Qian, X., Yang, J., et al.: Construction of Pt-free electrocatalysts based on hierarchical CoS₂/N-doped C@ Co-WS₂ yolk-shell nano-polyhedrons for dye-sensitized solar cells. *Electrochim. Acta* **340**, 135949 (2020)
187. Jiang, Y., Shen, H., Pu, T., et al.: High efficiency multi-crystalline silicon solar cell with inverted pyramid nanostructure. *Sol. Energy* **142**, 91–96 (2017)
188. Tang, Q., Yao, H., Xu, B., Ge, J.: Enhanced energy conversion efficiency of Al-BSF c-Si solar cell by a novel hierarchical structure composed of inverted pyramids with different sizes. *Sol. Energy* **208**, 1–9 (2020)
189. Balamurugan, J., Nguyen, T.T., Aravindan, V., et al.: Highly reversible water splitting cell building from hierarchical 3D nickel manganese oxyphosphide nanosheets. *Nano Energy* **69**, 104432 (2020)
190. e Asl, S.D., Sadrmezhaad, S.K.: Biphasic TiO₂ nanoleafed nanorod electrode for dye-sensitized solar cell. *Phys. E Low-dimensional Syst. Nanostruct.* **123**, 114206 (2020)
191. Li, Z., Yang, H., Zhang, L., et al.: Stainless steel mesh-supported three-dimensional hierarchical SnO₂/Zn₂SnO₄ composite for the applications in solar cell, gas sensor, and photocatalysis. *Appl. Surf. Sci.* **502**, 144113 (2020)
192. Williams, M.C.: Chapter 2 - Fuel Cells. In: Shekhawat, D., Spivey, J.J., Berry, DABT-FCT for FP (eds.), pp 11–27. Elsevier, Amsterdam (2011)
193. Lu, Q., Huang, J., Han, C., et al.: Facile synthesis of composition-tunable PtRh nanosponges for methanol oxidation reaction. *Electrochim. Acta* **266**, 305–311 (2018)
194. Van Dao, D., Le, T.D., Adilbish, G., et al.: Pt-loaded Au@ CeO₂ core–shell nanocatalysts for improving methanol oxidation reaction activity. *J. Mater. Chem. A* **7**, 26996–27006 (2019)
195. Shang, C., Guo, Y., Wang, E.: Facile fabrication of PdRuPt nanowire networks with tunable compositions as efficient methanol electrooxidation catalysts. *Nano Res.* **11**, 4348–4355 (2018)
196. Geng, J., Zhu, Z., Bai, X., et al.: Hot-injection synthesis of PtCu₃ concave nanocubes with high-index facets for electrocatalytic oxidation of methanol and formic acid. *ACS Appl. Energy Mater.* **3**, 1010–1016 (2020)
197. Lai, J., Lin, F., Tang, Y., et al.: Efficient bifunctional polyalcohol oxidation and oxygen reduction electrocatalysts enabled by ultrathin PtPdM (M= Ni, Fe, Co) nanosheets. *Adv. Energy Mater.* **9**, 1800684 (2019)
198. Sulaiman, J.E., Zhu, S., Xing, Z., et al.: Pt–Ni octahedra as electrocatalysts for the ethanol electro-oxidation reaction. *ACS Catal.* **7**, 5134–5141 (2017)
199. Wang, H.-M., Fang, Y., Yuan, P.-X., et al.: Construction of ultrasensitive label-free aptasensor for thrombin detection using palladium nanocones boosted electrochemiluminescence system. *Electrochim. Acta* **310**, 195–202 (2019)
200. Ren, G., Liu, Y., Wang, W., et al.: Facile synthesis of highly active three-dimensional urchin-like Pd@ PtNi nanostructures for improved methanol and ethanol electrochemical oxidation. *ACS Appl. Nano Mater.* **1**, 3226–3235 (2018)
201. Wang, H., Yin, S., Xu, Y., et al.: Direct fabrication of tri-metallic PtPdCu tripods with branched exteriors for the oxygen reduction reaction. *J. Mater. Chem. A* **6**, 8662–8668 (2018)
202. Du, N., Wang, C., Wang, X., et al.: Trimetallic TriStar nanostructures: tuning electronic and surface structures for enhanced electrocatalytic hydrogen evolution. *Adv. Mater.* **28**, 2077–2084 (2016)
203. Feng, Y.-G., Niu, H.-J., Mei, L.-P., et al.: Engineering 3D hierarchical thorn-like PtPdNiCu alloyed nanotripods with enhanced performances for methanol and ethanol electrooxidation. *J. Colloid Interface Sci.* (2020)
204. Deng, R., Xia, Z., Sun, R., et al.: Nanostructured ultrathin catalyst layer with ordered platinum nanotube arrays for polymer electrolyte membrane fuel cells. *J. Energy Chem.* **43**, 33–39 (2020)
205. Huang, H., Wang, X.: Recent progress on carbon-based support materials for electrocatalysts of direct methanol fuel cells. *J. Mater. Chem. A* **2**, 6266–6291 (2014)
206. Sun, S., Yang, D., Zhang, G., et al.: Synthesis and characterization of platinum nanowire–carbon nanotube heterostructures. *Chem. Mater.* **19**, 6376–6378 (2007)

207. Qazzazie, D., Yurchenko, O., Urban, S., et al.: Platinum nanowires anchored on graphene-supported platinum nanoparticles as a highly active electrocatalyst towards glucose oxidation for fuel cell applications. *Nanoscale* **9**, 6436–6447 (2017)
208. Xie, S., Tong, X.-L., Jin, G.-Q., et al.: CNT–Ni/SiC hierarchical nanostructures: preparation and their application in electrocatalytic oxidation of methanol. *J. Mater. Chem. A* **1**, 2104–2109 (2013)
209. Qin, X., Huang, Y., Wang, K., et al.: Novel hierarchically porous Ti-MOFs/nitrogen-doped graphene nanocomposite served as high efficient oxygen reduction reaction catalyst for fuel cells application. *Electrochim. Acta* **297**, 805–813 (2019)
210. Dong, B., Li, W., Huang, X., et al.: Fabrication of hierarchical hollow Mn doped Ni (OH)₂ nanostructures with enhanced catalytic activity towards electrochemical oxidation of methanol. *Nano Energy* **55**, 37–41 (2019)
211. Prieto, G., Tüysüz, H., Duyckaerts, N., et al.: Hollow nano- and microstructures as catalysts. *Chem. Rev.* **116**, 14056–14119 (2016)
212. Zhou, L., Zhuang, Z., Zhao, H., et al.: Intricate hollow structures: controlled synthesis and applications in energy storage and conversion. *Adv. Mater.* **29**, 1602914 (2017)
213. Gao, M., Sheng, W., Zhuang, Z., et al.: Efficient water oxidation using nanostructured α -nickel-hydroxide as an electrocatalyst. *J. Am. Chem. Soc.* **136**, 7077–7084 (2014)
214. Gong, C., Zhao, S., Tsen, W.-C., et al.: Hierarchical layered double hydroxide coated carbon nanotube modified quaternized chitosan/polyvinyl alcohol for alkaline direct methanol fuel cells. *J. Power Sources* **441**, 227176 (2019)
215. Perego, A., Giuffredi, G., Mazzolini, P., et al.: Hierarchical TiN nanostructured thin film electrode for highly stable PEM fuel cells. *ACS Appl. Energy Mater.* **2**, 1911–1922 (2019)
216. Kaur, P., Verma, G., Sekhon, S.S.: Biomass derived hierarchical porous carbon materials as oxygen reduction reaction electrocatalysts in fuel cells. *Prog. Mater. Sci.* **102**, 1–71 (2019)
217. Marinoiu, A., Andrulevicius, M., Tamuleviciene, A., et al.: Synthesis of well dispersed gold nanoparticles on reduced graphene oxide and application in PEM fuel cells. *Appl. Surf. Sci.* **504**, 144511 (2020)

Polymer Nanocomposites for Energy Storage Applications



Arij Naser Abougreen, Ahmed Esmail Shalan , Esraa Samy Abu Serea, and Mustafa K. A. Mohammed

Abstract Polymer based-nanocomposites (PNC) have attracted considerable industrial and research concerns thanks to their outstanding applications in various areas and it is expected to be one of the most useful functions for nanotechnology trends. PNC consists of a polymer with different nanofillers that scattered in a polymer matrix. The attained nanocomposites could have different shapes, structures, and geometry (for example, platelets, fibers, and spheres), but a range from 1 to 100 nm is accounted specially for one-dimension structure. They demonstrate unique merits that cannot achieved with individual compounds that act alone. Nanofillers enhance the characteristics of polymeric substances for their possible use as materials for advanced energy storage systems.

Polymer nanocomposites appear to have a very bright future for many applications due to their low average cost and ease of production, which make our life relaxed. The current chapter mainly focuses on different polymer nanocomposites and their applications for energy storage includes electrochemical capacitors and lithium-ion batteries.

Keywords Polymer · Nanocomposites · Energy · Storage · Applications

A. N. Abougreen (✉)

Electrical and Electronic Engineering Department, Faculty of Engineering, University of Tripoli, 13589 Tripoli, Libya

e-mail: a.abougreen@uot.edu.ly

A. E. Shalan (✉)

Central Metallurgical Research and Development Institute (CMRDI), P.O. Box 87, Helwan, Cairo 11421, Egypt

A. E. Shalan · E. S. A. Serea

BCMaterias-Basque Center for Materials, Applications and Nanostructures, Martina Casiano, UPV/EHU Science Park, Barrio Sarriena s/n, 48940 Leioa, Spain

M. K. A. Mohammed

Dijlah University College, Al-Masafi Street, Al-Dora, Baghdad 00964, Iraq

© The Author(s), under exclusive license to Springer Nature Switzerland AG 2022

A. E. Shalan et al. (eds.), *Advances in Nanocomposite Materials for Environmental and Energy Harvesting Applications*, Engineering Materials,

https://doi.org/10.1007/978-3-030-94319-6_22

1 Introduction

Nanocomposites are materials consists of at least one nanoscale layer which called nanofiller. This nanofiller is distributed in a matrix to take advantage of the properties of each component of the nanocomposite. Comparing nanofiller with traditional micrometer-sized filler that has the same concentration, it was found that nanofiller often enhances the properties. Polymeric nanocomposites (PNCs) were discovered by Toyota Research Group in the early 1990s [4, 28]. Conducting polymer is a promising electrode due to its high conductivity and rapid redox reactivity [1]. Several conductive polymers have been discovered including Polypyrrole (PPy) Polyaniline (PANI) and polythiophene (PTh) that can be used in different practical fields including energy storage application [2]. The most significant conductive polymer is PANI due to its low-cost, facility of fabricating from aniline monomer, good processability, fast doping and dedoping mechanism, environmental compatibility, superior electrical conductivity and ease of adjusting of conducting characteristics. PANI has received considerable attention for its usage as pseudocapacitive electrode for the supercapacitors [2, 3, 43, 44]. A supercapacitors based PPy electrode is commonly used owing to its easy preparation and processing, high environmental stability, inexpensive, fast redox activity, high conductivity, good flexibility, and high pseudocapacitivity merits [6, 46, 47].

Polymer nanocomposites have been gaining importance in recent years and it have been proven useful in numerous industrial fields including energy storage application [2]. Lithium-ion batteries (LIBs) is one of important application for PNCs due to its high performing voltage, low toxicity, high capacity and long cycling lifetime. Supercapacitors is another significant application for PNCs [13, 68]. Many researches have been performed on developing both anode and cathode which has the ability to provide high power density and energy density without any impact on its stability or cycle life. In addition, electrolyte receives the most attention as it is existed in between the electrodes and it remains active in both discharge and charge states. Also, the operation of the battery is highly dependent on the electrolyte. Most batteries rely on the liquid electrolyte. The batteries show high ionic conductivity however, low strength and their instability inhibits its employing in the commercial applications [36, 48]. Another issue is the dendrite growth which is result in short circuit in the battery. PNC is excellent in comparison to both liquid and electrolyte and the gel polymer electrolytes in several factors for example, dimension diversity, stability, flexibility, safety, and the price [36].

Energy storage systems like LIBs and supercapacitor have been used to improve zero-emission electric vehicle, large-scale smart grid, energy effective ships and locomotive and portable electronic applications [5]. Compared to the battery which stores the energy in the bulk material, supercapacitor stores the energy on the surface of the electrode or sub-surface layer. Supercapacitors are regarded to be one of the most popular energy storage system owing to their ability to provide high power as energy can be rapidly released from the surface or subsurface layer than from

the bulk. Also, supercapacitors show a superb cycling performance because charge–discharge mechanism happens on the surface which leads to maintaining the structure of the electroactive materials. Supercapacitors can be categorized relying on the way charge is stored into double layer capacitor (EDLC) and pseudocapacitor [3, 70]. The power is maintained in electrostatically on the electrode/electrolyte interfaces within the double layer of the EDLCs, whereas the charge storage happens through fast redox processes on the electrode surface of the pseudocapacitors. The classes of electrode materials for supercapacitor are categorized in three forms including carbon-based material, metal oxides (MOs)/hydroxides and conducting polymer [3].

This chapter is organized as follows: in Sect. 2 PNCs based materials for LIBs are presented and their properties are described. It also reviews synthesizing techniques used for obtain various PNCs materials for supercapacitors and the properties of these polymer nanocomposites are provided. Finally, in Sect. 3 some concluding observations are presented.

2 Polymer Nanocomposite for Energy Storage Application

Polymeric nanocomposite has been attracting the interest of many researchers to solve energy issue [2]. There is an urgent demand to produce energy resources because of the increased energy crisis resulting from the depletion of traditional fossil fuels. Also, renewable source is unstable, so it is necessary to find a stable method to obtain and store energy. Electrochemical energy storage systems (EESS) have gained significant research interest including supercapacitors and batteries [13].

2.1 PNCs Based Materials for Lithium-Ion Battery

Sony produced LIBs in 1990. LIBs have drawn the interest of researchers as energy storage device. These batteries have provided a solution to energy storage issues. They have become very popular batteries and they are the most widely used rechargeable batteries as they provide power to various portable devices such as cell phones and portable computers. It can also be used in electrical vehicles and in renewable energy systems [2].

LIB contains single Li cells which are connected in series for obtaining a suitable voltage while, they are connected in parallel when an increase in the output current is required. The fundamental Li-ion cell consists of two different electrodes, electrolyte and separator. The negative and positive electrodes are named as the anode and the cathode, respectively. The electrodes are isolated from each other by the electrolyte and separator which comprises of a small-sized polymer electrolyte that permits the movement of Li ions and does not permit the electrons to flow [2].

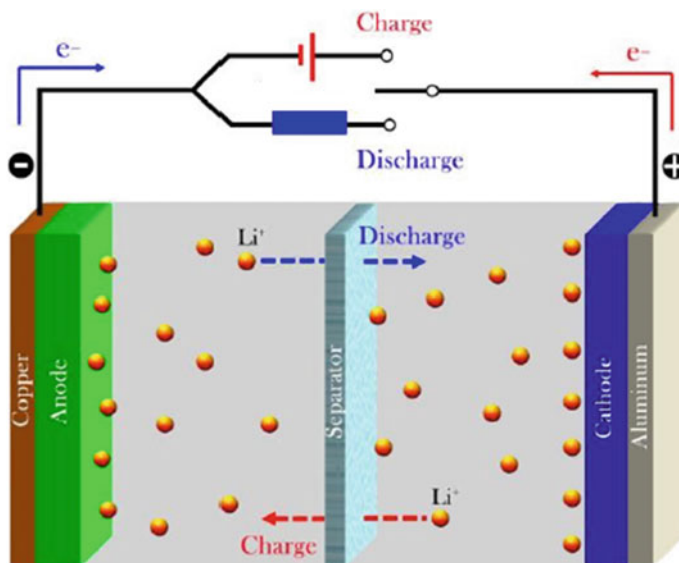


Fig. 1 Operation mechanism of a LIB [32]. Reprinted with permission from Long L, Wang S, Xiao M, Meng Y. Polymer electrolytes for lithium polymer batteries. *J Mater Chem A* 2016;4(26):10,038–69. Copyright (2016), the Royal Society of Chemistry

In Li-ion battery, carbon, silicon, and MOs are widely utilized as the anodic electrodes while $\text{Li}[\text{NiCoAl}]\text{O}_2$, $\text{Li}[\text{MnNiCo}]\text{O}_2$, LiCoO_2 , LiFePO_4 , and LiMn_2O_4 are used as the cathodic electrodes [13, 72]. Standard electrolytes are liquid and lithium salts like LiClO_4 , LiPF_6 , LiAsF_6 , LiCF_3SO_3 and LiBF_4 in non-aqueous organic materials for example, ethylene or polyethylene carbonate or dimethyl carbonates [2].

Figure 1 shows the working method of LIBs. To charge the battery, the electrodes must be connected to an external power source and thus the electrons will move from the positive electrodes to the negative electrodes via the outer circuit. Li^+ ions are also released as a result of an electrochemical reaction and these ions move from the cathode to the anode by the electrolyte. The opposite occurs during the discharge state, in which the electrons are released to move from the negative to the positive electrode and Li^+ ions also transfer internally by the electrolyte from the anode to the cathode [2].

Intrinsically conductive polymers (ICPs) have gained remarkable research interest to improve the properties of traditional LIB electrode materials.

2.1.1 PNCs as Electrolyte for the LIBs

Electrolyte exist between both the cathode and the anode. It is an essential component in LIB and it can communicate electronically with all the parts of the battery involving the electrodes and the separator. The main function of electrolyte is enabling the transferring of lithium ions from cathode to anode within charge process and an opposite movement in discharge state. Whereas, the operating temperature, operating potential, energy density, cyclic life and stability of the batteries rely upon at the electrolyte. So, electrolyte has a great impact on the overall performance [2, 60].

Liquid electrolyte dependent on organic solvents suffers from several defects which include high flammability, unhealthy gas production upon reaction and potential for leakage. In addition, LIBs with liquid-electrolyte are grown of dendrites which is an irregular microfiber made of metallic lithium that grow from the Li material during rapid charge and discharge states and can move through the electrolyte to the other electrode. When the applying current passes through these dendrites, it creates a short circuit in the batteries and the battery temperature will rise rapidly which could lead to a fire [2, 58, 59].

However, these disadvantages have no impact on the polymer electrolyte because the electrolyte does not contain any liquid. In addition, the polymer has several benefits as it resists changes that occur in the size of the electrode during charge and discharge states; thermally, mechanically and chemically stable; flexible; light weight and easy to process [2]. Thus, polymer electrolyte is significant part which is widely utilized in energy storage devices [62].

Nanocomposite polymer electrolyte has replaced the liquid electrolyte which leads to advanced LIB. In [74], a novel method was utilized to prepare nanocomposite polymer electrolyte. The authors have introduced an in-situ preparation approach of tin oxide nanostructures in the polyethylene oxide (PEO) resin. The fabricated polymeric electrolytes have demonstrated an ionic conductivity of about 1.1×10^{-4} S/cm at 300 K.

In [25], polymer nanocomposite has been synthesized. PEO has been used as polymeric resin and different contents of plasticizer LiCF_3SO_3 and nanostructured alumina (Al_2O_3) were employed as additive. It has been observed that adding plasticizer and nanostructured Al_2O_3 leads to increasing in the conductivity from 10^{-7} to 10^{-5} Scm^{-1} . The increasing in conductivity has been attributed to the decreasing in crystallinity when adding Li salt, nanostructured Al_2O_3 , and LiCF_3SO_3 into the SPE. The mechanical characteristics of PEO also reduce when adding lithium, nanostructured Al_2O_3 , and plasticizer salts.

Shim et al. have synthesized polymer nanocomposite electrolytes using the branched graft co-polymer (BCP) with poly (ethylene glycol) methyl ether methacrylate (PEGMA) and MA-POSS as polymeric resin and PEG-grafted graphene (PGO) as additive. Polymer nanocomposite composed of 0.2 wt% of PGO has demonstrated ionic conductivity of 2.1×10^{-4} Scm^{-1} at 30 °C where BCP has exhibited 1.1×10^{-5} Scm^{-1} at the same temperature. The mechanical and thermal stability of the nanocomposite have been enhanced even at the high temperatures above 150 °C [26].

2.1.2 PNCs as Cathode Electrode for the LIB

As stated previously, LIB contains two electrodes, one of them is positive, the cathode, and the other is negative and named as anode. Besides, the electrodes greatly influence the performance of LIB as it has a role in changing the energy density, power density, cyclability and cell voltage. The cathode represents 40% of the full battery cost. Therefore, several factors must be taken into account when selecting cathode material involving: the cathode material must demonstrate high free energy of reaction with lithium, thus it can exhibit high cathode voltage, must contain sufficient content of lithium, must possess high conductivity, should be inert toward the non-aqueous liquid-based electrolytes, should possess large capacity and charging/discharging long-term cycles, and should be nontoxic, inexpensive and not harmful to the environment [2, 85, 87].

In [23], a supramolecular structure of PANI and V_2O_5 has been prepared via electrostatic layer-by-layer process (ELBL). Powerful ionic interaction and hydrogen bonding between the ingredients resulted in special characteristics in ELBL film [2, 23].

The authors in [24] have synthesized a nanocomposite which contains PANI and vanadium oxide (V_2O_5) using reverse micelle technique. Also, the electrochemical performance of V_2O_5 and V_2O_5 /PANI nanofibers were assessed. It was observed that V_2O_5 nanofibers exhibit high capacity fading, however polymer nanocomposite with 30% PANI demonstrates capacity of 300 mAhg^{-1} . It was found that the polymer nanocomposite has maintained the morphology while V_2O_5 has changed it after electrochemical cycling. The PANI has the ability to suppress the stress produced by volume alters within cycling, giving rise performance and capacity [2, 24].

The sulfur cathode has been introduced as the future cathode for LIB owing to benefits involving its high theoretical capacity of 1672 mAhg^{-1} , its cheap price and its environment friendly. However, it has several disadvantages that inhibit its practical applications such as poor ionic and electronic conductivities, "shuttling reaction" because of the dissolving of polysulfide interfaces into electrolytes, and large volume alters during the charge/discharge mechanisms. Therefore, in the past decade, many reports have been performed to improve the features of sulfur (S) electrode employing a hybrid of carbon/polymer structure. Wu and coworkers have used chemical oxidation polymerization of PANI as a coat which has increased twist the multi-wall carbon nanotubes (MWCNTs)-core/S-shell nanocomposite. The MWCNT in the PANI/S/MWCNT hybrid has increased the conductivity and stability. The PANI decorating has formed an obstruction for dissolving of intermediate polysulfides, and has facilitated Li^+ transmission to the cathode. Therefore, all of that has enhanced in the electrochemical performance. The PANI/S/MWCNT electrode had an original discharge capacity of 1334.4 mAhg^{-1} and residual capacity of 932.4 mAhg^{-1} after 80 cycles. It was found that the rate of the PANI/S/MWCNTs was double that of the MWCNT/S electrode [35, 45].

In [22], freestanding V_2O_5 nanoarray-based cathode was fabricated. Firstly, a V_2O_5 nano-belt array (NBA) was grown onto a 3D graphene foam which is also named ultrathin graphite foam (UGF). After that, V_2O_5 was coated

with a mesoporous film of the poly(3,4-ethylenedioxythiophene) (PEDOT). The PEDOT/UGF/ V_2O_5 composite electrode has demonstrated an effective capacity of 297 mAhg^{-1} at 1°C .

2.1.3 PNCs as Anode Electrode for the LIBs

An important effort of research has been done to generate new materials to serve as an anode (negative electrode). The anode materials play a crucial role as it is responsible for the energy and power densities and life-cycle of the batteries [2].

Xu and coworkers have grafted the surface of $\text{Li}_4\text{Ti}_5\text{O}_{12}$ with PTh using an oxidative polymerization process which results in a core-shell nanocomposite. The fabricated structure demonstrated specific discharge capacity of 168.2 mAhg^{-1} at 1 C rate. The superb electrochemical merit can be attributed to the enhancement in the electronic conductivity which was obtained by PTh coating that can ease electron movement during the charging/discharging states [2, 20].

Li and coworkers have explored the synergistic advantages of nanocomposite electrode composed of on graphene, PEDOT and MnO_2 . The PEDOT/ MnO_2 /graphene hierarchical nanocomposite shows a high reversible Li capacity of 948 mAhg^{-1} over 15 cycles at $50 \text{ mA}\text{g}^{-1}$. The authors have attributed the enhancement in electrochemical performance to its special component. MnO_2 in the fabricated core-shell composite has properties of an open structures with distances between layers of about 72 \AA , promoting Li intercalation/deintercalation process for high Li storage. The high conductivity of 3-D graphene layers enhances the charge transmission to improve rate performance. The PEDOT decorating offers a flexibility features for MnO_2 develop and inhibits its ingathering for regular distribution, leading to better large volume extending during battery operation for the reversible capacity [34, 35].

Silicon (Si) is a hopeful negative electrode for future LIBs, nevertheless its applications is restricted owing to its low cyclability. Chen and coworkers have proposed a facile method to improve the long-term cyclability of Si anodes. They have synthesized a Si/PPP (polyparaphenylene) composite with core-shell design using Si nanoparticles into a conductive polymer of lithium ions. Si additives serve as effective Li-storage stage while the polymer accommodates the volume change and prohibits the direct interface of Si surface with electrolyte, in order to preserve the mechanical integrity of Si electrode. The nanocomposite shows an efficient capacity of 3184 mAhg^{-1} with a prime coulombic efficiency of 78%, a superior rate capability with capacity of 1670 mAhg^{-1} even at an elevated rate of 16 Ag^{-1} and a long-term cyclability. It retains 60% of capacity after 400 cycles, showing a great probability to work as anode for LIB application. Also, this core-shell structure can be employed for other Li-storable metals to serve as anode materials for LIBs [33].

In [77], PANI/Si composite as anode material for LIBs was synthesized using a chemical polymerisation of aniline in the presence of Si fillers. The composite exhibits a reversible specific capacity of 840 mAhg^{-1} after 100 cycles at a $100 \text{ mA}\text{g}^{-1}$ and superb cycling stability.

Kummer et al. used the gas-phase synthesis to produce Si nanoparticles. The electronic conductivity of Si nanoparticles was enhanced by adding one percent of boron. After that polymerization of the monomers was used in order to prepare PANI/Si nanocomposite. The obtained polymer nanocomposite consists of 50 PANI and 50% Si with a size of 40 nm. An anode that consists of 20% of the Si/PANI has achieved an primer charge capacity of 561 mAhg^{-1} with a Coulombic efficiency of 66%. After 300 cycles, the electrode exhibited discharge capacity of 390 mAhg^{-1} . It was observed that the existence of PANI has a great role in increasing electronic conductivity and providing pre flexible merit in the prepared composite as it also controls the volume changes of the silicon particles [2, 19].

Adding PANI has an important impact on titanium dioxide (TiO_2) additive as electrodes for LIBs. PANI- TiO_2 nanocomposite have been fabricated via mechanical mixing or solid coating procedure using different ratios of PANI. The maximum capacity of 281 mAhg^{-1} at 20 mA g^{-1} was achieved when 15% of PANI was used. Over 100 cycles, the composite with 15% PANI have maintained 43.7% of its original capacity, 168.2 mA g^{-1} at a high rate of 200 mA g^{-1} [2, 18].

A nanocomposite of reduced graphene oxide/ SnO_2 /PANI (rGO/ SnO_2 /PANI) was prepared and used as anodic electrode of LIBs. The synthesise process begins with scattering SnO_2 particles on the two-dimensional sheets of the GO, then SnO_2 is covered with a thin layer of PANI in order to improve the electric connection in the designed composite. Figure 2 (a) shows the cycling performance of three anodes utilizing SnO_2 , SnO_2 /rGO and rGO/ SnO_2 /PANI. In comparison with the pure SnO_2 electrode, it was observed that the anode material with the SnO_2 /rGO structure has showed low cyclic stability although it has demonstrated better cycling performance. The anode with the rGO/ SnO_2 /PANI structure showed considerable capacity of 1017 mAhg^{-1} for the second cycle. Beyond 200 cycles, its capacity still remained at a high magnitude of 1280 mAhg^{-1} . The rate performance of three anodes is illustrated in Fig. 2(b). The triple composite demonstrated excellent rate capability by providing 397 mAhg^{-1} capacity at a current density higher 10 A g^{-1} [2, 21].

In [61], core-shell with hollow SnO_2 /PPy composites with superior electrochemical feature have been prepared by a hydrothermal approach accompanied by a chemical-polymerization route. As an anode in LIBs, the nanocomposite has retained a large capacity of 448.4 mAhg^{-1} over 100 cycles with a coulomb efficiency of more than 97%. Moreover, the nanocomposite has a very good cycling stability owing to the special structured core-shell and a potential significant impact between the PPy covering sheet and the hollow SnO_2 sphere. The PPy covering prohibits the potential crunch of the SnO_2 nanoparticles, and it also prohibits the SnO_2 /Sn spheres from accumulating. In addition, the empty space inside the SnO_2 spheres efficiently reduces the massive volume alter pending charging-discharging process.

Graphite is commonly employed as anode electrode for LIB owing to its excellent cycling performance. However, it has a disadvantage of low theoretical specific capacity. Thus. There is an urgent need to discover an effective anode with large specific capacity. Si insufficient cyclic stability. To solve this issue, many researchers have prepared other materials as anode for LIBs [90]. In [78], (Si/graphite/PANI) nanocomposite has been synthesized using the polymerisation of aniline in the existence of nano-sized Si and graphite. The nanocomposite composed of nanosized

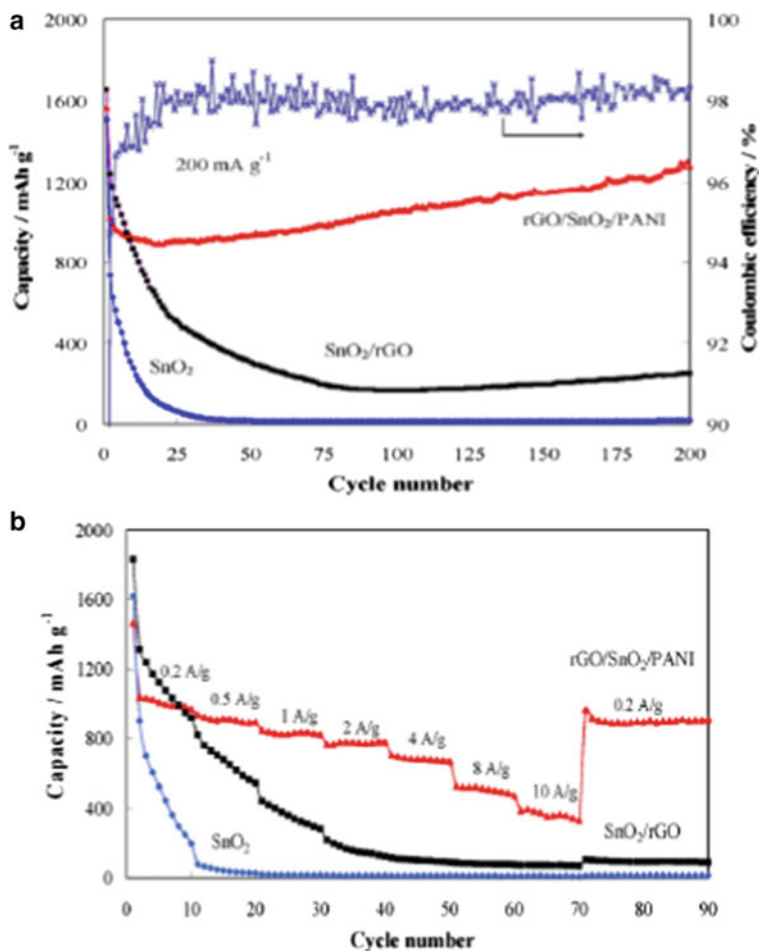


Fig. 2 **a** Cycling and **b** rate performance of the electrodes with SnO₂, SnO₂/rGO and rGO/SnO₂/PANI. Reprinted from Journal of Solid-State Ionics, Vol 294, Hao Liu, Bin Hong Liu, Zhou Peng Li, A rGO/SnO₂/PANI composite for the anode of LIBs, 12., Copyright (2016), with permission from Elsevier [21].

Si and graphite (G) with a uniform distribution in a PANI matrix. The nanocomposite demonstrates a high reversible specific capacity of 1392 mAhg⁻¹ for the first cycle and a stable capacity retention with 866 mAhg⁻¹ after 95 cycles. It was found that pure Si has only delivered reversible capacity of 888 mAhg⁻¹ and 425 mAhg⁻¹ for the first and the 95th cycles, respectively. The electrochemical performance has been improved owing to the good electric contact of active compositions, enhanced impregnation of Si additives, and high structural stability of the nanocomposite electrode through the charging-discharging process, which significantly arise from the existence of PANI.

In [79], A new nanocomposite composed of gas phase obtained nanosized Si, CNTs, and PANI has been prepared as a negative electrode for LIBs. Each component in the nanocomposite plays an important role. Si additives offer high capacity, CNTs providing great electric conductivity and flexibility system, and PANI improves the electrical conductivity. The nanocomposite has demonstrated a high reversible capacity of 2430 mAhg^{-1} .

In [86], silicon nanoparticles-PEDOT (SiNPs-PEDOT) composites have been fabricated by in situ thermal polymerization approach. The composite has employed as anode material and it has compared to ex-situ SiNPs-PEDOT nanocomposite. It was found that the in-situ polymerized nanocomposite has exhibited improved conductivity and rate capability.

2.2 PNCs Based Materials for Supercapacitor

Supercapacitor is one of the most common energy storage system [2]. It is named as electrochemical capacitor [69]. Supercapacitors offer higher energy densities than dielectric capacitor and higher power densities than battery [13]. In addition, charging and discharging in supercapacitors is very fast, owing to feature of the storage process without slow electrochemical reaction. Supercapacitor can retain performance for millions of charge/discharge cycles due to there is no any irreversible chemical reaction occurs at the electrodes in an electric double-layer capacitor, while batteries can only maintain performance for 1000 cycles [2, 56, 57].

The supercapacitor possess two electrodes detached via a dielectric electrolyte [2]. Within the improvement of a supercapacitor, the choice of the anodic electrode is one of the most significant parameters [54, 55].

2.2.1 The Impact of Conductive Polymers on Supercapacitors

Conductive polymer plays a vital role in pseudocapacitor. In [60], the impacts of various conductive polymers in electrode composites were investigated. In this paper, zinc sulfide/rGO (ZnS/RGO) nanocomposites have been fabricated by the hydrothermal approach. Also, in situ polymerization was employed to dope conductive polymers (PANI, PPy, PTH and PEDOT) on the ZnS/RGO composites. It was found that ZnS/RGO/PANI ternary electrode nanocomposite outperforms the other polymer-coated composites in capacitance performance and cyclic stability. For the three-electrode design, the discharge specific capacitance and cycle stability of ZnS/RGO/PANI were 1045.3 Fg^{-1} and 160% respectively at 1 Ag^{-1} after 1000 cycles. However, for a two-electrode design, the discharge specific capacitance and cycle stability were 722.0 Fg^{-1} and 76.1% at 1 Ag^{-1} after the same number of loops.

2.2.2 PANI and Metal Oxide Nanocomposites

PANI is commonly used in fabricating of supercapacitors due to its pseudocapacitive characteristic. However, PANI as a pure material has some defects. To solve this issue, nanocomposites can be prepared by merging PANI with other material [70]. Synthesis and experiments have been performed on components of PANI and MOs like MnO_2 , SnO_2 and MnWO_4 . In the PANI/MO composite, PANI not only acts as an electroactive material for energy storage, however also as a strong covering layer to prevent MOs from dissolving in acid electrolytes [3].

Chen and coworkers successfully prepared PANI – MnO_2 nanocomposite with excellent performance. The preparation steps were as follows: First, hydroxylated MnO_2 nanoparticles were adjusted on the surface using a silane coupling agent, triethoxysilylmethyl N-substituted aniline (ND42) which resulted in improvement in the interaction of MnO_2 and PANI, then the resulted surface modified MnO_2 (ND/ MnO_2) were cleaned and dried. The polymerization of aniline and ND/ MnO_2 composite was incorporated on a carbon cloth in an electrolyte dispersion having ND/ MnO_2 , aniline, H_2O_4 and $(\text{NaPO}_3)_6$. Successive cyclic voltammetric scans were preceded the co-polymerization. The electro-co-polymerization method was also used for the preparation of pure PANI and PANI/ MnO_2 composite. PANI/ND/ MnO_2 nanocomposite film has shown an average specific capacitance of 80 Fg^{-1} , with steady coulombic efficiency of 98% during 1000 cycles. It also has exhibited high intrinsic electronic conductivity and good kinetic reversibility. The authors has ascribed the superior characteristics to the enhanced interaction between PANI and MnO_2 and the increase in the effective surface area of the PANI – MnO_2 film as a result of the surface adjustment of MnO_2 nanoparticles using the silane coupling reagent. The findings also revealed that PANI/ND/ MnO_2 composites are

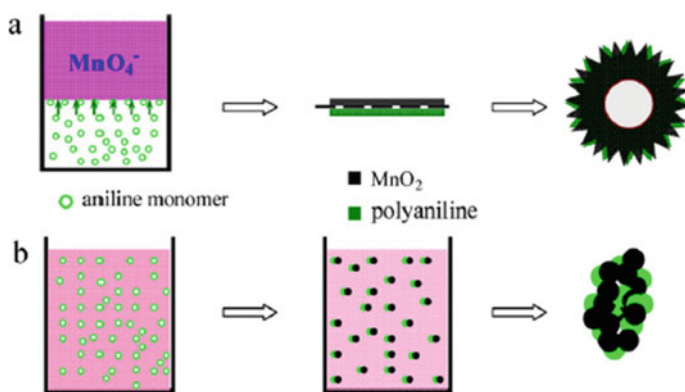


Fig. 3 Demonstration of the preparation mechanisms of MnO_2 /PANI nanocomposites: **a** interfacial synthesis and **b** chemical precipitation reproduced with permission from [10]

very fascinating electrodes with great potential to act as electrodes for supercapacitors and have demonstrated the significance of the interaction between PANI and MnO_2 which results in an improvement in capacitive properties [9].

Wang et al. have developed a creative way of synthesizing PANI– MnO_2 nanocomposites which is named interfacial synthesis method. The composite was prepared using the interface between an organic solution and an aqueous solution. Initially the organic solution was formed by dissolution of aniline monomers into inorganic Trichloromethane (CHCl_3) solution, then the aqueous solution was prepared by dissolution of potassium permanganate in filtered water and adding many drops of hydrochloric acid to the aqueous KMnO_4 solution to modify the pH value to 1. Once the second solution was inserted to the first solution, the interface was created instantly between the two phases and the reaction occurred [3, 10]. Aniline was spread from the organic solution to the interface through the reaction and was chemically oxidized into PANI. Simultaneously, MnO_4^- was reduced to manganese oxide deposit. Eventually, the MnO_2 – PANI composite was shaped and retained in the aqueous liquid. Also, the traditional MnO_2 – PANI composite was prepared using chemical co-precipitation for the aim of comparison [3, 10]. Both synthesis methods were illustrated in Fig. 3.

Figure 4 shows that MnO_2 – PANI composite that was synthesized by interfacial technique has a greater surface area ($124 \text{ m}^2 \text{ g}^{-1}$) and more uniform pore-size distribution than the nanocomposite that was fabricated by chemical precipitation method [3, 10].

The interfacial prepared MnO_2 /PANI nanocomposite electrodes show a higher specific capacitance of 262 F g^{-1} which is, approximately double the specific capacitance of chemical co-precipitation based MnO_2 – PANI composite. It also achieved better rate capability and stable cyclability. The authors rationalized the observed improved electrochemical features of the interfacial MnO_2 – PANI composite electrode to its special hollow microstructure, porosity and the presence of conducting PANI. It was found that the enhancement of MnO_2 – PANI composite offers promising applications in electrochemical capacitors [3, 10].

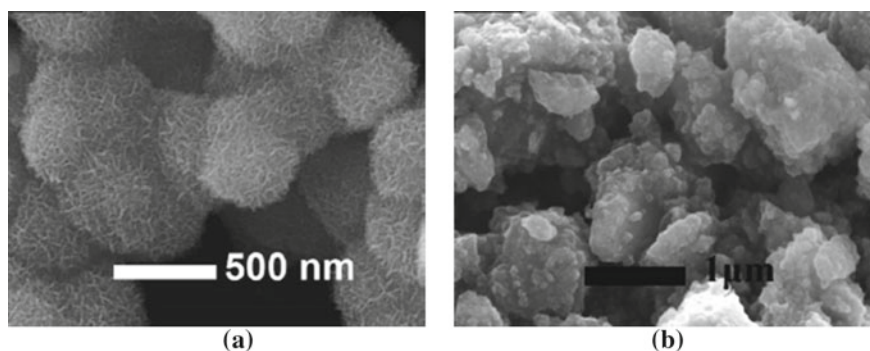


Fig. 4 SEM micro-images of MnO_2 -PANI nanocomposites fabricated via **a** interfacial synthesis and **b** chemical co-precipitation (reproduced with permission from ref. [10])

PANI – MnWO₄ composite was prepared using in situ polymerization through ultrasonication. The composite possesses good electrochemical characteristics with 50% of MnWO₄ loading. The PANI – MnWO₄ nanocomposites that fabricated using in situ polymerization demonstrate high specific capacitance of 475 Fg⁻¹ which is, much greater than that of the physical admixture of PANI and MnWO₄ (346 Fg⁻¹). PANI/MnWO₄ nanocomposites are considered to be appropriate electrode materials for supercapacitor application [11].

In [75], SnO₂ nanostructure and SnO₂/PANI composites have been prepared via a solution-route technique. Electrochemical characteristics of SnO₂ and SnO₂/PANI electrodes have investigated in a supercapacitor. The electrode of SnO₂/PANI was demonstrated larger specific capacity.

2.2.3 Supercapacitors Prepared from Graphene–PANI Composite Films

PANI has a high theoretical particular pseudocapacitance of 2000 Fg⁻¹, special rapid redox and acid–base doping/dedoping characteristics. Electrode materials have a huge effect on the performance of supercapacitor [63]. Combining graphene with PANI is one of the most significant research topics [63]. Graphene-based composites have gained increasing attention over the past years [71]. The graphene-PANI composites merge the advantages of electrical double-layer capacitance of graphene and pseudo-capacitance of PANI, leading to long cycle life and high energy densities [67].

Cheng and his colleagues have prepared a flexible and freestanding graphene/PANI nanocomposite paper by means of an in-situ anodic electrochemical of polymerized aniline into a PANI films on graphene sheet. Flexible graphene–PANI composite electrode has demonstrated significant advantages, such as a) enhanced electrical conductivity in PANI as a result of existence of the graphene sheet, and b) Accessibility of homogeneous ions and high interfacial charge uptake within the stacked design of the graphene–PANI composite. Graphene-PANI electrode exhibited an appropriate tensile strength (12.6 MPa). It also showed a volumetric capacitance and a gravimetric capacitance of 135 Fcm⁻³ and 233 Fg⁻¹, respectively [7].

In [64], graphene/PANI nanocomposites were chemically produced. The fabrication process depends on chemical reaction at liquid–liquid contacts, starts with benzene and aniline and at last produces composites as nanothick layers of polyaniline combined with graphene. The composites have demonstrated a specific capacitance of 267.2 135 Fcm⁻³.

Hierarchical nanocomposites have been fabricated by vertical alignments 1 – DPANI wire arrays on oxidized graphene substrate. Concentrations of aniline monomers and GO can be adjusted in order to modify the morphology of PANI nanowires. When utilized as electrodes in supercapacitor, the composite demonstrated a particular capacitance of 555 Fg⁻¹ at a low current density of 0.2 Ag⁻¹,

which is better than each electrode alone, owing to a mutual impact of PANI and graphene oxide [6, 49].

In [59], the authors have prepared hierarchically materials comprising of layered PANI nanowire forests non-covalently connected with single-layered graphene via a new fabrication approach. When tested as supercapacitor electrodes, the hierarchical nano-structures exhibited a specific energy density of 137 Whkg^{-1} and a power density of 1980 Wkg^{-1} for the three-layered structured electrodes. This research suggested an easy way to prepare an electrode for supercapacitors with high power density and high energy density [6, 50].

Phase-separated PANI/rGO composite was fabricated using electrochemical precipitation of PANI distributed exterior the rGO hydrogel. The composite electrode achieved a high specific capacitance of 783 Fg^{-1} at a high current density of 27.3 Ag^{-1} , which represents 99% of the result at a current density of 1.14 Ag^{-1} , exhibiting a superior performance. It was found that the phase-separated nanostructure is useful to the propagation of electrolyte, so the rate performance of the composite can be significantly enhanced [6, 38].

Another widely used procedure is physical combining of graphene and polymer in a given solvent because it is straightforward and allows easy processing of the solution. In [39], nanocomposite of chemically transformed graphene (CCG) and PANI nanofibers (PANI – NFs) has been fabricated using filtering the vacuum of the combined dispersions of both materials. It has showed a mechanical stability and a superior flexibility. Supercapacitor device which was fabricated using this composite film was demonstrated a high electrochemical capacitance of 210 Fg^{-1} at a discharge rate of 0.3 Ag^{-1} [6, 39].

The impact of graphene surface chemistry on the electrochemical performance of graphene/PANI composite as supercapacitor electrode has been investigated. GO, rGO, N-added rGO and amine-doped rGO were employed as carriers and loaded with PANI via non-covalent interaction. The surface chemistry has already performed a crucial role in the growth of PANI, which in turn has affected the amount of increment in specific capacitance. In the three-electrode system, the amine-modified rGO exhibited the maximum increment in specific capacitance of up to 500 Fg^{-1} at a scan rate of 2 mVs^{-1} and an increment in capacitance by a factor of 1.19 at 680 cycles. Nitrogen-doped rGO was employed as the cathode material whereas amine-modified rGO/PANI was used as anode material. The specific capacitance of the full cell was 79 Fg^{-1} at scan rate of 10 mVs^{-1} . This work illustrates the significance of graphene surface chemistry in the determination of final electrochemical performance [6, 37].

A hydrothermal treatment was used to fabricate a hierarchical PANI – rGO/cellulose fibers (CF) nanocomposite paper through “dipping and desiccation”. The PANI – rGO/CF paper with a PANI precipitation time of 72 h has demonstrated a specific capacitance of 464 Fg^{-1} at a current density of 1 Ag^{-1} , which was higher than the nanostructured rGO/CF paper and compact rGO/CF paper. The additional increase of the PANI precipitation time leads to a decline in the specific capacitance for the PANI – rGO/CF paper, owing to the decrease in both of the specific surface area and electrical conductivity. However, the nanostructured rGO/CF composite paper has showed a less decrease in specific capacitance when the

scan rate was increased. Also, the porosity in rGO/CF structure has proven effectiveness in preventing the rGO sheets from accumulation and allowing ion propagation. The specific capacitance of PANI – rGO/CF nanocomposite sheet in all solid supercapacitors is approximately 224 Fg^{-1} at a low current density of 0.1 Ag^{-1} , and the paper retained 89% of the maximum capacity after 1000 cycles [8].

Xiong et al. synthesized ternary cobalt ferrite/graphene/ PANI nanocomposite using a simple method. First, hydrothermal process was employed to obtain cobalt ferrite nanoparticles dispersed on graphene sheets. Then the surface of CoFe_2O_4 /graphene sheets was coated with PANI through in situ polymerization method then the gravimetric capacitance was measured in three electrodes system to be 1133.3 Fg^{-1} at rate of 1 mVs^{-1} [31]. After 5000 cycles the nanocomposite has retained more than 96% of the initial capacitance which indicates superior cycling stability. Figure 5 shows the preparing approach of cobalt ferrite/graphene/PANI nanocomposite. This work has studied CoFe_2O_4 /graphene/ PANI nanocomposites as electrode material for supercapacitors [31].

PANI has some drawbacks such as poor cyclic and mechanical stability. Carbon nanotubes (CNTs) are beneficial because they possess high electrical conductivity and high aspect ratios. rGO is another carbon nanomaterial which has a 2-D structure, and it is also have many benefits such as large specific surface area, high flexibility and tensile strength. These advantages of rGO leads to an increment in the cyclic stability [40–42]. PANI/CNT/rGO nanocomposite was prepared and tested as an electrode material for supercapacitor. PANI has offered pseudocapitance to the nanocomposite and CNT has increased the surface area which enhance electron transport. The ternary compound has achieved a specific capacitance of 312.5 Fg^{-1} and it had an excellent interfacial interaction between the CNT and PANI. CNTs have also decreased the restacking of GO. PANI/CNT/rGO nanocomposite is promising electrodes owing to its special structure and suitable interfacial interactions [40].

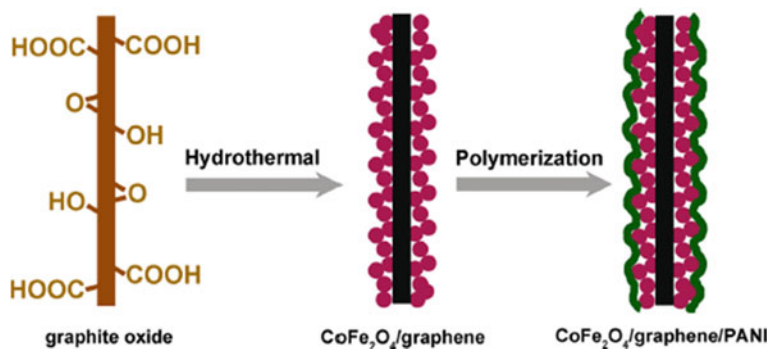


Fig. 5 Preparation of ternary CGP nanocomposites. Reprinted from Journal of Power Sources, Vol 245, Pan Xiong, Huajie Huang, Xin Wang, Design and synthesis of ternary cobalt ferrite/graphene/PANI hierarchical nanocomposites for high-performance supercapacitors, 938., Copyright (2014), with permission from Elsevier [31]

2.2.4 PANI–MoS₂ Nanocomposite

In [27] PANI–molybdenum disulfide composite (PANI –MoS₂) was prepared via in situ polymerisation of aniline onto MoS₂ utilizing HCl as the additives. PANI –MoS₂ nanocomposite demonstrates a highest specific capacitance of 687 Fg⁻¹ at a scan rate of 5 mVs⁻¹ through cyclic voltammetry (CV) and a C_{sp} of 612 Fg⁻¹ at a current density of 0.2 Ag⁻¹ employing chronopotentiometry (CP). Moreover, the nanocomposite shows a high energy density of 128 Whkg⁻¹ with a highest power density of 9.8 kWkg⁻¹ and a superb cyclic stability with 93% capacitance preservation after 2000 times charging/discharging cycle. cycles. These excellent electrochemical findings demonstrated the ability of PANI–MoS₂ composites to be an electrode for supercapacitor.

In [76], PANI–MoS₂ nanocomposite was prepared via self-stabilized dispersion polymerization approach. This nanocomposite has demonstrated high electrical conductivity of 28.6 Scm⁻¹. PANI–MoS₂ nanocomposite has showed larger energy density (4.7 Whkg⁻¹ at 1000 Wkg⁻¹) than traditional electrochemical capacitors.

2.2.5 PANI–MnFe₂O₄ Nanocomposite

In [80], a nanocomposite of magnetic PANI decorated with manganese ferrite was prepared using in situ polymerization as electrode material for supercapacitor. PANI–MnFe₂O₄ nanocomposite has demonstrated large capacitance of 371 Fg⁻¹ and superb cycle life.

2.2.6 PANI–NiFe₂O₄ Nanocomposite

In [81], PANI–NiFe₂O₄ nanocomposites have been fabricated using in situ-chemical oxidative polymerization approach. The nanocomposite with low percentage of NiFe₂O₄ loading has been demonstrated higher SC of 448 Fg⁻¹ compared to PANI (292 Fg⁻¹) and other PANI –NiFe₂O₄ nanocomposites. Thus, the fabricated PANI–NiFe₂O₄ nanocomposites can be used as appropriate electrodes for redox supercapacitor.

2.2.7 Graphene/PPy

PPy has also been employed as a conductive polymer for supercapacitor electrode due to its high electrical conductivity and high environmental stability and ease of manufacture [7, 73]. In the recent decades, graphene/PPy composites have been used extensively as electrode material for sucapacitors [6].

Biswas et al., prepared multilayer graphene/ PPy composite material by merging the nanolayered PPy with highly conductive graphene sheets to obtain high specific capacitance and low electronic resistance for supercapacitor electrode application.

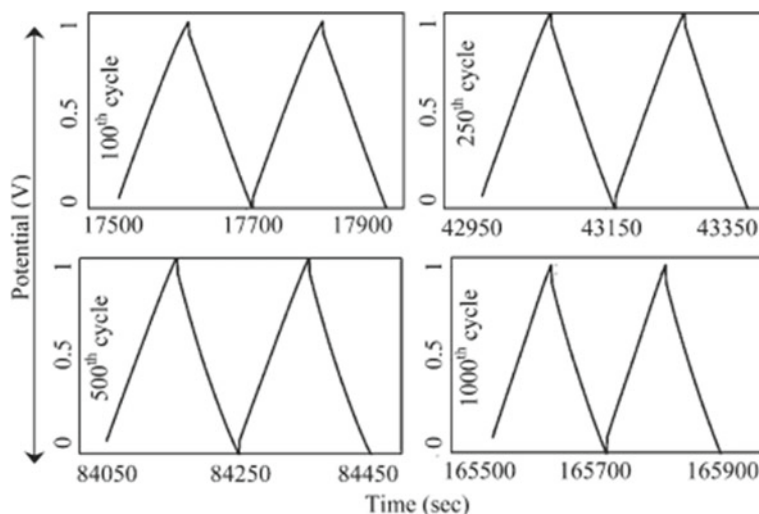


Fig. 6 Cyclic stability at 1Ag^{-1} constant current density. Reprinted with permission from (ref. [30]). Copyright (2010) American Chemical Society.”

The specific capacitance of synthesized multilayer composite electrode was 165 Fg^{-1} at current density of 1 Ag^{-1} discharge current density even after 1000 electrochemical cycles and high electrochemical cyclic stability. Figure 6 demonstrates that the multilayer composite of PPy and graphene nanosheets retain highly symmetric charging-discharging properties from 100 to 1000th electrochemical cycles [30].

In [66], Graphene/PPy has been prepared using chemical polymerisation approach. Electrochemical impedance spectroscopy (EIS) measurements were utilized for studying the frequency response characteristics of supercapacitor based on graphene/PPy composite. The conductive Graphene-PPy demonstrated higher knee frequency at 125 Hz than the knee frequency of pristine PPy at 36 Hz. The nanocomposite has demonstrated specific capacitances of 270 Fg^{-1} at 0.1 Hz and 112 Fg^{-1} at 125 Hz.

Another study was carried out by Lee et al. to develop an excellent nanoarchitecture composed of PPy and graphene sheets via polymerization method. graphene nanosheets act as a support medium for the electrochemical use of PPy and provide a path for electron transfer. The nanocomposite achieved a specific capacitance of 267 Fg^{-1} at a scan rate of 100 mVs^{-1} compared to 137 mVs^{-1} for PPy [7, 12]. Compared to individual graphene and PPy, graphene-PPy nanocomposite has an enhanced electrochemical performance which was ascribed to a) the oxidation or deoxidation of α - or β -C atoms in the PPy rings with the help of graphene nanosheets. b) Attaching PPy on the surface of GNS plays a role in decreasing the propagation and migration length and promoting the electrochemical use of PPy. c) Synergistic impact between PPy and GNS [12]. The energy density and power density were 94.93 Whkg^{-1} and 3797.2 Wkg^{-1} respectively. It was revealed that the specific capacitance has decreased only

by 10% after 500 cycles, showing an improvement of electrochemical cyclic stability of the nanocomposite [12].

Zhao and co-workers have used a general method to prepare layered GO nanostructures with sandwiched conducting polymers. This method depends on electrostatic interactions between GO sheets charged with a negative charge and surfactant micelles charged with a positive charge as shown in Fig. 7. For comparison, two different samples of GO – (conducting polymer) were synthesized. One of the samples is with fibrous morphology of the PPy and the other is with spherical PPy morphology. Electrochemical performance is highly dependent on morphology of the conducting polymer as indicated in Table 1. The GO–(fibrous PPy) nanocomposite, GO–PPy(F) has achieved a high specific capacitance of 510 Fg^{-1} . It was also found that when the current density was increased by 17 times, a high capacitance retention ratio (70%) was achieved [1].

The performance of the GO – (spherical PPy) compound, GO–PPy(S) was similar to that of GO–PPy(F) at low current density. however, when the current density rose, the performance of GO–PPy(S) was more regrettable than that of GO–PPy(F). It was observed that both the capacitance of GO–PPy(F) and GO–PPy(S) were much superior than that of net PPy. In addition, more than 70% of the initial capacitance was preserved for the compound electrode GO–PPy(FS) after 1000 cycles, whereas just 30% was maintained for the net PPy(F) electrode, demonstrating a better cycle capability of the compound material than the pure polymer electrode.

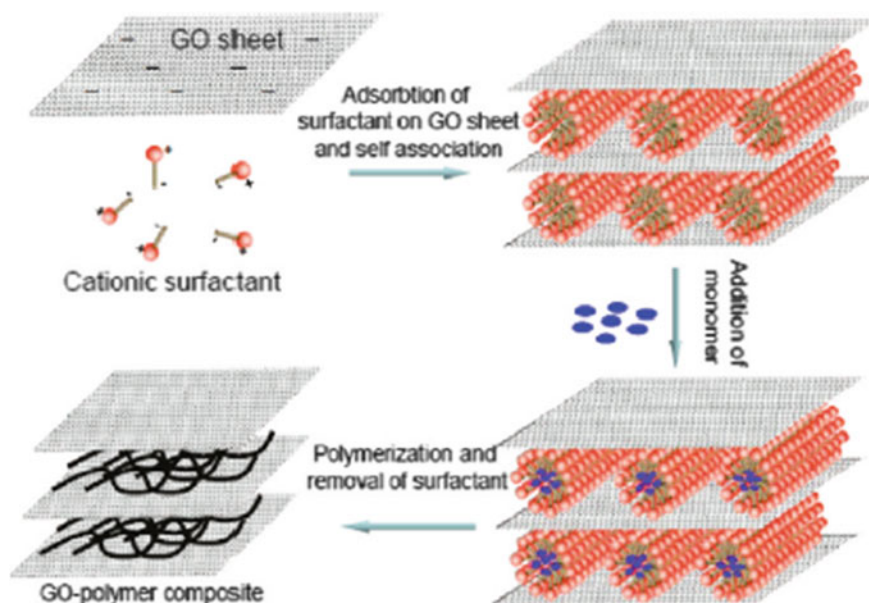


Fig. 7 The preparation mechanism of the GO–PPy composite. Reprinted with permission from [1] Copyright 2010, American Chemical Society

Table 1 Specific gravimetric capacitance of various electrodes at different current densities. GOR represents reduced GO in this table. Reprinted with permission from [1] Copyright 2010, American Chemical Society

Samples	0.3 Ag ⁻¹	0.5 Ag ⁻¹	1 Ag ⁻¹	2 Ag ⁻¹	3 Ag ⁻¹	5 Ag ⁻¹
GOR	124	98	92			
GO-PPy(F)	510	480	440	456	374	351
PPy(F)	360	250	175	150	120	130
GO-PPy(S)	528	483	364	307	276	255

Such fabulous findings for graphene-PPY compound electrodes are owing to a) the fact that the scaly GO sheets dispersed in solution yield a large available surface to attach the conductive polymer on both sides; b) the three dimensional layered structure improves the mechanical strength of the compound and stabilizes the polymers within the charging/discharging mechanism; c) the GO nanostructure with conductive polymer columns significantly reduces the dynamic resistance of electrolyte ions; and d) the easily attainable conductive polymers contribute pseudo-capacitance to the total energy storage to a large extent [1].

Subramanian and co-workers have fabricated a supercapacitor electrode by preparing graphene nanolayers using electrophoretic deposition of graphene then these graphene nanolayers have been used as a scaffold for the polymerization of PPy. As shown in Fig. 8, the nanocomposite electrodes structure was highly porous relative to that of the PPy electrodes (Fig. 8 a, b, e, f), and this porosity improved the electrode interaction with the electrolyte. In addition, PPy deposited on graphene uses a very high specific surface area of graphene, and the advantage of this mode of polymerization is that it reveals maximum surface locations for faradic redox reactions of the supercapacitor electrodes. Hence, these graphene-PPy nanocomposite electrode demonstrated a very high specific capacitance of 1510 Fg⁻¹, an area capacitance of 151 mFcm⁻², and a volume capacitance of 151 Fcm⁻³ at 10 mVs⁻¹ [7, 14].

In [6], graphene derivatives involving GO, rGO, NH₂-doped rGO and N-rGO were fabricated and merged with PPy as electrodes for supercapacitor to study the impact of surface functionalization and polymer hybridization on the performance. N-doped rGO/PPy, NH₂-modified rGO/PPy, GO/PPy and rGO/PPy electrodes have demonstrated a specific capacitance of 394 Fg⁻¹, 225 Fg⁻¹, 165 Fg⁻¹, 150 Fg⁻¹ respectively. N-doping of graphene has improved the electronic transfer efficiency and enhanced the surface wettability, which leads to the best electrochemical performance [15].

There are many methods to test the electrochemical performance of flexible supercapacitor under the influence of applying forces. The most common method is compression. 3D noncovalent rGO/PPy foam was used to acts as electrodes in highly compressible supercapacitor. It was found that the foam that was prepared has the ability to always withstand large compressive strains without any structural breakdown or springiness loss. Supercapacitors that are highly tolerant of compression and made from deformable foam electrodes demonstrated a specific capacitance of 360

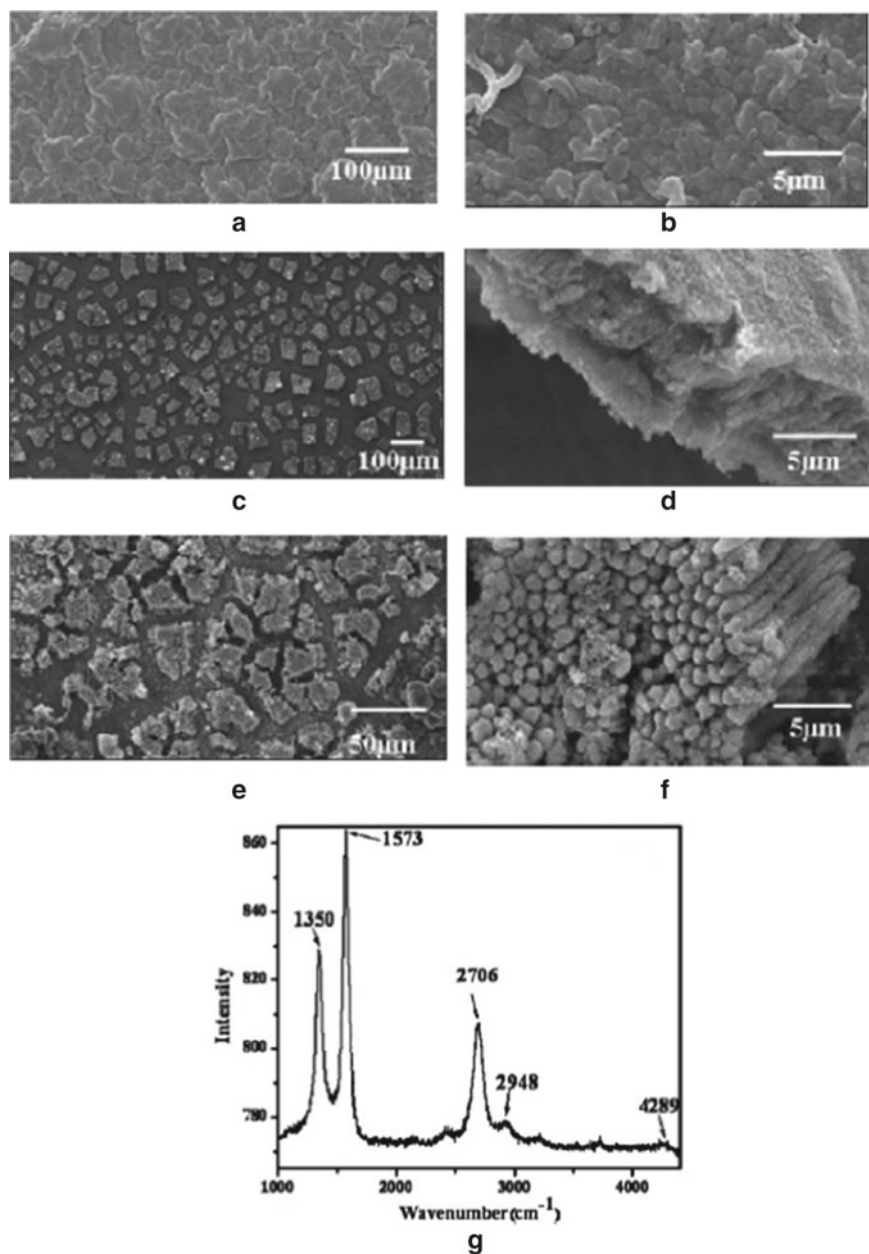


Fig. 8 **a** SEM image showing electropolymerized pyrrole on Ti; **b** magnified image of (a); **c** EPD of graphene on a Ti plate; **d** magnified cross sectional image of graphene platelets; **e** nucleation of polymerization on graphene platelets; **f** electropolymerization of pyrrole on graphene platelets; **g** Raman spectra of graphene. reprinted with permission. [14] Copyright 2011, Royal Society of Chemistry

Fg^{-1} at a current density of 1.5 Ag^{-1} , a good tolerance to compression without significant difference in capacity over 1000 compressive loading and unloading cycles. This research has provided a clear illustration of fabricating developed supercapacitor that shows superior tolerance to extreme conditions including mechanical compression and concussion [16].

Electrodepositing PPy on CVD fabricated nanotubular graphene was used to develop 3D interconnected nanotubular graphene–PPy hybrid material. The bi-continuous nanotubes materials that used as free-standing electrode in supercapacitor has demonstrated a specific capacitance of 509 Fg^{-1} at a low current density of 0.15 Ag^{-1} . In addition, all solid flexible supercapacitor prepared employing the composite materials and PVA/ H_2O_4 gel electrolyte have exhibited a specific capacitance of 514 Fg^{-1} at a low current density of 0.2 Ag^{-1} , an energy density of 21.6 Whkg^{-1} and a power density of 32.7 kWkg^{-1} [6, 17].

In [82], uniform graphene/PPy nanocomposites has been prepared using chemical modification for graphene nanosheets and in-situ polymerization for PPy layers. The nanocomposite has demonstrated a largest specific capacitance of 650 Fg^{-1} at 0.45 Ag^{-1} current density, a largest energy density of 54.0 Whkg^{-1} at 1 mA current, and a largest power density of 778.1 Wkg^{-1} at 5 mA current.

2.2.8 PPy/RGO/Iron Oxide

In [84], PPy/RGO/ Fe_2O_3 nanocomposite film has been prepared using electrodeposition approach. This nanocomposite is a promising electrodes for supercapacitor. Despite the fact that the exitance of Fe_2O_3 increased the electron transfer resistivity between the electrolyte and ternary nanocomposite, it hinders the disintegration of the nanocomposite produced by continuous expansion and contraction during the charging/discharge cycles. The nanocomposite film has demonstrated superb specific capacitance retention even after 200 cycles of charging/discharging.

2.2.9 Cobalt Monoxide (CoO)/PPy

Zhou and co-workers have developed a supercapacitor electrode which has consisted of well-aligned CoO nanowire that has deposited on a three-dimensional nickel foam with PPy uniformly restrained onto or strongly linked to each nanowire surface, Fig. 9(a). The structure of the electrode takes merit of high electrochemical activity from both the CoO and PPy, high electrical conductivity of PPy, and short ion propagation path in the arranged mesoporous nanowires. All of these benefits, coupled with the synergy between CoO and PPy result in a high specific capacitance of 2223 Fg^{-1} that close to the theoretical value, good rate capability, and cycling stability. Larger enclosed CV area in the CV curves, Fig. 9(b), and longer discharging time in the

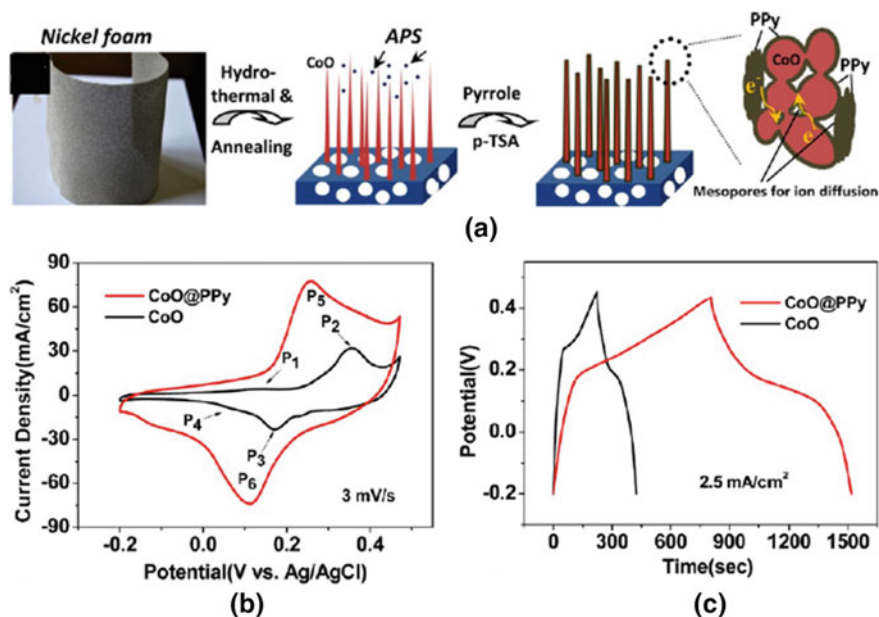


Fig. 9 **a** The representative synthetic method and structure details of the 3D hybrid CoO@PPy nanowire electrode **b** CV curves **c** charge – discharge curves **d** cycling performance of CoO@PPy and the pristine CoO electrodes. Reprinted with permission from (ref. [29]). Copyright (2013) American Chemical Society.”

charging/discharging curves, Fig. 9(c), proves an improved supercapacitive performance in the CoO@PPy electrode than CoO. The CoO@PPy electrode also demonstrates superior cycling stability by maintaining about 99.8% of the capacitance even after 2000 cycles [29].

2.2.10 PPy/CNT Nanocomposites

PPy/CNT nanocomposites are one of the most studied electrodes for supercapacitors [89].

2.2.11 PEDOT Nanocomposite

There are several benefits of PEDOT such as cost effectiveness, flexibility, and good electrical conductivity [65].

The graphene/conducting polymer nanocomposite has many advantages such as rapid charging/discharging mechanisms, high capacitance preservation, low cost and environmentally friendly. rGO/Ag/PEDOT nanocomposite has been fabricated using hydrazine hydrate. The nanocomposite demonstrated superior cycling stability with

retention of 101.8% of the original capacitance for 1000 cycles. The significantly improved specific capacitance is owing to the synergic impact of the two components of rGO, Ag nanoparticle and PEDOT. The composite also has a superb electrochemical characteristic and Environment friendly. owing to these benefits, it is promising electrode materials for supercapacitor [51].

2.2.12 Poly (Styrene Sulfonate)-PEDOT Nanocomposite

PEDOT–PSS is one of the most utilized conductive polymers and it outperforms other conductive polymers in many benefits such as adjustable conductivity, electrochemical performance, high transmittance, superior flexibility, good stability and processability [52, 53, 88]. Recently PEDOT–PSS has been studied as an important composite for optoelectronic applications and applications like solar cells and supercapacitors [52, 53].

In [52] a high-performance supercapacitor has been developed by incorporating rGO in PEDOT–PSS. Secondary doping of ethylene glycol (EG) with the help of rGO incorporation greatly improves the room temperature conductivity. The nanocomposite has exhibited long term stability with capacitance retention of more than 90% after 5000 cycles. The secondary doped PEDOT–PSS:EG/rGO nanocomposite have showed enhanced electrochemical performance with specific capacitance of 174 Fg^{-1} and energy density of 810 Whkg^{-1} .

In [88], ternary nanocomposite based on PEDOT: PSS doped with GO and glucose has been prepared. The nanocomposites solution (GGO-PEDOT) has been drop casted into a silicone mould and peeled off after water evaporation in order to obtain a flexible film. This approach has the advantage of simplicity. The nanocomposite has showed a specific capacitance of 16 Fg^{-1} which has indicated that this nanocomposite is appropriate to be employed as electrode material for flexible supercapacitors.

2.2.13 GO/PANI/PPy Nanocomposite

In [83], GO-based composites have been fabricated by in-situ polymerized aniline and pyrrole for studying the interaction of graphene oxide with PANI and PPy. Compared to pristine GO, specific capacitance of PPy coated GO enhanced by $\sim 122.73\%$. Also, the binding energy of PPy-GO has been found to be larger than PANI -GO owing to the absence of oxygen functional groups. Moreover, the storage capacity has been efficiently enhanced owing the synergistic effect of PPy coating on GO.

3 Conclusion

In conclusion, Polymer composites with the size of the filler in the nanoscale produce the polymer nanocomposites (PNC) and it is related to nanotechnology, which has been very hot topic. Recently, considerable attention has been paid to PNCs due to their unique properties, ease of manufacture and low cost. So, it will make our lives better. PANI, PPy, PTh are some of the discovered conducting polymers for various applications such as energy storage. This chapter has summarized the fundamental properties of different polymer nanocomposites and their application in energy storage including LIBs and electrochemical capacitors.

References

1. Zhang, L.L., Zhao, S., Tian, X.N., Zhao, X.S.: Layered graphene oxide nanostructures with sandwiched conducting polymers as supercapacitor electrodes. *Langmuir* **26**, 17624–17628 (2010)
2. Abdellatif Soliman, S.M., Sanad, M.F., Shalan, A.E.: Synthesis, characterization and antimicrobial activity applications of grafted copolymer alginate-g-poly(N-vinyl imidazole). *RSC Adv.* **11**, 11541–11548 (2021)
3. Batool, M., Nazar, M.F., Awan, A., et al.: Bismuth-based heterojunction nanocomposites for photocatalysis and heavy metal detection applications. *Nano-Struct Nano-Objects* **27**, 100762 (2021)
4. Abu Elella, M.H., Goda, E.S., Abdallah, H.M., et al.: Innovative bactericidal adsorbents containing modified xanthan gum/montmorillonite nanocomposites for wastewater treatment. *Int. J. Biol. Macromol.* **167**, 1113–1125 (2021)
5. Barhoum, A., Shalan, A.E., El-Hout, S.I., et al.: A broad family of carbon nanomaterials: classification, properties, synthesis, and emerging applications. In: *Handbook of Nanofibers*, pp. 1–40. Springer, Cham (2019)
6. Zhang, X., Samori, P.: Graphene/polymer nanocomposites for supercapacitors. *ChemNanoMat* **3**(6), 362–372 (2017)
7. Huang, Y., Liang, J., Chen, Y.: An overview of the applications of graphene-based materials in supercapacitors. *Small* **8**(12), 1805–1834 (2012)
8. Liu, L., Niu, Z., Zhang, L., Zhou, W., Chen, X., Xie, S.: Nanostructured graphene composite papers for highly flexible and foldable supercapacitors. *Adv. Mater.* **26**(28), 4855–4862 (2014)
9. Chen, L., Sun, L.J., Luan, F., Liang, Y., Li, Y., Liu, X.X.: Synthesis and pseudocapacitive studies of composite films of polyaniline and manganese oxide nanoparticles. *J. Power Sources* **195**(11), 3742–3747 (2010)
10. Wang, J.G., Yang, Y., Huang, Z.H., Kang, F.: Interfacial synthesis of mesoporous MnO₂/polyaniline hollow spheres and their application in electrochemical capacitors. *J. Power Sources* **204**, 236–243 (2012)
11. Saranya, S., Selvan, R.K., Priyadharsini, N.: Synthesis and characterization of polyaniline/MnWO₄ nanocomposites as electrodes for pseudocapacitors. *Appl. Surf. Sci.* **258**(11), 4881–4887 (2012)
12. Bose, S., Kim, N.H., Kuila, T., Lau, K., Lee, J.H.: Electrochemical performance of a graphene–polypyrrole nanocomposite as a supercapacitor electrode. *Nanotechnology* **22**, 295202 (2011)
13. Eivazzadeh-Keihan, R., Taheri-Ledari, R., Mehrabad, M.S., et al.: Effective combination of rGO and CuO nanomaterials through poly(p-phenylenediamine) texture: utilizing it as an excellent supercapacitor. *Energy Fuels* **35**, 10869–10877 (2021). <https://doi.org/10.1021/acs.energyfuels.1c01132>

14. Mini, P.A., Balakrishnan, A., Nair, S.V., Subramanian, K.R.V.: Highly super capacitive electrodes made of graphene/poly(pyrrole). *Chem. Commun.* **47**(20), 5753–5755 (2011)
15. Lai, L., et al.: Tuning graphene surface chemistry to prepare graphene/polypyrrole supercapacitors with improved performance. *Nano Energy* **1**(5), 723–731 (2012)
16. Zhao, Y., et al.: Highly compression-tolerant supercapacitor based on polypyrrole-mediated graphene foam electrodes. *Adv. Mater.* **25**, 591–595 (2013)
17. Kashani, H., Chen, L., Ito, Y., Han, J., Hirata, A., Chen, M.: Bicontinuous nanotubular graphene-polypyrrole hybrid for high performance flexible supercapacitors. *Nano Energy* **19**, 391–400 (2016)
18. Zheng, H., Ncube, N.M., Raju, K., Mphahlele, N., Mathe, M.: The effect of polyaniline on TiO₂ nanoparticles as anode materials for lithium ion batteries. *Springerplus* **5**(1), 1–7 (2016)
19. Kummer, M., et al.: Silicon/polyaniline nanocomposites as anode material for lithium ion batteries. *J. Electrochem. Soc.* **161**(1), A40–A45 (2014)
20. Xu, D., Wang, P., Yang, R.: Enhanced electrochemical performance of core-shell Li₄Ti₅O₁₂/PTh as advanced anode for rechargeable lithium-ion batteries. *Ceram. Int.* **43**(10), 7600–7606 (2017)
21. Liu, H., Liu, B.H., Li, Z.P.: A reduced graphene oxide/SnO₂/polyaniline nanocomposite for the anode material of Li-ion batteries. *Solid State Ionics* **294**, 6–14 (2016)
22. Chao, D., et al.: A V₂O₅/conductive-polymer core/shell nanobelt array on three-dimensional graphite foam: a high-rate, ultrastable, and freestanding cathode for lithium-ion batteries. *Adv. Mater.* **26**(33), 5794–5800 (2014)
23. Narasimha Reddy, Y., Reddy Mardi, R., Reddy, G.N., et al.: One-pot synthesis of novel substituted quinoxaline piperazine derivatives and their antimicrobial activities. *J. Mol. Struct.* **1253**, 132260 (2022). <https://doi.org/10.1016/j.molstruc.2021.132260>
24. Ponzio, E.A., Benedetti, T.M., Torresi, R.M.: Electrochemical and morphological stabilization of V₂O₅ nanofibers by the addition of polyaniline. *Electrochim. Acta* **52**(13), 4419–4427 (2007)
25. Klongkan, S., Pumchusak, J.: Effects of nano alumina and plasticizers on morphology, ionic conductivity, thermal and mechanical properties of PEO-LiCF₃SO₃ solid polymer electrolyte. *Electrochim. Acta* **161**, 171–176 (2015)
26. Shim, J., Kim, D.G., Kim, H.J., Lee, J.H., Baik, J.H., Lee, J.C.: Novel composite polymer electrolytes containing poly(ethylene glycol)-grafted graphene oxide for all-solid-state lithium-ion battery applications. *J. Mater. Chem. A* **2**(34), 13873–13883 (2014)
27. Raghu, M.S., Kumar, K.Y., Rao, S., Aravinda, T., Prasanna, B.P., Prashanth, M.K.: Fabrication of polyaniline–few-layer MoS₂ nanocomposite for high energy density supercapacitors. *Polym. Bull.* **75**(10), 4359–4375 (2018)
28. Safdari, M., Al-Haik, M.S.: A review on polymeric nanocomposites: effect of hybridization and synergy on electrical properties (2018)
29. Zhou, C., Zhang, Y., Li, Y., Liu, J.: Construction of high-capacitance 3D CoO@Polypyrrole nanowire array electrode for aqueous asymmetric supercapacitor. *Nano Lett.* **13**(5), 2078–2085 (2013)
30. Biswas, S., Drzal, L.T.: Multilayered nanoarchitecture of graphene nanosheets and polypyrrole nanowires for high performance supercapacitor electrodes. *Chem. Mater.* **22**(20), 5667–5671 (2010)
31. Xiong, P., Huang, H., Wang, X.: Design and synthesis of ternary cobalt ferrite/graphene/polyaniline hierarchical nanocomposites for high-performance supercapacitors This work is dedicated to Professor MIN Enze on the occasion of his 90th birthday. *J. Power Sources* **245**, 937–946 (2014)
32. Long, L., Wang, S., Xiao, M., Meng, Y.: Polymer electrolytes for lithium polymer batteries. *J. Mater. Chem. A* **4**(26), 10038–10039 (2016)
33. Chen, Y., Zeng, S., Qian, J.F., Wang, Y.D., Cao, Y.L., Yang, H.X., et al.: Li⁺-conductive polymer-embedded nano-Si particles as anode material for advanced Li-ion batteries. *ACS Appl. Mater. Interfaces* **6**(5), 3508–3512 (2014)

34. Guo, C.X., Wang, M., Chen, T., Lou, X.W., Li, C.M.: A hierarchically nanostructured composite of MnO₂/conjugated polymer/graphene for high-performance lithium ion batteries. *Adv. Energy Mater.* **1**, 736–741 (2011)
35. Li, Y., Ye, D.: 21. Carbon-Based Polymer Nanocomposite for Lithium-Ion Batteries. Elsevier Inc. (2018)
36. Eivazzadeh-Keihan, R., Asgharnasl, S., Moghim Aliabadi, H.A., et al.: Magnetic graphene oxide–lignin nanobiocomposite: a novel, eco-friendly and stable nanostructure suitable for hyperthermia in cancer therapy. *RSC Adv.* **12**, 3593–3601 (2022). <https://doi.org/10.1039/d1ra08640e>
37. Lai, L., et al.: Preparation of supercapacitor electrodes through selection of graphene surface functionalities. *ACS Nano* **6**(7), 5941–5951 (2012)
38. Wu, J., Zhang, Q., Zhou, A., Huang, Z., Bai, H., Li, L.: Phase-separated polyaniline/graphene composite electrodes for high-rate electrochemical supercapacitors. *Adv. Mater.* **28**(46), 10211–10216 (2016)
39. Wu, Q., Xu, Y., Yao, Z., Liu, A., Shi, G.: Supercapacitors based on flexible graphene/polyaniline nanofiber composite films. *ACS Nano* **4**(4), 1963–1970 (2010)
40. Kumar, M.S., Yasoda, K.Y., Batabyal, S.K., Kothurkar, N.K.: Carbon-polyaniline nanocomposites as supercapacitor materials. *Mater. Res. Express* **5**(4), 045505 (2018)
41. Yan, J., et al.: Preparation of graphene nanosheet/carbon nanotube/polyaniline composite as electrode material for supercapacitors. *J. Power Sources* **195**(9), 3041–3045 (2010)
42. Wang, H., Lin, J., Shen, Z.X.: Polyaniline (PANI) based electrode materials for energy storage and conversion. *J. Sci. Adv. Mater. Devices* **1**(3), 225–255 (2016)
43. Meng, C., Liu, C., Chen, L., Hu, C., Fan, S.: Highly flexible and all-solid-state paperlike polymer supercapacitors. *Nano Lett.* **10**(10), 4025–4031 (2010)
44. Wang, H., Hao, Q., Yang, X., Lu, L., Wang, X.: A nanostructured graphene/polyaniline hybrid material for supercapacitors. *Nanoscale* **2**(10), 2164–2170 (2010)
45. Wu, F., Chen, J., Li, L., Zhao, T., Chen, R.: Improvement of rate and cycle performance by rapid polyaniline coating of a MWCNT/sulfur cathode. *J. Phys. Chem. C* **115**, 24411–24417 (2011)
46. Yuksel, R., Alpugan, E., Unalan, H.E.: Coaxial silver nanowire/polypyrrole nanocomposite supercapacitors. *Org. Electron.* **52**, 272–280 (2018)
47. Wang, Z.L., He, X.J., Ye, S.H., Tong, Y.X., Li, G.R.: Design of polypyrrole/polyaniline double-walled nanotube arrays for electrochemical energy storage. *ACS Appl. Mater. Interfaces* **6**(1), 642–647 (2014)
48. Li, Q., Chen, J., Fan, L., Kong, X., Lu, Y.: Progress in electrolytes for rechargeable Li-based batteries and beyond. *Green Energy Environ.* **1**(1), 18–42 (2016)
49. Xu, J., Wang, K., Zu, S., Han, B., Wei, Z.: hierarchical nanocomposites of polyaniline nanowire arrays on graphene oxide sheets with synergistic effect for energy storage. *ACS Nano* **4**(9), 5019–5026 (2010)
50. Li, L., Zhang, X., Qiu, J., Weeks, B.L., Wang, S.: Reduced graphene oxide-linked stacked polymer forests for high energy-density supercapacitor. *Nano Energy* **2**(5), 628–635 (2013)
51. Ates, M., Caliskan, S., Ozten, E.: Preparation of rGO/Ag/PEDOT nanocomposites for supercapacitors. *Mater. Technol.* **33**(14), 872–883 (2018)
52. Khasim, S., Pasha, A., Badi, N., Lakshmi, M., Mishra, Y.K.: High performance flexible supercapacitors based on secondary doped PEDOT-PSS-graphene nanocomposite films for large area solid state devices. *RSC Adv.* **10**(18), 10526–10539 (2020)
53. Savva, A., Georgiou, E., Papazoglou, G., Chrusou, A.Z., Kapnisis, K., Choulis, S.A.: Photo-voltaic analysis of the effects of PEDOT:PSS-additives hole selective contacts on the efficiency and lifetime performance of inverted organic solar cells. *Sol. Energy Mater. Sol. Cells* **132**, 507–514 (2015)
54. Hu, C.C., Chang, K.H., Lin, M.C., Wu, Y.T.: Design and tailoring of the nanotubular arrayed architecture of hydrous RuO₂ for next generation supercapacitors. *Nano Lett.* **6**(12), 2690–2695 (2006)

55. Yang, G.W., Xu, C.L., Li, H.L.: Electrodeposited nickel hydroxide on nickel foam with ultrahigh capacitance. *Chem. Commun.* **48**, 6537–6539 (2008)
56. González, A., Goikolea, E., Barrena, J.A., Mysyk, R.: Review on supercapacitors: technologies and materials. *Renew. Sustain. Energy Rev.* **58**, 1189–1206 (2016)
57. Conway, B.E., Conway, B.E.: Similarities and differences between supercapacitors and batteries for storing electrical energy. *Electrochem. Supercapacitors* **2**, 11–31 (1999)
58. Ding, F., et al.: Dendrite-free lithium deposition via self-healing electrostatic shield mechanism. *J. Am. Chem. Soc.* **135**(11), 4450–4456 (2013)
59. Aryanfar, A., Brooks, D., Merinov, B.V., Goddard, W.A., Colussi, A.J., Hoffmann, M.R.: Dynamics of lithium dendrite growth and inhibition: pulse charging experiments and monte carlo calculations. *J. Phys. Chem. Lett.* **5**(10), 1721–1726 (2014)
60. Xu, Z.: Investigation on the role of different conductive polymers in supercapacitors based on a zinc sulfide/reduced graphene oxide/conductive. *RSC Adv.* **10**, 3122–3129 (2020)
61. Liu, R., et al.: Core – shell structured hollow SnO₂ – polypyrrole nanocomposite anodes with enhanced cyclic performance for lithium-ion batteries. *Nano Energy* **6**, 73–81 (2014)
62. Arya, A., Sharma, A.L.: Polymer electrolytes for lithium ion batteries: a critical study. *Ionics* **23**(3), 497–540 (2017)
63. Hong, X., et al.: Recent progress on graphene/polyaniline composites for high-performance supercapacitors. *Materials (Basel)* **12**(9), 1451 (2019)
64. Souza, V.H.R., Oliveira, M.M., Zarbin, A.J.G.: Bottom-up synthesis of graphene/polyaniline nanocomposites for flexible and transparent energy storage devices. *J. Power Sources* **348**, 87–93 (2017)
65. Zhao, Z., Richardson, G.F., Meng, Q., Zhu, S.: PEDOT-based composites as electrode materials for supercapacitors. *Nanotechnology* **27**(4), 42001 (2015)
66. Basnayaka, P.A., Ram, M.K., Stefanakos, L., Kumar, A.: Graphene/polypyrrole nanocomposite as electrochemical supercapacitor electrode: electrochemical impedance studies. *Graphene* **02**(02), 81–87 (2013)
67. Huang, Z., Li, L., Wang, Y., Zhang, C., Liu, T.: Polyaniline/graphene nanocomposites towards high-performance supercapacitors: a review. *Compos. Commun.* **8**, 83–91 (2018)
68. Demirocak, D.E., Srinivasan, S.S., Stefanakos, E.K.: A review on nanocomposite materials for rechargeable Li-ion batteries. *Appl. Sci.* **7**(7), 1–26 (2017)
69. Berrueta, A., Ursua, A., Martin, I.S., Eftekhari, A., Sanchis, P.: Supercapacitors: electrical characteristics, modeling, applications, and future trends. *IEEE Access* **7**, 50869–50896 (2019)
70. Chauhan, N.P.S., Solanki, M.S.: Approaches and challenges of polyaniline graphene nanocomposite for energy application, March. Elsevier Inc. (2018)
71. Divya, P., Prithiba, A., Rajalakshmi, R.: A comprehensive review on the nanocomposites of graphene and its derivatives in the application of supercapacitors. *Rasayan J. Chem.* **12**(1), 214–231 (2019)
72. Zheng, H., Kim, M.: Performance of modified graphite as anode material for lithium-ion secondary battery. *Carbon Lett.* **12**(4), 243–248 (2011)
73. Zhao, J., et al.: Facile synthesis of polypyrrole nanowires for high-performance supercapacitor electrode materials. *Prog. Nat. Sci. Mater. Int.* **26**(3), 237–242 (2016)
74. Tan, X., et al.: Preparation of nanocomposite polymer electrolyte via in situ synthesis of SiO₂ nanoparticles in PEO. *Nanomaterials* **10**(1), 157 (2020)
75. Channu, V.S.R., Rambabu, B., Kumari, K., Kalluru, R.R., Holze, R.: SnO₂/PANI nanocomposite electrodes for supercapacitors and lithium ion batteries. *Electrochem. Energy Technol.* **4**(1), 32–38 (2018)
76. Kim, M., Kim, Y.K., Kim, J., Cho, S., Lee, G., Jang, J.: Fabrication of a polyaniline/MoS₂ nanocomposite using self-stabilized dispersion polymerization for supercapacitors with high energy density. *RSC Adv.* **6**(33), 27460–27465 (2016)
77. Tao, H.C., Yang, X.L., Zhang, L.L., Ni, S.B.: Polyaniline encapsulated silicon nanocomposite as high-performance anode materials for lithium ion batteries. *J. Solid State Electrochem.* **18**(7), 1989–1994 (2014)

78. Chen, M., Du, C., Wang, L., Yin, G., Shi, P.: Silicon/graphite/polyaniline nanocomposite with improved lithium-storage capacity and cyclability as anode materials for lithium-ion batteries. *Int. J. Electrochem. Sci.* **7**(1), 819–829 (2012)
79. Xiao, L., Hwa, Y., Dobrowolny, S., Mahlendorf, F.: Novel Si-CNT/polyaniline nanocomposites as lithium-ion battery anodes for improved cycling performance. *Mater. Today Proc.* **4**, S263–S268 (2017)
80. Arsalani, N., Tabrizi, A.G., Ghadimi, L.S.: Novel PANI/MnFe₂O₄ nanocomposite for low-cost supercapacitors with high rate capability. *J. Mater. Sci. Mater. Electron.* **29**(7), 6077–6085 (2018)
81. Senthilkumar, B., Vijaya Sankar, K., Sanjeeviraja, C., Kalai Selvan, R.: Synthesis and physico-chemical property evaluation of PANI-NiFe₂O₄ nanocomposite as electrodes for supercapacitors. *J. Alloys Compd.* **553**, 350–357 (2013)
82. Liu, Y., et al.: Graphene/polypyrrole intercalating nanocomposites as supercapacitors electrode. *Electrochim. Acta* **112**, 44–52 (2013)
83. Pal, K., Panwar, V., Bag, S., Manuel, J., Ahn, J.H., Kim, J.K.: Graphene oxide-polyaniline-polypyrrole nanocomposite for a supercapacitor electrode. *RSC Adv.* **5**(4), 3005–3010 (2015)
84. Eeu, Y.C., Lim, H.N., Lim, Y.S., Zakarya, S.A., Huang, N.M.: Electrodeposition of polypyrrole/reduced graphene oxide/iron oxide nanocomposite as supercapacitor electrode material. *J. Nanomater.* **2013** (2013). Article ID 653890
85. Zhang, H., et al.: Recent progress in advanced electrode materials, separators and electrolytes for lithium batteries. *J. Mater. Chem. A* **6**(42), 20564–20620 (2018)
86. McGraw, M., et al.: One-step solid-state in-situ thermal polymerization of silicon-PEDOT nanocomposites for the application in lithium-ion battery anodes. *Polymer (Guildf)* **99**, 488–495 (2016)
87. Bensalah, N., Dawood, H.: Review on synthesis, characterizations, and electrochemical properties of cathode materials for lithium ion batteries. *J. Mater. Sci. Eng.* **5**(4), 1–21 (2016). <https://doi.org/10.4172/2169-0022.1000258>
88. Giuri, A., Colella, S., Listorti, A., Rizzo, A., Mele, C., Corcione, C.E.: GO/glucose/PEDOT:PSS ternary nanocomposites for flexible supercapacitors. *Compos. Part B Eng.* **148**, 149–155 (2018)
89. Afzal, A., Abulilwi, F.A., Habib, A., Awais, M., Waje, S.B., Atieh, M.A.: Polypyrrole/carbon nanotube supercapacitors technological advances and challenges. *J. Power Sources* **352**, 174–186 (2017)
90. Bai, Y., et al.: Electrochemical performance of Si/CeO₂/Polyaniline composites as anode materials for lithium ion batteries. *Solid State Ionics* **272**, 24–29 (2015)

Incorporation of Nanocomposite Thin Films as Effective Electrodes for Photovoltaic Devices Applications



Soraya Abdelhaleem and M. R. Balboul

Abstract The development of clean and renewable energy sources as an alternative to traditional energy sources like fossil fuel and oil has become one of the recent challenging issues in scientific researches. The photovoltaic device (PV), or solar cell, utilizes the most abundant renewable energy resource and it has the power to cover the world's electricity needs. Many articles already exist that discuss the basic principle of photovoltaic devices in detail. The key goal of this chapter is to highlight the different generations of PV devices, with a brief discussion on their structure and working principle. Besides, this article deals with the involvement of nanocomposite materials with the PV industry. Consequently, the types of nanocomposites are discussed herein with examples for the most commonly used nanocomposites in the production of photovoltaic devices. Recently, many studies have investigated the influence of utilizing nanocomposite materials in photovoltaic industry as well as their role in improving conversion efficiency of PV. This chapter utilizes many of these studies as references to emphasize the importance of using nanocomposites for photovoltaics.

Keywords Photovoltaic devices · Nanocomposite thin films · Clean energy · Solar cell

Abbreviations

PCBM	(6-6) Phenyl-C61-butyric acid methyl ester
a-Si	Amorphous silicon
BHJ	Bulk heterojunction

S. Abdelhaleem (✉)

Radiation Physics Department, National Centre for Radiation Research and Technology (NCRRT), Egyptian Atomic Energy Authority (EAEA), Nasr City, Cairo, Egypt

M. R. Balboul

Solid State Physics and Accelerators Department, National Centre for Radiation Research and Technology (NCRRT), Egyptian Atomic Energy Authority (EAEA), Nasr City, Cairo, Egypt

© The Author(s), under exclusive license to Springer Nature Switzerland AG 2022

725

A. E. Shalan et al. (eds.), *Advances in Nanocomposite Materials for Environmental and Energy Harvesting Applications*, Engineering Materials,
https://doi.org/10.1007/978-3-030-94319-6_23

CNT	Carbon nanotubes
CVD	Chemical vapor deposition
CIGS	Copper Indium Gallium Diselenide
CZTS	Copper Zinc Tin Sulfide
C-Si	Crystalline silicon
DLN	Diamond-like nanocomposite
DWCNTs	Double-walled carbon Nanotubes
DSSCs	Dye sensitized solar cells
ETM	Electron transporting material
FF	Fill factor
FTO	Fluorine-doped tin oxide
HOMO	Highest occupied molecule orbital
HTM	Hole transporting material
ITO	Indium tin oxide
LUMO	Lowest unoccupied molecule orbital
MOS	Metal oxide semiconductor
MWCNTs	Multi-walled carbon nanotubes
OPV	Organic photovoltaic
OSC	Organic solar cells
PSC	Perovskite solar cell
PV	Photovoltaic
PEDOT	Poly(3,4-Ethylenedioxythiophene)
P3HT	Poly-3-hexylthiophene
PCE	Power conversion efficiency
QDSSCs	Quantum-dot sensitized solar cells
rGO	Reduced graphene oxide
SWCNTs	Single-walled carbon nanotubes
TCO	Transparent conductive oxide
TFSCs	Thin Film Solar Cells

1 Introduction

The need for renewable and clean energy resources has become highly considerable due to the rise in global warming and environmental pollutions resulted from conventional energy sources such as oil, natural gas, and coal. Besides, the limitation of these sources has led to a significant increase in their cost [1]. The photovoltaic device (PV), i.e. solar cell, has emerged as the most powerful substitute to conventional energy resource, as it offers clean, abundant, unlimited, and sustainable energy [2]. The solar cell, is a device that affords direct conversion of the energy from sunlight to electricity based on the photovoltaic effect. In 1839, Becquerel created the first solar cell device [3, 4]. Since then, the development of the PV industry has attracted great interest in scientific research as it has been applied in many fields, including

daily life activities, industry, satellites, and spacecraft, etc. Based on the type of the absorber layer, solar cell technologies can be divided into four main generations: the first generation is mainly focused on crystalline silicon (c-Si), it dominates the photovoltaic market by 91% owing to its high efficiency [1], which has reached 26% [5]. However, because of the high manufacturing cost of this technology, the need for a substitutional technology that combines satisfying efficiency and low cost has increased over the last decades. This has led to the innovation of the second generation, which was initially introduced in the 1970s [6], by using amorphous silicon and thin-film solar cells including chalcogenides. This generation mainly aims to decrease the manufacturing cost by using low-cost and earth-abundant materials. The maximum efficiency of this technology has reached 23% [5]. However, reproducibility, production of homogeneous films over large areas, and manufacturing of highly efficient devices are still difficult to achieve. The third generation of solar cells is designed to combine both low cost and improved efficiency, it includes nanocrystalline films, dye-sensitized solar cell (DSSC), organic solar cell (OSC), perovskite solar cells (PSC), and quantum dot-sensitized solar cell (QDSSC) [7–9]. This technology has the advantage of operating perfectly under cloudy weather, which makes it a perfect device for indoor applications [4, 10, 11]. The fourth generation, which is known as “inorganics-in-organics”, offers reduced fabrication cost, better performance, and flexible solar cells. This technology combines polymer thin films with inorganic nanomaterials such as metal nanoparticles and metal oxides or organic nanomaterials, for instance, carbon nanotube (CNT) and graphene [12]. Figure 1 represents the schedule of the four generations of solar cell devices with examples for each generation.

Recently, applying nanomaterials in solar cell fabrication has gained great interest as it improves conversion efficiency as well as reducing the fabrication cost [1]. To fabricate a high-performance photovoltaic device, a wide range of nanomaterials have been used in buffer layers, absorber layers, and thin-film coating on the solar cell panels. Furthermore, the use of nanocomposite materials showed an improvement in the efficiency of photovoltaic cells. This chapter is devoted to giving a brief discussion on the basics of photovoltaics, and the role of nanocomposites in improving their efficiencies.

2 Nanocomposite Materials

One of the common techniques to take the advantage of two or more distinctly different components is to mix them to form a composite. When one of the constituent components has at least one dimension in the nanoscale range (10^{-9} m); the resultant material is referred to as nanocomposite [14]. The grain size in nanomaterials is ultra-fine, less than 50 nm. Nanomaterials have large surface-to-volume ratio, which gives rise to the inclusion of new quantum mechanical effects in such materials. Nanocomposites include a wide range of materials such as one-dimensional, two-dimensional,

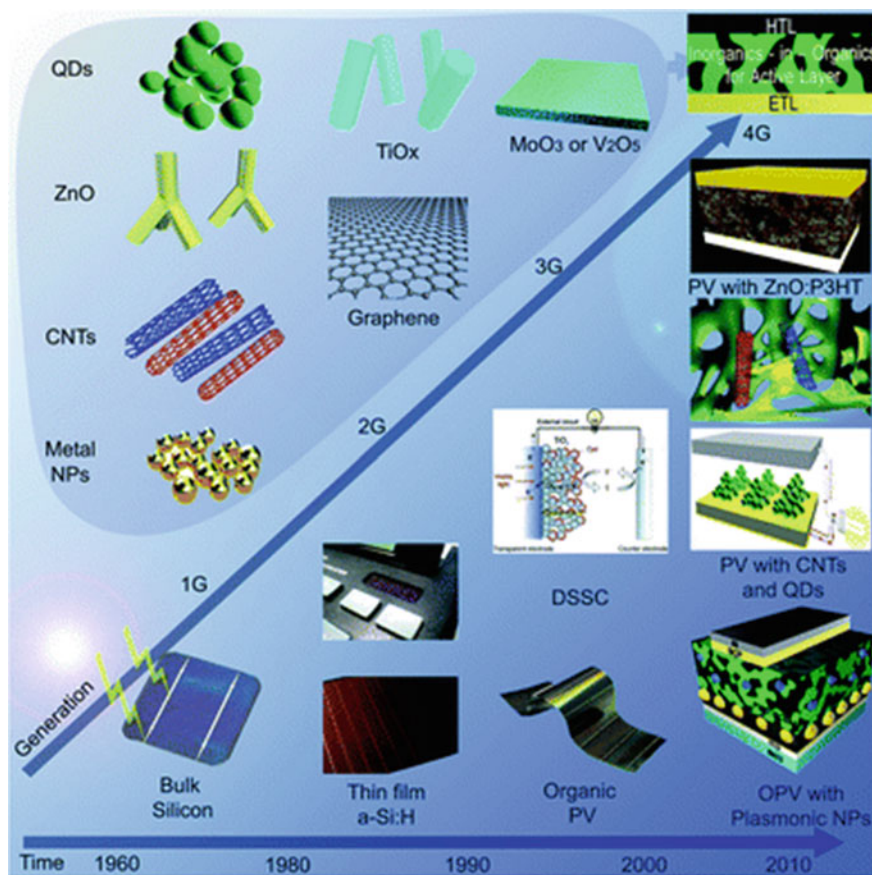


Fig. 1 The four generations of photovoltaic technology, with associated nanomaterial components. Taken from [13], with permission from The Royal Society of Chemistry

three-dimensional, and amorphous materials. The use of nanocomposites in industrial and commercial applications has become increasingly attractive. For instance, nanocomposites such as nanoparticles and nanospheres can be used as drug delivery and controlled-release drug systems. Hollow nanocomposites, which have an inner hollow space in their structure, can be used to store substances inside their cavities and release them for later use. Also, they can be used as fillers, coatings, capsules, etc., because of their convenient properties such as reduced density and optimum optical properties. Other applications such as polypropylene nanocomposites for furniture, machines, pinboards. Furthermore, nanocomposites are recently used in modern technology such as the manufacturing of bone cement, filter membranes, and photovoltaic devices [15, 16]. Most composites are prepared by combining two materials: one material (the matrix or binder) surrounds and binds together a bunch of fibers or fragments of a much stronger material (the reinforcement). These two

materials are mixed to combine the best properties of each type. To understand the roles of both the matrix and reinforcement in nanocomposites, imagine a block of concrete. Concrete is composed of a combination of fine and coarse aggregate, rock, and sand. It is not possible to use only cement in paving and building, as it is too thick and it would be prone to breaking. Consequently, mixing the additional materials with cement fills space, provides reinforcement, and forms a much stronger composite. Several types of nano-reinforcements can be used in nanocomposites, which include nanoparticles, nanotubes, nano-fibers, sheets, etc. Nanocomposites can be divided into three main types based on the bulk matrix: ceramic, metal, and polymer nanocomposites [14, 17].

3 Types of Nanocomposites

3.1 Ceramic Nanocomposites

A ceramic is an inorganic material, such as oxides, nitrides, carbides, etc., which has interesting properties like wear resistance, heat resistance, and high chemical stability. However, it is very strong, hard, and fragile, which makes it extremely weak under shearing and tension stresses. When ceramic material is combined with nanofiller such as whiskers, platelets, fibers, or nanoparticles, its fracture toughness is found to be increased [18]. These nanofillers or the so-called reinforcements to bridge the cracks and prevent their propagation through the ceramic material. Besides, mixing ceramics with a second phase leads to a phase transition accompanied by volume expansion, which generates a sealing force that heals the cracks [19]. One of the common examples of ceramic nanocomposites is $\text{Al}_2\text{O}_3/\text{SiC}$, in which the nano-reinforcements hinder the cracks, which lead to an increase in the fracture toughness [20].

3.2 Metal Nanocomposites

Metal matrix nanocomposites are formed by the combination of a metal which represents the matrix and a nano-reinforcement. Metal nanocomposites can be formed by combining metal with glass, ceramic, and polymer. Consequently, they are characterized by ductility and toughness along with high compressive and shear strength [18, 21].

Table 1 Examples of the different types of nanocomposites [21, 22]:

Type of nanocomposite	Examples
Metal	Fe–Cr/Al ₂ O ₃ , Ni/Al ₂ O ₃ , Co/Cr, Fe/MgO, Al/CNT, Mg/CNT, Cu/Al ₂ O ₃ , Nb/Cu
Ceramic	Al ₂ O ₃ /SiO ₂ , SiO ₂ /Ni, Al ₂ O ₃ /TiO ₂ , Al ₂ O ₃ /SiC, Al ₂ O ₃ /CNT, Si ₂ N ₄ /SiC, Al ₂ O ₃ /NdAlO ₃ , SiO ₂ /Fe
Polymer	Thermoplastic/thermoset polymer/layered silicates, polyester/TiO ₂ , polymer/CNT, polymer/ layered double hydroxides

3.3 Polymer Nanocomposites

When nano-reinforcements are dispersed into polymers, a new nanopolymer composite, that is ductile and lightweight, is formed [18, 21]. Table 1 shows some examples of the three types of nanocomposites.

4 Common Types of Nanomaterials used in Photovoltaics

4.1 Carbon Nanomaterials

Carbon nanomaterials can be classified according to their dimensions as follows [23]:

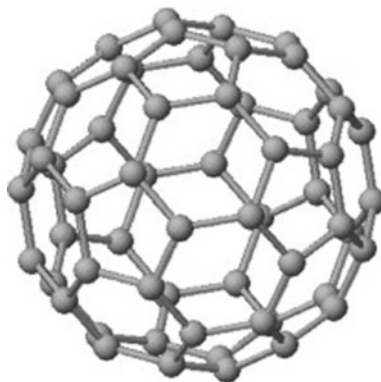
- (1) Zero-dimension carbon (0-D): such as Fullerenes, carbon onion, carbon dots (CDs), nanodiamonds;
- (2) One-dimension carbon (1-D): such as Carbon nanotubes (CNTs), carbon nanofibers;
- (3) Two Dimension carbon (2-D): such as Graphene.

In the following sections, we will discuss briefly the common carbon nanomaterials that are utilized in photovoltaic applications.

4.1.1 Fullerene

Fullerene is a molecule composed of symmetric nanocarbon molecules with a hollow sphere, ellipsoid, and other structures [24, 25]. These molecules were initially discovered by Kroto et al. in 1985 [26], they are stable at high temperatures with high electrical conductivity, which makes them suitable for application in nanocomposites [24]. Owing to delocalized π electrons, fullerene molecules have high nonlinear optical responses, large electron affinity with improved charge transport properties [24]. The most used fullerene molecule in photovoltaic applications is C₆₀, which is composed of 12 pentagons and 20 hexagons, It is commonly known as Buckminsterfullerene after it was discovered by an American architect called Richard

Fig. 2 Graphical illustration of C_{60} fullerene. Taken from [28], with permission



Buckminster Fuller [23]. Moreover, C_{60} can be fabricated by the laser ablation of graphite and arc-discharge methods. The C_{60} molecule possesses two different bond lengths; the 6:6 bonds which are regarded as “double bonds” and the longer the 6:5 bonds. C_{60} is not super-aromatic as it does not tend to form double bonds in the pentagons, causing poor electron delocalization. Consequently, C_{60} acts as electron-deficient alkenes and interacts easily with electron-rich alkenes [27]. Figure 2 shows a graphic illustration of the 60-carbon atoms comprising C_{60} fullerene.

4.1.2 Graphene

Recently, graphene is widely applied in several fields and industries [27]. It consists of nanocarbon with layered hexagonal crystal structures [24], in which each carbon atom is joined to its 3 nearest-neighbor carbon atoms by σ bonds with sp^2 hybrid orbitals. The distance between each carbon atom to its neighbor is approximately 1.42 Å as shown in Fig. 3.

Graphene has attracted great interest owing to its incredible features. It has remarkable electrical, thermal, and mechanical properties, extremely large electron-mobility ($15,000 \text{ cm}^2\text{V}^{-1} \text{ s}^{-1}$) with reduced scattering loss while traveling, and a huge surface area ($2630 \text{ m}^2/\text{g}$). Graphene has very good thermal conductivity, which ranges from 3000 to $6000 \text{ Wm}^{-1} \text{ K}^{-1}$, it also has an electrical conductivity of about $9.6 \times 10^7 \text{ S/m}$, stiffness, resistance against gases. Furthermore, graphene sheet has almost constant absorption, approximately 2.3%. Besides, graphene sheets have good flexibility and they are also chemically inert, which makes them a suitable material for applications such as protective coatings and electrodes [30]. These attractive features make graphene an outstanding choice to be utilized in photovoltaic devices. Besides, it can be incorporated with polymer nanocomposites and form Polymer/graphene nanocomposites which have been spotted as a promising candidate in solar cells [24].

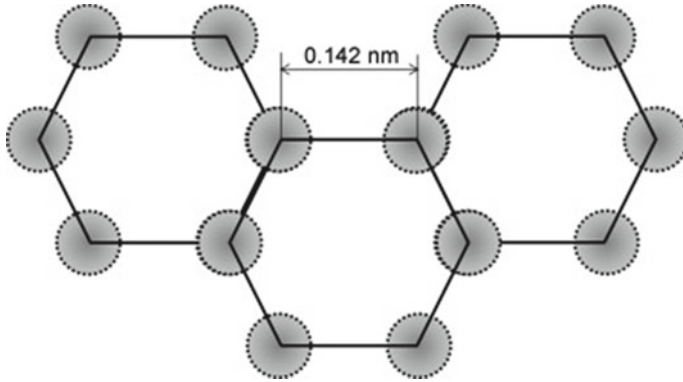


Fig. 3 Structure of graphene. Taken from [29], with permission

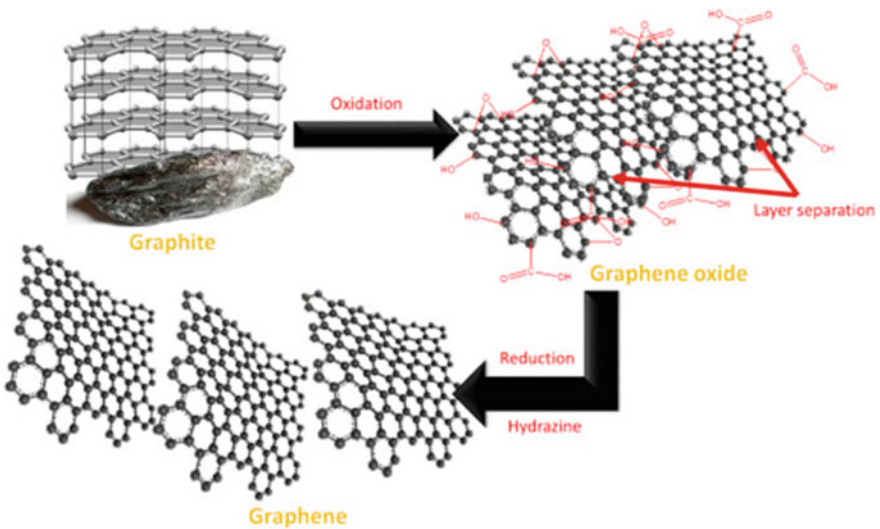


Fig. 4 Graphene generated from the reduction of graphene oxide. Taken from [24], with permission

Fabrication of graphene can be performed by numerous methods such as chemical vapor deposition, exfoliation, epitaxial growth, gamma-irradiation to graphite, and chemical and electrochemical routes. Recently, the oxidation of graphene, to form graphene oxide, followed by its reduction to form reduced graphene (rGO) has gained growing interest. RGO can be manufactured by utilizing several methods such as thermal annealing and chemical, photocatalytic, and plasma reduction [24, 27, 30]. Figure 4 displays the generation of graphene resulted from the reduction of graphene oxide.

4.1.3 Carbon Nanotubes (CNTs)

A carbon nanotube (CNT) is a cylindrical structure composed of single-layer carbon atoms wrapped in sheets with a diameter of a few nanometers, and a length ranging from a few microns to centimeters. As the ratio of length to diameter is large, CNTs are considered as one-dimensional nanostructured material. CNT was discovered in 1991 by Sumio Iijima. Since then, it has attracted interest from researchers working on nanomaterials. Due to its remarkable properties and unique structure, CNT can be applied in several applications [27]. CNTs have extraordinary strength and stiffness [31], they have an extraordinary strength that is 100 times larger than a steel cylinder with the same diameter but with a much lighter weight. They have an electrical and thermal conductivity higher than copper. CNTs can be classified into three categories: Single-walled carbon nanotubes (SWCNTs), Double-walled carbon nanotubes (DWCNTs), and Multi-walled carbon nanotubes (MWCNTs). Figure 5 shows the three different types of CNTs. SWCNTs have the simplest CNT structure as a single-walled graphene sheet rolled up in a cylindrical structure with a typical diameter in the range of 0.4–3 nm [24, 32]. The identification of the CNT structure depends on the chiral vector (n, m), as shown in Fig. 6. Therefore, nanotubes can be classified as armchair for $n = m$, chiral for $m > 0$, or zig-zag for $m = 0$. The chirality of nanotubes has a remarkable influence on the electronic properties of CNT, CNT can be either metallic or semiconductor, according to its chirality. Double-walled CNT (DWCNT) consists of exactly two concentric and overlapped nanotube cylinders [24]. MWNTs are composed of multiple coaxial cylinders with an interlayer spacing of about 0.34 nm which is approximately equivalent to the interlayer distance in graphite. They have an internal diameter that ranges from 0.4 nm to several nanometers, while their external diameter is determined by the number of outer layers and varies from 2 to 20–30 nm [27]. Since MWCNT comprises several layers of graphene with different chiralities for every layer, therefore, its electrical and physical properties are more complicated than SWCNT [24]. Typically, the MWCNT tends to agglomerate inside the TiO_2 matrix, and work as trapping locations that prevent the fast collection of the charges at the electrodes. Consequently, adding a small amount of MWCNT to TiO_2 can improve the performance of photovoltaic devices [31].

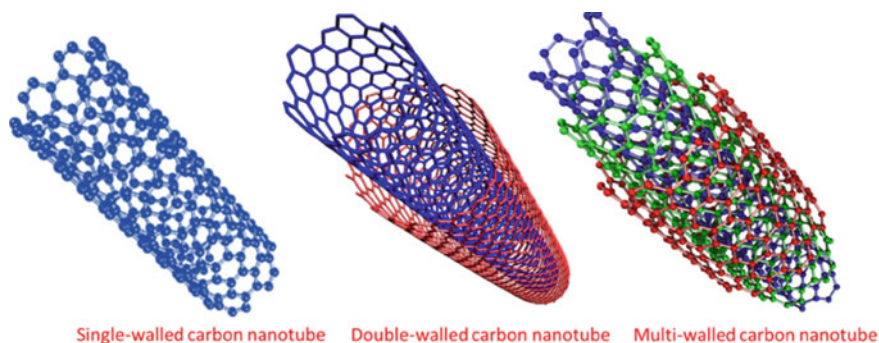


Fig. 5 Different types of CNTs. Taken from [24], with permission

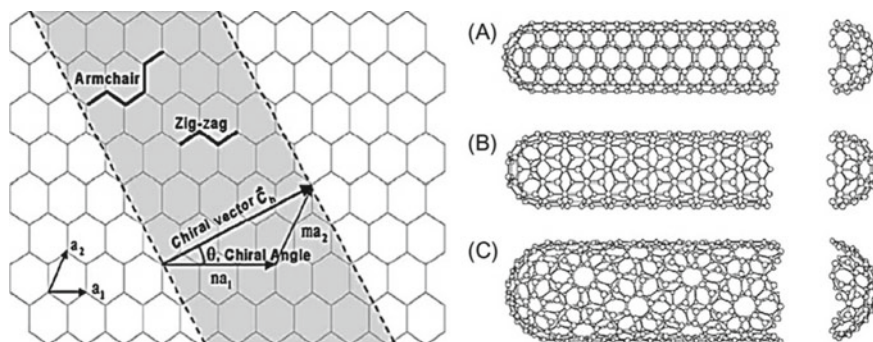


Fig. 6 Illustration of how a hexagonal sheet of graphene is Rolled-up to make a CNT with different chiralities (A: armchair; B: zig-zag; C: chiral). Taken from [24], with permission

CNTs have been widely used in several applications, such as electronic devices, supercapacitors, catalysis, photonics, etc. In photovoltaic devices, CNTs were applied as conductive and transparent electrodes, hole collection and transport layer, etc. CNTs can be produced by using several techniques, such as arc discharge, chemical vapor deposition, and laser ablation technique [27].

4.2 Titanium Dioxide (TiO_2)

Among the several types of metal oxide semiconductors, TiO_2 (also called titania or titanium (IV) oxide) nanomaterial has come out as a potential candidate owing to its attractive properties such as chemical inertness, optical stability, non-toxic, low cost, and resistance to corrosion [33]. The crystal structure of TiO_2 can be mainly classified into 3 types: anatase, rutile, and brookite. Both of the first two structures are usually regarded as the most powerful in the environment. Each of these structures possess different features and, hence, they have different usages and influences in the environment [34]. Figure 7 presents the crystallographic structures of the unit cells of anatase and rutile TiO_2 .

The physical and chemical properties of TiO_2 nanocrystals depend on their size, shape, arrangement, intrinsic electronic structure, and surface properties. Recently, the remarkable morphologies and features of TiO_2 have attracted much interest and several TiO_2 nanomaterials, such as nanotubes, nanorods, nanofibers, nanosheets, and interconnected structures, were applied in photovoltaics [33]. It is found that merging TiO_2 nanoparticles with other nanomaterials and applying them to the photovoltaic device can provide improved power conversion efficiency [31]. Usually, it is important to increase the surface area of TiO_2 to improve the interaction that occurs at the interface between TiO_2 and the interactive media. Additionally, the mobility of the electrons in TiO_2 nanomaterials should be high to collect the electrons introduced in their structure efficiently. Since the defects formed inside the grain boundaries

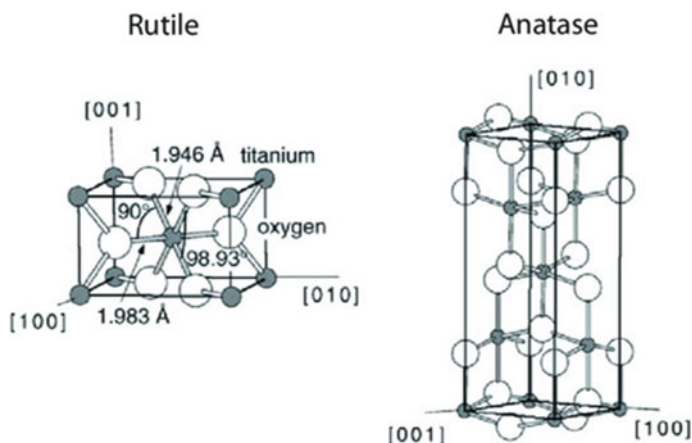


Fig. 7 Bulk structure of rutile and anatase. Taken from [35], with permission

at the interface between the nanoparticles may serve as electron traps, utilizing a network structure comprising TiO_2 single-crystal nanowire rather than nanosized TiO_2 particles is supposed to improve the fast electron transfer [33].

5 Development of Photovoltaic Technology

5.1 First Generation Solar Cells

First generation photovoltaics includes crystalline silicon (c-Si) and Gallium arsenide solar cells. C-Si solar cells predominate the photovoltaic market with a ratio of about 90%, it can be divided into two categories: monocrystalline and polycrystalline. On the other hand, GaAs is the most widely used in the production of solar panels [12]. We will discuss only c-Si silicon solar cells in this section.

Silicon solar cell is mainly fabricated from silicon which is a semiconductor material, semiconductors are promising materials as their conductivity can be modified when impurities are injected into their crystal structure. This impurity injection is referred to as the doping process [36]. Crystalline silicon (c-Si) has emerged as the first successful solar cell device. Since then, it is the most widely used in the photovoltaic market [37]. We will discuss briefly the working principle of c-Si. A pure silicon semiconductor can be doped with a pentavalent atom (donor) like phosphorus that creates four bonds with four neighboring atoms of silicon, which generate a free electron. As the phosphorus atom donates one electron, it loses its neutrality and becomes a positively charged immobile ion. Therefore, this region includes positively charged ions and free electrons, in this region, the majority carriers are electrons which makes it a negative region or the so-called n-type [36]. Similarly, when a

silicon semiconductor is doped with a trivalent atom (acceptor) like Boron, it forms three bonds with the neighboring atoms of silicon, which generate a free hole. As the boron atom accepts one electron, it loses its neutrality and becomes a negatively charged immobile ion. This creates a positive region or p-type in which the majority charge carriers are the free holes along with the negatively charged ions. When these two types are brought together, they form a p–n junction. Once this junction is created a portion of the free electrons from the n-region are diffused into the p-region and fill up some holes near the junction, leaving positively charged ions behind. Similarly, some of the holes diffuse into the n-type, and combine with the electrons, leaving negatively charged ions behind. These charges build up a space that is depleted from free carriers, forming the so-called depletion region. The charges in the depletion region create an electric field (ξ) which prevents further diffusion of electrons and holes. A graphical representation of the p–n junction is depicted in Fig. 8. To allow more diffusion of the charge carriers, an external voltage that is higher than the barrier potential (or the built-in voltage V_0) of the depletion region should be applied. We can therefore conclude that the movement of the charge carriers is controlled by two currents: diffusion current, which is generated by the carrier gradient that occurs as a result of flowing of the majority carriers through the junction, and drift current, which is flowing in the reverse direction of the diffusion current and caused by the electric field generated by the electrons and holes which are presented in the depletion region [38]. The previous model describes how the p–n junction works at the equilibrium state. However, applying an external voltage to the p–n junction can increase or reduce the height of the barrier potential. When the positive terminal of the external voltage supply is connected to the p-region and the negative terminal of the external voltage is connected to the n-region, the electrons and the holes are repelled towards the junction, which reduces the area of the depletion region, and the barrier potential

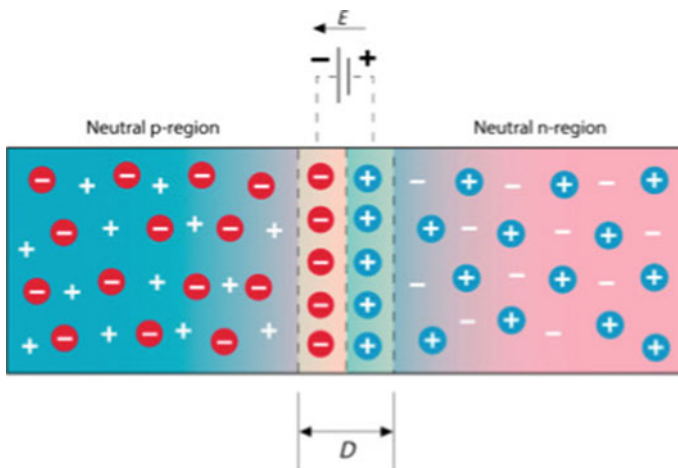
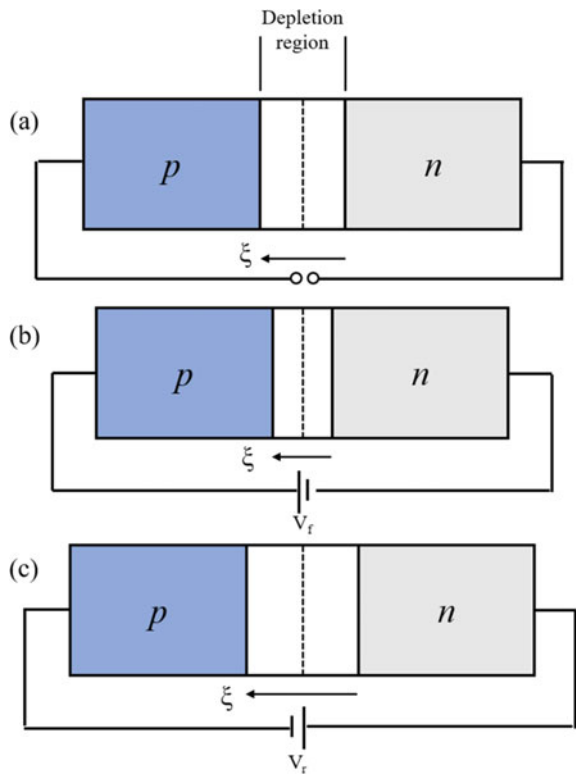


Fig. 8 Graphic illustration of the p–n junction showing the depletion region, the neutral regions, and the generated electric field. Taken from [38], with permission

is reduced to $V_0 - V_f$. As the external voltage is increased, the electrons will earn enough energy to overcome the barrier potential and start to diffuse across the junction, which allows the flow of the electric current. This connection is called forward bias. On the other hand, when the positive terminal of the external voltage supply is applied to the n-region, and the negative terminal of the external voltage is applied to the p-region, the electrons are attracted to the positive terminal and the holes are attracted to the negative terminal. In this case, the depletion region space is increased, this leads to an increase in the magnitude of the potential to $V_0 + V_r$, which prevents the flow of the electric current. This type of connection is called reverse bias [39]. Figure 9 summarizes the operation of the p–n junction under equilibrium, forward bias, and reverse bias.

Figure 10 shows the fundamental structure of a solar cell device, it mainly consists of a p–n junction, an anti-reflective coating, and finger electrodes. When the solar cell is illuminated by a light source, it easily absorbs almost all of the incident photons inside the depletion region. If the absorbed photons possess energy greater than the energy of the band gap energy of the semiconductor, electrons from the valence band are excited into the conduction band, which creates electron–hole pairs. These charge carriers are separated by the built-in electric field in the depletion region,

Fig. 9 A p–n: **a** under equilibrium, **b** under forward bias, and **c** under reverse bias



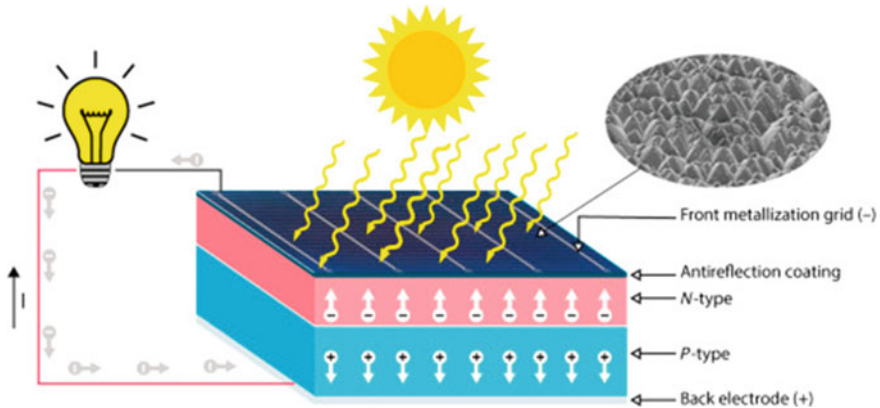


Fig. 10 The basic working principle of solar cell. Taken from [38], with permission

this electric field drives the electrons and holes to move out of the depletion region. Hence, electrons diffuse inside the n-region, and holes diffuse inside the p-region. The two electrodes on both sides of the junction then collect these carriers creating a potential difference between them. If an external load is connected, it offers a path for the electrons to move from the n-region, through this load and reach the p-region, which generates an electric current flow across this load. In this way, the solar cell device produces a direct current. The anti-reflective coating is an essential layer in the structure of a solar cell device, as it decreases the reflections from the incident sunlight and allows the absorption of more light into the device [4, 40].

There are significant parameters that describe the performance of a solar cell:

Short-Circuit Current

The short-circuit current (I_{sc}) is the current that flows across the external circuit when the voltage across the solar cell is zero, i.e. the two electrodes are short-circuited, and it represents the maximum current that flows through a solar cell device [37]. The short-circuit current depends on the area of the solar cell (A), therefore the short-current density (J_{sc}) is more commonly used, where: $J_{sc} = I_{sc}/A$.

Open-Circuit Voltage

The open-circuit voltage (V_{oc}) is the maximum voltage obtained from a solar cell when no load is applied, and consequently, the current flows in the external circuit is zero [4, 37].

Fill Factor

The fill factor (FF) is defined as the ratio of the maximum output electrical power ($P_m = V_m J_m$) obtained from a solar cell device and the multiplication of V_{oc} by J_{sc} [4, 37].

$$FF = \frac{V_m J_m}{V_{oc} J_{sc}} = \frac{P_m}{V_{oc} J_{sc}} \quad (1)$$

Theoretically, the optimum value of the fill factor should be 1. Practically, FF values larger than 0.75 are satisfying [30].

Conversion Efficiency

The conversion efficiency (η) is the ratio of the maximum power (P_m) and the incident power (P_s) [4]:

$$\eta = \frac{P_m}{P_s} \tag{2}$$

Figure 11 shows the IV characteristic curve and the main parameters of a solar cell device.

Silicon solar cell has gained a great interest in photovoltaics, as it is abundant in the earth’s crust, stable, and non-toxic element [12]. In 1954, researchers at Bell laboratories introduced the first c-Si device, with a 6% conversion efficiency [41]. In the 1990s, the c-Si solar cell has been produced on large scale and integrated into the industry. Since then, it has been used in several fields, such as housing, aerospace, electronic devices, etc. However, the fabrication cost of c-Si solar cells is still expensive when compared to the other traditional energy sources. Many efforts have been done to improve the conversion efficiency of crystalline silicon and to decrease the production cost [42]. One of the techniques that are used to increase the conversion efficiency is by applying nanostructured layer coating on the solar cell panel. In a recent study, the effect of different anti-reflective coating materials on the efficiency of silicon solar cells has been investigated [43]. Ashok Kumar et al. found that using CNT-TiO₂-SiO₂ as an anti-reflective coating gives the best result among the different used materials with an improvement in the conversion efficiency by 31.25% when compared to the uncoated cells. Figure 12 shows the I-V characteristic curve for coated/ uncoated devices.

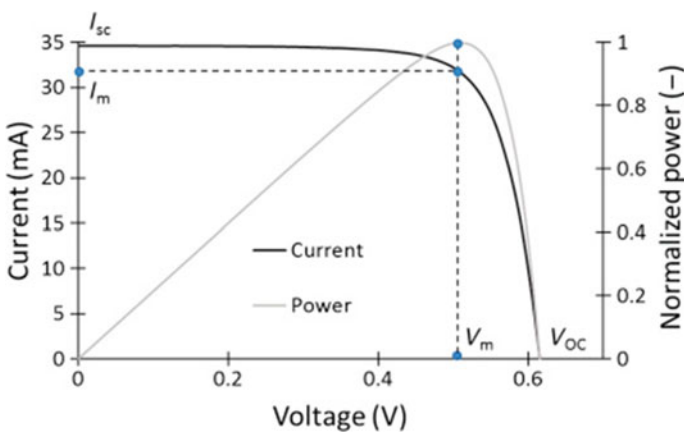


Fig. 11 IV characteristic curve of a solar cell device. Taken from [38], with permission

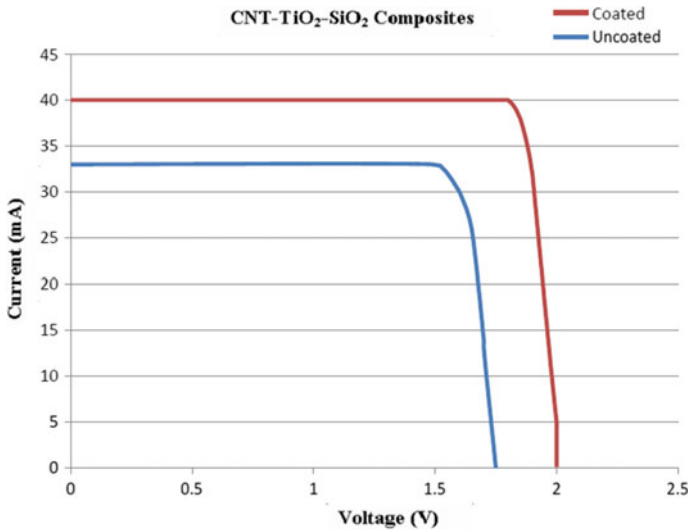
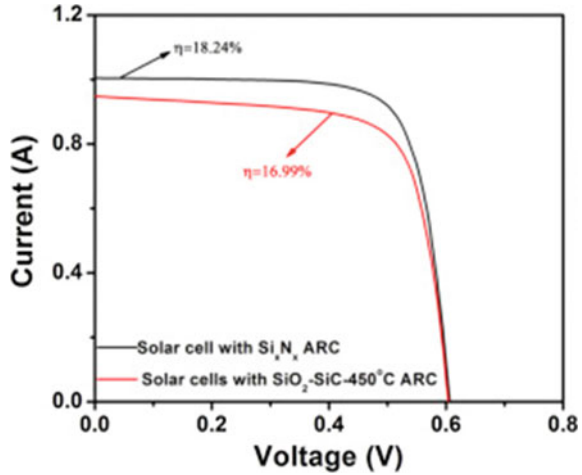


Fig. 12 I-V characteristic curve for CNT coated cell [43]

Jannat et al. used a low-cost deposition technique to deposit SiC-SiO₂ nanocomposite anti-reflective coating on P-type Si solar cell [44]. A SiC-SiO₂ nanocomposite layer was formed by two steps: the coating of the precursor solution by using spin coating, then the deposited layer was annealed at 450 °C. The study revealed that when the cell was coated by SiC-SiO₂ nanocomposite, the reflectance was reduced by 7.08% at a wavelength range from 400 to 1000 nm compared with the textured Si wafer. Furthermore, an improvement in the conversion efficiency by 18.24% was observed with SiC-SiO₂ nanocomposite anti-reflective coating when compared with the efficiency of the commercial Si_xN_x anti-reflective coating (16.99%). Figure 13 shows the enhancement in the conversion efficiency after the coating of SiC-SiO₂ nanocomposite. Gangopadhyay et al. used Diamond-like nanocomposite (DLN) thin film, which is based on amorphous carbon, as an anti-reflective coating for c-Si solar cell [45]. The reflectance loss of the textured crystalline silicon was found to be 8.31% in the wavelength range from 300 to 1100 nm, after coating with the anti-reflective nanocomposite-based material it was reduced to 2.25%. They also noticed an improvement in the conversion efficiency by 0.8% after coating the textured crystalline silicon with the anti-reflective nanocomposite material.

Besides the coating of an anti-reflective nanocomposite layer, many different ways can be utilized to enhance the conversion efficiency as well as reducing the losses in silicon solar cells. For instance, it is significant to decrease the thermalization losses in a solar cell device. The thermalization losses occur when photons having energy larger than the band gap energy are absorbed, consequently, an electron-hole pair that has an excess amount of energy is generated, this excessive energy is dissipated as heat at the conduction and valance band edges [46]. Down-shifting (or -converter) is an optical approach used to convert the high energy of the incident photon, that

Fig. 13 I–V characteristic curve of p-type Si solar cells coated with Si_xN_x and SiC-SiO_2 anti-reflective coatings at 450°C . Taken from [44], with permission



is not absorbed efficiently, into much lower energy that could be highly absorbed by the solar cell [47]. Dai Prè et al. used Mn-doped ZnS downshifting nanoparticles to reduce the thermalization losses [48]. They investigated the effect of different concentrations of ZnS:Mn nanoparticles on the conversion efficiency of silicon solar cell (0, 0.1, 0.2, and 0.5 wt%). An enhancement in the conversion efficiency of c-Si by 2% with a concentration of 0.1 wt% of the nanocomposites.

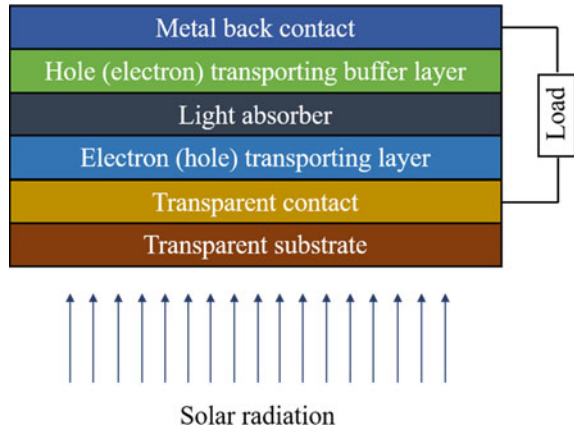
Nanocomposites can be also used as encapsulation materials to protect the solar cell from harmful environmental changes like humidity, UV radiations, etc. Oliveira et al. used ethylene–vinyl acetate copolymer/graphene oxide nanocomposites with different concentrations of graphene oxide (0.25, 0.50, 0.75, 1.00, 2.00% wt) [49]. They found that using a concentration of 0.25 wt% of graphene oxide is promising as an encapsulant material for the solar cell.

Xu et al. utilized p-type $(\text{CuS})_x:(\text{ZnS})_{1-x}$ nanocomposite to produce heterojunction p- $(\text{CuS})_x:(\text{ZnS})_{1-x}/n\text{-Si}$ solar cells [50]. They fabricated a p-type $(\text{CuS})_x:(\text{ZnS})_{1-x}$ transparent conductor by using a simple and cost-effective technique at low temperatures. They reached a large hole conductivity $> 1000 \text{ S cm}^{-1}$, an ideal V_{OC} value of 535 mV, and J_{sc} value of 21 mA/cm^2 . These results confirm that nanocomposite materials can be used to fabricate high-performance Si heterojunction by simple and low-cost solution-based techniques, and at low temperatures. Which may help in decreasing the production cost of Si solar cells in the future.

5.2 Second Generation Solar Cells

One of the major disadvantages of using silicon in PV applications is that it has an indirect bandgap, which requires the manufacturing of a thick layer with a thickness of around 180 to 300 μm to absorb photons. Besides, silicon has a band gap of around

Fig. 14 The basic structure of TFSC



1.1 eV, this prevents silicon solar cell from absorbing more than 50% of the visible spectrum. These drawbacks hinder the reduction of the manufacturing cost of silicon solar cells. This has led to the innovation of the second generation of solar cells, which is based on thin film solar cells (TFSCs) [51]. The essential goal of this generation is to decrease the fabrication cost by using low-cost materials with suitable optical and electrical properties. Cadmium telluride (CdTe), amorphous silicon (a-Si), and copper indium gallium diselenide (CIGS) are the most widely used thin-film solar cells in the PV market [52].

The working principle of thin-film solar cells follows the same concept as the traditional c-Si. When the sunlight strikes a TFSC device, photons with an energy greater than the band gap of the absorber are easily absorbed. Subsequently, the electron–hole pairs are generated in the absorber, which are separated by the electric field in the depletion region of the p–n junction. If the photon’s energy is lower than the band gap of the absorber, it will not separate electron–hole pairs and will completely pass through the absorber. Then, the two electrodes collect the created charge carriers [51]. As the concentration of the created carrier increases; the open-circuit voltage increases. Figure 14 represents the basic structure of a typical TFSC device.

5.2.1 Cadmium Telluride Thin Film Solar Cell

Cadmium telluride (CdTe) is a promising semiconductor for thin-film solar cell applications. It has a direct band gap of about 1.45 eV and a large absorption coefficient ($>5 \times 10^5/\text{cm}$), which allows CdTe solar cell to absorb about 99% of the incident photons having energy higher than the band gap in a very thin layer [53, 54]. Also, CdTe is stable, can be fabricated by low-cost techniques, and its maximum conversion efficiency has reached 22.1% when used in a solar cell device, these features make it one of the best thin-film solar cells in the PV market [55]. One of the techniques to

produce an efficient device is the selection and deposition of a suitable buffer layer (also called contact layer, carrier selective contact, carrier transport layer, etc.) that allows an efficient collection of the photogenerated charge carriers and transporting them out of the device with minimized losses [56]. It is possible to apply nanocomposite $(\text{CuS})_x(\text{ZnS})_{1-x}$ thin film as a buffer layer, or transparent hole transport layer (HTL) at the interface between CdTe and a metallization layer in CdTe solar cell [57]. A study has revealed that nanocomposite $(\text{CuS})_x(\text{ZnS})_{1-x}$ thin films are highly transparent in the visible region, and a free hole concentration of about 10^{21} cm^{-3} , which offers large electrical conductivity [50]. A study was done by Subedi et al. has investigated the effect of depositing a transparent conducting $(\text{CuS})_x(\text{ZnS})_{1-x}$ nanocomposite thin film as a back-contact interface layer between the CdTe and the standard Cu/Au back contact. $(\text{CuS})_x(\text{ZnS})_{1-x}$ nanocomposite thin films have shown p-type conductivity with high transmission ($>70\%$ at the visible region), and a large band gap of about 2.7 eV. The study has revealed that the introduction of the $(\text{CuS})_x(\text{ZnS})_{1-x}$ nanocomposite layer into the structure of the CdTe device can improve the conversion efficiency by 3.2% when compared with the device used only standard Cu/Au back contact. An efficiency of 13% was gained by utilizing $(\text{CuS})_x(\text{ZnS})_{1-x}$ nanocomposite thin film as a hole transport layer at the CdTe back contact [57].

Woods-Robinson et al. [56] studied the influence of the incorporation of p-type $\text{Cu}_x\text{Zn}_{1-x}\text{S}$ ($x = 0.30, 0.45, 0.60$) nanocomposite thin film as a back contact layer in CdTe solar cell. They found that the performance of this back contact is similar to the standard ZnTe:Cu back contacts with no decrease in external quantum efficiency. They also observed these cells remained stable over one year.

Cu–Zn–S thin films are highly conductive and transparency to light in the visible region. Bastola et al. used p-type Cu–Zn–S nanocomposite thin film as a back-contact hole transport layer in CdTe solar cell [58]. They observed that the conversion efficiency reached about 12.6% with an average of 12.4% with Cu–Zn–S as a back-contact, while for when Au was used only as a back-contact the efficiency reached 10.4% with an average of 9.8%. They also detected a reduction in the barrier height with Cu–Zn–S nanocomposite thin film.

5.2.2 Copper Indium Gallium Diselenide Thin Film Solar Cell

Copper indium gallium diselenide (CIGS) is another promising material for fabricating thin-films solar cells owing to its attractive properties such as large absorption coefficient, tunable bandgap, flexibility, and large conversion efficiency [59]. The highest conversion efficiency of CIGS solar cell has reached 23.35% [60]. Alhammadi et al. applied graphene–CdS nanocomposite as a buffer layer to enhance the conversion efficiency of CIGS thin film solar cells [61]. They found that the conversion efficiency is 8.62% using graphene–CdS nanocomposite buffer layer which is better when compared with the standard pure CdS buffer layer ($\sim 7.64\%$).

Wakefield et al. used mesoporous silica nanocomposite as an anti-reflective coating for Cu(In,Ga)Se₂ TFSC [62]. The idea of this study was to deposit efficient nanocomposite anti-reflective coating with a low-cost non-vacuum technique. They observed that using mesoporous silica nanocomposite as an anti-reflective coating layer reduced the Fresnel reflections, increased the short circuit current by 4.9%, and improved the quantum efficiency below 1000 nm.

5.2.3 Copper Zinc Tin Sulfide Thin Film Solar Cell

Although CIGS thin-film solar cell has recorded high conversion efficiency, the toxicity, rarity, and high cost of In and Ga have limited its commercial availability [63]. Copper zinc tin sulfide (CZTS) compound is an attractive alternative to CIGS. CZTS is a p-type semiconducting material with a direct band gap of 1.5 eV and a large absorption coefficient $> 10^4$. Owing to the non-toxicity, abundance in the earth's crust, and reduced-cost of its constituent elements, CZTS is more environmentally friendly and cost-effective when compared to CIGS [64].

Lin et al. [64] mixed CZTS with SnO₂ to synthesis CZTS@SnO₂ nanocomposites by an easy one-pot solvothermal process. They found that CZTS@SnO₂ nanocomposites show an increase in the photocurrents compared to pure CZTS samples. This increase is due to the p–n heterojunctions grown between CZTS and SnO₂, which can promote the separation of photoinduced electrons and holes.

5.3 Third Generation Solar Cells

Third generation offers both relatively high efficiency and low-cost devices. The main goal of this technology is to fabricate efficient photovoltaic devices using the thin film deposition methods that are applied for the second generation and/or new arrangements or materials. Besides, this technology uses non-toxic and abundant materials, which make it appropriate for large area deposition. Furthermore, the third generation utilizes nanostructured or organic materials that improve the conversion efficiency by phenomena such as the hot carrier-collection, the creation of various carriers (impact ionization), or modern semiconductor structures that include several energy levels [54].

The most significant technologies that exist in the third generation of PV devices are dye-sensitized solar cells, perovskite solar cell (PSC), quantum dot solar cells, and organic solar cells.

5.3.1 Dye-Sensitized Solar Cells (DSSCs)

Dye-sensitized solar cells (DSSCs) have gained great interest owing to their easy and reduced-cost manufacturing, simple structure, and relatively acceptable efficiency when compared to traditional solar cells [65–67]. Besides, DSSCs exhibit stable performance under different conditions such as incident angle, temperature, humidity, and irradiation [66]. The fabrication of DSSC was reported first in 1991 [68], and since then many efforts have been done to enhance the conversion efficiency. Although the conversion efficiency of DSSCs is much lower than the other solar cells, it is considered more desirable in terms of production cost [65]. The highest recorded power conversion efficiency for DSSC is 12.3%, while the efficiency of the laboratory scale has reached 14.3% [69]. A typical DSSC is formed between two transparent conductive oxide materials (TCO) that are deposited on glass substrates. The main construction of DSSC includes a transparent conducting working electrode (Photoanode), a sensitizer (dye), a counter electrode (cathode), and a redox electrolyte [66, 67, 70]. A schematic diagram for a traditional DSSC is shown in Fig. 15. Usually, the TCO-glass substrate is coated with a thick mesoporous layer of a nanocrystalline and wide band gap metal oxide semiconductor (MOS), such as TiO_2 , ZnO , and SnO_2 , this structure is referred to as photoanode. The mesoporous fabrication of the metal oxide layer affords a large surface area to maximize the dye absorption. To achieve the regeneration of dye molecules, a liquid electrolyte is inserted between the photoanode and the cathode. The cathode is a conductive glass that is commonly platinized and has the responsibility of the catalytic reaction between the charge from the external circuit and the mediator in the electrolyte [70].

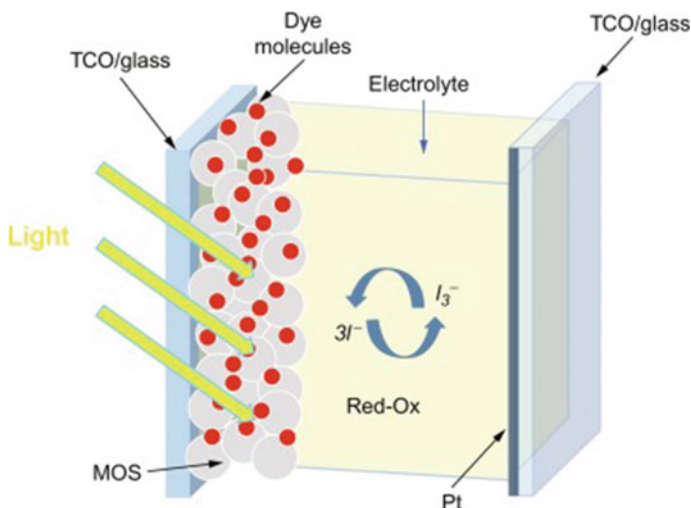


Fig. 15 A schematic representation of dye-sensitized solar cell. Taken from [70], with permission

The DSSC operates mainly in three main steps (i) the absorption of the photons and charge separation, (ii) transport and collection of charge, and (iii) dye regeneration [70]. When DSSC solar cell device is illuminated, the photons pass through the photoanode (let us assume it is made from TiO_2). Subsequently, photons with wavelength equivalent to the energy difference between the highest occupied molecule orbital (HOMO) and lowest unoccupied molecule orbital (LUMO) of dye sensitizer are absorbed. Subsequently, the electrons that exist in the ground state of dye are transferred to the excited state by the phenomenon termed photoexcitation of the dye. Excitation of the dye sensitizer results in the transfer of electrons from the excited state to the conduction band of TiO_2 , and then they are transferred through the semiconductor via the diffusion process and arrives at the conducting layer. The electrons start to flow to the cathode into the external circuit generating an electric current and then re-flow through the cathode, where they induce an oxidation–reduction process in the electrolyte solution. The electrolyte transfers the electron to the oxidized dye at the photoanode and recreates the dye molecule so that the process runs continuously. The current continues to flow through the circuit as long as the light strikes the cell [67].

Recent studies focus on designing an alternative counter electrode, to increase DSSC efficiency as well as to use low-cost material compared to the traditional counter electrode (cathode). Currently, novel materials are involved to fabricate an alternative counter electrode, such as Polymers, metal and polymer nanocomposites, and carbon-based materials [65]. A recent study by Bayram et al. has studied the effect of substituting the platinum (Pt) counter electrode with Graphene/polyaniline nanocomposite [65]. They observed that the power conversion efficiency with Graphene/polyaniline nanocomposite electrode varied from 0.56 to 1.36%, depending on the number of graphene layers. Furthermore, the efficiency for the cell with the conventional platinum-electrode was 1.1%. These results suggest that using Graphene/polyaniline nanocomposite as a counter electrode improves the conversion efficiency for DSSC. Another study by Younas et al. in which they used Pt-free electrode to improve the conversion efficiency and also to minimize the production cost [71]. In this study, Multiwall carbon nanotubes (MWCNT) were used as a Pt-free counter electrode. In addition, MWCNT- TiO_2 nanocomposites were used as a photoanode with four different mass ratios of MWCNT in TiO_2 ($n = 0.03, 0.06, 0.09$ and 0.12%). Using MWCNT in TiO_2 showed an improvement in the light absorption in the visible region, reduced electron recombination, and enhanced electron transportation. This has led to an improved conversion efficiency. The results have revealed that the DSSC with 0.06%- MWCNT- TiO_2 nanocomposites have the highest conversion efficiency (about 7.15%). This efficiency was better by about 13% when compared with the device made with the conventional Pt-counter electrode. In a different study, Mousavi and Taherpour used MWCNT/a- Fe_2O_3 as a counter electrode for DSSC [72]. Results reveal broad electroactive surface area, high response stability, and reduced resistance because of the high electrical conductivity and electrocatalytic activity of the MWCNT/a- Fe_2O_3 electrode. The conversion efficiency of DSSC with MWCNT/a- Fe_2O_3 counter electrode was about 6%, which is comparable to the efficiency of DSSC with Pt- electrode (that was about 7%). These

findings suggest the possibility of using nanocomposites as a low-cost alternative counter electrode to Pt-conventional electrode.

Recent studies revealed that using rGO in the structure of photoanode increases dye absorption. Javed et al. used Ag/rGO/TiO₂ ternary nanocomposite as a photoanode for plasmonic dye-sensitized solar cells [73]. Ag/rGO/TiO₂ ternary nanocomposite photoanode exhibited improved power conversion efficiency of 6.87%, which was about 15% higher when compared to the pure conventional TiO₂ based photoanode. Mehmood et al. also enhanced the conversion efficiency of DSSC by using co-sensitized nanocomposite photoanode [66]. They used a mixture of dye solutions of Ruthenium (N719) and organic dye (RK-1) for the sensitization of graphene/TiO₂ nanocomposite thin films. They obtained a conversion efficiency of 9.45% for the DSSC with the photoanode of graphene/TiO₂ based nanocomposite thin films co-sensitized with N719 and RK-1, which is improved when compared with the mixture of N719 and RK-1 with pristine TiO₂ films (the efficiency was about 8.45%). Kazmi et al. applied graphene –TiO₂ nanocomposite as a photoanode for DSSC with different percentages of graphene [67]. The results exhibited that the use of graphene thin film enhanced the performance of the DSSC. This enhancement has resulted from the increase in light absorption, the broad range of absorption wavelengths, the reduction of charge transportation distances, and the enhanced charge recombination resistance after incorporation of graphene nanocomposite. They observed an improvement in the conversion efficiency from 4.98 to 7.68%.

5.3.2 Perovskite Solar Cell (PSC)

Evolving from DSSCs, PSC has emerged as a new type of photovoltaic technology. It has attracted great interest owing to its reduced-cost and easy manufacturing among the various categories of photovoltaic devices. It has a smaller thickness, lighter weight, and more flexibility in comparison with the traditional c-Si [1]. Additionally, it has outstanding properties such as a large absorption coefficient, tunable band gap, reduced-temperature processing, and abundance of its constituent elements [74]. In the past 10 years, the conversation efficiency of PSC has improved from 3.8% to more than 25% since it was first produced in 2009, making them the fastest-growing technology in photovoltaic manufacturing [1, 75]. To date, the organometal halide CH₃NH₃PbX₃ (X = Cl, Br, I) is considered the most successful perovskite compound, as it provides the most attractive properties of optimum photovoltaic absorber such as high optical absorption, high mobility, and diffusion length of electrons and holes, surpassing structural defect-tolerance, low point defects, decreased surface recombination velocity, and benign grain boundary effects [74].

A typical PSC device structure consists of an intrinsic perovskite absorber layer (i) with a thickness of several hundred nanometers placed between an n-type electron transporting material (ETM) and a p-type hole transporting material (HTM) [74–76]. Therefore, the PSC structure can be classified into two different forms: a conventional type (n-i-p structure, which includes mesostructure) and an inverted type (p-i-n structure). Figure 16 shows the two different structures of PSC. When

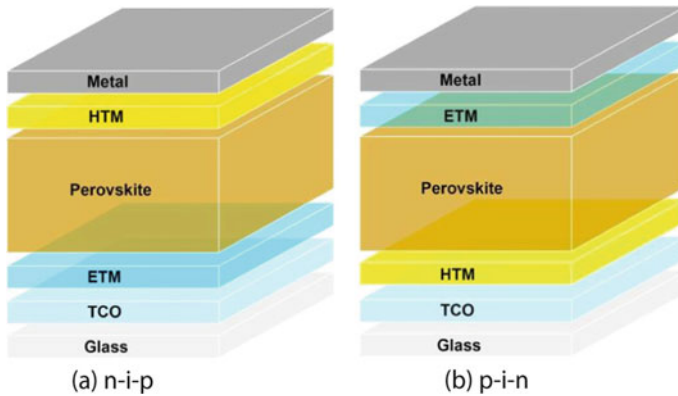


Fig. 16 The PSC device structure of **a** Conventional **b** inverted structures. Taken from [80], with permission

the sunlight strikes the device, photons are absorbed by the perovskite absorber layer followed by the generation of the charge carriers in the absorber. Consequently, electrons are introduced to the conduction band of ETM from the lowest unoccupied molecular orbital (LUMO) of the perovskite absorber layer. Similarly, holes are introduced into HTM from the highest occupied molecular orbital (HOMO) of the perovskite absorber layer. Afterward, the counter electrode will collect these photoexcited charge carriers. Both ETM and HTM play a vital role in the construction of PSC, as they transfer electrons and holes to the corresponding electrodes and prevent the diffusion of holes/electrons in the opposite direction, respectively [75]. The performance of PSC depends on many factors, among these factors the interface between the ETM and perovskite absorber layer has gained great attention due to its vital role in collecting electrons, and hence defining the performance of PSC. ETM usually consists of metal oxides TiO_2 , ZnO , SnO_2 , Al_2O_3 , Nb_2O_5 , Zn_2SnO_4 , and WO_3 [76]. Among these metal oxides, titanium dioxide (TiO_2) is the most frequently used ETM material to produce efficient PSC device, due to its fascinating properties such as superior electron-transporting features, low-cost, non-toxic, facial and variable deposition techniques, high chemical stability, and tunable electronic properties [76–78]. However, high-temperature processing is required to fabricate such materials to improve their crystallinity and increase the charge carrier mobility and hence lead to improved performance. Elevated-temperature sintering has many disadvantages as it increases the cost and slows the fabrication process, and can be applied only to hard, heat-resistant substrates, which prevents their usage with plastic and malleable metal foils and multijunction devices [79]. Wang et al. utilized the benefits of nanocomposites and presented a cost-effective, solution-based deposition process to produce nanocomposites of graphene and nanosized TiO_2 particles at low temperatures as an electron transport layer in meso-superstructured PSCs [79]. They successfully fabricated a highly efficient PSC device with an efficiency of about 15.6% at relatively low-temperature processing. Dadashbeik et al. presented

a simulation study in which they studied the influence of exploiting TiO₂/graphene nanocomposites as an electron transport layer in PSC by using [76]. An enhancement in the optical absorption in the active layer was found after using TiO₂/Gr nanocomposites. Furthermore, the conversion efficiency of PSC was increased to 17.01% when TiO₂/Gr(10%) nanocomposites were utilized rather than TiO₂ (the efficiency was about 14.42%).

Manibalan et al. utilized CeO₂-TiO₂ nanocomposite as an electrode material for PSC [81]. A device with pure TiO₂ showed an efficiency of about 8.07% with a short-circuit current density (J_{sc}) of 17.7 mA/cm², an open-circuit voltage (V_{oc}) of 0.74 V, and a fill factor (FF) of 0.69. While for the device with CeO₂/TiO₂ nanocomposites an improvement in solar cell parameters was observed, an efficiency of 10.51%, J_{sc} of 19.07 mA/cm², V_{oc} of 0.87 V, and FF of 0.63 were achieved.

5.3.3 Organic Solar Cell (OSC)

Recently, OSC has attained increased interest owing to its interesting advantages such as low-cost, mechanical flexibility, easy processing, suitable for large-area deposition, and environmentally-friendly [1, 82–84]. Moreover, the deposition of the active layers is simply done by solution-based processes such as spin-coating or printing, and hence it provides device fabrication at low temperature, which reduces the cost of the device [30]. The photoactive layer of OSC is composed of donor and acceptor organic materials [82]. The working principle of OSC differs from that of inorganic solar cells, as there is no generation of free charge carriers. Here, when the sunlight strikes the device, photons are absorbed by the donor, followed by the creation and confinement of excited states or the so-called excitons. An exciton is an electron–hole pair that is brought to each other by electrostatic force and can be dissociated into free electron–hole pairs by effective electric field force. Then, the electrons are collected from separated electron–hole pairs by the acceptor. OSCs can be divided into two types based on the chemical structure of the photoactive layer components, particularly the donor (p-type) materials: polymer solar cells and small-molecule solar cells [12, 30]. Polymer solar cells can also be transparent, and hence they can be employed in windows, walls, flexible electronics, etc. The major drawbacks of polymer solar cells are reduced conversion efficiency and photochemical degradation [30]. A typical polymer solar cell structure consists of a transparent conductive oxide electrode, usually an indium tin oxide (ITO) conductive coated glass, followed by a hole-transporting layer that made from poly(3,4-ethylenedioxythiophene):poly(styrenesulfonate) (PEDOT:PSS), then an active layer, an electron transport layer, and a metal electrode. The typical and inverted structure of polymer solar cells is depicted in Fig. 17. The efficiency of the polymer solar cell device depends on the type and the ordering of the layers and also the type of the metal electrode. The most common structure of polymer solar cell is the bulk heterojunction (BHJ) design, which is a blend of a donor polymer and a fullerene acceptor [30].

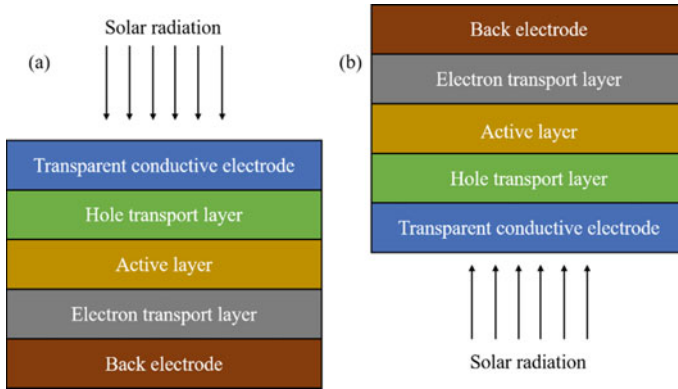


Fig. 17 Schematic representation of device structure of **a** typical polymer **b** inverted polymer

Similar to the conventional solar cell, the performance of the OSC is identified by three main parameters: the open-circuit voltage (V_{oc}), the short-circuit current density (J_{sc}), and the fill factor (FF). The conversion efficiency mainly depends on these parameters and the incident solar power (P_{in}). V_{oc} is mainly determined by the difference between the HOMO of the polymer donor and the LUMO of the fullerene acceptor, and J_{sc} is restricted by the multiplication of the photoinduced charge carrier density and the mobility inside the organic semiconductor [30].

Nanocomposites have been incorporated in the manufacturing of organic solar cells to improve their conversion efficiency. In a recent study reduced graphene oxide-germanium dioxide nanocomposite (rGO-GeO₂) was utilized in the photoactive layer of bulk heterojunction solar cells (BHJ SCs). A blend of poly-3-hexylthiophene (P3HT) and (6–6) phenyl-C₆₁-butyric acid methyl ester (PCBM) were used as donor and acceptor materials, respectively [82]. The conversion efficiency of BHJ solar cells with rGO-GeO₂ nanocomposite in the photoactive layer was increased by a ratio of up to 53%. Furthermore, the optical absorption and photocurrent were significantly improved when rGO-GeO₂ nanocomposite was incorporated in the photoactive layer. Besides, an increase in the short-circuit current density (J_{sc}) was achieved. The attained high J_{sc} implied that the incorporation of rGO-GeO₂ nanocomposite in the photoactive layer promoted exciton separation and generation of charge percolation pathways for charge transport to the electrodes, and hence limited charge recombination processes.

Mbuyise et al. induced a trimetallic nanocomposite (Ag:Zn:Ni) in the P3HT:PCBM photoactive layer of the organic solar cell [83]. An improvement in the conversion efficiencies of the solar cells was observed by 57 and 84% for 4 and 6% volume concentrations of the suspension of the metal particles, respectively. The improvement in the performance of the devices was assigned to the enhancement of light trapping into the photoactive layer and enhanced charge transport processes in the BHJ films after the incorporation of the trimetallic nanocomposite. Besides, the

induced nanocomposite worked as a separation center and an alternative transport channel to collect the photocurrents created by enlarged charge mobility.

Soultati et al. investigated the effect of using ZnO:ZnWO₄ nanocomposite as an electron transporting material on the performance of inverted BHJ OSCs (84). An improvement in the Voc, Jsc, and FF was achieved in the devices with the ZnO:ZnWO₄ nanocomposites. In addition, both of the inverted BHJ OSCs constituted of either poly (3-hexylthiophene) (P3HT): [6,6]-phenyl-C₇₁ butyric acid methyl ester (PC₇₁BM) or P3HT:indene-C₆₀ bisadduct (IC₆₀BA) photoactive blends exhibit improved efficiency, showing improvement by a 27 and 23%, respectively, in their efficiencies compared to the reference devices utilized pure ZnO. Additionally, the devices with ZnO:ZnWO₄ nanocomposite film show very good long-time stability, saving 95% of their initial conversion efficiency after storage for 500 h.

6 Conclusions and Perspectives

This chapter has presented a detailed discussion on nanocomposites and their types. It also provided some examples of the most common types of nanocomposites that were recently incorporated into photovoltaic materials to improve their conversion efficiency. For example, titanium dioxide and carbon nanomaterials including fullerene, graphene, and carbon nanotubes were discussed briefly. We also discussed the development of photovoltaic technology by presenting the four generations of the solar cells. The first generation introduced c-Si solar cells, which dominate the photovoltaic market with the highest recorded conversion efficiency. Nanocomposite materials were used in many studies in the fabrication of c-Si solar cells as anti-reflective coatings, which resulted in improved performance. Also, nanocomposites can be used as encapsulation materials to protect c-Si solar cells from environmental pollution, humidity, etc. The second generation, which includes thin-film solar cells, uses earth-abundant and low-cost materials to reduce the fabrication cost of solar cells. We discussed in this chapter the most common types of thin-film solar cells such as cadmium telluride, CIGS, and CZTS. Nanocomposite materials have been also incorporated inside the structure of thin-film solar cells, to improve their conversion efficiency. For the third generation, dye-sensitized solar cells, perovskite solar cells, and organic solar cells were discussed in detail. Several studies showed that introducing nanocomposites into the fabrication of the third generation helped to improve the performance of the device, as well as reducing the production cost. For instance, nanocomposite materials were used as an alternative for the costly platinum electrode. The tendency for manufacturing a highly efficient solar cell device is and will be the main target in the photovoltaic industry. Besides, the production of low-cost, easy processing, non-toxic, thin, and flexible solar cell devices will become more and more demanding. Therefore, it is expected to improve the performance as well as decreasing the production cost of the second and third photovoltaic generations to fulfill the requirements of the photovoltaic market. It is also expected to involve nanomaterials and nanocomposites more and more in the photovoltaic industry as it

provides an improvement in the conversion efficiency and can also replace the costly electrodes, thus it will help in reducing the fabrication cost.

References

1. Wu, C., et al.: Multifunctional nanostructured materials for next generation photovoltaics. *Nano Energy* **70**, 104480 (2020)
2. Valadi, K., Gharibi, S., Taheri-Ledari, R., et al.: Metal oxide electron transport materials for perovskite solar cells: a review. *Environ. Chem. Lett.* **19**, 2185–2207 (2021)
3. Becquerel, E.: Recherches sur les effets de la radiation chimique de la lumiere solaire au moyen des courants electriques [Research on sunlight chemical radiation effects using electrical currents.]. *C. R. Hebd. Seances Acad. Sci.* **9**, 145–149 (1839)
4. Isshiki, M., Wang, J.: II-IV semiconductors for optoelectronics: CdS, CdSe, CdTe. In: *Springer Handbook of Electronic and Photonic Materials*. Springer Handbooks, pp. 853–863. Springer, Cham (2017)
5. Nayak, P.K., Mahesh, S., Snaith, H.J., Cahen, D.: Photovoltaic solar cell technologies: analysing the state of the art. *Nat. Rev. Mater.* **4**(4), 269–285 (2019)
6. Wagner, S., Shay, J.L., Migliorato, P., Kasper, H.M.: CuInSe₂/CdS heterojunction photovoltaic detectors. *Appl. Phys. Lett.* **25**(8), 434–435 (1974)
7. Stathatos, E.: Dye sensitized solar cells as an alternative approach to the conventional photovoltaic technology based on silicon - recent developments in the field and large scale applications. In: Kosyachenko, L.A. (ed.) *Solar Cells - Dye-Sensitized Devices*, pp. 471–492. IntechOpen (2011)
8. Conibeer, G.: Third-generation photovoltaics. *Mater. Today* **10**(11), 42–50 (2007)
9. Green, M.A.: Third generation photovoltaics: ultra-high conversion efficiency at low cost. *Prog. Photovoltaics Res. Appl.* **9**(2), 123–135 (2001)
10. Granqvist, C.G.: Transparent conductors as solar energy materials: a panoramic review. *Sol. Energy Mater. Sol. Cells* **91**(17), 1529–1598 (2007)
11. Moharam, M.M., El Shazly, A.N., Anand, K.V., et al.: Semiconductors as effective electrodes for dye sensitized solar cell applications. *Top. Curr. Chem.* **379**, 20 (2021)
12. Luceño-Sánchez, J.A., Díez-Pascual, A.M., Capilla, R.P.: Materials for photovoltaics: state of art and recent developments. *Int. J. Mol. Sci.* **20**(4), 976 (2019)
13. Jayawardena, K.D.G.I., Rozanski, L.J., Mills, C.A., Beliatis, M.J., Nismy, N.A., Silva, S.R.P.: ‘Inorganics-in-Organics’: recent developments and outlook for 4G polymer solar cells. *Nanoscale* **5**(18), 8411–8427 (2013)
14. Twardowski, T.E.: *Introduction to Nanocomposite Materials: Properties, Processing, Characterization*. DEStech Publications, Inc., Lancaster (2007)
15. Kartsonakis, I.A., Charitidis, C.A., Kordas, G.C.: Synthesis and characterization of ceramic hollow nanocomposites and nanotraps. In: *Nanocomposites*, pp. 1–31. De Gruyter (2013)
16. Visakh, P.M.: Introduction for nanomaterials and nanocomposites: state of art, new challenges, and opportunities. In: *Nanomaterials and Nanocomposites*, pp. 1–19. Wiley-VCH Verlag GmbH & Co. KGaA (2016)
17. Zhang, Z., Chen, D.L.: Contribution of Orowan strengthening effect in particulate-reinforced metal matrix nanocomposites. *Mater. Sci. Eng. A* **483**(1), 148–152 (2008)
18. Rathod, V.T., Kumar, J.S., Jain, A.: Polymer and ceramic nanocomposites for aerospace applications. *Appl. Nanosci.* **7**(8), 519–548 (2017)
19. Sternitzke, M.: Review: structural ceramic nanocomposites. *J. Eur. Ceram. Soc.* **17**(9), 1061–1082 (1997)
20. Ferroni, L.P., Pezzotti, G., Isshiki, T., Kleebe, H.J.: Determination of amorphous interfacial phases in Al₂O₃/SiC nanocomposites by computer-aided high-resolution electron microscopy. *Acta Mater.* **49**(11), 2109–2113 (2001)

21. Sachinjith, K.R., Swathi Krishna, K.R.: A review on types of nanocomposites and their applications. *Int. J. Adv. Res.* **4**(6), 235–236 (2018)
22. Camargo, P.H.C., Satyanarayana, K.G., Wypych, F.: Nanocomposites: Synthesis, structure, properties and new application opportunities. *Mater. Res.* **12**(1), 1–39 (2009)
23. Barhoum, A., Shalan, A.E., El-Hout, S.I., et al.: A broad family of carbon nanomaterials: classification, properties, synthesis, and emerging applications. In: *Handbook of Nanofibers*, pp. 1–40. Springer, Cham (2019)
24. Eivazzadeh-Keihan, R., Taheri-Ledari, R., Mehrabad, M.S., et al.: Effective combination of rGO and CuO nanomaterials through poly(p-phenylenediamine) texture: Utilizing it as an excellent supercapacitor. *Energy Fuels* (2021). <https://doi.org/10.1021/acs.energyfuels.1c01132>
25. Holkar, C.R., Jain, S.S., Jadhav, A.J., Pinjari, D.V.: Scale-up technologies for advanced nanomaterials for green energy: feasibilities and challenges. In: *Nanomaterials for Green Energy*, pp. 433–455. Elsevier (2018)
26. Batool, M., Nazar, M.F., Awan, A., et al.: Bismuth-based heterojunction nanocomposites for photocatalysis and heavy metal detection applications. *Nano-Struct Nano-Objects* **27**, 100762 (2021)
27. Khan, Z.H., Kumar, A., Husain, S., Husain, M.: *Introduction to Nanomaterials. Advances in Nanomaterials*, pp. 1–23. Springer, New Delhi (2016)
28. Sastri, V.R.: Polymer additives used to enhance material properties for medical device applications. In: *Plastics in Medical Devices*, pp. 55–72. William Andrew Publishing (2010)
29. Zhen, Z., Zhu, H.: Structure and properties of graphene. In: *Graphene: Fabrication, Characterizations, Properties and Applications*, pp. 1–12. Academic Press (2018)
30. Díez-Pascual, A.M., Sánchez, J.A.L., Capilla, R.P., Díaz, P.G.: Recent developments in graphene/polymer nanocomposites for application in polymer solar cells. *Polymers (Basel)* **10**(2), 217 (2018)
31. Rakesh Tej Kumar, K., Ramakrishna, M., Durga Sukumar, G.: A review on PV cells and nanocomposite-coated PV systems. *Int. J. Energy Res.* **42**(7), 2305–2319 (2018)
32. Lin, X., Gao, P.: Graphene and carbon nanotube-based solar cells. In: *Nanomaterials for Solar Cell Applications*, pp. 603–660. Elsevier (2019)
33. Bai, Y., Mora-Seró, I., De Angelis, F., Bisquert, J., Wang, P.: Titanium dioxide nanomaterials for photovoltaic applications. *Chem. Rev.* **114**(19), 10095–10130 (2014)
34. Baalousha, M., Lead, J.R., Ju-Nam, Y.: Natural colloids and manufactured nanoparticles in aquatic and terrestrial systems. In: *Treatise on Water Science*, pp. 89–129. Elsevier (2011)
35. Diebold, U.: The surface science of titanium dioxide. *Surf. Sci. Rep.* **48**(5–8), 53–229 (2003)
36. Hersch, P., Zweibel, K.: *Basic Photovoltaic Principles and Methods*. United States (1982)
37. Smets, A., Jäger, K., Isabella, O., van Swaaij, R., Zeman, M.: *Solar Energy - The Physics and Engineering of Photovoltaic Conversion Technologies and Systems*. UIT Cambridge Ltd., Cambridge (2016)
38. Riverola, A., Vossier, A., Chemisana, D.: Fundamentals of solar cells. In: *Nanomaterials for Solar Cell Applications*, pp. 3–33. Elsevier B.V (2019)
39. Shur, M.: *Introduction to Electronic Devices* (1996)
40. Kasap, S.O.: *Principles of Electronic Materials and Devices*, 4th edn. McGraw-Hill Education, New York (2018)
41. Chapin, D.M., Fuller, C.S., Pearson, G.L.: A new silicon p-n junction photocell for converting solar radiation into electrical power. *J. Appl. Phys.* **25**(5), 676–677 (1954)
42. Xiao, S., Xu, S.: Status and progress of high-efficiency silicon solar cells. In: *High-Efficiency Solar Cells*, pp. 1–58. Springer, Cham (2014)
43. Ashok Kumar, B., Sivasankar, G., Sangeeth Kumar, B., Sundarapandy, T., Kottaisamy, M.: Development of nano-composite coating for silicon solar cell efficiency improvement. *Mater. Today Proc.* **5**(1 Part 1), 1759–1765 (2018)
44. Jannat, A., Lee, W., Akhtar, M.S., Li, Z.Y., Yang, O.B.: Low cost sol-gel derived SiC-SiO₂ nanocomposite as anti reflection layer for enhanced performance of crystalline silicon solar cells. *Appl. Surf. Sci.* **369**, 545–551 (2016)

45. Gangopadhyay, U., Jana, S., Das, S., Ghosh, P., Mondal, A.: Anti-reflective nanocomposite based coating for crystalline silicon solar cells with noticeable significance. *J. Renew. Sustain. Energy* **5**(3), 031607 (2013)
46. Heidarzadeh, H., Rostami, A., Dolatyari, M.: Management of losses (thermalization-transmission) in the Si-QDs inside 3C-SiC to design an ultra-high-efficiency solar cell. *Mater. Sci. Semicond. Process.* **109**, 104936 (2020)
47. Ahmed, H.A., Walshe, J., Kennedy, M., Confrey, T., Doran, J., McCormack, S.J.: Enhancement in solar cell efficiency by luminescent down-shifting layers. *Adv. Energy Res.* **1**(2), 117–126 (2013)
48. Dai Prè, M., et al.: Preparation and characterization of down shifting ZnS:Mn/PMMA nanocomposites for improving photovoltaic silicon solar cell efficiency. *Mater. Chem. Phys.* **139**(2–3), 531–536 (2013)
49. Oliveira, M.C.C., Soares, L.G., Viana, M.M., Diniz, A.S.A.C., Lins, V.F.C.: Development of ethylene-vinyl acetate copolymer/graphene oxide nanocomposites for crystalline silicon photovoltaic modules. *Int. J. Adhes. Adhes.* **100**, 102595 (2020)
50. Xu, X., et al.: Chemical bath deposition of p-type transparent, highly conducting (CuS)_x:(ZnS)_{1-x} nanocomposite thin films and fabrication of Si heterojunction solar cells. *Nano Lett.* **16**(3), 1925–1932 (2016)
51. Kodigala, S.R.: Thin Film Solar Cells from Earth Abundant Materials: Growth and Characterization of Cu₂ZnSn(SSe)₄ Thin Films and Their Solar Cells. Elsevier, Amsterdam (2014)
52. Lee, T.D., Ebong, A.U.: A review of thin film solar cell technologies and challenges. *Renew. Sustain. Energy Rev.* **70**, 1286–1297 (2017)
53. Ali, A.M., et al.: A computational study on the energy bandgap engineering in performance enhancement of CdTe thin film solar cells. *Results Phys.* **7**, 1066–1072 (2017)
54. Muhammad, J., et al.: Recent progressive status of materials for solar photovoltaic cell: a comprehensive review. *Sci. J. Energy Eng.* **7**(4), 77–89 (2019)
55. Li, C., et al.: Enhanced current collection of CdTe solar cells in the long wavelength region by co-evaporation deposition CdSe_xTe_{1-x} films. *Mater. Sci. Semicond. Process.* **121**, 105341 (2021)
56. Woods-Robinson, R., et al.: Sputtered p-type Cu_xZn_{1-x}S back contact to CdTe solar cells. *ACS Appl. Energy Mater.* **3**(6), 5427–5438 (2020)
57. Subedi, K.K., et al.: Nanocomposite (CuS)_x(ZnS)_{1-x} thin film back contact for CdTe solar cells: toward a bifacial device. *Sol. Energy Mater. Sol. Cells* **186**, 227–235 (2018)
58. Bastola, E., Subedi, K.K., Alfadhili, F.K., Phillips, A.B., Heben, M.J., Ellingson, R.J.: Room temperature processed transparent Cu-Zn-S nanocomposites as hole transport materials in CdTe photovoltaics. In: Conference Record of the IEEE Photovoltaic Specialists Conference (2019)
59. Youn, S.M., Park, M.J., Kim, J.H., Jeong, C.: Performance enhancement of CIGS thin-film solar cells with a functional-window NiO thin layer. *J. Alloys Compd.* **836**, 154803 (2020)
60. Nakamura, M., Yamaguchi, K., Kimoto, Y., Yasaki, Y., Kato, T., Sugimoto, H.: Cd-Free Cu(In, Ga)(Se, S) 2 thin-film solar cell with record efficiency of 23.35%. *IEEE J. Photovoltaics* **9**(6), 1863–1867 (2019)
61. Alhammedi, S., et al.: Performance of graphene–CdS hybrid nanocomposite thin film for applications in Cu(In, Ga)_{1-x}Se₂ solar cell and H₂ production. *Nanomaterials* **10**(2), 245 (2020)
62. Wakefield, G., Adair, M., Gardener, M., Greiner, D., Kaufmann, C.A., Moghal, J.: Mesoporous silica nanocomposite antireflective coating for Cu(In, Ga)Se₂ thin film solar cells. *Sol. Energy Mater. Sol. Cells* **134**, 359–363 (2015)
63. Abdelhaleem, S., et al.: Tuning the properties of CZTS films by controlling the process parameters in cost-effective non-vacuum technique. *J. Electron. Mater.* **47**(12), 7085–7092 (2018)
64. Lin, X., et al.: One-pot solvothermal synthesis of Cu₂ZnSnS₄@SnO₂ nanocomposites. *Mater. Lett.* **99**, 146–149 (2013)
65. Bayram, O., et al.: Graphene/polyaniline nanocomposite as platinum-free counter electrode material for dye-sensitized solar cell: its fabrication and photovoltaic performance. *J. Mater. Sci. Mater. Electron.* **31**(1), 10288–10297 (2020)

66. Mehmood, U., Ahmad, S.H.A., Khan, A.U.H., Qaiser, A.A.: Co-sensitization of graphene/TiO₂ nanocomposite thin films with ruthenizer and metal free organic photosensitizers for improving the power conversion efficiency of dye-sensitized solar cells (DSSCs). *Sol. Energy* **170**, 47–55 (2018)
67. Kazmi, S.A., Hameed, S., Ahmed, A.S., Arshad, M., Azam, A.: Electrical and optical properties of graphene-TiO₂ nanocomposite and its applications in dye sensitized solar cells (DSSC). *J. Alloys Compd.* **691**, 659–665 (2017)
68. O'Regan, B., Grätzel, M.: A low-cost, high-efficiency solar cell based on dye-sensitized colloidal TiO₂ films. *Nature* **353**, 737–740 (1991)
69. Tomar, N., Agrawal, A., Dhaka, V.S., Surolia, P.K.: Ruthenium complexes based dye sensitized solar cells: Fundamentals and research trends. *Sol. Energy* **207**, 59–76 (2020)
70. Calisir, M.D., Stojanovska, E., Kilic, A.: Polymer nanocomposites for dye-sensitized solar cells. In: *Polymer-Based Nanocomposites for Energy and Environmental Applications*, Woodhead Publishing Series in Composites Science and Engineering, pp. 361–396 (2018)
71. Younas, M., Gondal, M.A., Dastageer, M.A., Harrabi, K.: Efficient and cost-effective dye-sensitized solar cells using MWCNT-TiO₂ nanocomposite as photoanode and MWCNT as Pt-free counter electrode. *Sol. Energy* **188**, 1178–1188 (2019)
72. Mousavi, F., Taherpour, A.A.: A carbon nanotube-iron (III) oxide nanocomposite as a cathode in dye-sensitized solar cells: Computational modeling and electrochemical investigations. *Electrochim. Acta* **318**, 617–624 (2019)
73. Javed, H.M.A., et al.: Advanced Ag/rGO/TiO₂ ternary nanocomposite based photoanode approaches to highly-efficient plasmonic dye-sensitized solar cells. *Opt. Commun.* **453**, 124408 (2019)
74. Bin, S.T., et al.: Perovskite solar cells: film formation and properties. *J. Mater. Chem. A* **3**, 9032–9050 (2015)
75. Zhang, J., Zhang, W., Cheng, H.M., Silva, S.R.P.: Critical review of recent progress of flexible perovskite solar cells. *Mater. Today* **39**, 66–88 (2020)
76. Dadashbeik, M., Fathi, D., Eskandari, M.: Design and simulation of perovskite solar cells based on graphene and TiO₂/graphene nanocomposite as electron transport layer. *Sol. Energy* **207**, 917–924 (2020)
77. Hussain, I., Tran, H.P., Jaksik, J., Moore, J., Islam, N., Uddin, M.J.: Functional materials, device architecture, and flexibility of perovskite solar cell. *Emergent Mater.* **1**, 133–154 (2018)
78. Shahiduzzaman, M., et al.: Oblique electrostatic inkjet-deposited TiO₂ electron transport layers for efficient planar perovskite solar cells. *Sci. Rep.* **9**, 19494 (2019)
79. Wang, J.T.W., et al.: Low-temperature processed electron collection layers of graphene/TiO₂ nanocomposites in thin film perovskite solar cells. *Nano Lett.* **14**(2), 724–730 (2014)
80. Tonui, P., Oseni, S.O., Sharma, G., Yan, Q., Tessema Mola, G.: Perovskites photovoltaic solar cells: An overview of current status. *Renew. Sustain. Energy Rev.* **91**, 1025–1044 (2018)
81. Manibalan, G., Murugadoss, G., Thangamuthu, R., Mohan Kumar, R., Jayavel, R.: Facile synthesis of heterostructure CeO₂-TiO₂ nanocomposites for enhanced electrochemical sensor and solar cell applications. *J. Alloys Compd.* **773**, 449–461 (2019)
82. Amollo, T.A., Mola, G.T., Nyamori, V.O.: Improved short-circuit current density in bulk hetero-junction solar cells with reduced graphene oxide-germanium dioxide nanocomposite in the photoactive layer. *Mater. Chem. Phys.* **254**, 123448 (2020)
83. Mbuyise, X.G., Arbab, E.A.A., Mola, G.T.: The effect of a trimetallic nanocomposite in the solar absorber layer of organic solar cells. *RSC Adv.* **9**(11), 6070–6076 (2019)
84. Soultati, A., et al.: Organic solar cells of enhanced efficiency and stability using zinc oxide:zinc tungstate nanocomposite as electron extraction layer. *Org. Electron.* **71**, 227–237 (2019)

Recent Advances of TiO₂ Nanocomposites for Photocatalytic Degradation of Water Contaminants and Rechargeable Sodium Ion Batteries



Alaa El Din Mahmoud 

Abstract Nanocomposite term is broadly applied in material science. There are hundreds of various nanocomposites in literature. In this chapter, we selected titanium dioxide (TiO₂) due to its structural, optical, and electrochemical properties. Therefore, we highlight on the basics of TiO₂ nanocomposites and their recent applications. The optimized nanocomposites have the potential to be used in Environmental and Energy applications. One promising environmental application of TiO₂ nanocomposites is photocatalytic degradation of various contaminants. So far energy application is concerned, we focused on the utilization of TiO₂ nanocomposites in rechargeable sodium-ion battery. In recent times, tremendous efforts have been invested in the research activities on sodium-ion batteries across the globe which is a successor for lithium-ion batteries. One unique problem is the utilization of graphite as anode in sodium-ion batteries. Graphite miserably fails to electrochemically host enough Na⁺ ions in carbonate-based electrolytes. This instigated massive search for alternative anode materials for Na⁺-ion batteries. TiO₂ is an attracting and appealing candidate as anode for sodium-ion battery because it can electrochemically host Na⁺ ions at potentials <1 V. However, the Na⁺ ion storage capacity of TiO₂ is in general low (<200 mAhg⁻¹). In an effort to enhance the storage capacities, different types of nanocomposite of TiO₂ are investigated. This chapter describes the electrochemical properties of such nanocomposites of TiO₂ and their application in sodium-ion batteries.

Keywords Titanium dioxide · Nanomaterials · Semi-conductor · Environment · Pollution · Energy · Batteries

A. E. D. Mahmoud (✉)
Environmental Sciences Department, Faculty of Science,
Alexandria University, Alexandria 21511, Egypt
e-mail: alaa-mahmoud@alexu.edu.eg

Green Technology Group, Faculty of Science, Alexandria University, Alexandria 21511, Egypt

© The Author(s), under exclusive license to Springer Nature Switzerland AG 2022
A. E. Shalan et al. (eds.), *Advances in Nanocomposite Materials for Environmental and Energy Harvesting Applications*, Engineering Materials,
https://doi.org/10.1007/978-3-030-94319-6_24

757

List of Abbreviations

$^{\circ}\text{OH}$	Hydroxyl radicals
A	Ampere
AOP	Advanced oxidation process
BPA	Bisphenol A
CB	Conduction band
CEC	Emerging Concern Contaminants
CR	Congo Red dye
CTS-ZnO-TiO ₂	Ternary chitosan/zinc oxide/TiO ₂
Cu-TiO ₂ @C	Carbon-coated Cu-TiO ₂ nanocomposite
CV	Cyclic voltammetry
CV dye	Crystal Violet
e ⁻	Valence electrons
EB	Evans blue dye
g-C ₃ N ₄ -TiO ₂	Graphite-like carbon nitride nanocomposite
GO	Graphene oxide
G-TiO ₂	Graphene-TiO ₂ nanocomposite
Li ⁺	Lithium ion
mAh	Milliamperere hour
MB	Methylene blue
MgO	Magnesium oxide
Na ⁺	Sodium ion
N-G-TiO ₂	Nitrogen doped Graphene coated TiO ₂
Ni(OH) ₂	Nickel hydroxide
NR	Nanorods
NS	Nanospheres
NT	Nanotubes
ppb	Part per billion
PVA	Polyvinyl alcohol
rGO/TiO ₂	Reduced graphene oxide/TiO ₂ nanocomposite
rGO-ZnS-TiO ₂	Reduced graphene oxide-zinc sulphide-TiO ₂
RhB	Rhodamine B dye
TiO ₂	Titanium dioxide
VB	Valence band

1 Introduction

Nowadays, water pollution and energy consumption are a serious issue for everyone either individuals or sectors. Discharging the heavy metals and organic chemical compounds effluents, without proper treatment, have critical environmental impacts as well as on the human health effect [1, 2]. In another direction, the demand of global

energy is expected to rise 50% by 2050 [3]. Nanoparticles/nanocomposites can be part of the sustainable solution of the aforementioned issues. Herein, we focus on titanium dioxide or titania (TiO₂) because it is nontoxic material which possesses high chemical and photochemical stability with photocatalytic activity. Consequently, TiO₂ is one of the popular photocatalyst for decomposing contaminants [4].

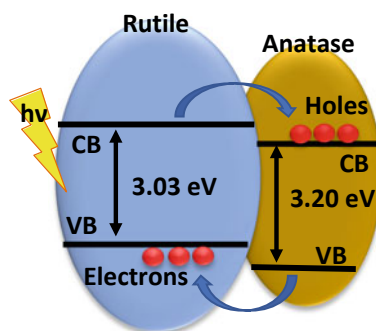
TiO₂ is also a semiconductor with large electronic bandgap of 3.03–3.20 eV [5]. The Structures TiO₂ can be anatase or rutile (a mineral has TiO₂). However, it is usually mixed between anatase and rutile phases. It is noting that anatase can be converted to rutile at temperatures between 550 and 1000 °C. Xiong et al. [6] concluded that the synthesized TiO₂ (55 anatase and 45% rutile) possessed high photoactivity because of its distinctive hierarchical structures.

The basic of photocatalysis is based on hitting the TiO₂ nanoparticles with energy radiation = or > its band gap energy to generate high energy electron–hole pairs. This can commence the photocatalytic reaction [4]. Therefore, TiO₂ shows low efficiency in utilizing sunlight and requires UV irradiation. As illustrated in Fig. 1, there is a recombination rate of electrons and hole pairs. when an electron migrates from the valence band of Rutile phase to the conduction band of anatase phase, the Fermi level will shift to more negative value (i.e.; Fermi level gradient) [7]. Such high recombination rate retards the practical application of TiO₂ nanoparticles in the visible region [8].

To overcome this drawback, tuning its optical band gap is necessary to absorb visible light. It is found that the optical properties of TiO₂ is dependent on the calcination temperatures [9]. As the calcination temperatures increased, its crystallinity is improved, and its phase transitioned from anatase to rutile.

TiO₂ could also be used in Li⁺-ion and Na⁺-ion batteries. There are unique advantages of utilizing TiO₂ as anode in sodium-ion battery. Although graphite is a well-known anode for Li⁺-ion battery, it could not be used in sodium-ion battery because Na⁺ ion does not intercalate in graphite. On the other hand, TiO₂ can host Na⁺ ion at relatively low voltage (potentials <1 V. However, TiO₂ is a poor electronic conductor. Therefore, nanocomposite of graphene, carbon nanotube, amorphous carbon and TiO₂ is used to enhance the electrochemical performance.

Fig. 1 Mechanism of the valence and conduction band for the anatase–rutile of TiO₂



Generally, nanoparticles have high surface-volume ratio which change their properties in comparison with the bulk particles [5]. Recently, the direction to nanocomposites is more on focus for various materials. The reasons can be due to [10]: i) nanocomposites are 1000 times tougher than the bulk materials, ii) the improved properties as electrical conductivity, thermal stability, and chemical resistance.

2 Photocatalytic Degradation of Water Contaminants

It is estimated that the consumption of water in industrial sectors is responsible for 22% of global water use. Hence, there are various contaminants with diversity in their properties and their concentrations (ng L^{-1} or $\mu\text{g L}^{-1}$ or mg L^{-1}) in water [11–13]. This not only indicates the complication of detection and analysis of all contaminants together but also makes a challenge for efficient water treatment [14, 15].

Emerging Concern Contaminants (CEC) is one of the major causes of water pollution. CECs include wide variety of pharmaceuticals, industrial chemicals, and personal care products, etc. [8, 16]. Furthermore, dyes are one of the major water pollutants worldwide.

The degradation of CECs and dyes can be conducted by advanced oxidation process (AOP) [17, 18]. The AOPs are classified either as homogeneous or heterogeneous processes where a wide range of these AOPs that are being studied for wastewater treatment. In this chapter, we focus on one of AOP which is photocatalysis process.

Photocatalysis technology is commonly used in water and air purification. Its process is based on the generation of hydroxyl radicals ($^{\circ}\text{OH}$) which are generated due to the interaction of light irradiation with semiconductor catalyst for the mineralization of pollutants to CO_2 and H_2O . The merit of $^{\circ}\text{OH}$ is possessing high oxidizing power and be able to oxidize organic contaminants [19].

Szczepanik [4] and Carp et al. [20] stated the advantages of photocatalysis based on TiO_2 . For instance, its ability to oxidize of pollutants in the range of part per billion (ppb), non-selective destruction of organics and inorganics under ambient temperature/pressure and can be adaptable to specially-designed reactor systems.

Simply, when TiO_2 is exposed to photons with energy with energy higher than its band gap, electrons will excite from the valence band (VB) to the conduction band (CB) creating an electron-hole pair as illustrated in Fig. 1. Hence, TiO_2 photocatalysts can decompose and mineralize organic compounds due to the series oxidation reactions from the generated holes (h^+) and hydroxyl radicals (OH) in the valence band, and electrons and superoxide anions (O_2^-) generated in the conduction band [9]. Further details regarding the TiO_2 reduction mechanism in the photocatalysis are summarized in Mahmoud [5].

The photocatalytic activity of TiO_2 nanoparticles is still limited due to i) potential photocatalyst loses with long time operation, ii) tendency of aggregation, iii) difficulty of separation and recovery, iv) scattering conditions of TiO_2 nanoparticles, and v) poor affinity to hydrophobic pollutants [21, 22].

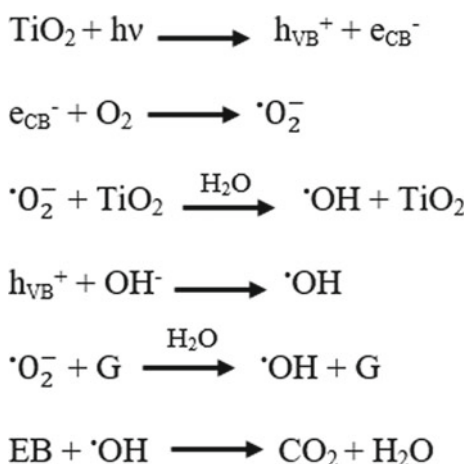
Nanocomposites with TiO₂ can increase its photocatalytic efficiency because it is possible to adjust the loading of a catalyst easily. Sutar et al. [8] found that 30% Graphite-like carbon nitride nanocomposite with 70% TiO₂ (g-C₃N₄-TiO₂) has the optimum efficiency for bisphenol A (BPA) and brilliant green dye (BG). This is due to the high surface area, lower band gap, and visible light absorption. The rate degradation constant of g-C₃N₄-TiO₂ nanocomposite is twice to that of bare TiO₂.

Another study by Monga and Basu [23], they synthesized also g-C₃N₄-TiO₂ but with various shapes of nanorods (NR), nanotubes (NT), and nanospheres (NS). They studied the photocatalytic degradation of Rhodamine B (RhB). The highest degradation of RhB was obtained with using g-C₃N₄-TiO₂ nanotubes within 80 min. The order of degradation efficiency is NT (97%), NR (94.5%), NS (92%), and commercial TiO₂ composite (74%).

Graphene-TiO₂ nanocomposite (G-TiO₂) was synthesized by Kumar et al. [24]. They tested G-TiO₂ as a photocatalytic nanocomposite for Evans blue (EB) dye in water. The mechanism of TiO₂ photocatalytic is illustrated in Scheme 1 where the EB dye was degraded using G-TiO₂. The valence electrons (e⁻) of TiO₂ are excited to the CB where the holes are formed in VB. As earlier mention in section, the formation of OH and $\cdot\text{O}_2^-$ are responsible for the dye degradation due to the electron mobility and the large surface area. Other research group worked on Graphene-TiO₂ nanocomposite which synthesized by electrostatic self-assembly method [25].

MgO coated Ag/TiO₂ nanocomposite was synthesized and used as a photocatalysis for phenol degradation by Scott et al. [26]. TiO₂-NR were holded with Ag and MgO nanoparticles to promote the absorption of the light through localized surface plasmon resonance and transfer of photo-induced electron-hole pairs within TiO₂. Furthermore, Ag is abundant, relatively low-cost, and possesses antibacterial activity for water treatment. It is found that 95% of phenol can be degraded using MgO coated Ag/TiO₂ nanocomposite within 120 min compared to Ag/TiO₂ nanocomposite with ~87% and TiO₂ with 75%.

Scheme 1 Reaction mechanism of photocatalytic dye degradation of Evans blue (EB) using Graphene-TiO₂ nanocomposite (G-TiO₂)



Chen et al. [27] constructed Carbon-coated Cu-TiO₂ nanocomposite (Cu-TiO₂@C) by thermal reduction. Cu-TiO₂@C was found effectively adsorb OH and enhancing the electron transfer between Cu and TiO₂ nanoparticles. The used Cu nanoparticles can promote the separation of e⁻ participate in the evolution of H₂ on the surface of TiO₂ particles. In addition, the coated carbon layer is accountable for the high photocatalytic stability of Cu-TiO₂@C in comparison with Cu-TiO₂ only.

Barakat et al. [19] fabricated solar active nickel (hydroxide (Ni(OH)₂) decorated on graphene oxide (GO) and modified TiO₂ nanocomposite for enhanced photocatalytic degradation of organic, and microbial contaminants.

Sonochemical preparation of TiO₂ nanocomposites is one the synthesis routes that stated in literature. Many researchers focused on this route because it is simple, fast reaction time, no high temperature is required as in the conventional synthesis methods, improve the phase purity (more crystalline), and its cavitation effect (the formation, growth and collapse of bubbles in a liquid) [28, 29].

Rhodamine B (RhB) was degraded using magnetic Fe₃O₄-TiO₂ that synthesized by a sonochemical route and the product could degrade RhB completely in 75 min [30]. Furthermore, the rate of photodecomposition decreased only to some extent after six cycles of the photocatalysis experiments. This could be due to the incomplete magnetic separation of the nanocomposite and its loss during the reaction. Generally, the merit of using magnetic nanoparticles and nanocomposites is their easy recovery in short time (~1 min) and the solution becomes transparent for further analysis.

Recently, magnetic Fe₃O₄-TiO₂ was also prepared with added graphene (Fe₃O₄-TiO₂-G) using the co-precipitation method [31]. The addition of graphene to the nanocomposite gave the advantage of combined adsorption and photocatalytic effect for methylene blue. Bhagwat et al. [32] prepared sonochemical Mg-TiO₂ nanocomposites for the purpose of Congo Red (CR) dye degradation from textile industry. They found that the prepared Mg-TiO₂ nanocomposites possess uniform morphology. Their optimum application was found at dose of 50 mg and pH = 4 to reach 98% of CR degradation.

Deshmukh et al. [33] synthesized reduced graphene oxide (rGO)/TiO₂ nanocomposite by following these steps (Fig. 2): i) dispersion of 1 g GO in 50 mL of isopropanol + 5 mL titanium (IV)isopropoxide, ii) 5 min sonication, iii) slowly addition of 1.35 M NaOH in the presence of sonication, iv) further sonication for 30 min. This nanocomposite was examined as a photocatalyst for methylene blue (MB) degradation of in the sun light. The maximum degradation of MB was observed ~91% at pH of 13.2 within 30 min and dose of 2 g L⁻¹.

There are also ternary nanocomposites that proved their efficiency and applicability as photocatalytic nanomaterials. Ternary chitosan-zinc oxide-TiO₂ (CTS-ZnO-TiO₂) nanocomposite was prepared by Bhanvase et al. [35]. It is found that 1 g L⁻¹ CTS-ZnO-TiO₂ nanocomposite can remove 80% of 50 mg L⁻¹ Crystal Violet (CV) dye. The used sonochemical technique shows advantages over the conventional mechanical stirring method. The prepared nanocomposite is more uniformly dispersed and exhibited higher adsorbing capacity for the CV removal than the prepared one by the mechanical stirring.

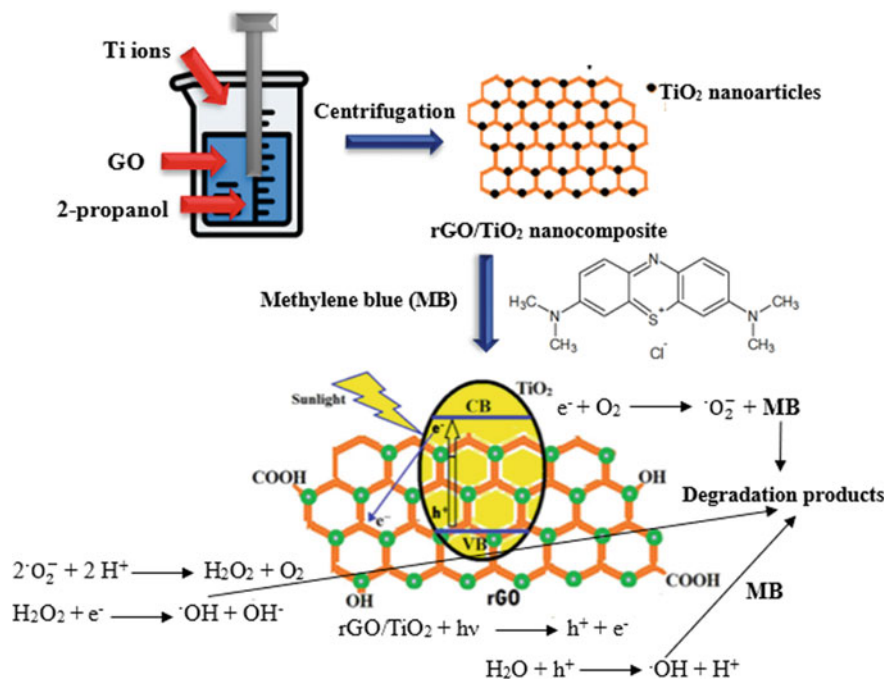


Fig. 2 The preparation of reduced graphene oxide (rGO)/TiO₂ nanocomposite using ultrasound assisted technique and its application as a photocatalyst. Adapted from Deshmukh et al. [33] and Mahmoud et al. [34]

Kale et al. [36] followed the same above-mentioned procedure but to synthesize reduced graphene oxide-zinc sulphide-TiO₂ (rGO-ZnS-TiO₂) nanocomposite. They reported that 0.4 g L⁻¹ rGO-ZnS-TiO₂ adsorbed and degraded 97.02% of 50 mg L⁻¹ CV dye at temperature of 35 °C but the adsorption only recorded 91.15%. It is quite interesting that the prepared nanocomposites displayed superior adsorption compared to its photocatalytic activity. The reason for that is most of CV dye molecules adsorbed and very low availability of the dye molecules for the photocatalytic degradation process.

ZnS nanoparticle is always chosen as a transition metal sulphide which extensively studied for their photocatalytic capabilities. However, it suffers from the occurrence of the particles' aggregation and the rapid recombination of photo-generated electron and hole pairs that significantly limits its outstanding photoelectric properties. Therefore, ZnS-TiO₂ nanocomposite have better photocatalytic activity due to quantum confinement effects [37].

3 TiO₂ Nanocomposites for Rechargeable Sodium Ion Batteries

The Na⁺-ion electrochemistry of TiO₂ was first investigated by Xu et al. [38]. The electrochemistry was explored with carbon coated TiO₂ nanocrystals. It was synthesized by adsorbing Ti precursor (C₁₂H₂₈O₄Ti) in cellulose-based filter paper followed by a hydrolysis and subsequent annealing. The anatase particle size is in the range of 10–15 nm. The cyclic voltammetry (CV) curves showed redox peaks at ~0.60 V (cathodic) and ~0.95 V (anodic) which were respectively attributed to the reversible sodiation and desodiation reactions in TiO₂. The material showed a highly stable reversible charge storage capacity of 150 mAhg⁻¹ over 100 cycles at a current density of 50 mA g⁻¹.

Similarly, Kim et al. [39] investigated the Na⁺-ion storage behavior in carbon coated anatase TiO₂ nanorod (Fig. 3a) derived from carbonization of pitch at 700 °C [38]. It is shown that carbon coating substantially improves the high rate performance. The recoverable charge capacity for carbon coated (2.9 wt%) anatase TiO₂ nanorod is 53 mAh g⁻¹ at extremely high current density of 33 A g⁻¹ (100 C), whereas pristine TiO₂ nanorod could sustain only 30 C-rate (10 A g⁻¹) with a capacity of 20 mAh g⁻¹ (Fig. 3b, c). The superior rate performance is ascribed to the five-order increase in the electronic conductivity of TiO₂ due to carbon coating. On the other hand, Oh et al. [40] demonstrated that optimized amount of carbon is necessary for improved electrochemical performance of anatase TiO₂. It is shown that 6.8 wt% carbon containing TiO₂ nanocrystals showed the best performance. The composite could sustain high current rate of 30 °C with a discharge capacity of 100 mAhg⁻¹ and coulombic efficiency greater than 95%.

Lee et al. [41] synthesized high surface area (215 m²g⁻¹) porous carbon-TiO₂ nanocomposite by polymerization method. When tested in Na-cell, it is found that this nanocomposite exhibits nearly 3 times greater gravimetric capacity the pristine TiO₂ nanoparticle. The discharge capacity is approximately 150 mAhg⁻¹ at a current rate of 42 mA g⁻¹ over 50 cycles. Again, Zhang et al. [42] observed a capacity of 140 mAhg⁻¹ for the carbon coated anatase TiO₂ hollow sphere, which shows a

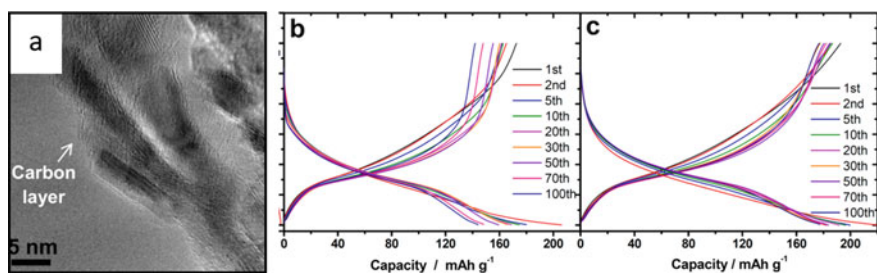


Fig. 3 TEM images of **a** carbon coated TiO₂ nanorod and Galvanostatic charge–discharge curves of **b** TiO₂ nanorod and **c** carbon coated TiO₂ nanorod. Reprinted with permission from Kim et al. [39], Copyright (2014) American Chemical Society

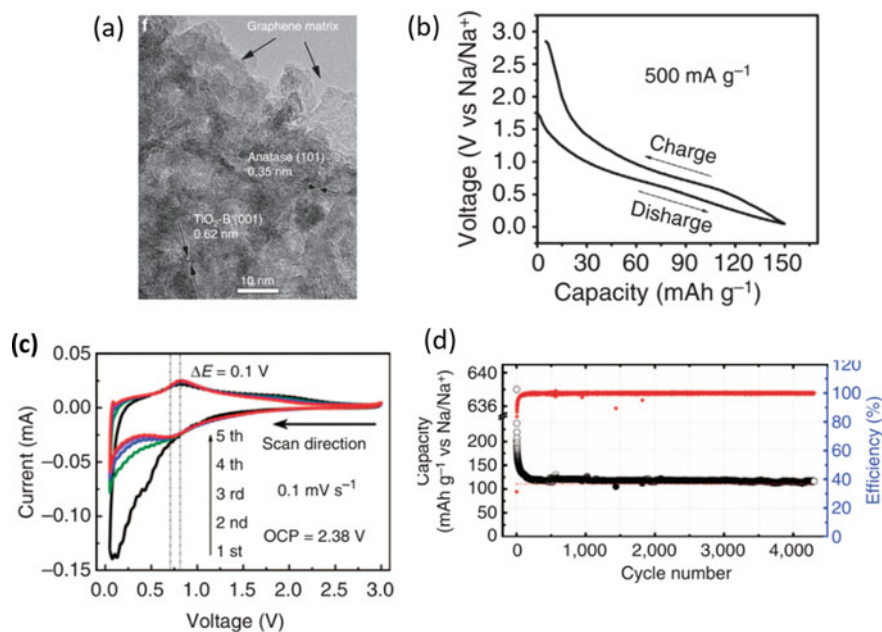


Fig. 4 **a** TEM images of graphene-TiO₂ nanocomposites, **b** Galvanostatic charge–discharge curves, **c** cyclic voltammogram and **d** capacity versus cycle number for graphene-TiO₂ nanocomposite. Reprinted by permission from Springer Nature: Nature Communication, Chen et al. [50] Copyright 2015

surface area of 103 m²g⁻¹, and it is stable for over 500 cycles at 5C current rate. On contrary, pristine TiO₂ hollow sphere could deliver a capacity of only 50 mAhg⁻¹ at 5C. The higher capacity of the carbon coated anatase TiO₂ hollow sphere is primarily attributed to the carbon coating high conductivity since the surface areas are identical.

Jung et al. [43] also showed that carbon coated TiO₂ nanofibers grown by electrospinning showed enhanced capacity than pristine TiO₂ nanofiber due to the reduced charge transfer resistance. Again, Shi et al. [44] performed an in-situ synthesis to obtain carbon-TiO₂ composites of high surface area (321 m²g⁻¹) from Ti-containing metal–organic framework (MIL-125). This method does not require any additional carbon source for carbon coating. It is seen that carbon-TiO₂ nanocomposites was assembled by numerous TiO₂ nanocrystals dispersed in an amorphous carbon matrix. This composite delivers discharge capacity of 148 mAhg⁻¹ after 500 cycles at current density of 500 mA g⁻¹. Chen et al. [45] synthesized size-tunable carbon coated mesoporous olive-like anatase TiO₂ using PVA as structure directing agent. This work shows that the size effects are more enormous at high charge–discharge rates for sodium storage, leading to the much rate performances for smaller sized mesoporous clusters. As shown, 80 nm clusters (primary particle size ~15 nm, area ~124 m²g⁻¹) show capacity of 125 mAhg⁻¹ at current rate of 3.36 Ag⁻¹ over 1000 cycles, whereas

150 nm clusters (primary particle size ~ 19 nm, area ~ 76 m²g⁻¹) show capacity of 96 mAhg⁻¹ at the same current rate over 1000 cycles.

Graphene is an excellent conductive additive for electrode preparation. Qin et al. [46] showed that N doped graphene-TiO₂ nanocomposite is far better for Na⁺ ion storage. It is seen that the capacity of N-G-TiO₂ is 471.3 mAhg⁻¹, whereas graphene-TiO₂ and pristine TiO₂ showed capacities of 320.6 mAhg⁻¹ and 240.7 mAhg⁻¹ at a current density of 10 mA g⁻¹. The enhanced capacity is attributed due to synergistic effect of pseudocapacitive storage of nitrogen doped graphene and overall enhanced electronic conductivity. It is also confirmed by impedance spectroscopy that the charge transfer resistance is considerably lower for N-G-TiO₂ than G-TiO₂ and pristine TiO₂. Cha et al. [47] also stated that N-G-TiO₂ nanocomposites showed excellent performance than the pristine analogue. It is seen that the specific capacity of N-G-TiO₂ nanocomposites is about 405 mAh g⁻¹ at a current rate of 50 mA g⁻¹, which is almost three times higher than that of pristine TiO₂ nanoparticles. It is attributed to the fast transfer of Na⁺ ions via open channels of the graphene.

Zhang et al. [48] also synthesized N-G-TiO₂ nanocomposites (size ~ 5 nm) by pyrolysis of GO wrapped metal organic frameworks. The most impressive feature of this nanocomposite (area ~ 154.8 m²g⁻¹) is the ultra-stable cycling performance. It delivers capacity of 117 mAhg⁻¹ with no obvious capacity loss even after 5000 cycles at a current of 1 Ag⁻¹, corresponding to a capacity retention of 93%. Similarly, Liu et al. [49] enhanced the insertion kinetic of Na⁺ ions in TiO₂ by applying rGO as a conductive matrix. It could be inferred from the reduced peak separation for sodiation and desodiation in case of GO-TiO₂ nanocomposite (0.14 V) than pristine (0.33 V) as shown in the cyclic voltammetry. At a current rate of 100 mA g⁻¹, GO-TiO₂ nanocomposite shows a capacity of 186 mAhg⁻¹ after 100 cycle.

Again, Chen et al. [50] used G-TiO₂ sandwich-like hybrid nanostructures (Fig. 4a) for Na⁺-ion storage study. This hybrid shows very small polarization (~ 0.1 V) between charge-discharge curves (Fig. 4b) at current density of 500 mA g⁻¹, which is also supported by CV curve (Fig. 4c). Moreover, the hybrid nanostructure exhibits stability over 4300 cycles with specific capacity of 120 mAhg⁻¹ at a current rate of 500 mA g⁻¹ (Fig. 4d). Kinetics analysis by CV reveals that Na⁺ ion pseudocapacitive behavior is predominant at high current rates, whereas both insertion/deinsertion and pseudocapacitive storage of Na⁺ ion is possible at slow current rates. DFT analysis indicates that the enhancement of electrochemical behavior is attributed to the fact that TiO₂ is chemically bonded with the graphene matrix which resulted in feasible pathways for enhanced electron transfer rate. Yeo et al. investigated graphene-wrapped anatase TiO₂ nanofibers [51]. This hybrid could show very stable behavior at all investigated current rates. For example, at a current rate of 5C, it shows a stable capacity around 120 mAhg⁻¹ where pristine TiO₂ nanofiber could deliver only 12 mAhg⁻¹ at the same current rate.

Feng et al. [52] incorporated TiO₂ into graphene could enhance the capacity by 40% over 400 cycles compared to pristine TiO₂. The observed stable discharge capacity is 102 mAhg⁻¹ at current of 100 mA g⁻¹ after 400 cycles. Zhu et al. also showed that sodium storage of commercial P25 TiO₂ can be incredibly enhanced by graphene wrapping [53]. After 300 cycles, the TiO₂@rGO electrode still delivered

a reversible capacity of 124 mAhg⁻¹, corresponding to a capacity retention of 87% at current of 66 mAg⁻¹. While the bare TiO₂ electrode delivers only 90 mAhg⁻¹ at 66 mAg⁻¹ and shows a capacity retention of only 70% over 300 cycles. The TiO₂-graphene could sustain over 1000 cycles at current rate of 1.65 Ag⁻¹ delivering average capacity of 60 mAhg⁻¹. EIS study reveals that the charge transfer resistance is quite lower for graphene-TiO₂ than pristine TiO₂. Fu et al. also showed significant improvement in sodium storage in anatase TiO₂ due to graphene incorporation. It is worth mentioning that a capacity of 117 mAhg⁻¹ is maintained even at a high current density of 5 Ag⁻¹ [54].

Another strategy to improve the electronic conductivity is via element doping. Yan et al. evaluated the Na⁺ ion storage capacity of Sn⁴⁺ doped TiO₂ nanotubes [55]. It is seen that 2.6 wt% Sn doped TiO₂ nanocomposite shows the highest discharge capacity of 257 mAhg⁻¹ after 50 cycles at current rate of 50 mAg⁻¹. Furthermore, these nanotubes sustain above 700 cycles at 5 Ag⁻¹ current rate with a discharge capacity of 103 mAhg⁻¹. It is also observed that charge transfer resistance decreases for Sn doped TiO₂ than pristine TiO₂. The charge-discharge profiles are identical to pristine TiO₂. The enhanced performance is attributed to the two-order increase in electron concentration due to doping of Sn (2.6 wt %) in TiO₂ as conformed via Hall measurements. Furthermore, Zhao et al. [56] investigated observed that 2 at. wt% Niobium doped TiO₂ nanocomposite showed better result than pristine TiO₂. At a current rate of 1.65 Ag⁻¹, 2 at. wt% Niobium doped TiO₂ showed two-time higher capacity than pristine TiO₂. The calculated Na⁺ ion diffusion coefficient for the 2% at. wt% Nb-doped TiO₂ is $4.31 \times 10^{-13} \text{ cm}^2\text{s}^{-1}$, 3.4 times higher than that of TiO₂ ($1.29 \times 10^{-13} \text{ cm}^2\text{s}^{-1}$), which reveals that Niobium doping increases the Na⁺-ion mobility of TiO₂. [57] investigated boron doped anatase TiO₂ and found that the capacity of this composite could reach 140 mAhg⁻¹ at a current rate of 660 mAg⁻¹ and the capacity decay is found to be only 8 mAhg⁻¹ over 400 cycles. The boron doping increases the unit cell volume. The charge transfer resistance also decreases for boron doped TiO₂ compared to pristine TiO₂. These two reasons helped to improve the electrochemistry of boron doped TiO₂.

4 Conclusions

Nanocomposites revealed improved photocatalytic degradation efficiency which is better than that of bare TiO₂. The photocatalytic degradation of the synthesized TiO₂ nanocomposites with sonochemical routes exhibited high degradation rate especially for dye molecules. To achieve the maximum activity of the photocatalytic of dye degradation, the addition of graphene to TiO₂ nanoparticles should be optimized. It is seen that addition of graphene, carbon nanotube and amorphous carbon significantly improves the electrochemical performance of TiO₂. It is also observed that nanostructuring and amount of additive play pivotal role in enhancing the Na⁺-ion storage capacity of TiO₂. The hybridization of graphene and TiO₂ enhances the sodium intercalation/deintercalation with low energy barrier due to the feasible

channel in the nanocomposite interface. Furthermore, the discharge of graphene/TiO₂ nanocomposites demonstrated higher reversible capacity than TiO₂ nanoparticles.

Acknowledgements The author would like to thank the support of Egypt's Academy of Scientific Research and Technology (ASRT) for the SA-Egypt Joint Project. Furthermore, the author thanks Dr. Shyamal Das (Tezpur University) for his assistance in Sect. 3.

References

1. Mahmoud, A.E.D., Fawzy, M., Hosny, G., Obaid, A.: Equilibrium, kinetic, and diffusion models of chromium(VI) removal using *Phragmites australis* and *Ziziphus spina-christi* biomass. *Int. J. Environ. Sci. Technol.* **18**, 2125–2136 (2020)
2. Badr, N.B.E., Al-Qahtani, K.M., Mahmoud, A.E.D.: Factorial experimental design for optimizing selenium sorption on *Cyperus laevigatus* biomass and green-synthesized nano-silver. *Alexandria Eng. J.* **59**, 5219–5229 (2020)
3. Batool, M., Nazar, M.F., Awan, A., et al.: Bismuth-based heterojunction nanocomposites for photocatalysis and heavy metal detection applications. *Nano-Struct Nano-Objects* **27**, 100762 (2021)
4. Szczepanik, B.: Photocatalytic degradation of organic contaminants over clay-TiO₂ nanocomposites: a review. *Appl. Clay Sci.* **141**, 227–239 (2017)
5. Mahmoud, A.E.D.: Nanomaterials: green synthesis for water applications. In: Kharissova, O.V., Martínez, L.M.T., Kharisov, B.I. (eds.) *Handbook of Nanomaterials and Nanocomposites for Energy and Environmental Applications*, pp. 1–21. Springer, Cham (2020)
6. Xiong, Z., Wu, H., Zhang, L., Gu, Y., Zhao, X.: Synthesis of TiO₂ with controllable ratio of anatase to rutile. *J. Mater. Chem. A* **2**, 9291–9297 (2014)
7. Protti, S., Albin, A., Serpone, N.: Photocatalytic generation of solar fuels from the reduction of H₂O and CO₂: a look at the patent literature. *Phys. Chem. Chem. Phys.* **16**, 19790–19827 (2014)
8. Sutar, R.S., Barkul, R.P., Delekar, S.D., Patil, M.K.: Sunlight assisted photocatalytic degradation of organic pollutants using g-C₃N₄-TiO₂ nanocomposites. *Arab. J. Chem.* **13**, 4966–4977 (2020)
9. Haider, A.J., AL-Anbari, R.H., Kadhim, G.R., Salame, C.T.: Exploring potential environmental applications of TiO₂ nanoparticles. *Energy Procedia* **119**, 332–345 (2017)
10. Okpala, C.C.: Nanocomposites—an overview. *Int. J. Eng. Res. Dev.* **8**, 17–23 (2013)
11. Mahmoud, A.E.D.: Graphene-based nanomaterials for the removal of organic pollutants: insights into linear versus nonlinear mathematical models. *J. Environ. Manag.* **270**, 110911 (2020)
12. Mahmoud, A.E.D., Fawzy, M., Radwan, A.: Optimization of Cadmium (Cd²⁺) removal from aqueous solutions by novel biosorbent. *Int. J. Phytoremediation* **18**, 619–625 (2016)
13. Mahmoud, A.E.D., Fawzy, M.: Statistical methodology for Cadmium (Cd (II)) removal from wastewater by different plant biomasses. *J. Bioremediat. Biodeg* **6**, 1–7 (2015)
14. Luo, Y., et al.: A review on the occurrence of micropollutants in the aquatic environment and their fate and removal during wastewater treatment. *Sci. Total Environ.* **473**, 619–641 (2014)
15. El Din Mahmoud, A., Fawzy, M.: Bio-based methods for wastewater treatment: green sorbents. In: Ansari, A.A., Gill, S.S., Gill, R., Lanza, G.R., Newman, L., (eds.) *Phytoremediation: Management of Environmental Contaminants*, vol. 3, pp. 209–238. Springer, Cham (2016)
16. Mahmoud, A.E.D., Stolle, A., Stelter, M.: Sustainable synthesis of high-surface-area graphite oxide via dry ball milling. *ACS Sustain. Chem. Eng.* **6**, 6358–6369 (2018)
17. Mahmoud, A.E.D., Franke, M., Stelter, M., Braeutigam, P.: Evaluation of bisphenol a removal from water bodies using eco-friendly technique. In: 4th International Congress on Water, Waste and Energy Management, Spain (2018)

18. Mahmoud, A., Stolle, A., Stelter, M., Braeutigam, P.: Adsorption technique for organic pollutants using different carbon materials. Abstracts of Papers of the American Chemical Society, Amer Chemical Soc 1155 16th st, NW, Washington, DC 20036 USA (2018)
19. Barakat, M., Anjum, M., Kumar, R., Alafif, Z., Oves, M., Ansari, M.O.: Design of ternary Ni (OH)₂/graphene oxide/TiO₂ nanocomposite for enhanced photocatalytic degradation of organic, microbial contaminants, and aerobic digestion of dairy wastewater. *J. Clean. Prod.* **258**, 120588 (2020)
20. Carp, O., Huisman, C.L., Reller, A.: Photoinduced reactivity of titanium dioxide. *Prog. Solid State Chem.* **32**, 33–177 (2004)
21. Dong, H., et al.: An overview on limitations of TiO₂-based particles for photocatalytic degradation of organic pollutants and the corresponding countermeasures. *Water Res.* **79**, 128–146 (2015)
22. Chen, D., et al.: Photocatalytic degradation of organic pollutants using TiO₂-based photocatalysts: a review. *J. Clean. Prod.* **268**, 121725 (2020)
23. Monga, D., Basu, S.: Enhanced photocatalytic degradation of industrial dye by g-C₃N₄/TiO₂ nanocomposite: role of shape of TiO₂. *Adv. Powder Technol.* **30**, 1089–1098 (2019)
24. Kumar, K.Y., Saini, H., Pandiarajan, D., Prashanth, M., Parashuram, L., Raghu, M.: Controllable synthesis of TiO₂ chemically bonded graphene for photocatalytic hydrogen evolution and dye degradation. *Catal. Today* **340**, 170–177 (2020)
25. Tao, E., Ma, Z., Yang, S., Li, Y., Ma, D., Xing, Z., Li, Y.: Enhanced electrical conductivity of TiO₂/graphene: the role of introducing Ca²⁺. *J. Alloys Compd.* **827**, 154280 (2020)
26. Scott, T., Zhao, H., Deng, W., Feng, X., Li, Y.: Photocatalytic degradation of phenol in water under simulated sunlight by an ultrathin MgO coated Ag/TiO₂ nanocomposite. *Chemosphere* **216**, 1–8 (2019)
27. Chen, S., Li, X., Zhou, W., Zhang, S., Fang, Y.: Carbon-coated Cu-TiO₂ nanocomposite with enhanced photostability and photocatalytic activity. *Appl. Surf. Sci.* **466**, 254–261 (2019)
28. Wang, Y., Sun, Y., Liu, S., Zhi, L., Wang, X.: Preparation of sonoactivated TiO₂-DVIDMS nanocomposite for enhanced antibacterial activity. *Ultrason. Sonochem.* **63**, 104968 (2020)
29. Biswas, M.R.U.D., Ali, A., Cho, K.Y., Oh, W.-C.: Novel synthesis of WSe₂-Graphene-TiO₂ ternary nanocomposite via ultrasonic techniques for high photocatalytic reduction of CO₂ into CH₃OH. *Ultrason. Sonochem.* **42**, 738–746 (2018)
30. Zhang, X., Jiang, W., Gong, X., Zhang, Z.: Sonochemical synthesis and characterization of magnetic separable Fe₃O₄/Ag composites and its catalytic properties. *J. Alloys Compd.* **508**, 400–405 (2010)
31. Fauzian, M., Taufik, A., Saleh, R.: The effects of adding Ag and graphene to Fe₃O₄/TiO₂ nanocomposites on adsorptive and sonophotocatalytic capabilities. *J. Phys. Conf. Ser.* **1442**, 012019 (2020)
32. Bhagwat, U.O., Wu, J.J., Asiri, A.M., Anandan, S.J.J.: Sonochemical synthesis of Mg-TiO₂ nanoparticles for persistent Congo red dye degradation. *J. Photochem. Photobiol. A Chem.* **346**, 559–569 (2017)
33. Deshmukh, S.P., et al.: Ultrasound assisted preparation of rGO/TiO₂ nanocomposite for effective photocatalytic degradation of methylene blue under sunlight. *Nano-Struct. Nano-Objects* **21**, 100407 (2020)
34. Mahmoud, A.E.D., Franke, M., Stelter, M., Braeutigam, P.: Mechanochemical versus chemical routes for graphitic precursors and their performance in micropollutants removal in water. *Powder Technol.* **366**, 629–640 (2020)
35. Bhanvase, B., Veer, A., Shirsath, S., Sonawane, S.: Ultrasound assisted preparation, characterization and adsorption study of ternary chitosan-ZnO-TiO₂ nanocomposite: advantage over conventional method. *Ultrason. Sonochem.* **52**, 120–130 (2019)
36. Kale, D.P., Deshmukh, S.P., Shirsath, S.R., Bhanvase, B.A.: Sonochemical preparation of multi-functional rGO-ZnS-TiO₂ ternary nanocomposite and its application for CV dye removal. *Optik* **208**, 164532 (2020)
37. Talebi, S., Chaibakhsh, N., Moradi-Shoeili, Z.: Application of nanoscale ZnS/TiO₂ composite for optimized photocatalytic decolorization of a textile dye. *J. Appl. Res. Technol.* **15**, 378–385 (2017)

38. Xu, Y., Lotfabad, E.M., Wang, H., Farbod, B., Xu, Z., Kohandehghan, A., Mitlin, D.: Nanocrystalline anatase TiO₂: a new anode material for rechargeable sodium ion batteries. *Chem. Commun.* **49**, 8973–8975 (2013)
39. Kim, K.-T., et al.: Anatase titania nanorods as an intercalation anode material for rechargeable sodium batteries. *Nano Lett.* **14**, 416–422 (2014)
40. Oh, S.-M., et al.: High electrochemical performances of microsphere C-TiO₂ anode for sodium-ion battery. *ACS Appl. Mater. Interfaces* **6**, 11295–11301 (2014)
41. Lee, J., Chen, Y.-M., Zhu, Y., Vogt, B.D.: Fabrication of porous carbon/TiO₂ composites through polymerization-induced phase separation and use as an anode for Na-ion batteries. *ACS Appl. Mater. Interfaces* **6**, 21011–21018 (2014)
42. Zhang, Y., et al.: Enhanced sodium storage behavior of carbon coated anatase TiO₂ hollow spheres. *J. Mater. Chem. A* **3**, 18944–18952 (2015)
43. Jung, K.-N., Seong, J.-Y., Kim, S.-S., Lee, G.-J., Lee, J.-W.: One-dimensional nanofiber architecture of an anatase TiO₂–carbon composite with improved sodium storage performance. *RSC Adv.* **5**, 106252–106257 (2015)
44. Shi, X., Zhang, Z., Du, K., Lai, Y., Fang, J., Li, J.: Anatase TiO₂@C composites with porous structure as an advanced anode material for Na ion batteries. *J. Power Sources* **330**, 1–6 (2016)
45. Chen, J., et al.: size-tunable olive-like anatase TiO₂ coated with carbon as superior anode for sodium-ion batteries. *Small* **12**, 5554–5563 (2016)
46. Qin, G., Zhang, X., Wang, C.: Design of nitrogen doped graphene grafted TiO₂ hollow nanostructures with enhanced sodium storage performance. *J. Mater. Chem. A* **2**, 12449–12458 (2014)
47. Cha, H.A., Jeong, H.M., Kang, J.K.: Nitrogen-doped open pore channeled graphene facilitating electrochemical performance of TiO₂ nanoparticles as an anode material for sodium ion batteries. *J. Mater. Chem. A* **2**, 5182–5186 (2014)
48. Zhang, Z., et al.: Metal–organic framework-derived graphene@ nitrogen doped carbon@ ultra-fine TiO₂ nanocomposites as high rate and long-life anodes for sodium ion batteries. *Chem. Commun.* **52**, 12810–12812 (2016)
49. Liu, H., Cao, K., Xu, X., Jiao, L., Wang, Y., Yuan, H.: Ultrasmall TiO₂ nanoparticles in situ growth on graphene hybrid as superior anode material for sodium/lithium ion batteries. *ACS Appl. Mater. Interfaces* **7**, 11239–11245 (2015)
50. Chen, C., et al.: Na⁺ intercalation pseudocapacitance in graphene-coupled titanium oxide enabling ultra-fast sodium storage and long-term cycling. *Nature Commun.* **6**, 6929 (2015)
51. Yeo, Y., Jung, J.-W., Park, K., Kim, I.-D.: Graphene-wrapped anatase TiO₂ nanofibers as high-rate and long-cycle-life anode material for sodium ion batteries. *Sci. Rep.* **5**, 13862 (2015)
52. Feng, J.-M., Dong, L., Han, Y., Li, X.-F., Li, D.-J.: Facile synthesis of graphene-titanium dioxide nanocomposites as anode materials for Na-ion batteries. *Int. J. Hydrogen Energy* **41**, 355–360 (2016)
53. Zhu, X., et al.: Graphene-modified TiO₂ microspheres synthesized by a facile spray-drying route for enhanced sodium-ion storage. *Part. Part. Syst. Charact.* **33**, 545–552 (2016)
54. Fu, C., et al.: Scalable synthesis and superior performance of TiO₂-reduced graphene oxide composite anode for sodium-ion batteries. *Ionics* **22**, 555–562 (2016)
55. Yan, D., et al.: Sn-doped TiO₂ nanotubes as superior anode materials for sodium ion batteries. *Chem. Commun.* **51**, 8261–8264 (2015)
56. Zhao, F., Wang, B., Tang, Y., Ge, H., Huang, Z., Liu, H.K.: Niobium doped anatase TiO₂ as an effective anode material for sodium-ion batteries. *J. Mater. Chem. A* **3**, 22969–22974 (2015)
57. Wang, B., et al.: Boron-doped anatase TiO₂ as a high-performance anode material for sodium-ion batteries. *ACS Appl. Mater. Interfaces* **8**, 16009–16015 (2016)

Major Trends and Mechanistic Insights for the Development of TiO₂-Based Nanocomposites for Visible-Light-Driven Photocatalytic Hydrogen Production



Ayat N. El-Shazly , Mahmoud A. Hamza , and Ahmed Esmail Shalan 

Abstract Hydrogen production *via* visible-light-driven photocatalytic processes based on the permanently available sunlight energy is considered as one of the most efficient strategies for solving energy issues facing human society and environmental crisis. TiO₂-based photocatalysts have been reported to be the most common and efficient photocatalysts, especially for water splitting; it is promoted as a suitable candidate because of its low cost, high stability, and being eco-friendly semiconductor. Although, TiO₂ photocatalysts have some drawbacks such as their wide bandgap, their high overpotential for the evolution of hydrogen, and their rapid electron–hole pair recombination rates, which impede its practical application. Therefore, numerous approaches are addressed for developing a variety of nanocomposites photocatalysts to be used in visible-light photocatalytic hydrogen production to overcome these shortcomings; these approaches can be categorized into four main strategies: doping, dye sensitization, semiconductor coupling, and coupling with carbon-based materials. These major trends displayed significant achievements in the design and construction of efficient visible-light-driven TiO₂-based photocatalysts by enhancing their sunlight absorption capability, the charge-carriers separation, and the corrosion resistance of the photocatalysts. In this chapter, the major trends and the corresponding mechanistic insights will be summarized with examples on the recent studies of visible-light-driven nanocomposites photocatalysts employed in photocatalytic hydrogen production.

Keywords Nanocomposite photocatalysts · Hydrogen production · Photocatalytic water splitting

A. N. El-Shazly, M. A. Hamza—Equally contributed to this work.

A. N. El-Shazly (✉) · A. E. Shalan
Central Metallurgical Research and Development Institute, P.O. Box 87, Helwan, Cairo, Egypt

M. A. Hamza
Chemistry Department, Faculty of Science, Ain-Shams University, Abbassia, Cairo, Egypt

A. E. Shalan
BCMaterials-Basque Center for Materials Applications and Nanostructures, Martina Casiano
UPV/EHU Science Park, Barrio Sarriena s/n, 48940 Leioa, Spain

Abbreviations

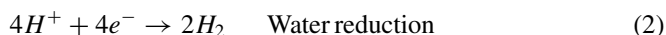
CB	Conduction band
CBM	Conduction band minimum energy level
E_g	Bandgap energy
e-h	Electron-hole pairs
e_{CB}^-	Photoinduced electron in the semiconductor's conduction band
E_J	Exa Joule (1 EJ = 10^{18} J)
H_2	Hydrogen gas
H^+	Proton
$h\nu$	Photon energy
h_{VB}^+	Photoinduced positive hole in the semiconductor's valence band
NHE	Normal hydrogen electrode
OER	Oxygen evolution reaction
O_2	Oxygen gas
PC	Photochemical
PEC	Photoelectrochemical
TM	Transition metal
VB	Valence band
VBM	Valence band maximum energy level

1 Introduction

The crucial need to reduce the continuing exhaustion of the non-renewable fossil fuels and to get rid of their negative impact on the whole environment can be considered as the chief engines to quest for renewable, cheap, and environment-friendly energy resources. The hydrogen gas (H_2) can act as an outstanding substitute to the traditional fossil fuels because of its clean combustion properties where the water vapor is the product of its combustion reaction, its renewability where water, the main resource on the earth, is its main raw material, and the high efficiency of its evolution from and conversion into electricity [1, 2]. Besides, the storage of hydrogen fuel could be achieved in many forms: gas, liquid, or metal hydride form, thus, it could be easily transported over a large distance in pipes and tankers [3]. In addition to this, compressed gaseous hydrogen exhibits a lower density than that of the liquid hydrogen, and exhibits greater content of energy than that of gasoline [3]. Hence, hydrogen can be considered as the most favorable carrier to store energy in such chemical form to be employed as efficient, environment-friendly, and renewable fuel [4, 5]. It is estimated that the worldwide hydrogen production rate is about 7.7 EJ/year, and this rate might be increased to about 10 EJ/year by 2050 [2]. Unfortunately, the employed approaches for hydrogen production depend on non-renewable energy sources, where 48% of the hydrogen production depend on natural gas, 30% *via* oil refining, and about 14% *via* coal gasification; however, only 4% of the worldwide hydrogen production depends on water electrolysis [6]. Thus, there is a crucial necessity to shift the worldwide hydrogen production to focus on efficient, renewable, and clean strategies, such as “green” semiconductor-assisted photocatalysis can

serve as efficient multidisciplinary technology merging physics, chemistry, chemical engineering with materials science and engineering for the efficient light employment for accelerating photochemical reactions and converting the permanently accessible solar energy into a much more useful form of energy [7–9].

In the semiconductor-assisted photocatalytic hydrogen evolution processes that occur on the photocatalyst (semiconductor) could be separated into three points: (i) illumination of the photocatalyst surface by photons exhibiting energy ($h\nu$) larger than the photocatalyst bandgap energy (E_g) causing the production of the photoinduced electrons (e_{CB}^-) that move from the valence band (VB) to the conduction band (CB) as well as the production of the photoinduced holes (h_{VB}^+) in the VB, which are commonly known as the e–h pair; (ii) the effective separation of the photoinduced electrons and photoinduced holes leading to the efficient utilization of the e–h pairs; and (iii) the redox reactions between the photoinduced e–h pairs and water molecules for achieving water splitting, where the holes are responsible for oxidizing the water molecules into O_2 gas (Eq. 1), and the electrons are responsible for reducing the water protons (H^+) to H_2 gas (Eq. 2) [10]. The initiation of the redox reaction requires a compatible band alignment of the employed photocatalysts with the redox potentials of water, where the lowest energy level in the CB, commonly known as the conduction band minimum (CBM), ought to be more negative than the potential of the hydrogen evolution reaction (E_{h^+/H_2} , 0 V vs. NHE), while the highest energy level of the valence band, commonly known as the valence band maximum (VBM), ought to be more positive than the potential of the oxygen evolution reaction (E_{O_2/H_2O} , 1.23 V vs. NHE) [11]. Hence, the bandgap energy (E_g) of an outstanding photocatalyst ought to be greater than 1.23 eV and smaller than 3.00 eV to have efficient photocatalytic water splitting upon the exposure of visible-light irradiation.



In general, there are two methods of photocatalytic water splitting, which are photochemical (PC) and photoelectrochemical water splitting (PEC). In PC systems (Fig. 1a), two types are known: one step and two-steps systems. In one-step system, the reduction and oxidation reactions of water molecules carry out within a single photocatalyst while in a two-steps (e.g. Z-scheme) system, two different semiconductors and a redox mediator are contacted, where each of the semiconductors will be used as an H_2 or O_2 evolution photocatalyst. As mentioned in Fig. 1b, in PEC systems, the reduction and oxidation reactions of water molecules carry out at different surfaces. If the material of the photoelectrode is an n-type semiconductor, it will act as a photoanode where the photoinduced holes will oxidize water molecules to form O_2 gas, while the photoexcited electrons will be migrated toward the Pt (counter electrode) through an external circuit to form H_2 . In the second case, if the material is a p-type semiconductor, it will act as a photocathode where the photoinduced electrons will reduce the protons to form H_2 gas, while the holes in which will

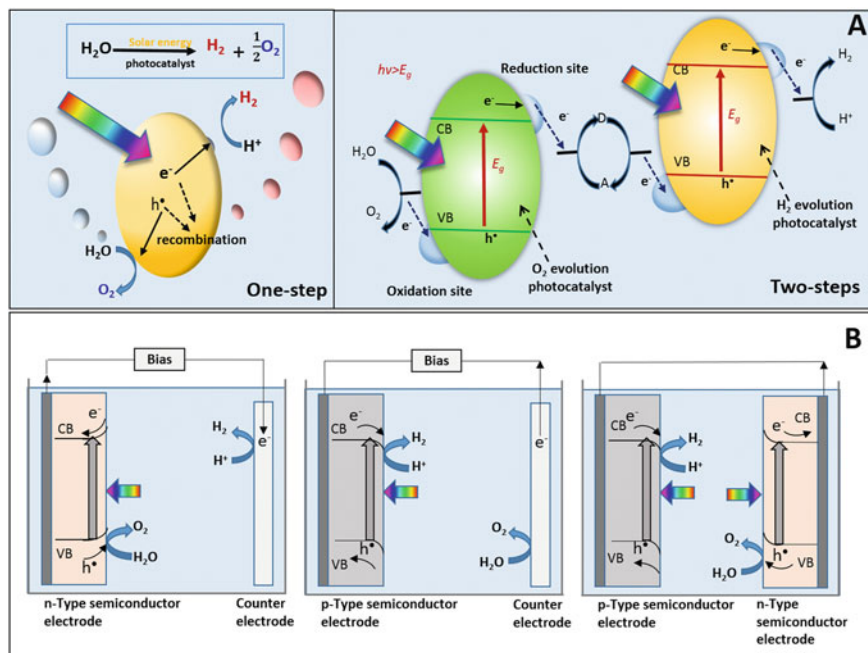


Fig. 1 Schematic of photocatalytic water splitting over powder photocatalysts, PC (A) and (PEC) (B), Ref [12] with permission from the Elsevier

migrate to the counter electrode and make the oxidation reaction of water molecules. In the third case, the utilization of a n-type semiconductor as the photoanode and a p-type semiconductor as the photocathode to form p-n junction can enhance the the efficiency of PEC water splitting. In PEC systems, to reduce the resistance of electrodes in the solution, a chemical bias or an external bias is applied to have efficient electron–hole pairs.

Generally, TiO_2 [13], ZrO_2 [14], ZnO [15], MoS_2 [16], $g-C_3N_4$ [17], CdS [18], Cu_2O [19], $SrTiO_3$ [20], and $BiVO_4$ [21], are promising candidates for photocatalytic hydrogen production. Figure 2 shows the bandgaps and the positions of the band edges of various photocatalysts compared to the redox potentials of water [22]. Among them, the positions of VB and CB of TiO_2 are compatible with the redox potentials of water, which make it classified as one of the suitable photocatalysts for H_2 production, because of its availability, non-toxicity, low cost, photostability, chemical stability in strongly acidic and alkaline media, as well as its outstanding photocatalytic performance [23, 24]. However, two prime drawbacks are affecting the photocatalytic activity of TiO_2 as a photoanode for water splitting; the former is the wide bandgap of TiO_2 excluding its absorption and its photocatalytic activity only under the UV irradiation, which resembles a very small percentage of the incident solar irradiation (2–4%), and the later is the rapid e^-h^+ recombination rate in TiO_2 leading to the reduction of its photocatalytic activity [23–25]. Recently, many approaches have been adapted for improving the photocatalytic performance of TiO_2 , including controlling the band structure by metal or nonmetal doping, coupling with

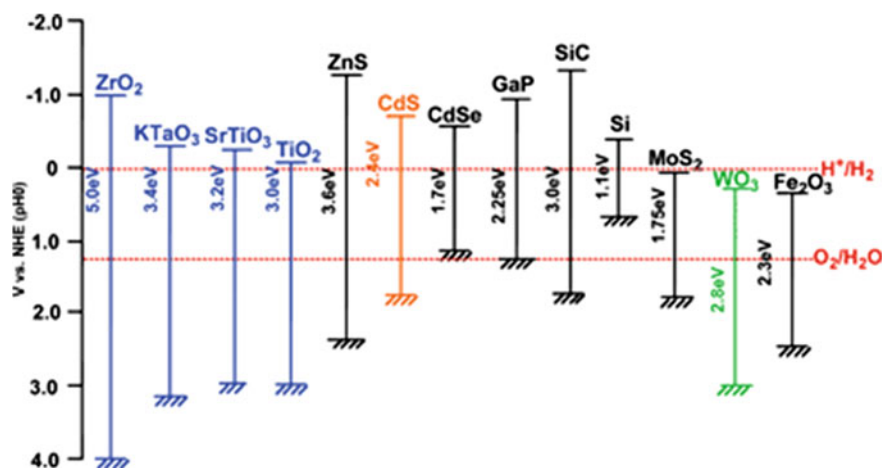


Fig. 2 The bandgaps and band edges of different semiconductors with respect to the redox potentials of water from Ref [22] with permission from the Royal Chemical Society

carbonaceous materials, photosensitization, and coupling with other semiconductors, as illustrated in Fig. 3.

Herein, we report the basics and the recent advances of various strategies to enhance the photocatalytic behavior of the TiO₂-based nanocomposites toward photochemical (PC) or photoelectrochemical (PEC) hydrogen production. Besides, the findings of these studies can prompt the employment of these nanocomposites in other essential photocatalytic fields such as solar cells, CO₂ reduction, ammonia production, and wastewater treatment.

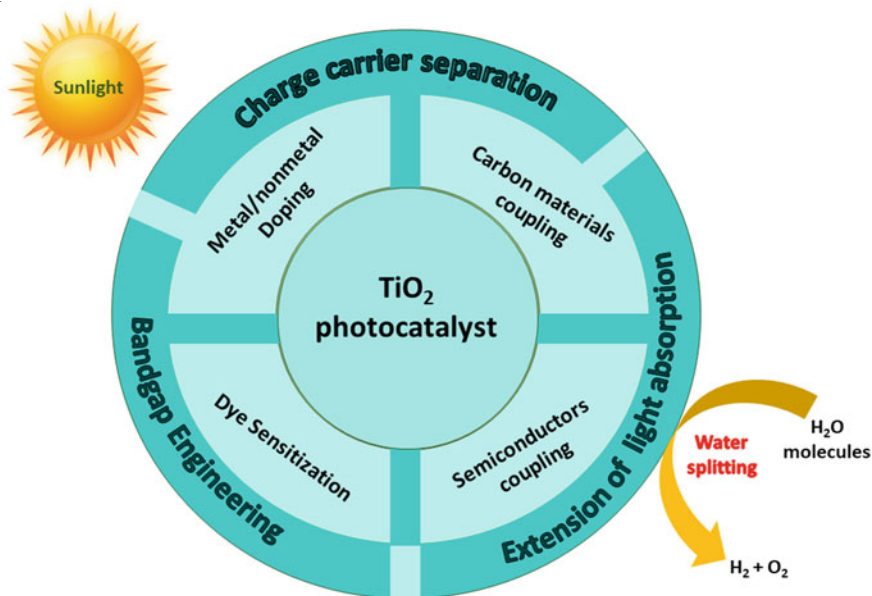


Fig. 3 Overview of approaches for enhanced TiO₂ performance for hydrogen generation

2 General Mechanisms of Photocatalytic Hydrogen Production using Heterojunctions

Generally, the construction of a hybrid structure or heterojunction can be considered as the most valuable approach for the enhancement of the efficiency of charge separation *via* providing extra pathways for various charge transfer processes, as illustrated in Fig. 4. It could be categorized into four types: Type I heterojunction, Type II heterojunction, Z-scheme heterojunction, and Schottky junction [26]. Figure 4a demonstrates the band alignment and the corresponding mechanism of Type I heterojunction in which the VB and CB of the first semiconductor (semiconductor A) straddle the bandgap of the second semiconductor (semiconductor B), where the positions of both VB and CB of semiconductor B are located between the VB and CB of semiconductor A; during the photocatalysis process, electrons

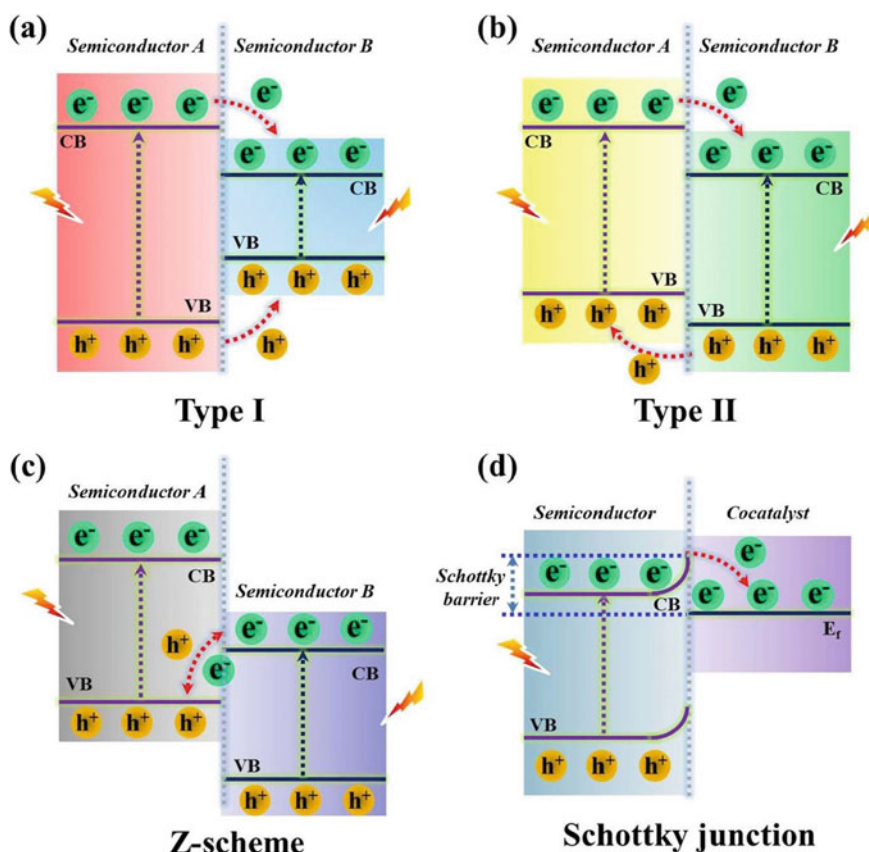


Fig. 4 Schematic illustration of four types of heterojunction mechanism. Reproduced from Ref. [27] with permission from Elsevier

and holes would migrate toward the semiconductor B and accumulate within it. On the contrary, Fig. 4b displays the staggered bandgap alignment in the Type II heterojunction (staggered bandgap). In other words, during the excitation process, photoinduced electrons transfer from the higher CB position (semiconductor A) to the lower CB position (semiconductor B), simultaneously holes migrate from the lower VB (semiconductor A) to the higher VB of semiconductor B, resulting in an efficient charge separation, as mentioned in Fig. 4b. Similarly, Z-scheme heterojunction (broken bandgap) (Fig. 4c), has a similar pathway as the Type II heterojunction; however, in this case, the electrons transfer from the CB of semiconductor B toward the VB of semiconductor A.

Additionally, Fig. 4d displays the Schottky junction, which is commonly observed upon the combination of semiconductor and metal, and the metal in this case commonly known as a co-catalyst. Notably, the metal's work function is greater than that of the semiconductor in this case, which means that the introduction of an extra level within the bandgap of the semiconductor; i.e., below the CB and above the VB; thus, the photoinduced electrons can move from the CB of the semiconductor into the metal (co-catalyst) through the interface. Thus, the establishment of the Schottky junction occurs because the semiconductor exhibit excess positive charge whereas the metal exhibit excess negative charge causing the construction of a space charge layer at the semiconductor/metal interface, commonly called the "Schottky barrier", which facilitate the electron trap (i.e. capture photoinduced electrons, and retard e-h recombination, causing a significant enhancement in the photocatalytic efficiency. Hence, the construction of any of the above-mentioned heterojunctions, especially Type II band alignment with a staggered bandgap alignment, can promote photocatalytic applications with enhanced charge separation performance because of the electric field built-in at the interface of the junction.

3 Metal/Nonmetal-Doped TiO₂ Nanocomposites

Doping TiO₂ with metal and/or nonmetal atoms/ions attempts can be considered as one of the most promising commonly-employed strategies, which showed substantial enhancement in the development of TiO₂-based photocatalysts to overcome the major disadvantages of the bare TiO₂ photocatalysts. The metal/nonmetal doping of TiO₂ can achieve a significant enhancement of its absorption capability for visible light, in addition to the occurrence of a suitable bandgap shift and reduction of the e-h recombination rates, which cause a remarkable improvement in the photocatalytic efficiency in the visible region as well as the UV region [28]. Many scientific articles reported several attempts for improving the photocatalytic properties of TiO₂ as well as its photocatalytic performance towards the production of hydrogen. In this section, we are going to explore the main types of doping (metal doping, nonmetal doping, and co-doping) as well as illustrating the corresponding general mechanisms for the metal/nonmetal-doped TiO₂, which must be presented to understand how metal/nonmetal-doped TiO₂ photocatalysts can overcome the drawbacks of the bare TiO₂ photocatalysts. Also, the main findings of some reported articles will be displayed and discussed.

Concerning the metal doping strategy, many metals such as gold (Au), silver (Ag), palladium (Pd), platinum (Pt), cobalt (Co), rhodium (Rh), ruthenium (Ru), nickel

(Ni), zinc (Zn), and copper (Cu), have been employed as efficient dopants to TiO₂-based photocatalysts to enhance their efficiency toward photocatalytic hydrogen production. Generally, doping TiO₂ with metal can achieve significant enhancement in the capabilities of visible light absorption in addition to the narrowing of the bandgap energy; thereby, improving the charge separation as well as the photocatalytic performance. The general mechanism of metal doping must be presented to understand how metal-doped TiO₂ photocatalysts can overcome the drawbacks of the bare TiO₂ photocatalysts, as shown in Fig. 5a. Firstly, metal doping can provide an extra energy level below the CB of TiO₂ as displayed in Fig. 5b, this new level (with lower energy than that of CB of the bare TiO₂) can act as an alternative CB for the metal-doped TiO₂ rather than the original CB in the undoped TiO₂, which leads to the decrease of the bandgap energy of metal-doped TiO₂ photocatalysts compared to the undoped TiO₂ photocatalysts. Additionally, this new level can act as may be used for trapping the photo-induced electrons, where these electrons may prefer to relax at this level rather than their returning to the VB of TiO₂ causing the decrease of the e-h recombination rate as well as the increase of the charge separation leading to the improvement of the photocatalytic efficiency of the metal-doped TiO₂ photocatalysts toward hydrogen production compared to the bare TiO₂ photocatalysts.

As a prime example, B. Liu et al. [29] proposed a scheme for the production of big amounts of fine single-crystalline TiO₂ nanowires through molten-salt flux, in addition to the *in-situ* incorporating of different transition-metals (TM) dopants (Cr, V, Fe, Mn, Co, Mo, Nb, and Rh) for tuning the electrical, optical, and photocatalytic characteristic. They stated that the as-synthesized TM-doped TiO₂ photocatalysts had various colors which differ from the original white color of the bare TiO₂ nanowires;

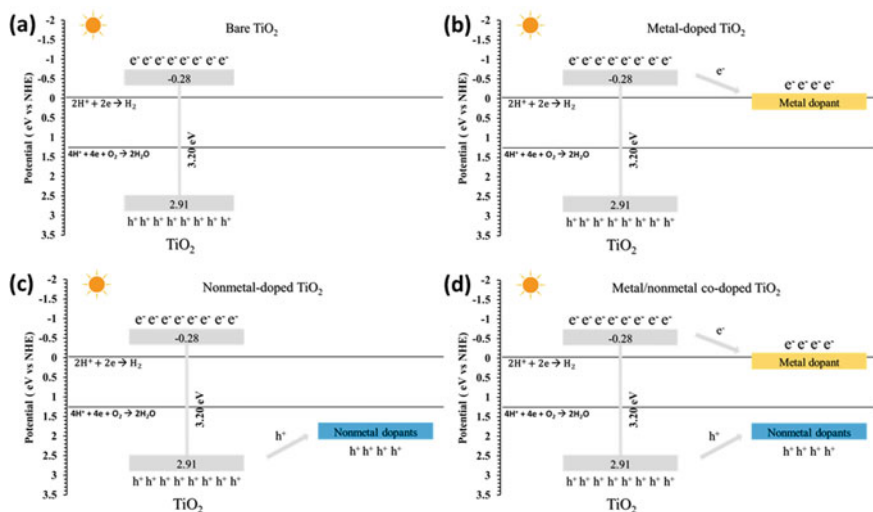


Fig. 5 The general mechanism of photocatalysis by bare TiO₂ (a), metal-doped TiO₂ (b), nonmetal-doped TiO₂ (c), and metal/nonmetal co-doped TiO₂ (d)

for example, 2%Rh-doped TiO₂ nanowires displayed a dark brown color gained due to the high absorption capabilities of the visible light, as displayed in Fig. 6a. In addition to this, the introduction of the metal dopants was found to decrease the overpotential in the water electrolysis, specifically that of the oxygen evolution reaction (OER), as shown in Fig. 6b, which could enhance the photoactivity of TiO₂, specifically for water oxidation, i.e. OER, and significantly reduce the kinetic loss in overpotential.

Unfortunately, the metal doping strategy exhibits various drawbacks such as the low stability of the doped nanomaterials and the metal leaching and probable toxicity impact limiting their application for water treatment trends. Also, the metallic atoms/ions may act as deep electron-trapping centers leading to the reduction of the photocatalytic activity. Besides, the incorporation of metal atoms/ions as dopants for TiO₂ were recognized by their contribution to the partial blocking of the active sites at the TiO₂ surface leading to the reduction of photocatalytic activity [30]. In addition to this, the doping with metals is expensive and the doping processes are hampered by some other disadvantages of some metals, for instance, the noble metals such as Au and Ag are relatively toxic; also, some of the metal centers in the metal-doped photocatalysts suffer from chemical corrosion or photocatalytic corrosion during the photocatalytic processes [28].

To avoid the drawbacks of metal dopants, such as the thermal instability and corrosion, using nonmetal atoms with large ionizing energy and high electronegativity, such as nitrogen (N), sulfur (S), carbon (C), boron (B), chlorine (Cl), and fluorine (F), are usually employed as effective alternatives for metals to dope TiO₂-based photocatalysts; this strategy can be considered as a feasible approach for developing the visible-light photocatalysts and enhancing their efficiency toward hydrogen production [28, 31]. Similarly, doping TiO₂ with nonmetal can achieve significant enhancement in the capabilities of visible-light absorption in addition to the narrowing of the

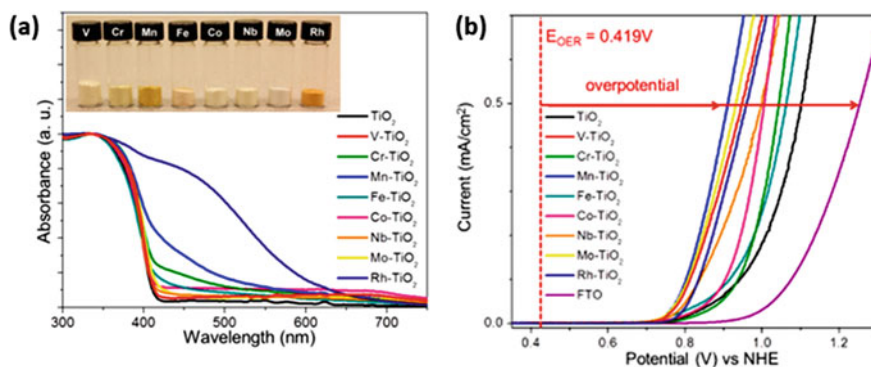


Fig. 6 DRS and the photographic picture of 2%TM-doped TiO₂ photocatalyst (a), and OER overpotential measurements using the electrodes (b) of bare TiO₂ and TM-doped TiO₂ deposited on FTO in alkaline media (at pH ~13.6); the dashed vertical line represents the redox potential of water oxidation. Reproduced from Ref. [29] with permission from the American Chemical Society

bandgap energy; thereby, improving the charge separation as well as the photocatalytic performance. Therefore, the general mechanism of nonmetal must be presented to understand how nonmetal-doped TiO_2 photocatalysts can overcome the drawbacks of the bare TiO_2 photocatalysts, as shown in Fig. 5c; it is clear that this mechanism is different from that of the metal doping approach. Firstly, nonmetal doping can provide an extra energy level above the VB of TiO_2 as displayed in Fig. 5c, this new level (with higher energy than that of VB of the bare TiO_2) can act as an alternative VB for the metal-doped TiO_2 photocatalysts rather than the original VB of undoped TiO_2 photocatalysts, which leads to the decrease of the bandgap energy of nonmetal-doped TiO_2 photocatalysts compared to the undoped one. Additionally, this new level may be used for trapping the photoinduced holes, where these holes may spontaneously transfer to this level rather than their relocation to their normal position at the CB of TiO_2 , leading to the reduction of the e-h recombination rates in addition to the increase of the charge separation and the improvement of the photocatalytic efficiency of the nonmetal-doped TiO_2 photocatalysts compared to the undoped one toward hydrogen production.

Among various nonmetal dopants, nitrogen (N) is the most commonly employed nonmetal dopant on TiO_2 for extending its absorption capability toward the visible-light region as well as promoting the charge separation; thereby, increasing the photocatalytic activity of N-doped TiO_2 photocatalysts toward hydrogen production [31]. However, the nonmetal doping strategy has many disadvantages; for instance, it was found that the amount of the nonmetal dopant could be decreased at the annealing stage leading to the reduction of the photoactivity of the as-prepared nonmetal-doped TiO_2 . Besides, some scholars proposed the decrease of the photocatalytic efficiency of nitrogen-doped TiO_2 can be attributed to the strong localization of N 2p states at the VBM, which could cause the trapping of photoinduced electrons and decrease the mobility of holes, and thereby, decrease the oxidation power of the photocatalyst. In addition to this, some researchers claim that the formation of the anion vacancies through nitrogen doping can be proposed as a reason causing the reduction of the photocatalytic activity.

Of course, various dopants exhibit different effects on the interface with the photoinduced holes and photoinduced electrons, which can be attributed to the difference in the positions of the various dopants in the lattice of TiO_2 . Besides, the coordination geometry and the positions of the dopants would be affected by the nature of the dopants themselves including the ionic radii, the work function, and the relative positions of the Fermi levels of the dopants; also the synthesis route and the method of the incorporation of the dopants play a crucial role in this regard. Various types of doping depend on the nature of the dopant itself (metal doping and nonmetal doping), as described above; also the mechanism of the co-doping is based on the number of different dopants in co-doping (double doping, and multi-doping) or the different types of the dopants (metal/nonmetal co-doping, nonmetal/nonmetal co-doping, and metal/metal co-doping).

Many attempts have reported the success of the co-doping strategy compared to the single-doping strategy where synergetic enhancements were achieved due to the combination of the various dopants at the same time. As a prime example for the multi-doping, our previous work reported by A. El-Shazly et al. [32], where unique multi-doped TiO_2 mesocrystals had been synthesized using a simple

sol-gel process followed by a topotactic transformation. It was found that the fabricated cobalt, carbon, titanium(III)-multi doped photoanodes (Co-C/Ti³⁺-TiO₂) exhibited an outstanding photocurrent density (25 mA/cm² at 1 V_{Ag/AgCl}), that was six-folds greater than that measured for the cobalt-free photoanode, C/Ti³⁺-TiO₂, (4.4 mA/cm²), as displayed in Fig. 7a; which also much higher than the reported results in the literature of the TiO₂ photoanodes [33]. We attributed the extraordinary photocurrent densities of the as-fabricated multi-doped TiO₂ photoanodes for the positive influence of the introduction of Co²⁺, Ti³⁺, and C dopants and their synergetic performance to prompt the formation of shallow impurity states, that are capable of reducing the e-h recombination rates, specifically in the case of the existence of cobalt ions. It was further evidenced by the shifts in the flat band potential (V_{fb}) of the Co-doped C/Ti³⁺-TiO₂ photoanode to a more negative value with respect to the V_{fb} of the C/Ti³⁺-TiO₂ photoanode, as estimated from the Mott-Schottky plots, as displayed in Fig. 7b. Finally, the proposed mechanism of the improved photocatalytic behavior of the as-fabricated Co-doped C/Ti³⁺-TiO₂ mesocrystals owing to the establishment of a Type-II heterojunction between CoO and TiO₂, along with

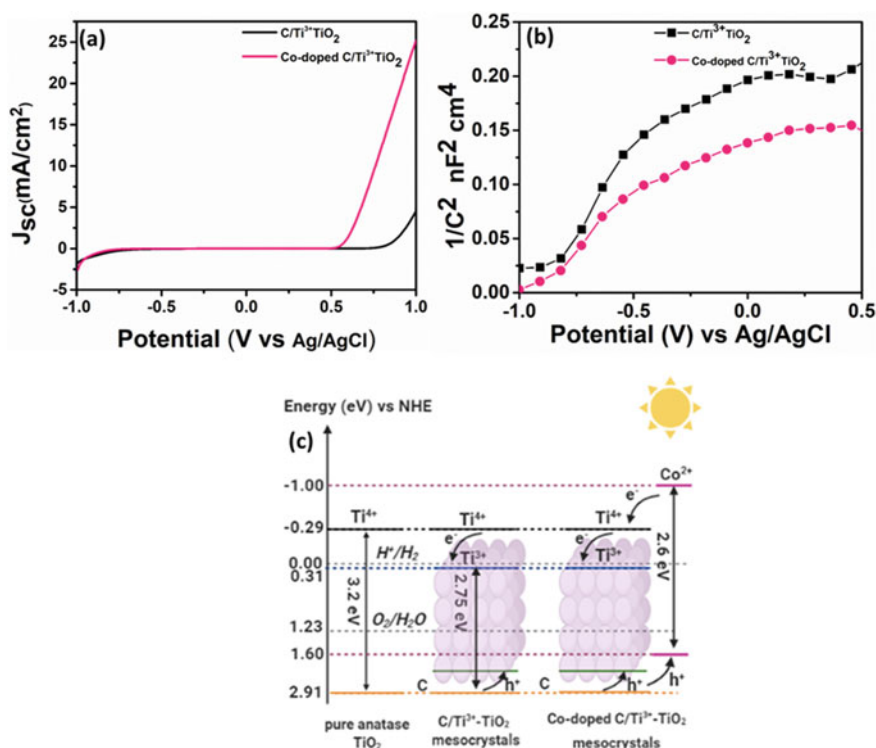


Fig. 7 The photoelectrochemical performance (a), Mott-Schottky plots (b), and the suggested mechanism (c) of the improved performance of the C/Ti³⁺-TiO₂ and Co-doped C/Ti³⁺-TiO₂ monocrytals thin-films. Reproduced from Ref. [32] with permission from Elsevier

the synergetic effects of the self-dopants (C and Ti^{3+}) which have a brilliant role in enhancing the conductivity and promotion of the charge separation, as demonstrated in Fig. 7c.

4 Carbon-Based TiO_2 Nanocomposites

Recently, the photocatalytic behavior of TiO_2 can be enhanced toward the visible-light region by incorporating the TiO_2 surface with carbonaceous materials such as carbon nanotubes, fullerenes, graphene oxide (GO), graphene, or reduced graphene oxide (RGO), etc., to fabricate carbon-based TiO_2 nanocomposites. Specifically, the coupling of graphene-based nanomaterials with TiO_2 nanoparticles exhibited innovative characteristics in the photocatalytic applications because of their high chemical stability, flexible structure, large specific surface area, perfect thermal conductivity, and outstanding electrical conductivities in addition to the unusual mobility of charge carriers at room temperature [34]; qualifying the graphene-based nanocomposites to be one of the most advantageous nanomaterials for enhancing the photocatalytic efficiency in the novel generations of photocatalysts. Additionally, with the extremely high specific surface area as support, graphene can play a significant role in gathering the photoexcited electrons from the CB of TiO_2 . L. Li *et al.* [35] investigated the preparation of the RGO/ TiO_2 nanocomposite *via* simple one-pot laser ablation in liquid (LAL) method. They achieved extension in optical absorbance from ultraviolet to the visible region and the prepared nanocomposites promoted charge conductivity and caused a substantial increase in the photocatalytic rate of hydrogen production, which was up to 23-folds compared to the bare TiO_2 . Besides, combining sol-gel with hydrothermal synthesis routes for the fabrication of nanocrystalline TiO_2 particles on RGO sheets showed improvement in the photocurrent density of 0.20 mA/cm^2 with respect to the bare TiO_2 photoanode of 0.11 mA/cm^2 [36]. The reason behind this enhancement is the introduction of the RGO sheets led to the establishment of shallow trap states that could improve charge carriers' separation and be highly efficient. When the fabricated hybrid materials are exposed to light, electrons will be excited and transferred to the CB of TiO_2 ; then some of these electrons could transfer to the RGO sheets while holes are left separated in the original VB of TiO_2 . Thus, RGO sheets acted as efficient electron acceptors and retarded the e-h recombination processes.

One of the drawbacks of utilizing graphene-based materials for photocatalytic trends is the fact that graphene itself exhibits zero bandgap energy; thus, to enlarge its practical application, creating a bandgap can affect its physical properties [37]. Therefore, if the size of graphene becomes closed to exciton Bohr radius, then the quantum confinement effect becomes important and considering the graphene quantum dot (GQDs). GQDs have fascinating properties derived from both graphene and carbon quantum dots, such as the size-dependent bandgap energy, outstanding electron conductivity, excellent photostability, unique ultraviolet and blue to green emission, and good dispersion in water and/or polar solvents [38]. Furthermore, various interesting photoelectronic features of GQDs could be good candidates for photocatalytic H_2 evolution applications. Besides, the PC and PEC efficiency of TiO_2

photocatalysts can be enhanced by coupling with GQDs to achieve visible-light-driven photocatalytic performance, where GQDs exhibit a dual function where they can act as a photosensitizer leading to the enhancement of the visible light absorption and electron reservoir causing an efficient charge separation and enhancement of the photocatalytic efficiency. X. Hao et al. [38] reported that about 100% enrichment for the produced amount of hydrogen using GQDs/TiO₂ compared to the bare TiO₂. Also, another work reported by A. Bayat et al. [39] found that the photocurrent enhancement for the composite of GQDs-x/TiO₂ was ~ 95% compared to bare TiO₂ nanoflowers. In another study, H. Zhang et al. [40] fabricated a nanocomposite of graphene quantum dots and hollow titanium dioxide nanosphere (GQDs/H-TiO₂), as shown in Fig. 8(a, b) the photocurrent response improvement of the as-synthesized GQDs/H-TiO₂ nanocomposite was about 3.5 folds greater than that of bare H-TiO₂ as show in Fig. 8(c, d), confirming that GQDs improved the electron-hole separation as suggested from the decrease of the charge resistance (Fig. 8e); thus, the photocurrent density was remarkably increased based on the sensitization of GQD and injection of electrons to the CB of TiO₂ as demonstrated in the proposed mechsism (Fig. 8f).

Compared to graphene nanomaterials, carbon nanotubes (CNTs) have superior properties as they exhibit high surface-to-volume ratio, rapid charge transfer, high thermal and electrical conductivity, as well as their large mechanical strength and great adsorption capacity allowing them act as promising candidates as a promoter for the charge transfer and as supports for photocatalysts. The coupling of TiO₂ with CNTs can be used as an advanced visible light nanocomposite for enhancing the separation efficiency of photoinduced charge carriers. This phenomenon is rationalized by (1) the stabilized e-h pairs that hinder the recombination rate and provide a longer lifetime; (2) when exposed to sunlight, the excited electrons could simply move to the CB of TiO₂ and (3) it can act as an impurity in TiO₂ lattice and create Ti - C or Ti - O - C vacancy sites that enhance the absorption capability of the visible light. Although MWCNTs-TiO₂ nanocomposites are more known in literature than those with single-walled carbon nanotubes (SWCNTs), (SWCNTs) have shown greater photocatalytic efficiency than that of multiwalled carbon nanotubes (MWCNTs) as the interphase contact of the surface of TiO₂ with the bundles of minor SWCNTs individuals is greater than that of MWCNT-TiO₂ [41].

5 Dye-Sensitized TiO₂ Nanocomposites

Dye sensitization can be considered as one of the commonly employed efficient methods for extending the practical applications of TiO₂ photocatalysts under visible irradiation as well as the enhancement of the charge separation. Generally, there is a large number of dye sensitizers such as natural dyes, synthetic organic dyes, metal-complex based dyes, and polymer dyes, which can be excited upon the absorption of visible light; then the excited electrons would be transferred to the CB of TiO₂, but this requires a Type-II band configuration and the dye sensitizer can act as a visible-antenna for the TiO₂ photocatalysts. The breakthrough for dye-sensitized solar cells (DSSCs) arose in 1991 upon the pioneering work of Grätzel and O'Regan, who built a DSSC device constituted by a Ru bipyridyl complex, nanocrystallineTiO₂

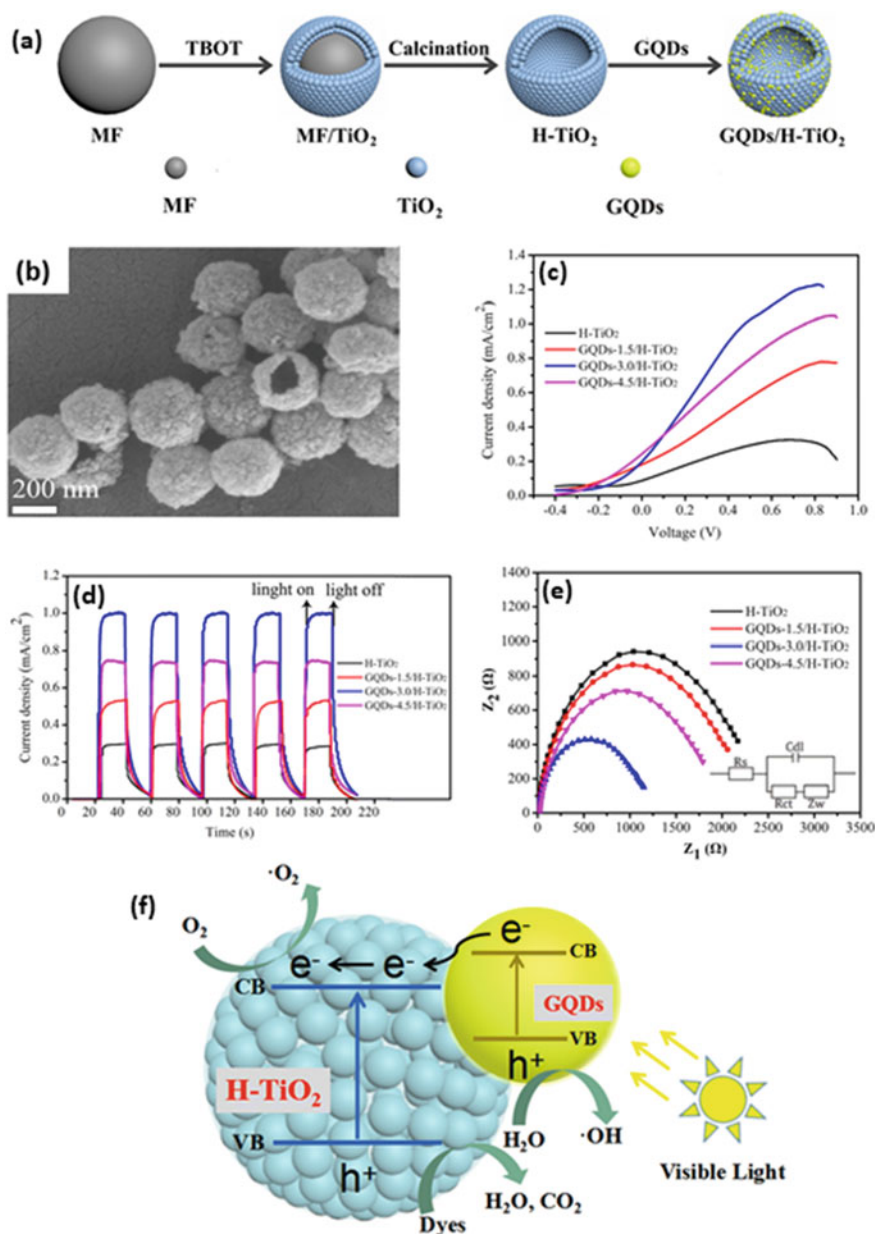


Fig. 8 The schematic diagram of fabrication of GQDs/H-TiO₂ composites (a), SEM image of GQDs-3.0/H-TiO₂ (b), J-V curves (c) and Transient photocurrent response spectra (d), and EIS spectra (e) of H-TiO₂, GQDs-1.5/H-TiO₂, GQDs-3.0/H-TiO₂, and GQDs-4.5/H-TiO₂, and the proposed mechanism of GQDs/H-TiO₂ composites (f). Reproduced from Ref. [40] with permission from Springer

thin-film electrode, and iodine-based redox electrolyte [42]. After that, Ruthenium metal complexes are the most popular and commonly used photosensitizers due to their relatively high efficiency, high absorption capabilities, suitable bandgap energies, and outstanding stability in aqueous solutions. Unfortunately, the toxicity, the high cost, and the resource scarcity of Ru metal impede its extensive real applications; however, no further systems are at par with Ru-based metal complexes [43]. Therefore, metal-free organic dyes become greatly investigated owing to their high molar extinction coefficients in the visible region, low-cost, and tunable structures [44]. Among various organic dyes, porphyrin-based compounds are predominantly efficient dye sensitizers because of their excellent photoelectrochemical property, remarkable chemical stability, as well as their high absorption coefficients of their Soret band (in the wavelength range 400–450 nm) and their Q-bands (in the wavelength range 500–700 nm). Besides, porphyrins exhibited intensive colors, and they were proposed to improve the whole photocatalytic response of TiO₂ to the visible light region in addition to the enhancement of the charge separation as confirmed by the increase in the lifetime of porphyrin-sensitized TiO₂ catalyst [23, 24].

For instance, H. Ding et al. [45] reported a brilliant work regarding the outstanding impact of the utilization of two organic heterocyclic compounds (indeno[1,2-b]thiophene-based dyes: S5 and S6) as dye sensitizers for Pt-doped TiO₂ in order to significantly enhance its photocatalytic efficiency toward hydrogen production by broadening the spectral response to the visible region and the near-infrared light region, as displayed in Fig. 9. The as-synthesized S6@Pt/TiO₂ and S5@Pt/TiO₂ samples exhibited an outstanding high and wide absorption peak at 500–700 nm, which were not observed in the Pt/TiO₂, as displayed in the recorded DRS spectra (Fig. 9a). Also, the DRS spectra confirmed that the as-synthesized dye sensitizers (S5 & S6) could be easily incorporated on the surface of Pt/TiO₂ and effectively utilize the visible light. Besides, because of the outstanding absorption capability in the visible region, it was found that the average hydrogen production rates of S5@Pt/TiO₂ and S6@Pt/TiO₂ were 11.3 and 3.9 times higher than that of the Pt/TiO₂, respectively. In addition to this, it was observed that about 95% of the photocatalytic activity of S5@Pt/TiO₂ was preserved after three cycles, as displayed in Fig. 9b, while about 70% of the photocatalytic activity of S6@Pt/TiO₂ was preserved, referring that the as-synthesized S5-based photocatalysts exhibited much better photostability and recyclability. All of this promising findings can be attributed to the enhancement in the charge separation which can be deduced from the substantial reduction in the PL intensity (Fig. 9c), the perfect stability of the transient photocurrent responses (*J-t*) curves (Fig. 9d), the decrease of the semicircle in Nyquist plot (Fig. 9e), and the increase of the apparent quantum efficiency (Fig. 9f). In addition to this, they proposed a mechanism (Fig. 9g) that describes the process of the injection of the excited electron from the LUMO levels of the S5 dye to the CB of TiO₂.

6 Semiconductor-Coupled TiO₂ Nanocomposites

As a competitive and alternative strategy, the construction of heterojunction between a wide-bandgap semiconductor such as TiO₂ and narrow-bandgap semiconductors seems to act as efficient visible-light-driven photocatalysts, because of the improved light absorbance and the enhanced charge separation of photoinduced e-h pairs through smoothing the charge transfer between TiO₂ and the coupled semiconductor,

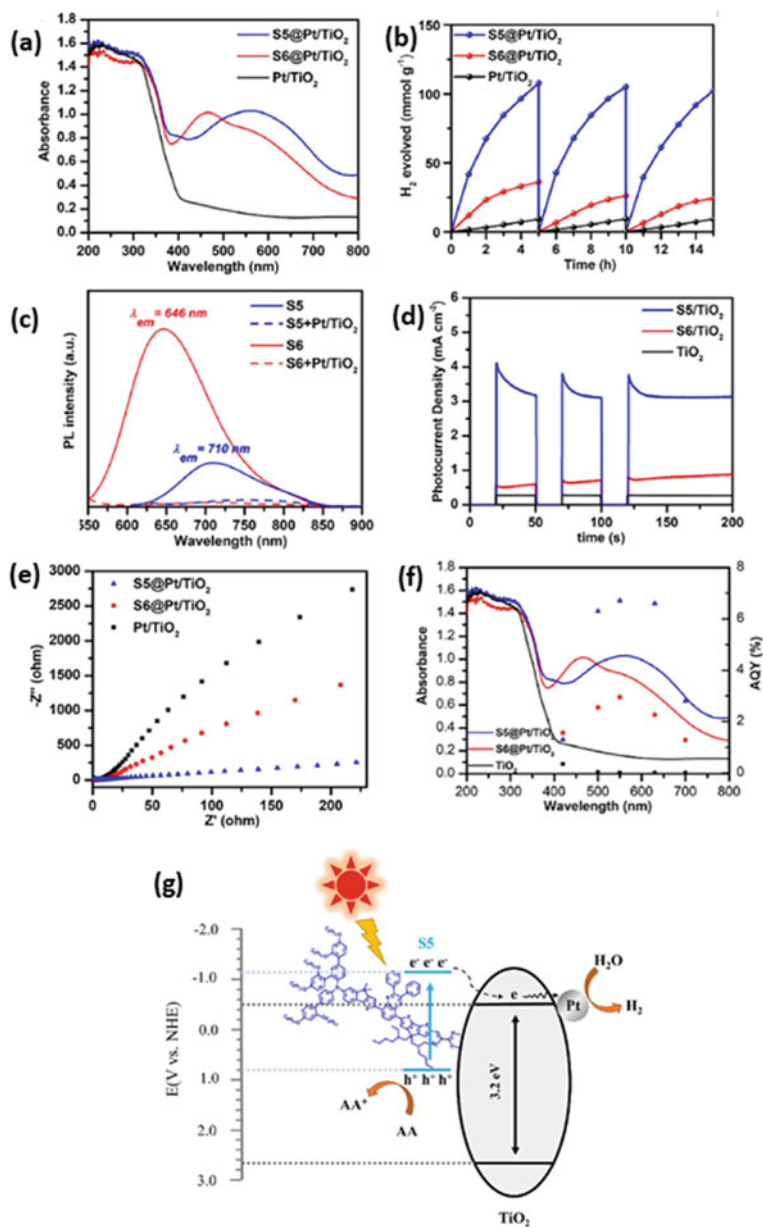


Fig. 9 The DRS spectra (a), Photostability for H_2 production for three cycles (b), PL spectra of S5 and S6 in THF solution without or with Pt/TiO_2 (0.67 g L^{-1}) (c), Transient current responses to on–off cycles of illumination (d), EIS Nyquist plots (e), Wavelength-dependent AQY values and DRS spectra (f), and The proposed mechanism of $\text{S5@Pt}/\text{TiO}_2$, $\text{S6@Pt}/\text{TiO}_2$ and Pt/TiO_2 (g) Reproduced from Ref. [45] with permission from Elsevier

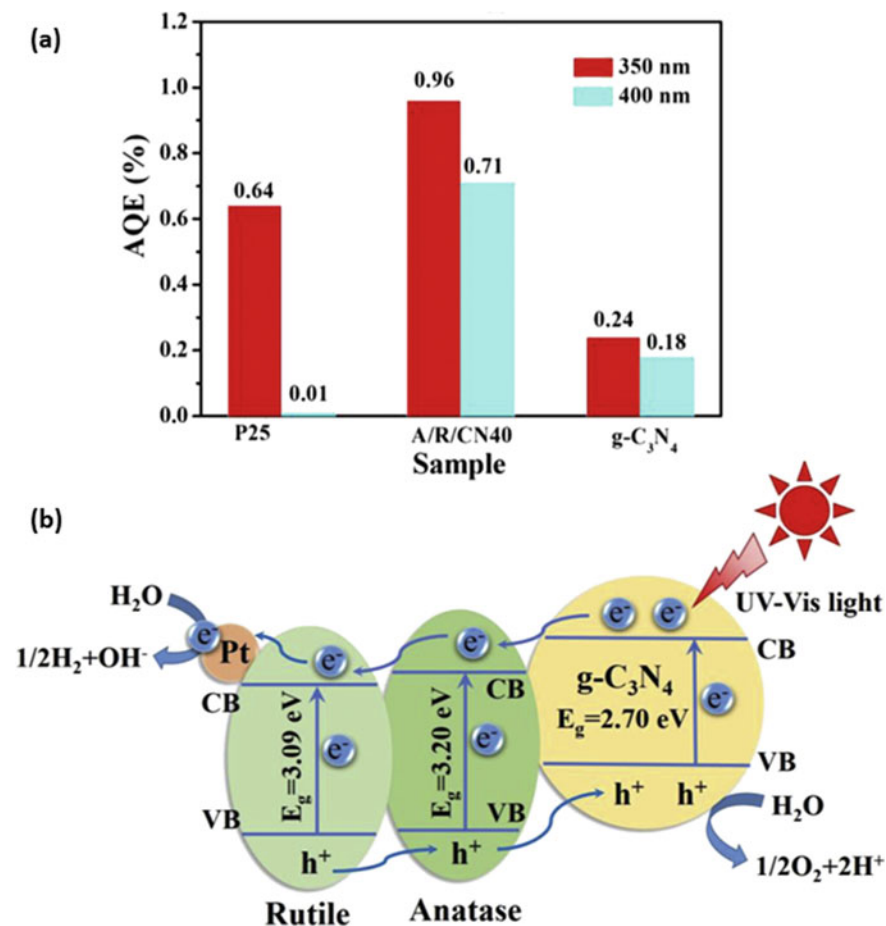


Fig. 10 The apparent quantum efficiency (a), and the schematic representation of photocatalytic hydrogen evolution (b) of P25, A/R/CN40 and g-C₃N₄ system. Reproduced from Ref. [51] with permission from Elsevier

but this requires a suitable band alignment such as Type II configuration. Recently, graphitic carbon nitride (g-C₃N₄) had been generated a lot of interest as a metal-free robust semiconductor for visible-light-driven photocatalytic applications, especially hydrogen production [46, 47]. Generally, the structure of g-C₃N₄ consists of strong covalent bonds between carbon and nitrogen atoms and shows good stability in acidic and alkaline medium, which is favorable for hydrogen production applications. g-C₃N₄ has fascinating characteristics such as the high thermal and chemical stability, the suitable band edges positions, and the low cost [48], in addition to the low bandgap of about 2.70 eV signifying that the absorbance of g-C₃N₄ is up to 460 nm [49]. Moreover, the presence of nitrogen atoms can anchor the active sites [50]. J. Wang et al. [50] developed g-C₃N₄/TiO₂ nanocomposites by calcining a mixture

of titanium precursor and melamine, they could achieve that the hydrogen production rate of the nanocomposite with 67 wt% melamine is about 5-folds enhancement compared to pristine g-C₃N₄ or bare TiO₂. Also, Y. Fang et al. [51] studied different proportions of g-C₃N₄ and TiO₂ to form novel anatase/rutile TiO₂/g-C₃N₄ multi-heterostructure photocatalysts displaying about double-increase in the average hydrogen production rate when the weight percent of g-C₃N₄ increased from 20 to 40%. However, by increasing the loading concentration of g-C₃N₄ to 50% and 60%, the rate of hydrogen production was suppressed, which was ascribed to the masking effect. The interesting results in this report are that the rate of hydrogen production of the optimal concentration of g-C₃N₄ (40%) is about 4-folds and 8-folds greater than that of bare P25 and g-C₃N₄, respectively [51]. They suggested a mechanism for the enhancement of the photoactivity is demonstrated in Fig. 10 where the g-C₃N₄/TiO₂ nanocomposite typically followed the Type II configuration, and the photogenerated electrons on the CB of g-C₃N₄ could spontaneously transfer to the lower CB of TiO₂ and efficiently reduce H⁺ to H₂ molecules.

Undoubtedly, the creation of TiO₂/transition metal oxides semiconductor materials nanocomposites offers an approach to accelerate the transport property, charge

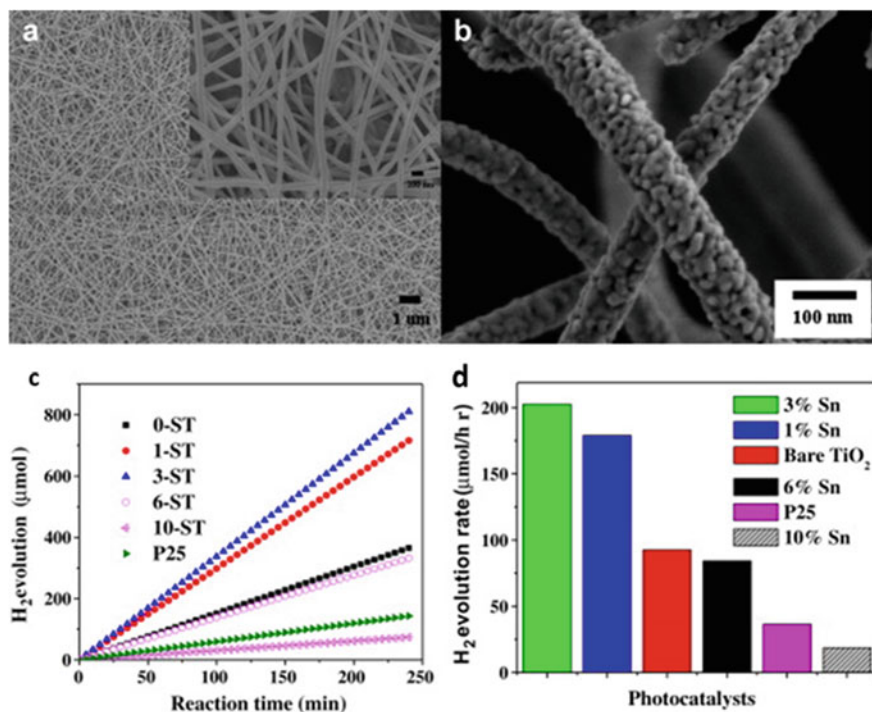


Fig. 11 SEM images (a, b), and amount of H₂ evolution over the irradiation time of 4 h (c), and the effect of Sn loading in photocatalysts on H₂ evolution rate (d) of TiO₂/SnO₂ nanofibers. Reproduced from Ref. [53] with permission from Elsevier

separation ability, and minimizing e-h recombination rates causing an increase in the photocatalytic activity of TiO₂ photocatalysts. Transition Metal oxides (TMOs) such as *n*-type semiconductors (ZnO, WO₃, SnO₂, Fe₂O₃, and MoO₃) and *p*-type semiconductors (NiO, CuO, and BiVO₄) offers a possibility of its coupling with TiO₂ for a photocatalytic H₂ production application. For example, TiO₂/SnO₂ nanotube photoanodes were fabricated by *M. Radecka* et al. [52] via the anodization of Ti-Sn films; the results revealed that solar-to-hydrogen (STH) efficiency had been enhanced via the incorporation of SnO₂ (2%), which was ascribed to the position of the CB of Sn⁴⁺ oxide located approximately at 0.5 eV which is more positive than the CB of TiO₂. Therefore, the formation of such composites is very promising because of the successful and efficient charge separation between different phases of oxides which increases their lifetime and retard their recombination. Lee and coworkers [53] carried out an interesting study by using TiO₂/SnO₂ nanofibers with innovative structures; SEM image of such composite is demonstrated in Fig. 11 a, b. Besides, a remarkable improvement in the photocatalytic efficiency had been observed in the case of the composite nanofibers with 3% SnO₂, showing the higher yield of H₂ generation (~200 μmol/h) as displayed in Fig. 11 c, d. The as-prepared 3%SnO₂/TiO₂ nanocomposite demonstrated a significant improvement in the hydrogen production rate by 2-folds and 5-folds times greater than that of bare TiO₂ nanofibers and P25 nanoparticles, respectively; this was ascribed to the synergistic effect of the formation of a ternary heterojunction composed of anatase TiO₂, rutile TiO₂, and rutile SnO₂ phases, long nanofibrous structure as well as the red-shifting in the light absorption toward the visible region.

Moreover, Bi-based oxides, such as CuBi₂O₄ [54], BiOIO₃ [55], Bi₂(CrO₄)₃ [2], BiNbO₄ [56], Bi₂MoO₆ [57], BiPO₄ [61], and BiVO₄ had been considered and profound photocatalytic performance toward water splitting. Specifically, the monoclinic BiVO₄ had been intensively investigated as a promising candidate for visible-light-driven water splitting because of its quite narrow bandgap energy of 2.4 eV [58–60]. However, BiVO₄ has some issues that limit its efficiency like instability and poor surface oxygen evolution reactivity, in addition to its short hole diffusion length (≈100 nm), and. Therefore the combination coupling of BiVO₄ with TiO₂ to form BiVO₄/TiO₂ heterojunction composite is an interesting candidate material for water splitting. Recently, H. Hou et al. [58] clearly illustrated the significance of the coupling of BiVO₄ and TiO₂ to accomplish efficient charge carriers separation via designing of BiVO₄@TiO₂ core-shell hybrid structure exhibiting high photocatalytic performance for water splitting. The as-prepared BiVO₄@TiO₂ core-shell provided high specific surface area in addition to the formation of the efficient staggered bandgap alignment (Type II heterojunction) leading to facilitate the charge separation, which significantly improved the efficiency of photocatalytic hydrogen production. M. Xie et al. [59] studied different weight ratios of TiO₂/BiVO₄ heterostructure; the results revealed that the photogenerated electrons-holes in the TiO₂/BiVO₄ heterostructure exhibited a longer lifetime than those in the bare TiO₂, see Fig. 12(a, b); they could demonstrate a better longer carrier lifetime of ≈3 ms which is greater than that of the bare BiVO₄. Interestingly, the amount of H₂ evolution in the presence of TiO₂/BiVO₄ heterostructure was 2.2 μmol h⁻¹ whereas that of BiVO₄ or TiO₂ could be negligible as shown in Fig. 12. It has been verified that the enhanced photo-generated charges' separation by the BiVO₄/TiO₂ heterostructure is mainly related to the unusual transfer of visible-light excited high-energy electrons from BiVO₄ to

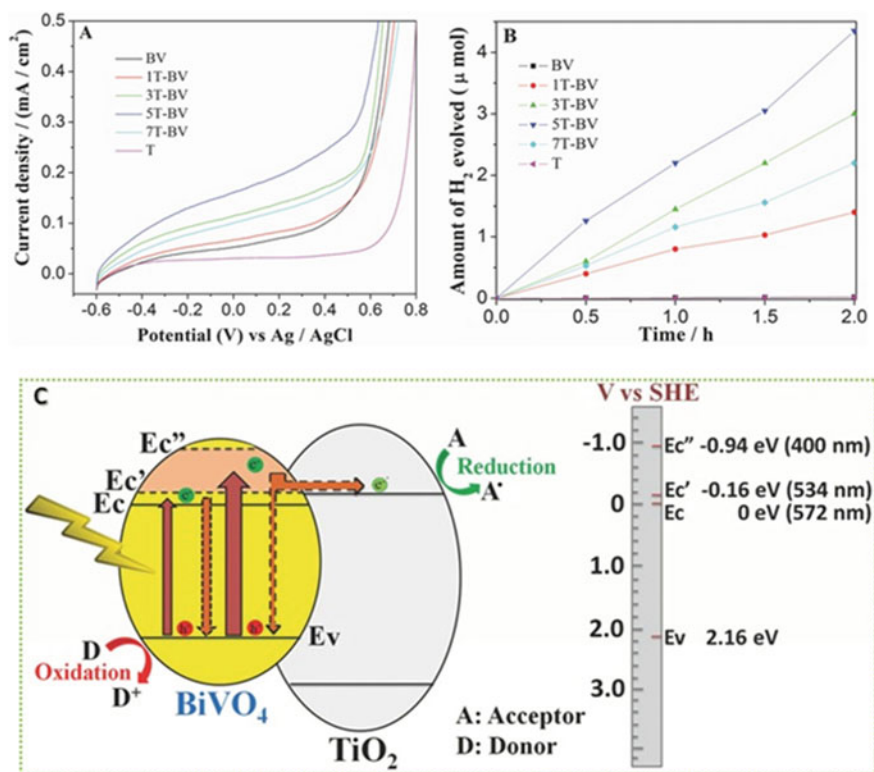


Fig. 12 The J - V curve (a), photocatalytic activity for producing H_2 (b), and the schematic diagram of the proposed pathway of the charge separation (c) of the fabricated $TiO_2/BiVO_4$ nanocomposite under visible illumination. Reproduced from Ref. [59] with permission from Wiley online library

TiO_2 as demonstrated in Fig. 12b. When $BiVO_4$ and TiO_2 are combined to form a nanocomposite, the Fermi levels (E_f) of both of them move to reach a balanced value because of the thermodynamic equilibrium of the system. The Fermi levels of $BiVO_4$ and TiO_2 had been estimated to be 0.9 eV and -0.1 eV, respectively [60]. However, after the coupling of $BiVO_4$ and TiO_2 , a heterojunction would be constructed and the equilibrium Fermi level would be generated. Briefly, it was stated that the position of TiO_2 energy-level would be lowered, while that of $BiVO_4$ would be raised to the equilibrium level. When the heterostructure photocatalyst is illuminated under visible light, the photoinduced electrons have to transfer from CB of $BiVO_4$ to the CB of TiO_2 , because the CB redox potential of $BiVO_4$ is more negative than that of TiO_2 , and these high-energy electrons are highly reactive for hydrogen production.

7 Conclusion

To sum up, at the beginning of the chapter, the fundamental basics of photocatalytic hydrogen based on TiO_2 photocatalysts were investigated either through photochemical or photoelectrochemical pathways. Besides, the main strategies of the development of TiO_2 -based nanocomposites as well as the corresponding mechanisms

including the types of heterojunctions were explored in this chapter. It was found that the various strategies including doping, carbon-based materials coupling, dye sensitization and semiconductor coupling, can achieve a significant and outstanding enhancement in the photocatalytic performance of TiO₂-based nanocomposites toward hydrogen production under visible light irradiation through the promotion of the optical and catalytic properties of TiO₂ either by narrowing the bandgap energy, extending the absorption ability toward the visible region, enhancing the charge separation, decreasing the e-h recombination rate, decreasing the charge transfer resistance, etc. Besides, several examples from the literature were displayed to investigate the promising results of the employed strategies in this regard. Finally, the findings of this chapter can prompt the employment of the explored TiO₂-based nanocomposites in other crucial photocatalytic applications such as solar cells, wastewater treatment, and CO₂ reduction.

Acknowledgement The authors would acknowledge the support of Ain Shams University and Central Metallurgical Research and Development Institute, and we would like to express our great appreciation and deep gratitude to **Dr. Nageh Allam** (Professor of Materials Science and Engineering and Director of Energy Materials Laboratory (EML) at the American University in Cairo), **Dr. Mohamed Rashad** (Professor of Materials Science and Engineering and Dean of Advanced Materials Institute at the Central Metallurgical Research and Development Institute), and **Dr. Zeinab Abou-Gamra** (Professor of Photochemistry and Chemical Kinetics at Ain Shams University) due to their priceless continuous support to us and their unforgettable positive impact on our career.

References

1. Rivero, M.J., Iglesias, O., Ribao, P., Ortiz, I.: Kinetic performance of TiO₂/Pt/reduced graphene oxide composites in the photocatalytic hydrogen production. *Int. J. Hydrogen Energy* **44**, 101–109 (2019). <https://doi.org/10.1016/j.ijhydene.2018.02.115>
2. Hamza, M.A., El-Shazly, A.N., Tolba, S.A., Allam, N.K.: Novel Bi-based photocatalysts with unprecedented visible light-driven hydrogen production rate: experimental and DFT insights. *Chem. Eng. J.* **384**, 123351 (2020). <https://doi.org/10.1016/j.cej.2019.123351>
3. Koohi-fayegh, M.A.R.S.: The prospects for hydrogen as an energy carrier: an overview of hydrogen energy and hydrogen energy systems. *Energy Ecol. Environ.* **1**, 10–29 (2016). <https://doi.org/10.1007/s40974-016-0005-z>
4. Yi, J., El-almi, W., Song, Y., et al.: Emerging surface strategies on graphitic carbon nitride for solar driven water splitting. *Chem. Eng. J.* (2019). <https://doi.org/10.1016/j.cej.2019.122812>
5. Aasadnia, M., Mehrpooya, M.: Large-scale liquid hydrogen production methods and approaches: a review. *Appl. Energy* **212**, 57–83 (2018). <https://doi.org/10.1016/j.apenergy.2017.12.033>
6. Arregi, A., Amutio, M., Lopez, G., et al.: Evaluation of thermochemical routes for hydrogen production from biomass: a review. *Energy Convers. Manag.* **165**, 696–719 (2018). <https://doi.org/10.1016/j.enconman.2018.03.089>
7. Kumaravel, V., Mathew, S., Bartlett, J., Pillai, S.C.: Photocatalytic hydrogen production using metal doped TiO₂: a review of recent advances. *Appl. Catal. B Environ.* **244**, 1021–1064 (2019). <https://doi.org/10.1016/j.apcatb.2018.11.080>
8. Xu, C., Anusuyadevi, P.R., Aymonier, C., et al.: Nanostructured materials for photocatalysis. *Chem. Soc. Rev.* **48**, 3868–3902 (2019). <https://doi.org/10.1039/C9CS00102F>
9. Hamza, M.A., El-Shazly, A.N., Allam, N.K.: Facile template-free one-pot room-temperature synthesis of novel m-Bi(OH)CrO₄ microspheres. *Mater. Lett.* **262**, 127188 (2020). <https://doi.org/10.1016/j.matlet.2019.127188>

10. Liao, C.H., Huang, C.W., Wu, J.C.S.: Hydrogen production from semiconductor-based photocatalysis via water splitting. *Catalysts* **2**, 490–516 (2012). <https://doi.org/10.3390/catal2040490>
11. Marepally, B.C., Ampelli, C., Genovese, C., et al.: Production of solar fuels using CO₂, 1st edn. Elsevier B.V. (2019)
12. Asri, M., Adnan, B., Arifin, K., Jeffery, L.: Titanate-based perovskites for photochemical and photoelectrochemical water splitting applications: a review. *Int. J. Hydrogen Energy* **43**, 23209–23220 (2018). <https://doi.org/10.1016/j.ijhydene.2018.10.173>
13. Ahmed, N., Ramadan, M., El Rouby, W.M.A., et al.: Non-precious co-catalysts boost the performance of TiO₂ hierarchical hollow mesoporous spheres in solar fuel cells. *Int. J. Hydrogen Energy* **3**, 21219–21230 (2018). <https://doi.org/10.1016/j.ijhydene.2018.10.012>
14. Amer, A.W., El-Sayed, M.A., Allam, N.K.: Tuning the photoactivity of zirconia nanotubes-based photoanodes via ultrathin layers of ZrN: an effective approach toward visible-light water splitting. *J. Phys. Chem. C* **120**, 7025–7032 (2016). <https://doi.org/10.1021/acs.jpcc.6b01144>
15. El-Shazly, A.N., Hegazy, A.H., Rashad, M.M., et al.: Ultrathin ALD TiO₂ shells for enhanced photoelectrochemical solar fuel generation. *J. Alloys Compd.* **739** (2018). <https://doi.org/10.1016/j.jallcom.2017.12.218>
16. Gupta, U., Rao, C.N.R.: Nano energy hydrogen generation by water splitting using MoS₂ and other transition metal dichalcogenides. *Nano Energy* **41**, 49–65 (2017). <https://doi.org/10.1016/j.nanoen.2017.08.021>
17. Cao, S., Yu, J.: g-C₃N₄-based photocatalysts for hydrogen generation. *J. Phys. Chem. Lett.* **5**, 2101–2107 (2014)
18. Li, J., Jiménez-Calvo, P., Paineau, E., Ghazzal, M.N.: Metal chalcogenides based heterojunctions and novel nanostructures for photocatalytic hydrogen evolution. *Catalysts* **10** (2020). <https://doi.org/10.3390/catal10010089>
19. Pan, L., Liu, Y., Yao, L., et al.: Cu₂O photocathodes with band-tail states assisted hole transport for standalone solar water splitting. *Nat. Commun.* **11**, 1–10 (2020). <https://doi.org/10.1038/s41467-019-13987-5>
20. Patial, S., Hasija, V., Raizada, P., et al.: Tunable photocatalytic activity of SrTiO₃ for water splitting: strategies and future scenario. *J. Environ. Chem. Eng.* **8** (2020). <https://doi.org/10.1016/j.jece.2020.103791>
21. Tayebi, M., Lee, B.K.: Recent advances in BiVO₄ semiconductor materials for hydrogen production using photoelectrochemical water splitting. *Renew. Sustain. Energy Rev.* **111**, 332–343 (2019). <https://doi.org/10.1016/j.rser.2019.05.030>
22. Kudo, A., Miseki, Y.: Heterogeneous photocatalyst materials for water splitting. *Chem. Soc. Rev.* **38**, 253–278 (2009). <https://doi.org/10.1039/b800489g>
23. Hamza, M.A., Abou-Gamra, Z.M., Ahmed, M.A.: The critical role of Tween 80 as a ‘green’ template on the physical properties and photocatalytic performance of TiO₂ nanoparticles for Rhodamine B photodegradation. *J. Mater. Sci. Mater. Electron.* (2020). <https://doi.org/10.1007/s10854-020-03017-2>
24. Ahmed, M.A., Abou-Gamra, Z.M., Medien, H.A.A., Hamza, M.A.: Effect of porphyrin on photocatalytic activity of TiO₂ nanoparticles toward Rhodamine B photodegradation. *J. Photochem. Photobiol. B Biol.* **176**, 25–35 (2017). <https://doi.org/10.1016/j.jphotobiol.2017.09.016>
25. Abou-Gamra, Z.M., Ahmed, M.A., Hamza, M.A.: Investigation of commercial PbCrO₄/TiO₂ for photodegradation of rhodamine B in aqueous solution by visible light. *Nanotechnol. Environ. Eng.* **2**, 12 (2017). <https://doi.org/10.1007/s41204-017-0024-9>
26. Guo, Y.: Photocatalytic activity enhanced via surface hybridization. 308–349 (2020). <https://doi.org/10.1002/cey2.66>
27. Hou, H., Zhang, X.: Rational design of 1D/2D heterostructured photocatalyst for energy and environmental applications. *Chem. Eng. J.* **395**, 125030 (2020). <https://doi.org/10.1016/j.cej.2020.125030>
28. Basavarajappa, P.S., Patil, S.B., Ganganagappa, N., et al.: Recent progress in metal-doped TiO₂, non-metal doped/codoped TiO₂ and TiO₂ nanostructured hybrids for enhanced photocatalysis. *Int. J. Hydrogen Energy* **45**, 7764–7778 (2020). <https://doi.org/10.1016/j.ijhydene.2019.07.241>

29. Liu, B., Chen, H.M., Liu, C., et al.: Large-scale synthesis of transition-metal-doped TiO₂ nanowires with controllable overpotential. *J. Am. Chem. Soc.* **135**, 9995–9998 (2013). <https://doi.org/10.1021/ja403761s>
30. Zangeneh, H., Zinatizadeh, A.A.L., Habibi, M., et al.: Photocatalytic oxidation of organic dyes and pollutants in wastewater using different modified titanium dioxides: a comparative review. *J. Ind. Eng. Chem.* **26**, 1–36 (2015). <https://doi.org/10.1016/j.jiec.2014.10.043>
31. Ismael, M.: A review and recent advances in solar-to-hydrogen energy conversion based on photocatalytic water splitting over doped-TiO₂ nanoparticles. *Sol. Energy* **211**, 522–546 (2020). <https://doi.org/10.1016/j.solener.2020.09.073>
32. El-Shazly, A.N., Hegazy, A.H., El Shenawy, E.T., et al.: Novel facet-engineered multi-doped TiO₂ mesocrystals with unprecedented visible light photocatalytic hydrogen production. *Sol. Energy Mater. Sol. Cells* **220** (2021). <https://doi.org/10.1016/j.solmat.2020.110825>
33. Liu, C., Wang, F., Zhu, S., et al.: Controlled charge-dynamics in cobalt-doped TiO₂ nanowire photoanodes for enhanced photoelectrochemical water splitting. *J. Colloid Interface Sci.* **530**, 403–411 (2018). <https://doi.org/10.1016/j.jcis.2018.07.003>
34. Atrees, M.S., Ebraheim, E.E., Ali, M.E.M., et al.: Synergetic effect of metal-doped GO and TiO₂ on enhancing visible-light-driven photocatalytic hydrogen production from water splitting. *Energy Sources Part A Recover. Util. Environ. Eff.* **43**, 484–494 (2021). <https://doi.org/10.1080/15567036.2019.1629130>
35. Li, L., Yu, L., Lin, Z., Yang, G.: Reduced TiO₂-graphene oxide heterostructure as broad spectrum-driven efficient water-splitting photocatalysts. *ACS Appl. Mater. Interfaces* **8**, 8536–8545 (2016). <https://doi.org/10.1021/acsami.6b00966>
36. Morais, A., Longo, C., Araujo, J.R., et al.: Nanocrystalline anatase TiO₂/reduced graphene oxide composite films as photoanodes for photoelectrochemical water splitting studies: the role of reduced graphene oxide. *Phys. Chem. Chem. Phys.* **18**, 2608–2616 (2016). <https://doi.org/10.1039/c5cp06707c>
37. Raghavan, A., Sarkar, S., Nagappagari, L.R., et al.: Decoration of graphene quantum dots on TiO₂ nanostructures: photosensitizer and cocatalyst role for enhanced hydrogen generation. *Ind. Eng. Chem. Res.* **59**, 13060–13068 (2020). <https://doi.org/10.1021/acs.iecr.0c01663>
38. Hao, X., Jin, Z., Xu, J., et al.: Functionalization of TiO₂ with graphene quantum dots for efficient photocatalytic hydrogen evolution. *Superlattices Microstruct.* **94**, 237–244 (2016). <https://doi.org/10.1016/j.spmi.2016.04.024>
39. Bayat, A., Saievar-Iranizad, E.: Graphene quantum dots decorated rutile TiO₂ nanoflowers for water splitting application. *J. Energy Chem.* **27**, 306–310 (2018). <https://doi.org/10.1016/j.jec hem.2017.09.036>
40. Zhang, H., Mo, Z., Pei, H., et al.: A synthesis of graphene quantum dots/hollow TiO₂ nanosphere composites for enhancing visible light photocatalytic activity. *J. Mater. Sci. Mater. Electron.* **31**, 1430–1441 (2020). <https://doi.org/10.1007/s10854-019-02657-3>
41. Vajda, K., Mogyorosi, K., Nemeth, Z., et al.: Photocatalytic activity of TiO₂/SWCNT and TiO₂/MWCNT nanocomposites with different carbon nanotube content. *Phys. Status Solidi Basic Res.* **248**, 2496–2499 (2011). <https://doi.org/10.1002/pssb.201100117>
42. O'Regan, B., Grätzel, M.: A low-cost, high-efficiency solar-cell based on dye-sensitized colloidal TiO₂ films. *Nature* **353**, 737–740 (1991). <https://doi.org/10.1038/353737a0>
43. Basheer, B., Mathew, D., George, B.K., Reghunadhan Nair, C.P.: An overview on the spectrum of sensitizers: the heart of dye sensitized solar cells. *Sol. Energy* **108**, 479–507 (2014). <https://doi.org/10.1016/j.solener.2014.08.002>
44. Choi, S.K., Yang, H.S., Kim, J.H., Park, H.: Organic dye-sensitized TiO₂ as a versatile photocatalyst for solar hydrogen and environmental remediation. *Appl. Catal. B Environ.* **121–122**, 206–213 (2012). <https://doi.org/10.1016/j.apcatb.2012.04.011>
45. Ding, H., Xu, M., Zhang, S., et al.: Organic blue-colored D-A- π -A dye-sensitized TiO₂ for efficient and stable photocatalytic hydrogen evolution under visible/near-infrared-light irradiation. *Renew. Energy* **155**, 1051–1059 (2020). <https://doi.org/10.1016/j.renene.2020.04.009>
46. Yan, J., Wu, H., Chen, H., et al.: Fabrication of TiO₂/C₃N₄ heterostructure for enhanced photocatalytic Z-scheme overall water splitting. *Appl. Catal. B Environ.* **191**, 130–137 (2016). <https://doi.org/10.1016/j.apcatb.2016.03.026>

47. Hashem, E.M., Hamza, M.A., El-Shazly, A.N., et al.: Novel Z-Scheme/Type-II CdS@ZnO/g-C₃N₄ ternary nanocomposites for the durable photodegradation of organics: kinetic and mechanistic insights. *Chemosphere* (2020). <https://doi.org/10.1016/j.chemosphere.2020.128730>
48. Hamza, M.A., Abd El-Rahman, S.A., El-Shazly, A.N., et al.: Facile one-pot ultrasonic-assisted synthesis of novel Ag@RGO/g-C₃N₄ ternary 0D@2D/2D nanocomposite with enhanced synergetic tandem adsorption-photocatalytic degradation of recalcitrant organic dyes: kinetic and mechanistic insights. *Mater. Res. Bull.* **142**, 111386 (2021). <https://doi.org/10.1016/j.matresbull.2021.111386>
49. Zhang, H., Liu, F., Wu, H., et al.: In situ synthesis of g-C₃N₄/TiO₂ heterostructures with enhanced photocatalytic hydrogen evolution under visible light. *RSC Adv.* **7**, 40327–40333 (2017). <https://doi.org/10.1039/c7ra06786k>
50. Wang, J., Huang, J., Xie, H., Qu, A.: Synthesis of g-C₃N₄/TiO₂ with enhanced photocatalytic activity for H₂ evolution by a simple method. *Int. J. Hydrogen Energy* **39**, 6354–6363 (2014). <https://doi.org/10.1016/j.ijhydene.2014.02.020>
51. Fang, Y., Huang, W., Yang, S., et al.: Facile synthesis of anatase/rutile TiO₂/g-C₃N₄ multi-heterostructure for efficient photocatalytic overall water splitting. *Int. J. Hydrogen Energy* **45**, 17378–17387 (2020). <https://doi.org/10.1016/j.ijhydene.2020.04.214>
52. Radecka, M., Wnuk, A., Trenczek-Zajac, A., et al.: TiO₂/SnO₂ nanotubes for hydrogen generation by photoelectrochemical water splitting. *Int. J. Hydrogen Energy* **40**, 841–851 (2015). <https://doi.org/10.1016/j.ijhydene.2014.09.154>
53. Lee, S.S., Bai, H., Liu, Z., Sun, D.D.: Electrospun TiO₂/SnO₂ nanofibers with innovative structure and chemical properties for highly efficient photocatalytic H₂ generation. *Int. J. Hydrogen Energy* **37**, 10575–10584 (2012). <https://doi.org/10.1016/j.ijhydene.2012.04.098>
54. Monny, S.A., Zhang, L., Wang, Z., et al.: Fabricating highly efficient heterostructured CuBi₂O₄ photocathodes for unbiased water splitting. *J. Mater. Chem. A* **8**, 2498–2504 (2020). <https://doi.org/10.1039/c9ta10975g>
55. Su, Y., Zhang, L., Wang, W.: Internal polar field enhanced H₂ evolution of BiOIO₃ nanoplates. *Int. J. Hydrogen Energy* **41**, 10170–10177 (2016). <https://doi.org/10.1016/j.ijhydene.2016.04.236>
56. Kuznetsova, M., Oliveira, S.A.A., Rodrigues, B.S., Souza, J.S.: Microwave-assisted synthesis of bismuth Niobate/Tungsten oxide photoanodes for water splitting. *Top Catal.* (2020). <https://doi.org/10.1007/s11244-020-01325-9>
57. Wu, M., Wang, Y., Xu, Y., et al.: Self-supported Bi₂MoO₆ nanowall for photoelectrochemical water splitting. *ACS Appl. Mater. Interfaces* **9**, 23647–23653 (2017). <https://doi.org/10.1021/acsami.7b03801>
58. Hou, H., Wang, L., Gao, F., et al.: BiVO₄@TiO₂ core-shell hybrid mesoporous nanofibers towards efficient visible-light-driven photocatalytic hydrogen production. *J. Mater. Chem. C* **7**, 7858–7864 (2019). <https://doi.org/10.1039/c9tc02480h>
59. Xie, M., Fu, X., Jing, L., et al.: Long-lived, visible-light-excited charge carriers of TiO₂/BiVO₄ nanocomposites and their unexpected photoactivity for water splitting. *Adv. Energy Mater.* **4**, 4–9 (2014). <https://doi.org/10.1002/aenm.201300995>
60. Sadeghzadeh-Attar, A.: Boosting the photocatalytic ability of hybrid BiVO₄-TiO₂ heterostructure nanocomposites for H₂ production by reduced graphene oxide (rGO). *J. Taiwan Inst. Chem. Eng.* **111**, 325–336 (2020). <https://doi.org/10.1016/j.jtice.2020.04.001>
61. El-Shazly, A.N., Hamza, M.A., Allam, N.K.: Enhanced photoelectrochemical water splitting via engineered surface defects of BiPO₄ nanorod photoanodes. *Int. J. Hydrogen Energy* **46**, 23214–23224 (2021). <https://doi.org/10.1016/j.ijhydene.2021.04.134>

Polymer/Carbon Nanocomposites: Synthesis, Properties and Application in Solar Energy



Ali Boumeftah, Abdelkader Belmokhtar, and Abdelghani Benyoucef

Abstract Conducting polymer/Carbon nanocomposites (CP/CM) have received a lot of attention due to their variety of applications in several fields, such as energy storage, biomedical, space and solar energy. This chapter is devoted to the different synthesis techniques of nanocomposites (CP/CM), as well as their properties and application in the solar energy field, as this is one of the best developed application areas for these materials due to the growing concern about energy issues.

Keywords Nanocomposite · Carbon · Polymer · Synthesis · Properties · Solar energy

Abbreviations

SWCNTs	Single-Walled Carbon Nanotubes
DWCNT	Double-Walled Carbon Nanotubes
MWNTs	Multi-Walled Carbon Nanotubes
GR	Graphene
GO	Graphene Oxide
rGO	Reduced Graphene Oxide
SPF Graphene	Solution-processed graphene material
PCBM	[6,6]-Phenyl C61 butyric acid methyl ester

A. Boumeftah (✉) · A. Belmokhtar
Laboratoire Matériaux Application et Environnement, Faculté des Sciences et de la Technologie,
Université Mustapha Stambouli de Mascara, BP 763, 29000 Mascara, Algérie
e-mail: ali.boumeftah@univ-mascara.dz

A. Belmokhtar
e-mail: a.belmokhtar@univ-mascara.dz

A. Benyoucef
Laboratoire des Sciences et Techniques de l'Eau, Faculté des Sciences et de la Technologie,
Université Mustapha Stambouli de Mascara, BP 763, 29000 Mascara, Algérie
e-mail: a.benyoucef@univ-mascara.dz

P3HT	Poly (3-Hexylthiophene)
PVA	Polyvinyl Alcohol
PEDOT: PSS	Poly (3,4 ethylenedioxythiophene):poly(4-styrenesulfonate)
ITO	Indium doped tin oxide
FTO	Fluorine-doped tin oxide
PET	Polyethylene terephthalate
PTB7	Poly [[4,8-bis[(2-ethylhexyl)oxy]benzo[1,2-b:4,5-b']dithiophene-2,6-diyl][3-fluoro-2-[(2-ethylhexyl)carbonyl]thieno[3,4-b]thiophenediyl]]
PEN	Poly (ethylene naphthalate)
PI	Poly (imide)
PMMA	Poly (methylmethacrylate)
PDMS	Polydiméthylsiloxane
PTAA	Poly (triaryl amine)
PCDTBT	Poly[N-9'-heptadecanyl-2,7-carbazole-alt-5,5-(4',7'-di-2-thienyl-2',1',3'-benzothiadiazole)]
MDMO-PPV	Poly (2-methoxy-5-(3,7-dimethyloctyloxy)-1,4-phenylene vinylene)
TCNQ	Tetracyanoquinodimethan
CVD	Chemical vapor deposition
PCE	The power conversion efficiency
OSC	Organic solar cell
OPV	Organic photovoltaic
PSCs	Polymer solar cells
ETL	Electron transport layer
HTL	Hole transport layer

1 Introduction

In recent years, conducting polymers (CPs) have been the subject of considerable research [1, 2] due to their interesting properties such electrical, mechanical, optical and thermal properties, as well as light weight and low cost [3–5].

The carbon materials such (activated carbon-AC, carbon black-CB, carbon nanotubes-CNT, carbon fibers-CF, graphene-G, fullerene, graphene oxide-GO, activated carbon fibers-ACF, graphite, etc.) have attracted enormous attention in most fields of science and technology because of their unique properties such mechanical electrical, thermal, optical and magnetic properties [6–8].

Carbon-based polymers materials have received most attention in research and industrial areas. Due to their combination of the properties of polymer and carbon [9, 10], these nanocomposites have been using in several fields such as solar cell, metal corrosion protection, advanced transistors, sensors/biosensors, biomedical, energy storage, electrochromicity, etc. [11–14]. Moreover, the most processing manners

have been used to synthesis several forms of carbon-based polymers materials are Solution Mixing, Melt Processing and In-situ Polymerization process. Recently, polymers/carbon nanocomposites have been considered as attractive and innovative materials to enhance the device efficiency in the future [15, 16].

Solar cells are one of the most studied applications of these nanocomposites because of the advantages provided by the two materials carbon and polymer. Fullerene, carbon nanotubes and graphene are types of carbon frequently utilized in photovoltaic cells. On the other hand, conducting polymers such polythiophenes (PT), polystyrene sulfonate (PSS) and polyphenylene vinylene (PPV) are also organic materials widely used in solar cells [17, 18].

This chapter describes a critical summary of the main works concerning the synthesis of carbon-based polymers, the properties of this nanocomposite and the applications of this material in different layers of solar cells.

2 Synthesis of Polymer/Carbon Composite

2.1 Solution Mixing Process

Solution mixing is the largest and most common process for the fabrication of polymer-carbon nanocomposites. In this technique, the carbon materials and the polymer are solubilized in the same solvent. Next, the elements are then blended by mechanical agitation or sonication. Finally, the precipitation is treated by chemical or thermal methods to remove the solvent [19]. Figure 1 shows representative diagram of solution mixing technique.

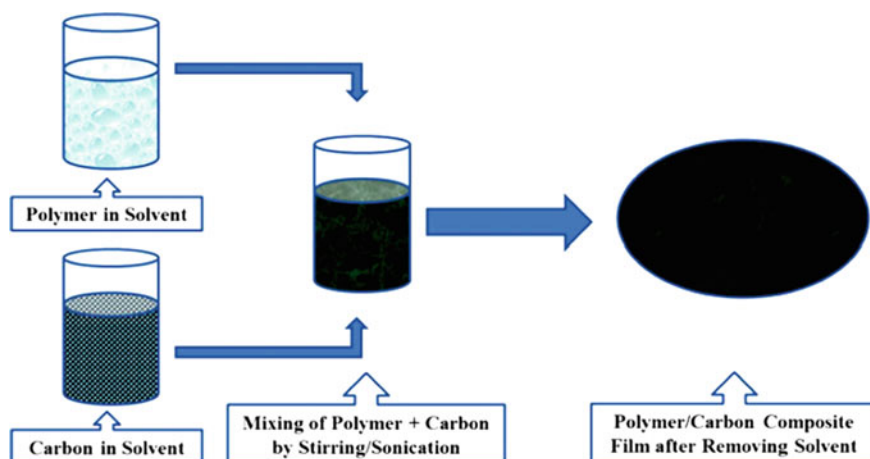


Fig. 1 Representative diagram of the steps of solution mixing technique for the fabrication of a polymer-carbon composite [20]

Different techniques of solution mixing have been utilized to prepare composite materials are (1) evaporative casting; hence the solvent is removed by evaporation in a controlled manner. (2) Vacuum filtration; in which elimination of solvent by vacuum filtration, the products washed with distilled water and methanol and oven drying just to simply detach the formed nanocomposites. (3) Fiber spinning depends on the use of the spinneret, which is operated by the extrusion method for the preparation of composite fibers. (4) Printing, hence a substance, typically ink is placed on a proper substrate to create a specific structure. The main printing techniques for making composite materials are divided into two methods: extrusion printing and inkjet [20].

One of the earliest studies concerning the solution mixing technique was the preparation of poly 3-hexyl thiophene (P3HT) and carbon nanotube. In this typical process, P3HT and carbon nanotube (with varying percentages) were dissolved in the solvent (dichlorobenzene). A solution containing two components was mixed by sonication for 2 h. Next, the product was dried at room temperature to remove the solvent. They reported that these nanocomposite films have shown a significant enhancement in electrical, mechanical and thermal properties, which indicates a good dispersion of carbon nanotube in the P3HT matrix [21–24].

2.2 Melt Blending

Melt blending is process frequently utilized for the synthesis of thermoplastic polymers in the industry. For the typical process, the temperature of the polymer is raised above its melting point to obtain a viscous liquid Fig. 2. Generally, the external and internal heating of the extruder screw are used to heat the polymer. Then carbon nanofillers are dispersed in the molten polymer using shear force to form composite materials.

To compare the melt blending method with other technique, the melt blending is simple process, more economical (because does not used any solvent), more environmentally friendly and is more compliant with many current industrial [19, 25]. However, previous studies have shown that the fusion mixture does not offer the same



Fig. 2 Representative diagram of the steps of Melt blending [20]

degree of fillers dispersion as in situ polymerization or the solvent mixing methods. This, in the fusion mixing method, the load dispersion is complicated because the polymer's higher viscosity rises to the melted state. Nevertheless, the high shear forces produced by the screw lead can have negative effects on carbon nanocharges (for example, graphite and GO) due to their thermal characteristics [26, 27].

The graphene nanoplatelets (GNP) and polypropylene (PP) composites were fabricated by melt blending technique. Firstly, polypropylene (PP) was heated at 180 °C and mixed for 3 min to obtain the melted polymer. Secondly, graphene nanofillers were added to the melted polymer and the mixture was agitated for 10 min. For this nanocomposite, the authors reported that there was no obvious change in the electrical properties of the graphene/PP nanocomposite even by increasing shear rate and shear stress. This is because of the low dispersibility of graphene in the PP matrix [28, 29].

Polymer/carbon black composites are also fabricated by melt blending method. For example, the thermoplastic polyurethane (TPU) was melted with carbon black (1%) at 190 °C and 220 r min⁻¹ for 3 min. The authors ensured good adhesion between the nanofillers and the TPU matrix. Consequently, Well-dispersed fillers provided considerable enhancement in mechanical, thermal, flammability, and electrical properties for this composite system [30, 31].

In other studies, many polymers such as poly (ether ether ketone) (PEEK), polystyrene (PS), polycarbonate (PC), and others were mixed with carbon materials to obtain the composites by this method in order to study their electrical, thermal and mechanical properties as well as their morphology [32–35].

2.3 *In situ Polymerization*

In situ polymerization is a largely utilized method for the production of polymer-carbon composites, which cannot be manufactured by mixing solutions (the unsolvable polymer) and melt blending techniques (thermally unstable polymer). As part of this process, carbon-based fillers are added to pure monomer (or several monomers), or solution of monomer. Then, the monomer polymerization may be triggered by distributing the initiator and the catalyst accompanied by radiation or heat treatment. Next, the mixture is then sonicated and blended to allow for growth. Finally, the precipitations are filtered and washed to remove the solvent and impurities, respectively [17, 20]. Figure 3 illustrates the in situ polymerization of polymer-carbon composites.

In situ polymerization is advantageous over the other two techniques due to the preparation of carbon-based polymer with a high filler fraction. In addition, thanks to the nano-sized monomers, this method guarantees a uniform dispersion of the charge in the polymer chain [19, 36].

Polyethylene (PE)-graphene nanocomposites synthesis was performed using the technique of in situ polymerization. The ethylene polymerization reaction was realized in a 500 mL glass reactor. Initially, the graphene filler, hexane (as solvent) and

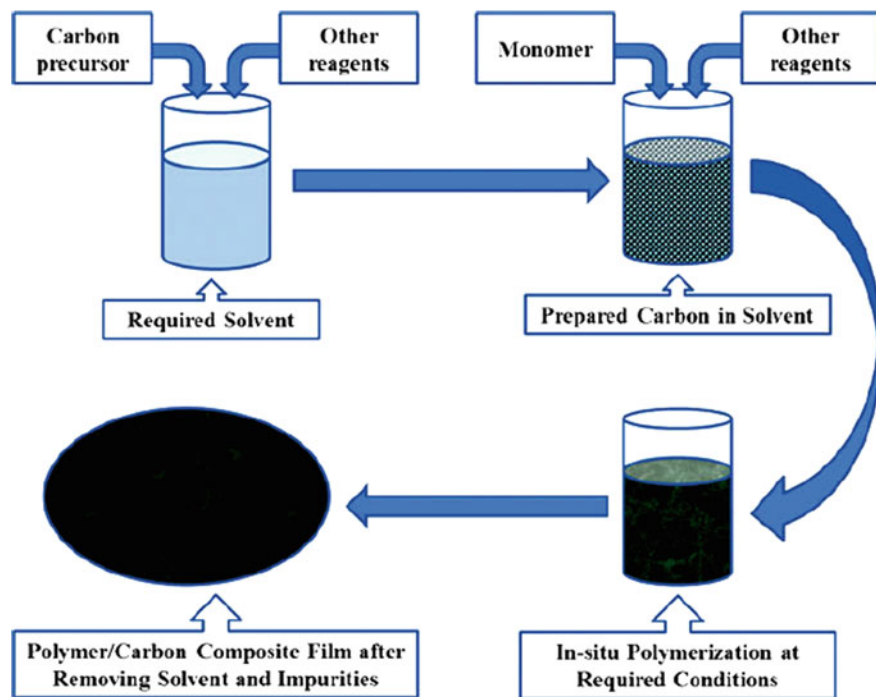


Fig. 3 Representative diagram of the steps of the in situ polymerization technique [20]

methylaluminoxane (MAO) (as catalyst) were placed in the reactor and ultrasonicated for 20 min. Then, the ethylene monomer was added and the polymerization was carried out for 1 h, 70 °C and 1 bar. Finally, the precipitated polymers were filtered, washed with ethanol, and dried at 60 °C. It was reported that the mechanical, electrical and thermal properties of PE/graphene nanocomposites were significantly increased. This may be due to the exfoliated of graphene in the PE matrix [37–39].

In another study, P3HT-DWCNT composite was synthesized via in situ polymerization for solar cell application. In the typical procedure, CHCl_3 solution and DWCNT was placed in a 250-mL double-neck, round-bottomed flask and the mixture was sonicated for 1 h at room temperature. Then, CHCl_3 solution containing FeCl_3 was added to the initial solution and further sonicated for 30 min. Next, 0.5 mL of 3HT monomer dissolved in a 25 mL of CHCl_3 solution was added dropwise and the mixture was stirred for 24 h at room temperature. The product was precipitated in methanol, filtered by Buchner funnel and washed with methanol, HCl, distilled water, and acetone. Finally, the resultant P3HT-DWCNTnanocomposite was dried at room temperature for 24 h. It was mentioned that the impressive conductivities and mobility values of the P3HT-DWCNT composite, even at low DWCNT loads, make it suitable for use in solar cell materials [36, 40].

3 Properties of Polymer/Carbon Composite

3.1 Mechanical Properties

Carbon-based polymer nanocomposites frequently show a remarkable enhancement in mechanical properties compared to pure polymers. These enhancements may comprise high modulus and increased strength. An interfacial interaction between the carbon layers and the polymer matrix is the key reason for the enhanced properties of these nanocomposites. The addition of reduced graphene oxide rGO in very low loading levels can increase the tensile strength and elastic modulus of polyimide. The addition of about 0.7% of rGO in PI enhances the tensile strength up to 103.12 MPa and elastic modulus up to 3.90 GPa. It was mentioned that the tensile strength and elastic modulus were increased by 74 and 65%, respectively. These reveals assigned to the better dispersion of rGO and the stronger chemical bonding linkage between rGO and polymer matrix [41–43].

The incorporation of MWNTs in the Polyvinyl Alcohol by wet-spinning process improved the mechanical properties of PVA film. The addition of 27.6 wt% of MWNTs in the polymer increase the Young's modulus from 6.7 to 12.8 GPa for the PVA-MWNT composite. Meanwhile, the Young's modulus steadily rising from 0.39 to 0.74 GPa for PVA-MWNT nanocomposite containing 14.4% wt of fillers MWNTs. The augmentation in mechanical strength was mainly associated to uniform dispersibility of the MWNTs in the VPA matrix and a highly stress transfer between the VPA matrix and the MWNTs [44, 45].

Fullerene C60 has also been used as a filler in carbon-reinforced composites due to their nanoscale size. The dispersion of low concentration (0.1–1.0 wt %) of Fullerene C60 into epoxy matrix was found to increase various mechanical properties such Young's modulus, fracture energy, tensile strength and fracture toughness. However, the presence of fullerene nanoparticles in the epoxy matrix has been shown to increase the composite bond strength and suppressed Fractures at the fiber interface. This significantly improved the matrix toughness [46, 47]. In other research, the mechanical properties of the fullerene [6,6]-phenyl C61 butyric acid methyl ester (PCBM) and poly(3-heptylth-iophene) (P3HpT), were studied at differing PCBM nanofiller loadings. It was found that with the increase in the filling load (0 to 50% by weight), the tensile modulus increased significantly. It was mentioned that P3HpT is an alternative to P3HT in organic solar cells thanks to its expandable, portable and mechanically robust solar cells [48].

3.2 Electrical Properties

The addition of various conductive carbon fillers in the polymer matrix allows the manufacture of electrically conductive composites. The molecular interactions between the fillers and polymer matrix play essential role in the enhancement of

electrical properties of the carbon-based polymer nanocomposite. However, the key parameters affecting the electrical properties of these nanocomposites are the nature of the filler and polymer, the method of production, filler concentration and dispersion state [8]. According to an earlier study, the electrical properties of the polycarbonate/MWCNT composites synthesized by micro twin screw extruder process were studied at various loadings of MWCNT nanofiller. The maximum conductivity of these composites was obtained at $1.27 \times 10^{-2} \text{ S cm}^{-1}$ for 10 wt. % filler loading and percolation level was determined at 0.21% by weight [49].

In another works, the melt-blended techniques are also applied to synthesis the polypropylene (PP)/CNTs nanocomposite. The conductivity was elevated by about 8 orders of magnitude to 10^{-7} S/cm at 0.75 wt% of CNT and the percolation threshold was significantly reduced from 0.75 to 0.36% by weight [50]. In previous studies, a better conductivity value of 1000 S/m was achieved at 64 wt% filler loading for both poly(phenylene sulfide)/MWNT and poly(para-phenylene vinylene)/SWNT nanocomposites prepared using a solution mixing method [51–53].

The dispersion of 5% percentage of GO increased the electrical conductivity of (PEDOT: PSS) from 18.49 to 90.00 Scm^{-1} . It was mentioned that the conductivity improvement of (PEDOT: PSS)/GO composite can be associated to the separation of PSS and PEDOT chains. The conductive path can be lengthened when the PEDOT chains link to the functional group of GO. In another study, the addition of graphene in the (PEDOT: PSS) matrix enhance various electrical properties of these composite. The short-circuit current density (J_{sc}), the open-circuit voltage (V_{oc}), energy conversion efficiency (η) and fill-factor (FF) is found to be 0.68 mAcm^{-2} , 0.68 V, 2.87 and 60.34%, respectively. However, The thickness of PEDOT:PSS layer for all the devices ranged from 50 to 90 nm. Due to the significant improvement of the electrical and morphological properties of these nanocomposites, the authors reported to the graphene based PEDOT: PSS composite has great potential in flexible OSC [54, 55].

The addition of Fullerenes to the conducting polymer was found to improve the electrical and optical properties of conjugated polymer/fullerene nanocomposite due to electron transfer from the valence band of conjugated polymer to Fullerenes. In this regard, new donor–acceptor heterojunctions devices have been realized in the composites of fullerene and conducting polymer. Moreover, the conductivity was found to increase with increasing fullerene volume fraction and photoconductivity of these nanocomposites was observed near the percolation threshold. An earlier study, P3HT as an electron donor was matched with PCBM as an electron acceptor in polymer solar cells. The electrical characteristics of PV were measured in the temperature 125 °C. The short-circuit current density (J_{sc}), the open-circuit voltage (V_{oc}), the power conversion efficiency (PCE) and fill-factor (FF) showed 10.60 mAcm^{-2} , 0.61 V, 4.37% and 0.67 respectively. It was mentioned that the P3HT-PCBM composite are promising material for the design of active layer in OSC devise [56–58].

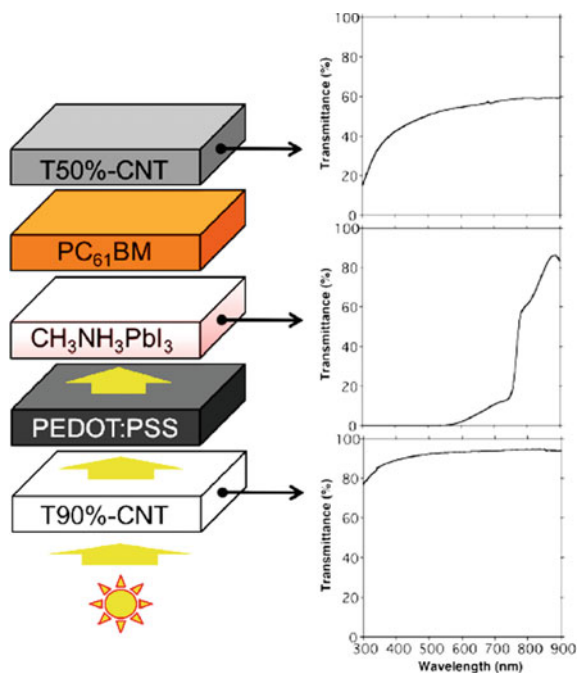
4 Carbon-Based Polymers for Solar Cell Applications

4.1 Electrodes

Indium doped tin oxide (ITO) and Fluorine-doped tin oxide (FTO) are widely utilized electrodes in organic solar cell (OSC) due to their high transparency and excellent conductivity. However, these materials have disadvantages such chemical instability (unstable in high and low pH), higher cost of preparation due to indium's lack of resources, its brittleness which can be readily cracked or broken on flexible substrates, toxicity and its environmental problems not yet seen. In this regard, the research has been re-launched to find new substitutes for the replacement of ITO and FTO. Recently, carbon-based materials served as a replacement for the transparent conducting oxide in OSC device due to their high electrical conductivity, transparency in thin films, ease of implementation, high flexibility and excellent mechanical properties. Consequently, carbon materials like carbon nanotubes (CNTs) and graphene are especially appealing as TCEs (transparent conducting electrodes) (anodes or cathodes) in polymer solar cells. [51, 59, 60].

Recently, CNT films produced by CVD method have been investigated as both the anode and the cathode in the same device. Referred as both CNT electrodes on OSCs (Fig. 4). Moreover, the CNT film was utilized as an electrode to replace the metal electrode since such a metal MAPbI₃ absorbs the better part of the solar spectrum..

Fig. 4 Schematics showing the solar light path and the transmittance spectra of the light-absorbing layers [62]



The HNO₃-doped CNT and CNT showed a transparency of 90 and 50% for anode and cathode, respectively. It was mentioned that the OSC devices containing CNT as both electrode yielded PCE of 7.32 compared to 9.8% for the device based on HNO₃-CNT anode and 10.5% for device based on CNT cathode. However, the main advantages of the both-CNT-electrode based PSCs are low consumption of raw materials and energy. It was mentioned that the enhancement of PCE of these PSCs are related by the improvements of CNT quality and structural optimization [61].

Beside, previous studies reported the SWCNT/MoO₃/PEDOT:PSS transparent electrodes in different heterojunction solar cell such P3HT/PCBM and PTB7/PCBM with metal as cathode [62]. All these electrode can be synthesized by coating or printing technique on PET or on glass substrates. The performances of these electrodes are compared in Table 1.

Graphene have also an organic materials has utilized as TCE for polymer solar cells due to its cheap, excellent optoelectric characteristic, light weight, mechanically flexible and easy to synthesis in large scale in the industries. However, the electrical conductivity of graphene is still inferior compared to the traditional ITO electrode, resulting in lower OSC performance. In this regard, the doping is the most widely used method of overcoming the problem of poor conductivity. Moreover, They adopt three types of strategies to increase the electrical conductivity of graphene: (i) “multilayer stack” technique of graphene films, (ii) Electrostatic graphene doping and (iii) “methods of chemical doping” using wet chemical dopants such AuCl₃, nitric acid and tetracyanoquinodimethane (TCNQ) [67].

Table 1 Comparison of previous research on SWCNT-based and ITO-based electrodes for organic solar cells

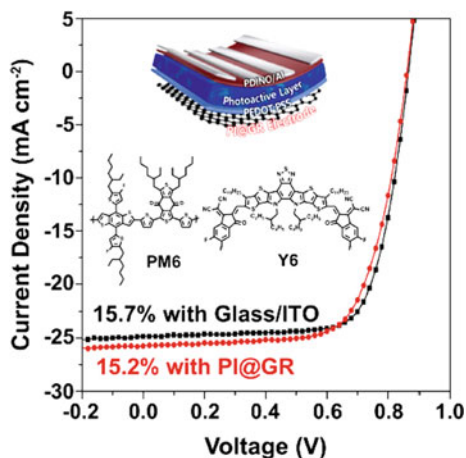
Substrate	Anode	Donor	V _{oc} (V)	J _{sc} (mA cm ⁻²)	FF	PCE _{best} (%)
Glass	ITO [63]	PBTZT-stat-BDIT 8	0.81	15	0.75	9.1
Glass	SWCNT [63]	PBTZT-stat-BDIT-8	0.8	12	0.46	4.4
Glass	HNO ₃ -CNT [63]	PBTZT-stat-BDIT-8	0.81	14.2	0.74	8.5
Glass	PEDOT:PSS-CNT [63]	PBTZT-stat-BDIT-8	0.8	14.3	0.70	8
Glass	ITO/MoO ₃ [62]	P3HT	0.6	9.42	0.5	2.83
Glass	ITO/MoO ₃ [62]	PTB7	0.74	15.5	0.64	7.31
Glass	MoO _x /65%SWCNT/MoO _x /PEDOT:PSS [62]	PTB7	0.72	13.7	0.61	6.04
Glass	PEDOT:PSS/MoO ₃ /65%SWCNT [62]	PTB7	0.7	12.7	0.58	5.27
PET	PEDOT:PSS/MoO ₃ /65%-SWCNT[62]	PTB7	0.69	12.6	0.45	3.91
Glass	ITO [64]	P3HT	0.48	7.42	0.40	2.3
Glass	SWCNT [64]	P3HT	0.54	11.39	0.55	3.37
Glass	PEDOT:PSS/ITO [64]	P3HT	0.59	10.8	0.55	3.5
Glass	PEDOT:PSS/SWNT [65]	P3HT	0.57	13.78	0.53	4.13
PET	PEDOT:PSS/Glass/SWNT [66]	P3HT	0.61	7.8	0.52	2.5

By applying a low-pressure CVD deposition technique for the preparation of n-doped graphene electrodes using a 25- μm thick copper foil. The authors reported that the high PCEs of 7.37 and 8.16% were obtained utilizing the graphene film as TCE and ZnO-NP as ETL for OSCs based on PTB7 or PTB7-Th, respectively. All these devices were demonstrated on PET substrates. It was mentioned that the graphene/ZnO-NP synthesized by an easy and uneconomic process can find applications in CSOs, flexible and portable optoelectronic devices [68].

Donghwan Koo et al. developed the TCE based on graphene by direct incorporation of PI containing (-CF₃ and -SO₂-) on graphene produced by CVD method. In this approach, PI plays a dual-functional role as substrate for the graphene and a carrier film for the transfer of this material. The PCE of the obtained PI-graphene electrode-based OSCs was 15.2% compared to 15.7% for ITO demonstrated on a glass substrate Fig. 5. It was reported that the PI-integrated graphene expose an ultra-clean surface together and better adequation with the substrate, resulting in an optical transmission greater than 92%, a low sheet resistance of 83 U/sq, thermal stability and outstanding mechanical robustness. It was mentioned that the electrode obtained have great potential for the used in different optoelectronic devices which require high efficiency and flexibility [69].

Raman et al. employed the thermal roll imprinted to synthesis graphene-covered Ag grids based transparent conductive electrodes (TCE) on PET substrate Fig. 6. It was reported that the Ag-graphene (TCE) showed a high transmittance of 77.73%, low sheet resistance of 14 Ω/sq and excellent PCE of 2.551% [70]. The comparison of graphene electrodes with other transparent electrodes in several OSC instruments shows in Table 2.

Fig. 5 Schematic of PI@GR and ITO based electrodes in the completed device structure and Corresponding Current density–voltage (J–V) diagram [69]



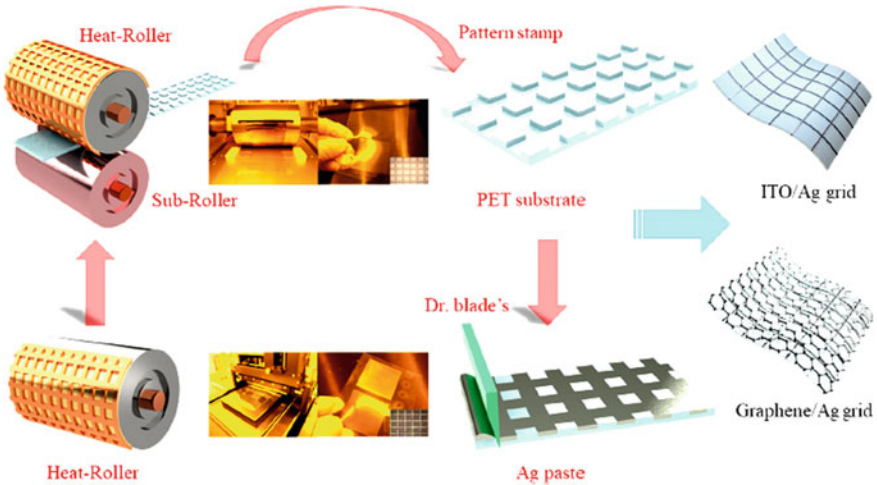


Fig. 6 Schematic illustration of Ag grid electrode integration [70]

Table 2 Past research on graphene materials utilized in solar cells as electrodes

Electrode	Configuration of solar cells	V_{OC} (V)	J_{SC} (mA cm^{-2})	FF (%)	PCE_{best} (%)	Ref.
Graphene	Al/Ca/PTB7:PC71BM/MoO3/PEDOT:PSS/graphene/PENa	0.72	14.1	69.5	7.1	[71]
ITO	Quartz/ITO-cathode based device	0.73	14.3	72.8	7.6	[71]
Graphene	Al/LiF/P3HT:PC61BMc/PEDOT:PSS/Graphene	0.59	8.5	51	2.5	[72]
ITO	Al/LiF/P3HT:PC61BM/PEDOT:PSS/ITO	0.58	9.2	57	3	[72]
Graphene oxide	Graphene oxide/AgNWs/PEDOT:PSS/Si	0.6	28.4	78.4	13.3	[73]
Ag grids	Si/PEDOT:PSS/Ag grids	0.59	24.6	69.5	10.2	[73]
Graphene/PMMA	PMMA/graphene/PEDOT:PSS/P3HT:PCBM/Cu	0.38	10.48	34.5	1.39	[74]
rGO	P3HT/ZnS/ZnO/reduced graphene oxide	0.61	3.86	43	1.01	[11]
TCNQ-graphene	Al/Ca/P3HT:PC61BM/PEDOT:PSS/TCNQ-graphene	0.57	8.9	48	2.58	[75]
HCl/HNO3-doped graphene	Al/LiF/P3HT:PC61BM/PEDOT:PSS/MoO3/HCl/HNO3-doped graphene	0.59	7	45	1.9	[75]
Graphene MoO3 + PEDOT:PSS	Al/LiF/P3HT:PC61BM/Graphene-MoO3 + PEDOT:PSS	0.59	4.8	43	1.23	[75]
Graphene-PEDOT:PSS	Al/LiF/P3HT:PC61BM/Graphene-PEDOT:PSS	0.42	1.2	24	0.12	[75]
Graphene	Al/LiF/P3HT:PC61BM/Graphene	0.5	2.4	29	0.35	[75]
ITO	Al/LiF/P3HT:PC61BM/PEDOT:PSS/ITO	0.58	9.2	51	2.5	[75]
Graphene	Grapheme/PEDOT:PSS + Au/P3HT:PCBM/Ag	0.59	10.61	50	3.17	[74]
EG – graphene	Au/PTAA/perovskite/PCBM/ZnO/EG – graphene	0.93	18.81	72	12.61	[50]
Graphene-Cu grids	PI/Graphene-Cu grids /PEDOT:PSS/perovskite/PCBM + ZnO/Ag	0.99	21.7	76	16.4	[76]
Graphene-PDMS	Graphene- PDMS/PTAA/perovskite/TiO2/Ti	1.08	18.7	74.4	15	[77]
Graphene/Al-TiO ₂	Ag/MoO ₃ /P3HT: PCBM/Al-TiO ₂ /graphene/Au				2.58	[78]
CVD-graphene	Graphite paste/CdTe/CdS/ZnO/graphene/glass				4.17	[78]
Au-graphene	ITO/ZnO/P3HT:PCBM/PEDOT:PSS/Au-graphene				3.04	[78]
rGO-CNT	Ca:Al/P3HT: PCBM/PEDOT:PSS/rGO-CNT/glass				0.85	[78]
rGO	Al/TiO ₂ /P3HT:PCBM/PEDOT:PSS/rGO/PET				0.78	[78]

4.2 Active Layer

Carbon materials such graphene, (SWCNT), fullerenes and their chemical derivatives are the most successful material used with polymer in the active layer of OSCs. The carbon materials play the role of acceptor while the polymer takes on the status of donor. This due to the physical properties of carbon based materials for PV such as optical absorption, good solubility in common organic solvents and good carrier mobility for the deposition from solution of thin solar cell active layers. Moreover, the deposition technique used for deposit active layers are spin coating, ink-jet printing, spray coating, slot-die coating, roller casting, or related methods, based on solutions [75, 79–81].

In one of the first such studies, the fullerene derivative PCBM was blended with MDMO-PPV to fabricate bulk heterojunction PV using the screen printing technique. MDMO-PPV:PCBM films situated between glass/ITO/PEDOT and aluminum electrode as active layer Fig. 7. The PCE of this device was 4.3% with thickness of 40 nm under monochromatic illumination. It was reported that the PCE will be enhance as the thickness of the film is upgraded and the interfaces are changed [82].

Fig. 7 a Schematic descriptions of the configuration of the connected OSC system b the technique of screen printing [82]

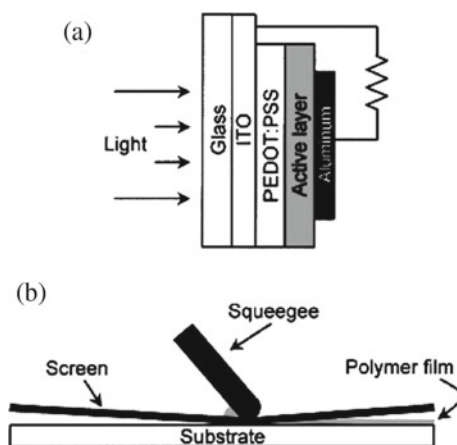
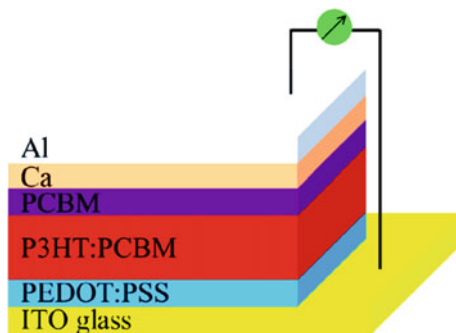


Fig. 8 Schematic configuration of the OSC based on P3HT: PCBM [83]



Similarly, the polymer solar cells based on bulk-heterojunctions between PCBM and P3HT have been developed Fig. 8. In this study, the PCBM film used as an active heterojunction layer for hole–electron separation. This signifies that the photogenerated carriers are isolated by the built-in field, while the holes and electrons are scattered to the P3HT and PCBM, respectively. The maximum PCE attained 4.24%, which is still far greater than 3.57% for P3HT: PCBM based device (traditional standard) [83].

In addition, Jagadamma and co-workers used PTB7: PC71BM as active layer for fabricating polymer solar cells, and compared them with P3HT:PC71BM based devices under similar experimental conditions. The PCE of 4.1% was achieved for P3HT:PC₇₁BM compared to 6.5% for low bandgap polymer donors PTB7:PC71BM on glass. This study demonstrated the manufacture of high-efficiency organic solar cells based on PTB7: PC₇₁BM with excellent shelf life stability in the nitrogen glove box after 3–13 months without encapsulation. [84].

Graphene has also been used in OSC (as an active layer) due to its high charge mobility and 2D conjugate structure, which makes it more adapted to chemical modification and adjustment of the energy band. and provides an efficient interface with the donor for quicker charge transfer and exciton separation. The PCE of graphene based solar cell was achieved in the ranges from 0.4 to 10% [75, 78].

In 2008, for first time, Cheng and his colleagues used organic (SPFGraphene) as a novel acceptor material with P3HT and P3OT as electron donor in active layer of organic solar cell device. The best PCE was obtained at 1.4% under simulated 100 mW cm² AM 1.5G light illumination. It was reported that SPF Graphene is a suitable candidate to replace PCBM in ETL of OSCs devices [85].

To demonstrate the graphene's role in OPV devices with different lateral dimensions. V. Gupta et al. fabricated aniline with graphene quantum dots (ANI-GQDs) and P3HT as active layer in the solar cell with a configuration of Al/LiF/P3HT:ANI-GQDs/PEDOT:PSS/ITO (anode) and compared to the P3HT and graphene sheets-aniline (GS-ANI). The maximum PCE of 1.14% was obtained for 1 wt % ANI-GQD in P3HT compared to 0.65% for 10 wt % GSs-ANI in P3HT. It was mentioned that ANI-GQDs enhanced OPV characteristics due to the improvement of optical and morphological properties of P3HT:ANI-GQDs [86].

The use of carbon nanotube in the active layer of OSC devices has also been investigated. One of the earliest studies involving the fabrication of active layer for OPV was the synthesis of SWCNT with poly (3-octyl thiophene) (P3OT). In this work, SWCNT is a role of charge separation and jump centres for hole transport. Moreover, the PCE of P3OT/SWCNT based OSCs was low of 0.1% because the poor interface area between the donor P3OT and the acceptor SWCNTs due to the insolubility of SWNTs in organic solvents. To solve this problem, The CNTs were functionalized to improve the solubility and consequently enhances the characteristic of OSCs device [59, 87].

Many strategies have been employed to improve the efficiency of OSC based on carbon naotube. Ren et al. used SWCNT/P3HT in OSC device as an active layer. The SWCNT/P3HT films prepared using spin-casting method. The devices showed a PCE of 0.72% for 3%wt of SWCNT in P3HT. This study indicated that the SWCNT is a good semiconducting material for the enhancement of the charge separation and transport in the OSCs devices active layer [88].

The effect of cadmium sulfide CdS on the photovoltaic properties of carbon naotube/P3HT heterojunction solar cells was investigated by Alvarado-Tenorio et al. In this study, the active layer of the OSC device consisted of the CdS- SWCNT and P3HT for the role of electron acceptor and the electron donor respectively. However, the P3HT:SWCNT/CdS as active layers revealed a PCE of 0.86% with 0.4 wt% of SWCNTs. Finally, it was confirmed that a good dispersion of SWCNT in P3HT has been shown to improve the electrical properties of P3HT films as well as the organic solar cell performance [89].

4.3 Charge Transport Layer (Hole/electron-Transport Layer) (HTL and ETL)

In OSCs, the charge transport layer (HTL or ETL) is a functional layer at the electrode/active layer interface to allow the collection and charge extraction and minimize recombined current leakage per active layer. However, these layers are very selective to let through one specific type of charge (electron or hole) and stop the other (hole or electron). In this respect, HTL is a purpose of electron blocking and establishing ohmic contact with donor polymer while the role of the ETL layer is the improvement of the cathode electrodes efficiency for collection and extraction of negative charge carriers. In general, HTL is a p-type material with broad band gap such as p-type metal oxides (V_2O_5 , NiO, MoO_3 , Cu_2O) and organic PEDOT:PSS while ETL is an n-type material such as n-type semiconductors (ZnO , TiO_2 , TiO_x ,) and n-type organic semiconductors (2,9-dimethyl-4, 10-phenanthroline, 7-diphenyl-1, BCP), and conducting polymer [90–94].

Je-Hong and co-workers used the PEDOT:PSS as HTL in OSCs using nanoimprint lithography technique. The PEDOT:PSS based device showed a high value of PCE 2.93%. This may be because the morphology of the PEDOT:PSS which results in greater mobility, increased the junction zone and decreased the reflectance [95].

To improve organic solar cell performance, Fang et al. were studied the effect of a modified fluorosurfactant PEDOT:PSS (as HTL) on the OPV device. In this study, PEDOT:PSS with Capstone Dupont FS-31 (CFS-31) films was synthesized using spin coating speed method. Moreover, the PEDOT:PSS-(CFS-31) based Ag/PEDOT:PSS:CFS-31/P3HT:PCBM/TiO_x/ITO/glass heterojunction solar cells exhibited a PCE of 3.1% with high stability under ambient conditions. This study showed that CFS-31 is more advantageous compared to standard surfactants in surmounting wettability problems encountered in the manufacture of solution-treated reverse OSCs devices [96].

Besides, the carbon based materials have been utilized in the HTL and ETL of OSC device. However, this application necessitated the creation of p- and n-type carbon materials. In this regard, There are many techniques such as doping to prepare the n and p-type materials. For example, S-, Pt-, B- and Au- doped carbon is p-type while Al-, N- and Cu- doped carbon is n-type materials [97, 98].

Heeger and his colleagues reported that graphene was used as ETL in OPV. In this work, the graphene was synthesized by solution-processed coating method. Firstly, the graphene was doped by HNO₃ to prepare graphene oxide (GO) and compared with the GO/TiO₂ and pure TiO_x utilized as the ETL in OSCs. However, the GO/TiO₂ showed a PCE of 7.5% in the PCDTBT/PC71BM based solar cell compared to 7.02 and 6.72% for pure TiO_x, and pur GO respectively. In addition, the GO and GO/TiO_x ETL exhibits the enhancement of 18 and 29% in JSC and PCE compared to the device without graphene ETL. It was demonstrated that the GO as ETL for BHJ solar cell is an encouraging architecture for the realization of high performance OPV devices [99].

Dai and co-authors used GO and GO-Cs as HTL and ETL, respectively, in the same OSC device configuration. In this study, GOs corresponds to both anode ITO and P3HT (HOMO level) is a role of the extraction of holes while the GO-Cs corresponds to both the Al level and the LUMO level of PCBM is the purpose of extraction of electrons. The device configuration of ITO (as anode) and Al (as cathode) showed a high PCE of 3.67% compared to 2.97% for reversed device of ITO (as cathode) and Al (as anode). Moreover, the authors demonstrated that GO is capable for used as both HTL and ETL in OSC [100].

Besides, the SWCNT as hole transport layer has been investigated. Kymakis and co-workers utilized SWCNT HTL between Bulk heterojunction phase and electrode in ITO/SWCNT/P3HT:PCBM/Al. The films SWCNT with 12.2 nm thickness prepared using Spin coated method exhibited the PCE of 3.05% compared to 2.84 and 1.16% for the devices with and without HTL based PEDOT:PSS. Finally, despite the good electron transfer in this device, SWCNTs do not have a noticeable effect on improving the efficiency of OSC, Currently several researchers are recomposing the use of SWCNTs in inorganic solar cells [101, 102].

5 Conclusions and Perspectives

Recently, several polymer-carbon nanocomposites were explored and used in organic photovoltaic device thanks to their excellent electrical, mechanical and optical properties and high stability in air. In this chapter, we have summarized the synthesis methods of polymer-carbon nanocomposites (in situ polymerization solution blending and melt blending) as the most adjustable, compatible and controllable methods for making carbon-based polymers. The properties of these nanocomposites are essentially related to its manufacturing process. In addition, carbon-based polymers are attractive alternative materials to replace conventional materials used in polymer solar cells. For example, graphene, carbon nanotube and these nanocomposites are suitable for TCE applications and replace ITO in the OSCs system. In addition, the derived from fullerenes PCBM, GR and SWCNT are also capable of replacing p- and n-type semiconductors in the HTL and ETL layers respectively.

Despite the advantages of OSCs (such the ability to absorb more higher energy photons with little energy loss, flexibility and easily fabricated at minimum cost), the polymer solar cell have low stability, efficiency, lifetime and low yield compared to silicon and inorganic solar cell. Nevertheless, many scientists, academia, and researchers are engaged to manufacture the ecofriendly OSCs at high efficiency, low cost, better lifetime and more stability. The work to improve PCE and select efficient materials for solar cell applications is currently underway. We look forward to the discovery of an efficient solar cell, which could exceed present efficiencies and achieve 80% or more.

References

1. Iqbal, S., Ahmad, S.: Recent development in hybrid conducting polymers: synthesis, applications and future prospects. *J. Ind. Eng. Chem.* **60**, 53–84 (2018)
2. Batool, M., Nazar, M.F., Awan, A., et al.: Bismuth-based heterojunction nanocomposites for photocatalysis and heavy metal detection applications. *Nano-Struct Nano-Objects* **27**, 100762 (2021)
3. Barhoum, A., Shalan, A.E., El-Hout, S.I., et al.: A broad family of carbon nanomaterials: classification, properties, synthesis, and emerging applications. In: *Handbook of Nanofibers*, pp. 1–40. Springer, Cham (2019)
4. Abu Elella, M.H., Goda, E.S., Abdallah, H.M., et al.: Innovative bactericidal adsorbents containing modified xanthan gum/montmorillonite nanocomposites for wastewater treatment. *Int. J. Biol. Macromol.* **167**, 1113–1125 (2021)
5. Akman, E., Shalan, A.E., Sadegh, F., Akin, S.: Moisture-resistant FAPbI₃ perovskite solar cell with 22.25% power conversion efficiency through pentafluorobenzyl phosphonic acid passivation. *Chemoschem* **14**, 1176–1183 (2021)
6. Abdellatif Soliman, S.M., Sanad, M.F., Shalan, A.E.: Synthesis, characterization and antimicrobial activity applications of grafted copolymer alginate-g-poly(N-vinyl imidazole). *RSC Adv.* **11**, 11541–11548 (2021)
7. Gebreegziabher, G.G., et al.: Polyaniline–graphene quantum dots (PANI–GQDs) hybrid for plastic solar cell. *Carbon Lett.* **30**(1), 1–11 (2019)

8. Kausar, A., Taherian, R.: Electrical conductivity behavior of polymer nanocomposite with carbon nanofillers. In: *Electrical Conductivity in Polymer-Based Composites: Experiments, Modelling and Applications*, pp. 41–72 (2019)
9. Cazorla-Amoros, D.: Grand challenges in carbon-based materials research. *Front. Mater. Sci.* **1**, 6 (2014)
10. Sun, Y., Miao, F., Li, R.: Bistable electrical switching and nonvolatile memory effect based on the thin films of polyurethane-carbon nanotubes blends. *Sens. Actuator A Phys.* **234**, 282–289 (2015)
11. Sookhakian, M., et al.: Enhanced photovoltaic performance of polymer hybrid nanostructure heterojunction solar cells based on Poly(3-hexylthiophene)/ZnS/ZnO/reduced graphene oxide shell-core nanorod arrays. *Ind. Eng. Chem. Res.* **53**(37), 14301–14309 (2014)
12. Abbasi, H., Antunes, M., Velasco, J.I.: Recent advances in carbon-based polymer nanocomposites for electromagnetic interference shielding. *Prog. Mater. Sci.* **103**, 319–373 (2019)
13. Gopalan, A.I., Lee, K.P., Ragupathy, D.: Development of a stable cholesterol biosensor based on multi-walled carbon nanotubes-gold nanoparticles composite covered with a layer of chitosan-room-temperature ionic liquid network. *Biosens. Bioelectron.* **24**(7), 2211–2217 (2009)
14. Simon, J., Flahaut, E., Golzio, M.: Overview of carbon nanotubes for biomedical applications. *Materials (Basel)* **12**(4), 624 (2019)
15. Tripathi, S.N., Rao, G.S.S., Mathur, A.B., Jasra, R.: Polyolefin/graphene nanocomposites: a review. *RSC Adv.* **7**(38), 23615–23632 (2017)
16. Mahmoud, W.E.: Morphology and physical properties of poly(ethylene oxide) loaded graphene nanocomposites prepared by two different techniques. *Eur. Polym. J.* **47**(8), 1534–1540 (2011)
17. Mutalib, M.A., Rashid, N.M., Aziz, F.: Carbon-based polymer nanocomposite for photovoltaic devices. In: *Carbon-Based Polymer Nanocomposites for Environmental and Energy Applications*, pp. 559–584. Elsevier (2018)
18. Mahmoudi, T., Wang, Y., Hahn, Y.-B.: Graphene and its derivatives for solar cells application. *Nano Energy* **47**, 51–65 (2018)
19. Spitalsky, Z., Tasis, D., Papagelis, K., Galiotis, C.: Carbon nanotube–polymer composites: chemistry, processing, mechanical and electrical properties. *Prog. Polym. Sci.* **35**(3), 357–401 (2010)
20. Rahaman, M., Aldalbahi, A., Bhagabati, P.: Preparation/processing of polymer–carbon composites by different techniques. In: *Carbon-Containing Polymer Composites*, pp. 99–124. Springer, Singapore (2019)
21. Hernández-Martínez, D., Nicho, M.E., Alvarado-Tenorio, G., García-Carvajal, S., Castillo-Ortega, M.M., Vásquez-López, C.: Elaboration and characterization of P3HT–PEO–SWCNT fibers by electrospinning technique. *SN Appl. Sci.* **2**(3), 1–9 (2020)
22. Aissa, B., et al.: Functionalized single-walled carbon-nanotube-blended P3HT-based high performance memory behavior thin-film transistor devices. *Nanotechnology* **31**(7), 075201 (2020)
23. Li, X., Zhu, Z., Wang, T., Xu, J., Liu, C., Jiang, Q., Jiang, F., Liu, P.: Improved thermoelectric performance of P3HT/SWCNTs composite films by HClO₄ post-treatment. *Compos. Commun.* **12**, 128–132 (2019)
24. Qu, S., Wang, M., Chen, Y., Yao, Q., Chen, L.: Enhanced thermoelectric performance of CNT/P3HT composites with low CNT content. *RSC Adv.* **8**(59), 33855–33863 (2018)
25. Kuilla, T., Bhadra, S., Yao, D., Kim, N.H., Bose, S., Lee, J.H.: Recent advances in graphene based polymer composites. *Prog. Polym. Sci.* **35**(11), 1350–1375 (2010)
26. Al-Saleh, M.H., Sundararaj, U.: A review of vapor grown carbon nanofiber/polymer conductive composites. *Carbon* **47**(1), 2–22 (2009)
27. Potts, J.R., Dreyer, D.R., Bielawski, C.W., Ruoff, R.S.: Graphene-based polymer nanocomposites. *Polymer* **52**(1), 5–25 (2011)
28. Al-Saleh, M.H.: Electrical and mechanical properties of graphene/carbon nanotube hybrid nanocomposites. *Synth. Met.* **209**, 41–46 (2015)

29. Karim, Z.A., Hafeez, A., Ismail, A.F.: The fabrication of carbon-based polymer nanocomposite. In: *Carbon-Based Polymer Nanocomposites for Environmental and Energy Applications*, pp. 3–25. Elsevier (2018)
30. Cruz, S.M., Viana, J.C.: Melt blending and characterization of carbon nanoparticles-filled thermoplastic polyurethane elastomers. *J. Elastomers Plast.* **47**(7), 647–665 (2014)
31. Zhang, Q., Zhang, B.Y., Guo, Z.X., Yu, J.: Tunable electrical conductivity of carbon-black-filled ternary polymer blends by constructing a hierarchical structure. *Polymers (Basel)* **9**(9), 404 (2017)
32. Yang, J., Wu, M., Chen, F., Fei, Z., Zhong, M.: Preparation, characterization, and supercritical carbon dioxide foaming of polystyrene/graphene oxide composites. *J. Supercrit. Fluid* **56**(2), 201–207 (2011)
33. Naffakh, M., Díez-Pascual, A.M., Gómez-Fatou, M.A.: New hybrid nanocomposites containing carbon nanotubes, inorganic fullerene-like WS₂ nanoparticles and poly(ether ether ketone) (PEEK). *J. Mater. Chem.* **21**(20), 7425–7433 (2011)
34. Bagotia, N., Choudhary, V., Sharma, D.K.: Synergistic effect of graphene/multiwalled carbon nanotube hybrid fillers on mechanical, electrical and EMI shielding properties of polycarbonate/ethylene methyl acrylate nanocomposites. *Compos. B. Eng.* **159**, 378–388 (2019)
35. Logakis, E., et al.: Low electrical percolation threshold in poly(ethylene terephthalate)/multi-walled carbon nanotube nanocomposites. *Eur. Polym. J.* **46**(5), 928–936 (2010)
36. Keru, G., Ndungu, P.G., Nyamori, V.O.: A review on carbon nanotube/polymer composites for organic solar cells. *Int. J. Energy Res.* **38**(13), 1635–1653 (2014)
37. Cruz-Aguilar, A., et al.: High-density polyethylene/graphene oxide nanocomposites prepared via in situ polymerization: morphology, thermal, and electrical properties. *Mater. Today Commun.* **16**, 232–241 (2018)
38. Zhang, H.-X., Park, J.-H., Yoon, K.-B.: Excellent electrically conductive PE/rGO nanocomposites: in situ polymerization using rGO-Supported MAO cocatalysts. *Compos. Sci. Technol.* **154**, 85–91 (2018)
39. Lee, J.S., Ko, Y.S.: Synthesis of petaloid graphene/polyethylene composite nanosheet produced by ethylene polymerization with metallocene catalyst adsorbed on multilayer graphene. *Catal. Today* **232**, 82–88 (2014)
40. Koizhaiganova, R., Kim, H.J., Vasudevan, T., Kudaibergenov, S., Lee, M.S.: In situ polymerization of 3-hexylthiophene with double-walled carbon nanotubes: studies on the conductive nanocomposite. *J. Appl. Polym. Sci.* **115**(4), 2448–2454 (2010)
41. Chen, M., Yin, J., Jin, R., Yao, L., Su, B., Lei, Q.: Dielectric and mechanical properties and thermal stability of polyimide–graphene oxide composite films. *Thin Solid Films* **584**, 232–237 (2015)
42. Wang, C., Lan, Y., Yu, W., Li, X., Qian, Y., Liu, H.: Preparation of amino-functionalized graphene oxide/polyimide composite films with improved mechanical, thermal and hydrophobic properties. *Appl. Surf. Sci.* **362**, 11–19 (2016)
43. Sun, G., et al.: Fabrication and mechanical, electrical properties study of isocyanate-based polyimide films modified by reduced graphene oxide. *Prog. Org. Coat.* **143**, 105611 (2020)
44. Lai, D., Wei, Y., Zou, L., Xu, Y., Lu, H.: Wet spinning of PVA composite fibers with a large fraction of multi-walled carbon nanotubes. *Prog. Nat. Sci.* **25**(5), 445–452 (2015)
45. Pantano, A.: Mechanical properties of CNT/polymer. In: *Carbon Nanotube-Reinforced Polymers*, pp. 201–232. Elsevier (2018)
46. Rafiee, M.A., Yavari, F., Rafiee, J., Koratkar, N.: Fullerene–epoxy nanocomposites-enhanced mechanical properties at low nanofiller loading. *J. Nanoparticle Res.* **13**(2), 733–737 (2010)
47. Okonkwo, A.O., et al.: High-toughness/low-friction ductile epoxy coatings reinforced with carbon nanostructures. *Polym. Test.* **47**, 113–119 (2015)
48. Savagatrup, S., et al.: Viability of stretchable poly(3-heptylthiophene) (P3HpT) for organic solar cells and field-effect transistors. *Synth. Met.* **203**, 208–214 (2015)

49. Babal, A.S., Gupta, R., Singh, B.P., Singh, V.N., Dhakate, S.R., Mathur, R.B.: Mechanical and electrical properties of high performance MWCNT/polycarbonate composites prepared by an industrial viable twin screw extruder with back flow channel. *RSC Adv.* **4**(110), 64649–64658 (2014)
50. Xu, X., et al.: Surface functionalization of a graphene cathode to facilitate ALD growth of an electron transport layer and realize high-performance flexible perovskite solar cells. *ACS Appl. Energy Mater.* **3**(5), 4208–4216 (2020)
51. Mirmohammadi, S.A., Sadjadi, S., Bahri-Laleh, N.: Electrical and electromagnetic properties of CNT/polymer composites. In: *Carbon Nanotube-Reinforced Polymers*, pp. 233–258. Elsevier (2018)
52. Yang, J., Xu, T., Lu, A., Zhang, Q., Fu, Q.: Electrical properties of poly(phenylene sulfide)/multiwalled carbon nanotube composites prepared by simple mixing and compression. *J. Appl. Polym. Sci.* **109**(2), 720–726 (2008)
53. Aarab, H., et al.: Electrical and optical properties of PPV and single-walled carbon nanotubes composite films. *Synth. Met.* **155**(1), 63–67 (2005)
54. Sarkhan, N.A., Rahman, Z.A., Zakaria, A., Ali, A.M.M.: Enhanced electrical properties of poly(3,4-ethylenedioxythiophene):poly(4-styrenesulfonate) using graphene oxide. *Mater. Today Proc.* **17**, 484–489 (2019)
55. Jayenta Singh, T., Singh, S., Masiul Islam, S., Get, R., Mahala, P., Jolson Singh, K.: Flexible organic solar cells with graphene/PEDOT:PSS Schottky junction on PET substrates. *Optik* **181**, 984–992 (2019)
56. Li, G., et al.: High-efficiency solution processable polymer photovoltaic cells by self-organization of polymer blends. *Nat. Mater.* **4**(11), 864–868 (2005)
57. Ganesamoorthy, R., Sathiyam, G., Sakthivel, P.: Review: fullerene based acceptors for efficient bulk heterojunction organic solar cell applications. *Sol. Energy Mater. Sol. Cells* **161**, 102–148 (2017)
58. Sachdeva, S., Singh, D., Tripathi, S.K.: Optical and electrical properties of fullerene C70 for solar cell applications. *Opt. Mater.* **101**, 109717 (2020)
59. Arici, E., Karazhanov, S.: Carbon nanotubes for organic/inorganic hybrid solar cells. *Mater. Sci. Semicond. Process* **41**, 137–149 (2016)
60. Anwar, H., George, A.E., Hill, I.G.: Vertically-aligned carbon nanotube counter electrodes for dye-sensitized solar cells. *Sol. Energy* **88**, 129–136 (2013)
61. Jeon, I., et al.: Perovskite solar cells using carbon nanotubes both as cathode and as anode. *J. Phys. Chem. C* **121**(46), 25743–25749 (2017)
62. Jeon, I., et al.: Direct and dry deposited single-walled carbon nanotube films doped with MoO(x) as electron-blocking transparent electrodes for flexible organic solar cells. *J. Am. Chem. Soc.* **137**(25), 7982–7985 (2015)
63. Jeon, I., et al.: Polymeric acid-doped transparent carbon nanotube electrodes for organic solar cells with the longest doping durability. *J. Mater. Chem. A* **6**(30), 14553–14559 (2018)
64. Tenent, R.C., et al.: Ultrasoother, large-area, high-uniformity, conductive transparent single-walled-carbon-nanotube films for photovoltaics produced by ultrasonic spraying. *J. Adv. Mater.* **21**(31), 3210–3216 (2009)
65. Barnes, T.M., et al.: Single-wall carbon nanotube networks as a transparent back contact in CdTe solar cells. *Appl. Phys. Lett.* **90**(24), 243503 (2007)
66. Rowell, M.W., et al.: Organic solar cells with carbon nanotube network electrodes. *Appl. Phys. Lett.* **88**(23), 233506 (2006)
67. Sinha, S., Swain, B.P.: graphene for the potential renewable energy applications. In: *Advances in Greener Energy Technologies*, pp. 439–450. Springer, Singapore (2020)
68. Jung, S., Lee, J., Seo, J., Kim, U., Choi, Y., Park, H.: Development of annealing-free, solution-processable inverted organic solar cells with N-doped graphene electrodes using zinc oxide nanoparticles. *Nano Lett.* **18**(2), 1337–1343 (2018)
69. Koo, D., et al.: Flexible organic solar cells over 15% efficiency with polyimide-integrated graphene electrodes. *Joule* **4**(5), 1021–1034 (2020)

70. Raman, V., Jo, J., Kim, H.-K.: ITO and graphene-covered Ag grids embedded in PET substrate by thermal roll imprinting for flexible organic solar cells. *Mater. Sci. Semicond. Process.* **120**, 105277 (2020)
71. Park, H., Chang, S., Zhou, X., Kong, J., Palacios, T., Gradecak, S.: Flexible graphene electrode-based organic photovoltaics with record-high efficiency. *Nano Lett.* **14**(9), 5148–5154 (2014)
72. Wang, Y., Tong, S.W., Xu, X.F., Ozyilmaz, B., Loh, K.P.: Interface engineering of layer-by-layer stacked graphene anodes for high-performance organic solar cells. *Adv. Mater.* **23**(13), 1514–1518 (2011)
73. Xu, Q., et al.: Solution-processed highly conductive PEDOT:PSS/AgNW/GO transparent film for efficient organic-Si hybrid solar cells. *ACS Appl. Mater. Interfaces* **7**(5), 3272–3279 (2015)
74. Liu, Z., Li, J., Yan, F.: Package-free flexible organic solar cells with graphene top electrodes. *Adv. Mater.* **25**(31), 4296–4301 (2013)
75. Singh, E., Nalwa, H.S.: Graphene-based bulk-heterojunction solar cells: a review. *J. Nanosci. Nanotechnol.* **15**(9), 6237–6278 (2015)
76. Jeong, G., et al.: Suppressed interdiffusion and degradation in flexible and transparent metal electrode-based perovskite solar cells with a graphene interlayer. *Nano Lett.* **20**(5), 3718–3727 (2020)
77. Heo, J.H., Shin, D.H., Lee, M.L., Kang, M.G., Im, S.H.: Efficient organic-inorganic hybrid flexible perovskite solar cells prepared by lamination of polytriarylamine/CH₃NH₃PbI₃/anodized Ti metal substrate and graphene/PDMS transparent electrode substrate. *ACS Appl. Mater. Interfaces* **10**(37), 31413–31421 (2018)
78. Yin, Z., et al.: Graphene-based materials for solar cell applications. *Adv. Energy Mater.* **4**(1), 1300574 (2014)
79. Ameri, T., Dennler, G., Lungenschmied, C., Brabec, C.J.: Organic tandem solar cells: a review. *Energy Environ. Sci.* **2**(4), 347–363 (2009)
80. Cheng, Y.-J., Yang, S.-H., Hsu, C.-S.: Synthesis of conjugated polymers for organic solar cell applications. *Chem. Rev.* **109**(11), 5868–5923 (2009)
81. Bernardi, M., et al.: Nanocarbon-based photovoltaics. *ACS Nano* **6**(10), 8896–8903 (2012)
82. Shaheen, S.E., Radspinner, R., Peyghambarian, N., Jabbour, G.E.: Fabrication of bulk heterojunction plastic solar cells by screen printing. *Appl. Phys. Lett.* **79**(18), 2996–2998 (2001)
83. Chi, D., Qu, S., Wang, Z., Wang, J.: High efficiency P3HT:PCBM solar cells with an inserted PCBM layer. *J. Mater. Chem. C* **2**(22), 4383–4387 (2014)
84. Jagadamma, L.K., et al.: Efficient inverted bulk-heterojunction solar cells from low-temperature processing of amorphous ZnO buffer layers. *J. Mater. Chem. A* **2**(33), 13321–13331 (2014)
85. Liu, Z., et al.: Organic photovoltaic devices based on a novel acceptor material: graphene. *J. Adv. Mater.* **20**(20), 3924–3930 (2008)
86. Gupta, V., Chaudhary, N., Srivastava, R., Sharma, G.D., Bhardwaj, R., Chand, S.: Luminescent graphene quantum dots for organic photovoltaic devices. *J. Am. Chem. Soc.* **133**(26), 9960–9963 (2011)
87. Pradhan, B., Batabyal, S.K., Pal, A.J.: Functionalized carbon nanotubes in donor/acceptor-type photovoltaic devices. *Appl. Phys. Lett.* **88**(9), 093106 (2006)
88. Ren, S., Bernardi, M., Lunt, R.R., Bulovic, V., Grossman, J.C., Gradecak, S.: Toward efficient carbon nanotube/P3HT solar cells: active layer morphology, electrical, and optical properties. *Nano Lett.* **11**(12), 5316–5321 (2011)
89. Alvarado-Tenorio, G., Cortina-Marrero, H.J., Nicho, M.E., Márquez Aguilar, P.A., Hu, H.: Improvement of photovoltaic performance of inverted hybrid solar cells by adding single-wall carbon nanotubes in poly(3-hexylthiophene). *Mater. Sci. Semicond. Process.* **56**, 37–42 (2016)
90. Irwin, M.D., Buchholz, D.B., Hains, A.W., Chang, R.P., Marks, T.J.: p-Type semiconducting nickel oxide as an efficiency-enhancing anode interfacial layer in polymer bulk-heterojunction solar cells. *Proc. Natl. Acad. Sci.* **105**(8), 2783–2787 (2008)

91. Shrotriya, V., Li, G., Yao, Y., Chu, C.-W., Yang, Y.: Transition metal oxides as the buffer layer for polymer photovoltaic cells. *Appl. Phys. Lett.* **88**(7), 073508 (2006)
92. Yip, H.L., Hau, S.K., Baek, N.S., Ma, H., Jen, A.K.Y.: Polymer solar cells that use self-assembled-monolayer-modified ZnO/metals as cathodes. *J. Adv. Mater.* **20**(12), 2376–2382 (2008)
93. Chu, T.Y., et al.: Bulk heterojunction solar cells using thieno [3, 4-c] pyrrole-4, 6-dione and dithieno [3, 2-b: 2', 3'-d] silole copolymer with a power conversion efficiency of 7.3%. *J. Am. Chem. Soc.* **133**(12), 4250–4253 (2011)
94. He, Z., et al.: Simultaneous enhancement of open-circuit voltage, short-circuit current density, and fill factor in polymer solar cells. *J. Adv. Mater.* **23**(40), 4636–4643 (2011)
95. Choi, J.-H., Choi, H.-J., Shin, J.-H., Kim, H.-P., Jang, J., Lee, H.: Enhancement of organic solar cell efficiency by patterning the PEDOT:PSS hole transport layer using nanoimprint lithography. *Org. Electron.* **14**(12), 3180–3185 (2013)
96. Lim, F.J., Ananthanarayanan, K., Luther, J., Ho, G.W.: Influence of a novel fluorosurfactant modified PEDOT:PSS hole transport layer on the performance of inverted organic solar cells. *J. Mater. Chem.* **22**(48), 25057–25064 (2012)
97. Hou, Y., Geng, X., Li, Y., Dong, B., Liu, L., Sun, M.: Electrical and Raman properties of p-type and n-type modified graphene by inorganic quantum dot and organic molecule modification. *Sci. China Phys. Mech.* **54**(3), 416–419 (2011)
98. Mahmoudi, T., Seo, S., Yang, H.Y., Rho, W.Y., Wang, Y., Hahn, Y.B.: Efficient bulk heterojunction hybrid solar cells with graphene-silver nanoparticles composite synthesized by microwave-assisted reduction. *Nano Energy* **28**, 179–187 (2016)
99. Wang, D.H., et al.: Transferable graphene oxide by stamping nanotechnology: electron-transport layer for efficient bulk-heterojunction solar cells. *Angew. Chem. Int. Ed. Engl.* **52**(10), 2874–2880 (2013)
100. Liu, J., Xue, Y., Gao, Y., Yu, D., Durstock, M., Dai, L.: Hole and electron extraction layers based on graphene oxide derivatives for high-performance bulk heterojunction solar cells. *J. Adv. Mater.* **24**(17), 2228–2233 (2012)
101. Kymakis, E., Stylianakis, M.M., Spyropoulos, G.D., Stratakis, E., Koudoumas, E., Fotakis, C.: Spin coated carbon nanotubes as the hole transport layer in organic photovoltaics. *Sol. Energy Mater. Sol. Cells* **96**, 298–301 (2012)
102. Ferguson, A.J., Blackburn, J.L., Kopidakis, N.: Fullerenes and carbon nanotubes as acceptor materials in organic photovoltaics. *Mater. Lett.* **90**, 115–125 (2013)

Graphene Based Nanocomposites: Synthesis, Characterization and Energy Harvesting Applications



Summan Aman, Maqzia Bashir, Muqaddas Baigum, Muhammad Faizan Nazar, Sajjad Hussain Sumrra, Syed Salman Shafqat, and Muhammad Nadeem Zafar 

Abstract Nanotechnology and nanoscience have emerged out as one of the most exciting areas of research today. As an inimitable morphological 2-D carbon material, graphene has triggered a gold rush in the nanomaterial society by introducing controlled functional building blocks. Besides, the mechanical, electrical, and optical properties of graphene make it an attractive contender for applications in solar energy conversion and electrochemical energy devices. Graphene based nanocomposites have been preferred greatly due to their low cost, low density, high electron mobility, exceptional optical transmittance, versatile process ability and excellent thermal conductivity. Subsequently, to encounter the global needs, energy scavenging has become an ultimate part of pervasive sensor network. A gold rush has been prompted all over the world for exploiting the possible applications of graphene-based nanomaterials. The best solution to this problem is to improve the photoconversion efficiencies by optimizing materials and device fabrication.

In this chapter, first of all we have discussed different synthesis methods of graphene nanocomposites like mechanical exfoliation, chemical vapor deposition, liquid phase exfoliation, electrochemical exfoliation and reduction of graphene oxide. For the elucidation of their structural and morphological characteristics, different techniques including SEM, TEM, Energy dispersive X-ray spectroscopy (EDX), UV/Vis absorption spectrum, Raman Spectroscopy, Photoluminescence spectroscopy (PL), X-ray photoelectron spectroscopy (XPS), XRD, Cyclic voltammetry, Impedance spectroscopy, DSC, FTIR and TGA have been discussed. Application potential analysis for graphene-based nanocomposites is discussed based on means including flexible and stretchable electronics, photocatalysis and electrochemical sensing, use in Li-ion batteries, supercapacitors, photovoltaic applications and

S. Aman · M. Bashir · M. Baigum · S. H. Sumrra · M. N. Zafar (✉)
Department of Chemistry, University of Gujrat, Gujrat 50700, Pakistan
e-mail: nadeem.zafar@uog.edu.pk

M. F. Nazar
Department of Chemistry, University of Education Lahore, Multan Campus, Multan, Pakistan

S. S. Shafqat
Department of Chemistry, University of Education, Lahore 54770, Pakistan

hydrogen production. Some of the future concerns have also been discussed related to their feasibility, controlled device fabrication of composites, stability and life span of composite, multistep heterogeneous catalysis and safe dumping of environmental contaminants.

Keywords Graphene based nanocomposites · Energy · Hydrogen production · Solar cells

Abbreviations

PMC	Polymer Matrix Composites
CNTs	Carbon Nanotubes
AFM	Atomic Force Microscopy
CVD	Chemical Vapor Deposition
G-PSS	Graphene [poly (sodium 4-styrene sulfonate)]
rGO	Reduced Graphene Oxide
ETOD	3,4-ethylenedioxythiophene
ATRP	Atom transfer radical polymerization
DMF	Dimethyl Formamide
MO	Metal Oxide
NMR	Nuclear Magnetic Resonance
MS	Mass Spectrometry
SEM	Scanning Electron Microscopy
FESEM	Field Emission Scanning Electron Microscopy
LTD	Low Temperature Decomposition
AP	Ammonium perchlorate
XPS	X-ray Photoelectron Spectroscopy
TGA	Thermogravimetric Analysis
CV	Cyclic Voltammetry
PON	Peroxydinitrites
MWCNTs	Multi-walled Carbon Nanotubes
AC	Alternating Current
ITO	Indium Tin Oxide
OER	Oxygen Evolution Reactions
NCs	Nanocomposites
GO	Graphene Oxide
STM	Scanning Tunneling Microscopy
NMP	N-methyl pyrrolidone
PSS	[Poly (sodium 4-styrene sulfonate)]
PEDOT	[Poly (3,4-ethylenedioxythiophene)]
APS	Ammonium peroxydisulfate
PFPA	Per fluorophenyl Azide
DMSO	Dimethyl Sulfoxide

PTA	Phosphotungstic Acid
XRD	Powder X-ray Diffraction
FTIR	Fourier Transform Infrared Spectroscopy
TEM	Transmission Electron Microscopy
DSC	Differential Scanning Calorimetry
HTD	High Temperature Decomposition
PSSA	Polyelectrolyte containing aromatic sulfonic acid
ESCA	Electron Spectroscopy of Chemical Analysis
EDX	Energy Dispersive X-ray
GCEs	Glassy Carbon Electrodes
PL	Photoluminescence
PVA	Polyvinyl Alcohol
ECs	Electrochemical Capacitors
LIBs	Lithium-Ion Batteries
ORR	Oxygen Reduction Reactions

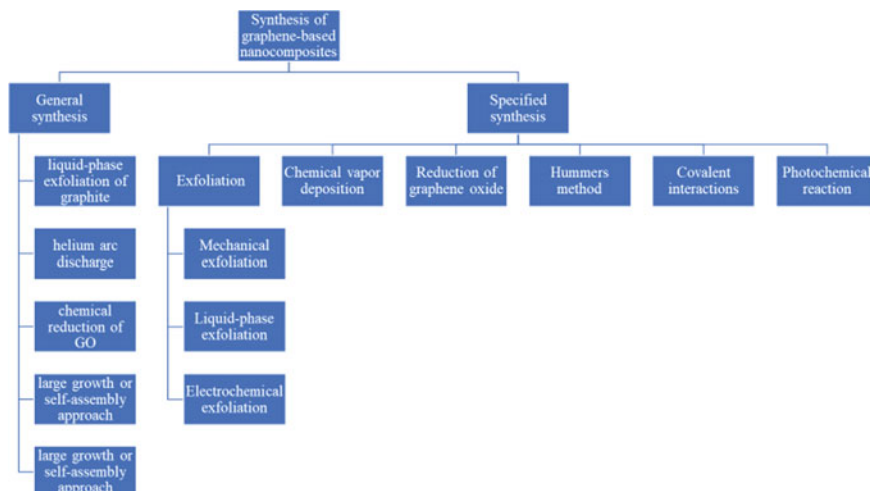
1 Introduction

An allotropic carbon having graphene stacks has upraised research in nanotechnology since its discovery. Graphene, a versatile twenty-first century material, is a single-atom-thick structure of sp^2 bonded C-atoms which arrange themselves in a structure like honeycomb, designated as an emerging class of nanomaterials with 2D arranged carbon atoms introducing the building blocks with controlled functionalities [1, 2]. The interfaces thus made contain efficient transport of the electrical energy with having substantial 2D planarity and layers with single atom thickness [3]. The transport of holes and electrons using field effect of electricity having ambipolar nature was allowed by specific characteristics of graphene like zero bandgap along with achievement of the 10^{13} cm^{-2} of carrier concentration and the mobility which can exceed from $15,000 \text{ cm}^2\text{V}^{-1}\text{s}^{-1}$ significantly at the room temperature [4, 5]. According to theoretical calculations, $2630 \text{ m}^2\text{g}^{-1}$ of surface area is possessed by the graphene along with $200,000 \text{ cm}^2\text{V}^{-1}\text{s}^{-1}$ of mobility at about 10^{12} cm^{-2} of carrier density with 80–95% of optical transparency having elevated electrical conductivity specifically at the room temperature [6–8]. Graphene contains robust mechanical properties with possession of the Young's modulus having value of 1 TPa along with 42 Nm^{-1} of the breaking strength and outstanding thermal conductivity having value $5000 \text{ Wm}^{-1} \text{ K}^{-1}$ with the fracture strains of ca. 25% which are very favorable for various graphene applications [9]. Due to prevailing environmental problems along with depletion of the fossil fuels in recent years, a great interest has been developed for designing alternative energy sources like devices with energy conversion and storage along with energy densities which can meet this increasing demand. Many properties of graphene like low density, nontoxicity, adjustable process ability and

high mobility of electrons makes the graphene a favorable material for several applications in industry. For the achievement of all these distinctive properties, a possible way is the formation of composite material by the integration of graphene sheets [9]. For example, in the formation of the Ag-nanoparticle films, graphene sheets perform an excellent role on nanoscale ad substrate. Formation of these films which accumulate on nanosheets having a single deposition layer having specific flexibility, forms stable aqueous suspensions [10, 11]. Due to possession of all the mentioned properties of graphene, it can be used for a number of purposes like strain sensors, in packaging industries, in antistatic coatings, electronic devices and as energy storage materials [12, 13]. The minute or the unbroken fibers of PMC (polymer matrix composite) fuse with the polymer matrix in such a way that load can be transferred in-between fibers via matrix. Both the industries and academic area raise significance of graphene-reinforced nanocomposites for study of their thermal and mechanical properties [14]. The special directions and specific geometry possessed by reinforced material can determine mechanical properties presented by nanocomposites [15, 16]. The properties of the nanocomposites like mechanical and electrical strength can be improved by the nanoscale interaction of host material with reinforced material [17]. Recently, researchers have found a considerable difference in special directions of NCs embedded graphene because of the different preparation methods and percentages of graphene in NCs [18]. The appropriate dispersion of the graphene significantly affects its distinctive properties. This issue can be resolved by optimizing materials and introducing controlled fabrication of composites. Consequently, there is a need of graphene having exorbitant qualities for its commercial applications [19]. An appreciating surface-to-volume ratio is possessed by the graphene as compared to the C-nanotubes. Due to presence of this property, graphene became more efficient with ultimate increase in the mechanical strength of composites of graphene with polymers. Graphene also contains the advantage of cost-effectiveness which means that graphene contains significantly low cost than CNTs due to its easy and large quantity availability from the precursors of graphite and from silicon carbide. A brief introduction is aimed to be described in this chapter about the graphene, the preparation methods of graphene nanocomposites followed by the characterization techniques and recent progress in energy harvesting application. At the end, summary and outlook is given to conclude this chapter [20, 21].

2 Synthesis of Graphene-Based Nanocomposites

Graphene was 1st time synthesized in 2004. Many synthesis methods were presented and some of which are given below in Scheme 1.



Scheme 1 Synthesis of graphene based nanocomposites

2.1 General Method for the Preparation of Graphene-Based Nanocomposites

As graphene is the fundamental material for synthesis of all functionalities of graphitic material, it faced problems in early research of fullerene and nanotubes [10]. For the utilization of advanced applications of graphene, there is the need for accessibility of the processable nanosheets of graphene in substantial amount. Up to now, two key paths are utilized: large-scale exfoliation and large-scale growth. Some of the techniques like exfoliation of the graphite in liquid phase [22], discharge of Helium arc [23], large scale growth or the self-assembly approach [24], deposition of chemical vapours [25] and the chemical reduction of the graphene oxide [26], have fascinated us to a step closer to the real-world applications for this material.

Among aforementioned approaches for the synthesis of the graphene-based composites, which need the preparation of graphene sheets on a large scale but also ought to be homogeneous distribution. The method of chemical reduction about GO (graphene oxide) appears as very much productive, having low cost and a way to produce mass production for the incorporation of the sheets of graphene into graphene hybrids. As evident from the Fig. 1, the presently focused procedure for the preparation of the graphene-based nanocomposites is by exfoliation of the graphene via combining sonication and oxidation methods accompanied by their reduction using chemical methods [26]. The GO is heavily oxygenated graphene comprising not only carbonyl, epoxy and the OH^- group on the fundamental plane but also the carboxylic group present on the boundary of carbon sheets [28]. The presence of functional groups on graphene oxide act as a presenter site and subsequently make the

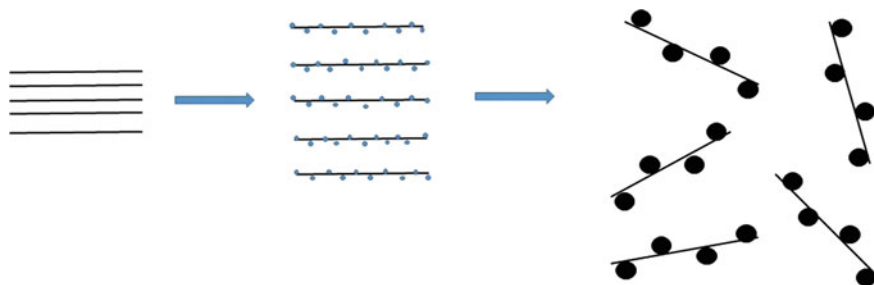


Fig. 1 Schematic route for attachment of nanoparticles on the graphene sheets. (1) Adsorption of metal ions on GO sheets (2) Anchorage of crystalline intercalation and growth of metal nanoparticles on exfoliated GO layers. Reproduced with permission from ref [27]. Copyright 2008, RSC

nanoparticles formed by in-situ synthesis to be embedded on active sites of surface and edges of the graphene oxide sheets. By the conversion of the planar geometry of carbon i.e., sp^2 -hybridization to distorted geometry i.e., sp^3 -hybridization, GO lost its exceptional electrical conductivity and thus ultimately it becomes electrically insulated [9]. For the recovery of properties of graphene like electrical properties and eliminate functional groups having O_2 for GO for the sake of regeneration of the aromatic graphene network in order to restore the network of graphene which is aromatic and essential.

2.2 Mechanical Exfoliation

The simplest method for the preparation of graphene is considered as mechanical exfoliation [12]. In this preparation method, a graphite piece is mostly used for the purpose of repetitive tape exfoliation which is then moved towards a substrate. Various devices and methods can be used like AFM (atomic force microscopy), Optical microscope, Raman spectroscopy and STM (scanning tunneling microscopy) which is used for the determination of the number of graphene layers. Appreciative quality crystals can be obtained by this preparative technique but have the limitation of only use in prototyping or the lab-scale experiments [29].

2.3 Chemical Vapor Deposition

This technique is helpful in preparing monolayer graphene with large quantity of structural polymers which can be used in several devices. Samples with considerable area can be prepared through exposure of the metals to the precursors of hydrocarbon nature at elevated temperature. It contains several techniques for CVD (chemical vapour deposition) like thermal CVD, plasma-enhanced CVD and the cold or hot

wall CVD etc. The development of the mechanism for the graphene depends on substrate development, which could be initiated by the C-atom growth. Generally observed that due to inertness of graphene to chemicals, it is difficult for the graphene to move from substrate, which results in wrinkles and defects in the material [22]. Chemical vapour deposition has originated as an effective method for production of graphene at large scale. Apart from this, CVD technique is turned out to be practicable technique for large scale fabrication of high-grade graphene [29].

2.4 Liquid-Phase Exfoliation

This method is widely used for graphene fabrication and contains three main steps as; (1) surfactant dispersion, (2) exfoliation (3) purification [30]. Primarily, ultrasound technique was used for exfoliation of the flakes of graphite in suitable solvent like NMP (N-methyl pyrrolidone) [31]. By increasing the time for sonication, we can achieve excessive graphene concentration. By the sonication process, material formed contains thick flakes and we can detach them by applying ultracentrifugation [32]. By increasing speed for centrifugation, we can achieve thinner graphene flakes with small lateral size of the material, mostly non suitable for the composites. In case of dispersion, yield obtained by the relation of graphene flakes for a single layer to total material gives the output of the procedure. Amongst all available variables, two main variables are rotational speed and sonication time. Moreover, the solvents with high reactivity generally increases cost of graphene and also contribute to pollution because graphene contains lower solubility thus uses more of the solvent. However, for purpose of upscaling of fabricated graphene, the most suitable technique is regarded as liquid-phase exfoliation [29].

2.5 Electrochemical Exfoliation

The use of electrical current and the liquid electrolyte comprises of electrochemical exfoliation, eventually utilizes electrodes made up of graphite. This process makes use of oxidation at anode and reduction at cathode for the electrode made up of graphite. For the formation of high-quality conductive layers of graphene, cathodic reaction techniques seemed to be more acceptable and eventually used in the applications like energy harvesting and optics [33]. Compared to pristine monolayer graphene, the material of anode comprises graphene layers in anodic oxidation possessing relatively poor yield and GO in oxidative state [34]. The main reason behind preferring the procedure of electrochemical exfoliation over many other procedures is its capability to yield in one step, easy to perform and requires only a small time of few minutes or few hours for its completion. In contrast, many techniques require a lot of completion time for many non-identical steps. Appropriate factor in nanocomposite development is based on flakes with lateral size, that

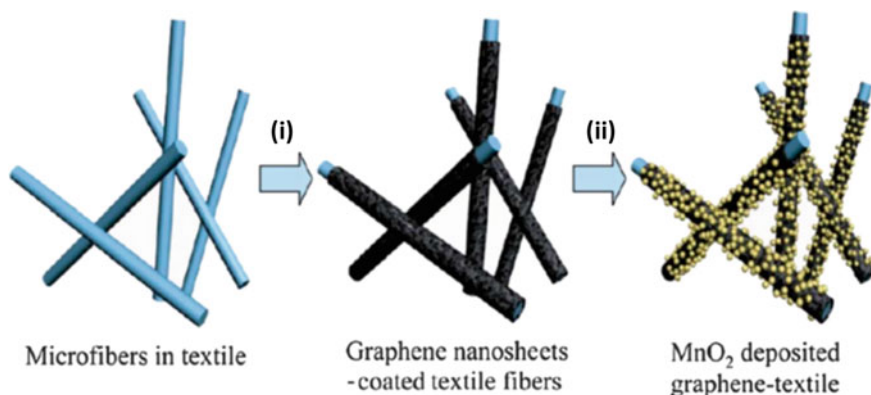


Fig. 2 Electrochemical deposition of MnO₂-graphene nanocomposites (Reproduced with permission from ref [36]. Copyright 2011, ACS)

is directly dependent upon graphite source along with providing exfoliation procedure with intercalation. Likewise, this process is made ecofriendly by using liquid electrolytes [35] (Fig. 2).

2.6 Reduction of Graphene Oxide

Park et al. developed the homogeneous suspension of graphene which was chemically treated in the aqueous media [37]. In this method, initially the graphite dispersion in water is prepared, in which added the aqueous KOH solution. In the opinion of Perk et al. when we treat the KOH which itself is a strong base with the reactive groups like OH, carboxylic acid or epoxy group, it gives a large negative charge on sheets of graphene producing sheets with considerable coating of positive and negative ions. For the stabilization of the potassium oxide modified GO for a long time, hydrazine monohydrate solution is added into it. It ultimately results in the development of the homogeneous suspension of above solution i.e., Hydrazine-potassium hydroxide modified GO, making it stable for about 4 months [38]. For Instance, G-PSS [Graphene poly(sodium 4-styrenesulfonate)] was initially produced by the reduction of aqueous suspension containing graphene oxide along with the hydrazine monohydrate present accompanied with polyelectrolyte of PSS. Performing this procedure, PSS [poly(sodium 4-styrenesulfonate)] was adsorbed onto rGO surface (Reduced Graphene Oxides) via noncovalent interactions of π - π bonds joining the rGO sheets at basal planes and the aromatic rings [39, 40]. PSS is called an ionic stabilizer in reactions containing rGO because it contains negatively charged ions like $-\text{SO}_3^-$ and produces homogeneous rGO suspensions in aqueous media. Afterwards, there is the formation of the hybrid materials of the G-PSS: PEDOT (Graphene [poly(sodium 4-styrenesulfonate)]: [poly(3,4-ethylenedioxythiophene)])

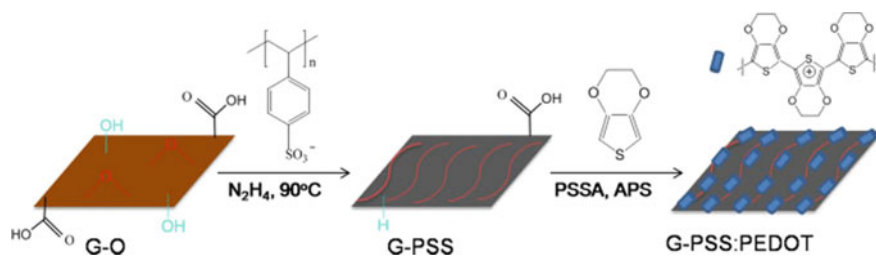


Fig. 3 Schematic formation of G-PSS: PEDOT nanocomposites (Reproduced with permission from [41]. Copyright 2011, SCI)

by the in-situ polymerization of the ETOD (3,4-ethylenedioxythiophene) along with APS (ammonium peroxydisulphate) in the presence of G-PSS. The rGO plates coated with PSS can function as the template in polymerization reactions to connect growing chains of PEDOT [poly(3,4-ethylenedioxythiophene)] on the G-PSS surface. The resulting material formed is hybrid nanomaterial of G-PSS: PEDOT (Fig. 3).

2.7 Hummers Method

Modified Hummers method was employed for the synthesis of the nanocomposites of the Ni/Graphene from the GO-precursors. GO-gel and the Ni(II)acetate tetrahydrate were used as the starting material in a ratio of Ni:C as 5%:95% of atomic ratio. For this purpose, adequate amount of Ni-acetate was dispersed in water followed by mixing with GO-gel. The mixture was changed to the dark brown shade before ultrasonication which was stirred slightly to get homogenized solution and then ultrasonicated at 25 °C for about 10 min. By adding 1 M NaOH solution, 10–12 pH was maintained for mixture while stirring. Prior to place the mixture was heated for 60 min at 70 °C in a closed container, solution was stirred again for 10 min. Gradually, heating was increased within next 60 min up to 95 °C.

Afterwards, centrifugation of the uniform solution was done and by double distilled water remaining contaminants were repeatedly rinsed and again centrifuged. Resultantly, the obtained precipitates were dried in vacuum to get precursor powder of Ni-hydroxide and graphene. Finally, by hydrothermal treatment for 3 h at 350 °C, the above nanocomposites were reduced to nanocomposites of Ni/graphene [42].

2.8 Covalent Interactions

The other suitable method for the fabrication of the nanocomposites of graphene is by covalent reaction. Covalent bonding of GO and graphene to the surface is done by using click chemistry, ATRP (atom transfer radical polymerization) amide

bonding or the diazonium salts [43]. Ionic liquids, per fluorophenylazide (PFPA), polymer, organic nitride, azidotrimethylsilane, p-phenyl-SO₃H, porphyrin as well as the nanoparticles can covalently bind to the graphene [44, 45]. The bonding present between the graphene sheets having covalent functionalities is amide bonding [46].

Stankovich et al. presented incorporation of GO with the isocyanate having organic nature by formation of esters of carbamate and amide with OH and carboxyl group on GO-surface [43]. Through amide bonding, the porphyrin ring of (aminophenyl)-10,15,20-triphenyl porphyrin containing amine functionality were also bonded covalently to the GO in DMF (dimethyl formamide) (Fig. 4a) [44]. Similarly, ionic liquids terminated at amine were made to attach at the graphene for polydisperse nanocomposite formation that can easily disperse in aqueous media, DMSO (dimethyl sulfoxide) and DMF for more than 3 months because of the presence of electrostatic forces in between different units of ionic liquid on the surface of graphene [45]. In other works, the amide bonding along with chemical reduction was used for the fabrication of the alkylated graphene papers via alkylation of GO [46]. Thus, produces the eternally conductive papers of alkylated graphene containing ordered structures having applications in supercapacitors, catalysis, Li-ion batteries and biocompatible materials.

Another way of covalent reaction is utilization of the diazonium salt for preparation of the graphene-based nanocomposites. In another research work, there occurs the sulfonation of the partially-reduced GO by aryl-diazonium salt that produces SO₃H group (sulfonated group) on sheets of graphene having S to C ratio of about 1:35. Moreover, the reduction of this sulfonated GO was done by hydrazine for removal of most of the surplus functional groups containing oxygen. The solubility of sulfonated graphene is about 2 mgmL⁻¹ at the pH of 3–10 [48]. Similarly, for the synthesis of the graphene hybrids with bulk of covalent functionalities without any of the oxidized defect, wet chemical method was opted. The intercalation of graphite with K was done in the presence of DME (1,2-dimethoxyethane) solution containing K/Na alloys in accompanied with exfoliation of the single-layer graphene. Due to addition of the diazonium salts, the graphene without oxidation defects was covalently functionalized and it causes no irreparable lattice damage on graphene layers [49]. The attachment of graphene to perfluorophenyl azide (PFPA) using diazonium bonding is due to its thermal and the photochemical activation. As compared to unmodified graphene, sheets of graphene having PFPA functionality were extremely soluble (Fig. 4b) [47]. In this method, the immobilization of the graphene sheet was done on the Si-substrate coupling agent of PFPA-silane, where silane ends get attach to the Si-substrate and PFPA-diazonium to graphene when they are subjected to thermal treatment [50].

For the graphene having covalent functionalities, ATRP (atom transfer radical polymerization) was also significant, starting by the initiator molecule accompanied with polystyrene chain present on the surface of graphene with grafting efficiency of above than 80% [51]. As compared to polystyrene, there is enhanced tensile strength by about 70% and the 57% of Young's modulus for the resulting material which are nanocomposites of polystyrene and graphene containing only the 0.9 wt% of the

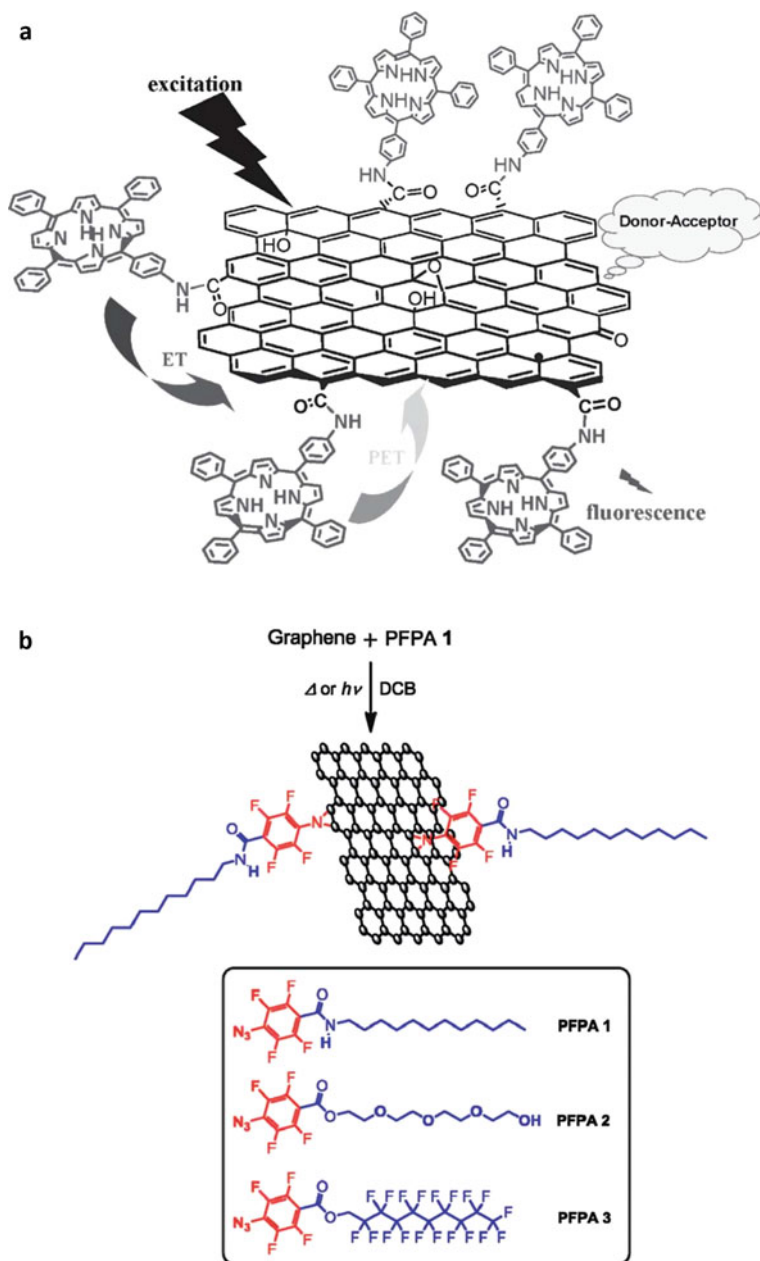


Fig. 4 **a** The hybrids of graphene-porphyrin fabricated through amine covalent bonding. Reproduced with permission from ref [41]. **b** The covalent bonding of graphene and PFPA via diazonium salt (Reproduced with permission from ref [47]). © 2009, John Wiley and Sons (a); © 2010, ACS (b)

graphene sheets. The resultant nanocomposites of polystyrene and graphene have enhanced thermal conductivity as compared to polystyrene by factor 2.6 with the 2 wt% of graphene [52].

2.9 Photochemical Reaction

For the preparation of the nanocomposites of graphene, favourable route is by photochemical reaction [53–56]. Some of the photochemical reactions occur in graphene presence by simple light irradiation resulting in formation of nanocomposites of graphene. For example, the nanocomposites of graphene-TiO₂ can be produced by careful mixing of TiO₂ and GO in ethanol by irradiating UV light in photochemical reactions. The TiO₂ is actually UV-active and when UV-light is irradiated, reduction of GO occurs by the electrons which get excited in the TiO₂ followed by production of nanocomposites of reduced graphene-TiO₂ [57]. Same procedure was adopted for synthesis of nanocomposites of BiVO₄- and WO₃-graphene by applying photocatalytic reaction in between GO and precursors. Instead of MO (metal oxide), the deposition of the nanoparticles of metals like Pb, Pt, Au and Ag can be done by the use of radiations [58, 59]. For the reduction of GO to graphene, one approach comprises the fabrication of metals like Pt, Au and Ag nanoparticles on surface of graphene by performing photolysis of PTA (phosphotungstic acid) (Fig. 5) [60]. Meanwhile, the in-situ reduction of metal precursors can be done by PTA which was photolyzed on the surface of graphene. Thus, attachment of metal nanoparticles on graphene surface can be done without using any of the molecular linker. The formation of fine dispersion of nanoparticles of noble metals like Pb, Au and Ag on graphene surface can be done using DMF by two-step photochemical technique. The very 1st step possesses the photochemical reduction of GO to the reduced graphene by using phosphotungstate with irradiation of UV-light. Secondly, formation of composites of graphene-noble metal nanoparticles is done by instant subjecting of metal ions or the compound precursors [53]. Through literature review, it is clear that the photochemical reaction for the production of nanocomposites of silver-reduced graphene can be initiated by the mixing of GO and ammonia-silver complexes using Ag-lamp of 450 W [60]. Similarly, the loading of Ag-NPs was done on GO-using radiations from visible light using photochemical reactions [54]. To prepare GO–Ag nanocomposites, photochemical depositions of Ag NPs on graphene oxide were also developed in an alkaline environment. For the preparation of nanocomposites of GO–Pt using photochemical deposition of the Ag-nanoparticles, photochemical deposition can be used. Pt–graphene nanocomposites were prepared in the same way irrespective of any reducing agent [58, 59].

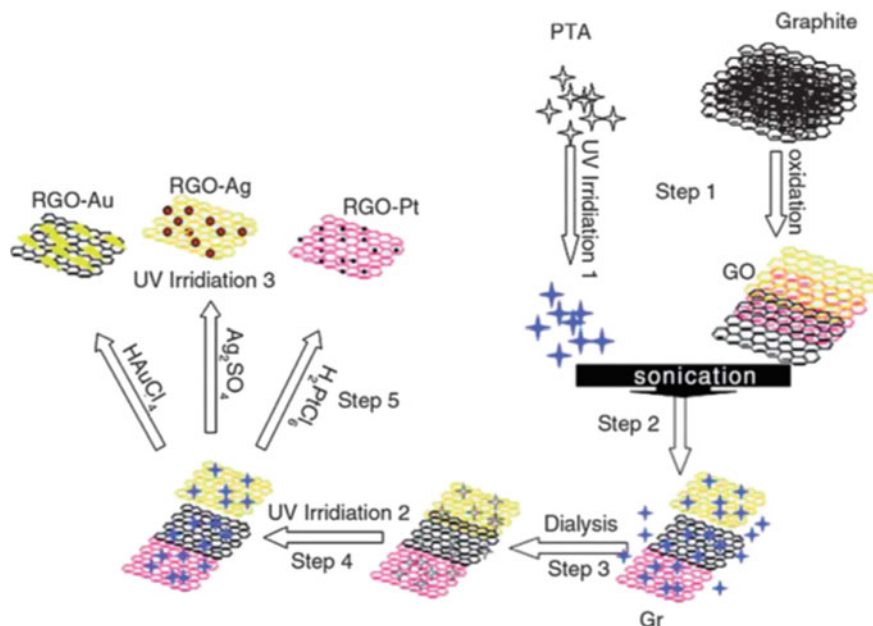


Fig. 5 Photochemical routes to metal NP-graphene nanocomposites (Reproduced with permission from ref [56]. © 2012, Elsevier)

3 Characterization of Graphene Based Nanocomposites

Nanocomposites are a combination of multilayers of nanomaterial with matrix support of another compound [61]. Hence, their characterization comprises several aspects [62]. The characterization of NPCs based upon analysis of morphological, optical, elemental, structural and functional properties is done by a number of techniques such as NMR, XRD, UV-Visible spectroscopy, MS, FTIR, XPS etc. Optical properties of NCs are recognized by two spectroscopic techniques, namely FTIR and UV-Visible spectroscopy [63].

3.1 TEM and FESEM Images of Silver Nanoparticles on GO-Sheets

SEM (scanning electron microscope) uses the highly focused high-energy beam of electrons for resolution of minor details of the specimen [64]. The signal produced by the interaction of sample and the beam reveals the important details of the sample which also contains information about material orientation, crystalline structure, morphology and the chemical composition of the sample [65]. However, SEM

contains a similar basic principle to light microscopy with the difference that it makes use of an electron beam instead of light. The resolution of SEM is better than a light microscope because of the smaller wavelength of electrons from the light [66]. Hence, SEM have power to reveal minor details of material about its internal structure, commonly as small as of the individual atoms [67].

The images for TEM (transmission electron microscope) and the FESEM (field emission scanning electron microscope) for the nanoparticles of silver on the GO-sheet are shown in figure below. In Fig. 6(a), 2D sheets of the graphene which are almost transparent were fabricated by Ag-particles. The nanosheets of carbon containing a single layer are so thin that it seems to be hard to distinguish them from the Cu-grid supported by carbon. However, edges of carbon sheets and their wrinkled silk waves lead to the conclusion that these particles are actually deposited on the support as given by Fig. 6(b). Instead of this, the Fig. 6(c and d), clearly shows that the synthesized nanoparticles of silver can accumulate on the substrate surface of graphene. Generally, there is presence of functional groups on the edges and planes of the GO. These functional groups (negatively charged) are used for the absorption of

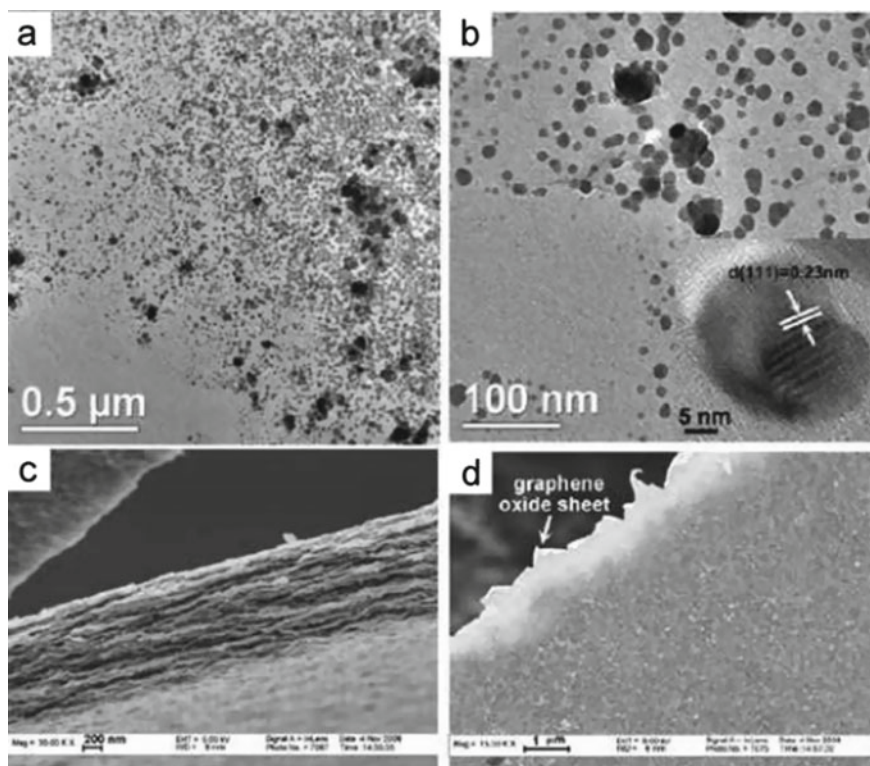


Fig. 6 TEM **a, b** and the FESEM **c, d** images for the deposited silver particles on the surface of GO-sheets (Reproduced with permission from ref [69]. © 2009, Wiley InterScience)

nanoparticles and inorganic materials on graphene surfaces. Thus, positively charged ions can easily interact with negative functionalities by using electrostatic interactions. In-situ reduction of ions using glucose permits the adsorption of nanoparticles of silver on GO-sheets. By applying this method, some nanoparticles get deposited on the GO-sheet surface and some on their edges [68].

It is clear from experiments that we can process aqueous solution of graphene-based sheets into the films and the paper like material [9, 26]. The sheets of GO coated with silver can easily be incorporated to form macroscopic film by drying it on substrate which contains a shiny luster of metal which shows mirror-like characteristics. But the film containing discrete GO-sheets contain very poor reflectivity. It is generally assumed that the origin of Ag-mirror films is due to assembly of Ag-nanoparticles on the substrate surface [70]. This system contains the formation of macroscopic films containing mirror-like appearance and can be characterized by restacking on nanoparticle film by silver (Fig. 6c).

3.2 TEM and FESEM Images of GO-Co₃O₄ Nanocomposites

From Fig. 7, SEM images of synthesized nanocomposite reveals that exfoliated sheets of GO were arbitrarily decorated by the particles of 100 nm size which are spherical in shape [27]. These nanoparticles formed by in-situ method result in the exfoliation of layered GO. In Fig. 8 the TEM images of the nanocomposites of GO-Co₃O₄ seemed to be brighter than those surrounded by thin film. This can be clearly seen that sheets of GO contain functional groups on its both sides including epoxy and OH group by which Co₃O₄ can easily get attached to the support [68].

3.3 Differential Scanning Calorimetry (DSC)

DSC (differential scanning calorimetry) is an electroanalytical technique which measures the heat flow across the system as a function of time or temperature when we expose the sample to controlled and programmed temperature. In this technique, we limit the specific heat capacity of pure compounds or mixtures and determine the catalytic effect of materials. Differential scanning calorimetry was conducted for the measurement of the catalytic effect produced by the nanocomposites of GO-Co₃O₄ produced by their thermal decomposition on ammonium perchlorate. Figure 9 shows the curve for DSC that contains decomposition of the AP (ammonium perchlorate) along with AP and GO, Co₃O₄ and the GO-Co₃O₄ nanocomposite [27]. Usually, the thermal decomposition of the ammonium perchlorate occurs in 3-main steps: (i) phase transition of the material at 240 °C for endothermic reaction, (ii) decomposition at low temperature of about 316 °C i.e., LTD (low temperature decomposition) and (iii) decomposition at high temperature of about 460 °C i.e., HTD (high

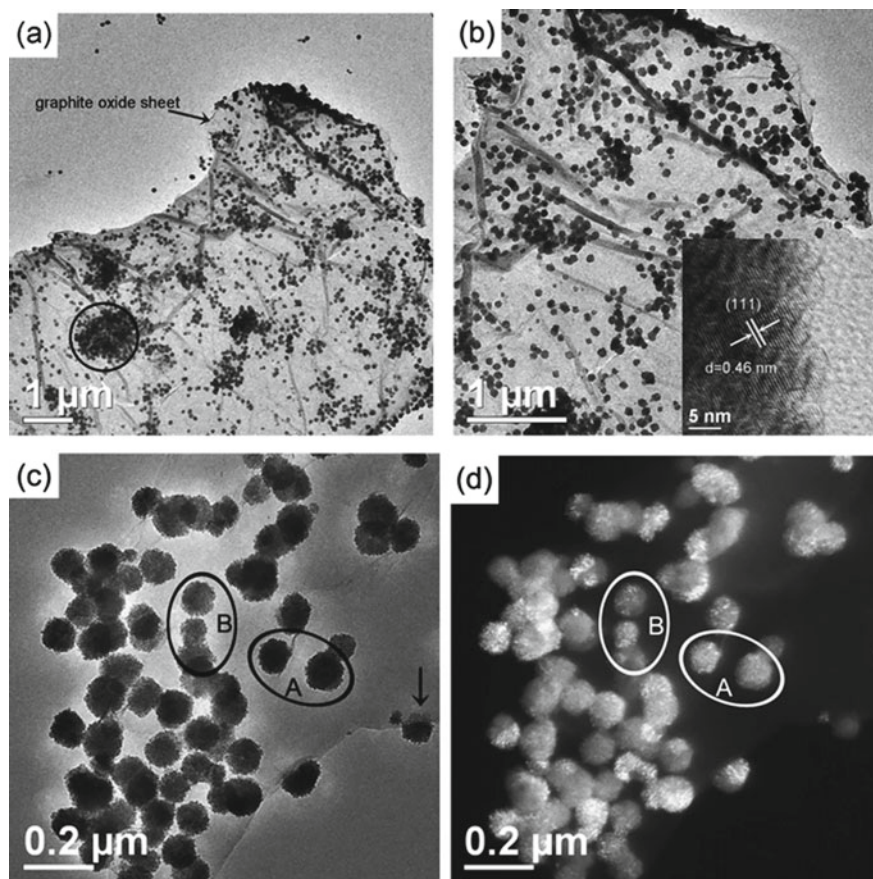


Fig. 7 FESEM images of GO-Co₃O₄ nanocomposites (Reproduced with permission from ref [27]. © 2008, RSC)

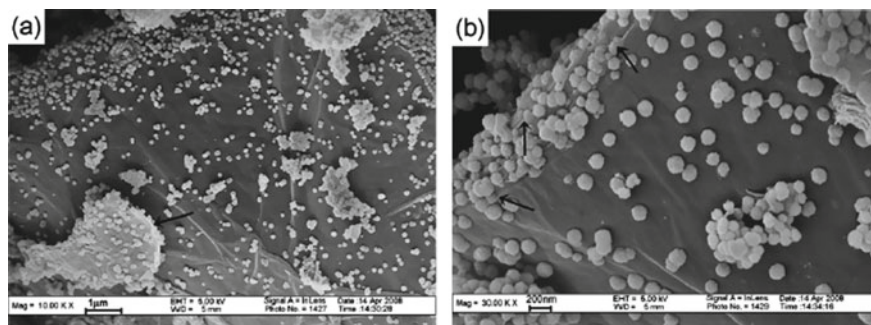


Fig. 8 TEM images of GO-Co₃O₄ nanocomposites (Reproduced with permission from ref [27]. ©2008, RSC)

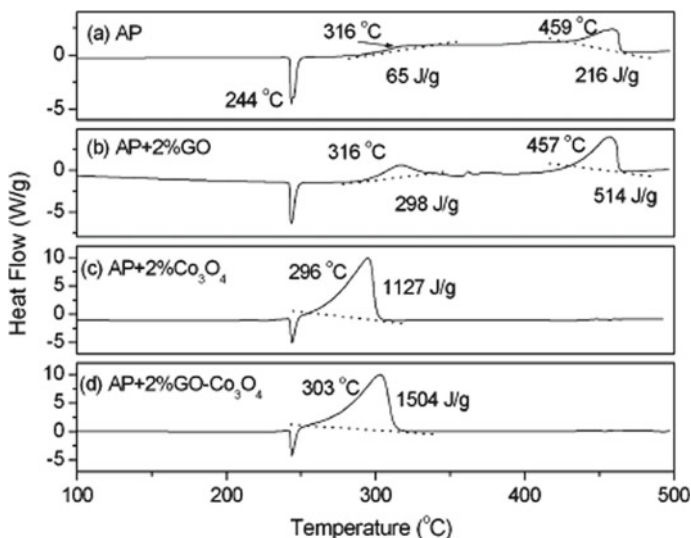


Fig. 9 Curves for DSC showing decomposition of the AP, AP with 2% GO, AP with 2% Co_3O_4 and the AP with nanocomposites of 2% Co_3O_4 -GO (Reproduced with permission from ref [27]. © 2008, RSC)

temperature decomposition). It is very critical to decrease decomposition temperature and increase endothermic heat for industrial applications of the AP. Two apparent exothermic peaks for AP can be observed when graphene was added in it, accompanying the new single peak of exothermic current at about 360 °C and it was observed that heat of these exothermic steps is more than AP [68]. This effect could be observed due to the catalytic nature of the GO. The introduction of the GO- Co_3O_4 and Co_3O_4 can reduce the temperature of the LTD and HTD and combine these steps into a single step. Decomposition temperature of 2% GO- Co_3O_4 (303 °C) and AP along with 2% Co_3O_4 producing exothermic reactions are nearly close to each other with quantities of 1504 and 1127% respectively. Therefore, for catalytic decomposition of AP due to cumulative effect of all distinct components, by adding GO- Co_3O_4 only decomposition is not increased but also resulted in an increase in the exothermic heat for AP, resulting in excellent catalytic properties of AP [27].

3.4 X-Ray Diffraction Analysis (XRD)

The crystal structure of a material can be best identified by using XRD along with interlayer distance of GO and graphene and its composition. XRD is based upon Bragg's law [71]. Figure 10(a) shows the XRD pattern for the GO, graphite and graphene. While the Fig. 10(b) represents composite of Ni and graphene before and after its reduction along with metallic Ni. Figure 10(a) shows that graphite contains

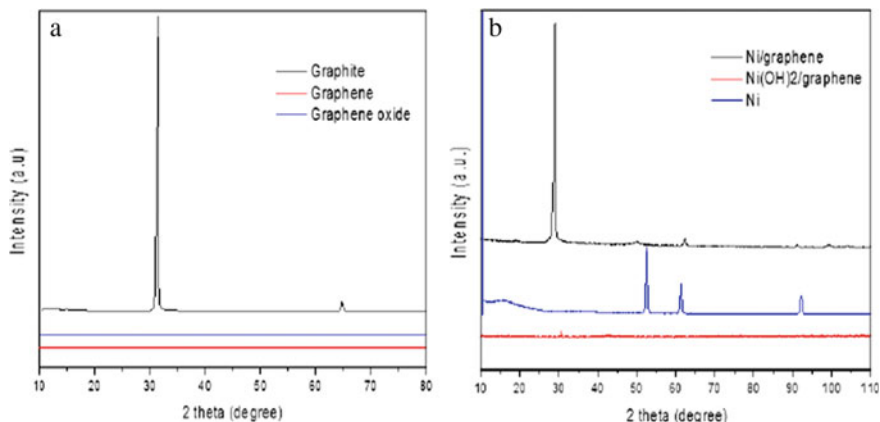


Fig. 10 (a) XRD spectra for graphite (black), GO (blue) and the graphene (red). (b) Ni (blue), Ni/graphene nanocomposite (black) and the Ni(OH)₂ precursor (red). (Reproduced with permission from ref [72]. © IOP Publishing Ltd)

diffraction peaks which are very sharp and contain high intensity at about $2\theta = 31^\circ$. We obtain (002) orientation with d-spacing of 0.33 nm. The peak for graphite disappears after oxidation and is proven by the appearance of blue and red lines for GO and graphene respectively. As evident from Fig. 10(b) after thermal reduction of hydrogen, the peak for Ni(OH)₂ disappears proving the reduction of Ni(OH)₂ into elemental Ni in formation of Ni/graphene composite. And there is an appearance of three-different peaks in its diffraction pattern i.e., at about $2\theta = 52.8, 61$ and the 93° corresponding to the reduction of Ni in Ni/graphene composite. Thus, these results clearly indicate that Ni gets reduced on graphene surface [72].

3.5 Raman Spectroscopy

Raman spectroscopy is a type of molecular spectroscopy which contains the interaction between light and matter for better investigation of material's characteristics. Information is gained by scattering of light. As it identifies the vibrational modes of interatomic bonding along with structure produced because of differences in structural features of molecules. This technique utilizes a monochromatic laser for interaction of phonons with molecular-vibration mode, resulting in movement of energy up and down in different energy levels by the inelastic scattering [73]. So, in order to elucidate the electronic distribution, Raman spectroscopy was performed. D and G bands are shown in spectra for characterization of graphene. G contains atoms with sp^2 -hybridization along with plane vibrational modes while D with sp^3 -hybridization show bands as defected bands. Figure 11 shows D and G bands which are present at 1578 cm^{-1} and 1658 cm^{-1} respectively. It has been observed that no shift produced in

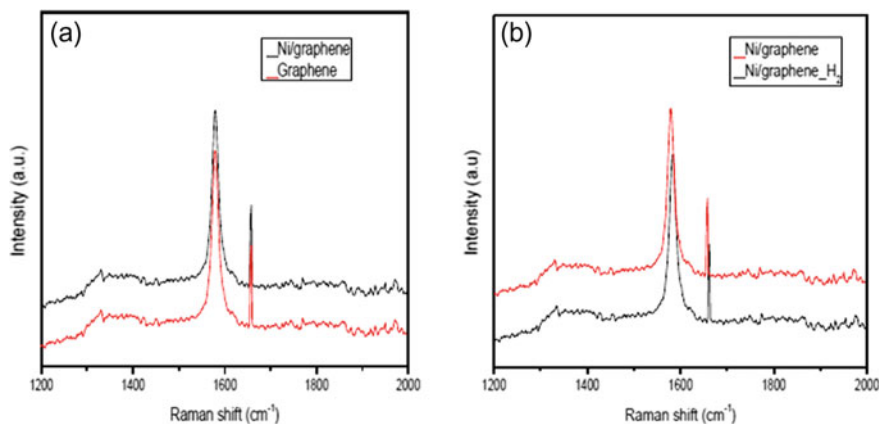


Fig. 11 Raman spectra of graphene, Ni/graphene, and Ni/graphene_{H₂} (Reproduced with permission from ref [72]. © IOP Publishing Ltd)

position of peak for Ni/graphene while when it gets charged with hydrogen it contains a peak. From their spectra, it is clear from D/G ratio that sp^2 -hybridization is strengthened while sp^3 is weakened. As the number of graphene sheets increases, there is an increase in high-frequency peaks due to their proportionality to number of vibrational modes. Hence, graphene platelet packing gives peaks with low intensity [72]. The shift in D-peaks of spectra can be observed due to restacking of platelets of graphene when Ni/graphene gets charged with hydrogen.

3.6 Fourier Transform Infrared Spectroscopy

FTIR spectroscopy is the technique employed to recognize vibrational modes in the molecules [74]. It is also known as vibrational spectroscopy. Comparison of FTIR spectra for nanocomposites of GO, G-PSS and the G-PSS: PEDOT is given in Fig. 12(a). Spectra for GO contains C=C peak at 1625 cm^{-1} while peaks for O-based functionalities like C=O, C-O (epoxide or ether), carboxy C-O and alkoxy C-O are present at 1730 , 1410 , 1230 and 1050 cm^{-1} respectively [75, 76]. A comparison of GO and G-PSS spectra exhibits a decrease in stretch intensities for C-O and C=O which suggest the reduction of RG-O (reduced graphene oxide) platelets. Furthermore, new bonds describing PSS polyelectrolyte appear at 1180 and 1088 cm^{-1} , showing introduction of PSS on RG-O surface. Peaks for G-PSS: PEDOT in FTIR spectra are present as; C=C at 1524 , C-C at 1320 , S-O at 920 and C-S at 680 cm^{-1} produced in PEDOT by thiophene ring, while peaks containing value of 1088 and 980 cm^{-1} represent the S=O stretching vibrations present in SO_3 -group [41]. Results predict the formation of PEDOT in the form of composites and in the form of association with the G-PSS [75].

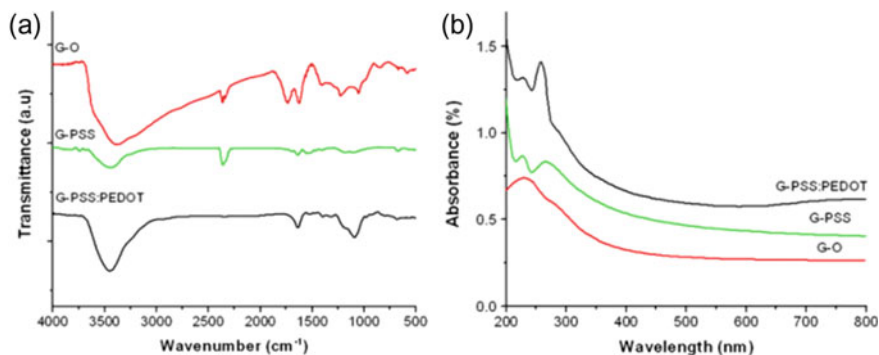


Fig. 12 **a** FTIR spectra for GO, G-PSS and G-PSS: PEDOT composite. **b** UV–Vis spectra for these composites (Reproduced with permission from ref [41]. © 2011, SCI)

Dispersions of above-mentioned composites in aqueous media were confirmed by UV–Vis spectra as given in Fig. 12b. Characteristic peak for GO in UV–Vis spectra was given at 232 nm and peak at 300 nm represents π – π^* transition in aromatic carbons and the n – π^* transition to C = O respectively. Two peaks at 226 and the 268 nm are given in spectra for G-PSS which were originally allocated to PSS-polyelectrolyte [77, 78] and the π – π^* transition RG-O contain red-shift from GO. For composite of G-PSS: PEDOT, peak at 275 nm due to PSSA (polyelectrolyte containing aromatic sulfonic acid) arises its broad absorption peak at 750 nm [79].

3.7 X-Ray Photoelectron Spectroscopy (XPS)

XPS (X-ray photoelectron spectroscopy) was commonly used to study surface characteristics along with analysis of biomedical polymers. This can also be called ESCA technique i.e., the Electron Spectroscopy of Chemical Analysis and employed for study of elements with mass ranging from 10–200, which are stable in vacuum conditions or made stable by just cooling the molecule. Moreover, it is not suitable for H₂ and He. This is regarded as the most informative surface technique providing other applications like most quantitative information about chemical information and readily interpretable technique as compared to other techniques [80]. For monitoring composition of graphene oxide, G-PSS and composites of GPSS: PEDOT, XPS was performed (Fig. 13) [41]. The XPS spectra for the GO can be divided into four-main parts showing C-atoms present in different O-containing functionalities i.e., C in C-O (286.6 eV), C = O (287.9 eV), non-oxygenated C (284.8 eV) and O-C = O (289.2 eV) [81, 82]. 1s C spectra for composites of G-PSS: PEDOT is given in Fig. 14. Same O-functionalities are present in both GO as well as G-PSS: PEDOT but contribution of oxygenated carbon is much less proving that many O-based functionalities are removed during reduction. Moreover, two supplementary peaks at about

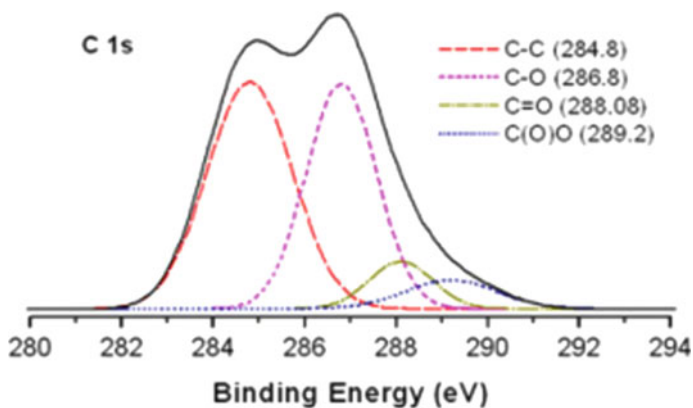


Fig. 13 C 1s XPS spectrum of G-O (Reproduced with permission from ref [41]. © 2011, SCI)

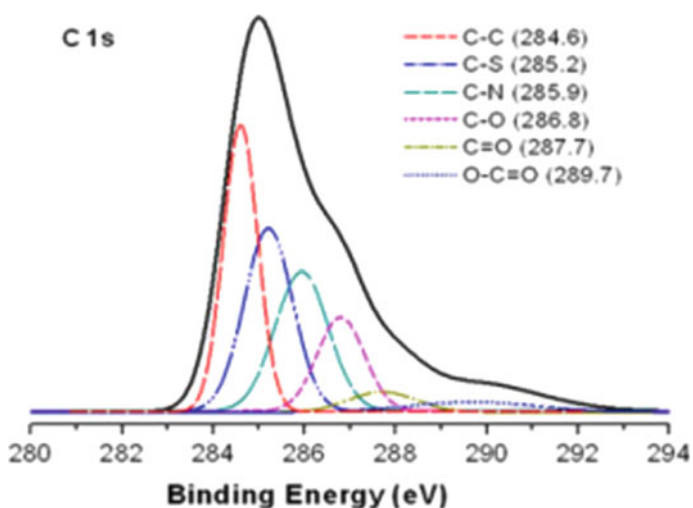


Fig. 14 C 1s XPS spectra of G-PSS: PEDOT composite (Reproduced with permission from ref [41]. © 2011, SCI)

285.2 eV and 285.9 eV are seen which are due to C-S in PSS as well as C-N in hydrazine respectively [82]. Hence, the PEDOT formation was confirmed by 2p S spectra (Fig. 15). Spin-split duplets show peaks for binding energy at 164.2 eV and 165.5 eV in case of S-atoms present in PEDOT, peak due to sulfonic acid ($\text{SO}_3\text{-H}^+$) group arise at 168.6 eV [41].

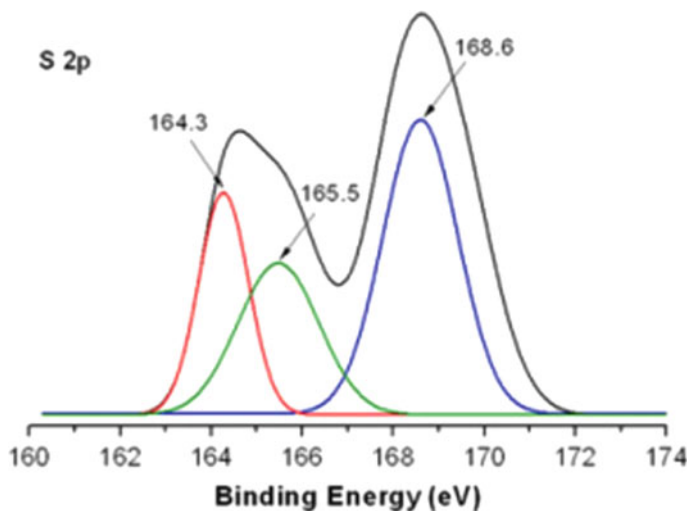
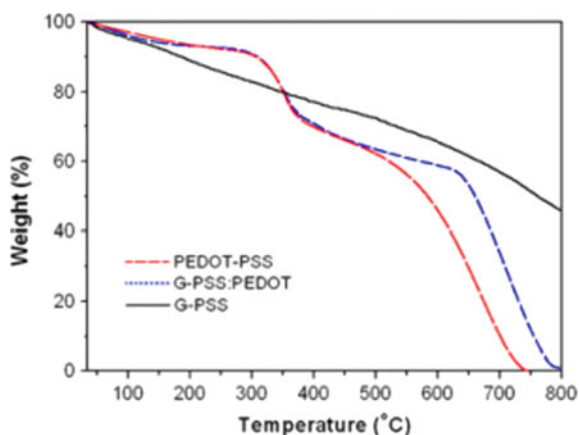


Fig. 15 S 2p XPS spectra of G-PSS: PEDOT composite (Reproduced with permission from ref [41]. © 2011, SCI)

Fig. 16 TGA spectra of G-PSS, PEDOT: PSS and G-PSS: PEDOT composites obtained at a heating rate of $10\text{ }^{\circ}\text{C min}^{-1}$ under nitrogen (Reproduced with permission from ref [41]. © 2011, SCI)



3.8 Thermogravimetric Analysis

TGA (thermogravimetric analysis) is a type of analysis which contains the measurement of the mass of the given substance over time when the sample is subjected to temperature and atmospheric changes. Consequently, information such as phase transitions, absorption, desorption, adsorption as well as thermal stability is determined. Hence, the thermal stability for the G-PSS: PEDOT hybrids was determined. The TGA data for the G-PSS: PEDOT, PEDOT: PSS and the G-PSS are given in Fig. 16. Both of the above samples contain good thermal stability only up to around $315\text{ }^{\circ}\text{C}$

which is 1st decomposition temperature employed, which also can be employed to the PSS decomposition. Whereas, PEDOT: PSS exhibits a relatively low temperature of 575 °C whereas G-PSS: PEDOT contains the enhanced thermal stability and shows 645 °C of 2nd decomposition temperature employed. Thus, it is clear that thermal stability of G-PSS; PEDOT is higher than PEDOT; PSS, which is due to effective hybridization present between RGO and PEDOT [41].

3.9 Energy Dispersive X-Ray (EDX)

The EDX (energy dispersive x-ray) spectroscopy which is also called EDAX or EDS analysis is actually x-ray technique which is used for the identification of elemental composition of given material. The peaks obtained give identification of each of the individual component of material in its true composition. Consequently, the analysis performed for the GO-MnO₂/hemin and a comparison were done with GO and the rGO/hemin when analyzed under same conditions. The ratio of relative atomic weight for many different samples is given in Table 1 [83].

In terms of iron and manganese peaks, difference in EDX spectra for rGO/hemin and the GO-MnO₂/hemin is shown in Fig. 17. The appearance of a new Mn peak for GO-MnO₂/hemin was expected which was absent in case of rGO/hemin and is in accordance with formation of nanocomposites of GO-MnO₂/hemin as shown in Fig. 17. Similarly, there has been an increase in atomic weight from 1.75 to 2.87 for Fe in rGO/hemin and GO-MnO₂/hemin respectively. The nanoneedle growth of MnO₂ with proper orientation was supported by Mn oxidation in the water-isopropanol system. It was assumed that this process causes exfoliation of sheets of GO [84]. Exfoliation of GO driven by the MnO₂ allows more interaction of hemin with graphene sheets for the formation of GO-MnO₂/hemin, which describes the increase in peaks of Fe in EDX spectra for nanocomposite material [83].

Table 1 %age weightage of the GO for EDX analysis along with GO after its treatment with the hemin for the formation of rGO/hemin and GO-MnO₂/hemin formed by treatment of GO-MnO₂ with hemin (Reproduced with permission from [83]. © 2018, ECS)

Atomic weight percentage (%)	GO	rGO/hemin	GO-MnO ₂ /hemin
C	68.13	70.78	30.40
O	31.70	25.32	41.73
Cl	–	2.15	0.59
Fe	–	1.75	2.87
Mn	–	–	24.41

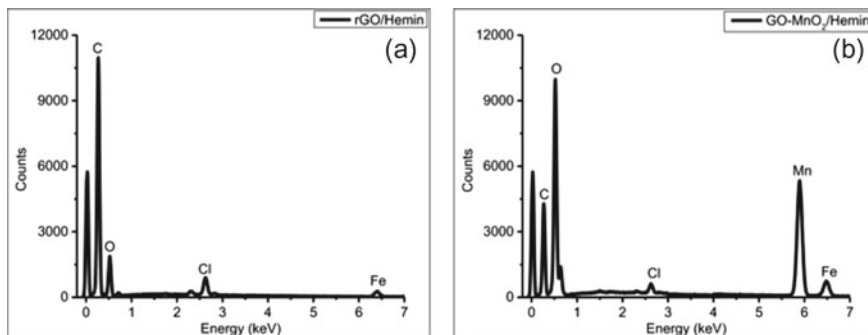


Fig. 17 EDX spectra for the nanocomposites of GO **a** EDX spectra for the rGO/hemin **b** EDX spectra for the GO-MnO₂/hemin (Reproduced with permission from ref [83]. © 2018, ECS)

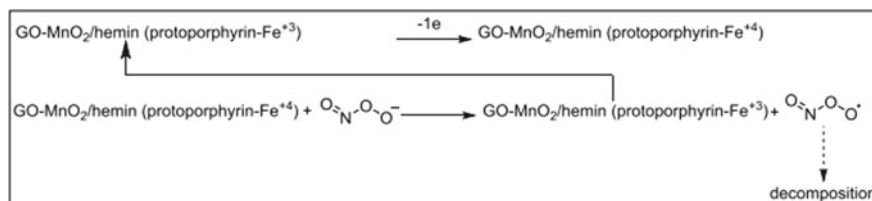


Fig. 18 The proposed mechanism for catalytic oxidation of the PON on the nanocomposites of GO-MnO₂/hemin using GCE interface (Reproduced with permission from ref [83]. © 2018, ECS)

3.10 Cyclic Voltammetry (CV)

Cyclic voltammetry is considered to be the influential technique which is used for investigation of oxidation and reduction processes occurring within the molecular species. The plot of CV is called voltammogram. Graphically, applied potential is shown on x-axis and resulting current on y-axis. CV data can be reported by two conversions i.e., oxidation and reduction [85]. So, electrochemical performance for the modified GCEs by GO-MnO₂/hemin and the rGO/hemin (glassy carbon electrodes) were determined at the same time using phosphate buffers. Now the suspensions for both of the above species with brown–red and brown-black color were deposited on the GCEs (glassy carbon electrodes) which were freshly polished and set them to dry before use. Typical response of these species for volumetric measurements in the presence and absence of the PON (peroxynitrite) was given in Fig. 18. In the phosphate buffer at 7.4 pH the solutions of PON made by 1 μM of SIN-1 stock solution were used. In presence of PON the oxidation peak or rGO/hemin was seen at +1.1 V which indicates catalytic oxidation of the PON supported by hemin present on graphene, the mechanism of which is reported in literature [86, 87]. GO-MnO₂/hemin contain a similar mechanism which is given in Fig. 18 [83].

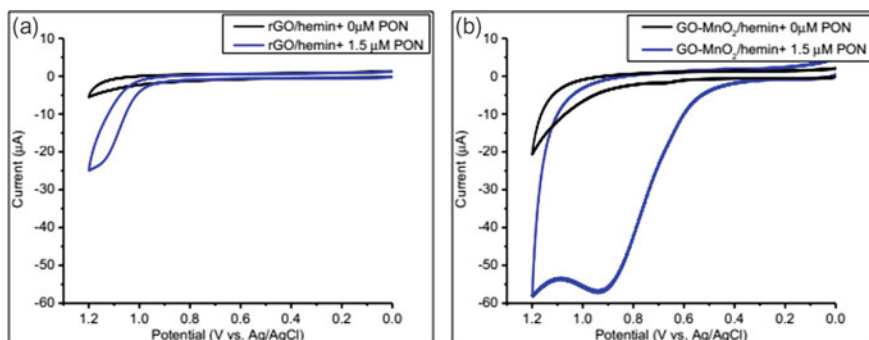


Fig. 19 CV of the GCEs which are modified by GO-MnO₂/hemin and rGO/hemin in the presence and absence of PON prepared by the stock solution of SIN-1 with 1 μM concentration and 7.4 pH. scan rate used for all the voltammograms was 0.1 v/s: **a** voltammetric response of the rGO/hemin in the presence and absence of PON of 1.5 μM **b** voltammetric response of GO-MnO₂/hemin in the presence and absence of PON of 1.5 μM (Reproduced with permission from ref [83]. © 2018, ECS)

In graphene/hemin composite, the integration of MnO₂ transfer the peak for catalytic oxidation of PON toward lower potential of about 200 mV. Therefore, a pronounced peak appears at +0.9 V for catalytic oxidation of PON versus Ag/AgCl as given in Fig. 19. The shift towards the lower positive potential in catalytic peak for MnO₂ shows that incorporation of MnO₂ with GO/hemin helps in lowering the barrier for the electrochemical oxidation of the PON on modified interfaces. Likewise, exfoliation of the graphene oxide supported by nanoparticles of MnO₂ support more incorporation of hemin catalyst with the nanocomposite material. When lower positive potential is applied, results in pronounced response of current [83].

3.11 Amperometric Measurements

Amperometry measurements include application of oxidizing and reducing potential to working electrode with consequent measurement of faradic current produced. During the measurement, optimized value of current and potential is made fixed even with variation of function of the time [88]. For the comparison of electrolytic activity of different materials, amperometric measurement are performed. For this purpose, the aliquot of PON prepared by stock solution of SIN-1 of 1 μM concentration was used. Thus, amperometric measurements were done for the PON modified electrodes along with comparison of rGO/hemin and GO-MnO₂/hemin after every injection for the sensors. Applied potential in both cases was +1 V. Figure 20 represents the response of induced current when PON aliquot was added to the electrochemical cell in the 7.4 pH phosphate buffer. A remarkable large response for the production of current by catalytic oxidation of PON was seen in CV measurements for GO-MnO₂/hemin as compared to rGO/hemin. There occurs a linear response between

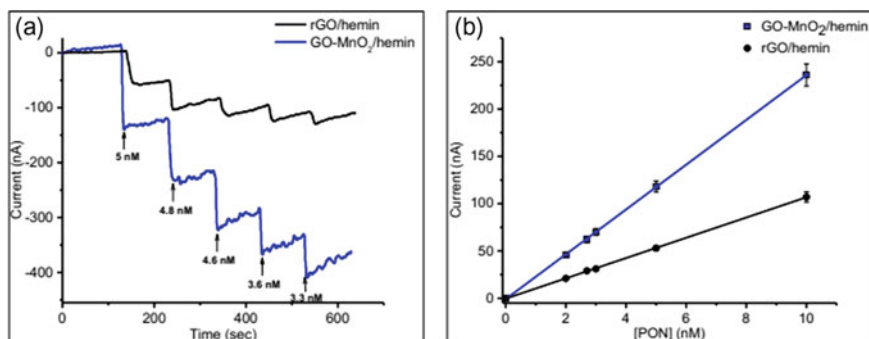


Fig. 20 Representative amperometric responses (nA) (Reproduced with permission from ref [83]. © 2018, ECS)

the added PON and measured current in amperometric measurements in 2.0–10.0 nM range (Fig. 20). Sensitivity of about 23.7 nA/nM in case of GO-MnO₂/hemin was analyzed in contrast with rGO/hemin of ~10 nA/nM. Relative detection limit for good stability of sensors with use of GO-MnO₂/hemin was 2.0 nM [83].

3.12 Photoluminescence Spectroscopy

The photoluminescence spectroscopy is the type of non-destructive spectroscopic technique for investigation of electronic structure for specified material. In this method, we expose light to the sample which absorbs the incident light and transfer excess light for excitation within the material that leads to photoluminescence. Therefore, PL (photoluminescence) spectrum of MWCNTs (multi-walled carbon nanotubes) for the excitation at about 325 nm and account for its structured band at 447 nm. p-p* transitions resulted from excitation of electrons of MWCNT from lower energy state to higher energy state as illustrated by the PL spectrum shown in Fig. 21. Eventually, recombination of the electron–hole at band edge for sp² clusters can be demonstrated by blue fluorescence obtained at shorter wavelengths having small band gap [89]. Band gap for the semiconductors of CNT was 1eV by which we can elucidate their structure at about 447 nm. When PVA (polyvinyl alcohol) is added to the MWCNT, fluorescence improvement was observed [90].

3.13 AC Impedance Spectroscopy

AC (alternating current) impedance spectroscopy is an electrical measurement technique used as a rapid, non-destructive tool for characterizing composite microstructure. It measures the properties of material like resistance and capacitance by applying

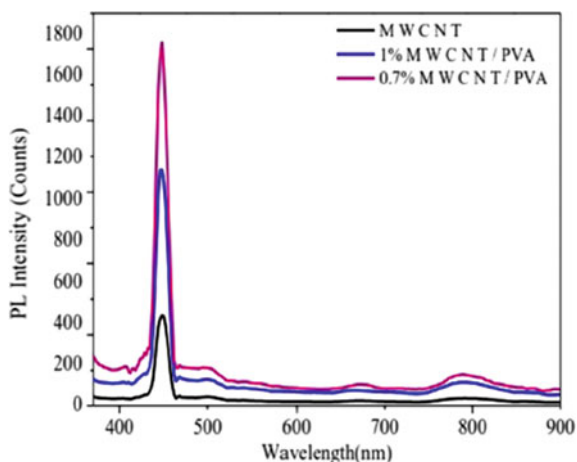


Fig. 21 PL Spectra of MWCNTs/PVA nanocomposites (Reproduced with permission from ref [90]. © 2016, Elsevier)

excitation signal for sinusoidal AC and is widely used in combination with engineered phase for sensing applications [91]. For the explanation of different properties of n-ZnO and reduced graphene oxide incorporated n-ZnO like gas sensing, AC impedance spectroscopy was performed. Both the rGO and the nZnO contain the analyte gas trapping ability and thus contribute to change in conducting properties [92]. Figure 22 illustrates imaginary parts for the impedance of n-ZnO/rGO for their exposure to air as well as different H₂S concentrations at 90 °C. The relaxation frequencies can also be indicated for ZnO/rGO-5 through this figure which can be evaluated by plotting impedance versus frequency (logarithmic frequency) [93]. When H₂S is employed, there is an observed decrease in the imaginary part of Im-(ZnO). With increase of H₂S concentration, additional electron flow was observed with decrease in barrier height. The shifting of peaks towards large frequency range can be related to easy flow of the charge carriers by using AC current [94–96].

4 Energy Harvesting Applications

The principle behind energy harvesting is all about the available environmental energy and its conversion to operable electrical energy. This energy is either used directly, collected or stored in the areas with no any grid power or the use of solar panels or wind turbines if inconvenient. To meet worldwide challenges, applications of energy harvesting have been playing an important part of universal sensor network. Because of the extraordinary application of graphene like low cost, non-toxicity and high flexibility, these are used as promising electrode for use in energy harvesting appliances. These devices are used for applications like self-powering biomedical

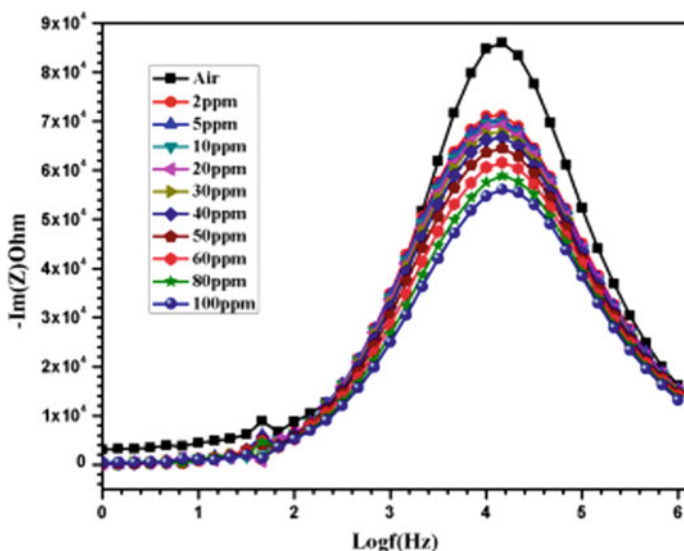


Fig. 22 Imaginary part of impedance for the n-ZnO/rGO-5 when exposed to the air along with H₂S gas with 2–100 ppm concentration at 90 °C (Reproduced with permission from ref [93]. © 2019, ACS)

sensors, portable electronic devices and sustainable environmental monitors, because of their ability to build a battery with long lifetime and development of a self-powered system [97].

4.1 Graphene-Based Flexible Logic Devices

In electronics, the promising applications of graphene are because of their large surface area of about $2630 \text{ m}^2\text{g}^{-1}$ along with capacity to accelerate transfer of holes and electrons along their 2D (2-dimensional) surface. Therefore, there is great importance of research for energy harvesting applications. An important example is nanogenerator which is used for conversion of mechanical energy into electrical energy. Logic devices which are flexible and stretchable, can maintain the apparent applications of bio-integrated and wearable electronics. Many efforts are being done for the development of such devices containing electrode materials which are oxide based, CNTs or polymer based [97–99]. However, even now after many years of intensive work, there are several challenges present regarding to the inherent electrical or mechanical weaknesses which are increasing problems due to its closeness to current fabrication technology. However, graphene also offers magnificent value for Young's modulus because of strong bonding of atoms along with mechanical flexibility, providing superlative electrical properties [100]. The electronic devices which contain stretchability, flexibility and conformal properties are best fit for this

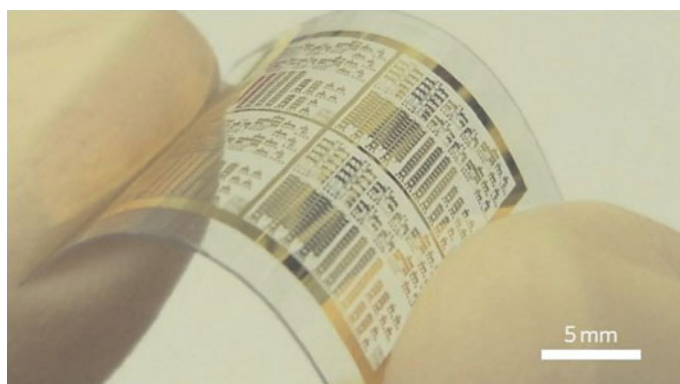


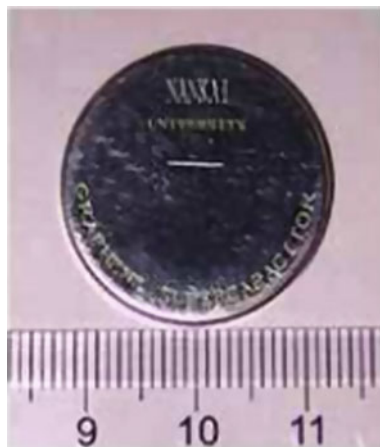
Fig. 23 Device fabrication on flexible and transparent PEN. (Reproduced with permission from ref [101]. © 2011, Macmillan Publisher Ltd)

purpose. Moreover, graphene with 2D nature provides distinctive advantages which are comparable with their fabrication methods. These exceptional advantages make graphene a favourable material for the stretchable or flexible electronics. The effective devices fabricated on a flexible and transparent PEN has been shown in Fig. 23.

4.2 Solar Energy Harvesting and Photocatalysis

There are two major challenges regarding the development of energy harvesting methods and protection of the environment. The possible solution is the conversion of solar energy into fuel or the electricity. For the best utilization of solar energy, three major processes containing ordered charge separation, maximum absorption of photons and the constructive use of separated charges. This major issue regarding energy harvesting needs the use of remarkable procedures in different environmental conditions. Hence, recent researches contain designing devices to concentrate the solar energy along with the improved understanding of the photovoltaic modules. If we increase the intensity of solar light, the response of photovoltaic devices can be improved. Especially, the important fields in utilization of solar energy are production of H_2 by water splitting, the conversion and storage of CO_2 operated through solar energy, development of solar cells which are sensitized to dyes, photocatalytic treatment of gas and waste water and the application of nanostructured material [102].

Fig. 24 An optical image of an industry-grade coin-shaped graphene-based supercapacitor device (Reproduced with permission from ref [103]. © 2009, ACS)



4.3 Supercapacitors

Supercapacitors, also known as the ultracapacitors or the ECs (electrochemical capacitors) form a unique energy storage system possessing environment friendly properties along with its low cost. It contains the advantage of easy storage and release of energy with a higher rate than that attainable with other batteries that are used for the purpose of energy storage. The energy density of these supercapacitors is greater than traditional dielectric capacitors. They can balance the high demand of energy by replacement of batteries for energy harvesting application. Since 1957, when General Electric established the practical application of electrochemical capacitors for the purpose of energy storage, supercapacitors with large reliability and small load cycles are regarded to be ideal along with sources for energy recapturing by forklifts, electrical vehicles and the load cranes [103]. Figure 24 shows the optical image of a industry grade coin-shaped graphene-based supercapacitor device.

4.4 Photovoltaic and Photoelectrochemical Devices

The photovoltaic and the photoelectrochemical devices based on graphene and its composites have notable applications for optical and electronic properties for production of electricity. Though, pure graphene was firstly presented as the transparent electrode material as applications in solar cells and these are turned out as successful electrode material for applications in photovoltaic and also the photoelectrochemical devices [104]. Nanocomposites of graphene give possible conductive electrodes to the ITO (indium tin oxide) porous films and sheets of pure graphene in the photovoltaic cells along with photoelectrochemical devices [105]. In this regard, sulphur particles are incorporated in graphene to be used in Li-S batteries as illustrated in Fig. 25.

Fig. 25 Wrapped S-particles (in graphene) for their use in Li-S batteries (Reproduced with permission from ref [111]. © 2011, ACS)



4.5 Electrochemical Energy Devices

4.5.1 Li-ion Batteries and Li-Batteries

The electrode material for the Li-ion batteries is provided by graphene due to its slight weight, greater surface area and the high conductivity [106]. Nanocomposites of graphene contain remarkable potential for many applications like enhancing cycling stability, rate performance and the capacitance in the LIBs (lithium-ion batteries) [107–110]. The nanocomposites of graphene with S, Si, metal oxides and the complex compounds are used as electrodes in LIBs. Graphene presence improves the performance of LIBs like Li-S batteries [111]. Graphene based nanocomposites have a high specific capacity of 900 mAhg^{-1} , great rate capability and cycling stability [108]. Graphene forms a porous structure along with a conductive pathway for easy diffusion of Li-ions. As formed hybrid film contains properties like high-rate capability along with cycling stability by having 496 mAhg^{-1} of specific capacity at about 100 mAhg^{-1} after about 40 cycles [109].

Beside of their use in Li-ion batteries, nanocomposites of graphene can also be directly used in LIBa or Li-S batteries [111–114]; and they have proven to be as excellent material for formation of cathode in rechargeable LIBs [111] (Fig. 25).

4.5.2 Na-ion Batteries

Recently, the Na-ion batteries has captivated interest researchers to use as energy storing devices due to its properties like inexpensive, environment friendly and most importantly its abundance on earth crust as it is 6th most copious element in earth crust [115–118]. As in Fig. 26 by applying charge and discharge current, there occurs back and forth movement of Na^+ between cathode and anode [119]. The ionic flow is managed by electronic movement from the circuit. Many materials can be used for the formation of electrode in Na-ion batteries like hard carbon, graphitic carbon, alloys of Na like P, Sn, Sb and Sn etc. along with some of the conversion materials like transition metal sulfide and oxide as the anode material and pyrophosphates, layered oxides and polyanionic phosphates ad the cathode material [116–118]. The organic materials are proven to be best suitable for the Na-ion batteries along with environment friendliness [120]. However, researches are being made for the selection

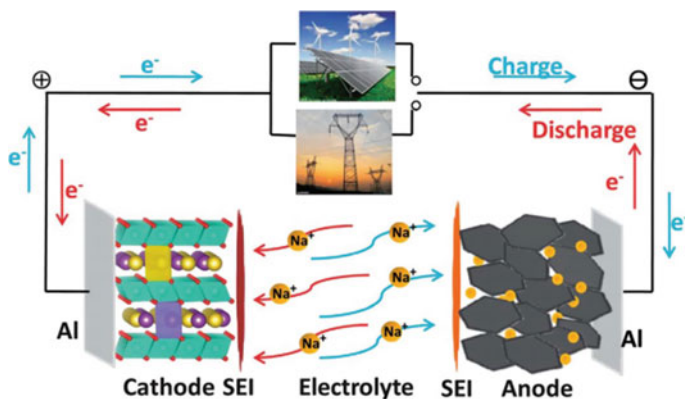


Fig. 26 Schematic diagram representing the Na-ion battery of rocking chair type with their working principle (Reproduced with permission from ref [119]. © 2013, RSC)

of suitable material in Na batteries. Due to the greater size of Na as compared to Li, limits the availability of the host materials [121].

4.5.3 Zn–Air Batteries

In the case of these batteries, the alkaline liquid electrolyte produces charge by mixing Zn with atmospheric O_2 (Fig. 27) [122]. The capacity of charge produced by Zn-air batteries is five times higher than Li-ion batteries. The capacity of charge produced by Zn-air batteries is five times higher than Li-ion batteries. Zn-air batteries are lighter, durable, safer and cheaper than that of Li-ion batteries with theoretical energy density of the order of 1086 WhKg^{-1} . Furthermore, many challenges are present in these batteries like formation of carbonates in air electrodes, small cell voltage as well as the slow-kinetic of the OER (oxygen evolution reaction) and ORR (oxygen reduction reaction). For the production of efficient and bifunctional batteries for OER and ORR processes, advanced researches are being done [123–127]. Nanosheets of graphene containing large surface area can present substrate for the growth of functional nanomaterials for the achievement of Zn-air batteries with high performance. In fact, there are advanced nanomaterials of graphene with bifunctional air-breathing cathode that perform efficient electrocatalytic activity that can reduce overpotential along with increase in cyclic stability of the rechargeable Zn-air batteries [128].

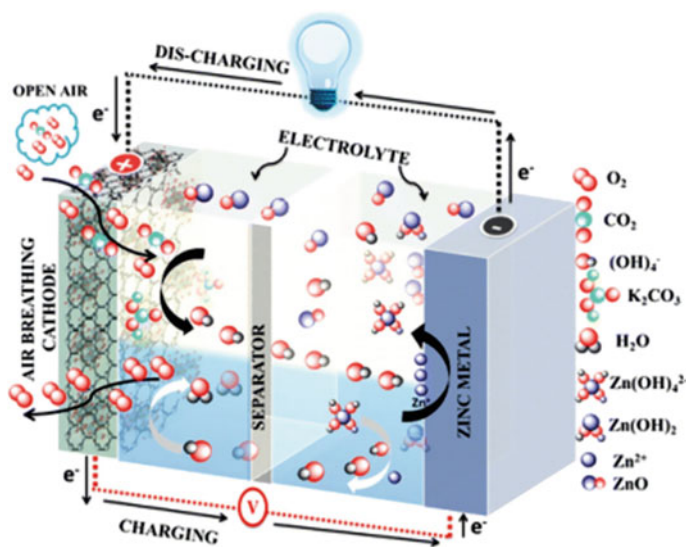


Fig. 27 Schematic diagram showing operation of the rechargeable aprotic Zn-air battery (Reproduced with permission from ref [122]. © 2014, ACS)

4.6 Photocatalytic Hydrogen Generation

Hydrogen is considered to be a type of clean and environment friendly fuel. By applying suitable photocatalyst, photocatalytic hydrogen evolution along with solar energy harvesting was regarded as a clean and efficient way for production of energy from hydrogen by using it as fuel [129, 130]. Many of the semiconductor photocatalysts are reported that are used for H_2 production from the H_2O [131, 132]. Many efforts are made for the utilization of nanocomposites of graphene for production of photocatalytic hydrogen. In this regard, activity of photocatalysts of graphene can be enhanced by incorporation with noble metals which are then used for production of photocatalytic hydrogen.

However, in early work, there was limited formation of H_2 -pairs on sheets of graphite due to its hindered adsorption on graphite surface [133], photocatalysts based on graphene can produce photocatalytic hydrogen on their surface. This is possible because of the accumulation of photogenerated electrons on the graphene surface. Therefore, C-atoms present on graphene sheets can reduce H^+ to H_2 by the use of electrons produced during photocatalytic reaction. For the production of H_2 from water, graphite oxide is proven to be the best catalyst because of the presence of suitable levels for oxidation to occur [132].

5 Summary and Outlook

There is increasing energy demands due to the increasing population of the world due to increased power consumption which is predicted to become double in coming few decades. Hence, there is a need for researchers and scientists to advance clean, sustainable and renewable energy technology, they can meet the growing challenges and demands of energy economically and should be environment friendly. [134–138]. The extensive use of the carbon fuels and their unfortunate environmental effects pushed this world in a paragon where there is need for the application of green methods and systems. Many of the environmental issues including acid rain and global warming are due to the unmediated response of excessive use of fossil fuels. The nanocomposites are based on graphene containing appreciable growth in the technology due to its applications. The use of H_2 as energy source is favourable due to its negligible release to the environment [126, 139, 140]. Along with many other materials, 2D carbon containing graphene is regarded as favourable material for storage of hydrogen because of its properties like lightweight, chemical stability, large surface area and the pronounced onboard reversibility [141].

For the production of the photocatalytic hydrogen, the photocatalysts based on graphene are demonstrated as favourable photocatalytic materials. In this regard, many researches have worked to prove the use of photocatalytic graphene-based materials for designing the procedure to produce photocatalytic H_2 . Presence of graphene has proven to be important in these materials for hydrogen production [129]. The effectiveness of the multicomponent photocatalysts based on graphene in the photocatalytic reactions is proven to be effective by recent results [131]. The effective charge distribution in different energy levels in multicomponent nanocomposites can be facilitated by adjusting band gap in energy levels of constituent materials. Significant improvement in photocatalysis can be achieved by optimal selection of shape, size and the composition of the multicomponent nanocomposites based on graphene. For designing and developing the photocatalytic material containing high performance, the best solution is the effective transfer of electron between the interface. Efforts are being made for the development of controlled and cost-effective methods to fabricate the 3D framework and its transformation along with development of the graphene doped with heteroatoms for the practical applications [142].

However, there are few challenges to be managed in order to manifest the capability of nanocomposites based on graphene regarding its applications, cost and synthetic methods. One of the main challenges is production of graphene and its composites on a large scale, which comprises enormous effects. Some of the challenges present are: (i) how we can prevent the formation of graphene clusters in matrix, (ii) how we can control most defects on the surface; and (iii) how we can tune application-based characteristics. Anyhow, there are many techniques to produce graphene, although few methods have been reported for commercialization of the energy storage appliances of graphene. To address these challenges, new methods and setups are needed for improvement of performance and properties of the graphene [143].

Their applications as fuel-cell batteries, supercapacitors and catalysts have been acknowledged with great exception during past few decades [136–138]. Certainly, the utilization of graphene-based composites in above mentioned applications is a new attempt presenting that research efforts in future will be profound. One challenge is the maintenance of the outstanding physical properties of the graphene for the synthesis of the nanocomposites [28]. One prediction is the development of elementary route via direct oxidation method of graphene by soft templating method for production of little bit functionalities as to furnish active sites of graphene with the nanoparticles. One important characteristic is that it has no need for composite reduction due to its lower oxidation condition, producing graphene framework with lesser defects [144].

The development in the field of hybrids and nanocomposites of graphene is notable. However, significant work is to be done in the field where they show applications as electrochemical devices and catalysts [145]. However, new probabilities are opened for utilization and better understanding of the graphene to overcome the knowledge gap [146]. Still, for the understanding of the fundamental application of the composites, significant attention is still needed.

References

1. Lee, C.-G., Park, S., Ruoff, R.S., Dodabalapur, A.: Integration of reduced graphene oxide into organic field-effect transistors as conducting electrodes and as a metal modification layer. *Appl. Phys. Lett.* **95**(2), 188 (2009)
2. Liao, K.-H., Kobayashi, S., Kim, H., Abdala, A.A., Macosko, C.W.: Influence of functionalized graphene sheets on modulus and glass transition of PMMA. *Macromolecules* **47**(21), 7674–7676 (2014)
3. Guo, C.X., Yang, H.B., Sheng, Z.M., Lu, Z.S., Song, Q.L., Li, C.M.: Layered graphene/quantum dots for photovoltaic devices. *Angew. Chem. Int. Ed.* **49**(17), 3014–3017 (2010)
4. Pletikosić, I., et al.: Dirac cones and minigaps for graphene on Ir (111). *Phys. Rev. Lett.* **102**(5), 056808 (2009)
5. Tang, L., Wang, Y., Li, Y., Feng, H., Lu, J., Li, J.: Preparation, structure and electrochemical properties of graphene modified electrode. *Adv. Funct. Mater.* **19**, 2782–2789 (2009)
6. Du, X., Skachko, I., Barker, A., Andrei, E.Y.: Approaching ballistic transport in suspended graphene. *Nat. Nanotechnol.* **3**(8), 491–495 (2008)
7. Huang, X., et al.: Graphene-based materials: synthesis, characterization, properties, and applications. *Small* **7**(14), 1876–1902 (2011)
8. Zhu, Y., et al.: Graphene and graphene oxide: synthesis, properties, and applications. *Adv. Mater.* **22**(35), 3906–3924 (2010)
9. Stankovich, S., et al.: Graphene-based composite materials. *Nature* **442**(7100), 282–286 (2006)
10. Novoselov, K.S., Geim, A.: The rise of graphene. *Nat. Mater.* **6**(3), 183–191 (2007)
11. Xu, C., Wang, X., Zhu, J.: Graphene–metal particle nanocomposites. *J. Phys. Chem. C* **112**(50), 19841–19845 (2008)
12. Geim, A.K., Novoselov, K.S.: The rise of graphene. *Nat. Mater.* **6**, 183–191 (2007)
13. Kim, H., Abdala, A.A., Macosko, C.W.: Graphene/polymer nanocomposites. *Macromolecules* **43**(16), 6515–6530 (2010)

14. Wu, S., Yin, Z., He, Q., Lu, G., Zhou, X., Zhang, H.: Electrochemical deposition of Cl-doped n-type Cu₂O on reduced graphene oxide electrodes. *J. Mater. Chem.* **21**(10), 3467–3470 (2011)
15. Schwierz, F.: Graphene transistors. *Nat. Nanotechnol.* **5**(7), 487 (2010)
16. Verdejo, R., Bernal, M.M., Romasanta, L.J., Lopez-Manchado, M.A.: Graphene filled polymer nanocomposites. *J. Mater. Chem.* **21**(10), 3301–3310 (2011)
17. Bortz, D.R., Heras, E.G., Martin-Gullon, I.: Impressive fatigue life and fracture toughness improvements in graphene oxide/epoxy composites. *Macromolecules* **45**(1), 238–245 (2012)
18. Yin, Z., et al.: Electrochemical deposition of ZnO nanorods on transparent reduced graphene oxide electrodes for hybrid solar cells. *Small* **6**(2), 307–312 (2010)
19. Shen, J., Shi, M., Yan, B., Ma, H., Li, N., Ye, M.: One-pot hydrothermal synthesis of Ag-reduced graphene oxide composite with ionic liquid. *J. Mater. Chem.* **21**(21), 7795–7801 (2011)
20. Shi, Y., et al.: Graphene wrapped LiFePO₄/C composites as cathode materials for Li-ion batteries with enhanced rate capability. *J. Mater. Chem.* **22**(32), 16465–16470 (2012)
21. Zhang, H., Lv, X., Li, Y., Wang, Y., Li, J.: P25-graphene composite as a high performance photocatalyst. *ACS Nano* **4**(1), 380–386 (2010)
22. Novoselov, K., Mishchenko, A., Carvalho, A., Neto, A.C.: 2D materials and van der Waals heterostructures. *Science* **353**(6298), aac9439 (2016)
23. Cao, A., et al.: A facile one-step method to produce graphene–CdS quantum dot nanocomposites as promising optoelectronic materials. *Adv. Mater.* **22**(1), 103–106 (2010)
24. Zhang, W., et al.: A strategy for producing pure single-layer graphene sheets based on a confined self-assembly approach. *Angew. Chem.* **121**(32), 5978–5982 (2009)
25. López, V., et al.: Chemical vapor deposition repair of graphene oxide: a route to highly-conductive graphene monolayers. *Adv. Mater.* **21**(46), 4683–4686 (2009)
26. Li, D., Müller, M.B., Gilje, S., Kaner, R.B., Wallace, G.G.: Processable aqueous dispersions of graphene nanosheets. *Nat. Nanotechnol.* **3**(2), 101–105 (2008)
27. Xu, C., Wang, X., Zhu, J., Yang, X., Lu, L.: Deposition of Co₃O₄ nanoparticles onto exfoliated graphite oxide sheets. *J. Mater. Chem.* **18**(46), 5625–5629 (2008)
28. Boukhalov, D.W., Katsnelson, M.I.: Modeling of graphite oxide. *J. Am. Chem. Soc.* **130**(32), 10697–10701 (2008)
29. Verma, D., Goh, K.L.: Functionalized graphene-based nanocomposites for energy applications. In: *Functionalized Graphene Nanocomposites and their Derivatives*, pp. 219–243. Elsevier (2019)
30. Niu, L., Coleman, J.N., Zhang, H., Shin, H., Chowalla, M., Zheng, Z.: Production of two-dimensional nanomaterials via liquid-based direct exfoliation. *Small* **12**(3), 272–293 (2016)
31. Ciesielski, A., Samori, P.: Graphene via sonication assisted liquid-phase exfoliation. *Chem. Soc. Rev.* **43**(1), 381–398 (2014)
32. Hernandez, Y., et al.: High-yield production of graphene by liquid-phase exfoliation of graphite. *Nat. Nanotechnol.* **3**(9), 563–568 (2008)
33. Raccichini, R., Varzi, A., Passerini, S., Scrosati, B.: The role of graphene for electrochemical energy storage. *Nat. Mater.* **14**(3), 271–279 (2015)
34. Abdelkader, A., Cooper, A., Dryfe, R., Kinloch, I.: How to get between the sheets: a review of recent works on the electrochemical exfoliation of graphene materials from bulk graphite. *Nanoscale* **7**(16), 6944–6956 (2015)
35. Ambrosi, A., Pumera, M.: Electrochemically exfoliated graphene and graphene oxide for energy storage and electrochemistry applications. *Chem.–Eur. J.* **22**(1), 153–159 (2016)
36. Yu, G., et al.: Solution-processed graphene/MnO₂ nanostructured textiles for high-performance electrochemical capacitors. *Nano Lett.* **11**(7), 2905–2911 (2011)
37. Lewandowska, M., Krawczyńska, A.T., Kulczyk, M., Kurzydowski, K.J.: Structure and properties of nano-sized Eurofer 97 steel obtained by hydrostatic extrusion. *J. Nucl. Mater.* **386**, 499–502 (2009)
38. Bekyarova, E., et al.: Electronic properties of single-walled carbon nanotube networks. *J. Am. Chem. Soc.* **127**(16), 5990–5995 (2005)

39. Baskaran, D., Mays, J.W., Bratcher, M.S.: Noncovalent and nonspecific molecular interactions of polymers with multiwalled carbon nanotubes. *Chem. Mater.* **17**(13), 3389–3397 (2005)
40. Haghseresht, F., Finnerty, J., Nouri, S., Lu, G.: Adsorption of aromatic compounds onto activated carbons: effects of the orientation of the adsorbates. *Langmuir* **18**(16), 6193–6200 (2002)
41. Trang, L.K.H., Thanh Tung, T., Young Kim, T., Yang, W.S., Kim, H., Suh, K.S.: Preparation and characterization of graphene composites with conducting polymers. *Polym. Int.* **61**(1), 93–98 (2012)
42. Zhou, C., Szpunar, J.A., Cui, X.: Synthesis of Ni/graphene nanocomposite for hydrogen storage. *ACS Appl. Mater. Interfaces* **8**(24), 15232–15241 (2016)
43. Stankovich, S., et al.: Synthesis of graphene-based nanosheets via chemical reduction of exfoliated graphite oxide. *Carbon* **45**(7), 1558–1565 (2007)
44. Xu, Y., et al.: A graphene hybrid material covalently functionalized with porphyrin: synthesis and optical limiting property. *Adv. Mater.* **21**(12), 1275–1279 (2009)
45. Yang, H., Shan, C., Li, F., Han, D., Zhang, Q., Niu, L.: Covalent functionalization of poly-disperse chemically-converted graphene sheets with amine-terminated ionic liquid. *Chem. Commun.* **26**, 3880–3882 (2009)
46. Putz, K.W., Compton, O.C., Segar, C., An, Z., Nguyen, S.T., Brinson, L.C.: Evolution of order during vacuum-assisted self-assembly of graphene oxide paper and associated polymer nanocomposites. *ACS Nano* **5**(8), 6601–6609 (2011)
47. Liu, L.-H., Lerner, M.M., Yan, M.: Derivatization of pristine graphene with well-defined chemical functionalities. *Nano Lett.* **10**(9), 3754–3756 (2010)
48. Si, Y., Samulski, E.T.: Synthesis of water soluble graphene. *Nano Lett.* **8**(6), 1679–1682 (2008)
49. Englert, et al.: Covalent bulk functionalization of graphene. *Nat. Chem.* **3**(4), 279–286 (2011)
50. Liu, L.-H., Yan, M.: Simple method for the covalent immobilization of graphene. *Nano Lett.* **9**(9), 3375–3378 (2009)
51. Fang, M., Wang, K., Lu, H., Yang, Y., Nutt, S.: Covalent polymer functionalization of graphene nanosheets and mechanical properties of composites. *J. Mater. Chem.* **19**(38), 7098–7105 (2009)
52. Fang, M., Wang, K., Lu, H., Yang, Y., Nutt, S.: Single-layer graphene nanosheets with controlled grafting of polymer chains. *J. Mater. Chem.* **20**(10), 1982–1992 (2010)
53. Chang, H., Wu, H.: Graphene-based nanocomposites: preparation, functionalization, and energy and environmental applications. *Energy Environ. Sci.* **6**(12), 3483–3507 (2013)
54. Moon, G.-h, Park, Y., Kim, W., Choi, W.: Photochemical loading of metal nanoparticles on reduced graphene oxide sheets using phosphotungstate. *Carbon* **49**(11), 3454–3462 (2011)
55. Ng, Y.H., Iwase, A., Bell, N.J., Kudo, A., Amal, R.: Semiconductor/reduced graphene oxide nanocomposites derived from photocatalytic reactions. *Catal. Today* **164**(1), 353–357 (2011)
56. Pasricha, R., et al.: Directed nanoparticle reduction on graphene. *Mater. Today* **15**(3), 118–125 (2012)
57. Zhang, Y., Yuan, X., Wang, Y., Chen, Y.: One-pot photochemical synthesis of graphene composites uniformly deposited with silver nanoparticles and their high catalytic activity towards the reduction of 2-nitroaniline. *J. Mater. Chem.* **22**(15), 7245–7251 (2012)
58. Tjoa, V., Chua, J., Pramana, S.S., Wei, J., Mhaisalkar, S.G., Mathews, N.: Facile photochemical synthesis of graphene-Pt nanoparticle composite for counter electrode in dye sensitized solar cell. *ACS Appl. Mater. Interfaces* **4**(7), 3447–3452 (2012)
59. Xu, F., Sun, Y., Zhang, Y., Shi, Y., Wen, Z., Li, Z.: Graphene–Pt nanocomposite for nonenzymatic detection of hydrogen peroxide with enhanced sensitivity. *Electrochem. Commun.* **13**(10), 1131–1134 (2011)
60. Chen, J., Zheng, X., Wang, H., Zheng, W.: Graphene oxide-Ag nanocomposite: In situ photochemical synthesis and application as a surface-enhanced Raman scattering substrate. *Thin Solid Films* **520**(1), 179–185 (2011)
61. Anandhan, S., Bandyopadhyay, S.: Polymer nanocomposites: from synthesis to applications. *Nanocompos. Polym. Anal. Methods* **1**, 1–28 (2011)

62. Akhrame, M.O., Fatoki, O.S., Opeolu, B.O., Olorunfemi, D.I., Oputu, O.U.: Polymeric nanocomposites (PNCs) for wastewater remediation: an overview. *Polym.-Plast. Technol. Eng.* **57**(17), 1801–1827 (2018)
63. Caro, C.: *UV/VIS Spectrophotometry—Fundamentals and Application*. Mettler-Toledo Publication (2015)
64. Moecher, D.P.: Characterization and identification of mineral unknowns: a mineralogy term project. *J. Geosci. Educ.* **52**(1), 5–9 (2004)
65. Argast, A., Tennis, C.F., III.: A web resource for the study of alkali feldspars and perthitic textures using light microscopy, scanning electron microscopy and energy dispersive X-Ray spectroscopy. *J. Geosci. Educ.* **52**(3), 213–217 (2004)
66. Williams, D.B., Carter, C.B.: *Transmission Electron Microscopy*. Springer, Boston (1996)
67. Hirsch, P.B., Howie, A., Nicholson, R.B., Pashley, D.W., Whelan, M.J.: Electron microscopy of thin crystals. *Phys. Today* **19**(10), 3 (1966)
68. Wang, X., Chen, S.: Graphene-based nanocomposites. In: *Physics and Applications of Graphene-Experiments*, pp. 135–168 (2011)
69. Xu, C., Wang, X.: Fabrication of flexible metal-nanoparticle films using graphene oxide sheets as substrates. *Small* **5**(19), 2212–2217 (2009)
70. Dikin, D.A., et al.: Preparation and characterization of graphene oxide paper. *Nature* **448**(7152), 457–460 (2007)
71. Chong, S.W., Lai, C.W., Hamid, S.B.A.: Green preparation of reduced graphene oxide using a natural reducing agent. *Ceram. Int.* **41**(8), 9505–9513 (2015)
72. Baloyi, S., Ngqalakwezi, A., Nkazi, D., Ntho, T.: Investigation of graphene-based nanocomposite for hydrogen storage. *IOP Conf. Ser. Mater. Sci. Eng.* **655**, 012029 (2019)
73. Gardiner, D.J.: Introduction to Raman scattering. In: *Practical Raman Spectroscopy*, pp. 1–12. Springer, Heidelberg (1989)
74. Prusty, K., Barik, S., Swain, S.K.: A correlation between the graphene surface area, functional groups, defects, and porosity on the performance of the nanocomposites. In: *Functionalized Graphene Nanocomposites and their Derivatives*, pp. 265–283. Elsevier (2019)
75. Han, Y., Lu, Y.: Characterization and electrical properties of conductive polymer/colloidal graphite oxide nanocomposites. *Compos. Sci. Technol.* **69**(7–8), 1231–1237 (2009)
76. Xu, Y., et al.: A hybrid material of graphene and poly (3, 4-ethyldioxythiophene) with high conductivity, flexibility, and transparency. *Nano Res.* **2**(4), 343–348 (2009)
77. McAloney, R.A., Sinyor, M., Dudnik, V., Goh, M.C.: Atomic force microscopy studies of salt effects on polyelectrolyte multilayer film morphology. *Langmuir* **17**(21), 6655–6663 (2001)
78. Schütte, M., Kurth, D.G., Linford, M.R., Cölfen, H., Möhwald, H.: Metallosupramolecular thin polyelectrolyte films. *Angew. Chem. Int. Ed.* **37**(20), 2891–2893 (1998)
79. Cutler, C.A., Bouguettaya, M., Kang, T.-S., Reynolds, J.R.: Alkoxysulfonate-functionalized PEDOT polyelectrolyte multilayer films: electrochromic and hole transport materials. *Macromolecules* **38**(8), 3068–3074 (2005)
80. Andrade, J.D.: X-ray photoelectron spectroscopy (XPS). In: *Surface and Interfacial Aspects of Biomedical Polymers*, pp. 105–195. Springer, Boston (1985)
81. Paredes, J., Villar-Rodil, S., Martínez-Alonso, A., Tascon, J.: Graphene oxide dispersions in organic solvents. *Langmuir* **24**(19), 10560–10564 (2008)
82. Stankovich, S., Piner, R.D., Chen, X., Wu, N., Nguyen, S.T., Ruoff, R.S.: Stable aqueous dispersions of graphitic nanoplatelets via the reduction of exfoliated graphite oxide in the presence of poly (sodium 4-styrenesulfonate). *J. Mater. Chem.* **16**(2), 155–158 (2006)
83. Kalil, H., Maher, S., Bose, T., Bayachou, M.: Manganese oxide/hemin-functionalized graphene as a platform for peroxynitrite sensing. *J. Electrochem. Soc.* **165**(12), G3133 (2018)
84. Hummers, W.S., Jr., Offeman, R.E.: Preparation of graphitic oxide. *J. Am. Chem. Soc.* **80**(6), 1339–1339 (1958)
85. Elgrishi, N., Rountree, K.J., McCarthy, B.D., Rountree, E.S., Eisenhart, T.T., Dempsey, J.L.: A practical beginner's guide to cyclic voltammetry. *J. Chem. Educ.* **95**(2), 197–206 (2018)
86. Oprea, R., et al.: Peroxynitrite activity of hemin-functionalized reduced graphene oxide. *Analyst* **138**(15), 4345–4352 (2013)

87. Peteu, S.F., Bose, T., Bayachou, M.: Polymerized hemin as an electrocatalytic platform for peroxyxynitrite's oxidation and detection. *Anal. Chim. Acta* **780**, 81–88 (2013)
88. Gee, B.: André Marie Ampère (1775–1836). *Phys. Educ.* **5**(6), 359 (1970)
89. Yan-Hong, Y., Run-Cai, M., Jin-Tao, B., Xun, H.: Photoluminescence of multiwalled carbon nanotubes excited at different wavelengths. *Chin. Phys.* **15**(11), 2761 (2006)
90. Goumri, M., Lucas, B., Ratier, B., Baitoul, M.: Electrical and optical properties of reduced graphene oxide and multi-walled carbon nanotubes based nanocomposites: a comparative study. *Opt. Mater.* **60**, 105–113 (2016)
91. Chung, W.-J., Sena, M., Merzlyak, A., Lee, S.-W.: Phages as Tools for Functional Nanomaterials Development (2011)
92. Lee, Y.-M., Huang, C.-M., Chen, H.-W., Yang, H.-W.: Low temperature solution-processed ZnO nanorod arrays with application to liquid ethanol sensors. *Sens. Actuators A Phys.* **189**, 307–312 (2013)
93. Balasubramani, V., Sureshkumar, S., Rao, T.S., Sridhar, T.: Impedance spectroscopy-based reduced graphene oxide-incorporated ZnO composite sensor for H₂S investigations. *ACS Omega* **4**(6), 9976–9982 (2019)
94. Barik, S., Choudhary, R., Mahapatra, P.: Impedance spectroscopy study of Na 1/2 Sm 1/2 TiO₃ ceramic. *Appl. Phys. A* **88**(1), 217–222 (2007)
95. Idrees, M., Nadeem, M., Mehmood, M., Atif, M., Chae, K.H., Hassan, M.: Impedance spectroscopic investigation of delocalization effects of disorder induced by Ni doping in LaFeO₃. *J. Phys. D Appl. Phys.* **44**(10), 105401 (2011)
96. Seitz, M., Hampton, F., Richmond, W.: Influence of chemisorbed oxygen on the AC electrical behaviour of polycrystalline ZnO. In: Additives and Interfaces in Electronic Ceramics Proc Special Conf held at Cincinnati 4–5 May 1982 *Advances in Ceramics* (1982)
97. Jang, S., et al.: Flexible, transparent single-walled carbon nanotube transistors with graphene electrodes. *Nanotechnology* **21**(42), 425201 (2010)
98. Klauk, H., Halik, M., Zschieschang, U., Eder, F., Schmid, G., Dehm, C.: Relationship between molecular structure and electrical performance of oligothiophene organic thin film transistors. *Appl. Phys. Lett.* **82**, 4175–4177 (2003)
99. Nomura, K., Ohta, H., Takagi, A., Kamiya, T., Hirano, M., Hosono, H.: Room-temperature fabrication of transparent flexible thin-film transistors using amorphous oxide semiconductors. *Nature* **432**(7016), 488–492 (2004)
100. Suo, Z., Ma, E., Gleskova, H., Wagner, S.: Mechanics of rollable and foldable film-on-foil electronics. *Appl. Phys. Lett.* **74**(8), 1177–1179 (1999)
101. Sun, D.-m., et al.: Flexible high-performance carbon nanotube integrated circuits. *Nat. Nanotechnol.* **6**(3), 156–161 (2011)
102. Tang, J., Dai, S., Darr, J.A.: Recent developments in solar energy harvesting and photocatalysis. *Int. J. Photoenergy* **2012**, 580746 (2012)
103. Wang, Y., et al.: Supercapacitor devices based on graphene materials. *J. Phys. Chem. C* **113**(30), 13103–13107 (2009)
104. Wu, J., Becerril, H.A., Bao, Z., Liu, Z., Chen, Y., Peumans, P.: Organic solar cells with solution-processed graphene transparent electrodes. *Appl. Phys. Lett.* **92**(26), 237 (2008)
105. Chang, H., Liu, Y., Zhang, H., Li, J.: Pyrenebutyrate-functionalized graphene/poly (3-octylthiophene) nanocomposites based photoelectrochemical cell. *J. Electroanal. Chem.* **656**(1–2), 269–273 (2011)
106. Li, X., et al.: Graphene-on-silicon Schottky junction solar cells. *Adv. Mater.* **22**(25), 2743–2748 (2010)
107. Hu, L.-H., Wu, F.-Y., Lin, C.-T., Khlbystov, A.N., Li, L.-J.: Graphene-modified LiFePO₄ cathode for lithium ion battery beyond theoretical capacity. *Nat. Commun.* **4**(1), 1–7 (2013)
108. Wang, H., et al.: Mn₃O₄– graphene hybrid as a high-capacity anode material for lithium ion batteries. *J. Am. Chem. Soc.* **132**(40), 13978–13980 (2010)
109. Yu, A., Park, H.W., Davies, A., Higgins, D.C., Chen, Z., Xiao, X.: Free-standing layer-by-layer hybrid thin film of graphene-MnO₂ nanotube as anode for lithium ion batteries. *J. Phys. Chem. Lett.* **2**(15), 1855–1860 (2011)

110. Zhou, X., Wang, F., Zhu, Y., Liu, Z.: Graphene modified LiFePO₄ cathode materials for high power lithium ion batteries. *J. Mater. Chem.* **21**(10), 3353–3358 (2011)
111. Wang, H., et al.: Graphene-wrapped sulfur particles as a rechargeable lithium–sulfur battery cathode material with high capacity and cycling stability. *Nano Lett.* **11**(7), 2644–2647 (2011)
112. Cao, Y., et al.: Sandwich-type functionalized graphene sheet-sulfur nanocomposite for rechargeable lithium batteries. *Phys. Chem. Chem. Phys.* **13**(17), 7660–7665 (2011)
113. Ji, L., et al.: Graphene oxide as a sulfur immobilizer in high performance lithium/sulfur cells. *J. Am. Chem. Soc.* **133**(46), 18522–18525 (2011)
114. Wang, J.-Z., Lu, L., Choucair, M., Stride, J.A., Xu, X., Liu, H.-K.: Sulfur-graphene composite for rechargeable lithium batteries. *J. Power Sources* **196**(16), 7030–7034 (2011)
115. Ji, L., et al.: Controlling SEI formation on SnSb-porous carbon nanofibers for improved Na ion storage. *Adv. Mater.* **26**(18), 2901–2908 (2014)
116. Kim, S., Seo, D., Ma, X., Ceder, G., Kang, K.: *Adv. Energy Mater.* **2**, 710 (2013). b) MD Slater, D. Kim, E. Lee, CS Johnson. *Adv. Funct. Mater.* 23:947 2012
117. Kim, S.W., Seo, D.H., Ma, X., Ceder, G., Kang, K.: Electrode materials for rechargeable sodium-ion batteries: potential alternatives to current lithium-ion batteries. *Adv. Energy Mater.* **2**(7), 710–721 (2012)
118. Yabuuchi, N., Kubota, K., Dahbi, M., Komaba, S.: Research development on sodium-ion batteries. *Chem. Rev.* **114**(23), 11636–11682 (2014)
119. Pan, H., Hu, Y.-S., Chen, L.: Room-temperature stationary sodium-ion batteries for large-scale electric energy storage. *Energy Environ. Sci.* **6**(8), 2338–2360 (2013)
120. Wang, L.P., Yu, L., Wang, X., Srinivasan, M., Xu, Z.J.: Recent developments in electrode materials for sodium-ion batteries. *J. Mater. Chem. A* **3**(18), 9353–9378 (2015)
121. Zhou, H., et al.: Outstanding hydrogen evolution reaction catalyzed by porous nickel diselenide electrocatalysts. *Energy Environ. Sci.* **10**(6), 1487–1492 (2017)
122. Prabu, M., Ramakrishnan, P., Nara, H., Momma, T., Osaka, T., Shanmugam, S.: Zinc–air battery: understanding the structure and morphology changes of graphene-supported CoMn₂O₄ bifunctional catalysts under practical rechargeable conditions. *ACS Appl. Mater. Interfaces* **6**(19), 16545–16555 (2014)
123. Lee, D.U., Choi, J.Y., Feng, K., Park, H.W., Chen, Z.: Advanced extremely durable 3D bifunctional air electrodes for rechargeable zinc–air batteries. *Adv. Energy Mater.* **4**(6), 1301389 (2014)
124. Lee, J.S., et al.: Metal–air batteries with high energy density: Li–air versus Zn–air. *Adv. Energy Mater.* **1**(1), 34–50 (2011)
125. Li, L., Manthiram, A.: Long-life, high-voltage acidic Zn–air batteries. *Adv. Energy Mater.* **6**(5), 1502054 (2016)
126. Li, Y., Dai, H.: Recent advances in zinc–air batteries. *Chem. Soc. Rev.* **43**(15), 5257–5275 (2014)
127. Xu, Y., Zhang, Y., Guo, Z., Ren, J., Wang, Y., Peng, H.: Flexible, stretchable, and rechargeable fiber-shaped zinc–air battery based on cross-stacked carbon nanotube sheets. *Angew. Chem.* **127**(51), 15610–15614 (2015)
128. Wang, K., et al.: Dendrite growth in the recharging process of zinc–air batteries. *J. Mater. Chem. A* **3**(45), 22648–22655 (2015)
129. Li, Q., et al.: Highly efficient visible-light-driven photocatalytic hydrogen production of CdS-cluster-decorated graphene nanosheets. *J. Am. Chem. Soc.* **133**(28), 10878–10884 (2011)
130. Maeda, K., Domen, K.: Photocatalytic water splitting: recent progress and future challenges. *J. Phys. Chem. Lett.* **1**(18), 2655–2661 (2010)
131. Xiang, Q., Yu, J., Jaroniec, M.: Enhanced photocatalytic H₂-production activity of graphene-modified titania nanosheets. *Nanoscale* **3**(9), 3670–3678 (2011)
132. Zhang, J., Yu, J., Zhang, Y., Li, Q., Gong, J.R.: Visible light photocatalytic H₂-production activity of CuS/ZnS porous nanosheets based on photoinduced interfacial charge transfer. *Nano Lett.* **11**(11), 4774–4779 (2011)
133. Casolo, S., Løvvik, O.M., Martinazzo, R., Tantardini, G.F.: Understanding adsorption of hydrogen atoms on graphene. *J. Chem. Phys.* **130**(5), 054704 (2009)

134. Chu, S., Majumdar, A.: Opportunities and challenges for a sustainable energy future. *Nature* **488**(7411), 294–303 (2012)
135. Dunn, B., Kamath, H., Tarascon, J.-M.: Electrical energy storage for the grid: a battery of choices. *Science* **334**(6058), 928–935 (2011)
136. Larcher, D., Tarascon, J.-M.: Towards greener and more sustainable batteries for electrical energy storage. *Nat. Chem.* **7**(1), 19–29 (2015)
137. Tarascon, J.-M., Armand, M.: Issues and challenges facing rechargeable lithium batteries. *Nature* **414**, 359–367 (2001)
138. Xu, K.: Electrolytes and interphases in Li-ion batteries and beyond. *Chem. Rev.* **114**(23), 11503–11618 (2014)
139. Schlapbach, L., Züttel, A.: Hydrogen-storage materials for mobile applications. *Nature* **414**, 353–358 (2001)
140. Wagemans, R.W., van Lenthe, J.H., de Jongh, P.E., Van Dillen, A.J., de Jong, K.P.: Hydrogen storage in magnesium clusters: quantum chemical study. *J. Am. Chem. Soc.* **127**(47), 16675–16680 (2005)
141. Chen, M.-L., Park, C.-Y., Choi, J.-G., Oh, W.-C.: Synthesis and characterization of metal (Pt, Pd and Fe)-graphene composites. *J. Korean Ceram. Soc.* **48**(2), 147 (2011)
142. Kumar, N.A., Baek, J.-B.: Doped graphene supercapacitors. *Nanotechnology* **26**(49), 492001 (2015)
143. Lightcap, I.V., Kamat, P.V.: Graphitic design: prospects of graphene-based nanocomposites for solar energy conversion, storage, and sensing. *Acc. Chem. Res.* **46**(10), 2235–2243 (2013)
144. Terrones, M., et al.: Interphases in graphene polymer-based nanocomposites: achievements and challenges. *Adv. Mater.* **23**(44), 5302–5310 (2011)
145. Chen, S., Zhu, J., Wang, X.: One-step synthesis of graphene–cobalt hydroxide nanocomposites and their electrochemical properties. *J. Phys. Chem. C* **114**(27), 11829–11834 (2010)
146. Zhou, M., et al.: Highly conductive porous graphene/ceramic composites for heat transfer and thermal energy storage. *Adv. Func. Mater.* **23**(18), 2263–2269 (2013)

Design of New High Energy Near Field Nanophotonic Materials for Far Field Applications



A. Guillermo Bracamonte

Abstract The aim of this Review of Literature was to discuss and show from the basis of different physics and chemical phenomena to Advanced Research below and beyond of the Nanoscale for Nano-; and Micro-devices design with multiple applications where the Energy signals of different nature were involucrated and transduced. In order to accomplish that it was showed and discussed different properties of Organic, Inorganic, and Hybrids Nanomaterials related with Energy Transfer (**ET**) for different applications from Nano-electronics to switchable Optical, Plasmonics, and Electro activated phenomena as Electromagnetism, Conductivity, Luminescence, Chemiluminescence and Enhanced properties. In order to do that, it was discussed different tuneable phenomena as Plasmonics (**P**) within the near field accompanied with applications in the Far field, as Plasmonic Resonators, Enhanced Plasmonics (**EP**) applied for Metal Enhanced Fluorescence (**MEF**), Fluorescence Resonance Energy Transfer (**FRET**); from where it was transduced and enhanced different types of signals. In addition it was discussed how these phenomena were tuned based on different Nanoplatforms as metallic Core-shell nanoparticles and Nano-cages, Organic Nanocomposites as Supramolecular nanoparticles, polymeric nanoparticles, and organized systems as micelles and vesicles. All the mentioned Nanoarchitectures depending of their compositions permitted variable properties within the near Field and Far filed as Enhanced Luminescence, Energy Transfers, Energy conductions and storage from nm and micrometer to higher lengths. Then, it was discussed different applications; from the fabrication of Lab.-on single particles and Multi-functional Nanostructured surfaces, Photonic surfaces for Nanophotonics to Biophotonics applications; and Nano-circuits for Micro-device fabrications.

Moreover, different experimental approaches and Set-Ups for different Research studies related with all the mentioned fields were showed and discussed as well; as for example Optical Fiber modifications, silica and organic waveguides, and In

A. G. Bracamonte (✉)

Instituto de Investigaciones en Físicoquímica de Córdoba (INFIQC), Departamento de Química Orgánica, Facultad de Ciencias Químicas, Universidad Nacional de Córdoba, Ciudad Universitaria, 5000 Córdoba, Argentina

Departement de Chimie et Centre d'optique, Photonique et Laser (COPL), Université Laval, Québec, QC G1V 06, Canada

© The Author(s), under exclusive license to Springer Nature Switzerland AG 2022

859

A. E. Shalan et al. (eds.), *Advances in Nanocomposite Materials for Environmental and*

Energy Harvesting Applications, Engineering Materials,

https://doi.org/10.1007/978-3-030-94319-6_28

Flow methodologies from Nanofluidics to Microfluidics coupled to different Optical detections.

Keywords Near field Energy Transfer (**NET**) · Plasmonics (**P**) · Enhanced Plasmonics (**EP**) · Optical Resonators (**OR**) · Plasmonic Resonators (**PR**) · Metal Enhanced Fluorescence (MEF) · Micro-devices · Lab-on nanophotonic platforms

List of Abbreviations

AFM	Atomic force microscopy
CD	Circular Dichroism
DEP	Dielectrophoresis
EELS	Electron Energy-Loss Spectroscopy
ET	Energy Transfer
EP	Enhanced Plasmonics
FWM	Four-wave mixing
LLs	Landau levels
LEDs	Light Emitter Devices
LSPR	Localized Surface Plasmon Resonances
MEF_{EF}	Metal Enhanced Fluorescence Enhancement Factor
NET	Near field Energy Transfer
NSOM	Near Field Scanning Optical Microscopy
NIR	Near Infrared Red
OLEDs	Organic Light-Emitting Diodes
OR	Optical Resonators
P	Plasmonics
PLEDs	Plasmonic Light Emitter Devices
MEF	Metal Enhanced Fluorescence
RET	Resonance Energy Transfer
SEM	Scanning Electron Microscopy
STEM	Scanning Transmission Electron Microscope
SMD	Single Molecule Detection
SEF	Surface Enhanced Fluorescence
SERS	Surface Enhanced Raman Spectroscopy
SPR	Surface Plasmon Resonance
TEM	Transmission Electronic Microscopy
UV	Ultra-Violet
FEM	Finite Element Method
FLIM	Fluorescence Lifetime Imaging
FRET	Fluorescence Resonance Energy Transfer

1 Introduction

For the fabrication and design of new Nanomaterials, Metamaterials and Quantum materials with different applications from the Quantum level to the near Field and far Field it should be considered many materials accompanied with tunable properties as well as synthetic pathways in order to develop targeted properties. In this manner it could be mentioned Plasmonics (**P**) [1], Enhanced Plasmonics (**EP**) [2], Semi-conductive and Super-conductive properties [3], Magnetic properties [4], Energy Transfer (**ET**) [5], Fluorescence Resonance Energy Transfer (**FRET**) [6], Metal Enhanced Fluorescence (**MEF**) [7]; Chemiluminescence [8] and Bioluminescence [9]; and metamaterial properties [10] based on variable composition of materials. Then these materials depending of their bottom-up and design joined to different Optical Set-ups variable applications could be developed. From these types of Research works it was generated different technologies at different scales as Nanodevices [11], Microdevices [12], Waveguides [13, 14], and Photonic surfaces [15] Chips, Photonics and Quantum Circuits [16], modified Optical fibers [17] and In Flow methodologies [18]. Then by this manner it could be incorporated within different instrumental approaches for variable Functionalities.

So, for targeted applications from Quantum to the Near and Far Field studies it should be accurately known and controlled the basis of the different phenomena as well as to discover new properties and metaproperties within the High Energy material Field.

In this manner, it should be discussed the power of the different properties and main variables to control them at the different levels.

So, to introduce the different scales focused on Energy, first it was discussed the near Field from the Plasmonics point of view. As it is known the Plasmon is defined as the electronic oscillation of a metallic surface obtained by an accurate excitation along the complete electromagnetic wavelength range depending of the material constitution [19, 20]. These phenomena are produced within shorter nm lengths that can be transduced to longer distances defined as the far Field. In addition these properties are close to the Quantum scale below 1–2 nm intervals.

In this way, within this Research Field at these scales it should be discussed as well the Fabrication and tuning of variable sizes and shapes of Nanoparticles, **EP** based on Nano-arrays [21], **MEF** based on Core-shell Nanoparticles [22], **FRET** coupled to **MEF** [23], and the incorporation of Molecular **ET** and **FRET** in different Nanoplatforms joined to Inorganic materials; where the Molecular **ET** occurs and their energies could be tuned, controlled [24], and harvested [25].

In this short Review it was showed and discussed some recent development done by us joined to recent examples from literature as well about the mentioned properties with applications of Non-classical light generation from subwavelength Nanoparticles to Light Emitter Devices (**LEDs**) and related, Semi-conductive materials, Ultra-luminescent materials, High Sensitive Sensors, micro-circuits, Microdevices and In Flow systems; and Energy Harvester materials.

2 Nanomaterials for Energy Transfer (ET) in the Nanoscale

The discovery and Research related with materials with potential applications on the Energy Field opened further studies about electronic configurations from Quantum phenomena below the Nanoscale to near Field related with closer distances between Quantic and Electromagnetic fields generated from different metallic surfaces to longer lengths known as the far Field. It could be well understood that the Quantum and Electromagnetic Energy within the near Field it should be transduced and enhanced to get impact on the Far field. By this manner from theoretical calculations and confined experimental measurements of these phenomena to Far Field applications there is a huge potential of Fundamental Research that it was reviewed along the next Chapters and sections.

2.1 *Conductive and Semiconductive Properties Based on Variable Material Constitution*

In order to contemplate different types of Energy conductions, It could be defined in a general way the conductive material as an object or type of material that allows Energy transfers; as for example from Electrical charges conductions, to the generation and conductions of Energy based on Photon-material interactions where the photon conductions are the basis of the success of the application. Moreover, it could be mentioned the Electronic conductions in the excited state that could produce light emission at different wavelengths depending of the material constitution; and the Electromagnetic waves conductions based on metal surface excitations at different wavelengths related with variable energies as well. These different mentioned types of energies could be transferred through different types of Organic, Inorganic and Hybrids materials that in the last time showed a large number of Research developments accompanied with different targeted applications that are still being in progress.

In this way, first of all, it could be showed how the Inorganic materials as Silica with excellent di-electrical properties were used for different Energy Transfer and storage applications. This material permitted the incorporation of different types of molecules, materials at different scales, etc. depending of the properties required. In the mentioned Research field, It should be mentioned the vital role of Silica on Photonics [26] studies from basic Research to real applications.

For example, for Solar Cells applications it was coupled TiO_2 nanoparticles as electron shuttles for improved electronic conductions generated by electron injections of perovskites [27] (Fig. 1).

In a similar manner organic polymers, based on their intrinsic molecular monomers, and variable compositions permitted Electronic conduction at the molecular level [28] and storage [29] accompanied with different applications that generated the addition of higher value to the materials based on their versatilities. For

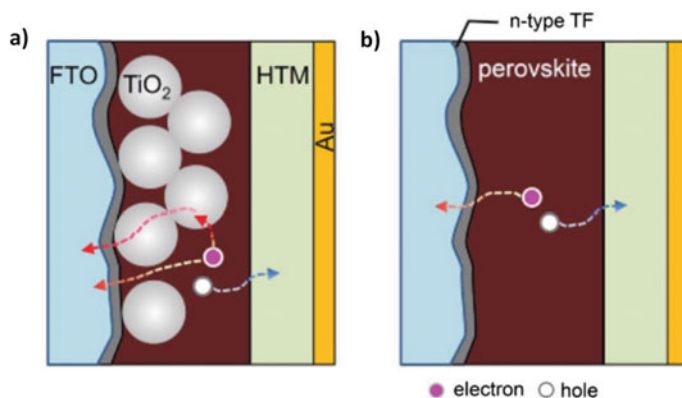


Fig. 1 **a** Mesoscopic perovskite solar cell with mesoporous TiO₂ layer and **b** planar structure without a mesoporous TiO₂ layer. Thin film (TF) on fluorine doped tin oxide (FTO) is an n-type semiconductor. HTM stands for hole transporting material. In the mesoscopic structure, electrons can be collected directly and/or via TiO₂ layer. Reprinted with permission from Ref [27] (N.-G. Park et al.). Copyright 2015 Small

examples, it could be mentioned from fabrication of chemical surface modifications from printable [3], flexible [30], and conductive at variable scales [31] and wearable devices [32], where the molecular and Nano-scale should be accurately controlled.

For example, well known conductive conjugated polymers based on polypyrrole and poly-anilines were largely used for electrical conductions. In particular it should be mentioned the use for organic electronics, the Poly(3,4-ethylenedioxythiophene):poly(4-styrenesulfonate) (PEDOT:PSS) as flexible and conductive material in many Chips and Microdevices [28]. However, even if this Polymeric material showed electronic conduction properties, it was showed some technical issues with PSS that they were overcome by a modification in the synthetic conditions that generated modified molecular weights with different crystal patterns of S-PEDOT accompanied with higher electronic conduction properties. So, in this example it was showed how sensitive was the electronic phenomena within the polymeric crystalline structures, even if the monomeric compositions were already studied and applied (Fig. 2).

It is very important the application of Polymers that can act as support of Organic conductive and Inorganic materials as well. For example the use of photo-curable resin with stretchable properties loaded with variable concentrations of graphene Nano-platelets generated bridged conductive Polymeric layers of graphene that permitted the electronic conduction and generation of switched on/off LEDs illumination by compression (Fig. 3) [33]. This practical material was evaluated to be incorporated within helmets as for example. So the meaning of the electronic conduction through the molecules below nm scales could be easily demonstrated at higher levels.

Moreover it should be mentioned that in the last years the use of mimetic Biomaterials and Natural materials by the right tuning permitted the development of different

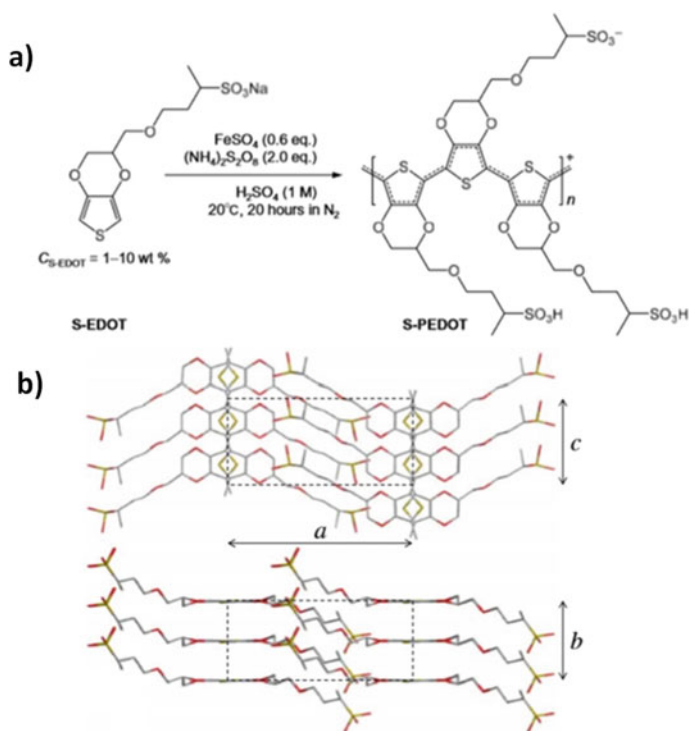


Fig. 2 **a** Synthesis of S-PEDOT by oxidative polymerization of the S-EDOT monomer; **b** Possible crystalline structure of S-PEDOT generated from analysis of X-ray diffraction (XRD) patterns of S-PEDOT films at different Concentrations of S-EDOT. a, b and c corresponded to the variable lengths recorded within Polymeric chains and between them. Reprinted with permission from Ref [28] (H. Okuzaki *et al.*). Copyright 2019 Sci. Adv

artificial Nano-Biomaterials for different applications. For example the fabrication of Porous Carbon Microspheres of Polyaniline for High-Rate Supercapacitors [34]. This material was based on a modified Chitin Carbon nanofibrous and porous microspheres (HCM) obtained by Pyrolysis; and joined within a substrate of polyaniline (PANI) to obtain the HCM – PANI composites. These HCM-PANI composites permitted the incorporation of ionic liquids that permitted higher ion flows with final properties as Supercapacitors (Fig. 4).

Moreover, within Semiconductive Nanomaterials it should be showed many high impact Luminescent materials already developed that they are still being studied and transferred to real applications. In this Research Field, it should be highlighted as well the previous examples the importance of the material constitution from Luminescence generation by classical emission of Individual Molecules with Optical excitation [35], to inter-molecular Fluorescence Resonance Energy Transfers [36, 37], and other non-classical Light states [38], emissions [39] and; Quantum materials as for example the well-known Organic [40] and Inorganic [41] Quantum's dots [42].

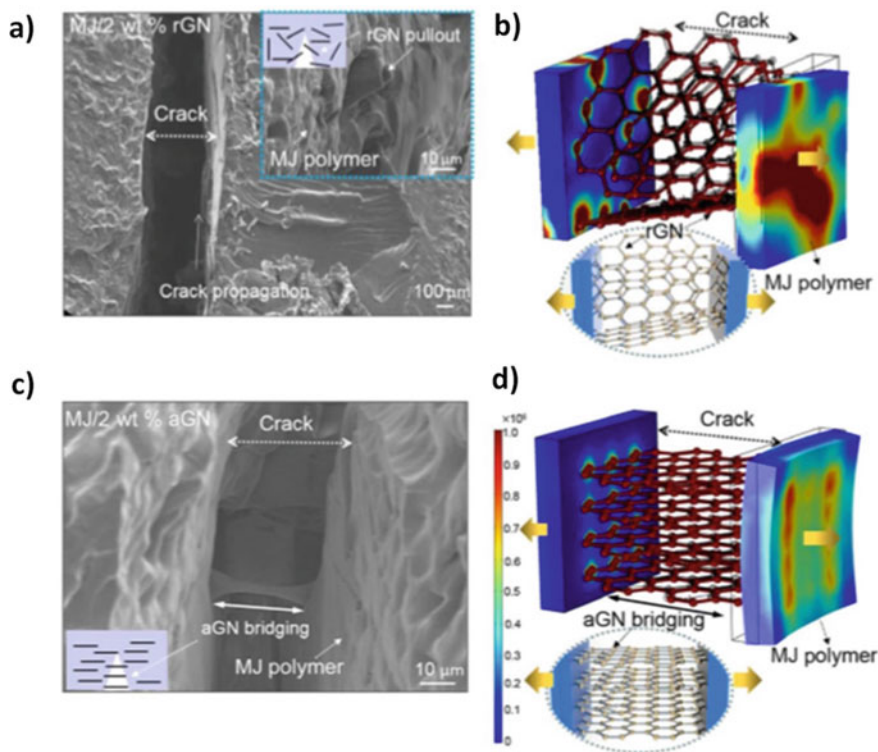


Fig. 3 **a** Crack propagation in MJ/rGNs; **b** Simulations of stress distributions of MJ/rGNs and MJ/aGNs by COMSOL Multiphysics; **c** Crack deflection of MJ/aGNs nacre and bridging and interlocking of aGNPs; **d** Simulations of stress distributions of MJ/aGNs by COMSOL Multiphysics. Notes: Photocurable resin: G⁺ from Maker-Juice notated as MJ; aligned Graphene Nano-Platelets notated as aGNs; random Graphene Nano-Platelets notated as rGNs. Reprinted with permission from Ref [34] (I. Chen et al.). Copyright 2019 Science Advances

In all the mentioned examples the electronic distributions between the basal and excited states based on their Energy bands gaps and chemical structure constitution [43–45], generated variable Luminescent emissions, quantum Yields and Luminescence phenomena [46]. So, in all the Luminescent materials the electronic flow between different but well overlapped Energy states generated variable emissions. These different Energy states could be generated within the same molecule or between different molecules and Nanomaterials.

For example, it was modulated the Photo- and Electroluminescence of based on a Photonic Molecular System. This Microdevice consisted in a Responsive p-Conjugated Donor–Acceptor Molecular System [47], that functioned by switching its emissions between green and orange in the solid state upon grinding, heating, and exposure to chemical vapor (Fig. 5). In this system it should be highlighted the design

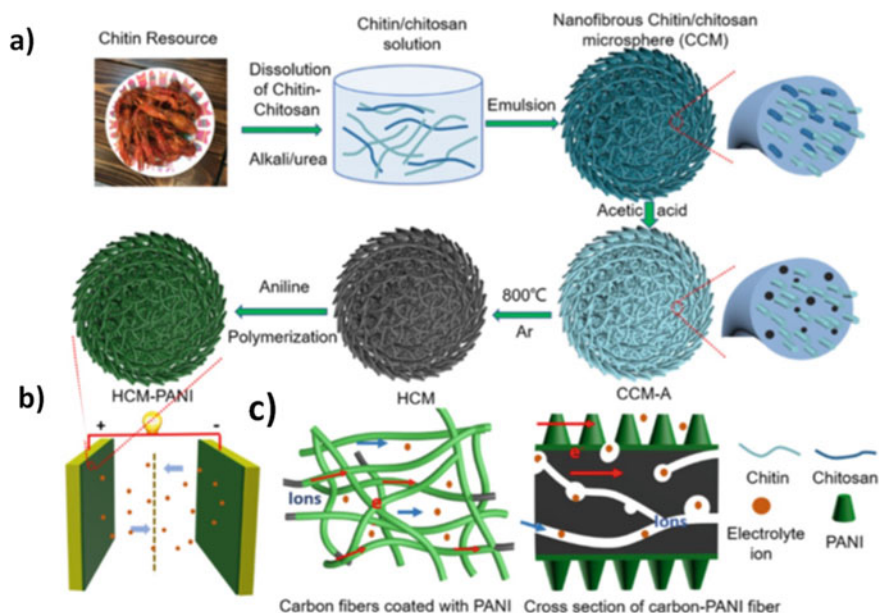


Fig. 4 Graphical illustrations of the formation process **a** two-electrode system **b** and porous structure of the nanofibers **c** for HCM – PANI. Reprinted with permission from Ref [35] (L. Zhang et al.). Copyright 2018 ACS Appl. Mater. Interfaces

of a Functional material external stimuli responsive electroluminescence with tunable two color in Organic Light-Emitting Diodes (OLEDs).

In this manner it could be tuned targeted Luminescent properties based on an accurate control of Functionalized shells as Luminescent layers with the incorporation of Semiconductive materials within multilayers to Fabricate different Luminescent OLEDs [48]. In these type of devices it could be observed the importance of the different constitutive parts with specific coupled functions in order to modulate their final properties, emissions and applications.

Finally it should be mentioned the electronic oscillation by the right excitation of metallic surfaces that could generate variable Electronic oscillations depending of the material constitution as well as the combination with other Optical active materials that could affect their intensities and wavelength bands intervals. Based on these physical properties new Research Fields were generated as Plasmonics and other Multidisciplinary Research Fields that they were considered and discussed their basis in the next section.

As example to understand the concept of the Energy translation or transference it could be discussed how from the electronic confinement within reduced sized Quantum Nanomaterials that generated discrete Energy states known as Landau levels (LLs) could be affected by different adjacent Semiconductive materials that generated as well Quantized states of Electromagnetic Energy. In this way it was studied their interactions between these two mechanisms and electronic interactions

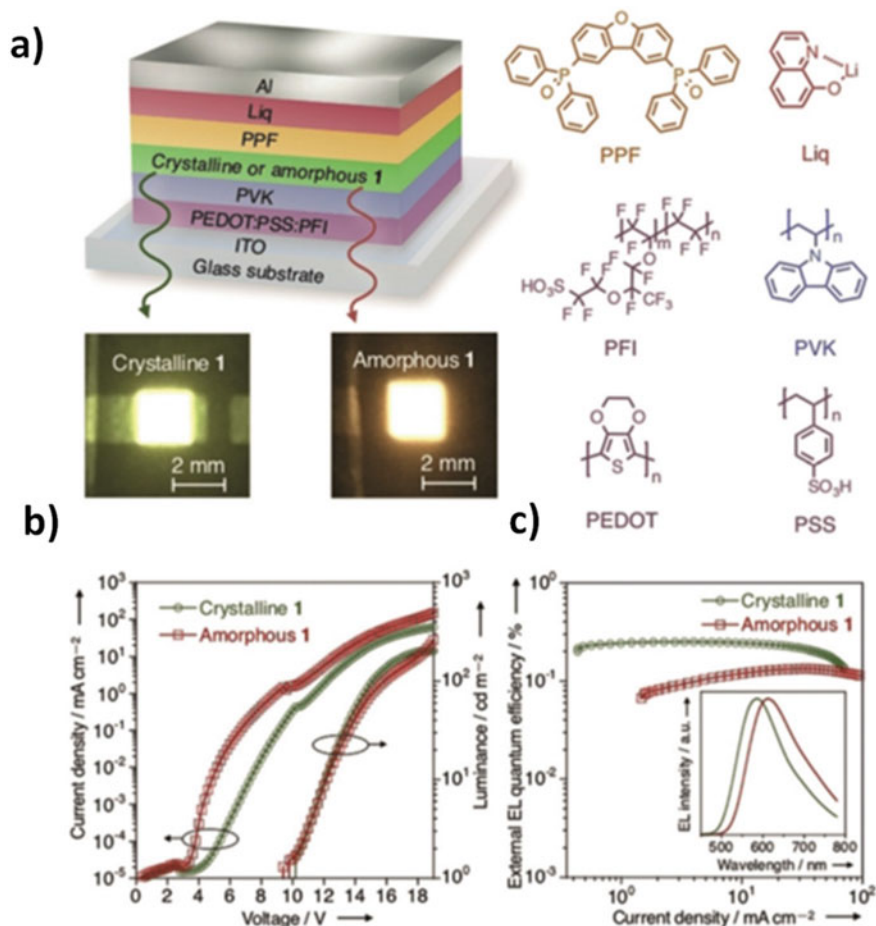


Fig. 5 **a** Schematic of the device structure and photos of green and orange EL emissions, **b** current density–voltage–luminance characteristics, and **c** external EL quantum efficiency–current density characteristics for the two-color emissive OLEDs. The inset in **c** shows the corresponding EL spectra measured at 10 mAcm². Reprinted with permission from Ref [48] (T. Yasuda et al.). Copyright 2018 Angew.Chem.Int. Ed.

in a circulator resonator made of graphene. The resonator is activated by an external magnetic field that afforded the electronic quantum states from atomic like states to LL-like states. Electronic interactions caused a characteristic wedding cake-like shape of electronic density at high fields [49].

3 High Energy Electromagnetic Fields from Nano-surfaces

3.1 Plasmonic and Enhanced Plasmonics (EP)

From the beginning of the Electromagnetic field Research studies, their interactions with matter, and enhanced spontaneous emissions developed by Purcell et al. [50] to Advanced developments within confined Micro-, and Nano-devices [51] there are a huge number of studies related with high Electromagnetic Energy fields generated from metallic surfaces within variable intervals of lengths. It should be highlighted that Purcell et al. were awarded with the Nobel prize in Physics 1952 for Nuclear Magnetic precision measurements [52]. These studies from the macroscale and microscale, then afforded further studies within smaller length scales.

Moreover, Plasmons described in the origins from dense electron gas by the Maxwell equations [53], and theoretical studies of electronic oscillations of Metallic surfaces described by the Mie Theory [54] (solution of the Maxwell equations) permitted later Advanced Experimental studies [55] contemplating a large number of fundamental Research and applied developments done as well as currently in progress.

These electronic oscillations produced different high Energy Electromagnetic Fields from the metallic surfaces that depending of their intrinsic material, and surrounding constitution generated variable emission wavelengths. In this context, different Nanomaterials showed particular spectroscopical properties along the entire Electromagnetic spectrum. By this manner it could be mentioned absorption from the UV to the IR ranges and longer wavelengths. Moreover, within each interval of wavelengths it could be used different approaches to generate Plasmonics properties. For example for the UV range, Localized Surface Plasmon Resonances (**LSPR**) were generated from large scale nanostructured aluminum films (Fig. 6a), and spherical nanoparticles (Fig. 6b) [56, 57] around 250–350 nm.

Moreover, it could be mentioned other Nanomaterials as Indium Nanoparticles [58] and semiconductors alloys [59]. Depending of the approach used many variables should be considered as design, synthesis, strategy of fabrication, chemical modification, and in particular their stabilization due to their intrinsic oxidation and reduction properties of the material.

Then, from the UV interval to longer wavelengths (within 400–550 nm intervals), it could be mentioned the generation of tunable Plasmons around 400 nm from silver films and spherical nanoparticles [60]; and around 520 nm for spherical gold Nanomaterials [61]. In general within short wavelength intervals the maximal Plasmonic band in the different regions mentioned, it could be tuned by modification of sizes and chemical modifications of the Nano-surfaces.

To understand and quantify the Plasmonic phenomenon it could be mentioned theoretical calculations based on Mie Theory that could generate contour plot of local field factor versus wavelengths and silica spacer thickness. Thus, by the study of spherical gold Core-shell Nanoparticle model it was showed the exponential decay proportional to $\cong 1/d^6$, [62, 63] being nominated d = spacer length from the gold

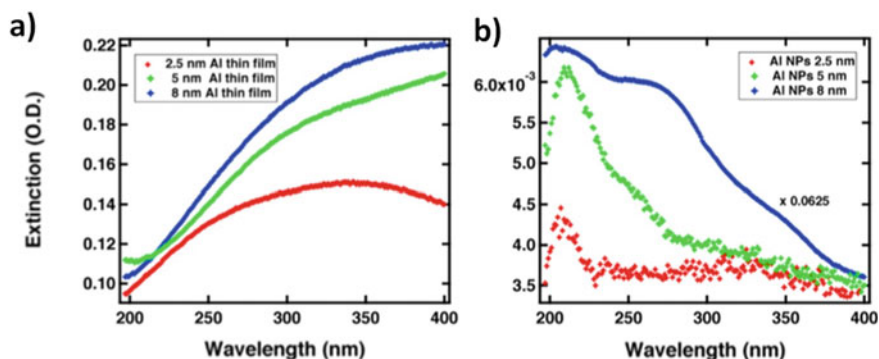


Fig. 6 Optical characterization of Al films and Al-NPs: **a** Extinction spectroscopy on a continuous aluminum film; **b** Extinction spectroscopy on annealed Al-NPs. The sizes indicated in the legend correspond to the original aluminum film thicknesses. The corresponding Al-NP diameters are given in Fig. 2. Note the different vertical scale for the blue curve. Reprinted with permission from Ref [57] (J. Plain et al.). Copyright 2013 Optical Matters Express

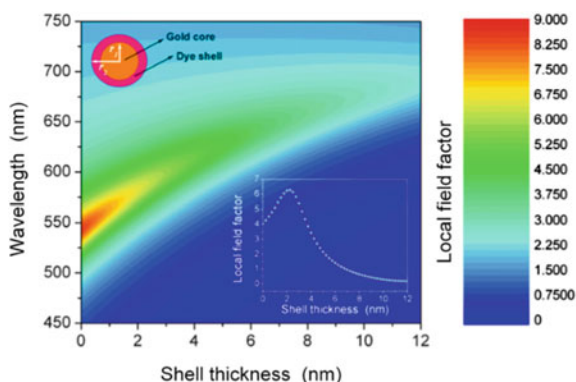


Fig. 7 Calculated contour plot of local field factor versus wavelength with different thickness of dye shell around gold Nanospheres. The up inset shows the geometry of the Core-shell model; and the down inset shows the local field factor as a function of dye shell thickness at a fixed wavelength of 590 nm. Reprinted with permission from Ref [65] (L.-q. Huang et al.). Copyright 2008 Physics Letters A, Elsevier

surface (Fig. 7). And, the Plasmonic intensity decrease from the Raman scattering decreased more rapidly than the surface enhanced fluorescence. By this manner for 30 nm gold Cores the maximal Local field factor was determined within shorter distances of 1–5 nm (Insert image of Fig. 7). Moreover, variable Electromagnetic fields wavelengths were recorded at the different shell thickness within the near field. At this point it should be mentioned that the near field was considered to closer distances where the Electromagnetic field could arrive to interact. For this example, it was arrived to longer distances than 10 nm [64]. And by this manner intermediate

and high intensities were generated within 500–650 nm wavelength. However the higher intensity interval of wavelengths was of 525–575, while the higher one centred at 545 nm.

Then, it should be mentioned that the electromagnetic Energy field's wavelengths could arrive to longer values as near-Infra-Red (**IR**) and Far-IR depending of their Nanomaterial constitutions, sizes and shapes. As for example from Mie theoretical calculations based on variation of axial and longitudinal distances that defined shapes from spheres to highly oblates generated wavelengths red shifting from 400 to 800 nm respectively. These results showed that the plasmon resonance depends strongly on particle shape. Thus, as for example when Nanoparticles become more oblate shift to the red [65]. Other shape to mention that contributed to Plasmonic properties within the IR interval, it was the triangular prisms [66]. These triangular Nano-prisms depending of their sizes and Nanomaterials variate Plasmonic wavelength bands from 600 to 800 nm and higher values calculated by DDA method. And it should be mentioned that the distribution of the high Energy Electromagnetic field was not uniform due to their shapes. It was showed higher Plasmonic emissions from the edges of the Nano-prisms than from the sides. In similar manner there were showed other shapes as Nano-stars with promising properties within the IR interval [67]. So, the new modes of Plasmonic resonances showed to be an interesting filed of Research by Lithography techniques as well as by chemical wet methods by modifications of the Colloidal dispersion reaction media [68]. Thus, it was obtained as well Nanorods [69] and Nanowires [70] with tunable properties within the IR as well. Finally, it should be mentioned the semiconductor Oxide Nanomaterials as IR Plasmonic materials as for example Zinc, Indium and Titanium Oxides [71] as well as other semiconductors [72] Nanomaterials.

Moreover, the Plasmonic properties showed to be highly affected for their surrounding media. Spherical metallic Nanoparticles in general showed homogeneous Electromagnetic fields around the Nano-surface, however even in presence of Silica with non-optical active properties accompanied with excellent dielectric constants produced variation in the Electromagnetic field wavelengths and distributions around the spherical Nanostructure [73].

In addition, it could be mentioned the deposition of spherical silver Nanoparticles on glass slides that showed strong intensities within the near field from non-homogeneous distributions (Fig. 8a). Thus, in presence of higher Electroactive materials higher interactions could affect more their near field distributions as well as their intensities.

By this manner, based on inter-Electromagnetic Fields interactions Enhanced Plasmonics (EP) [74] could be generated. As for example the deposition of the silver Nanoparticle over silver films produced strong hot spots of higher Electromagnetic fields between the silver film surface and the Nano-silver surface; while Enhanced on the other side of the Nanoparticle (Fig. 8b). These facts were related with the constructive and destructive sum of Electromagnetic field vectors based in the interaction of each component generated by the silver Nanoparticle and films. These intensities Enhancements were theoretically calculated by the Mie Theory and generated coloured images that could easily show the EP phenomena. Then, the challenge

Fig. 8 Electric field distribution for spherical silver particle positioned over the glass (left) and silver (right). Refractive index of surrounding medium was 1.33 (water). Reprinted with permission from Ref [75] (I. Gryczynski et al.). Copyright 2010 J. of Nanophotonics, SPIE

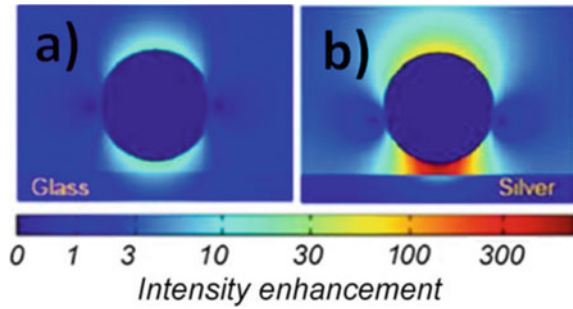
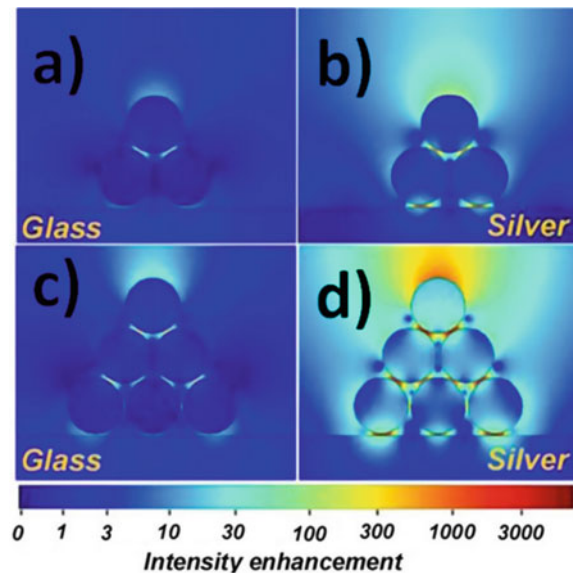


Fig. 9 Electric field distribution in the proximity of Silver colloidal assemblies formed over glass or metallic surface: **a** Trimmers over glass surface; **b** trimmers over Silver surface; **c** Higher Nano-arrays over glass surface; **d** Higher Nano-arrays over Silver surface. Reprinted with permission from Ref [75] (I. Gryczynski et al.). Copyright 2010 J. of Nanophotonics, SPIE



to overcome it was to design and fabricate Nanoarchitectures by different methodologies that permitted to exploit these phenomena for different applications. At this point it should be highlighted that this field still being the challenge within high impact fundamental Research studies and applications.

Moreover, it should be highlighted that the incorporation of addition silver Nanoparticles over glass slides, as trimeric forms, generated increased Electromagnetic fields within inter-Nanoparticles spacers (Fig. 9a) based as well by EP phenomena. However, if these additional Nanoparticles were added over silver films the effect of EP was even higher due to the additional Electromagnetic fields interactions of inter-Nanoparticles and silver films. So there was showed additional inter Electromagnetic fields interactions that generated higher Electromagnetic fields based on additional EP interactions. In addition, the effect of the incorporation of extra silver Nanoparticles within the Nano-array produced higher Electromagnetic

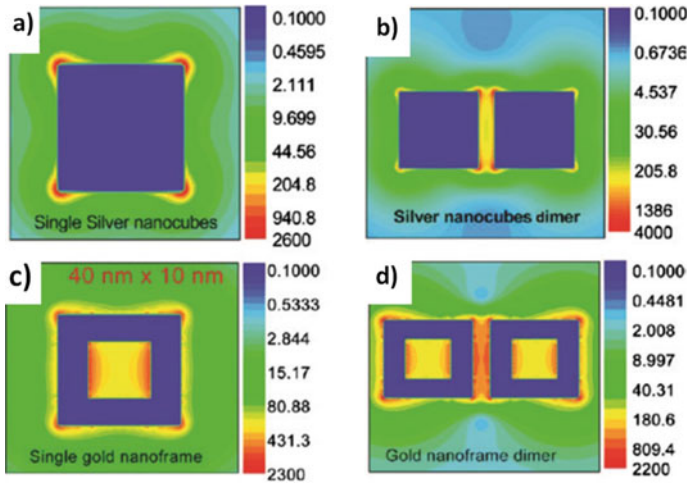


Fig. 10 DDA calculated plasmonic field distributions of solid Ag nanocubes and gold nanoframes: **a** individual Ag nanocube, **b** dimer of Ag nanocubes, **c** single Au nanoframe, **d** dimer of Au nanoframes Reprinted with permission from Ref [76] (J. Arbio et al.). Copyright 2017 Nanophotonics, De Gruyter

fields hot spots between inter-silver Nanoparticles on glass slides (Fig. 9c); while even higher factors were recorded on silver films (Fig. 9d).

By this manner it was showed the effect by physical phenomena from the Nanoscale within shorter lengths nominated as near Field that could be coupled to other physical and chemical phenomena.

However, other modes of Plasmonic interactions from confined hollowed Nanoarchitectures permitted the generation of EP properties within reduced sized cavities in the Nano-, and Microscale. In this manner, as for example from IR plasmonics of single Nanocubes (Fig. 10a), and EP between free spaces of Nanocube dimeric arrays (Fig. 10b) were generated single hollowed Nanocubes accompanied with Plasmonic outside and EP inside (Fig. 10c), and Multi-modal Plasmonic modes of hollowed dimeric Nanocube arrays (Fig. 10d) [75]. These structural modifications from confined Nanocavities generated new modes of Plasmonic resonances opening additional approaches to study Electromagnetic fields interactions.

Moreover, it should be mentioned the recently fabrication of hollowed metamaterials alloys by the incorporation of combination of gold and silver via a reduction assisted galvanic replacement approach [76] that permitted new modes of Enhanced control of Plasmonic properties (Fig. 11a). Modifying the Au:Ag ratios by 0.1, 0.25, 0.50, and 0.75 permitted to control the hollowed sizes from 70 to 80 nm within sizes of particles from 80 to 100 nm respectively (Fig. 11b–e). By this manner it was tuned Plasmons from 550 to 750 nm from smaller sizes to higher sizes accompanied with increasing values of their Extinction Coefficients close to 4.

Thus, it was achieved EP within a confined single Nanostructure, where it should be highlighted that the IR was known as a low energy field in comparison to shorter

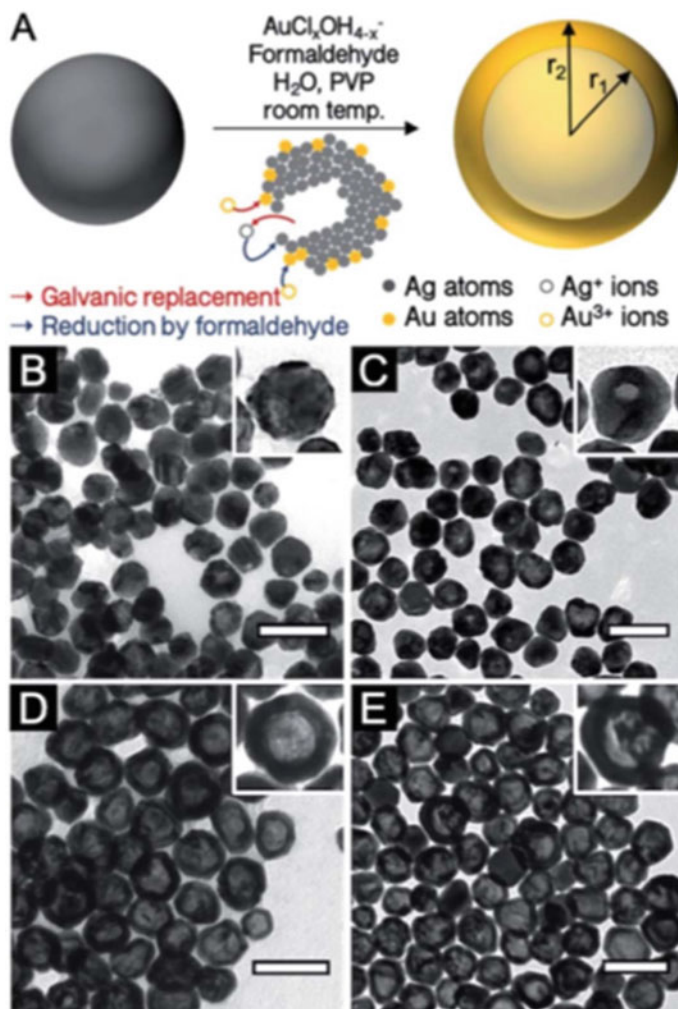


Fig. 11 a Schematic illustration of the co-reduction galvanic replacement procedure used. b–e TEM images of reaction products for different Au:Ag stoichiometries b 0.1Au:Ag, c 0.25Au:Ag, d 0.50Au:Ag, e 0.75Au:Ag. Reprinted with permission from Ref [77] (D. Boudreau et al.). Copyright 2019 RSC Advances, RSC. D. Boudreau, Enhanced control of Plasmonic properties of silver-gold hollow nanoparticles via a reduction assisted galvanic replacement approach, RSC Adv., 9 (2019) 389–396

wavelengths. So, the design and application of new approaches as the recently discussed could have high impact applications within this interval of wavelengths.

In order to conclude, it should be highlighted that the control and tuning of Electromagnetic fields within the near field could produce variable high Energy interactions with matter in their surrounding allowing the modification of the electronic properties of the Nanomaterial. In this manner it could be designed Optical Metamaterials [77],

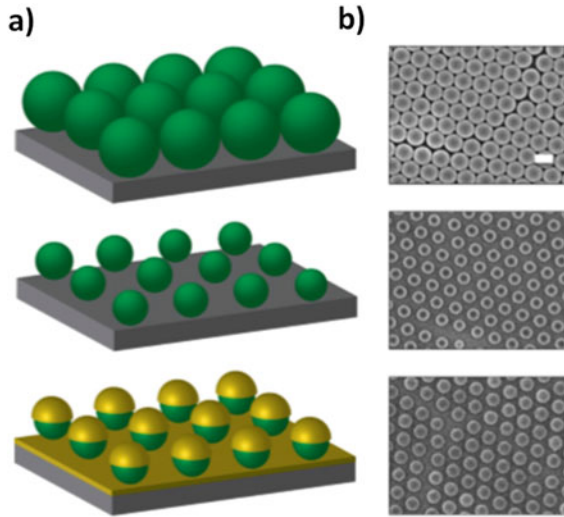


Fig. 12 **a** Schematic of the monodisperse gold nanocup fabrication technique with representative, **b** scanning electron micrographs for each step. Scale bar: 400 nm. Step: spin coat a monolayer of hexagonally close-packed polystyrene nanospheres on a silicon wafer. Step2: Briefly anneal to improve adhesion to the substrate and then use an oxygen plasma to uniformly etch the nanospheres to the desired size. Step3: Sputter a thin layer of gold (20 nm) at normal incidence to form nanocup structures. Reprinted with permission from Ref [82] (K. J. Alvine et al.). Copyright 2017 J. Nanophotonics, SPIE

Nanolasers [78], ring resonators [79], Plasmonic Light Emitter Devices (PLEDs) [80], and other functional Nanomaterials with high impact applications.

3.2 Enhanced Energy Properties

The high Energy fields generated within the near field could be used as sources of non-classical light generation for interaction with matter in their surroundings for: i) Energy detection in localized positions within the Nanoscale, ii) conversion, iii) transduction through Nanomaterials, iv) Metamaterials; and v) Energy storage. These different phenomena could be applied for different types of Energy. Thus, the number of studies and fundamental Research involucrated showed to be huge depending of the systems developed. Thus, in this section it was showed and discussed about a general overview of the Enhanced Energy properties based on recent and most representative reported publications within these topics.

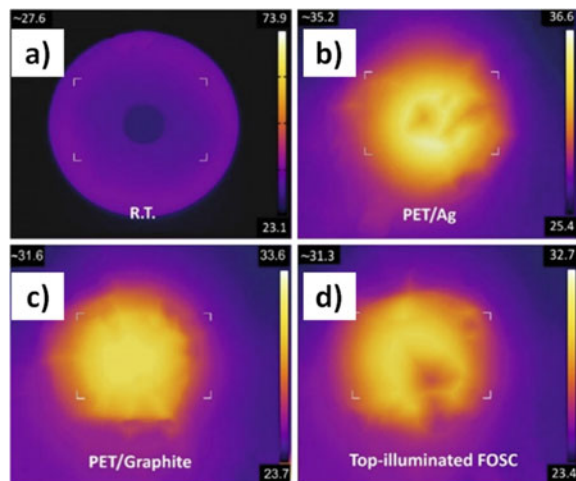
Targeted Enhanced Energy detection and transduction through Nanomaterials could be developed by Multi-resonant layered plasmonic films. These Metamaterials could be fabricated by many methodologies; however as example it could be mentioned by the deposition of polystyrene spheres silicon wafer and spin-coated

generated homogeneous Nano-patterned surfaces. The Nano-modified surfaces were etched with Oxygen plasma that generated Nano-cups templates to be modified with 20 nm gold depositions (Fig. 12a). This procedure permitted by TEM the determinations of sizes and depositions at each step of the synthesis (Fig. 12b). By this manner it was tuned sizes of gold depositions and spacers by incorporation of optical transparent polymers as poly(dimethylsiloxane) (PDMS), poly(methyl methacrylate) (PMMA), etc. The reflectance spectra and Transmitted light by illuminating the sample at normal incidence with a fiber-coupled deuterium/halogen light source generated controlled and Enhanced signals depending of their sizes and inter-nanoparticle spacers distances [81].

This proof of concept showed the coupling of light between the free inter-Nanoparticles spaces that generated higher Energies through the Metamaterial.

The in order to discuss the use of this proof of concept for developments directly related with the Energy field as Solar Energy, where the light should be captured from free photon coming from the sun to be transformed in other types of Energy depending of needs. In this Research field, innovation accompanied with improved properties was showed high impact on the application of different approaches to the design and synthesis of new materials for Solar Cells fabrication. Thus, the incorporation of silver Nanoparticles in flexible organic solar cells showed drastic modification on their capability to collect and transduce light through this modified hybrid Inorganic/Organic Nanomaterial. Briefly, a PET (poly(ethylene terephthalate) substrate was pre-coated with PDMS (poly-dimethylsiloxane) and modified with Graphite. Over this multi-layered Organic substrate were added silver Nanoparticles that generated higher IR emissions than in absence of them (Fig. 13) [25]. This fact could be explained by the previous resonant properties coupled to excellent semi-conductive properties form highly electronic conjugated organic structures as graphite.

Fig. 13 Thermal images taken with an IR camera for comparing the heat-insulation properties: **a** Thin metal object, **b** PET/Ag substrate, **c** PET/Graphite substrate, **d** Top-illuminated FOOSC. Reprinted with permission from Ref [83] (T. Xu et al.). Copyright 2019 Nanophotonics, Degruyter



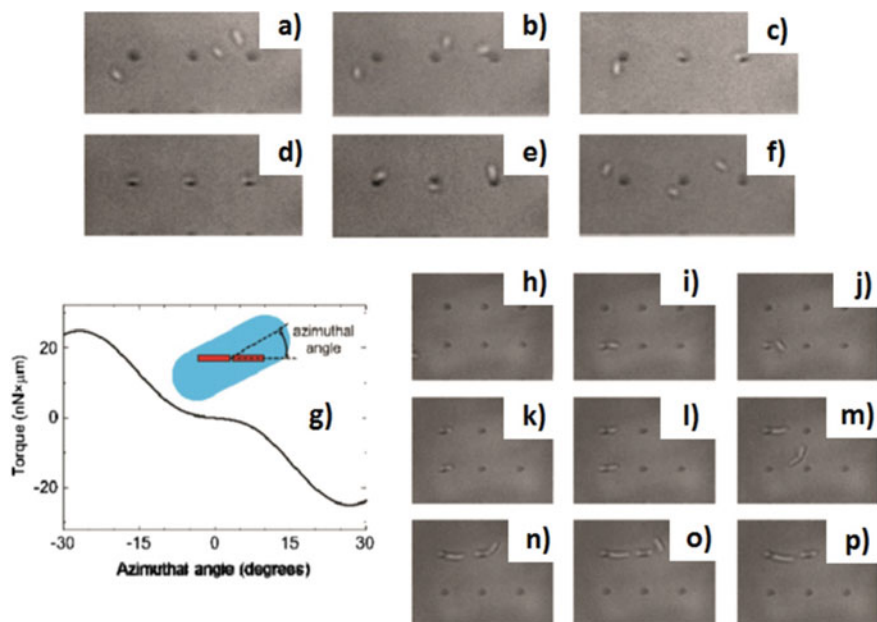


Fig. 14 **a-f** Successive frames showing simultaneous trapping of *E. coli* bacteria. The incident laser (800 nm) has been switched off just before recording frame *e*. **g** Calculated torque acting on the bacteria as a function of their angle relative to the rod axis, **h-p** Another sequence of trapping recorded over two hours, showing how the trapped bacteria keep on growing and dividing. Reprinted with permission from Ref [86] (R. Quidant et al.). Copyright 2009 Nano Lett, ACS

The Enhanced Energy properties generated from collective interaction between inter-Nanoparticles coupled to Semiconductive materials were generated from individual high Energy Nanostructures that by the right tuning could be extended to other applications as molecular and Biostructure detection.

Moreover it should be highlighted that the Enhanced Energy properties could be tuned by other approaches as strategies and Set ups based on the same physical phenomenon. In this way it could be mentioned the modification of the Optical gain in surface plasmon Nanocavity oscillators [82]. This approach was developed by a modified metal film as gain medium nanostrip, with a nanoled metal film deposited on the gain layer by coated Nanoparticles within the medium (e.g., an optically pumped semiconductor layer). By this manner was pumped and improved the Far field emission from the excited Near field.

So, if it is possible to achieve an accurate control of the Nanoarchitectures from the sizes of the Nanoparticles to the spacers between them if could be used the High Energy field generated within dimeric Nanoparticles to molecular detection based on the modification of Localized Surface Enhanced Raman Scattering (SERS) signaling in presence and absence of the targeted molecules. From theoretical calculations it could be determined the highest Electromagnetic field intensities at 0.25 nm

spacer lengths; however to shorter distances related with fused Nanoparticles showed the higher scattered light increasing in presence of few targeted molecules [83]. This fact was explained due to the localized phenomenon of **SERS** that showed more interaction between the electronic waves from reduced sizes as molecules and Electromagnetic champs generated in the close near Field.

In order to have an idea of the Energy and power of this High Electromagnetic field it could be discussed a visible example that it could be recorded by classical Transmission Bright Field Microscopy. The Nano-optical Trapping of Rayleigh Particles and Escherichia coli Bacteria was achieved by the accurate positioning of Nanoarrays of Rods structures to develop high EP properties that acted as Resonant Optical Antennas [84]. In this manner, it was permitted the trapping of Escherichia Coli bacteria in the surrounding of dimeric Nanorods controlled by Light activation of the **EP** properties (Fig. 14). The Optical trapping of the Biostructures and particles were explained as well based on the differences of the oscillating High Energy Electromagnetic waves from the metallic surfaces nominated as EP and Electronic properties of the Bacteria that produced attractive interactions.

Other approach based on **EP** properties from Optical Resonant cavities [85] showed the transduction of non-classical light through a Silicon photonic crystal. These microdevices were designed by accurate patterned linear unit cells of dimeric Nanocavities that acted as Resonant IR wavelengths by Laser excitation (Fig. 15). The fabrication was done over insulator wafers with 8 inch of silicon and 220 nm device layer and buried oxide layer using an electron beam lithography process. The excitation was done from the center of the Photonic device that generated Resonant emissions at both sides. These phenomena were generated through Enhanced Electromagnetic fields coupling from the near field within the Nanocavities to the Far field along the Photonic device. By this manner it was highlighted the drastic diminution of Energy losses obtained from the excitation to the Energy emitted of the non-classical light generated. This study was achieved from theoretical calculations to Experimental measurements done by Atomic force microscopy (**AFM**), Scanning Electron Microscopy (**SEM**) and Near Field Scanning Optical Microscopy (**NSOM**). Thus, it was clearly showed the effect of the Resonant Energy from EP that it showed potential applications as solar cells, including low power optoelectronics [86], non-linear Optics [87] and Quantum Optics [88, 89].

So, in the previous examples it was showed how from High Electromagnetic Energy within the Near field it could be transduced to the Far field with different impact on their surrounding depending of the matter constitution and tuning. In this manner these phenomena produced by different approaches permitted their direct visualization by standard and Advanced Optical set ups. Moreover it should be highlighted that for the previous developments different Nanomaterials and techniques were used to achieve targeted designs and generated properties based on the materials spatial accurately incorporated. Thus, it should be mentioned the use of Polymeric Nano-sheets, and films for Nano-patterned depositions and incorporation of different Nano-domains accompanied with the generation of particular properties. As for example, the well-ordered Inorganic Nanoparticle Arrays Directed by self-assembled block copolymer nanosheets with hexagonally-packed cylindrical

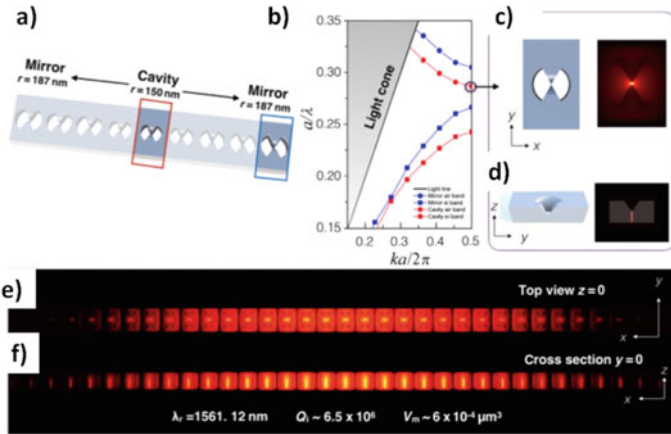


Fig. 15 Design of Silicon photonic crystal using a bowtie shaped unit cell: **a** the cavity is formed with a center unit cell of 150 nm radius and mirror unit cells of 187 nm radii on both sides of the cavity. The radius is gradually tapered from the center to the mirror segments. The photonic crystal lattice spacing is $a = 450$ nm, and the width of the waveguide is 700. The structure is designed with 220 nm silicon device layer and a $2 \mu\text{m}$ thick buried oxide layer, **b** Optical band structures of the cavity unit cell (red curve) and mirror unit cell (blue curve), **c** Top view (xy plane), **d** cross sectional view (yz plane) schematics and associated air band edge electrical energy in the center unit cell, **e** Log plot of the photonic crystal cavity electric energy distribution at the resonance wavelength in the xy plane at $z = 0$ (v -groove tip), **f** log plot of the photonic crystal cavity electric energy distribution at the resonance wavelength in the xz plane at $y = 0$ (bowtie tip). Figure S2 (A and B) shows the same mode profiles using a linear scale. Reprinted with permission from Ref [87] (S. M. Weiss et al.). Copyright 2018 Sci. Adv., Science

patterns within scaffolds of collapsed emulsion droplets [90]. Other example, Ultra-high-energy density lead-free dielectric films by incorporation of nanodomain structures in a BiFeO₃-BaTiO₃-SrTiO₃ solid solution that dramatically increased the energy density with potential high performance dielectrics applications [91].

In addition it should be mentioned that the discussed Plasmonic coupling could be extended their applications to longer wavelengths within Terahertz range [92, 93] related with many other applications from medical imaging, Biophotonics, to security screening and Wire-less communications. Thus, by the right tuning of Nanomaterials it was reported as for example the Enhanced plasmonic resonant excitation in a grating gated field-effect transistor with supplemental gate [94]. In addition, it should be mentioned the Silicon Nano-semiconductors patterned formed by Indium and Gadolinium, as InAs, GaAs, AlN/GaN, etc. for Terahertz emissions for their multiple applications [95].

Finally, it should be highlighted the possibility to tune light by interaction with Plasmonic Metamaterials. In this Research field, recently it was reported the study of nonlinear optical processes that can be enhanced by plasmonic resonances based on dipole Nanoantennas [96]. By this manner it was observed the quadrupolar third-harmonic response of dolmen-type plasmonic Fano structures. By this manner it was found that the third harmonic polarization field of the quadrupolar mode did not

Fig. 16 **a** Scheme of Second Harmonic (SH) spectroscopy of Al-nanoantennas that are resonant to the SH wavelength; **b** The background and the inset show tilted scanning electron micrographs of the investigated Nanoantennas sample that are resonant at frequency of Laser ω . Reprinted with permission from Ref [98] (H. Giessen et al.). Copyright 2016 ACS Photonics, ACS.

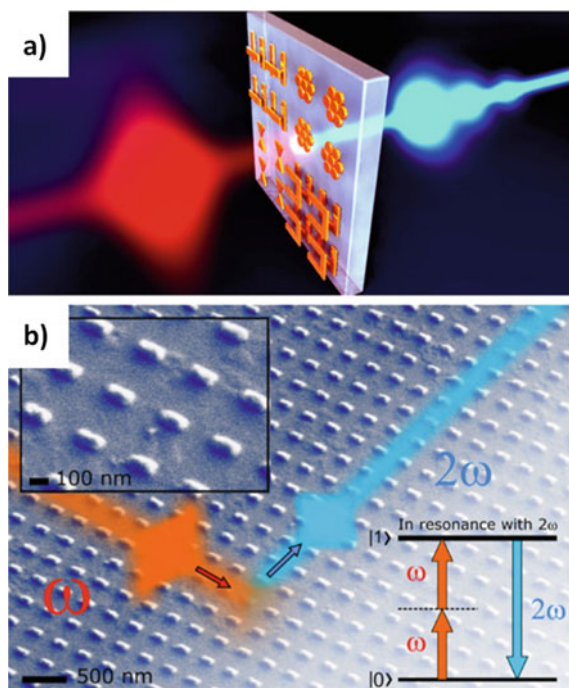
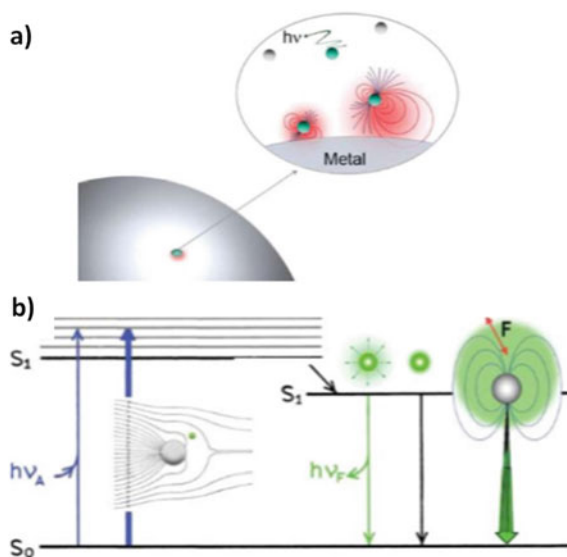


Fig. 17 **a** Fluorophore within the near Field of the Metallic surface, **b** Modified Jablonski diagram which includes metal fluorophore interactions. The thicker arrows represent increased rates of excitations and emissions. Reprinted with permission from Ref [101] (J. R. Lakowicz et al.). Copyright 2008 Analyst, RSC



radiate to the far-field due to destructive interference. So, depending of the Meta-material constitution the light interaction could produce variable emissions after interaction (Fig. 16). These type of developments showed potential applications in many other Research fields of high impact as well not related specifically with Energy as for example new non-classical modes of Light generations, Optical lens, and data encryption.

4 Nanomaterials for Enhanced Luminescence Emissions

4.1 *Core-Shell Nanoparticles for Metal Enhanced Fluorescence (MEF) and Fluorescence Resonance Energy Transfer (FRET)*

It could be mentioned and proposed different Enhanced emissions pathways; however the interaction of high Energy Electromagnetic Fields within the near Field with Luminescent emitters could drastically modify their excited state and emissions in controlled conditions. Thus, many approaches were used for the study of these interactions; as for example: a) metallic films, b) Nanostructured surfaces, and c) free metallic Nanoparticles in Colloidal dispersions.

Core-shell nanoparticles are well known for the enhanced luminescent properties where each part of the nanoparticle can be tuned in order to optimize their luminescent properties [22, 97, 98].

The Enhanced Luminescence properties are based on plasmonic effects known as Metal Enhanced Fluorescence (MEF). The MEF effect is a plasmonic effect that enhances the emission fluorescence of the emitter placed at an accurate distance from a metallic surface [99] (Fig. 17).

The MEF phenomenon depends of the distance of the fluorophore from the metallic surface due to the electromagnetic field intensity decays as an exponential function ($1/r^6$) with the distance (r) affecting by this manner drastically the fluorophore excitation [63, 100]. However, it should be highlighted the higher decrease of the near Field Intensity than the MEF Enhancements. For this reason in order to evaluate this parameter there are many studies developed using polymeric spacers as silica. In these Nanoarchitectures, the fluorophore is covalent bonded and the concentration can be controlled for maximal enhancements. These studies are in progress over surfaces [101] and colloidal dispersions [102], depending of the Nanoarchitecture design and applications.

It should be mentioned the main parameters to be controlled for optimal enhancements are the following: a) Plasmonic and spectroscopical properties overlapping, b) distance and spatial positions of dipolar momentum of the fluorophore from the metallic surface, c) concentration of fluorophores, and d) Nanoaggregation properties. Each of these parameters should be studied for optimal results depending of the targeted property and application.

Moreover, this phenomenon could be explained by different radiative pathways by the interaction of the fluorophore placed at an optimal distance to receive a high intense Electromagnetic field generated by the electronic oscillation of the Metallic core: a) by an enhanced absorption, b) augmented excitation of the fluorophores accompanied with increased emission; c) enhanced radiative decays accompanied, and d) diminished non-radiative decays. Depending of the fluorophores and Nanoarchitectures could variate the radiative pathways involucrated; however in presence of **MEF** effects the enhanced Fluorescence emissions were accompanied with Fluorescence Lifetime Decays shortening [103–105]. The enhancement factor depends of many variables as metal core used, shapes, sizes and 3D dimensions, [68] Intensity of the Electromagnetic field generated, [106–108] degree of fluorophore-Plasmon coupling and Quantum Yields [109]. So, in order to tune Luminescence properties many variables should be taken into account. And, Core-shell Nanoarchitectures formed by a metallic Core template covered with modified Optical transparent polymeric Silica shells with Fluorophores permitted an accurate control of many of the main mentioned variables that affect this phenomenon. As for example, 40 nm gold Core-shells Nanoplatforms modified with Rhodamine B (RhB) showed Enhanced Luminescence properties with **MEF** Enhancement factors (MEF_{EF}) of 9–10 in presence of Silica spacers shells of 10 nm, within Colloidal dispersions (Fig. 18) [110]. The absence of the metallic Core, generated by digestion with Sodium Cyanide addition, showed drastic diminutions in their emissions intensities accompanied with higher photobleaching properties by Static Fluorescence and Laser Fluorescence Microscopy (Inset images *i*) and *ii*) of Fig. 18). In this manner, by improving single Nanoparticles Laser excitation the MEF_{EF} raised close to 40, and permitted the Ultraluminescent Nano-Biolabelling of Single Escherichia Coli bacteria [111]. Moreover, it should be highlighted the use of individual Plasmonic properties for

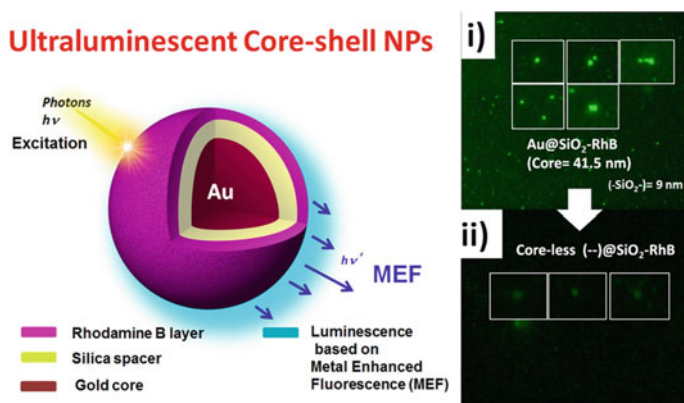


Fig. 18 a Gold Core-shell Nanoarchitecture with Ultraluminescent properties. Inset Images by Laser Fluorescence Microscopy *i*) Core-shell, and *ii*) Core-less emissions. Reprinted with permission from Ref [113, 114] (G. Bracamonte-D. Boudreau et al.). Copyright 2017 RSC Advances, RSC; and 2018 J. of Nanophotonics, SPIE

targeted emitter biomolecules incorporated within the membranes of genetically Engineered Escherichia Coli by the right Plasmonic tuning [112].

The right Plasmonic tuning should be based on optimal interactions of the Electromagnetic Field and Spectroscopical properties of the emitters. Different Nanomaterials showed variable Plasmonics properties within the large Electromagnetic Field interval of wavelengths depending of their intrinsic electronic constitutions as it was discussed on the previous sections. Thus, Optimal Plasmonics and Absorption

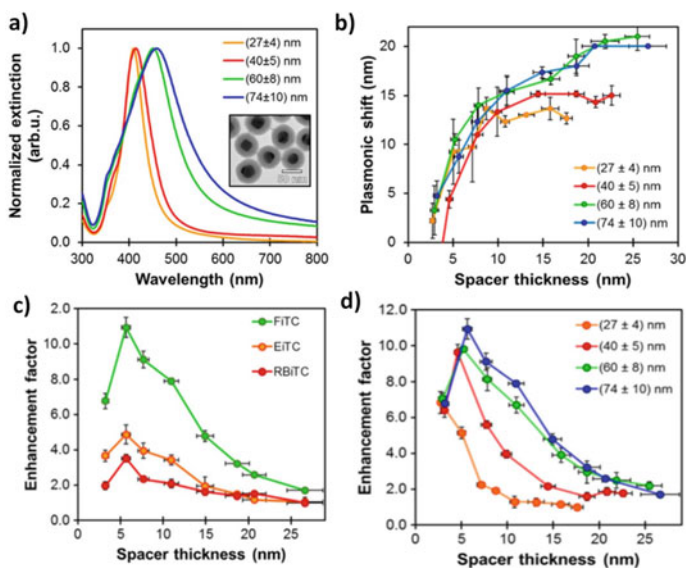


Fig. 19 a UV-VISextinctionspectrainH₂O, b Plasmonic shift as a function of shell thickness for different core sizes, c Enhancement factors for 74-nm cores with different xanthene fluorophores and silica spacer thickness d Fluorescence enhancement factors (EF) for Ag@SiO₂@SiO₂ + FITC ($\lambda_{exc} = 485$ nm, $\lambda_{em} = 520$ nm) with varying core sizes and silica spacer thickness (N = 3). Reprinted with permission from Ref [116] (D. Boudreau-et al.). Copyright 2016 Plasmonic, Springer

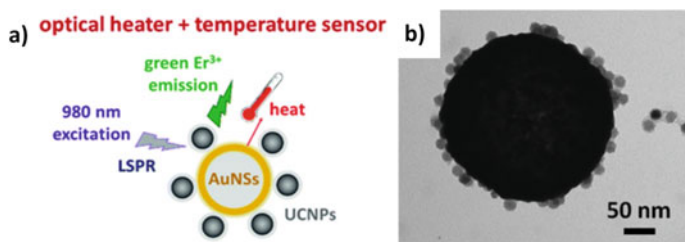


Fig. 20 a Scheme of gold nanoshells (AuNSs) decorated with lanthanide-based upconversion nanoparticles (UCNPs), b TEM image of AuNSs@UCNPs. Reprinted with permission from Ref [129] (D. Boudreau- J. L. Ribeiro et al.). Copyright 2017 J. of Material Chem. B, RSC

properties of the emitters should be evaluated considering the other variables in order to improve excitations within the Near Field.

For example, the use of silver Nanoparticles showed the strongest Plasmonic properties. However, even like that the phenomenon showed high sensitive effects [113]. Based on the control of their sizes, it was obtained maximal Plasmonic wavelengths from 400 to 500 nm within 27–74 nm intervals of sizes (Fig. 19a). In addition, it should be considered the surface coverage with Silica spacer shells that produced variable Plasmonic shifts depending of the Silica spacer lengths (Fig. 19b). So, when it was considered the strongest Plasmon from 74 nm sizes for coupling with variable absorption properties (at the right Silica spacer length), it was observed the higher MEF_{EF} for Optimal overlapping with Fluorescein (FiTC) in comparison to Eosin (EiTC) and Rhodamine B (RbiTC) (Fig. 19c). In a similar manner the effect of the Core size showed an influence in the Enhanced properties (Fig. 19d) based on their different intensities.

About the Quantum Yields, it should be highlighted that in general the higher enhancements recorded were in presence of lower values [109]. However other variables could affect the phenomenon; such as the orientation of the transition dipole [114, 115]. In particular this parameter it still being an experimental challenge to be achieved in order to compare it with theoretical studies.

All these considerations it should be taken into account within the entire Electromagnetic field; such from the UV region with Indium oxide Nanoparticles for Biological molecules [116] detection, toward the NIR interval [117], and longer wavelengths with other Nanomaterials, sizes and shapes. At this point it should be considered particular properties related with variable Plasmonic intensities based on different Plasmonic modes of Resonances generated from different shapes. These variations generated different Fluorescence Lifetime Decays shortening [118] based on Low, fast and Ultra-fast radiative decays mechanisms [119]. For example higher sizes of deposited single Silver Core-shell Nanoparticles on glass substrates generated stronger Plasmonic intensities that permitted NIR emitters coupling [120]. And therefore, it should be highlighted the Biophotonics applications within this interval of wavelengths due to the non-overlapping properties with the most common natural chromophores found in Biostructures. The most important applications could be considered from Biodetection by BioImaging [121] to Photo-thermal applications [122].

Other types of Core-shell Nanoparticles could be designed by different combinations of Inorganic and Organic materials. For example, Fluorescent Silica Core Nanoparticles Enhanced by the decoration of silver Nanoparticles [123], that it could be used as Bright Luminescent Nanoplatforms [124]. However, by the right tuning of Nanomaterials could be obtained different properties and Multi-modal approaches. By the deposition of Lanthanide Nanoparticles Cores (NaGdF₄:Yb₃ + :Er₃ +) over 250 nm gold Cores generated Bright and well-shaped Nanoarchitectures for induced NIR heating and thermometry (Fig. 20) [125].

The MEF effect was demonstrated as well for Single Quantum dot deposition over strong silver Plasmonic films [126] by Laser Fluorescence Microscopy. In a similar manner, it was studied the variation of different spacer lengths by the use

of Coated Metallic **AFM** tips [127]. Then, the High Energy near Field coupling with Quantum Dots from Nano-shell resonators permitted faster radiative decays that generated non-blinking properties [128]. Thus, it was demonstrated the impact on the non-classical Light generation by the right tuning of Plasmonic properties.

Other phenomena in the excited state that it should be mentioned and discussed; it was the effect of metallic surfaces on Resonance Energy Transfer (**RET**). This phenomenon is important due to the signal translation through different molecular entities accompanied with variable quantum yields and emissions with higher Stokes-shifts [104]. These characteristics could be used for Enhanced Fluorescence Energy routing for many applications as for example from Biophotonics studies to Nanotechnology developments.

This phenomenon in presence of modified microscope glass slides with silver Islands films (SIFs) showed Enhanced **RET** based on the interactions of the excited states of the fluorophores with the free electron of the metal, which polarize the metal and impose a reactive field on the fluorophore [129]. These early experiments were conducted in concentrated solutions of donor acceptor pairs in order to optimize inter-molecular distances below 10 nm for optimal **RET**. By this manner in presence of SIFs were recorded higher emissions of the acceptor than from the donor; while in absence of metallic surfaces it was observed higher emission from the donor than acceptor due to intrinsic differences in their Quantum Yields. Other approach used to improve distances between the donor/acceptor pairs, it was the use of labelled double stranded complementary DNA with fluorescent dyes. Thus, it was recorded higher emission of the donor accompanied with higher Fluorescence Lifetime Decays shortening just only in presence of the metallic films and acceptor dyes than in absence of both or just only in presence of one of them [130]. Moreover, it was showed Enhanced Förster Resonance Energy Transfer (**FRET**) on Single succinimidylated Silver Particle, Covalently Bound with aminated Donor-Labeled Oligonucleotide and linked with Complementary Acceptor-Labeled Oligonucleotide. In this study it was optimized donor – acceptor separations, particle Sizes, and distance from metal surfaces [130]. The increase of apparent distance (R_0/r) was dependent on the size of metal particle and the distance from the metal surface.

Then, it was showed **FRET** Enhancements based on accurate control of silica spacer shells and concentrations of donor acceptor pairs by Multilayered Silver Core-shell Nanoparticles [131]. These Nanoarchitectures showed Enhanced properties of the Fluorescent donor covalent bonded within modified Silica shell based on **MEF**. This phenomenon was coupled to Fluorescent acceptor dyes accurately separated by a Silica spacer shell. These Nanoplatfroms showed diminished photobleaching properties with higher emission than just only in presence of the **MEF** phenomenon. These observations were recorded from Colloidal dispersions by Static Fluorescence measurements as well as by Single Nanoparticle analysis with Imaging Fluorescence Cytometry (IFC). Therefore, further studies were developed for targeted applications. As for example for Biomolecules and DNA detections. So, non-covalent Polythiophene interactions with Proteins [132] and DNA [133] showed detection applications by colorimetric determinations. Moreover, it was showed Fluorescence signal amplification of intercalated Polythiophene within the double stranded DNA



Fig. 21 Principle of DNA detection on fluorescent multilayer Core-shell Nanoparticles: **A** Target ready NPs are prepared by complexing ssDNA probe-grafted NPs with polymer transducer, **B** hybridization of target DNA with ssDNA probes activates the polymer transducer as energy donor toward dye doped silica shell and excitation at 410 nm generates fluorescence emission by acceptor molecules at 550 nm. Reprinted with permission from Ref [141] (A. G. Bracamonte-D. Boudreau et al.). Copyright 2011 ACS NANO, ACS

by non-covalent interactions accompanied with 3D spatial arrangement in presence of the complementary DNA strand that generated an increased Quantum Yielded Supra-structure. This phenomenon was applied for ultrasensitive DNA detection [134]. Later, this proof of concept permitted the development of Plasmon Enhanced Resonance Energy Transfer from a non-covalent conjugated Polythiophene to **MEF** from Multilayered Silver Core shell Nanoparticles [135]. This Enhanced **FRET** permitted as well the development of a DNA Biosensor based on modified **MEF** Silver Core-shell Nanoparticles with targeted and labelled DNA strands with low Quantum Yielded Polythiophene that just only in presence of the complementary DNA strand showed Enhanced coupled **MEF-FRET** emissions (Fig. 21) [136]. These phenomena permitted limit of detection as low as 20 zmol in a volume of 20 μ L for perfectly matched 20-mer target corresponding to a conserved region of the *Candida albicans* yeast.

In this manner, as well it was optimized this Nanoarchitecture for SRY gene detection (sex determining region of Y chromosome) [137]. Thus, the target ready Core-shell Nanoparticles modified with 22-mer synthetic oligonucleotides showed **MEF** properties (Fig. 22a) within In Flow IFC from well dispersible Nanoplatforms that in presence of the targeted complementary strands higher Ultraluminiscent Nanoaggregates were recorded based on **MEF-FRET** coupling. The Nanoaggregation was generated from neutral charge development over the Nanoplatforms after interaction with the complementary double strands; that permitted higher inter-Nanoparticle interactions and aggregates formation proportional to added DNA concentrations (Fig. 22b). This Enhanced DNA detection by **MEF-FRET** coupling was used for free-PCR blood group genotyping [138]. Thus, these types of Core-shell Nanoarchitectures showed to be very versatile Nanoplatforms to control all the Nanoarchitecture parameters that affected these phenomena recorded within stable Colloid dispersions [139].

All these examples showed Enhanced Fluorescence Energy transfer through Plasmonic Core-shell Nanoplatforms; however the multilayered model could be used as well as resonant Nanostructures for Fluorescence Energy routing within Silica

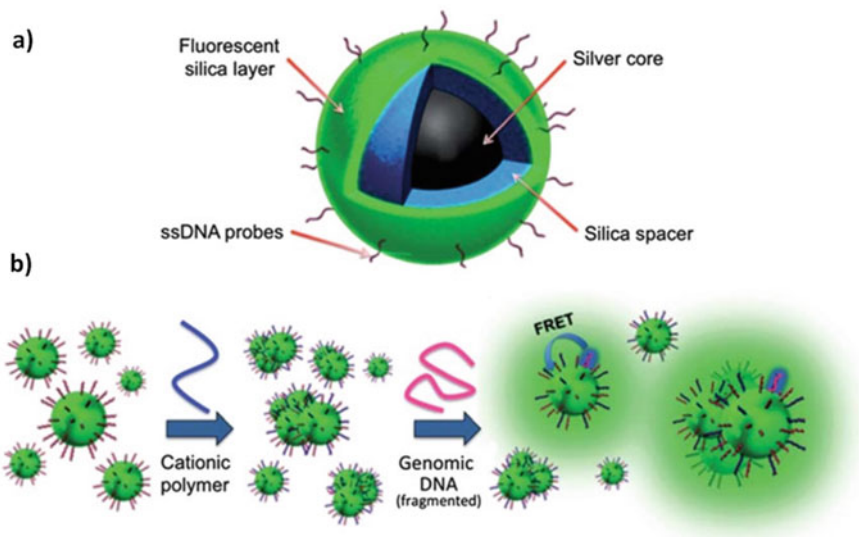


Fig. 22 **a** Scheme of targeted Ready NPs for SRY gene detection, **b** Steps of SRY gene detection. Reprinted with permission from Ref [142] (A. G. Bracamonte-D. Boudreau et al.). Copyright 2013 Analytical Methods, RSC

waveguides. Focusing on Nanotechnological studies for fabrication of Nanodevices, microdevices and Life Science applications based on Enhanced Electromagnetic Fields by **EP** within the near field, it could be highlighted the application of Enhanced Fluorescent Core-shell Nanoparticles accurately placed at fixed distances to translate interaction between propagating dark Plasmons within modified material coupling emission from nearby fluorophores [140] along patterned longitudinal axes. In addition the Multi-layered model could be used as well for tuning accurately spaced Fluorescent labelled Bioconjugates for large Fluorescence Enhancements on Nano-patterned Plasmonic substrates [141] at variable emissions wavelengths depending of the applications.

4.2 Plasmonic Resonators for Enhanced Energy Emissions

Plasmonic Resonators as Nanoarchitectures with localized **EP** properties generated high Electromagnetic Fields within the near field of adjacent metallic surfaces. These confined High Energy hot spots could be produced from different approaches depending of needs as it was described in the current section. Even if the State of the design and fabrication showed to be well developed, there are still existing needs and particular challenges to overcome that opened to Multidisciplinary Research fields Collaborations.

Plasmonic dimmers showed interesting high **EP** properties within inter-Nanoparticles. From theoretical calculations by the use of finite-difference time-domain method, it was calculated the total power of irradiance of a fluorophore placed between the High Energy Electromagnetic Field. When a fluorophore was oriented perpendicular to the metal surface, the total radiated power was increased in the close surrounding in presence of the dimeric system separated by 4 nm, in comparison to the isolated fluorophore and the case of a fluorophore near a single nanoparticle. While, when the fluorophore dipole was placed parallel to the metallic surface the emission was drastically quenched [142] (Fig. 23). By this manner it was correlated the Higher Electromagnetic fields intensities with the maximal total power of irradiances from it was determined until 450 times of enhancements within the hot spots.

These types of theoretical studies showed high impact and interest for the design of experimental approaches of Dimeric Resonators as well as supported previous experimental studies.

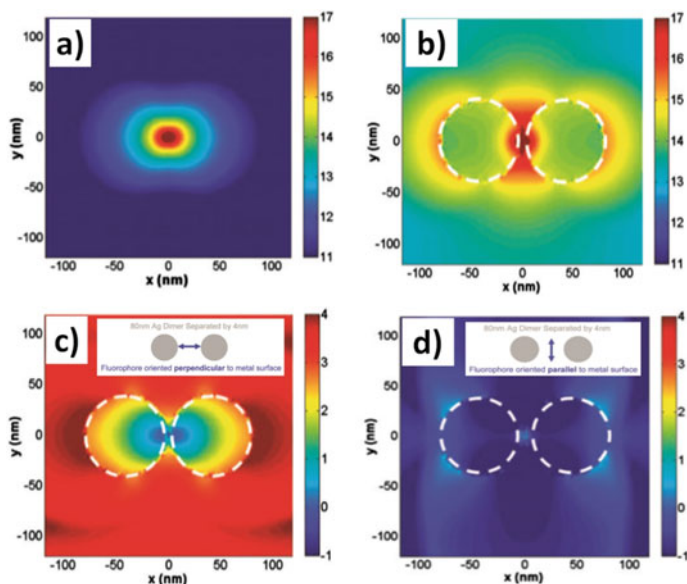


Fig. 23 Near-field intensity distribution around: **a** isolated perpendicular oriented dipole (along x-axis), **b** an 80-nm silver nanoparticle dimer with a gap space of 4 nm with the dipole in the middle of the dimer axis calculated using FDTD, **c** near-field enhancement and quenching. The white circle denotes the boundary of the nanoparticles, **d** near-field enhancement and quenching (with isolated parallel oriented dipole, along y-axis). The white circle denotes the boundary of the nanoparticles. Note all images are displayed in the log scale. Reprinted with permission from Ref [147] (M. H. Chowdhury-J. R. Lakowicz et al.). Copyright 2008 J Phys Chem C, ACS

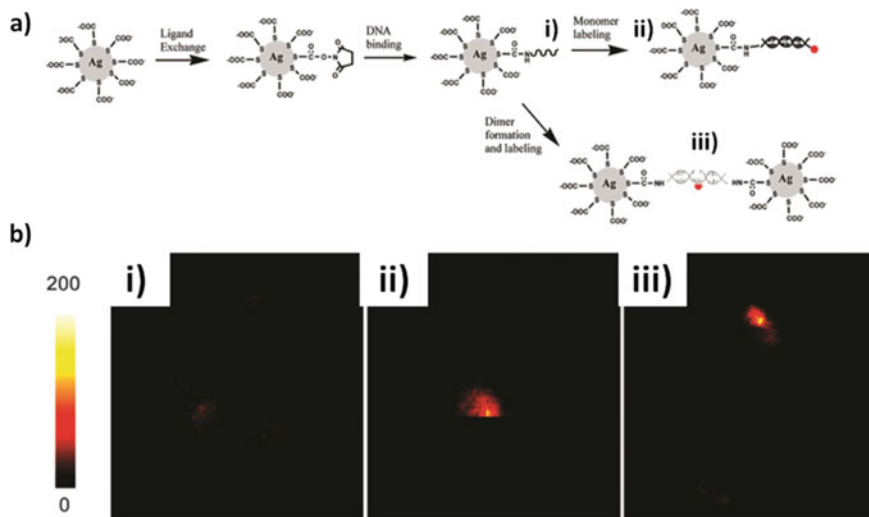


Fig. 24 **a** The Tiopronin-coated Silver Particle Was Succinimidylated via Ligand Exchange, Covalently Bound with Aminated Single-Stranded Oligonucleotide by Condensation, and Fluorescently Labeled by Complementary Single-Stranded Cy5-labeled Oligonucleotide to Generate the Labeled Metal Monomer, **b** Laser Fluorescence Microscopy of i) free Cy5 fluorescent dye. ii) single fluorophore on metal monomer. iii) on metal dimer. The $5\ \mu\text{m} \times 5\ \mu\text{m}$ images are $100\ \text{pixels} \times 100\ \text{pixels}$ with in integration time of 0.6 ms per pixel. Reprinted with permission from Ref [148] (M. H. Chowdhury-J. R. Lakowicz et al.). Copyright 2007 Nano Letters, ACS

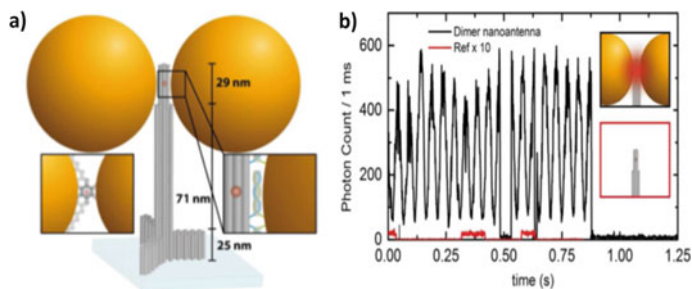


Fig. 25 **a** Sketch of the DNA origami pillar (gray) employed to build the optical nanoantenna with two $100\ \text{nm}$ Au nanoparticles together with a top-view (lower-left inset). The lower-right inset describes the "zipper" binding strategy to incorporate the Au nanoparticles to the origami structure, **b** Single-molecule fluorescence transients for a DN (black line) and for a DNA origami structure without nanoparticles (red line) obtained using ten times more excitation intensity. Reprinted with permission from Ref [152] (G. P. Acuna-P. Tinnefeld et al.). Copyright 2017 ACS Nano, ACS

For example based on the right chemical tuning of silver Nanoparticles with complementary DNA strands permitted the dimeric species formation. Tiopronin-coated Nano-surfaces covalent bonded by carboxyl group activations and nucleophilic substitutions with aminated Single-Stranded Oligonucleotide in presence of complementary Fluorescent labelled DNA strand permitted the dimeric Silver Nanoparticles formation (Fig. 24a). Thus, it was proof of concept of Enhanced Fluorescence emission application for DNA detection within dimeric Plasmonic Resonators. By Laser Fluorescence Microscopy, the free Fluorescent targeted complementary DNA strand at low concentration level showed very low emissions and photo-bleached hot-spots (Fig. 24b *i*)). While in presence of the modified Single-Stranded Oligonucleotide-silver Nanoparticles generated Enhanced Fluorescence emissions based on **MEF** from Localized Surface Plasmons accompanied with increased photobleaching properties (Fig. 24b *ii*)). However, Fluorescent double-length oligonucleotides complementary to modified Single-Stranded Oligonucleotide-silver Nanoparticles generated Higher Fluorescence emissions from dimeric species (Fig. 24b *iii*)). These Higher emissions were explained based on the interaction of the Fluorophore placed within a dimeric Plasmonic Resonator that produced **MEF-EP** coupling [143]. So, in this way, the study of associating and Dissociating Nano-dimer incorporated on lipidic bilayers permitted the quantification of Ultrasmall Amounts of DNA [144]. But, it should be highlighted that just at the moment as best of our knowledge there were not so many studies and developments reported.

Other designs that it should be highlighted were dimeric Resonators formed by DNA origamis architectures. By the use of accurate and targeted complementary DNA combinations, it was varied inter-10 nm gold Nanoparticle spacer lengths that permitted the study of Single Fluorophore emission and Quenching effect within the High Energy Plasmonic hot spot [145]. From the control of the spacer lengths within shorter distances within the near Field it was recorded the distance dependent quenching of fluorescence by Fluorescence Lifetime Imaging (**FLIM**). So, fitting with a model for nanosurface energy transfer yields, 10.4 nm spacer length was as the characteristic distance of 50% energy transfer. Moreover, in this communications it was discussed how the use of DNA nanotechnology with versatile characteristics by the use of attached Nanoparticles on DNA origami directly on the microscope coverslip paves the way for more complex experiments with potential applications in Genomics and Nano-Biotechnology by just only exploiting the interactions between Laser dyes and Nanostructures.

Moreover, based on 71 nm pillar DNA Origami with free side single DNA strands permitted the dimmer fabrication of modified complementary single stranded DNA 100 nm gold Nanoparticles (Fig. 25a) [146]. By this manner, it was possible an accurate control of inter-gold dimeric Nanoparticles. Theoretical calculations permitted the determination of higher Quantum Yield values within inter-nanoparticles spacer lengths higher than 10 nm. Thus, it was calculated QY within the **EP** hot spot of 0.78 and 0.85 for 12 and 17 nm spacer lengths respectively. So, by optimization of this DNA Origami dimeric Nanoarchitecture was achieved experimentally the detection of Single molecule Fluorescence transients (Fig. 25b). In optimal conditions of

Single Molecule Detection (**SMD**) within concentrated conditions it was determined from 5000 to 160,000 times of Fluorescence enhancements. Potential applications for Single Fluorophores diffusion detection within the high Electromagnetic hot spots was demonstrated in this way.

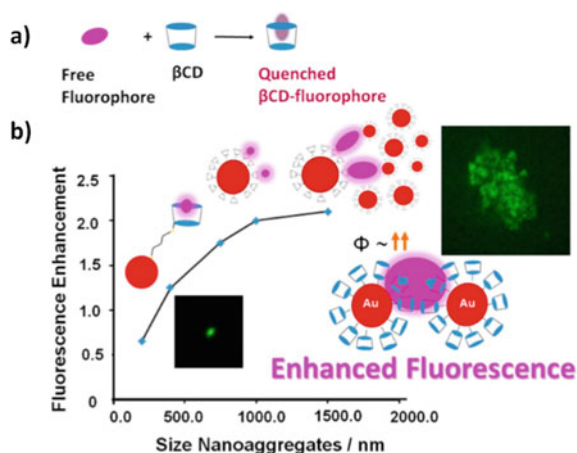
The Enhanced Plasmonics within the inter-Nanoparticle hot-spots showed a broadband Fluorescence Enhancement in different region of the Electromagnetic spectra interval by the right Nanomaterial tuning of dimeric Self Assembled Silver and gold Nanoparticles as Optical Antennas. Therefore, it was determined in the blue and green interval of emission wavelengths clear high Enhancements beyond 100 times for silver Nano-dimmers; while below 10 times for gold dimers. However, in the red region for silver and gold dimers similar enhancements beyond 150 times were recorded [147]. This fact could be explained by the non-homogeneous High Electromagnetic Energy Fields generated in the red region from different shapes of Plasmonic Nanomaterials with other modes Plasmonic Resonances. So, the synthesis of self-assembled Nanomaterials showed to be multi-factorial dependent. By this manner this Research Field is an open High Impact Research Field.

The control of the Nanoscale within the near Field phenomena overcame these shorter lengths to the Far Field by incorporating these Nanostructures as Nano-tools in advanced technological devices and Instrumentation for targeted applications. For example; the design and fabrication of a Plasmonics Enhanced Smartphone Fluorescence Microscopy [148]. This portable Fluorescence Microscopy it was based on Surface Enhanced Fluorescence (**SEF**) created by a thin metal film. In this Plasmonic design, the samples were placed on silver coated glass slides with a thin spacer distance, excitation by a Laser diode from the backside through a glass hemisphere generating by this manner the surface Plasmon polaritons. By this manner, 10 times of enhancements in Fluorescence intensity compared to bare glass substrates was achieved. This Photonic surface permitted the detection of the previous discussed silver Nano-dimmers DNA origami-based. Thus, it was at the best detected ~80 fluorophores per diffraction-limited spot.

Other example that it could be mentioned it was the Competitive Electromagnetic Field Enhancement at Silica/Silver Interfaces for Selective Intracellular Surface Enhanced Raman Scattering Detection [149]. This Nano-assembly it was based on the incorporation of 30 nm silver Nanoparticle in a poly(vinyl alcohol) adsorbed on Silica micro-sized particles. By applying Finite Element Method (**FEM**) analysis the Surface Enhanced Raman Spectroscopy (**SERS**) showed enhancements factors in the order of 10^{10} in presence of the Plasmonic Nanoplatforms. High values of this enhancement at the silver/silica interface of spherical geometry can be reached faster by using a 532 nm compared to 785 nm excitation wavelength. Using this Resonant Plasmonic platform it was differentiated the interaction of live fibroblasts with spread and round shapes for healthy and unhealthy state respectively. In similar manner it was detected in real time other types of Biostructures as amino-acids, proteins, cholesterol, and glucose.

Moreover, these types of Plasmonic Resonant materials were reported not only on surfaces. Within Colloidal dispersion, by the right tuning of 40 nm gold Core templates with short molecular spacers and supramolecular macrocycles it was

Fig. 26 Fluorescent phenomena of the Fluorescent Reporter RhodamineB (RhB) in the different media studied: **a** RhB in presence of β CD, **b** complexed RhB with gold Nanoparticles β CD grafted with 1,3-propanedithiol molecular spacer. Inset figures show Laser Fluorescence Microscopy Nanoimaging. Reprinted with permission from Ref [155] (A. G. Bracamonte et al.). Copyright 2019 Microchem. J., Elsevier



achieved different degrees of Nanoaggregation depending of the synthetic media used [150]. The supramolecular system applied was the β -Cyclodextrin (β CD) that formed host-guest complexes with Rhodamine B (RhB) as Fluorescent Reporter (Fig. 26a) on the modified Nanoplatforms. It should be highlighted that the free Supramolecular β CD-RhB complexes generated quenched emissions; however placed at a controlled distance from the Plasmonic Nano-surface the emission was overcome and protected. By this manner it was recorded Enhanced Fluorescence based on MEF from single Supramolecular modified gold Nanoparticles to higher Enhancements from bigger Plasmonic Resonant Nanoaggregates (Fig. 26b). These Ultraluminescent micro-sized Nano-aggregates were based on MEF-EP coupling that permitted low nM concentrations related with Single Molecule detections of complexed Fluorescent Reporter on modified Nanoplatforms.

In this way it should be mentioned the importance of the Bioconjugation, Multi-coloured Fluorescence tuning and non-covalent interactions between inter-Nanoplatforms for Biophotonics applications [151]. And the incorporation of silver Plasmonic Nanoarchitectures within polyacrylamide Polymeric networks for Nanotechnological applications [152]. At the same time it should be highlighted that these themes are currently developed and exist a huge interest and impact from different Research Fields.

In addition to the discussed approaches of Plasmonic Resonant Nanoarchitectures from single dimers to higher collective Resonant modes within Colloidal dispersions or deposited on controlled chemical modified Nano-surfaces and Micro-surfaces it should be mentioned and highlighted the design of larger modified surfaces and metamaterials with patterned Nanostructures. This control of larger and well-ordered Nano-patterned surfaces obtained by Lithography techniques permitted the fabrication of Microdevices and portable reduced sized instrumentation. In this Research field the In Flow Microfluidics showed to be in Advance for many applications with the use of reduced volumes and less time consuming methods. In this way, it could discussed the real time tunable lasing from plasmonic nanocavity arrays

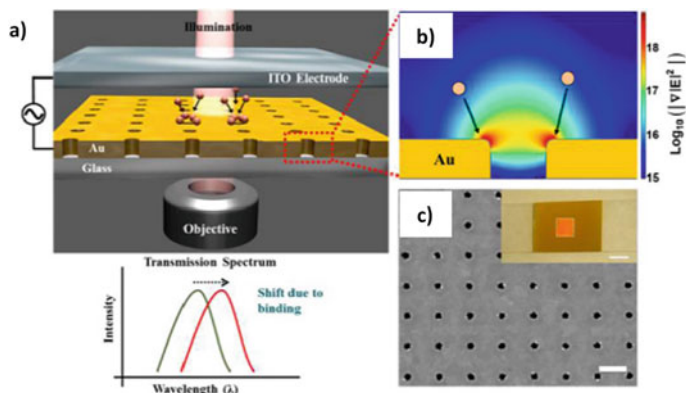


Fig. 27 **a** Schematic of the experimental setup, **b** Dielectrophoretic forces attract target molecules to the edge of each hole as the electric field intensity gradient is strongest (red color) along the rim of the holes, **c** The SEM image of the nanohole array (periodicity pitch $p = 600$ nm and nanohole diameter $d = 140$ nm), the scale bar here is 500 nm. Reprinted with permission from Ref [159] (M. Sun et al.). Copyright 2015 Nanophotonics, De Gruyter

obtained by Lithography; and incorporated within a Microfluidic Chip of reduced dimensions [153]. The Nano-patterned surface was by an accurately ordered cylindrical gold Nanoparticles design on substrates of polyurethane (PU) on glass. Larger surfaces in the order of $\sim\text{cm}^2$ were incorporated within the Microfluidic Chips. This device permitted the flow of different refractive index liquids (n) in presence of one unique IR Fluorescent reporter named as IR-140 that showed variable lasing with wavelengths from 853 to 896 nm by applying a fixed Laser excitation pumped at 800 nm (it was dissolved IR-140 in ethylene glycol with $n = 1.43$, DMSO with $n = 1.48$ and benzyl alcohol with $n = 1.54$). In summary, from the combination of metallic Plasmonic Resonant surfaces with accurate positioning in the Nanoscale and no-chemically modified to interact with a Fluorescent Reporter and by modifying the refractive index media with the application of a unique Laser excitation wavelength; it was collected thin Gaussian distributions of lasing emissions from the Laser dye reporter. Therefore, it was showed potential applications for In Flow Microdevices for Biodetection and Single Molecule Detection (SMD) with perspectives for signal Waveguiding as well. And it could be mentioned that these perspectives were generated from just only one approach from the near Field to the Far field.

In this manner, other design of larger Plasmonic Resonant surfaces that it could be discussed, it is based on gold Nanohole arrays with different Resonant modes generated by the intrinsic material constitution, shape and sizes of accurate patterned holes [154]. Thus a large-area of golden nanohole arrays integrated with conductive glass (indium tin oxide: ITO) (Fig. 27a) were used to demonstrate the application of dielectrophoresis (DEP) coupled to enhanced Surface Plasmon Resonance (SPR) (Fig. 27b). The incorporation of DEP permitted the controlled molecular diffusion within well-ordered Nano-holes array (Fig. 27c) by using AC electric field forces for sensing applications. By this manner, it was detected Bovine Serum Albumin

(BSA). It was found that the fabricated Nano-holes array permitted targeted label free molecules detections in real time for concentrations as low as 1 pM.

Finally from combination of approaches it could be designed as for example plasmonic antenna in box platform for enhanced single molecule detection. By this manner it was confined Plasmonic Resonant properties coupled to confined Plasmonic hole box from new properties could be generated as Enhanced Plasmonic properties and improved Molecular interaction within this confined Resonator [155].

In addition to the design and synthesis of 3D Nanostructures within Colloidal dispersion obtained by wet chemical methods, and modified surfaces by Lithography techniques; it should be mentioned and discussed the fabrication of individual hollowed Nanoarchitectures within Colloidal dispersion. In this way it was possible to get Single hollowed platforms with different shapes and sizes in the Nanoscale. In this Research Field even it was reported the fabrication of these type of Nanomaterials there are no so many developments done. But it should be highlighted the synthesis of hollowed resonators from gold Nano-cages as optical resonators for potential Biomedical applications [156]. To achieve future studies for different uses and applications it was tuned the large Electromagnetic field from UV to the IR.

Moreover it should be highlighted the recently opened possibility to manipulate Reversible Shapes and Plasmon Tuning in Hollow Ag/Au Nanorods [157]. The internal structure of hollow Ag/Au nanorods created by partial galvanic replacement was manipulated reversibly by Scanning Transmission Electron Microscope (STEM) probes and recorded by mapped with Electron Energy-Loss Spectroscopy (EELS) (Fig. 28a) without disturbing the internal structure. Thus, by the Electron beam irradiation it was created the solvated electrons and reactive radicals in an encapsulated solution-filled cavity into nanorods, Ag ions were reduced nearby the electron beam, reshaping the core of the nanoparticles without affecting the external shape. While by EELS it was measured their variable real time Energy loss positioning and reversible reshaping along the Nanorod structure (Fig. 28b). So, this new hollowed Nanomaterial opened potential applications in reprogrammable sensors, responsive materials, and optical memory units. Moreover, the liquid-filled nanorod cavity offers new opportunities for in situ microscopy of chemical reactions.

By this manner new studies from coupling of Surface Plasmon Modes and Refractive Index Sensitivity of hollow Nano-prism [158] to Quantum phenomena studies could be developed. At this point it should be highlighted that these studies could be developed by the accurate control of the atomic level within metamaterials and alloys.

So, tuned plasmons were sensitive to be coupled with different states of light and Localized Surface Plasmon Resonances (LSPR). For example, by the use bright entangled twin beams were applied to enhance the sensitivity of a plasmonic sensor used to measure local changes in the refractive index. It was demonstrated a 56% quantum enhancement in the sensitivity of a state-of-the-art plasmonic sensor when compared with the corresponding classical configuration and a 24% quantum enhancement when compared to an optimal single-beam classical configuration [159]. Moreover to don't leave at the side the importance of the light tuning

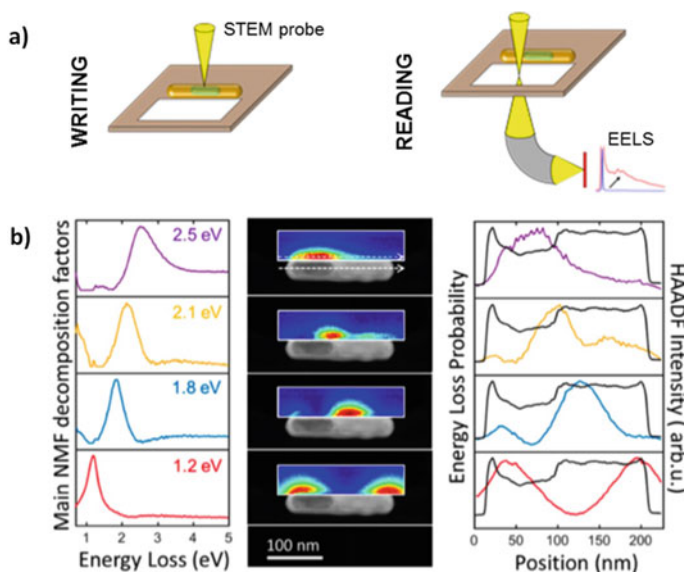


Fig. 28 a Write/read cycle and reversibility of interior restructuring in partially hollow AgAu nanorods. Ag migrates toward the beam when a solution-filled volume is illuminated. The void position and its effect on plasmon resonances can be interrogated without restructuring by acquiring electron energy-loss spectra (EELS) from the surroundings of the nanorod. **b** Successive reshaping states of the inner structure show reversibility of the HOLLOWED Plasmonic Nanorod. Reprinted with permission from Ref [162] (C. Schatz-D. Boudreau-E. Ringe et al.). Copyright 2016 Nanoletters, ACS

from external sources, the entangled twin beams were generated via a four-wave mixing (FWM) process based on a double- Λ configuration in hot 85Rb atoms.

Thus, it was demonstrated by many studies and developments, how from the atomic and Nanoscale control it was generated Quantum and Near Field interactions for Far Field phenomena.

4.3 Luminescent Hybrid Organic/Inorganic Nanomaterials

In order to add Multi-functionalities on Nanomaterials it should be combined different chemical structures and variable material compositions; where each part takes defined roles for a final targeted application. In this way, Organic materials by chemical variation permitted to be part of the whole Nanostructure from simple linkers, support material to add particular electronic and luminescence properties joined to Inorganic properties from metals, Semiconductors, and quantum emitters, etc.

By this manner it could be designed Multifunctional Hybrid Organic/Inorganic Nanomaterials for Enhanced non-classical light emissions tuning, Drug Delivery

applications, Molecular and Biomolecular detection, signal Waveguiding, etc.; as well as other Nanotechnological applications.

As proof of concept it should be discussed the use of gold Nanoplatfoms for chemical modification and tuning of variable Functionalities. For example, it could be mentioned the Nano-supramolecular complex synthesis for switch on/off enhanced fluorescence control and molecular release using a simple chemistry reaction [160]. This Nanoarchitecture was based on 50 nm gold Core templates modified by variable controlled lengths of Poly-ethylene (PEG) to link β -Cyclodextrin macrocycles (β CD). Thus, the gold Core permitted to generate strong Electromagnetic fields that Enhanced the Laser dye emitter sensing (Rhodamine B; RhB) via a **MEF** mechanism by Host-guest supramolecular complexation. By the incorporation of di-thianes within the short molecular spacers permitted the controlled Host-guest complex delivery (Fig. 29). Fluorescence Lifetime Decays shortening was observed from complexed RhB to modified β CD gold Nanoparticles (Fig. 29. Inset image *i*)) accompanied with Fluorescence Enhancements (Fig. 29. Inset image *ii*)). So, it was detected, enhanced, tracked and delivered few molecules per Nanoplatfom close to Single Molecule Detection (SMD) levels. It should be highlighted that **MEF** permitted to overcome the well-known quenching phenomena of the complexed Laser dye with β CD. These observations permitted to tune and develop **MEF** emission and Quenching protection effect with an optimized Host-guest Nanophotonic-supramolecular structure [161]. By grafting β CD on tuned gold NPs

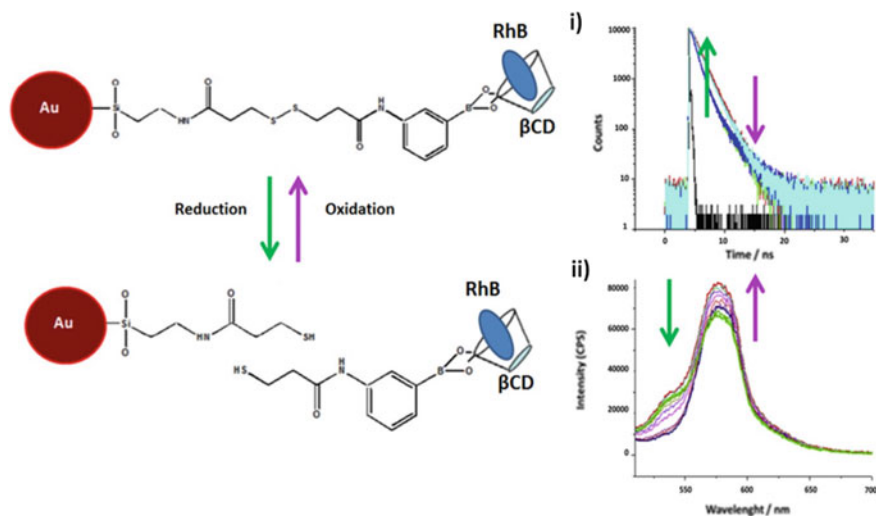


Fig. 29 Reduction reaction of disulfide covalent bond with DL-1,4-dithiothretol (DTT) for β CD complex delivery of Rhodamine B (RhB). *i*) RhB lifetime decays shortening from complexed RhB on covalent modified β CD on Au Nanoparticles, *ii*) Fluorescence spectra of RhB in the presence of Au@spacer_n- β CD (spacer 3,3'-dithiobis(sulfosuccinimidyl propionate: DTSSP) at time = 0 (blue line); 1 h period (red line); c) after 10 min of adding DTT (green line). Reprinted with permission from Ref [165] (A. G. Bracamonte-D. Boudreau et al.). Copyright 2016 Microchemical J., Elsevier

with compact and high conjugated Organic molecular spacers, it was possible to increase the sensitivity of RhB detection by 70, 80, and 294% when compared with solutions in phosphate buffer, with free β CD macrocycles, and in presence of the modified gold Nanoparticles, respectively. These results showed that the use of a supramolecular system attached to a metallic Nanoparticle could interact specifically with a dye to enhance its fluorescence emission through the **MEF** effect and increase the sensitivity of detection. Based on the previous discussed examples other types of Hybrids Organic/Inorganic Nanomaterials could be designed as Smart Multifunctional Nanoparticles as well [162].

So, metallic Nanoparticles could be used as Nano-templates and Nanoplatfoms for design and synthesis of new Nanomaterials and Metamaterials, accompanied with tuning and chemical modifications for targeted studies and applications. Within Life Sciences it should be highlighted the possibility the use of Bioconjugates techniques of antibody-antigen systems and their applications on Biophotonics, Biotechnology and Nanomedicine. While, for Photonics and other Nanotechnology developments by the right tuning and incorporation of controlled sizes, shapes, chemically modification, and Nanomaterials; it could be studied new potential physical and chemical properties.

Other type of Nano-, and Microparticles based on organic materials are the use of micelles and vesicles [163]. These Nanomaterials could add different ways of chemical modifications, molecule and tuned Nanostructures incorporation. This versatility joined to their intrinsically different properties in comparison to metallic Nanomaterials could be proposed to different studies and uses.

About tuneable vesicles with non-classical Luminescent properties it could be mentioned self-Assembled Vesicle Membranes with Amphiphilic Binding Sites and Reporter Dyes for Chemosensors uses [164]. In this example, it was used the well-known DSCP (1,2-distearoyl-sn-glycero-3-phosphocoline) for vesicles formation and combined with different amphiphilic fluorescent dyes based on the modification of the N-alkylated glutamic acid derivatives. In this manner it was showed the interaction of different amphiphilic artificial binding sites based on ZnII-cyclen (1,4,7,10-tetraazacyclododecane), CuII-NTA (nitrilotriacetic), and BACE (benzoaza crownether) structures, accompanied with incorporation of amphiphilic fluorescent reporter dyes derivates for different Biomolecules binding with phosphate anions, imidazole derivates, and ammonium anions. From Static Fluorescence Isotherms was recorded quenching and enhancements effects depending of the type of the chemical structures and interactions that affected the incorporated dyes emissions. The optical response of the Fluorescent dyes showed to be environment-sensitive on their structure and properties and also on their miscibilities with the substrate-free and occupied receptors.

Moreover, it was reported High-Affinity Peptide Binding Sites Assembled by Analyte-Induced Recruiting of Membrane Receptors [165]. This approach it was based on chemical modified vesicles with bi-functional Amphiphilic Binding Sites receptors for targeted two different amino acids interactions from short peptides it was showed the Dynamics of the lipidic bi-layer via **FRET** signaling (Fig. 30). The **FRET** signal it was collected from the Fluorescent reporters incorporated in

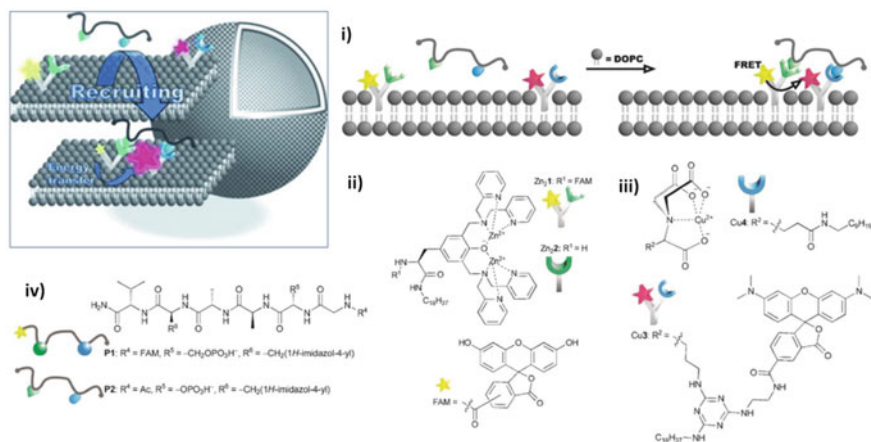


Fig. 30 Vesicular platforms for targeted non-covalent interactions and Fluorescence Resonance Energy Transfer (FRET) applications. i) Schematic representation of the recruiting of labeled membrane receptors by a peptide ligand resulting in FRET signaling; ii-iv) Structures of synthetic receptors and ligands (counterions omitted). Reprinted with permission from Ref [170] (Koenig et al.). Copyright 2012 Angew. Chem. Int. Ed, Wiley

the chemical structure of the Amphiphilic Binding Sites receptors. The Fluorescent Amphiphilic Binding Sites receptors showed their dynamics and mobility within the lipidic bi-layer in presence of the right peptide structure (Fig. 30). Inset image i)) that fixed the Fluorescent dyes reporters at optimal distances for FRET signaling. Then, these studies permitted the design of a Vesicular aptasensor for the detection of thrombin [165, 166]. Self-assembled phospholipid vesicles were functionalized with thrombin binding aptamers using a thiol-click reaction. The resulting aptasensors signal the binding of the analyte to the vesicle surface by changes of the emission properties of membrane co-embedded reporter dyes.

These previous examples showed how the vesicles could be used to graft varied molecules and functionalities. Thus these platforms with sizes within the Nano-, and the Micro-scale are potential Multi-functional Nanomaterials [167] based on the different chemical environments such as hydrophilic surfaces, hydrophobic bi-layers and internal polar cavity. The different parts permitted the design of compartmentalized functions as well inter-related or coupled for Multi-functional and targeted functions respectively. By this manner, smart polymer vesicles, pH responsive, thermos responsive, redox responsive, Light responsive, morphological changes by induced external stimulus, multifunctional applications within Life Sciences as imaging and drug delivery that still being a challenge due to their different types of synthesis, reproducibility, stability, loading efficiency, interaction with the media, cytotoxicity etc..

Other organic material with confined electronic properties with potential interactions with the near Field from metallic surfaces and Nanoparticles are the Carbon Quantum dots. These types of Quantum Nanomaterials showed high Quantum Yields

[168] with potential applications for Bioimaging. [169], and Bioconjugation applications [170]. In this way, it was opened the interest from studies related with their biocompatibility [171], their fabrication by low cost procedures and incorporation in Nanomaterials with high Social impact such as Solar cells [172]. But, it was not so many reported as best of our knowledge forming part of hybrid Luminescent Nanomaterials.

However, other type of organic Nanomaterial as graphene after their Nobel Prize award in Physics 2010, showed higher interest for their Electromagnetic properties and interactions within the near Field of Electromagnetic fields generated from metallic surfaces. It should be mentioned that this material was awarded for the ground-breaking experiments regarding the two-dimensional materials with applications in Nanoelectronics [173]. Moreover, it should be highlighted that graphene as a Nanomaterial formed just by carbon performed as well as cooper for electricity conductions. By this manner it was incorporated within electronic Micro-devices. Thus further studies were reported.

Graphene showed particular properties related how their electrons behave under the influence of an external magnetic field. Recently it was reported pseudo-magnetic fields from graphene through wafer scale epitaxial growth. Sallow triangular nanoprisms in the SiC substrate generate strain induced uniform fields of 41 T, that enabled the observation of strain induced Landau levels at room temperature by angle resolved photoemission spectroscopy. These observations were confirmed by model calculations and scanning tunneling microscopy measurements [174]. This work demonstrated the feasibility of exploiting strain induced quantum phases in two dimensional Dirac materials on a wafer platform that opened to new applications.

This level of quantum sensitivity permitted as well the light guiding within an optical fiber. In this Research work it was used carbon nanotubes to generate such guiding potential in graphene and create a single mode electronic waveguide [175]. This study it was based on a nanotube and graphene separated by a few nanometers. By this manner it was permitted to be controlled and measured independently. Therefore, it was observed the formation of a single guided mode in graphene by using the same nanotube as a probe.

Moreover, it is known the quantum performance of carbon from graphene nanostructures has remained stunted by an inability to alter the sp²-carbon lattice with atomic precision. So the tuning of these chemical Nanostructures showed particular interest by their modification with a precision at the atomic level to generate electronic vacancies and coherent spin centers. It should be mentioned that the coherent spin centers are a key ingredient of the quantum technologies. Thus, introducing controlled quantum-coherent centers it was predicted that the incorporated defects in conjugated carbon materials should also display long coherence times. By this manner it was showed superior quantum performances with these molecular modified graphene nanostructures (Fig. 31). These graphenoids with atomic modification control could lead to quantum electronic Nanomaterials with potential applications in carbon-based optoelectronic developments, electronic, and bioactive systems [176].

Moreover it should be highlighted the impact of organic microcavities at room temperature on reverse intersystem crossing (RISC) rates. This interaction permitted

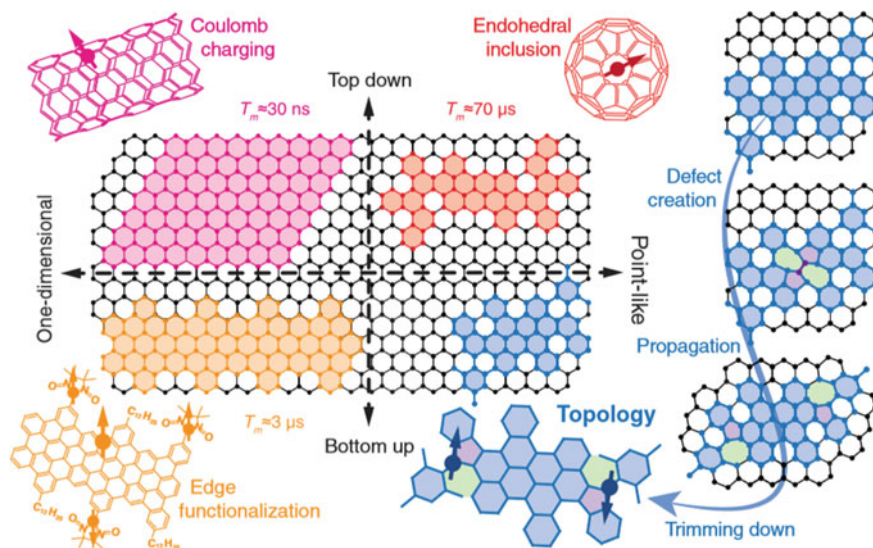


Fig. 31 Strategies toward obtaining aromatic quantum units. Quantum spin properties are introduced by heteroatom inclusion for endohedral fullerenes (red), Coulomb charging for carbon nanotubes (magenta), and side-functionalization in graphene nanoribbons (orange). Coherence times refer to room temperature, except for carbon nanotubes (mK). Topological stabilization of magnetic centers is obtained by rational synthetic tailoring of the lattice with atomic precision at preconceived sites (blue). The result is akin to a sequence (right) of introducing a Stone–Wales defect (purple and green), followed by propagation and trimming down. Reprinted with permission from Ref [181] (L. Bogani et al.). Copyright 2019 Science

thermally activated delayed fluorescence materials, that from strong light-matter coupling could be used to invert the ordering of singlet and triplet states and, in addition, enhance the RISC phenomena. By this manner It was demonstrated a Room-temperature superfluidity in a polariton condensate by a complete inversion of the singlet lower polariton and triplet excited states [177].

In addition, recently it was reported the enhanced current emission of carbon nanowalls (CNWs) by deposition of Ag, Au, In, and Mg as metal species [178]. The modified CNWs consisted of multi-layered graphene which is well-aligned vertically like walls. The morphology, coverage, chemical composition and crystallinity of the metal coating of 10 nm on CNWs were developed. The Ag-coated CNWs retained the highest current density for long-time emission at a constant applied field, while the non-coated CNWs have higher emission stability and a larger time constant of current degradation than the metal-coated ones.

From the differents examples given of graphene based on their intrinsic electronic properties it was showed varied measurable interaction with their environment such as light spin coupling, pseudo magnetic fields generation, electron shuttle, light guiding, and enhanced emissions.

In this manner, the electronic properties within the near field of organic materials permitted the design and fabrication of high density and high speed optoelectronic circuits. Thus, for example it was studied the Organic field-effect of highly conjugated organic semiconductor within optical waveguides [179]. The Organic semiconductor was based on carbazole nuclei (2,8-dichloro-5,11-dihexyl-indolo(3,2-b)carbazole named as CHICZ, Fig. 32). The CHICZ flexible crystals showed strong blue emission and less loss coefficients in long distance which showed potential properties to be incorporated within a Plasmonic Silica waveguide. The incident laser beam was

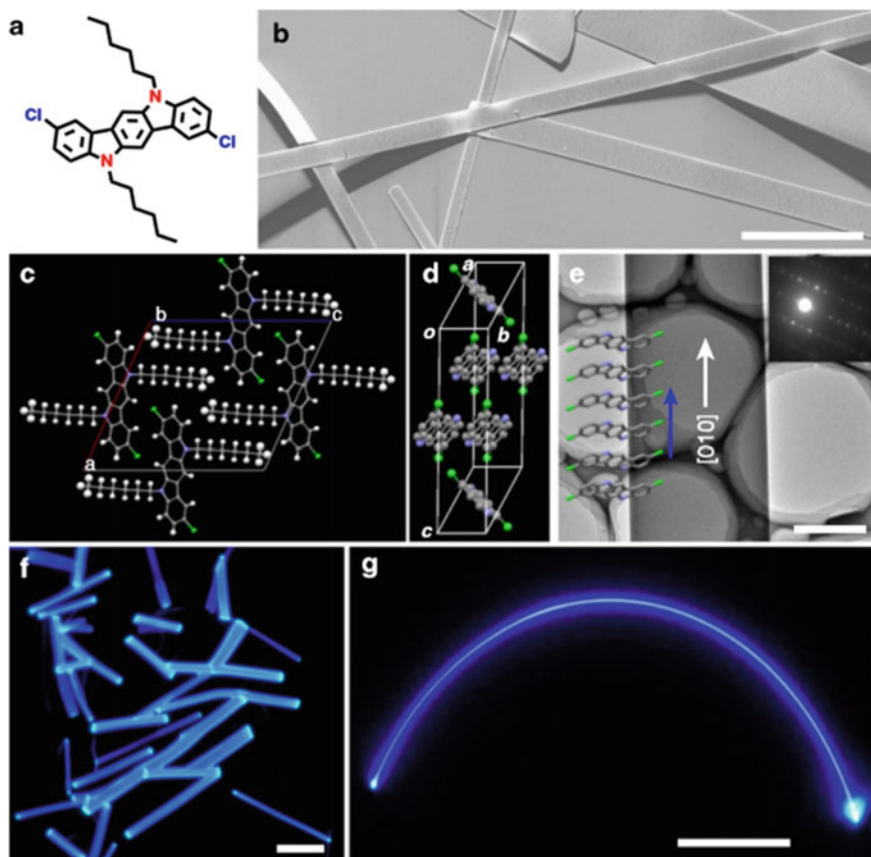


Fig. 32 Characterizations of CHICZ single crystals. **a** Molecular structure of CHICZ. **b** SEM image of CHICZ crystal ribbons. Scale bar: 20 μm . **c** and **d** Molecular packing in CHICZ single crystal seen from different directions. **e** TEM image and its corresponding SAED pattern of an individual CHICZ single crystal in which CHICZ molecules are packing along the b axis with $\pi - \pi$ stacking. Scale bar: 1 μm . **f** and **g** Fluorescence microscopy images of CHICZ ribbons showing less loss coefficients in long distance and good flexibility. Scale bar: 50 μm . Reprinted with permission from Ref [184] (W. Hu et al.). Copyright 2018 Nature Communications

guided into a CHICZ crystal through two possible ways: a) parallel, and b) perpendicular to the conducting channel of the transistors. In this manner it was evaluated the effect of electro-photo coupling. So, the propagation of optical waveguide in the active organic semiconductor could be tuned by the third terminal—the gate electrode of transistor, giving a controllable modulation depth as high as 70 and 50% in parallel and perpendicular directions of charge transport versus optical waveguide, respectively. Also, the optical waveguide with different directions can turn the field-effect of the device with the photodependence ratio up to 14,800. Therefore, It was achieved the integration of a field-effect transistor and optical waveguide together. This model system could be extended to more complicated fully conjugated systems.

Finally, it should be highlighted how from the control of the Nanoscale, it was arrived to high impact Research milestones with social impact such as Chips for computers with incorporation of graphene [180]; and Advanced Photonics Instrumentation for Biodetection with Plasmonic Resonators [140] The mentioned are just only two examples of many where hybrids Nanomaterials and Metamaterials were mainly involucrated for Nanotechnology developments.

4.4 Plasmonic Luminescent Organic Nanocomposites

This brief section intends to discuss how Organic Nanomaterials coupled to physical phenomena could lead to Advanced Luminescent Nanocomposites. These materials could be formed mainly by highly conjugated Carbon structures as support material as well as for their intrinsic properties. Small Organic molecules with Fluorescence properties were incorporated as Fluorescent reporters within Core-shell Nanoparticles and metallic Nanopatterned surfaces. The Fluorescent Nanoplatforms Bioconjugated with Biomolecules and antibodies showed enhanced Fluorescence emissions based on **MEF** with potential uses as emerging tools in biotechnology (Fig. 33) [7]. This Research Field still have being in progress accompanied with the generation of patents [181]. These Nanoplatforms showed impact on Single Nanoparticle Spectroscopy for Single Molecule Detection (**SMD**) applications [120].

The concept of the conjugation of an Organic molecule with metallic Nanosurfaces could be extended to higher conjugated Carbon allotropes with pseudo magnetic properties and Fluorescent emissions. These new Organic Luminescent Nanocomposites were not reported yet as best of our knowledge. However, there were many developed by us based on the combination of varied organic materials joined to inorganic Nanomaterials discussed in the previous sections of the present communication.

In addition, it should be mentioned and highlighted as well the importance of the control of the Nanoscales for developments of Micro-, and Nanodevices for Nanophotonics, Biophotonics and Nanomedicine applications [182]; where multidisciplinary Fields should be taken into account (Fig. 34). For all these developments the Organic materials showed to be important components of complex Nanoarchitectures for targeted studies and applications.

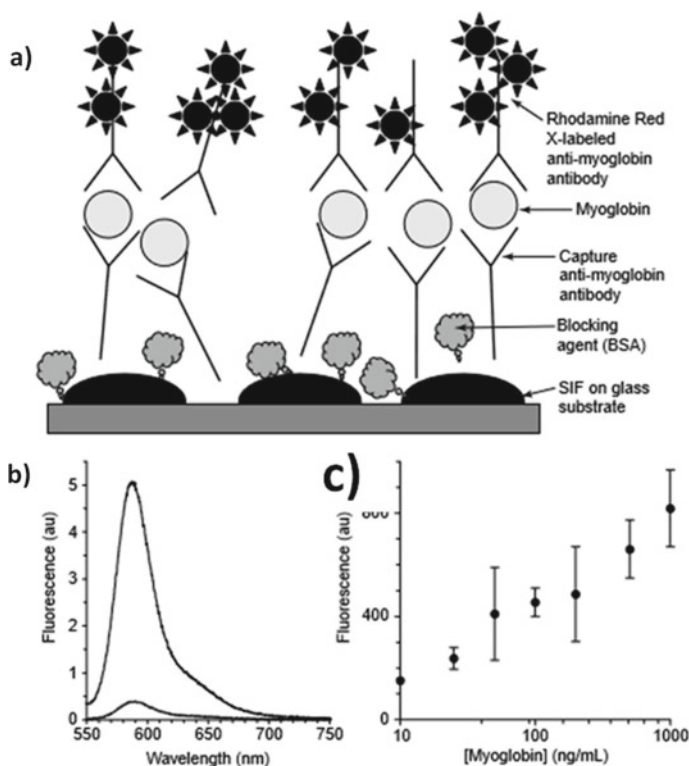


Fig. 33 Metal-enhanced planar immunoassays. **a** Schematic of a myoglobin-enhanced sandwich immunoassay on Silver Island Films (SiFs). **b** Fluorescence spectra of the Rhodamine Red-X-labeled anti-myoglobin antibody bound to the surface-immobilized myoglobin. The higher intensity corresponded from SiF on glass and the lower by on glass substrates. The concentration of myoglobin was 100 ng/mL on SiFs and on glass. **c** Fluorescence emission of Rhodamine Red-X-labeled anti-myoglobin antibody at different myoglobin concentrations on SiFs (excitation 532 nm). Reprinted with permission from Ref [186] (K. Aslan, I. Gryczynski, J. R. Lakowicz, C. D. Geddes et al.). Copyright 2005 Current Opinion in Biotechnology, Elsevier

So, Organic Nanocomposites with incorporation of Inorganic materials from different sources should show in the next years varied levels of developments in the Nanomaterial Research field for targeted applications.

5 Enhanced Chiro Optical Activity

The Chiro Optical activity from molecules to Nanoparticles and beyond based on the differentiation of the incident Electromagnetic Field of light between and after matter interaction showed to be very important in Life Sciences. In this section it was discussed the Enhanced Chiro-Optical properties based on the interaction of

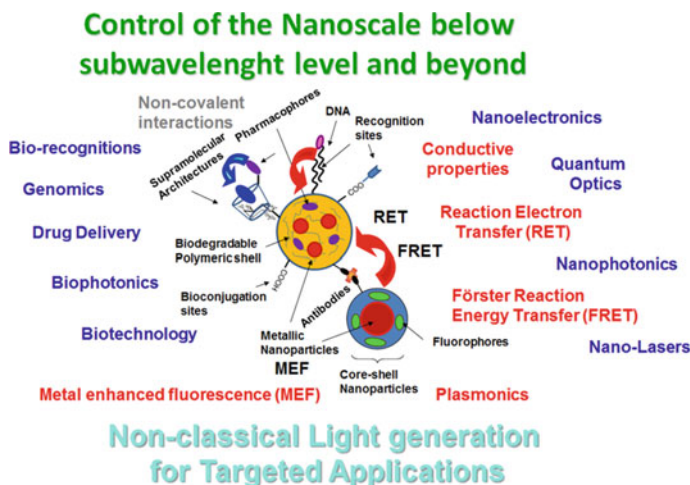


Fig. 34 Scheme of tuneable Nanoarchitectures for Targeted applications (written in blue) by exploiting different Photonic phenomena. Type of Nanoparticles, Chemical modifications and Physical properties developed are showed around them (written in black). Reprinted with permission from Ref [189] (A. G. Bracamonte et al.). Copyright 2020, Bentham Science Publishers

Chiral molecules with High Energy Electromagnetic Field from Plasmonic Nanostructures. As well, it was showed coupled Enhanced phenomena such as Luminescence and Dichroism signaling. Thus, it was opened new types strategies for molecular detection, Optical encryption and signal Waveguiding.

5.1 Basis of Chiral Light Differentiation

In order to begin this theme, it should be discussed the basis of the light discrimination in a typical Spectroscopy technique such as Circular Dichroism (CD). The CD is defined as the unequal absorption of left-handed and right-handed circularly polarized light. A beam of light has time dependent electric and magnetic fields associated with it. If the light is polarized by passing through suitable prisms or filters its electric field, E , will oscillate sinusoidally in a single plane. When viewed from the front, the sinusoidal wave can be visualized as the resultant of two vectors of equal length, which trace out circles, one which rotates clockwise (ER) and the other which rotates counter clockwise (EL). The two circularly polarized waves have physical existence. Thus, when an asymmetric molecule interacts with right and left circularly polarized light, it should be absorbed in different extents. By this manner the plane of the incident light wave is rotated and that the addition of the ER and EL vectors results in a vector that traces out an ellipse and the light is said to be elliptically polarized [183]. The CD spectroscopy is an excellent method for evaluation of secondary structure and folding of proteins.

And, as it is known the detection and differentiation of Chiral chemical structures is vital in nature due to the specificity of targeted interactions. Thus, from Biorecognition events to targeted drug administrations were ruled by Chiral selection. In the same way, the development in Nanoscience showed the importance and impact of engineered Nanoparticle Chiral selection by cell membranes. By this manner Supraparticles were designed to interact differentially with cells and proteins depending of their chemical modifications. The d-chirality modification demonstrated to be greater than threefold enhanced cell membrane penetration in breast, cervical, and multiple myeloma cancer cell [184]. So, Enhanced and improved Chiro-Optical strategies based on High Energy Electromagnetic Fields from Plasmonic interactions are currently investigated.

5.2 *Effect of Plasmonic Electromagnetic Fields on Chiro Optical Interactions*

In order to understand Enhanced Chiro-optical phenomena, it should be discussed first the Microscopic origin of the chiro optical response of optical media [185]. The CD intrinsically showed measureable signals at higher molecular concentrations than other classical spectroscopical techniques. However the development of engineered ultrathin optical devices within the Nanoscale permitted to enhance the CD response of Chiral media. At this point it is important to mention that the Chiro Optical response (CO) from Nano-Optical devices is not completely understood. But there is a recently reported theoretical model that contemplates the three main parameters that affects the CO response. It was defined a generalized Far field CO by the Optical Activity of the media (CO_{OA}) where it was contemplated a coupled electron oscillators system based on the Born-Kuhn model [186], then differential light absorption related with the planar interaction of a Chiral media and Near field absorption modes (CO_{abs}) [187], and the Axial CO that involucrate the birefringence physical phenomenon showed in all dielectric metamaterials (CO_{axial}) [188] (Fig. 35).

Each of the mentioned contributions showed independently considerable effect on the Far field CO signaling. By this manner the total Near field absorption modes could be considered as; $CO = CO_{OA} + CO_{abs} + CO_{axial}$. Thus, by tuning the matter media composition, it could be varied these phenomena with a consequent variation of the total CO signalling recorded.

In this way, for example it was developed Enhanced Circularly Polarized Luminescence from Reorganized Chiral Emitters on the Skeleton of a Zeolitic Imidazolate Framework [189]. The Chiral zeolitic imidazolate framework (ZIF) was obtained by modification their chemical surfaces with binaphthyl-derived (nominated as general structures: ZIF-8) with 4-(10-phenylanthracen-9-yl)phenyl and functional imidazole groups denominated as R-/S-1. These ZIF-8 Nanoplatfoms showed circularly polarized luminescence (CPL). These Chiral responsive Nanomaterials showed enhanced luminescent emissions in contact of enantioselective

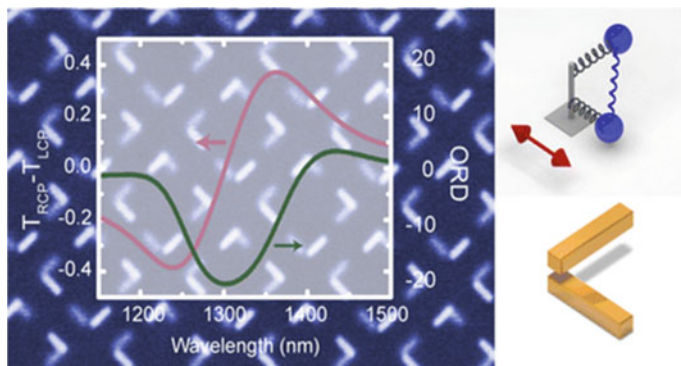


Fig. 35 Generation of natural optical activity in chiral media by coupled oscillator model of Born and Kuhn that consist in two identical, vertical, displaced and coupled oscillators. Inset images show modes of interactions from the classical Hook model applied. Reprinted with permission from Ref [193] (H. Giessen et al.). Copyright 2013, Nano Lett

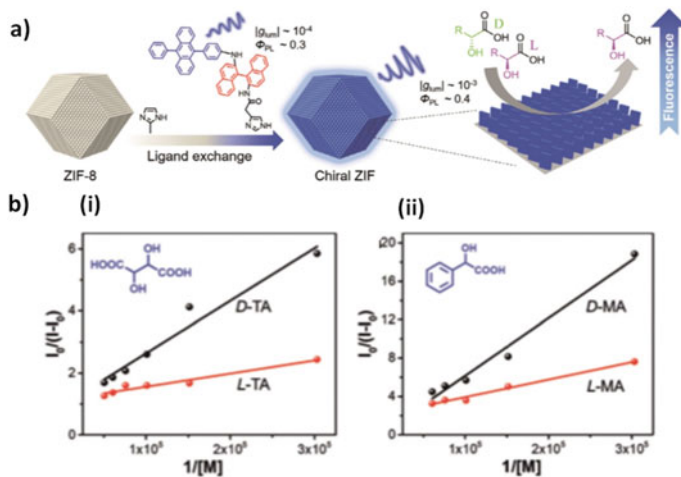


Fig. 36 a Amplified circularly polarized luminescence (CPL) and enantioselective recognition for α -hydroxycarboxylic acids of achiral ZIF. Crystal morphology of ZIF-8 and chemical structure of the chiral emitters and schematic representation of the ligand exchange at the surface of ZIF-8. The chiral emitters showed a well-ordered arrangement and rigid conformation on the skeleton, which resulted in the described properties. b (i) and (ii) corresponded to Benesi-Hildebrand plot of R-ZIF treated with l/d-TA and l/d-MA. Insets show the chemical structures of TA and MA, respectively. Reprinted with permission from Ref [196] (P. Duan et al.). Copyright 2019, Angew.Chem. Int. Ed

recognition of varied hydroxyl carboxylic acids (Fig. 36a). The presence of chiral binaphthyl and -NH- groups on the chiral emitters generated the enantioselective recognition of important α -hydroxycarboxylic acids such as tartaric acid (TA), and mandelic acid (MA) (Fig. 36b). These different sensitivities against the targeted

α -hydroxycarboxylic acids were based on their Association constants between the modified Chiral Nanoplatfoms and analytes, accompanied with variation of the media of the Fluorescent reporters.

In order to discuss the effect of High Energy Electromagnetic fields from Plasmons for Enhanced Circular Dichroism Spectroscopy [190]; it could be discussed a theoretical study related with a rigorous finite element method based study on the effects of various canonical plasmonic building blocks on the enhancement of molecular CD signals. These calculations were by the Mie theory by resolving the Maxwells equations contemplating the incorporation of a CO parameter. Thus, Plasmonic achiral nanorods did not showed CD signal; while in presence of a quiral media that interacted within High Energy hot spots generated between the Nanostructures enhanced DC signals. To quantify such enhancements it was defined the CD enhancement factor f as the ratio of the absolute values of the CD signals in presence of the plasmonic Nanoantennas and in absence of them. The Energy of the Electromagnetic Field generated took the main role in the enhancement factor f . By this manner it was showed a dependency of their enhancements values with planar inter-Nanorods spacer lengths. Optimal enhancements were determined within 5-10nm interval of values (Fig. 37). However, it should be highlighted that even with longer spacer lengths were determined appreciable enhancements with the configuration of Nanoantennas where Enhanced Plasmonic phenomena were generated as well. But, as near-field concentration played a crucial role, it was showed as well the effect of the spatial geometries of the conjunctions between the near fields of the

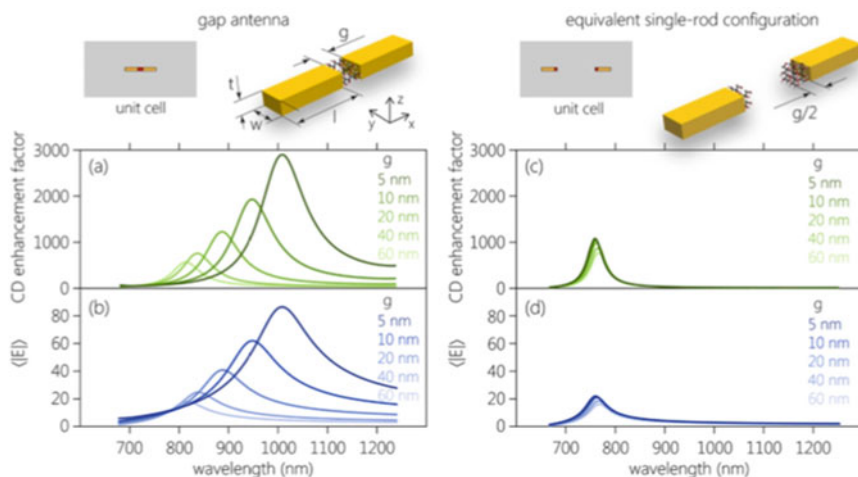


Fig. 37 Gap antenna and rod antenna enhancement factors. **a** CD enhancement factor for gap antennas of different gap sizes. **b** Averaged field enhancement within the volume occupied by the chiral medium in the case of gap antennas. **c** CD enhancement factor of the equivalent single rod antenna configuration for varying chiral medium volumes with side length g . **d** Averaged field enhancement within the volume occupied by the chiral medium in the case of rod antennas. Reprinted with permission from Ref [197] (T. Weiss et al.). Copyright 2016, ACS Photonics

Nanoantennas. But, at the best it was showed that planar configurations permitted better chiral-near field interactions for optimal interactions than other geometries such as vertically lifted out the plane. This fact was due to the standard planar gap antennas possessed the hot-spot electric field vectors parallel to the incident electric field vector.

By this manner, it was demonstrated the protein detection by Plasmon-coupled circular dichroism based on plasmonic nanoparticle-protein complexes [191]. To this study it was used Single particle Circular differential Scattering Spectroscopy coupled with electron imaging. Few proteins per inter-particle gaps of achiral Nanorods assemblies transferred and were responsible of the new Chiral properties of the Nanoassemblies. Therefore, potential applications in Biodetection are opened.

Moreover, it could be mentioned that the discussed properties could be incorporated in programmable optoelectronic devices. Thus, new Metamaterials with Enhanced Optical properties could be developed.

The fabrication of one dimensional nanomaterials with highly anisotropic optoelectronic properties are the key components for energy harvesting, flexible electronics, and biomedical imaging devices. For example it could be mentioned the 3D patterning of Perovskite nano-wire-block embedded within polystyrene-polyisoprene-polystyrene copolymer matrix with digitally programmable polarization anisotropy [192]. This proof of concept could be extended to other types of Nanomaterials with different properties depending of needs.

Finally, it should be mentioned that the design of new Metamaterials for active Optical properties by the incorporation of Plasmonic Nanomaterials permitted the tuning of emission of circularly polarized light by a linear dipole [193], the fabrication of Ultrathin Polarizing Plasmonic Metasurfaces [194], and Enhanced polarization sensitivity by plasmonic cavity in graphene phototransistors [195] (Fig. 38). So, the incorporation of High Energy Electromagnetic fields demonstrated to be important Optical Nanomaterial components for new Optical active materials for a large number of applications.

6 Future Perspectives in Enhanced Energy Fields

In the context to afford this final section, first it should be mentioned some general aspect in common for different developments that could add support to new designs. So, the perspectives related with Fundamental Research to Applied Research Developments with direct implications on design of new materials it could be mentioned many Research Fields involucrated.

In addition to propose new designs and materials from the Near field for Far fields applications it should be joined Multidisciplinary Fields as well.

As it was discussed in the different precedent sections to tune High Energy Electromagnetic fields it could be used different methodologies such as wet-chemistry

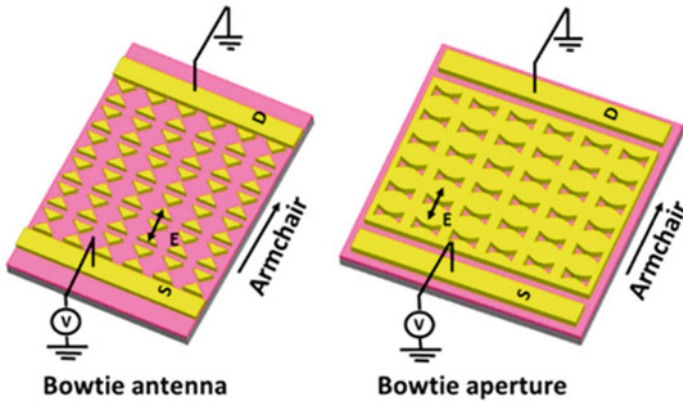


Fig. 38 Design of Plasmonic structures to show light polarization. The Bowtie antennas are used to increase the photocurrent in the armchair direction; while the Bowtie apertures are used for enhance the inherent polarization selectivity. Reprinted with permission from Ref [202] (X. Chen et al.). Copyright 2019, J. Appl. Phys

methodologies within Colloidal dispersions, chemistry of surfaces, and Lithography techniques that permitted the generation of Nanoplatfoms accompanied with particular properties depending of the intrinsic material used.

Moreover to the control of different High Electromagnetic fields and interaction with matter, each component should be tuned, from quantum properties to atoms, molecules and beyond within the Nanoscale for the generation of new Far field properties and phenomena. In this way, all type of new proposals and improved methods could find new interesting properties accompanied with potential applications, Functionalities or Multi-functionalities. Then, these Nanoarchitectures could be assembled in Nano-, and Microdispositives to develop or study other physical and chemical phenomena as well as to develop Functional devices.

Thus, it could be showed and discussed current directions of Fundamental Research with impact from basis of knowledge, proofs of concepts, and development of approaches, to real incorporation in Nanotechnology and technology such as Photonic devices and miniaturized instrumentation, etc. For example based on the control of the Nanoscale and patterning by Lithography techniques it could be highlighted the shaping of the Future of Nanotechnology and Biotechnology [196] that generated many patents in different technological fields. By this manner it was developed subwavelengths Optics [197], optical encryption and Quantum Optics [198] for targeted potential uses from Nanospectroscopy [11] to Quantum devices [199] and computing [200]. Moreover it should be highlighted the study the accurate incorporation of atoms within alloys, new drugs and organic molecules within Hybrids Nanocomposites, metallic and magnetic Nanoarchitectures with an accurate tuning of their surroundings. Then, highly conjugated organic allotropes from graphene to other carbon based materials were developed, incorporated within conductive materials, and currently are in progress too.

From all these developments as well it should be highlighted the innovation from combination of varied materials, as for example the use of well-known and largely applied rare metals within electronics for developments of Enhanced Luminescence based on MEF [201, 202].

Then, it could be mentioned how from inter-Near fields interactions, confined Nano-resonators were developed for multiple applications with impact on the frontiers of Nano-photonics and Quantum phenomena [203, 204]. By this manner, as well it was proposed new concepts as controlled light delivery within photonic plasmonic waveguides with potential impact on computer signaling [205]. In this theme as well it should be mentioned the fabrication of Organic materials for signal Waveguiding that even arrive to be compared with already developed silanized materials. To this subject it should be added the study of new properties from interaction of pseudo Electromagnetic fields such as from graphene and derivatives with Electromagnetic fields within the near field of metallic Nanoparticles.

Moreover, based on the control of Nanoscale and properties, it could be designed Nanocircuits and transistors by the development of hybrid quantum materials working at room temperature [206]. In this Research theme it should be highlighted how by diminishing sizes of Plasmonic Nanoplatforms it was arrived to study quantum phenomena from their Electromagnetic fields and interactions with surrounding [207].

Other example, related with the control below the Nanoscale where the matter constitution and control at the atomic level showed to be vital for studies such as Coherent spin manipulation of individual atoms on surfaces [208], for quantum applications and Enhanced electronic properties as Ultrafast optically induced spin transfer in ferromagnetic alloys [209].

But, the High Electromagnetic Energy within the Near field it was not used only for confined Far fields proofs of concepts and applications. This Energy was tuned as well for Nano-catalysis studies such as mechanistic studies of Plasmon Chemistry on Metal Catalysts [210, 211]. These studies have potential applications by their incorporation in Technology related with catalyzer. Moreover, to design and fabricate new materials towards solar cells such as top-illuminated flexible organic solar cells using ultrathin Ag-modified graphite-coated poly(ethylene terephthalate) substrates [25], and surface plasmon enhanced silicon solar cells [212]. These developments showed improved and Enhanced properties in comparison to in absence of the metallic Nanostructures.

Moreover, other example of real applications within the Far field based on a controlled Near field tuning, it is the development of Plasmonic Light Emitting Devices (P-LEDs), as for example AgNWs/AZO Composite Electrode for Transparent Inverted ZnCdSeS/ZnS Quantum Dot Light-Emitting Diodes [213]. In addition the design and fabrication of miniaturized instrumentation and multi-modal imaging based on Optical Fiber modifications. For all these developments the Nano-materials and control of their modifications were vital for the signal, light and energy transduction with high sensitivity. As for example it could be highlighted the design of Optrodes for combined optogenetics and electrophysiology applied in live animals, where it was showed how the light could be accurately delivered for targeted

Biomolecules [214]. Other related example it was the application of implantable devices and miniaturization of Light Emitting devices such as multisite micro-LED optrode arrays for neural interfacing, Neurophotonics [215]. This level of devices are close to Miniaturized Microscopies recently developed as well that arrived to be used to brain rodents monitoring in-vivo [216, 217]. At this level of technology, the use of Nano-tools as well it is well welcomed. This fact is showed in the development of many companies related with Life Sciences. By this manner, it could be mentioned the Synthetic non-classical luminescence generation by Enhanced Silica Nanophotonics based on Nano-Bio-FRET [218]; where non-classical light generated by Laser excitation was coupled to Optical active unicellular organism such as Cyanobacteria. In this Research field related with Biotechnology; as well it should be highlighted the use of strong Plasmonic Cores for coupling and enhancing emission of synthetic fluorophores from genetically engineered bacteria membranes [112]. Other example, that it could be mentioned, it is the use of Biocompatible MEF Nano-emitters based on gold Core-shell Nanoparticles for In Flow MEF-Bio-assays applications [219]. So, in this way the, there are many Research works from basic towards applied Research by the incorporation of varied High Energy Electromagnetic fields and coupled phenomena within the Nano-scale and beyond.

In this way the importance of the design and synthesis of materials and Metamaterials for Non classical light generation from the Nano-scale with interest in many Research fields such as Nanophotonics, Biophotonics, Nanomedicine [220], Waveguide signaling [221] are in progress. A well, it could be mentioned new concepts as targeted Functional Nano-materials [162], and Nano-, Micro-robots that showed in the last years many developments [222, 223].

Thus, it was briefly discussed and showed current Research directions based on Metamaterial and Hybrids materials with an accurate atomic, molecular and Nanoscale control, where chemistry and physics are joined to develop different High Energy emission and conduction modes.

Acknowledgements The author gratefully thanks to Professor Denis Boudreau from Département de chimie and Centre d'optique, photonique et laser (COPL), Québec, Canada, for the for the long standing collaboration Research work in progress. And to Professor Jesse Greener Dep. of Chem. of Laval University (CHM) to let me visit his Laboratory and support me within the Research field of Microfluidics. Moreover, to Professor Cornelia Bohne, from Department of Chemistry at University of Victoria, British Columbia, Canada, for her contribution in the field of Supramolecular Synthesis and Dynamics during the Postdoctoral position of the author. In addition to Professor Burkhardt Koenig from Institut für Organische Chemie, Universität Regensburg, Regensburg, Germany, for his motivation related with modifications of Organized systems and Photochemistry during a Research Visitor traineeship allowed to the author. In addition, specially thanks to Professor Nita Sahai from NASA Astrobiology Institute, University of Akron, Akron, Ohio, Unites States of America, where the author adquired knowledge from Origin of Life to Biotechnology during the Postdoctoral position of the author as well.

Finally it should be acknowledged the different grants and funds which allow to develop studies in this Research field and related. In particular, thanks to SECyT (Secretary of Science and Technology from the National University of Cordoba, UNC, Argentine) for the completion payment of the first Grant for Young Researchers that permit to work in this Research field. In addition to the Canadian Research Grants that permit the Research Collaborative work in progress.

References

1. Krenn, J.: Perspective on plasmonics. *Nat. Photonics* **6**, 714–715 (2012)
2. Romo-Herrera, J.M., Alvarez-Puebla, R.A., Liz-Marzan, L.M.: Controlled assembly of plasmonic colloidal nanoparticles clusters. *Nanoscale* **3**, 1–12 (2010)
3. Kamyshny, A., Magdassi, S.: Conductive nanomaterials for printed electronics. *Small* **10**(17), 3515–3535 (2014)
4. Briskina, C.M., Tarasov, A.P., Markushev, V.M., Shiryayev, M.A.: Magnetic field influence on the intensity of ZnO random lasing and exciton luminescence. *J. Nanophotonics* **12**(04), 1–4 (2018)
5. Zhao, W., et al.: Direct imaging of electron transfer band its influence on superconducting pairing at FeSe/SrTiO₃ interface. *Sci. Adv.* **4**, eaao2682, 1–7 (2018)
6. Patra, A., Koenen, J.-M., Scherf, U.: Fluorescent nanoparticles based on a microporous organic polymer network: fabrication and efficient energy transfer to surface-bound dyes. *Chem. Commun.* **47**, 9612–9614 (2011)
7. Aslan, K., Gryczynski, I., Malicka, J., Matveeva, E., Lakowicz, J.R., Geddes, C.D.: Metal enhanced fluorescence: an emerging tool in biotechnology. *Curr. Opin. Biotechnol.* **16**, 55–62 (2005)
8. Li, Q., Zhang, L., Li, J., Lu, C.: Nanomaterial amplified chemiluminescence systems and their applications in bioassays. *Trends Anal. Chem.* **1**(2), 1–13 (2011)
9. El Khamlichi, C., Reverchon-Assadi, F., Hervouet-Coste, N., Blot, L., Reiter, E., Morisset-Lopez, S.: Bioluminescence resonance energy transfer as a method to study protein-protein interactions: application to G protein coupled receptor biology. *Molecules* **24**(537), 1–21 (2019)
10. Talebi, N.: Electrons interacting with metamaterials: from few-photon sources to electronoptics. *SPIE Newsroom* (2017). <https://doi.org/10.1117/2.1201705.006891:1-3>
11. Huser, T.: Nano-biophotonics: new tools for chemical nano-analytics. *Curr. Opin. Chem. Biol.* **12**, 497–504 (2008)
12. Tang, Q., et al.: Micrometer and nanometer sized organic single crystalline transistors. *Adv. Mater.* **20**, 2947–2951 (2008)
13. Zhao, G., et al.: Organic field-effect optical waveguides. *Nat. Commun.* **9**, 4790, 1–7 (2018)
14. Kawachi, M.: Silica waveguides on silicon and their application to integrated optic components. *Opt. Quant. Electron.* **22**(5), 391–416 (1990)
15. Barnes, W.L., Kitson, S.C., Priest, T.W., Sambles, J.R.: Photonic surfaces. Microcavities and photonic bandgaps: physics and applications. In: Rarity, J., Weisbuch, C. (eds.) *NATO ASI Series (Series E: Applied Sciences)*, vol. 324. Springer, Dordrecht (1996)
16. Cheng, Z., Rios, C., Pernice, W.H.P., Wright, C.D., Bhaskaran, H.: On Chip photonic synapse. *Sci. Adv.* **3**, e1700160, 1–6 (2017)
17. Chang, H.M., et al.: Amplification of the signal intensity of fluorescence-based fiber-optic biosensors using a Fabry-Perot resonator structure. *Sensors* **15**, 3565–3574 (2015)
18. Gale, B.K., et al.: A review of current methods in microfluidic device fabrication and future commercialization prospects. *Inventions* **3**(60), 1–25 (2018)
19. Mi Kim, S., Woo Lee, S., Yi Moon, S., Young Park, J.: The effect of hot electrons and surface plasmons on heterogeneous catalysis. *J. Phys. Condens. Matter* **28**, 254002, 1–13 (2016)
20. Amendola, V., Bakr, O.M., Stellacci, F.: A study of the surface plasmon resonance of silver nanoparticles by the discrete dipole approximation method: effect of shape size, structure and assembly. *Plasmonics* **5**, 85–89 (2010)
21. Aroca, R.F.: Plasmon enhanced spectroscopy. *Phys. Chem. Chem. Phys.* **15**, 5355–5363 (2013)
22. Viger, M.L., Live, L.S., Therrien, O.D., Boudreau, D.: Reduction of self-quenching in fluorescent silica-coated silver nanoparticles. *Plasmonics* **3**(1), 33–40 (2008)
23. Asselin, J., Viger, M.L., Boudreau, D.: Metal-enhanced fluorescence and FRET in multilayer core-shell nanoparticles. *Adv. Chem.* **2014**, 1–16 (2014). Article no. 812313

24. Osmani, B., Töpfer, T., Müller, B.: Conducting and stretchable nanometer-thin gold/thiolfunctionalized polydimethylsiloxane films. *J. Nanophoton.* **12**(3), 033006, 1–11 (2018)
25. Wang, S., et al.: Towards all-solution-processed top-illuminated flexible organic solar cells using ultrathin Ag-modified graphite-coated poly(ethylene terephthalate) substrates. *Nanophotonics* **8**(2), 297–306 (2019)
26. Kafafi, Z.H., et al.: The role of photonics in energy. *J. Photonics Energy* **5**(050997–1), 1–44 (2015)
27. Suk Jung, H., Park, N.-G.: Perovskite solar cells: from materials to devices. *Small* **11**(1), 10–25 (2015)
28. Yano, H., Kudo, K., Marumo, K., Okuzaki, H.: Fully soluble self-doped poly(3,4-ethylenedioxythiophene) with an electrical conductivity greater than 1000 S cm^{-1} . *Sci. Adv.* **5**, eaav9492, 1–9 (2019)
29. Wang, X., Wu, D., Song, X., Du, W., Zhao, X., Zhang, D.: Review on carbon/polyaniline hybrids: design and synthesis for supercapacitor. *Molecules* **24**(2263), 1–18 (2019)
30. Schneider, F., Draheim, J., Kamberger, R., Wallrabe, U.: Process and materials properties of polydimethylsiloxane (PDMS) for optical MEMS. *Sens. Actuators A* **151**, 95–99 (2009)
31. Kewang, N., et al.: Compliant and stretchable thermoelectric coils for energy harvesting in miniature flexible devices. *Sci. Adv.* **4**, eaau5849, 1–7 (2018)
32. Nag, A., Mukhopadhyay, S.C., Kosel, J.: Wearable flexible sensors: a review. *Biosensors J.* **17**(13), 3949–3960 (2017)
33. Yang, Y., et al.: Electrically assisted 3D printing of nacre-inspired structures with self-sensing capability. *Sci. Adv.* **5**(4), eaau9490, 1–10 (2019)
34. Gao, L., et al.: Distinctive construction of chitin-derived hierarchically porous carbon-microspheres/polyaniline for high-rate supercapacitors. *ACS Appl. Mater. Interfaces* **10**, 28918–28927 (2018)
35. Wang, F., Beng, T.W., Zhang, Y., Fan, X., Wang, M.: Luminescent nanomaterials for biological labelling. *Nanotechnology* **17**, R1–R13 (2006)
36. Förster, Th.: 10th spiers memorial lecture. Transfer mechanisms of electronic excitation. *Discuss. Faraday Soc.* **27**, 7–17 (1959)
37. Selvin, P.R.: The renaissance of fluorescence resonance energy transfer. *Nat. Struct. Biol.* **7**, 730–734 (2000)
38. Tambasco, J.L., et al.: Quantum interference of topological states of light. *Sci. Adv.* **4**, eaa3187, 1–5 (2018)
39. Gordon, R.: Nanostructured metals for light-based technologies. *Nanotechnology* **30**, 212001, 1–21 (2019)
40. Wang, Y., Hu, A.: Carbon quantum dots: synthesis, properties and applications. *J. Mater. Chem. C* **2**, 6921–6939 (2014)
41. Owen, J., Brus, L.: Chemical synthesis and luminescence applications of colloidal semiconductor quantum dots. *J. Am. Chem. Soc.* **139**, 10939–10943 (2017)
42. Bera, D., Qian, L., Tseng, T.-K., Holloway, P.H.: Quantum dots and their multimodal applications: a review. *Materials* **3**, 2260–2345 (2010)
43. Qiu, X., Deng, H., Zhao, Y., Shi, Z.: Rhodium catalyzed, P-directed selective C7 arylation of Indoles. *Sci. Adv.* **4**, eaau6468, 1–9 (2018)
44. Zaja, D., Honisz, D., Łapkowski, M., Sołoducho, J.: Synthesis and properties of new Dithienosilole derivatives as luminescent materials. *Molecules* **24**, 2259, 1–10 (2019)
45. Woehrstein, J.B., et al.: Sub-100 nm meta-fluorophores with digitally tunable optical properties self-assembled from DNA. *Sci. Adv.* **3**(e1602128), 1–12 (2017)
46. Gmelch, M., Thomas, H., Fries, F., Reineke, S.: Programmable transparent organic luminescent tags. *Sci. Adv.* **5**, eaau7310, 1–6 (2019)
47. Isayama, K., Aizawa, N., Kim, J.Y., Yasuda, T.: Modulating photo- and electroluminescence in a stimuli-responsive p-conjugated donor-acceptor molecular system. *Angew. Chem. Int. Ed.* **57**, 11982–11986 (2018)

48. Ho, S., Liu, S., Chen, Y., So, R.: Review of recent progress in multilayer solution-processed organic light-emitting diodes. *J. Photonics Energy* **5**, 05761, 1–17 (2015)
49. Gutiérrez, C., et al.: Interaction-driven quantum Hall wedding cake–like structures in graphene quantum dots. *Science* **361**(6404), 789–794 (2018)
50. Purcell, E.M.: Spontaneous emission probabilities at radio frequencies. *Phys. Rev.* **69**, 681 (1946)
51. Su, Y., Chang, P., Lin, C., Helmy, A.S.: Record Purcell factors in ultracompact hybrid plasmonic ring resonators. *Sci. Adv.* **5**, eaav1790, 1–7 (2019)
52. Bloch, F., Purcell, E.M.: The Attraction of Spin, Nobel prize in Physics, Swedish Academy of Sciences (1952)
53. Pines, D., Bohm, D.: A collective description of electron interactions: II. Collective vs individual particle aspects of the interactions. *Phys. Rev.* **85**, 338, 1–10 (1952)
54. Mie, G.: Beitrage zur Optik truber Medien, speziell kolloidaller Metallosungen. *Annalen der Physik* **17**, 377–445 (1908)
55. Zhan, A., Gibson, R., Whitehead, J., Smith, E., Hendrickson, J.R., Majumdar, A.: Controlling three-dimensional optical fields via inverse Mie scattering. *Sci. Adv.* **5**, eaax4769, 1–5 (2019)
56. Martín, J., Proust, J., Gerard, D., Plain, J.: Localized surface plasmon resonances in the ultraviolet from large scale nanostructured aluminum films. *Opt. Matters Express* **3**(7), 954–959 (2013)
57. Mezziani, M.J., et al.: Formation and properties of stabilized aluminium nanoparticles. *Appl. Mater. Interfaces* **1**(3), 703–709 (2009)
58. Kind, C., Feldmann, C.: One-pot synthesis of In₀ nanoparticles with tuned particle size and high oxidation stability. *Chem. Mater.* **23**, 4982–4987 (2011)
59. Sharizal Alias, M., et al.: Review of nanophotonics approaches using nanostructures and nanofabrication for III-nitrides ultraviolet-photonics devices. *J. Nanophoton.* **12**(4), 043508, 1–56 (2018)
60. Rivero, P.J., Goicochea, J., Urrutia, A., Arregui, F.J.: Effect of both protective and reducing agents in the synthesis of multicolor silver nanoparticles. *Nanoscale Res. Lett.* **8**(101), 1–9 (2013)
61. Lee, J.-H., Cho, H.-Y., Kyu, C.H., Lee, J.-Y., Woo, C.J.: Application of gold nanoparticle to plasmonic biosensors. *Int. J. Mol. Sci.* **19**(2021), 1–14 (2018)
62. Wokaun, A., Lutz, H.P., King, A.P., Wild, U.P., Ernst, R.R.: Energy transfer in surface enhanced fluorescence. *J. Chem. Phys.* **79**(1), 509–514 (1983)
63. Lakowicz, J.R.: Radiative decay engineering: biophysical and biomedical applications. *Anal. Biochem.* **298**, 1–24 (2001)
64. Zhu, J., Zhu, K., Huang, L.-Q.: Using gold colloid nanoparticles to modulate the surface enhanced fluorescence of Rhodamine B. *Phys. Lett. A* **372**, 3283–3288 (2008)
65. Kelly, K.L., Coronado, E., Zhao, L.L., Schatz, G.C.: The optical properties of metal nanoparticles: the influence of size, shape, and dielectric environment. *J. Phys. Chem. B* **107**, 668–677 (2003)
66. Malinsky, M.D., Kelly, K.L., Schatz, G.C., Van Duyne, R.P.: *J. Am. Chem. Soc.* **123**, 1471 (2001)
67. Pylaev, T., Vanzha, E., Avdeeva, E., Khlebtsov, B., Khlebtsov, N.: A novel cell transfection platform based on laser optoporation mediated by Au nanostar layers. *J. Biophotonics* **12**, e201800166, 1–12 (2019)
68. Liz-Marzan, L.M.: Tailoring surface plasmons through the morphology and assembly of metal nanoparticles. *Langmuir* **22**, 32–41 (2006)
69. Moreau, L.M., et al.: The role of trace Ag in the synthesis of Au nanorods. *Nanoscale* **24**, 1–5 (2019)
70. Sun, Y.: Conversion of Ag nanowires to AgCl nanowires decorated with Au nanoparticles and their photocatalytic activity. *J. Phys. Chem. C* **114**, 2127–2133 (2010)
71. Matsui, H., Tabata, H.: Chapter 5. Oxide semiconductor nanoparticles for infrared plasmonic applications. In: *Science and applications of Tailored Nanostructures*, pp. 68–88 (2017). ISBN (eBook): 978-1-910086-19-3

72. Zhong, Y., Devi, M.S., Hamilton, T., Wasserman, D.: Review of mid-infrared plasmonic materials. *J. Nanophotonics* **9**, 093791, 1–21 (2015)
73. Hao, E., Schatz, G.C.: Electromagnetic fields around silver nanoparticles and dimers. *J. Chem. Phys.* **120**(1), 357–364 (2004)
74. Luchowski, R., et al.: Plasmonic platforms of selfassembled silver nanostructures in application to fluorescence. *J. Nanophotonics* **4**, 043516, 1–18 (2010)
75. Genç, A., Patarroyo, J., Sancho-Parramon, J., Bastús, N.G., Puentes, V., Arbio, J.: Hollow metal nanostructures for enhanced plasmonics: synthesis, local plasmonic properties and application. *Nanophotonics* **6**(1), 193–213 (2017)
76. Daniel, R., McCarthy, L., Ringe, E., Boudreau, D.: Enhanced control of plasmonic properties of silver-gold hollow nanoparticles via a reduction assisted galvanic replacement approach. *RSC Adv.* **9**, 389–396 (2019)
77. Park, J., et al.: Dynamic thermal emission control with InAs based plasmonic Metasurfaces. *Sci. Adv.* **4**, eaat3163, 1–7 (2018)
78. Osborne, I.S.: Switching on quantum dot lasers. *Science* **36**(6454), 652–655 (2019)
79. Su, Y., Chang, P., Lin, C., Helmy, A.S.: Record Purcell factors in ultra-compact hybrid plasmonic ring resonators. *Sci. Adv.* **5**, eaav179, 1–7 (2019)
80. Okamoto, K.: Chapter 2. Surface plasmon enhanced solid state light emitting devices. In: Wang, Z., Neogi, A. (eds.) *Nanoscale Photonics and Optoelectronics. Lecture Notes in Nanoscale Science and Technology*, vol. 9, Springer, New York (2010)
81. DeVetter, B.M., Bernacki, B.E., Bennett, W.D., Schemer-Kohrn, A., Alvine, K.J.: Multiresonant layered plasmonic films. *J. Nanophotonics* **11**(1), 016015, 1–8 (2017)
82. Liu, C.S., Tripathi, V.K.: Optical gain in surface plasmon nanocavity oscillators. *J. Nanophotonics* **10**(1), 016015, 1–11 (2016)
83. McMahan, J.M., et al.: Gold nanoparticle dimer plasmonics: finite element method calculations of the electromagnetic enhancement to surface-enhanced Raman spectroscopy. *Bioanal. Chem.* **394**, 1819–1825 (2009)
84. Righini, M., Ghenuche, P., Cherukulappurath, S., Myroshnychenko, V., Garcia de Abajo, F.J., Quidant, R.: Nano-optical trapping of Rayleigh particles and Escherichia coli bacteria with resonant optical antennas. *Nano Lett.* **9**(10), 3387–3391 (2009)
85. Hu, S., et al.: Experimental realization of deep subwavelength confinement in dielectric optical resonators. *Sci. Adv.* **4**, eaat2355, 1–6 (2018)
86. Altug, H., Englund, D., Vučković, J.: Ultrafast photonic crystal nanocavity laser. *Nat. Phys.* **2**, 484–488 (2006)
87. Schuller, J.A., Barnard, E.S., Cai, W., Chul, J.Y., White, J.S., Brongersma, M.L.: Plasmonics for extreme light concentration and manipulation. *Nat. Mater.* **9**, 193–204 (2010)
88. Tiecke, T.G., Thompson, J.D., de Leon, N.P., Liu, L.R., Vuletić, V., Lukin, M.D.: Nanophotonic quantum phase switch with a single atom. *Nature* **508**, 241–244 (2014)
89. Sipahigil, A., et al.: An integrated diamond nanophotonics platform for quantum optical networks. *Science* **354**, 847–850 (2016)
90. Yan, N., Liu, X., Zhu, J., Zhu, Y., Jiang, W.: Well-ordered inorganic nanoparticle arrays directed by block copolymer nanosheets. *ACS Nano* **13**, 6638–6646 (2019)
91. Pan, H., et al.: Ultrahigh-energy density lead-free dielectric films via polymorphic nanodomain design. *Science* **365**(6453), 578–582 (2019)
92. Popov, V.V., Fateev, D.V., Polischuk, O.V., Shur, M.: Enhanced electromagnetic coupling between terahertz radiation and plasmons in a gratinggate transistor structure on membrane substrate. *Opt. Express* **18**(16), 16771–16776 (2010)
93. Wang, L., Chen, X., Hu, W., Yu, A., Wang, S., Lu, W.: The absorption tunability and enhanced electromagnetic coupling of terahertz-plasmons in grating-gate AlN/GaN plasmonic device. *Opt. Express* **21**(9), 10821–10830 (2013)
94. Guo, N., Hu, W.-D., Chen, X.-S., Wang, L., Lu, W.: Enhanced plasmonic resonant excitation in a grating gated field-effect transistor with supplemental gate. *Opt. Express* **21**(2), 606–1614 (2013)
95. Lewis, R.A.: A review of terahertz sources. *J. Phys. D: Appl. Phys.* **47**(374001), 1–11 (2014)

96. Metzger, B., Hentschel, M., Giessen, H.: Ultrafast nonlinear plasmonic spectroscopy: from dipole nanoantennas to complex hybrid plasmonic structures. *ACS Photonics* **3**, 1336–1350 (2016)
97. Aslan, K., Wu, M., Lakowicz, J.R., Geddes, C.D.: Fluorescent core–shell Ag@SiO₂ nanocomposites for metal-enhanced fluorescence and single nanoparticle sensing platforms. *J. Am. Chem. Soc.* **129**(6), 1524–1525 (2007)
98. Lessard-Viger, M., Rioux, M., Rainville, L., Boudreau, D.: FRET enhancement in core shell nanoparticles. *Nano Lett.* **9**(8), 3066–30718 (2008)
99. Lakowicz, J.R., et al.: Plasmon controlled fluorescence: a new paradigm in fluorescence spectroscopy. *Analyst* **133**, 1308–1346 (2008)
100. Lackowicz, J.R.: Radiative decay engineering: Metal enhanced fluorescence and plasmon emission. *Anal. Biochem.* **337**, 171–194 (2005)
101. Ray, K., Chowdhury, M.H., Szmecinski, H., Lakowicz, J.R.: Metal-enhanced intrinsic fluorescence of proteins on silver nanostructured surfaces toward label-free detection. *J. Phys. Chem. C* **46**(112), 17957–17963 (2008)
102. Lessard-Viger, M., Brouard, D., Boudreau, D.: Plasmon Enhanced energy transfer from a conjugated polymer to fluorescent core shell nanoparticles: a photophysical study. *J. Phys. Chem. C* **115**(7), 2974–2981 (2011)
103. Lackowicz, J.R.: Radiative decay engineering 5: metal-enhanced fluorescence and plasmon emission. *Anal. Biochem.* **337**, 171–194 (2005)
104. Geddes, C.D., Lakowicz, J.R.: Metal-enhanced fluorescence. *J. Fluorescence* **12**(2), 121–129 (2002)
105. Geddes, C.D.: Metal-enhanced fluorescence. *Phys. Chem. Chem. Phys.* **15**, 19537 (2013)
106. Maier, S.A., Atwater, H.A.: Plasmonics: localization and guiding of electromagnetic energy in metal/dielectric structures. *J. Appl. Phys.* **98**, 011101, 1–10 (2005)
107. Sudiarte, I.W., Wallace Geldart, D.J.: Solving the Schrodinger equation for charged particle in a magnetic field using the finite time domain method. *Phys. Lett. A* **372**, 3145–3148 (2008)
108. Zhu, J., Zhu, K., Huang, L.-Q.: Using gold nanoparticles to modulate the surface enhanced fluorescence of Rhodamine B. *Phys. Lett. A* **372**, 3283–3288 (2009)
109. Dragan, A.I., Geddes, C.D.: Metal enhanced fluorescence: the role of quantum yield Q_0 in enhanced fluorescence. *Appl. Phys. Lett.* **100**, 093115, 1–4 (2012)
110. Rioux, M., Gontero, D., Veglia, A.V., Bracamonte, A., Guillermo, B.D.: Synthesis of ultraluminiscent gold core-shell nanoparticles as nanoimaging platforms for biosensing applications based on metal enhanced fluorescence. *RSC Adv.* **7**, 10252–10258 (2017)
111. Gontero, D., Veglia, A.V., Boudreau, D., Bracamonte, A.G.: Ultraluminiscent gold Core@shell nanoparticles applied to individual bacterial detection based on metal-enhanced fluorescence nanoimaging. *J. Nanophotonics* **12**(1), 012505, 1–12 (2018). Special issue Nanoplasmonics for Biosensing, Enhanced Light-Matter Interaction, and Spectral Engineering
112. Golberg, K., Elbaz, A., McNeil, R., Kushmaro, A., Geddes, C.D., Marks, R.S.: Increased bioassay sensitivity of bioactive molecule discovery using metal-enhanced bioluminescence. *Nanopart. Res.* **16**(2770), 1–14 (2014)
113. Asselin, J., Legros, P., Grégoire, A., Boudreau, D.: Correlating metal-enhanced fluorescence and structural properties in Ag@SiO₂ core-shell nanoparticles. *Plasmonics* **11**(5), 1369–1376 (2016)
114. Nie, S., Emory, S.R.: Probing single molecules and single nanoparticles by surface-enhanced Raman scattering. *Science* **275**, 1102–1108 (1997)
115. Senes, A., et al.: Increasing the horizontal orientation of transition dipole moments in solution processed small molecular emitters. *J. Mater. Chem. C* **5**, 6555–6562 (2017)
116. Magnan, F., Gagnon, J., Fontaine, F.-G., Boudreau, D.: Indium@silica core–shell nanoparticles as plasmonic enhancers of molecular luminescence in the UV region. *Chem. Commun.* **49**, 9299–9301 (2013)
117. Tam, F., Goodrich, G.P., Johnson, B.R., Halas, N.J.: Plasmonic enhancement of molecular fluorescence. *Nano Lett.* **7**(2), 496–501 (2007)

118. Seelig, J., et al.: Nanoparticle-induced fluorescence lifetime modification as nanoscopic ruler: demonstration at the single molecule level. *Nano Lett.* **7**(3), 685–689 (2007)
119. Le Ru, E.C., Etchegoin, P.G., Féliđj, N., Aubard, J., Lévi, G.: Mechanisms of spectral profile modification in surface-enhanced fluorescence. *J. Phys. Chem. C* **111**(44), 16076–16079 (2007)
120. Aslan, K., Wu, M., Lakowicz, J.R., Geddes, C.D.: Fluorescent core-shell Ag@SiO₂ nanocomposites for metal-enhanced fluorescence and single nanoparticle sensing platforms. *J. Am. Chem. Soc.* **129**, 1524–1525 (2007)
121. Wang, L., Song, Q., Liu, Q., He, Q., Ouyang, J.: Plasmon-enhanced fluorescence-based core-shell gold nanorods as a near-IR fluorescent turn-on sensor for the highly sensitive detection of pyrophosphate in aqueous solution. *Adv. Funct. Mater.* **25**, 7017–7027 (2015)
122. Zhao, T., et al.: Gold nanorod-enhanced two-photon excitation fluorescence of conjugated oligomers for two-photon imaging guided photodynamic therapy. *J. Mater. Chem. C* **7**, 14693–14700 (2019)
123. Zhang, J., Gryczynski, I., Gryczynski, Z., Lakowicz, J.R.: Dye-labeled silver nanoshell-bright particle. *J. Phys. Chem. B* **110**, 8986–8991 (2006)
124. Kalele, S.A., et al.: Optical detection of antibody using silica silver core-shell particles. *Chem. Phys. Lett.* **404**, 136–141 (2005)
125. Nigoghossian, K., Ouellet, S., Plain, J., Messaddeq, Y., Boudreau, D., Ribeiro, S.J.L.: Upconversion nanoparticle-decorated gold nanoshells for near-infrared induced heating and thermometry. *J. Mater. Chem. B* **5**, 7109–7117 (2017)
126. Fu, Y., Zhang, J., Lakowicz, J.R.: Silver-enhanced fluorescence emission of single quantum dot nanocomposites. *Chem Commun. (Camb.)* **3**, 313–315 (2009)
127. Walhorn, V., Paskarbit, J., Gotthard, F.H., Harder, A., Anselmetti, D.: Distance dependence of near-field fluorescence enhancement and quenching of single quantum dots. *Beilstein J. Nanotechnol.* **2**, 645–652 (2011)
128. Ji, B., et al.: Non-blinking quantum dot with a plasmonic nanoshell resonator. *Nat. Nanotechnol.* **10**, 170–175 (2015)
129. Lakowicz, J.R., et al.: Radiative decay engineering. 2 Effects of Silver Island films on fluorescence intensity lifetimes, and resonance energy transfer. *Anal. Biochem.* **301**, 261–277 (2002)
130. Zhang, J., Fu, Y., Chowdhury, M.H., Lakowicz, J.R.: Enhanced Förster resonance energy transfer on single metal particle. 2. Dependence on donor–acceptor separation distance, particle size, and distance from metal surface. *J. Phys. Chem. C* **111**(32), 11784–11792 (2007)
131. Lessard, V.M., Rioux, M., Rainville, L., Boudreau, D.: FRET enhancement in multilayer core-shell nanoparticles. *Nano Lett.* **9**(8), 3066–3071 (2009)
132. Najari, A., Anh, H.H., Leclerc, M.: Biosensors based on a cationic polythiophene detection of DNA and proteins. *Polymer Preprints* **48**(2), 3–4 (2007)
133. Ho, H.A., et al.: Colorimetric and fluorometric detection of nucleic acids using cationic polythiophene derivatives. *Angew. Chem.* **114**(9), 1618–1621 (2002)
134. Dore, K., Leclerc, M., Boudreau, D.: Fluorescence signal amplification for ultrasensitive DNA detection. In: Geddes, C.D. (ed.) *Reviews in Fluorescence*, pp. 179–197. Springer (2007)
135. Viger, M.L., Brouard, D., Boudreau, D.: Plasmon enhanced resonance energy transfer from a conjugated polymer to fluorescent multilayer core shell nanoparticles: a photophysical study. *J. Phys. Chem. C* **115**(7), 2974–2981 (2011)
136. Brouard, D., Lessard, V.M., Bracamonte, A.G., Boudreau, D.: Label-free biosensing based on multilayer fluorescent nanocomposites and a cationic polymeric transducer. *ACS Nano* **5**, 1888–1896 (2011)
137. Brouard, D., Ratelle, O., Bracamonte, A.G., St. Louis, M., Boudreau, D.: Direct molecular detection of SRY gene from unamplified genomic DNA by metal enhanced fluorescence and FRET. *Anal. Methods* **5**, 6896–6899 (2013)
138. Brouard, D., Ratelle, O., Perreault, J., Boudreau, D., St-Louis, M.: PCR-free blood group genotyping using a nanobiosensor. *Vox Sang.* **108**, 197–204 (2015)

139. Asselin, J., Viger, M.L., Boudreau, D.: Metal-enhanced fluorescence and RET in multilayer core-shell nanoparticles. *Adv. Chem.* **2014**(812313), 1–16 (2014)
140. Grégoire, A., Boudreau, D.: Chapter 28: Metal-enhanced fluorescence in plasmonic waveguides, Springer science business media dordrecht B. In: Bartolo, D., et al. (eds.) *Nano-Optics: Principles Enabling Basic Research and Applications*, NATO Science for Peace and Security Series B: Physics and Biophysics (2017). https://doi.org/10.1007/978-94-024-0850-8_28
141. Szmazinski, H., Badugu, R., Mahdavi, F., Blair, S., Lakowicz, J.R.: Large fluorescence enhancements of fluorophore ensembles with multilayer plasmonic substrates: comparison of theory and experimental results. *J. Phys. Chem. C Nanomater. Interfaces* **116**(40), 21563–21571 (2012)
142. Chowdhury, M.H., Pond, J., Gray, S.K., Lakowicz, J.R.: Systematic computational study of the effect of silver nanoparticle dimers on the coupled emission from nearby fluorophores. *J. Phys. Chem. C Nanomater. Interfaces* **112**(30), 11236–11249 (2008)
143. Zhang, J., Fu, Y., Chowdhury, M.H., Lakowicz, J.R.: Metal-enhanced single-molecule fluorescence on silver particle monomer and dimer: coupling effect between metal particles. *Nano Lett.* **7**(7), 2101–2107 (2007)
144. Kim, K., Oh, J.-W., Lee, Y.K., Son, J., Nam, J.-M.: Associating and dissociating nanodimer analysis for quantifying ultrasmall amounts of DNA. *Angew. Chem. Int. Ed.* **56**, 9877–9880 (2017)
145. Acuna Guillermo, P., et al.: Distance dependence of single fluorophore quenching by gold nanoparticles studied on DNA origami. *ACS Nano* **6**(4), 3189–3195 (2012)
146. Puchkova, A., Vietz, C., Pibiri, E., Wünsch, B., Sanz, P.M., Acuna, G.P., Tinnefeld, P.: DNA origami nanoantennas with over 5000-fold fluorescence enhancement and single-molecule detection at 25 μ M. *Nano Lett.* **15**, 8354–8359 (2015)
147. Vietz, C., Kaminska, I., Sanz, P.M., Philip, T., Acuna, G.P.: Broadband fluorescence enhancement with self-assembled silver nanoparticle optical antennas. *ACS Nano* **11**(5), 4969–4975 (2017)
148. Wei, Q., et al.: Plasmonics enhanced smartphone fluorescence microscopy. *Sci. Rep.* **7**(2124), 1–10 (2017)
149. Radziuk, D., Mohwald, H.: Surpassingly competitive electromagnetic field enhancement at the silica/silver interface for selective intracellular surface enhanced Raman scattering detection. *ACS Nano* **9**(3), 2820–2835 (2015)
150. Veglia, A.V., Bracamonte, A.G.: β -Cyclodextrin grafted gold nanoparticles with short molecular spacers applied for nanosensors based on plasmonic effects. *Microchem. J.* **148**, 277–284 (2019)
151. Li, S., Liu, Y., Xing, R., Yan, X.: Covalently assembled dipeptide nanoparticles with adjustable fluorescence emission for multicolor bioimaging. *ChemBioChem* **19**, 1–7 (2018)
152. Xia, B., He, F., Li, L.: Metal enhanced fluorescence using aggregated silver nanoparticles. *Colloids Surfaces A Physicochem. Eng. Aspects* **444**, 9–14 (2014)
153. Yang, A., et al.: Real time tunable lasing from plasmonic nanocavity arrays. *Nat. Commun.* **6**(6939), 1–7 (2015)
154. Dong, J., Zhang, Z., Zheng, H., Sun, M.: Recent progress on plasmon-enhanced fluorescence. *Nanophotonics* **4**, 472–490 (2015)
155. Punj, D., et al.: A plasmonic antenna in box platform for enhanced single molecule analysis at micromolar concentrations. *Nat. Commun.* **8**, 512–516 (2013)
156. Chen, J., et al.: Gold nanocages: engineering their structure for biomedical applications. *Adv. Mater.* **17**, 2255–2261 (2005)
157. Yazdi, S., Daniel, J.R., Large, N., Schatz, G.C., Boudreau, D., Ringe, E.: Reversible shape and plasmon tuning in hollow AgAu nanorods. *Nano Lett.* **16**, 6939–6945 (2016)
158. Zhang, K.J., Lu, D.B., Da, B., Ding, Z.J.: Coupling of surface plasmon modes and refractive index sensitivity of hollow silver nanoprism. *Sci. Rep.* **8**, 1599, 1–13 (2018)
159. Dowran, M., Kumar, A., Lawrie, B.J., Pooser, R.C., Marino, A.M.: Quantum-enhanced plasmonic sensing. *Optica* **5**(5), 628–633 (2018)

160. Guillermo, B.A., Brouard, D., Lessard-Viger, M., Boudreau, D., Veglia, A.V.: Nanosupramolecular complex synthesis: switch on/off enhanced fluorescence control an molecular release using a simple chemistry reaction. *Microchem. J.* **128**, 297–304 (2016)
161. Veglia, A.V., Bracamonte, A.G.: Metal enhanced fluorescence emission and quenching protection effect with a host-guest nanophotonic-supramolecular structure. *J. Nanophotonics* **12**(3), 033004, 1–12 (2018). Special Section on Nanoscience and Biomaterials in Photonics
162. Gontero, D., Lessard-Viger, M., Brouard, D., Bracamonte, A.G., Boudreau, D., Veglia, A.V.: Smart multifunctional nanoparticles design as sensors and drug delivery systems based on Supramolecular chemistry. *Microchem. J.* **130**, 316–328 (2017)
163. Wanzke, C., Jussupow, A., Kohler, F., Dietz, H., Kaila, V.R.I., Boekhoven, J.: Dynamic vesicles formed by dissipative self-assembly. *ChemSystemsChem*, **2**, e1900044, 1–7 (2020)
164. Gruber, B., Stadlbauer, S., Spath, A., Weiss, S., Kalinina, M., Konig, B.: Modular chemosensors from self-assembled vesicle membranes with amphiphilic binding sites and reporter dyes. *Angew. Chem. Int. Ed.* **49**, 7125–7128 (2010)
165. Gruber, B., Balk, S., Stadlbauer, S., Koenig, B.: Dynamic interface imprinting: high-affinity peptide binding sites assembled by analyte-induced recruiting of membrane receptors. *Angew. Chem. Int. Ed.* **51**, 10060–10063 (2012)
166. Muller, A., Konig, B.: Vesicular aptasensor for the detection of thrombin. *Chem. Commun. (Camb.)* **50**, 12665–12668 (2014)
167. Du, J., O'Reilly, R.K.: Advanced and challenges in smart and functional polymer vesicles. *Soft Matter* **5**, 3544–3561 (2009)
168. Liu, H., et al.: Synthesis of luminescent carbon dots with ultrahigh quantum yield and inherent folate receptorpositive cancer cell targetability. *Sci. Rep. Nat.* **8**(1086), 1–8 (2018)
169. Huang, C., Dong, H., Su, Y., Wu, Y., Narron, R., Yong, Q.: Synthesis of carbon quantum dot nanoparticles derived from byproducts in bio-refinery process for cell imaging and in vivo bioimaging. *Nanomaterials* **9**(387), 1–11 (2019)
170. Zhao, M.X., et al.: Synthesis, biocompatibility and cell labelling of L-arginine functional cyclodextrin modified quantum dot probes. *Biomaterials* **31**, 4401–4408 (2010)
171. Valizadeh, A., et al.: Quantum dots: synthesis, bioapplications, and toxicity. *Nanoscale Res. Lett.* **7**(480), 1–14 (2012)
172. Jiang, Z., et al.: Building a bridge from papermaking to solar fuels. *Angew. Chem. Int. Ed.* **58**, 14850–14854 (2019)
173. Geim, A., Novoselov, K.: For groundbreaking experiments regarding the two-dimensional material graphene. The Nobel Prize in Physics 2010, Press Release of the Royal Swedish Academy of Sciences (2010)
174. Nigge, P., et al.: Room temperature strain induced Landau levels in graphene on a wafer scale platform. *Sci. Adv.* **5**, eaaw5593, 1–7 (2019)
175. Cheng, A., Taniguchi, T., Watanabe, K., Kim, P., Damien, P.J.: Guiding dirac fermions in graphene with a carbon nanotubes. *Phys. Rev. Lett.* **123**(216804), 1–4 (2019)
176. Lombardi, F., et al.: Quantum units from the topological engineering of molecular graphenoids. *Science* **366**(1107–1110), 1–4 (2019)
177. Lerario, G., et al.: Room-temperature superfluidity in a polariton condensate. *Nat. Phys.* **13**, 837–842 (2017)
178. Kaneko, Y., Terada, K., Teii, K.: Field emission characteristics of metal nanoparticle-coated carbon nanowalls. *Nanotechnology* **31**, 165203, 1–8 (2020)
179. Zhao, G., Dong, H., Liao, Q., Jiang, J., Luo, Y., Fu, H., Hu, W.: Organic field-effect optical waveguides. *Nat. Commun.* **9**(4790), 1–9 (2018)
180. Hills, G., et al.: Modern microprocessor built from complementary carbon nanotube transistors. *Nature* **572**, 572–593 (2019)
181. Geddes, C.D.: Metal-enhanced fluorescence nanoparticles. United States, Patent Application Publication, Pub. No.: US 2009/0022766 A1, 22 January 2009
182. Bracamonte, A.G.: *Frontiers in Nano- and Micro-device Design for Applied Nanophotonics, Biophotonics and Nanomedicine*. Bentham Science Publishers, United States (2021)

183. Greenfield, N.J.: Using circular dichroism spectra to estimate protein secondary structure. *Nat Protoc.* **1**(6), 2876–2890 (2006)
184. Yeom, J., et al.: Chiral Supraparticles for Controllable Nanomedicine. *Adv. Mater.* **1903878**, 1–7 (2019)
185. Davis, M.S., Zhu, W., Lee, J.K., Lezec, H.J., Agrawal, A.: Microscopic origin of the chiroptical response of optical media. *Sci. Adv.* **5**, eaav8262, 1–10 (2019)
186. Yin, X., Schäferling, M., Metzger, B., Giessen, H.: Interpreting chiral nanophotonic spectra: the plasmonic Born-Kuhn model. *Nano Lett.* **13**, 6238–6243 (2013)
187. Eftekhari, F., Davis, T.J.: Strong chiral optical response from planar arrays of subwavelength metallic structures supporting surface plasmon resonances. *Phys. Rev. B* **86**, 075428 (2012)
188. Ma, Z., Li, Y., Li, Y., Gong, Y., Maier, S.A., Hong, M.: All-dielectric planar chiral metasurface with gradient geometric phase. *Opt. Express* **26**, 6067–6078 (2018)
189. Zhao, T., Han, J., Jin, X., Liu, Y., Liu, M., Duan, P.: Enhanced circularly polarized luminescence from reorganized chiral emitters on the skeleton of a zeolitic imidazolate framework. *Angew. Chem. Int. Ed.* **58**, 4978–4982 (2019)
190. Nesterov, M.L., Yin, X., Schäferling, M., Giessen, H., Weiss, T.: The of plasmon generated near fields for enhanced circular dichroism spectroscopy. *ACS Photonics* **3**(4), 578–583 (2016)
191. Zhang, Q., et al.: Unraveling the origin of chirality from plasmonic nanoparticle-protein complexes. *Science* **365**(6460), 1475–1478 (2019)
192. Zhou, N., et al.: Perovskite nano-wire-block copolymer composites with digitally programmable polarization anisotropy. *Sci. Adv.* **5**, eaav814, 1–9 (2019)
193. Neugbauer, M., Banzer, P., Nechayev, S.: Emission of circularly polarized light by a linear dipole. *Sci. Adv.* **5**, eaav7588, 1–5 (2019)
194. Chen, W., et al.: Large-area nanoimprinted colloidal Au nanocrystal-based nanoantennas for ultrathin polarizing plasmonic metasurfaces. *Nano Lett.* **15**, 5254–5260 (2015)
195. Zhang, D., et al.: Enhanced polarization sensitivity by plasmonic cavity in graphene phototransistors. *J. Appl. Phys.* **126**(074301), 1–7 (2019)
196. Darvill, D., Centeno, A., Xie, F.: Plasmonic fluorescence enhancement by metal nanostructures: shaping the future of bionanotechnology. *Phys. Chem. Chem. Phys.* **38**, 1–4 (2013)
197. Barnes, W.L., Dereux, A., Ebbesen, T.W.: Surface plasmon subwavelength optics. *Nature* **424**, 824–831 (2003)
198. Stobińska, M., et al.: Quantum interference enables constant time quantum information processing. *Sci. Adv.* **5**, eaau9674, 1–5 (2019)
199. Dutt, A., et al.: On-chip dual comb source for spectroscopy. *Sci. Adv.* **4**, e1701858, 1–9 (2018)
200. Song, C., Cui, J., Wang, H., Hao, J., Feng, H., Li, Y.: Quantum computation with universal error mitigation on a superconducting quantum processor. *Sci. Adv.* **5**, eaav5686, 1–6 (2019)
201. Derom, S., et al.: Metal enhanced fluorescence in rare earth doped plasmonic core-shell nanoparticles. *Nanotechnology* **24**, 495704, 1–8 (2013)
202. Sun, Y., Thiel, C.W., Cone, R.L., Equall, R.W., Hutcheson, R.L.: Recent progress in developing new rare earth materials for hole burning and coherent transient applications. *J. Lumin.* **98**, 281–287 (2002)
203. Rechcińska, K., et al.: Engineering spin-orbit synthetic Hamiltonians in liquid-crystal optical cavities. *Science* **366**(6466), 727–730 (2019)
204. Bracamonte, A.G.: New matter properties and applications based on hybrid graphene-based metamaterials. *Curr. Graphene Sci. (CGS)* **4**, 1–4 (2020). Special issue: design and synthesis of graphene based metamaterials
205. Haffner, C., et al.: Optoelectronics. Nano-opto-electro-mechanical switches operated at CMOS-level voltages. *Science* **366**, 860–864 (2019)
206. Pang, X.L., et al.: A hybrid quantum memory enabled network at room temperature. *Sci. Adv.* **6**, eaax1425, 1–8 (2020)
207. Du, L., et al.: Observation of new plasmon in the fractional quantum Hall effect: interplay of topological and nematic orders. *Sci. Adv.* **5**, eaav340, 1–5 (2019)

208. Yang, K., et al.: Coherent spin manipulation of individual atoms on a surface. *Science* **366**, 509–512, 1–4 (2019)
209. Hofferr, M., et al.: Ultrafast optically induced spin transfer in ferromagnetic alloys. *Sci. Adv.* **6**, eaay8717, 1–7 (2020)
210. Geonmonond, R.S., et al.: Marrying SPR excitation and metal–support interactions: unraveling the contribution of active surface species in plasmonic catalysis. *Nanoscale* **10**, 8560–8568 (2018)
211. Kazuma, E., Kim, Y.: Mechanistic studies of plasmon chemistry on metal catalysts. *Angew. Chem. Int. Ed.* **58**, 4800–4808 (2019)
212. Pillai, S., Catchpole, K.R., Trupke, T., Green, M.A.: Surface plasmon enhanced silicon solar cells. *J. Appl. Phys.* **101**, 093105, 1–8 (2007)
213. Jiang, X., et al.: AgNWs/AZO composite electrode for transparent inverted ZnCdSeS/ZnS quantum dot light-emitting diodes. *Nanotechnology* **31**(5), 1–10 (2019)
214. Dufour, S., De Koninck, Y.: Optrodes for combined optogenetics and electrophysiology in live animals. *Neurophotonics* **2**(3), 031205, 1–14 (2015)
215. McAlinden, N., et al.: Multisite microLED optrode array for neural interfacing. *Neurophotonics* **6**(3), 035010, 1–10 (2019)
216. Jacob, A.D., et al.: A Compact head-mounted endoscope for in vivo calcium imaging in freely behaving mice. *Curr. Protocols Neurosci.* **84**(1), 1–4 (2018)
217. Aharoni, D., Khakh, B.S., Silva, A., Golshani, J.P.: All the light that we can see: a new era in miniaturized microscopy. *Nat. Methods* **16**, 11–13 (2018)
218. Salinas, C., Ame, M.V., Bracamonte, A.G.: Synthetic non-classical luminescence generation by enhanced silica nanophotonics based on nano-bio-FRET. *RSC Adv.* **10**, 20620–20637 (2020)
219. Gontero, D., Veglia, A.V., Bracamonte, A.G.: In flow metal enhanced fluorescence for biolabelling and biodetection. *Photochem. Photobiol. Sci. RSC* **19**, 1168–1188 (2020)
220. Salinas, C.I., Bracamonte, A.G.: Design of advanced smart ultraluminous multifunctional nanoplatfoms for biophotonics and nanomedicine applications. *Front. Drug Chem. Clin. Res.* **1**(1), 1–8 (2018)
221. Salinas, C.I., Bracamonte, A.G.: From microfluidics to nanofluidics and signal waveguiding for nanophotonics, biophotonics resolution and drug delivery applications. *Front. Drug Chem. Clin. Res.* **2**, 1–6 (2019)
222. Alcântara, C.C.J., et al.: 3D fabrication of fully iron magnetic microrobots. *Small* **15**, 1805006, 1–9 (2019)
223. Justus, K.B., et al.: A biosensing soft robot: autonomous parsing of chemical signals through integrated organic and inorganic interfaces. *Sci. Robot.* **4**(31), eaax0765, 1–10 (2019)

Supramolecular Structures of Organic Molecules-Single Walled Carbon Nanotube Nanocomposites



Ahmed I. A. Abd El-Mageed and Takuji Ogawa

Abstract The merging of organic molecules and nanocarbons can potentially enhance the optoelectronic characteristics of the resultant nanocomposites, that will effectively lead to a significant development for the future of many applications i.e. environmental, energy harvesting, nanomolecular electronics, energy storage materials, gas storage materials, catalysis, polymer reinforcements, composite materials, nano-biotechnology and nano-medicine. Generally, the supramolecular structures of organic molecules on nanocarbons' surfaces have attracted much more attention for considerable nanoscience applications. Many nanocarbon candidates were used i.e. single-walled carbon nanotube (SWNT), highly oriented pyrolytic graphite (HOPG), fullerene as well as graphene. Compared to organic molecules/HOPG conjugates; the supramolecular structures of organic molecules/SWNT nanocomposites are less studied and still difficult to be predicted. One of the most efficacious tools to characterise and control the supramolecular behaviour of organic molecules/SWNT nanocomposites is the scanning probe microscopy (SPM) i.e. scanning tunneling microscopy (STM) and atomic force microscopy (AFM). This review highlights the efforts done to investigate the supramolecular structures of some organic molecules (i.e. porphyrins, polymer and other organic molecules) on SWNT surface characterized mainly by STM imaging technique supported by other measurements i.e. AFM, Ultraviolet (UV)-visible spectroscopy as well as theoretical calculations.

Keywords Nanocomposites · Scanning tunneling microscopy (STM) · Single-walled carbon nanotubes (SWNT) · Supramolecular structure · Porphyrin · Atomic force microscopy (AFM)

A. I. A. Abd El-Mageed (✉)

Chemistry Department, Faculty of Science, GALALA University, Galala City, Suez 43711, Egypt
e-mail: ahmed.abdelmageed@gu.edu.eg; ahmed.abdelmageed@mu.edu.eg

Chemistry Department, Faculty of Science, Minia University, Minia 61519, Egypt

T. Ogawa

Chemistry Department, Graduate School of Science, Osaka University, Machikaneyama 1-1, Toyonaka, Osaka 560-0043, Japan

Abbreviations

AFM	Atomic force microscopy
BDP	5, 15-bisdodecylporphyrin
CNTs	Carbon Nanotubes
DFT	Density Functional Theory
DOX	Doxorubicin
DWNT	double-walled carbon nanotubes
H ₂ TPP	5, 10, 15, 20-tetraphenyl-21H, 23H-porphine
HOPG	highly oriented pyrolytic
ITO	Indium Tin Oxide
MD	molecular dynamics
MM+	molecular mechanical modeling
MWNT	multi-walled carbon nanotubes
NIR	Near Infra-red
SAMs	self-assembled monolayers
SEM-EDS	Scanning electron microscopy with energy dispersive X-ray spectroscopy
SMM	single molecule magnet
SPM	scanning probe microscopy
STM	Scannig Tunneling Microscopy
STS	scanning tunneling spectroscopy
SWNT	Single-walled carbon nanotubes
TCNQ	tetracyanoquinodimethane
TEM	transmission electron microscopy
TTF	tetrathiofulvalene
UV	Ultraviolet
XPS	X-ray photoelectron spectroscopy

1 Introduction

Molecular Electronics [1]

Since the first model for single molecule-based device has been achieved by Arieh Aviram and Mark Ratner [2], in 1974, in which they have fabricated the first rectifier (electronic device) using tetracyanoquinodimethane (TCNQ) tetrathiofulvalene (TTF) and hemiquinone molecules; the molecular electronics field has attracted much more attention of various researchers [3–11]. Molecular electronics is a branch of science and/or nanotechnology in which single molecules, small group of molecules or nanoscale objects can be used as the principle active candidates in the electronic devices [3, 7]. Many various molecular building blocks can be utilized in the electronics device's fabrication i.e. molecules, nanoparticles, nanotubes and nanowires [12]. Unlike the solid-state devices which fabricated using “top-down” approach;

the single-molecule devices are mainly designed via “bottom-up” strategy in which molecular building blocks (i.e. atoms, molecules, nanoparticles and/or nanotubes) are emerged together to produce a very accurate design with specific and significant functionalities including diodes [13–15], memories [16–18], switches [19–23], logic gates [24–27], negative differential resistance [28], transistors [29–31] and wires [32].

There is another approach to fabricate the molecular electronic devices that is supramolecular chemistry techniques and/or self-assembly of organic molecules, carbon nanotubes, proteins and others. When molecules and/or atoms could be spontaneously organized giving regular arrays without any outside interference; this phenomenon known as self-assembly. The behavior of the electrochemically active molecules can be dramatically altered depending on the surrounded environment i.e. electrodes or any other materials; these are an interesting aspects in molecular electronic devices [7, 33].

Carbon Nanotubes (CNTs) [1]

Carbon nanotubes are hollow tubes of cylindrical-shaped sp^2 carbon atom with a radius of some nanometers and a few micrometers in length [34]; discovered by Iijima in 1991 [35, 36]. They are classified (based on the number of rolled-up graphene sheet) into single-walled (one graphene sheet) carbon nanotube (SWNT), double-walled (two graphene sheets) carbon nanotubes (DWNT) and multi-walled (more than two graphene sheets) carbon nanotubes (MWNT).

CNTs (especially SWNTs) have attracted much more attentions in the field of nanotechnology [37–40] as they can be used in a broad range of applications in numerous branches i.e. nano-molecular electronics, optoelectronics, sensors, energy storage materials, composite materials, nano-biotechnology, and nano-medicine. This mainly because SWNTs have a very promising and remarkable properties such as chemical stability, unique electronic and physical properties, high electrical and thermal conductivity as well as high surface area.

SWNT Functionalization [1]

The term SWNT functionalization means the physico-chemical modification of SWNT which can achieved by the interaction with other moieties and/or materials i.e. organic molecules, surfactants or polymers. In the supramolecular as well as molecular chemistry; SWNT can be functionalized with many approaches such as covalent sidewalls functionalization, non-covalent exohedral functionalization (i.e. formation of supramolecular adducts with surfactants or polymers or some organic molecules), endohedral functionalization with for example, C_{60} as well as defect functionalization [41].

Scanning Probe Microscopy (SPM) [1]

SPM behaves as one of the most powerful techniques that used in the measurement, characterization, manipulation and imaging substances in the material science as well as nanotechnology field. It is mainly producing images of the material surface by

scanning the sample surface using a physical probe. The most common types of SPM are scanning tunneling microscopy (STM) and atomic force microscopy (AFM).

The first STM has been invented by G. Binnig and H. Rohrer [42–44]; afterward STM become a powerful tool for the measurement, characterization, manipulation and imaging of the supramolecular structures of different organic molecules on different substrates [45–50]. STM measures the tunneling current (I) that is generated by a bias voltage (V) between the atomically sharp STM tip and conductive surface; by observing the tunneling current as the tip scans a surface; the surface morphology can be precisely detected. On the other hand, AFM is a very high-resolution SPM which used to analyze the surface features. It works by measuring atomic forces i.e. van der Waals forces, capillary forces, chemical bonding, mechanical contact force, magnetic forces, electrostatic forces, and other atomic forces.

In this review, we are highlighting the efforts done (to date) to investigate the supramolecular structures of different organic molecules (i.e. porphyrins, polymer and other organic molecules) on the SWNT surface characterized mainly by STM imaging technique supported by other measurements i.e. AFM, UV-visible spectroscopy as well as theoretical calculations. Incorporating of organic molecules with nanocarbons (especially SWNT) will lead to nanocomposite with enhanced properties i.e. conductive, mechanical and electrochemical which therefore can be applied directly in many low cost and economically viable applications i.e. energy storage materials, nanocomposites, nano-biotechnology, nano-medicine, environmental and energy harvesting.

2 Supramolecular Structures of Organic Molecules-SWNT Nanocomposites Characterized by STM Imaging Technique

Due to their distinctive advantages and unique properties i.e. high-speed fabrication, low cost, tunable electronic properties as well as low-temperature processing on flexible substrates; organic semiconductor molecules (like π -conjugated organic molecules and polymers) become more attractive compared to the traditional inorganic materials i.e. silicon. Moreover, it is possible to fabricate very promising devices and interesting designs via chemical synthesis, for instance molecular junctions-nanocarbons based devices. Furthermore, synthesis novel organic molecules (with new physical and electronic properties) will allow researchers to get novel dimensions and design flexibility which may be impossible to get using typical inorganic electronic materials. Additionally, merging synthetic molecules with other nano-building blocks will pave the way towards new and potentially useful applications. Consequently, single molecules become a promising candidate for the next generation of electronics [1, 7, 8, 33].

2.1 STM Studies of Porphyrin-SWNT Nanocomposites

Owing to their distinctive physical and optoelectronic properties, synthesis availability and high stability; porphyrins and its related materials are highly recommended to be utilized as main components in many fantastic applications i.e. enzymes simulation, catalysis, solar cells fabrication and energy conversion, organic light emitting devices, sensors, solar cells, light harvesting and molecular electronics applications. By changing the substituents which can bind to β - and/or *meso*- positions; the physical and electronic properties of porphyrins can be easily controlled. Furthermore, porphyrins (as divalent ligands) can be coordinated with almost every metal in the periodic table leading to much more enhancement of the optoelectronic properties of porphyrins [1, 51, 52].

Porphyrins can be arranged on the material surfaces via two common approaches; firstly, by the covalent attachment of porphyrins with the surface via well-established surface chemistries, this way is known as self-assembled monolayers (SAMs). However, the second approach in which porphyrins can be adsorbed (and/or self-organized) non-covalently onto surfaces forming giving two dimensional arrays and/or layers [1, 51, 52].

There are a few articles that described the STM identification for the supramolecular structures of porphyrin derivatives-SWNT nanocomposites. Basiuk and his research group have done a considerable effort in this regard during the period 2007–2013 [53–56], in which they have used the free base *meso*-tetraphenylporphine (or 5, 10, 15, 20-tetraphenyl-21H,23H-porphine, H₂TPP) and its complexes with Ni(II) and Co(II) (NiTPP and CoTPP, respectively), as well as hemin (a natural porphyrin) as target molecules that non-covalently adsorbed on the SWNT surface.

In their first report [54], they had studied the non-covalent interactions between porphyrin molecules (free base H₂TPP, CoTPP and NiTPP) with CNTs (MWNT and SWNT). They have stated from the experimental characterization that the adsorption strength can be in the order H₂TPP > CoTPP > NiTPP, respectively. According to their density functional theory (DFT) calculations, the interaction between H₂P and armchair (metallic) SWNT is stronger than that of CoP, however CoP can form stable complex with zigzag (semiconducting) SWNT than H₂P. Using STM measuring technique, they have measured only one composite sample (CoTPP/SWNT) under ambient conditions using HOPG substrate. Although, they have recognized some spots on the SWNT surface which may attributed to CoTPP molecules but they didn't realize any helical structure for the molecule on the tube surface due to the low image resolution. Consequently, one year later they tried to collect better STM images for CoTPP/SWNT composite [53], in addition to employing molecular mechanical modeling (MM+) to follow up how H₂TPP and CoTPP could be assembled on both HOPG and SWNT surfaces. From the MM+ modeling they have predicted (from an energetic point of view) that the free base H₂TPP molecules would rather form a monolayer than forming stacks on both HOPG and SWNT surfaces. Additionally, the H₂TPP molecules could assemble on SWNT sidewall forming long-period helix rather than short-period helix. The later finding was contradicted with their STM

measurements, where they have stated (based on their STM images) that CoTPP molecules prefer to assemble on the tube surface forming short-period helices rather than the long-period helical ones.

To confirm their previous study [53], in 2011, Basuik's group done another trial [55] to study again the self-assemble behavior of H₂TPP molecule on HOPG and SWNT surfaces using MM+ calculations and STM measurements. They have stated (using MM+ calculations) that H₂TPP molecules prefer energetically to self-assemble on SWNT surface forming long-period helices in which porphyrin molecules were aligned at right-angles interacting with the neighboring molecules. However, using STM (regardless the low image's resolution), they claimed that porphyrin molecules appear as a bright round spots on the SWNT surface with a full coverage forming interacting long-period helices.

In 2013, Basuik et al. [56] reported the non-covalent adsorption of H₂TPP, NiTPP, CoTPP, as well as hemin (a natural porphyrin) on SWNT surface characterized mainly by STM (in addition to other experimental techniques) and molecular mechanics calculations. They have stated that CoTPP can interact with SWNT stronger than the other molecules where it can disperse the SWNT bundles due to the intercalation. Consequently, CoTPP can assemble on the SWNT surface forming long-period interacting helices with different periodicity (Fig. 1) due to different SWNT sample properties i.e. diameter, chiralities. On the other hand, the other porphyrins (free base, NiTPP and hemin) can only adsorb on the SWNT bundle's surface owing to the weak interaction with SWNT, and hence, the authors couldn't characterize them accurately using STM measurements (Fig. 1).

Pham et al. [57], in 2017, studied the physical properties of SWNT functionalized with tetrathioacetyl porphyrin polymer (H₂P) (Fig. 2a) deposited on Au(111) substrate using scanning tunneling microscopy/spectroscopy (STM/STS) as well as classical molecular dynamics (MD) simulation to investigate the effect of sample annealing on the SWNT surface. They have proved the SWNT functionalization with porphyrin molecules using UV-visible spectroscopic and AFM measurements (Figs. 2b, c and d). By using STM measurements, they revealed that the sample annealing could alter the SWNT-H₂P hybrid's stability and hence the tube surface coverage degree decreased from 72 to 22% due to the unwrapping of the functionalizing porphyrin moieties (Fig. 2e, f and g).

Since 2018 to date, our group [58–61] is doing a significant effort in studying the supramolecular structures of different porphyrin molecules on SWNT surface characterized mainly by SPM imaging technique (with very high and clear resolution compared to other studies) supported with other experimental techniques as well as DFT calculations. We have used different porphyrin candidates in our studies (Fig. 3) i.e. 5,15-bis(3,5-bis(isopentyloxyphenyl))-10,20-bis(trimethylsilylethynyl)porphyrinato with different metal centers i.e. Zn, Ni, and Co [58], 5,15-bisdodecylporphyrin (BDP) [59] and its Ni(II) complex (Ni-BDP) [60] as well as Tb^{III}-5,15-bisdodecylporphyrin double-decker complex [61].

In 2018, we [58] studied the supramolecular structures of porphyrin derivative with its Zn(II), Ni(II), and Co(II) complexes (Fig. 3a) that non-covalently adsorbed on the SWNT surface. In addition to STM; the complexes have also characterized

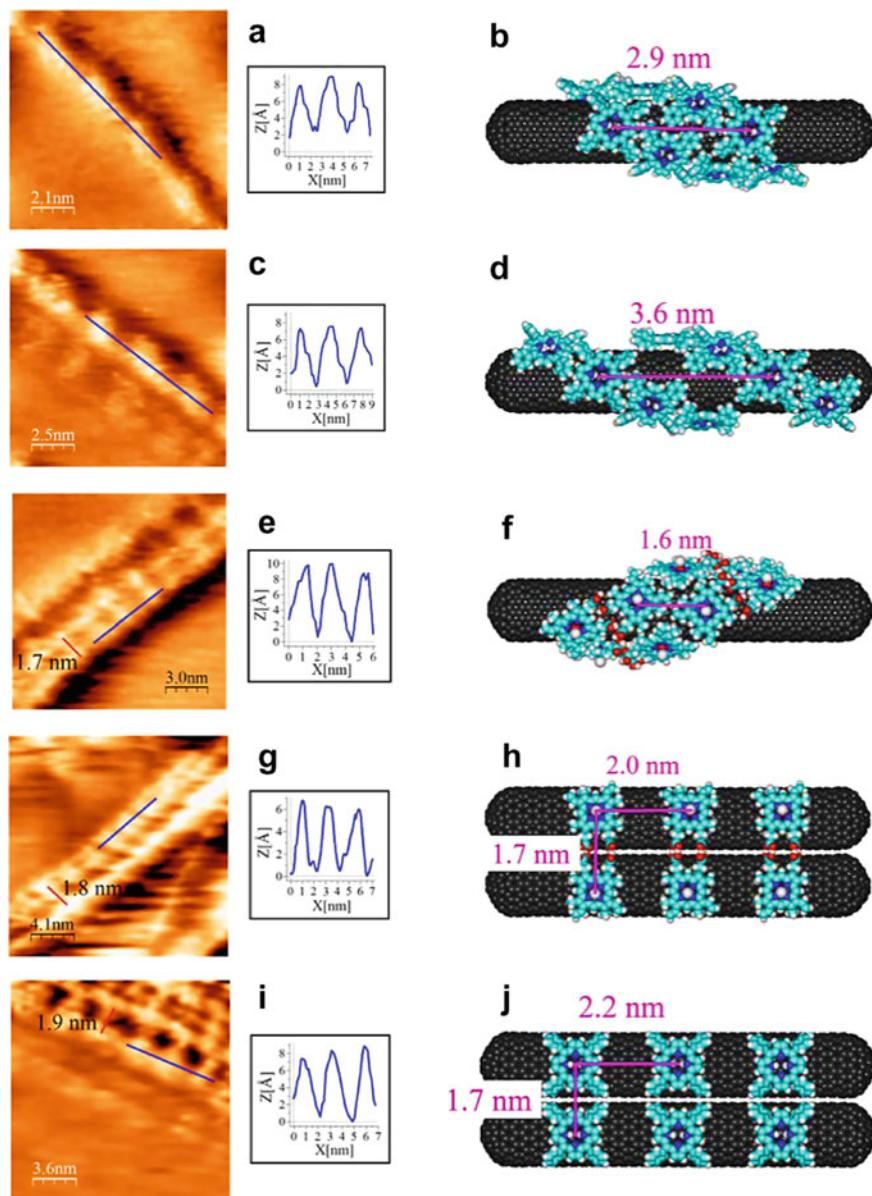


Fig. 1 STM images (together with the topographic profiles) for CoTPP/SWNT **a** and **c**, hemin/SWNT **e**, H₂TPP/SWNT **g**, and NiTPP/SWNT **i** complexes. STM imaging parameters: (a) $I_T = 1.1$ nA, $V = -0.5$ V; (c) $I_T = 0.9$ nA, $V = -0.5$ V; (e) $I_T = 1.0$ nA, $V = -0.5$ V; (g) $I_T = 0.6$ nA, $V = -0.5$ V; (i) $I_T = 0.9$ nA, $V = -0.5$ V. Optimized geometries suggested for CoTPP/SWNT **b** and **d** and hemin/SWNT **f** and **h** complexes, simulated using MM + force field. **j** Modeling shows the geometric arrays suggested for H₂TPP/SWNT and NiTPP/SWNT complexes, simulated using MM+ force field. Adapted from *Applied Surface Science* [56], copyright 2013, with permission from Elsevier

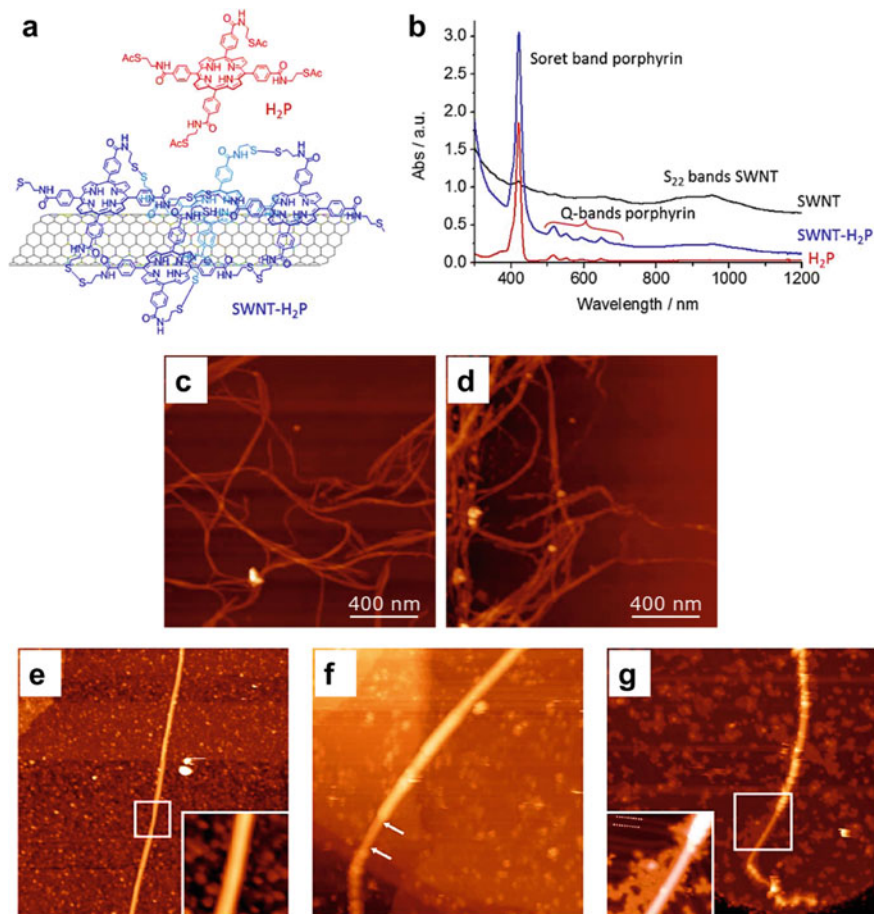


Fig. 2 **a** Chemical representation of porphyrin polymer derivatives (H₂P) and SWNT-H₂P hybrid. **b** UV–Vis–NIR absorption spectra of purified SWNT (black), free-base porphyrin H₂P (red) and SWNT-H₂P hybrid (blue). AFM images of carbon nanotubes deposited on Si/SiO₂, **c** before functionalization and **d** after functionalization. Typical STM images on Au(111) surface for **e** pristine nanotube, **f** SWNT-H₂P hybrid without annealing, and **g** SWNT-H₂P hybrid after annealing at 380 K. Adapted with permission of the American Chemical Society, copyright 2017 [57]

using transmission electron microscopy (TEM), scanning electron microscopy with energy dispersive X-ray spectroscopy (SEM–EDS), UV–visible spectroscopy as well as DFT calculations. Compared to Basuik’s study [56] we have succeeded to collect clearer STM images with better resolution. STM images revealed that the metalloporphyrins are apparently adsorbed on the SWNT surface (Fig. 4a–c) with clear debundling effect. ZnPor formed a supramolecular structure in the form of short helix-shaped arrays, however, NiPor formed a well-ordered arrays with long helix-structure (Fig. 4a and b). On the other hand, CoPor didn’t form any helical arrays on the tube surface (Fig. 4c) owing to the possibility of forming six-coordinate Co^{II}

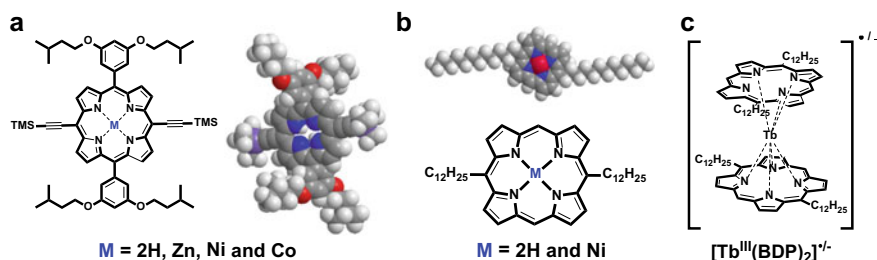


Fig. 3 Chemical structures of **a** 5,15-bis(3,5-bis(isopentyloxyphenyl))-10,20-bis(trimethylsilylethynyl)porphyrinato with its Zn(II), Ni(II), and Co(II) complexes. **b** 5,15-bisdodecylporphyrin (BDP) and its Ni(II) complex (Ni-BDP). **c** Tb^{III}-5,15-bisdodecylporphyrin double-decker complex

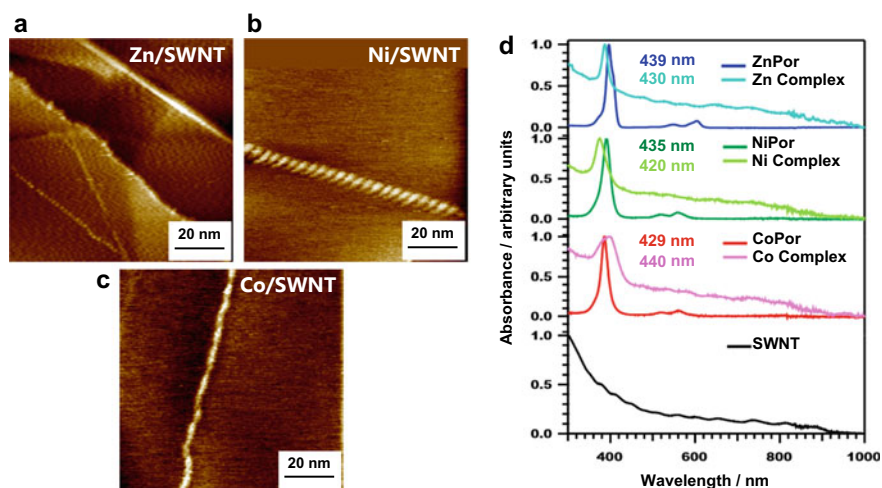


Fig. 4 STM images for the supramolecular structures (on HOPG surface) of **a** ZnPor/SWNT, **b** NiPor/SWNT, and **c** CoPor/SWNT complexes. STM imaging parameters: $V_{\text{sample}} = 0.100$ V and $I_t = 0.010$ nA, **d** UV–visible spectra of pristine SWNT and metalloporphyrins before and after the complexation, in CHCl_3 , accompanied by the λ_{max} values. Adapted from *Applied Surface Science* [58], copyright 2018, with permission from Elsevier

porphyrin with axial ligands i.e. water which obstructs forming any ordered pattern on the SWNT surface. The STM results are in consistent with UV–visible results in which the ZnPor and NiPor spectra were blue-shifted after complexing with SWNT, however the CoPor spectrum has red-shifted (Fig. 4d) due to the ligation with water molecules which led to the formation of J-aggregates. This study displayed that the incorporation of different metal centers inside the porphyrin ring will produce different supramolecular structures on the SWNT surface.

In 2019, we [59] have successfully investigated, for the first time, the experimental identification of SWNT absolute handedness-chirality using STM images

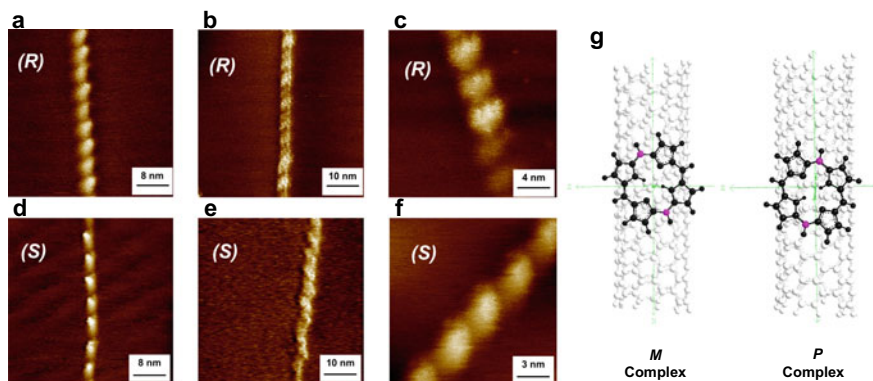


Fig. 5 a–f STM images of (*R*)-type (aligned to right) and (*S*)-type (aligned to left) of BDP/chiral-SWNT composites on HOPG surface under ambient conditions. STM parameters: $V_{\text{sample}} = 0.100$ V and $I_t = 0.010$ nA. **g** DFT optimized structures of *P*-(6,5)-SWNT/porphyrin complex (right) and *M*-(6,5)-SWNT/porphyrin complex (left), calculated using M05-2X/3-21G theoretical level. Adapted with the permission of Wiley, copyright 2019 [59]

of supramolecular structures of porphyrin derivatives (BDP, Fig. 3b). In this study, we confirmed that the supramolecular structures are sensitive to the chirality of SWNT beneath them. By utilizing this finding, the SWNT absolute-handedness chirality has been experimentally investigated using scanning tunneling microscopic images of supramolecular structures of porphyrin (BDP) for the first time. Two opposite chiral supramolecular structures have been observed based on the SWNT enantiomers handedness chirality (Fig. 5a–f). Beside STM, we have also identified the SWNT handedness-chirality using DFT calculations. Figure 5g shows the optimized structure of porphyrin/SWNT which displays the effect of SWNT handedness chirality on the alignment of porphyrin molecules on its surface. The possible geometries for BDP molecule to be aligned on SWNT surface as well as the whole supramolecular structures are displayed in Fig. 6a–q. The study is necessary as a key point to consider in designing and fabricating novel supramolecular architectures for porphyrin/SWNT-based devices with potential applications i.e. catalysts, sensors, optoelectronic, photonic and spintronic devices as an approach for the future development of molecular electronics field. Additionally, this study (first of its type) provides an obvious STM images with a very high resolution for porphyrin/SWNT supramolecular structures under ambient conditions.

In 2020, our recent work [60] reported the confirmation of SWNT absolute handedness-chirality identification using STM images (Fig. 7a–f) of supramolecular structures of metalloporphyrin (Ni-BDP, Fig. 3b). Additionally, this work illustrates that the metalation of porphyrin has no effect on the SWNT absolute handedness-chirality assignment, however, the main component is the porphyrin core with its large

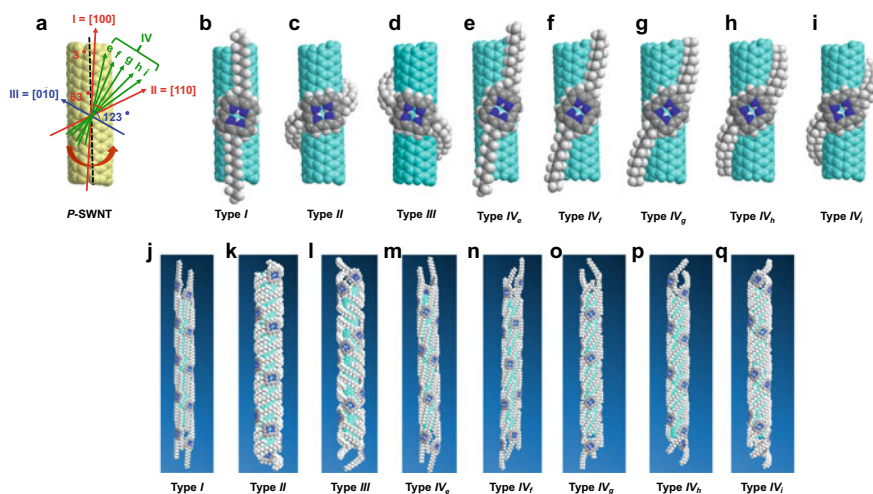


Fig. 6 **a–i** Models proposed to illustrate the possible geometries for one BDP molecule on the SWNT surface. **J–q** Models elucidate the whole supramolecular structures of BDP molecules on SWNT surface. Adapted with the permission of Wiley, copyright 2019 [59]

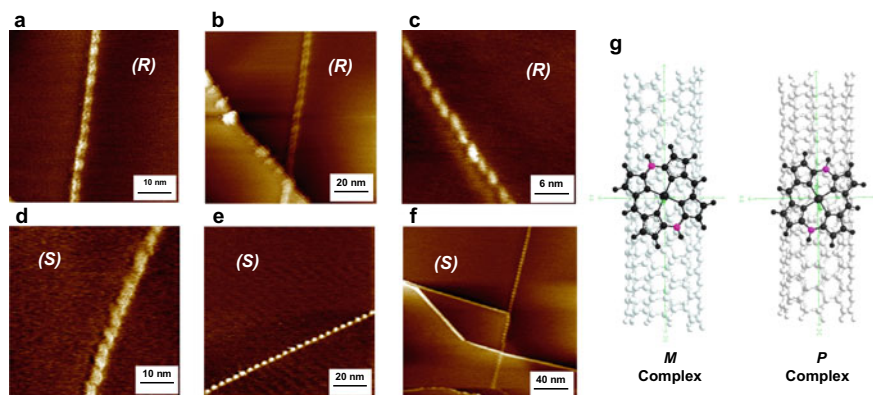


Fig. 7 **a–f** STM images of **(R)**-type (aligned to right) and **(S)**-type (aligned to left) of Ni-BDP/chiral-SWNT composites on HOPG surface. STM parameters: $V_{\text{sample}} = 0.100$ V and $I_t = 0.010$ nA. **g** DFT optimized structures of **P**-(6,5)-SWNT/Ni-porphyrin complex (right) and **M**-(6,5)-SWNT/Ni-porphyrin complex (left), calculated using M05-2X/3-21G theoretical level. Adapted with the permission of Wiley, copyright 2020 [60]

π -system. The study also provides an obvious STM images with a very high resolution for metalloporphyrin/SWNT supramolecular structures under ambient conditions. We have also supported our STM results with DFT calculations (Fig. 7g) which elucidates how the Ni-porphyrin obeys to the SWNT chiral structure beneath it.

To continue the considerable effort in this regard, we [61] have also studied (in 2019) the supramolecular structure of Tb^{III}-5,15-bisdodecylporphyrin double-decker complex (Fig. 3c) as single molecule magnet (SMM) on the SWNT surface using STM under an ultra-high vacuum and low temperature, AFM under ambient conditions and measuring the magnetic properties for the molecule and the composite as well. This is the first study of its type which reported the STM measurements of SMM/SWNT nanocomposites. STM images revealed that the molecule forms a well-ordered helix-shaped array with regular periodicity on the SWNT surface (Fig. 7a-g), some images displayed an interaction between both molecules and tubes as shown in Fig. 7f and 7g. AFM images (likewise STM) show strong debundling effect for SWNT due to the adsorption of SMM molecules on the tube surface, additionally, some helical arrays have been observed (Fig. 8a and d) and represented by modeling in Fig. 8h. Moreover, there are some interacted composites have been also observed (as in STM measurements) in Fig. 8e-g. We have measured some magnetic properties for the molecule before and after complexing with SWNT where the composite presents larger butterfly-shaped hysteresis loops than the molecule alone as an indication for longer relation time. Moreover, Due to the coupling between the SMM molecule and SWNT; the composite's magnetization increases almost linearly with decreasing temperature. This study opens the gate towards the future development of more advanced spintronic devices based on SMM/nanocarbon composites (Fig. 9).

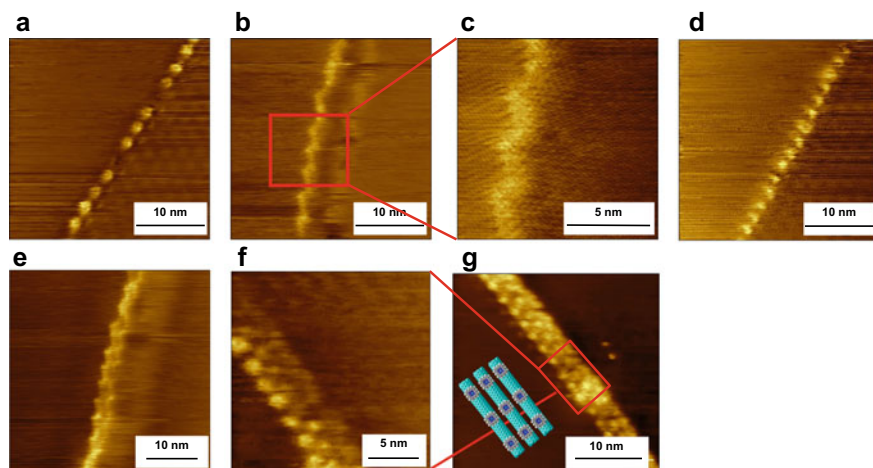


Fig. 8 a–g STM images of supramolecular structures of SMM/SWNT composites on HOPG surfaces. STM parameters: **a** $I_t = 0.1$ nA, $V_{\text{sample}} = 0.5$ V; **b** $I_t = 0.1$ nA, $V_{\text{sample}} = 0.3$ V; **c** $I_t = 0.1$ nA, $V_{\text{sample}} = 0.3$ V; **d** $I_t = 0.05$ nA, $V_{\text{sample}} = 0.2$ V; **e** $I_t = 0.1$ nA, $V_{\text{sample}} = 0.1$ V; **f** $I_t = 0.05$ nA, $V_{\text{sample}} = 0.1$ V; **g** $I_t = 0.05$ nA, $V_{\text{sample}} = -0.08$ V. The schematic model in Fig. g shows the side by side interaction of the composites. Adapted with the permission of The Royal Society of Chemistry [61]

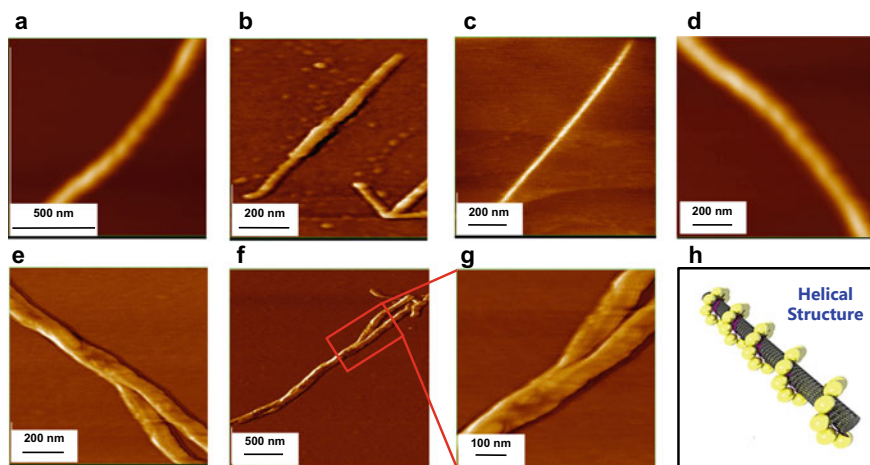


Fig. 9 a–g, AFM images of supramolecular structures of SMM/SWNT composites on HOPG surfaces under ambient conditions. **h** Schematic model shows the helical structure formed by the SMM molecule on the SWNT surface, as in Figures a and d. Adapted with the permission of The Royal Society of Chemistry [61]

2.2 STM Studies of Polymer-SWNT Nanocomposites

Polymer can interact with SWNT non-covalently via π - π stacking as well as van der Waal interactions. There are a few literatures which reported the supramolecular structures of different polymeric materials (i.e. [poly(*m*-phenylenevinylene-co-2,5-dioctoxy-*p*-phenylenevinylene), PmPV] [62], 1,8-diaminonaphthalene polymer [63], [regioregular poly(3-hexyl thiophene)] [64], [thiophene and 2-(2-thienyl) pyrrole] [65] and viologen polymer [66]) on SWNT surface characterized mainly by STM imaging technique supported by other experimental techniques and theoretical calculations.

In the first report, 2001, Carthy et al. [62], have functionalized SWNT with PmPV polymer where the SWNT has been coated with a polymer layer thirty time of the SWNT diameter. STM images on HOPG surface show the polymer wrapping on the tube surface. In addition to STM, they could characterize the PmPV/SWNT composite using STS and TEM.

Later in 2005, Tamburri et al. [63] prepared and measured the electrical properties for a novel category of layered composites in which SWNT was dispersed in 1,8-diaminonaphthalene polymer. This can be achieved by the electropolymerization of 1,8-diaminonaphthalene monomer in the presence of solution including SWNTs. Using this method, they could fabricate polymer/SWNT composite in which the polymer wasn't mixed directly with the SWNT. The STM measurements show that there is a contact between the polymer globules and SWNT bundles.

Goh et al. [64], in 2006, fabricated poly(3-hexylthiophene)/SWNT nanocomposites and characterized it using STM, TEM, Raman and UV–visible spectroscopies. They could image the polymer monolayers on SWNT surface using STM imaging technique which displayed the thiophene polymer chains wrapped around SWNT with chiral angle equals $41\text{--}48^\circ$ relative to the tube axis and interchain distance equals 1.68 \AA which is greater than that of polymer monolayers on HOPG surface (1.4 \AA).

In 2011, G. Kiani et al. [65] prepared a novel composite composed of (polythiophene-thienylpyrrole)/SWNT. The thiophene/thienylpyrrole monomers have firstly adsorbed on SWNT surface and then polymerized via chemical oxidative polymerization method. After adsorption, the electrical conductivity as well as thermogravimetric stability of the prepared composite have been enhanced compared to the bulk polymer and other similar composites. The STM measurements revealed that the SWNT surface has been successfully covered (partially or fully) with the polymer layer although there is no clear identification for the relative position of the two molecules on the tube surface.

One year later, in 2012, V-A. Constantin et al. [66] prepared two composites types composed of SWNT decorated with viologen polymer via electrochemical polymerization method. The synthesized composites have been characterized mainly by STM, Raman spectroscopy as well as XPS. The STM measurements (on ITO-glass electrode) demonstrated that molecules have been self-assembled on the tube surface before polymerization with almost full coverage, however, after polymerization they could observe some repeated viologen oligomer brushes along the SWNT.

2.3 STM Studies of Further Organic Molecules-SWNT Nanocomposites

There are some reports that provide an information about the supramolecular structures of nanocomposites formed of SWNT with further organic molecules (rather than porphyrin and polymer) i.e. linear-chain alkane and fatty acid molecules [67], thiol and thiophene [68], primary aliphatic amines [69], *t*-butyllithium [70], 9-aminoanthracene and 4-(pyren-1-yl)butanoic acid [71], peptide [72], benzoic acid [73], DNA [74] and doxorubicin [75].

In 2003, H. Ago et al. [67] studied the self-assemble structures of linear-chain alkane and fatty acid molecules on SWNT surface using STM imaging technique. Although, it was a bit difficult but they could sometimes observe seldomly some pattern for the target molecules on the tube surface, however, in comparison, these molecules can form clear lamellar structure on graphite surface. The authors attributed the reason due to the presence of different SWNT chiralities in the used sample. Figures 10a and b display the STM images for stearic acid and heptacosane, respectively, adsorbed on SWNT bundle surface, deposited in prior on HOPG surface.

L. Zhang et al. [68], in 2005, functionalized SWNT covalently with thiol and thiophene groups; they attached the function groups on the SWNT sidewalls via

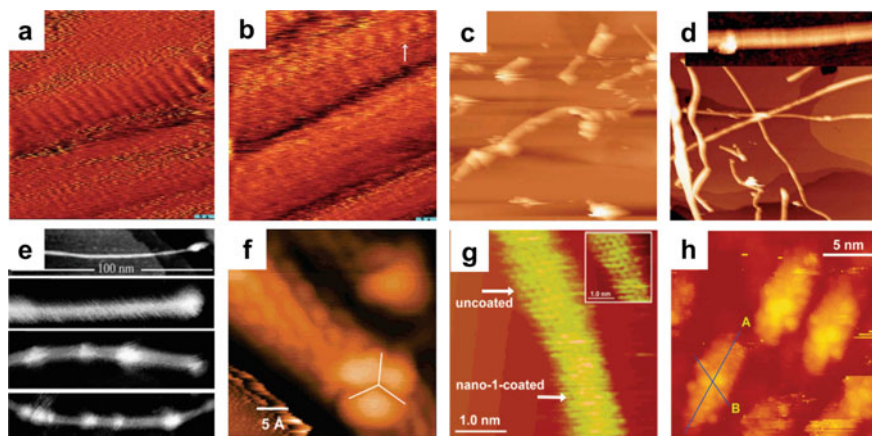


Fig. 10 STM image for **a** stearic acid, **b** heptacosane, casted on SWNT bundle surface deposited on HOPG surface. Adapted from *Chemical Physics Letters* [67], copyright 2003, with permission from Elsevier. STM images of **c** thiol-SWNT, **d** thiophene-SWNT on gold surface. Adapted with the permission of The Royal Society of Chemistry [68]. **e** STM images of 1-octadecylamine covalently attached to SWNT. Adapted with permission of the American Chemical Society, copyright 2006 [69]. **f** STM image of (*t*-Bu)₂ attached covalently to SWNT surface where the *t*-Bu group appears clearly as three-fold symmetry on the tube surface. Adapted with permission of the American Chemical Society, copyright 2006 [70]. **g** STM image shows part of SWNT coated with peptide molecule (lower part) as well as uncoated part (upper part) in which the atomic structure of SWNT is clearly appeared (inset). Adapted with permission of the American Chemical Society, copyright 2007 [72]. **h** STM image of DNA/SWNT composite on Si(110) substrate. Adapted with permission of the American Chemical Society, copyright 2009 [74]

substitution reaction of amine with fluoronanotubes. In order to follow up the SWNT functionalization they used AFM as well as gold nanoparticles as a marker. However, it's a good way but still it was difficult to assign exactly the functional groups distribution on the tube surface. Therefore, they have used STM to get an accurate information regarding the location of the substituted functional groups. Figures 10c and d provide STM images of thiol-SWNT and thiophene-SWNT, respectively, on gold surface in which the location of the functional groups was obviously observed.

In 2006, D. Bonifazi et al. [69] used some aliphatic amines i.e. 1-octylamine and 1-octadecylamine to functionalize SWNT covalently; where the reaction took place mainly on the nanotube ends. The attachment of the functional groups was characterized mainly using STM measurements where the molecules form a regular pattern and appear as a bright spots on the tube tips and sidewalls as well. Figure 10e display the STM images of 1-octadecylamine covalently attached to SWNT on both tips and sidewalls. On the same year, SWNT has been also covalently functionalized via the nucleophilic addition of *t*-BuLi to the SWNT sidewall producing *t*-Bu_nSWNT composite. By using STM measurements; R. Graupner and his coworkers [70] could observe the *t*-butyl groups attached covalently to the SWNT sidewall (as it's depicted in Fig. 10f) where the groups appear clearly as protrusions displaying the three-fold symmetry on the tube surface.

P. Lauffer et al. [71] functionalized the HiPCO-SWNT non-covalently with two organic molecules i.e. 9-aminoanthracene and 4-(pyren-1-yl)butanoic acid; the authors have evaluated the functionalization process with STM and STS measurements. However, the STM images didn't give a clear information about the actual functionalization degree, but still one can obviously observe the molecules attached successfully to the SWNT sidewalls. Although both molecules appear as protrusions on the SWNT sidewall but they are different; this can be clearly revealed from the STM images.

V. Z. Poenitzsch et al. [72], in 2007, used a designed peptide molecules to non-covalently adsorb on the SWNT surface via π - π stacking, additionally they have discussed the effect of electron-donating (hydroxyl) and electron-withdrawing (nitro) groups on the interaction between peptide and SWNT. They have characterized the resultant composite using AFM, STM, STS as well as Raman spectroscopy. The peptide molecule has been successfully adsorbed on the tube surface with a good coverage leading to SWNT dispersion; Fig. 10g shows STM image (on gold substrate) in which part of SWNT coated with peptide molecule (lower part) as well as uncoated part (upper part) in which the atomic structure of SWNT is clearly appeared (inset). STS and Raman measurements revealed that there is a weak charge transfer happened between the peptide and SWNT.

In the same year, C. RABOT et al. [73] studied the interaction between benzoic acid and SWNT co-adsorbed on Au (111) substrate. Although the benzoic acid molecules didn't adsorb directly on the SWNT walls; but there were some molecular arrays observed under the SWNT. These arrays were identified as dimers rows which hidden under the SWNT alignment; this suggested that the molecule-SWNT interaction is much weaker than the molecule-molecule interaction.

In 2009, D. A. Yarotski et al. [74] performed STM measurements for DNA-SWNT composite; Fig. 10h illustrates the STM image of DNA/SWNT composite on Si(110) substrate. The DNA molecule wrapped around the SWNT with a helical structure at 63° angle with a period of 3.3 nm which in a good agreement with the modelling built using CHARM FF simulations for DNA (20-mer) and (6,5) CNT chirality.

In 2016, Basiuk at his co-workers [75] combined the experimental and theoretical measurements to establish the structure of the anticancer antibiotic Doxorubicin (DOX) on SWNT surface via non-covalent interaction where SWNT can be used as a good carrier for DOX drug as a drug delivery process. They have used AFM to characterize the composite morphology, STM to get more details about the surface structure as well as long range corrected DFT calculations to study the non-covalent interaction between DOX and SWNT. AFM revealed that SWNTs-DOX conjugates exhibit some protrusions along the nanotube which cannot be found in unmodified SWNTs. STM measurements under ambient conditions demonstrated that DOX forms a periodic texture with alternating depressions where the molecule could be self-assembled on the tube surface forming a helical pattern with a protrusion's width equals around 0.6 nm that matches with the DOX molecular width. Moreover, the DOX molecule aligned with the tube principal axis with 50°. Among three DFT functionals (M05-2X, wB97X-D and LCBLYP) used for studying the DOX/SWNT system; M05-2X gave the most reliable data.

3 Conclusion

In Summary, we have highlighted the efforts done (up to date) to investigate the supramolecular structures of different organic molecules (i.e. porphyrins, polymer and other organic molecules) on the SWNT surface characterized mainly by STM imaging technique supported by other measurements i.e. AFM, UV-visible spectroscopy as well as theoretical calculations. Functionalization of SWNT with different organic molecules have been greatly developed due to the presence an effective and powerful characterization and/or identification techniques like scanning probe microscopy i.e. scanning tunneling microscopy (STM) and atomic force microscopy (AFM). Such kind of these promising techniques helped chemists and materials scientists to deeply study, understand and demonstrate the behavior, properties as well as supramolecular structures of the resultant nanocomposites. Consequently, this opens the gates towards more successful future development of many research fields for instance, environmental, energy harvesting, gas storage materials, energy storage materials, catalysis, polymer reinforcements, nanocomposites, nano-biotechnology, nano-medicine, due to the flexibility, high economic efficiency, diversity, and regulatory of supramolecular systems.

References

1. El-Mageed AIA. Study on the properties of organic molecule/nano-carbon conjugates. PhD thesis (chapter I), Osaka University, Japan, pp. 1–31 (2016)
2. Aviram, A., Ratner, M.A.: Molecular rectifiers. *Chem. Phys. Lett.* **29**(2), 277–283 (1974)
3. Carroll, R.L., Gorman, C.B.: The genesis of molecular electronics. *Angew. Chem. Int. Ed.* **41**(23), 4378–4400 (2002)
4. Andrews, D.Q., Solomon, G.C., Van Duyne, R.P., Ratner, M.A.: Single molecule electronics: increasing dynamic range and switching speed using cross-conjugated species. *J. Am. Chem. Soc.* **130**(51), 17309–17319 (2008)
5. Moth-Poulsen, K., Bjørnholm, T.: Molecular electronics with single molecules in solid-state devices. *Nat. Nanotechnol.* **4**(9), 551–556 (2009)
6. Kaneko, S., et al.: Site selection in single-molecule junction for highly reproducible molecular electronics. *J. Am. Chem. Soc.* **138**(4), 1294–1300 (2016)
7. Heath, J.R.: Molecular electronics. *Annu. Rev. Mater. Res.* **39**, 1–23 (2009)
8. Song, H., Reed, M.A., Lee, T.: Single molecule electronic devices. *Adv. Mater.* **23**(14), 1583–1608 (2011)
9. Huang, Z., Chen, F., Bennett, P.A., Tao, N.: Single molecule junctions formed via au-thiol contact: stability and breakdown mechanism. *J. Am. Chem. Soc.* **129**(43), 13225–13231 (2007)
10. Heath, J.R., Ratner, M.A.: *Molecular Electronics*. The National Academies Press, Washington, pp. 43–49 (2003)
11. Tour, J.M.: Molecular electronics. Synthesis and testing of components. *Acc. Chem. Res.* **33**(11), 791–804 (2000)
12. Vuillaume, D.: Molecular nanoelectronics. *Proc. IEEE* **98**(12), 2111–2123 (2010)
13. Metzger, R.M., et al.: Unimolecular electrical rectification in hexadecylquinolinium tricyanoquinodimethanide. *J. Am. Chem. Soc.* **119**(43), 10455–10466 (1997)
14. Metzger, R.M.: Unimolecular electrical rectifiers. *Chem. Rev.* **103**(9), 3803–3834 (2003)

15. Hihath, J., et al.: Inelastic transport and low-bias rectification in a single-molecule diode. *ACS Nano* **5**(10), 8331–8339 (2011)
16. Flood, A.H., Stoddart, J.F., Steuerman, D.W., Heath, J.R.: Whence molecular electronics? *Science* **306**(5704), 2055–2056 (2004)
17. Waser, R., Aono, M.: Nanoionics-based resistive switching memories. *Nat. Mater.* **6**(11), 833–840 (2007)
18. Liu, Z., Yasserli, A.A., Lindsey, J.S., Bocian, D.F.: Molecular memories that survive silicon device processing and real-world operation. *Science* **302**(5650), 1543–1545 (2003)
19. Liljeroth, P., Repp, J., Meyer, G.: Current-induced hydrogen tautomerization and conductance switching of naphthalocyanine molecules. *Science* **317**(5842), 1203–1206 (2007)
20. Koumura, N., Zijlstra, R.W., van Delden, R.A., Harada, N., Feringa, B.L.: Light-driven unidirectional molecular rotor. *Nature* **401**(6749), 152–155 (1999)
21. Browne, W.R., Feringa, B.L.: Making molecular machines work. *Nat. Nanotechnol.* **1**(1), 25–35 (2006)
22. Dulić, D., et al.: One-way optoelectronic switching of photochromic molecules on gold. *Phys. Rev. Lett.* **91**(20), 207402 (2003)
23. Auwärter, W., et al.: A surface-anchored molecular four-level conductance switch based on single proton transfer. *Nat. Nanotechnol.* **7**(1), 41–46 (2012)
24. Okawa, Y., et al.: Chemical wiring and soldering toward all-molecule electronic circuitry. *J. Am. Chem. Soc.* **133**(21), 8227–8233 (2011)
25. Collier, C., et al.: Electronically configurable molecular-based logic gates. *Science* **285**(5426), 391–394 (1999)
26. Kompa, K., Levine, R.: A molecular logic gate. *Proc. Natl. Acad. Sci.* **98**(2), 410–414 (2001)
27. Joachim, C., Renaud, N., Hliwa, M.: The different designs of molecule logic gates. *Adv. Mater.* **24**(2), 312–317 (2012)
28. Lam, H.Y., Natelson, D.: Transport in single-molecule transistors: Kondo physics and negative differential resistance. *Nanotechnology* **15**(10), S517 (2004)
29. Kubatkin, S., et al.: Single-electron transistor of a single organic molecule with access to several redox states. *Nature* **425**(6959), 698–701 (2003)
30. van der Zant, H.S., et al.: Molecular three-terminal devices: fabrication and measurements. *Faraday Discuss.* **131**, 347–356 (2006)
31. Liang, W., Shores, M.P., Bockrath, M., Long, J.R., Park, H.: Kondo resonance in a single-molecule transistor. *Nature* **417**(6890), 725–729 (2002)
32. Staykov, A., Areephong, J., Browne, W.R., Feringa, B.L., Y, K.: Electrochemical and photochemical cyclization and cycloreversion of diarylethenes and diarylethene-capped sexithiophene wires. *ACS Nano* **5**(2), 1165–1178 (2011)
33. Ratner, M.A., Davis, B., Kemp, M., Mujica, V., Roitberg, A., Yaliraki, S.: Molecular wires: charge transport, mechanisms, and control. *Ann. N. Y. Acad. Sci.* **852**(1), 22–37 (1998)
34. Dresselhaus, M., Dresselhaus, G., Jorio, A.: Unusual properties and structure of carbon nanotubes. *Annu. Rev. Mater. Res.* **34**, 247–278 (2004)
35. Iijima, S.: Helical microtubules of graphitic carbon. *Nature* **354**(6348), 56–58 (1991)
36. Iijima, S., Ichihashi, T.: Single-shell carbon nanotubes of 1-nm diameter. *Nature* **363**(6430), 603–605 (1993)
37. Yan, Y., Miao, J., Yang, Z., Xiao, F.-X., Yang, H.B., Liu, B., Yang, Y.: Carbon nanotube catalysts: recent advances in synthesis, characterization and applications. *Chem. Soc. Rev.* **44**(10), 3295–3346 (2015)
38. Singh, P., Campidelli, S., Giordani, S., Bonifazi, D., Bianco, A., Prato, M.: Organic functionalisation and characterisation of single-walled carbon nanotubes. *Chem. Soc. Rev.* **38**(8), 2214–2230 (2009)
39. Gao, C., Guo, Z., Liu, J.-H., Huang, X.-J.: The new age of carbon nanotubes: an updated review of functionalized carbon nanotubes in electrochemical sensors. *Nanoscale* **4**(6), 1948–1963 (2012)
40. Holister, P.: TEHaCRV, Nanotubes. CMP-Cientifica, Las Rozas, pp. 1–13 (2003)

41. Hirsch, A.: Functionalization of single-walled carbon nanotubes. *Angew. Chem. Int. Ed.* **41**(11), 1853–1859 (2002)
42. Binnig, G., Rohrer, H., Gerber, C., Weibel, E.: Surface studies by scanning tunneling microscopy. In: Neddermeyer, H. (ed) *Scanning Tunneling Microscopy. Perspectives in Condensed Matter Physics (A Critical Reprint Series)*, vol. 6, pp. 31–35. Springer, Dordrecht (1982)
43. Binnig, G., Rohrer, H., Gerber, C., Weibel, E.: Surface studies by scanning tunneling microscopy. *Phys. Rev. Lett.* **49**(1), 57 (1982)
44. Binnig, G., Rohrer, H., Gerber, C., Weibel, E.: 7×7 reconstruction on Si (111) resolved in real space. *Phys. Rev. Lett.* **50**(2), 120 (1983)
45. Teugels, L.G., Avila-Bront, L.G., Sibener, S.: Chiral domains achieved by surface adsorption of achiral nickel tetraphenyl- or octaethylporphyrin on smooth and locally kinked Au (111). *J. Phys. Chem. C* **115**(6), 2826–2834 (2011)
46. Murphy, B., et al.: Growth and ordering of Ni (II) diphenylporphyrin monolayers on Ag (111) and Ag/Si (111) studied by STM and LEED. *J. Phys. Condens. Matter* **24**(4), 045005 (2012)
47. Haq, S., Hanke, F., Sharp, J., Persson, M., Amabilino, D.B., Raval, R.: Versatile bottom-up construction of diverse macromolecules on a surface observed by scanning tunneling microscopy. *ACS Nano* **8**(9), 8856–8870 (2014)
48. Yoshimoto, S., Itaya, K.: Advances in supramolecularly assembled nanostructures of fullerenes and porphyrins at surfaces. *J. Porphyrins Phthalocyanines* **11**(05), 313–333 (2007)
49. Phan, T.H., Kosmala, T., Wandelt, K.: Potential dependence of self-assembled porphyrin layers on a Cu (111) electrode surface: In-situ STM study. *Surf. Sci.* **631**, 207–212 (2015)
50. Phan, T.H., Wandelt, K.: Self-assembly of metal free porphyrin layers at copper-electrolyte interfaces: dependence on substrate symmetry. *Surf. Sci.* **607**, 82–91 (2013)
51. Jurow, M., Schuckman, A.E., Batteas, J.D., Drain, C.M.: Porphyrins as molecular electronic components of functional devices. *Coord. Chem. Rev.* **254**(19), 2297–2310 (2010)
52. Smith, K.M., Falk, J.E.: *Porphyrins and metalloporphyrins*. Elsevier, Amsterdam (1975)
53. Basiuk, V.A., Bassioui, M.: Nanoassembly of meso-tetraphenylporphyrins on surfaces of carbon materials: initial steps as studied by molecular mechanics and scanning tunneling microscopy. *J. Nanosci. Nanotechnol.* **8**(1), 259–267 (2008)
54. Basiuk, E.V., Basiuk, V.A., Santiago, P., Puente-Lee, I.: Noncovalent functionalization of carbon nanotubes with porphyrins: meso-Tetraphenylporphyrin and its transition metal complexes. *J. Nanosci. Nanotechnol.* **7**(4–5), 1530–1538 (2007)
55. Bassioui, M., Álvarez-Zauco, E., Basiuk, V.A.: Self-assemblies of meso-Tetraphenylporphyrin ligand on surfaces of highly oriented pyrolytic graphite and single-walled carbon nanotubes: insights from scanning tunneling microscopy and molecular modeling. *J. Nanosci. Nanotechnol.* **11**(6), 5457–5468 (2011)
56. Bassioui, M., et al.: Noncovalent functionalization of single-walled carbon nanotubes with porphyrins. *Appl. Surf. Sci.* **275**, 168–177 (2013)
57. Pham, V.D., et al.: Properties of functionalized carbon nanotubes and their interaction with a metallic substrate investigated by scanning tunneling microscopy. *J. Phys. Chem. C* **121**(43), 24264–24271 (2017)
58. Abd El-Mageed, A.I., Ogawa, T.: Metal ion effect on the supramolecular structures of Metalloporphyrins on single-walled carbon nanotube surface. *Appl. Surf. Sci.* **462**, 904–912 (2018)
59. Abd El-Mageed, A.I., Handayani, M., Chen, Z., Inose, T., Ogawa, T.: Assignment of the absolute-handedness chirality of single-walled carbon nanotubes by using organic molecule supramolecular structures. *Chem. Eur. J.* **25**, 1941–1948 (2019)
60. Abd El-Mageed, A.I., Ogawa, T.: Single-walled carbon nanotube absolute-handedness chirality assignment confirmation using metalized porphyrin's supramolecular structures via STM imaging technique. *Chirality* **32**(3), 345–352 (2020)
61. Abd El-Mageed, A.I., Ogawa, T.: Supramolecular structures of terbium (iii) porphyrin double-decker complexes on a single-walled carbon nanotube surface. *RSC Adv.* **9**(48), 28135–28145 (2019)

62. Mc Carthy, B., Coleman, J.N., Czerw, R., Dalton, A.B., Carroll, D.L., Blau, W.J.: Microscopy studies of nanotube-conjugated polymer interactions. *Synth. Met.* **121**(1), 1225–1226 (2001)
63. Tamburri, E., et al.: Modulation of electrical properties in single-walled carbon nanotube/conducting polymer composites. *Carbon* **43**(6), 1213–1221 (2005)
64. Goh, R.G.S., Bell, J.M., Motta, N., Waclawik, E.R.: Microscopic and spectroscopic study of self-ordering in poly (3-Hexylthiophene)/Carbon nanotubes nanocomposites. *J. Nanosci. Nanotechnol.* **6**(12), 3929–3933 (2006)
65. Kiani, G., Sheikhoie, H., Rostami, A.: Highly enhanced electrical conductivity and thermal stability of Polythiophene/single-walled carbon nanotubes nanocomposite. *Iran. Polym. J. (English)* **20**(8 (134)), 623–632 (2011)
66. Constantin, V-A., Cao, L., Sadaf, S., Walder, L.: Oligo-viologen/SWCNT nano-composites: preparation and characterization. *Phys. Status Solidi B* **249**(12), 2395–2398 (2012)
67. Ago, H., Azumi, R., Ohshima, S., Zhang, Y., Kataura, H., Yumura, M.: STM study of molecular adsorption on single-wall carbon nanotube surface. *Chem. Phys. Lett.* **383**(5), 469–474 (2004)
68. Zhang, L., Zhang, J., Schmandt, N., Cratty, J., Khabashesku, V.N., Kelly, K.F., Barron, A.R.: AFM and STM characterization of thiol and Thiophene functionalized SWNTs: pitfalls in the use of chemical markers to determine the extent of sidewall functionalization in SWNTs. *Chem. Commun.* **43**, 5429–5431 (2005)
69. Bonifazi, D., et al.: Microscopic and spectroscopic characterization of paintbrush-like single-walled carbon nanotubes. *Nano Lett.* **6**(7), 1408–1414 (2006)
70. Graupner, R., et al.: Nucleophilic–Alkylation–Reoxidation: a functionalization sequence for single-wall carbon nanotubes. *J. Am. Chem. Soc.* **128**(20), 6683–6689 (2006)
71. Lauffer, P., Jung, A., Graupner, R., Hirsch, A., Ley, L.: Functionalization of single-walled carbon nanotubes by aromatic molecules studied by scanning tunneling microscopy. *Phys. Status Solidi B* **243**(13), 3213–3216 (2006)
72. Poenitzsch, V.Z., Winters, D.C., Xie, H., Dieckmann, G.R., Dalton, A.B., Musselman, I.H.: Effect of electron-donating and electron-withdrawing groups on peptide/single-walled carbon nanotube interactions. *J. Am. Chem. Soc.* **129**(47), 14724–14732 (2007)
73. Rabot, C., Clair, S., Kim, Y., Kawai, M.: Scanning tunneling microscopy observations of benzoic acid molecules coadsorbed with single-walled carbon nanotubes on Au(111) surface. *Jpn. J. Appl. Phys.* **46**(8B), 5572–5576 (2007)
74. Yarotski, D.A., et al.: Scanning tunneling microscopy of DNA-wrapped carbon nanotubes. *Nano Lett.* **9**(1), 12–17 (2009)
75. Rodríguez-Galván, A., Amelines-Sarria, O., Rivera, M., Carreón-Castro, M.D.P., Basiuk, V.A.: Adsorption and self-assembly of anticancer antibiotic doxorubicin on single-walled carbon nanotubes. *NANO* **11**(04), 1650038 (2016)

Structure and Properties Manipulations of Graphene: Towards Developing High Sensitivity Optical and Electrical Sensors



Mai Desouky, Ahmed Medhat, Mona Samir, Dina Salah, and Amal Kasry

Abstract Sensors that can be employed in environmental or biological applications require high sensitivity, specificity, quick and reproducible response, as well as low cost, to allow them to be integrated in a point-of-care packages. Surface sensors are of much higher sensitivity and specificity than the bulk sensors, due to the limited vicinity to probe the target to be detected. Optical and electrical sensors that can be employed as surface sensors are mostly based on surface plasmon resonance and field effect transistors, respectively. Optical sensors are of very high sensitivity, however they come with high cost, which makes their use in a point-of-care format quite limited. Electrical sensors could be fabricated with lower cost, and moderate sensitivity.

In order to achieve all the required properties of a reliable sensor, new materials need to be developed, in this work, we show our efforts to manipulate the graphene properties, through its structure modification, in order to enhance both its optical and electrical properties to the extent that it can be used as a sensor.

Graphene, since isolated in 2004, has attracted great attention to be used in several applications despite its unusual properties, such as the zero band gap that limits its electronic applications, and the very high optical transparency, leading graphene to defy any attempt for absorption in a wide range of wavelengths. To overcome the problem of the zero bandgap and consequently the optical absorption, we manipulate the structure of the single graphene sheet by creating regular and irregular holes in the range of 15–25 nm, with an interplanar distances of 40–60 nm, this structure is referred to as nanomembrane graphene (NMG). We investigate the effect of these structures on the change in the optical properties through probing the localized surface plasmon resonance (LSPR) generated at the edges of these holes by imaging via scanning near field optical microscopy. Our results are confirmed by

M. Desouky · M. Samir · A. Kasry (✉)

Nanotechnology Research Center (NTRC), The British University in Egypt (BUE), Suez Desert Road, P.O. Box 43, Cairo, El-Shorouk City 11837, Egypt
e-mail: amal.kasry@bue.edu.eg

M. Desouky · A. Medhat · D. Salah

Physics Department, Faculty of Science, Ain Shams University, Khalifa El-Maamon Street, Cairo 11566, Egypt

theoretical electromagnetic field mapping at the graphene membrane edges, which shows a noticeable absorption. The experimental results indicated that the wavelength is dependent on the holes' diameters and the inter-hole distances; therefore, this nanomembrane graphene can support light harvesting and consequently, could be used as a mid-IR biosensor with a sensitivity of 850 nm/RIU.

We also show that UV absorption in single-layer graphene can be enhanced by creating this nanomesh or nanomembrane structure. Density functional theory (DFT) is used to confirm our experimental results, which has indicated that the absorption peaks are due to the changes in the band structures of the NMG as a result of the pore super lattice.

Another application which depends on this structure manipulation is using graphene-gold nanoparticles hybrid, where the gold nanoparticles are embedded in the graphene holes. This hybrid was used as an electrical pH sensor by using the hybrid as a substrate in a capacitive metal oxide semiconductor (C-MOS) format, leading to a pH sensitivity of 86 mV/pH.

The presented applications in this work show the benefits of manipulating the structure of the graphene and how much it can lead to enhancing its properties.

Keywords Graphene · Nanomembrane graphene · Absorption · Localized plasmon resonance · IR biosensor · Gold nanoparticles · Hybrid · C-V sensor · pH sensor

Abbreviations

NMG	Nano-Membrane Graphene
SPs	Surface plasmons
GNR	Graphene nanoribbons
C-MOS	Capacitive-Metal Oxide Semiconductor
C-EIS	Capacitive-Electrolyte Insulator Semiconductor
s-SNOM	Scan near field optical microscope
GP	Graphene nanoPlatelets
GNPs	Gold Nanoparticles
GAH	Graphene nanoplatelets-Au-nanoparticles-Hybrid
SPR	Surface plasmon resonance
LSPR	Localized surface plasmon resonance
MOSFET	MOS-Field Effect Transistor
EISFET	EIS-Field Effect Transistor
C-V	Capacitance–Voltage measurement
V_{fb}	Flat-band voltage
V_g	Gate voltage
AFM	Atomic Force Microscopy
SEM	Scanning Electron Microscopy
EBL	Electron-beam lithography

1 Introduction

For couple of decades, detection of proteins has become one of the most elementary tasks in biomedical research, as well as in disease diagnosis and therapeutics. There is an extensive rise in the demand of early disease detection in order to facilitate early cure for patients [1]. Over the past decades, different types of biosensors have attracted enormous attention, e.g. optical, electrochemical, and piezoelectric [2–6]. Most optical biosensors have provided high sensitivity and high specificity as many studies have already shown [2, 4, 5, 7], this is despite that fact that some optical techniques are still time consuming, as for example single molecule spectroscopy [7], while others are expensive, e.g. mid IR spectroscopy [5]. The urge to develop higher sensitivity optical sensors, robust and cheap remains an aim for many researchers worldwide, to provide early disease detection and treatment. During the past two decades, an optical technique has become pervasive, named as surface plasmon polariton (SPR). This technique is based on high sensitivity plasmons accompanied with the surface plasmons excited on a metallic surface when shined by light. However, even though this technique has reported very high sensitivity values, it has some drawbacks, in which among is that it only operates within the visible wavelength range [8]. For that, further studies have been developed to study the sensitivity of the localized surface plasmon polaritons (LSPR) which mainly depends on plasmonic resonance of nanoparticle resulting in localized response which has shown higher sensitivity values as compared to the SPR [9]. Though being of higher sensitivity, LSPR has suffered some drawbacks in which among is the restricted operation within the visible regime and it mainly depends on chemically prepared metallic nano particles which suffers instability and agglomeration over time [10, 11]. Otherwise, LSPR has been reported for metallic spring ring resonators fabricated mainly by electron beam lithography technique (EBL) which is not feasible for mass production [12]. Thus, using them as an optical sensor is not a feasible mean for optical sensing.

The mid-IR wavelength range is an applicable range for infrared imaging, biomedical diagnostics, and chemo- and biosensing applications [13–17]. Vibrational/rotational modes in biomolecules are weak in the mid-IR regime which causes difficulties to detected because of the absence of appropriate mid-IR absorbing platforms [17]. Although plasmonics are widely used in optical biosensing, their natural resonance occurs mostly in the visible wavelength area -as previously highlighted - which is the case for Au and Cu [2, 14]. Discovery of materials with tunable plasmonic responses in the mid-IR wavelength range, which can be used for biological sensing applications, have become one of our main targets [2, 5, 6]. In the area of new emerging plasmonic materials, graphene has gained a great interest since its invention as a promising sensing material. The intriguing characteristics of graphene surface plasmons (SPs) have made it a remarkable candidate for sensing and photo detection [4, 18–24]. Graphene SPs can bear long relaxation times and since graphene is considered as a zero band gap material, it can be tuned across the mid-IR wavelength range through chemical doping or applying voltage, thus it is considered as a mid IR tunable material [23–26]. However, the one-atom-thickness of graphene layer

allows only 2.3% substantial absorbance in graphene which is insufficient value to be used as a sensing platform [18]. Previous studies have examined localized SPs in graphene nanostructures, including both nano-patterned graphene [4, 25, 26] and graphene nanoribbons (GNR) [24, 27] for two reasons, the first is to introduce sufficient absorption in the graphene layer, the second is using this absorption band for sensing applications. One further advantage of patterning the graphene layer, is overcoming the momentum mismatch between graphene SPs and the incident light which can be tackled by nanopatterning of the graphene layer, leading to strong field absorption [18, 19].

So far, the studies reporting doping of NMG or GNR have relied on applying external voltages or high level of chemical doping [4, 25–27]. Mid-IR absorption in highly-doped graphene nano disk arrays was studied via ionic gel with absorption value of 40% [26]. Other studies have reported absorption values as high as 90% in NMG [24], however, they included thick metallic substrate to suppress graphene transmission in addition to applying external voltage to introduce free charge carriers in graphene. Relying on metals in opto-electronic devices is not generally favored for CMOS compatible fabrication process [2, 9]. Thus, there is a great need to investigate 2D mid-IR absorbing structures, metallic free, tunable in order to harvest light energy to serve as a sensing platforms [28]. In general, NMG as a mid-IR absorber is highly valuable due to the atomic thickness of graphene, its lower losses, as well as the possibility to propose selective binding sites in the chemically active holes, which is a main requirement for biosensing applications [17, 29]. In order to achieve all of the required properties of a reliable sensor, new materials need to be developed, in this work, we show our efforts to manipulate the graphene properties, through its structure modification, in order to enhance both its optical and electrical properties to the extent that it can be used as a sensor.

In this chapter, we are mainly focusing on addressing, several new concepts the first is: demonstrating a partially new fabrication technique to fabricate NMG layer, which is a cheap methodology as compared to the currently reported ones in literature, secondly, studying the localized plasmonic response in NMG in the mid IR wave length regime with extensive details on the effect of variation of the size of the nano holes in graphene, and thirdly, investigating the possibility of using the NMG as a pH sensor incorporated with Au nano particles, which we refer to Graphene Nanoplatelet-Au Nanoparticles Hybrid (GAH).

2 Fabrication of NMG

Many studies have reported fabrication of patterned graphene using different techniques in which among is the EBL, photolithography and nano sphere lithography. EBL can pattern extremely small nano meshes in graphene reaching the size of 10 nm [17, 28, 30] which is not the case for photo lithography that can pattern holes of larger dimensions varying from 60–200 nm. Some cons are associated with the

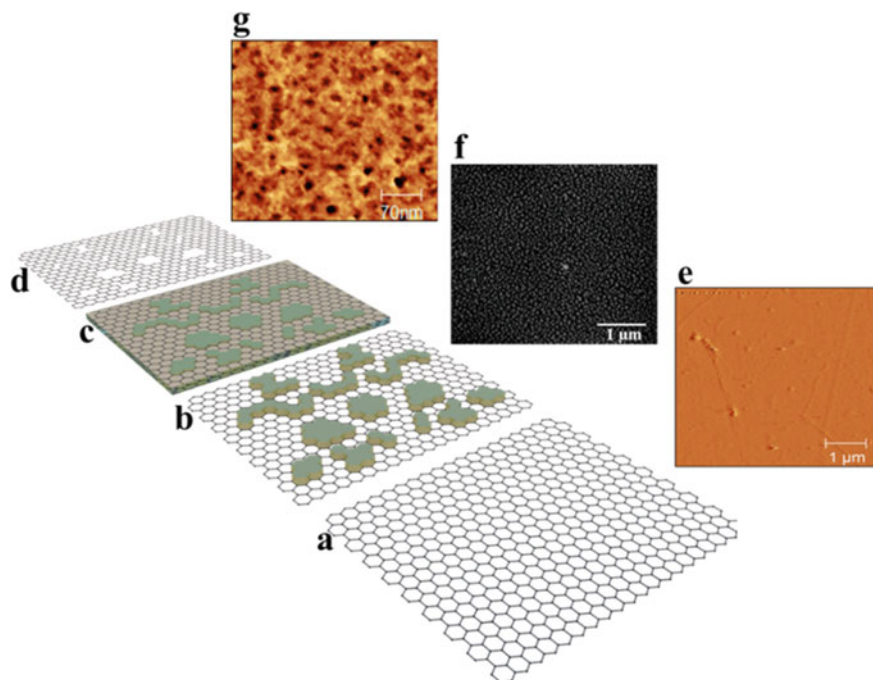


Fig. 1 A scheme of the NMG fabrication process. **a** Single layer CVD graphene on quartz slide; **b** Au nanoislands formed after annealing of a 10 nm sputtered gold layer; **c** a thin layer of sputtered Cr covering both the graphene and the nano islands; **d** NMG formed after both etching of the gold nano-islands and O₂ plasma treatment to etch the uncovered graphene; **e** AFM image of the single layer CVD graphene; **f** SEM image of the Au nanoislands after annealing; and **g** AFM image of the created NMG (Copyright © 2018, American Chemical Society)

aforementioned techniques; for example EBL is an expensive time-consuming technique which is not suitable for large scale sensor fabrication, whereas lithography techniques cannot be used for small hole nano-patterning [31]. Previous studies have shown that the size of the patterned hole can lead to absorption at a particular wave length range, and in order to excite the LSPR in the mid IR wave length regime small holes of dimension less than 60 nm are essential [2, 22–24], thus relying on photolithography in case as such is unattainable. Other techniques have been shown to fabricate nano holes of dimensions as small as 5 nm but unfortunately, they are mainly chemical based and extremely difficult to use [31].

A recent study has demonstrated new technique which is based on lithography for nano patterning but using Au nano particles as a mask (Desouky et al. 2018). Those Au nano islands are prepared by annealing of thin sputtered Au layer which leads to the formation of Au nano islands of variable dimensions. The holes have diameter varying between 5 to 30 nm and interatomic distance of 30 to 60 nm. The Au nano islands are then covered by Cr mask layer, followed by subsequent etching of the Au nano islands leaving exposed graphene sheet that is then etched with oxygen

plasma, leading to the formation of the NMG. The authors have referred to it as nano-membrane graphene (NMG) due to the variation in the holes' diameters and inter atomic distance. This technique is fast, and cheap as compared to the previously reported ones, and furthermore it has been shown that it can lead to the fabrication of nano holes of dimensions as small as 5 nm. The idea of this technique is illustrated in Fig. 1.

3 Absorption in NMG

As previously highlighted, fabrication of NMG aims to excite LSPR in order to be used as a sensing platform. Some previous studies have shown that, depending on the dimensions and shapes of the nano holes, absorption at particular wavelength takes place [2, 4, 13, 18, 21]. A theoretical study has shown that introducing zigzag edges patterned in graphene can lead to absorption of photon energy of up to 2.5 eV accompanied with external applied voltage of nearly 1 eV [22, 23]. Other study has shown that absorption in NMG can reach up to 40% using an ionic gel for doping of the graphene layer with charge carriers [26]. Using ionic gel in designing sensors is not feasible for practical applications, however the study showed the possibility of 40% absorption upon the excitation of LSPR in NMG when doped by charge carriers. Other studies have reported similar absorption values, however they included back thick metallic layers, and we previously mentioned that there is always an urge to search for CMOS compatible designs which are free from any metallic ingredients. In the previous shown metallic free nano membrane graphene (Fig. 1), no intentional doping or applied voltage were introduced. It was naturally-doped by charge carriers during the fabrication procedure, as the authors have proved [2]. Interestingly, the study showed the excitation of the LSPR in the nano membrane graphene using scan near field optical microscope (s-SNOM) and then theoretically showed the excitation of the LSPR using Lumerical finite difference time domain technique which leads to enhanced field confinement at the NMG edges.

Figure 2 (a) shows a scheme of the the LSPR excited and measured in NMG using the s-SNOM technique, where the highest field intensity has been found at wavelength of 11.1 μm , confirming the excitation of the LSPR in NMG. Although the nano membrane graphene include holes of variable dimensions, excitation at particular wavelength occurred as a result of the specific dimensions of the majority of holes; which was 25 nm diameter and 60 nm center-to-center distance. Figure 2 (b) shows that no optical signal is observed for the unpatterned graphene layer, while a change in the optical signal intensities and distributions are obvious in case of the NMG, depending on the excitation wavelength. As the wavelength increases the optical signal rises due to the excitation of the LSPR in nano membrane graphene reaching the maximum optical signal at 11.1 μm . The created optical signal leads to strong electric field confinement ($|E|^2$) at the nano membrane edges which has been confirmed by FDTD simulation and leads to field enhancement of a factor of 3×10^4 as compared to NMG at 14 μm (Fig. 3) which is far from the resonance wavelength (LSPR

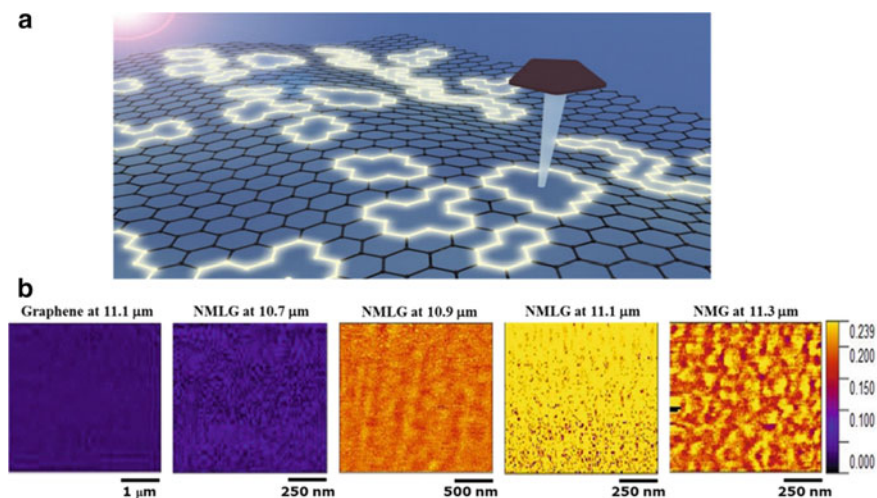


Fig. 2 **a** A scheme of the plasmonic at the edges of the NMG imaged by the s-SNOM technique **b** The s-SNOM images at the same color scale of single layer of CVD graphene at 11.1 μm where no optical signal is observed, and the NMG at different layer of wavelengths as indicated for each image, where the highest pronounced optical signal is obtained at a wavelength of 11.1 μm . (Copyright © 2018, American Chemical Society)

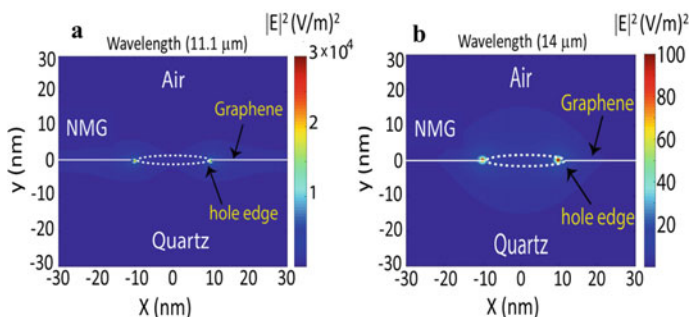


Fig. 3 **a** $|E|^2$ of the NMG at wavelength 11.1 μm with a field enhancement of 36,789; **b** $|E|^2$ of the NMG at wavelength 14.0 μm with a field enhancement of 199 (color scale represents the field intensity) (Copyright © 2018, American Chemical Society)

excitation wavelength). Figure 3) shows that the field enhancement is concentrated at the holes edges, the value of the calculated electric field belongs to the highest field point among the NMG edge.

LSPR is also dependent on the dimensions of the holes, i.e. the holes' diameter "d" and the center-to-center distance "a", this was theoretically investigated using FDTD simulations, the results are shown in Fig. 4 (a, c-d). For NMG, an absorption peak at 11.1 μm is produced, while at the same wavelength, graphene exhibits zero absorption (Fig. 4 (b), experimentally, this is shown in Fig. 4 (b), where the optical

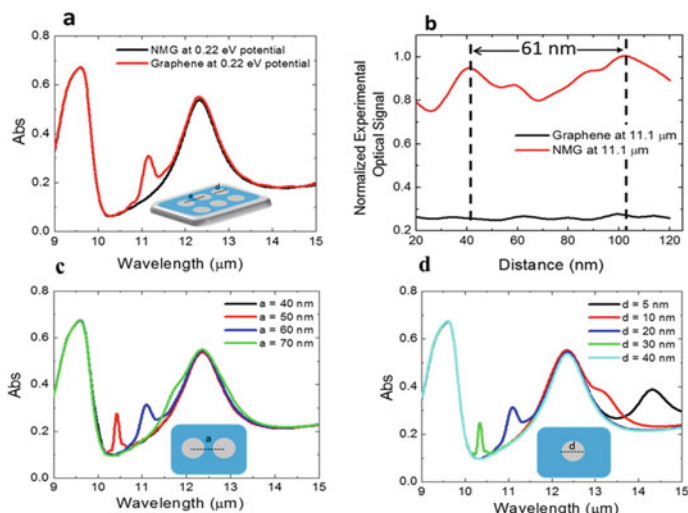
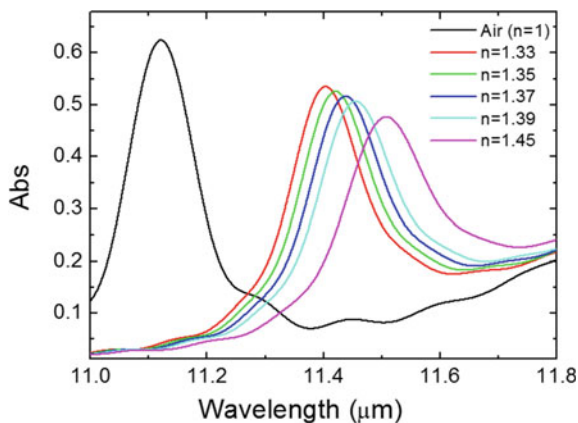


Fig. 4 **a** FDTD simulations of the absorption of the NMG at 0.22 V **b** Normalized experimental optical signal profile of both graphene and the NMG at 11.1 μm showing the enhancement at the hole's edges in case of the NMG, while it is flat in case of graphene (c and d) FDTD simulations of the absorption of NMG on quartz with different “a” at fixed “d = 20 nm” different “d” at fixed “a = 60 nm” (Copyright © 2018, American Chemical Society)

signal profiles of both graphene and NMG, extracted from the s-SNOM images, clearly indicates the optical enhancement at the edges of the holes in case of the NMG. Figure 4 (c) shows that increasing the center-to-center distances, the coupling strength between the NMG plasmons decreases leading to a red shift in the LSPR peak. Similarly, reducing the distances between the holes leads to increasing the confinement energy, resulting in a blue shift in the LSPR peak. However, when reducing the distance between two holes to 40 nm leads to no observable LSPR peak, indicating that there is an optimum center-to-center distance required to achieve the coupling between light and plasmons in NMG. The peaks at 9.6 μm and 12.05 μm are due to the quartz substrate [2, 32]. Figure 4 (d) shows the shift in the LSPR peak upon changing “d”, where reducing the holes' diameter results in red shifts in the absorption peak, while at 40 nm diameter, damping rises dramatically, diminishing the plasmon resonance. It is obvious that most of the holes have “d” varying only between 10 to 25 nm and center to center distances varying between 30 to 60 nm, however, the majority of holes were found to have **d** of 20 nm and **a** of 60 nm, this was the reason for the pronounced LSPR excitation at the 11.1 μm wave length which measured by the s-SNOM and theoretically confirmed by the FDTD simulations as shown in Fig. 4 (c-d).

Fig. 5 FDTD simulations of the NMG showing the change in absorption with increasing the refractive index of the surrounding media (Copyright © 2018, American Chemical Society)



4 Nano Membrane Graphene as a Sensor

The aim of this work was to develop a mid IR sensor for biomolecules. Mid-IR biosensors can be of significant importance in studying the structural signature of some proteins, as label-free sensors. The authors showed the possibility of investigating the NMG to be used as a sensitive medium for external stimuli. The authors theoretically investigated the shift in resonance due to the change in refractive index of the surrounding medium for the NMG [2]. They used different values of refractive indices (n) with increment of 0.2 which represents the index change by different biological molecules. Figure 5 shows the shift in the absorption wavelength upon changing “ n ”, where the slope of wavelength versus refractive index is 825, revealing a sensitivity of 825 nm/RIU. It is also obvious that the absorption value is as high as 40% and above which confirms the fact that this sensor can demonstrate high absorption values as compared to the reported ones in literature but of extra advantage that is being metallic free and no external voltage is applied. In addition, the great advantage of the nano -membrane graphene sensor is that it has been fabricated by cheap and fast technology which makes it feasible for mass production.

5 Conclusion

In this work, we explored the patterning of nanoscale holes with dimensions as small as 20 nm to create a graphene nanomembrane (NMG) structure using an easy and inexpensive lithography-free protocol. We report that Localized Plasmon Resonance (LSPR) can be excited in NMG without applying a potential, chemical doping, or reflective metallic layers. In the mid-IR wavelength range, LSPR was optically detected using the s- SNOM technique, where the NMG absorption approaches 35% at normal incidence and 39% at oblique incidence. These findings contradict the

previous belief that high doping levels, induced capacity, or modifying graphene edges into zigzag or armchair edges are needed to excite plasmons in graphene. In terms of practical applications, our findings can be an important platform to use mid-IR absorption in graphene for biosensing.

6 Graphene Nanoplatelets-Au Nanoparticles Hybrid as a pH Sensor

As mentioned in the introduction of this chapter, NMG has been reported many times as an effective way for optical biosensing due to LSPR which in turn produces a signal that can be detected by different optical techniques, e.g. UV–VIS spectroscopy or Raman Spectroscopy. Graphene nanoplatelets (GP) are a mixture between graphene and graphite, so their thicknesses can be from 0.34 nm to 100 nm according to the classification of GP [4, 33].

GP are known for their attractive properties such as light weight, high aspect ratio, electrical and thermal conductivity, mechanical strength, low cost, and flat structure. Furthermore, GP could be a smart choice for replacing various nanostructured fillers in material science, such as other carbon allotropes (i.e. carbon black or carbon nanotubes), metal nanoparticles, and clay [34, 35].

GP is an attractive material as a nanocomposite element, as they can easily and effectively be integrated into polymeric matrices [4, 36], they are less expensive than carbon nanofibers and nanotubes, and are comparable to nanofillers in improving the mechanical properties of polymers [37]. Additionally, the electrical conductivity of GP is higher than that of graphene oxides [38].

Gold nanoparticles (GNPs) have attracted great attention in the past two decades due to their significant properties including its high electrical conductivity, high thermal conductivity, biocompatibility, and easy fabrication [39–42], consequently, these properties led to using GNPs in many applications like biosensing and cancer therapy [40, 43–46]. GNPs can be prepared in different shapes like cubes, spheres, rods and stars, and they can be synthesized using either bottom up synthesis or top-down methods. Bottom-up methods depend on chemical and physical methods to assemble nanoscale structures into larger ones, they include chemical, photochemical, sonochemical, electrochemical, in addition to biosynthesis which depends on synthesis of GNPs using biomolecules extracted from biological cells [42, 47, 48]. Top down methods, e.g. photo- and electro-lithography, can be used to prepare high quality gold nanoparticles but they are quite expensive [49].

LSPR exhibited by GNPs when they interact with the incident light allow them to be used for optical biosensing [50–52], additionally, their biocompatibility is the best along with other metal nanoparticles, so GNPs were used for cancer therapy using laser beam by power confinement in the GNPs and consequently turning it to heat leading to killing cancer tumor [43, 44].

Electronic sensors based on electronic devices like Field-Effect Transistor (FET), including Metal-Oxide Semiconductor FET (MOSFET) and Electrolyte-Insulator Semiconductor FET (EISFET), Capacitive Metal Oxide Semiconductor (CMOS), and Capacitive Electrolyte-Insulator Semiconductor (C-EIS), have attracted attention in the recent years because of their easy fabrication and quick response [53–57].

Coupling the properties of graphene and GNPs, which refer to as Graphene-NP hybrid (GAH), is the main target of this work, in order to create a substrate for C-MOS that can be used as a pH sensor.

Capacitance–Voltage (C-V) measurement is a technique which depends on measuring the capacitance based on changing the applied gate voltage in adjusted certain range. C-V was used in sensing applications by measuring the shift in C-V curves which is due to the change of the flat band voltage (V_{fb}). V_{fb} represents the difference between work function of the metal layer and that of semiconductor in the case of C-MOS while it represents the difference between solution gate and the semiconductor layer in the case of C-EIS [58, 59].

The relation between the V_{fb} for C-MOS, the work function, and the maximum value of the oxide layer capacitance (C_{ox}) can be described by these equations: [60]

$$V_{fb} = \phi_{ms} - \frac{Q_0}{C_{ox}} \quad (1)$$

$$\frac{1}{C^2} = \frac{1}{C_{ox}^2} + \frac{2(V_g - V_{fb})}{A^2 q N_a \epsilon_s} \quad (2)$$

where ϕ_{ms} : the difference in the work function difference between the metal and the semi-conductor layers, in this case, it is the difference between the solution electrochemical potential and the semiconductor work function.

Q_0 : is the oxide layer charge,

q : electron charge,

N_a : acceptor concentration,

ϵ_s : the semiconductor permittivity,

A : electrode area.

For pH sensors, the C-V curves shift occurs by changing pH or target molecule concentration in the case of biosensors, due to the change in V_{fb} , so it is easy way for detection, at the same time, it represents easy and inexpensive fabrication of novel disposable sensors.

7 C-MOS Fabrication Process

For C-MOS fabrication, silicon (Si) chips with the size of $10 \times 10 \text{ mm}^2$, which is compatible with C-V system measurement cell, p-type silicon wafers with orientation $\langle 100 \rangle$ and diameter 100 mm, were used. Firstly, Si-wafer was cleaned using RCA

(Radio Corporation of America) cleaning process [61, 62]. Secondly, silicon dioxide (SiO_2) layer with 8 nm thickness was formed by thermal oxidation. Thirdly, Si wafer front side was coated by a photoresist (AZ 5214E) using spin coating at 3000 rpm for 30 s. Fourthly, buffer oxide etching was applied for 1 min to remove any remaining oxide ions in the back side of Si wafer. Sixthly, the back side was metallized by aluminum deposition with thickness of 300 nm and annealing at 550 °C for 30 min. Finally, the wafers were covered by poly methyl methacrylate (PMMA) and cut into chips with size $10 \times 10 \text{ mm}^2$ using wafer scribe.

8 GAH Formation

As previously indicated, GP has a thickness between 0.33 nm and 100 nm which means that GP can be in the form of multi-layer or mono-layer graphene. In this work, we used M25 class of GP which has graphene monolayers of 25 μm particle diameter of grade M GP with surface area of 120 to 150 m^2/gm . GP solution was prepared by sonication in 95% ethanol for 30 min at 150 W. Following the protocol of H. Yamaguchi et al., a 15 μL of 0.4 mg/mL of the solution was spin coated at 8000 rpm speed and a spinning time of 30 s, on a $10 \times 10 \text{ mm}$ Si-chip coated with 8 nm SiO_2 layer.

To prepare the GAH ensuring that the GNPs are embedded inside the GP film, 4 nm Au layer was deposited on Si-chips using Electron-beam deposition, at a deposition rate of 0.3 nm/min. Gold forms Au-nanoislands when deposited with thickness 4 nm, which shrink after annealing at high temperatures. Using this fact, the Au layer was annealed at 300 °C for 30 min in vacuum in order to form Au nanoislands with particle diameter of 20–25 nm. GAH film was prepared by depositing the nanoislands on the Si chips, followed by spin coating the GP film as shown in Fig. 6 (a). GAH and GP were characterized by Raman spectroscopy at laser wave length of 532 nm and

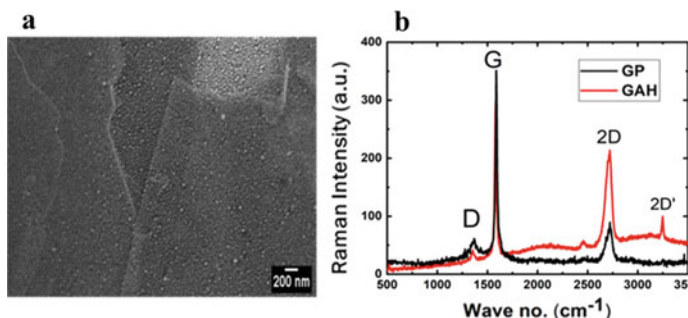


Fig. 6 **a** SEM image of the graphene-gold NPs hybrid film showing the particles are embedded in the graphene nanoplatelets film, **b** Raman spectra of the graphene film and the hybrid, showing an enhancement in the G and the 2D bands (Copyright © 2021, American Chemical Society)

power of 11.6 mW to ensure the difference between GP and GAH by embedding GNPs into GP film (Fig. 6 (b)). The Raman spectrum of GAH, compared to that of GP, shows higher intensity of 2D peak which is due to surface enhanced Raman scattering (SERS) because of using GNPs [63] and a new peak appeared after making the hybrid which is 2D' peak at 3250 cm^{-1} which corresponds to scattering of non-center optical phonons in the Brillion zone [64]. The enhancement of Raman signal after creating the GAH ensures the successful fabrication of the hybrid with embedded GNPs.

We characterized the fabricated C-MOS sensor with GAH layer as a substrate by C-V measurement at medium speed of 1 kHz frequency, sweep voltage of 100 mV and the number of points for every measured curve was 201.

The designed GP and GAH-CMOS were characterized at different pH values, from 2 to 10 which in turn showed positive shift in the C-V curves by increasing pH (Fig. 7 (a)) due to increasing of (V_{fb}) value. V_{fb} was calculated for every curve to calculate the sensitivity of GAH and consequently comparing it to that of GP (Fig. 7 (b)). GAH showed sensitivity of $53.3 \pm 4\text{ mV/pH}$ which was higher than that of

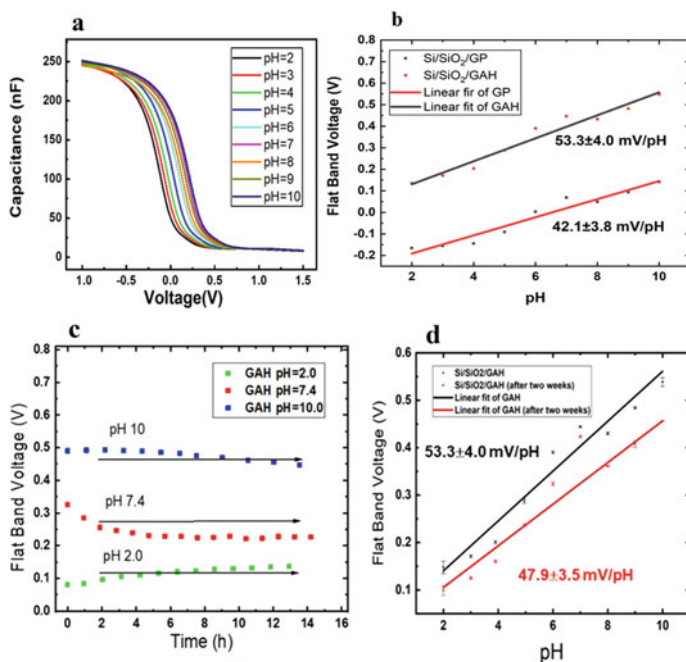


Fig. 7 **a** C-V measurements of the C-MOS structure with the hybrid at different pHs, **b** The change in the Flatband voltage of the hybrid with changing the pH, showing an increase in the V_{fb} values and consequently on the in the sensitivity. **c** Stability test of the hybrid at different pHs showing a stable V_{fb} for more than 14 h. **d** The change in the Flatband voltage of the hybrid with changing the pH of the same sample after 14 days, showing a decrease of 10% in the sensitivity, indicating a durable structure. (Copyright © 2021, American Chemical Society)

GP (42.1 ± 3.8). This means that making GAH enhanced the sensitivity by 26.7% compared to that of GP film only.

9 Conclusion

In this work, we present an easy protocol to fabricate, low cost, sensitive, and stable pH sensor based on graphene nanoplatelet-gold nanoparticles hybrid (GAH). The sensitivity of this GAH was found to be 53.3 mV/pH, which is close to the limit of the Nernst sensitivity. The sensitivity was enhanced by a factor of 26.7% after making the hybrid in comparison to GP only. This increase in sensitivity is referred to the increase in the surface potential of the GAH, due to the n-doping effect induced by the GNPs, which results in a change in the Fermi level of the graphene nanoplatelets. We introduce this sensor, as a sensitive and easy to use, which can be useful different important sensing applications.

References

1. Ma, G., Wan, Z., Yang, Y., et al.: Optical imaging of single-protein size, charge, mobility, and binding. *Nat. Commun.* **11**(1), 1–11 (2020). <https://doi.org/10.1038/s41467-020-18547-w>
2. Desouky, M., Anisur, M.R., Alba, M., et al.: Near-field mapping of localized plasmon resonances in metal-free, nano-membrane graphene for mid-infrared sensing applications. *ACS Appl. Nano Mater.* **1**, S1–S9 (2018). <https://doi.org/10.1021/acsnm.8b01631>
3. Etezadi, D., Warner, J.B., Ruggeri, F.S., et al.: Nanoplasmonic mid-infrared biosensor for in vitro protein secondary structure detection. *Light Sci. Appl.* **6**, e17029–e17110 (2017). <https://doi.org/10.1038/lsa.2017.29>
4. Afzali, A.A., Han, S.J., Kasry, A., Maarouf, A., Martyna, G.J., Nistor, R., Tsa, H.: US Patent 9102540 (2015). <https://patents.google.com/patent/US9102540B2/en>
5. Elsayed, M.Y., Ismail, Y., Swillam, M.A.: Semiconductor plasmonic gas sensor using on-chip infrared spectroscopy. *Appl. Phys. A Mater. Sci. Process* **123**, 1–7 (2017). <https://doi.org/10.1007/s00339-016-0707-2>
6. Chen, J., Badioli, M., Alonso-González, P., et al.: Optical nano-imaging of gate-tunable graphene plasmons. *Nature* **487**, 77–81 (2012). <https://doi.org/10.1038/nature11254>
7. Taylor, A.B., Zijlstra, P.: Single-molecule plasmon sensing: current status and future prospects. *ACS Sensors* **2**, 1103–1122 (2017). <https://doi.org/10.1021/acssensors.7b00382>
8. Koubová, V., Brynda, E., Karasová, L., et al.: Detection of foodborne pathogens using surface plasmon resonance biosensors. *Sens. Actuators B Chem.* **74**, 100–105 (2001). [https://doi.org/10.1016/S0925-4005\(00\)00717-6](https://doi.org/10.1016/S0925-4005(00)00717-6)
9. Desouky, M., Mahmoud, A.M., Swillam, M.A.: Tunable Mid IR focusing in in as based semiconductor hyperbolic metamaterial. *Sci. Rep.* **7**, 1–7 (2017). <https://doi.org/10.1038/s41598-017-15493-4>
10. Lee, K.S., El-Sayed, M.A.: Gold and silver nanoparticles in sensing and imaging: sensitivity of plasmon response to size, shape, and metal composition. *J. Phys. Chem. B* **110**, 19220–19225 (2006). <https://doi.org/10.1021/jp062536y>
11. Link, S., El-Sayed, M.A.: Spectral properties and relaxation dynamics of surface plasmon electronic oscillations in gold and silver nanodots and nanorods. *J. Phys. Chem. B* **103**, 8410–8426 (1999). <https://doi.org/10.1021/jp9917648>

12. Liu, P.Q., Luxmoore, I.J., Mikhailov, S.A., et al.: Highly tunable hybrid metamaterials employing split-ring resonators strongly coupled to graphene surface plasmons. *Nat. Commun.* **6**, 1–7 (2015). <https://doi.org/10.1038/ncomms9969>
13. Fei, Z., Goldflam, M.D., Wu, J.S., et al.: Edge and surface plasmons in graphene nanoribbons. *Nano Lett.* **15**, 8271–8276 (2015). <https://doi.org/10.1021/acs.nanolett.5b03834>
14. Desouky, M., Mahmoud, A.M., Swillam, M.A.: Silicon based mid-IR super absorber using hyperbolic metamaterial. *Sci. Rep.* **8**, 8–15 (2018). <https://doi.org/10.1038/s41598-017-18737-5>
15. Zhong, Y., Malagari, S.D., Hamilton, T., Wasserman, D.: Review of mid-infrared plasmonic materials. *J. Nanophotonics* **9**, 093791 (2015). <https://doi.org/10.1117/1.jnp.9.093791>
16. Law, S., Adams, D.C., Taylor, A.M., Wasserman, D.: Mid-infrared designer metals. 2012 IEEE Photonics Conf. IPC 2012 **20**, 786–787 (2012). <https://doi.org/10.1109/IPCCon.2012.6358858>
17. Hu, H., Yang, X., Zhai, F., et al.: Far-field nanoscale infrared spectroscopy of vibrational fingerprints of molecules with graphene plasmons. *Nat. Commun.* **7**, 1–8 (2016). <https://doi.org/10.1038/ncomms12334>
18. Koppens, F.H.L., Chang, D.E., García De Abajo, F.J.: Graphene plasmonics: a platform for strong light-matter interactions. *Nano Lett.* **11**, 3370–3377 (2011). <https://doi.org/10.1021/nl201771h>
19. Ni, G.X., Wang, L., Goldflam, M.D., et al.: Ultrafast optical switching of infrared plasmon polaritons in high-mobility graphene. *Nat. Photonics* **10**, 244–247 (2016). <https://doi.org/10.1038/nphoton.2016.45>
20. Ju, L., Geng, B., Horng, J., et al.: Graphene plasmonics for tunable terahertz metamaterials. *Nat. Nanotechnol.* **6**, 630–634 (2011). <https://doi.org/10.1038/nnano.2011.146>
21. Gao, W., Shu, J., Qiu, C., Xu, Q.: Excitation of plasmonic waves in graphene by guided-mode resonances. *ACS Nano* **6**, 7806–7813 (2012). <https://doi.org/10.1021/nn301888e>
22. De Abajo, F.J.G.: Graphene plasmonics: challenges and opportunities. *ACS Photonics* **1**, 133–152 (2014). <https://doi.org/10.1021/ph400147y>
23. Thongrattanasiri, S., Manjavacas, A., García De Abajo, F.J.: Quantum finite-size effects in graphene plasmons. *ACS Nano* **6**, 1766–1775 (2012). <https://doi.org/10.1021/nn204780e>
24. Thongrattanasiri, S., Koppens, F.H.L., García De Abajo, F.J.: Complete optical absorption in periodically patterned graphene. *Phys. Rev. Lett.* **108**, 1–5 (2012). <https://doi.org/10.1103/PhysRevLett.108.047401>
25. Kasry, A., Kuroda, M.A., Martyna, G.J., et al.: Chemical doping of large-area stacked graphene films for use as transparent, conducting electrodes. *ACS Nano* **4**, 3839–3844 (2010). <https://doi.org/10.1021/nn100508g>
26. Fang, Z., Wang, Y., Schlather, A.E., et al.: Active tunable absorption enhancement with graphene nanodisk arrays. *Nano Lett.* **14**, 299–304 (2014). <https://doi.org/10.1021/nl404042h>
27. Kim, S., Jang, M.S., Brar, V.W., et al.: Electronically tunable extraordinary optical transmission in graphene plasmonic ribbons coupled to subwavelength metallic slit arrays. *Nat. Commun.* **7**, 1–8 (2016). <https://doi.org/10.1038/ncomms12323>
28. Zheng, Z.B., Li, J.T., Ma, T., et al.: Tailoring of electromagnetic field localizations by two-dimensional graphene nanostructures. *Light Sci. Appl.* **6**, 1–8 (2017). <https://doi.org/10.1038/lsa.2017.57>
29. Kasry, A., Afzali, A.A., Oida, S., Han, S.-J., Menges, B., Tulevski, G.S.: detection of biomolecules via benign surface modification of graphene. *Chem. Mater.* **23**(22), 4879–4881 (2011). <https://doi.org/10.1021/cm201577k>
30. Zundel, L., Manjavacas, A.: Spatially resolved optical sensing using graphene nanodisk arrays. *ACS Photonics* **4**, 1831–1838 (2017). <https://doi.org/10.1021/acsphotonics.7b00405>
31. Liu, L., Zhang, Y., Wang, W., et al.: Nanosphere lithography for the fabrication of ultranarrow graphene nanoribbons and on-chip bandgap tuning of graphene. *Adv. Mater.* **23**, 1246–1251 (2011). <https://doi.org/10.1002/adma.201003847>
32. Kischkat, J., Peters, S., Gruska, B., et al.: Mid-infrared optical properties of thin films of aluminum oxide, titanium dioxide, silicon dioxide, aluminum nitride, and silicon nitride. *Appl. Opt.* **51**, 6789–6798 (2012). <https://doi.org/10.1364/AO.51.006789>

33. Cataldi, P., Athanassiou, A., Bayer, I.: Graphene nanoplatelets-based advanced materials and recent progress in sustainable applications. *Appl. Sci.* **8**, 1438 (2018). <https://doi.org/10.3390/app8091438>
34. Sengupta, R., Bhattacharya, M., Bandyopadhyay, S., Bhowmick, A.K.: A review on the mechanical and electrical properties of graphite and modified graphite reinforced polymer composites. *Prog. Polym. Sci.* **36**, 638–670 (2011). <https://doi.org/10.1016/j.propolymsci.2010.11.003>
35. Yang, S.Y., Lin, W.N., Huang, Y.L., et al.: Synergetic effects of graphene platelets and carbon nanotubes on the mechanical and thermal properties of epoxy composites. *Carbon N Y* **49**, 793–803 (2011). <https://doi.org/10.1016/j.carbon.2010.10.014>
36. Chung, D.D.L.: A review of exfoliated graphite. *J. Mater. Sci.* **51**, 554–568 (2015). <https://doi.org/10.1007/s10853-015-9284-6>
37. Zhang, M., Li, Y., Su, Z., Wei, G.: Recent advances in the synthesis and applications of graphene-polymer nanocomposites. *Polym. Chem.* **6**, 6107–6124 (2015). <https://doi.org/10.1039/c5py00777a>
38. Shen, J., Hu, Y., Li, C., et al.: Synthesis of amphiphilic graphene nanoplatelets. *Small* **5**, 82–85 (2009). <https://doi.org/10.1002/smll.200800988>
39. Kimling, J., Maier, M., Okenve, B., et al.: Turkevich method for gold nanoparticle synthesis revisited.pdf. *J. Phys. Chem. B* **110**, 15700–15707 (2006). <https://doi.org/10.1021/jp061667w>
40. Goldys, E., Xie, F.: Metallic nanomaterials for sensitivity enhancement of fluorescence detection. *Sensors* **8**, 886–896 (2007). <https://doi.org/10.3390/s8020886>
41. Daniel, M.C.M., Astruc, D.: Gold nanoparticles: assembly, supramolecular chemistry, quantum-size related properties and applications toward biology, catalysis and nanotechnology. *Chem. Rev.* **104**, 293–346 (2004). <https://doi.org/10.1021/cr030698>
42. Patra, S., Mukherjee, S., Barui, A.K., et al.: Green synthesis, characterization of gold and silver nanoparticles and their potential application for cancer therapeutics. *Mater. Sci. Eng. C* **53**, 298–309 (2015). <https://doi.org/10.1016/j.msec.2015.04.048>
43. Chadwick, S.J., Salah, D., Livesey, P.M., et al.: Singlet oxygen generation by laser irradiation of gold nanoparticles. *J. Phys. Chem. C* **120**, 10647–10657 (2016). <https://doi.org/10.1021/acs.jpcc.6b02005>
44. Bao, C., Conde, J., Polo, E., et al.: A promising road with challenges: where are gold nanoparticles in translational research? *Nanomedicine* **9**, 2353–2370 (2014). <https://doi.org/10.2217/nmm.14.155>
45. Wang, J., Shi, A., Fang, X., et al.: An ultrasensitive supersandwich electrochemical DNA biosensor based on gold nanoparticles decorated reduced graphene oxide. *Anal. Biochem.* **469**, 71–75 (2014). <https://doi.org/10.1016/j.ab.2014.09.023>
46. Gong, Y., Chen, X., Lu, Y., Yang, W.: Self-assembled dipeptide-gold nanoparticle hybrid spheres for highly sensitive amperometric hydrogen peroxide biosensors. *Biosens. Bioelectron.* **66**, 392–398 (2015). <https://doi.org/10.1016/j.bios.2014.11.029>
47. Rutherford, G., Xiao, B., Carvajal, C., et al.: Photochemical growth of highly densely packed gold nanoparticle films for biomedical diagnostics. *ECS J. Solid. State Sci. Technol.* **4**, S3071–S3076 (2015). <https://doi.org/10.1149/2.0081510jss>
48. Attar, A., Cubillana-Aguilera, L., Naranjo-Rodríguez, I., et al.: Amperometric inhibition biosensors based on horseradish peroxidase and gold sononanoparticles immobilized onto different electrodes for cyanide measurements. *Bioelectrochemistry* **101**, 84–91 (2015). <https://doi.org/10.1016/j.bioelechem.2014.08.003>
49. Shah, M.: Gold nanoparticles: various methods of synthesis and antibacterial applications. *Front. Biosci.* **19**, 1320 (2014). <https://doi.org/10.2741/4284>
50. Praig, V.G., McIlwee, H., Schauer, C.L., et al.: Localized surface plasmon resonance of gold nanoparticle-modified chitosan films for heavy-metal ions sensing. *J. Nanosci. Nanotechnol.* **9**, 350–357 (2009). <https://doi.org/10.1166/jnn.2009.J064>
51. Kazuhiko, F., Hidehiro, K., Nobuaki, O.: Gold nanoparticle monolayer formation on a chemically modified glass surface. *Anal. Sci.* **25**(2), 241–248 (2009). <https://doi.org/10.2116/anaisci.25.241>

52. Chegel, V., Rachkov, O., Lopatynskiy, A., et al.: Gold nanoparticles aggregation: drastic effect of cooperative functionalities in a single molecular conjugate. *J. Phys. Chem. C* **116**, 2683–2690 (2012). <https://doi.org/10.1021/jp209251y>
53. Zhu, D., Sun, Y., Shi, Z.: Research of CMOS biosensor IC for extracellular electrophysiological signal recording and pH value measuring. In: *International Conference on Solid-State and Integrated-Circuit Technology Proceedings, ICSICT 2557–2560* (2008). <https://doi.org/10.1109/ICSICT.2008.4735108>
54. Kutovy, Y., Zadorozhnyi, I., Hlukhova, H., et al.: Origin of noise in liquid-gated Si nanowire troponin biosensors. *Nanotechnology* **29**(17), 175202 (2018). <https://doi.org/10.1088/1361-6528/aaaf9e>
55. Waleed Shinwari, M., Jamal Deen, M., Landheer, D.: Study of the electrolyte-insulator-semiconductor field-effect transistor (EISFET) with applications in biosensor design. *Microelectron. Reliab.* **47**, 2025–2057 (2007). <https://doi.org/10.1016/j.microrel.2006.10.003>
56. Veeramani, M.S., Shyam, P., Ratchagar, N.P., et al.: A miniaturized pH sensor with an embedded counter electrode and a readout circuit. *IEEE Sens. J.* **13**, 1941–1948 (2013). <https://doi.org/10.1109/JSEN.2013.2245032>
57. Trinchi, A., Kandasamy, S., Wlodarski, W.: High temperature field effect hydrogen and hydrocarbon gas sensors based on SiC MOS devices. *Sensors. Actuators B Chem.* **133**, 705–716 (2008). <https://doi.org/10.1016/j.snb.2008.03.011>
58. Taur, Y., Ning, T.H.: *Fundamentals of Modern VLSI Devices*. Cambridge University Press, Cambridge (2009)
59. Park, B., Cho, K., Kim, H., Kim, S.: Capacitance characteristics of MOS capacitors embedded with colloiddally synthesized gold nanoparticles. *Semicond. Sci. Technol.* **21**, 975–978 (2006). <https://doi.org/10.1088/0268-1242/21/7/025>
60. Hu, C.: MOS Capacitor. In: *Modern Semiconductor Devices for Integrated Circuits*, pp. 157–192. Prentice Hall, Upper Saddle River (2010)
61. Kern, W.: *Handbook of Semiconductor Wafer Cleaning Technology*. New Jersey Noyes Publication, New Jersey, pp. 111–196 (1993)
62. Medhat, A., Salah, D., Boichuk, N., et al.: Graphene nanoplatelet–Au nanoparticle hybrid as a capacitive-metal–oxide–semiconductor pH sensor. *ACS Appl. Electron. Mater.* **3**, 430–436 (2021). <https://doi.org/10.1021/acsaelm.0c00968>
63. Kang, M., Park, S.G., Jeong, K.H.: Repeated Solid-state Dewetting of thin gold films for nanogap-rich plasmonic nanoislands. *Sci. Rep.* **5**, 1–7 (2015). <https://doi.org/10.1038/srep14790>
64. Chieu, T.C., Dresselhaus, M.S., Endo, M.: Raman studies of benzene-derived graphite fibers. *Phys Rev B* **26**, 5867–5877 (1982). <https://doi.org/10.1103/PhysRevB.26.5867>

Bulk and Nanocomposite Thermoelectrics: Synthesis, Properties, and Applications



Mustafa Shalaby, Salwa Hamdy, Ishtihadah Islam, Kulwinder Kaur, Aamer Nazir, and Shakeel Ahmad Khandy

Abstract Being a possible solution to avoid many environmental, political and economic issues, thermoelectric materials have been widely investigated for their ability to convert heat into electricity in the recent past as well as their benefit in reducing the dependence on fossil fuels. In this review we tried to highlight the challenges and possible strategies to synthesize efficient thermoelectric materials. The performance of thermoelectric power harvesting systems or thermoelectric generators (TEGs) relies on the improvement of the overall figure of merit (ZT) and the output power. Nanocomposite thermoelectrics display a vibrant augmentation of ZT and the strain engineering or band manipulation in bulk thermoelectrics prospect from the overall increase in efficiency of the TEGs. In this chapter, we will discuss the processing and feasible properties of the different nanocomposite and bulk thermoelectric systems. The physical or chemical methods of nanocomposite/bulk synthesis methods will be discussed, and the theoretical background of intrinsic transport coefficients will be highlighted in this regard. The possibilities of enhancement of the efficiency can be viewed in nanocomposites with special microstructures, which in turn

M. Shalaby

Thermal and Magnetic Lab, Solid State Physics and Accelerators Department, National Center for Radiation Research and Technology, Egyptian Atomic Energy Authority, B.O. Box 29, Nasr City, Cairo, Egypt

S. Hamdy

Cairo Regional Center, Egyptian Metrological Authority (EMA Weather), Cairo, Egypt

I. Islam

Department of Physics, Jamia Milia Islamia, New Delhi, India

K. Kaur

Department of Applied Sciences, Punjab Engineering College (Deemed to be University), Sector 12, Chandigarh 160012, India

A. Nazir

Department of Mechanical Engineering, National Taiwan University of Science and Technology, Taipei 10607, Taiwan

S. A. Khandy (✉)

Department of Physics, National Taiwan University, Taipei, Taiwan

© The Author(s), under exclusive license to Springer Nature Switzerland AG 2022

959

A. E. Shalan et al. (eds.), *Advances in Nanocomposite Materials for Environmental and Energy Harvesting Applications*, Engineering Materials, https://doi.org/10.1007/978-3-030-94319-6_31

scatter the phonons to minimize thermal conductivity while preserving or increasing the electrical conductivity and the Seebeck coefficient simultaneously. The benefits of these nanocomposites are to enhance ZT by 10–100% and increase the efficiency of thermoelectric devices. In the end, the future perspectives, developments, and challenges of bulk/nanocomposite thermoelectrics are put forward thoroughly.

Abbreviations

TE	Thermoelectric
ZT	Figure of merit
TEGs	Thermoelectric generators
S	Seebeck Coefficient
PGEC	Phonon glass-electron crystal
SEM	Scanning electron Microscope
XRD	X-Ray Diffraction
EDX	Energy Dispersive X-Ray
SAED	Selected area electron diffraction
HRTEM	High-resolution transmission electron microscopy
BF-TEM	Bright field transmission electron microscopy
FWHM	Full-width of at Half Maximum
EDTA	Ethylene diamine tetraacetic disodium salt
PAA	Porous anodic alumina
HOPG	Highly oriented surface of pyrolytic graphite
IGC	Inert-gas condensation
PLD	Pulsed laser deposition
vdW	van der Waals gaps
RGO	Graphene Oxide
DOS	Density of States
DFT	Density functional theory
TMR	Tunneling magnetoresistance

1 Introduction

Economically, current world faces a variety of issues related to energy production and its usage. Global oil supplies and demands continue to rise with the dramatically increase in the prices of Oil [1]. Environmentally, the global apprehensions of the rising impact of greenhouse gases, particularly carbon dioxide and the other carbon products is a prime concern. Politically, the lack of energy supplies will directly influence the poorer countries. Such issues claim the requirement of additional energy harvesting technologies. For the same purpose, several green-energy based modern

vehicle engines, transmissions, and related technologies are in progress to improve the performance of the vehicle transportation.

Still, the absence of one of these crucial problems from the modern-day technologies is quite appealing: most of the energy consumption would still generate unusable heat in the exhaust or cooling systems of the vehicles and other appliances. This waste in the form of heat is equal to two-thirds of the available power reserves of electric plants or the other industrial entities. So, thermoelectric (TE) materials provide a means of transforming this low-grade waste heat energy into electrical energy via the Seebeck effect which was discovered in 1821 [2, 3]. Similarly, a voltage gradient through the junction of a thermoelectric material generates a temperature gradient through the Peltier effect [4]. These categories of materials have been developed into numerous solid-state thermoelectric systems. Due to the significant advantages of thermoelectric harvesting energy systems: no moving parts, long service life, zero emissions, accurate temperature control and the ability to work in the extreme environment [5–7], the expectation of thermoelectric technologies is outstanding, particularly for power production and cooling systems. For power production, energy is collected from waste, environmental, or mechanical/hydraulic supplies and transformed into an exhaustible form — electricity by means of thermoelectric devices [7–10]. Thermoelectric materials are also capable of producing energy via solar radiations to generate a temperature difference throughout the installed thermoelectric materials [11, 12]. Nuclear reactors as well as radioisotope thermoelectric generators are used for propulsion and power supply in spacecrafts [14–17].

In refrigeration modes, air conditioner or micro thermoelectric cooling devices can be mounted in the integrated circuit to resolve the problem of heat dissipation. However flexible thermoelectric materials can be designed in uniforms or clothes of people who are employed in the extreme environment to operate as a wearable climate control system [18].

TE devices efficiency depends on the overall figure of merit (ZT) of the n & p-types thermoelectrics which is defined as [11, 12]:

$$ZT = \frac{S^2 \sigma T}{\kappa} = \frac{S^2 T}{\kappa \rho} = \frac{S^2 T}{\rho(\kappa_l + \kappa_e)} \quad (1)$$

where (S) represents the Seebeck coefficient, σ as well as κ are the electrical and thermal conductivities, respectively, T is the absolute temperature in Kelvin, ρ is the electrical resistivity, whereas the thermal conductivity (κ) consists of two parts: lattice thermal conductivity (κ_l) and electronic thermal conductivity (κ_e).

In the power generation mode, the efficiency (ϵ) can be calculated for both the components of the thermoelectric module (n & p-type) as follows:

$$\epsilon = \frac{T_h - T_c}{T_h} \frac{\sqrt{1 + ZT} - 1}{\sqrt{1 + ZT} + \frac{T_c}{T_h}} \quad (2)$$

For the cooling/refrigerator devices, the coefficient of performance (COP) is given by:

$$\text{COP} = \frac{T_h}{T_h - T_c} \frac{\sqrt{1 + Z\bar{T}} - \frac{T_c}{T_h}}{\sqrt{1 + Z\bar{T}} + 1} \quad (3)$$

where, T_h and T_c are the temperatures of hot and cold surfaces of the TE components, respectively. Also, ZT is occasionally known as the modified dimensionless value of figure of merit of TE devices while considering simultaneously the thermoelectric ability of p-type and n-type components from the materials involved in thermoelectric modules. So ZT may be described as:

$$ZT = \frac{(S_p - S_n)^2 \bar{T}}{(\sqrt{\rho_p \kappa_p} + \sqrt{\rho_n \kappa_n})^2} \quad (4)$$

where, \bar{T} is the average temperature gradient between the hot & cold faces of TE device. The subscripts n and p used to define both the types of the semiconductors p and n-type, respectively, after the geometrical shape optimization for the TE legs is achieved.

Nanostructured PbTe based compounds and alloys have the highest power generation efficiency = 20% with $ZT = 2.2$ by converting the thermal dissipations to electricity which is 30–40% smaller than the conventional systems [19].

There are limitations in the progression of thermoelectric materials despite the current achievements. The low values of $ZT (\leq 1)$ of the commercial TE and the efficiency is around 5% as shown in Fig. 1b. So, the competition to make large-scale thermoelectric devices with a high-power efficiency and higher ZT is demanded [20, 21].

To improve the thermoelectric properties of conventional materials, lot more efforts were made, seeking to improve ZT , especially the creation of the nanostructured materials, such as nanocomposite, superlattices, nanowires, and quantum dots. This has been revealed in Fig. 1a, which represents the remarkable progress accomplished for ZT through the past several decades. To promote thermoelectric practical devices and applications, ZT of the synthesized TE must be quite large.

Countless efforts in TE materials research have been evolved in improving the Seebeck coefficient and reducing the thermal conductivity (κ). Numerous reviews have studied the basic theory of nanostructured TE [21, 22] and the developments in bulk materials [23], nanoscale [24–26], or bulk nanostructured TE materials [1, 27, 28]. The impact of interfaces in low dimension TEs such as 1D nanowires or nanotubes [29–33], 2D superlattices (for example, the superlattices of $\text{Bi}_2\text{Te}_3/\text{Sb}_2\text{Te}_3$ and SiGe/Si , the quantum dot superlattices of $\text{PbSe}_{0.98}\text{Te}_{0.02}/\text{PbTe}$) [1, 34–40] and 3D nanograins [29, 41] can improve ZT by scattering the phonons at the interfaces, which in turn diminishes the thermal conductivity. The size of nanoscale materials results in quantum confinement and interface effects as well as significant changes in the density of state of the charge carriers. Quantum confinement impacts are being used to increase ZT by reducing the transport pathways inside the material. Because of the size of the material lower than the mean free path of the phonon, then it is

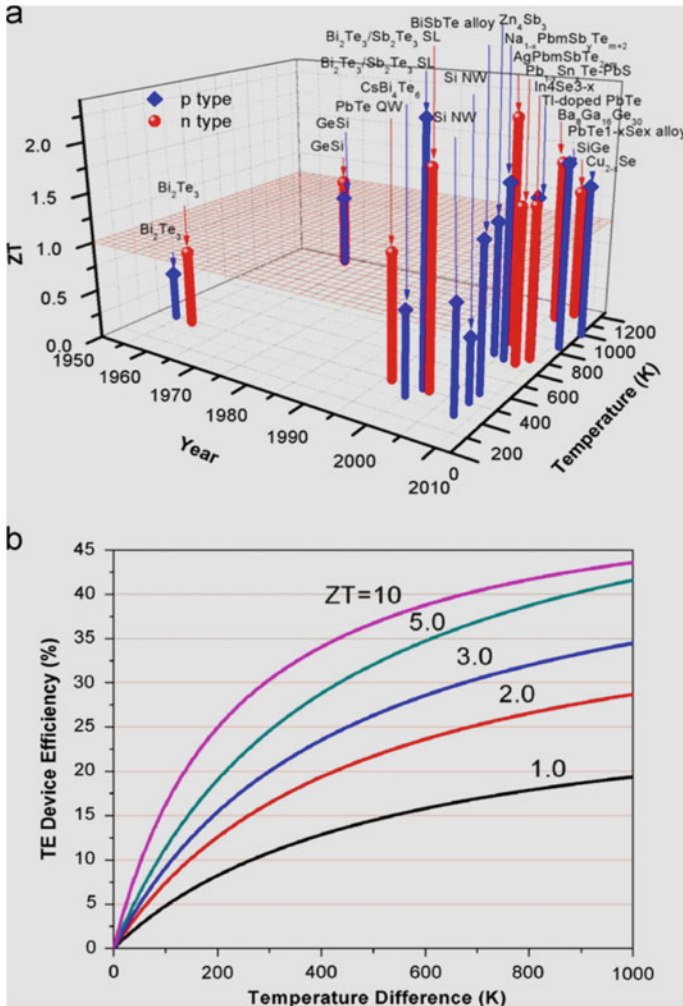


Fig. 1 a Figure of merit (ZT) temperature and year dependent data reveals the important achievements of thermoelectric materials taken from Ref. [20] for the available bulk and nano-thermoelectric materials; b The energy conversion of TE against ZT at $T_c = 300$ K [20]

restricted and no longer contributes to thermal conductivity and hence decreases reasonably. The main goal is to improve ZT and thermoelectric performance as well [42]. On the other hand, the grain size has a curial effect on thermal conductivity where the reduction in the grain size may decrease it to 1/3, at the same time Seebeck coefficient S and the electrical conductivity are not affected compared to the single crystal materials [43]. Thus, nanostructured TE's have a great impact on ZT: In Bi₂Te₃ nanograins ZT increased by 40%, in case of n-type semiconductor Si-Ge alloys ZT reduced by 40% [44], where P-type Si-Ge alloys 90% increase in ZT [45],

50% higher for both p-type half-Heuslers [46] and $\text{In}_4\text{Se}_{3-x}$ (n-type) [47], and by around 4 times larger in MgAgSb composites equal to 1.4 [48].

1.1 Nanocomposites and ZT Improvements

To maximize ZT, lot more attempts have been made and its value stayed stagnant around 1 over 50 years for all the temperature range. So, it became important to make advancements in the usage of new materials like alloys, thin films, bulk materials ...etc. In the 1990s, the most common two analogous methods were anticipated for ZT augmentation of thermoelectric materials: i) the first approach was based on new categories of superior bulk materials [49–51] called as rattlers in which the crystal structures contain weakly bound atoms or molecules with large vibrational amplitudes at partially filled structural sites acting as effective phonon scattering centers. The concept of phonon glass–electron crystal (PGEC) formulated by Glen Slack [52] has also been beneficial in guiding efforts in this direction. Material structures such as skutterudites (e.g., CoSb_3) [53–55], Clathrates (e.g., $\text{Ba}_8\text{Ga}_{16}\text{Ge}_{30}$) [56–58] and Zintl phases [60] fall within this group. ii) The second approach involves the use of low-dimensional materials (including quantum structures-wells/wires/dots) [60, 61] which would end up in the advancement of ZT via two strategies: i) nanoscale characteristics that endorse confinement effects resulting in an increase in the power factor $S^2\sigma$, and (ii) the existence of several interfaces in nanocrystals to increase phonon scattering rather than their counterparts (electrons) and thus reduce thermal conductivity without altering the electrical conductivity [29, 62].

The added value of this approach to the present research guidelines promotes the special design and synthesizing of the nanocomposite materials for improved TE performance. The three parameters S , σ and κ for the 3D-bulk materials are dependent and connected in somehow that restricted to controlling them indecently to enhance the overall ZT of the material. That is because, for example, S increase (by reducing carrier concentration) consequences in a frequent reduction in σ , where any increase in σ usually produce a rise in the electronic part of κ , owing to the Wiedemann–Franz relation. Conversely, if the dimensions of the material are reduced, the nano-scale lengths manage the properties of the material in the form of new effective variable. It is also conceivable to generate vivid changes in the density of states, permitting new prospects or chances to make S , σ , and κ vary in a quasi-independent fashion. One of the other effects of small dimensionality (e.g., less than ~ 100) is the appearance of quantum-confinement effects with respect to the decrease in number density of atoms in any of the 3D (x , y , or z) directions.

Also, the tunable dimensionality from 3D crystals to 2D (quantum wells) or to 1D (quantum wires) and lastly to 0D (quantum dots) leads to the new material properties like metal–semiconductor transition (as introduced for Bi nanowire composites) accomplish the new projections to alter S , σ , and κ individually. In addition, the

existence of various interfaces, scattering the phonons more efficiently than the electrons and the energy barriers filter the low-energy electrons, making the nano-sized materials appropriate for TE applications and devices with enhanced ZT's [29].

From the last few decades, theoreticians and experimentalists by wide use of quantum wells [61] and quantum wires [62] demonstrate the improvement of ZT. In this respect, PbTe superlattices grown by Harman et al. achieved a high ZT of ~ 1.7 (at 300 K) and 3.5 (at 570 K) [64]. Contrarily, the lattice thermal conductivity κ_l in the superlattices reduced to ~ 0.33 W/mK, being 6 times less than bulk PbTe (~ 2.4 W/mK). Further, the intensive experiments demonstrated that the ZT is actually increased by reducing the thermal conductivity and the augmentation in Seebeck coefficient makes no sense. Also, the exhibition of band alignment in these low dimensional materials (in Na-doped PbTeSe compound) elevates the ZT to 1.8.

p-type superlattices of Bi_2Te_3 - Sb_2Te_3 have been utilized by Venkatasubramanian et al. using the molecular beam epitaxy technique [36]. Now it became obvious that it is possible to improve the ZT of materials much beyond 1 by designing the thin films as proposed by the early works or by nanostructures. Besides, nanostructuring effectively raised ZT for Bi_2Te_3 , PbTe, and GeSe to over 1 near room temperature [20, 45]. However, SnTe nanocomposites are lead-free and ecofriendly thermoelectrics with $\text{ZT} \geq 1.2$ due to the exhibition of band convergence and introduction of nanoprecipitates [69–73]. On the other hand, SnSe nanocomposites and its doped forms (Na-doped materials) achieved $\text{ZT} \approx 2.6$ attracted the attention of the researchers [75–78].

1.2 The Basic Theory for ZT Enhancement

As mentioned previously, high ZT material/compound needs to have some features such as a high S, low carrier concentrations which existed in the semiconductors or insulators. However, a low electrical resistivity or a high electrical conductivity in metals is due to the plenty of carriers. So, the thermoelectric power factor could be maximized somewhere between the carrier concentrations of metals and semiconductors, as shown in Fig. 2 [25]. Particularly, the mathematical relation of Seebeck coefficient and carriers concentrations is given by:

$$S = \frac{8\pi^2 k_B^2}{3eh^2} m^* T \left(\frac{\pi}{3n} \right)^{2/3} \quad (5)$$

where k_B is the Boltzmann constant, e is the charge carrier, h is Planck's constant, m^* is the effective mass of the charge carrier, and n is the carrier concentration. The relationship between electrical conductivity and carrier concentration can be defined as

$$\sigma = ne\mu \quad (6)$$

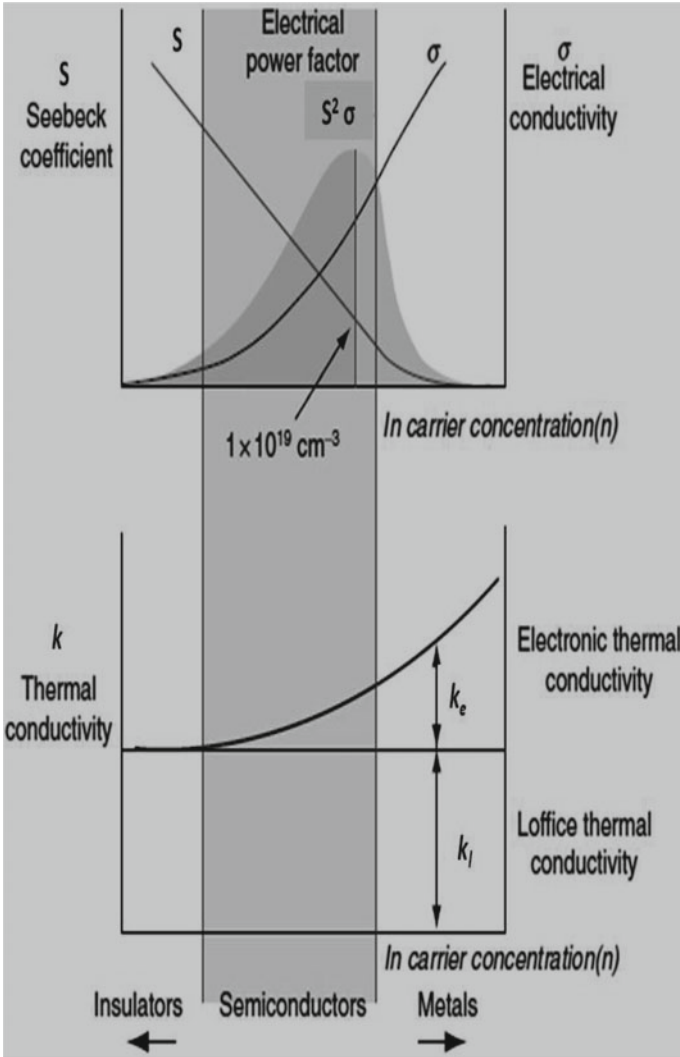


Fig. 2 The Seebeck coefficient(S), the electrical conductivity(s), the power factor ($S^2\sigma$), the electronic thermal conductivity (κ_e), and the lattice (κ_l) thermal conductivity variations on the charge carrier concentration n , for a bulk material

where, μ is the mobility of the carrier. Usually, the good TE's are the heavily doped semiconductor materials that have carrier concentrations up to 10^{19} – 10^{21} cm^{-3} [25]. A single type of carrier (n-type or p-type) is preferable to maximize the Seebeck coefficient, because the mixed n-type/p-type charge carriers would produce the opposite Seebeck effect, lowering the thermopower. To accomplish a single type of carrier, it is crucial to choose materials with proper energy band gaps and fitted doping,

wherein n-type and p-type ranges can be well defined. Therefore, efficient TE's are semiconductors (heavily doped) with energy band gap lower than 1 eV to achieve both single carrier type as well as sufficiently high carrier mobility. The decoupling of both the thermal and electronic terms control the ZT and hence, counting the electrical conductivity and Seebeck coefficient has been the key methodology to raise ZT.

The low thermal conductivity is also needed for more efficient TE materials. Whereas the two parts of the thermal conductivity are: κ_1 , that represents the transported heat from phonons itinerant through the crystal lattice and κ_e results from the heat carried by the charge carriers (such as electrons or holes) traveling through the crystal lattice. According to the Wiedemann–Franz Law

$$\kappa_e = L\sigma T \quad (7)$$

where L is the Lorenz number, as shown in Fig. 2, It is found that the electronic thermal conductivity (κ_e) is proportional to the electrical conductivity (σ). Consequently, to diminish the electronic part of the thermal conductivity for TEs is not always the best option, while it will inversely impinge on the electrical conductivity and has slight or no enhancement of ZT. Lattice thermal conductivity can be defined by

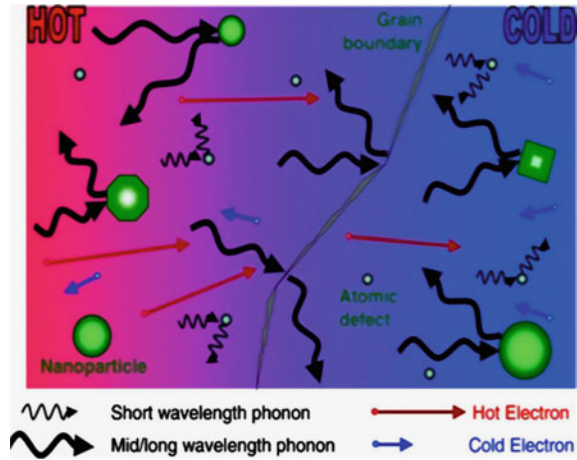
$$\kappa_1 = \frac{1}{3}(C_v v_s \lambda_{ph}) \quad (8)$$

where C_v is heat capacity, v_s is the velocity of sound, and λ_{ph} is mean free path of the phonon. It can be concluded that lattice thermal conductivity is the electronic structure independent parameter so that the improvement of ZT can be obtained by lattice thermal conductivity minimization.

The operational TE materials with a high ZT are the PGEC being the best practicable material with complex crystal structures, which contains voids (vacancies) and rattlers where the heavy element atoms, sited in the voids, could act as scattering centers to the phonons and hence lowering the lattice thermal conductivity (κ_1) notably. Also, the nanoscale materials were recommended to achieve large ZT because the structural arrangement of nanostructured materials foster the density of states (DOS) nearby Fermi level by quantum confinement effect and upsurge the thermopower, which grants a technique to decouple thermopower and electrical conductivity [26, 29].

Furthermore, nanostructuring is used to establish a wide density of interfaces wherein phonons can be more effectively and preferentially scattered over a large mean free path range than electrons, as demonstrated in Fig. 3. Thus, significantly lowers the thermal conductivity of the lattice while retaining carrier mobility and electronic conductivity. This can be accomplished by designing the nanostructures with reducing dimensions less than the mean free path of the phonons, but still longer than those of the charge carriers.

Fig. 3 Illustration of phonons scattering mechanisms and electronic transport of hot and cold electrons within TE materials [20]



1.3 Thermoelectric Nano-Structuring Methodologies

TE nanocomposites are typically produced by bottom-up strategies where the nanoparticles are fabricated first and then compacted into nanostructured bulk materials. The thermoelectric nanoparticles can be synthesized by several bottom-up methods (such as hydrothermal techniques, wet chemical reaction, and melt spinning method), and/or top-down methodologies (such as ball-milling). Amongst these approaches, ball-milling of high-energy type is an efficient and dominant processing strategy for nanoparticles in short times especially for the production of large quantities. Here the common strategies of ball-milling approach for nanoparticle fabrications will be discussed and reviewed.

1.3.1 Ball-Milles/Mechanical Attrition

Ball-Milling or Mechanical attritions are classified as one of the best common synthesis techniques for nanocomposites from bulk raw materials because they are more convenient, demand minimum specifications, less requirements of advanced equipments and flexibility in terms of the number of various categories of solid materials can be achieved by using this method.

Micro-sized TE particles were traditionally prepared by an old method of ball-milling in early 60s. It was found that the gradual reduction in the size of TE particles reached to micrometers in low energy environments. The final product of TE particles were packed in and ZTs were found to be enhanced slightly. SiGe composites have been prepared and used later in radioisotope thermoelectric generators (TEG).

The progress of the high-energy ball-milling technique was launched in the 70s and the mid of 80s to carry out the synthesis of variety of materials, including

superalloys, homogeneous composition ball-milled powders, amorphous alloys and severely deformed alloys. Till date, numerous types of high-energy ball mills were utilized to produce nanocomposites, for example, the shaker mills, the planetary mills, or the attrition mills.

The most popular types of ball mills differ in their specifications and the mechanisms used in the grinding media as the products of many companies. Figure 4 shows SPEX 8000 mixer/mill and the typical planetary ball mill.

Also, Table 1 describes the three types of high-energy ball mills with the calculations of ball velocities, the usage Kinetic energies for each impact; power and shock frequencies are reported as well. For instance, the ball mills from high-energy type have a high impact velocities as well as the impact frequencies especially for producing nanocrystalline materials for different grinding media. The used time for milling process relies on the energy and the frequency of impact of the mill balls. For instance, Just 20 min SPEX shaker milling is the counterpart to nearly 20 h of milling in the other types of low-energy mills like Invicat BX920/2. Also, it was known that the process of milling within SPEX shaker in few minutes is equivalent to hours in attritors and some days in a traditional low-energy mill. Although the usage of this technique in preparing TE materials is common but, there are some challenges such as the effectiveness of the reduction of the particle size is 0.1% in the traditional ball

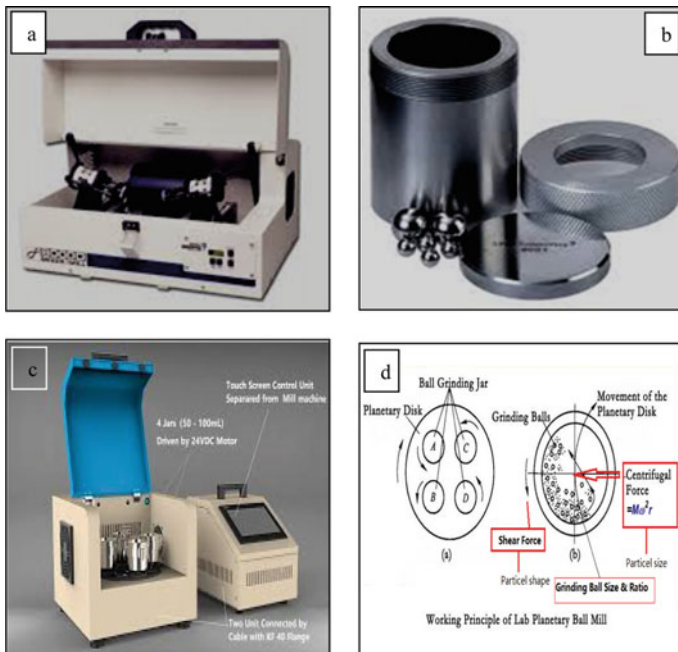


Fig. 4 a SPEX 8000 mixer/mill, b the vial and the balls, c planetary ball mill, and d the principle of the working of the planetary ball mill

Table 1 Three types of high-energy ball mills parameters

Parameter	Attritors	Shaker		Planetary ball mills		
		O ^a	SPEX mill	P5 ^a	G7 ^a	G5 ^a
Velocity of Balls (m/s)	0–0.8	0.14–0.24	<3.9	2.5–4.0	0.24–6.58	0.28–11.24
Power (W/g/ball or rod)	<0.001	0.005–0.14	<0.24	0.01–0.8	0–0.56	0–1.604
Kinetic energy (10–3 J/hit)	<10	3–30	<120	10–400	0.4–303.2	0.53–884
Shock frequency (Hz)	>1000	15–50	200	≈100	5.0–92.4	4.5–90.7
Atmosphere	Varied	Varied	Vacuum, gases	Varied	Varied	Varied
Capacity	Different capacities	Different capacities	0.2–10 gm	Different capacities	12 and 45 ml	Different capacities

^a FRITSCH Pulverisette

mills and <1% in high-energy ball milling. The balls may cause some contaminations in the product due to the difficulty in cleaning the balls. The destruction of the long-range ordered structure or even amorphous materials of different nanoparticles could be generated during this process.

1.3.2 Ball Milling/Attritions TE Nanocomposites

Milling or Mechanical attrition used in fabricating TE nanocrystals by transferring the structural decomposition of the raw materials of coarse grains into finer or smaller structures due to the plastic deformation achieved at room temperature. This procedure can be accomplished by any type of Ball milling route such as high-energy mills, the type of centrifugal, including vibratory mills types, or even by low energy tumbling mills. The ranging of the nanoparticle size achieved by attritors, horizontal mills or even the vibratory mills are in the range from 150 till 5–10 nm. The sensitivity of this procedure to the contamination and other infections from the milling environment urges the usage of a nicely atmospheric control and is vital in preserving the material purity, especially to avoid oxidation. Therefore, Ar and N gases are the most popular atmospheric gases employed in the fabrication of thermoelectrics. Another method for producing new phases in nanoscale is Mechanical alloying but it usually needs double-time more than the ordinary milling process to reach the nanoscale requirements.

Since 2008, mechanical attrition and high energy ball milling techniques have been employed widely in the fabrication of Fe-Si nanopowders, Si-Ge based alloys

[45], PbTe, PbSbTe alloys, SnTe, Bi₂S₃, BiSbTe alloys [97], MgSiSn, CoSb₃, Bi₂Te₃ nanoparticles [45, 102, 103], Zn₄Sb₃, MgAgSb, AgPb₁₈SbSe₂₀ (LAST), YbAgCu₄, half-Heuslers, In₄Se₃, skutterudites [113–115], including La_{3-x}Te₄ which display a challenge to be fabricated by the conventional approaches.

Table 2 records some conventional TE nanoparticles fabricated by the ball-milling route. The obtained crystallite sizes from ball-milling, power factor (PF), and the figure of merit (ZT) are also tabulated. Some of the TE nanoparticles were achieved by the mechanical milling technique where other TE's were produced through the mechanical alloying route.

Both of single-crystalline nanoparticles (such as Bi₂Te₃ and Zn₄Sb₃ nanoparticles with particle size 20 nm) as well as polycrystalline nanopowders can be obtained by

Table 2 Some conventional TE nanoparticles fabricated by ball-milling route

TE materials	Size	PF	Max ZT
Si ₉₅ Ge ₅	10–30 nm	40	0.95
Si ₈₀ Ge ₂₀	7 nm	N/A	1.5
Al _{0.05} La _{0.5} Co ₄ Sb ₁₂	N/A	40.2	1.36
Ce _{0.8} Fe ₃ CoSb ₁₂	94	21.6	0.68
Ce _{0.5} Yb _{0.5} Fe _{3.25} Co _{0.75} Sb ₁₂	104	22	0.93
Pb _{0.95} Ce _{0.05} Te	N/A	10	0.88
(Bi,Sb) ₂ Te ₃	5–50 nm	N/A	1.4
(Bi ₂ Te ₃) _{0.95} –(Bi ₂ Se ₃) _{0.05}	N/A	N/A	1.7×10^{-3}
Cu ₂ Te	<10 nm	N/A	N/A
Zn ₄ Sb ₃	5–20 nm	N/A	1.2
Bi _{100-x} Sb _x	N/A	N/A	1.4×10^{-3}
Ca ₅ Al _{1.9} Mn _{0.1} Sb ₆	1–10 μm	4.2	0.4
Ca _{4.8} Zn _{0.2} Al _{1.8} Sb ₆	1 μm	3.75	0.4
Ca _{2.94} Na _{0.06} AlSb ₃	50 μm	3.76	0.78
Ca ₅ Ga _{1.9} Zn _{0.1} Sb ₆	1–5 μm	0.546	0.35
Yb _{0.99} Zn ₂ Sb ₂	N/A	19.6	0.85
Sr ₅ In _{1.9} Zn _{0.1} Sb ₆	N/A	3.64	0.4
Mg _{3.2} Sb _{1.5} Bi _{0.49} Te _{0.01}	N/A	13	1.5
n-type Mg ₂ Ge	N/A	10.8	0.32
Sb doped Mg ₂ Ge	N/A	N/A	0.2
Bi-doped Mg ₂ Si _{0.6} Sn _{0.4}	>10 μm	N/A	1.36
V- dopedSrTiO ₃	1.4–3.5 μm	4.76	0.084
Y-doped SrTiO ₃	N/A	6.64	0.18
ZnO/Bi ₂ Te _{2.7} Se _{0.3}	>20 μm	22	~1.3
Ca _{0.96} Gd _{0.04} MnO _{3-δ}	110 nm	3.56	0.14

the mechanical milling process. TE ingots are prepared and then exposed to grinding process via ball-milling to fabricate TE nanocomposites which have finally the same chemical compositions. The ductile TE materials like half-Heuslers fragments can be grinded down to achieve polycrystalline nanoparticles by high-energy milling. Besides, Fig. 5 (a, b) illustrates bright-field transmission electron microscopic (BF-TEM) pictures of ball-milled Bi_2Te_3 and Zn_4Sb_3 nanosized particles, respectively. Figure 5c illustrates the images of TEM of ductile half-Heusler particles with nanocrystallites ranging from 50–100 nm.

It should be noted that the previous research pointed out that the speed and the time of milling are notably influencing on the achieved the crystal size of nanoparticles. Figure 6 illustrates how the crystalline size of Cu_2Te ball-milled nanoparticles changes at various ball-milling times. The nanoparticles of Cu_2Te were basically elemental powders of Cu and Te mechanically alloyed via the planetary milling at the room temperature. It was studied that the grain size estimated from XRD diffractograms decreased drastically at first while changing the time of ball-milling and then finally becomes constant with milling time.

The better and powerful technique used to identify the nanoparticle size accurately is TEM but also could be characterized by SEM where it usually gives the geometrical size not the crystalline size of the nanoparticles. Also, XRD may give better information for the nanoparticle grain size or crystalline size of any range by observing the changes in the peak positions and cell parameters. The grain size can be calculated utilizing the Rietveld method or by the traditional methods from Scherrer and Williamson–Hall equations to calculate both the grain size and the strain from The Full-width at Half Maximum (FWHM).

Also, the modified Scherrer equation is given below [43]:

$$B = \frac{0.9\lambda}{d \cos \theta} + \eta \tan \theta \quad (9)$$

The used parameters were d , λ , η that represent the crystallite size, the used wavelength of XRD beam and the strain, respectively, also B is the width at FWHM, and θ is the Bragg's angle. Thus, the procedure to calculate d and η , first plot $B \cos \theta$ against $\sin \theta$, from the obtained straight line, the slope is equal to η and $0.9 = \lambda/d$ is the intercept. So, d as well as η can be experimentally calculated from XRD diffractograms.

It should be noted that the agglomeration of the nanoparticles to compose several smaller particles usually happens significantly with ball-milled processing. Besides, each particle may perhaps consist of quite a few sub-particles identified as consistently diffracting grains/domains. So, it takes into consideration the careful determination of precise crystalline size/grain size from SEM techniques.

One of the observations of the obtained nanoparticles from ball-milling processing is the production of high density grain boundaries in TE nanoparticles. The various defects especially the grain boundaries can strongly scatter the phonons more than the other charge carriers that reduce the thermal conductivity and improve the ZT of

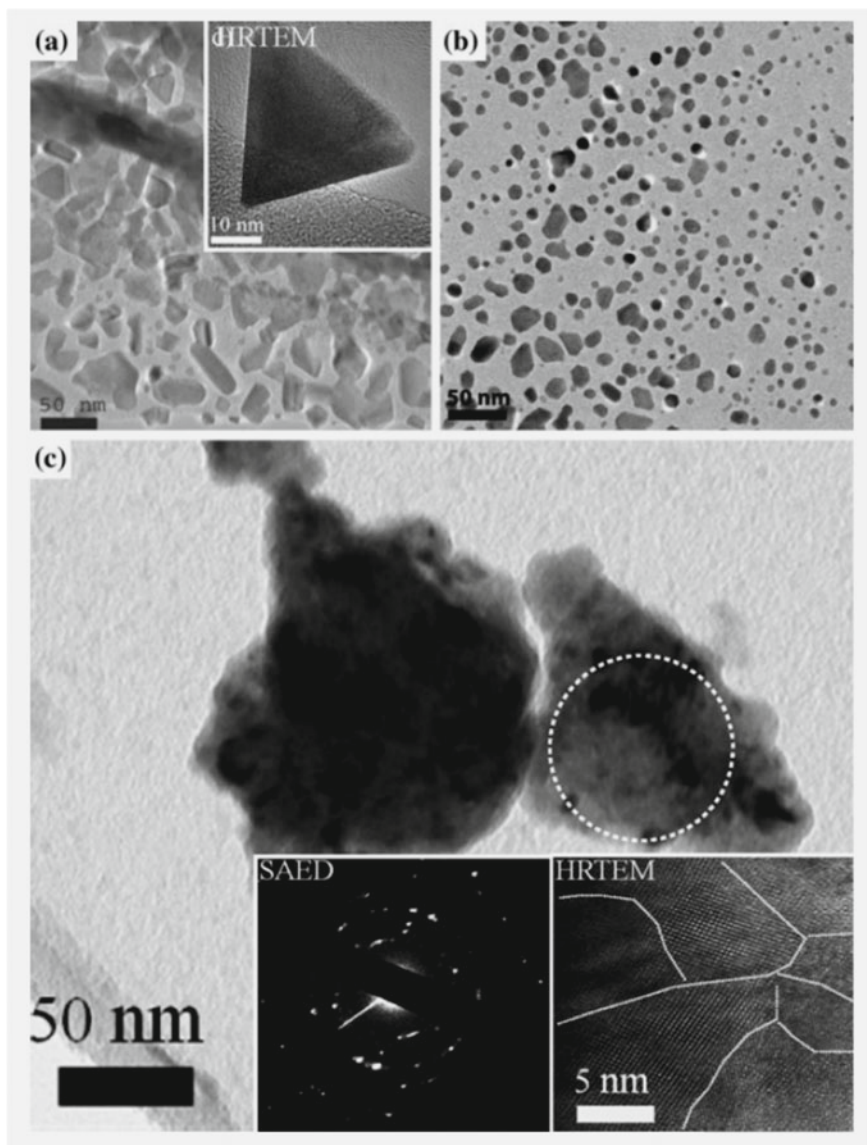
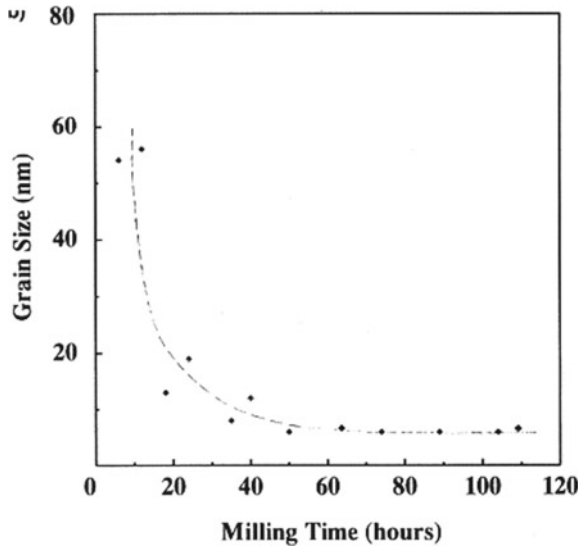


Fig. 5 The ball-milled nanosized particles of images for: **a** p-type Bi_2Te_3 . **b** Zn_4Sb_3 . **c** Half-Heuslers. The circle region is represented by SAED and HRTEM the right view

Fig. 6 Crystalline size of mechanical alloyed Cu_2Te nanoparticles



the nanocomposites. The TE nanocomposite fabrication methods will be discussed in the next section.

1.3.3 Wet Chemistry Synthesis

One of the outstanding techniques for nanocomposite fabrications in different shapes is the wet chemistry procedure. The solvo-thermal method (counting hydrothermal route) fabricates the nanostructures using the appropriate solvents of inorganic powders and precursors above the critical point/temperature of the solvent depending upon the self-formed pressures in an autoclave after the crystallization of the dissolved materials from the solution. In Comparison to other preparation techniques carried out at atmospheric pressure, increase of both the reaction temperature and the time in the solvothermal method may accelerate the crystal growth of the prepared compounds which come up with a smaller particle size distributions and improved crystallinity. One more benefit from this technique is that the nanocrystals may have different morphologies and shapes like, nanopowders, nanorods, nanoplates, multi-lateral nanosheets or nanoparticles, sheet-rods, etc. Also, the solubility of most of the materials in the different solvents by heat or pressure beyond the critical point makes this technique promising for synthesizing nanocomposites of numerous solid materials.

Hydrothermal method was used widely in the preparation of nanostructured TE materials such as Bi_2Te_3 based compounds, doped- Sb_2Te_3 , PbX ($X = \text{S}, \text{Se}, \text{Te}$), CoSb_3 , half-Heuslers, and $\text{Cu}_2\text{CdSnSe}_4$ etc. On the other hand, the tuning in the

preparation conditions like temperature, PH, time, the usage of different surfactants is the powerful tool in the fabrication of nanostructure particles within different shapes throughout an anisotropic growth process. Figure 5 illustrates different nanostructured forms of Bi_2X_3 ($\text{X} = \text{Se}, \text{Te}$), and Sb_2Te_3 that have the same layered rhombohedral crystal structure with D^{5}_{3d} (R3m) space group. The most common structure synthesized from the solvothermal technique is the hexagonal nanoplates where Fig. 7a shows a typical hexagonal nano-plate of Sb_2Te_3 . Here, the effect of the surfactant ethylenediaminetetraacetic disodium salt (EDTA) was added to the precursors through the usage of the hydrothermal processing. Bi_2Te_3 nano-capsules were obtained from polyhedral shell formations as illustrated in Fig. 7b. Contrarily, with the support of some polymer additive, nanowires can be developed by employing the same solvothermal process. Yu et al. articulated a synthesis technique of Te nanowires from the high-temperature decomposition of TeCl_4 in polydecene by the assistance of trioctylphosphine oxide in the form of surfactant. Tellurium nanowires act as a guide for the Bi_2Te_3 nanowire productions by making the reaction with $\text{Bi}[\text{N}(\text{SiMe}_3)_2]_3$ or BiPh_3 . Bi_2Te_3 nanowires are displayed in Fig. 7c. PbTe is one

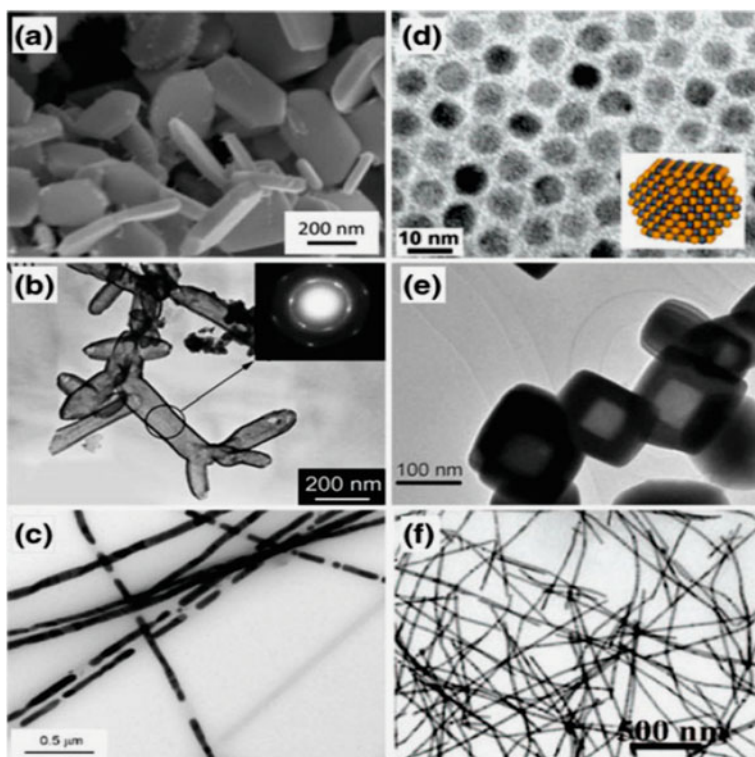


Fig. 7 Bi_2Te_3 TEM images with different nanoparticles shape: **a** nanoplates, **b** nanocapsules, **c** nanowires, and **d** represents PbTe nanoparticles; **e** nanoboxes, **f** and nanowires, the Figures were adapted from [157, 159]

of the classic TE materials but it has a cubic lattice structure. There are numerous chemical method synthesis procedures to grow the nanocomposites of PbTe that have been extensively studied. Figures 7d–f represents the different nanostructured forms, cuboctahedral nanoparticles, nanoboxes, and nanowires respectively, where they have been obtained by the assistance of solvothermal approaches. Chemical routes show well-defined nano shapes, for each particle and were supposed to have fewer defects than those obtained from the ball-milled technique and also have a high mobility carrier.

The final product materials bulk prepared from the different chemical routes may have different atomic defects at the grain boundaries. Small amounts of light elements, such as C, N, and O are residing at these boundaries contribute in producing little thermal conductivity.

Conversely, it is very unfavorable to the transportation of charge carriers in some systems. For instance, the carbons as well as the oxygen atoms, have been confirmed experimentally to have a considerable reduction in the mobility carriers of p-type Bi-Te system where oxygen atoms can be easily introduced during the production of Bi_2Te_3 nanoparticles via the chemical approaches. This makes the carrier concentrations to improve and the Seebeck coefficient (S) to reduce in n-type Bi-Te systems.

So far, the mechanism to transform the high-quality nanoparticles prepared by chemical routes with extraordinary characteristics for TE application is still a challenge and not an easy task.

1.3.4 Electrochemical Deposition

One of facile and effective methods to obtain nanostructured metal alloys is the electrochemical deposition technique [161]. First time the high-quality Bi_2Te_3 nanowires were obtained by Stacy's and co-researchers via the template-assisted (porous anodic alumina (PAA)) electrodeposition processing. This approach has the promotion in fabrication of nanowire arrays, such as doped n-type Bi_2Te_3 , doped p-type Bi_2Te_3 , Sb_2Te_3 , CoSb_3 , PbTe based compounds, etc. [164, 165]. This technique has an advantage in controlling the diameter and the length of the nanowires. The obtained diameter was ranging from 20–300 nm for as-prepared nanowires and is pore size dependent, whereas the length is directly proportional to electrodeposition time.

Also, the composition of the alloys is controlled by changing the electrolyte solution concentration. The arrays of nanowire orientations can be adjusted by varying the deposition potentials or via pulsed electrodeposition procedure. The electroplating can be used to develop a uniform growth of the arrays at low temperatures. Moreover, novel hollow TE nanocrystals can be realized within some special electrodeposition conditions. Li's group articulated the successful production of nanotube arrays of Bi. Zhu's et al. synthesized Bi_2Te_3 and its derived nanotubes arrays. In contrast, 1D chime like Bi-Sb nanocomposites were obtained by Li et al. without the support of

templates. Xiao et al. exemplified the PbTe cube shapes to be instantly deposited on a gold substrate with the polycrystalline structure. By the assistance of the cyclic electrodeposition or so-called stripping method, notable yields of long polycrystalline nanowires from Bi-Te were deposited wisely on the highly oriented surface of pyrolytic graphite (HOPG).

Heterostructures nano-materials can also be obtained by using the electrodeposition technique. The deposition potential is a crucial parameter when template-assisted pulsed electrodeposition is used in the preparation of TE materials. Wang and his group presented a detailed investigation of Bi-Sb-Te and efficiently controlled the growth of $\text{Bi}_2\text{Te}_3/\text{Sb}$ nanosystems in a very low time. The minimum period of as-synthesized $\text{Bi}_2\text{Te}_3/\text{Sb}$ heterostructures achieved low dimensions nearby 10 nm as depicted in (Fig. 8). On the other hand, they also prepared $\text{Bi}_2\text{Te}_3/\text{Te}$ heterostructure nanowire arrays by using the precipitation method to obtain a nano-confined structure

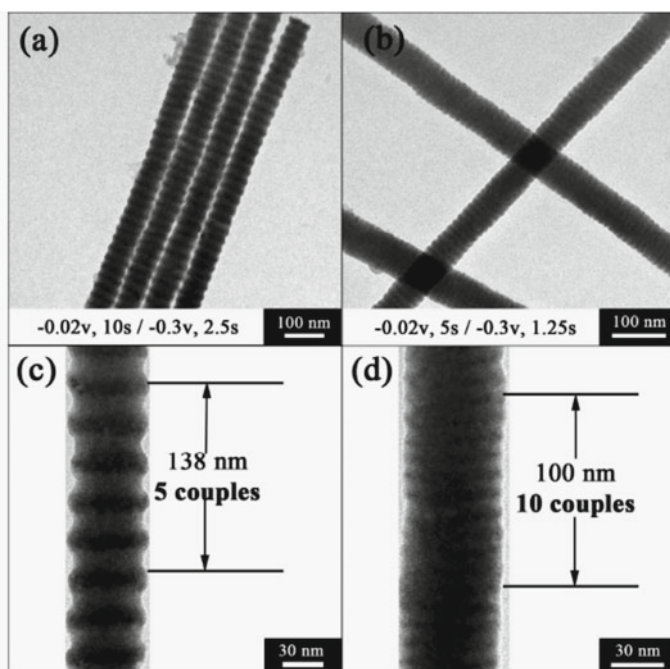


Fig. 8 a and b illustrate the TEM images of multilayered $\text{Bi}_2\text{Te}_3/\text{Sb}$ nanowires deposited in various conditions where c and d represent the corresponding highly magnified TEM images

1.3.5 Inert Gas Condensation Method

The inert-gas condensation (IGC) processing contains some important parameters such as evaporating, sputtering, or ablating materials that are inside of an evacuated chamber kept at a pressure of about 10^{-8} mbar and a low-pressure inert gas like helium is back-filled to the machine.

This route depends on the collision between the material atoms and the gas atoms inside the evacuated chamber, where they are losing their kinetic energy (K.E) and thereby finally condense in the form of small particles. The inert gas condensation approach generates equiaxed crystallites. The crystallite size of the powder obtained from this method ranges in nanometer scale and the size distribution is reduced. The inert gas pressure as well as the temperature, the evaporation/the sputtering or the ablation rate, and the gas type play a vital role in the crystal size formations.

IGC is an effective tool used today for obtaining experimental amounts of metallic nanocrystal and intermetallic powders as well. The best feature of this technique is the ability to generate non-agglomerated nano-powders, especially at low temperatures. First, an evaporative source produces the powder particles, and then the product is convectively carried out and collected on a cold substrate. The nanoparticles acquire in a thermalizing area just above the evaporative source, because of the interactions between the hot vapor species and the much colder inert gas atoms in the chamber typically at 1–20 mbar pressure. Lately, this technique has been accommodated for fabricating Si-Ge nanocomposites. Also, Magnetite (Fe_2O_3) thin films are promising TE's used for thermoelectric applications that were deposited on the surface of SiO_2/Si substrates using Pulsed laser deposition PLD at 300 °C.

1.3.6 Nanoprecipitation/Phase Separation Approach

The technique of nanoprecipitation is a successful solid-state route in the process of the fabrication of nanostructured bulk materials throughout the nano-inclusion. For example, PbTe-based nanocrystals including $\text{AgPb}_m\text{SbTe}_{2+m}$ (LAST-m) can be simply produced by this approach [184–188]. Throughout the cooling procedure of the molten material, nano-inclusions are obtained inside the matrix by phase separation or spinodal decomposition. Nevertheless, it is hard to manipulate the carriers from sample to sample due to the striving nature of the system and its phase diagram. So, the accuracy in controlling the temperature is a crucial point in this method of preparation. This technique is having the ability to fabricate a nanoscale lamellae structure. For systems like $\text{Sb}_2\text{Te}_3/\text{PbTe}$ and $\text{Pb}_2\text{Sb}_6\text{Te}_{11}$, the decomposing of the phase near the eutectic happened in PbTe and Sb_2Te_3 , where lamellae of nanostructured Sb_2Te_3 and PbTe are produced during the fast cooling process. The benefit of this approach is the one-stage method where nanoscale attachments or lamellae are produced simply by thermal treatment. Also, this technique is favorable for electronic transport because it presents coherent or semi-coherent interfaces.

Other chalcogenide materials not related to this shortcoming method are still being surveyed because it is outstanding in situ approach to prepare TE nanocomposites.

1.3.7 Spark Erosion Technique

One of the adjusted methods to fabricate TE nanoparticles with a particularly high synthesis yield is the spark erosion technique. It was initiated for producing fine powders of metals, alloys, and compositions on a micro-scale. Figure 9 schematically illustrates the components of this technique. The two electrodes in the left diagram are immersed into a dielectric liquid connected to a pulsed power supply on the upper side of the cell.

To generate a spark the applied field strength needs to be adequately high in the gap. The initiated spark may be generated from the breakdown inside the dielectric fluid, as described in the reaction zone in the magnified graph on the right side of Fig. 9. If the electric field is proposed to be improved to a high level, electrons can be released substantially and emitted from the cathode. These electrons plus the others in the gap collect the energy from the electric field, ionize the molecules of the dielectric fluid, and produce more ionized electrons and ions. In almost 10 ns of the electric field application, a very small diameter from plasma is established and temperature must be high (it may exceed 10,000 K).

The plasma column has a high temperature so it must be enveloped by a sheath of vaporized dielectric fluid which is controlled by the assistance of incompressible liquid as shown in Fig. 9. Besides, the kinetic energy states are transferred to the electrons and the ions into the anode and the cathode, respectively, which improves the temperature at the electrodes. Due to the much higher electron mobility than that of the ions; short spark times favor anode wear. Consequently, the applied pressure by the plasma channel enhances locally on the electrodes, the temperature of these heated local sections is increased higher than that of the boiling point of the metal. A quick reduction of the pressure takes place at the end of the voltage pulse producing a spark falls, the superheated sections may be boiled violently producing molten droplets and vapor also inside the dielectric liquid as well as liquid nitrogen (N), liquid argon (Ar), water, etc. The erosion process may be enhanced by the violent boiling of superheated regions or other mechanisms. For thermoelectric materials, spark erosion was used to fabricate Bi-Te nano-grained alloys by two different: (1) the development

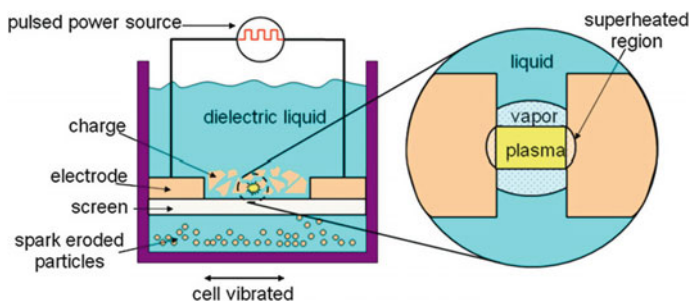
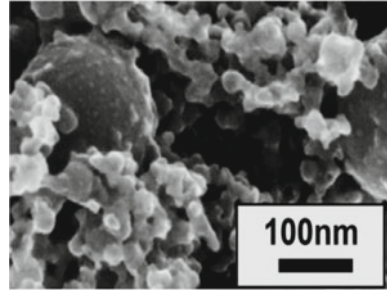


Fig. 9 Schematic diagram of the spark erosion technique for obtaining nanoparticles of a TE alloy

Fig. 10 SEM image
Bi-Sb-Te nanoparticles
prepared by spark erosion



of nanoparticles ranging from 20–30 in nm size, and (2) the establishment of micro-sized particles ranging from (0.1–10 μm) containing nano-grains as illustrated in Fig. 8.

Generally, the spark erosion method often produces a mixture of these two types of particles. For example, the spark-eroded nanocomposite $\text{Bi}_{0.5}\text{Sb}_{1.5}\text{Te}_3$ exhibits a high ZT value of 1.36 at 360 and the ZT values are analogous to those alloys synthesized by other top-down approaches. Spark erosion has a lot of benefits and advantages, especially the production of nano-particles, the rate of processing efficiency, and the scale-up potential K (see Fig. 10). Besides, the spark erosion method does not require crucible and the product has no contamination issues. Finally, oxygen-free preparation conditions are easily achieved.

1.4 Current Accomplishments in Bulk and Nanocomposite Thermoelectrics

Because of the interplay of the coefficients, and their strong dependence on temperature any TE material is limited to operate over the suitable temperature range. For the thermoelectric industry and applications, the classic inorganic and organic TEs are the most commonly used materials. So we will focus on the below discussion on the recent progress of the inorganic and organic TEs temperature range dependant.

1.4.1 Bismuth Telluride (Bi_2Te_3)

One of the most significant TE materials is Bi_2Te_3 based alloys & compounds which commonly used in the TE industry for enormous applications since 1960. They have a rhombohedral crystal structure composed of five thick lamellae, ($\text{Te}^1\text{-Bi-Te}^2\text{-Bi-Te}^1$) where they are also called quintuple layers (QL). The QL layers pack along the c-axis via van der Waals interactions, whereas the Te^2 atoms are hybridized (sp^3d^2) to six Bi-atoms as illustrated in Fig. 11. At room temperature, the unit cell parameters take the values $a = 4.345 \text{ \AA}$ and $c = 30.483 \text{ \AA}$. Moreover, the narrow semiconducting gap

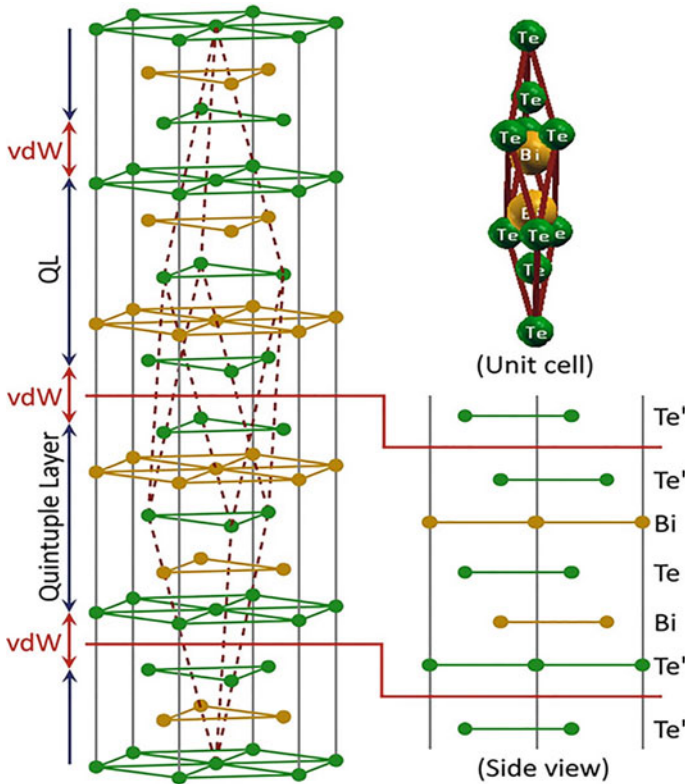


Fig. 11 Bi_2Te_3 Crystal structure showing van der Waals gaps (vdW) and the quintuple layers

at room temperature is equal to $E_g \sim 0.13$ eV makes these compounds beneficial for various TE applications. The excitations of the charge carriers are easier to excite into conduction band with increasing temperatures consequently, in the valence band an equivalent number of holes stay behind. These electron–hole pairs will play a part in the total heat conduction which may reduce the Seebeck coefficient (S). So, the usage of this material in high-temperature applications may enhance the energy gap also (Fig. 12).

The doping process results in a crucial outcome on Bi_2Te_3 starting from the type of the tuning and chaining the ZT values. The doping with Sb makes the Bi_2Te_3 alloys p-type semiconductor and the polycrystalline p-type $\text{Bi}_{0.5}\text{Sb}_{1.5}\text{Te}_3$ nanocomposites in bulk ($ZT = 1.2$ at 300 K & $ZT = 1.4$ at 373 K, respectively see Fig. 13). Also, the size reduction significantly condensed the thermal conductivity to $1.0 \text{ Wm}^{-1} \text{ K}^{-1}$ in the nanomaterials from $1.3 \text{ Wm}^{-1} \text{ K}^{-1}$ in the bulk ingots for the same materials, even though the electrical conductivity reduced slightly in the nano-composite. Finally, the achieved nanoscale materials enhance the ZT by 30% higher than that of bulk

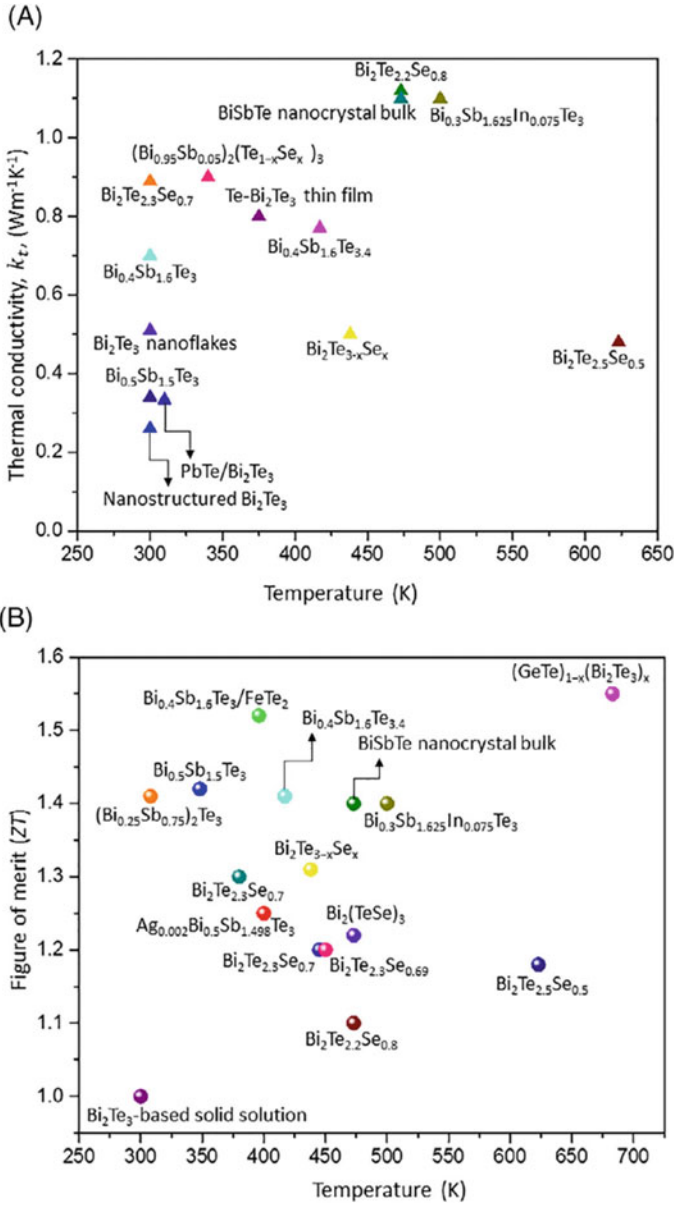


Fig. 12 Promising Bi₂Te₃ alloys displaying **a** ultra-low κ_T and **b** improved ZT values temperature dependence

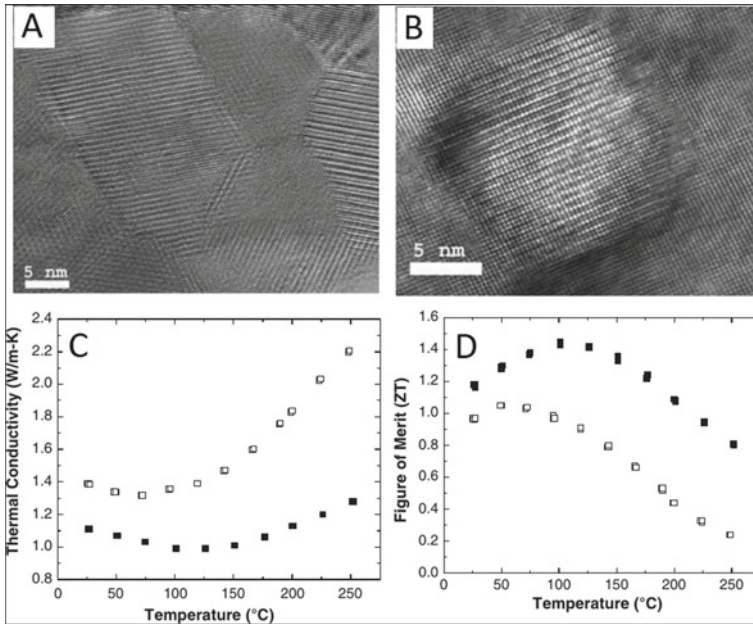


Fig. 13 High magnification TEM images of the hot-pressed $\text{Bi}_x\text{Sb}_{2-x}\text{Te}_3$ nanostructured materials: **a** showing the nanosize, high crystallinity, random orientation, and clean grain boundaries. **b** Nanodots without grain boundaries. **c** Thermal conductivity and **d** ZT of the $\text{Bi}_x\text{Sb}_{2-x}\text{Te}_3$ nanocomposites reproduced from Ref. Here white squares represent state-of-the-art p-type BiSbTe ingots and black squares display hot pressed bulk samples

ingots. To characterize the grain structure of the nanocomposite, Transmission electron microscopy (TEM) is illustrated in Fig. 8(a,c). From TEM data, it can be seen that the complex polygonal grain structures of few microns to a few nanometers size. At the same time, nanodots from Sb-rich ranged from 2 to 10 nm in diameter and a pure precipitate from Te with a diameter in the range 5–30 nm were also detected. The importance of these nanostructures could successfully scatter phonons with a wide wavelength, which improves the thermoelectric characteristics of the nanostructured Bi_2Te_3 composites. The more recent studies show other nanocomposites of p-type Bi_2Te_3 -based compounds enhance the ZT to 1.3 and 1.4 at 75 K and 373 K, respectively, but the figure of merit displays a value of nearly 1.04 at 398 K in n-type Bi_2Te_3 nanocomposites.

Different studies on the characteristics of Bi_2Te_3 -based nanocomposites display a wide variation in ZT values (0.4–1.7) at different temperatures. Such as a maxima in ZT equal to 1.5 at 390 K was obtained in p-type $(\text{Bi,Sb})_2\text{Te}_3$ nanocomposites when single elements of Bi, Sb, and Te are melt-spun simultaneously and further pursued by the spark plasma sintering technique. Values like ZT(1.47) and ZT(1.56) were accomplished in nanostructures synthesized by the hot-pressing method of Sb_2Te_3

and Bi_2Te_3 powders at nanoscale range with diameters less than 20 nm and p-type $\text{Bi}_{0.52}\text{Sb}_{1.48}\text{Te}_3$ nanocomposite with the diameter ranging from 5–15 nm precipitates.

Also, *Sharma* and his group achieved the highest ZT value at 700 K equal to 2.42 for Bi_2Te_3 (p-type) samples, whereas Bi_2Te_3 alloys in n-type form show large κ_T due to small E_g as well as minority carriers (electrons). Various studies have been put forward to improve E_g and simultaneously decrease κ_T of n-type Bi_2Te_3 by the different methods such as doping, alloying, nanostructuring, nanocomposites, nanoplates, quantum dots and twin boundary engineering are the most common routes.

Furthermore, Shalaby et al. synthesized a sulfur-doped $\text{Bi}_2\text{Te}_{2.85}\text{Se}_{0.15}$ nano composites from n-type semiconductors with achieved E_g of 0.14 eV. On the other hand, Bi_2Te_3 n-type nanocomposites were fabricated with the help of (NaOH) and the obtained E_g was 4.8 eV which was much higher than that of the pure Bi_2Te_3 (0.13 eV). The defects and other impurities like the existence of dislocations at the grain boundaries play a curial and non-invasive role in κ_T reduction by scattering the minority carriers and preventing them from contributing to the electronic transport properties.

On the other hand, a liquid-phase compaction method was used by *Kim* and his group to enhance dislocation arrays at grain boundaries having low-energy (see Fig. 13). The major purpose of this approach is to scatter and diffuse the phonons with medium frequency so that the phonon thermal conductivity (κ_1) reduces. They also pronounced the κ_1 reduction to $0.33 \text{ Wm}^{-1} \text{ K}^{-1}$ and an improvement of $ZT = 1.86$ at 320 K. Moreover, *Yang* and his co-workers fabricated n-type Bi_2Te_3 nanocomposites with ultra-low κ_1 of around $0.2 \text{ Wm}^{-1} \text{ K}^{-1}$ by creating high-density grain boundaries through dislocations. Additionally, the composite of $\text{Bi}_{0.36}\text{Sb}_{1.64}\text{Te}_3$ loaded with reduced Graphene Oxide (RGO) displayed a small κ_1 of $0.63 \text{ Wm}^{-1} \text{ K}^{-1}$.

Hydrothermal/solvothermal technique has also been used to fabricate Bi_2Te_3 nanostructures. *Ni* and his coworkers prepared nanopowders of Bi_2Te_3 using this approach and the hot-pressed method with zone-melted Alloy has been used with a ratio of 10:90. They found that the reduction in the size of powders to nanoscale decreases the thermal conductivity robustly than the electrical conductivity, which results in the improvement of ZT (0.83). Moreover, the possibility of the achievement of ZT of the nanocomposites materialized because of the usage of the suitable dopants and the structural optimization of the base alloys. Other Bi_2Te_3 -based nanocomposites demonstrate similar TE characteristics as that of pristine bulk Bi_2Te_3 , whereas some in contrast displayed poor performances. In conclusion, TE operations are related strongly to the structural and compositional characteristics of nanocomposites.

1.4.2 PbTe Based Nanocomposites

Lead telluride (PbTe) being one of the promising TE materials works at medium temperatures ranging from (450–800 K). Recently, The ZT of these compounds was

almost doubled to 1.5 at 773 K for Th doped PbTe via the improvement of the Seebeck coefficient (S). High ZT Th-doped PbTe nanostructured materials were observed and the density of PbTe nanocomposites was 95% as that of theoretical predictions. Such samples were fabricated by spark plasma sintering technique with nanoparticles ranging from 100–150 nm. The figure of merit of these nanocomposites was around 0.1 at room temperature. Doping elements such as potassium were observed to affect the structural and thermoelectric properties of PbTe nanocomposites.

Experimentally at room temperature, when the Potassium content increases the electrical conductivity was slightly enhanced also but at higher temperatures no effects have been indicated, where all samples exhibited a reduction with temperature. Also, it was found that all samples have nearly the same thermal diffusivity. A slight change in Seebeck coefficients for all samples has probably remarked a consequence of hole contributions w.r.t high carrier concentration. Figure 14a illustrates that the PF was enhanced by the increase in potassium content and registered a peak at 500 K. The maximum ZT value for $K_{0.015}Pb_{0.985}Te$ reached 1.3 at 673 K (Fig. 14b), in comparison to that of the Sodium-doped PbTe at the same temperature.

The ball-milling technique followed by a hot-pressed process was used in Al_xPbTe nanocomposites fabrication as depicted in Fig. 15a. In addition, the Aluminum doped PbTe nanocomposites show n-type semiconductor behavior with Seebeck parameter in the range -100 to -200 V/K and the electrical conductivity values of 3.6 – 18×10^4 S/m at 300 K, and the highest ZT of 1.2 is achieved for the $Al_{0.03}PbTe$ nanocomposites at 770 K. SEM image of a cracked surface of Al-doped PbTe nanocomposite is shown in Fig. 10b. The temperature dependence of the thermoelectric properties at different doping levels of Cr in Cr-doped PbTe nanocomposites is depicted in Fig. 15. It was found that Cr doping increased the power factor dramatically around the room temperature in contrast to the other n-type PbTe alloys. Also, the thermal conductivity reduces to 1.3 W/m/K (at 773 K) from 2.6 W/m/K at 300 K.

Figure 16 illustrates the thermoelectric properties at various temperatures for $Cr_{0.01}Pb_{0.99}Te_{1-x}Se_x$ ($x = 0.25, 0.5, 0.75, 0.85$) systems. It was found that the nanocomposites make a reduction in electrical conductivity values with the increasing

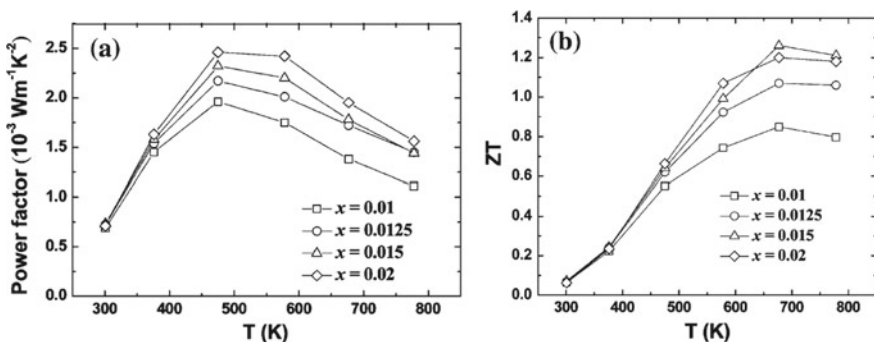


Fig. 14 The temperature dependence of: **a** power factor (PF) and **b** ZT of $K_xPb_{1-x}Te$ nanocomposite ($x = 0.01, 0.0125, 0.015, 0.02$)

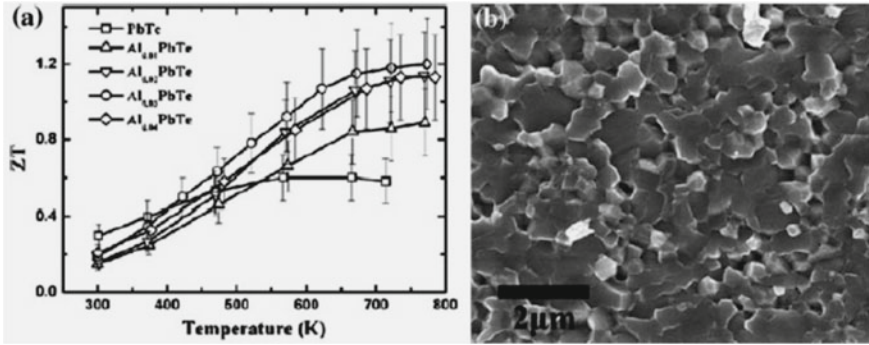


Fig. 15 The taken data for Al_xPbTe samples ($x = 0, 0.01, 0.02, 0.03, 0.04$). **a** Temperature versus ZT and **b** SEM images

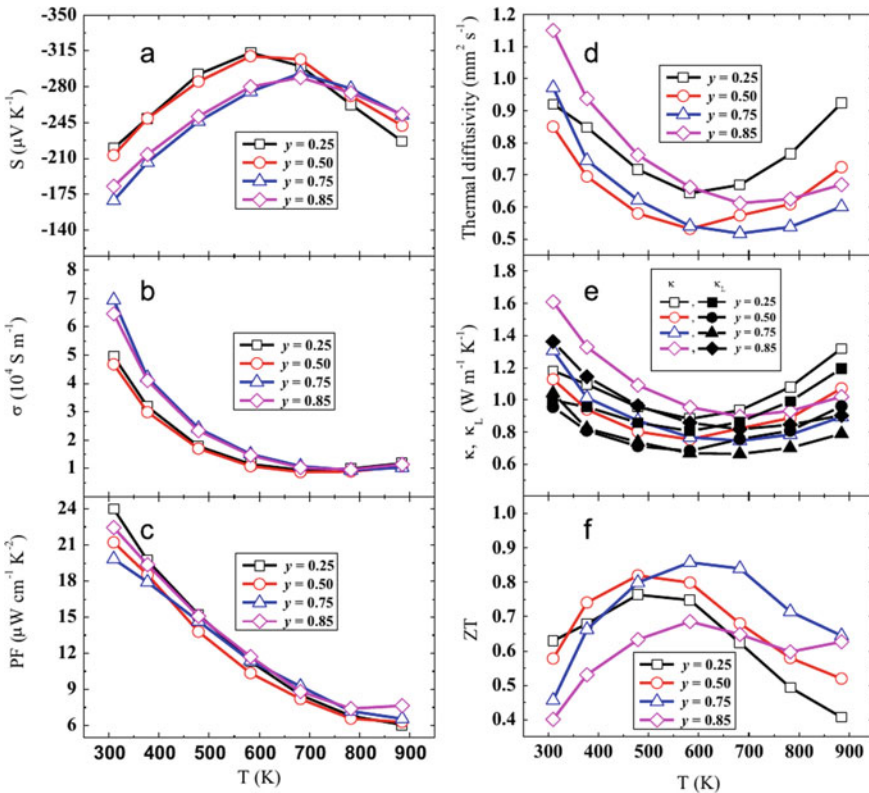


Fig. 16 Temperature-dependent thermoelectric parameters of $Cr_xPb_{1-x}Te$ nanocomposites ($x = 0.01, 0.015, 0.025, 0.03$) **a** Seebeck coefficient (S), **b** electrical conductivity, **c** power factor (PF), **d** thermal diffusivity, **e** total thermal conductivity (κ) and lattice thermal conductivity (κ_L), and **f** ZT

temperatures which is a characteristic of degenerate semiconductors. With enhancing Se content at a level of doping content into Cr site with 1 atomic %, the achieved Seebeck coefficient (S) reduced from 211 to 157 mV/K at room temperature. At higher temperatures, it was remarked that nanocomposites materials lower the Seebeck Coefficient because of the production of the bipolar effect. Generally, this effect shows a stronger behavior in samples with abundant Te concentration but it is still smaller in quantity than Se-rich samples. On the other hand, the increase of Se content to 75 atomic percent may enhance the electrical conductivity to the optimum because it drastically decreases when Se concentration was above 75 atomic %.

Se- rich- $\text{Cr}_{0.01}\text{Pb}_{0.99}\text{Te}_{0.25}\text{Se}_{0.75}$ sample revealed a high electrical conductivity and power factor throughout the temperature range. The enhancement was happened for the electrical conductivity due to the increase in the carrier concentrations to $(8.12 \times 10^{18} \text{ cm}^{-3})$ at room temperature proved from Hall measurements. This results show a remarkable drop in the thermal conductivity (κ), owing to the role of the defects resulting from alloying in phonon scattering, in comparison with the observed data from the Cr-doped PbTe nanocrystals.

At equal content of Te and Se in $\text{Cr}_{0.01}\text{Pb}_{0.99}\text{Te}_{0.5}\text{Se}_{0.5}$ nanomaterials, the thermal conductivity condensed to 0.8 W/m/K at 573 K. This was lower than 72% of the thermal conductivity achieved on PbTe for the same Cr doping level with 1% as depicted into Fig. 16. This decrease was expected theoretically and experimentally it was found to happen due to mass fluctuations when lattice distortion occurs. But the thermal conductivity at higher temperatures was registered and associated with the contribution of the heat transport from the minority carriers (holes). The highest figure of merit ZT for Se-rich $\text{Cr}_{0.01}\text{Pb}_{0.99}\text{Te}_{0.25}\text{Se}_{0.75}$ is 1 within the range of 573 K to 673 K. The maximum peak in ZT increased with increasing Se content.

It was found that Te-rich $\text{Cr}_{0.015}\text{Pb}_{0.985}\text{Te}_{0.75}\text{Se}_{0.25}$ nanocrystal has a maximum (ZT = 0.6) at room temperature due to the improvement of the thermoelectric performance by lowering κ , increasing (S = 220 mV/K) and the Hall mobility to $1120 \text{ cm}^2/\text{Vs}$ that improves the power factor. The figure of merit of Se-rich $\text{Cr}_{0.01}\text{Pb}_{0.99}\text{Te}_{0.25}\text{Se}_{0.75}$ samples was reported 0.5 at 573 and 1 at 673 K, respectively.

Besides, *Sie* and coworkers used Na_2Te as a doping material in PbTe alloy where a high S ($-112 \mu\text{VK}^{-1}$), σ (53.52 Scm^{-1}) and ZT of 0.81 were obtained. Also, *Jood* and his research group obtained a high ZT (~1.9) for the combinations (p-type $\text{Pb}_{0.953}\text{Na}_{0.040}\text{Ge}_{0.007}\text{Te}$) and (n-type $\text{PbTe}_{0.9964}\text{I}_{0.0036}$) legs by using between the dopants and the nanostructure of PbTe at ~805 K. Furthermore, *Xiao* et al. articulated the mix of Se with Sn and alloyed them into PbTe, where Se diminished the κ_T to ~1.21 from ~3 $\text{Wm}^{-1} \text{K}^{-1}$ but Sn improved both the carrier concentration (n) and the mobility (μ) of PbTe. They achieved the ZT of 1.2 at 673 K as well as the PF of ~14.6 $\mu\text{Wcm}^{-1} \text{K}^{-1}$ at 300 K in their work. Consequently, the key point to enhance ZT to the highest values for PbTe alloys is striking to improve DOS to obtain a high thermoelectric power coefficient (S), and the reduction of κ_1 value is also demanded with less effect on the electronic transport properties of these alloys.

1.4.3 Tin Selenide (SnSe) and Copper Selenide (Cu₂Se) Materials

Among the inorganic TE materials feasible in a medium temperature range with high performance and efficiency, SnSe based compounds are an asset. It reveals excellent features such as i) the long-range thermal stability, ii) simplistic nature or constitutes earth-abundant elements, iii) intrinsically ultralow lattice thermal conductivity κ_T , and iv) less toxicity. For crystal structure properties, SnSe takes NaCl structure and comprises a layered orthorhombic space group Pnma (Fig. 17a), and its unit cell dimensions are $a = 11.501 \text{ \AA}$, $b = 4.153 \text{ \AA}$, and $c = 4.445 \text{ \AA}$. On the other, it has a low indirect band gap of 0.86 eV with p-type conduction (i.e. hole concentration $\sim 10^{17} - 10^{18} \text{ cm}^{-3}$) and very high resistivity (ρ) ($\sim 10^1 - 10^5 \text{ \Omega cm}$) at 300 K. Consequently, one of the important issues is that the polycrystalline structure of SnSe material cannot be used for TE applications due to its very high room-temperature resistivity. The

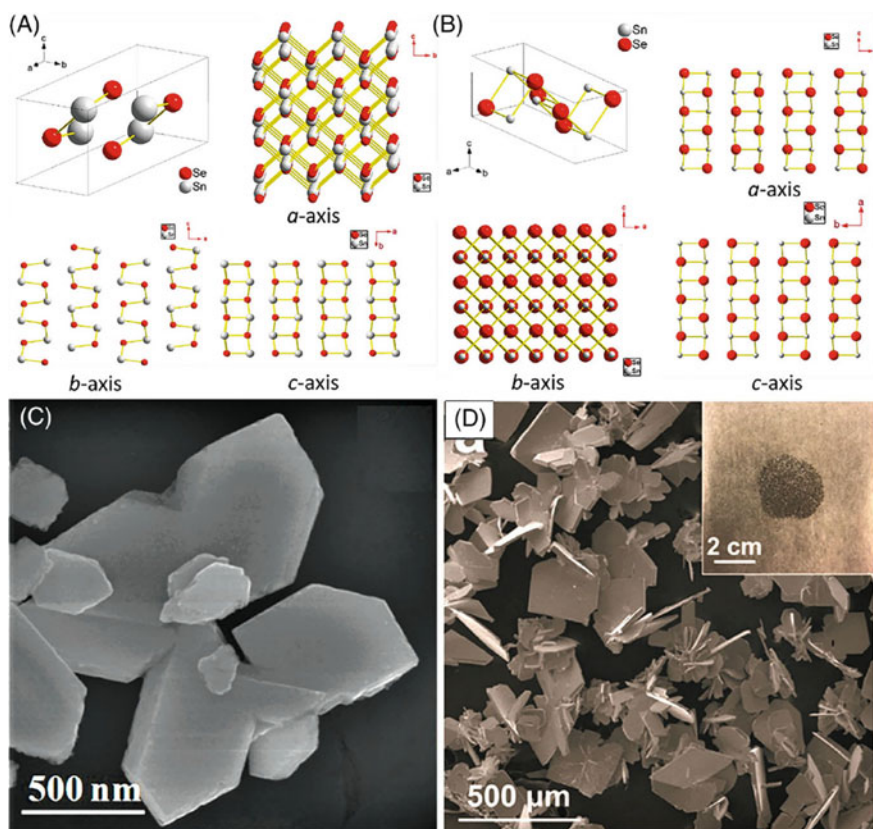


Fig. 17 SnSe Crystal structure with the common space groups **a** Pnma and **b** Cmcm, **c** Field Emission Scanning Electron Microscopy (FESEM) image of Sn_{0.97}Ge_{0.03}Se nanoplates and **d** SEM and optical image (right top view) of prepared Sn_{0.948}Cd_{0.023}Se microplates

increase in temperature $\sim 750\text{--}800$ K results in a remarkable phase change to Cmc m structure producing a further decrease in the energy gap to $E_g \sim 0.39$ eV and in lattice parameters to ($a = 4.31$ Å, $b = 11.70$ Å, and $c = 4.31$ Å) as shown in Fig. 16b. Polycrystalline SnSe usually displays low (μ) and thus shows low ZT value. The methods used to improve the performance of SnSe compounds are concluded to be suitable dopants as well as the low dimension scale or nanostructuring. For example, *Chandra* and his group used Ge doping elements to improve the n and diminish κ_T and their (Sn $_{0.97}$ Ge $_{0.03}$ Se nanoplates) morphology is presented in Fig. 17c. They pronounced a very low κ_T (≈ 0.18 Wm $^{-1}$ K $^{-1}$) and high ZT (≈ 2.1) at 873 K. Under similar conditions, *Shi* et al. revealed ~ 1.7 for ZT value of Sn $_{0.948}$ Cd $_{0.023}$ Se micro-plates (Fig. 17d). In addition, *Liu* et al. employed simultaneous techniques of doping and nanostructuring to improve PF (5.43 μ Wcm $^{-1}$ K $^{-2}$) and reduce κ_1 (0.13 Wm $^{-1}$ K $^{-1}$). SnSe nanocomposite was substituted by Pb and Zn atoms to form Sn $_{0.98}$ Pb $_{0.01}$ Zn $_{0.01}$ Se and maximum ZT (2.2) was recorded at 873 K. Due to the anisotropic transport characteristics of SnSe crystal system, mid-range TE performance was at its best. For example, a large ZT of 2.6 (at 923 K) and the ultralow thermal conductivities κ_T and κ_1 with values ~ 0.35 and 0.23 Wm $^{-1}$ K $^{-1}$ at 973 K, respectively were obtained for the SnSe single crystals within the orthorhombic unit cell. At 800 K, *Chang* and his group attained an exceptional ZT value of 2 by improving the important two factors μ and S with the help of Br dopants in SnSe (a -axis). Although the very good TE properties were achieved from single phase SnSe systems such as the ultralow κ_T and outstanding ZT values there were some unwanted properties such as i) the poor mechanical properties, ii) the inflexible crystal growth nature, and iii) the high fabrication cost which in aggregate made it unfavorable for large-scale production.

From the first principle study, *Anish* et al. discussed the SnSe as p-type material with indirect band gap E_g of 0.66 eV, where a phase separation occurred and n-type character with negligible indirect band gap E_g of 0.064 eV was entertained. They also revealed the existence of SnSe $_2$ as a minority phase, whereas the possibility of Cu $_2$ Se as a secondary phase is negligible because of its higher formation energy. Cu $_2$ Se system is similar to SnSe with a potential application as TE materials due to its abundance and pollution-free nature. It has two crystal structures viz., α and β -phase. The Cu $_2$ Se α -phase comprises a monoclinic structure with reasonably less symmetry at low temperatures. At 400 K, a remarkable structural change to a cubic system (β -phase within Fm-3 m space group) is observed, where Se atoms and Cu ions are redistributed on different interstitial sites and take up the simple face-centered cubic structure. The TE characteristics of Cu $_2$ Se (β -phase) exhibits larger ZT value than that of α -phase because of the improvement of S , σ , PF, and decrease in κ_T . Even though the improvement of n raised σ decreases S and vice versa, which is not favorable for PF of TE materials. Metallic Cu $_2$ Se β -phase reveals an outstanding PF (2.3 Wm $^{-1}$ K $^{-2}$) as well as ultra-high ZT value at 400 K. The doping and the nanostructuring strategies are widely used to elevate the TE performance of Cu $_2$ Se. *Liu* et al. for example used iodine (I) as a dopant to control the transition temperature of Cu $_2$ Se system and thus large ZT value of 2.3 was achieved at 400 K. At the same time, *Hu* and his group used alkaline metal (Li) in the doping process to increase S where they articulated ZT of 2.14 for Cu $_{1.98}$ Li $_{0.02}$ Se at 973 K. On the other hand,

Yang and his coworkers used a nanostructuring strategy to minimize the κ_1 up to $\sim 0.2 \text{ W m}^{-1} \text{ K}^{-1}$, which in turn shoots the ZT value to 1.82 at 850 K. Carbon-based alloys used in Cu_2Se to enhance the thermoelectric power (S) and lower the κ_T for more efficient TE performances have been lately introduced. Such as, *Hu* et al. doped carbon nanodots into the Cu_2Se system that improved S to $\sim 290 \mu\text{VK}^{-1}$ and diminished κ_T to $0.45 \text{ W m}^{-1} \text{ K}^{-1}$ which resulted in ZT equal to 1.98 at 973 K. Also, *Li* and his group used nanoparticles of carbon-coated boron in Cu_2Se system which displayed ZT ~ 2.23 at 1000 K. Likewise, *Li* et al. engineered graphene nanoplates inside a Cu_2Se matrix which drastically reduced κ_T to $\sim 0.4 \text{ W m}^{-1} \text{ K}^{-1}$ and hence the ZT ~ 2.44 at 873 K was obtained. All these considerable improvements indicate the benefits of both SnSe and Cu_2Se systems as strong candidates for TE applications.

1.4.4 Skutterudites Nanocomposites

Skutterudites being extensively studied for potential thermoelectric processing are considered as promising choices for next-generation TE materials and applications especially for power generation used in both solar source and waste heat managements. The significant characteristic of this kind of TE material is the open cage-like structure where the filled atoms act as rattlers for phonons. The “rattling” of these doped atoms scatter the phonons effectively and significantly decreases the thermal conductivity (κ).

Generally, the common chemical formula of Skutterudites was established by Oftedal and take (MX_3) formula, where (M) is a transition element (Co, Rh, Ir...) and (X) imply Pnictogen (P/As/Sb) atoms. Binary Skutterudites consists of an open casing structure with an Im3 space group in a cubic body-centered unit cell structure, whereas the void is produced by eight atoms surrounding octahedrally as depicted in Fig. 17a. Moreover, the unit cell is repositioned by $(1/4)$ distance diagonally across the body. On the other hand, the structure of Skutterudite composites contains two filled voids in each unit cell where the filler atoms are electropositive for example Yb, In, and Ti. An icosahedral cage-like structure surrounds these filler atoms taking the shape of pnictogen octahedral atoms (X). Moreover, the transition metal atoms (T) like Co, Rh, Ir, Ni, Pd are centered in this structure which takes the form of $\text{EP}_y\text{T}_4\text{X}_{12}$, depicted in Fig. 17b. This is called a “filled Skutterudite” and was first experimentally synthesized in 1977 by Jeitschko et al. (Fig. 18).

It is well known that most of the binary skutterudite TE materials exhibit high μ and n as mentioned in ref. [260]. For example, the CoSb_3 compound achieved a very high μ and n of $3445 \text{ cm}^2\text{V}^{-1} \text{ s}^{-1}$ and $4 \times 10^{17} \text{ cm}^{-3}$, respectively. On the other hand, the undoped p-type CoSb_3 exhibits a ZT value of about 0.2, and the doping in n-type crystals attains ZT = 0.52 at 600 K. The achieved figure of merit value in $(\text{Ni, Co})_4\text{Sb}_{12}$ nanocomposites is 0.7 without rattlers. Also, *Khovaylo* and his group achieved an ultra-low κ_T close to 1.25 and a high ZT value of ~ 1.5 at 725 K with the help of indium filler atoms embedded in skutterudite $\text{Co}_4\text{Sb}_{12}$ composition. Typically, the improvements in ZT were obtained with various kinds of atoms (such as Ce, La, Ca, Ba, Yb) to fill the cages structures. For instance, Yb-filled n-type $\text{Yb}_{0.19}\text{Co}_4\text{Sb}_{12}$

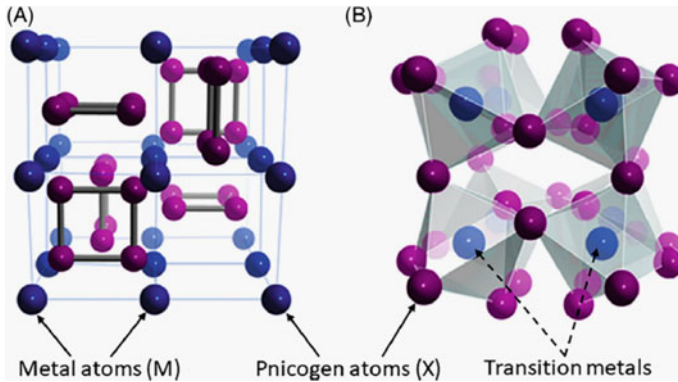


Fig. 18 The representative figures of **a** Binary Skutterudites structure with metal atoms (M), pnictogen atoms (X), and **b** general structure of filled $(EP_yT_4X_{12})$ Skutterudite

composition recorded a ZT peak close to 1 at 373 °C and ZT was about 0.7 value at 400 °C for n-type $Yb_{0.15}Co_4Sb_{12}$. While using the ball-milling and hot-pressing approach, the peak of ZT for $Yb_xCo_4Sb_{12}$ nanocomposites increased to 1.2. More categories of doped Co_4Sb_{12} nanocrystals have been articulated, like $Sn_yFe_3Co_5Sb_{24}$, $FeCo_3Sb_{12}$ as well as the rare-earth filled Fe_4Sb_{12} Skutterudite nanocomposites. *Zhou* and his group studied the p-type skutterudite nanocomposites $Co_{0.9}Fe_{0.1}Sb_3$ with $FeSb_2$ nano-inclusions. Generally, $FeSb_2$ is a chemically stable compound found as a secondary phase p-type skutterudite. For instance, the nanocomposite samples of $Co_{0.9}Fe_{0.1+x}Sb_{3+2x}$ with $x = 0.05, 0.1, \text{ and } 0.02$.

The lower Sb content is very sensitive in the constriction of $FeSb_2$ so rapid solidification was used to facilitate this process in the skutterudite stoichiometry. FESEM images on the fractured surface of the bulk $Co_{0.9}Fe_{0.1+x}Sb_{3+2x}$ nanocomposites are depicted in Fig. 19. Figure (19a) illustrates the zoomed-in examination of the circle region where nano-sized particles can be seen. It appears that the nanoparticles can be found in Fig. 19 (a–c) with different nominal (x) content where Fig. 19 (d) represents the parent sample $Co_{0.75}Fe_{0.25}Sb_3$ which is having the same Fe/Co ratio as $x = 0.2$ content and has the normal skutterudite composition MX_3 . It has appeared from Fig. 19d that the grain boundaries are much cleaner due to the Fe substations and shared in $FeSb_2$ skutterudites nanoparticles and it was found to be grown to the micron size. Even though the Skutterudites reveal high κ_T , but most of the Skutterudites give high $ZT \geq 1$ so it offers a strong potential for using them in high-efficiency TE applications.

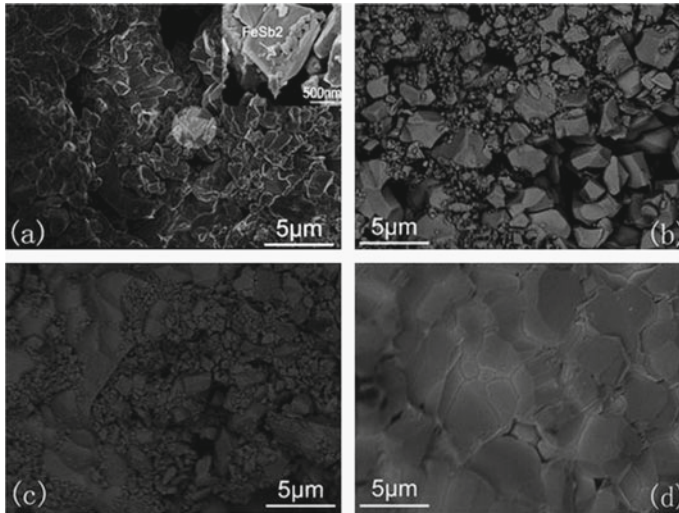


Fig. 19 FESEM images on fractured surface of $\text{Co}_{0.9}\text{Fe}_{0.1}\text{Sb}_{3+x}\text{FeSb}_2$ nanocomposites and reference sample $\text{Co}_{0.75}\text{Fe}_{0.25}\text{Sb}_3$. **a** $x = 0.05$, the circular region represents the nano-sized particles; **b** $x = 0.1$; **c** $x = 0.2$; **d** $\text{Co}_{0.75}\text{Fe}_{0.25}\text{Sb}_3$

1.4.5 Mg_2Si -Based Nanocomposites

Mg_2Si -Based Nanomaterials are considered as TE materials due to the exhibition of high ZT, abundant, non-toxic, and light elemental compositions e.g. $\text{Mg}_2(\text{Si}, \text{Sn})$, and become more attractive. A large ZT value of ~ 1.1 was achieved at 800 K for doped $\text{Mg}_2(\text{Si}, \text{Sn})$ typically in $\text{MgSi}_{0.4}\text{Sn}_{0.6}$ solid solutions, which is analogous to PbTe and filled skutterudite type materials. Zhang and his co-workers carried out the full microstructure study and thermoelectric properties of high ZT $\text{Mg}_2\text{Si}_{0.4-x}\text{Sn}_{0.6}\text{Sb}_x$ alloys. The obtained value of the lattice thermal conductivity κ_1 was in the range 1.5–2.1 W/mK at 300 K which is quite small when compared to undoped- Mg_2Si (7.9 W/mK) and 5.9 W/mK of Mg_2Sn composites. One of the important remarks on the synthesis procedure is the observation of the in situ formed nanodots by phase separation approach. So, it is proposed that the formations of the nanoscale compositional or the structural modulations are the reasons behind the reduction of thermal conductivity in these samples.

On other hand, $\text{Mg}_2\text{Si}/\text{Si}$ nanocomposites were prepared by Yalei Huang and his group and the compositions comprise Si nanosheet bundles. Also, the Mg_2Si deposited and formed on the Si nano-sheet bundles was prepared by the thermal annealing of CaSi_2 powders in MgCl_2 vapor. Figure 20 (a,b) illustrates the morphology obtained from SEM and TEM images of the $\text{Mg}_2\text{Si}/\text{Si}$ composites synthesized on the Si (111) substrate. The nanosheets were obtained with a thickness of several tens and up to one hundred nanometers and the stacked nanosheets also appeared with a small void space to form the bundles. Figure 20 (c,d) displays the

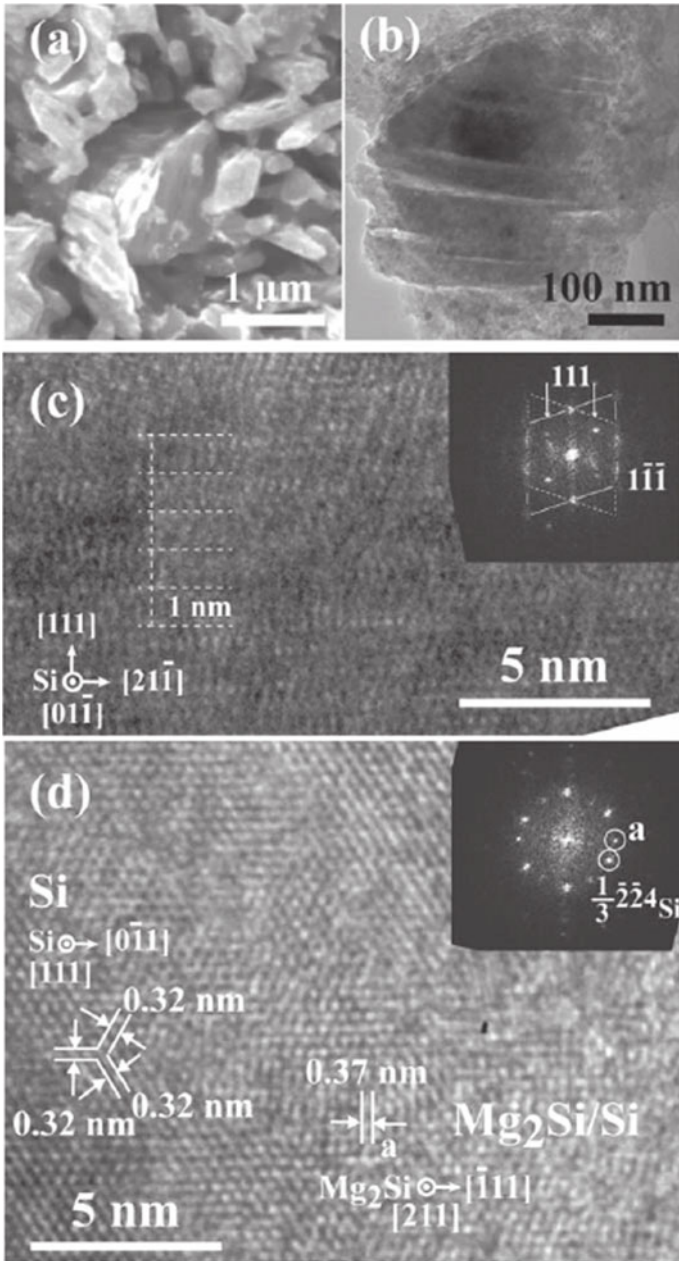


Fig. 20 A schematic diagrams for **a** Plan-view SEM image, **b** TEM image, **c** cross-sectional and **d** Plan view HRTEM images with an FFT pattern of the nano-sheet synthesized from CaSi_2 micro-walls on a Si (111) substrate by the thermal treatment approach at $600 \text{ }^\circ\text{C}$

cross-sectional and plan-view for HRTEM images with FFT patterns of the synthesized composites scratched off the substrate. Recently, *Souda* et al. carried out the modulation doping in Si–Mg₂Si system, where Mg₂Si was considered heavily doped phase and Si the undoped phase. Also, the Si–Mg₂Si nanocomposite ribbons were obtained by a melt spinning technique. The thermoelectric properties of the prepared samples are determined with a large power factor value equal to 2.7 mW m⁻¹ K⁻² at 773 K for these ribbons within the optimized structure and chemical compositions.

1.4.6 Si-Ge Nanocomposites

Alloys and nanocomposites of Si and Ge describe the solid solution Si_xGe_{1-x} thermoelectric materials operating at temperatures more than 1000 K. For instance, SiGe based alloys are being used in radio-isotope TE generators (RTG) for various space missions because of their ability to convert radio-isotope heat into electricity at large temperatures [52]. Generally, SiGe alloys possess potential applications in thermoelectric generators (TEG) to regain waste heat. Si and Ge in Si-Ge alloys crystallize in the diamond-like structure with the Fd-3 m space group which takes the face-centered cubic (FCC) Bravais lattice. SiGe composites have two well-known characteristics; viz the melting point is very high ~1300 K and outstanding stability at high temperatures. Also, Si_xGe_{1-x} solid solutions have good chemical stability at high temperatures, specifically against the oxidation process. A high figure of merit (<~1) entitles the fundamentals of TE use at a high-temperature range (1000–1200 K). Owing to their rigid and symmetric crystal structure, they display extremely small room temperature thermal conductivity (κ) (150 and 63 W/mK, respectively) to become promising thermoelectric materials. Nevertheless, the thermal conductivity has been decreased to nearly 5–10 W/mK due to the formation of a solid solution alloying. Recently, a lot of theoretical and experimental groups put forward massive efforts and achieved some success in improving the ZT of Si-Ge alloys. Nanostructuring using ball milling and other techniques is one of these efforts by which the thermal conductivity is reduced in comparison to the bulk alloys. The peak of ZT for both p-type and n-type Si-Ge alloys has been achieved [44, 45]. Particularly the figure of merit ZT of n-type Si-Ge nanocomposite has gone beyond 1 (at 1100 K). Figure 21 exhibits the power factor (PF) as well as the thermal conductivity (κ) of the Si₈₀Ge₂₀ systems synthesized by ball milling and hot-pressing approach. On the other hand, the Nanostructuring impact appears when the interfacial phonon scattering and the low dimensionality (nanoscale size) make the SiGe superlattices nanowires furnish a low κ_T . For example, *Usenko* and his research group synthesized the bulk sample of n-type Si-Ge nanostructures employing ball-milling and spark plasma sintering techniques. The obtained sample showed a little κ_T of about 2.47 Wm⁻¹ K⁻¹ at 300 K and an enhanced ZT value of 1.1 at 1073 K.

Various studies showed that the figure of merit (ZT) for n-type Si-Ge alloys (1 at 900–950 °C) is higher than p-type SiGe (0.65 at 900 °C) due to the large κ_T value and maximum n. In some cases, the ZT obtained for n-type Si-Ge alloy was about 1.3 with κ_T equal to 2.8 Wm⁻¹ K⁻¹ recorded at 1173 K, whereas p-type Si-Ge has reached a

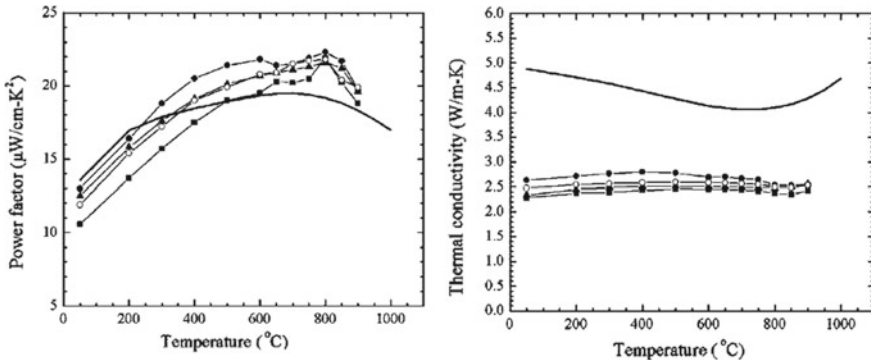


Fig. 21 Schematic diagrams for p-type $\text{Si}_{80}\text{Ge}_{20}$ nanocomposites: on the left) the power factor results, and on the right) thermal conductivity results of the samples prepared with the assistance of ball milling, hot pressing, and annealing approach

ZT value ~ 0.5 . Another effort has been endeavored to minimize κ_T and boost the ZT of Si-Ge alloys via doping. Typically, dopants have achieved a reasonable ZT value and lowered the κ_T values as well. *Usenko* et al. used boron as a dopant in $\text{Si}_{80}\text{Ge}_{20}$ via the spark plasma approach. They obtained a low κ_T value ($\sim 2.9 \text{ Wm}^{-1} \text{ K}^{-1}$) for the prepared samples and achieved a high ZT value of 0.72 at 1073 K. Later, *Peng* et al. exhibited a boron-doped Si-Ge thin film. They articulated an enhancement in S to $850 \mu\text{VK}^{-1}$ at 473 K but lowered the ρ to $1.3 \times 10^{-5} \Omega\text{m}$ where the PF improved to $5.6 \times 10^{-2} \text{ Wm}^{-1} \text{ K}^{-2}$. Also, the high-energy ball milling technique was used to obtain single-phase p-type (boron-doped) $\text{Si}_{80}\text{Ge}_{20}$ nanoparticles from elements [45]. (Fig. 22a) illustrates the single-phase synthesized $\text{Si}_{80}\text{Ge}_{20}\text{B}_x$ alloys. The crystalline nature of the mechanically alloyed Si-Ge nanocrystals differs from that of the ball-milled Bi_2Te_3 nanocrystals where Fig. 22(d) showed the polycrystalline nature of $\text{Si}_{80}\text{Ge}_{20}\text{B}_x$ nanoparticles. It appears that the mechanically alloyed Si-Ge is consisting of several sub-nanograins as depicted in (Fig. 22d). HRTEM image in Fig. 22(d) reveals the existence of a lot of defects inside the individual sub-grain since the formation of the nanograins was developed by a low temperature mechanical alloying technique rather than the melting and solidification method at higher temperatures.

Alternatively, the obtained n-type $\text{Si}_{80}\text{Ge}_{20}\text{P}_2$ samples prepared via mechanical alloy technique gave a single-phase nanoparticle shown in Fig. 23 (a). The particle size of the as-prepared nanopowders was ranging from 30–200 nm as depicted in Fig. 23 (b,c). These nanoparticles are like p-type mechanically alloyed Si-Ge nanoparticles where sub-grains from small crystals were visualized. The obtained sub-nanograins range from 5–15 nm as depicted in Fig. 23 (d). The main goal for thermoelectrics is to reduce κ_1 . So one of the interesting perspectives of Si-Ge alloy is the reduction of (κ_1) via different composites and preparation methods. For instance, *Kikuchi* and his coworkers used 10 nm diameter SiNWs to be embedded into $\text{SiGe}_{0.3}$. Bio-template masking and neutral beam etching methods were used to achieve SiNWs and then deposited via chemical vapor deposition route thermally.

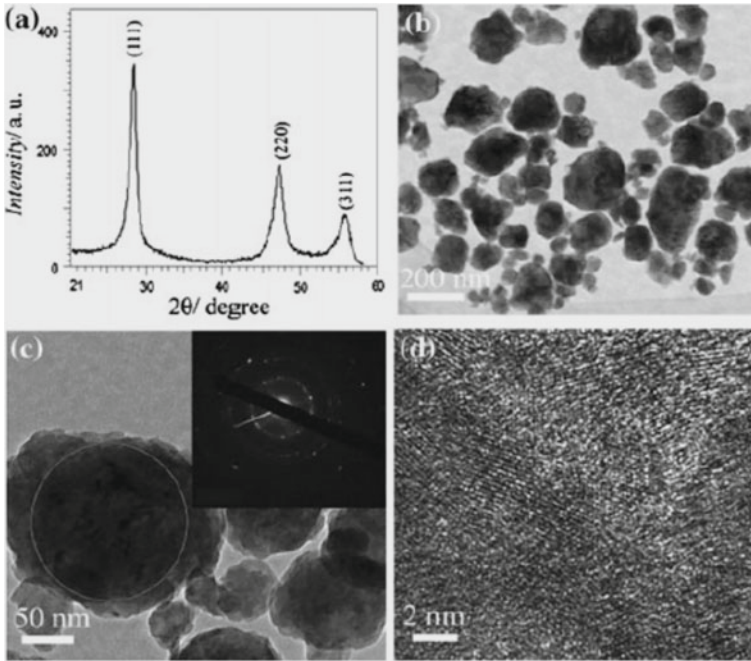


Fig. 22 Schematic diagrams for p-type $\text{Si}_{80}\text{Ge}_{20}\text{B}_x$ nanoparticles: **a** XRD pattern, **b** BF-TEM image, **c** medium magnification TEM image, **d** HRTEM image. The inset on the right of **c** is SAED of an individual grain revealing the polycrystalline structure of the grain [45]

They obtained from $\text{SiNW-SiGe}_{0.3}$ composite film a thickness of 100 nm, κ_T value of $3.5 \pm 0.3 \text{ Wm}^{-1} \text{ K}^{-1}$ in the temperature range 300 to 350 K. Furthermore, they observed the S and σ values at 873 K to be $4.8 \times 10^3 \mu\text{VK}^{-1}$ and $4.4 \times 10^3 \text{ Sm}^{-1}$, respectively. *Usenko* et al. fabricated the n-type $\text{Si}_{0.9}\text{Ge}_{0.1}\text{-Mg}_2\text{Si}$ composites. At 1073 K, they achieved a reduction in κ_1 up to $1.4 \text{ Wm}^{-1} \text{ K}^{-1}$ and observed an average value for ZT of ~ 0.8 .

1.4.7 Zintl Phases

The Zintl phases named after their discovery by a German chemist called Eduard Zintl and then were identified by Laves in the early 40s of the last century. A unified class of electropositive cations, mostly group I or II elements, reflect the Zintl phases. The second partner, which is a subset of inter-metallic compounds, was composed of post-transition metals or metal alloys from XIII, XIV, XV, XVI. Even though the application of Zintl phases as outstanding thermoelectrics is quite evident, their structure and chemical bonding details were fully investigated recently. Zintl phases may be widely used as TE materials due to the exhibition of the high thermoelectric

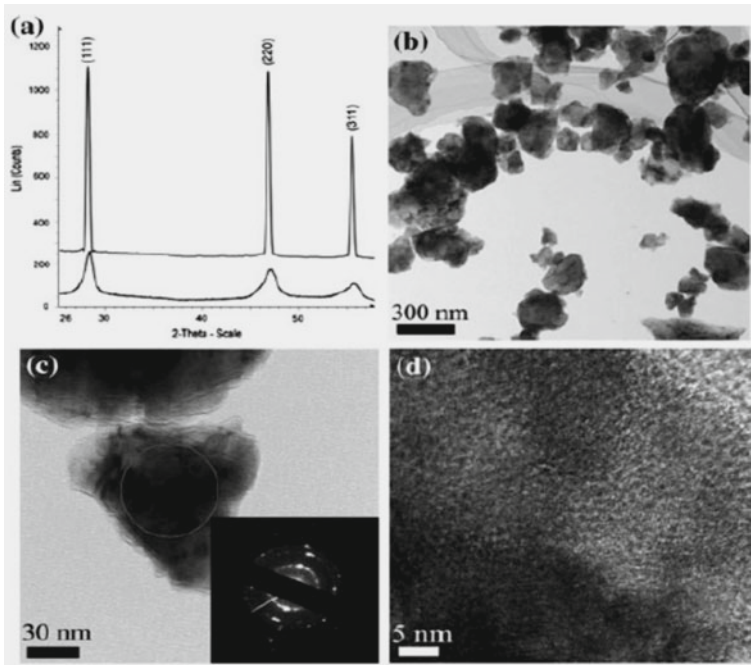


Fig. 23 Schematic diagrams of n-type $\text{Bi}_{80}\text{Ge}_{20}\text{P}_2$ nanoparticles as follow: **a** XRD diffractogram, **b** BF-TEM image, **c** BF-TEM image at medium magnification, and **d** HRTEM image. The inset on the right of **c** represents a SAED diagram of an individual nanoparticle [44]

power (S). For example, $\text{Yb}_{2-x}\text{Eu}_x\text{CdSb}_2$, $\text{Mg}_3\text{Pb}_{0.2}\text{Sb}_{1.8}$ and $\text{Yb}_{14}\text{MgSb}_{11}$ compositions registered the highest S values as follows $269 \mu\text{VK}^{-1}$, $\sim 280 \mu\text{VK}^{-1}$ and $279 \mu\text{VK}^{-1}$, respectively.

Additionally, the best advantage of these materials is the flexibility to work in wide temperature ranges. p-type and n-type of Zintl(1-2-2) phases exhibit outstanding characteristics among Zintl compounds in the low till the middle-temperature ranges wherein the range 975–1275 K demonstrates an improvement in the other p-type Zintl(14-1-1) families. One of the promising Zintl phases is of kind $\text{A}_{14}\text{MPn}_{11}$, where (A) element labels alkaline-earth or rare-earth metal, (M) element describes transition or main group metal, and (Pn) defines a pnictogen, respectively. For instance, $\text{Yb}_{14}\text{MnSb}_{11}$ is the most superior TE material for high-temperature applications. Al, Zn and La- $\text{Yb}_{14}\text{MnSb}_{11}$ have attained a $ZT = 1.1$ at 1275 K, 1.3 at 1223 K and 1.15 at 1150 K, respectively. Moreover, Snyder et al. articulated that $\text{Yb}_{14}\text{Mn}_{0.67}\text{Zn}_{0.33}\text{Sb}_{11}$ and $\text{Yb}_{14}\text{Mn}_{0.8}\text{Al}_{0.2}\text{Sb}_{11}$ compounds show the highest ZT among the other doped $\text{Yb}_{14}\text{MnSb}_{11}$ phases at 1200 K with values 1.7 and 1.76, respectively. Furthermore, there are numerous Zintl compounds like: n-type of KSnSb (with $ZT = 2.2$ at 800 K and 0.6 at 300 K), $\text{Ca}_{0.5}\text{Yb}_{0.5}\text{Mg}_2\text{Bi}_2$ ($Zt = 1$ at 873 K), $\text{Mg}_{2.985}\text{Ag}_{0.015}\text{Sb}_2$ records 0.15 at 725 K, EuZn_2Sb_2 and Yb- doped EuZn_2Sb_2 have ZT equal to 0.9 at 713 K and 0.68 at 773 K, ZnInSb compounds provide high ZT values of 1.4 at 700 K and

are commonly used for high-temperature applications. Lately, Mg_3Sb_2 based Zintl compositions with ZT value 0.6 at 773 K are very desirable for TE applications due to less toxicity, environment-friendly and earth-abundance characteristics.

More research has been carried out to study the possibility of transformation of p-type into n-type Mg_3Sb_2 compounds by terminating Mg vacancies and enhancing the number of carriers (n) to improve the TE performance of Mg_3Sb_2 . Li and his coworkers theoretically studied the electronic structure of n-type Mg_3Sb_2 via density functional theory (DFT) and reached a very high value of ZT with 3.1 at 725 K. Later in another example within the same DFT constraints, they touched a ZT value of 2.75 [305]. However, no experimental works or results have yet been achieved to reproduce the ZT value of more than 2 in such compounds. Figure 24 shows the (HRTEM) images and EDX obtained data of the nanostructured Mg_3Sb_2 and $Mg_3Sb_{1.8}Bi_{0.2}$ alloys [306] which generally exhibits the nanoscale characteristics and represents the uniform microstructures with nanoscale crystallites, together with some microstructure defects (Fig. 24 b–e) resulting from the long hours of the ball-milling procedure [306].

Bhardwaj et al. demonstrated that the nanostructured Mg_3Sb_2 and $Mg_3Sb_{1.8}Bi_{0.2}$ prepared via high energy ball milling and then followed by spark plasma sintering approach yield a ZT of ~ 0.4 and ~ 0.94 at 773 K, respectively. These are 54% to 56%, higher than that of bulk specimens. The observed ZT values for the $Mg_3Sb_{1.8}Bi_{0.2}$ nanocrystals w.r.t temperature are depicted in Fig. 25.

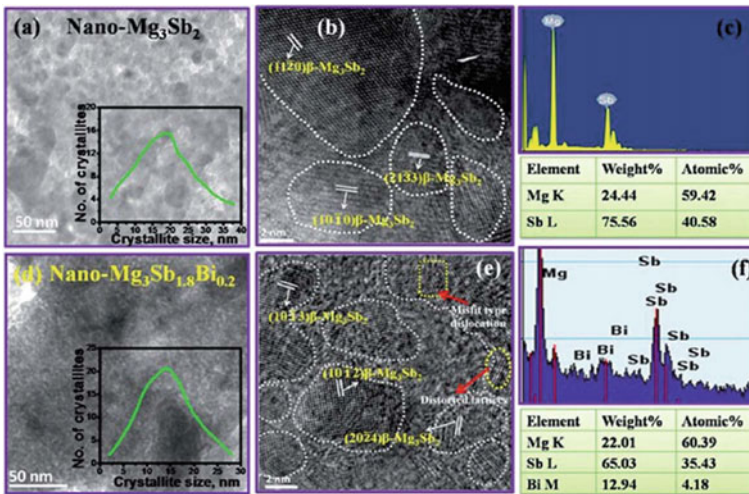
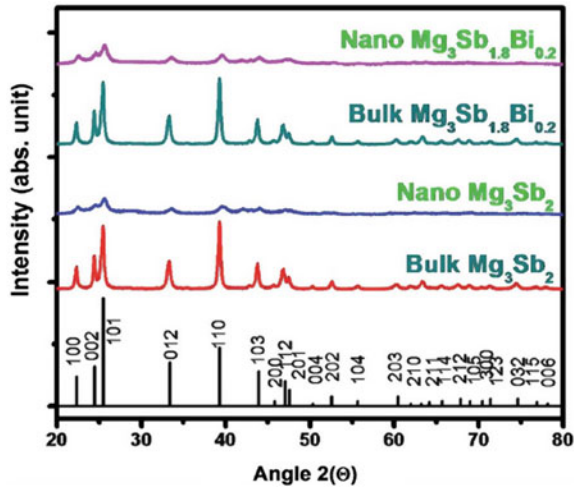


Fig. 24 Schematic diagrams nanostructured Mg_3Sb_2 and $Mg_3Sb_{1.8}Bi_{0.2}$ alloys: **a** TEM image of Mg_3Sb_2 sample; **b** nanostructured Mg_3Sb_2 lattice scale image with several orientations of the crystallographic planes; **c** EDAX-TEM designs for nanostructured Mg_3Sb_2 sample; **d** Obtaining data of bright field electron micrograph nanostructured $Mg_3Sb_{1.8}Bi_{0.2}$ sample; **e** The HRTEM of nanostructured $Mg_3Sb_{1.8}Bi_{0.2}$, showing distorted lattices; **f** The EDAX-TEM patterns obtained from the nanostructured $Mg_3Sb_{1.8}Bi_{0.2}$ specimen with the exact elemental analysis

Fig. 25 The obtained data for the temperature dependence of the thermoelectric figure of merit of bulk $\text{Mg}_3\text{Sb}_{2-x}\text{Bi}_x$ ($x = 0$ & 0.2) samples

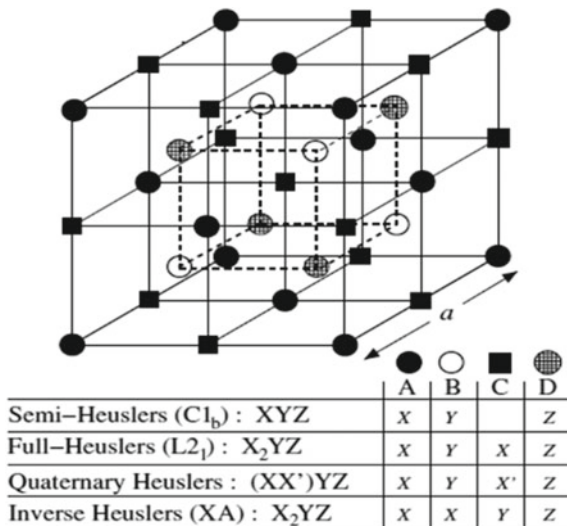


1.4.8 Heusler Materials

Heusler Alloys have long been discovered by F. Heusler in 1903. These alloys are broadly distributed in three categories according to the number of atoms in their unit cells. First, the Half-Heusler alloys having XYZ formula and are found in F-43 m space group. Here, the lattice positions are: X(0,0,0), Y(0.5,0.5,0.5) and Z(0.25,0.25,0.25). Second are the X_2YZ type Full Heusler alloys with L_21 structure (space group: Fm-3 m) and the atomic coordinates are X(0.75,0.75,0.75) and (0.25,0.25,0.25); Y(0,0,0) and Z(0.5,0.5,0.5). This class can be found in another stereotype called the inverse Heusler alloys with space group F-43 m but the position of X and Y atoms vary as: X(0,0,0) and (0.75,0.75,0.75), Y (0.5,0.5,0.5) and Z (0.25,0.25,0.25) depicted in Fig. 26. And the third one is the recent most category known as Quaternary Heusler Alloys with $\text{XX}'\text{YZ}$ formula and these can be found in F-43 m structure within type-I, type-II and type-III; where X, X', Y and Z locations vary as given in Fig. 25. Here, the X, X', Y are mainly transition metal elements but can be a rare-earth also and Z atom is generally a p-block element.

However, these materials lately flourished in various technological applications due to the exhibition of magnificent properties ranging from half-metallic ferromagnetism to superconductivity, large Curie temperature, semiconductor or topological behavior, robust spin polarization, and shape memory effects, etc., They found applications in tunneling magnetoresistance (TMR) devices, spin injectors or magnetic tunnel junctions and magnetic read heads. At the same time, the potential application in thermoelectric power generation has been the eminent among all such properties. In view of the electronic structure, this huge class of materials consist of magnetic, nonmagnetic, semiconductors, half-metals, semimetals (spin-gapless semiconductors, Dirac or Weyl semimetals, spin semimetals), etc. Non-magnetism and semi-conducting properties in Heusler alloys are preferably defined by Slater-Pauling rule

Fig. 26 Schematic representation of the half- and full-Heusler compounds' various structures. Note also that the lattice would simply be the b.c.c. if all atoms were identical



($M = N_v - 24$ or 28 or 18); where the valence electron count (N_v) is linked to the total magnetic moment (M) of the crystal. The rigorous degenerate valence bands and fully compensated spins in 12 or 8 bands create the possible semiconducting electronic structure of these alloys. However, in some cases, the crystal symmetry or d-electron splitting leads to spin semi-metallic or spin gapless nature also.

Thermoelectric resourcefulness of Heusler materials have been preceded by the recent discovery of $ZT = 5$ or 6 in a metastable $Fe_2V_{0.8}W_{0.2}Al$ Heusler thin film are illustrated into Fig. 27. It was supposed that the large differential density of states and a Weyl-like dispersion of electrons present around the Fermi level initiates a high mobility of charge carriers [316]. Experimentally found Ti/Sn doped NbFeSb [317] and TaFeSb [318] Heuslers achieved a ZT equal to 1.1 and 0.5, respectively. Also, the p-type alloys including Fe(V,Nb)Sb [319], TiPdSn [320] and XCoSb ($X = Ti, Zr, Hf$) and n-type XNiSn with quite high ZT s are among the few to note down here.

However, different strategic criteria and alterations are meticulously put forward to shape the maximum efficient Heusler materials to exhibit the augmentation of electricity from waste heat. Since then a huge database of Heusler thermoelectrics has been scrutinized and maintained but more research is yet needed to improve the efficiency of these new materials.

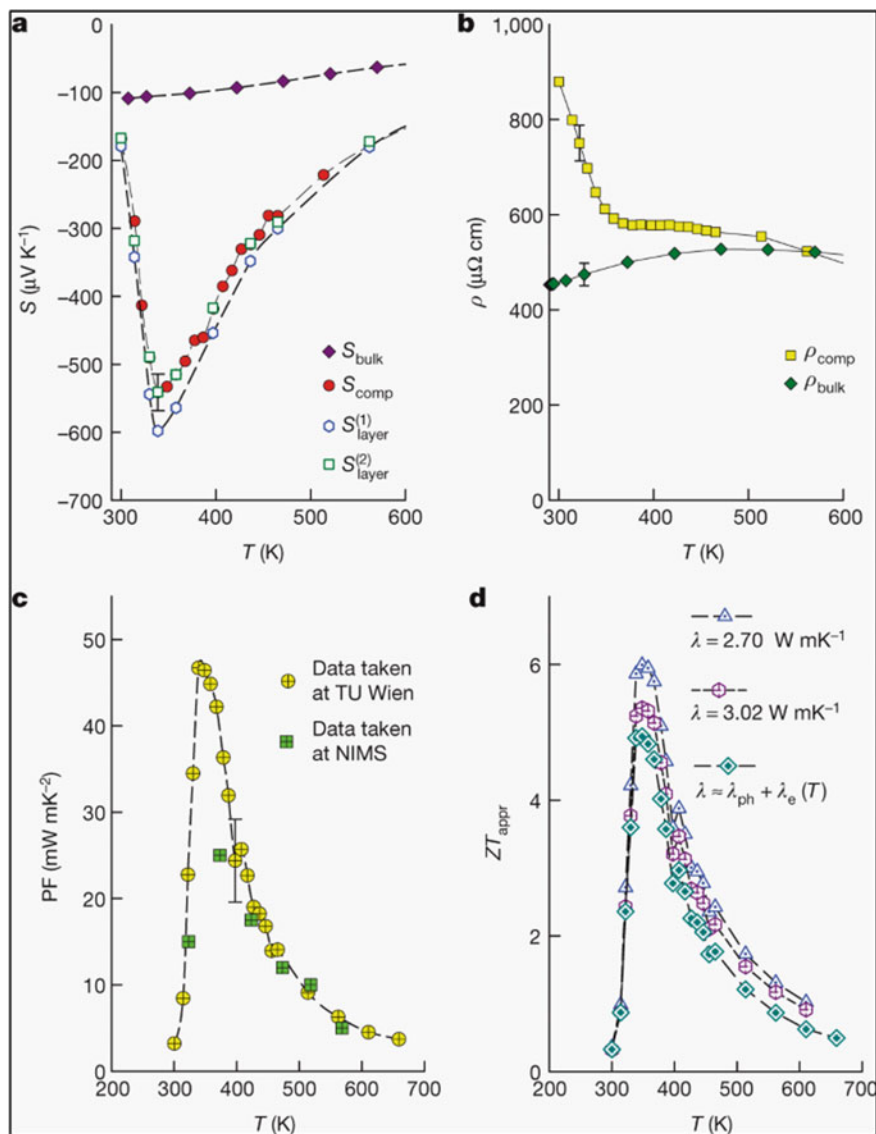


Fig. 27 Thin-film $\text{Fe}_2\text{V}_{0.8}\text{W}_{0.2}\text{Al}$ and its temperature-dependent thermoelectric properties. **a**, **b**, the Seebeck coefficient **a** and the electrical resistivity **b** of the entire composite (layer, interface and substrate), along with the $\text{Fe}_2\text{V}_{0.8}\text{W}_{0.2}\text{Al}$ thin-film. $S^{(1)}_{\text{layer}}$ and $S^{(2)}_{\text{layer}}$ are the Seebeck data with and without Fe_2Si as the interface, respectively. **c**, **d**, The power factor versus temperature **c** and the average merit figure **d**. ZT_{appr} is evaluated to a first approximation using the room-temperature (25°C) thermal conductivity ($\lambda_{\text{diff,RT}} = 2.70 \text{ W m}^{-1} \text{ K}^{-1}$; $\lambda_{\text{eff,RT}} = 3.02 \text{ W m}^{-1} \text{ K}^{-1}$ and keeping λ_{ph} constant). Open diamonds indicate the respective ZT_{appr} data

2 Conclusive Remarks

In this review, we have tried to highlight the advancements in thermoelectric materials and possible strategies to improve the thermoelectric efficiency of the traditional and newly designed TE materials. Further investigations are carried out on higher ZT enhancement of TE coefficients like S , σ at the same time the κ must be kept low values. The later has been found to be ultra-low in some 2D materials yet to be realized experimentally. It opens the window for the researchers to design the new strategies for practically synthesizable nanostructure materials. Hence, novel techniques to stabilize higher ZT in nanostructured metastable alloys like $\text{Fe}_2\text{V}_{0.8}\text{W}_{0.2}\text{Al}$ Heusler thin film and the TE application demands practically need to be acquired at elevated temperature for broader scope of this technology. Upcoming TE devices developed from these nanomaterials sought to be extensively used in cooling/refrigeration/air-conditioning applications at large scale and to launch a consistent, well-organized, eco-friendly energy consumption on our planet earth.

References

1. Snyder, G.J., Toberer, E.S.: Complex thermoelectric materials. *Nat. Mater.* **7**, 105–114 (2008)
2. Seebeck, T.J.: Magnetische polarisation der metalle und erze durch temperatur-differenz (magnetic polarization of metals and minerals by temperature differences), *Abhandlungen der Königlichen Akademie der Wissenschaften zu Berlin (Treatises of the Royal Academy of Sciences in Berlin)*, pp. 265–373 (1825)
3. Seebeck, T.J.: Ueber die magnetische polarisation der metalle und erze durch temperatur-differenz (on the magnetic polarization of metals and minerals by temperature differences). *Annalen der Physik und Chemie* **6**, 133–160 (1826)
4. Peltier, J.C.A.: Nouvelles expériences sur la calorificité des courants électrique (new experiments on the heat effects of electric currents). *Annales de Chimie et de Physique* **56**, 371–386 (1834)
5. Riffat, S.B., Ma, X.L.: Thermoelectrics: a review of present and potential applications. *Appl. Therm. Eng.* **23**, 913–935 (2003)
6. Tritt, T.M., Subramanian, M.A.: Thermoelectric materials, phenomena, and applications: a bird's eye view. *MRS. Bull.* **31**, 188 (2006)
7. Zhu, T., Liu, Y., Fu, C., Heremans, J.P., Snyder, J.G., Zhao, X.: Compromise and synergy in high-efficiency thermoelectric materials. *Adv. Mater.* **29**, 1605884 (2017)
8. Vining, C.B.: An inconvenient truth about thermoelectrics. *Nat. Mater.* **8**, 83 (2009)
9. Ibrahim, E.A., Szybist, J.P., Parks, J.E.: Enhancement of automotive exhaust heat recovery by thermoelectric devices. *P. I. Mech. Eng. Part D J. Automob. Eng.* **224**, 1097–1111 (2010)
10. Li, M., Xu, S., Chen, Q., Zheng, L.: Thermoelectric-generator-based DC–DC conversion networks for automotive applications. *J. Electron. Mater.* **40**, 1136–1143 (2011)
11. Schierle-Armdt, K., Hermes, W.: Thermoelektrik. *Chem. Unserer. Zeit.* **47**, 92 (2013)
12. Kraemer, D., et al.: Concentrating solar thermoelectric generators with a peak efficiency of 7.4%. *Nat. Energy*, **1**, 16153 (2016)
13. Kraemer, D., et al.: High-performance flat-panel solar thermoelectric generators with high thermal concentration. *Nat. Mater.* **10**, 532–538 (2011)
14. Friedensen, V.P.: Space nuclear power: Technology, policy, and risk considerations in human missions to Mars. *Acta Astronaut.* **42**, 395 (1998)

15. Yang, J.H., Caillat, T.: Thermoelectric materials for space and automotive power generation. *MRS Bulltin* **31**, 224 (2006)
16. O'Brien, R.C., Ambrosi, R.M., Bannister, N.P., Howe, S.D., Atkinson, H.V.: Safe radioisotope thermoelectric generators and heat sources for space applications. *J. Nucl. Mater.* **389**, 506–521 (2008)
17. He, J., Tritt, T.M.: Advances in thermoelectric materials research: looking back and moving forward. *Science* **357**, 6358 (2017)
18. Bahk, J.H., Fang, H., Yazawa, K., Shakouri, A.: Flexible thermoelectric materials and device optimization for wearable energy harvesting. *J. Mater. Chem. C* **3**, 10362–10374 (2015)
19. Biswas, K., et al.: High-performance bulk thermoelectrics with all-scale hierarchical architectures. *Nature* **489**, 414–418 (2012)
20. Bell, L.E.: Cooling, heating, generating power, and recovering waste heat with thermoelectric systems. *Science* **321**, 1457–1461 (2008)
21. Yang, J., Caillat, T.: Thermoelectric materials for space and automotive power generation. *MRS Bull.* **31**, 224–229 (2006)
22. Chen, Z.-G., Han, G., Yang, L., Cheng, L., Zou, J.: Nanostructured thermoelectric materials: current research and future challenge. *Prog. Nat. Sci. Mater. Int.* **22**, 535–549 (2012)
23. Pichanusakorn, P., Bandaru, P.: Nanostructured thermoelectrics. *Mater. Sci. Eng. R. Rep.* **67**, 19–63 (2010)
24. Zebarjadi, M., Esfarjani, K., Dresselhaus, M.S., Ren, Z.F., Chen, G.: Perspectives on thermoelectrics: from fundamentals to device applications. *Energy Environ. Sci.* **5**, 5147–5162 (2012)
25. Sootsman, J.R., Chung, D.Y., Kanatzidis, M.G.: New and old concepts in thermoelectric materials. *Angew. Chem. Int. Ed.* **48**, 8616–8639 (2009)
26. Vineis, C.J., Shakouri, A., Majumdar, A., Kanatzidis, M.G.: Nanostructured thermoelectrics: big efficiency gains from small features. *Adv. Mater.* **22**, 3970–3980 (2010)
27. Vaquero, P., Powell, A.V.: Recent developments in nanostructured materials for high-performance thermoelectrics. *J. Mater. Chem.* **20**, 9577–9584 (2010)
28. Bux, S.K., Fleurial, J.P., Kaner, R.B.: Nanostructured materials for thermoelectric applications. *Chem. Commun.* **46**, 8311–8324 (2010)
29. Minnich, A.J., Dresselhaus, M.S., Ren, Z.F., Chen, G.: Bulk nanostructured thermoelectric materials: current research and future prospects. *Energy Environ. Sci.* **2**, 466–479 (2009)
30. Kanatzidis, M.G.: Nanostructured thermoelectrics: the new paradigm? *Chem. Mater.* **22**, 648–659 (2009)
31. Dresselhaus, M.S., et al.: New directions for low-dimensional thermoelectric materials. *Adv. Mater.* **19**, 1043–1053 (2007)
32. Dresselhaus, M., Dresselhaus, G., Sun, X., Zhang, Z., Cronin, S., Koga, T.: Low-dimensional thermoelectric materials. *Phys. Solid State* **41**, 679–682 (1999)
33. Rao, A.M., Ji, X., Tritt, T.M.: Properties of nanostructured one dimensional and composite thermoelectric materials. *MRS Bull.* **31**, 218–223 (2006)
34. Hochbaum, A.I., et al.: Enhanced thermoelectric performance of rough silicon nanowires. *Nature* **451**, 163–167 (2008)
35. Boukai, A.I., Bunimovich, Y., Tahir-Kheli, J., Yu, J.-K., Goddard, W.A., III., Heath, J.R.: Silicon nanowires as efficient thermoelectric materials. *Nature* **451**, 168–171 (2008)
36. Hicks, L.D., Dresselhaus, M.S.: Thermoelectric figure of merit of a one-dimensional conductor. *Phys. Rev. B* **47**, 16631–16634 (1993)
37. Chen, G.: Thermal conductivity and ballistic-phonon transport in the cross plane direction of superlattices. *Phys. Rev. B* **57**, 14958–14973 (1998)
38. Venkatasubramanian, R., Siivola, E., Colpitts, T., O'Quinn, B.: Thin-film thermoelectric devices with high room-temperature figures of merit. *Nature* **413**, 597–602 (2001)
39. Harman, T.C., Taylor, P.J., Walsh, M.P., LaForge, B.E.: Quantum dot superlattice thermoelectric materials and devices. *Science* **297**, 2229–2232 (2002)
40. Böttner, H., Chen, G., Venkatasubramanian, R.: Aspects of thin-film superlattice thermoelectric materials, devices, and applications. *MRS Bull.* **31**, 211–217 (2006)

41. Heremans, J.P., Thrush, C.M., Morelli, D.T.: Thermopower enhancement in lead telluride nanostructures. *Phys. Rev. B* **70**, 115334 (2004)
42. Lee, S.-M., Cahill, D.G., Venkatasubramanian, R.: Thermal conductivity of Si-Ge superlattices. *Appl. Phys. Lett.* **70**, 2957–2959 (1997)
43. Yang, R., Chen, G.: Thermal conductivity modeling of periodic two-dimensional nanocomposites. *Phys. Rev. B* **69**, 195316 (2004)
44. Medlin, D.L., Snyder, G.J.: Interfaces in bulk low thermoelectric materials: a review for current opinion in colloid and interface science. *Curr. Opin. Colloid Interface Sci.* **14**, 226–235 (2009)
45. Lan, Y., Ren, Z.: Ch.11. In: Li, Q. (ed.) *Nanomaterials for Sustainable Energy, NanoScience and Technology*. Springer International Publishing, Switzerland (2016)
46. Wang, X.W., et al.: Enhanced thermoelectric figure of merit in nanostructured n-type silicon germanium bulk alloy. *Appl. Phys. Lett.* **93**, 193121 (2008)
47. Joshi, G., et al.: Enhanced thermoelectric figure-of-merit in nanostructured p-type silicon germanium bulk alloys. *Nano Lett.* **8**, 4670–4674 (2008)
48. Yan, X., et al.: Enhanced thermoelectric figure of merit of p-type Half-Heuslers. *Nano Lett.* **11**, 556–560 (2011)
49. Zhu, G.H., et al.: Effect of selenium deficiency on the thermoelectric properties of n-type $\text{In}_4\text{Se}_{3-x}$ compounds. *Phys. Rev. B* **83**, 115201 (2011)
50. Zhao, H., et al.: High thermoelectric performance of MgAgSb-based materials. *Nano Energy* **7**, 97–103 (2014)
51. Morelli, D.T., et al.: Low-temperature transport properties of p-type CoSb_3 . *Phys. Rev. B* **51**, 9622 (1995)
52. Caillat, T., Borshchevsky, A., Fleurial, J.P.: Properties of single crystalline semiconducting CoSb_3 . *J. Appl. Phys.* **80**, 4442 (1996)
53. Nolas, G.S., Slack, G.A., Schujman, S.B.: *Recent Trends in Thermoelectric Materials Research I*, vol. 69, p. 255. Academic Press Inc, San Diego (2001)
54. Rowe, D.M. (ed.): *CRC Handbook of Thermoelectrics*. CRC Press, Boca Raton, FL (1995)
55. Nolas, G.S., Morelli, D.T., Tritt, T.M.: Skutterudites: a phonon-glass-electron crystal approach to advanced thermoelectric energy conversion applications. *Annu. Rev. Mater. Sci.* **29**, 89–126 (1999)
56. Sales, B.C., Mandrus, D., Williams, R.K.: Filled skutterudite antimonides: a new class of thermoelectric materials. *Science* **272**, 1325–1328 (1996)
57. Sales, B.C., Mandrus, D., Chakoumakos, B.C., Keppens, V., Thompson, J.R.: Filled skutterudite antimonides: electron crystals and phonon glasses. *Phys. Rev. B* **56**, 15081 (1997)
58. Nolas, G.S., Cohn, J.L., Slack, G.A., Schujman, S.B.: Semiconducting Ge clathrates: promising candidates for thermoelectric applications. *Appl. Phys. Lett.* **73**, 178 (1998)
59. Blake, N.P., Mollnitz, L., Kresse, G., Metiu, H.: Why clathrates are good thermoelectrics: a theoretical study of $\text{Sr}_8\text{Ga}_{16}\text{Ge}_{30}$. *J. Chem. Phys.* **111**, 3133 (1999)
60. Iversen, B.B., et al.: Why are clathrates good candidates for thermoelectric materials? *J. Solid State Chem.* **149**, 455–458 (2000)
61. Kauzlarich, S.M., Brown, S.R., Snyder, G.J.: Zintl phases for thermoelectric devices. *Dalton Trans.* **21**, 2099–2107 (2007)
62. Hicks, L.D., Dresselhaus, M.S.: Effect of quantum-well structures on the thermoelectric figure of merit. *Phys. Rev. B* **47**, 12727 (1993)
63. Chen, G.: Thermal conductivity and ballistic-phonon transport in the cross-plane direction of superlattices. *Phys. Rev. B* **57**, 14958 (1998)
64. Heremans, J.P., Thrush, C.M., Morelli, D.T., Wu, M.C.: Thermoelectric power of bismuth nanocomposites. *Phys. Rev. Lett.* **88**, 216801 (2002)
65. Harman, T.C., Walsh, M.P., Laforge, B.E., Turner, G.W.: Nanostructured thermoelectric materials. *J. Electron. Mater.* **34**, L19–L22 (2005)
66. Harman, T.C., Reeder, R.E., Walsh, M.P., LaForge, B.E., Hoyt, C.D., Turner, G.W.: High electrical power density from PbTe-based quantum-dot superlattice uncouple thermoelectric devices. *Appl. Phys. Lett.* **88**, 243504 (2006)

67. Vineis, C.J., et al.: Carrier concentration and temperature dependence of the electronic transport properties of epitaxial PbTe and PbTe/PbSe nanodot superlattices. *Phys. Rev. B* **77**, 235202 (2008)
68. Pei, Y., Shi, X., LaLonde, A., Wang, H., Chen, L., Snyder, G.J.: Convergence of electronic bands for high performance bulk thermoelectrics. *Nature* **473**, 66–69 (2011)
69. Baxter, J., et al.: Nanoscale design to enable the revolution in renewable energy. *Energy Environ. Sci.* **2**, 559–588 (2009)
70. Moshwan, R., Yang, L., Zou, J., Chen, Z.G.: Eco-friendly SnTe thermoelectric materials: progress and future challenges. *Adv. Funct. Mater.* **27**, 1703278 (2017)
71. Tan, G., et al.: High thermoelectric performance of p-Type SnTe via a synergistic band engineering and nanostructuring approach. *J. Am. Chem. Soc.* **136**, 7006–7016 (2014)
72. Tan, G., et al.: Codoping in SnTe: enhancement of thermoelectric performance through synergy of resonance levels and band convergence. *J. Am. Chem. Soc.* **137**, 5100–5112 (2015)
73. Tan, G., et al.: Valence band modification and high thermoelectric performance in SnTe heavily alloyed with MnTe. *J. Am. Chem. Soc.* **137**, 11507–11516 (2015)
74. Tan, G., et al.: Extraordinary role of Hg in enhancing the thermoelectric performance of p-type SnTe. *Energy Environ. Sci.* **8**, 267–277 (2015)
75. Yang, L., Chen, Z.G., Dargusch, M.S., Zou, J.: High performance thermoelectric materials: progress and their applications. *Adv. Energy Mater.* **8**, 1701797 (2018)
76. Zhao, L.D., et al.: Ultralow thermal conductivity and high thermoelectric figure of merit in SnSe crystals. *Nature* **508**, 373–377 (2014)
77. Zhao, L.D., et al.: Ultrahigh power factor and thermoelectric performance in hole-doped single-crystal SnSe. *Science* **351**, 141–144 (2016)
78. Peng, K., et al.: Broad temperature plateau for high ZTs in heavily doped p-type SnSe single crystals. *Energy Environ. Sci.* **9**, 454–460 (2016)
79. DiSalvo, F.J.: Thermoelectric cooling and power generation. *Science* **285**, 703–706 (1999)
80. Chen, Z.G., Han, G., Yang, L., Cheng, L., Zou, J.: Nanostructured thermoelectric materials: current research and future challenge. *Prog. Nat. Sci.* **22**, 535–549 (2012)
81. Wood, C.: Materials for thermoelectric energy-conversion. *Rep. Prog. Phys.* **51**, 459–539 (1988)
82. Szczech, J.R., Higgins, J.M., Jin, S.: Enhancement of the thermoelectric properties in nanoscale and nanostructured materials. *J. Mater. Chem.* **21**, 4037–4055 (2011)
83. Rowe, D.M., Bunce, R.W.: The thermoelectric properties of heavily doped hot-pressed germanium-silicon alloys. *J. Phys. D Appl. Phys.* **2**, 1497 (1969)
84. Benjamin, J.S.: Mechanical alloying. *Sci. Am.* **234**, 40–49 (1976)
85. Suryanarayana, C.: Mechanical alloying and milling. *Prog. Mater. Sci.* **46**, 1–184 (2001)
86. Loeff, P., Bakker, H.: Amorphous gold-lanthanum alloy prepared by ball milling. *Scr. Metall.* **22**, 401–404 (1988)
87. Basset, D., Matteazzi, P., Miani, F.: Designing a high energy ball-mill for synthesis of nanophase materials in large quantities. *Mater. Sci. Eng. A* **168**, 149–152 (1993)
88. Yamada, K., Koch, C.C.: The influence of mill energy and temperature on the structure of the TiNi intermetallic after mechanical attrition. *J. Mater. Res.* **8**, 1317–1326 (1993)
89. Gusev, A.I., Rempel, A.A.: *Nanocrystalline Materials*. Cambridge International Science Publishing, Cambridge (2004)
90. Umemoto, M.: Preparation of thermoelectric β -FeSi₂ doped with Al and Mn by mechanical alloying (overview). *Mater. Trans. JIM* **36**, 373 (1995)
91. Davis, R.M., Koch, C.C.: Mechanical alloying of brittle components: silicon and germanium. *Scr. Metall.* **21**, 305–310 (1987)
92. Bouad, N., Marin-Ayral, R.M., Tedenac, J.C.: Mechanical alloying and sintering of lead telluride. *J. Alloy. Compd.* **297**, 312–318 (2000)
93. Kishimoto, K., Koyanagi, T.: Preparation of sintered degenerate n-type PbTe with a small grain size and its thermoelectric properties. *J. Appl. Phys.* **92**, 2544 (2002)
94. Bouad, N., Record, M.C., Tedenac, J.C., Marin-Ayral, R.M.: Mechanical alloying of a thermoelectric alloy: Pb_{0.65}Sn_{0.35}Te. *J. Solid State Chem.* **177**, 221–226 (2004)

95. Zhang, Q., et al.: High thermoelectric performance by resonant dopant indium in nanostructured SnTe. *Proc. Natl. Acad. Sci. USA* **110**, 13261–13266 (2013)
96. Liu, W., et al.: Bi₂S₃ nanonetwork as precursor for improved thermoelectric performance. *Nano Energy* **4**, 113–122 (2014)
97. Poudel, B., et al.: High-thermoelectric performance of nanostructured bismuth antimony telluride bulk alloys. *Science* **320**, 634–638 (2008)
98. Pierrat, P., Dauscher, A., Lenoir, B., Martin-Lopez, R., Scherrer, H.: Preparation of the Bi₈Sb₃₂Te₆₀ solid solution by mechanical alloying. *J. Mater. Sci.* **32**, 3653–3657 (1997)
99. Kim, H.C., Oh, T.S., Hyun, D.B.: Thermoelectric properties of the p-type Bi₂Te₃–Sb₂Te₃–Sb₂Se₃ alloys fabricated by mechanical alloying and hot pressing. *J. Phys. Chem. Solids* **61**, 743–749 (2000)
100. Schilz, J., Riffel, M., Pixius, K., Meyer, H.J.: Synthesis of thermoelectric materials by mechanical alloying in planetary ball mills. *Powder Technol.* **105**, 149–154 (1999)
101. Yang, J.Y., et al.: Synthesis of CoSb₃ skutterudite by mechanical alloying. *J. Alloy. Compd.* **375**, 229–232 (2004)
102. Ma, Y., et al.: Enhanced thermoelectric figure-of-merit in p-type nanostructured bismuth antimony tellurium alloys made from elemental chunks. *Nano Lett.* **8**, 2580–2584 (2008)
103. Kanatzia, A., Papageorgiou, C., Lioutas, C., Kyratsi, T.: Design of ball milling experiments on Bi₂Te₃ thermoelectric material. *J. Electron. Mater.* **42**, 1652–1660 (2013)
104. Yan, X., et al.: Experimental studies on anisotropic thermoelectric properties and structures of n-type Bi₂Te_{2.7}Se_{0.3}. *Nano Lett.* **10**, 3373–3378 (2010)
105. Liu, W.-S., et al.: Thermoelectric property studies on Cu-doped n-type Cu_xBi₂Te_{2.7}Se_{0.3} nanocomposites. *Adv. Energy Mater.* **1**, 577–587 (2011)
106. Zhu, G., et al.: The effect of secondary phase on thermoelectric properties of Zn₄Sb₃ compound. *Nano Energy* **2**, 1172–1178 (2013)
107. Sui, J., et al.: Effect of Cu concentration on thermoelectric properties of nanostructured p-type MgAg_{0.97-x}Cu_xSb_{0.99}. *Acta Mater.* **87**, 266–272 (2015)
108. Shuai, J., et al.: Study on thermoelectric performance by Na doping in nanostructured Mg_{1-x}Na_xAg_{0.97}Sb_{0.99}. *Nano Energy* **11**, 640–646 (2015)
109. Zhang, Q., et al.: Increased thermoelectric performance by Cl doping in nanostructured AgPb₁₈SbSe_{20-x}Cl_x. *Nano Energy* **2**, 1121–1127 (2013)
110. Koirala, M., et al.: Nanostructured YbAgCu₄ for potentially cryogenic thermoelectric cooling. *Nano Lett.* **14**, 5016–5020 (2014)
111. Yang, J., et al.: Solubility study of Yb in n-type skutterudites Yb_xCo₄Sb₁₂ and their enhanced thermoelectric properties. *Phys. Rev. B* **80**, 115329 (2009)
112. Dahal, T., et al.: Thermoelectric property enhancement in Yb-doped n-type skutterudites Yb_xCo₄Sb₁₂. *Acta Mater.* **75**, 316–321 (2014)
113. Dahal, T., et al.: Substitution of antimony by tin and tellurium in n-type skutterudites CoSb_{2.8}Sn_xTe_{0.2-x}. *J. Miner. Met Mater. Soc.* **66**, 2282–2287 (2014)
114. Dahal, T., Jie, Q., Lan, Y., Guo, C., Ren, Z.: Thermoelectric performance of Ni compensated cerium and neodymium double filled p-type skutterudites. *Phys. Chem. Chem. Phys.* **16**, 18170–18175 (2014)
115. Dahal, T., et al.: Effect of triple fillers in thermoelectric performance of p-type skutterudites. *J. Alloy. Compd.* **623**, 104–108 (2015)
116. Dahal, T., et al.: Thermoelectric and mechanical properties on misch metal filled p-type skutterudites Mn_{0.9}Fe_{4-x}Co_xSb₁₂. *J. Appl. Phys.* **117**, 055101 (2015)
117. Raihan, O., et al.: Parametric analysis of ball milling condition on thermoelectric performance of Bi_{0.6}FeCo₃Sb₁₂ skutterudite. *Mater. Res. Express* **5**, 105008 (2018)
118. May, A.F., Fleurial, J.P., Snyder, G.J.: Thermoelectric performance of lanthanum telluride produced via mechanical alloying. *Phys. Rev. B* **78**, 125205 (2008)
119. Zhu, G.H., et al.: Increased phonon scattering by nanograins and point defects in nanostructured silicon with a low concentration of germanium. *Phys. Rev. Lett.* **102**, 196803 (2009)

120. Bathula, S., et al.: Enhanced thermoelectric figure-of-merit in spark plasma sintered nanostructured n-type SiGe alloys. *Appl. Phys. Lett.* **101**, 213902 (2012)
121. Bashir, M.B.A., et al.: Enhancement of thermoelectric properties of Co₄Sb₁₂ Skutterudite by Al and La double filling. *J. Solid State Chem.* **284**, 121205 (2020)
122. Prado-Gonjal, J., Vaqueiro, P., Nuttall, C., Potter, R., Powell, A.V.: Enhancing the thermoelectric properties of single and double filled p-type skutterudites synthesized by an up-scaled ball milling process. *J Alloys Compd.* **695**, 3598–3604 (2017)
123. Li, J., Li, S., Wang, Q., Wang, L., Liu, F., Ao, W.: Effect of Ce-doping on thermoelectric properties in PbTe alloys prepared by spark plasma sintering. *J. Electron. Mater.* **40**, 2063 (2011)
124. Yang, J., Fan, X., Chen, R., Zhu, W., Bao, S., Duan, X.: Consolidation and thermoelectric properties of n-type bismuth telluride based materials by mechanical alloying and hot pressing. *J. Alloy. Compd.* **416**, 270–273 (2006)
125. Sridhar, K., Chattopadhyay, K.: Synthesis by mechanical alloying and thermoelectric properties of Cu₂Te. *J. Alloy. Compd.* **264**, 293–298 (1998)
126. Martin-Lopez, R., Dauscher, A., Scherrer, H., Hejtmánek, J., Kenzari, H., Lenoir, B.: Thermoelectric properties of mechanically alloyed Bi-Sb alloys. *Appl. Phys. A* **68**, 597–602 (1999)
127. Zevalkink, A., Swallow, J., Snyder, G.J.: Thermoelectric properties of Mn-doped Ca₅Al₂Sb₆. *J Electron. Mater.* **41**, 813–818 (2012)
128. Zevalkink, A., Toberer, E.S., Bleith, T., Flage-Larsen, E., Snyder, G.J.: Improved carrier concentration control in Zn-doped Ca₅Al₂Sb₆. *J. Appl. Phys.* **110**, 013721 (2011)
129. Johnson, S.I., Zevalkink, A., Snyder, G.J.: Improved thermoelectric properties in Zn-doped Ca₅Ga₂Sb₆. *J. Mater Chem A.* **1**, 4244–4249 (2013)
130. Zevalkink, A., Zeier, W.G., Cheng, E., Snyder, J., Fleurial, J.-P., Bux, S.: Nonstoichiometry in the Zintl phase Yb_{1–8}Zn₂Sb₂ as a route to thermoelectric optimization. *Chem Mater.* **26**, 5710–5717 (2014)
131. Chanakian, S., Zevalkink, A., Aydemir, U.: Enhanced thermoelectric properties of Sr₅In₂Sb₆ via Zn-doping. *J. Mater Chem A.* **3**, 10289–10295 (2015)
132. Tamaki, H., Sato, H.K., Kanno, T.: Isotropic conduction network and defect chemistry in Mg_{3+δ}Sb₂-based layered Zintl compounds with high thermoelectric performance. *Adv Mater.* **28**, 10182–10187 (2016)
133. Santos, R., Nancarrow, M., Dou, S.X., Aminorroaya Yamini, S.: Thermoelectric performance of n-type Mg₂Ge. *Sci Rep.* **7**, 3988 (2017)
134. Fan, W., et al.: Enhancing the zT value of bidoped Mg₂Si_{0.6}Sn_{0.4} materials through reduction of bipolar thermal conductivity. *ACS Appl. Mater. Interfaces* **9**, 28635–28641 (2017)
135. Khan, T.T., Mahmud, I., Ur, S.-C.: Synthesis and thermoelectric properties of the B-site substituted SrTiO₃ with vanadium. *Korean J. Mater. Res.* **27**, 416–421 (2017)
136. Khan, T.T., Ur, S.-C.: Thermoelectric properties of the yttrium doped ceramic oxide SrTiO₃. *J. Korean Phys. Soc.* **70**, 93–97 (2017)
137. Jiang, Q., Yang, J., Xin, J., Zhou, Z., Zhang, D., Yan, H.: Carriers concentration tailoring and phonon scattering from n-type zinc oxide (ZnO) nanoinclusion in p- and n-type bismuth telluride (Bi₂Te₃): leading to ultra low thermal conductivity and excellent thermoelectric properties. *J. Alloys Compd.* **694**, 864–868 (2017)
138. Löhnert, R., Stelter, M., Töpfer, J.: Evaluation of soft chemistry methods to synthesize Gd-doped CaMnO_{3-δ} with improved thermoelectric properties. *Mater. Sci. Eng. B.* **223**, 185–193 (2017)
139. Zhao, X.B., Ji, X.H., Zhang, Y.H., Zhu, T.J., Tu, J.P., Zhang, X.B.: Bismuth telluride nanotubes and the effects on the thermoelectric properties of nanotube-containing nanocomposites. *Appl. Phys. Lett.* **86**, 062111 (2005)
140. Gothard, N., Ji, X., He, J., Tritta, T.M.: Thermoelectric and transport properties of n-type Bi₂Te₃ nanocomposites. *J. Appl. Phys.* **103**, 054314 (2008)
141. Ni, H.L., Zhao, X.B., Zhu, T.J., Ji, X.H., Tu, J.P.: Synthesis and thermoelectric properties of Bi₂Te₃ based nanocomposites. *J. Alloy. Compd.* **397**, 317–321 (2005)

142. Wang, W., Wang, W., Poudel, B., Yang, J., Wang, D.Z., Ren, Z.F.: High-yield synthesis of single-crystalline antimony telluride hexagonal nanoplates using a solvothermal approach. *J. Am. Chem. Soc.* **127**, 13792–13793 (2005)
143. Yu, S.H., et al.: A new low temperature one-step route to metal chalcogenide semiconductors: PbE , Bi_2E_3 ($\text{E} = \text{S}, \text{Se}, \text{Te}$). *J. Mater. Chem.* **8**, 1949–1951 (1998)
144. Mi, J.L., Zhao, X.B., Zhu, T.J., Tu, J.P., Cao, G.S.: Solvothermal synthesis and electrical transport properties of skutterudite CoSb_3 . *J. Alloy. Compd.* **417**, 269–272 (2006)
145. Mi, J.L., Zhao, X.B., Zhu, T.J., Tu, J.P.: In-situ solvothermal and hot pressing preparation of micro-nano composite n-type CoSb_3 and its thermoelectric properties. *J. Inorg. Mater.* **23**, 715–718 (2008)
146. Makongo, J.P.A., et al.: Simultaneous large enhancements in thermopower and electrical conductivity of bulk nanostructured half-Heusler alloys. *J. Am. Chem. Soc.* **133**, 18843–18852 (2011)
147. Fan, F.J., et al.: Colloidal synthesis of $\text{Cu}_2\text{CdSnSe}_4$ nanocrystals and hot pressing to enhance the thermoelectric figure-of-merit. *J. Am. Chem. Soc.* **133**, 15910–15913 (2011)
148. Wang, D.B., et al.: Preparation and characterization of wire-like Sb_2Se_3 and flake-like Bi_2Se_3 nano crystals. *J. Cryst. Growth* **253**, 445–451 (2003)
149. Deng, Y., et al.: Solvothermal preparation and characterization of nanocrystalline Bi_2Te_3 powders with different morphology. *J. Phys. Chem. Solid* **63**, 2119–2121 (2002)
150. Wang, W.Z., et al.: High-yield synthesis of single-crystalline antimony telluride nano plate using a solvothermal approach. *J. Am. Chem. Soc.* **127**, 13792–13799 (2005)
151. Zhao, X.B., Sun, T., Zhu, T.J., Tu, J.P.: In-situ investigation and effect of additives on low temperature aqueous chemical synthesis of Bi_2Te_3 nanocapsules. *J. Chem. Mater.* **15**, 1621–1625 (2005)
152. Yu, H., Gibbons, P.C., Buhro, W.E.: Bismuth, telluride, and bismuth telluride nanowires. *J. Mater. Chem.* **14**, 595–602 (2004)
153. Urban, J.J., Talapin, D.V., Shevchenko, E.V., Murray, C.B.: Self-assembly of PbTe Quantum dots into nano crystal supper lattice and Glass Film. *J. Am. Chem. Soc.* **128**, 3248–3255 (2006)
154. Wang, W.Z., Poudel, B., Wang, D.Z., Ren, Z.F.: Synthesis of PbTe nanoboxes using a solvothermal technique. *Adv. Mater.* **17**, 2110–2114 (2005)
155. Tai, G.A., Zhou, B., Guo, W.L.: Structure characterization and thermoelectric transport properties of uniform single crystalline Lead telluride nanowire. *J. Phys. Chem. C* **112**, 11314–11318 (2008)
156. Gothard, N., Spowart, J.E., Tritt, T.M.: Thermal conductivity reduction in fullerene-enriched p-type bismuth telluride composites. *Phys. Status Solidi A* **207**, 157–162 (2007)
157. Schultz, J.M., McHugh, J.P., Tiller, W.A.: Effects of heavy deformation and annealing on electrical properties of Bi_2Te_3 . *J. Appl. Phys.* **33**, 2443–2450 (1962)
158. Oh, T.S., Hyun, D.B., Kolomoets, N.V.: Thermoelectric properties of the hot-pressed $(\text{Bi}, \text{Sb})_2(\text{Te}, \text{Se})_3$ alloys. *Scripta Mater.* **42**, 849–854 (2000)
159. Liu, W., Ren, Z., Chen, G.: *Thermoelectric Nanomaterials Book*, Chapter 11, Springer Series in Materials Science, vol. 182
160. Xiao, F., Hangarter, C., Yoo, B.Y., Rheem, Y.W., Lee, K.H., Myung, N.V.: Recent progress in electrodeposition of thermoelectric thin films and nanostructures. *Electrochim. Acta* **53**, 8103–8117 (2008)
161. Snyder, G.J., Lim, J.R., Huang, C.K., Fleurial, J.P.: Thermoelectric microdevice fabricated by a MEMS-like electrochemical process. *Nat. Mater.* **2**, 528 (2003)
162. Chen, L.J., Hu, H.N., Li, Y.X., Chen, G.F., Yu, S.Y., Wu, G.H.: Ordered CoSb_3 nanowire arrays synthesized by electrodeposition. *Chem. Lett.* **35**, 170–171 (2006)
163. Martin-Gonzalez, M., Prieto, A.L., Gronsky, R., Sands, T., Stacy, A.M.: High-density 40 nm diameter Sb-Rich $\text{Bi}_{2-x}\text{Sb}_x\text{Te}_3$ nanowire arrays. *Adv. Mater.* **15**, 1003–1006 (2003)
164. Jin, C.G., et al.: Electrochemical fabrication of large-area, ordered Bi_2Te_3 nanowire array. *J. Phys. Chem. B* **108**, 1844–1847 (2004)

165. Jin, C.G., Zhang, G.Q., Qian, T., Li, X.G., Yao, Z.: Large-area Sb_2Te_3 nanowire arrays. *J. Phys. Chem. B* **109**, 1430–1432 (2005)
166. Martin-Gonzalez, M., Snyder, G.J., Prieto, A.L., Gronsky, R., Sands, T., Stacy, A.M.: Direct Electrodeposition of highly dense 50 nm $\text{Bi}_2\text{Te}_{3-y}\text{Se}_y$ nanowire arrays. *Nano Lett.* **3**, 973 (2003)
167. Liu, W.F., Cai, W.L., Yao, L.Z.: Electrochemical deposition of well-ordered single-crystal PbTe nanowire arrays. *Chem. Lett.* **36**, 1362 (2007)
168. Wang, W., Qu, J.F., Lu, X.L., Zhang, G.Q., Li, G., Li, X.G.: Electrochemical Fabrication of $\text{Bi}_x\text{Te}_{1-x}$ ($0.4 \leq x \leq 0.7$) Nanowire Arrays. *Mater. Sci. Forum* **2171**, 546–549 (2007)
169. Li, L., Yang, Y.W., Huang, X.H., Li, G.H., Zhang, L.D.: Pulsed electrodeposition of single-crystalline Bi_2Te_3 nanowire arrays. *Nanotechnology* **17**, 1706 (2006)
170. Trahey, L., Becker, C.R., Stacy, A.M.: Electrodeposited bismuth telluride nanowire arrays with uniform growth fronts. *Nano Lett.* **7**, 2535 (2007)
171. Li, L., Yang, Y.W., Huang, X.H., Li, G.H., Ang, R., Zhang, L.D.: Fabrication and electronic transport properties of Bi nanotube arrays. *Appl. Phys. Lett.* **88**, 103119 (2006)
172. Li, X.H., Zhou, B., Pu, L., Zhu, J.J.: Electrodeposition of Bi_2Te_3 and Bi_2Te_3 derived alloy nanotube arrays. *Cryst. Growth Des.* **8**, 771 (2008)
173. Zhou, B., Li, X.H., Zhu, J.J.: Controllable synthesis of one-dimensional chinellike superstructures of homogeneous $\text{Bi}_{100-x}\text{Sb}_x$ alloys via a template-free electrodeposition. *Cryst. Growth Des.* **7**, 2276 (2007)
174. Xiao, F., Yoo, B.Y., Bozhilov, K.N., Lee, K.H., Myung, N.V.: Electrodeposition of single-crystal cubes of lead telluride on polycrystalline gold substrate. *J. Phys. Chem. C* **111**, 11397 (2007)
175. Menke, E.J., Li, Q., Penner, R.M.: Bismuth telluride (Bi_2Te_3) nanowires synthesized by cyclic electrodeposition/stripping coupled with step edge decoration. *Nano Lett.* **4**, 2009 (2004)
176. Xue, F.H., Fei, G.T., Wu, B., Cui, P., Zhang, L.D.: Direct electrodeposition of highly dense Bi/Sb superlattice nanowire arrays. *J. Am. Chem. Soc.* **127**, 15348 (2005)
177. Yoo, B., Xiao, F., Bozhilov, K.N., Herman, J., Ryan, M.A., Myung, N.V.: Electrodeposition of thermoelectric superlattice nanowires. *Adv. Mater.* **19**, 296 (2007)
178. Wang, W., Zhang, G.Q., Li, X.G.: Manipulating growth of thermoelectric $\text{Bi}_2\text{Te}_3/\text{Sb}$ multilayered nanowire arrays. *J. Phys. Chem. C* **112**, 15190 (2008)
179. Wang, W., Lu, X.L., Zhang, T., Zhang, G.Q., Jiang, W.J., Li, X.G.: Facile synthesis of a hierarchical PbTe flower-like nanostructure and its shape evolution process guided by a kinetically controlled regime. *J. Am. Chem. Soc.* **129**, 6702 (2007)
180. Dresselhaus, M.S., et al.: Materials and technologies for direct thermal-to-electric energy conversion. In: Yang, J., Hogan, T.P., Funahashi, R., Nolas, G.S. (eds.) *MRS Symposium Proceedings*, vol. 886, p. 3. Pittsburgh, PA (2005)
181. Benelmekki, M.: *Nanomaterials: The Original Product of Nanotechnology Book*, Chapter 2. IOP Publishing, Bristol (2019)
182. Johnsen, S., et al.: Nanostructures boost the thermoelectric performance of PbS . *J. Am. Chem. Soc.* **133**, 3460 (2011)
183. He, J.Q., et al.: Anomalous electronic transport in dual-nanostructured lead telluride. *J. Am. Chem. Soc.* **133**, 8786 (2011)
184. Androulakis, J., Todorov, I., He, J., Chung, D., Dravid, V., Kanatzidis, M.G.: Thermoelectrics from abundant chemical elements: high-performance nanostructured PbSe-PbS . *J. Am. Chem. Soc.* **133**, 10920–10927 (2011)
185. Girard, S.N., et al.: High performance Na-doped PbTe-PbS thermoelectric materials: electronic density of states modification and shape-controlled nanostructures. *J. Am. Chem. Soc.* **133**, 16588–16597 (2011)
186. Biswas, K., et al.: High thermoelectric figure of merit in nanostructured p-type PbTe-MTe ($M = \text{Ca, Ba}$). *Energy Environ. Sci.* **4**, 4675–4684 (2011)
187. Zhao, L., et al.: High performance thermoelectrics from earth-abundant materials: enhanced figure of merit in PbS by second phase nanostructures. *J. Am. Chem. Soc.* **133**, 20476–20487 (2011)

188. He, J., Androulakis, J., Kanatzidis, M.G., Dravid, V.P.: Seeing is believing: weak phonon scattering from nanostructures in alkali metal-doped lead telluride. *Nano Lett.* **12**, 343–347 (2012)
189. Hsu, K.F., et al.: Cubic $\text{AgPb}_m\text{SbTe}_{2+m}$: bulk thermoelectric materials with high figure of merit. *Science* **303**, 818–821 (2004)
190. Cook, B.A., Kramer, M.J., Harringa, J.L., Han, M.K., Chung, D.Y., Kanatzidis, M.G.: Analysis of nanostructuring in high figure-of-merit $\text{Ag}_{1-x}\text{Pb}_m\text{SbTe}_{2+m}$ thermoelectric materials. *Adv. Funct. Mater.* **19**, 1254–1259 (2009)
191. Ikeda, T., Collins, L.A., Ravi, V.A., Gascoin, F.S., Haile, S.M., Snyder, G.J.: Self-assembled nanometer lamellae of thermoelectric PbTe and Sb_2Te_3 with Epitaxy-like interfaces. *Chem. Mater.* **19**, 763 (2007)
192. Nguyen, P., et al.: Spark eroded $\text{Bi}_{0.5}\text{Sb}_{1.5}\text{Te}_3$ nanocomposites with enhanced thermoelectric performance and high production rate. Symposium JJ 2.6, MRS spring meeting and exhibition (2012), spark erosion: a high production rate method for producing $\text{Bi}_{0.5}\text{Sb}_{1.5}\text{Te}_3$ nanoparticles with enhanced thermoelectric performance. *Nanotechnology* **23**, 415604 (2012)
193. Berkowitz, A.E., Walter, J.L.: Spark erosion: a method for producing rapidly quenched fine powders. *J. Mater. Res.* **2**, 277–288 (1987)
194. Carrey, J., Radousky, H.B., Berkowitz, A.E.: Spark-eroded particles: influence of processing parameters. *J. Appl. Phys.* **95**, 823 (2004)
195. Serrano-Sánchez, F., et al.: Enhanced figure of merit in nanostructured (bi, Sb) $_2\text{Te}_3$ with optimized composition. *Sci. Rep.* **7**, 6277 (2017)
196. Goldsmid, H.J.: The Improvement of a Specific Material-Bismuth Telluride, Introduction to Thermoelectricity, pp. 85–107. Springer, Berlin (2016)
197. Sootsman, J.R., Chung, D.Y., Kanatzidis, M.G.: New and old concepts in thermoelectric materials. *Angew Chem. Int. Ed.* **48**, 8616–8639 (2009)
198. Park, K.H., Mohamed, M., Aksamija, Z., Ravaioli, U.: Ab initio lattice dynamics and thermochemistry of layered bismuth telluride (Bi_2Te_3). *J. Appl. Phys.* **117**, 015103 (2015)
199. Tanaka, S., Takiishi, M., Miyazaki, K., Tsukamoto, H.: Measurements of thermal conductivity of thin films by 3-omega method. In: International Conference on Micro/Nanoscale Heat Transfer, pp. 477–483. ASME, New York (2008)
200. Xu, Z., et al.: Attaining high mid-temperature performance in (bi, Sb) $_2\text{Te}_3$ thermoelectric materials via synergistic optimization. *NPG Asia Mater.* **8**, e302 (2016)
201. Tritt, T.M.: Thermal Conductivity: Theory, Properties, and Applications, pp. 1–9. Springer, Berlin (2005)
202. Hasan, M.N., Wahid, H., Nayan, N., Ali, M.S.M.: Inorganic thermoelectric materials: a review. *Int. J. Energy Res.* **44**, 1–53 (2020)
203. Lan, Y., et al.: Structure study of bulk nanograined thermoelectric bismuth antimony telluride. *Nano. Lett.* **9**, 1419–1422 (2009)
204. Yan, X., et al.: Experimental studies on anisotropic thermoelectric properties and structures of n-Type $\text{Bi}_{(2)}\text{Te}_{(2.7)}\text{Se}_{(0.3)}$. *Nano Lett.* **10**, 3373–3378 (2010)
205. Cao, Y.Q., Zhao, X.B., Zhu, T.J., Zhang, X.B., Tu, J.P.: Syntheses and thermoelectric properties of $\text{Bi}_{(2)}\text{Te}_{(3)}/\text{Sb}_{(2)}\text{Te}_{(3)}$ bulk nano-composites with laminated nanostructure. *Appl. Phys. Lett.* **92**, 143106 (2008)
206. Xie, W., Tang, X., Yan, Y., Zhang, Q., Tritt, T.M.: Highthermo- electric performance BiSbTe alloy with unique low-dimensional structure. *J. Appl. Phys.* **105**, 113713 (2009)
207. Xie, W., Tang, X., Yan, Y., Zhang, Q., Tritt, T.M.: Unique nanostructures and enhanced thermoelectric performance of melt-spun BiSbTe alloys. *Appl. Phys. Lett.* **94**, 102111 (2009)
208. Sharma, S., Schwingenschlöggl, U.: Thermoelectric response in single quintuple layer Bi_2Te_3 . *ACS Energy Lett.* **1**, 875–879 (2016)
209. Zhai, R., Wu, Y., Zhu, T.-J., Zhao, X.-B.: Tunable optimum temperature range of high-performance zone melted bismuth-telluride-based solid solutions. *Cryst Growth Des.* **18**, 4646–4652 (2018)
210. Hao, F., et al.: Enhanced thermoelectric performance in n-type Bi_2Te_3 -based alloys via suppressing intrinsic excitation. *ACS Appl. Mater. Interfaces* **10**, 21372–21380 (2018)

211. Yang, L., Chen, Z.-G., Hong, M., Han, G., Zou, J.: Enhanced thermoelectric performance of nanostructured Bi_2Te_3 through significant phonon scattering. *ACS Appl. Mater. Interfaces* **7**, 23694–23699 (2015)
212. Xu, B., Feng, T., Li, Z., Zhou, L., Pantelides, S.T., Wu, Y.: Creating zipper-like van der Waals gap discontinuity in low-temperature-processed nanostructured $\text{PbBi}_{2n}\text{Te}_{1+3n}$: enhanced phonon scattering and improved thermoelectric performance. *Angew. Chem. Int. Ed.* **57**, 10938–10943 (2018)
213. Soni, A., Yanyuan, Z., Ligen, Y., Aik, M.K.K., Dresselhaus, M.S., Xiong, Q.: Enhanced thermoelectric properties of solution grown $\text{Bi}_2\text{Te}_{3-x}\text{Se}_x$ Nanoplatelet composites. *Nano Lett.* **12**, 1203–1209 (2012)
214. Hong, M., et al.: N-type $\text{Bi}_2\text{Te}_{3-x}\text{Se}_x$ Nanoplates with enhanced thermoelectric efficiency driven by wide-frequency phonon scatterings and synergistic carrier scatterings. *ACS Nano* **10**, 4719–4727 (2016)
215. Li, S., et al.: Graphene quantum dots embedded in Bi_2Te_3 Nanosheets to enhance thermoelectric performance. *ACS Appl. Mater. Interfaces* **9**, 3677–3685 (2017)
216. Yu, Y., et al.: Simultaneous optimization of electrical and thermal transport properties of $\text{Bi}_{0.5}\text{Sb}_{1.5}\text{Te}_3$ thermoelectric alloy by twin boundary engineering. *Nano Energy* **37**, 203–213 (2017)
217. Shalaby, M.S., et al.: Preparation, structural characteristics and optical parameters of the synthesized nano-crystalline sulphur-doped $\text{Bi}_2\text{Te}_{2.85}\text{Se}_{0.15}$ thermoelectric materials. *J. Mater. Sci. Mater. Electron.* **31**, 10612–10627 (2020)
218. Rashad, M.M., El-Dissouky, A., Soliman, H.M., Elseman, A.M., Refaat, H.M., Ebrahim, A.: Structure evaluation of bismuth telluride (Bi_2Te_3) nanoparticles with enhanced Seebeck coefficient and low thermal conductivity. *Mater. Res. Innov.* **22**, 315–323 (2018)
219. Kim, S.I., et al.: Dense dislocation arrays embedded in grain boundaries for high-performance bulk thermoelectrics. *Science* **348**, 109–114 (2015)
220. Shin, W.H., et al.: Enhanced thermoelectric performance of reduced graphene oxide incorporated bismuth-antimony-telluride by lattice thermal conductivity reduction. *J. Alloys Compd.* **718**, 342–348 (2017)
221. Cao, Y.Q., Zhao, X.B., Zhu, T.J., Zhang, X.B., Tu, J.P.: Syntheses and thermoelectric properties of $\text{Bi}_2\text{Te}_3/\text{Sb}_2\text{Te}_3$ bulk nanocomposites with laminated nanostructure. *Appl. Phys. Lett.* **92**, 143106 (2008)
222. Ji, X., Zhang, B., Tritt, T.M., Kolis, J.W., Kumbhar, A.: Solution-chemical syntheses of nanostructured Bi_2Te_3 and PbTe thermoelectric materials. *J. Electron. Mater.* **36**, 721–726 (2007)
223. Ji, X.H., He, J., Su, Z., Gothard, N., Tritt, T.M.: Improved thermoelectric performance in polycrystalline p-type Bi_2Te_3 via an alkali metal salt hydrothermal nanocoating treatment approach. *J. Appl. Phys.* **104**, 034907 (2008)
224. Fan, S., Zhao, J., Guo, J., Yan, Q., Ma, J., Hng, H.H.: p-type $\text{Bi}_{(0.4)}\text{Sb}_{(1.6)}\text{Te}_{(3)}$ nanocomposites with enhanced figure of merit. *Appl. Phys. Lett.* **96**, 182104 (2010)
225. Fan, X.A., et al.: Bi_2Te_3 hexagonal nanoplates and thermoelectric properties of n-type Bi_2Te_3 nanocomposites. *J. Phys. D Appl. Phys.* **40**, 5975–5979 (2007)
226. Heremans, J.P., et al.: Enhancement of thermoelectric efficiency in PbTe by distortion of the electronic density of states. *Science* **321**, 554–557 (2008)
227. Martin, J., Nolas, G.S., Zhang, W., Chen, L.: PbTe nanocomposites synthesized from PbTe nanocrystals. *Appl. Phys. Lett.* **90**, 222112 (2007)
228. Pei, Y., LaLonde, A., Iwanaga, S., Snyder, G.J.: High thermoelectric figure of merit in heavy hole dominated PbTe . *Energy Environ. Sci.* **4**, 2085–2089 (2011)
229. Zhang, Q., et al.: Heavy doping and band engineering by potassium to improve the thermoelectric figure of merit in p-type PbTe , PbSe , and $\text{PbTe}_{1-y}\text{Se}_y$. *J. Am. Chem. Soc.* **134**, 10031–10038 (2012)
230. Zhang, Q., et al.: Effect of aluminum on the thermoelectric properties of nanostructured PbTe . *Nanotechnol.* **24**, 345705 (2013)
231. Chere, E.K., et al.: Enhancement of thermoelectric performance in n-type $\text{PbTe}_{1-y}\text{Se}_y$ by doping Cr and tuning Te: Se ratio. *Nano Energy* **13**, 355–367 (2015)

232. Paul, B., Banerji, P.: The effect of chromium impurity on the thermoelectric properties of PbTe in the temperature range 100–600 K. *J. Appl. Phys.* **109**, 103710 (2011)
233. Sie, F.-R., Liu, H.-J., Kuo, C.-H., Hwang, C.-S., Chou, Y.-W., Yeh, C.-H.: Enhanced thermoelectric performance of n-type PbTe doped with Na₂Te. *Intermetallics* **92**, 113–118 (2018)
234. Jood, P., Ohta, M., Yamamoto, A., Kanatzidis, M.G.: Excessively doped PbTe with Ge-induced nanostructures enables high efficiency thermoelectric modules. *Joule*, 1339–1355 (2018)
235. Xiao, Y., et al.: Synergistically optimizing thermoelectric transport properties of n-type PbTe via Se and Sn co-alloying. *J. Alloys Compd.* **724**, 208–221 (2017)
236. Shi, W., et al.: Tin selenide (SnSe): growth, properties, and applications. *Adv. Sci.* **5**, 1700602 (2018)
237. Chen, Z.-G., Shi, X., Zhao, L.-D., Zou, J.: High-performance SnSe thermoelectric materials: progress and future challenge. *Prog. Mater. Sci.* **97**, 283–346 (2018)
238. Zhou, Y., Zhao, L.D.: Promising thermoelectric bulk materials with 2D structures. *Adv. Mater.* **29**, 1702676 (2017)
239. Chen, Y.X., et al.: Understanding of the extremely low thermal conductivity in high-performance polycrystalline SnSe through potassium doping. *Adv. Funct. Mater.* **26**(37), 6836–6845 (2016)
240. Chandra, S., Biswas, K.: Realization of high thermoelectric figure of merit in solution synthesized 2D SnSe Nanoplates via Ge alloying. *J. Am. Chem. Soc.* **141**, 6141–6145 (2019)
241. Shi, X., et al.: High thermoelectric performance in p-type polycrystalline Cd-doped SnSe achieved by a combination of cation vacancies and localized lattice engineering. *Adv. Energy Mater.* **9**, 1803242 (2019)
242. Liu, J., et al.: Achieving high thermoelectric performance with Pb and Zn codoped polycrystalline SnSe via phase separation and nanostructuring strategies. *Nano Energy* **53**, 683–689 (2018)
243. Beretta, D., et al.: Thermoelectrics: from history, a window to the future. *Mater. Sci. Eng. R Rep.* **138**, 100501 (2018)
244. Chang, C., et al.: 3D charge and 2D phonon transports leading to high out-of-plane ZT in n-type SnSe crystals. *Science* **360**, 778–783 (2018)
245. Das, A., Kumar, A., Banerji, P.: First principles study of electronic structure and thermoelectric transport in tin selenide and phase separated tin selenide-copper selenide alloy. *J. Phys. Condens. Matter.* **32**, 265501 (2020)
246. Liu, H., et al.: Ultrahigh thermoelectric performance by electron and phonon critical scattering in Cu₂Se_{1-x}I_x. *Adv. Mater.* **25**, 6607–6612 (2013)
247. Byeon, D., et al.: Discovery of colossal seebeck effect in metallic Cu₂Se. *Nat. Commun.* **10**, 1–7 (2019)
248. Li, D., et al.: Chemical synthesis of nanostructured Cu₂Se with high thermoelectric performance. *RSC Adv.* **4**, 8638–8644 (2014)
249. Hu, Q., Zhu, Z., Zhang, Y., Li, X.J., Song, H., Zhang, Y.: Remarkably high thermoelectric performance of Cu_{2-x}Li_xSe bulks with nanopores. *J. Mater. Chem. A.* **6**, 23417–23424 (2018)
250. Yang, L., Chen, Z.-G., Han, G., Hong, M., Zou, Y., Zou, J.: High performance thermoelectric Cu₂Se nanoplates through nanostructure engineering. *Nano Energy* **16**, 367–374 (2015)
251. Hu, Q., Zhang, Y., Zhang, Y., Li, X.J., Song, H.: High thermoelectric performance in Cu₂Se/CDs hybrid materials. *J. Alloys Compd.* **813**, 152204 (2020)
252. Li, M., et al.: Ultra-high thermoelectric performance in graphene incorporated Cu₂Se: role of mismatching phonon modes. *Nano Energy* **53**, 993–1002 (2018)
253. Li, M., et al.: Ultrahigh figure-of merit of Cu₂Se incorporated with carbon coated boron nanoparticles. *Info. Mat.* **1**, 108–115 (2019)
254. Nolas, G.S., Cohn, J.L., Slack, G.A.: Effect of partial void filling on the lattice thermal conductivity of skutterudites. *Phys. Rev. B* **58**, 164–170 (1998)
255. Uher, C.: Skutterudites: prospective novel thermoelectrics. In: Tritt, T.M. (ed.) *Semiconductors and Semimetals*, vol. 69, pp. 139–253. Academic Press, San Diego, CA (2001)

256. Beretta, D., et al.: Thermoelectrics: From history, a window to the future. *Mater Sci Eng R Rep.* **138**, 100501 (2019)
257. Zhang, Q., et al.: Realizing high-performance thermoelectric power generation through grain boundary engineering of skutterudite-based nanocomposites. *Nano Energy* **41**, 501–510 (2017)
258. Zong, P.-A., et al.: Skutterudite with graphene-modified grain-boundary complexation enhances zT enabling high-efficiency thermoelectric device. *Energy Environ. Sci.* **10**, 183–191 (2017)
259. Khovaylo, V., Korolkov, T., Voronin, A., Gorshenkov, M., Burkov, A.: Rapid preparation of $\text{In}_x\text{Co}_4\text{Sb}_{12}$ with a recordbreaking $ZT=1.5$: the role of the in overfilling fraction limit and Sb over stoichiometry. *J. Mater. Chem. A.* **5**, 3541–3546 (2017)
260. Lei, Y., et al.: Structure and thermoelectric performance of Ti-filled and Te-doped skutterudite $\text{Ti}_x\text{Co}_4\text{Sb}_{11.5}\text{Te}_{0.5}$ bulks fabricated by combination of microwave synthesis and spark plasma sintering. *Mater. Lett.* **233**, 166–169 (2018)
261. Hu, C., et al.: Effects of partial La filling and Sb vacancy defects on CoSb_3 skutterudites. *Phys. Rev. B.* **95**, 165204 (2017)
262. Sales, B.C.: Filled skutterudites. In: Gschneidner, K.A., Jr., Bünzli, J.-C.G., Pecharsky, V.K. (eds.) *Handbook on the Physics and Chemistry of Rare Earths*, vol. 33, pp. 1–34. Elsevier, Amsterdam (2003)
263. Rull-Bravo, M., Moure, A., Fernandez, J., Martin-Gonzalez, M.: Skutterudites as thermoelectric materials: revisited. *RSC Adv.* **5**, 41653–41667 (2015)
264. He, Q., et al.: Nanostructured thermoelectric skutterudite $\text{Co}_{1-x}\text{Ni}_x\text{Sb}_3$ alloys. *J. Nanosci. Nanotechnol.* **8**, 4003–4006 (2008)
265. Chen, B., et al.: Low-temperature transport properties of the filled skutterudites $\text{CeFe}_{4-x}\text{Co}_x\text{Sb}_{12}$. *Phys. Rev. B* **55**, 1476–1480 (1997)
266. Keppens, V., et al.: Localized vibrational modes in metallic solids. *Nature* **395**, 876–878 (1998)
267. Puyet, M., Lenoir, B., Dauscher, A., Dehmas, M., Stiewe, C., Müller, E.: High temperature transport properties of partially filled $\text{Ca}_x\text{Co}_4\text{Sb}_{12}$ skutterudites. *J. Appl. Phys.* **95**, 4852–4855 (2004)
268. Chen, L.D., et al.: Anomalous barium filling fraction and n-type thermoelectric performance of Bay $\text{Co}_4\text{Sb}_{12}$. *J. Appl. Phys.* **90**, 1864–1868 (2001)
269. Li, H., Tang, X., Zhang, Q., Uher, C.: Rapid preparation method of bulk nanostructured $\text{Yb}_{0.3}\text{Co}_4\text{Sb}_{12+y}$ compounds and their improved thermoelectric performance. *Appl. Phys. Lett.* **93**, 252109 (2008)
270. Nolas, G.S., Kaeser, M., Littleton, R.T., Tritt, T.M.: High figure of merit in partially filled ytterbium skutterudite materials. *Appl. Phys. Lett.* **77**, 1855–1857 (2000)
271. Geng, H.Y., Ochi, S., Guo, J.Q.: Solidification contraction-free synthesis for the $\text{Yb}_{0.15}\text{Co}_4\text{Sb}_{12}$ bulk material. *Appl. Phys. Lett.* **91**, 022106 (2007)
272. Ur, S.-C., Kwon, J.-C., Kim, I.-H.: Thermoelectric properties of tin-filled skutterudites prepared by mechanical alloying process. *Met. Mater. Int.* **14**, 625–629 (2008)
273. Bao, S., et al.: Preparation of La-filled skutterudites by mechanical alloying and hot pressing and their thermal conductivities. *Mater. Sci. Eng. A* **438–440**, 186–189 (2006)
274. Bao, S., Yang, J., Zhu, W., Fan, X., Duan, X., Peng, J.: Preparation and thermoelectric properties of La filled skutterudites by mechanical alloying and hot pressing. *Mater. Lett.* **60**, 2029–2032 (2006)
275. Zhou, C., Sakamoto, J., Morelli, D., Zhou, X., Wang, G., Uher, C.: Thermoelectric properties of $\text{Co}_{0.9}\text{Fe}_{0.1}\text{Sb}_3$ -based skutterudite nanocomposites with FeSb_2 nano-inclusions. *J. Appl. Phys.* **109**, 063722 (2011)
276. Nolas, G.S., Wang, D., Beekman, M.: Transport properties of polycrystalline $\text{Mg}_2\text{Si}_{1-y}\text{Sb}_y$ ($0 \leq y < 0.4$). *Phys. Rev. B* **76**, 235204 (2007)
277. Huang, Y., et al.: Synthesis, structural and photoluminescence properties of $\text{Mg}_2\text{Si}/\text{Si}$ nanocomposites consisting of Si nanosheet bundles and Mg_2Si deposits. *Jpn. J. Appl. Phys.* **58**, SBBK04 (2019)

278. Zaitsev, V.K., et al.: Highly effective $\text{Mg}_2\text{Si}_{1-x}\text{Sn}_x$ thermoelectrics. *Phys. Rev. B* **74**, 045207 (2006)
279. Zhang, Q., He, J., Zhu, T.J., Zhang, S.N., Zhao, X.B., Tritt, T.M.: High figures of merit and natural nanostructures in $\text{Mg}_2\text{Si}_{0.4}\text{Sn}_{0.6}$ based thermoelectric materials. *Appl. Phys. Lett.* **93**, 102109 (2008)
280. Souda, D., Shimizu, K., Ohishi, Y., Muta, H., Yagi, T., Kurosaki, K.: High thermoelectric power factor of Si– Mg_2Si nanocomposite ribbons synthesized by melt spinning. *ACS Appl. Energy Mater.* **3**, 1962–1968 (2020)
281. Ioffe, A.F.: *Physics of Semiconductors*. Academic Press, New York (1960)
282. Slack, G.A., Hussain, M.A.: The maximum possible conversion efficiency of silicon–germanium thermoelectric generators. *J. Appl. Phys.* **70**, 2694–2718 (1991)
283. Mu, X., Wang, L., Yang, X., Zhang, P., To, A.C., Luo, T.: Corrigendum: ultra-low thermal conductivity in Si/Ge hierarchical Superlattice nanowire. *Sci. Rep.* **6**, 32904 (2016)
284. Wang, W., Zhang, G.Q., Li, X.G.: Manipulating growth of thermoelectric $\text{Bi}_2\text{Te}_3/\text{Sb}$ multilayered nanowire arrays. *J. Phys. Chem. C* **112**(39), 15190 (2008)
285. Usenko, A.A., et al.: Optimization of ball-milling process for preparation of Si-Ge nanostructured thermoelectric materials with a high figure of merit. *Scr. Mater.* **96**, 9–12 (2015)
286. Lan, Y., Ren, Z.: Thermoelectric nanocomposites for thermal energy conversion. In: Li, Q. (eds.) *Nanomaterials for Sustainable Energy*. NanoScience and Technology. Springer, Cham (2016). https://doi.org/10.1007/978-3-319-32023-6_11
287. Joshi, G., et al.: Enhanced thermoelectric figure of merit in nanostructured p-type silicon germanium bulk alloys. *Nano Lett.* **8**, 4670–4674 (2008)
288. Donmez Noyan, I., et al.: SiGe nanowire arrays based thermoelectric microgenerator. *Nano Energy* **57**, 492–499 (2019)
289. Usenko, A., et al.: Enhanced thermoelectric figure of merit of p-type $\text{Si}_{0.8}\text{Ge}_{0.2}$ nanostructured spark plasma sintered alloys with embedded SiO_2 nanoinclusions. *Scr. Mater.* **127**, 63–67 (2017)
290. Peng, Y., et al.: Improved thermoelectric property of B-doped Si/Ge multilayered quantum dot films prepared by RF magnetron sputtering. *Jpn. J. Appl. Phys.* **57**, 01AF03 (2017)
291. Kikuchi, A., Yao, A., Mori, I., Ono, T., Samukawa, S.: Composite films of highly ordered Si nanowires embedded in $\text{SiGe}_{0.3}$ for thermoelectric applications. *J. Appl. Phys.* **122**, 165302 (2017)
292. Usenko, A., et al.: Thermoelectric properties and cost optimization of spark plasma sintered n-type $\text{Si}_{0.9}\text{Ge}_{0.1}$ - Mg_2Si nanocomposites. *Scr. Mater.* **146**, 295–299 (2018)
293. Shuai, J., Mao, J., Song, S., Zhang, Q., Chen, G., Ren, Z.: Recent progress and future challenges on thermoelectric Zintl materials. *Mater. Today Phys.* **1**, 74–95 (2017)
294. Cooley, J.A., et al.: High Seebeck coefficient and unusually low thermal conductivity near ambient temperatures in layered compound $\text{Yb}_{2-x}\text{Eu}_x\text{CdSb}_2$. *Chem. Mater.* **30**, 484–493 (2017)
295. Hu, Y., Wang, J., Kawamura, A., Kovnir, K., Kauzlarich, S.M.: $\text{Yb}_{14}\text{MgSb}_{11}$ and $\text{Ca}_{14}\text{MgSb}_{11}$ -new mg-containing Zintl compounds and their structures, bonding, and thermoelectric properties. *Chem. Mater.* **27**, 343–351 (2014)
296. Bhardwaj, A., Misra, D.: Enhancing thermoelectric properties of a p-type Mg_3Sb_2 -based Zintl phase compound by Pb substitution in the anionic framework. *RSC Adv.* **4**, 34552–34560 (2014)
297. Kauzlarich, S.M., Brown, S.R., Snyder, G.J.: Zintl phases for thermoelectric devices. *Dalton Trans.* **2007**, 2099–2107 (2007)
298. Shi, X., Chen, L., Uher, C.: Recent advances in high-performance bulk thermoelectric materials. *Int. Mater. Rev.* **61**, 379–415 (2016)
299. Brown, S.R., et al.: Improved thermoelectric performance in $\text{Yb}_{14}\text{Mn}_{1-x}\text{Zn}_x\text{Sb}_{11}$ by the reduction of spin-disorder scattering. *Chem. Mater.* **20**, 3412–3419 (2008)
300. Toberer, E.S., et al.: Traversing the metalinsulator transition in a Zintl phase: rational enhancement of thermoelectric efficiency in $\text{Yb}_{14}\text{Mn}_{1-x}\text{Al}_x\text{Sb}_{11}$. *Adv. Funct. Mater.* **18**, 2795–2800 (2008)

301. Toberer, E.S., Brown, S.R., Ikeda, T., Kauzlarich, S.M., Jeffrey Snyder, G.: High thermoelectric efficiency in lanthanum doped $\text{Yb}_{14}\text{MnSb}_{11}$. *Appl. Phys. Lett.* **93**, 062110 (2008)
302. Snyder, G.J., Gascoin, F., Brown, S., Kauzlarich, S.: High efficiency thermoelectric power generation using Zintl-type materials. US Patent, 7728218 (2010)
303. Huang, D., et al.: Conjugated-backbone effect of organic small molecules for n-type thermoelectric materials with ZT over 0.2. *J. Am. Chem. Soc.* **139**, 13013–13023 (2017)
304. Shuai, J., et al.: Thermoelectric properties of bi based Zintl compounds $\text{Ca}_{1-x}\text{Yb}_x\text{Mg}_2\text{Bi}_2$. *J. Mater. Chem. A.* **4**, 4312–4320 (2016)
305. Zhang, H., et al.: A new type of thermoelectric material, EuZn_2Sb_2 . *J Chem Phys.* **129**, 164713 (2008)
306. Takagiwa, Y., et al.: Thermoelectric properties of EuZn_2Sb_2 Zintl compounds: zT enhancement through Yb substitution for Eu. *J. Alloys Compd.* **703**, 73–79 (2017)
307. Wei, P.-C., et al.: Enhancement of thermoelectric figure of merit in $\beta\text{-Zn}_4\text{Sb}_3$ by indium doping control. *Appl. Phys. Lett.* **107**, 123902 (2015)
308. Shuai, J., et al.: Thermoelectric properties of Na-doped Zintl compound: $\text{Mg}_{3-x}\text{Na}_x\text{Sb}_2$. *Acta Mater.* **93**, 187–193 (2015)
309. Li, J., Zheng, S., Fang, T., Yue, L., Zhang, S., Lu, G.: Computational prediction of a high ZT of n-type Mg_3Sb_2 -based compounds with isotropic thermoelectric conduction performance. *Phys. Chem. Chem. Phys.* **20**, 7686–7693 (2018)
310. Li, J., et al.: Designing high-performance n-type Mg_3Sb_2 -based thermoelectric materials through forming solid solutions and biaxial strain. *J. Mater. Chem. A.* **6**, 20454–20462 (2018)
311. Bhardwaj, A., Chauhan, N.S., Misra, D.K.: Significantly enhanced thermoelectric figure of merit of p-type Mg_3Sb_2 -based Zintl phase compounds via nanostructuring and employing high energy mechanical milling coupled with spark plasma sintering. *J. Mater. Chem. A* **3**, 10777 (2015)
312. Heusler, F.: *Verh. Deutsche Physikalische Gesellschaft.* **5**, S. 219 ff (1903)
313. Galanakis, I.: Theory of Heusler and Full-Heusler Compounds. In: Felser, C., Hirohata, A. (eds.) *Heusler Alloys*. Springer Series in Materials Science, vol. 222. Springer, Cham (2016). https://doi.org/10.1007/978-3-319-21449-8_1
314. Wollmann, L., Nayak, A.K., Parkin, S.S.P., Felser, C.: Heusler 4.0: tunable materials. *Annu. Rev. Mater. Res.* **47**, 247–270 (2017)
315. Gao, Q., Opahle, I., Zhang, H.: High-throughput screening for spin-gapless semiconductors in quaternary Heusler compounds. *Phys. Rev. Mater.* **3**, 024410 (2019)
316. Khandy, S.A., Chai, J.D.: Robust stability, half-metallic ferrimagnetism and thermoelectric properties of new quaternary Heusler material: a first principles approach. *J. Magn. Magn Mater.* **502**, 166562 (2020)
317. Khandy, S.A., Chai, J.D.: Thermoelectric properties, phonon, and mechanical stability of new half-metallic quaternary Heusler alloys: FeRhCrZ ($Z = \text{Si}$ and Ge). *J. Alloys Compd.* **127**, 165102 (2020)
318. Maat, S., Marley, A.C.: Physics and design of hard disk drive magnetic recording read heads. In: Xu, Y., Awschalom, D., Nitta, J. (eds.) *Handbook of Spintronics*. Springer, Dordrecht (2016)
319. Chadov, S., Wu, S.C., Felser, C., Galanakis, I.: Stability of Weyl points in magnetic half-metallic Heusler compounds. *Phys. Rev. B* **96**, 024435 (2017)
320. Chang, G., et al.: Room-temperature magnetic topological Weyl fermion and nodal line semimetal states in half-metallic Heusler Co_2Ti_X ($X = \text{Si}, \text{Ge}, \text{or Sn}$). *Sci. Rep.* **6**, 38839 (2016)
321. Hinterleitner, B., et al.: Thermoelectric performance of a metastable thin-film Heusler alloy. *Nature* **576**, 85–90 (2019)
322. Joshi, G., et al.: NbFeSb-based p-type half-Heuslers for power generation applications. *Energy Environ. Sci.* **7**, 4070–4076 (2014)
323. Zhu, H., et al.: Discovery of TaFeSb-based half-Heuslers with high thermoelectric performance. *Nat. Commun.* **10**, 270 (2019)

324. Fu, C., et al.: High band degeneracy contributes to high thermoelectric performance in p-type half-Heusler compounds. *Adv. Energy Mater.* **4**, 1400600 (2014)
325. Kaur, K., Kumar, R.: Ti based half Heusler compounds: a new on the screen with robustic thermoelectric performance. *J. Alloys Compd.* **727**, 1171–1177 (2017)
326. Liu, Y., et al.: Demonstration of a phonon-glass electron-crystal strategy in (Hf, Zr) NiSn half-Heusler thermoelectric materials by alloying. *J. Mater. Chem.* **3**, 22716 (2015)
327. Chen, S., et al.: Effect of Hf concentration on thermoelectric properties of nanostructured N-Type half-Heusler materials $\text{Hf}_x\text{Zr}_{1-x}\text{NiSn}_{0.99}\text{Sb}_{0.01}$. *Adv. Energy Mater.* **3**, 1210 (2013)

Nanodiamond/Conducting Polymer Nanocomposites for Supercapacitor Applications



Abdelrahman Zkria, Ali M. Ali, Imtenan Mahmoud, Abdalla Abdelwahab, Waleed M. A. El Rouby, and Tsuyoshi Yoshitake

Abstract Supercapacitors, known as electrochemical capacitors, are very attractive as energy storage devices due to their high-power density (up to 410 kW kg^{-1}), their unique ability to undergo charge/discharge quickly and their long cycling life (that could reach 4105 cycles). Efforts have been dedicated to develop various carbon-based nanomaterials for energy storage, specially supercapacitors. Carbon-based materials and conducting polymers (ie; Polypyrrole and Polyaniline) are considered the most promising candidates for capacitive materials, as they offer high charging capacity through diverse mechanisms. Among these carbon-based materials are nano-crystalline diamond (NCD) films, which were widely studied during the past decades due to their special features like; short-range sp^3 bonded carbon atoms and large surface to volume ratio. Artificial fabrication of NCD films was developed using various techniques like; high-pressure high-temperature (HPHT), chemical vapor deposition, plasma-discharge-stimulated, laser ablation, hot-filament technique, and coaxial arc plasma deposition. Although carbon-based nanomaterials display good stability in energy storage applications, the capacitance values are

A. Zkria (✉) · A. M. Ali · T. Yoshitake
Department of Applied Science for Electronics and Materials, Kyushu University, Fukuoka 816-8580, Japan
e-mail: abdelrahman_zkria@kyudai.jp

A. Zkria
Department of Physics, Faculty of Science, Aswan University, Aswan 81528, Egypt

A. M. Ali
Department of Physics, Al-Azhar University, Cairo 11884, Egypt

I. Mahmoud · A. Abdelwahab · W. M. A. El Rouby (✉)
Materials Science and Nanotechnology Department, Faculty of Postgraduate Studies for Advanced Science (PSAS), Beni-Suef University, Beni-Suef 62511, Egypt
e-mail: waleedmohamedali@psas.bsu.edu.eg

A. Abdelwahab
Faculty of Science, Galala University, Sokhna, Suez 43511, Egypt

yet limited by the microstructures within the materials; Therefore, their nanocomposites with conducting polymers provide higher performance and improved properties. This chapter aims to summarize and discuss the recent synthetic developments of nanocrystalline diamond/conducting polymer nanocomposites, and their applications to energy storage and supercapacitor.

Keywords Nanocrystalline diamond · Nanodiamonds · Nanodiamond films · Conducting polymers · Nanocomposite materials · Supercapacitors

List of Abbreviations

(NCD)	Nanocrystalline diamond
(HPHT)	high-pressure high temperature
(NDs)	nanodiamonds
(CNTs)	carbon nanotubes
(CVD)	chemical vapor deposition
(CAPD)	coaxial arc plasma deposition
(DC)	direct current
(UNCD)	ultrananocrystalline diamond
(MPCVD)	Microwave plasma assisted chemical vapor deposition
(HFCVD)	Hot filament assisted chemical vapor deposition
(PLA)	pulsed laser ablation
(PVD)	Physical vapor deposition
(rGO)	reduced graphene oxide
(3D)	three-dimensional
(CNF)	Carbon nanofibers
(BDND)	boron doped ND
(BDD)	boron doped diamond
(RTILs)	Room-temperature ionic liquids
(OLC)	Onion-Like-Carbon

1 Introduction

Recently, funds are poured for research focused on developing effective energy storage systems, including batteries, fuel cells, and supercapacitors. Among them, supercapacitors offer numerous advantages because of their high-power density (up to 410 kW kg^{-1}), fast charge/discharge process and long cycling life (up to 4105 cycles) [1, 2]. The existing problems of energy and power densities in batteries along with conventional capacitors (solid state-based SC and electrolytic-based SC) can be enhanced and even solved by development of supercapacitors properties. Historically, the first patent on supercapacitors was registered for Becker in 1957 [3].

Twelve years later, NEC (Japan) has developed under SOHIO company's license the commercial aqueous-electrolyte supercapacitors promoting them as power-saving units in electronics [4]. Currently, supercapacitors are the main power sources in various applications including electrical vehicles, pulse power applications and even portable devices.

In practical energy storage devices, the great challenge lies in material selection with elevated energy density. For achieving the best performance, the electrode materials must have a structure that enables high electrolyte accessibility, good electrical conductivity and they have to be mechanically and chemically stable. Therefore, materials such as monosaturated carbon materials, conducting polymers and transition metal oxides, are considered an optimum electrode materials for energy storage applications [5]. Among the carbon-based nanomaterials, nanodiamonds (NDs) stand for their promising features. This chapter will deliver an overview about the unique properties of ND, its growth methods and application in supercapacitor.

In this Chapter, we shall provide an outlook for the use of Nanodiamonds in Supercapacitors, going through the special qualities of Nanodiamonds and their potential as electrode materials in Supercapacitors, the different methods of synthesis for Nanodiamond and Doping approaches, we will review the effect of integrating Nanodiamonds within different composites with Carbon materials and with Polymers and the effect on increasing the performance in Supercapacitors. We will end the chapter reviewing some of the obstacles with this new emerging player in electrochemical application.

2 Carbon Based Nanomaterials in Energy Storage Systems

Carbon materials still hold onto its right as a central player in the field of energy whether it is renewable or non-renewable. The ability of carbon atoms to exist in a wide range of crystalline and disordered forms has enabled it to exist in numerous allotropic forms and sizes ranging from insulator diamond to layered semiconductor graphite to fullerenes. Carbon nanomaterials show extraordinary high surface areas, excellent electronic conductivity, improved capacitance, good electrolyte accessibility, and reprocessing ratibility over the traditional engineering probe materials. Thus, carbon nanomaterials with high accessible specific surface area are the dominant class of materials used as electrodes in supercapacitors. The discovery of carbon nanotubes (CNTs) was a major step that significantly accelerated the development of carbon as electrode materials. Due to the special aspects of 1D and 2D carbon structures, as shown in Fig. 1, CNTs and graphene are now a basic building blocks for various nanocarbon-based materials [6]. These nanocarbon-based structures are widely adopted as electrodes in supercapacitors, in which there is no need for insulating binder nor a low-capacitance conducting additives. Although carbon-based nanomaterials display good stability in energy storage applications, the values of the capacitance are impaired by the microstructures within these materials. Which is the major operating drawback for carbon-based electrodes.

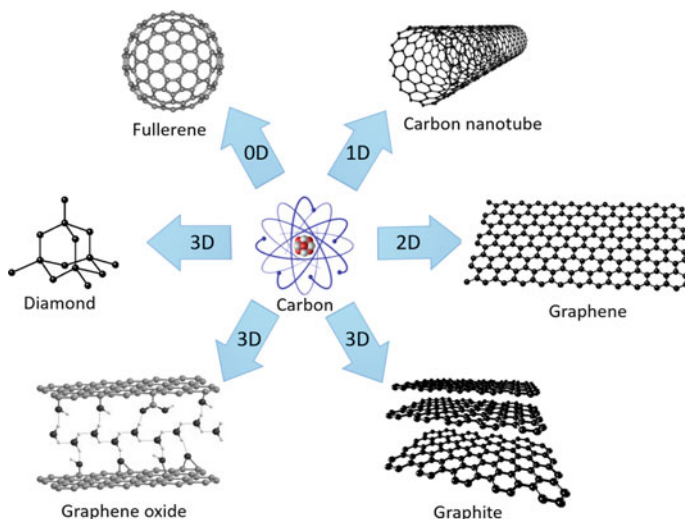


Fig. 1 Schematic representation of different allotropic forms of carbon [modified from 6]

3 Unique Properties of Nanodiamonds

Diamond is a very promising form of carbon nanomaterials. its unique features have fascinated researchers over the past years; like high carrier mobility, thermal conductivity that reach up to 25 W/cm.K, electric breakdown field of 107 V/cm, and hardness of 104 kg/mm². The superior electronic properties of diamond, along with the discovery of various fabrication methods for doped and non-doped diamond, have promoted it for future electronic applications. Additionally, NDs with nano-sized grains have dominated the interest of researchers within the last 10–12 years, as promising candidates for various applications. ND particles offer numerous advantages over the other carbon nanomaterials such as: (i) availability of single-digit size of only 4–5 nm. (ii) The ability to be doped with specific impurity defects that can be used in photoluminescence application; a step towards revolutionizing biological imaging and quantum optics applications. (iii) The increased chemical reactivity of the surface promoting them to participate in a wide range of chemical reactions. (iv) The ability to modify the surface chemical groups. (v) Their low toxicity compared to other carbon nanoparticles [7].

4 Nanodiamond Growth Methods

Diamond materials are available in single-, poly-, nano-, and ultra-nano-crystalline structures. For diamond artificial fabrication, several techniques have been invented

up until now such; the HPHT technique, the hot-filament technique, plasma-discharge-stimulated chemical vapor deposition (CVD), laser ablation, and coaxial arc plasma deposition (CAPD). Below we demonstrate a brief survey of the different ND particles and review some of the methods of their synthesis, which are summarized and illustrated in Fig. 2.

Diamond was first synthesized artificially at the beginning of 1960s using the energy of explosives. DeCarli and Jamieson demonstrated the formation of diamond powders with characteristic sizes of single particles in several micrometers by using shock wave compression of carbon materials like graphite and carbon black mixed with catalyst [8, 9]. Till the date, there are some attempts to transform graphite to diamond particles at the nanoscale using shock wave. Stefan J., et al. [10] successfully synthesized a hexagonal diamond in nanoscale by shock-compressed of graphite.

Another important method of artificially diamond production is HPHT method. The HPHT process converts graphite powder into diamond using high pressure of approximately 6 GPa and temperature of 1500 °C in the presence of a catalyst. This method is used to synthesis diamond with a particle size of 100–1000 μm [11, 12]. It is called polycrystalline diamond, and it is commercially available since the 1970s and widely used in the polishing industry. However, production of ND particles with small size of 4–5 nm and controlled surface function groups; cannot be achieved using explosives nor HPHT technique [13, 14].

Currently, nanoscale diamond structures are mostly prepared using CVD, ion irradiation of graphite, ultrasound cavitation, CAPD, along with laser ablation. These techniques produce many forms including: pure-phase NDs films, diamond particles, and doped ND with characteristic sizes in nanometer scale.

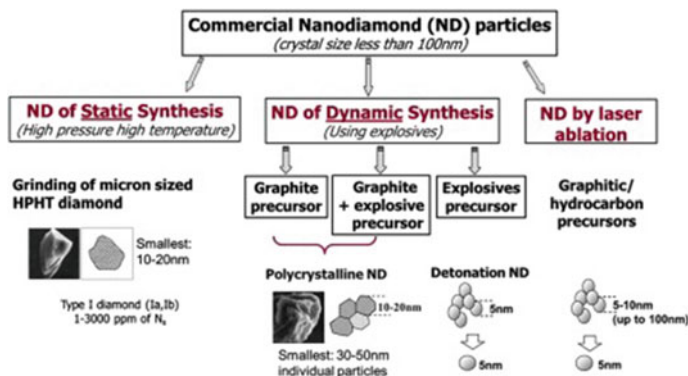


Fig. 2 Summary of artificial nanodiamond production techniques

5 Nanodiamond Produced by CVD

The conditions for depositing diamond are characteristic to each reactor design, the thing that affects many of their main properties. ND formation and growth onto a substrate surface using CVD technique depends mainly on the chemical reaction within energized gas mixture of carbon source. N. Setaka et al. at the National Institute for Research in Inorganic Materials was the first group to achieve the growth of ND particles using hot-filament method in 1981 and the microwave or radio frequency in 1982 for plasma assisted CVD process [15, 16]. In the late 1988, K. Kurihara et al. used a direct current (DC) arc plasma jet with an acetylene flame to assist CVD processes leading to increased deposition rate [17, 18].

In the late 1990s, ultra nanocrystalline diamond (UNCD) films with grain size of less than 5 nm was patented in the United States to Argonne National Laboratory [19]. These films were grown by microwave plasma assisted chemical vapor deposition (MPCVD) and hot filament assisted chemical vapor deposition (HFCVD) [20]. Nowadays, the smoothest films of UNCD material have been commercialized by advanced diamond technology. They exhibit many features applicable to a wide range of nano/ macro-scale multifunctional devices [21].

Consequently, in CVD methods, the parameters can be adjusted to control the structure of ND films such as; the inserted gas type, Carbon and Oxygen atoms concentration in the gas mixture, the process gas, and the type of the activation energy. Therefore, the CVD technique can be classified based on the energy source being used for excitation into thermal, electrical, chemical, or electromagnetic activation techniques [22, 23]. However, the required growth temperature and growth time of CVD nanodiamond are higher than 700 °C and 10 h respectively [24–27]. These requirements hinder the mass production of NDs and limit the substrate materials that can be used as a template of the deposition, especially in biological and electronic applications. One of the first attempts for growing NDs at low deposition temperature has been performed using MPCVD [28, 29]. The influence of surface wave plasma on the ability to deposit ND films at low temperature was studied. In that study, the deposition temperature was below 600 °C. In another study, Heiman et al. [30] employed a direct current glow discharge assisted CVD to deposit a nano-sized carbon composite containing a predominating diamond phase using a hydrogen–methane gas mixture. As shown in Fig. 3, the ND particles were grown at different temperatures (800–950 °C) demonstrating different nano-crystalline morphological structures. The direct current glow discharge activated the substrate surface and assisted the adhesion of the deposited films on the substrates.

Taylor et al. [31] and Mehedi et al. [32] used a linear antenna MPCVD to reduce the growth temperature of ND on different substrates. They have obtained films at different substrate temperatures of 500, 400 and 300 °C. The effects of substrate temperature on the morphological properties of the grown ND films are shown in Fig. 4. However, these preparation processes required complex power distributors and impedance matching system [33]. Low temperature CVD still has numerous

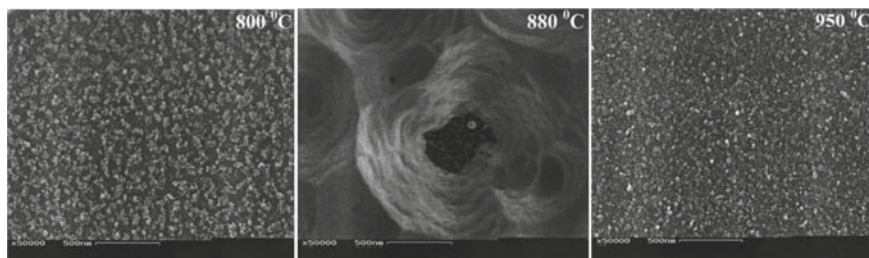


Fig. 3 SEM image of the ND films obtained by DC-glow discharge after 60 min at substrate temperatures of (a) 800 °C, (b) 880 °C, and (c) 950 °C [30]

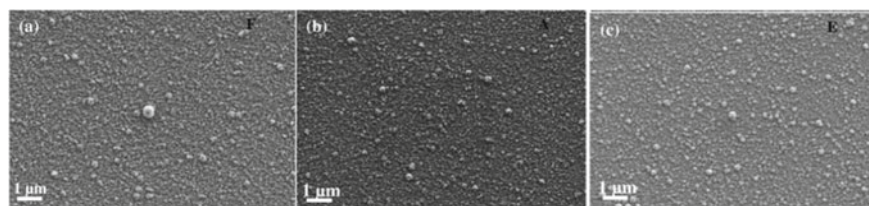


Fig. 4 Top-view SEM images of the NCD films, showing the effect of substrate temperature (a) 500, (b) 400 and (c) 300 °C (corresponding samples: F, A and E) [32]

problems, such as substrates plasma heating, the cooling process of the substrate holder, the poor nucleation and the slow growth rates.

In spite of the above-mentioned attempts, the low-temperature growth of CVD nanodiamonds was not of a great success due to the crucial role of substrate temperature in the growth mechanism of NDs, which is indispensable to activate the chemical reaction in the CVD reactors. In addition, the growth rate drastically decreases at low temperatures and the growing probability of carbon films dominates the nanodiamond growth [33, 34]. In conclusion, the substrate temperature is the most important parameter in deciding the overall growth rate as well as the quality of the nanodiamond. Accordingly, a high growth temperature is irreplaceable in the CVD reactors.

6 Nanodiamond Produced by Physical Vapor Deposition

Recently, pulsed laser ablation (PLA) and CAPD have been used as typical physical vapor deposition (PVD) methods, which offers many pros over the CVD growth techniques [35, 36]. Like; lower deposition temperature, higher growth rate, and enhanced control of morphology and thickness, as well as its applicability to versatile substrates without surface pretreatments or seeding process, are the main advantages of PVD to mention. The growth mechanism of ND films in PVD is totally different from that of CVD.

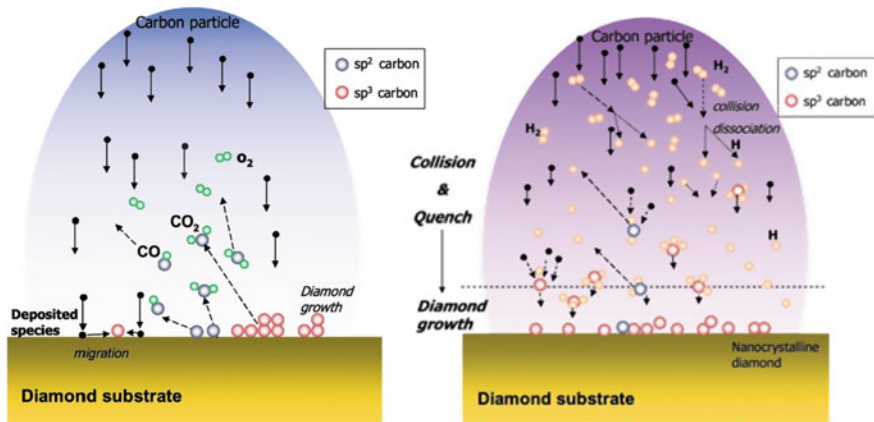


Fig. 5 Schematic of the diamond growth process by PLA technique in an (left) oxygen, and (right) hydrogen atmospheres [35]

The first studies on the formation of PLA-nanodiamonds were reported in 1992 and in 1998 by Ogale et al. and Polo et al. respectively; using PLA with a nanosecond laser irradiation directed towards the surface of a graphite target [37–39]. They obtained nanodiamond by laser ablation of graphite in a hydrogen atmosphere and a liquid-free environment. However, the synthesis of nanodiamond crystals was achieved by the ablation of graphite in combination with water and acetone as a liquid media. Yang et al. [40] reported cubic and hexagonal diamonds by the ablation of graphite immersed in different liquids, which was more effective and more adopted approach. As shown in the schematic diagram (Fig. 5), the synthesis of nanodiamonds with PLA is based on the interaction of a laser generated cavitation bubble with a solid boundary which facilitates the nucleation, growth, and solidification of the nanoparticles under the fast quenching conditions [41]

In recent years, CAPD method is drawing considerable interest for the fabrication of artificially structured nanomaterials specially UNCD with nano-sized grains about 2–4 nm. Hanada et al. [42] reported that, the growth process of UNCD by CAPD has some similarities to that by PLD such as; (i) pulsed deposition, (ii) employment of a graphite target as source material, and (iii) growth on untreated substrate. On the other hand, there are some specific features of CAPD over the PLD. The deposition rate per pulse in CAPD is (1.33 nm/pulse), which is two orders greater than PLD, and the size of UNCD crystallites formed with CAPD is (2.3 nm), smaller than that of crystallites formed by PLD (5 nm). In addition, a hydrogen atmosphere is not necessarily required for the UNCD crystallite formation while it is essential in PLD. During the growth of UNCD by CAPD, the arc gun was equipped with a cathodic graphite rod located inside an anodic cylinder that can provide a higher energetic carbon species (see Fig. 6). These ejected species can be accelerated toward the substrate with a controlled energy under the effect of negative bias voltage on the substrate [43]. So, by selecting the ion species and ion beam flux, the growth

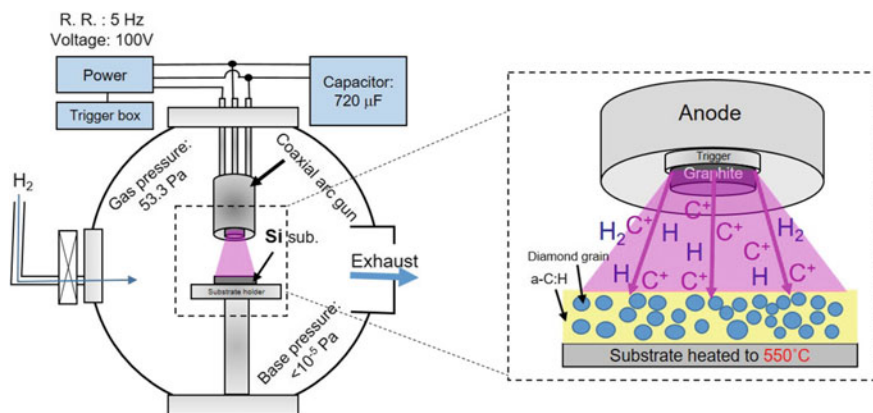


Fig. 6 Schematic of the growth mechanism of UNCD films by CAPD technique [46]

process can be precisely controlled, promoting a more hands-on structural and the chemical modifications of the resulting particles. Moreover, CAPD method facilitate the incorporation of various dopant elements during the deposition of UNCD films [44, 45]. CAPD-growth of UNCD film is physically carried out in a pulsed process, which enables the growth at low substrate temperature. Therefore, the substrate temperature can be separately controlled without hindering the deposition process.

Recently, Yoshitake group [47, 48] succeeded to grow the UNCD films by CAPD at substrate temperature as low as room temperature. Whereas, reducing the deposition temperature of nanodiamond films in general is the key factor to fabricate stress-free nanodiamond films which would open the door towards application in miniaturization technology (Fig. 7).

7 Nanodiamonds in Supercapacitors

The nanodiamond particle size is ranging between 1–100 nm which can be ultra-dispersed to extremely small size of 4–5 nm. Its large scale production with cheap methods would make it competitive with others carbon materials like graphene or carbon nanotubes [49]. The ND structure consists of crystalline diamond in the core with sp^3 bonding. While, the outer structure has both sp^2 (unsaturated) graphitic bonds and sp^2 (saturated) (Fig. 8). The unsaturated nature of the bonding in the ND surface is responsible for the redox chemistry at mild applied potentials [50].

The unique structure of NDs offer us excellent mechanical, thermal, and optical properties which promote them to be used in drug delivery, bio-imaging, and cellular marking. In addition, ND possess high surface area, tunable surface structure, and excellent chemical stability which facilitate its use in energy applications [51]. The undoped form of ND has a band gap of *ca.* 5.5 eV which is assumed to be an insulating

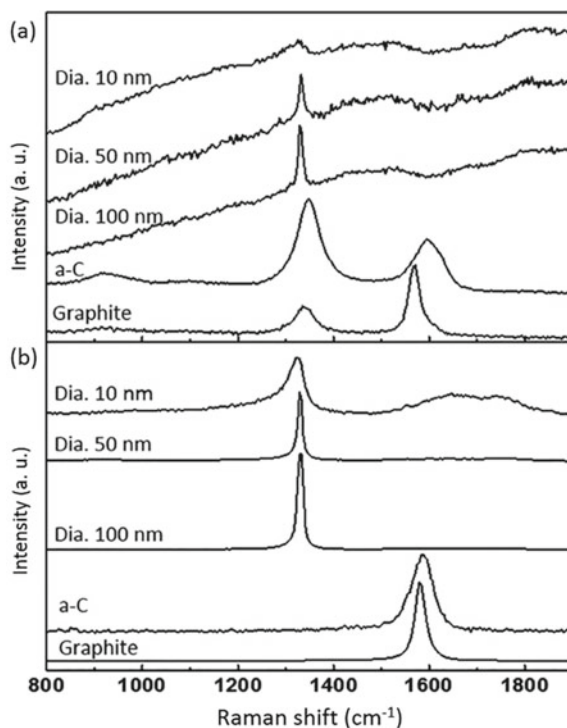


Fig. 7 Raman spectra of standard nanodiamond powder with different crystal sizes compared to amorphous carbon powder as well as graphite measured at 0.5 mW laser power and 60 s acquisition time with **a** 532 nm and **b** 224 nm excitation lasers. For better comparison, Raman spectra are plotted with an intensity offset [48]

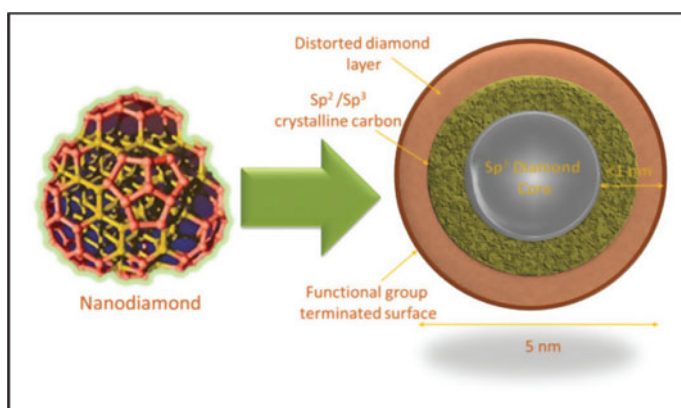


Fig. 8 Nanodiamond Structure [52]

material. One should expect that this substance does not have any chemical activity but on the contrary it was found practically that ND has electrochemical activity due to the small particle size and the high surface-to-bulk atom ratio [50]. The surface chemistry of ND is very important in the catalytic activity and electrochemical applications where the infrared spectroscopy (IR) reveals that the outer ND surface is highly oxidized due to the purification treatments (Fig. 9). The most oxidized carbon moieties are carbonyl (C = O) and carboxyl (COOH) groups at *ca.* 1680–1770 cm^{-1} .

Nanodiamond may also be doped with some elements or modify its surface chemistry to alter its electronic structure which would increase the conductivity, enhancing its application in energy fields (Fig. 10). For example, when diamond is doped with boron, it changes the diamond band gap by introducing new impurity bands, allowing for metallic conductivity.

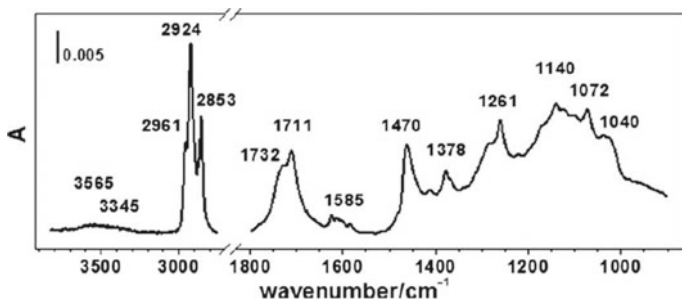


Fig. 9 IR absorption spectrum of untreated 5 nm nanodiamond [53]

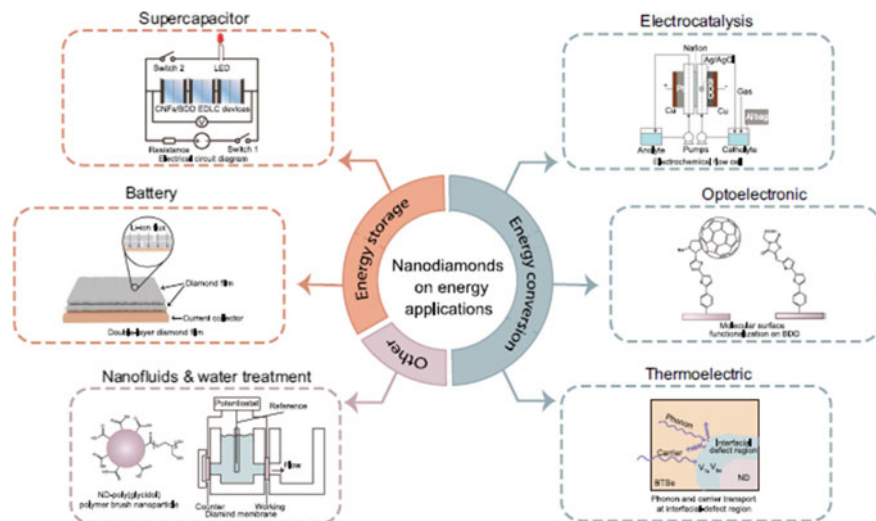


Fig. 10 Applications of nanodiamonds on energy related fields [51]

Some ND based electrodes have achieved a specific capacitance of 10 mFcm^{-2} and a specific energy of 10–100 Wh/kg in aqueous electrolytes [54], and can operate in potential windows around 3.2 V in aqueous and 4.6 in organic electrolytes [55]. Their wide potential window makes them a very special class of materials differ from the commonly used ones in electrochemistry [56]. The performance of diamond nanostructures is further improved by; (i) introduction of redox species into the electrolyte, (ii) forming surface terminations on the electrode (i.e.; pseudo capacitance); or by (iii) increasing the surface area [57].

8 Nanodiamond/Carbon Materials

Widely used sp^2 carbon materials in supercapacitors such as activated carbon, suffer from low stability and small potential window ($\sim 1 \text{ V}$) which limits their energy storage ability. On the contrary, conductive NDs are characterized by its mechanical stability and chemical inertness. Moreover, it has outstanding chemical stability at high current densities and high potentials. Thus, supercapacitors based on conductive NDs are considered a very good candidate for longer cycle life supercapacitors compared to the other carbon materials [58]. The most dominant feature of diamond is its wide potential window that arise from the inertness of diamond; the potential window far exceeds sp^2 -carbon based electrodes. Since the cell voltage is dependent on the used electrolyte, diamond enables the use of various (high-potential) stable electrolytes, and it can function with high stability under harsh operating conditions [52, 59]. The wide potential window is an exceptional feature regarding supercapacitors since the energy density and the power density are directly proportional to the square of the potential window; the higher the potential window, the greater the power and energy densities [60].

Growing of diamond on carbon based materials (such as carbon nanofibers, carbon fiber clothes, doped carbon fibers) forming hybrid compounds of sp^2/sp^3 is considered an interesting strategy for enhancing the electrochemical properties of ND materials [61–63]. The hybrid compounds of certain sp^2/sp^3 ratios are characterized by higher surface area-to-volume ratio that provide a highly active electrode material [64], this is an affordable option for supercapacitors' commercialization.

Ferreira et al. reported the fabrication of electric double-layer capacitor by using ND grown on carbon fiber substrate treated at different temperatures as in Fig. 11 (a and b). The materials' high porosity provided higher surface area that leads to a higher capacitive response. In addition, the growth of diamond on carbon fibers decreased the electric resistance of the electrode which improved the device performance [65]. The cyclic voltammogram curves of the prepared materials confirm the characteristic behavior of an ideal capacitor with rectangular curves as shown in Fig. 11(c and d). The measurements show that the diamond material treated at lower temperature (1300 K) had higher specific capacitance (2.6 mF/cm^2) at higher potential scan rate (100 mV/s) in aqueous acidic solution ($0.5 \text{ M H}_2\text{SO}_4$).

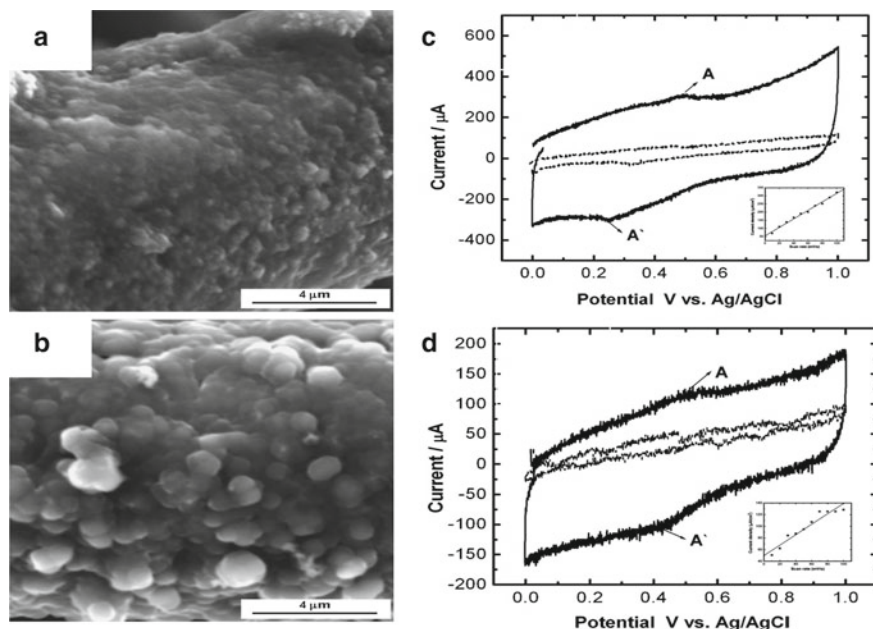


Fig. 11 SEM images of nanodiamond grown on carbon fibers treated at different temperatures of **a** 1300 and **b** 2300 K, respectively. Cyclic voltammograms of nanodiamond grown on carbon fibers treated at different temperatures of **c** 1300 and **d** 2300 K in aqueous solution of 0.5 M H_2SO_4 at different scan rate 100 mV/s (solid line) and 10 mV/s (dash line) [65]

As it is well known; the porous structure of carbons which provide a narrow size distribution of the sub-nanometer pores lead to higher capacitance properties [66]. The electrical double layer capacitance of most porous carbons is attributed to the micro-, meso- pores and outer surfaces of the particles that are available for ion adsorption. However, pinpointing the exact role of these different pores isn't an easy task. In case of CNTs, charge storage occurs at the outer surface, as in case of graphene layers. However, in case of carbon onion, the situation is different; there are no small sub-nanometer pores and all sites on the surface are nearly identical. The carbon onion-like particles of 5–15 nm in size with different pore texture and structure have been synthesized from NDs by means of calcination under controlled atmosphere and tested in electrical double layer capacitors [67]. The calcination of ND at 1200 °C causes graphitization of its surface forming the onions shape structure, however, the diamond cores are often still existed as seen in Fig. 12a. At higher calcination temperature (1200 °C), it was found that no diamond core could be obtained and the graphitic shells grow from the surface to the center (Fig. 12b). With the annealing of NDs, the electrical conductivity of carbon onions increased due to graphitization increment. The gravimetric capacitance increased with 10% upon thermal treatment of ND at 1200 °C. But with further increase in the calcination temperature, the

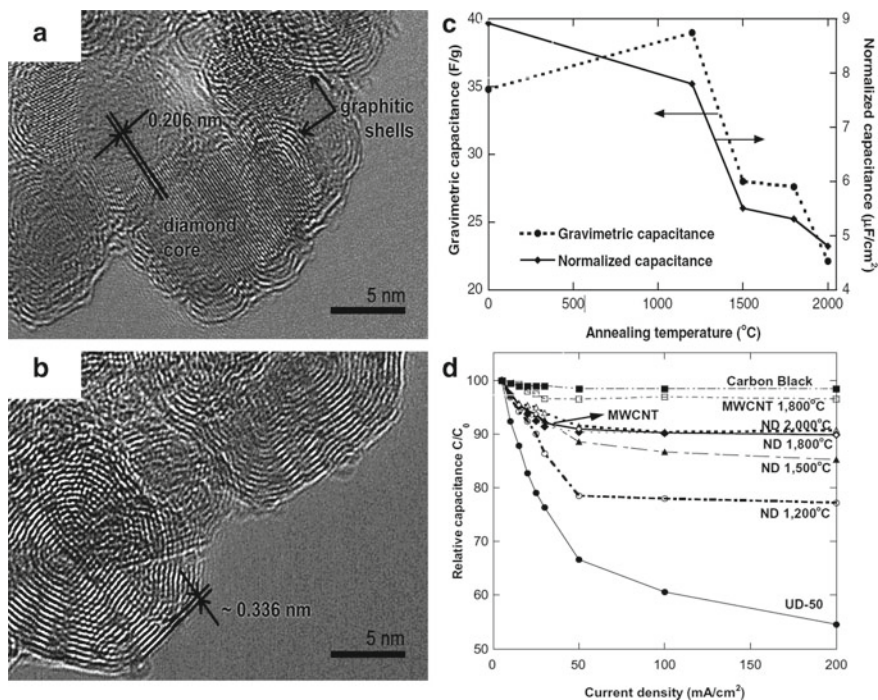


Fig. 12 HRTEM images of nanodiamond annealed at 1200 °C **a** and 1800 °C **b**. Effect of annealing temperature on capacitance of nanodiamond and carbon onions **c**. Relative capacitance (C/C_0) variation with current density **d** [67]

gravimetric capacitance was decreased (Fig. 12c). The smaller capacitance of as-received ND is due to the smaller specific surface area. As previously mentioned, the surface texture and porosity have great effect on ions transport and thus the capacitance. Ideally; supercapacitors at any current density should deliver the same energy. Yet, in real supercapacitors, the decreases in capacitance with increasing the current density is attributed to the presence of micro pores that increases the ohmic resistance of the structure due to the limitations in accessing the pores [68]. Figure 12d shows the variation in relative capacitance C/C_0 with the current density for the annealed ND at different temperature in comparison with carbon nanotubes treated at the same temperature and activated carbon. Since the porosity of all samples are almost the same, and the loss in capacitance was decreased with increasing the annealing temperature (Fig. 12d), the difference in performance must be attributed to the sample texture.

In the carbon material lattice, the edge planes or defects enhance the interaction with ions resulting in; increasing the capacitance and loss in capacitance under higher discharge currents [67].

Diamond exists in many forms and phases and there are so many doping approaches and all contribute to the overall performance of the material [54]. The

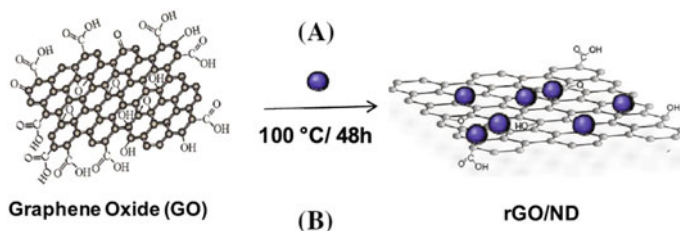


Fig. 13 Schematic diagram showing the preparation process of rGO/NDs nanocomposites [70]

different morphologies and various nanostructures along with the non-diamond carbon content all contribute to the material behavior. It was found that the more sp² carbon content within the diamond nanostructure, the smaller its potential window would be [56].

The enhanced chemical activity of diamond nanostructures can be attributed to the edge-bonds that can be terminated with desired (performance-boosting) atoms that contribute to the activity using different techniques and these surface species are able to promote the wettability, conductivity, electrochemical response and catalytic activity [53, 54]. Diamond has structural irregularities similar to graphene that further promote its electrochemical stability and enables the material to function at high potentials and high currents, and even withstand corrosive environments (ex; boiling mixture of HNO₃ and H₂SO₄ [69]). It also shows a stable capacitive behavior in aqueous and non-aqueous electrolytes [56, 59].

Nanodiamonds were also incorporated between reduced graphene oxide (rGO) layers forming a new composite (Fig. 13) with an overall suitable characteristic for supercapacitors.

In graphene-based materials, there are different oxygen functional groups on the surface which improve the wettability and hence the capacitance value [70, 71]. In addition, some of these function groups (quinone type) exhibits pseudo-capacitance characteristics through Faradic redox reactions especially at lower pH value (<3). When the ND was incorporated into the rGO, during the synthesis process these quinone function groups are formed on the surface ND and at the same time it was also available on the surface of rGO and both are contributing to the pseudo-capacitance behavior of the prepared composites. This clearly shows in the calculated capacitance from the cyclic voltammety measurements for rGO/nanodiamond samples with different ratio Fig. 14a. In addition to the pseudo-capacitance behavior, electrical double layer capacitance (EDLC) was observed from the well-known ideal rectangle-like shaped curves. The insertion ND between the rGO layer act as spacer for the sheets and prevent its staking. The specific capacitance in 1 M H₂SO₄ electrolyte for nanocomposites of different ND contents shows that the composite of 10/1 rGO/ND ratio has the highest capacitance of 186 F g⁻¹. These values of the specific capacitance were confirmed from the galvanostatic discharge curves (Fig. 14b) [70].

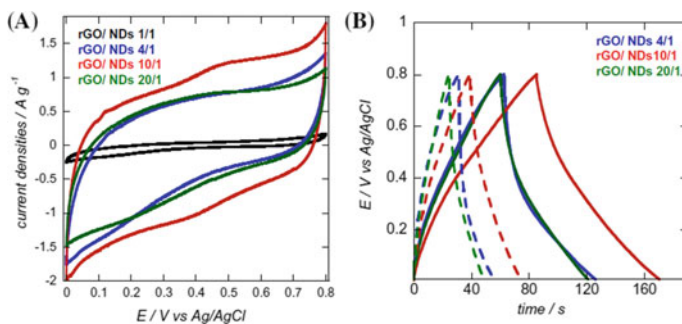


Fig. 14 Cyclic voltammograms in 1 M H_2SO_4 at 10 mV s^{-1} scan rate **a** and galvanostatic charge/discharge curves at current density of 1 A g^{-1} (full line) and 2 A g^{-1} (dotted line) in the potential window ranging (0–0.8 V) for the nanocomposites of different rGO/nanodiamond ratio [70]

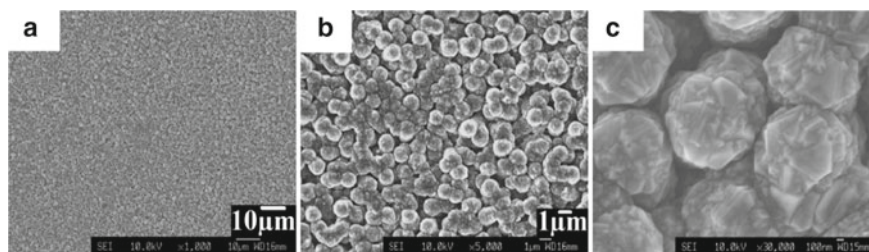


Fig. 15 (a-c) SEM images of nanodiamond grown by chemical vapor deposition on vertically aligned carbon nanotubes mats for 1 h [72]

When diamond is grown on vertically aligned carbon nanotube mats, the resulting composite exhibits high electrical double-layer capacitance in addition to a low electrochemical impedance which is very desirable in supercapacitors.

Diamond was grown on aligned carbon nanotubes to form a three-dimensional (3D) interconnected porous texture (Fig. 15). This structure facilitates the ion transport through lowering the resistance and decreasing the diffusion pathways; where it allows the current to move from the diamond surface to the charge collectors with low potential barrier at the junction [72, 73]. Moreover, the length of these aligned carbon nanotubes has had a great effect on the electrical double layer capacitance of the composite.

Carbon nanofibers (CNF) are considered an excellent support material for Nanodiamonds. Using the CVD technique Ferreira et al. [63] grew boron doped ND (BDND) and boron doped diamond (BDD) on CNF treated at different calcination temperatures and the produced core/shell structures have been coated with polyaniline (Fig. 16 show schematic illustration for the process). The CNF is critical for obtaining ND/CNF composites of high surface area, which is needed for high electrical double layer capacitors. In addition, during the coating of these nanocomposites with

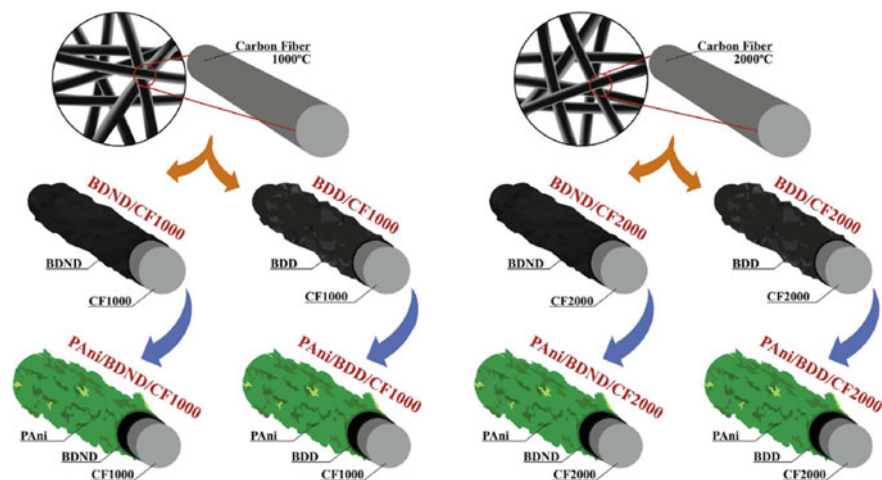


Fig. 16 Schematic diagram showing the fabrication of ternary polyaniline/diamond/CNF composites [5]

polyaniline, the smooth and long CNF morphology act as a template to the polyaniline chains orientation. This is very important in avoiding the volume variations which can occur during cycling, thus improving the stability of the supercapacitor.

Growth of diamond films in ternary composites leads to enhancement of polyaniline reversibility while when boron doped diamond films have been grown, the background current has been increased. Coating the binary composite with polyaniline film reduce the charge transfer resistance, enhancing the specific capacitance. Charge-discharge curves measured at 0.50 mA cm^{-2} for the binary and ternary composites electrodes, showed that the binary composites, BDD/CF2000 had the longest Charge-discharge time, and BDND/CF1000 had the lowest in binary composites (Fig. 17a). While in case of the ternary composites, polyaniline/BDD/CF2000 electrode had the highest charge storage capacity with specific capacitance of 526.5 F/g and polyaniline/BDND/CF1000 electrode show the lowest charge-storage (Fig. 17b).

Nanodiamond-carbon composites are also of great importance in the electrochemical applications because it changes the grain boundaries of ND. M. Y. Jiang et.al. [74] Studied the microstructure and electrochemical properties of nanocrystalline diamond and graphene films. In his study, the effect of growth pressure of ND by CVD on the resultant electrochemical properties was extensively studied. In low growth pressure range $1.0\text{--}1.3 \text{ kPa}$, graphene existed in high amounts in the composite with large size and better crystallinity which facilitated the electron exchange and reduced the potential window. With increasing the growth pressure to above 1.6 kPa , a reduction in graphene grain boundaries was observed and the amount of graphene in the final hybrid composite was reduced. Further increase of growth pressure to 2.2 kPa , graphene turned into small slices parallel to the ND

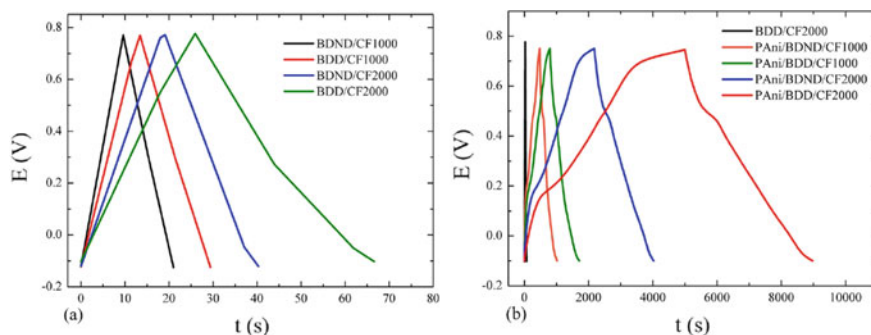


Fig. 17 Charge-Discharge curves of **a** binary composites electrodes (diamond/Carbon fibers) and **b** ternary composites electrodes (polyaniline/ diamond/Carbon fibers), including BDD/CF2000 for comparison [5]

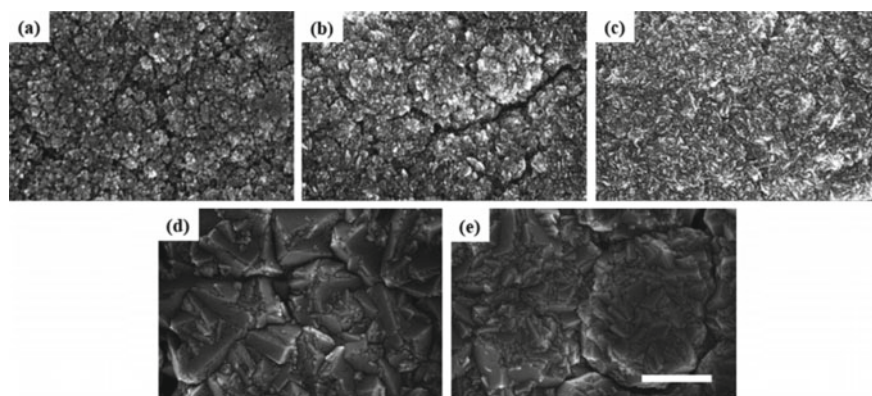


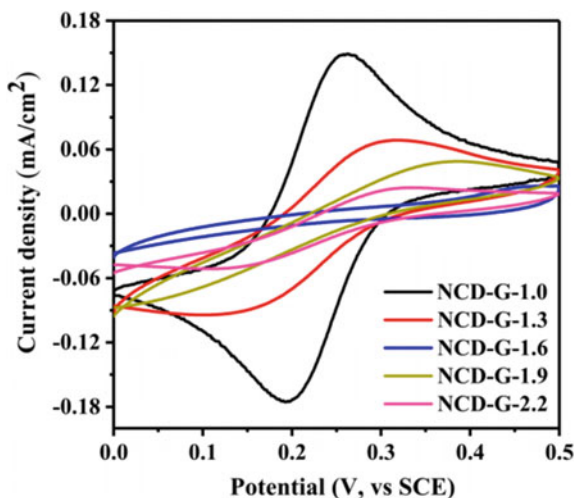
Fig. 18 surface morphology of nanodiamond-graphene hybrid films grown at different pressure **a** 1 kPa, **b** 1.3 kPa, **c** 1.6 kPa, **d** 1.9 kPa, and **e** 2.2 kPa [74]

grains, Fig. 18. As the diamond content increased with increasing growth pressure the potential window was enlarged and the background current decreased (Fig. 19).

9 Doped Nanodiamonds

Undoped ND are insulators; however, at the small nano-scale (i.e. 5 nm) the surface electrochemical properties begin to dominate the insulating aspect of the bulk ND and an electrochemical response can be observed. And the surface of the ND (even the undoped) contain a very wide range of chemical functionalities [75] which promotes chemical activity. Nanodiamond doping is achieved using a variety of elements (Boron, Nitrogen, Phosphorous, Oxygen, Sulfur...etc.) [76]. Doping changes the

Fig. 19 CV of nanodiamond-graphene hybrid films grown at different pressure[74]



properties of diamond from insulating to conducting. At low concentrations ($\leq 10^{19}$ atoms/cm³) the material acts as a semiconductor (n or P type, depending on the type of dopant) and acts as a semi-metal at high concentrations ($\geq 10^{20}$ atoms/cm³) [50, 77].

BDD nanostructures are the most used among doped-diamond nanostructures as boron can be added with higher concentrations than 10^{20} atoms/cm³ promoting the metal-like conductivity characteristics. Boron is an outstanding dopant as it's easily incorporated into the diamond's various structures and it has low charge-carrier activation energy [51, 53, 57]. Many chemicals can be used as the source of boron (diborane, trimethyl borane... etc.) [56] and with the change in materials and preparation method there exists a change in conductivity and bands energy of the resulted composite, which all affects the electrode performance. Soumen Mandal et.al. [78], prepared a boron ND composite by growing nanocrystalline diamond on boron nitride ceramic using MPCVD. The dielectric constant of the composite was enhanced after nanocrystalline diamond growth. This material was applied as superconducting composite which shows a transition temperature close to 3.4 K. Banerjee et. al. [79] prepared vertically aligned carbon nano-grass on top of boron-doped nanocrystalline diamond, HCNGs, by MPCVD technique. This composite was further applied as a supercapacitor electrode in two electrolytic solutions namely; (1 M Na₂SO₄) and (0.05 M K₃Fe(CN)₆/K₄Fe(CN)₆ in 1 M Na₂SO₄), Fig. 20 (a-d). This composite contains both advantages of excellent electrical conductivity of SP² and good electrochemical stability of SP³. Thus, the obtained specific capacitance of the hybrid composite reached 0.4 F.cm⁻² with stability retention of 95% after 10,000 cycles. Moreover, this electrode composite exhibited good power and energy density that arise from the wide operating potential window of -0.5 to 1 V, Fig. 20e.

Another work [80], studied the effect of surface chemistry of BDD on its wettability and electrochemical properties. The surface chemistry of BDD was modified by

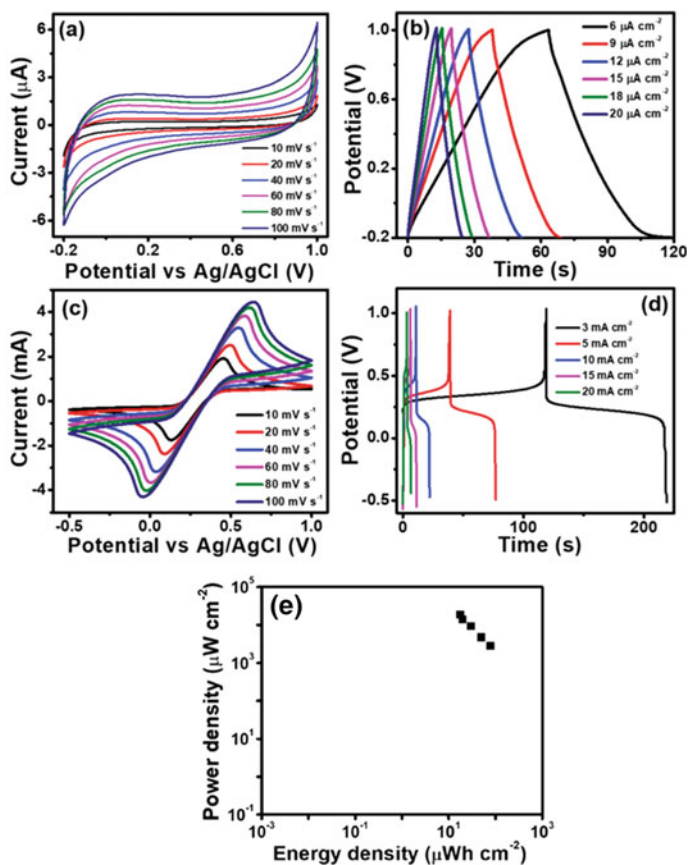


Fig. 20 The CV and GCD of HCNGs (a,b) in 1 M Na₂SO₄ and (c,d) in 0.05 M K₃Fe(CN)₆/K₄Fe(CN)₆ in 1 M Na₂SO₄; (e) Ragone plot of areal energy density vs. average power density of HCNGs [79]

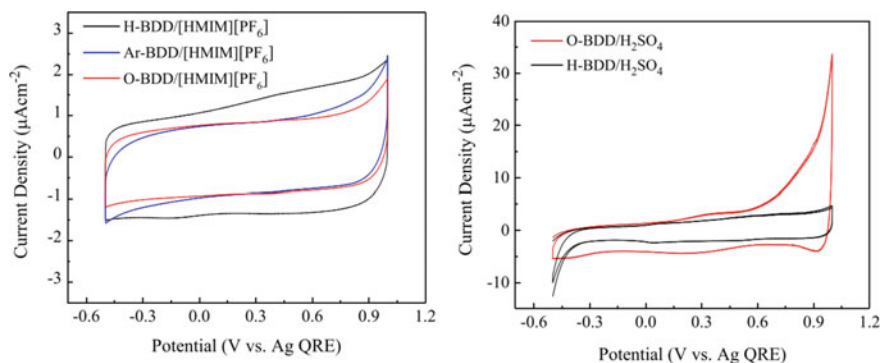
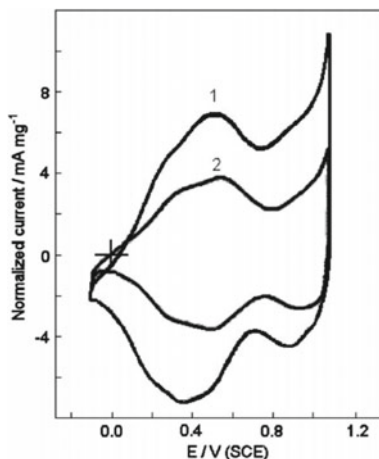


Fig. 21 The CV of H-BDD, O-BDD, and Ar-BDD in RTILs and 0.5 M H₂SO₄ [80]

Fig. 22 CV curves for; (1) BDD powder and (2) BDD film electrodes ($\text{RuO}_x \cdot n\text{H}_2\text{O}$ loading is the same in both samples; $0.5 \text{ M H}_2\text{SO}_4$ as electrolyte; 20 mV s^{-1} sweep rate) [81]



either microwave or radio-frequency plasma treatment in H_2 , denoted as H-BDD, Ar (Ar-BDD), or O_2 (O-BDD). Different trends were observed regarding the wettability in ultrapure water and in room-temperature ionic liquids (RTILs). In case of ultrapure water, the contact angle decreased from 110° for (H-BDD) to 41° for (O-BDD), indicating that the electrode becomes more hydrophilic with oxygen functionalities. While, in RTILs the contact angle increased from 20° for (H-BDD) to 50° for (O-BDD). The H-BDD electrode showed a capacitance range of $8\text{--}16 \mu\text{F}\cdot\text{cm}^{-2}$. Also, opposite behavior was observed in H_2SO_4 electrolyte, where the higher capacitance was obtained for the BDD with the highest surface oxygen content (O-BDD). This study illustrated the importance of surface wettability for ionic diffusion of ionic electrolyte which in turn affects the characteristic electrochemical properties, Fig. 20(a, b) (Fig. 21).

Nanodiamonds can also be used as support materials in supercapacitors [62, 63]. When BDD powders are used as support to $\text{RuO}_x \cdot n\text{H}_2\text{O}$, the deposition process was enhanced and the capacitance was increased (Fig. 22). [81].

Nitrogen-doped diamond have also shown similar and even higher performance compared to BDD, yet boron still dominates as it possess smaller atomic radius and hence lower distortion and higher metal-like conductivity [76]. Phosphorous is also a good candidate to be used with Nanodiamonds in supercapacitor, yet its relatively large atomic radius hinders the addition of high concentrations that could lead to imperfections and defects. It also has high activation energy (0.6 eV) which exceeds that of boron (0.37 eV) [56, 82].

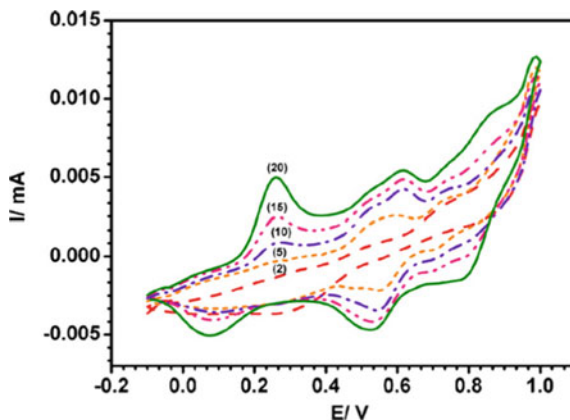
10 Conducting Polymers/Nanodiamond Composites

Conducting polymers are polymers that conduct electricity due to the presence of delocalized electrons that forms π bonds. It has a unique optical, electrical, electronic, and electrochemical properties that allow us to regulate design and electronic features. Thus, it finds application in energy storage systems, electronics and display devices [52]. The most common conducting polymers are polyaniline (PANI), polypyrrole (PPy) and polythiophene (PTh).

Polyaniline has superior advantages to other conducting polymers, including ease of preparation, low cost, high yield, and varying oxidation states. Conjugated polymers are also characterized by their availability to be doped using different elements and materials. For example, the undoped form of polyaniline (i.e. emeraldine) is an insulator with a conductivity in the range of 10^{-10} S/cm, while doping of polyaniline can improve its conductivity to more than 10^3 S/cm. There are many techniques that can be used for the formation of polymer/nanodiamond composites [49, 83–86]. Gopalan et al. [87] used the electrochemical method to graft PANI chains to ND supported on ITO, forming ITO/PANI-g-ND. Figure 23 shows the cyclic voltammogram of grafting PANI to ND surface with the electrochemical polymerization method.

Also, J.M. Zhang, et al. [49] prepared a ternary composite of carboxylated nanodiamonds(cNDs)/rGO@PANI, this composite was applied as electrode for electrochemical capacitors. In that study; first, the ND powders were annealed in air for 5 h at 425 °C removing any graphitic carbon impurities. Then, the carboxylate form of ND was synthesized by refluxing with a mixture of sulphuric acid and nitric acid (3:1) for 48 h at 120 °C. The electrochemical tests for this composite were performed in three electrodes electrochemical cell using 1 M H_2SO_4 as electrolyte. Different mass ratios were studied between cNDs and reduced graphene oxide namely cNDs:rGO; 1:4; 1:10, 1:20, 1:50 and the best composite for capacitor application was found to be cNDs/rGO(1:20)@PANI (Fig. 24 (a-c)). This composite was prepared in the form of

Fig. 23 Cyclic voltammogram recorded during chemical grafting of PANI on ND surface (Cycle number 2, 5, 10, and 20) [87]



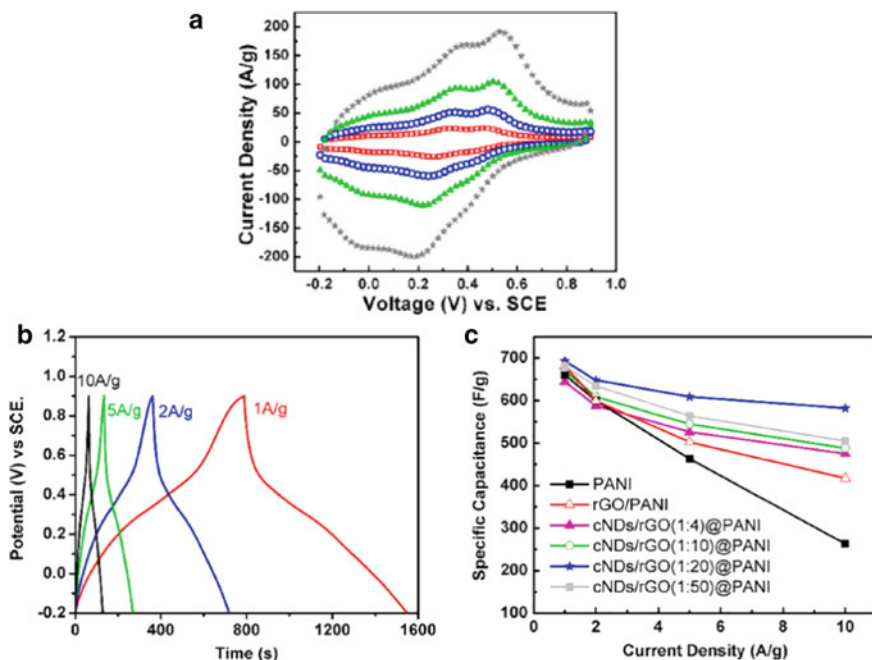


Fig. 24 (a) CV of cNDs/rGO(1:20)@PANI, (b) GCD curves of cNDs/rGO(1:20)@PANI at current densities between 1–10 A/g, (c) the capacitances of composites at different current densities [49].

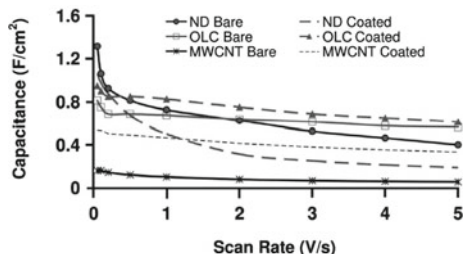
nanoclusters and nanorods and demonstrated a relatively high specific capacitance of 693 F/g and good cycling stability of 91% after 5000 cycle.

Polypyrrole/ ND composites are mainly employed as light harvesting entities in photovoltaic systems; as they conduct electricity, absorb light and generate free charges. Moreover, they are characterized by their stability due to bond formation between PPy and ND (covalent and non-covalent interactions). D. Miliaieva et al. [88] prepared a composite of ND and polypyrrole in colloidal solution and on surfaces using wet chemical process. The number of publications of polypyrrole ND composites are very low, especially in the supercapacitors application and needs more effort to understand their interactions and their electrochemical properties and potential.

11 Obstacles Towards Applicable Nanodiamond Electrodes

The reactive ion etching (RIE) method developed by Shiomi et al. [89] was used to prepare porous ND structures; yet when used alongside with growth on another nanostructure (like TiO₂ or SiNW) it results in deterioration of the diamond electrode [53].

Fig. 25 specific capacitance variance for ND soot, OLC, and MWCNT at different scan rates [90]



Most of the ND materials are subjected to post-synthesis treatments in order to attain the desired performance, the value of the capacitance of the material after treatment could be hundreds of times larger than the untreated material. However, the treatment is usually oxygen plasma-etching which subjects the material to the loss of a percentage of the diamond due to diamond etching, which increases the overall cost of fabrication, and limits the increase of surface area to approximately ten times; the plasma induced surface damage could lead to lower voltage operating windows, a less desired feature. [50–53, 68].

Nanodiamonds are a very promising candidates for supercapacitors. Yet their relatively low surface area (compared to other carbon nanomaterials) and high cost of fabrication hinders its progress compared to other low-cost carbon materials; it requires to be incorporated into other composites or using high energy post-synthesis treatments to increase the surface area in order to have the best possible performance [54]. Diamond electrochemistry is not widely studied like those of other carbons. Increasing the surface atoms over the bulk atoms is a mean of achieving higher performance, yet over processing the diamond could cause shortcomings such as instability, deformation and limited increase of surface area [50, 68].

Adding surface redox group could also cause a decrease in capacitance as the redox groups would cover the surface functional groups of the ND Fig. 25, even though the same mechanism would increase the capacitance when used with Onion-Like-Carbon (OLC) up to 0.6 F/cm^2 at 5 V/s [90].

The study of bonding and the role of sp^3 and sp^2 carbons on electrochemical behavior still needs further research and achieving the best material design would require a better understanding of the atomic level interactions. There are so many materials, designs and possibilities that could theoretically prevent us from reaching what we want if we don't know how to deal with what we have reached so far. All the upcoming materials and prospected composites; regarding diamond and other promising materials, will definitely show great performance compared to the existent materials. The goal should not only be about proposing different composites, and designing new materials. Rather it should be aimed mainly towards analyzing the data we already have, trying to create materials from abundant elements that would mimic the behavior of top electrochemical achievers; current understanding of atomic level interactions, surface chemistry, charge-carrier transfer, and conductivity are lacking in explaining much of what is (really) going on within an electrochemical beaker.

12 Conclusions and Future Perspectives

There are different preparation methods for NDs namely; CVD, ion irradiation of graphite, ultrasound cavitation, and laser ablation. Different morphologies of NDs with a wide range of particle sizes can be obtained depending on the used preparation process. For example, CVD is a distinctive process for synthesis of NDs with ultra-small particle sizes, but it requires applying high temperatures during its preparation. So, preparation of NDs with CVD process in low temperature is still a future challenge to reduce its production cost.

The unique properties of doped and un-doped nanodiamond together with its versatile preparation methods, makes nanodiamond composites excellent candidates for supercapacitors electrodes. There are wide range of elements that were used as dopants for NDs, these includes Boron, Nitrogen, and Phosphorous. These dopants promote NDs electrochemical activity.

It is well known that conductive polymers such as polyaniline have high specific capacitances due to storage of charges by faradaic reaction, but they suffer from long cycle life stability. Doping NDs with conductive polymers greatly enhances the electrode stability with good capacitance. Unlike activated carbon based materials that work in a potential window of about 1.5 V in aqueous electrolytes, NDs composites can work in a range of about 3.2 V which greatly enhance the produced energy density. The specific capacitance of conductive polymers/nanodiamonds composites still need to be developed to fulfill the modern industry requirements. The capacitance development can be achieved either by incorporation the transition metal oxides into the NDs composites or use asymmetric configuration.

References

1. Wang, S., Tongzhen, W., Zhiping, Q.: Supercapacitor energy storage technology and its application in renewable energy power generation system. In: Goswami, D.Y., Zhao, Y. (eds.) Proceedings of ISES World Congress 2007 (Vol. I–Vol. V), pp. 2805–2809. Springer, Heidelberg (2008)
2. Beardsall, J.C., Christopher, A.G., Moofik, A-T.: Energy storage systems: a review of the technology and its application in power systems. In: 2015 50th International Universities Power Engineering Conference (UPEC), pp. 1–6. IEEE (2015)
3. Becker, H.I.: Low voltage electrolytic capacitor. U.S. Patent 2,800,616, issued 23 July 1957
4. Boos, D.I.: U.S. Patent 3 536 963 (to Standard Oil, SO-HIO) (1970)
5. da Silva, L.M., et al.: Constituent material influence on the electrochemical performance and supercapacitance of PANi/diamond/CF composite. *Mater. Sci. Eng. B* **228**, 249–260 (2018)
6. de Barros, S.D.T., Jaqueline, D.S., Elizabeth, R.L., Luiz, F.B.M.: Metal-catalyzed cross-coupling reactions with supported nanoparticles: recent developments and future directions. *Catal. Rev.* **58**(4), 439–496 (2016)
7. Wang, F., Liu, J.: Nanodiamond decorated liposomes as highly biocompatible delivery vehicles and a comparison with carbon nanotubes and graphene oxide. *Nanoscale* **5**(24), 12375–12382 (2013)
8. Decarli, P.S.: Shock wave synthesis of diamond and other phases. *MRS Proc. Lib. Arch.* **383**, 21–31 (1995)

9. DeCarli, P.S., Jamieson, J.C.: Formation of diamond by explosive shock. *Science* **133**(3467), 1821–1822 (1961)
10. Turneure, S.J., Surinder, M.S., Travis, J., Winey, J. M., Yogendra, M.: Gupta. Transformation of shock-compressed graphite to hexagonal diamond in nanoseconds. *Sci. Adv.* **3**(10), eaao3561 (2017)
11. Bundy, F.P.: Direct conversion of graphite to diamond in static pressure apparatus. *Science* **137**(3535), 1057–1058 (1962)
12. Voronov, O.A., Tompa, G.S., Kear, B.H.: High pressure-high temperature device for making diamond materials. *Diam. Mater.* **7**(25), 264–271 (2001)
13. Xiao, H.Y., Qin, Y.K., Li, S.S., Liang, Z.Z., Ma, H.A., Jia, X.P.: Effects of additive boron on HPHT diamond single crystals grown by TGM. *Sci. China Phys. Mech. Astron.* **54**(12), 2186–2190 (2011)
14. Huang, G.F., et al.: Effects of additive NaN₃ on the HPHT synthesis of large single crystal diamond grown by TGM. *Sci. China Phys. Mech. Astron.* **53**(10), 1831–1835 (2010)
15. Matsumoto, S., Sato, Y., Kamo, M., Setaka, N.: Vapor deposition of diamond particles from methane. *Jpn. J. Appl. Phys.* **21**(4A), L183 (1982)
16. Kamo, M., Sato, Y., Matsumoto, S., Setaka, N.: Diamond synthesis from gas phase in microwave plasma. *J. Cryst. Growth* **62**(3), 642–644 (1983)
17. Kurihara, K., Sasaki, K., Kawarada, M., Koshino, N.: High rate synthesis of diamond by dc plasma jet chemical vapor deposition. *Appl. Phys. Lett.* **52**(6), 437–438 (1988)
18. Kurihara, K.K., Sasaki, M.K., Goto, Y.: Applications of Diamond Films and Related Materials (1991)
19. Sumant, A.V., Orlando, H.A., Derrick, C.M.: Ultrananocrystalline diamond films with optimized dielectric properties for advanced RF MEMS capacitive switches. U.S. Patent 8,354,290, issued 15 January 2013
20. Auciello, O., Sumant, A.V.: Status review of the science and technology of ultrananocrystalline diamond (UNCD™) films and application to multifunctional devices. *Diam. Relat. Mater.* **19**(7–9), 699–718 (2010)
21. Sumant, A.V., Auciello, O., Carpick, R.W., Srinivasan, S., Butler, J.E.: Ultrananocrystalline and nanocrystalline diamond thin films for MEMS/NEMS applications. *MRS Bull.* **35**(4), 281–288 (2010)
22. Schwander, M., Partes, K.: A review of diamond synthesis by CVD processes. *Diam. Relat. Mater.* **20**(9), 1287–1301 (2011)
23. Gottlieb, S., Wöhr, N., Schulz, S., Buck, V.: Simultaneous synthesis of nanodiamonds and graphene via plasma enhanced chemical vapor deposition (MW PE-CVD) on copper. *Springerplus* **5**(1), 568 (2016)
24. Yan, G., et al.: Mechanical properties and wear behavior of multi-layer diamond films deposited by hot-filament chemical vapor deposition. *Appl. Surf. Sci.* **494**, 401–411 (2019)
25. Tang, Y., Li, Y.S., Yang, Q., Hirose, A.: Deposition and characterization of diamond coatings on WC-Co cutting tools with W/Al interlayer. *Diam. Relat. Mater.* **19**(5–6), 496–499 (2010)
26. Heaney, P.J., Sumant, A.V., Torres, C.D., Carpick, R.W., Pfefferkorn, F.E.: Diamond coatings for micro end mills: enabling the dry machining of aluminum at the micro-scale. *Diam. Relat. Mater.* **17**(3), 223–233 (2008)
27. Xiao, X., Birrell, J., Gerbi, J.E., Auciello, O., Carlisle, J.A.: Low temperature growth of ultrananocrystalline diamond. *J. Appl. Phys.* **96**(4), 2232–2239 (2004)
28. Tsugawa, K., et al.: Nanocrystalline diamond growth in a surface-wave plasma. *Diam. Relat. Mater.* **20**(5–6), 833–838 (2011)
29. Popov, C., Kulisch, W., Boycheva, S., Yamamoto, K., Ceccone, G., Koga, Y.: Structural investigation of nanocrystalline diamond/amorphous carbon composite films. *Diam. Relat. Mater.* **13**(11–12), 2071–2075 (2004)
30. Heiman, A., Gouzman, I., Christiansen, S.H., Strunk, H.P., Hoffman, A.: Nano-diamond films deposited by direct current glow discharge assisted chemical vapor deposition. *Diam. Relat. Mater.* **9**(3–6), 866–871 (2000)

31. Taylor, A.P., et al.: Precursor gas composition optimisation for large area boron doped nanocrystalline diamond growth by MW-LA-PECVD. *Carbon* **128**, 164–171 (2018)
32. Mehedi, H.-A., et al.: Low temperature and large area deposition of nanocrystalline diamond films with distributed antenna array microwave-plasma reactor. *Diam. Relat. Mater.* **47**, 58–65 (2014)
33. Muranaka, Y., Yamashita, H., Miyadera, H.: Worldwide status of low temperature growth of diamond. *Diam. Relat. Mater.* **3**(4–6), 313–318 (1994)
34. Das, D., Singh, R.N.: A review of nucleation, growth and low temperature synthesis of diamond thin films. *Int. Mater. Rev.* **52**(1), 29–64 (2007)
35. Hara, T., et al.: Consideration of diamond film growth on various orientation substrates of diamond in oxygen and hydrogen atmospheres by reactive pulsed laser deposition. *Diam. Relat. Mater.* **13**(4–8), 622–626 (2004)
36. Yoshitake, T., et al.: Structural and physical characteristics of ultrananocrystalline diamond/hydrogenated amorphous carbon composite films deposited using a coaxial arc plasma gun. *Jpn. J. Appl. Phys.* **49**(1R), 015503 (2010)
37. Ogale, S.B., et al.: Synthesis of metastable phases via pulsed-laser-induced reactive quenching at liquid-solid interfaces. *Phys. Rev. B* **36**(16), 8237–8250 (1987)
38. Polo, M.C., Cifre, J., Sánchez, G., Aguiar, R., Varela, M., Esteve, J.: Pulsed laser deposition of diamond from graphite targets. *Appl. Phys. Lett.* **67**(4), 485–487 (1995)
39. Amans, D., et al.: Nanodiamond synthesis by pulsed laser ablation in liquids. *Diam. Relat. Mater.* **18**(2–3), 177–180 (2009)
40. Wang, J.B., Zhang, C.Y., Zhong, X.L., Yang, G.W.: Cubic and hexagonal structures of diamond nanocrystals formed upon pulsed laser induced liquid–solid interfacial reaction. *Chem. Phys. Lett.* **361**(1–2), 86–90 (2002)
41. Yoshitake, T., Nishiyama, T., Aoki, H., Suizu, K., Takahashi, K., Nagayama, K.: The effects of substrate temperature and laser wavelength on the formation of carbon thin films by pulsed laser deposition. *Diam. Relat. Mater.* **8**(2–5), 463–467 (1999)
42. Hanada, K., Yoshitake, T., Nishiyama, T., Nagayama, K.: Time-resolved spectroscopic observation of deposition processes of ultrananocrystalline diamond/amorphous carbon composite films by using a coaxial arc plasma gun. *Jpn. J. Appl. Phys.* **49**(8), 08JF09 (2010)
43. Ali, A.M., Egiza, M., Murasawa, K., Fukui, Y., Gonda, H., Sakurai, M., Yoshitake, T.: Negative bias effects on deposition and mechanical properties of ultrananocrystalline diamond/amorphous carbon composite films deposited on cemented carbide substrates by coaxial arc plasma. *Diam. Relat. Mater.* **96**, 67–73 (2019)
44. Zkria, A., Gima, H., Shaban, M., Yoshitake, T.: Electrical characteristics of nitrogen-doped ultrananocrystalline diamond/hydrogenated amorphous carbon composite films prepared by coaxial arc plasma deposition *Appl. Phys. Express* **8**, 095101 (2015)
45. Katamune, Y., Ohmagari, S., Al-Riyami, S., Takagi, S., Shaban, M., Yoshitake, T.: Heterojunction diodes comprising p-type ultrananocrystalline diamond films prepared by coaxial arc plasma deposition and n-type silicon substrates. *Jpn. J. Appl. Phys.* **52**, 065801 (2013)
46. Zkria, A., Abubakr, E., Egiza, M., Haque, A., Narayan, J., Yoshitake, T.: Structural evolution of laser-irradiated ultrananocrystalline diamond/amorphous carbon composite films prepared by coaxial arc plasma. *Appl. Phys. Express* **13**(10), 105503 (2020)
47. Naragino, H., Tominaga, A., Hanada, K., Yoshitake, T.: Synthesis method for ultrananocrystalline diamond in powder employing a coaxial arc plasma gun. *Appl. Phys. Express* **8**(7), 075101 (2015)
48. Ali, M.A., Deckert-Gaudig, T., Egiza, M., Deckert, V., Yoshitake, T.: Near-and far-field Raman spectroscopic studies of nanodiamond composite films deposited by coaxial arc plasma. *Appl. Phys. Lett.* **116**(4), 041601 (2020)
49. Zhang, J.M., et al.: High rate capability electrode from a ternary composite of nanodiamonds/reduced graphene oxide@ PANI for electrochemical capacitors. *Chem. Phys.* **526**, 110461 (2019)
50. Krueger, A., Williams, O.A.: The chemistry of nanodiamond. *Rsc Nanosci. Nanotechnol.* **2014**, 49–88 (2014)

51. Wang, H., Cui, Y.: Nanodiamonds for energy. *Carbon Energy* **1**(1), 13–18 (2019)
52. Kausar, A.: Review on conducting polymer/nanodiamond nanocomposites: essences and functional performance. *J. Plast. Film Sheeting* **35**(4), 331–353 (2019)
53. Nuzzo, R.: *Front Matter* (2014)
54. Siuzdak, K., Bogdanowicz, R.: Nano-engineered diamond-based materials for supercapacitor electrodes: a review. *Energ. Technol.* **6**(2), 223–237 (2018)
55. Yang, N., Foord, J.S., Jiang, X.: Diamond electrochemistry at the nanoscale: a review. *Carbon* **99**, 90–110 (2016)
56. Kraft, A.: Doped diamond: a compact review on a new, versatile electrode material. *Int. J. Electrochem. Sci* **2**(5), 355–385 (2007)
57. Yu, S., Yang, N., Jiang, X., Zhang, W., Liu, S.: Conductive diamond for electrochemical energy applications. In: Yang, N., Zhao, G., Foord, J. (eds.) *Nanocarbon Electrochemistry* (2020). <https://doi.org/10.1002/9781119468288.ch6>
58. Siyu, Y., et al.: High-performance supercapacitors using graphite@ diamond nano-needle capacitor electrodes and redox electrolytes. *Nanoscale* **11**(38), 17939–17946 (2019)
59. da Silva, L.M., et al. Constituent material influence on the electrochemical performance and supercapacitance of PANi/diamond/CF composite. *Mater. Sci. Eng B* **228**, 249–260 (2018)
60. Gao, F., Nebel, C.E.: Diamond-based supercapacitors: realization and properties. *ACS Appl. Mater. Interfaces*. **8**(42), 28244–28254 (2016)
61. Almeida, E.C., Diniz, A.V., Trava-Airoldi, V.J., Ferreira, N.G.: Electrochemical characterization of doped diamond-coated carbon fibers at different boron concentrations. *Thin Solid Films* **485**(1–2), 241–246 (2005)
62. Almeida, E.C., Trava-Airoldi, V.J., Ferreira, N.G., Rosolen, J.M.: Electrochemical insertion of lithium into a doped diamond film grown on carbon felt substrates. *Diam. Relat. Mater.* **14**(10), 1673–1677 (2005)
63. Ferreira, N.G., Silva, L.L.G., Corat, E.J.: Electrochemical activity of boron-doped diamond electrodes grown on carbon fiber cloths. *Diam. Relat. Mater.* **11**(3–6), 657–661 (2002)
64. Hian, L.C., et al.: Nanodiamond thin films on titanium substrates: growth and electrochemical properties. *J. Electrochem. Soc.* **150**(1), E59 (2002)
65. Almeida, E.C., Azevedo, A.F., Baldan, M.R., Braga, N.A., Rosolen, J.M., Ferreira, N.G.: Nanocrystalline diamond/carbon felt as a novel composite for electrochemical storage energy in capacitor. *Chem. Phys. Lett.* **438**(1–3), 47–52 (2007)
66. Raymundo-Pinero, E., Kierzek, K., Machnikowski, J., Béguin, F.: Relationship between the nanoporous texture of activated carbons and their capacitance properties in different electrolytes. *Carbon* **44**(12), 2498–2507 (2006)
67. Portet, C., Yushin, G., Gogotsi, Y.: Electrochemical performance of carbon onions, nanodiamonds, carbon black and multiwalled nanotubes in electrical double layer capacitors. *Carbon* **45**(13), 2511–2518 (2007)
68. Fuertes, A.B., Pico, F., Rojo, J.M.: Influence of pore structure on electric double-layer capacitance of template mesoporous carbons. *J. Power Sources* **133**(2), 329–336 (2004)
69. Hoffmann, R., et al.: Electrochemical hydrogen termination of boron-doped diamond. *Appl. Phys. Lett.* **97**(5), 052103 (2010)
70. Qi, W., et al.: Nanodiamond particles/reduced graphene oxide composites as efficient supercapacitor electrodes. *Carbon* **68**, 175–184 (2014)
71. Yang, J., Gunasekaran, S.: Electrochemically reduced graphene oxide sheets for use in high performance supercapacitors. *Carbon* **51**, 36–44 (2013)
72. Moreira, J.V.S., et al.: Diamond and carbon nanotube composites for supercapacitor devices. *J. Electron. Mater.* **46**(2), 929–935 (2017)
73. Hébert, C., Mazellier, J.P., Scorsone, E., Mermoux, M., Bergonzo, P.: Boosting the electrochemical properties of diamond electrodes using carbon nanotube scaffolds. *Carbon* **71**, 27–33 (2014)
74. Jiang, M.Y., et al.: Microstructure and electrochemical properties of nanocrystalline diamond and graphene hybridized films. *J. Appl. Phys.* **127**(1), 015301 (2020)
75. Holt, K.B.: *Electrochemistry of Nanodiamond Particles*. pp. 128–150. Royal Society of Chemistry, Cambridge (2014)

76. Yang, N., et al.: Conductive diamond: synthesis, properties, and electrochemical applications. *Chem. Soc. Rev.* **48**(1), 157–204 (2019)
77. Simon, P., Yury, G.: Materials for electrochemical capacitors. In: Peter, R. (ed.) *Nanoscience and technology: a collection of reviews from Nature journals*, Macmillan, London, pp. 320–329 (2010)
78. Mandal, S., Bland, H.A., Cuenca, J.A., Snowball, M., Williams, O.A.: Superconducting boron doped nanocrystalline diamond on boron nitride ceramics. *Nanoscale* **11**(21), 10266–10272 (2019)
79. Banerjee, D., et al.: Single-step grown boron doped nanocrystalline diamond-carbon nanograss hybrid as an efficient supercapacitor electrode. *Nanoscale* **12**(18), 10117–10126 (2020)
80. Bhardwaj, K., Parvis, F.S., Wang, Y., Blanchard, G.J., Swain, G.M.: Effect of surface oxygen on the wettability and electrochemical properties of boron-doped nanocrystalline diamond electrodes in room-temperature ionic liquids. *Langmuir* **36**(21), 5717–5729 (2020)
81. Spătaru, N., Zhang, X., Spătaru, T., Tryk, D.A., Fujishima, A.: Anodic deposition of RuO_x•nH₂O at conductive diamond films and conductive diamond powder for electrochemical capacitors. *J. Electrochem. Soc.* **155**(1), D73 (2007)
82. Yu, S., et al.: Phosphorus-doped nanocrystalline diamond for supercapacitor application. *ChemElectroChem* **6**(4), 1088–1093 (2019)
83. Kausar, A.: Mechanical, thermal, conductivity, and electrochemical behavior of poly (vinylidene fluoride)/poly (3, 4-ethylenedioxythiophene)/polyaniline-grafted-nanodiamond nanocomposite. *J. Thermoplast. Compos. Mater.* **33**(5), 628–645 (2020)
84. Ansari, M.O., Alshahrie, A., Ansari, S.A.: “Facile route to porous polyaniline@ nanodiamond-graphene based nanohybrid structures for dc electrical conductivity retention and supercapacitor applications. *J. Polym. Res.* **26**(3), 76 (2019)
85. da Silva, L.M., et al.: From electrode to device characterizations of polyaniline/micro and nanodiamond/carbon fiber as ternary composites applied as supercapacitor. *J. Solid State Electrochem.* **23**(6), 1871–1885 (2019)
86. Karami, P., Khasraghi, S.S., Hashemi, M., Rabiei, S., Shojaei, A.: Polymer/nanodiamond composites - a comprehensive review from synthesis and fabrication to properties and applications. *Adv. Colloid Interface Sci.* **269**, 122–151 (2019). <https://doi.org/10.1016/j.cis.2019.04.006>
87. Gopalan, A.I., Lee, K-P., Komathi, S.: Bioelectrocatalytic determination of nitrite ions based on polyaniline grafted nanodiamond. *Biosens. Bioelectron.* **26**(4), 1638–1643 (2010)
88. Miliaieva, D., Stehlik, S., Stenclova, P., Rezek, B.: Synthesis of polypyrrole on nanodiamonds with hydrogenated and oxidized surfaces. *Phys. Status Solidi (a)* **213**(10), 2687–2692 (2016)
89. Shiomi, H.: Reactive ion etching of diamond in O₂ and CF₄ plasma, and fabrication of porous diamond for field emitter cathodes. *Jpn. J. Appl. Phys.* **36**(12S), 7745 (1997)
90. Park, S., Lian, K., Gogotsi, Y.: Pseudocapacitive behavior of carbon nanoparticles modified by phosphomolybdic acid. *J. Electrochem. Soc.* **156**(11), A921 (2009)

Supercapacitors: Current Trends and Future Opportunities



Amira M. Bakry, M. M. Moharam, and F. Abdel Mouez

Abstract Day by day, energy storage systems have gained more and more great attraction owing to the growing needs of electrical power supply for moveable devices like mobile phones, electric vehicles and energy supply for fulfilling household's equipment. Supercapacitors (SCs) or ultracapacitors are considered the most encouraging energy storage applications as a result of their matchless, superior characteristics than conventional electrochemical capacitors, as well as higher power density than batteries and their environment-friendly nature. Electrode materials have enlarged much care through these last years, due to their major impact on the supercapacitor storage performance. Therefore, great efforts are focusing on developing supercapacitors and intensive studies have been stated to fabricate materials for electrodes with large specific capacitance and smart behavior. In this chapter, we have attempted to cover an extensive range for tested electrode materials used for improving supercapacitor efficiency. Carbon-based materials, metal oxides, conducting polymers and their nanocomposites materials have been considered a focus point and have showed up in excellent pose for energy storage.

Keywords Supercapacitors · Electrode materials · Nanocomposites · Energy storage · Specific capacitance · Power density

A. M. Bakry (✉)

Chemistry Department, Central Administration for Central Laboratories, Egyptian Mineral Resources Authority (EMRA), Ministry of Petroleum & Mineral Resources, Giza, Egypt
e-mail: amirabakry@sci.cu.edu.eg

M. M. Moharam (✉)

Chemical and Electrochemical Processing Department, Central Metallurgical Research and Development Institute (CMRDI), P.O. Box 87, Helwan 11421, Egypt
e-mail: mm.mohammed@psau.edu.sa

Chemistry Department, College of Arts & Science, Brince Sattam Bin Abdulaziz University, Wadi Al-dawaser, Alkharj, Saudi Arabia

F. A. Mouez

Corrosion Control & Surface Protection Department, Central Metallurgical Research and Development Institute (CMRDI), P.O. Box 87, Helwan 11421, Egypt

© The Author(s), under exclusive license to Springer Nature Switzerland AG 2022

1047

A. E. Shalan et al. (eds.), *Advances in Nanocomposite Materials for Environmental and Energy Harvesting Applications*, Engineering Materials,
https://doi.org/10.1007/978-3-030-94319-6_33

Abbreviations

1D	One dimensions
2D	Two dimensions
3D	Three dimensions
AC	Activated carbon
ALD	Atomic layer deposition
BMOs	Binary mixed metal oxides
BTMOs	Binary transition mixed metal oxides
CNF	Carbon nanofiber
CNTs	Carbon nanotubes
CPs	Conducting polymers
EDL	Electrochemical double layer
EDLCs	Electrochemical double-layer capacitors
DFT	Density functional theory
ESS	Electrochemical supercapacitors
GO	Graphene oxide
MOs	Metal oxides
MWCNT	Multi-walled CNT
NEC	Nippon Electric Company
NPs	Nanoparticles
NRs	Nanorods
NTs	Nanotubes
PANI	Polyaniline
PPy	Polypyrrole
PTh	Polythiophene
rGO	Reduced graphene oxide
SCs	Supercapacitors
SOHIO	Standard Oil of Ohio
SSA	Specific Surface Area
SWCNT	Single-walled CNT
TMOs	Ternary mixed oxides

1 Introduction

Recently, the energy accumulation and storage are in spotlight. It is one of the major focuses for world powers and scientific community [1]. Batteries are considered the most famous electrochemical energy storage systems applied for various fields. They are characterized by their high ability to accumulate considerable energy with a reasonably small weight and volume. Therefore, low power density, cycle life, and shelf life are the main difficulties for battery manufacture. Supercapacitors (SCs) gain prominence as electrochemical energy storage strategies and important complement

Table 1 Comparison between supercapacitors, batteries and fuel cells [3]

Property	Supercapacitors	Batteries	Fuel cells
Weight/kg	0.001–2	0.001–10	0.02–10
Charge/discharge time	ms–s	1–12 hrs	1–300 hrs
Life time	>100 000 cycles	150–1,500 cycles	1,500–10,000 hrs
Capacitance/F	0.1–2	N/A	N/A
Operating temperature/°C	–40 to + 85	–20 to + 65	+ 25 to + 1,000
Operating cell potential (DV)/V	2.3–2.75	1.25–4.2	0.6–1.0
Energy density/ (Wh/ kg)	1–5	5–600	300–3,000
Power density/ (kW/ kg)	10–100	0.005–0.4	0.001–0.1

for other energy storage or generation devices as secondary batteries and fuel cells. They are described due to their fast charging/discharging rate, unlimited life-cycle (>100 000 cycles), excellent cycle stability and great power density known to accumulate energy in the double-layer region or through supercapacitance as a function of practical potential [2]. Table 1 presented a comparison between supercapacitors, batteries and fuel cells [3].

Therefore, the basic challenge for supercapacitors is low energy density. So, the restriction issue for storage charge to the surface (or near surface) of supercapacitors results the energy density (or capacity) to be much lower than that of batteries [4]. Hence, great works have been done to raise their energy density (E). Also, it is recognized that the energy density of supercapacitor has been determined via the specific capacitance (F) of the electrode materials and the overall cell voltage (V). Consequently, it is urgent to improve electrode materials to reach to superior properties. In this perspective, through the past years, many works have been done for electrode materials fabrication. On the other wise, it is important to develop energy storage systems, in order to save the requirements of recent society and emerging environmental fears. Then, these systems should be friendly environment, high-performed and low-cost renewable energy storage devices. Therefore, this chapter presents a brief overview and state the most updated improvement performed of novel materials for supercapacitor electrodes.

1.1 How the Story of Supercapacitors Began?

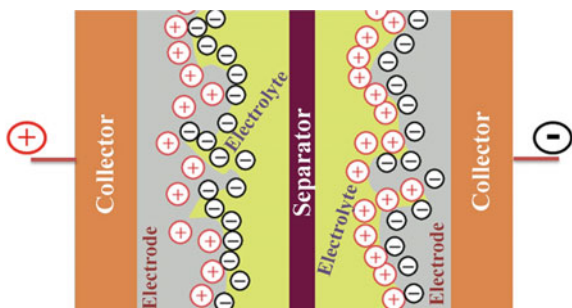
Supercapacitors are known as one of the prospective energy storage devices that have been recognized for over fifty years [2]. The story was begun in 1951 by engineers at General Electric Corporation when they started testing the porous carbon electrodes in the design of capacitors, from rechargeable batteries designing and fuel cells. After six years, in the same Corporation the first capacitor depends on high carbon surface area was developed by Becker [5]. In the year 1969 a team of researchers at Standard

Oil of Ohio (SOHIO) established an electric double layer capacitor. Hence, many efforts have been done for the market using porous carbon in a non-aqueous solvent that is containing a solution of dissolved tetra alkyl ammonium salt [6]. SOHIO did not commercialize their invention, which makes it in 1971 to license the technology to Nippon Electric Company (or NEC) of Japan. It is finally successful to make the first commercial device of double-layer capacitors under the name "supercapacitors" in 1978. It provides power backup for maintaining computer memory. Also, a number of companies were producing the electro-chemical capacitors by the 1980s but, they were still associated with low specific energy values. In 1991, much efforts have been by Conway to develop the electrochemical capacitors [7]. He reported the differences between battery and supercapacitor behavior at electrochemical energy storage. In addition to, he mentioned that, the increasing capacitance through surface redox reactions with faradaic charge transfer between ions and electrodes for "supercapacitor" term in 1999 [8]. According to his "supercapacitor" definition, a partially electrical charge is stored in the Helmholtz double-layer. So, as a result, a part of faradaic reactions with "pseudocapacitance" charge transfer of electrons and protons between electrolyte and electrode has occurred. While pseudocapacitors are chemically stored their charges through the redox reaction at the neighborhood (a few nanometers) of the surface [9, 10]. Conway and his researches, at the twentieth century extended greatly the knowledge of electrochemical capacitors and discussed the inclusive exposure of electrochemical supercapacitors (ESs) improvements. From that time Supercapacitor research has undergone immense growth and captured the attention of researchers in diverse areas to enhance its properties such as specific power, specific energy, and cycle stability. Also, manufacturing reduction cost is a great demand for high performing and long-lasting energy systems [9, 10].

2 Components of Supercapacitor

The supercapacitors design and components are analogous to that of the batteries. As seen in Fig. 1, it consists of: (i) Two electrodes, (ii) Electrolyte material, (iii) Separator which segregates the two electrodes electrically, (iv) Binder and (v) Current

Fig. 1 Schematic drawing for supercapacitor basic components



collector [11]. So, the electrode materials play a great role in the supercapacitor performance and considered as the most active supercapacitor components. Furthermore, the charge storage inside the supercapacitor affected according to the type of electrode-active material. However, the supercapacitor performance is controlled by parameter series, including the specific capacitance, power density, energy density, cyclic stability and retention capability [12]. Therefore, the specific capacitance is in a function of the Specific Surface Area (SSA) available by electrolyte, electrolyte interfacial double-layer capacitance, and density of the electrode materials. Thus, it is particularly dependent on the electrode material, the surface area and the pore-size distribution [2]. On the other hand, the power density (describing the efficacy in energy uptake/delivery in W/L or W/kg) and energy density (defining the quantity of electrical energy stored or deliverable in Wh/L or Wh/kg) are considered as tool to measure performance metrics for all kinds of conversion systems and energy storage [13]. Finally, Long cycle life of SC devices is one of many major advantages which leads to the so-called “fit-and-forget” benefits, highly required for certain applications.

3 Faradaic and Non-Faradaic Processes

There are two main feathers for electrode behavior Faradaic and non-Faradaic processes [12, 14], the basic differences between them are dictated in Table 2.

Table 2 The difference between faradaic and non-faradaic processes

	Faradaic	Non-Faradaic
Charge transfer	Redox reaction is occurred at the electrode surface.	No redox reaction at all. The processes are adsorption and desorption
	The transfer of charge happens during redox process.	No charge transfer occurs.
Conduction process	The charge at electrode surface must be done.	Conduction process has been done in electric double-layer capacitor (EDLC).
Examples	Acid batteries and fuel cells.	The charge transfer across metal solution and the interface is stopped.

4 Supercapacitors Types

Supercapacitors are classified into three main sets relying on the energy storage mechanism and also, the active materials, as shown in Fig. 2. The differences between the major characteristics for each group are summarized in Table 3.

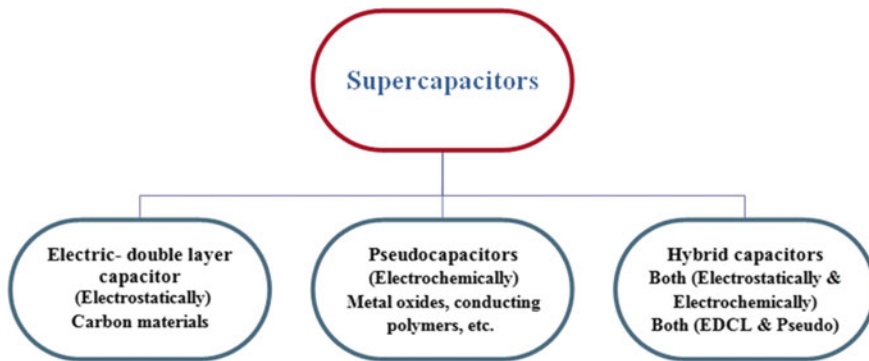


Fig. 2 Supercapacitors classification

Table 3 Comparison between electric double layer, pseudo and hybrid capacitors [9, 10, 12, 15]

	Electric- double layer capacitor	Pseudo capacitor	Hybrid capacitor
Mechanism of charge storage	Formation of double layer Physical, no chemical reaction.	Energy stored via charge transfer	Both Electric double layer and pseudo faradic reaction Combination.
Charge/ discharge process	Fast	Fast and reversible	Better than both capacitor types
Charge transfer	No charge transfer as faradic reaction	Redox process is responsible for charge transfer. Adsorption and intercalation will be on the surface of electrode material.	Involves charge transfer for electrode behaves as Pseudo capacitor and no transfer
Chemical reaction	No chemical reaction. The composition of electrode remains constant.	There is chemical reaction during process of charging & discharging process.	Combination of both EDLC and Pseudocapacitors
Cycle life	Long cycle life. High reversible capacity.	High reversible capacitance.	Exhibit high capacitance in compared to EDLC and redox capacitor
Types of process	Non- Faradic process	Faradic process	combining Faradaic process with non-Faradaic processes
Performance	Good	Excellent than EDLC	Excellent
Examples	Electrode with high surface area as activated carbon, graphene, carbon nanotube	Transition metal oxides, Conducting polymers.	Asymmetric electrode materials. One follows EDCL and the other is faradic

5 Electrode Materials for Supercapacitor

The selection of electrode material is a crucial factor in supercapacitor area. So, it determines the electrical properties [16]. It must have high conductivity, good chemical stability, temperature stability, corrosion resistance, and have lower cost additionally it should be environment-friendly [9]. Therefore, most studies are concerned on electrode materials improvement for developing supercapacitor technologies. The main types of supercapacitors are commonly described depending on the various active materials used. Carbon materials, metal nitrides, metal oxide and conducting polymers (CPs), in addition to nanocomposite based electrode materials. Figure 3 shows the different kind of electrode material used in supercapacitors.

5.1 Carbon Materials

Carbon materials have been used from the beginning of supercapacitors owing to their high specific surface area. Easy processing, nature abundance, low cost, non-toxicity, good electronic conductivity, high chemical stability, wide operating temperature range and environmental-friendliness make carbon the most choice materials until now [17]. Mainly, carbon materials save charges in an electrochemical double layer, which is created at the interface between the electrode and the electrolyte. Hence, the capacitance principally relies on the surface area available to the electrolyte ions. Within the last years, a tremendous number of researches were devoted to advance the performance of supercapacitors by developing new types of carbon materials, including activated carbon (AC), graphene, carbon nanotubes (CNTs), carbon aerogels and carbon xerogel. Every member of these materials has their own physical, electrical and morphological properties [18]. Table 4 demonstrated the special characteristics of carbon-based materials used in supercapacitor [19, 20].

(a) **Activated carbon (AC)** is still the major material employed to produce electrodes for the commercialization of supercapacitors (SCs), because of its advantages

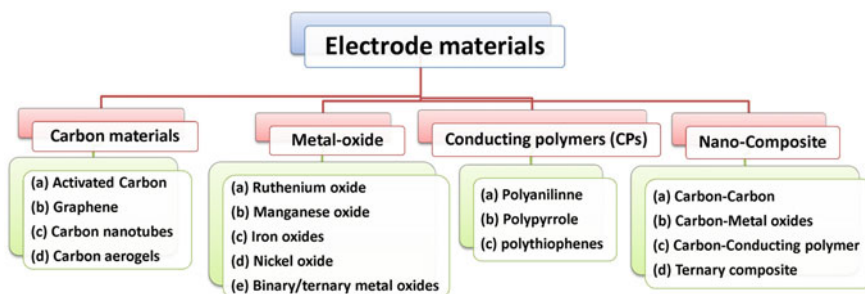
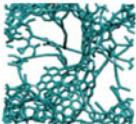
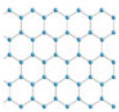
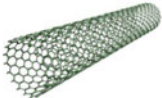


Fig. 3 Classification of electrode materials for supercapacitors system

Table 4. Characteristics of carbon-based materials [19, 20]

Material	Activated carbon	Graphene	Carbon nanotubes
Dimensionality	3D	2D	1D
Conductivity	Low	High	High
Volumetric capacitance	High	Moderate	Low
Cost	Low	Moderate	High
Structure			

including commercial availability, moderate cost, well-established production technologies, good electrical properties and large surface area [21]. Activated carbon can be prepared from any carbonaceous precursor by chemical activation with NaOH or KOH, which is considered a good method to produce activated carbons [22], usually in the form of fine powder, so making it conforms to monoliths or pellets an important area of research. On the other hand, it can be formed from a broad range of carbon-rich raw materials like coal and wood [23, 24]. The process of production includes mainly two steps, firstly, the carbonization of raw materials at low temperatures, then activation at higher temperature [25]. Many non-edible industrial and agricultural products were stated as a source for the raw materials to produce AC in the effort to preserve the environment and to reduce the production cost such as rice husk [25–27], ginkgo shells [28], argan seed shells [29], palm kernel shell [30], beer less [31], celtuce leaves [32], citrae peel [33], orange peels [34], sugarcane baggase [35], bamboo [36], conrncob [37], empty fruit bunches of oil palm [30] and camellia flower [38]. However, the limited energy storage capacity of commercial activated carbons (usually below 300 F/g) and rate capability limit their applications only to certain specialty markets. It is obvious that different electrolytes play an urgent role on the capacitance performance of AC, where its capacitance in organic electrolytes (<150 F/g) while give higher value in aqueous electrolytes (extending from 100–300 F/g) [16]. Table 5 listed some characteristics and properties of various activated carbon electrode materials studied on the literature at the last decade.

(b) **Graphene** has attracted enormous interest in the field of industry and academia. The graphene has a single layer graphite with close-packed conjugated hexagonal lattice structure. Currently, it looks like a rising star as an electrode material for energy storage applications, owing to its theoretically large specific surface area (2675 m²/g), chemical stability, high electrical conductivity [51]. On the other hand, the graphene-layered structure and the diverse redox states located on the reduced graphene oxide (rGO) surface enable it to be more popular and successful in this era [14]. The advantage of graphene as an electrode material related to that both major surfaces of graphene sheet are external and are easily accessible by electrolyte. Moreover, it doesn't rely on the spreading of pores in the solid state in comparison

Table 5 Various activated carbon electrode materials for supercapacitors

Electrode	Electrolyte	Specific capacitance (F/ g)	Power density (kW k/g)	Energy density (Wh k/g)	Retention capability	Ref.
Activated carbon						
AC	0.5 M Na ₂ SO ₄	135 at 0.2 A/g	–	~10	–	[39]
AC	1 M Li ₂ SO ₄	180 at 0.2 A/g	–	–	–	[40]
AC	1 M TEABF/ HFIP	110 at 1 mV/s	–	–	–	[41]
AC	0.7 M Et ₄ NBF ₄ / ADN	25 at 20 mV/s	–	~28	–	[42]
AC	1 M NaNO ₃	116 at 2 mV/s	–	–	–	[43]
AC fibers	1 M H ₂ SO ₄	280 at 0.5 A/g	–	–	99.3% after 2,000 cycles	[24]
Microporous carbon	1 M H ₂ SO ₄	100 at 0.2 A/g	~100	~3.8	–	[44]
AC	1.5 M SBP-BF ₄ / PC	122 at 0.1 A/g	–	52	–	[45]
AC (kernel shell)	1 M KOH	210 at 0.5 A/g	–	–	~95–97% after 1,000 cycles	[30]
AC (ACB)	1 M Na ₂ SO ₄	114 at 0.3 A/g	–	–	100% after 3,000 cycles	[46]
AC (kapok fibres)	1 M TEABF ₄	142 at 1 A/g	24	24	91% after 5,000 cycles	[47]
AC (Sargassum)	6 M KOH	336 at 1 A/g	2.44	44.42	85% after 10,000 cycles	[48]
AC (sawdust)	1 M TEABF ₄ /AN	160 at 0.25 A/g	–	49	97% after 5,000 cycles	[49]
AC (Corn husk)	6 M KOH	127 at 1 A/g	0.24	4.4	–	[50]
	1 M TEABF ₄ /AN	80 at 1 A/g	0.68	20	90% after 5,000 cycles	

to activated carbon and carbon nanotube [16]. Generally, the synthesis protocol and processes for designing the high purity electrode are strongly effect on the specific capacitance value of graphene. Also, the high costs and low yields have an effect in the capacitance value, In addition to the choice of electrolyte [52, 53]. On the other hand, the bulky scale manufacture for graphene with high value remains a goal even with using recent techniques. So, these are like electrochemical and chemical methods, arch discharge method, micromechanical exfoliation, chemical vapour deposition,

epitaxial growth, unzipping of CNTs, and intercalation methods in graphite [54]. But the major difficulty is the irreversible aggregation of graphene sheets during its synthesis, which origin the reduction of the effective surface area and influence on its electrochemical properties. Therefore, it is essential to inhibit graphene sheets agglomeration during all phases of graphene fabrication. Moreover, the next electrode production processes, can be confirmed by making graphene sheets with curvy shape, so it will not restack face to face, which enhances the attitude of these supercapacitors based graphene materials [16]. Furthermore, the lower experimental capacitance values were observed due to the hydrophobic nature, which restricts the allowed access ions of the aqueous electrolyte over the graphene surface. Thus, a technique to improve the hydrophilic graphene with less series resistance and more accessible surface area is highly wanted [14]. Graphene places the gold standard for potential electrochemical double layer (EDL) supercapacitors with a theoretical capacitance limit of ~ 550 F/g [53]. Some characteristics and properties of numerous tested graphene electrode materials were estimated and organized in Table 6.

(c) Carbon nanotubes: since 1991, CNTs have considerably enhanced the science of carbon materials and attracted extensive attention owing to their distinctive physical properties, including good chemical and mechanical stability in addition to their high electrical conductivity [62]. It's a higher dimensional form of graphene and can be categorized according to the orientation of the rolled-up graphene sheet to chiral, armchair or zigzag [53]. CNTs were suggested by Niu et al. in 1997 to be used

Table 6 Various graphene electrode materials for supercapacitors

Electrode	Electrolyte	Specific capacitance (F/g)	Power density (kW k/g)	Energy density (Wh k/g)	Retention capability	Ref.
Graphene						
Functionalized rGO film	Nafion	118.5 at 1 A/g	–	–	90% after 1,000 cycles	[55]
Carbon black pillared graphene film	1 M H ₂ SO ₄	215 at 0.1 A/g	414	–	97% after 10,000 cycles	[56]
3D N&B co-doped graphene hydrogel	1 M H ₂ SO ₄	239 at 1 mV/s	1.65	8.7	100% after 1,000 cycles	[57]
Functionalized graphene hydrogel	1 M H ₂ SO ₄	441 at 1 A/g	–	–	86% after 10,000 cycles	[58]
Graphene ribbon film	6 M KOH	407 at 2 mV/s	–	–	–	[59]
hydrothermal reduced graphene oxide	6 M KOH	341 at 1 A/g	–	–	91.58% after 5,000 cycles	[60]
N, S, P- tri-doped holey graphene oxide	2 M KOH	295 at 1 A/g	–	–	93.5% after 10,000 cycles	[61]

in supercapacitors [63]. Both single-walled CNT (SWCNT) and multi-walled CNT (MWCNT) are shaped when a graphite sheet is curled up into cylinders and have been known as prospective electrode materials for electrochemical supercapacitors. This is due to their distinctive properties like low resistivity, large surface area, low mass density, high chemical stability, and narrow distribution of mesopore sizes [64]. On the other hand, owing to the micropore volume, microtexture, catalyst and defects contamination of carbon nanotubes (CNTs), their specific capacitance is limited to low values. Therefore, significant efforts have been done to advance the capacitance of CNT-based supercapacitor electrodes through mixing with metal oxides and conducting polymers. Also, the modification of carbon nanotubes (CNTs) surface has gained considerable care via decoration with different functional materials. The excellent properties of functionally decorated CNTs merge the thermal conductivity and high electrical of CNTs and their optical and mechanical properties with the functional properties of other materials. Several procedures have been established to produce decorated CNTs, including chemical polymerization [65], chemical precipitation [66], electrodeposition [67], magnetron sputtering [68], pulsed laser ablation [69], atomic layer deposition [70]. Table 7 estimated and listed some characteristics and properties of different carbon nanotube electrode materials.

Table 7 Overview of examined CNT electrode materials for supercapacitors

Electrode	Electrolyte	Specific capacitance (F/ g)	Power density (kW k/g)	Energy density (Wh k/g)	Retention capability	Ref.
Carbon nanotubes (CNTs)						
SWNTs	1 M Et ₄ NBF ₄ /propylene carbonate	160 at 4 V	24	17	96.4% after 1,000 cycles	[71]
SWNTs	H ₂ SO ₄ /PVA gel	48 at 10 A/g	0.96	0.98	–	[72]
CNT(rubber)	H ₃ PO ₄ –PVA gel	18 at 0.1 A/g	–	–	90% after 1,000 cycles	[73]
CNT (functionalized by –OH, – COOH)	0.075 M hydroquinone + 1 M H ₂ SO ₄	3199 at 5 mV/s	–	–	70% after 350 cycles	[74]
SWNT	ion gel	51.8 at 1 A/g	1.48	15.7	96.6% after 3,000 cycles	[75]
N-doped CNT Spherical particles	1 M H ₂ SO ₄	215 at 0.2 A/g	–	–	99% after 1,500 cycles	[76]

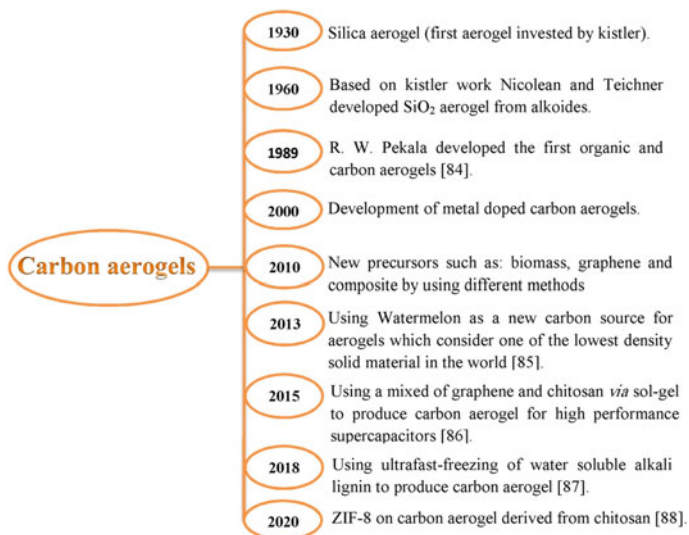


Fig. 4 Historical view of carbon aerogels with time

(d) Carbon aerogels: Recently, carbon aerogels have gained a great response as electrode materials owing to their interconnected microstructure, large electrical conductivity, high specific surface area and a density of 200 mg/cm³ [53, 77]. It is produced via the sol-gel method and is designed as a continuous network of conductive carbon nanoparticles with scattered mesopores [1, 53]. Carbon aerogels can be classified into three parts depending on the source of raw material. The first one is derivative from carbon nanomaterials such as graphene, CNTs, nanoribbons, and their hybrids [78, 79]. While, the second type is derived from biomass-based materials, like bacterial cellulose, cotton, watermelon, etc. [80, 81]. Finally, the third one is consequent from polymer-based aerogels [82]. All of these different categories have private special stamps permitting them as an appropriate for various sorts of applications. Therefore, many efforts are exerted to discover temporary precursors that are eco-friendly, inexpensive, abundant and easy to work with. The improvement of carbon aerogels over time is illustrated by Kobina et al. [83] and summarized in Fig. 4 according to the following reference [84–88]. Furthermore, Table 8 collated some characteristics and properties of different carbon aerogel electrode materials.

5.2 Metal-Oxide

Metal oxides have achieved large consideration as electrode materials for supercapacitor applications, owing to their low resistance and large specific capacitance which qualified them for high performance supercapacitors manufacture [16].

Table 8 Overview of various carbon aerogels electrode materials for supercapacitors

Electrode	Electrolyte	Specific capacitance (F/ g)	Power density (kW k/g)	Energy density (Wh k/g)	Retention capability	Ref
<i>Carbon aerogels</i>						
Carbon aerogel (watermelon)	6 M KOH	333.1 at 1 A/g	–	–	96% after 1,000 cycles	[85]
Graphene aerogel	0.5 M H ₂ SO ₄	325 at 1 A/g	7	45	98% after 5,000 cycles	[89]
Graphene aerogel	3 M KOH	4.76 at 0.4 A/g	4.08	0.26	95.5% after 10,000 cycles @ 200 mV/s	[90]
Carbon aerogel (cellulose)	1 M H ₂ SO ₄	328 at 0.4 A/g	–	–	96% after 5,000 cycles	[91]
Carbonaceous aerogel (seaweed)	6 M KOH	260.6 at 1 A/g	–	–	91.7% after 10,000 cycles	[92]
Carbon aerogel (Lignin)	1 M H ₂ SO ₄	189 at 1 A/g	1.0	26.25	97.4% after 10,000 cycles	[87]
Carbon aerogel (banana)	6 M KOH	178.9 at 1 A/g	0.05	3.23	98% after 10,000 cycles	[93]
Carbon aerogel (cellulose & Lignin)	6 M KOH	166 at 0.1 A/g	0.175	102	98.6% after 1,000 cycles	[94]
Carbon aerogel (agaric)	6 M KOH	340 at 3 A/g	2.0	25.5	91% after 10,000 cycles	[95]
Carbon aerogel (Bamboo fiber)	6 M KOH	120 at 20 A/g	–	–	100% after 30,000 cycles	[96]
Carbon aerogel (Rattan cane)	6 M KOH	221 at 0.5 A/g	–	–	100% after 10,000 cycles	[97]

Generally, metal oxide used in ES applications must satisfy certain criteria, such as: (1) electronically conductive, (2) coexisting in multiple oxidation states over a continuous range without changing in phase requiring irreversible, (3) dimensional structural modulations, and (4) the protons can facily insert into the oxide lattice on reduction (and out of the lattice on oxidation), permitting easy interconversion of $O^{2-} \leftrightarrow OH^-$ [98]. Ruthenium dioxide (RuO₂) [99], manganese oxide (MnO₂) [100–102], iron oxide [103–105], and nickel oxide (NiO) [106–108], are frequently used in supercapacitors owing to their cheap manufacturing costs and high theoretical specific capacitance from the faradaic charge transfer process [109].

(a) **Ruthenium oxide (RuO₂)** is suggested as an example for a mixed electronic–protonic conductor. Therefore, For supercapacitor applications, RuO₂ either amorphous or crystalline forms are the most characteristic among all other metal oxides owing to their metallic conductivity, long life cycle, highly reversible reduction–oxidation reaction and a broad working window with large specific capacitance [2]. Furthermore, the capacitance of RuO₂ is about ten times higher than that of carbon, which is owing to pseudocapitance from the surface reaction between H ions

and Ru ions [110]. Also, there are several techniques for RuO₂ synthesis, such as electrodeposition, reactive sputtering, sol-gel methods, and organometallic chemical vapor deposition, etc. [111]. Among all, electrochemical deposition is considered a promising candidate due to its environment-friendly. However, this allows many opportunities to change the nano-grain size by changing the synthesis parameters like current density, the deposition time, and various electrochemical techniques used as deposition at constant potential, or current density. As a result, it's noticed that changing in the electrochemical techniques imparts different morphological features in RuO₂. So, an expensive cost and limited occurrence become a major barrier for commercialization [112]. Hence, many studies at the last years are mainly concentrated on solving these problems by composite ruthenium oxide with cheap metal oxide materials or carbon materials to advance the application ratio of RuO₂ [113, 114].

(b) Manganese oxides: owing to their unique physical and chemical characteristics, low-cost commodity and low toxicity, manganese oxide has appeared as an attractive faradaic material, which can be utilized as promising alternatives for electrode materials [101, 109]. Manganese as a transition metal element can exist in variety of stable oxides as (MnO, Mn₂O₃, Mn₃O₄, MnO₂) and different crystallization types of crystal structures. So, Mn oxidation states have a high influence on electrochemical efficiency. For example, the trivalent Mn³⁺ in MnO_x have a lower conductivity than that of MnO₂ or amorphous manganese oxides [115]. However, these facts play a significant role in determining and optimizing the electrochemical properties when applying manganese oxides as electrode materials [101]. Also, the cycle stability for Mn oxides is controlled by the microstructure, but the chemical hydrous state effects on their basic capacitance [116]. On the other hand, for MnO_x fabrication, the hydrothermal process is very affective and easily to be controlled compared to other methods such as mechanical milling, co-precipitation, sol-gel, thermal decomposition and electrodeposition process [117]. Unfortunately, there are some issues that limited Mn oxides usage as ES materials. Firstly, there is a partial degradation of MnO₂ in the electrolyte during cycling which causing dissolution capacity of MnO₂ electrodes [118]. Secondly, the poor electronic conductivity of MnO₂ in addition to their poor surface area are the problems that inhibit MnO_x. Therefore, great works have been dedicated to adjust synthesis conditions in order to get desirable morphology of manganese oxides with defect chemistry, and crystal structures allow them for subsequent capacitance and power characteristics [102, 119].

(c) Iron oxides are another competitor for ES electrode material because of their abundant availability, ideal theoretical specific capacitances, wide working potentials, good redox activity, low cost and more environmentally friendly and less toxicity. Fe₂O₃ [105, 120, 121], Fe₃O₄ [122–124] and FeOOH [125–127] are famous iron oxides investigated in literature as electrode materials for supercapacitor applications. However, the limitation of using iron oxides is related to their poor conductivity and cycle stability [104]. Therefore, many researches concerned on solving this problem by several ways including elemental doping and the creation of oxygen vacancies [122], composite with other materials [121]. Also, designing special

nanostructures, which considered an efficient solution for poor conductivity, such as nanospheres, nanoflakes, nanorods (NRs), nanotubes (NTs), and nanoparticles (NPs) [105, 122, 123, 126].

(d) Nickel oxide is an extremely promising oxide for a supercapacitor electrode material. Nickel oxide has a high surface area, easily fabricated, reliable, accurate, non-toxic and cheap in cost [128]. Also, the morphologies nanostructured of NiO are including nanosheets [107], nanoribbons [129], nanoflakes [108], nanowires and NPs [130]. There are various synthesis methods available for easy preparation, such as chemical immersion, hydrothermal, microwave hydrothermal and electrodeposition processes [109]. Therefore, these features have increased their demand in many application areas.

(e) Binary/ternary metal oxides: metal oxide which suffers from low rate stability and poor cycle life for low conductivity in the process of charging and discharging it necessity to be improved by admixing electronically conductive phases. Along with modifying electrochemical performance of SCs, many studies have concentrated on mixing metal oxides for superior energy storage properties. In previous studies, binary mixed metal oxides (BMOs) of Mn-Fe [131], Co-Fe [132], Fe-Ni [133], Ni-Co [134–136], Ni-Mn [137], Co-Mn [138, 139], Mn-Ru [140] and ternary mixed oxides (TMOs) of Ni-Zn-Co [141], Ni-Co-Mn [142], Cu-Co-Fe [143], Ni-Co-Fe [143], Ni-Cu-Fe [143] were investigated to advance the capacitive performance of materials via disturbing synergistic effects into an electrode system. Several synthesis methods for mixed metal oxide electrodes were covered in several studies such as electro-deposition method [144], co-precipitation process [145], sol-gel process [146], chemical bath deposition [147], and hydrothermal method [148]. The challenges and the promising future of binary transition mixed metal oxides (BTMOs) are discussed in details by Zhang et al. [143], they review many eminent BTMOs in addition to their composites for supercapacitors application. On the other hand, the ternary mixed oxides exposed excellent performance in terms of specific capacitance and cost than pure oxide or binary oxides [149]. Therefore, huge research interest in recent years on the fabrication of novel ternary mixed oxides for next-generation supercapacitors [149–157]. Table 9 demonstrated an overview of several metal oxides and binary/ternary metal oxides electrode materials for supercapacitor applications.

5.3 Conducting Polymers (CPs)

CPs are organic polymers that conduct electricity via a bond conjugation system along polymer chain. Over the last years, CPs have attracted more attention when compared with carbon-based materials owing to their good conductivity (10^4 S/cm), environmental stability, large theoretical specific capacitance, ease of large-scale production, relatively cheap, financial viability, fast doping–undoping process and suitable morphology [2, 112, 166, 167]. Among all kinds of CPs, polyaniline (PANI) [168], polypyrrole (PPy) [169], polythiophene (PTh) [170] and some of their derivatives

consider a good choice for Supercapacitor electrode materials. Table 10 reveals the main advantages and disadvantages of PANI, PPy, and PTh based conducting polymers [167]. Generally, there is no singular technique for preparing conductive polymers from polymer. Polymerization can be realized by chemical or electrochemical processes, which provide films with various morphologies and thus different chemical and physical properties [171]. Electrochemical [172], chemical [173], template synthesis [174], photochemical [175], and ultrasonic assisted [176] were reported as a common method for conducting polymer preparation. The polymerization process greatly depended on the nature of the dopant anion and the synthesis conditions [177]. In conducting polymers, poor cycle stability owing to the extension and contraction phenomenon for the charge–discharge process, may be a problem. Consequently, many literature have interested on the electrochemical performance of these CPs electrodes and have examined several approaches to develop their properties [167].

(a) **Polyaniline (PANI)**: owing to its easy synthesis among conducting polymers, diverse structure, various oxidation states, excellent physical properties, special doping mechanism and high theoretical capacitance, (PANI) is the most broadly used for supercapacitors, directly as an electroactive material or indirect conducting agent [16, 112, 178]. Morphology of PANI is very important and critical to their electrochemical properties; thus, it's essential to find a high-efficiency and convenient synthesis method to prepare PANI. In this regard, various works have scrutinized the electrochemical performance of supercapacitor electrodes based on nanocomposites of PANI as reviewed and presented by Eftekhari et al. [179].

Table 9 Overview of various metal oxides and mixed metal oxides electrode materials for supercapacitors

Electrode	Electrolyte	Specific capacitance (F/g)	Power density (kW k/g)	Energy density (Wh k/g)	Retention capability	Ref.
Ruthenium oxide (RuO₂)						
Hydrous RuO ₂	1 M Na ₂ SO ₄	52.66 at 0.625 A/g	0.05	18.7	92% after 2,000 cycles	[99]
Hollow fusiform RuO ₂ ·xH ₂ O nanostructures	1 M H ₂ SO ₄	800 at 1 A/g	–	–	–	[158]
Manganese oxide						
MnO ₂ nanotube arrays	1 M Na ₂ SO ₄	320 at 20 mV/s	–	–	81% after 2,000 cycles	[159]
Porous Au/MnO ₂	2 M Li ₂ SO ₄	1145 at 50 mV/s	~16	~57	~80% after 500 cycles	[160]
Mesoporous MnO ₂	1 M Li ₂ SO ₄	284.24 at 1 mV/s	~0.07	~28.8	–	[100]

(continued)

Table 9 (continued)

Electrode	Electrolyte	Specific capacitance (F/g)	Power density (kW k/g)	Energy density (Wh k/g)	Retention capability	Ref.
Iron oxides						
α -Fe ₂ O ₃ nanotubes	1 M Li ₂ SO ₄	138 at 1.3 A/g	–	–	89% after 500 cycles	[161]
α -Fe ₂ O ₃	0.5 M Na ₂ SO ₃	300 at 1 A/g	–	–	73% after 1,000 cycles	[162]
α -Fe ₂ O ₃	1 M LiOH	681 mF/cm ² at 1 mA/cm ²	–	–	76.1% after 6,000 cycles	[120]
α -Fe ₂ O ₃ microrods	0.5 M Na ₂ SO ₃	346 at 2 mV/s	–	–	88% after 5,000 cycles	[103]
Nickel oxide						
Hexagonal NiO porous nanoplates	6 M KOH	286.7 at 1 A/g	–	–	–	[163]
NiO multi shelled nanospheres	2 M KOH	612.5 at 0.5 A/g	–	–	90.1% after 1,000 cycles	[106]
NiO nanoparticles	1 M KOH	549 at 1 mV/s	0.32	11	60.6% after 1,000 cycles	[164]
NiO	0.5 M Na ₂ SO ₄	458 at 5 mV/s	0.89	10.90	–	[165]
Binary/ternary metal oxides						
NiO/Co ₃ O ₄	6 M KOH	510 at 5 mA/cm ²	–	–	92% after 1,000 cycles	[134]
Ni _{0.37} Co oxide	6 M KOH	1000 at 10 A/g	–	–	98% after 15,000 cycles	[135]
Zn–Ni–Co nanowire arrays	6 M KOH	2481.8 at 1 A/g	0.19	35.6	94% after 3,000 cycles	[141]
Cu–Co–Fe	1 M KOH	221.1 at 5 mV/s	1711.95	7.90	–	[143]
Ni–Co–Fe	1 M KOH	60 at 5 mV/s	1426.23	4.79	–	[143]
Ni–Cu–Fe	1 M KOH	16.9 at 5 mV/s	1001.99	4.62	–	[143]

(continued)

Table 9 (continued)

Electrode	Electrolyte	Specific capacitance (F/g)	Power density (kW k/g)	Energy density (Wh k/g)	Retention capability	Ref.
Co ₃ O ₄ -NiO	2 M KOH	670 at 0.5 A/g	–	–	92% after 2,500 cycles	[144]
Mn-Co mixed metal oxides	1 M NaOH	679 at 5 mV/s	–	–	80% after 1,000 cycles	[138]
Co ₃ O ₄ /Fe ₃ O ₄	6 M KOH	143 at 1 A/g	–	–	79% after 3,000 cycles	[133]
NiO/Fe ₃ O ₄	6 M KOH	228 at 1 A/g	–	–	75% after 3,000 cycles	[133]
NiO/Co ₃ O ₄ /Fe ₃ O ₄	6 M KOH	~529 at 1 A/g	–	–	~86% after 3,000 cycles	[133]
Co ₃ O ₄ /Fe ₂ O ₃ nanocubes	3 M KOH	–	1.125	35.15	89.4% after 10,000 cycles	[132]
Zn-Mn-Co ternary oxide nanoneedle	3 M KOH	849 C/g at 1 A/g	–	–	81.6% after 8,000 cycles	[155]
P-doped Co _{0.21} Ni _{0.79} MoO ₄ on Ni foam	2 M KOH	1127.5 at 0.5 A/g	0.75	49.2	91% after 5,000 cycles	[154]
NiO/ZnMn ₂ O ₄ nanocomposites	0.5 M KOH	886 at 1 A/g	–	–	–	[157]
Zn-Ni-Co oxide (ZNCO-HU) nanosheets/nanowires	2 M KOH	1742 at 1 A/g	0.76	55.4	95.2% after 5,000 cycles	[150]

Table 10. Advantages and disadvantages of PANI, PPy, and PTh based conducting polymers [167]

	Conducting polymer		
	PANI	PPy	PTh
Advantages	<ul style="list-style-type: none"> • Flexibility • Ease of fabrication • Large specific capacitance range • Ease of doping /de-doping • High theoretical specific capacitance • Controllable conductivity 	<ul style="list-style-type: none"> • Flexibility • Ease of fabrication • Relatively high specific capacitance • High cycling stability • Applicable to neutral electrolytes 	<ul style="list-style-type: none"> • Flexibility • Ease of synthesis • Favourable cycling stability • Favourable environment stability
Disadvantages	<ul style="list-style-type: none"> • Specific capacitance being much relied on the synthesis conditions • Poor cycling stability • Only applicable to proton type electrolytes 	<ul style="list-style-type: none"> • Relatively low specific capacitance • Difficulty of doping/de-doping • Only for cathode materials 	<ul style="list-style-type: none"> • Poor conductivity • poor specific capacitance

(b) Polypyrrole (ppy): is a very promising conducting polymer as its high conductivity, strong mechanical properties, and easily prepared via chemical and electrochemical techniques in both aqueous and non-aqueous media [180, 181]. One of the most significant properties of this CP remains electrical conductivity. However, two essential factors control the conductivity of polypyrrole, the first one is the charge carrier number can be electrons or holes, and the second one is the charge carrier mobility. On the other hand, similar to traditional semiconductors, a reduction in temperature causes decrease in conductivity [182]. Preparing method, dopant, substrate, template beside the above factors effects on the properties and microstructure of PPy based electrodes. Usually, the electrochemical properties of PPy can be improved critically by adjusting these factors [167, 181].

(c) Polythiophenes (PTh): polythiophene and its derivatives have recently been in research spotlight due to their remarkable properties, such as long wavelength absorption, stable energy storage, high environmental stability, and high electrical conductivity [183, 184]. Polythiophene is an organic conducting polymer highly tuneable and stable in air and can be formed in bulk powder as well as in thin film shape [171]. As the other conducting polymer, PTh is produced using different approaches including electrochemical, photoelectrochemical, template synthesis, chemical, and ultrasonic assisted electrochemical [170]. Lately, polythiophene nanocomposites have received much more attention from researchers and scientific communities. A comprehensive review of polythiophenes nanocomposites for different applications has been collected and discussed by Husain et al. [185]. Table 11 estimated and listed some characteristics and properties of various supercapacitors based on conducting polymers (CPs) electrode materials.

Table 11 Overview of various supercapacitors based on conducting polymers (CPs) electrode materials

Electrode	Electrolyte	Specific capacitance (F/g)	Power density (kW k/g)	Energy density (Wh k/g)	Retention capability	Ref.
<i>Polyaniline (PANI)</i>						
PANI	1 M H ₂ SO ₄	503 at 10 mV/s	8.88	96.23	85% after 1,000 cycles	[168]
Sulfonated PANI	1 M H ₂ SO ₄	1107 at 1 A/g	14.8	31.4	94% after 5,000 cycles	[186]

(continued)

Table 11 (continued)

Electrode	Electrolyte	Specific capacitance (F/g)	Power density (kW k/g)	Energy density (Wh k/g)	Retention capability	Ref.
Polypyrrole (ppy)						
PPy	1 M KCl	576 at 0.2 A/g	–	–	82% after 1,000 cycles	[169]
PPy	2 M NaCl	325 at 0.6 mA/cm ²	0.14	26.7	63% after 500 cycles	[187]
PPy	3 M KCl	343 at 5 mV/s	–	47.64	91% after 4,000 cycles	[188]
PPy	1 M NaCl	120 at 0.25 mA/cm ²	35 μW/cm ²	1.16 μW h/cm ²	88% after 1,000 cycles	[189]
Polythiophenes (PTh)						
PTh	0.1 M LiClO ₄	252 at 5 mV/s	0.36	4.86	85% after 1,000 cycles	[171]
PTh	0.1 M LiClO ₄ /PC	300 at 5 mV/s	1.14	11.43	87% after 1,000 cycles	[170]

5.4 Nano-Composite

The main problem for effective contribution of metal oxides in supercapacitor applications is its poor conductivity. So, to challenge this problem, carbon materials are simply combined with metal oxides and conductive polymers (CPs), resulting in anisotropic and synergistic multi-element new electrode materials (single electrode). Hence, these novel and various carbon-based composites have a convenient application potential in the electrochemical field of supercapacitors, electrocatalysts and batteries [190]. Moreover, this single electrode will possess physical (non-faradaic) and chemical (faradaic) charge storage mechanisms [2]. The carbon by itself shows a capacitive response as a result of the charge gathering in EDL. In addition to, it provides a large surface area that is, raising the connection among the electrolyte and the deposited materials. Hence, the electrode capacitances of pseudocapacitive materials are growing through faradaic reactions. Therefore, the high performance of these materials for nanocomposite electrodes qualified them to be smart candidates in high capacitances and energy density supercapacitors manufacturing. Recently, Composites have been classified into two categories: (i) Binary composites, which use two different electrode materials and (ii) Ternary composites, that is using three different electrode materials to fabricate single electrode [16]. Finally, the synthesis conditions and composite morphologies have impact on the specific capacitances.

So, these composite materials exposed a specific capacitance exceeded that of the individual constituents.

(a) Carbon- Carbon Composite: carbon nanomaterials, especially graphene and CNTs are considered encouraging applicants of electrode materials for highly efficient supercapacitors. Therefore, they possess moderate electrical properties, high mesoporosity, effective specific surface area (SSA), and electrolyte accessibility [191]. For example, large-scale production of high quality graphene remains challenging using recent technologies graphene based supercapacitor. Moreover, the drawbacks of graphene sheets are formation of irreversible agglomerates and restacking to their graphite structure. So, the intrinsic capacitance determination becomes very complicated. This restacking issue is owing to the occurrence of Vander wall interactions among the adjacent sheets. It decreases its energy density accordingly to reduction of the surface area [18]. As a result, it is significant to overcome the aforementioned defects of graphene through hybridization with porous carbon, CNTs, and carbon nanofibers (CNFs), in order to boost their performance needs for their usage [192, 193]. Also, AC with large surface area is predominant electrode material for commercial supercapacitors. However, AC has limited capacitance largely because of its low mesoporosity and poor electrolyte accessibility. Then, many efforts have been done to combine carbon nanomaterials with AC for composite electrode synthesis, which have been applied in supercapacitors areas [194]. In this regard, CNTs [195], CNFs [196], and graphene [197] have been separately explored for this task. Unfortunately, the working of the final composite electrodes is limited, which is credited to the inefficient influences of these carbon nanomaterials in the composite composition. So, high-performance supercapacitors, which used new nanocomposite electrodes, combine the traditional high surface area AC and conductivity additive (carbon black) with carbon nanomaterials (CNT and CNF). [21].

(b) Carbon- Metal oxide Composite: composites with transition metal oxide are being recognized as a favorable higher energy density than that of carbon materials itself. In this regard, activated carbon and metal oxides composite exceeded these limitations of single components as metal oxide. However, they are able to store charge through Faradaic mechanism, which upsurges the specific capacitance of the SCs without reducing the carbon material stability of the [12]. On the other hand, the combination of graphene with other electrochemically active components, as metal oxides introduce high electrochemically available area and hints the improvements in mechanical strength, thermal stability, and electrical conductivity of the electrode. All of the reported characters reduce the restacking of graphene layers [198]. Mostly, sol-gel methods, solvothermal or hydrothermal synthesis, chemical in situ deposition, and wet-chemical techniques are usually used for the synthesis of graphene metal oxide composite [12]. Additionally, as well known, most of the metal oxide undergoes capacitance decay and poor electrical conductivity that is controlling on the electrochemical performance of these materials. Therefore, composites have been developed in which metal oxide can be combined with highly conductive materials including other metal nanoparticles, nanostructured carbon materials, and conducting polymers to solve these problems [104]. Currently, much study is

concerned on the combination of metal oxides with carbon nanotubes (CNTs) to get improved cyclability, rate performance and capacitance [199–201]. Actually, CNTs have several advantages, including high specific surface area and chemical stabilities, excellent electrical conductivity, unique hollow and layered structure, and suitable ion transport gaps [200]. Various routes describe the direct deposition of metal oxide species onto the CNTs surface as chemical vapor deposition [202], electrodeposition [203], hydrothermal treatment [204] and atomic layer deposition (ALD) [200]. Therefore, the fabrication route and metal oxide amount mostly effects on surface chemistry and electrochemical performance for the fabricated composites [12, 205].

(c) Carbon-Conducting Polymer Composite: the low cycling stability of conductive polymer materials is owing to the volume changes during the doping–dedoping processes. Also, their poor specific capacitance limits their application as electrode materials in SCs [12]. Therefore, a conjunction of carbon-based active materials with conductive polymers may defeat these challenges and improve the electronic conductivity of the active layer. This combination is between polymer materials with activated carbon [206], graphene [207] and CNTs [208, 209] which are extensively investigated as composite formulations for SC applications. The improved in the composite stability is because of, the composite carbon network regulating the difference in volumetric through the cycles of charge and discharge which enhanced the retention capability [210]. Also, this combination provides mechanical support for the polymer framework and hence critically develop the specific capacitance and cycling performance [210]. In the contrary, CNTs have restrictive surface areas in comparison to other microporous carbon blacks. So, they preserve rigid mechanically robust structures, which produce a three-dimensional electrode configuration. This network arrangement provides a porous structure. This facilitates the electrolyte species transport and introduces extremely electronically conductive pathways for the active materials redox centers. So, these exclusive electrode structures work successfully to rise the application of these redox centers throughout the bulk of conductive polymer materials [211].

(d) Ternary composite: indeed, the components of binary composites have not been realized all the necessities of a high-performed supercapacitor. Consequently, various processes have been utilized to propose the fabrication of ternary composites, through combining all three types of electroactive materials [12]. During the last years, many hard works have been done to advance some novel ternary composites. This work is based on two pseudocapacitive materials. They are metal oxides and CPs together with carbonaceous materials (nanotubes, graphene or carbon nanofibers) [212–214]. The specific capacitance of such a ternary composite reached over 1000 F/g with a good charge/discharge rate, cycling stability and satisfactory charge retention [178]. So, this combination put a synergic effect and collects the advantages of both pseudocapacitive materials which are being at the origin of supercapacitors new generation. Table 12 illustrates properties and characteristics of various nanocomposite electrode materials.

Table 12 Overview of various Nano-composites electrode materials for supercapacitors

Electrode	Electrolyte	Specific capacitance (F/g)	Power density (kW k/g)	Energy density (Wh k/g)	Retention capability	Ref.
Nano-composite						
Carbon- Carbon Composite						
Graphene/CNT	1 M KOH	290.6 at 0.5 A/g	–	–	100% after 1,000 cycles	[215]
Porous graphene/AC	6 M KOH	210 at 1 mV/s	0.03	22.3	94.7% after 5,000 cycles	[197]
3D graphene/CNT	6 M KOH	413 at 5 mV/s	–	–	115% after 5,000 cycles	[216]
Carbon dots/rGO	1 M H ₂ SO ₄	211.9 at 0.5 A/g	–	–	92.8% after 1,000 cycles	[217]
(N-AC/Gr)	6 M KOH	378.9 at 0.05 A/g	0.01	13.1	93% after 10,000 cycles	[218]
nitrogen-doped hierarchical porous carbon/CNTs	6 M KOH	293.1 at 1 A/g	0.87	27.46	99% after 10,000 cycles	[219]
N, O co-doped porous carbon/CNT	6 M KOH	287 at 0.2 A/g	12.5	4.5	95% after 20,000 cycles	[220]
Carbon- Metal oxides Composite						
TiO ₂ /AC	1 M H ₂ SO ₄	155 at 10 mV/s	–	–	–	[221]
CNT/RuO ₂	1 M H ₂ SO ₄	953 at 1 mV/s	5	16.8	98% after 2,000 cycles	[114]
3D MnO ₂ /graphene	0.5 M Na ₂ SO ₄	30 at 2 mV/s	0.06	6.8	82% after 5,000 cycles	[222]

(continued)

Table 12 (continued)

Electrode	Electrolyte	Specific capacitance (F/g)	Power density (kW k/g)	Energy density (Wh k/g)	Retention capability	Ref.
rGO/CuO	0.5 M K ₂ SO ₄	326 at 0.5 A/g	0.30	65.7	–	[223]
Highly porous graphene planes/MgO	6 M KOH	303 at 0.5 A/g	–	6.5	–	[224]
Activated Fe ₂ O ₃ @carbon Core-shell	5 M KOH	612 at 0.5 A/g	–	–	90% after 10,000 cycles	[225]
Co ₉ S ₈ /RGO	6 M KOH	1349 at 2.2 A/g	1.32	68.6	~96% after 1,000 cycles	[226]
α-Fe ₂ O ₃ /rGO	1 M KOH	903 at 1 A/g	–	–	70% after 1,000 cycles	[227]
MnO ₂ /AC	1 M KOH	1126 at 0.5 A/g	0.28	24	–	[228]
MnFe ₂ O ₄ /rGO	6 M KOH	271 at 0.5 A/g	0.32	15.9	104% after 5,000 cycles	[229]
CNT/MnO ₂	0.5 M Na ₂ SO ₄	910.2 at 10 mV/s	–	–	90% after 100 cycles	[230]
CNT/Co ₃ O ₄	2 M KOH	592 at 1 A/g	–	–	96.8% after 5,000 cycles	[231]
rGO/ZnO	1 M Na ₂ SO ₄	312 at 5 mV/s	–	–	95% after 1,000 cycles	[232]
MnO ₂ -RuO ₂ @ GNR	0.5 M Na ₂ SO ₄	156 at 1 A/g	14	60	–	[140]
3D graphene/ Ni _x Co _{1-x} O	6 M KOH	697.8 at 20 A/g	0.73	27.2	86% after 10,000 cycles	[136]

(continued)

Table 12 (continued)

Electrode	Electrolyte	Specific capacitance (F/g)	Power density (kW k/g)	Energy density (Wh k/g)	Retention capability	Ref.
rGO/NiFe ₂ O ₄	1 M Na ₂ SO ₄	210.9 at 0.5 A/g	0.23	23.7	94.2% after 5,000 cycles	[233]
Fe ₃ O ₄ /M-CNTs	0.5 M Na ₂ SO ₄	145.4 at 2 mV/s	–	–	87% after 3000 cycles	[234]
RGO/La ₂ O ₃	3 M KOH	156.25 at 0.1 A/g	1.56	21.7	78% after 500 cycles	[235]
CoFe ₂ O ₄ /MWCNTs	2 M KOH	390 at 1 mA/cm ²	0.32	26.7	92% after 2,000 cycles	[236]
(MCFEs) @ SnO ₂	6 M KOH	406 at 0.5 A/g	0.45	11.5	95% after 10,000 cycles	[237]
Carbon- Conducting Polymer Composite						
rGO-F/PANI	1 M H ₂ SO ₄	790 at 1 A/g	98	17.6	80% after 5,000 cycles	[238]
PANI/grafted rGO	1 M H ₂ SO ₄	1045.5 at 0.2 A/g	60	8.3	94.8% after 1,000 cycles	[239]
Poly(aniline-copolyrrole)/hybrid carbon	2 M naps + 0.1 M P-toluene sulphonic acid	337.35 at 10 mV/s	–	–	–	[240]
PPy/RGO	1 M KOH	336	–	21.1	64% after 500 cycles	[241]
PPy/Graphene	0.5 M H ₂ SO ₄	640.8 at 1 A/g	0.44	68.2	90% after 2,000 cycles	[242]
PANI deposited CNT fiber	1 M H ₂ SO ₄	182.6 at 0.2 A/g	–	–	77.3% after 5,000 cycles	[243]

(continued)

Table 12 (continued)

Electrode	Electrolyte	Specific capacitance (F/g)	Power density (kW k/g)	Energy density (Wh k/g)	Retention capability	Ref.		
							241.6 at 0.5 A/g	1183 at 1 A/g
ZIF-8/chitosan aerogel composite	2 M KOH		–	–		[88]		
PANI/MWCNT (2 wt%)	1 M H ₂ SO ₄		–	183.18		[244]		
(PET)/MOF/rGO	Poly(vinyl alcohol) + H ₂ SO ₄		0.6 mW/cm ³	64 μW h/cm ³		[245]		
Cyclodextrin polymer@ PANI /CNT	1 M H ₂ SO ₄		–	–		[246]		
Nitrogen doped GO/ PANI	1 M H ₂ SO ₄		0.8	31.14		[247]		
Ternary composite								
PANI/GNR/CNT	PVA/H ₃ PO ₄		29.6	–		[248]		
CoFe ₂ O ₄ /graphene/ PANI	1 M KOH		0.18	79.7		[249]		
RGO/CNT/NiO	2 M KOH		–	–		[250]		
PPy/Graphene/ layered double hydroxide nanowires	1 M KOH		–	17.5		[251]		

(continued)

Table 12 (continued)

Electrode	Electrolyte	Specific capacitance (F/g)	Power density (kW k/g)	Energy density (Wh k/g)	Retention capability	Ref.
Graphene/Polyamine/ C ₃ O ₄	6 M KOH	1247 at 1 A/g	0.19	90	100% after 3,500 cycles	[252]
VS ₄ /CNTs/RGO	0.5 M K ₂ SO ₄	558.7 at 1 A/g	13.85	174.6	–	[253]
N- GNS/PdNP/porous PANI	1 M H ₂ SO ₄	931 at 3.8 A/g	1.2	31.94	96% after 3,000 cycles	[254]
PANI/Aethylene black/MnCo ₂ O ₄	1 M KOH	1.51 F/cm ² at 1 mA/cm ²	0.11	18.2	90% after 3,000 cycles	[255]
<i>f</i> - CNFs/PPy/MnO ₂	1 M KCl	409.9 at 0.5 A/g	~0.3	42.53	86.3% after 3,000 cycles	[256]
PANI/NiO/SGO	6 M KOH	1350 at 1 A/g	–	–	92.23% after 5,000 cycles	[178]
PPy/cobalt oxyhy- droxide/cellulose fiber	0.6 M H ₂ SO ₄	571.3 at 0.2 A/g	–	–	93.02% after 1,000 cycles	[257]
ZnS/RGO/PANI	6 M KOH	1045.3 at 1 A/g	18	349.7	160% after 1,000 cycles	[258]
PPy/rGO/PbO ₂	1 M KCl	514 at 1 A/g	–	–	86% after 4,000 cycles	[259]
PANI/RGO/Fe ₂ O ₃ hydrogel@ carbon cloth	1 M H ₂ SO ₄	1124 at 0.25 A/g	~0.06	14.4	82% after 10,000 cycles	[260]

6 Future Prospects Should Be Considered for Extra Development of Supercapacitors

Great efforts and research have been conducted in the field of supercapacitor area to upsurge the performance characteristics and make them more commercially applicable. So, an important area should be deeply studied for supercapacitor applications are electrode materials. All of these research, studies and data are to seal the gap between supercapacitor and batteries. Some major points should be taken care to enhance the supercapacitor applications field are summarized as follows:

- (1) The recent configuration examination belongs to novel electrode materials, electrolytes and current collectors for supercapacitor applications are considered. All these supercapacitors components should be tested before entering the production scale. Therefore, the reduction cost for ES devices is an urgent issue for enhancing their commercial usage to be attractive materials. Also, the combination between highly performed electrolytes, electrode materials, current collectors and decreasing the cost for the aforementioned components is a smart solution to make this technology is globally attractive and efficient from the economic perspective. However, persistent research and work should concentrate on highly operated material synthesis as electrode materials with a non-expensive preparation route.
- (2) The porous nature and structure of the carbon materials will be studied according to the surface area and influence of the functional groups on the ionic adsorption. All of these factors should mention carefully to enhance the capability of energy storage. Moreover, active carbon materials with tunable textural properties will be involved. Until now, much research has interested on the construction of mesoporous materials. The well style for mesoporous materials is a perfect key for developing supercapacitor electrodes. As well as, the high surface areas, good mesopores linking, and the crystal frame nanostructure are all properties characterized mesoporous materials. All of these characteristics enlarge capacitance, make the charge-discharge cycle fast and improve the cycling capability. Furthermore, the carbon yields contents of heteroatom and tap densities should be taken into consideration. Moreover, an important matter for scale production with a suitable effective cost should be involved in improving the conversion efficiency of biomass precursors.
- (3) For supercapacitor applications, the evaluation of binary, ternary, and other mixtures of oxide materials is crucial and needed to improve the capability of energy storage. Therefore, transition metal nitride, which is one of the 2D nanomaterial families, has been selected as a supercapacitor electrode material owing to its excellent properties, as wonderful electronic conductivity and chemical stability. Also, transition metal nitride material is one of the likely materials due to the life span device increasing. On the other hand, great efforts will be taken to devolve the utilization of redox centers and energy storage limit by examining new conducting polymers and novel nanocomposite as electrode materials. However, the carbonaceous materials may use as a backbone, in

- the composite material along with redox-active materials like MOs and CPs. Also, it could be combined with novel 2D materials to prepare a suitable flexible film used as electrode material for flexible/transparent SCs. Moreover, performing more efficient, inexpensive, friendly environment electrodes for SC application through merging the bioderived functional groups and redox-active small molecules into the pseudocapacitive material have been deeply studied to improve the capacitance of the carbon-based material.
- (4) For supercapacitor performance, an extension of potential window is a basic issue. Recently, intelligent choice of electrolyte materials (solid, liquid, or gel) is also crucial as it would have serious influence on the ionic conductivity and device stability. Novel alternatives such as aqueous or highly concentrated electrolytes have been useful to solve the interfacial drawbacks. Otherwise, deep understanding of the phenomena happening in ES during charging, discharge and energy storage will be enhanced.
 - (5) Theoretical computational science will be helpful for screening a great range for hybrid materials or composites and will be useful for supercapacitors application, by optimizing the temperature tolerance, physical properties and electrical conductivity. The construction of adherent theoretical models to specify the capacitor mechanisms, molecular interactions and chemistry is a sign that helps researchers improve capacitance and define the corresponding dynamics and ion diffusion. The most recent computational studies concerned on the impact of pore sizes on double-layer capacitance. On the other hand, experimental proof proposes that pores smaller than the sizes of solvated ion species can effect on capacitance. This shows an evident deficiency of understanding of ion desolvation, transport, and adsorption in micropores. Density functional theory (DFT) has been used for these systems to understand specific mechanisms. Various charge storage mechanisms were applied for pore sizes in different size systems (microporous, mesoporous, and macroporous). Therefore, these types of research supply excellent and fundamental data that will be precious for creating novel electrode materials. Furthermore, the ion species with various electrode materials and electrolyte type will have important effects on the performance of ES. Also, the deep study of electrolyte dynamics system will help to suggest novel electrolytes with molecular interactions at the electrode interfaces and highly ion transport properties, which enhance the supercapacitor performance.
 - (6) Finally, The effective solution for the recent energy crisis is the fabrication of smart, clean and effective SCs. Also, all of these properties should be combined with easily and safely waste disposal of SCs. industry. By this manner, the waste disposal problem, carbon emission and energy issue can be controlled. The applications all of these suggestions sharing in getting clean air and effective energy sources with less pollution.

7 Concluding Remarks

Recently, tremendous effort has been done in a hot topic, which is a high-performance electrode material for supercapacitor systems. Specific selections for electrode materials come from its fatal role in improving the electrochemical performance of supercapacitors, which is considered as the most recent category for energy storage implementation. Therefore, the electrode materials should characterize with some special properties as high conductivity, good chemical stability, temperature stability, corrosion resistance, environmentally clean and a lower cost. The main electrode materials dedicated for this purpose are including carbon materials, metal oxides, conducting polymers and nanocomposite, which are concluded in these following points:

- 1: Carbon materials are the most preferable electrode according to its high specific area, a friendly environment, low cost, wide range of operating temperatures, and easy processing. There are many members of carbon family like activated carbon, graphene, carbon nanotubes and carbon aerogel.
- 2: Metal oxide is a promising electrode material for supercapacitors due to their distinctive characteristics. Ruthenium oxide is the first oxide used for supercapacitors, but recently, there are several kinds of metal oxides as nickel oxide, iron oxide and manganese oxide. The combination of binary and ternary metal oxides was investigated to advance the capacitive performance of the materials via disturbing synergistic effects into an electrode system. On the other hand, it is considered a solution for enhancing the poor behavior of metal oxide types.
- 3: The conducting polymers (CPs) have many fascinating characters to share in the electrodes fabrication for supercapacitor applications. They have good conductivity, environmental stability, large theoretical specific capacitance, ease of large-scale production and relatively cheap. Among all kinds of conducting polymers, PANI, PPy, PTh and some of their derivatives consider a good choice for Supercapacitor electrode materials.
- 4: Nanocomposites, which are formed through the combination between metal oxides, conducting polymers with carbonaceous materials (graphene, nanotubes or carbon nanofibers) have been effectively investigated to heal the singular electrode material problems. These composite materials exposed a specific capacitance exceeded that of the individual constituents with cycling stability, satisfactory charge retention and a good charge/discharge rate. By the way, carbon materials are simply merged with MO_x and CPs, creating anisotropic and synergistic multi-element new electrode materials (single electrode). Carbon-Carbon Composite especially graphene and CNTs are considered encouraging electrode candidate materials for highly efficient supercapacitors. Therefore, they possess effective specific surface area (SSA), moderate electrical properties, electrolyte accessibility, and high mesoporosity. Also, carbon-metal oxide composites have a hopeful application in the electrochemical field of supercapacitors, electrocatalysts and batteries as it overcomes the poor conductivity and exceeded these limitations of single components of metal oxide. While, a conjunction of carbon-based active materials with conductive polymers provides mechanical support

for the polymer framework and hence critically develop the specific capacitance and cycling performance.

Finally, we provide major points which have been suggested for Future perspective to upsurge the characteristics performance of supercapacitors.

References

1. Halper M.S., Ellenbogen, J.C., Supercapacitors: A brief overview. The MITRE Corporation, McLean, Virginia, USA, pp. 1–34 (2006)
2. Faraji, S., Ani, F.N.: The development supercapacitor from activated carbon by electroless plating—a review. *Renew. Sust. Energ. Rev.* **42**, 823–834 (2015)
3. Pollet, B., Staffell, I., Shang, J., Molkov, V.: Fuel-cell (hydrogen) electric hybrid vehicles. In: *Alternative Fuels and Advanced Vehicle Technologies for Improved Environmental Performance*. Woodhead Publishing, Sawston, pp. 685–735 (2014)
4. Kim, B.K., Sy, S., Yu, A., Zhang, J.: Electrochemical supercapacitors for energy storage and conversion. In: Jinyue, Y. (ed) *Handbook of Clean Energy Systems*, Wiley, Chichester, pp. 1–25 (2015)
5. Becker, H.I.: Low voltage electrolytic capacitor. U.S. Patent No. 2,800,616. Washington, DC: U.S. Patent and Trademark Office (1957)
6. Boos, D.L.: Electrolytic capacitor having carbon paste electrodes. U.S. Patent No. 3,536,963. Washington, DC: U.S. Patent and Trademark Office. (1970)
7. Conway, B.E.: Transition from “supercapacitor” to “battery” behavior in electrochemical energy storage. *J. Electrochem. Soc.* **138**(6), 1539 (1991)
8. Conway, B.E.: *Electrochemical Supercapacitors: Scientific Fundamentals and Technological Applications*. Kluwer Academic/Plenum Publishing, New York (1999)
9. Sharma, K., Arora, A., Tripathi, S.K.: Review of supercapacitors: materials and devices. *J. Energy Storage* **21**, 801–825 (2019)
10. Wang, R., Yao, M., Niu, Z.: Smart supercapacitors from materials to devices. *InfoMat* **2**(1), 113–125 (2020)
11. Samantara, A.K., Ratha, S.: Components of supercapacitor. In: *Materials Development for Active/Passive Components of a Supercapacitor: Background, Present Status and Future Perspective*. Springer, Singapore, pp. 11–39 (2018)
12. Kar, K.K.: *Handbook of Nanocomposite Supercapacitor Materials II*. Springer, Cham (2020)
13. Zhang, S., Pan, N.: Supercapacitors performance evaluation. *Adv Energy Mater.* **5**(6), 1401401 (2015)
14. Samantara, A.K., Ratha, S.: *Materials Development for Active/Passive Components of a Supercapacitor: Background, present status and future perspective*. Springer, Singapore (2017)
15. Libich, J., Máca, J., Vondrák, J., Čech, O., Sedlářková, M.: Supercapacitors: properties and applications. *J. Energy Storage* **17**, 224–227 (2018)
16. Iro, Z.S., Subramani, C., Dash, S.: A brief review on electrode materials for supercapacitor. *Int. J. Electrochem. Sci.* **11**(12), 10628–10643 (2016)
17. Wang, G., Zhang, L., Zhang, J.: A review of electrode materials for electrochemical supercapacitors. *Chem. Soc. Rev.* **41**(2), 797–828 (2012)
18. Dubey, R., Guruviah, V.: Review of carbon-based electrode materials for supercapacitor energy storage. *Ionics* **25**(4), 1419–1445 (2019)
19. Simon, P., Gogotsi, Y.: Capacitive energy storage in nanostructured carbon–electrolyte systems. *Acc. Chem. Res.* **46**(5), 1094–1103 (2013)
20. De, B., et al.: Transition metal oxide-/Carbon-/electronically conducting polymer-based ternary composites as electrode materials for supercapacitors. In: Kar, K.K. (ed.) *Handbook of Nanocomposite Supercapacitor Materials II, Performance Springer Series in Materials Science*, SSMS 302, vol. 302, Springer, Cham, pp. 387–434 (2020)

21. Cheng, F., Yang, X., Zhang, S., Lu, W.: Boosting the supercapacitor performances of activated carbon with carbon nanomaterials. *J. Power Sources* **450**, 227678 (2020)
22. Ruiz, V., et al.: An activated carbon monolith as an electrode material for supercapacitors. *Carbon* **47**(1), 195–200 (2009)
23. Zhang, Y., Cui, H., Ozao, R., Cao, Y., Chen, B.I.-T., Wang, C.-W., Pan, W.-P.: Characterization of activated carbon prepared from chicken waste and coal. *Energy Fuels* **21**(6), 3735–3739 (2007)
24. Jin, Z., Yan, X., Yu, Y., Zhao, G.: Sustainable activated carbon fibers from liquefied wood with controllable porosity for high-performance supercapacitors. *J. Mater. Chem. A* **2**(30), 11706–11715 (2014)
25. Teo, E.Y.L., Muniandy, L., Ng, E.-P., Adam, F., Mohamed, A.R., Jose, R., Chong, K.F.: High surface area activated carbon from rice husk as a high performance supercapacitor electrode. *Electrochim. Acta* **192**, 110–119 (2016)
26. Nguyen, T.D., Ryu, J.K., Bramhe, S.N., Kim, T.-N.: Performance of electric double layers capacitor using activated carbon materials from rice husk as electrodes. *Kor. J. Mater. Res.* **23**(11), 643–648 (2013)
27. Le Van, K., Thi, T.T.L.: Activated carbon derived from rice husk by NaOH activation and its application in supercapacitor. *Prog. Nat. Sci.* **24**(3), 191–198 (2014)
28. Jiang, L., Yan, J., Hao, L., Xue, R., Sun, G., Yi, B.: High rate performance activated carbons prepared from ginkgo shells for electrochemical supercapacitors. *Carbon* **56**, 146–154 (2013)
29. Elmouwahidi, A., Zapata-Benabithe, Z., Carrasco-Marín, F., Moreno-Castilla, C.: Activated carbons from KOH-activation of argan (*Argania spinosa*) seed shells as supercapacitor electrodes. *Bioresour. Technol.* **111**, 185–190 (2012)
30. Misono, I.I., Zain, N.K.M., Abd Aziz, R., Vidyadharan, B., Jose, R.: Electrochemical properties of carbon from oil palm kernel shell for high performance supercapacitors. *Electrochim. Acta* **174**, 78–86 (2015)
31. Lee, S.G., Park, K.H., Shim, W.G., Moon, H.: Performance of electrochemical double layer capacitors using highly porous activated carbons prepared from beer lees. *J. Ind. Eng. Chem.* **17**(3), 450–454 (2011)
32. Wang, R., Wang, P., Yan, X., Lang, J., Peng, C., Xue, Q.: Promising porous carbon derived from cellulose leaves with outstanding supercapacitance and CO₂ capture performance. *ACS Appl. Mater. Interfaces* **4**(11), 5800–5806 (2012)
33. Choi, J., Kim, N.R., Jin, H.-J., Yun, Y.S.: Nanoporous pyropolymer nanosheets fabricated from renewable bio-resources for supercapacitors. *J. Ind. Eng. Chem.* **43**, 158–163 (2016)
34. Arie, A.A., Kristianto, H., Halim, M., Lee, J.K.: Synthesis and modification of activated carbon originated from Indonesian local Orange peel for lithium ion Capacitor's cathode. *J. Solid State Electr.* **21**(5), 1331–1342 (2017)
35. Adinaveen, T., Kennedy, L.J., Vijaya, J.J., Sekaran, G.: Studies on structural, morphological, electrical and electrochemical properties of activated carbon prepared from sugarcane bagasse. *J. Ind. Eng. Chem.* **19**(5), 1470–1476 (2013)
36. Shrestha, L.K., et al.: Nanoporous carbon materials with enhanced supercapacitance performance and non-aromatic chemical sensing with C₁/C₂ alcohol discrimination. *Sci. Technol. Adv. Mater.* **17**(1), 483–492 (2016)
37. Adhikari, M.P., et al.: Nanoporous activated carbons derived from agro-waste corncob for enhanced electrochemical and sensing performance. *Bull. Chem. Soc. Jpn.* **88**(8), 1108–1115 (2015)
38. Zhang, J., Gong, L., Sun, K., Jiang, J., Zhang, X.: Preparation of activated carbon from waste camellia oleifera shell for supercapacitor application. *J. Solid State Electr.* **16**(6), 2179–2186 (2012)
39. Demarconnay, L., Raymundo-Pi, E., BÚguin, F.: A symmetric carbon/carbon supercapacitor operating at 1.6 aV by using a neutral aqueous solution. *Electrochem. Commun.* **12**(10), 1275–1278 (2010)
40. Fic, K., Lota, G., Meller, M., Frackowiak, E.: Novel insight into neutral medium as electrolyte for high-voltage supercapacitors. *Energy Environ. Sci.* **5**(2), 5842–5850 (2012)

41. Francke, R., Cericola, D., Kötzer, R., Weingarth, D., Waldvogel, S.R.: Novel electrolytes for electrochemical double layer capacitors based on 1,1,1,3,3,3-hexafluoropropan-2-ol. *Electrochim. Acta* **62**, 372–380 (2012)
42. Brandt, A., Isken, P., Lex-Balducci, A., Balducci, A.: Adiponitrile-based electrochemical double layer capacitor. *J. Power Sources* **204**, 213–219 (2012)
43. Abbas, Q., Pajak, D., Frąckowiak, E., Béguin, F.: Effect of binder on the performance of carbon/carbon symmetric capacitors in salt aqueous electrolyte. *Electrochim. Acta* **140**, 132–138 (2014)
44. Jiménez-Cordero, D., Heras, F., Gilarranz, M.A., Raymundo-Piñero, E.: Grape seed carbons for studying the influence of texture on supercapacitor behaviour in aqueous electrolytes. *Carbon* **71**, 127–138 (2014)
45. Yu, X., Ruan, D., Wu, C., Wang, J., Shi, Z.: Spiro-(1, 1′)-bipyrrolidinium tetrafluoroborate salt as high voltage electrolyte for electric double layer capacitors. *J. Power Sources* **265**, 309–316 (2014)
46. Momodu, D., et al.: Activated carbon derived from tree bark biomass with promising material properties for supercapacitors. *J. Solid State Electr.* **21**(3), 859–872 (2017)
47. Zou, Z., Liu, T., Jiang, C.: Highly mesoporous carbon flakes derived from a tubular biomass for high power electrochemical energy storage in organic electrolyte. *Mater. Chem. Phys.* **223**, 16–23 (2019)
48. Jia, X., Guo, F., Zhan, Y., Zhou, H., Jiang, X., Qian, L.: Synthesis of porous carbon materials with mesoporous channels from Sargassum as electrode materials for supercapacitors. *J. Electroanal. Chem.* **873**, 114353 (2020)
49. Eleri, O.E., et al.: Towards high-energy-density supercapacitors via less-defects activated carbon from sawdust. *Electrochim. Acta* **362**, 137152 (2020)
50. Rani, M.U., Nanaji, K., Rao, T.N., Deshpande, A.S.: Corn husk derived activated carbon with enhanced electrochemical performance for high-voltage supercapacitors. *J. Power Sources* **471**, 228387 (2020)
51. Kuila, T., Khanra, P., Kim, N.H., Choi, S.K., Yun, H.J., Lee, J.H.: One-step electrochemical synthesis of 6-amino-4-hydroxy-2-naphthalene-sulfonic acid functionalized graphene for green energy storage electrode materials. *Nanotechnology* **24**(36), 365706 (2013)
52. Raccichini, R., Varzi, A., Passerini, S., Scrosati, B.: The role of graphene for electrochemical energy storage. *Nat. Mater.* **14**(3), 271–279 (2015)
53. Hillier, N., Yong, S., Beeby, S.: The good, the bad and the porous: a review of carbonaceous materials for flexible supercapacitor applications. *Energy Rep.* **6**, 148–156 (2020)
54. Ramachandran, R., Saranya, M., Velmurugan, V., Raghupathy, B.P., Jeong, S.K., Grace, A.N.: Effect of reducing agent on graphene synthesis and its influence on charge storage towards supercapacitor applications. *Appl. Energy* **153**, 22–31 (2015)
55. Choi, B.G., Hong, J., Hong, W.H., Hammond, P.T., Park, H.: Facilitated ion transport in all-solid-state flexible supercapacitors. *ACS Nano* **5**(9), 7205–7213 (2011)
56. Yang, X., Zhu, J., Qiu, L., Li, D.: Bioinspired effective prevention of restacking in multilayered graphene films: towards the next generation of high-performance supercapacitors. *Adv. Mater.* **23**(25), 2833–2838 (2011)
57. Wu, Z.S., Winter, A., Chen, L., Sun, Y., Turchanin, A., Feng, X., Müllen, K.: Three-dimensional nitrogen and boron co-doped graphene for high-performance all-solid-state supercapacitors. *Adv. Mater.* **24**(37), 5130–5135 (2012)
58. Xu, Y., Lin, Z., Huang, X., Wang, Y., Huang, Y., Duan, X.: Functionalized graphene hydrogel-based high-performance supercapacitors. *Adv. Mater.* **25**(40), 5779–5784 (2013)
59. Sheng, L., Chang, J., Jiang, L., Jiang, Z., Liu, Z., Wei, T., Fan, Z.: Multilayer-folded graphene ribbon film with ultrahigh areal capacitance and high rate performance for compressible supercapacitors. *Adv. Funct. Mater.* **28**(21), 1800597 (2018)
60. Liu, Y.-Y., Luo, S.-H., Yan, S.-X., Feng, J., Yi, T.-F.: Green synthesis of reduced graphene oxide as high-performance electrode materials for supercapacitors. *Ionics* **26**(1), 415–422 (2020)

61. Liu, J., Zhu, Y., Chen, X., Yi, W.: Nitrogen, sulfur and phosphorus tri-doped holey graphene oxide as a novel electrode material for application in supercapacitor. *J. Alloys Compd.* **815**, 152328 (2020)
62. Pan, H., Li, J., Feng, Y.: Carbon nanotubes for supercapacitor. *Nanoscale Res. Lett.* **5**(3), 654–668 (2010)
63. Niu, C., Sichel, E.K., Hoch, R., Moy, D., Tennent, H.: High power electrochemical capacitors based on carbon nanotube electrodes. *Appl. Phys. Lett.* **70**(11), 1480–1482 (1997)
64. Zhang, L.L., Zhou, R., Zhao, X.: Graphene-based materials as supercapacitor electrodes. *J. Mater. Chem.* **20**(29), 5983–5992 (2010)
65. Zhu, Y., Shi, K., Zhitomirsky, I.: Polypyrrole coated carbon nanotubes for supercapacitor devices with enhanced electrochemical performance. *J. Power Sources* **268**, 233–239 (2014)
66. Hong, H., Kim, M., Lee, Y.-H., Yu, J., Lee, C.J., Min, N.: Spray deposition of LiMn_2O_4 nanoparticle-decorated multiwalled carbon nanotube films as cathode material for lithium-ion batteries. *Thin Solid Films* **547**, 68–71 (2013)
67. Chitturi, V.R., Ara, M., Fawaz, W., Ng, K.S., Arava, L.M.R.: Enhanced lithium-oxygen battery performances with Pt subnanocluster decorated n-doped single-walled carbon nanotube cathodes. *ACS Catal.* **6**(10), 7088–7097 (2016)
68. Wang, W., et al.: Silicon decorated cone shaped carbon nanotube clusters for lithium ion battery anodes. *Small* **10**(16), 3389–3396 (2014)
69. Imbrogno, A., Pandiyan, R., Barberio, M., Macario, A., Bonanno, A.: Pulsed-laser-ablation based nanodecoration of multi-wall-carbon nanotubes by Co–Ni nanoparticles for dye-sensitized solar cell counter electrode applications. *Mater. Renew. Sustain. Energy* **6**(2), 11 (2017)
70. Ding, H., et al.: TiO_2 quantum dots decorated multi-walled carbon nanotubes as the multi-functional separator for highly stable lithium sulfur batteries. *Electrochim. Acta* **284**, 314–320 (2018)
71. Izadi-Najafabadi, A., et al.: Extracting the full potential of single-walled carbon nanotubes as durable supercapacitor electrodes operable at 4 V with high power and energy density. *Adv. Mater.* **22**(35), E235–E241 (2010)
72. Niu, Z., et al.: Highly stretchable, integrated supercapacitors based on single-walled carbon nanotube films with continuous reticulate architecture. *Adv. Mater.* **25**(7), 1058–1064 (2013)
73. Yang, Z., Deng, J., Chen, X., Ren, J., Peng, H.: A highly stretchable, fiber-shaped supercapacitor. *Angew. Chem.* **125**(50), 13695–13699 (2013)
74. Wang, G., Liang, R., Liu, L., Zhong, B.: Improving the specific capacitance of carbon nanotubes-based supercapacitors by combining introducing functional groups on carbon nanotubes with using redox-active electrolyte. *Electrochim. Acta* **115**, 183–188 (2014)
75. Lee, J., Kim, W., Kim, W.: Stretchable carbon nanotube/ion-gel supercapacitors with high durability realized through interfacial microroughness. *ACS Appl. Mater. Interfaces* **6**(16), 13578–13586 (2014)
76. Gueon, D., Moon, J.H.: Nitrogen-doped carbon nanotube spherical particles for supercapacitor applications: emulsion-assisted compact packing and capacitance enhancement. *ACS Appl. Mater. Interfaces* **7**(36), 20083–20089 (2015)
77. Najib, S., Erdem, E.: Current progress achieved in novel materials for supercapacitor electrodes: mini review. *Nanoscale Adv.* **1**(8), 2817–2827 (2019)
78. Liu, R., Wan, L., Liu, S., Pan, L., Wu, D., Zhao, D.: An interface-induced co-assembly approach towards ordered mesoporous carbon/Graphene aerogel for high-performance supercapacitors. *Adv. Funct. Mater.* **25**(4), 526–533 (2015)
79. Nardecchia, S., Carriazo, D., Ferrer, M.L., Gutiérrez, M.C., Del Monte, F.: Three dimensional macroporous architectures and aerogels built of carbon nanotubes and/or graphene: synthesis and applications. *Chem. Soc. Rev.* **42**(2), 794–830 (2013)
80. Fang, K., et al.: Decorating biomass-derived porous carbon with Fe_2O_3 ultrathin film for high-performance supercapacitors. *Electrochim. Acta* **261**, 198–205 (2018)
81. Zhang, Y., et al.: Cotton wool derived carbon fiber aerogel supported few-layered MoSe_2 nanosheets as efficient electrocatalysts for hydrogen evolution. *ACS Appl. Mater. Interfaces* **8**(11), 7077–7085 (2016)

82. Zhang, Y., Fan, W., Huang, Y., Zhang, C., Liu, T.: Graphene/carbon aerogels derived from graphene crosslinked polyimide as electrode materials for supercapacitors. *RSC Adv.* **5**(2), 1301–1308 (2015)
83. Kobina Sam, D., Kobina Sam, E., Lv, X.: Application of biomass-derived nitrogen-doped carbon aerogels in electrocatalysis and supercapacitors. *ChemElectroChem* **7**(18), 3695–3712 (2020)
84. Pekala, R.: Organic aerogels from the polycondensation of resorcinol with formaldehyde. *J. Mater. Sci.* **24**(9), 3221–3227 (1989)
85. Wu, X.-L., Wen, T., Guo, H.-L., Yang, S., Wang, X., Xu, A.-W.: Biomass-derived sponge-like carbonaceous hydrogels and aerogels for supercapacitors. *ACS Nano* **7**(4), 3589–3597 (2013)
86. Hao, P., et al.: Graphene-based nitrogen self-doped hierarchical porous carbon aerogels derived from chitosan for high performance supercapacitors. *Nano Energy* **15**, 9–23 (2015)
87. Zhang, Y., Zhao, C., Ong, W.K., Lu, X.: Ultrafast-freezing-assisted mild preparation of biomass-derived, hierarchically porous, activated carbon aerogels for high-performance supercapacitors. *ACS Sustain. Chem. Eng.* **7**(1), 403–411 (2018)
88. Wang, M., et al.: Nitrogen-doped hierarchical porous carbon derived from ZIF-8 supported on carbon aerogels with advanced performance for supercapacitor. *Appl. Surf. Sci.* **507**, 145166 (2020)
89. Jung, S.M., Mafra, D.L., Lin, C.-T., Jung, H.Y., Kong, J.: Controlled porous structures of graphene aerogels and their effect on supercapacitor performance. *Nanoscale* **7**(10), 4386–4393 (2015)
90. Zhu, C., et al.: Supercapacitors based on three-dimensional hierarchical graphene aerogels with periodic macropores. *Nano Lett.* **16**(6), 3448–3456 (2016)
91. Zhuo, H., Hu, Y., Tong, X., Zhong, L., Peng, X., Sun, R.: Sustainable hierarchical porous carbon aerogel from cellulose for high-performance supercapacitor and CO₂ capture. *Ind. Crops Prod.* **87**, 229–235 (2016)
92. Cui, J., et al.: Prolifera-green-tide as sustainable source for carbonaceous aerogels with hierarchical pore to achieve multiple energy storage. *Adv. Funct. Mater.* **26**(46), 8487–8495 (2016)
93. Lei, E., Li, W., Ma, C., Xu, Z., Liu, S.: CO₂-activated porous self-templated N-doped carbon aerogel derived from banana for high-performance supercapacitors. *Appl. Surf. Sci.* **457**, 477–486 (2018)
94. Cai, T., Kuang, L., Wang, C., Jin, C., Wang, Z., Sun, Q.: Cellulose as an adhesive for the synthesis of carbon aerogel with a 3D hierarchical network structure for capacitive energy storage. *ChemElectroChem* **6**(9), 2586–2594 (2019)
95. Zhang, H., et al.: A chemical blowing strategy to fabricate biomass-derived carbon-aerogels with graphene-like nanosheet structures for high-performance supercapacitors. *Chemsuschem* **12**(11), 2462–2470 (2019)
96. Yang, X., Liu, X., Cao, M., Deng, Y., Li, X.: Tailoring porous carbon aerogels from bamboo cellulose fibers for high-performance supercapacitors. *J. Porous Mater.* **26**(6), 1851–1860 (2019)
97. Yang, X., Kong, L., Cao, M., Liu, X., Li, X.: Porous nanosheets-based carbon aerogel derived from sustainable rattan for supercapacitors application. *Ind. Crops Prod.* **145**, 112100 (2020)
98. Scibioh, M.A., Viswanathan, B.: *Materials for Supercapacitor Applications*. Elsevier, Amsterdam (2020)
99. Xia, H., Meng, Y.S., Yuan, G., Cui, C., Lu, L.: A symmetric RuO₂/RuO₂ supercapacitor operating at 1.6 V by using a neutral aqueous electrolyte. *Electrochem Solid-State Lett.* **15**(4), A60 (2012)
100. Li, S., Qi, L., Lu, L., Wang, H.: Facile preparation and performance of mesoporous manganese oxide for supercapacitors utilizing neutral aqueous electrolytes. *RSC Adv.* **2**(8), 3298–3308 (2012)
101. Wei, W., Cui, X., Chen, W., Ivey, D.G.: Manganese oxide-based materials as electrochemical supercapacitor electrodes. *Chem. Soc. Rev.* **40**(3), 1697–1721 (2011)

102. Ragupathy, P., Park, D.H., Campet, G., Vasan, H., Hwang, S.-J., Choy, J.-H., Munichandraiah, N.: Remarkable capacity retention of nanostructured manganese oxide upon cycling as an electrode material for supercapacitor. *J. Phys. Chem. C* **113**(15), 6303–6309 (2009)
103. Fu, C., Mahadevegowda, A., Grant, P.S.: Production of hollow and porous Fe₂O₃ from industrial mill scale and its potential for large-scale electrochemical energy storage applications. *J. Mater. Chem. A* **4**(7), 2597–2604 (2016)
104. Xu, B., et al.: Iron oxide-based nanomaterials for supercapacitors. *Nanotechnology* **30**(20), 204002 (2019)
105. Nithya, V., Arul, N.S.: Review on α -Fe₂O₃ based negative electrode for high performance supercapacitors. *J. Power Sources* **327**, 297–318 (2016)
106. Yang, Z., Xu, F., Zhang, W., Mei, Z., Pei, B., Zhu, X.: Controllable preparation of multishelled NiO hollow nanospheres via layer-by-layer self-assembly for supercapacitor application. *J. Power Sources* **246**, 24–31 (2014)
107. Cheng, G., Yang, W., Dong, C., Kou, T., Bai, Q., Wang, H., Zhang, Z.: Ultrathin mesoporous NiO nanosheet-anchored 3D nickel foam as an advanced electrode for supercapacitors. *J. Mater. Chem. A* **3**(33), 17469–17478 (2015)
108. Liu, Q., Yan, Q., Wu, S., Wang, J., Liu, H.: Ultrathin porous NiO nanoflake arrays on nickel foam as binder-free electrodes for supercapacitors. *Electrochemistry* **84**(4), 219–223 (2016)
109. Abdah, M.M., Azman, N.H.N., Kulandaivalu, S., Sulaiman, Y.: Review of the use of transition-metal-oxide and conducting polymer-based fibres for high-performance supercapacitors. *Mater. Des.* **186**, 108199 (2020)
110. Pandolfo, A.G., Hollenkamp, A.F.: Carbon properties and their role in supercapacitors. *J. Power Sources* **157**(1), 11–27 (2006)
111. Park, B.-O., Lokhande, C., Hyung-Sang, P., Jung, K.-D., Joo, O.-S.: Electrodeposited ruthenium oxide (RuO₂) films for electrochemical supercapacitors. *J. Mater. Sci.* **39**(13), 4313–4317 (2004)
112. Afif, A., Rahman, S.M., Azad, A.T., Zaini, J., Islan, M.A., Azad, A.K.: Advanced materials and technologies for hybrid supercapacitors for energy storage—a review. *J. Energy Storage* **25**, 100852 (2019)
113. Zhao, C., Zheng, W.: A review for aqueous electrochemical supercapacitors. *Front. Energy Res.* **3**, 23 (2015)
114. Bi, R.-R., Wu, X.-L., Cao, F.-F., Jiang, L.-Y., Guo, Y.-G., Wan, L.-J.: Highly dispersed RuO₂ nanoparticles on carbon nanotubes: facile synthesis and enhanced supercapacitance performance. *J. Phys. Chem. C* **114**(6), 2448–2451 (2010)
115. Zhang, S., Chen, G.Z.: Manganese oxide based materials for supercapacitors. *Energy Mater.* **3**(3), 186–200 (2008)
116. Chang, J.-K., Huang, C.-H., Lee, M.-T., Tsai, W.-T., Deng, M.-J., Sun, I.-W.: Physicochemical factors that affect the pseudocapacitance and cyclic stability of Mn oxide electrodes. *Electrochim. Acta* **54**(12), 3278–3284 (2009)
117. Hill, L.L., Verbaere, A., Guyomard, D.: Nanofibrous α , β , γ and α γ -manganese dioxides prepared by the hydrothermal-electrochemical technique: I. Synth. Charact. *J. Electrochem. Soc.* **150**(8), D135 (2003)
118. Brousse, T., Toupin, M., Dugas, R., Athouel, L., Crosnier, O., Belanger, D.: Crystalline MnO₂ as possible alternatives to amorphous compounds in electrochemical supercapacitors. *J. Electrochem. Soc.* **153**(12), A2171 (2006)
119. Ghodbane, O., Pascal, J.-L., Favier, F.: Microstructural effects on charge-storage properties in MnO₂-based electrochemical supercapacitors. *ACS Appl. Mater. Interfaces* **1**(5), 1130–1139 (2009)
120. Zheng, X., et al.: Spinous α -Fe₂O₃ hierarchical structures anchored on Ni foam for supercapacitor electrodes and visible light driven photocatalysts. *Dalton Trans.* **45**(16), 7094–7103 (2016)
121. Moysseowicz, A., Śliwak, A., Miniach, E., Gryglewicz, G.: Polypyrrole/iron oxide/reduced graphene oxide ternary composite as a binderless electrode material with high cyclic stability for supercapacitors. *Compos. B. Eng* **109**, 23–29 (2017)

122. Aghazadeh, M., Ganjali, M.R.: Samarium-doped Fe₃O₄ nanoparticles with improved magnetic and supercapacitive performance: a novel preparation strategy and characterization. *J. Mater. Sci.* **53**(1), 295–308 (2018)
123. Aghazadeh, M., Ganjali, M.R.: Evaluation of supercapacitive and magnetic properties of Fe₃O₄ nano-particles electrochemically doped with dysprosium cations: development of a novel iron-based electrode. *Ceram. Int.* **44**(1), 520–529 (2018)
124. Wang, L., et al.: Ultrasonic-assisted synthesis of amorphous Fe₃O₄ with a high specific surface area and improved capacitance for supercapacitor. *Powder Technol.* **256**, 499–505 (2014)
125. Gong, X., Li, S., Lee, P.S.: A fiber asymmetric supercapacitor based on FeOOH/PPy on carbon fibers as an anode electrode with high volumetric energy density for wearable applications. *Nanoscale* **9**(30), 10794–10801 (2017)
126. Chen, L.-F., et al.: Metal-like fluorine-doped β-FeOOH nanorods grown on carbon cloth for scalable high-performance supercapacitors. *Nano Energy* **11**, 119–128 (2015)
127. Shen, B., Guo, R., Lang, J., Liu, L., Liu, L., Yan, X.: A high-temperature flexible supercapacitor based on pseudocapacitive behavior of FeOOH in an ionic liquid electrolyte. *J. Mater. Chem. A* **4**(21), 8316–8327 (2016)
128. Zhang, S., Pang, Y., Wang, Y., Dong, B., Lu, S., Li, M., Ding, S.: NiO nanosheets anchored on honeycomb porous carbon derived from wheat husk for symmetric supercapacitor with high performance. *J. Alloys Compd.* **735**, 1722–1729 (2018)
129. Yin, B.-S., Wang, Z.-B., Zhang, S.-W., Liu, C., Ren, Q.-Q., Ke, K.: In situ growth of free-standing all metal oxide asymmetric supercapacitor. *ACS Appl. Mater. Interfaces* **8**(39), 26019–26029 (2016)
130. Wang, H., Yi, H., Chen, X., Wang, X.: Facile synthesis of a nano-structured nickel oxide electrode with outstanding pseudocapacitive properties. *Electrochim. Acta* **105**, 353–361 (2013)
131. Zhu, G., et al.: Porous Fe-Mn-O nanocomposites: synthesis and supercapacitor electrode application. *Prog. Nat. Sci.* **26**(3), 264–270 (2016)
132. Wei, X., et al.: A novel functional material of Co₃O₄/Fe₂O₃ nanocubes derived from a MOF precursor for high-performance electrochemical energy storage and conversion application. *Chem. Eng. J.* **355**, 336–340 (2019)
133. Song, F., Zan, G., Chen, Y., Wu, Q., Xu, Y.: In situ transformation of iron-group ternary metal oxides nanocubes from Co/Ni-PBA for high-performance supercapacitors. *J. Alloys Compd.* **741**, 633–641 (2018)
134. Fan, M., et al.: Facile synthesis of Co₃O₄ nanowires grown on hollow NiO microspheres with superior electrochemical performance. *Electrochim. Acta* **166**, 168–173 (2015)
135. Yu, L., Guan, B., Xiao, W., Lou, X.W.: Formation of yolk-shelled Ni-Co mixed oxide nanoprisms with enhanced electrochemical performance for hybrid supercapacitors and lithium ion batteries. *Adv. Energy Mater.* **5**(21), 1500981 (2015)
136. Zhou, Y., Wen, L., Zhan, K., Yan, Y., Zhao, B.: Three-dimensional porous graphene/nickel cobalt mixed oxide composites for high-performance hybrid supercapacitor. *Ceram. Int.* **44**(17), 21848–21854 (2018)
137. Majid, S.: High performance super-capacitive behaviour of deposited manganese oxide/nickel oxide binary electrode system. *Electrochim. Acta* **138**, 1–8 (2014)
138. Kadam, S., Mane, S., Tirmali, P., Kulkarni, S.: Electrochemical synthesis of flower like Mn-Co mixed metal oxides as electrode material for supercapacitor application. *Curr. Appl. Phys.* **18**(4), 397–404 (2018)
139. Guo, Y., Wu, C., Li, N.-W., Yuan, S., Yu, L.: Formation of Co-Mn mixed oxide double-shelled hollow spheres as advanced electrodes for hybrid supercapacitors. *J. Mater. Chem. A* **7**(44), 25247–25253 (2019)
140. Ahuja, P., Ujjain, S.K., Kanojia, R.: Electrochemical behaviour of manganese & ruthenium mixed oxide@ reduced graphene oxide nanoribbon composite in symmetric and asymmetric supercapacitor. *Appl. Surf. Sci.* **427**, 102–111 (2018)
141. Wu, C., et al.: Hierarchical mesoporous zinc-nickel-cobalt ternary oxide nanowire arrays on nickel foam as high-performance electrodes for supercapacitors. *ACS Appl. Mater. Interfaces* **7**(48), 26512–26521 (2015)

142. Zhao, J., et al.: Porous Ni-Co-Mn oxides prisms for high performance electrochemical energy storage. *Appl. Surf. Sci.* **425**, 1158–1167 (2017)
143. Zhang, Y., Li, L., Su, H., Huang, W., Dong, X.: Binary metal oxide: advanced energy storage materials in supercapacitors. *J. Mater. Chem. A* **3**(1), 43–59 (2015)
144. Zeng, Z., Xiao, B., Zhu, X., Zhu, J., Xiao, D., Zhu, J.: Flower-like binary cobalt-nickel oxide with high performance for supercapacitor electrode via cathodic electrodeposition. *Ceram Int.* **43**, S633–S638 (2017)
145. Wang, K., Zhang, Z., Shi, X., Wang, H., Lu, Y., Ma, X.: Temperature-dependent self-assembly of NiO/Co₃O₄ composites for supercapacitor electrodes with good cycling performance: from nanoparticles to nanorod arrays. *Rsc Adv.* **5**(3), 1943–1948 (2015)
146. Liu, M.-C., Kong, L.-B., Lu, C., Li, X.-M., Luo, Y.-C., Kang, L.: A sol-gel process for fabrication of NiO/NiCo₂O₄/Co₃O₄ composite with improved electrochemical behavior for electrochemical capacitors. *ACS Appl. Mater. Interfaces* **4**(9), 4631–4636 (2012)
147. Long, C., et al.: Amorphous Ni-Co binary oxide with hierarchical porous structure for electrochemical capacitors. *ACS Appl. Mater. Interfaces* **7**(44), 24419–24429 (2015)
148. Wang, X., et al.: Preparation and electrochemical properties of NiO-Co₃O₄ composite as electrode materials for supercapacitors. *Chem. Phys. Lett.* **667**, 260–266 (2017)
149. Biswal, A., et al.: Role of additives in electrochemical deposition of ternary metal oxide microspheres for supercapacitor applications. *ACS Omega* **5**(7), 3405–3417 (2020)
150. Acharya, J., et al.: Hybrid Electrodes based on Zn-Ni-Co ternary oxide nanowires and nanosheets for ultra-high-rate asymmetric supercapacitors. *ACS Appl. Nano Mater.* **3**(9), 8679–8690 (2020)
151. Dolla, T.H., Lawal, I.A., Billing, D.G., Pruessner, K., Ndungu, P.: Carbon encapsulated ternary Mn-Ni-Co Oxide nanoparticles as electrode materials for energy storage applications. *Electroanalysis* **32**(12), 2926–2935 (2020). <https://doi.org/10.1002/elan.202060294>
152. Ahsan, M.T., et al.: 3D Hierarchically mesoporous zinc-nickel-cobalt ternary oxide (Zn_{0.6}Ni_{0.8}Co_{1.6}O₄) nanowires for high-performance asymmetric supercapacitors. *Front. Chem.* **8**, 487 (2020)
153. Li, F., Sun, Z., Jiang, H., Ma, Z., Wang, Q., Qu, F.: Ion-Exchange Synthesis of Ternary FeCoNi-layered double hydroxide Nanocage toward enhanced oxygen evolution reaction and supercapacitor. *Energy Fuels* **34**(9), 11628–11636 (2020)
154. Xing, T., Ouyang, Y., Chen, Y., Zheng, L., Wu, C., Wang, X.: P-doped ternary transition metal oxide as electrode material of asymmetric supercapacitor. *J. Energy Storage* **28**, 101248 (2020)
155. Hussain, I., Mohamed, S.G., Ali, A., Abbas, N., Ammar, S.M., Al Zoubi, W.: Uniform growth of Zn-Mn-Co ternary oxide nanoneedles for high-performance energy-storage applications. *J. Electroanal. Chem.* **837**, 39–47 (2019)
156. Huang, Z.-H., et al.: Zinc-nickel-cobalt ternary hydroxide nanoarrays for high-performance supercapacitors. *J. Mater. Chem. A* **7**(19), 11826–11835 (2019)
157. Abel, M.J., Pramothkumar, A., Senthilkumar, N., Anbalagan, P.: Investigation on structural, optical and electrochemical behavior of NiO/ZnMn₂O₄ ternary nanocomposites via two-step synthesis approach for supercapacitor application. *Chemical Pap.* **75**, 641–651 (2021)
158. Wu, X., Zeng, Y., Gao, H., Su, J., Liu, J., Zhu, Z.: Template synthesis of hollow fusiform RuO₂-x H₂O nanostructure and its supercapacitor performance. *J. Mater. Chem. A* **1**(3), 469–472 (2013)
159. Xia, H., Feng, J., Wang, H., Lai, M.O., Lu, L.: MnO₂ nanotube and nanowire arrays by electrochemical deposition for supercapacitors. *J. Power Sources* **195**(13), 4410–4413 (2010)
160. Lang, X., Hirata, A., Fujita, T., Chen, M.: Nanoporous metal/oxide hybrid electrodes for electrochemical supercapacitors. *Nat. Nanotechnol.* **6**(4), 232–236 (2011)
161. Xie, K., et al.: Highly ordered iron oxide nanotube arrays as electrodes for electrochemical energy storage. *Electrochem. Commun.* **13**(6), 657–660 (2011)
162. Shivakumara, S., Penki, T.R., Munichandraiah, N.: High specific surface area α -Fe₂O₃ nanostructures as high performance electrode material for supercapacitors. *Mater. Lett.* **131**, 100–103 (2014)

163. Zhu, Z., Ping, J., Huang, X., Hu, J., Chen, Q., Ji, X., Banks, C.E.: Hexagonal nickel oxide nanoplate-based electrochemical supercapacitor. *J. Mater. Sci.* **47**(1), 503–507 (2012)
164. Jahromi, S.P., et al.: Influence of particle size on performance of a nickel oxide nanoparticle-based supercapacitor. *RSC Adv.* **5**(18), 14010–14019 (2015)
165. Navale, S., et al.: Electrochemical supercapacitor development based on electrodeposited nickel oxide film. *RSC Adv.* **5**(64), 51961–51965 (2015)
166. Das, T.K., Prusty, S.: Review on conducting polymers and their applications. *Polym. Plast. Technol. Eng.* **51**(14), 1487–1500 (2012)
167. Meng, Q., Cai, K., Chen, Y., Chen, L.: Research progress on conducting polymer based supercapacitor electrode materials. *Nano Energy* **36**, 268–285 (2017)
168. Dhawale, D., Vinu, A., Lokhande, C.: Stable nanostructured polyaniline electrode for supercapacitor application. *Electrochim. Acta* **56**(25), 9482–9487 (2011)
169. Li, M., Yang, L.: Intrinsic flexible polypyrrole film with excellent electrochemical performance. *J. Mater. Sci. Mater. Electron.* **26**(7), 4875–4879 (2015)
170. Patil, B., Patil, S., Lokhande, C.: Electrochemical characterization of chemically synthesized polythiophene thin films: performance of asymmetric supercapacitor device. *Electroanalysis* **26**(9), 2023–2032 (2014)
171. Patil, B., Jagadale, A., Lokhande, C.: Synthesis of polythiophene thin films by simple successive ionic layer adsorption and reaction (SILAR) method for supercapacitor application. *Synth. Met.* **162**(15–16), 1400–1405 (2012)
172. Pringle, J.M., Forsyth, M., Macfarlane, D.R., Wagner, K., Hall, S.B., Officer, D.L.: The influence of the monomer and the ionic liquid on the electrochemical preparation of polythiophene. *Polymer* **46**(7), 2047–2058 (2005)
173. Lee, S.J., Lee, J.M., Cheong, I.W., Lee, H., Kim, J.H.: A facile route of polythiophene nanoparticles via Fe³⁺-catalyzed oxidative polymerization in aqueous medium. *J. Polym. Sci. A Polym. Chem.* **46**(6), 2097–2107 (2008)
174. Ballarin, B., Facchini, M., Dal Pozzo, L., Martini, C.: Comparison of different porous sol–gel matrices: template synthesis of polythiophene. *Electrochem. Commun.* **5**(8), 625–631 (2003)
175. Voronkov, M., Tokareva, I., Dorofeev, I., Smirnov, V., Shagun, L.: Photochemical synthesis of polythiophenes and polythienylphenylenes. *Russ. J. Gen. Chem.* **80**(10), 2075–2077 (2010)
176. Reyman, D., Guereca, E., Herrasti, P.: Electrodeposition of polythiophene assisted by sonochemistry and incorporation of fluorophores in the polymeric matrix. *Ultrason. Sonochem.* **14**(5), 653–660 (2007)
177. Kamat, S., Tamboli, S., Puri, V., Puri, R., Yadav, J., Joo, O.S.: Post deposition heating effects on the properties of polythiophene thin films. *Arch. Phys. Res.* **1**(4), 119–125 (2010)
178. Huang, C., et al.: Synthesis of polyaniline/nickel oxide/sulfonated graphene ternary composite for all-solid-state asymmetric supercapacitor. *Appl. Surf Sci.* **505**, 144589 (2020)
179. Eftekhari, A., Li, L., Yang, Y.: Polyaniline supercapacitors. *J. Power Sources* **347**, 86–107 (2017)
180. Cherusseri, J., Kar, K.K.: Hierarchical carbon nanopetal/polypyrrole nanocomposite electrodes with brush-like architecture for supercapacitors. *Phys. Chem. Chem. Phys.* **18**(12), 8587–8597 (2016)
181. Ansari, R.: Polypyrrole conducting electroactive polymers: synthesis and stability studies. *J. Chem.* **3**(4), 186–201 (2006)
182. Khalkhali, R.A.: Effect of thermal treatment on electrical conductivities of polypyrrole conducting polymers. *Iran Polym. J.* **13**(1), 53–60 (2004)
183. Vijeth, H., Ashokkumar, S., Yesappa, L., Niranjana, M., Vandana, M., Devendrappa, H.: Camphor sulfonic acid assisted synthesis of polythiophene composite for high energy density all-solid-state symmetric supercapacitor. *J. Mater. Sci. Mater. Electron.* **30**(8), 7471–7484 (2019)
184. Ibáñez-Marín, F., Morales-Verdejo, C., Camarada, M.: Composites of electrochemically reduced graphene oxide and polythiophene and their application in supercapacitors. *Int. J. Electrochem. Sci.* **12**, 11546–11555 (2017)

185. Husain, A., Ahmad, S., Mohammad, F.: Preparation and applications of Polythiophene nanocomposites. *J. Eng. Sci. Comput. (JESC)* **I(III)**, 36–53 (2020)
186. Bandyopadhyay, P., Kuila, T., Balamurugan, J., Nguyen, T.T., Kim, N.H., Lee, J.H.: Facile synthesis of novel sulfonated polyaniline functionalized graphene using m-aminobenzene sulfonic acid for asymmetric supercapacitor application. *Chem. Eng. J.* **308**, 1174–1184 (2017)
187. Xu, J., et al.: Fabric electrodes coated with polypyrrole nanorods for flexible supercapacitor application prepared via a reactive self-degraded template. *Org Electron.* **26**, 292–299 (2015)
188. Rajesh, M., Raj, C.J., Kim, B.C., Cho, B.-B., Ko, J.M., Yu, K.H.: Supercapacitive studies on electropolymerized natural organic phosphate doped polypyrrole thin films. *Electrochim. Acta* **220**, 373–383 (2016)
189. Zhao, C., Jia, X., Shu, K., Yu, C., Min, Y., Wang, C.: Stretchability enhancement of buckled polypyrrole electrode for stretchable supercapacitors via engineering substrate surface roughness. *Electrochim. Acta* **343**, 136099 (2020)
190. Wang, X., Wu, D., Song, X., Du, W., Zhao, X., Zhang, D.: Review on carbon/polyaniline hybrids: design and synthesis for supercapacitor. *Molecules* **24**(12), 2263 (2019)
191. Wu, Z., Li, L., Yan, J.M., Zhang, X.B.: Materials design and system construction for conventional and new-concept supercapacitors. *Adv. Sci.* **4**(6), 1600382 (2017)
192. Wang, B., et al.: Graphene-based composites for electrochemical energy storage. *Energy Storage Mater.* **24**, 22–51 (2020)
193. Huang, Y., Liang, J., Chen, Y.: An overview of the applications of graphene-based materials in supercapacitors. *Small* **8**(12), 1805–1834 (2012)
194. Cheng, F., Yang, X., Dai, S., Song, D., Zhang, S., Lu, W.: Interweaving activated carbon with multi-dimensional carbon nanomaterials for high-performance supercapacitors. *J. Electrochem. Soc.* **167**(4), 040507 (2020)
195. Lu, W., Hartman, R., Qu, L., Dai, L.: Nanocomposite electrodes for high-performance supercapacitors. *J. Phys. Chem. Lett.* **2**(6), 655–660 (2011)
196. Li, Q., et al.: In situ construction of potato starch based carbon nanofiber/activated carbon hybrid structure for high-performance electrical double layer capacitor. *J. Power Sources* **207**, 199–204 (2012)
197. Zheng, C., Zhou, X., Cao, H., Wang, G., Liu, Z.: Synthesis of porous graphene/activated carbon composite with high packing density and large specific surface area for supercapacitor electrode material. *J. Power Sources* **258**, 290–296 (2014)
198. Yu, Z., Tetard, L., Zhai, L., Thomas, J.: Supercapacitor electrode materials: nanostructures from 0 to 3 dimensions. *Energy Environ. Sci.* **8**(3), 702–730 (2015)
199. Wang, J.-W., Chen, Y., Chen, B.-Z.: Synthesis and control of high-performance MnO₂/carbon nanotubes nanocomposites for supercapacitors. *J. Alloys Compd.* **688**, 184–197 (2016)
200. Li, M., He, H.: Study on electrochemical performance of multi-wall carbon nanotubes coated by iron oxide nanoparticles as advanced electrode materials for supercapacitors. *Vacuum* **143**, 371–379 (2017)
201. Wang, K., Gao, S., Du, Z., Yuan, A., Lu, W., Chen, L.: MnO₂-Carbon nanotube composite for high-areal-density supercapacitors with high rate performance. *J. Power Sources* **305**, 30–36 (2016)
202. Siddheswaran, R., Manikandan, D., Avila, R.E., Jeyanthi, C.E., Mangalaraja, R.V.: Formation of carbon nanotube forest over spin-coated Fe₂O₃ reduced thin-film by chemical vapor deposition. *Fuller Nanotub. Carbon Nanostruct.* **23**(5), 392–398 (2015)
203. Wu, M.-S., Lee, R.-H., Jow, J.-J., Yang, W.-D., Hsieh, C.-Y., Weng, B.-J.: Nanostructured iron oxide films prepared by electrochemical method for electrochemical capacitors. *Electrochem. Solid-State Lett.* **12**(1), A1 (2008)
204. Cheng, X., et al.: Three-dimensional α -Fe₂O₃/carbon nanotube sponges as flexible supercapacitor electrodes. *J. Mater. Chem. A* **3**(42), 20927–20934 (2015)
205. Yumak, T., Bragg, D., Sabolsky, E.M.: Effect of synthesis methods on the surface and electrochemical characteristics of metal oxide/activated carbon composites for supercapacitor applications. *Appl. Surf Sci.* **469**, 983–993 (2019)

206. Vighnesha, K., Sangeetha, D., Selvakumar, M.: Synthesis and characterization of activated carbon/conducting polymer composite electrode for supercapacitor applications. *J. Mater. Sci. Mater. Electron.* **29**(2), 914–921 (2018)
207. Moussa, M., El-Kady, M.F., Abdel-Azeim, S., Kaner, R.B., Majewski, P., Ma, J.: Compact, flexible conducting polymer/graphene nanocomposites for supercapacitors of high volumetric energy density. *Compos. Sci. Technol.* **160**, 50–59 (2018)
208. Meer, S., Kausar, A., Iqbal, T.: Trends in conducting polymer and hybrids of conducting polymer/carbon nanotube: a review. *Polym. Plast. Technol. Eng.* **55**(13), 1416–1440 (2016)
209. Afzal, A., Abuilaiwi, F.A., Habib, A., Awais, M., Waje, S.B., Atieh, M.A.: Polypyrrole/carbon nanotube supercapacitors: technological advances and challenges. *J. Power Sources* **352**, 174–186 (2017)
210. Gao, Y.: Graphene and polymer composites for supercapacitor applications: a review. *Nanoscale Res. Lett.* **12**(1), 387 (2017)
211. Yu, A., Chabot, V., Zhang, J.: *Electrochemical Supercapacitors for Energy Storage and Delivery: Fundamentals and Applications*. Taylor & Francis, Milton Park, p. 383 (2013)
212. Hou, Y., Cheng, Y., Hobson, T., Liu, J.: Design and synthesis of hierarchical MnO₂ nanospheres/carbon nanotubes/conducting polymer ternary composite for high performance electrochemical electrodes. *Nano Lett.* **10**(7), 2727–2733 (2010)
213. Wang, G., Tang, Q., Bao, H., Li, X., Wang, G.: Synthesis of hierarchical sulfonated graphene/MnO₂/polyaniline ternary composite and its improved electrochemical performance. *J. Power Sources* **241**, 231–238 (2013)
214. Wang, J.-G., Yang, Y., Huang, Z.-H., Kang, F.: Rational synthesis of MnO₂/conducting polypyrrole@ carbon nanofiber triaxial nano-cables for high-performance supercapacitors. *J. Mater. Chem.* **22**(33), 16943–16949 (2012)
215. Cheng, Q., Tang, J., Ma, J., Zhang, H., Shinya, N., Qin, L.-C.: Graphene and carbon nanotube composite electrodes for supercapacitors with ultra-high energy density. *Phys. Chem. Chem. Phys.* **13**(39), 17615–17624 (2011)
216. Yang, Z.-Y., et al.: Controllable growth of CNTs on graphene as high-performance electrode material for supercapacitors. *ACS Appl. Mater. Interfaces* **6**(11), 8497–8504 (2014)
217. Dang, Y.-Q., Ren, S.-Z., Liu, G., Cai, J., Zhang, Y., Qiu, J.: Electrochemical and capacitive properties of carbon dots/reduced graphene oxide supercapacitors. *Nanomater* **6**(11), 212 (2016)
218. Xie, Q., et al.: Sustainable low-cost green electrodes with high volumetric capacitance for aqueous symmetric supercapacitors with high energy density. *ACS Sustain. Chem. Eng.* **4**(3), 1422–1430 (2016)
219. Zhou, Y., et al.: Hierarchical nitrogen-doped porous carbon/carbon nanotube composites for high-performance supercapacitor. *Superlattices Microstruct.* **130**, 50–60 (2019)
220. Hao, J., et al.: Hierarchical structure N, O-co-doped porous carbon/carbon nanotube composite derived from coal for supercapacitors and CO₂ capture. *Nanoscale Adv.* **2**(2), 878–887 (2020)
221. Seo, M.-K., Park, S.-J.: Effect of nanosize titanium oxide on electrochemical characteristics of activated carbon electrodes. *Curr. Appl. Phys.* **10**(2), 391–394 (2010)
222. He, Y., et al.: Freestanding three-dimensional graphene/MnO₂ composite networks as ultralight and flexible supercapacitor electrodes. *ACS Nano* **7**(1), 174–182 (2013)
223. Purushothaman, K.K., Saravanakumar, B., Babu, I.M., Sethuraman, B., Muralidharan, G.: Nanostructured CuO/reduced graphene oxide composite for hybrid supercapacitors. *RSC Adv.* **4**(45), 23485–23491 (2014)
224. Wang, H., Sun, X., Liu, Z., Lei, Z.: Creation of nanopores on graphene planes with MgO template for preparing high-performance supercapacitor electrodes. *Nanoscale* **6**(12), 6577–6584 (2014)
225. Ye, Y., et al.: Core-shell structure carbon coated ferric oxide (Fe₂O₃@ C) nanoparticles for supercapacitors with superior electrochemical performance. *J. Alloys Compd.* **639**, 422–427 (2015)
226. Jana, M., et al.: Development of high energy density supercapacitor through hydrothermal synthesis of RGO/nano-structured cobalt sulphide composites. *Nanotechnology* **26**(7), 075402 (2015)

227. Quan, H., Cheng, B., Xiao, Y., Lei, S.: One-pot synthesis of α -Fe₂O₃ nanoplates-reduced graphene oxide composites for supercapacitor application. *Chem. Eng. J.* **286**, 165–173 (2016)
228. Zhou, M., Gomez, J., Li, B., Jiang, Y.-B., Deng, S.: Oil tea shell derived porous carbon with an extremely large specific surface area and modification with MnO₂ for high-performance supercapacitor electrodes. *Appl. Mater. Today* **7**, 47–54 (2017)
229. Tabrizi, A.G., Arsalani, N., Mohammadi, A., Namazi, H., Ghadimi, L.S., Ahadzadeh, I.: Facile synthesis of a MnFe₂O₄/rGO nanocomposite for an ultra-stable symmetric supercapacitor. *New J. Chem.* **41**(12), 4974–4984 (2017)
230. Mohan, R., Paulose, R., Parihar, V.: Hybrid MnO₂/CNT nanocomposite sheet with enhanced electrochemical performance via surfactant-free wet chemical route. *Ionics* **23**(11), 3245–3248 (2017)
231. Zhu, C., Wang, M., Li, T., Lu, T., Pan, L.: In situ synthesis of porous Co₃O₄ polyhedra/carbon nanotubes heterostructures for highly efficient supercapacitors. *Ionics* **23**(8), 2175–2183 (2017)
232. Jayachandiran, J., et al.: Synthesis and electrochemical studies of rGO/ZnO nanocomposite for supercapacitor application. *J. Inorg. Organomet. Polym. Mater.* **28**(5), 2046–2055 (2018)
233. Cai, Y.-Z., Cao, W.-Q., Zhang, Y.-L., He, P., Shu, J.-C., Cao, M.-S.: Tailoring rGO-NiFe₂O₄ hybrids to tune transport of electrons and ions for supercapacitor electrodes. *J. Alloys Compd.* **811**, 152011 (2019)
234. Nawwar, M., Poon, R., Chen, R., Sahu, R.P., Puri, I.K., Zhitomirsky, I.: High areal capacitance of Fe₃O₄-decorated carbon nanotubes for supercapacitor electrodes. *Carbon Energy* **1**(1), 124–133 (2019)
235. Zhang, J., Zhang, Z., Jiao, Y., Yang, H., Li, Y., Zhang, J., Gao, P.: The graphene/lanthanum oxide nanocomposites as electrode materials of supercapacitors. *J. Power Sources* **419**, 99–105 (2019)
236. Acharya, J., Raj, B.G.S., Ko, T.H., Khil, M.-S., Kim, H.-Y., Kim, B.-S.: Facile one pot sonochemical synthesis of CoFe₂O₄/MWCNTs hybrids with well-dispersed MWCNTs for asymmetric hybrid supercapacitor applications. *Int. J. Hydrog. Energy* **45**(4), 3073–3085 (2020)
237. Cao, M., Cheng, W., Ni, X., Hu, Y., Han, G.: Lignin-based multi-channels carbon nanofibers@SnO₂ nanocomposites for high-performance supercapacitors. *Electrochim. Acta* **345**, 136172 (2020)
238. Yu, P., Zhao, X., Huang, Z., Li, Y., Zhang, Q.: Free-standing three-dimensional graphene and polyaniline nanowire arrays hybrid foams for high-performance flexible and lightweight supercapacitors. *J. Mater. Chem. A* **2**(35), 14413–14420 (2014)
239. Liu, X., Shang, P., Zhang, Y., Wang, X., Fan, Z., Wang, B., Zheng, Y.: Three-dimensional and stable polyaniline-grafted graphene hybrid materials for supercapacitor electrodes. *J. Mater. Chem. A* **2**(37), 15273–15278 (2014)
240. Sharma, A.K., Bhardwaj, P., Dhawan, S.K., Sharma, Y.: Oxidative synthesis and electrochemical studies of poly (aniline-co-pyrrole)-hybrid carbon nanostructured composite electrode materials for supercapacitor. *Adv. Mater. Lett.* **6**(5), 414–420 (2015)
241. Xu, J., et al.: Polypyrrole/reduced graphene oxide coated fabric electrodes for supercapacitor application. *Org. Electron.* **24**, 153–159 (2015)
242. Pattanauwat, P., Aht-Ong, D.: Controllable morphology of polypyrrole wrapped graphene hydrogel framework composites via cyclic voltammetry with aiding of poly (sodium 4-styrene sulfonate) for the flexible supercapacitor electrode. *Electrochim. Acta* **224**, 149–160 (2017)
243. Lu, Z., Foroughi, J., Wang, C., Long, H., Wallace, G.G.: Superelastic hybrid CNT/graphene fibers for wearable energy storage. *Adv. Energy Mater.* **8**(8), 1702047 (2018)
244. Awata, R., Shehab, M., El Tahan, A., Soliman, M., Ebrahim, S.: High performance supercapacitor based on camphor sulfonic acid doped polyaniline/multiwall carbon nanotubes nanocomposite. *Electrochim. Acta* **347**, 136229 (2020)
245. Barakzahi, M., Montazer, M., Sharif, F., Norby, T., Chatzitikis, A.: MOF-modified polyester fabric coated with reduced graphene oxide/polypyrrole as electrode for flexible supercapacitors. *Electrochim. Acta* **336**, 135743 (2020)

246. Zhang, W., Kong, Y., Jin, X., Yan, B., Diao, G., Piao, Y.: Supramolecule-assisted synthesis of cyclodextrin polymer functionalized polyaniline/carbon nanotube with core-shell nanostructure as high-performance supercapacitor material. *Electrochim. Acta* **331**, 135345 (2020)
247. Ge, M., Hao, H., Lv, Q., Wu, J., Li, W.: Hierarchical nanocomposite that coupled nitrogen-doped graphene with aligned PANI cores arrays for high-performance supercapacitor. *Electrochim. Acta* **330**, 135236 (2020)
248. Liu, M., et al.: Hierarchical composites of polyaniline-graphene nanoribbons-carbon nanotubes as electrode materials in all-solid-state supercapacitors. *Nanoscale* **5**(16), 7312–7320 (2013)
249. Xiong, P., Huang, H., Wang, X.: Design and synthesis of ternary cobalt ferrite/graphene/polyaniline hierarchical nanocomposites for high-performance supercapacitors. *J. Power Sources* **245**, 937–946 (2014)
250. Bai, Y., Du, M., Chang, J., Sun, J., Gao, L.: Supercapacitors with high capacitance based on reduced graphene oxide/carbon nanotubes/NiO composite electrodes. *J. Mater. Chem. A* **2**(11), 3834–3840 (2014)
251. Li, X., Zhang, Y., Xing, W., Li, L., Xue, Q., Yan, Z.: Sandwich-like graphene/polypyrrole/layered double hydroxide nanowires for high-performance supercapacitors. *J. Power Sources* **331**, 67–75 (2016)
252. Lin, H., et al.: Self-assembled graphene/polyaniline/Co₃O₄ ternary hybrid aerogels for supercapacitors. *Electrochim. Acta* **191**, 444–451 (2016)
253. Ratha, S., Marri, S.R., Behera, J.: Rout CS (2016) High-energy-density supercapacitors based on patronite/single-walled carbon nanotubes/reduced graphene oxide hybrids. *Eur. J. Inorg. Chem.* **2**, 259–265 (2016)
254. Kalambate, P.K., Rawool, C.R., Karna, S.P., Srivastava, A.K.: Nitrogen-doped graphene/palladium nanoparticles/porous polyaniline ternary composite as an efficient electrode material for high performance supercapacitor. *Mater. Sci. Energy Technol.* **2**(2), 246–257 (2019)
255. Das, T., Verma, B.: Polyaniline based ternary composite with enhanced electrochemical properties and its use as supercapacitor electrodes. *J. Energy Storage* **26**, 100975 (2019)
256. MaaM, A., Rahman, N.A., Sulaiman, Y.: Ternary functionalised carbon nanofibers/polypyrrole/manganese oxide as high specific energy electrode for supercapacitor. *Ceram. Int.* **45**(7), 8433–8439 (2019)
257. Yang, S., Sun, L., An, X., Qian, X.: Construction of flexible electrodes based on ternary polypyrrole@ cobalt oxyhydroxide/cellulose fiber composite for supercapacitor. *Carbohydr. Polym.* **229**, 115455 (2020)
258. Xu, Z., et al.: Investigation on the role of different conductive polymers in supercapacitors based on a zinc sulfide/reduced graphene oxide/conductive polymer ternary composite electrode. *RSC Adv.* **10**(6), 3122–3129 (2020)
259. Abraham, S., Prasankumar, T., Kumar, K.V., Karazhanov, S.Z., Jose, S.: Novel lead dioxide intercalated polypyrrole/graphene oxide ternary composite for high throughput supercapacitors. *Mater. Lett.* **273**, 127943 (2020)
260. Gupta, A., Sardana, S., Dalal, J., Lather, S., Maan, A.S., Tripathi, R., Punia, R., Singh, K., Ohlan, A.: Nanostructured Polyaniline/Graphene/Fe₂O₃ composites hydrogel as a high-performance flexible supercapacitor electrode material. *ACS Appl. Energy Mater.* **3**(7), 6434–6446 (2020)